Tri-Service Corrosion Conference

14-18 January 2002

La Mansion Del Rio Hotel
San Antonio, TX

Editors: Dr. Robert A. Mantz and Dr. Paul C. Trulove

Report Documentation Page

Form Approved
OMB No. 0704-0188

1. REPORT DATE	2. REPORT TYPE	3. DATES COVERED
18 JAN 2002	**N/A**	**-**

4. TITLE AND SUBTITLE	5a. CONTRACT NUMBER
Tri-Service Corrosion Conference	5b. GRANT NUMBER
	5c. PROGRAM ELEMENT NUMBER
6. AUTHOR(S)	5d. PROJECT NUMBER
Dr. Robert A. Mantz; Dr. Paul C. Trulove	5e. TASK NUMBER
	5f. WORK UNIT NUMBER
7. PERFORMING ORGANIZATION NAME(S) AND ADDRESS(ES)	8. PERFORMING ORGANIZATION REPORT NUMBER
Air Force Office Of Scientific Research	**AFRL-SR-AR-TR-03-0349**
9. SPONSORING/MONITORING AGENCY NAME(S) AND ADDRESS(ES)	10. SPONSOR/MONITOR'S ACRONYM(S)
	11. SPONSOR/MONITOR'S REPORT NUMBER(S)

12. DISTRIBUTION/AVAILABILITY STATEMENT

Approved for public release, distribution unlimited

13. SUPPLEMENTARY NOTES

See ADM 001 660 for entire conference proceedings., The original document contains color images.

14. ABSTRACT

Proceedings of the 2002 Tri-Serive Corrosion Conference. The purpose of the conference is to promote interaction among the military services through a forum wherein the Federal Government's corrosion technologists and interested defense contractors have an open exchange of the latest corrosion issues relevant to military systems. Moreover, these conferences provide increased visability of DoD corrosion control and prevention efforts and promote novel and innovative solutions to DoD corrosion problems. The exchange of information encourages cooperative efforts aiding in the development of integrated corrosion prevention and control technologies.

15. SUBJECT TERMS

16. SECURITY CLASSIFICATION OF:			17. LIMITATION OF ABSTRACT	18. NUMBER OF PAGES	19a. NAME OF RESPONSIBLE PERSON
a. REPORT	b. ABSTRACT	c. THIS PAGE			
unclassified	**unclassified**	**unclassified**	**UU**	**1882**	

TABLE OF CONTENTS

Page

PROGRAM OVERVIEWS / COST / TRAINING 1

Overview of Air Force Corrosion Prevention and Control Program 2
Major Dan Bullock

The Implementation of Quality Assurance Training in Naval Ship Preservation Work 13
Norm Clayton and Jeff Duckworth

Methodology for Acquiring and Assessing the Cost of Corrosion for US Marine Corps Ground Vehicles and Selected Equipment 22
Michael Gallagher

Web Design for Information and Training in Corrosion Prevention & Control 31
P.R. Roberge

Fatigue Life, Corrosion and Safe-Life Issues 49
Vinod S. Agarwala and Basir Shafiq

POLLUTION PREVENTION / CASE STUDIES 63

Issues in the Measurement of Volatile Organic Compounds (VOC'S) in New-Generation Low-VOC Marine Coatings for the U.S. Navy 64
S. H. Lawrence, A.W. Webb, R. L. Foster, K. E. Lucas. E. D. Thomsas, P. M. Bizot, and C. E. Bevans

Elimination of MEK and Lacquer Thinner in Departmen of Defense Painting Operations 81
Joseph A. Lucas

Compressors for the 21st Century 89
Rick Miles, Ph. D. and David F. Ellicks

Bell Lab's Corrosion Preventive Compound (MIL-L-87177A Grade B) 95
David H. Horne,ChE., P.E.

The Operational Testing of the CPC ACF-50 on the US Navy's S-3B Viking Fleet 103
Edwin G. Mullin

Page

Failure Analysis of a HH-60 Helicopter External Fuel-Tank Pylon 117
John A. Newman and Robert S. Piascik, and Richard A. Lindenberg

Integrated Corrosion and Material Degradation Prevention Solutions Enhancing Readiness, Protecting Equipment, Preventing Pollution, and Lowering Life-Cycle Cost 134
Jim Martin

CORROSION CONTROL COATINGS: METALS 150

Development of Production-Scale Aluminum-Manganese Electrodeposition Process 151
Erin Beck, Dr. Michael J. Kane, Craig Matzdorf and Jim Green

Using Vanadium to Impart Self-Healing to Conversion Coatings for Aerospace Aluminum Alloys 167
M. Todd Coolbaugh, Howard P. Groger, Eugene C. Aquino, Sarah E. Morris, Jeanette E. Roberts, and Fred Pearlstein

Metallizing for Corrosion Protection 182
Dr. Douglas H. Neale, David F. Ellicks

Cerium-Based Corrosion Protection Systems for Aluminum Alloys 187
E. L. Morris, J. O. Stoffer, T. J O'Keefe, M. J. O'Keefe, W. G. Fahrenholtz, T. P. Schuman, P. Yu, S. Hayes, A. Williams, B. Rivera, and Chris Singleton

Low Temperature Retrogression and Re-Aging Heat Treatments for Thick Section Components of Aluminum Alloy 7075 for Aging Aircraft Refurbishment 205
C. P. Ferrer, M.G. Koul, B. J. Connolly, A. L. Moran

Environmentally Assisted Cracking Concerns for Cadmium Replacement 227
Scott Grendahl and Russell Kilbane

Evaluation of Barrier Properties of Sol-Gel Derived Coatings on AA2024-T3 246
N.N. Voevodin, V.N. Balbyshev, J.A. Johnson, and M.S. Donley

SCC and Corrosion Fatigue of HVOF Coated and Cr Plated AerMet 100 Steel 260
E. U. Lee, H. C. Sanders, and S. Hartle

Page

HEAT TREATMENTS AND METALLURGY 278

SCC and Corrosion Fatigue of Laser Formed Ti-6Al-4V Alloy 279
E. U. Lee and H. C. Sanders

Corrosion Behavior of Friction Stir Welded High Strength Aluminum Alloys 296
J. B. Lumsden, M. W. Mahoney, and G. A. Pollock

Strength, Corrosion, and Environmentally Assisted Cracking of A 7075-T6 Friction Stir Weld 308
C. S. Paglia, M. C. Carroll, B. C. Pitts, T. Reynolds, and R. G. Buchheit

Contributions of Hot Corrosion and Diffusional Processes Towards the Performance of High Temperature Materials 344
David A. Shifler

The Effect of Artificial Heat Treatment on the Chromate Conversion Performance of Al-Zn-Mg-Cu Alloy 363
Y. Yoon, V. Laget, and R. G. Buchheit

CORROSION DETECTION 378

Corrosion Sensing and Monitoring 379
C. S. Brossia, L. Yang, D. S. Dunn, and N. Sridhar

Riccati Equation Analysis of Light Transport in Simple and Fluorescent Paints 395
Jan D. Garmany

Microwave Corrosion Detectors (MCDS) for Inspecting Under Aircraft Paints and Appliqués 409
Alan V. Bray and Gary R. Schmidt

Corrosion Detection and Prioritization Using Scanning and Permanently Mountable MWM Eddy Current Arrays 419
Neil Goldfine, David Grundy, Vladimir Zilberstein, Darrell Schlicker, Ian Shay, Andrew Washabaugh, Mark Windoloski, Mark Fisher, Kenneth LaCivita, and Victor Champagne

The Corrosive Environment Monitoring (CEM) System: An Innovative Technique for Monitoring and Preventing the Formation of Corrosion on Aircraft Structure 443
John G. Moffatt, Fred S. Malver, and Sunil Menon, Ph.D.

Page

New Technological Challenges for Ultrasonic Guided Wave NDE 454
Thomas Hay, Joseph L. Rose, Vinod Agarwala, and J. E. Stephenson

Application of Remote-Field Eddy-Current Technique to Aircraft Corrosion Detection 466
Yushi Sun and Tianhe Ouyang

An Approach for Corrosion Classification based on Wavelet Analysis 488
Ajay Verma, Akif Ibragimov, and Richard Mayer

EVALUATION OF CORROSION CONTROL COATINGS 510

Outdoor Exposure Results for Pretreated and Topcoated Aluminum Armor Alloys 2519, 5083, and 7039 511
John V. Kelley and Brian E. Placzankis,

Evaluation of Zinc-Rich Primers for use on Army Vehicle Systems 539
I. Carl Handsy and John Repp

Atmospheric Exposure and Salt Fog Studies of the Corrosion Behavior of Electrodeposited Hard Chromium and HVOF Thermal Spray Coatings 555
S. H. Lawrence, P. M. Natishan, R. L. Foster, and B. D. Sartwell

GM 9540P Cyclic Accelerated Corrosion Analysis of Nonchromate Conversion Coatings on Aluminum Alloys 2024, 2219, 5083, and 7075 Using DoD Paint Sytems 568
Brian E. Placzankis, Chris E. Miller, and Craig A. Matzdorf

Low Volatile Organic Compound (VOC) Chemical Agent Resistant Coating (CARC) Application Demonstration/Validation 601
Lisa Weiser, Anthony Eng, David Fayocavitz, and Forrest Pilgrim

CLEANING / TESTING 617

The Effects of Chemical Rinse Agents on the Corrosion of Aerospace Alloys in. Marine Atmospheres 618
Louis MacDowell, Luz Marina Calle, Joseph Curran, Tim Hodge, Ronald Barile, and Robert H. Heidersbach,

Page

Effects of Testing Tank Geometry and Material on ICCP System Design 631
S. A. Wimmer, V. G. DeGiorgi, E. Hogan, K. E. Lucas

CORROSION CONTROL COATINGS: POLYMERS 649

Dual Use Interior Direct-To-Metal/Exterior Chemical Agent Resistant Coating Primer 650
Anthony Eng, David Fayocavitz, Steven Murray, Forrest Pilgrim, and Lisa Weiser

Polarization Behavior and Corrosion-Initiation Mechanisms of Mo Coated with Amorphous Hydrogenated Silicon Alloy Thin Ceramic Films 675
L.H. Hihara, A.S. Iwane, J. J. Yamane, and R.E. Rocheleau

Low Solar Absorbent Gray Coating for Topside Applications 694
Albert G. Holder and Robert F. Brady, Jr.

Advanced Coatings Systems for Corrosion Protection of Air Force Aircraft 701
Joseph H. Osborne

Development of Fluoropolymer Appliqués: Paintless Alternatives for Corrosion Protection in the Marine Environment 717
Terrence G. Vargo and Andrew W. Dalgleish

Cold Spray Technology for Military Applications 733
Vic Champagne and Wayne Ziegler

CORROSION CHARACTERIZATION 746

Corrosion of AA2024-T3 under Protective Coatings 747
M. Khobaib, J. P. Hoffmann, and M. S. Donley

Galvanic Behavior Database for Titanium-Steel Alloy Couples 764
Ralph P.I. Adler, Christopher E. Miller, and Brian E. Placzankis

Ion Beam Analysis Techniques for the Study of Material Surface Degradation 788
J. D. Demaree and J. K. Hirvonen

U.S. Army Experience with Corrosion Assessment and Analysis of Rotorcraft 805
Kevin S. Rees

Page

The Influence of Fuel Carbon Residue on Hot Corrosion **848**
David A. Shifler

Orientation Study of Fatigue Crack Initiation from Corrosion Damage **874**
M. Khobaib, C. Kacmar, and M. Donley

Corrosion Inhibitors for Aerospace Al Alloys **891**
M. Khobaib, Natalia Veovodin, L. Kasten, and M. S. Donley

Mechanisms of Military Coatings Degradation (PP-1133) Electrochemical Impedance Spectroscopy Subtask **910**
Kevin J. Kovaleski

The Applicability of EIS for Assessing Substrate Metal Mass Loss for Polymer-Coated Metals **930**
D. B. Mitton, S. L. Wallace, N. J. Cantini, N. Eliaz and R. M. Latanision, F. Bellucci, G. E. Thompson

The Function of Admixed Corrosion Inhibitors in Steel Reinforced Concrete **946**
Farrel J. Martin and Jan Olek

An Examination of Degradation Modes of Constructional Materials for Super Critical Water Oxidation System Fabrication **965**
D. B. Mitton, H. Kim, J. Zhang and R. M. Latanision

Rotating Disk Studies of Iron Corrosion in Water under Abiotic and Biotic Conditions **988**
Batric Pesic

The Role of Marine Bacteria in Stainless Steel Pitting **1012**
Richard I. Ray, Brenda Little, and Jason S. Lee

AFOSR 6.1 PROGRAM REVIEW **1026**

Inhibition of Oxygen Reduction by Chromate on AA2025-T3 **1027**
W. Clark, J. Ramsey, R. McCreery, and G. Frankel

Inhibition of Corrosion of Cu-Rich Aluminum Alloys by Cr(VI) Compounds **1041**
M. Kendig, R. Addison, S. Jeanjaquet , J. Waldrop, and M. Hon

Inhibition of Al Alloy Corrosion by Chromate **1057**
G. S. Frankel

Page

A Scanning Electrochemical Microscopy (SECM) Study of Heterogeneous Redox Activity at AA2024 Sufaces 1074
J. Seegmiller and D. A. Buttry

Aircraft Coatings Testing, Corrosion Sensors in Coatings and Mg-Rich Coatings as Cr-free Primers for Al 2024 T-3 1085
G. P. Bierwagen, S. Mabutt, L. He, X.Wang, M. Nanna, L. Ellingson and D. Tallman

Electrodeposition of Conducting Polymer Coatings on Active Metals using Electron Transfer Mediation 1112
D. E. Tallman, C. Vang, T. Underdahl, G. G. Wallace, and G. P. Bierwagen

Quantitative Use Of Spectroscopy and Effective Irradiation Dosage During Weathering 1127
S. G. Croll and A. D. Skaja

Evaluation of Functionalized Polysiloxanes as Aircraft Coating Primers 1158
P. Boudjouk, T. E. Ready, and S. B. Choi

Phenomenology of Localized Coating Failure on AA1100-H14 1171
J. M. Williams, O. M. Schneider, and R. G. Kelly

Corrosion of Al Alloy 2024-T3 1196
M. B.Vukmirovic, N. Dimitrov, and K. Sieradzki

Self-Assembled Nano-phase Particle (SNAP) Surface Treatments for Aerospace Aluminum Alloys 1209
L. S. Kasten, M. S. Donley, V. N. Balbyshev, and D. J. Gaspar

Development of Permanent Foundation Layer Coatings for Corrosion Protection of AA2024-T3 1228
J. A. Johnson, T. D. Dang, and N. N. Voevodin

Spectroscopic Investigation of SNAP Solution Chemistry 1247
R. A. Mantz, V. N. Balbyshev, and M. S. Donley

Acoustic and Thermal NDE Techniques for Characterization of Polymeric Coatings and Detection of Localized Corrosion 1258
J. Hoffmann, M. Khobaib, S. Sathish, and N. Meyendorf

The Development of a Multi-Functional Coating for Aerospace Applications Using Molecular- and Nano-Engineering Methods: A MURI Overview 1276
S. R. Taylor**,** J. R. Scully, R. G. Kelly, G. J. Shiflet, R.G. Buchheit, W. J. van Ooij, K. Sieradzki, C. J. Brinker, and A.L. Moran

Page

Opportunities for Nano-Structured 'Sol-Gel-Derived' Materials in Corrosion Inhibition **1301**
C. J. Brinker, Evelyn M. Bond, Hongji Chen, Yi Yang, George Xomeritakis, Hongyou Fan, Kui Yu, and Richardo Pardey

Amorphous Al-Co-Ce Alloy With Potential Excellent Corrosion Resistance **1323**
M. Gao, N. Unlu, M. Jakob, J. Scully, and G. J. Shiflet

The Rapid Discovery of New Corrosion Inhibitors Using Combinatorial Methods, **1331**
B. D. Chambers, S. R. Taylor, and M. W. Kendig

Corrosion Protection of AA 2024-T3 by Organofunctional Silanes **1345**
W. J. van Ooij, Anna Lamar, Danqing Zhu, and Matt Stacey

Photonic Crystal Structures as Nanoengineered Coatings **1368**
Karl Sieradzki

Transport of Chemical Species Through Epoxy Coatings **1377**
W. Gan, H. Wang, and R.G. Kelly

Augmentation of Coating Function Using Hydrotalcites **1387**
F. Wong, H. Guan, S. Mahajanam, and R. G. Buchheit,

Thermal Sprayed Aluminum Alloy Cladding for Aircraft Skin Replacements **1404**
B. J. Connolly, A. L. Moran, R. L. McCaw, J. Pugh, and K. Scandell

Localized Corrosion Resistance of $Al_{90}Fe_5Gd_5$ and $Al_{87}Ni_{8.7}Y_{4.3}$ Alloys in the Amorphous, Nanocrystalline and Crystalline States: Resistance to Micrometer-Scale Pit Formation **1427**
J. E. Sweitzer, G. J. Shiflet, and J. R. Scully

The Development of an Admicellar Polymerization Process for Depositing Coatings on Aluminum Alloys and Crevices. **1456**
Olga Matarredona, Kha Mach, Steven Merchant, Ed O'Rear, and Melissa Rieger

Transient Transport in Flake-filled Coatings Used for Corrosion Prevention **1472**
Nancy K. Lape, William H. Smyrl, and Edward L. Cussler

Flake Alignment in Composite Coatings **1488**
Chuanfang Yang, Allan Crasto, William H. Smyrl, and Edward L. Cussler

Synthesis of Self-assembled NAnoParticles (SNAP) from Alkoxysilane Solutions **1502**
Raj Makote, Mohammad Khobaib, Chenggang Chen, and Edward L. Cussler

Page

Localized Corrosion Growth Kinetics in Al Alloys 1512
G. S. Frankel

The Role of Coating Heterogeneities in the Long-Term Performance of Coated Aluminum Alloys: Delineation of Ionic Pathways Using a Molecular Probe 1527
P. Moongkhamklang and S. R. Taylor

In-Situ Confocal Laser Scanning Microscopy Surface Metrology Studies of Corrosion on AA2024-T3: Influence of Electrolyte Composition on the Corrosion Morphology of Bare AA2024-T3 1541
G. O. Ilevbare, O. Schneider, R. G. Kelly, and J. R. Scully

POSTER SESSIONS 1572

Development of an Exfoliation Test Procedure for USAF Aging Aircraft Program 1573
K. R. Cooper, C. Franck, and R.G. Kelly

Corrosion Chemistry Data Based on Correlations Between Electrochemical Spectroscopy and Surface Analyses 1589
L. S. Kasten, N. N. Voevodin, M. Khobaib, M. S. Donley and R. Osterday

Investigation and Evaluation of the Performance of Aircraft Coatings under QUV/Prohesion Alternating Exposure 1597
X. F.Yang, J. Li, A. M. Richter, D. E. Tallman, S. G.Croll and G. P. Bierwagen, J.Wegner, and J.T.Grant

Cerium Corrosion Inhibitor in Polysiloxane Primers 1611
Thomas E. Ready and Philip Boudjouk

Tunable ISAM Corrosion Prevention Coatings 1617
K. R. Cooper, Michael B. Miller, K. W. Furrow, and Robert G. Kelly

Design and Synthesis of Nanostructured Corrosion Resistant Coating for Aging Aircraft 1629
J. B. Mecham, R. J. Swavey, and R. O Claus

Monte Carlo Simulations of Environmental Degradation on Polymer Coatings 1635
Brian Hinderliter, and Stuart Croll

Studies of Corrosion and Pitting Initiation of AA2024-T3 Using Atomic Force Microscopy 1654
G. S. Frankel and P. LeBlanc

Page

An Electrochemical and Surface Study of Admicellar Coatings on Aluminum Alloys and Crevices 1670
K. Mach, O. Matarredona, S. Merchant, E. O'Rear and M. Rieger

Development of an Admicellar Polymerization Process for Creating Hydrophobic Coatings on Aluminum Alloys and Crevices 1682
O. Matarredona, E. O'Rear, and M. Rieger

Use of Electrochemical Noise Methods for in situ Corrosion Monitoring 1695
X. Wang, R. Bennett, K. Spenningsby, and G. Bierwagen

The Study of Polypyrrole as a Corrosion Inhibitor of Aluminum Alloy 2024-T3 1710
Victoria Johnston Gelling, Jie He, Dennis E. Tallman, Gordron P. Bierwagen, and Gordon G. Wallace

Coating Performance Evaluation Protocol Using Electrochemical Methods 1728
S. J. Mabbutt, J. Li, G. P. Bierwagen, and D. Tallman

Development of an Admicellar Polymerization Process for Depositing Polypyrrole on Aluminum Alloys to Inhibit Corrosion 1750
S. Merchant, M. Rieger, and E. O'Rear

Investigation of Integrated Coating System for Corrosion Protection 1764
Robert T. Parkhill, Olga Kachurina, Tammy L. Metroke, Edward T. Knobbe, John Ostrander, and Nicholas. A. Kotov

Fatigue Life Prediction of Corroded Parts using Artificial Neural Network Analysis of NDE Data 1778
E. B. Shell and R. G. Buchheit

Epoxy Adhesion to Hydrotalcite: Correlation with Contact Angle and Electrokinetic Measurements 1792
R. B. Leggat and S. R. Taylor,

US Army Tacom Adopted Corrosion Rating System 1802
I. Carl Handsy and John Repp

Prediction of Corrosion Protection System Aging by Theory-Based Data Mining 1810
Maria Inman, Patrick J. Moran, Paul Koola, Satheesh Ramachandran, and Perakath Benjamin

Nondestructive Quantification of Localized Corrosion and Prediction of Remaining Fatigue Life 1824
S. I. Rokhlin, J. Y. Kim, and B. Zoofan

Page

Corrosion Protection of 2024-T3 Aluminum Alloy by Bis-Nonfunctional Silanes **1842**
J. Anna Lamar, Danqing Zhu, and Wim J. van Ooij

Chromate Conversion Coating Characterization Using Multichannel Microelectrode Analyzer (MMA) **1857**
W. Zhang, B. Hurley, and R. G. Buchheit

PROGRAM OVERVIEW / COST / TRAINING

AIR FORCE CORROSION PREVENTION AND CONTROL PROGRAM

Daniel E. Bullock, Major, USAF

Chief, Air Force Corrosion Prevention and Control Office

AIR FORCE CORROSION PREVENTION AND CONTROL PROGRAM

The Air Force Corrosion Prevention and Control Program is an Air Force Headquarters (HQ USAF) level program, defined by Air Force Instructions, to prevent, detect, and control corrosion, and minimize its impact on Air Force systems. It is a maintenance support program, directed at the sustainment community, i.e., those who conduct corrosion prevention and control maintenance operations, as well as those who implement technologies for those operations.

AIR FORCE CORROSION PREVENTION AND CONTROL OFFICE

The Air Force Corrosion Prevention and Control Office (AFCPCO) is chartered and directed by HQ USAF to manage the program. Our office does this, in broad terms, by providing oversight of Air Force corrosion prevention and control operations, and by providing technical guidance to the Air Force corrosion community. We are the single USAF point of contact for all corrosion issues. Our customers are system managers, major command corrosion managers, depot corrosion personnel, and field-level maintainers across the Air Force; we support them in implementing and conducting the best possible corrosion prevention and control program.

We are not, of course, the only Air Force activity involved in corrosion prevention and control. Other organizations do research and development of new materials and processes; develop and conduct training of corrosion personnel; manage the sustainment of specific weapon

systems; and perform the actual maintenance actions. We work closely with these other partners, with other services, and with industry.

Our contribution is to ensure Air Force corrosion needs are met, in the most effective and efficient way, using the best available technologies, optimized for Air Force requirements. Our mission statement is to "Ensure the Air Force has an effective program to prevent, detect, and control corrosion, and minimize the impact of corrosion on Air Force combat capability." This paper discusses in greater detail how we accomplish our mission, and gives examples of some of our recent and on-going efforts.

TASKINGS AND TECHNICAL AREAS The AFCPCO is governed by Air Force Instruction 21-105, *Aerospace Equipment Structural Maintenance,* which directs us to do the following things:

- Provide leadership for the Air Force corrosion community
- Provide engineering management of eight general-series corrosion-related technical orders
- Provide engineering and technical assistance to all customers
- Conduct periodic corrosion surveys of major commands (MAJCOMs) and weapon systems
- Assist weapon system managers in managing their corrosion programs, in part through working groups called Corrosion Prevention Advisory Boards
- Conduct an annual, world-wide USAF corrosion conference
- Evaluate corrosion control technologies for applicability to Air Force requirements

We are involved in many corrosion-related technical areas:

- Coatings (powder coatings, flexible primers, metal wire-arc spray, non-chromated primers, conversion coatings)

- Paint stripping (environmentally acceptable chemicals, flashjet, laser, plastic media)

- Cleaning processes (scrub pads, aqueous parts washers, environmentally acceptable solvents)

- Corrosion preventive compounds and processes, including vapor corrosion inhibition and dehumidification

- Sealants and gaskets (conductive sealants, form-in-place gaskets)

- Process-related issues (facilities, air compressors)

- Corrosion management (modeling & prediction, severity assessments, material substitution, cost of corrosion)

- Training

- On-call customer support

SELECTED EXAMPLES OF CURRENT EFFORTS

TECHNICAL ORDERS

Technical Orders (T.O.s) direct Air Force maintenance processes, and are one of our most important responsibilities. Field maintainers overwhelmingly tell us their first priority is accurate, up-to-date, clear T.O.s. That's because they use the T.O.s for all corrosion maintenance, and all other corrosion-related technical data refers back to our general-series T.O.s. In essence, our T.O.s, applicable to all systems, define what can and cannot be done Air Force-wide. Keeping them up to date and accurate allows Air Force maintainers to use the best available materials and processes, with least effort, best results, and greatest safety and environmental compliance. Some recent details of our T.O. update efforts follow:

We completely revised T.O. 1-1-8, *Application and Removal of Organic Coatings, Aerospace and Non-Aerospace Equipment,* and republished it in April 2001. It has updated environmental, safety, occupational health information, based on current requirements. It authorizes the use of recently proven, more effective, more environmentally compliant materials and processes. It incorporates Air Force common insignia and markings, allowing us to rescind another, out-of-date technical order. We recently found that many bases were using contaminated plastic media for paint stripping, causing damage to critical components, so we immediately published a Safety Supplement to the T.O., which imposed heavy particle tests of the media to ensure safe use on aircraft structure.

T.O. 1-1-689, *Avionics Cleaning and Corrosion Prevention/Control,* is a joint T.O.; Navy is the lead service, and they published a major revision September 2000. The revision does not, however, include one change we requested: to authorize MIL-L-87177 corrosion preventive compound. Therefore, we have written a supplement to authorize it for Air Force maintainers.

We are making significant changes to T.O. 1-1-691, *Aircraft Weapon Systems Cleaning and Corrosion Control*. This also is a joint T.O., under Navy lead, and a full revision was published May 2001. We have found, however, that there are simply too many technical and programmatic differences between the way the Navy and the Air Force conduct corrosion maintenance. Currently the T.O. is largely Navy-specific, with an Air Force appendix that has exceptions and modifications to the Navy processes. Thus, the T.O. is difficult for Air Force users, with ambiguities about which materials and processes are authorized for Air Force use, and with a substantial amount of inapplicable content.

Therefore, with concurrence from HQ USAF and the MAJCOMs, we are extracting and updating the Air Force-applicable information. We will then republish T.O. 1-1-691 as Air

Force-only T.O. This will not affect the other services--they will maintain the existing T.O. as is, using their own current manual numbers.

We received engineering responsibility in September 2001 for four T.O.s for vehicles & support equipment. (T.O. 36-1-191, *Technical And Managerial Reference For Motor Vehicle Maintenance*; T.O. 35-1-3, *Corrosion Prevention, Painting and Marking of USAF Support Equipment (SE);* T.O. 35-1-4, *Processing and Inspection of Support Equipment for Storage and Shipment*; and T.O. 35-1-12, *Compounds and Procedures For Cleaning Support Equipment*.) These T.O.s came to us with many inaccuracies and incomplete information. Vehicles and support equipment, lacking the attention given to aircraft, are often poorly maintained, and we find major corrosion problems in the field that must be addressed. Corrosion of these assets accounts for direct maintenance costs to the Air Force of some $23 million a year. We have already provided some updates, fixing wrong mil-spec references, obsolete materials, and outdated processes. The T.O.s still require significant rewrite, however.

CORROSION SURVEYS

We survey each MAJCOM once every five years; the purpose is not to inspect every piece of equipment, but rather to evaluate the overall health of a command's corrosion prevention and control program. We visit a sample of bases within a command, and look at equipment, maintenance processes, materials used, training, scheduling, and hazardous materials management. We provide technical assistance on-site, and give briefings to unit and MAJCOM leadership to help them improve their programs.

Our most recent survey was of the Pacific Air Forces command (PACAF). Our survey team visited 10 locations in April-May 2001; what they found is typical of what we see throughout the Air Force.

- Aircraft were generally in good condition, though with some paint eroded from leading edges. Touchup is difficult, due to restrictions on spraying outdoors. Our recommendation is to perform interim touchup with brushes, rollers, or Sempens.

- Support equipment and vehicles, on the other hand, were in fair to poor condition overall. Often stored outdoors, and painted with inadequate coatings, much of this equipment has severe corrosion and needs attention soon.

- Unauthorized materials are sometimes used, such as cheap spray paint or industrial cleaning compounds that can damage equipment and violate environmental restrictions. Usually, in these cases, we can immediately provide information on the correct materials, including T.O. references and ordering information.

COATINGS REMOVAL

A coatings removal issue we resolved recently was the practice at some bases of sanding landing gear before repainting. At depot level, there are safe processes for removing landing gear coatings, but in the field, sanding causes damage to the substrate. This promotes crack initiation and corrosion, and thus is a safety of flight concern. We coordinated a response with MAJCOMs, system managers, and landing gear engineers; HQ USAF issued an official message that prohibits unapproved stripping and scuff-sanding methods.

RESPONSE TO FOOT AND MOUTH DISEASE DISINFECTION

In March 2001, we found several European countries were disinfecting Air Force aircraft landing gear against Foot and Mouth Disease (FMD). The disinfectants (bleach and other chemicals) are unauthorized, and promote corrosion, embrittlement, and materials degradation. As of 3 January 2002, 126 disinfections had been performed on 94 USAF aircraft of 16 types. The AFCPCO led the Air Force mitigation strategy, developing rinse and documentation

requirements and helping system managers determine long-term management actions to take with their affected aircraft. We worked with the Air Force Research Laboratory (AFRL), Navy, Boeing, and Department of Agriculture to have chemicals tested; based on the results, we recommended the "least risky" disinfectant and had it adopted for all disinfections. The recommended disinfectant at this time is a commercial product, Virkon S. The testing shows it to present a risk of hydrogen embrittlement to high-strength steel, but it is less damaging than other disinfectants to non-metallic materials, the most important being wiring insulation. (Note: there is no U.S. requirement to disinfect aircraft; our recommendation only applies when a foreign nation requires disinfection.)

AIRCRAFT WASH PADS

We are working with industry to develop and field test a new type of aircraft wash scrub pad. The current prototype, a proprietary design, shows potential to clean better while being less abrasive. Field testing is underway at various bases. If approved, and put into production, we will incorporate it into our technical orders to make it available to all units.

X-IT PREKOTE

We are in the first year of a six-year field evaluation of a new non-chromated pre-paint surface treatment for aluminum, X-It PreKote. It is environmentally friendly, non-toxic, and promotes adhesion; it has the potential to replace chromated conversion coatings, reducing chromium use. It is in use at Ogden Air Logistics Center on F-16s, but before we can recommend it for use Air Force-wide, we need more information on how it performs on different aircraft substrates. We have X-It PreKote now flying on four operational aircraft: two A-10's and two C-130's. AFRL is supporting us with additional lab testing. It is currently only being used with chromated primers, to assure adequate corrosion inhibition.

AQUEOUS PARTS WASHERS

The Air Force is struggling with problems caused by the introduction a few years ago of Aqueous Parts Washers (APW), replacing many solvent cleaning processes. A study we conducted documented the problems: APWs are not always effective in removing soils, requiring supplemental cleaning; they can cause corrosion of parts; the APWs themselves are corroding and failing at a rapid rate; they produce much more hazardous waste than originally predicted; they are not approved in many T.O.s; and they can cause hydrogen embrittlement. A follow-on study (Phase II) is defining and comparing potential solutions, testing improved APWs at operational bases, and refining designs. A Phase III effort, to start in 2002, will prototype and field test the most promising solutions at field units.

CORROSION FACILITIES GUIDE

We are developing an Air Force Corrosion Facilities Guide. Current civil engineering guidance is inadequate for corrosion maintenance operations. Many existing facilities have deficiencies, resulting in inadequate maintenance of the aircraft, increased risk to personnel, and environmental non-compliance. Commands cannot justify cost of adequate facilities without documentation justifying the requirements. We are determining MAJCOM requirements, documenting capabilities needed for effective performance of corrosion control tasks (light, heating/cooling, airflow, filtration, power, etc.), and evaluating available ways to achieve those capabilities. The final facility requirements guide will be coordinated with each MAJCOM and incorporated into technical orders.

CORROSION MANAGEMENT

AFCPCO is working with AFRL, in an effort being conducted for the Air Force Aging Aircraft System Program Office, to move the Air Force to a new philosophy of corrosion management.

The intent is to move away from the current "find-and-fix" process to an ability to "anticipate and manage." This effort is developing tools to better predict, detect, understand, and manage corrosion. Projects are ongoing in environmental severity, modeling, cost of corrosion, analysis of corroded structure, materials substitution, and corrosion suppression. The goal is to to be able to safely fly aircraft with known corrosion, deferring repair, and thus saving up to hundreds of millions of dollars a year.

ANNUAL CORROSION PROGRAM CONFERENCE

AFCPCO conducts the annual Air Force Corrosion Program Conference, targeted primarily at field-level and depot-level corrosion maintainers, weapon system and MAJCOM corrosion managers, and those who support them. It emphasizes solutions to current and near-term concerns (other conferences adequately review longer term research and development). Last year we had 441 participants, representing all MAJCOMs, all Air Force depots, 124 field units, all sister services, HQ USAF, AFRL, system managers, and industry. It's one of our primary means to communicate changes in guidance, newly authorized materials, and lessons learned to the entire Air Force corrosion community.

CURRENT CONCERNS FACING THE AIR FORCE

Overall, we consider the most pressing concerns that face the Air Force Corrosion Prevention and Control Program today to be, in general terms:

- The continual need for education and communication. Many users do not know what is already authorized or prohibited. They don't understand the technical reasons for certain process requirements. In this downsized Air Force, many haven't had enough on-the-job training. Most calls for assistance we receive don't require new technology: the answer is known, it just needs to be communicated.

- Continued use of unauthorized materials. Many users have been erroneously compelled by environmental authorities to abandon T.O.-mandated materials and use "green" materials that damage aircraft. In most cases, there are environmentally acceptable authorized materials that can be used instead. In other cases, users simply use whatever's convenient or available, because they don't understand the impact of using the wrong material.

- Management of out-sourced corrosion work. While contracting out such tasks as painting and depainting can help units deal with personnel shortages, it creates the need for new skills at the unit level. Corrosion personnel now need to know how to ensure necessary requirements are included in contracts. They also need to know what recourse they have when the finished product does not meet the requirements.

- The environmental pressure to use less hazardous materials is likely to increase. For example, we fully expect to have to cut back further on the use of chromium as a corrosion inhibitor.

- Because of limited funding, technical solutions to all these issues need to also be affordable.

TECHNOLOGY NEEDS

Looking ahead to the future, we have identified the highest priority technology needs for the Air Force R&D community to address to meet upcoming corrosion challenges:

- Better methods to predict, detect, and manage corrosion

- Non-chromium corrosion-inhibiting coatings
- Improved corrosion preventive compounds
- Materials to prevent degradation of advanced composites
- Improved, environmentally acceptable plating or surface treatment technologies
- Advanced coatings removal technologies

SUMMARY

In summary, the AFCPCO manages the Air Force corrosion program for HQ USAF. We are the Air Force's single, central point of contact with resident expertise--experienced engineers, technicians, and senior enlisted staff. We provide formal technical guidance and on-call problem solving for MAJCOMs, depots, system managers, and field units. We address cross-cutting corrosion problems, provide continuity throughout the Air Force corrosion community. We serve as a bridge between developers and users, helping transition technologies into operational use.

For more information, contact:

Major Dan Bullock
Chief, Air Force Corrosion Prevention and Control Office
AFRL/MLS-OLR
325 Richared Ray Blvd.
Robins AFB GA 31098-1639
DSN 468-3284
478-926-3284
daniel.bullock@robins.af.mil or afcorr@robins.af.mil

THE IMPLEMENTATION OF QUALITY ASSURANCE TRAINING IN NAVAL SHIP PRESERVATION WORK

Norm Clayton & Jeff Duckworth

Naval Surface Warfare Center, Carderock Division
Ship Systems Engineering Station – Philadelphia

BACKGROUND

The cost of preservation work on Naval vessels is a significant portion of the Navy's overall maintenance cost. For tanks alone, data collected in the 1990's estimated the annual cost of coatings work to be $244 million dollars. While the Navy's ship preservation processes have long been well defined, until the early 1990's the requirements for the oversight of the processes were minimal. Considering the increasing costs of shipboard preservation, the Navy decided to invest in efforts that would extend coating performance and provide significant lifecycle cost reductions. These efforts were concentrated on the implementation of both high performance coatings in selected areas, and effective Quality Assurance (QA) for the entire coating process. These two efforts came together in the mid-1990's, with emphasis on those areas of a ship that had the greatest preservation cost: tanks, underwater hulls, bilges, exterior surfaces, flight decks, and the well deck overheads of amphibious ships. Much has been written previously on the Navy's adoption of high performance, high solids coatings for many of its more critical coated areas.[1-4] This paper describes the parallel efforts to increase the quality of the preservation process.

PRESERVATION PROCESS QA

There are several elements to a comprehensive QA program for the preservation process:

- The documentation or specification of process requirements.
- The use of specific test methods and acceptance criteria.
- The definition of checkpoints in the process where the tests are to be performed.
- The record-keeping required for the process.
- The training and certification of personnel involved with the process.

US Navy coating policy documents are the starting point for all of the above requirements, since they define the test methods and criteria, the appropriate checkpoints, and the type of training required. For Naval vessel preservation work, there are five primary documents that define the requirements:

- Naval Ship Technical Manual (NSTM) Chapter 631, *Preservation of Ships in Service*, Volumes 1-3.
- Naval Ship Technical Manual (NSTM) Chapter 634, *Deck Coverings*.
- NAVSEA Standard Item 009-32, *Cleaning and Painting Requirements.*
- Submarine Preservation Maintenance Standard, SUBMEPP MS No. 6310-081-015
- Preservation Process Instructions (PPI)

The applicability of these documents varies according to vessel and coating type, and to the facility performing the work (Naval activity or shipyard vs. commercial contractor). However, coating inspectors that have been trained and certified are required for process QA for critical coated areas by all of these documents. Two training and certification programs are recognized for this purpose: the Navy's "NAVSEA Basic Paint Inspector" (NBPI) course, or Session 1 of the NACE International Coating Inspector Program (CIP). This paper focuses on the training provided by the NBPI course.

THE NAVSEA BASIC PAINT INSPECTOR (NBPI) COURSE

The NBPI course was developed in 1995, and has evolved in parallel with changes in the Navy's specification and test requirements. The organization of the course was originally modeled after the well-known course administered by NACE International, but the content is very specific to Naval vessel coating requirements. Successful completion of the week-long course results in a certification that is valid for four years before a student must go through a re-certification process. Students are evaluated based on written quizzes and final exam, their demonstration of proficiency with the inspection instruments taught in the course, and on coating inspection log books that they create during a hands-on practical day. Several team exercises are used throughout the week to give students time to use each of the inspection instruments as they are introduced, to apply their new knowledge to case histories, and to familiarize them with important process documents.

The course curriculum basically follows the preservation process, from surface preparation through curing of the final coat and evaluation of workmanship and coating defects. An introductory section deals with corrosion basics, covering common forms of corrosion and the corrosion behavior of the most common alloys used in ship construction. Standard methods of evaluating in-service coatings, such as degree of rusting and blistering, are also described. Time is also spent in familiarizing students with the complex and frequently changing coatings policy documents, particularly NSTM Chapter 631 and NAVSEA Standard Item 009-32.

Surface preparation methods that are described in the course cover a wide range that may be encountered, from simple methods used by ship's force, to more complex industrial and shop processes that may be encountered in a shipyard. Non-mechanical surface cleaning methods

reviewed include solvent cleaning, acid cleaning, pickling, steam cleaning, and alkaline cleaning. Hand and power tool cleaning methods are described, followed by abrasive blasting and hydroblasting. The surface preparation topic is concluded by a description of alternative methods intended for either sensitive substrates or environmental compliance.

The instruments and test methods used by a coatings inspector are introduced and demonstrated in the order that each would be used in the preservation process. Those that apply to surface preparation include the evaluation of surface cleanliness according to written and visual standards, the measurement or surface profile, and the measurement of pertinent environmental conditions such as relative humidity, dew point, and surface temperature. The measurement of invisible surface salt contaminants is also demonstrated, in terms of both the extraction of salts from the surface, and the measurement of either chlorides or conductivity in the fluid that was extracted. For each of these techniques, specific Navy requirements for sampling rate or frequency, and acceptance criteria are described.

The course then moves into coatings, covering different types used on Naval vessels according to their resin systems and curing mechanisms. Coatings with special functional purposes are also described, such as anti-fouling, non-skid, fire retardant, and intumescent paints. Paint storage and mixing requirements are covered, as are application methods such as spraying using conventional air, airless, high volume low pressure, and plural component equipment. At this point, both wet and dry film thickness test methods are described, with special emphasis on dry film thickness (DFT) measurement in accordance with the industry standard SSPC-PA-2.[5]

The instructional material concludes with a description of common coating failures and defects, the use of wet sponge, low voltage holiday detectors, and a discussion of specialty substrates and coatings. These include painting over composites and signature reduction

materials, and the use of powder coatings and thermal spray aluminum coatings. The course also has a section covering safety for the coating inspector at various stages in the preservation process, and a summary of the roles and responsibilities of coatings inspectors in Naval ship work.

A summary of the instruments and test methods taught, and the common Navy criteria for the tests, is shown in Table 1. Not all of these tests are invoked for all preservation work.

RESPONSIBILITIES OF NAVY COATING INSPECTORS

The responsibilities of a Navy Paint Inspector will vary with the type of work being performed. While coating inspectors are required for all critical coated area preservation work performed when a vessel is in a maintenance availability, they are also used to document the Navy's many shipboard coating test initiatives. Their roles may vary from simply verifying key measurements made by contractors, to having greater responsibility and stop-work authority. Some of the more significant specific requirements are listed below (following the table). Many others can be found in NSTM Chapter 631, Table 631-11-1.

TABLE 1.
Naval Ship Preservation Process Tests and Criteria

Test	Instrument	Criteria
Surface Degreasing	Black Light	No visual evidence of grease or oil.
Environmental Conditions • Relative Humidity • Surface Temperature • Dew Point	 • Sling Psychrometer • Temperature Gages • Psychrometric Tables	During surface prep.- • Less than 85% or 50%. • 5^0F above dew point
Surface Cleanliness • Hand & Power Tool • Abrasive Blasting • Hydroblasting	SSPC Written & Visual Standards • SP-3, SP-11, VIS-3 • SP-10, SP-5, VIS-1 • SP-12, VIS-4	Prepared surface must meet cleanliness level specified for job.
Surface Profile	Profile tape and micrometer	Within specified range.
Surface Salts • Chlorides • Conductivity	Extraction methods plus… • Bresle titration • Conductivity meter	Non-immersed//immersed: • ≤5 // 3 μg/cm^2 • ≤70 // 30 μsiemens/cm
Environmental Conditions • Relative Humidity • Surface Temperature • Dew Point	 • Sling Psychrometer • Temperature Gages • Psychrometric Tables	During coating- • Less than 85% or 50%. • 50^oF – 100^oF, and… • 5^0F above dew point
Dry Film Thickness (DFT)	Magnetic Pull-Off gages and Constant Pressure Probe Gages	Minimums, maximums, and averages within specified ranges as per SSPC-PA-2.
Film Defects & Holidays	Visual inspections and low voltage wet sponge holiday detector	No defects as defined in job specification.

- Review of all applicable documentation (job specifications, Navy policy documents, paint manufacturers data sheets, etc.) in order to identify and resolve potential conflicts.

- Verification of abrasive blast media certification to applicable specification.

- Verification of coating receipt inspection conformance tests.

- Verification of shelf life of coatings to be used.

- Measurement of environmental conditions throughout preservation process, from abrasive blasting through curing of the final coat.

- Verification that specified cleanliness level was achieved prior to priming.
- Measurement of surface profile.
- Measuring residual surface chlorides or conductivity prior to priming.
- Verification of masking of items not to be painted.
- Verification that coatings are properly mixed, and that any required induction times are observed.
-
- Verification of stripe coating of edges and welds.
- Measurement of the DFT of each coat and of the overall paint system.
- Verifying that correct overcoat times (time between coats) are followed.
- Inspection for workmanship, holidays, and other application defects.
- Completing all record-keeping requirements.

In addition to the shipboard areas defined in NSTM Chapter 631, trained and certified coating inspectors are being required to oversee repainting efforts on selected types of equipment. Current equipment where certified coating inspectors are required includes combat system radomes, and the weather deck surfaces of Vertical Launching System (VLS) modules.

Coating inspectors in the Navy community that have been trained by either NBPI or the NACE International course are now required for related work in assessing the condition of the coatings in tanks and voids. Trained inspectors are required to collect data that will help make maintenance decisions as to whether a coating needs complete replacement, touch-up spot repair, or no action at all. This is largely based on evaluating the degree of rusting of specified zones in a tank per ASTM D 610[6], and evaluating any blisters in the paint per ASTM D 714[7].

CURRENT SITUATION

At the end of 2001, there have been over 1100 people who have taken the NBPI course from the three activities that have taught it over the past six years. These students represent virtually every facet of the Navy coatings community. Approximately 93% percent of the students have successfully passed the course. The re-certification process has begun, with approximately 70 people out of 250 expired people applying to recertify.

FUTURE DIRECTIONS

The major challenge in the near future for the NBPI course is a transition to private sector instruction. Currently, the course is instructed by three different organizations: South Tidewater Association of Ship Repairers (STASR), the Port of San Diego Ship Repair Association (PSDSRA), and Naval Surface Warfare Center, Carderock Division (NSWCCD). The STASR and PSDSRA facilities provide a locally available course for a significant portion of those performing preservation work for the Navy, while NSWCCD travels to other sites to provide local training (Portsmouth Naval Shipyard, Pearl Harbor Naval Shipyard, Trident Refit Facilities, commercial shipyards, etc.). At the current time NSWCCD offers the course five to six times a year in different locations. In order to increase the availability of the course, NAVSEA has decided to allow SSPC to instruct the course, utilizing instructors that have met criteria drafted by NAVSEA and SSPC. With the present schedule SSPC should begin offering classes in the March—April 2002 timeframe. As with the other organizations that offer the course, NAVSEA will continue to maintain the content of the NBPI course.

REFERENCES

1. B. Appleman & J. Helsel, *Improving the Quality of Preservation Work on U.S. Navy Ships,* JPCL Aug 2001, pp. 55-58.

2. G. Kuljian, A. Kaznoff, & A. Parks, *State of the Art Procedures for Ensuring Optimum Coating Longevity in Navy Tank Coating Operations,* in "Technologies for Diverse Industries", SSPC Report 96-08, SSPC, Pittsburgh, PA 1996, pp. 70-79.

3. E. D. Thomas & A. Webb, *The U.S. Navy's Advances in Coating Ship Tanks,* JPCL Feb 2001, pp. 29-41.

4. W. Mathe', J. Rudroff, and P. Parson, *Evaluating the Use of Plural-Component Spray Equipment on U.S. Navy Ships,* JPCL, Feb. 2000, pp. 42-46.

5. SSPC-PA-2, *Paint Application Standard No. 2 – Measurement of Dry Coating Thickness with Magnetic Gages.*

6. ASTM D 610, *Standard Test Method for Evaluating Degree of Rusting on Painted Steel Surfaces.*

7. ASTM D 714, *Standard Test Method for Evaluating Degree of Blistering of Paints.*

METHODOLOGY FOR ACQUIRING AND ASSESSING THE COST OF CORROSION FOR U. S. MARINE CORPS GROUND VEHICLES AND SELECTED EQUIPMENT

Mike Gallagher
Naval Surface Warfare Center Carderock Division
Marine Coatings and Corrosion Engineering Branch
Philadelphia, PA 19112

ABSTRACT

In 1999, the U.S. Marine Corps Corrosion Prevention and Control (CPAC) program office tasked the Naval Surface Warfare Center Carderock Division (NSWCCD) to develop a methodology for assessing the Cost of Corrosion for U. S. Marine Corps ground vehicles and selected equipment. The approach taken, including the assumptions and lessons learned, is presented. The utilization of the On-Line Analysis Processing (OLAP) capability resident in Microsoft Office is also presented as a desktop tool for interactive assessment and evaluation of the findings.

The methodology presented is an attempt to acquire all direct corrosion cost elements over a given time period and to deliver them in a format to be used at various administrative levels to determine where corrosion is occurring and to quantify the associated costs. Recognizing, and being able to quantify, where corrosion costs occur would assist in: determining and prioritizing future research and development efforts; identifying unreliable components, systems or designs; providing data that may identify emerging operational and maintenance corrosion problems by base, platform type, maintenance echelon, and various levels of systems, components and parts; and provide both a baseline and an on-going measurement for candidate corrosion reduction/cost improvement programs.

The proof-of-concept effort concluded with cost of corrosion results for FY97 through FY99. A follow on effort is currently being conducted to update the results through FY01.

INTRODUCTION

The U. S. Marine Corps annually spend millions of dollars combating corrosion. The "Cost of Corrosion" effort, funded by the Corrosion Prevention and Control (CPAC) program resident at Marine Corps Systems Command, is an attempt to develop a methodology and process to quantify that cost. The approach taken relies heavily upon correlating existing data

resources and interviews with the Fleet Marine Force. The data resources included the three primary maintenance and supply information management systems as well information from Principle End Item Stratification Sheets and various informal tracking systems used by individual maintenance offices. With the exception of Marine Maintenance Officer (MMO) tracking of Corrosion Control and Coating (C3) expenditures, none of the data resources identify any particular cost or repair/maintenance action as corrosion related. Nevertheless, these data sources provide a complete as possible cost, count and stratification of Marine Corps equipment, maintenance and repair records, and parts acquired or exchanged for repair and maintenance. When combined with the interview results, which identify and quantify those parts whose replacement is related to corrosion, a cost can be derived for corrosion material and labor associated with principle end item Table of Authorized Material Control Numbers (TAMCN) and Equipment Identification Numbers (IDN), as well as the equipment owner, the repair activity, the regional area code (RAC) and the level of maintenance.

The results of the effort are presented in an On-Line Analysis Processing (OLAP) database. The OLAP cube file is a multi-dimensional database in the form of a Pivot Table or Pivot Chart that enables a user at any administrative level, from Platform Manager (PM) to repair company, to interactively explore applicable data without having to construct individual queries. The PM can ascertain total corrosion costs or identify potential areas of concern or improvement for their given equipment, the Marine Expeditionary Force (MEF) MMO can identify costs expended and quantity of repair actions within any given unit, and a repair unit can identify and track areas of improvement for maintenance and repair of a given part. The OLAP cube provides not only a means of deriving costs and quantity, but also a tool for tracking and monitoring internal Marine Corps corrosion cost improvement programs.

APPROACH

This effort was two-fold: (1) to develop a methodology whereby corrosion costs for U. S. Marine Corps ground vehicles and selected engineering equipment could be assessed and (2) to deliver that information in a means that could be most utilized by administrators and program managers. The corrosion cost elements considered for this task were: (1) 1st echelon "Rust Busting", (2) 2nd through 4th echelon maintenance and repair, (3) Corrosion Control and Coating (C3) Program expenditures, and (4) consumables. Indirect costs, such as administrative and facility overhead, were not included in this study, the exception being the C3 program, which is almost exclusively outsourced. Facility costs are intended to be included in the future. The primary costs represented are material and labor. Included in labor costs is consideration for what has been termed, for this effort, "adjacent labor". Adjacent labor is intended to capture time spent, due to corrosion, in repair or preparation of areas adjacent to the primary repair. Examples of this might be preparation and coating of a bulkhead prior to mounting a piece of equipment; drilling and tapping bolt holes where a rusted bolt snapped (especially common when repairing some exhaust systems); and cleaning and preparing electrical connections. In each of these cases, the original cause of part failure was not necessarily corrosion, but additional time was added to the job because of corrosion.

The equipment focus group included nine equipment categories, containing 79 TAMCNs and 130 IDNs. The equipment categories were the following:

- AAV - all configurations of amphibious assault vehicles (AAV).
- Engineer-Motor - motored engineer equipment including, cranes, road grader, scoop loaders, motorized rollers, tractor scrapers, tractors, fork lifts and material trucks.

- Engineer-Trlr - trailered engineering equipment including, fixed bridge, fuel pump module, water pump module, pneumatic tool, power distribution unit, pump assemblies, pumps and water purification unit.
- Generator - all diesel generator units.
- HMMWV - all configurations including; radio set, radio terminal set, truck ambulance, and truck utility of the High Mobility Multi-purpose Wheeled Vehicle (HMMWV).
- LAV - all configurations of light armored vehicles (LAV).
- LVS - power unit and all trailers of the Logistics Vehicle System (LVS).
- Trailer - miscellaneous trailers including, trailer chassis, dolly trailer, tank semi-trailer, cargo trailer, low bed trailer and tank trailer.
- Truck 5T - all configurations of 5-ton trucks: tractor truck, cargo truck, dump truck and wrecker truck.

To be most useful, the information needed to differentiate between all the variants of the equipment population, as well as maintain identification of the command, the equipment owner and who conducted the repair.

DISCUSSION

The methodology developed utilizes, as much as possible, real values obtained through U. S. Marine Corps maintenance information management systems: Marine Corps Integrated Maintenance Management System (MIMMS), the Supported Activities Supply System (SASSY), and the newly implemented Asset Tracking Logistics and Support System (ATLASS II+). Additional data sources used were Principle End Item Stratification Sheets, and various field, on-site, informal tracking systems. None of these systems, however, identify any particular

repair action or part replacement as corrosion related. Nevertheless, these systems are the most comprehensive records of vehicle/equipment count and disbursement, and of maintenance and repair actions available. Incorporating this information provides a foundation for quantifying the data and findings.

Of the four cost elements considered, C3 and consumables costs are the most directly available. The Marine Corps Corrosion Control and Coating (C3) program is an annually funded line item for extending the service life of Marine Corps equipment, decreasing future maintenance costs and increasing readiness. By definition, all C3 expenditures were considered corrosion related. Similarly, a list of CPAC approved products was compiled and the national stock numbers were queried through SASSY for all material acquisitions.

Assessing corrosion costs accrued through maintenance and repair actions was more difficult. In order to identify and quantify which parts were replaced and what maintenance/repair actions were conducted due to corrosion, an extensive interview process was developed. Using the MIMMS data, lists were compiled of all parts replaced for the principal end items within the focus group. The original MIMMS data was for all maintenance actions conducted during FY97 and FY99. During this three-year period over 1.5 M records were generated for the focus group equipment and over 40,000 different National Stock Numbers (NSN) were identified as parts replaced. An assumption made when developing the parts lists for the focus equipment was that a majority of the corrosion problems and resultant costs were due to a minority of parts. It was recognized, however, that although a particular part may be replaced rarely, its replacement cost was of such magnitude that it could not be ignored as a corrosion problem simply because of an infrequent replacement history. Therefore, two parts lists were developed for each equipment category in the focus group and an “80-20” rule was

applied to both. The first parts list was "COST" and ranked all parts in order of their sum total replacement cost, regardless of quantity, and was cut off when the aggregate cost achieved 80% of the total parts cost. The second parts list was "QUANTITY" and ranked all parts in order of their sum total replacement quantity, regardless of cost, and was cut off when the aggregate quantity achieved 80% of the total parts count. The two lists then, when combined, account for high material cost items with very little associated labor cost as well as high labor cost items (due to quantity) with very little associated material cost. These parts lists formed the basis of the interviews.

The major premise behind the interview process was, "The people who can best identify what parts are most frequently affected by corrosion are the people who have to maintain the equipment". Accordingly, interviews were conducted with mechanics and their direct supervisors. Multiple units within each MEF were chosen for interviews based upon the volume of focus group maintenance/repair actions generated in MIMMS. Each of these units was interviewed with parts lists for all of the vehicle/equipment categories maintained by their respective unit. The unit interviews averaged between one and two hours, depending upon the number of equipment categories maintained by the unit and the length of the individual part lists (the parts list for HMMWVs exceeded 700 parts).

Five questions were asked during the interview. The first question "Is this part ever replaced due to corrosion or is there ever adjacent work performed because of corrosion?" was a screening question; negative responses quickly passed to the next part. Positive responses required providing estimates for (1) the number of times out of ten the part is replaced due to corrosion, (2) approximately how long does it take to change out this part, (3) how often out of ten times is there adjacent work due to corrosion, and (4) what is the average amount of time

spent on adjacent work? Two additional and similar questions (how often? and how much?) were asked during visits to 3rd and 4th echelon maintenance battalions to include cost considerations for parts sent out for rebuild or disposal. All positive response were compiled and averaged for cross-reference with the MIMMS and ATLASS II + records to derive an applied corrosion cost for parts replaced due to maintenance and repair.

Derivation of corrosion costs for maintenance and repair was conducted separately for each of the Regional Area Codes (RAC) to account for the geographic and environmental differences between the various MEFs. Further, although there is one master list of "secondary repairable" items for the Marine Corps, each MEF maintains its own, slightly different list. Therefore, secondary repairable item lists were acquired from each of the MEFs. Multiple queries were constructed accounting for focus group equipment, RAC, level of maintenance (echelon), secondary and non-secondary repair material, and interview responses and the resultant corrosion costs for material and labor were appended under separate fields to each applicable MIMMS and ATLASS II + record.

In addition to the above maintenance and repair questions, unit maintenance and operations officers were interviewed for estimates of time spent "Busting Rust". First echelon equipment operators are responsible for performing all preventive maintenance on their vehicles/equipment, which includes periodic inspections and subsequent corrosion corrective actions (generally requiring use of a wire brush and coating application). Also included was time spent performing pre- and post-deployment corrosion prevention procedures. Results from these interviews were also compiled and averaged and the cross-referenced with Equipment Stratification Tables to derive a total time spent busting rust for the MEF.

Processing of all data and information was accomplished exclusively through Microsoft Access. The final table includes all maintenance actions from the maintenance information systems (both corrosion and non-corrosion related) as well as the C3, consumables and rust busting cost elements. The applied corrosion costs are related to a principal end item (PEI), as identified by both the TAMCN and the IDN, as well as to a either a C3 expenditure, Rust Busting, or a specific replacement part when applicable, identified by national stock number (NSN). Consumables are related to RAC. This final table is then presented in an OLAP cube file via Microsoft Excel. The OLAP capability enables a user to interactively view the data in a number of different formats, from a macro (total corrosion cost for HMMWVs) to a micro (how many starters at a specific command were replaced for a particular kind of generator) perspective.

The Cost of Corrosion for U. S. Marine Corps ground vehicles and engineering equipment has been updated to reflect cost for FY00 and FY01. The process is self-contained so that future updates can be processed and re-distributed, assuming timely receipt of new information, in approximately 2 to 3 weeks. It is feasible, given the ability to transfer data via the Internet, that a methodology and procedure could be implemented to provide quarterly updates of a revolving two year cost of corrosion assessment.

CONCLUSIONS

It was apparent during the course of this effort that corrosion is a topic of high concern to the Marine Corps. During the interviews, personnel at all echelon levels were extremely cooperative and willingly talked about the problems they faced maintaining their equipment and the time invested combating corrosion. More than a few times we found that the unit to be

interviewed had already filled out the part lists with their estimates for the interview questions; minimizing the interview process to a review. In all of these cases it was evident that the personnel had taken considerable time and care to review the lists and provide as comprehensive an appraisal as possible.

Similarly, when it became clear what structure the OLAP cube was going to take, preliminary results were presented to various MEF representatives for their assessment and input. Most representatives expressed the opinion that this tool would be very useful, providing them a handle for quantifying and assessing their corrosion problems. That the representatives felt the program had promise was rewarding; their interest and enthusiasm, however, was a reflection of the need.

This task has grown from an initial concept to derive a cost of corrosion for U. S. Marine Corps ground vehicles to stratification of corrosion costs across product lines and owners, to incorporation of a desk top tool for interactive assessment of costs across various dimensions. The OLAP cube file as a deliverable for this effort cannot be considered the final product as modifications may be required to address the specific needs of the users and for inclusion of corrosion costs at the depot levels. Nevertheless, the methodology used and the OLAP deliverable demonstrate a means of acquiring a corrosion cost for a broad spectrum of equipment and commands and then delivering that information in a package form that can easily provide measurable data across numerous dimensions.

WEB DESIGN FOR INFORMATION AND TRAINING IN CORROSION PREVENTION & CONTROL

P.R. Roberge

Department of Chemistry and Chemical Engineering Royal Military College,
Kingston, Ontario, Canada, K7K 7B4
roberge-p@rmc.ca or http://corrosion-doctors.org

ABSTRACT

Web based training (WBT) is slowly becoming an accepted training method in many professional fields. With modern Web editing tools, it is possible to design highly effective WBT material to meet the training needs of a diverse population. In order to introduce these technologies in the classroom, new paradigms have to be developed to satisfy requirements specific to training. However, technical changes usually impact educational methods very slowly. The introduction of the overhead projector in the classroom, for example, has yet to replace the use of chalk, a very small change indeed. Most of the successes in WBT have so far been achieved for courses in software and computer engineering. In such cases the medium is also the training breadboard. For hard courses in other engineering disciplines, progress will be much more difficult for two main reasons: the first and probably most obvious is the effort required to transform the training material into a computerized format. Such endeavor has been estimated to be of the order of one hundred hours of preparation for a typical university lecture. The second obstacle is subtler and maybe more challenging than the first since it is psychological in nature. As much as software engineers understand the mechanics to produce and run a WBT course, the opposite is true of many specialists in other disciplines. This paper presents a relatively inexpensive and progressive approach to the introduction of WBT as a training aid by building-up adequate features into an existing information Web site.

INTRODUCTION

The exponential growth in Internet technologies has made Web-based training (WBT) a viable alternative for delivering training to individuals anywhere in the world at any time. This delocalization of supply and demand opens new challenges and opportunities that are quite exciting in specialized areas of expertise, for which experts often are unavailable for such

mundane tasks as teaching and training. Education and training via the Web are growing rapidly. Reduced training costs, world-wide accessibility, and improved technological capabilities have made electronic instructional delivery to adult learners a viable alternative to classroom instruction.

It is estimated that technology-assisted training will represent half of all training methods by the year 2002. Particularly appealing to industry are the cost savings such training affords. PNC Bank Corp in Pittsburgh, for example, recently installed a system for self-paced online training through which it expects to save as much as 40 percent per user in training expenses.[1] MCI WorldCom slashed approximately $3 million in travel, facility, and labor costs over a year by offering 20 percent of its classes over the Web. The company expected to increase this to 50 percent in 1999.[2] By switching from classroom to WBT, some companies have realized up to 75 percent savings in their training budgets, making this mode of training especially appealing to companies that have large numbers of employees to train.[3] Travel expenses, instructor fees, facility costs, materials, and office equipment costs, in addition to the cost of lost time on the job when employees are in training represents some of the savings that are realized through WBT.

While the possibilities to offer adequate training via the Internet or Intranet are probably the areas of greatest predictable growth in the field of professional training. Most corrosion Web sites are mostly the presentation of information that was never designed to fit into an intellectual schema for training. In spite of the tremendous advantages offered by these new technologies, experience has shown that an enormous investment in professional time in planning and developing course material is required. Fortunately, some Web sites are readily designed to support WBT. The Corrosion Doctors site is an excellent example of such sites. Some of the perceived WBT benefits are:

- **Reduced Learning Time:** Studies show typical reductions in training time, "learning compression," of 40-60% using WBT training primarily due to the increase in student interactivity;
- **Reduced Training Costs:** Overall costs with WBT instruction are reduced due to overall delivery costs being lower for WBT training even though initial development costs are higher with computer-based instruction;
- **Consistency:** Training consistency is maximized using WBT instruction. Courses delivered in an interactive multimedia format do not vary from class to class, day to day or location to location;
- **Just-In-Time:** Interactive multimedia systems are being used worldwide to deliver training when it's most needed, on the job, at the employee location;
- **Self-Paced and Individual Learning:** Interactive Multimedia systems provide a level of responsive feedback and individual involvement that is highly motivating in both individual and classroom environments. Further, interactive learning systems focus attention and reduce distraction;
- **Student Feedback:** Interactive WBT can provide feedback immediately to student responses and activity. Plus, unlike classroom instruction, interactive systems can be designed to ensure that each student masters current material before moving forward;
- **Enhanced Ability to Track and Evaluate Student Performance and Progress:** Courseware developed with a comprehensive Course Management System makes it easier to administer enrollment and track student performance and progress.

This paper presents an incremental approach to WBT development that will hopefully help avoid many of the pitfalls facing the introduction of a new technology in the classroom, while providing the means to test new concepts before the creation of full-scale training packages.

THE CORROSION DOCTORS' WEB SITE

Quite a few Web sites provide various forms of corrosion information. A search of the generic term "corrosion" would typically reveal the existence of more than one million Web pages with references to the subject. The following sections will discuss various aspects related to the creation, development, and operation of the Corrosion Doctors Web site. From its launching in mid August 1999, the site has reached an interesting level of Web traffic in its first two years of existence, with positive indicators that the site is actually fulfilling its initial goal of bridging large distances across many disciplines.

EARLY HISTORY

In the early 1980s, the Royal Military College was tasked to organize a corrosion short course for National Defense engineering personnel, with attendants and instructors coming from various branches of the Department and from all possible locations in Canada. In the context of downsizing and restructuring, the organization of the Corrosion and Prevention short course became increasingly difficult. The decision was then made to explore other ways to dispense corrosion training. Two information modules and one Aircraft Corrosion Newsletter were developed in the early part of 1997. The main goal of these Web pages was to improve the communication of complex data and concepts between distant locations. The Web pages were created using a very efficient tool, Frontpage 97, requiring a minimum of programming skills.

However, while these pages were developed in a relatively straightforward manner, they had to be transferred to a UNIX based Web server by a different team, with a few levels of bureaucratic annoyances. In practice this meant that the pages turnover was very slow and limited to HTML coding.

The interest and need to interface to a largely distributed community were reexamined in a study carried out by an external advisor in the first part of 1999. One obvious conclusion of the study was to seek a Web service adapted to the development tools chosen and free of local politics. The reengineered site was launched in mid August 1999 as the ***Corrosion Doctors***. It was decided, early in the existence of the site, to build it on feedback and collaborations from the broadest community possible. Most of the first months of the Web site development were spent learning the rudiments of information for Web delivery while conducting surveys designed to reveal specific aspects of the corrosion engineering profession.

SITE FEATURES

Many of the Corrosion Doctors Web site features have been described in a recent publication.[4] One important exercise in designing a Web site is to analyze its features in terms of development effort as a function of the dynamic potential of these features and interest shown by visitor frequency (Figure 1). The dynamic potential axis in Figure 1 represents the easiness to change, add, or subtract from each page or feature. While both the Journal, a feature that was canceled following this simple analysis, and the Training Center were designed to provide depth to the site, directly designing training feature made much more sense in terms of efficiently developing a Web site with limited resources and funding support. The following sections will highlight some important aspects of the site for its use in training.

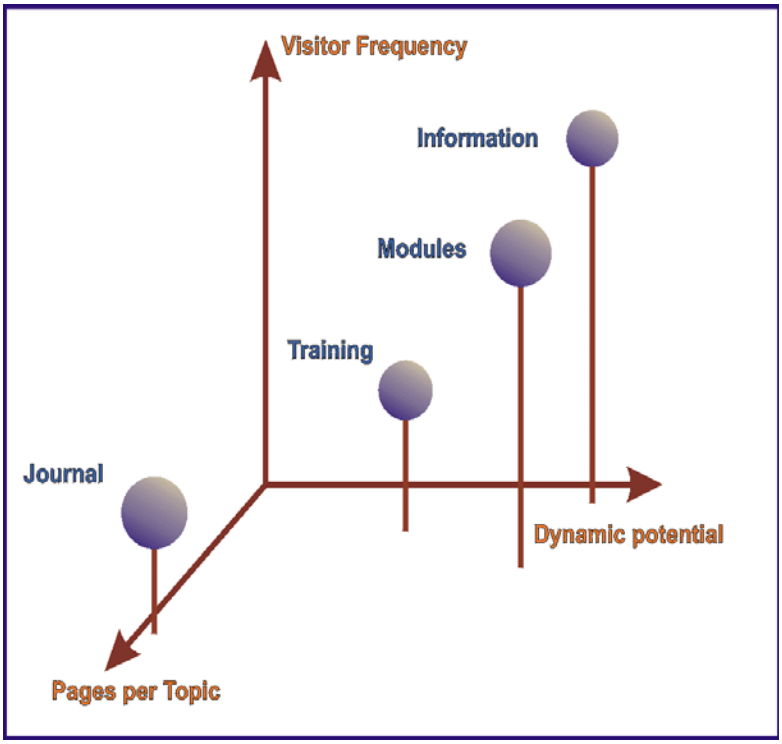

FIGURE 1. Schematic representation of four features as a function of visitor frequency, number of pages per topic, and dynamic potential.

SITE STRUCTURE

The Corrosion Doctors Web site presently contains approximately one thousand pages mostly organized in a series of modules designed in frames since such display of information can provide an excellent training structure. Figure 2 illustrates the frame organization in a module

specifically designed for training. As visible in Figure 2, a visitor coming to the information presented in a frame from a module entry (Figure 3) would be guided by a table of contents that would remain visible independently of the page in focus.

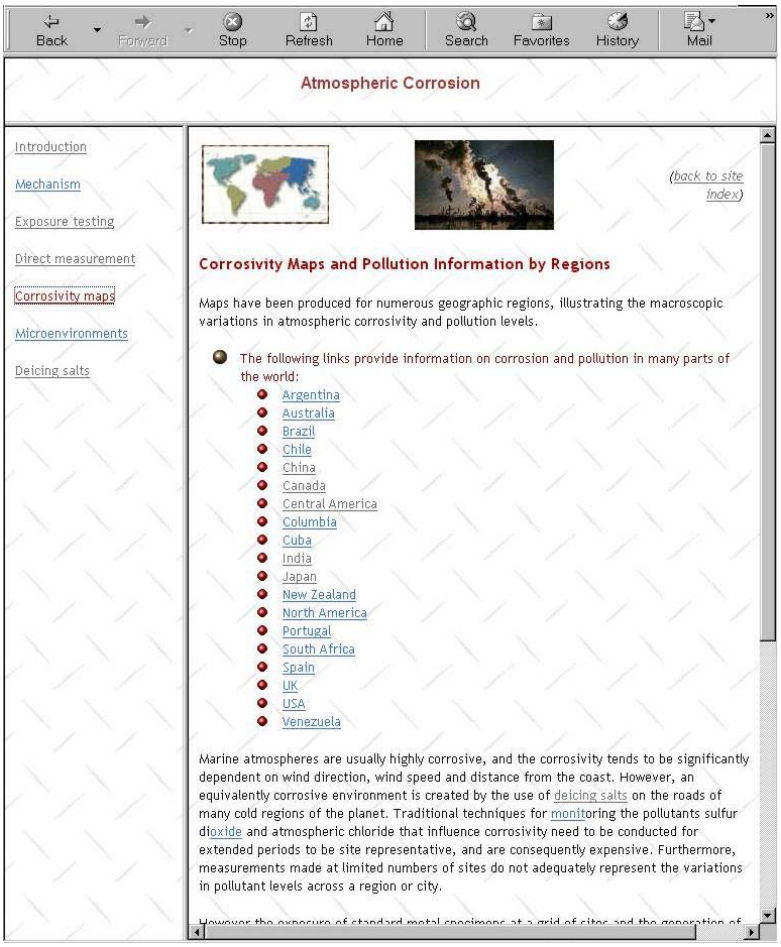

FIGURE 2. Example of a frame organization in the Corrosion Doctors' Web site.

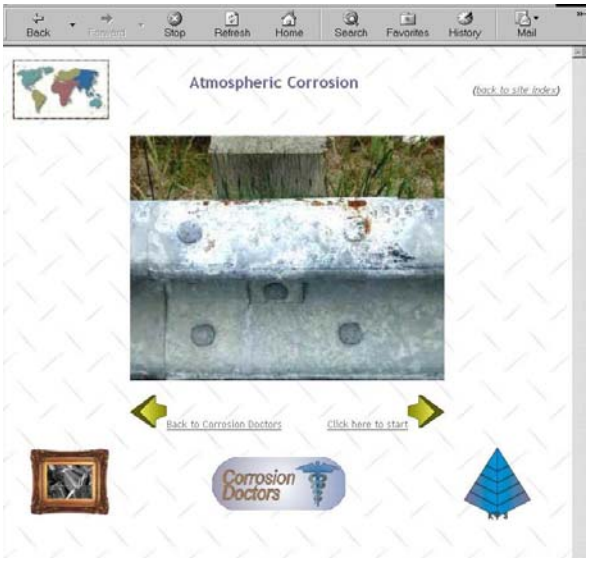

FIGURE 3. Module entry for the frame-based information displayed in Figure 2.

The site also contains a core navigational structure based on twenty pages describing general information concerning links to other Web sites or events and various lists providing access to the Modules themselves. Figure 4 illustrates the appearance of a page belonging to the navigational core structure with general common links on the left and specific hyperlink buttons on the top.

FIGURE 4. Example of a page that belongs to a navigational structure.

SITE INDEXES

One feature that was immediately accepted by both human and machine visitors was the site main Index. The alphabetical Index was created to overcome the partitioning caused by the use of frames in designing information modules. Navigating through the Web site had become increasingly complex as the number of information modules with its associated pages had grown into a real maze. The site Index lists, for each letter of the alphabet, hypertext references to most pages of the site that, in turn, have a return link to the Index. The main difficulty was to decide how each page would be referenced for the site Index as well as for visiting spiders and crawlers. However, the effort was not done in vain since many of the keywords used in the indexing process have now reached the highest level of citation with most of the popular search engines. The latest indexing scheme is based on icons reflecting specific themes that a visitor could be

tempted to explore in parallel to an initial query Figure 5). Other useful indexes have also been created for many topics such as:

- Landmarks
- Corrosivity maps (Figure 2)
- Pictures
- Biographies

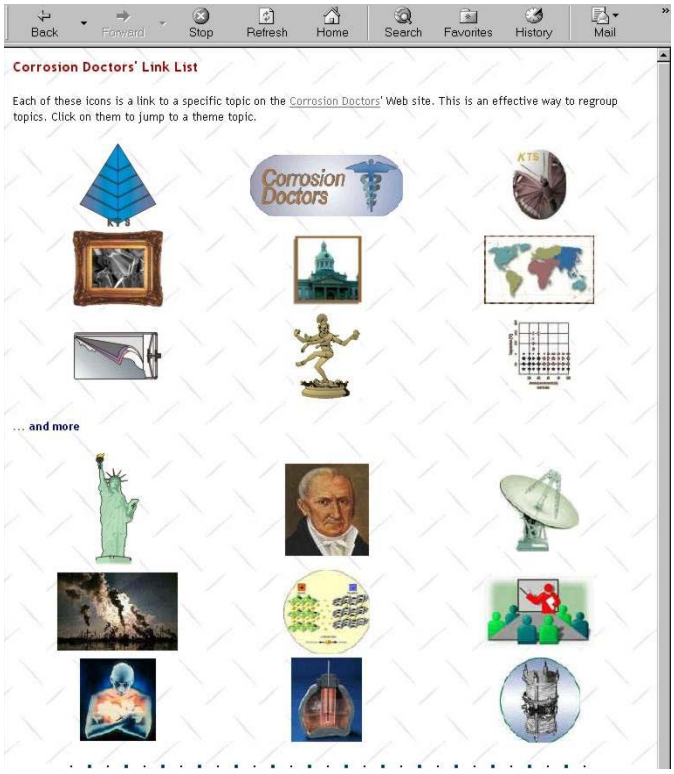

FIGURE 5. Icons that be found throughout the Web site.

USING THE WEB SITE FOR TRAINING

The Training Center was built in the Web site after more than one year of existence. It was considered to be a prudent approach for testing some concepts of WBT before developing full-scale training packages. These experiments were deemed necessary since development

guidelines, market analyses, or accreditation requirements are greatly missing in this new promising field of communication and information processing.

EDUCATORS' LIST

A survey was designed to help define who could be interested to use the Corrosion Doctors site as a support medium for training in corrosion science and engineering. Filling up this survey was the first step in joining the Corrosion Doctors Educators' list. This survey, as with all the surveys carried so far on the site, was constructed in a manner that could be answered in a few mouse clicks. There was also room for more elaborate comments. The survey participants were asked to provide contact information and some details on their teaching experience and actual teaching involvement. Following this preamble, the participants were asked to select the most useful topics amongst a list of twenty-four titles corresponding to Modules of the site. Forty-four participants have answered this particular survey and the results obtained are summarized in Table 1.

TABLE 1.
Results of the survey on using information modules in support of training.

Corrosion Basics	Interested	% interest
Atmospheric Corrosion	22	50
Causes and Forms of Corrosion	35	**80**
Hot Corrosion	15	34
Kinetics	24	55
Elements of Risk	20	45
Microbiologically Influenced Corrosion	16	36
Natural Waters	17	39
Reference Electrodes	17	39
Reinforced Concrete	11	25
Seawater	27	**61**
Soil Corrosion	13	30
Thermodynamics	24	55
Corrosion Prevention and Control		
Anodic Protection	12	27
Cathodic Protection	23	52
Corrosion Inhibitors	23	52
Corrosion Monitoring – Basics	28	**64**
Inspection	21	48
Life Prediction	21	48
Materials Selection	26	59
Protective Metallic Coatings	31	**70**
Protective Organic Coatings	22	50
Corrosion Testing		
Corrosion Testing – Basics	35	**80**
Electrochemical Test Methods	33	**75**
Testing for Pitting and Crevice Susceptibility	18	41

TRAINING ENGINEERS

To organize materials for on-line teaching and training, it is useful to consider a standardized pedagogical framework to describe what engineering students should learn. This is not a trivial question.[5] Engineers do need to learn on their own, deal with unexpected situations and solve problems. Following the example provided by Bourne, the types of things that engineering students should learn have been classified into two well-known taxonomies in

education.[5] Barrett's taxonomy proposes that learning should be divided into four categories: literal recognition (recall), inferential comprehension, evaluation, and appreciation.[6] Merrill's taxonomy uses a performance-context matrix that includes the actions of remember, use, or find (create).[7] The content is classified as fact, concept (classification), procedure or principle. The taxonomies appear to be useful for classifying learning outcomes in engineering and in selecting the technology required for on-line implementation. Table 2 presents some typical learning outcomes that may serve as a basis for classification of how we should structure engineering learning scenarios (adapted from reference 5). Examples are given in the right hand column of particular engineering problems in the area of corrosion engineering.

Most learning outcomes presented in Table 2, with the exception of the Literal (Barrett) or Remember (Merrill) outcomes, can be advantageously supported in a Web format by numerical questions. Typical engineering tasks require that specific goals be reached using a diversity of mathematical tools varying with contexts and situations. The main virtue of regular assignments, when teaching an engineering topic, is to keep the students focused on reasons and methods to accomplish specific tasks. Teaching corrosion engineering means going through detours in various fields that do not necessarily seem to be related, at least to an average student. The breadth of information presently on the site can be used to build questions on specific themes. The level of difficulty of each problem is indicated in decreasing order, with 5 corresponding to the most difficult and 1 to the easiest.

1. Thickness of a galvanized coating: Knowledge of metallic coatings and atmospheric corrosion (level 2)

2. Corrosion inhibition in cleaning acids: Knowledge of electrochemical methods and corrosion inhibition (level 3)

3. Copper sulfate reference half cell potential: Knowledge of basic thermodynamics (level 3)

4. Choosing the material of construction of a heat exchanger: Knowledge of corrosion economics (level 2)

5. Galvanic coupling causing galvanic corrosion: Knowledge of corrosion kinetics (level 4)

6. Choosing a paint schedule: Knowledge of corrosion economics (level 2)

7. Anodic vs. cathodic corrosion inhibition: Knowledge of corrosion kinetics and corrosion inhibitors (level 4)

8. Cathodic protection and calcareous deposits: Knowledge of corrosion kinetics, seawater, cathodic protection and basic corrosion rates (level 5)

A course program can be designed by threading the course content to meet the specific objectives required to complete this type of engineering problems. Once a structure is adopted the problems themselves can be reworked quite easily since they all require different sources of knowledge.

Table 2.
Examples of typical learning outcomes.

Typical Engineering Knowledge	**Barrett**	**Merrill**	**Sample Problems**
What is . . . (identification)	Literal	Remember fact	What are the units of corrosion penetration rates? Relate these to Faraday's law
Recall characteristics	Literal	Remember concept	State the characteristics of each type of corrosion testing studied.
Describe a process	Literal	Remember process	Describe how the linear polarization method can yield corrosion rates.
How to do something	Literal	Remember procedure	List the procedure to draw an Evans' diagram.
Set up a problem using guidelines	Literal	Remember principle	State the guidelines to design an anodic protection system.
Recognize types of corrosion inhibitors	Inferential	Use a concept (classify things into categories)	Given these five corrosion inhibitors, identify which are passivators.
What will happen if?	Inferential	Use principle	What will happen if the pH of a steel vessel was to drop below 6.2 from 10.2?
Apply a learned pattern or sequence	Appreciation	Use procedure	Using the information in the cathodic protection module, calculate the number of sacrificial anodes that would be required to form a calcareous deposit on a steel pile immersed in seawater.
Linkage between theory and practice	Appreciation	Use principles (laws and heuristics) to solve a problem	Use the Pourbaix diagram of Cr to determine the control current and potential for the anodic protection of a S43000 stainless steel vessel.
Linkage to real world complexity	Appreciation	Use principles	Using straight value depreciation, decide between two copper-nickel alloys for the design of a heat exchanger.
Creating specifications and implementing	Evaluation	Find principles	Evaluate the corrosion monitoring needs of this section of a chemical processing plant and design a cost effective strategy to generate reliable data.
Finding out (analyzing)	Evaluation	Find principles	Create a set of guidelines to determine the points of a plant susceptible to localized corrosion.

SUMMARY

One of the most significant capabilities that can be supplied to users is interaction. Presentation of text and graphic materials in hypertext form is indeed useful; however, Web-based materials are significantly more interesting when they are interactive. For example, a common technique is to add forms to hypertext markup language (HTML) documents so that the user can interact with the Web page. In an on-line classroom setting, this type of capability can be useful for creating surveys, tests, and shared materials. With a Web browser, it is very simple to embed access to file transfer protocol (FTP). Thus, if there are files that students need to download, this capability can be embedded directly in the HTML document. Animation, tutorial systems, and access to bulletin boards can also provide additional capabilities. However, there are many indications that these fancy features could become more a distraction than real training tools.

With the tools at hand today, it is possible to craft highly effective WBT to meet the training needs of a diverse population. However, these opportunities are presently perceived as any other research activities by training institutions. Most of the successes in WBT have so far been achieved for courses in software and computer engineering. In such cases the medium is also the training breadboard. For hard courses in other disciplines progress will be much more difficult for two main reasons: the first and probably most obvious is the effort required to transform the training material into a computerized format. Such endeavor has been estimated to be of the order of one hundred hours of preparation for a typical university lecture. The second obstacle is subtler and maybe more challenging than the first since is psychological in nature. As much as software engineers understand the mechanics to produce and run a WBT course, the

opposite is true of many specialists in other disciplines. This lack of familiarity can easily turn into an obstinate opposition to an estranging technology.

REFERENCES

1. McGee MK. Train on the Web 101-105. Informationweek 1999; 101-5.

2. Greengard S. Web-based Training Yields Maximum Returns. Workforce 1999; **78:** 95-6.

3. Cole-Gomolski B. Web Training Requires Different Educational Approach 33, no. 8 (February 22, 1999): 44. Computerworld 1999; **33:** 44.

4. Roberge PR. The Creation and Management of a Successful Corrosion Information Web Site. Corrosion Reviews 2001; **19:** 177-205.

5. Bourne JR, .Brodersen AJ, Campbell JO, Dawant MM, Shiavi RG. A Model for On-Line Learning Networks in Engineering Education. Journal of Engineering Education 1996; **85**.

6. Smith RJ, Barrett TC. *Teaching Reading in the Middle Grades*. Reading, MA: Addison-Wesley, 1974.

7. Merrill MD. The Descriptive Component Display Theory. In: Merrill MD, Twitchell DG, eds. Instructional Design Theory. Englewood Cliffs, NJ: Educational Technology Publications, 1994; 111-57.

FATIGUE LIFE, CORROSION, AND SAFE LIFE ISSUES

Vinod S. Agarwala* and Basir Shafiq**

*Senior Scientists, Research and Engineering Group
48110 Shaw Road Unit 5
Naval Air Systems Command, Patuxent River, MD 20670
Phone: (301) 342-8002
Fax: (301) 757-1895
Email: agarwalavs@navair.navy.mil

**Associate Professor, Department of General Engineering
Box 9044
University of Puerto Rico, Mayagüez, PR 00681
Phone: (787) 832-4040 ext.2094
Fax:(787) 265-3816
Email: a_basir@rumac.uprm.edu

ABSTRACT

Fatigue experiments performed on 7075-T6 Al alloy at various frequencies, stress levels and under alternating wet and dry environments indicate that simultaneous action of corrosion and fatigue substantially accelerates crack initiation and growth rates as compared to pure fatigue (dry air) condition. In experiments performed under alternating wet and dry test conditions, the fatigue process (crack growth rate) appears to adapt rapidly to the changing environment. Sudden reduction in crack growth rates are observed at transition points between dry and wet cycles. However, at every transition point, crack growth rate reduction is followed by a rapid increase to the velocity of respective dry or wet environment. Lowering the frequency or increasing the stress level substantially reduces crack initiation time and overall lifetime. S-N curves show a continuous downward trend without reaching a plateau or threshold.

NOMENCLATURE

CFCG – corrosion fatigue crack growth
Δk – change in stress intensity
E/M - electrochemical/micromechanical
ACT - crack tip subject to corrosive solution
ICT – crack tip subject to dry air conditions
CGR – crack growth rate
δ - crack opening displacement
R – stress level ($\sigma_{min}/\sigma_{max}$)
MD – Metal Dissolution
HE – Hydrogen Embrittlement

INTRODUCTION

Severity of service environment has forced U.S. Navy to adopt safe-life policy in determining the lifetime of aircraft metallic structures. Since Navy has a large inventory of aging aircraft, the concerns related to remaining life of aircraft are highly dependent on their structural integrity issues. It is also a fact that material degradation due to effects of corrosion and fatigue can pose a serious threat to mission readiness and reliability. Under the conjoint action of mechanical fatigue and corrosion, the mechanisms of failure become highly complex and simple models, which relate to pure fatigue or electrochemical actions or simple superposition of the two, do not apply.[1] A comprehensive CFCG model is yet to appear that can accurately predict lifetime (stages for crack initiation and propagation) of aircraft structures. The primary difficulty appears to be the lack of experimental techniques/tools which are required to obtain crack tip E/M parameters, such as corrosion current density, hydrogen generation and absorption, and microcracking, etc.

EXPERIMENTAL SETUP

It has been shown that in the presence of chloride ions the pH of crack tip can be acidic even when the bulk solution is almost neutral.[2] This occurs due to hydrolysis of corroding species such as aluminum. Since pH of naval (service) environment can vary anywhere between 3 to 5, a mild 1%NaCl solution of pH ~ 2.5 (simulating crack tip pH) was selected for CFCG testing. In order to study the effects of pre-corrosion, ACT/ICT and frequency on the CGR characteristics, testing was performed at a constant load (=972-N, about 5.5% of the static load) and R(=0.1), while the frequency was varied from 1 to 30-Hz. Tests under various stress levels (7% to 18% of the static load) and three different frequencies (0.2-1.0-Hz) were performed to

study the effect of frequency on S-N behavior of the material under ACT conditions. To study CFCG under alternating crack tip environments, two sets of test were performed at a constant frequency (=1hz); one at a constant K(=6.6-MPa-$m^{1/2}$) and R(0.4) and the second one at a constant load(=1335-N about 8% of the static load) and R(=0.4). Crack initiation (taken equal to 0.25-mm) was carried out under ACT conditions, except for the specimens tested under ICT, which were pre-cracked according to ASTM E399-95 standard.

LOADING AND ENVIRONMENTAL EFFECT

EFFECT OF PRE-CORROSION

Irrespective of the extent of pre-corrosion at any frequency, test results indicated a sharp decrease in the crack initiation time under ACT condition. The results of ACT and ICT on CFCG behavior beyond crack initiation suggested that the effects of pre-corrosion do not contribute in the ensuing fatigue CGR. However, significantly reduced lifetime is observed in the crack propagation stage in ACT specimens due to the presence of corrosive species. A comparison of fatigue crack growth behavior under ACT and ICT conditions at two pre-corrosion times is as shown in Fig. 1.

EFFECT OF FREQUENCY

To study the effect of frequency (time) on CFCG, specimen crack tips were kept active during testing. Figure 2 shows the dramatic difference in CFCG rates of specimens tested in ICT/ACT conditions. Increasing frequency (from 1 to 30-hz) increased the fatigue life in ACT specimens reaching a threshold at around 10-hz, beyond which further increase in life was not significant. ACT specimens exhibited an up to five fold increase in the CGR. Increase in the CFCG at a lower frequency is associated with longer time per cycle for electrochemical reactions

to occur such as ionic transport, anodic dissolution, and hydrogen diffusion and embrittlement. Figure 2 indicates that CFCG rate decreases as the frequency is increased, however, it never approaches the CGR of ICT specimens, indicating the presence of corrosion effects even at very high frequencies (or short times).

EFFECT OF STRESS

S-N curves provide a useful indication of the remaining life of the material and can be subsequently used in a predictive lifetime model. Figure 3 shows an up to one order of magnitude reduction in lifetime (of 0.25-mm) in ACT specimens as compared to ICT specimens. ICT specimens reached an infinite life below 13% stress level (test terminated at 500,000 cycles) mainly because crack initiation never took place. However, an infinite life is never obtained and instead a continuous downward trend is observed in the S-N curves of the material subject to corrosive (ACT) environments, as shown in Figures 3,4. Since corrosion is a time dependent phenomenon, the S-N curves of CFCG strongly depend on the test frequency. Hence Fig. 4 shows a significant reduction in corrosion fatigue life as the frequency is reduced from 1 to 0.2 Hz.

U.S. Navy's current safe-life policy dictates a crack tolerance of no more than 0.25-mm whereas a damage tolerant design can, in principle, allow the crack to grow to a significant length beyond safe life limit. Comparisons of lifetimes shown in Fig. 3 indicate an up to 50% increase in life during each increment of 0.25-mm.

DISCUSSION

The observed increase in CFCG maybe explained in terms of various E/M processes simultaneously taking place at the crack tip, such as, MD, HE and crack tip microcracking etc.[1-3]

In MD process, potential differences are created between distinct anodic and cathodic sites at high and low stress points, respectively. The crack tip which is smallest in area and highest in stress (becomes an anode) and develops a very high current density, thus accelerating the dissolution of the crack tip. In an open-circuit system, anodes and cathodes with small potential differences and area ratios result in much lower corrosion current density. At the crack tip under corrosion-assisted fatigue stresses, the CGRs are, therefore, significantly higher.[1,2]

Diffusion of hydrogen and formation of hydrides may occur simultaneously at the crack tip, which causes critical stress intensity to decrease allowing crack to propagate into brittle hydride phase. In addition, the chemical potential of solute hydrogen and hydrides are reduced at tensile stress conditions such as crack tips. The greatly decreased stress intensity factor and reduced chemical potential allows rapid crack propagation when the applied stress is only moderately increased.[1,2,4] Furthermore, as a material fatigues, it develops a zone of microcracks, which are formed in the vicinity of the crack tip. This facilitates diffusion of salt laden moisture and acid (H^+ ions) at the crack tip, which in turn accelerate MD and HE.

The surface morphology of cracked specimens showed severe effects of corrosion. The specimens tested under ICT conditions showed typical grain pullout and irregular cracked surface, whereas, the ACT specimens exhibited a smoother cracked surface with pits and crevices, a typical feature of corroded surface (Figures 5(a), 5(b)). It is generally accepted that the predominant environmental crack growth mechanism in high strength Al alloys is HE.[1,2,5,6] SEM results strongly hint at MD taking an active role in the overall crack growth behavior that HE is unlikely to cause such crack faces. Furthermore, considerably smaller closing strains (δ_{min}) were obtained under ACT conditions, a behavior that generally speeds up the CGR and indicates the presence of MD.

The complicated nature of CFCG during crack initiation and propagation stages suggest that better crack detection and monitoring techniques are needed which could be readily utilized on an aircraft carrier before relaxing U.S. Navy's strict crack tolerance policy.

EFFECTS OF ALTERNATING ENVIRONMENT/CRACK ARREST

An operational aircraft structure is invariably exposed to varying humidity, temperature and chemical environments. In order to gain further understanding of how a changing environment may affect actual fatigue life of an aircraft, alternating ACT/ICT cycle tests were conducted.

Crack driving mechanisms not only depended on the applied stress level but also on the relative crack tip strain, i.e., the ratio of δ_r ($= \delta_{max}/ \delta_{min}$). Lowering the δ_r lowers the crack driving force. Crack arrest was observed to be more severe going from ICT to ACT conditions as δ_r decreased due to sudden and temporary increase in δ_{min}. During ACT to ICT transition, hardly any crack arrest was noticed, as no significant change in δ_r took place.

Under ICT conditions, the surface grains pulled out during failure get lodged in the crack opening. This does not allow the crack to close perfectly. As soon as the fluid is put in the crack tip, the spacing between the crack faces increases and δ_{min} gets a sudden jump, which (temporarily) decreases the actual crack tip driving Δk and retards crack growth. Given time, the corrosive solution during ACT cycle dissolves pulled out grains at the crack-tip and smoothens crack surfaces, that leads to a decrease in δ_{min} (and consequently an increase in δ_r) resulting in enhanced effective ΔK at the crack tip – thus giving a faster CGR. The increase in CGR is also aided by the corrosion at the crack tip, which is a very rapid process.

It is a well-known fact that tension/compression condition is more severe than tension/tension condition at the crack tip.[7] This idea can be extended to contend that the ratio of $\sigma_{max}/\sigma_{min}$ (proportional to $\delta_{max}/\delta_{min}$) would have similar effect on the CGR. A higher ratio would be more severe at the crack tip than a lower one. During the initial stages of ACT cycle, with solution in the crack profile, the minimum crack tip opening (δ_{min}) increases while the compression effects decrease, which tend to slow down the crack growth. It is also evident that at higher stress levels, corrosion rate increases as crack arrest durations become shorter.

It was observed that crack arrest was either non-existent or comparatively short going from ACT to ICT conditions. Stable ACT conditions (beyond transition point) give rise to a higher δ_r, as discussed above. When solution is suddenly sucked out of the crack area during ICT-cycle, δ_{min} suddenly experiences a decrease leading to a higher δ_r. However, ICT environmental conditions rapidly take over the crack growth kinetics, thus reducing CGR. In time the δ_{min} increases due to grain pullout, etc., thus further reducing the crack driving ΔK. This behavior is more prominent in the stable crack growth regime, Figure 6(a). To further accentuate the role δ_r plays in crack arrest mechanism, a non-dimensional form of δ was obtained as given in Eq. 1 and shown in Figure 6(b). It may be noted from Figure 7(b) that during stable crack growth regime, the ICT cycle δ_{ICT} was lower than the ACT cycle δ_{ACT}. However, this effect disappears at higher ΔK values.

$$\delta_n = \frac{\delta_{\max}}{\delta_{\min}} \left(\frac{\delta_{final}}{\delta_{initial}} \right) \tag{1}$$

Constant load test hinted at the ΔK dependence of CGR. To understand alternating environment and crack arrest phenomena as a function of ΔK, constant K test was performed at 6.6-MPa-$m^{1/2}$ and 0.4R. The constant K test results indicate a sharp change in crack speeds

when the environment is changed. Figure 7(a) shows sharp difference in the crack growth behavior during ACT and ICT environments. Crack arrest mechanism is slightly more enhanced in this case, as the CGRs were fairly constant under constant ΔK. This occurred as a result of lower effective crack tip driving ΔK; a conclusion arrived from Figure 7(b) where δ_n values at ICT cycle are markedly lower than the ones obtained during the ACT cycle throughout the testing. It is noteworthy that the difference in δ_n during ACT and ICT cycles increased as the crack grew, thus relating it to crack driving forces and crack tip corrosion. At later stages of the crack growth, substantial load decrease to maintain constant K causes the crack-tip strains to drop below a level required for crack advance during the ICT cycle. However, it is interesting to note from Figure 7(a) that at the same low crack tip strain, a change in environment to ACT conditions sped up the crack growth due to corrosion occurring at the crack tip.

CONCLUSIONS

A better understanding of crack tip E/M processes is required before a reliable prediction methodology can be developed. This conclusion is based on the following observations and results:

- Even a mildly aggressive environment has a detrimental effect on the lifetime of metal aircraft structures, irrespective of frequency (time of exposure) or stress level.
- The so-called infinite life generally obtained under ICT conditions is never obtained under ACT conditions, even at extremely low stress levels and high frequencies.
- Pre-corrosion and/or presence of corrosive environment at the crack tip drastically reduces crack initiation time, while keeping ACT during crack propagation stage results in significant increase in CGR rate at all frequency and stress levels as compared to ICT conditions.

- Changing crack tip environment alters CGR quite rapidly. Severe crack arrest is observed at ICT to ACT environment transition points especially at lower Δk and R-values. Whereas, crack closure effects reduce as δ_{min} is increased.

REFERENCES

1. Turnbull, A., "Modeling of Environment Assisted Cracking, Corrosion Science, Vol.34, No.6, 1993, pp. 921-960.

2. Agarwala, V. S., "An In-Situ Experimental Study of the Mechanisms of Catastrophic Damage Phenomena," in Hydrogen Effects on Material Behavior, Eds. N.R. Moody and A.W. Thompson, The Mineral, Metals and Materials Society, Warrendale, PA, 1990, pp. 1033-1045.

3. Ford, F. P., "Corrosion Fatigue Crack Propagation in Aluminum-7% Magnesium Alloy," Corrosion, Vol.35, No.7, 1979, pp.281-287.

4. Gingell, A. and King, J., "The Effect of Frequency and Microstructure on Corrosion Fatigue Crack Propagation in High Strength Aluminum Alloys", Acta Materialia, Vol.45, No.9, 1997, pp.3855-3870.

5. Parkins, R., " Stress Corrosion Cracking. Environment Induced Cracking of Metals," eds. R. Gangloff and M. Ives, NACE, Houston, 1990, pp.1-20.

6. Wei, R. and Gao, M., "Hydrogen Embrittlement and Environmentally Assisted Crack Growth." NACE, Houston, 1990, pp.789-816.

7. Schijve, J., "Cumulative Damage Analysis in Aircraft Structures and Materials", The Aeronautical Journal, Vol.74, 1970, pp.517-532.

FIGURES

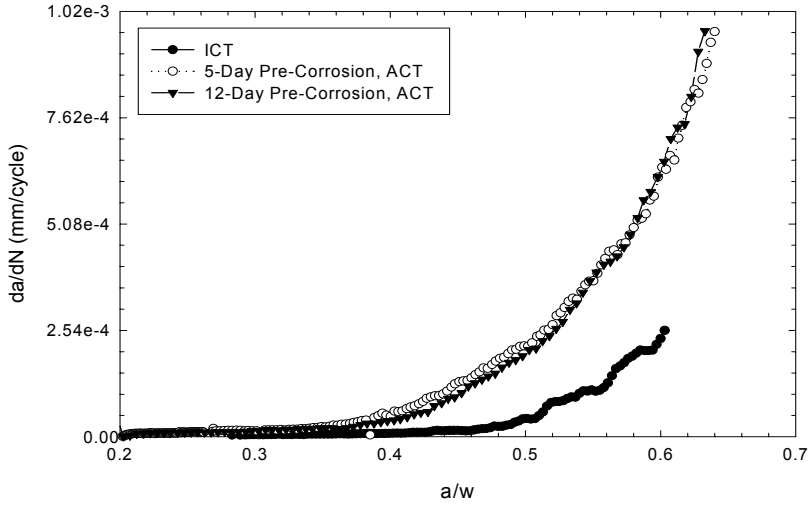

FIGURE 1. Test results under ACT and ICT conditions. Significant jump in fatigue CGR is observed in the case of ACT condition.

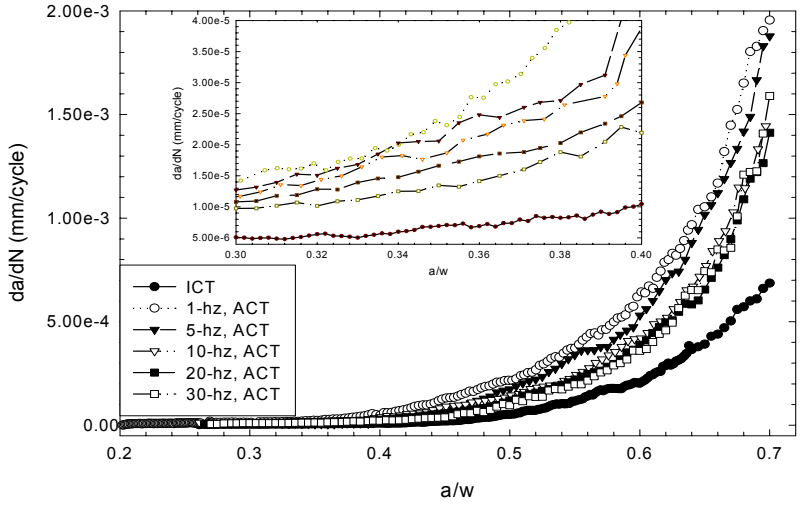

FIGURE 2. Comparison of fatigue CGR results for tests conducted at different frequencies under a constant load condition.

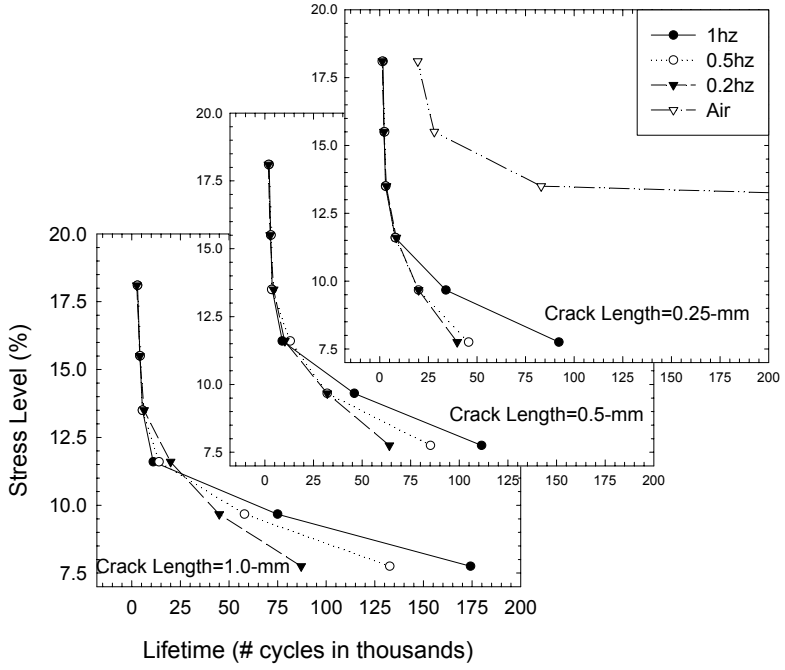

FIGURE 3. S-N curves at various crack lengths and frequencies.

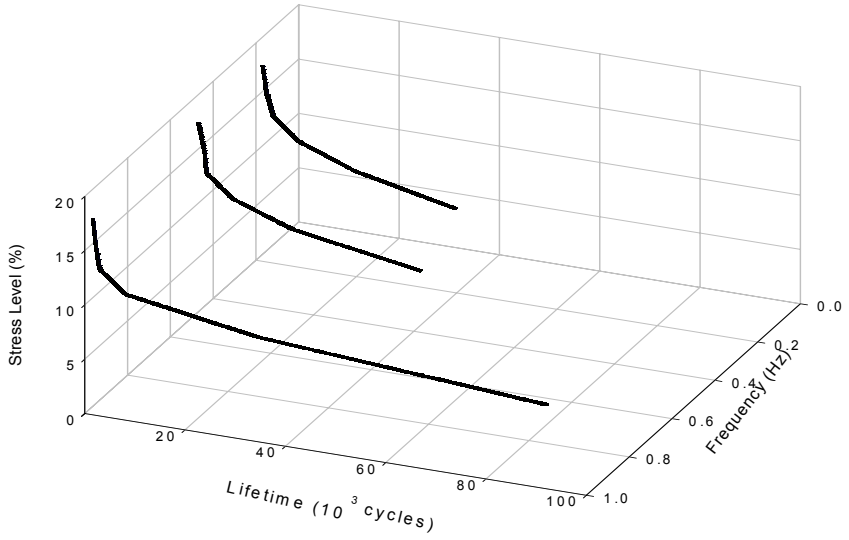

FIGURE 4. 3-D plot of stress level (7-18%), frequency (1-30hz) and lifetime.

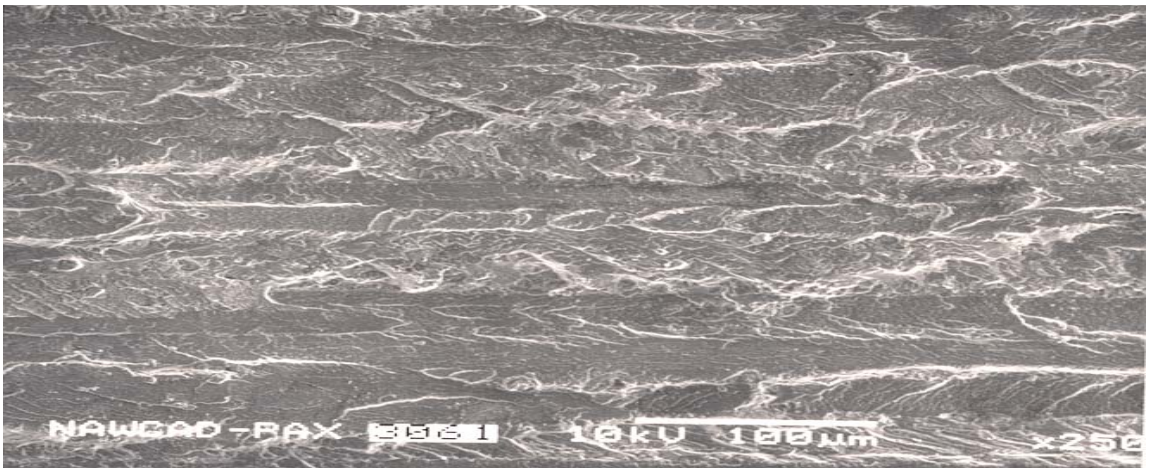

FIGURE 5(A). Surface morphology of cracked specimen tested under ICT condition. Typical surface roughness of ductile failure is observed.

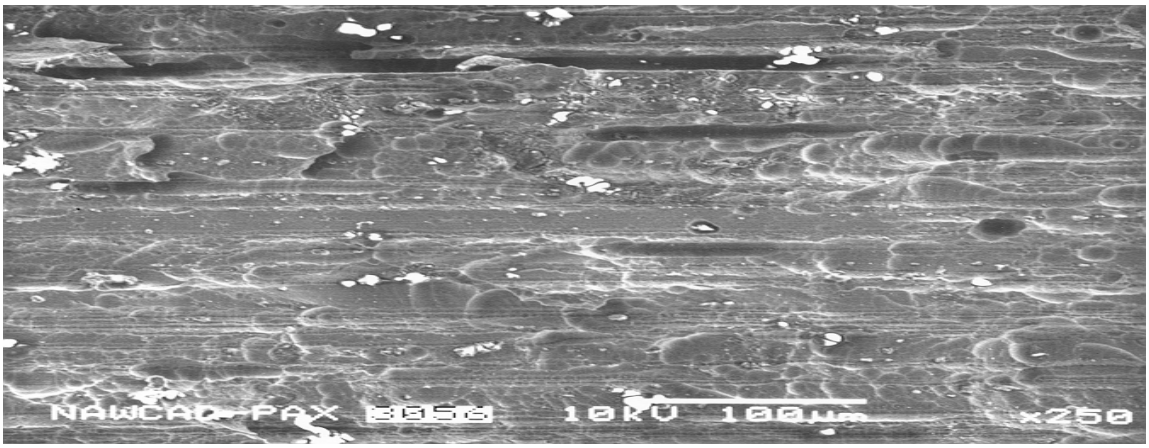

FIGURE 5(B). Surface morphology of cracked specimens tested under ACT condition. Smoother surface with crevices and holes is observed.

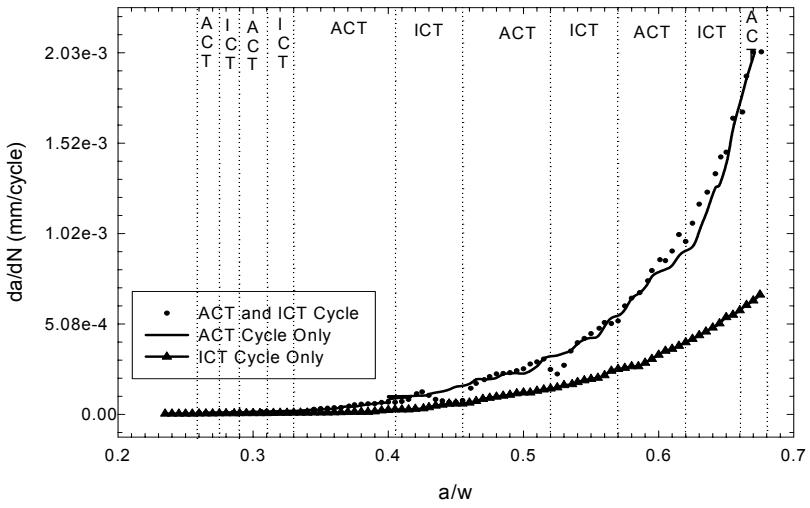

FIGURE 6(A). Fatigue CGR's in alternating ACT and ICT conditions under constant load testing.

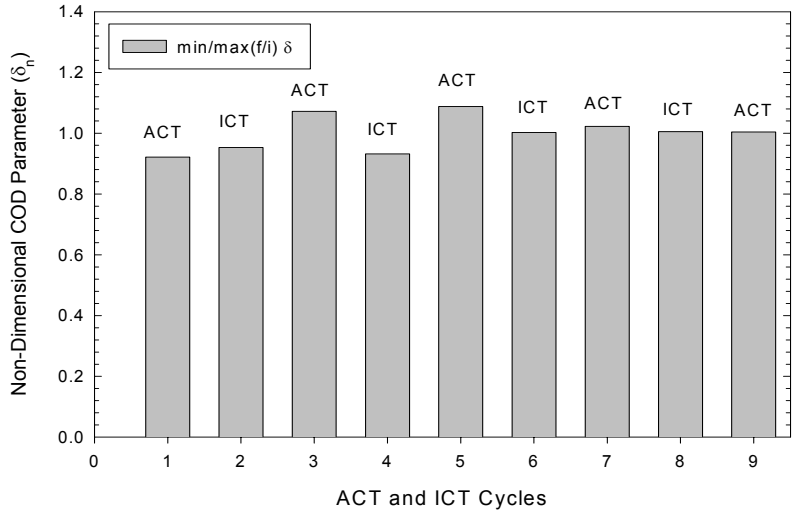

FIGURE 6(B). Non-dimensional δ values obtained from alternating ACT and ICT environment test conducted under constant load.

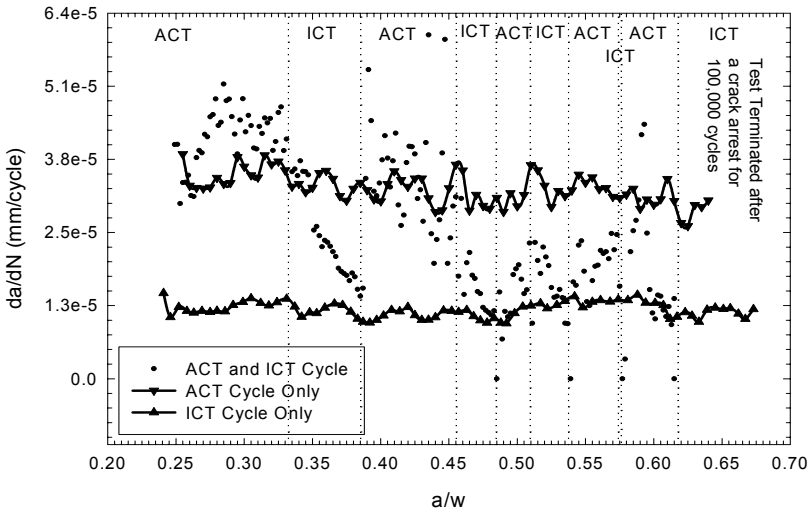

FIGURE 7(A). Test conducted under alternating ACT and ICT environment under constant stress intensity condition.

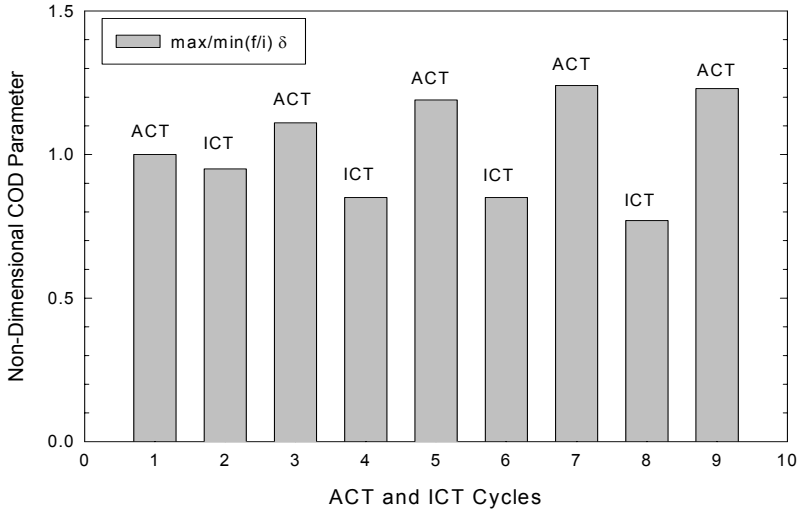

FIGURE 7(B). Non-dimensional δ values obtained from alternating environment test conducted under constant stress intensity condition.

POLLUTION PREVENTION / CASE STUDIES

ISSUES IN THE MEASUREMENT OF VOLATILE ORGANIC COMPOUNDS (VOC'S) IN NEW-GENERATION LOW-VOC MARINE COATINGS FOR THE U.S. NAVY

S.H. Lawrence[1], A.W. Webb[1], R.L. Foster[1], K.E. Lucas[1], E.D. Thomas[2], P.M. Bizot[3], and C.E. Bevans[3]

[1] U.S. Naval Research Laboratory, Code 6130, Washington, DC 20375
[2] U.S. Naval Sea Systems Command, SEA 05M, Washington, DC 20376
[3] Geo-Centers, Clinton, MD 20749

ABSTRACT

Marine coatings under evaluation for use by the Navy have been tested for the quantity of volatile organic compounds (VOC's) they contain. This has been done in accordance with *EPA Reference Method 24* and (by incorporation) *ASTM Standard Test Method D 2369*. High solids two-component systems were of particular interest. We report here a summary of some of those results, and discuss issues in the testing conducted in our laboratory and elsewhere, which may affect the accuracy and precision of the data.

Data precision was lower for those samples with reduced absolute VOC contents. For individual samples, particularly those with lower VOC contents, results varied considerably with changes in testing procedure (all in accordance with the testing standard). Efforts to discern other correlations between testing procedure and collected data yielded somewhat more ambiguous results.

INTRODUCTION

This paper addresses the issue of quality of data acquired in accordance with *ASTM D 2369*, "Standard Test Method for Volatile Content of Coatings",[1] details of which are incorporated in *Federal (EPA) Reference Method 24*, "Determination of Volatile Matter Content, Density, Volume Solids, and Weight Solids of Surface Coatings" (referred to hereafter as *"EPA Method 24"*). Specifically, this article is concerned with the measurement of volatile organic compound (VOC) content in coatings being evaluated for use by the U.S. Navy, including the two-component high solids systems finding increasing use because of their lower VOC contents.

The problem of smog, and recognition of the major role played by tropospheric ozone in its formation, resulted in passage of the Clean Air Act of 1970, along with subsequent amendments. Because VOC's were known to play a role in the formation of ozone, this legislation included regulations for controlling their emissions.[2] The U.S. EPA was charged with monitoring compliance with these rules, as well as formulating standards by which compliance could be determined. In response, *ASTM D 2369* was incorporated into law as part of *EPA Method 24*,[3] and this method was in turn incorporated into *ASTM D 3960*, "Standard Practice for Determining Volatile Organic Compound (VOC) Content of Paints and Related Coatings."[4]

This legislation has had a major and continuing impact on the coatings industry. Compliance with the new regulations has required wholesale reformulation of paints to reduce, or remove entirely, the organic (VOC) solvents previously used to enable their flowability and sprayability. One response by the industry has been the introduction of water-based low-VOC latex formulations, which have found increasing use in domestic commercial markets, but are generally unacceptable for marine applications. Another response has been to employ as solvents "VOC-exempt" volatile organic compounds, so designated because they have been shown to not cause ozone formation, and are thus exempt from the regulations normally imposed on VOC-emitting activities. The marine coatings community does not currently employ VOC-exempt coatings extensively, for reasons based on cost and performance.

Another approach involves formulation of high solids coatings with "reactive diluents" which facilitate mixing and spraying, but unlike the volatile nonreactive solvents they are intended to replace, are chemically incorporated into the coating during its cure. Such coatings are finding greater use in USN applications, often in conjunction with the increased use of high

solids two-component formulations such as epoxies, urethanes, and silicones, since these are the most prevalent commercial products suitable for a marine environment.

As these reduced VOC coatings have been introduced to the market, there have been reports of concern regarding the accuracy and precision (reproducibility/repeatability) of VOC analyses conducted in accordance with *EPA Method 24/ASTM D 2369*. Some of these reports deal mostly with the water-based latex systems, for which it is necessary to calculate VOC content by measuring total volatiles and water content, then subtract the latter from the former.[5-7] Mania[5] conducted a study of 45 paints of known formulations with VOC's ranging from 7 to 562 g/L, and concluded that the error between the known and measured VOC's increased exponentially as the VOC content declined below about 250 g/L. This error reached 200% at VOC's below 50 g/L. Their study dealt primarily with latexes, but also included data on solvent-based systems. Elsewhere, Ferlauto[8] provided a useful discussion of chemistry-based sources of discrepancies in VOC measurements, although it is for a melamine crosslinked high-solids polyester system.

However, there is considerably less information in the open literature concerning the specific issue of VOC evaluation of high solids coatings of the type suitable for marine applications. Based on searches of several online technical databases,[9-10] only a 1993 article by Ancona *et al.*,[11] discussing a round-robin study of two-component high solids coatings, appears to offer the most direct discussion to date of using *ASTM D 2369* for VOC analysis of this class of coatings. The authors reported higher than expected VOC levels, with large standard deviations in their results.

As a further historical note, it was found that versions of *ASTM D 2369* have evolved significantly over the years in their treatment of multicomponent coatings, with the 1987 version

excluding from testing such coatings "wherein one or more parts may, at ambient conditions, contain liquid coreactants that are volatile until a chemical reaction has occurred with another component of the multipackage coating" *(paragraph 1.3*). Since at least 1995, subsequent versions have substituted this phrase with one that claims suitability of the test standard for such coatings. This change was presumably the outcome of round-robin studies carried out sometime between 1987 and 1995, and referred to ("*Note* 2") in later versions.

Here we discuss some of our experiences with conducting VOC measurements in accordance with the aforementioned *ASTM/EPA* methods, and we will compare these with observations reported by other workers. These results may have implications for the validity of using *ASTM D 2369/EPA Method 24* for measuring the VOC content of these high solids coating systems.

EXPERIMENTAL

For the nonaqueous coatings systems discussed in this paper, measurements were conducted in accordance with the appropriate sections of *EPA Reference Method 24*/*ASTM D 3960-01*. Density of the liquid coating was determined using *ASTM D 1475-98*,[12] and volatile content using *ASTM D 2369-01*. This article does not address issues related to the former, e.g., entrapment in samples of air bubbles, which give rise to low values in the density measurement.

Distilled to its very basics, practice of *ASTM D 2369-01* for water-free samples calls for the reaction (1 hr "pre-dilution reaction time"), dispersion/dilution with ~3mL solvent (e.g. toluene or MEK), drying (25ºC, over a 1 - 24 hr "induction time") and baking (110ºC) of a thoroughly mixed and carefully weighed sample (0.3 & 0.1g, to nearest 0.1 mg). The post-bake

sample weight is subtracted from the initial sample weight, and from this, and measurement of the sample density as described above, VOC content is calculated.

Two different approaches were used in this study:

- The first round of tests utilized existing EPA methodology and extensions of the methodology. VOC measurements were made on a total of 39 paints with vendor-claimed VOC's ranging from 0 g/L to 359 g/L. Paint types included latexes, and solvent-borne epoxies, polyurethanes, alkyds, and a polyurea. The specific tests run included:
    - 1 hour induction time, 110°C bake, use of solvent
    - 23 hour induction time, no bake, use of solvent
    - 23 hour induction time, 110°C bake, use of solvent
    - 1 hour induction time, 110°C bake, no use of added solvent
    - 23 hour induction time, no bake, no use of added solvent

  These analyses were primarily of single samples (very limited data on precision – minimal reproduction of analyses)
- In the second round of tests, data was collected which provided both information on precision (each sample was in triplicate) and variation of induction times ranging from 1 through 24 hours. Data on four paints has been collected to date, with vendor-claimed VOC's ranging from 72 to 340 g/L. All of these tests included the use of solvent and a bake at 110°C. All of these paints were epoxies.

RESULTS

Presentation of the results of the first round of testing is simpler by grouping the paints into three separate categories:

- High Solvent Paints, i.e., vendor-claimed VOC's greater than 200 g/L
- Low Solvent Paints, i.e., vendor-claimed VOC's between 50 and 150 g/L
- Very Low Solvent Paints, i.e., vendor claimed VOC's of less than 50 g/L

Results are summarized in Figure 1. The simplified result of testing the high solvent paints is that the measured VOC is not significantly affected by either the use of additional solvent, or by the length of the induction time before baking. It should also be noted that these tests exhibit little variation from the vendor-claimed VOC's – measured and claimed VOC's fall within 3-4% of one another.

For the low solvent paints, VOC's measured with a 1 hour induction time and added solvent roughly match the vendor-claimed VOC's (as did the high solvent paints), but for the very low solvent paints, the use of solvent, a bake and a 1 hour induction period yielded measured VOC's much higher than the vendor-claimed VOC's (averages: 90 g/L VOC measured; 9 g/L VOC claimed)

Table 1 compares averages of data provided by the vendors to averages of our VOC data measured in strict accordance with *EPA Method 24* procedures, and shows considerable variability (middle column). This table also indicates the effect of the solvent level on the ratio of the VOC's measured with 1-hour-induction time to those measured with a 24-hour induction time (both measurements were carried out with solvent and a bake).

The second approach to testing provided more information on the impact of induction time on measured VOC, as well as information on the precision of the tests. Figure 2 indicates

that (high) solvent-based epoxy has a range of 6% in the variation between 1 and 24 hours. The variation in measured VOC's of the low solvent epoxies ranges from 35% to 50%, and depends on the choice of induction time (between 1 and 24 hours).

In the laboratory, all samples were prepared simultaneously, and solvent was added in the sequence of induction times (e.g. the 1-hour induction sample was mixed with solvent first, and the 24-hour induction sample was mixed last.) Mixing all of the triplicate samples with solvent required about 100 minutes. Figure 3 indicates that the measured VOC decreases with induction time. This is plausible and intuitive – as the paint cures some of the solvent may be trapped within the paint film; also reactive diluents, which may show up as solvents with a short induction time, will be incorporated into the polymer chain at long induction times.

It is apparent from Figure 3, and especially Figure 4, that the scatter in data increases as a function of induction time. Other data, not shown here, indicates that this source of data scatter is more significant than the time interval between solvent addition and final (dried) sample weighing.

DISCUSSION

Except for the high solvent paints, the variability of the VOC data increases as the VOC decreases, and the measured VOC tends to decrease as the induction time increases (see Table 1). Both of these trends are consistent with the increasing use of reactive diluents as the "solvent" level of paints decreases. It is plausible that a short induction time, i.e. one hour, may cause a higher level of reactive diluents to be volatized from a paint sample than if a longer induction time is used. The inherently higher viscosity of "solvent-free" paints using reactive diluents as opposed to straight solvents probably contributes to variability, as it will be more difficult for any entrapped solvent to be released from the paint film. Furthermore, the addition

of solvent in the test may be slowing down the incorporation of the reactive diluent molecules into the coating resin polymer chains, leaving them more susceptible to volatilization, thus contributing to a (falsely) high measured VOC value.

The nature of the paint resins, curing agents, catalysts, and reactive diluents which are used in high solids paints supports the hypothesis that reactive diluents might be baked out of paint systems prematurely, yielding too high a VOC. Table 2 illustrates these physical properties. Whereas traditional solvent-based coatings employ resins and curing agents with molecular weights typically in the 500 to 1000 amu range, and with boiling temperatures typically greater than 350ºC, the new resins and curing agents typically have molecular weights between 175 to 150 amu and boil at temperatures closer to the 110ºC value called for in *EPA Method 24/ASTM D 2369*. It is plausible that the induction period is too short or the bake temperature is too high.

Further work is required on the sources of variability of these measurements. Both this study and previous literature[5] indicate that variability, as well as error, increase at lower levels of VOC's. Data from Mania[5] is graphically represented in Figure 5. In their study, "true VOC" was known from formulation knowledge and analysis of all of the raw materials for this study. Laboratories other than those of the paint manufacturer will not normally have this much information.

The existing published literature, including the above study, focuses on water reducible paints (latexes), and errors associated with the measurement of water. Water reducible paints currently utilized by the Navy contain relatively high solvent (e.g. > 300 g/L). Similar to all high-solvent paints, measurement of VOC's for these paints is marked by low variability (high precision), so this published literature is of little utility for the Navy's immediate concern.

However, VOC content in latex paints is expected to become a bigger issue for the Navy in the future.

Both the EPA and ASTM state precision criteria that are based on the measurement – the precision should be between 1.5% and 5%, regardless of whether the measured VOC is 5 g/L or 500 g/L. Possible resolutions to this include varying the required precision inversely with the claimed VOC level, or perhaps using an absolute precision value (e.g. 20 g/L).

Precision: Table 3 provides a summary of the precision of data from our study and that of Mania,[5] in comparison with the criteria set forth in *EPA Method 24/ASTM D 2369*. Several points arise from this comparison:

- There is insufficient openly published data that addresses VOC measurement of low solvent (high solids) solvent-borne paints.
- The VOC measurement data for low VOC paints has far more scatter (variability) than is accepted by the EPA and ASTM standards. In fact, using EPA/ASTM guidelines would result in rejection of most of our data. The Mania[5] study presents data that has even higher scatter than this study, and they expended far more effort obtaining precision data than we did. The Mania study utilized 20 duplicates for each data point, while this study used only triplicate samples.
- The final four rows of Table 3 indicate that the precision (scatter) of the data for low solvent paints is approximately 10 times worse than the ASTM guidelines, and that this scatter gets worse as the solvent (VOC) level drops.

In effect both the EPA and ASTM standards call for precision on the order of 1.5% repeatability of the actual VOC measurement, regardless of whether the VOC is 5 g/L or 500 g/L. As the VOC decreases, scatter in the measurement increases, at least in part the result

of trying to measure very small weight differences of a very small sample. At a level of zero VOC, some of the measures of this scatter become undefinable (i.e., involve division by zero). A recommended resolution is to establish an absolute level of precision, e.g. ± 20 g/L VOC.

Further study to address VOC measurements of high solids solvent-borne paints should address the following questions:

1. To what extent does the VOC test actually predict the in-service emission of volatilized solvents (i.e. non-reactive diluents)?
2. During VOC testing, how do the emissions of volatilized reactive diluents vary with induction time?
3. How can the procedure be modified to improve the precision -- perhaps use of larger samples, or use of a single fixed induction time, determining the optimum amount of additional solvent, optimizing the baking time and temperature, etc.?

As a final note, a development which may impact the future of *ASTM D 2369/EPA Method 24* is the improved understanding of the atmospheric reactivity of volatile organic compounds, particularly their differentiation with respect to their relative reactivities with oxygen and nitrogen oxides (NO_x) in the presence of sunlight (ozone-producing conditions). A much-cited 1990 article by Carter[13] discusses this issue in considerable detail, and such work has led to the conclusion that volatile organic compounds cannot be considered alike in their capability for facilitating ozone formation. Such research concerning the "maximum incremental reactivity" (MIR) values for different VOC's, has provided the impetus for recently proposed amendments to California regulations for reducing VOC emissions.[14]

CONCLUSIONS

1. Measured VOC tends to fall off with induction time, for all but the high solvent paints. This is consistent with the higher use of reactive diluents in place of solvents in "solvent free" paints.
2. The variability of VOC measurement increases, roughly in inverse proportion to the level of VOC's present.
3. Further work on measurement of VOC of solvent-borne paints should focus on those paints with low and very low levels of VOC's. Since higher solvent paints exhibit relatively low variability and low apparent error, further study of those paints should be limited to verification of whatever techniques are developed for low or very low solvent paints.
4. One source of error in measurement is the "pre-dilution reaction time" of paint samples, i.e., that interval between the time components are mixed, and solvent dispersant is added. Our observations suggest that significant reduction in random error could be realized by keeping this time to a minimum, preferably under 15 minutes. However, the effect of reducing this time on the overall completeness of curing (including resin incorporation of reactive diluents) is not readily predictable.
5. Two very different approaches are possible in further investigations. The first approach would involve a reexamination of existing *ASTM D 2369* test parameters such as the film thickness during paint incubation and baking, sample size, the impact of using (or not using) dispersing solvents, induction time, and oven (bake) temperature.
6. A second approach would be based on full quantitative analysis of all the VOC's in a coating. This scenario would seem particularly likely if future VOC regulations are based on adopted MIR values (see the end of the last section).

REFERENCES

1. ASTM International, West Conshohocken, PA; throughout this paper, the suffix designating year of adoption for versions of individual standards (e.g., *ASTM D 2369-**89***) has been omitted, except when relevant.
2. "Manual on Determination of Volatile Organic Compound (VOC) Content in Paints, Inks, and Related Coating Products," 2nd Edition, (J.J. Brezinski, ed.), 1993, p.1 [ASTM Manual Series **MNL 4**; ASTM, West Conshohocken, PA].
3. Code of Federal Regulations, 40 CFR 60, Appendix A, Method 24; first published in its original form in the October 1980 *Federal Register.*
4. J. Berry, "D2369: The Stealthy Defender of Public Health," ASTM Standardization News **27** *(2)*, 26-29 (Feb. 1999).
5. D.J. Mania, M.L. Bruck, S. Fezzey, and F. Louis-Floyd, "Sources of Error in VOC Determination via EPA Method 24," J. Coat. Tech. **73** *(919)*, 111-117 (Aug. 2001).
6. C.M. Fobar, V.C. Jenkins, and C.N. Millner, Jr., "VOC Testing Comparison: EPA Method 24 Versus the Cal Poly Pomona Method," J. Coat. Tech. **70** *(879)*, 49-53 (Apr. 1998).
7. V.C. Jenkins, J.C. Reilly, B. Sypowicz, and M.T. Wills, "VOC Testing Comparison: EPA Method 24 Versus the Cal Poly Method," J. Coat. Tech. **67** *(841)*, 53-59 (Feb. 1995).
8. E.C. Ferlauto, "Comparison of Volatile Organic Content (VOC) and Volatiles Released from a melamine Crosslinked High-Solids Polyester," J. Coat. Tech. **60** *(764)*, 51-59 (Sept. 1988).
9. Various databases, OCLC Online Computer Library Center, Inc., Dublin, OH.
10. The Web of Science, Institute for Scientific Information (ISI), Philadelphia, PA.
11. B. Ancona, R. Alexander, J. Aviles, et al., "Suitability of ASTM Test Method D 2369 for Determination of VOC in High Solids Coatings," J. Coat. Tech. **65** *(820)*, 45-50 (May 1993).
12. ASTM D 1475, "Standard Test Method for Density of Liquid Coatings, Inks, and Related Products."
13. W.P.L. Carter, "A Detailed Mechanism for the Gas-Phase Atmospheric Reactions of Organic Compounds," Atmospheric Environment **24A** *(3)*, 481-518 (1990).
14. "Initial Statement of Reasons for the Proposed Amendments to the Regulation for Reducing Volatile Organic Compound Emissions from Aerosol Coating Products and Proposed Tables of Maximum Incremental Reactivity (MIR) Values, and Adoption of Proposed Amendments to Method 310, 'Determination of Volatile Organic Compounds in Consumer Products'," State of California Air Resources Board (2000) – available on the Internet at http://www.arb.ca.gov/regact/conspro/aerocoat/aerocoat.htm (URL verified as active at time of manuscript submission).

TABLE 1.
Summary of Variations in VOC Data

Solvent Level	**Average Variation between Measured (Authors) and Claimed (Vendor) VOC, %**	**1-hour induction VOC / 24-hour induction VOC (expressed as %)**
High Solvent	3%	98%
Low Solvent	35%	139%
Very Low Solvent	50%	249%

TABLE 2.
Physical Properties of Various Raw Materials

Material	**Molecular Weight**	**Vapor Pressure (mmHg) @ 21ºC**	**Viscosity (Poise, P) @ 25ºC**	**Boiling Point (ºC)**
Bisphenol A Epoxy Resin	957 (avg.)	< 0.01	110-150 (like molasses)	500*
Bisphenol F Epoxy Resin	312(avg.)	< 0.01	25-45 (viscous liquid)	450*
Benzyl Alcohol	108	0.08	1 (like water)	206
K54	265	< 0.01	Solid	135 @ 1 mmHg
Isophorone Diamine	265	< 0.01	3 (light oil)	247
Triethylenetetraamine		< 0.01	25-35 (like motor oil)	267
Triethanolamine		< 0.01	35-40	335
Amido Amine Curing Agent	Mixture	4.95	6.5	> 340
Cycloaliphatic Amine	Mixture	10.33	1	205
C12-C14 Glycidyl Ether	205-234	0.6	7-12	216

***** Homopolymerizes and/or decomposes depending on sample volume

TABLE 3.
Precision: Paints Tested by Standards Agencies and in this study

Agency	Parameter	Paints	Criteria or Data Value
ASTM	REPEATABILITY Accept/reject variability	Solvent-borne multicomponent 35-72% volatile	1.7%
EPA	REPEATABILITY Accept/reject variability	No explicit information provided; probably same data/paints as ASTM	1.5%
Mania [5]	Error (difference between Measured and true VOC)	38 paints, 0-560 g/L VOC, median paint had 250 g/L	96%
ASTM	Repeatability: Coefficient of Variation	Solvent-borne multicomponent	0.5%
This study	Repeatability: Coefficient of Variation	340 g/L VOC solvent-borne multicomponent (epoxy) paint	2.4%
This study	Repeatability: Coefficient of Variation	144 g/L VOC solvent-borne multicomponent (epoxy) paint	6.4%
This study	Repeatability: Coefficient of Variation	72 g/L VOC solvent-borne multicomponent (epoxy) paint	10.0%
This study	Repeatability: Coefficient of Variation	22 g/L VOC solvent-borne multicomponent (epoxy) paint	15.5%

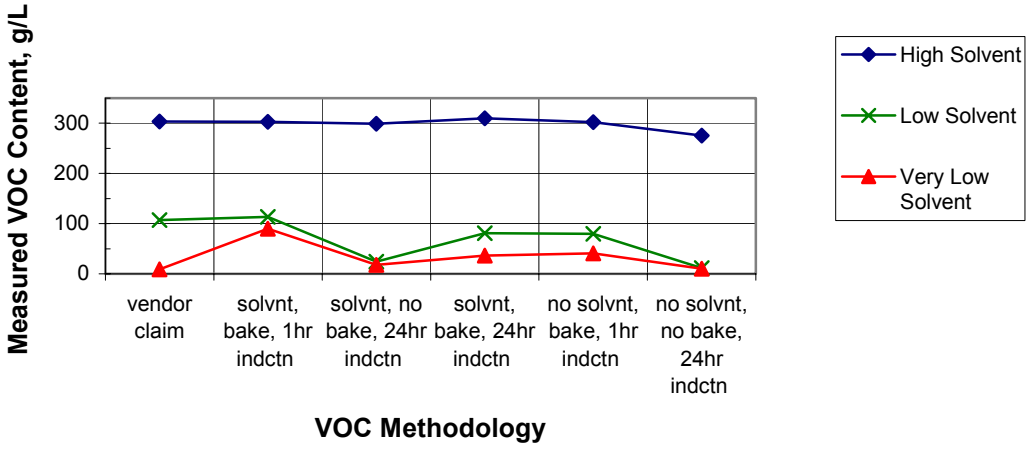

FIGURE 1. Summary of Average VOC Data by Solvent Content

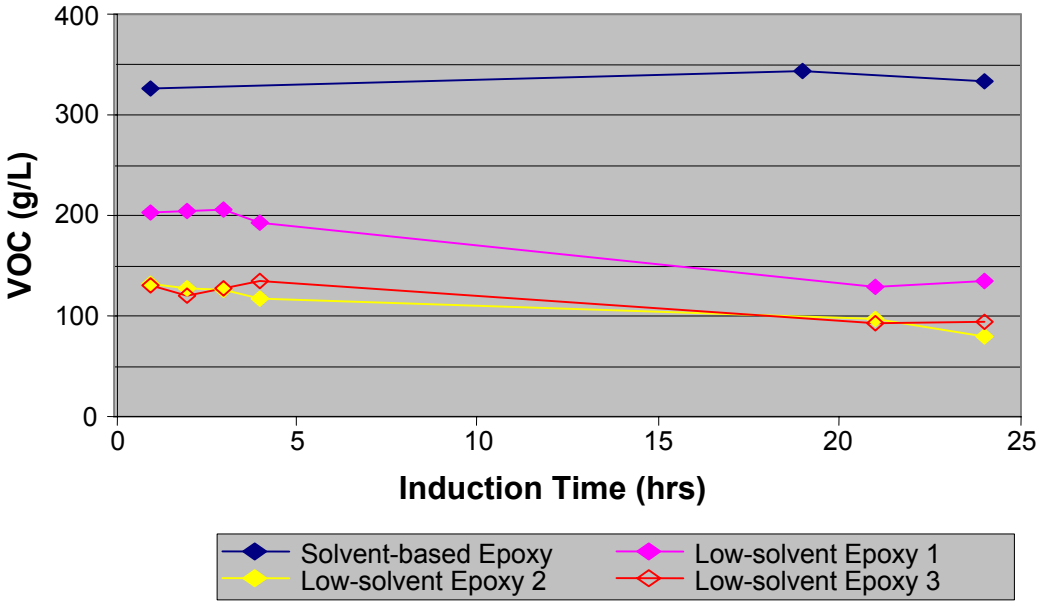

Figure 2. VOC vs. Induction Time

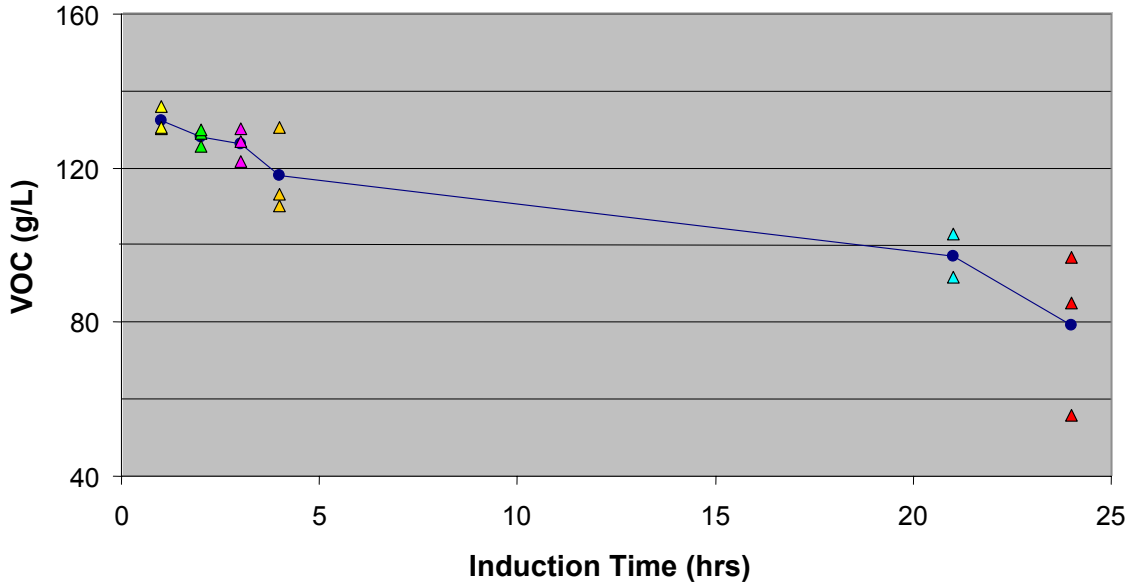

FIGURE 3. Measured VOC (Low Solvent Epoxy #2) Vs. Induction Time.

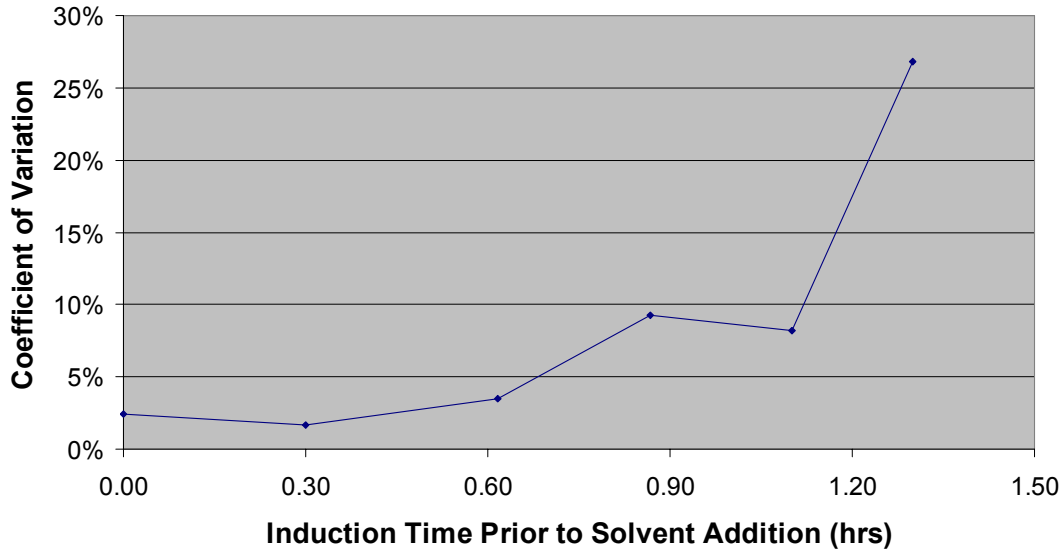

FIGURE 4. Coefficient of Variation vs. Induction Time Prior to Solvent Addition (Low-solvent Epoxy 2).

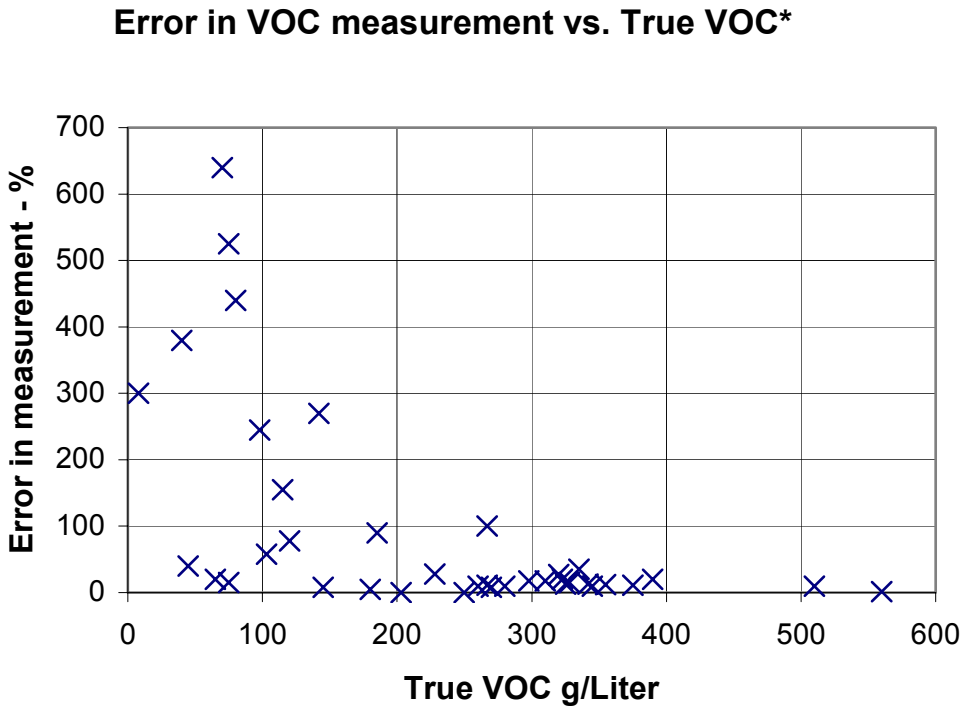

FIGURE 5. Error in VOC Measurement vs. True VOC. *from Mania, DJ; et al. [Reference 5].

ELIMINATION OF MEK AND LACQUER THINNER IN DEPARTMENT OF DEFENSE PAINTING OPERATIONS

Mr. Joseph A. Lucas

Inland Technology Incorporated
401 East 27th Street
Tacoma, WA 98421
(253) 383-1177
inland@inlandtech.com

ABSTRACT

Painting operations at aerospace and Department of Defense facilities create large and problematic waste streams as well as major emissions of hazardous air pollutants and VOC's. Some of these emissions are a result of the composition of the paints used, and as a result, create a waste stream that can only be addressed by a reformulation of the specific paints and coatings. However, the greatest percentage of waste and emissions generated by painting operations is a result of the use of MEK and lacquer thinner in clean up and surface preparation activities. Usage of these hazardous materials account for an excess of 50% of the overall waste generated by a painting facility. The successful elimination of MEK and lacquer thinner for these painting activities would clearly assist these facilities in meeting the requirements of the Aerospace NESHAPS and Executive Order # 12856, and would facilitate a considerable reduction in the overall generation of hazardous waste.

This presentation is an exemplary representation of successful replacement projects that have taken place at civilian manufacturers, aerospace, and Department of Defense installations. It will detail the substitution process from a chemical development standpoint, and will discuss the equipment validation procedures, work practice changes, and training required to make the substitution process successful. In each case study, the end result was a replacement process and chemistry that was more environmentally responsible and less regulated than the original process. In addition, each substitution project resulted in demonstrable cost savings.

CASE STUDY # 1

US Army, Aberdeen Proving Ground had a strong incentive to reduce the hazardous waste generation caused by the use of paint thinner as a cleaning solvent at the Auto Body Shop. Ms. Amy Borman and Mr. Keith Katz determined the necessity for a substitution project,

following an environmental audit which the safety and environmental officers conducted. The pre-existing conditions were; paint gun cleaning that consumed 70 or more gallons of lacquer thinner each month, and evaporative loss and contamination from usage, creating the need for frequent disposal of dirty lacquer thinner and replenishment with fresh material. This frequent disposal of lacquer thinner makes the cleaning process a major source of emissions and hazardous waste. The challenge for the research team was to provide a cleaning solution that would eliminate these problems. It was first necessary to develop a technology that would make the alternative material cost effective to use. The new cleaning solution ideally would contain no hazardous air pollutants, be non-flammable, and have minimal worker exposure risks associated with its use. The new material, therefore, would present considerable differences in behavior, even while accomplishing the cleaning task it was designed to do. Additionally, training procedures and work practice modifications required development in order to accommodate the differing characteristics between the new cleaner and the old style thinner. The research team took these criteria into the laboratory for experimentation.

THE SOLUTION-FROM A CHEMICAL STANDPOINT

Inland Technology developed and patented "a low toxicity solvent composition" known as EP 921™. This solvent alternative was developed to mimic the Hansen's Solubility Parameters of MEK almost perfectly. It contains less than 1% VOC, has no ozone depleting or EPA 17 chemicals in the formula, and has a flashpoint of 156° F, EP 921™ eliminating the fire risks associated with lacquer thinner or MEK. This new cleaner proved effective in the removal of all uncured and semi-cured paints used by the Army, including the chemical resistant CARC coating. In December of 1998 EP 921™ was awarded a toxicity clearance from the US Army Center for Health Promotion and Preventative Medicine.

THE SOLUTION - FROM AN EQUIPMENT STANDPOINT

In order to maximize the cost effectiveness of the new cleaning compound, new equipment was engineered for the cleaning process. The Edge Tek™ Filtration System filters the EP 921™ on line as the cleaning station is being used. The system filters down to .1 micron nominal, and removes a major portion of the paint solids. This allows the EP 921™ to be re-used for a measure of months. Typically, the only wastes being disposed of are the filter elements, and a small amount of settled paint solids. The volume of hazardous waste disposed is reduced by greater than 85%.

THE SOLUTION -WORK PRACTICES, TRAINING AND PUTTING IT ALL TOGETHER

Since there is no evaporative loss associated with EP 921™, most of the training and work practices necessary for the implementation of EP 921™ into a paint shop involve conservation techniques. It is also critically important to develop techniques for the removal of unevaporated EP 921™ from the surfaces of the painting equipment. Conservation techniques involve cascading the extremely dirty EP 921™ into a gross-cleaning operation, capture of the rinsate material, separation of the paint solids from the EP 921™, and filtration of that material in order to extend the usable life of the cleaner. The EP 921™ is unique in that its chemistry is able to attract the paint from the surfaces of the application equipment (paint lines, spray guns, pressure pots and cups) and form micelles of the free-floating paint. However, the paint has no opportunity to bond with or emulsify within the EP 921™. The greater specific gravity of the paint allows the paint to settle out, or to be easily filtered out, of the EP 921™. This lack of emulsification also prevents the EP 921™ from losing effectiveness, since the cleaner is not

becoming saturated with paint. This exemplifies the nature of EP 921™ as a use-specific product which cannot be used as a surface preparation or thinner for paint or coating.

Final removal of EP 921™ from painting equipment involves the wiping of the surfaces with a dry rag inside the cup or pot and outside of the cup and gun head. Either rinse the inside of the cup with Teksol EP®, or, refill the cup or pot with fresh paint, and shoot it through the gun head into the waste paint container. The painter is now ready to begin the next painting job. It is of the utmost importance that the painter do a "pattern check" spray, (this takes 5 seconds or less spraying) to make sure all the EP 921™ is out of the gun head.

THE RESULTS

In May of 1996, two paint gun cleaning stations were filled with an initial charge of 5 gallons of EP 921™ and were put into service. A review of the performance was conducted 48 months later. It is notable that these same gun cleaning stations are still in use today. The records show that the total purchases for the stations during that 48 month period, consist of 95 gallons of EP 921™ and 15 cases of 12 Edge Tek™ Filter Elements, however, not all of these had been consumed after the 48 months. Emissions of hazardous air pollutants, VOC's, and EPA 17 chemicals have been cut to nearly zero. In a cost comparison with lacquer thinner, 48 months usage would have been 3,290 gallons at a cost of approximately $ 2.00 per gallon for a total of $ 6,580.00. The disposal volume for that same period would have been approximately 1,645 gallons, at a cost of $ 5.00 per gallon totaling $ 8,225.00 The costs of the traditional method of painting equipment cleaning had a total cost of $ 14,805. By comparison, the use of EP 921™ and the Edge Tek™ Filter System was: Acquisition of 95 gallons of EP 921™ at a cost of $ 28.95 per gallon, totaling $ 2,702.75, and the Edge Tek™ Filters, at a cost of $ 13.33 per filter element, totaling $ 2,079.48. The disposal cost for the 156 filter elements was $

360.00. These filter elements were contained in one 55 gallon sized drum. The total cost for the 48 months usage of the EP 921™ was $ 5,142.23. This represents a cost savings of nearly 300%! This cost savings is strictly a monetary assessment, while volume of airborne emissions was reduced from 11,515 pounds of hazardous air pollutants from the cleaning process to zero pounds.

CASE STUDY #2

Another example of the opportunity for minimization of airborne emissions from the painting equipment cleaning operations took place at Eglin Air Force Base. The point of contact was Mr. Al Holley, Painting Supervisor for the small parts painting shop. The mission at hand was to replace MEK in use as a clean-up solvent for the painting equipment. The replacement cleaner would have to be non-VOC, non-HAP, contain no ozone depleting chemicals, and contain none of the EPA 17 chemicals. The alternative clean-up solvent would need to be effective in the removal of uncured epoxy primers and polyurethane topcoat paints, as well as have a compatibility with the gaskets and seals present in the painting equipment.

The previous conditions that were encountered at the small parts painting shop were: five full time painters who worked a day shift and a swing shift using high solids epoxy primers, and polyurethane top coats. The yearly consumption for the cleaning of the paint guns was approximately 5,200 gallons of MEK. The blend of waste paint and MEK accounted for 27,400 pounds of hazardous waste generated by this small shop per year. Additionally, the air emissions assessment for this shop showed more than 14,000 pounds of hazardous air pollutants and VOC emitted per year. Incoming MEK purchases totaled $ 6,000.00 per year, however, add to that the hazardous waste disposal cost of $ 12,450.00 per year.

The combined Eglin AFB, Inland Technology Task Force gathered data in order to develop and implement the ideal solution both for the air emission and solid waste issues. From interviews with the painters, it was learned that the current cleaning tanks were inefficient at cleaning all of the small openings and valves in the paint guns that were in use. After the paint guns were flushed in the tanks, the painters needed to disassemble the guns and hand detail all of the parts with a small bucket of MEK and a brush. The ideal piece of equipment would allow for both flushing of the gun heads, as well as detail work. This would be done preferably in the same piece of equipment, and with a non-hazardous cleaner. The performance criteria are the same as the previous case study, with a special emphasis on cleaning of high solids paints. If the paint is not completely removed from the equipment, the gun head will clog or spray in an erratic pattern. The high solids paints are also very prone to "clabbering" or congealing in the presence of water or incompatible solvent cleaners. The congealing of the paint in the gun head will cause such severe clogging, that the gun will need to be detailed with a stripper compound. This takes a long time, and the strippers are often destructive to the seals inside the gun head. The environmental criteria was driven by the need to reduce the generation of hazardous waste, with an emphasis on worker health and safety. Determination was made (using off-line trials) that the EP 921™ would remove the uncured and semi-cured paints used at Eglin AFB. The next order was to comply with the request for a piece of equipment which would allow for the flushing of the gun head assemblies, cleaning of the cup interiors, and cleaning of the cup and gun exteriors. Such a machine would need an air-operated pump, and would utilize the Edge Tek™ Filter System to minimize the disposal of the used EP 921™. The cleaning unit would need to be of a stainless steel construction in order to assure a long usable life for the unit. Based upon the requests of the environmental officers and the painting crew, the IT-45SSER™ was conceived.

UNIT SPECIFICATIONS FOR THE IT-45SSER™ PAINT GUN WASHER

Measurements: 37" x 31" x 74" high, constructed of 14-gauge schedule 304 stainless steel, utilizes an air-operated diaphragm pump, and is equipped with the Edge Tek™ Filter System including a 25-micron resin prefilter.

The training procedures for implementing the EP 921™ and the IT-45SSER™ were overseen by the environmental officers, as well as the Paint Quality Assurance Team. Initially the new unit was placed along side the old style cleaning tanks. This provided a "security blanket" for the painters while they were becoming accustomed to using the non-evaporating EP 921™. After several days, in which the painters discovered that the EP 921™ was even more effective in the cleaning of the orifices of the gun heads, the old tanks were removed. The most radical change the painters experienced was the ability to clean the guns and cups in an open tank, without breathing the unpleasant fumes of the MEK. The other change was the need to follow the cleaning with a dry rag wipe to the exterior surfaces of the gun head and cup, as well as the interior of the cup. The EP 921™, which remained in the "barrel" of the gun head, was completely flushed away by the initial pattern-check spray of the next charge of paint. All of the various types of paint and primer that were cleaned in the old style washer were successfully tested in the IT-45SSER™ exhibiting no degradation of the gun seals, and no clogging of the spray ports in the gun heads.

After an assessment period of 14 months, the IT-45SSER™ at Eglin AFB showed these results: The shop now uses no MEK, and as a consequence, the paint shop emits zero Hazardous Air Pollutants or VOC's from the cleaning process. Additionally, the shop generates only 30 gallons (or 240 pounds) per year of hazardous waste from the cleaning of the painting equipment. Perhaps the most startling outcome is that the initial charge of 25 gallons of EP

921™ has lasted over one year. This is a comparable chemical purchase cost of $ 723.75 instead of $ 6,000.00. In addition, a volume reduction of hazardous waste of more than 27,000 pounds! The IT-45SSER™ Paint Gun Washer and EP 921™ have now been given National Stock Numbers, and are currently in use in all branches of the Department of Defense.

In conclusion, these case studies are examples of successful process substitution projects. It should be noted that no one chemical, or piece of equipment, should be supposed to solve all environmental concerns. The greatest efforts were those involving the training and modifying of the SOP's (Standard Operating Procedures) for cleaning of the painting equipment and handling of the resultant wastes. It is a testimony to those training efforts, more than simply purchase of a new product, which resulted in the dramatic reduction of hazardous wastes from these sites.

COMPRESSORS FOR THE 21ST CENTURY

Rick Miles, Ph. D.
NCI Information Systems, Inc.
325 Richard Ray Blvd., Bldg. 165
Robins AFB, GA 31098

David F. Ellicks
US Air Force Corrosion Prevention and Control Office
325 Richard Ray Blvd., Bldg. 165
Robins AFB, GA 31098

ABSTRACT

Air compressors are currently used in everyday operations throughout the Air Force. Current fielded models are either electrical or gas driven piston systems. Many of these air compressors are required when a unit deploys overseas. The footprint for these compressors can be rather large. The compressors also are very noisy and have numerous moving parts that require lubrication. In addition, the compression process results in large amounts of heat generation. Resonance air compressors solve all of these problems. This presentation will discuss a three-year initiative through the PRAM (Productivity, Reliability, Availability, and Maintainability) program to produce an innovative compressor prototype for use in Air Force paint and corrosion control shops. Development of the compressor will be performed in three stages. The first stage consists of the development of a low pressure, low volume (15 PSIG, 9 SCFM) compressor that will be used to supply compressed air to a paint pot. The second stage will involve the development of a higher pressure (90 PSIG, 15 SCFM) compressor appropriate for servicing one painter in paint application at a base level paint shop. The final stage will be determined based on the technology development of the first two stages. This paper will cover the development, testing and qualification, and future potential for these types of compressors.

INTRODUCTION

With the switch throughout the military to HVLP (high-volume, low pressure) paint guns to increase the transfer efficiency of applying high solids coatings, the selection of an appropriate compressor for supplying air flow to the gun has increased in significance. In most Air Force paint shops one air compressor is used to supply air for several functions (painting, grinding,

blasting, etc.). This places a large demand on the compressor and may result in insufficient air to atomize high solids coatings[1]. Pressure losses between the compressor and pressure regulators also must be minimized in order to prevent a paint job that exhibits the "orange peel" effect.

Air compressors are currently used in everyday operations throughout the Air Force. Current fielded models are either electrical or gas driven piston systems. Many of these air compressors are required when a unit deploys overseas. The footprint for these compressors can be rather large. The compressors also are very noisy and have numerous moving parts that require lubrication. In addition, the compression process results in large amounts of heat generation.

The traditional type of compressor used in everyday Air Force shop operations usually has a large footprint and is extremely heavy. The compressor usually requires a holding tank in order to provide constant pressure and flow without any pressure surges. The air is usually compressed by driving multiple piston cylinders up and down. In order to prevent seizure of the pistons in the assembly the pistons must be well lubricated. If breathable air is required, a separate compressor must be used. This compressor will have a large filtration system that purifies the air produced by the compressor.

Currently, there is a three-year initiative through the PRAM (Productivity, Reliability, Availability, and Maintainability) program to produce a linear resonance compressor prototype for use in Air Force paint shops. Development of the compressor will be performed in three stages. The first stage will be the development of a low pressure, low volume (15 PSIG, 7.5-12 SCFM) compressor that will be used to supply compressed air to a paint pot. The second stage will involve the development of a higher pressure (90 PSIG, 15 SCFM) compressor appropriate

for providing shop level support. The final stage will be determined based on the technology development of the first two stages.

The development of the compressor technology began with the entire resonator drive system that used the mechanical resonance of the pump (resonator and valve head) to generate a dynamic pressure (acoustic standing wave). This provided variable capacity, simple linear motor design, and short stroke/high frequency operation. The entire resonator drive was modified so that only the diaphragm had to be moved to generate the dynamic pressure. This eliminated concerns over having to drive large pieces of hardware. While the diaphragm drive performed well, a need arose to be able to produce the same dynamic pressure in a smaller area. In order to maintain the acoustic standing wave the shape of the resonator was critical. The acoustic resonance was replaced with pneumatic resonance. This reduced the noise level and cost by eliminating the large resonator section. The maximum decibel level allowed by the Air Force without a distance requirement is 85 decibels (dB). The linear resonance compressor while producing large amounts of sound energy within the resonator cavity produces approximately only 60 dB of noise outside of the cavity. For comparison, normal conversation produces about 55 dB. The decibel level may change due to the particular application.

The development of the first generation compressor took place in 4 phases. The first phase concentrated on improving the overall design of the compressor module. The second phase focused on integrating the compressor modules into a system and analyzing the scalability of the technology. Does putting two compressors producing 15 psig at 3 cfm in parallel result in 15 psig at 6 cfm? This linear scalability was confirmed. Phase III concentrated on improving system reliability. The first generation compressor prototype was delivered to NCI Information Systems for Phase IV performance confirmation testing in December 2001.

Unfortunately, with scaling up of the compressor the noise level produced by the machine was also increased significantly. A welded steel frame enclosure was used to encapsulate the compressor modules. A baffle was created at the top of the compressor unit to reduce the direct noise exiting the vent opening. Composite panels of aluminum and foam board were used due to their relative specific stiffness to minimize vibration and weight. The panels were lined with sound absorbing material to minimize any acoustic standing waves that might be created from the compressor modules. The suspension was made of silicone rubber O-rings to aid in isolating the vibrating modules from the enclosure.

The lubrication requirement for currently fielded air compressors results in the need for filters in order to use a compressor for breathing air. The linear resonance compressor has no lubrication requirements allowing a compressor producing breathable air without the need for a filter.

This technology has already been licensed to a major appliance manufacturer and a major computer manufacturer. The appliance manufacturer will use this technology to replace current compressors on its line of refrigerators and the computer manufacturer will be using the technology to constantly cool the computer. Linear resonance compressors for both applications will reduce the noise level and required maintenance.

COMPRESSOR TECHNOLOGY

The Phase I compressor developed for the Air Force uses the RMS technology in a modular system. Each module features high frequency pumping and variable output microprocessor control. Oilless pump construction and simple linear motor design provide the compressor with high reliability and maximum durability. The modularity provides scalable capacity and redundancy for maximum up-time and serviceability.

To accomplish these objectives, NCI has been working with a vendor to design and develop prototype hardware as well as develop a new military compressor specification for this unique technology. NCI also is developing a test plan for the field testing of the compressor that will determine the overall performance, safety, and reliability of the compressor system. NCI will also develop cost data for Return on Investment calculations and develop and deliver a database of requirements and test results.

The vendor has developed and patented a new technology that allows sound waves to carry significantly more energy than previously thought. This patented technology creates a "standing" sound wave in a closed resonator with an energy density thousands of times greater than previously achieved. The key to this technology is the shape of the resonator cavity. The acoustic compressor arose from the fact that this standing wave within the resonator can generate large amounts of oscillating pressure.

RESULTS

NCI has reviewed military and commercial compressor specifications in order to begin development of a new specification for oil-free linear resonance air compressors. NCI also began development of a test plan for the Phase I field test. Preliminary testing of a multiple stage compressor has been accomplished by the vendor. Results have indicated that an almost linear scale up in flow from a single stage compressor is possible. The vendor is currently investigating possible modifications to reduce the weight and footprint of the multi-stage compressor. The vendor has concluded life cycle and reliability testing on the first prototype and is compiling a report of their test results. The single stage compressor has passed fatigue cycling up to 10E7 cycles. An upper use temperature limit of 150 degrees Celsius has been added as a design criterion in order to avoid failure of the laminate adhesive in the motor. It has also been

determined that the compressor must produce 17 psig at the outlet of the compressor in order to produce 15 psig at the outlet of the attached quick disconnect hose. Currently the vendor has a working 4-stage compressor that produces 17 psig at the outlet at 6 SCFM as shown below.

The current multi-stage compressor features high frequency pumping with variable output microprocessor control. The oil-free all metal pump construction and simple linear motor design will provide high reliability and maximum durability. The compressor contains no rotating parts, no sliding seals, and requires no lubrication. The modularity of the compressor provides scalable capacity and redundancy for maximum up-time and serviceability. Should one of the compressor stages fail to operate only it needs to be removed and replaced. This allows for the compressor stage to be repaired and overhauled while the actual compressor remains in service.

CONCLUSIONS

Linear resonance pump technology while in its infancy has the potential to be used in numerous military and commercial applications.

REFERENCES

1. Joseph, Ron. "Brief Description of Observations of Air Force Spray Booth." Pollution Prevention Conference. San Antonio, TX. 2000.

BELL LAB'S CORROSION PREVENTIVE COMPOUND (MIL-L-87177A GRADE B)

David H. Horne, ChE, P.E.
Aerospace Engineer,
F-16 Structural/Mechanical Branch, OO-ALC/YPVS
Hill AFB, Utah 84056-5828

ABSTRACT

The Bell Laboratories invented a corrosion preventive compound (CPC) to stop the corrosion of their electrical switching systems and connector contacts that were causing very large maintenance expenses. The Air Force Materials Laboratory wrote a military specification to describe the CPC, MIL-L-87177. The CPC was used by the F-16 System Program Manager to prevent corrosion of the electrical contacts in the F-16 aircraft Main Fuel Shutoff Valve (MFSOV) that had experienced many uncommanded closures and had caused at least six aircraft crashes. When the order to treat the MFSOV actuator connectors with the Bell Lab's CPC was issued the uncommanded closures ceased.

The F-16 System Manager tasked the Battelle Labs to investigate the MFSOV control system to determine the causes of the MFSOV anomalies and recommend permanent corrective actions. Wright-Patterson AFB funded Battelle to research and compare the effectiveness of CPCs sold to the Air Force. Battelle found six of the 12 CPCs actually accelerated corrosion. Battelle then performed an on-aircraft study to determine the effects of treating the electrical connectors of avionics units on the F-16. The MTBF of some avionics units increased 20 times; the Mission Capable (MC) Rate at one Base increased 16%; and a calculated cost savings greater than 50 times the study cost was realized.

The F-16 cost savings office estimated that by treating the F-16 fleet avionics connectors with this CPC will result in an continual cost avoidance of about 500 million dollars per year.

BACKGROUND

The Bell Laboratories were asked to invent a means to identify and prevent the frequent and extensive electrical signal transmission and switching equipment failures occurring in the Bell System Divisions throughout the country. These failures occurred in both environments believed benign to corrosion damage but more frequently in known highly corrosive atmospheres. The task

was assigned to Dr. George Kitchen, a Chemical Engineer who was expert in oils and lubricants. Fred Meyer, a NACE corrosion specialist, in the Air Force Materials Laboratory learned of Bell's CPC, obtained the physical and some chemical characteristics of the CPC and wrote a procurement specification to describe its parameters.

Numerous *uncommanded* MFSOV closures puzzled AF personnel from the beginning of the F-16 tests at Edwards AFB. However, in 1987 a flameout of an F-16 that very nearly resulted in a crash prompted the Air Force to investigate the possible causes of that and other aircraft which had similar flameouts. Corrosion had been seen in many of the MFSOV connectors. The Army's lead corrosion scientist, Lloyd O. Gilbert, a NACE Corrosion Specialist, recommended the Bell Lab's CPC to treat the MFSOV electrical connector which had been found to have tin plated pins in the MFSOV actuator and gold plated sockets in the connecting harness. Dissimilar metals were found in many electrical connectors on the F-16, however at the Air Force's demand many such connector sets already had been changed to gold to gold. After the order to treat the MFSOV actuator connectors with the Bell Lab's CPC was issued the uncommanded closures ceased for about seven months. However, the AF later recognized that the F-16 maintenance personnel probably did not have the Bell CPC as specified, because the corrosion prevention was short in duration.

INVESTIGATION AND TESTING

MFSOV Failsafe Module corrosion was observed and reported. Obvious iron oxide in some connectors revealed the tin-plating on the pins had been corroded enough to breach the tin some even found with water puddle in the connectors. Some MFSOV actuators received by San Antonio ALC for overhaul had connectors with pins that had completely corroded off. SA-ALC saw so many corroded connectors that they adopted the practice to replace the connectors on all MFSOV actuators overhauled.

The F-16 System Manager tasked the *Battelle Labs* in Columbus, OH to investigate the MFSOV control system to determine the causes of the MFSOV anomalies and recommend permanent corrective actions. Battelle found that tin reacts with oxygen in the air much like aluminum which produces tin oxide. The gold plated sockets which immediately exposed more tin to the oxygen in the air easily wiped off the tin oxide, and the corrosion process was repeated. The tin plated connector contacts were experiencing fretting corrosion that proceeds as long as the tin could contact some other surface that in a vibration environment would rub away the tin oxide. However, Battelle also revealed that a light oil like MIL-L-87177A Grade B could shield the oxygen from the tin.

Battelle also found a silicone grease had contaminated the microswitch fulcrums in the MFSOV actuators thus causing them to stick in the "open" position preventing current to pass to the "open" windings to keep the valves open.

The Wright Patterson AFB FACTS Office (acronym for Fasteners, Actuators, connectors, Tools, and Subsystems) funded and tasked the Battelle Labs to perform laboratory and field tests using CPCs that were being purchased and used by the DoD and determine their true corrosion preventive abilities. For the two year test at ten CONUS locations, twelve CPCs were identified

eleven of which were claimed to conform to either MIL-C-83109E Type II or III or to MIL-L-87177A Grade B. Laboratory salt spray cabinet and other tests using AA 6061, AA7075, silver, copper, and mild steel test plates that were spray treated with each CPC being investigated. Also Amphenol 50-position double sided card edge connectors with "60-m" nickel, "30-m" hard gold over oxygen free high conductivity copper contacts were used in the tests.

Six of the formulations (five of which were qualified to MIL-C-81309E) actually accelerated corrosion in some tests, but two were excellent in the tests.

The FACTS Office also funded flight tests on the F-16 using the two best CPCs identified in the lab and field tests to determine what reliability and cost effects would occur. The Bell Lab's CPC was one of them. Using the REMIS maintenance tracking system, the number and rate of line replaceable units that had been treated with the CPC in their electrical connectors that were "pulled" for backshop maintenance or were sent to be overhauled were monitored and compared on a flight hour basis with the rate of pulls and overhauls from aircraft that had not been treated with the CPC in their electrical connectors. In addition, maintenance man-hours, mission capable rate, and change in electrical resistance across connector sets were tracked and recorded. The connector sets treated in the flight tests all had gold to gold contacts.

DISCUSSION OF RESULTS

IMPROVED RELIABILITY OF ELECTRONIC CIRCUITS

It is important to know that almost every time we briefed electrical maintenance personnel and described what we were trying to learn by the research study we were asking them to do with us by treating electrical connectors with a CPC they would say that it was universal practice when an electrical problem existed that simply disturbing the corrosion between the contacts by dismating, blowing out the corrosion in the connector, and remating the connector would make the equipment

work okay. For this study an increase of ten milliohms across a connector set was specified as the failure threshold, and thousands of measurements were taken during the tests. A demonstration of the differences of environments was seen after a year between Nellis AFB where only 3% of the *unlubed* connector sets exceeded the 10-milliohm increase and Homestead ARS where 47% of the *unlubed* connector sets exceeded the 10-milliohm increase.

In contrast, after a year at both Nellis AFB and Homestead ARS, 96% of the Bell Lab's CPC *lubed* connectors statistically showed no increased resistance, and none exceeded the 10-milliohm threshold.

However, after a year, a compilation of resistance changes at all Bases showed that all of Bell Lab's CPC lubed connectors that were *undisturbed* and 98% of the Bell Lab's CPC lubed connectors that were *disturbed* passed with less than 10-milliohms increase. But only 62% of *the unlubed, undisturbed* and 73% of the *unlubed* but *disturbed* connectors passed. However the resistance of more than 24% of all the *unlubed* connectors increased more than 100-milliohms.

After one year 86% of the *unlubed* connectors at McEntire ANGB, 46% at Homestead ARS, and 4% at Nellis AFB increased more than 10-milliohms failing the acceptable criteria.

For all Bases 36% of *unlubricated, undisturbed* and 34% *of unlubricated, disturbed* connectors exceeded 10-milliohms. Although all of the *lubricated, undisturbed* passed, 2% of the *lubed, disturbed* connectors exceeded 10-milliohms and the resistance of 1% exceeded 78-milliohms. Thus, connectors that are disturbed must be relubed to assure their continued reliability.

RELIABILITY

The normal events when LRUs are pulled to check them in the backshop many are BCS and are returned to service, but after two or so times a specific S/N LRU fails in flight and again is found BCS with the AIS station the backshop personnel are convinced something is wrong with it that they cannot detect, so they send it to be overhauled. So the REMIS data revealed or at least suggested that lubed connectors on some LRUs that increased their MTBF 19 of 20 times meant LRUs normally sent for overhaul were serviceable except for the corrosion in their connectors.

Scientific studies require controls in the universe being examined. The Sioux City Air National Guard agreed to be a control for the first 12-months for the flight study. At the end of seven months after Sioux City ANG cleaned its avionics LRU connectors the cumulative BCS rate was only 0.57/1,000-flight hours while the ANG average was 7/1,000-flight hours. Then for the next four months (until the Sioux City ANG completed its obligation to just clean its connectors) its BCS rate increased to 6.75/1,000-flight hours, almost the same as the ANG fleet. However, after it lubed its avionics connectors its rate flattened out to 0.0-BCS/1,000-flight hours for the next three months, and its rate at the end of the test after lubing was 1.1-BCS/1,000-flight hours, like other Bases that lubed. Remember, in 1988 after the TCTO to treat MFSOV actuator connectors was issued, no problem reports were received by the F-16 engineering office for about seven months but then began again. It appears at that time to accomplish the TCTO' demands, substitute CPCs for the prescribed Bell Labs CPC must have been used to treat the actuator connectors. Months later it was determined that the CPC Item Manager had no record that any field unit had requested the prescribed CPC at that time.

COST SAVINGS

Based on the reductions in LRUs sent to be overhauled by the Bases participating in the three-year flight test program, a savings from reduced LRU overhauls of about $60-million for the participating Bases. Thus, the $5000 spent for the CPC equates that about $100 was saved for each penny of CPC. The ratio of savings to study cost is greater than 50 to 1. From these numbers the F-16 cost savings office estimated that the implementation of the lubrication throughout the F-16 fleet will result in saving about $500-million/year to the Bases operating the F-16s by reducing overhaul costs.

IMPORTANT AEROSPACE WEAPONS SYSTEMS PARAMETERS OF BELL LABS' CPC

CPC spreads protecting all surfaces;

Low vapor pressure 50-mm Hg, to prevent evaporation even at 60,000-ft altitudes;

Low surface tension to displace water or surface moisture;

Liquid to minus 70-deg F; and stable to about 450-deg F, decomposes without evaporation;

No known health, safety, or environmental problems;

RECOMMENDATIONS

The Bell Labs' CPC is considered to be entirely safe for personnel and on the aircraft. Two MIL-L-87177A Grade B sources are available,. One is NSN stock listed as a 16-ox aerosol can: NSN 6850-01-328-3617.

Treat all electrical connectors especially dissimilar metal connectors.

CONCLUSIONS

MISSION CAPABLE RATES INCREASED

At Homestead ARS the average aircraft mission capable (MC) rate for the aircraft on which the avionics LRU connectors were lubricated was 16% higher than aircraft with unlubed connectors.

NO FLIGHT OR PERSONNEL SAFETY IMPACTS REPORTED

Every participating Base was asked to report any flight or personnel safety impacts, and at the end of the test program all Bases reported no impacts had been seen.

ELECTRICAL RESISTANCE THROUGH UNDISTURBED BELL LABS' CPC LUBRICATED CONNECTORS PASSED CRITERIA

98% showed no statistical change in resistance.

Virtually all unlubricated connectors failed the 10-milliohm maximum increase in resistance.

The study was terminated before a trend appeared to indicate that relubrication was warranted.

Disturbed connectors should be relubed before remating.

MAINTENANCE REQUIREMENTS WERE REDUCED SIGNIFICANTLY

A reduction of maintenance man-hours of approximately one third was recognized on aircraft which had been treated with the Bell Labs' CPC. That MMH reduction is not expected to reduce maintainer costs, but it will provide for faster turn around of aircraft improving MC rates and allow maintainers to concentrate on other important duties.

The investigation to determine the results of lubricating the electrical connectors of avionics LRUs was a spectacular success. The technology is transportable to other electronic equipment which have gold to gold connectors including aircraft, naval craft, computers, land vehicles, and aerospace vehicles.

THE OPERATIONAL TESTING OF THE CPC ACF-50 ON THE US NAVY'S S-3B VIKING FLEET

Edwin G. Mullin
F/A-18 Structures Fleet Support Team: [4.1.6.0.0] F/A-18FST.3
Naval Air Depot North Island
P.O. Box 357058
San Diego, CA 92135-7058
U.S.A.
Voice: 619/545-0745 FAX: 619/545-5160
e-mail: MullinEG@navair.navy.mil

ABSTRACT

Corrosion is the number one maintenance degrader of Aviation Weapon Systems in the Navy today. Because of the high cost of materials and the high number of maintenance man hours spent repairing and replacing corroded components and surfaces on the aircraft every year; any action that can be taken to reduce these expenditures should be aggressively pursued. The S3 Fleet Support Team [S3FST] has evaluated ACF-50, an ultrathin Corrosion Preventive Compound (CPC) that is used on aircraft in the Civilian Aviation Industry. ACF-50 provides a flexible but durable coating that displaces moisture on the aircraft structure and supplements the existing aircraft finish system.

During 1996, ACF-50 application and effectiveness were tested on an ES-3A aircraft assigned to VQ-5. Prior to the ACF-50 application, the aircraft received a Material Condition, Aircraft Service Period Adjustment [ASPA] Inspection to determine the overall condition of the Weapon System. All corrosion discrepancies were noted as to their Maintenance Level O, I or D [Organizational, Intermediate or Depot] and their severity [Minor, Major or Critical]. After the ASPA Inspection was completed, ACF-50 was applied to the entire interior surfaces of the airframe. The high pressure/low volume application of the CPC took approximately 4 hours and consumed approximately 20 Liters of ACF-50.

12 Months later [7 of which the aircraft was carrier deployed to the Persian Gulf] this same ES-3A again received a thorough Material Condition [ASPA] Inspection. To ensure consistency this second inspection was accomplished using the same ASPA inspection team and procedures used for the initial ASPA inspection. Again, all corrosion discrepancies were noted as to Maintenance Level and Severity. In comparison of these two ASPA Inspections; a **47%** reduction in corrosion discrepancies was noted. As a side note, all maintenance accomplished on the ES-3A during the 12 month evaluation period was routine. No special corrosion preventative tasks were accomplished. Further research into this product determined that it has been commercially available World Wide since the mid 1980s. ACF-50 is currently approved for use by the United States Coast Guard, the Federal Aviation Administration and various

Original Equipment Manufacturers [OEMs], including Beech Aircraft, British Aerospace, McDonnell Douglas, and Sikorsky.

Based on the proceeding research and prototyping; it is conservatively anticipated that a 20% reduction in overall organizational level maintenance man hours expended looking for and repairing corrosion discrepancies will be realized if the application of the CPC ACF-50 is accomplished at the 308 Day IMC interval. All of the required materials and application tools are readily available off-the-shelf from Pacific Corrosion Control Corporation. After initial ACF-50 application, maintenance of the film protection consists of inspection of treated areas at subsequent 308 day inspections and touch-up as necessary. It is also anticipated that a reduction in material cost expenditure will be realized both for O and D-Level Corrosion Discrepancies and D-Level Maintenance Man-Hours (MMHRS) expended addressing corrosion. However, at this point the S3FST is unable to quantify those cost savings.

During the first week in June 2000, 8 S-3B aircraft under the custody of Sea Control Wing Atlantic [WINGLANT] were fogged at Naval Air Station, Jacksonville, Florida. In addition to these 8 fogged aircraft the S-3 Fleet Support Team is also tracking corrosion on 5 additional control S-3B aircraft that were not fogged. During the first week in October 2000, 8 additional S-3B aircraft under the custody of Sea Control Wing Pacific [WINGPAC] were fogged at Naval Air Station, North Island, San Diego California. In addition to these 8 fogged aircraft the S-3 Fleet Support Team is also tracking corrosion on 7 additional control S-3B aircraft that were not fogged. As each aircraft reached its Special 308 Day Corrosion Inspection; reports are being generated and submitted to S-3 Reliability & Maintainability [R&M]. The last of these corrosion reports was expected be submitted to R&M in July 2001. The S-3 Fleet Support Team [North Island] was tasked by the S-3 Program Management Office [NAVAIRHQ] to submit a formal Engineering Paper, with S-3 Engineering's recommendation to either incorporate or not incorporate the routine application of the CPC ACF-50 across the S-3 Community. This final paper was submitted to NAVAIRHQ in August 2001.

BACKGROUND

The S-3A was initially developed as an Anti-Submarine Warfare [ASW] Platform. Over the years this ASW capability has been enhanced and expanded. The current Type/Model/Series [T/M/S] designator is S-3B. The platform has also been modified for the Aerial Tanker Mission. In addition, the S-3B has also progress from a Sea Control platform into additional missions in surveillance and attack.

In the fall of 1995, R&M under the S3FST was tasked to evaluate the commercially available Corrosion Preventive Compound [CPC], ACF-50 and determine if it was a product that would be useful and/or beneficial to the US Navy.

Because the initial ACF-50 development work that was accomplished yielded only a single data point. And because other questions regarding the effectiveness of ACF-50; additional evaluations were pursued under the guidelines of the Aging Aircraft Program [AAP], the Affordable Readiness Initiatives [ARI] Program & the Aircraft Equipment Reliability and Maintainability Improvement Program [AERMIP]. The proceeding abstract paragraph gives a good synopsis of what has been accomplished by the S3FST to date.

APPLICATION DEVELOPMENT, TOOLING AND LESSONS LEARNED

The proto-type application of ACF-50 was accomplished on an ES-3A [Signal Intelligence/Electronic Intelligence] T/M/S S-3 in the summer of 1996. The ES-3A T/M/S has since been retired from the Navy's inventory. Application of the CPC was accomplished by a licensed Airframe & Power Plant [A&P] Mechanic from Pacific Corrosion Control Corporation. The application was accomplished in a fleet hanger at North Island while the airframe had all of its panels removed and access doors open. Direct application to the airframe was accomplished via a High Pressure / Low Volume Pump System. This High Pressure / Low Volume technique yields a very fine atomization, a fog, that permeates the entire interior structure of the aircraft. The Nozzle Pressure during this application was 1200 PSI. This fogging type of application allows the CPC to wick its way into the entire airframe via capillary action. A Lesson Learned during this evolution was that first, the dispersion of the CPC is more effective if the airframe

structure has fewer panel and doors open. And secondly, with fewer panel and doors open, dispersion of the CPC in the Hanger Spaces is less intrusive.

During the week of 5 Jun 2000, fogging was accomplished on 8 S-3Bs at WINGLANT. In addition, 5 non-fogged S-3Bs from WINGLANT were also identified as control aircraft. During the week of 2 Oct 2000, fogging was also accomplished on 8 S-3Bs at WINGPAC. In addition, 7 non-fogged S-3Bs from WINGPAC were also identified as control aircraft. All fogging was accomplished by O-Level maintenance personnel. In addition, technical representatives from Lear Chemical & Pacific Corrosion Control were on-site to train the O-Level Sailors and be available to resolve technical issues. Also on-site was an S3FST R&M Engineer to develop a maintenance program for ACF-50 and also resolve engineering issues.

Prior to the application of ACF-50, all S-3Bs that were to be fogged were inspected and photographed for corrosion and general material condition. Also the aircraft Log Books were review and Flight Data Information was recorded. The non-fogged aircraft were not photographed or inspected at that time. However, non-fogged aircraft Log Books were review and Flight Data Information was recorded. Some hard to access areas of the fogged airframes were inspected via Electronic Bore Scope Camera and Monitor.

In addition, Technical Documentation development was also accomplished during the fogging applications. Such things as Airframe Preparation, Specific Panel Removal Requirements, Sequence of Application of ACF-50 and which application tooling [fogging wands] best suited for each area of the aircraft were identified. The Team also identified specific precautions to be taken to prevent damage to systems. The following are the main precautions that were taken:

- The Parachutes and Seat Pans were removed from the Cockpit to prevent the possible intrusion of the CPC which could cause parachute fabric to stick together and/or also contaminate emergency rations located in the Seat Pan. The cockpit and also the internal avionics tunnel were not fogged. These areas are occupied by the crew during flight.
- The LOX [Liquid Oxygen] Bottle was removed from its compartment. The LOX Lines were seal with double plastic bags. Initial fogging of ACF-50 was accomplished inside the LOX Compartment. However, R&M has determined that even though ACF-50 leaves no residue from fogging; safety precautions would dictate that petroleum products should not be in close proximity to Liquid Oxygen. All future fogging of the S-3B will be accomplished with the LOX Compartment Door Closed
- The FLIR [Forward Looking Infrared] was extended and the FLIR Optical Lens was masked to protect its special coating.
- The ES-3A contains a number of Avionic Boxes with very close tolerance Digital Membrane Pads. During the Proto-type fogging of this T/M/S, the Team masked these pads as a precaution in the event any of these membranes may have had pre-existing damage.

Another point R&M wishes to highlight; ACF-50 is authorized under MIL-C-81309 for both Class II and Class III applications. As a result, no other precautions were required with regard to electrical systems or equipment. One area that Lear Chemical identifies for General Aviation Aircraft is that if the aircraft contain an Auto Pilot that uses friction pads; these pads should be masked [protected from CPC intrusion].

During the fogging of all S-3Bs, R&M tracked the Elapsed Maintenance Time required to Fog each aircraft. In addition, the amount of ACF-50 consumed was also recorded. The Team also tried to determine the optimal number of Maintenance Personnel required to accomplish the most efficient application flow. Based on these engineering evaluations the following information applies:

- The optimal number of maintenance personnel needed to accomplish the efficient fogging of an S-3B is 4.
- The average number of hours required to fog an S-3B is 4 Hours
- The average amount of ACF-50 consumed during the fogging of an S-3B is 12 liters.

One other Technical Modification the Team made was to the S-3 Maintenance Requirement Cards [MRC] Deck, NA 01-S3IMC-6-3. With regard to lubrication requirements after the Special 14 Day Aircraft Washing/Cleaning requirements. R&M locally modified the pertinent Maintenance Requirement Cards to require the use of ACF-50 in aerosol cans in-lieu-of MIL-C-81309 and VV-L-800. These locally modified requirements primarily effect such items as piano hinges and electrical cannon plugs. Finally, as a Lessons Learned precaution from the ES-3A proto-type, WINGLANT and WINGPAC S-3B's were fogged outdoors at the Squadron's Wash Racks. This was done so the first, any dripping CPC from the airframe would be contain. And secondly, dispersion of the CPC in Hanger Spaces would not occur.

One of the major Lessons Learned during the fogging evolution is that although ACF-50 can be washed off with soap & water; it is still a viable product for use in aircraft Wheel Wells, Wing & Fin Fold Wells and Bomb Bays. The reason being is that although the CPC will be washed off of the surfaces of these areas during the aircraft's next 14 Day wash interval, the CPC has been applied via direct pressure spraying in these areas. What this application does is that

the capillary action of the CPC wicks its way into all the cracks and crevices and under nuts, bolts, joints, rivets etc. and displaces any moisture that may be present. The capillary action has a direct impact on inhibiting corrosion at internal/external boundaries of the airframe structure. This phenomenon impacted corrosion percentage calculations and will be discussed further in the Inspection and Evaluation paragraphs of this paper. In addition, during the aircraft's next 14 Day wash interval, the CPC remains in place to continue to block the intrusion of moisture.

The following are a number of other Lessons Learned concerning application Equipment. R&M would like to point out that all tooling problems identified and recommendations made during the fogging evolution at WINGLANT in June 2000 were taken for action by Lear Chemical. By the time the WINGPAC aircraft were fogged in October 2000, all the identified modifications to tooling had been accomplished and these modified tools were supplied to both Wings at no additional cost to the government.

- The 25 foot hoses that run from the Pump to the Spray Gun were extended to 35 ft. On two of the WINGLANT aircraft, the Fins were unable to be folded and the Team was unable to Fog the Fin Tip without manually elevating the Pump System.
- The 5 wheel catty that the Pump System sits in was unstable in an operational ramp environment. The wheels were too small and they were spaced too close together. As a result, Lear Chemical replaced the 5 wheel catty with a Two Wheel Cart System.
- The Brass Quick Disconnects [QDs] that the Pump System initially used were too soft for a military environment. Lear Chemical replaced most of them with Steel QDs.
- The Cone Head QD Nozzle [about ½ inch in thickness and the diameter of a quarter] that was used to Fog the Wheel Wells, Wing & Fin Butts and Bomb Bays was inadvertently shot into the interior bilges of the Bomb Bay Door on one of the Fogged Birds. This

Nickel Plated Brass Fitting, FOD [Foreign Object Damage], took a Boring Tool and a number hours to retrieve and then patch the door. As a result, Lear Chemical has installed a lanyard on this one fitting to prevent future FODing.

- Lear Chemical also provided us with an experimental fogging wand for testing. The team found this experimental wand to be one of the most useful tools used during fogging. The tool was excellent for fogging into drain holes. The Team identified that if another foot was added to the wand hose; it would be perfect. Lear Chemical has accomplished the modification and supplied one to each Wing.
- During the WINGLANT Fogging, one of the Plastic Hose Flex Wands crimped [folding crease] at its QD. Lear Chemical Improved the design by installing a 6 inch length of spring at the QD to prevent this crimping. Lear Chemical has also supplied these to each WING.

During the third day of fogging aircraft at WINGLANT, the Team fogged an S-3B that was undergoing an Integrated Maintenance Concept [IMC], Planned Maintenance Interval [PMI]. The Horizontal Stabilizer was off this aircraft for an In Service Repair for major corrosion of the Stab's Rear Spar. The Stab was on a stand and there was no rear spar installed. As a result, the entire interior structure of the Stab was open for visibility. This Stab was fogged as we had accomplished on the 6 previous aircraft. We were able to identify that we were not getting adequate atomization for complete distribution of the CPC through out the internal structure. By experimenting with the shop air pressure into the pump and the atomization pressure at the spray nozzle; we were able to determine the optimum settings for best atomization pressure was 80 psi shop air in and 400 psi out, at the nozzle. Because of this Lesson Learned, the Team has used these pressure setting on all of the additional S-3Bs that have been fogged to date.

CORROSION INSPECTION & EVALUATION

The S-3B has the following Routine Maintenance Cycles: Daily, Turnaround, 7, 14 & 28 Day Inspections. In addition the Viking has an additional Maintenance Cycle of 308 Days, 616 Days and IMC PMIs. The PMIs are broken into 3 "Phases". Each Phase addresses different specific areas of the aircraft. A PMI is accomplished every 616 Day. The Daily through 616 Day Maintenance Cycles are accomplished by Organizational and/or Intermediate Level Maintenance Personnel only. The IMC PMIs are accomplished by all three Personnel Maintenance Levels; O, I and D. During the 308 Day Maintenance Cycle, the MRC Deck identifies a thorough Corrosion Inspection of the entire Weapon System. These Corrosion Inspection requirements are identified in Card 65 Series of NA 01-S3IMC-6-3.

Each S-3B that was part of the ACF-50 Operational Evaluation was at a different point in its 308 Day Maintenance Cycle. None of the fogged nor non-fogged aircraft were purposely based lined. Some of the S-3Bs were at the beginning of their 308 Day Maintenance Cycle. Some of the S-3Bs were in the middle and some were at the end of their 308 Day Maintenance Cycle. As each S-3B reached its 308 Day Inspection interval; R&M requested that specific Operational Data and all corrosion inspections results be reported to them by each VS Squadron via the squadrons appropriate WING. R&M has received all of these reports for the 8 Fogged and 5 Non-Fogged S-3Bs assigned to WINGLANT. With regard to the 8 Fogged and 7 Non-Fogged S-3Bs at WINGPAC, R&M has only received 50% of the reports to date. However, R&M was able to retrieve NALCOMIS, Equipment Condition Analysis [ECA], Malfunction [MAL] Code 170 [MAL Code 170 is Corrosion] Data, for the 10 month period from October 2000 to July 2001. As a point of information; within the Naval Aviation Maintenance Program, anytime maintenance is accomplished on aircraft, that maintenance must be documented using what the

Navy calls a Maintenance Action Form [MAF]. Contained on these MAFs are specific data areas the require entries. One of these data areas requires the type of Malfunction that is being addressed. Corrosion is one example. Cracked, Broken, Out of Adjustment, etc. are other types of malfunction examples. As a result, engineering is able to query the MAF Reporting Data Base that is located in NALCOMIS and retrieve the number of specific MAL Code hits an aircraft may receive during an identified period of time.

The type of Operational Data that R&M was requesting were such thing as total number of flight hours flown during the evaluation period. Other Operational Data that was collected were the number of catapult launches accomplished and also the number of arrestments completed during the evaluation period. This Operational Data allowed R&M to better understand each S-3B's, by BUNO, usage and environment experienced during the evaluation period. From WINGLANT, 4 of the Fogged and 4 of the Non-Fogged aircraft belonging to VS-30 deployed to sea for 6 months starting in July 2000. The 4 Fogged and 1 Non-Fogged aircraft belonging to VS-24 remained at Jacksonville during the entire evaluation period. From WINGPAC, 4 of the Fogged and 4 of the Non-Fogged aircraft belonging to VS-29 deployed to sea for 6 months starting in November 2000. The 4 Fogged and 3 Non-Fogged aircraft belonging to VS-33 remained at North Island for 6 months after fogging and are now operationally deployed. Because of these current Operational Commitments, R&M has only received 50% of the reports on the WINGPAC aircraft. R&M intends to incorporate additional VS-33 data into R&M's ACF-50 evaluation as it becomes available.

Other factors that have had an impact on the data that is being complied is that some S-3Bs have been transferred to other squadrons. Some of the evaluation S-3Bs underwent an IMC PMI during the evaluation period. Also, some of the squadron personnel that were involved in the

initial ACF-50 developmental work have now rotated to other activities. And, new squadron personnel have had to pick up the reporting requirements with very little or no background information on what is attempting to be accomplished. All of these items have had some degree of impact on the overall program. However, R&M is making every attempt to ensure that all collected data properly reflect what has actually occurred and is as accurate as possible.

Another point that R&M wishes to make is that through our total evaluations, we have determined that ACF-50 has impacted what we have identified as Airframe Structural Boundaries. What is meant by this is that because of the active capillary action of the CPC wicking its way throughout the entire aircraft structure, those area of the structure that did not receive a direct application of the CPC, are still experiencing benefits from this active CPC. Over the operational life of naval aircraft, NAVAIR Engineering has determined that the majority of corrosion initiates at structural interfaces. A structural interface is where two pieces of an aircraft structure come together. These interfaces primarily see corrosion because of moisture. Moisture can be trapped in these area which creates an active conduit for a corrosion cell.

During the review of the corrosion data collected, a question arose as to whether R&M should only count the Corrosion hits against those areas that received an application of ACF-50. Or, whether all corrosion hits, external as well as internal, should be considered in the final percentage calculation. Because the corrosion percentage calculations that were accomplished during the ES-3A proto-type used total corrosion numbers; R&M wishes to remain consistent with the current aircraft being evaluated. However, R&M also wishes to emphasize that if only the corrosion hits applicable to the those areas of the airframe that were Fogged were counted;

the percentage of corrosion between Fogged and Non-Fogged S-3Bs would be substantially higher in favor of the Fogged airframes.

After review of all the data that was available to R&M, final calculations indicate that the Fogged WINGLANT S-3Bs had **31.6%** less corrosion then Non-Fogged S-3Bs. In addition, R&M calculations have reflected that the Fogged WINGPAC S-3Bs had **37.5%** less corrosion then Non-Fogged S-3Bs.

One other final point that R&M wishes to emphasize is that during this entire operational evaluation of ACF-50; not one negative feedback was received by the S-3FST. The CPC, ACF-50 had no negative impact with regard to paint adhesion, seal deterioration, loosening of faying surfaces or any other type of material degradation to date.

SUMMARY AND RECOMMENDATIONS

R&M has accomplished a Reliability Centered Maintenance [RCM] Analysis on all of the data that has been complied on the ACF-50 Operational Evaluation. Some of the questions that R&M asked during this evaluation are:

- **Is there a return on our investment?** Or more clearly stated, is there a return to the Navy if the routine application of the CPC, ACF-50, is incorporated into the S-3B's Maintenance Plan? Cost analysis shows that there is an initial cost investment for the Heavy Duty Application System #90032 of $2450.00 Ea. This cost is derived from the 2001-2002 GSA Contract Consumables amount to approximate 12 liters of CPC from a 20 liter pale, NSN: 8030 01 438 4086-ACF-50, at a cost of $307.45 per 20 liter pale. These costs also come from the 2001-2002 GSA Contract And finally the cost of a case aerosol cans, NSN: 8030 01 438 4079-ACF-50, used at the Special 14 Days interval for

spot application at a cost of $119.73 per case. In addition, there is the Maintenance Man-Hours [MMHRS] cost of the application of ACF-50 on one S-3B. This amounts to the organization labor cost of 4 fleet sailors times approximately 4 MMHRS per S-3B. Or, the cost to fog one S-3B of approximately $200 in ACF-50 bulk material cost. Plus, approximately $300 in ACF-50 Aerosol material cost to maintain the aircraft every 308 Days. The Organizational Labor cost amounts to approximately $1000. **These totals amount to approximately $1500 in Labor and Material Costs per S-3B fogged every 308 Days.** The initial investment of $2450 for the Heavy Duty Application System can be pro-rated over a period of time. For the purpose of this ACF-50 Evaluations, the AERMIP Program Office purchased one application system for each WING. In addition the AERMIP Program Office purchased enough bulk and aerosol ACF-50 to fog and maintain the 16 Fogged S-3Bs for the evaluation period. It is the recommendation of R&M that there be a minimum of 2 Heavy Duty Application Systems at each Naval Air Station. This allows for aircraft to still be fogged if one system should be down for parts. Maintenance requirements for the application system are negligible.

- **Will the incorporation of the routine application of the CPC, ACF-50, increased or decreased the Organizational Level Maintenance Workload [Corrosion Control MMHRS]?** Additional impact on O-Level Maintenance requires the new need to apply the CPC, ACF-50, after each Special 308 Day Inspection and also at the completion of each IMC Planned Maintenance Interval. However, base on the percentage seen during the R&M ACF-50 evaluation; the trade off is a substantial reduction in total Corrosion Control MMHRS.

- **Have or will other levels of Maintenance [Intermediate and/or Depot] be impacted by the routine application of ACF-50 on the S-3B Weapons System?** Again, base on the percentage seen during the R&M ACF-50 evaluation; the trade off is a substantial reduction in total Corrosion Control MMHRS at all levels of maintenance.
- **What impacts will be made on O/I/D Material requirements and cost by the routine application of ACF-50 on the S-3B Weapons System?** Again, base on the percentage seen during the R&M ACF-50 evaluation; it becomes quite apparent that the potential material cost saving should be substantial at all levels of maintenance. If there is a reduced requirement to replace aircraft structure, aircraft material or system components, due to corrosion; logic dictates that material cost should be less.

Based on our Fleet Supports Teams analysis; R&M's recommendation is that the use of the CPC ACF-50 be incorporated into the S-3B's regular Maintenance Plan at the earliest possible date. In closing, the R&M Team would like to reiterate a quote from one of the VS Squadrons Maintenance Control Chief's that was made during the ACF-50 evaluation. The quote reads:

"ACF-50 Is Not a Silver Bullet. However, It Is a Very Useful and Productive Tool That Enhances the Ability of Our White Hats to Maintain Our Fleet Assets at an Acceptable Operational Level!"

FAILURE ANALYSIS OF A HELICOPTER EXTERNAL FUEL-TANK PYLON

John A. Newman
U.S. Army Research Laboratory
Vehicle Technology Directorate,MS 188E
Hampton, VA 23681

Robert S. Piascik
NASA Langley Research Center
Metals and Thermal Structures Branch, MS 188E
Hampton, VA 23681

Richard A. Lindenberg
U.S. Coast Guard Aircraft Repair and Supply Center
Elizabeth City, NC 27906

ABSTRACT

An eight-inch-long (0.2 m) crack was found in an external helicopter fuel-tank pylon. The damaged pylon was removed from service and analyzed at NASA Langley Research Center to determine the cause of the crack. Results of the analysis revealed that crack initiation occurred at corrosion pits in a fastener hole and crack propagation was a result of fatigue loading.

INTRODUCTION

At the U.S. Coast Guard air station in Elizabeth City, North Carolina, an eight-inch-long (0.2 m) crack was found in an external fuel-tank pylon of a HH-60 “Jayhawk” helicopter. External fuel tanks are used to extend the range and operation times of U.S. Coast Guard (USCG) helicopters and are fastened to pylons attached to the helicopter fuselage. Fuel-tank pylons are fabricated from 7075 aluminum alloy forgings that are machined into the final configuration. The HH-60 is capable of carrying three external pylon-drop fuel tanks: one 80-gallon (300 L) tank and two 120-gallon (450 L) tanks. The crack was found in a 120-gallon tank pylon. Photographs of a Coast Guard HH-60 helicopter are shown in Figure 1. The photograph of the entire helicopter fuselage in part (a) shows the location of a 120-gallon fuel tank. As seen in part (b), the pylon that connects the fuel-tank assembly to the fuselage is normally covered and

hidden from view. A photograph of a fuel-tank pylon is shown mounted to the fuselage in part (c); the pylon is visible because the covering has been removed for inspection.

The failure analysis reported herein concentrated on finding evidence of fatigue loading and/or corrosion that could lead to cracking of the fuel-tank pylon. Helicopter components are known to experience fatigue (cyclic) loading resulting in possible fatigue cracking.[1, 2] Additionally, USCG helicopters are routinely exposed to corrosive marine environment and cracking may be exacerbated by environmental-load interactions that produce brittle crack growth resulting from stress corrosion cracking and/or corrosion fatigue.[3] After the crack was detected, the damaged pylon was removed from service and shipped to NASA Langley Research Center in Hampton, Virginia for detailed destructive examinations to determine the cause of cracking.

INITIAL VISUAL INSPECTION

A photograph of the cracked pylon is shown as Figure 2a. The left curved-side of the pylon was mounted vertically to the helicopter fuselage; the arrow in the upper-right corner of Figure 2a indicates the vertical-up direction. The fuel-tank assembly was attached to the pylon through the two holes on the far right side of Figure 2a. Loads applied to the pylon are nominally expected in the vertically downward direction, applied at the end of the horizontal (cantilever) portion of the pylon, creating high bending stresses in the corner region of the pylon as indicated in Figure 2a. The crack appears to have initiated at fastener holes in this high stress region and propagated in a vertically downward direction. Eventually the crack propagated into a vertical stiffener and appeared to have arrested. Figure 2b is a more detailed view of the crack region outlined in Figure 2a. The dashed line in Figure 2b parallels the crack from the apparent region of crack initiation (fastener holes in the upper flange) to crack arrest at a vertical stiffener.

The top of the pylon upper flange, in the crack initiation region, is shown in Figure 3a. Here, the crack is seen bisecting two fastener holes, each $^{3}/_{16}$-inch (4.8 mm) in diameter; presumably, the crack initiated at one of these holes. The bottom surfaces of the upper flange near these fastener holes are shown in Figures 3b and 3c. The two smaller holes adjacent to the

large hole located on the left of Figure 3a were used to attach the bracket shown in Figure 3b. Results presented later in this paper indicate that crack initiation occurred at the fastener hole shown in Figure 3b.

DESTUCTIVE EXAMINATION

To perform detailed examination of the crack surface, the pylon was broken by carefully applying a load at the end of the horizontal cantilever while the curved vertical portion was locked into position. This loading allowed the horizontal cantilevered portion of the pylon to rotate and fracture the remaining ligament without disturbing the crack surfaces. A photograph of the broken pylon is shown in Figure 4a. Only the crack surface associated with the smaller piece of the pylon was examined; the larger piece was preserved for future examination. A photograph of the crack surface in the upper flange (where crack initiation appeared to occur), and a portion of the web, is shown in Figure 4b. Visual inspection of the crack surfaces revealed dark-colored regions on the crack surfaces, primarily near the fastener holes where the crack appeared to initiate. These dark spots, indicated in Figure 4b, are corrosion products (likely oxide debris) that are typically produced during fatigue crack growth of aluminum alloys in an aggressive environment.[4, 5] A photograph of the crack surface as it propagated from right to left into the vertical stiffener is shown in Figure 5. To the right of the curved final crack front, the fatigue crack surface is covered with a uniform dark colored corrosion product layer. To the left of the crack front, the fracture surface (produced as the cracked pylon was broken) is clean and free of corrosion products.

FRACTOGRAPHY

A more detailed examination of the crack surface was performed with a scanning electron microscope (SEM). The smaller piece of the broken pylon, shown in Figure 4a, was too large for SEM examination and was cut into smaller pieces. First, a single cut was made (indicated in Figure 6a by the dashed line) parallel to the crack so that the entire crack surface was contained in a strip of material approximately 12-inches (0.3 m) long. Five additional cuts were made normal to the crack surface (indicated in Figure 6b with dashed lines) dividing the crack surface into six pieces, each approximately

2-inches (50 mm) long. The six pieces of the crack surface were small enough to be accommodated in the SEM. Care was taken not to cut through regions containing important crack-surface features.

Crack-surface corrosion products made SEM analyses difficult. Therefore, the crack surface was ultrasonically cleaned in a 50% nitric acid (HNO_3) solution for 60-second intervals. After the crack surface was removed from the acid solution, it was thoroughly rinsed with water, and the cleaning procedure was repeated before the crack surface was thoroughly cleaned. (A third 60-second exposure was not needed.) This technique has been used at LaRC to remove oxides from crack surfaces without altering crack-surface features of interest.

Features and characteristics of the crack surface are used to provide information about the history and cause of the crack. The crack-surface features of primary interest to this study are markings that result from crack-tip deformation; herein, called deformation markings. Deformation markings are useful because they indicate the location and shape of the crack front at an instant in time. Crack surfaces produced during constant-amplitude fatigue loading typically have periodic deformation markings that are nearly equally spaced.[6] Where cracks are known to advance during each load cycle, the spacing between these markings (commonly called striations) is the increment of crack advance per load cycle, termed as the fatigue crack growth rate (For aluminum alloys, striated fatigue crack growth (one striation per load cycle) is known to occur for $\Delta K > 7$ MPa$\sqrt{m}$. Multiple load cycles may occur between crack-surface marks at lower values of ΔK.[7, 8]). This is useful because the fatigue crack growth rate can be related to the crack-tip load parameter, ΔK. Most structures (including helicopter pylons) experience irregular variable-amplitude fatigue loading. Complex load interactions occur during variable-amplitude loading, possibly resulting in irregular fatigue crack growth rates or crack arrest (*i.e.*, cracks become non-propagating). In general, it is difficult to distinguish between striation markings (produced as a crack propagates) and crack arrest marks (produced as a crack arrests). Therefore, it is difficult to determine fatigue crack growth rates with deformation markings produced during variable-amplitude loading.[9] Even in cases of complex variable-amplitude loading, a great deal of information about the crack history

can be obtained from crack-surface markings. For example, both striations and crack arrest marks indicate the progression of the crack front, so no distinction between these markings is needed to determine the crack initiation site. During the early stages of crack growth, the crack propagates in radial directions from the crack initiation site producing curved crack-surface markings (concave toward the crack initiation site) that can be used to determine where crack initiation occurred.

SEM examination of the clean crack surface revealed crack-surface deformation markings, evidence that crack propagation was a result of fatigue loading. The majority of the crack surface did not exhibit deformation markings, but those that were found revealed that crack initiation occurred at corrosion pits in the fastener hole of Figure 3b. The photograph of the crack surface in Figure 7a shows the region of crack initiation; crack initiation occurred at the fastener hole in the upper right corner of the figure, highlighted with a box. The crack surface in Figure 7b is a higher-magnification image of the crack initiation region highlighted (box) in Figure 7a. A region of corrosion pitting is noted in Figure 7b along the inside edge of the fastener hole (right side of the photograph). The region of crack initiation noted in Figure 7b is shown at higher magnification in Figure 7c. Corrosion pits are seen as a rough-textured region on the right side of Figure 7c. Deformation markings on the crack surface are barely visible in Figure 7c. The curved dotted line in Figure 7c shows the curvature of the deformation marks (concave to the right) indicating that crack initiation occurred at the corrosion pits seen on the right side of the figure. These marks are better seen at higher magnification in Figure 7d.

SEM images of the crack initiation region of Figure 7 are shown at a different angle in Figure 8 to illustrate the complex nature of the crack surface and to highlight regions of pitting that did not result in crack initiation. Here, the crack surface was viewed at an angle 45^{o} from the direction normal to the crack surface, and the specimen is rotated 90^{o} (with respect to the orientation of Figure 7) so the fastener hole is oriented horizontally. In Figure 8a, the intersection of the crack surface with the edge of the fastener hole is indicated with a dashed horizontal line; the surface of the hole and the crack surface are below and above the dashed line, respectively. The upper and lower surfaces of the upper flange (shown in Figure 3) are the edges seen on the extreme right and left sides of Figure 8a, respectively. The boxes in

Figure 8a identify two regions of corrosion pitting in the fastener hole: one where cracks did not initiate (left box) and one where cracks did initiate (right box). These regions are shown at higher magnification in Figures 8b and 8c, respectively.

Evidence of crack-surface deformation marks at three locations along the crack surface is shown in Figure 9. These three locations, identified in Figure 9a as b, c, and d, are shown at high-magnification in Figures 9b, 9c, and 9d, respectively. The markings observed in Figures 9b and 9c are not equally spaced, possibly suggesting that complex variable-amplitude loading occurred. The deformation markings shown in Figure 9d are equally spaced and exhibit the morphology typical of fatigue striations. The average spacing between deformation markings is determined by counting the number of marks intersecting lines along the crack growth direction (*i.e.* normal to the marks). In Figure 9b, 8 marks are counted along a line 100 μm long. For Figures 9c and 9d, 10 marks and 20 marks are counted along lines 15 μm and 30 μm long, respectively. If each deformation mark was produced by a single load cycle, the average fatigue crack growth rates corresponding to Figures 9b, 9c, and 9d would be 1.2×10^{-5} m/cycle, 1.5×10^{-6} m/cycle, and 1.5×10^{-6} m/cycle, respectively. The markings in Figures 9b and 9c are not regularly spaced and may not have been produced by single load cycles. Therefore, these markings do not permit a good estimation of fatigue crack growth rates. The crack-surface markings seen in Figure 9d are likely striations, each produced by a single load cycle. Therefore, the calculated fatigue crack growth rate of 1.5×10^{-6} m/cycle is likely a good estimate for the crack surface of Figure 9d. Based on laboratory 7075 aluminum data, the fatigue crack growth rate for Figure 9d corresponds to values of ΔK between 15 MPa$\sqrt{m}$ and 20 MPa$\sqrt{m}$.[10, 11]

DISCUSSION

The results of detailed destructive examinations show that crack initiation occurred at corrosion pits that formed in a fastener hole. Corrosion problems are greater for USCG helicopters because they operate in a marine environment where exposure to salt-water spray – known to corrode aluminum alloys

– is likely. Fastener holes create a crevice-like environment that entraps water resulting in a corrosive environment where pitting is likely.[12] Pitting damage is difficult to detect because the damage is highly localized (*e.g*. may be hidden in a fastener hole) and only affects a small amount of material.

The crack found in the fuel-tank pylon initiated at corrosion pits in the region where the highest stresses were expected. As shown in Figure 2a, vertical-downward loading on the pylon creates a high-stress region in the corner where the cantilever meets the vertical portion of the pylon. The stress concentration effect of fastener holes in this region further increases the local stress state near these discontinuities.[13] Finally, corrosion pitting in these fastener holes creates rough surfaces that further increase the severity of the local stress state.[14-16] Due to these three factors (pylon loading, fastener hole geometry, and corrosion pits) the highest local stress occurred at the fastener hole of Figure 3b, the crack initiation site.

Deformation markings on the crack surface were used to identify the crack initiation site. However, care must be taken when using fatigue striations to quantify the fatigue crack growth rate. Researchers have suggested that a single striation may not be the result of a single load cycle.[7, 8] Unpublished research for aluminum alloys by Piascik has revealed similar findings; Paris regime fatigue crack growth ($\Delta K > 7$ MPa$\sqrt{m}$) exhibits single load cycle per striation behavior, but near the fatigue crack growth threshold ($\Delta K < 5$ MPa$\sqrt{m}$) multiple load cycles are required per striation because more complex crack-tip damage processes are operative. As the crack propagated through the webbing, clear evidence of striation markings was found on the crack surface indicating a fatigue crack growth rate of approximately 10^{-6} m/cycle (recall Figure 9d). Test data for similar materials indicates this occurs for values of ΔK between 15 MPa$\sqrt{m}$ and 20 MPa$\sqrt{m}$; in the range of ΔK where each load cycle is expected to produce one striation. Striations in Figures 9b and 9c were not well defined possibly because the values of ΔK were low, *i.e*. near the fatigue crack growth threshold.

The striation markings seen in Figure 9d indicate that rapid crack propagation occurred in the pylon webbing (approximately 1.5 mm of crack growth per 1000 load cycles). As the crack grew,

increases in ΔK and fatigue crack growth rates likely occurred. Pylon failure was prevented because a vertical stiffener deflected the crack causing crack arrest. Cracks tend to propagate in the direction perpendicular to the principal (largest) normal stress, the orientation where the mode I stress intensity factor (K_I) is at its maximum value and the mode II stress intensity factor (K_{II}) is zero.[17] This stiffener likely diverted the crack from principal stress directions, resulting in mixed-mode crack-tip loading (*i.e.* both K_I and K_{II} are non-zero) and a reduction in K_I, the crack driving force. Crack arrest was likely a result of a reduction in crack driving force and crack-face contact due to mode II (sliding-mode) displacements further reducing the fatigue crack driving force.[18, 19] The crack surface corrosion product in Figure 5 were likely produced by sliding-mode contact of rough crack surfaces.

Failure of this pylon was prevented when the vertical stiffener diverted and arrested the propagating fatigue crack. However, prevention of similar cracking problems in the future should focus on preventing the corrosion pitting that lead to crack initiation. In other words, preventing crack initiation (here caused by corrosion pitting) is preferable to, and likely more successful than, relying on techniques to arrest cracks after they develop.

CONCLUSIONS

A failure analysis was performed to determine the cause of an eight-inch-long crack found in a U.S. Coast Guard HH-60 helicopter external fuel-tank pylon. Based on the failure analysis results presented in this paper, it is believed the following sequence of events occurred and resulted in the crack.

1. **Corrosion pitting** – The initial damage occurred when corrosion pits formed in a fastener hole. Fasteners are known to provide a crevice-like environment where entrapped water can form a highly corrosive environment where pitting is likely to occur.

2. **Crack initiation** – Crack initiation occurred in a region of high local stress; at corrosion pits in a fastener hole, near the corner with the highest bending stress; all three factors greatly increases local state of stress.

3. **Fatigue crack propagation** – Crack-surface markings indicate that crack propagation was a result of fatigue, or cyclic, loading. Corrosion products on the crack surfaces suggest that fatigue crack growth occurred in a corrosive environment. The presence of fatigue loading and corrosive environment exacerbates cracking; fatigue cracks contained in 7000 series alloys exposed to air with 90% humidity will continue to grow at extremely low loads.

4. **Crack arrest** – After propagating through approximately 80% of the pylon web, the crack intersected a vertical stiffener and was diverted. Diverting the crack likely lowered the crack-tip driving force resulting in crack arrest.

REFERENCES

1. J.W. Lincoln, in Aeronautical Fatigue in the Electronic Era, ed. A. Berkovits, held June 21-23, 1989 (Warley, UK: International Committee on Aeronautical Fatigue), p. 263.
2. R.A. Everett and W. Elber, Journal of the American Helicopter Society 45 (2000): p. 3.
3. R.P. Gangloff, Environment-Induced Cracking of Metals, eds. R.P. Gangloff and M.B. Ives, (Houston, TX: NACE, 1990), p. 55.
4. S. Suresh, A.K. Vasudevan, and P.E. Bretz, Metallurgical Transactions 15A (1984): p. 369.
5. A.K. Vasudevan and S. Suresh, Metallurgical Transactions 13A (1982): p. 2271.
6. C. Laird, Fatigue Crack Propagation, ASTM STP 415 (Philadelphia, PA: ASTM, 1967), p. 131.
7. D.L. Davidson and J. Lankford, International Materials Review 37 (1992): p. 45.
8. H.J. Roven, M.A. Langoy, and E. Nes, in Fatigue ’87, vol. 1, eds. R.O. Ritchie and E.A. Starke (West Midlands, UK: England Engineering Materials Advisory Services, 1987), p. 175.
9. J. Schijve, Fatigue and Fracture of Engineering Materials and Structures 22 (1999): p. 87.
10. P.E. Bretz, R.J. Bucci, R.C. Malcolm, and A.K. Vasudevan, Fracture Mechanics: 14th Symposium, ASTM STP 791 (Philadelphia, PA: ASTM, 1983), p. II-67.
11. C.S. Oh, and J.H. Song, International Journal of Fatigue 23 (2001): p. 251.

12. M.G. Fontana, Corrosion Engineering, 3rd ed. (New York, NY: McGraw Hill, 1986), p. 51.

13. S. Suresh, Fatigue of Materials (Cambridge, UK: Cambridge University Press, 1991), p. 272.

14. P.S. Pao, S.J. Gill, and C.R. Feng, Scripta Materiallia 43 (2000): p. 391.

15. K.K. Sankaran, R. Perez, and K.V. Jata, Materials Science and Engineering A297 (2001): p. 223.

16. G.S. Chen, K.C. Wan, M. Gao, R.P. Wei, and T.H. Flournoy, Materials Science and Engineering A219 (1996): p. 126.

17. F. Erdogan and G.C. Sih, Journal of Basic Engineering, December (1963): p. 519.

18. E.K. Tschegg, Acta Metallurgica 31 (1983): p. 1323.

19. X. Yu and A. Abel, Fatigue and Fracture of Engineering Materials and Structures 23 (2000): p. 151.

FIGURES

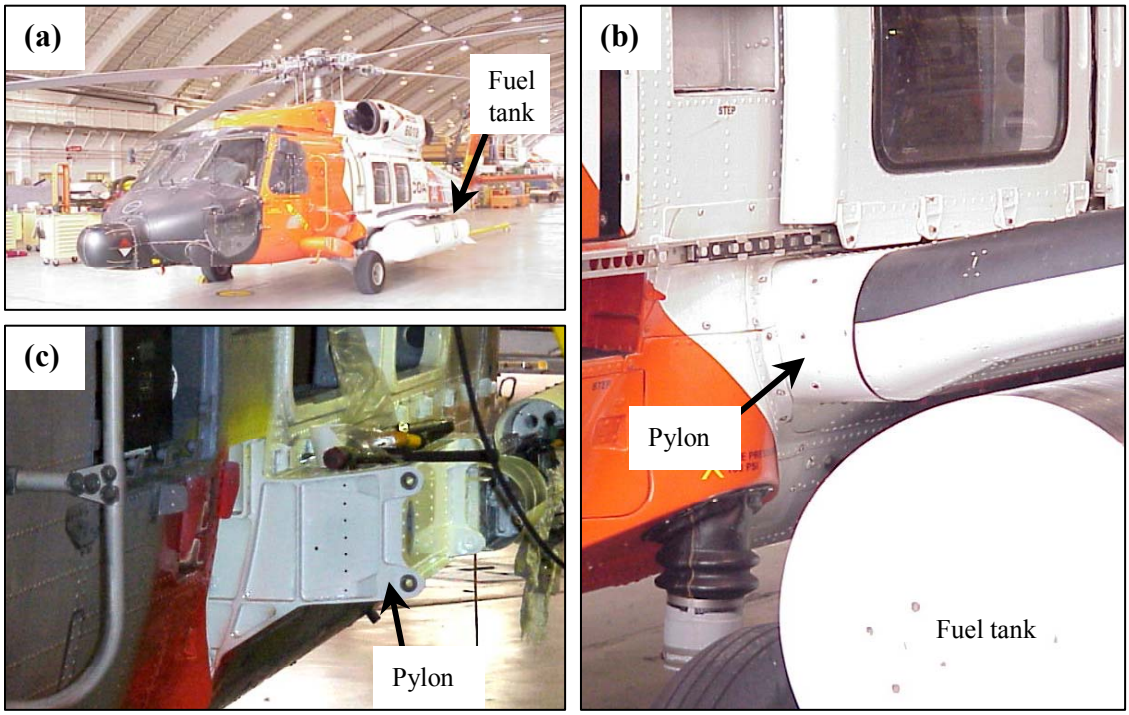

FIGURE 1. Photographs are shown of the external pylon-mounted fuel-tank assembly on the HH-60 helicopter. (a) A 120-gallon fuel tank is shown on the fuselage. (b) A more detailed photograph of the fuel-tank pylon attachment is shown. (c) A pylon is seen after the fuel-tank assembly was removed for inspection.

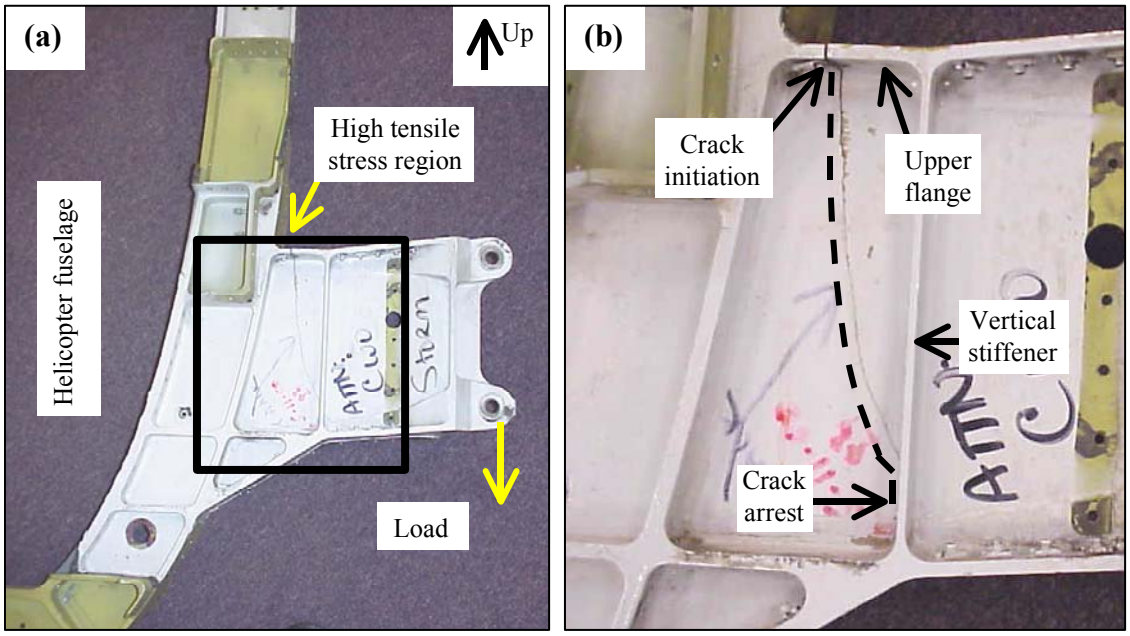

FIGURE 2. Photographs of the cracked pylon are shown. (a) A photograph of most of the pylon is shown. (b) A more detailed image is given of the cracked region.

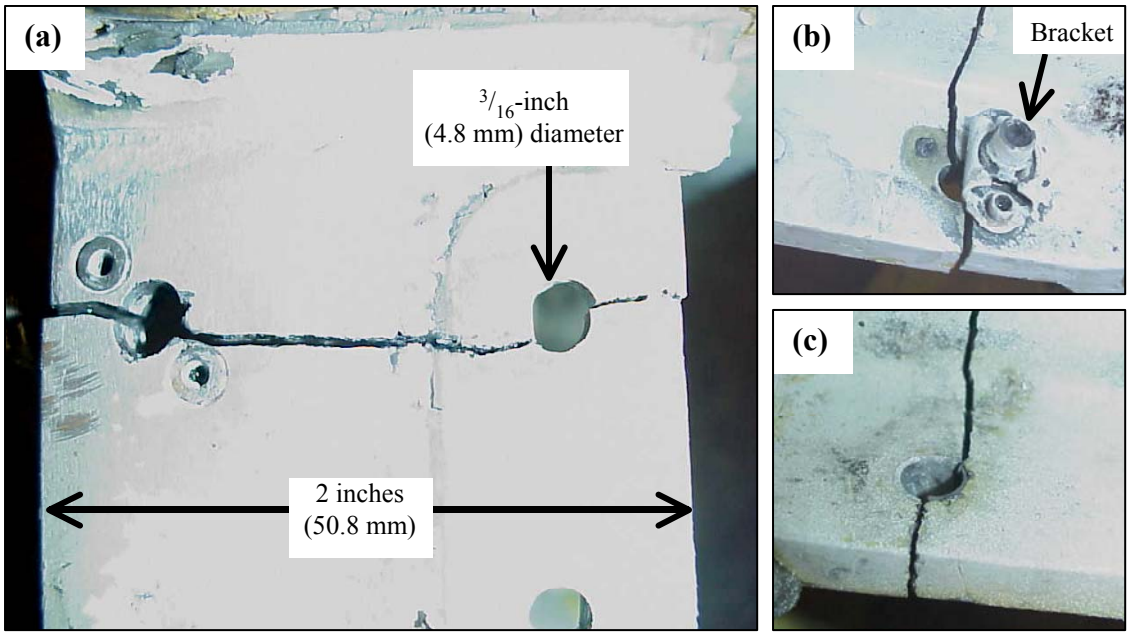

FIGURE 3. Photographs of the crack initiation region are shown. (a) A photograph of the crack intersecting two fastener holes on the top of the upper flange is shown. (b) The fastener hole on left of (a) is shown from the underside of the flange. (c) The fastener hole on right of (a) is shown from the underside of the flange.

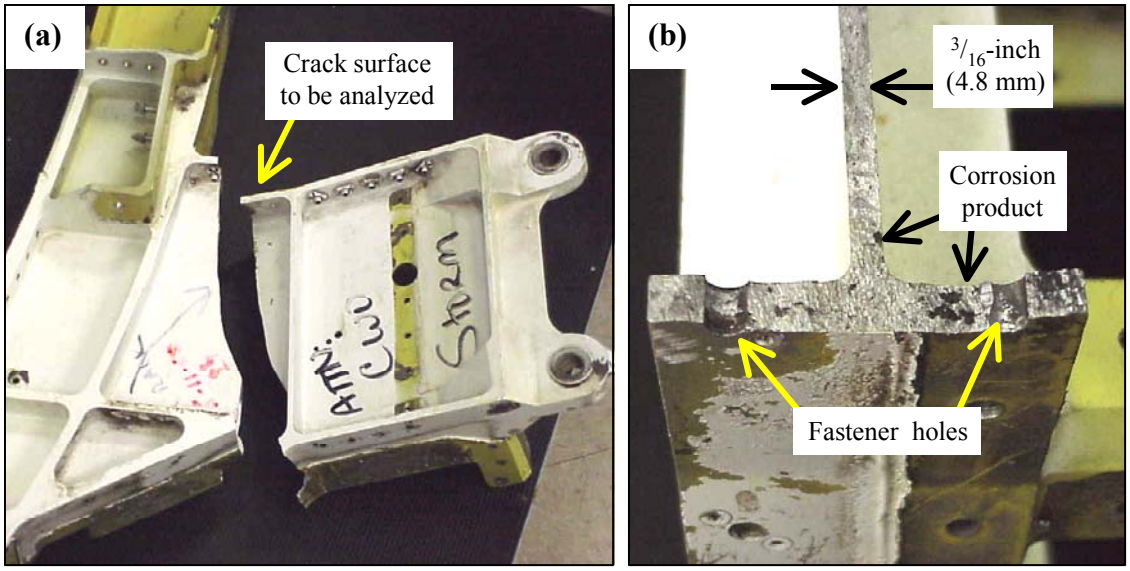

FIGURE 4. Photographs of the broken pylon are shown. (a) A photograph of the broken pylon is shown. (b) A detailed photograph is given of the crack surface in the crack initiation region.

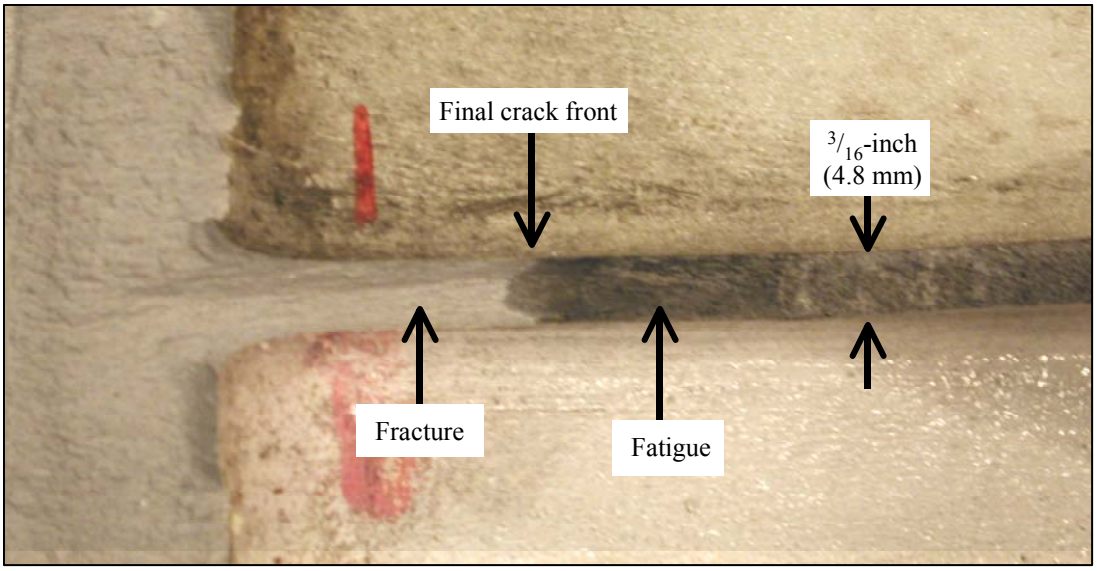

FIGURE 5. A photograph of the crack surface as the crack propagated into the vertical stiffener is shown.

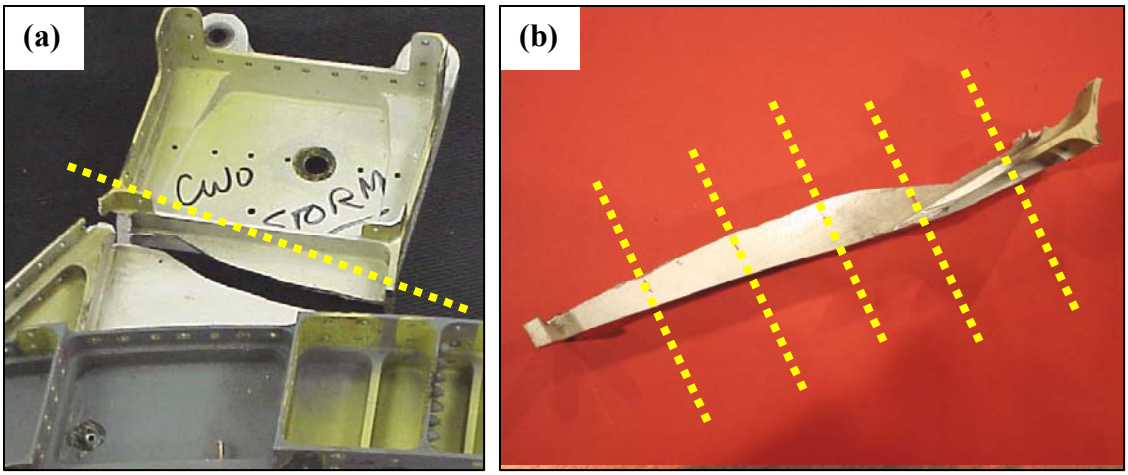

FIGURE 6. Two photographs are shown to illustrate how the broken pylon was cut for SEM analysis. (a) The first saw cut removed the crack surface from the pylon. (b) The crack surface was then cut into six smaller pieces.

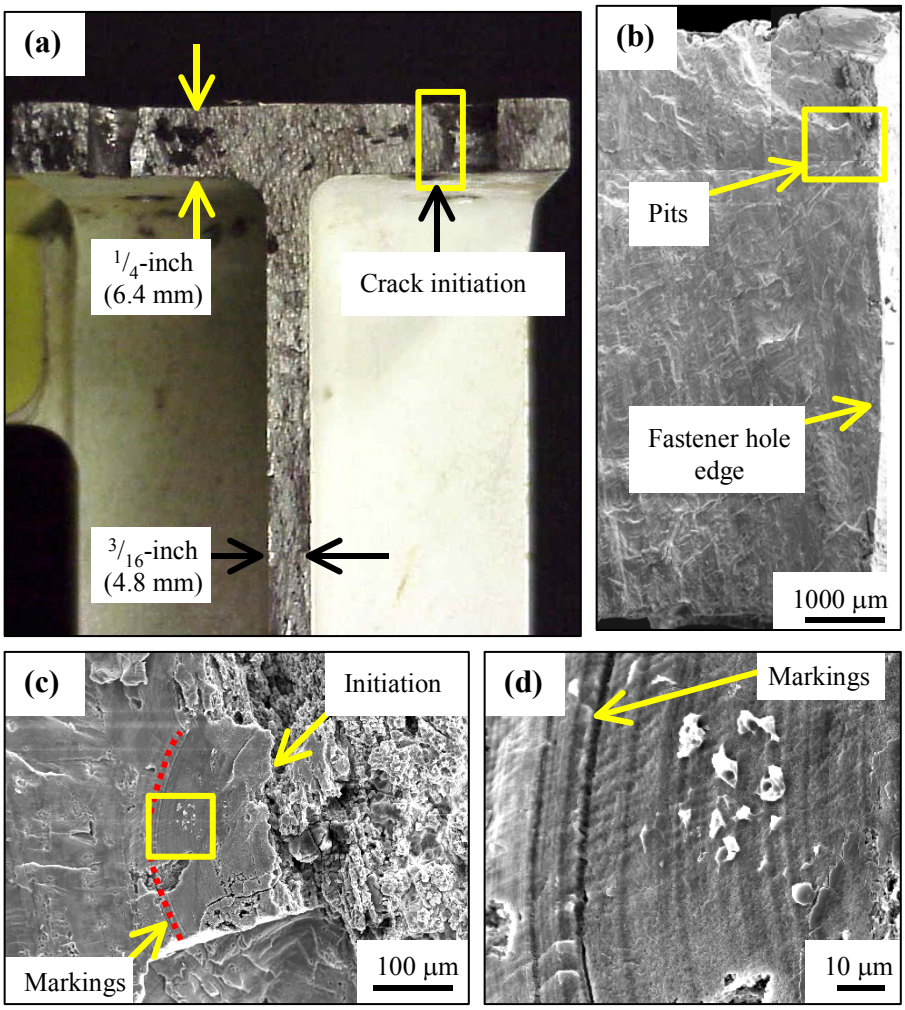

FIGURE 7. The crack initiation region is shown in a series of images, at increasing magnification. (a) Photograph of the crack surface in the pylon upper flange region is shown. Also shown are micrographs of (b) crack surface at edge of fastener hole surface, (c) crack initiation at corrosion pits, and (d) crack surface markings at high-magnification in crack initiation region.

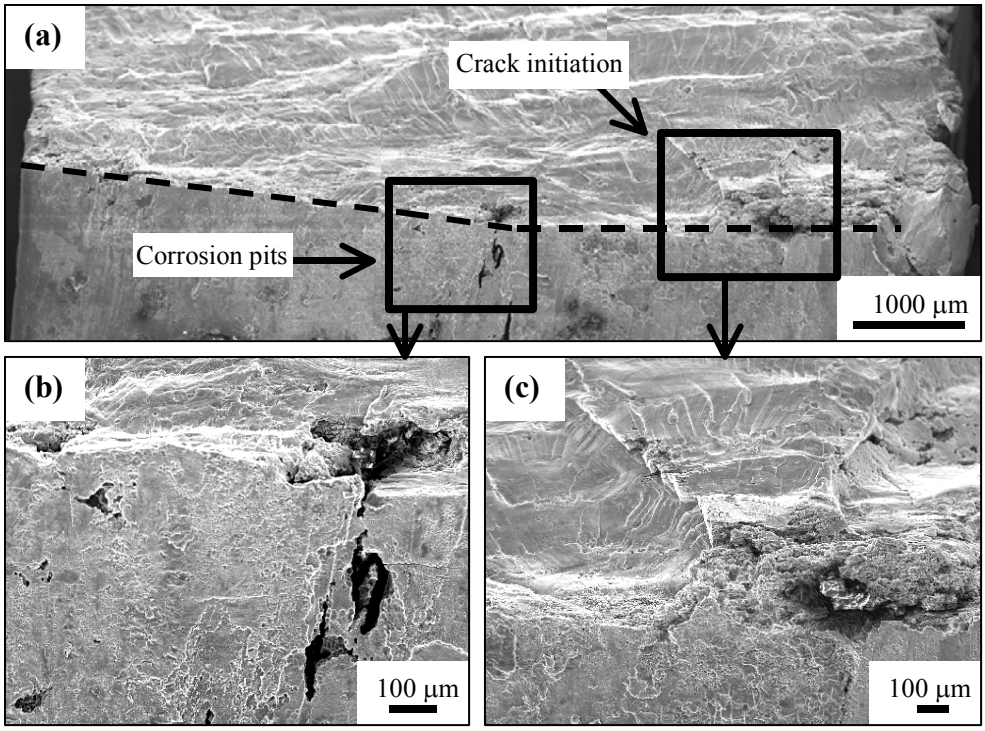

FIGURE 8. Micrographs of the crack initiation region, viewed at a 45^{o} angle to the crack surface, are shown. (a) The crack surface at the edge of the fastener hole surface is shown. High-magnification micrographs are shown of corrosion pits (b) where cracks did not initiate and (c) where cracks initiation occurred.

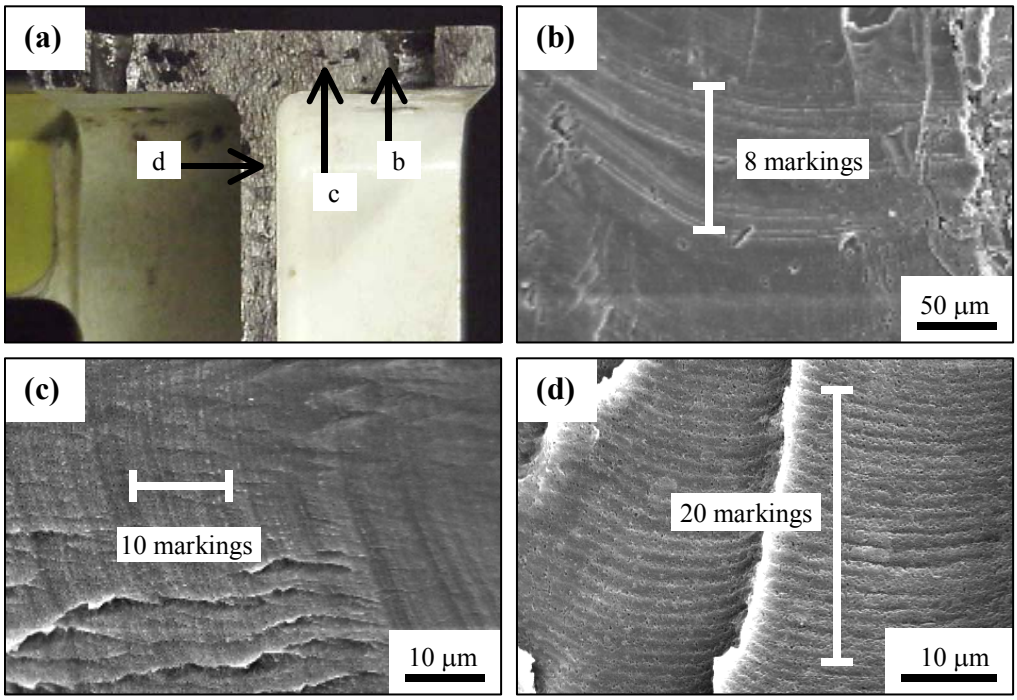

FIGURE 9. Micrographs of crack-surface markings are shown at high magnification. (a) A photograph of the crack surface in the pylon upper flange region is shown. High-magnification micrographs are shown of the crack surface (b) near the crack initiation region, (c) between the fastener hole and the web, and (d) in the pylon web.

INTEGRATED CORROSION AND MATERIAL DEGRADATION PREVENTION SOLUTIONS—ENHANCING READINESS, PROTECTING EQUIPMENT, PREVENTING POLLUTION, AND LOWERING LIFE-CYCLE COST

James H. Martin

LOGIS-TECH,inc.
5775 Barclay Drive, Suite #4
Alexandria, Virginia
22315-5710

ABSTRACT

This paper covers a core maintenance technology that arrests atmospheric material degradation: Controlled Humidity Protection (CHP) systems. Naval Aviation and Army National Guard doctrine cite Controlled Humidity Protection (CHP) as the preferred method of equipment and weapon system protection. The Army Reserve is reengineering their equipment management doctrine to take advantage of CHP applications. The most widely installed CHP applications in the U.S. military are Environment Stabilization Systems (ESS®). These systems stop corrosion and other moisture-related material degradation, enhance readiness, reduce maintenance costs and improve equipment reliability. ESS® allows customers to redesign their maintenance programs for maximum efficiency based on operational requirements and capability. The benefits of ESS® include corrosion prevention, improved wiring insulation performance, mold and mildew prevention, pollution prevention, hazardous waste stream reduction, and reduced manpower requirements. The success of controlled humidity systems in military application resulted in ESS® being offered by the Army National Guard and Navy under Indefinite Delivery Indefinite Quantity (IDIQ) contract vehicles. The Department of Defense Inspector General, the Government Accounting Office and the Center for Naval Analysis completed studies that documented a Return on Investment (ROI) of up to 8:1 on installed, operational systems.

INTRODUCTION

Dynamic dehumidification applications prevent and suppress atmospheric corrosion and other moisture-induced materiel degradations.

Corrosion can be defined as a natural degradation of engineering materials due to interactions with the environment. For metals and alloys most corrosion is an electrochemical

process. Although usually associated only with metals and alloys, degradation of non-metallic materials is more and more being considered corrosion. Degradation can occur to physical, performance or aesthetic characteristics of a material.

There are three disciplines in corrosion control: prevention, detection, and treatment. Investment in prevention pays the highest dividends by lowering the resource requirements for detection and treatment.

The discipline of corrosion prevention includes corrosion suppression: stopping corrosion from progressing.

Four core processes are available for corrosion prevention and suppression: dynamic dehumidification, coatings and compounds applications, anodic and cathodic protection, and materials selection and treatment.

Dynamic dehumidification has been recognized as an effective method to preserve and protect weapon systems and used by many countries since the 1930s. It was initially used to preserve equipment that was planned to be out of service for long periods, such as mothballed ships and propositioned equipment. The use of dehumidification on operational equipment or short-term rotation of equipment began in several countries during the past fifty years. The development of more cost-effective dehumidification equipment has increased the use of this technology.

In many United States Department of Defense weapons and equipment applications, dynamic dehumidification is often referred to as Controlled Humidity Protection or Controlled Humidity Preservation, or “CHP”.

FACTS

Battelle Labs reports that corrosion costs to the United States economy exceed $300 billion per year. Sandia National Labs reports that corrosion is the leading cause of weapons stockpile degradation. The Army Material Command reports that corrosion damage in DOD exceeds $10 billion per year. The Air Force Corrosion Prevention and Control Office reported FY97 aircraft corrosion cost $800 million. The Naval Air Systems Command reported Navy/USMC aviation corrosion costs of $1.2 billion in FY99 and $1.4 billion in FY01, stating corrosion was their largest single cost driver. Navy/USMC also expends up to 2 million man-hours per year at the organizational maintenance level to troubleshoot and repair aircraft wiring system problems. All services report that corrosion-related processes are their greatest source of hazardous waste.

SCIENCE BEHIND CONTROLLED HUMIDITY PROTECTION (CHP)

The most prevalent form of atmospheric corrosion and material degradation is moisture-induced and abetted. Relative humidity (RH), temperature, dew point, heat content of surfaces, time-of-wetness, and the daily transient profiles and interactions of these properties play a key role in moisture-induced damage.

Relative humidity alone has a profound effect on corrosion rates. Corrosion starts when the surrounding relative humidity is higher than 45% RH. Above 50% RH the corrosion rate of ferrous metals increases exponentially.[1] Some non-ferrous metal at relative humidity rises also exhibits increased rates of corrosion: brass, nickel copper, zinc, and copper. In the United States, the relative humidity exceeds this critical level more that 90% of the time. Pollutants tend to shift Vernon's curve to the left making corrosion rates increase even more. Even in most desert climates the relative humidity peaks above 50% daily during the period of midnight to 9:00 a.m.

Due to the high thermal energy retention of many weapons systems, this daily cycle causes tremendous amounts of condensation and exacerbates the time-of-wetness contribution to the corrosion problem.

Salts and electrolyte combine near the seacoast to increase corrosion.[2] Salt collection rates and weight loss of AISI 1008 steel charted nearly parallel patterns of exponential increase as the seacoast was approached. Nearly flat from 200 miles to only 2 miles proximity, the curves sharply increase between 3000 to 1000 feet from the coast, increasing even more steeply approaching 100 feet from the sea.

Selecting a controlled humidity band of 30% RH to 40% RH provides optimal protection to materials in military weapons and equipment: steels, non-ferrous metals, gold contacts, wire insulation, elastomers, electronics, fuels and lubricants.

A protective relative humidity of 35% is normal for electronics.[3] More humidity causes corrosion and less humidity causes static electricity problems. Environmental variables have a significant effect on failure rates displaying an exponential corrosion-related failure rate above 50% RH similar to that for metals.[4]

Corrosion attacks on gold plating used for contacts on circuit boards have been quantified, showing that a dramatic increase occurs above 50% relative humidity.

Military Specification (MILSPEC) avionics and electronics are sensitive to moisture.[5] These include conformal-coated hermetically sealed parts. As these systems are replaced with commercial grade plastic encapsulated integrated circuits and discrete semiconductors, sensitivity to moisture will increase.

High relative humidity causes electrical current leakage and corrosion in avionics. [6]

Relative humidity-induced wire insulation performance degradation causes costly problems. A wiring system's insulation resistance is inversely proportional to the relative humidity. Reduced insulation resistance lowers insulating performance and causes faulty signals, stray currents, and results in false component removals that result in no-fault-found at higher maintenance levels. For example, a PVC insulation's designed resistance of 10^{14} ohms (Ω) begins to sharply deteriorate as the relative humidity exceeds 50%, dropping to 10^{12} Ω at 80% RH, 10^{11} Ω at 90% RH, and below 10^{9} Ω at 100% RH. Similarly, Nylon insulation's designed resistance of 10^{11} ohms (Ω) sharply deteriorates above 50% RH, dropping to 10^{8} Ω at 80% RH, 10^{6} Ω at 90% RH, and 10^{5} Ω at 100% RH.

Mold and mildew attack affects fuels, lubricants, fabrics, textiles, and other materials common in military weapons and equipment. Warm and humid conditions promote a faster rate of mold and bacteria growth. Above 50% relative humidity mold growth can occur provided nutrients and spores are available with warm temperatures (above 40° F).

There has been concern regarding the long-term effect of lowered relative humidity on military equipment. It has been verified that storage of equipment for long periods in air controlled at appropriate levels of lowered humidity has no detrimental effects. Some examples include:

ITEM	STORAGE LIFE
Leaded Gasoline	4 years
Diesel Fuel	8 years
Motor Oil	8 years
Transmission Oil	8 years
Coolant	8 years
Rubber goods (14 types)	No attack at 30-50% RH
Electronics	No static at 30-50% RH

No matter how good or poor the material or design, controlling relative humidity helps.

DEPARTMENT OF DEFENSE POLICY REGARDING CONTROLLED HUMIDITY PROTECTION (CHP)

Controlled Humidity Protection and dehumidified storage is a proven concept accepted throughout the military services.

The DOD and Service Department's policy, from the Joint Service Manual (JSM) for Storage and Material Handling, states "schedules for cyclic inspection will normally be extended for items under CH (Controlled Humidity) storage".[7] This capability to *stop the clock* and defer preventative maintenance and inspections for equipment in a sheltered controlled humidity environment is a crucial force-multiplier for the military.

Naval and Marine Corps aviation policy states "dehumidification is the preferred method of preservation" applicable to all aircraft, components, Support Equipment (SE), Armament Weapons Support Equipment (AWSE), and Weapons Handling Equipment (WHE).[8] For systems placed in dehumidified protection "all scheduled special inspections may be deferred until the system is removed from preservation". The period is from "0 days to indefinite". Methods for applying dynamic dehumidification are delineated.[9]

Inspection frequencies for various storage conditions:[10]

- Open yard: 5 months.
- Under shed: 12 months.
- Non controlled temperature warehouse: 24 months.
- Controlled temperature warehouse: 30 months.
- Controlled Humidity warehouses: 60 months.

A forthcoming Marine Corps Order delineating the U.S. Marine Corps Corrosion Prevention and Control (CPAC) program will include Controlled Humidity Protection as one of the cornerstone policies. A subsequent Handbook is in work to address implementation.

BENEFITS OF CONTROLLED HUMIDITY PROTECTION (CHP)

Controlled Humidity Protection supports the Department of Defense in transformation. As a result of force structure downsizing, the mission-required equipment and operational tempo are mismatched to only a percentage of the resources required to sustain them.

The ability to *stop the clock* and defer preventative maintenance and inspections for equipment in a sheltered controlled humidity environment is a crucial force-multiplier for the military.[8] By placing a portion of weapons and equipment in Controlled Humidity Protection 100% of mission requirements can be met with only a portion of the resources previously available.

For equipment that is planned to be out of service for extended periods of time, dehumidification ensures the equipment will be taken out of storage in the same condition it was when placed into storage. No deterioration means no corrosion growth (eliminating grinding, repairing, blasting, cleaning, coating, priming, painting and sealing), no electronics failures, no electronics false removals resulting in no-fault-found, no mold or mildew to remove, no rotten insulation or upholstery to replace. It means elimination of the maintenance tasks that would accrue in unprotected storage of equipment and elimination of the scheduled maintenance tasks that are required on equipment placed in an open storage environment (coatings, bags, tape, sealant, preservation compounds, lubricants, etc.).

When used in support of equipment that is in regular use, dehumidification improves reliability, thus reducing the maintenance tasks which again has a favorable impact on the environment. Equipment can be portable and travel to the field.

General Controlled Humidity Protection benefits include:

- CHP directly supports the war-fighter by putting more warriors on the battlefield and improving the tooth-to-tail ratio.
- CHP is environmentally friendly: dry air cannot pollute and forgoing the use of other products significantly reduces waste streams.
- Low risk: CHP is a COTS application proven effective by the services in the early 1990's, being fielded to operational forces since 1995.
- Affordable: multiple government audits of installed operational CHP systems cite returns on investment (ROI) up to 8:1.
- CHP is easy to use and tailorable to unique service, unit and equipment operational profiles.
- Reduction of cyclic preventative maintenance and inspections.
- Reduction of corrosion-induced failures and repairs.
- Reduction of false removals resulting in no-fault-found at higher echelons of maintenance.
- Reduction in spares requirements and cannibalization.
- Improves weapon reliability and availability.
- Improves Mean Time Between Failure (MTBF) of systems, Line Replaceable Units (LRUs), and components.
- Improves affordability and service life potential.
- Lowers Total Ownership Cost by drastically slashing Operations and Support expenditures.

Independent studies and analyses of Army National Guard CHP program by the Government Accounting Office (GAO), the Department of Defense Inspector General (DOD IG) and the Army Center for Economic Analysis (CEAC) validated returns on investment (ROI) of up to 8:1 and the following specific results:

- MTBF for electronics improved by 30%.
- Maintenance times reduced between 30% to 50%.
- Preservation costs reduced between 20% to 30%.
- By placing 25% of their mobilization and training equipment in long term Controlled Humidity Protection and the remainder in operational Controlled Humidity Protection, the Army National Guard could accrue $1.65 billion in benefits during a ten-year period.

Studies have been performed that suggest dehumidification can apparently effect a 20% reliability improvement (indicating substantial moisture sensitivity) in assemblies using conformal-coated hermetic parts.[5]

Controlling relative humidity to maintain between 30% RH and 40% RH would significantly reduce corrosion of stored aircraft.[11] Dehumidified aircraft storage is recommended where practical.[12]

Naval Air Warfare Center-Aircraft Division, Patuxent River Maryland and ARINC Research Corporation conducted an evaluation of improvements for the Navy EP-3 ARIES III aircraft in VQ-1 squadron at NAS Agana, Guam using dehumidification when the aircraft was on deck from May 1993 to April 1994:

- Avionics reliability improved 25%.
- Intermediate level maintenance labor reduced 40%.
- Depot Level Repairable costs reduced 26%.

- Mission Capability increased 4-6%.
- Reduced maintenance man-hours per flight hour 4-22%.
- Increased MTBF 7-30%.
- Estimated $1.4 million annual savings on a $1.2 million investment.
- Return on investment achieved in 6 to 9 months.

The AV-8B Harrier Remanufacturing Program compared Controlled Humidity Protection storage to the AMARC at Davis-Monthan AFB. Sheltered CHP in place at MCAS Cherry Point resulted in:

- Better environment for corrosion protection.
- Lower cost.
- Faster and cheaper return to service.

The measures of effectiveness have typically been readiness, maintenance hours and cost. Additionally, the Naval Engineering Leadership Program's (NELP) Pollution Prevention Equipment Program (PPEP) quantified reductions in the waste stream obtained during a thorough evaluation of dehumidification of aviation support equipment and armament support equipment:[13]

- Stored equipment maintenance reduced by 80%.
- Hazardous materials and hazardous waste reduced by 74%.
- Increased equipment availability.
- OPNAV code N-45 (Logistics) now funds CHP equipment and installation for Navy fleet units.

The Multiple Launch Rocket System (MLRS) Program Manager (PM) directed Northrup Grumman (TASC) to explore ways of reducing the Total Ownership Cost of the MLRS. TASC

assessed the results of the Florida Guard's MLRS's being placed into sheltered CHP during CY2000:

- The top ten cost drivers in the battalion dropped 78%, from $413K in 1999 to less than $92K in 2000.
- LRU's on the launcher are the most costly to the system and accounted for over 50% of the cost for repair parts in 1999. There were zero demands for LRU's in 2000.
- Applying these findings across all 643 Army MLRS systems yields potential savings in excess of $11 million per year.

The Minnesota Army National Guard placed ten operational H-1 Cobra helicopters in sheltered CHP in the fall of 1997. No preventative maintenance or inspections were performed for twelve months. In September 1998 they were removed from sheltered CHP and operational tests were conducted:

- All controls functioned normally.
- No leaks.
- No corrosion.
- Pressures of all fluid systems normal on run-up.

A Marine Aircraft Logistics Squadron (MALS–29) conducted an evaluation of storing aircraft ground support equipment. 392 items of equipment were placed in Controlled Humidity Protection storage and the maintenance hours compared with this and normal preventative maintenance for out-of-service support equipment.

- Normal storage of the equipment would have expended 535 maintenance hours annually for preservation.

- The one-year storage of the 392 items in Controlled Humidity Protection storage required 8 preservation maintenance hours, a 98% reduction.

MALS-14 documented material and maintenance costs of start-up, equipment preparation, scheduled and unscheduled maintenance, and HAZMAT for dehumidified storage of 201 items of aviation ground support equipment compared to normal preservation:

- Savings first year: $183,831 ($7,964 HAZMAT)
- Projected 8-year savings: $1,624,530.

Sweden uses dynamic dehumidification in operational aircraft:

- Avionics MRBF improved 26%.
- Aircraft availability improved 5%.
- CHP costs recovered in six months.

German fighter squadrons use dynamic dehumidification on operational Tornado aircraft. Avionics failures were reduced 45%.

IMPLEMENTATION OF CONTROLLED HUMIDITY PROTECTION (CHP)

LOGIS-TECH's Environment Stabilization System (ESS®) technology was developed as part of a Small Business Innovative Research (SBIR) program through the Naval Air Systems Command (NAVAIR) to pioneer Controlled Humidity Protection technologies for the military. The SBIR program is a three-phased, government-to-industry initiative designed to encourage development of moderate-to-high risk ventures that can benefit the public and private sector. Phases I and II are competitively awarded and define and develop the concept for the Government. Phase III is commercialization of the concept for application in both Government and industry. LOGIS-TECH has received multiple Phase III contract awards for application of ESS®.

Environment Stabilization Systems (ESS®) are uniquely tailored solutions that achieve valid Controlled Humidity Protection by guarantying relative humidity below 40% RH more than 90% of the time, and below 50% RH 100% of the time. Control and monitoring systems must be in place that will maintain the above-prescribed atmosphere and provide prompt indication of any out of limit condition. CHP applications generally fall into two broad categories:

- Sheltered CHP can consist of pre-engineered steel structures, tension-fabric structures, or an existing building converted specifically for CHP use. Since cyclic preventative maintenance, inspections and services are deferred for equipment in sheltered CHP; this is the preferred method of CHP.
- Unsheltered CHP uses the vehicle hull or equipment enclosure as the envelope to contain the humidity-controlled atmosphere. Cyclic preventative maintenance, inspections and services are not deferred for equipment in unsheltered CHP.
  - ✓ Operational Protection (OP) typically consists of multiple equipment items parked so as to facilitate ducting dry air into the equipment via flexible hose and vehicle interface adapters. Usually accommodating at least five vehicles, some OP systems provide CHP to as many as twenty pieces of equipment.
  - ✓ Single Vehicle Environment Stabilization Systems (SVESS®) consist of individual, portable deployable dehumidification systems custom tailored to a particular weapon or equipment item. These are typically powered in a manner that accommodates the unit's deployment condition.

Modern Controlled Humidity Protection systems are as environmentally friendly as they are energy efficient, long lasting and generate only water in the form of condensate or vapor as a

by product. Generally electrically powered and using electrical energy for heat regeneration of the desiccant, the regeneration can also be provided by other sources of energy such as natural gas, propane, or steam.

Over 600 Environment Stabilization Systems (ESS®) now provide the military Controlled Humidity Protection at 135 sites in 41 states and 10 overseas locations. Most are remotely monitored and controlled, with customer visibility provided via Internet access to system performance trends. A worldwide network of Contractor Logistics Support (CLS) is in place to ensure system performance guarantees are met and to service these installations.

SUMMARY

Controlled Humidity Protection (CHP) systems stop corrosion and other moisture-related material degradation, enhance readiness, reduce maintenance costs and improve equipment reliability. CHP allows customers to redesign their maintenance programs for maximum efficiency based on operational requirements and capability. The benefits of CHP include corrosion prevention, improved wiring insulation performance, mold and mildew prevention, pollution prevention, hazardous waste stream reduction, and reduced manpower requirements. Controlled Humidity Protection systems enjoy a government-audited return on investment of up to 8:1. CHP systems are available to all DOD components through an Indefinite Delivery Indefinite Quantity (IDIQ) contract vehicle administered by Naval Air Warfare Center-Aircraft Division (NAWC-AD) Lakehurst, New Jersey: N68335-01-D-0096.

CHP Points of Contact

NAVY IDIQ N68335-01-D-0096
NAWC-AD Lakehurst, New Jersey
Tom Hill or Rita Brownlee 732-323-2103

ARNG IDIQ DAHA90-98-D-0009
National Guard Bureau Headquarters
Alexandria, Virginia
Ms. Barbara Mather 703-607-1260

USMC Material Command, CPAC
Albany, Georgia
Ms. Debra Mixon 229-639-7267

LOGIS-TECH, inc.
5775 Barclay Drive, Ste. 4
Alexandria, Virginia 22315-5710
www.logis-tech.com
Jim Martin 703-921-1038 x114
Jmartin@logis-tech.com

REFERENCES

1. W. H. J. Vernon, Second experimental report to the Atmospheric Research Committee, British Non-ferrous metals Research Association (1926).

2. Kennedy Space Center, Relative corrosivity of atmospheres at various distances from the seacoast, MTB 099-74 (1980).

3. Defense Systems Management College, DSMC—Acquisition Logistics Guide, December 1997, Part II, Chapter 10, paragraph 10.4.2.1 (1997).

4. Sandia National Laboratories, U.S. Army Aviation and Missiles Command Life Cycle Systems Engineering Workshop, 4-5 November, 1997.

5. Air Force, Air Force SBIR Solicitation AF97-172 (1997).

6. Society of Automotive Engineers; SAE Aerospace Recommended Practice 987 Rev A.

7. Joint Service Manual (JSM) for Storage and Material Handling; DOD 4145.19R, DLAM 4145.42, TM38-400, AFMAN 23-210, MCO 4450-14, NAVSUP PUB 572; Section VII

Operations in CH (Controlled Humidity) Space, Section 3-52 Material Protection Factors, paragraph i.

8. OPNAVINST 4790.2; Naval Aviation Maintenance Plan (NAMP), Volume I, paragraph 12.1.16 Preservation Procedures and Responsibilities

9. NAVAIR 15-01-500; Preservation of Naval Aircraft, Chapter 6 Environmental Control, Section II Dynamic Dehumidification, Section IV Dehumidification Installation.

10. Defense Logistics Agency, Defense Logistics Agency Manual DLAM 4145.12.

11. Air Force, USAF Scientific Board (1994).

12. National Materials Advisory Board, 1997; Interim report: Aging of U.S. Air Force Aircraft, (March 1997).

13. Navy Environmental Leadership Program (NELP); Pollution Prevention Equipment Program (PPEP), NAWC-AD Lakehurst New Jersey, www.lakehurst.navy.mil\p2\docs\fr\265.htm.

CORROSION CONTROL COATINGS: METALS

DEVELOPMENT OF PRODUCTION-SCALE ALUMINUM-MANGANESE ELECTRODEPOSITION PROCESS

Erin N. Beck, Dr. Michael J. Kane, Craig A. Matzdorf, and Jim L. Green

Naval Aviation Systems Command
Research and Engineering Group, Code 4.3.4.1
Patuxent River, MD 20670-1908

ABSTRACT

The Department of Defense (DoD) is reducing use of cadmium-based coatings for defense systems due to cadmium's environmental and health hazards, specifically toxicity and human carcinogenicity. One potential alternative to cadmium is aluminum-manganese. The researchers have successfully demonstrated laboratory-scale electrodeposition of aluminum-manganese on steel. Neither aluminum nor manganese is toxic or carcinogenic as defined by the Resource Conservation and Recovery Act or International Agency for Research on Cancer, respectively.

The researchers have developed a proposed production-scale aluminum-manganese plating process based on laboratory-scale experimentation. Aluminum-manganese electroplating is conducted in a molten salt solution of 79% aluminum chloride, 10% sodium chloride, 10% potassium chloride, and 1% manganese chloride by weight. Laboratory-scale plating equipment includes a Pyrex glass vessel, electric heating mantle, glass stirrer, power supply, and ventilation. Production-scale plating equipment includes Glasteel-lined plating tank, heat tape, Glasteel-coated agitator, upper plenum, power supply, and ventilation with scrubber.

The goal of this effort is implementation of the production-scale process at Naval Aviation Depot (NADEP) North Island, and eventual tri-service replacement of cadmium coatings.

INTRODUCTION

Military aircraft are often exposed to environmental conditions that accelerate corrosion of metallic components. Cadmium electroplating is the current technology used to slow corrosion of steel aircraft components. Although cadmium plating is a simple, straightforward process, strict environmental regulation of cadmium is driving the search for a replacement to cadmium.

Alternatives to cadmium plating include tin-zinc, zinc-nickel, Ion Vapor Deposited (IVD) aluminum[1], Alumiplate[2], and aluminum-manganese plating. The zinc-based alternatives have a more active open circuit potential than cadmium or aluminum-based alternatives. As such, the in-service production of hydrogen is more thermodynamically favorable for zinc-based alternatives, which may lead to environmentally assisted cracking of high strength steels. IVD aluminum has limited ability to coat complex shapes and internal diameters. Alumiplate utilizes a hazardous toluene-based plating solution. Aluminum-manganese plating has potential to be an affordable alternative for cadmium plating that can coat complex shapes and internal diameters.

BACKGROUND

Cadmium electroplating is a relatively simple process. First, the aircraft components are prepared for plating through several cleaning steps. Then the components are dipped into a cadmium-cyanide plating tank. After plating is complete the components are dipped into a water rinse tank to remove residual plating solution.

Cadmium and cyanide waste products are generated during all stages of the cadmium plating lifecycle. The cadmium plating process itself, refurbishment of cadmium plated components, and washing of Defense systems that contain cadmium plated components all result in generation of cadmium or cyanide waste products. Wastes that produce Toxicity Characteristic Leaching Procedure (TCLP) extract ≥ 0.1 mg/l cadmium are D006 hazardous waste (toxicity characteristic) per Title 40, Part 261, Section 24 of the Code of Federal Regulations (CFR). Plating, refurbishing, and washing wastes typically exceed 0.1 mg/l cadmium. Wastewater treatment sludge from electroplating operations are F006 hazardous waste per Title 40, Part 261, Section 31 of the CFR. Spent cyanide plating bath solutions from

electroplating operations are F007 hazardous waste per Title 40, Part 261, Section 31 of the CFR. Therefore, the military is required to handle and dispose of these wastes in accordance with hazardous waste regulations. Compliance with hazardous waste regulations requires strict handling, storage, and disposal procedures, and expensive disposal fees.

In addition to requiring compliance with hazardous waste requirements, cadmium plating poses a serious health risk to workers. The Navy Environmental Health Center (NEHC) evaluated the general toxicity and carcinogenicity of cadmium, as well as the chemical constituents of potential alternative coatings.[3,4] NEHC's evaluation of cadmium determined that cadmium poses a significant health hazard to exposed workers. Cadmium inhalation exposure is proven to cause serious acute and chronic respiratory effects, as well as reproductive effects. Inhaled cadmium is easily absorbed into human organ tissue, and then very slowly eliminated. Cadmium is recognized as a known human carcinogen by the International Agency for Research on Cancer (IARC) and the National Toxicology Program (NTP).

Workers are exposed to cadmium during the plating process, as well as during refurbishing and washing cadmium plated components. Workers may be exposed to cadmium through the inhalation route during initial bath makeup and refurbishment of cadmium plated components. Cadmium salt in powder form is typically used to charge the plating tank, and may result in generation of cadmium dust at a concentration greater than the Occupational Safety and Health Administration (OSHA) Permissible Exposure Limit (PEL) of 5 $\mu g/m^3$. Refurbishment of aircraft components includes grinding of the components as part of the preparation and cleaning process. Grinding also results in generation of cadmium containing dust, potentially exposing workers to harmful levels of cadmium dust on a regular basis.

In addition to inhalation, workers may also be exposed to cadmium through the ingestion route at all stages of the cadmium plating lifecycle. Cadmium may be easily transferred onto the surface of the skin when a worker touches a cadmium plated component or plating rack. If proper hygiene is not exercised then transfer of cadmium from hand to mouth is highly likely.

The scope and breadth of cadmium usage within the Department of Defense is enormous. Due to the complexity and high volume usage of cadmium in military applications the pursuit of several cadmium alternatives is necessary. Aluminum-manganese is one potential alternative that is being pursued by the Department of Defense.

The aluminum-manganese electroplating process is fairly straightforward. First, aircraft components are cleaned and prepared similar to parts prepared for cadmium electroplating. Next, parts are dipped into a 190°C aluminum-manganese plating tank. Finally, the components are dipped into a water rinse tank to remove residual plating solution. The entire process should be more enclosed and require relatively more ventilation than cadmium plating to contain aluminum chloride fuming.

Electroplated aluminum-manganese is expected to reduce some of the environmental and health issues associated with the use of cadmium. Unlike cadmium, aluminum-manganese plating, refurbishing, and washing wastes will not be hazardous waste due to toxicity characteristic. Waste aluminum-manganese plating solution may be hazardous waste due to corrosivity and reactivity characteristic per Title 40, Part 261, Sections 22 and 23 of the CFR. The spent plating solution may be simply treated with sodium hydroxide solution to form non-hazardous solid waste. A hazardous waste permit may be required to perform treatment due to reactivity characteristic. Eliminating refurbishing, washing, and most plating wastes from

hazardous waste classification may significantly reduce handling and disposal costs, as well as regulatory reporting burden.

In addition to reducing environmental regulatory burden, aluminum-manganese plating poses a smaller health risk to workers when compared to cadmium. The OSHA PELs for aluminum and manganese are 5 mg/m^3, three orders of magnitude greater than the PEL for cadmium. The study conducted by NEHC reported that exposure to manganese dust or fumes can cause central nervous system and respiratory effects, as well as eye irritation.[4] And, that inhalation of aluminum can cause respiratory effects, dementia and convulsions. The researchers also had toxicity testing conducted on aluminum-manganese powder.[5,6,7,8] The powder composition was 30 weight percent manganese, roughly twice that of the nominal composition of the electroplated aluminum manganese coating. The toxicity results for Al/Mn 70:30, - 100 Mesh Batch #98-9082S were as follows: LD_{50} is greater than 2,000 mg/kg of body weight, is not a dermal irritant, is an ocular irritant but is not corrosive. Finally, neither manganese nor aluminum are known or suspected carcinogens per IARC and NTP. As a result, the in-service costs associated with environmental and health compliance of aluminum-manganese coatings will be comparable to other cadmium alternatives, all of which will be much less than costs for cadmium coatings.

TECHNOLOGY DEMONSTRATION OBJECTIVES

Based on successful laboratory-scale experimentation, the researchers have developed a proposed production-scale aluminum-manganese plating process. A 200-gallon production representative aluminum-manganese plating process will be designed and installed as a technology demonstration at the Naval Aviation Depot (NADEP) North Island, CA. If

successful, aluminum-manganese plating could be used as a one-for-one replacement for the cadmium-cyanide plating currently performed at the depot. A larger plating tank would be required to accommodate all aircraft components.

The goals of this demonstration project are to demonstrate and validate that electroplating of aluminum-manganese from a molten salt bath is technically feasible and commercially viable for a production-scale process, and to transition aluminum-manganese coatings for use on high strength steel flight critical components currently coated with cadmium.

TECHNOLOGY DESCRIPTION

Electroplating of aluminum-manganese is conducted in a molten salt bath of nominal weight percent composition of 79% aluminum chloride, 10% sodium chloride, 10% potassium chloride, and 1% manganese chloride. Application of direct current to 1100 aluminum alloy anodes causes an aluminum-manganese deposit of 13 wt% manganese to form on the steel component surface. The deposit provides anodic protection of the steel, hill-and-valley surface probably amenable to paint adhesion (see Figure 1), and possible lubricity similar to a cadmium plated surface.

An overall schematic of the proposed aluminum-manganese plating process sequence is shown in Figure 2. Figure 3 exhibits the proposed aluminum-manganese plating equipment configuration.

First, clean dry parts would be masked. Teflon tape may be used at present, and other maskants are planned for suitability testing by the researchers.

Next, the component would be cleaned to remove iron oxides and grease, dirt, and oil from handling. Cleaning may be done one of two ways. The component may be grit blasted

with aluminum oxide, or the component may go through a sequence of vapor degrease, electrolytic cleaning, hot water rinse, room temperature water rinse, acid dip, and water rinse.

After cleaning, the component should be attached to its fixture (racked) and dipped into the plating solution as soon as possible to minimize iron oxide formation on the component surface. Once the component is racked the crane would move the fixture into the upper plenum. The upper plenum side door would close, and the plating tank lid would slide to the open position.

Next, the crane would lower the fixture into the plating tank, and electrical connections would be made. The fixture would include a lid shaped to close off the open top of the plating tank while the fixture is located in the plating tank. The power supply would be turned on and a pre-programmed plating sequence chosen. Plating would be performed at 180 amps/sqft. direct current and 190°C with forced convection. The plating tank would be heated by heating tape wrapped around the outside of the tank, and insulation would cover the heating tape. A glass coated impeller would supply forced convection. The plating rate would be approximately 1 mil to 3 mils per hour.

After plating is complete the crane would lift the fixture into the upper plenum, and the plating tank lid would slide to the closed position. After fuming of the component has subsided the upper plenum side door would be opened, and the crane would move the fixture over and down into the water rinse tank. The time required for fuming to subside while in the upper plenum is unknown at this time. The crane would lift the fixture above the rinse tank, and water would be sprayed on the fixture as a second and final rinse.

Finally, the component would be unracked and baked within four hours. Baking parameters are undetermined at this time.

KEY DESIGN CRITERIA

There are numerous key design criteria in the proposed aluminum-manganese plating process:

FUMING/MOISTURE

- Upper plenum, ventilation, and scrubber will be required to minimize exposure to hydrogen chloride fumes. At operational temperatures the high vapor pressure of aluminum chloride generates vapors that react with moisture in the air to produce hydrogen chloride fumes. Fuming of a laboratory-scale open molten salt bath was easily addressed using a properly sized conventional fume hood as described below.

A rectangular 10-gallon tank was constructed and operated in a fume hood by the researchers. The surface area of the molten salt in the 10-gallon tank was 1.5 square feet. At operational temperatures fuming of the molten salt bath was minimal when the tank was covered, based on visual observation. When uncovered the tank generated a large volume of white fumes; however, fume generation did not exceed the capacity of the fume hood. Dregar tubes were used to analyze for hydrogen chloride around the tank after the cover was removed from the tank. Hydrogen chloride was undetectable outside the hood. Inside the hood, on all sides below the top of the tank, the hydrogen chloride level was 1.5 ppm or less. No visible fuming was observed on the sides of the tank. Above the tank and along the underside of the top of the fume hood white visible fumes were present. In the area where fuming was observed the hydrogen chloride concentration exceeded 10 ppm. The PEL for hydrogen chloride is 5 ppm.

Figure 3 exhibits production representative molten salt plating equipment with proposed ventilation. A vacuum would maintain slight negative pressure within the upper plenum and

draw the fumes to a scrubber before release to the atmosphere. In addition, slotted ventilation would surround three sides of the area in which the plating tank and rinse tank are located. The slotted ventilation would capture any fumes generated during transfer of the fixture from the upper plenum to the rinse tank.

- Dry nitrogen blanket on plating solution surface will be required to minimize moisture addition to plating solution; backup argon cylinder will be required for use in the event of a power outage.

EQUIPMENT

- Glasteel 9115-lined carbon steel plating tank will be required to prevent chemical attack.[9] Materials tested by the researchers for weight loss due to plating solution attack include Titanium Grade 2, Nickel 400, Nickel 200, Hastelloy B2, Tungsten, Incolloy 825, Tantalum, 6Al4VTi, Inconel 600, Glasteel 9115, Teflon PTFE, Teflon LFP. Tantalum and Glasteel 9115 did not gain or lose weight. Teflon PTFE and Teflon LFP gained weight and color. All other materials lost significant weight.
- Heat tape and insulation will be required to uniformly heat plating solution and to provide ability to re-heat plating solution in the event the solution cools to solid form.

PROCESS CONFIGURATION

- The molten salt plating process will need to be designed so that water will not come into contact with molten salt in the event of a spill to minimize fume generation.

OPERATING PARAMETERS

- Manganese content in the plating solution dictates manganese content in the deposit (determined in laboratory experiments conducted by the researchers).

- 13 wt% manganese content in deposit is required to provide anodic protection of components (determined in laboratory experiments conducted by the researchers).
- Optimal operating temperature is 190°C (determined in laboratory experiments conducted by the researchers).
- Direct current at 180 amps/sqft. (optimal current sequence determined in laboratory experiments conducted by the researchers).
- Mild forced convection is required with Glasteel 9115-coated impeller (need for forced convection determined in laboratory experiments conducted by the researchers).
- Hot rinse water may be required to maximize residue removal (optimal temperature undetermined at this time).
- pH-basic rinse water may be required to minimize hydrogen embrittlement (optimal pH undetermined at this time).
- Hydrogen embrittlement relief may be required for aluminum-manganese plated steel components. High strength steels are embrittled by the decomposition of aluminum chloride and formation of hydrogen chloride during rinsing. Post-baking components relieves hydrogen embrittlement by driving hydrogen out of the component structure. Operating parameters for post-baking aluminum-manganese plated steel components are unknown at this time.
- Aluminum-manganese coatings are removed using a caustic solution. Residual manganese products may remain and can be removed by light scrubbing with an abrasive pad.

ENVIRONMENTAL, HEALTH, AND SAFETY

- The rinse water will contain aluminum oxides, aluminum hydroxides, and manganese, and may be discharged to public wastewater treatment facilities depending on local regulations.

None of the rinse water constituents, or the rinse water characteristics (after neutralization), will cause it to be labeled hazardous waste.

- Waste plating solution may require hazardous waste label for corrosivity and reactivity characteristics, and possibly due to F006 designation for plating wastes.
- Aluminum-manganese plating includes several processes in which worker health and safety must be protected.
  - Chemical additions to the plating tank will result in generation of aluminum chloride dust, and possibly manganese chloride dust, in excess of OSHA PELs. Workers will be required to wear full-face respirators during chemical additions to the plating tank if engineering controls and operating procedures cannot adequately reduce the concentrations of chemicals below their OSHA PELs.
  - Electrical connections may need to be made manually, potentially exposing workers to hot metal surfaces and hydrogen chloride fumes. Workers will be required to wear thermal/chemical protective gloves and a full-face respirator.
  - Hard hats and steel toed safety shoes may also be required, as well as safety glasses with sides shields. Consultation with an industrial hygienist will be necessary to determine if additional protective equipment will be needed.

OTHER ISSUES

- Aluminum chloride vapor condenses and crusts on cool surfaces. Procedures must be developed to eliminate or minimize crust formation, and to remove crust once formed. Surfaces likely to develop crust are the inside wall of the plating tank above the plating solution level, the underside of the plating tank lid, and the inside walls of the upper plenum.

SUMMARY

Continued use of cadmium electroplating to protect steel from corrosion is becoming less practical due to environmental, safety, and health issues associated with cadmium. Numerous alternatives to cadmium plating exist, each with benefits and drawbacks.

Aluminum-manganese plating exhibits the potential to be an affordable alternative to cadmium plating that can be utilized for high strength steel applications. Based on laboratory-scale experimentation, a production-representative aluminum-manganese plating process has been developed for technology demonstration at NADEP North Island, CA. The goals of the demonstration are to demonstrate that production-scale aluminum-manganese plating is technically feasible and commercially viable, and to transition aluminum-manganese coatings for use on high strength steel flight critical components currently coated with cadmium.

ACKNOWLEDGMENTS

This is a DoD-unique project, which originated in the Strategic Environmental Research and Development Program. The project has continued with support from the Aviation Pollution Prevention Technology Program (CNO 45) and the Environmental Security Technology Certification Program.

REFERENCES

1. Ivadizer is name brand of the ion vapor deposition chamber.
2. AlumiPlate, Incorporated. Minneapolis, MN. Phone 888-258-6475.
3. 'Evaluation and Report of General Toxicity and Carcinogenicity of Cadmium, Cadmium Oxide and Cadmium Hydroxide,' Ser IH6/01349. Department of the Navy, Navy Environmental Health Center, 13 July 2000.

4. ‘Evaluation and Report of General Toxicity and Carcinogenicity of Potential Cadmium Replacement Coatings,’ Ser IH6/01227. Department of the Navy, Navy Environmental Health Center, 26 June 2000.

5. ‘Volume I, Acute Oral Toxicity/LD50 in Rats, Al/Mn 70:30.’ MB Research Laboratories, 19 December 2000.

6. ‘Volume II, Acute Dermal Toxicity in Rabbits/LD50 in Rabbits, Al/Mn 70:30.’ MB Research Laboratories, 18 December 2000.

7. ‘Volume III, Acute Dermal Irritation in Rabbits, Al/Mn 70:30.’ MB Research Laboratories, 20 December 2000.

8. ‘Volume IV, Acute Eye Irritation in Rabbits, Al/Mn 70:30.’ MB Research Laboratories, 18 December 2000.

9. Glasteel is a registered trademark of Pfaudler, Incorporated. Rochester, NY. Phone 716-235-1000.

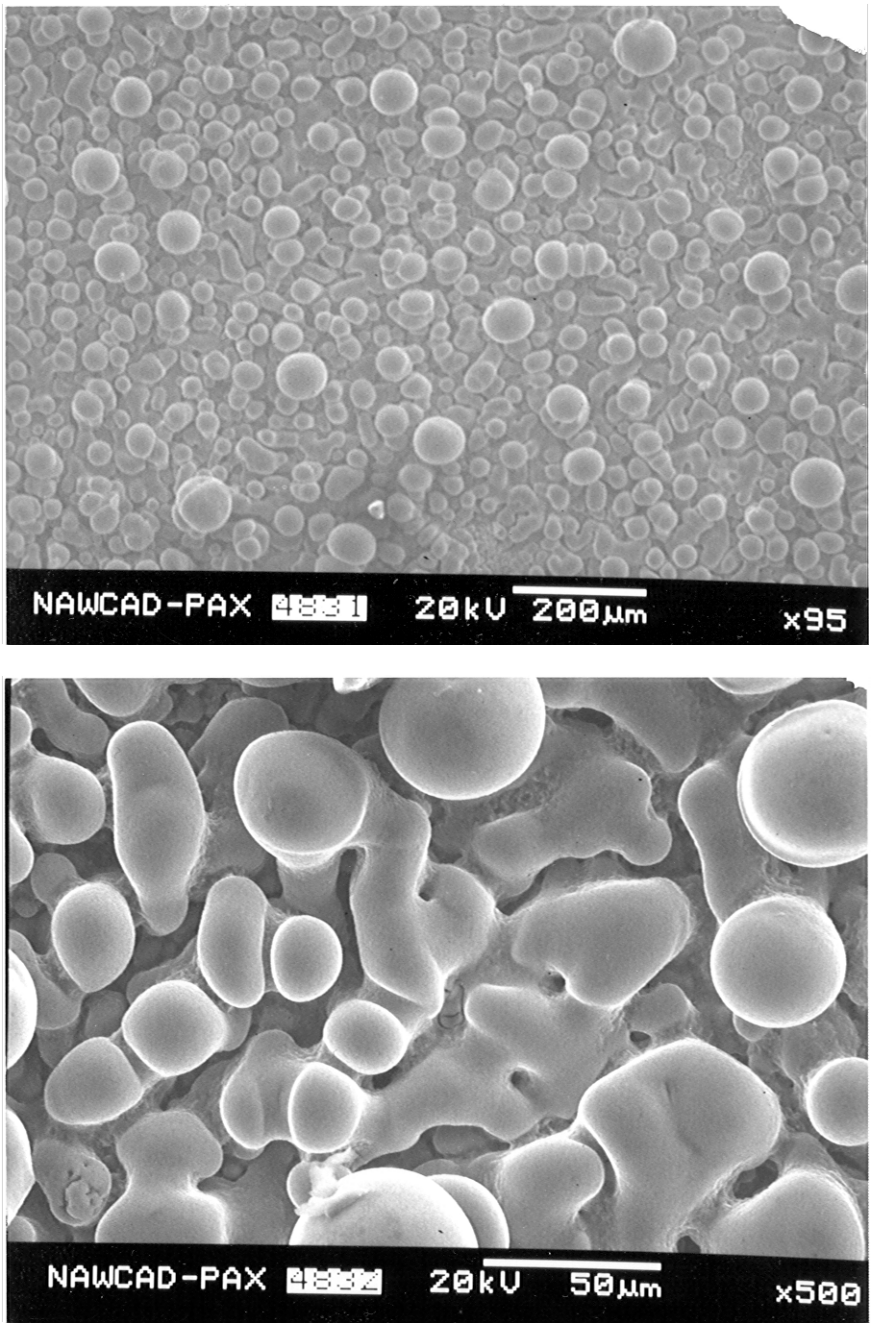

FIGURE 1: Micrographs of Aluminum-Manganese Deposit with 15wt% Manganese

Proposed Aluminum-Manganese Electroplating Process Sequence

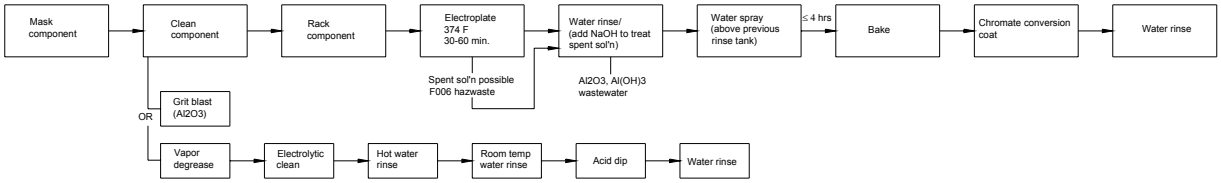

Existing Cadmium-Cyanide Electroplating Process Sequence

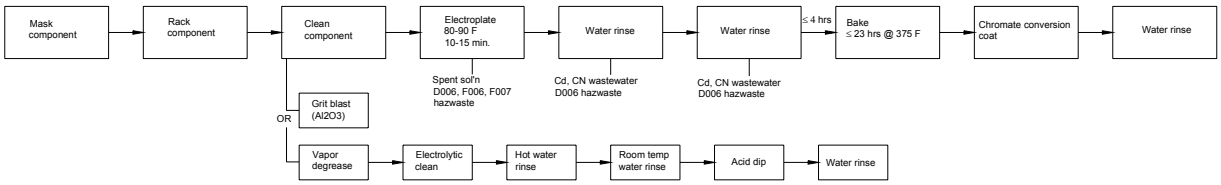

FIGURE 2: Proposed and Existing Electroplating Process Sequences

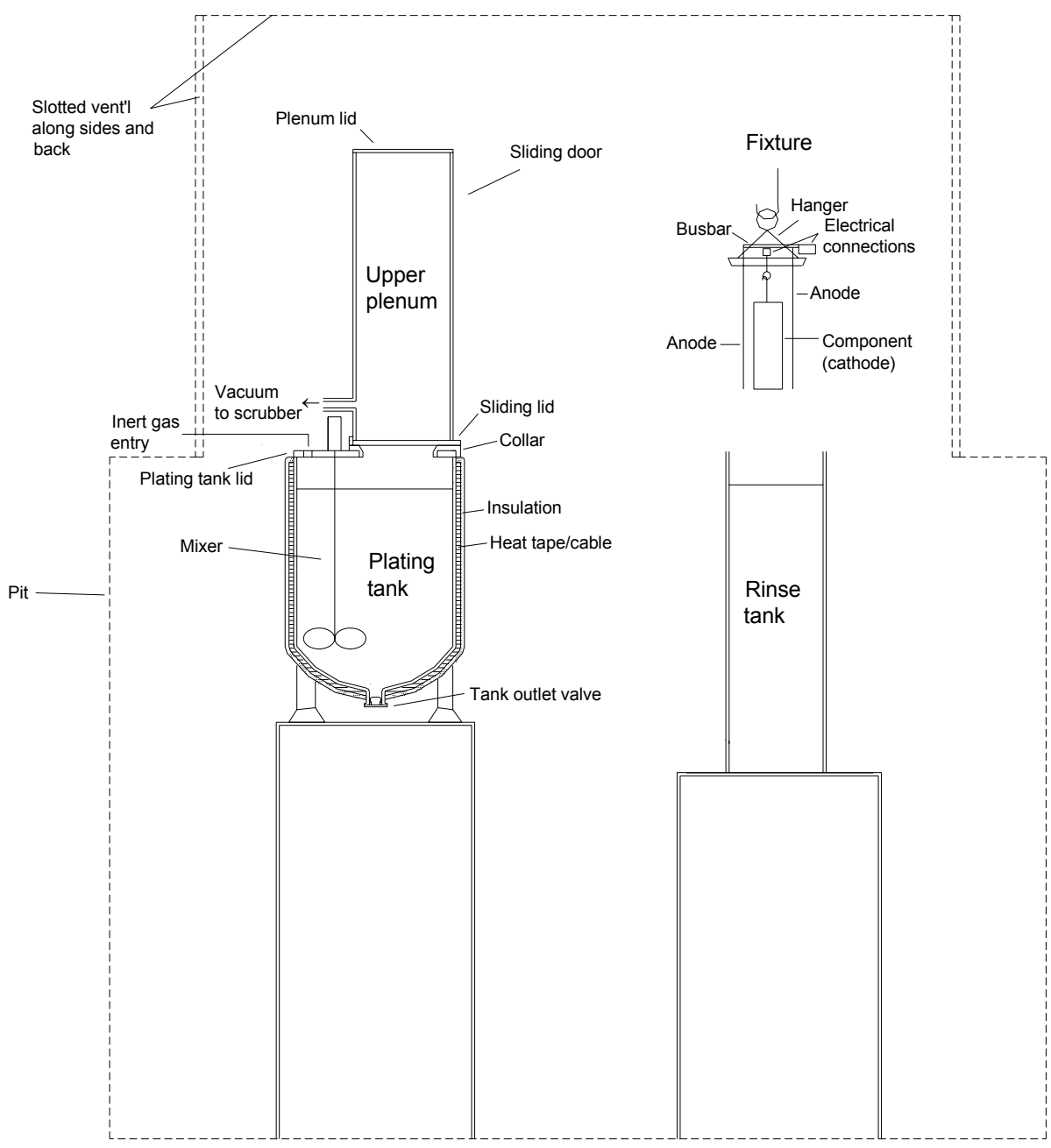

FIGURE 3. Molten Salt Plating Equipment Configuration

USING VANADIUM TO IMPART SELF-HEALING TO CONVERSION COATINGS FOR AEROSPACE ALUMINUM ALLOYS

M.T. Coolbaugh, H.P. Groger, E.C. Aquino, S.E. Morris, and J.E. Roberts
American Research Corporation of Virginia
Radford, Virginia

F. Pearlstein
Philadelphia, PA

ABSTRACT

A new conversion coating pretreatment for aerospace aluminum alloys has been developed. Laboratory testing has shown that the new coating can afford up to 336 hours of neutral salt-spray corrosion protection to AA2024-T3 and passes modified wet-tape adhesion tests. One particularly intriguing aspect of the new coating is its apparent ability to self-heal during salt-spray testing. A range of surface analytical methods was used to study the morphology and structure of the coating. It is postulated that the new coating contains vanadium rich inclusions in a zirconium hydroxide matrix. Self-healing is thought to arise from passivation of bare aluminum surfaces *via* leaching of vanadate, i.e. V^{5+}, species from the coating during salt-spray testing.

INTRODUCTION

Chromate (hexavalent chromium) conversion coatings are applied to aluminum surfaces as a base for paint to provide enhanced adhesion and protection against corrosion. Increasing concern about the health and environmental effects of toxic industrial wastes and by-products has created demand for more benign alternatives to chromate coating. Chromium in the hexavalent state presents chronic and acute threats to the health of humans and to the environment. Treatment of Cr6+ in waste streams to an acceptable level is a costly process. A

need exists for the replacement of chromate conversion coatings by an environmentally favorable coating method[1]

One of the more interesting aspects of the chromate conversion coatings is their ability to self-heal. Self-healing refers to the apparent ability of damaged areas of a chromate conversion coating metal to resist corrosion. For example, an aluminum specimen scribed after the application of a chromate conversion coating will not show any corrosion in the scribe even after several hundred hours of neutral salt-spray exposure. This phenomenon is generally regarded as arising from passivation of the bare metal surface in the scribe by chromate species leaching from the conversion coating. There is great interest in developing pretreatments that possess self-healing characteristics.

American Research Corporation of Virginia has been active in the development of a trivalent chromium conversion coating (tccc) pretreatment originally invented by the U.S. Navy.[2,3] The tccc have been shown to be very effective and the weight of scientific evidence supports the conclusion that the trivalent form of chromium is much less toxic and mutagenic than the hexavalent form. However, the U.S. Environmental Protection Agency has proposed very stringent discharge limits based on total chromium concentrations. This paper reports the results of research sponsored by the U.S. Navy that have demonstrated that zirconium, zinc and vanadate, i.e. V^{5+}, can be used to develop pretreatment formulations in which the chromium can be greatly reduced or eliminated. These coatings are of great potential interest since they show evidence of self-healing.

EXPERIMENTAL PROCEDURES

The main objective of the research reported here was the development of field-usable pretreatments for aerospace aluminum alloys. To meet this objective work was concentrated on developing pretreatments that could be spray applied to aircraft under conditions commonly encountered during re-paint and maintenance conditions. The bulk of the testing was performed on AA2024-T3 as this is the most difficult of the commonly encountered alloys to protect from corrosion. AA2024-T3 sheets were obtained from commercial vendors and cut into specimens. Specimens were cleaned and deoxidized prior to the application of the coating. The coating formulation was an aqueous solutions prepared from concentrates at the time of use. The conversion coatings were aged 24 hours. Coated specimens were subjected to neutral salt-spray testing per ASTM B117. The majority of salt-spray testing was performed in-house but Ashely Labs, Ltd., an independent testing facility, was employed to perform confirmatory salt-spray tests. Adhesion-to-paint was determined by the modified wet-tape adhesion test as described in ASTM D-3359. Treated AA2024-T3 specimens were coated with a two-part non-chromated epoxy primer that was allowed to cure for one week. Adhesion testing was performed after the specimens had been immersed in deionized water for 24 hours at 23°C and then 168 hours at 65°C. Upon removal, two parallel scribes 3/4 inch apart were cut through the coating and an "X" mark was subsequently scribed through the coating between the two initial scribes. A strip of masking tape was applied firmly to the coating surface and was then removed by seizing the free end and pulling it off rapidly at an angle of 180°. The specimens were examined for removal and uplifting of the coating from the substrate and the adhesion rating based on the percentage of coating remaining on the surface was recorded.

A number of surface analytical techniques were used to gain insight into the performance of the coatings. X-ray photoelectron spectroscopy (XPS), auger electron spectroscopy (AES), time-of-flight secondary ion mass spectrometry (TOF SIMS) and reflection-absorption infrared spectroscopy (RAIRS) were used to characterize the composition of coatings before and after salt-spray testing. Scanning electron microscopy and energy dispersive X-ray spectrometry (EDAX) were used to study the morphology and chemical composition of the coatings. TOF SIMS measures the masses of ions ejected from the surface of a specimen following impact by beam of high-energy ions. TOF-SIMS is very surface sensitive and can be used in situations where energy overlaps limit either XPS or AES. TOF SIMS generally does not provide oxidation state information. Some inferences concerning the chemical bonding in the specimen can be made based on the nature of ions observed in the mass spectrum. RAIRS is a surface analytical method that provides information about thin coatings on infrared-reflective surfaces. In essence a beam of infrared (IR) light is directed at the aluminum specimen bearing a coating. The beam passes through the coating to the metal substrate, which is highly reflective in the IR frequency range. After reflection, the light passes out through the coating and is eventually passed to a detector. Light intensity is lost from the beam due to excitation of molecular and lattice vibrations within the coating. Vibrational frequencies can often be directly related to local atomic ordering, i.e. molecular structure, thereby providing valuable insight into the chemical identity of the coating not directly available from the surface analytical techniques discussed earlier in this paragraph.

RESULTS AND DISCUSSION

COATING PERFORMANCE

Table 1 presents the results of ASTM B117 testing performed by an independent laboratory on AA2024-T3 specimens treated with the zirconium-zinc-vanadium (ZZV) coating. Figure 1 presents photographs of two AA2024 specimens following 336 hours of salt-spray exposure. One specimen was treated with a solution of potassium hexafluorozirconate (K_2ZrF_6, PFZ) while the other was treated with the ZZV formulation. Both specimens had been scribed near their bottom edges subsequent to treatment. The PFZ treated specimen shows extensive corrosion while the ZZV treated specimen is essentially uncorroded after 336 hours. Note that the scribe in the ZZV treated specimen shows little or no corrosion. Figure 2 shows the result of a wet-tape adhesion test on a ZZV treated specimen that had been coated with a non-chromated epoxy primer. These results indicate that the ZZV coating has potential as a drop-in replacement for chromate conversion coatings for field use during aircraft repaint operations.

COATING FORMATION AND STRUCTURE

The major component of "trivalent chromium" conversion coatings is in fact zirconium oxide or hydroxide with the chromium concentrated toward the aluminum-coating interface. One possible mechanism for the formation of a zirconium oxide/hydroxide coating is suggested by work performed to develop “liquid phase deposition” (LPD) of silica and titanium oxide coatings. Films are deposited from acidic solutions that are supersaturated with respect to the oxide and that also contain a high concentration of the complex fluoride species, e.g. SiF_6^{2-}. A substrate is immersed into the solution and is surrounded by a metallic aluminum cage. The Al^{3+} ions, generated by oxidation with H^+, have a very high affinity for F^- and react with the complex fluoroions as illustrated in the scheme below for SiO_2 deposition.

$$SiF_6^{2-} + Al^{3+} \rightarrow Si^{4+} + AlF_6^{3-} \quad (1)$$

$$Si^{4+} + 2\,H_2O \rightarrow SiO_2 + 4\,H^+ \quad (2)$$

The conversion coating solutions are neither highly acidic nor saturated with respect to zirconium oxide. However, the solubility of zirconium is extremely low (10^{-10} M) at pH = 4. Experiments conducted at ARCOVA have shown that addition of Al^{3+} to a solution of PFZ leads to the formation of a zirconium precipitate at pH =4. The reaction between PFZ and aluminum takes place with or without other species present, as apparent from surface analysis and RAIRS.

Tccc coating formulations are most effective when the PFZ concentration is around 1.0-g/L whereas the ZZV coatings are only effective when the PFZ concentration is around 10-g/L. Increasing PFZ concentrations lead to striking changes in the appearance of the coatings. Low PFZ coatings are thin, 50 - 100 nm, and essentially transparent. High PFZ coatings are a readily apparent dull gray. The transition may be followed by RAIRS as shown in Figure 3. The IR spectra indicate that the coating thickness increases as the PFZ concentration increases. The dominant spectral features become quite sharp indicating a transition to a crystalline structure. The crystalline nature of the films is apparent in the SEM images shown in Figure 4. Figure 4A shows that the ZZV coating consists of an array of columnar crystals approximately 1 μm thick. Globular structures are found interspersed through the columnar crystals. Figure 5A gives EDAX spectra of a region containing only the columnar crystals while the spectra in Figure 5B was obtained in a region centered on one of the globular clusters. These spectra suggest that the majority of the vanadium and zinc components of the coating are localized in the globular structures.

MECHANISM OF SELF-HEALING

One of the remarkable characteristics of the high PFZ-ZS-SV-SW coatings is their apparent self-healing ability. After the specimens are conversion coated, a scribe was cut through the coating into the metal substrate so that an uncoated area is present on the specimens during salt-spray testing. The ZZV coated specimens show little or no corrosion in these scribed areas after 336 hours of salt-spray testing, as shown in Figure 1. Surface spectroscopic methods were used to further examine this phenomenon. Auger depth profiling of regions both inside and adjacent to a self-healed section of a scribe on a specimen that had been subjected to 336 hours of neutral salt-spray testing show that the scribed area of the specimen appears to have developed a thin (ca. 25nm) coating having an apparent Al:O ratio of 1:2, suggestive of AlOOH. Traces of fluorine and zinc are seen in the scribe, but zirconium is not observed. Unfortunately, AES has great difficulty in detecting vanadium in the presence of large amounts of oxygen. To overcome this difficulty, the specimen was examined with Time of Flight- Secondary Ion Mass Spectrometry, TOF-SIMS. TOF-SIMS has very high spatial resolution and is quite rapid and allows elemental mapping. The result of a surface mapping study is shown in Figure 6. Mapping shows very strong signal from aluminum in the scribe and essentially no zirconium in the region of the scribe. Vanadium is observed both inside, and outside of the scribed region.

SEM imaging of post-salt-spray specimens was also performed and representative images are shown in Figure 4B. The most significant difference between the non-tested and tested specimens, e.g comparing Figures 4A and 4B, is the disappearance of the globular structures. Based on the spectroscopic and imaging studies, and the observation that ZZV coatings provide very little corrosion protection without the incorporation of vanadium, it is postulated that self-healing arises from dissolution of vanadium rich phases in the coating during salt-spray

exposure. Vanadium is known to be a very good inhibitor of pitting corrosion for aluminum. Oxidation of aluminum by vanadium (V) is a thermodynamically favorable process.

CONCLUSIONS

Reactions between aluminum and complex fluorides such as ZrF_6^{2-} provide facile routes to the preparation of oxide coatings. The versatility of this approach is demonstrated in the preparation of highly protective coatings from solutions containing relatively low levels of ZrF_6^{2-} and Cr^{3+} or higher levels of ZrF_6^{2-} with smaller amounts of Zn^{2+} and V^{5+}. The latter coatings are of interest because they appear to possess some ability to self-heal scribed regions during salt-spray exposure. The experimental evidence suggests that the mechanism of self-healing involves the release of vanadate species from localized structures within the coating that migrate to and pacify the bare metal of the scribe.

ACKNOWLEDGEMENTS

The research reported here was funded through the Small Business Innovation Research Program. Grateful acknowledgement is given to the U.S. Air Force Research Laboratory ("Aqueous Non-chromate Conversion Coatings for Aluminum Alloys," SBIR Phase II Contract Number F08637-99-C-6003 and SBIR Phase I Contract Number F33615-98-C-5126) and the U.S. Navy Office of the Secretary of Defense (SBIR Phase II Contract Number N00421-97-C1202). Special gratitude is due to the Technical Contract Monitors, Capt. Gina Grazziano, 1Lt David Kempisty and Maj. Bernard Ghim of the U.S. Air Force and Dr. Vinod Agarwala of the U.S. Navy.

REFERENCES

1. Hinton, R.W. Metal Finishing, 89, pp. 55-61.

2. Pearlstein, F., Agarwala, V.S., J. Plating and Surf. Finishing, (1994),July, p. 50.

3. Pearlstein, F. and Agarwala, V.S., "Trivalent Chromium Conversion Coatings for Aluminum," U.S. Patent 5,304,257, (1994).

TABLES

TABLE 1.
Salt Spray Corrosion Test Results for Spray Applied ZZV Conversion Coatings on Al2024-T3 Tested at Ashley Laboratories.

	Number of Pits After Salt Spray	
Specimen	*168 hrs*	*336 hrs*
1	0	0
2	0	0
3	1	1
4	0	2
5	0	1

FIGURES

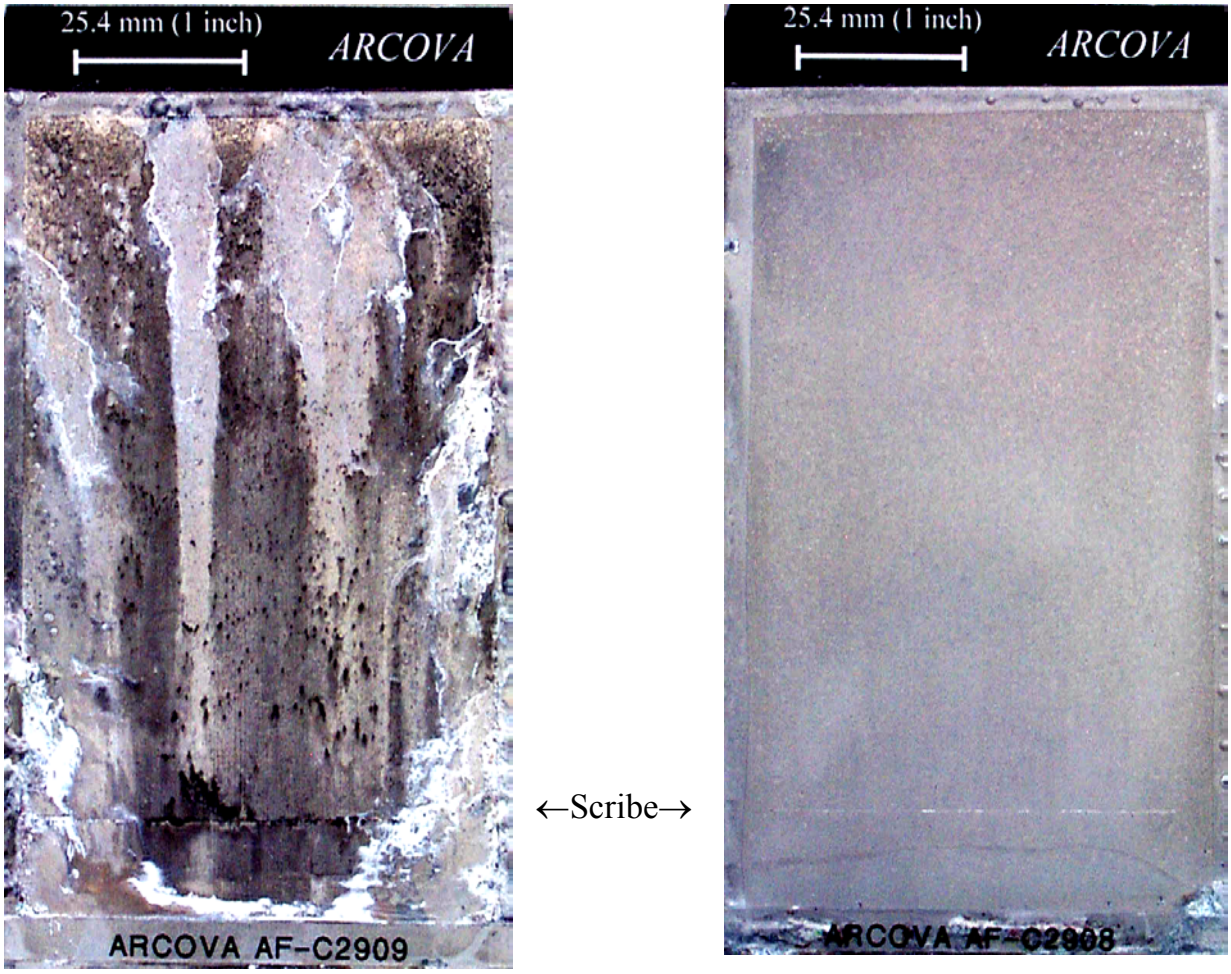

A B

FIGURE 1. Photographs of Test Specimens After 336 Hours of Salt Spray Exposure per ASTM B-117. Specimen A was Treated with PFZ only; Specimen B was Treated with the ZZV Formulation.

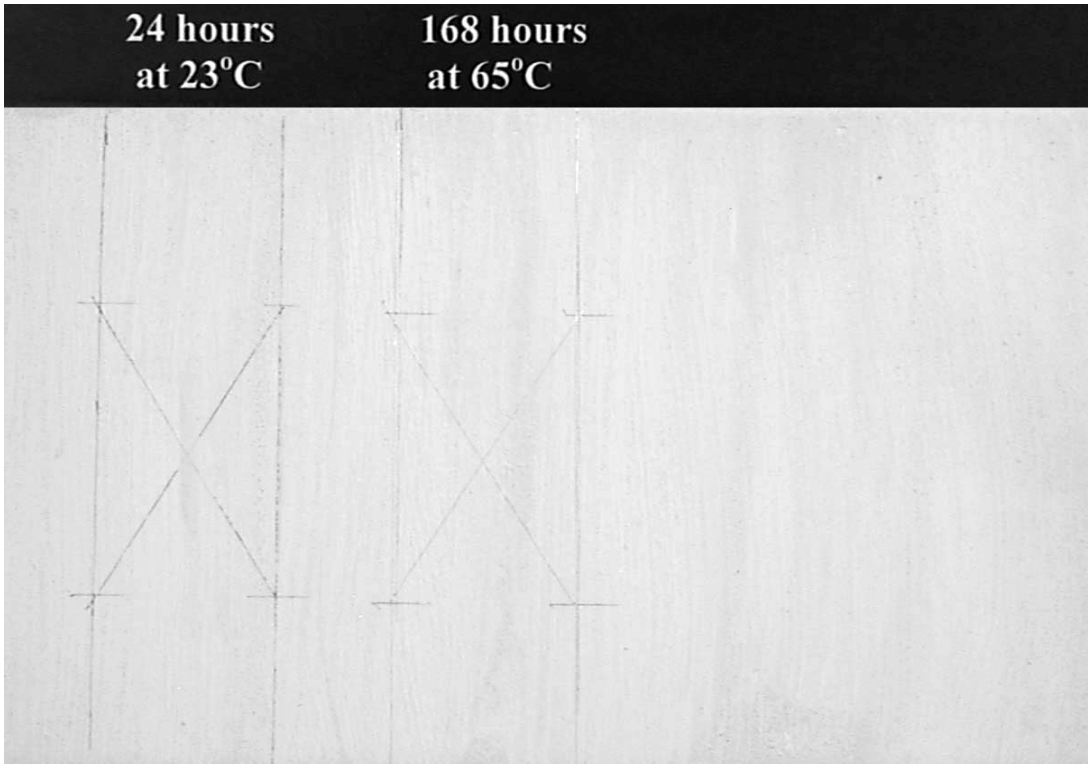

FIGURE 2. Photograph of a ZZV Treated Adhesion Specimen after Testing. Specimens were Coated with a Non-chromated Epoxy Primer (Deft 44-W-18.) The 24 Hour Test is on the Left and the 168 Hour Test is on the Right.

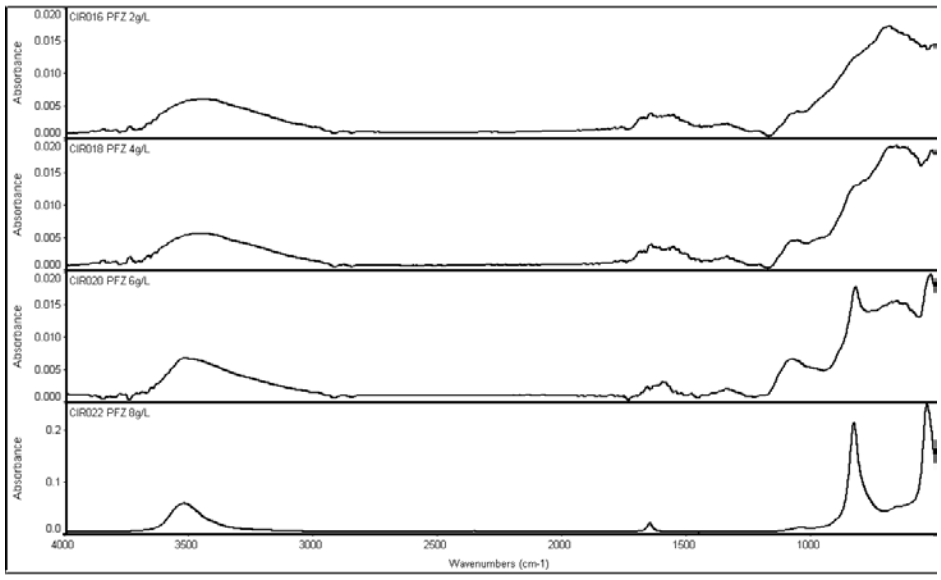

FIGURE 3. Specular Reflectance FTIR Spectra of Spray Applied PFZ Coatings. Potassium Hexafluorozirconate Concentrations Increase from 2g/L in the Top Figure, to 8g/L in the Bottom Figure, Increasing by 2g/L per Figure.

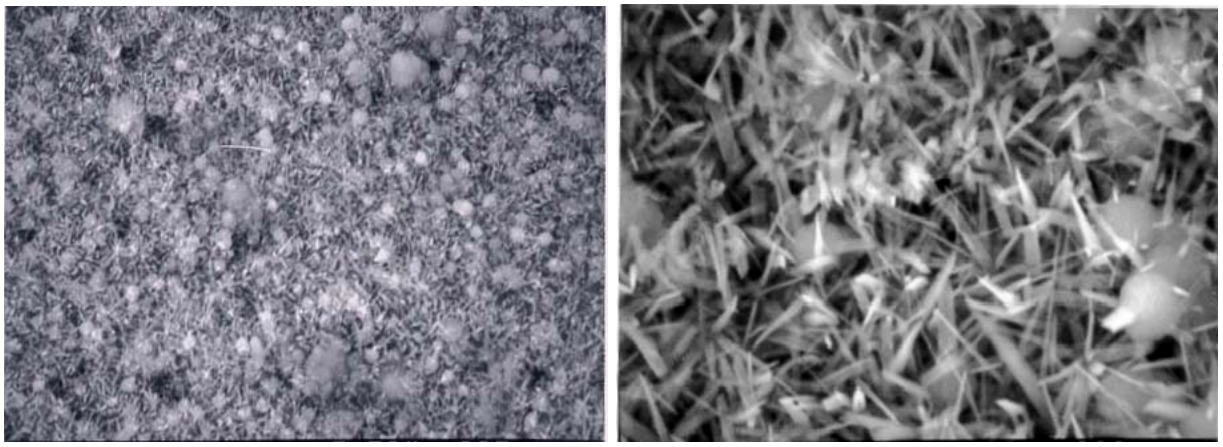

1900 X 10000 X

A

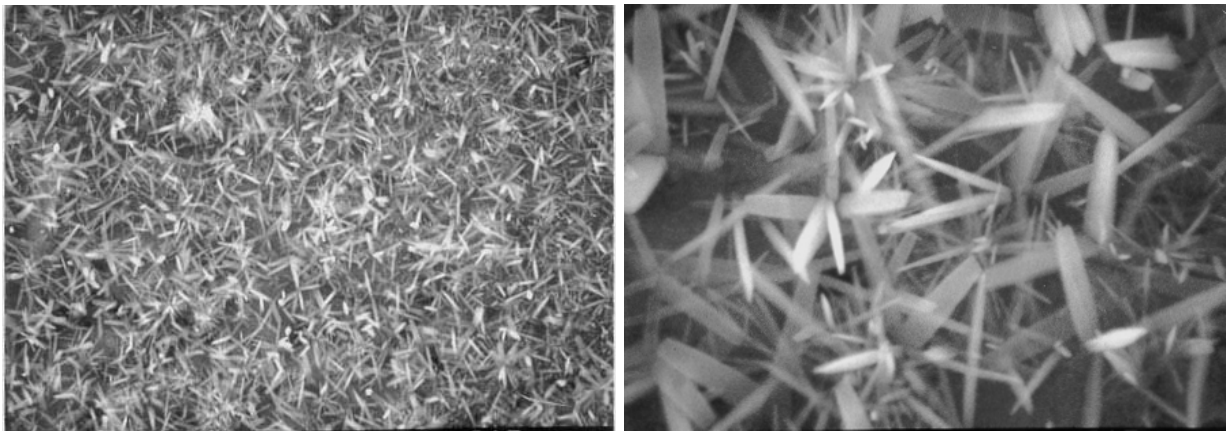

2000 X 10000 X

B

FIGURE 4. SEM Images of a ZZV Conversion Coatings, A) before Salt-spray Testing, Showing Columnar Crystals and Gobular Structures and B) Following Salt-spray Testing. Note the Absence of the Globular Structures Following Salt Spray Testing.

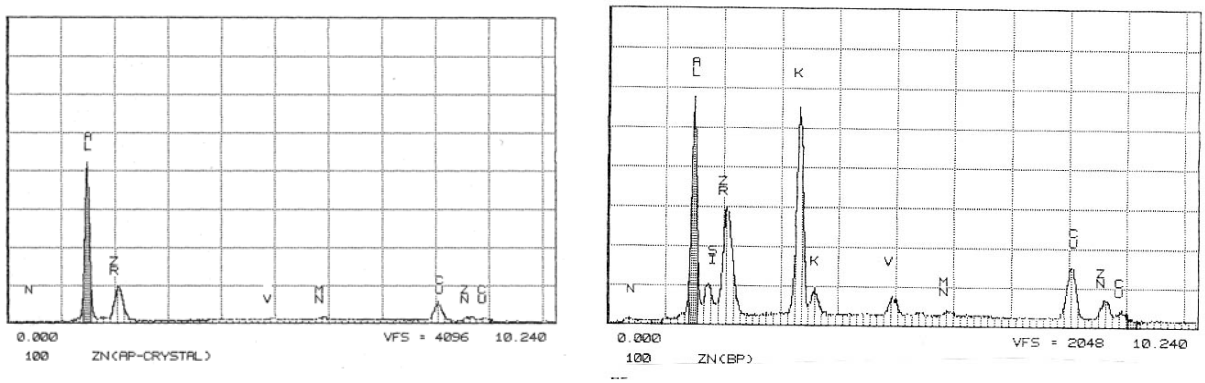

A B

FIGURE 5. EDAX Spectra of A) Columnar Crystals and B) Globular Components of Conversion Coating Prepared by Spray Application of a ZZV Coating.

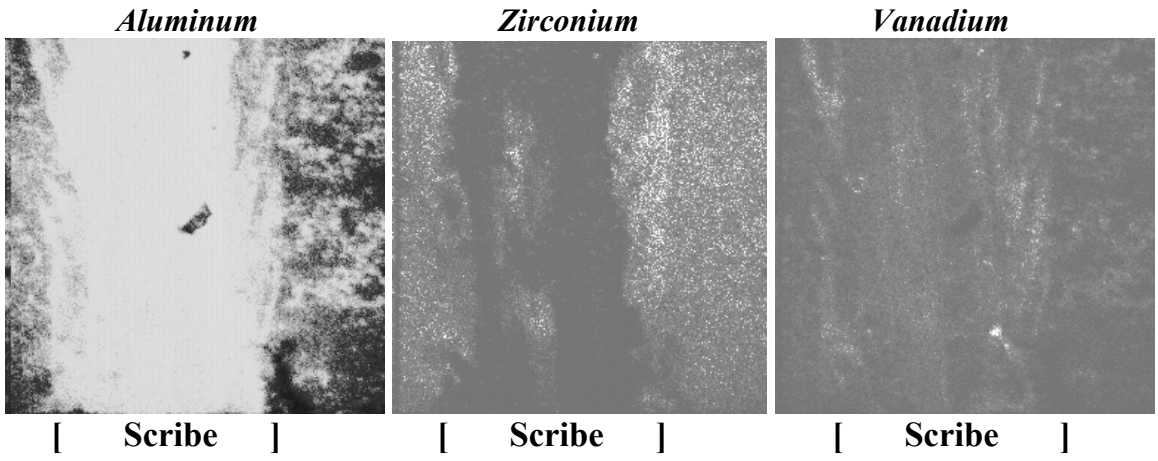

FIGURE 6. Time-of-flight Secondary Ion Mass Spectroscopic Surface Mapping of Aluminum, Zirconium and Vanadium in the Scribed Region of a ZZV Conversion Coated Specimen that Showed Self-healing During Salt-spray Testing. Light shading indicates a higher count rate for that pixel.

METALLIZING FOR CORROSION PROTECTION

Douglas H. Neale, Ph.D
NCI Information Systems, Inc.
2663 River Oak Dr.
Decatur. Georgia 30033-2804

David F. Ellicks
AFRL/MLS-OLR
325 Richard Ray Blvd., Bldg. 165
Robins AFB, Georgia 31093

ABSTRACT

The effectiveness of zinc and aluminum coatings for sacrificial corrosion protection of steel substrates has been well understood for many years. In addition to zinc galvanizing and conventional coatings loaded with zinc or aluminum metallic particles, these protective metals or their alloys can be applied using one of several thermal spray technologies ("metallizing"). Thermal spray techniques melt the selected coating metals and deposit them onto substrates for which protection is desired. The earliest approaches employed metal dusts sprayed though gas flames. This technique has evolved into "plasma" and "HVOF" systems used today for sophisticated modification of surface properties (e.g. increased hardness for wear, lubricity enhancement to decrease friction, etc.) using exotic metals and ceramics. Thermal spray technology also evolved from employing powders to using single wires fed through flames to allow higher application rates for such applications as metal fill and corrosion protection. In the last 20 years, wire arc spray technology employing two electrically charged wires of opposite polarity has been developed to further increase spray/deposit rates and has enabled the technology to graduate from shop to large-scale field applications. This brief paper is intended to familiarize its readers with wire arc spray technology; its applications, performance, limitations, costs and operational parameters.

INTRODUCTION

The use of sacrificial metals for corrosion protection ("cathodic protection") has been employed for hundreds of years. Electrochemically active materials such as zinc and aluminum can provide effective protection for less active materials such as iron and steel when placed in intimate, electrical contact with those materials in corrosive environments. In addition to

chemical galvanizing or coating with conventional paints loaded with metallic powders, cathodic protection can be applied by melting and directly depositing the active metals using thermal spray technologies ("metallizing"). The earliest thermal spray techniques employed gas flames or plasmas for melting metal powders and single wires. These techniques (HVOF, "D-Gun", Plasma systems) are still currently in use for applying corrosion protection as well as for more sophisticated protective coatings that yield enhanced surface properties for specialized applications. Wire and powder techniques, however, are somewhat limited in their application rates and use in the field for production coating applications. Development of wire arc spray over the last two decades has enabled metallizing to enter the realm of field duty for use on large iron/steel structures and high volume applications for the purpose of corrosion protection.

WIRE ARC SPRAY TECHNOLOGY

Wire arc spray systems employ welding techniques and hardware to apply sacrificial metal coatings to surfaces requiring corrosion protection. The protective metals are provided in wire format. In these machines, the two separate wires are given opposite electrical polarities with a standard welding power supply and are continuously fed by a controlled drive system into the spray gun. In the gun, the wires are brought into close proximity resulting in an electric arc that heats and melts the wire. The molten metal is propelled to and deposited on the target with a compressed air stream introduced behind the arc producing a pattern similar to conventional paint spray guns. The molten metal immediately re-solidifies as it impacts the surface forming a uniform protective coating. Depending on the thickness and alloy applied, these coatings commonly provide superior corrosion protection in excess of 25 years under a variety of aggressively corrosive environments. Metallizing has been demonstrated in field production

operations with portable commercial units on bridges, dams, offshore drilling platforms, water and gas storage tanks, communications towers, aircraft maintenance stands, general-purpose bomb casings, launch towers, aerospace ground support equipment (AGE), truck/trailer frames, pipelines and shipboard applications. This technology is currently gaining wide recognition and acceptance in State and Federal Departments of Transportation for corrosion protection of the infrastructure.

Parameters, features and requirements of metallizing technology are summarized below:

Substrate Surface Preparation:

- Abrasive blast with angular grit to produce 2mil – 3 mil anchor profile
- SSPC-SP 10/ NACE No. 2 finish: "near white metal" for non-marine applications
- SSPC-SP 5/NACE No. 1 finish: "white metal" for marine applications
- Dust/debris free

Coating Parameters/Characteristics:

- 6 – 10 mils total thickness (2-3 mils per pass, typical)
- Clean/dry compressed air @ 80-100 Psig
- Application rates: 50 – 200 square feet per hour
- Cost relative to conventional military epoxy/polyurethane system (application dependent)
    - Material/application cost: 150% - 250%
    - Life cycle cost: 5% to 50 %
- Fine/Medium sandpaper-like finish
- Excellent adhesion to substrate (> 500 psi)
- Excellent flexibility (10 mil coating passes 1/2 inch dia. mandrel bend test)
- Porous coating – accepts topcoats/sealers well
- Moderate substrate heating
    - Typically less than 10 degrees F for substrates thicker than ¼"
    - Controllable with application technique for substrates less than ¼" thick
- Topcoat/sealer optional
    - Cosmetics
    - Corrosion protection service life modestly enhanced
    - Chemical compatibility important (e.g., non-alkyd)

Health/Safety:

- Arc spray process regarded as a welding process
- High levels of dust and smoke produced
    - High levels of ventilation/filtration for enclosed spray operation (booths)

    - Full respirator helmet with fresh air supply for manual application operator
    - Welding fumes
    - Aluminum and/or zinc oxide waste dust – disposable/reclaimable
- High level of ultra-violet radiated from arc
    - Eye protection with 3-6 welding shade number when gun shield is used
    - Eye protection with 9-12 welding shade number when no gun shield is used
- High noise levels produced (116 dBA at source, typical)
    - Ear plugs AND earmuffs for manual application operator
    - Ear plugs or earmuffs for personnel within 10 - 50 feet range from arc spray gun
- Personnel protective equipment (PPE) required
    - Goggles/full-face shields
    - Gloves
    - Full body cover

Equipment:

- Portable, rugged application equipment
- Machines, wire materials commercially available, stock listed
- Cost: ~ $25K per mobile spray unit (electric power, compressed air sources not included)

Materials (sacrificial corrosion protection):

- Zinc, aluminum, zinc/aluminum alloy
- Material selection depends on application and environment
- Typical wire sizes: 1/8" and 3/16"
- Wire supply formats:
    - 40 pound reels (mobile machine)
    - 500 pound drums (fixed machine)

Utilities (per gun):

- Compressed air: 75 scfm @ 100 psig (~25 HP compressor)
- Electric: 230/460 Vac, 3 phase (30 amps @ 460 Vac)

Sample Supporting Standards And Specifications for Wire Arc Thermal Spray Process:

"Application of Thermal Spray Coatings (Metallizing) of Aluminum, Zinc, and Their Alloys and Composites for the Corrosion Protection of Steel"*

"Application of Thermal Spray Coatings (Metallizing) of Aluminum, Zinc, and Their Alloys and Composites for the Corrosion Protection of Steel, Part B Guide"*

* These documents are joint draft standards under development by the American Welding Society (AWS C2B), National Association of Corrosion Engineers (NACE TG 146) and the Society for Protective Coatings (SSPC C.1.2.B)

MIL-STD-2138, “Metal Sprayed Coatings for Corrosion Protection Aboard Naval Ships”

“Thermal Spraying: Practice, Theory, and Application”, American Welding Society

“Guide for the Protection of Steel with Thermal Sprayed Coatings of Aluminum and Zinc and their Alloys and Composites”, ANSI/AWS C2.18-93

“Guide for Thermal Spray Metallic Coating Systems”, SSPC Coating System Guide No. 23.00

SUMMARY

Wire arc spray is a mature technology for field application of sacrificial corrosion protection coatings on iron/steel equipment and structural applications. These metallized coatings, when applied correctly, offer extended protection that yields life cycle costs substantially lower than conventional liquid coating systems. The commercially available application equipment is versatile, rugged, maintainable and mobile. Metallizing has been successfully demonstrated in a wide variety of commercial and military production applications and the technology promises to become an essential and effective asset to Military corrosion protection and prevention maintenance activities.

CERIUM-BASED CORROSION PROTECTION SYSTEMS FOR ALUMINUM ALLOYS

E.L. Morris, J.O. Stoffer, T.J O'Keefe, M. O'Keefe, W. Fahrenholtz,
T. Schuman, P. Yu, S. Hayes, A. Williams, B. Rivera and Chris Singleton.

University of Missouri-Rolla, Rolla, MO 65409.

ABSTRACT

A cerium-based conversion coating has been developed which appears to meet the military requirement of 336 hour corrosion protection in neutral salt spray conditions. The oxidation state and phase of the condensed cerium has been shown to be an important aspect of the corrosion protection properties provided by the film. Because of the strong influence of the solution chemistry and operating parameters on film performance, a basic knowledge of the system stability is essential. Towards this end, a revised E-pH diagram was developed for the Ce-H_2O system. In addition, cerium-based conversion coatings in conjunction with various corrosion inhibitor containing primer formulations appear to meet the military requirement of 2000 hour neutral salt spray exposure as defined by Mil-P-85582 for a scribed primer system. Results indicate that cerium is a promising candidate as a drop in replacement for chrome in conversion coating and primer formulations.

INTRODUCTION

Chromating is the most commercially used surface pre-treatment for the corrosion protection of aluminum alloys in the aircraft and the aerospace industries. However, hexavalent chromium, a known carcinogen, is a primary component in this process. Because of this, alternative methods to chromating, such as cerium-based conversion coatings and inhibitors in primers which were developed by Stoffer *et al.,* appear to meet the military corrosion protection requirements of 2000 hours scribed salt spray exposure for a complete coating system .[1, 2]

Other toxic chemicals, such as cyanides and fluorides, may be present in commercial chromate conversion baths.[3] Major reasons for the widespread use of chromium-based protective coatings are their self-healing nature, excellent corrosion resistance and their ease of

application.[4,5] However, current environmental legislation is moving towards total exclusion of hexavalent chromium, Cr^{6+}, due to its toxic nature. Regulatory pressure to reduce the hazardous waste of chromium supports development of non-toxic alternative methods of corrosion protection. Potential candidates for the replacement of toxic chromium, which include cerium based salts are currently being developed into various e-coat, paint formulations and tested.[2]

The purpose of this present study was the evaluation of cerium-based conversion coatings and corrosion inhibiting pigments for primer systems for the future replacement of chromium in military and aerospace application. Classical ASTM methods, such as ASTM B-117 salt fog, were used to evaluate the corrosion protection of the conversion coatings and inhibitor containing primer formulations. Electrochemical evaluation results were correlated to ASTM B-117 performance.

EXPERIMENTAL

To observe the phase transformations of cerium in aqueous solution, titration studies for pH change and cerium hydrolysis were conducted. The tests were made at ambient temperature ($25 \pm 1\ ^0C$) using 100 mL of aqueous cerium solution, normally containing 0.01 mol/L of Ce(III) or Ce(IV). For Ce(IV), the solution was made from commercial 0.5N stock solutions of $Ce(ClO_4)_4$ which contained some free $HClO_4$. For Ce(III), a commercial $Ce(ClO_4)_3$ solution (40 % w/w) was used. Solution pH was monitored continuously. With continuous solution agitation provided by a magnetic stirrer, the solution pH was slowly increased by addition of concentrated (45.3 % w/w) KOH solution in 10 or 20 :L increments using a 25-:L syringe. As the cerium ions underwent hydrolysis, the pH, solution color, and the formation of solid phases were noted when the pH became stable. The experiments were made either open to air or with Ar sparging.

The 7075-T6 aluminum alloy specimens (89% Al-5.9% Zn-1.4% Cu-1.1% Mg-1.0% Si-0.2% Cr) used in this study were manufactured by Pioneer Kaiser. The pretreatment of the alloy was in accordance with Boeing-St. Louis specification which included rinsing with acetone followed by immersion in 5% "Turco" alkaline cleaner for 10 to 15 minutes. Cleaning can be followed by a deoxidizing treatment performed in a solution containing 2.5 wt% Amchem #7 and 10 vol% nitric acid or sulfuric acid at ambient temperature for 5 minutes. Cleaned and deoxidized panels were thoroughly rinsed with de-ionized water prior to coating.

The non-spontaneous cerium electrolyte was prepared by dissolving 30 mM $Ce(NO_3)_3X6H_2O$ into a solution containing 0–75 vol% propylene glycol and 0–17 wt% hydrogen peroxide. The coatings were deposited galvanostatically using direct current (DC) plating with a DSA (dimensionally stable anode) or platinum wire mesh anode at a current density between 5 and 15 mA/cm^2 for 1 to 5 minutes. Once the deposition was completed, specimens were removed from the electrolyte, rinsed with deionized water, and sealed in boiling water for 5 minutes.

The cathodic e-coat was prepared by first adding the surfactant Triton CF-10 to the distilled water while stirring at 890 rpm using a 3.5" Cowell's blade. The titanium dioxide and any inhibiting pigments were then slowly added while stirring at 890 rpm. Once added, the speed was then increased to 1420 rpm and until a dispersion of about 6+ on the Hegman scale was obtained. A typical dispersion time was 30 minutes. Then distilled water was added to the pigment paste and allowed to stir moderately using magnetic stirring overnight. The emulsion was then blended into the e-coat bath under slow stir. If no severe settling appeared, the e-coat bath stirred for 1 additional hour prior to use. Samples were then e-coated at 200 V for 2

minutes. A stainless steel anode was used. All e-coated samples were rinsed with distilled water, air dried, and allowed to cure in an oven at 150 ^{o}C for 30 minutes.

To evaluate the corrosion protection provided by these paint inhibitors, the inhibitor containing formulations were exposed to 2000 hour salt spray testing which was performed in accordance with ASTM B-117 methods. All scribes were made using a standard carbide tipped pen. To ensure a uniform and deep enough scribe, 4 to 6 passes were made. SEM/EDX analysis of the scribed region was used to ensure that a deep enough and clean scribe was obtained. The edges of each panel were then covered using non-conductive, electrical tape. Neutral salt spray testing was performed at both UMR and Boeing-St. Louis. All sea salt/SO_2 exposure tests were performed at Boeing-St. Louis in accordance with ASTM methods. Elemental characterization and high magnification micrographs were obtained using a Hitachi S4700 SEM/EDX.

RESULTS AND DISCUSSION

REVISED Ce-H_20 E-pH DIAGRAM

The oxidation state and phase of the condensed cerium has been shown to be an important aspect of the corrosion protection properties provided by the film. Because of the strong influence of the solution chemistry and operating parameters on film performance, a basic knowledge of the system stability is essential. Towards this end, a revised E-pH diagram was developed for the Ce-H_2O system.

One motivating factor for re-examining the cerium E-pH diagram is the recent application of cerium films for corrosion protection of aluminum alloys. The use of Ce in conversion coatings is the subject of several papers and patents and a number of representative

examples can be found in the literature.[1,2,5,6] Also, to a lesser extent, there has been some interest in using cerium compounds as a substitute for chromate in paint and primer-type coatings.[2,7]

The general mechanism of cerium conversion coating deposition has been described previously.[5,8] In both the non-electrolytic and electrolytic cerium deposition processes, an increase in solution pH at the cathode interface leads to precipitation of the cerium compounds. In two patented processes,[1,2,5] the increase in interfacial pH is achieved by cathodic polarization of the substrate. One patent claims that the final coating is initially deposited as an oxide or hydroxide with a Ce(IV) oxidation state, with the possibility of inclusion of some Ce(III). [1] In this application, a soluble cerium (III) salt is used in the electrolyte with an oxidant, such as hydrogen peroxide, added to assist in forming a final Ce(IV) state. Reactions that would increase pH include:

$$2H_2O + 2e^- \rightarrow H_2 + 2OH^- \quad \text{(R1)}$$

$$2H^+ + 2e^- \rightarrow H_2 \quad \text{(R2)}$$

$$H_2O_2 + 2H^+ + 2e^- \rightarrow 2H_2O \quad \text{(R3)}$$

$$H_2O_2 + 2e^- \rightarrow 2OH^- \quad \text{(R4)}$$

The reactions for precipitation and film formation are thought to be:

$$Ce^{3+} + 3OH^- \rightarrow Ce(OH)_3 \quad \text{(P1)}$$

$$Ce^{3+} + OH^- + \tfrac{1}{2} H_2O_2 \rightarrow Ce(OH)_2^{2+} \quad \text{(P2)}$$

$$Ce(OH)_2^{2+} + 2OH^- \rightarrow Ce(OH)_4 \quad \text{(P3)}$$

Correlation of film characteristics and properties with cerium film formation are needed to better understand the influence of deposition parameters, such as pH and cerium species, on corrosion protection performance. Interest in the thermodynamic stability of various cerium species has thus led to a review of recently published data on cerium species, construction of a revised E-pH diagram using these data and some precipitation experiments to verify the derived

E-pH diagram. The E-pH diagram constructed in this study is significantly different from the one published earlier in Pourbaix's Atlas[9] (Fig.1). Of particular practical importance is the need to clarify the low pH regions where the precipitation of the cerium compounds seems to occur during processing.

DIAGRAM CONSTRUCTION

The perchlorate system was chosen because ClO_4^- has little tendency to form complexes with cerium ions, so the cerium behavior is equivalent to the Ce-H_2O system.

Example Calculation - Ce^{4+}/Ce^{3+} Equilibrium

The basic electrochemical reaction between Ce^{3+} and Ce^{4+} is

$$Ce^{3+} \rightarrow Ce^{4+} + e \tag{1}$$

Using the updated standard molar Gibbs energy of formation at 298.15 K, ΔG_f^0, of the two ions (Lide, 2000), the standard potential is

$$E^0 = \frac{(\Delta G^0_{f,Ce^{4+}} - \Delta G^0_{f,Ce^{3+}})}{nF} = \frac{-503{,}800 + 672{,}000}{1 \times 96485} = 1.743V \tag{2}$$

$$E = 1.743 + \frac{RT}{nF} ln \frac{[Ce^{4+}]}{[Ce^{3+}]} = 1.743 + 0.05916 \log \frac{[Ce^{4+}]}{[Ce^{3+}]} \tag{A1}$$

When $[Ce^{4+}] = [Ce^{3+}]$, E = 1.743 V.

Using a similar approach, the other equilibrium reactions can be calculated. Reaction types would include those involving electron transfer, pH, or a combination of electron transfer and pH. When all the proposed expressions are plotted together, the regions of stability are defined resulting in the E-pH diagram shown in Figure 2.

The major difference noted with the revised diagram was that the theoretical pH for Ce(IV) precipitation was much lower than indicated in the original diagram. In 0.01 mol/L $Ce(ClO_4)_4$ solution, the $Ce(OH)_4$ precipitation starts at pH values less than 5.

Precipitation tests confirmed that the newly constructed E-pH diagram seemed reasonable in light of the experimental results. In perchlorate solution, $Ce(OH)_2^{2+}$ is a more stable ionic form than $Ce(OH)^{3+}$ and $Ce(OH)_3^{+}$ in the Ce(IV) hydrolysis process. The morphology of the cerium conversion coatings prepared using a precipitation process is given in Figure 3.

SALT SPRAY EVALUATION OF CERIUM CONVERSION COATINGS

Cerium-coated 7075-T6 alloy panels 3×6 inches have been evaluated using ASTM-B117 salt spray testing for 336 hours in parallel with chromated specimens at the Boeing-St. Louis laboratories. Well-prepared coatings on 7075-T6 exhibited no sign of corrosion or discoloration after the salt fog exposure. Side by side comparison of bare, chromium and cerium conversion coated panels after 336 hours of neutral salt fog testing is shown in Figure 4. Overall, the surface is uniformly covered by cerium compounds, and no major corrosion areas were found after the tests.

SALT SPRAY EVALUATION OF CERIUM-BASED PRIMERS

E-coat primers have been used extensively in the automotive industry, because of their ability to coat metal substrates with irregularly shaped parts. The e-coat provides excellent surface coverage using a low VOC primer. One major problem with e-coat systems is their inability to contain corrosion inhibitors, which would allow for passivation and protection of exposed metal defects. The e-coat provides an exceptional barrier coating, but once the primer is compromised, the underlying substrate is easily corroded. It is the instability of the e-coat

emulsion due to the nature of the precipitation reactions of film formation, which makes the incorporation of corrosion inhibitors into the primer system extremely difficult. However, cerium-based inhibitors have successfully been incorporated into e-coat primers by Stoffer *et al*.[1, 2] The cerium-based corrosion inhibiting pigments have successfully been incorporated into several commercially available e-coat formulations. Figure 5 shows several e-coat primer formulations applied over bare, chrome, and cerium conversion coatings for Al 7075 T-6 and Al 2024 T-3 after 2000 hours neutral salt fog testing. Results indicate that the incorporation of cerium-based corrosion inhibiting pigments into the e-coat formulations does indeed provide protection to the underlying metal substrate when the primer integrity is compromised.

SUMMARY OF THE E-COAT SYSTEMS TESTED AND BOEING-ST. LOUIS

Promising candidates were formulated, coated, and sent to Boeing-St. Louis for testing. The tests conducted at Boeing-St. Louis were 12 weeks cyclic prohesion and four weeks sea salt SO_2 evaluation. A summary of the results for only the promising prohesion and SO_2 results obtained from Boeing-St. Louis is given in Table 1. The quality of each coating system is based upon the average of the representative panels that were tested. The amount and degree of corrosion is recorded in millimeters of migration from the scribe. Since variations in the way a scribe is cut into a panel can affect the degree of corrosion that occurs, Boeing machine scribed all of the panels to ensure a uniform scribe width and depth.

Based upon the Boeing-St. Louis tests, e-coat formulations containing cerium-based inhibitors performed comparably to Boeing's currently used chromated primers in cyclic prohesion tests. The cerium containing e-coat performed significantly better than the chromated primer system in SO_2 exposure. Photos of these actual panels after prohesion and SO_2 exposure are shown in Figures 6 and 7. The paint/primer on some panels shown was removed in order to

better examine the actual extent of corrosion to the underlying metal. Advanced weathering results obtained in our lab and confirmed at Boeing-St. Louis, confirmed that cerium nitrate, when incorporated into a cathodic e-coat formulation, played an active role in the corrosion protection of high strength aluminum alloys.

CONCLUSIONS

A revised E-pH diagram was developed for the Ce-H_2O system using more recent thermodynamic data on cerium species not available for the original diagram published in Pourbaix's Atlas. The major difference noted with the revised diagram was that the theoretical pH for Ce(IV) precipitation was much lower than indicated in the original diagram. In 0.01 mol/L $Ce(ClO_4)_4$ solution, the $Ce(OH)_4$ precipitation starts at pH values less than 5. Precipitation tests confirmed that the newly constructed E-pH diagram seemed reasonable in light of the experimental results. In perchlorate solution, $Ce(OH)_2^{2+}$ is a more stable ionic form than $Ce(OH)^{3+}$ and $Ce(OH)_3^{+}$ in the Ce(IV) hydrolysis process.

Based on the revised E-pH diagram, a cerium-based conversion coating has been developed which appears to meet the military requirement of 336 hour corrosion protection in neutral salt spray conditions. Cerium-based conversion coatings have been successfully produced by cathodically polarizing aluminum alloys in an electrolyte containing cerium. Well-prepared coatings on 7075-T6 alloys passed 336-hour salt spray tests with no observable corrosion or discoloration. In general, the cerium-based coating is a promising candidate to replace the chromating system.

In addition, cerium-based conversion coatings in conjunction with various corrosion inhibitor containing primer formulations appear to meet the military requirement of 2000 hour neutral salt spray exposure. These cerium-based primers also performed well in corrosive

environments during advanced weathering tests. ASTM G 85 cyclic prohesion and sea salt/SO_2 were performed at Boeing-St. Louis. E-coat formulations containing cerium nitrate as an inhibitor, performed comparably to Boeing's currently used chromated primers and e-coat in cyclic prohesion tests, and cerium nitrate performed significantly better than these systems in sea salt/SO_2 exposure.

Again, it is clear that the use of cerium appears to be a promising candidate for the future replacement of chromium in aerospace applications.

ACKNOWLEDGMENTS

The authors would like to thank AFOSR, AFRL, Boeing-St. Louis, the National Science Foundation, and the Missouri Department of Economic Development for their support.

REFERENCES

1. J.O. Stoffer, T.J. O'Keefe, X. Lin, E.L. Morris, P. Yu, and S.P. Sitaram, Electodeposition of Cerium-Based Coatings for Corrosion Protection of Aluminum Alloys, U.S. Patent 55,932,083 (1999).

2. E.L. Morris, J.O. Stoffer, T.J. O'Keefe, P. Yu, and X. Lin, Plym. Mater. Sci. Eng., 78, 172 (1998).

3. R.G. Buchheit, M.D. Bode and G.E. Stoner, Corrosion-Resistant, Chromate-Free Talc Coatings for Aluminum, *Corrosion Science*, 50 [3] 205-214 (1994).

4. D. Gilroy, P.J. Eddowes, etc., *Metal Finishing*, Oct., 26 (1996).

5. F. Mansfeld, M.W. Kendig, *J. Electrochem. Soc*., 135, 828 (1998).

6. Hinton, B., Hughes, A., Taylor, R., Henderson, M., Nelson, K., Wilson, L., *ATB Metall*., **37 (2-3-4)**, 165-168 (1997).

7. Baldwin, K.R., Gibson, M.C., Lane, P.L., Smith, C.J.E., *7th European Symposium on Corrosion Inhibitors--Proceedings.* **2**, Universita degli Studi di Ferrara, 771-785 (1990).

8. Lin, X., Ph.D. Thesis, University of Missouri-Rolla (1998).

9. Pourbaix, M., *Atlas of Electrochemical Equilibria in Aqueous Solutions*, NACE (1974).

TABLE

TABLE 1
SUMMARY OF THE PROHESION AND SO_2 RESULTS

Description	Inhibitor Present In E-Coat/Primer	Avg. Scribe Migration[a] Prohesion	Avg. Scribe Migration[a] SO_2
Boeing E-Coat on CrCC 7075 T-6	None	6.25	2.55
Chrome Primer on CrCC 7075 T-6	Chromium	0.65	2.50
UMR E-Coat on CrCC 7075 T-6	Commercial	6.00	NA
UMR E-Coat on CrCC 7075 T-6	Cerium Compound	1.10	0.20

a = Migration in mm from center of scribe at the region of the panel with the most corrosion.

FIGURES

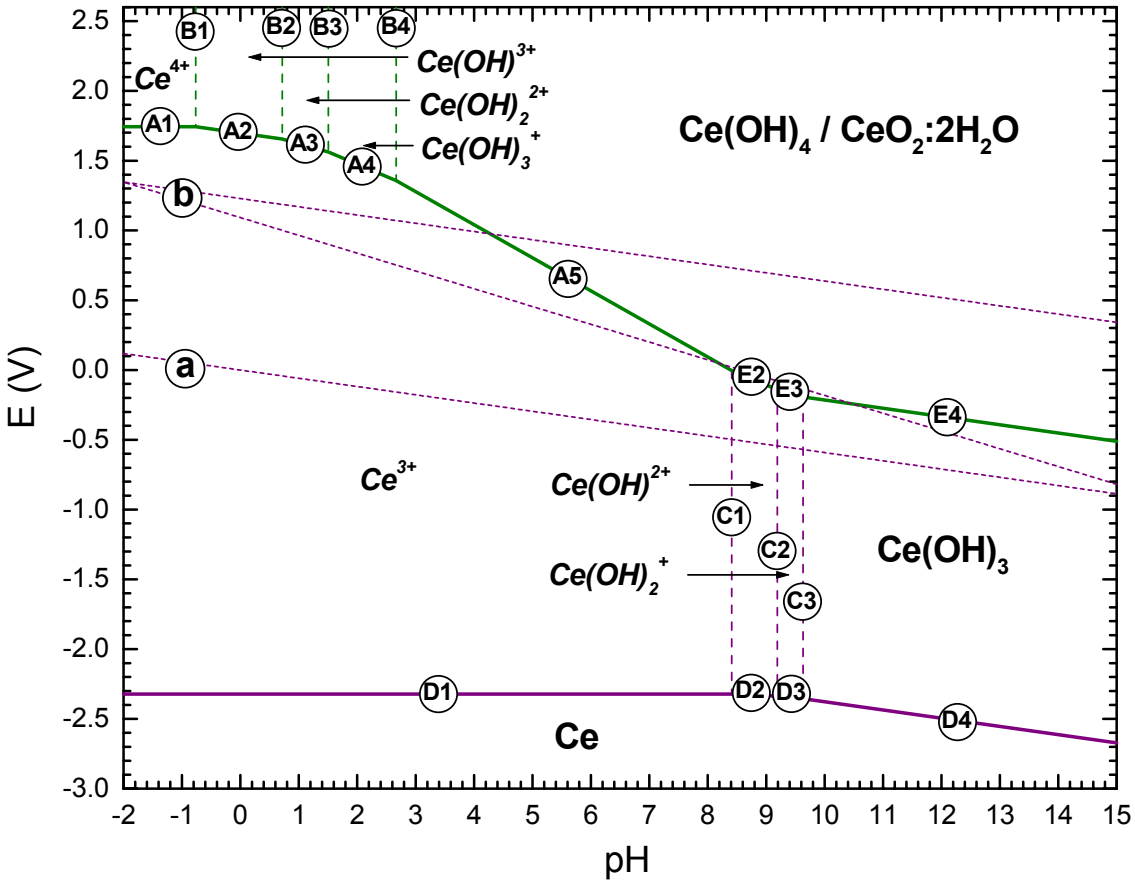

FIGURE 1. Previously published Pourbaix Diagram for cerium. (Pourbaix, 1974)

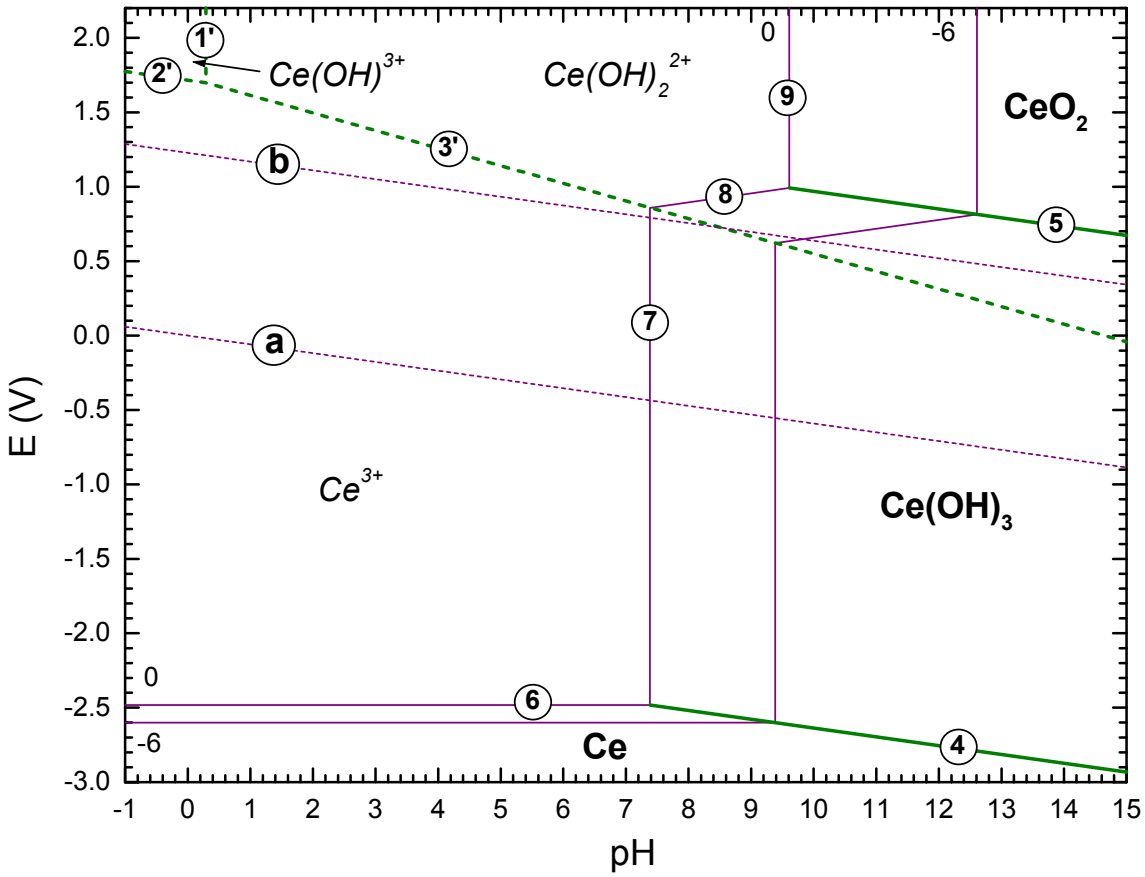

FIGURE 2. An updated Pourbaix Diagram for cerium in aqueous perchlorate solution.

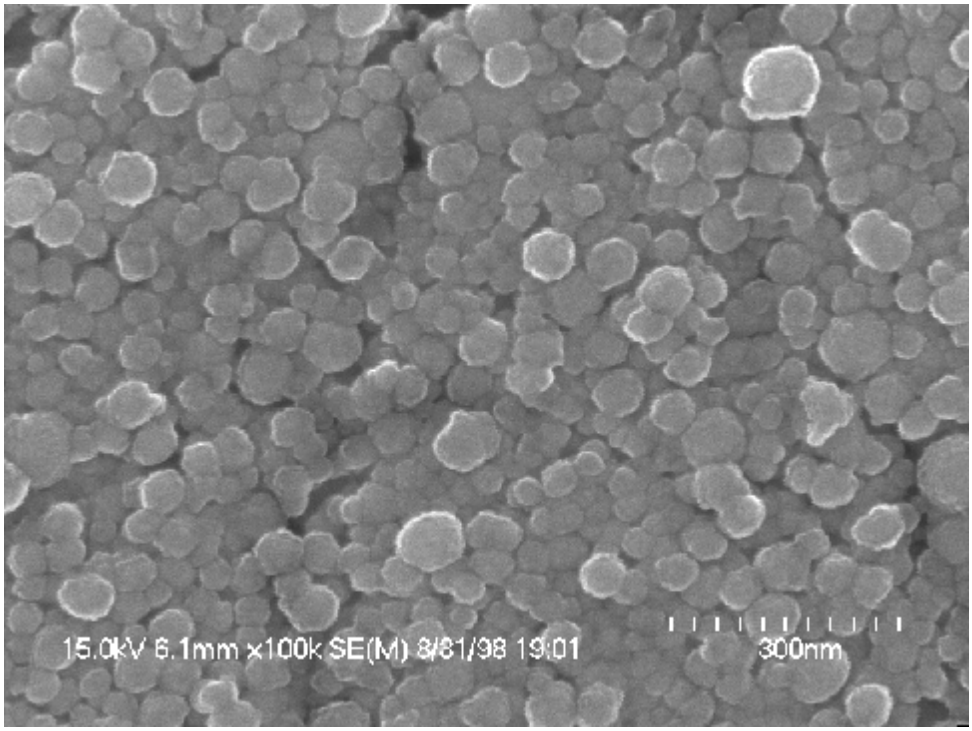

FIGURE 3. SEM image of a cerium coating on 7075-T6 aluminum panel.

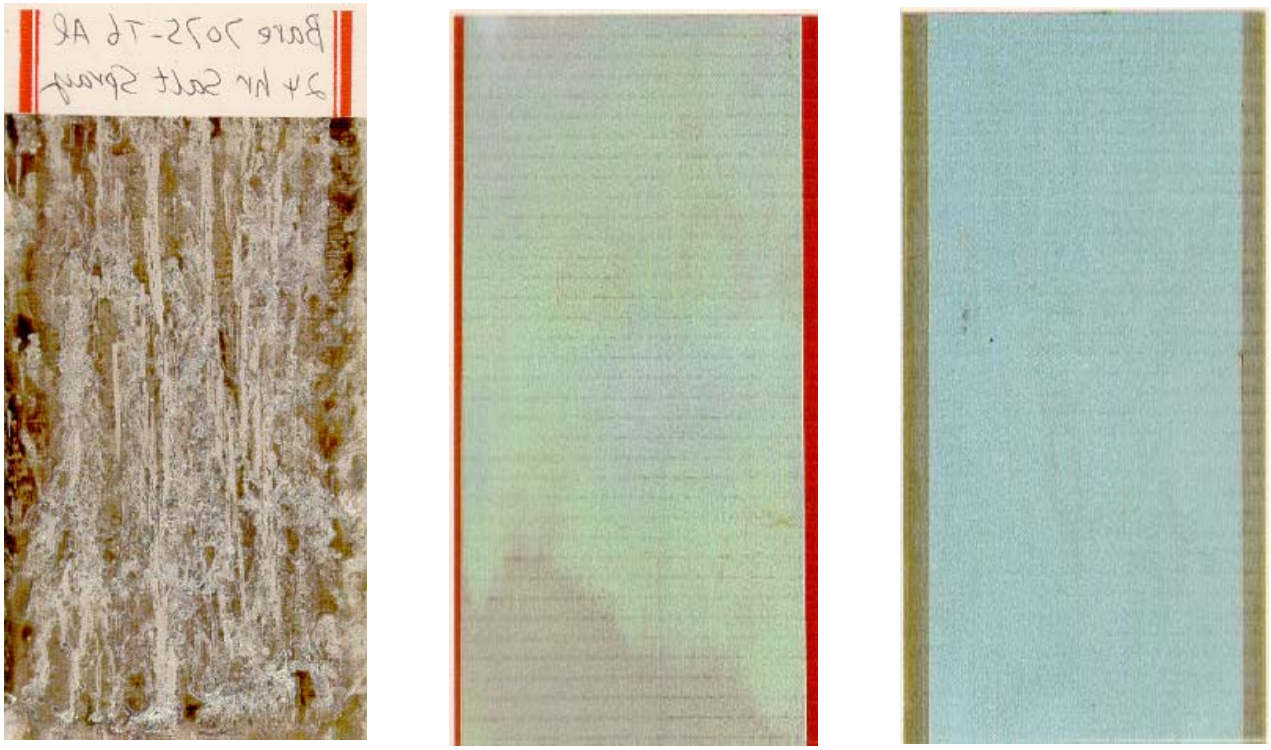

Bare 7075 T-6
24 Hours
Salt Fog Exposure

CeCC 7075 T-6
336 Hours
Salt Fog Exposure

CrCC 7075 T-6
336 Hours
Salt Fog Exposure

FIGURE 4. Comparison of Bare, Cerium and Chromium Conversion Coated Al 7075-T6 Panels After Salt Fog Testing.

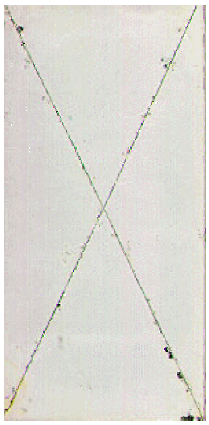

Bare Al 7075-T6
No Inhibitor

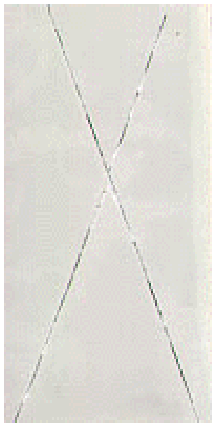

CrCC Al 7075-T6
No Inhibitor

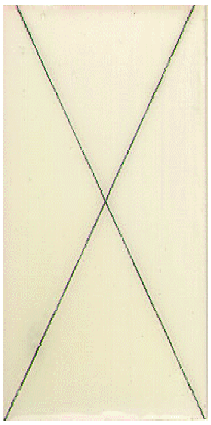

CrCC Al 7075-T6
Primer + Inh. I

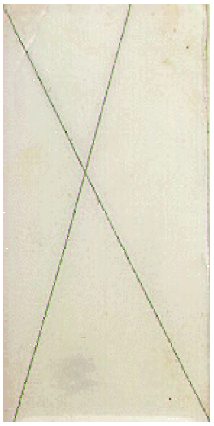

CeCC Al 7075-T6
Primer + Inh. I

Bare Al 2024-T3
No Inhibitor

CrCC Al 2024-T3
No Inhibitor

CrCC Al 2024-T3
Primer + Inh. I

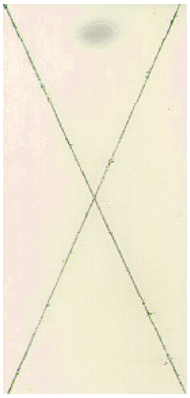

CeCC Al 2024-T3
Primer + Inh. I

FIGURE 5. Representative Al 7075 T-6 And Al 2024 T-3 Panels After 2000 Hours ASTM Salt Spray.

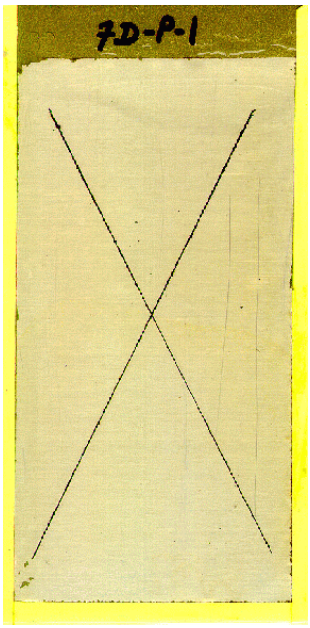

Chromated Al 7075 T-6
Chromated Primer

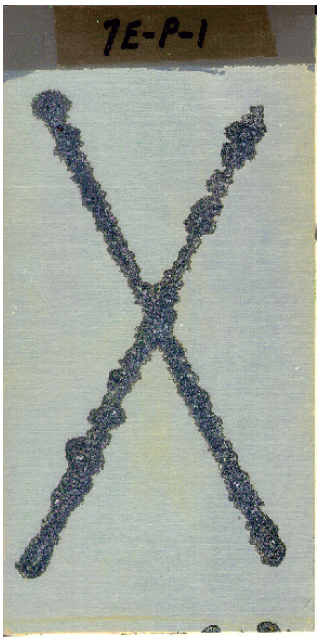

Chromated Al 7075 T-6
Boeing E-Coat + No Inhibitor

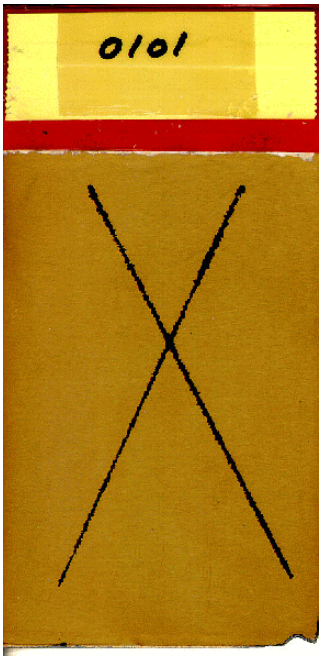

Chromated Al 7075 T-6
UMR E-Coat + Cerium

FIGURE 6. Various E-Coats on Chrome Conversion Coated Al 7075 T-6 Panels After 12 Weeks ASTM Prohesion At Boeing-St. Louis.

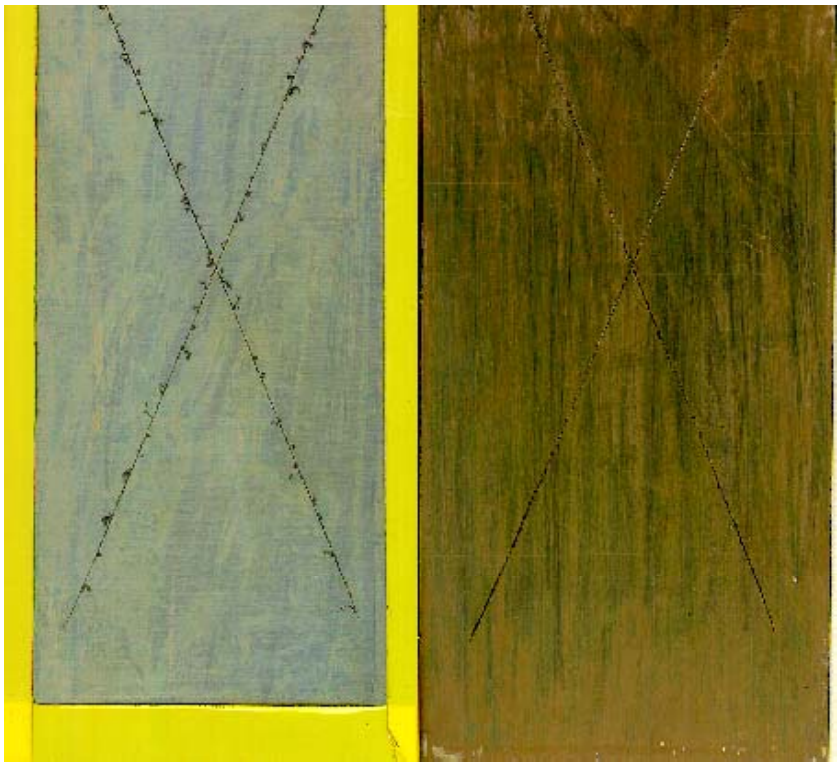

CrCC 7075 T-6
Chrome Primer
Heavy Chromated

CrCC 7075 T-6
UMR E-coat
Cerium Compound

FIGURE 7. Various E-Coats on Chrome Conversion Coated Al 7075 T-6 After 12 Weeks Sea Salt/SO_2 At Boeing-St. Louis.

LOW TEMPERATURE RETROGRESSION AND RE-AGING HEAT TREATMENTS FOR THICK SECTION COMPONENTS OF ALUMINUM ALLOY 7075 FOR AGING AIRCRAFT REFURBISHMENT

Charles P. Ferrer, Michelle Gaudett Koul, Brian J. Connolly, Angela L. Moran
United States Naval Academy
Annapolis, MD 21402

ABSTRACT

Aluminum alloy 7075, commonly used on military aerospace platforms, is susceptible to intergranular stress-corrosion cracking (SCC) in the peak strength T6 temper. The susceptibility of this temper to SCC is alleviated through the use of the T73, or overaged temper, that provides improved SCC resistance, but with a 10-15% strength loss compared to the T6 temper. Experimental test results by Cina and Ranish[1] indicated that retrogress and re-aging (RRA) heat treatments reduce the trade-off between T6 strength and T73 SCC resistance. However, the short time heat treatment used limited the applicability of RRA to thin sections of material. The primary goals of this research effort were to determine if lower retrogression temperatures could be used in the RRA process to extend the applicability of this heat treatment to thick section aircraft components and to quantify any observed improvements. Alternate immersion (AI) and double-cantilever beam (DCB) tests were conducted in an 0.6 M NaCl solution to evaluate the SCC resistance of various tempers. Improvements in properties were demonstrated using RRA heat treatments at lower temperatures and longer times than those previously investigated. In general, the various RRA tempers below 200°C produced strengths similar to that of T6 with improved SCC properties. The RRA temper with retrogression at 160°C for 660 minutes produced the greatest improvement, with only a 4% reduction in strength below T6. As an added benefit, heat transfer analysis indicated the RRA tempers with lower retrogression temperatures and longer retrogression times are more viable for use in industry for thick section components.

INTRODUCTION

The principal alloy of this study, AA7075 in the T6 temper, is a high strength alloy used extensively for structural aircraft components. This precipitate-age hardened Al-Zn-Mg-Cu alloy has remained attractive for such applications primarily because of its high strength to

weight ratio. The heat treatment steps utilized to obtain the T6 temper include a solution heat treatment at approximately 480°C for 30-120 minutes, quenching to room temperature, and aging at 120°C for 24 hours. One of the major problems with the aluminum 7075-T6 and other Al-Mg-Zn-Cu high-strength alloys is that they are highly susceptible to stress-corrosion cracking. The T73 temper is an over-aged temper, which involves solution heat treatment followed by a two-step aging process and results in better SCC resistance than the T6 condition, but a 10-15% reduction in strength. This difference in strength is significant to the aerospace industry, where higher strengths allow for a smaller section size and significant weight savings.

Efforts have been made to alleviate the tradeoff between high-strength and stress corrosion cracking resistance in high strength aluminum alloys. Cina[1] reported a heat treatment known as retrogression and re-ageing (RRA), which resulted in the corrosion resistance of 7075 in the T73 temper while maintaining T6 level strengths. The RRA heat treatment was conducted on material already in the T6 condition, and involves a short-time treatment at a temperature between 200-280°C, followed by re-ageing for 24h at 120°C. It has been shown that during the retrogression heat treatment step, strength falls rapidly from the T6 level to a minimum, increases to a local maximum (that is below the T6 strength level), and then falls off with increasing retrogression time. After re-ageing of the retrogressed material, the strength recovers and the T6 level strength can be obtained up to a limiting retrogression time. The trends indicate for a constant retrogression temperature, the Stage II stress corrosion crack growth velocity decreases with increasing retrogression times beyond the local maximum in strength.

Studies have also been conducted to characterize the microstructural differences between the T6 and T73 conditions in order to gain insight into which microstructural parameters control the SCC susceptibility of this alloy[2,3,4,5,6,7]. One difference of note is that the microstructure of

AA7075-T73 shows grain boundary precipitates that are much coarser than those of the T6 temper. Park and Ardell[8] showed that an increase in grain boundary precipitate size correlates with increased stress corrosion cracking resistance. Furthermore, it has been shown that longer retrogression times during the RRA process corresponds to grain boundary precipitates coarsening, which resemble the T73 temper. Thompson *et. al.*[7] hypothesized that the increased size of the grain boundary precipitates creates a smaller cathode to anode ratio. In this sense, the stress corrosion cracking behavior along the grain boundaries is analogous to the galvanic corrosion between dissimilar metals.

Previous research has attempted to identify the optimal retrogression time for a given retrogression temperature as defined by the maximum improvement in SCC resistance for a strength level comparable to the T6 condition. Independent evaluations[2,3,9] indicated that the optimal time for the retrogression portion of the RRA treatment does not correspond to the local minimum in strength. They found that the optimal conditions occur at the maximum retrogression time that retains the T6 strength after re-aging. In either case, the time of the retrogression heat treatment at the temperatures they examined (200-280°C) was typically less than ten minutes. These heat treatments are therefore limited to thin section components.

Due to the trends observed in the literature, it is hypothesized that the optimal retrogression time at a given temperature is the longest time that results in the T6 level strength after re-aging. Although Cina and Ranish[1] utilized temperatures greater than 200°C for the retrogression process, it has been shown that the similar strength variations occur with the use of lower temperatures.[5] The retarded precipitation kinetics at lower retrogression temperatures would result in a longer optimal regression times, allowing the RRA heat treatment to be performed on thick sections. The objectives of this study is to quantify the effect of RRA

treatments with retrogression temperatures at and below 200°C on the strength and stress corrosion cracking resistance of AA7075 and characterized the viability of using the RRA heat treatment on thick section components.

EXPERIMENTAL PROCEDURES

MATERIALS AND HEAT TREATMENT

Aluminum alloy AA7075 (Al-5.93wt% Zn-2.28wt% Mg-1.57wt% Cu-0.21wt% Cr) was received in three-inch thick plates in both the T6 and T73 tempers. All of the specimens for testing were machined from the "as received" condition prior to further heat treatment.

The plates received from the manufacturer were processed such that the material developed characteristic grain orientations. Figure 1 shows the longitudinal or rolling direction (L), transverse (T), and short transverse (S) directions. Figure 1 also shows that all the specimens were machined such that the S and SL orientations were evaluated. This orientation was chosen because it results in the highest SCC susceptibility for this material.

RRA heat treatments were conducted on the pre-machined specimens in the T6 temper. This is consistent with previous research where the RRA heat treatment was applied to material received in the T6 condition.

METRICS USED TO DETERMINE CANDIDATE RRA TREATMENTS

An initial survey of the retrogression and re-aging heat treatment was performed on one-inch cubic test blocks removed from the T6 plate. The test blocks, which were initially in the T6 condition, were retrogressed (heat treated) at 200, 180, and 160°C for various times. Following the retrogression heat treatments, all of the blocks were re-aged for 24 hours at 120°C. This re-aging treatment is the same artificial aging treatment that is applied to materials to give the high-

strength T6 condition. Based on previous research, altering the time of the re-aging heat treatment had a relatively minor effect on the strength and corrosion properties of aluminum.[10] Therefore, this variable was not investigated in this research and was kept constant for all of the RRA heat treatments.

Hardness was used as an initial metric to determine/select candidate RRA heat treatments. Rockwell B (HRB) measurements were obtained for each of the blocks following the retrogression and after the full RRA heat treatment. RRA treatments were chosen based on the HRB versus retrogression time plots.

Electrical conductivity was used as a subsequent metric to determine/select candidate RRA heat treatments. Electrical conductivity measurements for selected RRA conditions were performed on 8.0 x 0.5 x 0.5-inch bars using 1 Ampere of current. Electrical conductivity was used due to its known relationship to SCC susceptibility of AA7075 when aged from the T6 condition to the T73 condition.[11, 12, 13, 14, 15]

STRESS CORROSION CRACKING SUSCEPTIBILITY VIA ALTERNATE IMMERSION TESTING

The alternate immersion (AI) test was performed within the guidelines of ASTM G44. Alternate immersion tensile specimens were machined in the (S) direction (Figure 1). The specimens were loaded under displacement control to 30%, 60%, and 90% percent of their yield strengths. Once the specimens were loaded, the frames were coated to expose only the gage length of the AI specimen to the corrosion environment. The specimens were immersed for 10 minutes out of every hour in a 3.5% NaCl solution and allowed to dry for the remaining 50 minutes in laboratory air. Specimens were monitored daily and were pulled from testing upon complete specimen fracture.

STRESS CORROSION CRACK GROWTH VIA DOUBLE CANTILEVER BEAM TESTING

Bolt-loaded double-cantilever beam tests were used to complement the AI testing by quantifying the SCC resistance in pre-cracked specimens. The SL DCB specimens employed were approximately 6-in long in the (L) direction with specimen thickness (B) and height (2h) equal to 1.0-in. The DCB specimens were fatigue pre-cracked and bolt-loaded; followed by the measurement of the deflection at the load line (ν) and initial crack length (a). The bolt-loaded end of each specimen was coated to eliminate any galvanic interaction between the steel bolts and the aluminum specimen. The DCB specimens were exposed to a corrosive environment by dripping 3.5% NaCl solution into the crack mouth several times daily. This particular exposure was chosen for two reasons. The first is that DCB SCC crack growth data in the literature has been obtained using this particular exposure and a comparison of results was desired. Secondly, previous research has indicated that K vs. da/dt behavior of AA7075-T6 with dropwise 3.5% NaCl is very similar to full immersion in NaCl solutions of various pH levels[16].

The crack length as a function of time was optically measured for each specimen. The applied stress intensity (K_I) as a function of crack length (a), load-line displacement (ν) and specimen half-height (h) was calculated based on the following equation:[16]

$$K_I = \frac{vEh[3h(a+.6h)^2 + h^3]^{1/2}}{4[(a+.6h)^3 + h^2 a]} \qquad (1)$$

RESULTS AND DISCUSSION

HARDNESS PROFILE

The profiles of Rockwell B hardness measurements conducted on samples retrogressed at 160°C, 180°C, and 200°C are shown in Figures 2a, b, and c respectively. These figures show that the hardness value of the material decreases during the initial stages of retrogression heat treatment for all retrogression temperatures examined. After reaching a minimum, the hardness value increases to a local maximum. Following this peak in hardness, continued retrogression will cause the hardness to decrease as the material overages. These results are similar to results obtained in previous research performed at higher temperatures.[2,5,17] However, the time to reach the initial minimum on the retrogression curve was much shorter for the higher retrogression temperatures. Hardness performed after re-aging indicates that the hardness of the RRA condition increases to a maximum, then decreases as a function of retrogression time.

The purpose of the survey experimentation with test blocks was to find the maximum retrogression time that retained T6 strength upon re-aging for each of the three retrogression temperatures. The selection of the RRA heat treatments for more extensive mechanical and corrosion property evaluations was based on the experimental results of the test blocks. Best-fit curves were generated for each set of data for the different retrogression temperatures. In order to account for experimental error of the test block results, two different heat treatments for each retrogression temperature were chosen for continued experimentation.

For each of the three retrogression temperatures, the time that corresponded to a Rockwell B hardness of 88.0 was selected for further experimentation. This was done in order to standardize the expected hardness after the RRA heat treatment for each different temperature.

Furthermore, an HRB of 88.0 is at the low end for minimum acceptable hardness for aluminum 7075 in the T6 temper. For each of the three retrogression temperatures, another RRA heat treatment was selected based on the point where the best-fit curve crossed the average T6 hardness value for the test blocks. Table 1 shows the final RRA heat treatments selected for the first phase of experimentation.

ELECTRICAL CONDUCTIVITY PROFILE

Due to the marginal SCC resistance (i.e., marginal SCC crack growth rates and marginal failure rate in AI testing) of the RRA tempers selected using the initial test metric (i.e., hardness profile), a second phase of testing was performed. Since electrical conductivity has been correlated to SCC resistance, conductivity measurements were used to select RRA times for the second phase of testing. Electrical conductivity specimens were retrogressed at 160°C and 180°C for various times, and the conductivity and hardness of each of the samples were measured. As expected, Figure 3 shows that the electrical conductivity increases with increasing retrogression time (aging time). Figures 4a and b display the hardness versus electrical conductivity for each measured temper of AA7075 aluminum. Based on these measurements, two more RRA treatments with electrical conductivities similar to that of the T73 temper were chosen for additional corrosion testing. These two heat treatments, also given in Table 1, maintain hardness (strength) while maximizing electrical conductivity values.

TABLE 1.
Retrogression and re-aging (RRA) heat treatments selected for corrosion testing.

	Retrogression Temperature (°C)	Time (min)	Reaging Temperature (°C)	Reaging Time (hr)
Phase I	200	8 35	120	24
	180	35 50	120	24
	160	250 275	120	24
Phase II				
	160	660	120	24
	180	120	120	24

STRESS CORROSION CRACKING SUSCEPTIBILITY VIA ALTERNATE IMMERSION TESTING

The results of the alternate immersion test are shown in Table 2. The data are shown as the percentage of yield strength of the material versus days to failure. The alternate immersion test is an accelerated means of providing comparative data of corrosion susceptibility of various materials. Those materials with higher resistance to SCC will generally have a larger number of days to failure in alternate immersion. As expected, the T73 temper exhibited the longest lifetimes and remained unbroken for the total testing time (see Table 2). The results of the alternate immersion indicate the low temperature, long time regression heat treatments (160^{o}C/ 660 min, 180^{o}C/120 min) performed better than T6 condition.

TABLE 2.
Alternate immersion test results for AA7075 T6, T73 and various retrogressed and re-aged (RRA) conditions.

TEMPER	APPLIED LOAD (% σ_{vs})	NUMBER FAILED	DAYS UNTIL FAILURE (max exposure time = 135 days)**
T6	30%	2 OF 2	4,4
	60%	1 OF 1	3
	90%	1 OF 1	3
T73	30%	0 OF 2	---
	60%	0 OF 2	---
	90%	0 OF 2	---
RRA RETRO 160°C/250 MIN	30%	2 OF 2	3,5
	60%	2 OF 2	3,3
	90%	2 OF 2	1,3
RRA RETRO 160°C/275 MIN	30%	2 OF 2	3,5
	60%	2 OF 2	3,4
	90%	2 OF 2	1,3
RRA RETRO 160°C/660 MIN	30%	0 OF 2	---
	60%	1 OF 2	55
	90%	2 OF 2	14,45
RRA RETRO 180°C/35 MIN	30%	2 OF 2	3,4
	60%	2 OF 2	3,3
	90%	2 OF 2	1,3
RRA RETRO 180°C/50 MIN	30%	2 OF 2	3,4
	60%	2 OF 2	1,4
	90%	2 OF 2	1,1
RRA RETRO 180°C/120 MIN	30%	0 OF 2	---
	60%	1 OF 2	89
	90%	2 OF 2	87,87
RRA RETRO 200°C/8 MIN	30%	2 OF 2	3,3
	60%	2 OF 2	3,3
	90%	2 OF 2	1,1
RRA RETRO 200°C/35 MIN	30%	1 OF 2	41
	60%	1 OF 2	2
	90%	2 OF 2	2,2

** The T73 temper was exposed for a maximum of 250 days. The RRA 160C/600, RRA 180C/120, and RRA 200C/35 were exposed for a maximum of 101 days.

STRESS CORROSION CRACK GROWTH VIA DOUBLE-CANTILEVER BEAM TESTING

DCB testing was conducted to evaluate the SCC behavior of a material in the presence of a flaw. This constant displacement test is useful in determining the Stage II crack growth rate of a material when it is subjected to a corrosive environment. Data from a double-cantilever experiment are typically shown as the crack growth rate (da/dt) versus stress intensity (K) and

selected results are shown in Figure 5. The scatter observed in this data is typical for these experiments. Tests were not conducted for long enough time periods to observe crack arrest and measure K_{ISCC}.

All of the RRA tempers exhibited lower crack growth rates than that of the T6 temper. However, the crack growth rates of some of the RRA tempers were still much higher than that that of the T73 temper. A significant improvement in SCC resistance was obtained for the low temperature, long time retrogression heat treatments (180°C/120 min and 160°C/660 min). Figure 5 shows that substantially lower crack growth rates compared to the T6 temper were obtained for these conditions. These results are consistent with the results obtained from the alternate immersion testing.

Figure 6 shows all of the tempers investigated in this research via a plot of yield strength versus the average stage II crack growth rate. In general, the various RRA tempers produce strengths similar to that of T6 with lower crack growth rates. Figure 6 also indicates that the trade-off between the T6 and T73 tempers is reduced with the use of the RRA tempers. For a given yield strength, the crack growth rate is lower with the use of this temper. Most significantly, the RRA temper with retrogression at 160°C for 660 minutes produced the greatest improvement, with only a 4% reduction in strength below T6.

HEAT TRANSFER ANALYSIS

A heat transfer analysis for the thermal treatment of AA7075 was performed in this work to justify why the RRA heat treatment that Cina[1] proposed in 1973 is only appropriate for thin sections of material and to provide a realistic model of the RRA heat treatment on thicker sections of material. An important issue in the heat treatment process is the time for the material to reach the intended temperature, which is equal to the furnace temperature.

All of the following calculations are analyzed using a constant thickness plate. Consider a slab of thickness 2L at an initial temperature, T_i, both sides of which are exposed suddenly to a medium of temperature T_∞. The heat transfer coefficient (ϕ) is assumed to be equal on both sides of the plate. For unidirectional conduction, the temperature distribution of the material is assumed to depend only on the distance from the centerline of the material (x) and time (t). The excess temperature function is given by:

$$\theta(x,t) = T(x,t) - T_\infty \tag{2}$$

The complete mathematical statement is as follows:

$$\frac{\partial^2\theta}{\partial x^2} = \frac{1}{\alpha}\frac{\partial\theta}{\partial t} \quad \text{(conduction equation),}$$

$$\theta = \theta_i \quad \text{at t = 0,}$$

$$\frac{\partial\theta}{\partial x} = 0 \quad \text{at x = 0,}$$

$$-k\frac{\partial\theta}{\partial x} = \phi\theta \quad \text{at x = L,}$$

where: k = thermal conductivity coefficient of Al (167 W/m-K)
α = thermal diffusivity of Al (0.667 cm^2/s)
ϕ = typical heat transfer coefficient for a gas at atmospheric pressure (100 W/m^2-K)
$\theta_i = T_i - T_\infty$.

The temperature at the center of a plate with a given time is specified in dimensionless form and the solution is determined graphically through the use of Heisler charts.[18]

In order to make the calculation more realistic, the unidirectional heat conduction was extended to three dimensions. In the three-dimensional case, the dimensionless temperature for conduction in three dimensions is the product of the dimensionless temperatures in each of the

three different dimensions. A 3x3x(h) inch block (with height h specified for each analysis) was modeled, assuming an initial temperature of 25°C (Figure 7).

The heat transfer model was utilized to compare the use of high and low retrogression temperatures during the RRA process. The high retrogression temperature heat treatment of 220°C for 5 minutes and the low retrogression temperature heat treatment of 160°C for 660 minutes were chosen. The 220°C temperature and time has been shown to produce reduced Stage II crack growth rates compared to the T6 temper.[16] The 160°C temperature and time was shown to produce favorable strength and SCC resistance in this research (Figure 6).

Figure 7 displays theoretical temperature at the center of a cubic block following the retrogression heat treatment for four values of h. The analysis indicates that the higher retrogression temperature heat treatment (i.e., 220ºC / 5 minutes) is not a feasible heat treatment to perform on thicker sections (3 inches or greater) of material because the center of the block does not achieve the desired temperature within the heat treatment time. Therefore, the center of the material would not exhibit the desired properties for the heat treatment. This analysis shows that the use of lower retrogression temperatures allows the entire block to reach the furnace temperature during the allotted heat treatment time. In addition, this analysis shows that an approximate thickness of 0.06 inches is required in order for the center of the material to reach a regression temperature of 220ºC in 5 minutes, which limits the use of this particular temperature to sheet specimens.

SUMMARY/CONCLUSIONS

The results of this research indicate that the T6 temper exhibits strengths that are ten to fifteen percent higher than the T73 temper, but has crack growth rates that are approximately ten

times faster than T73. Furthermore, the T6 temper fails much more quickly when subjected to 3.5% NaCl in the alternate immersion test.

The RRA temper alleviates the trade-off in properties between these two tempers. However, the use of a high retrogression temperatures limit the use to thinner sheets of material. This research proved that lower retrogression temperatures and corresponding longer retrogression times alleviates the trade-off between the T6 and T73 temper for AA 7075. The improvements in properties are summarized as follows.

- RRA tempers with retrogression temperatures down to 160°C produced crack growth rates lower than that of the T6 temper during the double-cantilever beam experiment.
- RRA tempers with retrogression temperatures down to 160°C lasted substantially longer than T6 in the alternate immersion test.
- Heat transfer analysis and results of the corrosion tests indicate the RRA temper with lower retrogression is a more viable temper for use in industry. Longer retrogression times (8-11 hours) render the heat treatment applicable to thick sections of material.

ACKNOWLEDGEMENTS

The authors would like to acknowledge the assistance and contributions of the Alcoa Technical Research Center, Naval Air Warfare Center Aircraft Division, Loyola Marymount University and Professor Rick Link, Mr. Steve Crutchley and Mr. Tony Antenucci from the United States Naval Academy.

REFERENCES

1. B. Cina, B. Ranish, "New technique for reducing susceptibility to stress corrosion cracking of a high strength aluminum alloy," Israel Aircraft Industries Ltd., Lod Airport, Israel, unpublished work, 1973.

2. K. Rajan, W. Wallace, J. Beddoes, "Microstructural Study of the High-Strength Stress Corrosion Resistant 7075 Aluminum Alloy," *Journal of Materials Science,* V17 (1982), pp.2817-2824.

3. J. K. Park, "Influence of Retrogression and Reaging Treatments on the Strength and Stress Corrosion Resistance of Aluminum Alloy 7075-T6," *Materials Science and Engineering,* A103 (1988), pp. 223-231.

4. M. Kanno, I. Araki, Q. Cui, "Precipitation Behavior of 7000 Alloys During Retrogression and Reaging Treatment," *Materials Science and Technology,* V10 (1994), pp.599-603.

5. W. Wallace, J. Beddoes, M. DeMalherbe, "A New Approach to the Problem of Stress Corrosion Cracking in 7075-T6 Aluminum," *Canadian Aeronautics and Space Journal,* V27 (1981), pp. 225-232.

6. A. Uguz, J. Martin, "The Effect of Retrogression and re-ageing on the Ductile Fracture Toughness of Al-Zn-Mg Alloys Containing Different Dispersoid Phases," *Journal of Materials Science,* V30 (1995), pp. 5923-5926.

7. J. Thompson, E. Tankins, V. Agarwala, "A Heat Treatment for Reducing Corrosion and Stress Corrosion Cracking Susceptibilities in 7xxx Aluminum Alloys," NACE (1987), pp. 45-51.

8. J. K. Park, A. J. Ardell, "Effect of Retrogression and Reaging Treatments on the Microstructure of Al-7075-T651," *Metallurgical Transactions A,* V15A (1984), pp. 1531-1543.

9. K. Ural, "A Study of Optimization of Heat-Treatment Conditions in Retrogression and Reageing Treatment of 7075-T6 Aluminum Alloy," *Journal of Materials Science Letters,* V13 (1994), pp.383-385.

10. P. Fleck, J. Barba, H.M. Oh, J. Peraza, J. Foyos, E.W. Lee, and O.S. Es-Said,"Retrogression and Reaging of 7075 T6 Aluminum Alloy", Aluminum Alloys – Their Physical and Mechanical Properties: Proceedings of the 7th International Conference ICAA7, Charlottesville, VA, (April, 2000): pp.649-654.

11. T. C. Tsai, T. H. Chuang, "Technical Note: Relationship Between Electrical Conductivity and Stress Corrosion Cracking Susceptibility of Al 7075 and Al 7475 Alloys," *Corrosion*, V52 (1996), pp. 414-416.

12. J. S. Robinson, S. D. Whelan, R. L. Cudd, “Retrogression and Re-aging of 7010 Open Die Forgings,” *Materials Science and Technology,* V15 (1999), pp. 717-724.

13. J. Y. Barghout, G. W. Lorimer, R. Pilkington, B. Prangnell, “The Effects of Second Phase Particles, Dislocation Density, and Grain Boundaries on the Conductivity of Aluminum Alloys,” *Materials Science Forum,* V217-222 (1996), pp. 975-980.

14. P. Olafsson, R. Sandstrom, A. Karisson, “Electrical Conductivity of Aluminum Alloys,” *Materials Science Forum,* V217-222 (1996), pp. 981-986.

15. C. W. Bartges, “Changes in Solid Solution Composition as a Function of Artificial Ageing Time for Aluminum Alloy 7075,” *Journal of Materials Science Letters,* V13 (1994), pp. 776-778.

16. M. Hyatt, “Use of Precracked Specimens in Stress Corrosion Testing of High Strength Aluminum Alloys,” Corrosion-NACE V26 (1970), pp.487-503.

17. N. Danh, K. Rajan, W. Wallace, “A TEM Study of Microstructural Changes During Retrogression and Reaging in 7075 Aluminum”, *Metallurgical Transactions A,* V14A (1983), pp. 1843-1850.

18. A. Bejan, Heat Transfer. John Wiley & Sons, Inc: New York (1993), pp.143-177.

FIGURES

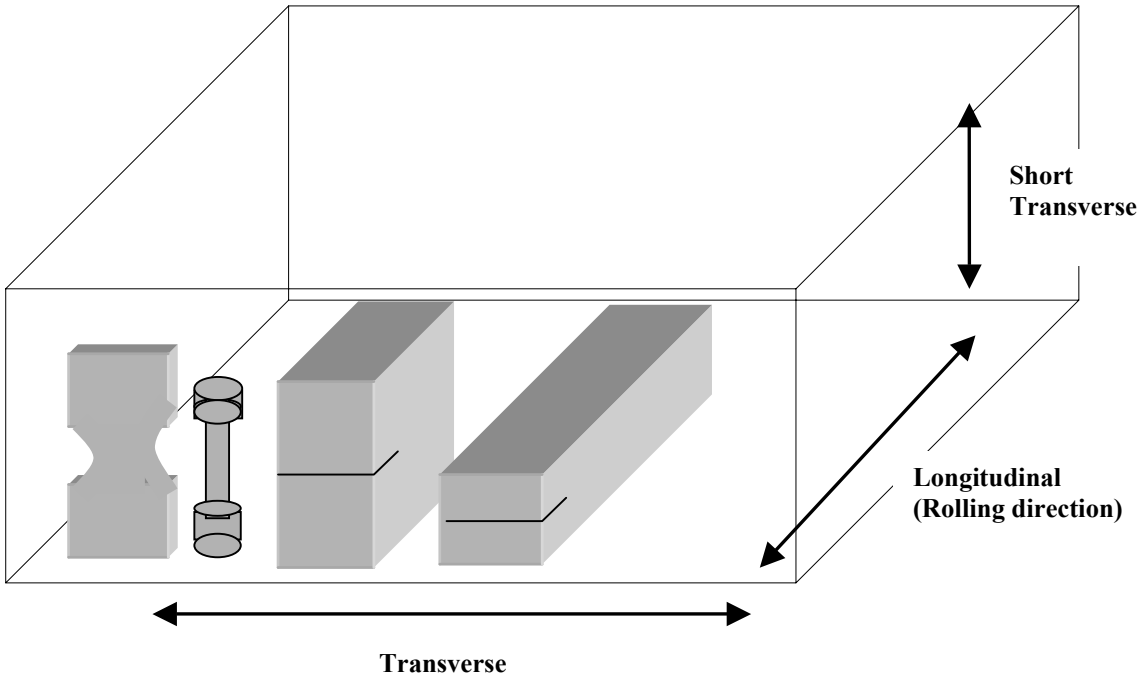

FIGURE 1. Schematic depicting specimen orientations with respect to rolling direction of AA7075 plate used in this study.

a)

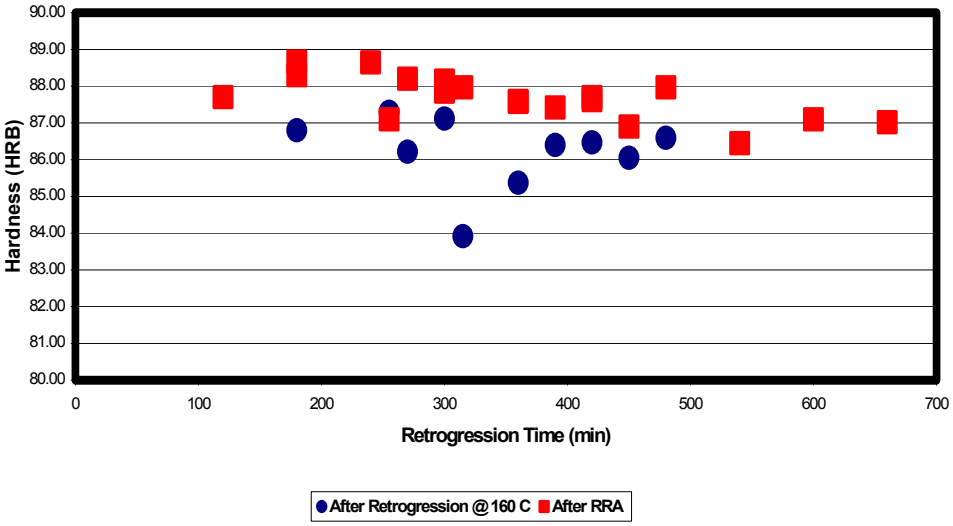

b)

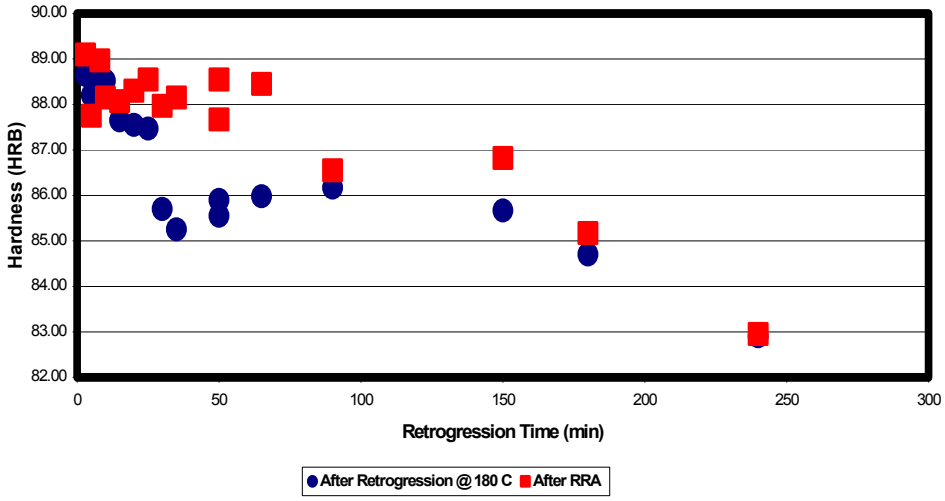

c)

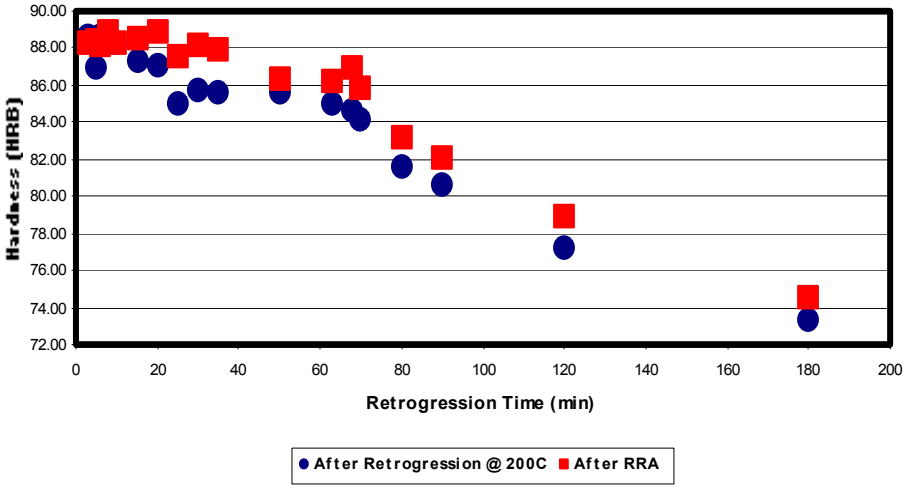

FIGURE 2. Rockwell B (HRB) hardness for: **a)** retrogression at 160°C for various times and for retrogression (160°C for various times) + reaging (24h at 120°C, RRA), **b)** retrogression at 180°C for various times and for retrogression (180°C for various times) + reaging (24h at 120°C, RRA), **c)** retrogression at 200°C for various times and for retrogression (200°C for various times) + reaging (24h at 120°C, RRA)

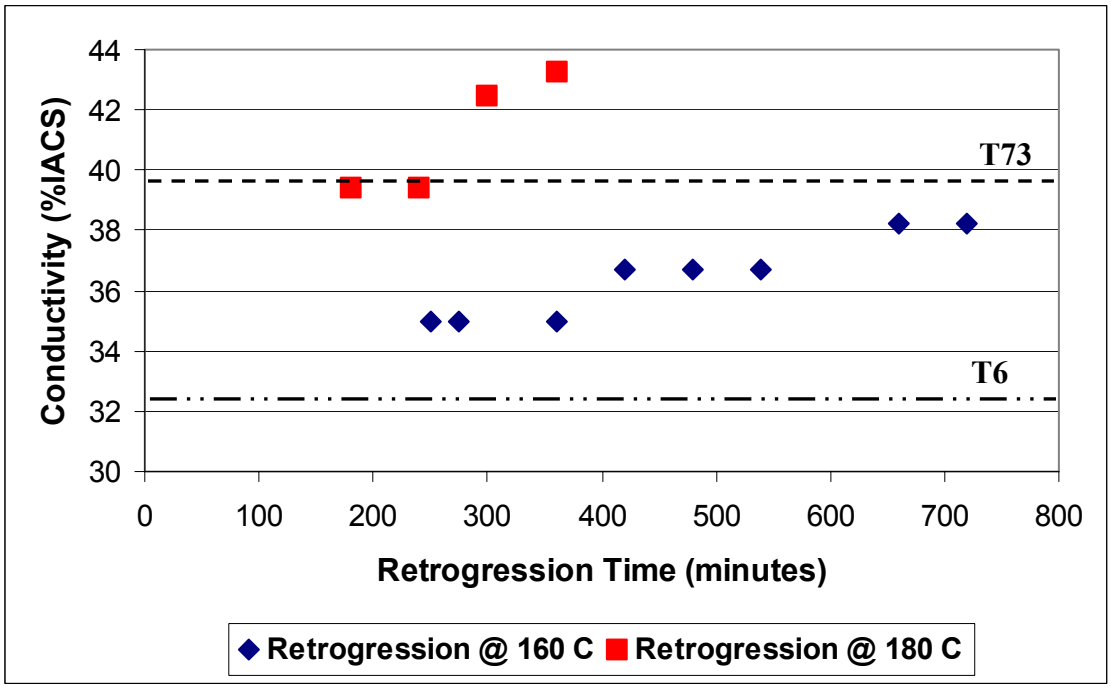

FIGURE 3. Electrical conductivity versus regression time for two RRA heat treatments of AA7075.

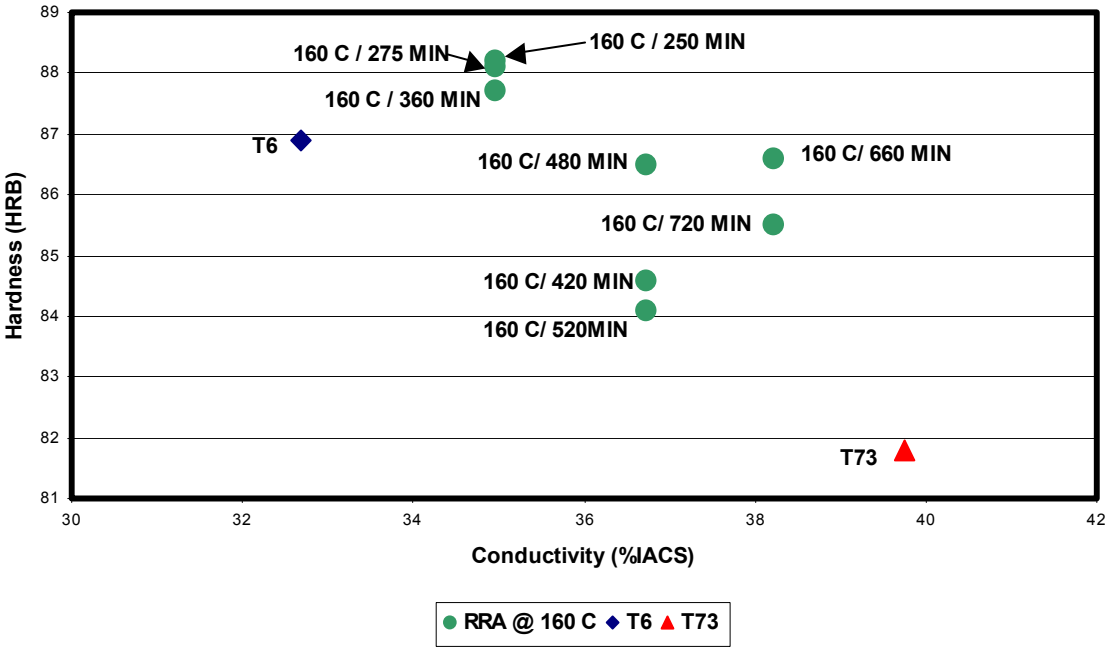

FIGURE 4a. Plot of HRB versus conductivity for AA7075 in the T6, T73, and various RRA tempers (retrogression @ 160°C).

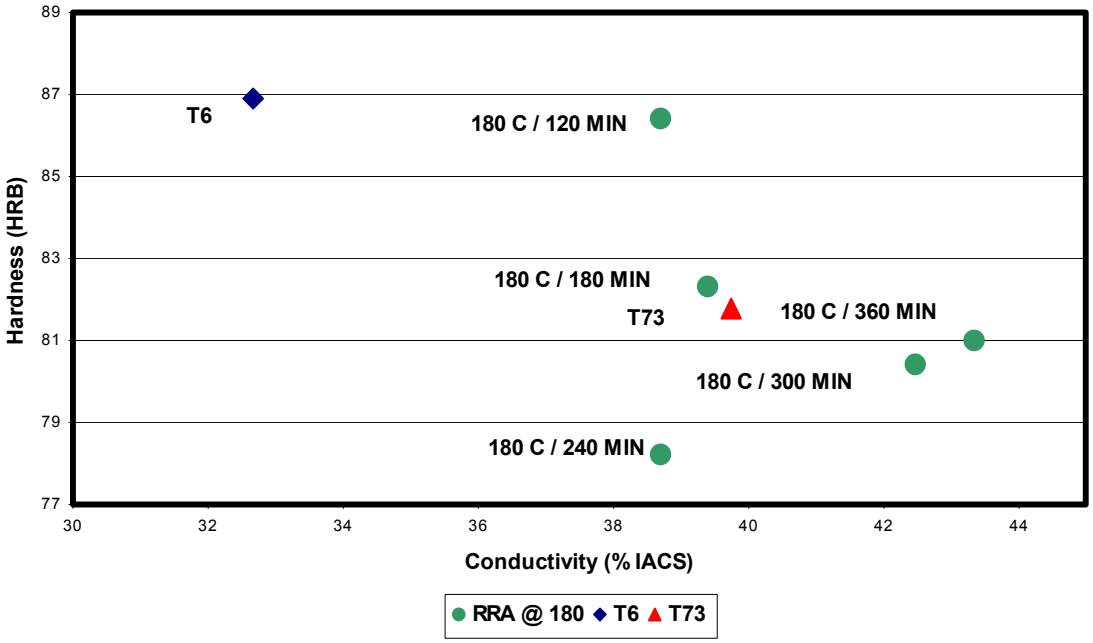

FIGURE 4b. Plot of HRB versus conductivity for AA7075 in the T6, T73, and various RRA tempers (retrogression @ 180°C).

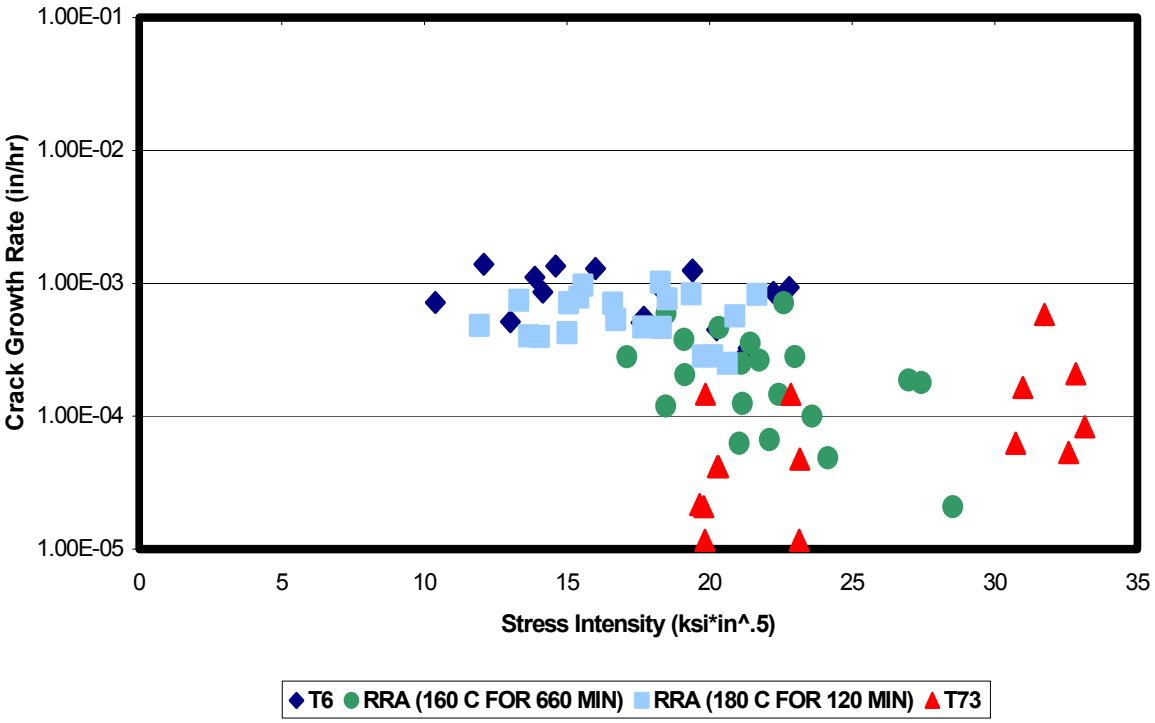

Figure 5. Crack growth rate versus stress intensity for AA7075 in the T6, T73, and two RRA tempers: (1) 160º/660 min + 120ºC/24 hr (2) 180ºC/120 min + 120ºC/24 hr.

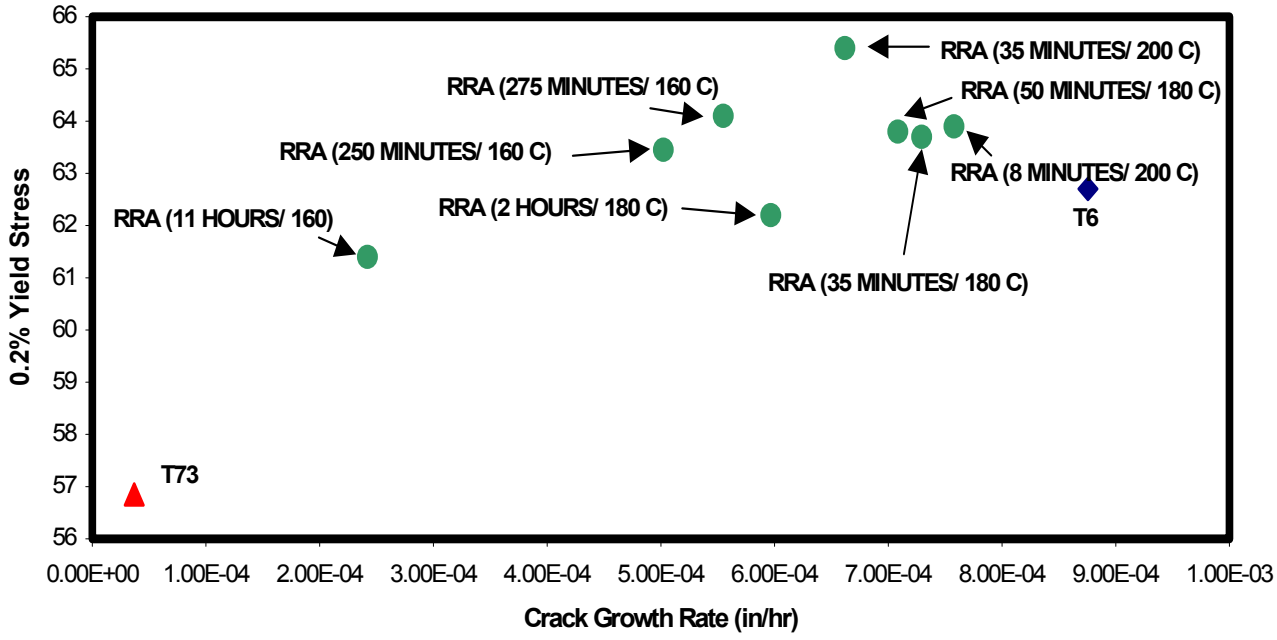

FIGURE 6. 0.2% yield stress versus crack growth rate for AA7075 in the T6, T73, and various RRA tempers.

h (inches)	160°C for 660 minutes	220°C for 5 minutes
.06 **	160°C	220°C
3	160°C	77.8°C
6	160°C	71.5°C
12	160°C	65.2°C

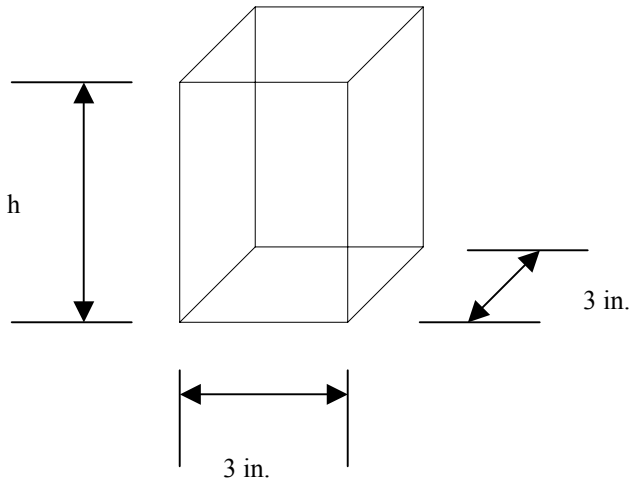

FIGURE 7. This figure/table gives the temperature at the center of a rectangular block following the respective retrogression heat treatment. **Please note that the analysis of the h = 0.06 in. case is approximated due to the limits of the Heisler charts.

ENVIRONMENTALLY ASSISTED CRACKING CONCERNS FOR CADMIUM REPLACEMENT

Scott Grendahl, Russell Kilbane

U.S. Army Research Laboratory
Weapons and Materials Research Directorate
Aberdeen Proving Ground, MD 21005
sgrenda@arl.army.mil
Voice: (410) 306-0819
Fax: (410) 306-0806

ABSTRACT

Recently, cadmium replacement has become the topic of an Environmental Security Technology Certification Program (ESTCP). As a direct result of this program, replacement coating systems will be developed and scrutinized. A fundamental starting point for corrosion resistant coatings development work consists of a target for the overall chemical potential (galvanic series) and pH of the coating system and the substrate. This work developed the data necessary to determine the target for several high strength steels. Hydrogen is widely recognized as having a detrimental embrittling effect on high strength materials, especially high strength steel. Many of these materials show a strong dependence of hydrogen on chemical potential and pH. This work focused on determining the effect of hydrogen on the environmentally assisted cracking critical stress intensity values (K_{IEAC}) for several common high strength structural steels. Evaluating the effects of hydrogen on K_{IEAC} over a range of chemical potential and pH will make the optimum chemical potential and pH evident for each material. It then becomes possible for the coating system designers to tailor a prospective coating system around those optimum values with the various substrates. If a system were designed at the optimum values for chemical potential and pH, the substrate material would be at the most tolerant conditions for resisting detrimental hydrogen effects regardless of the source of the hydrogen.

INTRODUCTION

Cadmium coatings are currently utilized in every major land, sea, and air defense system in a wide variety of system critical applications. Cadmium plays an important role in the substrate-coating relationship. The functional performance of the coating system contributes to

the longevity and mechanical performance of any coated component. In the case of high strength steels, the functional performance of cadmium coatings as part of the substrate-coating system evolved over several decades of in-service use. Due to the wide range of environmental regulation and costs associated with the utilization, handling, and disposal of cadmium containing components and processes, the government has determined a replacement must be found. A fundamental starting point for the research required to accomplish this task begins with the determination of the materials that are common substrates for the cadmium containing coating systems.

These materials, most commonly high strength steels, are deleteriously affected by hydrogen generated at or near the surface from the natural corrosion process of the environment, particularly when possessing yield strengths above 1400 Mpa.[1] This deleterious effect of hydrogen on high strength material by the environment is typically referred to as environmentally assisted cracking (EAC). Failures of military grade steels with cadmium containing coating systems have been reported extensively in literature.[2-7] Since all substrates reach equilibrium in the environment (in terms of pH and electrochemical potential) with their respective coating systems, it would be extremely beneficial to know the optimum pH and electrochemical potential where the tolerance of the high strength material to EAC is at the maximum level. A coating system could then be designed around those parameters for each individual material. If a coating system were designed with no regard for the equilibrium pH and electrochemical potential, it is quite possible that the system could fail prematurely, since high strength materials demonstrate a strong dependence on these parameters. Although there are a number of standard procedures for assessing the susceptibility of high strength steel to hydrogen

assisted cracking,[9-21] none of these methods address the effect of electrochemical potential and pH, both of which are real characteristics of the environment where these steels are utilized.

Determination of the optimum pH and electrochemical potential where a material is most tolerant to hydrogen can be achieved in several ways. One way is to measure the critical stress intensity, K_I, at various artificially generated electrochemical potentials and over a range of pH. Although artificially created, the resulting data could be referred to as the critical stress intensity for environmentally assisted cracking, K_{IEAC}, with the understanding that equilibrium conditions in the environment will be established with the coated substrate that include these parameters. The equilibrium potential for the hydrogen proton reaction in water is as follows:

$$E_{H^+/H_2} = -0.059\,pH - \left(\frac{0.059}{2}\right)\log \rho_{H_2} \qquad (1)$$

The potential varies as a function of pH and hydrogen pressure. Therefore the likelihood to produce hydrogen gas or monatomic hydrogen increases as electrochemical potential and pH decrease. Strong effects of these parameters on the measured critical stress intensity have been demonstrated.[8]

EXPERIMENTAL PROCEDURE

It was concluded, based upon numerous ESTCP conversations, that the most frequently utilized high strength steels in critical military applications were vacuum arc remelted (VAR) 4340 at various strength levels, PH 13-8 Mo steel in the H1000 condition, and 4335V steel. The VAR material was tested in the HRc 38 and HRc 52 conditions. The VAR 4340 had two heat treatments; a) an 845 C austenitizing treatment for 30 minutes followed by an oil quench and a 340 C, 1-hour temper yielding a hardness of 52 HRc, and b) an 845 C austenitizing treatment for

30 minutes followed by an oil quench and a 470 C temper for 1 hour yielding a hardness of 38 HRc. The supplied chemical composition and mechanical properties are presented in Tables 1 and 2.

TABLE 1
Chemical Composition of Supplied Experimental Materials

Element	**VAR 4340**	**PH 13-8 Mo**	**4335**
Carbon	0.42	0.032	0.36
Manganese	0.77	0.03	0.72
Silicon	0.28	0.05	0.28
Phosphorus	0.009	0.007	0.008
Sulfur	0.002	0.0004	0.009
Chromium	0.76	12.45	0.75
Nickel	1.76	8.25	1.83
Molybdenum	0.23	2.20	0.37
Cobalt	NA	0.02	NA
Aluminum	NA	1.03	NA
Nitrogen	NA	0.0030	NA
Titanium	NA	0.018	NA
Vanadium	NA	0.02	0.20
Oxygen	NA	0.0002	NA
Iron	Remainder	Remainder	Remainder

TABLE 2
Mechanical Properties of Supplied Experimental Materials

Mechanical Property	**VAR 4340 HRc 38**	**VAR 4340 HRc 52**	**PH 13-8 Mo**	**4335**
Yield Strength, MPa	1070	1550	1460	1450
Tensile Strength, MPa	1200	1875	1520	1655
Elongation %	16	-	15	10
Reduction of Area %	-	-	63	-
Hardness, HRc	38	52	46	-
PS Fracture Toughness	105 MPa√m	60 MPa√m	100 MPa√m	100 MPa√m

This work utilized precracked charpy impact specimens in an 8-10 hour slow strain, constant displacement rate (0.005 mm/min), double cantilever beam experiment on an Instron Model 4301 testing apparatus to determine K_{IEAC}. Schematics of the test specimen and testing apparatus are presented in figures 1 and 2, respectively. The test specimens were manufactured in accordance with ASTM-E-399.[19] The precracking was carried out utilizing three separate stages, incorporating decreasing loading levels. In the initial precracking stage, the load was maintained to keep stress intensity values below 80% of the estimated experimental critical stress intensity and the stress ratio ($\sigma_{max}/\sigma_{min}$) was kept between –1 and +0.1. During the final stage of precracking, the load was reduced so the final value of K_{max} was unlikely to exceed 60 % of the estimated value for K_I during experimentation. Additionally, the final value for K_{max}/E did not exceed 0.0032 $m^{1/2}$, where E is Young's Modulus. Precrack length, represented by the dimensionless expression a/W (crack length over specimen width), was maintained near 0.5.

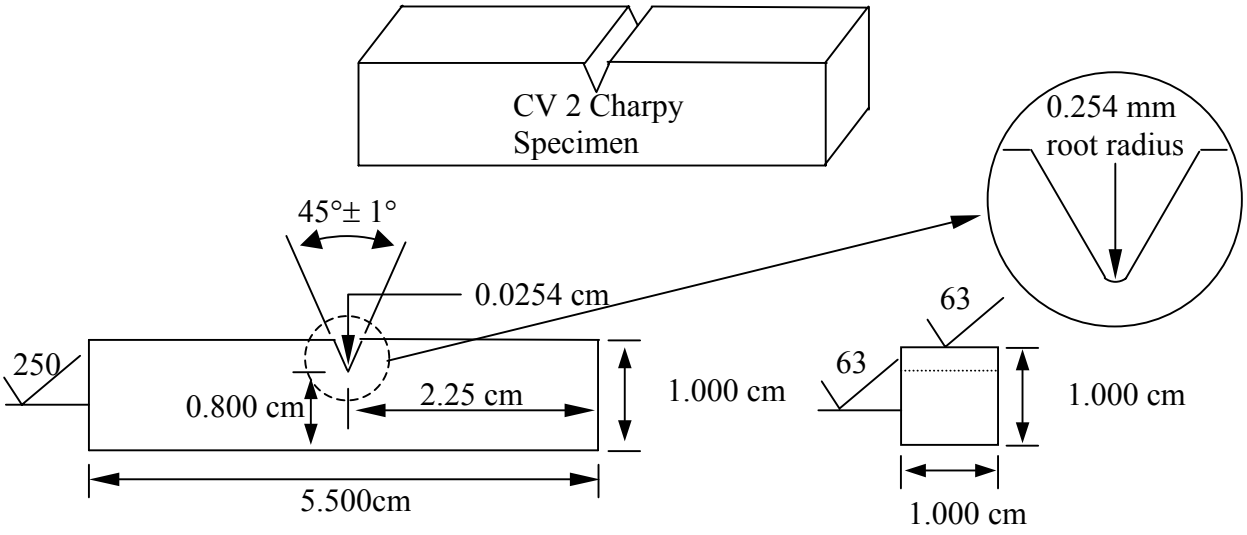

Notes:

1. Tolerances, unless noted.

Squareness	⊥ perpendicular ± 0.001 TIR
	|| parallel ± 0.001 TIR
Decimal	.XX ± 0.127 mm
	.XXX ± 0.0254 mm
	.XXXX ± 0.0127 mm

FIGURE 1. Schematic of the K_{IEAC} fracture specimen.

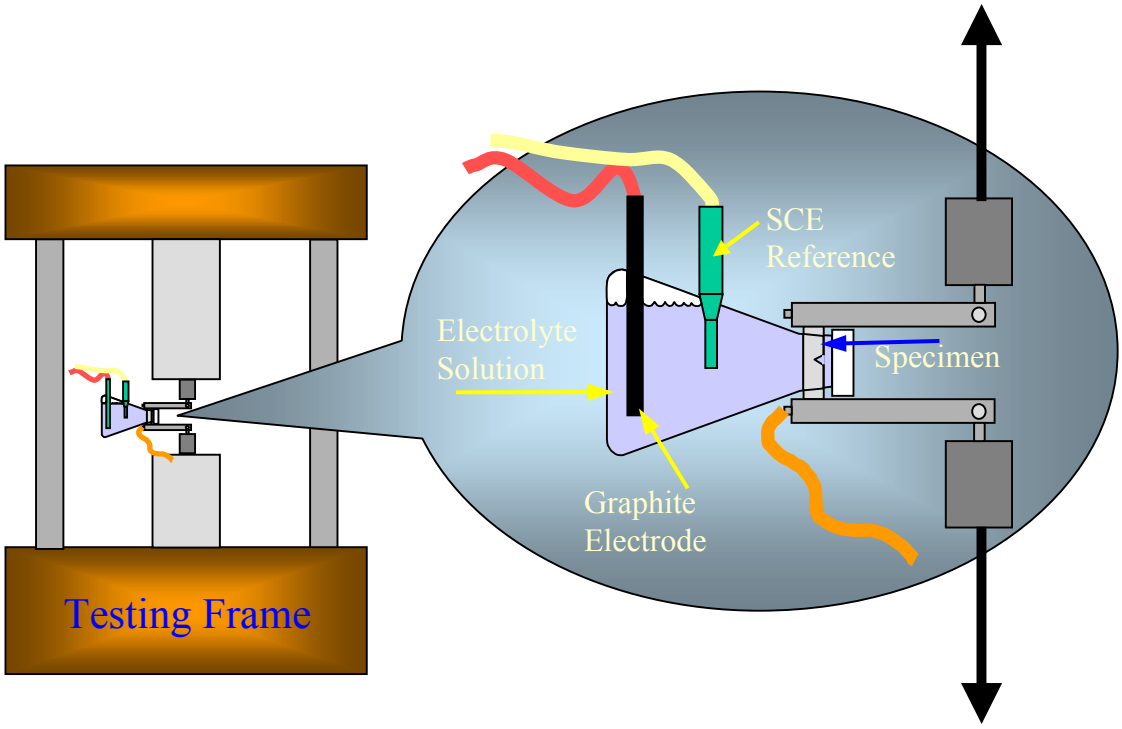

FIGURE 2. Schematic of the K_{IEAC} fracture apparatus.

The calculation for the onset of environmentally assisted cracking, or K_{IEAC}, was derived as follows for cantilever bending from the four point bending expression.

$$K_{IEAC} = \left(\frac{6M_{IEAC}\sqrt{\pi a}}{BW^{3/2}} \right) x f(a/W) \tag{2}$$

where:

$$f(a/W) = 1.122 - 1.40(a/W) + \left(7.33(a/W)^2 - 13.08(a/W)^3\right) + 14.00(a/W)^4 \tag{3}$$

where:

M_{IEAC} = the applied moment necessary to induced cracking,
B = the specimen thickness,
W = the specimen depth, and
a = the initial crack length.

For double cantilever bending, the term M_{IEAC} becomes $P_{IEAC}S$, where P_{IEAC} is the load necessary to induce critical cracking and S is the length of the moment arm. This yields the utilized expression for K_{IEAC}.

$$K_{IEAC} = \left(\frac{6P_{IEAC} S\sqrt{\pi a}}{BW^{3/2}} \right) x f(a/W) \tag{4}$$

where: *f(a/W)* varies between 2.3 and 3.2 for *a/W* values between 0.45 and 0.55, respectively.

Overall crack length was determined from optical fractographs of each specimen. The final crack length was determined from the average of the summation of length measurements perpendicular to the crack front. Computer software digitally analyzed the data. First, the photo was digitized, and then the software outlined the edges of the notched and precracked region. Next, the software filled the notched and precracked area, and subsequently calculated lengths across this filled area. The lengths were then averaged. This method is depicted in Figure 3 with a step size of 20 shown for clarity. The method utilized had a step size of one for maximum accuracy.

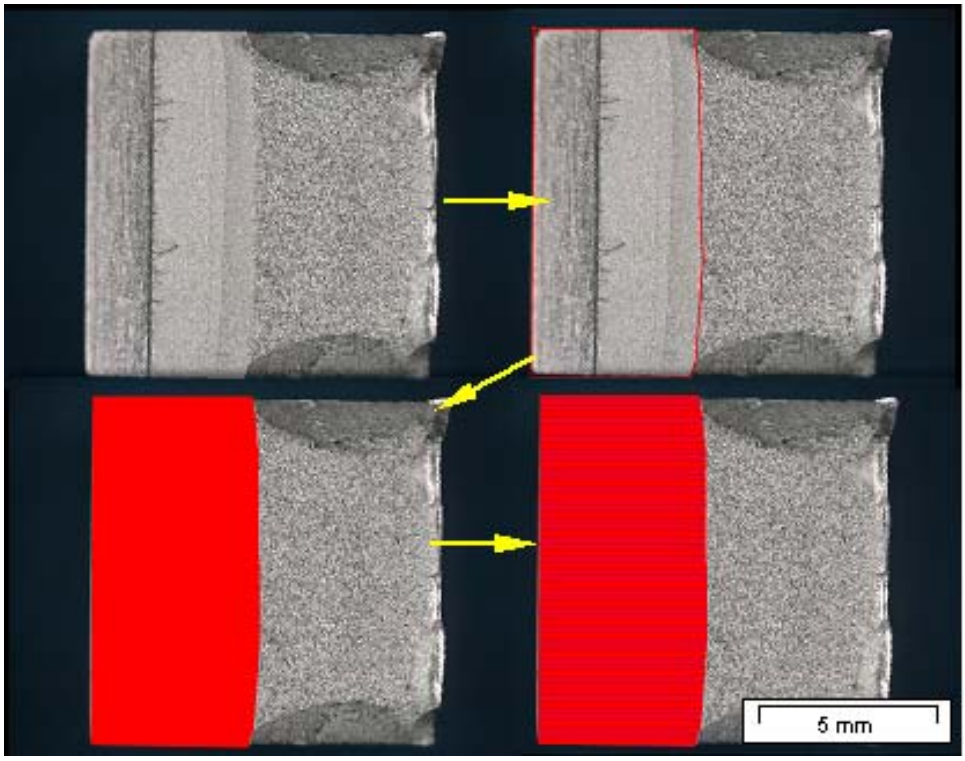

FIGURE 3. Crack length determination procedure.

Experimentation was conducted in a range of electrochemical potentials and pH. Each material was subjected to neutral 3.5% NaCl solution at four different electrochemical potentials, -0.6, -0.8, -1.0, and -1.2 V_{SCE}. Electrochemical potential was maintained with the utilization of an AMEL Instruments Model 2051 potentiastat and a potassium chloride reference saturated calomel electrode (SCE). Tests were conducted in dilute sulfuric acid at pH 2, and in dilute sodium hydroxide at pH 11, at both -0.6 and -0.8 V_{SCE}. Open circuit experiments were also conducted in neutral 3.5% NaCl. Five specimens were tested for each group.

RESULTS

Figure 4 presents the results from the VAR 4340 steel heat-treated to HRc 52. These results were obtained in the 3.5 % NaCl, and in the diluted sulfuric acid and sodium hydroxide solutions. This material showed the least dependence on electrochemical potential and pH of all the materials investigated. The measured K_{IEAC} values were greatest, 22 MPa√m, in the NaCl and pH 11 solutions at -0.6 V_{SCE}, while the lowest measured K_{IEAC} values, 16 MPa√m, were obtained from the NaCl solution at -1.2 and -1.0 V_{SCE}. The measured open circuit K_{IEAC} value in 3.5% NaCl was approximately 17.5 MPa√m at the measured open circuit potential of -0.57 V_{SCE}. The caustic pH levels slightly increased the measured K_{IEAC} values at -0.8 V_{SCE}, while they did not appear to significantly increase them at -0.6 V_{SCE} versus those obtained in 3.5% NaCl solution at the same potential. Additionally, the acidic solution generally decreased the measured value of K_{IEAC} at both -0.8 and -0.6 V_{SCE} versus those obtained in 3.5% NaCl solution at the same potentials.

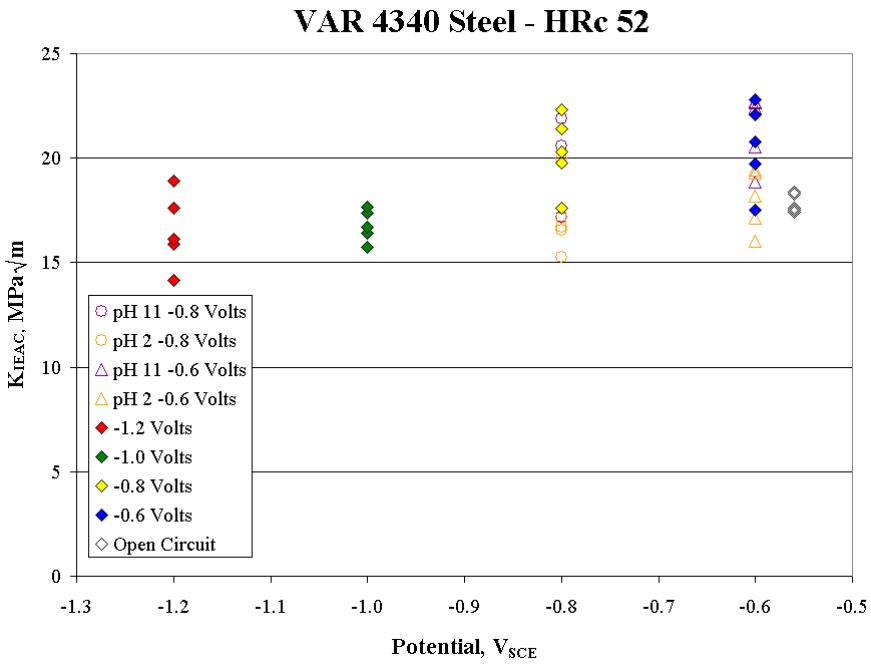

FIGURE 4. K_{IEAC} Results for VAR 4340 HRc 52.

The results obtained from VAR 4340 steel heat-treated to HRc 38 are presented in figure 5. The 3.5 % NaCl, pH 2 and pH 11 solutions were utilized. The material demonstrated a great dependence on both pH and electrochemical potential. The greatest measured K_{IEAC} value, 90 MPa√m, was obtained at -0.8 V_{SCE} in the pH 11 solution. The lowest measured K_{IEAC} value, 18 MPa√m, was obtained at -1.2 V_{SCE} in the NaCl solution. The pH 11 solution tended to increase the measured K_{IEAC} values, considerably at -0.6 V_{SCE}, versus those obtained in 3.5% NaCl solution at the same potential. Additionally, the acidic solution decreased the measured value of K_{IEAC} significantly at -0.8 V_{SCE}, while the measured K_{IEAC} values remained largely unaffected at -0.6 V_{SCE} versus those obtained in 3.5% NaCl solution at the same potentials. The measured open circuit K_{IEAC} value in 3.5% NaCl was approximately 65 MPa√m at the measured open circuit potential of -0.59 V_{SCE}.

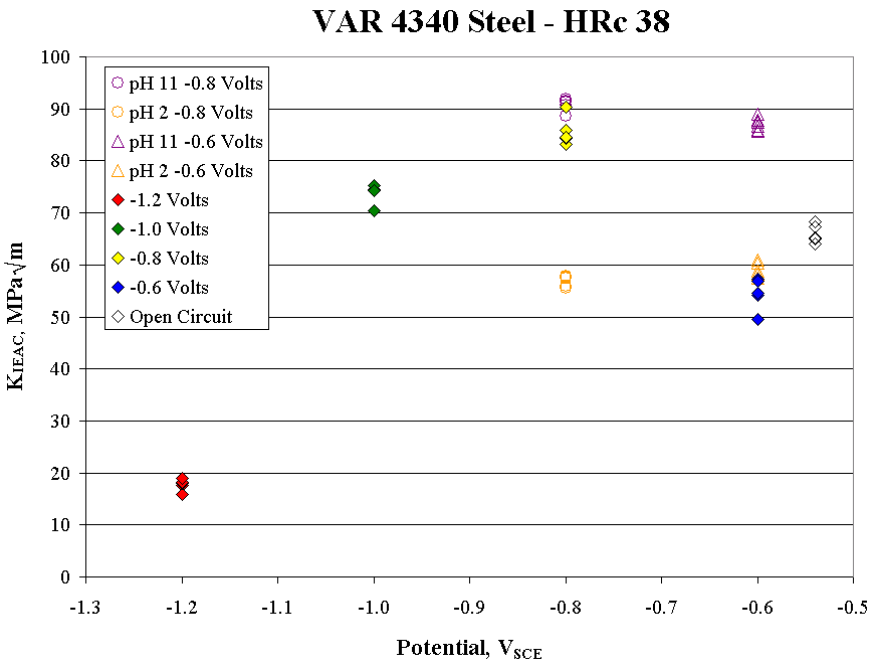

FIGURE 5. K_{IEAC} Results for VAR 4340 HRc 38.

The results from the PH 13-8 Mo in the H1000 condition are presented in figure 6. Again, K_{IEAC} values were obtained from all three solutions. The highest measured K_{IEAC} values were 78 MPa√m and were obtained from the pH 11 solution at -0.8 V_{SCE}. The lowest measured K_{IEAC} value, 9 MPa√m, was obtained at -1.2 V_{SCE} in the NaCl solution. The measured open circuit potential of -0.76 V_{SCE}, yielded a K_{IEAC} value in 3.5% NaCl of 72 MPa√m. Similar to the other materials, the pH 11 solution raised the measured K_{IEAC} values while the pH 2 solutions lowered the measured values.

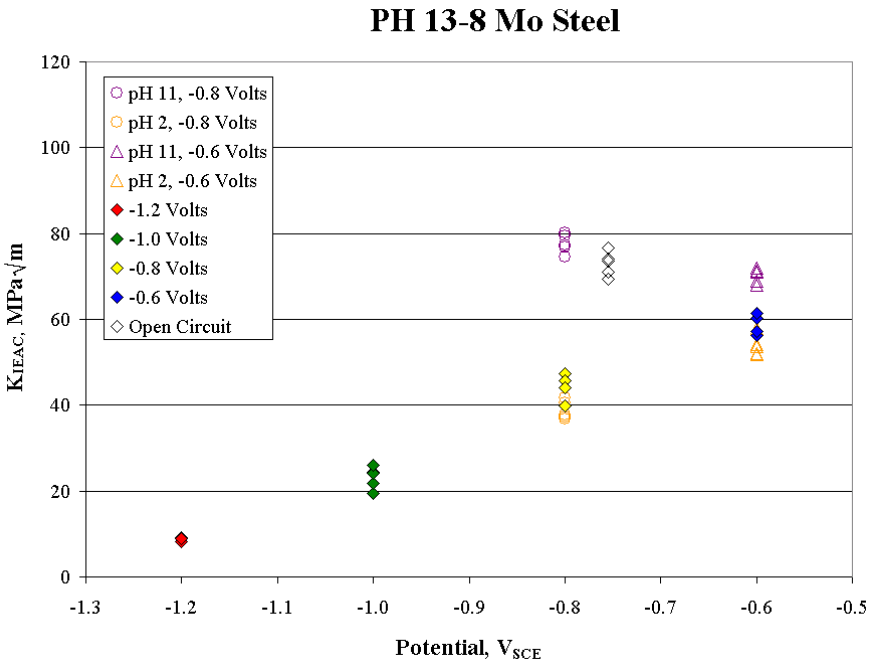

FIGURE 6. K_{IEAC} Results for PH 13-8 Mo.

The 4335 material exhibited the same general trend as the other materials. The results for this material are presented in figure 7. The highest measured value for K_{IEAC}, 84 MPa√m, was obtained in the pH 11 solution at -0.8 V_{SCE}. The lowest measured value was again at -1.2 V_{SCE}, and was approximately 22 MPa√m in 3.5 % NaCl. The measured open circuit K_{IEAC} value was 67 MPa√m at the measured open circuit potential of -0.59 V_{SCE}.

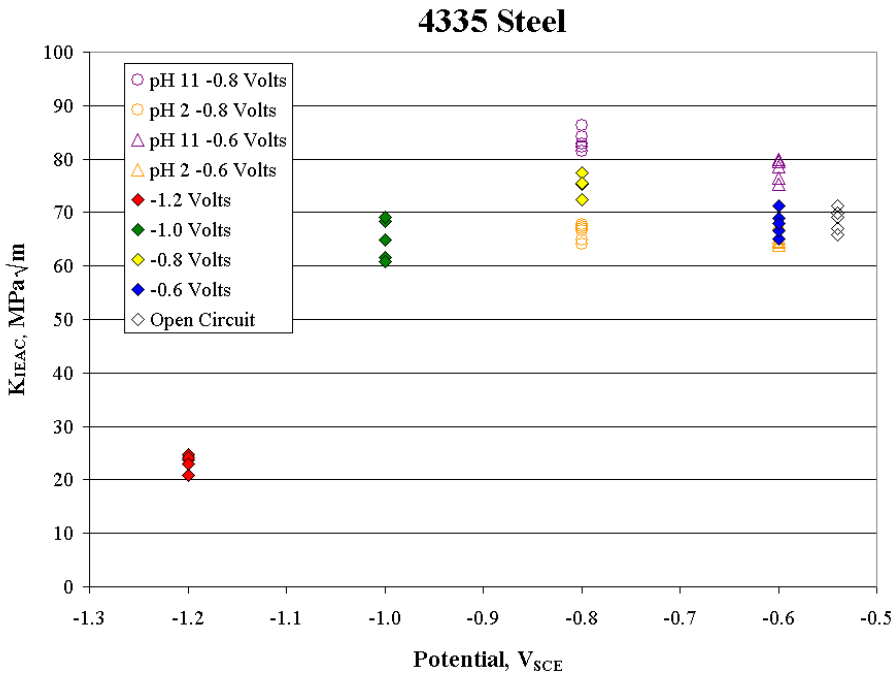

FIGURE 7. K_{IEAC} Results for 4335 Steel.

The surfaces of the fractured specimens were characterized for fracture morphology within the different regions. Each of the three regions; a) cyclic fatigue transgranular fracture, b) hydrogen affected brittle intergranular or semi-intergranular fracture, and c) semi-ductile or ductile fracture were observed in the materials investigated. Figures 8 through 11 depict the three zones of fracture for VAR 4340 HRc 52, VAR 4340 HRc 38, PH 13-8 Mo, and 4335 steel, respectively.

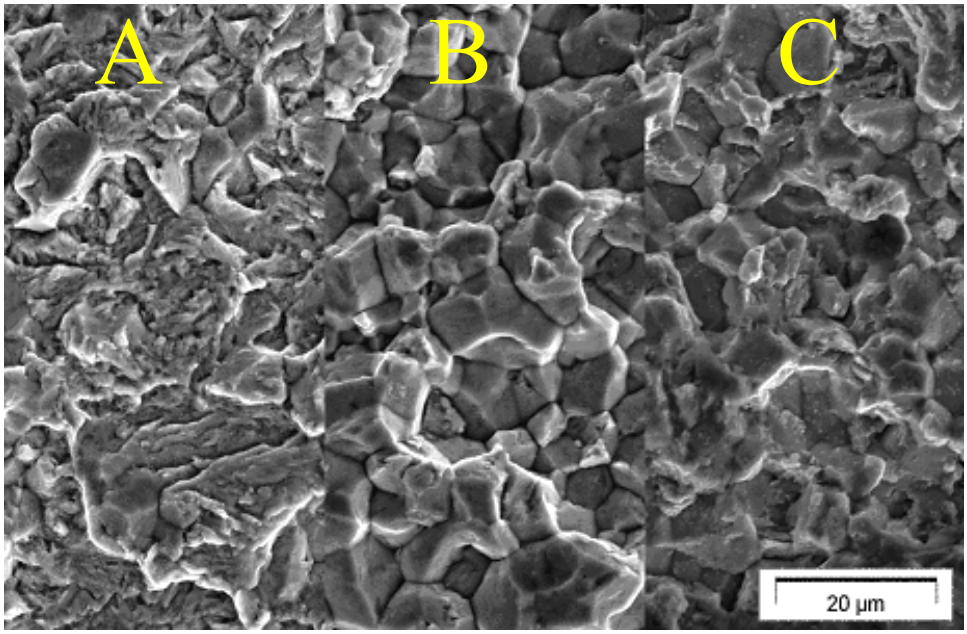

FIGURE 8. Fracture Morphology Zones for VAR 4340 HRc 52 Steel.

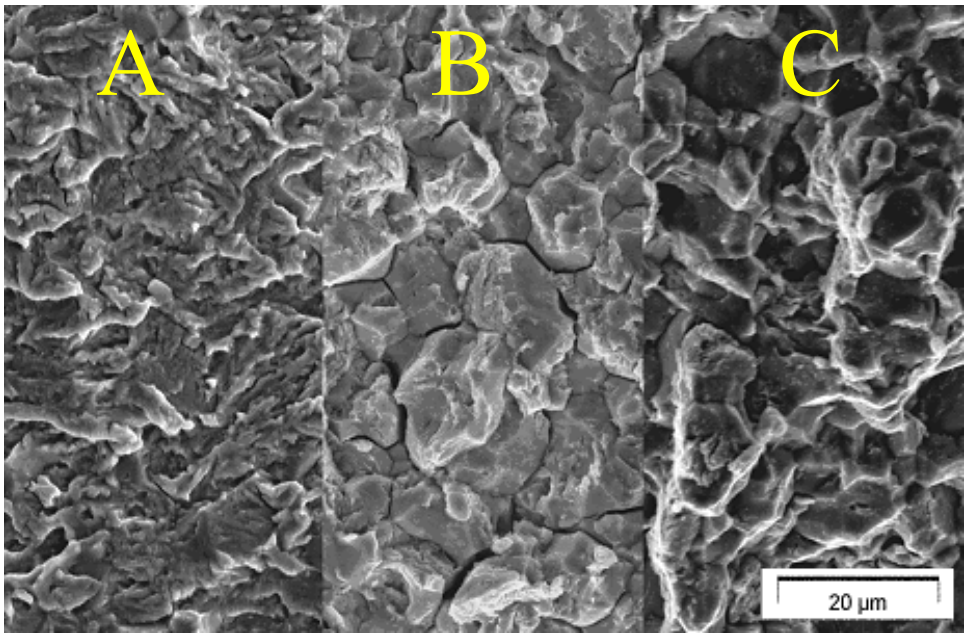

FIGURE 9. Fracture Morphology Zones for VAR 4340 HRc 38 Steel.

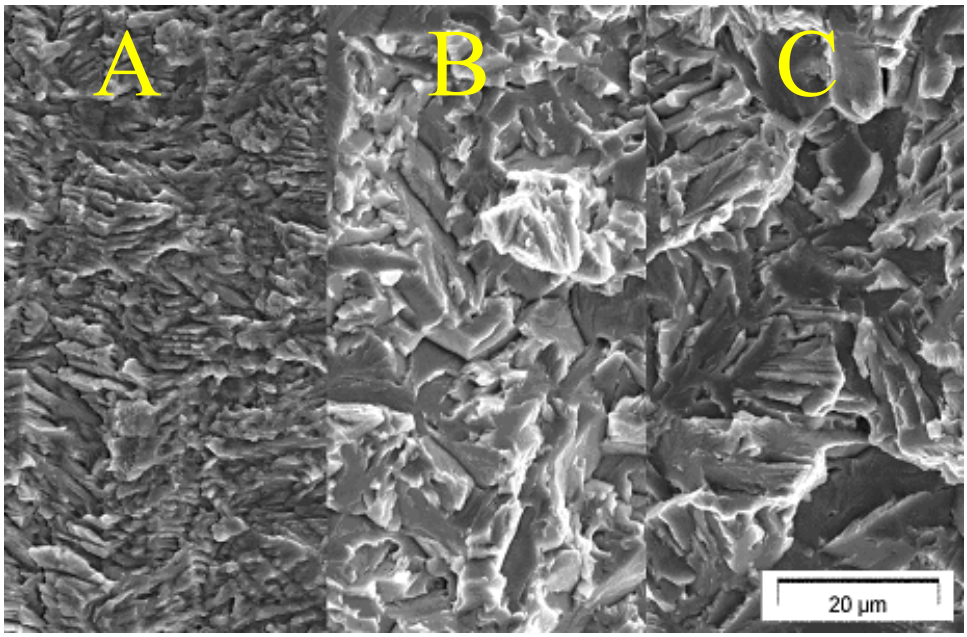

FIGURE 10. Fracture Morphology Zones for PH 13-8 Mo Steel.

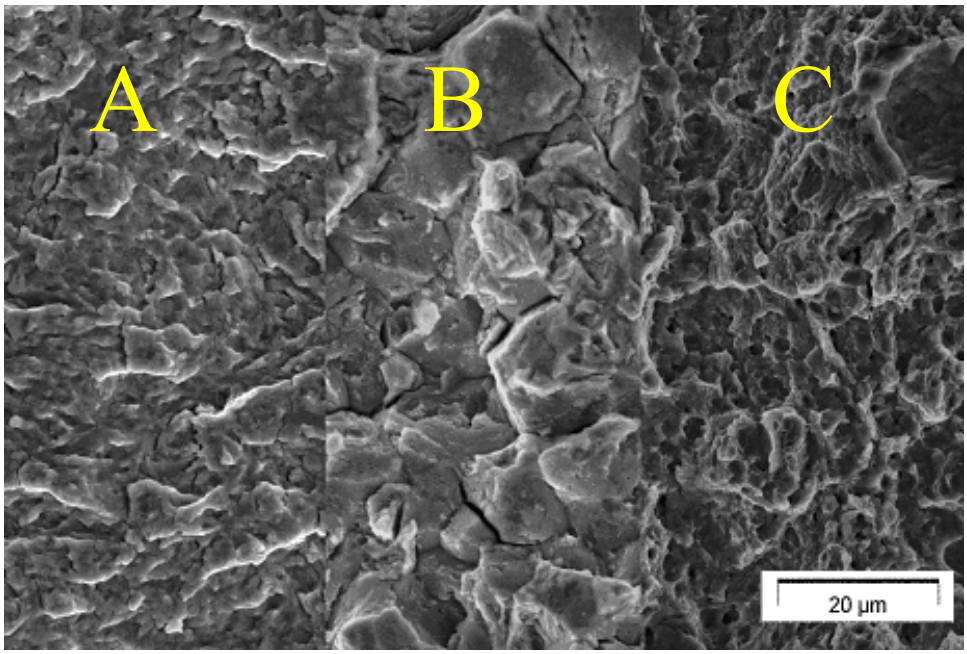

FIGURE 11. Fracture Morphology Zones for 4335 Steel.

DISCUSSION

The materials demonstrated strong dependence on potential. Additionally, the general trend of the pH 11 solution to increase the measured K_{IEAC} values while the pH 2 solution decreased the measured values held true for all materials. It appeared that the initial relationship governing the dissociation of the hydrogen proton reaction dominated the K_{IEAC} experimentation. It was interesting to note that the PH 13-8 had a near direct relationship with potential, as potential decreased so did the measured K_{IEAC} value. VAR 4340 in the HRc 52 condition remained largely unaffected by electrochemical potential and pH probably due to the sensitivity of the material to hydrogen and the fact that general corrosion of 4340 in 3.5 % NaCl was sufficient to introduce enough hydrogen in the solution to deleteriously affect the steel. The fracture toughness of the materials decreased dramatically in the presence of excess hydrogen. The K_{IEAC}/K_{Ic} ratios for the tested materials are presented in table 3.

TABLE 3.
K_{IEAC}/K_{Ic} Ratios for the Tested Materials

Material	PS K_{Ic} (MPa√m)	K_{IEAC} (MPa√m) at -1.2 V_{SCE}	K_{IEAC}/PS K_{Ic}
VAR 4340 HRc 52	60	17	0.28
VAR 4340 HRc 38	105	17	0.16
PH 13-8 Mo	100	9	0.09
4335	100	23	0.22

Since most of these materials are used in conjunction with sacrificial coatings due to their poor corrosion resistance, designers must be careful to account for hydrogen damage when attempting to avoid critical flaws. This case is more extreme for PH 13-8 Mo for example, since its K_{IEAC}/K_{Ic} ratio is 0.09. A designer would be more likely to allow a critical flaw in this material, when ignoring hydrogen, then in VAR 4340 HRc 52. The K_{IEAC} values in the presence

of excess hydrogen are actually very similar. Realistically, this is an exaggeration due to the extreme amount of hydrogen at -1.2 V_{SCE}, but the trend can certainly be seen, even at other potentials, in the plotted data. The minimum and maximum measured K_{IEAC} data is summarized in table 4. Coating system designers can use this data in their designs. By tailoring the coating to push the overall potential of the coated substrate toward -0.8 V_{SCE} and toward the basic end of the pH scale, a design would yield the most hydrogen tolerant system possible for each material, although the specific values vary slightly from case to case.

TABLE 4.
Maximum and Minimum measured K_{IEAC} Values for the Tested Materials

Material	**PS K_{Ic} (MPa√m)**	**Maximum K_{IEAC} (MPa√m), Potential and pH at Max.**	**Minimum K_{IEAC} (MPa√m), Potential and pH at Min.**
VAR 4340 HRc 52	60	21.4, -0.6 V_{SCE}, pH 11	16.5, -1.2 V_{SCE}, neutral 3.5% NaCl
VAR 4340 HRc 38	105	91.2, -0.8 V_{SCE}, pH 11	17.4, -1.2 V_{SCE}, neutral 3.5% NaCl
PH 13-8 Mo	100	78.3, -0.8 V_{SCE}, pH 11	9.1, -1.2 V_{SCE}, neutral 3.5% NaCl
4335	100	84.2, -0.8 V_{SCE}, pH 11	23.4, -1.2 V_{SCE}, neutral 3.5% NaCl

CONCLUSIONS

The detrimental effect of hydrogen on K_{Ic} was characterized over a wide electrochemical potential and pH range for the high strength steels investigated in this work. Most of the materials demonstrated extreme dependence of K_{IEAC} on both electrochemical potential and pH. PH 13-8 Mo proved to be the most affected. The K_{IEAC} value was lowered to approximately 10% of the known plane strain fracture toughness, K_{Ic}, value in the presence of hydrogen. The other materials behaved similarly, but were not as severe. The maximum K_{IEAC} values for the materials investigated in neutral 3.5% NaCl were as follows: VAR 4340 HRc 52, 21 MPa√m; VAR 4340 HRc 38, 86 MPa√m; PH 13-8 Mo, 59 MPa√m; and 4335 steel, 75 MPa√m.

REFERENCES

1. Bruce, Craig, "Hydrogen Damage," Metals Handbook Ninth Edition, Vol. 13, p 168.

2. Champagne, Victor K., Jr.; Wechsler, Gary; Pepi, Marc S.; Bhansali, Kirit J., "Failure Analysis of the Apache Mixer Pivot Support" MTL-TR-91-25, APG, MD, 1991.

3. Levy, M., P. Buckley, J. Beatty, R. Brown , R. Huie and K. Bhansali, "Failure Analysis of the Main Rotor Retention Nut from the AH-64 Helicopter," MTL-TR-92-39, Watertown, MA, 1992.

4. Krutsan, H. M., Zdanovs'kyi ,V. H., Karvats'kyi LM, Khoma MS , "Causes of Damages to Fan Blades of the Generator of a Steam Turbine," Materials Science 33: (3) 371-374 May-Jun 1997.

5. Rinker, J. G., Hochman, R. F., "Hydrogen Embrittlement of 4340 Steel as a Result of Corrosion of Porous Electroplated Cadmium," Corrosion 28: (6) 231-& 1972.

6. Champagne, Victor K., Jr.; Ziegler, Wayne; Pepi, Marc S., "Failure Analysis of the Main Rotor Retention Nut," Letter Report, APG, MD, 1999.

7. Champagne, Victor K., Pepi, Marc S., Ziegler, Wayne, and Grendahl, Scott, "Failure Analysis of the AH-64 Input Flange," Letter Report, APG, MD, 1999.

8. Buckley, P.F., Brown R., et al, "Corrosion Behavior of High Strength Steels for Aerospace Applications," Metallic Materials for Lightweight Applications, Proceedings of the 40th Sagamore Army Materials Conference, 30 Aug-2 Sept. 1993, Plymouth, MA, p. 449 ff.

9. ASTM G49-95, Standard Practice for Preparation and Use of Direct Tension Stress-Corrosion Test Specimens, ASTM, Philadelphia, PA, 1995.

10. ASTM F1624-95, Standard Test Method for Measurement of Hydrogen Embrittlement in Steel by the Incremental Load Technique, ASTM, Philadelphia, PA, 1995.

11. ASTM G129-95, Standard Practice for Slow Strain Rate Testing to Evaluate the Susceptibility of Metallic Materials to Environmentally Assisted Cracking, ASTM, Philadelphia, PA, 1995.

12. ASTM G38-73, Standard Practice for Making and Using C-Ring Stress Corrosion Test Specimens, ASTM, Philadelphia, PA, 1995.

13. ASTM G30-97, Standard Practice for Making and Using U-Bend Stress Corrosion Test Specimens, ASTM, Philadelphia, PA, 1997.

14. ASTM G39-99, Standard Practice Preparation and Use of Bent-Beam Stress Corrosion Test Specimens, ASTM, Philadelphia, PA, 1999.

15. ASTM F 1940-98, Standard Test Method for Process Control Verification to Prevent Hydrogen Embrittlement in Plated or Coated Fasteners, ASTM, Philadelphia, PA, 1998.

16. ASTM B 849094, Standard Specification for Pre-Treatments of Iron or Steel for Reducing Risk of Hydrogen Embrittlement, ASTM, Philadelphia, PA, 1994.

17. ASTM F1113-87, Standard Test Method for Electrochemical Measurement of Diffusible Hydrogen in Steels (Barnacle Electrode) ASTM, Philadelphia, PA, 1994.

18. ASTM F 1459-93, Standard Test Method for Determination of the Susceptibility of Metallic Materials to Gaseous Hydrogen Embrittlement, ASTM, Philadelphia, PA, 1998.

19. ASTM F326-96, Standard Test Method for Electronic Measurement for Hydrogen Embrittlement from Cadmium-Electroplating Processes, ASTM, Philadelphia, PA, 1996.

20. ASTM B850-98, Standard Guide for Post-Coating Treatments of Steel for Reducing Risk of Hydrogen Embrittlement, ASTM, Philadelphia, PA, 1998.

21. ASTM E-399-97, Standard Test Method for Plane Strain Fracture Toughness of Metallic Materials, ASTM, Philadelphia, PA, 1998.

EVALUATION OF BARRIER PROPERTIES OF SOL-GEL DERIVED COATINGS ON AA2024-T3

N.N. Voevodin[1], V.N. Balbyshev[2], J.A. Johnson, and M.S. Donley

Air Force Research Laboratory, Wright-Patterson Air Force Base, OH 45433-7750, USA
[1] University of Dayton Research Institute, 300 College Park, Dayton, OH 45469-0168, USA
[2] Universal Technology Corp., 1270 N. Fairfield Rd., Dayton, OH 45432-2600, USA

ABSTRACT

The Air Force requires development of environmentally compliant aircraft coating systems that perform adequately in terms of corrosion protection. Current Air Force corrosion inhibitor paint chemistry relies heavily on the use of Cr(VI) compounds, which are incorporated into both the surface pretreatment and the primers. These corrosion inhibitor systems are very effective, but are known carcinogens and therefore must be eliminated. Sol-gel based surface treatments are being investigated as a potential replacement for the current chromate-based approach. Surface modifications based on the conventional epoxy-zirconate sol-gel and the self-assembled nanophase particle (SNAP) siloxane coatings have been investigated. The formation of a SNAP coating relies on aqueous solution processes to generate nanoscale particles with an inorganic functionality. SNAP coatings provide epoxy functionality for bonding to appropriate substrates and tailorable chemistry for interaction with subsequent polymer layers. It has been demonstrated in a 2000 hr salt spray test that coating systems with SNAP surface treatment and a chromated primer perform as well as systems with Alodine™ pretreatment and a chromated primer. Superior adhesion and corrosion protection characteristics make SNAP surface treatment a promising environmentally benign alternative to chromate pretreatments.

INTRODUCTION

Aircraft coating systems are a major technological concern for DoD, and one in which continual improvement is sought. Estimates indicate that aircraft painting/stripping/repainting and handling of the hazardous waste associated with these materials cost in excess of $150M per year for the USAF. The problems associated with corrosion are the number one maintenance cost for the USAF estimated at $700M per year, and 15% of this cost is associated with paint related corrosion (1). A typical aircraft paint system consists of a surface treatment, a primer,

and a topcoat. The surface treatment is applied to the substrate (typically aluminum alloy AA2024-T3 or AA7075-T6) to provide a surface morphology for optimum primer adhesion and typically contains inhibitors for corrosion protection (2,3). The primer also contains corrosion inhibitors which assist in providing the function of corrosion prevention. There must be a compatible interface between the surface treatment and the primer for optimal performance. Finally, the topcoat provides signature control, acceptable optical and physical appearance, and a protective barrier to the outside environment (i.e. sunlight, water, mechanical abrasion, etc.). Each component plays an important role in the protection from environmental factors, but components must be compatible with each another in a complete coating system package.

The corrosion protection requirements of coating systems are more demanding for aging aircraft. With shrinking budgets and the enormous cost of new weapon systems, fewer new aircraft are being developed. This directly results in the continued use of the current aircraft far longer than they were intended. While structural integrity of the aircraft is crucial, the first line of defense to the outside environment is the coating system. As the service life of the weapon systems becomes longer, the demands on coating systems become greater. Therefore, there are large economic incentives to improve upon existing coating systems and at the same time reduce hazardous air pollutants (HAPs) and volatile organic compounds (VOCs). Conventional surface treatment and primer components rely solely on hexavalent chromium (Cr^{6+}) as the corrosion inhibitor, which also must be eliminated to comply with environmental regulations. These traditional coating chemistries, with their established protocols, applications, and performance, will eventually be restricted from use. New classes of materials for surface treatments, corrosion inhibitors, polymer resin systems, and solvent application systems must be established. They

must perform the multi-functional role of an air force aircraft coating system which consists of three main attributes: 1) corrosion protection, 2) survivability, and 3) cosmetic appearance.

EXPERIMENTAL

The were applied to 4" x 6" AA2024-T3 panels. The surface cleaning protocol and experimental procedures for the synthesis of the epoxy-zirconate and SNAP sol-gels have been previously described (4, 5). The surface of the panels with the chromate conversion coating (CCC) was treated using the Warner-Robins surface treatment, which uses B & B Regel alkaline cleaner (MIL-PRF-87937), Octabrite 5096 acid etch (Mil-C-10578D), and Turco Alumigold B chromate conversion coating (MIL-C-81706 material SPEC, and MIL-C-5541 process SPEC). Paints used in this study were those currently used for the maintenance of C-130 aircraft. Chromated primer Deft 23377G epoxy (MIL-PRF-23377) was applied at 77°F (± 3°F) and 50% (± 5%) relative humidity to a dry film thickness of 15-23 μm. Panels were allowed to cure for two hours before the topcoat was applied. Topcoat Deft 85285 polyurethane (MIL-C-85285B), Type 1, Color 36173 was applied under the same experimental conditions as the primer to a dry film thickness of 55-80 μm. The appliqué film was 3M 500 series standard type film qualified to AMS 3603 (MIL-FP-500). A listing of these coating systems is presented in Table 1. Corrosion resistance was tested using the salt spray test according to ASTM B117 for 2000 hrs (6). After the test, the bottom halves of the panels were stripped for visual inspection. Scans of the backs of the panels were taken for a qualitative comparison of the two sol-gel systems without any other protective coating in the salt spray chamber.

EIS tests were performed in triplicate in dilute Harrison's solution (aqueous solution of 0.35wt.% $(NH_4)_2SO_4$ and 0.05wt.% NaCl) using model PC3-300 Gamry potentiostat (Gamry

Instruments Inc.) coupled with Gamry Corrosion Measurements System CMS 100 and CMS 300 software. EIS spectra were collected in the frequency range from 0.02 Hz to 100 kHz. A representative scan from each set was selected and is shown in the figures presented in this report.

An adhesion test consisting of 4 hour submission in boiling water was performed to qualitatively compare the adhesion of sol-gel coatings. Several 4" x 6" AA2024-T3 panels were dip-coated with the solution of the self-assembled nanophase particle (SNAP) silicon sol-gel. The experimental procedure for forming the SNAP sol-gel has been previously described (4). The panels were dip-coated in such a manner that the sol-gel was only applied to the bottom half of the Al panels, leaving the upper portion of the panel uncoated. After the application of the sol-gel, the entire area of the Al panels was coated with an epoxy-polyamide system (Shell Epon Resin 828 and Shell Epi-Cure 8290-Y60) tinted with a blue pigment dispersion (Elementis Tint-Ayd ST 8292) in order to enhance visual indication of the paint coverage. After the coated panels were air-dried for one week, they were immersed in boiling water for 4 hours. Upon completion of the test, the panels were subjected to visual inspection.

TABLE 1.
Description of Coating Systems

	Surface Treatment	Primer	Top Coat	Performance 2000 h Salt Spray
AC 1-3 (control)	Alumigold CCC	Chromated Primer (23377)	Top Coat (85285)	Excellent-passed on the scribe and on the back
AC 2-3	Alumigold CCC	Chromated Primer (23377)	3M Applique (Perforated)	Excellent-passed on the scribe and on the back
AC 8-6	SNAP	Chromated Primer (23377)	3M Applique (non-Perforated)	passed on the scribe, satisfactory on the back
AC 7-6	Epoxy-Zr	Chromated Primer (23377)	3M Applique (non-Perforated)	passed on the scribe, not passed on the back
AC 8-17	SNAP	none	3M Applique (non-Perforated)	slight corrosion on the scribe and on the back
AC 7-17	Epoxy-Zr	none	3M Applique (non-Perforated)	significant corrosion on the scribe and on the back

RESULTS AND DISCUSSION

The traditional salt spray coating evaluation technique was used by the Coatings Technology Integration Office (CTIO) to test the performance of a new appliqué system. All coating systems were tested in replicates; however, for the sake of discussion, only one representative panel from each group is described here. Similar observations can be made about the other panels from the sets of replicates. The backsides of the panels were examined after the salt spray test due to the fact that only sol-gel treatment had been applied to the back of the panel. While the backsides were not subjected to the same exposure conditions as the front of the panels, and experimental parameters could not be monitored or controlled, visual inspection of

the backsides can provide valuable information about relative performance of the two types of sol-gels without additional polymer layers.

A panel with the conventional Air Force paint system, containing chromate conversion coating, chromated primer and a topcoat, was used as control and is displayed in Fig. 1 on the left. After 2000 hrs in the salt spray chamber, the scribe on the panel remained shiny with no visible signs of corrosion. The appliqué panel, where the topcoat was replaced by a perforated laminant, did not show significant signs of corrosion in the scribe, as shown in Fig. 2 on the left. The unscribed backs of panels AC1-3 and AC2-3 (images on the right of figures 1 and 2) showed no visual indication of corrosion.

The SNAP and epoxy-zirconate sol-gel pretreatments for Al were tested in the salt spray chamber alongside the control panel AC1-3 and the appliqué panel AC2-3. Panel AC8-6 with a SNAP sol-gel treatment, chromated primer, and a non-perforated appliqué is shown in Fig. 3. The bottom half of front side (image on the left) had been stripped for better visual observation. There were no signs of corrosion or undercutting; however, the scribe was not as shiny as on the control panel AC1-3. The back of the panel, which only had the pretreatment (SNAP sol-gel in this case), showed no defects or substrate deterioration.

When the chromated primer was removed from the system, as in Panel AC8-17 shown in Fig. 4, leaving only the SNAP sol-gel and the appliqué to protect the substrate in the salt spray chamber, corrosion products were observed in the scribe. However, no corrosion was detected outside the scribe, and no undercutting was present.

FIGURE 1. AC1-3 (control): Alumigold chromate conversion coat, 23377 chromated primer, 85285 topcoat.

FIGURE 2. AC2-3: Alumigold chromate conversion coat, 23377 chromated primer, 3M appliqué (perforated).

In comparison to the SNAP sol-gel system, similar panels with epoxy-zirconate sol-gel were tested. Panel AC7-6 (Figure 5) contained a chromated primer and a non-perforated appliqué (compare with AC8-6, Figure 3), and panel AC7-17 (Figure 6) only contained the epoxy-

zirconate sol-gel pretreatment and the appliqué. In the case of AC7-6, no significant corrosion products were found in the scribe after the test. The stripped bottom half of the front side of the panel revealed no undercutting. However, the backside of the panel showed severe damage to the film and the Al substrate. The epoxy-zirconate/appliqué panel without the chromated primer, as shown in Figure 6, had significant accumulation of corrosion products in the scribe, and severe undercutting (up to 1 cm away from the scratch) was detected. The backside of the panel had some of the sol-gel pretreatment removed during the test, thus exposing Al to the aggressive environment of the salt spray chamber.

FIGURE 3. AC8-6: SNAP sol-gel pretreatment, 23377 chromated primer, 3M appliqué (non-perforated).

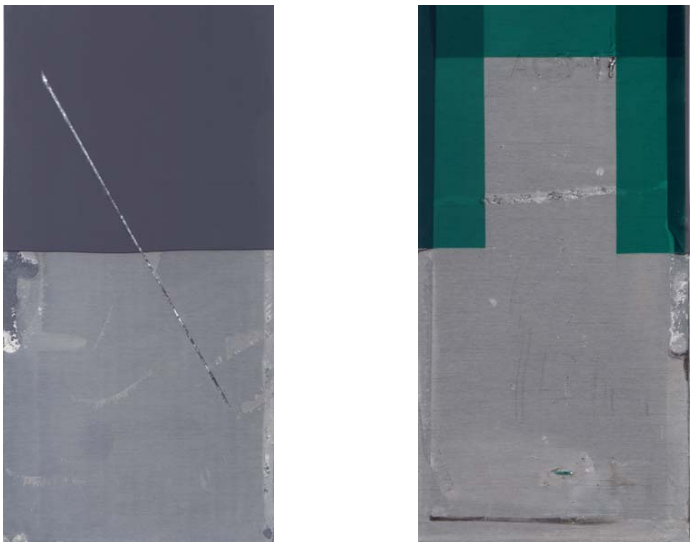

FIGURE 4. AC8-17: SNAP sol-gel pretreatment, 3M appliqué (non-perforated).

FIGURE 5. AC7-6: Epoxy-zirconate sol-gel pretreat-ment, 23377 chromated primer, 3M appliqué (non-perforated).

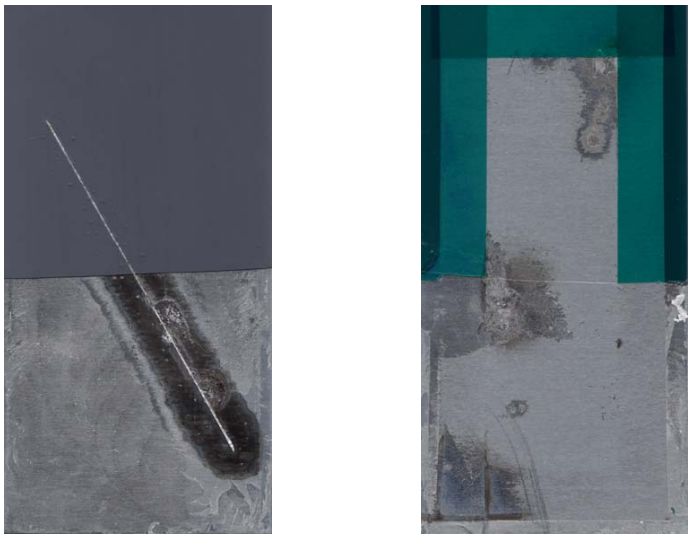

FIGURE 6. AC7-17: Epoxy-zirconate sol-gel pre-treatment, 3M appliqué (non-perforated).

Based on the observations from the scribed panels, we can conclude that the epoxy-zirconate sol-gel system does provide some level of corrosion protection when used in systems with a chromated primer. However, it appears that this sol-gel coating alone does not provide adequate corrosion protection comparable to that of the chromate conversion coating.

In contrast to the epoxy-zirconate sol-gel, the SNAP coating performed equally well with or without a chromated primer in the system. The difference in the behavior of the two sol-gels could be explained by the fact that SNAP sol-gel formation is based on a process that produces dense, defect-free films because the coating is formed by crosslinking the nanophase particles – the sol-gel chemistry is completed in solution prior to film application. Conversely, the epoxy-zirconate sol-gel coating relies on condensation reactions occurring on the coated substrate after the film is applied. Comparison of the backsides of the panels with two types of sol-gels also suggests that SNAP sol-gel forms films that are less susceptible to attack in corrosive environment. All the epoxy-zirconate panels exhibited corrosion degradation on the back whereas all SNAP panels did not. The failure of a sol-gel pretreatment occurs through ingress of

electrolyte into the film followed by the loss of adhesion. The SNAP coating, being a more dense coating , is more effective at providing a protective barrier to electrolyte. Absence of delamination in this case suggests that adhesion characteristics of SNAP are superior to those of the epoxy-zirconate sol-gel.

In order to verify the improvements of hydrolytic stability with concomitant adhesion enhancements brought about by incorporation of the SNAP surface treatment into coating formulation, a simple boiling water test was set up. Upon removal of the panels from boiling water after 4 hours, the upper portions of the panels that had not been treated by SNAP were marked by severe blistering of the blue epoxy-polyamide coating as shown in Figure 7. The bottom halves of the panels showed no paint delamination and no blisters had formed. This test demonstrates that SNAP coating acts as an adhesion promoter when applied to Al substrate.

Another important characteristic of SNAP films that is necessary for an adequate level of corrosion protection is barrier properties. Superior adhesion of SNAP films makes it resistant to corrosive electrolyte containing Cl^- ions. The results of the immersion studies by EIS are shown in Figure 8. The low-frequency |Z| remained almost unchanged for almost 2 months of constant immersion in dilute Harrison's solution. A |Z| value of 4×10^7 Ω cm^2 and a capacitive profile were observed at the low frequencies of the impedance spectra at immersion times between 0 and 42 days. After approximately 60 days, the low-frequency |Z| value started to decrease, approaching the 1×10^6 Ω cm^2 mark and showing a low-frequency plateau. After 80 days of immersion, the |Z| stabilized around 1×10^6 Ω cm^2 and remained unchanged for up to 167 days, at which point the panels were taken off the test. Even though the |Z| value after 167 days is indicative of corrosion protection afforded by a rather poor coating, it should be noted that SNAP films are on the order of 1 μm in thickness and are not full coating systems. These EIS

immersion test results demonstrate that SNAP sol-gel films applied to the aluminum substrate maintain hydrolytic stability in a corrosive environment.

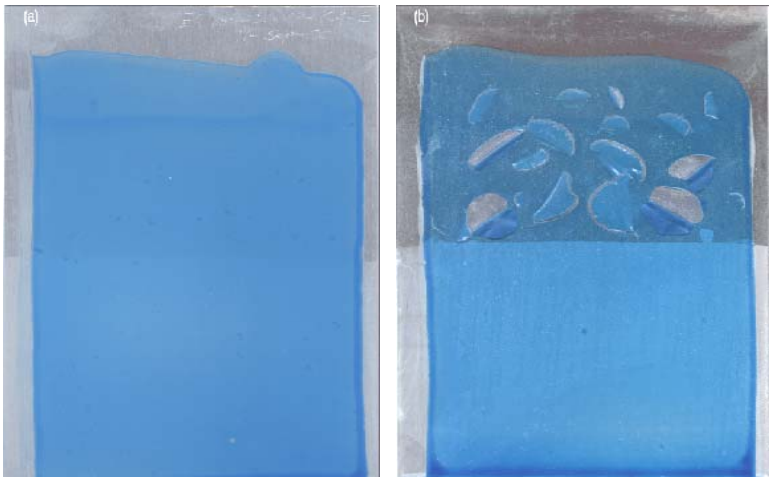

FIGURE 7. Boiling water test of SNAP surface treatment.

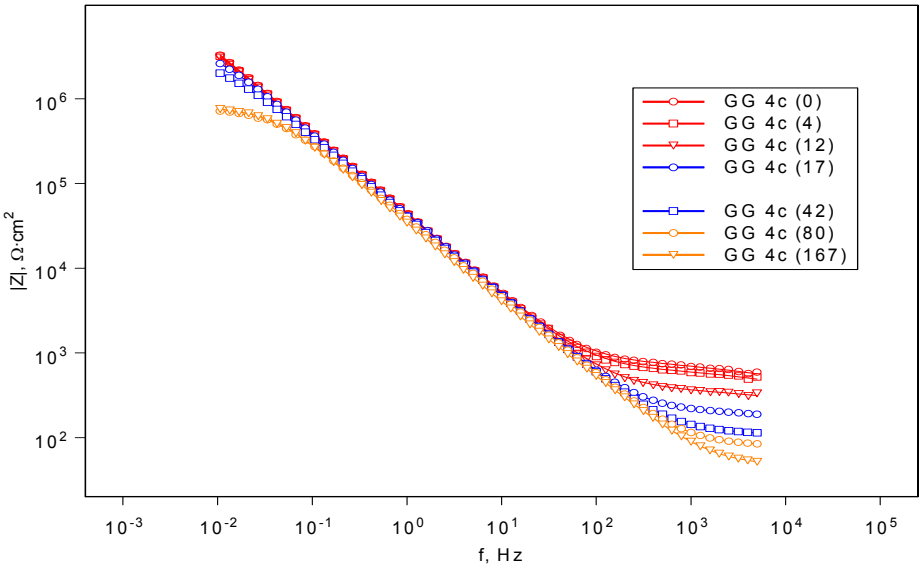

FIGURE 8. EIS studies of SNAP sol-gel as a function of immersion time.

CONCLUSIONS

Corrosion protection afforded by incorporation of a sol-gel pretreatment layer into a full coating system has been studied in a 2000 hr salt spray test. Paint systems with both epoxy-zirconate and SNAP sol-gels exhibited adequate corrosion protection when used with a chromated primer. However, paint systems with epoxy-zirconate sol-gel without a chormated primer revealed severe undercutting. At the same time, SNAP sol-gel was found to be more effective than epoxy-zirconate when used in a system without a chromated primer, showing no film undercutting around the area of the scribe. Undercutting develops in the areas of weak adhesion to the substrate, and therefore can be considered a relative ranking scale for the strength of adhesive bonds at the metal-coating interface. SNAP sol-gel performed as well as the systems with Alodine pretreatment and a chromated primer or with a chromated primer alone. Strong hydrolytic stability of SNAP on Al substrate was experimentally demonstrated in a 4-hour boiling water test, where paint blistering was prevented by the SNAP film preapplied to AA2024-T3. Overall, superior adhesion and corrosion protection characteristics make SNAP surface modification a promising environmentally benign alternative to chromate pretreatments.

REFERENCES

1. R.N. Miller, R. Summit and F.H. Meyer, NACE, Vol. II, 1440 (1994).
2. U.S. Pat. 5,132,003 (1992) M. Mitani, “Process for Surface Tratment of Aluminum or Aluminum Alloy.”
3. U.S. Pat. 4,963,198 (1990) G.A. Reghi, “Process for Corrosion resisting Treatments for Aluminum Surfaces.”
4. A.J. Vreugdenhil, V.N. Balbyshev, M.S. Donley, Journal of Coatings Technology, **73** (915), 35 (2001).

5. N.N. Voevodin, et.al., Progress in Organic Coatings, **41** (4), 288-292 (2001).

6. ASTM B117-90, "Standard Method of Salt Spray (Fog) Testing," ASTM, Philadelphia, PA, 1990.

SCC AND CORROSION FATIGUE OF HVOF COATED AND CR PLATED AERMET 100 STEEL

E. U. Lee, H. C. Sanders and S. Hartle
Naval Air Warfare Center Aircraft Division
Patuxent River, MD 20670

ABSTRACT

The stress corrosion cracking (SCC) and corrosion fatigue behavior of an AerMet 100 steel was studied, employing three groups of specimens. The first group was coated with 83% WC-17% Co powders by High Velocity Oxygen Fuel (HVOF) thermal spray. The second one was Cr electoplated. The third one was bare. The SCC was investigated under sustained tension in 3.5% NaCl solution of pH 7.3, employing rising step loading technique. The threshold stress for SCC, $(\sigma_{th})_{scc}$, increased to a peak and then decreased with increasing cathodic potential from -1.2 to -0.5 volt. Furthermore, it was lower for the HVOF coated and Cr plated specimens than for the bare one. The lower SCC resistance is attributed to the galvanic corrosion of the base metal at the interface in the presence of the more noble HVOF coating and Cr plating and 3.5% NaCl solution. At the open circuit potential, the values of $(\sigma_{th})_{scc}$ were 1324, 1531 and 1724 MPa (192, 222 and 250 ksi) for the HVOF coated, Cr plated and bare specimens, respectively. The fatigue resistance was determined by stress-life fatigue testing in 3.5% NaCl solution of pH 7.3 and air. In 3.5% NaCl solution, it was greater for the HVOF coated specimen, intermediate for the Cr plated ones, and lowest for the bare one. In air, it was similar for the three groups of specimens at higher stresses but lower for the Cr plated one at lower stresses. The HVOF coating and Cr plating were flaked during SCC and fatigue loading in both of the environments.

INTRODUCTION

Various steel components of aircraft, such as landing gear, actuator, piston and shock absorber, have been Cr electroplated to prevent corrosion and wear and/or to rebuild worn or undersized components. However, this process has some problems. The elctroplating bath contains hexavalent Cr, a human carcinogen,[1] and so the air emission and solid waste disposal from the electroplating operation must be minimized or eliminated. In addition, the Cr eletroplating induces hydrogen embrittlement in the base metal, and the post-plating baking is

required to mitigate hydrogen effect. Because of these problems, its replacements have been sought. As a potential candidate, HVOF thermal spray coating has emerged.[2,3]

In the HVOF coating process, fuel, usually propane or hydrogen, is mixed with oxygen and burned in a barrel of spray gun. The combustion products are allowed to expand through a nozzle where the gas velocity becomes supersonic. Powders are introduced in the nozzle, heated and accelerated. They become fully or partially melted droplets and propelled toward the workpiece or substrate. On impact, the droplets flow into thin lamellae, adhering to the surface, overlapping and interlocking as they solidify. The benefits of HVOF coating are absence of hexavalent Cr and hydrogen embrittlement, and high bond strength and low porosity. However, its integrity and applicability to aircraft components remain to be determined.

The components of carrier-based aircraft are under static and cyclic loading in corrosive environments, and susceptible to SCC and corrosion fatigue. The resistance to SCC and corrosion fatigue is a key factor for the integrity and applicability of HVOF coating to the Navy aircraft. This study aims at clarifying this and comparing with those for Cr electroplating and bare AerMet 100 steel.

Residual stress in thermal spray coatings, such as HVOF coating, is unavoidable due to the high temperature associated with thermal spray and the difference in thermal expansion coefficient and Young's modulus between the coating and base materials. Therefore, it is essential to know the residual stress level in the base metal and its influence on SCC and fatigue resistance. The other objective of this study is to measure and compare the residual stresses in HVOF coated and Cr plated specimens and to define the effect on SCC and fatigue resistance.

EXPERIMENTAL PROCEDURE

BASE METAL

A forged slab of AerMet 100 steel, 25.4 mm (1 inch) thick, was used as the base metal. Its chemical composition is shown in Table 1. It was solution treated at 885°C for 75

TABLE 1.
Chemical Compostion of AerMet 100 Steel

Element	Weight %
C	0.230
Mn	< 0.01
Si	0.01
P	0.003
S	0.0008
Cr	3.11
Ni	11.07
Mo	1.19
Co	13.40
Ti	0.010
Al	0.005

minutes in argon, cooled in nitrogen, frozen in dry-ice and alcohol, and aged at 482°C for 5 hours in air. The microstructure is shown in Figure 1. The mechanical properties are yield strength 1724 MPa (250 ksi), ultimate tensile strength 2069 MPa (300 ksi), elongation 14% and fracture toughness 126 MPa√m (115 ksi√in).

SPECIMAN

Two types of specimen, buttonhead and hourglass, were used for SCC and fatigue tests, respectively. Their gage lengths and diameters were 25.4 mm (1 in) and 4.1 mm (0.160 in) for the buttonhead specimen,[4] and 49.3 mm (1.940 in) and 6.4 mm (0.251 in) for the hourglass (or specimen with a continuous radius between ends),[5] respectively. All specimens were machined to have the longitudinal axis parallel to the rolling direction of the base metal, AerMet 100 steel slab.

Each type of specimen was divided into three groups. The first group was coated with 83% WC-17% Co powders by means of HVOF thermal spraying. The second one was Cr electroplated and baked at 375°F for 24 hours in vacuum. Prior to the HVOF coating and Cr plating, the specimen was shot-peened. The thickness of the HVOF coating and Cr plating was 76 μm (3 mil). The third one was bare.

RESIDUAL STRESS MEASUREMENT

The HVOF coating and Cr plating were removed by electropolishing, and the residual stress was measured at various depths in the base metal by X-ray diffraction.

SCC TEST

The SCC test was conducted with a buttonhead specimen, employing an accelerated test method of rising step loading,.[6] in 3.5% NaCl solution of pH 7.3 at room temperature. The test machine included a loading device for sustained tension, an environmental chamber, a pump for circulation of electrolyte and a potentiostat. During the test, the specimen was the working electrode in a three-electrode cell with a saturated calomel reference electrode and a platinum counter-electrode in 3.5% NaCl solution. Cathodic potentials, ranging from –1.2 to –0.5 volt, were applied to generate various amounts of hydrogen at the advancing crack tip of a specimen under sustained tension.

Since the threshold stress intensity factor for SCC, K_{ISCC}, can not be determined with a coated or plated specimen, having no pre-crack, the threshold stress for SCC, $(\sigma_{th})_{scc}$, was determined at various cathodic potentials.

FATIUGE TEST

The fatigue test was conducted in a MTS machine of 90 KN (20 kip) capacity, using an hourglass specimen, in air and 3.5% NaCl solution of pH 7.3. The specimen was subjected to

constant amplitude cyclic loading of sinusoidal waveform at load ratio 0.1 and frequencies 1 and 20 Hz in air and 3.5% NaCl solution. A stress-life (S-N) curve was developed for each type of coating, plating and environment.

RESULTS AND DISCUSSION

RESIDUAL STRESS

The residual stress in the base metal, beneath the HVOF coating and Cr plating, was determined to be compressive and changing with depth, as shown in Figure 2. In the HVOF coated specimen, the compressive residual stress increases to the peak, -600 MPa (-87 ksi), at depths, ranging from 40 to 100 μm (1.6 to 3.9 mil), and then diminishes with increasing depth. Its layer is about 190 μm (7.5 mil) deep. In the Cr plated specimen, the compressive residual stress peak is -917 MPa (–133 ksi) at depth 38 μm (1.5 mil), and its layer is about 100 μm (4 mil) deep. Compared to the Cr plated specimen, the HVOF coated specimen has a lower peak but a deeper layer of compressive residual stress.

McGrann[7] also observed similar features of compressive residual stress distribution in 83% WC-17% Co HVOF coated and Cr electroplated 4130 steel specimens. In this case, the peak residual stress was greater in the HVOF coated specimen than in the Cr plated one.

SCC

The SCC threshold tensile stress, $(\sigma_{th})_{scc}$, was found to vary with potential, V_{SCE}, under sustained tension in 3.5% NaCl solution. The variation is shown for the bare, Cr plated and HVOF coated specimens in Figure 3. At V_{SCE} = -1.2 volt, the $(\sigma_{th})_{scc}$ is lowest for all three groups of specimen. With increasing V_{SCE}, the $(\sigma_{th})_{scc}$ increases to the peak at V_{SCE} = -0.8 volt, and then decreases. At V_{SCE} = -0.5 volt or the open circuit potential, $(\sigma_{th})_{scc}$ = 1724, 1531 and

1324 MPa (250, 222 and 192 ksi) for the bare, Cr plated and HVOF coated specimens, respectively. For a given V_{SCE}, the bare specimen has the greatest, the Cr plated one the intermediate, and the HVOF coated one the minimum $(\sigma_{th})_{scc}$. This indicates that the Cr plating and HVOF coating reduce the SCC resistance of AerMet 100 steel in 3.5% NaCl solution.

During the SCC test, the HVOF coating and Cr plating on the buttonhead specimens were flaked, as shown in Figure 4. The flaking was not localized at any particular site, but it occurred all over the gage length portion.

Figure 5(a) shows a cross-section of a buttonhead specimen, normal to the longitudinal axis, in the immediate vicinity of flaked Cr plating. The plating was cracked obliquely to its surface and flaked along its interface during the SCC test. Corrosion pits are visible on the interface of the base metal. Presumably the corrosion pits were formed by galvanic corrosion of the base metal in the presence of more noble Cr plating and 3.5% NaCl solution, which was seeped into the interface through plating cracks and flakes. Furthermore, it is believed that the galvanic corrosion enhanced the SCC of the base metal. Figure 5(b) shows a cross-section of a buttonhead specimen in the immediate vicinity of flaked HVOF coating. Similar flaking of the coating and corrosion pits on the base metal interface are seen.

FATIGUE

Figure 6 shows the stress-life (S-N) curves for the bare, HVOF coated and Cr plated specimens, fatigue tested in air. The three curves nearly overlap each other, indicating similar fatigue resistances, at the higher stress level. However, the fatigue resistance appears to be lower for the Cr plated specimen at the lower stress level. The bare specimen was not shot-peened, whereas the base metal of the HVOF coated and Cr plated specimens was shot-peened and had compressive residual stress in the vicinity of the interface, as shown in Figure 2. If only the

residual stress effect is considered, the Cr plated specimen should show greatest, the HVOF coated one intermediate and the bare one the lowest fatigue resistance. However, the reverse was observed. Apparently, there must be the other effects on fatigue resistance for the Cr plated and HVOF coated specimens.

Sartwell[8,9] reported that Cr plating on 4340 steel led to substantially lower and HVOF coating somewhat lower fatigue resistance, compared to the bare one. For both of the coating and plating, the reduction of fatigue resistance was greater at lower stress levels.

Bodger[10] showed that the fatigue performances of HVOF coated and Cr plated E35NCD16 (a French ultrahigh strength steel) specimens were more-or-less similar but inferior to that of the bare one.

Figure 7 shows the S-N curves for the bare, HVOF coated and Cr plated specimens, fatigue tested in 3.5% NaCl solution. The HVOF coated specimen has the greatest, the Cr plated one the intermediate and the bare one the lowest fatigue resistance at the lower stress level. This observation evidences that both of the coating and plating can provide the base metal some protection against corrosion fatigue in 3.5% NaCl solution, more obvious at lower stress levels.

Figure 8 shows the S-N curves for the bare specimens, fatigue tested in air and 3.5% NaCl solution. The fatigue life of the bare specimen was reduced by 3.5% NaCl solution, more at the lower stress level.

Figure 9 shows the S-N curves for the HVOF coated specimens, fatigue tested in air and 3.5% NaCl solution. The two curves nearly overlap each other, indicating similar fatigue resistances in both environments and HVOF coating protection against corrosion fatigue in 3.5% NaCl solution.

Figure 10 shows the S-N curves for the Cr plated specimens, fatigue tested at frequencies 1 and 20 Hz in air and 3.5% NaCl solution. At frequency 20 Hz, the S-N curves for the both environments overlap each other, indicating little or no effect of 3.5% NaCl solution on fatigue life. But at frequency 1 Hz, the fatigue life is shorter in 3.5% NaCl solution than in air at the low stress level, indicating the effect of corrosive environment at a lower frequency.

Figure 11 shows flaking of HVOF coating, occurred during fatigue test in air and 3.5% NaCl solution. The flaking is localized in the immediate vicinity of the fracture, the site of highest stress, in the both environments. The base metal in the flaked area shows red corrosion product in the specimen, fatigue test in 3.5% NaCl solution.

Figure 12 shows flaking of Cr plating, occurred during fatigue test in air and 3.5% NaCl solution. The flaking is also localized in the immediate vicinity of the fracture in the both environments.

SUMMARY AND CONCLUSION

The residual stress is compressive near the interface of the HVOF coated and Cr plated specimens, and it changes with depth in the base metal. In the HVOF coated specimen, the compressive residual stress reaches its peak –600 MPa (–87 ksi) at depths 40 – 100 μm (1.6 – 3.9 mil), and decreases with increasing depth. In the Cr plated specimen, the compressive residual stress reaches its peak –917 MPa (–133 ksi) at depth 38 μm (1.5 mil) and decreases with increasing depth. Compared to the Cr plated specimen, the HVOF coated one has lower peak but deeper layer of compressive residual stress.

- The SCC threshold stresses are 1724, 1531 and 1324 MPa (250, 222 and 192 ksi) at the open circuit potential for the bare, Cr plated and HVOF coated specimens, respectively.

The reduction of SCC resistance is attributed to the galvanic corrosion of the base metal at the interface in the presence of more noble plating or coating and 3.5% NaCl solution.

- In air, the fatigue resistances are similar for the bare, HVOF coated and Cr plated specimens at higher stresses, but lower for the Cr plated one at lower stresses.
- In 3.5% NaCl solution, the fatigue resistance is greatest for the HVOF coated, intermediate for the Cr plated and lowest for the bare specimens.
- The fatigue resistance of the bare and Cr plated specimens is lower in 3.5% NaCl solution than in air, whereas that of the HVOF coated specimen is similar in air and 3.5% NaCl solution.
- The HVOF coating and Cr plating are flaked under sustained tension in 3.5% NaCl solution and fatigue loading in air and 3.5% NaCl solution.

REFERENCES

1. ASM Handbook, Vol. 5: Surface Engineering, (Materials Park, OH: ASM International, 1994), p. 925.

1. Proceedings of the International Thermal Spray Conference & Exposition, held 28 May – 5 June 1992 (Orlando, FL),p. 127.

2. Jerry D. Schell and Merk Rechesteiner, Plating and Surface Finishing (July 2000): p. 17.

3. Metals Handbook, Vol. 8: Mechanical Testing, 9th ed. (Materials Park, OH: ASM International, 1985), p. 314.

4. ASTM Standard E 466-96, “Standard Practice for Conducting Force Controlled Constant Amplitude Axial Fatigue Tests of Metallic Materials” (West Conshohocken, PA: ASTM, 1996).

5. Metals Handbook, Vol. 8: Mechanical Testing, 9th ed. (Materials park, OH: ASM International, 1985), p. 539.

6. Proceedings of the 15th International Thermal Spray Conference, ITSC'98, held May 1998, (Nice, France), p. 557.

7. Bruce D. Sartwell and Philip E. Bertz, Advanced Materials and Processes (Aug. 1999): p. 25.

8. Bruce D. Sartwell, Welding Journal (July 2000): p. 39.

9. B. E. Bodger, R. T. R. McGrann and D. A. Somerville, Plating and Surface Finishing: (Sept. 1997):, p. 28.

FIGURES

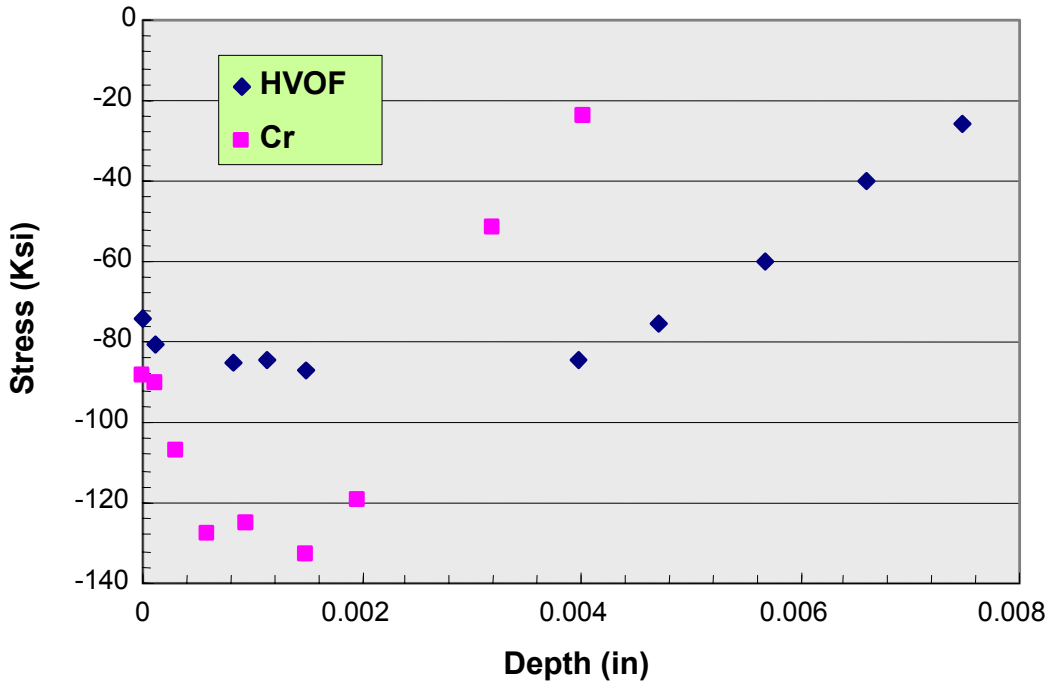

FIGURE 2. Profile of Residual Stress in Base Metal

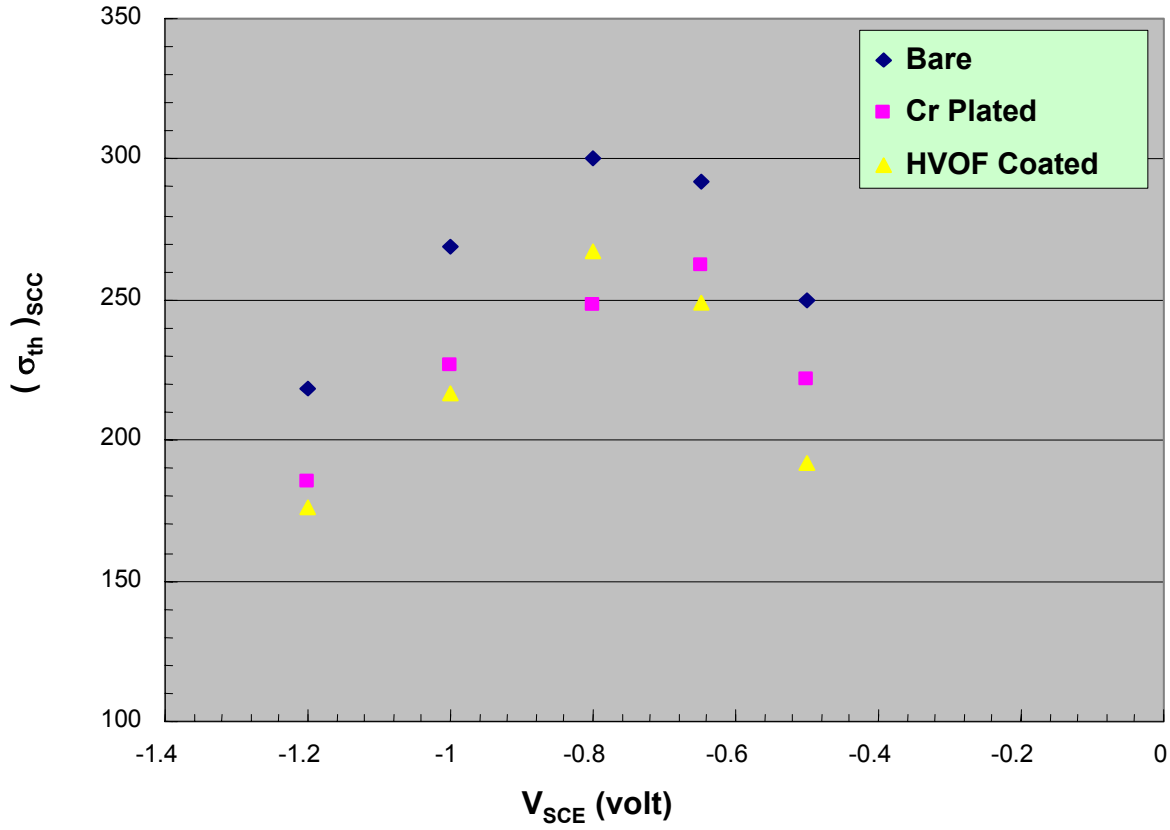

FIGURE 3. Variation of SCC Threshold Stress, $(\sigma_{th})_{SCC}$, with Potential, V_{SCE}

FIGURE 4(a) Flaking of Cr Plating during SCC Test

FIGURE 4(b) Flaking of HVOF Coating during SCC Test

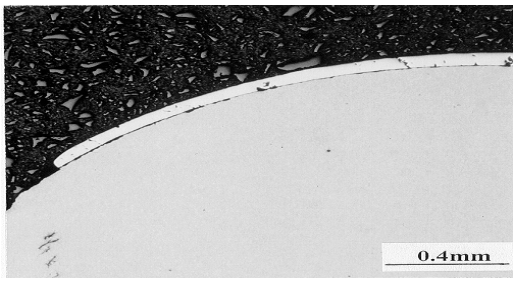

As Polished

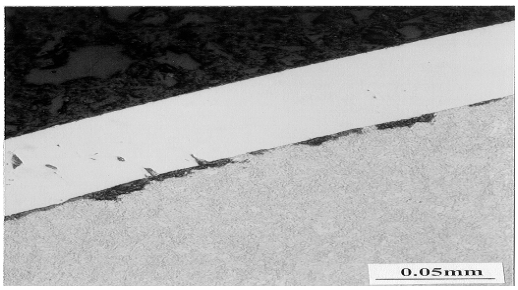

Polished & Etched

FIGURE 5(a). Cross-Section of Specimen, showing Flaking of Cr Plating and Corrosion Pits on Base Metal Interface.

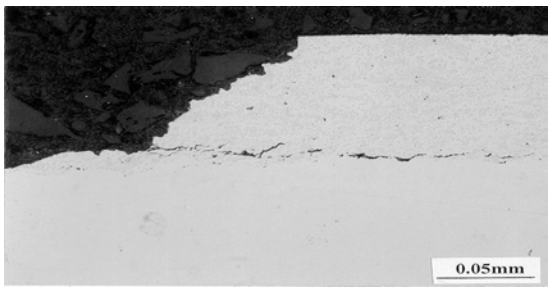

As Polished

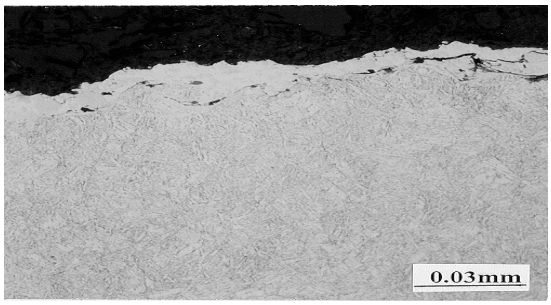

Polished & Etched

FIGURE 5(b). Cross-Section of Specimen, showing Flaking of HVOF Coating and Corrosion Pits on Base Metal Interface.

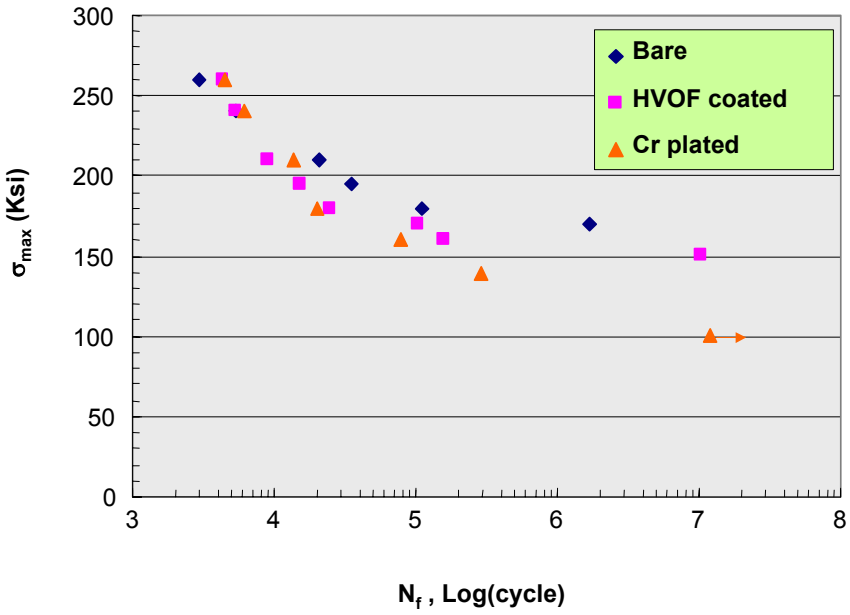

FIGURE 6. S-N Curves for Bare, HVOF Coated and Cr Plating Specimens, Fatigue Tested in Air

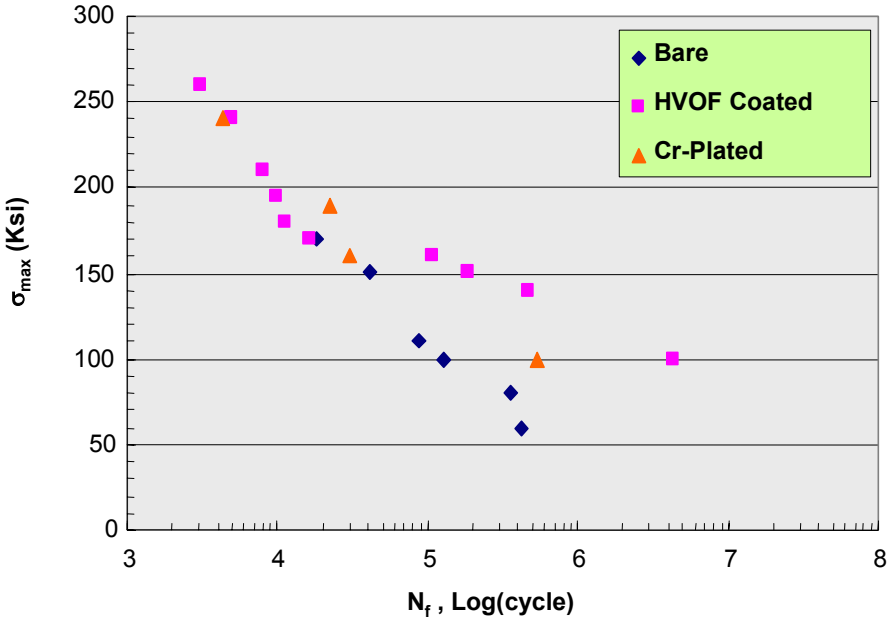

FIGURE 7. S-N Curves for Bare, HVOF Coated and Cr Plating Specimens, Fatigue Tested in 3.5% NaCl Solution

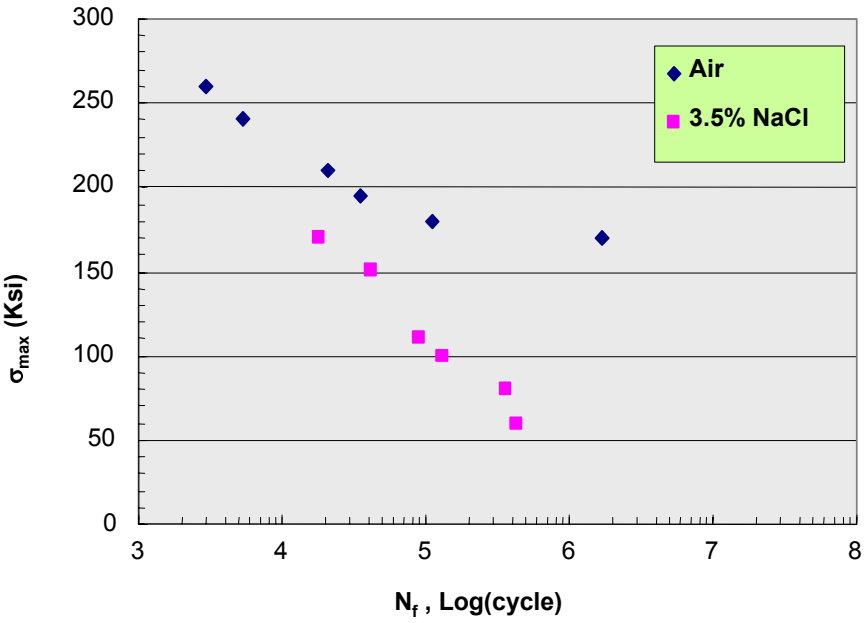

FIGURE 8. S-N Curves for Bare Specimens, Fatigue Tested in Air and 3.5% NaCl Solution.

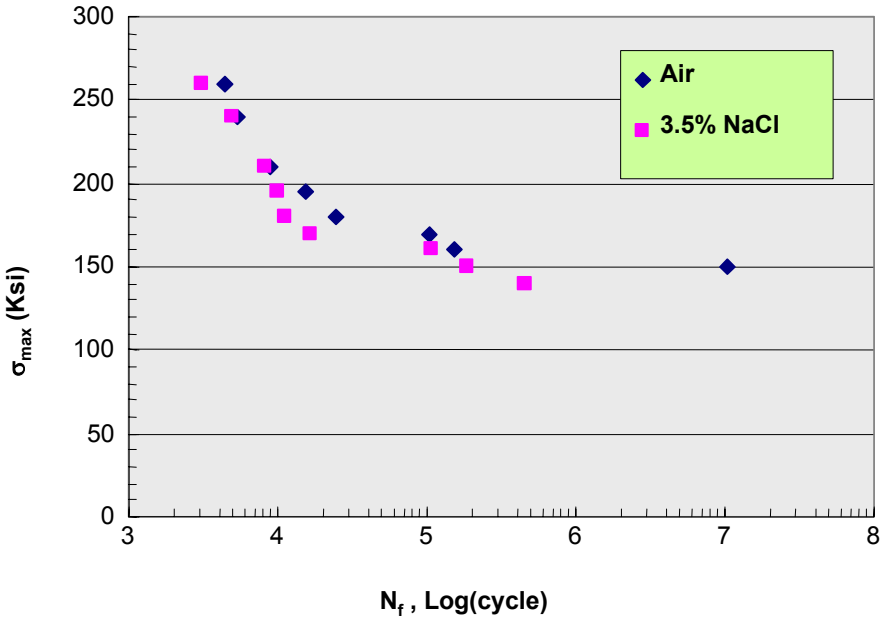

FIGURE 9. S-N Curves for HVOF Coated Specimens, Fatigue Tested in Air and 3.5% NaCl Solution

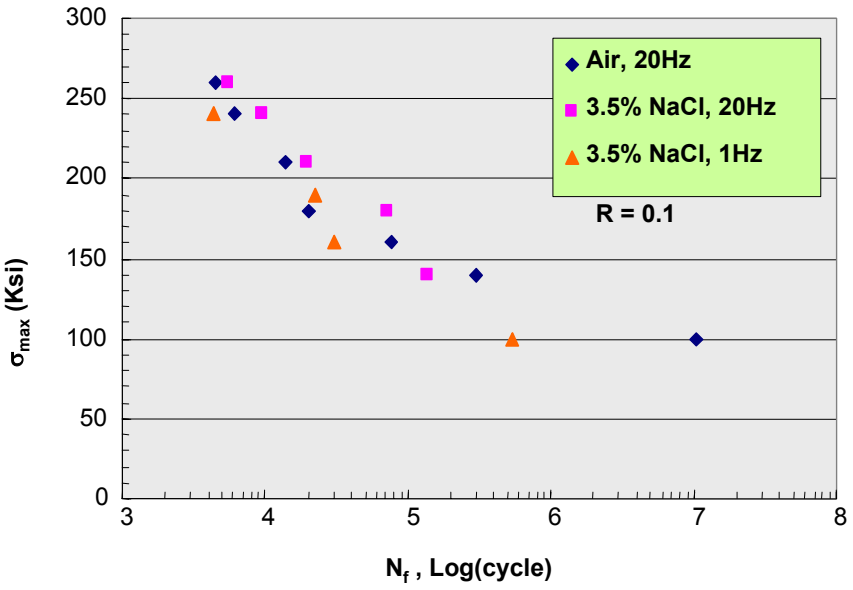

FIGURE 10. S-N Curves for Cr Plated Specimens, Fatigue Tested in Air and 3.5% NaCl Solution

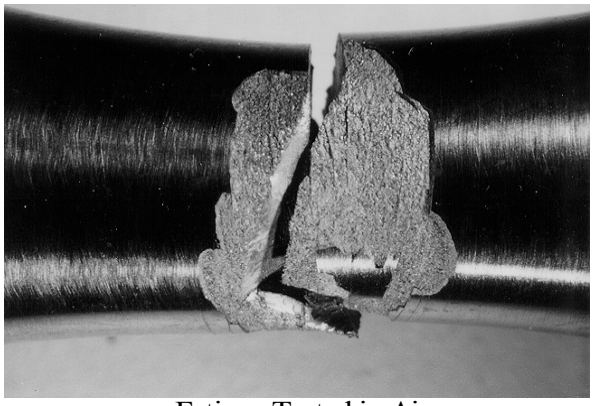

Fatigue Tested in Air

Fatigue Tested in 3.5% NaCl Solution

FIGURE 11. Flaking of HVOF Coating during Fatigue Test

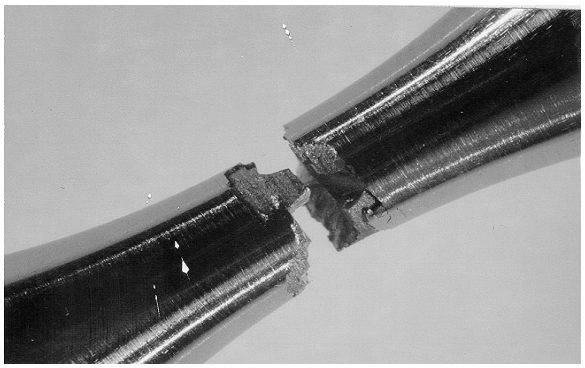

Fatigue Tested in Air

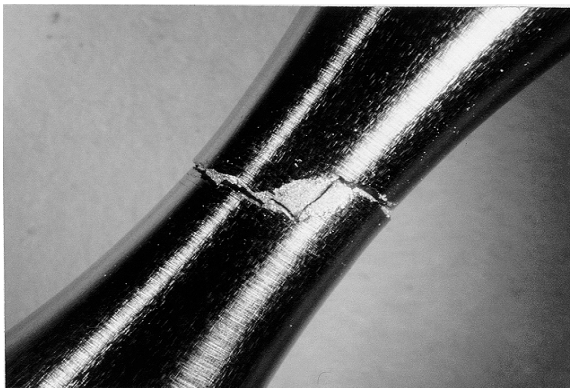

Fatigue Tested in 3.5% NaCl Solution

FIGURE 12. Flaking of Cr Plating during Fatigue Test

HEAT TREATMENTS AND METALLURGY

SCC AND CORROSION FATIGUE OF LASER FORMED Ti-6Al-4V ALLOY

Eun U. Lee and Henry C. Sanders
Naval Air Warfare Center Aircraft Division
Patuxent River, MD20670

ABSTRACT

The stress corrosion cracking (SCC) and corrosion fatigue of Laser formed and wrought Ti-6Al-4V alloys were studied and compared. The SCC was investigated in 3.5% NaCl solution of pH 7.3, employing rising step loading technique. The threshold stress intensity for stress corrosion cracking, K_{ISCC}, decreased initially and leveled off subsequently with increasing cathodic potential from –1.2 to -0.2 volt. The K_{ISCC} values at the open circuit potential were determined to be 33 MPa√m (30 ksi√in) for the Laser formed Ti-6Al-4V alloy of X-Y orientation, and 16.5 and 33 MPa√m (15 and 30 ksi√in) for the wrought one of L-T and T-L orientations, respectively. The fatigue crack growth was measured at various stress ratios in air and 3.5% NaCl solution of pH 7.3. The variation of threshold stress intensity range for fatigue crack growth, ΔK_{th}, with stress ratio, R, was evaluated. The ΔK_{th} decreased and the crack growth rate, da/dN, increased with increasing R. The resistance to fatigue crack growth was greater for the Laser formed Ti-6Al-4V alloy than for the wrought one in air. However, it was similar for the both alloys in 3.5% NaCl solution. The SCC and fatigue crack paths were transgranular, deflecting and branching, in the both alloys.

INTRODUCTION

The manufacturing process for many aircraft components includes forging and machining of metallic materials. To cut down the time-consuming and costly process and fabricate near-net shape components without wasting materials, Laser forming has been developed. It consists of Laser heating and depositing pre-alloyed or blended elemental powders directly into a near-net shape component without any mold or die in argon-environment. Subsequently, the component is subjected to the post-forming heat treatment and final machining to the net shape.

Although the Laser forming process has a merit of cost saving, the integrity and applicability of its product to aircraft components remain to be determined. Especially, the SCC and corrosion fatigue behavior of the Laser formed alloy has not been fully understood. Carrier-based aircraft components are under static and cyclic loading in corrosive environments, and susceptible to SCC and corrosion fatigue. The resistance to SCC and corrosion fatigue is a key factor for the integrity and applicability of Laser formed alloys to Navy aircraft. This has been investigated, employing a Laser formed Ti-6Al-4V alloy, and the results are reported in this paper.

EXPERIMENTAL PROCEDURE

SPECIMAN MATERIALS

A Laser formed Ti-6Al-4V alloy was supplied by AeroMet Corp., Minneapolice, MN. This was initially Laser formed, HIPed at 1650^{o}F under 103 MPa (15 ksi) pressure for 2 hours, and then heat treated. The heat treatment consisted of solution treating at 1675^{o}F for 2 hours, cooling in argon, aging at 1000^{o}F for 4 hours, and furnace cooling. The resultant hardness was Rockwell C 35.

A wrought Ti-6Al-4V alloy of hardness Rockwell C 34 was used as a reference material. The chemical compositions of the Laser formed and wrought Ti-6Al-4V alloys are shown in Table 1.

TABLE 1.
Chemical Compositions (wt %) of Laser Formed and Wrought Ti-6Al-4v Alloys.

Element	Laser Formed	Wrought
C	0.041	0.011
Fe	0.164	0.19
Al	5.95	6.60
V	3.97	4.0
O	0.200	0.170
N	0.019	0.016
H	0.003	0.002
Ti	Balance	Balance

SPECIMENS

Two types of specimen were used. One was a square bar specimen of 10x10x70 mm (0.39x0.39x2.75 in), having a single edge 60^{o} V-notch, for the SCC test, and the other a compact tension specimen of width 38 mm (1.5 in) and thickness 5 mm (0.2 in) for the fatigue test. These specimens were machined to have the crack plane orientations X-Y and X-Z for the Laser formed Ti-6Al-4V alloy and L-T and T-L orientations for the wrought one.

STRESS CORROSION CRACKING TEST

Since the cantilever bend and double cantilever beam tests take a long time, an accelerated test method of rising step loading[1] was employed. The square bar specimen was fatigue-precracked ½ thickness and then step-loaded in four-point bending under constant displacement control at room temperature, while held at a predetermined potential in 3.5% NaCl solution of pH 7.3. The load was increased at 2% of the ultimate bending strength each hour until load dropped. The load drop corresponded to the threshold crack growth. The stress intensity factor was calculated as a function of applied bending moment and crack length, using the following equation.

$$K = \sigma\sqrt{\pi a} * F(a/W) \quad (1)$$

where
K: stress intensity factor
σ: gross stress = $6M/bW^2$
M: bending moment = Pc
P: applied load
c: moment arm length
b: specimen thickness
W: specimen width
a: crack length
$F(a/W) = 1.122 - 1.40(a/W) + 7.33(a/W)^2 - 13.08(a/W)^3 + 14.0(a/W)^4$

During the test, the specimen was the working electrode in a three-electrode cell with a saturated calomel reference electrode and a platinum counter-electrode. Cathodic potentials, ranging from –1.2 volt to the open circuit potential –0.2 volt, were applied to generate various amounts of hydrogen at the advancing crack tip. The threshold stress intensity for SCC, K_{ISCC}, was determined at various potentials.

After the SCC test, the crack path was examined with an optical microscope.

FATIGUE TEST

The fatigue tests were conducted in air and 3.5% NaCl solution of pH 7.3 at room temperature in a vertical MTS machine of 90 KN (20 kip) capacity and a horizontal test machine of 45 KN (10 kip) capacity, respectively. The specimen was subjected to constant amplitude cyclic loading of sinusoidal waveform with stress ratios, R, ranging from 0.1 to 0.9, at a frequency of 10 Hz. The fatigue crack growth rate, da/dN, and the threshold stress intensity range for fatigue crack growth, ΔK_{th}, were determined. Subsequently, the variation of ΔK_{th} with R were evaluated, and the fatigue crack path was examined with an optical microscope.

RESULTS AND DISCUSSION

STRESS CORROSION CRACKING

Figure 1 shows the variation of threshold stress intensity for stress corrosion cracking, K_{ISCC}, with potential, V_{SCE}, in 3.5% NaCl solution for the Laser formed Ti-6Al-4V alloy in X-Y orientation. K_{ISCC} is greatest at the minimum employed potential V_{SCE} = -1.2 volt, decreases with increasing V_{SCE}, and levels off at V_{SCE} = -0.7 volt. At the open circuit potential, V_{SCE} = -0.2 volt, K_{ISCC} is 33 MPa√m (30 ksi√in).

Figure 2 shows the variation of K_{ISCC} with V_{SCE} in 3.5% NaCl solution for the wrought Ti-6Al-4V alloy in L-T and T-L orientations. As for the Laser formed Ti-6Al-4V alloy, K_{ISCC} is greatest at the minimum potential V_{SCE} = -1.2 volt, decreases with increasing V_{SCE}, and levels off at V_{SCE} = -0.8 volt. Within the range of employed potential V_{SCE}, -1.2 to –0.2 volt, K_{ISCC} is greater for T-L orientation than for L-T orientation. The K_{ISCC} values at the open circuit potential -0.2 volt are 16.5 and 33 MPa√m (15 and 30 ksi√in) for the L-T and T-L orientations, respectively.

Beck and Blackburn[2], and Beck[3] studied the SCC susceptibility of a duplex annealed Ti-8Al-1Mo-1V alloy, determining the fracture load under tensile loading with crosshead speed of $5x10^{-3}$ cm/min, in KCl, KBr and KI solutions. The fracture load decreased with increasing potential from –1500 mV to –500mV. This feature is similar to the observation made in this study. However, such a variation for titanium alloy is quite different from that for high strength steels. In high strength steels, K_{ISCC} is minimum at V_{SCE} = -1.2 volt and increases with increasing V_{SCE}, greatly in AerMet 100 steel or little in 300M steel.[4]

Figure 3 shows SCC path in the Laser formed Ti-6Al-4V alloy specimen of X-Y orientation. The crack path deflects, branches, and mostly crosses grain boundaries and α

platelets of the basket-weave structure. Some portion of a crack passes along a grain boundary or a needle of the basket weave structure. A similar SCC path feature is observable in the wrought Ti-6Al-4V alloy specimen of L-T orientation, as shown in Figure 4.

Similar crack paths were also reported for Ti-6Al-4V[5], Ti-8Al-1Mo-1V[5] and Ti-7Al-2Cb-1Ta[6] alloys, during SCC tests in salt atmosphere[5] and sea waters of various pH levels[6]. In those cases, the cracks propagated and branched transgranularly with little regard to the orientation of the α platelets.

FATIGUE

The typical variation of fatigue crack growth rate, da/dN. with stress intensity range, ΔK, is shown for the Laser formed and wrought Ti-6Al-4V alloys, tested at different stress ratios in air and 3.5% NaCl solution, in Figures 5-7. With increasing stress ratio, the threshold stress intensity range for fatigue crack growth, ΔK_{th}, decreases and the crack growth rate, da/dN, increases in the both environments, though there is some difference in the magnitude of change. Similar features have also been observed by a number of investigators for the other alloys.[7-27]

For comparison, typical relative fatigue crack growth behaviors are illustrated for the Laser formed and wrought Ti-6Al-4V alloys, tested in air and 3.5% NaCl solution, in Figures 8 and 9. Under an identical loading condition, the da/dN is greater and the ΔK_{th} is smaller in 3.5% NaCl solution than in air throughout the near-threshold fatigue and Paris regimes. This evidences that 3.5% NaCl solution accelerates fatigue crack growth. However, in steels, the da/dN vs ΔK curve for the test in NaCl solution has been observed to cross over that for the test in air within the near-threshold fatigue regime. This is attributed to the crack closure induced by corrosion product at the crack tip.[12-14,19] Apparently, such a corrosion-product-induced crack closure is absent or not appreciable in the Ti-6Al-4V alloys, Laser formed or wrought.

The variation of ΔK_{th} with R is shown for the Laser formed and wrought Ti-6Al-4V alloys, tested in air and 3.5% NaCl solution, in Figures 10-12. For the both alloys, within the R range employed, ΔK_{th} is less in 3.5% NaCl solution than in air. Besides, ΔK_{th} decreases with increasing R and eventually levels off.

Figures 13 and 14 compare the variations of ΔK_{th} with R for Laser formed alloys in X-Y and X-Z orientations in air and 3.5% NaCl solution. The ΔK_{th} value is slightly greater in X-Z orientation than in X-Y orientation at a given R in both of the environments.

The maximum stress intensity, K_{max}, has a relationship with ΔK_{th}, given by the equation,

$$K_{max} = \Delta K_{th}/(1-R) \quad (2)$$

The curve of ΔK_{th} vs K_{max} is called Fundamental Fatigue Threshold Curve.[11] A fatigue crack can grow above the curve but can not below the curve. Therefore, this curve indicates the fatigue crack growth resistance of a material in a given environment and a given metallurgical condition.

Figures 15 and 16 show the fundamental fatigue threshold curves for the Laser formed and wrought Ti-6Al-4V alloys, fatigue tested in air and 3.5% NaCl solution. These curves confirm that the fatigue crack growth resistance of the both alloys is lower in 3.5% NaCl solution than in air.

Figures 17 and 18 compare the fundamental fatigue threshold curves for the Laser formed and wrought Ti-6Al-4V alloys in air and 3.5% NaCl solution. The curve for the Laser formed alloy is located above that for the wrought one, indicating the Laser formed alloy having greater resistance to fatigue crack growth than the wrought one, in air. However, those curves for the tests in 3.5% NaCl solution overlap each other, indicating the both alloys having similar resistance to fatigue crack growth, in 3.5% NaCl solution.

The fatigue crack path was observed to be transgranular, deflecting and branching, in the both alloy and both environments.

SUMMARY AND CONCLUSION

1. Stress Corrosion Cracking

   - The threshold stress intensity for SCC, K_{ISCC}, is maximum at cathodic potential, V_{SCE} = -1.2 volt, decreases with increasing V_{SCE}, and eventually levels off for the Laser formed and wrought Ti-6Al-4V alloys.
   - K_{ISCC} values at open circuit potential are 33 MPa√m (30 ksi√in) for the Laser formed alloy specimen of X-Y orientation, and 16.5 and 33 MPa√m (15 and 30 ksi√in) for the wrought alloy specimens of L-T and T-L orientations, respectively.
   - The SCC path is transgranular, deflecting and branching, in the both alloys.

2. Fatigue Crack Growth

   - The threshold stress intensity range for fatigue crack growth, ΔK_{th}, decreases and the fatigue crack growth rate, da/dN, increases with increasing stress ratio, R.
   - The FCG resistance is greater for the Laser formed Ti-6Al-4V alloy than for the wrought one in air, but it is similar for the both alloys in 3.5% NaCl solution.
   - The fatigue crack path is transgranular, deflecting and branching, in the both alloys and both environments.

REFERENCES

1. ASM Handbook, Vol. 8, Mechanical Testing, (Materials Park, OH: ASM International, 1995), p. 539.

2. T. R. Beck and M. J. Blackburn, AIAA Journal, 6,2 (1968): p. 326.

3. Proceedings of Conference on Fundamental Aspects of Stress Corrosion Cracking, held September 11-15, 1967, (Houston, TX: NACE, 1969), p. 605.

4. Eun U. Lee, Henry Sanders and Bhaskar Sarkar, in Proceedings of 1999 Tri-Service Conference on Corrosion, held Nov. 15-19, 1999 (Myrtle Beach, SC: 1999).

5. M. J. Donachie, Jr., W. P. Danesi, and A. A. Pinkowish, Stress-Corrosion Cracking of Titanium, ASTM STP 397, (West Conshohocken, PA: ASTM, 1966), p. 179.

6. D. A. Litvin and B. Hill, Corrosion, 26, 3 (1970): p. 89.

7. B. R. Kirby and C. J. Beevers, Fatigue of Engineering Materials and Structures 1, (1979): p.203.

8. G. R. Yoder, L. A. Colley and T. W. Crooker, Scripta Met 16, (1982): p. 1021.

9. M. Lafarie-Fernot and C. Gase, Fatigue of Engineering Materials and Structures 6 (1983): p.329.

10. Proceedings of the International Symposium on Fatigue Crack Growth Threshold Concepts, held October 1983 (Warrendale, PA: The Metallurgical Society of AIME, 1984), p. 25.

11. A. K. Vasudevan and K. Sadananda, Metallurgical and Materials Trans. A 26A, (1995): p. 1221.

12. R. O. Ritchie, S. Suresh and C. M. Moss, Journal of Engineering Materials and Technology, ASME Trans. 102, (1980): p. 293.

13. A. T. Stewart, Engineering Fracture Mechanics 13, (1980): p. 463.

14. S. Suresh, G. F. Zaminski and R. O. Ritchie, Metall. Trans. A. 12A, (1981): p. 1435.

15. Y. Nakai, K. Tanaka and T. Nakanishi, Engineering Fracture Mechanics 15, (1981): p. 291.

16. Proceedings of the International Symposium on Fatigue Crack Growth Threshold Concepts, held October 1983 (Warrendale, PA: The Metallurgical Society of AIME, 1984), p. 263.

17. G. T. Gray,III, J. C. William and A. W. Thompson, Metall. Trans. A, 14A, (1983): p. 421.

18. Proceedings of the International Symposium on Fatigue Crack Growth Threshold Concepts, held October 1983 (Warrendale, PA: The Metallurgical Society of AIME, 1984), p. 205.

19. P. K. Liaw, T. R. Leax and J. K. Donald, Acta Metall. 35, (1987): p. 1415.

20. Proceedings of the International Symposium on Fatigue Crack Growth Threshold Concepts, held October 1983 (Warrendale, PA: The Metallurgical Society of AIME, 1984), p. 281.

21. Proceedings of the International Symposium on Fatigue Crack Growth Threshold Concepts, held October 1983 (Warrendale, PA: The Metallurgical Society of AIME, 1984), p. 299.

22. R. O. Ritchie, Journal of Engineering Materials and Technology, ASME Trans. 99, (1977): p. 195.

23. R. O. Ritchie, International Metals Reviews, 5 & 6 (1979): p. 205.

24. H. Doker and G. Marci, International Journal of Fatigue, 5, (1983): p. 187.

25. S. Suresh, A. K. Vasudevan and P. E. Bretz, Metall. Trans. A, 15A (1984): p. 369.

26. L. X. Han and S. Suresh, Journal of American Ceramic Society 72 (1989): p. 1233.

27. A. K. Vasudevan and K. Sadananda, Scripta Met. 28 (1993): p. 837.

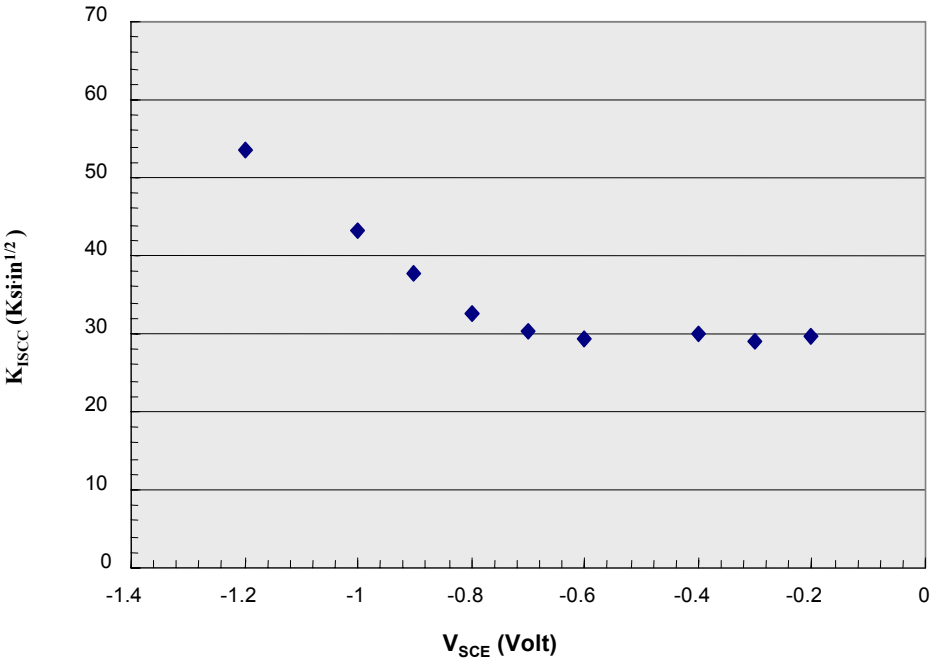

FIGURE 1. Variation of Threshold Stress Intensity for Stress Corrosion Cracking, K_{ISCC} , with Potential, V_{SCE}. (Laser Formed Ti-6Al-4V Alloy, X-Y Orientation)

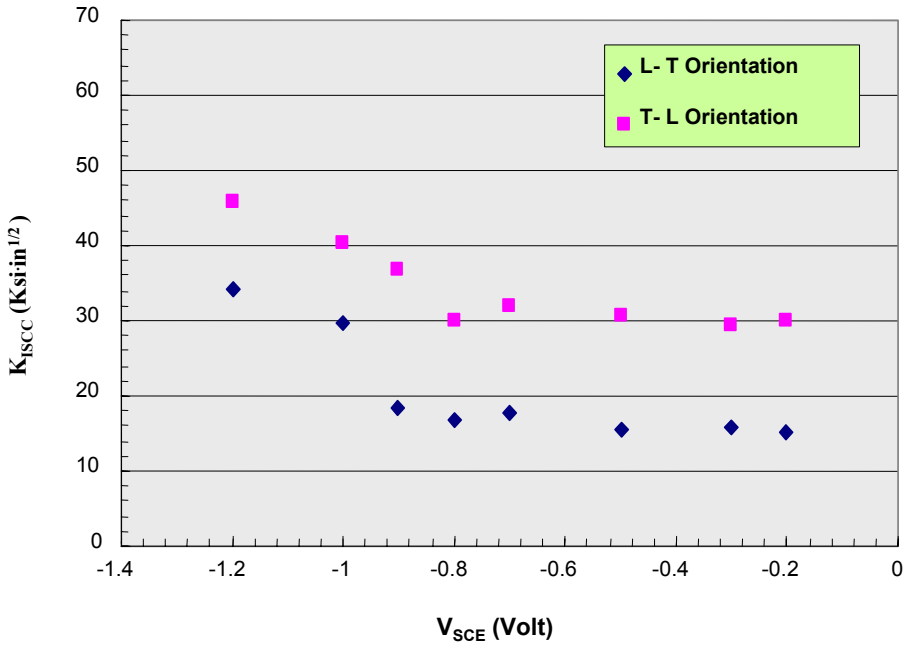

FIGURE 2. Variation of Threshold Stress Intensity for Stress Corrosion Cracking, K_{ISCC} , with Potential, V_{SCE}. (Wrought Ti-6Al-4V Alloy, L-T & T-L Orientations)

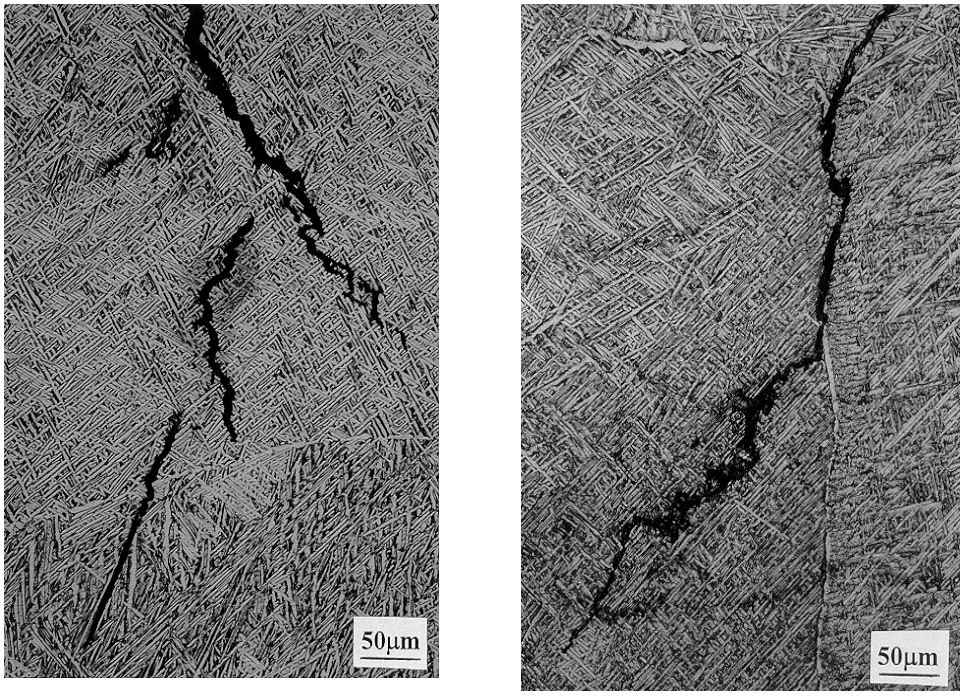

FIGURE 3. SCC Path in Laser Formed Ti-6Al-4V Alloy of X-Y Orientation

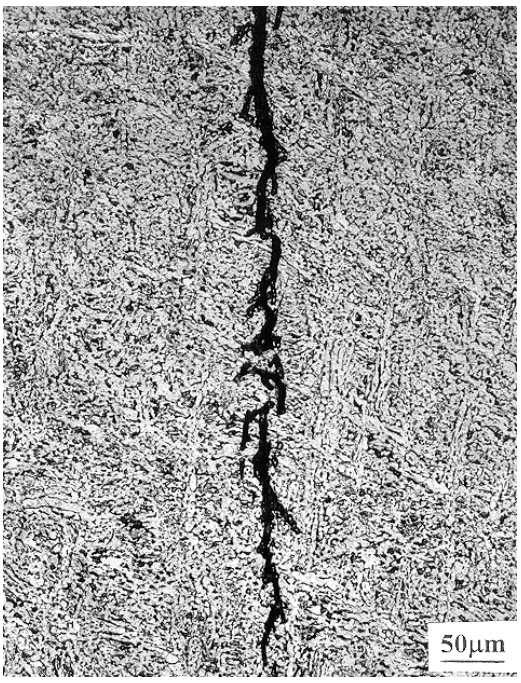

FIGURE 4. SCC Path in Wrought Ti-6Al-4V Alloy of L-T Orientation

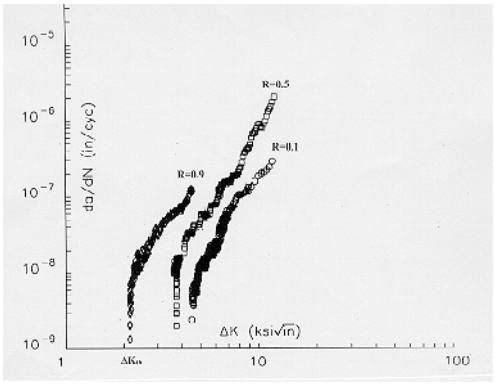

FIGURE 5. Variation of Fatigue Crack Growth Rate, da/dN, with Threshold Stress Intensity Range for Fatigue Crack Growth, ΔK_{th}, in Air. (Laser Formed Ti-6Al-4V Alloy, X-Y Orientation)

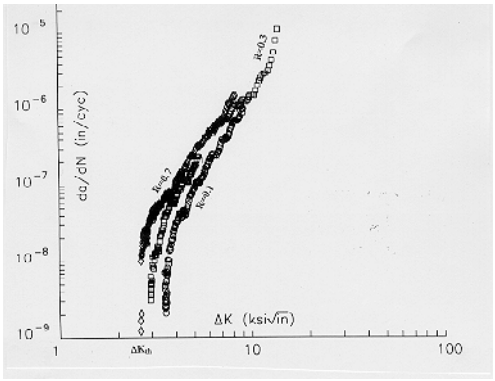

FIGURE 6. Variation of Fatigue Crack Growth Rate, da/dN, with Threshold Stress Intensity Range for Fatigue Crack Growth, ΔK_{th}, in 3.5% NaCl Solution. (Laser Formed Ti-6Al-4V Alloy, X-Z Orientation)

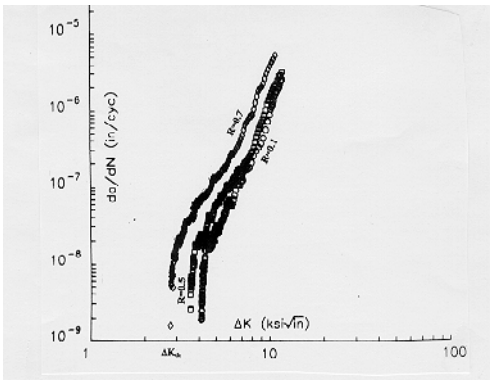

FIGURE 7. Variation of Fatigue Crack Growth Rate, da/dN, with Threshold Stress Intensity Range for Fatigue Crack Growth, ΔK_{th}, in Air. (Wrought Ti-6Al-4V Alloy, L-T Orientation)

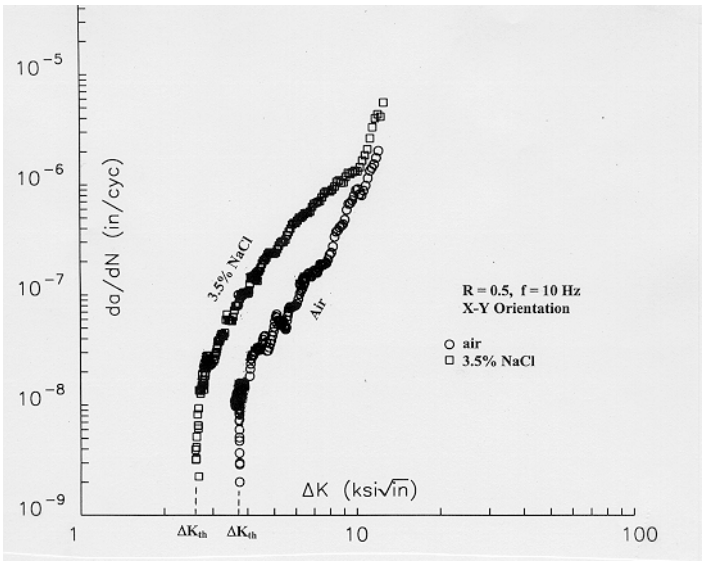

FIGURE 8. Variation of Fatigue Crack Growth Rate, da/dN, with Threshold Stress Intensity Range for Fatigue Crack Growth, ΔK_{th}, in Air and 3.5% NaCl Solution. (Laser Formed Ti-6Al-4V Alloy, X-Y Orientation)

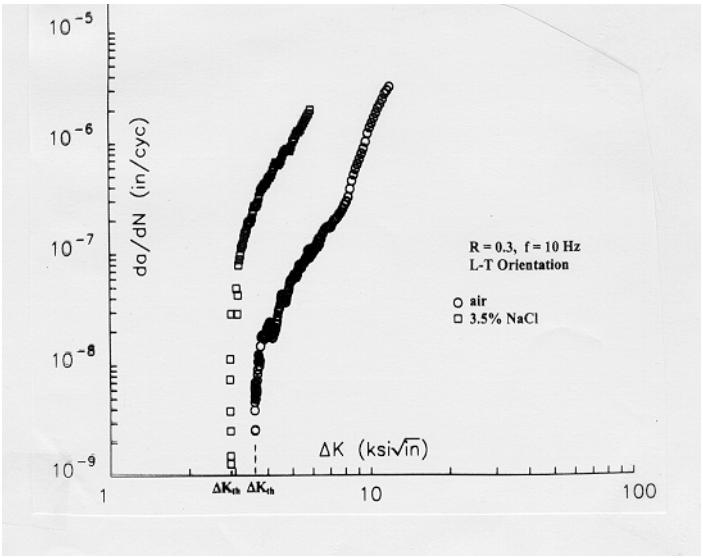

FIGURE 9. Variation of Fatigue Crack Growth Rate, da/dN, with Threshold Stress Intensity Range for Fatigue Crack Growth, ΔK_{th}, in Air and 3.5% NaCl Solution. (Wrought Ti-6Al-4V Alloy, L-T Orientation)

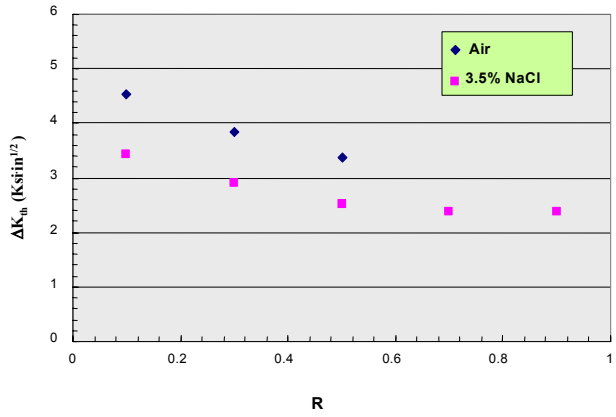

FIGURE 10. Variation of Threshold Stress Intensity Range for Fatigue Crack Growth, ΔK_{th}, with Stress Ratio, R, in Air and 3.5% NaCl Solution. (Laser Formed Ti-6Al-4V Alloy, X-Y Orientation)

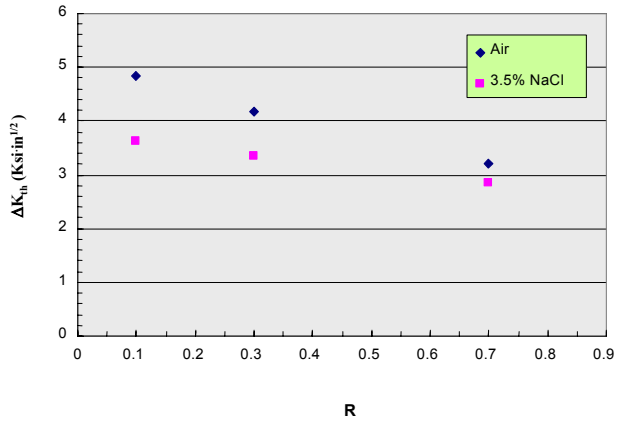

FIGURE 11. Variation of Threshold Stress Intensity Range for Fatigue Crack Growth, ΔK_{th}, with Stress Ratio, R, in Air and 3.5% NaCl Solution. (Laser Formed Ti-6Al-4V Alloy, X-Z Orientation)

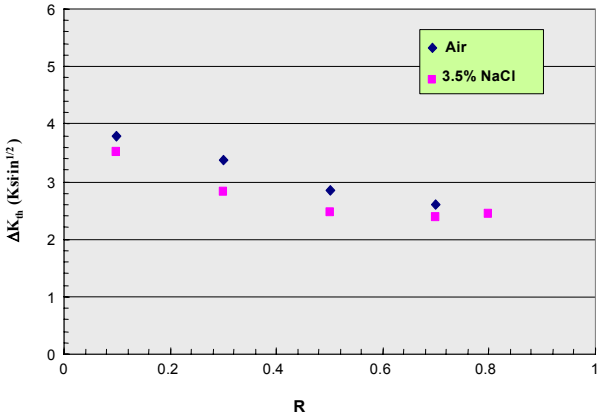

FIGURE 12. Variation of Threshold Stress Intensity Range for Fatigue Crack Growth, ΔK_{th}, with Stress Ratio, R, in Air and 3.5% NaCl Solution. (Wrought Ti-6Al-4V Alloy, L-T Orientation)

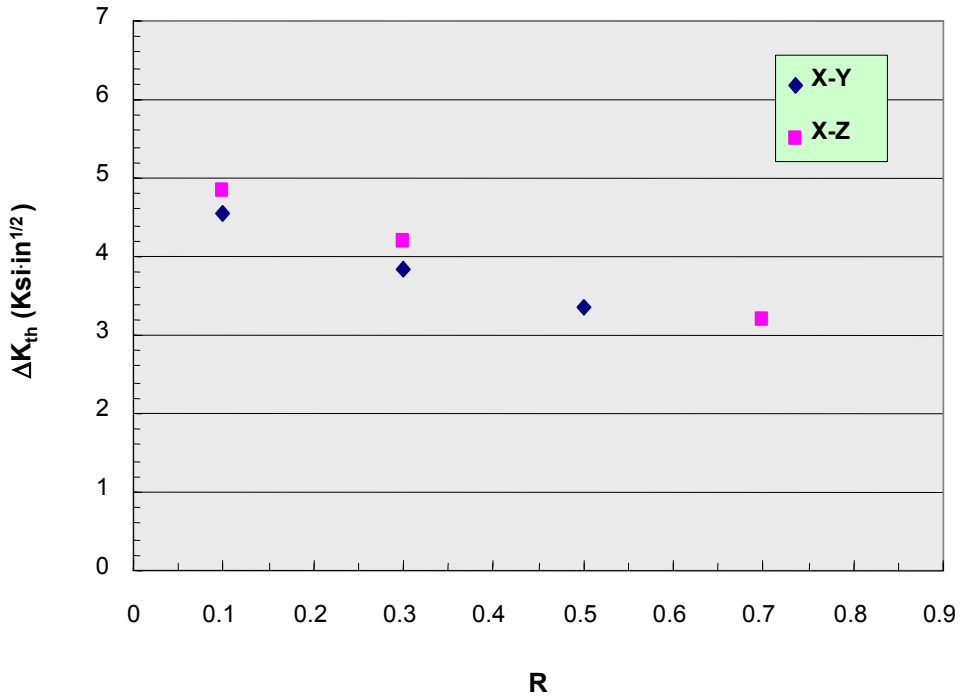

FIGURE 13. Variation of Threshold Stress Intensity Range for Fatigue Crack Growth, ΔK_{th}, with Stress Ratio, R, in Air. (Laser Formed Ti-6Al-4V Alloy, X-Y & X-Z Orientations)

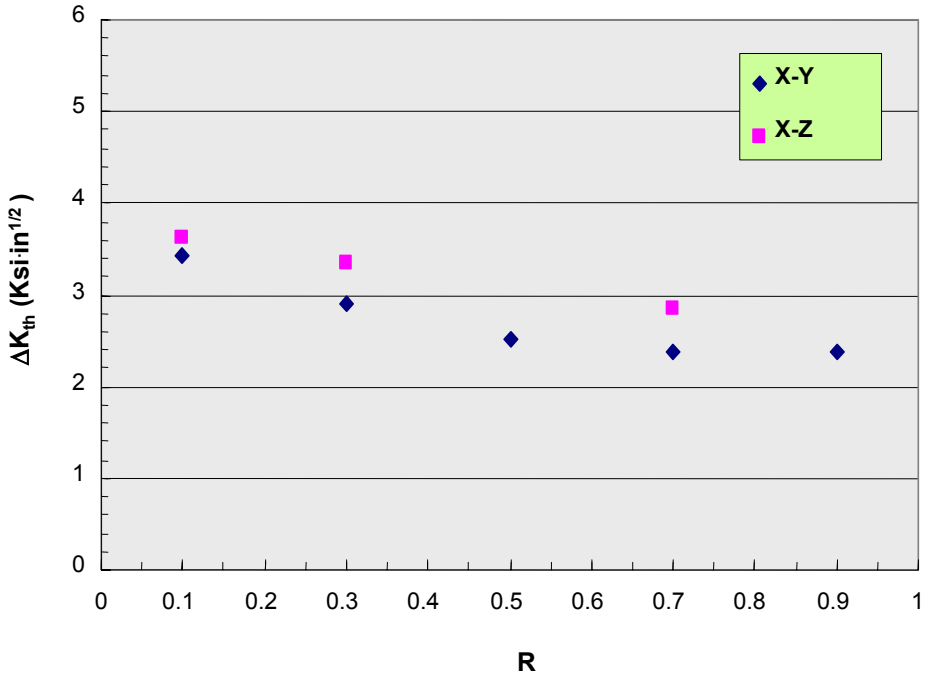

FIGURE 14. Variation of Threshold Stress Intensity Range for Fatigue Crack Growth, ΔK_{th}, with Stress Ratio, R, in 3.5% NaCl Solution. (Laser Formed Ti-6Al-4V Alloy, X-Y & X-Z Orientations)

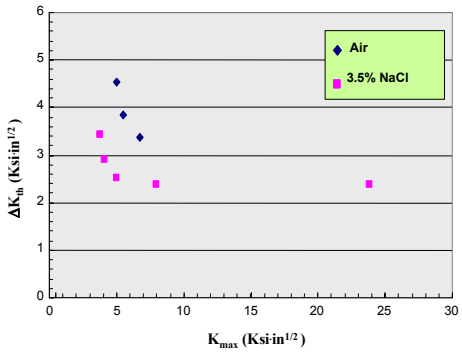

FIGURE 15. Fundamental Fatigue Threshold Curves for Fatigue Test in Air and 3.5% NaCl Solution. (Laser Formed Ti-6Al-4V Alloy, X-Y Orientation)

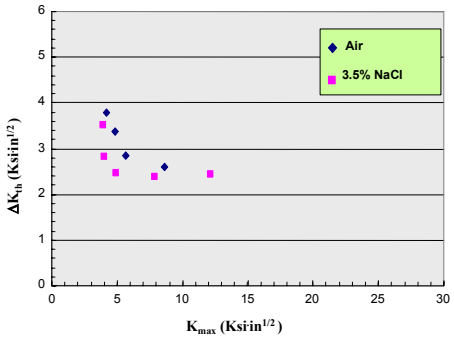

FIGURE 16. Fundamental Fatigue Threshold Curves for Fatigue Test in Air and 3.5% NaCl Solution. (Wrought Ti-6Al-4V Alloy, L-T Orientation)

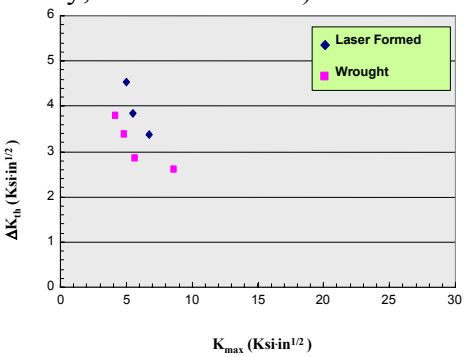

FIGURE 17. Fundamental Fatigue Threshold Curves for Fatigue Test in Air. (Laser Formed and Wrought Ti-6Al-4V Alloys of X-Y and L-T Orientations, respectively)

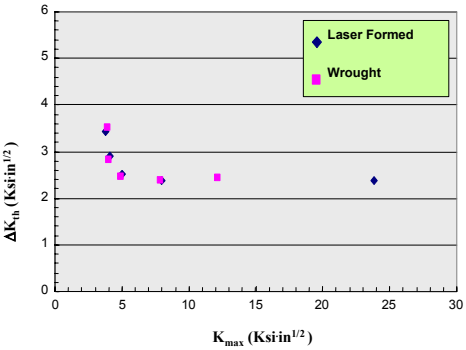

FIGURE 18. Fundamental Fatigue Threshold Curves for Fatigue Test in 3.5% NaCl Solution. (Laser Formed and Wrought Ti-6Al-4V Alloys of X-Y and L-T Orientations, respectively)

Corrosion Behavior of Friction Stir Welded High Strength Aluminum Alloys

J. B. Lumsden, M. W. Mahoney, and G. A. Pollock
Rockwell Scientific, 1049 Camino dos Rios, Thousand Oaks, CA 91360, USA

ABTRACT

Friction stir welding (FSW), a relatively new solid state joining process, is used to join aluminum alloys of all compositions including alloys essentially considered unweldable. During FSW, a rotating tool provides a continual hot working action, plasticizing metal within a narrow zone at the join line, while transporting metal from the leading face of the probe to the trailing edge as the tool moves along the interface. Although melting does not occur during FSW, temperatures are sufficiently high and times at temperature sufficiently long to cause dissolution, nucleation, and/or coarsening of strengthening precipitates. The temperature-time profile changes with distance from the nugget causing a gradient in microstructure and precipitate morphology. The altered microstructure in the weld zone becomes sensitized in some high strength aluminum alloys. Results presented assess the pitting, intergranular, and SCC corrosion behavior of FSW 7XXX and 2XXX alloys. Progress in understanding the changes in microstructure responsible for the sensitization will be discussed. The presentation also will include evaluations of approaches for corrective measures.

INTRODUCTION

Friction stir welding (FSW) is a solid state joining process invented at TWI in 1991. This technology makes it possible to join aluminum alloys, which are difficult or impossible to weld by conventional techniques.[1-10] FSW does not require expensive, sophisticated machinery or operators with highly specialized skills. It is environmentally friendly and does not need shielding gas, large power supplies, protection against radiation, or generate toxic welding fumes. The process can be completely automated and replace labor intensive mechanical joining and welding procedures. In addition, substantial weight savings can be realized by elimination of rivets and fasteners.

A schematic illustration of the FSW process is shown in Figure 1. To friction stir weld either a butt or lap joint, a specially designed cylindrical tool is rotated and plunged into the joint line. The tool has a small diameter entry probe with a concentric larger diameter shoulder. When descended to the part, the rotating entry probe contacts the surface and rapidly heats and softens a small column of metal. As the probe penetrates beneath the surface, part of this metal column is extruded above the surface. The tool shoulder and length of probe control the penetration depth.

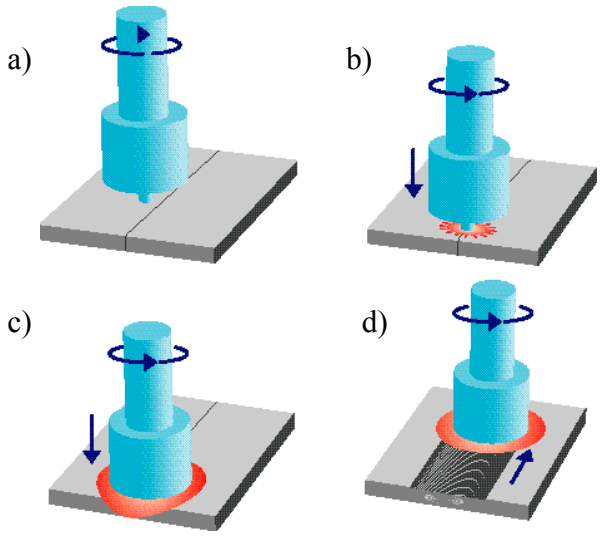

FIGURE 1. Schematic illustration of friction stir welding: a) rotating tool prior to contact with the plate; b) tool pin makes contact with the plate, creating heat; c) shoulder makes contact, restricting further penetration while expanding the hot zone; and d) plate moves relative to the rotating tool, creating a fully recrystallized, fine grain microstructure.

When the shoulder contacts the metal surface, its rotation creates additional frictional heat and helps to plasticize a larger cylindrical metal column around the inserted probe. The shoulder provides a forging force that contains the upward metal flow caused by the tool probe. During welding, the metals to be joined and the tool are moved relative to each other such that

the tool tracks the weld interface. The rotating tool provides a continual hot working action, plasticizing metal within a narrow zone. As the tool translates along the joint line, plasticized material is stirred and forged behind the trailing edge of the pin where it consolidates and cools, not solidified, to form a recrystallized fine grain microstructure.

Although melting does not occur during FSW, temperatures are sufficiently high and times at temperature sufficiently long to cause dissolution, nucleation, and/or coarsening of strengthening precipitates. The temperature-time profile changes with distance from the nugget causing a gradient in microstructure and precipitate morphology. The altered microstructure can have corrosion resistant properties significantly different from those of the parent alloy.

EXPERIMENTAL

Material used in this study was 6.35 mm thick AA2024-T351, AA7050-T7651, AA7075-T7651, and AA7075-T651. Samples were friction stir welded using conventional friction stir welding practices[1]. Following welding, samples were tested after naturally aging for five months.

The range in corrosion resistant properties of the various weld zones was determined using several approaches. The degree of sensitization of the FSW material was determined by microscopic examination of specimens after exposure to a 10% dilution composition of the solution used in the ASTM G34 Constant Immersion Exfoliation (EXCO) test. Pitting potentials were measured in deaerated 0.6 M NaCl using the potentiodynamic polarization technique in accordance with ASTM G-61. For these measurements, test samples from the heat affected zone (HAZ) were obtained by cutting parallel to the HAZ/nugget boundary and 0.5 mm into the HAZ. A cut made through the center of the nugget, perpendicular to the weld axis, was used to determine the pitting potential of the nugget. Susceptibility to stress corrosion cracking (SCC)

was evaluated using the slow strain rate (SSR) method described in ASTM Standards G-129 and G-49. Tensile specimens were machined transverse to the weld with the gauge section perpendicular to the rolling direction. Gage cross section dimensions were 6.35mm x 3.18mm. The gauge length included the weld nugget and both HAZ's. Specimens, electrically insulated from the grips, were mounted in a 1.5 liter cell. A 0.6M NaCl solution open to the air was continuously recirculated through the cell from a 5 liter reservoir.

RESULTS AND DISCUSSION

Figure 2 is a macrograph of the nugget and the adjacent zones of FSW AA 7050-T7651. This is typical of all of the FSW aluminum alloys investigated. The onion ring appearance is associated with fine bands of very fine grain microstructure (3μm) with a high density of second phase particles alternately dispersed between bands of fine grain microstructure (5μm) with a lower volume fraction of second phase precipitates. The nugget microstructure consists of recrystallized equiaxed fine grains (3 to 5 microns). The FSW process generates zones adjacent to the weld nugget with two different microstructures. A heat affected zone (HAZ) is created a short distance from the weld nugget where the metal has experienced a thermal transient but no deformation. Immediately adjacent to the weld nugget is a partially recrystallized zone (PRZ) where the microstructure has experienced both deformation, as well as the thermal transient. The PRZ in Figure 2 is the region with the redirected grains adjacent to the weld nugget.

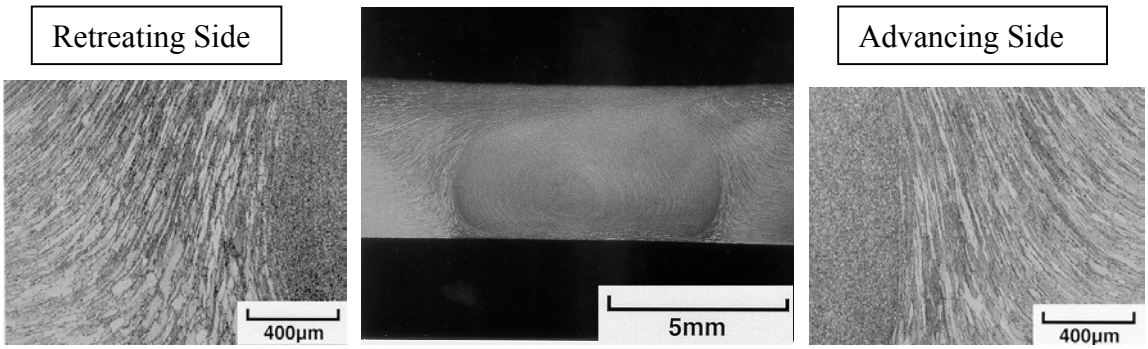

FIGURE 2. Aluminum alloy AA 7050-T7651 following friction stir welding, transverse view in the direction of travel. Nugget has a fine grain fully recrystallized microstructure. A partially recrystallized zone with uplifted grains is adjacent to the nugget.

Earlier work in this program[11-12] and results of others[13-14] demonstrated that FSW sensitizes microstructures in the weld zone of some high strength aluminum alloys. A simple immersion test illustrates weld zone sensitized regions. Figure 3 shows examples of immersion test results on friction stir welded AA2024-T351, AA7050-T7651, and AA7075-T7651. These photomicrographs were taken following exposure to a modified composition of the ASTM G34 EXCO solution used to determine exfoliation resistance. The attack is different for each alloy. Intermetallics are preferentially attacked in the HAZ of AA2024-T351 resulting in deep pits. Intergranular attack occurs in AA7050-T7651 initiating at the nugget/PRZ interface and spreading into the nugget. Intergranular attack also occurs in AA7075-T7651, but it initiates at the PRZ/HAZ interface and spreads into the HAZ.

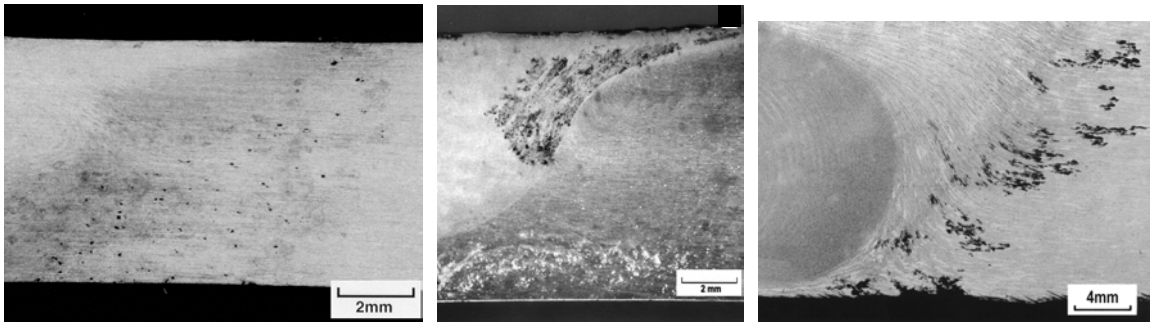

a) AA2024-T351 b) AA7050-T7651 c) AA7075-T7651

FIGURE 3. Attack in the sensitized zones of a) AA2024-T351, b) AA7050-T7651, and c) 7075-T7651 by immersion in modified ASTM G34 EXCO solution.

The results of potentiodymanic polarization in deaerated 3.5% NaCl give additional insights into the effects of FSW on corrosion behavior. These results (Figure 4) show that the pitting potentials in the weld zone are lower than those in the parent metal. In the materials tested, the pitting potential of the HAZ was always the lowest except in AA7050-T7651 where the nugget had the lowest pitting potential. The pitting resistance in the nugget and HAZ of the T7 temper is reduced more than that in the T6 temper.

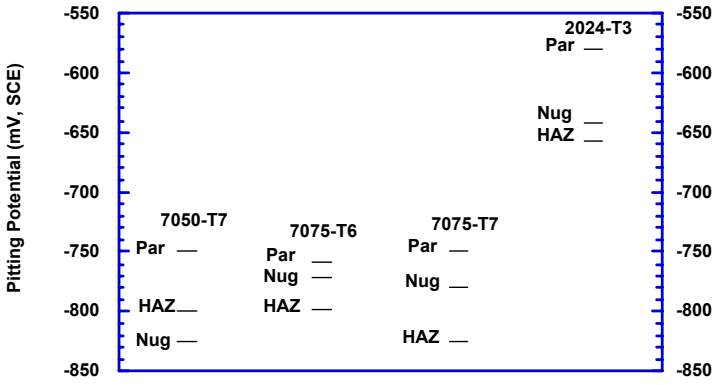

FIGURE 4. Pitting potentials of four high strength aluminum alloys, following FSW, comparing values in the heat affected zone (HAZ) and nugget (Nug), with the parent metal (Par).

The SSR results show that the weld zones of AA7050-T7651 (Figure 5) and AA7075-T7651 (Figure 6) are susceptible to SCC. These measurements, made during exposure to 3.5% NaCl, showed loss of ductility in the FSW materials. Susceptibility to SCC is expressed as the strain rate dependence of the elongation in the NaCl solution. All of the FSW Al alloys tested had strain rate independent elongations in dry air. Both FSW AA7050-T7651 and FSW AA7075-T7651 had the same elongation in air and solution at the highest strain rate used, 3 X 10^{-4} s^{-1}. The elongation of FSW AA7050-T7651 in solution decreased much more rapidly than that of FSW AA7075-T7651 as the strain rate decreased. This suggests that the SCC crack growth rate in FSW AA7050-T7651 is greater than that in FSW AA7075-T7651, and thus more susceptible to SCC. Conversely, the parent material AA7075-T7651 is more susceptible to SCC than the parent AA7050-T7651.

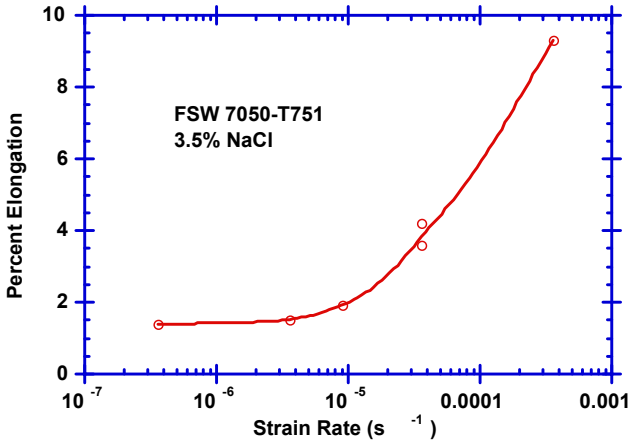

FIGURE 5. Strain rate dependence of the elongation of AA7050-T7651 from the SSR results in 0.6 M NaCl open to the air.

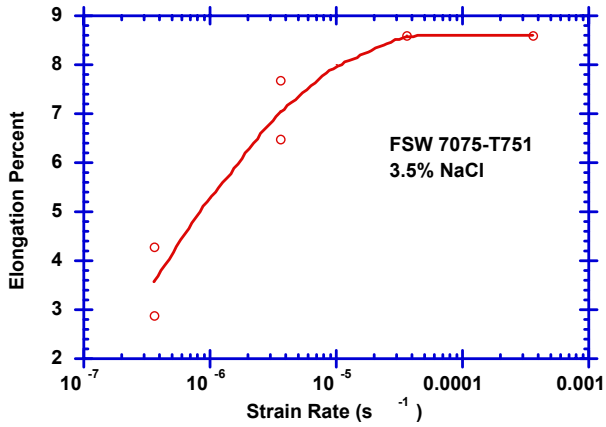

FIGURE 6. Strain rate dependence of the elongation of AA7075-T7651 from the SSR results in 0.6 M NaCl open to the air.

Figure 7 shows an optical cross sectional view of the FSW AA7050-T7651 specimen pulled to failure in solution at a strain rate of 10^{-6} s^{-1} and an SEM view of the fracture surface. The optical macrograph shows a fracture path along the nugget/PRZ interface on the weld advancing side. The SEM micrograph shows an intergranular fracture advancing through the nugget fine grain microstructure. This is consistent with the immersion results illustrating that

the most highly sensitized region is the interface between the prz and the nugget. The post-test fractrography for AA7075-T7651 (Figure 8) shows intergranular fracture on the advancing side of the weld in the large grain region of the HAZ. This is again consistent with the immersion tests showing that in this case, the most highly sensitized region is in the HAZ. SEM fracture surface micrographs showed deep grooves on the specimen edges where the elongated grains pulled out when decohesion occurred in the grain boundaries. (The tensile axis is in the long transverse direction). The center of the specimen failed by ductile fracture when failure occurred by overload as the load carrying cross section decreased as the SCC cracks propagated from the edges. As shown in Figure 9, FSW does not decrease the SCC resistance of AA2024-T351 in the 3.5% NaCl solution, but, as discussed above, the HAZ of FSW 2024 is highly susceptible to pitting.

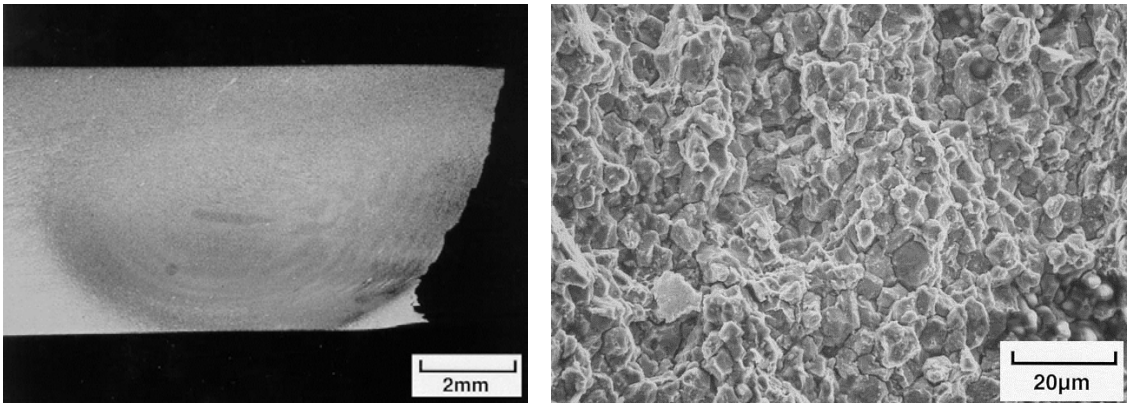

a) b)

FIGURE. 7. SCC fracture in FSW AA7050-T751 a) Optical macrograph showing cross sectional view and b) SEM photomicrograph of the fracture face.

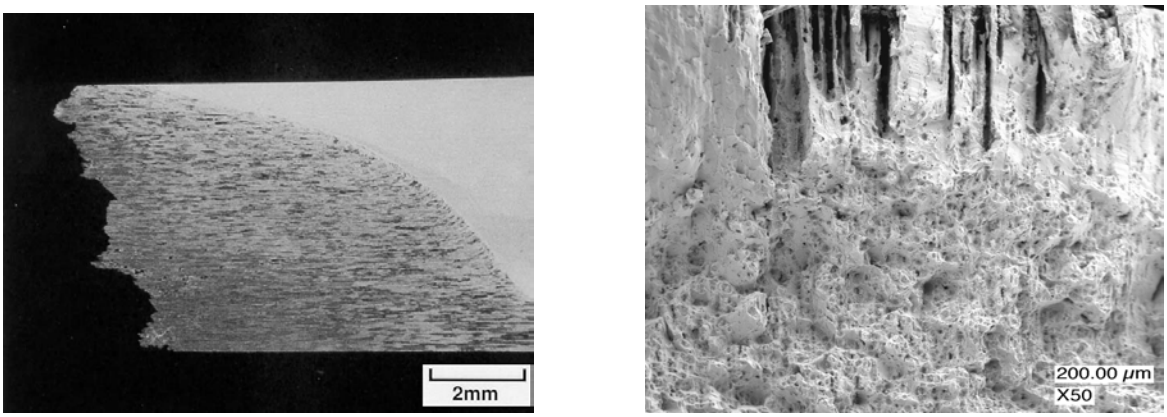

a) b)

FIGURE 8. SCC fracture in FSW AA7075-T751 a) Optical macrograph showing cross sectional view and b) SEM photomicrograph of the fracture face.

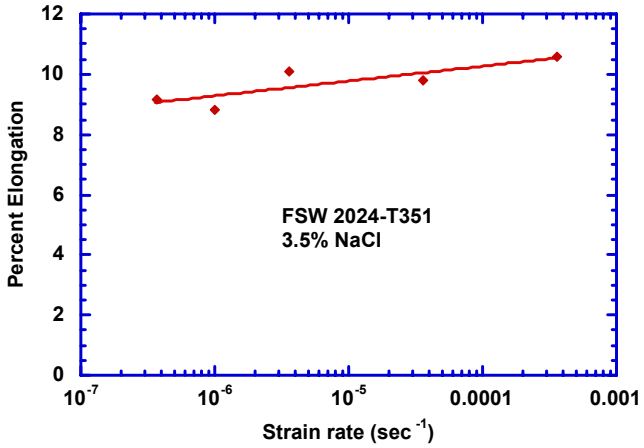

FIGURE 9. Strain rate dependence of the elongation of AA2024-T351 from the SSR results in 0.6 M NaCl open to the air.

In summary, the 2XXX (Al-Cu-Mg) and 7XXX (Al-Zn-Mg-Cu) series high strength aluminum alloys investigated in the program are sensitized by FSW. The results illustrate a strong alloy composition dependence on the sensitization process. Small changes in alloy composition (AA7050-T7 vs. AA7075-T7) cause the location of the sensitized microstructure in the weld zone to change. Large changes in alloy composition can change the type of corrosion attack that occurs in the sensitized microstructure (AA2024 vs. AA7075 and AA7050). The

2XXX and 7XXX alloys derive their high strength from the intermetallic compounds which precipitate either during natural aging at room temperature or artificial aging at intermediate temperatures. The compositions of the precipitates and grain boundaries are changed by the thermal transients generated during FSW. Preliminary analytical electron microscopy measurements of the sensitized microstructures do not conclusively indicate a grain boundary, precipitate free zone, or precipitate chemistry, which correlates with sensitization. These chemistries are complex and vary with distance from the center line of the weld and with alloy.

Six procedures for preventing sensitization or restoring the SCC resistance of FSW precipitation hardened aluminum alloys are being investigated. Active/passive cooling during FSW and the use of Sc as an alloying addition are aimed at preventing composition changes in precipitates and grain boundaries responsible for the sensitized microstructure. Pre/post-weld heat treatment, laser treatment, and friction stir processing of friction stir welds have the potential to restore the corrosion resistance in sensitized weld zones to that of the parent metal. Post weld treatment by low plasticity burnishing (LPB) will change the residual stress if performed after FSW. If LPB is performed prior to FSW, the resulting deformation could alter the deleterious nucleation and growth kinetics of the precipitates during welding.

ACKNOWLEDGEMENT

Support of this work by ONR Contract# N0014-99-C-0153/P00002 is gratefully acknowledged, John Sedriks Program Manager.

REFERENCES

1. W.M. Thomas, et al, "Friction Stir Butt Welding", International Patent Appl. No. PCT/GB92/02203, GB Patent Appl. No. 9125978.8, Dec. 1991, and U.S. Patent No. 5,460,317, (Oct. 24, 1995).

2. C.J. Dawes and W.M. Thomas, *TWI Bulletin 6* (Nov./Dec. 1995): p. 124.

3. M. Ellis and M. Strangwood, *TWI Bulletin 6* (Nov/Dec 1995): p.138.

4. C.J. Dawes and W.M. Thomas, *Welding Journal*, 75, 3 (1996): p. 41.

5. O.T. Midling, "Material Flow Behavior and Microstructural Integrity of Friction Stir Butt Weldments", *Proc. 4th Int'l. Conf. on Aluminum Alloys*, Atlanta GA, (Sept. 1994).

6. M.W. Mahoney, *Welding and Joining*, (Jan./Feb. 1997): p. 18.

7. S. Kallee and D. Nicholas, *Welding and Joining*, ((Feb. 1998): p. 18.

8. C. J. Dawes, *Welding & Metal Fabrication*, (January 1995): p. 14.

9. C.G. Rhodes, M.W. Mahoney, W.H. Bingel, R.A. Spurling, and C.C. Bampton, *Scripta Met*.36 (1997): p 69.

10. M.W. Mahoney, C.G. Rhodes, J.G. Flintoff, R.A. Spurling, and W.H. Bingel, *Metallurgical and Materials Trans.* 29A (July 1998): p. 1955.

11. Jesse Lumsden, Murray Mahoney, Gary Pollock, Doug Waldron, and Angelo Guinasso, "Stress Corrosion Susceptibility in 7050-T751 Aluminum Following Friction Stir Welding", *Proc. First Friction Stir Welding Symposium,* (TWI, London, 1999).

12. Jesse Lumsden, Murray Mahoney, Gary Pollock, Cecil Rhodes, Corrosion 55, 12 (1999): p. 1127.

13. 13. A.J. Leonard, Proceedings of the Third International Symposium on Friction Stir Welding, Kobe, Japan, September, 2001.

14. G.S. Frenkel, Z. Xia, Corrosion, 55 (1999), p. 139.

STRENGTH, CORROSION, AND ENVIRONMENTALLY ASSISTED CRACKING OF A 7075-T6 FRICTION STIR WELD

C.S. Paglia, M.C. Carroll, B.C. Pitts, T. Reynolds, and R. G. Buchheit

The Ohio State University
Department of Materials Science and Engineering
477 Watts Hall
2041 College Road
Columbus, OH 43210-1179

ABSTRACT

The microstructure and hardness of a friction stir welded (FSW) 7075-T6 alloy has been investigated and correlated with corrosion and environmental cracking behavior for transverse and longitudinal orientations. Microstructural characterization reveals significant differences in the grain size, orientation, subgrain structure, strengthening precipitate distribution, and localized deformation adjacent to the weld region. The weld nugget is comprised of equiaxed grains and exhibits different crystallization bands, along with deformation features such as folds and grain alignments in particular in the outer region. The strength and ductility of the micro-zones is controlled by grain size, the presence and size of the small, coherent intragranular precipitates, along with the degree of sensitization achieved during the weld process. The mechanical properties of the nugget, are probably also influenced by its microstructural refinement. The corrosion behavior of the different weld micro-zones has been examined using conventional polarization sweep techniques as well as micro-electrochemical measurements. A comparison of the investigated micro-zones indicate that the heat affected zones demonstrate slightly lower pitting potentials than for the other areas of the weld zone. Localized corrosion generally initiates at constituent particle sites such that the differences in the pitting potentials were attributable to the precipitate distribution and additional grain boundary precipitate phases which have been formed, or selectively sensitized, during the FSW process. Furthermore, constant extension rate measurements (CERT) revealed the highly sensitized heat affected zone in the advancing side of the weld (HAS) to be the most susceptible to environmentally assisted cracking.

INTRODUCTION

Friction stir welding is a relatively new solid state welding process introduced by The Welding Institute (TWI) in 1991.[1] Despite limited transient melting on contact surfaces

(asperity-melting) that has been reported,[2] the melting point of the material being joined is generally not reached during this welding process.[3] This allows for a better overall weld in terms of a lowered incidence of weld defects and lower residual stresses. The high weld quality of this new method enables the effective joining of 7xxx series high-strength aluminum alloys, which are notoriously difficult to weld with conventional welding techniques,[4,5] and as such have contributed to the rising interest of the aerospace industry in developing and understanding this promising welding technique.[6]

The FSW process,[7] mainly consists of a rotating, non-consumable, high strength pin which is plunged between the work pieces to be joined. The pin extend from a cylindrical shoulder and rotates at several hundreds revolutions pro minute moving along the weld line (Figure 1). The material is effectively heated by friction and is plastically deformed adjacent to the rotating pin. During a longitudinal weld, the tool and the material are moved relative to one another.

In the past, microstructural characterization has been performed on different types of friction stir welded alloys, such as 2024, 6061, and 7075,[3,8,9] but limited research has been carried out with respect to general corrosion characteristics,[7,10] and environmentally-assisted cracking of stir welded high strength aluminum alloys. It has been generally reported that the weld zones are more susceptible to corrosion than the parent metal both in 2024-T3[11] and 7075-T6.[7] In the latter case, the decrease in the corrosion resistance was attributed to Cu depletion along the grain boundaries and in the associated precipitate-free zones.[7]

The aim of the present work is to investigate the aforementioned corrosion behavior as well as the environmentally-assisted cracking behavior of friction stir welded 7075-T6. Since the high degree of thermo-mechanical deformation and the sharp temperature gradient that occurs

during FSW causes the formation of distinct microstructural zones across the weldment, the investigations were carried out for each of these micro-zones individually on both transverse and longitudinal sections.

EXPERIMENTAL PROCEDURES

MATERIAL AND WELDING PARAMETERS

Aluminum 7075-T6 plates (30.48 x 10.16 x 0.953 cm) were friction stir welded at a travel speed of 14.18 cm/min applying a Z force of 6136.36 Kg and an X force of 978.5 Kg. The head angle was 2.5 ^{o} and the rotation speed was 240 rpm. The final welding length was 26.04 cm. All the investigations were carried out approximately 5 months after welding.

SAMPLE ORIENTATION AND IDENTIFICATION

Samples were sectioned in both transverse and longitudinal orientations with respect to the weld, as depicted in Figure 2. The resulting micro-zones can be classified as five distinct zones in the welded area between the two joined sections unaffected parent metal (PM): the heat affected zones on both the advancing side (HAS) and the trailing side (HTS), the weld nugget formed directly by the rotating pin, and the highly deformed narrow regions sandwiched between the heat-affected zones and the weld nugget designated the thermo-mechanically affected zones (TMAZ).

OPTICAL, ELECTRON MICROSCOPY AND MICROHARDNESS

The metallographic investigations were carried out on polished surfaces in a 1 μm slurry and etched using Keller's reagent. The images were taken both with an Olympus SZ H10 equipped with a Hitachi camera VK-C370 as well as a Nikon COOLPIX990 digital camera, and were processed with a Clenex Vision$_{PE}^{TM}$ software.

An XL 30 ESEM-FEG field emission environmental scanning electron microscope operating at 10-15 KV was used to characterize the fracture surfaces.

A Philips CM200 LaB_6 transmission electron microscope operating at 200 kV was used for the characterization of the microstructure. TEM foils were prepared by punching 3mm samples that were subsequently thinned by electropolishing on a twin jet polisher at 15V, -20^{o}C, in a 25% nitric acid/75% methanol solution.

The Vicker' s micro-hardness was measured on polished surfaces (1 μm) across the weld 0.5, 4 and 7 mm below the surface (plate thickness 9.53 mm) from the advancing side to the trailing side of the weld from parent metal to parent metal. Hardness data was obtained utilizing a MICROMET ® II Digital Microhardness Tester, with a test load of 300 g and a load time of 20 seconds.

POTENTIODYNAMIC POLARIZATIONS

Test samples (Figure 2) were polished to 6 μm and rinsed with alcohol just prior to taking measurements. The surfaces were masked with lacquer to limit the testing area to 0.425 cm^2. The electrochemical cell was purged for 30 minutes with Ar and filled with a 3.5 wt% NaCl solution under continuous Ar flow to maintain a deareated solution. The open circuit potentials were measured for 20 minutes followed by a potentiodynamic scan run at 0.2 mV/s. A platinum net was used as a counter-electrode while a saturated calomel electrode (SCE) was used as an external reference. The potentiostat used was an EG&G 263 A.

MICRO-ELECTRICAL MEASUREMENTS

The micro-electrochemical technique was first utilized in order to study MnS inclusions in corroding stainless steels,[12] and has already been reported in detail.[13] The micro-electrochemical cell utilizes glass micro-capillaries which are ground to a flat opening and sealed

against the sample surface by using silicon rubber to avoid any leakage of solution during the measurement.[13] This technique greatly reduces the exposed area being evaluated; typical flat cells measure areas on the order of cm^2, while the micro-capillary technique can allow the study of localized corrosion phenomena in areas on the order of μm^2 (Figure 3).

Based on the success of recent studies on pit initiation on intermetallic particles,[14] the previously described technique was used in the present work to compare the corrosion behavior of intermetallic-containing and intermetallic-free areas across the FSW micro-zones. Since the identification of the intermetallic constituent-containing areas was done optically and no chemical analysis was made to distinguish between the intermetallic constituents, the resulting polarization curves indicate the corrosion susceptibility of the measured areas without differentiating the cathodic or anodic behavior of the constituent particles with respect to the matrix. A 40 μm diameter capillary was placed on a polished weld zone surface directly in each of the zones to be measured. The OCP was measured for 1 minute, followed by potentiodynamic scans run at 5mV/s in an areated solution. At least 9 measurements were made within every micro-zone on intermetallic-free and intermetallic-containing areas. The electrolyte consisted of a 3.5 weight % NaCl solution.

CONSTANT EXTENSION RATE TESTS (CERT)

CERT investigations were carried out using M-CERT™ rig[15] on tensile specimens oriented both longitudinally and transverse to the weld (Figure 3a) in an areated 3.5 wt % NaCl solution. The gage length of the transverse sections included the weld and the HAZs (Figure 3b). Each micro-zone of interest was first tested in air in order to provide baseline reference data. The as-machined gage length was ground to 800 grit sandpaper to obtain a uniform surface. In order to avoid additional crevice corrosion of the samples tested in solution, the interface gage length-

grip was coated with a lacquer and further wrapped with a Teflon tape. Tests were conducted at an extension rate of 2.5 x 10 –5 mm/s with an initial load of 36 Kg.

RESULTS

MICRO-HARDNESS ACROSS THE WELD

The most extreme dip in the measured hardness values (on the order of 115 HV), are found within the heat affected zones on both the advancing and trailing side of the weld. The parent metal, being at a maximum-strength temper, naturally maintains highest microhardness values with an average of 165 HV. The weld nugget and the highly deformed zones adjacent to it (TMAZ) show hardness values ranging somewhere between the parent metal and the heat affected zones (Figure 4). The width of the zones in a transverse orientation does not remain constant through the thickness of a welded section; from the top of the welded section the nugget narrows somewhat while both the HAS and HTS widen toward the bottom of the plate.

MICROSTRUCTURAL CHARACTERIZATION

An optical overview of the weld cross section shows a distinct weld nugget region, with plastic deformation rings and regions adjacent to it with highly deformed grains (Figure 5a). TEM study demonstrates that the nugget is comprised of equiaxed grains ranging in diamater from 2 to 5 μm; the appearance is closer to that of an as-cast material than an aging temper. Large, blocky, incoherent intergranular precipitates are prevalent (Figure 6a). Moving toward the trailing side of the weld, the equiaxed grains of the nugget region form a sharp boundary with the strongly bent larger grains of the highly deformed adjacent zone (Figure 5d). Towards the advancing side of the weld, the boundary between nugget and the highly deformed zone adjacent to it is less pronounced, and deformational features such as folds are observed within

the nugget region (Figure 5c). The parent metal exhibits a typical elongated grain structure (Figure 5e) with grain interior strengthening precipitates varying from blocky or highly elongated 80-100 nm particles to a fine dispersion of 10-12 nm particles. This relatively bimodal distribution reflects the two common forms of the η-phase precipitates – large particles which are less susceptible to re-dissolution during thermal transients (hence their continued presence in the nugget) and the fine dispersion of strengthening precipitates brought out by strengthening aging treatments applied to the parent metal. In addition to the precipitate structure, there are narrow precipitate-free zones (PFZ) lining grain boundaries, and some presence of distinct grain boundary precipitates can be observed. Cr-bearing dispersoids with average size of approximately 100 nm are also present (Figure 6a). In the heat affected zones between the re-solutionized nugget and the relatively unaffected parent material, the thermal weld transient has caused a distinct coarsening of the fine dispersion of coherent strengthening precipitates (Figure 5f), along with a widening of the PFZ and enhanced growth of the grain boundary precipitates (Figure 6c, d). Optically, both the heat affected zones present subgrain growth (Figure 5f), whereas for the nugget narrow rings mark the advancing of the weld tool in the longitudinal direction (Figure 5b).

CORROSION BEHAVIOR

Polarization scans indicate similar trend for the parent metal both longitudinally and transverse to the weld with two breakdown potentials typical for the 7075-T6 tempers (Figure 7a). The nugget generally shows lower breakdown potentials compared to the parent metal for both the transverse and the longitudinal direction (Figure 7b). In some cases, however, higher breakdown potentials and the appearance of a second breakdown takes place in particular for the transverse orientation. The two heat affected zones (HAS, HTS) show one breakdown potential

with slightly lower values for the transverse orientation. Generally both heat affected zones show slightly lower breakdown potentials, particularly in the transverse direction (Figure 7c, d). The surface morphology after 20 minutes of exposure of transverse samples reveals areas of localized corrosion for both of the heat affected zones as well as for the parent metal, with a slightly higher corrosion for the heat affected zones. Within the nugget, the corrosion attack appears more fine grained and less localized so that a direct comparison with the previous micro-zones is difficult (Figure 8). ESEM investigations indicate that corrosion initiates within intermetallic-containing areas both through anodic dissolution of the intermetallic constituent itself or through dissolution of the surrounding matrix.

Micro-electrochemical measurements indicate a breakdown potential of -0.767 ± 0.033 V SCE for the intermetallic-free and -0.808 ± 0.006 for the intermetallic-containing areas, following 72 measurements within the micro-zones. These results indicate that within the micro-zones the intermetallic-free areas generally show higher breakdown potentials than those areas containing intermetallics. This difference in potential is of the same order of magnitude as potential differences observed between the micro-zones during potentiodynamic scans. Additionally, a comparison between the measurements carried out within the different micro-zones transverse to the weld on intermetallic-contaning areas indicates a lower breakdown potential for each of the heat affected zones when compared to the parent metal. The lowest overall breakdown potentials are observed for the nugget (Table 1).

MECHANICAL PROPERTIES AND FRACTOGRAPHY IN AIR

The main mechanical parameters observed from the constant extension rate tests are summarized in Table 2. Generally, the strain and the time to failure nearly double for each of the samples tested longitudinally. Higher maximum stresses are observed for the parent metal when

compared to the weld in the transverse direction. Longitudinally, it should be emphasized that the lowest values are detected within the heat affected zone in the advancing side of the weld. These latter low values coincide with the maximum stress obtained transverse to the weld.

The fracture surface transverse to the parent metal exhibits a slanted, smooth morphology with the presence of elongated flat regions, presumably grains, separated by equiaxed dimples. In the flat regions, narrow striations-like features are occasionally observed (Figure 9a). Transverse to the weld, the fracture always occurs within the heat affected zone, and always in the advancing side (Figure 12). The fracture surface is generally rougher with the presence of dimples alternated by aligned voids (2-4 μm) transverse to the crack propagation direction. Within these latter voids second phase particles are occasionally present (Figure 9b). The flat regions observed previously are still present. Among the different micro-zones tested longitudinally, the parent metal fracture surface shows irregular facet-like structures (Figure 10a), probably corresponding to grains and the presence of micro-voids. The nugget reveals a rough and irregular surface, with intergranular-like fracture morphologies superimposed by the high density of micro-voids (Figure 10b), which contribute to the high ductility of the nugget. For both heat affected zones, the facet-like features are less prevalent when compared to the parent metal and the fracture surfaces are generally smooth. Striations are more commonly present in particular in the flat fracture regions of the heat affected zone in the advancing side. Alternating zones of cleavage, tongue-like morphologies, and a number micro-voids elongated in the fracture propagation direction are also present. As for the fracture surface transverse to the weldment, two generations of micro-voids are present (Figure 10c). Within the heat affected zone in the trailing side, each of these latter morphologies, and particularly the micro-voids, are blunted (Figure 10d).

DYNAMIC LOADING OBSERVATIONS AND ENVIRONMENTAL SUSCEPTIBILITY

The CERT investigations transverse to the weld exhibit lower strain values when compared to the individual micro-zones tested longitudinally (Figure 11a, b). The maximum stresses exhibited by the samples tested transverse correlate with those measured longitudinally in the isolated heat-affected zones. The high embrittlement (lowest ductility ratio) of the heat affected zone in the advancing side of the weld as compared to that in the trailing side also need particular attention (Figure 11b). In the former case, the specimens tested in air show a slanted fracture surface whereas a strong necking with a fracture surface perpendicular to the tensile axis is observed for the ones tested in solution.

For the specimens tested transverse to the weld, visual inspection reveals that the two main regions of high plastic deformation are isolated to both of the heat affected zones. Obvious regions of necking are observed, particularly within the heat affected zone on the advancing side of the weld. Not surprisingly, this is also the region most likely to fracture in each of the samples tested transverse to the weld (Figure 12). A closer examination of the tensile sample surface indicates a triangle-like pit initiation away from the fracture zone, closer to the nugget. Conversely, when approaching the fracture region within the highly deformed heat affected zone on the advancing side, the corrosion characteristic is indicative of intergranular attack (Figure 12b). Compared to parent metal, the weld samples tested in solution show a high number of intergranular initiation sites on the cylindrical surface just before the fracture (Figure 13). The fracture surface indicates intergranular-like features close to the initiation site, which then appear to change to a transangular path at the fracture end where overload becomes dominant.

The environmental susceptibility of the parent metal and associated weld zones was also investigated by observing the general corrosion features of the fracture surfaces. For the samples

tested in the transverse direction, an intergranular morphology with secondary cracks around grains is observed in the parent metal (Figure 14a), and an increased extent of attack with both intergranular and intersubgranular morphologies is present in the weld zones (Figure 14b). In this latter case, the fracture surface is rough, with elongated, step-like features which may be linked to the presence of aligned micro-voids previously observed in the specimens tested in air. For the samples tested longitudinally, secondary cracks and an intergranular path of attack are both observed for the facet-like structures of the parent metal (Figure 15a) and the equiaxed grain structure of the nugget (Figure 15b). The samples of the heat affected zone on the advancing side of the weld consistently demonstrate a higher susceptibility to intergranular and intersubgranular attack (Figure 15c) when compared to the samples of the heat affected zone in the trailing side (Figure 15d).

DISCUSSION

THE RELATIONSHIP BETWEEN MECHANICAL PROPERTIES AND MICRO-ZONES.

The different strengthening precipitates observed across the weld could likely be indexed as $Mg_{32}(Al,Zn)_{49}$ or $Mg(Zn_2,AlCu)$ for the larger particles in the 80 nm range, whereas the fine 10-12 nm particles have been reported to be too small to be identified by diffraction analysis.[9] Grain boundary precipitates have been reported as be $MgZn_2$.[16] Within the weld nugget the small 12 nm precipitates disappear and the larger ones become incoherent with the parent metal. This is a manifestation of the reversion of these small particles back into solution during the high temperature weld pass.[9] Both of the narrow thermo-mechanically affected zones adjacent to the weld nugget show a similar precipitate distribution as observed in the nugget, although the intragranular 80 nm precipitates in the TMAZ are highly oriented and the grains are distinctly

elongated. This observation is consistent with the similar hardness values for the TMAZ and the nugget (Figure 4), although a strong difference in the grains can be observed optically. Rather than the recrystallized, equiaxed grain structure found in the nugget, the TMAZ is comprised of elongated, highly deformed grains (Figure 5d).

The comparatively low strength values observed in each of the heat affected zones was likely due to the coarsening of the fine intragranular precipitates (Figure 6c, d), as has been reported in a previous work.[3] The low hardness values observed in each HAZ correlate with the low maximum stresses achieved via CERT for not only the isolated HAZ samples pulled longitudinally but also to the entire weld zone when tested in the transverse direction (Table 2). When the weld is tested in the transverse direction, the fracture invariably occurs in the weaker regions of the weld, i.e. the heat affected zones, as has been reported in other work.[3] Additionally, the fracture surface exhibits ductile features; it is apparent that the second phase particles present within the larger voids act as initiation sites for ductile fracture (Figure 9b). It should be reemphasized that in the transverse direction the strain may not be uniformly distributed across the span of different micro-zones. The weld nugget appears to withstand deformation more effectively than do the HAZs, mainly as a result of isotropic strain behavior of the equiaxed grains and the associated high ductility, resulting in necking that is mainly observed in the soft HAZ.[3] Furthermore, from the CERT measurements it appears that the nugget is more prone to work hardening than the heat affected zones.

Based on the aforementioned results, a good correlation exists between the hardness measurements and the maximum stresses achieved within the micro-zones tested longitudinally (Figure 4, Table 2). The lower hardness and stress values of the nugget as compared to that of the parent material tested longitudinally are presumably caused by the disappearance of the

extremely fine distribution of intragranular strengthening precipitates (Figure 6b) and the reduction of preexisting dislocations due to the thermal transient of the weld pass.[9] The slightly higher hardness and maximum stresses values for the nugget compared to the heat affected zones are most likely due to the coarsening of the fine strengthening precipitates, resulting not only in a loss of strain hardening from the dispersion of coherent precipitates (when compared to the parent material), but also a lack of solid-solution strengthening apparent in the nugget from the reversion of these fine precipitates. All of the micro-zones indicate high ductility when tested longitudinally. It is clear, therefore, that while the precipitate structure differs across the weld zone, the thermal transient from the weld pass has effectively drawn the strength temper from each of the micro-zones. The result of this thermal transient can also be seen in the larger PFZs (Figure 6c, d) and the higher strain achieved within the HAZs compared to the parent metal (Tab. 2). Presumably, the more ductile PFZ fail by micro-void coalescence (Figure 10c, d),[3] although a failure through micro-void coalescence at grain boundary may not be ruled out. The nugget show the presence of grain boundary particles without PFZs. Particles can be seen entrapped in grain boundaries, not as a result of precipitation along boundaries but more likely due to pinning processes by preexisting particles of thermally-activated mobile boundaries. The presence of high ductility and grain boundary particles without PFZs correlate well, however, with previously reported results on alloy systems,[17] as well as on similar friction stir welded alloys,[3] and further support the failure starting through the formation of micro-voids at grain boundary particles.

The narrow striation-like features generally present on the flat regions of the fracture surfaces may well indicate a discontinuous nature of the crack advance.

MICROSTRUCTURAL FEATURES AND CORROSION CONTROLLING FACTORS

In spite of the distinctly different microstructures obtained across the FSW zone (Figure 5), only slight differences in the first breakdown potentials between the micro-zones are observed (Figure 7). Being that the differentiation between the micro-zones has thus far been largely based on hardness profiles, the narrow thermo-mechanically affected zone adjacent to the nugget was not evaluated in these corrosion investigations. These narrow, highly deformed zones appear to corrode only in the presence of very aggressive solutions,[7,10] however, and do not appear to represent initiation sites for corrosive attack. In fact, mild corrosion tests revealed the heat affected zone to be the primary initiation region for corrosion.[10] Both the advancing side and trailing side heat affected zones show slightly lower breakdown potentials (Figure 7a, c, d) and a slightly higher incidence of pits (Figure 8a, c) when compared to the parent metal, particularly for samples tested in the transverse orientation. This agrees with results obtained for the same type of alloy,[7] as well as other types of high strength aluminum alloys such as 7010-T7651 and 2024-T351.[10] The pitting potentials of the nugget (Figure 7b) which indicate lower values compared to the parent metal but slightly higher values compared to the heat affected zones in particular for the transverse orientation well correlate with previously reported results[7,10] Nonetheless, some measurements, in particular in the transverse orientation, indicated the appearance of a second breakdown. To this end, it is probably wise not to speculate on the highly inhomogeneous “onion ring” structure,[3,11] (Figure 5) as a cause for some scattering of the pitting potentials in the transverse direction.

The lower pitting potentials showed by the micro-electrochemical measurements for the intermetallic-containing areas along with the slightly lower breakdown potentials found for the nugget and the heat affected zones compared to the parent metal (Table 1) suggest that the

temperature gradient occurring during welding may not only have selectively sensitized grain boundaries through the formation of discrete precipitates (Figure 6c, d), but also affected the electrochemical behavior of the intermetallic constituents. Grain boundary sensitization in these particular zones was also reported in a previous work on the same type of alloy.[7] It generally appears that the higher the temperature within the weld zone, the higher the susceptibility of the intermetallic constituents or intermetallic-containing areas to corrosive attack (Table 1). Within the heat affected zones, the lower breakdown potentials correlate with the low pitting potentials of the intermetallic-containing areas. For the nugget, however, no distinct correlation is found. The reason for this might be found in the inhomogeneous structure of the nugget, which occasionally indicates a partial reduction of the average size of the second phase particles, as was observed for a previously reported alloy system.[11] This may promote a general fine-grained pitting as observed in Figure 8b, and influence the large scale breakdown potentials (Figure 7b).

Different reports on high strength aluminum alloys have associated the presence of two breakdown potentials on T6 tempers on two particular forms of attack; pitting, intergranular, or a combination of the two.[18,19] In this work, two breakdown potentials were also found for the parent metal while generally only one breakdown potential was found for the nugget and each of the heat affected zones. The occurrence of one breakdown potential in the nugget, as well in the hottest region of the heat affected zone, was reportedly controlled by grain boundary attack.[7] This particular study, however, showed corrosion to initiate on or around intermetallic constituents, and it is known that intermetallic compounds exhibit very different electrochemical behavior compared to the matrix.[20] Similar observations were made in FSW AA2024-T351 following 21 hours of exposure to 0.1 M NaCl,[10] and the increase in the reaction rate at cathodic sites along with an increase in free Cu on the surface is known.[21,22] Since Cu was detected in

some of the intermetallic constituents, its contribution to enhanced corrosion may also take place, although in this study the main influence of second phase particles was detected at early stages. Furthermore, it appears that either the second phase particles themselves or the matrix surrounding them show a susceptibility to corrosion, depending on the micro-zone in which they are located (Table 1). In the latter case, a good correlation was found between the pitting potential of the intermetallic-containing areas and the general pitting potentials for the heat affected zone and the parent metal. Although in this study no tests were performed to independently study intergranular corrosion, and no electrochemical distinction between the intermetallic particles was made, it is clear that the role of the intermetallic constituents in controlling the pitting potentials of the weld zones may not be ruled out. There is a tendency of the intermetallic precipitates to concentrate on grain boundaries, in the parent metal and particularly in the heat affected zones (Figure 5e, f) where subgrain formation takes place; corrosion could therefore conceivably initiate directly within grain boundary regions. The pitting potentials measured with potentiodynamic scans, however, appear to be controlled by both intermetallic constituents as well as by grain boundary chemistry,[7] which, as will be discussed in the next section, influence the susceptibility to environmental cracking.

EMBRITTLEMENT AND DISCRIMINATION BETWEEN THE HEAT AFFECTED ZONES

At first look, the results of the ductility ratios of the weld as compared to the parent metal in the transverse direction (Figure 11a) may be misleading with respect to the embrittlement susceptibility of these materials. As has been observed in a different study when assessing the mechanical properties of the same stir friction welded alloy,[3] the deformation across the weld is mainly concentrated within the HAZs, resulting in necking in both regions. Thus, the inhomogeneous distribution of the strain across the weld compared to the parent metal would

require due care when interpreting the degree of embrittlement based solely on strain to failure evaluations. The high deformation taking place within the HAS as compared to the parent metal may somehow mask the degree of embrittlement based on dynamic loading observations.

Contrary to what the ductility ratios in the transverse direction the weld, particularly in the HAS, exhibits a higher susceptibility to environmental attack when compared to the parent metal (Figure 12). In the longitudinal direction, generally, the more homogeneous distribution of the strain during testing allows for better reliability of recorded ductility ratios. Within the soft HAS region, localized intergranular attack zones are present (Figure 12), although the fracture surface indicates a slight intergranular attack on the crack initiation site (Figure 13c). Intergranular attack regions are observed, however, on the cylindrical surface of the specimens just before the fracture location (Figure 13a, b). It may therefore be argued that the entire soft HAS region is more susceptible to corrosive attack. This results in the formation of localized intergranular attack regions on the specimen surface, the location from which fracture originates. The weld nugget reveals its susceptibility to environmental attack as was reported in recent work on 7050-T7451,[23] although the comparison of results with different specimen geometry must be considered.

The main observation, however, remains that despite very similar microstructures in both of the HAZ regions, all fractures occurs within the HAS rather that within the HTS. The higher environmental corrosion susceptibility of the HAS as compared to the HTS appears to be supported by the longitudinal CERT test (Figure 11b) which demonstrate the lowest ductility along with a higher degree of intergranular and intersubgranular attack (Figure 15c, d). Despite the lack of obvious microstructural differences between these two zones (Figure 6 c, d), and the similarity of the pitting potentials on large scale measurements (Figure 7c, d), it appears that the

HAS may qualitatively develop a more susceptible microstructure with regard to the formation of grain boundary precipitates and solute depleted zones (Figure 6c, d). Other published work,[24] gives credence to the level of Cu depletion at grain boundaries as a direct contributor to overall SCC resistance; further studies are evaluating differences in Cu depletion across the individual weld zones.

It is important to note that the two heat affected zones present slight differences in microstructural features, but significant differences in performance with regard to SCC resistance. It would appear that for the FSW process conditions outlined above, the two heat affected zones have achieved differing levels of sensitization. The diffuse boundary of the nugget with the present of folds towards the advancing side of the weld (Figure 5c) and the sharp boundary and absence of particular deformational features towards the trailing side (Figure 5d) might be one clue as to the asymmetric material response to FSW deformation. Such differences in observable features likely also indicate an associated asymmetrical temperature distribution. Welding parameters such as head angle, pin speed, or advancing speed may thus all have a distinct effect on thermal response of the alloy. Moreover, the capability of the FSW rig to provide symmetrical heat transfer from the welding plates to the backing plate may also be critical in determining the level of sensitization, and therefore the future environmental susceptibility, of the finished weld. In this context, it may be only speculated that the dependency of the corrosion behavior on the plate thickness,[10] may be the results of different welding conditions.

SUMMARY AND CONCLUSIONS

The characteristics of a friction stir welded section of Al-7075-T6 was evaluated with regard to the distinct weld zones. Microstrucural features of individual micro-zones were investigated and correlated with strength, hardness, ductility, corrosion and environmental assisted cracking behavior.

1. The strength and ductility of the different micro-zones appears to be controlled mainly by the size and distribution of the small intragranular η-phase strengthening precipitates as well as the microstructure of the grain boundary regions. In the hardened T6 condition (parent material), strength is provided mainly by the fine dispersion of coherent precipitates. In the HAZ, these precipitates coarsen and strength is lost. Closer to and within the nugget region, the more extreme thermal conditions allow a complete re-solutionizing of the small η-phase particles, resulting in a loss of precipitate strengthening, but also some gain in solid solution strengthening.

2. The temperature gradient taking place during FSW appears to have a different effect on the level of sensitization across each individual weld zone. The resulting level of sensitization in each zone will have a direct effect on the overall corrosion behavior of the weld.

3. Despite the similarity in microstructure and breakdown potentials between the two heat affected zones, both on the advancing and trailing side, the heat affected zone in the advancing side of the weld (HAS) exhibits the highest environmental susceptibility among the investigated micro-zones. The HAS is inherently the failure zone for samples tested transverse to the weld pass under SCC-enhanced conditions.

ACKNOWLEDGEMENTS

The authors would like to thank the University of South Carolina for welding the materials as well as the Fontana Corrosion Center at the Ohio State University for technical support and the Wright-Patterson Air Force Base for the financial support.

REFERENCES

1. W. M. Thomas, et. al., Friction Stir Butt Welding. GB 9125978.8, (1991), (1995), U.S. 5,460,317.

2. O. T. Midling, O. Grong, A Process Model for Friction Welding. Acta Metall. Mater., 42, (1994), p. 1595-1609.

3. M. W. Mahoney, et al., Properties of Friction-Stir-Welded 7075 T651 Aluminum. Met. Trans. A, 29A, (1998), p. 1955.

4. C. J. Dawes, W.M. Thomas, TWI Bulletin, 11/12, (1995), p. 124.

5. C. J. Dawes, W.M. Thomas, Weld. J., 75, (1996), p. 41.

6. D. Lohwasser, Application of Friction Stir Welding for Aircraft Industry. The Second International Symposium on Friction Stir Welding. Gothenburg, Sweden (2000).

7. J. B. Lumsden, et al., Intergranular Corrosion Following Friction Stir Welding of Aluminum Alloy 7075-T651. Corrosion, 55, 12, (1999).

8. Y. Li, L.E. Murr, J.C. McClure, Flow Visualization and Residual Microstructures Associated with the Friction-Stir Welding of 2024 Aluminum to Aluminum 6061. Materials Science and Engineering, A271, (1999), p. 213-223.

9. C. G. Rhodes, et al., Effects of Friction Stir Welding on Microstructure of 7075 Aluminum. Scripta Materialia, 36, 1, (1997): p. 69-75.

10. F. Hannour, A.J. Davenport, M. Strangwood. Corrosion of Friction Stir Welds in High Strength Aluminum Alloys. 2nd International Symposium on Friction Stir Welding. Gothenburg, Sweden (2000).

11. G. Biallas, et al. 1st International Symposium on Friction Stir Welding. Thousand Oaks, California (1999).

12. H. Boehni, T. Suter, A. Schreyer, Micro-and Nanotechnologies to Study Localized Corrosion. Electrochimica Acta, 40, 10, (1995): p. 1361-1368.

13. T. Suter, Ph. D. Thesis in Materials Science No. 11962, ETH Zurich (1997).

14. T. Suter, R.C. Alkire, Microelectrochemical studies of Pit Initiation at Single Inclusions in Al 2024-T3. Journal of the Electrochemical Society, 148. 1, (2001): p. B36-B42.

15. ASTM G129, Standard Practice for Slow Strain Rate Testing to Evaluate the Susceptibility of Metallic Materials to Environmentally Assisted Cracking (American Standards for Testing and Materials, revised ed.).

16. G. W. Lorimer, Precipitation Processes in Solids, ed. K.C. Russell, H.I. Aaronson, Warrendale, PA: Met. Soc. AIME. 87 (1978).

17. A. K. Vasudevan, R.D. Doherty, Acta Metall., 35, (1987): p. 1193-1219.

18. S. Maitra, G.C. English, Met. Trans., 12, A, (1981): p. 535.

19. T. Ramgopal, G.S. Frankel, Role of Alloying Elements and Intermetallic Particles in the Intergranular Corrosion of AA7150. Corrosion and Corrosion Prevention of Low Density Metals and Alloys, ed. B.A. Shaw, R.G. Buchheit, J.P. Moran., (Pennington NJ: The Electrochemical Society, 2000), p. 411-421.

20. R. G. Buchheit, J. Electrochemical Soc.,142(1995): p. 3994.

21. R. G. Buchheit, et al., J. Electrochemical Society, 144, (1997): p. 2.621.

22. N .Dimitrov, N., J.A. Mann, K. Sierdazki, J. Electrochemical Society, 146, (1999): p. 98.

23. J. Lumsden, M. Mahoney, G. Pollock, Stress Corrosion Susceptibility in 7050 T7451 Aluminum Following friction Stir Welding. 2001. To be published.

24. J. K. Park, A.J. Ardell, Acta Metall. Mater., 39, (1991): p. 591.

25. K. V. Jata, S. L. Semiatin, Continuos Dynamic Recrystallization During Friction Stir Welding of High Strength Aluminum Alloys. Scripta mater., 43, (2000): p. 743-749.

TABLES

TABLE 1.
Microelectrochemical measurements of the intermetallic-contaning areas within the different microzones. The data indicate the average of 9 independent measurements within each microzone.

	Parent metal	Nugget	Heat zone (Adv. side)	Heat zone (Trail.Side)
OCP	-0.846 (Std 0.020)	-0.866 (Std 0.026)	-0.813 (Std 0.022)	-0.855 (Std 0.027)
1 breakdown	-0.798 (Std 0.05)	-0.813 (Std 0.052)	-0.810 (Std 0.045)	-0.808 (Std 0.023)

TABLE 2.
Mechanical data for the micro tensile CERT specimens tested in air. Average standard deviations: stress: 20.82; strain: 0.29; TTF: 0.07.

Sample	Max. Stress [Mpa]	**Max. Strain [%]**	TTF [days]
Parent metal (transverse)	468.85	9.58	2.3
Weld (transverse)	364.4	6.54	1.57
Parent metal (longitudinal)	500.97	11.52	2.76
Nugget (longitudinal)	450.68	15.201	3.63
Heat affected zone advancing side (longitudinal)	373.76	14.217	3.40
Heat affected zone trailing side (longitudinal)	380.82	12.705	3.04

FIGURES

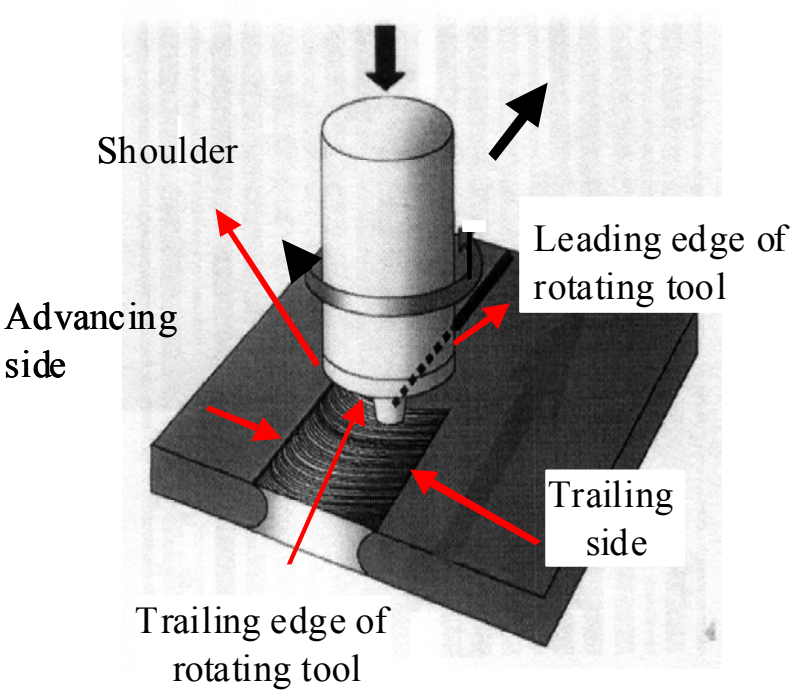

Figure1. Schematic representation of the FSW process. Modified from [25].

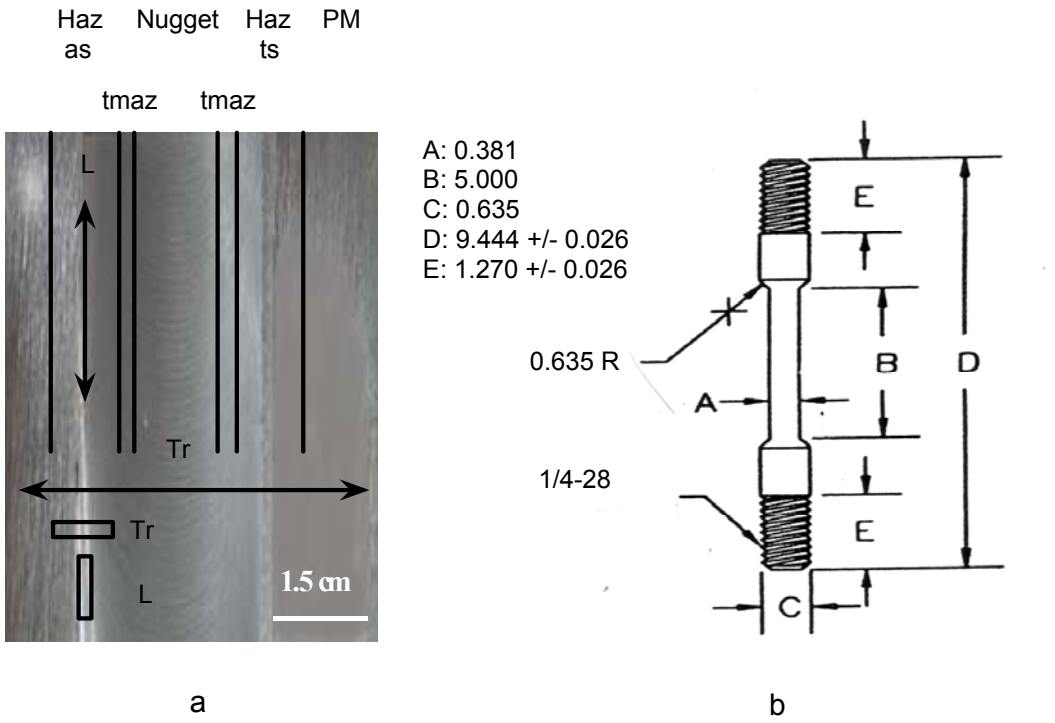

Figure 2. Tensile specimen (arrows) and corrosion samples (rectangles) orientation with respect to the weld (a). CERT specimen dimension (b). Drawing not to scale.

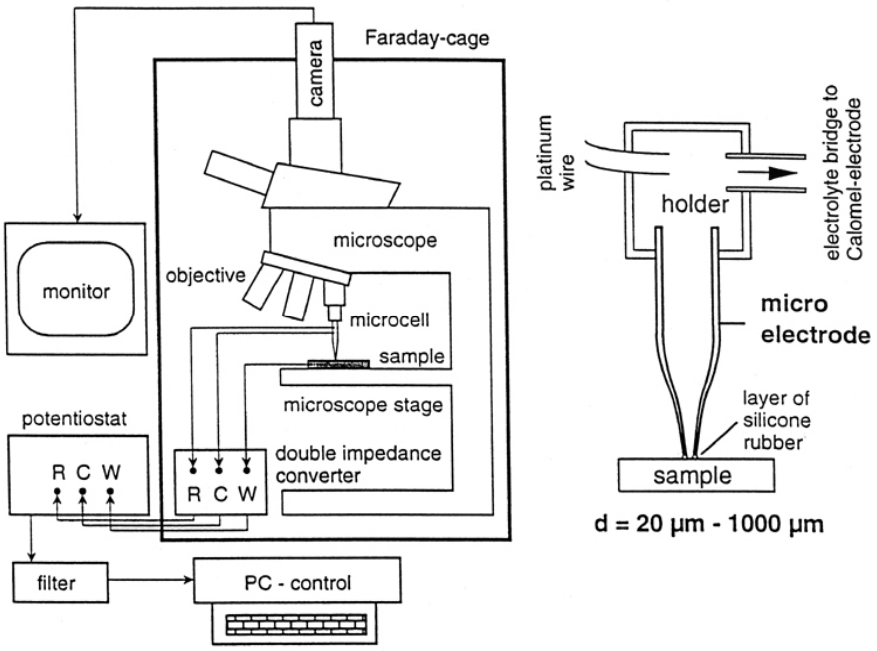

a b

Figure 3. Schematic of the micro-capillary electrochemical cell set up (a) and the micro-capillary holder (b) [13].

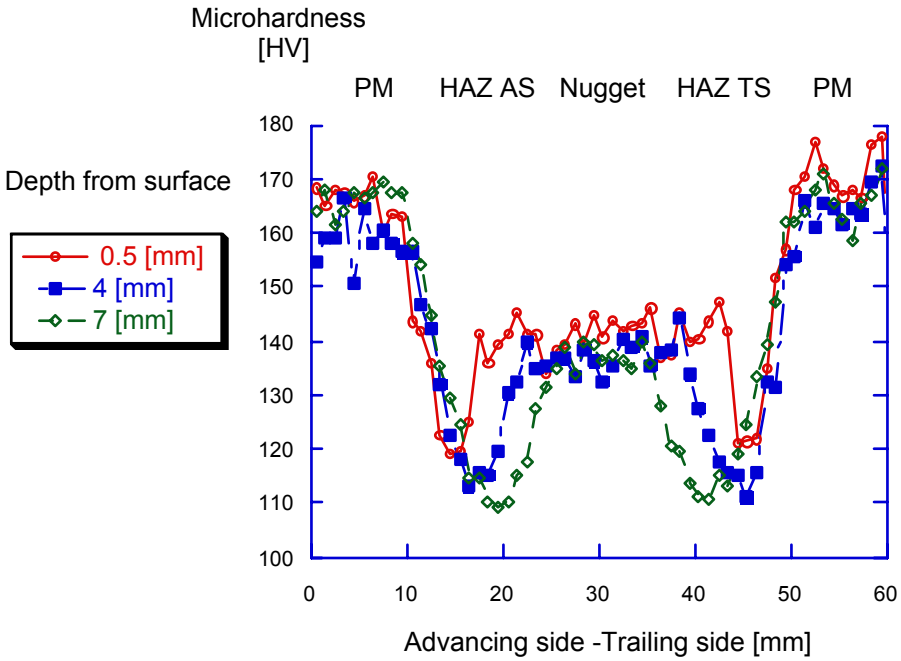

Figure 4. Microhardness profiles across the weld.

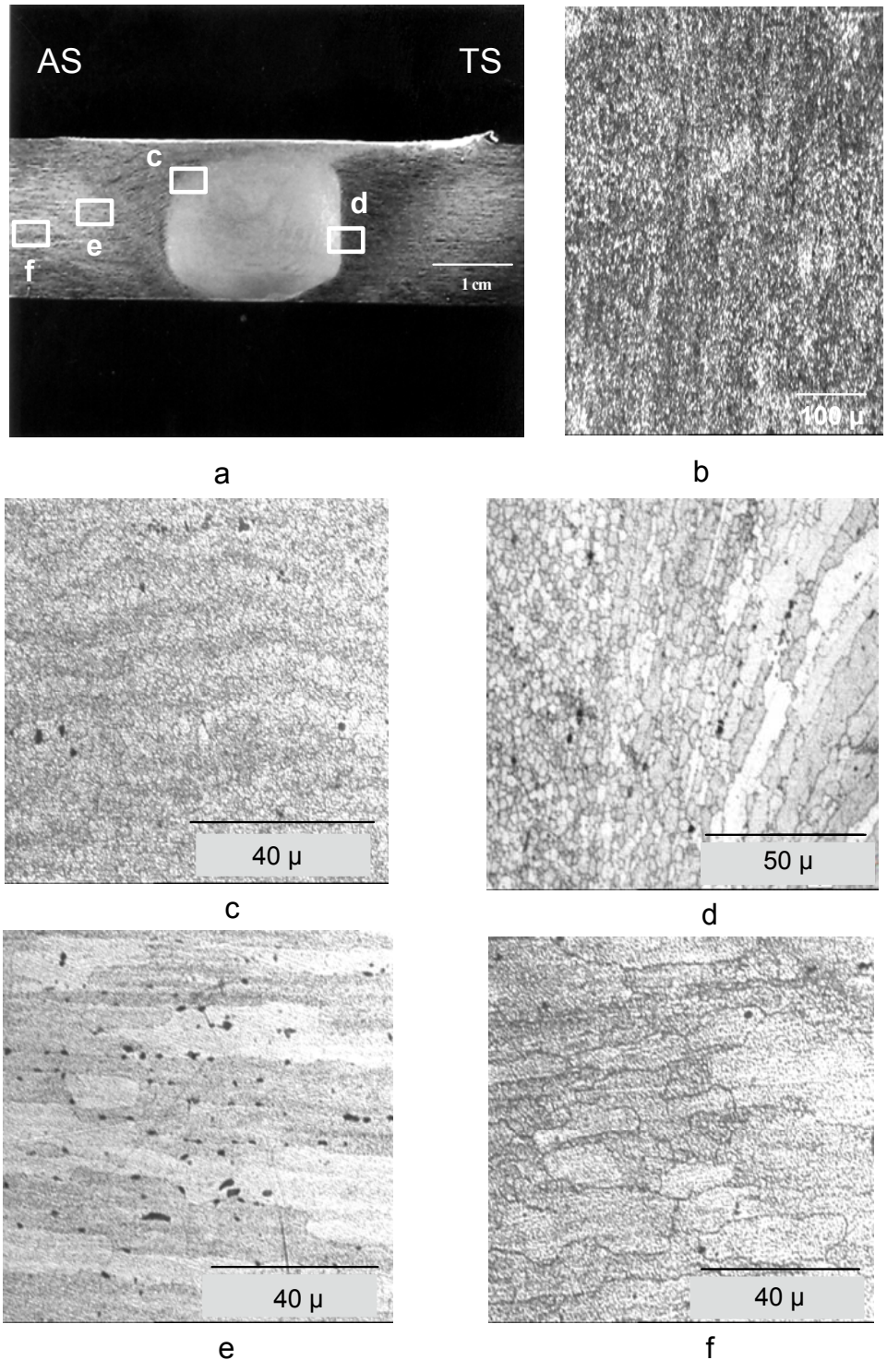

Figure 5. a: Weld cross section with advancing (AS) and trailing (TS) side. b: Weld nugget longitudinal section. c: folds in the weld nugget. d: sharp boundary between nugget and thermo-mechanically affected zone. e: parent metal. f: heat affected zones subgrain formation (AS).

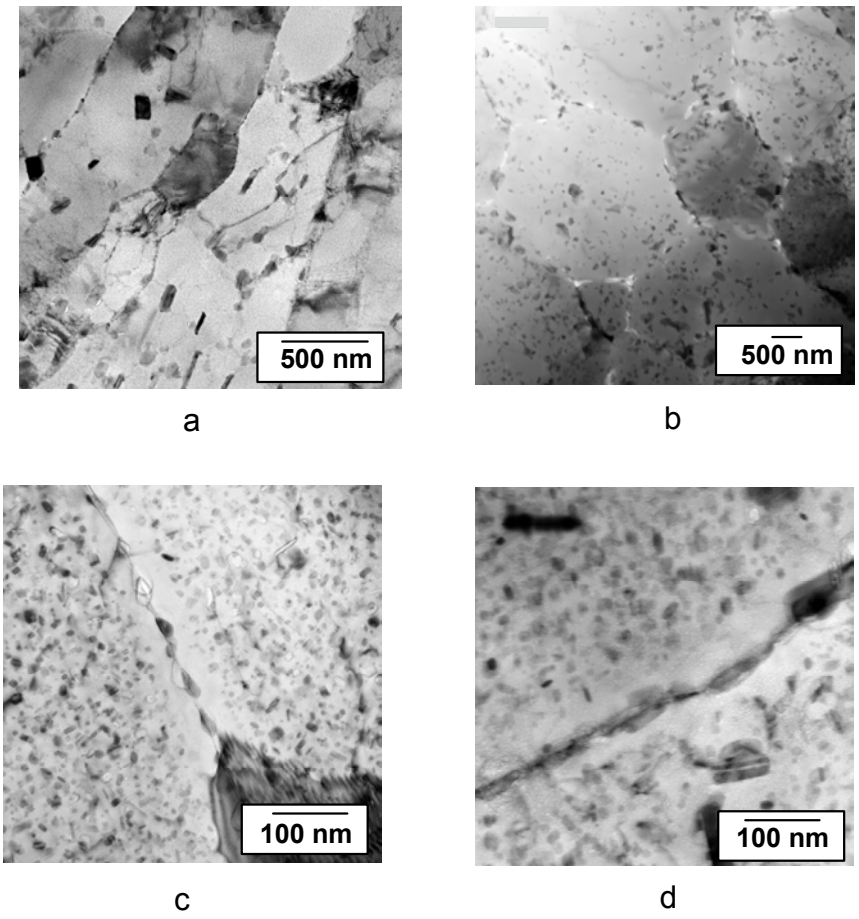

Figure 6. Microstructural features of parent metal (a), nugget (b), heat affected zone advancing side (c) and trailing side (d).

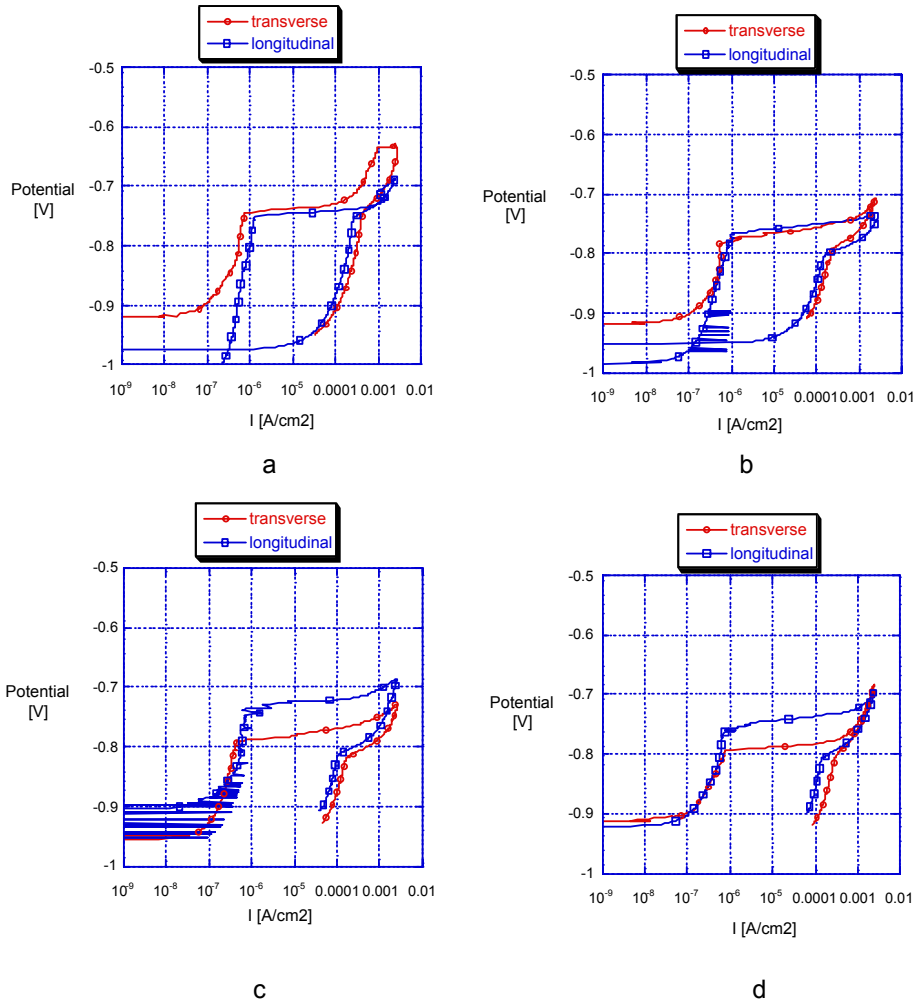

Figure 7. Representatives polarization curves for the microzones transverse and longitudinally to the welding direction. a: parent metal. b: nugget. c: heat affected zone advancing side. d: heat affected zone trailing side.

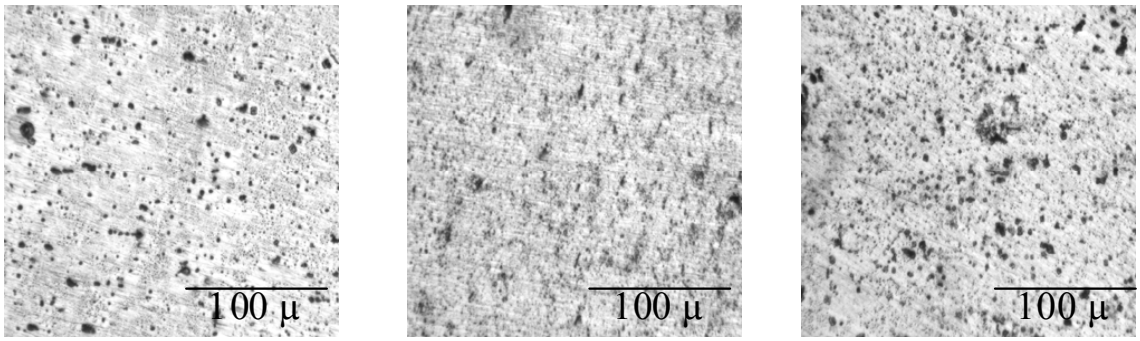

a b c

Figure 8. Corrosion features of the microzones transverse to the weld after 20 minutes exposition to 3.5 wt. % NaCl. a: parent metal. b: nugget. c: heat affected zone.

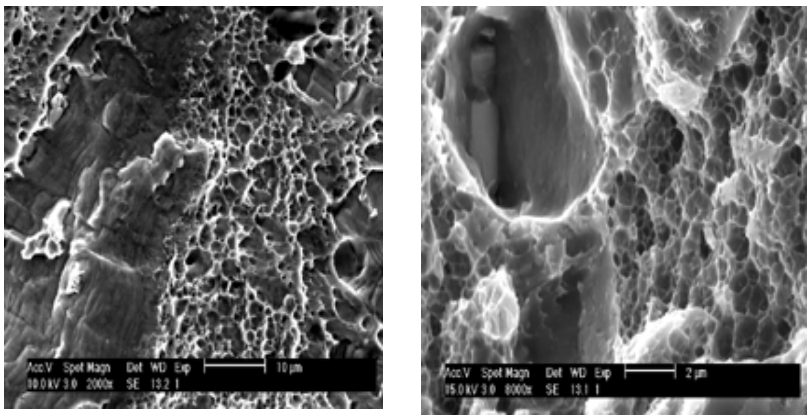

a b

Figure 9. Fracture surface of parent metal (a) and weldment (b) in the transverse direction.

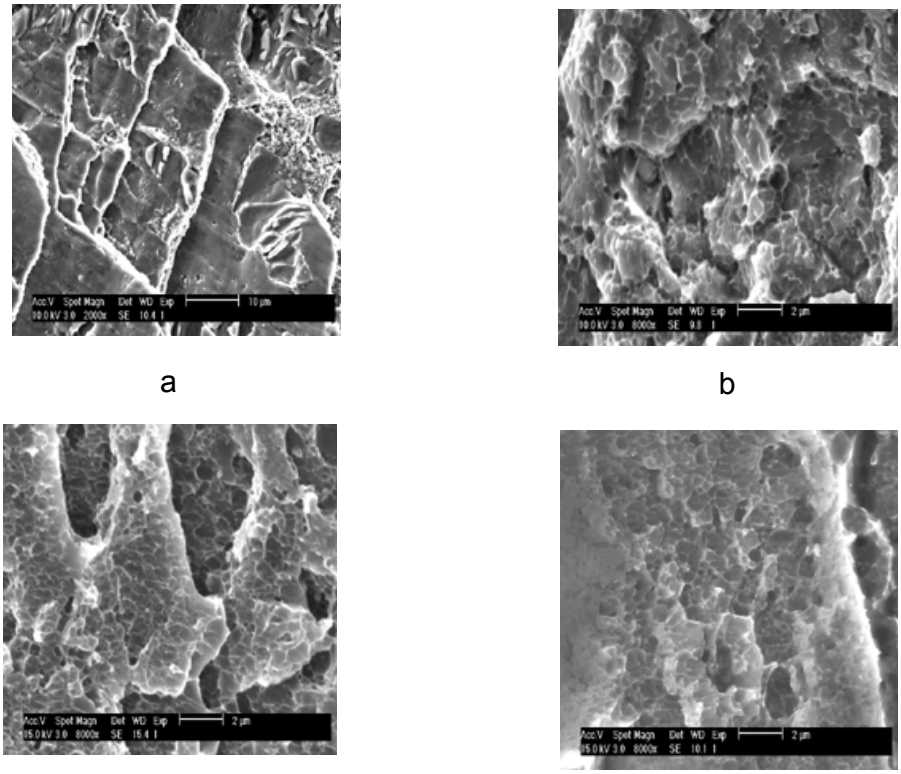

a b c d

Figure 10. Fracture surfaces of parent metal (a), nugget (b), HAS (c) and HTS (d) in the longitudinal direction.

Sample	Ductility ratio
Parent metal	0.77
Weldment	0.86

a

Sample	Ductility ratio
Parent metal	1.05
Nugget	0.85
Heat affected zone advancing side	0.32
Heat affected zone trailing side	1.31

b

Figure 11. CERT data and ductility ratios for the specimens tested transverse (a) and longitudinally (b) to the weld. The graphs display representatives measurements, whereas the ductility data are averages of two measurements.

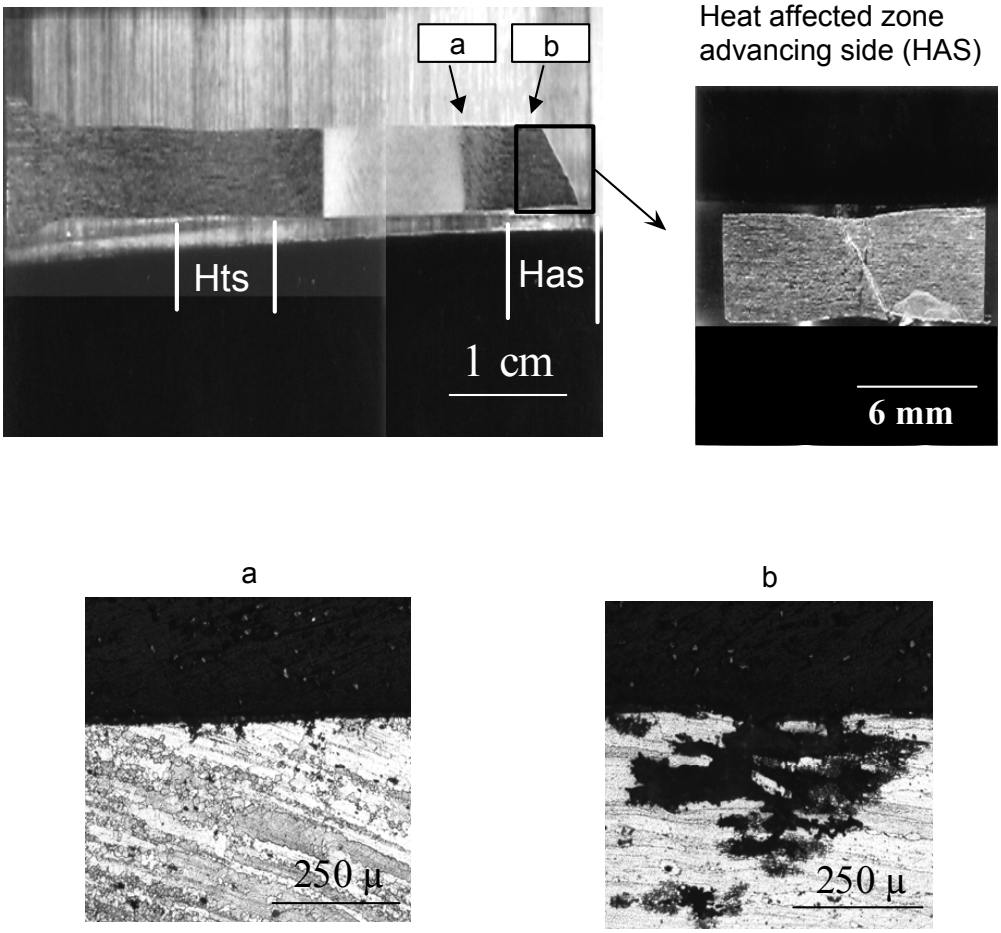

Figure 12. Section of a tensile specimen tested in solution transverse to the weld. Note the necking in both heat affected zones particularly for the advancing side (Has) and the development of an intergranular-type attack close to the fracture location (b).

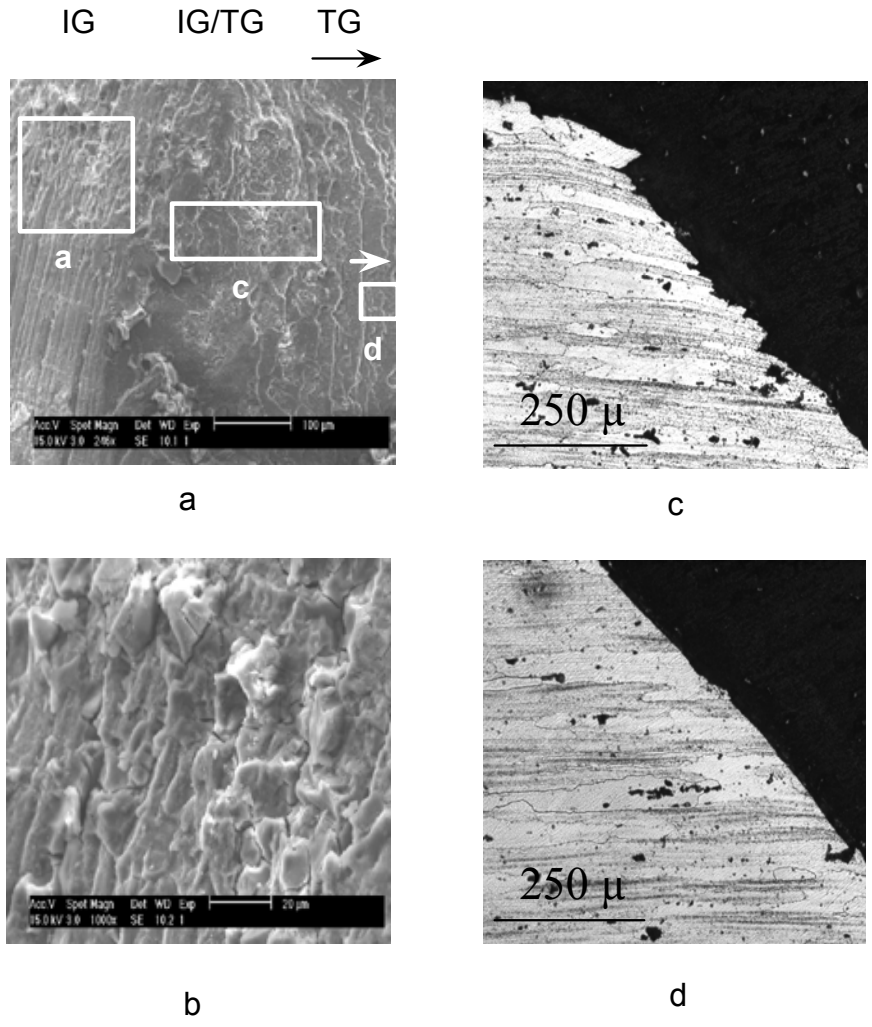

Figure 13. Fracture morfology of samples tested in solution transverse to the welding showing intergranular attack (IG) on the cylindrical specimen surface close to the fracture initiation site (a). Detail of the IG zone (b). The fracture surface show IG-like features close to the initiation zone (c) and transangular morfology (TG) in the overload region (d).

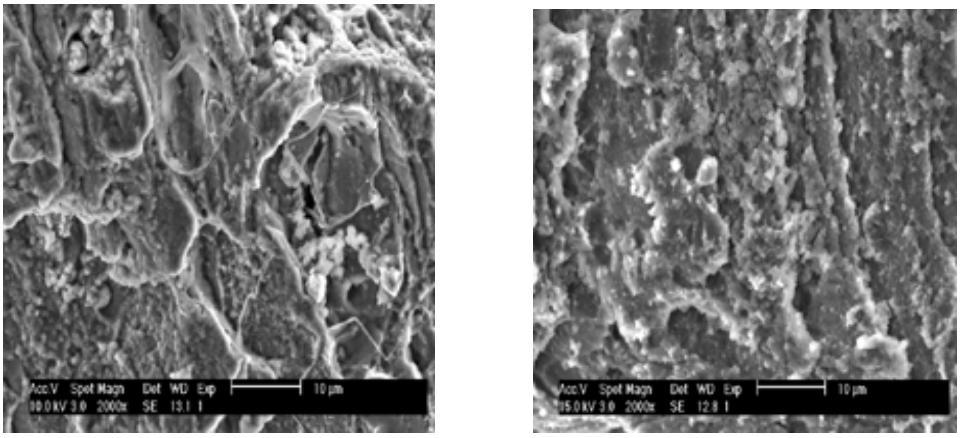

a b

Figure 14. Fracture surface of parent metal (a) and weld (b) tested in solution in the trasverse direction. Note the intergranular-subgranular attacking morfology of the weld.

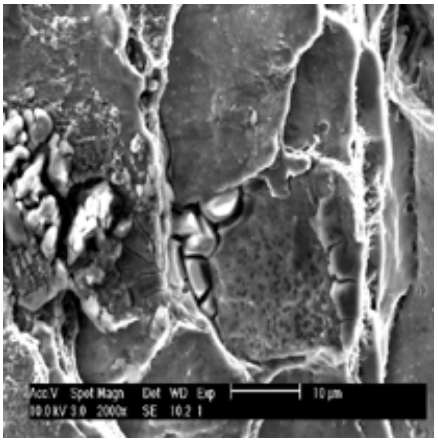

a

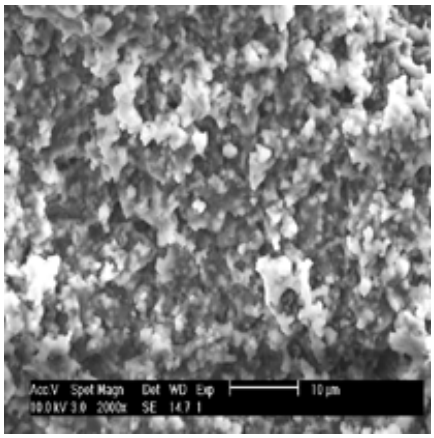

b

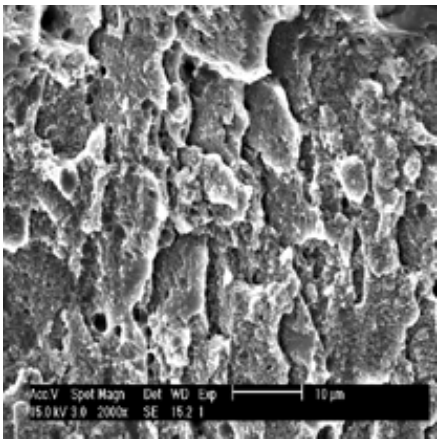

c

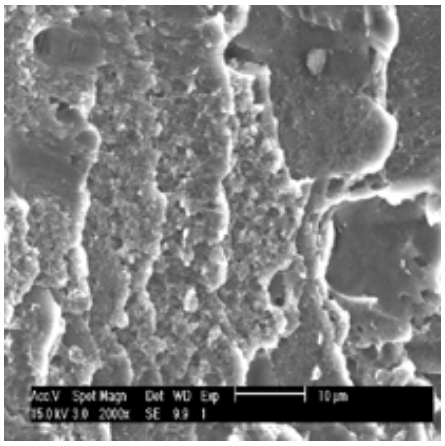

d

Figure 15. Environmental susceptibility of the different microzones tested longitudinally. a: parent metal; b: nugget; c: heat affected zone advancing side; d: heat affected zone trailing side.

CONTRIBUTIONS OF HOT CORROSION AND DIFFUSIONAL PROCESSES TOWARDS THE PERFORMANCE OF HIGH TEMPERATURE MATERIALS

David A. Shifler
Carderock Division, Code 613
Naval Surface Warfare Center
West Bethesda, MD, 20817-5700

ABSTRACT

During a recent high-temperature work, it was discovered that a high-temperature coating on a single crystal casting had completely failed after 1000 hours of exposure in a hot corrosion environment. Though previous tests showed this coating was somewhat resistant to hot corrosion at 1650 °F (899 °C), our results revealed catastrophic corrosion penetration of both the coating and the alloy substrate.

Differences in chemical compositions between a coating and a substrate alloy can lead to interdiffusion between these materials that can modify the oxidation and corrosion resistance of the coating and the mechanical properties of the coating-substrate system. The stress state may also significantly influence and increase the magnitude of the interdiffusion that may lead to deleterious precipitation reactions. The crystal orientation or alloy phase of the substrate may also contribute to interdiffusion rates.

This paper will look at the chemistry of a high-temperature coating and a substrate alloy before and after exposure to a hot corrosion environment to evaluate the degree of interdiffusion and discern what mechanistic pathways may cause precipitation reactions deleterious to alloy/coating performance.

INTRODUCTION

High temperature coatings provide a barrier from corrosive or highly oxidative environments that may degrade the substrate alloy. To provide optimum performance coatings need to have good adherence to the substrate, ductility to resist thermal cycling, avoid defects that may provide easy pathways to deleterious gases, and maintain corrosion resistance over the design life of the high temperature component.

Aluminide coatings on transition metals and alloys such as iron, nickel and cobalt are β-FeAl, β-NiAl, and β-CoAl, respectively. Diffusion aluminide coatings are typically processed via pack

cementation, slurry-diffusion or chemical vapor deposition.[1] Subsequent heat treatments help develop the proper mechanical properties and trigger further diffusion within the coating. The principal protective oxide generated by the high-temperature oxidation of these aluminide intermetallics is Al_2O_3 which causes subsequent improved oxidation and corrosion resistance of aluminide coatings, although less protective oxides can form if other alloying elements are present in the substrate, either in solution or as precipitated phases.[2]

Two diffusional growth mechanisms are: (a) low activity aluminide and (b) high activity aluminide that characterize the pack aluminizing process on nickel-base superalloys depending on the relative aluminum activity.[3]

Low activity coatings grow predominately by outward diffusion of nickel from the substrate to form a two-zone structure. The outer zone is a single-phase β-NiAl layer saturated with other substrate alloying elements such as chromium, cobalt, titanium, and molybdenum that diffuse outwardly with the nickel from the substrate.[3] The content of any foreign element in the outer zone is limited by its solubility in NiAl. β-NiAl stoichiometry varies with aluminum content decreasing from the outer surface towards the inner coating zone. The inner zone is β-NiAl containing a variety of second phases such as carbides and σ phase.[3] The effects of nickel outward diffusion can lead to the enrichment of elements such as chromium, cobalt, and molybdenum, in certain cases, in the substrate underlying the coating proper.[3]

High activity coatings grow by inward diffusion of aluminum resulting in the formation of a Ni_2Al_3 layer. A single diffusion layer typifies this coating type, prior to heat treatment. Since the coating is formed by predominantly inward aluminum diffusion, the substrate structure is reproduced in the coating, with all alloy elements being diluted in proportion to the amount of aluminum introduced. High activity coatings subjected to heat treatment convert the initial Ni_2Al_3 layer into more ductile and oxidation resistant β-NiAl. During this transformation aluminum diffuses from the

Ni_2Al_3 to meet and react with the nickel diffusing from the substrate to form a 3-zone coating structure. This gives rise to an outer zone after heat treatment that consists of a β-NiAl matrix saturated with foreign elements and containing numerous precipitates due to their lower solubility in the β-NiAl phase, a single-phase β-NiAl in the middle zone along with varying amounts of substrate alloying elements,[3] and an inner zone with β-NiAl with a variety of dispersed phases created by outward diffusion of the nickel from the substrate similar to the diffusion zone in a low activity coating.

Modified aluminide coatings designate aluminide coating classes that are altered by the addition of a secondary element like chromium, platinum, a reactive element, or a combination of these elements.[1] These coatings are generated by either: (1) incorporating the secondary element into the coating by pack codeposition, or (2) deposition of the modifying element prior to an aluminization process by electroplating, electrophoresis sputtering, chemical vapor deposition, or pack cementation.[1]

Chromium-modified aluminide coatings result in a microstructure that contains layers of chromium and NiAl.[4] One commercial chrome-modified aluminide coating displayed a 3-zone structure after thermal treatment: an outer zone consisting of a fine dispersion of α-Cr in a hyper-stoichiometric β-NiAl matrix, a middle zone containing stoichiometric β-NiAl, and an inner zone with α-Cr in a hypo-stoichiometric β-NiAl.[5]

Platinum, a relatively inert metal, is added to improve the hot corrosion resistance of an aluminide coating. This effect is strongly influenced by processing procedures for the coatings.[6] Platinum has shown significant benefits on the oxidation resistance of both low activity and high activity PtAl coatings.[7] Platinum promotes the formation of thinner and purer Al_2O_3 scales during the early stages, lowers the rate of β-NiAl degradation, and delays the onset of scale spallation. Platinum-modified aluminide coatings develop a spectrum of two-zone and three zone structures of standard aluminides depending on processing and the heat treatments involved.[8] In PtAl systems, platinum diffusional

processes behave in a similar manner as does nickel in NiAl where stoichiometry plays a strong role.[8] Pt is relatively immobile in the Al-rich NiAl phase and highly mobile in the Ni-rich NiAl phase.

A chromium-silicon aluminide coating is formed by inward diffusion of the aluminum and silicon constituents generated during heat treatment from a molten metallic slurry on the surface of the substrate.[8] Aluminum diffuses to nickel and silicon diffuses to chromium to form a composite monolayered coating consisting of β-NiAl and chromium silicide ($CrSi_2$).[9] A multistage process, developed to redistribute these key elements and structures, generates a multilayered coating that is more resistant to cracking and more stable at higher temperatures.[10] The silicon content is limited on the outer surface of the coating and layers of fine chromium silicides are distributed throughout the β-NiAl in discrete bands.[10]

Some additional details of chromium-modified platinum aluminide, palladium-modified aluminide, yttrium-modified aluminide, hafnium-modified aluminide, and other reactive element-modified aluminide coatings are discussed elsewhere.[1]

Hot corrosion is a complex process involving both sulfidation and oxidation.[11] Hot corrosion is a form of accelerated oxidation which affects alloys and coatings exposed to high-temperature gases contaminated with sulfur and alkali metal salts.[12] These contaminants combine in the gas phase to form alkali metal sulfates; if the temperature of the alloy or coating surface is below the dew point of the alkali sulfate vapors and above the sulfate melting points, molten sulfate deposits are formed.[12] Molten sodium sulfate is the principal agent in causing hot corrosion.[13,14]

Chloride salts can act as a fluxing agent and dissolve protective oxide films. Air in a marine environment ingested into the combustion zone of any marine gas turbine engine will be laden with chlorides unless properly filtered. NaCl has been viewed as an aggressive constituent in the hot corrosion of gas turbine components in the marine environment.[15-17] Attack by halogens at elevated temperatures occurs due to reaction product volatility.

Two forms of hot corrosion exist. Type I, high temperature hot corrosion (HTHC) occurs through basic fluxing and subsequent dissolution of the normally protective oxide scales by the molten sulfate deposits at metal temperatures ranging from 850 to 950 °C (1562-1742 °F). Type I hot corrosion generally involves broad attack caused by internal sulfidation above 800 °C; alloy depletion is generally associated with the corrosion front.

Type II, low temperature hot corrosion (LTHC) occurs from 650 to 750°C (1202-1382 °F) where pSO_3 is relatively high or melts are deficient in the oxide ion concentration leading to acidic fluxing that results in pitting attack where the sulfides are found in the pitted area.[12]

EXPERIMENTAL

Table 1 shows that Coating A, a slurry coating of chromium, silicon-modified β-NiAl, was applied on two different alloy substrates that represent materials used in a marine gas turbine engine. Coating A was applied onto each alloy substrate as per specified, proprietary specifications of the engine manufacturer using a slurry process where a metal-filled coating is deposited and the coated part is heated in a protective atmosphere so that aluminum and silicon can form intermetallics with the substrate.[9] In the coating the aluminum reacts with nickel to form β-NiAl and silicon reacts with chromium to form $CrSi_2$.[9]

The chemical composition of the alloy substrates that were coated for low-velocity, atmospheric-pressure (LVBR) testing are listed in Table 2. Both Alloy C10 and 738 are nickel-base, which are designed for high-temperature strength and generally provide some high-temperature oxidation and corrosion resistance. Iron is minimized in these alloys to lessen corrosion and the development of undesirable iron-derived crystallographic transformations. Aluminum, rhenium, tungsten, and other elements are added to improve the passive film of the alloys at high temperatures.

LVBR exposures were utilized to test the hot corrosion resistance of typical hot-section gas turbine materials. Details of burner-rig operation have been presented earlier.[18,19] The burner-rig test was run at 1650 °F (899 °C) for 1000 hours since that is typically the temperature where Type I, HTHC is often maximized. The fuel, NATO F-76, was doped with di-tertiary butyl disulfide to increase the sulfur concentration to one percent by weight, the maximum sulfur level specified in diesel fuel for shipboard use. Sea salt (10 ppm) was injected into the fuel combustion zone during the LVBR test to simulate the salt ingestion that occurs in marine environments and induce high-temperature reactions that occur in the hot section of marine gas turbine engines. Air/fuel ratios during these LVBR tests were 30:1.

A rotating carousel with individually isolated pins enhanced equal high temperature exposure of all test specimens. This fixture generally was removed from the burner-rig once every 24 hours and was allowed to cool to room temperature in ambient air for about one hour. This simulated the thermal cycling that is experienced from the off-and-on nature of shipboard gas turbine operation. Stresses in the oxide scales induced by thermal cycling increase the spallation of surface oxides thereby increasing the propensity towards high-temperature corrosion of the alloy. There were 38 thermal cycles during the 1000-hour LVBR test.

After the LVBR test, the hot corrosion attack on each section was measured by metallographic examination at 200X magnification every 20 degrees around the specimen circumference. The readings at each site around the circumference consisted of the outer diameter of the remaining coating material, if present, and the inner reading marking the maximum corrosion penetration at that specific 20-degree interval site. The following measurements are reported:

1. Average Coating Loss on a Radius. Loss in coating thickness due to all forms of oxidation and sulfidation. An average of 54 measurements (18 per cross section: top, middle, and bottom) were made per pin. Sites that either displayed no remaining coating and/or

displayed corrosion into the alloy substrate were recorded as having 0.00 mil (0.00 μm) remaining coating.

2. Maximum Coating Penetration on a Radius. This is a measurement of the deepest attack found on any of the three cross-sections. This number yields a measurement of maximum depth of coating or, if the coating is absent, substrate attack. Maximum penetration numbers are typically used to rank coatings performance in LVBR tests under the assumption that once the coating has been completely penetrated, it no longer provides the substrate the corrosion/oxidation protection that was intended. Although the average coating loss may be considerably less than the maximum penetration, the greatest degree of attack is determined to be the most critical measurement.

Some samples were further examined using a JEOL 6400V scanning electron microscope. Energy dispersive spectroscopy (EDS) was utilized to provide standardless semi-quantitative elemental analysis of alloy and coating constituents and to provide X-ray mapping to display the elemental distribution of these constituents.

RESULTS AND DISCUSSION

Untested examples of Alloy C10/Coating A and Alloy 738/Coating A are shown in Figures 1a and 1b, respectively. Coating A on both alloys shows a 3-layered coating structure.

Results of the corrosion measurements after LVBR 1000-hr. exposures are given in Table 3. The mean value for the remaining Coating A on Alloy C10 was 0.91 mils (23.0 μm). The degree of the Coating A that remained on Alloy C10 pins was highly variable, ranging from 0.05 to 2.00 mils (1.3 to 50.8 μm). The average loss of Coating A on Alloy C10 pins was 4.48 mils (113.7 μm) or 83 % of the original Coating A thickness. Full penetration of Coating A into the Alloy C10 alloy substrate

occurred at numerous locations, particularly at the top pin elevation, either through coating spallation or enhanced hot corrosion.

Alloy 738/Coating A showed a mean value of 1.38 mils (35.0 μm) remaining coating thickness on a radius. This translates to an average coating loss on a radius of 2.70 mils (68.5 μm) or about 66% of the original Coating A thickness after the LVBR exposure at 1650 °F (899 °C) exposure for 1000 hours burning NATO F-76. Coating A was fully penetrated at a minimum of one site for each Alloy 738/Coating A test pin.

Hot corrosion severely attacked Coating A on both Alloys C10 and 738 during the 1000-hr LVBR test at 1650 °F (899 °C). Figure 2a shows that hot corrosion/sulfidation of Coating A on Alloy C10 leads to delamination or spalling that proceeds along the coating and along the coating/substrate interface. A magnified view (Figure 2b) displays the banded sulfidation attack between the different phases in the coating structure. The presence of sulfur at these interfacial regions was confirmed by X-ray energy dispersive spectroscopy. Complete penetration and loss of Coating A led to severe attack of and penetration into the Alloy C10 substrate.

The hot corrosion behavior of the Alloy 738/Coating A after the 1000-hr, LVBR exposure at 1650 °F (899 °C) burning the NATO F-76 was vastly different than the Alloy C10/Coating A results. First, sulfidation that occurred on Coating A on Alloy 738/Coating A test pins (Figure 3) led to pit-like attack in the coating which sometimes completely penetrated through Coating A. Secondly, though Coating A on Alloy 738 generally experienced severe attack, there were some areas along the coated pin specimens that displayed relatively minor hot corrosion. Finally, the hot corrosion/sulfidation on Alloy 738/Coating A, unlike the observations of Alloy C10/Coating test pins, did not lead to delamination or spalling of the coating from the alloy substrate.

Coated test pins LVBR-exposed for 1000 hours at 1650 °F (899 °C) showed that Coating A on both alloys experienced severe coating losses due to HTHC and sulfidation as shown in Figure 2 and

3.[20] Coating A suffered severe corrosion in this hot corrosion environment as $CrSi_2$ was converted to CrS precipitates while silicon and titanium oxides were formed.[5]

The aluminide coating losses were affected by the substrate alloy chemistry.[20] In addition to hot corrosion caused by fluxing reactions, the high temperature environment may cause interdiffusion reactions among constituents in the coating and/or between the coating and substrate chemical components that may lead to precipitation along the coating/substrate interface. Coating A has an average chromium content of 15 wt.%; because of the intentional coating structure the chromium is unevenly distributed in Coating A and is concentrated at the $CrSi_2$ precipitates. While Alloy 738 has a chromium content of 16 wt.%, Alloy C10 has a chemistry containing only 2 wt.% Cr.

Chromium is an element added to alloys,[21,22] and coatings to improve the hot corrosion resistance of these materials. However, the difference in chromium content of Coating A and Alloy C10 may induce Cr interdiffusion between these materials leaving an alloy surface enriched in Cr and a coating depleted in Cr. This interdiffusion reaction may be quite rapid as suggested by an apparent diffusion front shown in Figure 4.

X-ray analysis was conducted at various sites of an Alloy C10/Coating A specimen after 1000 hours LVBR exposure at 1650 °F (899 °C). The results of the X-ray standardless analysis are listed in Table 4. The refractory (Ta, W, Re) elemental concentrations in the bulk Alloy C10 were somewhat higher than the nominal Alloy C10 chemistry listed earlier in Table 2. Both sulfur and silicon were detected in the bulk alloy, although neither element should be present. The sulfur may be detected due to the presence of molybdenum which is present in Alloy C10 and whose L_α peak is very near to the sulfur K_α peak. Aluminum detected in the alloy is about half of its proper concentration.

Standardless EDS analysis should be viewed only as a semiquantitative analysis method. Tantalum and silicon appears to be enriched by about 50% along an alloy void site near the

coating/alloy interface as compared to the bulk Alloy C10 chemistry. Aluminum, tungsten, rhenium were also slightly enriched.

The aluminum content in Coating A was higher than detected in Alloy C10. Though not reportedly constituents of Coating A,[9] Re, W, and Ta were detected ahead of the apparent corrosion as viewed in Figure 4. Behind the corrosion front W and Ta were still detected, but Re was not. Compared to their content ahead of the front, the amount of silicon decreased while the chromium concentration increased in the coating suffering attack. The greatest change detected in Coating A was the change in sulfur concentration behind the corrosion front where Coating A suffered sulfidation. The sulfur increased by 19 times in the attacked region behind the front as compared to the coating A region ahead of the front. Such HTHC/sulfidation attack caused swelling of the coating thickness.

X-ray mapping of selected elements around the corrosion front in Coating A are shown in Figure 5. Cr shows some apparent concentration decrease behind the corrosion front as compared to ahead of the lateral corrosion front in Coating A. The sulfur X-ray map shows a definite change in concentration between the two coating regions; the sulfur content steeply increased in the sulfidized area behind the corrosion front Further, more detailed analysis is needed to better define the diffusion and corrosion processes and their underlying causes.

A fundamental importance of surfaces, interfaces, grain boundaries, coating structures and associated structural defects, enrichment-segregation phenomena, and transport properties are essential towards understanding corrosion degradation mechanisms.[23] Phase transformations and surface reactions of the coating during hot corrosion are basically the same as those that take place during oxidation, except that the overall rates during hot corrosion are faster.[24]

Degradation of aluminide coatings may be initiated by basic fluxing of Al_2O_3 and propagated, eventually, by both basic fluxing and sulfide oxidation leading to HTHC.[2] If molybdenum or tungsten is present in the coating derived from their presence in the substrate, acidic fluxing of the protective

oxides can occur.[2] While functioning at high temperatures, Al_2O_3 is formed on the surface of aluminide coatings while just below this oxide, aluminum is depleted in the coating, leading to destabilization of β-NiAl and transformation to Ni_3Al. Cracking of aluminide coatings may also occur by creep if the service temperatures are below the ductile-to-brittle transition temperature.[25]

Sulfur can be transported through the Al_2O_3 and Cr_2O_3 protective scales under certain conditions resulting in discrete sulfide precipitates at the scale/alloy interface.[26] Sulfide concentrations above about 10-20 ppm have been shown to modify the adhesion strength and cyclic oxidation resistance of the protective oxide scales. Numerous corrosion processes are controlled along grain boundaries and other easy diffusion pathways.[23] Sulfur was detected on the outer coating surface and was viewed behind the lateral-moving corrosion front. The lateral movement may have been caused by a crack or break in Coating A.

Coatings and superalloy substrates generally have widely diverse compositions due to the functional requirements of balancing mechanical properties and corrosion resistance. As observed for the samples exposed to a hot corrosion environment during our LVBR tests, chemical potential gradients between the coating and superalloy substrate may cause interdiffusion phenomena to occur. Interdiffusion between the coating and the substrate,[27] can modify the oxidation and corrosion resistance of the coating and the mechanical properties of the coating-substrate system. Interdiffusion slowly changes the chemical composition and subsequently, may alter the microstructure of the coating and/or the substrate. The presence of sulfide species in the coating may also lead to diffusion via grain boundaries or other relatively easy diffusion pathways into the substrate and/or the coating. This may alter the long-term performance of a coating/alloy system in a hot corrosion environment in way that would not occur in an oxidation environment. Furthermore, sulfidation may decrease the free chromium content (or as $CrSi_2$) in Coating A, rendering the coating more prone to further hot corrosion.

Interdiffusion is a complex process that requires use of multivariable diffusion couples in a phase field approach,[28] or knowledge of diffusion pathways in multicomponent phase diagrams,[29] to model the process and provide an understanding of the contributions to interdiffusion. These methods are based on Onsager's formalism of Fick's law, which includes diffusion interactions among the components.[30]

Precipitates at or near the coating/substrate interface may act as a diffusion barrier, thereby suppressing interdiffusion. Precipitates may also induce spallation if there is a change in the molar volume fraction relative to the alloy or to the coating matrix. Small changes in chemical composition of a susceptible alloy may lead to phase transformations due to instabilities that develop.

Refractory metals such as W, Mo, and Ta, and chromium show a higher resistance to degradation by interdiffusion.[31] The addition of reactive elements may act as reservoirs to slow sulfur diffusion along grain boundaries and mitigate sulfur segregation at the coating/substrate interface.

CONCLUSIONS

High temperatures coatings such as aluminide coatings are used to protect alloy substrates in corrosive environments. The oxidation and corrosion resistance of aluminide coatings can be improved by proper selection of secondary elements additions, by proper coating design, and by use of proper coating processes.

Degradation of aluminide coatings in hot corrosion environments can occur through acidic or basic fluxing with sulfur-containing species. In our testing, Coating A suffered extensive, high temperature hot corrosion and sulfidation. Coating A on Alloy C10 delaminated or spalled from the alloy substrate after Type I hot corrosion attacked the coating. Coating A on Alloy 738 experienced pitting in the coating, but did not spall from the alloy substrate.

The resultant corrosion differences of the Coating A (silicon + chromium-modified aluminide) on the two test alloys may have been exacerbated by differences in the elemental chemistries between the coating and the substrate (and between coating zones) resulting in interdiffusion. The degree of interdiffusion between the coating and Alloy C10 substrate has not been determined at this time. Further, more detailed analysis is needed to better define the diffusion and corrosion processes and their underlying causes. Future work is planned to discern the contribution of stress, if any, to interdiffusion processes.

Selected elements may be added to coatings to act as barriers to interdiffusion or reservoirs to "getter" deleterious species.

REFERENCES

1. R. Streiff, in Elevated Temperature Coatings: Science and Technology II, N.B. Dahotre, J.M. Hampikian, Eds., The Minerals, Metals, and Materials Society, Warrendale PA, 407 (1996).

2. G.W. Goward, "Protective Coatings for High Temperature Alloys: State of Technology" in Proceedings of the Symposium on 'Properties of High Temperature Alloys', Z.A. Foroulis, F.S. Pettit, eds, PV 77-1, The Electrochemical Society, Pennington, NJ, 806 (1976).

3. G.W. Goward, D.H. Boone, *Oxidation of Metals*, v. 3 (5), 475 (1971).

4. G. Marijnissen, in High-Temperature Protective Coatings, M. Khobaib, R.C. Krutenat, Eds., The Metallurgical Society, Warrendale PA, 27 (1984).

5. G. McAdam, S.G. Russo, Proceedings of the 13th International Corrosion Congress, paper 314, Australasian Corrosion Association, Clayton Vic, Australia (1996).

6. R. Streiff, D.H. Boone, L.J. Purvis, in Surface Engineering, NATO ASI Series, Kossowski, Singhal, Eds., Martinus Nijhoff Publishers, Dordrecht, 469 (1984).

7. Y. Niu, W.T. Wu, D.H. Boone, J.S. Smith, J.Q. Zhang, C.L. Zhen, in High Temperature Corrosion III, R. Streiff, J. Stringer, R.C. Krutenat, M. Caillet, Eds., (Editions de Physique, Paris), 511 (1993); and *Journal de Physique IV*, v. 3, 511 (1993).
8. R. Streiff, O. Cerelier, D.H. Boone, *Surface and Coatings Technology*, v. 32, 111 (1987).

9. B.G McMordie, A.K. Isaacs, "Slurry Aluminide Coating Processes for Gas Turbine Components at Overhaul", presented at The Annual Gas Turbine Conference and Exhibition, The Institution of Diesel and Gas Turbine Engineers, at Harrogate, UK, November 1, 1991).

10. D. Barry, M.C Meelu, B.G. McMordie, T.A. Kircher, 95-GT-359, International Gas Turbine & Aeroengine Congress, American Society of Mechanical Engineers, New York (1997).

11. A.U. Seybolt, P.A. Bergman, M. Kaufman, "Hot Corrosion Mechanism Study, Phase II", Final Report under contract No. N600 (61533) 65595, MEL 2591, Assignment 87-122, prepared for NSRDC, Annapolis, MD (30 June 1966 to 31 October 1967).

12. S.R. J. Saunders, in Guidelines for Methods of Testing and Research in High Temperature Corrosion: Working Party Report, H.J. Grabke, D.B. Meadowcroft, Eds., European Federation of Corrosion, Number 14, The Institute of Materials, London, 85 (1995).

13. E.L. Simons, G.V. Browning, H.A. Liebhafsky, *Corrosion*, v.11 (12), 505t (1955).

14. R.K. Ahluwalia, K.H. Im, *Journal of the Institute of Energy*, v. 64, no. 461, 186 (1991).

15. R.L. Jones, Naval Research Laboratory Report 6170-859 (1975).

16. J.F. Conde′, B.A. Wareham, Proceedings: Gas Turbine Materials in the Marine Environment Conference, MCIC-75-27, 73 (1974).

17. D.A. Shores, D.W. McKee, H.S. Spacil, Proceedings: Properties of High Temperature Alloys with Emphasis on Environmental Effects, PV 77-1, Z.A. Foroulis, F.S. Pettit, eds., The Electrochemical Society, Pennington, NJ, 649 (1976).

18. H. von E. Doering, P.A. Bergman, *Materials Research and Standards*, v. 9 (9), 35 (1969).

19. G.C. Booth, R. L. Clarke, *Materials Science and Technology*, v. 2, 272 (1986).

20. D.A. Shifler, **CORROSION/2001**, paper 167, Houston, TX (2001).

21. R.T. Grant, "High Chromium, High Nickel Alloys for High Temperature Corrosion Resistance", presented at the Elevated Temperature Symposium, paper 66052, NACE International (1966)

22. G.L. Swales, Australian Corrosion Engineering, v. 7, 33 (1963).

23. P. Kofstad, *Materials Science and Engineering*, A120, 25 (1989).

24. N.R. Lindblad, *Oxidation of Metals*, v. 1, 143 (1969).

25. S.M. Saad, J.R. Nicholls, P. Hancock, in High Temperature Corrosion, NACE-6, R.A. Rapp, ed., NACE International, Houston, TX, 568 (1983).

26. I.G. Wright, "High Temperature Corrosion", in Corrosion, vol.13, Metals Handbook, 9th Ed., ASM International, Materials Park, OH, 99-100 (1987).

27. A. Sanz, L. Llanes, J.P. Bernadou, M. Anglada, M.B. Rapaccini, in Elevated Temperature Coatings: Science and Technology II, N.B. Dahotre, J.M. Haampikian, Eds., The Minerals, Metals, and Materials Society, Warrendale, PA, 373 (1996).

28. E. Basuki, A. Crosky, B. Gleeson, *Materials Science and Engineering*, A224, 27 (1997).

29. K. Wu, Y. Wang, J.E. Morral, in Elevated Temperature Coatings: Science and Technology IV, N.B. Dahotre, J.M. Hampikian, J.E. Morral, Eds., The Minerals, Metals, and Materials Society, Warrendale PA, 133 (2001).

30. L. Onsager, *Physical Review*, v. 37, 405 (1931); *Physical Review,* v. 38, 2265 (1932).

31. M. Göbel, A. Rahmel, M. Schütze, M. Schorr, W.T. Wu, *Materials at High Temperatures*, v. 12 (4), 301 (1994).

TABLES

TABLE 1.
Test Matrix for Low-Velocity, Atmospheric Pressure Burner-Rig Test of a Marine Gas Turbine Engine Materials

ENGINE LOCATION	ALLOY	COATING	TEST TEMPERATURE
Intermediate Pressure Blade	Alloy C10	Coating A (Cr_2Si_2 + NiAl)	1650 °F (899 °C)
High Pressure Blade	Alloy 738	Coating A (Cr_2Si_2 + NiAl)	1650 °F (899 °C)

TABLE 2.

Chemical Composition of Alloy Substrates used in Low-Velocity, Atmospheric Pressure Burner-Rig Testing (Wt. Percent)

Elements (wt. %)	**Alloy C10 (nominal)**	**Alloy 738**
C		0.106
S		0.0008
P		< 0.005
Si		0.05
Mn		< 0.01
Cr	2	15.94
Mo	0.4	1.66
Fe		0.06
Ti	0.2	3.34
Al	5.7	3.35
Co	3	8.43
Ni	Bal. (~69.5)	Bal. (~61.5)
W	5	2.50
Nb	0.1	0.90
Ta	8	1.76
Re	6	0.02
Zr		---
Hf	0.03	< 0.02

TABLE 3.

Corrosion Measurements of Gas Turbine Materials LVBR Tested for 1000 hours at 1650 °F (899 °C) Using NATO F-76 Fuel.

Coating Designation	Pin I.D	Substrate Alloy	Calculated Original coating Thickness (mils)	Average Remaining Coating on a Radius (mils) (54 sites)	Average Coating Loss on a Radius (mils) (54 sites)	Maximum Coating Penetration on a Radius (mils)
Coating A	2	Alloy 738	4.16	1.29	2.87	into substrate
	5	Alloy 738	4.05	1.30	2.75	into substrate
	8	Alloy 738	3.79	1.18	2.61	into substrate
	12	Alloy 738	3.97	1.28	2.69	into substrate
	15	Alloy 738	4.40	1.84	2.56	into substrate
Coating A	4	Alloy C10	5.00	0.09	4.91	into substrate
	7	Alloy C10	5.47	0.50	4.97	into substrate
	11	Alloy C10	4.88	0.05	4.83	into substrate
	14	Alloy C10	5.80	1.89	3.91	into substrate
	17	Alloy C10	5.76	2.00	3.76	into substrate

TABLE 4.

Standardless Elemental Analysis of Specific Sites of Alloy C10 and Coating A (Wt. Percent)

Elements	Bulk Alloy C10	Alloy C10 @ voids below interface	Coating A ahead of front	Coating A behind front, coating attack
Al	2.72	3.97	9.52	6.98
Si	2.93	4.53	2.88	1.71
S	1.01	1.18	0.68	13.19
Cr	1.82	2.02	0.66	1.70
Co	2.83	2.85	2.75	2.99
Ni	64.50	52.70	72.09	66.39
Ta	9.48	13.36	3.90	2.67
W	7.45	9.50	4.76	4.38
Re	7.26	9.88	2.77	0.00

FIGURES

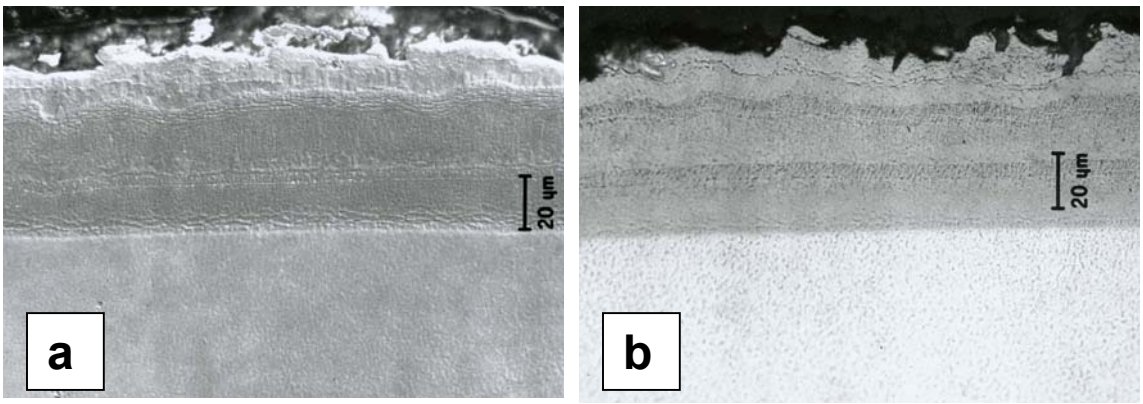

FIGURE 1. Alloy C10/Coating A (a) and Alloy 738/Coating A (b), untested. Both Photo (a) via differential interference contrast and optical Photo (b) display the 3-layered structure of the Coating A before LVBR exposure. 500X

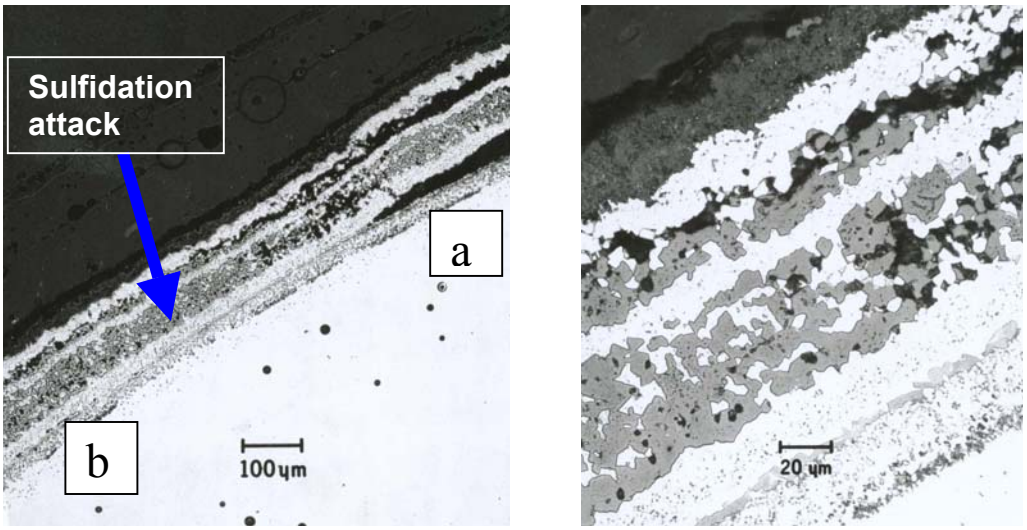

FIGURE 2. Alloy C10/Coating A specimen after 1000-hr exposure to NATO F-76 @ 1650 °F (899 °C). Delamination/spalling (a) is occurring at the coating zone interfaces after coating is attacked by hot corrosion/sulfidation (b).

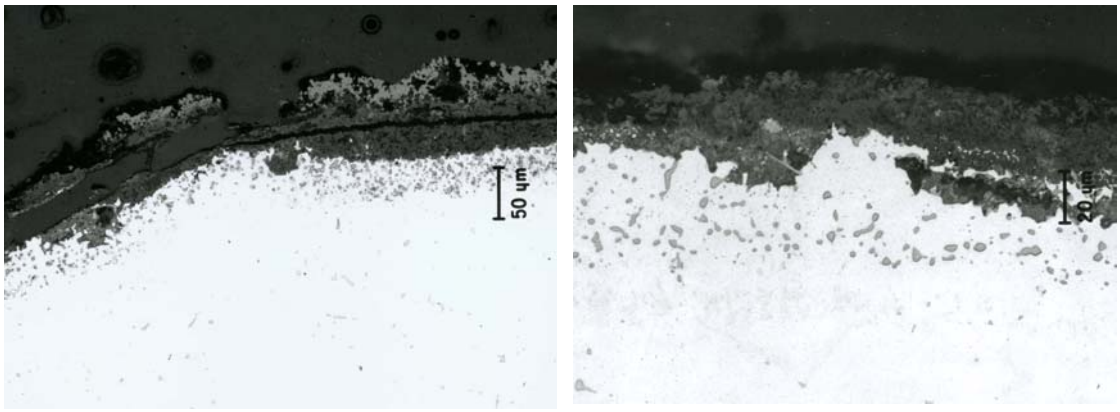

FIGURE 3. Alloy 738/Coating A specimens after 1000-hr exposure to NATO F-76 @ 1650 °F (899 °C). Coating is severely attacked by hot corrosion/sulfidation but shows no evidence of delamination.

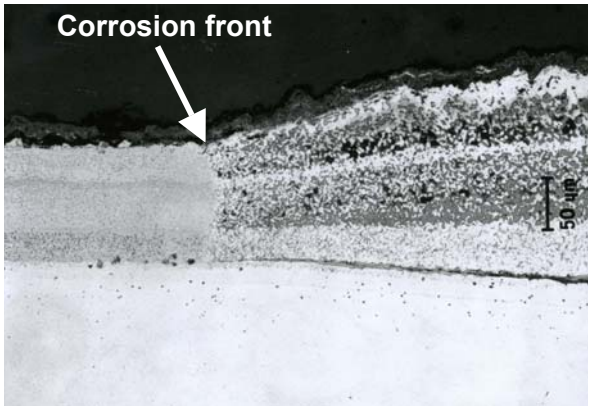

FIGURE 4. Alloy C10/Coating A specimen after 1000-hr exposure to undyed NATO F-76 @ 1650 °F (899 °C). Corrosion leads to swelling of coating thickness and precipitation at coating/substrate interface.

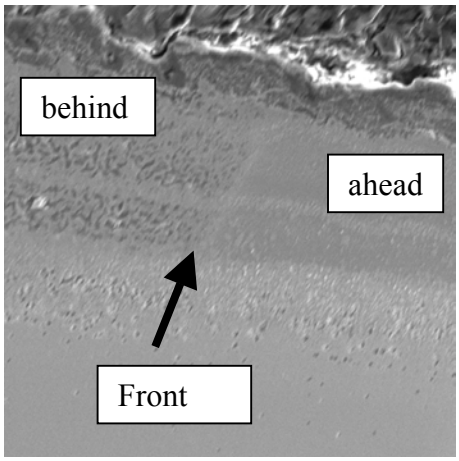

SEM , 600X

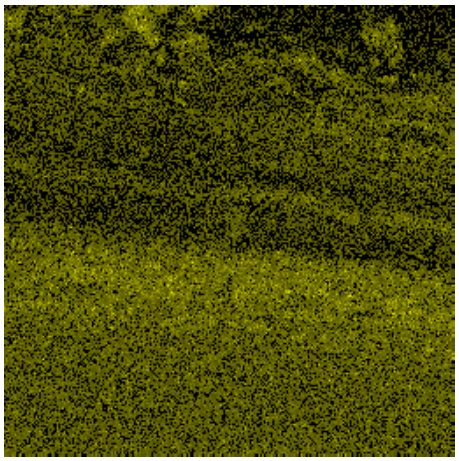

Silicon X-ray map

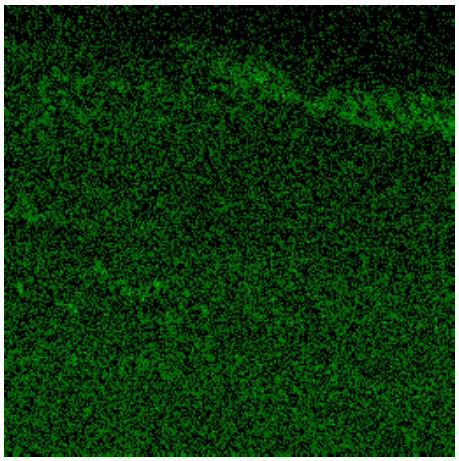

Aluminum X-ray map.

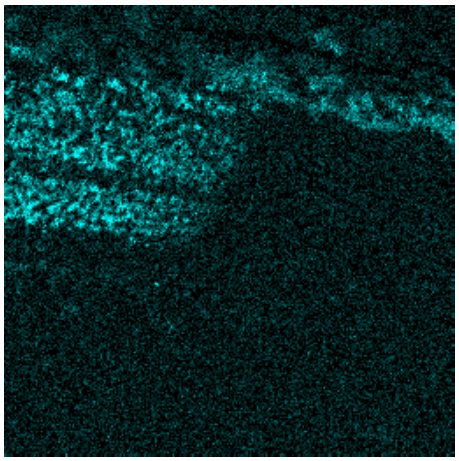

Sulfur X-ray map.

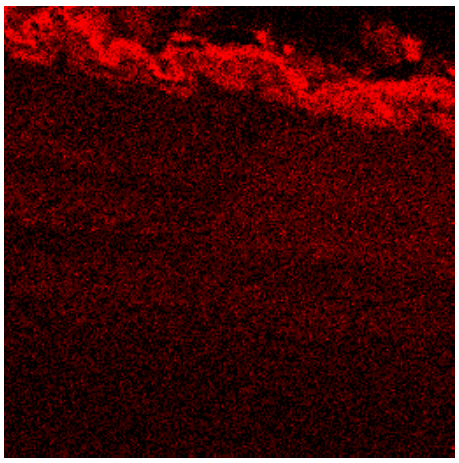

Chromium X-ray map.

FIGURE 5. SEM and elemental X-ray maps of selected elements analyzed ahead and behind the corrosion front found in an Alloy C10/Coating A pin sample, 600X.

THE EFFECT OF ARTIFICIAL HEAT TREATMENT ON THE CHROMATE CONVERSION PERFORMANCE OF AL-ZN-MG-CU ALLOYS

Y. Yoon, V. Laget and R. G. Buchheit

Fontana Corrosion Center
Department of Materials Science and Engineering
The Ohio State University
Columbus, OH 43210

ABSTRACT

Anecdotal reports in the literature suggest that formation and breakdown of chromate conversion coatings (CCC) on 7xxx alloys are strongly dependent on temper. To quantitatively characterize and ultimately understand this phenomenon, the corrosion behavior and CCC performance of heat-treated Al-Zn-Mg-Cu alloys was investigated in polarization, electrochemical impedance spectroscopy (EIS), X-ray absorption near edge spectroscopy (XANES), and scanning Kelvin probe force microscopy (SKPFM) experiments. Specimens were examined in W, T6, T7, and retrogression and re-aging (RRA) tempers. Anodic polarization curves of bare AA7475 measured under deaerated conditions showed that the pitting and repassivation potentials of T7 and RRA tempers were slightly more positive than those of T6 and W tempers. Cathodic polarization curves showed that CCC inhibited cathodic reaction on this alloy. The coating resistances of chromate conversion coated AA7475 in all of the tempers were determined by EIS after 24 hours of exposure to 0.5 M NaCl solution. The coating resistance of T7 temper was higher than that of T6 temper in 3-min CCC as well as 1-min CCC. The results indicate the chromate conversion performance of AA7475 is strongly dependent on alloy temper. In addition, T7 temper has a higher Cr(VI) than T6 temper in 3-min CCC from XANES. However, much more Cr(VI) is leached from a 3-min CCC during contact with an aqueous chloride solution. Scanning Kelvin probe force microscopy shows that the intermetallic compound (IMC) particles having Cu and Fe have a higher surface potential and are changed to lower surface potential than the matrix after CCC.

INTRODUCTION

Chromate conversion coatings (CCCs) are applied to 7xxx alloys for resistance to localized corrosion. Although CCCs provide excellent inhibition to aluminum alloys, the use of chromate has been under pressure for environmental regulations due to its toxic and carcinogenic nature. Extensive studies have been directed at characterizing CCCs, and at developing chromate-free coatings that are environmentally benign. The exact mechanism of corrosion inhibition by chromate is still unclear and there is no replacement that is equivalent with the performance of chromate.

In order to find promising replacements for CCCs, it is necessary to better understand CCCs formation and breakdown. It is well known that subtle changes in Al alloy microstructure due to heat treatment can influence the mechanical and corrosion properties Al-Zn-Mg-Cu alloys.[1] For instance, while T6 temper has higher tensile strength than T7 temper, the T7 temper has higher stress corrosion cracking (SCC) resistance. Industrial reports have indicated that corrosion protection by CCC is inferior on T7 temper than on T6 temper.[2] Why this change in CCC protection occurs is not clear. For this reason, we have begun to characterize the effect of 7xxx alloy temper on CCC formation and breakdown.

EXPERIMENTAL PROCEDURES

MATERIALS

The materials used in this study were commercial AA7475 and AA7075. The compositions were measured by inductively coupled plasma mass spectrometry (ICP-MS), and are shown in Table 1. For this study, specimens were heat-treated to the W temper (495 °C /1hr, followed by quenching in cold water), the T6 temper (W + 115 °C /24hr), the T7 temper (W +

99 °C /4~8hr + 160 °C /24~30hr), and a retrogression and re-aged temper, RRA (W + T6 + retrogression, 204 °C /1hr + re-aging, T6). The RRA temper was designed to increase the tensile strength and SCC resistance.[3] Figure 1 shows the microstructure of the plate form in which samples were prepared.

POTENTIODYNAMIC POLARIZATION MEASUREMENT

Anodic polarization curves were collected at a scan rate of 0.2 mV/sec in 0.5 M NaCl deaearted solution after immersion at open circuit potential (OCP) for 2 hours. The initial sweep of anodic polarization curve was initiated at 30 mV below corrosion potential. When the measured current reached an apex potential *i.e.* 0.5 $V_{SCE,}$ or apex current 10^{-3} A/cm^2, the sweep-direction was reversed and a cathodic sweep was conducted. The typical forward and reverse sweeps are shown on Figure 2. From these plots, three characteristic potentials were determined: corrosion potential (E_{corr}), pitting potential (E_{pit}), and repassivation potential (E_{rp}). The cathodic polarization curves were measured from bare AA7475 as well as from the chromate conversion coated samples in 0.5M NaCl aerated solution after immersion at open circuit potential for 24 hours.

The experiments were performed in a three-electrode cell. A saturated calomel electrode (SCE) and a platinum mesh were used as reference and auxiliary electrodes, respectively. The electrolyte was a 0.5 M NaCl solution which was deaerated by bubbling an argon through the solution for at least 1 hour before immersing the specimen. Each specimen was abraded with 2400 grit silicon carbide paper, rinsed in deionized water, degreased in acetone and then masked along its edges with black wax exposing surface area about 0.15-0.2 cm^2.

CHROMATE CONVERSION COATING PREPARATION

The chromate conversion coating process is given in Table 2.

ELECTROCHEMICAL IMPEDANCE SPECTROSCOPY (EIS).

EIS was conducted using a 10 mV sinusoidal voltage signal. Spectra were collected at the open circuit potential over a frequency range of 10 kHz to 10 mHz. Measurements were made on a 1cm^2 specimen area in contact with a 0.5 M NaCl solution open to air.

X-RAY ABSORPTION NEAR EDGE SPECTROSCOPY (XANES)

XANES is a powerful tool for the study of CCCs.[4,5] XANES was performed at the Brookhaven National Laboratory of the National Synchrotron Light Source on beam line X-19A. Spectra were obtained at the Cr K edge (E_0 = 5989 eV) on samples tilted at 45^o to the incident beam. XANES for Cr is distinguished by pre-edge peak for Cr(VI) at 5994 eV and an absorption edge for total Cr at 6250 eV which are shown in Figure 3. EIS data were collected for the sample exposed to solution for 7 days. The normalized edge height is a measure at total Cr content in the coating, and the ratio of the normalized pre-edge peak height to the absorption edge height is a relative measure of Cr(VI) content.

SCANNING KELVIN PROBE FORCE MICROSCOPY (SKPFM)

SKPFM is also a powerful tool for the study of the localized corrosion and the chromate inhibition of CCC.[6-9] SKPFM can measure the surface topography and the surface potential at the same surface. SKPFM was conducted by using Dimension 3000 series of Digital Instruments. During first scan, the surface topography could be measured by tapping mode and the second scan of the same trace could get the surface potential by lift mode. The tip was conductive Pt/Ir-coated silicon.

RESULTS AND DISCUSSION

Figure 4 summarizes the results from anodic polarization curves. The pitting potential (E_{pit}) was shifted slightly to noble potentials in the sequence of W, T6, RRA, and T7. This suggests that T7 temper has a higher resistance to localized corrosion than T6 temper. Repassivation potentials (E_{rp}) follow a similar trend to E_{pit}. Additionally, the anodic polarization behavior was independent of the orientation.

Figure 5 shows the cathodic polarization curves of bare AA7475 in the T6 and T7 tempers, and 1-min CCC on AA7475 in all tempers. Curves were collected in aerated 0.5 M NaCl after 24 hours immersion. Cathodic kinetics were observed to decrease in the following order:

T6-bare > T7-bare > T6-1min CCC >7-1min CCC

This trend indicates that cathodic reactions are inhibited by the presence of CCC.

A simple equivalent circuit model was used for EIS analysis is shown in Figure 6. The resistance (R_s) corresponds to the solution resistance. The coating resistance (R_{coat}) is the resistance related to the presence of the chromate conversion coated surface. The constant element phase (CPE) accounts for the capacitive response of the surface.

Figure 7 shows the coating resistances of AA7475 in 1-min and 3-min CCC as function of exposure time. The coating resistances of T7 tempers are always higher than those of T6 tempers for 7 days in 1-min CCC as well as in 3-min CCC. There is a large difference in coating resistance between T6 temper and T7 temper. This result, however, conflicts with reports suggesting that the performance of AA7075-T6 was much better than that of AA7075-T7 for salt spray corrosion resistance test (2). There are two possible factors leading to the conflict. The first

factor is the different experimental methods, which are salt spray test and EIS test. The second one is the difference in purity level between AA7075 and AA7475.

X-RAY ABSORPTION NEAR EDGE SPECTROSCOPY

Figure 8 (a) and (b) shows the normalized pre-edge peak at 5994 eV which is the representative Cr(VI) and the ratio between pre-edge peak and edge peak. The pre-edge height of T7 temper is much higher than that of T6 temper in 3-min CCC. During immersion in chloride solution, the 3-min CCC release much more Cr(VI) content than the 1-min CCC, which may be related to the CCC performance in Figure 9. For example, the release of Cr(VI) of T7 temper with 3-min CCC is 0.92 and those of W and RRA tempers are 0.93 and 0.95 respectively. The coating resistances increase in the sequence of W, T7 and RRA tempers. In 1-min CCC case, the release of Cr(VI) of T7 temper is 0.27 and that of RRA temper is 0.17. The coating resistance of T7 temper is higher than that of RRA temper. Figure 8 (b) shows that the ratio of pre-edge peak over edge peak in 1-min CCC and 3-min CCC is around 25~30 %, which is consistent with reports in literature.[4,5]

SCANNING KELVIN PROBE FORCE MICROSCOPY

Figure 11 shows the SKPFM image of IMCs (a) surface topography, (b) surface potential after polishing and (c) surface topography, (d) surface potential for a 30-sec CCC at room temperature, and (e) SEM image of the same region in SKPFM. The bare IMCs have 20~40 nm height and 200~400 mV increase in surface potential compared to the matrix. However, the relative height of IMCs is decreased up to 100 nm and the potentials of intermetallic particle sites are decreased about 10~20 mV compared to the matrix after 30 sec of conversion coating. Decreasing the surface potential difference between IMCs after CCC may be related to the

increased corrosion resistance. Figure 11 indicates that the shapes of IMC with CCC do not change during exposure to 0.5 M NaCl up to 2 days.

Initial formation of CCC at the IMCs of the aluminum alloys is important for the understanding of CCC inhibition. Figure 12 shows SKPFM images of CCC formed on IMCs in 7xxx alloys with T6 and T7 tempers by immersion for 5 sec at 5 °C. The IMC chemistry was examined by EDS. Most IMCs exhibiting a high surface potential contained Fe and Cu. After coating for 5 seconds, the IMCs of AA7075-T6 were still present, but the other IMCs were eteched and the potential differences were dramatically decreased.

CONCLUSIONS

The anodic polarization curves show that the pitting and repassivation potentials of T7 and RRA tempers are slightly more noble than those of T6 and W tempers. Cathodic polarization curves showed that the reduction kinetics are inhibited by chromate conversion coatings, and chromate coated T7 temper has higher cathodic inhibition than chromate coated T6 temper. The coating resistance of the alloy in the T7 temper is higher than those of T6 tempers in 1-min and 3-min CCC. The release of Cr(VI) in 3-min CCC is much higher than 1-min CCC. The IMCs except AA7075-T6 are depressed and surface potential difference between IMCs and matrix are reduced after conversion coating.

ACKNOWLEDGEMENT

This project is funded by the Strategic Environmental Research and Development Program under contract number DACA72-99-C-0002.

REFERENCES

1. S. Maitra and G. C. English, Metall. Trans. A, 12A (1981): p. 535.

2. L. J. Bailin, P. Fitzpatrick, and M. J. Joyce, "Evaluation of Unpainted Alodine chromate conversion coating for corrosion resistance and electrical conductivity" (Report LMSC-FO35575, Lockheed Missiles & Space Co., 1985).

3. B. Cina, U.S. Patent 3856584 (1974).

4. M. W. Kendig, A. J. Davenport and H. S. Isaacs, Corros. Sci., 34 (1993): p. 41.

5. C. S. Jeffcoate, H. S. Isaacs, A. J. Aldykiewics Jr, and M. P. Ryan, J. Electrochem. Sci., 147 (2000): p. 540.

6. P. Schmutz and G. S. Frankel, J. Electrochem Soc., 145 (1998): p. 2285.

7. P. Schmutz and G. S. Frankel, J. Electrochem Soc., 145 (1998): p. 2295.

8. P. Schmutz and G. S. Frankel, J. Electrochem Soc., 146 (1999): p. 4461

9. J. R. Waldrop and M. W. Kendig, J. Electrochem Soc., 145 (1998): p. L11.

TABLES AND FIGURES

TABLE 1.

The composition of 7xxx alloys. (wt %)

AA	Zn	Mg	Cu	Cr	Fe	Si	Mn	Ti
7475	5.64	2.27	1.35	0.22	0.05	0.021	0.001	0.044
7075	5.52	2.44	1.41	0.17	0.28	0.019	0.029	0.033

(Average of three separate samples by Perkin-Elmer Sciex ELAN 6000 ICP-MS)

TABLE 2.

Chromate conversion coating process for Al 7475 alloys.

Steps	**Process**
Cleaning & degreasing	32 g/L Na_2SiO_3 48 g/L Na_2CO_3 at 65 °C for 2 min Rinse
Deoxidizing	72 ml/L HNO_3 30 g/L Sanchem1000 at 55 °C for 3 min Rinse
Chromate conversion coating	7.55 g/L Alodine® 1200S Ajust pH to 1.5 ~ 1.7 by HNO_3 at room temp.for 1 and 3 min Rinse Drying for 24 hours

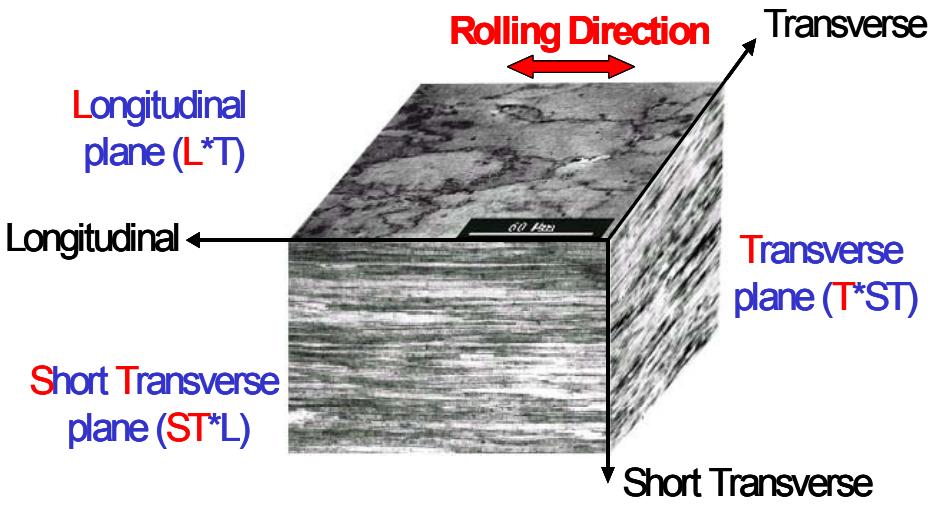

FIGURE 1. SEM image of AA7475-T7.

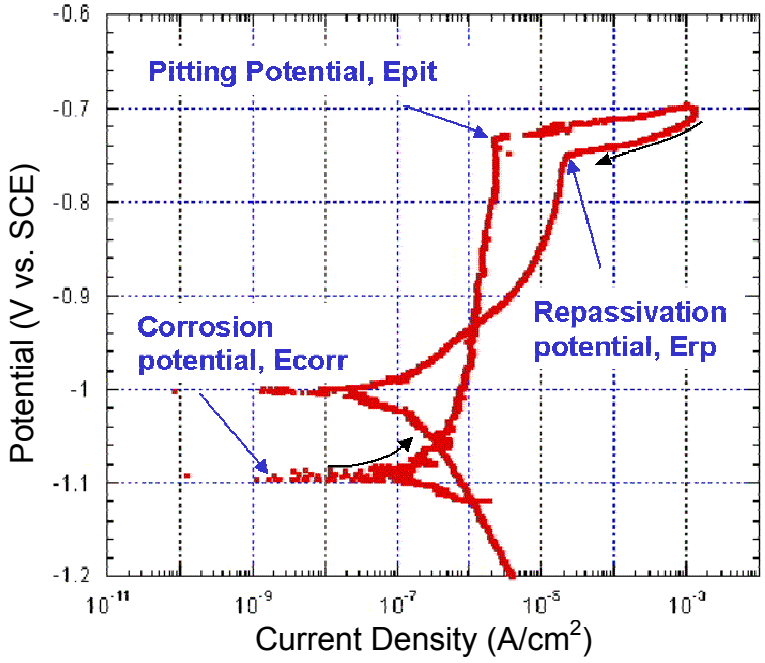

FIGURE 2. Anodic polarization curve of AA7475-T7 after 2hr open circuit potential in 0.5 M NaCl deaerated solution.

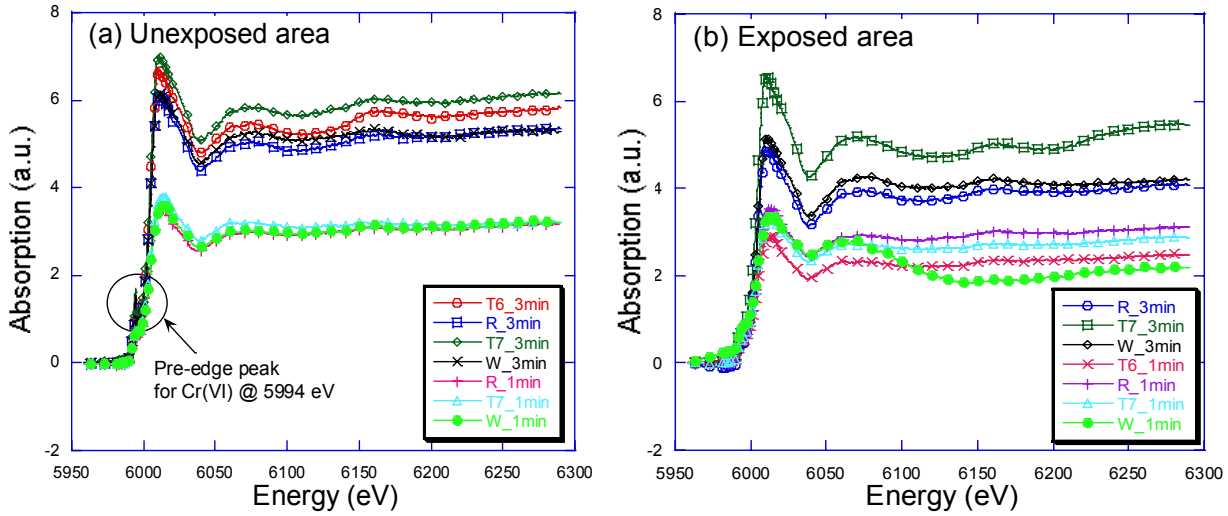

FIGURE 3. X-ray absorption near edge spectroscopy of AA7475 (a) unexposed area and (b) exposed area in 0.5 M NaCl for 7 days.

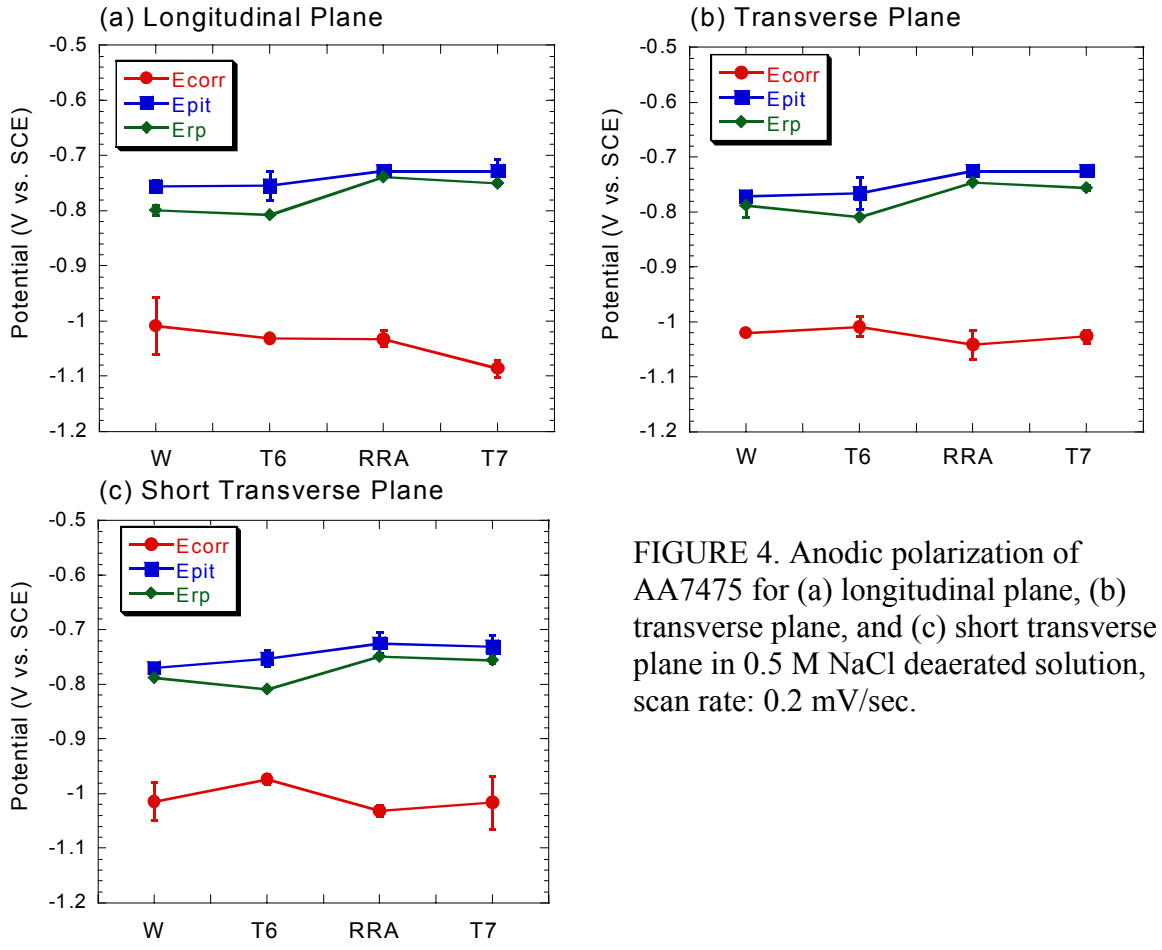

FIGURE 4. Anodic polarization of AA7475 for (a) longitudinal plane, (b) transverse plane, and (c) short transverse plane in 0.5 M NaCl deaerated solution, scan rate: 0.2 mV/sec.

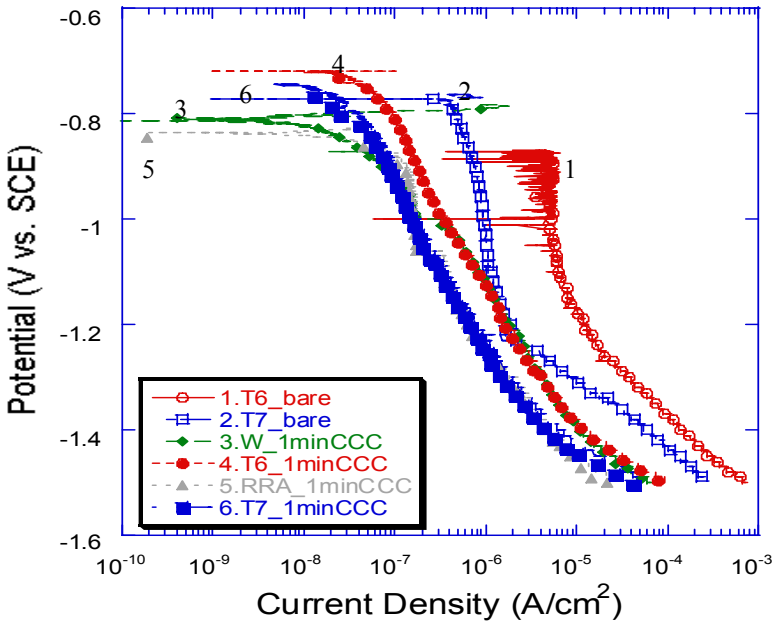

FIGURE 5. Cathodic polarization curves for uncoated and chromate conversion coated AA7475 in aerated 0.5 M NaCl after 24 hours immersion.

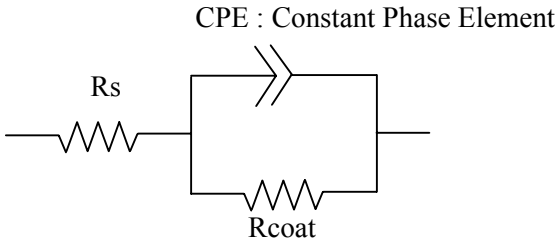

FIGURE 6. Equivalent circuit diagram for chromate conversion coating of 7xxx alloys.

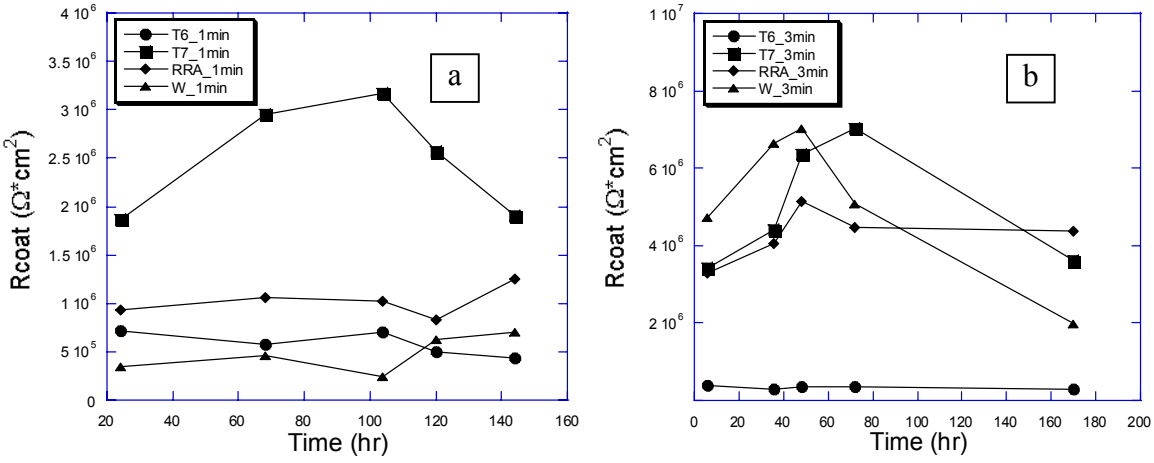

FIGURE 7. Coating resistance of AA7475 in 1-min and 3-min CCCs as function of exposure time to 0.5 M NaCl aerated solution.

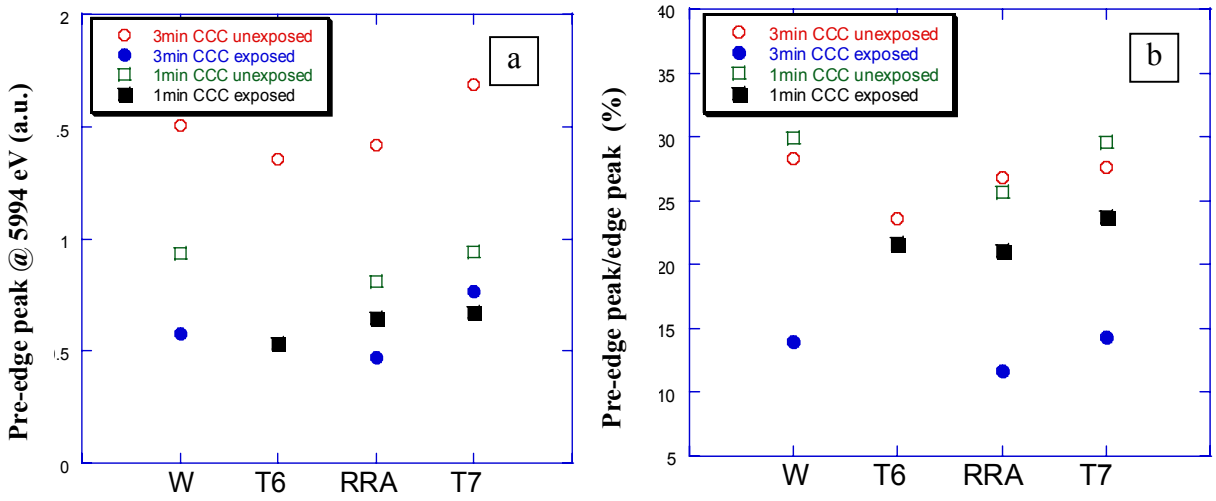

FIGURE 8. Pre-edge peak and ratio of pre-edge peak/edge peak in 1-min and 3-min CCCs in 0.5 M NaCl for 7 days.

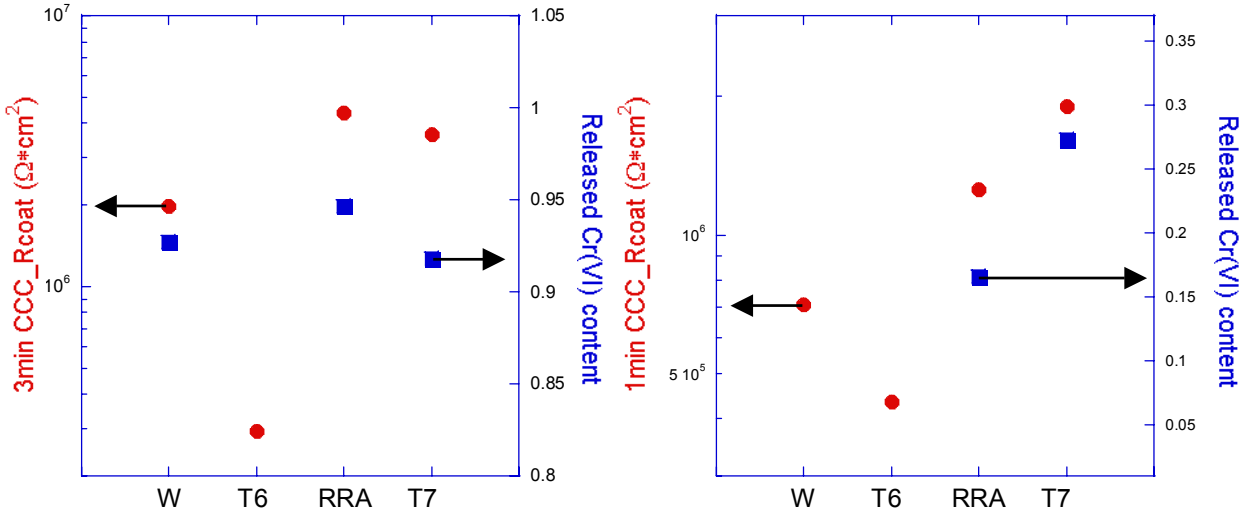

FIGURE 9. The comparison between coating resistance and released Cr(VI) in 1-min and 3-min CCCs in 0.5 M NaCl.

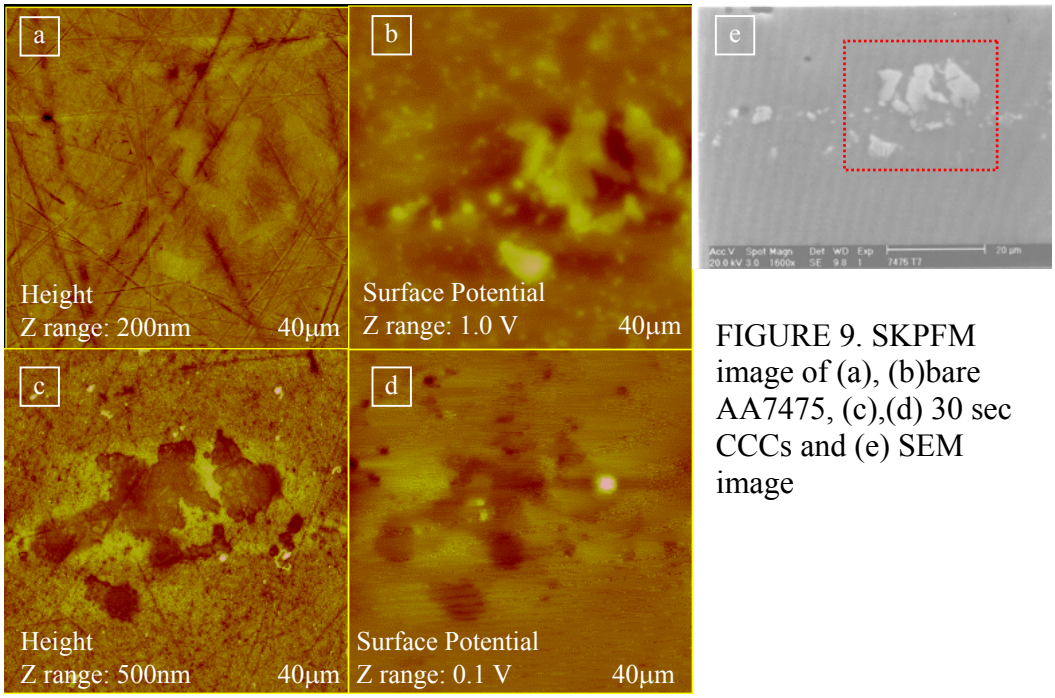

FIGURE 9. SKPFM image of (a), (b)bare AA7475, (c),(d) 30 sec CCCs and (e) SEM image

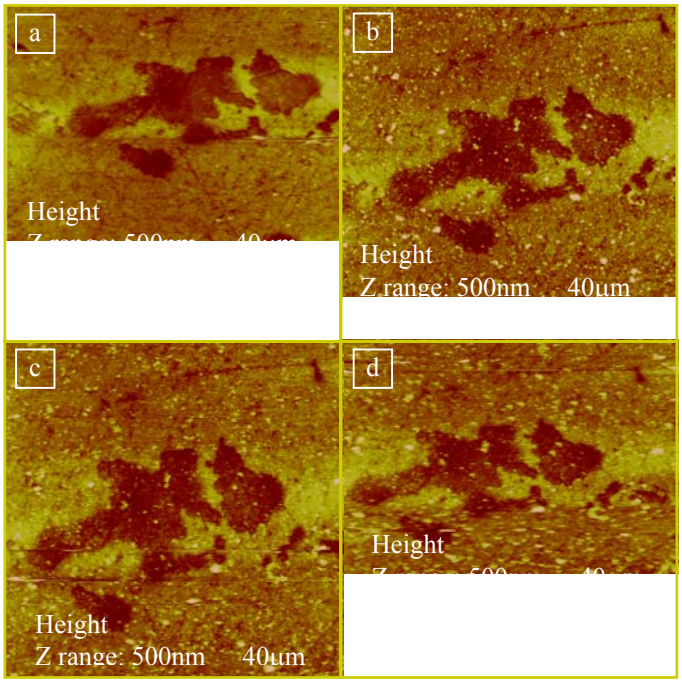

FIGURE 10. SKPFM surface morphology during exposure to 0.5 M NaCl solution for (a) 2min, (b) 8hr, (c) 24hr, and (d) 2 days.

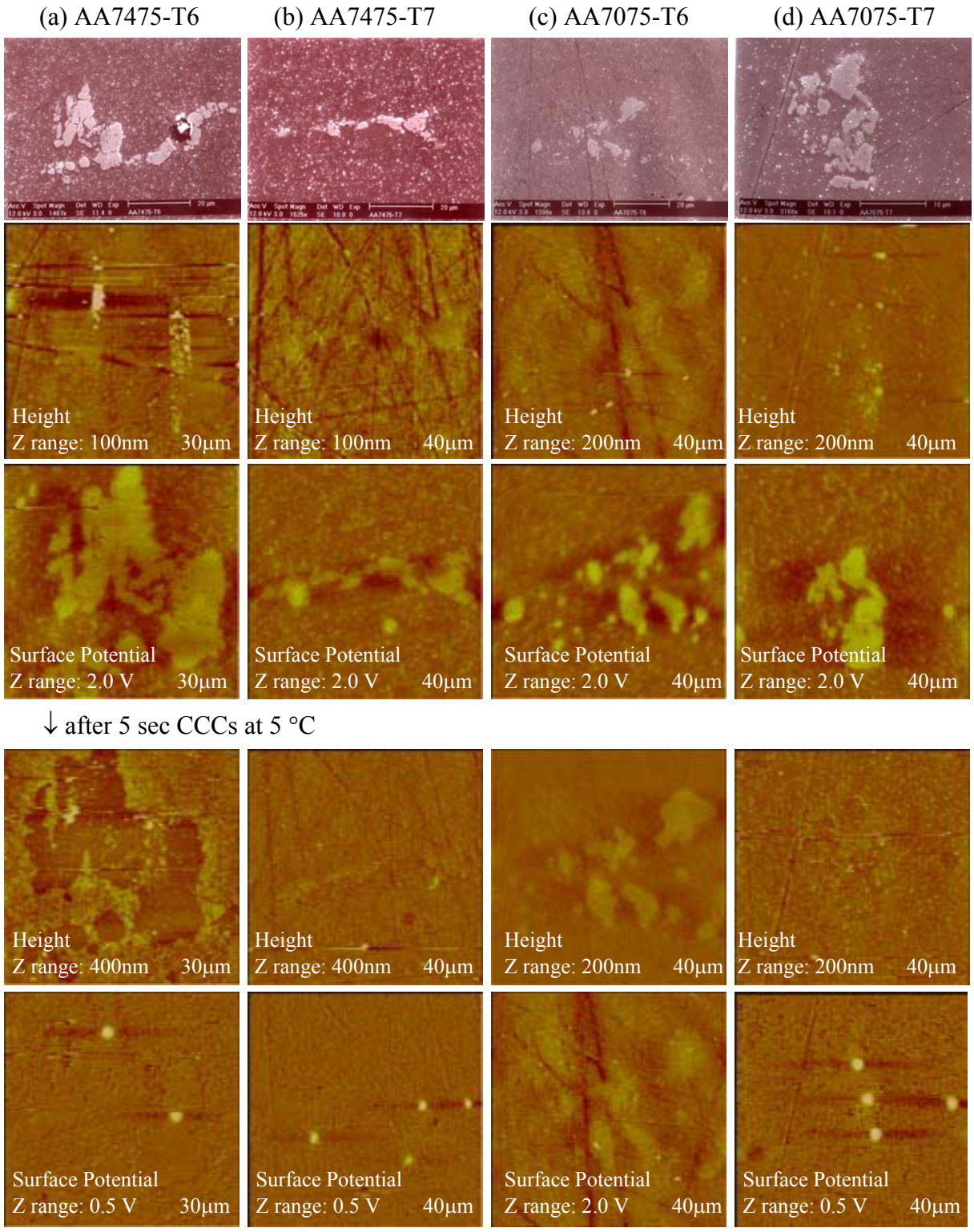

FIGURE 11. SKPFM image of intermetallic compounds in (a) AA7475-T6, (b) AA7475-T7, (c) AA7075-T6, and (d) AA7075-T7 before and after 5 sec CCCs at 5 °C.

CORROSION DETECTION

CORROSION SENSING AND MONITORING

C.S. Brossia, L. Yang, D.S. Dunn, N. Sridhar

Southwest Research Institute
San Antonio, TX 78238

ABSTRACT

Atmospheric corrosion of steels, aluminum alloys, and Al-clad aluminum alloys is a problem for many commercial and military vehicles, aircraft, and support equipment. Paint-based coating systems are usually the primary means to prevent the corrosion of many of these assets. Under ideal conditions, the coating provides a continuous layer that is impervious to moisture. At present, maintenance cycles for commercial and military aircraft and ground vehicles is based on experience and visual appearance rather than a quantitative determination of readiness from a corrosion perspective. To aid in maintenance decisions and reduce costs, sensors are often used to monitor corrosion. The present suite of corrosion sensors, however, generally are not aimed at determining coating integrity nor do they examine other key aspects of asset viability including the effects of other metallic component corrosion (e.g., stainless steel structural member corrosion on aluminum aircraft components), as well as asset washdown and storage procedures. Additionally, uncertainties in asset location and variability in exposure conditions make condition-based maintenance and life prediction decisions difficult. Several sensor concepts have been developed with the goal of addressing the shortfalls of previous sensor designs and results from evaluating these sensors are presented and discussed.

INTRODUCTION

Atmospheric corrosion of steels, aluminum alloys, and Al-clad aluminum alloys is a problem for many civil engineering structures, commercial and military vehicles, and aircraft. Paint is usually the primary means to prevent the corrosion of steel bridge components, automobiles, trucks, and aircraft. Under ideal conditions, the coating provides a continuous layer that is impervious to moisture. At present, maintenance cycles for commercial and military

aircraft and ground vehicles, as well as engineered structures, is often based on experience and visual appearance rather than a quantitative determination of system integrity. In many cases limitations to experience arising from new component or coating use, variations in exposure conditions, and the possibility of extensive corrosion damage occurring in hidden areas such as seams and lap joints are serious drawbacks to the present methodology used to determine maintenance schedules. These factors can result in considerable unnecessary costs. For example, it has been reported that the U.S. Air Force spends an average of $800M annually on corrosion control measures, of which coating maintenance operations are the majority.[1] To counter this and reduce costs, sensors are often used to monitor corrosion.

Monitoring the corrosion of engineered structures and vehicles has been proposed using a variety of corrosion sensors.[2-7] The level of complexity of the proposed sensors varies from simple designs, where the magnitude of either a galvanic or an impressed current is monitored over time,[4] to more advanced designs that incorporate multiple miniaturized electrodes including reference, chloride, and pH electrodes.[3,8-10] The simple galvanic sensor design is robust, has been shown to be effective as a time of wetness sensor, and can be used to assess the corrosivity of the environment.[4] Sensors with integrated reference, pH, and chloride ion selective electrodes can be

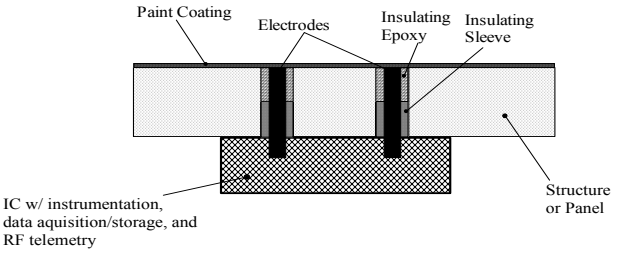

FIGURE 1. Cross-section schematic of coating integrity sensor concept.[11]

used to measure corrosion rate and collect more detailed information on the variations in environment chemistry. The present suite of corrosion sensors, however, generally is not aimed at determining coating integrity nor do they examine other key aspects of asset viability including the effects of other metallic component corrosion (e.g., stainless steel structural member corrosion on aluminum aircraft components), as well as asset washdown and storage procedures.

Present work at Southwest Research Institute has been aimed at developing sensor technologies that facilitate in-situ examination of coating integrity, inhibitor efficacy, localized corrosion, and environmental corrosivity. Efforts in each of these areas are described and results obtained are presented.

EXPERIMENTAL APPROACH

COATING INTEGRITY SENSOR

The basic coating integrity sensor is shown in Figure 1.[11] Initial efforts utilized standard electronic component passthroughs using gold pins and a pin spacing of between 3.5 and 11 mm, with the instrumentation and other components separate from the sensor assembly. After mounting, the pins were initially left slightly raised with respect to the substrate surface and then were ground back flush to the surface and the panels were painted.

The carbon steel panels were painted using a single polyurethane primer coat and three polyurethane top coats. After painting, the backside and edges of all the panels were coated with wax to prevent corrosion of the panel edges. In addition, half of the panels were scribed with a

7.5x7.5 cm “X”-shaped defect to expose the underlying substrate. All scribing was performed using a carbide tipped stylus with no scribe lines intersecting the sensor electrodes. Furthermore, duplicate panels without mounted sensors were included to determine if the sensors themselves adversely effected coating performance.

Two different aluminum alloys commonly used in aerospace applications, AA2024-T3 and AA7075-T6, were also examined, but without prior surface treatments such as a chromate conversion coating. For these panels, a series of coating variations was examined: a three-coat polyurethane coating system, a one-coat polyurethane coating, and a one-coat enamel coating. The enamel coating was chosen to represent a paint system that would likely perform poorly and served as a basis for comparison with the polyurethane coatings. Furthermore, the enamel color was black to facilitate visual detection of white aluminum corrosion products. The effects of surface contamination by hydraulic fluid prior to painting were also examined, as hydraulic fluid/oil contamination of the surface prior to painting has been reported. The panels were exposed in a programmable environmental chamber using the following exposure sequence:

- Spray 5 wt% NaCl solution at 55 EC for 3 min
- 80 – 90 %RH at 55 EC for remainder of day
- Repeat daily

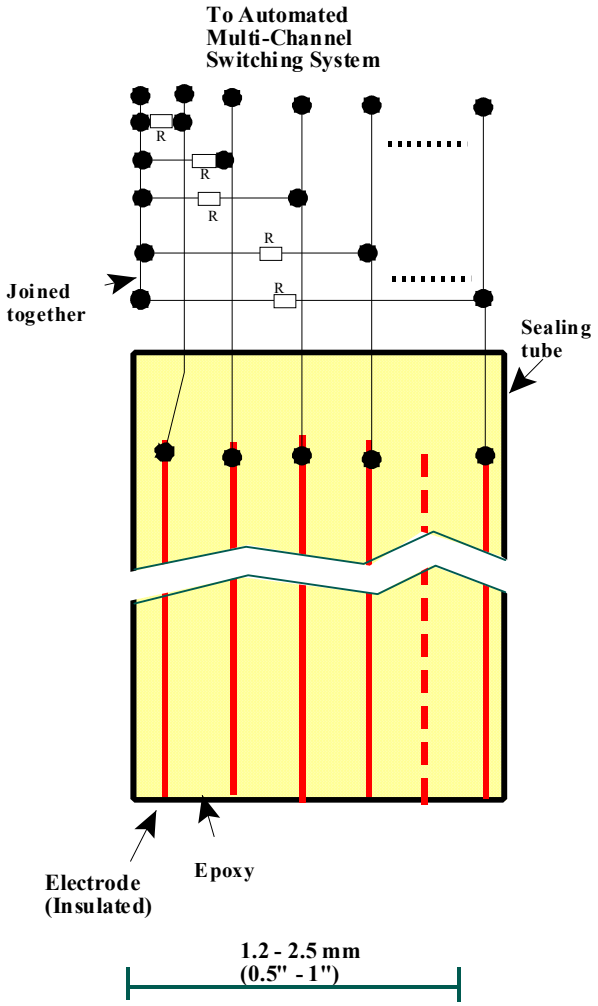

FIGURE 2: Schematic of coupled multi-electrode sensor.

Figure 2 shows a schematic diagram of the coupled multi-electrode localized corrosion/corrosivity sensor. A resistor is used between each electrode and the common connection point, and a multi-channel voltmeter is used to measure the voltage across the resistors to derive the current flowing through each electrode (with a positive value being cathodic and a negative value being anodic). If the potential drop across the resistors are negligibly low, the collection of the interconnected electrodes in the sensor simulates a large

metal area. The cathodic sites supporting corrosion on an electrode can be on the corroding electrode itself or can be on other electrodes through the external circuit. Therefore, the current flowing from the external circuit, I^{ex}, is a fraction of the total corrosion current, I, on the corroded electrode may be expressed as follows,[12]

$$I = \frac{I^{ex}}{\varepsilon} \tag{1}$$

where ε is a current distribution factor that represents the fraction of the current resulting from corrosion that flow through the external circuit. The value of ε may vary between 0 and 1, depending on parameters, such as the surface heterogeneities on the metal, the corrosion environment, the size, and the number of the sensing electrodes. If an electrode is severely corroded and significantly more anodic than the others in the sensor, the ε value for this electrode would be close to 1. On the other hand, if in an aqueous solution, no electrode is more anodic than the others in the sensor (in the case of uniform corrosion), the external current is close to zero since most of the current is distributed within the anodic and cathodic sites within each electrode. The maximum anodic current, obtained either directly from the most anodic current of the all the measured currents from different electrodes or from statistical analysis of the measured currents from different electrodes, was used as the corrosion current.[12]

RESULTS AND DISCUSSION

COATING INTEGRITY SENSOR

To quantify the performance of the coatings, a new parameter N' was developed and then normalized to a scale with a maximum value of 1. N' was determined by finding the product of the phase angle in radians and the magnitude of the impedance at a given frequency, as shown below,

$$N' = \frac{\phi |Z|}{10^8} \tag{2}$$

where Z is the impedance and N is the phase angle. Values of N' greater than 10^{-1} were considered to be indicative of a good, intact, protective coating. This value is reasonable based on a determination of N' values for applique coatings currently used by the U.S. Air Force, which exhibited N' values greater than this. Coatings with N' values between $5x10^{-3}$ and 10^{-1} were considered marginal, and coatings with N' values less than $5x10^{-3}$ were considered poor based on observations of coating performance during testing. To detect defects (hole, scribe), a criterion of 10^{-1} was also used, with values less than this indicating the presence of a coating defect.

The values of N' for scribed and unscribed carbon steel panels as a function of exposure time are shown in Figure 3. Based on N', the coating on the unscribed panel was still protective even after prolonged exposure. The scribed panel, however, exhibited a sharp decrease in N' between 17-28 days of exposure. This decrease indicated that the defect (the scribe) was detected rather than an indication that the coating was degrading. It should be noted that the unscribed panel has shown no decrease in N' over time. This conclusion was also supported by the physical

appearance of the panels as shown in Figure 4, where extensive coating creep back along the scribe length reached nearly 7 mm in many locations along with considerable blistering of the coating along the scribe. The remaining coating areas away from the scribe were still intact and similar in appearance to the unscribed panel. It should be noted, though, that significant corrosion of the scribed panel was observed even after 5 days of exposure despite no detectable change in N' until much later. As a result of this observation, the sensor design was modified to facilitate detection of defects by connecting one lead of the sensor to the back of the panel.

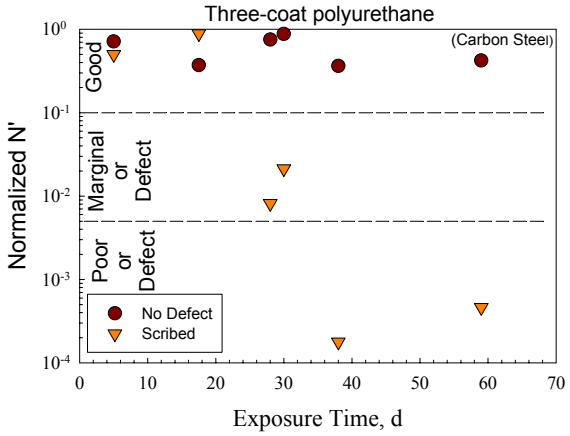

FIGURE 3: Sensor response for carbon steel panel with and without scribe defect.

FIGURE 4: Physical appearance of carbon steel panels after testing.

Figures 5 and 6 show the results obtained using the AA7075 panels for the various coatings examined and their physical appearance after testing. The three-coat polyurethane coating was still protective even after 30 days of exposure (N' was greater than 10^{-1}). The one-coat polyurethane showed slightly poorer results, remaining protective for the first few days but eventually falling into the marginal range (N' ~ 10^{-2}). Visual examination comparing the three-coat and one-coat panels did not reveal any notable differences. The panels that were contaminated with hydraulic fluid prior to painting exhibited results similar to the one-coat polyurethane panels. In this case, the contaminated panel initially showed fairly good performance with N' ~ 10^{-1}. After a few days, however, N' decreased below $5x10^{-3}$, indicating poor performance. Visual examination of the panels did not reveal any indication of coating degradation beyond the appearance of the "fish eyes" created from the surface contamination. It is thought that the surface contamination by oil prior to painting resulted in the creation of local weak spots in the coating as the oil acted as a paint solvent. Detection of the contamination may also arise from a loss of adhesion or from a change in the interfacial impedance at the contamination spot. Though it is unclear exactly what has changed by the presence of the contamination, it is evident that its effects are clearly detectable. When the enamel coating was examined, it showed poor performance even after a single day of exposure, with N' being nearly constant at $3x10^{-4}$ during the entire testing period. Examination of the enamel coated panels revealed the presence of white aluminum corrosion products on the surface, indicating that complete coating penetration failure had occurred at least in some locations on the panel surface. In addition, visual comparison of the instrumented and non-instrumented panels did not reveal any differences and close examination at the sensor mounting location did not reveal any evidence that the sensor introduced coating failure, nor did it promote corrosion.

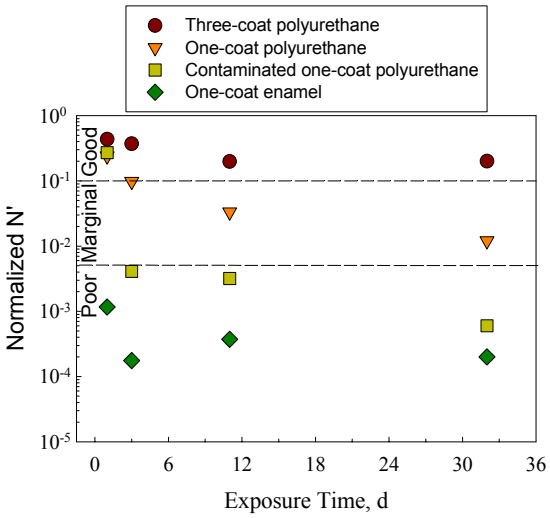

FIGURE 5: Sensor response for different coatings on AA7075, including prior surface contamination.

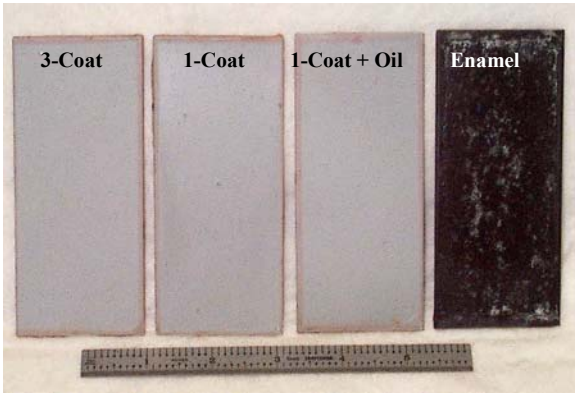

FIGURE 6: Physical appearance of AA7075 panels after exposure.

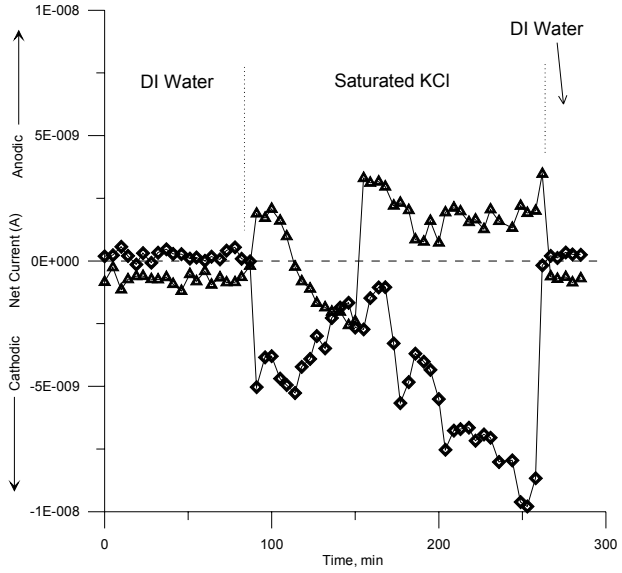

FIGURE 7: Response of two Type 304 stainless steel electrodes in a multi-electrode array indicating localized corrosion.

COUPLED MULTI-ELECTRODE LOCALIZED CORROSION/CORROSIVITY SENSOR

Localized corrosion of steel and stainless steel components and structural members in ground vehicles and aircraft is also an important consideration in assessing the readiness and integrity of an asset. The response of two of the Type 304 stainless steel electrodes in a 25 electrode array sensor when exposed to different environments is shown in Figure 7. On the transition from deionized water to saturated KCl, one electrode becomes predominantly anodic and the other predominantly cathodic. It should be noted that the net currents do not balance in this representative case because the responses of the other electrodes are not shown. Because one (or more) electrodes become predominantly anodic and others cathodic, it serves as an indication that localized corrosion is taking place. The anodic current measured roughly corresponds to a corrosion rate of 25 μm/y which is quite low compared to reported localized corrosion

propagation rates.[13-15] This current, however, represents an underestimation for two main reasons: some of the electrode surface still may be cathodic thus reducing the net anodic current measured and the area of the electrode undergoing localized corrosion is only a fraction of the total exposed area. To better estimate the localized corrosion propagation rate, alternative sensor designs are being explored to reduce the electrode diameter from 0.5 – 1 mm down to values approaching 10 μm. The reduction in electrode diameter will tend to solve both issues with respect to estimating the total anodic current.

The same sensor concept was also used to evaluate corrosion inhibitors (Figure 8). In this case, carbon steel (1010) electrodes were used and were evaluated in air-saturated tap water. Prior to the addition of the inhibitors, the corrosion currents were on the order of 10^{-4} A/cm^2 which is roughly equivalent to 1.3 mm/yr. When either a commercial nitrite-based inhibitor or benzotriazole were added, the corrosion rate decreased by a factor of ~ 100. The addition of $NaNO_3$, at least up to concentrations of 47 mM, were not effective at inhibiting carbon steel corrosion. From these results it is clear that inhibitor efficacy can be monitored. This could be utilized in a vehicle washdown system that incorporates corrosion inhibitors and recycles rinse water to reduce effluent streams. Such a system could have a predetermined set point at which new water and additional inhibiting chemicals are added to maintain the desired chemistry.

This system has also been used to monitor atmospheric corrosion under surface contamination conditions. In this case, the sensor surface was contaminated with NaCl prior to placing the sensor in a humidity chamber. The humidity was then controlled over time and the current monitored. Based on the known deliquescence point (the relative humidity where the salt in question is in thermodynamic equilibrium with a saturated solution of the salt) for NaCl, it would be expected that significant corrosion would occur only at RH > 74%. Figure 9, however,

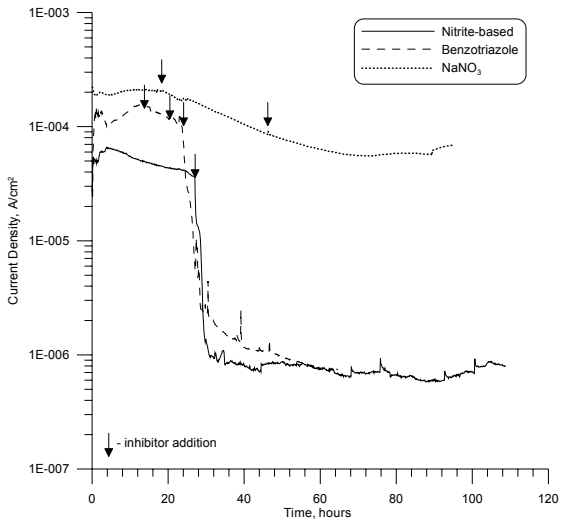

FIGURE 8: Carbon steel multi-electrode sensor response in tap water with the additional of different corrosion inhibitors.

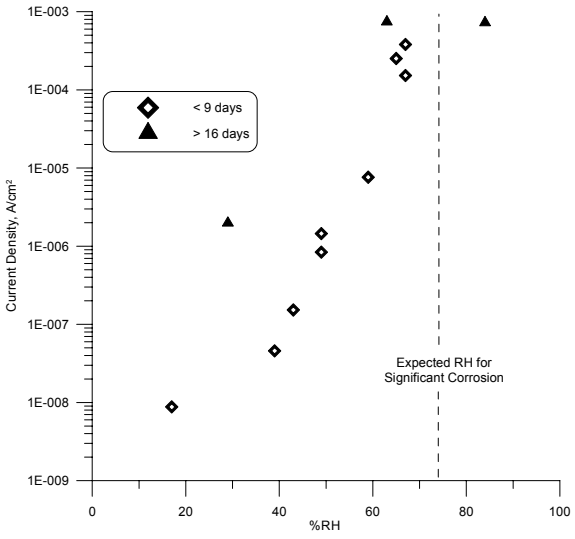

FIGURE 9: Carbon steel multi-electrode response when contaminated with NaCl as a function of %RH.

shows that currents > 10^{-4} A/cm^2 are still observed at RH < 74%. In fact, after exposure for periods longer than 16 days, when the RH was held at 30% the current increased from values

near 10^{-8} to over 10^{-6} A/cm^2. This indicates that significant corrosion can still occur at low RH when the surface is contaminated with salt. This observation is important given the plans for long-term storage of assets in controlled humidity buildings. A situation could arise in which assets that have recently been through over-sea transport or are stationed near ocean sites are placed in storage and are not subjected to prior thorough washdown. Given that the typical RH of these buildings is about 40%, substantial corrosion of components and hidden areas may still occur if sea spray or other salts contaminate them. For example, archeological objects that have been dug up from marine sites continue to corrode in storage when the RH values are near 40%. Incorporation of this sensor as the assets are going into storage could provide an indicator of possible problems without the need for active visual inspection. Thus, when the sensor indicates a high corrosion rate the particular asset or storage building can then be inspected. This offers distinct advantages over the current proposed practice of solely monitoring the %RH of the building as this would not account for any salts that may be present.

CONCLUSIONS

Effective corrosion monitoring and maintenance of ground vehicles, aircraft, and support equipment is a complex and challenging problem for the military. Recent work has led to the development and evaluation of sensor technologies that can monitor the integrity of coating systems prior to the onset of substrate corrosion. Other efforts have also led to the construction of a sensor design that can detect localized corrosion and can also be used to monitor the efficacy of inhibitors as well as environmental corrosivity. These issues become important as a diversity of materials are utilized such that individual component corrosion may then subsequently led to early failure of surrounding components and structures. Monitoring the corrosion of critical

assets under long-term storage may be important because previously corroded and hidden areas can continue to corrode even when the nominal RH is about 40%. From these efforts it is clear that a single sensor concept that answers the wide array of corrosion-related issues facing extended asset retention and use is unlikely to succeed and a multi-sensor approach is needed.

ACKNOWLEDGEMENTS

Various aspects of this work was funded by the Southwest Research Institute Advisory Committee for Rarch. The aluminum panels used were generously supplied by Alcoa and James Moran and are gratefully acknowledged.

REFERENCES

1. Cooke, G., G. Cooke, Jr., G. Kawanishi, T. Higginbotham, P. Miller, S. Wacksman. *A study to determine the annual direct cost of corrosion maintenance for weapon systems and equipment in the United States Air Force, Final Report*. Contract # F09603B95BDB0053, DO 0006, CDRL No. A001. 1998.

2. Chawala, S.K. T. Anguish, and J.H. Payer. Microsensors for corrosion control. *Corrosion* 45(7): 595-601. 1989.

3. Diwan, R.M., A. Raman, P.K. Bhattacharya, and R. Lee. Atmospheric corrosion microsensor development: A review. *Proceedings of the Corrosion/95 Conference.* Paper No. 227. Houston, TX: NACE International. 1995.

4. Shinohara, T., S. Tsujikawa, S. Motoda, Y. Suzuki, W. Oshikawa, S. Itomura, T. Fukushima, and S. Izumo. Evaluation of corrosivity of marine atmosphere by ACM (Atmospheric Corrosion Monitor) type corrosion sensor. *International Symposium on Plant Aging and Life Prediction of Corrodible Structures*. Sapporo, Japan: Japan Society of Corrosion Engineering. 1995.

5. Sridhar, N., D.S. Dunn, C.S. Brossia, and O. Moghissi. Corrosion monitoring techniques for thermally driven wet and dry conditions. *Proceedings of the Corrosion 2000 Conference*. Paper No. 283. Houston, TX: NACE International. 2000.

6. Brossia, C.S., D.S. Dunn, O.C. Moghissi, N. Sridhar. *Assessment of Methodologies to Confirm Container Performance Model Predictions*. CNWRA 2000-06, San Antonio, TX: Center for Nuclear Waste Regulatory Analyses. 2000.

7. Agarwala, V.S., S. Ahmad. Corrosion detection and monitoring – a review. Corrosion/2000, Paper 00271, Houston, TX: NACE International, 2000.

8. Desmond, D., B. Lane, J. Alderman, J.D. Glennon, D. Diamond, D.W.M. Arrigan. Evaluation of a miniaturized solid state reference electrodes on a silicon based component. *Sensors and Actuators* B 44: 389B396. 1997.

9. Suzuki, H., A. Hiratsuka, S. Sasaki, I. Karube. Problems associated with the thin-film Ag/AgCl reference electrode and a novel structure with improved durability. *Sensors and Actuators* B46: 104-113. 1998.

10. Suzuki, H., A. Hiratsuka, S. Sasaki, I. Karube. An integrated three-electrode system with a micromachined liquid junction Ag/AgCl reference electrode. *Analytica Chemica Acta* 387: 103-112. 1999.

11. Brossia, C.S., D.S. Dunn. Apparatus and Method for Detecting the Degradation of a Coating Using Embedded Sensors, U.S. Patent (filed), 2001.

12. Yang, L., N. Sridhar, O. Pensado, D. Dunn. *Corrosion*, submitted for publication. 2001.

13. Dunn, D.S., G.A. Cragnolino, N. Sridhar. Localized corrosion initiation, propagation, and repassivation of corrosion resistant high-level nuclear waste container materials. *Corrosion/96 Conference*. Paper No. 97. Houston, TX: NACE International. 1996.

14. Cramer, S.D., J.P. Carter. Corrosion in geothermal brines of the Salton Sea known geothermal resource area. *Geothermal Scaling and Corrosion*. ASTM STP 717, p. 113. Casper and Pinchback, eds. West Conshohocken, PA: ASTM International. 1984.

15. Cramer, S.D., J.P. Carter, R.K. Conrad. Corrosion and scaling of nickel alloys in Salton Sea geothermal environments. *Proceedings of the International Symposium on Solving Corrosion and Scaling Problems in Geothermal Systems*, p. 215. Houston, TX: NACE International. 1984.

RICCATI EQUATION ANALYSIS OF LIGHT TRANSPORT IN SIMPLE AND FLUORESCENT PAINTS

Jan D. Garmany
Systems & Processes Engineering Corp.
101 W. 6th Street Suite 200
Austin, TX 78701

INTRODUCTION

Johnson and Agarwala[1] proposed the use of fluorescent indicators to disclose and monitor hidden corrosion beneath coatings. Visible indicators have also been proposed and used, notably by Zhang and Frankel[2] and by Isaacs et al.[3] All of these applications were under clear coatings or intended for laboratory use. Our experience with the use of indicators in opaque coatings shows that it is best to distribute the indicator throughout the coating, or at least throughout the surficial layer of coating. As the chemical effects of corrosion at the base of the coating transform the indicator, the presence of corrosion is revealed by the altered appearance of the surface before coating failure. However, environmental effects may transform the indicator in a thin layer at the surface of the coating, introducing the possibility of false alarms. We have examined this problem by detailed modeling of fluorescent paint. We present the theory of this modeling and some numerical results to test vulnerability to false alarms.

Kubelka and Munk[5] first analyzed the one-dimensional transport of light in paints. This work was extended by Fukshansky and Kazarinova[6] to include the possibility of fluorescence. The differential systems for simple paint are straightforward, since they only need to account for light absorption and scattering at single wavelengths. Analysis of the fluorescent case is more difficult, since an incident photon may excite fluorescence at different wavelengths throughout the emission spectrum. In particular, the emission spectrum may overlap with the fluorescence-

related absorption spectrum, creating a re-excitation feedback path. This feedback is ultimately lossy and reduces the strength of the fluorescence. In the exposition below, we first review the features of modeling simple paint. We then present a simplified model of fluorescent paint to motivate the generalization to a more complete model. This final generalization adequately approximates the integrodifferential system in Fukshansky and Kazarinova [1980] for fluorescent coupling of dissimilar wavelengths.

SIMPLE PAINT

We consider a strongly scattering medium that varies only with depth and which is uniformly illuminated at its surface. While the scattering is isotropic in three dimensions, we invoke symmetry to conclude that the light intensities only vary with depth. The depth into the coating is denoted by z. The total volume scattering of light of intensity I from a layer of thickness dz is $2\beta I\, dz$, where it is assumed that the scattering is equally divided between the forward and backward directions. We also suppose that the the absorption of light in a layer of thickness dz is $\gamma I\, dz$. Setting $\alpha=\beta+\gamma$, we may write the differential system for one-dimensional transport of light intensity in a simple paint coating as

$$\frac{d}{dz}\begin{pmatrix} f \\ b \end{pmatrix} = \begin{pmatrix} -\alpha & \beta \\ -\beta & \alpha \end{pmatrix}\begin{pmatrix} f \\ b \end{pmatrix}. \tag{1}$$

Here, the functions f and b represent the intensities of forward and backward propagating light, respectively. This system was first derived by Kubelka and Munk [1931]. For a coating with constant properties, the analytical solution of this system is straightforward for $\gamma > 0$ and has been well studied.

Problems involving the calculation of a reflectance lend themselves to analysis in terms of a Riccati substitution, $b = Rf$, and solving for dR/dz. After eliminating f from the result, we obtain a nonlinear differential equation (the Riccati equation) for R:

$$\frac{dR}{dz} = 2\alpha R - \beta(1 + R^2) \tag{2}$$

The initial value of R may range from 0 (totally absorbing substrate, no reflection) to 1 (totally reflecting substrate) at $z = 0$. We note that because the forward propagation is taken to be in the positive z direction, we must integrate toward negative z in building up the coating thickness. Alternatively, we may start at $z = h$ for some positive depth h and integrate toward $z = 0$.

We may calculate the saturation reflectance achieved at infinite thickness by setting $dR/dz = 0$. We write this condition as

$$R^2 - 2\frac{\alpha}{\beta}R + 1 = 0 \tag{3}$$

For realistic scattering media, we have that the dimensionless ratio $\alpha/\beta > 1$, and the physically valid solution ($R < 1$) is given by

$$R_{sat} = \frac{\alpha}{\beta} - \left(\frac{\alpha^2}{\beta^2} - 1\right)^{\frac{1}{2}} \tag{4}$$

For weak absorption, $\alpha/\beta = 1 + \varepsilon$, where $\varepsilon << 1$. In this limit,

$$R_{sat} \to 1 + \varepsilon - \sqrt{2\varepsilon} \tag{5}$$

For strong absorption, $\alpha/\beta = N >> 1$, we obtain

$$R_{sat} \to \frac{1}{2N} \tag{6}$$

SIMPLIFIED MODEL OF FLUORESCENT PAINT

As an intermediate step, we consider a simplified model of fluorescent paint. This model should be adequate when the overlap of the absorption and emission spectra is small. We suppose that the wavelengths may be separated into two independent bands, denoted U (ultraviolet or short wavelength) and V (visible or long wavelength). The forward and backward propagating intensities now have U and V components, and the differential system governing them may be written as

$$\frac{d}{dz}\begin{pmatrix} f_U \\ f_V \\ b_U \\ b_V \end{pmatrix} = \begin{pmatrix} -\alpha_U & 0 & \beta_U & 0 \\ \varphi\theta & -\alpha_V & \varphi\theta & \beta_V \\ -\beta_U & 0 & \alpha_U & 0 \\ -\varphi\theta & -\beta_V & -\varphi\theta & \alpha_V \end{pmatrix}\begin{pmatrix} f_U \\ f_V \\ b_U \\ b_V \end{pmatrix} \tag{7}$$

where

$$\alpha_U = \gamma_U + \beta_U + 2\theta \tag{8}$$

$$\alpha_V = \gamma_V + \beta_V \tag{9}$$

The subscripted quantities are generalizations of α, β, and γ introduced in the study of simple paint. The quantity θ represents the absorption of the fluorescent species, and φ is the quantum efficiency of the fluorescence. The factor of 2 multiplying θ in (8) accounts for the absorption required to yield potential fluorescent emission in both the forward and backward directions. In contrast, there is no factor of 2 on any scattering coefficient β since there is no wavelength change and half the scattered energy is restored to the original direction of the incident intensity. If we introduce the notation

$$\mathbf{A} = \begin{pmatrix} \alpha_U & 0 \\ -\varphi\theta & \alpha_V \end{pmatrix} \tag{10}$$

$$\mathbf{B} = \begin{pmatrix} \beta_U & 0 \\ \varphi\theta & \beta_V \end{pmatrix} \tag{11}$$

we may rewrite (7) in the form

$$\frac{d}{dz}\begin{pmatrix} \mathbf{f} \\ \mathbf{b} \end{pmatrix} = \begin{pmatrix} -\mathbf{A} & \mathbf{B} \\ -\mathbf{B} & \mathbf{A} \end{pmatrix}\begin{pmatrix} \mathbf{f} \\ \mathbf{b} \end{pmatrix} \tag{12}$$

where **f** and **b** are the 2-vectors of forward and backward propagating intensities. The structure of the transport equation (12) obviously resembles (1), and is characteristic of one-dimensional transport.

The Riccati substitution **b** = **Rf** leads to the matrix Riccati system

$$\frac{d}{dz}\mathbf{R} = -\mathbf{B} + \mathbf{AR} + \mathbf{RA} - \mathbf{RBR} \tag{13}$$

Let

$$\mathbf{R} = \begin{pmatrix} a & b \\ c & d \end{pmatrix} \tag{14}$$

It can be shown that if b=0 initially, then it is always zero, because of the placement of the zero elements in (10) and (11). This result is appropriate physically, since b is the (unexpected) excitation of short wavelength emissions by long wavelength incident light. Under these conditions, we can analytically determine the saturation reflectances and the saturation fluorescence when the coating has constant properties. We set $d\mathbf{R}/dz$=0, and after some algebra, we find

$$a_{sat} = \frac{\alpha_U}{\beta_U} - \left(\left(\frac{\alpha_U}{\beta_U} \right)^2 - 1 \right)^{\frac{1}{2}} \tag{15}$$

$$d_{sat} = \frac{\alpha_V}{\beta_V} - \left(\left(\frac{\alpha_V}{\beta_V} \right)^2 - 1 \right)^{\frac{1}{2}} \tag{16}$$

for the short and long wavelength saturation reflectances, respectively. These are identical in form to the simple paint case. We also obtain

$$c_{sat} = \frac{\varphi\theta(1+a_{sat})(1+d_{sat})}{\alpha_U + \alpha_V - \beta_U a_{sat} - \beta_V d_{sat}} \tag{17}$$

as the saturation fluorescence.

We have studied the solution of (13) numerically, showing that the generalized reflectance matrix converges to the theoretical saturation value.

GENERAL MODEL OF FLUORESCENT PAINT

The continuous model of the 1-D evolution of strong scattering in a fluorescent paint may be written as

$$\frac{df(\lambda)}{dz} = -\alpha(\lambda)f(\lambda) + \beta(\lambda)b(\lambda) + \varphi\eta(\lambda)\int_{\lambda_1}^{\lambda_2} d\lambda'\theta(\lambda')[f(\lambda') + b(\lambda')] \tag{18}$$

$$\frac{db(\lambda)}{dz} = \alpha(\lambda)b(\lambda) - \beta(\lambda)f(\lambda) - \varphi\eta(\lambda)\int_{\lambda_1}^{\lambda_2} d\lambda'\theta(\lambda')[f(\lambda') + b(\lambda')] \tag{19}$$

where

$$\alpha(\lambda) = \beta(\lambda) + \gamma(\lambda) + 2\theta(\lambda) \tag{20}$$

The notation is consistent with prior usage, but now the scattering, coating absorption, and fluorophore absorption (β, γ, and θ respectively) are functions of a continuous wavelength variable λ. The fluorophore absorption spectrum $\theta(\lambda)$ is nonzero between λ_1 and λ_2. We denote

this interval as Λ_θ. The emission spectrum is denoted by $\eta(\lambda)$, which is taken to be nonzero over a finite range between λ_3 and λ_4, which we denote as Λ_η.

For practical numerical calculations, we use a discretization of the functions of wavelength, using a piecewise constant approximation, e.g.

$$(\boldsymbol{\alpha})_i = \frac{1}{\Delta\lambda_i}\int_{\Delta\lambda_i} \alpha(\lambda)d\lambda \tag{21}$$

Thus, the ith element of each coefficient array is the average value of the continuous function in the ith wavelength interval. We also define the intensity vectors formed by the simple integrals of the wavelength dependent intensity functions, e.g.,

$$(\mathbf{f})_i = \int_{\Delta\lambda_i} f(\lambda)d\lambda \tag{22}$$

With these definitions, we may write

$$\mathbf{A} = diag(\boldsymbol{\alpha}) - \varphi\boldsymbol{\eta}\boldsymbol{\theta}^T \tag{23}$$

$$\mathbf{B} = diag(\boldsymbol{\beta}) + \varphi\boldsymbol{\eta}\boldsymbol{\theta}^T \tag{24}$$

The notation *diag*(**x**) means a diagonal matrix with nonzero entries given by the elements of **x**. If the number of wavelength intervals is n, then the matrices **A** and **B** are $n\times n$. The resulting full differential system is identical in form to (12), and is of order $2n$. We may no longer distinguish between U and V wavelength ranges, since the absorption and emission spectra may (and most commonly do) overlap. This overlap leads to coupling introduced by nonzero elements in the upper triangles of the $n\times n$ submatrices. This effect is illustrated in Fig. 1. The Riccati substitution

yields an $n \times n$ generalized reflectance matrix from which we may predict an arbitrary reflectance spectral response due to an arbitrary illumination spectrum.

NUMERICAL RESULTS AND CONCLUSIONS

Our numerical results are illuminating. We elected to use synthetic absorption and emission spectra (Figs. 2-4) for demonstration purposes and simplicity. The fluorescent emission is a broad function centered in the blue, and the fluorescence absorption and emission spectra overlap considerably. The intensities have an arbitrary linear scale that starts at zero. The results for red (Figs. 5 and 6) and blue coatings (Figs. 7 and 8) show the resulting emission spectra for progressive quenching of fluorescence from the top (false indication) and the bottom (true indication). The wavelength notations on the spectra are merely suggestions: no actual physical properties have been used or measured in this model experiment.

The most striking result is for the red coating. The "false" indication shows a progressive redward shift of the peak fluorescence emission as quenching increases. Conversely, the "true" indication shows the emission to be shifted blueward as quenching increases. This is intuitively expected. For the true indication, the fluorescence is from a thin layer near the surface, so the short path through the colored coating has less effect on the spectrum. When the fluorescence is confined to the bottom of the layer, wavelengths near the color of the coating are favored on the long path.

When the intrinsic emission peak and the coating reflectivity peak are closer, the shifts in the fluorescence peak are less pronounced. To resolve the ambiguous indication, it may be necessary to scratch or abrade the surface to see if a superficial quenched layer disappears. There

may be a considerable advantage to tailoring the indicator to have an emission peak displaced from the reflectivity peak. Less can be done about neutral or very dark colored coatings.

We have outlined the development of a practical scheme for the calculation of reflectance and emission from a fluorescent paint. The treatment is sufficiently general to provide accurate predictions of fluorescent paint behavior, which we expect to be of particularly great use in the monitoring of corrosion indicators.

REFERENCES

1. R.E. Johnson and V.S. Agarwala, Materials Performance 33 (1994), p. 25.

2. J. Zhang, G.S. Frankel, Corrosion 55, 10 (1999), p. 957.

3. H.S. Isaacs, G. Adzic, C.S. Jeffcoate, Corrosion 56, 10 (2000), p.971.

4. P. Kubelka and F. Munk, Zeitschrift fur technische Physik 12 (1931), p. 593.

5. L. Fukshansky and N. Karazinova, J. Opt. Soc. Am. 70 (1980), p. 1101.

FIGURES

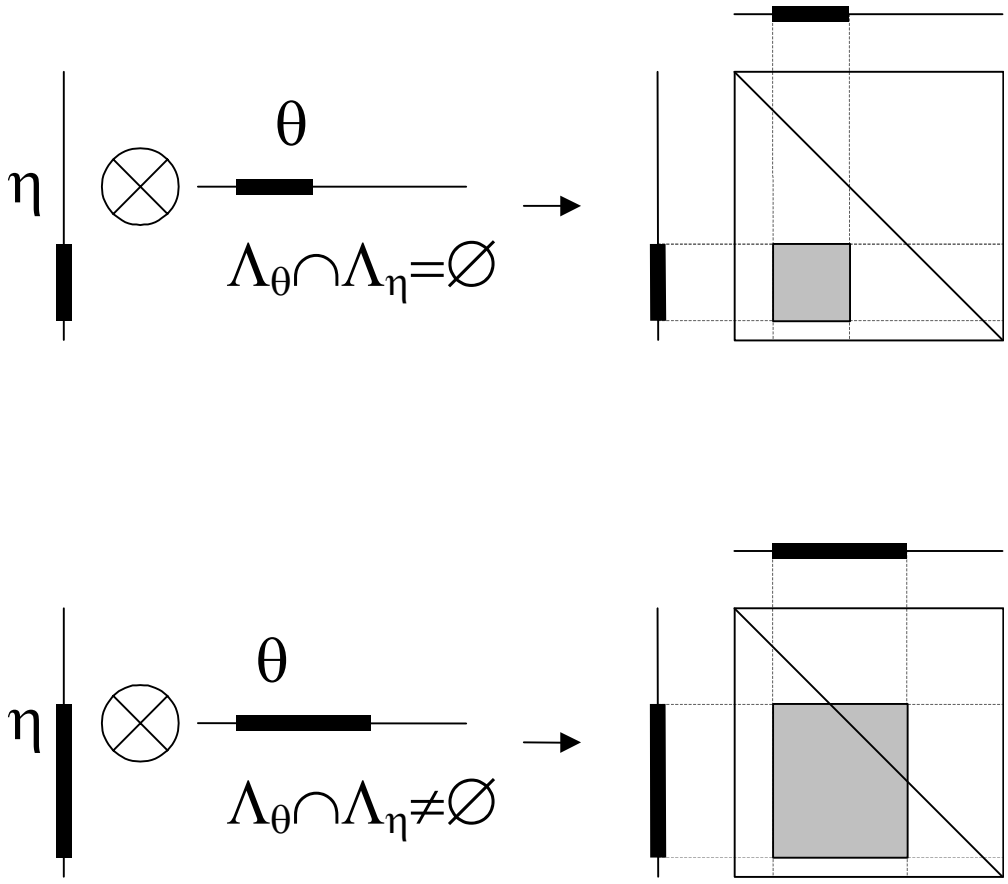

FIGURE 1. Differences in coefficient matrix structure for non-overlapping (top) and overlapping absorption and emission spectra. Nonzero vector elements are bold lines, resulting nonzero matrix elements are gray rectangles.

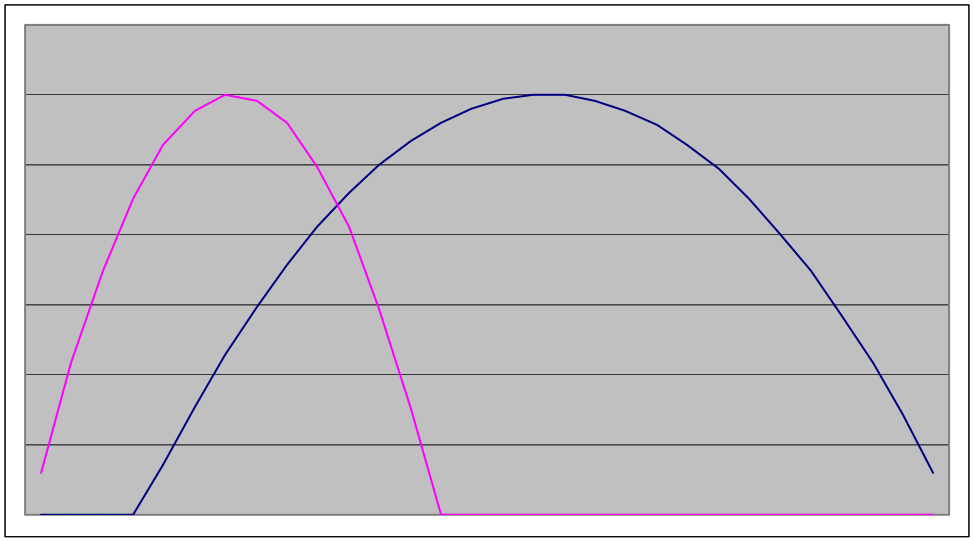

200 nm Nominal wavelength 800 nm

FIGURE 2. Absorption and emission spectra used in modeling fluorescent indicator.

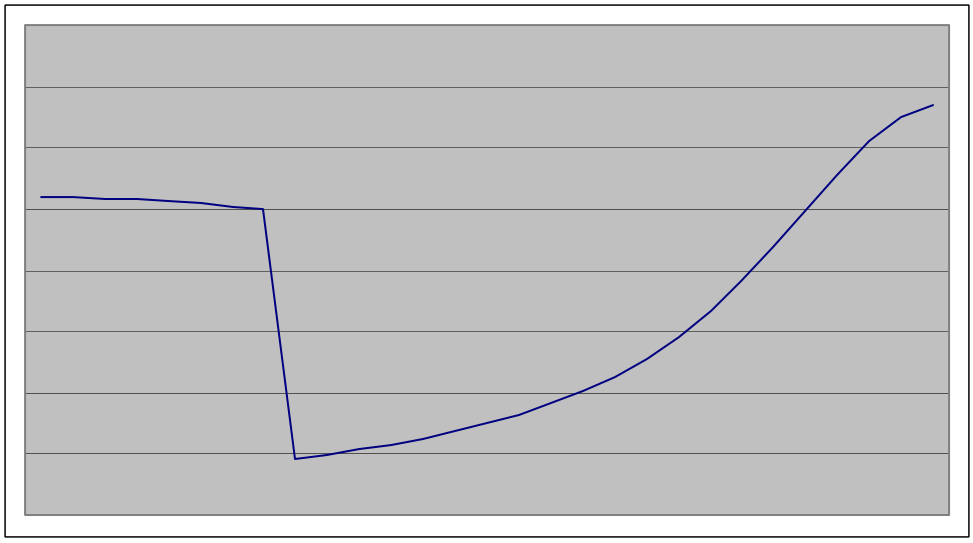

200 nm Nominal wavelength 800 nm

FIGURE 3. Reflectivity spectrum of red coating.

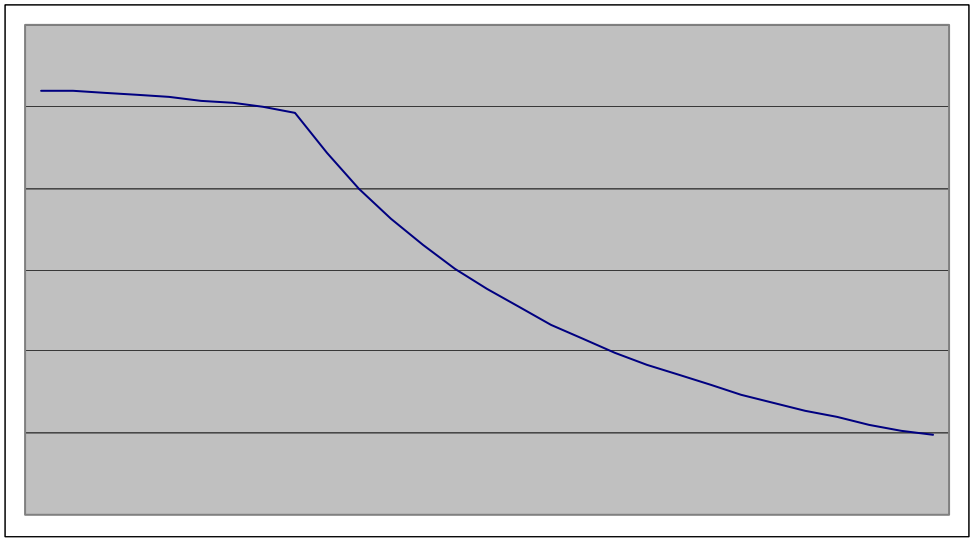

200 nm Nominal wavelength 800 nm

FIGURE 4. Reflectivity spectrum of blue coating.

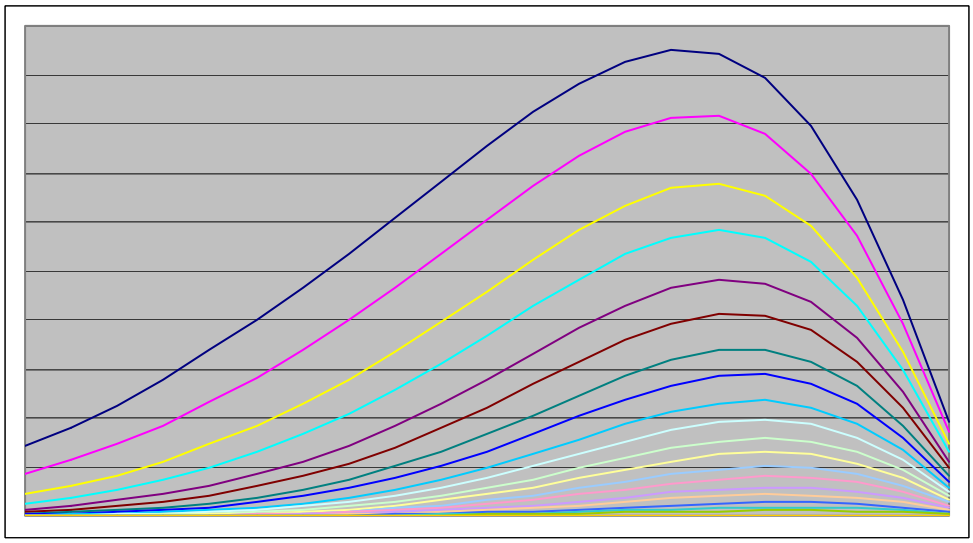

400 nm Nominal wavelength 800 nm

FIGURE 5. Fluorescent emission spectra in red coating showing effects of progressive quenching from the top of the coating. Note rapid initial drop in intensity and redward shift of emission peak. Quenching is in 5% increments of the total depth.

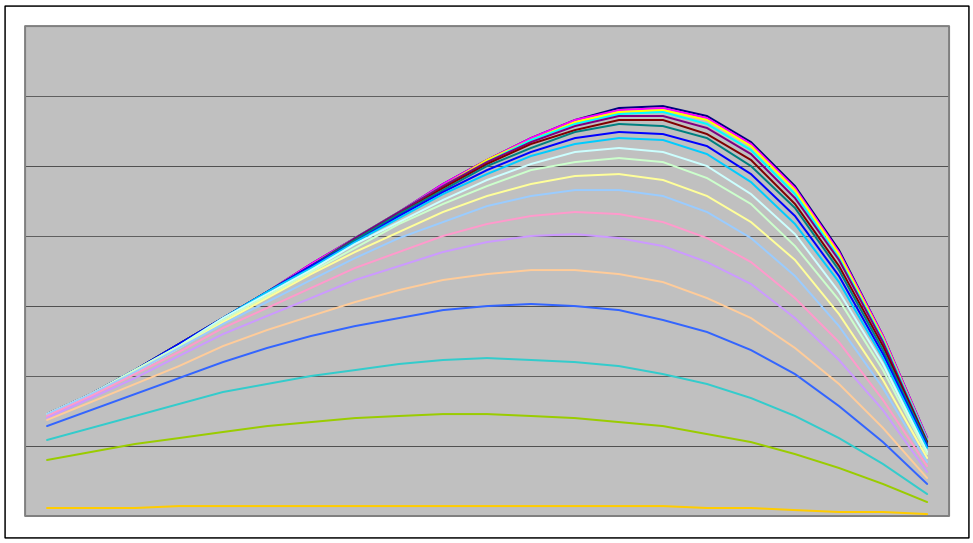

400 nm Nominal wavelength 800 nm

FIGURE 6. Fluorescent emission spectra in red coating showing effects of progressive quenching from the bottom of the coating. This case shows a slow initial drop in intensity and blueward shift of emission peak.

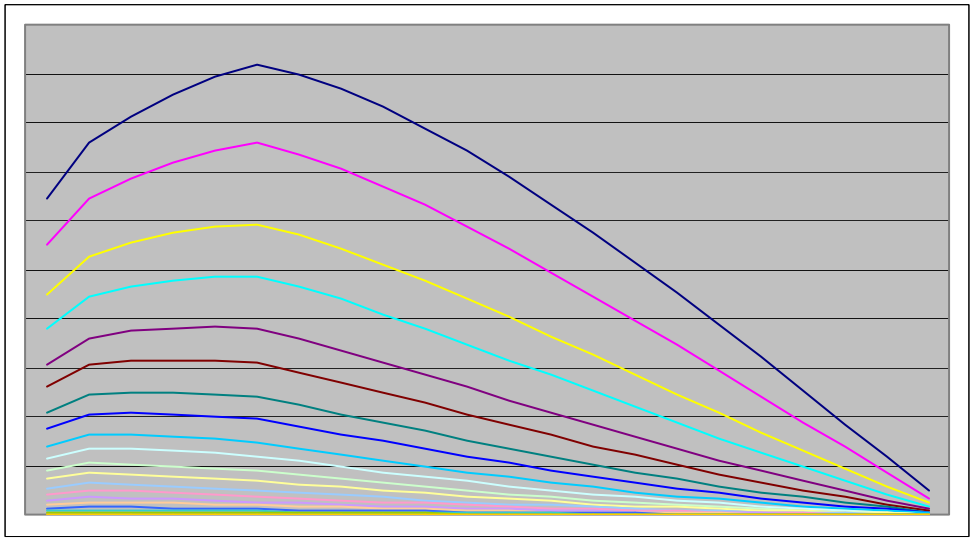

400 nm Nominal wavelength 800 nm

FIGURE 7. Fluorescent emission spectra in blue coating showing effects of progressive quenching from the top of the coating.

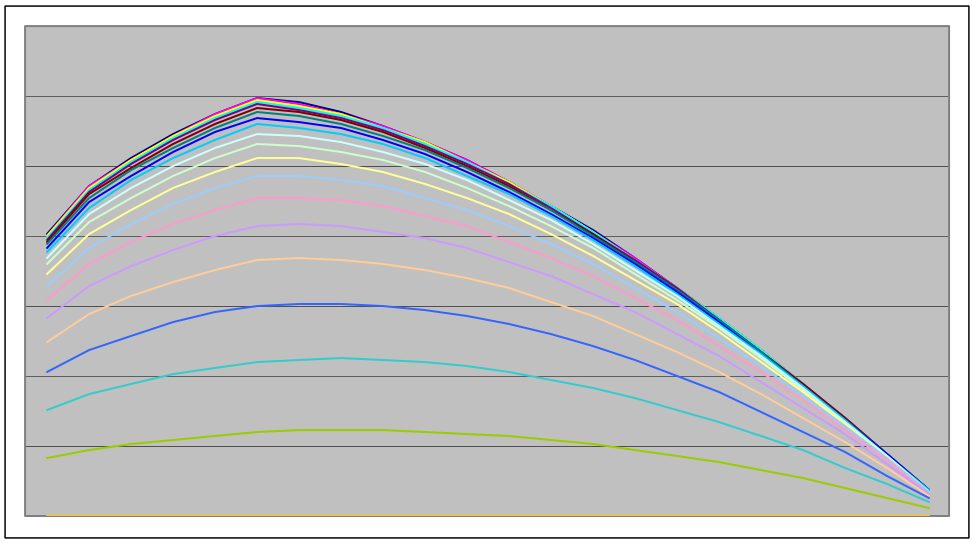

400 nm Nominal wavelength 800 nm

FIGURE 8. Progressive quenching from bottom in blue coating. Near coincidence of the reflectivity and emission peaks causes only modest shift in peak. The kink is due to overlap of absorption and emission fluorescence spectra.

MICROWAVE CORROSION DETECTORS (MCDS) FOR INSPECTING UNDER AIRCRAFT PAINTS AND APPLIQUÉS

Alan V. Bray and Gary Schmidt

System & Materials Research Corp. (SMRC)
19300 Crosswind Circle
Spicewood, Texas 78669

ABSTRACT

When corrosion erupts beneath a painted surface a microwave signal reflected from the area is different than when corrosion is not present. Two factors are responsible for this change: corrosion products change the dielectric characteristic of the area; and, changes in the distance between the coating top and base metal result from pitting, swelling, and corrosion product build-up. In this project an NDE tool is being developed to exploit this phenomenon for aircraft paints and appliqués. Design issues include separating the effect of altitude variations and tilt angle of the sensor from corrosion-influenced signal changes. In addition a series of operating logic sequences are developed to minimize the occurrence of false positive and negative responses to the question "corrosion-no corrosion." The project is currently in an early build stage and a pre-prototype microwave corrosion detector (MCD) is in alpha test. The ability of an MCD to detect corrosion was correlated with the exposure time of the corrosion specimens in previous work[1], and is extended here to provide a relative assessment of the degree of corrosion. The onset of corrosion is an important demarcation in inspecting paints and appliqués – as corrosion products build to the point they are visible to the naked eye it is too late to take preventive measures. The pre-prototype MCD threshold for corrosion detection will be known better after alpha and beta level testing. The project goal is to be able to reliably and economically detect corrosion onset in aircraft skins.

INTRODUCTION

Microwave NDE is an emerging technology that uses the interaction between incident microwave radiation and the changes in the reflected signal to detect fatigue cracks, corrosion, composite moisture content and delamination, and other phenomena that produce a change in the dielectric characteristic of the item being inspected. Microwave NDE methods take advantage of

the way in which incident radiation interacts with changes in layered dielectric media.[2,3] As the dielectric characteristics under the aperture of the wave guide change, the reflected signal changes. In addition corrosion can cause a change in altitude from the top of the coating to base metal through pitting, swelling, and the build-up of corrosion products. These changes in altitude relative to base metal are readily detected, but must be distinguished from other sources of altitude change, such as non-uniform paint thickness, to avoid false positive or negative indications. On an aircraft the layers of materials over bright aluminum typically include an anti-corrosion coating, a primer and topcoat, or an applique. These dielectric layers effect the transmission characteristics of the microwave signal in a relatively constant fashion on the skin of the aircraft, although changes in paint thickness and paint type also affect the uncorroded signal return. If a layer of corrosion products begins to develop on the surface of the aluminum, or in the vicinity of a scratch in the anti-corrosion coating, the dielectric characteristic changes, and may be accompanied by an altitude change, affecting a change in the reflected signal. An alpha level microwave corrosion detector (MCD) design and initial test data are presented.

APPROACH

The microwave sensors are commercial-off-the-shelf components used in automatic door openers and police radar guns. The sensors are first characterized by their altitude versus output signal from a bare aluminum plate, essentially tracing the standing wave pattern as a function of standoff distance. These data are then used to develop the dynamic range and operating region for the MCD. A number of waveguide types and configurations were characterized in this fashion to select a design baseline. The alpha MCD configuration uses a microwave horn that is an integral part of the MCD mechanical system.

In order to minimize detection errors in an MCD design it is critical that altitude and tilt angle from the inspection surface be kept as constant as possible. When the altitude and tilt angle are kept to within a fixed range the signal change that results from the presence of corrosion is discernible, and without that control corrosion impacted signals can be lost. For contoured surfaces such as those in aircraft this means that the scanning system must be flexible enough to maintain perpendicularity, while carefully controlling altitude above the work. The alpha level design uses a spring loaded scanning contact to accomplish this. The horn antenna provides a spot size of roughly 250 by 190 mm for the inspection.

An important concern in the design of any NDE tool is minimizing the occurrence of false positives and negatives in making a decision as to the status of the inspected work. The approach taken in the alpha MCD design is to identify those conditions that are indicative of good and poor detection performance, and build these into a logical series of queries for data quality. These queries are then implemented in a programmable microcontroller that insures the conditions for good performance are at hand before registering a corrosion level indication.

DEVELOPMENT PROCEDURES

SENSOR CHARACTERIZATION AND SELECTION

The sensors are K band (24 GHz) transmitter/receivers, and the antenna is a rectangular horn. This selection was made to increase the spot size over the waveguide aperture used in the earlier work. The primary means of characterizing these sensors for this application is to measure the output voltages from the sensor as a function of altitude above the work. The sensors is equipped with integrated (I) and quadrature (Q) outputs from the factory. Figure 1 shows the characteristic curve for the final horn design. The Y axis is the digitized voltage count

for both I and Q. Two other horns, a Mylar coated plastic and a zinc horn of roughly the same size were also considered, and had a similar shape to the curve in figure 1

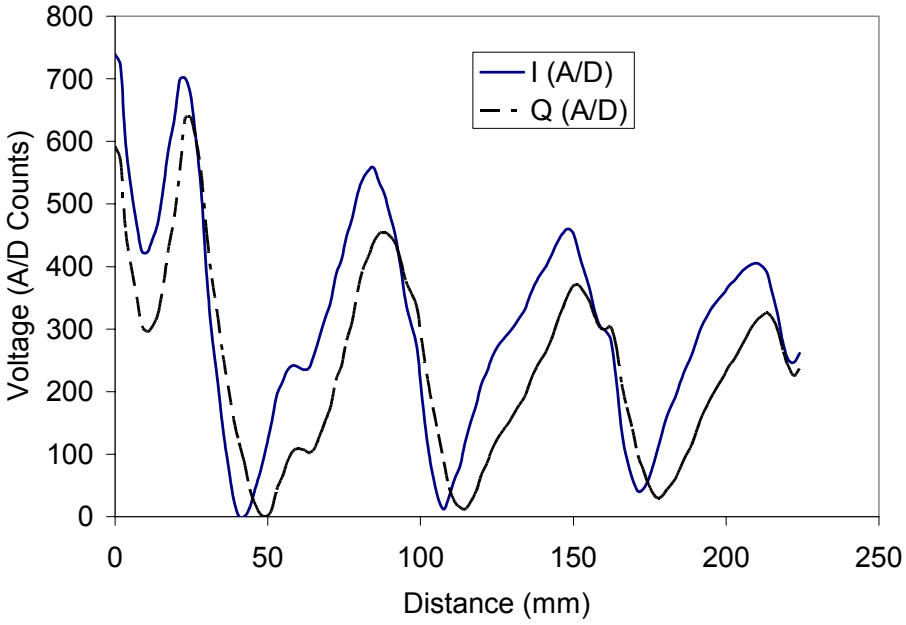

FIGURE 1. Distance From a Flat Plate Versus I and Q Sensor Outputs

The region selected for operation was the in the 30 to 40 mm range. This selection was based on a number of factors:

- Both I and Q are falling off linearly in this region.
- This standoff distance is controllable mechanically and keeps the sensor poised above the work at a convenient altitude for scanning.
- This region has the highest dynamic range of any other similar portion of the sensor characteristic curve.
- Q > I on all down sloping portions of the curve, and provides a data quality check to insure that the operating range is correct.
- This region was the most sensitive to the presence of corrosion.

The Mylar and Zinc horns had more "bumps" in their characteristic curves, but not enough to preclude them from consideration. The most compelling reasons for selecting an integrated antenna design was the ease of mounting, the ruggedness of the horn assembly, and the simplification of the interface to the mechanical system.

When the substrate is corroded the slopes of I and Q versus distance change in proportion to the degree of corrosion being sensed. The presence of corrosion can itself cause a change in the altitude of the sensor above the work – heavy corrosion product formation being thicker. Unfortunately this same effect can result from increases in paint thickness or scanning altitude errors. Thus an MCD design challenge is to separate the effects of altitude and corrosion in designing the NDE tool. I and Q are independent variables, and each reacts differently to the presence of corrosion. The ratio Q/I for an uncorroded specimen at any altitude from base metal is essentially a constant. By forming the ratio Q/I another independent variable is formed that is also independent of altitude change. This is being investigated as another means of minimizing detection decision errors.

Figure 2 shows a measurement of I and Q for each of a number of corrosion specimens (prepared to ASTM 3490 - modified for a nitric acid bath

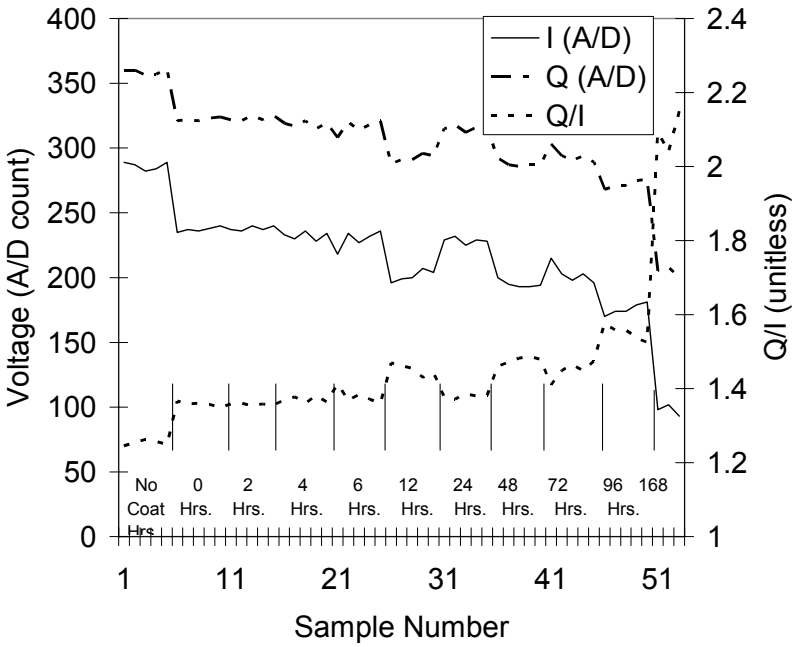

FIGURE 2. I, Q, and Q/I for 10 Corrosion Levels Defined by Plaque Hrs. of Exposure

in the same manner described in [1]). The corrosion specimens range from 0 to 168 hours. The specimens are corroded in the baths and then covered with appliqué. I and Q for each specimen plaque are shown by the 5 measurement replicates at each corrosion level. The ratio Q/I varies with increasing exposure level, starting slowly and beginning to show significant increase around 6 hours of exposure. It ranges from roughly 0.32 to 0.62 over the 168 hour exposure range of the specimens – essentially going from corrosion free to very heavily corroded in a dynamic range of 0.30 in Q/I. The alpha version is configured with a detection scheme based on how I changes with exposure. Newer MCD versions will attempt to add Q/I as a corrosion discriminator. This should make them less dependent on the state of the sensor from the factory and to small variations in altitude above base metal.

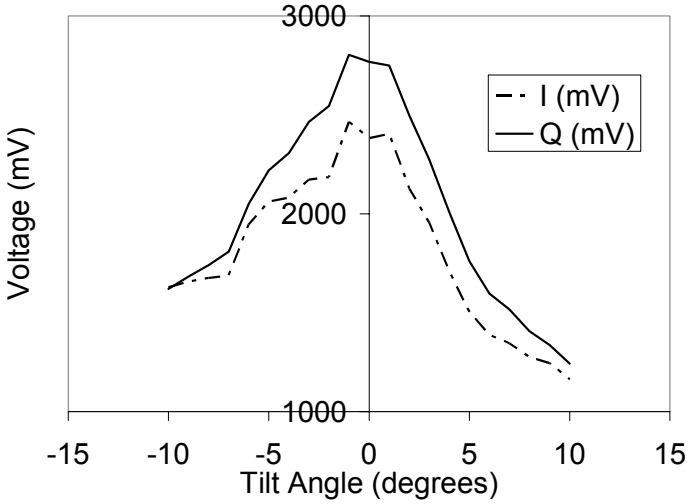

FIGURE 3. MCD Tilt Angle versus Output

MECHANCIAL SYSTEMS

Controlling altitude and tilt angle of the sensor above the work is critical to collecting consistent MCD data. Tilting loses energy to the outside of the horn, and altitude errors as small as 0.005 inches can change the output significantly. Figure 3 illustrates the sensitivity to tilt errors. A tilt of 2 degrees reduces the outputs by nearly 10%.

The mechanical design includes a spring loaded mount that keeps a downward pressure of roughly a pound on the three-wheeled truck under the microwave sensor. Since the horn is an integral part of the assembly its structure provides the attachment point for the wheels. Figure 4 is a photograph of the alpha MCD from the bottom showing the sensor truck assembly.

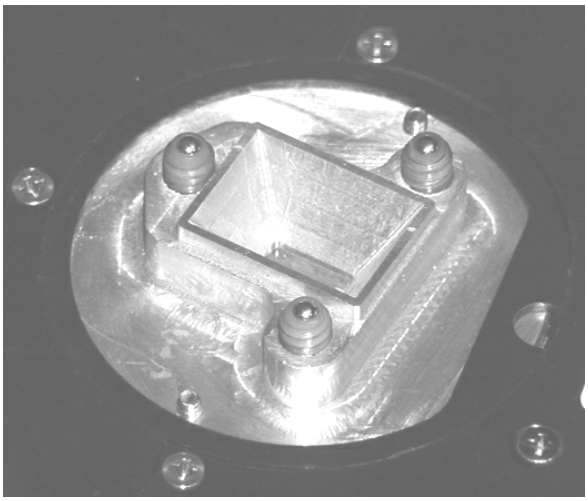

FIGURE 4. Sensor Truck Assembly

SYSTEM DESIGN

The mechanical system maintains height and tilt angle above the work, and the sensor system provides a DC signal proportional to corrosion product build up under the coating. The MCD system design takes these inputs and makes a real time corrosion/no-corrosion decision. The signals from the sensor are digitized and routed to a programmable microcontroller. In addition the microcontroller gets inputs from deadman switch that indicates the sensor has been lifted from the work, battery voltage from the set of 3 – AAA batteries, input form the operator via a main clicker and a mode switch. Some of the functions these signals can initiate include:

- Tripping of the deadman switch turns power off to the sensor. This is a safety issue as well as a power conserving and data checking action.
- If Q < I an error signal is issued and no data can be collected.
- Changing mode - the I value is split up into 8 categories in a pre programmed tables to light the LEDs and send signals to the audio jack on the unit that indicate corrosion severity. Each table is a different “mode” of operation, and up to 8 tables can be stored.

- Battery voltage is checked and an error signal issued if lower than threshold.
- The main clicker – initiates system self-test, starts the inspection, and turns power on and off.

The major modes identified to date include aircraft paint, appliqués, and painted rivets. The first two include sensitivity ranges of medium, course, and fine. These are made increasingly more sensitive by increasing the lower limit in the table and dividing the remaining dynamic range into 8 parts. The rivet mode involves centering the MCD over a rivet for a dwell time of 5 – 10 seconds - sight lines are provided for positioning the MCD over the rivet.

RESULTS

The alpha build MCD development data shown in Figures 1 and 2 are representative of the data collected on corrosion specimens in the laboratory. Recent tests on static aircraft displays and large corrosion specimens have shown:

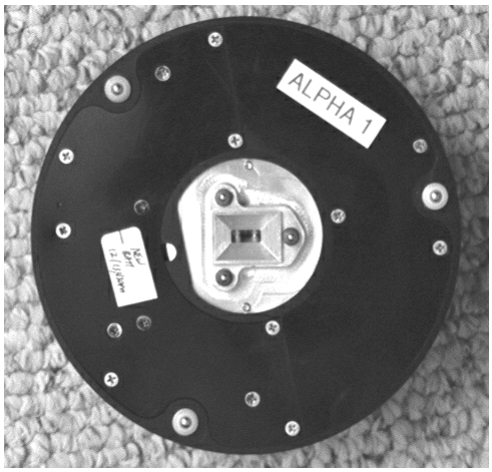

FIGURE 5. Bottom View of MCD

1. Older aircraft paints, particularly those that have developed a chalky surface, can be marred by the inner and outer wheels of the unit. These will be modified to insure that aircraft paint isn't scratched or marred during inspection. Both wheel sets are shown the bottom view of Figure 5.
2. Battery life is roughly 10 hours for continuous inspection.
3. Scan rates to 0.2 meters/second have been demonstrated without data loss.

4. Minimization of false positives and negatives has been reasonably successful to date. As bad data conditions are identified they are countered with program modifications to the microcontroller.

The alpha test program is just getting underway, and a modification to the trucks to handle item 1 above will be made before resuming the test program.

CONCLUSIONS

To date the development of microwave corrosion detectors (MCDs) for inspecting under aircraft paint and appliqués appears promising. The biggest hardware challenges that remain include finalizing the mechanical scan system – primarily in the truck assemblies, and continuing to identify and reduce sources of false positive and negative indications. A testing challenge is to develop a corrosion detection test that includes unknown locations and severities (a blind test). This is a difficult task using simulated corrosion specimens, but may be possible on an aircraft that is scheduled for repainting. After alpha testing is complete, and modifications are made to accommodate shortfalls, a small (10 unit) prototype production run will be made. These units will be tested at selected Navy and commercial airline beta test sites.

REFERENCES

1. A. V. Bray, H. Stretz, S. C. Buckner, "Coating Effects in Microwave NDE in the Detection of Corrosion for Aircraft Applications," NACE 2000, Orlando FL, (March 2000).
2. N. A. Qaddoumi, Shroyer, R. Zoughi, "Microwave Detection of Rust Under paint and Composite Laminates," Research in Nondestructive Evaluation, vol.9, no. 4, (1997).

3. N. Qaddoumi, L. Handjojo, T. Bigelow, J. Easter, A. Bray and R. Zoughi, “Microwave Corrosion Detection Using Open-Ended Rectangular Waveguide Sensors,” To be published in Materials Evaluation (1999).

4. A. V. Bray, K. E. Jenne, N. Qaddoumi, J. K. Easter, T. Bigelow, R. Zoughi, “Microwave NDE Methods for Detecting Corrosion Under Paint,” American Society of Naval Engineers Condition Based Maintenance Symposium, Arlington VA, (June 1998).

CORROSION DETECTION AND PRIORITIZATION USING SCANNING AND PERMANENTLY MOUNTED MWM EDDY CURRENT ARRAYS

Neil Goldfine, David Grundy, Vladimir Zilberstein, Darrell Schlicker,
Ian Shay, Andrew Washabaugh, Mark Windoloski, Mike Fisher
JENTEK Sensors, Inc., Waltham, MA 02453-7013
Phone: 781-642-9666; email: jentek@shore.net

Kenneth LaCivita
AFRL/MLSA, Wright Patterson Air Force Base, Dayton, OH
Phone: (937) 255-3590; email: Kenneth.LaCivita@wpafb.af.mil

Victor Champagne
United States Army Materials Technology Laboratory, Aberdeen Proving Ground, MD
Phone: (410) 306-0822; email: vchampag@arl.army.mil

ABSTRACT

Conformable eddy current sensor arrays, known as Meandering Winding Magnetometer Arrays (MWM-Arrays®), provide the potential to detect, quantitatively characterize, and prioritize near-surface and sub-surface hidden corrosion in structural components. These arrays can be used in a scanning mode, e.g., for wide area imaging, or as permanently mounted sensors for monitoring of corrosion fatigue after a corrosion site has been identified and characterized. When used on metals, MWM-Arrays are eddy current sensor arrays. The MWM-Array has a single drive winding to impose a shaped magnetic field and a linear array of inductive sensing elements to provide high-resolution imaging. Specific advantages over more conventional eddy current arrays, that are composed of individual eddy current sensors, include the following: (1) for hidden corrosion, the single MWM drive can provide deep magnetic field penetration (e.g., similar to a large diameter eddy current coil), while numerous small inductive (or magnetoresistive) sensing elements provide high-resolution imaging (this decouples the depth of penetration from the image resolution, permitting high resolution imaging of hidden corrosion); (2) the Cartesian coordinate design of the MWM-Array (i.e., rectangular as opposed to cylindrical), permits accurate imaging of buried features near edges (e.g., imaging hidden corrosion or detecting cracks at the last row of fasteners in a lap joint); and (3) relatively low cost "sensor tips" (fabricated with standard etching processes) provide registered linear arrays of sensing elements that can be scanned manually (with a simple position encoder) to produce two-dimensional C-scan type images without requiring expensive scanners and with minimal setup time. This paper describes the following demonstrated results: (1) detection and imaging of

corrosion through an insulating layer (to demonstrate detection and imaging of surface corrosion without paint removal), (2) detection and imaging of hidden corrosion for a single-layer structure, e.g., a floor board, and (3) detection and imaging of hidden corrosion in multi-layer structures, e.g., lap joints. Specific examples include (1) imaging of corrosion and material loss from grinding repairs on a C-130 flight deck chine plate section, (2) hidden material loss imaging for second-layer material loss for simulated lap joint material loss specimens, and (3) surface pitting and exfoliation/intergranular corrosion imaging for coupons removed from a corrosion test. Funding for this research was provided in part by the U.S. Air Force, the U.S. Army, and JENTEK Sensors, Inc.

INTRODUCTION

Imaging of damage in aircraft structures with eddy current sensors has proven valuable for assessment of both cracks and corrosion. Typically, individual eddy current sensors are used with scanners that move the sensors back and forth to acquire data for building an image. This is similar to the sewing-stitch patterns used for engine disk slot inspection. The scanners used with conventional eddy current sensor inspections must provide accurate two-dimensional positioning of the sensor to build reliable images. There are some major disadvantages to such "raster scanning" with automated scanners: (1) throughput limitations are substantial when wide areas must be inspected, (2) costs can be high and significant maintenance and setup time may be required, (3) wide area scanners are often only practical for nearly flat surfaces, and these scanners can cover limited scanning areas at a time, requiring constant repositioning to scan large areas, such as a lap joint on an aircraft.

For some applications, a registered linear array that can be scanned rapidly and manually across complex features by available personnel with minimal training may be the ideal solution. It has been suggested by professionals at military aircraft depots that an array on the end of a long pole that is simply scanned manually down a lap joint would be ideal. The problem is

achieving high quality field inspection results with such a low cost scanning apparatus and with minimal setup time and minimal training of available personnel.

Complex components may also require inspection of regions not generally accessible with complex scanners. Inspection systems should be versatile enough to meet field and depot inspection requirements with simple adaptations, e.g., using interchangeable sensor and manual/semi-automated scanner configurations. For example, the inspection of the C-130 flight deck chine plate without removal of wires and on-board equipment requires a thin sensor that can be scanned within a confined area.

Finally, detection of corrosion damage is a minor part of the problem. The real problem is prioritizing detected corrosion for subsequent maintenance and repair efforts. Stories from Air Force and Navy field and depot engineers indicate that a check for corrosion damage in out-of-sight areas is sometimes done by "sticking your thumb through the skin" of a helicopter. Sometimes, corrosion in the fuel tanks, e.g., in the P-3 Orion, has only been discovered after the "fuel starts to leak." Programs requiring comprehensive visual inspection have improved this situation. For example, according to specialists at Tinker AFB, hidden corrosion loss of more than 10% on the KC-135 can generally be detected visually, e.g., due to pillowing and then verified with eddy-current sensors.

However, many situations exist where simply detecting corrosion, visible or hidden, is not sufficient. Corrosion damage must not be prioritized based solely on material loss (in percent). Recent focus on developing damage tolerance methods for corrosion damage requires a more detailed assessment of corrosion damage in terms of its impact on residual strength. Corrosion fatigue life prediction is still difficult, but limited information about the shape and nature of corrosion damage can provide useful information for prioritization of detected

corrosion damage. Decision support for maintenance and repair for individual aircraft, as well as for depot and fleetwide initiatives, requires such information. For example, identifying intergranular corrosion/exfoliation or estimating stress concentration from material loss would support prioritization and might alter the order of maintenance and repair actions.

The MWM-Array technology described here addresses this need for quantitative, low cost, high throughput corrosion imaging. The examples of corrosion imaging described here include manual scanning, with and without position encoders, as well as automated scanning.

MWM-ARRAY TECHNOLOGY

Figure 1 shows two MWM-Array sensor configurations. The MWM-Array in Figure 1a has a relatively wide drive winding spacing of 0.3 in. (7.6 mm) for imaging of hidden corrosion located at up to 0.1 in. (2.5 mm) depth. This sensor has a linear array of rectangular 0.08 in. by 0.04 in. sensing elements. The MWM-Array in Figure 1b has a relatively small drive winding spacing of 0.07 in. (1.8 mm), with relatively small, 0.04 in. by 0.04 in. square sensing elements, for detection and imaging of surface corrosion and surface-connected cracks, e.g., for inspection without paint removal. Note that low-frequency MWM-arrays using enhanced inductive and giant magnetoresistive sensing elements, under development in on-going efforts, should permit inspection of structures with thickness up to at least ½ in.

The MWM-Array drive winding is driven with an electric current at a prescribed frequency (e.g., 6 kHz to 20 MHz). The ratio of the voltage measured at the terminals of each sensing element to the drive current provides the transfer impedance value. A fully parallel architecture instrument with parallel architecture probe electronics, shown in Figure 2, is used to measure the magnitude and phase of the transfer impedance at each sensing element.

This high-speed, low noise parallel architecture instrumentation (e.g., with 37 channels providing absolute impedance magnitude and phase measurements in less than 10 milliseconds) combined with C-scan (2-D) imaging software and position measurement encoders provide rapid

manual or automated scanning, e.g., 2 in./sec. with a 1 to 3 in. wide or wider MWM-Array. High-resolution capabilities also permit imaging of internal geometric features and wall thickness for components with complex surface shape or internal features. This is valuable for manufacturing quality control and repair assessments, e.g., assessment of remaining wall thickness near complex internal features after grinding repairs.

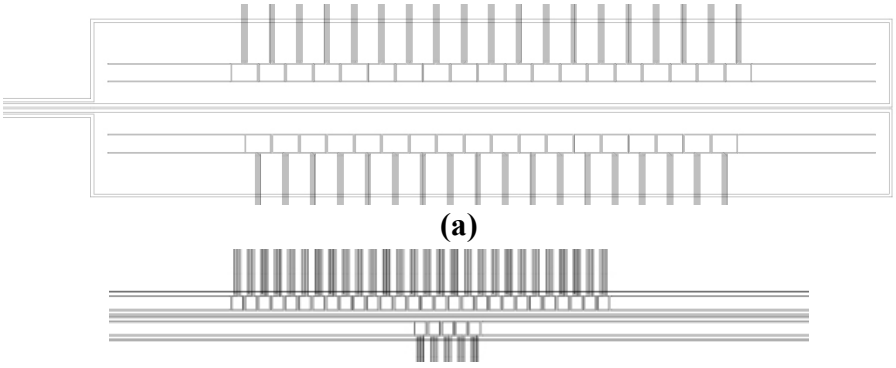

FIGURE 1. (a) MWM-Array with a wide drive winding spacing of 0.3 in. (7.6 mm) for imaging of hidden corrosion up to 0.1 in. (2.5 mm) depth (b) MWM-Array with a smaller drive winding spacing of 0.07 in. (1.8 mm), and small sensing elements for imaging surface corrosion and small cracks without paint removal.

FIGURE 2. (a) MMW-Array probe with up to 37 channels, (b) fully parallel instrumentation with 7 to 39 channels, and (c) interchangeable MWM-Array sensor tips.

To provide accurate imaging of geometric (e.g., metal loss or remaining wall thickness) and metallurgical properties (e.g., heat treatment condition), the MWM-Array impedance instrumentation must provide (1) accurate and precise impedance measurements over a wide frequency range, and (2) predictable sensor responses to variations in the material under test properties. Also, measurements must be fast, calibration and setup must be simple, and required

training and operator experience must be minimal. Available personnel should be able to perform inspections in field and depot environments without significant special training.

To address these requirements, MWM-Arrays are designed so that interactions with multilayer media (such as a lap joint) could be easily modeled from basic physical principles. Then, databases of sensor responses, called measurement grids, are generated in advance to permit direct measurement of two unknowns. Three specific examples of two-unknown problems are described below.

RESULTS

This section provides results for three specific examples: (1) hidden corrosion and geometric feature imaging on a C-130 flight deck chine plate removed from service, (2) second layer material loss imaging for a lap joint standard, and (3) higher resolution surface corrosion imaging on specimens removed from Army Corrosion Retardant Additive Testing after a 1-year exposure at a seaside test facility.

C-130 FLIGHT DECK CHINE PLATE: HIDDEN CORROSION AND GEOMETRIC FEATURE IMAGING

A C-130 flight deck chine plate is shown in Figures 3a and 3b. The plate thickness between the reinforcing ribs varies between 0.043 and 0.047 in. Figure 3a shows the normally inaccessible backside with local areas of corrosion visible in the photograph. Figure 3b shows the exposed surface of the chine plate, with areas of material removal by local grinding. Figure 3a is inverted (left-right flipped) to permit easy visual correlation with MWM-Array thickness (material loss) images. Three regions were scanned with the MWM-Array for corrosion imaging

capability demonstration purposes. In practice, the entire plate requires scanning. Figures 4, 5, and 6 provide results of these demonstration scans performed at a frequency of 10 kHz.

Several specific capabilities have been demonstrated to date:

1. Remaining wall thickness measurement and imaging
2. Imaging near edges
3. Imaging of internal geometric features
4. Calibration in air without standards
5. Rapid manual scanning

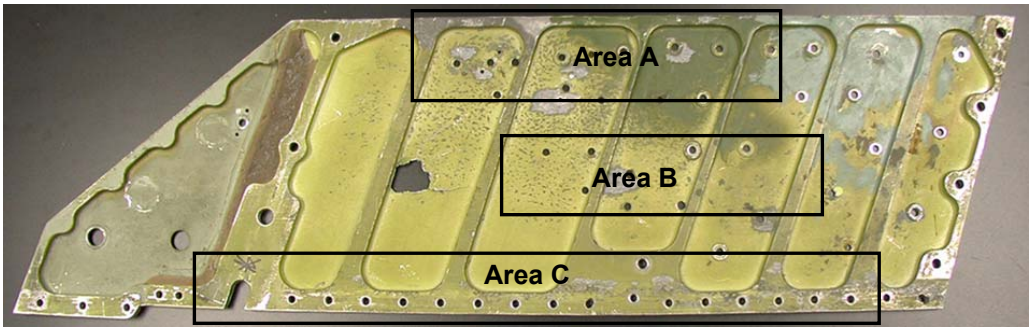

(a) Inaccessible side, inverted photo.

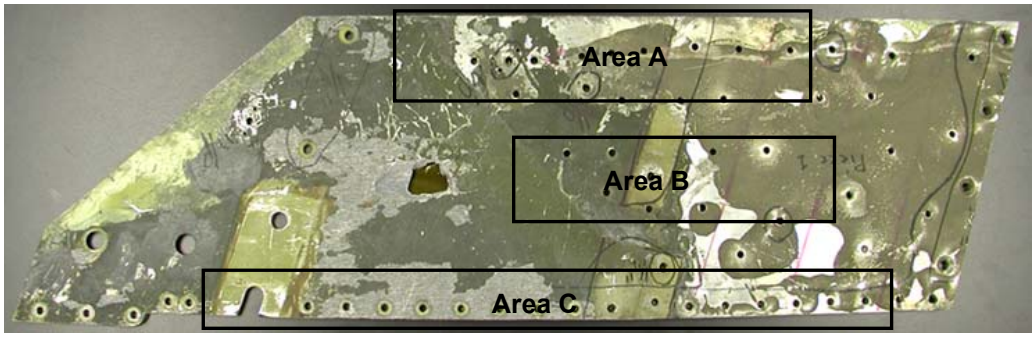

(b) Accessible side.

FIGURE 3. Photographs of (a) inaccessible side, inverted photo (b) accessible side of C-130 flight deck chine plate. Note: For MWM thickness images of Area A, see Figure 4; for Area B, see Figure 5; and for Area C, see Figure 6.

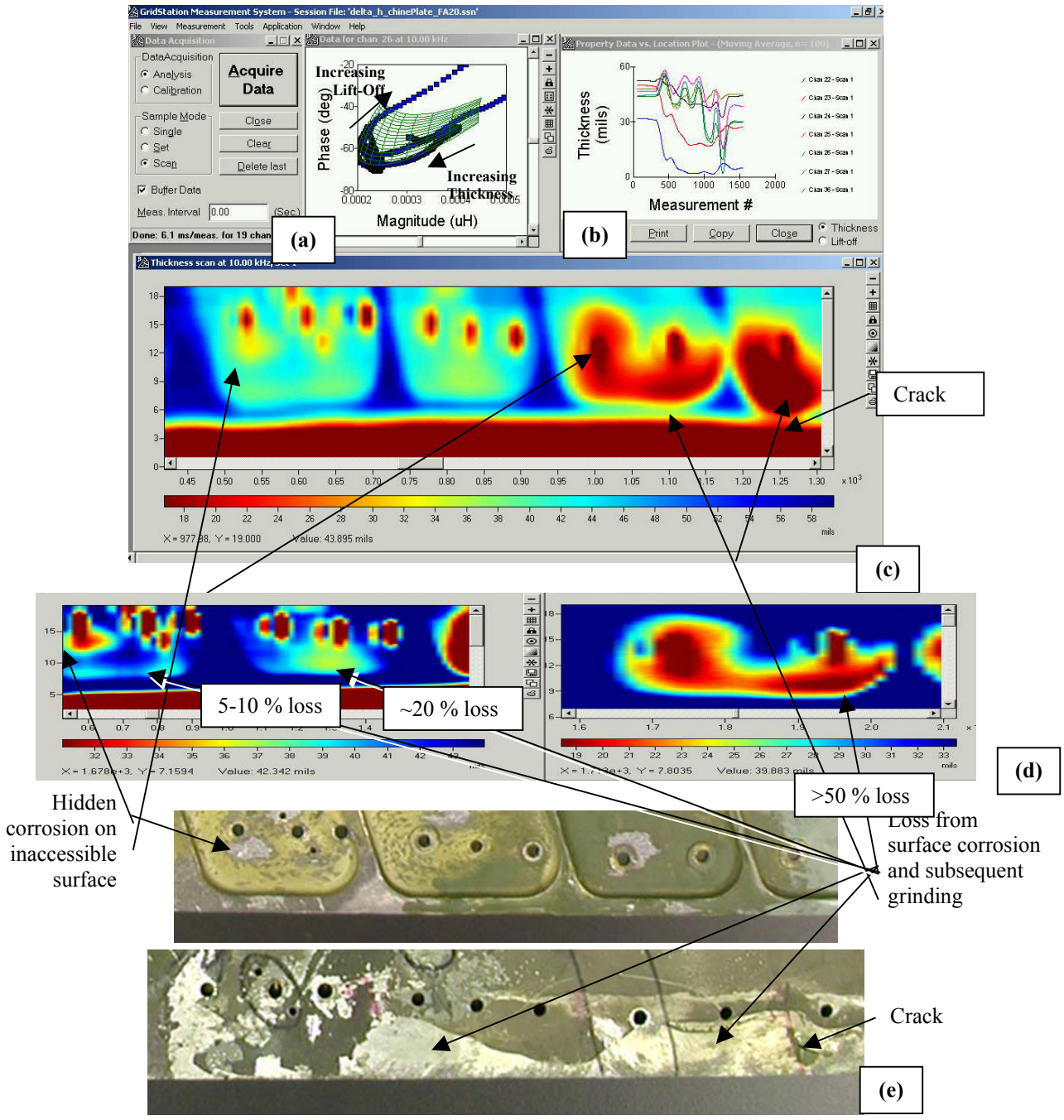

FIGURE 4. MWM-Array scanning of the flight deck chine plate Area A (see Figure 3): (a) measurement grid for two unknowns: plate thickness and lift-off, (b) MWM-Array individual channel thickness measurement responses as a function of scan position along chine plate, (c) two-dimensional **thickness** image for scan along one edge of the chine plate showing regions of material loss due to grinding on accessible side and local areas of corrosion on inaccessible side (this image was obtained by scanning from right to left which resulted in an inverted, i.e., left-right flipped image), (d) blow ups of local areas of MWM-Array thickness image with thickness scale set to highlight local material loss areas, and (e) photographs of the area on the accessible (inverted) and inaccessible sides of chine plate (both photographs are rotated 180° relative to Figure 3).

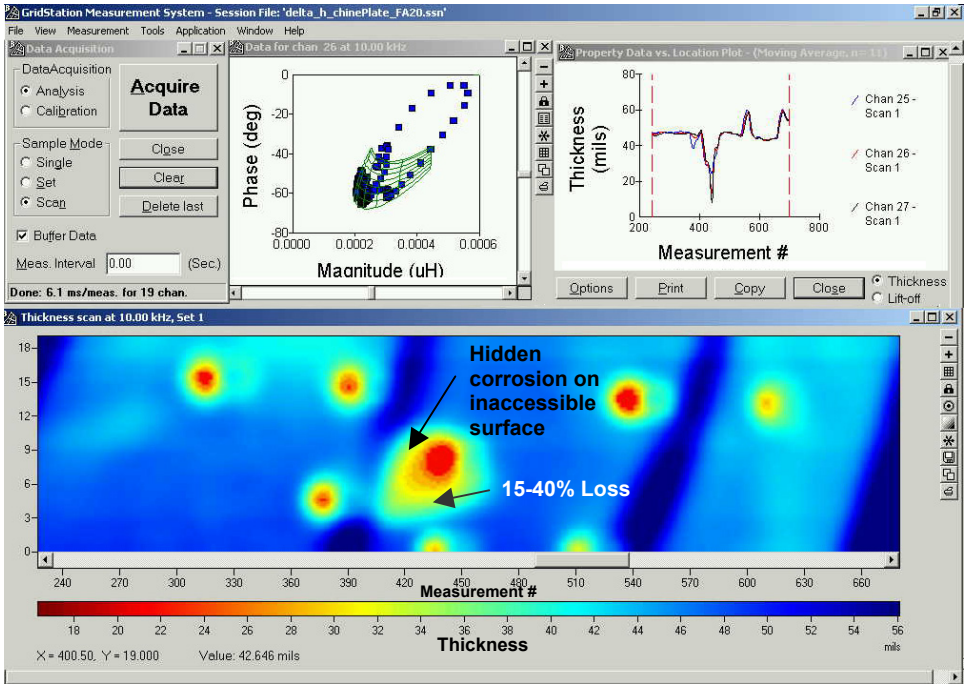

(a)

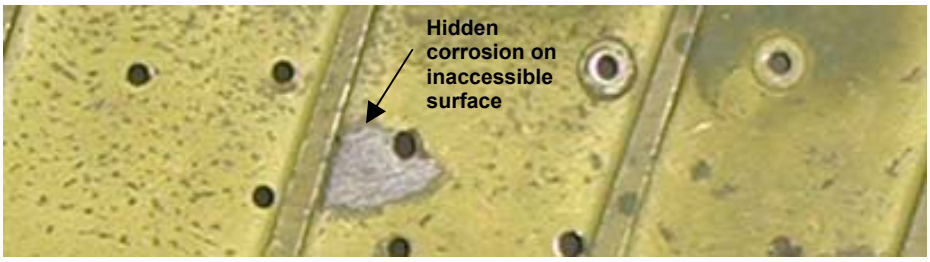

(b)

FIGURE 5. (a) MWM-Array GridStation software windows showing results for Area B. The photo in (b) has been inverted for visual comparison (as shown in Figure 3a).

As illustrated in Figure 4(a), a measurement grid is used to convert the magnitude and phase measurements at each sensing element into estimates of plate thickness and lift-off, where lift-off is the proximity of the sensor to the outer metal surface, including contributions from roughness and paint. The result is an image of the plate thickness, automatically corrected for lift-off variations. This permits scanning without paint removal, which is essential for this chine plate inspection application. Figure 4(b) shows the individual channel thickness data as a function of scan position, while Figure 4(c) provides the two-dimensional image of the region of

the chine plate identified in Figure 3 as Area A. Note that the numbers along the vertical axis in the C-scan images shown in Figures 4 through 6 correspond to channel numbers. Each channel covers a 0.1-in wide area. As illustrated here, the plate was scanned with the MWM-Array shown in Figure 1a, partly overhanging the edge of the chine plate. This permits imaging of internal geometric features and material loss close to complex features such as edges and integral stiffeners (shown in dark blue). This image also illustrates the value of simple expansion of the color scale to highlight material loss as in Figure 4(d) and 4(e).

Note that there are two substantially different types of material loss illustrated in Figure 4. The thickness loss near the leftmost fastener is material loss from hidden corrosion on the inaccessible surface near a fastener hole. The thickness loss that is most significant, however, is the loss shown in Figure 4(e) and on the right of Figure 4(c). This thickness loss is the result of surface corrosion on the accessible surface that was ground out manually to the point that 50 percent to nearly 100 percent of the material has been removed in some cases.

In Figure 5, a thickness image for a section in the center of the chine plate (Area B in Figure 3) is shown. It illustrates a region of substantial corrosion on the opposite side. This is similar to the loss at the leftmost fastener in Figure 4(c).

In Figure 6, a thickness image for the lower edge of the chine plate (Area C in Figure 3) shows similar results. This Figure also illustrates distinct internal geometric features compared to photographs and the scan in Figure 4.

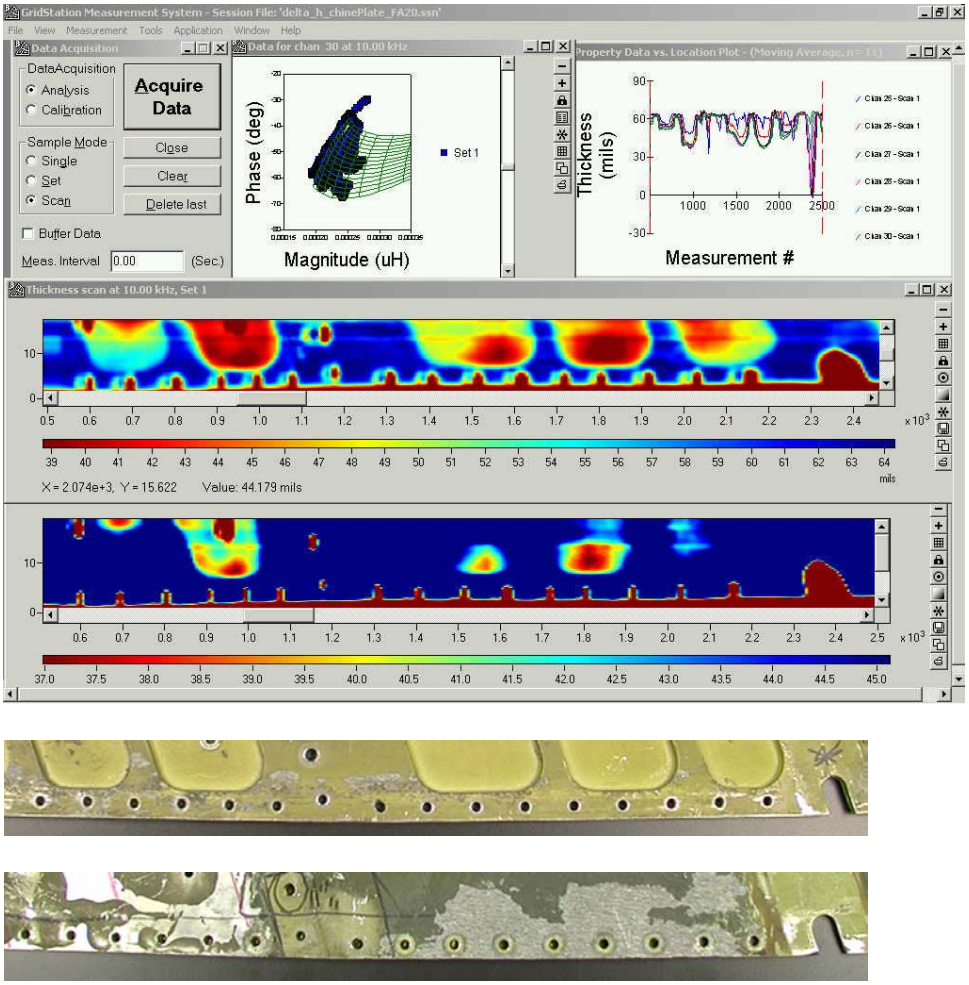

FIGURE 6. MWM-Array thickness images for C-130 flight deck chine plate regions (Area C) where corrosion that occurred primarily on accessible surface was removed by grinding. The two MWM-Array images are shown with different thickness scales to emphasize regions of interest. (Note that the photo of the accessible side is inverted for visual comparison).

LAPJOINT TEST SPECIMEN: SECOND LAYER MATERIAL LOSS IMAGING

This section describes preliminary work on a two-layer test specimen simulating hidden corrosion loss in a lap joint. This specimen was provided by the Air Force. Images of the corrosion loss on the inside of the second layer were taken with the MWM-Array at a frequency of 10 kHz. Improper assumptions regarding the location of the corrosion loss may result in errors in the material loss estimates. For corrosion detection alone, this may not be important. However, erroneous assumptions will affect sensitivity and robustness, and, for prioritization

based on actual material loss percentages, it is critical to account properly for the material loss location. Figure 7a and b provide the responses of a single channel of the MWM-Array to material loss between two layers as the element is scanned across the loss region. For first or second layer material loss, the nature of the MWM-Array response varies significantly with material loss location.

The work described here illustrates the high resolution imaging capability of the MWM-Array and demonstrates its high sensitivity to material loss of 5 percent, with apparent sensitivity to material loss below 1 percent and relative thickness resolution potentially to a small fraction of a percent. Figures 8 and 9, respectively, provide scans of 5 percent and 10 percent loss specimens for both first and second layer loss. The simulated material loss in these specimens had a domed shape with the loss on the inside of the second layer.

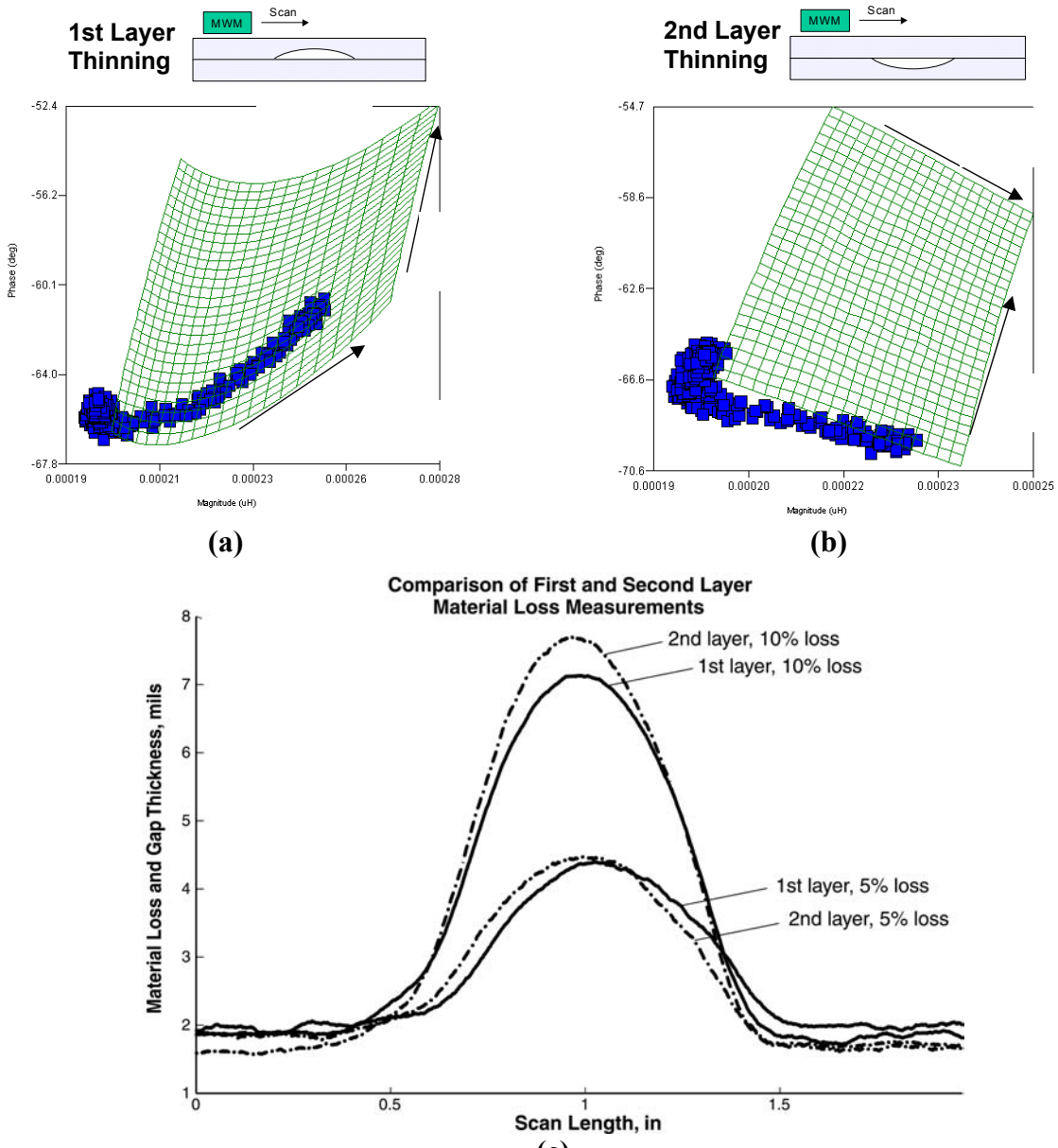

FIGURE 7. Responses of a single channel of the MWM-Array to material loss between two layers as the element is scanned across the loss region: (a) first layer thinning, (b) second layer thinning, and (c) plot of first and second layer material loss for individual MWM sensing elements scanned across the maximum loss point for reported 5 and 10 % material loss.

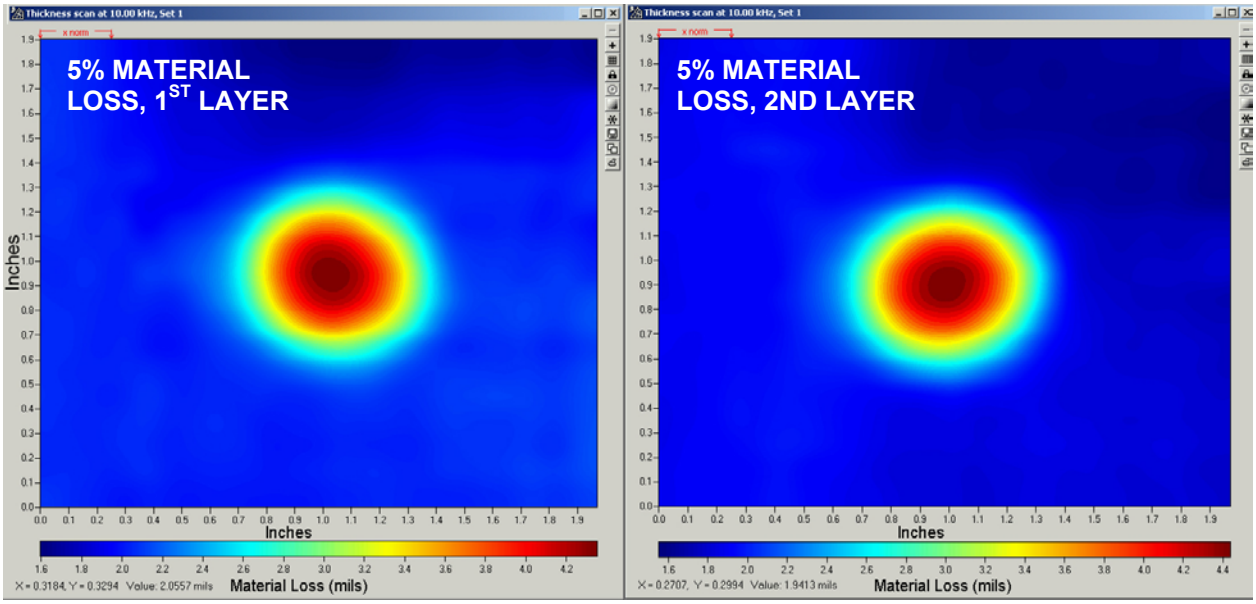

FIGURE 8. MWM-Array generated images of the 5 percent maximum material loss, represented by a dome-shaped cavity on the inside first layer surface (left image) between two 0.04-in. thick aluminum skins; inside second layer surface (right image) between two 0.04-in. thick aluminum skins.

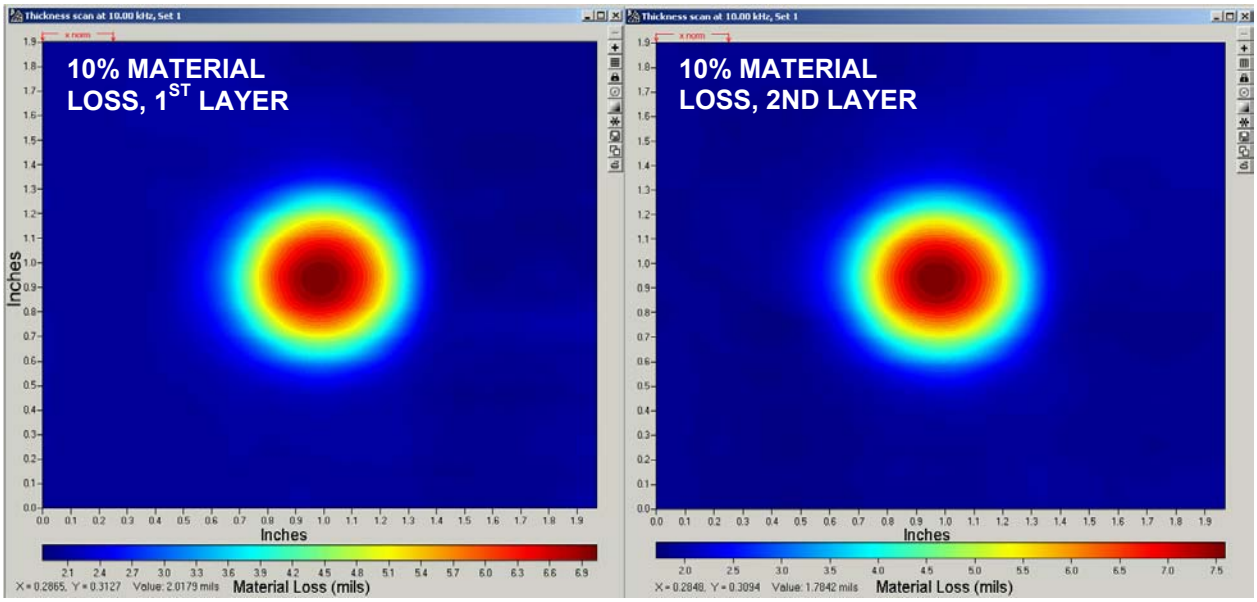

FIGURE 9. MWM-Array generated images of the 10 percent maximum material loss, represented by a dome-shaped cavity on the inside first layer surface (left image) between two 0.04-in. thick aluminum skins; inside second layer surface (right image) between two 0.04-in. thick aluminum skins.

The capability to determine which layer the corrosion loss is occuring (1st, 2nd, 3rd …) for complex structures is critical to prioritization. Here a single frequency method was used. Multiple frequency methods, currently under development, should be significantly more capable.

CORROSION IMAGING FOR COATED AND UNCOATED SURFACES

The goal of the work described here is to demonstrate the capability to map corrosion damage and the potential to determine the depth of pitting and the apparent extent of intergranular corrosion and exfoliation near pits. This paper presents only preliminary results for two coupons removed from Army Corrosion Retardant Addititive Testing after a 1-year exposure at a seaside test facility and a reference coupon (i.e., unexposed coupon).

As part of an ongoing program funded by the Army Research Laboratory (ARL), JENTEK is characterizing corrosion damage for numerous samples of various materials including two aluminum alloys (2024-T3 with two different coatings and uncoated 7075-T6), a magnesium alloy, Ti-6Al-4V, and three steels (only results for 7075-T6 aluminum coupons are provided here).

These coupons were exposed to a harsh marine environment for one year, with weekly rinses using various rinse agents. Details of the U.S. Army corrosion testing program can be found elsewhere.[1]

In the following, preliminary results are presented for three Al 7075 coupons including (1) a reference coupon not exposed to the environment, (2) a coupon with moderate corrosion including pitting, intergranular corrosion and crevice corrosion, and (3) a coupon with more pronounced and more extensive corrosion. During the corrosion testing, coupons (2) and (3) were rinsed weekly, each with different rinsing agents.

Figure 10 provides MWM-Array images of Al 7075 coupons obtained at 1 MHz, through an approximately 0.004 in. thick nonconductive (paper) layer to demonstrate detection through paint. The image in Figure 10 is for the reference coupon with no damage (left side), and the coupon with the more significant corrosion damage (right side). This is an image of the electrical conductivity, corrected for lift-off using a conductivity/lift-off measurement grid. This lift-off is the spacing between the conducting material surface and the MWM-Array winding plane (not including the thickness of the coating on the sensor). These images were taken during the same scan, with the coupons placed on an automated scanner adjacent to each other. The sensor used for this scan is shown in Figure 1b. The sensing elements for this sensor are squares with approximately 0.04 in. (1 mm) sides and center spacing. Thus, the vertical axis in the C-scan images shown in Figures 10 through 14 has units of millimeters. The horizontal scan distance is approximately 4 in. (100 mm).

Figures 11 and 12 provide images of the reference panel with the corrosion coupons (2) and (3), respectively, at two different frequencies with a 0.001 in. insulating shim to protect the surface. There is reasonably good agreement between the images for coupon (3) with a 0.001 in. lift-off and the image with a 0.004-inch lift-off shown in Figure 10. Figure 13 provides a comparison of two repeated images of the reference part and corrosion coupon (3) to illustrate the MWM-Arrays measurement repeatability. Only a very close examination may reveal minor differences. Figures 11, 12 and 13 illustrate that the MWM-Array images can provide not only a measure of relative corrosion damage, but also, judging by the scans of coupon (3) at different frequencies, can reveal, at lower frequencies, additional features that represent intergranular corrosion below the surface. Further investigations of multiple frequency MWM-Array intergranular corrosion/exfoliation assessment are planned to confirm this observation.

For some military aircraft applications, it may be desirable to detect only pits that exceed a certain depth, for example 0.01 in., and to detect all areas experiencing intergranular corrosion/exfoliation. Shallow pits with exfoliation might be ground out if extensive subsurface intergranular corrosion/exfoliation is not present, while individual deep pits and shallow pits with extensive exfoliation may require replacement of skin panels.

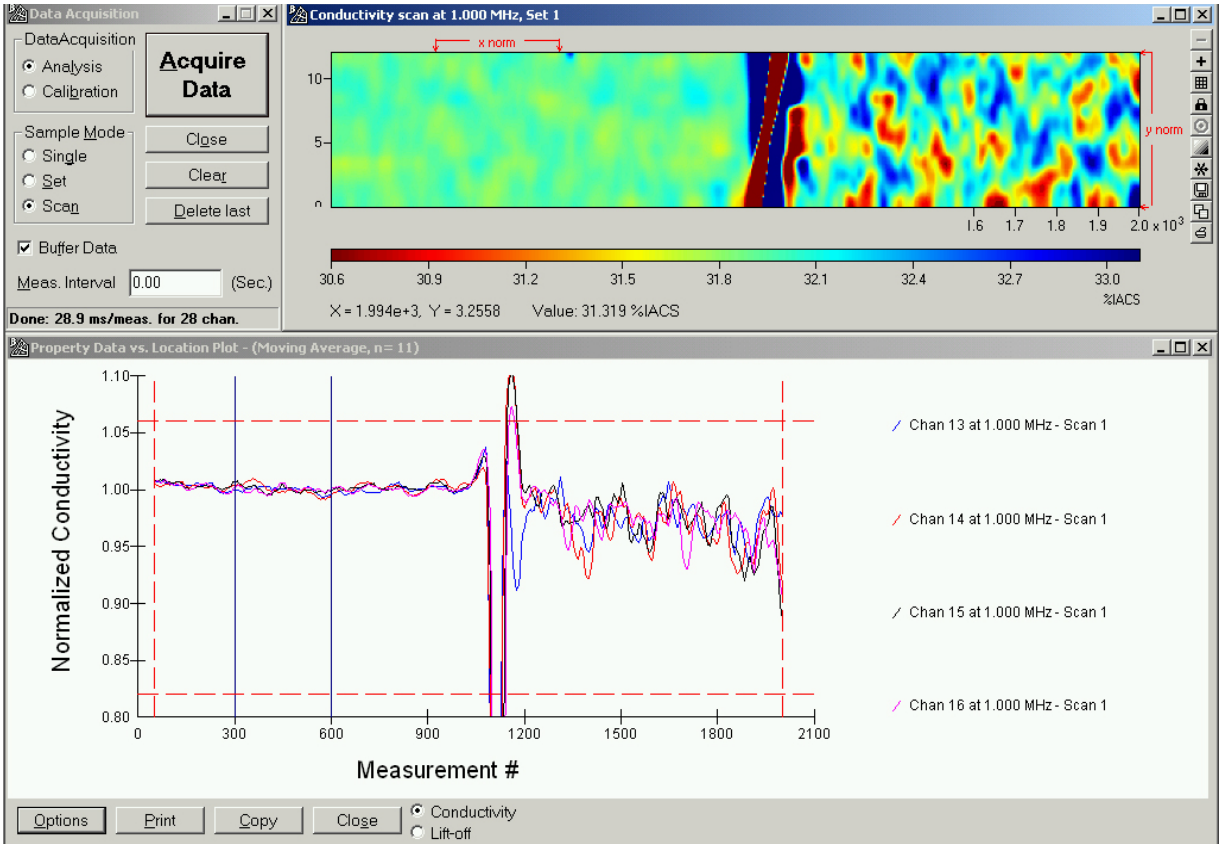

FIGURE 10. MWM-Array conductivity images and MWM responses of selected channels for the reference Al 7075 coupon (left image and responses) and the more severely corroded Al 7075 coupon (3) (right image and responses) obtained at 1 MHz, using the sensor in Figure 1b. The scan was made with a 0.004 in. lift-off (using a piece of paper to simulate a layer of paint). The scan width is about 0.5 in (12 mm), and the scan length is about 4 in. (100 mm).

The MWM-Array image shown in Figure 14 reveals discrete round pits simulated with drilled holes of varying depth in an aluminum alloy plate. This plate sample (provided by

Raytheon Aircraft Integration Systems) had simulated pits with depths ranging from 0.005 in. to 0.05 in. and diameters of approximately 0.015, 0.03 and 0.047 in. The scan in Figure 14 is of the smaller "pits" in the sample, with depths of 0.005, 0.01, 0.02 and 0.03 in. and a diameter of 0.015 in. From Figure 14a it is clear that the MWM-Array signal is sensitive to the depth of pits if the depth of sensitivity is beyond the depth of the deepest pit. Thus, the 158 kHz signal is sensitive to depth while the 1 MHz data is not. A reliable depth measurement can be obtained with the sensor design optimized for a specific application and with a multiple frequency signature derived to obtain a reliable signal to depth correlation. However, it appears from actual corrosion results that individual pit characterization may not be as critical as determination of the depth of the deepest intergranular corrosion/exfoliation.

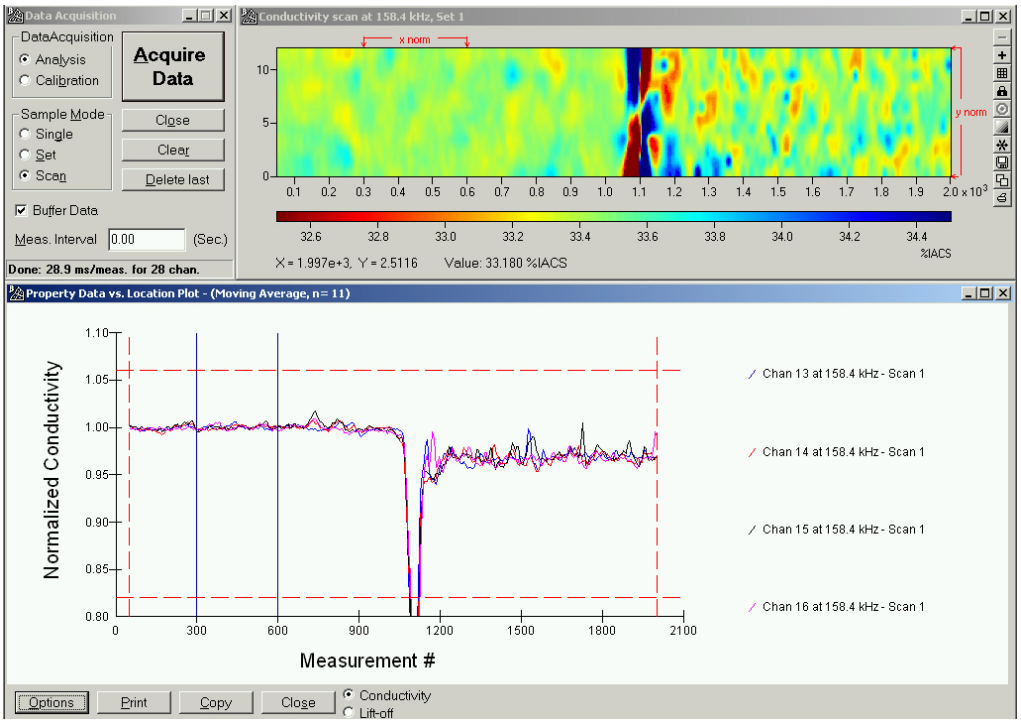

(a)

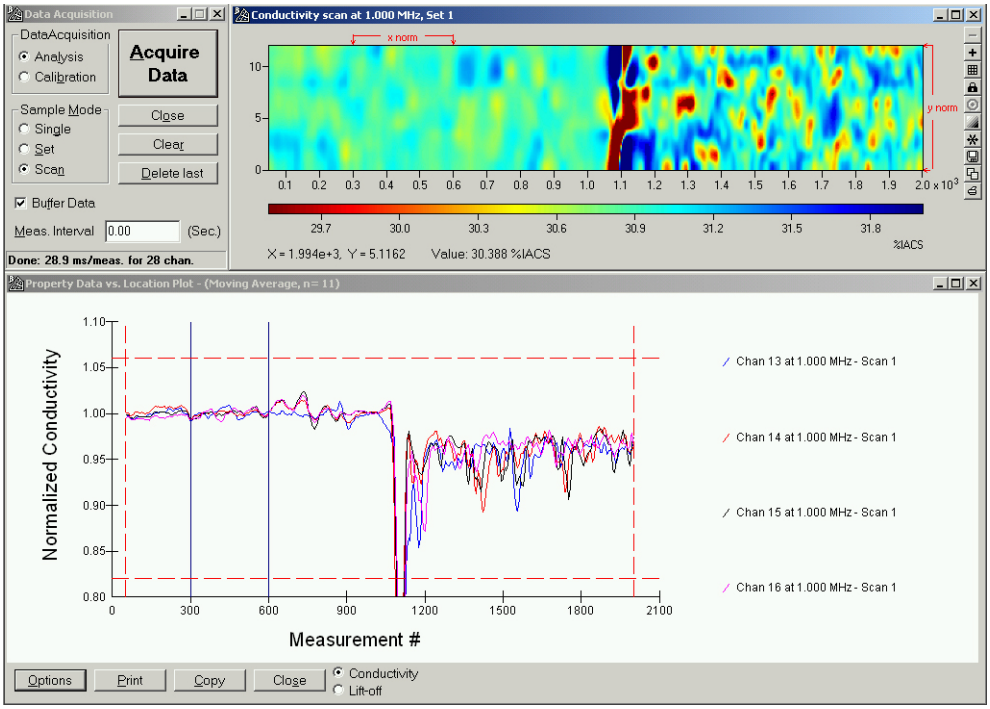

(b)

Figure 11. MWM-Array conductivity images and MWM responses of selected channels, using the MWM-Array shown in Figure 1b, for the reference coupon (left images and responses) and corrosion coupon (2) (right images and responses), at (a) 158 kHz, and (b) 1 MHz, with a 0.001-in. lift-off.

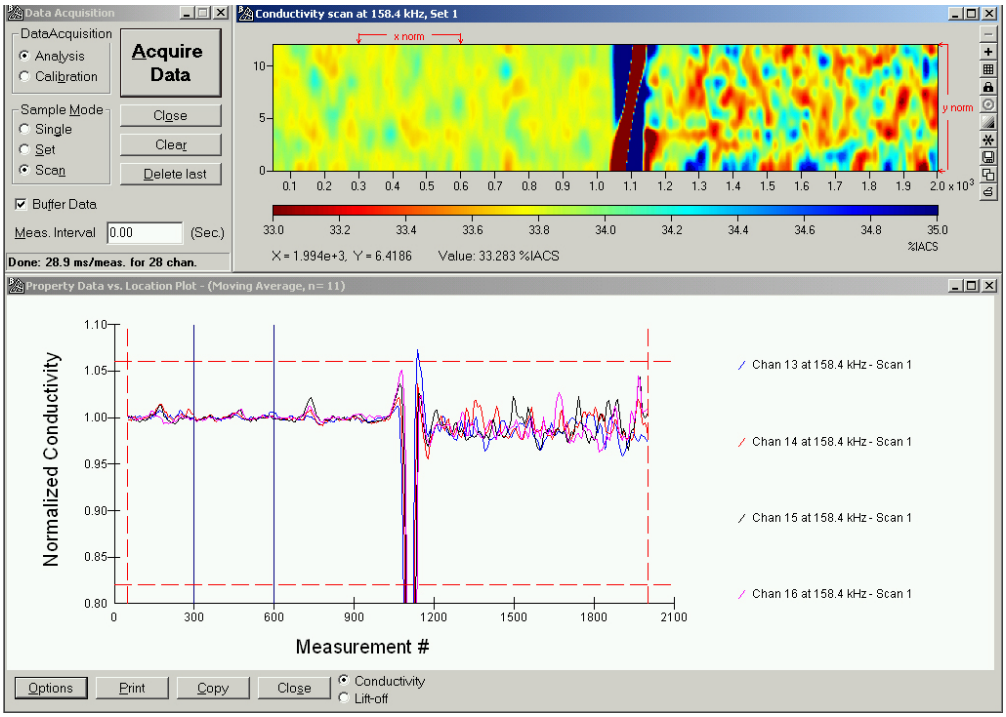

(a)

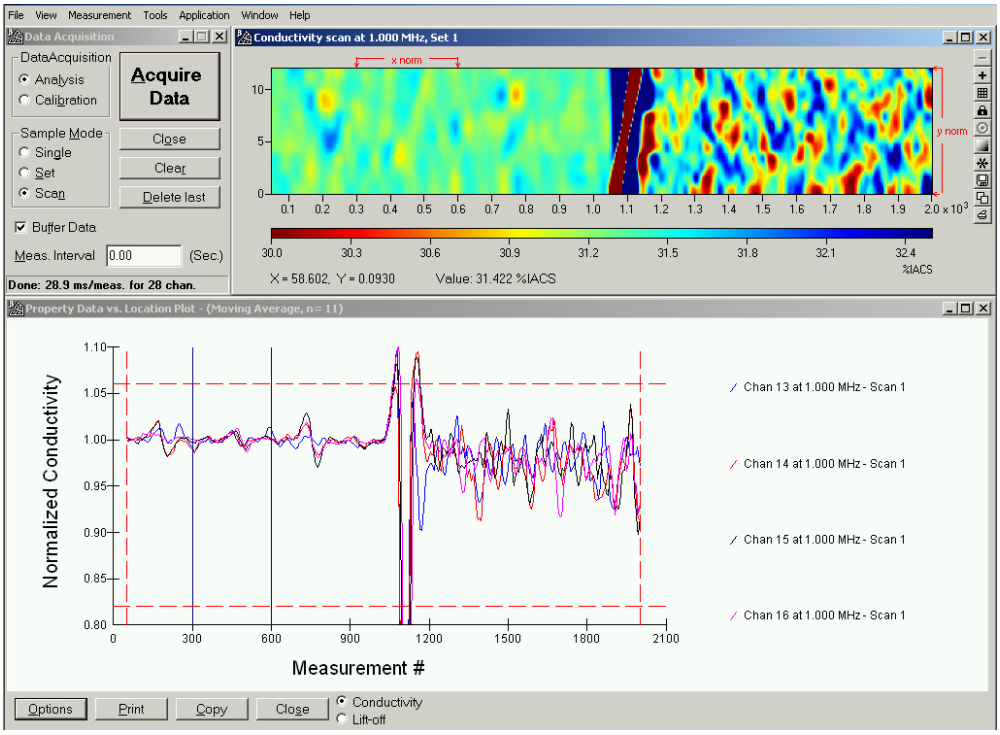

(b)

FIGURE 12. MWM-Array conductivity images and MWM reponses of selected channels, using the MWM-Array shown in Figure 1b, for the reference Al 7075 coupon (left images and responses) and the corrosion coupon (3) (right images and responses), at (a) 158 kHz, and (b) 1 MHz, with a 0.001-in. lift-off.

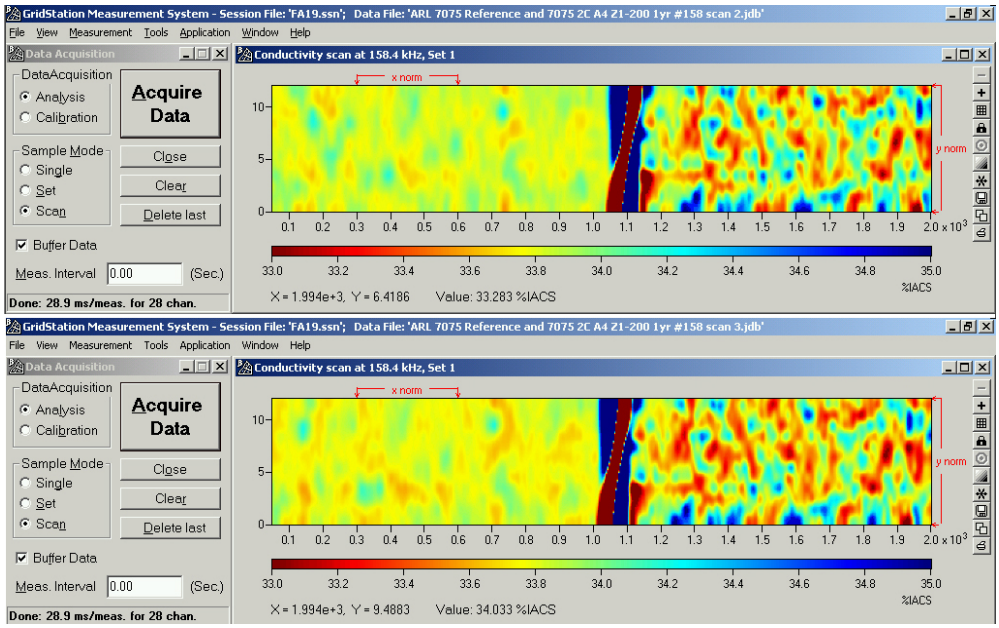

(a)

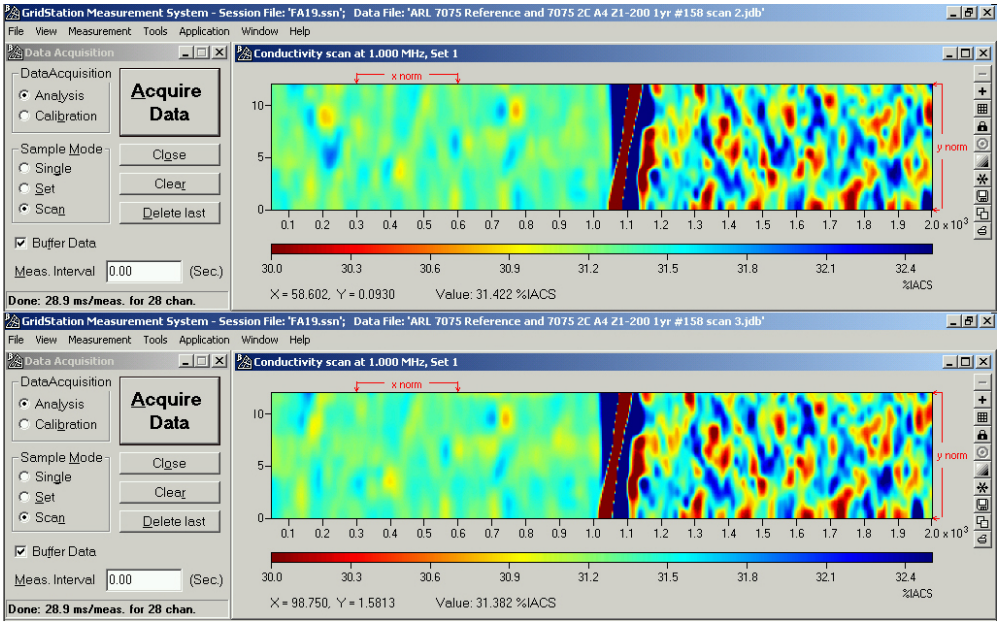

(b)

FIGURE 13. Repeated MWM-Array conductivity images, using the sensor shown in Figure 1b, for the reference panel (left images) and the third corroded specimen (right images), at (a) 158 kHz, and (b) 1 MHz, with a 0.001 in. lift-off. Note that the start and end positions of the scan, from left to right are offset by about 200 measurement points. The scan width is about 0.5 in. (12 mm) and the length is about 4 in. (100 mm).

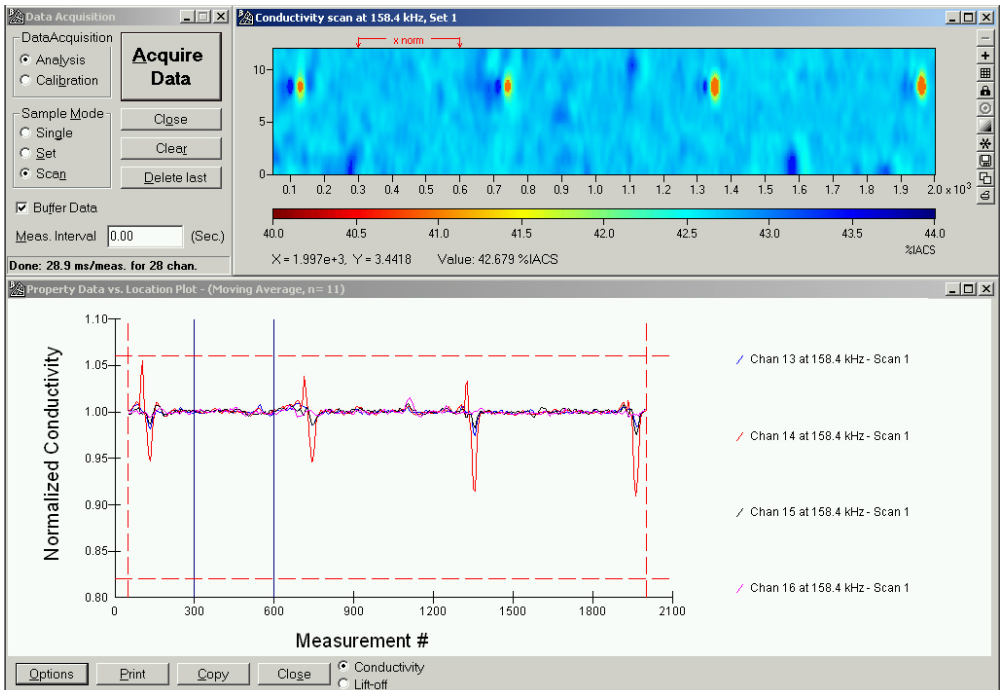

(a)

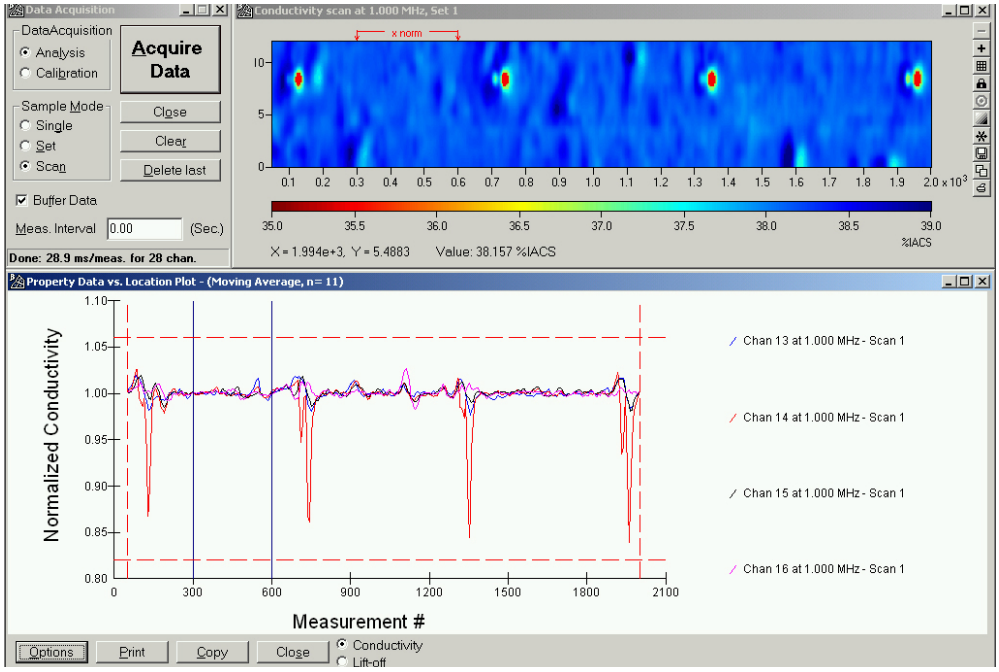

(b)

FIGURE 14. MWM-Array conductivity images and MWM responses from selected channels at (a) 158 kHz and (b) at 1 MHz for the aluminum alloy plate sample with pits simulated by drilled holes. The scan covers four holes with depths of 0.005, 0.01, 0.02, and 0.03 in. and a diameter of approximately 0.015 in.

PERMANENTLY MOUNTED MWM-ARRAYS FOR CORROSION FATIGUE MONITORING

Figure 15 illustrates the potential configurations for permanently mounted rosette and linear MWM-Arrays. These might be used for corrosion fatigue test monitoring and monitoring of difficult-to-access locations on aircraft.

FIGURE 15. (a) Illustration of corrosion-fatigue monitoring with permanently mounted MWM-Arrays. Examples of permanently-mountable MWM-Rosette (b) and linear MWM-Array (c) configurations. Numerous other configurations can be provided.

SUMMARY AND CONCLUSIONS

This paper has described three examples of MWM-Array imaging of corrosion damage and material loss: (1) hidden corrosion on the inaccessible surface of a single layer specimen - a C-130 flight deck chine plate, (2) hidden material loss on simulated lap joint specimens to demonstrate first and second layer corrosion loss imaging, and (3) surface corrosion damage imaging with and without a simulated paint layer.

The MWM-Array can provide relatively rapid imaging of up to several inches per second for the first two examples, with slower speeds required for assessment of pitting and intergranular corrosion. For surface corrosion, characterizing individual pits would require high-resolution imaging at relatively slow speeds (e.g., 0.1in./sec.).

The MWM-Array technology with parallel architecture instrumentation is field portable and suitable for field and depot inspections of flat and curved surfaces. MWM-Arrays can be used with a simple linear (roller or string) encoder to record position, as accomplished for the

hidden corrosion lap joint specimens, or with an automated scanner as for the surface corrosion images.

Also, MWM-Arrays can be used in a permanently mounted configuration after corrosion damage has been identified to permit in-service or laboratory monitoring of corrosion fatigue.

REFERENCES

1. L. MacDowell, J. Curran, T. Hodge, R. Barile, R. Heldersbach, "The Effects of Chemical Wash Additives on the Corrosion of Aerospace Alloys in Marine Environments," presented at the Tri-Service Conference, San Antonio, TX, 2002.

THE CORROSIVE ENVIRONMENT MONITORING (CEM) SYSTEM : AN INNOVATIVE TECHNIQUE FOR MONITORING AND PREVENTING THE FORMATION OF CORROSION ON AIRCRAFT STRUCTURE

John G. Moffatt
U.S. Army Aviation Applied Technology Directorate
Ft. Eustis, Virginia, jmoffatt@aatd.eustis.army.mil

Fred S. Malver.
Honeywell Technologies Center, Honeywell Inc.
Minneapolis, Minnesota, malver_fred@htc.honeywell.com

Sunil Menon, Ph. D.
Honeywell Technologies Center, Honeywell Inc.
Minneapolis, Minnesota, smenon@htc.honeywell.com

ABSTRACT

The detection and prevention of corrosion on military aircraft is vitally important in operation and support (O&S) costs and mission readiness. Due to reduced military budgets and overall downsizing, the Army aviation fleet continues to age. Therefore, maintaining these resources is critical. A recent study concluded that savings of billions of dollars annually could be realized through proper implementation of anti-corrosive practices such as early detection and maintenance. The goal of Corrosive Environment Monitor (CEM) System is to save O&S costs by conducting inspections only when necessary and to detect corrosion before damage occurs to the aircraft. Characteristics of the CEMS is its ability to monitor ionized intrinsic corrosive components that can accumulate inside hidden or inaccessible locations, such as sub-floor regions. Honeywell Inc. is developing the CEM under a contract funded by the Aviation Applied Technology Directorate (AATD) located at Fort Eustis, Virginia.

BACKGROUND

This program expands on work originally developed for the U.S Air Force's Wright-Patterson Laboratory Materials Directorate in Dayton Ohio, in a program entitled the smart aircraft fastener evaluation (SAFE). The SAFE program's goal was to detect corrosion developing in the lap joints of aircraft skins or within aircraft structural members. An innovative

product that spawned from this effort was a micro-sensor array capable of sensing corrosive parameters on a fastener head and surrounding environment that was developed by the Lawrence Livermore National Laboratory.

A follow-on effort was conducted which made modifications to the SAFE technology by replacing the micro-sensor array with full-size commercial off the shelf (COTS) sensors. Also an interchangeable free-potential electrode made with the material that is being evaluated was added to the system. The free-potential electrode functions as a galvanic cell incorporating the material being monitored. The interchangeability of the free-potential electrode provided a relatively simple way to enable monitoring different materials. Changing the sensor configuration enabled monitoring larger more global areas.

CURRENT PRACTICES FOR CORROSION INSPECTIONS

Currently, inspections to check for corrosion are done on an elapsed time basis determined by geographic location. Areas located near water sources have required frequent inspection intervals. Conversely, areas located further away from water sources have relatively longer inspection intervals. A chart showing elapsed inspection intervals relative to city locations is shown at Figure 1. The time intervals are broadly based and do not account for changes of seasonal weather. For example, the summer weather on the East Coast is generally hot and humid, while the fall and springs are typically milder and less humid. As it stands now, coastal areas require basic inspections of aircraft every 15 days, and in-depth inspections every 30 days. Although this may be reasonable for the severe summer weather, it is probably excessive for the more temperate months. Regardless, weather is highly unpredictable and not a completely reliable means of determining inspection intervals. The CEM solves this problem as the actual environmental conditions the aircraft is being exposed to are recorded. Furthermore,

this data is incorporated in an algorithm, which calculates when inspections for corrosion accumulation should be conducted. The CEM will be used to monitor hard to access locations such as the sub-floor region of the aircraft.

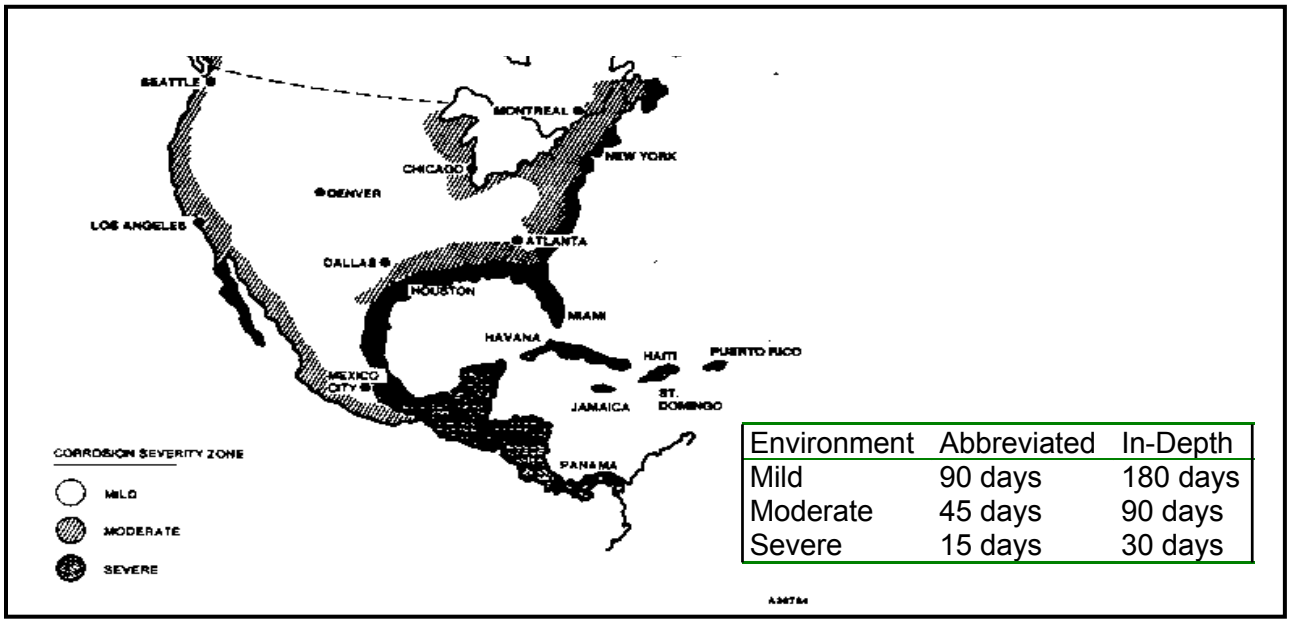

Environment	Abbreviated	In-Depth
Mild	90 days	180 days
Moderate	45 days	90 days
Severe	15 days	30 days

FIGURE 1. Current Calendar-Based Inspection Requirements.

CORROSION ALGORITHM DEVELOPMENT

In order to understand how the CEM algorithm calculates incipient corrosion, one must understand how corrosion develops. Corrosion is the partial or complete wearing away, dissolving or weakening of any structure by chemical or electrochemical reaction with its environment. Examples of corrosive agents to aircraft metals include water, salt, and air. The CEM uses commercial off the shelf (COTS) sensors to monitor temperature, humidity, chloride-ion, and pH levels. An additional sensor is a free potential electrode fabricated with the same metal that is being monitored which acts reference monitor. An algorithm is being developed that weights the relative levels of these monitored parameters to the development of corrosion. This algorithm and the associated parameters are shown at Figure 2. The algorithm will

consider chemistry concepts, empirical laboratory and flight testing data. Scaling of the parameters being monitored will determine a relative corrosion exposure index. Statistical analysis of breadboard tests and field data will verify the scaling parameters. Once the algorithm calculates a given exposure level an inspection of the monitored area is recommended. Thus, the exposure level acts as a corrosion odometer telling the user when to inspect for possible formation of corrosion.

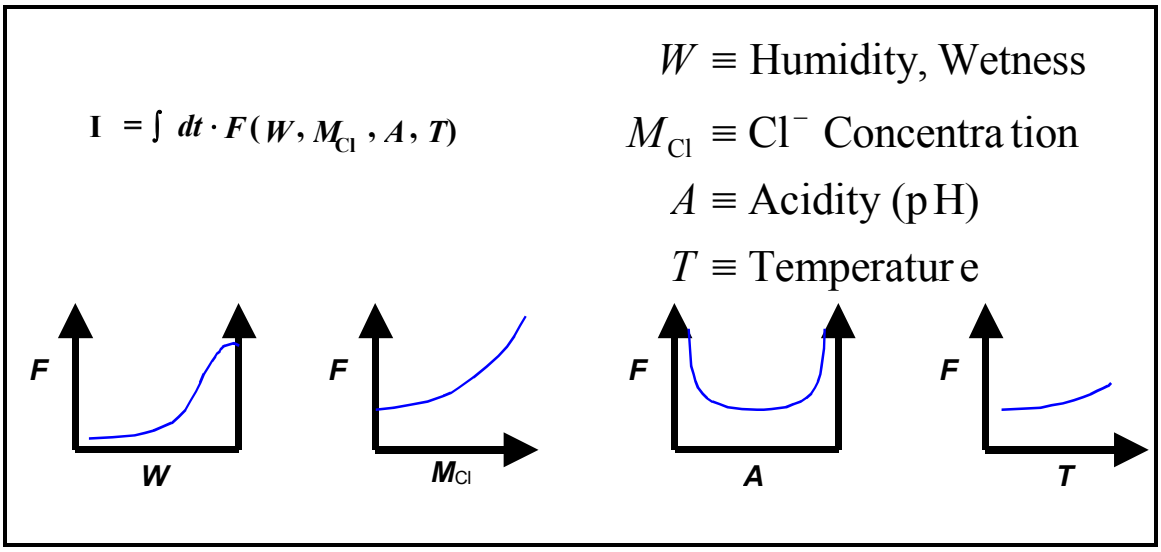

FIGURE 2. Algorithm Development

CEM SYSTEM HARDWARE

The hardware consists of two modules, one to monitor corrosion parameters and a second box to show the user the calculated exposure level. They are designated as the Sensor module (SM) and the electronics support module (ESM), respectively. It is configured this manner so that the SM can be installed in remote hard to reach areas, while the ESM can be placed in an area easily accessible to the maintainers of the aircraft. A long shielded cable is used to connect the two modules. The system is simply powered by four AA batteries. Other features of the CEM include a real-time clock that controls the sampling rate and time-tags the data. The CEM

has been designed to draw very little battery power both when sampling and displaying the data. Since environmental changes normally are gradual, a sample of one per hour would be a reasonable rate. Drawings of the modules are shown in Figures 3 & 4. The ESM features a digital display of the relative corrosion index value and the current individual parameter readings. This provides a "snapshot" of the prevalent conditions of the monitored area.

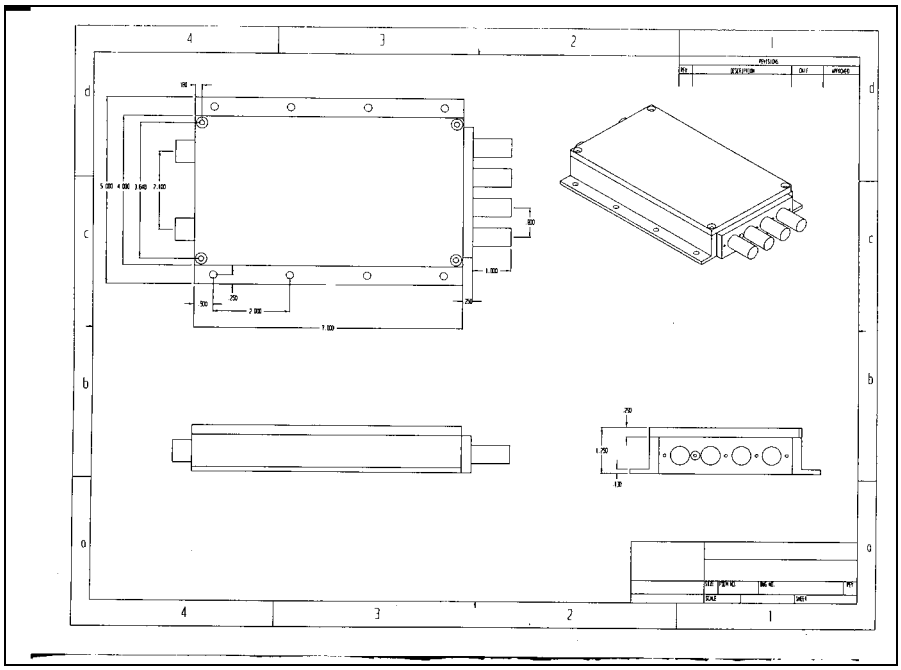

FIGURE 3. Sensor Module (all dimensions in inches).

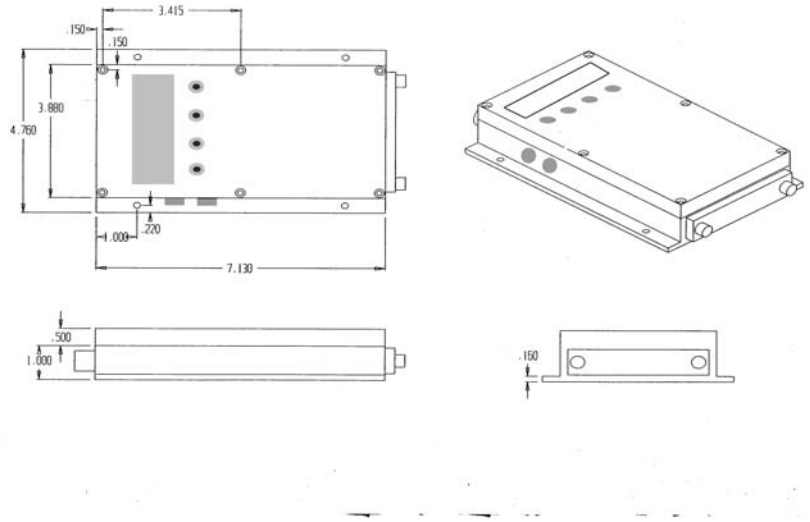

FIGURE 4. Electronics Support Module (all dimensions in inches).

The CEM will be demonstrated in actual field testing at Felker field on CH-47D aircraft used by an Army Reserve Unit. A full inspection of this aircraft can take as long as two days. This is due to the inspection requirement of the large sub-floor area, which often retains moisture and is susceptible to the formation of corrosion. Much of the time is spent removing and reinstalling access panels, which run the length of the aircraft and are attached with a multitude of bolts. Obviously, maintenance officers would prefer to conduct a full inspection only when there is high probability that corrosion is beginning to occur.

CEM SYSTEM INSTALLATION

Installation of the system is simple. The modules are lightweight and are connected by a shielded cable. For the demonstration phase at Ft. Eustis, the modules will be "C" clamped to existing structure. A view of the installation location of the SM is shown at Figures 5 and 6. This area is underneath the floor and is located at the rear of the aircraft near the back cargo bay door, which is sometimes submerged in water. Often water can leak into this area and cause damaging corrosion. The SM will be attached to a honeycomb configured cross beam. The ESM will be installed against the wall behind the last troop seat. It will be accessible by

removing the wall cover that is fastened via Velcro methods. A total of four CEM systems will be used during the test. Two aircraft will use one CEM system each, while a third aircraft will have two CEM systems. Demonstration Phase

It is anticipated that during the one year demonstration phase, the CEM units will prove the current inspection intervals are overly conservative. The reserve unit will conduct their normal inspection practices, while the CEM systems will operate and collect data. Maintenance logs will be correlated with the CEM data and conclusions with recommendations will be made. Ideally, the CEM corrosion meter will recommend inspections at much lower rate than the Reserve fleet practices. Also, when the corrosion meter indicates an inspection should be conducted, it is desired that the monitored area show signs of corrosive activity.

BENCH TEST AND FIELD TESTS

Bench tests were conducted in humidity and salt-fog chambers at Honeywell facilities in Minneapolis. Experiments were performed for a period of 6 months. Coupons were fabricated of 2024-T6 aluminum with dimensions of 2 1/8" x 2 1/8" x 3/16". These specimens were glass bead blasted to obtain smooth, uniform surfaces. In order to document results the coupons were weighed and digitally photographed weekly. Imaging processing software developed by Honeywell was used to quantify corrosion effects on the coupons.

Tests to quantify humidity effects were conducted at 100 degrees Fahrenheit, 80% humidity for four weeks. Nominal corrosion damage resulted from these tests. Saltfog tests resulted in visible damage to the test specimens. Figure 7 shows Coupon #11 after four weeks of 95 degrees Fahrenheit and salt solution 5% by weight. Corrosion pitting locations are documented by white specs on the processed image.

Currently, there is one CEMS installed on a CH-47 D at Felker field. There are plans to install four more units on three aircraft. With two units located in different locations on one aircraft and one unit each on two different aircraft. Data has been downloaded and relayed to Honeywell for analysis and correlation with bench test data. Figure 8 is a plot of the Humidity sensor information for a period of 3 months. A spike occurred during the power wash event. This maintenance action involves high pressure cleaning liquid inside and out on the aircraft.

ALGORITHM MODIFICATIONS

In conjunction with bench tests, field tests and the International Organization for Standardization (ISO) 9223 Corrosion of metal and alloys – Corrosivity of atmospheres – Classification, an algorithm relating the measured parameters to relative exposure rates is being developed by Honeywell. Equations correlating physics of corrosion coupled with empirical data is being constructed. Tables from the ISO 9223 that relate corrosion rate, time of wetness and airborne salinity for aluminum are being coded in the algorithm. These tables are based on years of experimental data. Various assumptions were also made while incorporating data information into the algorithm.

PRELIMINARY COST BENEFITS ANALYSIS

Lastly, the costs and benefits should be considered. Costs of ownership include acquisition, installation, operating and repair/replacement costs. Another cost will be costs due to false alarms. Weighed against the costs are the benefits, which include: reduction of inspections, increased mission readiness, repairs savings and extended aircraft life. It is anticipated the benefits will outweigh the costs and the breakeven point will be reached relatively quickly.

FIGURE 5. Sensor Module Installation Location

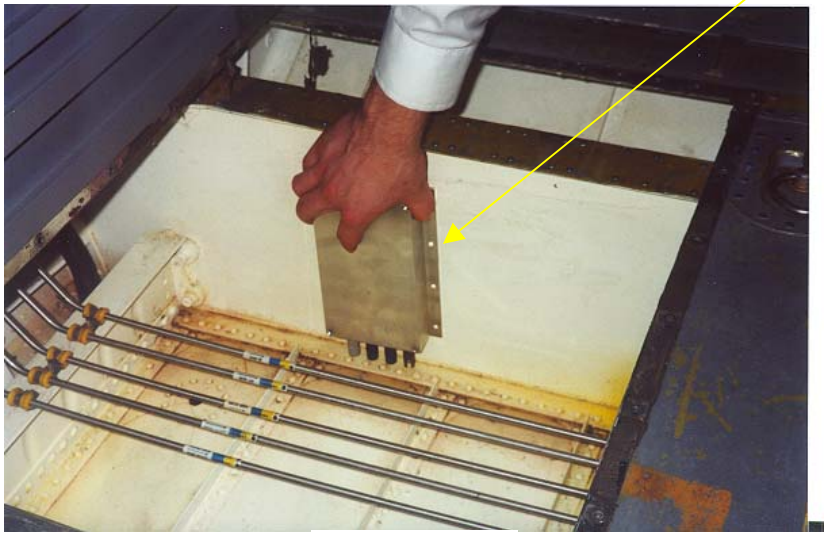

FIGURE 6. Sensor Module Positioned on Sub-Floor Cross Member.

CONCLUSIONS

In summary, the Army is developing a monitoring system, which will aid the maintainer of the aircraft. Actual environmental conditions of inaccessible areas will be known. Therefore, the maintenance officer will be able to practice condition based maintenance which will save on operation and support (O&S) costs and increase mission readiness.

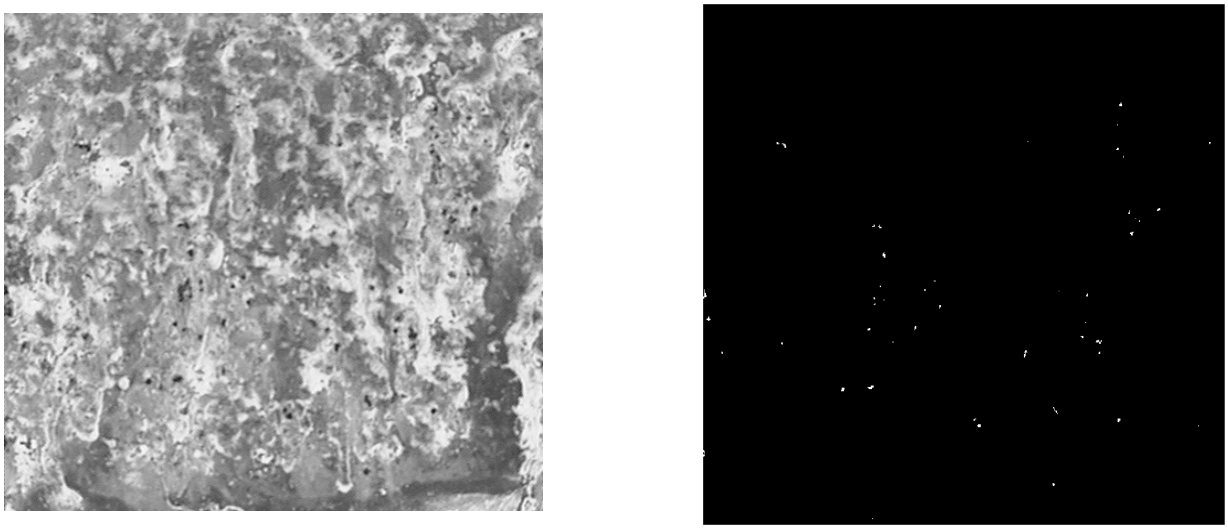

FIGURE 7. Coupon # 11 After Four Weeks Of Salt Fog Tests

Digitized Image Processed Image

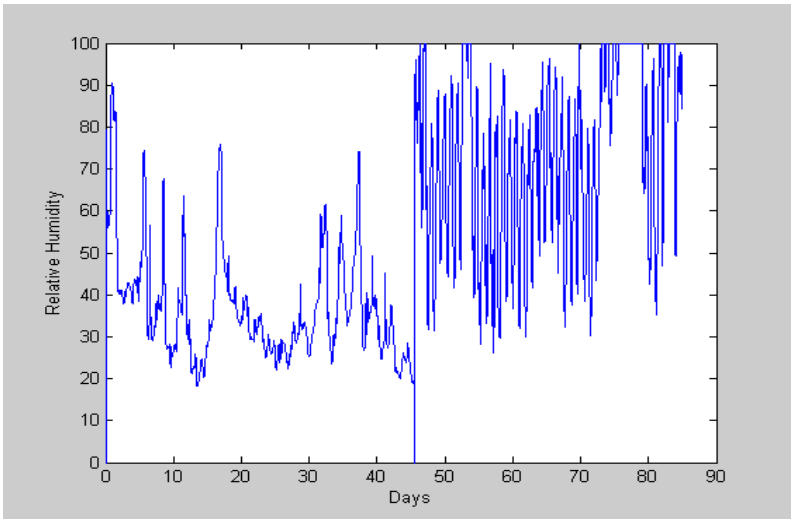

FIGURE 8. Field Test Humidity Data For CH-47 D Sub-floor Area

REFERENCES

1. "Honeywell Corrosive Environment Monitor (CEM) for Health and Usage Monitoring", Fred Malver, Steve Lewis, Ron Jiracek, John Volk, Sunil Menon, Darryl Busch, John Moffatt, Robert Crane, (56th AHS International Forum, Virginia Beach, Virginia, May 2 –4 2000).

2. International Standard ISO 9223:1992(E) Corrosion of metals and alloys – Corrosivity of atmospheres – Classification, First edition (1992-02-15).

NEW TECHNOLOGICAL CHALLENGES FOR GUIDED WAVE NDE

Mr. Thomas R. Hay
The Pennsylvania State University
Engineering Science & Mechanics Department
The Pennsylvania State University
411E Earth & Engineering Sciences Building
University Park, PA 16802
Telephone: 814-863-8026
trh157@psu.edu

Dr. Joseph L. Rose
Paul Morrow Professor
Email: jlresm@engr.psu.edu

Dr. Vinod Agarwala
Naval Air Warfare Center
Aircraft Div. Code 434000A-MS3
Patuxent River, MD 20670-5304
Telephone: 301-342-800
Email: agarwalavs@navair.navy.mil

Mr. J. E. Stephenson
Naval Air Warfare Center
Email: stephensonje@navair.navy.mil

ABSTRACT

This paper summarizes the current research effort focusing on development of ultrasonic guided wave technology suitable for condition based maintenance (CBM) of military aircraft. Early detection of fatigue cracking in the transmission support beam of the SH-60 helicopter is an example of a problem that can be tackled using guided waves. New developments in sensor technology and guided wave instrumentation have made the possibility of embedding sensors permanently on the beam. The sensor can be controlled remotely and valuable information on the condition of fatigue cracking can be obtained using a portable personal computer. The current research thrust is concentrating on integrating wireless communication into the system.

INTRODUCTION

Ultrasonic guided wave technology has been applied to many aircraft inspection applications and is now ready to be implemented as a tool in maintenance of the military's aging aircraft. The challenge now is to integrate sensor technology, wireless communication, and portable data acquisition and analysis hardware into one complementary technology. Although there are many conventional and new innovative NDE technologies that maintenance personnel may select to monitor for damage [1-3] guided waves have emerged as a natural choice for some aircraft applications due to their ability to propagate over long distances, multi-layer inspection capability, and dispersive characteristics [4-9]. In the past, a significant amount of research has been devoted to developing guided wave sensors, instrumentation, and the associated wave mechanics for a given structure. Very little work has actually focused on integrating the complimentary technology. The following discussed the motivation for developing guided wave technology for CBM and the sensors and instrumentation required for realization.

SH-60 TRANSMISSION SUPPORT BEAM MAINTENANCE

The fatigue cracking (Fig.1) in the SH-60 transmission support beam generally initiates close to the middle of the beam and grows outward axially. Table 1 shows the transmission beam cold working chart. Note that repairs occur in 1/64" increments. If the crack is detected early enough, it can be milled out. Currently, the aircraft is inspected every 200 flight hours or 6,000 landing cycles and can be unnecessary since cracking may not be present. By using a condition based maintenance (CBM) approach instead of a time based maintenance (TBM) approach, unnecessary inspections and the associated costs can be avoided. Fig. 2 shows that the current one day inspection of the beam contributes to only 1% of the total maintenance cost of the beam which includes the tear-down, replacement, and parking costs.

COMB SENSOR DEVELOPMENT

Piezocomposite comb sensors were used for the feasibility study since they were readily available from the manufacturer and also because their performance could be easily predicted. The final sensor, however, will use a piezopolymer as the substrate since this material is 10-100 times cheaper than the piezocomposite. A typical prototype piezocomposite sensor can cost up to $500 while in high volume applications the unit cost can be potentially reduced to $100. Prototype PVDF transducers can be manufactured for less than $100 and for high volume applications it may be possible to develop individual sensors for $25-50. See Fig. 3 for a cost comparison of the different sensors that can be used to excite guided waves. Notice that the piezopolymer sensor is the only viable candidate for high volume applications.

AUTOMATED INSPECTION DEVELOPMENT

Each helicopter has transmission beam 16 critical zones, 8 on each beam, where monitoring for cracks is required. The controlling instrumentation can record data from 8 sensors by using a built in multi-plexer to switch from sensor to sensor. This approach minimizes the inspection setup time since only one cable connection is required for 8 transducers. Special built-in software gates are used to analyze the data with analysis tools including real time peak detection, real time signal profile extraction, and real time reference signal correlation analysis. Built-in alarms can then be implemented for each feature. Fig. 4 shows the gate concept.

It was also necessary to develop a protocol for transducer performance and transducer coupling diagnostics. Since it is possible for the sensors to become damaged and/or unattached during flight it is required to perform a pre-inspection test to verify that the transducer is still attached to the beam and functional. This is accomplished by recording the transducer response

before installation and after it is bonded to the structure. The correlation of these two signals will serve as a reference for future data taken from the bonded sensor when compared to that from the initial installation. Any significant deviation from the correlation of the reference signals will alert the operator

Phase 1 of the work focused on the detection of severe cracking and the supporting instrumentation. The instrumentation was developed such that little or no modification would be needed to upgrade the system for smaller crack detection as outlined in the cold work chart above. The only major difference between the systems is the transducer used to inspect for cracking and the detection gates. As a result, the hardware, software, and inspection routines are applicable to both types of crack detection.

The transducer position and wave propagation direction are shown in Fig. 5. The thinner section of the beam is 2.5 mm thick and the 30 mm long. The comb transducer finger spacing was 0.7 mm which closely matched the wavelength of the A_0 in the thinner section at 2 MHz (see Fig. 7). Experimental measurement of the group velocity gave a value of 2.85 mm/us which closely matched the theoretical value of 2.93 mm/us shown in Fig. 6. Tests were performed using the HELIUS system developed jointly by Penn State Ultrasonics Lab and TISEC Inc. The system outputs a gated sinusoid in the 50 kHz to 15 MHz frequency range at a maximum voltage of 300V. The receiver has an output level of 4V and a dynamic range of 70 dB. Sample RF waveforms are provided in Fig. 4 from a crack free and cracked zone. The critical information is found in the 20-24 *u*s and 29-35 *u*s windows corresponding to the crack gate and back edge gates, respectively. As the crack propagates from hole to hole the echo from the back edge diminishes while that from the crack increases.

FUTURE WORK

The next phase of work will focus on the development of wireless sensors and the supporting instrumentation. One approach to implementing wireless technology is shown in Fig. 8. The signal from the local comb transducer is conditioned and amplified then digitized. Following digitization the signal is acquired by a digital signal processor and stored. The stored waveform is then processed as discussed above and the results are transmitted back to the host PC via a telemetry link notifying the operator on the condition of the beam.

CONCLUSIONS

An ultrasonic guided wave system for the condition based monitoring of the SH-60 Sea Hawk helicopter was presented. It was shown that it is possible to monitor for cracking in the transmission support beam using embedded guided wave comb transducers. The design and installation is strongly influenced by the local geometry and access of the beam adjacent to the cracking. The supporting instrumentation development was discussed focusing on the detection gates, real-time feature analysis, pre-inspection diagnostics, and inspection automation. The building blocks for a wireless system that is currently being developed was also presented.

REFERENCES

1. N. Qaddoumi, E. Ranu, J.D. McColskey, R. Mirshahi and R Zoughi, “Microwave Detection of Stress Induced Fatigue Cracks in Steel and Potential for Crack Opening Determination,” RNDE, vol. 12, no. 2, pp. 87-103, 2000.
2. J.S. Sandhu, P. Sincebaugh, H. Wang, W.J. Popek, “New Developments in Acoutography for Fast Full-Field, Large Area Ultrasonic NDE,” in NDE of Aging Materials and Composites IV, George Y. Baaklini, Carol A. Lebowitz, Eric S. Boltz, Editors, Proceedings of SPIE Vol. 3993, 2000.

3. T.R. Schmidt, “The Remote Field Eddy Current Inspection Technique”, Materials Evaluation, 42, 2 (1984): pp. 225-230.

4. J.L. Rose, Ultrasonic Waves in Solid Media, (New York: Cambridge University Press 1999).

5. J.L. Rose, K. Rajana, K. Hansch, “Ultrasonic Guided Waves for NDE of Adhesively Bonded Structures,” Journal of Adhesion, 50 (1995): pp. 71-82.

6. W. Zhu, J.L. Rose, J.M. Barshinger, V. Agarwala “Ultrasonic Guided Wave NDE for Hidden Corrosion Detection,” RNDE, 10, 4 (1998): pp. 205-225.

7. J.L. Rose, L. Soley, “Ultrasonic guided waves for the detection of anomalies in aircraft components”, Materials Evaluation, 50, 9 (September 2000): pp. 1080-1086.

8. D.N. Alleyne and P. Cawley, “Long range propagation of Lamb waves in chemical plant pipe work,” Mater. Eval., 45, 4 (April 1997): pp.504-508.

9. R.S.C. Monkhouse, P.D. Wilcox, P. Cawley, Flexible interdigital PVDF Lamb wave transducers for the development of smart structures”, QNDE (1996): pp 884-887.

10. J. L. Rose and L. Soley, “Ultrasonic Guided Waves for the Detection of Anomalies in Aircraft Components”, Materials Evaluation, 50, 9 (September 2000): pp. 1080-1086.

TABLES

TABLE 1.
Cold Work Chart for Navy H-60 Aircraft

Fastener	Starting Hole Diameter	Initial Ream Diameter	Cold Expanded Hole Diameter	Final Hole Diameter	Mandrel
	Range	Min./Max			
HL20PB-6-X	0.171-0.180	0.177-0.180	0.181-0.183	0.184-0.187	CX6-0-N
HL64PB-6-X	0.180-0.195	0.192-0.195	0.197-0.199	0.199-0.201	CX6-1-N
HL220PB-6-X	0.195-0.212	0.209-0.212	0.213-0.215	0.215-0.217	CX6-2-N
HL224PB-6-X	0.212-0.228	0.225-0.228	0.229-0.231	0.230-0.233	CX6-3-N
HL20PB-8-X	0.228-0.238	0.235-0.238	0.241-0.243	0.244-0.247	CX8-0-N
HL64PB-8-X	0.238-0.253	0.250-0.253	0.255-0.257	0.261-0.264	CX8-1-N

FIGURES

FIGURE 1: Close up of SH-60 transmission beam fatigue crack

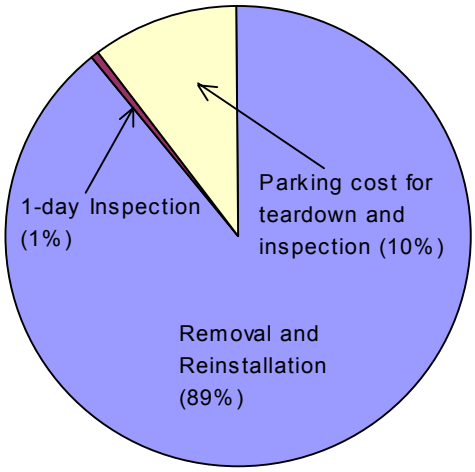

FIGURE 2. Current maintenance cost breakdown.

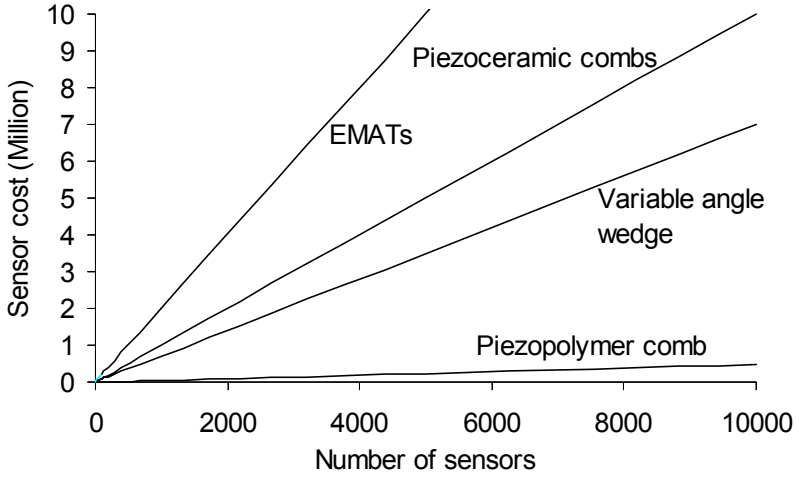

FIGURE 3. High volume application of guided wave sensors

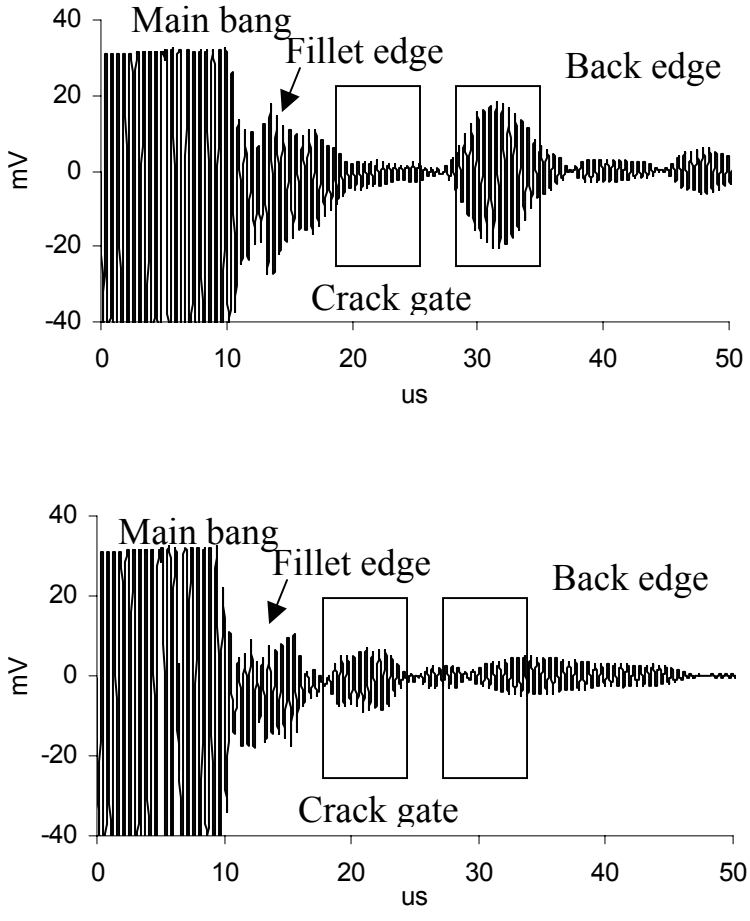

FIGURE 4. Example software gates for analysis of data.

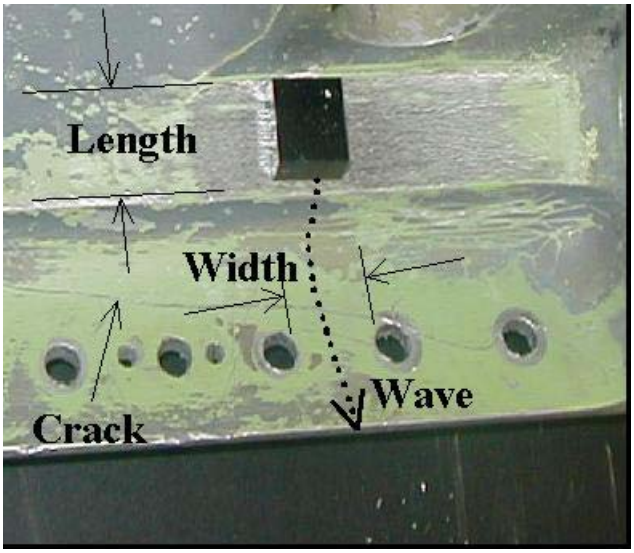

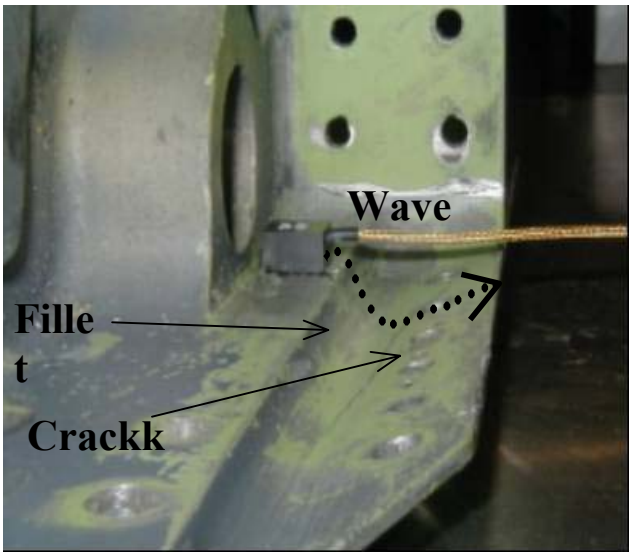

FIGURE 5. Transducer position and wave propagation direction.

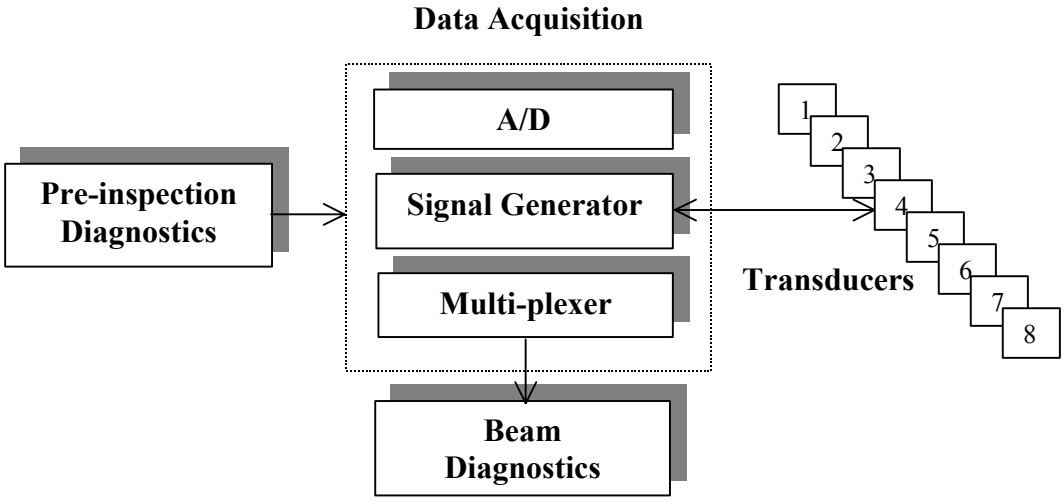

FIGURE 6. Inspection

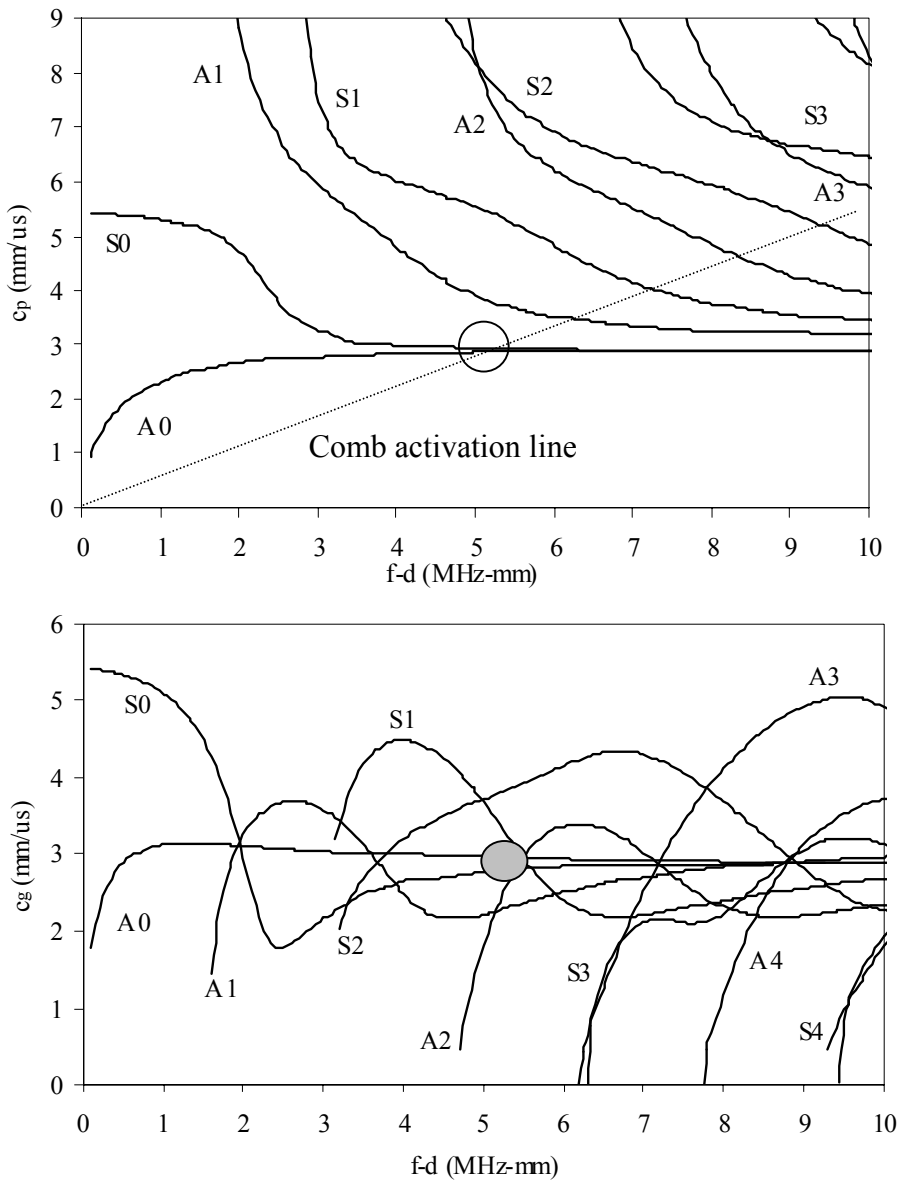

FIGURE 7. Phase (top) and group (bottom) velocity curves for an aluminum plate.

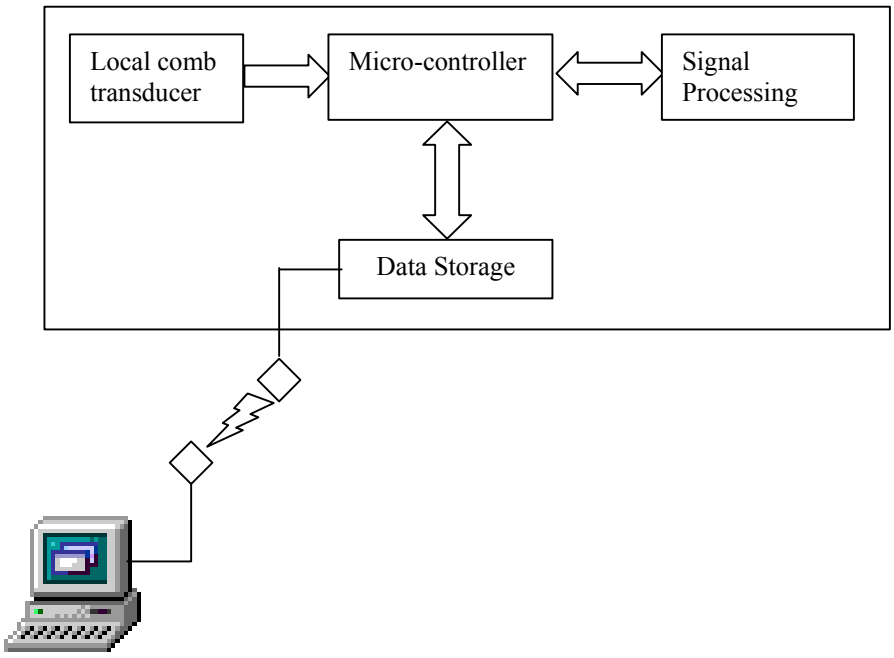

FIGURE 8. Wireless communication with guided wave sensor.

APPLICATION OF REMOTE-FIELD EDDY-CURRENT TECHNIQUE TO AIRCRAFT CORROSION DETECTION

Yushi Sun, Tianhe Ouyang
Innovative Materials Testing Technologies, Inc.., 2501 N. Loop Drive, Ste 1610, Ames, IA 50010
Tel. 515-296-5328, Fax. 515-296-9910
Email. suny@iastate,edu.

ABSTRACT

Aircraft have to operate in corrosive environments. Interlayer regions, lap-joint sections, and areas around fastener holes are all candidates where corrosion can easily take place. Corrosion cannot be totally prevented. However, it can be detected and controlled before it becomes a major problem. Current aircraft corrosion NDE methods include ultrasonic waves, eddy-current, and many other NDE approaches. Few, if any, of these are suitable for such applications, especially for thick and multi-layer structures.

Recently developed highly sensitive Remote Field Eddy Current (RFEC) System shows promise for detecting deeply embedded flaws in aircraft multiple layer structures.

The RFEC system has experienced rapid advances in last few years. The current test data show that the system is capable of detecting deeply embedded discontinuities. Examples include:

1. Aluminum material discontinuity 1.0" below the inspection surface;
2. A 12.7mm x 12.7mm x 0.15mm corrosion thinning 9.5mm below the surface, that is 1.6% thinning;
3. A 12.7mm x 12.7mm x 0.05mm corrosion thinning 4.95mm below the surface, that is 1.0% thinning;A 2.3mm diameter and 0.1mm deep backside machined pitting on a 3.2mm thick 7075-T6 specimen.

A brief introduction of RFEC phenomenon and the RFEC system will be included in the paper. The latest test results will also be illustrated there.

INTRODUCTION

The detrimental impact of corrosion on aircraft surfaces and structural components has been widely recognized for years. Aircraft have to operate in corrosive environments. Interlayer regions, lap-joint sections, and areas around fastener holes are all candidates where corrosion can easily take place. Severe maritime environments, that are often encountered in practice, increase the chance of corrosion and its growth. Corrosion is a major contributory factor both in the initiation and growth of fatique cracks which are formed due to the cyclical nature of loads.

Corrosion cannot be totally prevented. However, it can be detected and controlled before it becomes a major problem. Therefore, corrosion prevention and control technologies help extend the service life of aircraft. Unfortunatley, Aircraft structural components are often hidden by overlying panels and airframe skin. Corrosion and fatigue damage can go unnoticed until the damage is severe. Inspection technologies that are currently used are incapable of detecting corrosion in such inaccessible areas. Maintanance teams have to take sections of the aircraft apart periodically for inspection, with the Navy spending nearly $200,000 per aircraft/year on preventive maintenance. A significant portion of this cost is incurred for taking sections apart. Accordingly, there is a strong need for developing practical and affordable methodologies to mitigate corrosion, to detect and monitor the onset of corrosion processes, to inspect corrosion damage, and to predict corrosion-assisted fatigue of aircraft without requiring sections of aircraft to be taken apart

Current aircraft corrosion NDE methods include ultrasonic waves, eddy-current, and many other NDE approaches. Few, if any, of these are suitable for such applications. Ultrasonic and thermal wave methods are not good candidates due to the air gaps between the layers and are hence limited to the detection of anomalies present in the first two layers. Conventional eddy current techniques (ECT) are limited by the skin-depth effect. Significant improvement must be made to existing ECT to meet the demand for detecting flaws that are hidden deep below the inspection surface

Much effort has been focused on improving the capabilities of ECT for detecting deep flaws. Applications of low frequencies and pulsed eddy current, that contains low frequency components, have improved the deep flaw detectability of ECT in a certain extent. However, the tremendous total-signal/flaw-signal ratio limits the capability of ECT in detecting deep flaws

Currently there are primarily two fundamental approaches used to improve the performances of ECT. The first approach is trying to cancel or compensate the large surface, useless signal by altering probe design or using software. Self-Nulling Probe (SNP)[1] serves a good example of this approach that alters probe design. The sensor and the drive coil of a self-nulling probe are separated by a ferromagnetic cylinder called "flux focusing lens" to minimizes the sensor signal coming directly from the drive coil. Pulsed Eddy Current Techniques (PECT)[2] serves an excellent example that compensates non-flaw signal using software. A flaw signal is obtained by subtracting a previously measured non-flaw signal from the signal measured at the suspected flaw location. Special algorithms have also developed to correct errors due to the difference in lift-offs for the two measurements.

The second approach involves applications of highly sensitive magnetic sensors, including Hall element, Magneto-Resistive (MR) element[3] sensors, Giant Magneto-Resistive (GMR) elements, and Super-conducting Quantum Interface Device (SQUID)[4] sensors. Coils sensors measure variation rates of magnetic fields and do not fit low-frequency applications that are necessary for deep flaw detection. The abovet-mentioned magnetic sensors measure the magnetic fields themselves and work as well in low-frequency ranges as they work at high frequencies.

There is a trend in recent few years that the two fundamental approaches are combined together in a single technique. Examples include: PECT is combined with Hall elements,[5] SNP combined with Giant Magneto-Resistive (GMR) elements.[6]

Remote Field Eddy-Current Technique (RFECT)[7] can be classified as one member of the first approach that altering the probe design and minimizing the signal coming directly from the drive coils. Its major difference of an RFEC probe from an SNP consists of the completeness of

the so-called remote field eddy current effect that makes the domination of the indirect-couple signal in the sensor location.

REMOTE FIELD EDDY CURRENT PHENOMENON

The RFEC effect was first noticed and investigated in conducting pipes. When a coil excited by an alternating current is placed in a pipe as shown in Figure 1, the energy diffuses along two different paths. The interaction between the two fields results in what is often referred to as the remote field eddy current effect. Studies indicate that the energy diffusing via the direct path attenuates very rapidly due to the induced eddy currents inside the conductive pipe wall. The signal received by the pick-up coil that is located a certain distance away from the excitation coil is primarily due to the energy diffusing via the indirect path. This portion of the energy passes the wall twice before arriving at the pick-up coil. Therefore, the signal received by the pickup coil is closely related to the pipe wall conditions, its thickness, conductivity, and permeability. The signal phase angle is linearly proportional to the wall thickness independently from the coil lift-off or wobbles.

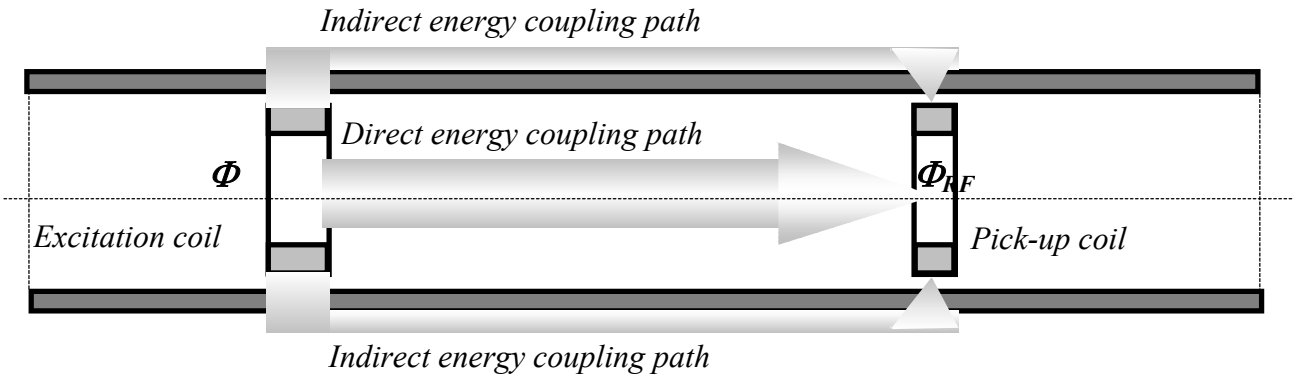

FIGURE 1. Energy transmission paths in an RFEC device inspection pipelines

Recent years have seen the use of the RFECT for inspecting objects with flat geometries. Figure 2 shows the schematic drawing of such a RFEC probe.

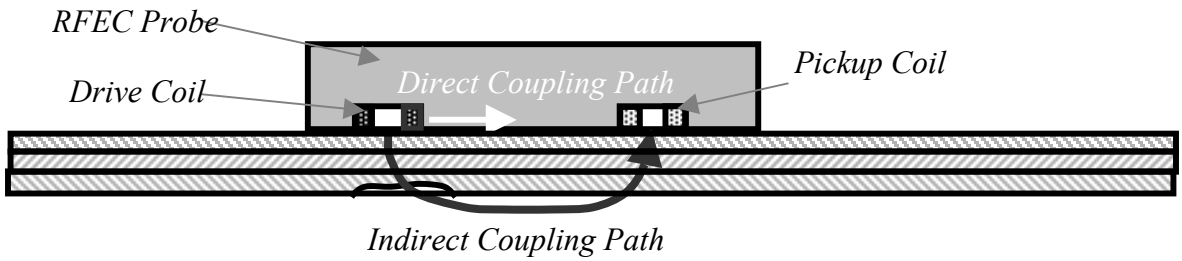

FIGURE 2. Schematic drawing of an RFEC probe inspecting objects of flat geometries.

If two coils, a drive coil and a pickup coil, alone are placed on top of a conductive object of flat geometries, the majority of the energy released from the drive coil goes along the top surface of the object directly to the pickup coil. There will not be any RFEC effect can be seen. The signal measured from the pickup coil has basically no relation to the conditions of the lower portion of the wall.

A special structure including shields and magnetic-circuit is designed and built, see.[7] Extensive finite element simulations were used to obtain the dimensional and parametric relations that guarantee the occurrence of the RFEC phenomenon at the pickup coil location. Experimental measurements have shown that with the existence of the RFEC probe structure the direct coupling path has been basically blocked. The energy release from the drive coil is forced to go downward into the object wall. Then, a portion of the penetrated energy goes back to the wall top at the pickup coil location.

RFECT VERSUS OTHER ECTS

Why RFECT is absolutely necessary to be introduced in ECT for detecting deeply hidden flaw? To answer the question some fundamental study of the detection principles of different eddy current techniques have to be investigated.

Working Principle of the conventional ECT. Coil impendence, Z, or induced voltage in a pickup coil, V, is usually used as the output signal of an eddy current nondestructive evaluation (NDE) system. Theory tells that both Z and V are functions of the total flux, Φ, generated by the excitation coil, see Figure 1. The two quantities increase monotonically with increase of Φ. Magnetic sensors measure flux density, B, at a location close to the excitation coil. This does not vary the Φ-dependent feature of an ECT signal.

Experimental data show that a flaw causes a very limited change in Φ and hence in Z or V_i. Typical values of such changes are in the order of a few percents or a few tenths of a percents. The change in Φ caused by a deeply hidden flaw may be less than 0.01%. In conventional ECT a flaw signal is obtained by subtracting a reference signal, e.g. a non-defect signal, from the signal obtained at the flaw condition, it will be called later on *Acquired-Signal*. Since practically one can never obtain a reference signal at a condition identical to that where the

corresponding acquired signal is measured, the difference from such a subtraction includes the entire contribution from the condition difference of the two measurements. This should be okay in inspections of surface or subsurface flaws where a flaw signal is still dominating in the subtraction difference. However, in detection of deeply hidden flaws when a flaw signal becomes comparable with, or even smaller than, the signal caused by the condition difference of the two measurements, the situation changes.

Working Principle of some new ECTs. In the newly developed eddy current techniques, such as PEC, SQIUD and SNP, some new ideas are included to improve their performances. However, there has been no change in the Φ-dependent feature of an ECT signal. Subtracting a non-flaw signal from an acquired-signal is still the basic method for obtaining a flaw signal.

As mentioned earlier, two fundamental approaches have been used to improve their performances. The first approach involves to improvement of the accuracy of the subtraction and more efficient use of the signal difference. SNP uses a flux-focusing lens to minimize the sensor signal coming directly from the drive coil. Unfortunately, the authors believe, the cancellation is far from complete. PECT makes use of the board frequency spectrum of a transient signal from a pulse-driven probe, uses sophisticated software to analyze the subtracted difference and obtain more detailed information of a flaw. Special algorithms have also been developed to correct the errors due to the difference in lift-offs for the two measurements. However, there is no change in the Φ-dependent feature of an ECT signal. Subtraction of data from the two measurements is still a fundamental step of the method.

The second approach involves applications of highly sensitive magnetic sensors with no alteration of the working principles of the conventional ECT.

Working Principle of some RFECT. RFECT is based on the measurement of the voltage, V_i, induced in a pick-up coil by the flux, Φ_{RF}, which has passed the test object twice as shown in Figure 1. A flaw causes a significant change in Φ_{RF} and hence in V_i. The change in the phase of Φ_{RF} caused by a flaw has a linear relationship with the changes in the wall thickness of an object.

Although the ECT probe signal level is high, the perturbation caused by a flaw is small, i.e. the flaw-signal/acquired-signal ratio is low. This limits the maximum gain that one can employ. In the case of RFECT although the probe signal level is low, the flaw-signal/acquired-signal ratio is high. This allows higher gain levels to be used.

SUPER SENSITIVE EDDY CURRENT (SSEC) SYSTEM RF01A SSEC system has been developed to accommodate RFECT probes. A conventional eddy current system was modified for the purpose. The system is capable of providing an extremely high gain, up to 135 dB, for amplifying the remote-field probe signal.[8] The system has been used to test the samples simulating aircraft structures and shows excellent performance with respect to penetration depth and sensitivity to deeply hidden cracks and corrosion.

A solution to increase the penetration depth for ECT and RFECT is to use low frequencies since the field attenuation in conducting materials decreases with decrease in frequency. However, this does not help when coil sensors are employed. The use of low excitation frequency may result in a change in the magnitude of magnetic flux, but the signal level may not increase due to lower induction at lower frequencies. Sensors capable of measuring the absolute values of a magnetic field directly, including Hall elements, MR, and GMR sensors, etc., should be considered when low frequencies are used in ECT and RFECT.

Unlike most commercially available ECT systems the super-sensitive RFEC system is designed to be able to accommodate these new magnetic sensors. Furthermore, a multi-phase power supply is built into the system for generating a traveling/rotating magnetic wave on the surface of a conducting object. This allows the users to perform a stationary scan thereby eliminating noise due to mechanical movements.

CURRENT STATUS OF RFECT

Recent development shows promise of the RFECT in deep flaw detections. Three typical and frequently used RFEC probes are shown in Figure 3. Some typical test results will be given in later sections of the paper.

RF-4mm V.3
Footprint: 22mm x 55mm

RF-2mm V.3
Footprint: 7.6mm x 15.8mm

RF-2mm ROT
Footprint: 7.6mm x 15.6mm

FIGURE 3. Photo-pictures for three typical RFEC Probes

Four criteria have been chosen to show the advantages of the RFECT over other ECTs. These include:

1. *Maximum detectable depth* of an ECT is defined as the maximum depth in a multi-layered aluminum structure where the ECT probe is still capable of detecting the material discontinuity of the structure.
2. *Detectable depth for a 0.05mm thinning* of an ECT is defined as the maximum depth in a multi-layered aluminum structure where a 0.05mm deep large area thinning can be detected by a probe of the ECT.

3. *Detectable depth for a 1.25mm thinning* of an ECT is defined as the maximum depth in a multi-layered aluminum structure where a 1.25mm deep large area thinning can be detected by a probe of the ECT.
4. *Detectable depth for a 0.75mm ~ 1.5mm crack* of an ECT is defined as the maximum depth in a multi-layered aluminum structure where a 0.75mm ~ 1.5mm long fatigue crack can be detected by a probe of the ECT.

The comparisons are shown in the following four charts shown in Figures 4 – 7.

The four charts indicate that SQUID has about the same capability as the RFECT does. However, an SQUID probe is about 1000mm in its length, while an RFEC probe is about 20mm ~ 50mm long. Comparing to SQUID the RFECT has mush greater flexibility.

Moreover, our estimation tells that the overall cost of an SQUID system would be at least a few dozens times the cost of an RFEC system.

TEST 1 – DETECTING DEEP MATERIAL DISCONTINUITY

The test setup is shown in Figure 8a. A thick aluminum bulk is placed blow a stack consisting of three pieces of aluminum plates of 61.1mm, 8.6mm, and 8.8mm, respectively. Figure 8b shows the imaginary, or Y, component of the raw signal when an RF4mm probe was moving along the top surface of the three-layered, 25.7mm thick aluminum stack and passing over the edge, forward and backward, of the aluminum bulk below.

TEST 2 – DETECTING SIMULATED WALL THINNING

The test set is comprised of two thicker aluminum plates of 8.6mm and 6.6mm thick, respectively, see Figure 9a. Additional five thinner 2024T3 sheets are attached to the two thicker plate stack. The thickness of the structure varies step-wise from 15.2mm to 21.1mm. Figure 7b shows the real, X, and imaginary, Y, components of the raw signal when an RF4mm probe was

moving along the top surface of the seven-layered structure. Figure 9c shows the corresponding points of each step in the complex plane trajectory.

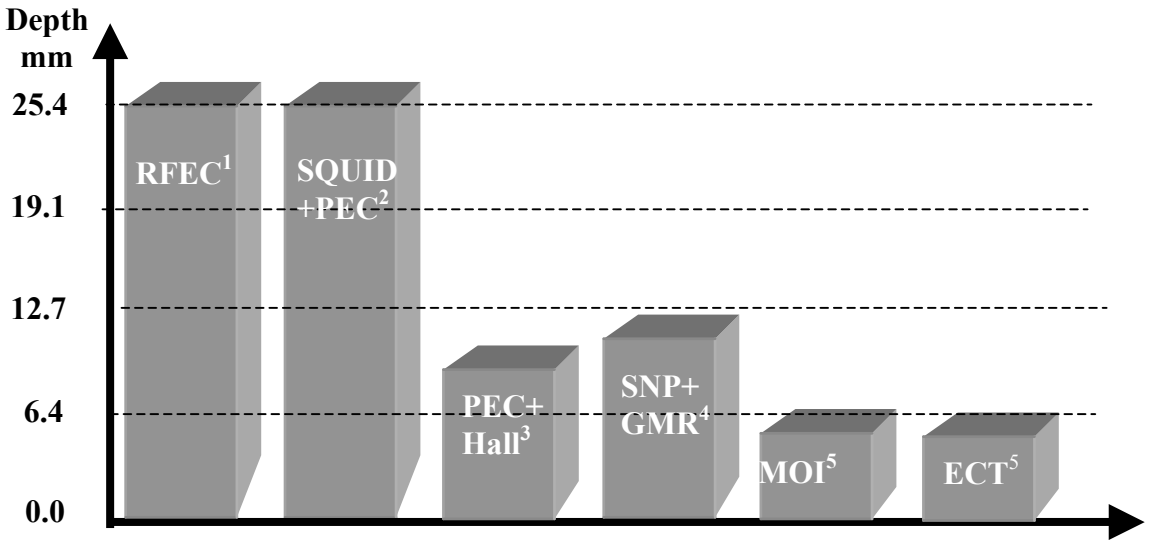

Figure 4. Comparison of RFECT with other ECTs
No. 1 Maximum detectable depth
[1]RFEC – Remote field eddy current technique
[2]SQUID+PEC – Super-conductive quantum interface device plus pulsed eddy current
[3]PEC+Hall – pulsed eddy current plus Hall element
[4]SNP+GMR – Self-nulling probe plus giant magneto-resistive element
[5]MOI – Magneto-optic image
[5]ECT – Conventional eddy current technique

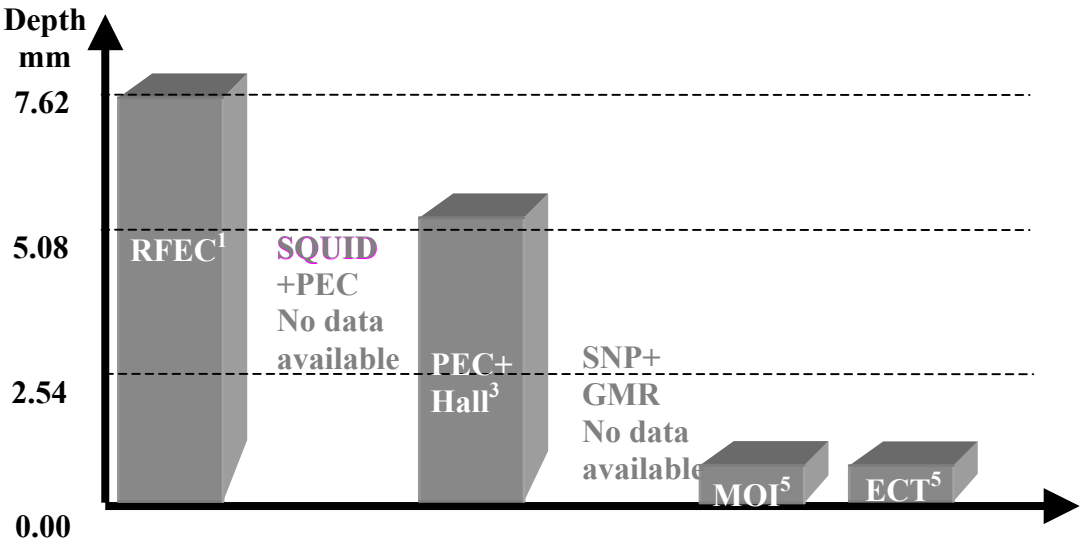

FIGURE 5. Comparison of RFECT with other ECTs No. 2. Detectable depth for a 0.05mm thinning

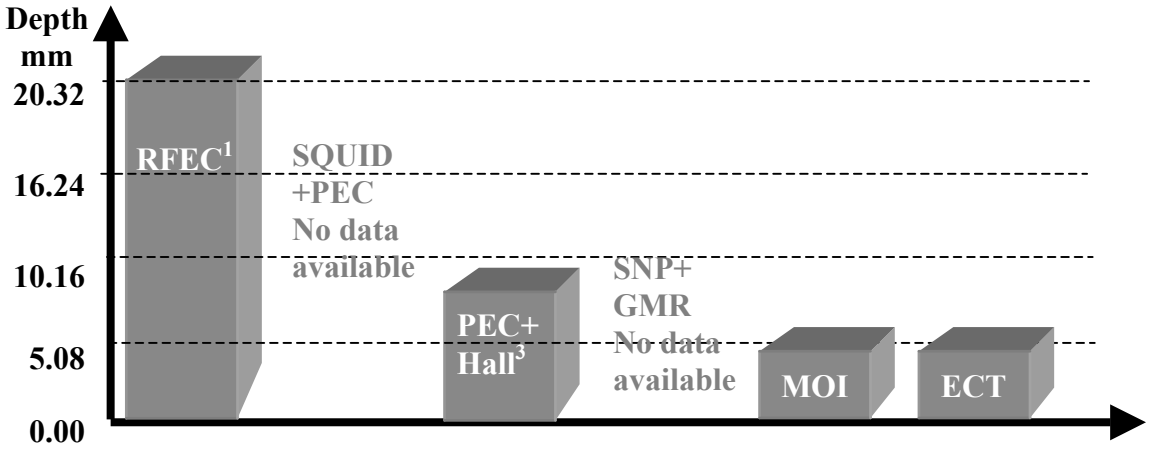

FIGURE 6. Comparison of RFECT with other ECTs No. 3. Detectable depth for a 1.25mm thinning

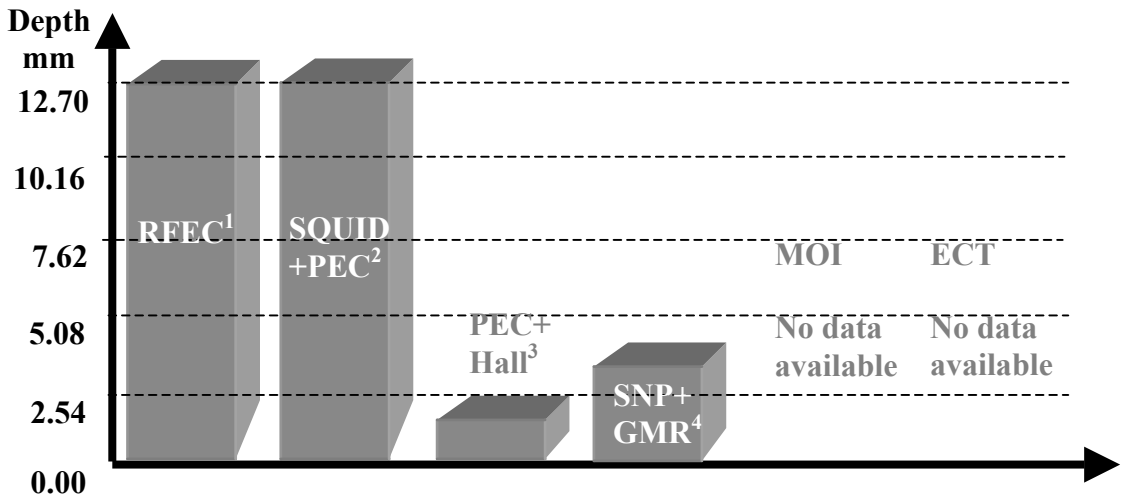

FIGURE 7. Comparison of RFECT with other ECTs
No. 4 Detectable depth for a 0.75mm – 1.50mm crack

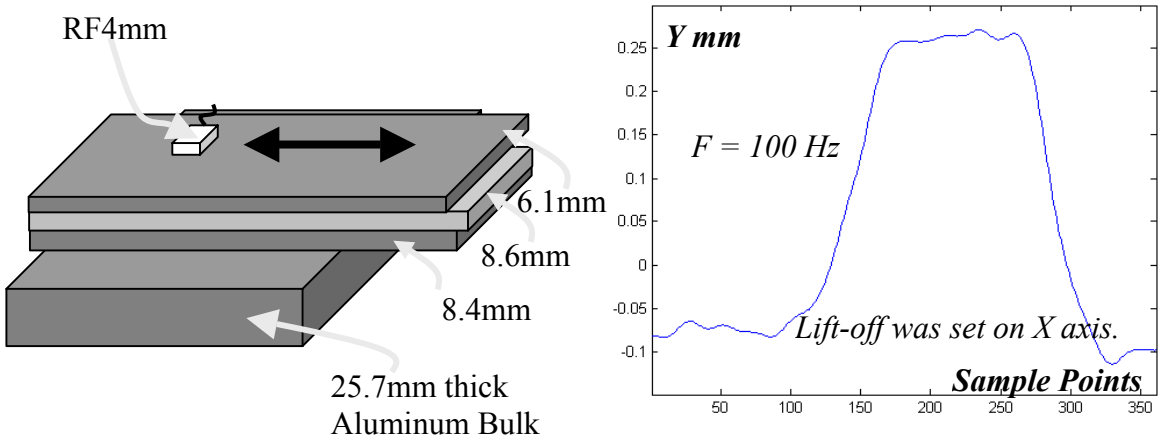

FIGURE 8. Detecting material discontinuity 25.7mm below the surface of inspection.
a. Test setup.
b. Y-component when probe passing over the edge of bulk below the 25.7mm thick stack.

TEST 3 – DETECTING SIMULATED CORROSION THINNING

CNDE corrosion specimen #5 is used in the first subtest. In the specimen chemical corrosion thinning patches of 0.15mm deep with different areas. They are made on one side of a 1.6mm (0.063") thick 2024T3 sheet, see Figure 10a. Two aluminum plates of 6.6mm and 1.25mm thick, respectively, are placed on the non-flaw side of the specimen. An RF4mm probe

is scanned over the top surface right above the 12.7mm × 12.7mm × 0.15mm patch made on the specimen. Figure 10b shows the 3-dimensional signal magnitude response obtained from the scan.

CNDE Corrosion Specimen #1 was used for the second subtest. It is identical to CNDE Corrosion Specimen #5 but the chemical thinning patch are made of 0.05mm deep, three times shallower than that of Specimen #5, see Figure 11a. Three aluminum plates of 0.8mm, 1.25mm and 1.25mm thick, respectively, are placed on the non-flaw side of the specimen. An RF2mm

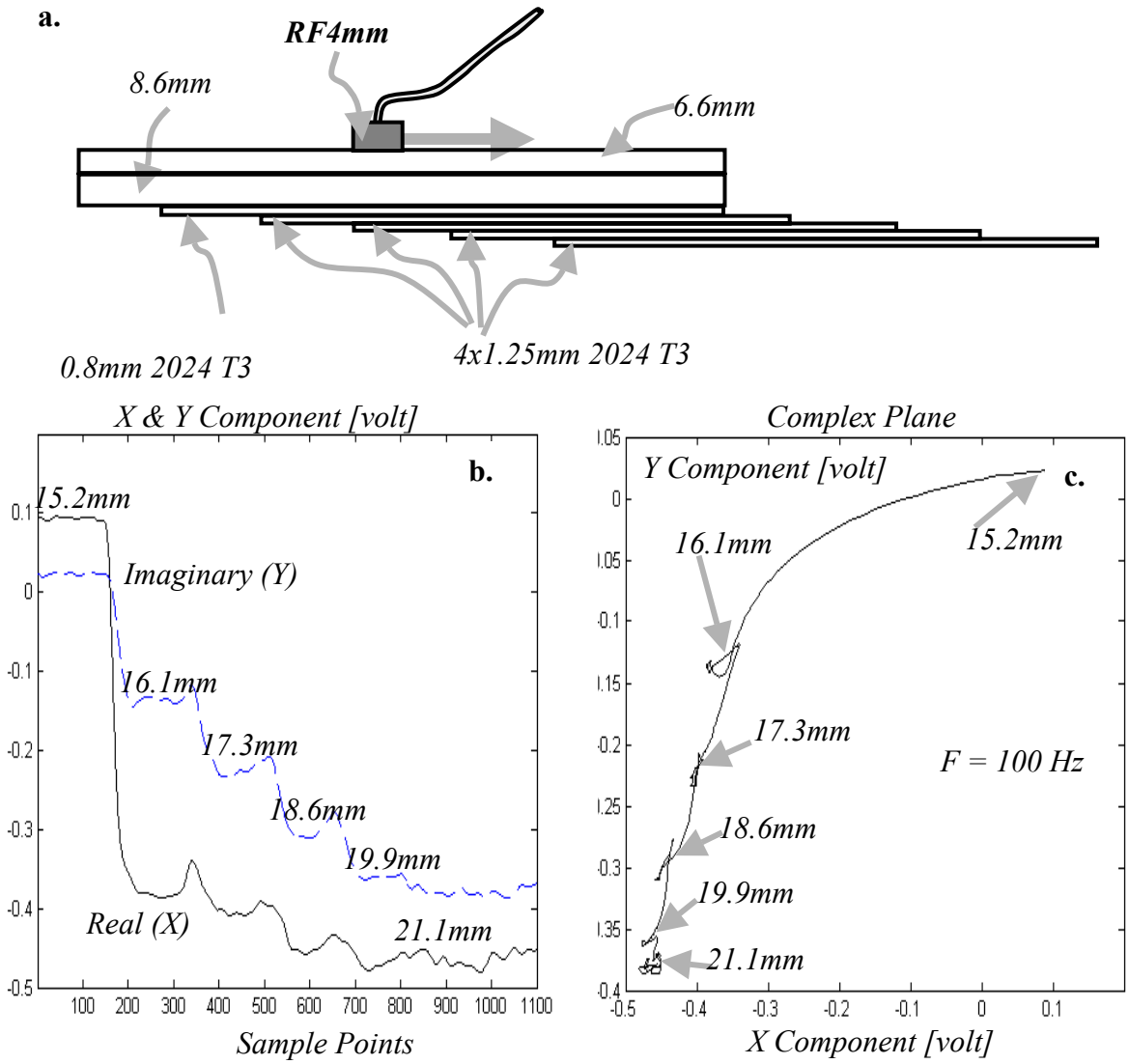

FIGURE 9. Detecting simulated wall thinning
a. Test setup. b. X and Y-components when probe passing over the top surface of the thickness-varying stack. c. Corresponding points of each step in the complex plane trajectory.

probe is scanned over the top surface right above a 12.7mm × 12.7mm × 0.15mm patch made on the specimen. Figure 11b shows the image representing signal magnitude obtained from the scan.

Figure 12 shows the complex plane trajectories obtained where the specimen in place at different layers of the four-layer test stack.

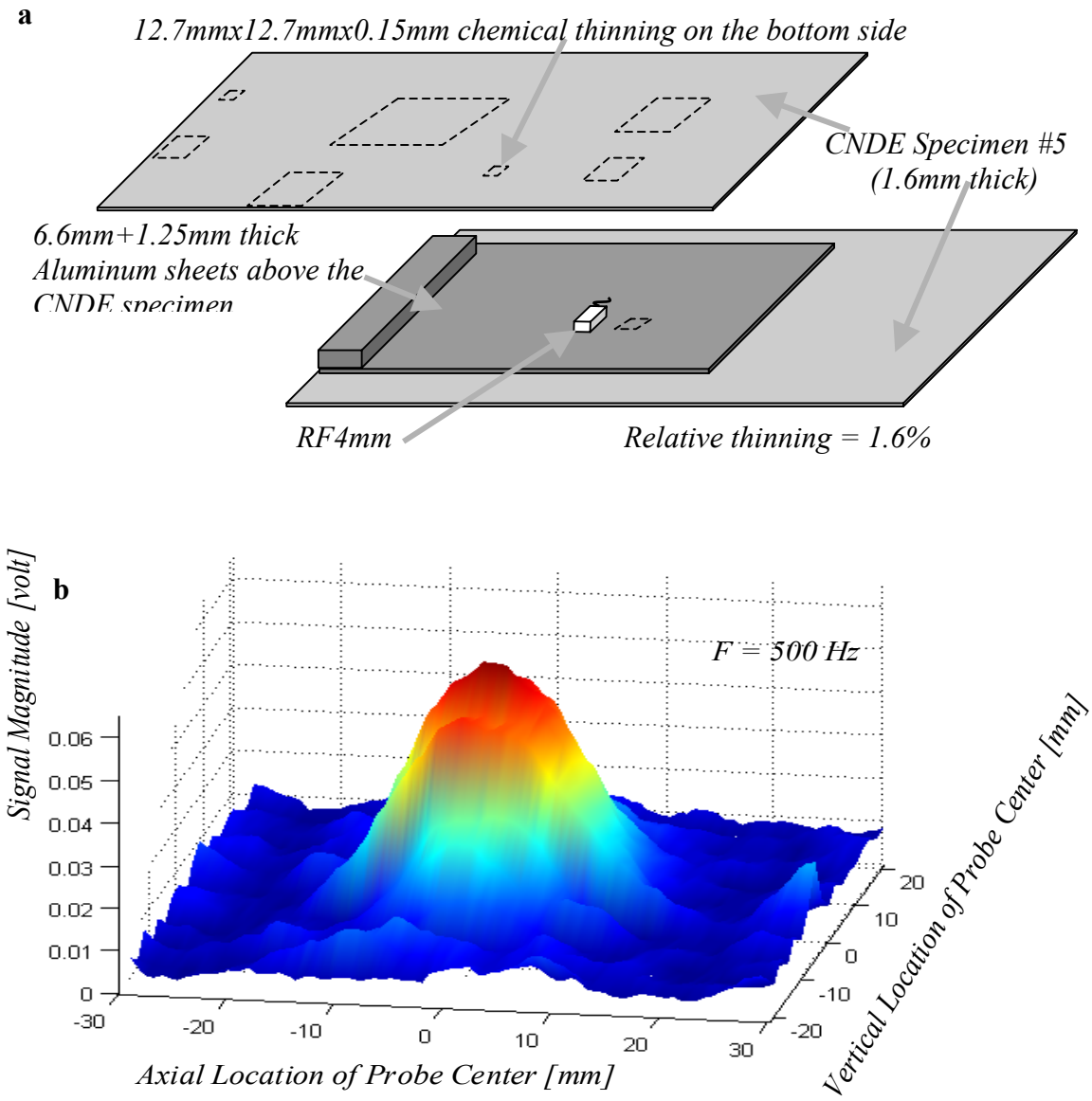

FIGURE 10. Detecting a 12.7mm × 12.7mm × 0.15mm patch simulating corrosion thinning that is 9.3mm below the surface of inspection (1.6% thinning).
a. - Test setup. b. – Signal response when scanning the patch using an RF4mm probe.

TEST 4 – DETECTING SIMULATED CORROSION PITING

A NAVYAIR specimen, see Figure 13, is used in the test. In The specimen is comprised of a 3.2mm thick 7075-T6 sheet with nine mechanically machined holes of different diameters and different depths to simulation corrosion pitting. Two A-scans are made on the backside of the

specimen along Row #2 and Row #3. Figures 14a and 14b show the imaginary components of the signals for the A-scans.

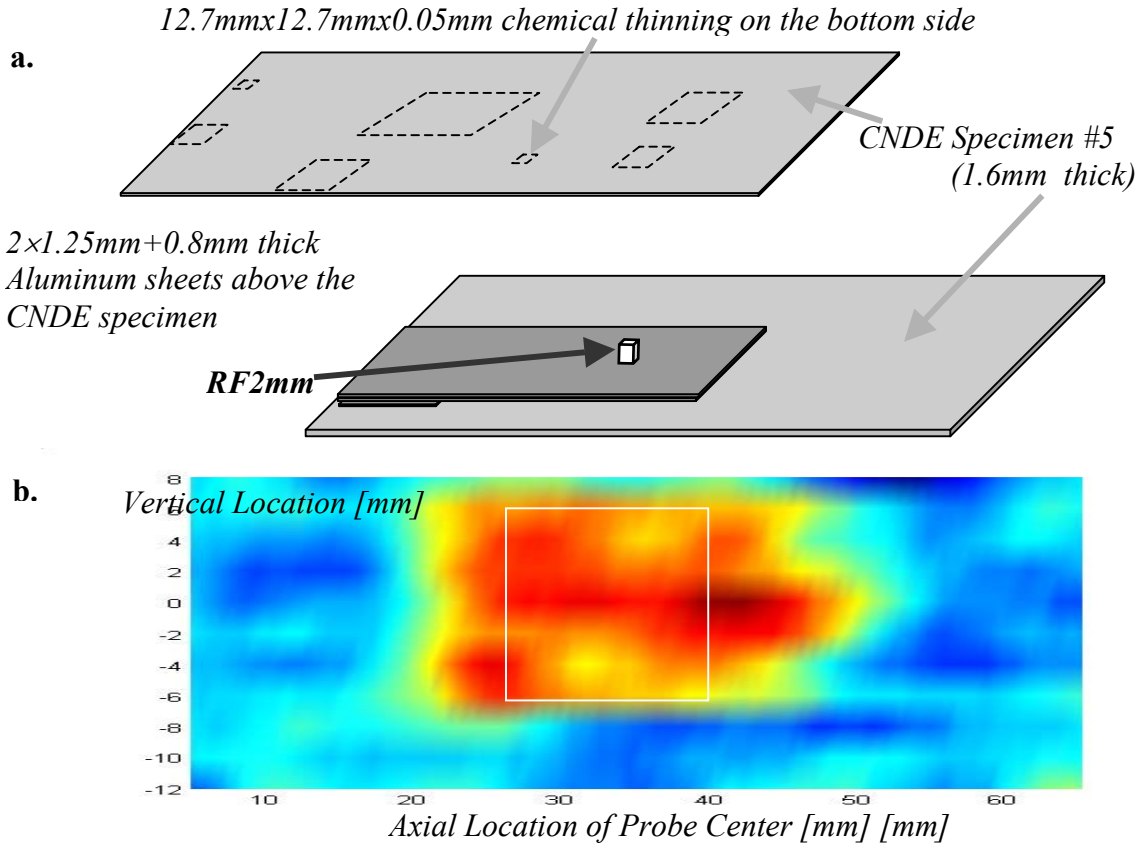

FIGURE 11. Detecting a 12.7mm × 12.7mm × 0.05mm patch simulating corrosion thinning that is 4.9mm below the surface of inspection (1.03% thinning).
a. - Test setup. b. – Signal magnitude when scanning the patch using an RF2mm probe.

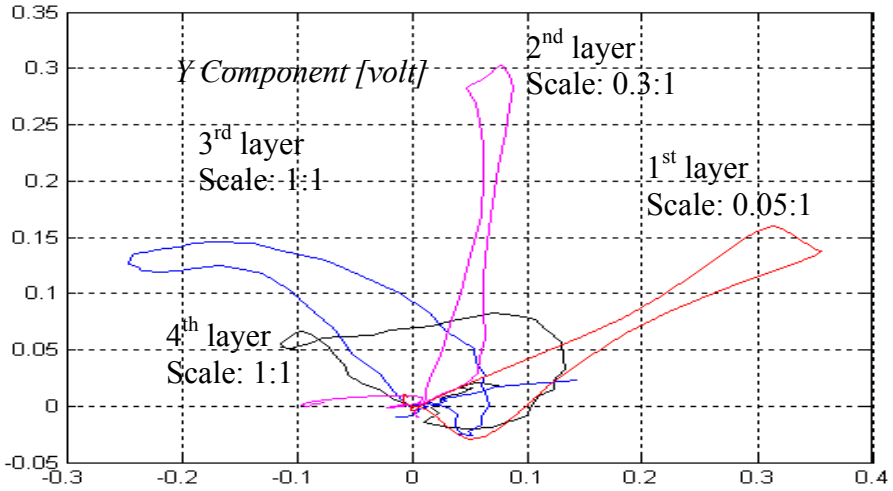

FIGURE 12. Detecting a 12.7mm × 12.7mm × 0.05mm patch simulating corrosion thinning that is located at different depth of a four-layer and 4.9mm thick aluminum stack.

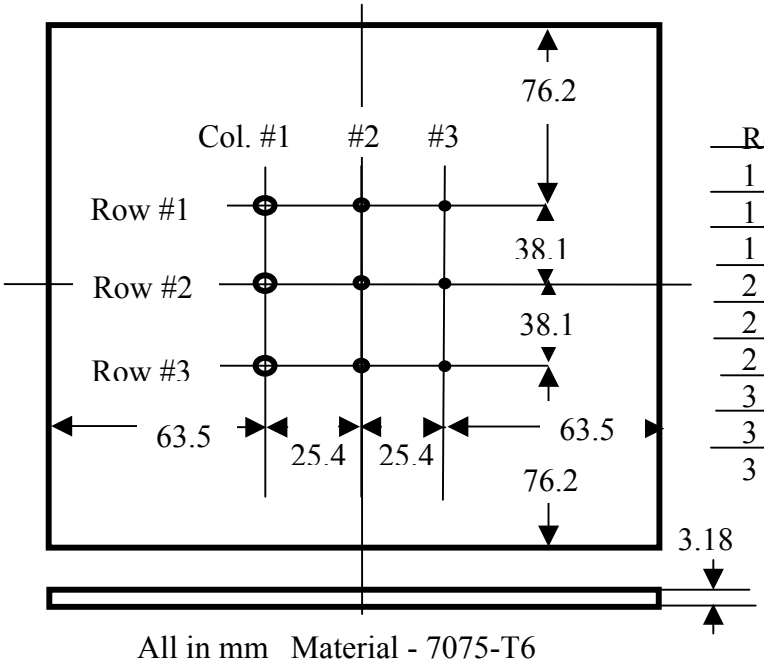

Table 1. Hole Dimensions [mm]

Row #	Col. #	Diameter	Depth
1	1	3.2	0.2
1	2	2.3	0.2
1	3	1.6	0.2
2	1	3.2	0.1
2	2	2.3	0.1
2	3	1.6	0.1
3	1	3.2	0.025
3	2	2.3	0.025
3	3	1.6	0.025

FIGURE 13. NAVYAIR Specimen simulating corrosion pitting.

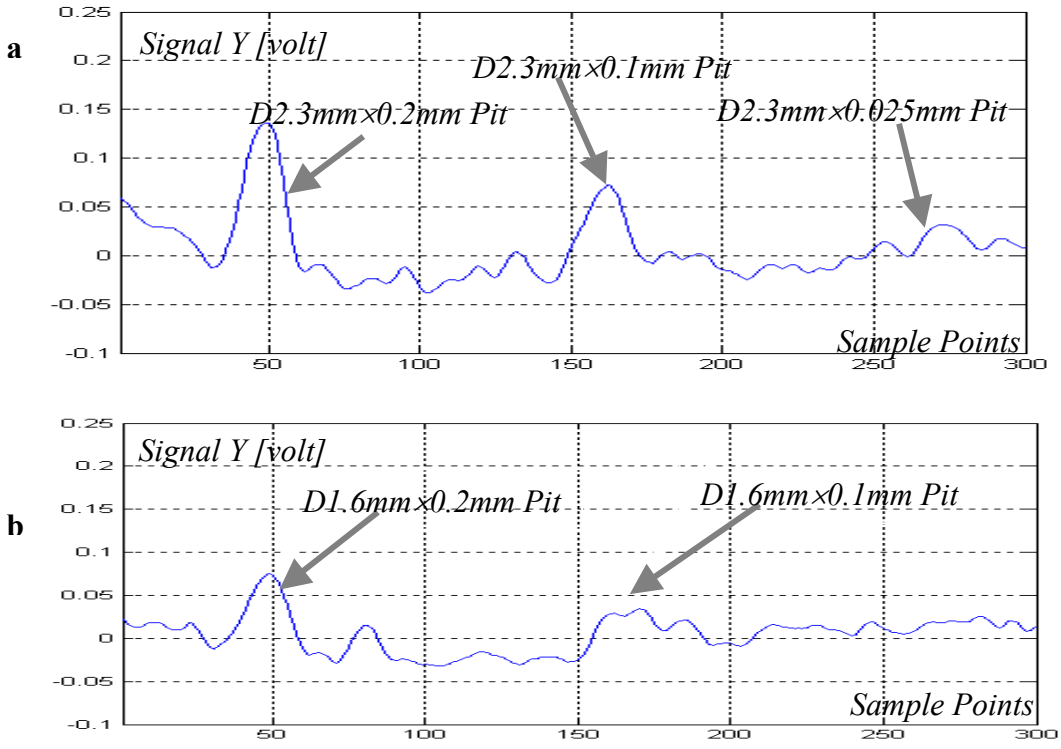

FIGURE 14. Imaginary components of signal two A-scans along Row #2 and Row #3 of the NAVYAIR Specimen using an RF2mm probe. a. Along Row #2. b. Along Row #3.

TEST 5 – DETECTING FATIGUE CRACK

The system was used to test fatigue crack specimens made by the Lockheed Georgia Company in 1980. In previous works[9] a linear, or raster, scan mode was used. Our recent study has shown that much better crack distinguishability can be obtained in a rotation scan mode. The preliminary results of detecting fatigue cracks using rotational scan mode and RFECT are illustrated in this section.

The specimen consists of two 7075T3 aluminum layers. To generate fatigue cracks on the fastener holes, at first, ten small holes were drilled on each layer of the specimens and an artificial crack was initiated on a selected hole. The artificial crack was initiated at one of the four locations: on the counter-sunk surface; on the bottom surface of the first layer; on the top

surface of the second layer; or on the bottom surface of the second layer. A cyclical load was then applied to the specimens until the fatigue crack grew to the required length. Finally, the artificial crack was removed by increasing the diameter of the holes and the two layers are assembled and finished. All fasteners except one were made of titanium; one of the ten fasteners was made of carbon steel.

Figure 15 shows one of the specimens, B4-1, where a 0.79mm long fatigue crack was made on the bottom surface of the second layer of the specimen. Figures 16a and 16b show the signal Y components obtained from scanning clockwise and anti-clockwise, respectively. Figure 16c show a typical signal Y obtained from scanning a non-cracked rivet hole. Figures 16d, 16e and 16f show the corresponding derivatives of Y obtained from the above three data set.

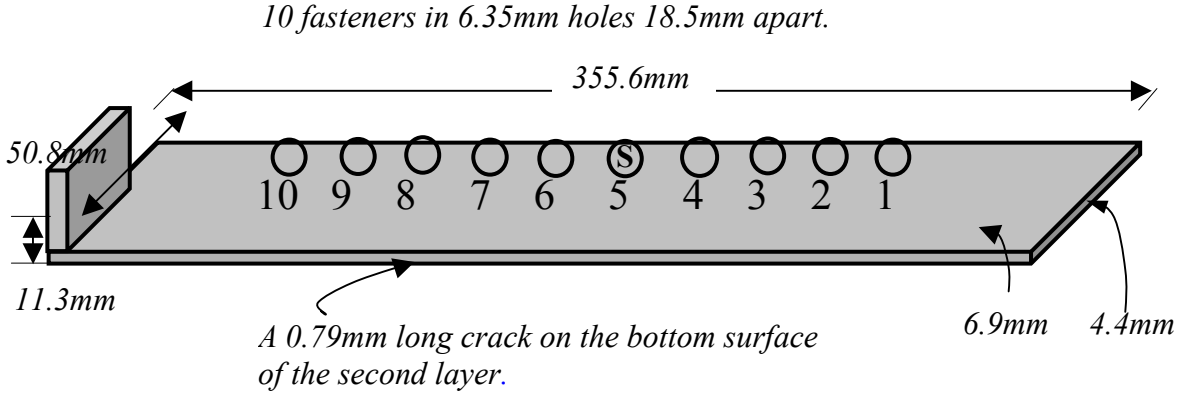

Figure 15. Fatigue crack specimens, B4-1 made by the Lockheed Georgia Company.

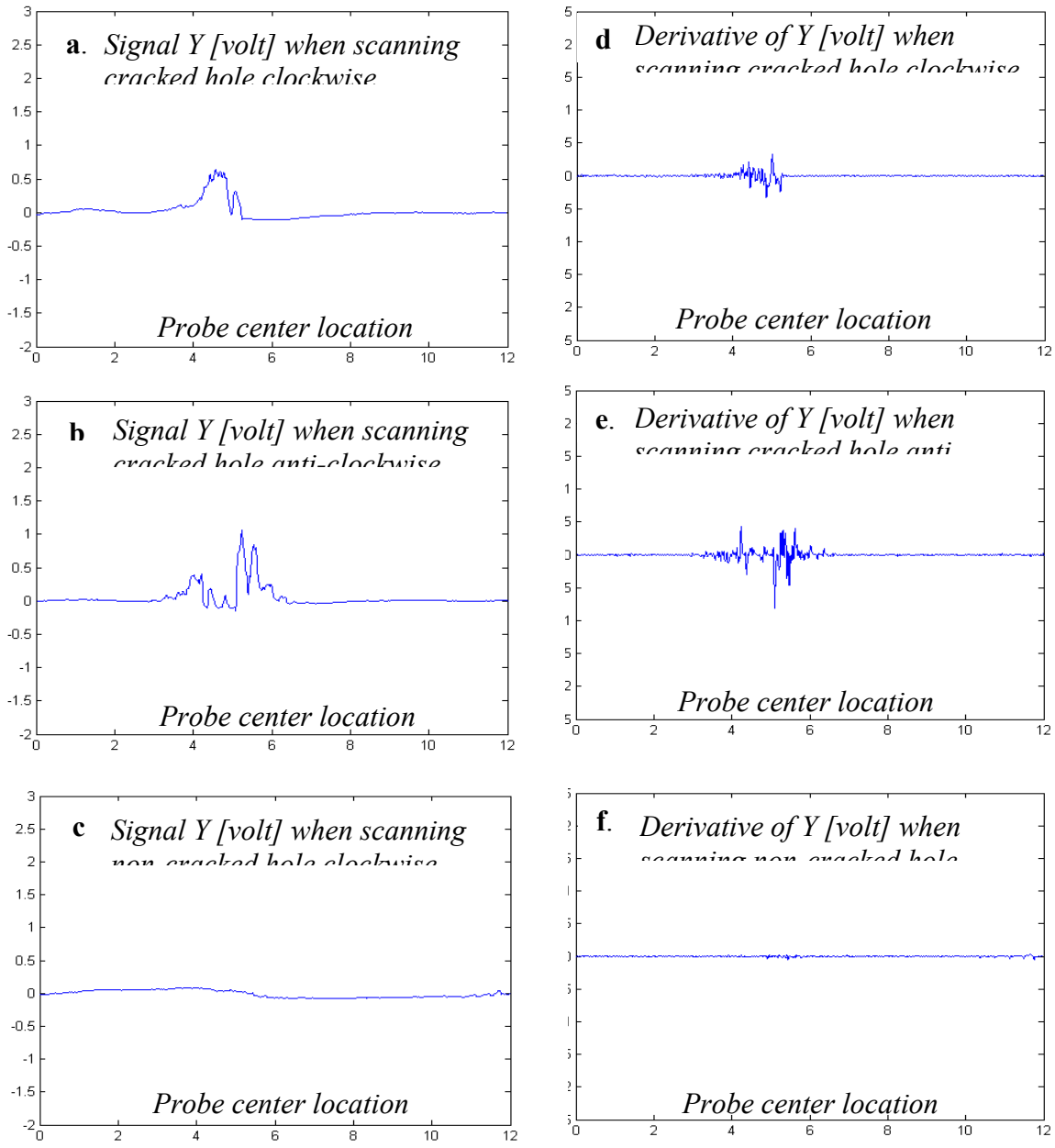

FIGURE 16. Signal imaginary, Y, components obtained from scanning rivet holes

a. Signal Y - scanning cracked hole # 8 clockwise.
b. Signal Y - scanning cracked hole #8 anti-clockwise.
c. Signal Y - scanning non-cracked hole #2 clockwise.
d. Derivative of Y – scanning cracked hole # 8 clockwise.
e. Derivative of Y - scanning cracked hole #8 anti-clockwise.
f. Derivative of Y - scanning non-cracked hole #2 clockwise

ACKNOWLEDGEMENT

The authors would like to thank Dr. Matt J. Golis, AQC, for his great contributions including instructions, comments, corrections, as well as editorial work to this paper.

REFERENCES

1. R. A. Wincheski, et al., US Patent #5,648,721, "Rotating Flux-Focusing Eddy Current Probe for Flaw Detection." (July 15, 1997).

2. J.A. Bieber, C.C. Tai, and J. Mouder, Review of Progress in Quantitative Non-Destructive Evaluation, 17A, PP. 315-322.

3. W. F. Avrin, "Eddy-current measurements with magnetoresistive sensors: third-layer flaw detection in a wing-splice structure 25mm thick", Proceedings of SPIE, Nondestructive Evaluation of Aging Aircraft ,Airport, and Aerospace Hardware IV, Chair/Editor Ajit K. Mal, 7-8 March 2000, (Newport Beach, California) PP. 29-36.

4. W. Podney, "Electromagnetic Microscope for Automated Inspection of C-141 Wings", Presented on The Fourth Joint DoD/FAA/NASA Conference on Aging Aircraft, (15-18 May, 2000, St. Louis, MO).

5. R. Smith (DERA, UK), G. Hugo, (DSTO, UK), "Transient Eddy-Current NDE for Aging Aircraft - Capabilities and Limitations", Presented on The Fourth Joint DoD/FAA/NASA Conference on Aging Aircraft, (15-18 May, 2000, St. Louis, MO).

6. B. Wincheski and M. Namkung, (NASA), "Magnetoresistive Based Rotating Probe System for Detection of Deep Fatigue Cracks in Aircraft Structures with Fasteners", Presented on The Fourth Joint DoD/FAA/NASA Conference on Aging Aircraft (15-18 May, 2000, St. Louis, MO).

7. Y. Sun, US Patent #6,002,251 entitled Electromagnetic-field-focusing remote-field eddy-current probe system and method for inspecting anomalies in conducting plates, (December 14, 1999).

8. T. Ouyang, US Pending, US Patent Application Serial No. 09/540,370, Super-Sensitive Eddy-Current System and Method, (filed on March 31, 2000).

9. Yushi Sun, Tianhe Ouyang, and Robert J. Lord, “Detecting 1st and 2nd Layer Simulated Cracks in Aircraft Wing Spanwise Splice Standards Using Remote-Field Eddy Current Technique”, presented at Aging Aircraft Conference 2001, (Kissimmee, Florida, September 10~13, 2001).

AN APPROACH FOR CORROSION CLASSIFICATION BASED ON WAVELET ANALYSIS

Ajay Verma, Akif Ibragimov and Richard Mayer
Knowledge Based Systems, Inc.
College Station, TX – 77840

ABSTRACT

The main goal of this paper is to present techniques that can be used for detection and classification of corrosion. This technology can be used to analyze corrosion in critical areas such as lap joints for the aging aircraft. In this paper we present a wavelet analysis based *corrosion feature extraction* method from the nondestructive inspection (NDI) data, which is then used by a *neural net classification model* for detection and classification of corrosion. From past experience, it has been seen that not any single sensor is sufficient for corrosion detection as each sensor has its limitations. In this paper we also show that *data fusion* of multiple sensor signals improves the probability of detection and better assessment of corrosion damage. We will also present a *data standardization* process to bring data from different sensors to a common standard or scale, so that they can be compared directly before any data fusion. We use Ultrasonic and Eddy current sensor data for analysis as these are widely used methods of nondestructive inspection for corrosion detection. In this paper we will also concentrate on detecting "region of interest" or ROI for corrosion evaluation and classification. This method can be used for the identification of the ROI in the specimen, the markup of the image and the annotation of the markups with their assessments.

INTRODUCTION

There are various challenges and serious problems faced by both civilian and military industry in monitoring corrosion in the aging aircraft fleet. The corrosion is predominantly found in the lap joints of the aircraft, where some moisture is trapped and triggers corrosion. The presence of corrosion in critical areas can violate the structural integrity of the aircraft. It has been demonstrated that less than 5% of thickness loss can reduce up to 50% of fatigue life in certain lap joint specimens. Currently, there are no proven structural models which can predict

the limits on corrosion level that can be tolerated for air worthiness. The Federal Aviation Administration has directives, which allow aircraft to operate with up to 10% material loss in lap slice joints[2,7]. In some military industries, currently, a NDI scan is performed and the image obtained from them is sent for identification of the potential "Region of Interest" (ROI). The NDI engineers mark-up the results of the generated images. The identification of the ROI, the markup of the image and the annotation of the markups with their assessments are all performed manually.

The main aim of this paper is to present a technique that can be used for detection and classification of corrosion. This technology can be used to analyze corrosion in critical areas such as lap joints for the aging aircraft. A single sensor is not adequate for inspecting different types and levels of corrosion. To cover all the dimensions of corrosion, multiple sensors are required. The two most promising sensors that have been employed for non-destructive inspection (NDI) are the ultrasonic and the eddy current sensors. Each sensor may measure some features, which may not be detected by other sensor. Hence, more reliable information can be deduced by fusing the data of multiple sensors. From industry's perspective, before any corrosion is analyzed or classified, there is a need to develop a functionality that can determine the ROI for evaluation in a given specimen and our intent is to develop a neural net (NN) model for *corrosion classification* based on *features extraction* from sensor data using *wavelet analysis*. With proper training of a NN model, this technique can be used with any individual sensor signal or signal obtained by data fusion of multiple sensors. We will also present wavelet-based techniques for enhancing the corrosion signal by *data fusion* of one or more sensors, and determining the *region of interest* (ROI) in the specimen for corrosion evaluation. For data fusion of images we will also present a technique for data standardization of signals.

Presently, various signal-processing techniques exist which can be utilized to analyze a signal whether it is one dimensional (for example, an audio signal) or two-dimensional (for example, an image). In recent years, the wavelet has emerged as a powerful tool for signal processing. The main advantage of wavelet processing is that the signal processing can be accomplished at various resolutions. The wavelet coefficients measure the degree of irregularity of the signal at various levels or resolutions. Another advantage of wavelet analysis is that the localized features (i.e. in time domain or spatial domain) can be identified to an extent as determined by the Heisenberg uncertainty principle. Note that in signal processing using the Fourier analysis, there is no information of local behavior of the signal. These advantages of wavelet analysis makes it very suitable to capture the sharp abruptly changing features buried in a signal such as the corrosion features found in images. An additional advantage of wavelet transformation is that the information of the signal can be captured in fewer coefficients, which results in large data compression. We used "Discreet Wavelet Transform" (DWT) extensively for the image processing requirement in building the NDE technology.

PROBLEM DISCUSSION

In this paper we will analyze two types of signals, namely, the ultrasound signal, and the eddy current signal. Generally, NDE techniques are classified based on the energy source that is utilized for evaluation.[1,4] Most of the techniques can be classified in the categories of acoustic, electromagnetic, optical, x-ray energy sources as well as physical methods such as liquid penetrants. Ultrasonic techniques provides good resolution for thickness loss in plates due to corrosion but these techniques are sensitive to an uneven scanning surface and coupling as the probe must have good contact with the test specimen. While eddy current is an electromagnetic phenomenon and can be modeled as a diffusion process, the ultrasonic method of testing relies

on wave propagation of energy. Eddy current methods overcome some limitation of ultrasonic techniques as it does not require contact and hence it is insensitive to surface roughness. But these methods have resolution problems and are sensitive to "lift-off" variations.

Note that all the NDI techniques result in a measurement across the surface area of the specimen. This measurement can be represented by a two-dimensional function (signal) of intensity, say $\phi(x, y)$. Usually, this measurement is presented in an image form, hence, each NDT scan of specimen produces an image. These images are stored in different formats. One of the popular formats that is usually used to store the image is the bitmap format. Normally, these images are colored images so as to obtain better resolution. The hue variation in the image gives the intensity signal across two dimensions. The intensity data obtained from different sensors result in a data having different scales. Even when the same sensor is used at different times, the scales could be different depending upon how the calibration is performed. Hence, we see that there is no one-to-one correspondence between the NDI data for two different scans of the same specimen. For data fusion, this necessitates a normalization process of all sensor data so that it can be brought to a common standard before it can be used.

When multiple sensors are used for NDI, the challenge is how to consolidate the information obtained by different sensors. We overcome the problem of consolidating the information by developing a *wavelet fusion model* that uses an advance wavelet-based data fusion technique to fuse the data from two images. The enhanced image that combines the features obtained from multiple images is then used for classification of the corrosion in the specimen. Using ROI detection, the regions for evaluation are determined. The classification for any region of the specimen is based on the corrosion features present in the region. We compute the energy associated with the wavelet coefficients for a given region to put a **m**easure on the

image **f**eatures (MIF) corresponding to the corrosion. A Neural Net classification model based on theses extracted features was then developed.

IMAGE PROCESSING AND WAVELETS

In literature, there are various techniques that are used to analyze and interpret a signal. Some examples of these techniques are Fourier analysis, Windowed Fourier (or short time Fourier) analysis, Wavelet analysis, Local Cosine transform analysis, and Q-transform analysis. All of these analyses consist of the signal transformation and establishment of signal properties in different domains. Most of the analysis tools are defined for a one-dimensional signal, however, they can easily be extended to two dimensional signals such as image data. Fourier analysis is very useful for the signals that are time-invariant. However, if the signal contains localized features, the Fourier analysis is not suitable as it is unable to capture the short time or the transient behavior of the signal. This is particularly applicable to most of the image data, including images obtained from NDT techniques, as the images normally contain localized features. To capture the localized features in time and frequency domain, the localized time-frequency signal processing is required. Windowed Fourier transforms and Wavelet transforms fall under this category. Unlike signal in time domain, where energy spread in frequency is infinite, and Fourier transform of the signal, where the energy spread in time is infinite, the energy spread in windowed Fourier and wavelet transform is finite both in time as well as frequency domain. FIGURE 1 shows the energy spread in time and frequency domain for windowed Fourier and wavelet atoms. An added advantage of wavelet transform is the multi-resolution analysis as it measures the time frequency variations of the spectral components, with a varying time frequency resolution (see FIGURE 1).

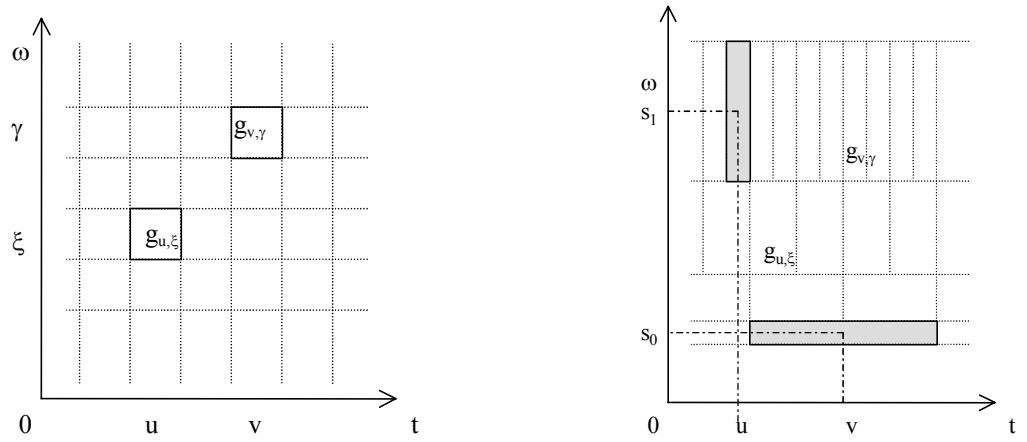

FIGURE 1. Time-frequency boxes representing the energy spread for windowed Fourier and wavelets atoms.

The discrete wavelet transform (DWT) uses a function whose dilation and translation forms a set of complete orthonormal basis. For computer applications such as image processing, the discrete wavelet transform results in tremendous data compression. The image is stored as a decomposition over the discrete orthonormal wavelet basis functions[11]. The discrete wavelet functions $\psi_{m,n}(t)$ and coefficients $w_{m,n}$ are defined as

$$\psi_{m,n}(t) = \frac{1}{\sqrt{2^m}}\psi\left(\frac{t - 2^m n}{2^m}\right)_{(m,n)\in Z^2} \tag{1}$$

$$w_{m,n} = \left\langle f, \psi_{m,n} \right\rangle \tag{2}$$

where $\psi(t)$ is the mother wavelet function and wavelet coefficients are the dot product of the signal f and the wavelet functions, provides a measure of a degree of irregularity in the region of support of the wavelet function. A more regular signal implies a smaller wavelet coefficient. Wavelet coefficients at different scales measure the irregularity of the image features at different resolutions. A majority of the wavelet coefficients are small and can be ignored without much alteration of the signal. This results in significant data compression.

Any finite energy signal f can be represented as

$$f = \sum_{m=-\infty}^{+\infty} \sum_{n=-\infty}^{+\infty} \langle f, \psi_{m,n} \rangle \psi_{m,n} \text{ or } f = \sum_{m=-\infty}^{\infty} d_m \tag{3}$$

where partial sum d_m is defined as

$$d_m = \sum_{n=-\infty}^{+\infty} \langle f, \psi_{m,n} \rangle \psi_{m,n}, \tag{4}$$

and it is interpreted as detail variation at the scale 2^m. These layers of details are added at all scales to progressively improve the approximation of the original signal. When the signal is discrete and of finite length, the signal f can be decomposed only in a few finite number of scales and an approximate signal. If the signal f is decomposed in N scales, then it can be represented as

$$f = \sum_{m=0}^{N-1} d_m + a_N, \tag{5}$$

where a_N is the approximation on an N^{th} scale level. If the signal contains noise, it can be removed by filtering the data by ignoring details at very fine scale levels. For a two dimensional signal, detailed variation is split into three orientations (o) corresponding to horizontal (h) details, vertical (v) details and diagonal (d) details and Equations (4) and (5) takes the form as

$$d_{m,o} = \sum_{n=-\infty}^{+\infty} \langle f, \psi_{m,o} \rangle \psi_{m,o}, \quad o = h, v, d \tag{6}$$

$$f = \sum_{o} \sum_{m=0}^{N-1} d_{m,o} + a_N. \tag{7}$$

FIGURE 2 represents the function decomposition graphically.

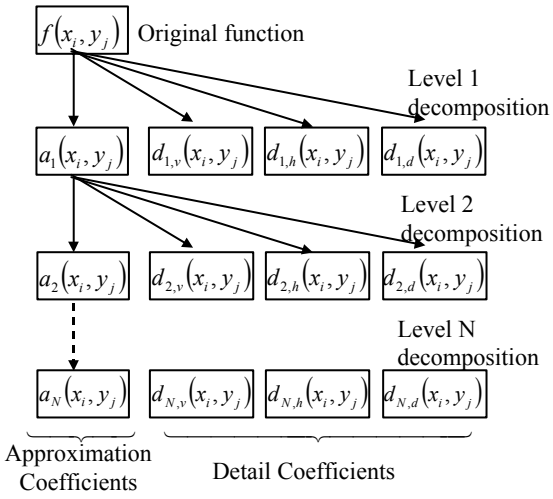

FIGURE 2. Function decomposition into approximation and detail variation.

REGION OF INTEREST (ROI) DETECTION

From an industry perspective, before any corrosion is analyzed or classified, there is a need to define a functionality that can determine the "Region of Interest" (ROI) for evaluation in a given specimen. For detecting an ROI based on the corrosion level, first we define an elementary window $A^{M,N}$ in wavelet coefficient domain(WDC). As each wavelet coefficient represents a feature of a region of finite length ("region of support"), the window size cannot be chosen arbitrarily small. Let $R_{\Gamma_{\text{roi}}}$ be a ROI to be detected based on an elementary window $A^{M,N}$. Note that Γ_{roi} is a set of coordinates that is used to define $R_{\Gamma_{\text{roi}}}$. Hence, the ROI $R_{\Gamma_{\text{roi}}}$ can be defined fully by appropriately populating Γ_{roi}. Note that the wavelet coefficients are a measure of the degree of irregularity in the signal and the approximation coefficient gives an average value of the signal in a region of its influence or support. The total energy $E_t^{M,N}(i,j)$ of a window $A^{M,N}$ gives a measure of corrosion in that window. Let E_{th} be a constant which defines a threshold value for selecting coordinates (i,j) of a window $A^{M,N}$. The total energy

$E_t^{M,N}(i,j)$ of the selected window size greater than a given threshold implies that the window is included in the region of interest. Hence, we can now formally define Γ_{roi} as:

$$\Gamma_{\text{ROI}} = \{(i,j): E_t^{M,N}(i,j) \geq E_{\text{th}}\}. \quad (8)$$

FIGURE 3 shows an example of ROI detection. On the left FIGURE 3 shows the image data corresponding to an ultrasound sensor scan of a specimen, on the right we show the result of ROI analysis. The blue region defines the ROI. By definition $R_{\Gamma_{\text{roi}}}$ is a multi-connected region with smooth boundaries. But for the practical region the signal data is scanned with the given window size at a step of a half window length. This will result in ROI having a zigzag boundary (as seen in the FIGURE 3) instead of a smooth boundary. Note that all the groups of overlapping windows will form separate fully connected region of interest.

If multiple values of threshold are used, a contour map of ROI is obtained as shown in FIGURE 3. The ROI for higher threshold values are always smaller in size and fully contained within the ROI for the smaller threshold.

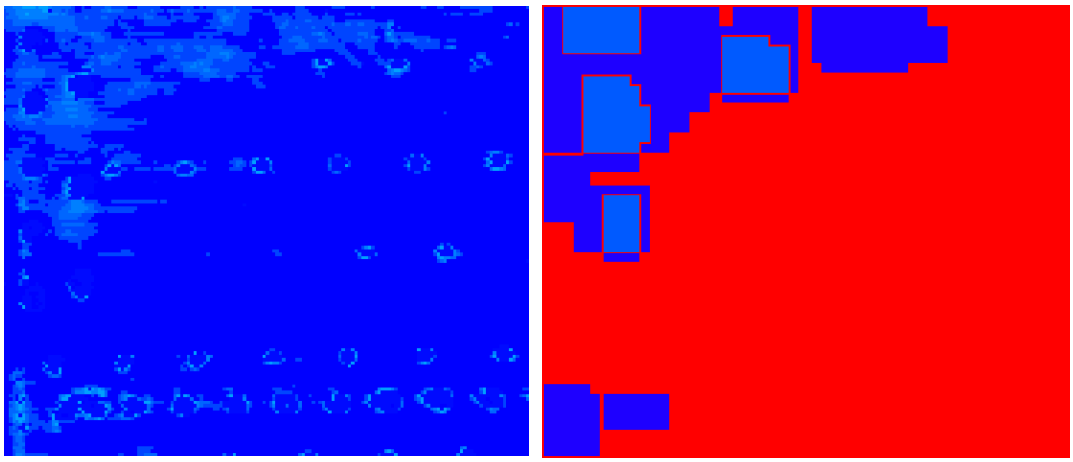

FIGURE 3: Region of Interest (ROI) Detection

IMAGE DATA FUSION

The motivation for the image fusion is that that each image may capture certain features, but it may miss others. By fusing the two images, the goal is to capture all the features and provide a total picture or image. But before even attempting image fusion, it must be noted that the two images being considered for the fusion are supposedly obtained from different types of sensors. Obviously, the data of the two signals is most likely to be an entirely different representation of the same physical property. Hence, as a first step before fusion, we require data standardization. We also require that the images are registered with respect to the axis system. In this work we assume that all the images are already registered.

DATA STANDARDIZATION

The purpose of the signal data standardization is to bring a different signal to a common standard reference so that it can facilitate data fusion. For a common standard reference, one signal is chosen as a base standard representation, while other signals are transformed to the standard representation The transformed Ultrasonic signal $Th(x,y)$ in standard representation is shown in FIGURE 6. For minimization of norm between Eddy Current and transformed Ultrasonic signals, only about 70% of the data is used, the underlying assumption is that although images may capture different features, but approximately 70% of the features are common to both images.

DATA FUSION

After standardization, the two data signals $f(x,y)$ and $Th(x,y)$ undergo the wavelet transformation. In our example three levels of wavelet decomposion are used for the purpose of data fusion. After wavelet decomposition, using Equation (7) the two signals can be represented as

$$f(x,y) = \sum_{m=1}^{3} d_{m,h}^{f}(x,y) + \sum_{m=1}^{3} d_{m,v}^{f}(x,y) + \sum_{m=1}^{3} d_{m,d}^{f}(x,y) + a_{3}^{f}(x,y)\,,$$

$$\mathrm{T}h(x,y) = \sum_{m=1}^{3} d_{m,h}^{h}(x,y) + \sum_{m=1}^{3} d_{m,v}^{h}(x,y) + \sum_{m=1}^{3} d_{m,d}^{h}(x,y) + a_{3}^{h}(x,y)\,, \qquad (9)$$

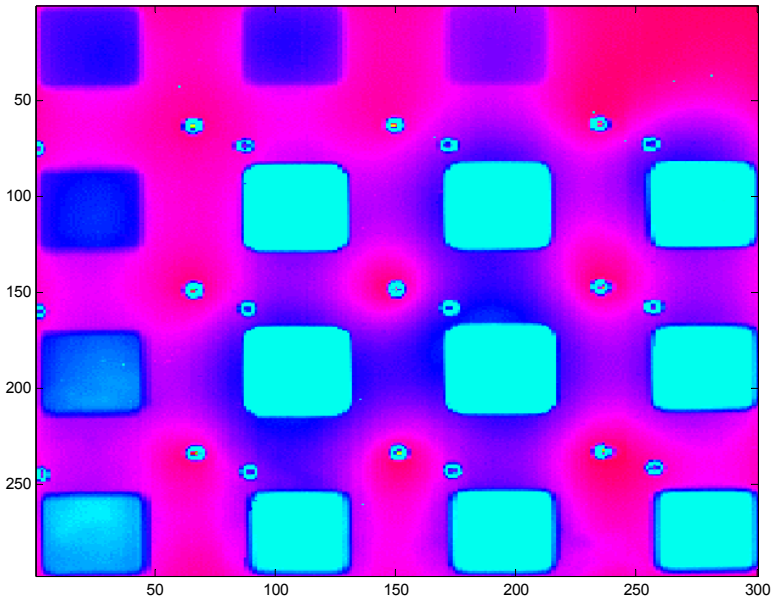

FIGURE 4. Eddy Current Sensor Data

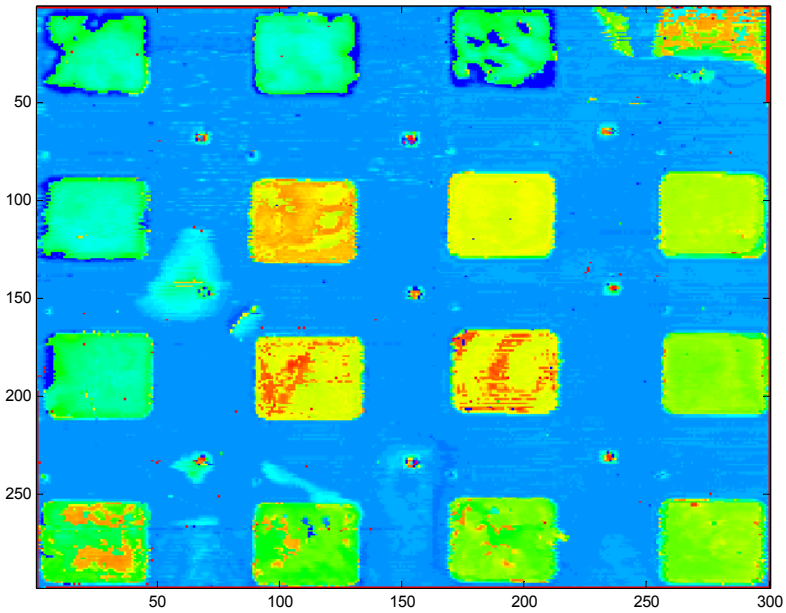

FIGURE 5. Ultrasonic Sensor Data (Original)

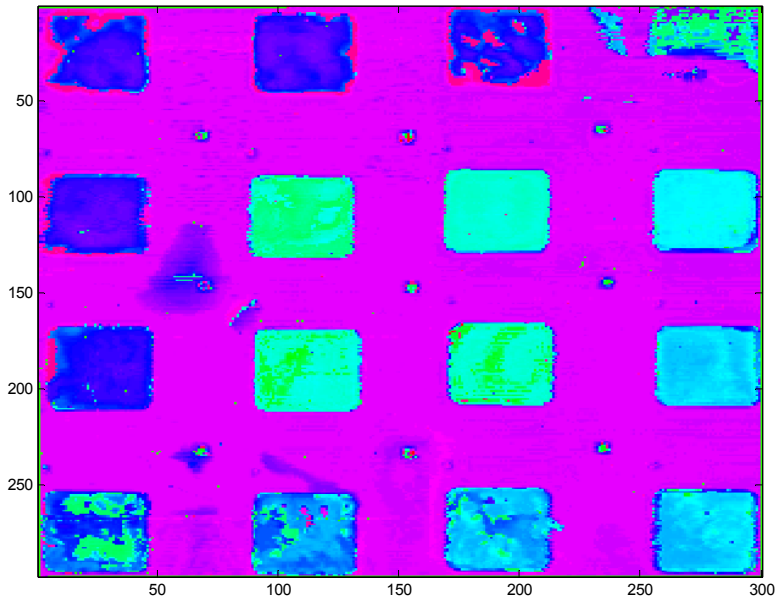

FIGURE 6. Ultrasonic Sensor Data (After Transformation)

where $d^f_{m,h}$, $d^f_{m,v}$ and $d^f_{m,d}$ represent the horizontal, vertical and diagonal details at level m and $a^f_3(x,y)$ give the approximation at level 3. The superscript f and h are introduced to differentiate between the details for the two signals. The fusion algorithm[5] compares the local energy $E^{M,N}_{m,o}(x,y)$ for each wavelet coefficint $w_{m,o}(x,y)$ identified by location (x,y), scale m, and orientation o for both images. The inverse transform of the fused coefficient returns the fused image, which contains all the features that have been captured in different images (See FIGURE 7).

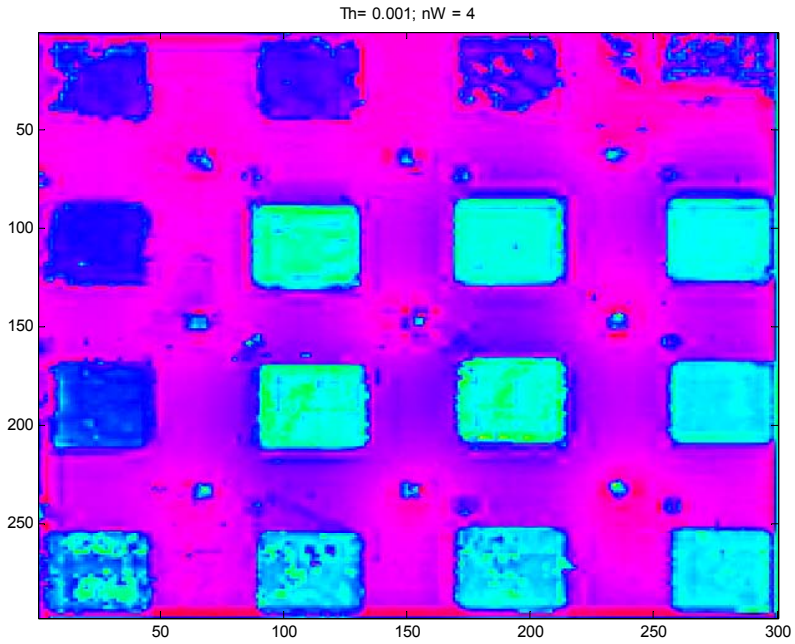

FIGURE 7. Fused Data

NEURAL NET-BASED CLASSIFIER MODEL

The main goal of this research was automatic evaluation and classification of a given region according to corrosion pattern. We know that corrosion is distributed randomly at varying strengths. To classify any region of interest, it is helpful to extract features, which can capture and measure the irregularity or the randomly distributed corrosion. For this we use a set of three-window MIF values (MIF-Measure of Image Features, certain quantitative characteristic of the image features). We scan the region of interest with the given window sizes and then determine the highest *total energy* windows in WCD. A neural net classifier was designed to take the input from these scans and produce as output a classification of the material loss (see FIGURE 8).

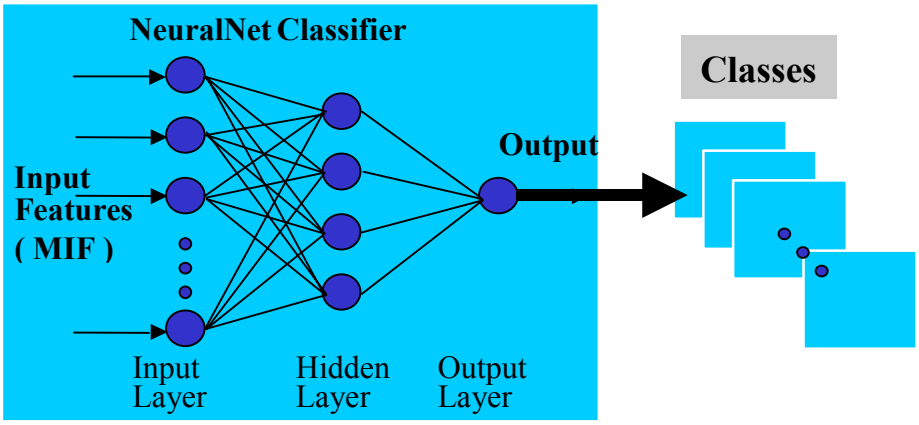

FIGURE 8. Architecture for Neural Net Classifier

NEURAL NET TRAINING DATA PREPARATION

FIGURE 7 shows the image after data fusion. The specimen tested contained 15 patches made by machining out the material, in order to simulate different levels of material loss. These patches were divided in three classes, the first class consisting of the first five patches with smallest thickness loss; the second class consisting of the next five patches with smallest thickness, and finally, the third class consists of the remaining five patches with the most thickness loss. For data preparation, five sets of data were created from each patch, totaling 75 exemplars. For training, four exemplars from each patch totaling 60 exemplars and ordered in a random fashion were used. The testing set consisted of the remaining 15 independent exemplars, one from each patch. Similar training and testing data were also prepared from Ultrasonic data alone as well as Eddy Current sensor data alone for comparison purposes.

RESULTS

Three neural nets were trained for fusion data, ultrasonic data and eddy current sensor data. The output of the NN classifier for test data corresponding to fusion image are tabulated in Table 1 and summarized in Table 2. The first column gives the actual classes of all fifteen

exemplars. Three output values from the neural net are shown in columns 3 to 5. Based on the nearest class center, the predicted classes are shown in the last column. We see that only the 6th exemplar was predicted incorrectly as class 1. This gives an accuracy of 93%. The output values of the neural network is also seen graphically in FIGURE 9.

TABLE 1.
NN Classifier Results.

	Exemplar	***Output 1***	***Output 2***	***Output 3***	**Prediction**
Class 1		0.8396	0.1617	0.0063	
	1	0.8397	0.1616	0.0063	Class 1
	2	0.8397	0.1616	0.0063	Class 1
	3	0.8397	0.1616	0.0063	Class 1
	4	0.8397	0.1616	0.0063	Class 1
	5				Class 1
Class 2	6	0.8261	0.1307	0.0183	Class 1
	7	-0.0404	0.9902	0.0253	Class 2
	8	-0.0338	1.0460	-0.0433	Class 2
	9	-0.0311	1.0484	-0.0464	Class 2
	10	0.0334	0.9836	0.0193	Class 2
Class 3	11	-0.0432	-0.0067	1.0097	Class 3
	12	-0.0395	0.0189	0.9848	Class 3
	13	-0.0424	-0.0091	1.0116	Class 3
	14	-0.0409	0.0345	0.9711	Class 3
	15	-0.0424	-0.0095	1.0120	Class 3

TABLE 2.
Summary of Classification Results

Prediction Actual	**Class 1**	**Class 2**	**Class 3**
Class 1	**5**	**0**	**0**
Class 2	**1**	**4**	**0**
Class 3	**0**	**0**	**5**

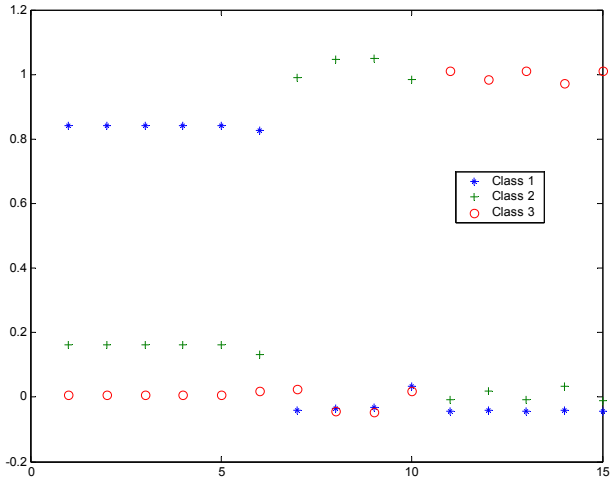

FIGURE 9. NN Classifier Results

NDE CORROSION DETECTION TOOLKIT AND ITS FEATURES

We have developed a NDE corrosion detection toolkit for experimentation with the above described Wavelet NN techniques on the Windows 2000 operating system. It has a user-friendly interface that allows the user to perform various analysis starting from the basic operation of loading image data to advanced operations such as image fusion, ROI detection, selection of a region for evaluation, features evaluation and corrosion classification. The tool performs directly on the image data obtained through the non-destructive inspection of the specimen. The tool has been developed using MATLAB and a NeuroSolutions as COTS component. Most of the image processing components, including wavelet processing has been developed using MATLAB. The wavelet-based neural net classifier is simulated using NeuroSolutions engine

BASIC FEATURES

The toolkit has three windows for holding graphic images and a list box with names of previously loaded images. Using the *Load Image* and *Remove Imag*e buttons, the image data files can be loaded or removed from the toolbox. The toolbox accepts any bitmap file or MATLAB

data file. The top left window is the *active window* and holds the *active* image, which is being analyzed. The image in the active window is loaded by selecting the image from the image list. For an operation where two images are required, for example fusion or normalization, the top right window or the *secondary window* is used to hold the *secondary* image. Any image in the active window can be transferred to the secondary window using the right arrow window.

The right bottom window is the *result window* that holds an image produced by some action performed in the toolbox. If an operation doesn't produce an image, the result window will either remain empty or continue to hold any previous image. Any output image can be placed in the list box for further operations by pressing the left arrow button.

Any message from the software is presented in the bottom panel. A panel on the right side allows various operations to be performed. There are four panels – Fusion, Normalize, DataPrep, and ROI, which provide various operations to be performed on the images. Any panel can be activated by pressing the corresponding button on top of the panel. The available functionality in various panels are briefly defined below.

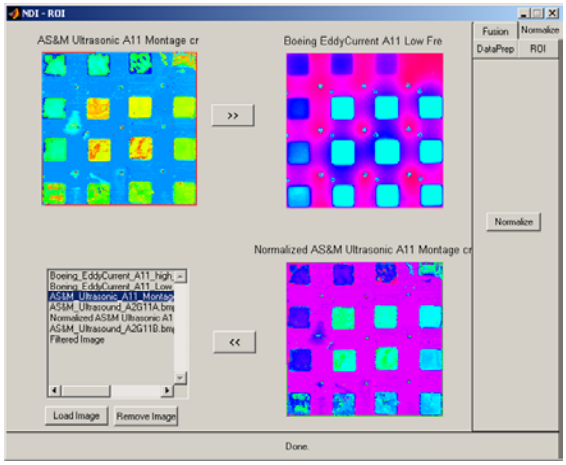

FIGURE 10. NDE Toolbox - Normalization Panel

STANDARDIZATION

First a base image is selected and transferred to the *secondary window.* The image to be normalized is enteredin the *active window*. The normalize button in the panel is pressed to start the normalization process. The output image (normalized) is produced in the *result window*. FIGURE 10 shows the toolbox with the *Normalize* panel and an example of normalization. In this example, the ultrasound image in the active window is normalized using low frequency eddy current image as the base for normalization.

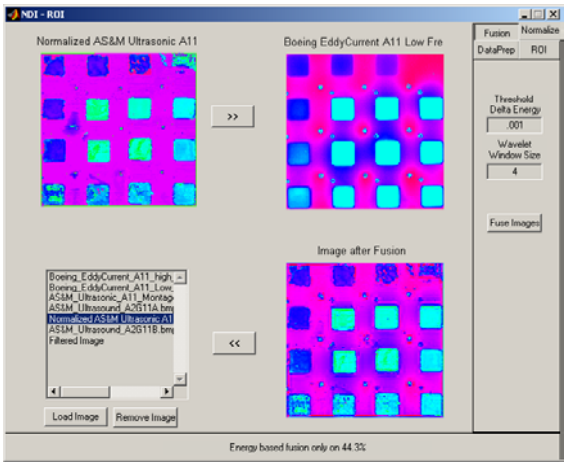

FIGURE 11. NDE Toolbox - Fusion Panel

FUSION

The two images to be fused are loaded in the *active* and *secondary* windows. In the fusion panel, the user- defined wavelet window size and the threshold delta energy values are specified. Pressing the *Fuse Images* button will fuse two images and produce the output image in the *result window*. FIGURE 11 shows an example of fusion images using this tool. In this example the image produced by low frequency eddy current inspection and the normalized image obtained by ultrasonic inspection are fused. The resulting fusion image can be seen in the *result window*.

DATA PREPARATION FOR CLASSIFICATION

For data preparation, only an active window is used for the input image, while the output is an ascii formatted data file. Hence, the secondary window and the result window continue to hold the previous images if any. This panel provides two functionalities, namely, i) the region selection, and ii) feature extraction. The data preparation consists of feature extractions from the specified regions, which can be later used for corrosion classification. The user can select or deselect the regions to be processed for classification with the click of the mouse in the *active window*, after pressing the *Get Input* button. The selection of an input region for classification can be saved to or loaded from a user-defined data file. The user has the option to change the window size of the region to be classified. The user can also define the number of windows to be used for feature extraction in any given region. After selection of the regions, the *Create Data* button begins the feature extraction algorithm and the output data is saved in a text file. FIGURE 12 shows an example of region selection from a calibration block to generate feature data for the purpose of training the neural net classification model.

ROI DETECTION

The ROI detection panel allows two operations, i) Image Filtering and ii) ROI Detection for Corrosion. Both operations use one input image, which is loaded in the active window, and produces an output image. The secondary window is inactive and continues to hold any previous image. The image filtering operation can be used to filter out Rivets and Spot Welding from the image. An image filter coefficient can be defined by the user which determines the intensity to which the original signal is retained. The filtered image can be reloaded to the active window after adding it to an image list for ROI detection operation. This tool allows multiple (graded) levels of ROI detection, by inputting multiple threshold energy values. The user can also define

other parameters used for ROI detection. The ROI detection algorithm is started by pressing the *Get ROI* button. FIGURE 13 shows an original image in the secondary window (for comparison) and the filtered image in the active window, while the output window shows two levels of ROIs.

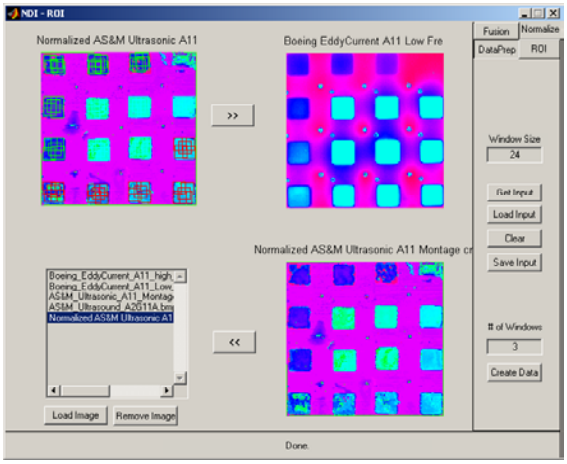

FIGURE 12. NDE Toolbox – Data Preparation Panel (Feature Extraction)

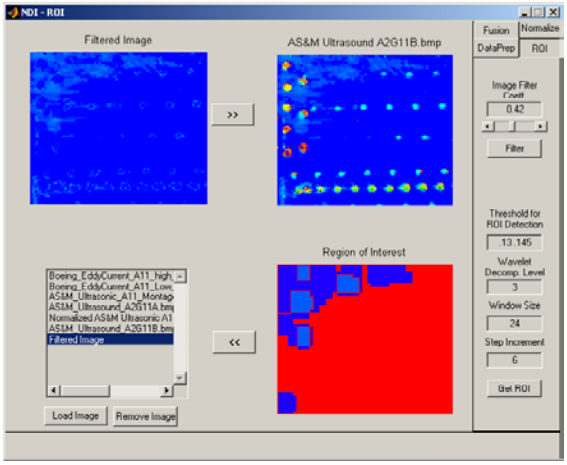

FIGURE 13. NDE Toolbox – ROI Panel

NEURAL NET-BASED CLASSIFICATION

The Neural Net model developed for corrosion classification was implemented using the NeuroSolutions package. It loads the data file containing the extracted feature data. The data file contains one exemplar for each region to be classified. The model should be trained before being

utilized for classification. Usually, the training will be done on the data generated from the calibration block. Here, the user has the option of running the program either in training mode or testing mode.

CONCLUSIONS

The main focus of this work was how to extract features from an image and map them to a given set of clases. From the application point of view, the goal was to develop techniques that can be used for detection and classification of corrosion from various NDE sensor images. We developed *Energy Metric Set (EMS)* and then defined a *Measure of Image Feature (MIF),* to develop a method for image *feature extraction*, which is then used by a *neural net classification model* for detection and classification of corrosion. This technology can be used to analyze corrosion in critical areas such as lap joints for aging aircraft. As presented in this paper our result showed that *data fusion* of multiple sensors improves the probability of detection and better assessment of corrosion damage. We also developed a *data normalization* process to map data from different sensors to a common standard or scale. This was useful as the data in the common standard can be compared directly and data can be fused. In this research we also concentrated on detecting "region of interest" or ROI for corrosion evaluation and classification. This method can be used for the identification of the ROI in the specimen, the markup of the image and the annotation of the markups with their assessments. The demonstrate the successful implementation of the techniques developed.

REFERENCES

1. R. Halmshaw, Non-Destructive Testing, (London and Baltimore: Edward Arnold Publishers Ltd., 1987).

2. G.G. Eastaugh, A.A. Merati, D.L. Simpson, P.V. Straznicky, D.V. Krizan, "The Effects of Corrosion on the Durability and Damage Tolerance Characteristics of Longitudinal Fuselage Skin Splices",*1998 USAF Aircraft Structural Integrity Program Conference*, San Antonio, 1-3 December 1998.

3. Federal Aviation Administration (FAA) Airworthiness Directive 94-12-09

4. J. Yim, S.S. Udpa, L. Udpa, M. Mina, W. Lord, "Neural Network Approaches to Data Fusion", Review of Progress in Quantitative Nondestructive Evaluation, Volume: 14A, Page Numbers: 819-826

5. B.J. Matuszewski, L.K. Shark, M.P. Varley, "Region-Based wavelet fusion of ultrasonic radiographic and shearographyc non-destructive testing images" 15th World Conference on Nondestructive Testing, Roma (Italy), October 15-21, 2000

6. D. S. Forsyth, "Nondestructive and Teardown Inspections of Lap Joint Specimenn 604-15 B" Institute for Aerospace Research, Report No. SMPL-LTR-2000-0167, June 2000

7. D. S. Forsyth, J.P. Komorowski, "The Role of Data Fusion in NDE for Aging Aircraft", SPIE Aging Aircraft, Airports, and Aerospace hardware IV, Newport Beach, SPIE Vol. 3994 paper 6, March 2000

8. J.Yim, S.S. Udpa, L. Udpa, "Image Fusion Using Multi-Resolution Decomposition Techniques" Proceedings of the 4th Annual Midwest Electro-Technology Conference, Ames, IA, 1995

9. K. Sun, S. Udpa, L.Udpa, T. Xue, W. Lord, "Registration Issues of Eddy Current and Ultrasound NDE Data using Q-Transform

10. J.R. Zhao, Y.Ma and H. Gao, "Denoising Method of AE Signal by Using Wavelet Transform" 15th World Conference on Nondestructive Testing, Roma (Italy), October 15-21, 2000

11. S. Mallat "A Wavelet Tour of Signal Processing", Academic Press, San Diego, 1999

EVALUATION OF CORROSION CONTROL COATINGS

OUTDOOR EXPOSURE RESULTS FOR PRETREATED AND TOPCOATED ALUMINUM ARMOR ALLOYS 2519, 5083 AND 7039

John V. Kelley, and Brian E. Placzankis

US Army Research Laboratory, Weapons and Materials Research Directorate
Aberdeen Proving Grounds, Maryland 21009

ABSTRACT

Over the last few decades it has been determined that chemical treatments containing hexavalent chromium (Cr+6) are risks to both human health and the environment. One of the mainstays in corrosion prevention of aluminum alloys has been the use of chromate conversion coatings to promote adhesion and inhibit corrosion. Because of the push to reduce the use of Cr+6, many non-chromate treatments have been evaluated over the years. This paper compares the relative performance of six non-chromate pretreatments with grit-blasted and chromated control samples in outdoor exposure at Cape Canaveral FL. Recently obtained outdoor exposure data have been analyzed to determine the effectiveness of the pretreatments and indicates a different failure mode than typically seen in accelerated corrosion chambers. Corrosion attack at the edges is prevalent in outdoor exposure while attack at scribe is uncommon. The substrate of most concern, aluminum 2519, seemed to be less of a factor than originally anticipated when no pretreatment was used. All samples have been monitored throughout the test using electrochemical impedance spectroscopy. Adhesion tests were performed upon completion of outdoor exposure. The data is compared with earlier accelerated corrosion data performed on matching samples.

INTRODUCTION

The automotive and defense industry have been relying on accelerated corrosion data to determine relative corrosion performance of alloys and coating systems for decades. These methods are particularly valuable in determining the ability of coatings to protect steel from corrosion. However the use of salt fog testing to determine the corrosion behavior of coated aluminum alloys is not as accurate.[1] For this reason, outdoor exposure is a useful tool to validate accelerated corrosion data and is the most realistic method of evaluating corrosion performance.

The U.S. Army is continually seeking to lighten the force in an effort to increase its mobility, and deployability. The use of aluminum armor alloys in the construction of armored vehicles is one of the most efficient ways to achieve this. But aluminum armor can introduce new challenges in corrosion protection. For example, the mainstay in corrosion prevention of aluminum alloys, and the most effective to date has been the use of chromate conversion coatings. Aluminum alloys are often pretreated with chromate conversion coatings to stabilize the native oxide on the surface of the metal to promote adhesion, and inhibit corrosion. However, over the last few decades it has been determined that chemical treatments containing hexavalent chromium (Cr+6) are risks to both human health and the environment. Therefore, the Army and private industry have been challenged with developing environmentally benign pretreatments for aluminum armor alloys.

Al 5083-H131 and 7039-T64 are used for the bulk of light-weight armor applications. Currently Al-Mg 5083 is the most widely used aluminum armor alloy because of its high ductility and resistance to stress corrosion cracking (SCC).[2] It's been used in armored systems such as the Amphibious Assault Vehicle (AAV), and the Bradley Fighting Vehicle. Alloy 7039 has high strength and provides better ballistic protection but is more susceptible to stress corrosion cracking and is less suitable for structural applications in marine / tropical environments. The continuous need to lighten the force while improving armor protection has led to the investigation of other aluminum alloys.

In recent years, Al 2519-T87 has been looked at as a possible replacement for 5083 in some applications. It's superior ballistic performance and high strength to weight ratio would help lighten the overall weight of the vehicle while providing better ballistic protection. Alloy 2519 was recently selected for the Advanced Amphibious Assault Vehicle (AAAV). The AAAV is one of the weapon systems presently under development by the Marine Corps and will

eventually replace the AAV. Alloy 2519 must be used with care in marine applications because of its susceptibility to pitting corrosion.[3] Chemical Agent Resistant Coating (CARC) coated 2519 samples have performed poorly in accelerated corrosion tests regardless of the pretreatments used.

Avoiding corrosion of the metallic components in armored vehicles has always been a challenge. Since the Environmental Protection Agency has targeted hexavalent chrome for elimination, and 2519 is becoming more common in armored systems, the task becomes even more difficult. There are many non-chromate alternatives on the market today but, as yet, none have proven to be as effective as chromate in various accelerated corrosion tests.

The US Army Research Laboratory (ARL) Weapons and Materials Research Directorate developed and executed a research program under the auspices of the Department of Defense Strategic Environmental Research and Development Program (SERDP) to examine commercially available non-chromate alternatives for protection of aluminum alloys.

The goal of this effort was to assess the effectiveness of several non-chromate alternatives on coated test panels of three aluminum armor alloys. Included in the program were samples that were subjected to outdoor marine exposure. A study conducted by Dante, Petry and Peeler,[1] suggests that to get meaningful results from outdoor exposure tests, longer than two years is needed. The results in this report are of samples that completed 4 years outdoor exposure and will be used to attempt to validate the earlier accelerated corrosion data, and gage the relative corrosion performance of three aluminum alloys. Electrochemical impedance spectroscopy (EIS), and adhesion tests were also used to evaluate the condition of the topcoats.

EXPERIMENTAL PROCEDURE

The selection of non-chromate conversion coatings to be tested was done in conjunction with the National Center for Manufacturing Sciences (NCMS), University of Michigan study partners.[4] Thirteen vendors of non-chromate coatings were asked to coat test panels. Of these, four vendors (for a total of 6 non-chromate coatings) agreed to have their coatings evaluated. For control purposes a chromate conversion coating and a grit blasted condition were also included.[5] The notations used to identify all of the pretreatments and coatings in this study are listed in Table 1.

At the beginning of the program, a total of approximately 300 aluminum panels nominally 4 in x 6 in x 0.375 in, (10 cm x 15 cm x 1 cm) of alloys 2519-T87, 7039-T64, and 5083-H131 were machined from rolled armor plate stock and sent to vendors and Army depots for coating application. Twelve panels for each conversion coating/alloy combination were prepared. From each set of twelve panels, 5 were painted with an epoxy primer[6] and CARC[7] topcoat, 3 panels were coated with the epoxy primer only, and 4 panels were left in the conversion coated state.

From the 5 sets painted with the CARC system, 2 sets (a total of 48 panels) were selected for outdoor exposure and are the topic of this study. All specimens and their designations are tabulated in Appendix A. Each of these panels was "X" scored using a hardened steel scribe with a static load of 5 kg, and placed on a rack on the beach at Cape Canaveral Air Force Base Florida (Figure 1). A hole was drilled in each panel near the edge, and was used to attach the “working electrode” lead with a screw for impedance measurements. The panels were propped up at about 30 degrees from horizontal with screw holes on top so water would drain away from hole. The racks were positioned approximately 100 yards away from and facing the ocean. Each panel was held in place about 1.25 inches above the surface of the rack using Teflon brackets. Teflon was

used because of its inert qualities, durability and electrical insulating properties (Figure 2). The other seven sets of panels were tested in an earlier study using accelerated test methods and EIS.[5] Periodic visual inspections were performed at 6, 9, 19, and 48 months outdoor exposure and the condition of the surface of the panel was estimated and recorded in terms of percent area failed. At the end of the 48 months exposure, the surface of the panel was evaluated according to ASTM D 1654. Procedure B was used to rank the areas away from the scribe, and procedure A was used to obtain ratings for creepage outward from the scribe. The rating criteria for ASTM D 1654 are outlined in Table 2 and Table 3.

Electrochemical Impedance Spectroscopy was employed to monitor coating condition over time. A portable EIS apparatus was designed to allow measurements to be taken at remote sites in the field (Figure 4). It consisted of a Schlumberger 1280 combination frequency response analyzer (FRA) / potentiostat, a 12 volt DC to 120 volt AC power inverter with 12 volt battery, and a Toshiba laptop computer. Periodic measurements were taken at 6, 9, 19, and 48 months of exposure using the cell configuration illustrated in Figure 3. The cell was filled with 25 mL of 0.5 N NaCl solution and allowed to equilibrate for at least 2 hours prior to taking measurements. The software package Zplot was used for data acquisition, and Zview for data analysis. Measurements were taken at the corrosion potential of the sample over the frequency range of 100 KHz-0.01Hz. The single sine technique was utilized, with a sinusoidal potential impressed upon the open circuit corrosion potential of the substrate (-0.930 V vs. SCE) and an applied amplitude 80mv. An attempt was made to attach the cell and take measurements on a different spot on the panel for each inspection period. That wasn't always possible because, as the samples degraded over time, the amount of defect free area to perform EIS became limited on some samples.

The EIS data was plotted and evaluated in Bode and Nyquist formats. The Bode formats display the magnitude (log | Z |) and phase angle (θ) of the impedance as a function of applied frequency (log f). The total impedance of the specimen, defined as the log | Z | value at 10 mHz in the Bode magnitude plot, was also plotted as a function of exposure time for comparison of the effectiveness of each coating system.

Post exposure paint adhesion tests were performed using a HATE Mark VII coating adhesion tester (Figure 5) in accordance with ASTM D 4541.[8] A loading fixture commonly referred to as a "dolly" is secured normal to the coating surface using a cyanoacrylate adhesive. After allowing the adhesive to cure for 24 hours in laboratory conditions (Table 4), the attached dolly was inserted into the test apparatus. The load applied by the apparatus was gradually increased and monitored on the gauge until a plug of coating was detached. The failure value in lbs/in^2 (psi) was recorded and the failure mode characterized. For this test to be accurate, the panels must be of sufficient thickness to ensure that the coaxial load applied during the removal stage does not distort the substrate material and cause a bulging or a "trampolining effect." On a thin specimen, the resultant bulge causes the coating to radially peel away outwards from the center instead of uniformly pulling away in pure tension and thus results in significantly lower readings. All of the panels used in this study were made from 0.375 inch thick aluminum armor and were of adequate thickness for the pull-off test procedure.

RESULTS

VISUAL INSPECTION

At each of the inspection intervals, every panel was visually examined and any defects were noted. Some key photos are presented in Figures 15 though 18. Regardless of the orientation of the photos, the bottom edge of the panel refers to the edge opposite the screw hole.

One of the first observations made of all panels was of the noticeable fading of the paint at the 9 months inspection. At that time it was also apparent that corrosion had begun on the edges of panels B, J, O, P, in set A, and panels A, I, L, O, Q, R in set B (see appendix A). At 37 months, 2 of the sample sets were removed from the test because of excessive corrosion damage. They were P (7039 / Patclin 2) and L (2519 / Turcoat). All other samples completed the 48 months of exposure. When the test was terminated after 48 months, all samples were given a final thorough visual inspection. First a general overall condition of the panels was estimated, and the average of each alloy-pretreatment combination was taken. These results are illustrated in Figure 6. Unlike the subsequent evaluations done according to ASTM 1654, these data represent the overall condition of the top surface of the panel and take into account the corrosion near the edges and along the scribes.

Measurements of corrosion creepage outward from the scribes, and the condition of the unscribed areas of the panels was done according to ASTM D 1654 procedure A and procedure B respectively. These results are shown in Figure 7 and 8. For the evaluations of areas away from the scribe, an effort was made to discount any corrosion within 0.5 inches from the edges and any corrosion initiating from the scribes. Despite these efforts, in several cases the corrosion undercutting from the edges went beyond the 0.5-inch boundary and therefore were included.

ELECTROCHEMICAL IMPEDANCE SPECTROSCOPY (EIS)

EIS was used to measure the dielectric response of the coating as it degraded over the 48 months of outdoor exposure, and compared with previously recorded laboratory measurements. The procedure for the laboratory measurements taken on immersion samples is described elsewhere [5]. For the outdoor experiment, a total of 4 measurements were recorded for each sample over the 48 months. These results are given in Figures 9-13. The initial measurement was made in the lab on a similarly prepared sample. Measurements made at 6, 9 and 19 months

were made on site at Cape Canaveral AFB. The final impedance measurement was taken at 48 months for all samples and was done in the laboratory when the exposure test was terminated.

COATING ADHESION

Post-exposure coating adhesion tests were performed on all samples exposed. A total of 2 “pull-off” tests per panel were done and the results for each alloy/pretreatment combination were averaged and illustrated in Figure 14. All of the pull-off results, along with the statistics are tabulated in Appendix B. The mode of failure for each pull-off was noted and is given in Appendix C.

DISCUSSION

The objective of this effort was to evaluate commercially available non-chromate conversion coatings against a baseline of hexavalent chromate (Alodine 1200), and to characterize the corrosion mechanisms and adhesion performance of the coatings systems. This discussion will focus on two areas: 1) The performance of the pretreatments on each alloy in outdoor exposure, and 2) a comparison of the corrosion observed and the relative performance of these coatings in outdoor exposure and accelerated corrosion tests.

The three alloys used in the study (Al alloys 2519, 7039 and 5083) have very different general corrosion characteristics. Alloy 2519 is generally very susceptible to pitting corrosion, and is considered difficult to pretreat due to the Cu containing precipitates and constituent particles found in the alloy microstructure. Alloy 5083, the most commonly used aluminum armor alloy, is very resistant to pitting corrosion, even if the alloy is tested "bare." Alloy 7039 is somewhat susceptible to pitting, and can also suffer from stress corrosion cracking. Thus, it is anticipated that the conversion coating/organic coating systems will behave differently on each alloy.

Despite the general corrosion resistance of alloy 5083, some of the pretreatments performed poorly on this alloy. As shown in Figure 7, most of the alloy/coating combinations showed no appreciable creepage from the scribes. However, creepback was observed for both the Turcoat and Bulk Chemical pretreatments on alloy 5083. ASTM ratings of the unscribed areas are given in Figure 8, and again two pretreatments (Patclin 3 and grit blasting) showed significant performance drops on this alloy. The impedance plots for the coatings on 5083 are shown in Figure 10, while the post-exposure adhesion results are shown in Figure 14. Neither the total impedance measurements nor the post-exposure adhesion results provide a simple explanation for this behavior. Overall, several of the non-chromate conversion coatings performed well on this alloy, as did the Alodine 1200 control.

Alloy 7039 displayed the greatest resistance to creepage from the scribes, but still had significant attack away from the scribe for some pretreatments (Figures 7 and 8). The Patclin 2 and grit blasted panels had ratings of 2 and 4 respectively for unscribed regions. Again, results from impedance as a function of exposure (Figure 11) and post-exposure adhesion (Figure 14) do not provide much insight to this behavior. The impedance values of both these pretreatments are within the scatter band. The post-exposure adhesion strength of the grit blasted panels was somewhat lower (1515 psi) than the average value of 2367 psi attained by all the alloy 7039 specimens, but the Patclin 2 adhesion was 2505 psi, which was the third highest. Again, as with 5083, several of the non-chromate pretreatments performed well, as did the chromate control samples.

As previously mentioned, the high copper contents found in 2000 series aluminum alloys make them difficult to pretreat, and alloy 2519 is no exception. Despite this, several of the non-chromate pretreatments and the Alodine 1200 control performed quite well when tested in conjunction with the organic coating system in outdoor exposure. Five pretreatments showed

no creepage from the scribe (Figure 7), and five pretreatments had ASTM ratings of 9 or 10 for unscribed areas. Most surprising was the fact that the grit blasted panels with no pretreatment fell into both these groups, and compared extremely well with the chromate controls. Figure 17 shows scanned images of the grit blasted 2519 panels after 48 months exposure, showing no creepback of the coating whatsoever. The only defect visible is a small blister beside the hole used to attach the working electrode contacts for impedance measurements, earning it a rating of 9. This result was so surprising that the alloy content of each 2519 panel was re-verified via energy dispersive spectroscopy in a scanning electron microscope.

The second area of this discussion will compare the performance results of accelerated corrosion tests with the results of the same alloy pretreatment combinations in outdoor exposure. Observations of the predominant failure modes will also be discussed. The initial evaluation of these non-chromate conversion coatings was based on ASTM B117 salt fog, and GM 9540P data,[5] and the outdoor exposure results will attempt to validate the initial findings.

After 100 cycles of GM 9540P, 7039 had only 2 cases of blistering near the scribe, fewest of the 3 alloys. Because all of the pretreatments on 7039 performed relatively well compared to chromate, no one non-chromate conversion coatings emerged as the best for 7039. In outdoor exposure 7039 samples had no measurable corrosion attack initiating at the scribes, again, the fewest cases of all 3 alloys. Corrosion initiating at the edges of samples caused the majority of the damage on this alloy in outdoor exposure. Chemcote was marginally better at resisting corrosion at the edges than the other non-chromate pretreatments for 7039 in outdoor exposure. But none was as good as chromate at resisting undercutting at the edges.

Accelerated corrosion testing proved to be disastrous for non-chromate conversion coatings on 2519. Total failure was seen on 2519 with all but 3 surface treatments: grit blasted, chromate, and Chemcote, with chromate performing best. However, as mentioned earlier, the

2519 samples performed much more admirably in outdoor exposure, with the biggest apparent surprise being the grit blasted 2519 samples with no pretreatment. Although unexpected, the impressive performance of the grit blasted 2519 panels was not in conflict with the accelerated corrosion results. In the earlier work, the grit blasted 2519 was one of three that did not experience "total failure" after 100 cycles of GM 9540P. Also in agreement was the good corrosion performance of the Chemcote on 2519. Turcoat (Figure 15) and all the Patclin treatments on 2519 did not fair as well which is also consistent with the previous work.

The exceptional resistance to general corrosion of 5083 is evident in the results of the accelerated testing data. In general 5083 was clearly the best performer of all 3 alloys as long as it was pretreated. However, when 5083 is grit blasted and without a pretreatment, significant blistering occurs. This correlated well with the outdoor exposure data where 6 out of the 7 pretreatments on 5083 rated a 9 or above (Figure 8) and grit blasted only scored a 6 rating. Alodine 1200 performed best in both accelerated corrosion and outdoor exposure tests on 5083. However, if not for the corrosion along the edges of the panel, an argument could be made for Chemcote and Patclin 2 as the best in outdoor exposure.

In outdoor exposure corrosion attack at the scribe was relatively uncommon, which is in contrast to what is typically seen in accelerated corrosion tests. Only 5 out of the 24 pretreatment / alloy combinations (about 21%) experienced any measurable creepage from the scribe. Thus most of the corrosion that was observed initiated at the edges of the samples. In outdoor exposure the edges and bottom of the panels stay wetter longer than the sun exposed top surface. The usual "edge effects" (residual stress, thinning of the paint) coupled with UV embrittling of the coating contributed to the edge attack not typically seen in accelerated corrosion chamber tests.

The total impedance of a representative set of samples tested in outdoor exposure are given in Figures 9 through 11. There was no real correlation between total impedance and corrosion performance of the pretreatment. Several samples had good corrosion performance and low impedance while others had high impedance values with poor corrosion performance. That said, samples with high impedance and blistering may indicate that the pretreatment relies on barrier properties for protection and offers little resistance to undercutting. If the opposite is true, as in the case of chromate, the pretreatment may have inhibiting "self healing" qualities and provides better resistance to undercutting, but offers less barrier protection.

Figures 12 and 13 offer a comparison of the impedance values of the two controls in outdoor exposure with the laboratory impedance measurements of similarly prepared control samples in laboratory immersion samples. There appears to be a similar trend with both sets of data, especially with the grit blasted samples, which eventually leveled off at about 10^5 ohms. There is clearly more noise in the chromate data for both outdoor exposure and laboratory, perhaps as a product of the inhibiting qualities of chromate. Nevertheless, this comparison is offered as a verification of the degradation trends of the like prepared control samples in outdoor exposure.

CONCLUSIONS

- The mode of failure in outdoor exposure was distinctly different from that typically seen in accelerated corrosion chambers. Corrosion attack at the edges is prevalent in outdoor exposure while attack at scribe is uncommon.
- All samples maintained good adhesion (above 1500 psi) regardless of corrosion performance. A slight correlation between post exposure adhesion, and corrosion performance was observed within samples of a given surface treatment.

- Post exposure adhesion was a function of surface treatment and not alloy dependant. Samples with a chemical pretreatment tend to maintain adhesion better than those without a chemical pretreatment. The exception being grit blasted 2519 samples where post exposure adhesion was comparable to all others including chromate.
- Alloy 2519 grit blasted with no pretreatment did surprisingly well performing best of all the samples without a pretreatment, and nearly as well as chromate.
- Because of its superior ability to retard undercutting and inhibit corrosion, chromate was best at protecting the edges of samples as well as guarding against attack at the scribe. No other pretreatment was more consistent at protecting all 3 alloys than chromate.
- Regardless of the mode of failure observed in outdoor exposure, there was agreement with the performance results from accelerated corrosion tests and outdoor exposure. In both tests, Brent Chemcote performed best of the non-chromate pretreatments on all 3 alloys.

ACKNOWLEDGEMENTS

The authors would like to thank several people for their technical contribution. Most notable is Mr. Russell Kilbane who methodically performed many of the laboratory impedance measurements, pull-off adhesion tests, and compiled and presented data in graphical format. Mr. Cliff Hubbard who painstakingly performed the EDS alloy verifications, and consultations with Dr. John Beatty, and Christopher Miller aided in the understanding of coating technology. Finally we would like to thank the Strategic Environmental Research and Development Plan (SERDP) program for the original funding of this program.

REFERENCES

1. Comparison of Laboratory Corrosion Test Methods and Outdoor Corrosion Test for Air Force Coating Systems, J.F. Dante, L. Petry, D.T. Peeler, 1999 Tri-Service Corrosion Conference Proceedings, Nov 1999.

2. Weldability Study of 2519-T87 Aluminum Armor, Daniel Nowak, U.S. Army Materials Technology Laboratory, Watertown MA, TN May 1990.

3. Aluminum Armor 2519: A Review of Literature Relevant to the Advanced Amphibious Assault Vehicle, Joseph Pickens, Concurrent Technologies Corp, Johnstown PA, TR No 99-95 Jan 13, 2000.

4. National Center for Manufacturing Sciences "Alternatives to Chromium for Metal Finishing" Final Report NCMS # 0273RE95 Ann Arbor, MI October 1995.

5. Evaluation of Non-Chromate Conversion Coatings on Aluminum Armor Alloys, Brian E. Placzankis, John H. Beatty, John V. Kelley, Lorrie Krebs, Corrosion 97, paper no. 532.

6. MIL-P-53022 "Primer, Epoxy Coating, Corrosion Inhibiting, Lead and Chromate Free." February 1992.

7. MIL-C-53039A "Coating, Aliphatic Polyurethane, Single Component, Chemical Agent Resistant." 23 November 1988.

8. ASTM D 4541, “Standard Test Method for Pull-Off Strength of Coated Specimens Subjected to Corrosive Environments,” American Society for Testing and Materials, Philadelphia, PA, 1989.
9. Corrosion Tests and Standards, Application and Interpretation, Robert Baboian editor, ASTM Philadelphia PA, 1995.

TABLES AND FIGURES

TABLE 1.
Descriptions for notations used for coatings and pretreatments

Notation	Coatings/Pretreatment
Gritblasted	Grit blasted panel with no conversion coating
Chromate	Alodine 1200
Chemcote	Brent Chemcoat L497260A
Turcoat	Turco Alcoat 6787
Patclin 1	Patclin 1910A
Patclin 2	Patclin 1910B
Patclin 3	Patclin 1910C
Bulk Chem	Bulk Chemical E-CLPS 923
CARC / Topcoat	Chemical Agent Resistant Coating MIL-C-53039A.
Primer	Epoxy Primer MIL-P-53022-10.

TABLE 2.
Rating criteria for evaluating creepage from scribe of painted panels subjected to corrosive environments, ASTM D 1654

Rating of Failure at Scribe (Procedure A)		
Representative Mean Creepage From Scribe		
Millimetres	Inches (Approximate)	Rating Number
Over 0	0	10
Over 0 to 0.5	0 to 1/64	9
Over 0.5 to 1.0	1/64 to 1/32	8
Over 1.0 to 2.0	1/32 to 1/16	7
Over 2.0 to 3.0	1/16 to 1/8	6
Over 3.0 to 5.0	1/8 to 3/16	5
Over 5.0 to 7.0	3/16 to 1/4	4
Over 7.0 to 1 0.0	1/4 to 3/8	3
Over 10.0 to 13.0	3/8 to 1/2	2
Over 13.0 to 16.0	1/2 to 5/8	1
Over 16.0 to more	5/8 to more	0

TABLE 3.
Rating criteria for evaluating unscribed areas of painted panels subjected to corrosive environments, ASTM D 1654

Rating of Unscribed Areas (Procedure B)	
Area Failed (%)	Rating Number
No failure	10
0 to 1	9
2 to 3	8
4 to 6	7
7 to 10	6
11 to 20	5
21 to 30	4
31 to 40	3
41 to 55	2
56 to 75	1
Over 75	0

TABLE 4.
Laboratory Conditions for Pull-Off Adhesion ASTM D 4541

Adhesive type	Cyanoacrylate
Cure time (hours)	24
Temperature (C)	25
Relative Humidity (percent)	31
Substrate Materials	Al 2519 / 5083 / 7039
Coating type	CARC 53022 / 53039A
Coating thickness (mils)	~4.0

FIGURE 1: Exposure racks at Cape Canaveral

FIGURE 2: Teflon hold-down brackets

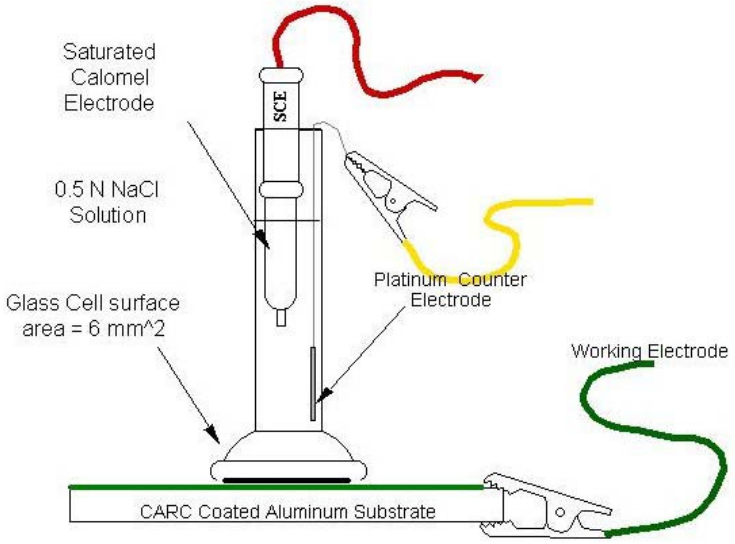

FIGURE 3: Schematic of EIS Cell used for field measurements

FIGURE 4: Portable EIS set up at outdoor exposure test site, Cape Canaveral FL

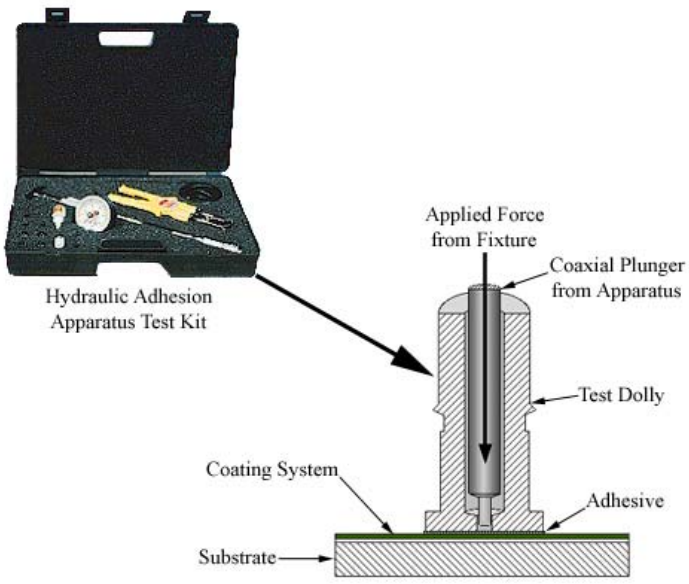

FIGURE 5: Schematic of the pull-off adhesion test performed on all exposed samples

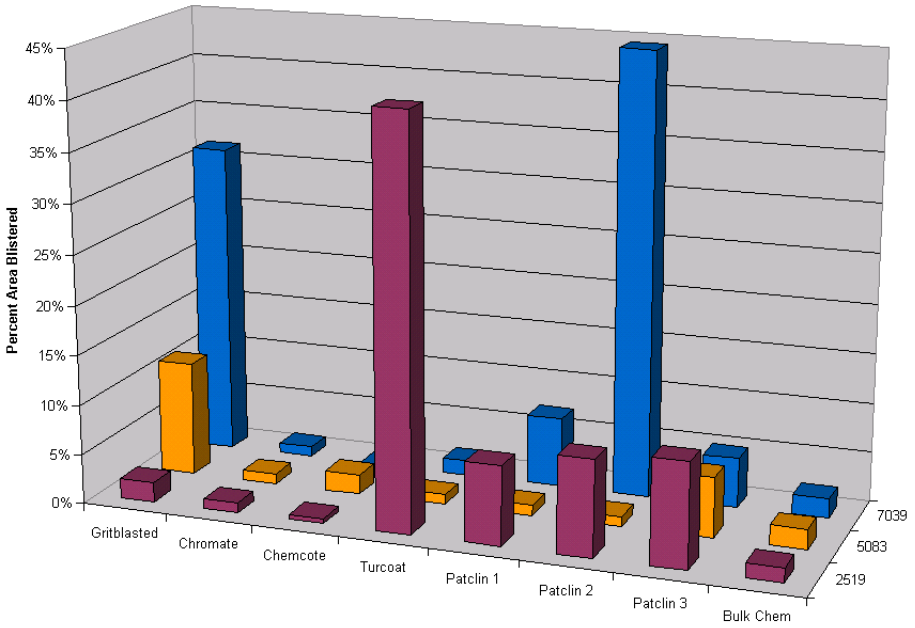

FIGURE 6: Average area failed of both sets of panels after 48 months (208 weeks) outdoor exposure

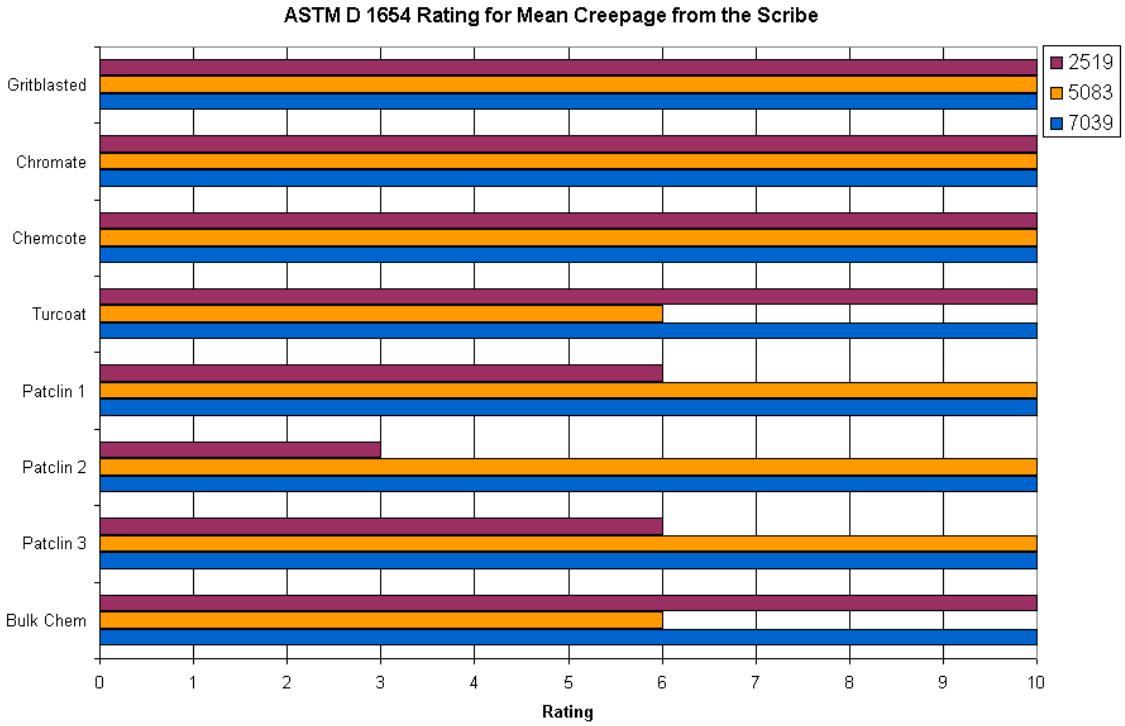

FIGURE 7: ASTM 1654-Procedure A ratings for panels in outdoor exposure

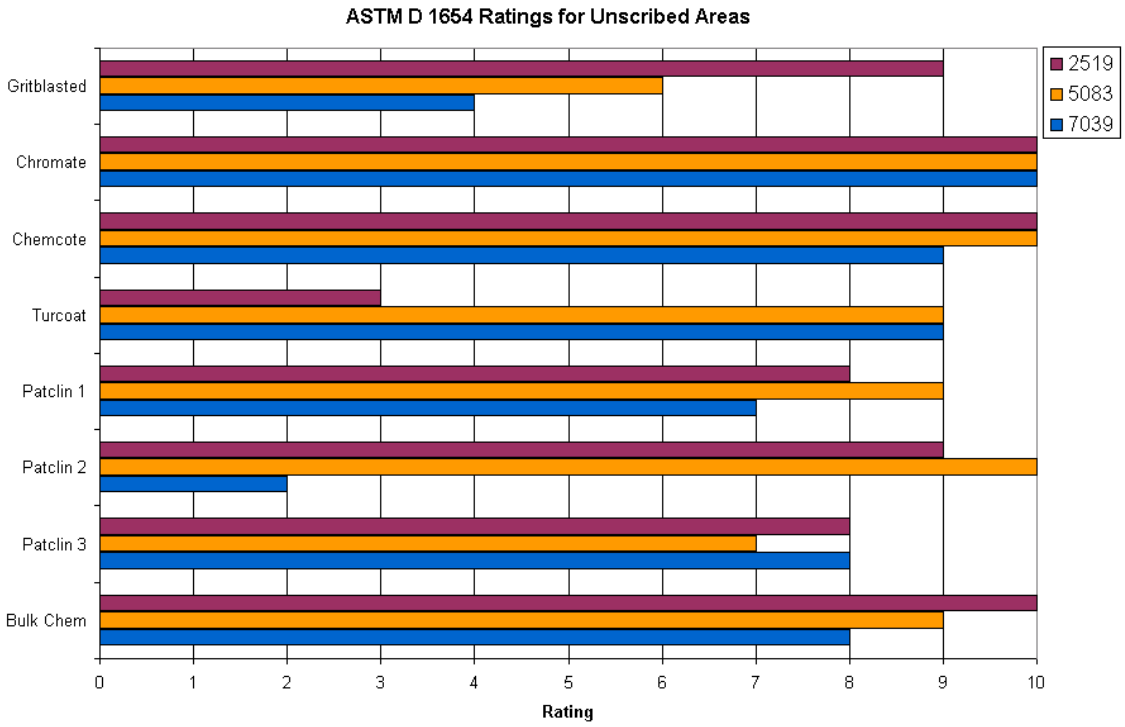

FIGURE 8: ASTM 1654-Procedure B ratings for panels in outdoor exposure

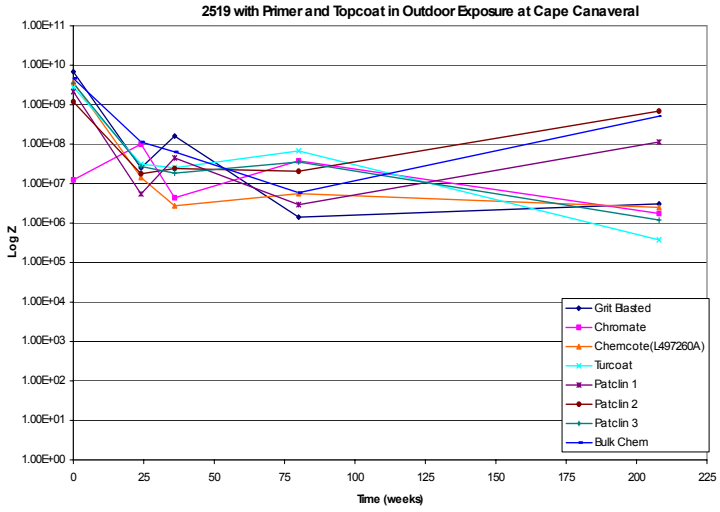

FIGURE 9: 2519 in outdoor exposure

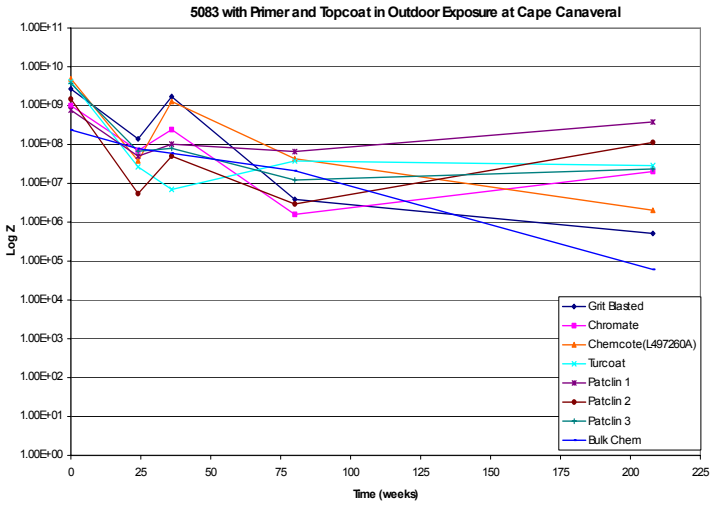

FIGURE 10: 5083 in outdoor exposure

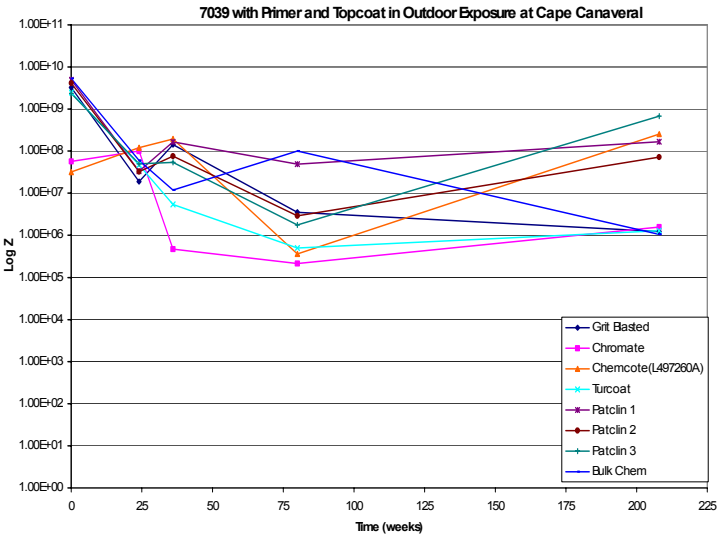

FIGURE 11: 7039 in outdoor exposure

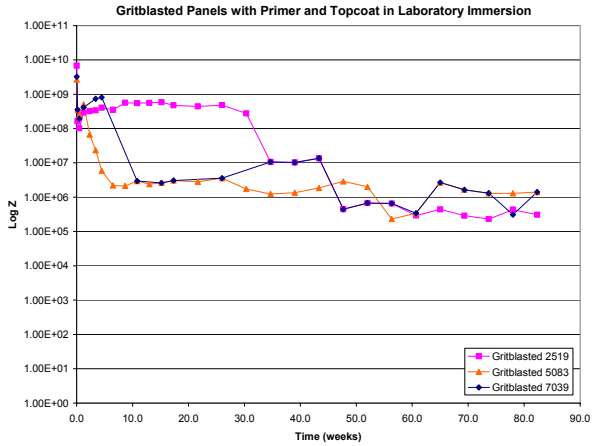

FIGURE 12a: Grit blasted panels in lab immersion

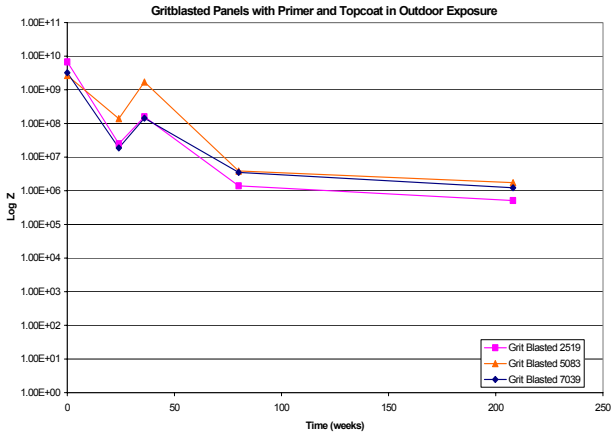

FIGURE 12b: Grit blasted panels in outdoor exposure

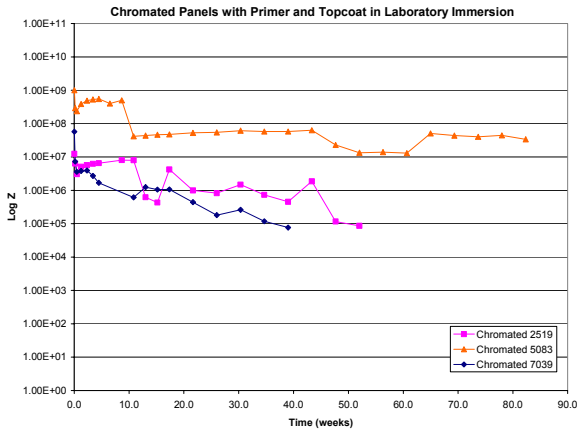

FIGURE 13a: Chromated panels in lab immersion

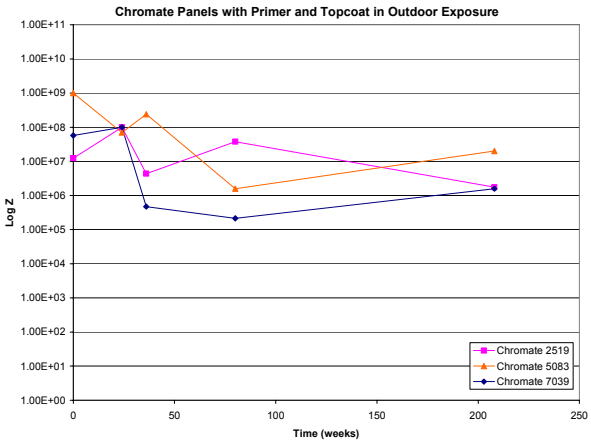

FIGURE 13b: Chromated panels in outdoor exposure

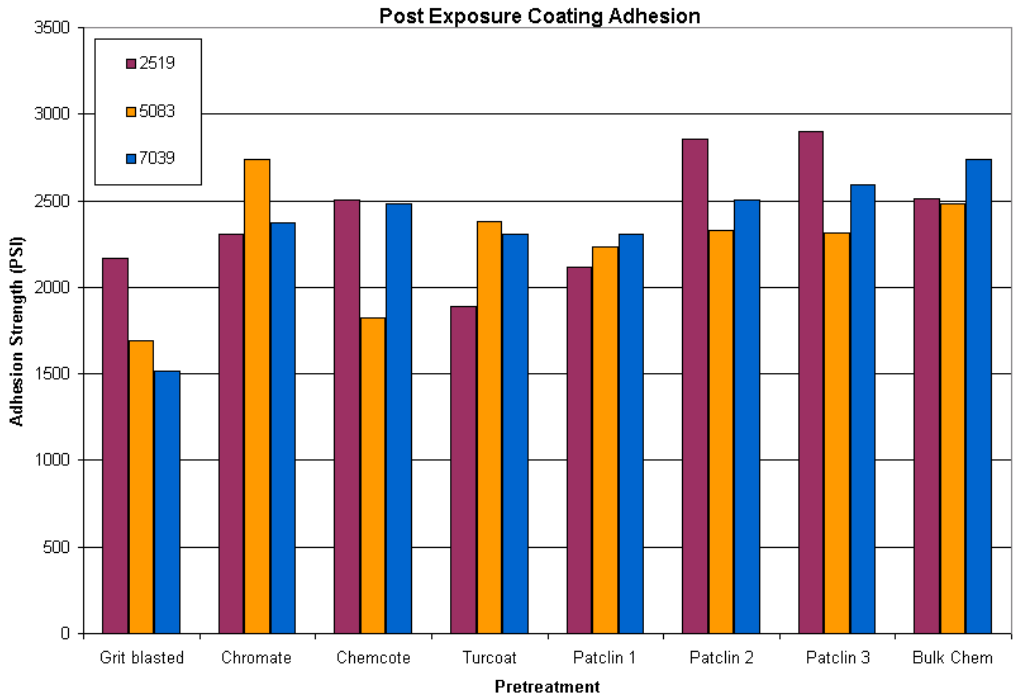

FIGURE 14: Averaged post exposure pull-off coating adhesion strength data

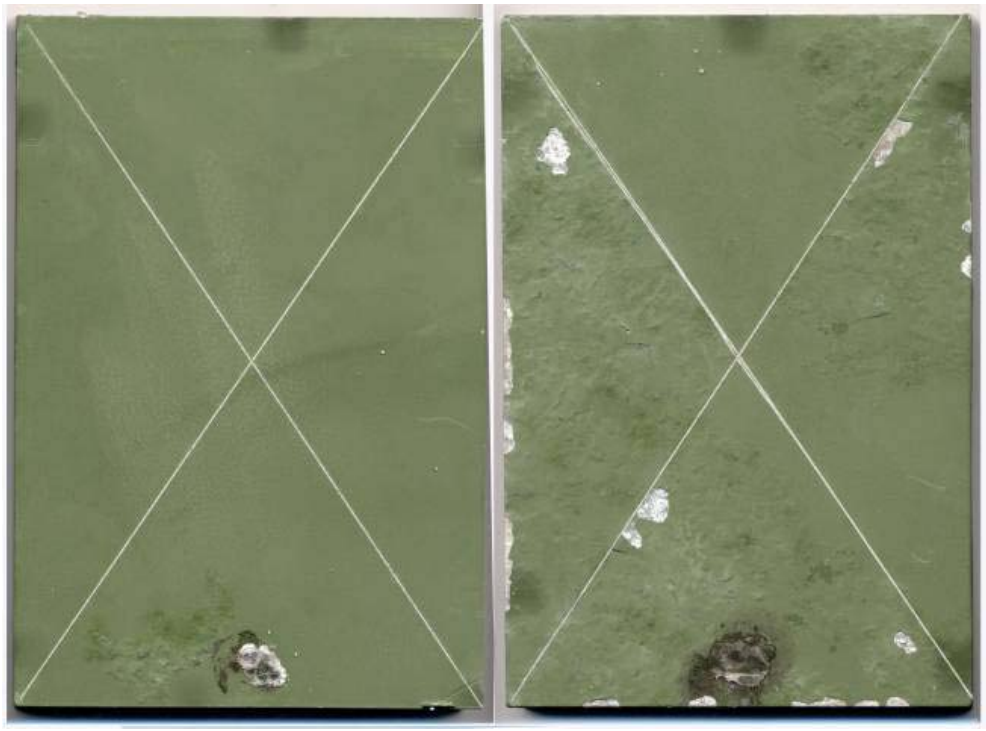

A B

FIGURE 15: Alloy 2519 pretreated with Turcoat

A B

FIGURE 16: Alloy 7039 pretreated with Patclin 2

A B

FIGURE 17: Grit Blasted 2519 after 48 months exposure

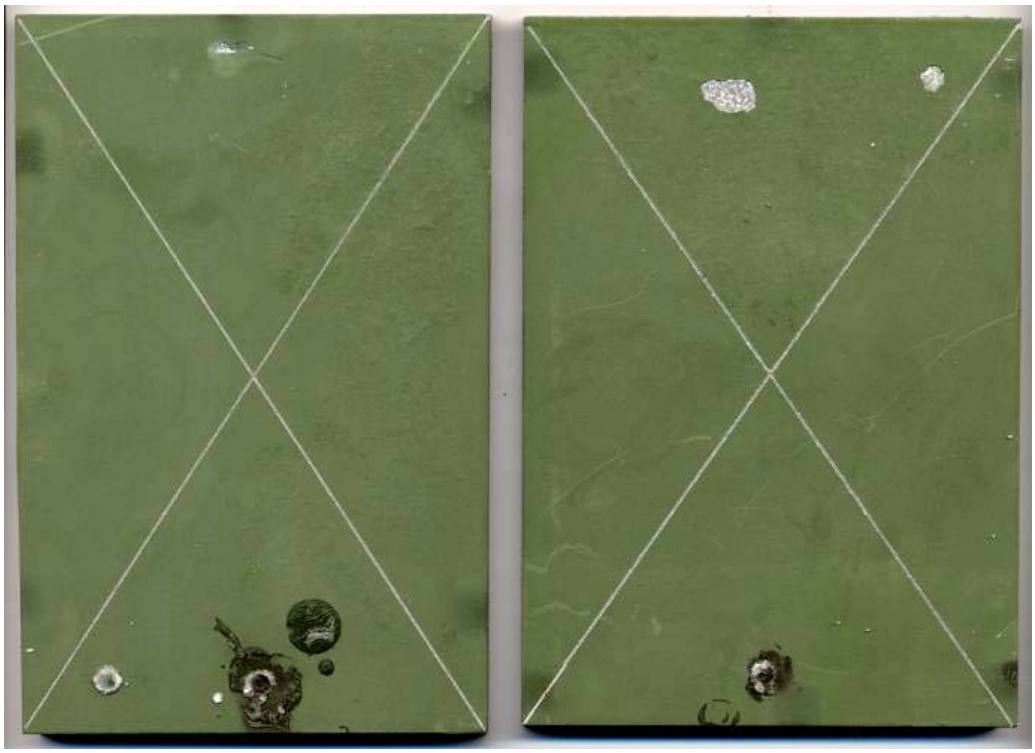

A B

FIGURE 18: Grit Blasted 7039 after 48 months exposure

Appendix A: Sample designations, pretreatments and alloy combinations

EDS Verification of Aluminum Alloy Substrates				
Panel Identification	**Set #**	**Alloy Element**	**Alloy Designation**	**Pretreatment Type**
A	a	Cu	2519	Grit blasted / no conversion coating
	b	Cu	2519	Grit blasted / no conversion coating
B	a	Mg	5083	Grit blasted / no conversion coating
	b	Mg	5083	Grit blasted / no conversion coating
C	a	MgZn	7039	Grit blasted / no conversion coating
	b	Mgzn	7039	Grit blasted / no conversion coating
D	a	Cu	2519	Chromate - Alodine 1200
	b	Cu	2519	Chromate - Alodine 1200
E	a	Mg	5083	Chromate - Alodine 1200
	b	Mg	5083	Chromate - Alodine 1200
F	a	MgZn	7039	Chromate - Alodine 1200
	b	MgZn	7039	Chromate - Alodine 1200
G	a	MgZn	7039	Nochromate - Brent Chemcoat L497260A
	b	MgZn	7039	Nochromate - Brent Chemcoat L497260A
H	a	Mg	5083	Nochromate - Brent Chemcoat L497260A
	b	Mg	5083	Nochromate - Brent Chemcoat L497260A
I	a	Cu	2519	Nochromate - Brent Chemcoat L497260A
	b	Cu	2519	Nochromate - Brent Chemcoat L497260A
J	a	Mg	5083	Nonchromate - Turcoat Alcoat 6787
	b	Mg	5083	Nonchromate - Turcoat Alcoat 6787
K	a	MgZn	7039	Nonchromate - Turcoat Alcoat 6787
	b	MgZn	7039	Nonchromate - Turcoat Alcoat 6787
L	a	Cu	2519	Nonchromate - Turcoat Alcoat 6787
	b	Cu	2519	Nonchromate - Turcoat Alcoat 6787
M	a	Mg	5083	Nonchromate - Patclin 1910A
	b	Mg	5083	Nonchromate - Patclin 1910A
N	a	MgZn	7039	Nonchromate - Patclin 1910A
	b	Cu	2519	Nonchromate - Patclin 1910A
O	a	Cu	2519	Nonchromate - Patclin 1910A
	b	Cu	2519	Nonchromate - Patclin 1910A
P	a	MgZn	7039	Nonchromate - Patclin 1910B
	b	MgZn	7039	Nonchromate - Patclin 1910B
Q	a	Mg	5083	Nonchromate - Patclin 1910B
	b	Cu	2519	Nonchromate - Patclin 1910B
R	a	Cu	2519	Nonchromate - Patclin 1910B
	b	Cu	2519	Nonchromate - Patclin 1910B
S	a	Mg	5083	Nonchromate - Patclin 1910C
	b	Mg	5083	Nonchromate - Patclin 1910C
T	a	Mgzn	7039	Nonchromate - Patclin 1910C
	b	MgZn	7039	Nonchromate - Patclin 1910C
U	a	Cu	2519	Nonchromate - Patclin 1910C
	b	Cu	2519	Nonchromate - Patclin 1910C
V	a	Cu	2519	Nonchromate - Bulk Chemical E-CLPS 923
	b	Cu	2519	Nonchromate - Bulk Chemical E-CLPS 923
W	a	MgZn	7039	Nonchromate - Bulk Chemical E-CLPS 923
	b	MgZn	7039	Nonchromate - Bulk Chemical E-CLPS 923
X	a	Mg	5083	Nonchromate - Bulk Chemical E-CLPS 923
	b	Mg	5083	Nonchromate - Bulk Chemical E-CLPS 923

Appendix B: Post exposure pull-off adhesion results with statistics

ASTM D 4541 Coating Adhesion (PSI)									
Test Sample		Reading Number*						Statistics	
Alloy	Pretreatment	1	2	3	4	5	6	Average	Std Dev
2519	Grit Blast	1710	1750	2800	2400	--	--	2165	528
2519	Chromate	2500	2650	2400	1680	--	--	2308	431
2519	Chemcote	2320	2700	2790	2200	--	--	2503	287
2519	Turcoat	2010	2100	1350	2100	--	--	1890	362
2519	Patclin 1	1920	1810	2280	2450	2200	2050	2118	237
2519	Patclin 2	3200	2800	2560	2850	2700	2510	2770	249
2519	Patclin 3	2820	2600	2980	3200	--	--	2900	254
2519	Bulk Chem	2200	2640	2500	2710	--	--	2513	226
5083	Grit Blast	1800	1490	1180	2300	--	--	1693	478
5083	Chromate	2600	2950	2700	2710	--	--	2740	149
5083	Chemcote	2410	1700	2390	800	--	--	1825	759
5083	Turcoat	2150	2220	2350	2800	--	--	2380	292
5083	Patclin 1	1890	2000	2580	2450	--	--	2230	336
5083	Patclin 2	2190	1900	--	--	--	--	2045	205
5083	Patclin 3	1620	2200	2910	2530	--	--	2315	547
5083	Bulk Chem	2590	2450	2500	2400	--	--	2485	81
7039	Grit Blast	1780	1400	1480	1400	--	--	1515	181
7039	Chromate	2310	2400	2690	2090	--	--	2373	249
7039	Chemcote	2950	2000	2700	2275	--	--	2481	425
7039	Turcoat	2500	2025	2300	2400	--	--	2306	205
7039	Patclin 1	2690	2300	--	--	--	--	2495	276
7039	Patclin 2	2480	2600	2490	2450	--	--	2505	66
7039	Patclin 3	2310	2450	2890	2710	--	--	2590	260
7039	Bulk Chem	2840	2900	2620	2600	--	--	2740	152

Appendix C: Failure mode recording for each pul-off set.

Pull-Off Adhesion Test Failure Modes			
Panel Identification	**Set #**	**1st Reading**	**2nd reading**
A	a	substrate	substrate
	b	substrate	adhesive/substrate
B	a	substrate	substrate
	b	substrate/adhesive	substrate/adhesive
C	a	substrate	substrate
	b	substrate	substrate
D	a	adhesive/intralayer	adhesive/intralayer
	b	adhesive	adhesive
E	a	adhesive/substrate	intralayer
	b	intralayer	interlayer
F	a	substrate/adhesive	adhesive
	b	adhesive/substrate	substrate
G	a	substrate	adhesive/substrate
	b	Adhesive/substrate	intralayer
H	a	intralayer/substrate	intralayer/substrate
	b	substrate	substrate
I	a	substrate	intralayer
	b	adhesive	adhesive
J	a	adhesive/substrate	adhesive/substrate
	b	substrate	adhesive/substrate
K	a	adhesive/substrate	substrate/adhesive
	b	substrate	adhesive/substrate
L	a	substrate	substrate
	b	substrate/adhesive	substrate/adhesive
M	a	adhesive/substrate	adhesive/substrate
	b	intralayer	adhesive/substrate
N	a	adhesive	adhesive
	b	substrate	substrate
O	a	substrate/adhesive	adhesive/intralayer
	b	substrate	substrate
P	a	intralayer	intralayer
	b	adhesive/substrate	adhesive/substrate
Q	a	substrate	substrate
	b	adhesive	adhesive
R	a	adhesive/substrate	adhesive/substrate
	b	adhesive	intralayer
S	a	substrate/adhesive	substrate
	b	adhesive/substrate	adhesive
T	a	adhesive	adhesive
	b	adhesive	adhesive
U	a	adhesive	adhesive
	b	adhesive	adhesive/substrate
V	a	adhesive	adhesive/substrate
	b	intralayer	intralayer
W	a	adhesive/intralayer	adhesive/substrate
	b	substrate	adhesive/substrate
X	a	adhesive	substrate
	b	intralayer	adhesive

EVALUATION OF ZINC-RICH PRIMERS FOR USE ON ARMY VEHICLE SYSTEMS

I. Carl Handsy
US Army Tank-automotive Armaments Command
AMSA-TR-E/MEPS
Warren, MI 48397-5000
Handsyi@tacom.army.mil

John Repp
Corrpro Companies, Inc.
50 Tennessee Ave.
Ocean City, NJ 08226
Jrepp@corrpro.com

ABSTRACT

Army vehicles (like other DOD weapon systems) are a continually aging fleet. With reductions in acquisition and maintenance dollars, vehicles are being used beyond their original design life. To prolong the service life of this equipment, while reducing maintenance costs, improved technologies are needed for repair and maintenance of these vehicles. One of the biggest areas of concern is corrosion of these fielded weapon systems, which costs the Army $2-3 billion per year. This can affect the readiness of our troops and reduce their effectiveness during peace and war times.

Zinc-rich coatings have been used on existing weapon systems during maintenance and repair activities. These coatings are used to provide sacrificial corrosion protection to steel substrates (where no sacrificial protection was present or existing galvanizing has been removed during repair). However, despite its use on weapon systems, little or no relevant testing in an Army military environment has been conducted. TACOM/TARDEC initiated a program to evaluate two zinc-rich coating materials to show key performance factors as related to Army military equipment.

INTRODUCTION

Zinc-rich coatings are used in the corrosion protection of steel structures. These paints use zinc dust or particles as the pigment, providing sacrificial cathodic protection. These

coatings are traditionally used on steel structures in natural atmospheric exposure (i.e., bridge and highway structures) to mitigate corrosion of the substrate. Recently these coatings have been implemented on Army vehicles to reduce corrosion.

These coatings are used for the repair of damaged components and the upgrade of existing fielded equipment. Despite being used for many years in the bridge and highway industries, the long-term performance of these coatings is unknown in an Army vehicle environment. Often zinc-rich coatings are choosen either arbitrarily or based on product datasheets written for other industries and structures. This test program was developed to evaluate two zinc-rich coating materials for relative performance compared with control samples.

EXPERIMENTAL APPROACH

Testing was performed using standardized test procedures to relatively compare the performance between the two zinc-rich coated, steel and galvanized steel test panels, using a standard chemical agent resistance coating (CARC) system. The test methods used to evaluate these samples are discussed below.

SAMPLE PREPARATION

Steel and galvanized test panels along with existing 5-ton truck doors were prepared to evaluate the performance of zinc-rich and control coating systems. Various substrate preparations and conditions were evaluted including unexposed, smooth and pre-rusted steel substrates. Prior to coating application, unexposed substrates were abrasive blasting to a Steel Structures Paint Council (SSPC) SP-10 condition, with a 50-76-μm (2-3-mil) profile. Pre-rusted steel substrates were prepared to a SSPC SP-3 condition. Galvanized and smooth test panels were solvent cleaned, only, prior to coating application.

Following surface preparation, samples were solvent cleaned and coating application was performed in accordance with the manufacturer's recommendations. On test samples only, application included priming with one of two zinc-rich primers (A or B). All samples were then either left uncoated or were over-coated using a MIL-P-53022 epoxy and/or MIL-C-46168 polyurethane CARC topcoat, depending on the test being performed. Table 1 shows the coating systems applied based on tests being performed.

Following application test samples were left exposed to ambient conditions for a minimum of seven days, or as required by the coating manufacture, allowing for full cure. After complete cure, samples for corrosion testing were preconditioned by either scribing through the coating system to the steel substrate or damaging the coating system using a gravelometer (chipping). Scribing was performed on test panels and 5-ton truck doors. Chipping was performed on test panels only, simulating random damage that might be expected during normal vehicle operations.

ACCELERATED CORROSION TESTING

Accelerated corrosion testing was performed in accordance with GM 9540P, "Accelerated Corrosion Test." Test samples were exposed to a cycle of:

- Four salt solution (0.9% NaCl, 0.1% CaCl, 0.075% $NaHCO_3$ and deionized water) spray events, spaced 90-minutes apart;
- Ambient atmospheric exposure between salt spray events and and additional 210-minutes after the final spray event;
- High temperature (49° C) and high humidity (100% RH) exposure for eight hours and
- High temperature (60° C) and low humidity (<30% RH) for eight hours.

Each cycle of events requires 24-hours to complete and represents one test cycle. A total of 120-cycles (15 test years, with 8-cycles equivalent to one test year) were performed to evaluate the coating materials. During this test periodic evaluations of the test samples were performed. These evaluations were visual inspections of the samples in accordance with the Army's Corrosion Rating System (scale of 0 to 4, with 0 being no corrosion and 4 being perforation of the substrate) for rusting, ASTM D714 for blistering and maximum cutback (in millimeters) from the intentional scribe. For reporting purposes the blistering data (which is an alphanumeric raiting) was converted to a composite rating of 0 to 10 as shown in table 2. GM 9540P testing was performed by Corrpro and Army Research Laboratories (ARL) for inter-laboratory analysis.

SEASHORE EXPOSURE TESTING

Seashore exposure testing was performed at Corrpro Companies Inc.'s Sea Isle City, NJ (SIC) and Kennedy Space Center's Cape Canaveral, FL (KSC) beachside exposure sites. Both sites represent a natural, harsh marine coastal environment. The SIC site represents a North-East marine environment with a wide annual temperature range, is in close proximity to the Atlantic Ocean and experiences high airborne chlorides and atmospheric pollutants. The KSC site is typical of a South-East marine environment and is below the flight path of the space shuttle launch trajectory, resulting in high pollutant fallout immediately following launches.

Samples were exposed for a period of six months, with periodic evaluations for corrosive attack. Samples were evaluated for rusting in accordance with the Army's Corrosion Rating System, blistering in accordance with ASTM D714 and maximum cutback from the intentional scribes (in millimeters). Following six months of testing, the samples were left exposed at each location for future evaluations.

REPAIRED DOORS

To fully evaluate the performance of the coating systems under simulated service conditions, test patches were prepared on existing 5-ton truck doors exposed at the KSC site. These doors were originally exposed in the mid 1980's to evaluate the corrosion resistance of the Army's CARC coating system. Each of these doors experienced varying levels of corrosive attack during this exposure, but the majority of base metal remained intact. The substrate of these doors was prepared by abrasive blasting to remove all paint and corrosion products. The doors were then divided into four test sections to evaluate various coating systems. Figure 1 shows a representative test door and a sketch of the coating systems applied to this door.

Test doors were prepared and exposed with test panels. Following six months of testing these samples remain exposed at the KSC site for future evaluations.

ADHESION TESTING

Adhesion testing was performed using both pull-off (ASTM D4541) and crosscut (ASTM D3359) test methods. Testing was performed on samples as applied and following 120-cycles of GM 9540P testing. The pull-off adhesion test is performed until disbondment of the test dollies occurred and the failure strength and location were recorded. The crosscut adhesion testing was used to attempt to remove the coating material from the panel substrate. The amount of coating material removed is rated on a scale of 0 to 5 (with 5 being no removal) and used to compare relative adhesion between coating systems.

MANDREL BEND TEST

Mandrel bend testing was performed in accordance with ASTM D522 using a conical mandrel. Testing was performed on samples as applied and following 120-cycles of GM 9540P testing. Samples were placed at the narrow end of a conical mandrel and bent approximately

180° using a metal roller. The furthest distance that cracking, if any, propagates from the smallest diameter of the mandrel is used to compare the flexibility of the intact coating systems.

RESULTS AND DISCUSSION

A battery of laboratory corrosion and performance tests were performed in accordance with the methods listed above. The results of these tests are discussed below.

COATING APPLICATION

Coating application was performed by Corrpro personnel in accordance with the coating manufacturer's recommendations. Coating application was performed at Corrpro's facilities in Ocean City, NJ at at KSC. Application at Corrpro's facilities was accomplished using air powered spray equipment. Application at KSC was performed using brush application.

During coating application at Corrpro's facilities, an incompatibility between the Zinc-Rich A, MIL-P-53022 and MIL-C-46168 coating was observed, as indicated by bubbling of the over-coat material (MIL-P-53022 or MIL-C-46168). Further review of the product literature and conversations with the manufacturer identified this as a known incompatibility between the solvents used in Zinc-Rich A and the MIL spec coatings. A wash primer (DOD-P-15328, which is part of the CARC coating system) was used as an intermediate coat between Zinc-Rich A and the epoxy or CARC coatings, eliminating bubbling. This was also used on the steel control samples, before coating system application.

ACCELERATED CORROSION TESTING

Accelerated corrosion testing was performed in accordance with GM 9540P for 120-cycles (15 test years). Samples were periodically evaluated for signs of corrosive attack. Table 3 shows the cycles following which corrosive attack was first observed on the samples tested by

Corrpro and the average final rating of each coating system after GM 9540P testing. This data shows that, in general, Zinc-Rich B had better overall performance than Zinc-Rich A. Testing also showed that those systems applied over a SSPC SP-10 substrate had better performance than the same systems applied over a SSPC SP-3 substrate. The test was able to differentiate performance between the zinc-rich coating systems.

Table 4 shows the ARL data following 120-cycles of GM 9540P testing. Although the ratings observed were not the same as Corrpro's, similar trends were observed. Differences in ratings may be a result of the subjective nature of this and other visual rating systems. Measured data, which is not as subjective (here scribe cutback) was similar for both ARL and Corrpro tests and suggests similar performance.

The data in tables 3 and 4 also shows that samples preconditioned by chipping experienced accelerated degradation versus those preconditioned by scribing. This suggests that ranodmized preconditioning representative of damage that may occur during actual fielding results in more aggressive attack of samples, further delineating between performance differences. Figure 2 shows examples samples at the completion of testing.

SEASHORE EXPOSURE TESTING

Seashore exposure testing was performed at SIC and KSC for a period of six months. At the completion of six months of exposure samples were evaluated for corrosive attack. Table 5 shows the average final ratings at the completion of this exposure. No data is presented for blistering, since blistering was not observed on any test panel.

Similar to the samples in accelerated corrosion testing, those preconditioned by chipping experienced accelerated degradation versus those preconditioned by scribing. However, no significant corrosive attack was observed on most samples, except those chipped and exposed at

KSC. Here the SP-3 samples were more heavily corroded than the same systems applied over a SP-10 substrate. Test samples remain exposed at both locations for future evaluations, if desired. Future evaluations would help further delineate between the performance of alternative coating systems.

REPAIRED DOORS

Repaired doors were exposed at KSC for a period of six months. Following this exposure, no blistering was observed. Stage 1 corrosion was observed on all sections of the repaired doors. However, this corrosion was only observed at limited locations throughout the test sections. Cutback from the intentional scribes was also observed on the test sections, with all sections having only minimal cutback (average of 2-mm). These samples remain exposed for future evaluations, if desired.

ADHESION TESTING

Pull-off and cross-cut adhesion testing was performed on as applied samples and panels completing 120-cycles GM 9540P testing. Figure 3 shows the average failure strength of pull-off adhesion testing. This figure shows that the final failure strengths for each coating system were typically less than the initial value. At the completion of testing most systems had a final adhesion strength above 500-psi. The two systems that had values below 500-psi were SP-3/ Zinc-Rich A and SP-3/ Zinc-Rich B.

In addition to evaluating the failure strength of these panels, the failure location must also be considered. Although the failure strength will demonstrate the force required to disbond a pull stub, the failure location identifies the weak point in the system. Table 6 shows the failure location for each system. This table shows that the control systems (Control and Galvanized) had failures at the adhesive both before and after 120-cycles of GM 9540P testing. This

indicates that the bonding strength of the complete coating system to the substrate is greater than the failure strength shown in figure 11. All other systems (except SP-10/Zinc-Rich B) had failures to the substrate. A change in failure location and/or decrease in strength indicates that exposure may have affected the bond strength of the coating systems. The values in figure 11 can be used to relatively compare the two zinc-rich primers since all achieved substrate failures. These values show that the Zinc-Rich B primed panels achieved similar or better performance than the Zinc-Rich A primed panels over both SP-10 and SP-3 substrates.

Figure 4 shows the results of cross-cut adhesion testing. This figure shows that most systems had average adhesion ratings of 5 before and after 120-cycles of GM9540P testing. The only systems to achieve an average rating below 4 were the SP-10/Zinc-Rich A/CARC, SP-10/Zinc-Rich B/CARC and SP-3/Zinc-Rich B. This may suggest a possible incompatibility between zinc-rich primer and CARC topcoats. Further testing would be necessary to verify this.

MANDREL BEND TEST

Mandrel bend testing was performed on as-applied samples and samples following 120-cycles of GM 9540P testing. Following testing the length of any crack originating in the coating was measured, in millimeters. Figure 5 shows the length of these cracks. This figure shows that as applied the flexibility of the zinc-rich coatings is similar to the as-applied and post-test flexibility of the epoxy/CARC and galvanized/epoxy/CARC systems. After testing only Zinc-Rich A had worse performance than both control systems. When the zinc-rich systems were over-coated with CARC or an epoxy/CARC system flexibility was significantly reduced.

CONCLUSIONS

Based on the results of these tests, the following conclusions were made.

1. The zinc-rich coatings tested (moisture cure urethane, 90%+ zinc content) have shown improved corrosion performance versus the steel control.
2. The zinc-rich coatings tested did not have equivalent performance to galvanizing, suggesting that they be used primarily for repair and/or upgrade activities.
3. Evaluation of test samples showed that those preconditioned by chipping, which might be encountered during normal operations, exhibited accelerated degradation versus other samples, further delineating performance differences.
4. Inter-laboratory results showed similar performance, although actual rating varied.
5. Testing suggests that Zinc-Rich B may have better long-term performance than Zinc-Rich A.
6. Other zinc-rich paints (chemistry and zinc content variations) should be qualified for use prior to implementation.

FIGURES AND TABLES

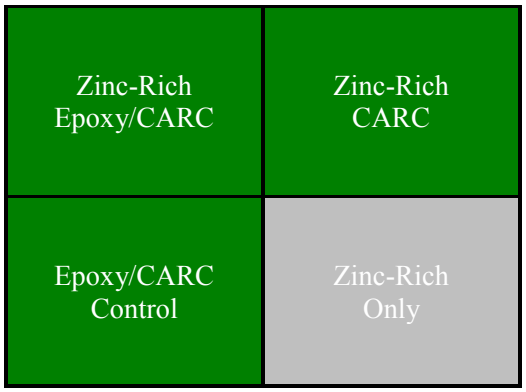

FIGURE 1. Representative Test Door.

SP-10, Zinc-Rich A. SP-3, Zinc-Rich A/ CARC.
SP-10, Zinc-Rich B. SP-3, Zinc-Rich B/CARC.

FIGURE 2. Representative Photos of Zinc-Rich Samples After 120-Cycles GM 9540P.

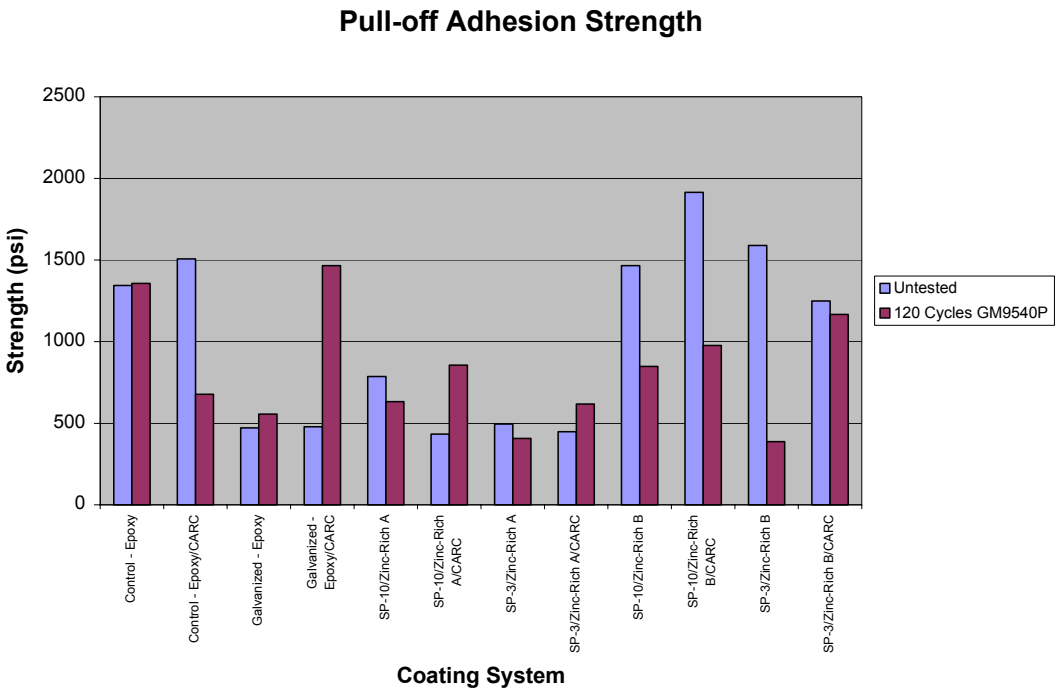

FIGURE 3. Average Pull-Off Adhesion Failure Strength.

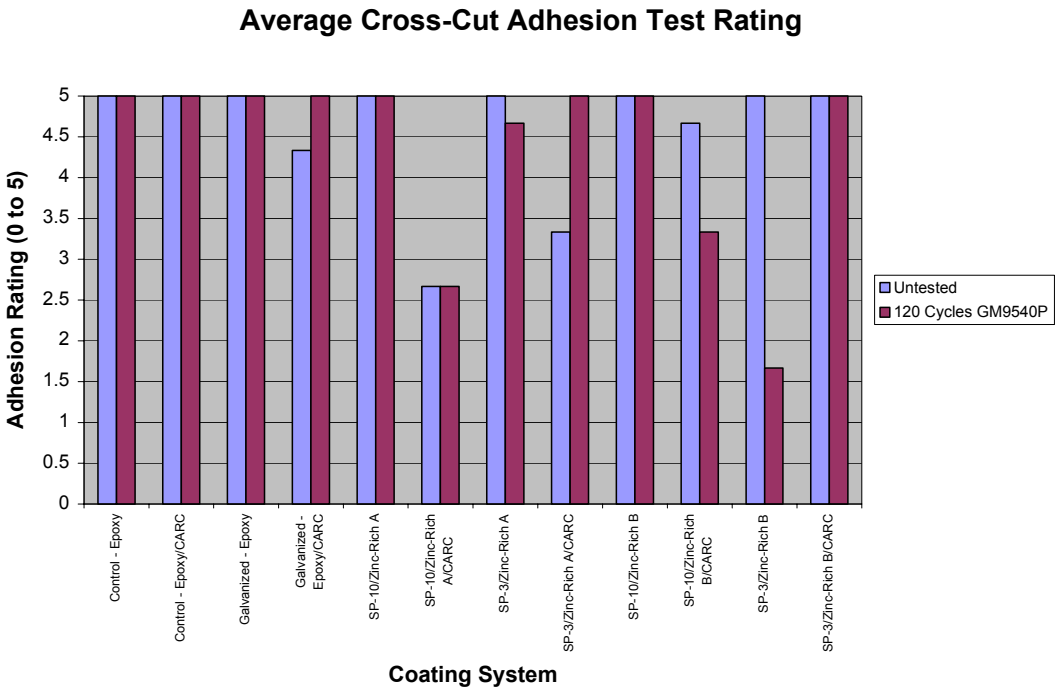

FIGURE 4. Crosscut Adhesion Test Results.

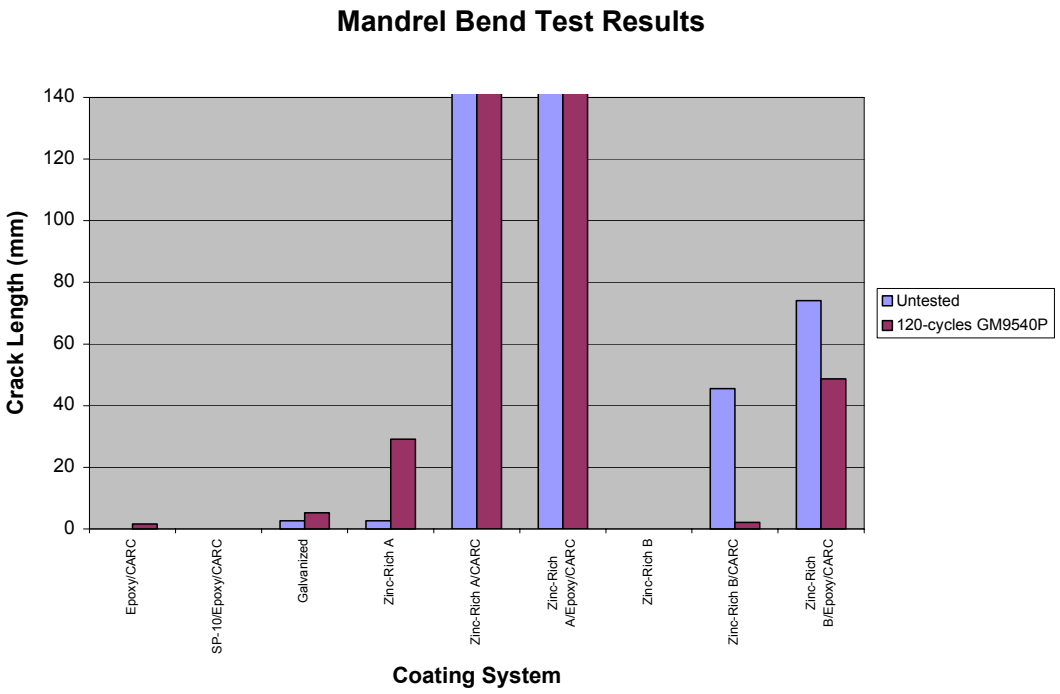

FIGURE 5. Mandrel Bend Crack Length.

TABLE 1
Test Sample Coating Systems

Test	Substrate Pretreatment		Substrate Preparation			Zinc-Rich	MIL-P-53022	MIL-C-46168
	Cold Rolled	Galvanized	Smooth	Rusted (<5%)	Blast (SP-10)			
Cyclic corrosion testing (GM-9540P)	√				√		√	√
		√	√				√	√
	√			√		√		√
	√				√	√		√
	√			√		√	√	√
	√				√	√	√	√
Seashore exposure sites – KSC (a) & SIC (b)	√				√		√	√
		√			√		√	√
	√			√		√		√
	√				√	√		√
	√			√		√	√	√
	√				√	√	√	√
Repaired doors (KSC only)					√		√	√
					√	√		
					√	√		√
					√	√	√	√
Adhesion testing – pull-off & cross-cut	√				√		√	
	√				√		√	√
		√	√				√	
		√	√				√	√
	√			√		√		
	√				√	√		
	√				√	√	√	
	√				√	√		√
Mandrel bend test	√		√				√	√
	√				√		√	√
		√	√				√	√
	√		√			√		√
	√				√	√		√
	√		√			√	√	√
	√				√	√	√	√

TABLE 2
Composite Blister Rating Index.

Size	Density			
	Few (F)	Medium (M)	Medium Dense (MD)	Dense (D)
10	10.0	10.0	10.0	10.0
9	9.22	8.75	8.00	4.80
8	8.44	7.50	6.00	3.50
7	7.67	6.25	4.60	1.60
6	6.89	5.00	3.70	1.10
5	6.11	4.40	3.00	0.90
4	5.33	3.80	2.50	0.75
3	4.56	3.20	2.10	0.55
2	3.78	2.60	1.65	0.35
1	3.00	2.00	1.00	0.00
0	0.00	0.00	0.00	0.00

TABLE 3
GM 9540P Initial Observation and Final Corrosion Rating of CORRPRO Samples.

Coating System	Corrosion Rating (Scribed/Chipped)		Blistering (Scribed/Chipped)		Cutback (Scribed)	
	Initial	Final	Initial	Final	Initial	Final (mm)
Control	120+/8 cycles	0.0/2.0	120+/48 cycles	10.0/3.00	24 cycles	16.7
Galvanized	120+/48 cycles	0.0/2.0	120+/120 cycles	10.0/6.89	120+ cycles	0.00
SP-10/Zinc-Rich A/ CARC	120+/8 cycles	0.0/2.0	120+/112 cycles	10.0/8.44	120+ cycles	0.00
SP-3/Zinc-Rich A/ CARC	96/8 cycles	2.0/2.0	96/56 cycles	6.89/6.89	56 cycles	3.67
SP-3/Zinc-Rich A/ Epoxy/ CARC	96/8 cycles	0.3/2.0	96/72 cycles	9.48/5.33	56 cycles	2.33
SP-10/Zinc-Rich B/ CARC	120+/16 cycles	0.0/1.0	120+/120+ cycles	10.0/10.0	120+ cycles	0.00
SP-3/Zinc-Rich B/ CARC	96/8 cycles	1.0/2.0	96/112 cycles	8.44/5.33	112 cycles	2.67
SP-3/Zinc-Rich B/ Epoxy/ CARC	96/8 cycles	0.3/2.0	120+/48 cycles	10.0/5.85	112 cycles	3.00

TABLE 4
GM 9540P Initial Observation and Final Corrosion Rating of ARL Samples.

Coating System	Corrosion Rating (Scribed/Chipped)		Cutback (Scribed)	
	Initial	Final	Initial	Final (mm)
Control	90/40 cycles	1.0/2.0	12 cycles	13.1
Galvanized	120+/12 cycles	0.0/2.0	12 cycles	0.63
SP-10/Zinc-Rich A/ CARC	120+/12 cycles	0.0/2.0	12 cycles	1.80
SP-3/Zinc-Rich A/ CARC	30/12 cycles	1.0/2.0	12 cycles	4.27
SP-10/Zinc-Rich B/ CARC	12/12 cycles	1.0/2.0	12 cycles	0.77
SP-3/Zinc-Rich B/ CARC	12/12 cycles	1.0/2.0	12 cycles	5.53

TABLE 5
Average Corrosive Attack After Six Months Marine Exposure

Coating System	Corrosion - Scribed (SIC/KSC)	Corrosion - Chipped (SIC/KSC)	Cutback (mm) (SIC/KSC)
Control	0/0	1/2	0/0
Galvanized	0/0	0/0	0/0
SP-10/Zinc-Rich A/ CARC	0/0	1/1	0/0
SP-3/Zinc-Rich A/ CARC	0/0	1/2	0/0
SP-3/Zinc-Rich A/ Epoxy/ CARC	0/0	1/2	0/2
SP-10/Zinc-Rich B/ CARC	0/0	1/1	0/0
SP-3/Zinc-Rich B/ CARC	0/0	1/2	0/0
SP-3/Zinc-Rich B/ Epoxy/ CARC	0/0	1/2	0/0

TABLE 6
System Failure Locations

System	Failure Location	
	Pre-Test	120-cycles GM 9540P
Control – Epoxy	Adhesive	Adhesive
Control – Epoxy/CARC	Adhesive	Adhesive
Galvanized – Epoxy	Adhesive	Adhesive
Galvanized – Epoxy/CARC	Adhesive	Adhesive
SP-10/Zinc-Rich A	Substrate	Substrate
SP-10/ Zinc-Rich A /CARC	Substrate	Substrate
SP-3/ Zinc-Rich A	Intracoat	Substrate
SP-3/ Zinc-Rich A /CARC	Intercoat	Substrate
SP-10/ Zinc-Rich B	Substrate	Adhesive
SP-10/ Zinc-Rich B /CARC	Substrate	Substrate
SP-3/ Zinc-Rich B	Intracoat	Substrate
SP-3/ Zinc-Rich B /CARC	Substrate	Substrate

ATMOSPHERIC EXPOSURE AND SALT FOG STUDIES OF THE CORROSION BEHAVIOR OF ELECTRODEPOSITED HARD CHROMIUM AND HVOF THERMAL SPRAY COATINGS

S. H. Lawrence[1], P. M. Natishan[1], R. L. Foster[2], and B. D. Sartwell[1]

Naval Research Laboratory

Washington, DC [1] and Key West, FL[2]

ABSTRACT

The corrosion behavior of several coating/substrate combinations was determined during a three-year atmospheric exposure and using the ASTM B117 Salt Fog Test. The coatings were electrodeposited hard chromium (EHC) and two high-velocity oxygen-fuel (HVOF) thermal-sprayed coatings, tungsten-carbide/cobalt (WC/Co) and Tribaloy® T400. The substrates were 4340 steel and 7075 aluminum. The results from the B117 and atmospheric exposure tests differed. The WC/Co coating on 4340 steel protected the substrate significantly better during atmospheric corrosion that the other coatings. Whereas in the B117 test, the EHC and WC/Co performed essentially the same but did not protect the substrate well. For the aluminum substrate, the EHC had the best overall performance with WC/Co coating showing promise. However, samples with the HVOF WC/Co coating applied to the edges as well as the face performed better than the EHC coatings in the atmospheric exposure. In general, the T400 ranked below the WC/Co and EHC coatings in its ability to protect aluminum substrates.

INTRODUCTION

Electrodeposited hard chrome (EHC) plating is commercially used to produce hard, wear-resistant coatings on new or refurbished parts. However, the plating baths contain hexavalent chromium, which has adverse health and environmental effects[1]. As a result, wastes generated from plating operations must be disposed of as hazardous waste and plating operations must abide by emissions standards and permissible exposure limits for workers as established by government regulatory agencies. In the United States, increasingly stringent environmental and worker-safety regulations are making chromium plating more expensive for manufacturers and repair facilities. Therefore, finding acceptable replacements is desirable.

A replacement coating for EHC must possess fatigue, wear, corrosion, impact, and mechanical properties equal to or better than those of hard chrome. A promising technique to produce hard, wear resistant coatings that could replace EHC plating in a number of applications is high-velocity oxygen-fuel (HVOF) thermal spray coating [2,3]. In HVOF, an explosive gas mixture ignites in the barrel of a spray gun, which partially melts the powdered coating material and propels it in a carrier gas toward the substrate at supersonic speeds. HVOF uses oxygen and a fuel gas as the combustion propellant. The HVOF process is capable of depositing metal alloy, ceramic/metal composite, and polymer coatings rapidly and to thickness values comparable to those of EHC plating.

In this paper we review work published elsewhere [4]. This work compares how well the EHC and HVOF coatings provide protection against corrosion to 4340 steel and 7075 aluminum substrates during a three-year atmospheric exposure and ASTM B117 testing.

EXPERIMENTAL PROCEDURE

Commercial samples of 4340 steel and 7075 aluminum were used. The substrate dimensions for all but two samples were 4 x 6 x 0.2 inches. Two 7075-aluminum substrates that received HVOF WC/Co coatings had dimensions of 3 x 4 x 0.2 inches. The substrates were prepared for deposition by degreasing and blasting with aluminum oxide. For the EHC samples 180 - 220 grit was used and for the HVOF samples 54 grit was used**.** The angle of impingement was 90 degrees. On the 7075 aluminum alloy samples, a 37-micron coating of nickel sulfamate was electrodeposited (from a nickel sulfamate solution) prior to deposition of the EHC, which was applied according to United States military standard MIL-STD-1501. The WC/Co coatings were deposited at the Naval Aviation Depot in Jacksonville, Florida using a Sulzer Metco Diamondjet hybrid HVOF system with hydrogen as the fuel gas. The WC/Co powder material was Sulzer-Metco Diamalloy 2005 with a composition of 83% WC and 17% Co. The Tribaloy 400 coatings were deposited at Southwest Aeroservice, Inc. in Tulsa, Oklahoma using a Stellite Jet Kote II HVOF system with hydrogen as the fuel gas. The Tribaloy T400 powder material was designated as T400 and was manufactured by Stellite with a composition of 60% Co, 28% Mo, 9% Cr, and 3% Si. The HVOF coatings were deposited so they retained residual compressive stress as indicated on an Almen N strip, with deflections ranging from 0.005 inches to 0.010 inches. The porosity was less than 1.5% and the oxide content was less than 2.5%. The average Vickers microhardness for the coatings (100-gram load) was 950 for the EHC, 1150 for the WC/Co and 700 for the T400. The nominal thickness for all of the coatings was 100 □m (0.004 inches). All the coatings were tested in the as-deposited condition. At least five samples were produced for each coating/substrate combination. The T400 coatings covered the entire sample

including the edges. For the EHC, the coatings were applied to an area of 4 x 4 inches, with both faces and edges within that area being coated. For the WC/Co on the 4340 substrates, the coatings were applied to one face and the edges but not the reverse face. For the WC/Co coating on the 7075 substrates there were two conditions. In the first, the coating was applied only to one face over an area of 4 x 4 inches with no coating applied to the edges. In the second case, the coating was applied to one complete face and the edges but not to the reverse face. There were two of the latter samples and the dimensions of these samples were 4 x 3 inches. All uncoated areas on the samples were sealed using epoxy. The samples were placed in the atmospheric exposure rack at the Naval Research Laboratory facility in Key West, FL. The exposure racks are at an angle of 45 degrees. The test duration was three years.

After exposure, the samples were cleaned with an abrasive pad to remove the corrosion products**.** After the corrosion products were removed, blisters and undercutting of the coating were noted. The blisters and undercut coating were mechanically removed to better assess the extent of the corrosion, i.e., to determine the area of the substrate that was no longer protected by the coating. Each sample was then assigned a protection rating based on the ASTM B537-70 [5] standard and these results are summarized in Table 1. This standard only considers the face of the samples for rating but in this work, the sample edges were also assigned a protection rating. The protection rating is an indication of how well the coating was able to prevent/slow corrosion of the substrate.

RESULTS AND DISCUSSION

4340 STEEL SUBSTRATE

Figures 1 and 2 show a series of photos taken before and after cleaning, respectively, for the coatings on 4340 steel after the three-year atmospheric exposure. Once the samples were cleaned, it was possible to identify surface defects such as blisters or pits. Removing the blisters and portions of the coating that were undercut by corrosion provided a better representation of affected areas, as shown in Figure 2. This surface condition was used to determine the protection ratings for the front face and edges.

Table 2 and Figure 3 present the protection ratings for the coatings on 4340 steel. The front face of all samples coated with T400 showed significant undercutting, with the percentage of the surface affected ranging from 10 to 50%. The protection ratings for sample faces ranged from 1 to 3, with an average of 1.9. For the edges, more than 50% were corroded with a significant amount of undercutting of the coating. The average protection rating for the edges was rated as negligible and given a 0 rating. The T400 samples were very heavily corroded near the edges and it appeared that the undercutting started at the edges and moved toward the center of the face.

The front face of all EHC samples showed that the coating was severely undercut similar to the T400. The protection ratings for individual samples ranged from 0 to 2, with an average of 0.5. The edges were also heavily corroded with significant undercutting. The average protection rating was 0.2 for the edges with the individual values ranging from 0 to 1.

The face and edges of the WC/Co samples showed no sign of corrosion. The protection rating for the individual samples, both the front face and edges, was 10. In general, the

surface of the WC/Co coatings became darker in color during exposure. Upon cleaning the dark layer was removed and it was apparent that the coating itself had undergone general corrosion. This was likely due to dissolution of the cobalt binder. The HVOF WC/Co coating clearly outperformed the EHC and HVOF T400 coatings in terms of providing protection to both the face and edges.

7075 ALUMINUM ALLOY SUBSTRATE

The series of photos in Figures 4 and 5 for the three coatings on 7075 aluminum were taken before and after cleaning, respectively. Once the samples were cleaned pits were more evident as indicated in Figure 5. The cleaned surfaces were used to obtain protection ratings. The protection ratings for the coatings on the 7075 aluminum are presented in Table 2 and Figure 6.

Small pits were seen on the face of all samples with the T400 coating. The pits were propagating into the bulk and there was no noticeable undercutting at the coating/metal interface. The average protection rating for both the face and edges was determined to be 1.0.

The WC/Co samples provided a very interesting result. The average protection ratings for the samples for which the edges were coated were 10 and 6 for the face and edges, respectively. These ratings were markedly different than those for the faces of the samples for which the edges were not coated. These samples had an average protection rating of 3.3. Individual values ranged from 3 to 4. The pits on these samples were large relative to those on the T400 coating. For the sample with the WC/Co coating shown in Figures 4 and 5, there is concentration of pits near the interface between the coating and the epoxy mask. However, other aluminum samples with the WC/Co coating did not show this trend or any discernible pattern of pitting. No undercutting was noted next to the pits. General corrosion of the WC/Co coating was also noted.

The average protection ratings for the face and edges of the EHC samples were 7.2 and 3.2, respectively. Individual values for the face ranged between 5 and 10, while the individual values for the edges ranged from 2 to 6. Overall, on 7075 aluminum the EHC coating performed best compared to the HVOF coatings. However, the samples where the HVOF WC/Co coating was applied to the edges performed better than the EHC coatings. The results for the EHC samples are in part due to the effect of the nickel sublayer.

COMPARISON WITH B117 TESTING

Previous work [4,6] reported on the corrosion behavior of HVOF T400, HVOF WC/Co, and EHC coatings that had undergone ASTM B117 testing. Table 3 provides a summary of the B117 results for coating/substrate combinations identical to those used in the atmospheric studies, with the coatings being applied at the same time. The samples that had undergone atmospheric testing and ASTM B117 performed differently. In the B117 test, none of the coatings protected the 4340 steel and the EHC and WC/Co coatings performed about the same (also see Figure 7). Both had an average protection rating for the faces of about 3 (see Table 3). The T400 had an average protection rating of 1.6. However, in the atmospheric exposure the HVOF WC/Co coating protected the steel significantly better than the other two coatings. Again, general corrosion of the WC/Co coating was noted following the atmospheric exposure.

In the B117 test, the EHC coating had the best performance on the 7075 aluminum substrate as no pits or blisters were noted on the front face or edges (also see Figure 8). The WC/Co coatings showed no pitting or blistering on the front face but had a significant amount of pitting along the edges. The T400 coating face had pitting in 83% of the samples. The edges of the samples with the T400 coating also had a significant

amount of pitting. Pitting and blistering were noted beneath the label of the T400 coating on aluminum after B117 testing, indicating a susceptibility to crevice corrosion. In the case of the samples exposed in the atmospheric test, only 1 of 7 samples had a pit undercutting the label on the T400 coating. For the atmospheric exposure, the EHC coating protected the aluminum better than the other coatings with the exception of the WC/Co coating that was applied to the edges as well as the face.

In general, the three-year atmospheric exposure was a more severe test for most of the coating/substrate combinations. The exception was the WC/Co on 4340 steel and the WC/Co on the 7075 aluminum substrates that also had the edges coated. Additional testing is needed to clarify the performance of the WC/Co coatings on aluminum.

SUMMARY

1. The results from the B117 and atmospheric exposure tests differed. In the atmospheric exposure testing, the WC/Co coating on 4340 steel protected the substrate significantly better that the other coatings. Whereas in the B117 test, the EHC and WC/Co performed essentially the same, although neither protected the substrate well.

2. For the aluminum substrate, the EHC had the best overall performance with WC/Co coating showing promise. However, samples with the HVOF WC/Co coating applied to the edges as well as the face performed better than the EHC coatings in the atmospheric exposure. In general, the T400 ranked below the WC/Co and EHC coatings in its ability to protect aluminum substrates.

REFERENCES

1. B. Meyers and S. Lynn, “Chromium Elimination”, in ASM Handbook, Volume 5, Surface Engineering, ASM International (1994), p. 925.

2. K. O. Legg, M. Graham, P. Chang, F. Rastagar, A. Gonzales, and B. Sartwell, Surf. Coat. Technol., 81 (1996): p. 99.

3. K. O. Legg, Plating and Surface Finishing, 83(7), (July, 1996): p. 12.

4. P. M. Natishan, S. H. Lawrence, R. Foster, and B. D. Sartwell, Corrosion, in press.

5. ASTM Standards for Corrosion Testing of Metals, ATSM B537-70, ASTM Committee G-1, ASTM, Philadelphia, PA (1990) p. 38.

6. P. M. Natishan, S. H. Lawrence, R. L. Foster, J. Lewis, and B. D. Sartwell, "Corrosion Behavior of HVOF Thermal Spray Coatings Compared to Electrodeposited Hard Chromium", Surface and Coatings Technology, 130, (2000): p. 218.

TABLES AND FIGURES

TABLE 1.
Protection rating versus area of defect from ASTM B 537-70 [4].

Area of Defect (in percent)	Rating
0	10
to 0.1	9
0.1 to 0.25	8
0.25 to 0.5	7
0.5 to 1.0	6
1.0 to 2.5	5
2.5 to 5.0	4
5 to 10	3
10 to 25	2
25 to 50	1
greater than 50	0

TABLE 2.
Average value of the protection rating for samples that had undergone a three-year atmospheric exposure.

Coating	Substrate	Protection - Face	Protection - Edge
T400	4340 steel	1.9	0
WC/Co	4340 steel	10.0	10.0
EHC	4340 steel	0.5	0.2
T400	7075 Al	1.0	1.0
WC/Co*	7075 Al	3.3	-
WC/Co**	7075 Al	10.0	6
EHC	7075 Al	7.2	3.4

* edges not coated, sealed with epoxy

** edges received HVOF coating

TABLE 3.
Average value of the protection rating for samples that had undergone1,000 hours of ASTM B117 testing.

Coating	Substrate	Protection - Face	Protection - Edge
T400	4340 steel	1.6	1.0
WC/Co	4340 steel	3.4	3.2
EHC	4340 steel	3.2	2.0
T400	7075 Al	9.0	3.0
WC/Co	7075 Al	10	2.0
EHC	7075 Al	10	10

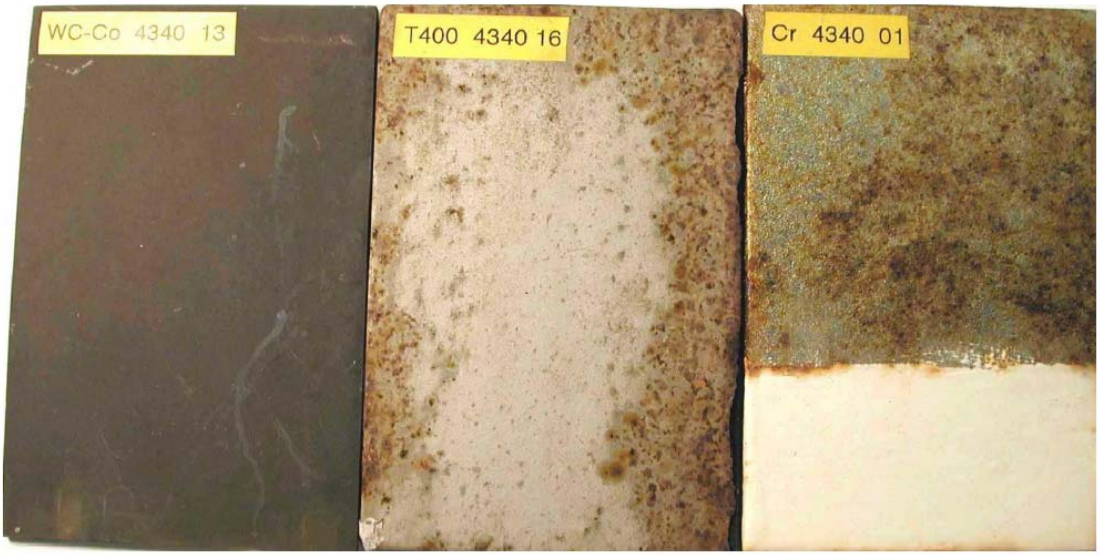

FIGURE 1. HVOF WC/Co, HVOF T400 and EHC coatings on 4340 steel before cleaning.

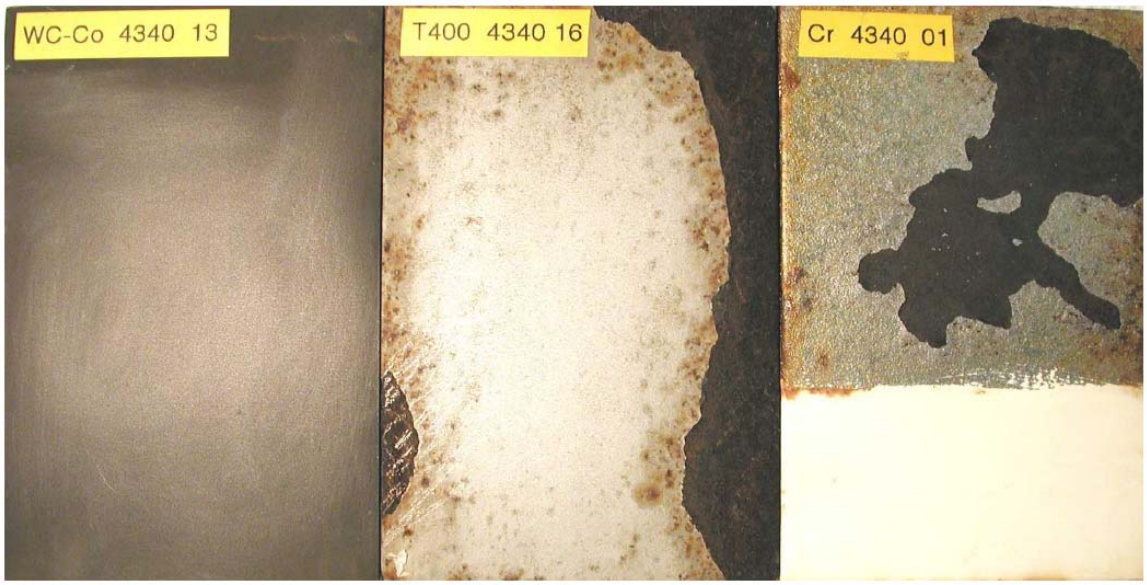

FIGURE 2. HVOF WC/Co, HVOF T400 and EHC coatings on 4340 steel after cleaning.

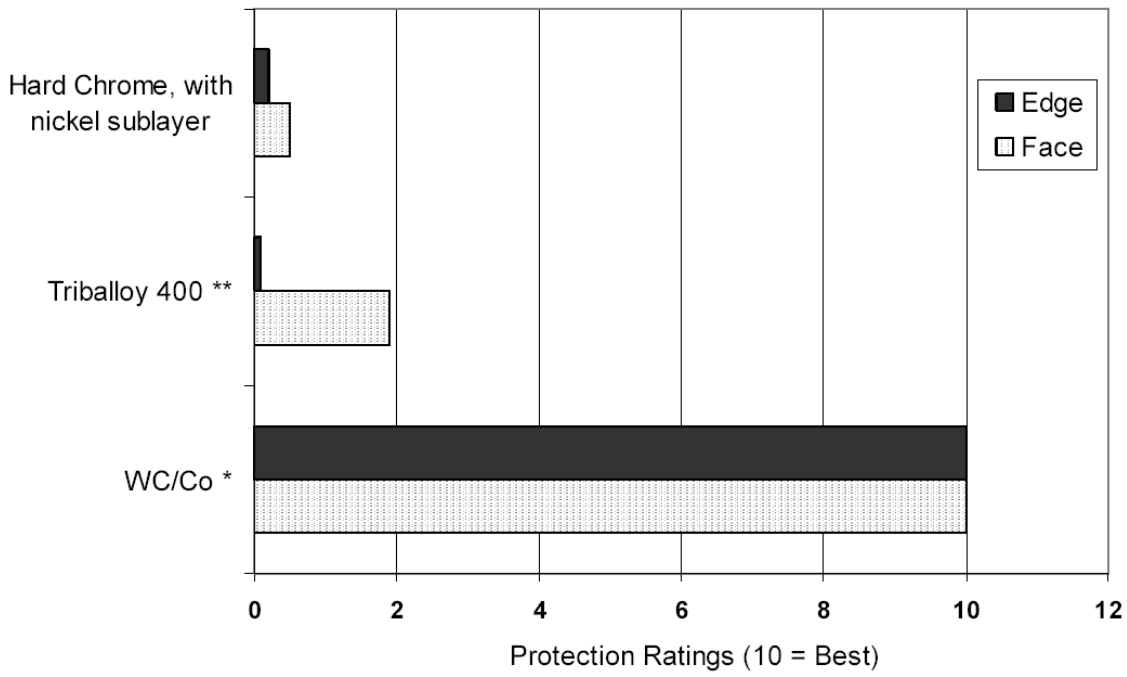

FIGURE 3. Protection ratings for the 4340 steel samples.

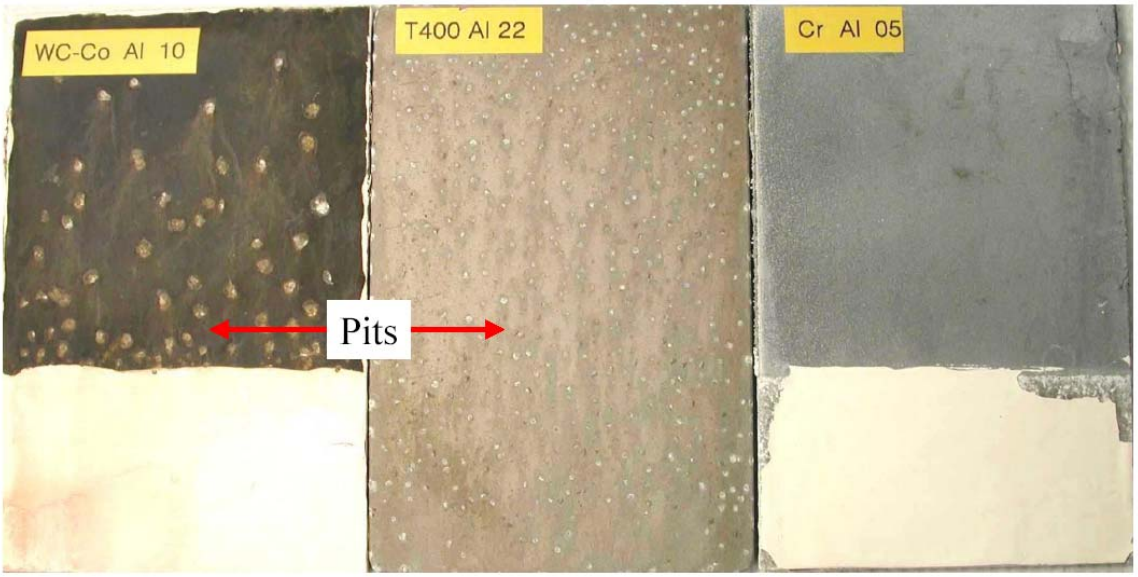

FIGURE 4. HVOF WC/Co, HVOF T400 and EHC coatings on 7075 aluminum before cleaning.

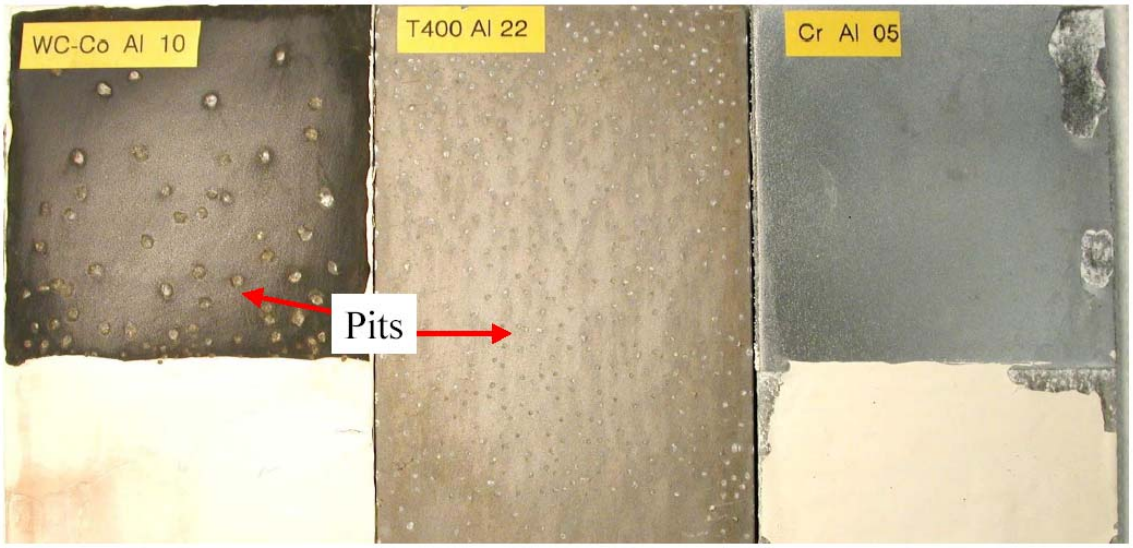

FIGURE 5. HVOF WC/Co, HVOF T400 and EHC coatings on 7075 aluminum after cleaning.

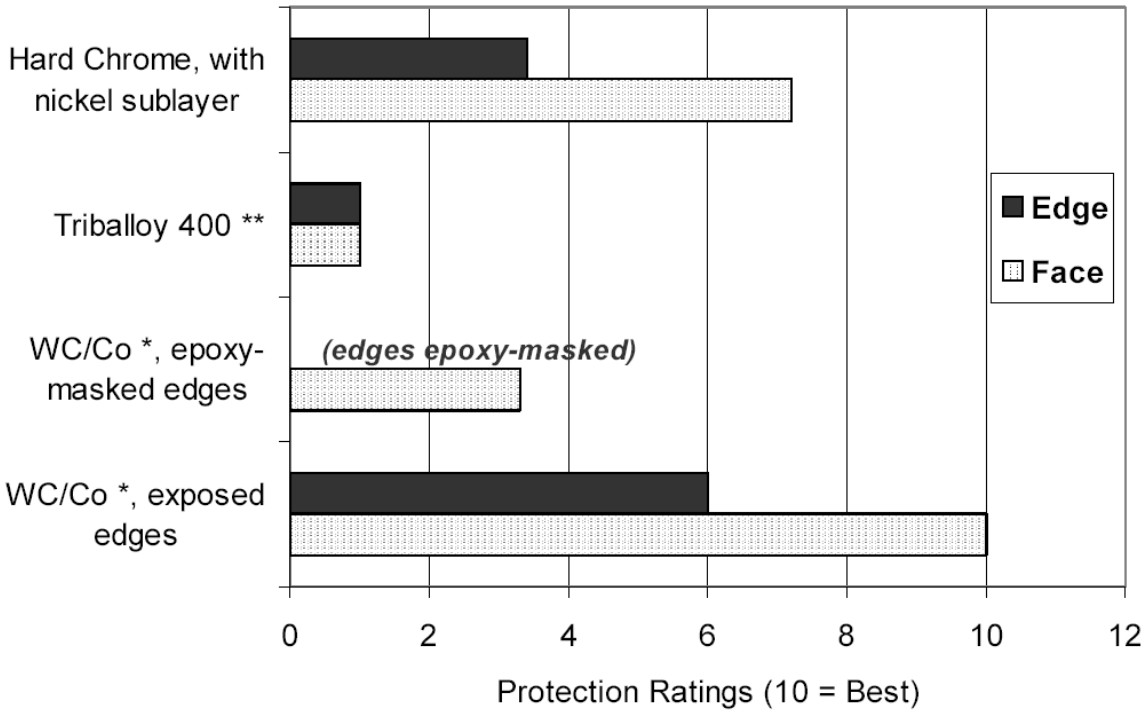

FIGURE 6. Protection ratings for the 7075 aluminum samples

GM 9540P CYCLIC ACCELERATED CORROSION ANALYSIS OF NONCHROMATE CONVERSION COATINGS ON ALUMINUM ALLOYS 2024, 2219, 5083, AND 7075 USING DOD PAINT SYSTEMS

Brian E. Placzankis and Chris E. Miller
U.S. Army Research Laboratory, Weapons and Materials Research Directorate
Aberdeen Proving Ground, Maryland 21005-5066

Craig A. Matzdorf
NAVAIR, Code 4.3.4.1
48066 Shaw Road, BLDG 2188, Unit 5
Patuxent River, MD 20670-1908

ABSTRACT

This study examines corrosion resistance of eight nonchromate conversion coatings versus hexavalent chromium based Alodine 1200 controls on scribed coated test panels of aluminum alloys 2024, 2219, 5083, and 7075. Five representative DoD primer/topcoat organic coating systems were evaluated for each of the conversion coating/alloy combinations. Scribed panels were exposed using GM 9540P for 120 cycles duration and were photographed and measured at 20 cycle intermediate intervals for scribe creepback using method ASTM D 1654. Differences in pretreatment performance based upon variation in coating type as well as alloy were noted. How these data may relate with respect to implementation of nonchromate pretreatments for different military applications is discussed.

INTRODUCTION

Eight candidate Cr^{+6} free conversion coatings for study on aluminum alloys were selected based upon feedback from Navy, Air Force, Army, and NASA activities at an initial meeting with personnel representing the Environmental Security Technology Certification Program (ESTCP) and the Joint Group on Pollution Prevention (JG-PP). Overall funding for this study was provided through these organizations. The overall nonchromate study consists of two phases: Phase I laboratory validation of alternatives through extensive coupon tests to evaluate

paint adhesion, corrosion resistance and other criteria; and Phase II field testing and process validation of selected alternatives at various user facilities.

This report expands upon a previous report[1] by adding additional data on aluminum alloy 2219 and also includes *complete* data obtained throughout the GM 9540P exposure period. As in the previous study, the focus of this particular report is constrained to a portion of Phase I laboratory data, specifically GM 9540P accelerated corrosion using exposure of aluminum alloys 2024, 2219, 5083, and 7075 specimens treated with eight candidate hexavalent chromium free pretreatments as well as one hexavalent chromium based pretreatment (Alodine 1200S) for a controlled comparison. In order to closely match conditions found in currently fielded equipment, five organic coating systems commonly used in fielded DoD systems were selected.

EXPERIMENTAL PROCEDURE

Aluminum panels (225 each nominally 7.62 cm x 12.7 cm) of alloys 2024-T3, 2219-T87, 5083-H131, and 7075-T6 were obtained. Prior to pretreatment and testing, all coupons were clearly labeled using a mechanical scribe to permanently affix the experimental designation. Twenty-five panels with each pretreatment combination were prepared for each alloy for GM 9540P exposure. Each set of 25 panels was further subdivided to 5 groups, one for each of the 5 selected DoD coatings. The five DoD coating systems applied were:

(1) MIL-PRF-23377[2] high solid epoxy primer with MIL-PRF-85285[3] high solid polyurethane topcoat (USAF/Navy)

(2) MIL-PRF-85582c1[4] waterborne epoxy with MIL-PRF-85285 topcoat (Navy)

(3) MIL-PRF-85582nc[4] waterborne epoxy chromium free formulation with MIL-PRF-85285 topcoat (Experimental/JG-PP/Air Force/Navy/Boeing)

(4) MIL- P-53030[5] water reducible epoxy primer with MIL-C-53039[6] chemical agent

resistant single component polyurethane topcoat (Army/USMC)

(5) MIL-P-53022[7] epoxy primer with MIL-C-53039 polyurethane topcoat (Army/USMC).

The first 2 coating systems: 23377/85285 and 85582/85285 each contained hexavalent chromium compounds in their formulations, therefore elimination of Alodine 1200S would only reduce the total hexavalent chromium present for these cases. The remaining 3 coating systems were chromium free. The 2 Army/USMC coating systems meet Chemical Agent Resistant Coating (CARC) specifications.

Prior to painting, all of the panels were cleaned and pretreatments were applied per each of the pretreatment manufacturers specifications at NAVAIR facilities. The coating system's respective primer coats were applied within 24 hours subsequent to pretreatment application to each group of five panels for each pretreatment for each alloy. The topcoats were applied after 24 hour primer cure. The full coating system was then cured at ambient conditions for 14 days. The panels were then delivered from NAVAIR to ARL test facilities. Figure 1 depicts a schematic detailing the GM 9540P test matrix.

Three cyclic corrosion test chambers (CCTC) were used to evaluate the coated aluminum test panels. In order to maximize uniformity of test conditions, each alloy was given its own specific chamber. Immediately prior to exposure, the panels were all "X" scribed using a standard carbide tipped hardened steel scribe. The scribed panels were placed into the chambers (Figure 2) and tested using GM Standard Test 9540P[8], that provides more dynamic accelerated conditions versus conventional ASTM B 117 saltfog.[9] The GM 9540P test consists of 18 separate stages that include the following: saltwater spray, humidity, drying, ambient, and heated drying. The environmental conditions and duration of each stage for one complete 9540P cycle are provided in Table 1. The standard 0.9% NaCl, 0.1% $CaCl_2$, 0.25% $NaHCO_3$ test

solution was used. In addition each chamber was calibrated with standard steel mass loss calibration coupons described in GM Standard Test 9540P and supplied by GM . In order to visibly chronicle the corrosion, one representative panel of each of the five test panels was chosen at 20 cycles of exposure and digitally scanned at 600 dpi resolution. Subsequent scans of the same representative panel were made at every 20 cycles until the conclusion of 120 cycles or until specimen group failure. Specimens were numerically rated for damage at each 20 cycle interval using method ASTM D 1654.[10] Specimen group failures were defined by a rating of 0 under ASTM D 1654 for 3 or more of the panels in a particular alloy/pretreatment/coating set. In order to facilitate easier viewing of the inevitable large portions of data from this matrix, color codes were assigned based upon ranges of ASTM D 1654 ratings. Table 2 depicts the ASTM D 1654 rating parameters and also defines the colors and their respective rating ranges.

RESULTS

With the exception of premature failures under ASTM D 1654, the coated panels were all subjected to 120 cycles of GM 9540P. The creepback ratings at 20 cycle intervals are characterized in Tables 3-22. Final 120 cycle creepback ratings for all panels are listed and characterized in Appendix A. The prevalent failure mode for the most of the panels was blistering along the scribe. In addition to the color coding assigned in Table 2, additional corrosion characterization is provided in the tables. Figure 3 details these additional characterizations and provides examples. In cases where blistering occurred in regions *away from the scribe*, the table cells appear with *diagonal* cross-hatching. In situations where coating creepback from the scribe resulted from *adhesion loss*, *vertical* cross-hatching was used. In rare

situations, mixed failure mode consisting of nonscribe blistering with adhesion loss at the scribe occurred. In these situations a finer textured cross-hatching pattern was used.

ALUMINUM 2024

For Al 2024, the top performing pretreatments were clearly defined. For this particular alloy it was the coating system selection that aided in revealing the better performers. For the hexavalent chromium bearing 23377/85285 coating system, all of the pretreatments performed well for the most part and completed 120 cycles with the highest ratings among the coating systems (Table 3).

Although the 85582c1/85285 coating system also contains hexavalent chromium, overall it performed much worse when compared versus the 23377/85285 system for the same pretreatments. In addition to scribe creepback this coating system was very susceptible to blistering away from the scribe with two exceptions. The 2 exceptions for this system with the best performance were Alodine 1200S and Boegel (Table 4).

For the remaining three coating systems: 85582nc/85285, 53030/53039, and 53022/53039, the best performance was provided by the NAVAIR TCP and Alodine 1200S pretreatments (Tables 5-7 and Figures 4 and 5). In the specific case of the waterborne primed 53030/53039 CARC system, the TCP pretreatment even *exceeded* the performance for Alodine 1200S. Alodine 5200 pretreatment rendered respectable performance at or near the leaders for these chromium free coating systems.

ALUMINUM 2219

Of all the Al alloys examined in this study, Al 2219 with its high Cu content is by far the most corrosion prone and provides a difficult task for even hexavalent based Alodine 1200S. For the chromate based 23377/85285 coating system, although all pretreatments lasted the full 120

cycle duration, significant corrosion damage occurred on many of the pretreatments. The best performers for this coating system were Alodines 1200 and 5200 and Oxsilan. TCP showed mixed performance among its 5 respective replicates but overall still performed much better than the remaining pretreatments (Table 8, Appendix A). For the chromate containing 85582c1/85285 system, the best performers were Alodines 1200 and 5200, NAVAIR TCP, Oxsilan and Boegel. The remaining pretreatments performed in the intermediate range with ratings ranging from 5 to 7 (Table 9, Figures 6 and 7).

For the three chromate free coating systems : 85582nc/85285, 53030/53039, and 53022/53039, there was significant corrosion damage and most of the pretreatments were unable to endure 120 cycles without early specimen group failure. Although the corrosion damage was severe, the most consistent performers for these systems were NAVAIR TCP, and Alodines 1200 and 5200. Oxsilan rated only marginally better than the remaining pretreatments for the chromate free coatings but only by virtue of not completely failing as soon (Tables 10-12).

ALUMINUM 5083

Al 5083, an alloy known for its stable protective oxide layer, does not usually significantly corrode, even under accelerated conditions. Due to its widespread use in tactical ground systems, accelerated corrosion methods such as GM 9540P are still necessary for this alloy for quality assurance and also for detecting potential coating adhesion issues. As expected, for Al 5083, most pretreatments sustained the full 120 cycle duration without any noticeable damage across all 5 coating systems as seen in Tables 13 through 17. As in Al 2024 the 23377/85285 coating system proved superior and there was no significant creepback resulting from corrosion or coating system delamination. For 85582c1/85285, there were adhesion issues with the Sanchem 7000 pretreatment which rated a 7 by 60 cycles and then stabilized for the

balance of the 120 cycles. For the nonchromium based formulation 85582nc/85285, the problems with the Sanchem process were more pronounced with more severe creepback resulting from actual corrosion. Any damage for Al 5083 is significant since even in a bare uncoated and untreated condition this alloy will not significantly corrode. For this same coating system, the Chemidize 727ND pretreatment also showed blistering though to a somewhat less severe degree along the scribe. For the waterborne 53030 primer based CARC system, Sanchem exhibited damage due to adhesion failure similarly as noted above. For the solvent primer based 53022/53039 CARC system, the only noticeable damage occurred on the Bi-K Aklimate of the University of Maryland Baltimore Campus and Gerard Chaney of Harford County Community College for assistance in preparing hundreds of test panels for exposure. Geoff Hoerauf and Mike Starks (Red River Army Depot) of the Bradley Fighting Vehicle Systems Environmental Management Team for providing additional Army background information and a phase 2 demonstration validation site. Tom Landy and Carl Handsy of TARDEC for supplying initial Army ground vehicle materials input for this study. Steve Carr of AMMCOM for providing continuous input to the study concerning pretreatment issues on Army missile systems. Finally we thank NAVAIR's Michael Kane, ESTCP, and JG-PP for sponsoring this study.

pretreated system.

Aluminum 7075

With the exception of Al 2519, Al 7075 specimens surprisingly exhibited the most severe damage from corrosion during GM 9540P exposure. For the coating system 23377/85285 as in the other alloys, most all of the pretreatments performed well with little or no damage to the scribed region. The exception for this case was Alodine 5200 with damage characterized by coating delamination from the scribed regions (Table 18).

For the 85582c1/85285 system, the top performers with little or no damage were Alodine 1200S, TCP, X-IT PreKote, and Boegel. Other pretreatments for this system were disqualified either by lower ratings due to corrosion, delamination, or both. Sanchem 7000 pretreatment failed across the majority of its 5 panels by 100 cycles (Table 19).

For the chromate free 85582nc/85285 system the only top performers were Alodine 1200S and TCP (Table 20 and Figure 9). The next best performing alternatives containing no chrome whatsoever were the distant runners up Alodine 5200 and Boegel which both rated a "5" through 120 cycles. Panels failing the exposure for this coating system were Sanchem and Bi-K Aklimate. In particular, the failure for Sanchem was severe with partial series failures at 20 cycles and specimen group failure by 40 cycles exposure.

As in previous alloys, the CARC systems were more susceptible to corrosion attack than their aircraft coating counterparts. For the waterborne primer system 53030/53039 chronicled in Table 21, Alodine 1200S, and TCP pretreatments performed best. The mode of creepback progression on the TCP treated panel was due to delamination of the coating. The next best performers for this coating system were Alodine 5200 and Boegel however their performance at best was fair with both pretreatments only rating a "4" at the conclusion of 120 cycles. Series that failed prior to completion of 120 cycles in order of decreasing severity included: Chemidize 727ND, Bi-K Aklimate, and Sanchem 7000.

A comparison between Tables 21 and 22 shows the 53022/53039 system performance for all pretreatments overall was better than for the waterborne primer CARC series for Al 7075. The NAVAIR TCP pretreatment was clearly superior for this group as shown in Figure 10. Next best finishers were Alodine 5200 and Alodine 1200S with ratings at 120 cycles of "6" and "5" respectively. Boegel rated a "3" with the others all rating a "2" or lower at 120 cycles. The only

failure prior to 120 cycles was the Chemidize 727ND pretreatment which failed as a set by 60 cycles.

DISCUSSION

This purpose of this study was to provide GM 9540P accelerated cyclic corrosion performance data for alternatives to Cr^{+6} based Alodine 1200S. It should be stressed that good performance in accelerated corrosion testing alone does not guarantee a good conversion coating. Other factors such as coating system adhesion, visible color changes to the substrate surface (for quality control) upon pretreatment application, toxicity issues other than Cr^{+6}, as well as the logistics and costs of process application steps, all play significant roles in selection of a viable pretreatment alternative. In order to obtain the most information possible, this overall ESTCP/JG-PP effort includes additional laboratory procedures such as saltfog, SO2 saltfog, and adhesion methods, all conducted on the same alloy/pretreatment/coating combinations investigated in this portion of the study. Variations in application procedures such as surface preparations, bath conditions for dip processes, and spray applications are also included. These additional results will follow in subsequent ESTCP reports. Information on these documents should become available in time via ESTCP/JG-PP contacts. Ultimately, this compiled database will be offered to help users identify potential alternatives to chromate conversion coatings currently in use by OEM's and depots.

It should be noted that it is likely that in various situations more than one pretreatment may be suitable to replace Alodine 1200S. As seen from data in this study as well as previous studies,[11-13] different pretreatments that often work well on one aluminum alloy, may not always work well for another. However, this does not necessarily mean that a unique pretreatment is

needed for every unique situation. For simplicity as well as economies of scale, the best possible benefit for replacing Alodine 1200S would be gained by minimizing the number of finalists to as few as possible. A pretreatment that has well rounded performance across many aluminum alloys would be the most desirable. In this particular study, the best all around non Cr^{+6} performer was the Cr^{+3} based TCP pretreatment patented by NAVAIR. Toxicity studies on trivalent chromium exposure indicate no carcinogenic or other hazards similar to those found in Cr^{+6} pretreatments such as Alodine 1200S.[14,15] Nevertheless, environmental regulatory bodies such as those found in California and the European Union have implemented or indicated future stricter guidelines concerning the use of chromium containing pretreatments.

If trivalent chromium based pretreatments such as TCP are not acceptable or are denied for implementation due to their total chromium content, the next best performing pretreatments were Alodine 5200 and Boegel. For the most part, performance between these two pretreatments for each alloy was roughly comparable when performance across all variations of coating systems was examined. There are two factors that may favor Alodine 5200 over Boegel. The first is its performance on the Cr^{+6} free organic coating systems 85582nc/85285, 53030/53039, and 53022/53039. For the more corrosion prone Al alloys 2024 and 7075, Alodine 5200 either met or exceeded Boegel in GM 9540P creepback performance when these chromium free coating systems were used. Previous laboratory and automotive proving ground[16] studies involving Alodine 5200 have also shown good performance on a variety of Al alloys using 53022/53039 based CARC coating systems.[11-13] Second is that Boegel is currently limited to spray and wipe application methods due to mixing and solution shelf life once mixed (1 day maximum).

Currently many prospective Cr^{+6} free pretreatments may simply just be able to "get by" when coated over by Cr^{+6} enhanced organic coating systems. In order to truly determine the enhanced corrosion resistance gained from a hexavalent chromium free pretreatment, a hexavalent chromium free organic coating system must be used when performing corrosion test methods. Current and future acquisition systems such as the Armored Amphibious Assault Vehicle (AAAV) and the Interim Armored Vehicle (IAV) are already mandating Cr^{+6} free organic coating systems. This trend is likely to continue and potentially may even be applied to some fielded DoD vehicles and weapon systems. In order to clearly delineate the best possible Cr^{+6} free pretreatment(s), additional experimental results in addition to field tests on actual systems from NAVAIR and other participating DoD activities will be critical.

CONCLUSIONS

1. Pretreatment performance varied with varying alloys

2. DoD coating systems formulated with Cr^{+6} additives provided significantly enhanced corrosion resistance versus coatings without Cr^{+6}

3. Alodine 5200 and NAVAIR TCP Cr^{+3} performed best overall in GM 9540P cyclic accelerated corrosion among non Cr^{+6} based pretreatments with performance at or near Cr^{+6} based Alodine 1200S across all alloys and coating systems examined.

4. Commercially available Alodine 5200, in conjunction with the chromium free organic coatings tested in this study, provides a completely chromium free coating system with good corrosion resistance.

ACKNOWLEDGEMENTS

The authors would like to thank additional people who contributed to this study. Russel Kilbane.

REFERENCES

1. B. Placzankis, C. Miller, C. Matzdorf, “Analysis of Nonchromate Conversion Coatings on Aluminum Alloys 2024, 5083, and 7075 with DoD Coatings Using GM 9540P Cyclic Accelerated Corrosion Exposure,” Proceedings from the Triservice Conference on Corrosion, San Antonio, TX, January 2002.

2. MIL-PRF-23377G, “Primer Coatings, Epoxy, High Solid,” U.S. Department of Defense, Washington, DC, September 1994.

3. MIL-PRF-85285, “Coating, Polyurethane, High Solids,” U.S. Department of Defense, Washington, DC, April 1997.

4. MIL-PRF-85582, “Primer Coatings, Epoxy, Waterborne,” U.S. Department of Defense, Washington, DC, September 1997.

5. MIL-P-53030A, “Primer, Epoxy Coating, Water Reducible, Lead and Chromate Free,” Revision A, Amendment 2, U.S. Department of Defense, Washington, DC, 1992

6. MIL-C-53039A, “Coating, Aliphatic Polyurethane, Single Component, Chemical Agent Resistant,” U.S. Department of Defense, Washington DC, May 1993.

7. MIL-P-53022-10, “Primer, Epoxy Coating, Corrosion Inhibiting, Lead and Chromate Free,” U.S. Department of Defense, Washington DC, February 1992.

8. GM 9540P, “Accelerated Corrosion Test; GM 9540P,” General Motors Engineering Standards, 1997

9. ASTM B117 – 90, "Standard Method of Salt Spray (Fog) Testing," ASTM, Philadelphia, PA. 1990

10. ASTM D 1654-79A, “Standard Method for Evaluation of Painted or Coated Specimens Subjected to Corrosive Environments,” ASTM, Philadelphia, PA 1984

11. B. Placzankis, C. Miller, B. Mullis, “Examination of Nonchromate Conversion Coatings for Aluminum Armor from Three Final Candidates Using Accelerated Corrosion and Adhesion Test Methods,” ARL-TR-2601, September 2001

12. B. Placzankis, C. Miller, J. Beatty, "Accelerated Corrosion Analysis of Nonchromate Conversion Coatings on Aluminum Alloys 5083, 7039, and 6061 for DoD Applications," Proceedings from the Triservice Conference on Corrosion, Myrtle Beach, SC, November 1999.

13. B. Placzankis, C. Miller, J. Beatty, "Accelerated Corrosion Analysis of Aluminum Armor Alloy 2519 With Nonchromate Conversion Coatings for DoD Applications," Proceedings from the U.S. Navy and Industry Corrosion Technology Information Exchange, Louisville, KY, July 1999.

14. Appendix - Toxicology Report, M.B. Research Laboratories, Spinnerstown, PA, MB Project #98-7031, December 1998.

15. H. Gibb, P. Lees, P. Pinsky, B. Rooney, "Lung Cancer Among Workers in Chromium Chemical Production," American Journal of Industrial Medicine, pp. 115-126 Volume 38, Issue 2, Published Online: 7 Jul 2000

16. S. King, "U.S. Army Aberdeen Test Center Accelerated Corrosion Test Facility," U.S. Army Research, Development, and Acquisition, Jan/Feb 1999 Issue, pp. 41-43.

TABLE 1.
GM 9540P Cyclic Corrosion Test Details

Interval	Description	Time (min)	Temperature (±3C)
1	Ramp to Salt Mist	15	25
2	Salt Mist Cycle	1	25
3	Dry Cycle	15	30
4	Ramp to Salt Mist	70	25
5	Salt Mist Cycle	1	25
6	Dry Cycle	15	30
7	Ramp to Salt Mist	70	25
8	Salt Mist Cycle	1	25
9	Dry Cycle	15	30
10	Ramp to Salt Mist	70	25
11	Salt Mist Cycle	1	25
12	Dry Cycle	15	30
13	Ramp to Humidity	15	49
14	Humidity Cycle	480	49
15	Ramp to Dry	15	60
16	Dry Cycle	480	60
17	Ramp to Ambient	15	25
18	Ambient Cycle	480	25

TABLE 2.
Evaluation of Coated Specimens Subjectedto Corrosive Environments - ASTM D 1654.

Rating of Failure at Scribe (Procedure A)		
Representative Mean Creepage From Scribe		Rating
(Millimeters)	(Inches)	Number
Over 0	0	10
Over 0 to 0.5	0 to 1/64	9
Over 0.5 to 1.0	1/64 to 1/32	8
Over 1.0 to 2.0	1/32 to 1/16	7
Over 2.0 to 3.0	1/16 to 1/8	6
Over 3.0 to 5.0	1/8 to 3/16	5
Over 5.0 to 7.0	3/16 to 1/4	4
Over 7.0 to 1 0.0	1/4 to 3/8	3
Over 10.0 to 13.0	3/8 to 1/2	2
Over 13.0 to 16.0	1/2 to 5/8	1
Over 16.0 to more	5/8 to more	0

TABLE 3.
ASTM D 1654 Scribe Creepback Ratings for Al 2024 Coated with 23377/25285

panel #	pretreatment	20 Cycles	40 Cycles	60 Cycles	80 Cycles	100 Cycles	120 Cycles
2-51	Alodine 1200S	10	10	9	8	8	8
2-151	TCP10	10	10	9	9	8	8
2-251	Alodine 5200	9	9	9	8	8	8
2-351	Sanchem 7000	9	9	9	9	9	9
2-451	X-IT PreKote	10	10	10	8	7	7
2-551	Oxsilan AL-0500	9	9	9	9	9	8
2-651	Chemidize 727ND	10	9	9	8	8	8
2-751	Bi-K Aklimate	10	10	10	7	7	7
2-851A	Boegel	10	9	9	9	9	9

TABLE 4.
ASTM D 1654 Scribe Creepback Ratings for Al 2024 Coated with 85582c1/25285

panel #	pretreatment	20 Cycles	40 Cycles	60 Cycles	80 Cycles	100 Cycles	120 Cycles
2-56	Alodine 1200S	9	9	9	8	8	8
2-156	TCP10	10	9	7	7	7	7
2-256	Alodine 5200	9	9	9	8	8	8
2-357	Sanchem 7000	5	5	5	0	0	
2-456	X-IT PreKote	9	7	6	5	5	5
2-557	Oxsilan AL-0500	9	9	9	7	7	7
2-656	Chemidize 727ND	9	9	7	7	6	5
2-756	Bi-K Aklimate	9	9	9	9	9	9
2-856A	Boegel	10	10	9	9	9	8

TABLE 5.
ASTM D 1654 Scribe Creepback Ratings for Al 2024 Coated with 85582nc/25285

panel #	pretreatment	20 Cycles	40 Cycles	60 Cycles	80 Cycles	100 Cycles	120 Cycles
2-61	Alodine 1200S	9	9	8	7	6	6
2-163	TCP10	9	9	9	7	6	5
2-264	Alodine 5200	9	7	6	6	6	6
2-361	Sanchem 7000	5	0				
2-461	X-IT PreKote	9	7	7	5	5	5
2-561	Oxsilan AL-0500	9	7	7	7	7	6
2-661	Chemidize 727ND	8	6	4	2	2	2
2-761	Bi-K Aklimate	6	4	4	4	3	3
2-862A	Boegel	9	5	4	4	4	4

TABLE 6.
ASTM D 1654 Scribe Creepback Ratings for Al 2024 Coated with 53030/53039

panel #	pretreatment	20 Cycles	40 Cycles	60 Cycles	80 Cycles	100 Cycles	120 Cycles
2-66	Alodine 1200S	9	9	8	7	7	7
2-169	TCP10	9	9	9	8	8	8
2-266	Alodine 5200	9	7	7	7	7	6
2-366	Sanchem 7000	9	7	5	3	3	3
2-470	X-IT PreKote	7	7	5	5	5	5
2-567	Oxsilan AL-0500	9	5	5	5	4	3
2-666	Chemidize 727ND	9	5	3	2	0	0
2-766	Bi-K Aklimate	9	7	5	5	5	5
2-866A	Boegel	9	5	5	4	4	4

TABLE 7.
ASTM D 1654 Scribe Creepback Ratings for Al 2024 Coated with 53022/53039

panel #	pretreatment	20 Cycles	40 Cycles	60 Cycles	80 Cycles	100 Cycles	120 Cycles
2-71	Alodine 1200S	9	8	7	7	7	6
2-172	TCP10	9	9	7	6	6	6
2-271	Alodine 5200	9	8	8	8	7	6
2-371	Sanchem 7000	9	6	5	0	0	0
2-471	X-IT PreKote	9	7	5	4	4	3
2-571	Oxsilan AL-0500	9	9	8	6	5	4
2-672	Chemidize 727ND	9	4	4	0	0	0
2-771	Bi-K Aklimate	9	9	9	9	9	7
2-871A	Boegel	9	7	7	6	6	6

TABLE 8.
ASTM D 1654 Scribe Creepback Ratings for Al 2219 Coated with 23377/25285

panel #	pretreatment	20 Cycles	40 Cycles	60 Cycles	80 Cycles	100 Cycles	120 Cycles
9-51	Alodine 1200S	10	10	10	10	10	10
9-153	TCP10	10	10	9	9	9	7
9-251	Alodine 5200	10	10	10	10	10	10
9-351	Sanchem 7000	10	10	6	6	6	6
9-451	X-IT PreKote	10	10	10	9	9	9
9-551	Oxsilan AL-0500	10	10	10	10	10	10
9-651	Chemidize 727ND	7	6	5	5	5	5
9-751	Bi-K Aklimate	10	10	8	6	5	5
9-853A	Boegel	10	10	6	6	5	4

TABLE 9.
ASTM D 1654 Scribe Creepback Ratings for Al 2219 Coated with 85582c1/25285

panel #	pretreatment	20 Cycles	40 Cycles	60 Cycles	80 Cycles	100 Cycles	120 Cycles
9-56	Alodine 1200S	10	10	10	10	10	10
9-156	TCP10	10	10	10	10	9	9
9-256	Alodine 5200	10	10	10	10	9	9
9-358	Sanchem 7000	10	10	6	6	6	6
9-457	X-IT PreKote	10	10	10	10	9	7
9-556	Oxsilan AL-0500	10	10	10	10	10	10
9-656	Chemidize 727ND	7	5	5	5	5	5
9-756	Bi-K Aklimate	10	10	10	10	7	7
9-859A	Boegel	10	10	9	9	9	9

TABLE 10.
ASTM D 1654 Scribe Creepback Ratings for Al 2219 Coated with 85582nc/25285

panel #	pretreatment	20 Cycles	40 Cycles	60 Cycles	80 Cycles	100 Cycles	120 Cycles
9-64	Alodine 1200S	10	7	6	5	4	4
9-161	TCP10	10	6	6	5	4	4
9-261	Alodine 5200	8	7	6	5	5	5
9-364	Sanchem 7000	5	1	0	0		
9-461	X-IT PreKote	6	2	0			
9-564	Oxsilan AL-0500	8	5	4	4	3	3
9-661	Chemidize 727ND	4	2	0	0		
9-764	Bi-K Aklimate	5	2	0			
9-861A	Boegel	4	1	0	0		

TABLE 11.
ASTM D 1654 Scribe Creepback Ratings for Al 2219 Coated with 53030/53039

panel #	pretreatment	20 Cycles	40 Cycles	60 Cycles	80 Cycles	100 Cycles	120 Cycles
9-66	Alodine 1200S	8	4	3	3	2	0
9-166	TCP10	6	4	2	0	0	0
9-266	Alodine 5200	7	4	2	1	0	0
9-366	Sanchem 7000	4	2	0			
9-467	X-IT PreKote	3	1	0			
9-566	Oxsilan AL-0500	4	0	0			
9-666	Chemidize 727ND	2	0				
9-766	Bi-K Aklimate	2	0				
9-869A	Boegel	2	0				

TABLE 12.
ASTM D 1654 Scribe Creepback Ratings for Al 2219 Coated with 53022/53039

panel #	pretreatment	20 Cycles	40 Cycles	60 Cycles	80 Cycles	100 Cycles	120 Cycles
9-71	Alodine 1200S	10	5	0	0	0	0
9-171	TCP10	7	5	5	5	3	2
9-271	Alodine 5200	6	5	3	2	1	0
9-371	Sanchem 7000	3	0	0	0		
9-473	X-IT PreKote	2	0	0			
9-573	Oxsilan AL-0500	5	1	0			
9-671	Chemidize 727ND	2	0				
9-771	Bi-K Aklimate	2	0	0			
9-871A	Boegel	5	4	2	1	0	

TABLE 13.
ASTM D 1654 Scribe Creepback Ratings for Al 5083 Coated with 23377/25285

panel #	pretreatment	20 Cycles	40 Cycles	60 Cycles	80 Cycles	100 Cycles	120 Cycles
5-51	Alodine 1200S	10	9	9	9	9	9
5-151	TCP10	9	9	9	9	9	9
5-251	Alodine 5200	9	9	9	9	9	9
5-351	Sanchem 7000	9	9	9	9	9	9
5-451	X-IT PreKote	9	9	9	9	9	9
5-551	Oxsilan AL-0500	10	10	10	10	10	10
5-651	Chemidize 727ND	10	10	10	10	9	9
5-751	Bi-K Aklimate	10	9	9	9	9	9
5-851A	Boegel	10	10	9	9	9	9

TABLE 14.
ASTM D 1654 Scribe Creepback Ratings for Al 5083 Coated with 85582c1/25285

panel #	pretreatment	20 Cycles	40 Cycles	60 Cycles	80 Cycles	100 Cycles	120 Cycles
5-56	Alodine 1200S	10	10	10	9	9	9
5-156	TCP10	10	9	9	9	9	9
5-256	Alodine 5200	9	9	9	9	9	9
5-360	Sanchem 7000	8	8	7	7	7	7
5-456	X-IT PreKote	10	9	9	9	9	9
5-556	Oxsilan AL-0500	9	9	9	9	9	9
5-656	Chemidize 727ND	9	9	9	9	9	9
5-756	Bi-K Aklimate	10	9	9	9	9	9
5-856A	Boegel	9	9	9	9	9	9

TABLE 15.
ASTM D 1654 Scribe Creepback Ratings for Al 5083 Coated with 85582nc/25285

panel #	pretreatment	20 Cycles	40 Cycles	60 Cycles	80 Cycles	100 Cycles	120 Cycles
5-61	Alodine 1200S	9	9	9	9	9	9
5-161	TCP10	9	9	9	9	9	9
5-261	Alodine 5200	9	9	9	9	9	9
5-364	Sanchem 7000	7	5	5	5	3	3
5-462	X-IT PreKote	9	9	9	9	9	9
5-561	Oxsilan AL-0500	10	10	9	9	9	9
5-661	Chemidize 727ND	8	7	7	7	7	7
5-761	Bi-K Aklimate	9	9	9	9	9	9
5-861A	Boegel	9	9	9	9	9	9

TABLE 16.
ASTM D 1654 Scribe Creepback Ratings for Al 5083 Coated with 53030/53039

panel #	pretreatment	20 Cycles	40 Cycles	60 Cycles	80 Cycles	100 Cycles	120 Cycles
5-66	Alodine 1200S	9	9	9	9	9	9
5-167	TCP10	9	9	9	9	9	9
5-266	Alodine 5200	9	9	9	9	9	9
5-366	Sanchem 7000	8	7	7	7	7	7
5-466	X-IT PreKote	9	9	9	9	9	9
5-566	Oxsilan AL-0500	9	9	9	9	9	9
5-666	Chemidize 727ND	9	9	9	9	9	9
5-766	Bi-K Aklimate	9	9	9	9	9	9
5-866A	Boegel	9	9	9	9	9	9

TABLE 17.
ASTM D 1654 Scribe Creepback Ratings for Al 5083 Coated with 53022/53039

panel #	pretreatment	20 Cycles	40 Cycles	60 Cycles	80 Cycles	100 Cycles	120 Cycles
5-71	Alodine 1200S	9	9	9	9	9	9
5-171	TCP10	9	9	9	9	9	9
5-271	Alodine 5200	9	9	9	9	9	9
5-371	Sanchem 7000	9	9	9	9	9	9
5-471	X-IT PreKote	10	9	9	9	9	9
5-571	Oxsilan AL-0500	9	9	9	9	9	9
5-671	Chemidize 727ND	9	9	9	9	9	9
5-771	Bi-K Aklimate	9	8	8	7	7	7
5-871A	Boegel	9	9	9	9	9	9

TABLE 18.
ASTM D 1654 Scribe Creepback Ratings for Al 7075 Coated with 23377/25285

panel #	pretreatment	20 Cycles	40 Cycles	60 Cycles	80 Cycles	100 Cycles	120 Cycles
7-51	Alodine 1200S	10	10	10	9	9	9
7-151	TCP10	10	9	9	9	9	9
7-253	Alodine 5200	6	6	6	6	6	6
7-351	Sanchem 7000	9	8	8	8	8	8
7-451	X-IT PreKote	10	10	10	10	9	9
7-551	Oxsilan AL-0500	10	10	10	10	9	9
7-651	Chemidize 727ND	9	9	9	9	9	9
7-751	Bi-K Aklimate	10	10	10	10	9	9
7-851A	Boegel	10	10	10	10	9	9

TABLE 19.
ASTM D 1654 Scribe Creepback Ratings for Al 7075 Coated with 85582c1/25285

panel #	pretreatment	20 Cycles	40 Cycles	60 Cycles	80 Cycles	100 Cycles	120 Cycles
7-56	Alodine 1200S	10	10	10	9	9	9
7-156	TCP10	9	9	9	9	9	9
7-259	Alodine 5200	6	5	5	5	5	5
7-357	Sanchem 7000	4	3	1	0		
7-456	X-IT PreKote	10	10	10	9	9	9
7-556	Oxsilan AL-0500	10	9	9	7	7	6
7-656	Chemidize 727ND	7	7	7	6	6	6
7-756	Bi-K Aklimate	10	9	9	9	9	9
7-856A	Boegel	10	10	10	10	10	9

TABLE 20.
ASTM D 1654 Scribe Creepback Ratings for Al 7075 Coated with 85582nc/25285

panel #	pretreatment	20 Cycles	40 Cycles	60 Cycles	80 Cycles	100 Cycles	120 Cycles
7-61	Alodine 1200S	9	9	8	8	8	8
7-161	TCP10	10	10	10	10	10	9
7-261	Alodine 5200	6	5	5	5	5	5
7-361	Sanchem 7000	0					
7-461	X-IT PreKote	9	6	6	4	3	1
7-561	Oxsilan AL-0500	9	9	8	7	6	6
7-661	Chemidize 727ND	8	7	5	3	2	1
7-765	Bi-K Aklimate	7	3	2	0		
7-861A	Boegel	9	7	7	5	5	5

TABLE 21.
ASTM D 1654 Scribe Creepback Ratings for Al 7075 Coated with 53030/53039

panel #	pretreatment	20 Cycles	40 Cycles	60 Cycles	80 Cycles	100 Cycles	120 Cycles
7-66	Alodine 1200S	9	9	8	8	7	7
7-166	TCP10	8	8	7	7	7	7
7-268	Alodine 5200	6	5	4	4	4	4
7-366	Sanchem 7000	5	4	2	1	0	
7-466	X-IT PreKote	7	5	4	3	3	2
7-568	Oxsilan AL-0500	7	4	3	3	2	0
7-669	Chemidize 727ND	2	0				
7-769	Bi-K Aklimate	2	1	0			
7-866A	Boegel	9	7	7	5	5	4

TABLE 22.
ASTM D 1654 Scribe Creepback Ratings for Al 7075 Coated with 53022/53039

panel #	pretreatment	20 Cycles	40 Cycles	60 Cycles	80 Cycles	100 Cycles	120 Cycles
7-71	Alodine 1200S	9	9	9	7	5	5
7-174	TCP10	10	9	9	9	9	9
7-271	Alodine 5200	9	9	7	7	7	6
7-371	Sanchem 7000	4	4	3	3	2	1
7-473	X-IT PreKote	6	5	4	3	3	1
7-571	Oxsilan AL-0500	9	4	3	3	3	2
7-674	Chemidize 727ND	3	0				
7-771	Bi-K Aklimate	3	3	3	2	2	1
7-871A	Boegel	9	5	5	4	3	3

FIGURE 1: GM 9540P Test Panel Matrix Breakdown

FIGURE 2: Test Chamber Configuration Used for GM 9540P

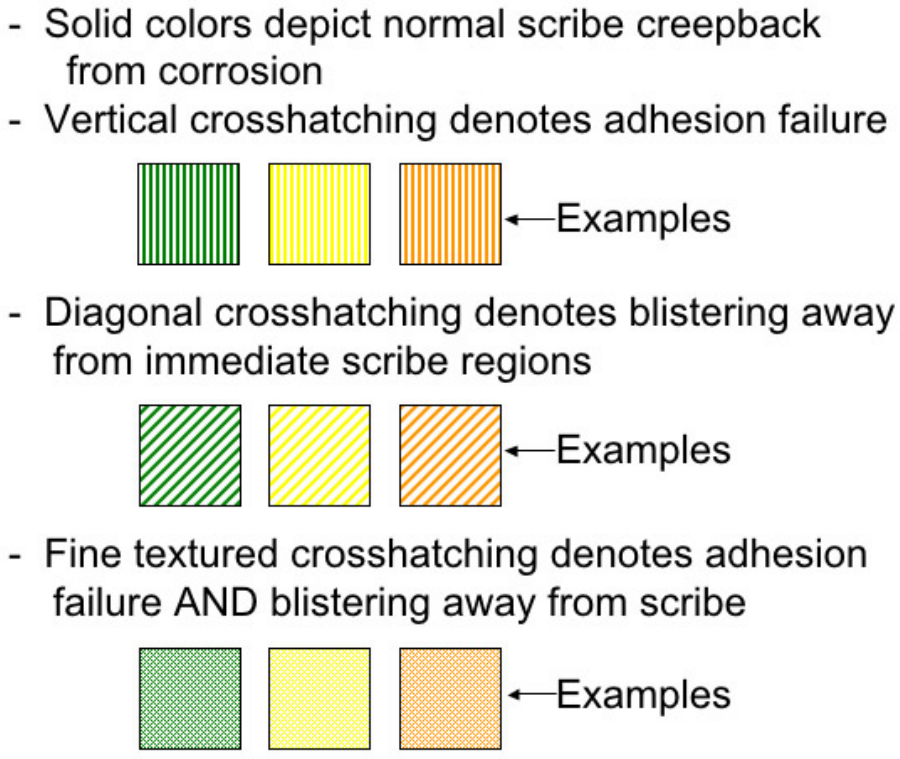

FIGURE 3: Color Code Shading Patterned for Detailed Descriptions

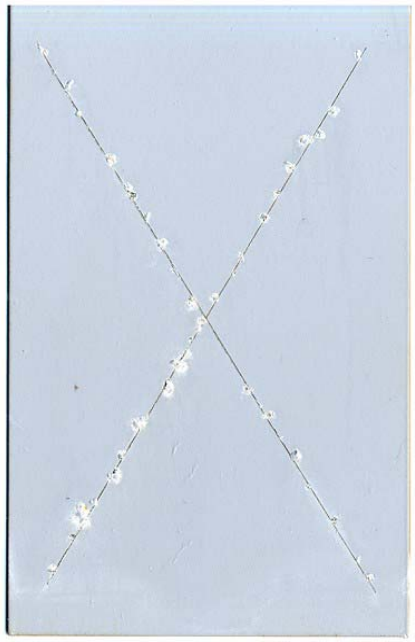

(a) Alodine 1200S

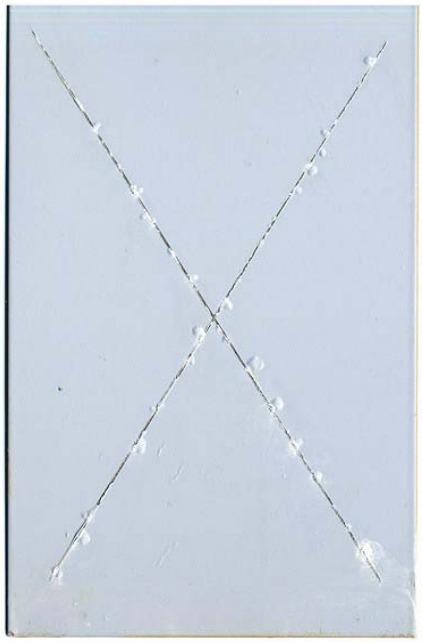

(b) TCP

(c) Alodine 5200

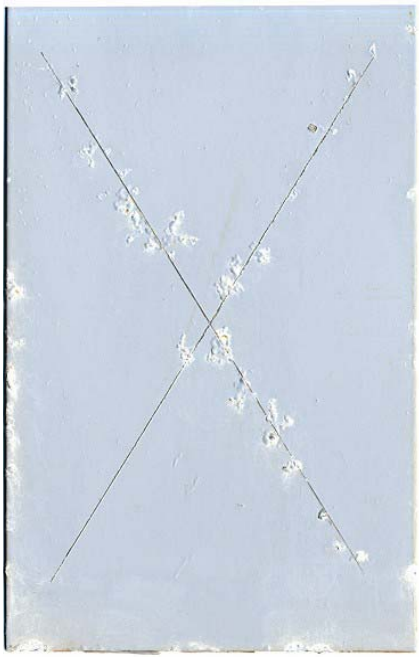

(d) Boegel

FIGURE 4: Al 2024 with 85582nc/85285@120 Cycles GM 9540P

(a) Alodine 1200S

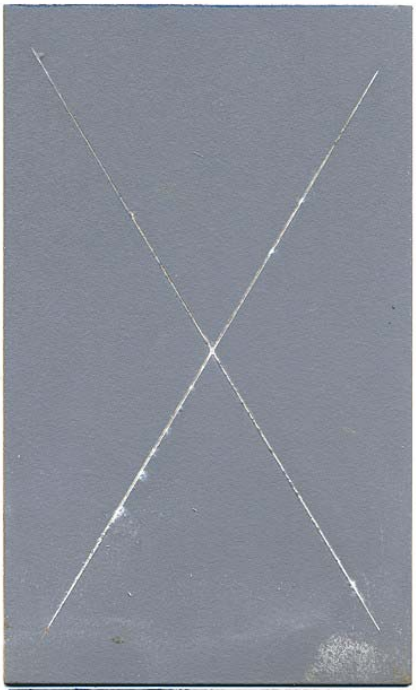

(b) TCP

(c) Alodine 5200

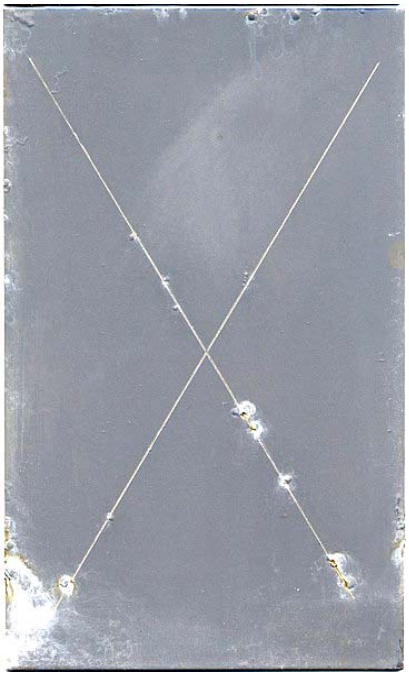

(d) Boegel

FIGURE 5: Al 2024 with 53030/53039@120 Cycles GM 9540P

(a) Alodine 1200S

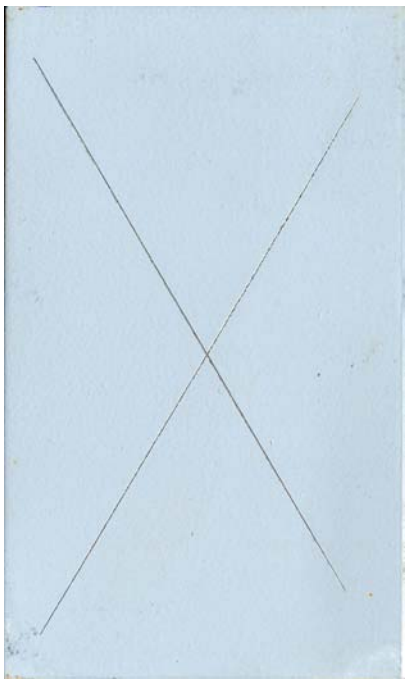

(b) TCP

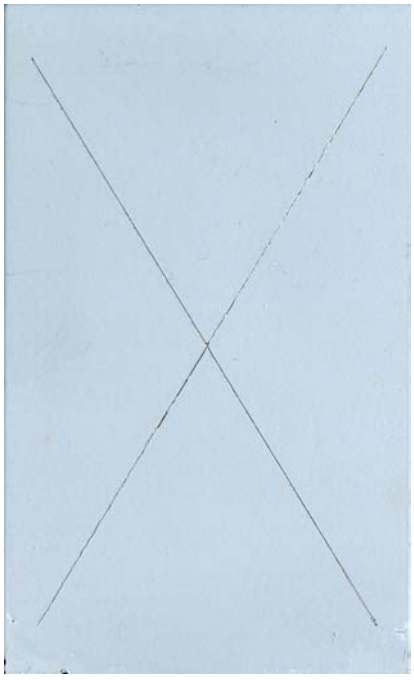

(c) Alodine 5200

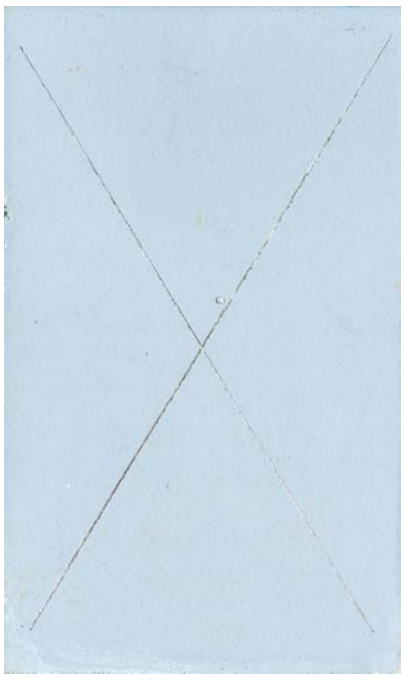

(d) Oxsilan AL-0500

FIGURE 6: Al 2219 with 85582c1/25285@120 Cycles GM 9540P

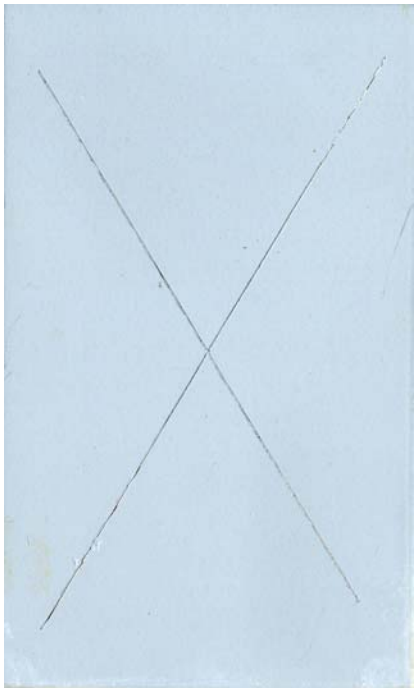

(a) X-IT PreKote

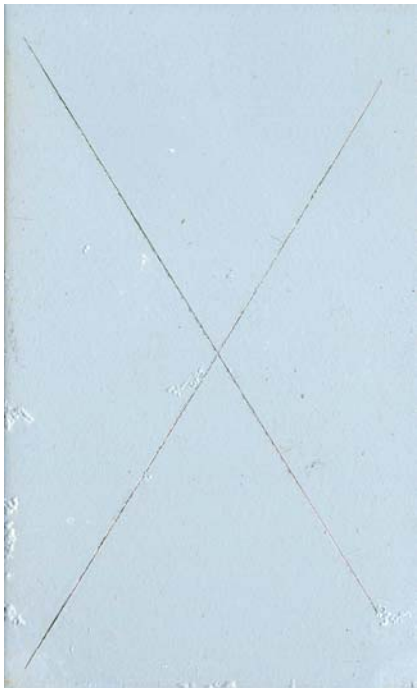

(b) Chemidize

(c) Bi-K Aklimate

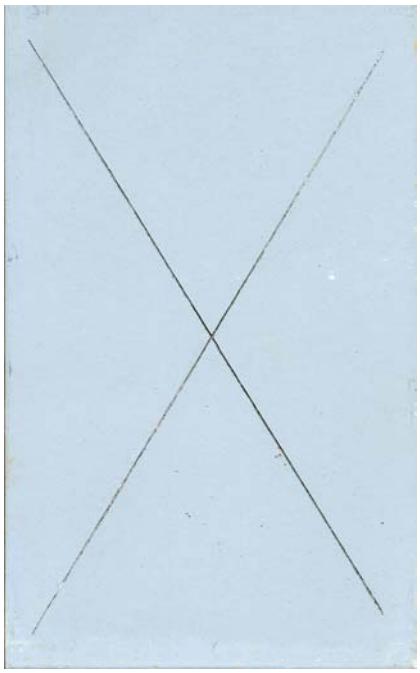

(d) Boegel

FIGURE 7: Al 2219 with 85582c1/25285@120 Cycles GM 9540P

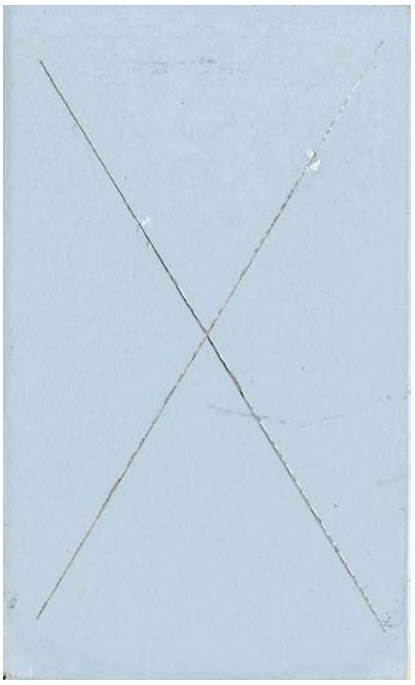

(a) Alodine 1200S

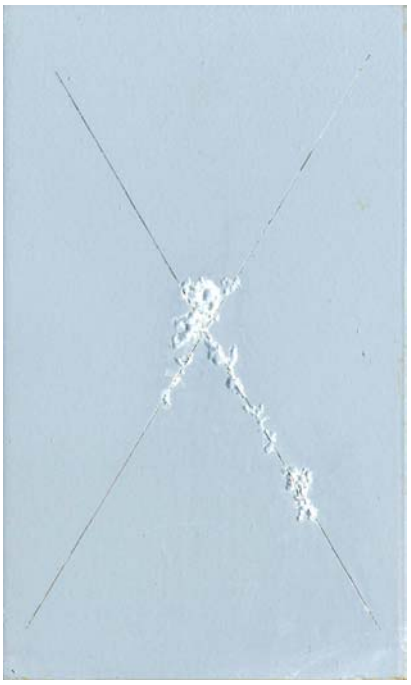

(b) TCP

(c) Alodine 5200

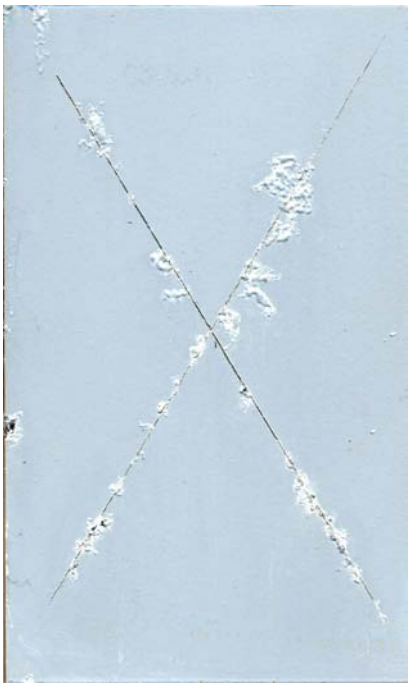

(d) Oxsilan AL-0500

FIGURE 8: Al 2219 with 85582nc/85285@120 Cycles GM 9540P

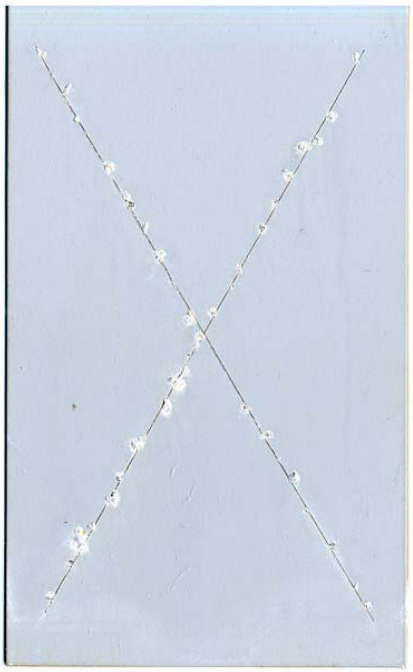

(a) Alodine 1200S

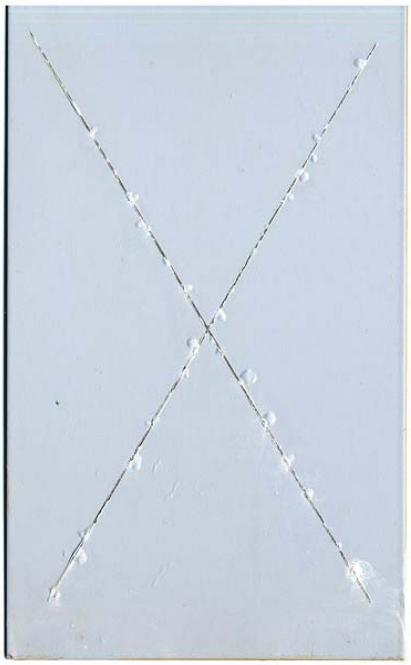

(b) TCP

(c) Alodine 5200

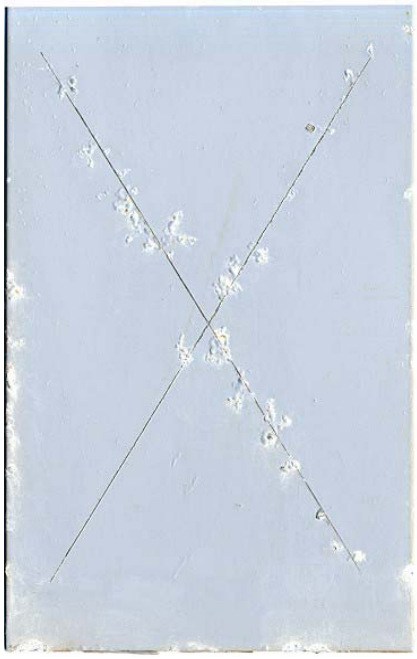

(d) Boegel

FIGURE 9: Al 7075 with 85582nc/85285@120 Cycles GM 9540P

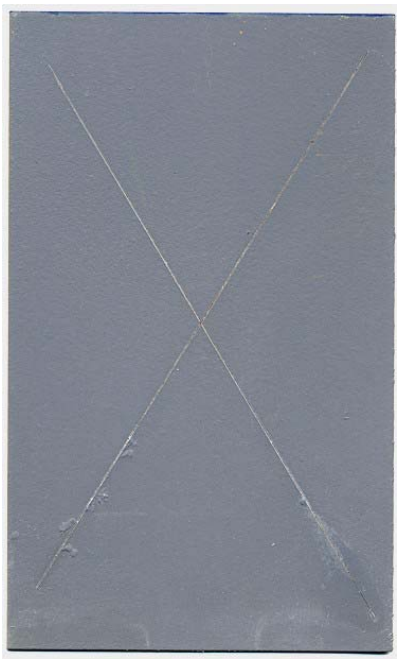

(a) Alodine 1200S

(b) TCP

(c) Alodine 5200

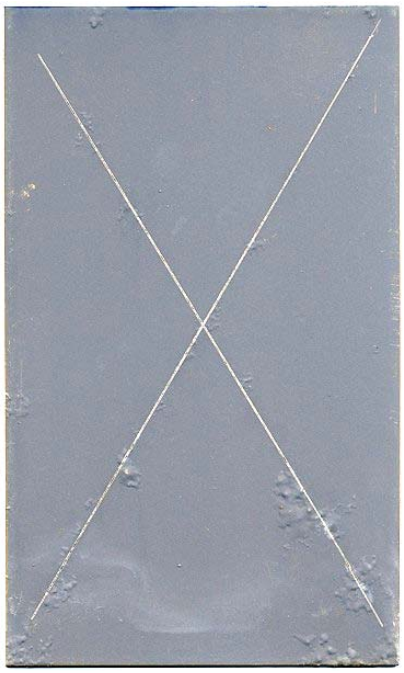

(d) Boegel

FIGURE 10: Al 7075 with 53022/53039@120 Cycles GM 9540P

APPENDIX A.
Complete 120 Cycle GM 9540P Cyclic Corrosion ASTM D 1654 Creepback Ratings

Aluminum 2024 - T3 Panel Designation, Coating System, and Ratings															
Pretreatment	23377/85285					85582c1/85285					85582nc/85285				
Alodine 1200S	2-51	2-52	2-53	2-54	2-55	2-56	2-57	2-58	2-59	2-60	2-66	2-62	2-63	2-64	2-65
Rating	8	9	9	9	9	8	8	8	9	8	6	6	7	7	6
TCP10 (NAVAIR)	2-151	2-152	2-153	2-154	2-155	2-156	2-157	2-158	2-159	2-660	2-666	2-662	2-663	2-664	2-665
Rating	8	9	8	9	8	7	8	9	8	9	5	5	5	6	6
Alodine 5200	2-251	2-252	2-253	2-254	2-255	2-256	2-257	2-258	2-259	2-260	2-266	2-262	2-263	2-264	2-265
Rating	8	8	8	8	9	8	8	7	8	8	7	6	6	6	5
Sanchem 7000	2-351	2-352	2-353	2-354	2-355	2-356	2-357	2-358	2-359	2-360	2-366	2-362	2-363	2-364	2-365
Rating	9	8	5	7	9										
X-IT PreKote	2-451	2-452	2-453	2-454	2-455	2-456	2-457	2-458	2-459	2-460	2-466	2-462	2-463	2-464	2-465
Rating	7	7	7	7	7	5	5	7	7	7	5	4	4	5	5
Oxsilan AL-0500	2-551	2-552	2-553	2-554	2-555	2-556	2-557	2-558	2-559	2-560	2-566	2-562	2-563	2-564	2-565
Rating	8	8	8	8	9	1	7	4	4	4	6	6	6	5	5
Chemidize 727ND	2-651	2-652	2-653	2-654	2-655	2-656	2-657	2-658	2-659	2-660	2-666	2-662	2-663	2-664	2-665
Rating	8	7	7	8	7	5	6	7	6	6	2	3	2	0	2
BI-K Aklimate	2-751	2-752	2-753	2-754	2-755	2-756	2-757	2-758	2-759	2-760	2-766	2-762	2-763	2-764	2-765
Rating	7	7	8	8	9	9	8	7	8	7	3	0	0	0	0
Boegel	2-851A	2-852A	2-853A	2-854A	2-855A	2-856A	2-857A	2-858A	2-859A	2-860A	2-866A	2-862A	2-863A	2-864A	2-865A
Rating	9	9	9	9	6	8	9	9	9	7	2	4	2	4	2

Aluminum 2024 - T3 Panel Designation, Coating System, and Ratings										
Pretreatment	53030/53039					53022/53039				
Alodine 1200S	2-66	2-67	2-68	2-69	7-70	7-71	7-77	7-73	7-74	7-75
Rating	7	6	6	7	6	6	5	6	6	6
TCP10 (NAVAIR)	2-666	2-667	2-668	2-669	7-170	7-171	7-177	7-173	7-174	7-175
Rating	8	8	9	8	6	9	6	7	9	8
Alodine 5200	2-266	2-267	2-268	2-269	7-770	7-771	7-777	7-773	7-774	7-775
Rating	6	8	7	7	5	6	6	7	7	6
Sanchem 7000	2-366	2-367	2-368	2-369	7-370	7-371	7-377	7-373	7-374	7-375
Rating	3	5	4	4	4	0	2	3	2	2
X-IT PreKote	2-466	2-467	2-468	2-469	7-470	7-471	7-477	7-473	7-474	7-475
Rating	4	4	5	5	5	3	3	3	0	2
Oxsilan AL-0500	2-566	2-567	2-568	2-569	7-570	7-571	7-577	7-573	7-574	7-575
Rating	4	3	3	4	3	4	5	6	3	4
Chemidize 727ND	2-666	2-667	2-668	2-669	7-670	7-671	7-677	7-673	7-674	7-675
Rating	0	1	2	3	0	3	0	2	4	3
BI-K Aklimate	2-766	2-767	2-768	2-769	7-770	7-771	7-777	7-773	7-774	7-775
Rating	5	0	0	1	0	7	3	2	0	2
Boegel	2-866A	2-867A	2-868A	2-869A	7-870A	7-871A	7-877A	7-873A	7-874A	7-875A
Rating	4	2	3	2	0	6	1	3	3	2

Aluminum 2219 - T87 Panel Designation, Coating System, and Ratings															
Pretreatment	23377/85285					85582c1/85285					85582nc/85285				
Alodine 1200S	9-51	9-52	9-53	9-54	9-55	9-56	9-57	9-58	9-59	9-60	9-66	9-62	9-63	9-64	9-65
Rating	10	10	10	9	6	10	10	9	10	9	7	7	6	4	6
TCP10 (NAVAIR)	9-151	9-152	9-153	9-154	9-155	9-156	9-157	9-158	9-159	9-660	9-666	9-662	9-663	9-664	9-665
Rating	7	9	7	9	8	9	9	9	7	9	4	6	5	5	5
Alodine 5200	9-251	9-252	9-253	9-254	9-255	9-256	9-257	9-258	9-259	9-260	9-266	9-262	9-263	9-264	9-265
Rating	10	10	9	9	9	9	9	9	9	9	5	5	7	7	6
Sanchem 7000	9-351	9-352	9-353	9-354	9-355	9-356	9-357	9-358	9-359	9-360	9-366	9-362	9-363	9-364	9-365
Rating	6	7	5	9	7	6	7	6	5	8					
X-IT PreKote	9-451	9-452	9-453	9-454	9-455	9-456	9-457	9-458	9-459	9-460	9-466	9-462	9-463	9-464	9-465
Rating	9	3	9	4	2	7	7	6	6	7					
Oxsilan AL-0500	9-551	9-552	9-553	9-554	9-555	9-556	9-557	9-558	9-559	9-560	9-566	9-562	9-563	9-564	9-565
Rating	10	10	9	9	9	10	9	9	9	9	4	4	3	3	3
Chemidize 727ND	9-651	9-652	9-653	9-654	9-655	9-656	9-657	9-658	9-659	9-660	9-666	9-662	9-663	9-664	9-665
Rating	5	4	4	5	5	5	7	7	9	9					
BI-K Aklimate	9-751	9-752	9-753	9-754	9-755	9-756	9-757	9-758	9-759	9-760	9-766	9-762	9-763	9-764	9-765
Rating	5	8	8	7	7	7	6	5	4	4					
Boegel	9-851A	9-852A	9-853A	9-854A	9-855A	9-856A	9-857A	9-858A	9-859A	9-860A	9-866A	9-862A	9-863A	9-864A	9-865A
Rating	6	3	4	9	9	9	7	6	9	7					

Aluminum 2219 - T87 Panel Designation, Coating System, and Ratings										
Pretreatment	53030/53039					53022/53039				
Alodine 1200S	9-66	9-67	9-68	9-69	9-70	9-71	9-77	9-73	9-74	9-75
Rating	0	5	5	5	4	0	0	0	0	0
TCP10 (NAVAIR)	9-666	9-667	9-668	9-669	9-170	9-171	9-177	9-173	9-174	9-175
Rating	0	1	4	3	2	2	2	2	1	1
Alodine 5200	9-266	9-267	9-268	9-269	9-770	9-771	9-777	9-773	9-774	9-775
Rating	0	3	4	3	3	0	4	4	4	4
Sanchem 7000	9-366	9-367	9-368	9-369	9-370	9-371	9-377	9-373	9-374	9-375
Rating										
X-IT PreKote	9-466	9-467	9-468	9-469	9-470	9-471	9-477	9-473	9-474	9-475
Rating										
Oxsilan AL-0500	9-566	9-567	9-568	9-569	9-570	9-571	9-577	9-573	9-574	9-575
Rating										
Chemidize 727ND	9-666	9-667	9-668	9-669	9-670	9-671	9-677	9-673	9-674	9-675
Rating										
BI-K Aklimate	9-766	9-767	9-768	9-769	9-770	9-771	9-777	9-773	9-774	9-775
Rating										
Boegel	9-866A	9-867A	9-868A	9-869A	9-870A	9-871A	9-877A	9-873A	9-874A	9-875A
Rating										

Aluminum 5083 - H131 Panel Designation, Coating System, and Ratings															
Pretreatment	23377/85285					85582c1/85285					85582nc/85285				
Alodine 1200S	5-51	5-52	5-53	5-54	5-55	5-56	5-57	5-58	5-59	5-60	5-66	5-62	5-63	5-64	5-65
Rating	9	9	9	9	9	9	9	9	9	9	9	9	9	9	9
TCP10 (NAVAIR)	5-151	5-152	5-153	5-154	5-155	5-156	5-157	5-158	5-159	5-660	5-666	5-662	5-663	5-664	5-665
Rating	8	9	9	8	9	9	9	9	9	9	9	9	9	9	9
Alodine 5200	5-251	5-252	5-253	5-254	5-255	5-256	5-257	5-258	5-259	5-260	5-266	5-262	5-263	5-264	5-265
Rating	9	9	9	9	9	9	9	9	9	9	9	9	9	9	9
Sanchem 7000	5-351	5-352	5-353	5-354	5-355	5-356	5-357	5-358	5-359	5-360	5-366	5-362	5-363	5-364	5-365
Rating	9	9	9	9	3	9	8	8	6	7	4	3	5	3	0
X-IT PreKote	5-451	5-452	5-453	5-454	5-455	5-456	5-457	5-458	5-459	5-460	5-466	5-462	5-463	5-464	5-465
Rating	9	9	9	9	9	9	9	9	9	9	7	8	9	9	8
Oxsilan AL-0500	5-551	5-552	5-553	5-554	5-555	5-556	5-557	5-558	5-559	5-560	5-566	5-562	5-563	5-564	5-565
Rating	9	9	10	10	10	9	9	9	10	9	9	9	9	9	9
Chemidize 727ND	5-651	5-652	5-653	5-654	5-655	5-656	5-657	5-658	5-659	5-660	5-666	5-662	5-663	5-664	5-665
Rating	9	9	9	9	10	9	9	10	10	9	7	9	7	6	6
BI-K Aklimate	5-751	5-752	5-753	5-754	5-755	5-756	5-757	5-758	5-759	5-760	5-766	5-762	5-763	5-764	5-765
Rating	9	9	9	9	9	9	9	9	9	9	9	9	9	9	6
Boegel	5-851A	5-852A	5-853A	5-854A	5-855A	5-856A	5-857A	5-858A	5-859A	5-860A	5-866A	5-862A	5-863A	5-864A	5-865A
Rating	9	9	9	9	9	9	9	9	9	9	9	9	9	9	9

Aluminum 5083 - H131 Panel Designation, Coating System, and Ratings										
Pretreatment	53030/53039					53022/53039				
Alodine 1200S	5-66	5-67	5-68	5-69	5-70	5-71	5-77	5-73	5-74	5-75
Rating	9	9	9	9	9	9	9	9	9	9
TCP10 (NAVAIR)	5-666	5-667	5-668	5-669	5-170	5-171	5-177	5-173	5-174	5-175
Rating	9	9	9	9	9	9	9	9	9	9
Alodine 5200	5-266	5-267	5-268	5-269	5-770	5-771	5-777	5-773	5-774	5-775
Rating	9	9	9	9	9	9	9	9	9	9
Sanchem 7000	5-366	5-367	5-368	5-369	5-370	5-371	5-377	5-373	5-374	5-375
Rating	7	6	7	7	5	9	9	9	9	6
X-IT PreKote	5-466	5-467	5-468	5-469	5-470	5-471	5-477	5-473	5-474	5-475
Rating	9	9	9	9	9	9	9	9	9	9
Oxsilan AL-0500	5-566	5-567	5-568	5-569	5-570	5-571	5-577	5-573	5-574	5-575
Rating	9	9	9	9	9	9	9	9	9	9
Chemidize 727ND	5-666	5-667	5-668	5-669	5-670	5-671	5-677	5-673	5-674	5-675
Rating	9	7	5	9	9	9	7	5	9	6
BI-K Aklimate	5-766	5-767	5-768	5-769	5-770	5-771	5-777	5-773	5-774	5-775
Rating	9	9	9	9	9	7	9	9	9	5
Boegel	5-866A	5-867A	5-868A	5-869A	5-870A	5-871A	5-877A	5-873A	5-874A	5-875A
Rating	9	9	9	9	9	9	9	9	9	9

Aluminum 7075 - T6 Panel Designation, Coating System, and Ratings															
Pretreatment	23377/85285					85582c1/85285					85582nc/85285				
Alodine 1200S	7-51	7-52	7-53	7-54	7-55	7-56	7-57	7-58	7-59	7-60	7-66	7-62	7-63	7-64	7-65
Rating	9	9	9	9	9	9	9	9	9	9	8	9	7	8	8
TCP10 (NAVAIR)	7-151	7-152	7-153	7-154	7-155	7-156	7-157	7-158	7-159	7-660	7-666	7-662	7-663	7-664	7-665
Rating	9	9	9	9	9	9	9	9	9	9	5	7	7	7	8
Alodine 5200	7-251	7-252	7-253	7-254	7-255	7-256	7-257	7-258	7-259	7-260	7-266	7-262	7-263	7-264	7-265
Rating	7	7	6	5	5	6	7	5	6	6	5	6	5	7	5
Sanchem 7000	7-351	7-352	7-353	7-354	7-355	7-356	7-357	7-358	7-359	7-360	7-366	7-362	7-363	7-364	7-365
Rating	8	8	9	9	9										
X-IT PreKote	7-451	7-452	7-453	7-454	7-455	7-456	7-457	7-458	7-459	7-460	7-466	7-462	7-463	7-464	7-465
Rating	9	9	9	9	9	9	9	9	9	9	1	3	2	3	2
Oxsilan AL-0500	7-551	7-552	7-553	7-554	7-555	7-556	7-557	7-558	7-559	7-560	7-566	7-562	7-563	7-564	7-565
Rating	9	9	9	9	9	6	5	7	7	6	6	7	6	9	7
Chemidize 727ND	7-651	7-652	7-653	7-654	7-655	7-656	7-657	7-658	7-659	7-660	7-666	7-662	7-663	7-664	7-665
Rating	9	9	9	9	9	6	6	5	7	5	1	0	0	0	2
BI-K Aklimate	7-751	7-752	7-753	7-754	7-755	7-756	7-757	7-758	7-759	7-760	7-766	7-762	7-763	7-764	7-765
Rating	9	9	9	9	9	9	9	9	9	9					
Boegel	7-851A	7-852A	7-853A	7-854A	7-855A	7-856A	7-857A	7-858A	7-859A	7-860A	7-866A	7-862A	7-863A	7-864A	7-865A
Rating	9	9	9	7	9	9	9	9	9	9	5	5	4	5	5

Aluminum 7075 - T6 Panel Designation, Coating System, and Ratings										
Pretreatment	53030/53039					53022/53039				
Alodine 1200S	7-66	7-67	7-68	7-69	7-70	7-71	7-77	7-73	7-74	7-75
Rating	7	7	8	6	7	5	6	5	5	4
TCP10 (NAVAIR)	7-666	7-667	7-668	7-669	7-170	7-171	7-177	7-173	7-174	7-175
Rating	7	7	6	7	6	3	5	8	9	9
Alodine 5200	7-266	7-267	7-268	7-269	7-770	7-771	7-777	7-773	7-774	7-775
Rating	3	2	4	5	6	6	3	3	5	4
Sanchem 7000	7-366	7-367	7-368	7-369	7-370	7-371	7-377	7-373	7-374	7-375
Rating						1	0	0	2	3
X-IT PreKote	7-466	7-467	7-468	7-469	7-470	7-471	7-477	7-473	7-474	7-475
Rating	2	2	1	0	2	1	2	1	1	2
Oxsilan AL-0500	7-566	7-567	7-568	7-569	7-570	7-571	7-577	7-573	7-574	7-575
Rating	1	3	0	1	1	2	6	4	2	2
Chemidize 727ND	7-666	7-667	7-668	7-669	7-670	7-671	7-677	7-673	7-674	7-675
Rating										
BI-K Aklimate	7-766	7-767	7-768	7-769	7-770	7-771	7-777	7-773	7-774	7-775
Rating						1	0	0	0	2
Boegel	7-866A	7-867A	7-868A	7-869A	7-870A	7-871A	7-877A	7-873A	7-874A	7-875A
Rating	4	3	2	3	3	3	3	1	2	3

LOW VOLATILE ORGANIC COMPOUND (VOC) CHEMICAL AGENT RESISTANT COATING (CARC) APPLICATION DEMONSTRATION/VALIDATION

Lisa Weiser, Anthony Eng, David Fayocavitz, Forrest Pilgrim
Naval Surface Warfare Center, Carderock Division, Code 624

ABSTRACT

The Strategic Environmental Research and Development Program (SERDP) funded a tri-Service effort to develop a low Volatile Organic Compound (VOC) Chemical Agent Resistant Coating (CARC) for use on Army, Marine Corps, and Air Force equipment. As part of this effort, the Army Research Lab (ARL) has developed a high performance low VOC water dispersible (WD) CARC polyurethane topcoat (MIL-DTL-64159), Naval Surface Warfare Center, Carderock Division (NSWCCD) performed the application studies, and Wright Research Labs (WRL), along with Southwest Research, Inc., performed the de-paint or stripping studies. Under Environmental Security Technology Certification Program (ESTCP) sponsorship, NSWCCD along with the other members of the team, conducted demonstration/validation (dem/val) tests of this new formulation to determine the success of application of this coating under production conditions at various Department of Defense (DoD) depot locations.

The dem/val tests for coating application performed at Army, Air Force, and Marine Corps. facilities demonstrated that this coating is a viable "drop-in" replacement for currently used material. The new WD CARC coating was easily applied utilizing existing equipment at the various sites in a cost-effective manner. The properties of the applied coating were confirmed via laboratory testing, results indicating an improvement in performance as compared to the standard CARC. A transition program to implement this coating has been established within the Marine Corps Systems Command.

BACKGROUND

The Strategic Environmental Research and Development Program (SERDP) funded a tri-Service effort to develop a low Volatile Organic Compound (VOC) Chemical Agent Resistant Coating (CARC) - Project PP #1056, for use on Army, Marine Corps, and Air Force equipment. The chemical agent resistant and camouflage coating must comply with current/anticipated regulatory requirements for VOC and eliminate hazardous air pollutants (HAPs) and toxic

solvents used in current CARC formulations. Additionally, the new formulation must meet performance requirements for all three Agencies. The effort was initiated in fiscal year (FY) 1997 and was funded by SERDP through FY 1999.

The technical effort was divided into three phases - formulation, application, and stripping, with each Agency overseeing one of the phases. The Army Research Lab (ARL) conducted the formulation efforts, Naval Surface Warfare Center, Carderock Division (NSWCCD) performed the application studies, and Wright Research Labs (WRL), along with Southwest Research, Inc., performed the de-paint or stripping studies. Administrative management of the overall program was performed by the Army Armament Research, Development and Engineering Center (ARDEC).

Using recent developments in polymer and pigmentation technology, ARL was successful in developing a high performance water dispersible (WD) CARC polyurethane topcoat.[1] The formulation developed under the SERDP Project succeeded in meeting the VOC objective of 1.8 lb/gal and has eliminated hazardous air pollutants as well. In addition to be being fully environmentally compliant, the new coating shows significant performance enhancements via laboratory data, i.e. low temperature flexibility, mar resistance, and weathering durability as compared to the standard solvent borne CARC (MIL-C-46168D) system.[2] ARL has drafted the specification for this material, which is due for release. The specification will be designated MIL-DTL-64159—Water Dispersible Aliphatic Polyurethane Chemical Agent Resistant Coating. There are two types of this material. Type I has siliceous extender pigments. Type II has polymeric bead extenders, which was the version formulated and investigated in the SERDP efforts. The Type II version will be referred to as WD CARC hereafter in this report, unless stated otherwise.

NSWCCD Code 624 is currently a member of a tri-service team (consisting of the same members as above) funded by the Environmental Security Technology Certification Program (ESTCP). ESTCP's charter is to demonstrate/validate promising technologies, developed under the SERDP program or other science and technology (S&T) initiatives, which may result in a positive environmental impact. The technology to be demonstrated/validated during FY-00—FY-02 timeframe under this ESTCP effort, is the WD CARC.

The objective of the dem/val project is to prove that the application of the new low VOC WD CARC formulation to defense materiel, under production conditions is viable. The trials will also serve to obtain costs associated with application and performance data of the cured film, applied under production conditions. Stripping trials will also be performed to validate that the new WD CARC can be applied and stripped utilizing existing equipment at the depots, in a cost-effective manner, when following the process guidelines as developed by the SERDP effort.

Field trials were planned at three facilities, one at each of the services that will be utilizing the WD CARC. The following locations were selected and participated in the program:

United States Marine Corps – Marine Corps Logistics Base (MCLB) – Barstow, CA
United States Army – Tobyhanna Army Depot, Tobyhanna, PA
United States Air Force – Ogden Air Logistics Center, Ogden, UT

From these ESTCP efforts, the WD CARC material was proven as a viable coating, and a "drop in" replacement for currently used material. The United States Marine Corps (USMC) has fully adopted this material and mandated its use throughout the Marine Corps.[3] To help ease the transition and implementation, MARCORSYSCOM has funded trials of the new material at most of the major USMC depot facilities. These facilities include MCLB Albany, Kaneohe Bay Hawaii (Pearl Harbor Naval Shipyard), and Okinawa Japan. This paper discusses the demonstration conducted at MCLB Barstow, CA.

FIELD APPLICATION TRIALS

Four vehicles were selected for the application of WD CARC at Barstow. The vehicles selected were two HMMWV, a 5-ton Truck, and an LAV-AT. All four vehicles were steam cleaned and blasted to bare metal using almandite garnet 36 mesh blast media. The fiberglass areas on the HMMWV were scuff sanded and any substrate defects repaired.

After completion of the steam cleaning and blasting, all the metal surfaces of the vehicles were coated with a wash primer, DOD-P-15328D. The vehicles were primed using MIL-P-53030A, epoxy primer, manufactured by Deft Chemical Coatings. The primer was applied to the vehicles at an acceptable Dry film thickness (DFT) with no obvious sags, runs, or other defects.

Aluminum and steel test panels were also provided for concurrent application of the WD CARC system. These panels were used for laboratory testing to characterize the coating. The tests include adhesion, specular gloss, color difference, viscosity, and taber abrasion. The results are provided in this report. Additional panels were also exposed to accelerated weathering for 10 months prior to being used in the ESTCP stripping study scheduled for July 2001 at MCLB Barstow.

The panels were pretreated prior to application of the WD CARC. The steel panels had a zinc phosphate pre-treatment (TT-C-490 Type I) while the aluminum panels had a chromic acid anodized pre-treatment (MIL-A-8625 Type I) or a chromate conversion pre-treatment (MIL-C-5541, Class 1A).

The epoxy primer, MIL-P-53030 manufactured by Deft, Inc. was also applied to all the test panels. The average DFT of the applied primer onto the test panels was between 1.5 and 2 mils. The coating was applied with no sags, runs, or other defects.

WD CARC APPLICATION

MIXING

Sherwin Williams manufactured the WD CARC applied to the panels and four vehicles. The only color of WD CARC available at the time of the demonstration was color #34094 of FED-STD 595B, also known as Green 383. Initially, two batches of paint were mixed. The component A was placed on a shaker for five minutes prior to the mixing. In each five-gallon pail, two gallons of component A were mixed with one gallon of component B using a squirrel mixer for approximately 3 minutes. As stated on the manufacturer's data sheet, three quarts of water (0.75 parts) were then added, for a mix ratio of 2:1:0.75.

The WD CARC (2:1:0.75 mix ratio) was applied to the test panels and both HMMWV"s using Binks HVLP Mach 1 conventional system guns. The average wet film thickness (WFT) applied was approximately 5 mils. Multiple runs or sags were noticed on each vehicle, which is acceptable considering this was the painter's first use of the material.

On the same day, four additional batches of paint were mixed to support the remaining vehicles. The mixing process was the same as used on the first batch, except only two quarts (0.5 part) of water were added (2:1:0.5 mix ratio). The water concentration adjustment was based on the expertise of the painters who determined that the viscosity was slightly lower than optimal for their application techniques and process goals.

Viscosity of the WD CARC, using Zahn #3 (Signature series) cup, was accomplished in order to quantify the rheological effects of water dilution with respect to paint application performance (i.e., atomization, leveling, sag resistance tendencies). Viscosity was also used to quantify the working life of the paint in the liquid state. The viscosity of all six batches of WD

CARC material used during the demonstration varied from about 14 to 16 seconds for the two batches with a ratio of 2:1:0.75 to about 20 to 26 seconds for those with a 2:1:0.5 ratio.

The WD CARC (2:1:0.5 mix ratio) was applied to the LAV-AT and 5 ton truck. Eight runs or sags were noted on the vehicle, which as with the HMMWVs, is acceptable. The increase in the absolute number of sags is tempered by the size of the vehicle and thus the amount of material applied to the truck.

Atomization, film formation and leveling were satisfactory at either water dilution concentration. However, at the lower water dilution level, which equates to a higher volume solids level (40% for 0.5 parts water versus 37% for 0.75 parts water), superior film buildup was realized. While the tendency of a paint to sag and/or run can be influenced by the physical constraints of the parts being painted (i.e. recessed areas, sharp edges, raised rivets, etc.) as well as the skill of the applicator (i.e. technique, ability to make equipment adjustments, ability to minimize duration of learning curve, etc), this tendency appeared to be minimized at 0.5 parts water based on the overall appearance and minimal runs/sags.

POST APPLICATION TESTING

Gloss. Specular gloss characteristics were quantified using a portable HunterLab ProGloss-3 at 60^{o}, and 85^{o} orientations. Specular gloss measurements orient the light source as well as the detection optics at equal angles of incidence. In general, as the gloss of a topcoat decreases, the probability of visual detection correspondingly decreases. Thus, superior survivability properties are obtained with gloss values that are minimized. Typically, minimized gloss values are obtained by the scattering of light by pigments that protrude through the upper surface of a topcoat[4] although gloss control can also be manipulated via alteration of the polymer reactivity of distinct regions of a polymeric blend.[5]

The day following application, gloss data was collected for the two HMMWV's and the 5-ton truck. The 60^o and 85^o gloss values averaged for each vehicle were all very low and less than the maximum allowable per the MIL-C-46168 specification and the proposed WD CARC specification.

Color. Color was quantified using a portable spectrophotometric colorimeter (Applied Color Systems, Inc., Datacolor PCS-500D) conforming to ASTM D 2244 using the CIELAB color scale with D65 illuminant and 10^o observer instrument settings. Color conformance or difference (ΔE) is mathematically defined as:

$$\Delta E = [(L_{std} - L_{test})^2 + (a_{std} - a_{test})^2 + (b_{std} - b_{test})^2]^{1/2} \quad (1)$$

and generally, a ΔE value of 1.0 or less is considered imperceptible to individuals with normal vision. The instrument settings were identical to those used in a previous study.[6] The CIE LAB standard values are based on color #34094 of FED-STD-595B (383 green). Color data was generated for the two HMMWV's and the 5-ton truck at approximately the same time as the gloss tests described above. ΔE data for the two HMMWV's and the 5-ton truck ranged from 1.695 to 1.982.

The values obtained for all the vehicles are slightly superior to the lab data (ΔE=2.76) generated previously.[2] Also, ΔE for the vehicles when converted to the National Bureau of Standards (NBS) color system units were within the 2.0 NBS units as required in the CARC topcoat specifications.

Dry Film Thickness. Dry film thickness (DFT) obtained of the WD CARC system, includes the thickness of the primer. To calculate the WD CARC topcoat thickness, the average primer DFT for the vehicles was subtracted from the total system DFT. The two HMMWV's had low film thickness, which is obviously undesirable, nonetheless it is encouraging that the 5-ton

truck attained the desired average vehicle DFT of just above the 1.8 mil DFT, as required in MIL-C-53072. This was most likely due to the reduced amount of water used to mix the batches of WD CARC for the 5-ton (from 0.75 part water for the HMMWV batches to 0.5 part water for the remaining batches), which correspondingly increased the volume solids level from about 37% to 40%.

This strongly suggests that in order to get the proper film build it is advantageous to use the lower water concentration mix ratio of 2:1:0.5. While the deficient thickness of the topcoat on the HMMWV's is not expected to cause any major problems, overcoating the 383 green with black and brown to complete the camouflage pattern should help to allay these concerns.

APPLICATION SURVEYS

Following application of the WD CARC on the four vehicles and test panels, the three painters completed a WD CARC Field Trial Application Survey developed by NSWCCD. Included in this survey were questions concerning the mixing and spraying characteristics of the WD CARC, as compared to the solvent based CARC and the Water-borne Camouflage Coating (WBCC per MIL-C-29475, an interim coating authorized for use prior to implementation of MIL-DTL-64159). In addition, a general opinion of the WD CARC as compared to the solvent based CARC and the WBCC was also requested.

Based on these surveys, response choices were given a rating from 1 to 5. The rating of 1 corresponds with the much more difficult, much slower, and much worse response choices. On the other extreme, the rating of 5 corresponds to the much easier, much quicker, and much better response choices. Based on the numerical ratings, the mixing of the WD CARC with regard to complexity, ease, and time required was about the same (3 rating) compared to the currently used paints. The spray properties with regard to spray ease, spray quality, application rate, and applied

film quality were considered better (4 rating) compared to the currently used paints. Overall, the WD CARC was considered better (4 rating) by the depot applicators than both the solvent based CARC and the WBCC.

TEST PANEL RESULTS

DYNAMIC MECHANICAL THERMAL ANALYSIS (DMTA)

A Dynamic Mechanical Thermal Analysis (DMTA) was performed on Barstow and baseline WD CARC samples. The coatings were applied to 1010 cold rolled steel substrates and tested in dual cantilever or 3 point bending load cells. The glass transition temperature shifted only slightly from 98°C to 103°C for the Barstow sample. This is a good indication that the bulk properties are very similar and have remained essentially unchanged.

TENSILE ADHESION TESTING (ASTM D4541)

Tensile adhesion tests performed on the coated panels are used to quantify the amount of force necessary to break the bond of the coating to the substrate and identify the mode of failure (MOF). A type VI PATTI self-alignment adhesion tester was used with an F-8 piston per ASTM D4541-95, "Standard Test Method for Pull-off Strength of Coatings Using Portable Adhesion Testers." Adhesion is determined by measuring the force necessary to pull off a button adhered to the surface of the test panel. After adhering the button to the surface to be tested, a piston with an air collar is attached to the button and compressed air is forced into the collar until the button is pulled off the surface and the pull-off-strength (POS) noted. MOF is noted as a percentage with the failure either being cohesive (within a particular coating layer) or adhesive (between two layers).

A two component epoxy (Miller-Stephenson 907) adhesive was used to adhere two test buttons to the surface of each of the WC CARC coated steel panels. The objective of the testing was to compare the data obtained from the Barstow application to that obtained from baseline testing of the same coating system applied in a laboratory setting.

Results of the PATTI adhesion testing produced an average pull-off-strength (POS) of 2312 pounds per square inch (psi), as shown in Table 1. This correlates well with the results obtained from the baseline SERDP testing, which produced an average POS of 2543 psi for WD CARC to steel and 1992 psi for primer (MIL-P-53030) and WD CARC to steel.[6] MOF results were not recorded during the SERDP testing, therefore a comparison cannot be made. However, it is important to note that most of the failures were considered adhesive between the epoxy adhesive and the WD CARC or between the adhesive and the surface of the button. This suggests that the adhesive strength of the epoxy was exceeded prior to the adhesive or cohesive strength of the WD CARC.

ABRASION RESISTANCE

Resistance to abrasion was determined using ASTM D4060-95, "Standard Test Method for Abrasion Resistance of Organic Coatings by the Taber Abraser", however with slight deviation. Instead of using the resilient (rubber and abrasive grain) wheels, a much more rigid and coarse H-10 (vitrified) wheel with a 500 g weight was chosen. This was accomplished in order to gain more significant wear data in an efficient time span such that minor changes in application processes could be characterized.

The 4" x 4" steel panels coated with WD CARC were abraded by rotating the panels under weighted abrasive wheels. Abrasion resistance was calculated as total weight loss, as

weight loss per cycle (wear index), and as percent loss in coating thickness. The data from the panels is presented in Table 2.

After 750 cycles, the total (average) weight loss was 84.5mg and the reduction in DFT was 1.0 mil. These results are comparable to the baseline WD CARC samples from above, and indicate that the Barstow samples exhibited excellent abrasion resistance and obvious superior abrasion resistance compared to the solvent-borne system (MIL-C-46168D).

ACCELERATED WEATHERING

The Army coordinated the accelerated weathering testing. Results of this testing were used to determine how the coating would perform with regard to colorfastness. The Xenon Arc accelerated weathering included exposure in an Atlas Ci-65 chamber with 108 minutes of light and 12 minutes of light plus deionized water spray on the front of the panels. The panels were exposed for 1000 hours in accordance with ASTM G155-00, "Standard Practice for Operating Xenon Arc Light Apparatus for Exposure of Non-Metallic Materials." The panels, however, have remained in the Xenon Arc accelerated weathering chamber in order to obtain additional data.

The results of the colorfastness were graphed as shown in Figure 1. The NBS color difference is shown versus total hours of exposure. A color change value of 2.5 units is the maximum allowable color change as specified in MIL-C-46168. A NBS color change of about 1.6 units at 4200 hours of exposure has been obtained with the WD CARC applied at Barstow. The solvent borne CARC (MIL-C-46168D) and WD CARC with siliceous extenders (MIL-DTL-64159, Ty I) did not perform as well as the WD CARC with polymeric beads (MIL-DTL-64159, Ty II). The WD CARC with polymeric beads, applied in the laboratory and at Barstow, demonstrates exceptional accelerated weathering resistance.

COST ANALYSIS

The cost of the WD CARC along with data on the other topcoats approved for use on USMC tactical vehicles and support equipment is shown in Table 3. The paint cost data was provided by the paint manufacturer (Sherwin Williams) that participated in this ESTCP sponsored demonstration. Based on similar process variables, the amount of time and material required to paint a vehicle with MIL-C-29475 is essentially identical to that of WD CARC. Thus application-related labor and the overhead/facilities costs do not have an effect on this analysis.

Based solely on cost per gallon of the various paints for a 100 gal order, these values range from $38.00 to $51.67 for the MIL-C-53039 and WD CARC, respectively. The cost per square foot at the recommended dry film thickness (1.8 mils) ranges from $0.08361 to $0.14569 for the MIL-C-53039 and WD CARC, respectively. Thus, assuming that a vehicle has a wetted surface of 1000 square feet, it would cost $83.61 for the MIL-C-53039 versus $145.69 for the WD CARC based on the cost and the theoretical coverage characteristics of the paint. The cost per square foot of MIL-C-29475 (the current standard topcoat used at MCLB Barstow) would obviously fall between that of the MIL-C-53039 and WD CARC. This cost analysis is more relevant to immediate or short term costs, while a long term or life cycle cost analysis would certainly take into account the durability or frequency of repainting required.

Other factors, not included in the above cost analysis, that would affect cost can be attributed to decreased VOC emissions, decreased waste generation, and increased worker safety. Avoidance of the need to implement hard controls (i.e., thermal/catalytic/ regenerative oxidizer, adsorption filter equipment, etc.), which can cost up to $5M per depot facility along with the associated operating costs which can be as high as $250,000 per year per facility can be attained with the implementation of this type of low VOC technology versus the higher VOC CARC's.

Since the WD CARC utilizes polymeric bead extenders in place of silica extender pigments (which are contained in all the other CARCs), health-related ailments of maintenance workers exposed to air-borne silica (i.e., silicosis) would be avoided along with the associated costs related to health remediation and/or litigation. Utilization or realization of any of these environmental cost benefits individually and/or collectively would easily decrease the overall cost of the WD CARC to significantly less than any of the other standard CARC's from a life cycle standpoint.

CONCLUSIONS AND RECOMMENDATIONS

The application of the WD CARC on the four vehicles at MCLB Barstow demonstrated the "drop-in" nature of the WD CARC system. The WD CARC was applied to the vehicles with similar application performance compared to the standard CARCs. The surveys completed by the depot applicators at MCLB Barstow indicated that the WD CARC was considered overall to be a better coating than both MIL-C-46168D and MIL-C-29475. In addition, the laboratory testing completed on the coated panels resulted in similar test results to the SERDP program testing of the baseline WD CARC.

The DFT values obtained on the vehicles indicated that in order to obtain the proper film build, it is necessary to use a lower water concentration mix ratio (2:1:0.5). Therefore, it is recommended that the WD CARC be mixed at 2 parts A: 1 part B: 0.5 part water, providing environmental conditions and equipment allow. Any increase in the amount of water should be made in small increments to avoid unnecessary recoating.

The cost analysis indicated that the WD CARC is similar to the MIL-C-46168D based on paint material costs, coverage, and life cycle. When the expected durability based on critical

laboratory performance data is considered, the cost analysis indicates that the WD CARC is superior to MIL-C-46168D and MIL-C-29475. The economic benefit of WD CARC should be realized, in comparison to MIL-C-53039, as full production and widespread implementation of the WD CARC material is accomplished. After taking into account the environmental cost benefits, the WD CARC is lucidly shown to be the most cost efficient and thus the most prudent option.

REFERENCES

1 U.S. Patent # 5,691,410, "Water Dispersible Low Reflectance Chemical Resistance Coating Composition," J.A. Escarsega and K.G. Chesonis, U.S. Army, 25 November 1997.

2 R.W. Katz, "Low Volatile Organic (VOC) Chemical Agent Resistant Coating (CARC)," SERDP Project # PP1056, U.S, Army Armament Research, Development and Engineering Center, April 2000.

3 Commandant Marine Corps, Logistics Plans, Policies, and Strategic Mobility Division (LP) Naval Message, 260101Z MAY 00, "Chemical Agent Resistant Coating (CARC) Paint Requirement And Policy For Marine Corps Ground Equipment."

4 T.C. Patton, "Paint Flow and Pigment Dispersion", 2nd Edition, Wiley Interscience, 1979, pp 185, 510.

5 Dr. P. Thometzek, Dr. U. Freudenberg and M. Grahl, "Tailor Made Polyurethane Powders for High-Quality Coatings," Paint and Coating Industry, Vol XVI, No. 6, June 2000, pp 54-56.

6 M. Patel, A. Eng, F. Pilgrim, L. Weiser, "Low Volatile Organic Compound (VOC) Chemical Agent Resistant Coating (CARC) Application Study—Final Report," CARDIVNSWC-TR-62-00-03, March 2000.

TABLES AND FIGURES

TABLE 1.
PATTI Adhesion Results of Barstow Panels

			Mode of Failure						
Panel	POS	Avg	Adhesive: Substrate/ Primer	Cohesive: Primer	Adhesive: Primer/ Topcoat	Cohesive: Topcoat	Adhesive: Topcoat/ 907	Cohesive: 907	Adhesive: 907/ Button
1.1	1991	2195					65%		35%
1.2	2398		20%				75%		5%
2.1	2439	2419					60%		40%
2.2	2398		60%				20%		20%
3.1	1950	2154	50%				10%		40%
3.2	2358		40%				35%		25%
4.1	1788	2480	5%				5%		90%
4.2	3172		20%				15%		65%
	AVG	**2312**							
	SD	**427.9**							

TABLE 2.
Taber Abrasion Results of Barstow Panels

	Total Weight Loss (mg)			Wear Indices (μg/cycle)			DFT (mils)		
Sample	*250 Cycles*	*500 Cycles*	*750 Cycles*	*250 Cycles*	*500 Cycles*	*750 Cycles*	*Initial*	*Final*	Thickness Loss (%)
1	28.0	43.0	75.0	112	86	100	4.6	3.8	17.4
2	49.0	69.0	92.0	196	138	123	4.7	3.7	21.3
3	41.0	81.0	92.0	164	162	123	4.4	3.4	22.7
4	28.0	69.0	79.0	112	138	105	4.7	3.5	25.5
AVG	**36.5**	**65.5**	**84.5**	**146**	**131**	**113**	**4.6**	**3.6**	**21.7**

Note: H-10 wheel, 500 gram weight
Note: Final appearance of test area - smooth green surface. even coating wear, no exposed substrate.

TABLE 3.
Cost Analysis Based on Paint Materials Cost and Coverage

Paint Co	Prod Name	Admixed (% Solids)	$/Gal (100 gal order)	Coverage 1 mil DFT (Sq Ft)	$/Sq Ft (@ 1 mil DFT)	$/Sq Ft (@1.8 mils DFT)	$/Sq Ft/Yr (@ 1.8 mils DFT)
The Sherwin Williams Co.	MIL-DTL-64159, Ty II	39.8	51.67	638.392	0.08094	0.14569	0.01619
	MIL-C-46168D, Ty IV	38.1	47.30	611.124	0.07740	0.13932	0.02322
	MIL-C-53039	51	38.00	818.04	0.04645	0.08361	0.01394
	MIL-C-29475	48.2	44.61	773.128	0.05770	0.10386	0.01731

Note: admixed vol% solids for MIL-DTL-64159, Ty II based on mix ratio of 2 Parts A : 1Part B : 0.5 Part H2O
Note: coverage data is based on 100% application transfer efficiency
Note: recommended DFT for all CARC is 1.8 mils (minimum)
Note: paint life cycle is based on the following data: 9 yr for 64159 Ty II vs. 6 yr for others

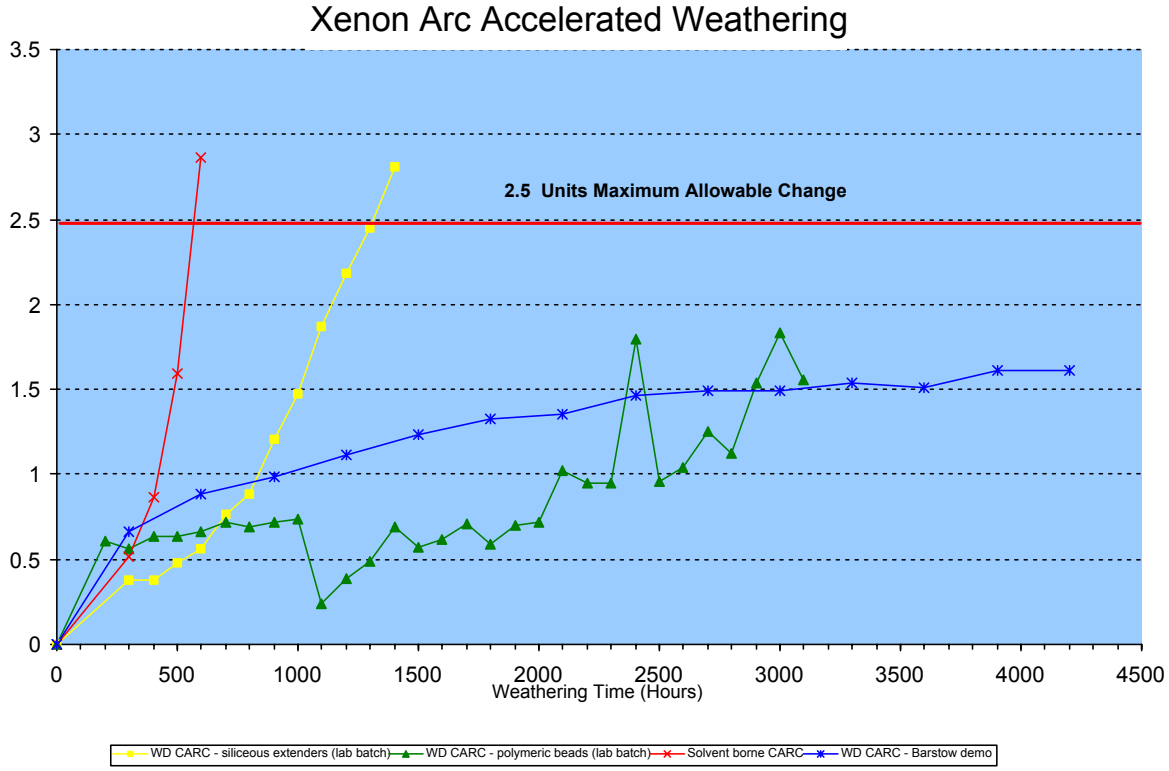

FIGURE 1. Xenon arc accelerated weathering of various coatings

CLEANING / TESTING

THE EFFECTS OF CHEMICAL RINSE AGENTS ON THE CORROSION OF AEROSPACE ALLOYS IN MARINE ENVIRONMENTS

Louis MacDowell and Luz Marina Calle
NASA
Kennedy Space Center, FL 32899

Joseph Curran, Tim Hodge, and Ronald Barile
Dynacs, Inc.
Kennedy Space Center, FL 32899

Robert Heidersbach
Materials Engineering Department
California Polytechnic State University
San Luis Obispo, CA 93407

ABSTRACT

This paper presents the methodology for comparing the relative effectiveness of four Chemical Rinse Agents (CRAs) used for rinsing aircraft. The products were applied on a weekly basis to a series of flat alloy panels exposed to an oceanfront, marine environment for one year. The results are presented and compared to those obtained from exposures of the same alloys that were not washed, were washed with seawater, or washed with demineralized (DM) water.

INTRODUCTION

AIRCRAFT CORROSION

Corrosion is a very difficult problem that costs commercial air fleet operators millions of dollars annually. The costs of corrosion in terms of military readiness cannot be measured, but they are believed to be even higher than for commercial operators. Military hardware must often be shipped in haste to remote locations where it is operated in harsh environments with less time for maintenance and with limited maintenance facilities.

Fig. 1 shows a typical Army refueling station during the deployment to the Persian Gulf in 1991. The facilities at forward installations like this are very limited and maintenance of equipment takes a back seat to operational demands. As a result of this combination of limited facilities and high operational demands, military aircraft often experience substantial corrosion damage during field deployment. Fortunately, much of the equipment spends a fair amount of its time in rear locations where facilities are not this limited and attempts at corrosion control and remediation are possible.

FIGURE 1. Helicopter refueling operation during Operation Desert Storm [1]

A number of proprietary products are marketed for rinsing aircraft for both the civilian and military markets. Unfortunately, these products have not been impartially evaluated, and government decision-makers do not have reliable data for making decisions on whether or not these products work and are worth their expense.

The purpose of this project was to determine if a number of proprietary CRAs could be used to prolong the life of Army aircraft deployed under circumstances such as those shown in Fig. 1. The project was undertaken to compare the efficiencies of a number of commercial rinsing products and to determine if they offered measurable advantages over rinsing with water having no detergents or other chemical additives. A secondary purpose was to determine if these same products would reduce corrosion during training and other operations at rear areas where maintenance facilities are less limited.

ATMOSPHERIC CORROSION TEST SITE

The NASA Kennedy Space Center Beach Corrosion Test Site (BCTS) has the highest corrosivity of any long-term exposure site in North America. This is documented in Table 1, which compares the corrosivity of the Kennedy beach side location with other test sites. For this reason, the Army initiated a program to test alloys and corrosion control methods at this site. Fig. 2 shows the rapid decrease in corrosion rates as distance from the beach increases. Any deployment of Army aircraft to locations other than the BCTS would result in an exposure that would be less corrosive.

TABLE 1.
Comparison of corrosion rates of carbon steel at various test locations[2]

Location	Type Of Environment	µm/yr	Corrosion rate (a) mils/yr
Esquimalt, Vancouver Island, BC, Canada	Rural marine	13	0.5
Pittsburgh, PA	Industrial	30	1.2
Cleveland, OH	Industrial	38	1.5
Limon Bay, Panama, CZ	Tropical marine	61	2.4
East Chicago, IL	Industrial	84	3.3
Brazos River, TX	Industrial marine	94	3.7
Daytona Beach, FL	Marine	295	11.6
Pont Reyes, CA	Marine	500	19.7
Kure Beach, NC (80 ft. from ocean)	Marine	533	21
Galeta Point Beach, Panama CZ	Marine	686	27
Kennedy Space Center, FL (beach)	Marine	1070	42

(a) Two year average

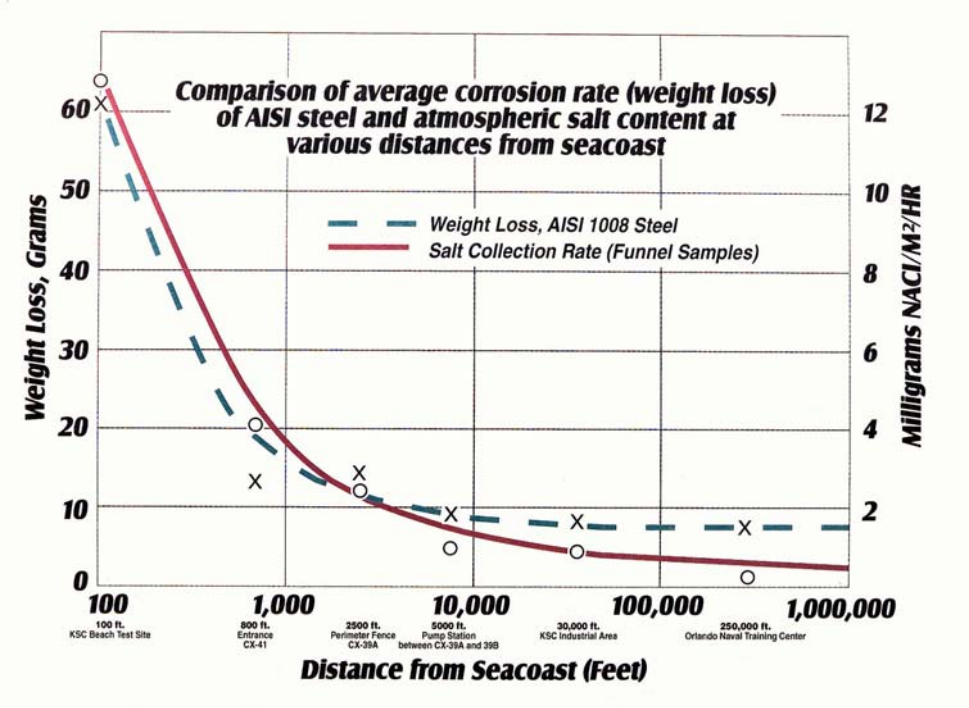

FIGURE 2. Changes of corrosion rate with distance from the ocean[3]

EXPERIMENTAL PROCEDURES

ALLOYS TESTED

The alloys shown in Table 2 were chosen by the Army as being representative of the kinds of alloys most commonly used on military aircraft. The relative corrosion resistance of these alloys was evaluated in comparison tests where the alloys were exposed to the marine atmosphere with no rinsing, rinsing with ocean water, and rinsing with DM water as a control.

TABLE 2.
Alloys tested in this program

UNS Alloy Designation	Military Handbook 5 Designation	Military Handbook 5 Common Name	Composition	Designation This Study	Comments
G43400	1206	4340	Fe, 0.4 C, 1.8 Ni, 0.8 Cr, 0.25 Mo	4340	
S45850	1220	18Ni(250) Maraging	Fe, 18 Ni, 7.5 Co, 5 Mo, Ti, Al	C-250	
S35500	1505	AM-355	Fe, 15.5 Cr, 4.5 Ni, 3 Mo	AM-355	
S13800	1510	PH 13-8 Mo	Fe, 13 Cr, 8 Ni, 2 Mo	PH 13-8 Mo	
A92024	3203	2024	Al, 4.5 Cu, 1.5 Mg, 0.6 Mn	2024-T3/8625	Anodized IAW Mil 8625 Type 1
J9100	3204	2024	Al, 4.5 Cu, 1.5 Mg, 0.6 Mn	2024-T3/5541	Alodined Mil 5541
A97075	3207	7075	Al, Zn 5.6, 2.5 Mg, 1.6 Cu, 0.3 Cr	7075-T6	
M11311	3601	AZ31B	Mg, 3 Al, 1 Zn	4377/3171 or AZ31B-H24	Surface treated IAW SAE-AMS-M-3171
R65400	3607	Ti-6Al-4V	Ti, 6 Al, 4 V	Ti-6Al-4V or Ti	

CRAS TESTED

Table 3 shows the chemical analyses of the proprietary CRAs tested. The analyses were done using ion chromatography. Several of them are marketed with trade names implying that they will eliminate salt or chlorides.

EXPOSURE TESTING

Flat panel specimens were exposed to the marine atmosphere environment in racks manufactured in accordance with standard industrial procedures (Fig. 3). [4] The alloys discussed above are undergoing a two-year exposure test at the KSC Beach Corrosion Site. The coupon size was nominally 4 by 6 inches by 1/16 to 3/16 inches thick, weighing 40 to 1200 grams each.

RINSING PROCEDURES

The specimens were rinsed once each week with a commercial pressure sprayer and the proprietary chemicals listed in Table 3 diluted according to the manufacturer's instructions.

TABLE 3.
Chemical analyses of CRAs tested

	Concentration, ppm			
Sample ID	#1	#2	#3	#4
ANIONS				
Fluoride	nd	nd	3,477	nd
Chloride	110	60	nd	232
Nitrite	91	131	nd	314
Nitrate	94	nd	166	9,511
Phosphate	25,191	65	80	nd
Sulfate	1,152	92	227	529
CATIONS				
Sodium	7,930	2,367	1,453	nd
Ammonium	nd	1,919	134	36,053
Potassium	5,537	116	280	1,023
Magnesium	nd	nd	nd	nd
Calcium	48	56	60	nd

Nd: not detected, below lower detection limit

FIGURE 3. View of Beach Corrosion Site and coupon configuration

CORROSION REMOVAL AFTER EXPOSURE

The coupons were placed outdoors at the BCTS September 29, 2000, and were retrieved after one year of exposure on October 5, 2001 to be photographed before the cleaning process. A cleaning process was determined for each metal type using ASTM G-1, Standard Practice for Preparing, Cleaning, and Evaluating Corrosion Test Specimens, as a guideline. All coupons were first cleaned by using a pressure washer to remove the gross corrosion products, followed by a five-minute ultrasonic bath, dried, and weighed. After the pressure water wash process, the coupons were chemically cleaned in a specific solution according to metal type. The given solution was chosen to remove the corrosion products with minimal dissolution of the base metal. The chemical cleaning process was repeated on each specimen several times, and the mass loss determined after each cleaning until a constant weight was reached. The removal of the corrosion products was confirmed by examination with a low power microscope. After the coupons were cleaned, they were re-tagged, photographed, and bagged for storage and further analysis.

RESULTS

WEIGHT LOSS

Only the 4340 alloy coupons lost a significant amount of mass, in the range of 4 to 18 grams, or 0.5 to 3 % weight. The relatively large weight loss is due to the exposure of uncoated metal. All other alloy coupon weight changes were insignificant, in the range of 0.01-gram weight gain for titanium, to 1.0-gram average weight loss for alloy AZ31B (magnesium) with 3171 coating. Therefore, weight loss data was only applied to the 4340 alloy for rating CRA performance. For metals that displayed pitting corrosion damage such as the aluminum and magnesium alloys, pit ratings were conducted using ASTM G-46, Practice for the Examination and Evaluation of Pitting Corrosion as a guideline. The weight loss of all metals related to CRAs and controls is shown in Table 4.

APPEARANCE OF COUPONS

As expected, the 4340 steel showed the most severe corrosion due to its low alloying and lack of coating (e.g., DM rinse, Fig. 4). Both the 2024/8625 and the 2024/5541 aluminum showed minor surface pitting while the AZ31B and the 7075 aluminum (Fig. 5) showed moderate to high pit densities. The 7075 also showed exfoliation indicative of intergranular corrosion along the edges of the panels with some of the rinse agents (Fig. 6). The titanium (Ti-6Al-4V), AM-355, and the PH 13-8 Mo showed no significant changes in appearance due to the exposure, regardless of CRA.

TABLE 4.

Coupon weight loss in grams, showing coupon with worst-case loss and average loss of replicate samples

ARMY Coupon Weight Loss/ Corrosion Analysis

Metal:	Rinses	Worst Case	Avg. Weight
4340 Steel	CRA #1	13.888	10.653
	CRA #2	14.625	10.923
	CRA #3	11.315	10.696
	CRA #4	9.996	7.631
	DM Water	17.177	13.509
	Exposure	14.312	11.278
	Seawater	16.107	15.714
Magnesium AZ31B	CRA #1	0.775	0.770
	CRA #2	1.016	0.994
	CRA #3	1.186	1.118
	CRA #4	0.95	0.932
	DM Water	0.898	0.887
	Exposure	0.947	0.916
	Seawater	1.038	1.020
2024/ 8625 Aluminum	CRA #1	0.149	0.067
	CRA #2	0.091	0.056
	CRA #3	0.089	0.068
	CRA #4	0.302	0.128
	DM Water	0.403	0.170
	Exposure	1.173	0.437
	Seawater	1.299	0.459
PH 13-8 Stainless Steel	CRA #1	0.047	0.041
	CRA #2	0.036	0.034
	CRA #3	0.064	0.058
	CRA #4	0.017	0.009
	DM Water	0.045	0.041
	Exposure	0.059	0.059
	Seawater	0.052	0.047
2024/ 5541 Aluminum	CRA #1	0.035	0.029
	CRA #2	0.395	0.139
	CRA #3	0.227	0.200
	CRA #4	0.116	0.086
	DM Water	0.232	0.091
	Exposure	0.067	0.051
	Seawater	0.041	0.028
AM-350 Stainless Steel	CRA #1	0.03	0.026
	CRA #2	0.029	0.027
	CRA #3	0.029	0.028
	CRA #4	0.026	0.026
	DM Water	0.035	0.031
	Exposure	0.041	0.036
	Seawater	0.035	0.035
7075 Aluminum	CRA #1	0.687	0.279
	CRA #2	0.121	0.294
	CRA #3	0.865	0.521
	CRA #4	0.938	0.623
	DM Water	0.548	0.231
	Exposure	1.607	0.606
	Seawater	0.243	0.140
Titanium Ti-6Al-4V	CRA #1	-0.014	-0.009
	CRA #2	-0.022	-0.010
	CRA #3	-0.011	-0.007
	CRA #4	-0.013	-0.008
	DM Water	-0.022	-0.014
	Exposure	-0.005	-0.001
	Seawater	-0.017	-0.010

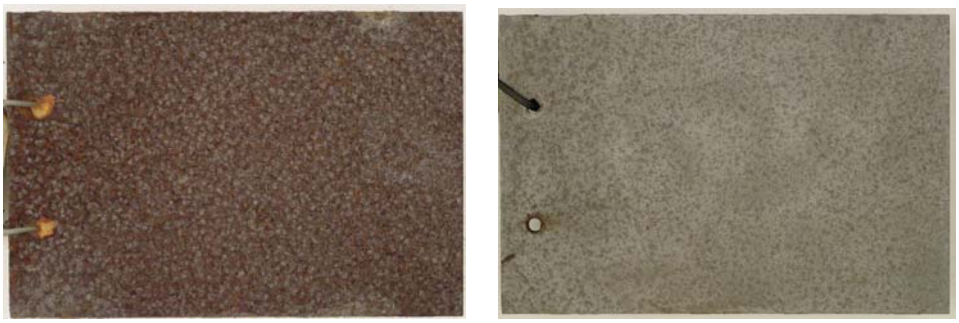

4340 CRA DM Un-Cleaned 4340 CRA DM Cleaned

FIGURE 4. Typical 4340 steel coupon - 0.4x

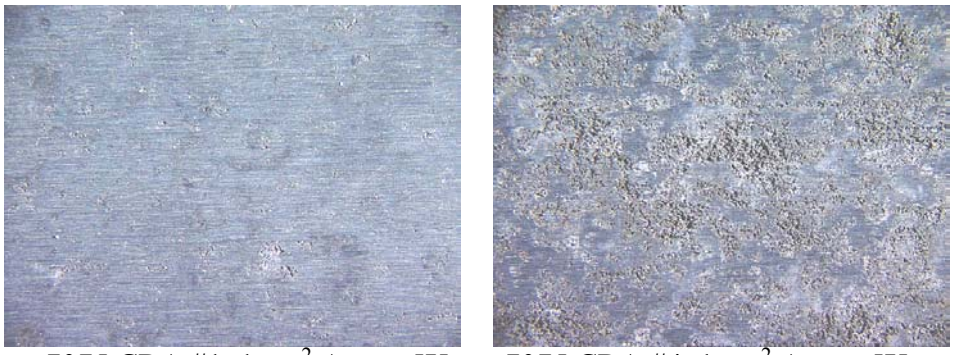

7075 CRA #1, 1 cm^2 Area - 5X 7075 CRA #4, 1 cm^2 Area - 5X

FIGURE 5. Pit density effects for different rinse agents (cleaned coupons)

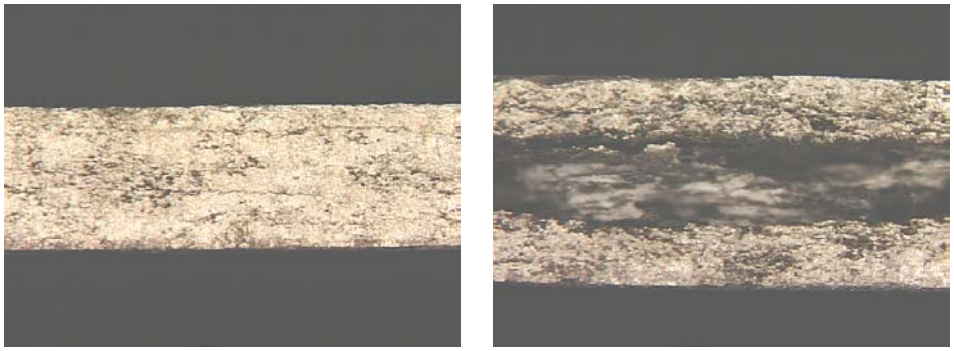

7075 Edge View, CRA #1 - 10X 7075 Edge View, CRA #4 - 10X

FIGURE 6. Intergranular corrosion effects for different rinse agents

PITTING ANALYSIS

Table 5 shows the results of rating the coupons using the ASTM G-46 standard chart as a guideline. The pitting density ratings of <2500 (A-0), 2500 (A-1), 10,000 (A-2), 50,000 (A-3), 100,000 (A-4), and 500,000 pits/m^2 (A-5), per ASTM G-46 are included. Pit ratings B and C are shown, each with five levels, 1 through 5:

- Pit area average of 0.0 (0), 0.0 - 0.5 (B-1), 0.5 - 2.0 (B-2), 2.0 - 8.0 (B-3), 8.0 - 12.5 (B-4), and 12.5 - 24.5 mm^2 and greater (B-5)
- Pit depth average of 0.0 (0), 0.0 - 0.4 (C-1), 0.4 - 0.8 (C-2), 0.8 - 1.6 (C-3), 1.6 - 3.2 (C-4), and 3.2 - 6.4 mm and greater (C-5).

TABLE 5.
Analysis of coupons with significant pitting

7075 Rinse	ASTM rating	Area mm^2	ASTM rating	Depth mm	ASTM rating
CRA #1	A-3	0.0038	B-1	0.018	C-1
CRA #2	A-3	0.0079	B-1	0.036	C-1
CRA #3	A-4	0.0038	B-1	0.024	C-1
CRA #4	A-5	0.0064	B-1	0.052	C-1
DM H_2O	A-3	0.0020	B-1	0.032	C-1
Exposure	A-3	0.0113	B-1	0.044	C-1
Seawater	A-4	0.0133	B-1	0.034	C-1

Mg(AZ31B) Rinse	ASTM rating	Area mm^2	ASTM rating	Depth mm	ASTM rating
CRA #1	A-3	0.0707	B-1	0.092	C-1
CRA #2	A-4	0.2552	B-1	0.184	C-1
CRA #3	A-4	0.3318	B-1	0.125	C-1
CRA #4	A-4	0.1963	B-1	0.042	C-1
DM H_2O	A-4	0.1590	B-1	0.124	C-1
Exposure	A-4	0.2827	B-1	0.128	C-1
Seawater	A-3	0.5281	B-2	0.098	C-1

2024/8625 Rinse	ASTM rating	Area mm^2	ASTM rating	Depth mm	ASTM rating
CRA #1	A-0	0.0000	0	0.000	0
CRA #2	A-2	0.0020	B-1	0.004	C-1
CRA #3	A-2	0.0079	B-1	0.040	C-1
CRA #4	A-1	0.0095	B-1	0.022	C-1
DM H_2O	A-0	0.0000	0	0.000	0
Exposure	A-0	0.0000	0	0.000	0
Seawater	A-1	0.0028	B-1	0.020	C-1

2024/5541 Rinse	ASTM rating	Area mm^2	ASTM rating	Depth mm	ASTM rating
CRA #1	A-2	0.0133	B-1	0.046	C-1
CRA #2	A-2	0.0095	B-1	0.030	C-1
CRA #3	A-2	0.0314	B-1	0.032	C-1
CRA #4	A-3	0.0380	B-1	0.050	C-1
DM H_2O	A-0	0.0000	0	0.000	0
Exposure	A-0	0.0000	0	0.000	0
Seawater	A-1	0.0452	B-1	0.046	C-1

DISCUSSION

As can be seen from the data, variations of corrosion performance were documented for the different rinse agents on different alloy/coating combinations. No single rinse agent consistently displayed beneficial effects on all metals; conversely, some displayed detrimental effects such as intergranular corrosion on some aircraft alloys when compared to the demineralized water rinse control. Some of this could be explained due to the low level of attack in the short, one-year exposure period. Some coated specimens were not attacked until recently when the corrosion began through the coating. The corrosion damage was slight on these panels and significant variations in rinse performance were not seen. However, this exposure continues at the KSC Beach Corrosion Site with duplicate panels exposed with the one-year panels. At the end of the two year cycle, it is anticipated that the corrosion damage will be much more significant allowing a more clear cut ranking of CRA rinse performance.

ACKNOWLEDGEMENTS

This project was sponsored by the US Army Aviation and Missile Command Research, Engineering, and Development Center, Aviation Engineering Directorate (AMSAM-RD-AE-S-M), Redstone Arsenal, AL. Wayne Marshall of NASA/KSC Microchemical Analysis Lab performed the chemical analysis of CRAs. Handling, tagging, weighing, rinsing, and many other tasks were done by a Dynacs Corporation team including Ray Springer, Rubie Vinje, Jerry Curran, Jerry Staub, and Phil Read. The Launch Equipment Test Facility group including Dave Early and Richard Sapp, fabricated stands for coupon exposure.

REFERENCES

1. Army Black hawk helicopter being refueled by 101st Airborne Division, February, 1991, http://www.army.mil/cmh-pg/photos/gulf_war/146-03.jpg, (August 2001).

2. S. Coburn, Atmospheric Corrosion, in Metals Handbook, 9th ed, Vol. 1, Properties and Selection, Carbon Steels, American Society for Metals, Metals Park, Ohio, (1978): p.720

3. J.D. Morrison, Report on the Relative Corrosivity of Atmospheres at Various Distances from the Seacoast, NASA-Kennedy Space Center Report MTB 099-74.

4. Standard Practice for Conduction of Atmospheric Corrosion Tests on Metals, ASTM G-50-76 (97).

EFFECTS OF TESTING TANK GEOMETRY AND MATERIAL ON ICCP SYSTEM DESIGN

S. A. Wimmer[1], V. G. DeGiorgi[2], E. Hogan[3], K. E. Lucas[4]

[1]Nova Research, Inc., Alexandria, VA

[2]Multifunctional Materials Branch, Naval Research Laboratory, Washington, DC

[3]Material Science and Technology Division, Naval Research Laboratory, Washington, DC

[4]Center for Corrosion Science and Engineering, Naval Research Laboratory, Washington, DC

ABSTRACT

Shipboard impressed current cathodic protection (ICCP) systems have been successfully modeled using a boundary element method approach. This computational approach is well suited for handling a large volume of electrolyte and for handling the LaPlace equation, the governing differential equation for electrochemical corrosion. Computational methods also have the advantage of being able to predict the performance of a large number of configurations and conditions in a relatively short period of time.

Past work has shown the accuracy of computational results by direct comparison with experimental results previously validated by comparison with real ship data. The computational models used were designed to represent a ship in the open sea; however, the experimental work is performed in a tank. Distance between the ship model and tank boundaries, tank geometry and wall materials will have an influence on experimental results.

This paper focuses on determining the effect of the tank's geometry and material. Various testing tank geometries and material conditions are modeled. The polarization curve for the walls of the testing tank is approximated as insulated and painted steel. The facility at NRL Key West is modeled, as well as other combinations of tank geometry and material. Some combinations were created to determine the effects of variations and do not represent actual tanks. Accuracy, modeling assumptions and limitations of the computational approach are discussed.

INTRODUCTION

The performance of ICCP systems is a complex response to a variety of factors, including, but not limited to, geometry, conductivity of the surrounding medium, material polarization response and material interactions. The ability to predict performance under a variety of changing conditions is becoming increasingly important in this era of time and cost consciousness. The use of computational methods has become an accepted practice in many fields of study to supplement experiments. The use of computational methods for corrosion problems, boundary elements (BE) in particular, is well documentd.[1,2,3,4]

Increasingly, computational modeling is being done in tandem with physical scale modeling (PSM). The concept of an unified approach between computational modeling and PSM is highly desired. The unified approach uses validated computational tools to examine hull geometry, boundary conditions and other experimental parameters to determine a refined set of PSM experiments that should be completed to design the ICCP system for the hull. Traditionally, many PSM experiments have to be conducted to determine the proper ICCP system under a wide variety of operational conditions. These experiments can be costly and time consuming depending upon the number of conditions studied. Computational simulations in tandem with PSM can reduce the overall cost and time needed to design an optimum and versatile ICCP system.

To help better define a set of PSM experiments, the PSM environment must be understood. This paper looks at how test tank geometries and materials could affect measured and computed results. Computational simulations are performed to model different tank sizes and to model painted versus perfectly insulated testing tanks. Two different experimental set ups are modeled: a dipole and a ship model. Both physical experiments were conducted at NRL's

Key West facility. Computational results are presented along with some measured results. It is not the purpose of this work presented here to predict actual system performance, rather the purpose of this work is to examine variations that are a direct result of the tank testing environment.

The computational models presented in this paper were created in or imported into MSC PATRAN.[5] The geometry was then translated via a custom program to create input files for the two BE commercial codes used in this paper; BEASY-CP[6] and FN Remus Detailed Modeler (FNR or FNREMUS).[7] The results from both commercial codes are post-processed using another custom program that extracts and translates pertinent data, which is then plotted using Tecplot.[8]

DIPOLE

A simple electric field test was performed to create a dipole. The source and sink poles were spaced 250 cm apart at a depth of 82.398 cm in a cylindrical tank of 10 m diameter and filled with 264.16 cm of scaled conductivity water. Use of scaled conductivity seawater is a standard procedure in PSM testing. The cylindrical tank is made of galvanized steel and has a 30 mil neoprene liner. Natural sea water (18.5 ohm-cm resistivity) was scaled, by adding fresh water, to obtain a resistivity of 740 ohm-cm (1/40 scale). The dipole had a strength of 4.69 mA. An electric field sensor was passed under the dipole centerline at a depth of 47.5 cm. The sensor has four half cells as seen in Figure 1. The sensor provided two curves of differential potential values, which are referred to as the vertical (z-direction) and longitudinal (x-direction) potentials. Figure 2 shows the measured potentials at depth for three sensor sweeps under the dipole centerline.

A BE model of this experiment was created using the same dimensions as the experiment and is show in Figure 3b.The dipole source and sink points were modeled as 1 cm cubes. The

cubes and the tank were meshed using nine-noded quadratic quadrilateral elements. To model the neoprene liner, the walls of the tank were assumed to be perfect electrochemical insulators and given a zero current flux boundary condition. The water surface was modeled as a symmetry boundary. Internal node points were positioned along the sensor's path for each of the half cells. The values from the half cells were then differenced to calculate differential potentials at depth.

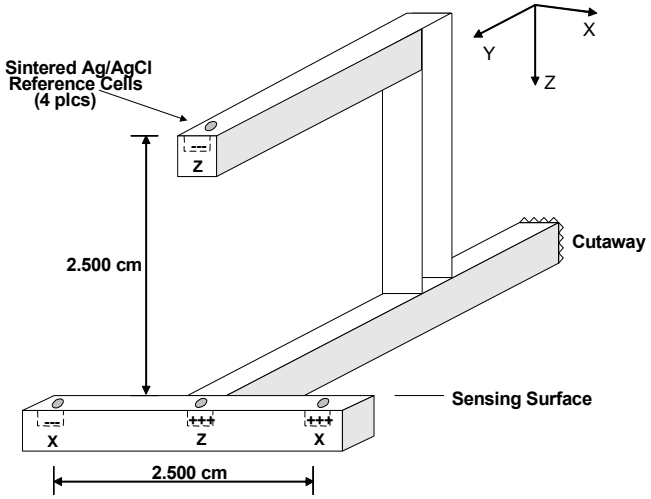

FIGURE 1. Electric field sensor

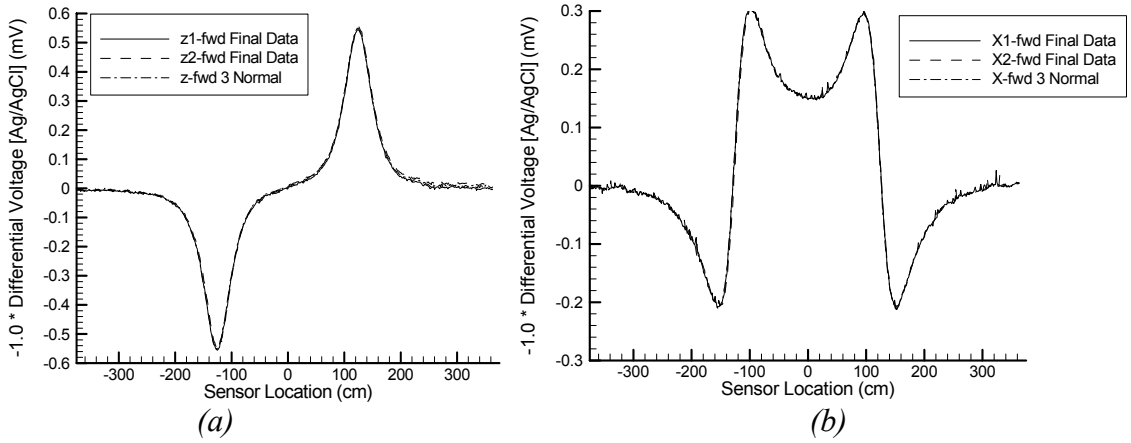

FIGURE 2. Experimental measurements: (a) vertical and (b) longitudinal.

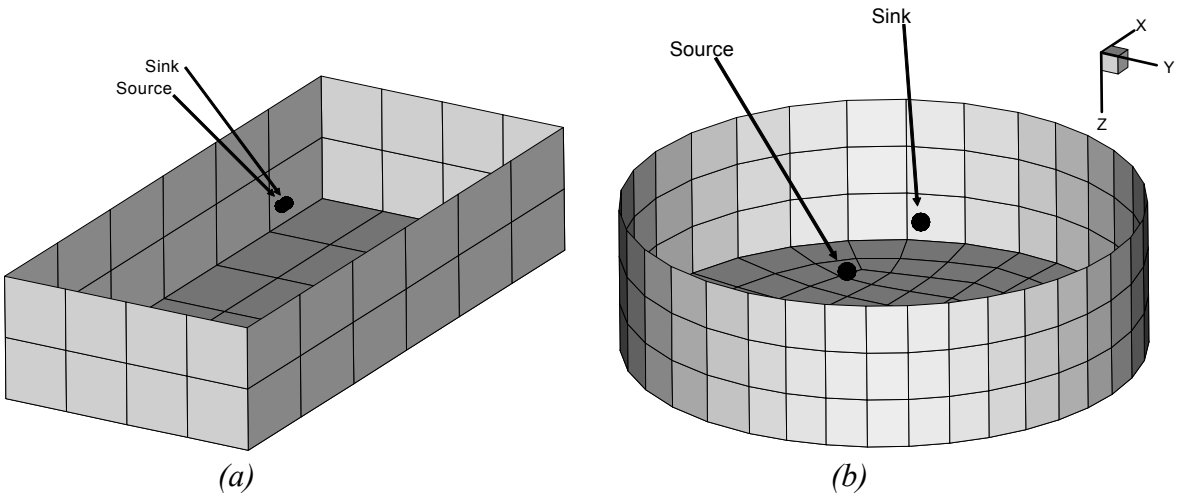

FIGURE 3. Computational boundary element meshes for the dipole model using (a) the far field boundary or (b) the cylindrical tank.

This model was used in two commercial BE programs: BEASY-CP and FNREMUS. The dipole strength was divided by the surface area of the cube to determine the proper normal current flux boundary condition (±0.78167 mA/cm) for the BE solver BEASY-CP. For the FNREMUS program, the dipole strength was divided by the number of elements in the cube to determine the proper element current flux boundary condition (±0.1954 mA). A comparison of the measured to the computed differential potential at depth is seen in Figure 4. The BEASY-CP simulation under predicts the vertical and longitudinal potentials, while the FNREMUS simulation over predicts the vertical and under predicts the longitudinal potentials. The reason for the discrepancy in computational solutions is not clear and requires further study. The differences between measured and calculated results could have multiple causes. Possible sources of variations are the sensor being tilted while taking measurements or numerical approximations. Since the focus of this paper is the differences due to tank material and geometry, the computational discrepancies and the differences between measured and calculated results will be reported in a future article.

A second boundary mesh (Figure 3a) was created in order to examine the effects of a nearly infinite domain. The mesh is a 1/40 scale version of a computational far field boundary condition commonly used by the authors when modeling ICCP systems on ships. Figure 5 compares the results obtained using this far field boundary to the results obtained using the experimental cylindrical tank. Results from both BE codes are shown. The far field boundary produces differential potentials that are slightly lower than the cylindrical tanks for both BE codes. This implies that even though the boundaries are perfect insulators, the size of electrolytic space is important.

Another result of interest is the potential distribution along the tank and far field boundary. Figure 6 shows representative contour plots for the dipole and tanks modeled. While the contour pattern is the same for BEASY-CP and FNREMUS, the values are slightly larger for the FNREMUS solution. The far field boundary shows potential values of small magnitudes, suggesting that it is indeed a far field boundary and the modeled source cannot throw that far.

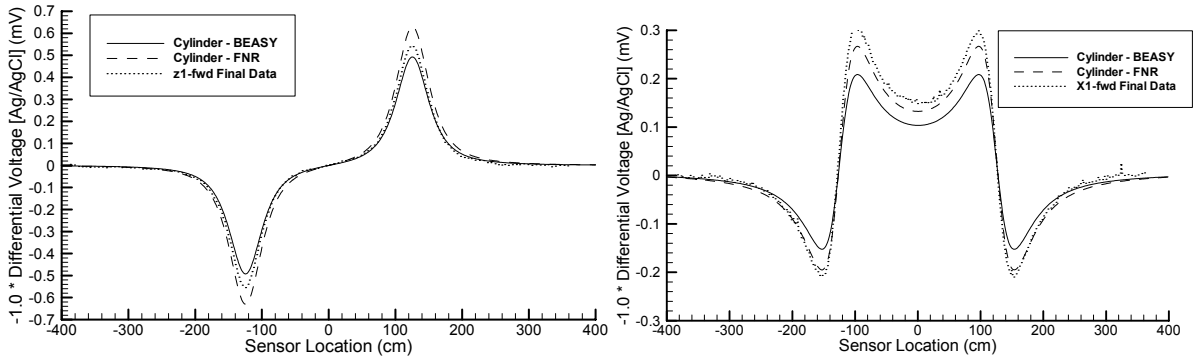

(a) (b)

FIGURE 4. Comparison of BE results using the cylindrical tank boundary to experimental measurements: (a) vertical and (b) longitudinal.

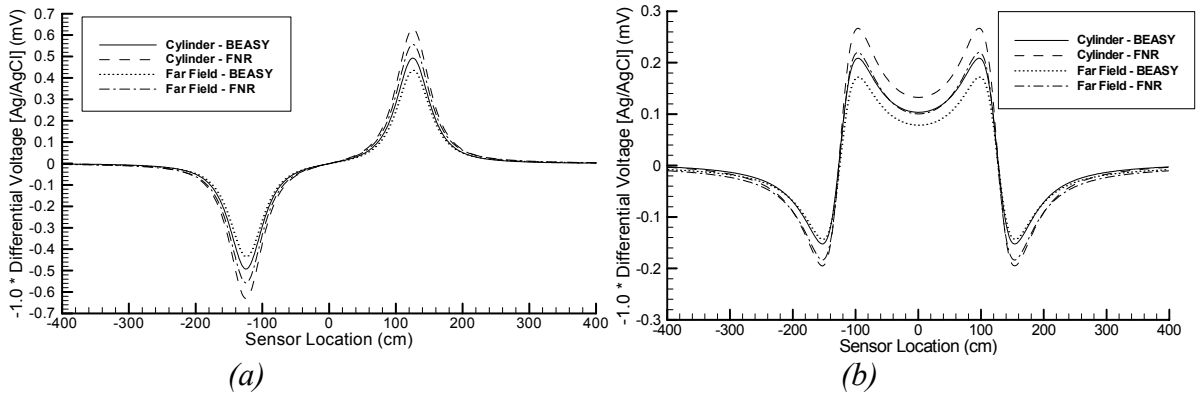

FIGURE 5. Comparison of BEM results for dipole model for both boundaries: (a) vertical and (b) longitudinal.

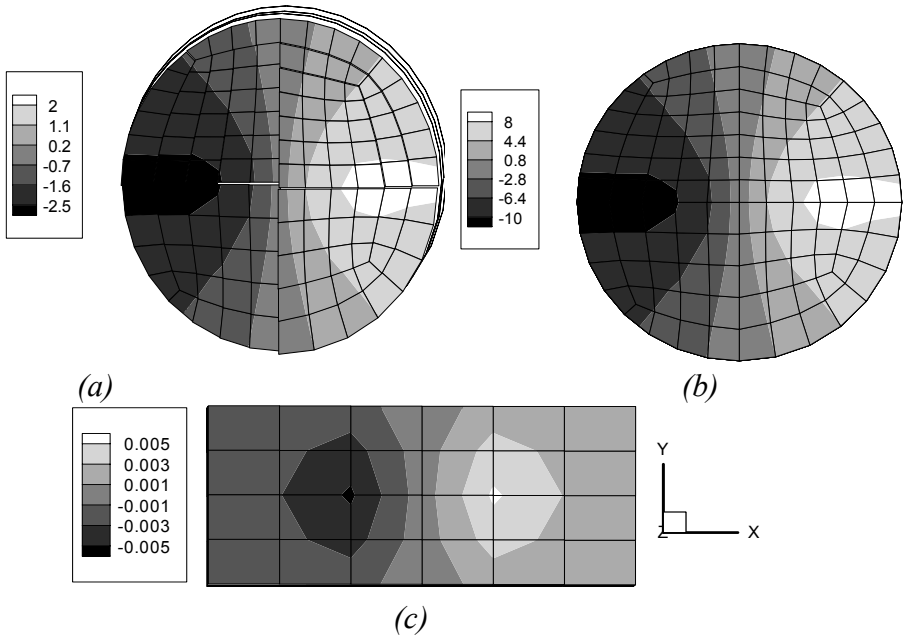

FIGURE 6: Contour plots of potential values on the bottom surface of the boundaries: (a) cylindrical tank solved by BEASY-CP, (b) cylindrical tank solved by FNREMUS and (c) far field boundary solved by BEASY-CP.

If the tank walls are assumed to be painted steel instead of a perfect insulator, the resulting potential changes. Figure 7 shows the differential potentials for the painted steel condition versus perfect insulation. The polarization curve used in these calculations is a 1/1000 scale of the bare steel polarization curve (see reference 9 for more details). These results

demonstrate how great an effect the boundary condition has on the computational solution and how important it is for the experimentalist to account for the boundaries material properties. The assumption of perfect insulation on the surface of the cylindrical tank is the most appropriate boundary condition the authors can use, since the tank at NRL Key West contains a neoprene liner.

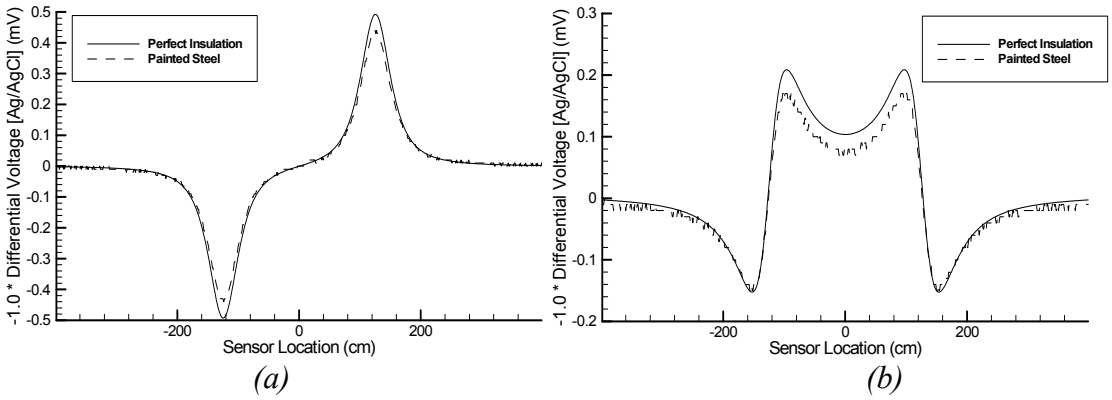

FIGURE 7: Comparison of dipole model results for the cylindrical tank solved by BEASY-CP, assuming the boundary is a perfect electrochemical insulator or is merely painted: (a) vertical and (b) longitudinal.

SHIP

The dipole model discussed above is a simple system. In this section, a more complex system involving a ship within various boundaries is examined. Two different testing tanks were modeled. Instead of scaling the ship and electrolyte properties down to the size of the tank, the geometry of the tank was scaled up. The far field box and the two tanks are shown in Figure 8. The far field box is about 12 x 5 x 5 ship lengths. The cylindrical tank is scaled from its actual testing size to real life, resulting in a diameter of about three ship lengths and a depth of about one ship length (3 x 1 ship lengths). The small rectangular tank is about 1.92 x 0.38 x 0.24 ship lengths. The seawater is not scaled (full strength) and has a resistivity of 0.198 ohm-m. A

different viewing scale was used to show each tank in Figure 8, however, the same ship is shown in each tank. To save computational time, the ship and boundary is considered symmetric about the centerline. Symmetry conditions are also applied at the water surface. All simulations of the ship are run using BEASY-CP.

For each simulation, the same ICCP system is used and held at a constant state. The hull and rudder of the ship are comprised of a mixture of painted and bare steel (damaged paint). The propellers are nickel aluminum bronze (NAB). The ICCP system was determined experimentally by Lucas et al.[10] This ICCP system was computationally modelled using the far field boundary by specifying the anode potentials along the hull surface.[9,11] The ICCP state and polarization curves in the previously cited publications are used in this paper. For all simulations shown, the same ICCP system state, hull geometry, hull materials, material spatial location on the hull, and polarization curves were used.

Initially, the tanks are assumed to be perfectly insulated (i.e. no current flux). Figure 9 shows the centerline and three meter profiles for measured and calculated results. The measured results were previously published in[10,11] were determined from experiments performed in the cylindrical tank. The potential results are displayed along the length of the ship denoted by frames. A frame length is the distance between structural frames on the ship. The voltage spikes indicate the high potentials observed at an anode location. Figure 10 shows contour plots of the hull potentials. For each boundary, the ICCP system protects the system adequately. As seen on Figure 9 and Figure 10, the far field boundary and the cylindrical tank yield the same computed solution. However, the small tank has the bow of the ship less protected, that is less cathodic. Unlike the dipole model, the cylindrical tank does not differ from the far field boundary result.

Therefore, the diameter of the tank is adequate to represent an open sea condition for the defined ship.

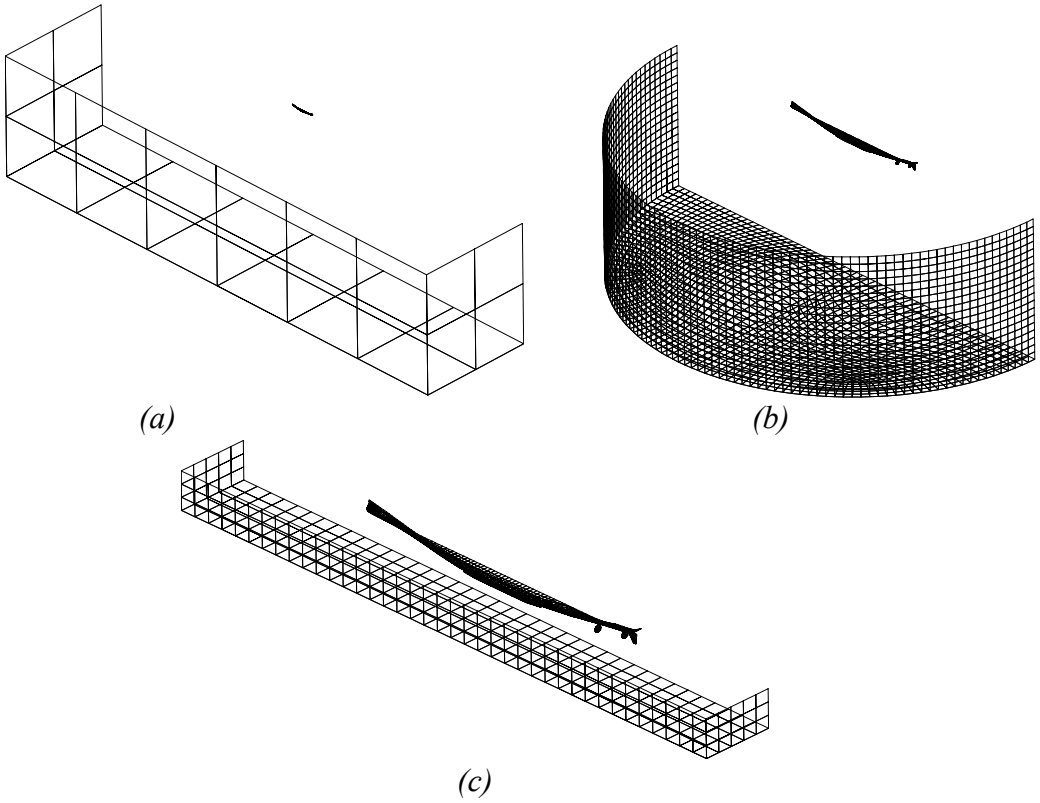

FIGURE 8: Computational boundary element meshes for the ship model using (a) the far field boundary, (b) the cylindrical tank or (c) a small rectangular tank.

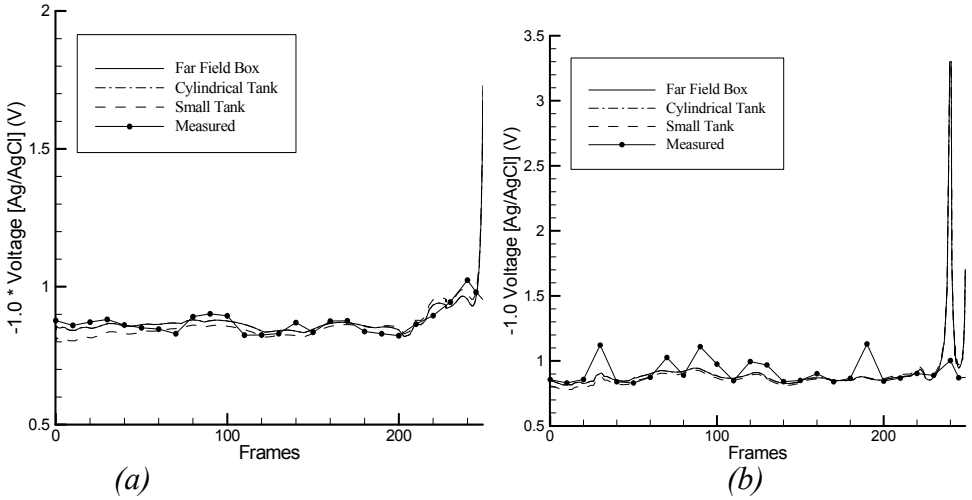

FIGURE 9: Comparison of ship model results: (a) centerline profile and (b) three meter profile.

FIGURE 10: Contour plots of on-board potential values for (a) far field boundary, (b) cylindrical tank and (c) small rectangular tank.

Figure 11 shows the off-board half-cell and differential potentials. Figure 11a is the potentials associated with two strings of internal node points lying below the centerline of the hull. The two strings are about one meter vertically apart. Using these two lines of internal points, the ICCP system contribution to the electronic signature is calculated (Figure 11b). The plots of internal node points and differential potentials show that the size of the tank affects the solution; however, the size of the tank does not greatly affect the ICCP signature contribution.

Since all the tanks wall were defined with a boundary condition of zero current flux, it was expected that the potential values on the tank walls would be a constant value. For the far field and the cylindrical tank the potential values on the wall were indeed a constant value of approximately -0.885 V (±0.001 V). However the small tank does not have a constant potential value (see Figure 12). Instead the walls of the small tank have potential values that range of -0.8 to -1.0 V.

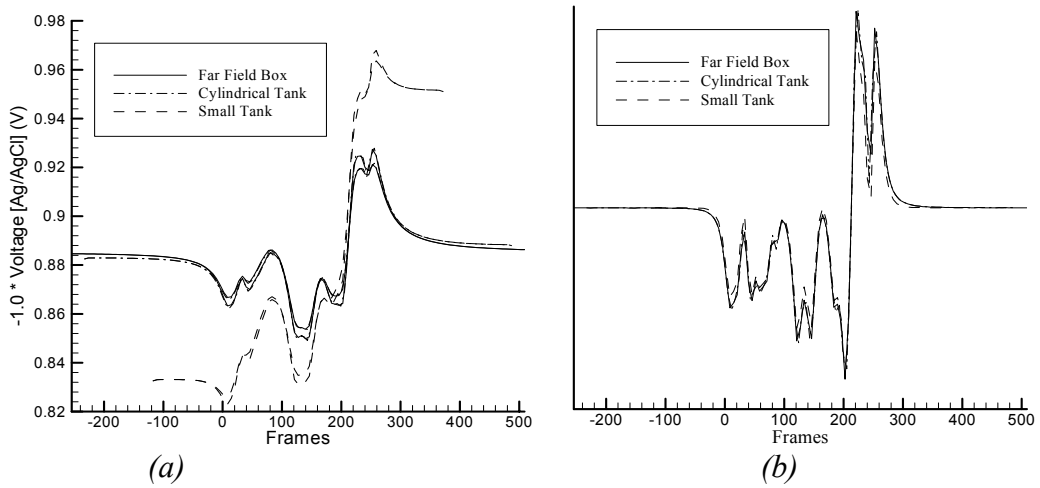

FIGURE 11: Comparison of ship model result: (a) internal node point solution and (b) ICCP signature contribution.

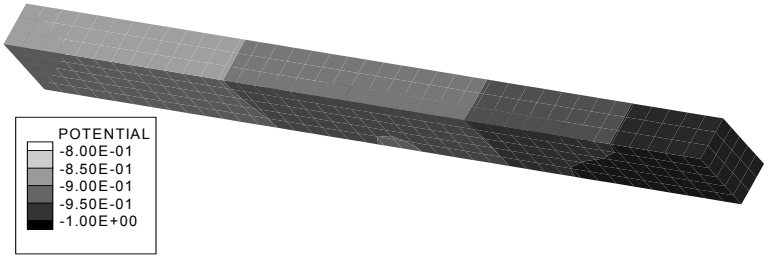

FIGURE 12: Contour plots of potential values on the boundaries for the small rectangular tank.

In reality, many testing tanks may not use insulated liners, but instead use paint to insulate the interior surface. This would inevitably result in a tank wall with some degree of imperfection. Both tank simulations and the far-field simulation were repeated assuming that the walls were painted steel. The paint assumption does not affect the shape of the on-board potential, but it lowers the profiles, as seen in Figure 13. Computationally, the polarization curve was implemented by the author's in BEASY-CP with a lower limit of -0.6 V. Since the ICCP system is held constant, corrosion begins to occur for the far field and cylindrical tanks along most of the hull (Figure 14). Contrarily, the smaller tank shows a less corrosive state, with only the bow and propellers experiencing corrosion.

The assumption of paint on the boundaries greatly affects the potential and the ICCP signature contribution for all tanks. The small tank is the most affected. Figure 15 shows the internal node point potential values and the ICCP signature contribution. The far field and the cylindrical tank have almost the same values, while the small tank has higher internal node point potential values and a different ICCP signature contribution. The resulting ICCP signature contributions for the painted boundaries differ from the ICCP signature contributions for perfectly insulated boundaries. However, the change in the ICCP signature contribution, from perfect insulation to paint, is the smallest for the small tank.

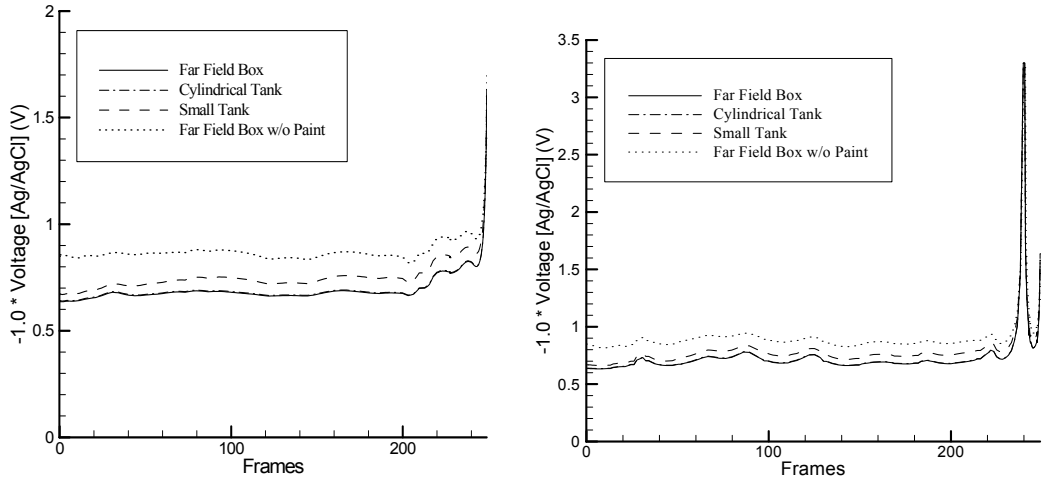

FIGURE 13: Comparison of ship model results, assuming the boundaries are painted: (a) centerline profile and (b) three meter profile.

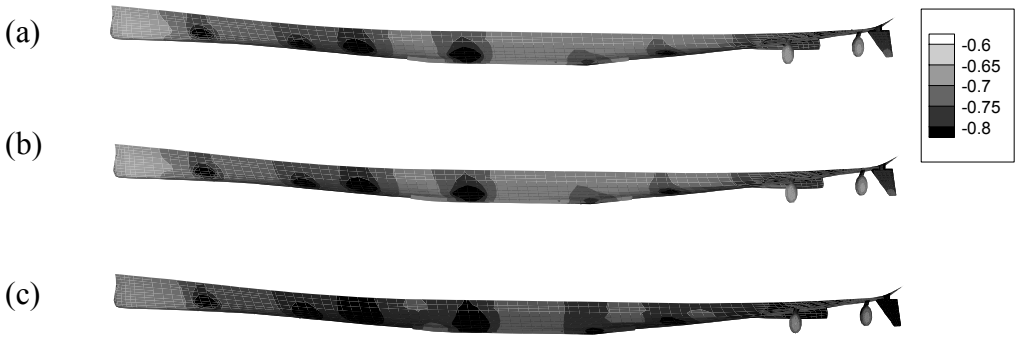

FIGURE 14: Contour plots of on-board potential values, assuming the boundaries are painted, for (a) far field boundary, (b) cylindrical tank and (c) small rectangular tank.

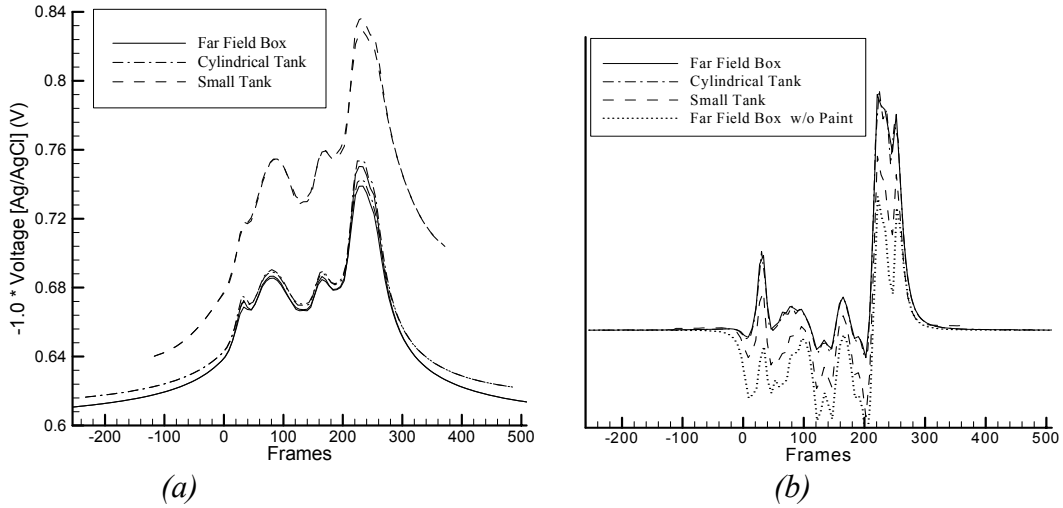

(a) *(b)*

FIGURE 15: Comparison of ship model results, assuming the boundaries are painted: (a) internal node point solution and (b) ICCP signature contribution.

The contour plots of potential values on the boundary and tank surfaces are seen in Figure 16. Not shown is the far field boundary which has a constant contour of -0.65 V and is indeed far enough away to not be affected. The cylindrical tank, when paint is assumed, is just beginning to show slight deviations from the far field solution, as seen by the slightly non-uniform contour plot of potential values on the surface of the cylindrical tank. The small tank, however, show a larger discrepancy from the far field solution and about a 2 V variation in potential values on its tank.

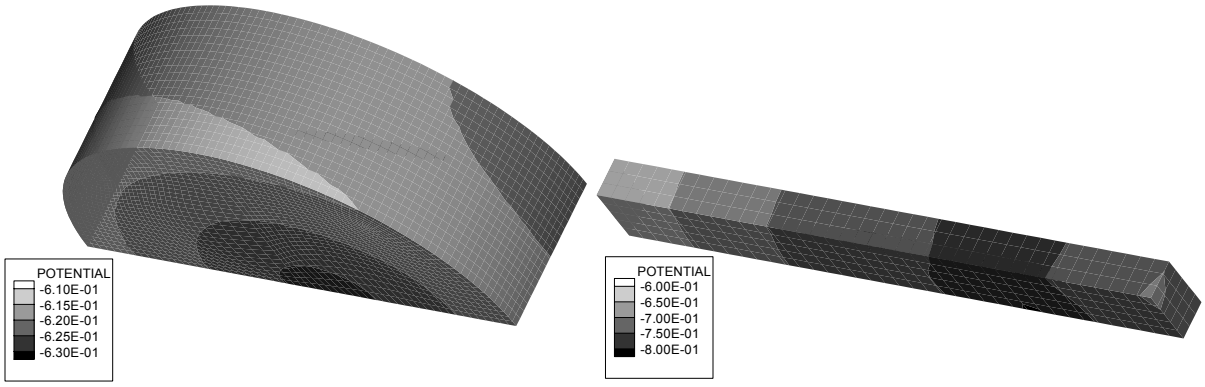

FIGURE 16: Contour plots of potential values on the boundaries, assuming the boundaries are painted, for (a) cylindrical tank and (b) small rectangular tank.

SUMMARY

Previous work has concentrated on determining the accuracy of computational models by detailed comparison with experimental results; primarily with physical scale model results. Experimental results have been used as truth-values in these comparisons. Any differences in results were attributed to limitations in the computational modeling process. However, computational models have been built to represent ships in open sea. PSM is performed in finite volume tanks. As in any experimental process, there are issues with boundary constraints that are a result of the experimental set up. In this paper a systematic study is made of the affects that tank size and material has on predicted results. Two models were used; a simple dipole and a more complex model consisting of a ship with a defined ICCP system. The effects of tank size, geometry and material were examined in terms of at depth potentials, on-board and off-board potentials as well as calculated ICCP signature contributions. Two commercial boundary element codes that deal specifically with electrochemical corrosion were used in the studies. In summary the studies presented indicate that:

Detailed evaluation of parameter studies completed indicates that all results of interest are affected to some degree by tank geometry and tank wall material. The trends observed are important to the understanding of system behavior. The characteristics are equally important for both the experimentalist and computational modeler. The trends determined are important to correctly evaluate measured values, correctly interpret differences in experimental and computational results and to more fully understand the physical performance of simple and complex electrochemical systems.

ACKNOWLEDGMENTS

The support of Dr. Alexis Kaznoff and Mr. E. Dail Thomas, Naval Sea Systems Command, is gratefully acknowledged.

REFERENCES

1. R. A. Adey and S. M. Niku, "Computer Modeling of Corrosion Using the Boundary Element Method," Computer Modeling in Corrosion, ASTM STP 1154, (West Conshohocken, PA: American Society of Testing and Materials, 1992), p. 248.

2. R. S. Munn, "A Review of the Development of Computational Corrosion Analysis for Spatial Modeling Through It's Maturity in the Mid 1980's," Computer Modeling in Corrosion, ASTM STP 1154, (West Conshohocken, PA: American Society of Testing and Materials, 1992), p. 215.

3. P. O. Gartland, et al, "Innovations Developed Through the 1980'ies in Offshore CP Design Computer Modeling and CP Inspection," CORROSION/93, paper 522 (NACE, 1993).

4. V. G. DeGiorgi, "A Review of Computational Analyses of Ship Cathodic Protection Systems," Boundary Elements XIX (Southhampton, UK: Computational Mechanics Pub., 1997), p. 829.

5. MSC PATRAN 2001 User's Manual (Los Angeles, CA: MSC Software Corporation, 2001).

6. BEASY v. 7 User's Manual (Billerica, MA: Computational Mechanics International, 2000).

7. FN Remus Detail Modeler: User Guide (Dorking, Surrey, UK: Frazer-Nash Consultancy Limited, 2000).

8. Tecplot v. 9.0 User's Manual (Bellevue, WA: Amtec Engineering, Inc., 2000).

9. V. G. DeGiorgi, A. Kee, K. E. Lucas, and E. D. Thomas, "Examination of Modeling Assumptions for Impressed Current Cathodic Protection Systems," CORROSION/99, (Houston, TX: NACE, 1999).

10. K. E. Lucas, E. D. Thomas, A. I. Kaznoff, and E. A. Hogan, "Design of Impressed Current Cathodic Protection (ICCP) Systems for U.S. Navy Hulls," 1999, Designing Cathodic Protection Systems for Marine Structures and Vehicles, ASTM STP 1370 (Norfolk, VA: American Society for Testing and Materials, 1998), p. 17.

11. V. G. DeGiorgi and K. E. Lucas, "Computational Design of ICCP Systems: Lessons Learned and Future Directions," 1999, Designing Cathodic Protection Systems for Marine Structures and Vehicles, ASTM STP 1370 (Norfolk, VA: American Society for Testing and Materials, 1998), p. 87.

CORROSION CONTROL COATINGS: POLYMERS

Dual Use Interior Direct-To-Metal/Exterior Chemical Agent Resistant Coating Primer

Anthony Eng, David Fayocavitz, Steven Murray, Forrest Pilgrim, and Lisa Weiser;

Naval Surface Warfare Center, Carderock Division, Code 624, Philadelphia, PA

ABSTRACT

Paint and depaint operations are a costly source of hazardous emissions and waste generation at all levels of military equipment maintenance. Reduction in emissions via individual component improvements and/or optimization of a materials system or process can be extremely advantageous from a regulatory, as well as from a financial perspective. The U.S. Marine Corps is attempting to achieve and realize these types of improvements by identifying and characterizing the properties of commercial off-the-shelf low volatile organic compounds coatings for use in a dual-function role: as an interior direct-to-metal coating and as an exterior chemical agent resistant coating (CARC) primer. Forty-nine candidate coatings were down-selected to nine coatings in the first phase of the effort. In the subsequent phase, an extensive laboratory analysis effort was used to determine the best three candidate coatings to satisfy these dual function requirements. Critical coating properties such as chemical agent resistance, corrosion resistance, adhesion, and abrasion resistance were some of the full battery of tests that were used as a basis to characterize and identify the best coatings. The top performers are currently being evaluated in field demonstrations.

INTRODUCTION

The current organic coating system for military vehicles consists of an epoxy primer and either an epoxy topcoat (interior) or a polyurethane topcoat (exterior). The U.S. Marine Corps (USMC) Systems Command and their logistics bases (i.e., depot maintenance facilities) desire a low/no volatile organic content (VOC) coating that can be used as both a direct-to-metal (DTM) coating for the interior of vehicles and as a primer beneath the chemical agent resistant coating (CARC) topcoat on the exterior of vehicles. By developing and specifying one coating for both purposes, the U. S. Marine Corps expects to reduce VOC emissions, decrease hazardous material

generation, streamline maintenance processing rate, and optimize procurement and inventory requirements. Ultimately, these improvements should also decrease life-cycle costs.

This paper documents a performance evaluation of commercial-off-the-shelf coating systems for use as both a DTM with high visibility characteristics for the interior of USMC vehicles and as a primer underneath CARC topcoats on the exterior of the vehicles. Approved coating systems are to be applied employing currently used application equipment at the USMC logistics bases.

EXPERIMENTAL

An initial group of 49 candidates were generated based on a general solicitation of the paint and coatings industry via review of military/federal paint specification qualified products lists (QPL), paint journals, and internet-search responses. These companies were only allowed to submit technical data (i.e., product literature and material safety data sheets). Then based on a multi-attribute decision analysis method known as the Analytical Hierarchy Process[1] (AHP) and the associated AHP software[2], the top eight candidate coatings plus one control coating (MIL-P-53030) were down-selected from the original group of 49 paints (as shown below):

A. 2 Component, Water-Borne Epoxy (control)

B. 1 Component, Water-Borne Acrylic

C. 2 Component, Solvent-Borne Epoxy

D. 2 Component, Solvent-Borne Epoxy

E. 1 Component, Water-Borne Acrylic

F. 2 Component, Water-Borne Urethane

G. 2 Component, Solvent-Borne Epoxy

H. 2 Component, Water-Borne Epoxy

I. 2 Component, Water-Borne Urethane

The names of the candidate coatings have been omitted from this paper due to proprietary issues.

The standard solvent-borne CARC, MIL-C-46168, and the recently developed water dispersible CARC[3] (MIL-DTL-64159, Type II) were utilized as control topcoats when the candidate coatings were evaluated as primers. These control topcoats are two-component, polyurethane coatings with VOC contents of 420 g/l and 216 g/l, respectively. The MIL-C-46168 was applied at a dry film thickness of approximately 3.5 mils while the MIL-DTL-64159 was applied at about 2.0 mils.

Solvent-borne epoxy MIL-P-53022 and water-borne epoxy MIL-P-53030 are the standard state-of-the-art primers used by both U. S. Army and USMC for both interior and exterior applications for military assets. Solvent-borne epoxy MIL-PRF-22750 is the standard state-of-the-art coating used for interior topcoat applications in both these services. The results of the most rigorous test methods from these three specifications were used to determine performance ratings for this dual-functional coating analysis effort.

The standard substrate used for coated metal coupon characterization tests was a SAE 1010 low carbon steel coupon with approximately 0.5 mil anchor tooth profile. The dimensions of these panels were 4 × 6 × 0.062 inch. The exceptions to this general substrate standard were as follows:

a) Panels for flexibility testing consisted of 4 × 6 × 0.01 inch cold rolled steel (CRS).

b) 5083-H32 aluminum panels (4 × 6 × 0.062 inch with about 0.5 mil profile) were used for the GM 9540 accelerated cyclic corrosion exposure testing. The standard

substrates as well as the test panels in a) and b) of this section were obtained from the Metal Samples Co. of Munford, AL.

c) CRS panels of 4 × 4 × 0.032 inch dimensions were used for the abrasion resistance analysis (Taber Industries, N. Tonawanda, NY).

d) Leneta charts (7 5/8 x 11 3/8 inch) obtained from the Paul N. Gardner Co. (Pompano Beach, FL) were the substrates used to determine contrast ratio and sag resistance of the candidate coatings.

e) Also, free films (6 x 8 inch) were prepared for dynamic mechanical thermal analysis (DMTA) testing by applying the coatings onto Tedlar polyvinyl fluoride release film (DuPont Inc, Buffalo, NY). The free films were separated from the release film three days after application.

All of the metal coupons were wiped with ACS grade acetone prior to paint application. The test specimens were horizontally oriented during paint application. The equipment used to apply the candidate paints to the appropriate substrates described above consisted of a conventional air-atomizing spray gun with a siphon cup (Graco, Inc., Minneapolis, MN) with a 0.070 inch diameter fluid nozzle. In two of the nine candidate coatings; however, the viscosity was significantly high to preclude the use of conventional equipment. In these two cases, products were manually applied by brush. All coatings were applied in cross-coats (i.e., 90^{o} offset between two successive deposition passes) and allowed to cure at ambient temperature (approx. 75^{o}F) and humidity for at least four weeks.

RESULTS AND DISCUSSION

ACCELERATED STORAGE STABILITY

For elevated temperature storage stability water-borne coating systems were evaluated in accordance with military specification MIL-P-53030 (52^{o}C, 14 days) while solvent-borne coating systems were evaluated using military specification MIL-C-22750F (60^{o}C, 7 days). Freeze/thaw storage stability testing of all coating system components was conducted in accordance with MIL-P-53030 that consisted of four 24 hour cycles of 16 at -7^{o}C followed by 8 hours at 24^{o}C. Subsequent to exposure to elevated temperature storage, the base component of water-borne coating system I became stiff and crumbly and exhibited a significant increase in viscosity. There were no abnormalities associated with any of the other paint system components in this test. In all cases, the combined paint components formed a smooth homogeneous mixtures and formed smooth films after draw down bar application. Thus, coating I was given a failing rating while all others were passing as shown in Table 1. Following freeze/thaw testing for both water-borne and solvent-borne coating systems, the single component water-borne coating systems B and E and multi-component water-borne coating I failed this test regimen. The solvent and pigment of Coating B showed significant stratification while Coating E was observed to be a spongy mass; both coatings could not be remixed. The base component of Coating I was found to be very grainy and subsequently, this graininess was maintained in the draw down film application. All of the other coatings passed this test.

SPRAYING PROPERTIES

The qualitative description of the general spray characteristics and film forming properties of the nine candidate coatings were determined based on FTMS #141C, Method 4331.1. Coatings A, F, H, and I were the easiest to spray out into a continuous and defect-free

film. These coatings were given a satisfactory or passing rating as shown in Table 1. Interestingly, these coatings were all water-borne systems. Coatings C and G, which were both solvent-borne, did not atomize nor flow as well as the previous coatings, and, consequently, required more attention and effort to produce a uniform film. However, the fact that they were effectively but not efficiently sprayable and that minor surface effects (i.e., orange peel, textured surface) were produced earned these two coatings a rating of "borderline." Although coating D was sprayable (barely), it was given a failing rating due to its poor atomization and poor leveling which is likely a manifestation of its high viscosity. Also, coating D did not form a continuous film until a dry film thickness (DFT) of 4 mils was attained and at this DFT, a severely orange peeled surface was clearly evident. Due to their extremely high viscosity, coatings B and E were given failing ratings. These coatings were so viscous that the efflux viscosity could not be determined with the Zahn cup with the largest orifice (#5).

RHEOLOGY

Rheological data was collected for each of the nine candidate primers using a stress-controlled rheometer with a stationary double walled stainless steel couette cup and a rotating titanium bob. Steady stress sweep tests that produced viscosity profiles—shear strain rate as a function of viscosity—were performed using each of the candidate coatings. An overlay of the viscosity profiles for each of the coatings is shown in Figure 1. The coatings exhibiting the lowest viscosities at high strain rates should theoretically prove to be the easiest to spray apply, and that was precisely the case. When these coatings were applied in the laboratory, coatings A, F, H, and I were found to be the easiest to spray as indicated by the rheometric plots.

It is also true that the coatings that exhibited a high viscosity at low strain rates should be less prone to sag. In general, the tendency to sag after application was observed to be generally

consistent with that predicted by the flow curves—the highest viscosity materials at low strain rates (coatings B, C, G, D, and E) show good sag resistance (i.e., >8 mils anti-sag index), while some of the lower viscosity materials (coatings A and F) demonstrate lesser sag resistance (i.e., anti-sag index of ~2.5 mils). It is interesting that the two lowest viscosity materials (coatings H and I) show surprisingly good sag resistance (>6 mils anti-sag index) in laboratory observations; however, other factors can be involved, such as rapid solvent evaporation during film formation, rapid coalescing/curing, etc., which could lead to this result.

SOLVENT RESISTANCE

The methyl ethyl ketone (MEK) solvent resistance of the coating systems was evaluated in accordance with ASTM specification D 5402. This test is a relative indicator of cure and cross-linking of thermoset paints[4] . The requirement set forth in MIL-PRF-22750 (i.e., no substrate exposure after 50 passes) was used as the guideline for rating performance. The MEK resistance of the coating systems was exceptionally good for all but two of the coating systems. Coating system B dissolved in MEK during the first 25 double rub cycle and was completely removed down to the substrate after 50 double rubs. Coating E softened and adhered to the cloth; however, was not removed down to the substrate following 100 double rub cycles. This coating was considered satisfactory along with the remaining coatings as shown in Table 1.

OPERATIONAL FLUID RESISTANCE

Military performance standard MIL-PRF-22750, MIL-P-53022, MIL-P-53030, ASTM D1308, and ASTM D714 were used for test criteria and evaluation of the coatings following operational chemical immersion exposure tests. Coating B softened and formed a dense to medium dense blister pattern with size no. 2 blisters on the immersed panel surface exposed in the MIL-L-23699 synthetic lubricating oil resistance test (see Table 1). Coating E softened and

easily peeled away when scratched with a fingernail, although it did not exhibit blistering. These two coatings were obviously unsatisfactory while the remaining coating systems satisfied the specification requirements since none displayed coating defects upon exposure to this operational fluid immersion test. All of the candidate coating systems exposed to immersion in MIL-H-5606 hydraulic fluid displayed no evidence of paint defects. After exposure to the hydrocarbon fluid or JP-8 fuel, all coating systems passed except for coating B which softened and formed a medium dense blister pattern with size no. 6 blisters on the exposed panel surface.

DS2 AND CHEMICAL AGENT RESISTANCE

All of the candidate coatings were tested for decontaminating solution (DS2) resistance via color (2.5 units change maximum) and pencil hardness (2 level change maximum) by colleagues at the U.S. Army Research Laboratory (Aberdeen, MD). DS2 material is specified under MIL-D-50030. The coatings that performed well in the DS2 testing were subsequently tested for chemical agent resistance (i.e., HD blistering agent) utilizing 4 replicates per coating where the maximum amount of desorbed agent allowed was 40 micrograms. Coatings A, D, G, and H passed the DS2 color and hardness screening tests as shown in Table 2. Coating C was considered to possess borderline DS2 performance since this coating displayed a very low color change and the change in hardness was within specification limits at the longer dwell times (24 hr, 7 days). Coatings B, E, F, and I were rated as deficient and not tested for agent resistance. Four replicates were used for the agent resistance test. As displayed in Table 2, all the coatings tested for agent resistance clearly exceeded the minimum requirement per the standard CARC topcoat specifications.

DE-IONIZED WATER IMMERSION RESISTANCE AND TAPE ADHESION

Testing per ASTM D1308 involves exposing an organic coating to a reagent to determine adverse affects. This procedure required immersion exposure of the candidate coatings on the standard test coupon (two replicates) to de-ionized water at room temperature (23°C) for 24 hours, then removing the panels and examining (as per MIL-P-53022 and MIL-P-53030) for any defects, i.e. discoloration, blistering, and loss of adhesion. The tape adhesion test (ASTM D 3359, method B) is used to assess the adhesive strength of a coating by applying and removing tape to a dry film of the test coating. This adhesion test was performed before and after water immersion. The three different types of coating chemistries (i.e., epoxy, acrylic, and urethane) exhibited distinct performance characteristics following water immersion. For water immersion resistance, the epoxies (coatings A, C, D, G and H) generally performed the best compared to the other two resin chemistry types as displayed in Table 1. Epoxies are often used in a marine environment, either partially or completely immersed, as an anticorrosive barrier coating. As expected, they held up well showing little to no negative effects from the exposure. Each coating had only minor edge effect corrosion and no apparent hardness change after the 24-hour exposure. Coatings B and E were given borderline ratings due to apparent loss in hardness. Coatings F and I were given failing ratings due to dense and medium dense blistering, respectively. Although all of the coatings displayed satisfactory (rating $\geq$3) dry tape adhesion as seen in Figure 2, coatings F and I displayed significant decreases in wet tape adhesion performance to the point of being considered failures. This expectedly corresponds to the water resistance performance. Interestingly, coating C had a slight increase in its wet tape adhesion value probably due to the fact that cutting a crosshatch pattern on the dry, non-immersed panels

produced some scribing delamination while those same cuts on the immersed panels were less destructive. This was probably a result of plasticization due to water absorption into the film.

PATTI ADHESION

ASTM D 4541 is used to quantify the adhesive strength of a coating by adhering and subsequently removing a sandblasted and cleaned aluminum pull-stub from the painted test coupon (4 replicates using the standard substrate) in a tensile or normal direction via a pneumatic device. A commercially specified adhesive (Epoxy#**907**, Miller-Stephenson Chemical Co, Inc.) and a U.S. Navy specified epoxy adhesive (NAVSEA DWG 5808332, DTNSRDC-2844-**1102**) were utilized in the evaluation of the candidate coatings as DTMs. Only the Epoxy#907 was used in the evaluation of the candidate coatings as primers. This tensile adhesion test is not currently used in Army or USMC CARC system (primer and topcoat) specifications. It is used in this paper merely as supplemental data. DTM data indicated that most coatings demonstrated good adhesion at the level of the control coating A (~2500 psi) as shown in Figure 3. The exceptions to this statement were coatings B and F, particularly with respect to the 1102 adhesive. The candidate coatings as primers with topcoats, as shown in Figure 4**,** indicated that again coating B and to some degree coating F displayed relatively poor adhesion properties. Although the standard deviation of many of the data sets were fairly high in this study (from 4% to 53 % of the adhesive strength), the general magnitude of the high performance coatings were equivalent to similar military specification coatings types studied in a previous report involving CARC primers.[3]

ABRASION RESISTANCE

Resistance to abrasion was determined using ASTM D4060. A Taber Abraser with resilient calibrase wheels (No. CS-17) and a 1000 gram weight were used in this test. Abrasion

resistance was quantified every 500 cycles up to a total of 1500 cycles. CS-17 wheels were resurfaced every 500 cycles by using an abrasive (S-11) disk. Four replicates were used for each coating system. Coatings for high performance industrial applications typically produce a wear index of less than 50 μg per cycle[5]. Coatings A, C, G, H, and I were the superior performers with average wear indices within this range as displayed in Table 1. Coating D falls just outside of this high performance range with an index of 53 μg per cycle followed by coatings F, E, and B. Even though this is not a test in the standard CARC military specifications, this test is used to more thoroughly quantify the performance of the candidate coatings and to assist in the differentiation between the coatings.

MANDREL BEND TEST

The Mandrel Bend Test was performed on all coatings in accordance with ASTM D 522. The purpose of this test is to rate each coating's resistance to cracking and to determine the total elongation of each coating. This test, performed on the nine candidate coatings, demonstrated that coatings B, E, and F were extremely flexible as shown in Table 3. These 3 coatings when bent over the smallest mandrel diameter (1/8 inch) did not show any signs of cracking and the elongation of these coatings were all greater than 30%. Coatings A and I had small cracks within the paint after being bent over the 1/8 inch mandrel. However, both of these coatings were free of defects at the 0.25-inch mandrel diameter. All of the other coatings failed to satisfy the 0.25-inch requirement in MIL-P-53022 and MIL-P-53030. It is of interest that these coatings, identified as urethanes (F, I) and acrylics (B, E), are generally considered to be relatively flexible. In comparison, epoxy coatings C, D, G, and H do not meet the requirements of the primer specifications. These coatings could be best described as brittle, since cracking was evident quite easily through the entire thickness of coating revealing bare metal. In addition to

performance attributable to general resin classes, the thicknesses of these failed epoxy coatings were generally higher than the others, which can have a detrimental effect on its mandrel bend resistance. It is important to note that coating A satisfies the mandrel bend resistance requirement as stated above, regardless of its epoxy matrix content. Again, a liberal stance would seem wise, since this test produces relative mandrel cracking resistance performance data. Another point to keep in mind is that while this resistance test is common, it does not simulate the typical failure mode of operational assets.

IMPACT RESISTANCE

Impact resistance is a paint property that quantitatively characterizes the durability of a coating with respect to a rapid impact event. This characteristic is thought to be dependent on both adhesion and flexibility[6]. After about five weeks of cure at ambient laboratory conditions, the impact resistance test was performed on the candidate coatings based on ASTM D 2794. There are clearly two groups of coatings. Coatings B, E and F had relatively high impact resistance ($\geq$ 38 in-lb) while all of the other coatings have relatively low and similar values (1 to 4 in-lb) as shown in Table 3. This data also corresponds to the mandrel bend data when two broad regimes ($\geq$ 30% elongation or 1/8 mandrel vs. others) are created. While, in general, it is desirable to have a large impact resistance value, a low value in this test does not necessarily equate to premature failure. As an example, although coating A produced the lowest impact resistance value, it currently conforms to MIL-P-53030 and is currently the standard water-borne primer for all U.S. Army and USMC vehicles. In addition, this coating has not been shown to be deficient from a field durability perspective. Again, this test is used to better understand the breadth of performance properties of the various coatings.

DYNAMIC MECHANICAL THERMAL ANALYSIS (DMTA)

In a dynamic temperature ramp test using DMTA equipment, a sinusoidal stress is imposed and a resulting sinusoidal strain with the same frequency is measured along with the associated phase lag (δ). The energy stored elastically by the sample is quantified via the storage modulus (E')that is also called the elastic modulus. The energy dissipated through heat generation is quantified via the loss modulus (E") that is also known as the viscous modulus. Storage modulus is related to stiffness or solid-like behavior while the loss modulus is related to the damping ability or liquid-like character of a material. The tangent of the phase lag between the in-phase E' and the out-of-phase E" responses is known as tan δ or the loss tangent. The tan δ is mathematically equal to the ratio of E"/E'. The peak in this loss tangent response is commonly used to define the glass transition temperature (T_g)[6-8]. E', E", and tan δ were measured as a function of temperature using the DMTA at a temperature ramp rate of 3^o per minute and a frequency of 1 Hz. Free film specimens of the candidate coatings were produced with a rectangular die of 25.4 mm x 8 mm dimensions. DMTA was performed only on those coatings which had passed chemical agent resistance testing (coatings A, C, D, G, and H).

The glass transition temperature via the peak temperature in the tanδ response corresponds to 77°C (coating C), 78°C (coating H), 81°C (coating G), 83°C (coating D), and 95°C (coating A) as shown in Figure 5. These temperatures are all well above the operating temperatures these coating would normally experience. Assuming the degree of cure is near or at the ultimate level, these comparatively high T_g values would tend to reduce polymer segment mobility and free volume change. This generally tends to promote consistency related to minimization of ion transfer and general permeability properties. In the glassy region of the elastic modulus response (upper plateau on the lower temperature portion of the spectra) in

Figure 6, the coatings exhibited moduli in the 5×10^9 Pa to 8×10^9 Pa range. Coatings C and H entered an earlier transition from the glassy to rubbery state (lower plateau) than did the other coatings; this could result in property changes if the coating were exposed to temperatures greater than 40°C to 50°C (where the transition started for C and H). At about 25°C (in the glassy region), coatings C and D exhibited slightly lower modulus values, and thus greater flexibility, than the other coatings (A, G, and H). At this temperature, the storage modulus of coatings A, G, and H were nearly identical. It is important to note that this data does not correspond to the impact and mandrel bend resistance data. This is probably due to the film thickness dependence of those two resistance tests.

ACCELERATED CORROSION TESTING

Accelerated corrosion testing was performed using both a neutral salt fog test per ASTM B 117 and an accelerated cyclic corrosion test per GM9540P by colleagues at the U.S. Army Research Laboratory. The evaluation of creep via corrosion at the scribe was performed in accordance with ASTM D 1654, while the size and frequency of the blistering away from the scribe was determined by utilizing ASTM D 714. Five test coupons per candidate coating were used for each of the corrosion tests. Table 4 shows the corrosion responses for the maximum duration in each test along with intermediate data for only the steel substrates in B 117 and GM9540P.

The analysis of the panels exposed in the B 117 for 168 hours indicated that, on average, the rating number was no less than 7, meaning that less than 2 mm of creep was observed at the scribe. The only exception was coating B, which had slightly higher amount of creep with a rating of approximately 5. The amount of creep could not be measured on coating E panels due to the large amount of blisters at the scribe area. As a result, these panels were removed from

further testing. Coatings C, D, and G were performing the best at this point in the test since they inexperienced no blisters. At 336 hours, coatings A, B, F, H, and I were removed from the salt fog test due to the amount of creep at the scribe and a blistering rating number of 4. At the final inspection at 2,748 hours, coating G performed the best, with the least amount of creep from the scribe and no blisters. Coatings D and C trailed in both creep and blister formation. It is important to note that the current corrosion resistance test requirement (per MIL-P-53022 and MIL-P-53030) allows for trace rusting and five scattered blisters (1 mm diameter) on an un-scribed test substrate in 336 hours of ASTM B 117 exposure. Also, it should be noted that the current test substrates were abrasively profiled without subsequent inorganic pretreatment (to more closely simulate the harshest field procedures).

For the GM9540P test, five coatings (B, E, F, H, I) on steel were removed from the chamber prior to the 43 cycle interval due to excessive corrosion and/or defects. As shown by the blister rating in Table 4, the area away from the scribe was being adequately protected after 43 cycles for coatings A, C, D, and G. From an absolute magnitude perspective, the scribe ratings for these coatings are fairly low. However, again it should be noted that no conversion treatment was used to prepare and assist in the corrosion control of these substrates prior to the organic coating application. Although the creep ratings are low, they appear to be relatively uniform between the coating replicates with apparent rating performance differentiation between the candidate coatings. After 125 cycles, no blisters were observed on any of the three remaining candidate coatings, as indicated by the ASTM rating of 10. However, coating A experienced the least creep from the scribe followed by coatings C and D.

The coatings applied to the aluminum panels performed very well with regard to resistance to creep and blistering in the GM9540P exposure chamber. The good corrosion

resistance data for aluminum versus the relatively poor response on steel were not surprising since 5000 series Al is generally more resistant to corrosion than low carbon steel. Only coating F samples on Al were removed after 56 cycles due to the frequency (medium-dense to dense) and size (rating#8) of the blisters. After 125 cycles, coatings G, D, C, and A performed the best, with no blistering and relatively minor creep at the scribe (see Table 4).

ANALYTICAL HIERARCHY PROCESS

The Analytic Hierarchy Process[1] (AHP) is a multi-attribute decision analysis method that allows one to set priorities and make logical decisions when both qualitative and quantitative aspects of a decision need to be considered. Designed to reflect the way people actually think, AHP was developed more than 20 years ago by Dr. Thomas Saaty, while a professor at the Wharton School of Business, and continues to be extensively reviewed and applied in the literature. AHP involves breaking down complex decisions into smaller parts, proceeding from the *goal* to *criteria* to *subcriteria*, down to the *alternative* courses of action. Simple pairwise (or one-to-one) comparison *judgments* throughout the hierarchy are used to arrive at overall *priorities* for the alternatives. A relatively intuitive and user-friendly software package[2] allows for the development of AHP models with user defined importance weightings. Using this model, the final rankings for the 9 candidate coatings were determined as provided in Table 5. An obvious separation in performance via the AHP model occurs between the 5th (coating H) and the 6th (coating E) ranked coatings that corresponds to AHP scores of 0.800 and 0.352, respectively. All of the epoxy coatings (both water-borne and solvent-borne) reside above this performance chasm while the acrylic and urethane coatings remain below. The spread between the two groups of coatings while, being indicative of all of the test discussed in this report, were highly influenced by the DS2 and chemical agent resistance test which had a composite global

weighting of 0.556 which was approximately 5 times larger than any other major criteria. Nonetheless, the AHP rankings generally correlate well to a comparison of all the raw tabulated and graphical data compared in the traditional time-tested, although unsophisticated, method of combining all data into one large and all inclusive table (or spreadsheet) and slowly whittling away the deficient contenders.

SUMMARY/CONCLUSIONS

Nine candidate commercial off-the-shelf coatings were thoroughly tested in the laboratory and analyzed for paint performance using MIL-P-53030 and MIL-PRF-22750 as guidelines. These specifications and the commercial materials qualified to each of these specifications are currently in use in the USMC as interior/exterior primers and as interior topcoats, respectively. The candidate coatings were tested per a composite of the most rigorous of the methods and requirements in the above specifications. In addition, coating material performance analysis was supplemented by evaluations utilizing viscosity profile, glass transition and modulus (via DMTA), tensile adhesion, GM9540P accelerated corrosion exposure, abrasion resistance, DS2 resistance, and chemical agent resistance. Finally, the AHP methodology was effectively utilized in the final coating performance analysis phase of this effort. In the final evaluation of the candidate coatings as an exterior primer/interior DTM, the AHP model indicated relative rankings of coatings A, G and C coatings as the first, second, and third best coatings. As a confirmation of the validity of the AHP, the traditional, time-tested, and labor intensive manual collation of tabular and graphical data was also performed. Removal of the deficient candidates produced a group of 5 contending coatings (A, C, D, G, and H) without hierarchy. Engineering judgment further reduced this group of top performers to 3 coatings (A,

C, and G), again without definitive individual hierarchy. The performance of these three coatings clearly indicates superior performance and thus warrants appropriate field level application demonstrations on operational vehicles and ground support equipment. Associated field demonstration evaluation reports and specification development and implementation will also be forthcoming to facilitate the transition of these materials.

REFERENCES

1. T.L. Saaty, *The Analytical Hierarchy Process: Planning, Priority Setting, Resource Allocation, McGraw-Hill*, New York, NY, 1980.

2. Expert Choice (Version 2000), Decision Support Software, Inc., Pittsburgh, PA, 1993.

3. R.W. Katz, "Low Volatile Organic Compounds (VOC) Chemical Agent Resistant Coating (CARC)," Final Technical Report, SERDP Project # PP1056, U.S. Army Armament Research, Development, and Engineering Center, April 2000.

4. G. Chu and F.N. Jones, "Low-Temperature Curing Higher-Solids Polyester Coatings with Melamine Formaldehyde Resin Crosslinkers," *Journal Of Coatings Technology*, Vol. 65, No. 819, April 1993.

5. S. Mokashi, "Creating Performance Specifications for Coating and Lining Concrete," *Journal Of Protective Coatings and Linings*, Vol. 16, No. 12, December 1999.

6. L. Hill, "Mechanical Properties of Coatings," Federation Series on Coatings Technology, Federation of Societies for Coatings Technology, Blue Bell, PA, April 1987.

7. R.B. Prime, "Thermosets," Chapter 6, Thermal Characterization of Polymeric Materials, 2nd Ed., Vol. 2, E.A. Turi (Ed.), Academic Press, Inc., SanDiego, CA, 1981.

8. R.P. Chartoff, P.T. Weissman, and A. Sircar, "The Application of Dynamic Mechanical Methods to T_g Determination in Polymers: An Overview," *Assignment of the Glass Transition*, *ASTM STP 1249*, R.J. Seyler (Ed.), American Society for Testing and Materials, Philadelphia, PA, 1994, pp 88-107.

TABLES AND FIGURES

TABLE 1.
Miscellaneous Paint Tests

Test Performed	Ctg A	Ctg B	Ctg C	Ctg D	Ctg E	Ctg F	Ctg G	Ctg H	Ctg I
Elevated Temp Storage Stability	Pass	Pass	Pass	Pass	Pass	Pass	Pass	Pass	Fail
Freeze/Thaw Storage Stability	Pass	Fail	Pass	Pass	Fail	Pass	Pass	Pass	Fail
Spray Properties	Pass	Fail	Borderline	Fail	Fail	Pass	Borderline	Pass	Pass
Solvent Resistance	Pass	Fail	Pass	Pass	Pass	Pass	Pass	Pass	Pass
Lube Oil Resistance	Pass	Fail	Pass	Pass	Fail	Pass	Pass	Pass	Pass
Hydraulic Fluid Resistance	Pass	Pass	Pass	Pass	Pass	Pass	Pass	Pass	Pass
Hydrocarbon Fluid Resistance	Pass	Fail	Pass	Pass	Pass	Pass	Pass	Pass	Pass
Water Resistance	Pass	Borderline	Pass	Pass	Borderline	Fail	Pass	Pass	Fail
Abrasion Resistance (average wear index, μg/cycle)	45	132	47	53	123	62	42	39	23

TABLE 2.
DS2 and Chemical Agent Resistance

Ctg	***DS2 Pencil Hardness***						**DS2 Exposure**	***Agent Resistance***
	2 hr		*24 hr*		*7 day*			
	No DS2	*DS2*	*No DS2*	*DS2*	*No DS2*	*DS2*	*NBS Color Change*	*HD (micrograms)*
A	6H	4H	6H	5H	6H	5H	0.8584	0
B	2H	HB	3H	2H	2H	2B	0.3475	NA
C	6H	3H	5H	4H	5H	3H	0.3770	22
D	6H	4H	5H	4H	5H	4H	1.5797	15
E	4H	F	3H	F	2H	HB	1.4128	NA
F	HB	3B	HB	5B	2B	6B	4.5374	NA
G	4H	3H	6H	4H	6H	4H	0.2882	15
H	4H	2H	4H	2H	4H	2H	0.8708	15
I	4H	H	5H	4H	4H	3H	0.5931	NA

TABLE 3.
Mandrel Bend and Impact Resistance

	Impact Resistance	**Mandrel Bend**			
Coating	*Impact Resistance (in-lb)*	*General Ranking*	*Dry Film Thickness (mils)*	*Resistance to Cracking (Mandrel Diameter, in)*	*Total Elongation (%)*
A	1	Pass	1.17	1/4	14.8
B	$\geq$ 60	Pass	2.67	1/8	>31.8
C	4	Fail	7.67	1	4.9
D	3	Fail	4.17	3/4	5.5
E	55	Pass	3.17	1/8	>32.4
F	38	Pass	1.50	1/8	>30.1
G	4	Fail	11.50	1	5.7
H	4	Fail	3.5	3/8	10.8
I	4	Pass	3.67	1/4	16.6

TABLE 4.
Corrosion Resistance

Coating System		A	B	C	D	E	F	G	H	I
		B117 – Steel Substrate								
168 hrs	*Creep*	7.3	5.7	7.3	7.5	IMM	7.0	7.3	7.7	7.0
	Blister	8.0	7.4	10.0	10.0	4.8	7.0	10.0	9.2	6.6
2748 hrs	*Creep*	*	*	2.3	3.5	*	*	4.0	*	*
	Blister	*	*	5.6	6.5	*	*	10.0	*	*
		GM9540P – Steel Substrate								
43 cycles	*Creep*	4.4	*	3.4	4.2	*	*	2.0	*	*
	Blister	10.0	*	10.0	10.0	*	*	10.0	*	*
125 cycles	*Creep*	2.8	*	2.0	1.8	*	*	*	*	*
	Blister	10.0	*	10.0	10.0	*	*	*	*	*
		GM9540P – Aluminum Substrate								
125 cycles	*Creep*	8.0	6.8	8.4	8.8	7.2	*	9.0	7.8	4.6
	Blister	10.0	8.0	10.0	10.0	9.0	*	10.0	8.0	7.6

* Sample removed before test duration; IMM = immeasurable

TABLE 5.
AHP Rankings Of Candidate Coatings

Designator	*Classification*	*AHP Score*
A	Water-Borne Epoxy	0.868
G	Solvent-Borne Epoxy	0.839
C	Solvent-Borne Epoxy	0.833
D	Solvent-Borne Epoxy	0.806
H	Water-Borne Epoxy	0.800
E	Water-Borne Acrylic	0.352
B	Water-Borne Acrylic	0.323
I	Water-Borne Urethane	0.294
F	Water-Borne Urethane	0.294

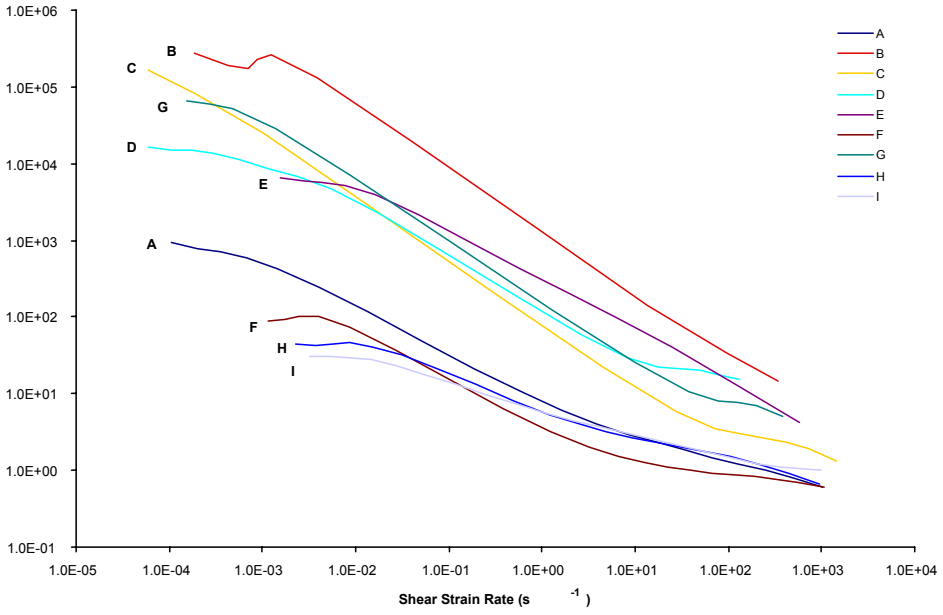

FIGURE 1: Viscositv Profile

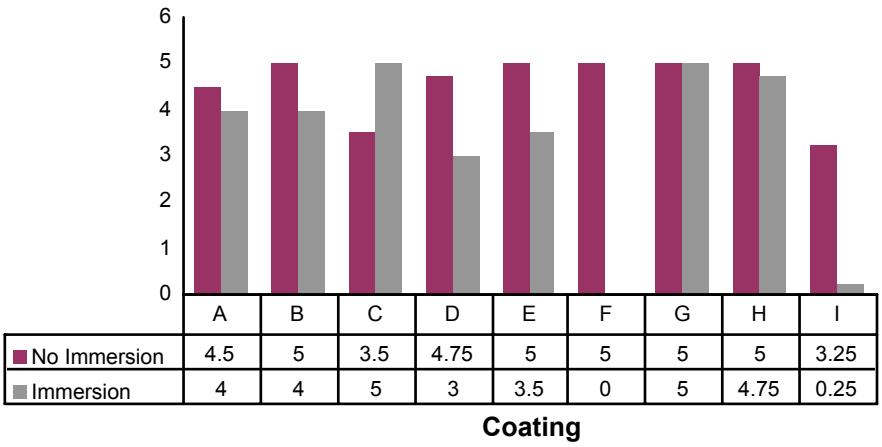

FIGURE 2: Tape Adhesion

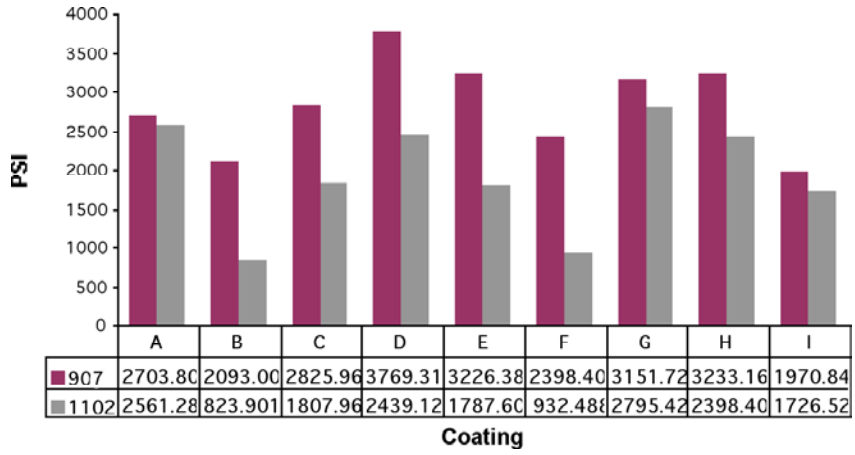

FIGURE 3. PATTI Adhesion, DTM Coating Only

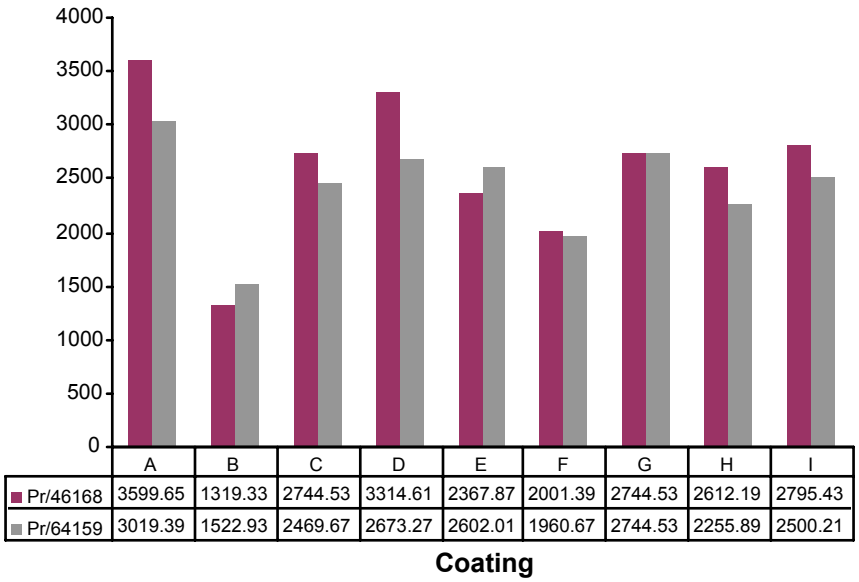

	A	B	C	D	E	F	G	H	I
Pr/46168	3599.65	1319.33	2744.53	3314.61	2367.87	2001.39	2744.53	2612.19	2795.43
Pr/64159	3019.39	1522.93	2469.67	2673.27	2602.01	1960.67	2744.53	2255.89	2500.21

FIGURE 4. PATTI Adhesion, Primer + Topcoat

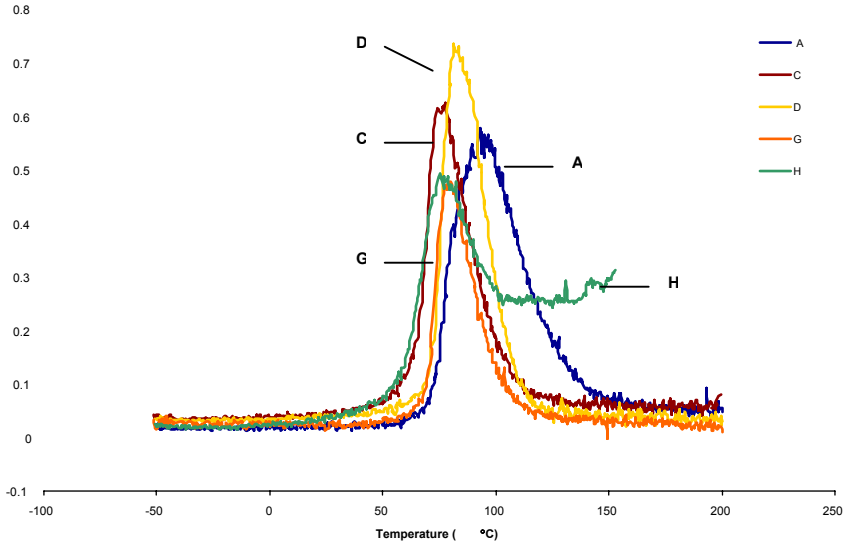

FIGURE 5: Tanδ as a Function of Temperature

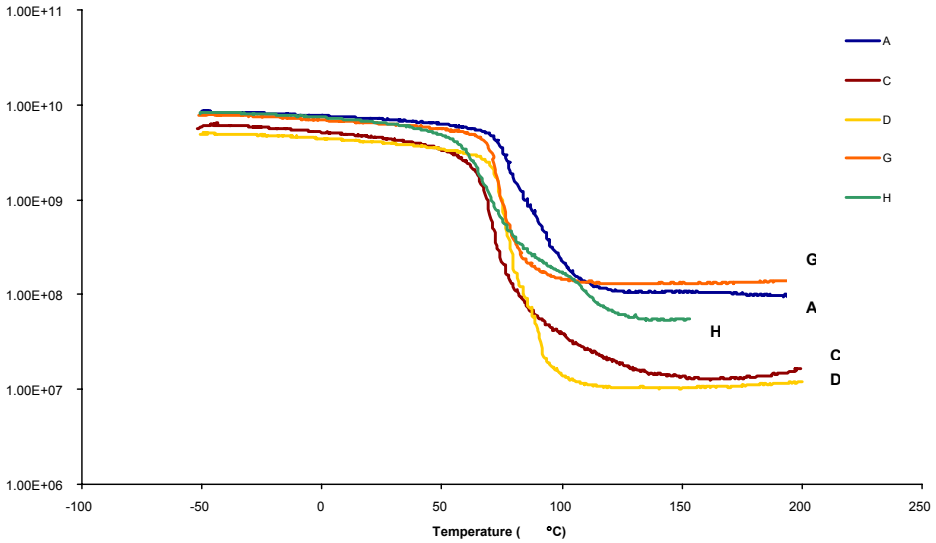

FIGURE 6. Elastic Modulus as a Function of Temperature

POLARIZATION BEHAVIOR AND CORROSION-INITIATION MECHANISMS OF MO COATED WITH AMORPHOUS HYDROGENATED SILICON ALLOY THIN CERAMIC FILMS

L.H. Hihara[a], A.S. Iwane[a], J.J. Yamane[a], and R.E. Rocheleau[b]

[a]Department of Mechanical Engineering
University of Hawaii at Manoa,
Honolulu, HI 96822, USA

[b]Hawaii Natural Energy Institute
University of Hawaii at Manoa
Honolulu, HI 96822, USA

ABSTRACT

Amorphous hydrogenated silicon, silicon nitride, and silicon-carbon films on molybdenum substrates were anodically and cathodically polarized in NaCl and Na_2SO_4 solutions at 30°C. The silicon films showed signs of extensive deterioration; where as, the silicon nitride and silicon-carbon films were inert, but lead to pitting of the Mo substrate predominantly at pre-existing coating breaches. Analysis of the corrosion morphology, and comparisons of actual polarization diagrams to those generated by an electrochemical model indicated that submicron cracks accounted for most of the breaches, while larger breaches, such as those caused by coating spallation were less frequent. To a lesser degree, pits also initiated from regions lacking pre-existing breaches during the later stages of anodic polarization.

INTRODUCTION

Silicon-alloy thin films deposited using plasma-enhanced chemical vapor deposition (PECVD) are generally considered to be inert chemical resistant materials. The effectiveness of

silicon-alloy thin films as corrosion barriers, however, has been compromised by film defects that lead to localized substrate corrosion. Silicon-alloy films have been previously studied as corrosion barriers for integrated circuits[1-3] and medical implants.[4] The studies demonstrated that silicon nitride[1,3] and silicon carbide[4] films generally improved corrosion resistance, but could not prevent localized corrosion of the substrate at film defects. Corrosion initiation sites on substrates coated with thin silicon alloys have been identified in a recent study[5] as regions of spallation, microcracks, and localized areas where no visible film defects could be detected using scanning electron microscopy. Since the utility of using PECVD silicon-alloy thin films as effective corrosion barriers hinges on their ability to prevent or substantially reduce corrosion, further research is needed to develop a comprehensive understanding of the localized-corrosion mechanisms.

In this study, polarization experiments were conducted on pure Mo, and Mo substrates coated with amorphous, hydrogenated a-Si:H, a-SiN_x:H, and a-SiC_x:H thin films to study the degradation mechanisms of the coated substrates. The experiments were conducted in deaerated and oxygenated 0.5 molar (M) Na_2SO_4 and 3.15 weight percent (wt.%) NaCl solutions. Chlorides are particularly aggressive towards metals with naturally occurring passive films and, hence, it was of interest to determine if chlorides had a similar effect on metals coated with the synthetic films. Molybdenum was chosen as the substrate material since its polarization behavior is very similar when exposed to either 0.5 M Na_2SO_4 or 3.15 wt% NaCl. Hence, differences in corrosion behavior of the coated Mo specimens which may appear in the sulfate and chloride solutions are likely to be attributable to the effect of Cl^- and SO_4^{2-} on the films rather than their effect on Mo.

The a-Si:H coatings did not provide corrosion protection and resulted in general corrosion. Both the a-SiN_x:H and a-SiC_x:H coatings were chemically inert and provided general protection of the Mo substrate, but could not prevent localized corrosion at coating breaches. The corrosion morphology and anodic polarization behavior of the a-SiC_x:H/Mo and a-SiN_x:H/Mo specimens were compared to that predicted using an anodic-polarization model to identify processes by which localized substrate corrosion occurs. The anodic-polarization model by Hihara that was used in this study was based on the hypothesis that localized corrosion predominantly initiates from preexisting coating defects during the initial stages of polarization, and not from the nucleation of new defects.[6] Pre-existing defects would serve as nucleation sites for localized corrosion because neither the silicon-alloy films nor the substrate Mo have the ability to heal coating defects. Data from the scanning-vibrating electrode technique, which provided localized cathodic and anodic current-density maps, provided further evidence that pits primarily nucleate from pre-existing coating breaches. Analyses on both a-SiC_x:H/Mo and a-SiN_x:H/Mo rendered similar conclusions, but only results from the a-SiC_x:H/Mo specimen will be presented here due to limitations on space.

MATERIALS

THIN FILMS

The deposition parameters and composition of the silicon alloy films have been described elsewhere.[5] The a-Si:H, a-SiN_x:H, and a-SiC_x:H films were deposited to a thickness of 0.7 μm on 1 mm-thick, 5 cm-by-5 cm pure Mo (99.98%) plates. The samples are denoted as a-Si:H/Mo, a-SiN_x:H/Mo, and a-SiC_x:H/Mo, respectively.

ELECTRODES

To make planar electrodes, the coated Mo specimens were sectioned into pieces. Electrical contact was made with the back side of the metallic substrates by attaching a copper wire with conductive silver paint. The back and sides of the electrodes were sealed with an epoxy adhesive (0151 EPOXY-PATCH of Dexter Corp., Seabrook, NH). The exposed surface area of the films was approximately 0.5 cm^2. The samples were cleaned in reagent grade alcohol (89.9% ethyl, 5.0% methyl, 5.0% isopropyl, 0.1% water) and rinsed in deionized 18 MΩ•cm water prior to polarization experiments. Pure Mo (99.98%) electrodes were prepared from 1.27 cm-diameter wafers sectioned from a rod. Electrical contact was made with the backside of the wafer. The backside and circumference of the wafer were sealed with the epoxy adhesive. To form a planer electrode surface, the front side of the wafer was ground and polished to a 0.05 μm finish immediately prior to immersion in the electrolyte.

ELECTROLYTES

Near neutral 0.5 M Na_2SO_4 and 3.15 wt.% NaCl solutions were prepared from reagent grade chemicals and ultrapure 18 MΩ•cm resistivity water. The electrolytes were either deaerated with prepurified (99.99%) N_2 gas or oxygenated with pure (99.74%) O_2 gas for at least one hour prior to and during the polarization experiments. The electrolyte temperature was maintained at 30°C.

EXPERIMENTAL METHODS

POLARIZATION EXPERIMENTS

Potentiodynamic polarization experiments were conducted with a Model 273 PAR potentiostat/galvanostat (EG&G, Princeton, NJ). The electrodes were stabilized at their

corrosion potential prior to polarization. Potentials were measured against a saturated calomel electrode (SCE). Each polarization experiment was performed at least three times to verify reproducibility. In generating the polarization diagrams, the logarithm of the current density was averaged over three experiments and plotted as a function of potential. The only diagram to have been plotted from a single anodic polarization scan is that of the a-SiC_x:H/Mo that is compared to the diagram generated from the anodic polarization model.

SCANNING VIBRATING ELECTRODE TECHNIQUE (SVET)

A scanning vibrating electrode system by Applicable Electronics was used to obtain localized current maps. The vibrating microprobe consisted of platinum/iridium (20% Pt, 80% Ir) microelectrodes fabricated by Micro Probe Inc. The tips of the microprobes were plated with platinum black to increase capacitance. The vibrating microprobe was scanned at a height of 100 μm over the specimen surface. A Zeiss AxioPlan Reflected Light Microscope in concert with a Hitachi KP-C501 All Solid State Color Camera was used to observe and record video images of the specimen in situ.

The SVET experiments were conducted in quiescent 0.5 M Na_2SO_4 solutions at room temperature exposed to laboratory air in a polymethyl methacrylate cell. The specimen potentials were controlled with a variable DC power supply consisting of a DC battery and a variable resistor circuit, which was necessary to eliminate noise which was encountered when using a PAR EG&G potenitostat. The potentials were allowed to stabilize prior to scanning. A fixed area of the a-SiC_x:H/Mo specimen was scanned at least three times at a given potential to verify reproducibility. Cathodic current maps were generated first followed by the generation of the anodic current maps over the same region.

MICROSCOPY

All of the anodically polarized electrodes were inspected with a Nikon SMZ-2T stereo microscope to assess the corrosion morphology. The a-SiC_x:H/Mo electrode that was selected for pit-size documentation was typical of the other a-SiC_x:H/Mo electrodes exposed to the same conditions. The entire electrode surface was sequentially photo-micrographed at 50 times magnification using an optical Zeiss Axioskop metallurgical microscope. Pits were counted and measured from the entire electrode surface. The electrode was further examined at higher magnifications.

RESULTS

POLARIZATION DIAGRAMS

The polarization behavior of pure Mo was studied to provide base-line data for comparison to the ceramic-coated Mo substrates. Comparisons of anodic and cathodic polarization diagrams of Mo exposed to deaerated and oxygenated 0.5 M Na_2SO_4 and 3.15 wt% NaCl are presented (Figure 1).

Anodic polarization behavior of a-Si:H/Mo, a-SiN_x:H/Mo, and a-SiC_x:H/Mo were compared to that of pure Mo in deaerated 0.5 M Na_2SO_4 (Figure 2) and 3.15 wt% NaCl solutions. The polarization diagrams of the coated specimens in the 3.15 wt% NaCl (not shown) solution were similar to those in the 0.5 M Na_2SO_4 solution.

SCANNING VIBRATING ELECTRODE TECHNIQUE

Localized cathodic (Figure 3a) and anodic (Figure 3b) current-density maps were measured over the a-SiC_x:H/Mo specimen exposed to 0.5 M Na_2SO_4. Cathodic current measurements were conducted first followed by anodic current measurements over the same

region. It was assumed that cathodic measurements did not induce degradation of the coating and, therefore, did not affect the subsequent anodic measurements. Cathodic and anodic current densities were high over the same regions.

MICROSCOPY OF ANODICALLY POLARIZED SPECIMENS

In 0.5 M Na_2SO_4 and 3.15 wt% NaCl, pure Mo and a-Si:H/Mo specimens exhibited general corrosion. The a-Si:H films did not provide protection. The a-SiN_x:H and a-SiC_x:H films were inert, but the subtrate was subjected to highly localized corrosion in both 0.5 M Na_2SO_4 and 3.15 wt% NaCl. The pit-size histogram for the a-SiC_x:H/Mo electrode in the Na_2SO_4 solution is shown in Figure 4. Thorough examination of a-SiC_x:H/Mo electrodes anodically polarized in 0.5 M Na_2SO_4 and 3.15 wt% NaCl (Figure 5) revealed only sporadic and very rare coating defects among the pits.

DISCUSSION

The effect of Cl^- and SO_4^{2-} on bare Mo and the coated substrates was determine by comparison of the polarization diagrams. Further insight into the polarization behavior and corrosion initiation mechanism of the inert a-SiC_x:H and a-SiN_x:H coatings was gained by 1) comparison of the cathodic and anodic current-density maps, and 2) comparison of the actual polarization diagram of the a-SiC_x:H coated substrate to that generated by the anodic electrochemical-polarization model.

COMPARISON OF CERAMIC-COATED SUBSTRATES TO BARE SUBSTRATES

Pure Mo has relatively similar polarization behavior in 0.5 M Na_2SO_4 and 3.15 wt% NaCl (Figure 1). Therefore, if the coated-substrates display different anodic behavior in 0.5 M Na_2SO_4 and 3.15 wt% NaCl solutions, the variation should be attributable to the effect of Cl^- and

SO_4^{2-} ions on the coatings rather than on the Mo substrate. The anodic polarization diagrams of a-Si:H/Mo, a-SiN_x:H/Mo, and a-SiC_x:H/Mo exposed to both 0.5 M Na_2SO_4 (Figure 2) and 3.15 wt% NaCl solutions showed similar behavior, indicating that Cl^- and SO_4^{2-} generally had similar effects on the coatings. Differences in the polarization behavior among the various coatings, however, were prominent. The a-Si:H films did not provide protection and may have consisted of unprotective subsilicides or formed silicomolybdic complexes when Si reacts with hexavalent Mo in the electrolyte.[5] Both the a-SiN_x:H and a-SiC_x:H films were chemically inert and resulted in current densities of approximately two orders of magnitude less than that of the bare Mo.

COMPARISON OF CATHODIC AND ANODIC CURRENT DENSITY MAPS

A current-density hotspot was observed in identical locations for both the cathodic and anodic (Figure 3) current-density maps of the a-SiC_x:H/Mo polarized in 0.5 M Na_2SO_4. Since the cathodic map was generated prior to the anodic map, the region of the current-density hotspot could not have been generated by coating breakdown induced by anodic polarization. The location of the hotspot was a pre-existing coating defect with a radius of approximately 15 μm. The results indicate that pre-existing coating defects are a source of pitting initiation sites in these coated materials.

ANALYSIS OF ANODIC POLARIZATION DIAGRAMS

Analyses of the anodic polarization diagrams, corrosion morphology, and pit-size distribution data were very useful in elucidating the mechanisms by which the a-SiC_x:H/Mo and a-SiN_x:H/Mo specimens underwent degradation. An electrochemical polarization model by Hihara [6] was used to incorporate the electrochemical data and pit-size distribution data obtained from microscopic analysis to predict the shape of the experimental a-SiC_x:H/Mo polarization diagram. The anodic polarization model[6] accounts for the growth of concave hemispherical pits

at preexisting coating breaches, but does not account for the initiation of coating breakdown. In this study, film breakdown was not assumed to occur during anodic polarization, because the electric field generated through the silicon alloy films was assumed to be insufficient to cause breakdown during the initial stages of anodic polarization.

Anodic Polarization Model. The anodic polarization model[6] is based on the assumption that the anodic current density i_A of a coated Mo substrate is the sum of that originating on the coating, $i_{A,coat}$, and on bare Mo, $i_{A,Mo}$, exposed at pre-existing coating breaches:

$$i_A = i_{A,Coat}\, x_{Coat} + i_{A,Mo} \sum_j x_{Mo\,j} \tag{1}$$

$$i_A = i_{A,Coat} \left(1 - \sum_j x_{Mo\,j}\right) + i_{A,Mo} \sum_j x_{Mo\,j} \tag{2}$$

where,

$$x_{Coat} + \sum_j x_{Mo\,j} = 1. \tag{3}$$

The parameter x_{Coat} is the area fraction of the ceramic coating and x_{Moj} is the area fraction of Mo exposed at coating breaches having an initial radius r_{oj}. During potentiodynamic anodic polarization, the current density of the coating $i_{A,Coat}$ was assumed to be constant and independent of potential as that of an ideal passive film. The current density at coating breaches was assumed to be that of bare Mo exhibiting Tafel behavior:

$$i_{A,Mo} = \exp_{10} \frac{E - a_A}{\beta_A} \tag{4}$$

The parameter E is the applied potential, and the polarization constants a_A and β_A (Tafel slope) are determined experimentally from bare Mo electrodes. It was also assumed that the area fraction x_{Moj} increases with the growth of hemispherical pits that undercut the coating at breaches. An expression for x_{Moj} was derived by coupling Faradays law to the growth of hemispherical pits. The expression of x_{Moj} is a function of the applied potential E; starting polarization potential E_o; Mo polarization constants a_A and β_A; scan rate E; initial coating breach

size r_{oj}; breach density ρ_j (defects per unit area of initial size r_{oj}); Mo density ρ_{Mo}; Mo atomic weight AW_{Mo}; Mo valence n; and the Faraday F.

$$x_{Mo\,j} = 2\pi \left(r_{o\,j} + \frac{3}{2\pi} \frac{AW_{Mo}}{\rho_{Mo}\, nF} \frac{\beta_A}{2.3\dot{E}} \left\{ \exp_{10} \frac{E - a_A}{\beta_A} - \exp_{10} \frac{E_o - a_A}{\beta_A} \right\} \right)^2 \rho_j \tag{5}$$

An anodic polarization diagram can be generated by estimating a value for $i_{A,Coat}$, tabulating values of $i_{A,Mo}$ (equation 4) and x_{Moj} (equation 5) as functions of E, and substituting the results in equation 2 to obtain i_A as a function of E.

At potentials somewhat positive to E_{corr}, where the cathodic component of the net current is negligible, the anodic polarization diagram generated by the model (i.e., E vs. log i_A) can be compared to that of the actual anodic polarization diagram. At potentials closer to the open-circuit potential where the cathodic component is not negligible, a comparison between the model and actual polarization diagram requires that the net current i_{Net} be plotted as a function of potential.

$$i_{Net} = |i_A - i_C| \tag{6}$$

For many cases, i_C has the form

$$i_C = \exp_{10} \frac{E - a_C}{\beta_C} \tag{7}$$

where a_C and β_C are constants determined from cathodic polarization diagrams of the coated substrates.

Determination of Polarization Model Parameters. A typical a-SiC_x:H/Mo specimen anodically polarized in 0.5 M Na_2SO_4 was selected for detailed analysis. This specimens showed typical characteristics of localized corrosion.

The utilization of the model requires the input of the parameters E, a_A, β_A, a_C, β_C, E_o, r_{oj}, ρ_j, and $i_{A,Coat}$, which are tabulated in Table 1 for the a-SiC_x:H/Mo specimen exposed to Na_2SO_4. The parameters have been obtained by various methods, which are discussed below.

The scan rate E was set by the experiment and equal to 0.1 mV/sec. The constant a_A and Tafel slope β_A are averaged values obtained from anodic polarization diagrams of bare Mo. The constants were based on data in the high current range since the growth of pits were dominated at high current densities. Note that the model also extrapolates beyond 10^{-2} A/cm^2, which could introduce some departure from the actual current density.

The cathodic constants a_C and β_C are not needed for comparisons that are in a potential range significantly positive to that of E_{Corr}, where i_{Net} (i.e.,$|i_A - i_C|$) is approximately equal to i_A. It is in this potential range that the effects of pit growth become evident and the model has the most significance. Taking i_C into account helps only to render the curve generated by the model significantly similar to that of the actual polarization curve near E_{Corr}. Values of β_C were measured from cathodically polarized specimens in the potential region just outside of E_{Corr} where it was most relevant to the model. The relatively large values of β_C indicated that they were not likely associated with hydrogen evolution. The slopes β_C for each specimen type were relatively consistent varying less than 15% of the average value. The parameter a_C shifts the polarization curves either to the right or left, which also varied from specimen to specimen. The value of a_C was chosen so that the open-circuit potential of the model coincided with that of the experimental polarization diagram. The selection of the value of a_C was done solely for the purpose of rendering E_{Corr} of the model similar to that of the actual diagram. It should be emphasized again that the significance of the model is important well into the anodic regime away from E_{Corr}.

For simplicity, the anodic current density of the coating $i_{A,Coat}$ was assumed to be constant and independent of potential as that of an ideal passive film. This was reasonably consistent with other silicon alloy coatings deposited on Si, which either exhibited no dependency or only slight dependency on potential.[3] The anodic current density of the coating $i_{A,Coat}$ cannot be directly measured unless the coating is defect free or if the substrate has a dissolution current density significantly lower than that of the coating (see equation 1). Since the coatings were not defect free and were deposited on Mo which has high dissolution current densities, a value of $i_{A,Coat}$ had to be estimated. An estimate of $i_{A,Coat}$ was obtained by the adjusting the value of $i_{A,Coat}$ in the model until correlation between the model and experimental diagram was achieved. The value of log $i_{A,Coat}$ obtained for a-SiC_x:H (-7.25) was in the same order of magnitude of other silicon alloy films on Si substrates.[3]

The parameters E_o, r_{oj}, and ρ_j were extracted from the specific experiment that was used for comparison to the model. The model requires the actual starting potential E_o of the polarization experiment, and a reliable estimate of the defect density ρ_j and corresponding initial defect size of radius r_{oj}. The distribution of pit sizes for the a-SiC_x:H/Mo specimen (Figure 4) suggest that several r_{oj}-ρ_j pairs could be used. For simplicity, however, only two pairs r_{o1}-ρ_1 and r_{o2}-ρ_2 were implemented to test the model, leaving further refinement for later if necessary. The r_{o1}-ρ_1 pair was used for very small preexisting defects. Scanning electron microscopy (SEM) has shown evidence that some pits nucleate under small cracks in a-SiN_x:H and a-SiC_x:H coatings.[5] Under these circumstances, the substrate is likely to be exposed by virtue of a fine coating crack rather than a loss of coating material. The value of r_{o1} was, therefore, chosen to be 0.1 μm. For a fixed defect density, the polarization curves generated by the model converge when the defect sizes become less than about 0.1 μm since the growth rate of the pits is not proportional to pit

size.[6] The r_{o2}-ρ_2 pair was used for larger preexisting defects. The value of r_{o2} was estimated as 15 μm corresponding to regions of spallation found on virgin a-SiC_x:H/Mo specimens examined using SEM,[5] and the pre-existing defect found on the specimen subjected to current mapping (Figure 3). The value of ρ_1 was estimated to be equal to the total defect density of the actual specimens less ρ_2 corresponding to defects having an initial size of r_{o2}. The value of ρ_2 was selected as that corresponding to pits in the histogram bin of the largest radii (Figure 4). It was assumed that the largest pits originated from defects having the largest initial radii of r_{o2}.

Comparison Between Model-Generated and Actual Anodic Polarization Diagrams. The comparison between the actual and model-generated anodic polarization diagrams for the a-SiC_x:H/Mo specimen (Figure 6) showed good correlation in the overall shape of the diagrams, using the simplified two pit-size distribution (i.e., r_{o1}-ρ_1 and r_{o2}-ρ_2 pairs). Both diagrams show pseudo pitting potentials E_{psp} at which the current density markedly increased. The value of E_{psp} is dependent on the initial value of x_{Mo},[6] and not due to coating breakdown. There was relatively good correlation between the anodic slopes of the actual and model-generated diagrams (Table 2) at potentials greater than E_{psp}, which provided more insight into the degradation process. Based on the model [6] at potentials greater than E_{psp}, the anodic slope is limited between that of bare Mo $\beta_{A,Mo}$ and one-third of this value. The slope should tend toward that of bare Mo $\beta_{A,Mo}$ when either r_o or x_o or both are relatively large, and should tend toward $\beta_{A,Mo}/3$ if both r_o and x_o are relatively small or as the potential becomes significantly larger than E_o. Since the slopes can change with current density, measurements were made over two current ranges using the least squares method.

For the a-SiC_x:H/Mo specimen exposed to the sulfate solution, the anodic slopes of the actual and model-generated polarization diagrams (0.076 V/dec) were identical in the current

range from 3 x 10^{-7} to 2 x 10^{-5} A/cm^2, but noticeably less than that of bare pure Mo (0.104 V/dec). Based on the model, a slope less than that of bare Mo is an indication that both r_o and x_o were relatively small, which was also corroborated with the relatively low pit density of the a-SiC_x:H/Mo specimen (Figure 4). At higher potentials in the current density range from 2 x 10^{-5} to 3 x 10^{-3} A/cm^2, the slope of the model-generated diagram (0.038 V/dec) approached the lower limit 0.035 V/dec ($\beta_{A,Mo}/3$), but that of the actual diagram was significantly less (0.014 V/dec). A possible explanation is that the nucleation of new pits during the later stages of anodic polarization would further increase the current density resulting in an anodic slope less than that predicted by the model. The nucleation of only a few new pits could have a noticeable affect on the anodic slope since the a-SiC_x:H/Mo specimen had a relatively low pit density (82 pits/cm^2). Evidence of pit nucleation during the later stages of polarization was evident on a a-SiC_x:H/Mo specimen polarized in 3.15 wt% NaCl (Figure 5). The coating defects and small size of the pits indicate that they nucleated in the later stages of the polarization experiment. The large pit on the lower left of the micrograph, which was of typical size observed on the sample, was believed to have formed from a pre-existing coating breach. Similar evidence was also observed on the a-SiC_x:H/Mo specimen polarized in the 0.5 M Na_2SO_4 solution.

CONCLUSIONS

The Cl^- and SO_4^{2-} ions had similar effects on the uncoated and coated Mo specimens. The Cl^- ions were not found to be any more aggressive than the SO_4^{2-} ions regarding the silicon alloy films. The a-Si:H films were not protective in either the 0.5 M Na_2SO_4 or the 3.15 wt% NaCl solution; whereas, the a-SiC_x:H and a-SiN_x:H films were chemically inert in both solutions.

The general shape of the curve generated by the anodic polarization model showed relatively good correlation to the actual polarization curve of the a-SiC_x:H/Mo specimen. This correlation rendered a degree of validity on the initial assumption that localized corrosion primarily initiated from pre-existing coating defects on the a-SiC_x:H/Mo and a-SiN_x:H/Mo specimens. Deviations in the anodic slope between the model and actual polarization curves suggested that additional pits nucleated during the later stages of anodic polarization at higher potentials. The presence of very small pits and coating defects, though very rare and sporadic, revealed by microscopic analysis provided supporting evidence for occasional pit nucleation during the later stages of polarization.

ACKNOWLEDGEMENTS

The financial support of the National Science Foundation (Grant No. DMR-9057264), the National Renewable Energy Laboratory, and the TRW Foundation is gratefully acknowledged. The authors are particularly grateful to Dr. B.A. MacDonald of the National Science Foundation; and Dr. Reynold Kajiwada and Mr. Aaron Oki, TRW Technical Fellow, of TRW.

REFERENCES

1. R.K. Ulrich, D. Yi, W.D. Brown, and S.S. Ang, Corros. Sci. 33 (1992): p403.
2. R.K. Ulrich, D. Yi, W.D. Brown, and S.S. Ang, Thin Solid Films 209 (1992): p.73.
3. R. E. Rocheleau, Z. Zhang, A. Iwane, and L.H. Hihara, J. Electrochem. Soc. 141 (1994): p.1938.
4. C. Sella, J. Lecoeur, Y. Sampeur, and P. Catania, Surface and Coatings Technology 60 (1993): p.577

5. L.H. Hihara, A. Iwane, S. Voss, R.E. Rocheleau, and Z. Zhang, Corros. Sci. Vol. 41 (1999): p.1417.

6. L.H. Hihara, to be submitted to Corros. Sci.

TABLES

Table 1.
Table of Parameters for Anodic Model

	a_A * (mV)	β_A * (mV)	a_C ** (mV)	β_C ** (mV)	E_o (mV)	r_{o1}	r_{o2}	ρ_1	ρ_2	log $i_{A,Coat}$ [A/cm^2]
						μm		cm^{-2}		
a-SiC_x:H/Mo□ Na_2SO_4	0.408	0.104	-3.012	-0.312	-0.75	0.1	15	74	8	-7.25

* - for pure uncoated Mo in current density range 10^{-4} to 10^{-2} A/cm^2.
** - in region near the open-circuit potential prior to hydrogen evolution regime.

TABLE 2:
Anodic Current Slopes

	SiC_x:H/Mo in Na_2SO_4	
Anodic slope (actual) (V/dec)	0.076	0.014
Anodic slope (model) (V/dec)	0.076	0.038
Log current range [A/cm^2]	-6.5 to –4.8	-4.8 to –2.5

FIGURES

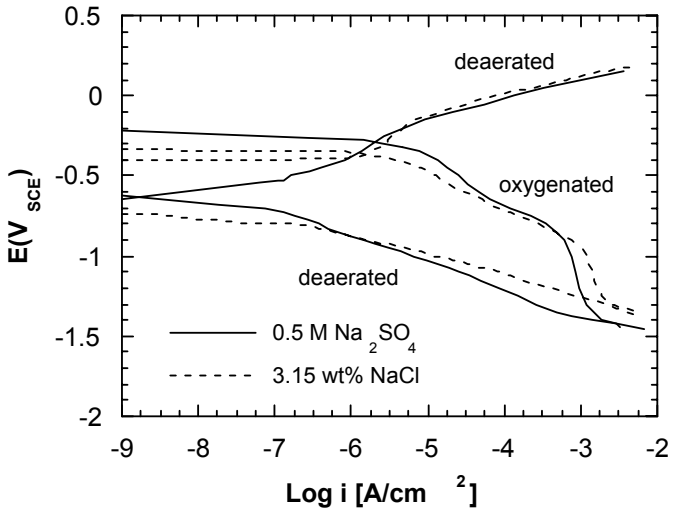

FIGURE 1. Anodic and cathodic polarization diagrams of bare pure Mo exposed to deaerated and oxygenated 3.15 wt% NaCl and 0.5 M Na_2SO_4 at 30°C. Scan rate = 0.1 mV/s.

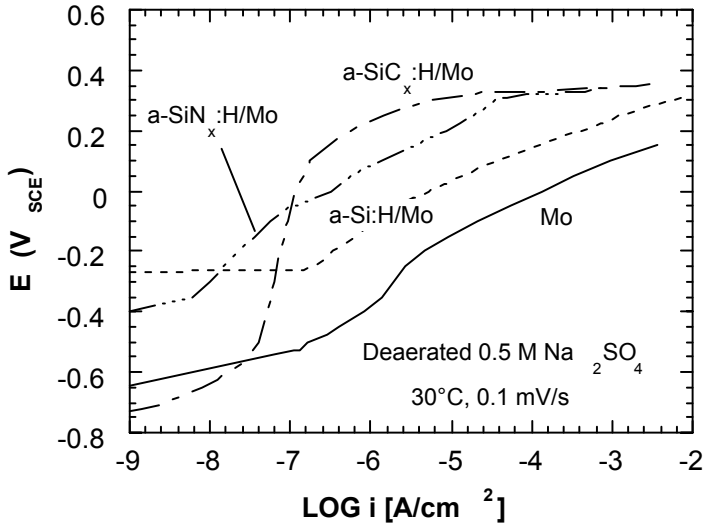

FIGURE 2. Comparison of anodic polarization diagrams of bare pure Mo, a-Si:H/Mo, a-SiN_x:H/Mo, and a-SiC_x:H/Mo exposed in deaerated 0.5 M Na_2SO_4 at 30°C, and scan rate = 0.1 mV/s.

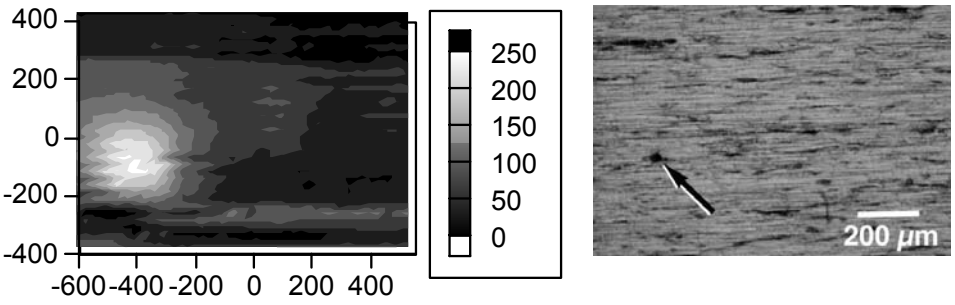

FIUGRE 3a: Cathodic-current density map of a-SiC_x:H/Mo in air-exposed 0.5 M Na_2SO_4, and micrograph (on right) of corresponding region. Notice pre-existing defect at arrow. Defect radius was measure to be approximately 15 μm. Current density in $\mu A/cm^2$. E = -1.3 V_{SCE}

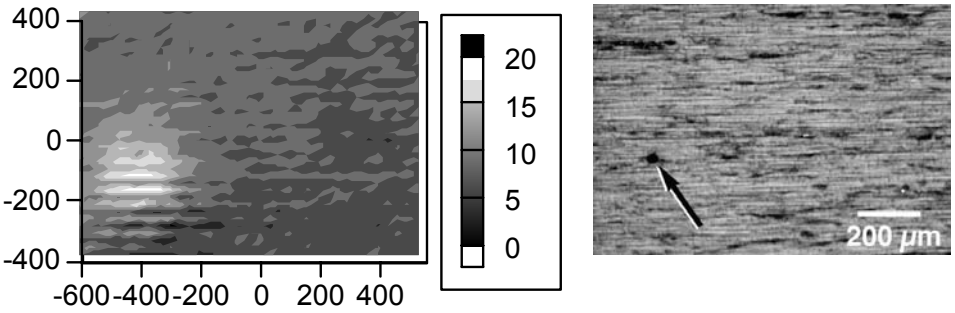

FIGURE 3b: Anodic-current density map, and micrograph of corresponding region, over same area as in Figure 3a. Current density in $\mu A/cm^2$. E = 0.1 V_{SCE}

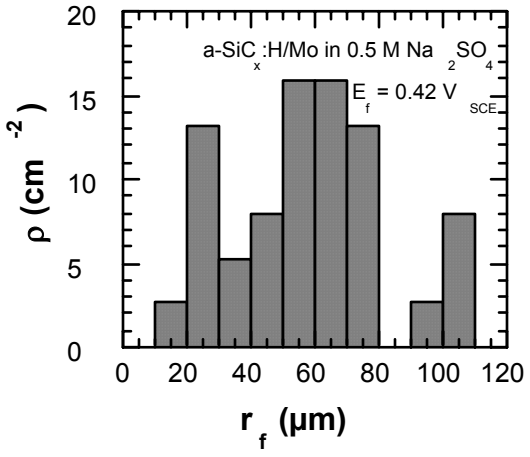

FIGURE 4. Pit-size distribution histogram of a-SiC_x:H/Mo anodically polarized in 0.5 M Na_2SO_4 at 30°C and 0.1 mV/s.

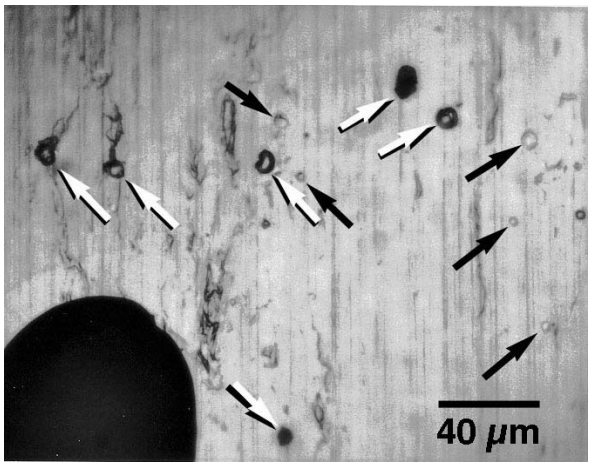

FIGURE 5. Optical micrograph of a-SiC_x:H/Mo anodically polarized in 3.15 wt% NaCl. Large pit on lower left was of typical size. Black arrows point to coating defects and white arrows point to newly formed pits. The occurrence of the defects and newly formed pits was extremely sparse over the specimen, and only detected in this region.

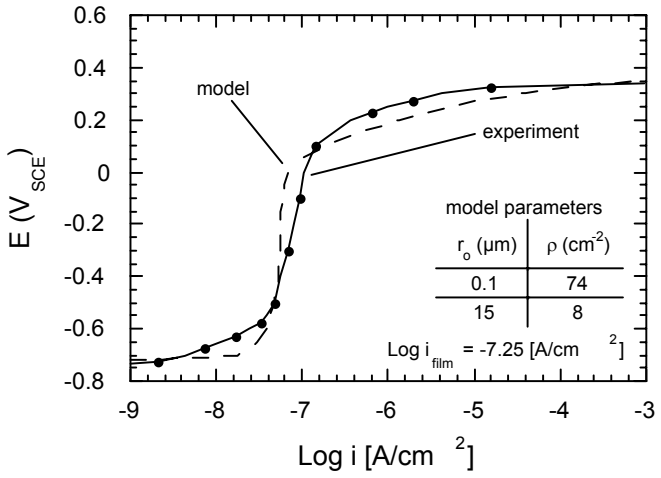

FIGURE 6. Comparison of anodic polarization diagram of actual a-SiC_x:H/Mo and that generated by anodic polarization model for 0.5 M Na_2SO_4 at 30°C and 0.1 mV/s scan rate.

LOW SOLAR ABSORBENT GRAY COATING FOR TOPSIDE APPLICATIONS

Albert Holder (Code 641)

Naval Surface Warfare Center
9500 MacArthur Blvd
West Bethesda, MD. 20817-5700
Voice Telephone 301-227-4787
Fax 301-227-4814
e-mail HolderAG@NSWCCD.Navy.Mil

Dr. Robert Brady (Code 6132)

Naval Research Laboratory
4555 Overlook Ave. SW
Washington DC 20375
Voice Telephone 202-767-2268
Fax 202-767-4642
e-mail Brady2@ CCF.NRL.Navy.Mil

ABSTRACT

Our task was to develop a coating to meet the Navy requirements of color and gloss retention, low solar absorbance, shorter cure time and harder film with easy clean up using detergent wash or only hydro-washing below 200 psi. Also, our goal was to reduce volatile organic compounds (VOC) in the reformulated coating. The VOC content of the currently used silicone-based alkyd paint (MIL-E-24635) is 2.8 lbs/gal or 340 g/l of solvent

INTRODUCTION

The Mil-E-24635 coating is used on the hull, decks, superstructures, and wherever haze grey (MIL-STD-26270) is the required color. This material does not meet the needs of the Navy, therefore NAVSEA has been evaluating a new reformulated Low Solar Absorbance (LSA) Anti-Stain Coating. Unfortunately the polymer, **silicone alkyd** is the same resin as the old Mil-E-24635 and gives the same end result of long cure time allowing airborne extraneous material to become embedded into the relatively soft film and preventing washing off. Ship Commanding

Officers see side shell rust bleed as being unacceptable, and this requires many hours of sailors time, so over-coating for aesthetic value is the only alternative.

Further, the chelating agent addition to the silicone-alkyd has reduced the shelf-life to approximately half the original shelf life storage. The air drying properties of the applied films are affected by the increase of tack free time and hard dry. Just- in-time purchasing is the solution, if the manufacturing date is recent. It appears that the chelating agent is absorbing the metallic cobalt driers. An acrylic latex emulsion (Mil-E-24763A) type is being tried on the Navy ship radomes, but often weather conditions such as low temperature or high humidity, which are common in the coastal ports, are not favorable to its applications.

At the present time the silicone-based alkyd paint (MIL-E-24635) used extensively on hull, deck, and superstructures is not satisfactory due to UV absorption, gloss reduction, color change, chalking and dirt retention. The Mil-E-24635 silicone –alkyd coating is applied extensively at sea by the Sailors, for touch-up. This means the on - board paint locker stocks the product for this purpose. We are aware that the paint has 2.8 lbs per gallon of solvent for each can and these solvents may contribute to a fire hazard situation. Therefore, reduction of the solvents will improve this safety situation.

Therefore, as requested by NAVSEA 05M1, this task attempts to improve the present Silicone – Alkyd for cleanability, reduction of VOCs, improve the dry ability of the paint, and improve the LSA Haze Gray in the near infra-red range.

EXPERIMENTAL PROCEDURE

Resin technology, acrylics, polyesters, polyurethane modified alkyds and even polyureas are available today that may produce a lower volatile organic compound (VOC) coatings that can

may be formulated to improve on the weaknesses of the present Mil-E-24635C Silicone Alkyd. To improve the LSA Haze Gray in the near infra-red range the black pigment was removed and replaced by less heat absorbing pigments as shown in Table 1.

The reformulation will provide the following benefits:

- Resistance to chalking
- Color and gloss retention
- Quicker drying film for reduced air borne material pick - up
- Easier cleaning of the coating film
- Reduced VOC
- Low solar absorbance

The coating is being or is in the process of evaluation by the following accelerated ASTM tests:

- ASTM B-117 Salt – Fog
- ASTM D-3359 Adhesion Tape Test on Mil-P-24441 and bare metal
- ASTM D-870 Immersion in water.
- ASTM D-4585 Condensation Resistance
- Shelf- life at 40^{o}F, 78^{o}F and 120^{o}F Viscosity check and application
- ASTM D-4587 UV exposure
- ASTM D-1014 45^{o} South natural weather exposure.
- ASTM D-2486 Scrub Resistance
- ASTM D-4039 Gloss Readings
- ASTM D-659 Chalking

During this investigation, the following is also planned:

1. Literature Search

2. Work with Industry to formulate a new resin, if required.

3. Work with industry to formulate an acceptable coating

4. Prepare coupons for testing

5. Begin Physical Tests

   a. Viscosity (ASTM D-562)

   b. Tack free time at 25°C (ASTM D-1640)

   c. Adhesion to epoxy primer (ASTM D-4541)

   d. Sag Resistance (ASTM D-4400)

   e. Settling (ASTM D-869)

   f. Fineness of grind (ASTM D-1210)

   g. Washability (ASTM D-3450)

CONCLUSION

This is an on going project. All testing for 2001 has been completed and the results are being reviewed. The 2002 testing is in-process and results will be obtained in summer for a conclusion of the project with a report. The laboratory results will be forwarded to NAVSEA 05M1 for ship on-site evaluation.

ACKNOWLEDGEMENTS

This work was supported by Joseph F Korczynski of the Signature Materials Branch, Naval Surface Warfare Center, Carderock Division, Code 642 and Craig Bevans of Geo-Centers, INC., working out of Naval Research Laboratory.

REFERENCES

1. All ASTM test procedures refer to the ASTM, 100 Barr Harbor Drive, PO Box C700, West Conshohocken, PA 19428-2959

2. Fed. Test Methods Std 141D – Method 6041.3 may be obtained from http://www.dodssp.daps.mil/

TABLES

TABLE 1.
Reflectance Results of MIL-E-24635C Enamel, Silicon Copolymer Haze Gray 26270

WITH BLACK PIGMENT	WITH NO BLACK PIGMENT
VISIBLE WAVELENGTH 380nm 11.2 % Reflectance 88.8 % Absorption 700nm 23.42 % Reflectance 76.58 % Absorption	VISIBLE WAVELENGTH 380nm 11.81 % Reflectance 88.19 % Absorption 700nm 25.21 % Reflectance 74.79 % Absorption
NEAR INFRA-RED WAVELENGTH 710nm 23.16 % Reflection 76.84 % Absorption 1000nm 18.07 % Reflection 81.93 % Absorption	NEAR INFRA-RED WAVELENGTH 710nm 23.00 % Reflectance 77.00 % Absorption **1000nm 82.44 % Reflectance** 17.56 % Absorption

• THE GREATER THE REFLECTANCE THE COOLER THE PAINT AND SUBSTRATE
• BLACK PIGMENT WAS REPLACED USING TWO INORGANIC PIGMENTS – YELLOW OXIDE AND RED OXIDE AND ONE ORGANIC PIGMENT – PHTHALOCYANINE BLUE

TABLE 2.
Dry Time (FED-STD-141D Method 4061.3)

Paint No.	Dry-to-Touch (hrs)	Dust-Free (hrs)	Score
1	0.5	0.5	10
2	1.0	>3.0	0
3	1.0	2.0	5
4	1.0	1.0	8
5	0.5	0.5	10
6	0.5	0.5	10
7	0.5	3.0	2
8	0.5	2.0	5
9	0.5	2.0	5
10	0.5	1.5	7
11	0.5	1.0	8
12	0.5	1.0	8
13	1.5	2.5	3
14	1.5	2.5	3
15	1.0	2.5	3
16	3.0	3.0	2

Dust-Free Time (hrs)	Score
0.5	10
1.0	8
1.5	7
2.0	5
2.5	3
3.0	2
>3.0	0

Scoring Range
10 – Best
5 – Baseline
0 - Worst

TABLE 3.
Washability (ASTM D3450)

Paint No.	Before Washing Y (R1)	After Washing Y (R2)	ΔE (ASTM D2244)	Reflectance Recovery (%)	Score Based on RR
1	17.4	19.8	2.93	114	5
2	22.5	26.1	3.70	116	4
3	23.6	26.9	3.20	114	5
4	23.2	26.3	3.16	113	5
5	22.8	25.8	3.02	113	5
6	23.4	25.8	2.41	110	6
7	23.3	26.1	2.83	112	6
8	23.3	25.8	2.55	111	6
9	24.3	27.1	2.68	112	6
10	23.0	25.4	2.45	111	6
11	23.2	25.6	2.42	110	6
12	24.2	26.5	2.22	110	6
13	23.5	25.5	2.03	109	6
14	23.4	26.9	3.44	115	5
15	23.2	26.4	3.14	114	5
16	52.8	51.3	2.58	97	10

Reflectance Recovery (%) Range	Score
93-97	10
98-102	9
103-107	7
108-112	6
113-115	5
116-120	4

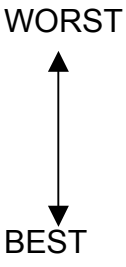

TABLE 4.
Pencil Hardness (ASTM D3363)

Paint No.	Scratch Hardness	Gouge Hardness	Score
1	2B	2B	8
2	4B	4B	6
3	5B	5B	5
4	4B	4B	6
5	2B	2B	8
6	2B	2B	8
7	2B	B	9
8	2B	B	9
9	2B	B	9
10	B	HB	10
11	2B	B	9
12	2B	B	9
13	5B	5B	5
14	5B	5B	5
15	5B	5B	5
16	<8B	<8B	<2

Hardness Key	Score
6H	
5H	
4H	
3H	
2H	
H	
F	
HB	10
B	9
2B	8
3B	7
4B	6
5B	5
6B	4
7B	3
8B	2

Harder

Softer

TABLE 5.
Water Immersion (ASTM D1308)

Paint No.	Initial Gouge Hardness	Final Gouge Hardness	ΔE (ASTM D 2244)	Score
1	2B	2B	0.00	10
2	4B	5B	1.27	0
3	5B	6B	0.30	8
4	4B	4B	0.10	10
5	2B	2B	0.00	10
6	B	2B	0.37	7
7	2B	2B	0.00	10
8	B	2B	0.45	6
9	B	2B	0.41	6
10	HB	HB	0.21	8
11	B	2B	0.45	6
12	B	2B	0.40	7
13	5B	5B	0.00	10
14	5B	5B	0.00	10
15	5B	5B	0.37	7
16	<8B	<8B	0.06	10

Range	Score
0 - 0.1	10
0.11 - 0.2	9
0.21 - 0.3	8
0.31 - 0.4	7
0.41 - 0.5	6
0.51 - 0.6	5
0.61 - 0.7	4
0.71 - 0.8	3
0.81 - 0.9	2
0.91 - 1	1
1.01 - 1.1	0

ADVANCED COATING SYSTEMS FOR CORROSION PROTECTION OF AIR FORCE AIRCRAFT

Joseph H. Osborne

The Boeing Company
Phantom Works, Seattle, WA

ABSTRACT

The U.S. Air Force, Navy, and DARPA have sponsored several programs aimed at increasing performance of and reducing hazardous materials used in exterior coatings applied to aluminum structured military aircraft. The DoD sponsored programs have been successful in developing a high performance topcoat, conversion coatings, and primers that have acceptable performance. The Air Force Aging Aircraft office is sponsoring an Advanced Technology Demonstration program that will bring together these advanced technologies into a coating system for use on operational Air Force vehicles. The coating system to be demonstrated includes a Boeing developed sol-gel conversion coating, a chromated primer, and the Deft Advanced Performance polyfluorourethane topcoat (APC). An outline of the program plan is presented.

Laboratory test data shows that the demonstration coating system has corrosion performance equivalent to a fully chromated coating. Neutral salt spray corrosion testing shows equivalent performance of the control and demonstration coating system on panels and on a "rig" assembly. Cyclic corrosion (Prohesion) results for panels parallel the salt spray results but the alloy steel fasteners in the "rigs" are severely attacked. Electrochemical Impedance Spectroscopy shows that coating systems exposed to uv light have a different failure mode than those exposed to neutral salt spray or constant immersion.

INTRODUCTION

As the average age of USAF aircraft continues to climb it is increasingly important to develop and implement cost effective materials and processes that will maintain the capability and readiness of the fleet. While there are a number of issues that concern aging aircraft, corrosion of the airframe and components is the number one aging aircraft problem with respect to costs and aircraft availability.[1] A number of technical issues prevent accurate prediction of the cost of maintenance and availability of aircraft due to corrosion events. Corrosion is difficult to

accurately detect and quantify and the maintenance database is poorly maintained. Corrosion prediction is difficult and the uncertainties in projections are large. In practice, many corrosion findings are surprises making corrosion management reactive rather than proactive.

In addition to the problems of predicting and managing corrosion on the fleet, increasingly stringent environmental regulations are making the use of traditional materials more and more costly. Hexavalent chromium is the most effective corrosion inhibitor available for aluminum, magnesium, and steel and is widely used in corrosion protection materials. The use of volatile organic materials used in paints, lubricants, and corrosion prevention compounds is being significantly reduced. The USAF, AFOSR, and DARPA have invested significant funding over the past ten years to identify new materials that can replace hexavalent chromium and other hazardous materials to both reduce costs from environmental compliance requirements and to improve overall system performance.

This paper describes a coating system that combines elements of several development programs and the technology transition program to demonstrate its operational performance. The Advanced Aircraft Corrosion Protection (AACP) program will define producibility operations and develop a performance data package to support application of the coating system at a maintenance depot and flight test the coating system to verify coating system performance on fielded aircraft. The focus of this paper is the corrosion performance aspects of the Advanced Coating system.

EXPERIMENTAL PROCEDURES

Test panels and coupons were prepared using standard aerospace coating and cleaning procedures. Coupon substrates are aluminum alloy 2024-T3 unless otherwise specified. Standard panel preparation included solvent wiping and deoxidizing by immersion in a nonchromated acidic solution. Alodine 1200S or Alodine 600 were used for the control conversion coatings. Boegel EPII as developed at The Boeing Company was used for the nonchromate conversion coating.[2]

Primers used were purchased from Akzo Nobel or Deft and are qualified to MIL-PRF-23377 or MIL-PRF-85582. The topcoat used is Deft 99-GY-001 fluorourethane Advanced Performance Coating (APC, MIL-PRF-85285).

Accelerated corrosion testing was accomplished using neutral salt spray (ASTM B117) or cyclic corrosion exposure (ASTM G85 Annex 5, also known as the "Prohesion" cycle). Samples were exposed to UV light in an Atlas Xenon Weather-O-Meter model CI4000 in accordance with ASTM G26. Operating conditions were 63°C black panel temperature, 42°C dry bulb temperature, 50% relative humidity, 0.35 W/m² irradiance at 340 nm, and 2 hour cycles of 18 minutes water spray and 102 minutes dry.

The EIS system included an EG&G Princeton Applied Research (PAR) model 273A potentiostat-galvanostat, a Schlumberger model SI 1260 impedance/gain-phase analyzer, and a personal computer. Data were obtained using an applied alternating voltage of 40 mV at the open circuit potential. Specimens were tested in a PAR model K0235 Flat Cell using 5% NaCl electrolyte. The corrosion resistance for the coatings was calculated using the method of Kendig and Jeanjaquet.[3]

CORROSION “RIGS”

The exteriors of aircraft are a complex mixture of materials including aluminum, titanium, and composites. The skin materials intersect at butt and overlap joints. Fasteners of aluminum, titanium, and alloy and stainless steel penetrate the surfaces at regular intervals. Galvanic and crevice corrosion can occur at these joints and fastener locations. To better approximate some of these effects a corrosion test “rig” was devised based on configurations found in older aircraft. The test rig is shown in FIGURE 1. A sandwich of AA2024-T3 aluminum sheet is held together with three alloy steel fasteners. Test coatings were applied to the assembled rigs; no coatings were applied to the fay surface between the aluminum panels. The left fastener was scribed through the aluminum substrate and fastener, the middle fastener was spun to break the coating and create a crevice between the fastener and substrate, while the right fastener was used as a “control”. At right, in FIGURE 1 is a section from a B-52 that shows a longeron strap fastened to the airframe using alloy steel fasteners. Corrosion clearly shows through the coating system at several of the fasteners.

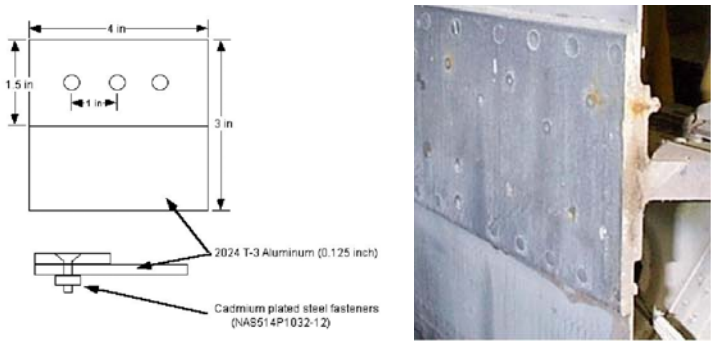

FIGURE 1. Corrosion Test "rig"

DESCRIPTION OF DEMONSTRATION COATING SYSTEM

The ATD demonstration coating system combines elements from programs sponsored by AFRL and DARPA. Elements of the coating process currently used for depot repainting of aircraft and those for the demonstration coating system are shown in FIGURE 2.

Operation	Present	ATD Demonstration	Benefits
Clean and deoxidize	Alkaline cleaner Acidic brightener	Solution (acid deoxidizer, MIL-C-38334, Chemidize 727) Solid State ($NaHCO_3$, Spongejet)	Reduced waste treatment, better performance
Conversion Coating	Alodine 1200	Boegel EP-II/AC-131	Eliminate Cr(VI) waste treatment
Primer	MIL-PRF-23377 or MIL-PRF-85582	MIL-PRF-23377 or MIL-PRF-85582	Chromate primer for corrosion protection
Topcoat	MIL-PRF-85285	Deft 99-GY-001 (APC)	Increased Performance

FIGURE 2. Description of Demonstration Coating System

The demonstration coating system has two recently developed materials that improve the overall performance and reduce environmental hazards. These are the nonchromated adhesion promoter that replaces chromated conversion coat and the Advanced Performance Coating (APC) topcoat. The Boegel adhesion promoter was developed at Boeing initially for adhesive bonding and is now available commercially. The coating solution is a dilute aqueous mixture of zirconium alkoxide and a silane coupling agent. The coupling agent is chosen to be compatible with the organic coating component of the coating (or bonding) system. The coating solution dries in place on the metal surface to form a thin (~50 – 250 nm) gradient coating that is principally zirconium oxide at the metal interface changing to the organic coupling agent at the surface.

The Advanced Performance Coating uses a fluorinated polyurethane resin system and was developed for the C-17 transport aircraft. It has increased durability and cleanability as

compared with conventional polyurethane topcoats. The APC coating is currently used as the topcoat on C-17 and is approved for use on F-15, and KC-135.

A key feature of the AACP program is to evaluate the coating system as a whole, not as individual components. Evidence from a number of studies shows that overall performance of coating systems is a function of the choice of coating system components. In years past, more corrosion was noticed under some colors on camouflage painted F-4 Phantom aircraft. A recent study of the resistance of the APC coating to QUV exposure shows that the ΔE is influenced by the primer used.[4] The measured ΔE is less with a waterborne primer than with a solvent borne primer. This effect has not been studied to any great extent and the cause is not known.

The use of the Boegel conversion coating has two ramifications in the choice of other system components. First, the requirement for a rigorous deoxidizing or "brightening" of the aircraft surface is relaxed. The brightening step is critical when a chromate conversion coating (CCC) is used since a reactive metal surface is needed for the CCC to properly form and adhere. However, the strong acids used to brighten the metal surfaces are thought to contribute to corrosion damage seen on aircraft. The sol-gel based Boegel coating adheres to the thin native oxide on the metal surface and to thicker oxides as well. Cleaning steps that produce a clean water break free surface with tightly adhered oxides may be sufficient to provide adequate paint adhesion using Boegel.

The second consequence of the choice of the Boegel conversion coating is that a chromated primer is required. Previous studies have shown that adequate corrosion protection is not achieved with nonchromated coating systems available today.[5] Some chromate is required either in the CCC or in the primer for the coating system to have adequate protection of damage areas. Primers contain much more chromate inhibitors than does a CCC. Coating systems that

contain a chromated primer have equivalent corrosion performance regardless of the conversion coating used provided the coating passes adhesion requirements.

From strictly a chromate-reduction standpoint, replacing the primer would appear to be most beneficial and, indeed, if the goal were simply to reduce overall hexavalent chromium in the coating system, the primer would be the principal target. However, the chromate conversion coating and the resin based primer present different containment and personal protective equipment requirements from a processing viewpoint. Locales where waste water treatment requirements are strict and the consequences of an aqueous spill are significant might be best served with the nonchromated cleaning and conversion coatings to be demonstrated here. Where airborne emissions and spray application of chromated materials is highly regulated, then a coating system using a nonchromated primer might be a better choice. Ideally a nonchromated coating system, conversion coating and primer, is desired but the current state-of-the-art nonchromate inhibitors are not sufficiently robust to provide adequate performance of a completely nonchromated coating system.

AACP WORK PLAN

The Advanced Aircraft Corrosion Protection program work plan is divided into two phases. Coating system performance verification and optimization will be performed in Phase I. Techniques to verify the presence of the Boegel coating after application to the vehicle and optimization of the Boegel conversion coating combined with the primer and topcoat is one task in this phase. Developing procedures and processes aimed at producibilty in a depot setting will be the second major task in Phase I. Procedures to clean the vehicle prior to applying the Boegel coating will be developed, as discussed above. Kitting of the Boegel coating ingredients and

techniques for applying the coating to large areas will also be developed. Procedures and materials that will remove primers and Boegel from the vehicle will be defined.

Phase II is the operational testing portion of the program. The coating system defined in Phase I will be applied to components on operational vehicles and monitored for performance. The coatings will be applied by depot personell to verify the adequacy of the application procedures. Coupons prepared along with the operation vehicle will be simultaneously tested to allow comparison of the coating system performance in laboratory exposure procedures with field performance.

DEMONSTRATION COATING SYSTEM CORROSION PERFORMANCE

Table 1 shows a summary of the best performing coating systems from the ACRAC program,[5] their rating,[6] and the exposure hours at which they were rated. The demonstration coating system is the highest rated although differences between the top coatings is slight.

TABLE 1.
Summary of Corrosion Testing

Coating Code	Primer / Topcoat	Filiform	NSS @ hours	CCT @ Hours
PC	Boegel/85582/APC gray	9	9.5 / 5688	
FC	Alodine/85582/APC gray	9	9 / 5688	7 / 2544
PC	Boegel/85582/APC gray	8	9 / 5688	
LC	Alodine/10PW22-2/APC gray		8 / 5688	
FC	Alodine/85582/APC gray	9	10 / 2500	7 / 2544
PC	Boegel/85582/APC gray		10 / 2500	10 / 2544
PC	*Boegel/85582/APC gray		10 / 2500	
PC	*Boegel/85582/APC gray		9.5 / 2500	
NC	*Boegel/---/TT-P-2756		8 / 2500	
LC	Alodine/---/TT-P-2756		7 / 2500	7 / 2544

* panels deoxidized with NaHCO3 blasting. All other panels acid etch deoxidized.

Some of the coatings in Table 1 have been exposed well beyond the typical military specification requirement of 2000 hours and commercial requirement of 3000 hours. This was done in an attempt to differentiate between the coating systems. At the specification limit all of

the top performing coating systems were indistinguishable. Any of these coating systems should be interchangeable on a weapon system. One coating that deserves comment is the LC coating with the Akzo Nobel/Dexter 10PW22-2 primer. This low chromate coating is one of the best performers on the Boeing JG-PP NonChromated Primer study.[4] The results presented here corroborate the testing on that program.

Figure 3 shows the top four panels from Table 1 after 5688 hours of continuous exposure to neutral salt spray (NSS). All of the coating systems show only minor darkening at isolated points along the scribe line. The duplicate panels are similar except for the low chromate system (Alodine plus nonchromate 10PW22-2 primer) where the duplicate panel showed much more corrosion and was pulled from the salt spray chamber after approximately 3500 hours.

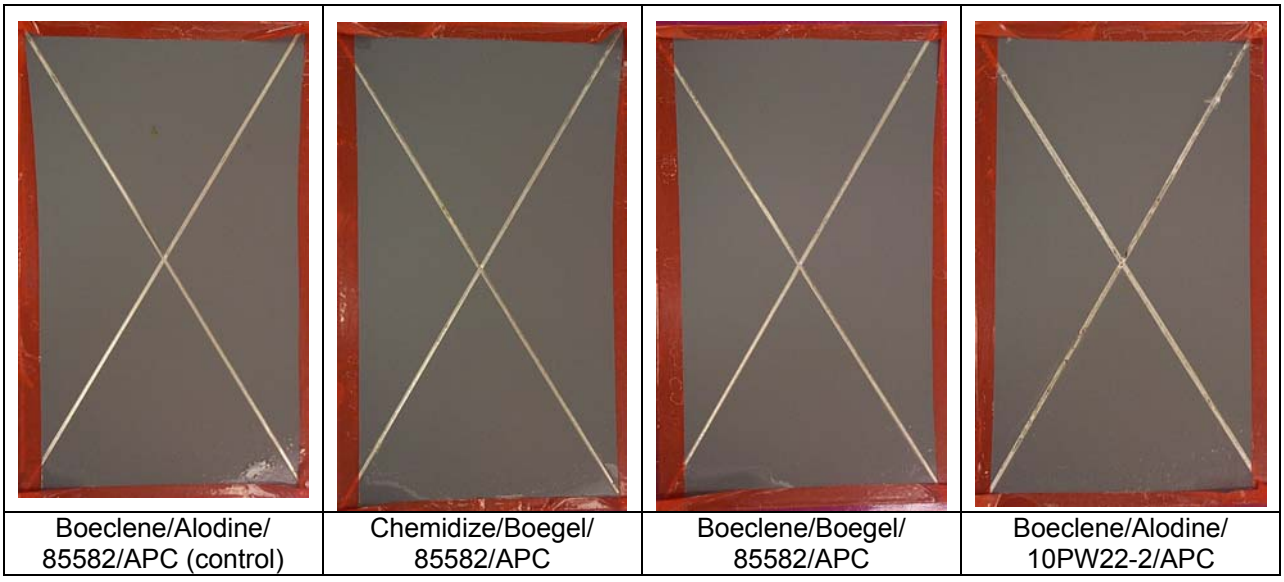

FIGURE 3. Coatings at 5488 Hours Neutral Salt Spray Exposure Panel Salt Spray Corrosion Results.

Air Force maintenance depots typically use solvent borne MIL-PRF-23377 primers when repainting aircraft due to its reduced sensitivity to organic soils such as leaking hydraulic fluid and fuel as compared to the waterborne MIL-PRF-85582 primers. In addition, the typical

corrosion test is of the primer without topcoat. Figure 4 shows panels of the control and demonstration coating system after approximately 2500 hours in salt spray. The topcoated panels are comparable to those shown in Figure 3. All panels show excellent corrosion resistance. The topcoated panels show slight corrosion, more than the primer only panels. This is typical and is be associated with the decreased mobility of hexavalent chromium in the topcoated panels. There is no apparent difference, at this exposure duration, between the waterborne MIL-PRF-85582 and solvent borne MIL-PRF-23377 or between chromated and nonchromated conversion coatings. Cyclic corrosion testing of these coating systems showed similar corrosion modes and acceleration factors to the neutral salt fog testing.

The equivalent performance of the demonstration coating system to the chromated control coating indicates that independent corrosion protection from the conversion coating is not necessary for long term corrosion protection. The chromated primer, that contains a significant quantity of hexavalent chromium in a “slow release” form, provides the long term corrosion protection. The principal function of the conversion coating is to provide adhesion of the primer to the substrate. This is similar to the use of unsealed anodize coatings on Boeing Commercial airplanes when using a chromated primer. The unsealed anodize coating provides little or no corrosion protection to the substrate but results in superior adhesion of the primer to the substrate. The overall coating system with the chromated primer provides the required long term corrosion protection.

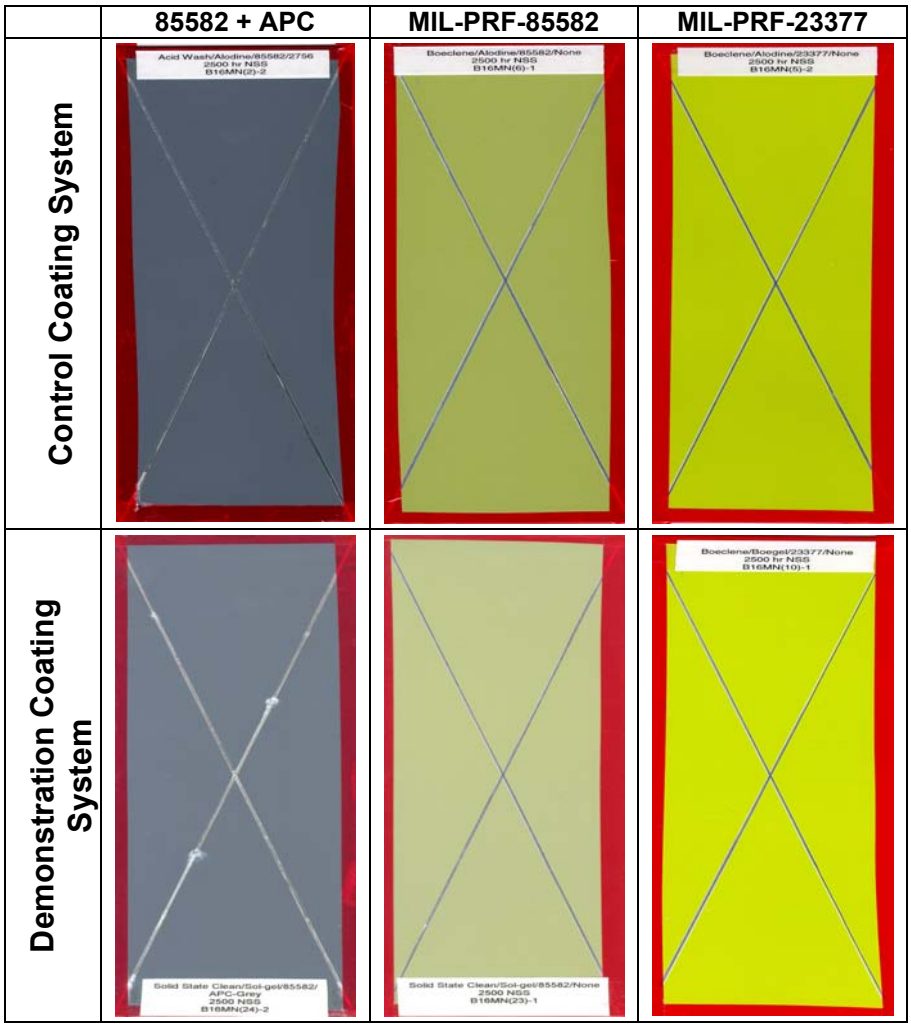

FIGURE 4. Corrosion Results of Panels with Chromated Control and Demonstration Coating Systems – 2500 hours exposure to ASTM B117 Salt Spray.

"RIG" RESULTS

The rigs that contain alloy steel fasteners coupled to aluminum show very different performance depending on the corrosion exposure testing. The results from exposure to neutral salt spray and cyclic corrosion testing are shown in Figure 5. Exposure of the rigs to ASTM B117 salt spray gives results that are consistent with the panel results. With the chromated control coating and the demonstration coating systems there is little corrosion of the aluminum at scribe areas and the alloy steel bolt is protected from corrosion.

The same coating systems in cyclic corrosion testing (ASTM G85 Annex 5) show good performance on the aluminum scribes. However, red rust appeared on the scribed cadmium plated steel fastener within the first 168 hours of exposure. Some small patches of white corrosion also occur on the aluminum portions but most of the scribe remains bright bare metal.

Rusting of the scribed bolt is common to all of the rigs placed in cyclic corrosion testing regardless of coating system. This result is surprising since aluminum is electrochemically active relative to steel and should protect the steel substrate. There are at least two explanations for the rusting of the bolt in contact with aluminum. The first regards the potential passivation of the scribed aluminum during a dry cycle. This could lead to a reversal in potential where the steel becomes active relative to the aluminum. The steel would then act as the anode protecting the aluminum surface. There is some data that suggests that aluminum does, indeed, passivate in "benign" environments and that an aggressive environment such as salt spray is required to keep it active.[7]

Another explanation is that the aluminum does protect the steel fastener while wet. During the dry-off cycle, however, the steel fastener becomes isolated from the aluminum and rusting occurs directly with oxygen in atmosphere. This will require electrically decoupling the steel fastener from the aluminum substrate, a process that probably does not happen completely as moisture will remain in the fay surfaces between the alloy steel fastener and the aluminum substrate.

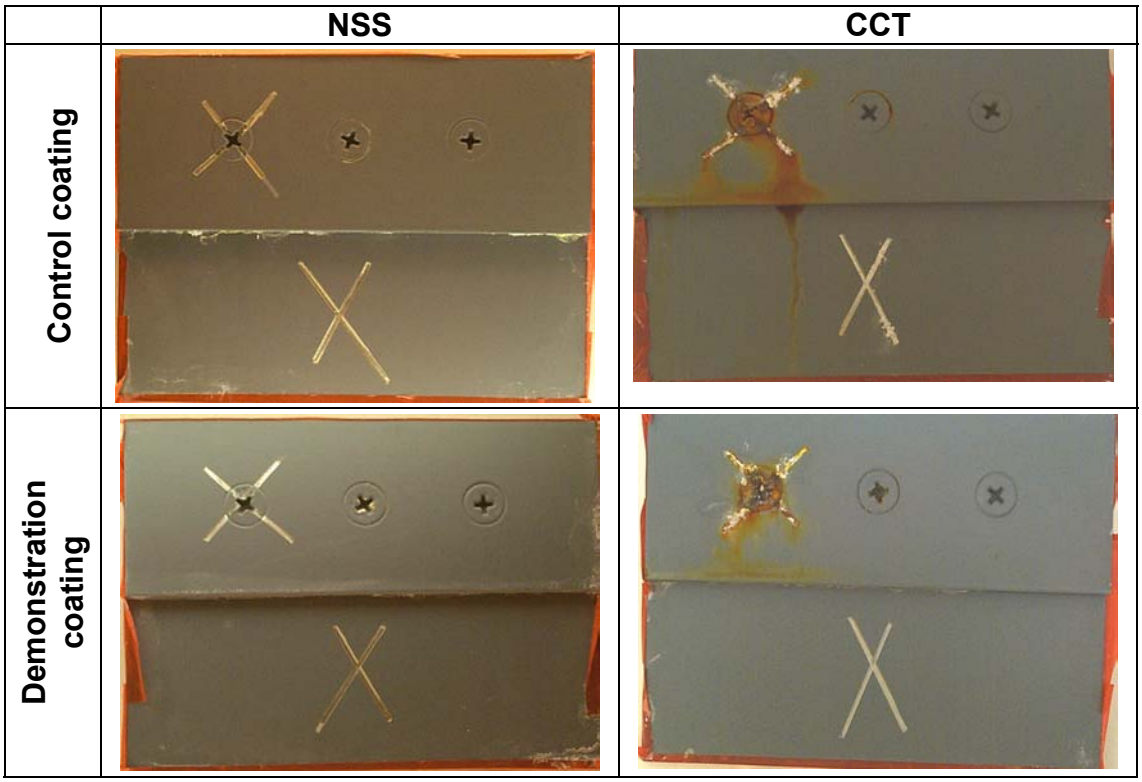

FIGURE 5. Corrosion Results of Rigs after ~2500 hours exposure

CYCLIC EXPOSURE ELECTROCHEMICAL RESULTS

Introduction. Electrochemical impedance spectroscopy is a nondestructive method used to evaluate coating systems. It is sensitive to many subtle changes in the coating system. While the interpretation of the EIS data to predict corrosion performance remains controversial, its use to show a "fingerprint" of coating systems to show the effect of exposure might prove useful.

EIS spectra were obtained on coating systems using three different protocols: constant immersion in sodium chloride solution, periodic measurements of coupons that were exposed to neutral salt spray, and periodic measurements of coupons that were exposed to a cycle of uv light for three days followed by 4 days exposure to salt spray.

Data presented here was obtained on undamaged areas of the coated panel and is typical of a variety of coating systems studied. No corrosion or coating degradation was noticed on the

panels. The uv exposure produced a barely noticeable lightening of the matt gray coating, ΔE for the coatings studied was less than 0.35 over the exposure period. The EIS results are summarized in Figure 6. Impedance and phase plots are shown for reach of the exposures as well as a plot of Rx calculated using a simple single time constant model and an image of a scribe that was present on each panel.

Preliminary analysis shows several interesting features. First, EIS data for the neutral salt spray exposure and immersion are very similar. Conceptually this is reasonable as in both cases the coating is continuously wet with electrolyte. The primary difference in the exposures is that the electrolyte is oxygenated and continuously refreshed in salt spray exposure.

The EIS data for the coatings that were exposed to the uv/salt spray cycle all show a significant change in both the impedance and phase data after about 40-60 days of exposure. This indicates that there may be a "breakthrough" time when uv light might be able to penetrate through the topcoat and begin to affect the epoxy primer. The "breakthrough" time is readily seen in the plots of Rx, calculated from a simple single time constant model. The salt spray and immersion data show slow decrease in Rx while the uv/NSS sample shows a sharp drop starting about day 50.

This preliminary data shows that EIS is sensitive enough to indicate subtle differences in coating systems. This sensitivity and the nondestructive nature of the EIS technique lead to the possibility of developing a procedure for monitoring coatings on-aircraft for overall "health" and a protocol to determine when a coating system is no longer providing sufficient protection and needs replacing. Cyclic exposure data will be obtained during development and flight test phases of the AACP program to build a database from which a monitoring protocol can be developed.

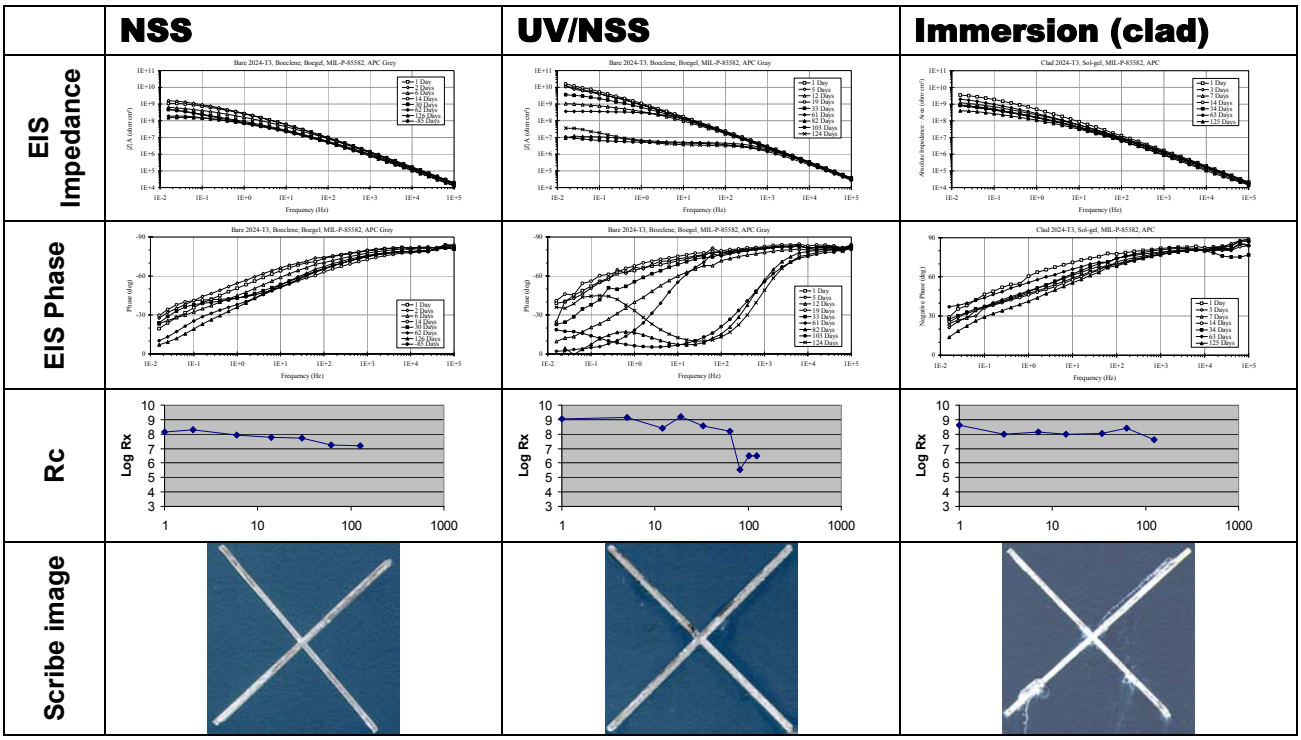

FIGURE 6. EIS Results for Cyclic Exposure Tests, Boegel/85582/APC coating system.

ACKNOWLEDGEMENTS

This work was partially funded by DARPA/AFRL Contract F33615-96-C-5078. Dr. Michael Donley was the technical monitor of the DARPA/AFRL contract. Dr. Martin Kendig performed the calculations for Rx. Dr. Dennis Dull and Mr. Glen Rasmussen obtained the EIS spectra.

REFERENCES

1. Dr. Jack Lincoln, presentation at aging aircraft TIM, Sacramento, CA, 6/6/2001

2. The Boegel EPII formulation is now available commercially as AC-131 from Advanced Chemistry and Technology, Garden Grove, CA. The term “Boegel” will be used in this paper to indicate both the Boeing developed solution and AC-131.

3. M. Kendig and S. Jeanjaquet, "Simplified and Rapid Analysis of Paint Impedance", in 'Advances in Corrosion Protection by Organic Coatings III', I. Sekine, M. Kendig , D. Scantlebury and D. Mills, eds., , PV-97-41, Electrochemical Society, Princeton, NJ, USA (1998).

4. Larry Triplett, Boeing-St. Louis, Unpublished Data.

5. Advanced Corrosion Aircraft Coatings final report, JG-PP Nonchromate Primers program, Boeing internal test reports.

6. Boeing Materials Technology rating system. 10=no corrosion, 7=marginal pass.

7. The Boeing Company, unpublished data.

DEVELOPMENT OF FLUOROPOLYMER APPLIQUÉS: PAINTLESS ALTERNATIVES FOR CORROSION PROTECTION IN THE MARINE ENVIRONMENT

Terrnece G. Vargo and Andrew Dalgleish

Integument Technologies, Inc.
70 Pearce Avenue
Tonawanda, NY 14150
716.873.1199
Fax 716.873.1303

INTRODUCTION

The chemical inertness and high temperature resistance of fluoropolymers have long made them one of the corrosion industry's top engineering materials of choice for service environments that demand resistance to the harshest chemicals at elevated temperatures.[1] In the past, the challenge has always been, "How does one achieve sound adhesion to substrates from a class of materials that are known for having low surface energy 'non-stick' properties as a primary characteristic?" Specifically, the serviceability and usefulness of this class of high-performance plastics is severely limited because of the inability to achieve strong adhesive bonds between fluoropolymer surfaces and other materials such as adhesives, plastics, ceramics, metals, glass, etc. More importantly, would greater adhesion capabilities expand the potential uses of fluoropolymers by making them a commercially feasible alternative to traditional coating and lining materials? Additionally, can this be achieved without sacrificing any of the superior performance properties of the polymer? To answer that question, this paper will present a novel cold gas plasma treatment process that now makes it possible to permanently bond adhesives and coatings to thin films and sheets of fluoropolymers in such a manner that adhesion remains

strong and permanent even under extreme conditions while maintaining the performance properties of the treated fluoropolymers.

TRADITIONAL FLUOROPOLYMER TECHNOLOGY

Traditionally fluoropolymer coatings and linings are applied in a powder, liquid or sheet form. The powders are spray applied and baked on in a multi-step process. Liquid dispersion solvent-based coatings are applied in a similar fashion. The number of steps required to achieve any significant thickness, from 10 mils DFT or more, can be commercially prohibitive in terms of costs, curing equipment, safety and handling of solvents, etc. Further, the process requires thorough quality assurance, monitoring and testing throughout the many steps necessary for a proper coating application.

Alternatively fluoropolymers sheet linings, from 40 to 100 mils DFT or greater, are manufactured by incorporating a glass fabric backing into the sheet during the extrusion process. The backing then allows the sheet lining to be installed by mechanically adhering the fabric to a substrate by use of an adhesive, which is usually an epoxy. This process is expensive as a result of the high raw material costs associated with the thicker sheets and glass backing. Additionally, this precludes the use of easy to apply, flexible thin films which have recently come under increased scrutiny as possible paint replacement coatings systems for various Navy and Marine applications (including appliqués for state-of –the-art aircraft).

Accordingly, various methods for promoting adhesion of thin fluoropolymer sheets and films have been developed using chemical and actinic radiation etch processes.[2-7] In general however, these processes adversely affect the chemical and morphological characteristics of the surface by physically destroying and altering the fluorinated surface of the polymer to promote adhesion. The resultant surface is an oxidized carbonaceous oxide overlayer, which over time

degrades the adhesive bond when exposed to various environmental or application conditions such as thermal stress and exposure to UV radiation from sunlight.

PLASMA SURFACE SCIENCE

A new process using a cold gas plasma treatment has been developed for modifying fluoropolymer surfaces in a manner that promotes adhesion to a variety of materials including other polymers, adhesives, ceramics, and metals. In the late 1980's, researchers at the State University of New York at Buffalo discovered that a radio frequency (rf) glow discharge (cold gas plasma) of hydrogen, in combination with vaporized liquids, created a distinctive surface modification at fluoropolymer surfaces.[8-10] By utilizing a hydrogen plasma as a fluorine scavenger in concert with vaporized liquids, the oxygen incorporation into the surface matrix of a fluoropolymer material was found to be highly controllable. The research discovered that the plasma surface modification enabled the subject material to retain its morphology, chemical resistance, and hydrophobic properties comparable to that of the original, unmodified fluoropolymer while effectively creating highly reactive sites for bonding other materials.

The research demonstrated that the oxygen functionalities created on these fluoropolymer surfaces were chemically reactive and permanent. It is this chemical functionality that allows various adhesives and polymers to form a covalent bond to the modified fluoropolymer surface. What's more the treatment does not significantly affect the film's surface tension properties. In other words it remains the "non-stick," easy-to-clean material that fluoropolymers are famous for.

By judiciously selecting the process gas and conditions used during an RF plasma surface treatment we have demonstrated the ability to enhance various desired surface properties of many different materials. In the application specific to halogenated polymers, a mixture of

hydrogen and H_2O or MeOH vapor co-reactant is used to generate the plasma. This combination partially defluorinates the fluoropolymer surface and concurrently adds permanently stable –OH functionalities at the defluorinated sites. The -OH functionality adjacent to fluorinated carbon groups is extremely stable, yet chemically reactive to various chemistries. The resultant reactivity is ideal for forming tenacious bonds with selective adhesives and polymers.

INNOVATIVE THIN PROTECTIVE COATING SYSTEMS FOR CORROSION PROTECTION IN THE MARINE ENVIRONMENT

The objectives of this project were to:

1. Examine the effectiveness of (2) different adhesive backed fluoropolymer films (both of which were treated using the plasma technology described above) with respect to their ability to provide corrosion protection to aircraft grade aluminum (2024-T3).
2. Examine the corrosion protection effectiveness of the above (2) fluoropolymer films on aircraft grade aluminum in conjunction with corrosion inhibitors incorporated into the coatings system.

The first fluoropolymer that was investigated was a surface modified ethylene-chloro-trifluoroethylene (ECTFE). The second material was a surface modified perfluorinated alkoxy (MFA) fluoropolymer. Both of these films were backed with a pressure sensitive (peel-and-stick) acrylic adhesive (ADCHEM 747). These appliqué films were then evaluated on aircraft grade aluminum that was either untreated, or pretreated via deoxidation followed by a chromate conversion coating by as per MIL-C-5541 using MIL-C-81706 (the aluminum test panels were prepared and generously supplied by the Naval Air Warfare Center (NAWCAD) at Patuxent River, MD). Additionally, both fluoropolymer film coatings were tested on untreated and pretreated aluminum that was subsequently treated with several different corrosion inhibitors.

The evaluation of these films involved peel strength tests of the composite films and subsequent corrosion testing at NAWCAD.

In order to choose relevant corrosion inhibitors to be investigated in this study we had detailed discussions with R & D personnel at Cortec Corporation (Cortec specializes in corrosion inhibitors for military applications). Our discussions were based on the project goals related to finding a non-toxic (or low toxicity) corrosion inhibitor that could:

1) Be used effectively with our fluoropolymer appliqués for enhancing corrosion protection on aluminum substrates
2) Be formulated into our currently used acrylic based pressure sensitive adhesive system (or other similar adhesive system) so that an all in one coating system might eventually result from this work.

Based on these discussions, Cortec personnel recommended several of their corrosion inhibitors that they have targeted for exactly the uses described above as our project goals. Specifically, several corrosion inhibitors were supplied that were non-toxic aqueous based coatings that have been formulated so that they may also be used as an additive that could be directly incorporated into various adhesive systems.

Additionally, we also were interested in studying a microencapsulated DNBM corrosion inhibitor system developed previously by Dr. Agarwala of NAWCAD. Agarwala[11-13] has described several new compounds that have been successfully demonstrated for retarding corrosion, fatigue, and stress corrosion cracking of various aerospace materials such as 7075-T6 aluminum alloys. These materials have been named DNBM, an acronym for a dark brown, highly viscous, 100% solids mixture of quaternary ammonium dichromate, nitrate, borate, and molybdate. Each panel was prepared by first making a 5% by volume solution of each of Cortec

VCI corrosion inhibitor in distilled water and a 5% by volume solution of DNBM in toluene. Next each test panel was immersed for several minutes in each prepared corrosion inhibitor solution, removed from solution, and then dried with a hot air gun. Finally, we coated each panel with ITI's pressure sensitive adhesive backed fluoropolymer film and let cure for 24 hrs.

SUMMARY RESULTS

A total of 60 aircraft grade aluminum (2024-T3) test panels with different fluoropolymer thin film coatings were supplied to NAWCAD for ASTM B-117 Salt Fog and ASTM G-85 SO_2 Salt Fog corrosion testing. Final analysis of the coatings systems have resulted from 2000 hrs of ASTM B-117 Salt Fog exposure followed by an additional 500 hr exposure to an SO_2 Salt Fog (ASTM G 85). Additionally, 40 test panels having the same coatings systems applied were subjected to adhesion tests in order to evaluate the adhesion characteristics of each coating on the aluminum substrates.

Legend and Table 1 below lists: (1) the test panel and coating, (2) the results of 2000 hrs of Salt Spray exposure as per ASTM B-117, (3) the results of 500 hrs of SO_2 salt spray exposure as per ASTM G-85, and (4) the peel strength values for each system.

LEGEND 1.
For deoxidized, chromate pretreated aluminum test panels

XA - 5 mil MFA fluoropolymer with 4 mil acrylic adhesive PSA on deoxidized, chromate pretreated aluminum test panel

YA - 5 mil ECTFE fluoropolymer with 4 mil acrylic adhesive PSA on deoxidized, chromate pretreated aluminum test panel

1A - 5 mil MFA fluoropolymer with 4 mil acrylic adhesive PSA on deoxidized, chromate pretreated aluminum test panel that was additionally treated with DNBM w/o chromate

2A 5 mil MFA fluoropolymer with 4 mil acrylic adhesive PSA on deoxidized, chromate pretreated aluminum test panel that was additionally treated with DNBM with chromate

3A 5 mil MFA fluoropolymer with 4 mil acrylic adhesive PSA on deoxidized, chromate pretreated aluminum test panel that was additionally treated with Cor-tec VCI M 370-A

4A 5 mil MFA fluoropolymer with 4 mil acrylic adhesive PSA on deoxidized, chromate pretreated aluminum test panel that was additionally treated with Cor-tec VCI M 5120

5A 5 mil ECTFE fluoropolymer with 4 mil acrylic adhesive PSA on deoxidized, chromate pretreated aluminum test panel that was additionally treated with DNBM w/o chromate

6A 5 mil ECTFE fluoropolymer with 4 mil acrylic adhesive PSA on deoxidized, chromate pretreated aluminum test panel that was additionally treated with DNBM with chromate

7A 5 mil ECTFE fluoropolymer with 4 mil acrylic adhesive PSA on deoxidized, chromate pretreated aluminum test panel that was additionally treated with Cor-tec VCI M 370-A

8A 5 mil ECTFE fluoropolymer with 4 mil acrylic adhesive PSA on deoxidized, chromate pretreated aluminum test panel that was additionally treated with Cor-tec VCI M 5120

TABLE 1.
Corrosion and adhesion results of coatings on, deoxidized, and chromate pre-treated aluminum test panels.

Test Panel	**Corrosion Results**		**Adhesion Results** **(ASTM D 903-93 lbs/lin.in.)**	**± Error: % Error Adhesion results**
	2000 hrs Salt Spray; ASTM B-117	500 hrs SO_2 Salt Spray; ASTM G85		
XA	No Corrosion	No Corrosion	14.2 = (2550 N/m)	0.43: 3.0%
YA	No Corrosion	No Corrosion	32.4 = (5680 N/m)	1.40: 4.3%
1A	No Corrosion	No Corrosion	**5.8 = (1050 N/m)**	**1.79: 30.1%**
2A	No Corrosion	No Corrosion	6.1 = (1075 N/m)	0.46: 7.5%
3A	No Corrosion	No Corrosion	21.6 = (3791 N/m)	1.10: 5.1%
4A	No Corrosion	No Corrosion	14.2 = (2550 N/m)	0.92: 6.5%
5A	No Corrosion	No Corrosion	**14.0 = (2460 N/m)**	**8.51: 60.8%**
6A	Med. Corr. In Scribe	Med. Corr. In Scribe	10.2 = (1794 N/m)	0.23: 2.3%
7A	Slight Corr. in Scribe	Corr. in Scribe	31.2 = (5460 N/m)	1.99: 6.4%
8A	No Corrosion	Slight Corr. in Scribe	31.8 = (5580 N/m)	2.80: 8.8%

Legend and Table 2 below lists: (1) the test panel and coating, (2) the results of 2000 hrs of Salt Spray exposure as per ASTM B-117, (3) the results of 500 hrs of SO_2 salt spray exposure as per ASTM G-85, and (4) the peel strength values for each system.

LEGEND 2.
For "as received", untreated aluminum test panels

XB - 5 mil MFA fluoropolymer with 4 mil acrylic adhesive PSA on aluminum test panel without any prior pre-treatment or chromate protection

YB - 5 mil ECTFE fluoropolymer with 4 mil acrylic adhesive PSA on aluminum test panel without any prior pre-treatment or chromate protection

1B - 5 mil MFA fluoropolymer with 4 mil acrylic adhesive PSA on aluminum test panel treated only with DNBM w/o chromate

2B 5 mil MFA fluoropolymer with 4 mil acrylic adhesive PSA on aluminum test panel treated only with DNBM with chromate

3B 5 mil MFA fluoropolymer with 4 mil acrylic adhesive PSA on aluminum test panel treated only with Cor-tec VCI M 370-A

4B 5 mil MFA fluoropolymer with 4 mil acrylic adhesive PSA on aluminum test panel treated only with Cor-tec VCI M 5120

5B 5 mil ECTFE fluoropolymer with 4 mil acrylic adhesive PSA on aluminum test panel treated only with DNBM w/o chromate

6B 5 mil ECTFE fluoropolymer with 4 mil acrylic adhesive PSA on aluminum test panel treated only with DNBM with chromate

7B 5 mil ECTFE fluoropolymer with 4 mil acrylic adhesive PSA on aluminum test panel treated only with Cor-tec VCI M 370-A

8B 5 mil ECTFE fluoropolymer with 4 mil acrylic adhesive PSA on aluminum test panel treated only with Cor-tec VCI M 5120

TABLE 2.
Corrosion and adhesion results of coatings on "as received", untreated, aluminum test panels.

Test Panel	**Corrosion Results**		**Adhesion Results** **(ASTM D 903-93 lbs/lin.in.)**	**± Error: % Error Adhesion results**
	2000 hrs Salt Spray; ASTM B-117	500 hrs SO_2 Salt Spray; ASTM G85		
XB	Slight Corr. in Scribe	Slight Corr. in Scribe	13.5 = (2355 N/m)	1.11: 8.2%
YB	Slight Corr. in Scribe	Corr. in Scribe	31.7 = (5554 N/m)	2.41: 7.6%
1B	Slight Corr. in Scribe	Slight Corr. in Scribe	7.8 = (1373 N/m)	0.81: 10.4%
2B	Slight Corr. in Scribe	Slight Corr. in Scribe	5.5 = (965 N/m)	0.58: 10.5%
3B	**No Corrosion**	**No Corrosion**	**> 18.4 = (3217 N/m)**	**6.00: 32.6%**
4B	Slight Corr. in Scribe	Slight Corr. in Scribe	13.0 = (2275 N/m)	0.52: 4.0%
5B	Medium Corr. in Scribe	Medium Corr. in Scribe	**15.2 = (2656 N/m)**	**4.25: 28.0%**
6B	Slight Corr. in Scribe	Slight Corr. in Scribe	10.3 = (1812 N/m)	0.49: 4.8%
7B	Medium Corr. in Scribe	Corr. in Scribe	31.5 = (5514 N/m)	0.86: 2.7%
8B	Slight Corr. in Scribe	Medium Corr. in Scribe	19.4 = (3395 N/m)	1.11: 5.7%

RESULTS

SALT SPRAY CORROSION TESTS

Tables 1 and 2 list the results of a 2000 hr Neutral Salt Spray exposure (ASTM B-117) followed by 500 hrs of exposure to an SO_2 Salt Spray test (ASTM G 85). These exposure tests were performed on (2024 -T3) aluminum test panels that were coated with various films and corrosion inhibitors. All of the samples labeled with an "A" (Legend and Table 1) were pretreated using the following steps:

(1) Alkaline clean with Oakite 164 at 135 °F for 15 minutes

(2) Warm water rinse

(3) Deoxidize with Turco Smut – Go NC at ambient temps for15 minutes

(4) Warm water rinse

(5) Chromate conversion coating with Alodine 1200S at ambient temp for 3 minutes

(6) Cold water rinse, deionized water rinse, air dry

(7) Allow chromate gel to set overnight

Samples labeled with a "B" (Legend and Table 2), were provided without any prior treatment or cleaning and, other than a degreasing process using a mild alcohol solution were used "as received". Each test panel was prepared in triplicate for corrosion testing and all of the test panels were first cross-scribed before testing in order that corrosion evaluation could be measured both under regions that were coated and in regions where the coating was compromised.

Corrosion Tests (Table 1). Corrosion results of all coatings tested on the aluminum panels that were first deoxidized and pre-treated with chromate (as per standard pre-treatments for aluminum military aircraft) all passed both the 2000 hr neutral salt spray and the following 500 hr SO2 salt spray tests. In fact, Table 1 shows a series of seven coatings that showed no visual corrosion – even in the scribed areas. Note, that upon magnified (10X) inspection one could identify the onset of minor pockets of corrosion strictly limited to scribed regions.

Samples 6A, 7A, and 8A all developed small degrees of visual corrosion that were confined to areas within the scribed regions of the films. Based on the ASTM test criteria, the degree of corrosion measured on these test panels was inhibited to the degree that the coatings on these panels were given a passing grade.

Basically, all of the coatings systems applied and evaluated in this project all passed the rigorous testing methods standardized for coatings systems on aircraft grade aluminum. In fact, both the MFA and ECTFE (with acrylic pressure sensitive adhesive) fluoropolymers, (having no additional corrosion inhibitor added to the coating system), showed no corrosion on any portion

of the aluminum panels (even under magnified (10X) inspection) other than that in the scribed area.

Corrosion Tests (Table 2). Table 2 lists results from test panels labeled with a "B". These aluminum test panels were identical to the test panels used in Table 1 (i.e. those labeled with and "A") except for the fact that they were coated "as received" without any prior deoxidation and coating with a conversion coating. Other than a mild alcohol solution used for degreasing, the aluminum test panels were used "as received".

The results listed in Table 2 shows that without the deoxidation step and chromate pre-treatment used for the test samples in Table 1, the onset of corrosion results for almost all of the samples. Although visual corrosion is observed on all samples except 3B (3B showed results like those found for panels "A" where corrosion could only be observed under magnified conditions), the degree of corrosion is only minor and based on the test criteria (i.e., pass/fail) for ASTM B-117 and G 85, all of the coating systems on the test panels listed in Table 2 are still considered passes.

The coating system used for test panel 3B was an MFA fluoropolymer backed with an acrylic PSA applied to an "as received" aircraft grade aluminum test panel that was first degreased by ultrasonicating in a mild alcohol solution and then coated with an aqueous based corrosion inhibitor obtained from CORTEC's line of vapor corrosion inhibitors: VCI M 370-A.

Based on these results and adhesion results that will be discussed later, the fluoropolymer appliqué/VCI M 370-A coating system appears to be an exciting development. Essentially, the data shows that this coating system provides excellent corrosion protection even on aluminum substrates that are not deoxidized or coated with a chromate conversion coating. These results have initiated subsequent work in our laboratories that is focused on the development of a new

adhesive formulation that will incorporate a corrosion inhibitor (having similar chemistry to the VCI M 370-A corrosion inhibitor) directly into the PSA (pressure sensitive adhesive) system. From this development we hope to fabricate a single peel and stick coating system that has the potential for: (1) eliminating the laborious practice of deoxidizing and pretreating aluminum surfaces and; (2) providing an easy to install coating system that is capable of protecting aluminum systems and components from severe environments common to the marine environment.

ADHESION TESTS

Tables 1 and 2 list the adhesion test results obtained by Advanced Plastic and Material Testing Inc. The American Association accredits APMT for Laboratory Accreditation. The peel adhesion tests were performed as per ASTM D 903-93.

The peel adhesion results (listed in Tables 1 and 2) show the variability in surface adhesion for each test panel preparation (i.e., the variability indicates the degree of homogeneity and effective coverage of the surface preparation by the calculated % error). In general, we observe that each coating system has (within error limits) the same results whether they have been measured on deoxidized, chromate pre-treated aluminum (Table 1) or the "as received" aluminum test panels (Table 2). This indicates that the standard deoxidation step and subsequent chromate pre-treatment used on current aluminum based military aircraft has no effect on the adhesion strength for this particular system. This is supported by the fact that the fluoropolymers applied to test panels XA and YA have similar adhesion strengths as the fluoropolymers applied to panels XB and YB. The major difference is the base fluoropolymer where the measurements show that the PSA backed MFA bonds with strengths between 13PLI and 14 PLI, as opposed to the PSA backed ECTFE fluoropolymer which bonds significantly stronger with peel strengths

exceeding 30 PLI. Since the PSA used for both the MFA and ECTFE fluoropolymer is the same (ADCHEM acrylic adhesive 747), the difference in peel strengths is probably related to the difference in stiffness or surface modulus exhibited by each respective fluoropolymer, (ECTFE has a higher surface modulus (ca. 8000 psi) than MFA (ca. 3500 psi) which is more flexible and elongates easier). In both cases however, (e.g., 13 PLI and greater) is expected to provide the required adhesion for any marine application. (Note: obviously other conditions may prevail such as humidity, immersion in seawater, etc.).

Another objective of this project was to determine the effectiveness of applying a fluoropolymer appliqué to aluminum in conjunction with other corrosion inhibitors as discussed previously. Thus, experiments were performed where we coated three uniquely different corrosion inhibitors directly onto both pre-treated aluminum and "as received" aluminum test panels as described above.

There were three different corrosion inhibitors investigated in this study. The first one was DNBM, which was applied to the test panels by spraying a dilute solution of DNBM (5% by volume) in Toluene directly onto the test panel. The other two, (CORTEC VCI M 370-A and M 5120) were applied by dipping the test panels into an aqueous based solution containing 5% of the corrosion inhibitor solution by volume as described above.

The results in Tables 1 and 2 show that the least effective corrosion inhibitor (with respect to obtaining good adhesion) was the DNBM material that had % error ranging from 7.5% to over 30%. During the application of DNBM (i.e., spraying from toluene) we noted that the coating procedure produced surfaces having a large variability in homogeneity with respect to coverage and coating thickness. The large disparities in adhesion strengths shown in Tables 1 and 2 effectively support this observation and indicate a need to develop a different procedure

for applying this coating. The results obtained from test panels that were coated with M 5120 all have % errors that are within expected experimental errors normally associated with hand applied coatings and as such, suggests that M 5120 can be easily applied to aluminum components and structures using water based application procedures. Finally, corrosion inhibitor M 370-A showed a large % error on only test panel 3B. Note however, that the adhesion strength value is >18.4PLI where the ">" sign indicates that the MFA fluoropolymer material either stretched or tore during the peel testing. This accounts for the large % error and does not suggest any non-homogeneity in coating coverage or thickness**. Thus, corrosion inhibitor M 370-A also represents a good candidate for continued study**.

CONCLUSIONS

Based on both the corrosion and adhesion results described above, it appears that all of the coatings systems are effective for corrosion protection. Specifically, for use on deoxidized and chromate pre-treated aluminum, the fluoropolymer films (i.e., MFA and ECTFE) demonstrate outstanding corrosion protection without the use of any additional treatments using other corrosion inhibitors. In the case that the aluminum is not pre-treated, the most effective coatings system appears to be the MFA fluoropolymer used in conjunction with CORTEC's VCI M 370-A. This system demonstrated a capability to provide superior effectiveness with respect to preventing corrosion under the salt spray test conditions evaluated at NAWCAD. Additionally, the M 370-A also shows good compatibility to MFA films backed with our acrylic PSA based on the measured adhesion strengths that are expected to be more than sufficient for providing good adhesion to various aluminum components subjected to the marine environment.

The results obtained in this project have demonstrated the potential of this paint replacement system that may result in a novel appliqué technology that can be:

(1) Easily applied, removed and repaired

(2) Used without pretreatment on various marine vehicles and components including aircraft hull, wings or components

(3) Pigmented for various military uses around the world

(4) Capable of integrating additional characteristics like E^3 protection, as well as providing corrosion protection, and rapid decontamination and substrate protection from chemical and/or biological agents.

ACKNOWLEDGEMENTS

The Authors would like to thank the personnel at the Naval Air Warfare Center – Aircraft Division at Patuxent River MD for both technical and financial support under the Navy's Small Business Innovative Research program. Special thanks to Jim Muller and Kevin Kovaleski for the technical support in preparing and donating the aluminum test panels and Dr. Agarwala for supplying the DNBM materials. Finally, we would also like to thank Cortec Corporation for their help and generous donation of the VCI materials used in this project. This project was supported by the Navy's SBIR topic N99-177 Contract No. N68335-00-C-0129.

REFERENCES

1. A.E. Feiring, J.F., Imbalzano, D.L., Kerbow, *Trends in Polymer Science*, 2(1), (1994): p. 26.
2. R.R. Rye, K,M, Chi, M., Hampden-Smith, T.T., Kodas, J. Electrochem. Soc., 139, (1992): L60.
3. M.H. Hung, R.R. Burch R.R., J. Appl. Polym. Sci., 55(4), (1995): p. 549.
4. C.A. Costello, T.J. McCarthy, Macromolecules, 20, (1987): p. 2819.
5. R.C. Bening, T.J. McCarthy, Macromolecules, 23, (1990): p. 2648.
6. L.M. Siperko, R.R. Thomas, J. Adhes. Sci. Technol., 3, (1989): p. 157.

7. H. Meyer, et. al., in Metallized Plastics 2: Fundamental and Applied Aspects, K. L. Mittal, Ed. (Plenum, New York, 1991), p. 121.

8. T.G. Vargo, J.A. Gardella, Jr., A.E. Meyer, R.E., Baier, J. Polym. Sci. Part A: Polym.Chem., 29, (1991): p. 555.

9. J.A. Gardella, Jr., and T.G. Vargo, U.S. Patent 4,946,903, 1990.

10. J.A. Gardella, Jr., and T.G. Vargo, U.S. Patent 5,266,309, 1993.

11. V.S. Agarwala, "Inhibition of Corrosion Fatigue Assisted Failures in High Strength Alloys, Corrosion Inhibition, R.H. Hausler, ed. (Houston TX: NACE, 1988), p. 79.

12. L.J. Bailin, V.S. Agarwala, "Development of Microencapsulated DNBM Quaternary Ammonium Inhibitors for Paints," Proc. 1987 Tri-service Conference on Corrosion, Air Force Wright Aeronautical Labs, Wright Patterson Air Force Base, AFWAL-TR-4139, Vol. II, pg. 111, May 1987.

13. K.L. Vasanth, "Corrosion Inhibition in Naval Vessels," Proc. Corrosion 96 the 1996 NACE International Annual Conference and Exposition, Paper 233, p. 4.

COLD SPRAY TECHNOLOGY FOR MILITARY APPLICATIONS

V. K. Champagne and W. Ziegler

US Army Research Laboratory
Weapons and Materials Research Directorate
Building 4600
Aberdeen Proving Ground, MD 21005-5069

ABSTRACT

This paper will discuss an emerging technology commonly referred to as 'cold spray' and its possible use as a metal deposition technique to form wear and corrosion resistant coatings for DOD applications. Cold spray is a material deposition process whereby metal powder particles are utilized to form a coating or a free-standing structure by means of ballistic impingement upon a suitable substrate. Conventional methods of surface preparation of the substrate, such as grit blasting, which are necessary for thermal spray processes, are often not required for cold spray. In the cold spray process, a supersonic stream of compressed gas accelerates metal powder particles. The spray nozzle design incorporates the use of a converging-diverging throat through which the preheated gas stream is expanded to attain supersonic velocities, with an accompanying decrease in temperature. The informal term "cold spray" arose due to the relatively low temperatures of the expanded gas and particle stream that exits the nozzle. The advantages of cold spray over current and emerging technologies are to be realized in terms of economics, environmental compliance and performance. Cold spray coatings offer certain advantages over those applied by conventional thermal spray techniques in that they can contain less oxidation since they are applied below the melting temperature and do not experience the effects of thermal stress as a result of resolidification. In addition, some cold spray coatings have been shown to adhere to the substrate by a solid state bonding mechanism having much higher bond strengths.

BACKGROUND

The cold gas-dynamic spray method or "cold spray" was originally developed in the mid-1980's by Dr. Anatoli Papyrin and colleagues at the Institute of Theoretical and Applied Mechanics (Russian Academy of Sciences).[1,2] Cold spray is a material deposition process

whereby metal powder particles are utilized to form a coating or a free-standing structure by means of ballistic impingement upon a suitable substrate. Since, in some instances, research has indicated that the deposited material appears to adhere to the substrate as a result of a metallurgical bond, conventional methods of surface preparation, such as grit blasting, which are necessary for thermal spray processes, are often not required for cold spray. Additionally, in the initial stages of the cold spray process, before the individual particles begin to adhere to the surface, the substrate is in fact being grit blasted, which may facilitate in bonding. The metal powders range in particle size from <5–50 μm and are accelerated by a supersonic (300-1200 m/s) stream of compressed gas. The spray nozzle design incorporates the use of a converging-diverging throat through which the preheated gas stream is expanded to attain supersonic velocities, with an accompanying decrease in temperature. The informal term "cold spray" arose due to the relatively low temperatures (-17°C to 704°C) of the expanded gas and particle stream that exits the nozzle. It is important to note that the temperature of the gas stream is always below the melting point of the particulate material and the resultant coating and/or freestanding structure is formed in the solid state. Currently, the types of carrier gases most often used in the cold spray process are nitrogen and helium. Atmospheric air may also be used but then oxidation of the powder particles may become an issue and higher velocities that are required to deposit some of the harder materials cannot be achieved. Since adhesion of the metal powder to the substrate, as well as the cohesion of the deposited material, is accomplished in the solid state, the characteristics of the cold spray deposit are quite unique in many regards. There are a variety of metals that have been successfully deposited by the cold spray process including iron, stainless steel, nickel, copper, aluminum, zinc, cobalt, titanium, molybdenum, silver, tin, cadmium, bronze, Inconel 718, nickel based super alloys and many other alloys.

ADVANTAGES AND APPLICATIONS

The cold spray process does not use thermal energy to melt the particles to be deposited, but instead relies upon the ability of the particles, which are accelerated by a supersonic jet of compressed gas (300-1200 m/s)[3], to plastically deform upon impact with a substrate and cause cratering (Figure 1).[4] The bonding mechanism of cold spray has been compared to that of explosive welding[5,6] whereas the formation of a solid-state jet of metal occurs at the impact point between the particle and substrate.[4] The same phenomena is believed to occur between particles, such that residual stresses in cold sprayed samples have been reported to be predominately compressive rather than tensile.[7] Theoretically, such a condition can be substantiated by the fact that the subsequent solid particles impacting previously deposited material at these high velocities would be continuously peening the surface as the coating is built up.[8] Recrystallization and evidence of severe cold work have been reported, to support this claim. There has been no indication that melting occurred during impact but significant plastic deformation has been observed of the particle and the substrate. Figure 2 shows the high velocity impact of a single copper particle against a stainless steel substrate. It is well understood that shot-peened metallic surfaces result in the formation of compressive stress layers. Since the bonding mechanism appears to be directly related to the plasticity of the powder used, it stands to reason that the cold spray process is limited to powders that are predominately metallic. However, research has shown that a metallic powder can be doped with a significant amount of non-metallic powder and be successfully deposited. Amateau and Eden have demonstrated this by applying a coating of Al-9-Ce5Cr-2.8Co + 15 volume percent SiC onto an aluminum substrate.[9] Other hard

materials such as chromium-carbide (Cr3C2) have also been applied after being mixed with 25 percent metallic powder serving as a binder. [9]

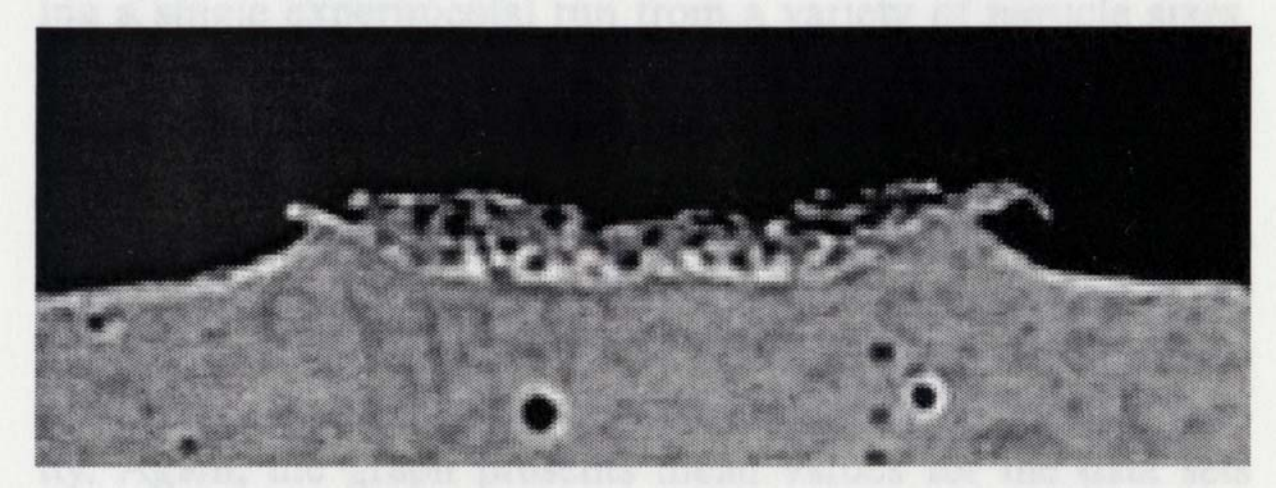

FIGURE 1. Cross-section of the impact site between a copper particle and a stainless steel substrate. [4]

The most significant advantage of cold spray is the ability to apply metal and metal alloy particles at temperatures much lower than the melting points of either the coating or the substrate. This characteristic of the cold spray process alone overcomes a multitude of problems associated with coatings applied by conventional thermal spray techniques such as phase transformation, recrystallization, oxidation and residual stress. Figure 3 shows the operating temperatures and particle velocities of the cold spray method as compared with other thermal coating methods. The exceptional adhesion of cold spray coatings is, in part, due to the low temperatures at which the coatings are deposited. One of the most deleterious effects of depositing coatings at high temperatures is the residual stresses that develop, especially at the coating-substrate interface, upon solidification from the molten state. This problem is compounded when the substrate material has a significantly different thermal expansion coefficient from the coating material. This variation often causes the metal coating to debond

from the substrate upon cooling. Sometimes the residual stresses may not be enough to cause the coating to separate from the substrate but may weaken it and reduce its effective service life. This problem can be minimized when cold spray is used.

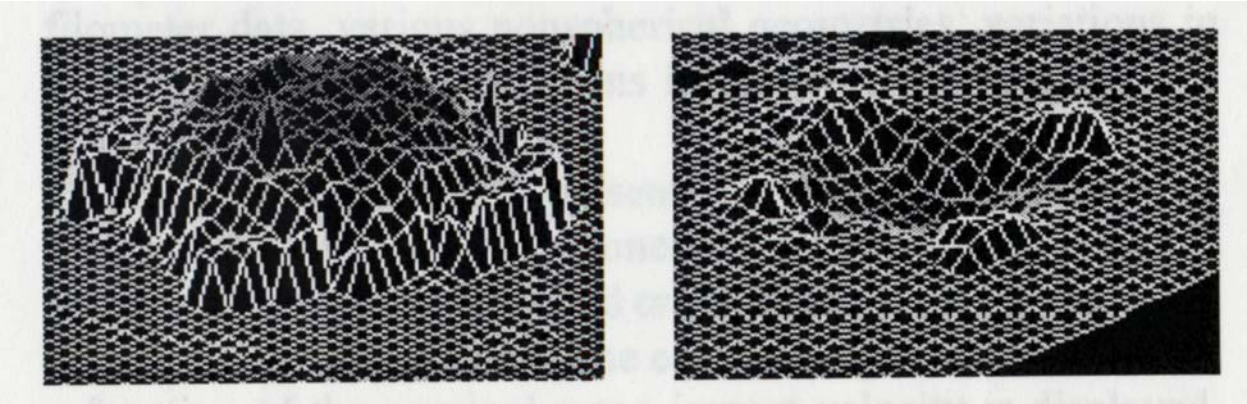

FIGURE 2. Profilometry results before and after removal of copper splat from a 600 m/s impact.[4]

Another important attribute of cold spray is the high coating density that can be achieved with minimal oxide content, which is a distinct advantage over that of thermal spray coatings. Surface oxides are broken up during impact, exposing a clean metal surface, which promotes good bonding and low oxide content. The resultant cold spray coating retains the properties of the original metal powder, such as thermal and electrical conductivity, making it a good candidate for applications in the electronics industry. High deposition rates are another significant advantage. Deposition rates exceeding 15 kg/min have been achieved [9] compared to approximately 0.23 kg/min for high velocity oxygen fuel (HVOF)[10]. The high deposition rates, combined with low oxide and residual stress levels, allow for increased adhesion and extremely thick coatings (>2.54 cm in a matter of minutes), as well as the formation of freestanding structures. This characteristic makes cold spray a possible alternative to laser rapid prototyping.

Since cold spray is performed below the melting temperatures of the materials being deposited the process is inherently safer and there are no metal fumes to contend with.

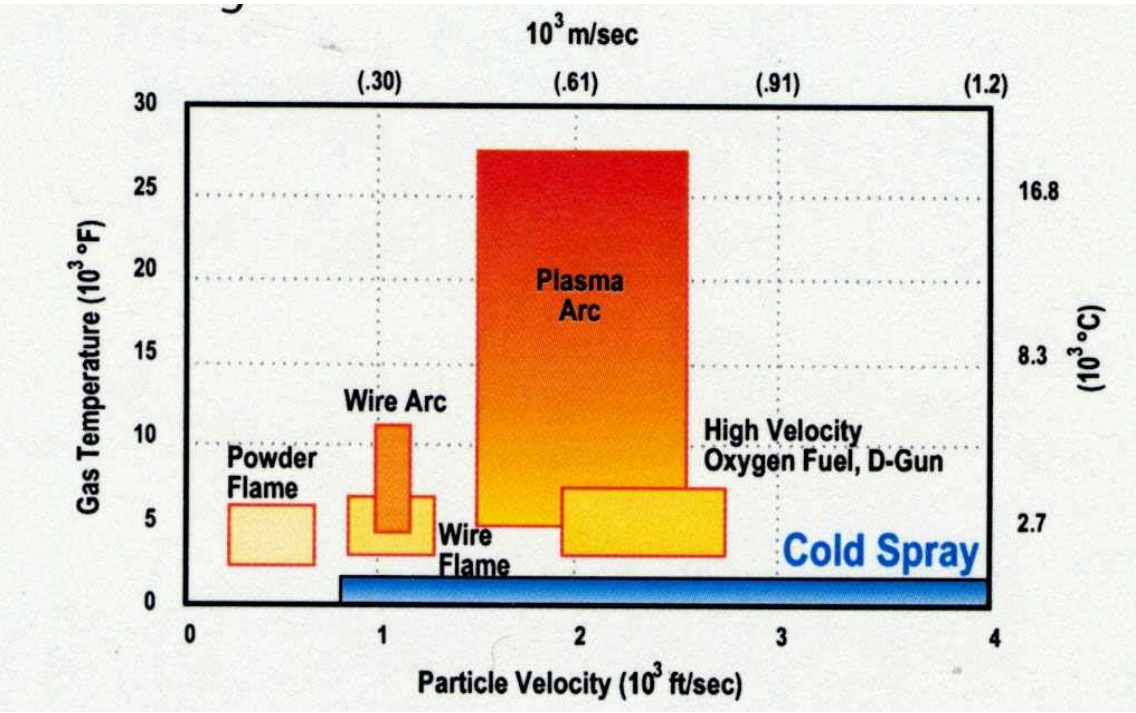

FIGURE 3. Comparison of thermal spray and cold spray particle velocity and gas temperature.[11]

THE ARL COLD SPRAY SYSTEM

The ARL cold spray facility consists of a liquid nitrogen source and compressor; a gas control module that regulates the high-pressure gas; a gas heater; a powder feeder; the supersonic nozzle; and a data acquisition and control system. A schematic of the major components and flow diagram is shown in Figure 4.

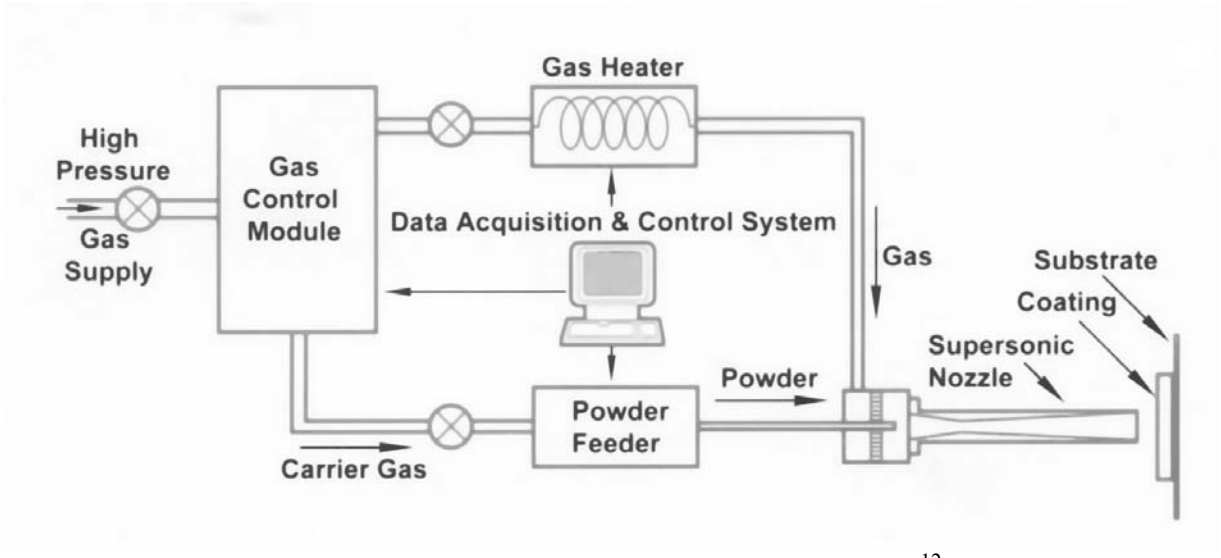

FIGURE 4. Flow diagram of the cold spray process.[12]

Liquid nitrogen is evaporated and then compressed to a working pressure of 500 psi. A 400-gallon storage tank serves as a buffer between the compressor and the Gas Control Module (GCM). The GCM ties the control inputs from the operator to the hardware operation. Instructions to the GCM are conveyed from the operator via the Data Acquisition System (DACS). The GCM splits the nitrogen flow into two streams – the main gas flow to the gas heater and nozzle and the feeder flow to the powder feeder. The pressures are controlled and the flow rates are measured for each stream. The gas heater heats the main gas flow to the selected operating temperature. This is accomplished by means of a 25 KW heating coil. Current to the coil is controlled by the DACS. Bulk powder feedstock is contained in the powder feeder. Slots in a rotating wheel within the powder feeder fill with powder, and the wheel's rotation transfers powder to the exit port. Varying the rotation rate through the DACS controls the powder feedrate. The flow of nitrogen from the GCM transports the powder from the powder feeder to the nozzle. The heated main gas flow from the gas heater and the powder flow from the powder feeder combine at the nozzle prechamber. The prechamber mixes the powder with the heated main gas for subsequent acceleration into and through the supersonic nozzle. The nozzle can be

stainless steel or silicon carbide and has a 0.079" throat diameter. Depending on the gas pressure and temperature as set by the DACS, the gas exit velocity can reach up to Mach 4 (Table 1). Figure 5 shows the major components and the arrangement of the cold spray system at ARL. The cold spray process is able to deposit pyrophoric materials such as titanium and aluminum that are difficult to apply by conventional thermal spray techniques and the noise levels are lower. Additionally, cold spray systems are less complex than those of thermal spray and in most cases the powders can be reclaimed improving the economics of the process. Efforts are also underway to produce a helium recovery system to make the use of helium more practical.

TABLE 1.
The ranges of gas and powder conditions of the cold spray system.

Parameter	Value
Main Gas Stagnation Pressure	100 to 500 psi
Main Gas Stagnation Temperature	0 to 1300 degree F
Main Gas Flow Rate	30 to 100 CFM
Powder Feeder Gas Flow	40 to 110 CFM
Powder Feed Rate	10 to 30 pounds/hour
Gas Heater Power	0 to 25 KW

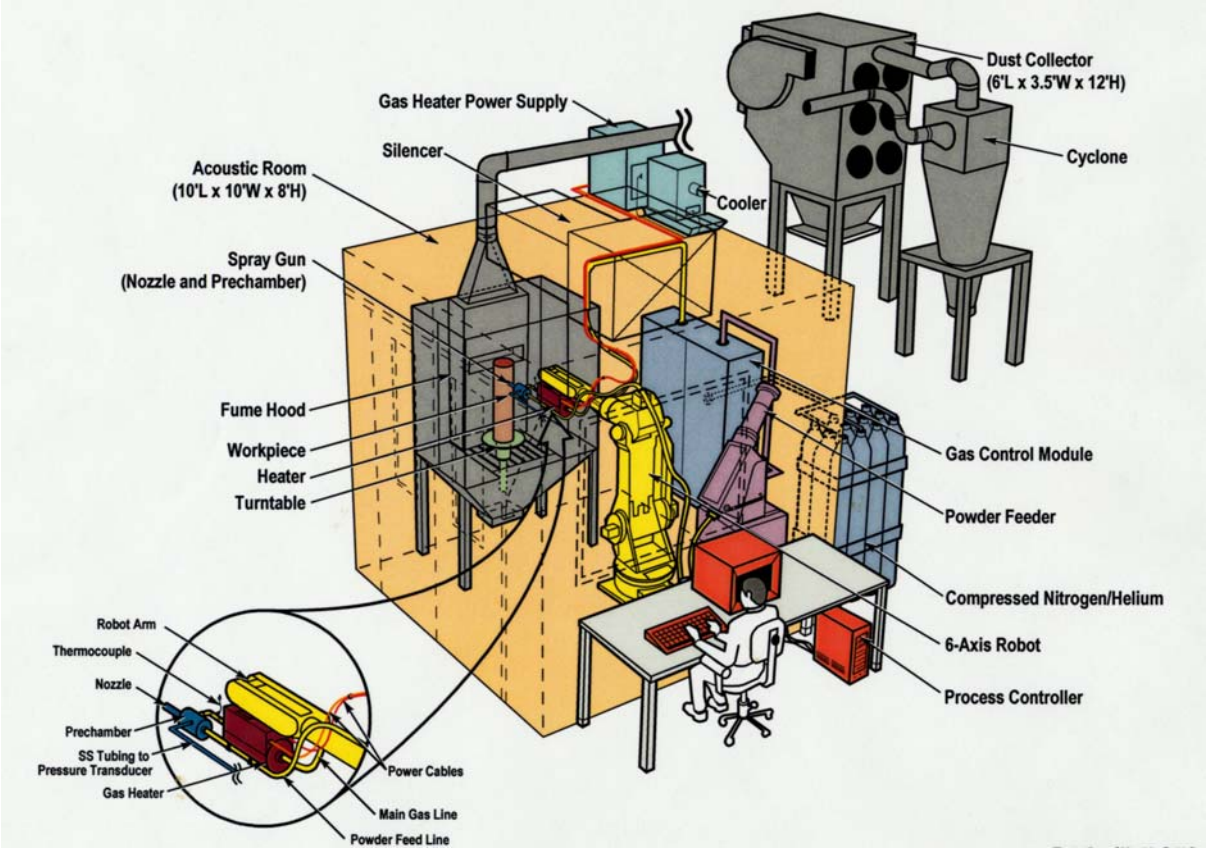

FIGURE 5. Schematic of the cold spray system.[12]

MILITARY APPLICATIONS FOR COLD SPRAY

The cold spray process shows immediate promise in electronics since the deposited material has nearly the same properties as the original powder, such as electrical and thermal conductivity. This is a result of low oxide contamination and high density. Potential applications include electrical conductors for integrated circuit boards, electrical contacts in bomb fuzes, heating elements and electrical insulation coatings for metals, ceramics and polymeric materials.

Sacrificial coatings for use on steel and aluminum are very good candidates for cold spray. Amateau and Eden have produced data indicating that the corrosion rate of aluminum, zinc and 85zinc-15aluminum coatings sprayed onto steel were lower than those produced by thermal spray (Figure 6). The corrosion tests were conducted at the La Que Center for Corrosion

Technology in Wrightsville Beach, North Carolina and at PennState. Sections of the appliqué steel armor of the AAV (Amphibious Assault Vehicle) were coated by the cold spray process and also thermal spray. The tests performed at the La Que Center were accomplished by immersing the panels in filtered seawater for 1 hour followed by a 23 hour drying cycle. This procedure war repeated over the course of 6 months to represent an accelerated corrosion test. Penn State conducted similar tests where the immersion cycle was 10 minutes in the seawater and 50 minutes in air. The corrosion rates were derived from polarization measurements taken over time.

The cold spray process has been demonstrated for the Advanced Amphibious Assault vehicle (AAAV) by work conducted by Amateau and Eden under a U.S. Navy MANTECH Program addressing an alternative road wheel design on the track system. A wear and corrosion resistant coating comprised of Al-9Ce-5Cr-2.8Co+15 volume percent SiC was proposed to replace a steel wear ring riveted to the side of the aluminum road wheel. The new lightweight coating applied by the cold spray process resulted in a weight savings of 191 kgs. (420 lbs.) since each vehicle has 28 wheels and a weight savings of 6.8 kgs. (15 lbs.) was realized for each wheel. The wear performance of the cold spray coated road wheels has been demonstrated on an actual test vehicle driven for over 1610 miles.

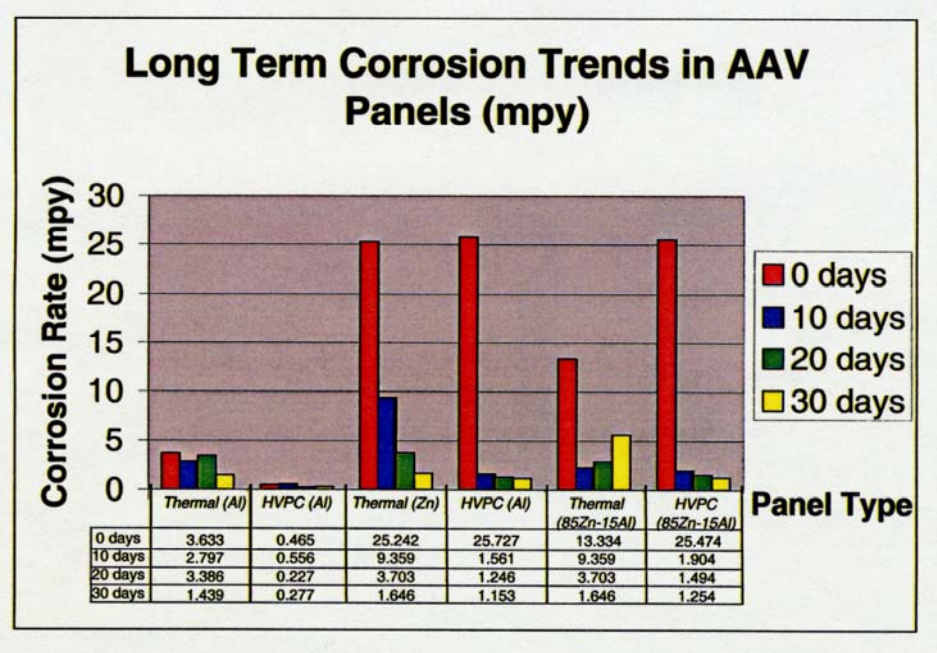

FIGURE 6. Corrosion rates for AAV appliqué armor panels coated with Al, Zn and 85Zn-15Al.[9]

Cold spray technology can also be applied to the repair and build-up worn parts. The US Army Research Laboratory (ARL) is currently participating in an effort with Corpus Christi Army Depot to address possible alternatives to nickel and chrome electroplating plating for Army rotorcraft components. Included in this study, is the CH47 servo actuator which is fabricated from 7075 aluminum electroplated with nickel and chrome on the hydraulic contact surface to prevent wear and corrosion pitting. Another candidate is the SH-60 landing gear manufactured from 300M steel, which also contains a nickel and chrome electroplating for wear and corrosion resistance. The Navy is experiencing severe corrosion pitting on the exposed portion of the plated, wear surface. The remaining part of the gear is IVD aluminum coated. Cold spray has also been proposed for a series of T-700 engine parts including; impellors, shafts, tie rods as an alternative to chrome electroplating. It is anticipated that cold spray will be used in

certain applications currently dominated by thermal spray techniques where bond strength plays a predominate role.

RESEARCH EFFORTS

ARL will be focusing its efforts in developing military applications for cold spray technology and generating much needed materials characterization data. There is limited published research on such important aspects of the cold spray process as bond strength, coating density, deposit efficiency and corrosion resistance to name just a few. ARL plans to establish processing parameters for a variety of coating and substrate combinations that will be dictated by the specific applications targeted. Currently, ARL has several applications it is exploring, including the coating of ceramic substrates with titanium. Research is also being conducted to cold spray tungsten penetrators with materials such as stainless steel and nickel. The cold spray process is also being investigated for use in munition applications, replacing conventional welding techniques. The cold spray process will not be a total replacement for thermal spray simply due to its inability to deposit very hard materials such as ceramics, although progress has been made demonstrating the capability to spray mixtures of ceramic and metal powders containing significant amounts of ceramic particles. The high deposition rates associated with cold spraying titanium makes this application attractive for rapid prototyping and an area that ARL will also be exploring in the future.

REFERENCES

1. A.P. Alkhimov, A.N. Papyrin, V.F. Dosarev, N.I. Nesterovich, and M.M. Shuspanov, “Gas Dynamic Spraying Method for Applying a Coating,” U.S. patent 5,302,414,12 April 1994.

2. A. O. Tokarev, Structure of Aluminum Powder Coatings Prepared by Cold Gas Dynamic Spraying, Met. Sci. Heat Treat; Vol. 38 (No. 34), 1996, p. 136-139.

3. R. Dykhuisen and M. Smith, "Gas Dynamic Principles of Cold Spray," Journal of Spray Technology, Volume 7, No. 2, 1998.

4. R. Dykhuisen, et al, "Impact of High Velocity Cold Spray Particles," Journal of Spray Technology, Vol. 8, No. 4, p. 564, Dec. 1999.

5. B. Crossland, "Explosive Welding of Metals and its Application," Clarendon Press, Oxford, 1982.

6. H. El-Sobky, "Mechanics of Explosive Welding," Explosive Welding Forming and Compaction, T. Blazynski, Ed., Applied Science Publishers, London, 1983.

7. R. McCune, et al, "Thermal Spray: Practical Solutions for Engineering Problems," C. Berndt, Ed., ASM International Proceedings, 1996.

8. M. Smith, et al, "Cold Spray Direct Fabrication-High Rate, Solid State, Material Consolidation," Materials Research Society Proceedings, Nov. 1998.

9. M. Amateau and T. Eden, "High-Velocity Particle Consolidation Technology," IMAST Quarterly, p.4, No.2, 2000.

10. M. Thorpe, "Try Thermal Spray for Specialty Metal and Carbide Coatings," Chemical Engineering Progress, p. 55, November, 1991.

11. R. McCune, et al, "An Exploration of the Cold Gas-Dynamic Spray Method for Several Materials Systems," Proceedings of the 8th National Thermal Spray Conference, September, 1995.

12. Ktech Cold Spray Operator's Manual, Revision 0, Oct. 10, 2001; pg ix.

CORROSION CHARACTERIZATION

Corrosion of AA2024-T3 under Protective Coatings

M. Khobaib[1], J. P.Hoffmann[1], and M.S. Donley

Air Force Research Laboratories, Wright Patterson Air Force Base, Ohio

[1]University of Dayton Research Institute, Dayton,

ABSTRACT

Polymer coatings provide an excellent corrosion barrier for Al-skinned military aircraft. However, the degradation and damage of the coatings in their service life over time leads to the initiation of corrosion damage at the substrate level. Early detection and negation of such activity can provide extensive cost savings. Several Electrochemical and Non Destructive Evaluation (NDE) techniques show promise in detecting the onset of corrosion under such coatings. Current accelerated testing of aircraft coating systems for corrosion protection relies heavily on salt spray methods. Electrochemical techniques such as Electrochemical Impedance Spectroscopy (EIS) and Electrochemical Noise Methods (ENM) provide insight into the global properties of a coating system, and both techniques are being used on a limited basis. However, there is a need to investigate corrosion events with greater spatial resolution under coatings at the metal/coating interface. Such corrosion activity may be related to coating defects and variations in the surface chemistry of the underlying metal. The Scanning Vibrating Electrode Technique (SVET) has been developed to allow the investigation of localized corrosion activity with high spatial resolution.

Electrochemical and NDE techniques were used to investigate the early stage of AA2024-T3 substrate corrosion activity under protective coatings. Coatings in this investigation ranged from a simple epoxy amine to commercially used military aircraft polyurethane coatings. SVET testing of panels with intact high-resistance barrier coatings could not reveal corrosion damage under normal testing conditions because of little or no corrosion activity within the limited exposure time. Chemical, mechanical, and electrochemical means of accelerating the corrosion damage were utilized to obtain results in a reasonable time frame. Corrosion initiation and its progress under the coating were studied in detail and the results are discussed here. Complimentary high-resolution NDE techniques, such as Scanning Acoustic Microscopy (SAM) and Fan Thermography (FT) measurements were used to identify the corrosion sites. The overall objective of this investigation is to establish a correlation between the electrochemical and NDE techniques.

INTRODUCTION

Polymer coatings provide an excellent corrosion barrier for Al-skinned military aircraft. These coatings constitute multi-layer with different additives to satisfy all the requirements of military aircraft coatings. Current coating-systems consist of surface pretreatment (chromate conversion coating), primer (mainly epoxies pigmented with chromates) and topcoat (polyurethanes).[1-3] The corrosion protection is mainly provided by the surface pretreatment and primer through a complex mechanism of inhibition and barrier functionality. The factors contributing to corrosion initiation include defects, pores in the primer coating, and polymer degradation and resulting changes in transport properties of primer coatings, which allows the ingress of environment to substrate, and, of course, a corrosion prone multi-component metallic surface. Such ingress of environment to the substrate is a key element in the corrosion initiation process. Early detection and negation of such activity can provide extensive cost savings. Nondestructive characterization of corrosion protective coatings is of exceptional importance to enhance usability of coating systems and thus, to reduce the costs of aircraft maintenance and to avoid extensive environmental pollution. The possible failure of the coating leads to insufficient corrosion protection and finally to the failure of the Al alloy. Determination of mechanical and physical properties of the coating and the condition of the interface are required, both under different types of load and environmental exposure. Furthermore, it is necessary to detect corrosion damage in the aluminum alloy below the coating. To achieve this, the employment of state of the art electrochemical technique and high-resolution NDE is necessary

Several Electro chemical sensors and NDE techniques show promise in detecting the onset of corrosion under such coatings. Current accelerated testing of aircraft coating systems for corrosion protection relies heavily on salt spray methods. Electrochemical techniques such

as EIS and ENM provide insight into the global properties of a coating system, and both techniques are being used on a limited basis.[4-8] However, there is a need to investigate corrosion events with greater spatial resolution under coatings at the metal/coating interface. Such corrosion activity may be related to coating defects and variations in the surface chemistry of the underlying metal. The SVET has been developed to allow the investigation of localized corrosion activity with high spatial resolution.[9-12] Such activity may be associated with coating defects or galvanic coupled regions of the metal surface.

The SVET has been developed to allow in-situ examination of localized corrosion activity through the detection of minute D.C. current variations associated with corrosion. The technique offers high resolution in current measurements of the order of 0.5 $\mu A/cm^2$ and is able to detect the initiation and progression of corrosion activity under a protective coating. A video image of the sample, captured after each scan, pinpoints the site of corrosion initiation, and calculated current density vectors can be superimposed on the video image to determine the precise location of a corrosion current source. A repeat scan function quantifies corrosion progression with time by allowing the user to choose multiple consecutive scans and observe the growth or repassivation of corrosion sites. The difference in initial corrosion activity under various coatings can be correlated to the failure life of the coatings.

High-resolution NDE techniques, such as SAM[13,14] and FT[15] offer opportunities to characterize corrosion events on high strength aluminum alloy airframe structures under polymeric protective coatings**.** SAM can be utilized to map either coating or interface properties (C-scans). A detailed analysis of such scans provides information on the curing quality of the coatings. It is also possible to detect small corrosion pits under delaminated areas. Furthermore, the reflections of surface waves, which are generated and detected by the same probe enables the

examination of the substrate/coating interface which can lead to the detection of sites of weak adhesion or corrosion pitting underneath an intact coating. Flash thermography is a well-established method to characterize defects under coatings. FT (hot air heating) uses all the principles of flash thermography with additional advantage of its simplicity and lower cost. The flash lamp is replaced with hot air gun or fan. The IR camera observes the heating process of the material. In comparison to the flash lamps this heating method deposits considerably less energy per time on the surface of examination. The sample heats up much slower, which allows observing the material response over longer periods of time. The lower heat deposition energy reduces the risk of destroying the coating.

In this study, early indications of corrosion under a protective coating was detected and mapped by SVET. Some of these corrosion sites were allowed to grow at different levels of corrosion. These samples were then characterized by SAM and FT to detect the loss of adhesion and the presence of corrosion under the coating. The findings were complimentary and at the same time the combined data provided extensive details about the state of the substrate under the coating.

EXPERIMENTAL DETAILS

The state of corrosion under a coating was studied initially by mapping local current density of several proprietary and a few known laboratory formulated coatings through the use of SVET. The coatings were exposed to Harrison's solution, an electrolyte containing 5.00 grams NaCl and 35.00 grams $(NH_4)_2SO_4$ in 1.00 liter of water. In each instance, AA2024-T3 served as the substrate. Initially, the specimen coatings were intact (with no artificial damage), and the

progress of corrosion activity was recorded by scanning a small area within the cell. The cell was formed by gluing a 1/8" high, 2" diameter slice of acrylic pipe to the coated sample surface.

It was noted that in case of high barrier coating systems, the coating performed so well that, under normal immersion, no corrosion damage was detected, even after weeks of continuous electrolyte exposure. In order to establish an accelerated test methodology and obtain results in a reasonable amount of time (days vs. months), corrosion damage would have to be intentionally excited to initiate corrosion, allowing the subsequent observation of corrosion progression. As a result, various chemical, mechanical, and electrochemical methods were used to artificially damage the coating and/or the metal substrate to study corrosion initiation. These techniques included placing drops of 10 % $CuCl_2$ under the coating, scribing the sample, and applying an external potential. These studies were carried out with AA2024-T3 panels, coated with a clear, water-based epoxy primer. The coated samples were characterized by SAM and FT after a complete SVET scans and analysis of the specimens with various degrees of corrosion.

RESULTS AND DISCUSSION

SVET has the advantage of locating the site of corrosion activity , because of its ability to produce one to one correspondence with the corrosion current measurement and the active sites on thespecimen. This is achieved by obtaining a video image of the sample captured immediately following a SVET scan and placing it in 1:1 correspondence next to a 2-D current vector plot.

The details of this are described in a previous paper [16] where the two different regions – an intact and a delaminated area in a degraded coating was clearly established by SVET. A similar study demonstrated the initiation and progression of corrosion in defective and degraded

coatings within days of exposure.[17] However, it quickly became evident that under normal testing conditions, little corrosion damage was detected in panels coated with a high resistance barrier coating, even after prolonged electrolyte exposure. [17]

Figure 1 shows a 2-D current density mapping of a coated aluminum panel with currently used coating for U.S. Air Force aircraft. The specimen was exposed for over two weeks with maximum current density level of less than 25 $\mu A/cm^2$. This was repeated with three samples and the results were very similar. These experiments also demonstrated that under normal testing conditions, little corrosion damage was detected in panels coated with a high resistance barrier coating, even after prolonged electrolyte exposure.

To obtain results in a shorter period of time, the creation of artificial corrosion damage was planned. Placing a small drop of an aggressive salt solution on the bare alloy surface was investigated as one method of chemically creating damage under the coating. A drop of 10.0 % $CuCl_2$ was placed on the metal panel, which was then coated with a clear, water-soluble primer (thickness = 26-29 μm). Although the drop of salt solution was not visible under the clear coating, each sample was masked and positioned on the SVET sample holder such that the location of the salt drop was in the approximate center of the scanned region.

Figure 2(a) shows the 2-D current density mapping of a sample after 7 hours of total electrolyte exposure. The cathodic region in the center corresponding to the salt drop increased in size with exposure time. In addition, the magnitude of both the anodic and the cathodic current densities increased. Figure 2(b) shows the corresponding vector overlay diagram. In the video image, which was captured immediately after the scan, the coated panel with the 10.0 % $CuCl_2$ drop was visible. The dark circular region in the approximate center of the scanned region represents the drop. Comparison of the 2-D mapping after 7 hours of exposure with the

corresponding vector overlay clearly identifies the sites of corrosion. However, the corrosion activity did not proceed after exposure of several more days. Hence, a scribe was introduced into the center of the panel as a mechanical means of creating artificial corrosion acceleration.

In the second set of experiments, coated panels were scribed (mechanical acceleration of corrosion) and the scribed area was exposed to electrolyte followed by SVET scan. The corrosion activity was noticed in the initial few hours which subsided with extended exposure possibly due to passivation. Therefore, $CuCl_2$ powder was sprayed on the scribe to further accelerate the corrosion. Figure 3(a) shows a representative scan of this sample taken 2 hours after $CuCl_2$ addition (112 hours total electrolyte exposure). The 2-D current density mapping revealed that the magnitude of both the anodic and cathodic current densities had further increased. In addition, the area corresponding to cathodic current density had also increased in size. Figure 3(b) shows the corresponding vector overlay that was created using the SVET software. In the video image, which was captured immediately after the scan, the coated panel containing the $CuCl_2$-filled scribe is visible. The length of each vector is determined by the magnitude of the current density. The vector tail represents the origin of the current source. Vectors that point upward represent anodic current density while vectors that point downward represent cathodic current density. Comparison of the 2-D scan after 112 hours with the corresponding vector overlay verified that the Cu-containing region was cathodic while the adjacent area was anodic. This analysis provided a complete detail of the corrosion activity under a coating although no visible corrosion was present.

Again, in another attempt to study corrosion activity under a coating, a sample with currently used coating for U.S. Air Force aircraft was exposed to Harrison's solution. The current density mappings obtained between 7 and 25 hours of total electrolyte exposure revealed

no significant changes in current activity as shown in Figure 4a, so an external potential was applied to electrochemically accelerate the corrosion activity at the substrate. Figure 4b shows the resulting 3-D current density mapping of the sample after applying a potential at 25 hours of total electrolyte exposure. The inverted cone-like shape corresponds to the salt drop region. The magnitude of the anodic current density increased significantly to almost 8000 $\mu A/cm^2$. Upon applying the potential (polarizing in anodic direction), the coating "broke" and violent bubbling occurred at the drop site. Again SVET provided complete details of the corrosion activity even under very accelerated condition.

It must be emphasized that the corrosion activity under coating with short exposure is possible even without artificial acceleration. However, this requires coatings with conductive pathways and defects [17]. In the interest of time, such coatings were used to continue NDE investigation.

NDE of coated specimens were conducted after establishing reliable methods of creating and analyzing corrosion events by SVET on AA2024-T3 panels protected by polymeric coating. An AA2024-T3 panel was coated with a proprietary clear epoxy formulation for this purpose. The panel was exposed to Harrison's solution and corrosion damage was created by imposing a small amount of external potential to the sample. The specimen was scanned by SVET and several damage sites were identified. The specimen was then scanned by SAM and both coating and substrate reflections were obtained. The resulting C-scans for this sample are represented in Figure 5, with particular reference to three spots. Spot 'a' was selected as a reference or control where no indication of corrosion was evident. Spot 'b' showed some indication of delamination and corrosion damage under the coating was clearly evident at spot 'c'.

In the substrate reflection C-scan, additional bright spots can be observed within delaminated regions (Figure 5b, position c). As a first assumption we considered these spots to reflect a corrosion feature.

Additionally the A-scans corresponding to the positions a, b and c are shown in Figure 6 (right side). At the undamaged position only the two reflections from the coating and the substrate occur (Figure 6a). This is shown schematically on the left side of Figure 6. At a site of delamination, these two reflections are more separated in time as the distance between the two surfaces increases. This concept is illustrated on the left side in Figure 6b. An additional reflection from the coating backsurface/water interface can be observed as shown on the right side of Figure 6b. Apparently the ingress of water or humidity delaminated the region separating the two materials. This reflection reveals negative amplitude, because the change of acoustic impedance from coating to water is negative as well. The bright spots in Figure 5b are corresponding to large reflections, i.e. a large acoustic impedance change must occur. This happens when the wave has to propagate from the water into a hydrogen gas bubble as shown schematically in Figure 6c. This bubble indicates the presence of a corrosion pit. This process is illustrated in Figure 6c (left side) The H_2 bubble is captured within the delaminated region. Eventually a small substrate reflection can be seen that occurs slightly later than in Figure 6a or 6b. This is also due to a small corrosion pit.

Figure 6 shows results of SVET, FT and SAM images of the same sample area. At first SVET measurements were carried out. Figure 7a presents a vector overlay mapping of electrochemical current density superimposed over a video image. Delamination can be observed in the video image. The longer vectors indicate corrosion activity underneath these delaminated regions. Coating delamination or sites of corrosion are thermal barriers. If the test

object surface is heated the heat diffusion into the aluminum plate is inhibited in the delaminated or corroded region. A thermal response appears. The time for the maximum contrast at the surface is called response time. This time depends upon the thermal properties of coating and substrate and the coating thickness. Figure 7b shows a thermal contrast for corrosion below a polymeric coating. The spatial resolution was improved with a microscopic optic used in combination with the camera. The bright spots (higher surface temperature) indicate regions of reduced heat diffusion and correlate well with the SVET image. Furthermore, the actual grid structure of the substrate surface is visible providing the possibility to detect sites of corrosion as disturbances in a well-defined surface topography.

The SAM scan clearly identifies the same three spots observed by SVET and FT (Figures 7a and 7b). At the same time some additional spots are visible. This could be due to the rather poor performance of this coating and the fact that repeated heating and additional exposure in a water bath has a deteriorating effect on the sample. The results presented demonstrate that the electrochemical and NDE techniques provide complimentary information. At the same time these techniques used together can provide detailed information about the state of the coating and there is a good possibility of integrating the information that can provide the details of the health of the substrate beneath a coating exposed to corroding environment

CONCLUSIONS

The SVET was successfully used to monitor the initiation and progress of corrosion in coated panels exposed to Harrison's solution. A variety of chemical, mechanical, and electrochemical techniques were investigated, and a relatively controlled method of creating

artificial corrosion damage was established. It was possible to cause extensive corrosion damage to occur in just a few minutes by imposing external voltage.

SAM has proven to be an excellent laboratory technique. Both SAM and FT were also successfully employed to detect sites of delamination and localized corrosion in aluminum alloy substrate under the coating. Reasonable correlation was obtained amongst SVET, SAM and FT. The results from all the three techniques provided a complete detail of the damage state at the substrate under various coatings. Ongoing work is concentrated to distinguish corroded and delaminated regions.

ACKNOWLEDGMENTS

The work presented in this paper is sponsored by the Defense Advanced Projects Agency (DARPA) Multidisciplinary University Research Initiative (MURI), under Air Force Office of Scientific Research grant number F49620-96-1-0442. The authors would like to thank Ms. Angela Mahan and Dr. Joel Johnson, for their contributions and support.

REFERENCES

1. M. Khobaib, final report for US Air Force, contract-number F 33615-94-C-58-04, (1997).
2. J. Hoffmann et al., 3rd Annual Report for DARPA-MURI, Grant Number F49620-96-1-0442, (1999).
3. C.S. Jeffcoate et al., in Proceedings of 43rd International SAMPE Symposium and Exhibition , Vol.43, (1998), pp. 2113-2122.
4. Taylor, S. R., “Assessing the Moisture Barrier Properties of Polymer coatings Using Electrical and Electrochemical Methhods”, IEEE Transactions on Electrical Insulation., Vol. 24, No. 5, Oct 1989
5. Mansfeld, F., “Analysis and Interpretation of EIS Data for Metals and Alloys”, Issue AA: February 1993, Schlumberger Technologies,, Billerica, MA.

6. Jeffcoate, C. S., Wocken, T. L., and Bierwagon, G. P., "Electrochemical Assessment of Spray-Applied Thermoplastic Coating Barrier Properties," J. Materials Eng. & Performance, 6 (1997) pp. 417-420.

7. Amirudin, A., and Thiery, D., "Application of Electrochemical Impedance Spectroscopy to Study the Degradation of Polymer-Coated Metals", Progress in Organic Coatings, 26, 1-28, (1995).

8. Macdonald, J. R., "Impedance Spectroscopy", Wiley, New York, 1987.

9. Isaacs, H. S., Aldykiewicz Jr., A. J., Thierry, D., and Simpson, T. C. "Measurements of Corrosion at Defects in Painted Zinc and Zinc Alloy Coated Steels Using Current Density Mapping", *Corrosion*, Vol. 52, No. 3, (1996) pp.163-168.

10. Applicable Electronics, Inc., 22 Buckingham Drive, Sandwich, MA 02563.

11. Aldykewicz Jr., A. J., Isaacs, H. S., and Davenport, A. J. "The Investigation of Cerium as a Cathodic Inhibitor for Aluminum-Copper Alloys", *Journal of the Electrochemical Society*, Vol. 142, No. 10, (1995) pp.3342-3350.

12. Isaacs, H. S., Davenport, A. J., and Shipley, A. "The Electrochemical Response of Steel to the Presence of Dissolved Cerium", *Journal of the Electrochemical Society*, Vol. 138, No. 2 (1991) p.391.

13. V.K. Kinra, V.R. Iyer, Ultrasonics, Vol.33, (1995), pp. 95-109.

14. A. Briggs, Acoustic Microscopy, Oxford University Press, New York, (1992).

15. U. Netzelmann, G. Walle, Photoacoustic and Photothermal Phenomena, 10th International Conference, Rome, Italy, 1998, published in AIP Conference Proceedings, Vol.463, American Institute of Physics, Woodbury, New York, (1999), pp. 401-403.

16. Khobaib, M., Rensi, A., Matikas, T., and Donley, M.S., "Real Time Mapping of Corrosion Activity Under Coatings", Progress in Organic Coatings, 41 (2001), 266-272.

17. Buchanan, A., Khobaib, M., Matikas, T., and Donley, M.S., "Investigation of Corrosion Initiation Using The Scanning Vibrating Electrode Technique", Proceedings of 1999 Tri-Service Conference on Corrosion, November 15-19, 1999, Martyle Beach, SC., The U.S. Army Research Laboratory, Aberdeen Proving Ground, MD.

FIGURES

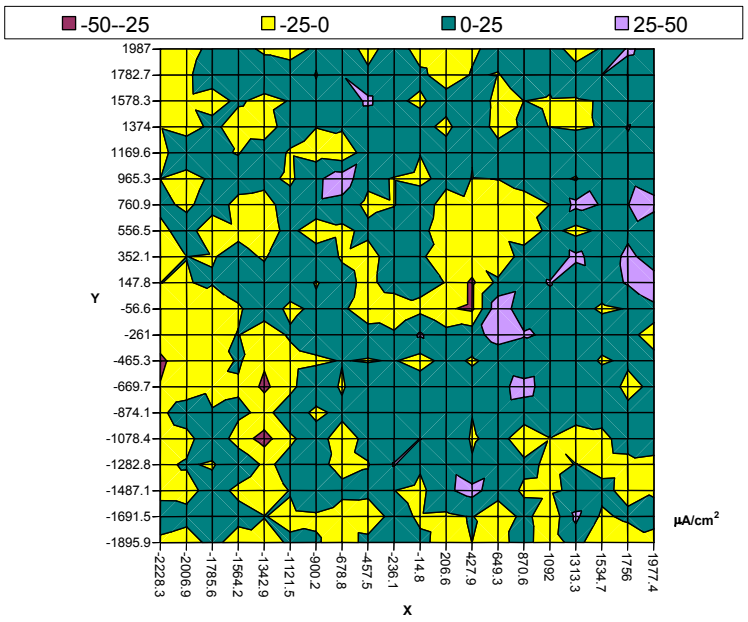

FIGURE 1. 2-D Current Density Map of Corrosion Activity Under a High Barrier Resistance Coating.

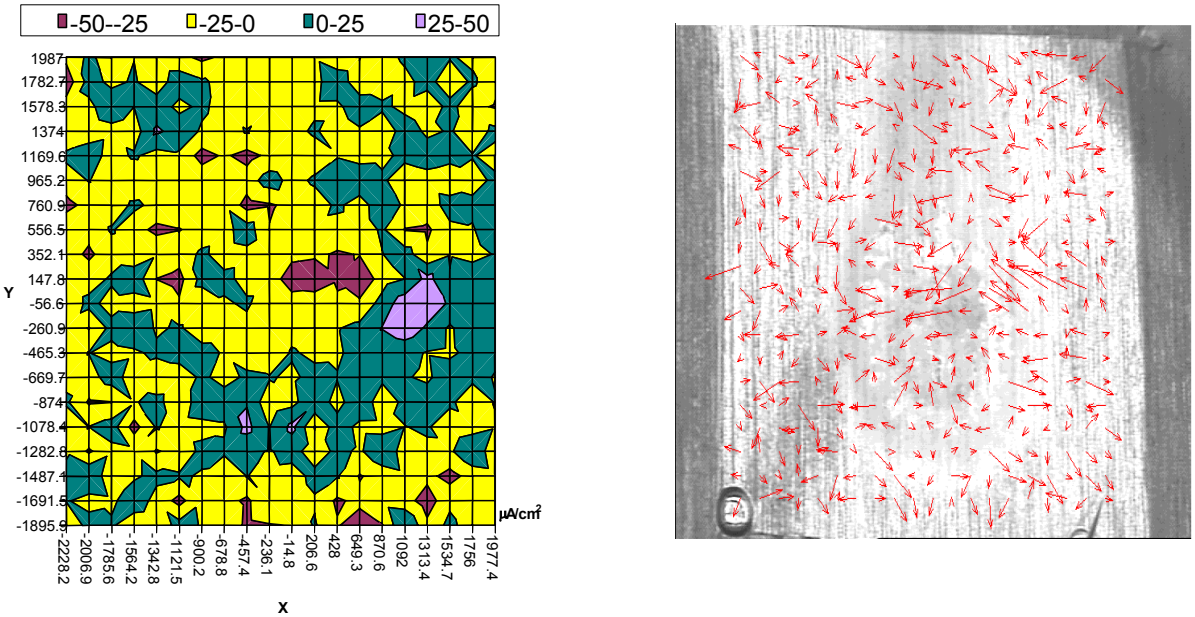

FIGURE 2. Corrosion Current Map Under a Proprietary Coating a) 2-D Current Density Map and b) Current Vector Over-lay Imposed over Video Image of the Scanned Area.

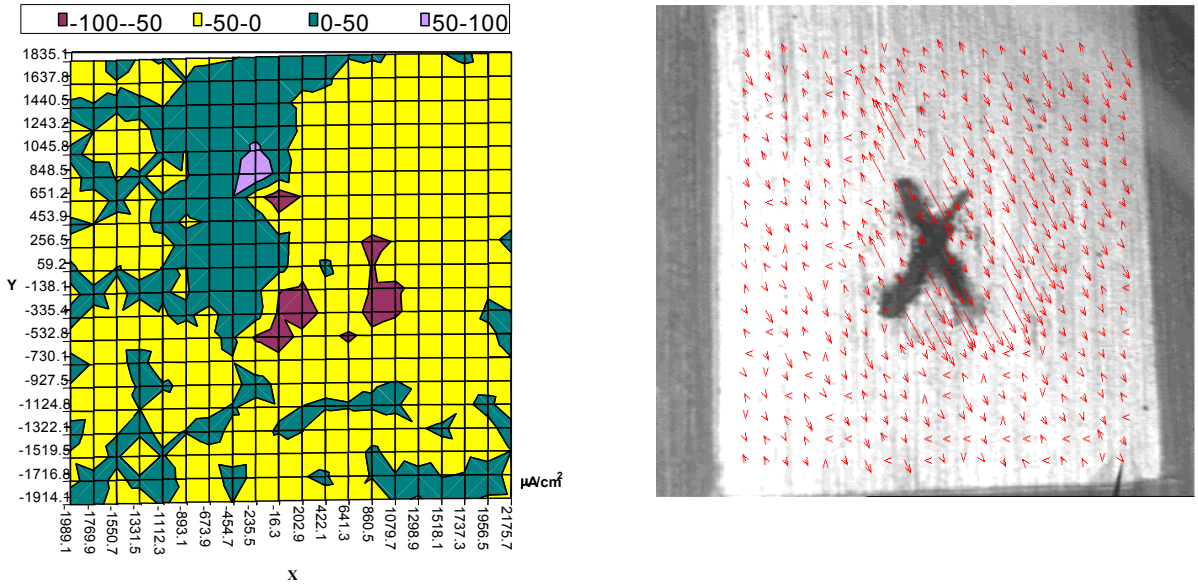

FIGURE 3. Current Density Map around Scribed Region: a) 2-D Current Density Map and b) Current Vector Overlay Imposed over Video Image of the Scanned Area.

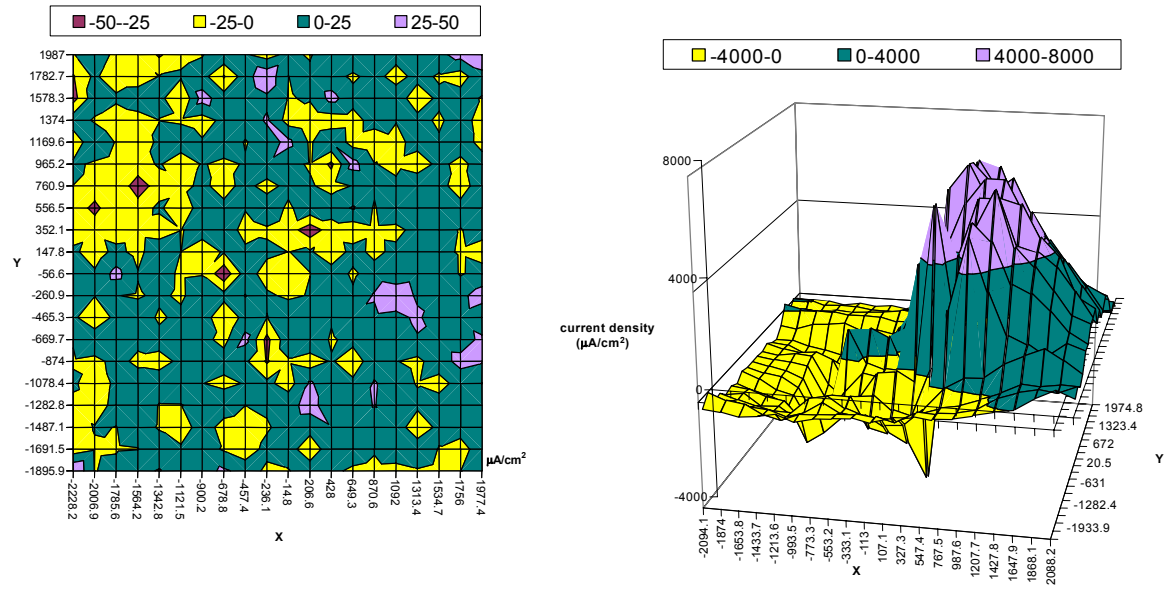

FIGURE 4. Current Density Maps Under a Proprietary Coating: a) 2-D Current Density Map at Open Circuit Potential and b) 3-D Current Density Map Obtained After Imposing External Potential.

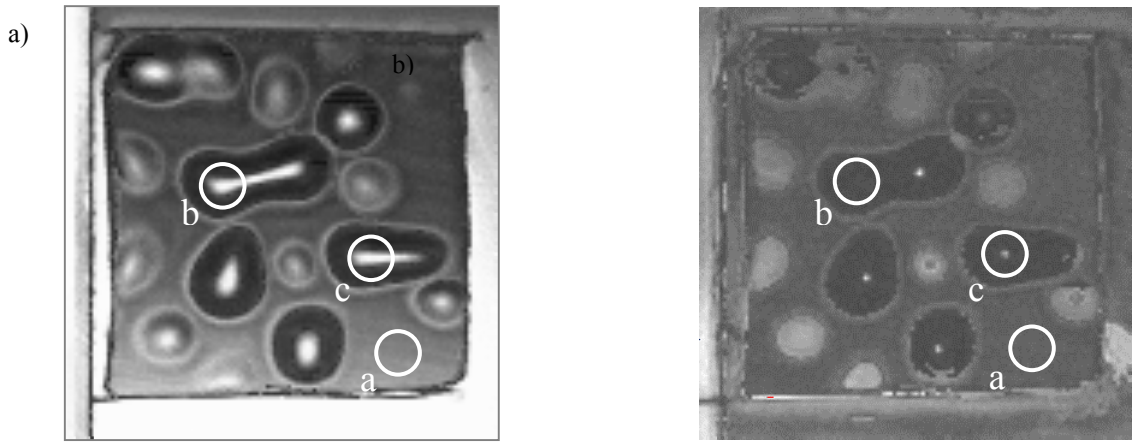

FIGURE 5. C-scans of Bulk Wave Reflection Amplitudes: a) Interface Reflection b) Surface Wave Reflection (38-µm Thick Artificially Damaged Epoxy Coating, Scan Area: 6x6 mm^2, Stepwidth: 50 mm, Lens in focus) Position a: Undamaged Region; Position b: Delaminated Region; Position c: H_2-Bubble Above Corrosion Pit.

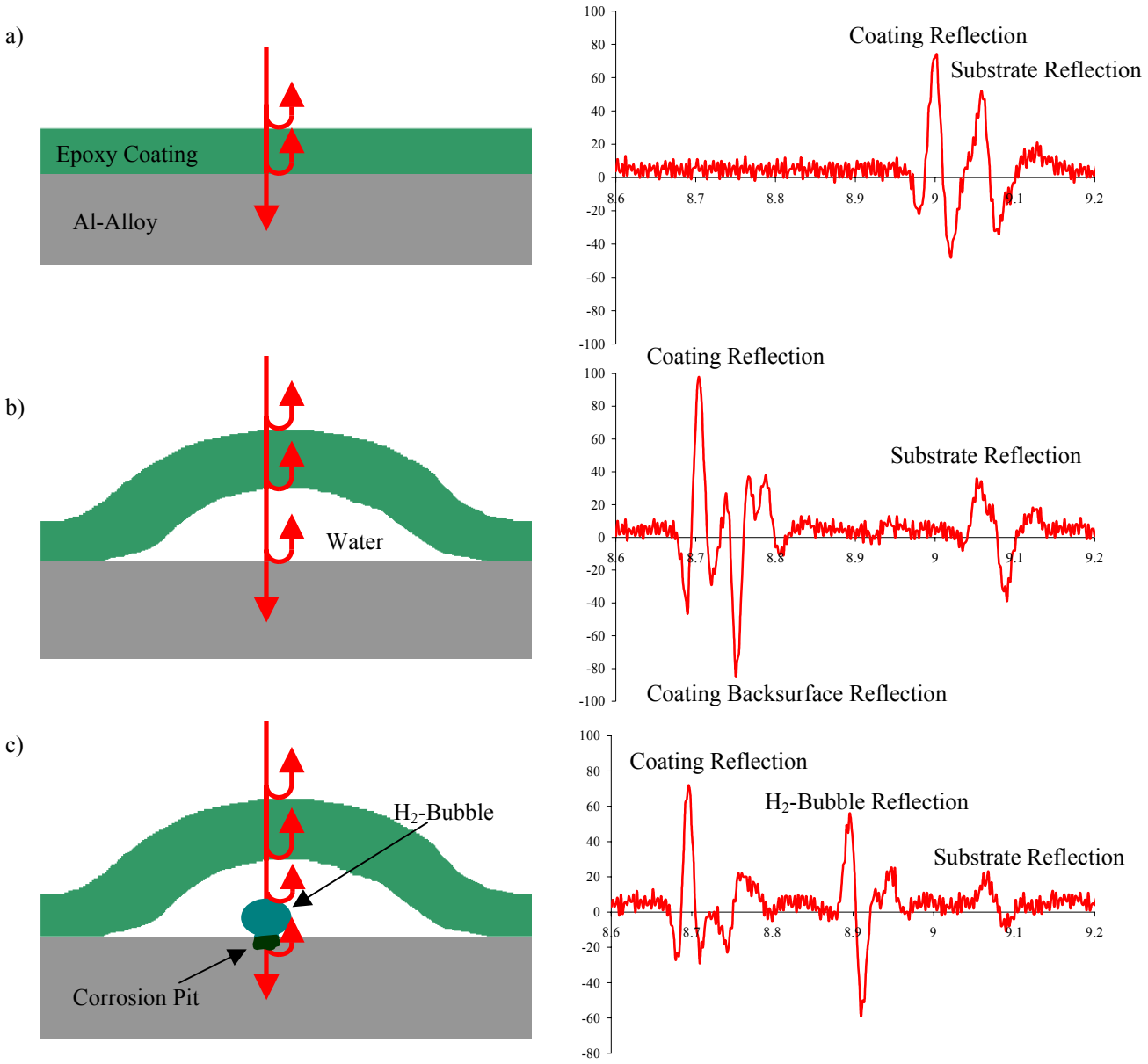

FIGURE 6. A-Scans and Schemes for Positions Shown in Figure 4. a) Undamaged Region, b) Delaminated Region, c) H_2-Bubble Above Corrosion Pit.

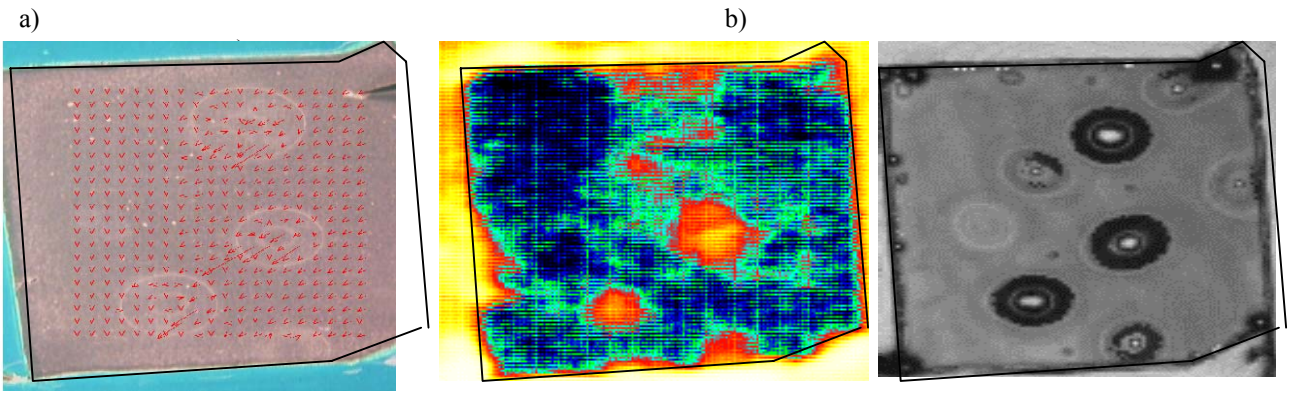

FIGURE 7. NDE Imaging of Same Sample: 50-mm Thick Artificially Damaged Epoxy Coating; a) SVET Video Image + Current Density Vector Overlay (Vector Area: 4x4 mm^2), b) Fan Thermography Image (Image Area: 6x6 mm^2), c) SAM Substrate Reflection C-Scan (Scan Area: 6x6 mm^2, Stepwidth: 50 mm, Lens in Focus).

Galvanic Behavior Database for Titanium-Steel Alloy Couples

Ralph P.I. Adler, Christopher E. Miller, and Brian E. Placzankis

US Army Research Laboratory; Weapons and Materials Research Directorate
Weapons Materials Division; Metals and Ceramics Research Branch
AMSRL-WM-MC
Aberdeen Proving Ground, MD 21005-5066

ABSTRACT

Future lightweight armor materials will be required for the next generation of lighter, more lethal and more survivable materiel. The probable use of titanium alloy components will form galvanic couples with structural and armor steels or other materials. The resulting couples may induce corrosion phenomena dramatically accelerating the corrosion rate of those metals less noble than titanium. The specific objective of this project was to evaluate the magnitude of galvanic corrosion effects between typical ferrous and titanium alloys. Electrochemical and accelerated corrosion measurements were taken from both bare and CARC coated Ti/steel samples to determine accelerated corrosion rates and whether these reach unacceptable rates. Samples with and without X-scribed defects in the CARC coating were evaluated. Electrochemical studies on bare samples validated accelerated steel corrosion rates but found that intact CARC coatings effectively mitigate corrosion in Ti/steel couples. Even for X-scribed samples, the rapid buildup of corrosion products in the defect reduced galvanic currents by two orders of magnitude. Engineering studies with TACOM "Joint A Assembly" CARC coated samples (Phase I: bolted sets of Ti/steel plates with intact CARC seals) had virtually no iron corrosion product at the couple interface. After breaking apart and examination, the same samples (rebolted with compromised CARC seals) were given a second accelerated corrosion cycle (Phase II); the consequent intrusion of moisture caused a severe buildup of iron corrosion product at the couple interface. Thus mixed Ti/Fe interfaces protected from the environment by defect-free CARC coatings have not exhibited unacceptable buildups of iron corrosion products.

INTRODUCTION

Future lightweight armor materials will be required for the next generation of “lighter and more lethal and more survivable” materiel. This will involve the use of state-of-the-art, low cost titanium alloy components (1) that will most likely be in electrical contact with structural and

armor steels as well as other materials. The resulting galvanic couples thus may induce galvanic corrosion phenomena and could dramatically accelerate the corrosion rate of the metal that is usually less noble than the titanium alloy. The specific objective of this project was to evaluate the magnitude of galvanic corrosion effects between typical ferrous and titanium alloys. Electrochemical and accelerated corrosion measurements were taken from both bare and CARC (**C**hemical **A**gent **R**esistant **C**oatings) coated Ti/Steel samples to determine the galvanically accelerated corrosion rates and whether these reach unacceptable rates when a liquid electrolyte is present. This gives an indication of the maximum galvanically assisted corrosion rates expected since Army vehicles are often covered with (a film of) water. Comparison between bare couples and those with CARC coatings (with and without "defects") in an aqueous environment will indicate the magnitude of the phenomenon and whether further corrosion prevention/inhibition remedies are necessary. For CARC coated Ti/steel couples there must be a demonstration that the 15 year corrosion resistance performance is met with a CARC system that also meets the EPA compliance goals for FY05.

EXPERIMENTAL PROCEDURE

EXPERIMENTAL TEST PLAN

Scientific Assessment of Galvanic Corrosion

Potentiodynamic Testing

Alloy:	Conc. Of NaCl in Cell Electrolyte
Ti 6/4	3.5%
AISI4130	3.5%

Galvanic Corrosion Cell Testing (Ti 6/4 against 4130)

Condition:	Conc. Of NaCl in Cell Electrolyte
bare couple	0.005N
bare couple	0.5N
CARC coating (w/o defects)	0.005N
CARC coating (w/o defects)	0.5N
CARC coating (w/ scratch defect)	0.005N
CARC coating (w/ scratch defect)	0.5N

Engineering Assessment of Galvanic Corrosion. Accelerated corrosion testing using "Salt Fog Testing" per ASTM B117-90 (2) and cyclic corrosion testing per the GM9540P Protocol (3) was performed on CARC coated “TACOM Joint A Assembly” samples (4). Specific combinations (Ti/Ti; Ti/Fe; and Fe/Fe) of Ti 6/4 and 4130 plates were through-hole bolted together with a Grade 8 fastener followed by thorough CARC coating. Both Phase I accelerated corrosion testing protocols involved testing each assembly with an intact interface sealed by the CARC coating. After Phase I, each couple was disassembled and the internal common plate interface examined. The re-assembled sample with its broken CARC interface seal-- that then allows fluid entrainment-- was then re-subjected to a second series (Phase II) with an identical sequence of Phase I accelerated testing exposures.

SAMPLE PREPARATION

Scientific Test Samples. Samples for electrochemical and engineering testing were produced from existing supplies of Titanium 6/4 (6 w/o Aluminum, 4 w/o Vanadium) alloy and AISI 4130 steel. All scientific test samples had two parallel faces, but size and shape varied. Prior to potentiodynamic or galvanic corrosion cell testing, the "bare" specimens were abraded with 600-grit silicon carbide paper, rinsed in distilled water, degreased in acetone, rinsed again in distilled water, and then dried. One square centimeter of each bare specimen was exposed to the test solution. The "coated" samples had the machined surfaces pretreated with DoD-P-15328 (5), then primed with MIL-P53022 (6), and topcoated with MIL-C-53039(7). One square centimeter of each "coated" specimen with or without an "X-scribed" defect was exposed to the test solution.

Engineering Test Samples. Engineering samples were assembled to the “TACOM Joint A Assembly” configuration that is described schematically in Figure 1. 2”x 2” x 1” plates of Ti and steel were individually grit-blasted to a near-white finish. Then specific combinations (Ti/Ti; Ti/Fe; and Fe/Fe) of these plates were through-hole bolted together with a Grade 8 fastener torqued to 180 foot-pounds. Each assembly, including the bolt/nut and washer, was then pretreated with DoD-P-15328, then liberally primed with MIL-P53022, and then topcoated with MIL-C-53039 that formed an effective seal against fluid intrusion.

TESTING PROTOCOL

Testing Protocol for Scientific Samples. More specific details and a description of the equipment used can be found in Reference 8. Figure 2 depicts the electrochemical cell assembly that was used for both series of scientific tests.

Potentiodynamic Tests. Potentiodynamic tests were conducted at room temperature in an aerated cell containing about 400 ml of the test solution. The model K0235 cells were manufactured by Princeton Applied Research (PAR), with a Platinum-plated electrode at one end of the cell and a sample holder at the other end. A computer-controlled Schlumberger SI 1280 electrochemical measurement unit was used. The open-circuit potentials were measured against a saturated calomel electrode (SCE) for one hour before the scans commenced. A scan rate of 0.1667 mV/s was utilized. Potentiodynamic scans were performed in standard 3.5% NaCl aqueous solutions.

Galvanic Tests. Galvanic tests were performed in two concentrations of salt solutions (0.5N and 0.005N NaCl). [but could not be performed in distilled water (due to its high resistivity).]. For high humidity atmospheric exposures, the 0.5N NaCl solution may be too severe but was still run for comparative reasons. A modified version of the PAR K0235 with sample holders at both ends for coupling the Ti 6/4 and 4130 specimens was used for the galvanic corrosion tests (Figure 2). In this test setup, a Keithley Multiplexer with single-pole double-throw switches was used to sequentially multiplex between each of the six (nitrogen) aerated cells and a PAR 273 Potentiostat/Galvanostat. A potential difference between samples of 0V was maintained (an effective short circuit) while simultaneously measuring the galvanic current (I) that is proportional to the corrosion rate. The galvanic currents were measured over a minimum of two weeks (for the bare and defect-free coated samples) or four weeks for the coated samples with X-scribed defects (to reach an apparent steady state current value).

Testing Protocol for Engineering Samples.

Salt Fog Testing (SFT). Salt Fog Testing of TACOM Joint A Assembly samples were performed according to ASTM B117 protocol in two phases. Figure 3 shows the Salt Fog Test

Chamber and lists the exposure parameters. The Phase I exposure of 2500 hours was performed with an unbroken CARC seal. After unbolting and breaking the CARC seal, the interface was examined for any corrosion phenomena. Subsequently each couple, after one plate was rotated by 90 degrees and rebolted to snug fit state, was given a second 2500 hour exposure (Phase II) without the benefit of the original CARC seal. Sample interface characterization was then again documented.

Cyclic Corrosion Testing (CCT). Cyclic Corrosion Testing of another series of Joint A Assembly samples were performed according to GM 9540P protocol in two phases. Figure 4 shows the Cyclic Test Chamber and lists the exposure parameters. The Phase I exposure of 100 cycles was performed with an unbroken CARC seal. After unbolting and breaking the CARC seal, the interface was examined for any corrosion phenomena. Subsequently each couple, after one plate was rotated by 90 degrees and rebolted to snug fit state, was given a second 100 cycle exposure (Phase II) without the benefit of the original CARC seal. Sample interface characterization was then again documented.

RESULTS AND DISCUSSION:

SCIENTIFIC EVALUATIONS

Potentiodynamic Scans. The Potentiodynamic Scans for the Ti and Steel samples in 3.5% NaCl aqueous solution are shown in Figure 5. The various electrochemical parameters were estimated as: a) Corrosion Potential for Ti 6/4= -0.35 V; b) Corrosion Potential for AISI 4130 = -0.8V; and c) Mixed Corrosion Potential (for Ti 6/4 with AISI 4130) = -0.75V. Note that the Mixed Corrosion Current was an order of magnitude greater than that for the Corrosion Current for AISI 4130.

Galvanic Current. Galvanic current is a useful indicator of the behavior of two different materials that are in electrical contact with each other in a specific environment. Larger currents indicate that galvanically assisted corrosion is occurring that is proportional to the effective contact area and the galvanic potential difference between the materials in the coupled sample. Smaller currents indicate that either there is a small galvanic differential between the materials or that the kinetics of the corrosion reaction are quite slow. If the current decreases with exposure time, it may be that the buildup of corrosion products acts as a partial barrier. In the present case, the galvanic current (I) provides an assessment of the relative corrosion rates as a function of electrolytic salt concentration for bare and CARC coated samples as well as CARC coated samples with deliberately X-scribed defects. The results and observations are listed in Table 1. Characterization of the corrosion products on the bare iron substrates is depicted in Figure 6 for samples exposed to 0.005N and 0.5N NaCl solutions (samples #4 and #2, respectively) and has also been included in the next series of tables.

X-ray results were obtained using a "2 theta" flat sample diffractometer with Cu K-alpha radiation (9). By measuring and then ratioing the intensities of the strongest diffraction peaks from the iron substrate and the two iron oxide phases (i.e. magnetite Fe_3O_4 and hematite Fe_2O_3), information about the corrosion products formed on the 4130 steel substrate during the “bare”galvanic current tests can be obtained. The relevant x-ray diffraction data is listed in Table 2. Analysis of this X-ray diffraction data has been interpreted to show that the concentration of NaCl in the electrolyte produces differences in total oxide thickness and the relative volume fraction of the hematite and magnetite phases and is presented in Table 3.

The resultant observations are that: a) the total oxide layer thickness for the sample exposed to the 0.5N NaCl solution was about twice that for the sample exposed to the 0.005N

NaCl solution; b) the sample exposed to the 0.5N NaCl solution had an outer layer of Fe_2O_3 (hematite) with a layer Fe_3O_4 (magnetite) adjacent to the steel with some residual NaCl in these oxides; c) the sample exposed to the dilute 0.005N NaCl solution had thinner layers of both Fe_3O_4 and Fe_2O_3 compared to the thicker ones from the more concentrated 0.5N NaCl exposed sample; and d) the relative volume fraction of the Fe_2O_3 phase in the total oxide coating was larger for the 0.5N NaCl exposed sample compared to that for the sample exposed to a lower concentration of NaCl.

ENGINEERING EVALUATIONS

After exposure of Joint A Assembly samples to either SFT or CCT (for both Phase I or II) the common interface was examined for corrosion products. An arbitrary, qualitative ranking methodology was devised to assign a metric for the extent of corrosion product formed at this interface and has been listed in Table 4. Observations of these common interfaces were qualitatively described and given a rating (where "zero" means no corrosion was observed; and "10" means the most extensive corrosion product buildup was observed) after either Phase I or II exposures.

Salt Fog Exposure Results. Table 5 provides the Interface Corrosion Assessment after salt fog exposure. Illustrative macrophotos of these interfaces after salt fog exposures are provided for the Ti-steel interfaces for Phase I (Figure 7a) and Phase II (Figure 7b).

Cyclic Corrosion Exposure Results. Figure 8 depicts the external macrostructure of all "Joint A Assembly" samples after Phase II GM9540P accelerated testing exposure. Table 6 provides the Interface Corrosion Assessment of these samples after Phase I and II Cyclic Corrosion exposures. Illustrative macrophotos of these interfaces after Salt Fog exposures are provided for the Ti-steel interfaces after Phase I (Figure 9a) and Phase II (Figure 9b). To be

noted is that the buildup of interfacial corrosion products is even greater in the comparable Fe-Fe samples as listed in Tables 5 and 6 and illustrated in Figure 10a for Salt Fog and Figure 10b for Cyclic Corrosion Phase II exposures. Clearly the CCT protocol provides a more aggressive accelerated testing environment due to the programmed cyclic changes in thermal and chemical conditions compared to the constant exposure conditions within the SFT accelerated testing chamber.

X-ray Characterization of Interface Corrosion Products from post Phase II (CCT and SFT)"Joint A Assembly" Samples. After Phase II exposures, scrapings/flakes of the interfacial corrosion product were examined using the same x-ray diffraction techniques as were used for the previous scientific samples. The intent was to qualitatively determine if differences in the relative volume fractions of hematite and magnetite in the oxide occurred due to the two different accelerated testing methodologies. The results listed in Table 7 indicate that at Fe/Fe interfaces the salt fog exposures produced a primarily hematite oxide phase while the cyclic corrosion produced a primarily magnetite product. For samples with Ti/Fe interfaces, the volume fraction of the minority oxide seems to be increased for either testing protocol.

CONCLUSIONS

SCIENTIFIC STUDIES

An initial Ti (6/4)-Fe (AISI 4130) galvanic corrosion database for an aqueous environment was established. Potentiodynamic scans using a conventionally accepted open cell with a 3.5% NaCl aqueous solution validated that a more noble Ti cathode increased the mixed couple galvanic current by an order of magnitude, thus increasing the corrosion rate at the (4130) steel anode.

During galvanic cell testing of the bare Ti/Fe couples, the buildup of an oxide layer on the Fe anode was faster and thicker in the 0.5N NaCl than in the 0.005N NaCl electrolyte cell. The presence of this oxide layer effectively increased the electrical resistance of this circuit for either concentration electrolyte cell nominally reducing the steady state galvanic current to half of the initial maximum current observed. In both cases magnetite was the major oxide phase formed but the minority volume fraction was higher for the hematite phase formed in the 0.5N NaCl cell; this shift may be a result of the differences in the kinetics of oxide formation.

No galvanic current was measured during galvanic cell testing of the CARC coated Ti/Fe couples for either NaCl concentration cell; thus the CARC layer was very protective in isolating both the anode and cathode from the electrolyte. For both NaCl concentration cells, even deliberate "X-scribed" defects in the CARC experienced rapid buildup of a corrosion product in the defect. Thus, compared to the bare couples, the measured galvanic current was reduced by two orders of magnitude for the 0.005N NaCl cell and three orders of magnitude for the 0.5N NaCl cell respectively. This means that as a practical matter, small defects in CARC should experience a rapid buildup of an oxide product that could partially block subsequent electrolyte access to the rest of the steel substrate.

ENGINEERING STUDIES

Accelerated "Joint A Assembly" salt fog testing of Phase I samples that had unbroken CARC seals between the Ti/Fe plates had virtually no corrosion along the contacting iron interface since there was no fluid intrusion. Similar accelerated "Joint A Assembly" cyclic corrosion testing of Phase I samples had minor corrosion along the contacting iron interface due to localized compromises in the CARC seal between the Ti/Fe plates. Thus in most cases the

presence of a quality CARC coating can help exclude electrolytes between contacting dissimilar metal plates thus mitigating galvanically induced corrosion product buildup.

During Phase II accelerated "Joint A Assembly" salt fog and cyclic corrosion testing the absence of the CARC seal allowed the intrusion of moisture/electrolyte into the crevasse between the two bolted plates leading to corrosion at the contacting iron interface. Thus there was a significant buildup of Fe corrosion products in the crevasse between both Fe/Fe and Ti/Fe interfaces during salt fog exposures. For Fe/Fe couples, hematite was the primary oxide phase with a minor amount of magnetite; for Ti/Fe couples the presence of Ti apparently produced a nearly even mix of both magnetite and hematite but the total quantity of corrosion product was less than for the Fe/Fe couples.

For cyclic corrosion Phase II exposures there was severe oxidation/exfoliation of corrosion products again due to the presence of moisture/electrolyte in the crevasse between either the Fe/Fe or Ti/Fe interfaces. For Fe/Fe couples, magnetite was the primary oxide phase with a minor amount of hematite; for Ti/Fe couples the presence of Ti 6/4 apparently caused the formation of an oxide mixture of mainly magnetite with some hematite but the quantity of corrosion product was again less than for the Fe/Fe couples.

To be noted is that Phase II CCT Fe/Fe samples produced the greatest amount of interfacial corrosion products for all samples examined in this study. Thus clearly for an engineering Corrosion Propensity Screening tool, the CCT protocol-- due to the programmed cyclic changes in thermal and chemical conditions compared to the constant exposure conditions within the SFT accelerated testing chamber-- provides a more rigorous and aggressive accelerated testing methodology.

Thus mixed Ti/Fe interfaces that are protected/sealed from the environment by CARC coatings will not experience unacceptable galvanically accelerated corrosion phenomena. Accordingly mixing titanium and steel components on Army materiel, provided they are protected by a quality CARC coating, will not cause adverse durabilty problems or lead to increased maintenance issues and costs.

ACKNOWLEDGEMENTS

The authors want to recognize the following colleagues for their contributions to this paper. Russell A. Kilbane who was responsible for the setup and experimental measurement of potentiodynamic scans and galvanic corrosion cell testing for galvanic corrosion. Dr. Paul F. Buckley for his initiation of and technical contributions to this project. Dr. Daniel J. Snoha for his expertise in operating the x-ray diffraction equipment and providing quality powder diffraction results. Finally, Dr. John H. Beatty for his technical leadership and professional advice.

REFERENCES

1. Montgomery, J.S., M.G.H. Wells, B. Roopchand, and J.S. Ogilvy, “Low-Cost Titanium Armors for Combat Vehicles,” *Journal of Metals,* vol. 49, No. 5, pp 45-47, May 1997

2. American Society for Testing and Materials. Standard Method of Salt Spray (Fog) Testing," ASTM B117, West Conshohocken, PA, 1990

3. General Motors. "Accelerated Corrosion Test GM9540P." General Motors Engineering Standard GM 9540P, 1997.

4. Levy, M, B.E. Placzankis, R. Brown, R. Huie, M. Kane, and G. McAllister, “The Effects of Co-Mingling Dissimilar Fastener Coatings on the Corrosion Behavior of Steel Bolt Assemblies,” MRL TR 92-40, US Army Materials Technology Laboratory, July 1992

5. U.S. Department of Defense. "Primer (Wash) Pretreatment (Formula No. 117 for Metals)" DoD-P-15328, Revision D, Amendment 2, Washington, DC, March 1991.

6. U.S. Department of Defense. "Primer, Epoxy Coating, Corrosion Inhibiting, Lead and Chromate Free." MIL-P-53022-10, Washington, DC, February 1992.

7. U.S. Department of Defense. "Coating. Aliphatic Polyurethane, Single Component, Chemical Agent Resistant." MIL-C-53039A, Washington, DC, May 1993.

8. Miller, C.E., J.H. Beatty, J.V. Kelley, B.E. Placzankis, and P.F. Buckley, “Galvanic and Potentiodynamic Corrosion Studies of Depleted Uranium and Sabot Materials,” ARL-TR-2047, Army Research Laboratory, September 1999

9. Cullity, B.D., "Elements of X-ray Diffraction," Second Edition, Addison-Wesley, chapters 6,7, and 10.

TABLES AND FIGURES

TABLE 1.
Assessment of Galvanic Current Parameters for Ti/Fe Couple

Parameters		Max. Current		Steady State Current		Comments
Solute Conc 0.xN NaCl	Sample	Magnitude (μA/sq. cm.)	Nominal Time (Days)	Magnitude (μA/sq. cm.)	Nominal Time (Days)	
0.005	Bare Couple	20	2	10	6-14	similar behavior for bare couples whether in 0.5 or 0.005 solns.
	CARC-coated with X-scribed Defect	0.18	5	0.12	20	very small steady state Galvanic current
	CARC-coated, Defect Free	zero		zero		CARC very protective, no Galvanic current
0.5	Bare Couple	18	2	6 - 8	4-10	rapid build-up of thicker corrosion product reduces current relative to 0.005N exposures
	CARC-coated with X-scribed Defect	Approaches steady state		0.006	7-14	rapid buildup of corrosion product in defect significantly reduces Galvanic current relative to 0.005N exposure
	CARC-coated, Defect Free	zero		zero		CARC very protective, no Galvanic current

TABLE 2.
Xray Diffraction Data for Iron Oxide Phase Analysis

Raw Xray Diffraction Data: for Corrosion Products Phase Analysis

Most Intense Fe and Oxide Phase Lines (Fe substrate from Galvanic Cells)

			Primary Peak XRD Intensity (arb. Units) for:		
Phase	Bragg Angle	d-spacing	Bare Fe	#2: 0.5N NaCl	#4: 0.005N NaCl
Fe (110)	44	2.0302	3800	1063	1332
Fe_2O_3	37	2.4699		384	350
Fe_3O_4	36	2.5311		640	692

TABLE 3.
Interpretation of Corrosion Products from Galvanic Cell Fe Substrates

	Sample (bare or 0.xN NaCl exposed Fe)				
line	Peak Intensity Ratios	Bare Fe	#2: 0.5N NaCl	#4: 0.005N NaCl	Interpretation
a	Fe oxidized/Fe bare	1	0.28	0.35	#2 oxide layer twice as thick as #4
b	Fe_3O_4/Fe oxidized	-	0.6	0.52	#2 has more Fe_3O_4 than #4
c	Fe_2O_3/Fe oxidized	-	0.36	0.26	#2 has more Fe_2O_3 than #4
-	ratio of c/b	-	0.6	0.5	Relative Ratio of Fe_2O_3/Fe_3O_4
-	-	-	-	-	Phases is greater in #2 than #4

TABLE 4.
"Joint A Assembly" Interface Corrosion Rating System

Rating	Qualitative Description	Reference
0(zero)	**No** Interface Corrosion	SF & GM Phase I for Ti/Ti
1	**No Significant** Corrosion	SF Phase I for Ti/Fe & Fe/Fe
2	**Slight** Corrosion (greater than for SF Ph I = #1)	GM Phase I for Ti/Fe
3	**Some** Corrosion (greater than GM Ph I for Ti/Fe=#2)	GM Phase I for Ti/Fe
4		
5	**More** Corrosion (greater than GM Ph I for Fe/Fe=#3)	SF Phase II for Ti/Fe
6		
7	**Severe** Corrosion (greater than SF Ph II for Ti/Fe=#5)	SF Phase II for Ti/Fe
8		
9	**Very Severe** Corrosion; Rust Exfoliation (less than for Fe/Fe=#10)	GM Phase II for Ti/Fe
10	**Most Severe** Corrosion; Major Rust Exfoliation	GM Phase II for Fe/Fe

TABLE 5.
"Joint A Assembly" Interface Corrosion Assessment After Salt Fog Exposure

Couple	Rating	B117-90 Test Chamber Exposure, Phase I Qualitative Description	Rating	ASTM B 117-90 Test Chamber Exposure, Phase II Qualitative Description
Ti/Ti	0	**No** Corrosion CARC Coating Sealed Out Moisture	0	**No** Ti Corrosion Moisture Intrusion into Common Interface
Ti/Fe	1	**No Significant** Corrosion of Fe CARC Coating Sealed Out Moisture	5	**More** Fe Corrosion (more than Ph I GM: Fe/Fe) Moisture Intrusion into Common Interface
Fe/Fe	1	**No Significant** Corrosion of Fe CARC Coating Sealed Out Moisture	7	**Severe** Fe Corrosion (more than Ph II SF : Ti/Fe) Moisture Intrusion into Common Interface

TABLE 6.
"Joint A Assembly" Interface Corrosion Assessment After Cyclic Corrosion Exposure

Couple	Rating	Cyclic Corrosion Test Chamber Exposure, Phase I Qualitative Description	Rating	Cyclic Corrosion Test Chamber Exposure, Phase II Qualitative Description
Ti/Ti	0	**No** Corrosion Thermal Cycles Slightly Compromised CARC Seal --leading to slight moisture intrusion	0	**No** Ti Corrosion Moisture Intrusion into Common Interface
Ti/Fe	2	**Slight** Corrosion of Fe (more than Ph I SF :Ti/Fe) Thermal Cycles Slightly Compromised CARC Seal --leading to slight moisture intrusion	9	**Very Severe** Fe Corrosion (more than Ph II SF : Fe/Fe) --Rust Exfoliation Moisture Intrusion into Common Interface
Fe/Fe	3	**Some** Fe Corrosion (more than Ph I SF : Fe/Fe) Thermal Cycles Slightly Compromised CARC Seal --leading to slight moisture intrusion	10	**Most Severe** Fe Corrosion; Major Rust Exfoliation Moisture Intrusion into Common Interface

TABLE 7.
Interface Oxidation Products for Joint A Assembly Samples from X-ray Diffraction Analysis

Sample Descriptors			Estimated Amounts of Interface Corrosion Product(s) after Phase II	
ID	Couple	Comments	After Salt Fog Exposure	After GM 9540 Exposure
A	Fe/Fe		**Fe_2O_3** Primary Phase; Fe_3O_4 minor	
B	Fe/Fe			**Fe_3O_4**Primary Phase; Fe_2O_3 minor
E	Ti/Fe	Ti & Fe side scrapings	Mix of **Fe_3O_4**(55%) & **Fe_2O_3**	
V	Ti/Fe	Fe side scraping only	Nearly equal mix of **Fe_3O_4** & **Fe_2O_3**	
R	Ti/Fe	Scrapings only from Ti side		Mix of **Fe_3O_4**(60%) & **Fe_2O_3**(40%)
X	Ti/Fe	Flakes only from Fe side		Major **Fe_3O_4** Phase; very minor Fe_2O_3
Y	Ti/Fe	Fine powder only from Fe side		Major **Fe_3O_4** Phase; very minor Fe_2O_3

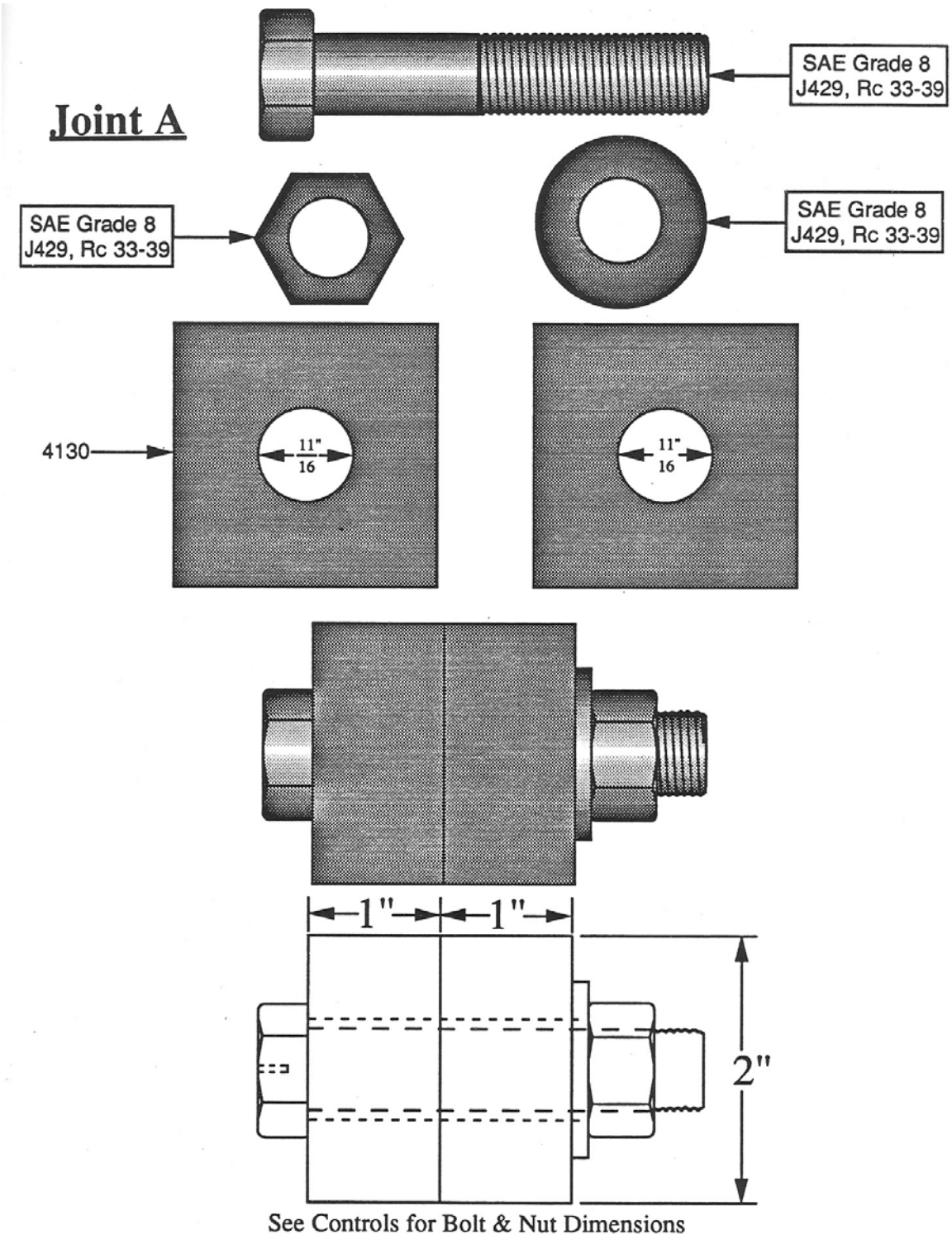

FIGURE 1. Engineering Samples Assembled to the "TACOM Joint A Assembly" Configuration[4]

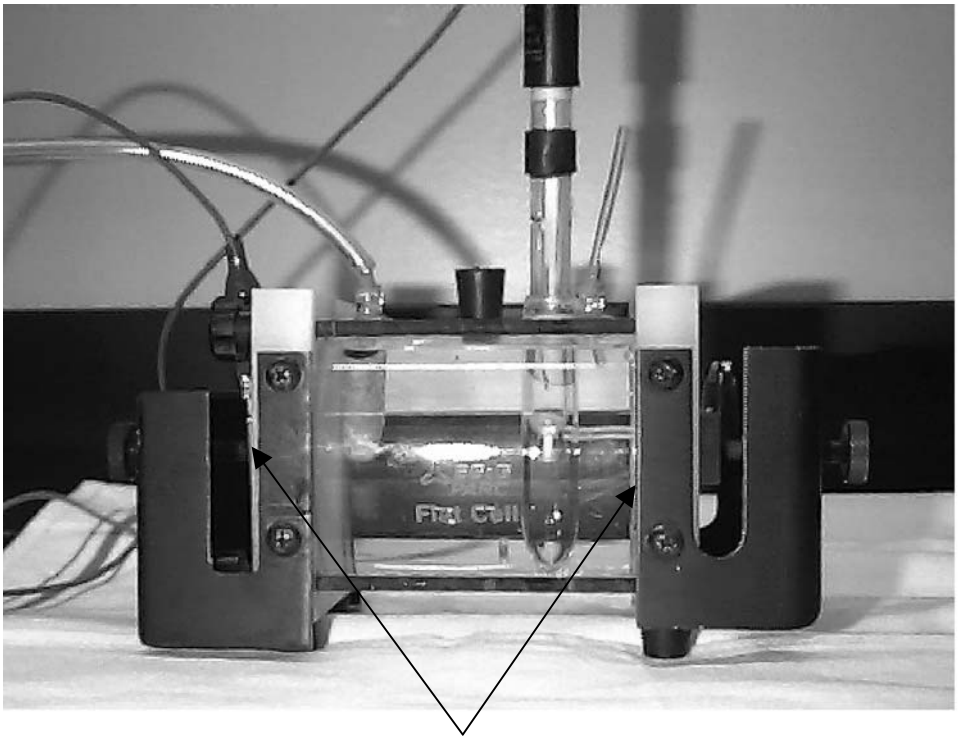

Specimen Locations

FIGURE 2. Electrochemical Cell Assembly for Scientific Testing

ASTM B117-90 Test Chamber

- 95 F @ 100% RH
- 5% (by weight) NaCl Solution
- Compressed Air Atomized Fog

FIGURE 3. ASTM B117 Salt Fog Test Chamber

GM 9540P Cyclic Test Chamber

- 0.9% NaCl
- 0.25 $NaHCO_3$
- 0.1% $CaCl_2$

FIGURE 4. GM9540 P Cyclic Test Chamber

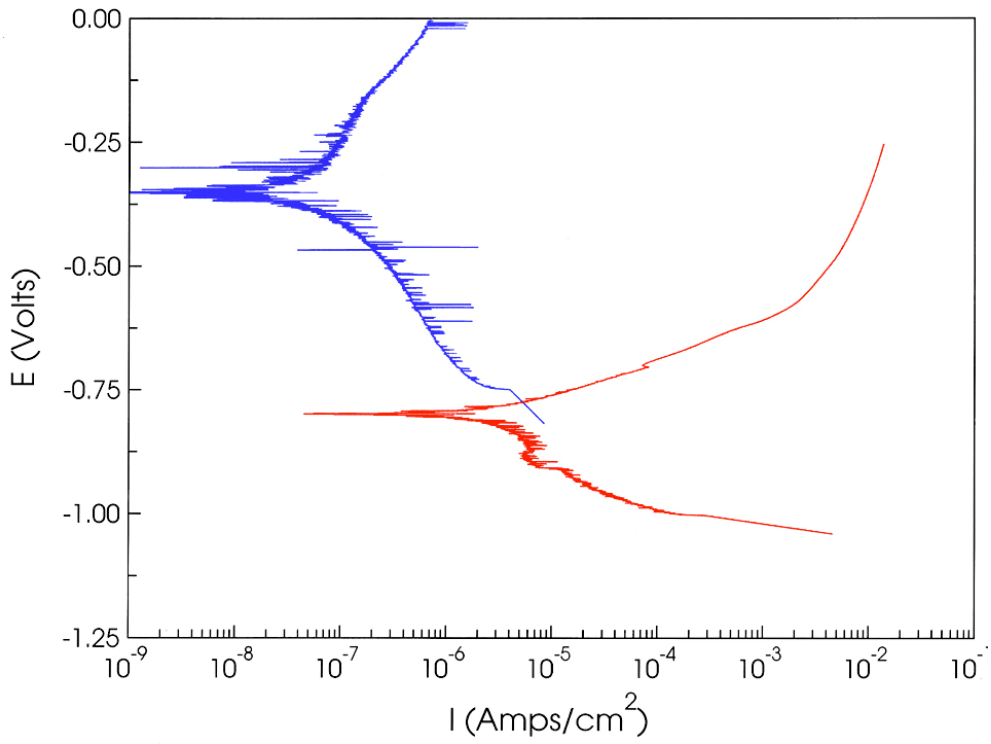

FIGURE 5. Potentiodynamic Scans for Ti (upper trace in blue) and Fe (trace in red)

FIGURE 6. Corrosion Products on AISI 4130 after 14 Days Galvanic Cell Test (left sample #4 exposed to 0.5N NaCl; right sample #2 exposed to 0.005N NaCl).

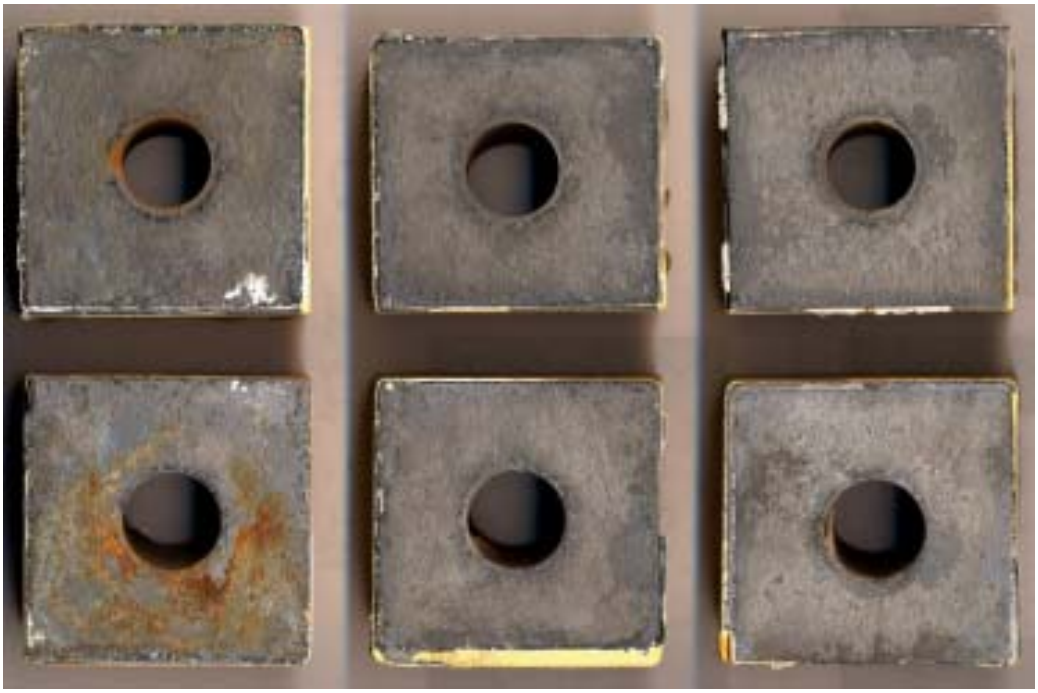

FIGURE 7a. Macrophotos of Ti-steel Interfaces after Phase I Salt Fog Exposure

FIGURE 7b. Macrophotos of Ti-steel Interfaces after Phase II Salt Fog Exposure

FIGURE 8. Assembled Armor Mockup Couples after Phase II GM 9540P Testing Exposure

FIGURE 9a. Macrophotos of Ti-steel Interfaces after Phase I Cyclic Corrosion Exposure

FIGURE 9b. Macrophotos of Ti-steel Interfaces after Phase II Cyclic Corrosion Exposure

FIGURE 10a. Macrophotos of Fe-Fe Interfaces after Phase II Salt Fog Exposure

FIGURE 10b. Macrophotos of Fe-Fe Interfaces after Phase II Cyclic Corrosion Exposure

ION BEAM ANALYSIS TECHNIQUES FOR THE STUDY OF MATERIAL SURFACE DEGRADATION

J. D. Demaree and J. K. Hirvonen

Weapons & Materials Research Directorate, Army Research Laboratory
Aberdeen Proving Ground, Maryland 21005-5066

ABSTRACT

The environmental degradation of metals and other materials often depends critically on the chemistry of the outermost atomic layers of that material. High-energy ion accelerators provide a variety of techniques to non-destructively measure the surface composition, and can thus be invaluable tools in the development of corrosion-, erosion-, and wear-resistant materials. The most common ion beam measurement technique, Rutherford backscattering spectrometry (RBS), yields elemental depth concentrations near the surface, and is quick and non-destructive, with near-surface depth resolutions on the order of 10 nm. The RBS technique is mass sensitive, and is most useful in the depth profiling of heavy (high Z) elements since the scattering yield is proportional to the square of the atomic number. Lighter elements (hydrogen, carbon, oxygen) are therefore more difficult to detect with this technique, since elastic scattering from low-Z nuclei is less likely. For these lighter elements another technique, nuclear reaction analysis (NRA), can provide a non-destructive, highly quantifiable measure of surface compositions of thin oxides, nitrides, or hydrogen-charged materials.

At ARL's accelerator facility at Aberdeen Proving Ground, these and other ion beam techniques have been used to study various materials science problems, including the diffusion and trapping behavior of hydrogen and carbon in steels, combustion-induced surface modification of gun steel during firing, and the development of environmentally-friendly alternative coating materials to replace electroplated chromium. Insights provided by these ion beam analyses have helped ARL's computer modelers and material scientists design next-generation materials for future Army systems.

INTRODUCTION

Ion accelerator-based analysis techniques[1,2] have found many applications in materials science, especially with regard to surface-mediated phenomena like aqueous corrosion, thermal oxidation, and tribology. Accelerators capable of producing ions with energies from 1 to 10 MeV are able to penetrate the first few micrometers of the surface of a material, where they

undergo elastic and inelastic scattering reactions with electrons and nuclei, or (more rarely) nuclear reactions with specific target atom nuclei. These ion-solid interactions can provide unique "fingerprints" of the presence of particular elements or isotopes in the target material, and can often provide highly sensitive elemental information of the outermost atomic layers of a material. In the study of environmental degradation and other surface property mediated processes, it is these outermost layers that are usually most important in determining the overall performance of the material.

Rutherford backscattering spectrometry (RBS) is the most commonly used ion analysis technique, and provides a nondestructive means of depth profiling elements in the outermost 1-2 micrometers of a material. The technique involves the measurement of the energy spectrum of light ions (usually incident monoenergetic 1.5 – 3.0 MeV He^+ ions) that have been elastically backscattered from nuclei of near-surface atoms. Typically 1 in 10^5 to 1 in 10^6 incident ions undergoes such backscattering events. Using simple billiard ball kinematics, as well as accounting for the nearly-linear "viscous drag" slowing of ions by electron interactions in this energy range, the energy spectrum can often be deconvoluted to provide elemental depth profiles of the target material. This technique is mass sensitive, and cannot easily distinguish between elements of similar mass, and is much more sensitive to elements with high atomic numbers than to light elements, and usually requires no calibration standards. It is an excellent tool for many applications involving near surface composition, and provides a nondestructive complement to other depth profiling methods (Auger electron spectroscopy, secondary ion mass spectrometry, etc.) that can provide complementary chemical information lacking in RBS analysis, but which often require calibration standards.

In the study of environmental interactions with materials, however, the most important interactions are often with light elements like oxygen, nitrogen, carbon, and hydrogen. For the detection and profiling of light elements such as these, nuclear reaction analysis (NRA) can be a more useful tool than RBS, since nuclear reactions are isotopic-specific and (in certain circumstances) can have reaction rates greatly above any interfering background. Hundreds of nuclear reactions have been investigated and catalogued from prior nuclear physics experiments and these data are directly applicable to materials studies. The choice of the best nuclear reaction to exploit requires consideration of both the ion beam species and energies available, as well as the desired sensitivity and required depth resolution of the measurement.

At the Army Research Laboratory's accelerator facility, located at Aberdeen Proving Ground, Maryland, both of these ion beam analysis techniques have been used to study materials systems for enhanced durability in electronic materials, in ground and air vehicle components, and in critical weapon components. In the following pages, several examples are given to illustrate the usefulness of ion beam analysis for understanding the environmental degradation of materials.

RUTHERFORD BACKSCATTERING SPECTROMETRY (RBS)

OXIDATION OF SILICON-CONTAINING DIAMONDLIKE CARBON COATINGS.

Researchers at ARL have studied the synthesis of diamond-like carbon (DLC) coatings using ion beam assisted deposition (IBAD) for several years, primarily for tribological applications. Liquid hydrocarbon precursors, like tetraphenyl-tetramethyl-trisiloxane (704 Dow-Corning diffusion pump oil), are vapor deposited onto the substrate to be coated, while the deposited, condensed vapor on the substrate is simultaneously bombarded with 40 keV argon ions. The

energetic ion beam converts the thin condensed oil layer into a very hard, low friction coating via molecular disassociation. The presence of silicon in the coating material has been shown to substantially increase the resistance of the coating to humidity effects, which can degrade the low-friction properties of conventional (i.e., non Si containing) DLC coatings. In general, conventional DLC coatings cannot be used for elevated temperature applications because of their poor thermal stability above 350°C, but several researchers have reported an increase in thermal stability when additional elements are present in the coatings.

Si-DLC coatings deposited at ARL were annealed in air at temperatures up to 600 °C, and RBS was used to examine the coatings after exposure to such oxidizing conditions.[3] RBS analysis showed that the composition of the films (excluding hydrogen, which cannot be detected by RBS) remained the same up to 300°C, but at higher temperatures the coating began to oxidize, forming a layer of SiO_2 at the outer surface of the coating. Figure 1 shows backscattering spectra for coatings before annealing, and after annealing at 500°C and 600°C for 30 minutes. After the 500°C anneal, only 22 percent of the initial Si-DLC film remained buried beneath a SiO_2 oxide layer, which did not contain any carbon or argon. Absence of carbon from the oxide, as well as increased porosity noted by optical microscopy, suggested that carbon is removed by CO_2 formation. After 600°C anneals, the DLC coating was completely oxidized, and only a SiO_2 layer remained. The presence of such a SiO_2 "cap" on the Si-DLC coating at high temperatures, clearly and readily detected by RBS, helped to explain the increased resistance to oxidation seen in Si-containing DLC. These Si-DLC coatings may be used for protective applications at temperatures up to 100°C higher than conventional DLC, because of this protective capping layer.

Ion beam analysis of H can, however, be accomplished using 1) forward recoil elastic scattering [FRES] of protons [H] by heavier ions at concentration levels of 0.1 at. % or higher (FRES technique not discussed here) or by 2) highly sensitive nuclear reaction analysis (described in a later section).

STABILITY OF SIC OHMIC CONTACTS

High power, high temperature electronic materials based on silicon carbide hold great promise for next-generation DoD vehicle propulsion and weapons systems. The thermal stability of ohmic contacts in SiC devices is critical for performance at the high temperatures (up to 600° C) at which these devices will be expected to perform. ARL researchers have been investigating a number of methods for producing stable, low resistivity contacts to *n*-SiC, and RBS has been used to assess the extent of interfacial diffusion between the contact metallization and the underlying SiC [4,5].

Multilayer contacts of Ni/WSi/Ti/Pt were deposited by sputtering, with Ni closest to the SiC to form a silicide contact. The contact is first annealed at temperatures of 950°C or 1000°C in order to form a silicide contact with good ohmic properties, but then are subjected to long-term aging tests at temperatures closer to the proposed operational temperatures. Figure 2 shows a portion of the RBS spectrum showing ions that have backscattered from Pt and W. This peak corresponds to a depth profile with the surface at the highest energy position and the rear of the film at the lowest energy due to energy loss of the He ions as they penetrate and scatter from progressively deeper portions of the film. The lower energy edge of the large peak corresponds to backscattering from the interface between the contact and the underlying SiC, and RBS reveals that the contacts formed using an initial 1000°C anneal are more stable than those formed at 950°C. The back edge of the 950°C contact shows additional movement during aging at

650°C, indicating an incomplete reaction during the initial contact formation. This observed difference had a strong effect on the electronic performance of the contact as well, and indicates that these ohmic contacts require higher temperature anneals in order to be thermally stable enough to survive potential Army applications.

NUCLEAR REACTION ANALYSIS (NRA)

HYDROGEN DETECTION AND PROFILING IN HIGH STRENGTH STEELS AND IN POLYMER SEGREGATION

Hydrogen has a strong effect on the chemical, mechanical, and electrical properties of nearly all materials, and an understanding of these effects is critical for durability and performance of many Army materiel systems. Despite its ubiquity, the presence of hydrogen is extremely difficult to detect. Conventional surface analysis techniques (e.g., Auger electron spectroscopy, ESCA/XPS) are "blind" to H since it has only one electron shell. Nuclear reactions between hydrogen nuclei (protons) and light element nuclei are fairly common, however, and often produce high-energy reaction by-products (gamma rays, charged particles) that are readily detected and useful for quantitative H detection and depth profiling. It should be noted that these capabilities are unique to ion beam analysis of hydrogen. An ion accelerator can be used to accelerate specific light element nuclei to the energy range necessary to induce these reactions (generally 3-10 MeV), and the presence of characteristic reaction products (e.g., gamma rays) upon hitting a target is indicative of the presence of hydrogen in the target material. The $^{1}H(^{15}N, \alpha\gamma)^{12}C$ reaction is most often used because of the extremely high reaction cross-section and the very narrow (i.e., resonance) energy range (6.385 ± 0.005 MeV) over which it occurs. This narrow energy range can be used to depth profile hydrogen in a material by varying

the incident ion energy so that the reaction energy occurs at various depths in the material. This nondestructive method for hydrogen depth profiling in materials yields sensitivities as low as 50 atomic ppm, with near surface depth resolutions as low as 1-5 nm.

At ARL's accelerator facility, this reaction has been used to detect hydrogen in high strength steels, polymer blends, diamondlike carbon films, gun barrel alloys & coatings, and other materials. Figure 3 shows the results of hydrogen profiling (using the ^{15}N reaction) in ESR-4340 steel with and without Pt implantation in the outermost 100 nm of the surface, after generating hydrogen on the surface via an electrochemical reaction. NRA analysis shows that the presence of Pt acts to reduce the amount of hydrogen underneath the steel surface, either by encouraging hydrogen recombination, or by facilitating the migration of hydrogen away from the surface and into the bulk. It is thought that this might reduce hydrogen embrittlement problems in critical load bearing components.

Figure 4 (reproduced from reference 6) shows how hydrogen depth profiling can be used to study surface segregation in polymer blends. In work done with researchers at the University of Akron,[6] blends of deuterated and hydrogenated polymers with different polymer architectures were examined with NRA to assess the extent of surface segregation caused by entropic effects. The blends shown in Figure 4 were hydrogenated 6-arm "star" polystyrene, in a matrix of deuterated linear polystyrene. The dotted line shows the expected hydrogen profile if no segregation is present; clearly, the star polymers segregate preferentially to the air/polymer interface, as was expected from entropic theory. Because the stopping power of ions in polymers is much lower than in metals, the depth resolution of H profiling in polymers is roughly 5 nm (using the system at ARL); achievable depth resolutions in metals can be as low as 1 nm.

CARBON AND NITROGEN IN GUN BARREL MATERIALS

Just as light-element ion beams can be used to detect hydrogen in materials, hydrogen ion beams (that is, protons) can be used to detect light elements in materials using the inverse of the same nuclear reactions described above. For example, one can impinge high energy H^+ ions onto a material to detect and profile the ^{15}N atom distribution in the near surface region. Since many environmental degradation mechanisms involve reactions with water, oxygen, carbon or nitrogen, NRA is particularly useful in the study of corrosion, oxidation, and erosion processes.

The erosion of gun tubes during firing is a critical limitation to the development of new more energetic propellants, and a better understanding of gun tube erosion is desirable for the optimal design of future weapons systems. The Army has long studied gun tube erosion in new and proposed weapons systems through direct measurement of erosion (that is, mass loss after firing), and is currently using advanced computer modeling to better understand the chemical interactions between gun steels and hot propellant gases as they contribute to overall erosion. The direct measurement of light elements in the near surface of gun steels by NRA currently supports the modeling efforts by providing diffusion coefficients in gun steel, as well as examining the role of light erosive elements (e.g., C, N) in and on steel surfaces after exposure to next-generation propellants.

It is thought that carbon interactions with gun steel (primarily from carbon monoxide in the propellant gas) are critical to the understanding of tube erosion and the failure of gun tube liners (usually electroplated chromium). Future gun tubes may be lined with sputtered or clad tantalum coatings instead, to avoid the environmental safety and health impacts of electroplating. In order to model the chemical reactions during gun firing, one must account for the diffusion of carbon in gun barrel steel, Cr and Ta. To measure this by NRA, samples of all three materials

were implanted with carbon-13, an isotope with a resonant nuclear reaction with protons that produces high-energy gamma radiation, and then progressively annealed at various temperatures. NRA was used to profile the implanted carbon after each annealing treatment, and Figure 5 shows some results from that study. The implanted C profile decreases monotonically with increasing anneal temperature presumably to the interior and possibly to the surface.

While carbon migrates readily at relatively low temperatures in both steel and Cr, the profile seems to become static after some time, which probably indicates the trapping of carbon in precipitate form. In tantalum, no carbon migration is seen until very high temperatures are reached, indicating that tantalum liners are likely to be inert to carbon reactions at the temperature expected during firing. There is, however, the possibility that carbon migrating in the steel might accumulate at its interface with the relatively carbon-impenetrable tantalum, leading to interface failure. This may be addressed in future studies by covering the implanted steel with sputtered tantalum and repeating the annealing studies.

Erosive gases from next-generation propellants may have significantly different compositions than traditional propellants, leading to very different erosion behavior. Specifically, greater amounts of nitrogen in the hot propellant gas may lead to the formation of a nitride layer on the gun steel surface, which may help reduce more damaging interactions with carbon species. Using the inverse of the hydrogen profiling reaction described above, a beam of protons was accelerated onto gun steel test nozzle samples exposed to various propellant gases in a simulated gun firing rig. Remnant ^{15}N present in a nitride (^{15}N ~0.37% of nitrogen in nature) can be depth profiled by detecting the high-energy gamma rays produced by the nuclear reaction. Figure 6 shows a series of nitrogen (isotope-15) depth profiles over a depth of approximately 1-2 micrometers obtained when gun steel is exposed to propellants containing

various amounts of nitrogen. The amount of nitrogen at the surface ranges from negligible to as high as 8 atomic percent, indicating significant differences in the amount of nitride formed and migrating inward during the test firing. This work showed for the first time evidence for "combustion induced nitriding" of the gun barrel surface, which appeared to be correlated with reduced erosive wear (weight loss of the nozzle during test firing). Current work focuses on correlating these measurements with observed erosion behavior, as well as experiments designed to understanding the possible competition between nitrogen and carbon reactions at the surface that may contribute to the decreased erosion seen with some of the high-nitrogen propellants currently being tested.

CONCLUSIONS

Accelerator-based ion beam analysis techniques provide a sensitive, nondestructive means of examining the outermost atomic layers of a material, where critical interactions with the environment occur. Rutherford backscattering spectrometry (RBS) is a versatile, fast method for elemental depth profiling which requires no external calibrations and is best suited for detecting medium- to high-Z near-surface elements in relatively simple materials systems. Nuclear reaction analysis (NRA) is more time-consuming, but can offer highly sensitive, isotope-specific detection of light elements (e.g. hydrogen, carbon, and nitrogen) that can be of primary importance in environmental degradation of materials.

ACKNOWLEDGMENTS

The case studies described in this paper are primarily the work of other researchers at ARL, or university researchers working on Army-funded programs, all of who used the

accelerator laboratory at ARL to help understand their particular materials systems. Interested parties are encouraged to contact them directly; questions regarding the application of ion beam analysis techniques are encouraged to contact the authors of this paper. Dr. Costas Fountzoulas (ARL) developed the Si-DLC coatings for low-friction applications and wear resistance. Dr. Melanie Cole (ARL) heads the development of rugged contacts to silicon carbide electronics. Surface segregation of polymer blends is an interest of Professor Mark Foster at the University of Akron, sponsored by ARO. Hydrogen migration in steels was studied by Dr. R.P.I. Adler, Paul Buckley, and others at ARL. Gun barrel erosion is a topic of great current interest, with Paul Conroy (ARL) coordinating many of the current efforts at ARL-WMRD. Work on the role of light erosive elements in gun barrel erosion was sponsored by the Environmental Quality Basic Research and Development Program (POC: T. Sachar - IEC/Picatinny Arsenal).

REFERENCES

1. Handbook of Modern Ion Beam Analysis, eds. J.R. Tesmer and M. Nastasi (Materials Research Society, Pittsburgh, PA, 1995).

2. Backscattering Spectrometry, W.-K. Chu, J.W. Mayer and M.-A. Nicolet (Academic Press, New York, NY, 1978).

3. C.G. Fountzoulas, J.D. Demaree, L.C. Sengupta and J.K. Hirvonen, "Thermal Annealing Behavior of Si-DLC IBAD Coatings", Materials Research Society Symposia Proceedings, **438** (1997) 587

4. M.W. Cole, P.C. Joshi, F. Ren, C.W. Hubbard, M.C. Wood, M.H. Ervin, "The Materials Properties of a Nickel Based Composite Contact to n-SiC for Pulsed Power Switching", Materials Research Society Symposia Proceedings, **622** (2000) 587

5. M.W. Cole, P.C. Joshi, C. Hubbard, J.D. Demaree and M. Ervin, "The thermal stability and performance reliability of Pt/Ti/WSi/Ni Ohmic contacts to *n*-SiC for high temperature and pulsed power device applications", submitted for publication.

6. C. C. Greenberg, D. M. Teale, M. D. Foster, C. M. Turner, S. Corona-Galvan, E. Cloutet, R. P. Quirk, C. F. Majkrzak, D. Demaree, "Surface Segregation in Blends of Linear and Regularly Star Branched Polystyrene", submitted to Macromolecules.

FIGURES

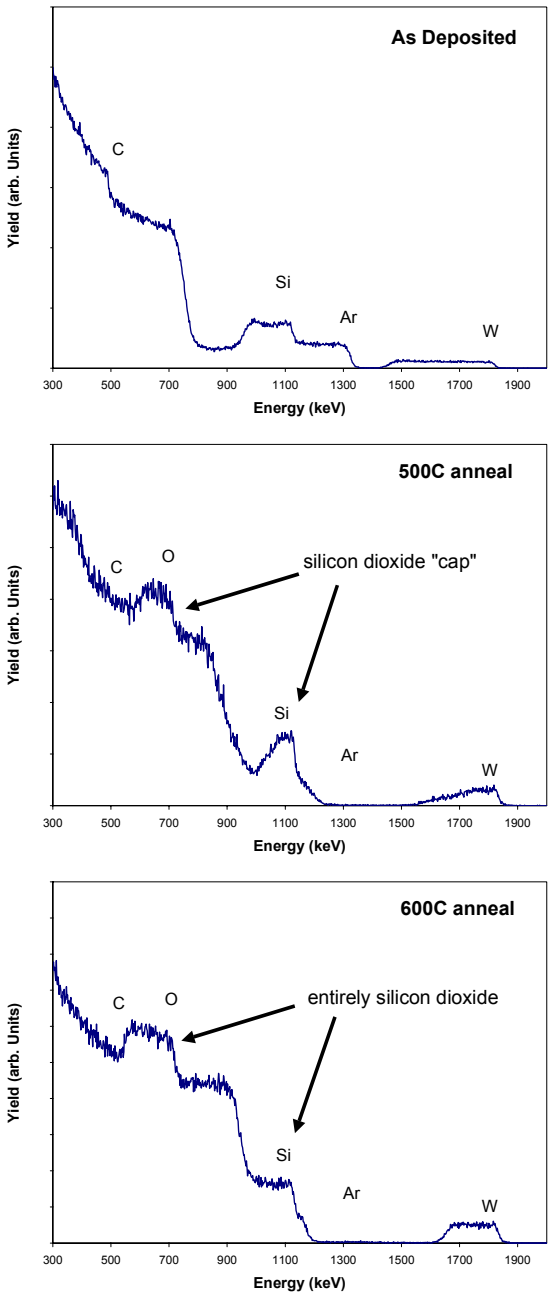

FIGURE 1. Rutherford backscattering spectra of silicon-containing diamond-like carbon (Si-DLC) coatings after deposition, and after 30 minute anneals in air at 500°C and 600°C. Note: There are trace amounts of Ar and W retained in the coatings from IBAD synthesis of Si-DLC, from the W-filament Ar^+ ion source. Despite the small concentration (about 0.1 atomic percent), the backscattering yield for W is high because of its high cross section for elastic scattering (proportional to Z^2, where Z is the atomic number of the element).

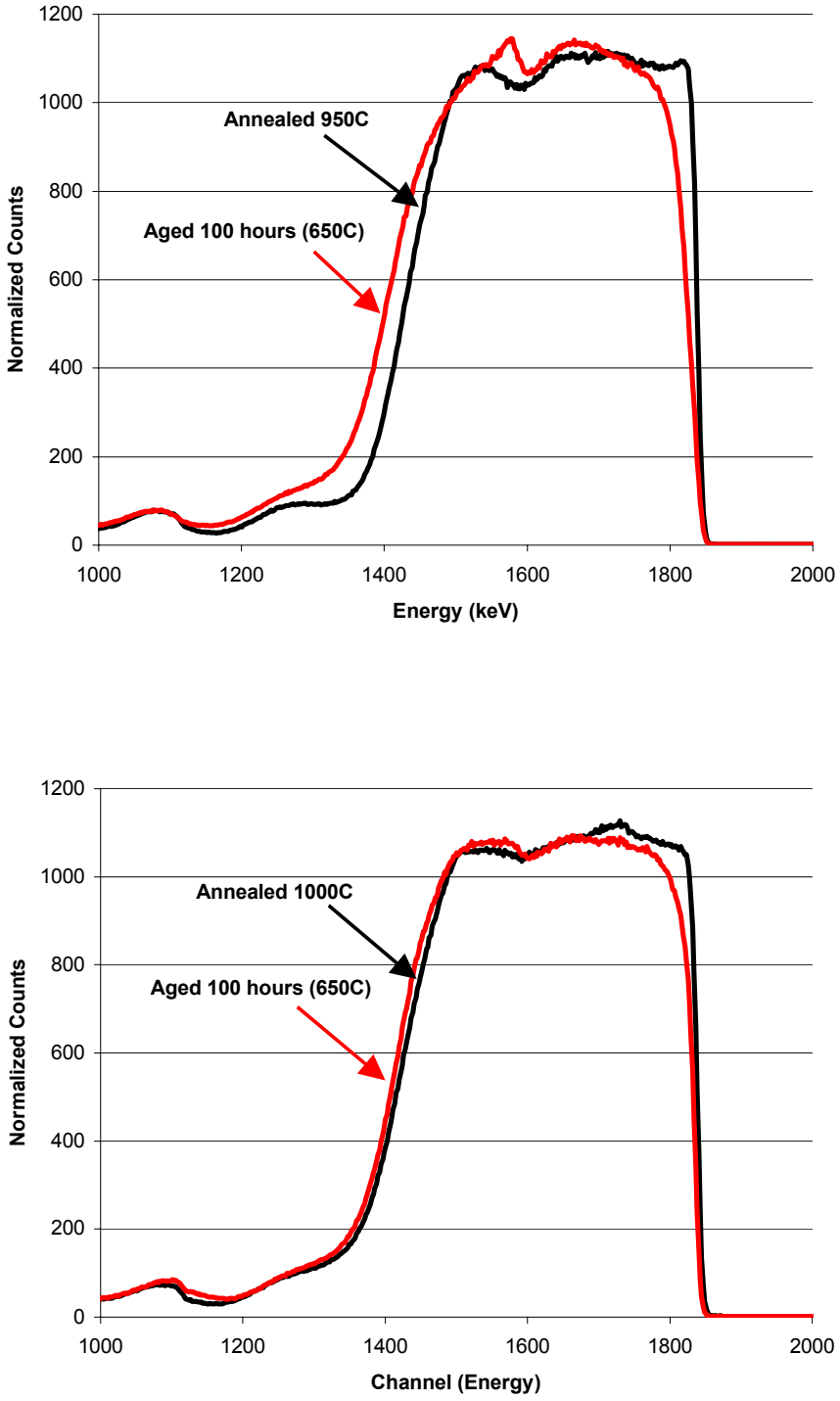

FIGURE 2. Rutherford backscattering spectra from composite ohmic contact to SiC before and after additional 650°C aging. Top spectra are for initial 950°C anneal, and bottom spectra are for initial 1000°C anneal.

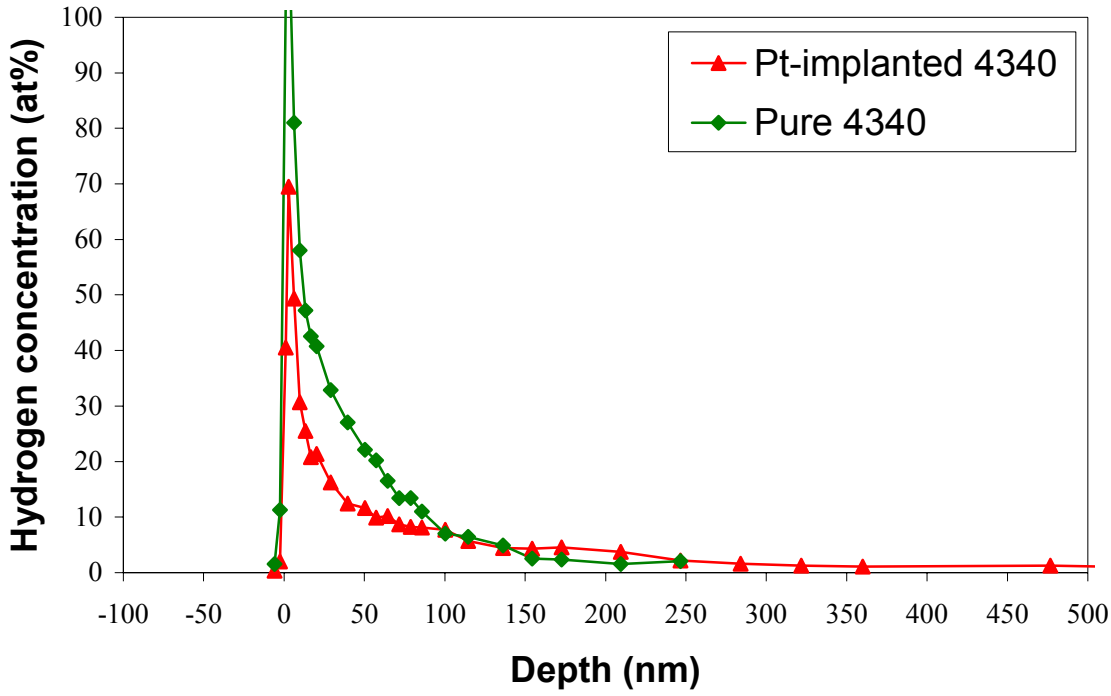

FIGURE 3. Hydrogen depth profile obtained using NRA for ESR 4340 with and without platinum implantation in outermost 100 nm of the steel, after hydrogen charging. Sharp spike at depth "zero" corresponds to H in surface contaminants (H_2O and adventitious hydrocarbons).

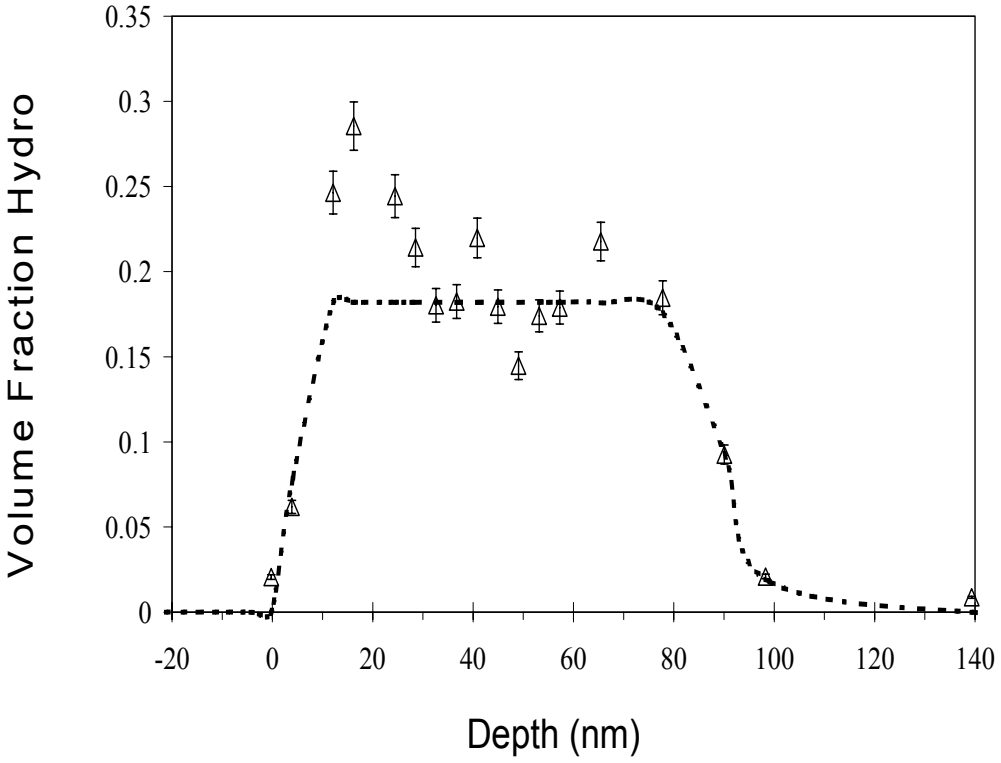

FIGURE 4. Hydrogen depth profiles of hydrogenated 6-arm "star" polystyrene in deuterated linear polystyrene (from reference 6), showing segregation of the hydrogenated polymer to the surface. The dashed line is an approximation of the profile expected should no segregation occur.

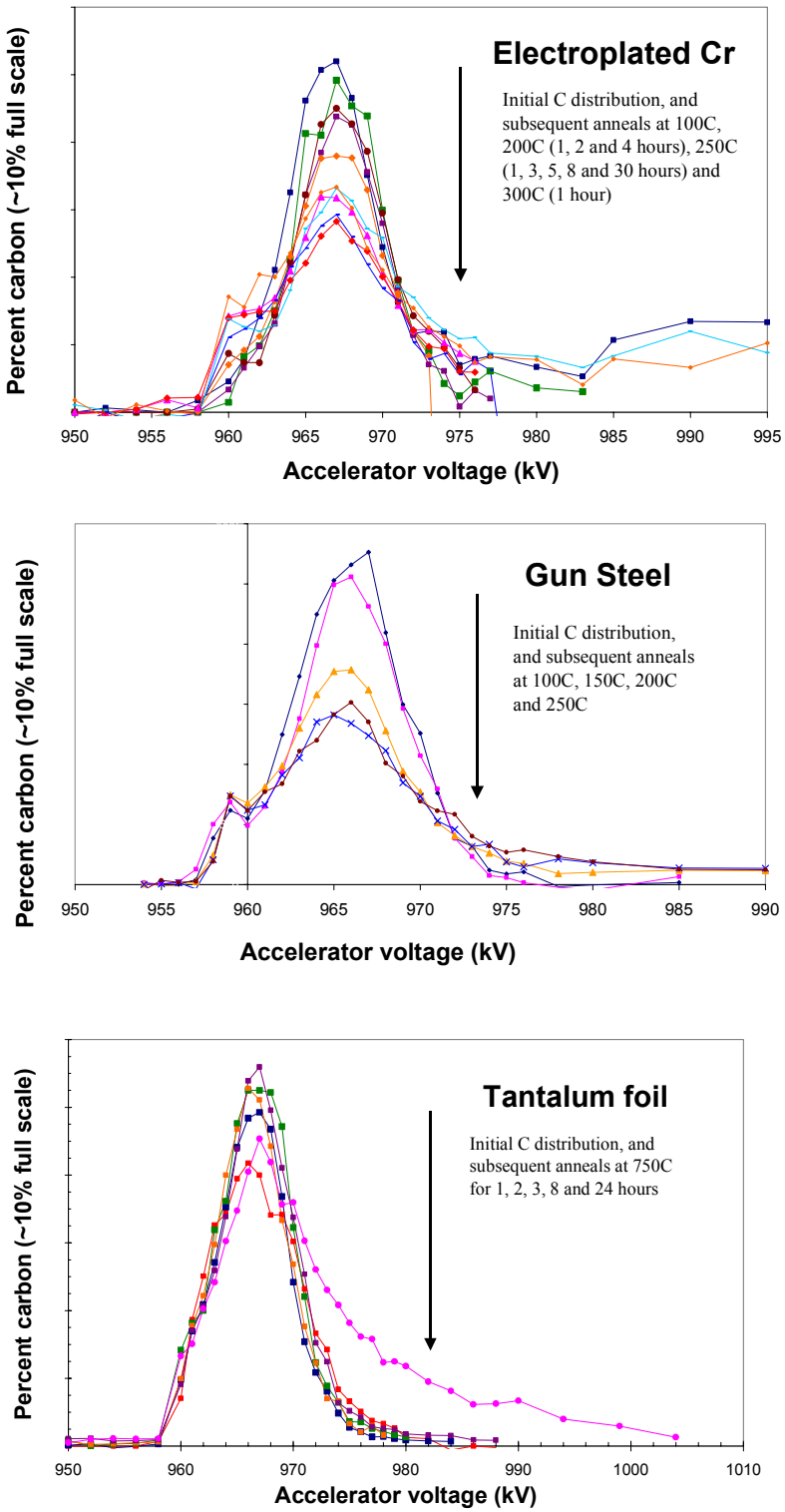

FIGURE 5. Carbon-13 depth profiles in a) gun steel, b) chromium electroplate and c) tantalum foil, after various heat treatments to assess carbon diffusion, as measured by NRA. Arrows indicate evolution of carbon profile after annealing.

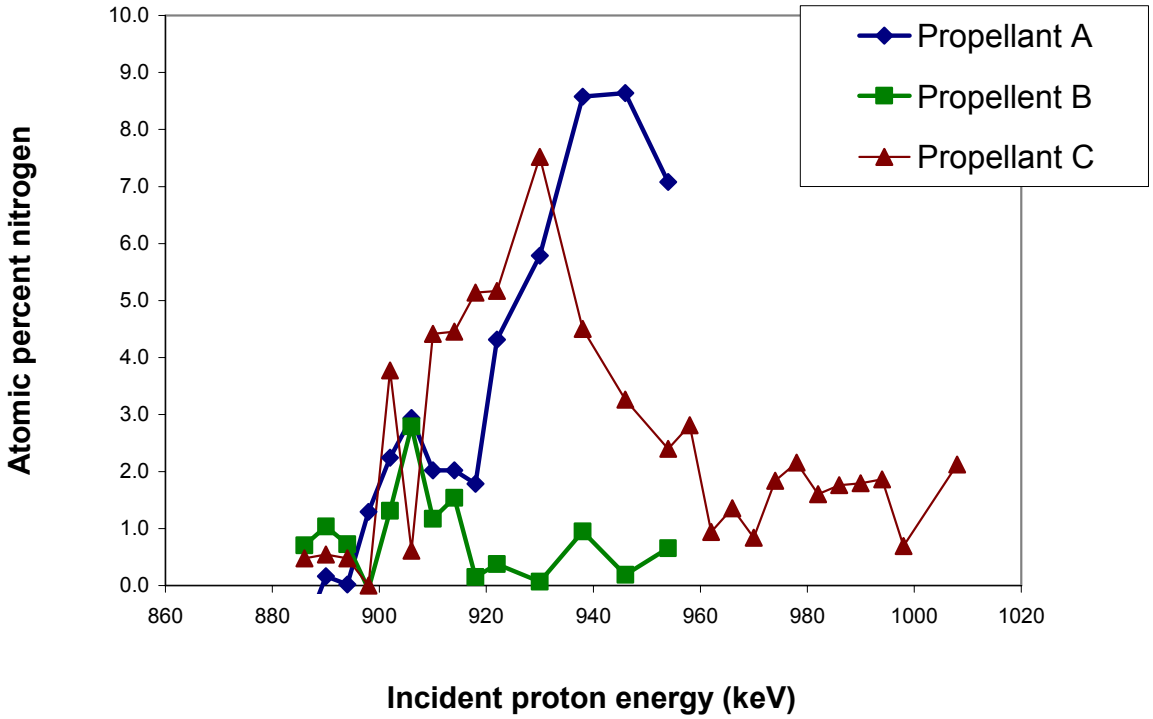

FIGURE 6. Nitrogen depth profiles measured by NRA on gun steel exposed to various propellant gases during test firing. Propellants containing high amounts of nitrogen (A and C) showed nitrided surface layers (> 1 micrometer thick), while a conventional propellant (B) showed little nitrogen retention.

U.S. ARMY EXPERIENCE WITH CORROSION ASSESSMENT AND ANALYSIS IN ROTORCRAFT

Kevin S. Rees

ABSTRACT

The Airframe Condition Evaluation (ACE) program is used to conduct an annual structural evaluation of every helicopter in the Army fleet. The ACE assesses the condition of the fleet and identifies aircraft requiring depot maintenance. A corrosion data collection task was added to the ACE program in 1998. This paper discusses the Army's efforts to evaluate corrosion data collected through the ACE program for the entire Army helicopter fleet. A number of significant discoveries and conclusions are presented. An evaluation of ACE corrosion findings is presented revealing that pitting, exfoliation, and corrosion fatigue are not widespread problems on the UH-60 helicopter while general surface corrosion and filiform corrosion are significant problems in some areas of the aircraft. Data describing the variety of corrosion observed in all front-line Army aircraft is also presented. It is anticipated that this data describing the occurrence of corrosion in Army helicopters will prove useful for future efforts aimed at preventing or correcting the conditions observed.

INTRODUCTION

The U.S. Army currently uses the ACE methodology to conduct fleet surveillance and prioritize aircraft for induction into programmed depot maintenance. ACE includes an annual evaluation of virtually every helicopter in the Army fleet. ACE uses visual indicators to estimate the amount and scope of airframe degradation and corrosion. ACE is the primary driver for depot maintenance of Army helicopters, with no consideration given to flight hours or calendar time. Corrosion indicators for aircraft components were added to the ACE during 1998. However, these component (gearbox, rotorhead, engine, etc.) indicators were not scored and did not contribute to the return of any aircraft for depot maintenance during 2000. The ACE has always contained some structural corrosion indicators, but these corrosion indicators were not

scored independently from other structural issues. Prior to this ACE improvement project, corrosion had not been a significant factor in determining which aircraft should undergo depot maintenance.

This paper will discuss progress in an ongoing effort to improve the condition of the Army fleet through the ACE process. Areas of discussion will include an analysis of the current ACE methodology and a discussion of the role of corrosion in helicopter structural degradation. Also included are significant data describing the occurrence of corrosion in the Army fleet and how ACE is being used by the Army to improve the condition of the fleet with regards to corrosion.

ACE PROGRAM METHODOLOGY

PURPOSE

The ACE program is designed to identify Army rotorcraft that have experienced structural deterioration to such an extent that they require programmed depot level maintenance to restore them to full serviceability.[1,2] The result of the ACE is a discrete score for each aircraft that can be used to rank order the entire rotorcraft fleet according to their condition while also identifying all aircraft that require depot maintenance. Ideally, ACE will enhance the safety and readiness of the fleet while reducing depot costs when compared to time based overhaul programs. Time-based depot maintenance scheduling must consider absolute worst case operating conditions, by design, in order to maintain aircraft safety and readiness. The conservatism required in a time-based scheme generates a much larger depot maintenance requirement than the depot maintenance requirement developed by a condition-based system such as ACE.

The ACE evaluation system is also required to include readiness considerations in identifying aircraft for depot maintenance.[1] The purpose of including readiness considerations in the ACE is to select aircraft for depot maintenance that are creating a significant drag on unit level maintenance resources. The maintenance burden associated with these aircraft can degrade the "go-to-war" ability of a unit. Examples of readiness related indicators include deferred field level tasks, impending field inspection or maintenance requirements, and a low aircraft mission capability rate. However, the current incarnation of the ACE does not include significant weight for factors directly related to aircraft readiness.

The ACE technique is based on the principles of reliability-centered maintenance.[2,3,4,5] Specifically, the ACE implements the on-condition maintenance aspect of reliability-centered maintenance. On-condition maintenance actions are those determined to be necessary based on an actual evaluation of the component or system during a scheduled inspection or screening. On-condition maintenance is a valid and desirable approach to determining maintenance requirements for equipment such as rotorcraft.[5,6] If a sound evaluation interval is selected, on-condition maintenance ensures that required maintenance actions are performed while unnecessary maintenance actions are minimized. So, if the cost of the evaluation is small when compared to the cost of the maintenance action (as is the case with ACE and depot maintenance), on-condition maintenance will result in a very cost-effective maintenance scheme that maintains the inherent reliability of a system. The entire fleet-wide ACE evaluation program costs the Army less than 50% of the cost of one aircraft overhaul per year. The ACE is also currently used by the U.S. Air Force to help identify their H-60 helicopter depot maintenance candidates. Foreign countries operating U.S. designed military helicopters in Asia, Europe, Africa, and around the world also use the ACE to enhance the readiness of their aircraft fleets.

DESCRIPTION OF THE ACE METHODOLOGY

ACE is an annual evaluation consisting of a visual inspection and a review of historical records for every helicopter in the Army. The ACE evaluators utilize mirrors, borescopes and other tools to aid their visual inspection, but more sophisticated non-destructive inspection techniques are not a part of the current ACE. During an ACE evaluation a team of two evaluators examines the aircraft based on predefined indicators of aircraft condition. Definitions of some of the terms of interest in the ACE are as follows:

- Indicators: model specific inspection locations for the structural condition of the aircraft
- Condition Codes: descriptions of defect types & severity for each indicator
- Weights: points associated with each unique indicator/condition code possibility
- Profile Index: the sum of the indicator/condition code findings for a given aircraft
- Threshold: a predetermined point that dictates the minimum profile level requiring depot maintenance

The U.S. Army Aviation and Missile Command's Aviation Engineering Division reviews field performance data, depot tear-down analysis, and other failure records for each aircraft Mission/Design/Series to empirically develop ACE indicators and condition codes. Once the ACE is established for a Mission/Design/Series, the results of the evaluations are reviewed to establish or modify the weights. The results of the ACE are a listing of the worst-case condition code observed for each indicator on an individual aircraft. Once the appropriate weights are applied to these indicators, a profile index (or score) is generated for the aircraft. This profile will dictate whether or not an individual aircraft is a depot maintenance candidate. A sample portion of a table of ACE indicators and condition codes is included as Table 1

The number of indicators for each aircraft is always less than 100, and typically numbers approximately 60. There are 23 different condition codes defined for the ACE and included in Table 1. However, all 23 codes are not applicable to every indicator. Once the complete list of ACE indicators is rank-ordered, engineering judgment is used to assign the final weights to each indicator. The sum of all of the worst case weights for each indicator is 1000 points.

ANNUAL ACE CYCLE

The ACE process is an orderly annual cycle that is essentially the same for all Army aircraft. This cycle is designed to provide Army decision-makers key information needed to prioritize depot maintenance returns. These decision-makers use the ACE results to lay out a depot maintenance induction schedule based on budget limitations and the aircraft availability needs of the Army's war-fighters and trainers. The first step in the ACE cycle is the development or modification of ACE indicators for each aircraft. Potential indicators are selected empirically using expert engineering judgment based on aeronautical importance, depot versus field maintenance capability, and potential for continuing aircraft deterioration.[2] These potential indicators are then analyzed using operational data from both field and depot maintenance activities. For ongoing ACE programs the findings from the previous year's evaluations are reviewed against actual depot findings and indicators are added, dropped, or fine-tuned.

Once the final indicator/condition code selections have been made, the ACE documentation for the evaluators is updated. Army Maintenance Engineers prepare this documentation in the form of an AMCOM Engineering Directive as supplemental data to the appropriate Army publication.[7,8] These documents need to be in place prior to conducting the annual ACE evaluator training and certification, the next step in the annual cycle. Arrangements

are made for a training location where at least one example of each aircraft model of interest will be available. ACE evaluators from worldwide locations come in for a single two-week session where all indicators and condition codes are reviewed and discussed. All questions are answered and the evaluators break up into teams and perform actual ACE evaluations on the aircraft. The teams then compare their results and any discrepancies are reviewed and resolved. The goal is to insure that all evaluators are looking at and scoring the indicators to a common standard. Tips on using mirrors, borescopes and other inspection devices are shared with all evaluators simultaneously. Relative terms such as "excessively worn" and "moderate corrosion" are explained with both photographs and aircraft exhibits. Once the evaluators have completed this training the Army is satisfied that the potential for misinterpretation and multiple standards has been minimized. After successful completion of the training, evaluators are issued ACE certifications valid for the next 12 months.

Immediately following the ACE training the evaluators begin performing their evaluations. The results of these evaluations are fed back to the master ACE database (stored in Microsoft Access) where they are scored. Meanwhile, the Army Maintenance Engineers have finished developing a preliminary set of indicator weights for each aircraft Mission/Design/Series. These proposed weights are applied to the individual aircraft results as they are generated. Once the Army Maintenance Engineers have had a chance to apply the proposed weights to approximately 10% of the fleet, and are satisfied that the results are valid, the indicator weights are finalized. The ACE evaluators continue to perform their evaluations and the Maintenance Engineers review results, answer questions, and begin working on any required revisions for the next year's cycle.

Some aircraft are identified as requiring immediate depot maintenance due to the criticality of the ACE findings and the potential for unsafe aircraft operations. The Maintenance Engineers work with the ACE evaluators and Depot Program Managers to identify these aircraft and make arrangements for their immediate induction into depot maintenance. The final step in the cycle is the evaluation of the year's ACE results for budget implications and depot program development. Once this evaluation is completed, and the final depot candidates are identified, this information is shared with Army field commanders at the Worldwide Aviation Logistics Conference. Once the depot candidate selection and induction schedule is finalized at the conference, the cycle is complete.

ADDITION OF CORROSION INDICATORS

The ACE has always included an extensive visual evaluation of primary aircraft structural members. This structural evaluation identifies cracks, working rivets, punctures, improper repairs, misalignment, scratches/dents, and corrosion pitting (as shown in Table 1). The inclusion and importance of these condition codes depends on the particular structural member being examined. During the first 22 years of the ACE program (from 1975 – 1997), collection of data documenting the occurrence of corrosion in the Army fleet was not a part of the ACE process. If corrosion was not the most severe condition code for an indicator on any given aircraft, which is often the case, then the ACE would not have noted the presence of the corrosion. In October 1997 the Army's Aviation Engineering Division was directed to take immediate action to begin collecting data on the state of the Army helicopter fleet in terms of corrosion degradation. The team first selected a number of unscored corrosion indicators to add to the ACE in order to begin this fleet-wide assessment.[9] The team also took action to ensure that all structural corrosion indications (D codes) were captured in the database even if the D

codes were not scored due to the occurrence of a more significant condition code on the same structural member. Since the ACE was already dictating an annual fleet-wide aircraft evaluation, the team was able to add visual corrosion indicators for aircraft components (gearboxes, rotorhead, controls, etc.) to the procedure at very little additional cost. However, these new component corrosion data points were not treated as actual scored indicators.

The corrosion data being collected through the ACE is called the Corrosion Prevention and Control Evaluation. The corrosion evaluation includes collection of environmental, operational and maintenance data. The corrosion evaluation also includes a visual evaluation of the actual condition of the aircraft structure and components. The environmental data collected includes how the aircraft is stored (e.g., hangar or tarmac), geographic location, location of operations during the past year, and other related data. These data are required to provide some environmental context to the other information collected on each aircraft. Maintenance data are also collected to provide a more complete picture of what actions are required in the field to maintain the level of preservation observed for a given aircraft. Maintenance data collected includes component replacement records, types of corrosion preventive compounds used, aircraft and engine wash frequency, and the source of the wash water. The ACE evaluators also collect aircraft condition data, including indications of corrosion such as blistering paint, pitting, exfoliation, powdery residue, etc. Each instance of corrosion is coded to identify the type of observation and what corrective maintenance action will be required (e.g., clean and treat, patch, or remove and replace). An example of an ACE component corrosion evaluation sheet is shown in Table 2. The actual data collected are stored in a Microsoft Access database along with all other ACE data. All findings are recorded in the database including required maintenance action and level of corrosion damage. Corrosion damage is classified as mild surface corrosion,

medium corrosion damage (approximately 5-10% loss of parent metal), or severe corrosion damage (more than 10% loss of parent metal).[10] These ACE corrosion results have been collected for a three-year period and are now being evaluated for use as scored indicators. The actual types of corrosion being considered as indicators will be discussed later in this paper.

CURRENT ACE STRUCTURAL RESULTS

The ACE program results in a fleet-wide assessment of every aircraft in the Army on an annual basis. Since each aircraft Mission/Design/Series has its own unique indicators, aircraft ACE scores are only compared within one Mission/Design/Series family (and not across aircraft lines). In other words, the UH-60 fleet condition is ranked by ACE score separately from the AH-64 fleet, which is also ranked separately from the CH-47 fleet. Illustrations of the results obtained through the ACE are included in Figures 1 through 4. Each of these Figures displays the annual findings from recent ACE evaluations. The Figures are arranged as histograms that display intervals of ACE profile scores versus the number of aircraft achieving these scores. Reviewing a particular ACE distribution in this manner can give Army leadership a sense of the actual structural condition of a particular aircraft fleet. The distribution suggests the extent of the depot level maintenance workload needed to restore the fleet's condition in the coming years. The ACE results can be used to provide an accurate snapshot of the condition of the fleet if relevant indicators and weights are used. These data can be a significant tool in monitoring the condition of the fleet, developing future maintenance budgets, and planning for major system modifications or upgrades. Army Maintenance Engineers must routinely review these histograms to evaluate the state of repair of the fleet and to determine how well current ACE indicators and weights are discriminating between the best and the worst aircraft currently in operation. Recent analysis of ACE scores and the physical aircraft condition led to the

conclusion that for some aircraft the ACE has not been fully capturing the structural deterioration of the Army's fleet. Some aircraft with fairly low ACE scores have displayed significant structural degradation due to corrosion damage.

ROTORCRAFT DEGRADATION ASSOCIATED WITH CORROSION

Corrosion is a significant issue affecting the availability and safety of the Army's helicopter fleet. The purpose of this discussion is to first review existing research and publications concerning the general effects of corrosion on aircraft. This discussion is followed by a more detailed examination of a number of specific types of corrosive attack known to affect Army aircraft. This existing knowledge is then evaluated and applied specifically to the ACE program and potential ACE indicators. The results of the analysis indicate that the effects of corrosion on current Army helicopter operations can be severe. In light of the findings presented below it appears that corrosion should play a larger role in Army aircraft condition evaluation, specifically through the ACE program.

RELEVANCE TO MILITARY ROTORCRAFT

Premature Failures. Corrosion has been linked to a wide variety of premature failures in aircraft and their components.[11,12,13] Although corrosion is seldom the sole contributing factor in a severe mishap or major catastrophe, it's insidious effects on reliability and availability cannot be denied. Corrosion can increase effective stress levels due to uniform thickness loss. Corrosion pits can act as fatigue crack initiation sites. Depending on the environment, material, and application, the deleterious affects of corrosion can be quite varied. The one common denominator is typically reduced service life.

Safe-Life Designs Vulnerable. Aircraft that have been designed using safe-life techniques (rather than damage tolerance) may be especially susceptible to failure due to corrosion damage.[11,13] In the past, the safe-life approach often led to the choice of high strength alloys (especially aluminum) with very low fracture toughness. These materials perform well in the laboratory environment and even during accelerated component fatigue testing. These qualification exercises normally take place in a clean, dry environment. However, when exposed to harsh environments over long periods of time, these same materials are often sensitive to stress-corrosion cracking and corrosion fatigue. The flaws induced due to this environmental exposure can dramatically reduce actual component lifetimes from those predicted through the safe-life methodology. This is a very important consideration for military helicopter operations since all Army aircraft have been designed using safe-life techniques.

Time Dependency. The occurrence of corrosion in aircraft is primarily dependent on calendar time rather than flight hours.[12,13,14] While some corrosion is related to service conditions (such as marine operations) much of the actual damage occurs during aircraft downtime rather than during operations. This fact suggests that scheduling corrosion inspection and maintenance activity as a function of flight hours rather than calendar time is inappropriate. The time dependency of corrosion makes this an issue of growing concern to the Army. Over the past several years flying hour budgets have been reduced, requiring Unit Commanders to fly each aircraft fewer hours per year. Meanwhile, corrosion damage, which is dependent on time in-service, continues to accrue. Therefore, corrosion damage is becoming more significant compared to flight-induced damage than it has been in the past.

Periodic Inspections. One of the most dependable methods of dealing with the occurrence of corrosion in aviation systems is periodic inspection.[14,15] Periodic inspections are

critical since corrosion in aircraft can never be entirely eliminated. Corrosion prevention treatments should be followed and sound design practices that minimize the opportunity for corrosion to occur are essential. However, many of the materials installed on existing Army aircraft (alloys developed prior to the 1970's) have a tendency to corrode, and no prevention or treatment regime is 100% effective for these materials. All aircraft operators rely on periodic inspections to detect and correct corrosion related defects before they cause a system failure. This should be especially true of operators of aging systems, such as the Army.

Inspection for stress corrosion cracking, corrosion fatigue cracks, and other corrosion-related problems is a part of every Army aircraft inspection. Concern for corrosion damage is a part of the routine pre-flight inspection as well as the intensive phase maintenance inspection (which occurs every 200-500 hours depending on aircraft model). The ACE evaluation, while not an inspection, complements the normal aircraft inspection activities conducted by field units. In order to fully complement normal aircraft inspection activities it is quite logical that ACE should also address corrosion issues. In fact, in order to be comprehensive the ACE must include an assessment of deterioration due to corrosion.

MANIFESTATIONS OF CORROSIVE ATTACK

There are a wide variety of manifestations of corrosion in aircraft. Materials used include aluminum, high strength steel, magnesium, titanium, and composites (both metallic and non-metallic). These materials are joined in a wide variety of ways and are coated with many different compounds. Therefore, corrosion inspections and the ACE evaluation should be tailored to detect the most likely type of corrosion in each component or structural member. A discussion of a few of the more common types of corrosion found in aircraft applications follows.

Exfoliation. One of the manifestations of corrosion in older, heavily rolled, high strength aluminum alloys, such as 2024-T3 and 7075-T6, is exfoliation. In exfoliation, the presence of corrosion leads to layering and flaking. This flaking causes delamination of the surface grains that are pushed out by underlying corrosion product.[16] Exfoliation is essentially a severe form of environmentally assisted cracking occurring in the direction of the grain flow. The grain has been flattened and elongated during the rolling operation. As this exfoliation progresses, and pieces of the aluminum surface are dislodged, the thickness of the piece reduced. This thickness loss results in a smaller cross-sectional area to carry the design load, and an increase in stress levels. As exfoliation continues, and the thickness is further reduced, the part may actually fail due to an overstress condition. Exfoliation is seldom uniform and normally results in increased surface roughness.[12] The degree of this surface roughening should be detectable by an inspector or evaluator and can serve as a useful indicator of the depth of attack of the corrosive activity. Once actual thickness loss can be measured using routine field level maintenance procedures it is normally advisable to replace the component. The presence of metal flaking or surface roughness can be used as an ACE indicator of exfoliation in certain instances.

An evaluation of all UH-60 corrosion data collected during the past two years revealed very few reported instances of exfoliation or "flaking". Physical examination of UH-60 aircraft during pre-shop analysis at the depot has confirmed that exfoliation does not appear to be a major source of corrosion damage for the UH-60. The one area of the UH-60 where exfoliation has been consistently observed is around the doors and door latches, as shown in Figure 5. The exfoliation corrosion damage observed on the aircraft doors is of little structural significance and can be corrected with basic field maintenance procedures. However, this corrosion damage is maintained as an indicator of the effectiveness of a unit's corrosion prevention and control

program for the aircraft under evaluation. It appears from the analysis conducted during this project that exfoliation corrosion is not a major source of structural damage for the UH-60 aircraft.

Pitting. Formation of corrosion pits is very common in magnesium and high strength aluminum, especially the 7075-T6 alloy common in Army helicopter structures.[12,17] These corrosion pits normally form in aluminum where constituent particles with an electrochemical potential difference with the surrounding matrix (e.g. $Al_{23}CuFe_4$ and Al_2Cu) are present at the surface of the component.[18] These corrosion pits can have a serious effect on the expected life of any component exposed to fatigue loading. Corrosion pits are often deep and narrow enough to serve as significant points of stress concentration.[16] Also, these pits are often accompanied by environmentally assisted cracks at their base. Therefore, inspection for corrosion pits in aircraft structure and components is an important part of any corrosion inspection scheme. Corrosion pits in fatigue sensitive structures should be significantly weighted indicators.

An evaluation of two years of UH-60 corrosion data has highlighted a significant problem with corrosion pitting in the magnesium housings of the input and intermediate gearboxes. A picture of an intermediate gearbox center housing with corroded mounting feet is included as Figure 6. These magnesium housings are treated with a baked resin coating system. Corrosion pits can compromise the structural integrity of the gearbox housing if they are not detected. The housing cannot be repaired if the corrosion pits are more than 0.020 inches deep or cover more than 30% of the surface area of a given mounting foot. Corrosion pitting in the mounting feet of these gearbox housings is a significant expense to the Army since many of these gearbox housings are found to be corroded beyond repair limits. These gearbox housings can be replaced through normal field maintenance procedures. Corrosion pitting in these

magnesium components is an indication of the corrosiveness of the aircraft's operational environment as well as the effectiveness of the unit's corrosion inspection and prevention program. Operational experience and depot tear-down data indicates that one can expect to find other hidden corrosion damage on an aircraft if serious corrosion pitting is observed in these gearboxes.

Filiform Corrosion. One of the most insidious forms of corrosive attack in aircraft structures is filiform corrosion. This corrosion occurs beneath cladding or coatings and can progress undetected for a significant period of time.[19] Filiform corrosion occurs on aluminum, steel, and magnesium surfaces that have organic coatings, typically paint. Fine filaments randomly emanating from one or more point sources characterize the corrosive attack. The source of initiation is often a defect or mechanical scratch in the protective coating. Filiform attack normally occurs when the relative humidity is between 65% and 90%. The typical corrosive filament growth rate is 0.1mm per day in length and may be as deep as 0.015 mm. Filiform corrosion has been widely observed in aircraft on both 2024 and 7000-series aluminum alloys.[19]

The Army has experienced significant filiform attack to the aluminum skin of our UH-60 aircraft. One particularly striking example of filiform corrosion was detected on external skin underneath the main cabin area of an UH-60 aircraft. The initial indication of the corrosive attack is shown in Figure 7. However, additional inspection conducted once the external filiform was detected revealed extensive corrosion damage on the internal surfaces of this same skin, located under the aircraft fuel cells (Figure 8). The corrosion apparently began on the interior of the aircraft skin and the filiform attack progressed to the exterior of the skin through drain holes. As a result of this finding a new ACE indicator has been added to this area of the aircraft

requiring utilization of a borescope inserted through the drain holes to inspect for filiform and other corrosion under the aircraft fuel cells.

Environmentally-Assisted Cracking. Environmentally assisted cracking occurs when environmental factors either initiate or accelerate crack formation or development beyond that experienced in a more benign environment. Environmentally- assisted cracking usually affects grain boundary regions and can produce a network of corrosion cracks, better known as intergranular cracking, on the metal surface (leading to the exfoliation described above). Two types of environmentally assisted cracking, involving an interaction between the environment and loading conditions, are of particular interest in aviation applications. Theses two types of environmentally assisted cracking are stress corrosion cracking and corrosion fatigue.

Stress corrosion cracking occurs when an aggressive environment causes crack initiation in the presence of a sustained stress, where this crack would not have occurred or progressed in a more benign environment.[16] The stress necessary to cause stress corrosion cracking can be either external (applied) or internal (residual). Failure due to stress corrosion cracking can occur before substantial network cracking occurs.[16] Stress corrosion cracking has been known to occur in Army aircraft components primarily where fasteners are applied, or in conjunction with lap joint pillowing. Corrosion inspections and evaluations must seek and detect stress corrosion cracking in order to preserve the structural integrity of the aircraft and its components.

Corrosion fatigue can occur when a component is exposed to cyclic mechanical loading in a harsh environment. Corrosion fatigue occurs when a fatigue crack grows faster in this harsh environment than that experienced in a more benign environment.[16] Virtually all helicopter components and structures are exposed to some level of cyclic loading or vibration. These same components are also exposed to a harsh flight or ground environment during some period of their

service. Since the corrosion fatigue phenomenon can affect virtually all helicopter components, and since the mechanisms of corrosion fatigue are complex and not widely understood this issue is of particular importance to Army helicopter operations. Therefore, the phenomenon of corrosion fatigue will now be examined in greater detail.

CORROSION FATIGUE

Corrosion fatigue occurs whenever material cracks due to the combined actions of cyclic loading (fatigue) and a corrosive environment (gaseous or liquid). Characteristics of corrosion fatigue include crack growth rates that can be substantially higher in the corrosive environment than those observed in a benign environment. These corrosion fatigue crack growth rates depend on a wide variety chemical, electrochemical, and mechanical variables. The phenomenon of corrosion fatigue is of particular relevance to the ACE program since corrosion fatigue may compromise the structural integrity of Army helicopters and should be reflected in ACE indicator weighting in these instances. Corrosion fatigue has been known to result in crack growth rates which are 2 -10 times higher than what would be expected from normal fatigue.[15,17,20,21,22,23] The magnitude of this crack growth rate acceleration varies widely depending on a number of factors that will be discussed below. This crack growth rate acceleration is manifested as both shorter times to crack nucleation/initiation as well as higher large crack growth rates. There are currently no widely accepted and reliable algorithms and models capable of predicting corrosion fatigue behavior across a variety of materials or environments.[24,25] Each combination of material, environment and load spectrum must be tested or analyzed individually in order to obtain valid estimates of corrosion fatigue crack growth rates.

The surface condition of metallic materials is always critical to their fatigue performance since fatigue cracks typically are initiated at the surface in the high cycle fatigue regions.[15] This is especially true in the case of corrosion fatigue, since surface imperfections serve not only as stress concentrators, but also as potential sources of concentrated corrosive attack. The formation of surface imperfections is particularly critical in high cycle fatigue scenarios since 80-90% of typical high cycle fatigue life is spent in the crack nucleation stage.[26] Therefore, corrosion pits, intergranular attack, and other surface defects due to corrosion can speed up crack formation by an order of magnitude.[16,20,22,23] Clearly, corrosive surface attack of aircraft structural components can greatly compromise structural integrity. Poor surface condition due to corrosive attack can also render any fatigue life calculations based on a benign environment totally invalid.

CORROSION FATIGUE RATE AFFECTED BY MANY FACTORS

The rate of crack initiation and growth under conditions of corrosion fatigue is highly variable and is affected by a wide variety of factors. These factors include mechanical variables (load frequency, stress range, stress ratio, etc.), environmental variables (temperature, humidity, corrosive agent, etc.) and material variables (alloy composition, heat treatment, contact with dissimilar materials, etc.). The interaction of this plethora of factors makes corrosion fatigue behavior difficult to predict. It is important that Army Maintenance Engineers understand the potential for corrosion fatigue, and the variables that affect its behavior, in order to develop valid ACE indicators and weightings. A discussion of a few of the considerations of most significance to helicopter maintenance follows.

Cyclic Load Frequency. Load frequency is the most important variable one must consider, after the actual environment itself, when evaluating the potential for corrosion

fatigue.[16,27] Corrosion fatigue actually causes higher crack growth rates when the cyclic load frequency is slower.[28] This may seem counter-intuitive at first glance to an engineer used to performing traditional fatigue calculations (where failure will occur in fewer hours of operation if the load frequency increases). However, when one considers that crack growth rate acceleration due to corrosion fatigue relies on the electrochemical, time-dependent processes of corrosion to occur, one can understand why lower frequencies will result in higher rates of corrosion fatigue. Low frequencies of cyclic loading (less than 5 Hz) are necessary to allow a significant opportunity for the corrosion to occur. The effect of corrosion fatigue normally disappears when load frequencies exceed 10 Hz.[27,28]

The potential for corrosion fatigue should be considered as a possibility in many rotorcraft structural components. Most helicopters have main rotor speeds in the neighborhood of 300 revolutions per minute, which translates into a frequency of 5 Hz. Some helicopter structure and components may be excited at a one-per-rev frequency, which is within the frequency range necessary for some modest corrosion fatigue activity in older high strength aluminum alloys.[29,30] Specific load magnitudes and frequencies for military helicopter structures are normally contained in structural design reports from the manufacturer and should be consulted to determine predicted load levels and frequencies for any given component. The frequency of fatigue loading should be considered as a starting point when Maintenance Engineers are developing ACE indicators and weights associated with fatigue cracking in corrosion prone areas.

Cyclic Load Waveform. Although cyclic load waveform has little effect on fatigue crack growth rate in benign environments, it appears that corrosion fatigue behavior is significantly affected by the waveform of the cyclic load. The effects of corrosion fatigue appear to increase

when the cyclic waveform has a significant period of rising load such as sinusoidal, triangular, and positive sawtooth.[31] These types of waveforms (especially sinusoidal) will be generated by a rotary mechanism such as a main or tail rotor head. The types of load waveforms generated by rotary wing aircraft reinforce the fact that corrosion fatigue should be a concern for the Army's helicopter fleet.

Stress Ratio. The stress ratio, R, is the ratio of the minimum stress to the maximum stress during cycling. The stress ratio may affect corrosion fatigue crack growth rates in certain environment/alloy combinations. Typically, a larger positive R-value will result in a higher crack growth rate for the same □K.[32] The limiting value of R is 1.0 in a constant tension load situation. A stress ratio of 1.0 describes the situation where stress corrosion crack growth occurs in some high strength aluminum alloys. The effect of high stress ratios on corrosion fatigue crack growth rates should also be considered in rotorcraft maintenance engineering analysis.

Stress Intensity Range. Crack growth rates normally increase with increasing stress intensity in embrittling environments.[23] However, the precise dependence of crack growth rate on the stress intensity range, □K, varies markedly by material and environment. Stress intensity range does effect crack growth rates for a given material in all types of environments, ranging from highly aggressive to a vacuum. In some instances, such as with some aluminum, the increased crack growth rate occurs during all three regimes of crack growth (near threshold, power law, and fast fracture). In other instances, such as with some Titanium alloys, the changes in crack growth rate behavior are much more complex.[33] In general, the aircraft Maintenance Engineer can expect increased stress intensity range to result in a faster crack growth rate. If more precise and detailed performance information is needed, laboratory tests for the expected alloy/environment combination should be consulted.

Temperature and Humidity. Crack growth rates associated with corrosion fatigue increase with increased humidity and temperature.[22,28] This is to be expected since the occurrence of corrosion fatigue is dependent on the electrochemical reactions causing the corrosive attack. Most electrochemical processes, including those causing corrosion, increase in activity as the temperature increases. The oxidation reactions associated with corrosive attack of metallic components also rely on moisture to occur, so the relationship between increasing humidity and higher crack growth rate is also to be expected. The maintenance engineer should consider the environmental variables surrounding the local area of the potential fatigue crack in his corrosion fatigue analysis. For example, the bilge area of most aircraft retains moisture for long periods of time after it is wetted. Floor beams in these bilge areas are at a higher risk for corrosion fatigue that beams in drier areas. Similarly, areas near the turboshaft engines and gearboxes are much warmer than ambient conditions. The potential for serious corrosion fatigue should be addressed when developing ACE indicators in any similar warm and/or wet regions of the aircraft.

Alloy. The initiation and progress of corrosion fatigue is highly dependent on the actual alloy under attack. This is to be expected as well since alloy composition and microstructure has a significant impact on normal corrosion behavior.[16] Corrosion fatigue behavior is also affected by material properties such as temper, yield strength, and forming method.[34] Any good corrosion fatigue analysis should include a consideration of the alloy and the method of forming for the component being evaluated.

Corrosion Fatigue Analysis for UH-60 308 Frame. The ACE has detected a significant number of aircraft with coincident fatigue cracks and corrosion in the vicinity of the fuselage station (FS) 308 frame and the Butt Line (BL) 34.5 beam, as shown in Figures 9 and 10. The BL

34.5 beam is the outermost longitudinal bending member of the upper fuselage of the UH-60 aircraft. It spans the cargo door cutout with splices at FS 308 and 379. The BL 34.5 beam is a built-up "I" beam made from a 0.063" channel formed of 7075-T6 aluminum on the inboard side. The 34.5 beam also includes an extruded angle at the upper outboard cap and 0.063" nested angles forming the lower outboard cap. Cracking has been detected in both the left and right lower cap splices at FS 310 at 1000-3000 flight hours, with the right side being the most critical location.[35] The dominant source of fatigue loading in this area of the aircraft structure comes from the rotor head and blades and has a predominant frequency of 4 times main rotor speed (since there are 4 blades). This translates into a load frequency of roughly 18 Hz, well above the corrosion fatigue regime. This dominant high load frequency tends to diminish the significance of corrosion fatigue as a factor in crack propagation in the BL 34.5 beam; the load fluctuates too quickly for corrosive action to play a major role.

A second factor affecting corrosion fatigue is the waveform of the applied fatigue loads. The waveform of the load in the BL 34.5 beam area of the aircraft will undoubtedly be fairly sinusoidal in nature since a smoothly rotating rotor head generates it. There will be some high frequency vibration in the waveform due to drive train vibration, but the general shape of the wave from will resemble a sine wave much more than it will resemble a square wave. This sinusoidal waveform, with a relatively long period of rising load level, would tend to aggravate the corrosion fatigue effect. A third factor affecting corrosion fatigue is the stress ratio. The stresses in this area of the aircraft cycle between compressive and tensile, with a typical ratio of –0.10 to –0.20 depending on the fastener hole being considered.[35] The effect of corrosion fatigue is aggravated by high positive stress ratios. Therefore, the negative stress ratio occurring in the BL 34.5 beam will tend to minimize the effect of corrosion fatigue. A fourth factor

affecting corrosion fatigue is the environment, specifically temperature and humidity. The area around the BL 34.5 beam of the aircraft does experience temperatures above ambient conditions due to its proximity to the main transmission and the insulating effect of the soundproofing and panels of the cabin roof. This elevated temperature would tend to accelerate the effect of corrosion fatigue. The final factor considered in this corrosion fatigue analysis is the alloy itself. The 7075-T6 alloy of the 34.5 is quite susceptible to corrosion fatigue and stress corrosion cracking.[34] Most tempers of the 7075 alloy exhibit some susceptibility to corrosive attack, but the T6 temper is especially vulnerable to environmentally assisted cracking.

As can be seen from this discussion, the BL 34.5 beam area of the UH-60 has factors that would tend to both aggravate and ameliorate the potential for corrosion fatigue. The elevated temperature in the area of the 34.5 beam, the sinusoidal loading regime and the susceptibility of the alloy to corrosion would argue for a significant potential for corrosion fatigue. However, the negative stress ratio and high load frequency suggest that corrosion fatigue will not be a major issue for this area of the aircraft. The high number of load cycles and large extremes in loading result in fairly rapid crack growth, and therefore reduce the potential for corrosion to act at the crack tip. The current ACE provides indicators for both corrosion and cracking at the FS 308 frame location. This means that an aircraft profile index can accumulate points for both corrosion and cracking at this area simultaneously. The minimal potential for corrosion fatigue identified through the analysis presented above suggests that there is no need to assign additional weight to this area (through coupling these corrosion and crack indicators) to account for the potential of corrosion fatigue.

SYNOPSIS

Corrosion is a significant threat to helicopter reliability and availability. A careful consideration of the potential for the various types of corrosive attack must be made when developing specific ACE indicators. The examples of potential corrosion indicators discussed above illustrate how the ACE can account for corrosion damage as it affects aircraft condition. Corrosion fatigue is an especially complex phenomenon as it applies to helicopter operations. A thorough and detailed analysis of the potential for corrosion fatigue behavior should be conducted whenever helicopter components experiencing fatigue loading are also subjected to significant corrosive attack. If the potential for corrosion fatigue is significant, then weighting (and possibly coupling) of the appropriate ACE indicators should reflect this possibility. The potential for all types of significant corrosion damage in a particular helicopter Mission/Design/Series must be assessed when formulating ACE indicators. This is being accomplished for the current ACE cycle on the UH-60 aircraft. A separate corrosion index will be now reported as a part of the overall ACE score for each UH-60 aircraft evaluated during the coming year. A final weight of the UH-60 corrosion indicators in the overall ACE score has not been assigned, but it is expected that somewhere between 10% and 30% of the potential overall ACE score for each aircraft will be attributable to the corrosion index. A final decision on the actual weight of the ACE corrosion index will be reached once at least 10% of the fleet has been evaluated. This same philosophy will be applied to other Army aircraft as personnel become available.

CORROSION DATA

Since the Army recognizes the serious impact that corrosion can have on the structural integrity and availability of our helicopters, it is only logical that the extent of corrosive attack should be considered as a uniquely visible factor when selecting aircraft for depot maintenance. Therefore, the Army has recognized the requirement to examine each aircraft Mission/Design/Series to determine what corrosion indicators should be evaluated as a separate corrosion dimension of the ACE, and how much weight these individual indicators should carry. The analysis necessary to support the addition of scored corrosion indicators to the UH-60 ACE has just recently been completed. As a result of this analysis the UH-60 ACE will contain a corrosion index that includes more than 50 indicators of aircraft structural corrosion and 30 indicators of component (gearbox, engine, servos, etc.) corrosion. These indicators were selected based on a review of three years worth of ACE corrosion data. Tables containing the UH-60 ACE structural and component corrosion findings for the year 2000 are included in Tables 6 and 7. The new scored ACE corrosion indicators for the UH-60 were selected based on an analysis of this data, and the indicators shown in Tables 6 and 7 are representative of the actual ACE corrosion indicators selected for use on the UH-60 aircraft.

Preliminary weights for each of these corrosion indicators have been developed. The decision was made to score three separate levels of corrosion (mild, medium, and severe) based on an analysis of the corrosion data previously collected, as well as physical inspections of a large number of aircraft. Many corrosion test, measurement and evaluation schemes recognize four or more levels of corrosion.[10] The ACE corrosion data collection scheme used from 1998 – 2000 also used a four level classification scheme. However, evaluation of three years worth of aircraft data indicates that there are almost no instances of very severe (level IV) corrosion

observed in operational aircraft. This result should not be unexpected. With the routine pre-flight and operational inspections conducted on aircraft on a regular basis, very severe (level IV) corrosion does not go undetected or uncorrected. Lesser levels of corrosion damage have been routinely observed, but less than a dozen instances of very severe damage were reported from the entire UH-60 fleet over a three-year period. Since there are so few occurrences of very severe corrosion damage, the decision has been made to only recognize three levels of corrosion damage in the ACE for scoring purposes. In the rare event that very severe corrosion is detected, it will be assigned the same number of points as a severe occurrence. The ACE process must allocate a limited number of points to the indicators selected, so these must be significant indicators of aircraft deterioration. If points are assigned to an extremely rare occurrence then they are not available to be assigned to a more common occurrence. Since the goal of the program is to distinguish between the best and worst aircraft in the fleet, there is no value (and some detriment) to assigning points to indicator condition codes that are never observed. In order to meet the objective of making significant distinctions between aircraft, all ACE corrosion indicators will be scored on a three level of severity basis (mild, medium, and severe).

Corrosion results collected on the CH-47, AH-64, and OH-58 aircraft were also briefly reviewed as a part of preparing this paper. These results are presented in Tables 5-10. The data presented in these tables indicate some additional corrosion problem areas in the Army fleet requiring additional attention. For example, the CH-47 aircraft experiences significant structural corrosion on the walkways between the forward and aft pylons and significant component corrosion to the landing gear. The OH-58 aircraft experiences corrosion in the lower cockpit shell as well as in the avionics compartment. The AH-64 aircraft experiences structural corrosion in the engines mounts as well as significant corrosion to the main and tail rotor heads

and swash plates. The ACE corrosion data collected on all Army aircraft will be reviewed to improve both corrosion data collection procedures and aircraft maintenance practices as resources permit.

CONCLUSIONS

The ACE has proven to be a very useful and robust tool for selecting and prioritizing Army helicopters for programmed depot maintenance. However, in addition to fulfilling this basic mission of selecting aircraft for depot maintenance, the ACE has also proven very useful in assessing overall fleet condition and of collecting information regarding corrosion in the Army fleet. The basic corrosion findings presented in this paper suggest that there is significant room for improvement in both aircraft maintenance practices and aircraft component design. The ACE detected significant costly and preventable corrosion throughout the Army fleet.

This paper presented an analysis of aircraft corrosion in general, and Army experience in particular, and concluded that there is real value in including corrosion as a separately scored ACE index. A number of types of corrosive attack were discussed in detail, and presented along with case studies. A particularly interesting conclusion is that corrosion fatigue is not a serious threat to most UH-60 structures due to the relatively high frequency of the fatigue load spectrum.

In order to take full advantage of the corrosion data collected to date, the ACE structural and corrosion findings presented here should be reviewed in detail to identify specific aircraft design and maintenance weaknesses. These data can also be used to justify the investment necessary to implement future design changes.

The Army has collected data that provides insight into the types of corrosion being experienced in out aircraft fleet. The next step is to complete detailed analysis of the data and make the changes necessary to improve the corrosion performance of our aircraft.

REFERENCES

1. Army Regulation 750-1, "Army Maintenance Policy and Retail Maintenance Operations", Headquarters Department of the Army Washington, D.C. 1 July 1996, pp. 5.18 – 5.24.

2. ACE/AACE Inspection and Analysis Handbook, Nondestructive Testing Information Analysis Center (U.S. Army Aviation Systems Command, Corpus Christi, TX: April 1985), Part I pp. 1-6, Part II pp. 11-18.

3. Army Regulation 750-40, "Guide to Reliability-Centered Maintenance for Fielded Equipment", Headquarters Department of the Army Washington, DC February 1980, pp. 26 - 29.

4. AMC Pamphlet, 750-2, "Guide to Reliability-Centered Maintenance", Headquarters Department of the Army Washington, DC June 1985, pp. 2 - 6.

5. MSG-3 "Airline/Manufacturers Maintenance Planning Document", Air Transport Association, Washington, DC October 1980, pp. 2 - 4.

6. R.T. Anderson & L. Neri, Reliability-Centered Maintenance (New York NY: Elsevier Science Publishers, 1990), pp. 250 - 275.

7. ATCOM Pamphlet 750-1(2), (5), (16), "Airframe Condition Evaluation Requirements for Army Model OH-58 (CH-47 and AH-64)", U.S. Army Aviation & Troop Command 14 April 1993, pp. 1-1 through 3-2.

8. Army TB 1-1520-237-25-2, "Joint Airframe Condition Evaluation", U.S. Army Aviation & Missile Command, 15 March 1997, pp. 1 - 8.

9. AMCOM Engineering Directives AED-A1806A, A1808, A1813, A1815, "Corrosion Evaluation in the ACE", U.S. Army Aviation & Missile Command, 1998, pp. 1 - 11.

10. ASTM G34-99, "Standard Test method for Exfoliation Corrosion Susceptibility of 2XXX and 7XXX Series Aluminum Alloys", American Society for Testing and Materials, 2000, pp. 2 - 5.

11. R.A. Everett, Jr. and W. Elber, "Damage Tolerance Issues as related to Metallic Rotorcraft Dynamic Components", (Washington, DC: American Helicopter Society Forum Proceedings, 1988), pp. 8 - 10.

12. J. N. Scheuring and A. F. Grandt, "Quantification of Corrosion Damage Utilizing a Fracture Mechanics Based Methodology", (Albuquerque, NM: 3rd Joint FAA/DOD/NASA Conference on Aging Aircraft, September 1999), pp. 2 - 7.

13. Ulf G. Goranson, "Aging Jet Transport Structural Evaluation Programs", (15th Symposium of the International Committee on Aeronautical Fatigue, June 1989), pp. 2 - 9.

14. CFR Title 14, Part 25.609, "Protection of Structure", Federal Aviation Administration, Washington DC.

15. R.J. Bucci and C.J. Warren, "Material Solutions & Related Structural Integrity Assessment Issues for Aging Aircraft", (Solomons, MD: Proceedings of 4th International Aircraft Corrosion Conference, August 2000), pp. 4 - 6.

16. M.G. Fontana & N.D. Greene, Corrosion Engineering, (New York: McGraw-Hill, 1978), pp. 91-115.

17. P.S. Pao, S. Gill, C.R. Feng, "Fatigue Crack Initiation from Corrosion Pits in Aluminum Alloys", (Albuquerque, NM: 3rd Joint FAA/DOD/NASA Conference on Aging Aircraft, September 1999), pp. 3 – 5.

18. H. Bohni and H.H. Uhlig, Journal of the Electrochemical Society, Vol. 116, 1969, page 906

19. Aircraft Corrosion: Causes and Case Histories, Vol. I, Advisory Group for Aerospace Research and Development (AGARD) Corrosion Handbook, AGARD-AG-278, 1985.

20. M.R. Achter, "Effect of Environment on Fatigue Cracks", Fatigue Crack Propagation, STP 415, ASTM, 1967.

21. Dr. Vinod Agarwala & Dr. Bashir Shafiq, "Aircraft Structural Integrity and Life Time in Aggressive Environments", (Solomons MD: Proceedings of 4th International Aircraft Corrosion Conference, August 2000), pp. 3 - 7.

22. T.W. Cooker and B.N. Leis, "Corrosion Fatigue: Mechanics, Metallurgy, Electrochemistry and Engineering", STP 801, ASTM, Philadelphia, 1984.

23. A.J. McEvily and R.P. Wei, "Fracture Mechanics and Corrosion Fatigue" in Corrosion Fatigue: Chemistry, Mechanics, and Microstructure, ed. O.F. Devereux, A.J. McEvily, and R.W. Staele, National Association of Corrosion Engineers, 1973, pp. 381-395.

24. J.T. Jong, ASTM Standard News, VOL 13 Number 11, NOV 1985, pp. 59-63.

25. R.P. Gangloff and R.P. Wei, Metallurgical Transactions, A, Vol. 8A, 1977, pp. 1043-1053

26. K. Tanaka, Fracture Mechanics: Perspectives & Directions (20th Symposium) STP 1020, ASTM, 1989.

27. K. Endo and K. Komai, "Effects of Stress Wave Form and Cycle Frequency on Low Cycle Corrosion Fatigue", Corrosion Fatigue: Chemistry, Mechanics, and Microstructure, ed. O.F. Devereux, A.J. McEvily, and R.W. Staele, National Association of Corrosion Engineers, June 1971, pp. 437-450.

28. R.P. Wei, P.S. Pao, R.G. Hart. and G.W. Simmons, Met. & Mat. Transactions A, VOL 11, page 151.

29. G. Eastaugh, A. A. Merati, P. V. Straznicky, D. V. Krizan, and J. Cook, "Experimental Study of the Effects of Corrosion on the Fatigue Durability and Crack growth of Longitudinal Fuselage Splices", (St. Louis, MO: 4th Joint FAA/DOD/NASA Conference on Aging Aircraft, May 2000).

30. Mr. D. E. Nieser, "Effects of Corrosion on Structural Life and Flight Safety of the C/KC-135 to 2040", (St. Louis, MO: 4th Joint FAA/DOD/NASA Conference on Aging Aircraft, May 2000).

31. S.T. Rolfe and J.M. Barsom, Fracture and Fatigue Control of Structures: Application of Fracture Mechanics, (New York, NY: Prentice Hall, 1987).

32. B. Tompkins and P.M. Scott, Metal Technology, VOL 9, 1982, pp. 240-248.

33. D.B. Dawson and R.M. Pelloux, Metallurgical & Materials Transactions A, VOL 5 1974, pp. 723-731.

34. MIL-HDBK-5H, Metallic Materials and Elements for Aerospace Vehicle Structures, Department of Defense, 1 DEC 1998, pp. 3-344 through 3-370.

35. W. Fujimoto, C. Anderson, E. Golski, Structural Analysis MH-60G Airframe Selected Fatigue Critical Sites, Document # SEL-6894, Sikorsky Aircraft, 21 April 1995, pages 2.10, 4.0, 6.10, and A10.23-33.

TABLES

TABLE 1.
Sample H-60 ACE indicators

ITEM NO.	INDICATOR	CONDITION CODE
1	TRANSMISSION SUPPORT BEAMS	I E G H D U X A R
2	CABIN FRAME FS 308	I E D X U H G R
3	SERVO BEAM RAILINGS AND T-ANGLE SUPPORTS	I E D A X H G R
4	CABIN FRAME, FS 379	I E D A B J H G Y R
5	TAIL CONE, CANTED HINGE BULKHEAD, FS 647	I E D A X U R
6	MAIN LANDING GEAR/DRAG BEAM ATTACHMENT	E D A X U H G R
7	CABIN FRAME FS 247	E D B J H G Y R
8	FS 485: FRAMES/FITTINGS	E D B P H G Y R
9	CABIN FRAME FS 295	I E D B J H G Y R
10	ESSS AND SHOCK STRUT ATTACHMENT FITTINGS, L/H & R/H	E D B H G Y R
11	NOSE SEC. FRAMING, FS 162-247, AND AFT BULKHD, FS 247	E D X H G R
12	TAIL CONE BULKHEAD, FS 605	E B U X D R
13	BEADED PANELS FS 295 – FS 308 L/H & R/H	E B D J G Y S R
14	FS 34.5 BEAMS FS 308 – FS 398 L/H & R/H	E D H G Y R
15	CABIN FRAME FS 265.5	I E D B J H G Y R
16	CARGO HOOK SUPPORT FITTINGS	E D A X H G R
17	TAIL CONE, INTERIOR	E B D H G Y R
18	TRANSITION SECTION, TAIL ROTOR DRIVESHAFT SUPPORTS	E D H G P R
19	TAIL CONE SHEAR DECK FS 605 TO FS 646 W.L. 215	E B D H G Y R
20	TRANSITION SECTION INT. STRINGERS AND SHEETMETAL	E D B H G R
21	TRANSITION FRAME FS 421	E D B J H G Y R
22	TRANSITION FRAME FS 464	E D B J H G Y R
23	OIL COOLER SUPPORT BRACKET	E D A H G Y R
24	AIRFRAME AROUND FLIGHT CONTROL SUPPORT STRUCTURE	E D P H G F R
25	FLIGHT CONTROL DECK	E D A H G R
26	ENGINE MOUNT LUGS AND SUPPORTING STRUCTURE	E D R
27	CABIN DOOR FRAMES, TRACKS, AND LATCH KEEPS	E D B F H G Y S R

Note: Condition Codes for Table 1

A	Worn Excessively	M	Good
B	Buckled	N	Loose
C	Deteriorated	P	Bent
D	Corroded	Q	Minor
E	Cracked	R	No defect
F	Mis-aligned	S	Previous Repair
G	Loose rivets	T	Improper hardware
H	Major	U	Dent
I	Oxidized	X	Scratch
J	Punctured	Y	Temporary repair
K	Poor	Z	Bolts in Lieu of Rivets
L	Fair		

TABLE 2.
Sample UH-60 Corrosion Checklist

CPC Indicator Nomenclature	**Condition**				
Date Arrived Current Location (MM/YY)					
Previous Location (City, State, Country)					
Date Arrived Previous Location (MM/YY)					
Operational Environment (mark multiple)	□ Marine □ Urban Industrial □ Non-combat □ Recent Deploy. □ Float				
Local Prevention Program (mark multiple)	□ Corrosion Prevention Compounds Used □ Routinely Hangared				
Wash Water Quality (mark one)	□ Untreated Nat. Source □ Treated Nat. Source □ Municipal □ Softened				
Airframe Wash/Preservation Cycle	□ None □ Daily □ Weekly □ Bi-weekly □ Monthly □ Quarterly				
Engine Wash Cycle (mark one)	□ None □ Daily □ Weekly □ Bi-weekly □ Monthly □ Quarterly l				
	Maintenance Required	**Defect Class**	**Intrusive**	**Protection**	**Indirect Indication**
STRUCTURE:					
ACE Items With 'D'-Corroded Reported	T P N	See ACE			
External Stores Support Beams	T P N R	I II III			
COMPONENTS:					
Nose Compartment Electrical/Electronic	T P N R	I II III			
Instrument Panel/Consoles Electronic	T P N R	I II III			
Main/Tail Rotor Servos and Actuators	T P N R	I II III			
Pre-Actuator Flight Controls	T P N R	I II III			
Main Rotor Head	T P N R	I II III			
Main Rotor Blades	T P N R	I II III			
Main Transmission	T P N R	I II III			
Input Modules	T P N R	I II III			
Post-Actuator Flight Controls	T P N R	I II III			
Engines and Engine Sequencing Units	T P N R	I II III			
Auxiliary Power Unit and Fuel Control	T P N R	I II III			
Main Rotor Pylon Electrical/Electronic	T P N R	I II III			
Misc. Comp.--Forward Main Rotor Pylon	T P N R	I II III			
Misc. Comp.--Aft Main Rotor Pylon	T P N R	I II III			
Misc. Comp.—Cockpit and Cabin Section	T P N R	I II III			
Cabin and Transition Section Electronic	T P N R	I II III			
Miscellaneous Comp.—Transition Section	T P N R	I II III			
Drive Shafts	T P N R	I II III			
Intermediate Gearbox	T P N R	I II III			
Tail Rotor Head	T P N R	I II III			
Tail Rotor Blades	T P N R	I II III			
Misc. Comp.—Tail Boom and Empennage	T P N R	I II III			
Miscellaneous Airframe Hardware	T P N R	I II III			
Miscellaneous Components, Other Areas	T P N R	I II III			

Maintenance Action Codes

T	Clean and Treat
P	Patch or Fill
N	Replace with new item
R	No Defect

Corrosion Damage Codes

I	Mild
II	Medium
III	Severe or Very Severe

TABLE 3.
Year 2000 UH-60 ACE Structural Corrosion Results

UH-60 ACE STRUCTURE CORROSION FINDINGS FOR CY 2000		
INDICATOR – NOMENCLATURE	**POSSIBLE CONDITION CODES**	**NUMBER OF CORROSION "HITS"**
CABIN DOOR FRAMES, TRACKS, AND LATCH KEEPS	E D B F H G Y S R	59 D Codes
TAIL CONE, INTERIOR	E B D H G Y R	29 D Codes
TRANSITION SECTION INT. STRINGERS & SHEETMETAL	E D B H G R	22 D Codes
TAIL PYLON INTERIOR	E D A H G P Y R	18 D Codes
TRANSITION SECTION, EXTERIOR SHEETMETAL	E P D J B H G Y R	17 D Codes
OTHER CABIN INTERIOR STRUCTURE	E D A B J H G Y R	14 D Codes
FS 34.5 BEAMS FS 308 – FS 398 L/H & R/H	E D H G Y R	9 D Codes
CABIN SECTION, EXTERIOR SHEETMETAL, FS 247-379	E D J B H G Y R	8 D Codes
TAIL CONE BULKHEAD, FS 605,	E B U X D R	8 D Codes
CABIN FRAME FS 265.5	I E D B J H G Y R	6 D Codes
TAIL PYLON, ANTENNA MOUNTS (HH/MH-60A/G/K/L)	E D P H G C R	6 D Codes
ENGINE MOUNT LUGS AND SUPPORTING STRUCTURE	E D R	6 D Codes
FS 485: FRAMES/FITTINGS	E D B P H G Y R	5 D Codes
NOSE SECTION FRAMING, FS 162-247, AFT BLKHD	E D X H G R	3 D Codes
CABIN FRAME FS 247	E D B J H G Y R	3 D Codes
CABIN FRAME, FS 379	I E D A B J H G Y R	3 D Codes
TRANSITION FRAME FS 464	E D B J H G Y R	3 D Codes
TAIL PYLON, INTER, AND TAIL GEARBOX MOUNTS	I E D H G C R	3 D Codes
MAIN ROTOR PYLON FIREWALLS, COVER TRACKS	E D A H G R	3 D Codes
NOSE SECTION, TRANSPARENCY FRAMING	C E D H G R	2 D Codes
COCKPIT FLOOR AND AVIONICS RACKS, NOSE	E D J B H G R	2 D Codes
TRANSMISSION SUPPORT BEAMS	I E G H D U X A R	2 D Codes
TRANSITION BULKHEAD FS 398	E D B J H G Y R	2 D Codes
TAIL CONE STRINGERS	E B D H G Y R	2 D Codes
ESSS AND SHOCK STRUT ATTACH. FITTINGS	E D B H G Y R	1 D Code
CABIN, GUN SUPPORT BEAMS	E D B J H G Y R	1 D Code
BEADED PANELS FS 295 – FS 308 L/H & R/H	E B D J G Y S R	1 D Code
CABIN FRAME FS 308	I E D X U H G R	1 D Code
TAIL CONE, EXTERIOR SHEETMETAL	E D J B H G Y S R	1 D Code
TAIL PYLON, STABILATOR	E A D P H G R	1 D Code
OIL COOLER SUPPORT BRACKET	E D A H G Y R	1 D Code

TABLE 4.
Year 2000 UH-60 ACE Component Corrosion Results

UH-60 ACE COMPONENT CORROSION FINDINGS FOR CY 2000	
Component Corrosion Indicator	**# of Corrosion "Hits"**
Main and Tail Rotor Servos and SAS Actuators	90
Nose Compartment Electrical/Electronic	85
Misc. Components, Other Areas	62
Misc. Airframe Hardware	60
Tail Rotor Head	49
Instrument Panel/Consoles Electrical/Electronic	48
Misc. Components—Tail Cone and Empennage	43
Cabin and Transition Section Electrical/Electronic	43
Input Modules	19
Main Rotor Head	18
Pre-Actuator Flight Controls	15
Main Rotor Pylon Electrical/Electronic	14
Intermediate Gearbox	10
Engines and Engine Sequencing Units	10
Misc. Components--Transition Section	8
Misc. Components—Cockpit and Cabin Section	7
Main Rotor Blades	7
Tail Rotor Gearbox	6
Misc. Components—Forward Main Rotor Pylon	6
Post-Actuator Flight Controls	5
Tail Rotor Blades	5
Misc. Components--Aft Main Rotor Pylon	4
Main Transmission	2
Drive Shafts	2
Auxiliary Power Unit and Fuel Control	1

TABLE 5.
Year 2000 CH-47 ACE Structural Corrosion Results

CH-47 ACE STRUCTURE CORROSION FINDINGS FOR CY 2000		
INDICATOR – NOMENCLATURE	**POSSIBLE CONDITION CODES**	**NUMBER OF CORROSION "HITS"**
Aft, Upper Walkway Honeycomb Panel	S C D Y J R	5
Fwd, Upper Walkway Honeycomb Panel	S C D Y J R	4
Frame / Panel FS 440	B E D S G Y R	4
Center, Upper Walkway Honeycomb Panel	S C D Y J R	3
Frame / Panel FS 360	B E D S Y R	3
Rear Ramp Hinges (Castings)	E D G R	2
Fuel Pod, Honeycomb Panel, Aft, R/H	S C D Y J R	2
Frame, FS 534	E D G Y R	1
Fuel Pod, Honeycomb Panel, Center, R/H	S C D Y J R	1
Frame/Panel, FS 400/Hook Beam/Ftg Dblr, FS 420	B E D S G Y R	1
Frame, FS 502 R/H	E D G Y R	1
Frame / Panel, FS 482 R/H	E B D S Y R	1
Frame / Panel, FS 280	B E D S Y R	1
Frame / Panel FS 482 L/H	B E D S Y R	1
Exterior Engine Mounts, Fwd L/H & R/H	E D X Y G R	1
Aft Pylon Bulkhead, FS 482, 2 Or More Cracks	V D R	1
Fuel Pod, Honeycomb Panel, Aft, L/H	S C D Y J R	1

TABLE 6.
Year 2000 CH-47 ACE Component Corrosion Results

CH-47 ACE COMPONENT CORROSION FINDINGS FOR CY 2000	
Component Corrosion Indicator	**# of Corrosion "Hits"**
Miscellaneous Airframe Hardware	67
Miscellaneous Components, Other Areas	43
Engines	41
Landing Gear	34
FWD Rotor Head and Swashplate	21
Instrument Panel/Consoles Electrical/Electronic	21
Nose Compartment Electrical/Electronic	16
Combiner Transmission	16
Pre-Actuator Flight Controls	14
Aft Rotor Head and Swashplate	13
FWD transmission	8
Miscellaneous Components - Aft Pylon	4
Aft Transmission	4
Ramp	3
Avionics Compartment Electrical/Electronic	3
Auxiliary Power Unit	3
Miscellaneous Components - Aft Cabin	2
Miscellaneous Components - Cockpit Section	2
Engines	1
Aft Rotor Blades	1
Hydraulic Reservoirs / Coolers	1
Auxiliary Power Unit	1
Drive Shafts	1
Engine Transmissions	1
Miscellaneous Components, Heater Component	1
Miscellaneous Components, Other Areas	1

TABLE 7.
Year 2000 OH-58 ACE Structural Corrosion Results

OH-58 ACE STRUCTURE CORROSION FINDINGS FOR CY 2000		
INDICATOR – NOMENCLATURE	**POSSIBLE CONDITION CODES**	**NUMBER OF CORROSION "HITS"**
Passenger Lower Shell, L/H	S C Y J D U R	4
Co-Pilots Lower Shell, L/H	S C Y J D U R	4
Baggage Floor	S C Y J D U R	3
Passenger Lower Shell, R/H	S C Y J D U R	2
Fuel Cell Fwd Bulkhead, Fs 121	S C Y J D U R	1
Fuel Cell Shell, L/H Side	S C Y J D U R	1
Roof Panel Exterior, L/H	S C Y J D U R	1
Roof Panel Exterior, R/H	S C Y J D U R	1
Roof Panel Interior, R/H	S C Y J D U R	1
Fuel Cell Shell, Lower, L/H Side	S C Y J D U R	1
Fuel Cell Shell, Lower, R/H Side	S C Y J D U R	1

TABLE 8.
Year 2000 OH-58 ACE Component Corrosion Results

OH-58 ACE COMPONENT CORROSION FINDINGS FOR CY 2000	
Component Corrosion Indicator	**# of Corrosion "Hits"**
Miscellaneous Airframe Hardware	80
Miscellaneous Components - Aft Fuselage	53
Aft Avionics Compartment Electrical / Electronic	53
Miscellaneous Components, Other Areas	37
Other Ace Structure	24
Engine	17
Instrument Panels / Consoles Electrical/Electronic	12
Main Transmission	4
Tail Rotor Gear Box	4
Main Rotor Head	3
Other Ace Structure	2
Miscellaneous Components - Main Rotor Pylon Area	2
Cabin Electrical / Electronic	2
Miscellaneous Components – Nose	1
Miscellaneous Components - Cockpit and Cabin	1
Engine	1
Other Ace Structure	1
Post Actuator Flight Controls	1
Swashplate	1
Transmission Support Beams	1
Tail Rotor Head and Blades	1
Tailboom and Stabilizers	1
Drive Shafts	1

TABLE 9.
Year 2001 AH-64 ACE Structural Corrosion Results

AH-64 ACE STRUCTURE CORROSION FINDINGS FOR CY 2001		
INDICATOR – NOMENCLATURE	**POSSIBLE CONDITION CODES**	**NUMBER OF CORROSION "HITS"**
Engine Mounts, L/H & R/H	E D G Y R	12
Canopy Structure and Doors R/H	E D B G Y R	5
Fuselage Structure , FS 280-370 R/H other than Deck	E D B A G Y R	2
Equipment Deck Fwd L/H	E D B G Y R	1
Fuselage Structure , FS 280-370 L/H other than Deck	E D B A G Y R	1
Mast Support Base	E D G Y R	1
Tailboom Fwd, FS 370 - 450 R/H & L/H	E D B G Y R	1
Tailboom Structure (Other Than Skins), FS 370 - 450	E D B G Y R	1

TABLE 10.
Year 2000 AH-64 ACE Component Corrosion Results

AH-64 ACE COMPONENT CORROSION FINDINGS FOR CY 2000	
Component Corrosion Indicator	**# of Corrosion "Hits"**
Miscellaneous Airframe Hardware	70
TADS / PNVS	53
Miscellaneous Components, Other Areas	53
Miscellaneous Components – XMSN and Eq. Bays	48
Tail Rotor Head and Swashplate	47
Main Rotor Head and Swashplate	42
Main Rotor Blades	40
Miscellaneous Components -- Main Rotor	25
Miscellaneous Components – Nacelles	25
Engines	17
Tail Rotor Gear Box	16
Forward Avionics Bays Electrical/Electronic	15
Aft Avionics Compartment Electrical/Electronic	12
Intermediate Gear Box	9
Main Rotor Head and Swashplate	7
Instrument Panel / Consoles Electrical/Electronic	4
Misc. Components -- Tail Boom and Empennage	3
Main and Tail Rotor Servos	3
Nose Gear Box Assemblies	2
Drive Shafts	2
Miscellaneous Components	2
Main Rotor Struts and Stationary Mast	2
Main Transmission	1
Tail Rotor Gear Box	1
Auxiliary Power Unit	1
Wing Assemblies	1
Post Actuator Flight Controls	1

FIGURES

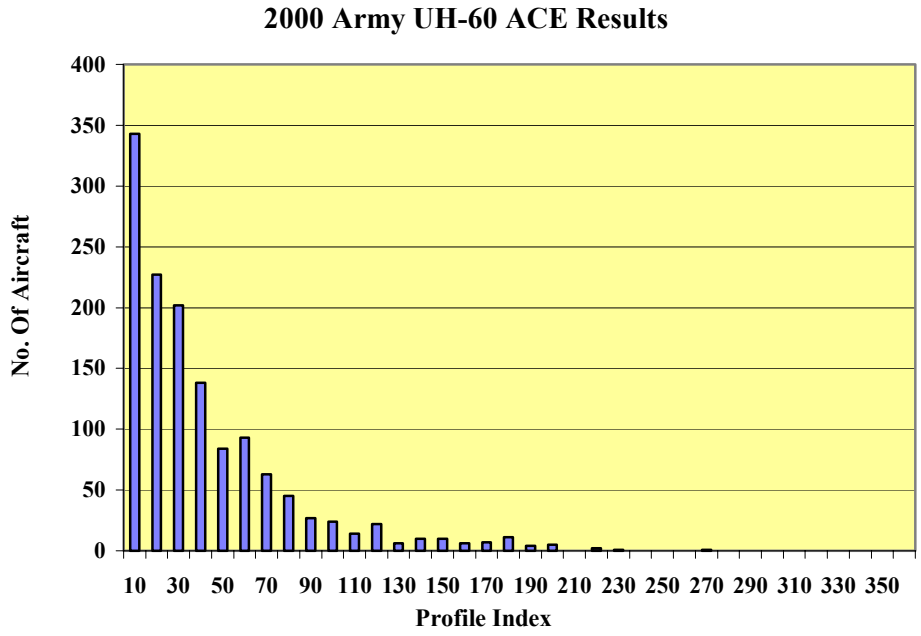

FIGURE 1. Year 2000 ACE Scores for UH-60 Aircraft

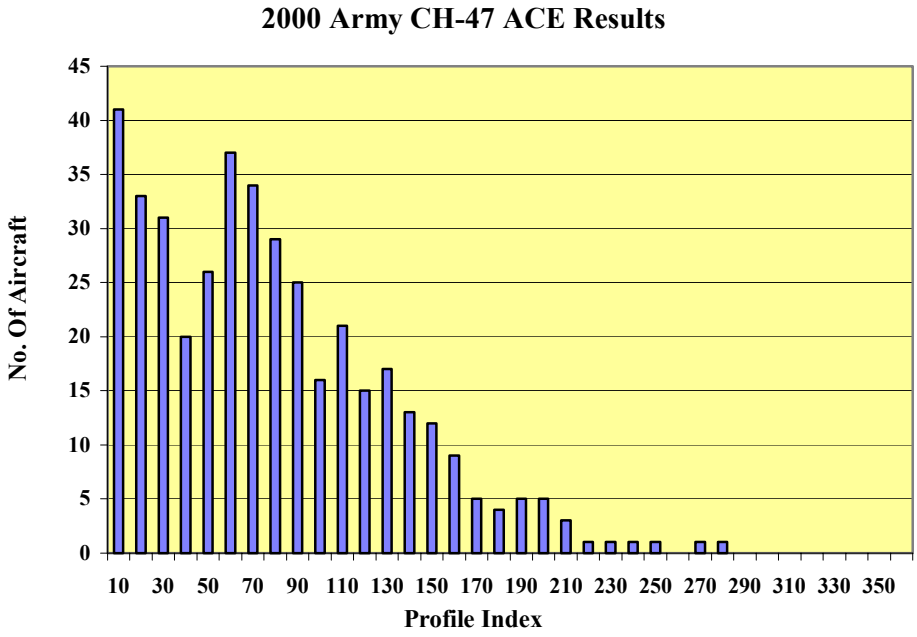

FIGURE 2. Year 2000 ACE Scores for CH-47 Aircraft

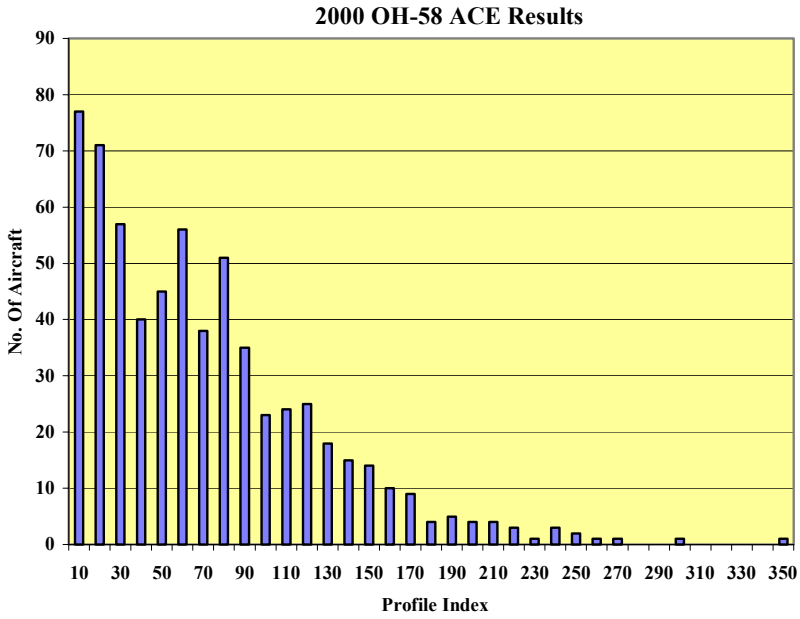

FIGURE 3. Year 2000 ACE Scores for OH-58 Aircraft

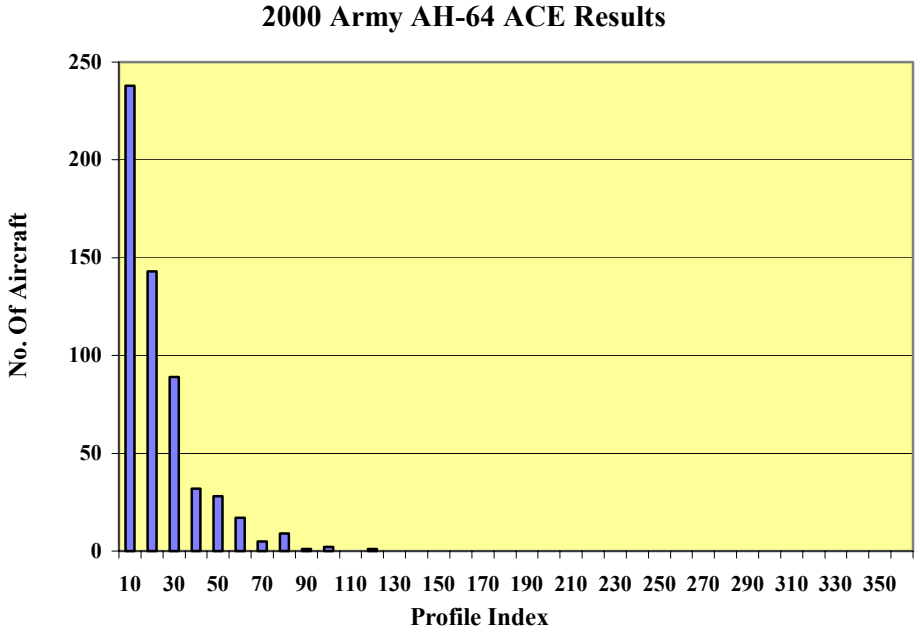

FIGURE 4. Year 2000 ACE Scores for AH-64 Aircraft

FIGURE 5. UH-60 Cargo Door Tracks

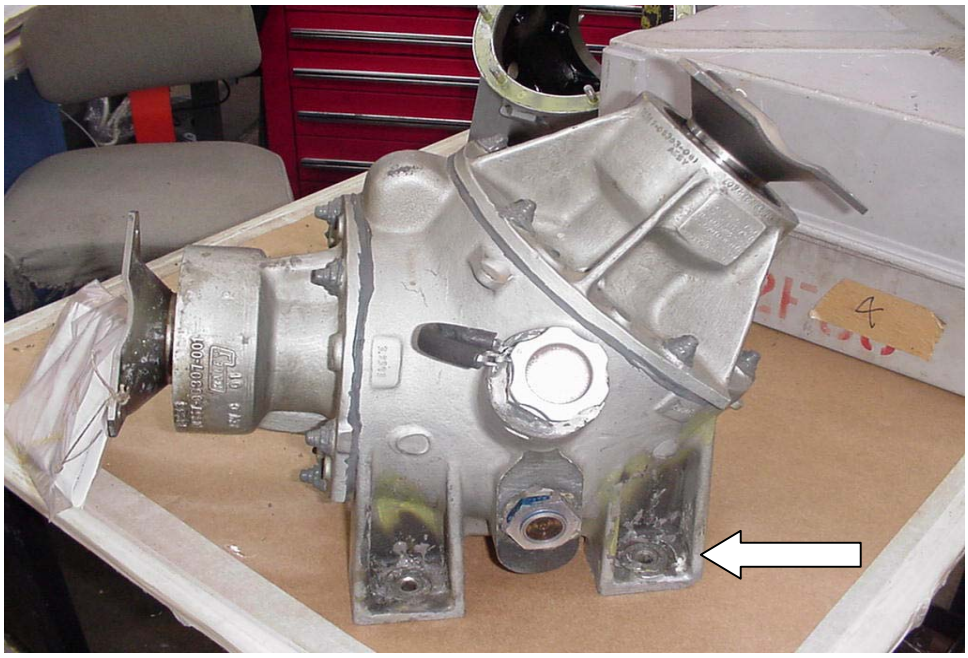

FIGURE 6. Corrosion Pitting in UH-60 Intermediate Gearbox

FIGURE 7. External Filiform Corrosion on UH-60 Skin

FIGURE 8. Internal Filiform Corrosion on UH-60

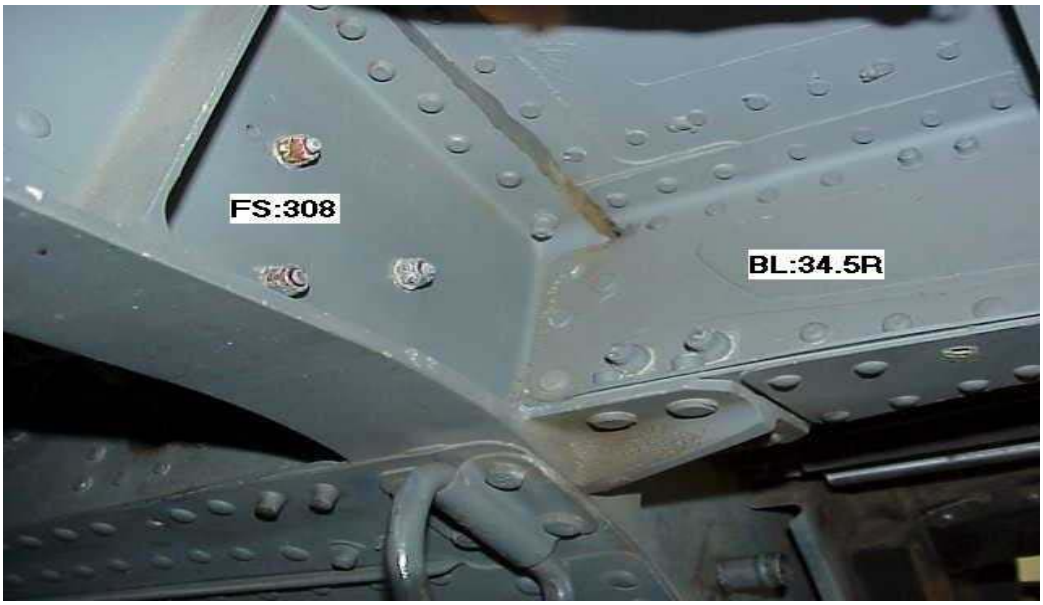

FIGURE 9. Overview of UH-60 308 Frame/ 34.5 Beam

FIGURE 10. Crack on UH-60 34.5 Beam

THE INFLUENCE OF FUEL CARBON RESIDUE ON HOT CORROSION

David A. Shifler

Carderock Division, Code 613
Marine Corrosion Branch
Naval Surface Warfare Center
9500 MacArthur Boulevard
West Bethesda, MD 20817-5700

ABSTRACT

The unavailability and cost of certain fuels commonly used by the U.S. Coast Guard sometimes promoted the use of alternative, commercial marine gas oil (MGO) fuels to operate their gas turbine engines. This paper evaluates the effects of the carbon residue content of commercial distillate-type fuel specifications, on the Type II hot corrosion resistance of marine gas turbine engine materials.

The gas turbine materials consist of bill-of-material high-temperature nickel-based and cobalt-based superalloys with specified aluminide coatings used in the hot section components of a marine gas turbine engine. The hot corrosion of these gas turbine materials was evaluated over a period of 1000 hours in a low-velocity, atmospheric-pressure burner rig (LVBR). These hot corrosion results were compared to LVBR hot corrosion tests using the Navy's primary fuel.

INTRODUCTION

The US Coast Guard (USCG) serves as the chief agency for protecting life and property, for enforcement of maritime laws on the high seas and in navigable waters of the United States, for maintenance of aids to navigation, and for providing search and rescue. The USCG has worldwide duties that involve clearing clogged harbors on the North Atlantic and Alaskan coasts and on inland lakes, rivers, and canals, locating and locating icebergs in the shipping lanes in the North Atlantic and other polar regions, enforcing illegal immigration by sea, and interdicting drugs into the United States. Its unique maritime and enforcement responsibilities spread Coast Guard cutters and patrol boats to various ports and stations worldwide.

To fulfill its mission, the USCG has a fleet of several hundred vessels ranging from small patrol boats to the 420-ft, 16,700-ton Healy class icebreakers. Various diesel and gas turbine engines power these boats and ships. The Coast Guard regularly operates in sparsely populated or remote areas around the world, and therefore USCG ships often need to refuel where Navy military specified fuels are unavailable. Shipboard Navy fuels are NATO F-76 Naval distillate fuel covered by MIL-F-16884J[1] and JP-5 (NATO F-44) aviation turbine fuel purchased under MIL-DTL-5624 military specification.[2] NATO F-76 is the primary fuel and JP-5 is the "acceptable substitute" to F-76. These fuels require separate transport modes, storage facilities, and transfer procedures. These fuels have specific physical and chemical properties that promote satisfactory operation in all Navy aircraft (JP-5 only) and in all shipboard diesel engines, gas turbine engines, and steam boilers (F-76 and/or JP-5). When NATO F-76 and JP-5 are unavailable, the USCG resorts to purchasing commercial fuels to minimize operational impact and continue its mission. Generally, this commercial fuel is bought under a Defense Energy Support Center (DESC) bunker contract that meets the Naval Sea Systems Command (NAVSEA) Marine Gas Oil (MGO) Purchase Description.[3] NAVSEA Purchase Description MGO (MGO PD) fuel is subjected to standard commercial practice quality controls rather than the extensive handling and storage requirements for MIL-SPEC fuels.

Several reports indicate that use of MGO PD fuel increases hot corrosion of gas turbine components and has limited storage stability. A conservative storage stability estimate of six weeks has been established for complete use of MGO PD in USCG and Navy ships; however, this has been viewed as operationally unrealistic. NATO F-76, on the other hand, has a minimum storage life of 3 years as defined by ASTM D 5304.[4] Three distinct mechanisms have been suggested for fuel instability: (1) chemical degradation of the fuel; and (2) the potential for

incompatibility when new fuel is mixed with remaining fuel in tanks; and (3) microbiological contamination. Any remaining commercial MGO-type fuel left in storage tanks can act as a catalyst to degrade newly introduced MIL-SPEC fuels or other MGO-type fuels. The USCG is addressing this issue under another program.

To assure greater fuel availability and lower costs, the USCG developed a program to define the operational and maintenance impact of using MGO PD versus NATO F-76 fuel. The USCG has compiled the detailed fuel requirements of all the engine manufacturers that have engines in the USCG fleet whether using NATO F-76 or MGO PD-type fuel. In particular, the manufacturer of USCG propulsion gas turbine engines has expressed the concern that continuous operations using MGO-type fuel would increase maintenance requirements and would require more frequent inspections to monitor the anticipated higher hot corrosion rates.

The Coast Guard has identified storage stability, acidity, particulate contamination, carbon residue content, ash content, cetane number, and sulfur content as possible areas of concern when MGO PD-type fuels are burned in gas turbine engines. Although most fuel properties between NATO F-76 and MGO PD are nearly identical, but there is no MGO PD property for storage stability, maximum particulate contamination, demulsification, and trace metals. NATO F-76 lists 23 fuel property parameters while MGO PD only lists 13 property specifications. The MGO PD has less restrictive requirements for acidity, carbon residue, or ash content as compared to NATO F-76. Table 1 compares nominal values of NATO F-76 properties and the properties of the MGO PD fuel.

Fuel contamination can adversely affect fuel storage and thermal stability and the performance life of gas turbine engine components, particularly in the engine hot sections. Copper, if present, affects fuel thermal stability, lead forms low-temperature eutectics, sodium

and potassium contribute to increased hot corrosion while sub-ppm (≥ 0.3 ppm) levels of vanadium have been shown to accelerate hot corrosion. The amount of sulfur in the fuel will determine the degree by which hot corrosion may occur.[5-7] Calcium acts as surface glue that entraps fuel contaminants and enhances corrosion.

Therefore, the objectives of this investigation are to: (1) examine the relative hot corrosion of gas turbine coating materials via low-velocity burner-rig (LVBR) testing by burning MGO PD-type fuel with carbon residue of 0.19 wt.% and 0.33 wt.% and (2) utilize the experimental results as the basis to validate that the 0.19 wt.% carbon residue level is appropriated as the new fuel carbon residue maximum limit for commercial fuels bought to the MGO PD for both the USCG and the Navy.

EXPERIMENTAL PROCEDURE

MATERIALS – FUEL

The test objective was to evaluate the materials representative of those current hot-section materials of Coast Guard gas turbines using NATO F-76 fuel as the baseline condition. Di-tertiary butyl disulfide was added to this diesel fuel to increase the sulfur concentration to one percent by weight, the maximum prescribed sulfur level under MIL-F-16884J.[1]

Sulfur-doped NATO F-76-based fuel was blended with a soluble bottoms product residue (drilling mud) removed from Kuwaiti Crude to produce a high-carbon residue MGO fuel that complied with ASTM D3244 specifications.[8] The analysis of the NATO F-76 base fuel and the blended fuels containing 0.19 wt.% or 0.33 wt.% fuel carbon residue (herein referred to as MGO-CG1 and MGO-CG2, respectively) are listed in Table 2.

MATERIALS – ALLOYS AND COATINGS

Materials common in the first and second stage blades and vanes from the USCG marine gas turbine engine was selected for examination. As listed in Table 3, these alloys were either nickel-based (Alloy 738, Alloy 792) or cobalt-based (Alloy M509). The chromium content in these alloys ranged from about 12 to 23.5 weight percent. Iron is kept to a minimum in these alloys to minimize corrosion and development of iron-derived crystallographic transformations. Aluminum and other elements are added to improve the passive film at high temperatures.

Pure diffusion aluminide coatings procedures were applied to each alloy substrate as per specified, proprietary specifications of an engine manufacturer. The alloy substrates and coatings, as identified in Table 4, are materials found in the first or second stage blade or vanes of a marine gas turbine engine. The coatings, referred to herein as Coating A (NiAl diffusion coating) and Coating B (CoAl diffusion coating) are used to protect the alloy substrates from hot corrosion and reduce the effective temperature experienced by the alloy substrates.

Figure 1 shows examples of untested Coating A and Coating B aluminide coatings. The outer layer consists of non-metallic dispersions, while an inner layer consists of an inter-diffusion zone. The coating thicknesses discussed in this report will include both inner and outer layers. The average original coating thickness of Coating A over the both nickel-base substrates was 2.89 to 3.54 mils (73-90 μm). The average original thickness of Coating B over the cobalt-based alloy was 1.45-2.35 mils (37-60 μm). Two thicknesses, 1.47 mils (37.3 μm) initially and later 2.08 mil (52.8 μm) of Coating B, were applied to Alloy M509 test pin substrate because the original thickness of Coating B was less than the minimum specified for this engine application.

Standard pins were included in the LVBR test to serve as controls.[9] The substrate of the standard pins were Alloy 333 and the coating was a plasma sprayed CoCrAlY or NiCrAlY. The nominal chromium content of these overlay coatings was approximately 39 wt.%.

BURNER-RIG TEST PROCEDURES

A low-velocity, atmospheric pressure burner-rig (LVBR) was utilized to evaluate the hot corrosion resistance of the hot-section gas turbine coated alloys using the NATO F-76 baseline, MGO-CG1, and MGO-CG2 fuels, respectively. Details of burner rig operation were described in previous papers.[10,11] The gases added to the fuel stream are thoroughly mixed by the swirling action of air entering through the tangential slots in the combustion tube. Sea salt (10 ppm) was injected into the burner-rig combustion zone to duplicate high-temperature reactions that can occur in gas turbines in marine environments. Downstream, the test pin specimens were exposed to the products of combustion in a carousel rotating at 29 rpm to assure uniform temperature exposure of all test specimens. The air/fuel ratio during these LVBR tests was 30:1.

LVBR tests for the three alloy/coating combinations listed earlier in Table 4 were run for 1000 hours at 1300 °F (704 °C) since this is roughly the midpoint temperature range where low-temperature, Type II hot corrosion of materials is observed. In addition to the five cylindrical pin specimens (0.125-inch diameter x 2.5-inch length) for each alloy/aluminide coating combination, two standard pins coated with CoCrAlY, as described earlier, were tested.

Thermal cycling of the test pins was performed during the LVBR test to simulate the off-and-on nature of shipboard gas turbine engine operation. Stresses in oxide scales induced by thermal cycling increase the possibility of spallation of a coating thereby increasing the tendency towards more severe high-temperature corrosion of the coating. When the specimen carousel was removed from the burner-rig, the specimens were allowed to cool to room temperature in

ambient air. Specimens were also visually examined to observe any signs of coating degradation during this time.

BURNER RIG TEST SPECIMEN EVALUATION PROCEDURE

The hot corrosion attack of each pin was measured at three cross-sections (top, middle, and bottom) cut along the length of its exposed area. These measurements were achieved by metallurgical examination. The examination determined an average coating loss on a radius and a maximum coating penetration for each test pin. Details of the measurement procedure are found in earlier papers.[12,13]

RESULTS

PIN MEASUREMENTS AFTER BURNER-RIG TESTING

Results of the corrosion measurements after 1000-hr. exposures from burner-rig testing using NATO F-76, MGO-CG1, and MGO-CG2 fuels are found in Tables 5, 6, and 7, respectively. Hot corrosion of the standard pin with plasma sprayed CoCrAlY coating resulted in an average 10% loss of the original coating thickness. The average Type II hot corrosion loss at 1300 °F (704 °C) from the 1000-hr. LVBR 1000-hr. exposure to NATO F-76 fuel combustion (1.3 mils {33 μm}) was greater than the average hot corrosion from MGO-CG1 fuel combustion (0.90 mil {23 μm}) and MGO-CG2 fuel combustion (0.48 mil {12 μm}). The maximum penetration of the control pins burning MGO-CG2 was 1.04 mils (26 μm). The typical degree of hot corrosion attack experienced on the CoCrAlY coatings after a 1000-hr LVBR test is shown in Figure 2.

Burner-Rig Results for Alloy 738/Coating A. Alloy 738 with Coating A showed a mean value (based on the results of five test specimens) of 1.02 mils (25.9 μm) average coating loss on

a radius or about 33% of the original coating thickness after the 1300 °F (704 °C) exposure for 1000 hours using the sulfur-modified NATO F-76, Table 5. The coating had fully penetrated at one site each for two Alloy 738/Coating A test pins. Other specimens had a maximum penetration of 82 to 97 percent of the 3.10 mil (79 μm) original Coating A thickness.

Alloy 738/Coating A test pins demonstrated a mean value of the average coating loss on a radius was 2.72 mils (69 μm) or about 92% of the original Coating A thickness after a 1000-hr. LVBR exposure burning MGO-CG1 fuel, Table 6. Unlike the behavior after 1000-hr burner-rig exposures with NATO F-76, the entire loss of the Coating A was observed at numerous sites (an average of 21 per 54 measurement sites) on Alloy 738/Coating A either through coating spallation or increased coating loss due to hot corrosion.

LVBR pin measurement results for Alloy 738/Coating A test pins after the 1000-hr LVBR test using MGO-CG2 fuel are shown in Table 7. Alloy 738/Coating A pins (5 test specimens) experienced a mean coating loss on a radius of 0.87 mils (22.2 μm) or about 28% of the original coating thickness after exposure for 1000 hours at 1300 °F (704 °C). Coating A was fully consumed at a minimum of one site for two Alloy 738/PWA 73 coated test pins, and penetration had progressed to the alloy/coating interface on two other Alloy 738/Coating A test pins. The last Alloy 738/Coating A test pin experienced a maximum penetration of 77% of its 3.03 mil (77 μm) original coating thickness. Figure 3 shows the typical performance of Coating A on Alloy 738 as a function of fuel carbon residue.

Burner-Rig Results for Alloy 792/Coating A. The hot corrosion behavior of Alloy 792 coated with Coating A resulted in a mean value from five test specimens of 0.99 mil (25.2 μm) average coating loss on a radius. This represents approximately 33% of the original coating thickness from the 1300 °F (704 °C) exposure for 1000 hours using the sulfur-modified NATO

F-76. There were no complete penetrations of the Coating A on the Alloy 792 substrate. The maximum coating penetration on a radius was 2.57 to 2.87 mils (65.3 to 72.9 μm) or 86 to 97% of the original Coating A thickness.

The hot corrosion of Alloy 792/Coating A test pins was greatly increased after a 1000-hr, 1300 °F (704 °C) LVBR exposure burning the MGO-CG1 fuel. Unlike the behavior after 1000-hr burner-rig exposures with NATO F-76, the entire loss of the Coating A was observed at numerous sites either through coating spallation or increased hot corrosion. Figure 8 shows the spalling of either Coating A or salt deposits on the pin coating. The mean value of the average coating loss (five pins) on a radius was 2.83 mils (72 μm) or about 94% of the original Coating A thickness on Alloy 792 pin substrates. The maximum penetration had exceeded the full coating thickness and had begun to attack the Alloy 792 substrate.

The hot corrosion behavior of Alloy 792/Coating A after a 1000-hr., 1300 °F (704 °C) LVBR exposure burning the MGO-CG2 fuel resulted in a mean value, from five test specimens, of 1.21 mil (30.7 μm) average coating loss on a radius or approximately 37% of the original coating A thickness. Complete coating penetration was observed on three of the Alloy 792/Coating A pins. The maximum penetration of the fourth pin was located at the alloy/coating interface while the maximum coating penetration on a radius of the fifth Alloy 792/Coating A test pin was 2.99 mils (75.9 μm) or 84% of the original PWA 73 coating thickness. The typical performance of Coating A on Alloy 792 as a function of fuel carbon residue was similar to its performance on Alloy 738 (Figure 3).

Burner-Rig Results for Coating B. The hot corrosion behavior of the Alloy M509/Coating B aluminide after the 1000-hr, 1300 °F (704 °C) exposure with baseline NATO F-76 was vastly different than the Coating A results. The mean value for five test pins was 1.35

mils (34.3 μm) average coating loss on a radius or 92% of the original Coating B thickness. Full penetration of Coating B had occurred at numerous locations, particularly at the top pin elevation either through spallation of the aluminide coating or enhanced hot corrosion.

The hot corrosion behavior of the Alloy M509/Coating B aluminide after the 1000-hr, 1300 °F (704 °C) exposure burning the MGO-CG1 fuel displayed some apparent improvement of the hot corrosion resistance versus the results from sulfur-doped NATO F-76, 1000-hr LVBR exposure. The mean value for the average coating loss on a radius was 1.21 mils (30.7 μm) or 82% of the original Coating B thickness. Much of this improvement was due to better retention of Coating B on Alloy M509 (average of 27 per 54 measured sites per pin) during the LVBR exposure burning MGO-CG1 compared to the 1000-hr burner-rig exposure burning NATO F-76 (14 of 54 measured sites per pin). However, there was a tendency for the hot corrosion attack of the Alloy M509 substrate to be more severe during the MGO-CG1 exposure than during the NATO F-76 combustion.

The mean value of the average coating loss on a radius for the five (nominally 1.47 mil (37.3 μm) thick) Coating B coated test specimens was 1.35 mils (34.3 μm) or 83% of the average (actual 1.62 mil (41.2 μm)) original Coating B thickness in an LVBR test burning MGO-CG2. Full penetration of Coating B had occurred at numerous locations, particularly at the top pin elevations. Hot corrosion had attacked the Alloy M509 substrate at these bared sites.

The mean value of the average coating loss on a radius for the five thicker (nominally 2.08 mil (52.8 μm)) Coating B coated test specimens was 1.66 mils (42.1 μm) or an average 78% of this original (actual 2.14 mil (54.3 μm)) Coating B thickness during the LVBR test combusting MGO-CG2. Again, full penetration of Coating B had occurred at numerous

locations, particularly at the top pin elevations. The hot corrosion degradation of Coating B on Alloy M509 as a function of different fuel carbon residue concentration is shown in Figure 4.

However, the thicker, 2.08 mil (52.4 μm) Coating B (slightly greater than the minimum coating thickness specified for the USCG marine gas turbine engine, refer to Table 2) provided some additional protection to the Alloy M509 substrate than the substandard 1.47 mil (37.3 μm) thick Coating B, leading to less overall penetration into Alloy M509 during the 1000-hr. LVBR test. The mean maximum penetration on a radius of the five nominally 1.47 mil-thick Coating B on Alloy M509 pins was 5.24 mil (133 μm) (including penetration into the substrate) when measured at the top pin elevations while the mean value of the maximum penetration on a radius of the five (nominally 2.08 mil (52.4 μm) thick Coating B on Alloy M509 pins was 2.66 mil (67.6 μm) at the top pin sites.

DISCUSSION

A summary of the average coating losses of the aluminide coatings as a function of the carbon content is illustrated in Figure 5. Combustion of either the baseline NATO F-76 or the MGO-CG2 fuels during the 1000-hr LVBR tests at 1300 °F (704 °C) yielded similar average losses (30% to 35%) of the original Coating A aluminide thickness on either nickel-base alloy. By raising the carbon residue content to 0.33 wt.% (on 10% bottoms) as contained in the MGO-CG1 fuel, the coating loss on the radius of Coating A increased to approximately 92% of its original thickness on the pin specimens.

The losses Coating B on the cobalt-base Alloy M509 test pins yielded severe Type II hot corrosion attack after 1000-hr LVBR tests burning baseline, sulfur-doped NATO F-76, MGO-CG2, or MGO-CG1 test fuels. Average coating losses in the range of 82 to 102% of the original

coating thickness were measured. The initial Coating B thickness was nominally 1.47 mil (37 μm) thick which was not within the required thickness criteria for the gas turbine (Table 2). Though several pins were later nominally recoated to the minimum specified coating thickness (~ 2.08 mil; 53 μm), the average coating loss measured after the 1000-hr LVBR test using MGO-CG2 was still 78% of original coating thickness. The thicker Coating B tended to show that substrate attack decreased as the carbon residue content in the fuel decreased as measured at the most severely corroded, usually top elevation, sites of each test pin.

The composition, the processing, and the test exposure conditions of the aluminide-coated specimens in these tests can affect test results. Diffusion aluminide coatings are typically processed via slurry-fusion or pack cementation. Subsequent heat treatments help develop the proper mechanical properties and allow further coating diffusion. The principal protective oxide, which provides improved oxidation and corrosion resistance of aluminide coatings is Al_2O_3, although less protective oxides can form if other alloying elements are present in the substrate, either in solution or as precipitated phases.[14] Aluminide coating degradation may be initiated by basic fluxing of Al_2O_3, and proceed by both basic fluxing and sulfide oxidation.[14] If molybdenum or tungsten is present in the coating from diffusion from the substrate, acidic fluxing of the protective oxides can occur.

Higher carbon content in the fuel can increase corrosion rates because the resulting char particles can trap sulfides on the surface of turbine airfoils causing increased hot corrosion rates. Higher carbon content may also create a more luminous flame, causing slightly increased temperatures of the combustion chamber liners, but this alone should not cause a significant change in combustion chamber distress. Viscosity levels can have a detrimental effect on fuel atomization and will contribute to combustion chamber distress. A rise in carbon residue content

in the fuel can cause fuel coking and plugging and streaking of the fuel nozzle. Streaking can cause burning of the combustion chamber liners and turbine nozzle guide vanes.

In general, reducing environments appear to have a more severe effect on hot corrosion of gas turbine materials than oxidizing environments.[15,16] Carbon deposition from unburned fuel on hot metal surfaces can sometimes generate a localized reducing environment even in bulk conditions that are normally oxidizing.[16,17] During burner-rig operations, burning of MGO-CG1 or MGO-CG2 tended to deposit carbon on the nozzle tip; burning NATO F-76 fuel vastly decreased any of these carbon deposits. Carbon production or carbon formed on surfaces may be extremely erosive as well.[16]

The major difference among the NATO F-76, MGO-CG1, and MGO-CG2 fuels was the amount of carbon residue (10% on bottoms). Carbon promotes hot corrosion by reducing sodium sulfate to sodium sulfide, thus increasing sulfidation. Sodium sulfide has been detected in sodium sulfate/carbon mixtures after cooling from the melt.[18,19] The reduction of sodium sulfate to sodium sulfide by carbon occurs according to the reaction:[19]

$$Na_2SO_4 + 4C \Leftrightarrow Na_2S + 4CO \quad K = 9.2 \times 10^9 \qquad (1)$$

Sulfate reduction will occur even under low concentrations of carbon as low as [C] = 3×10^{-4}. Bessen and Fryxell stated that small amount of carbon in the deposit could accelerate hot corrosion by as much as a factor of 10.[20] According to one engine manufacturer, the maximum carbon residue (on 10% bottoms) specified for a distillate fuel such as MGO or NATO F-76 fuel is 0.25 wt%.

Carbon deposition from hydrocarbon gases such as methane or by the formation of carbon monoxide has been observed. Gas phase hydrocarbons can decompose by catalytic action on hot alloy surfaces to form solid carbon that is not readily oxidized, thus promoting

local reducing conditions and accelerated hot corrosion.[17,21,22] or almost catastrophic sulfidation.[23] The effect of solid carbon in promoting sodium sulfate-induced hot corrosion will depend on the concentration of carbon in the condensate and on the size and crystalline structure of the particles formed on the alloy.[22]

Ni, Co, and Fe have been found to promote decomposition of hydrocarbons to yield solid carbon deposits and attack nickel-base alloys by Na_2S to form Ni_2S_3.[19] However, local reducing conditions are unlikely to reduce Cr_2O_3 directly[19] thus providing some explanation to the increased resistance of the CoCrAlY coating in the control pin specimens.

In the molten salt state, carbon could also act as a noble material relative to the coatings and the alloys and promote localized galvanic corrosion of the active species in the coatings. Carbon production or carbon formed on surfaces may be extremely erosive as well.[17, 23]

Aluminide coatings should suffer higher corrosion rates than chromia-forming coatings subjected to molten Na_2SO_4-NaCl mixtures. It is well known from work in aqueous solutions that both aluminum has a more electronegative potential chromium and that aluminum oxide is more prone to pitting attack in chloride environments than chromium oxide.

Although it is not known how the chlorides were involved with carbon residue in this work since it was not a primary task objective, chlorides are expected to enter the marine gas turbine engine primarily through the salt-laden combustion air from the marine environment. Restall observed synergistic effects of both salt and carbon in accelerating hot corrosion.[23] Two common mechanisms for the participation of chlorides in accelerating hot corrosion of high-temperature alloys are: (1) its involvement is forming lower temperature molten phases with the sodium or potassium sulfate salts, and (2) chlorides actively disrupt the oxide films in either the alloys or some coatings.

The plasma sprayed CoCrAlY coating on the standard pins was found to be more resistant than either aluminide coating. The chromium content in this coating was unknown. Earlier work in U.S. Navy coating development programs evaluated hot corrosion performance of MCrAlY coatings. Both Aprigliano[24] using electron beam physical vapor deposited (EB-PVD) high-chromium CoCrAlY coatings and Clarke[25] using both EB-PVD and plasma sprayed CoCrAlY coatings found this thermal barrier coating that were resistant to Type II or low temperature hot corrosion. These results agreed with an earlier conclusion that chromia-forming coatings were more resistant to Type II hot corrosion than alumina-forming coatings.[26]

CONCLUSIONS

Carbon residue was shown to adversely affect gas turbine materials if the carbon residue is above a threshold concentration. Above the threshold concentration, carbon accelerates hot corrosion by reducing sodium sulfate to sodium sulfide and increasing sulfidation.

The hot corrosion resistance of the CoCrAlY coating that was exposed to LVBR combustion of MGO-CG2 fuel was superior to the hot corrosion resistance of either of the aluminide coatings.

The average coating losses via Type II hot corrosion of Coating A on both Alloy 738 and Alloy 792 nickel-base substrates were very similar. Maximum penetration experienced after a 1000-hr. LVBR exposure at 1300 °F (704 °C) burning the MGO-CG2 fuel, was slightly greater than observed for NATO F-76 but much less than either Alloy 738 or 792 pins coated with Coating A that were LVBR-exposed for 1000 hours burning MGO-CG1 fuel.

Coating B consistently appeared to be less resistant to Type II hot corrosion than Coating A pins in all LVBR tests. Either spallation or increased hot corrosion of the Coating B resulted

in numerous sites where no coating was present on the cobalt alloy substrate after 1000 hours of LVBR exposure burning MGO-CG2 fuel. Alloy M509/Coating B pins showed similar Type II hot corrosion behavior to that observed after LVBR testing using NATO F-76. However, a thicker applied Coating B did lead to less Type II hot corrosion penetration into the cobalt-base alloy substrate.

MGO-CG2 fuel did not cause significant accelerated Type II hot corrosion of USCG aluminide-coated gas turbine alloys compared to NATO F-76 results.

The LVBR test results verify that the upper carbon residue limit for MGO PD commercial fuel specification should be revised to 0.20 wt% (10% bottoms) as is currently specified for MIL-SPEC NATO F-76 fuel distillate.

ACKNOWLEDGEMENTS

This work was supported by the U.S. Coast Guard with the program managed by Mr. Tom Gahs of the Coast Guard Engineering Logistics Center, Code 026. High temperature corrosion testing was performed David Greenlaw of the Marine Corrosion Branch, NSWCCD Code 613 under the supervision of Mr. Robert J. Ferrara. Albert Brandemarte and Rick Stockhausen of the Metallography Laboratory (Code 612) performed the polishing and metallographic work.

RERERENCES

1. MIL-F-16884J, “Military Specification Fuel, Naval Distillate” 31 May 1995.
2. MIL-DTL-5624T, "Detail Specification: Turbine Fuel, Aviation, Grades JP-4, JP-5, and JP-5/JP-8ST", 18 September 1998.

3. Marine Gas Oil (MGO) Purchase Description, NAVSEA Serial No. 03M3/45 (August 9, 1996).

4. D5304-94, " Standard Test Method for Assessing Distillate Fuel Storage Stability by Oxygen Overpressure", Committee D02.14, American Society of Testing and Materials, West Conshohocken, PA. (1994).

5. S. Mrowec, *Oxidation of Metals*, v. 44, 177 (1995).

6 . J.A. Goebel, F.S. Pettit, G.W. Goward, *Metallurgical Transactions*, v. 4, 261 (1973).

7. R.A. Rapp, Y.S. Zhang, *JOM*, v. 46, No. 12, 47 (Dec. 1994).

8. "Standard Practice for Utilization of Test Data to Determine Conformance with Specifications", D3244-97, ASTM, West Conshohocken, PA (1997).

9. D.A. Shifler, "Effects of Fuel Carbon Residue on the Hot Corrosion Resistance of Materials in Marine Gas Turbines", 1999 Tri-Service Conference on Corrosion", November 15-19, 1999, Myrtle Beach, SC, DoD Tri-Service Corrosion Committee.

10. H. von E. Doering, P.A. Bergman, "Construction and Operation of a Hot-Corrosion Test Facility", *Materials Research and Standards*, v. 9, No. 9, 35 (1969).

11. G.C. Booth, R. L. Clarke, *Materials Science and Technology*, v. 2, 272 (1986).

12. D.A. Shifler, **CORROSION/2000**, paper 243, NACE International, Houston, TX (2000).

13. D.A. Shifler, **CORROSION/2001**, paper 167, Houston, TX (2001).

14. G.W. Goward, in Proceedings of the Symposium on 'Properties of High Temperature Alloys', Z.A. Foroulis, F.S. Pettit, eds, PV 77-1, The Electrochemical Society, Pennington, NJ, 806 (1976).

15. E.L. Simons, G.V. Browning, H.A. Liebhafsky, *Corrosion*, v.11, 505t, (1955).

16. C.G. McCreath, *Materials Science and Technology*", v. 3, 494 (1987).

17. D.W. McKee, G. Romeo, *Metallurgical Transactions*, v. 4, 1877 (1973).

18. J. Stringer, in Proceedings of the Symposium on 'Properties of High Temperature Alloys', Z.A. Foroulis, F.S. Pettit, eds, PV 77-1, The Electrochemical Society, Pennington, NJ, 541 (1976).

19. V. Vasantasree, M.G. Hocking, B.A. Nagaraj, in Proceedings of 3rd US/UK Navy Conference on ' Gas Turbine Materials in a Marine Environment', Bath, Session V, paper 4(a) (1976).

20. I.I. Bessen, R.E. Fryxell, in Proceedings of 1st US/UK Navy Conference on 'Gas Turbine Materials in a Marine Environment', Hyattsville, MD, 73-84 (1974).

21. D.W. McKee, G. Romeo, *Metallurgical Transactions*, v. 5, 1127 (1974).

22. D.W. McKee, G. Romeo, Proceedings of 1974 Gas Turbine Materials in the Marine Environment Conference, J.W. Fairbanks, I. Machlin, eds., Castine, ME during July 1974, MCIC 75-27 (June 1975).

23. J.E. Restall, in Proceedings of 3rd US/UK Navy Conference on 'Gas Turbine Materials in a Marine Environment', Bath England, Session V, paper 10 (September 1976).

24. L.F. Aprigliano, in Proceedings of the 4th US.UK Conference on ' Gas Turbine Materials in a Marine Environment', Annapolis, MD, 151 (1979).

25. R.L. Clarke, in Proceedings of the 4th US.UK Conference on ' Gas Turbine Materials in a Marine Environment', Annapolis, MD, 189 (1979).

26. A.F. Taylor, B.A. Wareham, C.G. Booth, J.F.G. Conde, in Proceedings of 3rd US/UK Navy Conference on ' Gas Turbine Materials in a Marine Environment', Bath, Session III, paper 3 (1976).

TABLES

TABLE 1.
MGO PD Fuel Specifications versus Nominal and Specified NATO F-76 Values

Property	Units	ASTM Method	MGO PD Requirements	NATO F-76 MIL-F-16884J Requirements	NATO F-76 Test Baseline
Viscosity @ 40 °C	mm^2/s	D 445	1.7-4.5	1.7-4.3	3.35
Appearance @ 21°C or ambient (whichever is higher)		Visual	Clear and bright	Clear and bright	Clear and bright
Carbon Residue on 10% bottoms	wt %	D 524	0.35	0.20 max	0.10
Sulfur	wt %	D 4294/D 129	1.0 max	1.0 max	0.99[c]
Cloud Point	°C	D 2500	-1.1 max	-1 max	-10
Pour Point	°C	D 97	--	-6 max	-5
Distillation 90 % Pt	°C	D 86	357	357 max	319
Color	--	D 1500	3 max	3 max	< 1.0
Flash Point[(a)]	°C	D 93	60 min	60 min	93
Particulates	mg/l	D 6217	--	10 max	5
Hydrogen Content	wt %	D 4808	--	12.5 min.	--
Density @ 15.6 °C	kg/m^3	D 1298	876 max	876 max	840
Ash	wt %	D 482	0.01 max	0.005 max	< 0.001
Water & Sediment	vol %	D 2709	0.05 max	0.05 max	< 0.005
Water Content	ppm	D 1744	--		190
Cetane Number or Cetane index[(b)]		D 613 D 976	42 min 43 min	42 min 43 min	--
Corrosion @ 100°C max		D 130	3 max	1 max	--
Aniline Point	°C	D 611	--	60 min	--
Acid Number	mg KOH/g	D 974, D 664	--	0.30 max	--
Demulsification	Minutes @ 25°C	D 1401	--	10 max	--
Ca	ppm	[(d)]	--	1.0 max	< 0.1
Cu	ppm	[(d)]	--	--	<0.1
Pb	ppm	[(d)]	--	0.5 max	< 0.1
Ni	ppm	[(d)]	--		< 0.1
K +Na	ppm		--	1.0 max	
V	ppm	[(d)]	--	0.5 max	< 0.1

[a] The flash point value is absolute and no value less than 60 °C is permissible.
[b] Cetane index requirement shall apply to base fuel without cetane improving additives. Where cetane index is reported, the value shall be reported as the cetane index.
[c] NATO F-76 after sulfur doping with di-tertiary butyl disulfide ($C_8H_{18}S_2$; M.W. 178.35).
[d] Trace metals shall be determined by whatever industry-accepted method – such as AA or ICP-AES – which affords the level of detection required. The producer shall specify the method used.

TABLE 2.

Property and Compositional Analysis of NATO F-76 Fuel versus MGO-CG1 and MGO-CG2 Fuels Used for Burner Rig Testing at 1300 °F (704 °C)

Property	Units	ASTM Method	NATO F-76 baseline	MGO-CG1 [a]	MGO-CG2 [b]
Viscosity @ 40 °C	mm^2/sec	D 445	3.243	3.169	3.27
Carbon Residue on 10% bottoms	wt%	D524	0.099	0.33	0.19
Sulfur	wt%	D 4294/D 129	0.99	0.99	0.99
Cloud Point	degs C	D 2500	-8	-8	-4
Pour Point	degs C	D 97	-10	-12	-26
Distillation 90% Pt.	degs C	D 86	325	326.1	316.1
Color		D 1500	1	5.5	4.0
Flash Point	degs C	D 93	97	90	88
Particulates	mg/l	D 6217	6	10	6.99
Density @ 15.6 °C	kg/m^3	D 1298	838.3	837.8	839.7
Ash	wt%	D 482	0.005	0.01	0.01
Water and Sediment	vol%	D 2709	<0.001	< 0.005	---
Water Content	ppm	D 1744	49	190	---
Metals	ppm	ICP[c]			
Al	ppm		< 0.1	< 0.1	---
Ca	ppm		0.4	0.7	0.011
Cu	ppm		0.2	0.3	0.3
Fe	ppm		< 0.1	< 0.1	---
Pb	ppm		< 0.1	< 0.1	---
Ni	ppm		< 0.1	< 0.1	<0.015
Si	ppm		0.16	0.19	---
K	ppm		0.4	0.69	0.002[d]
Na	ppm		0.2	0.27	0.081[d]
V	ppm		< 0.1	< 0.1	0.041

[a] MGO-CG1 fuel formulated and analyzed by USX Engineering Consultants, Fuels and Lubricants Lab, 4000 Tech Center Drive, Monroeville, PA. 15146, (412)-825-2165.

[b] MGO-CG2 fuel formulated at NSWCCD and analyzed by NAVAIR, CODE 4.4.5, Fuels and Lubricants Division, Patuxent River, MD 20670-1534. Both MGO-CG1 and MGO-CG2 fuels consist of a blend of the high-sulfur NATO F-76 listed above and a bottoms product residue (drilling mud) removed from a Kuwaiti Crude by vacuum distillation (Kuwait Residue-PARC-PTMOS-PR845-9-960ATB). This residue material was obtained from UEC, Inc (USX Engineers Consultants, Inc.), USS Technical Center, 4000 Tech Center Drive, Monroeville, PA 15146. [c] Intercoupled plasma spectroscopy [d] Analyzed by atomic adsorption rather than ICP

TABLE 3.
Nominal Composition of the Substrate Alloys

Elements	Alloy 738 PWA 1451	Alloy 792 PWA 1456	MAR-M-509 PWA 647
	Composition (weight percent)		
C	0.117	0.11	0.63
S	0.0009	0.0005	0.0007
P	<0.005	< 0.010	< 0.010
Si	0.020	0.02	0.10
Mn	<0.01	< 0.10	0.01
Cr	16.14	11.87	23.48
Mo	1.69	1.91	0.050
Fe	0.06	0.06	0.21
Ti	3.36	3.98	0.19
Al	3.33	3.47	0.18
Co	8.37	8.96	Balance (~54)
Ni	Balance (~ 61.5)	Balance (~ 61)	10.10
W	2.62	4.01	6.93
Zr	0.034	0.043	0.41
B	0.009	0.016	< 0.01
Nb	0.90	----	< 0.02
Ta	1.80	4.04	3.51
Hf	<0.02	0.53	---

TABLE 4.
Typical Gas Turbine Alloys Coating Tested

Alloy	Coating	Type	Typical Location
Alloy 738	Coating A	Pure Aluminide	1st stage Vane
Alloy 792	Coating A	Pure Aluminide	1st stage Blade
Alloy M509	Coating B	Pure Aluminide	2nd stage Vane 2nd, 3rd stage Blades

TABLE 5.

Corrosion Measurements of Gas Turbine Materials Burner-Rig Tested for 1000 hours at 1300 °F (704 °C) Using NATO F-76 Fuel

Coating	Pin I.D	Substrate Alloy	Original Coating Thickness (mils)	Average Coating Loss on a Radius (mils)	Maximum Coating Penetration on a Radius (mils)
CoCrAlY	1	HA 188	11.3	1.19	1.92
	9	HA 188	11.7	1.44	2.44
Coating A aluminide	2	Alloy 738	3.10	1.21	3.00
	5	Alloy 738	3.10	0.78	2.70
	8	Alloy 738	3.10	1.11	3.10*
	12	Alloy 738	3.10	1.33	3.10*
	15	Alloy 738	3.10	0.65	2.55
Coating A aluminide	3	Alloy 792	2.97	1.06	2.82
	6	Alloy 792	2.97	1.04	2.87
	10	Alloy 792	2.97	0.89	2.72
	13	Alloy 792	2.97	1.15	2.77
	16	Alloy 792	2.97	0.80	2.57
Coating B aluminide	4	Alloy M509	1.47	1.27	into substrate
	7	Alloy M509	1.47	1.43	into substrate
	11	Alloy M509	1.47	1.32	into substrate
	14	Alloy M509	1.47	1.39	into substrate
	17	Alloy M509	1.47	1.36	into substrate

* penetration to coating/substrate interface

TABLE 6.

Corrosion Measurements of Gas Turbine Materials Burner-Rig Tested for 1000 hours at 1300 °F (704 °C) Using MGO-CG1 Fuel

Coating	Pin I.D.	Substrate Alloy	Original Coating Thickness (mils)	Average Coating Loss on a Radius (mils)	Maximum Coating Penetration on a Radius (mils)
CoCrAlY	1	HA 188	11.3	0.77	2.02
	9	HA 188	11.7	1.02	1.34
Coating A aluminide	2	Alloy 738	2.98	2.84	into substrate
	5	Alloy 738	2.93	2.36	into substrate
	8	Alloy 738	2.99	2.94	into substrate
	12	Alloy 738	2.96	2.79	into substrate
	15	Alloy 738	2.89	2.69	into substrate
Coating A aluminide	3	Alloy 792	2.96	2.34	into substrate
	6	Alloy 792	3.02	2.96	into substrate
	10	Alloy 792	3.02	3.00	into substrate
	13	Alloy 792	3.06	2.92	into substrate
	16	Alloy 792	2.94	2.91	into substrate
Coating B aluminide	4	Alloy M509	1.47	1.18	into substrate
	7	Alloy M509	1.47	1.18	into substrate
	11	Alloy M509	1.47	1.24	into substrate
	14	Alloy M509	1.47	1.33	into substrate
	17	Alloy M509	1.47	1.16	into substrate

TABLE 7.

Corrosion Measurements of Gas Turbine Materials, After 1000-hr LVBR Test at 1300 °F (704 °C) Burning MGO-CG2 Fuel.

Coating	Pin I.D.	Substrate Alloy	Original Coating Thickness (mils)	Average Coating Loss on a Radius (mils)	Maximum Coating Penetration on a Radius (mils)
CoCrAlY	1	Alloy 333	11.10	0.76	1.00
	12	Alloy 671	10.42	0.20	1.07
Coating A NiAl	2	Alloy 738	3.03	0.53	2.34
	6	Alloy 738	3.21	0.87	3.21*
	10	Alloy 738	3.30	0.96	3.30*
	15	Alloy 738	2.65	0.80	into substrate
	19	Alloy 738	3.17	1.21	into substrate
Coating A NiAl	3	Alloy 792	3.26	1.35	into substrate
	7	Alloy 792	3.54	1.06	2.99
	11	Alloy 792	3.24	1.54	into substrate
	16	Alloy 792	2.81	0.94	into substrate
	20	Alloy 792	3.34	1.15	3.34*
Coating B CoAl 1.47 mil	4	Alloy M509	1.47	1.17	into substrate
	8	Alloy M509	1.50	1.19	into substrate
	13	Alloy M509	1.65	1.34	into substrate
	14	Alloy M509	1.85	1.69	into substrate
	17	Alloy M509	1.65	1.29	into substrate
Coating B CoAl 2.08 mil	5	Alloy M509	2.10	1.42	into substrate
	9	Alloy M509	2.35	1.53	into substrate
	14	Alloy M509	2.08	1.99	into substrate
	18	Alloy M509	2.08	1.98	into substrate
	22	Alloy M509	2.08	1.37	into substrate

- penetration to coating/substrate interface

FIGURES

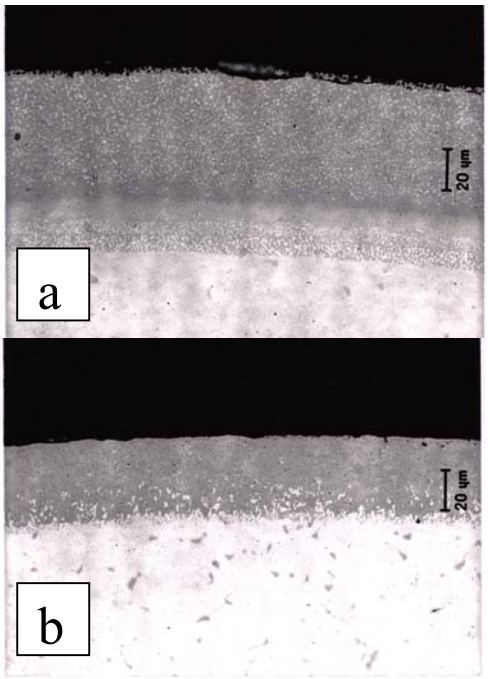

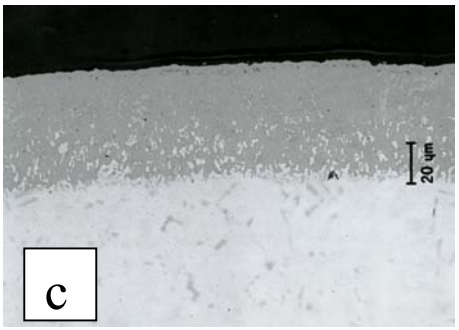

FIGURE 1. Aluminide coatings, untested. (a) Coating A on Alloy 738. (b) Coating B on Alloy M509, 1.47 mil nominal thickness. (c) Coating B on Alloy M509, 2.08 mil nominal thickness. All coatings display an outer layer consisting of non-metallic dispersions while inner layer displays a diffusion zone.

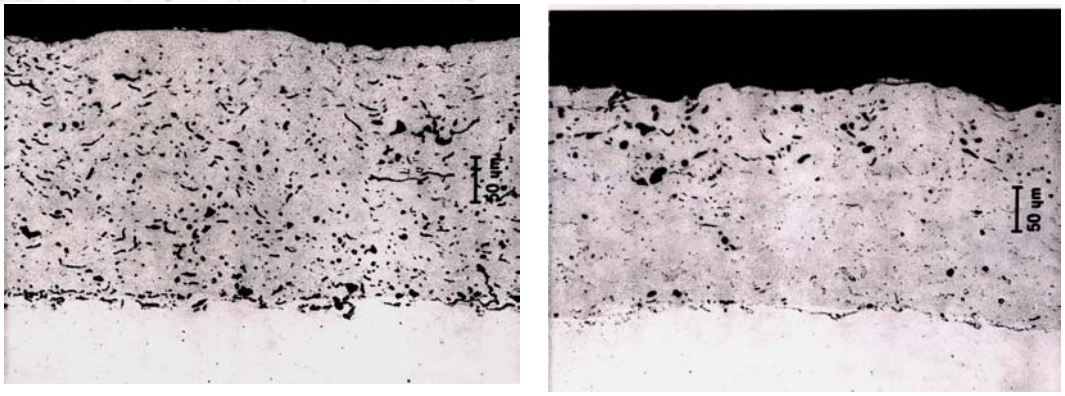

FIGURE 2. Standard CoCrAlY coating (a) before any LVBR testing and (b) after 1000 hours of LVBR exposure at 1300 °F (704 °C) burning NATO F-76 fuel. Similar performance was also observed after 1000 hours of LVBR exposure at 1300 °F (704 °C) using MGO-CG1 and MGO-CG2 fuels.

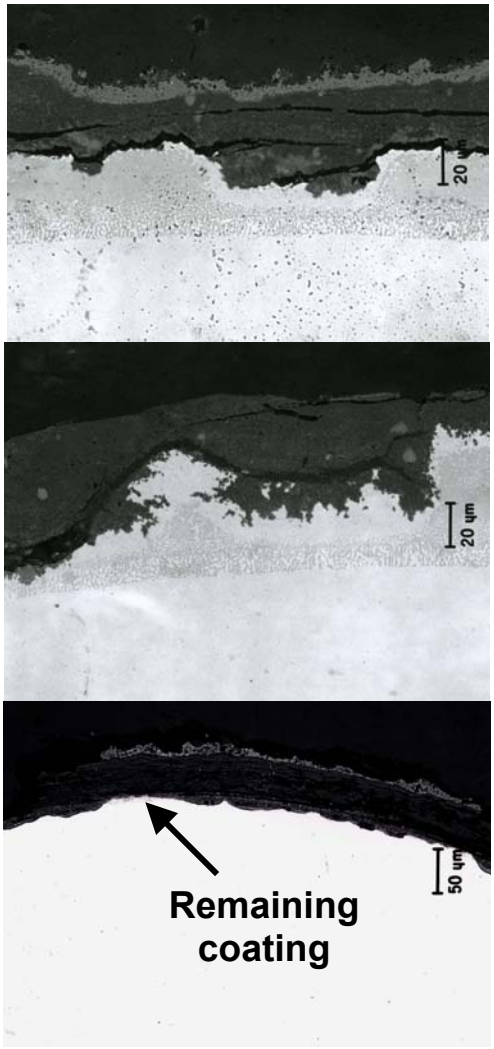

Performance of Alloy 738/Coatng A after 1000-hr. LVBR Exposure to NATO F-76, 0.099 wt.% carbon residue

Performance of Alloy 738/Coatng A after 1000-hr. LVBR Exposure to MGO-CG2, 0.19 wt.% carbon residue

Performance of Alloy 738/Coatng A after 1000-hr. LVBR Exposure to MGO-CG1 0.33 wt.% carbon residue

FIGURE 3. Alloy 738/Coating A after 1000-hr LVBR exposure at 1300 °F (704 °C) burning different fuels. The typical coating losses increased as the carbon residue content in the fuel increased. Coating degradation caused by Type II hot corrosion. Performance of Alloy 792/Coating A is similar.

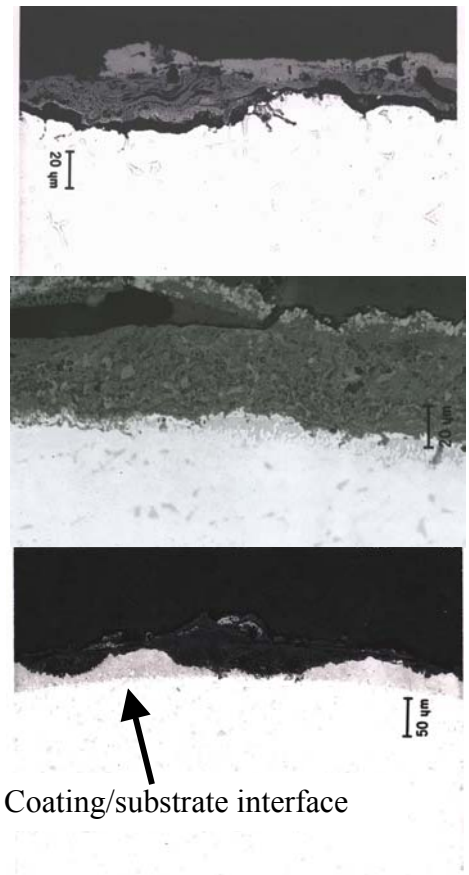

FIGURE 4. Alloy M509/Coating B after 1000-hr LVBR exposure at 1300 °F (704 °C) burning different fuels. The typical coating losses were similar for fuels with carbon residue from 0.099 to 0.33 wt.%. Coating B degradation caused by Type II hot corrosion.

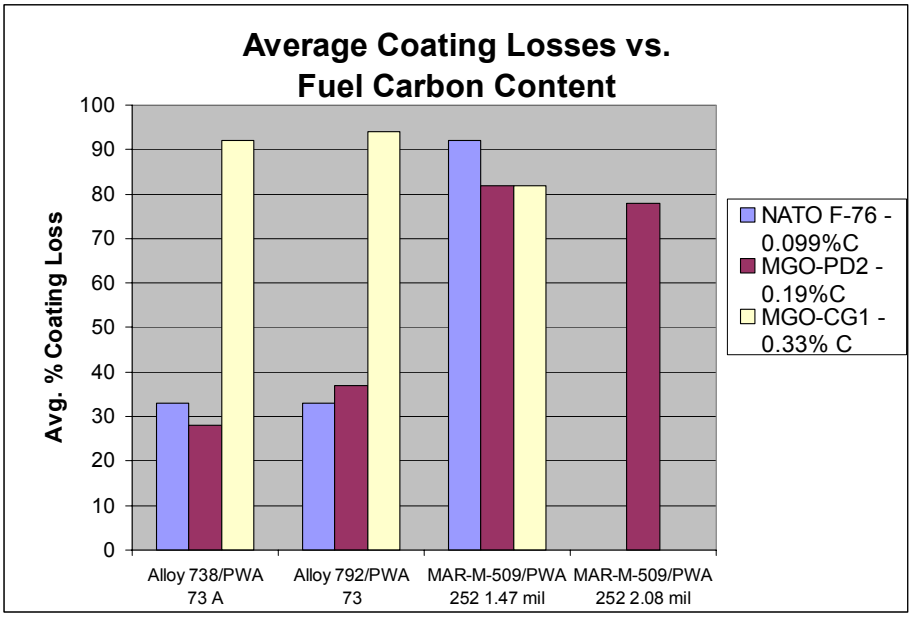

FIGURE 5. Summary of average coating losses for each alloy/coating combination as function of carbon residue content.

Orientation Study of Fatigue Crack Initiation from Corrosion Damage

M. Khobaib[1], C. Kacmar[1], and M. Donley[2]

[1]University of Dayton, Dayton, OH

[2]Air Force Research Laboratories, Wright-Patterson AFB, OH

ABSTRACT

Fatigue crack nucleation from corrosion damage is drawing considerable attention in the aging aircraft research community. Localized corrosion, such as corrosion pits, is a potential stress raiser and provides active sites for fatigue crack initiation. The detailed knowledge of the metrics of early stages of corrosion damage and transition to fatigue cracks is critical to the accurate life prediction of the structure. High strength aluminum alloys are known to be very sensitive to orientation and this could play a critical role in both pitting and the resulting fatigue damage.

Fatigue experiments on dog bone specimens of AA2024-T3 with known pit morphology were conducted to investigate the crack initiation and growth behaviors of cracks nucleating from pits. The corrosion pits were grown electrochemically in a controlled fashion and samples were prepared with pit depth varying from 3 to nearly 130 μm. These pits were characterized using white light interferometer; surface parameters such as average roughness and morphology were determined before fatigue testing. Specimens were aligned in L-T, T-L, L-S, S-L, S-T and T-S directions to investigate the effect of orientation on pitting and fatigue characteristics.

The fractured surface was analyzed after the fatigue test and stress intensity calculations were made based on these observations. No clear effect of orientation could be seen from the limited test data. However, the crack growth behavior of the crack nucleating from these pits was typical of a short crack. The results provide the details of the critical pit size that can lead to fatigue crack initiation as well as supply information about the growth behavior of cracks nucleating from corrosion pits.

INTRODUCTION

Corrosion of high strength aluminum alloy structures poses a serious problem in extending the life of aging aircraft fleet. The United States military has a large fleet of aging aircraft which is expected to grow further due to budgetary restriction. Most of these aircraft will be in operation for longer than they were originally designed to be.[1] Consequently, the Air Force is concerned about the growing number of aging aircraft that require extensive maintenance. The older these aircraft get; the maintenance of their structural integrity becomes increasingly critical for life sustainment. Hence, increased attention is required towards structural damage modeling, repair and life prediction.

Aircraft structures experience a variety of environmental influences even under normal service conditions and some of these are synergistic while others are cumulative. Some of the main causes of failure of aging aircraft are the cumulative corrosion damage, fatigue cracking and their synergistic interactions. These problems are bound to worsen with the continued service use of these aircraft. The Department of Defense is addressing these issues with research initiatives related to corrosion problem facing aging aircraft, structural testing and developing analytical tools for qualifying the effects of corrosion on structural integrity.[2]

Pitting is the type of corrosion most commonly observed in these high strength aluminum alloys. Although it is well known that the conjoint action of corrosion and stress leads to accelerated loss in the structural integrity of aircraft, the critical stage of damage where, under stress, a corroded area leads to crack initiation is not understood at all. One example of this mechanism is the transition of pitting corrosion to active notch. The corrosion is recognized as one of the main nucleation sites for fatigue crack formation in a wide range of steels and high strength aluminum alloys.[3-10]

The most significant problems are usually associated with airframe components, such as rivets, fasteners and joints. To date, the most practical solution for inspection of corrosion damage in these areas is to completely strip the paint from the plane. This method is naturally quite expensive, and time consuming and sometimes no corrosion are found. There is no predictive tool to assess the life of structure from any corrosion metrics. Quantitative measures such as pit dimensions and surface roughness as corrosion metrics have been used along with crack growth tools in estimating fatigue life of components subjected to corrosion.[11] Other studies have focussed on measuring and applying a large number of candidate metrics for quantifying corrosion in aging KC-135.[12] However, these results can be used to predict specific cases, because the very sensitive issue of orientation was ignored in all these investigations.

This study was initiated under the sponsorship of Department of Defense, to quantitatively investigate the role of corrosion damage on the fatigue behavior of high strength aluminum alloys. It must be emphasized that the pitting effect on fatigue is not yet well understood. A large number of laboratory investigations have studied the effects of prior corrosion and the presence of a corrosive environment on fatigue crack initiation and growth of high strength aluminum alloys.[13,14] These studies, however, have not addressed the early stages of corrosion and its transition to fatigue cracking in structural materials. The information presented in this study about short-term as well long-term effects of corrosion is vital to understanding the early stages of damage evolution in aircraft structure whose operational mechanical and environmental spectra are not adequately represented in laboratory experiments. Nakajima and Tokaji[15] have found that a crack emanates from a pit during simultaneous corrosion fatigue only if the pit grows to the level when the stress intensity factor reaches a certain threshold value. Phillips and Neuman[16] demonstrated that the fracture mechanics of long

crack fatigue growth in AA2024-T3 alloy leads to substantial exaggeration of the fatigue life for a very small initial size. They established the importance of the short crack analysis and experimentally found Paris constants for short and long crack growth in AA2024-T3 alloy.

It is very critical to understand the effect of specimen orientation on the crack initiation process, since AA2024-T3 is very sensitive to microstructure. In this study controlled pits were grown in standard dog-bone fatigue samples fabricated with tensile axes parallel to L-T, T-L, L-S, S-L, S-T and T-S orientation. These specimens were then tested under fatigue condition in laboratory air. The high strength aluminum alloys are known to be orientation dependent.[17,18] The primary objective of this study is to develop a relationship between a pitting parameter and a structural integrity parameter. The overall objective is to formulate a life prediction model based on pitting parameters obtained from nondestructive evaluation tool used in the service and expected fatigue spectra of the aircraft. Initially a method was developed to produce controlled pitting, so that pits of varying sizes, morphologies and distributions could be created on fatigue samples fabricated from AA2024-T3. A number of AA2024-T3 dog-bone fatigue samples were electrochemically pitted. The pit morphology was characterized using optical microscopy, white light interference microscopy (WLIM), and scanning electron microscopy (SEM). All samples were fatigued under the same conditions. The fracture surface of all the specimens after failure was characterized using optical microscopy and SEM and pit dimensions and crack geometry and parameters were obtained. The stress intensity factor calculations were made using Neuman-Raju approximation[19] and, finally the crack growth behavior was obtained through software package, CRACKS.[20]

EXPERIMENTAL

Standard dog–bone fatigue samples of AA2024-T3 were machined with L-T, T-L L-S, S-L, S-T and T-S orientations. The dimensions for the fatigue specimens are shown in Figure 1. Each sample was cleaned and prepared at a time. The gage section of the sample was sanded up to 600 grit SiC paper. The sample was then rinsed with distilled water and dried with a stream of air. Most of the specimen's surface was covered with a waterproof tape. A small portion in the center of the gage section was initially left exposed as shown in Figure 1, and later covered with a thin coat of micro-stop. Two fine holes were created in the microstop coating after the film had dried. This was intentionally done to provide desired site/sites for pit initiation. The sample thus prepared was then glued into an electrolytic cell for electrochemically producing pit/pits on the surface.

A solution of 0.1M NaCl was used as the pitting electrolyte. A Saturated Calomel Electrode (SCE) was used as the reference while platinum meshed disc served as the counter electrode. The pitting was produced in the area of the exposed gage section using a potentiostatic scan. An initial potential of -450 mV (SCE) was applied for 10 minutes, and then the potential was lowered to -520 mV (SCE) for the remainder of the scan. Various scan times were used to obtain pits of varying depth. The sample was promptly removed from the cell, after the potential scan, cleaned with running distilled water and dried in a stream of air. The pit morphology and depth measurements were determined using optical microscopy, SEM and WLIM. The samples were then fatigued within 24 hours of being removed from the electrolytic cell. Fatigue tests were conducted on a single machine under the same conditions at a stress ratio, R = 0.1, maximum stress = 256 Mpa, and a frequency = 15 Hz. All the samples were analyzed after fracture to determine the exact location of crack initiation from a particular pit.

The fracture surface was analyzed to obtain the crack parameters. The stress intensity factor for each sample was calculated using Newman–Raju approximation[19] and crack growth behavior was obtained through CRACK calculation.[20]

RESULTS AND DISCUSSION

The test matrix was designed to generate a wide range of pit size and depth. Controlled potentiostatic polarization scheme was used to produce a wide range of pit sizes in a relatively short amount of time. Figure 2 shows a representative optical micrograph of a pit in L-S oriented specimen that was anodically polarized with the substrate coated with the imperfect layer of microstop coating. The polarization times range from four hours to 24 hours. For longer polarization times, larger and deeper pits were observed. The pit morphology was characterized using WLIM. Figure 2b to 2d shows the details of pit morphology obtained using different options available with WLIM. Figure 2c shows the maximum contrast while Figure 2d provides a detailed 3-D morphology of the pit. SEM was also used to characterize a few select samples. A more extensive display of these profiles can found in reference.[20] Since SEM is a well-established method, it was used to mainly compare the qualitative surface features with those shown in the WLIM surface profiles.

The sample shown in Figure 2 was coated with the micro-stop to restrict the number of sites for pit nucleation and to allow formation of a few large pits on the sample surface. A number of specimens were pitted to establish some parameter which results in one or two dominant pit. These parameters were later used to create controlled pitting, one or some times two, out of which one became dominant with increasing polarization time. The polarization times for the sample ranged from 4 hours to 24 hours. The longer polarization times produced

larger pits. As the polarization times increased, the pit depths also increased. However, the sample polarized for twenty hours had deeper pits than the sample polarized for twenty-four hours.[21] In this case, instead of growing deeper, the pits expanded during the extra polarization time. This behavior is shown in Figure 3.which is a plot of polarization time vs. critical pit depth. All data points were determined to be statistically valid using the average deviation method.[22]

A two-dimensional analysis was performed for each sample using WLIM as described in reference[21] to determine the dimensions of the pits produced on these samples. The pitted samples were fatigued after the surface pit morphology was characterized completely. The samples were fatigue tested at a stress ratio, R = 0.1 and a frequency, f = 15 Hz. The main goal was to determine a relationship between pit depth and stress intensity factor, K. The critical pit size is assumed as the size of the pit that initiates fatigue crack. Figure 4 schematically illustrates such a fatigue crack initiation and growth process from a pit.[23]. This figure represents a flow chart of the experimental procedure. Step 1 simply shows the dog-bone fatigue sample with the load direction and a small area of the gage section where pits are to be initiated. Step 2 shows three pits created by controlled accelerated technique. One of these pits initiates fatigue crack on fatigue loading and a semi-elliptic crack appears to grow. This stage is depicted in Step 3. Step 4 is a two dimensional scheme of the crack initiation and growth process with the two important parameters of the pit depth and diameter (length) used in stress intensity factor calculation.

A detailed analysis of fracture surface indicated that crack always started from the pit at the corroded surface. In most cases the crack initiated from a single pit and a single semi-elliptical surface crack grew to a critical size leading to the failure of the specimen. In some

cases, the cracks initiated from two or more adjacent pits. In these cases, the cracks linked together to form a single semi-elliptic crack that eventually caused the failure. Figure 5 shows several optical micrographs of a sample before and after it was failed under fatigue. The pitted face was examined first to determine the area in which the crack developed. The fractured surface was then examined for the initiation site of the crack. The crack appeared to be centered around the left pit. The left pit is the crack initiating pit and it corresponds with the top pit shown in Figure 5(a). The depth and diameter of this pit were calculated using the WLIM two-dimensional analysis.

Once the parameters of interest were obtained using WLIM, the stress intensity factor for each specimen was calculated. The stress intensity factor was used as the key fatigue parameter in developing a relationship between pit depth and fatigue parameter. The stress intensity factor for each sample was calculated using a program developed at the University of Dayton Research Institute.[20]

One of the main objectives of this study is to develop a relationship between a structural integrity parameter and a pitting parameter. Such a relationship is shown in Figure 6. The stress intensity factor was plotted against critical pit depth. There appears to be a linear relationship between the two parameters. This relationship can be used to predict the life of structure. Fatigue crack growth model developed by University of Dayton Research Institute CRACKS model was used to predict the crack growth behavior of fatigue cracks initiating from a pit. A single semi-elliptical surface crack is assumed to develop from the critical pit. The model uses the stress intensity factor number from previous calculation and the crack growth data is generated from the initial and final crack size measured. Crack growth is assumed to start from

the first applied cycle with no crack initiation period. Such an assumption is a reasonable approach because majority of the fatigue life of pitted sample comprises of growth stage.[24]

Crack growth data in the form of da/dN vs. stress intensity factor is shown in Figure 7. The data shown as open squares are taken from notched compact tension specimen representing long crack growth.[21] The closed squares represent the data from pitted samples used in this study. It appears that the crack growth behavior of cracks initiating from pit is typical of short crack growth behavior. However, a transition to long crack growth behavior is quite evident suggesting that pits deeper than 80 μm behave similar to standard notched specimen representing long crack growth data. More tests are required with critical pit depths in the range of 100-200 μm.

Figure 6 shows the plot of pit diameter Vs. K for three orientations. There is a lot of scatter in the data, but it is encouraging to note a trend. More tests are required to make any conclusion. However, when the stress intensity factor is plotted against the pit depth, the scatter is significantly reduced. The results are shown in Figure 7. Some layering of data is observed for LT and TL orientations at higher pit depths. The relationship can be used to predict the life of structure. The data from the pit characterization and fracture surface analysis were the main input into the CRACKS model developed by University of Dayton Research Institute which has been used here to predict the crack growth behavior of fatigue cracks initiating from a pit. A single semi-elliptical surface crack is assumed to develop from the critical pit. The model uses the stress intensity factor number from previous calculation and the crack growth data is generated from the initial and final crack size measured. Crack growth is assumed to start from the first applied cycle with no crack initiation period. Such an assumption is a reasonable approach because majority of the fatigue life of pitted sample comprises of growth stage.[25]

Crack growth data for LS, TL and LT orientation in the form of da/dN vs. stress intensity factor is shown in. Figure 8. The data shown with filled squares are taken from notched compact tension specimen representing long crack growth.[22] It appears that the crack growth behavior of cracks initiating from pit is typical of short crack growth behavior. However, a transition to long crack growth behavior is quite evident suggesting that pits deeper than 80 mm behave similar to standard notched specimen representing long crack growth data. More tests are required with critical pit depths in the range of 100-200 μm

SUMMARY

A select number of pits were created on dog-bone fatigue sample by an electrochemical technique. The pit depth increased with increasing polarization time. However, this relationship failed at polarization times longer than 20 hours. All the pits were characterized using WLIM and SEM. Important parameters such as length and depth of the pits were determined. The fracture surface was analyzed to determine the initiation and failure locations on the surface. Stress intensity factors were calculated using all the parameters measured. A linear relationship was observed between critical pit depth and K. Fatigue crack growth initiating from a pit was observed to be typical of short crack. Sign of possible transition to long crack growth behavior was observed for pits deeper than 80 μm.

ACKNOWLEDGMENTS

Effort sponsored by the Defense Advanced Projects Agency (DARPA) Multidisciplinary University Research Initiative (MURI), under Air Force Office of Scientific Research grant

number F49620-96-1-0442. Technical assistance from Y. Ding, N. Schell, P.C. Mieldar and L. Simon are gratefully acknowledged.

REFERENCES

1. Rokhlin, S. I., and Kim, J.Y., "Fracture Mechanical Analysis of Fatigue Crack Initiation and Growth from Pitting Corrosion", Second Annual Report for DARPA-MURI Under AFOSR Grant Number F49620-96-1-0442, (1998) p. A24-2.

2. Groner, D. J., "US Air Force Aging Aircraft Corrosion", Current Awareness Bulletin, Structures Division, AFRL/FIBD, Aerospace Structures Information and Analysis Center, WPAFB, OH, Spring 1997.

3. Chen, G.S., Wan, K.C., Gao, M., Wei, R. P., and Flourney. Materials Science & Engineering, A 219, p. 126, 1996.

4. Congleton, J., Olieh, R. A., and Parkins, R. N. Met Technol. 9, p. 94, 1982.

5. Kondo, Y. " Prediction of Fatigue Crack Initiation Life Based on Pit Growth", *Corrosion*, Vol. 45, no. 1, (1989) p. 7.

6. Ahn, S. H., Lawrence Jr., F. V., and Metzger, N. M. Fatigue Fracture Eng. Mater. Struct. 15, p. 625, 1992.

7. Chen, G. S., and Duquette, D. J., Matall. Trans. 23A, p. 1563, 1992.

8. Huang, Y. H., and Alkire, R. C., J. Electrochem. Soc. 136, p. 2763, 1989.

9. Piascik, R. S., and Willard, S. A. "The Growth of Small Corrosion Fatigue Cracks in Alloy 2024", *Fatigue and Fracture of Engineering Materials and Structures,* Vol. 17, No. 11, (1994) pp. 1247-1248.

10. Harmsworth, Clayton L. "Effect of Corrosion on the Fatigue Behavior of 2024-T4 Aluminum Alloy", ASD Technical Report 61-121, (1961).

11. Perez, R., "Metrics Exploration and Transformation Development for Corrosion/Fatigue", Final Report, Delivery Order 0005, USAF Contract F33615-95-D-3216, November 1996.

12. Mitchell, G., "Application of Corrosion Quantification Techniques to the USAF KC-135 Stratanker", Proceedings of the Air Force 4th Aging Aircraft Conference, United States Air Force Academy, CO, July 1996, p. 251.

13. Wanhill, R. J. H., “Aircraft Corrosion and Fatigue Damage Assessment”, Proceedings of the US Air Force ASIP Conference, San Antonio, TX, December 1995, p.9.

14. Cole, G. K., Clark, G., and Sharp, P.K., “The implications of Corrosion with Respect to Aircraft Structural Integrity”, Aeronautical and Maritime Research Laboratory, Melbourne, Australia, Research Report DSTO-PR-0102, AR-010-199, March 1997.

15. Nakajima, M., and Tokaji, K., “A Mechanical Condition of Fatigue Crack Initiation from Corrosion Pits”, Fatigue 1996, Proceedings of the Sixth International Fatigue Congress, Berlin, Germany, pp. 697-702, 1996.

16. Philips, E. P., and Neuman, J. C., “Impact of Small Crack Effect on Design Life Calculations"” Experimental Mechanics, pp. 221-225, 1989.

17. P. Doig and P.E.J. Flewitt, *Mechanisms of Environment Sensitive Cracking of Materials*, Metals Society, University of Surrey, p. 113 (1977).

18. T.H. Sanders, Jr., *et al*., *Effect of Microstructure on Fatigue Crack Growth of 7xxx Aluminum Alloys Under Constant Amplitude and Spectrum Loading*, Report 56-78-AF8, Contract N00019-76-C-0482, Aluminum Company of America, ALCOA Center, PA, (April, 1978).

19. Newman, J. C., and J. Raju, I. S., “Stress-Intensity Factor Equations for Cracks in Three-Dimensional Finite Bodies”, Fracture Mechanics: Fourteenth Symposium-Volume 1: Theory and Analysis. ASM STP 791, (1983) pp. I-238-I-265.

20. John, R., Personal communication, AFRL, Wright Patterson Air Force Base, Ohio.

21. Simon, L. B., “Influence of Pitting Corrosion on the Loss of Structural Integrity in Aluminum Alloy 2024-T3”, Master’s Thesis

22. Wilson, L., Quantitative Analysis: Gravimetric, Volumetric and Instrumental Analysis, 3rd Edition, Mohican Textbook Publishing Co., Loudonville, Ohio, (1995) pp. 50-58.

23. Shankaran, K. Shankaran. “Validation of Accelerated Corrosion Tests for Aging Aircraft Life Prediction: Effects of Pitting Corrosion on the Mechanical Behavior of 7075-T6 Aluminum Alloy”, Final Report, 1998, F33615-96-D-5835, Delivery Order: 0026-02, AFRL, Wright-Patterson AFB, OH.

24. Bray, G.H., Bucci, R.J., Colvin, E.L., and Kulak, M., “Effect of Prior Corrosion on the S/N Fatigue Performance of Aluminum Alloys 2024-T3 and 2524-T3”, Effects of the Environment on the Initiation of Crack Growth, ASTM STP 1298, 1997, p. 89.

FIGURES

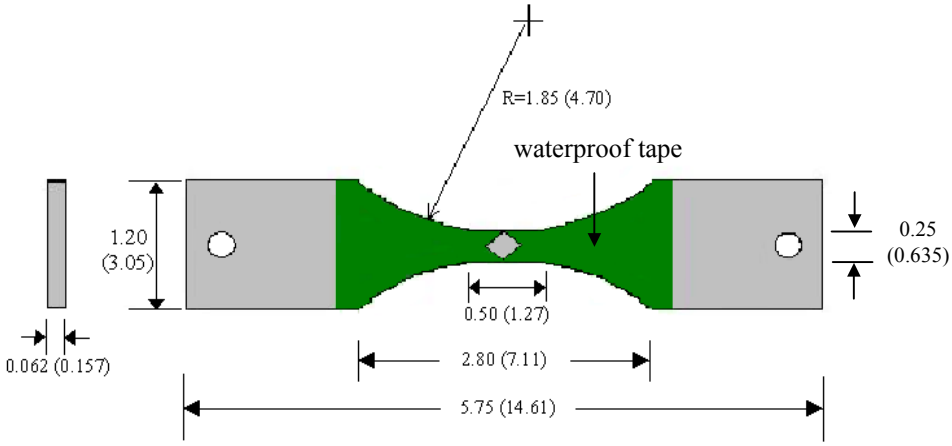

FIGURE 1. Geometry of Dog-Bone Fatigue Sample Made of AA2024-T3. Primary dimensions are in inches, and dimensions in parentheses are in cm.

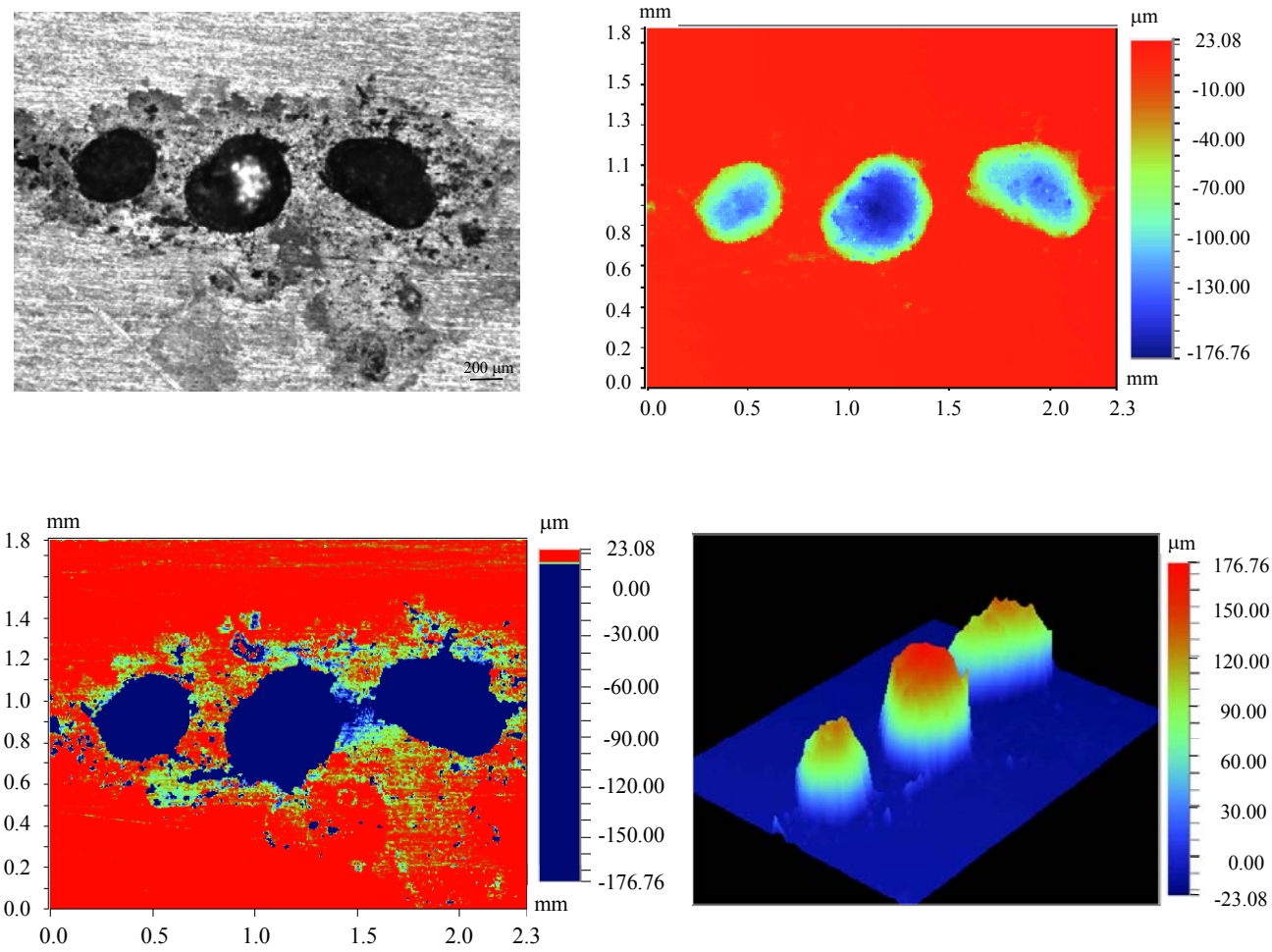

Figure 2. Characterization of Pit Morphology: (a) Optical Micrograph, (b) WLIM Surface Profile, (c) WLIM Maximum Contrast and (d) 3-D Image of the Pits.

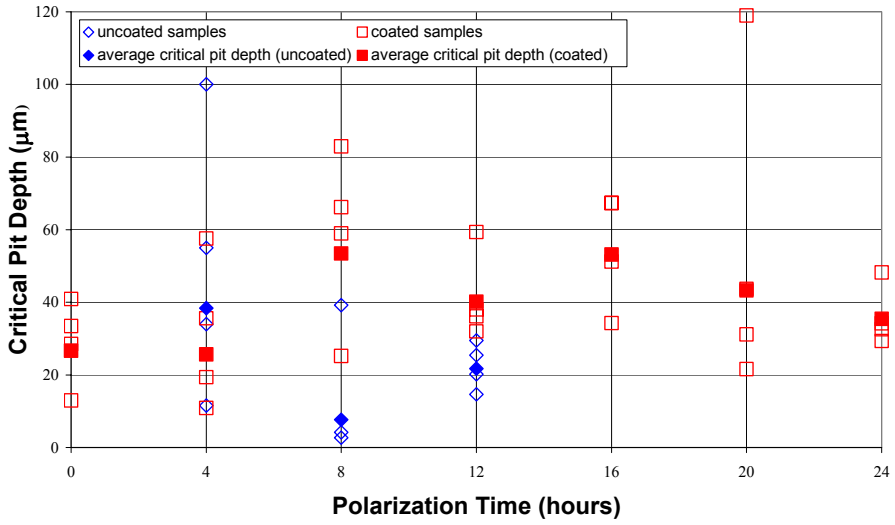

FIGURE 3. Change in Critical Pit Depth with Increasing Polarization Time.

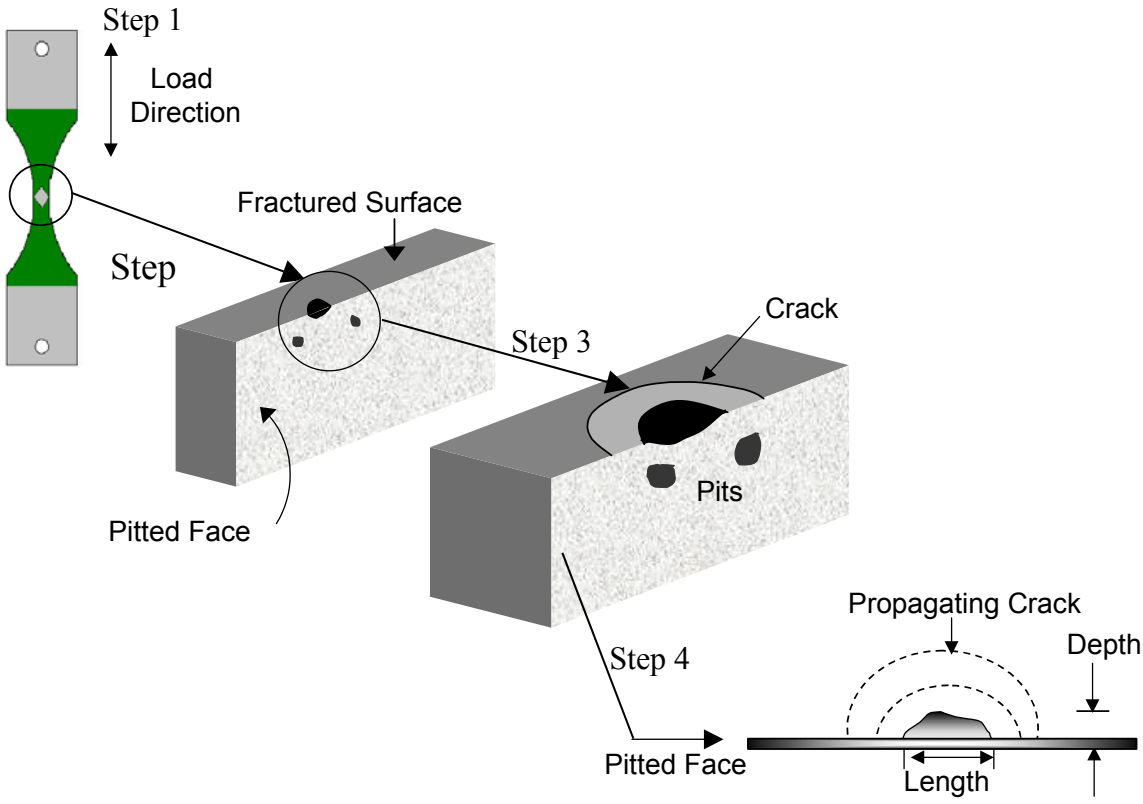

FIGURE 4. Crack Growth Schematics.

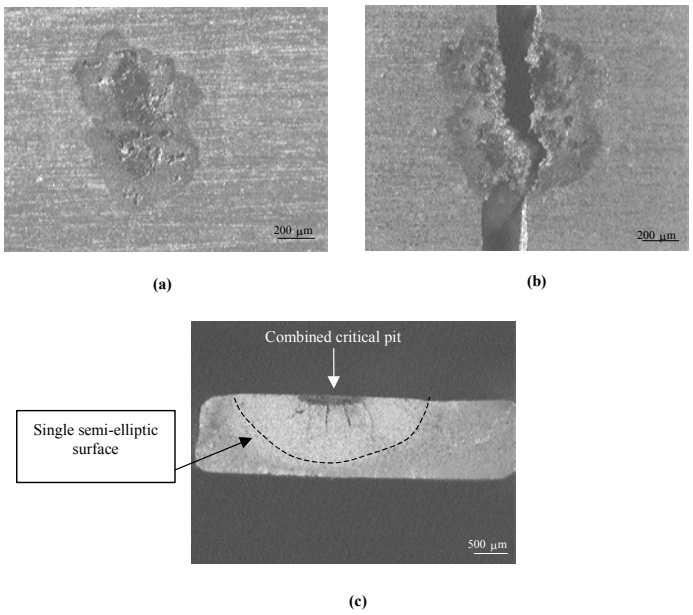

FIGURE 5. Fractured Microstop Coated Dog-Bone Sample Polarized for 20 Hours (a) Optical Micrograph of Pitted Surface Before Fracture (b) Optical Micrograph of Pitted Surface After Fracture (c) Fractured Surface Showing Semi-Elliptic Crack.

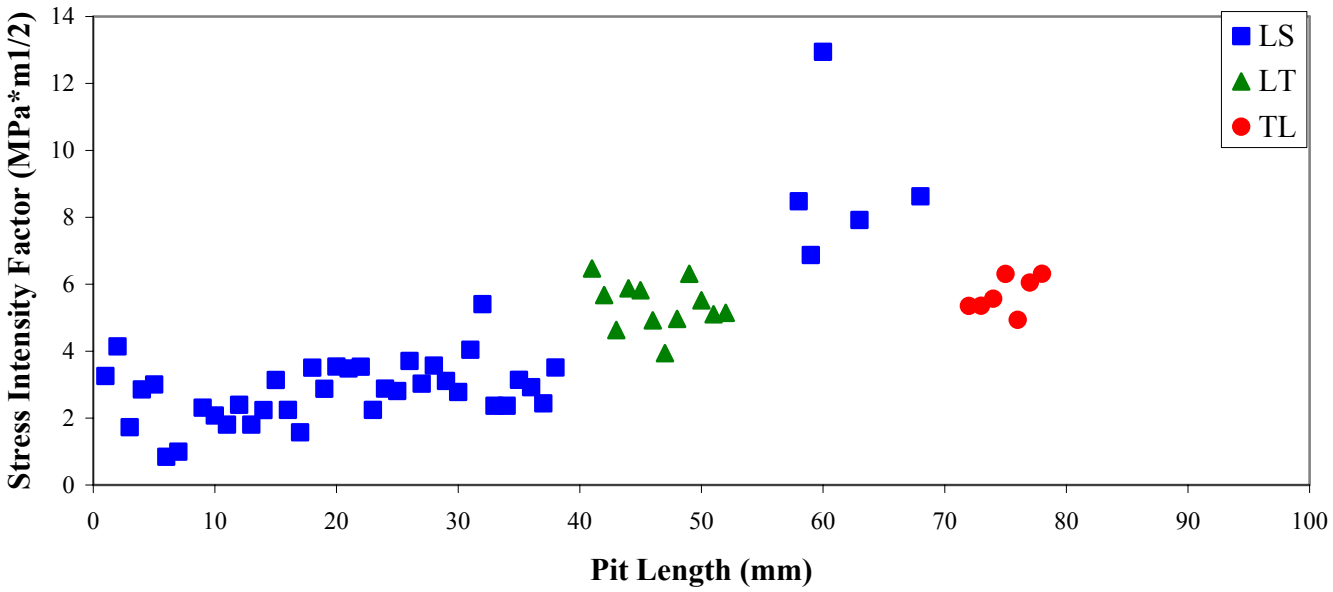

FIGURE 6. The Variation of Stress Intensity Factor with Pit Length.

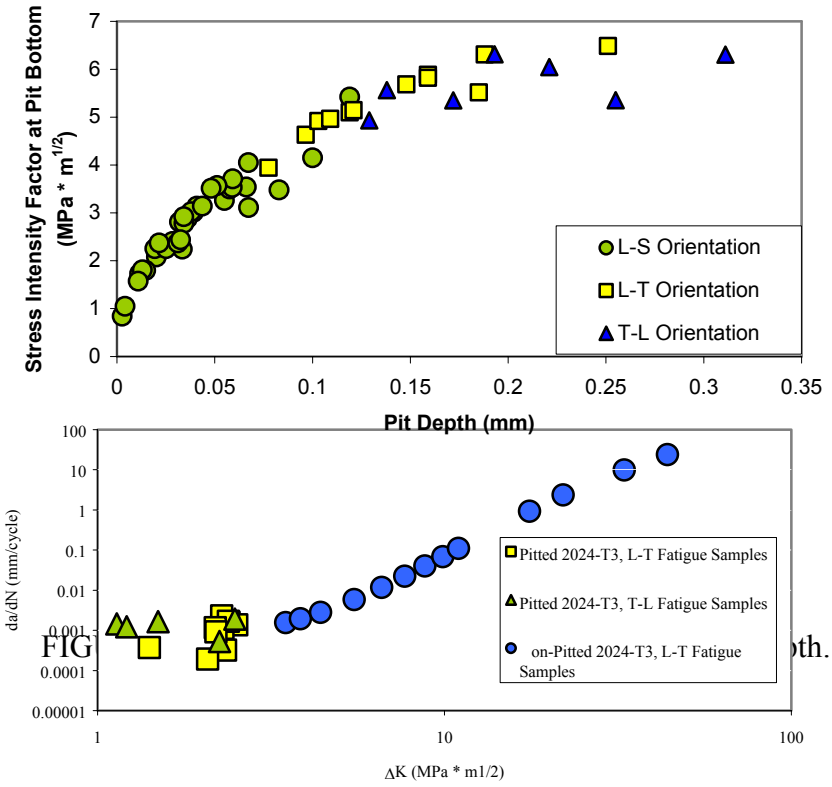

FIG th.

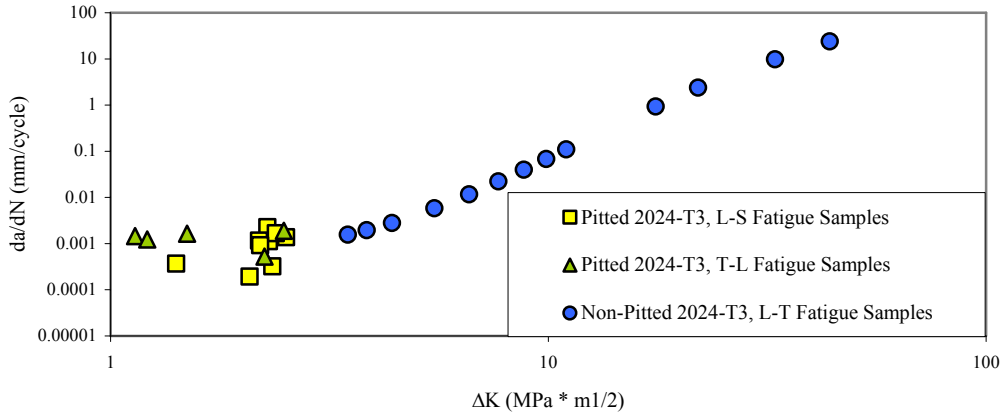

FIGURE 8. Crack-Growth Rate Versus ΔK.

CORROSION INHIBITORS FOR AEROSPACE AL ALLOYS

M. Khobaib, [1] N. Voevodin,[1] L. Kasten[1] and M. S. Donley[2]

[1]University of Dayton Research Institute, Dayton, Ohio

[2]Air Force Research Laboratories, Wright-Patterson AFB, OH

ABSTRACT

The heterogeneous microstructure of high strength aluminum alloys makes them very susceptible to localized corrosion in service environment. Hence, any long-term application of these materials requires the presence of active inhibitors. Current Air Force inhibitor paint chemistry relies heavily on the use of chromate, which is incorporated into both the surface treatment and primers. Chromium is a known carcinogen and extensive efforts are underway at the Air Force Research Laboratory to develop environmentally friendly alternatives. The main focus is directed towards organic inhibitors, which can be introduced into the primer as fixed/mobile entities. Mercaptobenzotriazole has been used for decades to inhibit the corrosion of copper and could play a role in reducing the corrosion of copper bearing AA2024-T3.

A number of amines, phosphonates, sulfonates and thiols were tested to investigate their corrosion prevention properties. Select proprietary commercial formulations were also included in this investigation. Scanning vibrating probe, anodic polarization and immersion data indicate effective inhibition provided by a number of laboratories developed formulations. Detailed surface analysis was conducted to investigate the role of thiols in forming a complex with corrosion active metal sites.

INTRODUCTION

Corrosion inhibitors are chemicals, which reduce, slow down or prevent corrosion of metallic materials in contact with corrosive environment. In the paint and coating industry, they are added mainly to primer to enhance the corrosion prevention characteristic of coatings, since paint is like a membrane and an organic coating is not a perfect barrier separating a metal substrate from its environment. Current Air Force corrosion inhibitor paint chemistry relies on the heavy use of metal chromate in the form of strontium chromate, which is incorporated into

both the surface pretreatment and the primers as highly effective corrosion inhibitor additives. Environmental regulations are forcing paint materials and processing technology to move away from chemistries involving chromates, and these compounds will soon be substantially reduced or eliminated from the paint tech base.

Chromate is the key ingredient in conversion coating of aluminum alloys and constitutes a considerable portion of primer pigment. The main reason for the widespread use of chromate conversion coatings is their self-healing nature, the ease of application and their high electrical conductivity. However, the environmental health risks associated with the use of chromate ions are prohibitive.[1] The aluminum alloys constitute most of the substrate in an aircraft structure, which require corrosion prevention scheme. Hence, all the discussion relates to the inhibition of aluminum alloys only.

Because of the increased pressure to eliminate the use of chromium, a number of alternatives have been explored for environmentally compliant corrosion prevention systems.[2] Currently sol-gel treatments, in which organometallic monomers are condensed into polymers or ceramers, are gaining acceptance as corrosion prevention surface treatments. An example of this is a polymetallosiloxane coating on an aluminum substrate.[3-4] Sol-gel films have been demonstrated as potential replacement for chromate treatments of aluminum alloys and other metals.[5-11] In a recent review article, M. Guglielmi[8] has discussed the potential of sol-gel coatings as corrosion inhibiting system for metal substrate. Other sol-gel coatings, particularly anisotropic films (changing in composition from metal substrate to top of the coating) have shown promise in corrosion resistance and substrate adhesion, but need further optimization. The sol-gel method is being applied to obtain a thin protective coating of cerate, molybdate and other rare-earth compounds on aluminum substrate through environmentally friendly process.

However, these inorganic compounds are not expected to provide long-term protection over extended period of 30+ years. Recently developed self-assembled, nano-phase particle (SNAP) sol-gel film[12] offers excellent barrier resistance to aluminum substrate, but will require the incorporation of inhibitor for any long-term protection. Hence the viable approach is to develop organic inhibitor formulations with proper functionality to be incorporated into sol-gel film as a fixed or mobile entity. The primary objective is to develop environmentally friendly organic formulation, which can provide better or equivalent corrosion prevention to aluminum alloy substrate as compared with currently used chromate compounds.

Several commercial inhibitors are available for various service applications including paints and coatings. The thrust in paint industry appears to be towards water- soluble inorganic salts. These formulations are normally combination of several classes of inhibitor compounds, some functioning as anodic and others as cathodic inhibitors. Commercial experience has shown that such combinations are often more effective due to some synergistic effect. Unfortunately most of these are optimized for specific application. On the other hand, the chemistry is generally proprietary and, the more components that make up an inhibitor formulation; the more difficult it will be to incorporate in a sol-gel film.

A large number of organic compounds have been used as corrosion inhibitors. Over 100 basic structures are noted by one reviewer.[13] A large number of these are patented and most of them are tailored for specific application. Many of these formulations are based on amines, phosphonate and sulfonate compounds. The largest classes of organic inhibitors belong to amine group. Aliphatic and aromatic amines, mono-, di-, or poly- amines and their salts, all are used as corrosion inhibitors. Organic compounds containing both N and S atoms have been reported as superior corrosion inhibitors to those containing N and S atoms alone.[14] The most popular

inhibitive formulations currently being used are based on phosphonates.[15-17] The inhibition of AA2024-T3 offers a challenge due to its complex chemistry and the leaching and redistribution of copper during some cleaning process prior to conversion coating.

A number of select commercial inhibitor formulations were investigated and some more are still being screened for their effectiveness as corrosion inhibitor for aluminum alloy. Promising results were obtained from some formulations developed in our laboratory. Almost all the testing was done in 3.5 percent NaCl solution. The first and foremost criterion in the selection of inhibitor was the question of toxicity.

EXPERIMENTAL

Since the inhibitor was being developed for incorporation into a sol-gel film intended to replace the currently used chromate conversion coating, the high strength AA2024-T3 was selected as the test substrate. Standard 60 x 30 x 3.125 mm test coupons were used for immersion tests. Potentiodynamic polarization tests were conducted on 100 mm square area exposed to the electrolyte. The specimen was carefully mounted on a commercially available electrochemical test set up. A smaller area of 5 mm x 5 mm was used for scanning vibrating electrode technique (SVET) test. All the specimens were polished with emery paper upto 600 grit, cleaned thoroughly in acetone and alcohol, and in several instances finally degreased with petroleum ether. The specimen for surface analysis was polished to a mirror finish of 6 micron.

The polarization tests were carried out in accordance with ASTM standard G5-72, “Standard Recommended Practice for Standard Reference Method for Making Potentiostatic and Potentiodynamic Standardization Measurements”. The measurements were conducted using

Gamry Inc., CMS 100 electrochemical system. SVET tests were conducted using Applicable Electronics Model 1200.

RESULTS AND DISCUSSION

From the hundreds of immersion, polarization and SVET tests that were conducted in this investigation, a number of representative results have been chosen for discussion in the paper. It is important to understand that optimizing inhibitor formulations for aggressive environment such as 3.5 percent NaCl solution in water requires much more than conducting these discriminating tests. However, the results provide important information for select down process.

The immersion tests were used as foolproof test and the criterion for pass-fail was based entirely on visual inspection. Some of the samples were continuously immersed in 3.5 percent NaCl solution along with inhibitor for over a year with intermittent visual inspection.

Figure 1 compares the anodic polarization behavior of AA2024-T3 in 3.5 percent NaCl solution with two percent piperidine and two percent phosphonate compounds. Both these are mixed in 3.5 percent NaCl solution. Again the passivation offered by piperidine compound is quite clear. However, the open circuit potential is noted to shift cathodic. Again the surface of the specimen had a dark adherent layer. The protective nature of the film is shown in Figure 2. Figure 2 shows SVET scans of a panel treated in 1.0 percent piperidine solution for 24 hours followed by an air drying of 24 hours at room temperature, which was immersed in 3.5 percent NaCl solution. Hardly any current response is noted after the initial 15 minutes of exposure. The current density remains very low almost to the level of noise even after 24 hours of exposure, as shown in Figure 2b. The corrosion resistance and the throwing power of piperidine

film were tested by creating a dent to expose the fresh alloy in the center of the panel. Figure 3 shows the results of SVET scans from such a panel immersed in 3.5 percent NaCl. Initially, a current peak corresponding to the freshly exposed area is observed as shown in Figure 3a. This high current density drops down with time as shown in Figure 3b and almost no corrosion activity is observed after 27 hours of exposure as seen in Figure 3c.

The immersion results of the phosphonate base formulations were very promising and several other compounds were studied. Figure 4 shows the structures of few select compounds. The comparative polarization behavior of two phosphonate compounds is shown in Figure 5. The diphosphonate appears to provide higher passivity, although its open circuit potential dips cathodic. Figure 6 shows a similar plot for high strength AA7075-T6. It is quite clear from these two plots (Figures 5 and 6) that the inhibition offered to AA7075-T6 by both phosphonate compounds is better for AA7075-T6. The immersion results also showed such a trend.[18] Hence, the remaining study was concentrated on AA2024-T3.

The inhibitor efficiency of the phosphonate base formulation was increased by small addition of sodium mercapto benzo thiazole (NaMBT).[18] NaMBT has been used for inhibition of copper and apparently a small addition of NaMBT to 3.5 percent NaCl restricts the galvanic action of Cu present in the precipitates distributed all over the surface of AA2024-T3. Figure 7 shows the structure of few select thiols which were studied for their effectiveness in inhibiting the corrosion of AA2024-T3 in an aggressive solution of 3.5 percent NaCl. The interesting point is to note that in some cases both N and S can form bond with active metal sites of AA2024-T3, while in other case only S is available to do so. Figure 8 shows the comparison of the polarization behaviors of AA2024-T3 in 0.2 percent thiol + 3.0 percent phosphonate and 0.2 percent thiol + 0.3 percent imidazole with 1.0 percent sodium dichromate in 3.5 percent NaCl

solution after an exposure of one hour. Small difference in the behavior is noted and 1.0 percent sodium dichromate shows slightly better inhibitive properties over the other two formulations. However, the situation changes with longer exposure and a mixture of 0.2 percent thiol + 0.3 percent imidazole shows the best performance after 24 hours exposure as shown in Figure 9. The open circuit potential is nearly 250 mV more noble than that produced by 1.0 percent sodium dichromate, and the current at passivity is also reduced by over five times. The mixture of thiol+ phosphonate also over performs 1.0 percent sodium chromate in longer exposure. No sign of corrosion was observed after nine months of exposure for all three formulations and the coupons appear as bright and shiny as when they were initially immersed.

The behavior of thiol base formulation was studied by SVET also. Figure 10 shows SVET scans, both in two (Figure 10a) and three dimensions (Figure 10b) for a SNAP sol-gel coated AA2024-T3 panel. The panel was exposed to a very aggressive solution of a mixture of dilute Harrison and 2.0 percent CuCl2 solution. The high current density of over 600mAmp/cm2 can be easily noticed. Figure 11 shows SVET scans of the same panel after the introduction of the inhibitor (0.2 percent thiol + 0.3 percent imidazole). The corrosion current completely subsides and no current activity is noticed after one hour (Figure 11a) of exposure. Little or no current activity is observed after 24 hours of exposure as shown in Figure 11b. The specimen was left exposed for five days and Figure 12 shows the 3-D scan (Figure 12a) and current vector overlay (Figure 12b). No current activity was observed for such an extended period indicating excellent inhibition.

Figures 13–15 show the results of surface analyses of a polished AA2024-T3 specimen exposed to 3.5 percent NaCl solution with a mixture of 0.2 percent thiol + 0.3 percent imidazole. The surface of this specimen was analyzed just after polishing before any treatment and again

after it was immersed in the inhibited electrolyte. Figure 13 shows a representative SEM photograph of this polished untreated specimen. Two areas of interest were selected and marked for identification. Area 1 shows a large precipitates, while area 2 represents the background. Figure 14 (a and b) shows XPS scan of area 1, before (Figure 14a) and after (Figure 14b) 40 hours of immersion in the inhibited bath. The amounts of Cu, Mg and Fe are noted to be significantly reduced after the treatment. Figure 15 shows similar spectra for area 2 and the results are very encouraging. Although no Fe is observed in either case, and the amount of Cu and Mg in the untreated case is lower than that present in area 1, it must be noted that Cu and Mg is completely absent after the treatment in this case also. This could be the result of complete surface coverage with thin layer of adsorbed inhibitor or there could be selective inhibitor adsorption to Cu, Mg and Fe sites. There is a remote possibility of Cu, Mg and Fe chelation followed by dissolution into the electrolyte. More work is needed before a meaningful conclusion can be made.

REFERENCES

1. Sax, N.J, "Dangerous Properties of Industrial Materials", 5th ed., New York: Van Nostrand Reinhold, 1993.

2. Jeffcoate, C.S., Voevodin, N.N., Khobaib, M., Reynolds, L.B., Kuhn, W.K., and Donley, M.S., "Trends in Future Nonchromate Corrosion Inhibitors", Proceedings of 43rd Int. SAMPE Symposium, May 31 - June 4, 1998, Anaheim.

3. Lizlovs, E.A, Corrosion 32 (1976): 263.

4. Parkhill, R.L., Reynolds, L.B., Grebasch, N., Khobaib, M., Kuhn, W.K., Knobbe, E.T., Liang, J.D., and Donley, M.S., "Corrosion Resistant Sol-gel Coatings for Aircraft Aluminum Alloys", The Symposium: Proceedings of 1997 Tri-Service Corrosion, Nov 17-21, 1997, Wrightsville Beach, NC.

5. Kato, K., "Enhancement of the Corrosion Resistance of Substrate by Thin SiO2 Coatings Prepared from Alkoxide Solution without Catalyst", J. Mater. Sci. 28, 4033 (1993)

6. Sugama, T., and Taylor, C., "Pyrolysis-induced Polymetallosiloxane Coatings for Aluminum Substrates", J. of Mater. Sci. 27, 1723-34 (1993).

7. Schmidt, H., and Wolter, H., "Organically Modified Ceramics and their Applications", J. Non-Cryst. Solids, 121, 428-35 (1990).

8. Guglielmi, M., "Sol-gel Coatings on Metals", J. Sol-gel Sci. & Tech. 8, 443-49, (1997)

9. Atik, M., Luna, F.P., Messaddeq, S.H., and Aegerter, M.A., "Ormocer (ZrO2-PMMA) Films of Stainless Steel Corrosion Protection", J. Sol-gel Sci. & Tech. 8, 517-522, (1997).

10. De Santics, O., Gomez, L., Pellegri, N., Parodi, C., Marajofsky, A., and Duran, A., "Protective Glass Coatings on Metallic Substrates", J. Non-Cryst. Sol. 121, 338-43, (1990).

11. Barrow, D., Applications of Sol-gel Ceramic Coatings", Key Eng. Mater. 122-124, 443-50, (1990).

12. Vreugdenhil, A.J., Balbyshev, V.N., and Donley, M.S., J. of Coatings Technology, vol 73, No. 915, April 2001.

13. Rigg.Jr. O. L., Corrosion Inhibitors (Houston, TX. NACE, 1973), p. 7-27

14. Quaraishi, M. A., Khan, M. A. W., Ajmal, M., Muralidharan, S., and Iyer, S. V. K., "Influence of Molecular Structure of Substituted Benzothiozoles on Corrosion Inhibition and Permeation Through Mild Steel in Sulfuric Acid", Brit. Corros. J. , 32 (1997), p. 72.

15. Thevissen, P., Cleuren, W., De Crom, A., Coleman, I., and Kerremans, S., "Development of an All Organic Program for Open Evaporation Cooling Water Systems Based on a New Copolymer", Proc. 7 SEIC Ann. Univ. Ferrara, N. S. Sez. V, Suppl. 9 (Ferrara, Italy, Univ. Fertrara, 1990), p. 485.

16. Kuznetsow, Yu. I., Trunov, E. A., and Isaev, V. A., "Protection of Low-Carbon Steel by Zinc Phosphatews", Prot. Met. 23 (1987), p. 63.

17. Boffardi, B. P., "Control of Environmental Variables in Water Recirculating Systems", in Metals Handbook, vol. 13, 9^{th} ed. (Materials Park, OH., ASM International. 1987), p. 494.

18. Khobaib, M., Voevodin, N., and Donley, M.S., "Organic Inhibitors for High Strength Al-Alloys", Proceedings of 2000 DoD/Industry Aerospace Coatings Conference, May 21-25, 2000, Norfolk, VA.

FIGURES

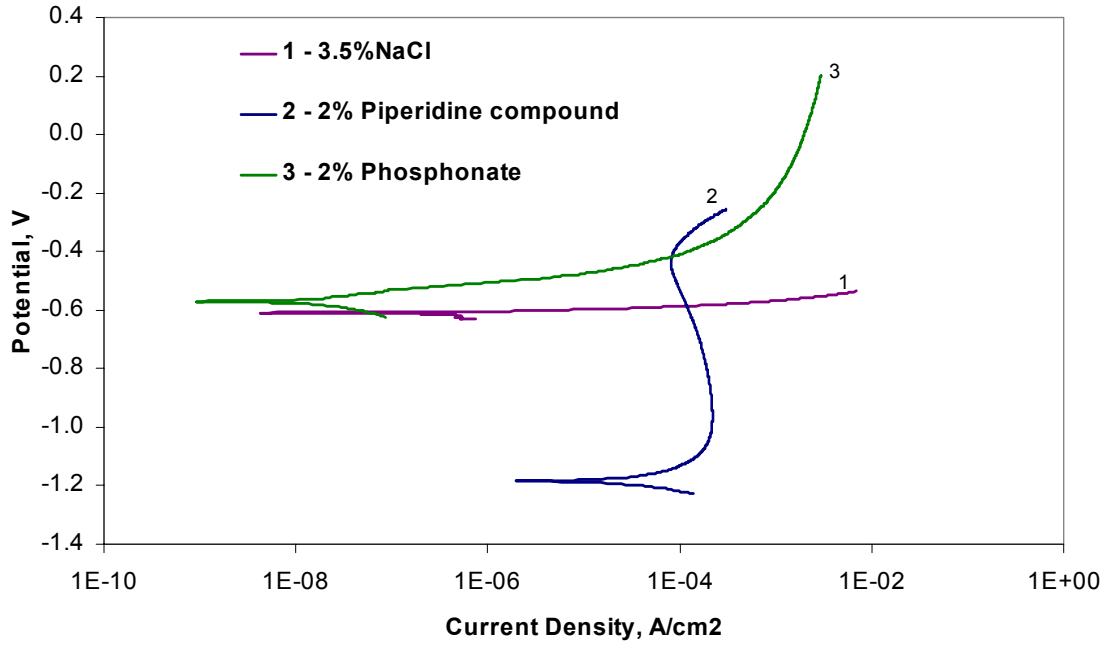

FIGURE 1. Anodic Polarization Behaviors of Al 2024-T3 in 3.5 Percent NaCl, 3.5 Percent NaCl + 2.00 Percent Piperidine and 3.5 Percent NaCl + 2.00 Percent Phosphonate Compound.

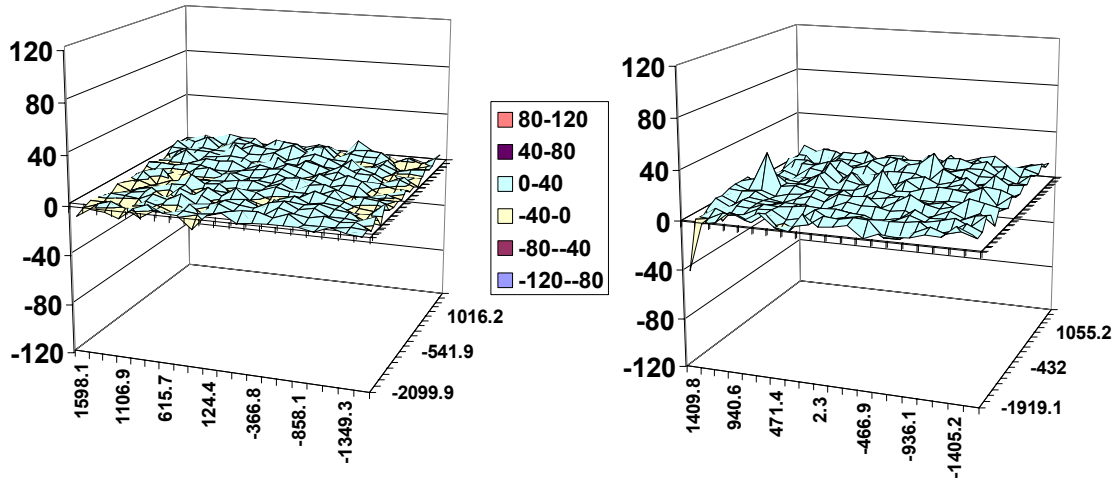

FIGURE 2. SVET Scans of 1.0 Percent Piperidine Treated AA2024-T3 Panel Exposed to 3.5 Percent NaCl Solution.

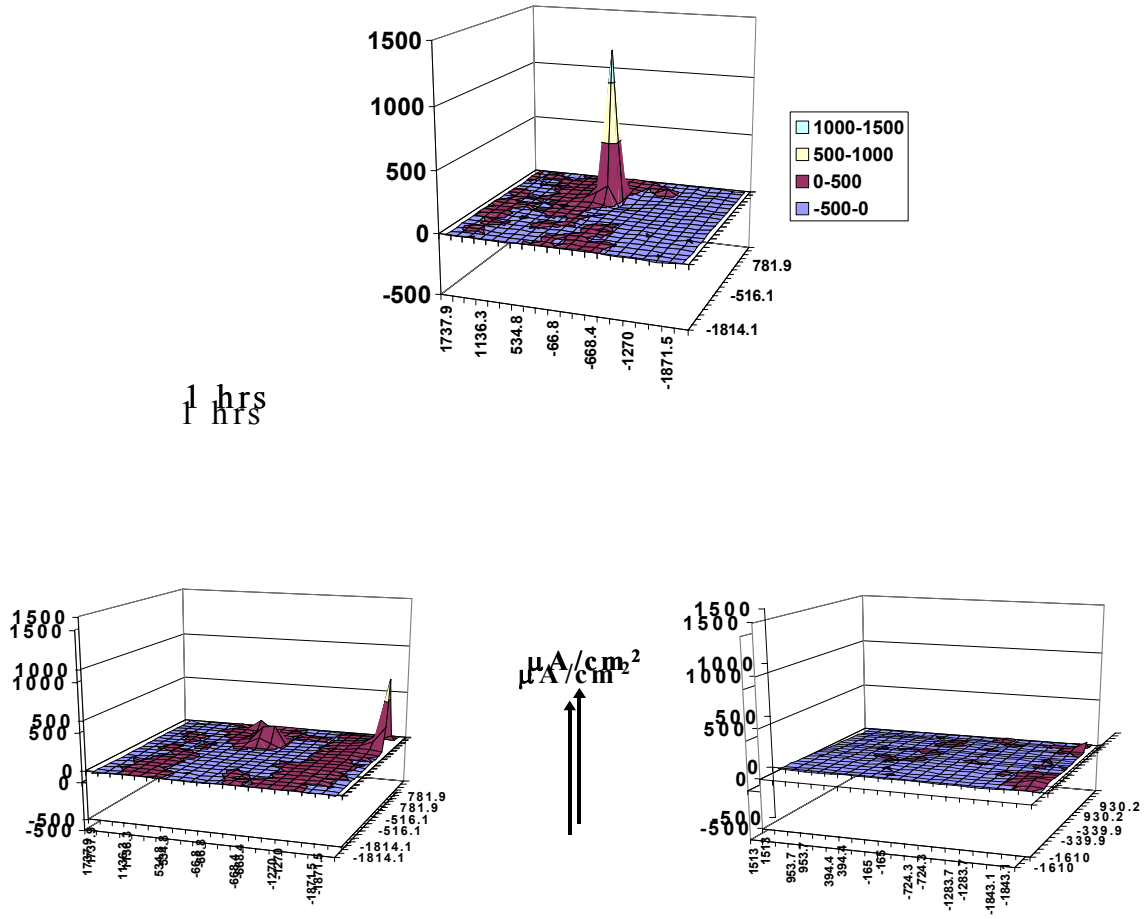

FIGURE 3. SVET Maps of an AA2024-T3 Panel Treated with 1.0 Percent Piperidine Solution, Followed by Exposure in Inhibited Solution.

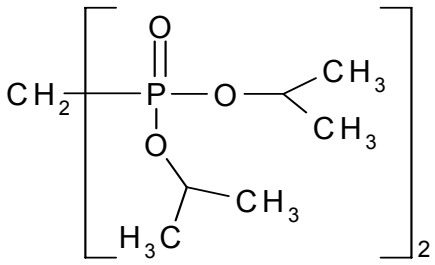

Tetraisopropyl Methylenediphosphonate

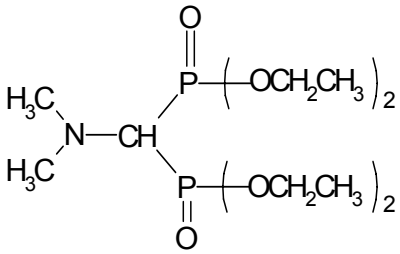

Tetraethyl Dimethylenediphosphonate

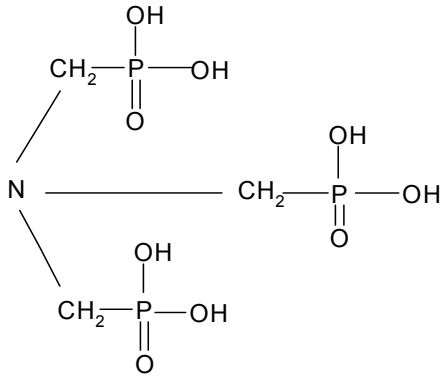

Amino-tris-methylenephosphonic Acid

FIGURE 4. Chemical Structures of Three Select Phosphonate Compounds.

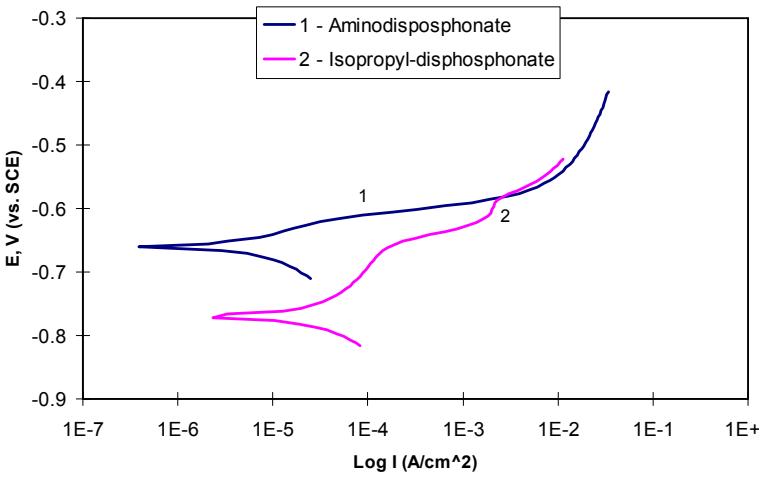

FIGURE 5. Comparative Polarization Scans of AA2024-T3 Inhibited by Two Phosphonate Base Compounds.

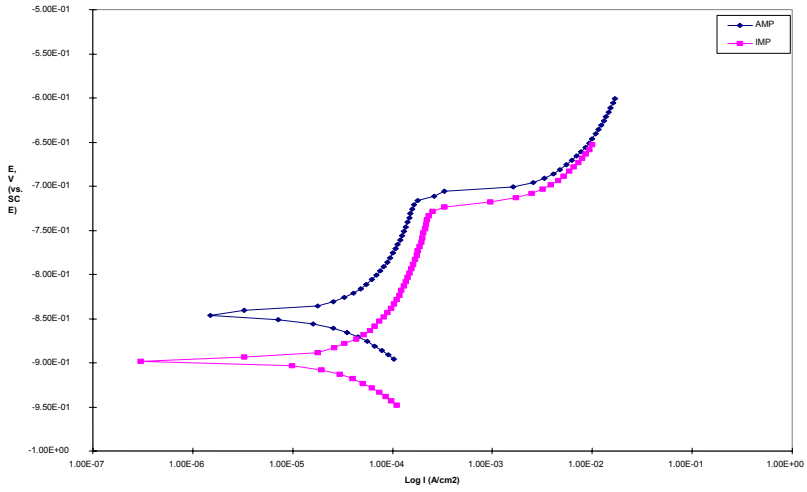

FIGURE 6. Comparative Polarization Scans of AA7075-T6 Inhibited by Two Phosphonate Base Compounds.

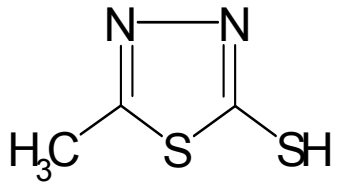

2-Mercapto-5-Methyl-1,3,4-Thiazol

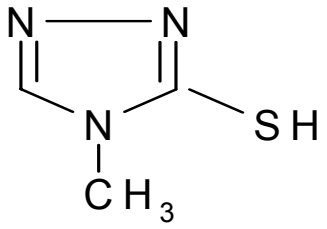

3-Mercapto-4-Methyl-1,2,4 Triazole

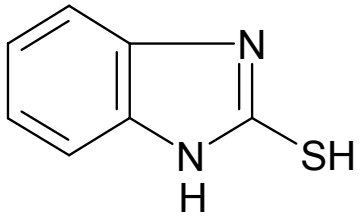

Mercaptobenzimidazole

FIGURE 7. Chemical Structures of Select Thiols.

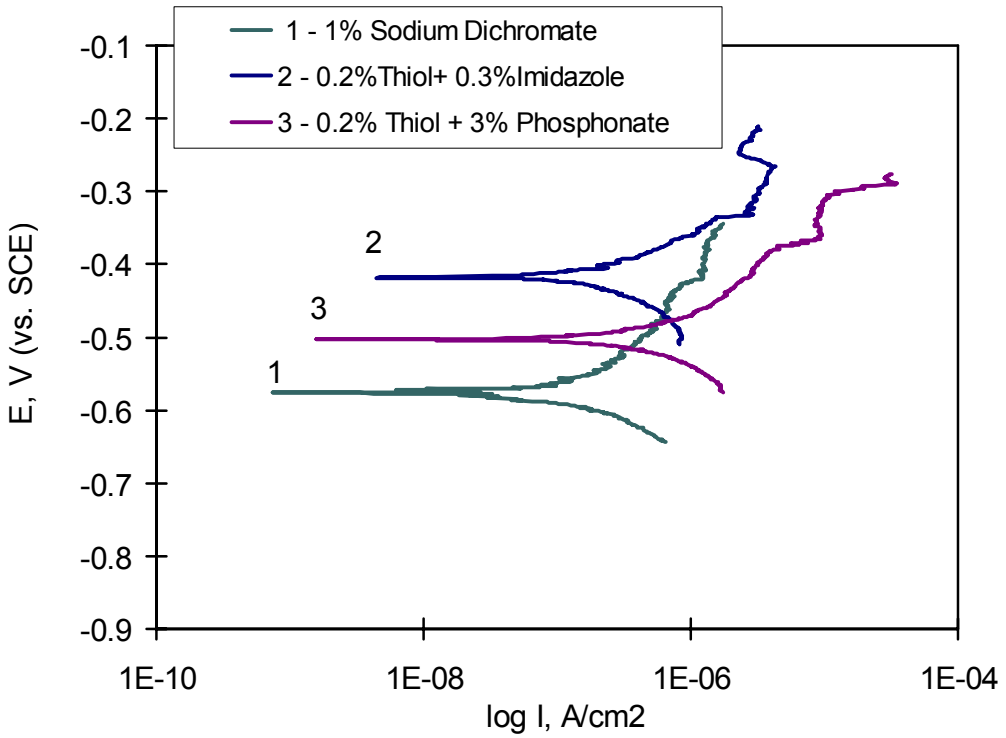

FIGURE 8. Comparative Polarization Behaviors of AA2024-T3 in 1.0 Percent Sodium Dichromate, 0.2 Percent Thiol + 0.3 Percent Imidazole and 0.2 Percent Thiol + 3.0 Percent Phosphonate with 3.5 Percent NaCl, after One Hour Exposure.

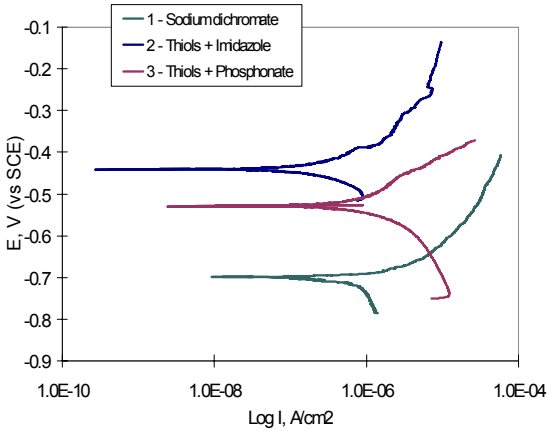

FIGURE 9. Comparative Polarization Behaviors of AA2024-T3 in 1.0 Percent Sodium Dichromate, 0.2 Percent Thiol + 0.3 Percent Imidazole and 0.2 Percent Thiol + 3.0 Percent Phosphonate with 3.5 Percent NaCl, after 24 Hours of Exposure.

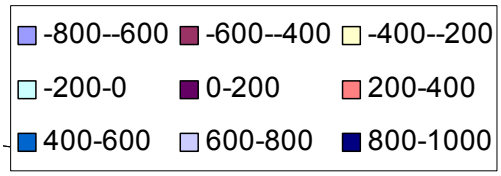

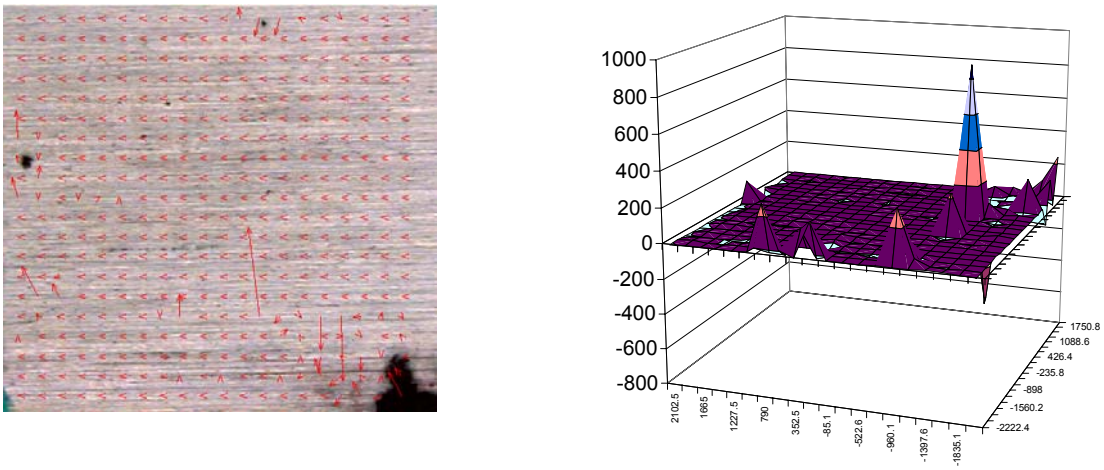

FIGURE 10. SVET Maps of SNAP Coated AA2024-T3 Exposed to a Mixture of Diluted Harrison's + 2.0 Percent $CuCl_2$.

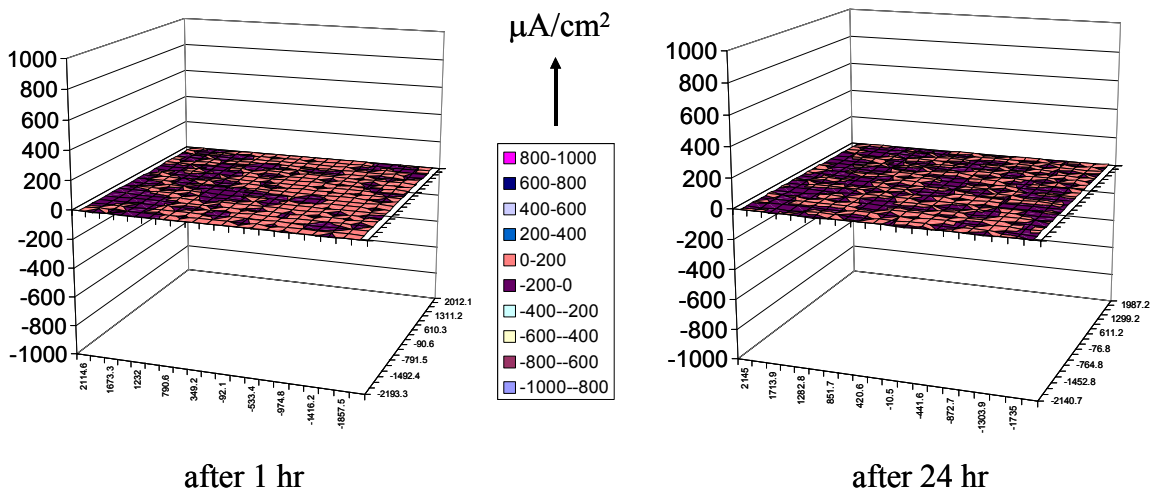

FIGURE 11 SVET Maps of SNAP Coated AA2024-T3 Exposed to Electrolyte in Figure 10 Along with 0.2 Percent Thiol + 0.3 Percent Imidazole.

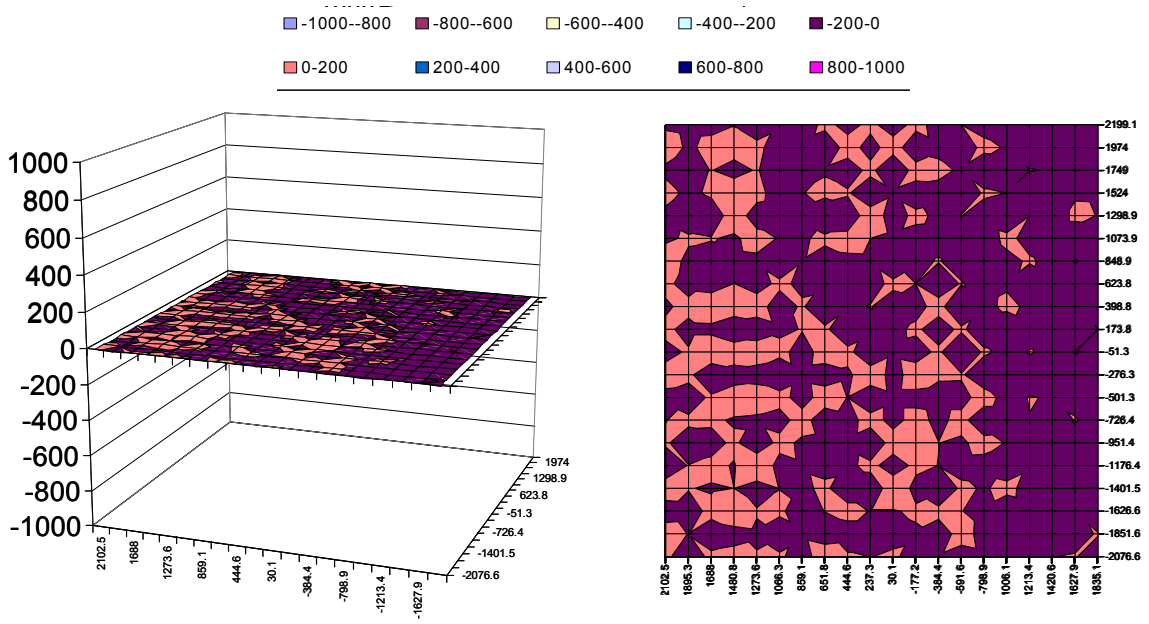

FIGURE 12. SVET Maps of SNAP Coated AA2024-T3 Exposed to Electrolyte in Figure 10 Along with 0.2 Percent Thiol + 0.3 Percent Imidazole, Exposed for Five Days.

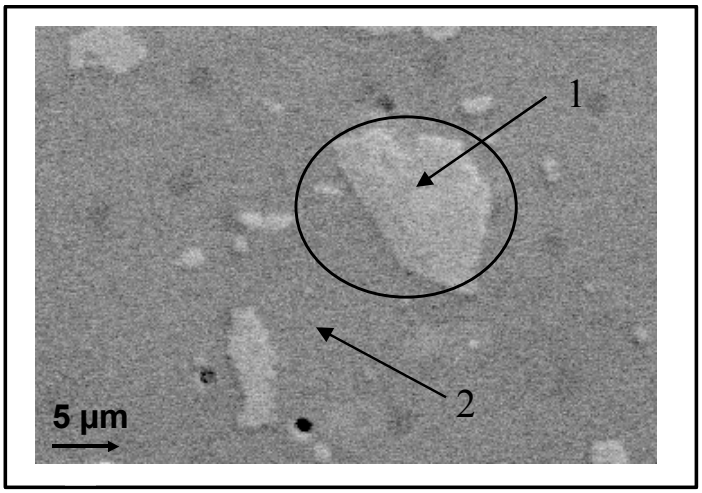

FIGURE 13. SEM Photograph Showing the Select Precipitate Area and the Background.

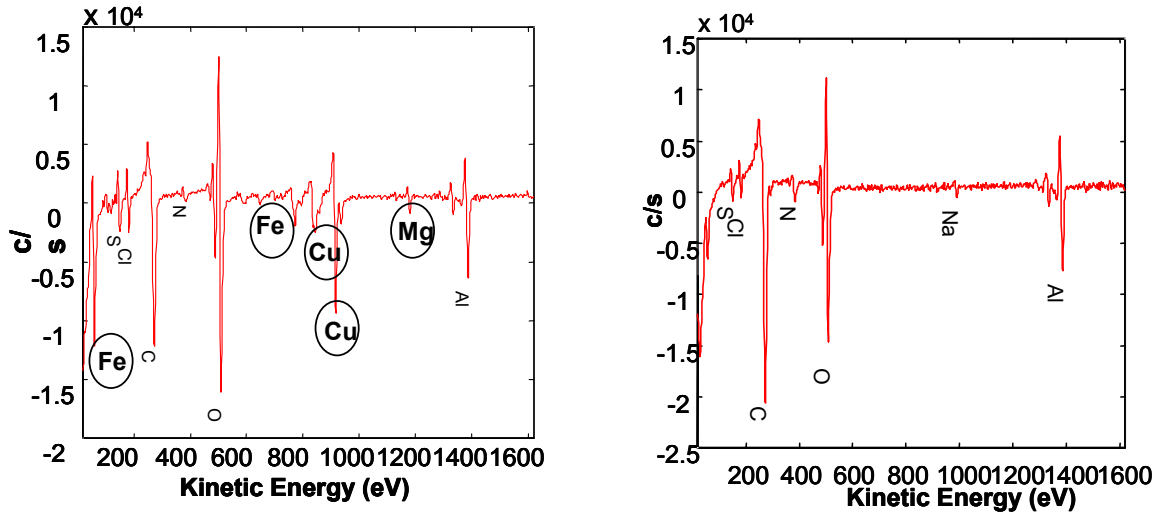

(a) (b)

FIGURE 14. XPS Spectra of AA2024-T3 Surface; (a) Untreated and (b) Treated with Inhibitor.

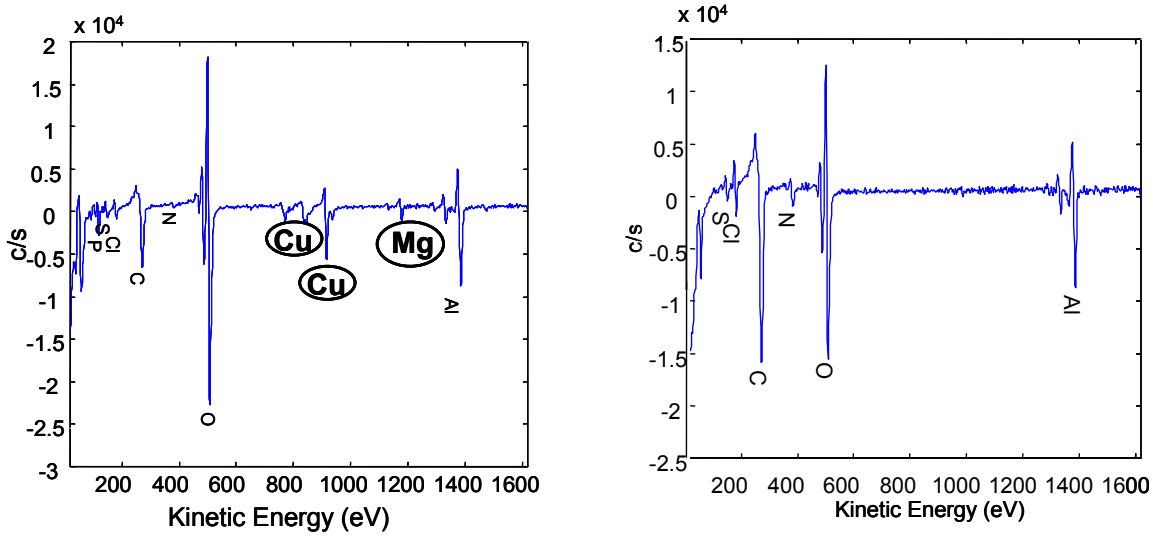

(a) (b)

FIGURE 15. AES of Area 2 of Figure 13; (a) Before Treatment and (b) After Inhibitor Treatment AA2024-T3.

MECHANISMS OF MILITARY COATINGS DEGRADATION (PP-1133) ELECTROCHEMICAL IMPEDANCE SPECTROSCOPY SUBTASK

Kevin J. Kovaleski

Naval Air Warfare Center Aircraft Division, Patuxent River, MD
Kevin J. Kovaleski, NAWCAD Principal Investigator,
Edward W. Lipnickas, Navmar Applied Sciences
Bldg. 2188
Aerospace Materials Division
NAWCAD
48066 Shaw Road Unit 5
Patuxent River, MD 20670-1908
Phone: (301) 342-8049
E-mail: kovaleskikj@navair.navy.mil

BACKGROUND

Due to environmental restrictions, coatings research has focused on the development of systems with less organic solvents and toxic corrosion inhibitors. This fact has caused concerns in the user communities that the new coating systems will not provide the same level of protection as their non-environmentally compliant counterparts under the harsh operating conditions experienced by the military. A better understanding of how coatings degrade needs to be developed to insure that new systems will be designed that meet or exceed the performance of the older systems while reducing volatile organic compounds (VOCs) and toxic corrosion inhibitors.

OBJECTIVE

This project was initiated to identify, model, and predict degradation mechanisms that lead to military coating system failures and force depaint/paint operations to occur. Efforts will

focus on primer/topcoat systems that are being fielded to comply with environmental legislation and regulations. Two important failure modes that lead to repainting were examined. First, degradation of topcoat appearance and protective ability due to exposure to ultraviolet radiation and moisture was quantified and modeled. Also, the effect of topcoat degradation on corrosion resistance and primer-substrate adhesion was analyzed quantitatively and related to service life. Accelerated testing methodologies were developed and implemented to facilitate a more rapid fielding of future environmentally compliant coating systems with greater confidence and understanding.

During FY 2001, sample preparation was completed. Characterization of the coating system behavior utilizing electrochemical impedance spectroscopy (EIS) for both standard and environmentally friendly coating systems was completed. In addition, wet tape adhesion tests were performed on panels subjected to laboratory and static field aging.

TECHNICAL APPROACH

EIS data were obtained in accordance with the Aerospace Materials Division's Quality Manual using a standardized procedure. The EIS system consisted of an EG&G Princeton Applied Research Model 283 potentiostat/galvanostat interfaced to a computer-controlled EG&G Princeton Applied Research Model 1025 frequency response detector. The impedance spectra were determined from 1 MHz to 0.01 Hz using AC amplitude of 50mV at open circuit DC potential. A schematic diagram of the apparatus is shown in Figure 1.

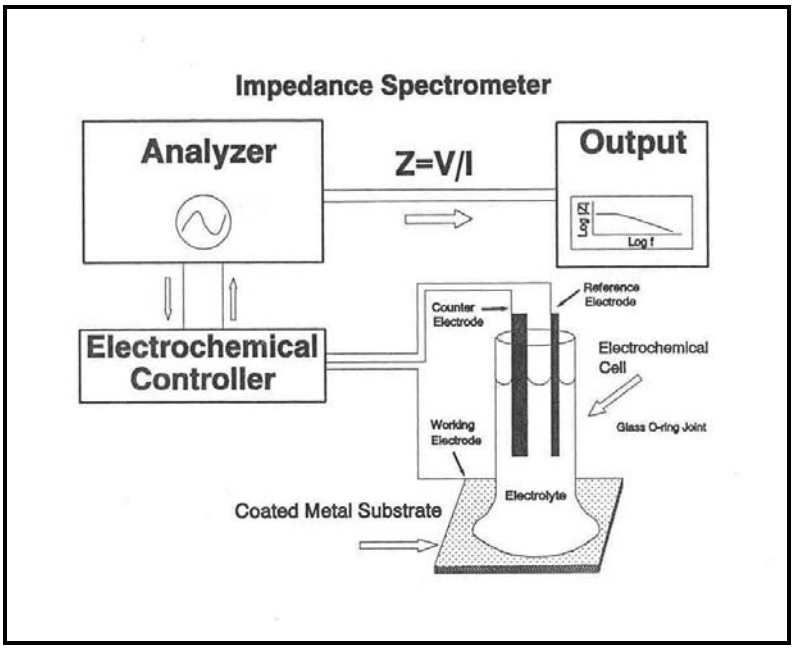

FIGURE 1. Schematic diagram of the EIS experimental set-up.

The cell was a glass cylinder clamped and O-ring sealed to the sample surface, as shown in Figure 1 above. The seal exposed 7.75 cm^2 of sample surface area to the test solution medium. The reference electrode was saturated calomel and a platinum wire/disk assembly served as the counter electrode.

Baseline samples were conditioned by continuous immersion using the assembly above in either 3.5% NaCl solution or a solution of 1% NaCl and 0.1% $CaCl_2$ (GM9540P). Measurements were made after 1, 4, and 7 days, then after 2, 4, 8, 12, and 16 weeks.

EIS was performed on panels that were exposed to either laboratory or static field aging. Different sets of laboratory-aged panels were exposed to neutral salt spray/fog (ASTM B 117), accelerated artificial weathering (QUV-A), and cyclic corrosion (GM9540P). Different sets of static field-aged panels were exposed at sites in Arizona, and Florida. The laboratory and static field-aged samples were conditioned by immersion using the assembly above for one hour in 3.5% NaCl solution before the EIS measurements were made.

Four EIS spectra were obtained for each coating system for each baseline interval and each laboratory/static field exposure test to ensure reproducibility of the data. Due to time constraints and good reproducibility, it was determined during the testing that only two spectra would suffice for the purposes stated above. For simplicity, one representative EIS spectrum per coating system was fitted for each exposure condition for tests conducted after laboratory/field aging and for each time interval for both solutions for specimens under immersed conditions.

Wet tape adhesion tests were performed on laboratory/field-aged panels following the EIS tests. The tests were performed in the center of the panel, between the areas where the electrochemical cell was attached. These tests were conducted in accordance with the Aerospace Materials Division's Quality Manual using a standardized procedure. The panels were immersed in distilled water at 120°F for four days and inspected for peel away and blistering. Peel away was evaluated as per ASTM D 3359, Method A and blistering was evaluated as per ASTM D 714.

Coating systems are summarized in Table 1. Exposure was quantified in time for samples subjected to neutral salt spray and cyclic corrosion tests. For QUV-A and field aging the exposure was quantified in UV irradiance. Wet tape adhesion data is summarized elsewhere.[1]

TABLE 1.
Summary of coatings evaluated in program.

Coating System	Primer	Topcoat	Substrate	Description
A	MIL-P-53022	MIL-C-46168, Type IV	Steel	Army Control
B	MIL-P-53030	MIL-C-64159	Steel	Army Future
C	MIL-PRF-23377, Type II, Class C	MIL-PRF-85285, Type I	Aluminum	Navy/AF Control
*D	MIL-PRF-85582, Type II, Class N	Deft Zero-VOC Topcoat	Aluminum	Navy Future

*Coating D was found to have poor performance and the IR signature of properly formulated Coating D versus the questionable sample was investigated. A strong signature for epoxy component A (polymer of diglycidyl ether of bisphenol-A) was found, which normally disappears when properly mixed with component B for the primer portion. Hence, it was concluded that improper mixing of the 2 components caused poor primer adhesion resulting from insufficient cure.

The EIS data for waterborne coatings B,D was initially fit to a 7-element circuit [2]. It is desirable to have as few elements as possible while maintaining a minimal systematic deviation between measured and fitted result[3]. After further investigation it was decided to refit the data to a 5-element circuit (Figure 2) for the following reasons: EIS published in literature generally use 100 kHz as the high frequency limit; this is because most systems are only capable of handling data up to this frequency. The system consists of a frequency response analyzer interfaced to a potentiostat to make the impedance measurements over a frequency range. The potentiostats used cannot make reliable measurements at frequencies above 100 kHz and thus the data in the 100 kHz to 1 MHz range was questionable. Fitting the program in this area resulted in an additional time constant in the100 kHz to 1 MHz interval, necessitating a 7-element circuit. By eliminating the frequencies in the 100 kHz to 1 MHz range, the data was successfully fitted (including D coatings) to the circuit in Figure 2.

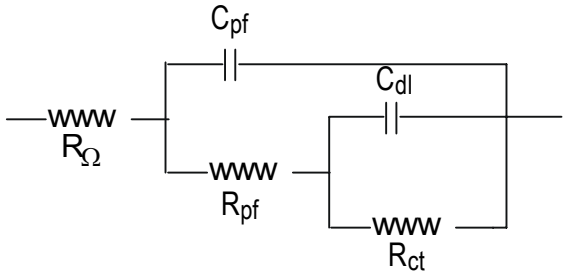

FIGURE 2. 5-Element Equivalent Circuit model

The equivalent circuit model (ECM) was utilized to determine resistive and capacitive parameters and their logarithmic values plotted vs. time/UV exposure. Capacitances were fit using constant phase elements (CPE's), a circuit element that more accurately describes the behavior of the "real world " systems. These systems are generally inhomogeneous (porous) and the true "capacitance" is a distribution of values. A factor *n,* is associated with the CPE value; it ranges from 0 to 1 and indicates the degree of inhomogeneity. A perfect capacitor would have a value of 1.0. Due to size limitations for conference papers, the EIS data appear for baseline samples immersed in 3.5% NaCl solution as Figures 1-4 in Reference 1 and for baseline samples immersed in GM9540P solution in Figures 5-8 in Reference 1. Equivalent circuit plots are presented for specimens subjected to A) neutral salt spray in Figures 9-12, B) GM9540P in Figures 13-16, C) QUV-A in Figures 17-20, D) natural exposure in Arizona in Figures 21-24, E) natural exposure in Florida in Figures 25-28. The *n* values for the CPE's are summarized in Table 3. Once again, Figures 9-28 and Table 3 are contained in Reference 1.

RESULTS

NACL AND GM9540P IMMERSIONS

Figures 3-8 are presented as examples of the ECM parameter changes as a function of exposure (immersion, QUV, B117, outdoor, etc.). The complete set of figures is contained in Reference 1. Figures 3-8 appear at the end of the "Results" section.

The ECM representing immersion behavior of Coating A panels in 3.5% NaCl solution over time (Figure 3; Figure 1, Reference 1) exhibited gradual electrolyte penetration with decreasing paint film resistance (R_{pf}) over the 16-week exposure, the most significant change in R_{pf} occurring in the 4-16 week interval. Corrosion is not significant after 16 weeks.

The ECM representing immersion behavior of Coating B panels in 3.5% NaCl solution over time (Figure 2, Reference 1) exhibited decreasing R_{pf} and increasing C_{pf} suggesting electrolyte penetration. A decreasing *n* value of the paint film at 16 weeks is observed, indicating an increasingly imperfect capacitor or paint film degradation, most likely due to larger or more numerous pores in the film. Corrosion is not significant after 16 weeks.

The ECM representing immersion behavior of Coating C panels in 3.5% NaCl solution over time (Figure 3, Reference 1) exhibited a constant R_{pf} value throughout the 4-16 week exposure. There is a sharp increase in the values of C_{dl}, and C_{pf} at 8 weeks that is attributed to solution uptake and the presence of water and ions at the coating/metal interface. However, at 16 weeks the values return to those observed at 4 weeks. The R_{ct} value remains above 10^8 Ω/cm^2 throughout and it is believed that there is very little corrosion occurring even after 16 weeks of exposure. It is unclear if the data at 8 weeks showed a significant change in the overall coating properties.

The ECM representing immersion behavior of Coating D panels in 3.5% NaCl solution over time (Figure 4, Reference 1) showed that all protective properties are destroyed after one week as indicated by the low resistance values.

The ECM representing immersion behavior of Coating A panels in GM9540P solution over time (Figure 5, Reference 1) exhibited a gradual decrease in R_{pf}, suggesting electrolyte penetration. Corrosion is not significant after 16 weeks.

The ECM representing immersion behavior of Coating B panels in GM9540P solution over time (Figure 6, Reference 1) exhibited low R_{pf} values, indicating poor barrier properties throughout the exposure. The R_{ct} values are less than 10^7 Ω/cm^2 , this is indicative of significant corrosion under the film.

The ECM representing immersion behavior of Coating C panels in GM9540P solution over time (Figure 7, Reference 1) showed no change in coating integrity over the 32-week exposure period.

The ECM representing immersion behavior of Coating D panels in GM9540P solution over time (Figure 8, Reference 1) showed that all protective properties are destroyed in one week as indicated by the low R_{pf} values.

NACL AND GM9540P CYCLIC TEST

The ECM representing Coating A panels exposed to B-117 neutral salt spray (Figure 9, Reference 1) showed at 18-48 weeks a decreasing R_{ct} and an increasing C_{dl}, indicating coating/metal interfacial activity, due to the onset of significant corrosion. A decrease in R_{pf} is observed at 12-48 weeks of exposure, indicating formation of the conductive pathways in the bulk film, this was confirmed with adhesion and blistering data (Table 2, Reference 1).

The ECM representing Coating B panels exposed to B-117 neutral salt spray (Figure 4; Figure 10, Reference 1) exhibited a decreasing R_{pf} in the 18-48 week interval, this is indicative of increasing electrolyte penetration. This coincides with changing R_{ct} and C_{dl} at 12-48 weeks, indicating significant corrosion and electrolyte at the coating/metal interface. The presence of corrosion product may be the reason for the sharp increase in R_{ct} at 48 weeks.

The ECM representing Coating C panels exposed to B-117 neutral salt spray (Figure 11, Reference 1) exhibited insignificant coating/metal interfacial activity as observed with minor changes in both R_{ct} and C_{dl} over the 0-18 week B117 exposure interval. This is confirmed with good adhesion and no observed blistering (Table 2, Reference 1). A change of R_{ct}, R_{pf} and C_{dl} in the 18-48 week interval suggests chromates filling the bulk coating pores, resulting in continuing corrosion protection.

The ECM representing Coating D panels exposed to B-117 neutral salt spray (Figure 12, Reference 1) showed that protective properties are destroyed after one week as indicated by low resistance values.

The ECM representing Coating A panels exposed to the GM 9540P cyclic corrosion test (Figure 13, Reference 1) exhibited decreasing R_{pf} up to the 3-week point, suggesting solution ingress. At 6-18 weeks decreasing R_{pf} is observed, indicating the formation of conductive pathways through the coating. Increased R_{ct} at 6-18 weeks may be due to the leaching of inhibitor from the coating to the interface and the filling of the bulk coating pores. The paint film CPE *n* value (Table 3, Reference 1) is at a minimum at the 48 week period, predicting that water, ions, and inhibitor are present at the coating/metal interface. R_{ct} is declining and corrosion of the substrate is imminent. This was confirmed with poor adhesion and blistering.

The ECM representing Coating B panels exposed to the GM9540P cyclic corrosion test (Figure 14, Reference 1) exhibited little coating/metal interfacial activity or coating degradation up to the 18-week interval. At the 18-48 week interval inhibitor may be filling the coating pores and increasing R_{pf}, resulting in continued corrosion protection.

The ECM representing Coating C panels exposed to the GM9540P cyclic corrosion test (Figure 5; Figure 15, Reference 1) exhibited insignificant coating/metal interfacial activity with minor changes in both R_{ct} and C_{dl}, over the 0-12 week interval with little coating degradation (R_{pf}). At 12-48 weeks changes in C_{dl} and R_{pf} are observed, probably due to chromates filling the bulk coating pores.

The ECM representing Coating D panels exposed to the GM9540P cyclic corrosion test (Figure 16, Reference 1) exhibited low resistance values indicating that protective properties are destroyed after one week.

UV EXPOSURE

The ECM representing Coating A panels exposed to QUV-A weathering (Figure 17, Reference 1) shows that at ~ 200 MJ/m^2 of UV exposure the the *n* value of the paint film CPE is at a maximum. This is indicative of increased barrier properties, due to residual curing/crosslinking of the coating. This was confirmed with an increase of density (ρ) (Appendix 1, Reference 1) and T_g (Appendix 2, Reference 1), and a high R_{pf} value. There are minor changes in both R_{ct} and C_{dl} in the 75-447 MJ/m^2 interval, suggesting insignificant coating/metal interfacial activity. This is confirmed with good adhesion and no blistering.

The ECM representing Coating B panels exposed to QUV-A weathering (Figure 6; Figure 18, Reference 1) exhibited that at ~298 MJ/m^2 of UV exposure the *n* value of the paint film CPE and R_{pf} are at a maximum. This is indicative of increased barrier properties, due to

residual curing/crosslinking of the coating; this is confirmed with good adhesion and no blistering. There was no density (ρ) or T_g data available in this interval for Coating B. There is insignificant interfacial activity as is seen with the minor change in both R_{ct} and C_{dl} in the 75-447 MJ/m^2 interval.

The ECM representing Coating C panels exposed to QUV-A weathering (Figure 19, Reference 1) exhibited that at ~447 MJ/m^2 of UV exposure the *n* value of the paint film CPE is at a maximum, and R_{pf} is increasing. This is indicative of increasing barrier properties, due to residual curing/crosslinking of the coating. There was no density (ρ) or T_g data available in this interval for Coating C. There is a significant increase in R_{ct} and a decrease in C_{dl} in the 298-447 MJ/m^2 interval, suggesting another curing phase or the filling of the pores with chromates. Poor adhesion was exhibited throughout the duration of exposure, this suggests that the panels may have had contaminants present at the coating/metal interface that affected adhesion.

The ECM representing Coating D panels exposed to QUV-A weathering (Figure 20, Reference 1) exhibited that at ~75 MJ/m^2 of UV exposure the *n* value of the paint film CPE is at a maximum. This is indicative of increasing barrier properties, due to residual curing/crosslinking of the coating. This was confirmed with an increase of density (ρ) and T_g. Exposing Coating D to QUV-A significantly enhanced its barrier properties.

The ECM representing Coating A panels subjected to natural exposure in AZ (Figure 7; Figure 21, Reference 1) exhibited that at ~200 MJ/m^2 of UV exposure the *n* value of the paint film CPE is at a maximum. This is indicative of increased barrier properties, due to residual curing/crosslinking of the coating. This was confirmed with an increase of density (ρ) and T_g. There are minor changes in both R_{ct} and C_{dl} in the 65-305 MJ/m^2 interval, suggesting

insignificant coating/metal interfacial activity, this is confirmed with good adhesion and no blistering.

The ECM representing Coating B panels subjected to natural exposure in AZ (Figure 22, Reference 1) exhibited that at ~305 MJ/m^2 of UV exposure the *n* value of the paint film CPE is at a maximum and an increase in R_{pf} is observed. This is indicative of increased barrier properties, due to residual curing/crosslinking of the coating. There was no density (ρ) or T_g data available in this interval for coating B. There is insignificant interfacial activity as is seen with the minor change in both R_{ct} and C_{dl} in the 65-305 MJ/m^2 interval, this is confirmed with good adhesion and no blistering.

The ECM representing Coating C panels subjected to natural exposure in AZ (Figure 23, Reference 1) exhibited that at ~305 MJ/m^2 of UV exposure the *n* value of the paint film CPE is at a maximum, and R_{pf} is increasing. This is indicative of increasing barrier properties, due to residual curing/crosslinking of the coating. There was no density (ρ) or T_g data available in this interval for Coating C. Poor adhesion was exhibited throughout the duration of exposure. Similar adhesion and blistering characteristics were observed here as when exposed to QUV-A.

The ECM representing Coating D panels subjected to natural exposure in AZ (Figure 24, Reference 1) exhibited that at ~65 MJ/m^2 of UV exposure the *n* value of the paint film CPE is at a peak and R_{pf} is increasing. This is indicative of increasing barrier properties, due to residual curing/crosslinking of the coating. This was confirmed with an increase of density (ρ) and T_g.

The ECM representing Coating A panels subjected to natural exposure in FL (Figure 8; Figure 25, Reference 1) exhibited that at ~ 120 MJ/m^2 of UV exposure the *n* value of the paint film CPE is at a maximum. This is indicative of increased barrier properties, due to residual curing/crosslinking of the coating. This was confirmed with an increase of density (ρ) and T_g.

The low R_{pf} values in the 151-271 MJ/m^2 interval suggest that coating barrier properties have decreased but have not yet affected the coating/metal interface, because of the minor changes in both R_{ct} and C_{dl}. The coating degradation is probably due to the deleterious combination of humidity and UV exposure. The R_{ct} and C_{dl} values predict insignificant coating/metal interfacial activity, this is confirmed with good adhesion and no blistering.

The ECM representing Coating B panels subjected to natural exposure in FL (Figure 26, Reference 1) exhibited that at ~271 MJ/m^2 of UV exposure the *n* value of the paint film CPE is at a maximum and an increase in R_{pf} is observed. This is indicative of increased barrier properties, due to residual curing/crosslinking of the coating. There was no density (ρ) or T_g data available in this interval for coating B. There is insignificant interfacial activity as is seen with the minor change in both R_{ct} and C_{dl} in the 57-271 MJ/m^2 interval, this is confirmed with good adhesion and no blistering.

The ECM representing Coating C panels subjected to natural exposure in FL (Figure 27, Reference 1) showed that at ~271 MJ/m^2 of UV exposure the *n* value of the paint film CPE is at a maximum, and R_{pf} is increasing. This is indicative of increasing barrier properties, due to residual curing/crosslinking of the coating. There was no density (ρ) or T_g data available in this interval for coating C. There is coating/metal interfacial activity as is seen with the change in C_{dl} in the 57-271 MJ/m^2 interval. This may be due to increased charge species due to the migration of chromates and H_2O through the coating and the availability of sufficient chromates to inhibit corrosion. Poor adhesion was exhibited throughout the duration of exposure.

The ECM representing Coating D panels subjected to natural exposure in FL (Figure 28, Reference 1) showed that at ~91 MJ/m^2 of UV exposure the coating appeared to have reached its maximum curing/crosslinking, this is observed with increasing T_g. The density, adhesion, and

blistering data were inconclusive for this exposure. The increasing *n* and R_{pf} in the 91-271 MJ/m^2 interval may be due to the migration of inhibitors filling the bulk coating pores and their availability to protect against corrosion. The changing C_{dl} may be due to H_2O and increased charge species at the coating/metal interface.

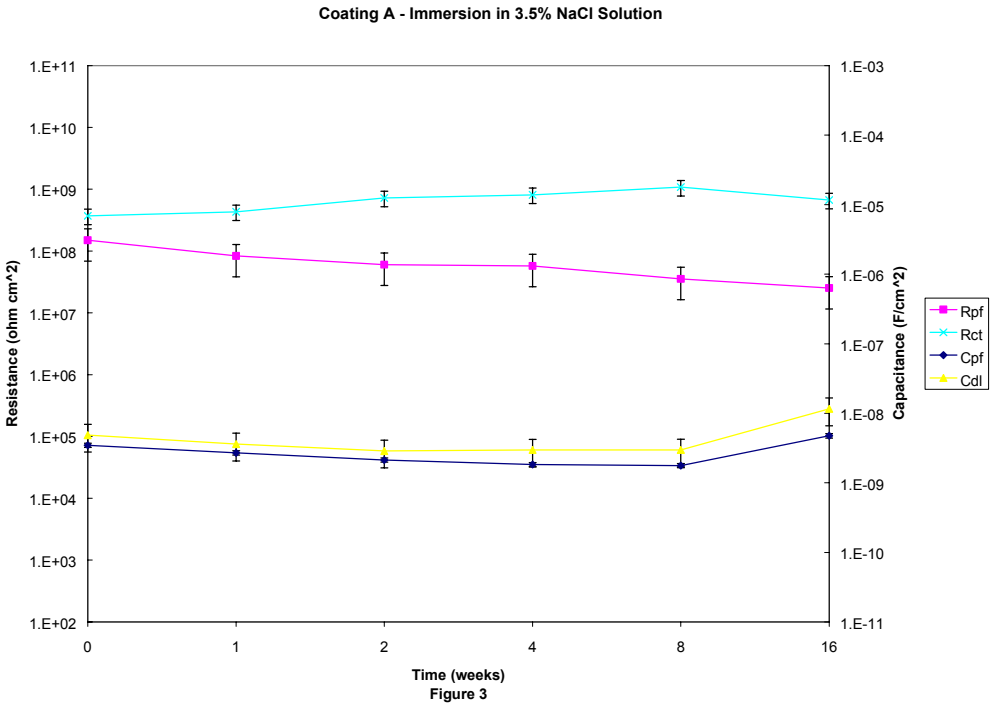

FIGURE 3. Coating C ECM Results after Immersion in 3.5% NaCl Solution.

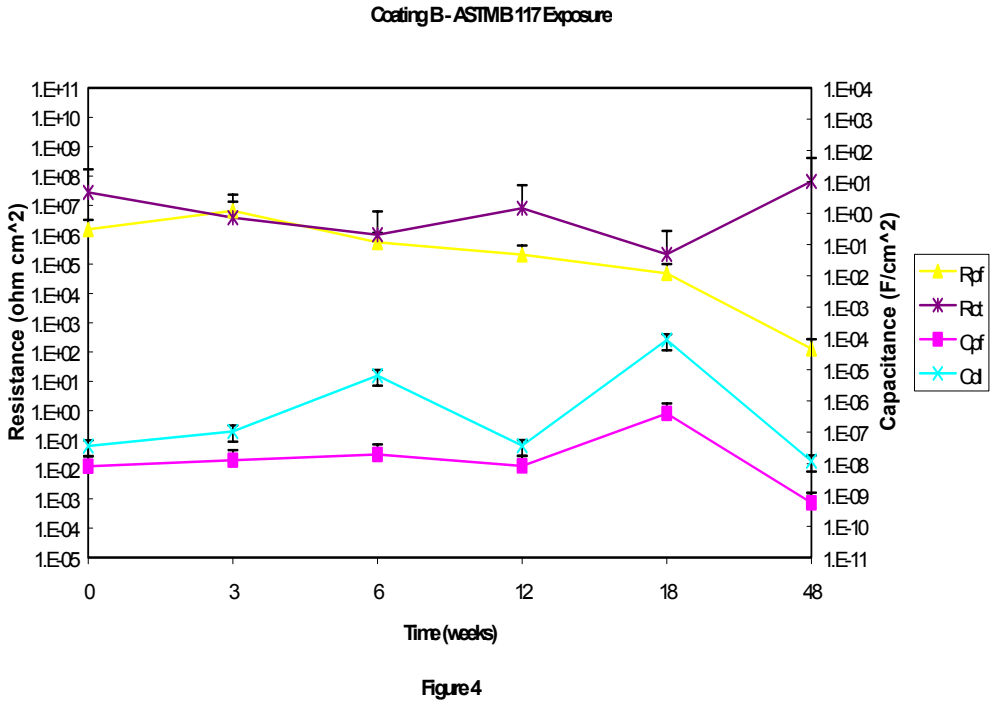

FIGURE 4. Coating C ECM Results after ASTM 117 Exposure.

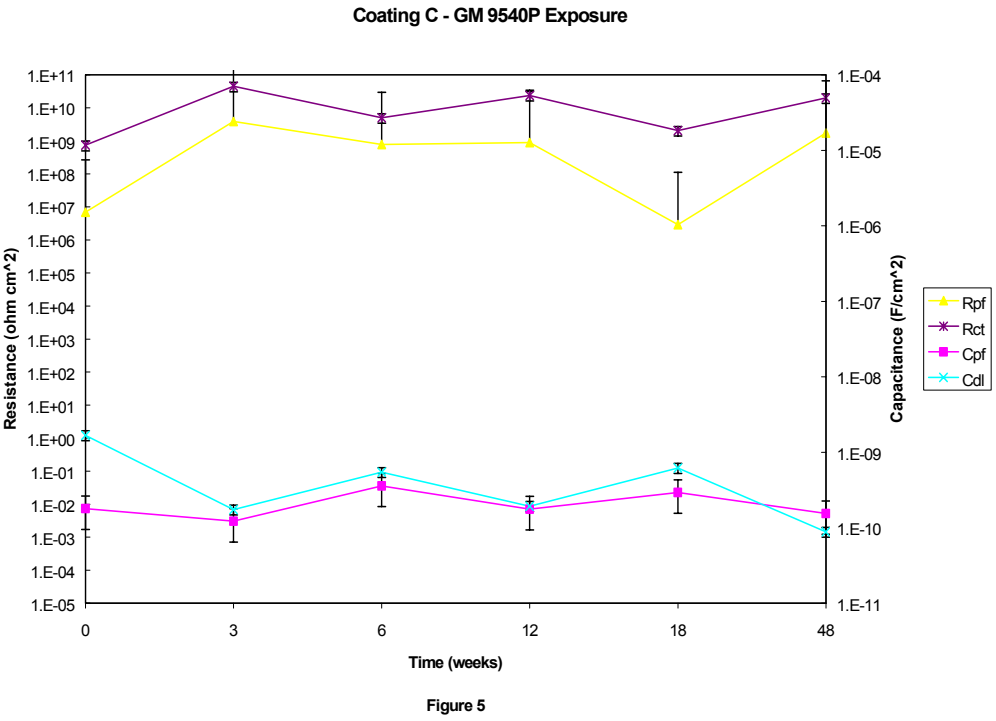

FIGURE 5. Coating C ECM Results after GM9540P Exposure.

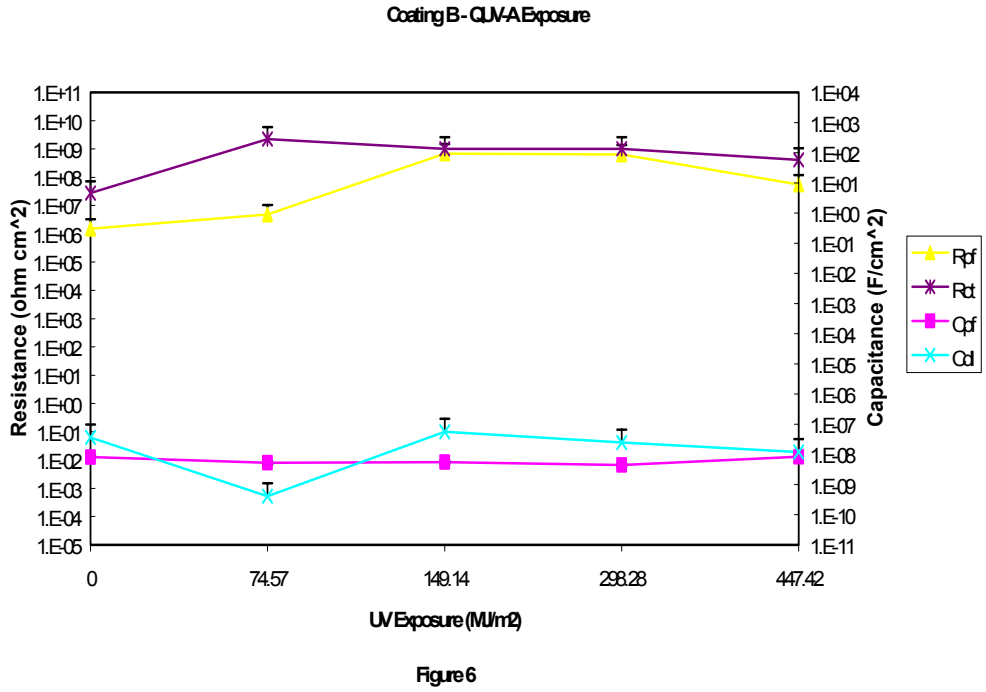

FIGURE 6. Coating B ECM Results after QUV Exposure.

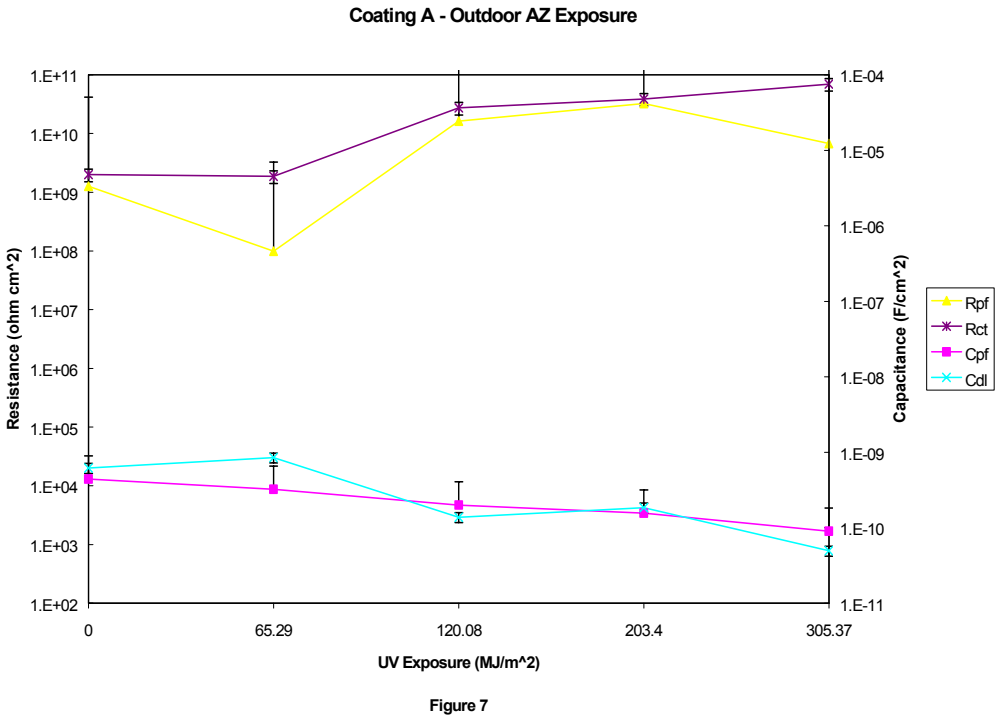

FIGURE 7. Coating A ECM Results after Outdoor AZ Exposure.

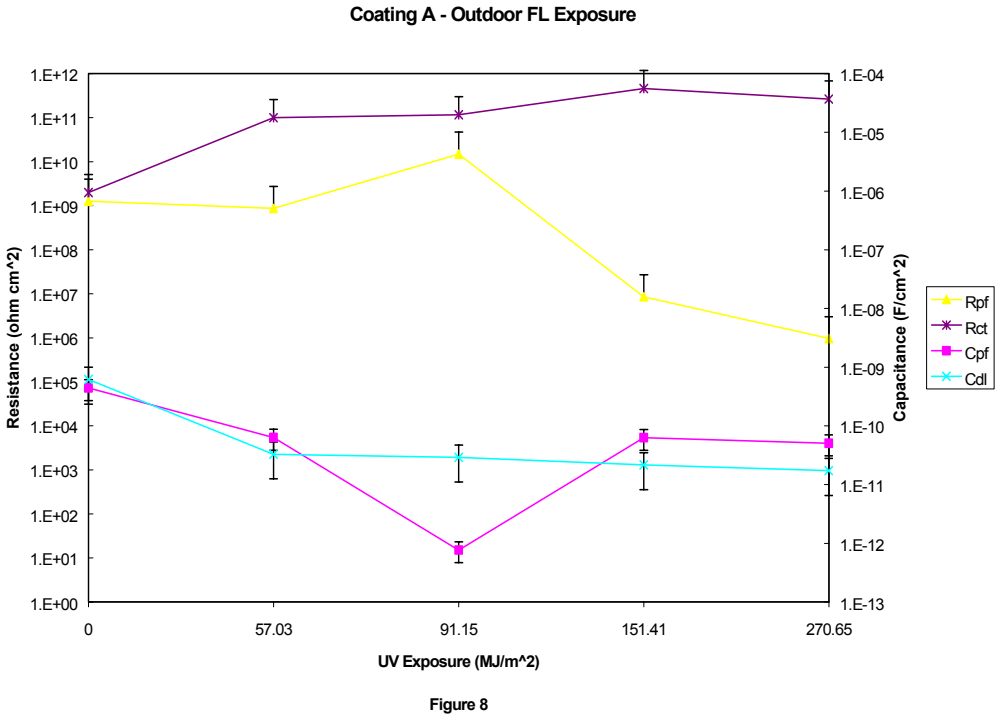

FIGURE 8. Coating A ECM Results after Outdoor FL Exposure.

CONCLUSIONS

An abrupt increase or decrease of any ECM parameters is an indicator of changes within the system, deleterious or advantageous. The ability to approximately determine the system behavior and to attribute changes of the ECM parameters to anticipated behavior would be of immeasurable importance in the evaluation of coatings systems.

COATINGS A AND B

Coating A was found to attain its maximum degree of cure at ~ 200 MJ/m^2 of UV exposure for the QUV, and AZ weathering conditions and ~ 120 MJ/m^2 for the FL exposure. The decrease in curing irradiance in FL is attributed to the deleterious effect of humidity, and chain scission being more dominating than crosslinking at ~ 120 MJ/m^2 of exposure. The QUV

exposure had the most stable ECM parameter behavior followed by AZ and finally FL, due to the increasing humidity in the weathering conditions.

The B117 solution is more aggressive than the GM9540P solution to Coating A, based on the steady decline of R_{pf} and R_{ct}. By 48 weeks of exposure to B117 salt spray Coating A offers little protection against corrosion. Adhesion and blistering data confirm this finding. Coating B was found to attain its maximum degree of curing at 270-305 MJ/m^2 of UV exposure for the FL, QUV, and AZ weathering conditions, suggesting most complete cure at ambient conditions. The QUV exposure had the most stable ECM parameter behavior followed by AZ and finally FL.

Coating B is a more porous coating than Coating A, this is seen with its lower Rpf and paint film CPE *n* values. This coating also tended to degrade more gradually than did Coating A: this is attributed to the more rigid ring structure present in the polymer backbone of B. Ring structures reduce polymer chain movements resulting in more even distributions of voids where conductive pathways can form and remain. Coating A does not have ring moieties in its backbone and is thus capable of more segmented movement. Conductive pathways can form and be interrupted, possibly explaining the cyclic behavior of the R_{pf} values observed for Coating A for many of the exposure conditions.

The B117 salt spray is much more aggressive than the GM9540P testing. This was confirmed with adhesion and blistering data and the large changes in the ECM parameters.

COATINGS C AND D

Coating C exhibited the best barrier properties of all the coatings tested. Exposure to GM9540P cyclic corrosion testing and B117 salt spray did not seriously affect the barrier properties of the coating. One unique feature of Coating C was the increase in R_{pf} and R_{ct} after ~300 MJ/m^2 of irradiance in QUV testing, a sharp decrease was also observed in C_{dl}. This

behavior is attributed to the formation of allophonates by further reaction of the urethane backbone with residual isocynates[4]. Coating C is formulated to contain fewer crosslinks than either coating A or coating B to enhance flexibility. The additional crosslinking observed does enhance barrier properties, but may adversely affect such properties as flexibility and impact resistance.

Coating C exhibited the poorest adhesion of all the coatings, possibly due to poor surface preparation.

Coating D exhibits additional curing from ~65-91 MJ/m^2 in the QUV, FL and AZ exposures. Coating D is the most porous of all the coatings having the lowest paint film resistance (R_{pf}). Both GM9540P and B117 salt spray testing were detrimental to the barrier properties of Coating D. This was confirmed with adhesion and blistering data, and low resistance values in the ECM. Coating D had the quickest increase in barrier properties of all the coatings after exposure to UV, supporting the earlier statement that the coating did not sufficiently cure at ambient conditions. Heat associated with the UV exposure was sufficient for the reactants to reach the activation energy required for full cure.

FUTURE WORK

It is apparent that UV exposure alone does not significantly degrade the bulk barrier properties of these coatings. In some cases, it can actually enhance them. It is when moisture is introduced in conjunction with UV that deleterious effects are observed. EIS testing at elevated temperatures on panels subjected to various amounts of UV may be able to show the combined effects of UV, water, and temperature in a few hours compared to weeks when done separately. Experiments will be conducted to determine if this is so by comparing EIS spectra of panels

subjected to QUV containing wet cycles predictive capability of elevated temperature EIS can be realized.

It was suggested that an additional curing stage was observed in coating C after exposure to more than 300 MJ/m^2 of UV radiation. IR spectroscopy performed on panels subjected to different irradiance values of UV to determine if such groups as allophonates appear after certain exposure amounts. Although the presence of additional crosslinking appears to be beneficial, properties such as flexibility can be lost, resulting in cracking.

REFERENCES

1. K. Kovaleski, E. Lipnickas, "Mechanisms of Military Coatings Degradation (PP-1133), Electrochemical Impedance Subtask" (Annual Report submitted to the Strategic Environmental Research and Development Program, December 2001).

2. K. Kovaleski, D. Dumsha, "Mechanisms of Military Coatings Degradation (PP-1133): Electrochemical Impedance Spectroscopy Part 1", Naval Air Warfare Center Report NAWCADPAX/TR-2001/55, Patuxent River, MD, June 2001.

3. E.P.M. van Westing, G. M. Ferrari, Corr. Sci. 36, 8 (1994): p. 1323.

4. C. Hare, Protective Coatings: Fundamentals of Chemistry and Composition (Pittsburgh, PA: Technology Publishing Company, 1994), p. 245.

THE APPLICABILITY OF EIS FOR ASSESSING SUBSTRATE METAL MASS LOSS FOR POLYMER-COATED METALS

D.B. Mitton, S.L. Wallace, N.J. Cantini, N. Eliaz and R.M. Latanision

H.H. Uhlig Corrosion Laboratory,
Massachusetts Institute of Technology,
Cambridge, MA 02139, USA.

F. Bellucci

Department of Materials and Production Engineering,
University of Naples Federico II,
P.Le Tecchio 80125, Naples, Italy

G.E. Thompson

Corrosion and Protection Centre
University of Manchester Institute of Science and Technology
Manchester M60 1QD, U.K.

ABSTRACT

Research has been carried out to evaluate the correlation between substrate mass loss and data generated by electrochemical impedance spectroscopy (EIS). Experiments were carried out as a function of exposure time for both polymer-coated and bare samples. Substrate metal mass loss was determined in-situ and in real time with a vibrating sample magnetometer (VSM). In all cases, the sample was held potentiostatically at the open circuit potential (ocp) while EIS data were collected. Mass loss data calculated from electrochemical impedance (EI) spectra were then compared to equivalent data generated on the VSM. Although previous research has investigated the correlation for bare samples, establishing this relationship for a coated substrate is more convoluted. The difficulty results from errors associated with solution uptake within the polymer, and corrosion product entrapment. Such errors obviate the use of traditional gravimetric techniques and, until now, the relationship between substrate metal mass loss and EIS has not been established for polymer-coated samples. Although the current research indicates that EIS can accurately define the mass loss for a bare sample, the correlation for coated samples has, generally, not been as good.

INTRODUCTION

Organic coatings are frequently employed to reduce the degradation of a metallic substrate exposed to a corrosive environments. They may also serve as reservoirs for inhibiting compounds.[1] Such coatings are, however, not impervious to aqueous solutions, which can ultimately result in underfilm corrosion.[1, 2] The corrosion rate cannot be assessed in this case by direct mass loss measurements due to water absorption in the coating, trapped corrosion products beneath the coating, and the non-uniform character of underfilm corrosion.[3]

EIS has been widely employed to study corrosion protection by organic coatings. Advantages of this technique over *dc* and conventional techniques include the absence of significant perturbation to the system, its applicability to the assessment of low-conductivity media such as polymers, and a frequency component that may provide mechanistic information.[1,4] EIS, however, has some significant drawbacks. At low frequencies, where underfilm corrosion reactions are probed, experimental difficulties and time constraints can complicate precise determination of the charge-transfer resistance (R_{ct}, describing the electrochemical reaction under activation control) and the double-layer capacitance (C_{dl})[5]; additionally, the Warburg impedance may have a masking effect,[6, 7] and inductive loops or new time constants are sometimes observed.[8] Moreover, due to the long measurement time required, both the corrosion rate and corrosion potential can change during the experiment. There has also been no evidence that R_{ct} can be equated to the polarization resistance (R_p) and used in the Stern-Geary equation to calculate the underfilm corrosion rate.[9] In-depth mechanistic and kinetic information on the corroding interface can easily be overlooked in EIS by modeling the system with an oversimplified equivalent circuit.[4]

Magnetic measurements may also be used to monitor corrosion.[10-12] The saturation magnetic moment (μ_s) of a ferromagnetic material is a structure-insensitive material property; thus, it only changes with mass (volume) of the material. Since the signal from a ferromagnetic substrate is much larger than the signals of either a polymer coating or non-ferromagnetic corrosion products, decreases in μ_s can be measured and used to assess the mass loss due to corrosion.[13, 14]

The operating principle of the VSM involves the detection of a dipole field from a magnetic sample vibrating perpendicular to a uniform magnetizing field.[16-17] Changes in magnetic moment on the order of 10^{-5} -10^{-6} emu can be measured permitting the accurate determination of very low mass losses (micrograms).

The objective of this work is twofold: to verify the applicability of the VSM for measuring the corrosion rate of bare and coated ferromagnetic materials, and to suggest a way of using it to enhance the interpretation of EIS data. Once a correlation between electrochemistry and mass loss is unequivocally established, there will no longer be any obstacle to the use of EIS for monitoring the corrosion rate of an organic-coated metal.

EXPERIMENTAL DETAILS

Cobalt was chosen for this work since it is ferromagnetic and produces non-ferromagnetic oxides.[18, 19] Sample size was an important consideration in this research. On the one hand, since small amounts of corrosion were expected (given the presence of a coating and short exposure times), the initial volume of the cobalt had to be sufficiently small to ensure significant change in saturation magnetic moment; *i.e.*, larger than the sensitivity of the VSM (±0.25%). In addition, the sample had to be placed within a reduced VSM pole gap (to achieve

increased magnetic fields) and satisfy the magnetic dipole approximation.[20] The need to achieve increased magnetic fields mainly results from the strong magnetic anisotropy of cobalt,[21] there is only one easy axis of magnetization, which corresponds to the [0001] axis of hexagonal symmetry. Consequently, the experimental intrinsic magnetization curves depend on the relative orientation of the magnetic moments in the sample to the applied field. However, at sufficiently high applied fields, the saturation magnetic moment is the same for all different orientations.

Sample size, on the other hand, needed to be large enough to avoid ohmic errors during electrochemical tests due to sheet resistance phenomena,[22] and to provide a sufficiently large exposed area for the electrochemical measurements to be meaningful.

To prepare the samples, silicon wafers were electron-beam deposited with a 3200 Å-thick pure cobalt layer. The wafers were then sectioned into rectangular samples of approximately 0.7 cm by 2.3 cm. Selected samples were coated with a transparent acrylic varnish. The polymer coating was prepared by mixing 100 g Viacryl VSC 5754/60 resin with 36 g Maprenal MF800, both from Vianova Resins. Acetone was added to the mixture to obtain the proper viscosity. The samples were subsequently dipped in a bath of the varnish and allowed to air-dry for a short time prior to curing in an oven at 115°C for 30 min. The polymer was intentionally undercured to make it more permeable to moisture and ions by decreasing the degree of cross-linking. A shielded copper wire was attached to the cobalt as an electrical contact for the electrochemical measurements. The back and the edges of the sample were masked to prevent localized corrosion phenomena.

VSM and EIS tests were performed *in situ* and in real time on the cobalt samples using a novel miniature cell design (Figure 1).[23] This cell design satisfied the previous sample dimension requirements and used weakly diamagnetic and paramagnetic materials. A Pyrex tube

of 11 mm inner diameter and 13 mm outer diameter was cut to a length of approximately 45 mm. One end of the tube was dipped in a five-minute epoxy gel. After the solid epoxy plug was established, three holes of adequate diameter were drilled to permit positioning of the inner components. The sample and a platinum electrode, the latter serving as a counter/auxiliary electrode in electrochemical measurements, were glued inside the tube, facing each other. The platinum electrode was prepared in advance by spark welding a high-purity platinum wire to a high-purity platinum foil. The bottom end of the tube and the two holes through which the sample and the counter electrode were inserted were subsequently sealed with epoxy. A glass rod was glued along the axis of the cell and a removable plug was adjusted to seal the third hole during VSM runs.

The cell was filled with a 0.5 M NaCl (pH 7) solution, daily refreshed from a reservoir through which purified air was continuously bubbled. For EIS measurements, a modified three-electrode setup was used, in which a miniature reference electrode (EG&G model K0265 Ag/AgCl) was immersed directly in the cell. The standard potential of the relevant half-cell reaction is +0.222 V *vs.* SHE (standard hydrogen electrode).[24] The electrode was filled with a solution of 17%, 3 M NaCl in distilled water, saturated with AgCl. Under such conditions, the electrode potential is +0.194 V *vs.* SHE. A Schlumberger Solartron 1286 Electrochemical Interface and a Solartron 1250 Impedance / Gain-Phase Analyzer, connected to a PC by an IEEE/GPIB interface, were used. The open circuit potential (OCP) was monitored for more than 20 minutes before each sweep. Frequency ranges of 10 kHz to 10 mHz and 65 kHz to 5 mHz were selected for the uncoated and polymer-coated samples, respectively. The amplitudes of the superimposed potential were 5 and 20 mV for the uncoated and coated samples, respectively. EIS data was analyzed with ZView, a software package developed by Scribner Associates.

Potentiodynamic measurements were carried out with a traditional three-electrode setup in order to estimate the Tafel slopes for bare cobalt. A 0.5 M NaCl solution and a saturated calomel electrode (SCE) were used. Before each measurement, the OCP was monitored for at least 10 min. Scans were subsequently generated from –250 mV relative to the OCP to +700 mV (with respect to the SCE), at a sweep rate of 1 mV/s, using Scribner Associates DC Corrware software package.

Corrosion rates were obtained from electrochemical measurements, using the expression:

$$r = \frac{a \cdot i_{corr}}{nF} \tag{1}$$

where a is the atomic mass of the corroded metal (58.933 g/mol), n the number of electrons transferred in the reaction (2 equiv./mol), F is Faraday's constant (96,487 C/equiv.), and i_{corr} the corrosion current density. Substituting the Stern-Geary relation for i_{corr}, the following equation is obtained:

$$r = \frac{a}{nFAR_p} \cdot \frac{\beta_a |\beta_c|}{2.3(\beta_a + |\beta_c|)} \tag{2}$$

where A is the exposed surface area, R_p the polarization resistance, and β_a and β_c the anodic and cathodic Tafel slopes, respectively. The cumulative mass loss was subsequently obtained by integrating the normalized time-dependent corrosion rate on time:

$$\Delta m = \int_{t_0}^{t_n} rA\,dt \tag{3}$$

Magnetic measurements were carried out at room temperature with a Model 880 VSM from Digital Measurement Systems, Inc. The instrumentation was controlled by a commercial software package capable of measuring all basic magnetic properties. Firstly, calibration was carried out using a standard high-purity nickel disc. The voltage gain of the VSM was

automatically redefined to obtain a standardized value for the reference sample. Secondly, the reference electrode was removed from the miniature cell, and the cell was entirely filled with solution, sealed with a conical plug and tightly mounted onto a glass rod (cell holder). Thirdly, the sample was positioned at the saddle point of the magnetic field. Finally, the magnetic moment of each cell was recorded six times in the range 8050-10000 Oe. To collect the magnetic moment data, an averaging technique was employed, in which the average moment value was computed over thirty measurements every 50 Oe. Eventually, the saturation magnetic moment (μ_s) was calculated by averaging the values obtained from four of the six runs, ignoring the other two extreme values. Employing this procedure, very accurate values of μ_s were obtained; typically with $STDEV / \overline{\mu}_S < 0.25\%$, where $STDEV$ is the standard deviation and $\overline{\mu}_S$ the mean saturation magnetic moment.

The total magnetic moment of the system, $\mu(H)$, included contributions from the ferromagnetic cobalt and from all of the remaining paramagnetic and diamagnetic materials present in the cell. This can be expressed by:

$$\mu(H) = (1-\alpha)\cdot V_0 \cdot M(H) + (\Sigma \alpha_i V_0 \chi_i + V_p \chi_p + \Sigma V_j \chi_j)\cdot H \qquad (4)$$

where $\alpha \equiv \Sigma \alpha_i$ is the volume fraction of cobalt that has been corroded/oxidized, α_i the volume fraction of cobalt that has turned into a corrosion/oxidation product i, V_0 the initial volume of ferromagnetic Co, $M(H)$ the magnetization of Co, H the applied magnetic field, χ_i the magnetic susceptibility of the i^{th} corrosion/oxidation product, V_p the volume of the polymer coating, χ_p the magnetic susceptibility of the polymer, V_j the volume of the material of the j^{th} constituent of the cell (other than cobalt, polymer coating, and corrosion/oxidation products), and χ_j its magnetic susceptibility.

When the applied field exceeds the saturating field of the ferromagnetic material, the magnetization is no longer dependent on the applied field; *i.e.*, $M(H) \equiv M_s$, the saturation magnetization (the maximal magnetic moment density). Thus, the signal of the system becomes a straight line, and μ_s of cobalt can be separated readily from the contributions of the paramagnetic and diamagnetic materials by linear regression.

It should be noted that intrinsic magnetization curves were recorded for the different constituents of the cell. The Pyrex tube, made from a diamagnetic material, exhibited good linearity with a reasonably low slope of approximately -1.0×10^{-7} emu/Oe. The platinum electrode, made from a paramagnetic material, also revealed excellent linearity with a slope of approximately 5.0×10^{-7} emu/Oe. The electrolyte (0.5 M NaCl) exhibited exceptional linearity with a slope of the order of -2.0×10^{-7} emu/Oe. The remaining constituents of the cell (gray paint, epoxy, solder material, glass rod, glass capillary, copper wire, plastic conical plug, and silicon wafer) all exhibited negligible signals (lower than 10^{-5} emu) when tested individually. Due to compensations between the diamagnetic and the paramagnetic materials, the slope of the linear signal from the cell filled with electrolyte was approximately 2.0×10^{-7} emu/Oe. The signal from the cobalt sample ($\sim 3.5 \times 10^{-2}$ emu) was thus prominent within the range of 8050-10000 Oe.

Several other factors are noteworthy with regard to the magnetic measurements. First, the core of the cell was chosen to be a long hollow cylinder of semi-infinite geometry in order to minimize disruptions of the magnetic flux lines. Second, the core was glued to a glass rod to prevent any relative rotation between the cell and its holder. Third, to avoid effects of dynamic resonance due to extra vibrations under the VSM, the cell was entirely filled with electrolyte and sealed with a plug. Moreover, cobalt is an extremely stable ferromagnetic material, with a Curie temperature as high as 1115°C.[25] In the vicinity of room temperature, where all measurements

were carried out, the variation of M_s with temperature is insignificant.[26] The saturation magnetization is defined as a constant quantity for the bulk material. In the case of films, such as metallic wafers, this definition may no longer be legitimate. Since ferromagnetism arises from atomic interactions of a cooperative nature, it is anticipated that, as the number of atom layers in a film is reduced, three-dimensional effects will begin to disappear at some critical thickness and the behavior of the film will approach that of a paramagnetic material.[27] Fortunately, as the critical thickness at which M_s is reduced is typically of the order of 30 Å for most common ferromagnetic materials,[27, 28] the initial saturation magnetization of the cobalt films studied in this research (3200 Å-thick) could be equated to the saturation magnetization of the bulk material (1400 emu/cm^3).[25] This was supported by calculating a theoretical saturation magnetization of 1369 emu/cm^3 for a 3200 Å-thick *hcp* cobalt film grown by electron beam deposition.[23] Finally, the detection coil geometries are usually described by assuming that the sample acts as a pure dipole, which is true only for ellipsoidal samples or when the sample dimensions are very small compared to the dimensions of the detection coils. Therefore, corrections for sample size were applied to the calculated values of $\mu_{s,}$[23] following the procedure suggested by Zieba and Foner.[20]

Assuming that the value of the saturation magnetization, M_s, is not affected by corrosion phenomena, the mass loss due to corrosion was calculated by:

$$\Delta m = \frac{\mu_{s,0} - \mu_{s,f}}{\mu_{s,0}} \cdot m_0 \qquad (5)$$

where $m_0 = \frac{\mu_{s,0}}{M_{s,b}}\rho$ is the initial mass of cobalt, $\mu_{s,0}$ the saturation moment before exposure to the electrolyte, $\mu_{s,f}$ the saturation moment after a certain exposure time, $M_{s,b}$ the bulk cobalt saturation magnetization, and ρ the density of cobalt (8.832 g/cm^3). Corrosion rates were

calculated by plotting the cumulative mass loss *versus* time, performing polynomial fitting, differentiating the fitting expressions over time, and normalizing to the exposed area.

RESULTS AND DISCUSSION

BARE SAMPLES

The average corrosion potential of cobalt on silicon wafer was found to be approximately –390 mV *vs.* SCE. This value lies between the standard potentials of cobalt and oxygen (–518 mV and –159 mV, respectively, *vs.* SCE). A series of potentiodynamic measurements were carried out and the anodic (β_a) and cathodic (β_c) Tafel constants were obtained by linear regression. The values obtained in this way were: β_a = 81 mV and $|\beta_c|$ = 367 mV, which are reasonable for these constants.[29, 30]

Excellent correlation between the cumulative mass loss values measured by EIS and VSM is evident for uncoated silicon/cobalt wafers (Figure 2). Measurements reported elsewhere by the authors[31] indicate an excellent correlation between VSM and gravimetric mass loss. Thus, the VSM is considered to be applicable for mass loss measurements. Sweeps (Figure 2) performed at times longer than 69 h of immersion yielded spectra which could not be deconvolved for analysis. Such behavior may result from the significantly reduced volume of cobalt and the exposure of the silicon wafer.

It is evident from Figure 2 that the corrosion rate (proportional to the slope of the curve) decreases with time. This behavior is typical for corrosion of bare metals.[32] Finally, the curve exhibits asymptotic behavior, which indicates that all of the initial mass of cobalt in the exposed area (~170 μg) was consumed by corrosion after immersion for about 120 h.

COATED SAMPLES

In the case of polymer-coated samples, EIS analysis could only be made after some immersion time, when the cobalt beneath the polymer was clearly exposed. This was reflected by the appearance of a second semicircle at low frequencies (Nyquist plot). EIS analysis was also not possible after long immersion times, likely due to masking effects of diffusion through corrosion products, which had formed at the bottom of defects in the coating, and/or exposure of the silicon substrate. Figure 3 reveals the underfilm corrosion rates of polymer-coated cobalt samples, as obtained by both EIS and VSM measurements. The corrosion rates increase with exposure time, reach peak values and subsequently decrease, as typical for coated samples.[32] Moreover, lower mass losses were observed for the coated samples in comparison with the uncoated samples (Figure 2), as anticipated. Visual and microscopic observations indicated that corrosion initiated at defects, and usually progressed in a branch-like fashion.[33] Reasonable agreement between the corrosion rate values obtained from EIS and VSM measurements is apparent. Discrepancies in data between the two techniques may result from changes in the Tafel parameters with time and inaccurate determination of R_{ct} from the Bode and Nyquist plot. The good agreement between EIS and VSM results supports, for the first time, the validity of using R_{ct} and the Stern-Geary relation (equation 2) for underfilm corrosion rate evaluation. However, as shown here, such an evaluation can be made on the basis of EIS only well after corrosion initiates, and when diffusion (or other) processes do not mask the appearance of the substrate in the EIS spectra.

CONCLUSIONS

Based on *in situ* measurements of the corrosion rate for both bare and acrylic-coated cobalt samples by means of EIS and a VSM, the following conclusions are drawn:

1. Measurements of the saturation magnetic moment allow accurate *in situ* monitoring of corrosion rates of bare and polymer-coated cobalt.

2. Magnetic measurements may be used to improve the interpretation of EIS data, especially with respect to underfilm corrosion.

3. When the charge-transfer resistance can be determined unambiguously from EIS spectra, underfilm corrosion rates can be measured.

ACKNOWLEDGEMENTS

This work is partially supported by the National Science Foundation (NSF) through grant number DMR-9708148.

REFERENCES

1. D.A. Jones, *Principles and Prevention of Corrosion*, (Macmillan Publishing Company, New York, 1992), pp. 475-493.

2. E.L. Koehler, in *Corrosion Control by Organic Coatings*, edited by H. Leidheiser, (NACE, Houston, TX, 1981), p. 87.

3. W.J. Lorenz and F. Mansfeld, Corrosion Science, **21** (9), 647 (1981).

4. J.R. Macdonald (editor), *Impedance Spectroscopy – Emphasizing Solid Materials and Systems*, (Wiley, New York, 1987).

5. F. Mansfeld, S.L. Jeanjaquet, and M.W. Kendig, Corrosion Science, **26**, 735 (1986).

6. P. Bonora, F. Deflorian, and L. Fedrizzi, Electrochimica Acta, **41**, 1074 (1996).

7. J. Dawson and D. John, Journal of Electroanalytical Chemistry, **110**, 37 (1980).

8. G.W. Walter, Corrosion Science, **26** (9), 681 (1986).

9. F. Mansfeld, Corrosion, **36**, 301 (1981).

10. J.G. Bellingham, M.L.A. MacVicar, M. Nisenoff, and P.C. Searson, Journal of the Electrochemical Society, **133** (8), 1753 (1986).

11. V. Poulbot, H. Glénat, N. Kernevez, F. Coulet, F. Dalard, and J.J. Rameau, in *Progress in the Understanding and Prevention of Corrosion*, edited by J.M. Costa and A.D. Mercer, (Vol. 2, The Institute of Materials, London, 1993), p. 1463.

12. H. Suzuki, Y. Shiroishi, S. Hishiyama, T. Ohno, Y. Matsuda, F. Matsunaga, and N. Tsumita, IEEE Trans. on Magnetics, **5**, 3411 (1987).

13. S.L. Wallace, *The Correlation of Electrochemical and Magnetic Techniques for Use in Characterization of Underfilm Corrosion*, M.Sc. Thesis (Dept. Materials Science and Engineering, MIT, Cambridge, MA, 1999).

14. D.B. Mitton, *Degradation of Thin Metal/Alloy Films (for Magnetic Recording)*, Ph.D. Thesis (UMIST, Manchester, 1989).

15. S. Foner, Review of Scientific Instruments, **27** (7), 548 (1956).

16. K.D. McKinstry, C.E. Patton, C.A. Edmondson, P.J. McClure, and S. Kern, Review of Scientific Instruments, **62** (3), 779 (1991).

17. S. Foner, Review of Scientific Instruments, **30** (7), 548 (1959).

18. W. Betteridge, *Cobalt and its Alloys*, (ELLIS Horwood Limited, England, 1982).

19. R. Bozoroth, Ferromagnetism, (IEEE Press, New York, 1951), p. 293.

20. A. Zieba and S. Foner, Review of Scientific Instruments, **53** (9), 1344 (1982).

21. R. Pauthenet, Cobalt, **26**, 3 (1965).

22. A. Kuhn and J. Wellwood, British Corrosion Journal, **21**, 228 (1986).

23. N.J. Cantini, *In-Situ Characterization of Underfilm Corrosion by Magnetic and Electrochemical Techniques*, M.Sc. Thesis (Dept. Materials Science and Engineering, MIT, Cambridge, MA, 2000).

24. D.A. Jones, *Principles and Prevention of Corrosion*, (Macmillan Publishing Company, New York, 1992), pp. 64-67.

25. C. Kittel, *Introduction to Solid State Physics*, (7th ed., John Wiley & Sons, New York, 1996), p. 449.

26. N. Cusack, *The Electrical and Magnetic Properties of Solids*, (John Wiley & Sons, New York, 1958), pp. 320-340.

27. J.E. Thompson, *The Magnetic Properties of Materials*, (Newness Books, Feltham, England, 1968), pp. 121-139.

28. W. Schwarzacher, The Electrochemical Society Interface, **8** (1), 20 (1999).

29. D.A. Jones, *Principles and Prevention of Corrosion*, (Macmillan Publishing Company, New York, 1992), p. 80.

30. M. Stern and E.D. Weisert, Proceedings ASTM, **32**, 1280 (1959).

31. N.J. Cantini, D.B. Mitton, N. Eliaz, G. Leisk, S.L. Wallace, F. Bellucci, G.E. Thompson, and R.M. Latanision, Electrochemical and Solid-State Letters, **3** (6), 275 (2000).

32. L.M. Callow and J.D. Scantlebury, Journal of the Oil and Colour Chemists' Association, **64**, 119 (1981).

33. D.B. Mitton, N. Eliaz, S.L. Wallace, N.J. Cantini, G. Leisk, F. Bellucci, G.E. Thompson, and R.M. Latanision, Journal of the Electrochemical Society, submitted.

34. R.S. Tebble and D.J. Craik, *Magnetic Materials*, (Wiley-Interscience, London/New York, 1969), pp. 9-27.

FIGURES

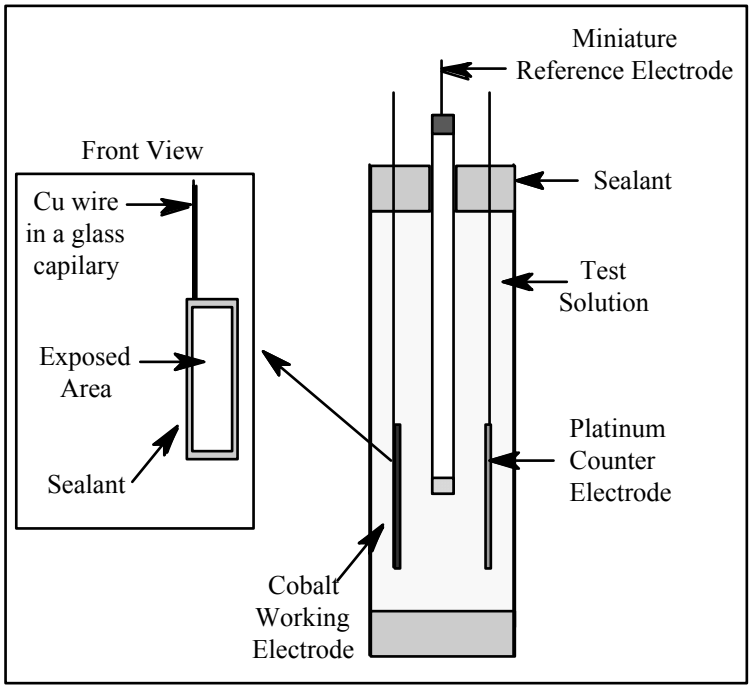

FIGURE 1. Schematic representation of the miniature cell employed during the research.

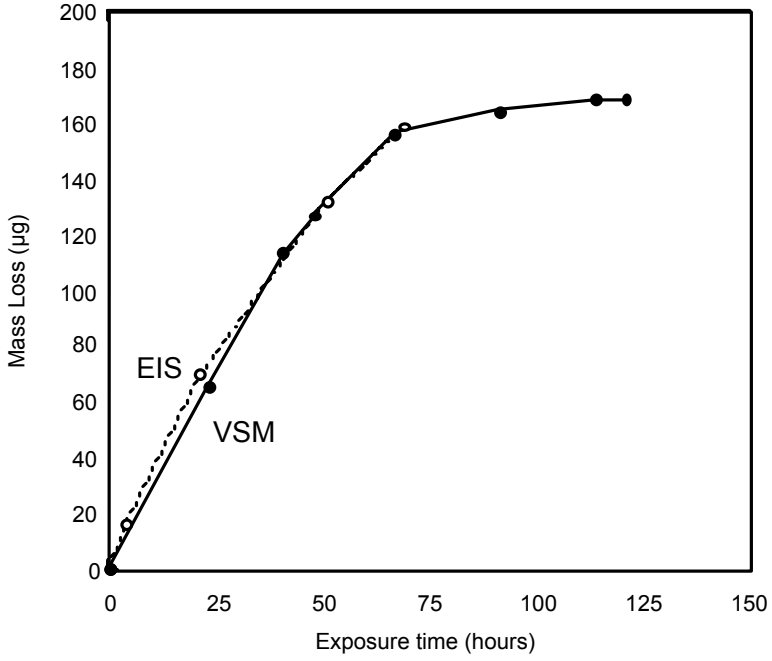

FIGURE 2. Cumulative mass loss for bare Co obtained from EIS and VSM data.

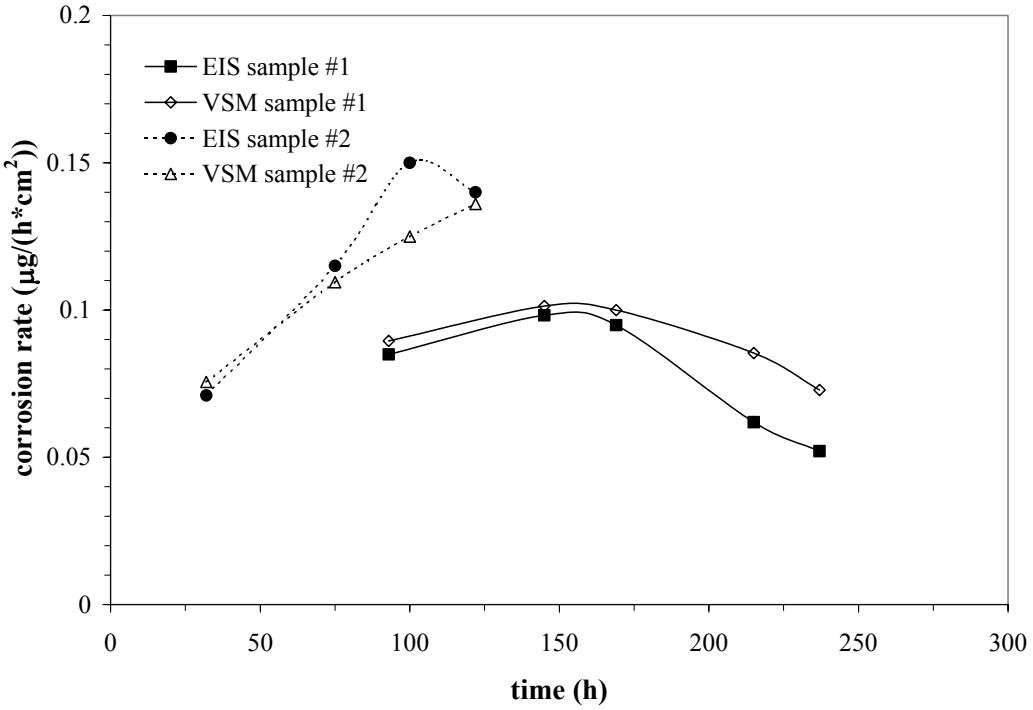

FIGURE 3. Underfilm corrosion rates of polymer-coated cobalt samples, as obtained from EIS and VSM measurements.

THE FUNCTION OF ADMIXED CORROSION INHIBITORS IN STEEL REINFORCED CONCRETE

F. J. Martin*,+ and J. Olek*

*School of Civil Engineering
Purdue University
West Lafayette, IN 47907

+GEO-Centers, Inc.
Fort Washington, MD 20749

ABSTRACT

The methods of corrosion inhibitor interaction with reinforcing steel are investigated in the present work, with particular emphasis on effects associated with corrosion inhibitors admixed into Portland cement paste. It is demonstrated that the principal objective in reinforcing steel corrosion inhibition is preservation of the naturally passive steel surface condition established by the alkaline environment. Availability of inhibitors to the steel surface and their inherent tendency to stabilize passive film defects are of critical importance. It is observed that pore solution concentrations of inorganic inhibitors tend to be lower than the admixed concentration, while pore solution concentrations of organic inhibitors tend to be higher than the admixed concentration.

INTRODUCTION

The nation's reinforced concrete infrastructure represents a significant capital investment, and annual costs related to infrastructural degradation, loss of service and consequent repair also represent an appreciable expense. The largest single mechanism of concrete degradation is corrosion of steel reinforcement embedded inside concrete. This type of corrosion is particularly insidious because the visual signs of reinforcing steel corrosion (cracking of concrete and rust-staining of the concrete surface) are merely indicators that the problem is beyond preventive maintenance and requires costly repair. This is an infrastructural cost to which the Armed Forces are not immune. Any reinforced concrete structure in a severe service environment (seaside piers

and buildings, bridges and parking structures exposed to deicing salts) can become subject to this type of degradation.

A great deal is already understood about concrete chemistry and the reinforcing steel corrosion process, although a complete fundamental view of reinforcing steel passivity and depassivation is arguably incomplete[1]. It requires remarkably little corrosion of steel reinforcement (only about 50μm) in order to cause fracture and spalling of the surrounding concrete[2]. Concrete is a porous medium, and contains small amounts of highly alkaline solutions (pH ~ 13-14) in its pore structure. It is a generally accepted notion that the alkalinity of pore solutions in "pristine" concrete helps to stabilize passivity of reinforcing steel exposed to concrete, and that steel exposed to these conditions may serve nearly indefinitely without corrosion-related failures[3]. However, small chemical changes to concrete chemistry (i.e.: carbonation or exposure to chloride) can evoke a devastating effect on the corrosion rates of embedded reinforcing steel[2]. For reinforcing steel in concrete, the degree to which chloride ions can damage passivity is related to alkalinity of the environment. In alkaline conditions free of chloride ions, the passive film on mild steel breaks down at a potential of +560 mV_{SCE}[4]. As chloride ions are introduced to the steel surface, the breakdown potential decreases, and becomes a joint function of chloride content and pore solution pH[5]. The $[Cl^-]/[OH^-]$ ratio provides insight into the relative stability of a passive film in concrete, where a $[Cl^-]/[OH^-]$ ratio below 0.3[6] (or alternatively below 0.6[7]) is believed to provide a sufficiently stabilizing environment to sustain passivity.

Admixtures are capable of modifying the pore solution chemistry of hydrated Portland cement. The set accelerator calcium chloride has long been recognized as detrimental to reinforcing steel corrosion due to residual dissolved chloride ions retained in pore solutions of

mature concrete[8]. Sodium and potassium bearing admixtures have been connected with elevating pore solution alkalinity due to residual alkali cations retained in pore solution after hydration[9]. Excessive pore solution alkalinity can be accompanied by self-destruction of a concrete due to chemical reactions between aggregates and pore solutions[9]. Corrosion inhibiting admixtures are intended to modify the pore solution chemistry through addition of inhibitive ions, such as the nitrite anion (NO_2^-)[10,11].

With few exceptions, the majority of corrosion inhibition studies for reinforcing steel in concrete are concerned with whether a specific compound will inhibit corrosion, and not how it is inhibited. Anodic inhibitors investigated in the course of published research include phosphates[12], silicates[13], molybdates[14,15], borates[16], nitrites[17], and many other compounds. Cathodic inhibitors include ammonium carbonates[18], polyphosphates[19], and amines[20] and others.

Calcium nitrite is the most widely-used corrosion inhibiting admixture for reinforcing steel in concrete[3]. Calcium nitrite was first patented as a reinforcing steel corrosion inhibitor in 1978[17], and the nitrite protection mechanism has been perhaps more intensely researched than any other inhibitor used in reinforced concrete. As an anodic inhibitor, calcium nitrite reportedly enhances passive film repair through a reaction that converts iron (II) ions to an iron (III) oxyhydroxide phase[21]. Field use of the inhibitor has confirmed that admixed calcium nitrite delays the loss of passivity for chloride-contaminated structures[22-24]. Despite stabilizing the passive film at open-circuit potentials, calcium nitrite has been observed to decrease the breakdown potential of the passive film in simulated pore solutions[4,25]. Synergistic inhibition has been reported for inhibitor formulations that contain nitrite anions and various organic cathodic inhibitors[26-28]. Calcium nitrite accelerates the set of concrete [11] (a potentially negative side effect of its use), but it possesses a desirable absence of alkali cations[21]. Sodium nitrite is occasionally

used as a corrosion inhibitor for reinforcing steel,[29,30] although the risk of detrimental effects due to alkali unsoundness prevent its widespread use in the United States.

Carboxylic acids have a history of corrosion inhibition in aqueous environments, and have also found application as corrosion inhibiting admixtures in concrete despite a strong retarding influence on the hydration of cement paste[31]. Sodium benzoate[29,30] is the most widely used, although continuing development with carboxylic acids as corrosion inhibitors in this field has resulted in at least one pertinent patent[32]. Mechanistic studies in neutral-pH solutions have shown that benzoate is able to stabilize passivity only in presence of dissolved oxygen[33], but this is a mechanism that has not been verified in concrete or alkaline aqueous studies.

Amines are the functional chemical basis for another class of organic corrosion inhibiting admixtures, and for vapor-phase corrosion inhibitors as well. Simulated pore solution studies have demonstrated that amines[34,35] and aminoalcohols[20] are Higher-order, self-assembling organic inhibitors have been explored by Incorvia et al[36,37], who used polyalkylenepolyamines and alkanedioic acids to produce amidoamine, an inhibitive reaction product. Amine adsorption on steel surfaces has been explored by Grunze et al[20], whose work in simulated pore solutions demonstrated that aminoalcohols are chemisorbed onto a steel surface, and are capable of displacing adsorbed ions in the process. Following the arguments of McCafferty[38] for neutral-pH inhibition, one might expect that amine-based inhibitors require more time to passivate a surface than nitrites or benzoates – a feature that has been observed in simulated pore solutions[4].

The relative absence of information on inhibitor protection mechanisms stems from the difficulty encountered in accurately assessing the passivity of steel embedded in reinforced concrete[1,39,40], and the timescales of natural reinforcing steel corrosion processes that make it difficult to conduct laboratory studies[39]. The only available ASTM-directed experimental method

for evaluating the effects of corrosion inhibiting admixtures in concrete is the galvanic macrocell technique[41], which provides at best a coarse measurement of inhibitor effectiveness. It is not uncommon for concrete-based corrosion studies to admixed chlorides and inhibitors into fresh concrete[42,43]. Admixing chlorides into concrete causes immediate depassivation of reinforcing steel (a situation not encountered in service). The intent of using admixed chloride is to shorten duration of an experiment to a period of days, weeks, or months, instead of year, although it does not provide a chloride-free passivation time required for some inhibitors to function[4]. Electrochemical experiments on mild steel coupons in "simulated pore solutions" have become the norm for screening inhibitors[4,25] due to much shorter experimental periods (hours or days), but these experiments do not take into account any elements of the concrete microstructure[44] which may affect interfacial transport processes and the actual inhibitor corrosion protection mechanisms in concrete.

The present communication is intended to provide mechanistic information for two principal admixed corrosion inhibitor types: nitrites and amines. Mechanistic information is derived from an experimental procedure that provides for natural interaction between inhibitors, hydrating Portland cement paste, and a reinforcing steel surface. Chloride-induced corrosion is observed on a laboratory timescale (28-56 days) without the need for admixing chlorides into cement paste. Electrochemical experiments are coupled with analyses of pore solutions extracted from hydrated cement pastes to gauge the influence of an inhibitor on pore solution chemistry and corrosion electrochemistry.

EXPERIMENTAL

Electrochemical experiments were conducted in a cell that employs a thin film of inhibited cement paste cured in-place on a reinforcing steel surface. The experimental cell and

accompanying procedure have been described elsewhere[45], consequently only a brief description is provided in the present communication. The cell shown in Figure 1 accommodates a cement paste film 2-6 mm thick, cast in place against a polished reinforcing steel surface. A Teflon™ (DuPont, Wilmington, DE) PTFE o-ring forms the watertight seal that serves as a casting form for the cement paste, and a fitted PTFE forming tool (not shown in Figure 1) is used to control thickness of the cement paste film. No chlorides are admixed into the fresh cement paste. Initial curing occurs in a 100% RH humidity chamber, in an atmosphere free of chloride ions. After three days of initial curing the PTFE forming tool is removed, the specimen chamber and solution chamber are assembled, and the solution chamber is filled with a 1M NaCl solution. Diffusion of chloride ions to the reinforcing steel surface through the cement paste film occurs in a matter of days due to the thinness of the cement paste film. The chloride solution is saturated with $Ca(OH)_2$ to limit atmospheric carbonation of the cement paste film during the two-month experimental period. Drying shrinkage of cement paste is avoided due to the continual exposure of moisture to the cement paste film. The cell is constructed from alkaline-resistant materials, which will not degrade during exposure to the cement paste or lime-saturated chloride solution. Reinforcing steel surfaces not exposed to cement paste are maintained completely dry. Electrical connections to the reinforcing steel are made to a dry steel surface.

Electrochemical experiments are conducted by communication with the reinforcing steel surface through the cement paste film. The three-electrode configuration is suitable for monitoring electrochemical noise, electrochemical impedance spectroscopy, and for performing polarization studies. Frequency response of the cell is optimized in part by maintaining a conductive solution in the Luggin capillary, rather than filling the capillary with lower conductivity cement paste[46]. Polarization resistances are determined using linear polarization

curves which are either measured directly or re-constructed with mathematical simulations using a measured electrochemical impedance spectrum. Electrochemical measurements are conducted with either a BAS-Zahner IM6 (BioAnalytical Systems, West Lafayette, IN) impedance analyzer, or a Gamry PC3 (Gamry Instruments, Willow Grove, PA) potentiostat.

Steel specimens are commercial-grade GR60 reinforcing steel, for which the chemical composition is listed in Table 1. Steel specimens are prepared by sectioning and polishing the flat crosscut surface to a 600-grit finish. The polished surface is then degreased using acetone, rinsed with deionized water and dried with dry inert gas (such as N_2). After polishing and degreasing, the steel specimen is then loaded into the specimen chamber prior to casting of the inhibited cement paste film.

Cement paste having a water to cement ratio (*w/c*) of 0.5 is prepared using a mechanical mixer in accordance with ASTM C305[47], or by hand mixing for small quantities of cement paste. Chemistry of the Type I/II Portland cement (Lonestar Industries, Greencastle, IN) is shown in Table 2. After mixing, a small amount of cement paste (1-3 ml) is cast against the exposed reinforcing steel surface of the specimen chamber. In addition, a minimum of 250 ml of cement paste is retained in a separate container for pore solution expression and analysis. Pore solution analysis specimens are not exposed to chloride solutions, and are each maintained in a humid curing chamber for a minimum of 56 days prior to pore solution expression and analysis.

Pore solution expression is performed following the method of Barneyback and Diamond[48]. In this procedure, each cement paste sample is inserted into a punch and die assembly, then pressed until water exudes from ports in the mechanical assembly. The compressive force is many times the compressive strength of the cement paste, and causes a collapse of the cement paste capillary pore structure that permits collection and analysis of pore

solutions. Pore solution analysis is performed using ion chromatography and UV-Vis spectroscopy.

Two commercial corrosion-inhibiting admixtures are evaluated in the present study, along with several laboratory formulations of organic and inorganic compounds intended to be representative of different classes inhibitors: nitrites, nitrates, phosphates, benzoates, amines, and chromates. Table 3 lists the admixed inhibitors evaluated in the present work, and concentrations of each inhibitor admixed into cement paste. Nitrite-based inhibitors include sodium nitrite, calcium nitrite, and a commercially available calcium nitrite-based corrosion-inhibiting admixture (CNIA). The commercial calcium nitrite formulation contains a nominal amount of calcium nitrate in a 10:1 nitrite to nitrate ratio. Amine-based corrosion inhibiting admixtures include dimethylaminoethanol (DMAE), the disodium salt of ethyldiamenetetraacetate (EDTA), and a commercially available organic inhibitor (OCIA). Other inhibitor formulations include sodium phosphate monobasic, benzoic acid, disodium chromate, and sodium nitrate.

RESULTS AND DISCUSSION

A plot of corrosion potential versus time for several conditions is shown in Figure 2. Three groupings of potentials are observed during the experimental period. The most noble potentials are associated with passive control specimens containing no inhibitor and not exposed to chlorides, indicated by (●) in Figure 2. After 28-day exposure these specimens exhibit potentials between +0mV$_{SCE}$ and +100mV$_{SCE}$. Moderately less noble potentials are observed for presumably passive reinforcing steel specimens exposed to both inhibitors and chlorides, indicated by (◆) in Figure 2. Potentials at 28 days for this grouping of specimens occur in the range between –250 mV$_{SCE}$ and –75mV$_{SCE}$. A third grouping of corrosion potentials indicated by

(■) include specimens exposed to: a) chloride solutions and do not contain admixed inhibitors in cement paste films, and b) admixed inhibitors and chloride solutions. These specimens manifested presumably active corrosion potentials. Active potentials were generally measured in the range between $-600mV_{SCE}$ and $-500mV_{SCE}$. Dashed lines in Figure 2 highlight a typical feature of the corrosion potential response for a single chromate-inhibited experiment. Note that the highlighted behavior follows the passive group of corrosion potentials for the first 40 days of experimentation, then decreases precipitously and settles into the lower band of corrosion potentials. Specimens containing no corrosion inhibiting admixtures made this passive to active potential transition within the first few days of exposure, while some of the inhibited specimens maintained passive corrosion potentials for weeks or longer prior to transitioning to active corrosion potentials.

Figure 3 shows polarization resistance behavior for the same experimental conditions displayed in Figure 2. In Figure 3, the difference between passive and active conditions is also clearly delineated. Passive corrosion conditions correspond to polarization resistances in excess of 1 Mohm-cm², while active corrosion conditions correspond to polarization resistances between 10 kohm-cm² and 100 kohm-cm². Dashed lines and open circles in Figure 3 trace the development of polarization resistance for a single chromate-inhibited experiment (the same experiment highlighted in Figure 2). The precipitous drop in polarization resistance for this chromate-inhibited specimen corresponds with the drop in corrosion potential for the same experimental timeframe.

The active and passive groupings in Figures 2 and 3 suggest that there might be a correlation between corrosion potential and polarization resistance (hence, corrosion rate) for the present experimental conditions. Figure 4 is a plot of polarization resistance versus corrosion

potential for this experimental data set. Two groupings of data are clearly visible in this plot: passive conditions and active conditions. The tightness of these two groups seems to suggest that corrosion protection (as well as depassivation) occurs by a common process, regardless of the inhibitor. One would not expect an amine and a nitrite to inhibit corrosion in exactly the same way – the former being a film-forming inhibitor and the latter being an oxide repair enhancer – except if the two different compounds are working to stabilize the same process. The common element that each of these different inhibitors share is that they must each interact with the naturally-formed oxide film, preserving passivity so long as the oxide remains stabilized. Nitrites are particularly well suited to this task because the proposed mechanism by which they operate is enhancing passive film repair. Amines are not as well suited to stabilize the passive film at lower concentrations because their primary function is formation of surface-wide film (not defect-specific interaction) that protects against offensive ions by steric hinderance[38]. Amines are, however, capable of stabilizing passivity if present in sufficient quantity to isolate passive film defects from approaching chlorides.

Some of the interactions of corrosion inhibitors with cement paste chemistry are shown in Table 3. The inorganic inhibitors undergo a decrease in concentration during hydration of the cement paste, indicating that some portion of the inhibitor becomes incorporated into (or adsorbed onto) hydrated phases of the cement paste. Interaction between hydrating cement paste and a nitrite inhibitor admixed at 100mM concentration results in a pore solution concentration of 22mM, a reduction of about 80%. The appreciable corrosion protection afforded by low admixed concentrations of nitrite ions (and undetectable amounts of nitrite in pore solutions) suggests that nitrites interact with the steel surface immediately upon exposure, prior to removal from pore solution. Phosphate inhibitors appear to be entirely removed from pore solution by the

cement paste during hydration. Each of the organic inhibitors in Table 3 increases concentration in pore solution during hydration, indicating that the inhibitors are retained in solution while the mix water is consumed by hydration reactions.

Na:K ratios are listed in Table 3 as a relative alkalinity index. Na^+ and K^+ are common impurities in Portland cement, and are the primary reason for the pore solution pH's to climb to values above 12.5. The cement used in these experiments is a low alkali cement because TA (total alkalinity) is less than 0.64[49]. However, due to quantities of alkali impurities that are present in the cement, naturally occurring concentrations of Na^+ and K^+ in pore solutions are around 0.06M and 0.30M, respectively. None of the admixed inhibitors contain K^+ ions, thus a ratio of Na^+ to the natural background concentration of K^+ can serve as an internal standard for coarse estimates of inhibitor-contributed Na^+ alkalinity. Table 3 shows that appreciable Na^+ contributions are present for higher concentrations of sodium nitrite, sodium nitrate, and sodium phosphate.

Increases in pore solution alkalinity due to Na^+ persistence results in a lower $[Cl^-]/[OH^-]$ ratio, causing increased stability of the passive film. The sodium phosphate inhibitor produced the strongest increase in pore solution alkalinity of all inhibitors admixed in a 0.1M concentration for the present study. Despite the alkalinity-induced passivity that inherently exists in Portland cement paste, additional alkalinity-induced passive film stabilization by admixtures is *not* a desirable property due to the increased risk of alkali-aggregate for a concrete containing highly alkaline cement pastes. Calcium nitrite was the only inorganic inhibitor evaluated in the current study that did not elevate pore solution alkalinity because it was the only inorganic admixture that did not deliver additional sodium cations to pore solution.

CONCLUSIONS

It has been shown that the primary function of admixed corrosion inhibitors for reinforcing steel in Portland cement paste is to stabilize the naturally occurring passive film. For the experimental technique employed in the present work, an abrupt transition in corrosion potential and polarization resistance accompany the loss of passivity. Passive conditions for this experimental procedure consisted of corrosion potentials between –250 and –75 mV_{SCE}, with polarization resistances greater than 1 Mohm-cm^2. Active corrosion conditions were characterized by corrosion potentials between –600 and –500 mV_{SCE}, with polarization resistances between 10 and 100 kohm-cm^2. Sufficient doses of admixed corrosion inhibitors delayed the time-to-depassivation in these experiments. Nitrite anions effectively stabilized the passive film at lower concentrations than amines.

Corrosion inhibitor interaction with pore solution chemistry has been explored. Pore solution concentrations of inorganic corrosion inhibiting anions were shown to decrease during hydration due to binding of the inhibitor by cement paste hydration reaction compounds. Pore solution concentrations of organic inhibitors increased during hydration due to the partial consumption of mix water during hydration. Changes in pore solution alkalinity caused by Na+ persistence in pore solutions have also been identified. The use of calcium nitrite did not cause an increase in pore solution alkalinity.

ACKNOWLEDGEMENTS

The authors gratefully acknowledge financial and technical support from the NSF Center for Advanced Cement-Based Materials (ACBM) at Northwestern University, as well as the Naval Research Laboratory in Washington, DC for sponsoring the publication of this work at the Tri-Services Corrosion Conference.

REFERENCES

1. K. Videm, in Proceedings of the International Conference on Corrosion and Rehabilitation of Reinforced Concrete Structures, Orlando, Florida, 1998

2. C. Andrade and M. C. Alanso, in *Application of Accelerated Corrosion Tests to Service Life Prediction of Materials, ASTM STP 1194* (American Society for Testing and Materials, Philadelphia, 1994).

3. A. Bentur, S. Diamond, and N. S. Berke, *Steel Corrosion in Concrete*, 1st ed. (E & FN Spon, New York, 1997).

4. F. J. Martin and J. Olek, in Proceedings of the ASCE Materials Congress, Washington, D.C., 1996

5. S. Goni and C. Andrade, Cement and Concrete Research **20**, 525 (1990).

6. S. Diamond, Cement, Concrete and Aggregates **8** (2), 97 (1986).

7. D. A. Hausman, Materials Protection **6** (11), 19 (1967).

8. ACI 222R-95, in *ACI Manual of Concrete Practice, Part 1: Materials and General Properties of Concrete* (Detroit, Michigan, 1995), pp. 1.

9. L. Struble, Purdue University, 1987.

10. A. A. Jeknavorian, D. Chin, and L. Saidha, Cement, Concrete, and Aggregates, **17** (1), 48 (1995).

11. J. Corbo and H. Farazam, ACI Materials Journal **86** (5), 498 (1989).

12. L. Dhouibi, E. Triki, and A. Raharinaivo, in Proceedings of the Conference on Understanding Corrosion Mechanisms in Concrete, Boston, MA, 1997

13. N. H. Zaid, USA Patent No. 5595679 (January 21, 1997 1997).

14. S. Hettiarachchi and A. T. Gaynor, USA Patent No. 5366602 (December 11,1989 1994).

15. B. A. Miksic, C. Chandler, M. Kharshan, A. Furman, B. Rudman, and L. Gelner, USA Patent No. 5750053 (May 12, 1998 1998).

16. J. D. Dillard and J. O. Glanville, USA Patent No. 5092923 (March 3, 1992 1992).

17. A. M. Rosenberg and J. M. Gaidis, USA Patent No. 4092109 (1978).

18. C. N. Hansen, USA Patent No. 5383962 (January 24, 1995 1995).

19. Garber, USA Patent No. 4803007 (February 7, 1989 1989).

20. M. Grunze, A. Welle, N. Blank, and U. Maeder, in Proceedings of the Conference on Understanding Corrosion Mechanisms in Concrete, Boston, MA, 1997

21. N. S. Berke and M. C. Hicks, in Proceedings of the Conference on Understanding Corrosion Mechanisms in Concrete, Boston, MA, 1997

22. N. S. Berke and M. C. Hicks, in *Corrosion forms and control for infrastructure (ASTM STP 1137)* (ASTM, Philadelphia, PA, 1992), pp. 417.

23. Y. P. Virmani, K. C. Clear, and J. Pasko, T. J, Report No. HFWA/RD-83/012, 1983.

24. R. Cigna, G. Familiari, F. Gianetti, and G. Peroni, in Proceedings of the Conference on Understanding Corrosion Mechanisms in Concrete, Boston, 1997

25. M. Tullmin, L. Mammoliti, R. Sohdi, C. M. Hansson, and B. B. Hope, Cement, Concrete & Aggregates **17**, 134 (1995).

26. N. S. Berke, D. F. Shen, M. C. Hicks, and E. M. Gartner, USA (June 18, 1996 1996).
27. N. S. Berke and M. C. Hicks, USA (June 3, 1997 1997).

28. N. Kudo and H. Ibe, USA Patent No. 3976494 (1976).

29. O. M. Villemur and M. R. Barbosa, Informacion Tecnologica **8**, 51 (1997).

30. G. Batis, N. Kouloumbi, and A. Katsiamboulas, Cement, Concrete & Aggregates **18**, 118 (1996).

31. K. K. Sagoe-Crentsil, V. T. Yilmaz, and F. P. Glasser, Cement and Concrete Research **23**, 1380 (1993).

32. B. A. Miksic, C. Chandler, M. Kharshan, A. Furman, B. Rudman, and L. Gelner, USA Patent No. 5597514 (January 28, 1997 1997).

33. H. H. Uhlig and R. W. Revie, *Corrosion and corrosion control: an introduction to corrosion science and engineering*, 3rd. ed. (Wiley & Sons, New York, 1985).

34. A. Phanasgaonkar, B. Cherry, and M. Forsyth, in Proceedings of the Conference on Understanding Corrosion Mechanisms in Concrete, Boston, MA, 1997

35. J. K. Buffenbarger, M. A. Miltenberger, and S. L. Amey, in Proceedings of the Corrosion '96, 1996

36. M. J. Incorvia, Jr., R. W. Chobin, Jr., and T. Hegge, Jr., USA Patent No. 5891364 (April 6, 1999).

37. M. J. J. Incorvia, USA Patent No. 6071436 (June 6, 2000).

38. E. McCafferty, in *Corrosion Control by Coatings*, edited by Jr. Henry Leidheiser (Science Press, Princeton, NJ, 1978), pp. 279.

39. J. A. Gonzalez, M. Benito, S. Feliu, P. Rodriguez, and C. Andrade, Corrosion **51**, 145 (1995).

40. U. Bertocci, in *Electrochemical Noise Measurement for Corrosion Applications (ASTM STP 1277)*, edited by J R Kearns, J R Scully, P R Roberge et al. (ASTM, Philadelphia, PA, 1996), pp. 39.

41. ASTM G109-99a, in *ASTM Book of Annual Standards* (ASTM, Philadelphia, 1999).

42. C. Andrade, M. Keddam, X. R. Novoa, M. C. Perez, C. M. Rangel, and H. Takenouti, Electrochimica Acta **46**, 3905 (2001).

43. P. Gu, S. Elliott, R. Hristova, J. J. Beaudoin, R. Brosseau, and B. Baldock, ACI Materials Journal **94** (5) (1997).

44. A. Raharinaivo, J.-P. Guilbaud, G. Chambazian, and F. Derrien, Corrosion Science **33** (10), 1607 (1992).

45. F. J. Martin and J. Olek, submitted to Review of Scientific Instruments (2002).

46. S. Fletcher and M. D. Horne, J. Electroanal Chem **297**, 297 (1991).

47. A. C305-87, in *Annual Book of ASTM Standards* (Philadelphia, 1993), pp. 197.

48. R. S. Barneyback and S. Diamond, Cement and Concrete Research **11** (2), 279 (1981).

49. P. K. Mehta and P. J. M. Monteiro, *Concrete Structure, Properties, and Materials*, 2 ed. (Prentice-Hall, Englewood Cliffs, NJ, 1993).

TABLES AND FIGURES

TABLE 1
Chemical composition (w%) of ASTM A615 Grade 60 reinforcing steel, compared to AISI 1020HR mild steel (w%)

Steel	C	Mn	P	S	Si	Cu	Ni	Cr	Mo
GR60	0.40	1.13	0.014	0.048	0.20	0.34	0.13	0.14	0.05

TABLE 2
Chemical analysis (w%) of Type I/II Portland Cement used in cement paste studies

SiO_2	Al_2O_3	Fe_2O_3	CaO	MgO	SO_3	Na_2O	K_2O	TA (Na_2O)	LOI
20.70	5.44	2.04	64.12	1.49	2.67	0.09	0.37	0.33	2.07

TABLE 3.

Inhibitor mix concentrations, resulting pore solution chemistry, and time required to depassivate in electrochemical testing.

Inhibitor Species	Admixed Conc. (10^{-3}M)	Pore Solution Conc. (10^{-3}M)	Pore Solution Na:K Ratio	Time to corrosion (d)
None	N/A	N/A	0.20	5
Benzoic Acid	1	2.6	0.21	> 56
Calc. Nitrite	1 †110	*0.0 22.4	0.21 0.19	12 > 28
Disod. Chromate	1	0.4	0.29	40
Disod. EDTA	1	2.6	0.22	> 56
DMAE	10	49	0.21	14
Sod. Nitrite	0.01 0.1 1 10 100	*0.0 *0.0 *0.0 0.7 21.7	0.20 0.21 0.21 0.25 0.56	40 > 56 > 56 > 56 > 56
Sod. Nitrate	0.01 10	*0.0 0.5	0.20 0.25	5 > 28
Sod. Phosphate	1 100	*0.0 *0.0	0.21 0.60	9 > 28
OCIA	‡1%	**0.5%	N/A	§8 thru > 28

* Pore solution concentration below limit of detection (0.1 mM)

† Admixed as CNIA, 1% by weight of cement

‡ Admixed as 1% by weight of cement.

** OCIA inhibitor changed chemical structure during hydration. Single UV-Vis absorption peak prior to hydration became multiple UV-Vis peaks after hydration.

§ Depassivation time was extended by a supplemental inhibitor treatment to the cement paste prior to chloride introduction into cell.

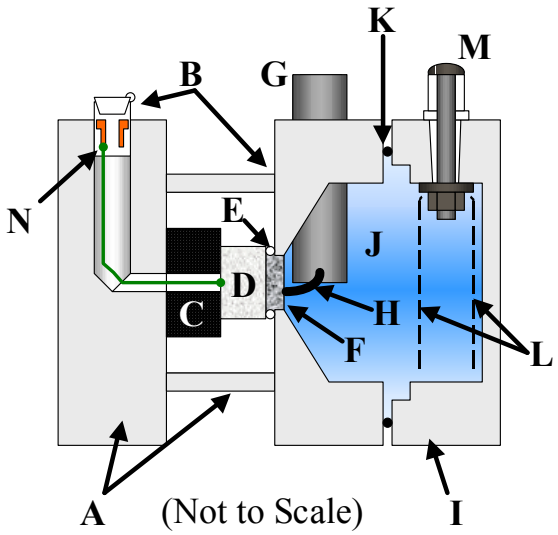

FIGURE 1. Cutaway view of experimental cell used for cement paste film studies. Features indicated include: A) specimen chamber, B) watertight cell body seals, C) specimen holder, D) polished steel specimen, E) Teflon o-ring, F) 2-3 mm paste/mortar film, G) RE holder, H) Luggin capillary, I) solution chamber, J) electrolyte cavity, K) solution chamber o-ring, L) CE mesh, M) CE leads, N) WE leads

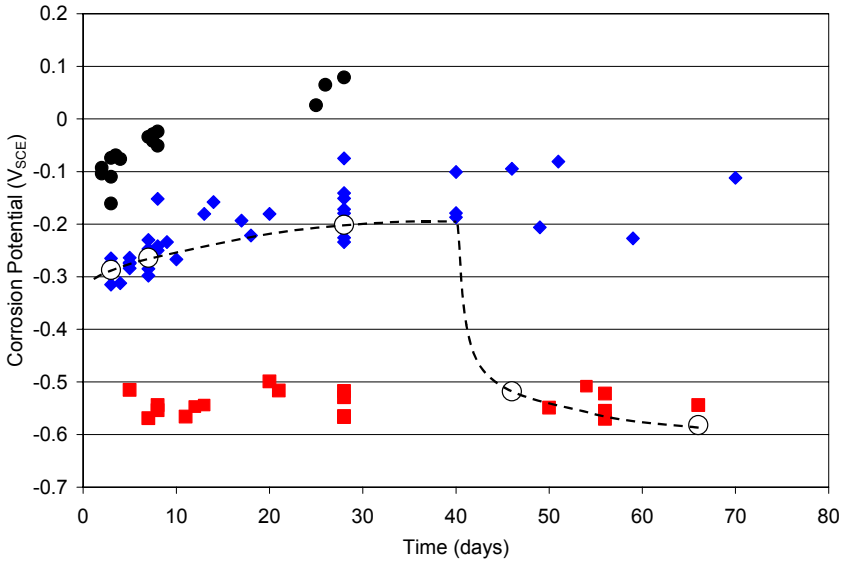

FIGURE 2. Corrosion potential versus time for reinforcing steel specimens exposed to chloride solutions (1M NaCl), some cement pastes contain admixed inhibitors and some do not. Markers indicate: (●) passive steel with no chlorides present, (◆) passive steel with chloride present at steel surface, (■) depassivated steel in presence of chlorides. Dashed lines indicate the corrosion potential history for a single experiment, also highlighted with (○).

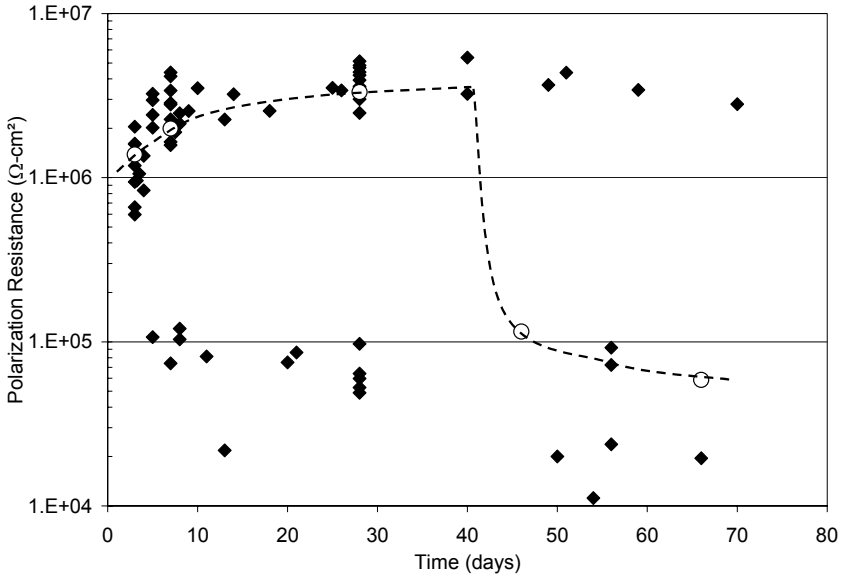

FIGURE 3. Polarization resistance versus time for reinforcing steel specimens exposed to chloride solutions (1M NaCl). Note the separation of polarization resistances between passive ($>10^6$ ohm-cm^2) and active ($<10^5$ ohm-cm^2) corrosion states. Open circles indicate experimental history for highlighted specimen from Figure 2.

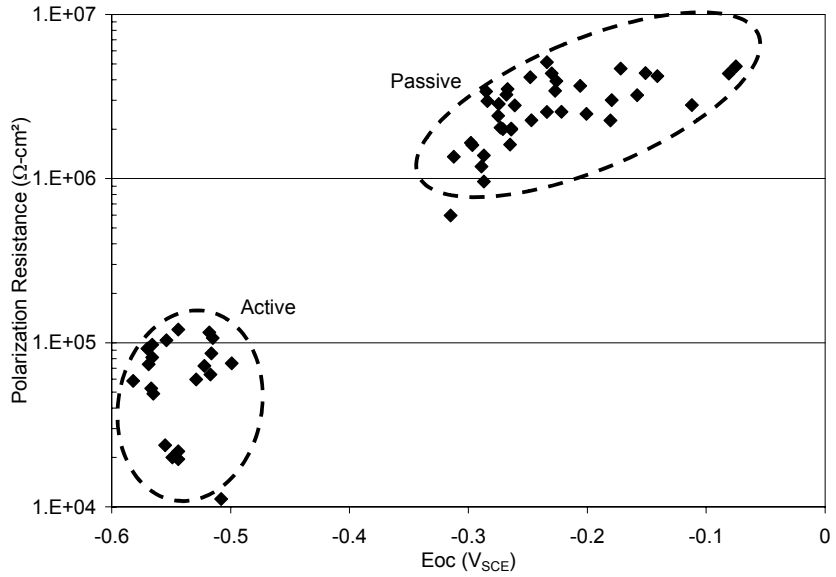

FIGURE 4. Plot of polarization resistance versus open-circuit corrosion potential shows two groupings: passive conditions and active conditions.

AN EXAMINATION OF DEGRADATION MODES OF CONSTRUCTIONAL MATERIALS FOR SUPERCRITICAL WATER OXIDATION SYSTEM FABRICATION

D.B. Mitton, H. Kim, J. Zhang and R.M. Latanision

H.H, Uhlig Corrosion Laboratory
Massachusetts Institute of Technology
Cambridge, MA, U.S.A. 02139

ABSTRACT

There is a need to destroy both military and civilian hazardous waste and an urgency, mandated by public concern over traditional waste handling methodologies, to identify safe and efficient alternative technologies. One very effective process for the destruction of such waste is supercritical water oxidation (SCWO). By capitalizing on the properties of water above its critical point, (374˚C and 221 atm for pure water), this technology provides rapid and complete oxidation with high destruction efficiencies at typical operating temperatures. Nevertheless, corrosion of the materials of fabrication is a serious concern and the practicality of SCWO may be limited by the ability to control corrosion. This paper reviews the current literature and presents experimental results for a number of candidate materials of fabrication. Among the potential modes of degradation, stress corrosion cracking (SCC) appears to be the most likely to result in catastrophic failure of a system component.

BACKGROUND

During the Workshop on Corrosion in Supercritical Water Oxidation (SCWO) Systems held at MIT in 1993 the attendees recognized the potential that corrosion problems could restrict the commercialization of SCWO for aggressive waste streams. At that time, the group consensus was that a material of fabrication universally applicable to all sections of a SCWO system was extremely unlikely. While the data base for the potential materials of fabrication for SCWO systems has increased significantly since then, the group consensus still holds. The corrosion of the materials of fabrication remains a serious concern and a significant amount of

research remains to be carried out to identify materials or methods to reduce degradation within all sections to an acceptable level.

There is in excess of 23,000 tons of chemical agent stockpiled at eight sites within the continental U.S. The composition and nomenclature for a number of agents are presented in Table 1.[1] While production was stopped in the late 1960's, some of this waste may have originated as long ago as the 1940's.[2] In addition to stockpiled munitions, there exists a significant, but unknown, quantity of non-stockpiled waste that also needs to be considered for destruction,[3, 4] which is a growing technical challenge due to the variety and circumstances in which it is found.[1, 3, 4] The Chemical Weapons Convention (CWC), which was signed by 130 countries seeks to eliminate chemical weapons and their production early in the new millennium.[2, 5] In order to be able to accomplish this, a safe, efficient and economical waste disposal methodology needs to be identified. While a number of traditional destruction methodologies such as landfill or incineration do currently exist, they face significant public opposition.[6] Further, the economics of incineration requires a relatively high concentration of waste in the feed and the practice of permitting aqueous waste concentration by evaporation in open ponds prior to disposal is no longer acceptable.

In addition to chemical agents, there is a need for DOE to address the clean up of in excess of 160,000 m^3 of mixed waste in its charge. While SCWO is demonstrably capable of destroying such wastes, many of the DOE wastes contain solvents or oils that are high in chlorine or other potentially corrosive precursors (e.g. fluorine, sulfur, tributyl phosphate). During destruction by SCWO, these can be oxidized to acidic products. In the case of chemical agents (Table 1), the oxidation of Sarin (GB) produces a mix of hydrofluoric and phosphoric acids; the oxidation of VX results in sulfuric and phosphoric acids; and finally, the oxidation of

mustard agent (HD) produces hydrochloric and sulfuric acids.[7] Such acidic conditions may result in significant corrosion of the process unit and, in the context of the development of scaled-up systems,[8-10] corrosion may ultimately be the deciding factor in the commercial application of this technology.

THE CHARACTERISTICS AND BENEFITS OF THE SCWO PROCESS

This is a promising technology applicable to many dilute organic wastes[11-13] in the range 1-20%, which are not suitable for disposal by either incineration or landfill.[6] As the critical point is approached, the density of water changes rapidly as a function of changes in either temperature or pressure. In this regime, the density is intermediate between that of liquid water (1 gcm^{-3}) and low pressure water vapor (<0.001 gcm^{-3}). Typically, at SCWO conditions, water density is approximately 0.1 gcm^{-3} and, consequently, the properties of supercritical water are significantly different from liquid water at ambient conditions. The dielectric constant of water at 25 MPa drops from approximately 80 at room temperature to 2 at 450˚C and the ionization constant decreases from 10^{-14} at room temperature to 10^{-23} at supercritical conditions. These changes result in supercritical water acting essentially as a non-polar dense gas with solvation properties approaching those of a low-polarity organic. Under these conditions, hydrocarbons generally exhibit high solubility in supercritical water and, conversely, the solubility of inorganic salts is very low. The solubility of NaCl, for example, drops from about 37 wt% at 300˚C to only 120 ppm at 550˚C. The combination of the solvation and physical properties make supercritical water an ideal medium for the oxidation of organics. When organic compounds and oxygen are dissolved in water above the critical point, kinetics are fast and the oxidation reaction proceeds rapidly to completion. While the products of hydrocarbon oxidation are CO_2 and H_2O, heteroatoms are converted to inorganic compounds (usually acids, salts or oxides in high

oxidation states). As a result of the relatively low temperature of operation NO_x and SO_2 are not produced.[11] The latter may be particularly important during the destruction of explosives, which produce nitrogen oxides during incineration.[14]

Figure 1 presents a schematic diagram of a waste treatment system based on SCWO technology.[12] In this process, aqueous organic waste (1), which may be neutralized with a caustic solution (2) or have fuel (3) injected for startup is initially pressurized from ambient to the pressure of the reaction vessel and pumped through a heat exchanger (4). This helps to bring the stream up to the desired temperature before reaching the reactor. At the head of the reactor (5), the stream is mixed with air or oxygen. In some cases, an oxidant such as hydrogen peroxide (H_2O_2) may be utilized in preference to either air or oxygen; however, this is not economically advantageous. The reaction occurs in the top zone (6), where spontaneous oxidation of the organics liberates heat and raises the temperature to levels as high as 650˚C. Organic destruction occurs quickly with typical reactor residence times of one minute or less. As a result of their low solubility, salts precipitate and impinge on the lower zone (7), which is at a temperature of about 200˚C. The salts may be continuously taken off as a brine (8) or removed periodically as solids. The primary effluent (9) passes out the top of the reactor into a separator (10) where the gas (11) and liquid (12) are quenched and separated. Finally, while a portion of the liquid remains in the system and is recycled (13) some is taken off as an effluent (14). Heat can be recovered from the treatment process stream and used to preheat the feed (4) or potentially to produce steam for electric power generation.[11]

CORROSION PROBLEMS IN SCWO SYSTEMS

The major disadvantages of SCWO revolve around high pressure ($P > 23$ MPa), potential solids handling problems, and, for some waste streams, corrosion.[11] Although SCWO is

technologically able to destroy hazardous wastes, the process must be carried out in a reactor capable of accommodating elevated temperatures, pressures, and degradation problems[15-33] that may result from aggressive feed streams.

As high-nickel materials have traditionally been employed for severe service applications,[21] they have been utilized during fabrication of a number of bench-scale and pilot plant reactors. The current data base, nevertheless, suggests that these materials may not be suitable for the most aggressive "untreated" SCWO feed streams[7, 8, 15, 17, 22-27] as they can exhibit both significant weight loss and localized effects including pitting, SCC and dealloying in such environments.

As early as 1990,[29] dealloying of Cr and Mo (I-625) or Cr, Mo and W (C-276) was recognized as a potential contributor to degradation within SCWO systems. Based on effluent analysis, results suggested loss of chromium for non-chlorinated feeds, while selective dissolution of the main alloying element, Ni, was apparent for chlorinated feeds.[30] Corroboration was subsequently provided[24, 25] by metallographic examination during analysis of a failed C-276 SCWO preheater tube, which, for acidic chlorinated conditions, revealed severe depletion of Ni. Interestingly, this analysis also suggested that the most severe corrosion was associated with a high subcritical temperature[25] and that, at supercritical conditions, in the absence of salt precipitates, corrosion may actually be minimal for alloys such as C-276.[31] At supercritical temperatures for an untreated acidic chlorinated feed,[32] high-nickel alloys I-625, C-22 and I-686 apparently follow a general trend in which the corrosion rate decreases between 400 and 600˚C; however, a significant increase was recorded above 600˚C. Conversely, within the same temperature range the corrosion rate of C-276 increased with increasing temperature. While one report suggests no apparent pattern in the location of localized corrosion for alloy

625,[23] there is significant evidence to suggest that the potential for corrosion of Ni alloys exposed to SCWO conditions is more pronounced in the high subcritical regime[24-26, 33] and that the aggressiveness of the solution may decrease above the critical point.[34, 35] Care is, however, necessary in extrapolating such behavior, as cracking has also been reported at supercritical temperatures after extended exposure times.[8] In addition, to some extent, the upper temperature limit for severe corrosion depends on the pressure and, thus, density of the solution, with higher densities favoring corrosion.[33] While an Inconel 625 tube exposed to an aqueous feed stream containing 1800 ppm HCl without the addition of oxygen, revealed only general corrosion[16] a 10 fold increase in the concentration (18000 ppm) resulted in transgranular SCC within the subcritical temperature zone (300˚C) after exposure for only 46 hours. Under more complex low pH conditions, others[27] report both transgranular and intergranular cracking of I-625 at subcritical, but not at supercritical, temperatures. Hong has, however, previously reported observing SCC and pitting of I-625 exposed to a mixed methylene chloride isopropyl alcohol feed neutralized with NaOH after extended times at supercritical temperatures (300 hours at 580˚C).[8] In general, when tested in chemical agent simulant feeds, corrosion of the nickel alloys (C-22, C-276, 625, 825 and HR-160) was unacceptably high for both chlorinated and non-chlorinated simulants.[7] When exposed to a highly chlorinated feed at 600˚C for a short duration (66.2 hours) HR-160 exhibited reasonable performance based on weight loss data; however, in regions where the surface oxide layer was locally disrupted severe grain boundary corrosion was apparent.[19] There is some evidence for a correlation between Cr content and corrosion resistance for Ni alloys in SCWO systems.[36] The high Cr alloys such as G-30 (≈30% Cr) exhibit reasonable corrosion resistance.[10, 19, 37] For a maximum temperature of 350˚C, results[20] indicate a rate of approximately 4 mmpy for G-30 exposed to an acidic chlorinated feed.

POTENTIAL METHODOLOGIES FOR REDUCING CORROSION DAMAGE

A recognition of materials degradation as one of the central challenges to the ultimate commercialization of this technology, has precipitated a number of potential methodologies for corrosion mitigation.

Corrosion Resistant Liners and Coatings. One potential methodology for reducing corrosion damage during the destruction of aggressive feeds would involve the use of a corrosion resistant liner in conjunction with a pressure-bearing wall. Although some progress has been made in circumventing corrosion problems in this way, liners have not been extensively tested in these systems and, as previously mentioned, there are conflicting reports on corrosion of basic materials. In addition, the liner materials (titanium and platinum) most frequently suggested for aggressive feed streams tend to be expensive.

Feed Modification. One possible alternative (or addition) to the use of corrosion resistant liners would be to adjust the feed stream chemistry such that serious degradation is minimized. It may be possible to accomplished this by reducing the chloride concentration, or by altering the pH and oxidizing conditions such that the most favorable thermodynamics are obtained.

Sufficient dilution of an aggressive feed can potentially reduce the risk of corrosion by lowering the chloride concentration and, thus, permit processing by SCWO. The required dilution may, however, be so large as to make such a procedure economically unattractive. For example a dilution of 1000-10000 for wastes high in solvents such as carbon tetrachloride may be required to reduce feeds to acceptable levels.[38]

Although feed neutralization, with NaOH for example, has seen some success in SCWO systems for acidic feeds, it has been carried out without a full understanding of its effect on corrosion within a system. Typically, feed neutralization involves stoichiometric quantities of

neutralizer; however, there is evidence[25] that a limited E-pH region exists within which the stability of Ni, Cr and Fe is thermodynamically favored for high subcritical conditions. Thus, the addition of the incorrect quantity of neutralizer may result in corrosion of systems fabricated from alloys containing these elements.

Reactor Design. Over the years, a number of new or modified reactor designs have emerged. In general, these designs, attempts to reduce exposure of the pressure bearing wall to the process fluid and to limit potential problems with plugging. In its simplest form design modification has involved the use of a liner with deionized water between the vessel wall and the liner.[39] More complex designs have included, the dual shell pressure balanced vessel (DSPBV),[40] the transpiring wall reactor and the reactor concept of a filmcooled coaxial hydrothermal burner (FCHB),[41, 42] In the latter case, while the authors were initially optimistic about the design,[41] subsequent experiments revealed problems including corrosion of the core tube tip and coaxial tubes.[42]

RECENT RESULTS

FAILURE ANALYSIS

Figure 2 presents both a schematic representation of an experimental plug flow reactor (PFR) and a number of micrographs of the tube cross-section at selected locations within the PFR. This system is employed to study the kinetics and reaction mechanisms of the destruction of organics in supercritical water. The organic preheaters were employed to heat an aqueous methylene chloride (CH_2Cl_2) feed solution (0.017 to 0.057 mol l^{-1} CH_2Cl_2) to the temperature of the reactor. Although isothermal conditions were maintained in the reactor (450°C-600°C) during individual experiments, the preheater temperature varied from ambient at the entrance to

supercritical at the exit. The alloy C-276 tubes employed as organic preheaters were approximately 250-300 cm long and had an outside diameter (OD) of 1.6 mm. The total time of exposure to the feed solution prior to failure was 104 hours for the first, 45 hours for the second and 56 hours for the third preheater.

Ultimately, all three units failed by the development of an axial intergranular crack, Figure 2 (a). In general, the inner diameter of the tube wall in the region of the failure site displayed dealloying[25] of Ni, Fe and Mo and enrichment of Cr. It is significant that although different conditions (temperature, feed type and composition) were employed during the various experiments, the three individual failures all occurred in the same general region of tube between 37.5 and 59 cm from the inlet end of the preheater.

There was no appreciable corrosion either at the preheater inlet (Figure 2 (b)), which was at near ambient temperature, or at the preheater exit (Figure 2(c)), which experienced significant HCl concentrations at supercritical conditions. The exit to the preheater (Figure 2(c)) and inlet to the cool-down heat exchanger (Figure 2(d)), which are known to be at supercritical conditions, both reveal low rates of corrosion. A short distance into the cool-down heat exchanger (Figure 2(e)), crack development is observed. The form of corrosion observed within the cool-down heat exchanger echoes the corrosion morphology seen within the preheater, and elemental analysis indicates selective dissolution of Ni, Fe and Mo as well as enrichment of Cr. Finally, beyond this point the corrosion rate within the cool-down heat exchanger decreases (Figure 2(f)) as a function of decreasing temperature.

No thermocouple was located in the vicinity of the preheater failure site. Nevertheless, as corrosion tended to be minimized within known supercritical regions, cracking was assumed to develop preferentially within a high subcritical regieme.[25] Rapid crack development could

compromise system integrity and, thus, foreknowledge of the probable location of maximum degradation would be important during system design. A subsequent section of this paper deals with this in more detail.

CORRELATION BETWEEN THERMODYNAMICS AND CORROSION

In general, during the failure analysis dealloying of Ni, Mo and Fe, and enrichment of Cr was observed. We previously suggested,[25] the potential that an E-pH region thermodynamically favorable to the stability of Ni-base alloys may be obtainable by feed modification. It was apparent from the results that there was a region of the E-pH diagram were thermodynamic conditions favored both the formation of insoluble chromium and soluble Ni, Fe and Mo. Additionally, it became clear during that analysis that a moderate increase in pH could result in a significant change in the corrosion behavior of the C-276 alloy. It was hypothesized that an increase in pH could either favor the stability of Cr, Ni and Fe (less oxidizing conditions) or the loss of Cr stability in conjunction with the formation of a stable Ni oxide (more oxidizing conditions).

Figure 3 presents both (a) the experimentally determined[43] relative concentration of Ni, Cr and Mo in the effluent for an Inconel 625 reactor exposed to various feed pH values and (b) a combination E-pH diagram for Ni, Cr and Mo at 300˚C.[25] The concentration of Ni, Cr and Mo in the effluent were experimentally determined at three ambient pH values: 1.3, 7.0 and 12.7 at a high subcritical maximum test temperature (Tmax ≈ 350˚C) and tabulated in the literature.[43] Figure 3 (a) was derived from the tabulated data and presents the relative concentration of Ni, Cr and Mo in the effluent for an Inconel 625 reactor exposed to various feed pH values. These data have been presented in Figure 3 (a) using the same abscissa (pH) as the E-pH diagram presented

in Figure 3 (b). By presenting the data in this way, a number of interesting features become apparent:

Acidic chlorinated feed. (pH 1.3) For these conditions, while the nickel concentration in the effluent is appreciably higher than the nominal alloy value, the Cr and Mo effluent concentrations are significantly lower than nominal. In agreement with our previous work indicating dealloying of alloy C-276 in acidic chloride media,[25] these data indicate that conditions are such that Ni is unstable while Cr is stable, resulting in selective dissolution of Ni. From the E-pH diagram (Figure 3 (b)), this suggests the probability of conditions associated with the stability of Ni^{2+} and CrOOH (shaded region). The pH of the feed was slightly more acidic (1.3) than the soluble/insoluble Cr species line (pH≈2). The E-pH diagram, however, represents conditions at 300˚C, while the pH of the feed was determined at ambient conditions. The metal (Ni, Cr, Mo) loss for this experiment was approximately 1589 ppm after 15 hours.

Neutral chlorinated feed. (pH 7), With the shift in pH from acidic to more neutral conditions, there has been a significant decrease in the relative concentration of Ni and an appreciable increase in the relative concentration of Cr in the effluent. Thus, while the Ni in the effluent is now lower than the nominal value, Cr is appreciably higher than nominal for this alloy. This indicates that conditions now favor stable Ni. At this pH, as previously indicated,[25] these data suggest selective dissolution of chromium for oxidizing environments. Nevertheless, the measured total metal dissolution is significantly less (40 ppm after 15 hours of exposure). The decreased corrosion rate results from the increase in feed pH, altering the thermodynamic stability of Ni from soluble (Ni^{2+}) to insoluble (NiO). Assuming that the experimentally indicated selective Cr depletion suggests $HCrO_4^-$ stability, it may be possible to decrease corrosion further by reducing the oxidizing potential of the feed to region 3 in Figure 3 (b).

Alkaline chlorinated feed. (pH 12.7), A further increase in pH results in data that again indicate selective dissolution of Cr. The total metal in the effluent has, however, decreased to a value 600 times lower than that recorded for the acidic feed (2.6 ppm after a 15 hours). While this may be indicative of the potential for successful corrosion control by this methodology, longer-term exposure experiments are, needed.

The results presented in Figure 3 are particularly interesting as the behavior of the Inconel-625 alloy exposed to aqueous HCl was predicted quite accurately by the hypothesis developed during the failure analysis of a C-276 tube exposed to methylene chloride.[25] This suggests that such results may be valuable not only for specific alloys but may also be employed in a more general way to provide information on other alloys.

INSTRUMENTED TUBE EXPERIMENTS

In order to provide a more controlled assessment of the correlation between temperature and corrosion rate, a number of experiments have been carried out in which an alloy C-276 tube was instrumented with thermocouples. These experiments were designed to correlate as closely as possible to conditions associated with the failure of the organic preheaters previously discussed. As one of the major products of the hydrolysis of CH_2Cl_2 occurring in the preheaters is hydrochloric acid, during the instrumented tube experiment, an aqueous HCl feed was introduced at a supercritical temperature and allowed to cool as it traversed the length of the tube. The ambient pH of the feed and the effluent were both approximately 2. During previous work[31] the following broad regions were delineated: (i) a region at high temperature in which no corrosion was identified, (ii) a transition zone at a somewhat lower temperature with some disconnected dealloying, (iii) a region in which a well established dealloyed layer with little evidence of cracking was apparent. The thickness of this layer was inversely proportional to the

measured temperature, exhibiting a tendency to thicken as the temperature decreases, (iv) a region in which both a dealloyed layer and intergranular cracking were observed. While the most severe cracking was associated with a subcritical temperature, the results were also interpreted to suggest the potential for crack development at higher temperatures during extended exposure.

While some temperature measurement problems were encountered during the previous experiment as a result of insufficient contact area between the tube and thermocouple, this problem was overcome in subsequent experiments by employing sub-miniature thermocouples.[44] Preliminary results are presented in Figures 4 (a-j).

Figure 4 presents the results for an alloy C-276 tube exposed to a 365 ppm aqueous HCl feed (pH≈2) for a total test time of 19.5 hours at a pressure of 24.6-25.3 MPa. Similar to results reported for the preheaters[31] the depth of cracking and dealloying generally track each other closely (Figure 4 (a)) as a function of temperature.

There is a distinct increase in degradation as the temperature decreases into the subcritical regime. The higher rate of degradation continues over a range of approximately 30˚C prior to decreasing again at approximately 345˚C. At the highest temperature assessed during this examination (Figure 4 (b)), the morphology reflects disconnected dealloying similar to that reported previously.[31] As the temperature approached the critical point (Figures 4 (c)), the dealloying and cracking became well established. Within the high subcritical region the extent of cracking and dealloying tend to remain constant or increase slightly as the temperature is decreased (Figures 4 (d)); however, below approximately 345˚C the depth of penetration decreased significantly. Finally, at a temperature of approximate 292.5˚C (Figure 4 (e)) the degradation is minimal

These results corroborate the hypothesis developed during the preheater failure analysis and initial instrumented tube experiment that maximum degradation for Ni-base alloys may be associated with high subcritical temperatures. However, this was a simple non-salt forming feed and, in the presence of salt precipitates, corrosion behavior will change. Additionally, these were short duration experiments and cracking has been reported for Ni-base alloys, even at supercritical temperatures, after extended exposure.[8] Great care needs to be exercised, therefore, in extending these data to longer times or to systems where salts may develop.

EXPOSURE STUDIES

Samples positioned within the top zone of the Modar reactor (Figure 1) were exposed for 66.2 hours to a test temperature of approximately 600˚C in a highly chlorinated oxygenated organic feed stream containing C, H, O, N, Cl, S, Na, K, Si and F, with small additions of Ce, Pb and Zn. The materials chosen for testing included four nickel-base alloys (Inconel-625, Hastelloy C-276, C-22 and G-30) an austenitic stainless steel (316-L), a duplex stainless steel (Ferralium 255) and a high-cobalt alloy (HR-160). Either non-welded or welded and non-welded coupons of each alloy were exposed and, in addition, u-bend samples of Inconel-625, Hastelloy C-276 and stainless steel type 316-L were included. Coupons were mounted on a titanium rod and insulated from the rod and each other by means of alumina spacers.

As indicated by the corrosion rate data (Figure 5), alloy G-30 reveals the best corrosion resistance and alloy HR-160 (high Co) also exhibits good performance. The Ni-base alloys, C-22, C-276 and I-625 exhibit comparable rates, while the Fe-based duplex steel (Ferralium-255) reveals a rate similar to the Ni alloys. On the other hand, the austenitic stainless steel, 316-L, displayed the highest corrosion rate.

All samples were covered with both a salt layer and a black, tenacious oxide layer, which remained on the surface of the various samples even after removal of the salt layer by ultrasonic cleaning. Such salt deposits may be the precursors of severe corrosion[36] and have been linked to underdeposit corrosion of titanium.[45] Typically, the thickness of the oxide layer formed on alloy C-22, C-276, I-625, and 316-L is about 360µm, 550µm, 840µm, 1800µm respectively. As this order also reflects increasing corrosion rate (Figure 5), it suggests the oxide layer does not provide any significant corrosion protection. EPMA analysis for the various elements present within the oxide layer of the nickel alloys indicated nickel depletion in all cases.[19]

Both alloy C-276 and alloy I-625 exhibited pitting (Figure 6) and, in the case of C-276 some intergranular attack. Alloy C-22 revealed resistance superior to both alloy C-276 and I-625. For the conditions tested, alloy G-30 exhibited the best corrosion behavior.

SUMMARY AND CONCLUSIONS

It is apparent that there is a region of the E-pH diagram were thermodynamic conditions favor the formation of insoluble Cr, Ni and Fe at a high subcritical temperature (300˚C). Maintaining this region by feed chemistry control during waste destruction may reduce degradation.

Test results corroborate the strong correlation between feed pH and the relative dissolution of Ni and Cr for nickel base alloys. Acidic conditions tend to favor Ni dissolution and basic conditions tend toward Cr dissolution.

During the failure analysis, it was recognized that corrosion was minimized within known supercritical regions and cracking was, therefore, assumed to develop preferentially within a high subcritical regime. This was corroborated by subsequent instrumented tube

experiments designed to closely reflect conditions associated with the preheaters. These data were, however, for short duration experiments and a simple non-salt forming feed. As cracking of Ni-base alloys has been reported[8] at supercritical temperatures after extended exposure, great care needs to be exercised in extending these data to longer times or to systems where salts may develop.

ACKNOWLEDGEMENTS

The authors gratefully acknowledge funding from the U.S. Army Research Office under the supervision of R. Shaw through awards DAAH04-95-1-0302, and DAAD19-00-1-0446, and the Consortium on SCWO Constructional Materials (Haynes International, Krupp-VDM, NiDI, Special Metals).

REFERENCES

1. The NATO Advanced Workshop, Destruction of Military Toxic Waste, Naaldwijk, the Netherlands, May 22-27, 1994, US Army Research Office Report.

2. L. Drake, Selecting Technologies for Destruction of the Chemical Weapons Stockpile" MIT Energy Laboratory Seminar, February 9, 1993.
3. Aqua fortis, US Army Research Office 1993, Vol. 2, No. 2.

4. Aqua fortis, US Army Research Office 1994, Vol. 3, No. 1.

5. Aqua fortis, US Army Research Office 1993 Vol. 2, No. 1.

6. K.C. Swallow and D. Ham, The Nucleus 1993, 11, p. 11.

7. K.W. Downey, R.H. Snow, D.A. Hazlebeck, and A.J. Roberts, *Science and Technology*; ACS Symposium Series, 608, p. 313: ACS, Washington, DC, 1995.

8. R.M. Latanision, R.W. and Shaw, Co-Chairs, Corrosion in Supercritical Water Oxidation Systems -Summary of a Workshop held at MIT May 6-7, 1993, Report No. MIT-EL 93-006.

9. D.B. Mitton, J.C. Orzalli, and R.M. Latanision, Proc. 3rd Int. Symp. on Supercritical Fluids, 1994 Vol. 3, p. 43.

10. A.J. Thomas, and E.F. Gloyna, Corrosion Behavior of High Grade Alloys in the Supercritical Water Oxidation of Sludges, 1991, University of Texas at Austin Technical Report, CRWR 229.

11. J.W. Tester, H.R. Holgate, F.J. Armellini, P.A. Webley, W.R. Killilea, G.T. Hong, and , H.E. Barner, *Emerging Technologies for Waste Management III*; ACS Symposium Series, 518. p 35: ACS, Washington, DC, 1993.

12. M. Modell, *Standard Handbook of Hazardous Waste Treatment and Disposal*, McGraw Hill: New York 1989.

13. E.U. Franck, *High Temperature, High Pressure Electrochemistry in Aqueous Solutions;* NACE: Houston, 1976.

14. C.A. LaJeunesse, B.E. Mills, and B.G. Brown, Supercritical Water Oxidation of Ammonium Picrate, 1994, Sandia report SAND95-8202•UC-706.

15. S. Tebbal, and R.D. Kane, Corrosion 98, Paper 413, 1998, NACE, Houston, TX. (16)Boukis, N.; Landvatter, R.; Habicht, W.; Franz, G. First Experimental SCWO Corrosion Results of Ni-Base Alloys Fabricated as Pressure Tubes and Exposed to Oxygen Containing Diluted Hydrochloric Acid at $\leq 450^{\circ}C$, P=24 MPa, First Int. Workshop on Supercritical Water Oxidation, 1995, Jacksonville Florida.

17. D.B.Mitton, J.C. Orzalli, and Latanision, R.M. 12th ICPWS, p. 638, Begell House: New York, NY 1995.

18. D.B. Mitton, S-H Zhang, E-H Han, K.E. Hautanen, and R.M. Latanision, Proc. 13th ICC, Melbourne, Australia 1996.

19. D.B. Mitton, Y.S. Kim, J.H. Yoon, S. Take, and R.M. Latanision, Corrosion 99, Paper 257, 1999, NACE, Houston, TX.

20. J. Konys, S. Fodi, A. Ruck, and J. Hausselt, Corrosion 99, Paper 253, 1999, NACE, Houston, TX.

21. ASM Handbook, Vol 13, Corrosion, 9th ed., p. 641 ASM International, Materials Park, OH 1987.

22. J.C. Orzalli, Preliminary Corrosion Studies of Candidate Materials for Supercritical Water Oxidation Reactor Systems, Master's Thesis, Department of Materials Science and Engineering, MIT 1994.

23. B.C. Norby, "Supercritical Water Oxidation Benchscale Testing Metallurgical Analysis Report," Idaho National Engineering Laboratory, 1993, Report, EGG-WTD-10675.

24. R.M. Latanision, Corrosion, 1995, 51, 4, p. 270.

25. D.B. Mitton, P.A. Marrone and R.M. Latanision, J. Electrochem Soc. 1996, 143, p. L59.

26. D.B. Mitton, J.C. Orzalli, and R.M. Latanision, *Science and Technology*; ACS Symposium Series, 608, p. 327: ACS, Washington, DC, 1995.

27. R.D. Kane and D. Cuellar, Literature and Experience Survey on Supercritical Water Corrosion, 1994, CLI International Report, No L941079K.

28. G.P. Wozaldo and W.L. Pearl, Corrosion, Vol. 21, p. 355 (1965).

29. T.T. Bramlette, B.E. Mills, K.R. Hencken, M.E. Brynildson, S.C. Johnston, ; J.M. Hruby, H.C. Feemster, B.C. Odegard, and M. Modell, Destruction of DOE/DP Surrogate Wastes with Supercritical Water Oxidation Technology, 1990, Sandia National Laboratories Report, SAND90-8229.

30. S.F. Rice, R.R. Steeper, and C.A. LaJeunesse, Destruction of Representative Navy Wastes Using Supercritical Water Oxidation, 1993, Sandia Report SAND 94-8203 UC-402.

31. D. B. Mitton, S-H Zhang, M.S. Quintana, J.A. Cline, N. Caputy, P.A. Marrone and R.M. Latanision, Corrosion 98, Paper 414, 1998, NACE, Houston, TX.

32. G.T. Hong, D.W. Ordway and V.A. Ziberstein, Materials Testing in SCWO Systems, First Int. Workshop on Supercritical Water Oxidation, 1995, Jacksonville Florida.

33. P. Kritzer, N. Boukis, and E. Dinjus, Corrosion 98, Paper 415, 1998, NACE, Houston, TX.

34. S. Huang, K. Daehling, T.E. Carleson, M. Abdel-latif, P. Taylor, C. Wai, and A. Propp, Electrochemical Measurement of Corrosion of Iron Alloys in Supercritical Water *Supercritical Fluid Science and Technology*; ACS Symposium Series, 406. p 287: ACS, Washington, DC 1989.

35. L.B. Kriksunov and D.D. Macdonald, J.Electrochem. Soc. 1995, p. 4069.

36. K.M. Garcia, and R. Mizia, Corrosion Investigation of Multilayered Ceramics and Experimental Nickel Alloys in SCWO Process Environments, First Int. Workshop on Supercritical Water Oxidation, 1995, Jacksonville Florida.

37. S. Fodi, J. Konys, J. Hausselt, H. Schmidt and V. Casal, Corrosion 98, Paper 416, 1998, NACE, Houston, TX.

38. C.M. Barnes, R.W. Marshall, R. Mizia, J.S. Herring and E.S. Peterson, Identification of Technical Constraints for Treatment of DOE Mixed Waste by Supercritical Water Oxidation, 1993, EGG-WTD-10768.

39. G.T. Hong, personal communication, 1997.

40. A.G. Fassbender, R.J. Robertus and G.S. Daverman, The Dual Shell Pressure Balanced Vessel: A Reactor for Corrosive Applications, First Int. Workshop on Supercritical Water Oxidation, 1995, Jacksonville Florida.

41. H.L. LaRoche, M. Weber, and Ch. Trepp, Rationale for the Filmcooled Coaxial Hydrothermal Burner (FCHB) for Supercritical Water Oxidation (SCWO), First Int. Workshop on Supercritical Water Oxidation, 1995, Jacksonville Florida.

42. M. Weber, B. Wellig, R . von Rohr, Corrosion 99, Paper 258, 1999, NACE, Houston, TX.

43. P. Kritzer, N. Boukis and E. Dinjus, Corrosion, 1998, 54, 824.

44. J.A. Cline, Experimental and Ab Initio Investigations of Corrosion in Supercritical Water Oxidation Systems, Ph.D. Dissertation, MIT 2000.

45. Garcia, K.M. Supercritical Water Oxidation Data Acquisition Testing, 1996, INEL report INEL-96/0267.

TABLES AND FIGURES

TABLE 1.
The composition and nomenclature for a number of chemical agents.[1]

Agent	Composition
GB (Sarin)	Isopropyl methylphosphonofluoridate
VX	O-ethyl S-diisopropylamino-methyl methylphosphonothiolate
HD (Mustard)	Bis-2-(chloroethyl)sulfide
GF	Cyclohexyl methylphosphonofluoridate
GD (Soman)	Pinacolylmethyl-phosphonofluoridate
GA (Tabun)	O-ethyldimethyl-amidophosphorylcyanide

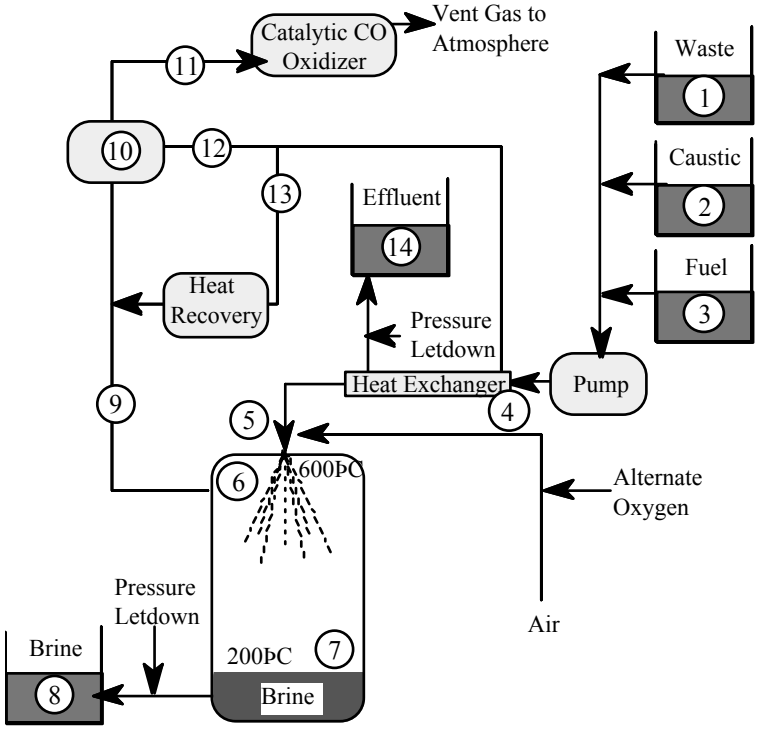

FIGURE 1. Schematic representation of a waste treatment system based on SCWO technology.

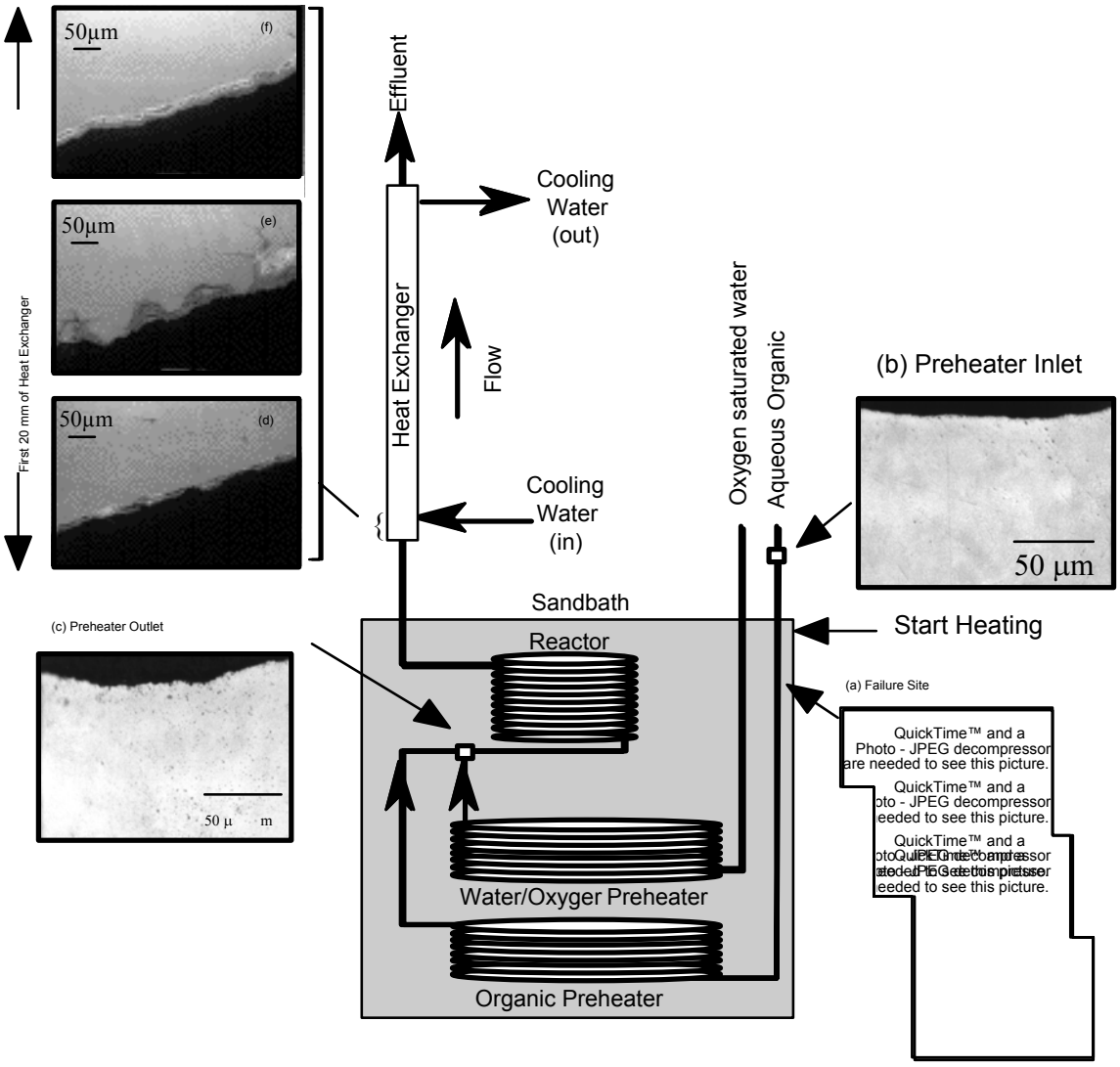

FIGURE 2. A schematic representation of an experimental plug flow reactor (PFR) and a number of micrographs(a-f) of the tube cross-section at selected locations within the PFR.

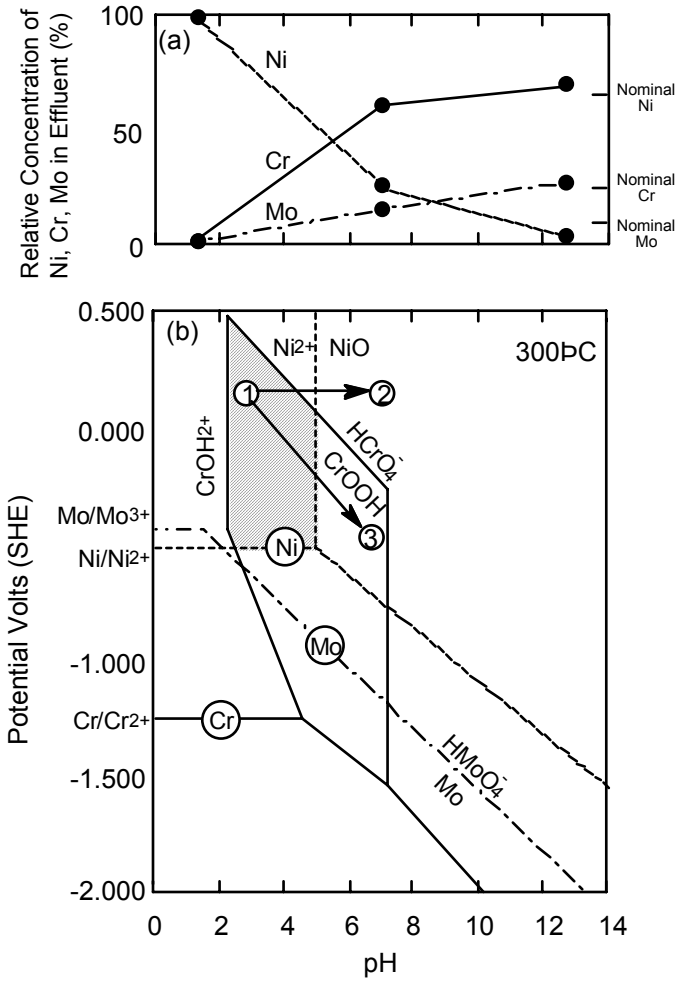

FIGURE 3. (a) the experimentally determined[43] relative concentration of Ni, Cr and Mo in the effluent for an Inconel 625 reactor exposed to various feed pH values and (b) a combination E-pH diagram for Ni, Cr and Mo at 300˚C.[25]

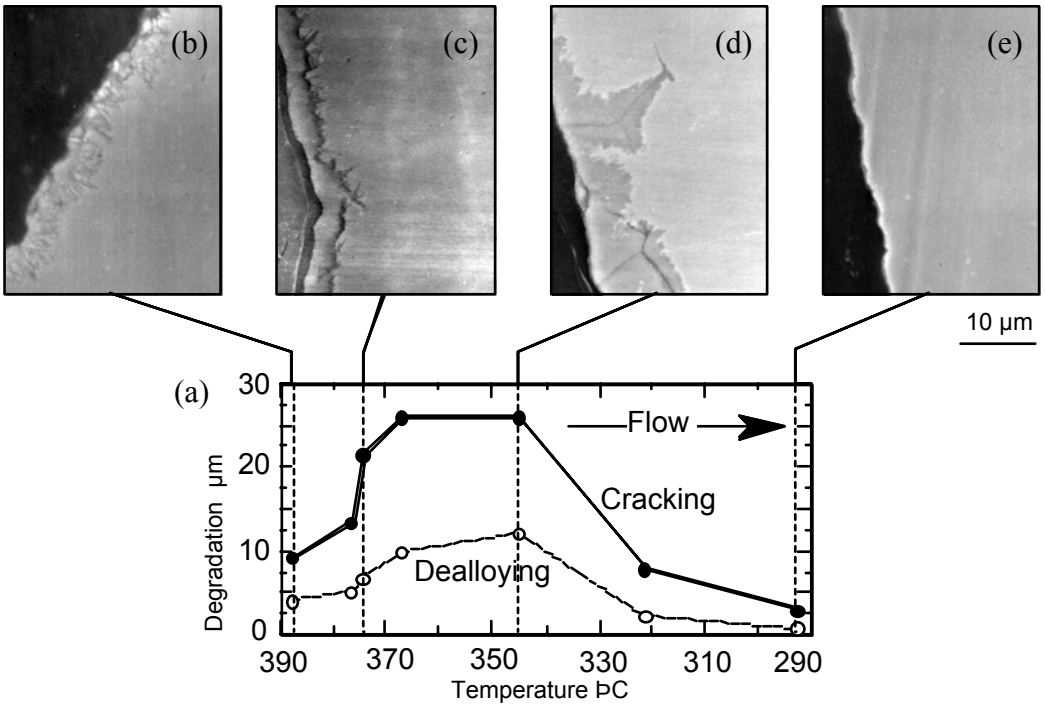

FIGURE 4. The results from an instrumented alloy C-276 tube as a function of temperature (a) the extent of cracking and dealloying and (b-e) the appearance of the inner tube diameter. The tube was exposed to an HCl feed (pH≈2) for a total test time of 19.5 hours.

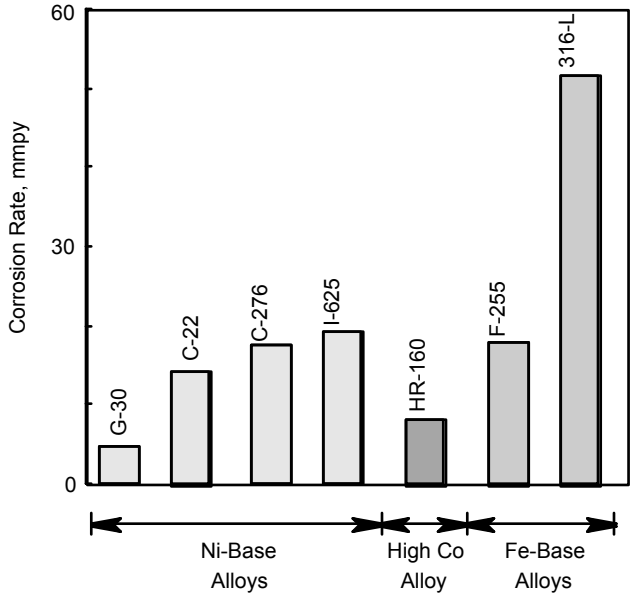

FIGURE 5. Mass loss data in millimeters per year (mmpy) for the various alloys exposed to an aggressive chlorinated SCWO feed stream.

ROTATING DISK STUDIES OF IRON CORROSION IN WATER UNDER ABIOTIC AND BIOTIC CONDITIONS

Batric Pesic

Department of Metallurgical, Materials Science and Engineering
University of Idaho
Moscow, Idaho 83844-3024
e-mail: pesic@uidaho.edu

ABSTRACT

Dissolution reactions of iron in water and medium salt solutions were examined by using conventional kinetic studies and the rotating disk technique. Reactions of iron were examined as a function of the following kinetic parameters: pH, oxygen concentration, temperature, ferrous and ferric ion concentration, type of solution, the presence of anions and cations, and the presence of bacteria, *Thiobacillus ferrooxidans.* The effect of pH was studied by using either H_2SO_4 or HCl for acidity adjustment. The above parameters were also examined in the medium salt solution. It was found that there were two iron dissolution regions with respect to pH. The iron dissolution independent of pH, and the iron dissolution dependent on pH with a negative two reaction order with respect to hydrogen. The range of pH independence was a function of oxygen concentration. There were two iron dissolution with respect to oxygen concentration too. The reaction orders with respect to oxygen were 1.0, when the concentration of O_2 was higher than 21%, and 0.5, when the concentration of O_2 was lower than 21%. *T. ferrooxidans* because of its poor adhesion onto iron surface had no effect on iron dissolution. Among anions, phosphate ions had the most negative effect. Among cations, V^{5+} had a strong positive effect, and Mo^{6+} had a strong negative effect on iron dissolution. Silver from silver nitrate even of 1.0 mg/l concentration had a strong positive effect on iron dissoluton.

INTRODUCTION

Iron is one of the most important metals to civilization. Its importance stems from its abundance and physical-chemical properties. Among the properties, the mechanical strength and the ability to dissolve various metals and elements are the most important. Steel is its most important derivative. Corrosion, the resistance to environmental degradation, of iron and steel is another important property which must always be considered and evaluated. Due to its

importance, the properties of iron in contact with aqueous solutions have been extensively studied. However, it is interesting to note that almost all studies have been based on the electrochemical principles, i.e. the typical corrosion studies. Of the abundant literary contributions to the corrosion of iron, the two monographs by Drazic[1] and Plonski[2] are the most extensive. Drazic's focus was on the review of literature concerned with the electrochemistry of iron in an active state, while Plonski reviewed dissolution of iron in acid media as a function of surface structure and adsorption phenomena.

It is rather interesting to note that among an enormous literature body on the subject of iron corrosion no publication was found that examined the rate of iron dissolution by utilizing conventional kinetic techniques. The lack of such data is rather intriguing considering ubiquitous and important nature of iron. Such data are very important and should serve as a control when comparing its reactivity with the reactivity of its various alloys. It was the task of this laboratory to launch such a conventional study and provide the fundamental information on the kinetics of iron dissolution. The kinetic parameters studied were: the effect of pH, temperature, ferrous and ferric ion concentration, type of solution, oxygen concentration, the effect of anions and cations and the effect of presence of bacteria, *Thiobacillus ferrooxidans*. In the previous dissolution study[3], iron was in the form of particulates. In this study, the reaction surface area was controlled by utilizing flat surface geometry, an iron disk in a rotating disk technique. H_2SO_4 and HCl were used for pH adjustment. In addition, the iron dissolution studies were performed in medium salt solution used for growth of *T. ferrooxidans*.

EXPERIMENTAL

MATERIALS AND PROCEDURE

Pure iron plate (99.99% Fe, AESAR) was used to cut 12.5 mm iron disks. An iron disk

was imbedded into a plastic cylinder with a shaft, which further was mounted onto a rotator assembly. The speed of disk rotation was controlled by an electric motor controller. During the experimentation, a disk was immersed 2-3 mm into a solution. The solution samples were taken at certain time intervals and analyzed for concentration of iron by using atomic absorption spectrophotometer (Varian Spectra 10/20). Analytical grade reagents and diionized water were used for solution preparation. Solution temperature was controlled by a temperature controller.

Standard experimental conditions are given in Table 1.

Table 1.
Standard Experimental Conditions

Volume	200 ml	Temperature	25 oC
pH	1.5	Rotation speed	800 rpm
Oxygen	21% (air)		

RESULTS

EFFECT OF ROTATING SPEED

In the rotating disk technique experiments, the first parameter that has to be studied is the speed of rotation. The iron dissolution data always fall on a straight line from which the rate of iron dissolution (line slopes) can be calculated. The calculated rates are further incorporated into Levich (4) equation, equation (1):

$$\frac{1}{A}\frac{dn}{dt} = J = 0.62 D^{2/3} v^{-1/6} \omega^{1/2} Co \qquad (1)$$

where,

dn/dt	rate of a reaction (M/min)
A	surface area (cm^2)
J	flux ($M/cm^2 sec$)

D	diffusion coefficient (cm^2/sec)
ν	kinematic viscosity (cm^2/sec)
ω	angular speed of rotation (rad/sec)
Co	concentration of chemically active species (M)

Levich equation was derived for reactions controlled by mass transfer through a uniform laminar film, and as such it represents a powerful technique for evaluation of diffusion coefficients of chemically active species. According to equation (1) a plot of the rates (slopes of lines from raw dissolution data) versus $T^{1/2}$ should produce a straight line with the intercept at zero. The Levich plot is given in Figure 1 for iron dissolution in sulfuric acid and medium salt solutions. Straight lines were obtained but these did not pass through the origin. The presence of intercept is a strong diagnostic that iron dissolution in acid medium does contain a kinetic control contribution.

EFFECT OF PH

Effect of pH was studied in three different atmospheres, air, oxygen and argon, each study repeated in three different solutions, H_2SO_4, HCl and medium salt. The dissolution data are given in Figure 2a-c. Iron dissolution was the fastest in oxygen atmosphere (Figure 2b) and the slowest in argon (Figure 2c). The role of pH during iron dissolution can be deciphered from the reaction order plot, ln(rate) vs. pH. An excellent presentation on the effect of pH is obtained in consequent Figure 3a-c. It was found that, for each atmosphere, there are two distinct pH regions, the iron dissolution rate region independent of pH and, the iron dissolution rate region dependant on pH with a negative second reaction order with respect to hydrogen ion. Accordingly, the role of oxygen is to define the length of horizontal lines representing the independence of iron dissolution rate on pH. The independence of the rate of dissolution from pH was the shortest in 100% O2 atmosphere (up to about pH 2.5), and the longest in oxygen free

atmosphere, i.e. argon, (up to about pH 4.0). In air, the iron dissolution rate was independent of pH up to around pH 3.0. These results were reproducible in each solution studied, H_2SO_4, HCl, and medium salt.

Both pH regions are readily explainable from the mechanistic point of view. The reactions corresponding to iron dissolution in the independence from pH region are identical to those proposed by corrosion scientists. The common accepted mechanism, in this region, is the so called BDD, Bockris-Despic-Drazic, mechanism[1]. Accordingly the first step in iron reactions with water is the adsorption, reaction (2),

$$Fe + H_2O \leftrightarrow FeOH_{ads} + H^+ + e \quad (2)$$

followed by the reaction of iron oxidation, reaction (3).

$$FeOH_{ads} \rightarrow FeOH^+ + e, \ (r.d.s.) \quad (3)$$

Iron reports into solution according to reaction (4),

$$FeOH^+ + H^+ \leftrightarrow Fe^{2+} + H_2O \quad (4)$$

The rate determining step is the reaction (3), which is H^+ independent, thus in acidic to moderately neutral solutions the rate of iron dissolution is pH independent. The data presented in Figure 3a-c confirm this mechanistic explanation.

The second pH region, in which the rate of iron dissolution decreases with the decrease of hydrogen ion concentration on power of two, does not reflect the kinetic but rather the thermodynamic phenomena. As the iron dissolution is responsible for production of ferrous ions, these species are not stable in the presence of oxygen. Oxidation of Fe^{2+} with oxygen is a function of pH. In low pH region, pH 0-2, in which Fe^{3+} is soluble, the rate of Fe^{2+} oxidation, reaction (5), is very slow.

$$4Fe^{2+} + 4H^+ + O_2 \rightarrow 4Fe^{3+} + 2H_2O \quad (5)$$

According to Mathews and Robins[5], reaction (5) proceeds according to the rate expression (6),

$$\frac{1}{4}\frac{d[Fe^{3+}]}{dt} = 1.32x10^{11} \times \frac{[Fe^{3+}][O_2]^{1.01}}{[H^+]^{0.25}} \times e^{(-17.6\times10^3/RT)}, M/\min \quad (6)$$

Above pH 2, Fe^{3+} is unstable and consequently the reaction of Fe^{2+} oxidation is different, reaction (7).

$$Fe^{2+} + 5/2H_2O + 1/4O_2 = Fe(OH)_3(s) + 2H^+ \quad (7)$$

The rate of ferrous ion oxidation according to reaction (7) is very sensitive to pH. Thus, according to Stumm and Lee[6], Sung and Morgan[7], the rate of iron oxidation increases with increase of $[OH^-]$ on power of two, equation (8),

$$\frac{-d[Fe^{2+}]}{dt} = k[Fe^{2+}][pO_2][OH^-]^2, M/\min \quad (8)$$

The expression (8) can be rewritten to reflect H^+ instead of OH^- in which case the reaction order with respect to hydrogen ions would become negative two. The value of slopes in Figure 3a-c are very close to -2. It is conclusive, therefore, that the straight lines with negative slopes in Figure 3a-c represent the rate of ferrous ion oxidation and not the rate of iron dissolution.

EFFECT OF OXYGEN CONCENTRATION

The effect of oxygen concentration on dissolution rate of iron, in all three solutions, was studied at pH 1.5. The raw data are presented in Figure 4a-c. These data were used to produce the reaction order plots, Figure 5a-c. According to the reaction order plots, dissolution of iron occurs according to two different mechanisms depending on oxygen concentration. It is interesting to note that the concentration of oxygen corresponding to air is the rate changing point. In solutions in contact with the atmosphere containing higher than air concentrations of oxygen iron dissolves according to the first order of reaction. As all diffusion controlled

reactions are of the first order, under high oxygen concentration conditions iron dissolution is controlled, perhaps, by diffusion of oxygen (non-electrochemical phenomenon). A half-reaction order is obtained for solutions in contact with the atmosphere with oxygen concentration lower than in air. A half-reaction order is most often assigned to the electrochemical reaction control mechanisms. The data for points for air atmosphere belong to both reaction mechanisms, thus the reactions in air atmosphere have to follow mixed kinetics mechanism.

The role of oxygen in corrosion of iron mechanisms is not a well resolved issue. The major controversy is on the mechanism of oxygen reduction on bare and passive iron surface[8,9]. It is generally assumed that oxygen reduction proceeds via *4e* pathway, with or without the formation of H_2O_2 as an intermediary, reactions (9) and (10):

$$O_2 + 4H^+ + 4e \rightarrow 2H_2O \quad (9)$$

$$O_2 + 2H_2O + 4e \rightarrow 4OH^- \quad (10)$$

EFFECT OF TEMPERATURE

Effect of temperature on dissolution of iron was studied in three different atmospheres, 10% O_2, air, and 100%O_2, Figure 6a-c. The temperature range was 25-55 ^oC. Three different solutions, H_2SO_4, HCl and medium salt were adjusted at pH 1.5. The rotation speed was 800 rpm.

The Arrhenius plots are given in Figure 7a-c with the relevant activation energies. It can be observed that the activation energy of iron dissolution was less than 5.0 Kcal/mole for each solution in contact with 100% O_2, indicating diffusion reacion control mechanisms. In the 10% O_2 atmosphere, the activation energy was above 5.0 Kcal/mole, a diagnostic value for reaction controlled mechanisms. The activation energies in the case of air atmosphere were right around 5.0 Kcal, again the border line when the reaction of iron dissolution changes its mechanism.

FERRIC IRON CONCENTRATION

This parameter is difficult to study because the reaction product is also iron, which is therefore difficult to distinguish from iron initially added. Nevertheless, ferric iron concentration effect was examined for very small initial concentration, 0.0005M, 0.001M and 0.002M Fe^{3+}, in air, in sulfuric, hydrochloric acid, and medium salt solutions, Figure 8a-b. It was found that the reaction order with respect to ferric iron was close to 2.0, for both solutions. This reaction order with respect to ferric ion is different from the close to 0.5 value obtained with powdered iron[10].

EFFECT OF *T. FERROOXIDANS*

T. ferrooxidans is a well known ferrous ion oxidizing bacteria in the pH region 1-3.5. As the reaction product of oxidation is ferric iron, it was expected that the adhesion of *T. ferrooxidans* on iron surface would have profound effects on the iron dissolution rates, especially when considering that any produced ferrous would be rapidly converted to ferric iron, thus converting the system to ferric dissolution conditions. The effect of pH study, in the presence of *T. ferroxidans*, however revealed neither the effect of pH, nor the effect of bacteria on iron dissolution (compared to control), Figure 9a-b. This is a rather surprising result and one explanation could be that the cells did not have an affinity for adhesion to pure iron surface.

Bacteria presence had an effect, however, if ferrous ion was initially added, Figure10a-d. A positive effect of *T. ferrooxidans* on iron dissolution, Figure 10c-d, was obtained compared to the same experimental conditions under abiotic conditions, Figure 10a-b. Initial presence of ferrous ion alone was ineffective as the oxidation of ferrous to ferric with oxygen in low pH solutions is very slow.

EFFECT OF ANIONS

Six different anions, each of 0.1M concentration, were examined with respect to their

effect on the rate of iron dissolution. The anions examined were SO_4^{2-}, Cl^-, $H_2PO_4^-$, HPO_4^-, PO_4^{3-}, and Br^-. The effects were examined in air and 100% O_2 atmosphere, each for three different solution, H_2SO_4, HCl, and medium salt, at pH 1.5. No effect of any anion was found in the air atmosphere, Figure 11a. However, in the 100% O_2 atmosphere, the anions had a negative effect in the following decreasing order: $>SO_4^{2-}$, $>Cl^-$, $>PO_4^{3-}$, $> Br^-$, $>H_2PO_4^-$, $>HPO_4^-$. Accordingly, sulfate ion had no or very little effect on iron dissolution. There is abundant literature on this subject, which will not be reviewed here, and for further information the monograph by Drazic[1] should be consulted.

EFFECT OF CATIONS

Effect of cations was also examined in two atmospheres, air and oxygen. Cations examined were: Ni^{2+}, Co^{2+}, Cr^{3+}, Mn^{2+}, Ca^{2+}, Mg^{2+}, Ag^+ (as sulfate and nitrate), Mo^{6+} and V^{5+}. The concentration of each cation was 0.01M, except of silver which was present in concentration of 1.0 mg/l.

In the air atmosphere, Figure 12a-c, V^{5+} had a significant positive effect on dissolution of iron in H_2SO_4 and medium salt solutions. In HCl solutions, V^{5+} was on opposite side with the most negative effect. The presence of Mo^{6+} cation decreased the iron dissolution rate the most, in each solution. Exactly same effect with respect to V^{5+} and Mo^{6+} was observed in oxygen atmosphere. The effect of Ag^+ from nitrate should be noted. In both atmospheres, the presence of silver in silver nitrate form had the most positive effect. Silver from silver sulfate was not as effective as silver from silver nitrate. As the concentration of silver was only 1.0 mg/l this effect cannot be assigned to the nitrate ion as its concentration would be too low for the effect of an anion. (Nitrate anion effect was not studied, unfortunately.) The mechanism for positive effect of Ag^+ in HCl solutions is not known. Silver from silver sulfate and silver nitrate was stable (no

noticeable precipitation) in both atmospheres (air and oxygen) and both solutions (H_2SO_4). The galvanic action of silver chloride precipitated on the surface of iron would have been the best approach to explain the positive effect of silver, if the silver concentration decreased with time. This parameter deserves further study by using in-situ surface morphology characterization techniques such atomic force microscopy.

The effect of other cations Ni^{2+}, Co^{2+}, Cr^{3+}, Mn^{2+}, Ca^{2+}, Mg^{2+} was almost indistinguishable from the control results when no cation carrying salt was added.

CONCLUSIONS

1. Pure iron dissolves in two characteristic pH regions in aqueous solutions. In acidic solutions iron is independent of pH. The range of pH independence is a function of oxygen concentration and increases with the decrease of such concentration. In the pH dependent region, hydroxide ion concentration increase has a negative effect on iron dissolution. The reaction order with respect to OH^- is about 2, or negative two with respect to H^+.

2. With respect to content of oxygen in the atmosphere iron dissolves, again, in two kinetically characteristic regions. When the concentration of oxygen is lower than 21% (air), the reaction order with respect to oxygen is about 0.5. When the concentration of oxygen is higher than 21%, the reaction order become 1.0. The break point between these two mechanisms is the oxygen content corresponding to air, 21%. Thus, in air iron dissolves according to mixed kinetics mechanisms.

3. The activation energy calculations also confirmed the change of mechanisms of iron dissolution with the concentration of oxygen. When the atmosphere contained more than 21% O_2, the activation energy was less than 5.0 Kcal/M, a diagnostic value for diffusion controlled

reactions. The activation energy in atmosphere with less than 21%O_2 was in the range 6.0-7.0 Kcal/mole, a diagnostic range for electrochemically controlled mechanisms. In air atmosphere, the activation energy was about 5.0 Kcal/mole, the value that can belong to both reaction mechanisms.

4. *T. ferrooxidans* did not adhere on iron surface, thus it had no effect on iron dissolution. The presence of bacteria had a positive effect when ferrous iron was initially presents. This effect was caused by oxidation of ferrous to ferric iron, and contribution of ferric iron to overall iron dissolution.

5. Anions, especially those from phosphate salts, had a negative effect on dissolution of iron.

6. Among examined cations, V^{5+}, Mo^{6+} and Ag^{+} had the most pronounced effects. V^{5+} had a strong positive effect, while Mo^{6+} had a strong negative effect. V^{5+} also had a negative effect in water acidified with HCl. The reasons for positive effect of Ag^{+} from silver nitrate are not known.

ACKNOWLEDGMENT

This work has been sponsored by the U.S. Department of Defense, Department of the Navy, Office of Naval Research, Grant Number N000149810533.

REFERENCES

1. D.M. Drazic, Modern Aspects of Electrochemistry, No. 19, (Plenum Press, New York, 1989), p. 69.

2. I. -H. Plonski, Modern Aspects of Electrochemistry, No. 29, (Plenum Press, New York, 1996), p. 203.

3. B. Pesic and V.C. Storhok, EPD Congress 2001, (The Publication of The Minerals, Metals &Materials Society, 2001), p. 471.

4. Yu.V. Pleskov and V.Yu. Filinovskii, The Rotating Disk Electrode, (Consultants Bureau, New York, 1976).

5. C.T. Mathews and R.G. Robins, Proc. Aust. Inst. Min. Met., No. 242, (June 1972): p. 47.

6. W. Stumm and G.F. Lee, Industrial and Engineering Chemistry, 53, No. 2 (1961): p. 143.

7. W. Sung and J.J. Morgan, Environmental Science & Technology, 14, No. 5 (1980): p. 561.

8. V. Jovanicevic, and J.O'M. Bockris, J. Electrochemical Society, vol. 133, No. 9, 1986.

9. Comments, J. Electrochemical Society, vol. 137, No. 1, 1990.

FIGURES

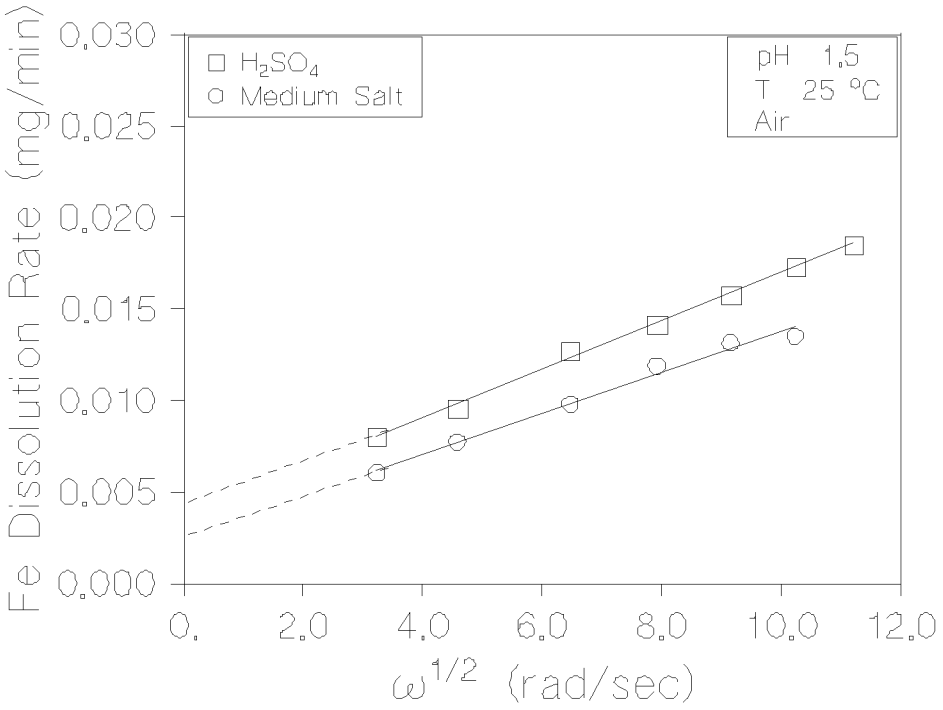

FIGURE 1. Levich Plots for dissolution of iron in water and medium salt soltuion.

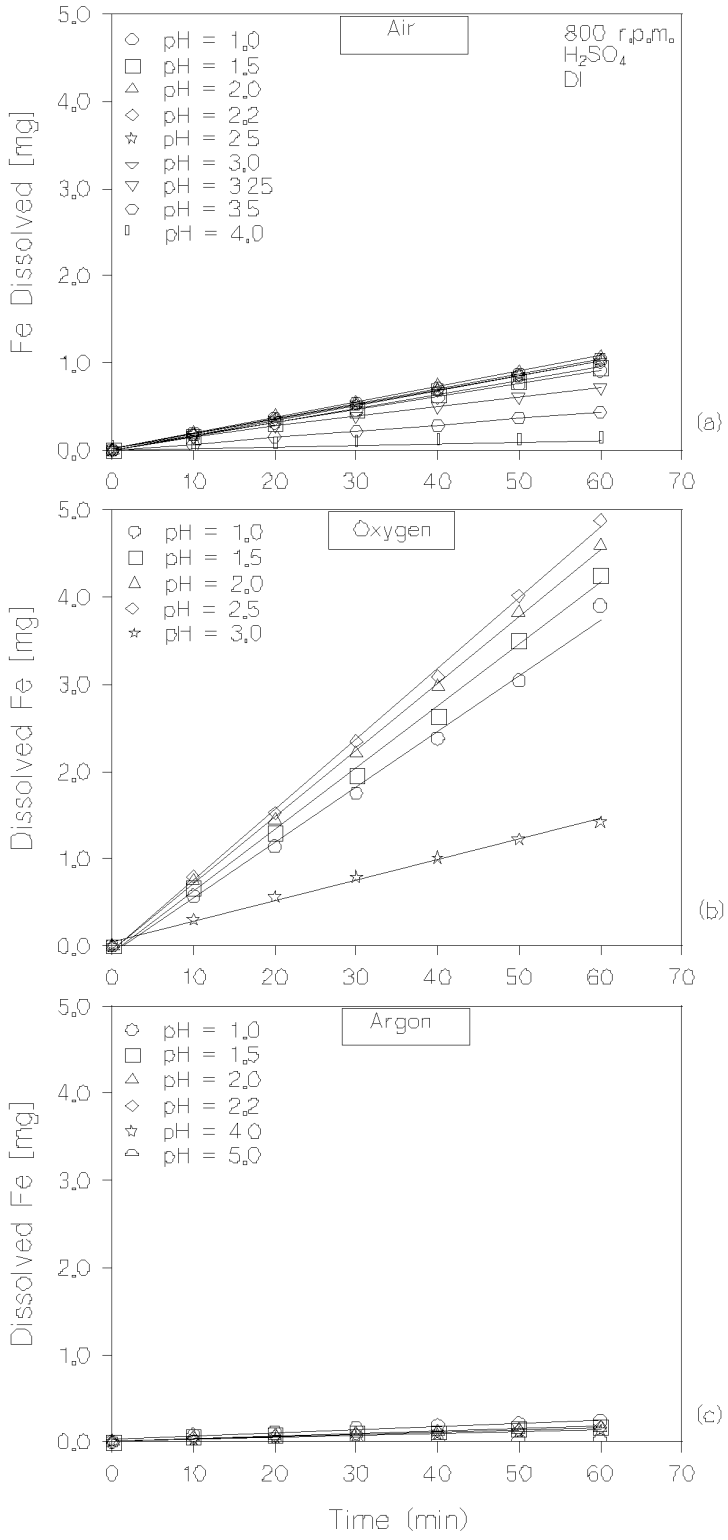

FIGURE 2. Effect of pH on iron dissolution.

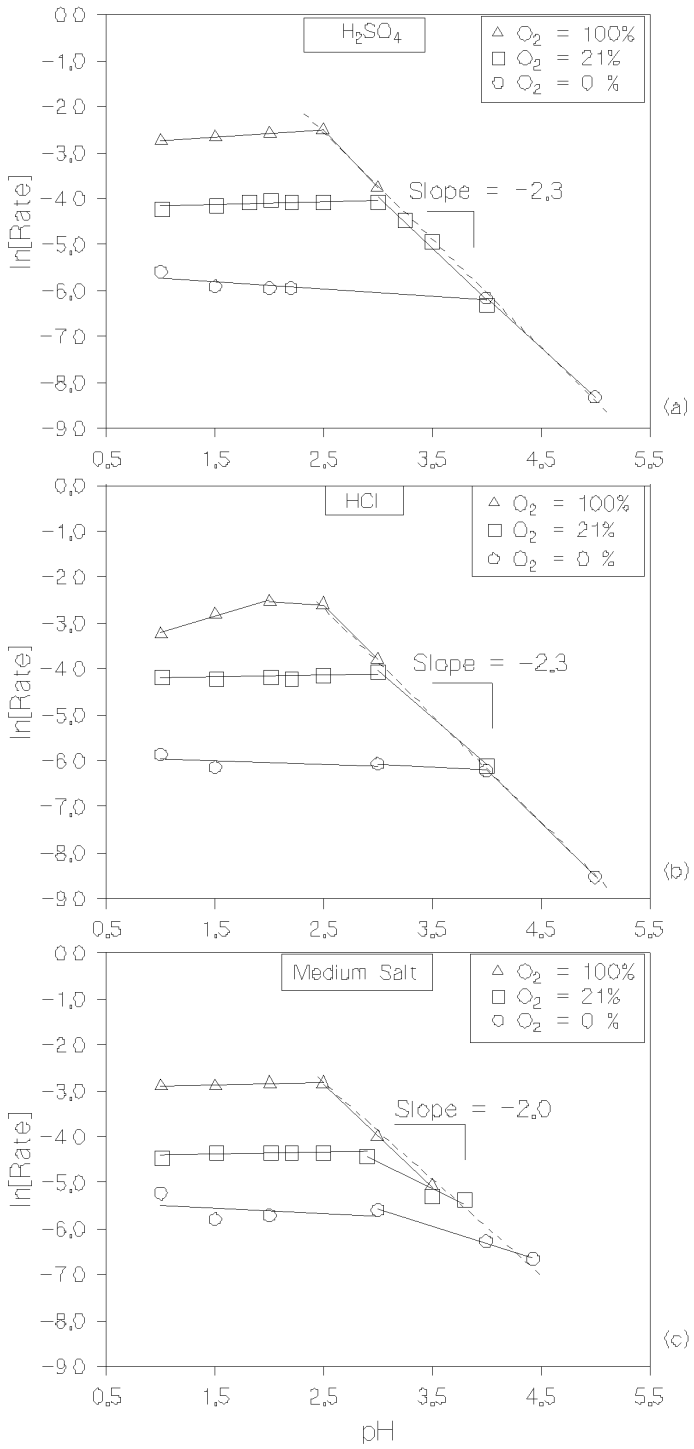

FIGURE 3. Reaction order with respect to oxygen plots.

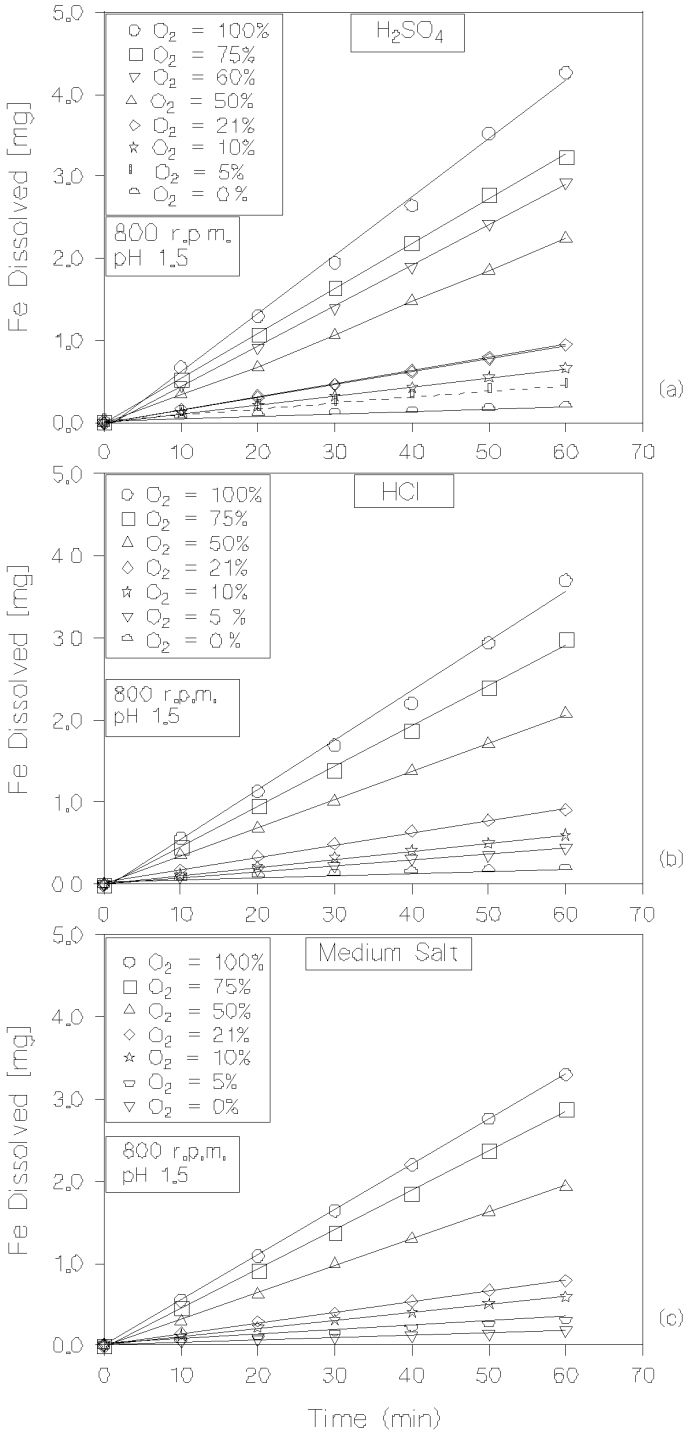

FIGURE 4. Effect of oxygen on dissolution of iron.

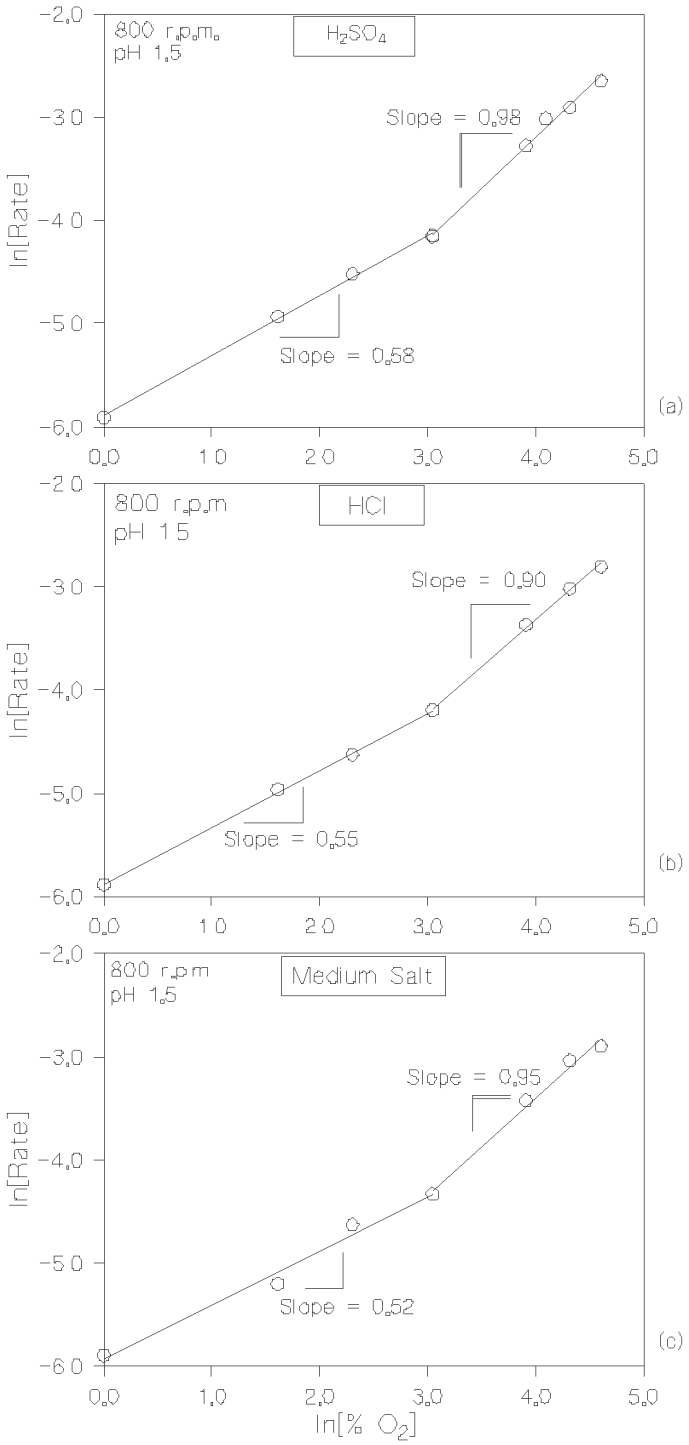

FIGURE 5. Reaction order with respect to oxygen plots.

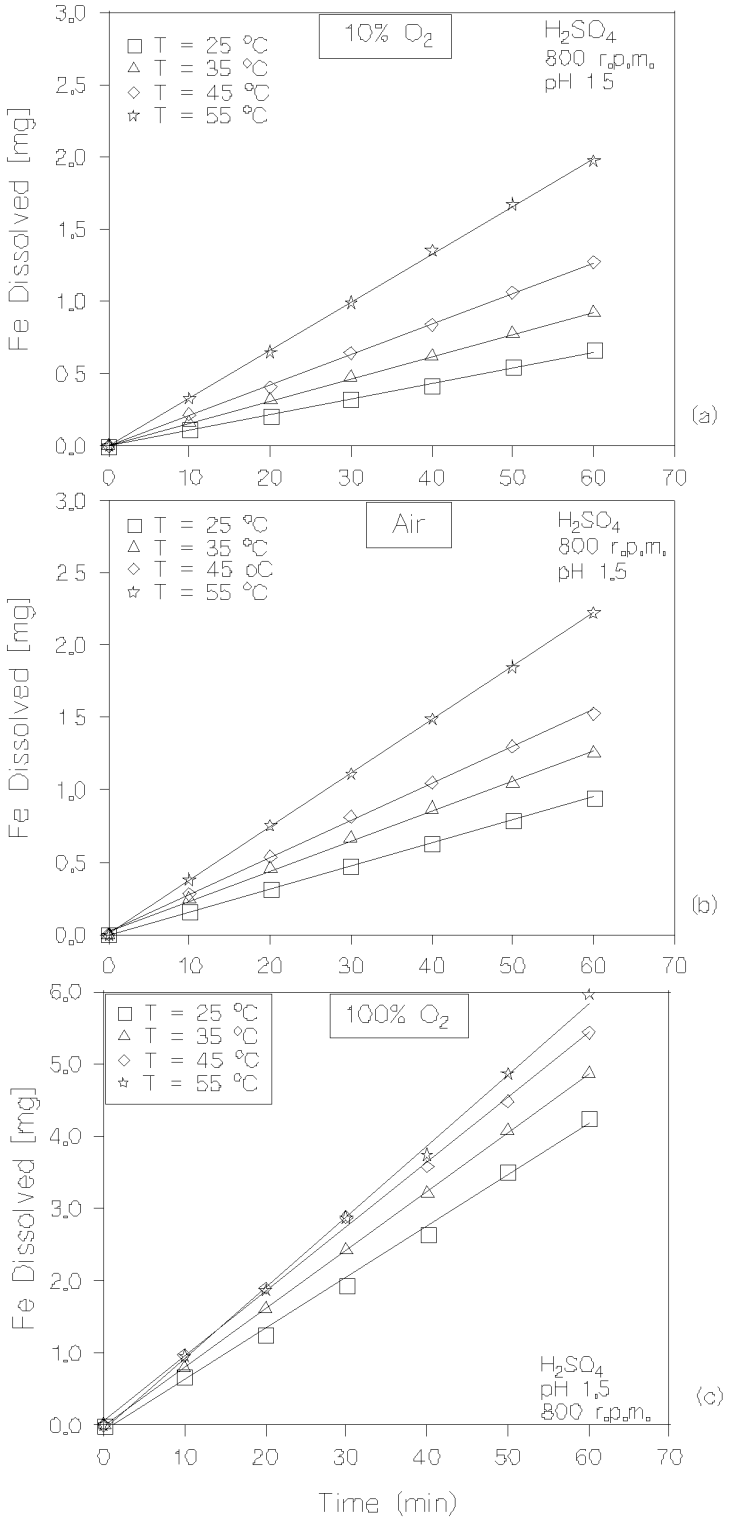

FIGURE 6. Effect of temperature on dissolution of iron.

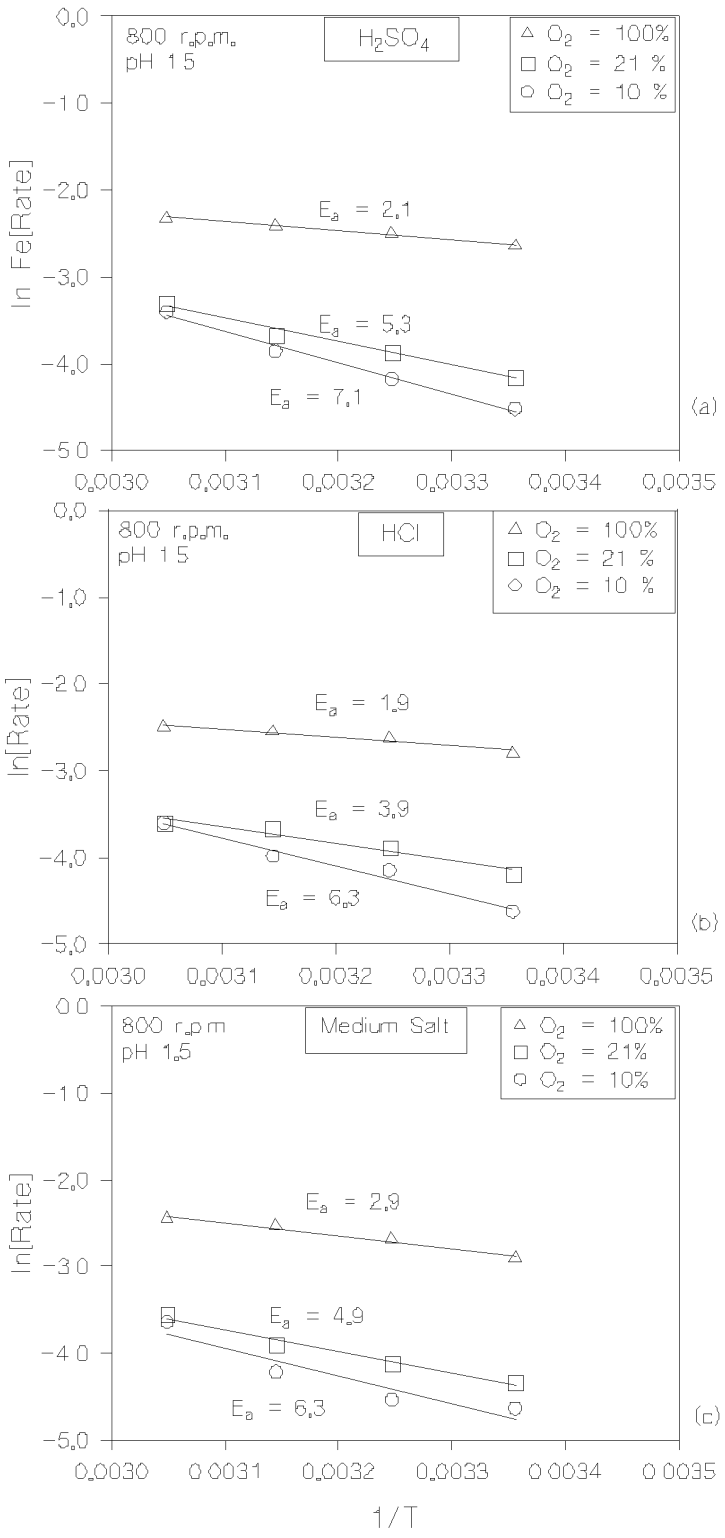

FIGURE 7. Arrhenius plots for dissolution of iron under specified conditions.

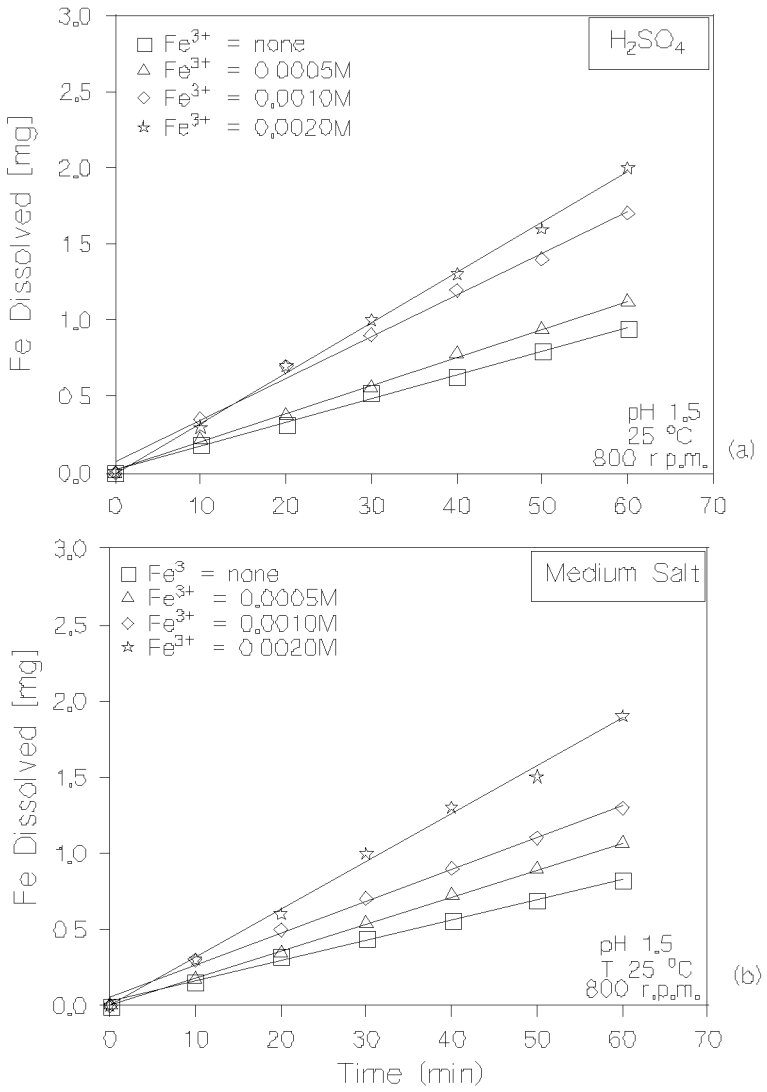

FIGURE 8. Effect of Fe^{3+} concentration on iron dissolution.

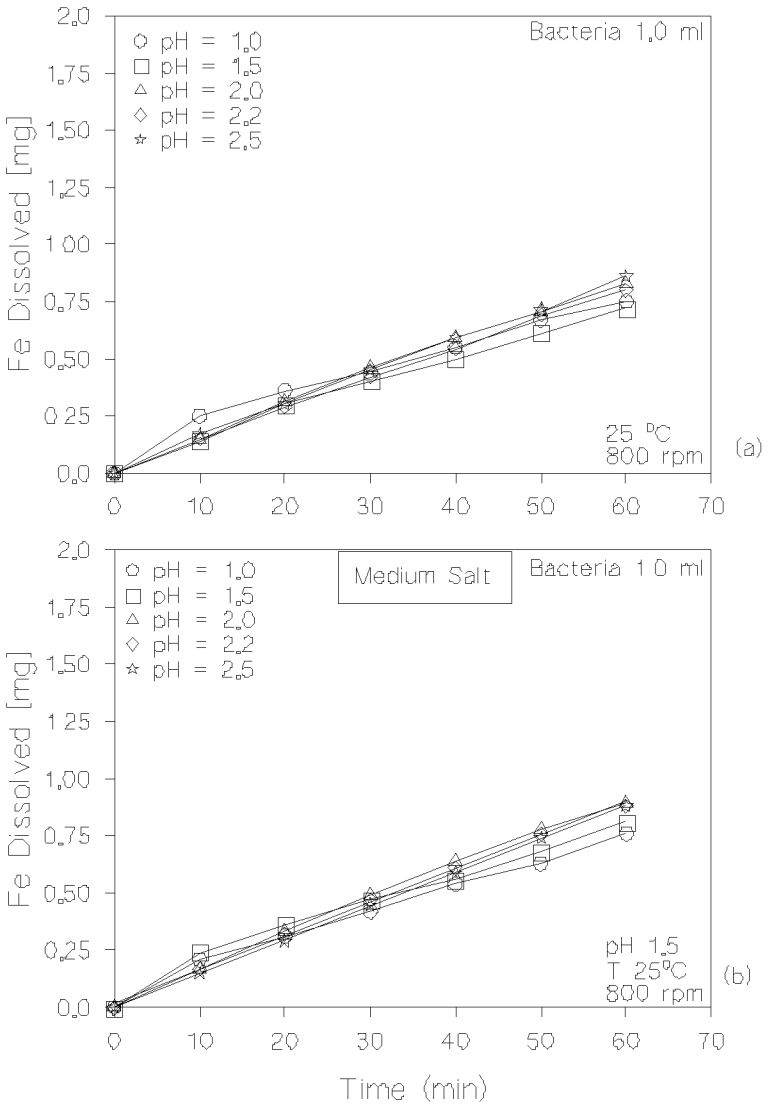

FIGURE 9. Dissolution of iron in the presence of *T. ferrooxidans* Effect of pH.

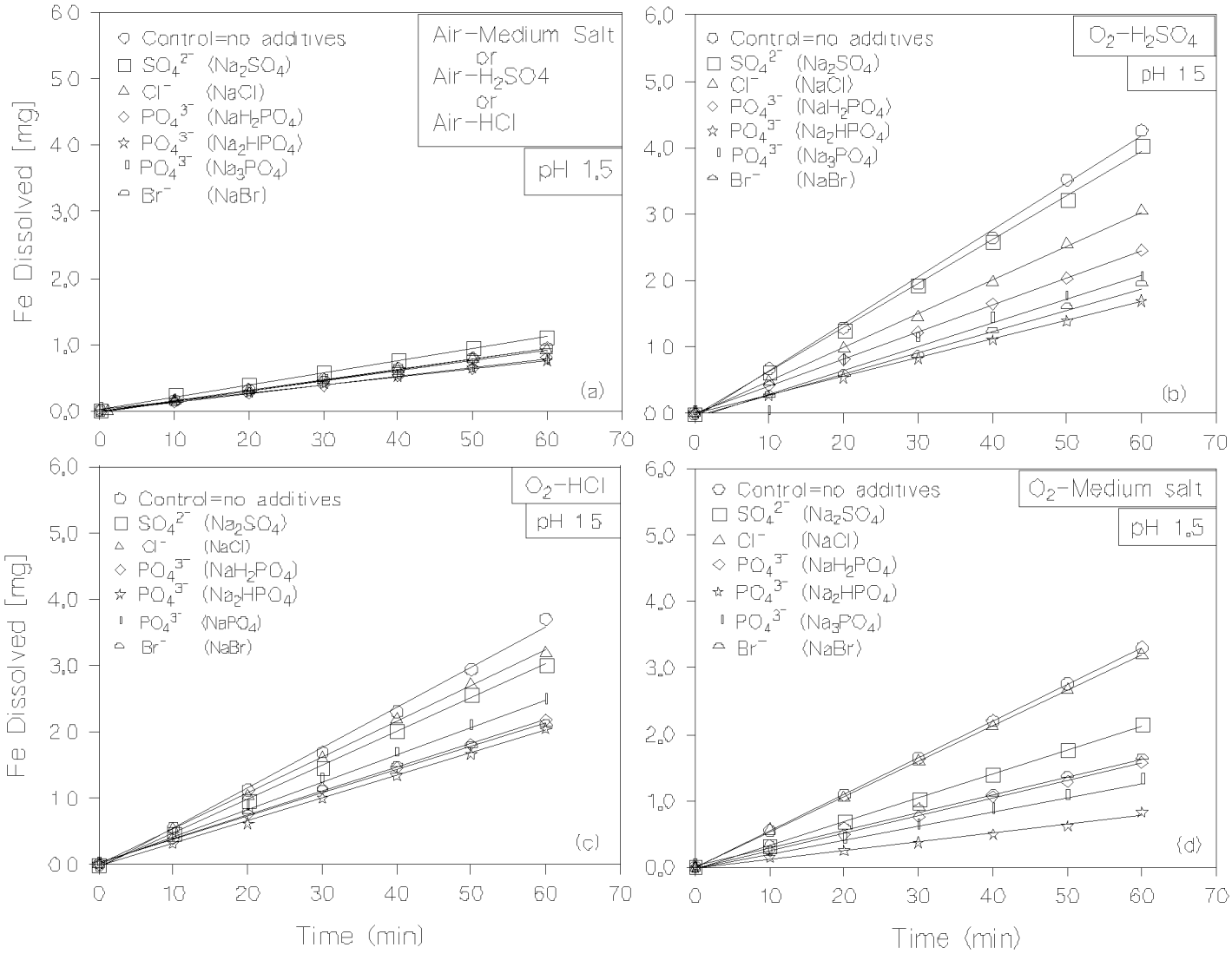

FIGURE 10. Effect of Fe^{2+} on iron dissolution under abiotic and biotic (*T. ferrooxidans*) conditions.

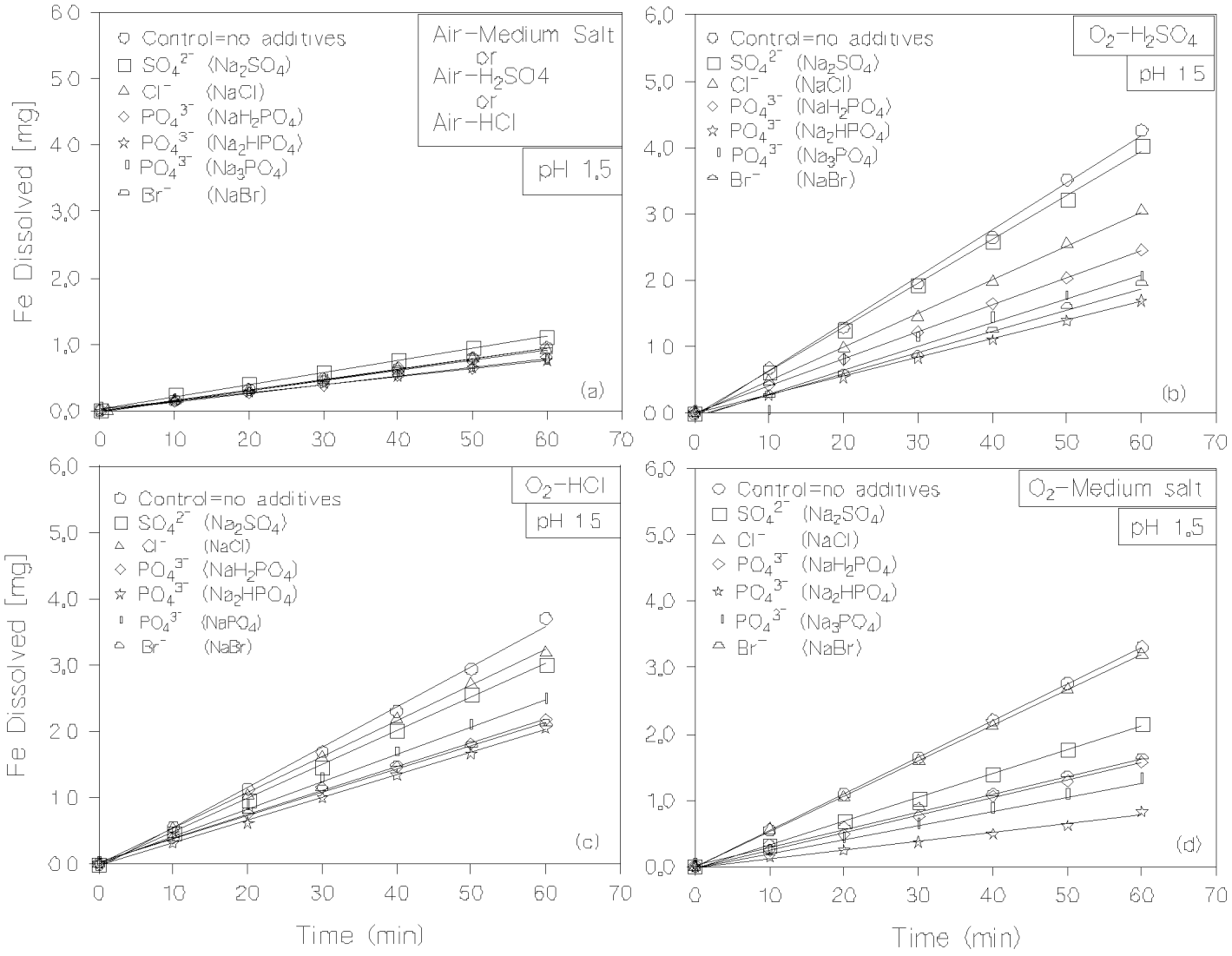

FIGURE 11. Effect anions on dissolution rate of iron.

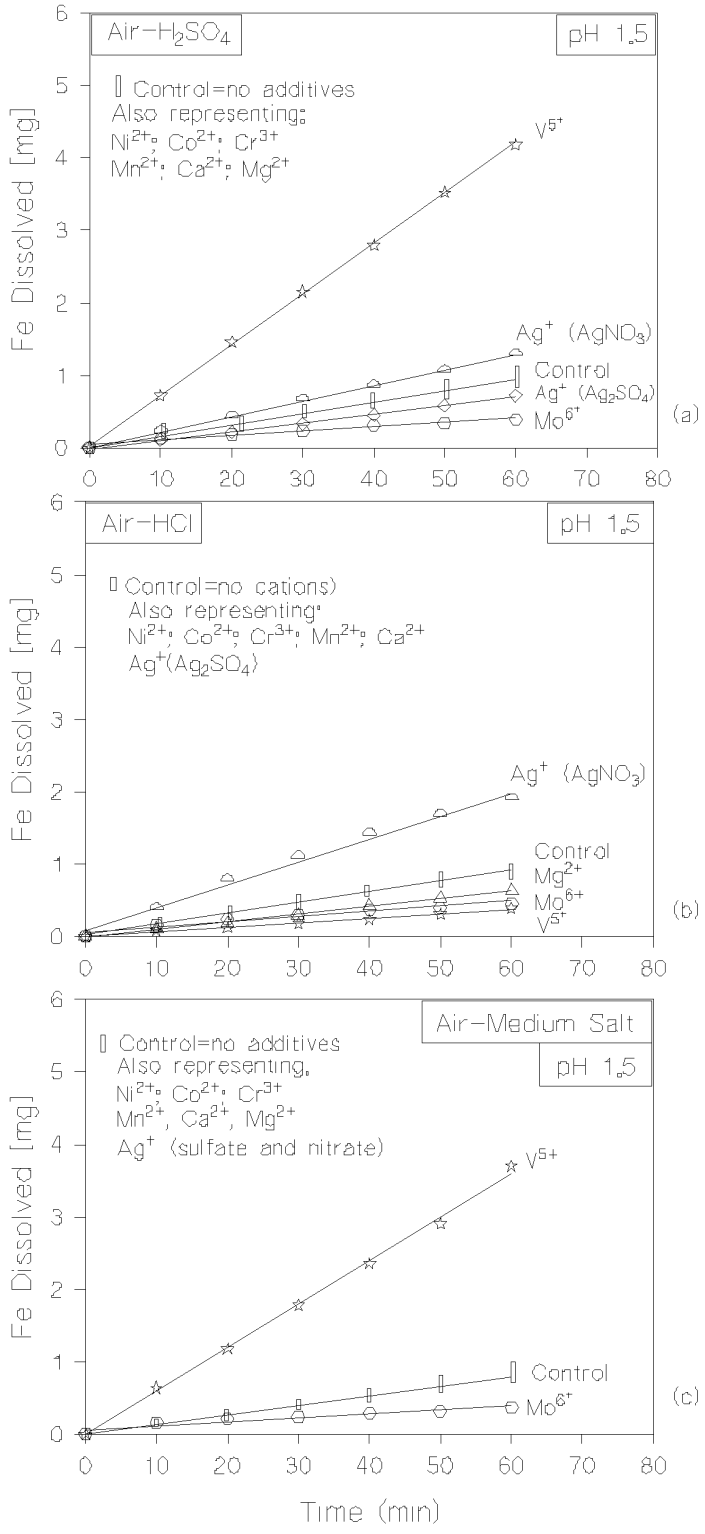

FIGURE 12. Effect of cations on dissolution of iron-air atmosphere.

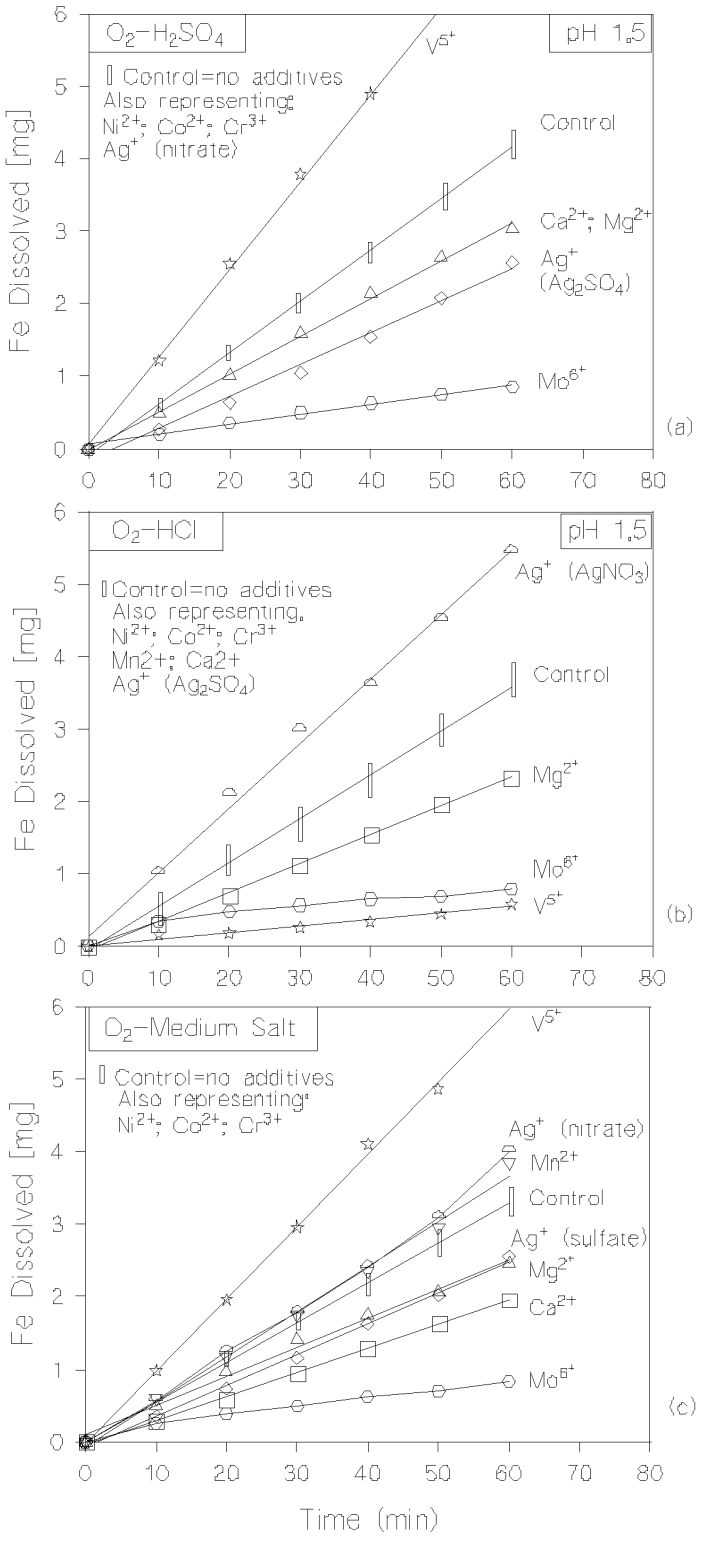

FIGURE 13. Effect of cations on iron dissolution-oxygen atmosphere.

THE ROLE OF MARINE BACTERIA IN STAINLESS STEEL PITTING

Richard I. Ray, Brenda J. Little and Jason S. Lee

Naval Research Laboratory/Code 7330 & 7303
Stennis Space Center, MS 39529-5004
ray@nrlssc.navy.mil
blittle@nrlssc.navy.mil
jason.lee@nrlssc.navy.mil

ABSTRACT

Flat plate and welded stainless steel coupons (316L, Nitronic 50 an AL6XN) were evaluated for potential microbiologically influenced corrosion in seawater. No pitting was observed in flat plate or welded AL6XN under the exposure condition after one year. Pits were located at welds of Nitronic 50 and 316L stainless steels after six- and eight-week exposures. In all cases, large numbers of bacteria were associated with the corrosion products. No corrosion was located on flat plate coupons of 316L or Nitronic 50.

INTRODUCTION

Microbiologically influenced corrosion (MIC) is used to designate corrosion due to the presence and activities of microorganisms. The spatial relationship between bacterial cells and pitting of weldments in austenitic stainless steels exposed in fresh water is well documented. [1-11] However, the reason for preferential microbial colonization at weldments has not been satisfactorily explained. Several case histories document selective attack at 316L stainless steel weldments exposed in marine environments.[12-14] It is generally accepted that the weld material is less resistant to pitting than the base metal because of differences in composition and structure resulting from heating and cooling. Welds typically contain ferrite, not found in the base metal. Little et al.[15] demonstrated that marine bacteria are co-located with iron corrosion product even when the bacteria were not responsible for the corrosion. Experiments in this paper were

designed to determine the potential for MIC in stainless steel weldments and to document the electrochemical impact of marine organisms on welded austenitic stainless steels.

MATERIALS AND METHODS

EXPOSURE CONDITIONS

Flat coupons (10 cm x 10 cm x 3.2 mm) were prepared of three stainless steels (316L, Nitronic 50 and AL6XN). Coupons were also prepared with a tungsten inert gas butt weld across the width in the center of the coupon. The welds on the coupons were not burnished and no attempt was made to remove surface oxides. 316L and Nitronic® coupons were welded with matching fillers. AL6XN was welded with Inconel 625 and Hastelloy C-276. See Table 1 for USN numbers and alloy compositions. Samples were cleaned and degreased by rinsing consecutively in isopropyl alcohol, acetone, and blown dry with nitrogen gas. Experiments were conducted in natural seawater in Key West, Florida and in abiotic artificial seawater with a salinity of 35 ppm. Two coupons of each material were exposed to flowing seawater for one year. Serial dilutions of the natural seawaters were tested with MICkit V® (BioIndustrial Technologies, Georgetown, TX) to quantify aerobic bacteria (AERO), acid-producing bacteria (APB), sulfate-reducing bacteria (SRB), iron-related bacteria (IRB), and low-nutrient bacteria (LNB). Coupons were examined monthly until the end of the test period (one year). Location and general description of corrosion was noted.

TABLE 1.
USN Numbers and Alloy Compositions

Name	USN #	Nominal Concentration (wt%)
316L	S31603	Cr(16.0-18.0), Mo(2.0-3.0), Ni(10.0-14.0), C(0.035 max), Fe(bal)
AL6XN	N08367	Cr(20-22), Mo(6-7), Ni(23.5-25.5), Cu(0.75 max), N(0.18-0.25), C(0.03 max), Fe(bal)
Nitronic 50	520910	Cr(22), Mo(2.25), Ni(12.5), Mn(5), Si(1 max), N(0.3), Fe(bal)
Inconel	N06625	Cr(21.5), Mo(9.0), Nb + Ta (3.6), Ni(bal) (61.0)
Hastelloy	N10276	Cr(15.5), Mo(16.5), W(3.8), Fe(5.5), Ni(bal) (57.0)

MICROSCOPY.

At the end of the exposure periods, surface topography and chemistry (i.e., corrosion products, biological deposits, and inorganic deposits) were documented using an ElectroScan® Model E-3 environmental scanning electron microscope (ESEM). Stainless steel samples were removed from the exposure medium, fixed in 4% glutaraldehyde in abiotic seawater, carried through a series of water washes with a final distilled water wash and examined directly from distilled water. Samples were attached to a Peltier® stage, maintained at 4 ^{o}C and imaged in a water vapor environment at 2-5 torr to maintain samples in a hydrated state. Coupons were x-rayed for 20 minutes at 100 kV/3 mAmps.

ELECTROCHEMISTRY.

Anodic polarization scans were performed on 316L samples using a PAR horizontal flat cell with a defined working electrode area of 1 cm^2 with a knife-edge crevice-free gasket. Duplicate scans were performed at sites along the weld and approximately 2.5 cm away from the weld on the flat plate. A Pt-Nb mesh (2.5 cm^2) and a saturated calomel electrode (SCE) were used as counter and reference electrodes, respectively. The open-circuit potential (OCP) was recorded for 10 minutes before scans were initiated. Scan range was from OCP to 0.7 V vs. SCE at a scan rate of 1 mV/sec.

Corrosion of the weld area was initiated by polarizing to 200 mV above OCP for 20 minutes in a Princeton Applied Research (PAR) Tait corrosion cell where the 316L coupon was at the bottom of the cell facing up. A glass tube (6.25 cm diameter) was placed on top of the sample with a rubber gasket seal. The top was sealed and the entire cell was clamped together using exterior bolts. Significant tightening was required to seal the bottom of the cell due to the height difference of the weld and the rest of the sample. The cell was filled with 200 mL of artificial seawater. The value of 200mV was chosen to drive active corrosion along the weld but not on the unwelded plate. Polarizations of welded and flat plate areas were conducted in duplicate. At the conclusion of the 20-minute polarization, OCP was monitored vs. SCE for two days. After two days, 20 mL of natural seawater were added to each system. Coupons were allowed to corrode freely for an additional four days.

RESULTS

EXPOSURE TESTING.

Key West natural seawater contained low levels (10 cells mL^{-1}) of AERO, APB, SRB, IRB, LNB. Flat coupons of Nitronic 50 and 316L exposed in natural seawater showed no signs of corrosion (Figure 1). Nitronic 50 and 316L showed visible corrosion in welds at six weeks in flowing seawater. Through-wall pitting was observed for 316L after an eight-week exposure (Figures 2a-c). In all cases corrosion was limited to weld areas. ESEM micrographs of the well-developed corrosion products demonstrated the presence of numerous microorganisms (Figure 3). There were no accumulations of bacteria on the unwelded plates or in areas away from the welds. Flat plate and welded AL6XN coupons did not show any visible corrosion after one-year exposures.

FIGURE 1. Nitronic 50 flat coupon exposed to flowing seawater.

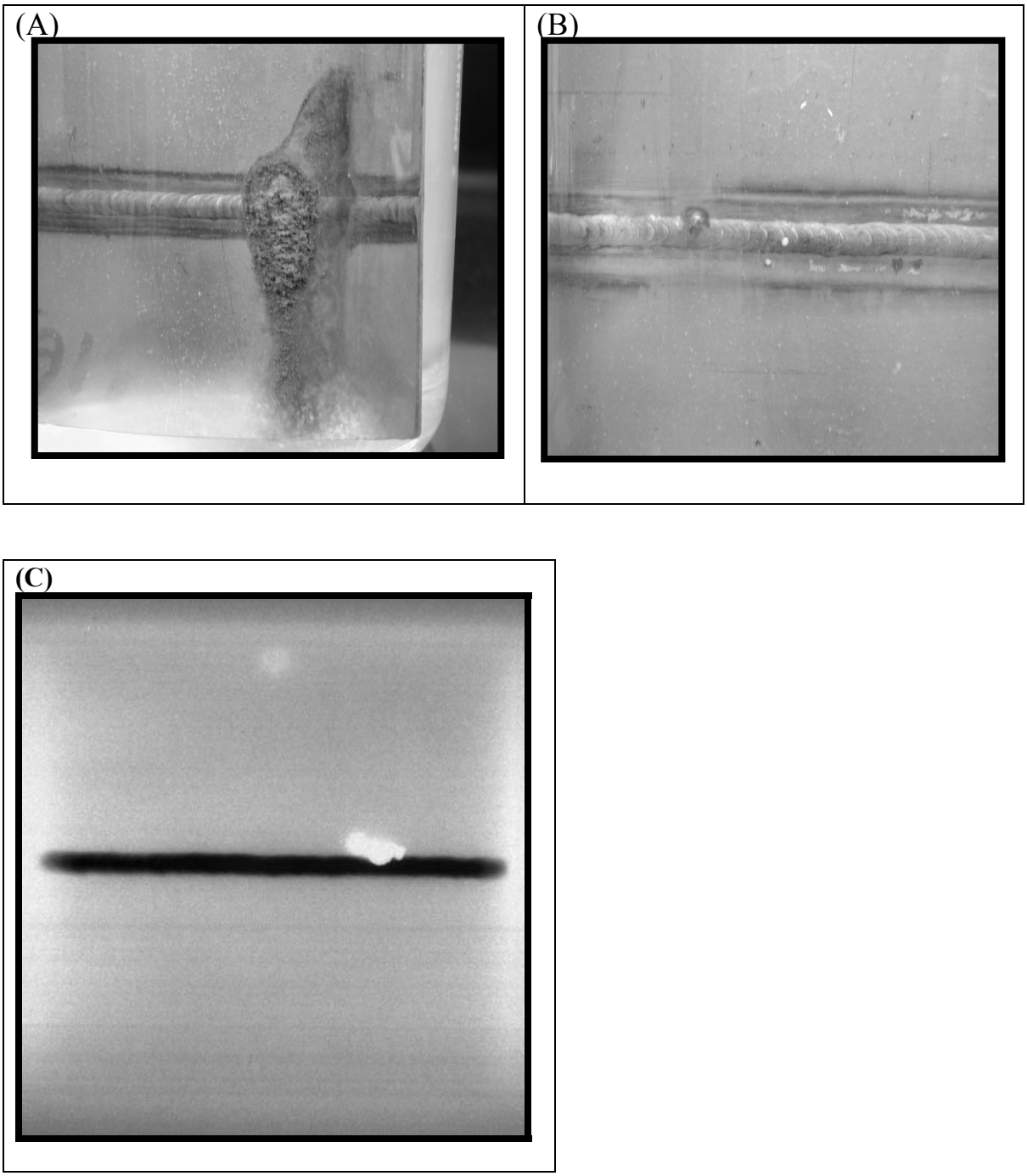

FIGURE 2. 316L stainless steel coupon with a center weld exposed to flowing seawater for 10 weeks:

(A) Pit with corrosion product (B) Penetration through the wall

(C) X-ray of the weld after exposure

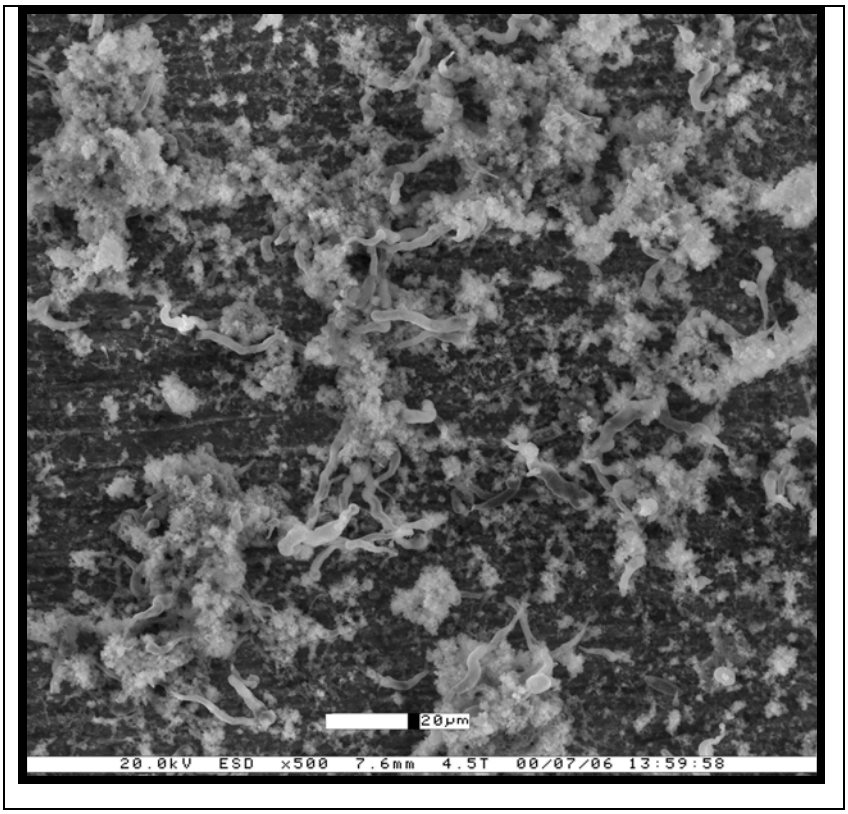

FIGURE 3. 316L welded coupon exposed to flowing seawater for 10 weeks.

OCP values for the welded 316L were ~70 mV lower than the ones recorded for the plate (Figure 4). The polarization scans of the welds indicate that there is a lack of passive behavior and that active corrosion initiated immediately above the OCP with a steady increase in current density with increasing potential. Anodic polarization scans of the flat plate indicated a distinct passive region between 0 and 450 mV where the maximum current density increased one order of magnitude with a maximum of 0.1 $\mu A/cm^2$. Current densities measured at the weld started at 0.1 $\mu A/cm^2$ and increased five orders of magnitude over the same range. Breakdown potentials were observed at 450 and 550 mV in scans for the two flat plate samples. No discernable breakdown potential was observed for the welded metal.

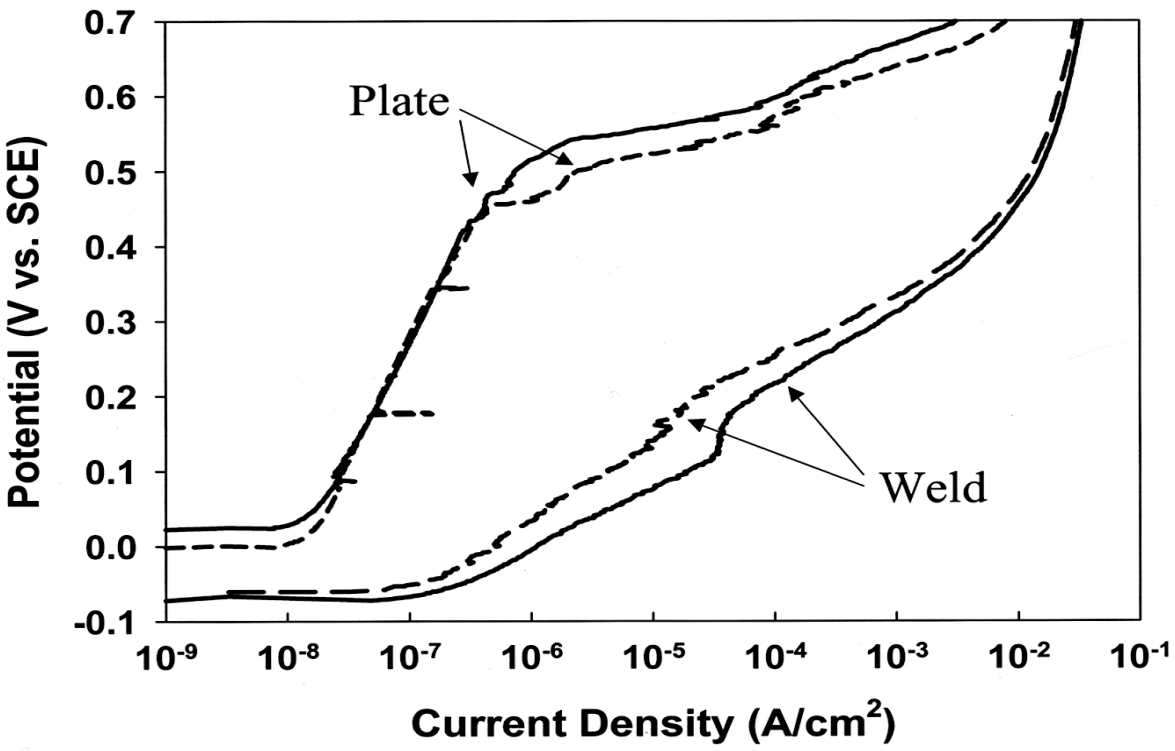

FIGURE 4. Anodic polarization scans of welded and as-received 316L plate.

Polarization at 200 mV produced varying amounts of corrosion on duplicate samples — heavy corrosion in one sample and less corrosion in a second sample as demonstrated in time transient OCP (vs. SCE) (Figure 5). OCP for the sample with less corrosion started at 155 mV and fluctuated in the initial 15 minutes of exposure with a minimum value of 60 mV. After 15 minutes, OCP returned to 155 mV and remained relatively stable over the next hour. During this hour, only a slight orange-red discoloration was observed at the weld indicating light corrosion. In contrast, the sample with more corrosion had an initial OCP of –50 mV. OCP dropped over the first 25 minutes of exposure with a minimum value of -90 mV. OCP returned to the initial value of –50 mV over the next hour. Over this period, significant orange-red discoloration was observed on the weld surface, indicating significant corrosion.

The time transient OCP for the two previously polarized samples (Figure 6) indicate two different responses after addition of natural seawater. The immediate impact of the additions can be seen on the figure as two small fluctuations in the first 0.25 hour. Over the next two days increases were observed in OCP for both samples. OCP for the lightly corroding sample increased from 150 mV to 210 mV, while the OCP for the sample with more corrosion increased from –50 mV to 0 mV. Addition of viable cells to the electrolyte of the sample with heavier corrosion had no influence on the OCP over 40 hours and OCP remained at 0 mV. In contrast the OCP for the sample with minor corrosion fluctuated over the next 40 hours with a minimum value of 160 mV. During this time, the weld continued to discolor. Over the next three days (six days after the initial anodic polarization) OCP increased for both samples — 250 mV and 160 mV for the lightly corroding and heavily corroding samples, respectively.

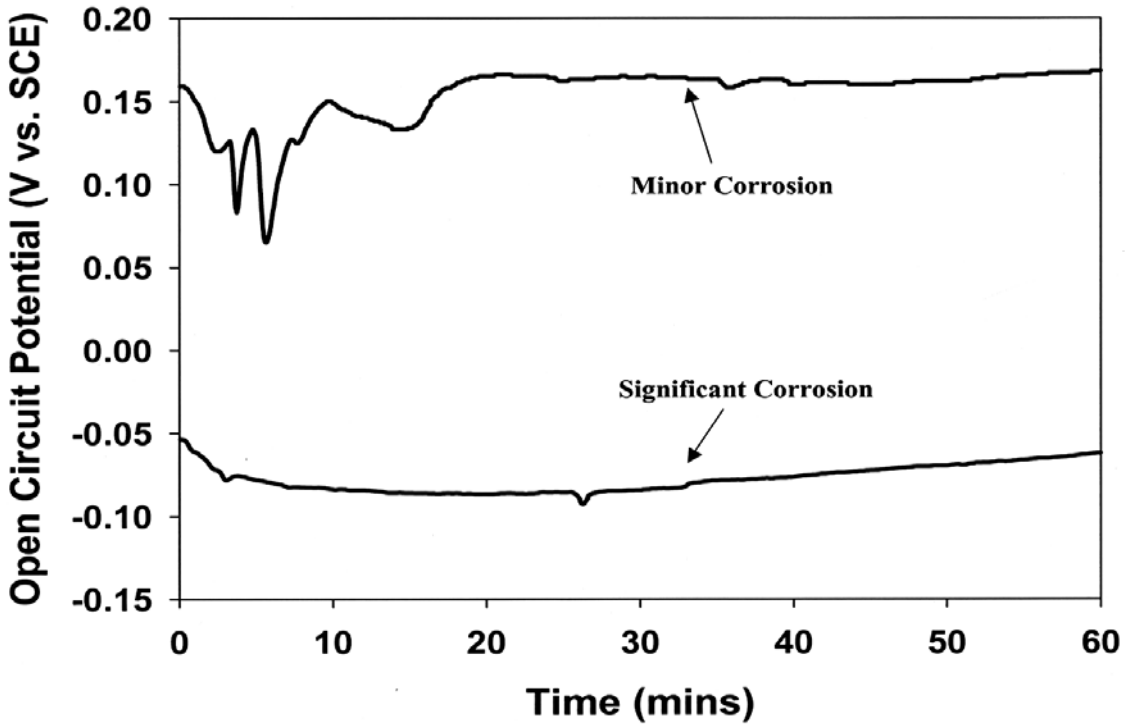

FIGURE 5. OCP measured after potential holds at 200 mV above the initial OCP.

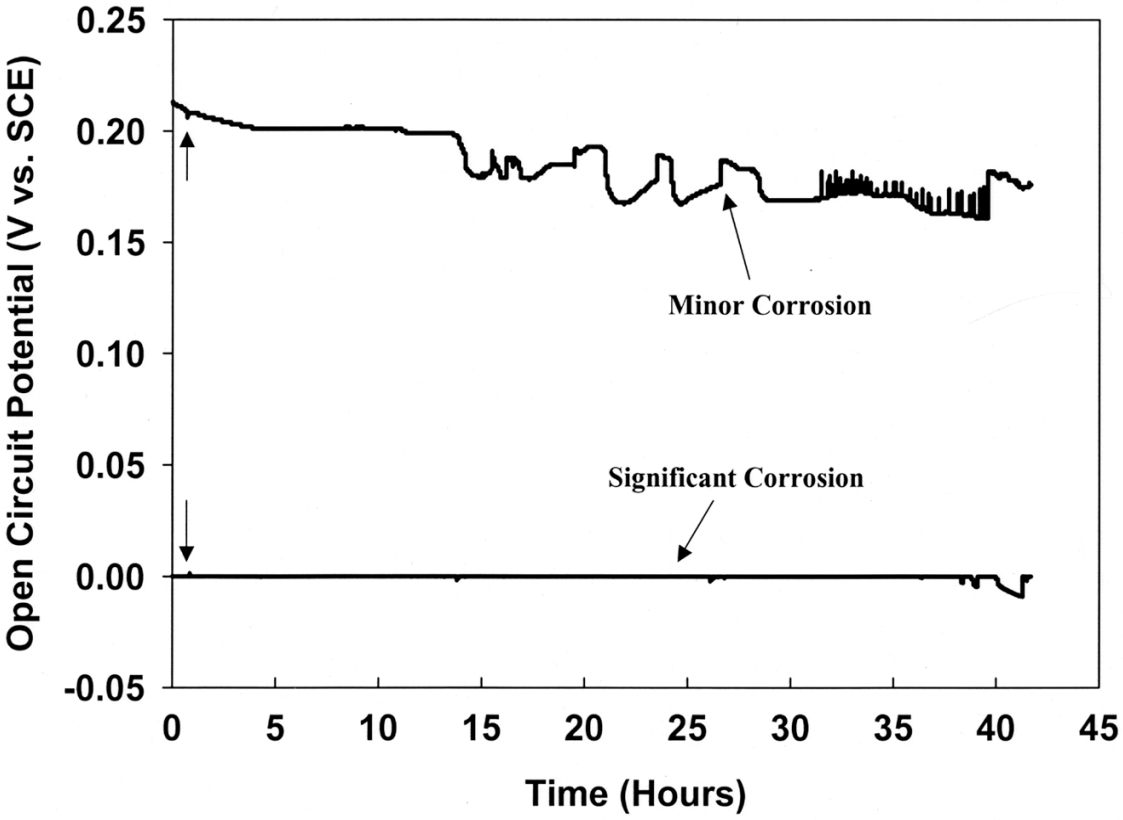

FIGURE 6. OCP measured two days after the anodic potential holds. Natural seawater was added at 0.25 hours as indicated by the vertical arrows.

There are many reports of MIC localized at welds in 300 series stainless steels exposed in fresh natural and chlorinated waters.[1-11] In these cases MIC is attributed to biomineralized deposits, resulting from oxidation of ferrous to ferric and accumulation of tubercle-like deposits of ferric hydroxide [$Fe(OH)_3$].[16] The oxidation can be carried out by a variety of organisms including bacteria, yeast, and fungi, but is particularly associated with genera of the so-called iron and manganese bacteria, *Siderocapsa, Gallionella, Leptothrix, Sphaerotilus, Crenothrix,* and *Clonothrix*. All are common in soil and groundwater. Deposits of cells and metal ions create oxygen concentration cells that effectively exclude oxygen from the area immediately under the deposit and initiate a series of events that are individually or collectively very corrosive. In an oxygenated environment, the area immediately under individual deposits becomes deprived of

oxygen. That area becomes a relatively small anode compared to the large surrounding oxygenated cathode. Cathodic reduction of oxygen may result in an increase in pH of the solution in the vicinity of the metal. Metal cations form at anodic sites. If the metal hydroxide is the thermodynamically stable phase in the solution, metal ions will be hydrolyzed by water with the formation of H^+ ions. If cathodic and anodic sites are separated from one another, the pH at the anode will decrease, and that at the cathode will increase. In addition, Cl^- ions from the electrolyte will migrate to the anode to neutralize any charge buildup, forming heavy metal chlorides that are extremely corrosive. Under these circumstances, pitting involves the conventional features of differential aeration, a large cathode to anode surface area, and the development of acidity and metallic chlorides.

This widely accepted mechanism does not account for the specificity of the attack at weldments. Several theories have been advanced, but none has been accepted. The two-phase weld metal appears to be the most susceptible, although the relative susceptibilities of ferrite and delta phases have not been clearly defined.[1] Garner[17] reported that the pitting potential and the critical pitting temperature were lower for welded than unwelded steel. Stein[2] determined that sensitization of the 300 series stainless steels does not affect susceptibility to MIC. The higher tendency for MIC of welds compared to unwelded material has been attributed to surface roughness or chemical composition that facilitates colonization. Pope et al.[18] speculated that more nutrients accumulated at roughened areas i.e., welds, causing increased biofilm formation. However, Holthe[19] showed that the increase in potential that accompanies biofilm development is just slightly more rapid on a rough surface than on a polished one. Eashwar and Dexter[20] published a paper entitled "Relation of Bacterial Settlement Patterns to Anodic Activity on Stainless Steel Weldments," but there are no data in the paper to support the title. Franklin et

al.,[21] working with a phosphate-buffered freshwater medium, demonstrated that an aerobic bacterium was attracted to anodic sites on flat plate carbon steel coupons and that pit propagation was related to microbial settlement.

Preferential attack at welds is common to both freshwater and marine exposures. However, there are fewer reports of MIC localized at welds in 300 series stainless steels exposed in seawater, possibly because there are fewer applications of 300 series stainless steels in chloride-rich media. Little et al.[12] reported MIC localized at weldments of 300 series stainless steel causing through wall pitting of .032 cm plate after six to eight weeks exposed to flowing or stagnant seawater. They further demonstrated that in the absence of microorganisms anodic sites initiated at welds but those sites were not sustained and did not develop into pits. In the presence of marine bacteria stable anodic sites formed within four weeks.

Despite the attraction of bacteria to anodic sites on steel substrata in both fresh and marine waters the mechanism for pit propagation may differ in the two environments. Freshwater contains a higher concentration of reduced iron, a lower concentration of chloride, and a different population of microorganisms. The concentration of total iron in open marine waters is in the nM range. The generally cited causative organisms are not prevalent in seawater environments. The chemical oxidation rate of iron in seawater at pH 8.2 is so high that microbial oxidation is not competitive. In the ocean, iron-oxidizing bacteria are found primarily in bottom waters and seeps, where ferrous iron is seeping into the ocean from anaerobic groundwater, or where it is being produced in the sediments by iron-reducing organisms.

CONCLUSIONS

Experiments presented in this paper demonstrate that welded 316L corrodes at a lower potential than does the unwelded plate, and that over short exposure times the electrochemical impact of marine bacteria varies between aggressively corroding sites and those that are producing lower current densities. It appears that under all circumstances marine bacteria are attracted to anodic sites that occur preferentially at welds. Under some circumstances the attraction produces an electrochemical impact and in other cases the cells have no impact.

ACKNOWLEDGEMENTS

This work was funded under program element 0601153N and by the Office of Naval Research (Dr. John Sedriks). NRL Contribution Number NRL/PP/7303/02/0001.

REFERENCES

1. S.W. Borenstein, Microbiologically Influenced Corrosion Handbook, (New York, NY: Industrial Press Inc, 1994), p. 152.

2. A. Stein, "Microbiologically Influenced Corrosion-An Overview, Third International Symposium on Environmental Degradation of Materials in Nuclear Reactors, held August 30-September 3, 1987, (Traverse City, MI: 1987).

3. S.W. Borenstein, P.B. Lindsay, "Microbiologically Influenced Corrosion Failure Analyses," CORROSION/87, paper no. 381 (Houston, TX: NACE, 1987).

4. R.E. Tatnall, MP 19 (1980): p.88.

5. G. Kobrin, MP 15 (1976): p. 38.

6. G. Kobrin, Biologically Induced Corrosion (Houston, TX: NACE International, 1986), p. 33.

7. J. Kearns, S. Borenstein, "Microbiologically Influenced Corrosion of Welded Stainless Alloys for Nuclear Power Plant Service Water Systems," CORROSION/91, paper no. 279, (Houston, TX: NACE, 1991).

8. S.W. Borenstein, P.B. Lindsay, “Why Does Microbiologically Influenced Corrosion Occur preferentially at Welds?,” CORROSION/91, paper no. 286 (Houston, TX: NACE, 1991).

9. J. Kearns, S.W. Borenstein, “Microbiologically Influenced Corrosion of Welded Stainless Alloys for Nuclear Power Plant Service Water Systems,” CORROSION/91, paper no. 279, (Houston, TX: NACE, 1991).

10. S.W. Borenstein, MP 27, 8 (1998): p. 62.

11. S.W. Borenstein, MP 30, 1 (1991): p. 52.

12. R.I. Ray, B.J. Little, J. Jones-Meehan, “A Laboratory Evaluation of Stainless Steels Exposed to Tap Water and Seawater,” Research Technical Symposium: Corrosion 2002, (Houston, TX: NACE International, 2002).

13. W.R.N. Howell, Jr., “An Analysis of Possible Microbiologically Influenced Crevice Corrosion of 316 Stainless Steel in a Seawater Environment,” (Thesis, Massachusetts Institute of Technology, 1996).

14. N.J.E. Dowling, M. Franklin, D.C. White, C.H. Lee, C. Ludin, “The Effect of Microbiologically Influenced Corrosion on Stainless Steel Weldments in Artificial Sea Water,” CORROSION/89, paper no. 187, (Houston, TX: NACE International, 1989).

15. B.J. Little, P.A. Wagner, K.R. Hart, R.I. Ray, “Spatial Relationships Between Bacteria and Localized Corrosion,” CORROSION/96, paper no. 278, (Houston, TX: NACE International, 1996).

16. B. Little, P. Wagner, F. Mansfeld, Inter. Mater. Rev. 36 (1991): p. 253.

17. A. Garner, Corrosion 35, 3 (1979) p. 108.

18. D.H. Pope, D.J. Duquette, D.C. Wagner, Jr., A.H. Johannes, “Microbiologically Influenced Corrosion: A State of the Art Review,” (Columbus, OH: Materials Technology Institute of the Chemical Process Industries, 1984) p. 76.

19. R. Holthe, “The Cathodic and Anodic Properties of Stainless Steels in Seawater,” (Ph.D. diss., Norwegian University of Science and Technology, 1988).

20. M. Easwar, S.C. Dexter, “Relation of Bacterial Settlement Patterns to Anodic Activity on Stainless Steel Weldments,” Corrosion/99, paper no. 174, (Houston, TX: 1999).

21. M. Franklin, B.J. Little, D.C. White, R. Ray, R. Pope, Biofouling 15, 1-3, (2000) p. 23.

AFOSR 6.1 PROGRAM REVIEW

INHIBITION OF OXYGEN REDUCTION BY CHROMATE ON AA2024-T3

William J. Clark, Jeremy D. Ramsey, and Richard L. McCreery

Department of Chemistry
The Ohio State University
100 West 18th Avenue
Columbus, OH 43210-1185

Gerald S. Frankel

Department of Materials Science and Engineering
The Ohio State University
105 West Woodruff Avenue
Columbus, OH 43210

ABSTRACT

This paper summarizes some aspects of the activities in the McCreery research group carried as part of 5-year Multidisciplinary University Research Initative (MURI) program funded by the Air Force Office of Scientific Research (AFOSR).

OVERVIEW

During the course of the MURI project, the McCreery group collaborated with other MURI investigators to investigate mainly three issues:

1. Formation and structure of chromate conversion coating (CCC).
2. Storage and release of Cr^{VI} in CCC, including the role of Cr^{VI} as active inhibitor.
3. The mechanism of corrosion inhibition on AA2024-T3 by Cr^{VI}.

The results are summarized below, with sections divided as indicated above and references to the list of publications at the end of this section. The formation of a CCC was shown to involve Cr^{VI}

reduction to Cr^{III}, followed by formation of an insoluble Cr^{III}-Cr^{VI} oxide (section 4.1.1).[1-3] This mixed oxide has the important property of reversible binding of Cr^{VI}, so that Cr^{VI} is incorporated into the CCC film at about 1/3 the molar concentration of Cr^{III}. The formation of the CCC is catalyzed by redox mediation by ferricyanide,[2] and is not homogeneous over the AA2024-T3 alloy.[3] We demonstrated that the Cr^{III}-Cr^{VI} mixed oxide can release Cr^{VI} into dilute aqueous solution, with an equilibrium that is similar to a Langmuir adsorption isotherm (section 4.1.2).[4-6] The "released" Cr^{VI} is capable of migrating to an unprotected alloy region, where it provides corrosion protection.[6,7] The storage, release, and migration of Cr^{VI} is responsible for the critically important "self-healing" action of chromate conversion coatings and pigments. Section 4.1.3 addresses the action of dilute Cr^{VI} on AA2024-T3 and related materials. We showed that Cr^{VI} adsorbs on AlO_x surfaces, to form both an Al^{III}-Cr^{VI} mixed oxide[7-9] and Cr^{III}-Cr^{VI} mixed oxide.[4] In fact, Cr^{VI} forms an approximate monolayer of Cr^{III} on copper, platinum, or carbon surfaces.[10,11] This monolayer inhibits anodic reactions on corroding alloys, but has a profound effect on oxygen reduction kinetics.[10] Inhibition of corrosion by Cr^{VI} is "locked in" by reduction to Cr^{III}, but this happens only at the monolayer level. The combination of storage, release, migration and irreversible inhibition is critical to the excellent properties if Cr^{VI} for corrosion protection.

1. STRUCTURE AND FORMATION OF CCC FILMS.

Elemental analysis and vibrational spectroscopy were used to probe the chemical structure of the CCC film. Synthetic oxides containing Cr^{III}, Cr^{VI}, and Al^{III} were synthesized to attempt to reproduce the structure of a CCC prepared on AA2024-T3. A Cr^{III}/Cr^{VI} mixed oxide was found to have spectroscopic and physical properties quite similar to a CCC formed on the alloy.[12] The CCC formation process is summarized in Figure 2, and involves simultaneous

polymerization of Cr^{III} hydroxide and adsorption of Cr^{VI}. The CCC and the chromium III/VI mixed oxide had the following properties:

1. Negligible aluminum content.
2. 3:1 Cr^{III}:Cr^{VI} molar ratio.
3. Raman band at 858 cm^{-1} that is pH and temperature independent.
4. Solubility at pH <2 and >9.
5. IR bands at 960, 919, 817 and 1621 cm^{-1}.
6. The ability to release soluble Cr^{VI} species and protect initially untreated AA2024-T3.

A structure proposed for the CCC and mixed oxide involving a covalent Cr^{III}-O-Cr^{VI} bond is shown in Figure 3. The structure is consistent with the vibrational spectra and D_2O and $H_2{}^{18}O$ isotope effects[1] as well as EXAFS and XPS reports in the literature. We propose that the Cr^{III}/Cr^{VI} mixed oxide binds and releases Cr^{VI} according to the mechanism of Figure 3.

The chemistry of the mixed oxide is important to corrosion protection, since it can reversibly bind Cr^{VI} and can support “self healing”, as summarized below. We conclude that the Cr^{III}/Cr^{VI} mixed oxide is a major component of the CCC on AA2024-T3.

Ferricyanide is an “accelerator” in “Alodine” coating baths, but its role and acceleration mechanism were not previously understood. Raman and FTIR spectroscopy were used to determine the fate of $Fe(CN)_6^{-3}$ in the CCC, and to examine its chemistry during CCC formation[1,2] with the following conclusions:

1. Ferricyanide is incorporated in the CCC as physisorbed $Fe(CN)_6^{-3}$ and as a Fe-CN-Fe polymer known as Berlin Green.

2. Ferricyanide rapidly oxidizes Al in AA-2024.
3. Ferrocyanide rapidly reduces $Cr_2O_7^{-2}$ to Cr^{III}.
4. Acceleration depends on a redox mediation mechanism, in which the slow reduction of $Cr_2O_7^{-2}$ to Cr^{III} is catalyzed by ferri/ferrocyanide as a consequence of points 2 and 3 above.
5. Several redox systems beside $Fe(CN)_6^{-3/-4}$ can act as mediators, including $Fe^{+3/+2}$ and $IrCl_6^{-3/-2}$. These mediators lead to effective CCC's similar to those produced from Alodine.
6. There is no evidence that ferricyanide is involved directly in the anticorrosion properties of the CCC, although that possibility cannot be completely ruled out.

We examined CCC formation on a composite of 5 phases of Al, Cu, and Mg and on AA2024-T3[3,13]. The copper rich phases show significantly thinner CCC films than adjacent Al-rich phases. Similar effects are apparent on AA2024, with thinner CCC films observed on Cu or Fe inclusions and intermetallic particles. The observation of adsorbed CN^- on Cu phases implies that ferricyanide decomposition on Cu may inhibit redox mediation, resulting in a thinner CCC on Cu phases.

2. RELEASE OF CR^{VI} FROM CCC TO EFFECT "SELF HEALING".

CCC treated and bare AA2024-T3 samples were placed face to face in an "artificial scratch" cell (figure 4) containing 0.1 M NaCl to determine if corrosion protection of the untreated alloy results from its proximity to the CCC sample.[6] Raman spectroscopy was used to monitor the release of chromate species from the CCC and the formation of Cr^{III}/Cr^{VI} species on initially untreated alloy. Micrographs show that an initially untreated sample is protected from

corrosion by migration from the CCC, while the control sample is seriously damaged. The polarization resistance of the remotely protected sample is comparable to that of a CCC on AA2024-T3. The split cell shows clearly that a CCC can protect a nearby exposed alloy surface, but it does not reveal the identity of the migrating species, nor the equilibria involved. We examined both Cr^{VI} speciation and the nature of the "release" equilibrium using UV-Vis and vibrational spectroscopy of the solution near a CCC.

Both old and recent literature on the speciation of Cr^{VI} in solution was examined, and new data from Raman spectroscopy were added to what has become a controversial area. The Cr-O-Cr linkage is observable with Raman, providing a definitive probe of the presence of dinuclear chromate species. By monitoring the Raman spectrum at different pH and Cr^{VI} concentration, it was possible to demonstrate that bichromate, $HCrO_4^-$ must exist at low [Cr^{VI}] and in the pH range 2-6.[5] Above pH 6, only CrO_4^{-2} exists in solution, while in the range of 2-6, both $Cr_2O_7^{-2}$ and $HCrO_4^-$ are present. At the low concentrations expected during release of Cr^{VI} from a CCC, $HCrO_4^-$ is the predominant species. The main point relevant to corrosion inhibition by dilute Cr^{VI} is that below pH 6 Cr^{VI} is primarily $HCrO_4^-$, and above pH, it is CrO_4^{-2}. $Cr_2O_7^{-2}$ is a minor species for total Cr^{VI} levels below 10^{-3} M.

By observing the solution composition above a CCC in salt solution, we established that Cr^{VI} in solution is in equilibrium with Cr^{VI} in the CCC.[4] This equilibrium was examined by spectroscopically monitoring the solution concentration of Cr^{VI} above a CCC. Plots of [Cr^{VI}] vs. time for various area to volume ratios showed "saturation" in which the [Cr^{VI}] in solution reached a constant value upon release from a CCC. In addition, solution Cr^{VI} adsorbed to Cr^{III} hydroxide, to a level that depended on the area/volume ratio. These equilibrium Cr^{VI} concentrations are consistent with a Langmuir adsorption mechanism, involving formation of a

Cr^{III}-O-Cr^{VI} bond. The release of Cr^{VI} into solution is pH dependent, with higher pH shifting the equilibrium toward desorption. Under the low pH and relatively high [Cr^{VI}] during Alodine treatment, adsorption of Cr^{VI} is favored. At higher pH and low Cr^{VI}, such as might occur in the field, desorption is favored. The adsorption/desorption is reversible with repeated pH excursions. This observation may explain why Cr^{VI} **adsorbs** during Alodine treatment, but **desorbs** and migrates in the field, in order to bring about 'self healing". In addition, the basic conditions near cathodic sites promote Cr^{VI} release and self healing.

Overall, the observations are consistent with the Langmuirian equilibrium between Cr^{VI} and Cr^{III} shown in figure 3. The kinetics of Cr^{VI} release from the CCC were studied in conjunction with the Frankel group, and are reported in another section of this report. The main conclusion of the efforts on Cr^{VI} storage and release are:

1. Cr^{VI} is released by the CCC, mainly as as $HCrO_4^-$ or CrO_4^{-2}, depending on pH.
2. Chromium is deposited on initially untreated alloy or defects, and is partially reduced to Cr^{III}.
3. The initially untreated alloy is protected from corrosion, as judged by appearance, polarization resistance, and polarization curves.
4. The rate of release of Cr^{VI} from the CCC depends on aging time of the original coating, with lower release rates for longer aging, and faster release at high pH.

3. IN-SITU RAMAN MICROSCOPY OF CHROMATE EFFECTS ON ALUMINUM ALLOY

Now that we know that self-healing by CCC films results from release of Cr^{VI}, the major question remains of how dilute Cr^{VI} inhibits corrosion. The interaction of dilute chromate with corroding alloy is responsible for passivation and protection. As a first step in establishing the

mechanism of corrosion inhibition, we used spatially resolved Raman spectroscopy to observe chromate interactions with pits in AA2024-T3 immersed in salt water.[8] The approach permitted localized monitoring of chromate in and near pits, and Raman spectra revealed the composition of the corrosion products.

Our working hypothesis for the protection of aluminum alloys by a CCC is based on migration of soluble chromate from the CCC to an actively corroding site, possibly followed by reduction to a Cr^{III} oxide and formation of the Cr^{III}/Cr^{VI} mixed oxide. To further explore this hypothesis, we have used in-situ Raman spectroscopy to monitor Cr^{VI} species in and near an active pit in AA2024-T3 immersed in 0.1 M NaCl. The spatial resolution of Raman was used both to localize the Raman measurement to the pit interior and to obtain Raman images of the Cr^{VI} species after interaction with the pit. After exposure to dilute Cr^{VI}, the Raman spectrum inside the pit exhibits a band at 850 cm^{-1}, whose appearance coincides with cessation of H_2 evolution. This band is not identical to the CCC Raman band, although they are quite similar. Dynamic Raman monitoring of alloy pits revealed the following:

1. The Raman bands for chromate species formed in pits differs slightly from that in a CCC, but the difference is significant. Mild heat treatment of the corrosion product causes changes in the Raman spectrum which differ greatly from those observed in a CCC.
2. The pH inside the pit appears to be higher than expected. Chromate reduction to Cr^{III} requires 8 H^+, and may partially neutralize protons generated by pit growth.
3. The migration of dichromate into the pit **precedes** formation of mixed oxide. Presumably a certain amount of dichromate is reduced to Cr^{III} by the active aluminum surface before mixed oxide is formed.

4. The growth of the pit, judged both visually and from H_2 evolution, stops after entry of Cr^{VI} into the pit and formation of the 850 cm^{-1} band.
5. The spectra of the product of the chromate interaction with an initially active pit corresponds to spectra of synthetic $Al(OH)_3$/chromate compounds, and to spectra of anodized alumina treated with chromate. These structures appear to involve covalent and/or electrostatic binding between Al^{III} hydroxide and Cr^{VI} species.

Comparison of dilute Cr^{VI} interactions with pits in AA-2024 to the chemistry of CCC formation in Alodine reveal some important differences. The low pH, high [F^-], $Fe(CN)_6^{-3}$ and relatively high [Cr^{VI}] in Alodine favors formation of the Cr^{III}/Cr^{VI} mixed oxide by dissolving Al oxides and creating a high Cr^{+3} concentration. In the pit, however, the absence of accelerator and fluoride puts Cr^{VI} in contact with $Al(OH)_x$, thus favoring formation of the Al^{III}/Cr^{VI} mixed oxide.[8,9]

Now that we know what compounds and structures form in the CCC and 2024 corrosion pit, how do they inhibit corrosion? The effects of Cr^{VI} on cathodic and anodic reactions were examined with an unusual split cell which permitted isolation of cathodic and anodic regions.[10,11] Several experiments using pure Cu and Al electrodes were performed initially, to characterize the cell and determine chromate effects, with an example shown in Figure 5. Strong inhibition of oxygen reduction was observed when dilute chromate was added to a cell containing a Cu cathode, while no effect was observed when chromate was added to a pure Al anode. With 2024, both cathodic and anodic inhibition by chromate was observed. Two manuscripts are under consideration by The Journal of the Electrochemical Society on the conclusions from the split cell approach. These observations were combined with many others from the MURI group to formulate a hypothesis that the primary mechanism of corrosion protection by chromate is

inhibition of oxygen reduction on Cu sites, through formation of chemisorbed Cr^{III} oxide, possibly followed by a second layer of adsorbed Cr^{VI}. We showed that the reduction of Cr^{VI} is spontaneous on Cu, Pt, and glassy carbon, and stops at approximately one monolayer due to inhibition of electron transfer by the Cr^{III} layer. This monolayer (and possibly the additional Cr^{VI} layer) inhibits O_2 reduction both by blocking catalytic sites and by inhibiting outer sphere electron transfer.[10] Figure 6 shows a schematic of Cr^{III} monolayer formation and Cr^{VI} adsorption.

Overall, the important properties of Cr^{VI} coatings, in the form of a CCC or as a chromate containing primer, which determine its outstanding corrosion protection performance may be summarized as:

- Mobility - Chromate is stored in anticorrosion coatings and primers in a form which can migrate to damaged areas long after coating application. This property results in "self healing" of coating defects or damage over an extended period of time. The chemical identity and properties of the storage mechanism were determined.
- Adsorption - Mobile chromate interacts with corrosion sites selectively, both on aluminum pits and on copper-containing cathodic sites. This adsorption is responsible for decreasing the loss of alloy from pitting and inhibiting the reactions of oxygen, which ultimately drive the corrosion process.
- Reduction - Once chromate is adsorbed to active sites, it may be reduced to Chromium III, which is substitution inert, nonmobile and permanent. This step forms a new Cr^{III} film and permanently inhibits corrosion activity at the formerly active site. At least one action of this Cr^{III} layer is O_2 reduction inhibition.

Overall, the MURI revealed that chromate acts like a "smart weapon" which stays dormant until needed, is released when damage occurs, then migrates to the damage site, adsorbs to it, and is transformed to a permanent, inhibiting form. The MURI identified the unusual combination of properties that underlies the effectiveness of chromium VI as a corrosion inhibitor. Since chromium VI is destined to be replaced by environmentally benign substitutes, the MURI conclusions about inhibition mechanism provide an excellent basis for designing chromate replacements.

REFERENCES

1. L. Xia, *Chemistry*, The Ohio State University, Columbus, (2000), p. 237.
2. L. Xia and R. L. McCreery, *J. Electrochem. Soc.*, **146**, 3696 (1999).
3. W. R. McGovern, P. Schmutz, R. G. Buchheit , and R. L. McCreery, *J. Electrochem. Soc.*, **147**, 4494 (2000).
4. L. Xia, E. Akiyama, G. Frankel, and R. L. McCreery, *J. Electrochem. Soc.*, **147**, 2556 (2000).
5. J. D. Ramsey, L. Xia, M. W. Kendig, and R. L. McCreery, *Corros. Sci.*, **43**, 1557 (2001).
6. J. Zhao, G. Frankel, and R. L. McCreery, *J. Electrochem. Soc.*, **145**, 2258 (1998).
7. J. Zhao, L. Xia, A. Sehgal, D. Lu, R. L. McCreery, and G. Frankel, *Surf. Coat. Technol.*, **140**, 51 (2001).
8. J. D. Ramsey and R. L. McCreery, *J. Electrochem. Soc.*, **146**, 4076 (1999).
9. J. D. Ramsey, *Chemistry*, The Ohio State University, Columbus, (2001), p. 277.
10. W. J. Clark and R. L. McCreery, submitted.
11. W. J. Clark, J. D. Ramsey, R. L. McCreery, and G. Frankel, JES, in press

12. L. Xia and R. L. McCreery, *J. Electrochem. Soc.*, **145**, 3083 (1998).

13. W. R. McGovern, *Chemistry*, Ohio State University, (1999), p. 121.

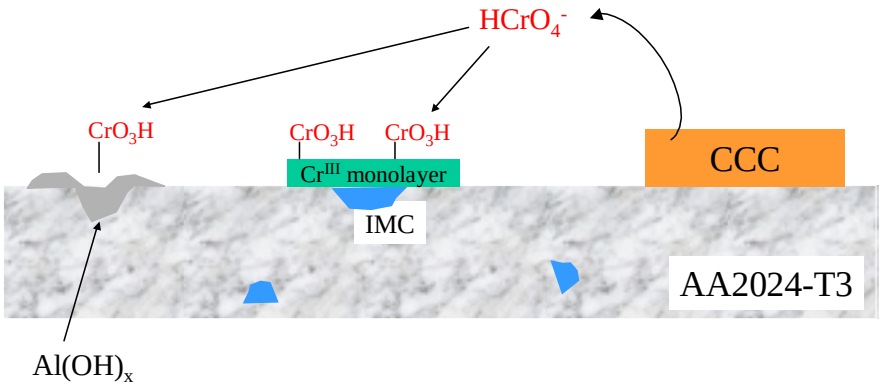

FIGURE 1. Schematic of self healing mechanism exhibited by chromate conversion coatings on AA 2024-T3 alloy.

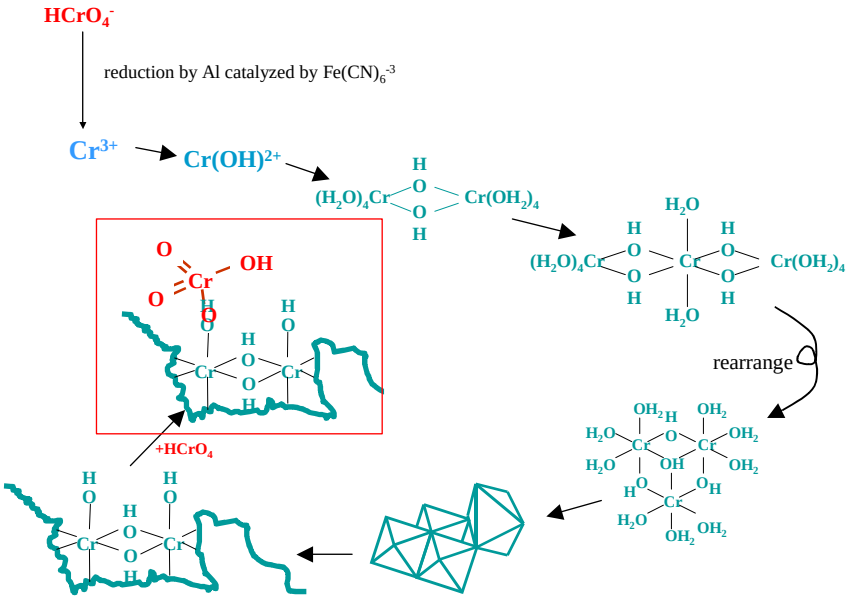

FIGURE 2. Summary of CCC formation during Alodine 1200 treatment, showing olymeriaztion of Cr^{III} hydroxide and adsorption of Cr^{VI}.

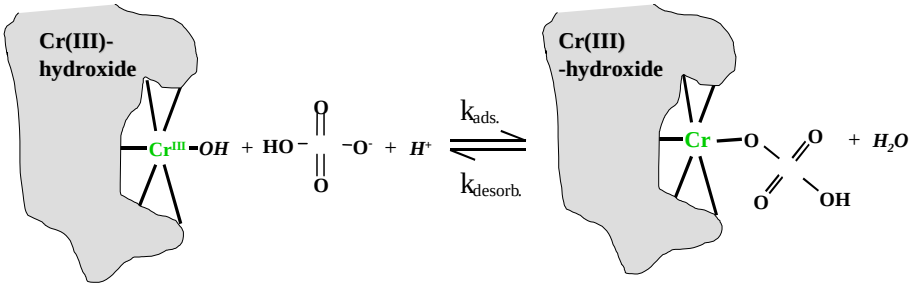

FIGURE 3. Most likely structure of Cr^{VI}-Cr^{III} mixed oxide, showing dynamic adsorption of Cr^{VI} by insoluble Cr^{III} oxy-hydroxide.[4]

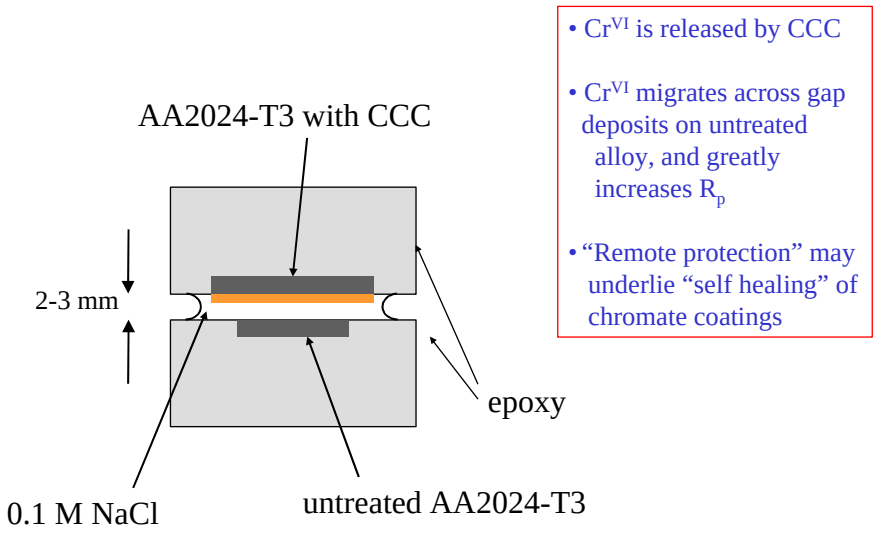

FIGURE 4. Artificial scratch cell used to demonstrate remote protection of bare AA2024-T3 by a nearby CCC.[6]

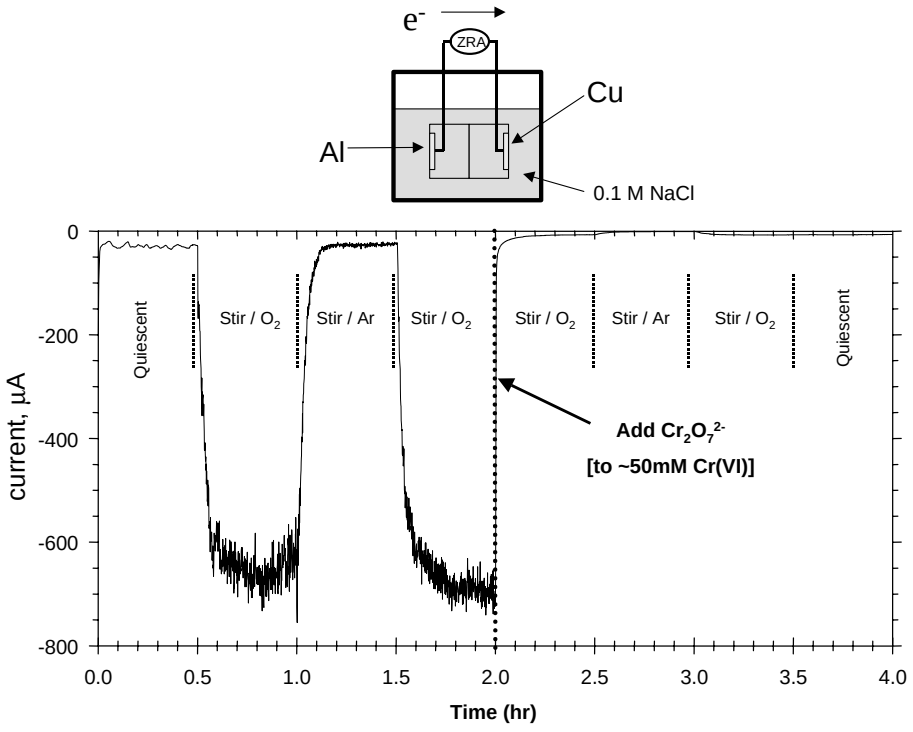

FIGURE 5. Galvanic current in a Al/Cu cell with variation in dissolved gas concentration. O_2 promotes a galvanic current from Al to Cu, but this current is severely inhibited by Cr^{VI} injection.

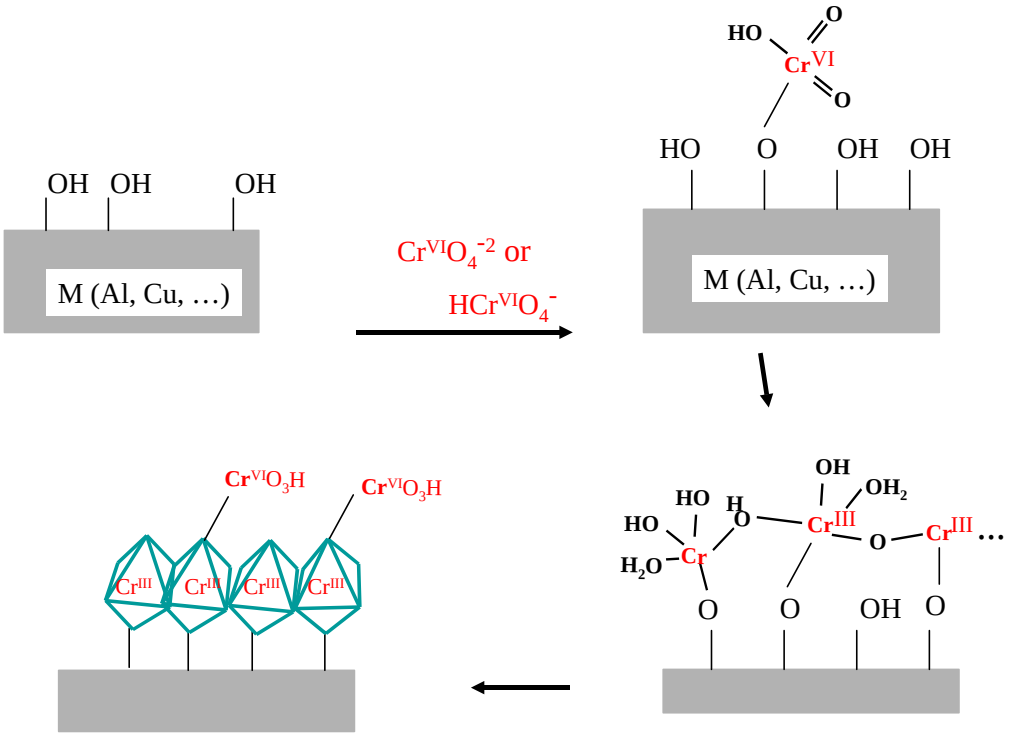

FIGURE 6. Likely mechanism for adsorption and reduction of Cr^{VI} to form a Cr^{III} monolayer, followed by adsorption of additional Cr^{VI}.

INHIBITION OF CORROSION OF Cu-RICH ALUMINUM ALLOYS BY Cr(VI) COMPOUNDS

M. Kendig, R. Addison, S. Jeanjaquet, J. Waldrop and M. Hon

Rockwell Scientific Company LLC
1049 Camino dos Rios
Thousand Oaks, CA 91360

ABSTRACT

Results from a number of experiments performed over the past several years focused on understanding the role played by hexavalent chromium compounds, typically chromate and dichromate, in inhibiting corrosion of Al and its alloys.

Anionic oxo-Cr(VI) easily adsorbs on aluminum oxide to lower its zeta potential thereby discouraging chloride adsorption. Cr(VI) oxo anions adsorb on active cathodes on Al alloys with subsequent rapid reduction so as to inhibit oxygen reduction and depolarization by other cathodic reactions.

Although Cr(VI) inhibits mainly by the slowing of oxygen reduction, it also inhibits anodic dissolution of unstable intermetallics.

INTRODUCTION

Over this past five years work Rockwell Scientific has participated with a team investigating the mechanism by which hexavalent chromium compounds inhibit corrosion in Al and its alloys, particularly in the difficult to protect Cu-rich high strength material AA 2024-T3. This presentation summarizes our major scientific results from which we draw a number of conclusions.

BACKGROUND

The oxo-anionic compounds of hexavalent chromium (referred to in the technical literature as chromate or dichromates) have a seemingly unique capability for protecting light metals and alloys from corrosion. Unfortunately these compounds are both toxic and

carcinogenic. Elimination of hexavalent chromium from the environment during the manufacturing of aircraft and aerospace vehicles requires a clear understanding of the mechanism by which hexavalent chromium protects aluminum and its alloys, particularly the difficult to protect Cu-rich 2000 series materials.

By hypothesis, chromate conversion coatings form from the reaction of hexavalent oxo-chromium (VI) anions with aluminum to generate a mixed chromium(III) oxide/aluminum oxide film that retains releasable Cr(VI). The residual Cr(VI) can move from the coating in the presence of a corrosive environment to defects in the film where it provides subsequent inhibition. An activity of oxo-Cr(VI) anions in the environment has been hypothesized to inhibit corrosion primarily by limiting the oxygen reduction reaction occuring at cathodic sites on the alloy surface, but it also passivates anodically active phases. In addition, Cr(VI) adsorbs on aluminum oxide so as to stabilize the oxide in the presence of chloride.

While other members of the MURI team confirmed the active inhibiting behavior and structure of the releasable chromate in conversion coatings, and galvanic nature of intermetallic phases, Rockwell Scientific's effort focussed on the following:

- Characterization of the nucleation of chromate conversion coatings on Al 2024-T3
- Characterization of the adsorption of hexavalent chromium on anodized aluminum oxide
- Implications of the speciation of oxo-Cr(VI) in aqueous environments
- Influence of hexavalent chromium on the oxidation and reduction kinetics at Cu-rich intermetallics
- Mechanism of inhibition of the oxygen reduction reaction (ORR) by Cr(VI) in neutral electrolytes.

SCIENTIFIC GOALS

The overall scientific goal of this program has been to elucidate the details of the mechanism by which hexavalent chromium inhibits corrosion of aluminum alloys, particularly the difficult to protect 2000 series alloys. Rockwell Scientific's specific goal was to determine how the ionic species of oxo-Cr(VI) interact with intermetallic phases and aluminum oxide to achieve an overall corrosion inhibition.

EXPERIMENTAL APPROACH

PEK EXPERIMENT

Previously reported work on hexavalent chromium-sealed anodized aluminum suggests that chromate does not actually 'seal' porous anodized aluminum in the sense that it plugs pores,[1] rather chromate seals with a reinforcement of the pore-wall[2] as compared to the completely-plugging hot-water sealing. One way that a small quantity of oxy-chromium (VI) anions improves corrosion resistance without plugging the pores is by changing the surface charge of the oxide so as to discourage adsorption and transport of chloride. Such a mechanism has been shown to occur for ferrous oxide films[3,4] and has been proposed for aluminum oxide covered surfaces.[5-11]

Fortunately there exists a rather elegant method for interrogating the surface of the pore of anodized aluminum as to its surface charge. In the mid 1980's, Bernstein and White reported that when an ultrasonic wave passes through an anodic film immersed in an electrolyte it shears the double layer in the pores of the film so as to produce an alternating voltage.[12] An alternative approach for acoustically assessing the zeta potential of a porous medium entails applying a high frequency electrical signal while observing the acoustic response.[13] In the former Bernstein and White approach, the piezo-electrokinetic (PEK) response results from oscillation in the streaming

potential produced within the porous aluminum oxide in response to an applied acoustic pulse. In principle, the magnitude of this signal relates to the magnitude and sign of the zeta potential, ζ, of the oxide and the phase depends on the sign of ζ. Note that ζ and the surface charge, σ, are related to each other through the following equation:

$$\sigma = D\zeta/(4\pi\gamma) \quad (1)$$

where σ = surface charge, γ = Debye length (constant with constant ionic strength and dielectric constant) and D = the diffusion coefficient for the ions of the double layer. According to the model developed in ref 12, the normalized piezo-kinetic response has the following form:

$$V_{out}/u(0) = \pi n R^2 \sigma\gamma/(2\omega^{1/2} \varepsilon_{pore} \alpha^{1/2} \mu^{1/2}) \quad (2)$$

where ε = dielectric constant of the fluid in the pore, α = the fluid's compressibility , ω = angular frequency of the acoustic signal, and R = the pore diameter.

Using a test cell similar to that described previously,[12] the PEK response for sulfuric acid anodized high purity aluminum, exposed to electrolytes typically of constant ionic strength, has been determined as a function of pH and oxo-Cr(VI) anion concentration. The results for the chromate-containing solutions were compared to those for a nitrate-containing solution since the nitrate has been shown not to specifically adsorb on aluminum oxide surfaces.[14]

AFM ANALYSIS OF THE NUCLEATION OF CHROMATE CONVERSION COATINGS

Al 2024-T3 specimens were polished to a 0.01 μm finish in a non aqueous environment as described previously and exposed for short times in cold (5C) Alodine 1200 chromating reagent so as to just initiate the chromate conversion coating process. The resulting specimens

were rinsed in distilled water and stored in a vacuum dessicator before examining using an atomic force microscope (AFM).[15]

EIS OF CHROMATE INHIBITED INTERMETALLICS

Intermetallic specimens of theta phase $CuAl_2$ prepared as previously described were exposed to NaCl solution with and with out 10 mM Cr(VI). An electroplater's mask was used to isolate single grains of the material for the electrochemical analysis. Alternatively, a microelectrochemical cell approach previously described by Sutter et al.[16] and implemented at Ohio State University was used to perform potentiodynamic polarization on individual s-phase Cu,Mg aluminide grains.

CYCLIC VOLTAMMETRY

Copper and gold rotating disk electrodes (RDEs) were used for evaluating the electrochemical reduction kinetics of oygen and hexavalent chromium in near neutral (pH 6.1) solution.

PHASE TRANSFER CATALYST

In order to establish the degree of ionization of oxo-chromium anions at low pH a phase transfer compound, Adogen 464, was used to form ion complexes with oxo-Cr(VI) anions. The ion complexes can dissolve in an organic phase (hexane). Extraction of chromate into hexane occurs when the Cr(VI) compound exists as an anion. Extraction of Cr(VI) was detected as a yellowing of the hexane phase. In this way the pH range (under acidic conditions) over which oxo-Cr(VI) anions exist could be established.

SUMMARY OF RESULTS

IONIC INTERACTIONS WITH OXIDES

The pH dependence of the PEK signals for the anodized Al 1100 is summarized in Figure 1. For some of the data points in Figure 1 a scaled waveform has been superimposed to illustrate the phase and, hence, justify the assignment of the sign to the signal. The PEK signal for the sample in the nitrate solution remains high and of the same phase over the accessible pH range (pH 4 - pH 11). Higher pHs were not evaluated since the oxide becomes unstable to rapid dissolution. The error bars for the variation of pH were determined from the pH measured before and after the experiment. The pH of the oxo-Cr(VI) buffer solutions was stable during an experiment. Despite efforts to buffer the nitrate solutions, rather extensive pH variation was observed. Hence the large error bars for the high pH, non-chromate nitrate solutions. As can be seen the PEK signal changes phase which indicates a change of sign at high pH. The pH, where the sign changes, is called the pH of zero charge (pzc).

Chromate significantly lowers the surface charge (zeta potential) within the porous anodized layer on sulfuric acid anodized aluminum for pH above 4. For very low pH, chromate does not lower the zeta potential as evidenced by no lowering of the PEK signal. This is a result of complete protonation of the chromate or dichromate anion. The pH of zero charge for the interior surface of the porous anodic film is above 10.5 in the non-complexing sodium nitrate. This pzc exceeds that typically reported for alumina particles and reflects the properties specific to the pore interior. The presence of just 0.01 M oxo-Cr(VI) lowers the pzc of the pore interior to 8.2. Furthermore, the presence of dilute chromate substantially lowers the surface charge on the surface of aluminum oxide without being converted irreversibly to Cr(III) oxide. Hence, we conclude that hexavalent chromium provides corrosion inhibition to anodized aluminum without

reductively converting to an inert Cr(III) oxide species. The oxo-Cr(VI) anions accomplish this by specific adsorption on the oxide surface so as to discourage the adsoptionadsorption of chloride. The reader can find additional details of these results in the published literature.[17]

Cr(VI) SPECIATION

Using data available in the literature, the relative concentrations of the different oxo-Cr(VI) anions can be calculated. The distribution depends on total Cr(VI) concentration and pH. The calculated distributions have been shown in collaboration with McCreery et al. to be consistent with spectroscopic observation.[18] An important result of this work has been the observation that, depending on total chromate concentration, for a sufficiently low pH, the chromate oxyanions are completely protonated and are not active. This can be seen from the relative extraction of yellow Cr(VI) into an organic phase from water by a long chain alkyl ammonium cation. If the the pH of the aqueous phase is sufficiently low, no anions are present to be extracted by the organic cation (see Figure 2). Hence for a sufficiently active and acidic pit, Cr(VI) would not effectively inhibit anodic dissolution. This is consistent with observations by that Cr(VI) does not inhibit in very acidic anodically formed pits.[19]

NUCLEATION OF CHROMATE CONVERSION COATINGS

The formation of a chromate conversion coating on a highly polished Al 2024-T3 specimen initiates on the more cathodic, blocky shaped Fe, Mn Cu aluminides as shown in Figure 3.[15] Once nucleated, the film inhibits further reaction.

INHIBITION OF OXYGEN REDUCTION

Inhibition of the cathodic oxygen reduction reaction (ORR) on a Cu cathode does not require formation of a three dimensional film, but rather results from a sub-mololayer

electrosorption of a Cr(III) species. Furthermore, such an adsorbed film inhibits bulk conversion of Cr(VI) to Cr(III) as well as reduction of oxygen. The current vs voltage data presented in Figure 4 for a rotating Cu cathode illustrate these points.[29] In the absence of any inhibitors, a current plateau appears between –0.6 and –1.1 V vs SCE due to diffusion-limited oxygen reduction. In the presence of Cr(VI), the current between –0.6 and –0.8 volts is dramatically decreased as a result of the inhibition of oxygen reduction. The current increases to a plateau more negative than –0.8 V as a result of chromate reduction. Note that –0.8 V represents an extremely large overvoltage for chromate reduction indicating that the process that inhibits oxygen reduction also inhibits chromate reduction. Ce(III) does not seem to provide the same degree of inhibition of the ORR as does the Cr(VI) oxo-anions. Clark and McCreery will publish similar conclusion based on their work on the reduction of Cr(VI) on glassy carbon electrodes.[30] Cyclic voltammetry (Figure 5) in the –0.4 to –0.6 volt range provides evidence that the adsorption process giving rise to this inhibition involves a reduction process, presumably that of Cr(VI) to Cr(III). Ilevbare and Scully had previously demonstrated the effectiveness of Cr(VI) as an irreversible ORR inhibitor on a variety of cathodes.[20-22]

INHIBITION OF ANODIC REACTIONS

The sigma phase Cu, Mg aluminides are particularly reactive. Scully et al. demonstrated the formation of metallic Cu cathodes by the corrosion of this phase.[23] The Cu,Mg aluminide phase dealloys to produce a very active Cu-rich cathodic site for initiating adjacent pitting.[24-25] Alternatively these phases may anodically dissolve to form Cu clusters which disperse into the corrosive environment where, once disconnected from the base metal, corrode and redeposit as Cu cathodes.[26] Cr(VI) oxo-anions in dilute, slightly acidic chloride not only inhibits the high cathodic activity of the dealloyed phase, but also passivates these surfaces to produce a low

passive current.[27] Electrochemical impedance analysis of the inhibition shows that a two dimensional passive film is formed by the chromate.[28]

Cr(VI) has significant effects on the reaction kinetics of the dealloyed layer formed on the S phase. Figure 6 shows a potentiodynamic scan at 10 mV/s from –1.40 V to 0.00 V vs SCE for S phase in 10mM NaCl with and without 5mM Cr(VI). As can be seen, addition of chromate lowers the cathodic current density for the S phase between the open circuit potential and –1.20 V. Chromate appears to inhibit the oxygen reduction reaction. The chromate also shows anodic passivation (with a passive current density below 1 uA/cm^2 from open circuit up to a potential of –0.4 V where the anodic current rises). A breakdown potential, E_{br}, measured in chloride/chromate solutions is not very reproducible, but generally falls below the E_{br} measured in chromate-free solutions for which the intermetallic phase had already dealloyed to form a pseudo-passive porous Cu layer.[27]

These results suggest that the oxo-Cr(VI) species at this pH of 4.3 effectively inhibits the dealloying of the intermetallic. As a result of both the lack of dealloying and the presence of an adsorbed chromate layer (either as Cr(VI) or Cr(III)), the rate of oxygen reduction in the open-circuit to –1.2 V region remains substantially lower than that observed on the dealloyed intermetallic in the absence of chromate. Furthermore, the intermetallic shows some actual passivity above open circuit with a current density limited to about 1 μA/cm^2. However, the surface passivated by chromate becomes active with polarization above a rather low E_{br} value compared to the polarization required for the dealloyed pseudo-passive, cathodically active surface.[27]

CONCLUSIONS

The results show that hexavalent chromium behaves primarily as a good inhibitor of ORR at cathodic sites on high-strength Al alloys. The mechanism of ORR inhibition entails electrosorption of a sub-monolayer of a Cr(III) surface compound that inhibits both ORR and further chromate reduction. Cr(VI) readily adsorbes as the unreduced anion on Al oxide to lower the zeta potential and the pH of zero charge of the oxide. As such, adsorption of the chromate discourages chloride adsorption and destabilization of the oxide. Chromate appears to inhibit the anodic dissolution of the very active intermetallic Cu,Mg aluminide phase. This also limits the formation of sites for oxygen reduction. Speciation of the hexavalent chromium is important as the anionic form provides the active inhibition. At very low pH such as in active pits the chromate anion(s) can become completely protonated and rendered inactive.

ACKNOWLEDGEMENT

We gratefully acknowledge support by the Air Force Office of Scientific Research under contract F49620-96-1-0479. Interactions with the other members of the MURI team lead by Dr. G. Frankel of The Ohio State University are gratefully acknowledged. We also wish to recognize effort provided by two interns, David Powers and Eric Cheng.

REFERENCES

1. F. Mansfeld and M. Kendig, *J. Electrochem. Soc*.,135(4), 828 (1988).
2. J. P. Hoar and G. C. Wood , *Electrochim Acta*, 7, 333 (1962).
3. M. Sakashita and N. Sato, *Corros. Sci.,* 17, 473 (1977)
4. N. Sato, *Corrosion,*45(5), 354 (1989).
5. P. M. Natishan, E. McCafferty and G. K. Hubler, *J. Electrochem. Soc*., 135, 321 (1988)

6. E. McCafferty, *Corros. Sci*., 37(3), 481 (1995)
7. P. M. Natishan, E. McCafferty, G. K, Hubler, *J. Electrochem. Soc.,* 133, 1061 (1986)
8. Z. Szlarska-Smialowska, *Corros. Sci*., 33 (8), 1193 (1992).
9. M. A. Petrunin, V. D. Gil'dengorn, T. A. Yurasova, G. V. Kuryavtsev, A. P. Nazarov, V. V. Lisichkin, *Russian J. of Phys. Chem.,* 66(9), 1323 (1992)
10. A. P. Nazarov, M. A. Petrunin, Yu. N. Mikhailoskii, *Protection. of Metals,* 28(4), 432 (1992)
11. M. A. Petrunin, V. D. Gil'dengorn, A. P. Nazarov, *Protection of Metals,* 30(2), 130 (1994)
12. J. J. Bernstein and White, *J. Electrochem. Soc.*, 131(5), 1050 (1984).
13. N. P. Miller, J. C. Berg, *Colloid and Surfaces,* 59, 119 (1991)
14. R. Alwitt, *Colloid and Interface Science*, 40(2), 195 (1972).
15. J. Waldrop and M. Kendig, J. Electrochem. Soc. J. Electrochem. Soc., 145(1), L11 (1998).
16. T. Suter, H. Bohni, Electrochim. Acta, 42, 3275 (1997).
17. M. Kendig, R. Addison, S. Jeanjaquet, "The Influence of Oxo-Cr(VI) Species on the Zeta Poetential in the Porous Oxide of Anodized Aluminum", J. Electrochem. Soc., 146(12),4419 (1999)
18. J. Ramsey, L. Xia, M. Kendig, R. McCreery, "Raman spectroscopic Analysis of the Speciation of Dilute Chromate Solutions", Corrosion Science 43(8), 1557 (2001)
19. E. Akiyama and G. S. Frankel, submitted to *J. Electrochem. Soc.,* 1999
20. G. O. Ilevbare, J. R. Scully, *Corrosion*, 57(2), 134 (2001)
21. G, Ilevbare, C. Jeffcoate, J. R. Scully in 'Passivity and Localized Corrosion, Sato Symposium, ECS PV 99-27, 269 (1999).
22. G. Ilevbare, J. R. Scully, *J. Electrochem. Soc.*, 148(5), 196 (2001).

23. J. R. Scully, T. O. Knight, R. G. Buchheit, E. E. Peebles, *Corros Sci* 35, 185 (1993).
24. R.G. Buchheit, R.P. Grant, P.F. Hlava, B. McKenzie, G.L. Zender, *J. Electrochem. Soc.*, 144, 2621 (1997).
25. V. Guillaumin and G. Mankowski, *Corr. Sci.*, 41, 421 (1999).
26. R. Buchheit, M. A. Martinez and L. P. Montes, *J. Electrochem. Soc*, 147:(1) 119-124 (2000)
27. M. Kendig, R. Buchheit, H. Guan, R. Leard "Electrochemical Aspects of Dealloyed Al_2CuMg" Proceedings of the Electrochemical Society, April 2001.
28. M. Kendig, S. Jeanjaquet, R. Addison and J. Waldrop, *Surf. Coat. Tech.*,140(1), 58 (2001).
29. M. Kendig and S. Jeanjaquet "Cr(VI) and Ce(III) Inhibition of Oxygen Reduction on Copper", to be published, *J. Electrochemical Society* (2001)
30. W. Clark and R. McCreery, "Inhibition of Corrosion-related Reduction Processes via Chromium Monolayer Formation", to be published, *J. Electrochem. Soc.* (2001)

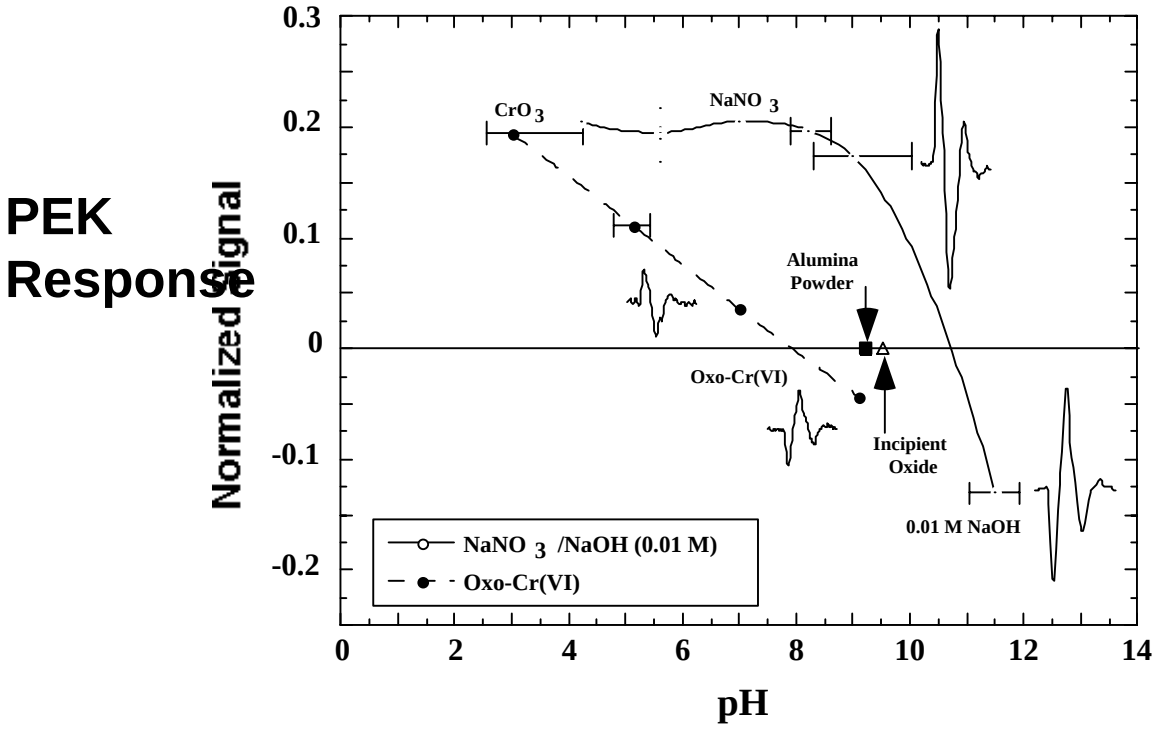

FIGURE 1. PEK response (relative amplitude) as a function of pH. The sign is determined by the phase.

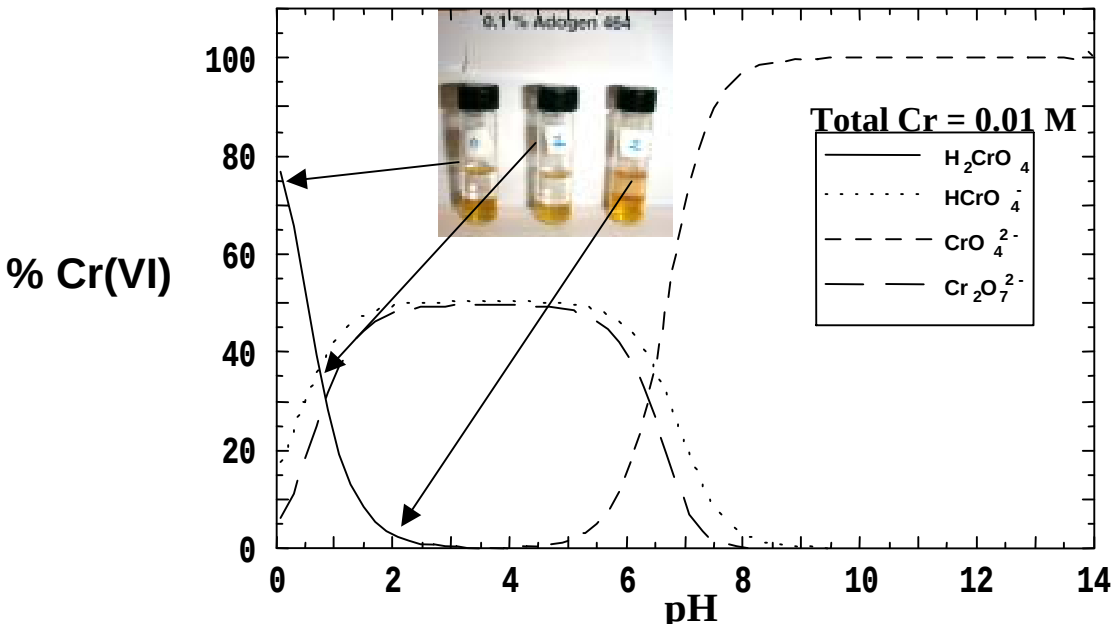

FIGURE 2. Calculated distribution of oxo-Cr(VI) species and a photograph of the extraction of ion pair chromate complexes from an aqueous phase to an organic phase using the Adogen 464 quaternary ammonium phase transfer catalyst. Note that when the chromate anion is sufficiently protonated at pH 0-1, no anion extraction into the upper organic phase occurs.

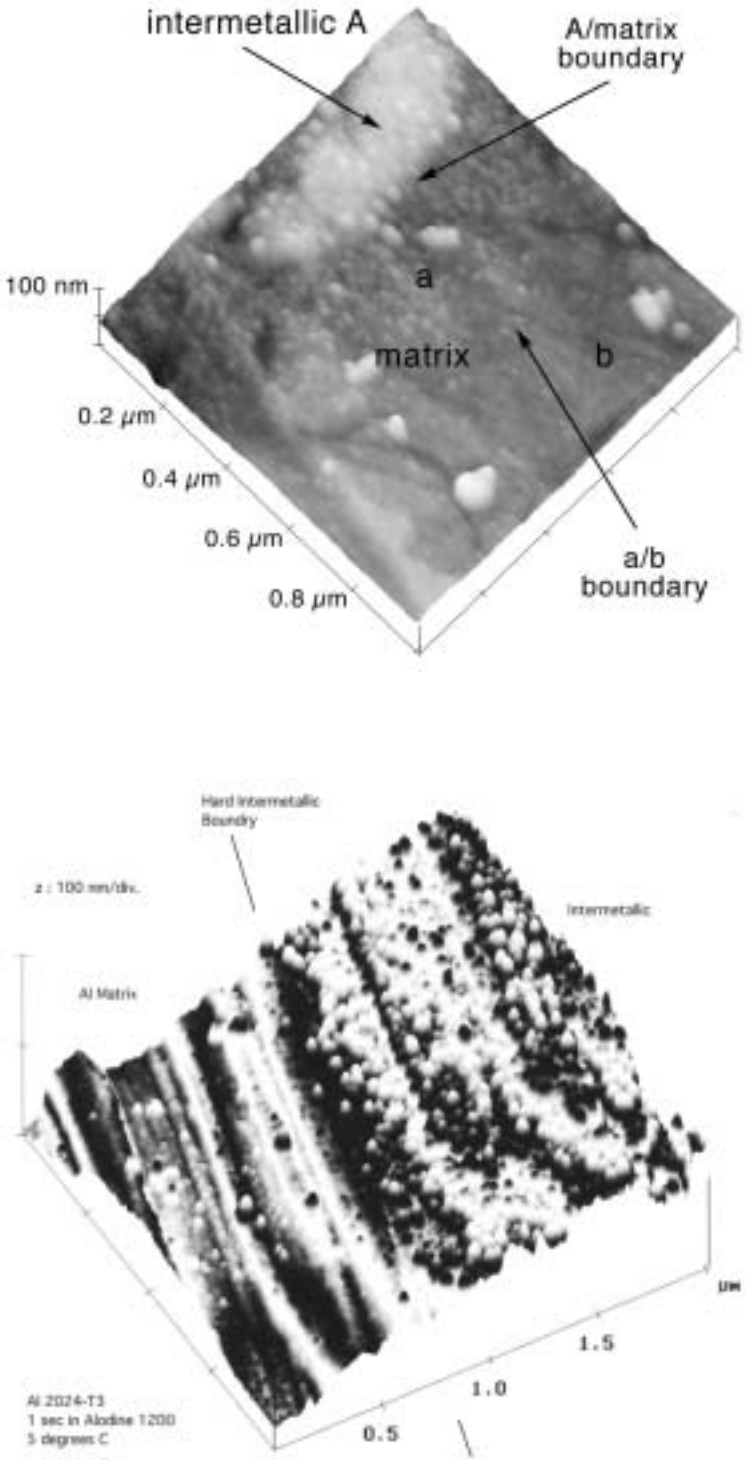

FIGURE 3. Two AFM images showing the nucleation stages resulting in the formation of chromate conversion coating on the cathodic Fe Mn aluminides.

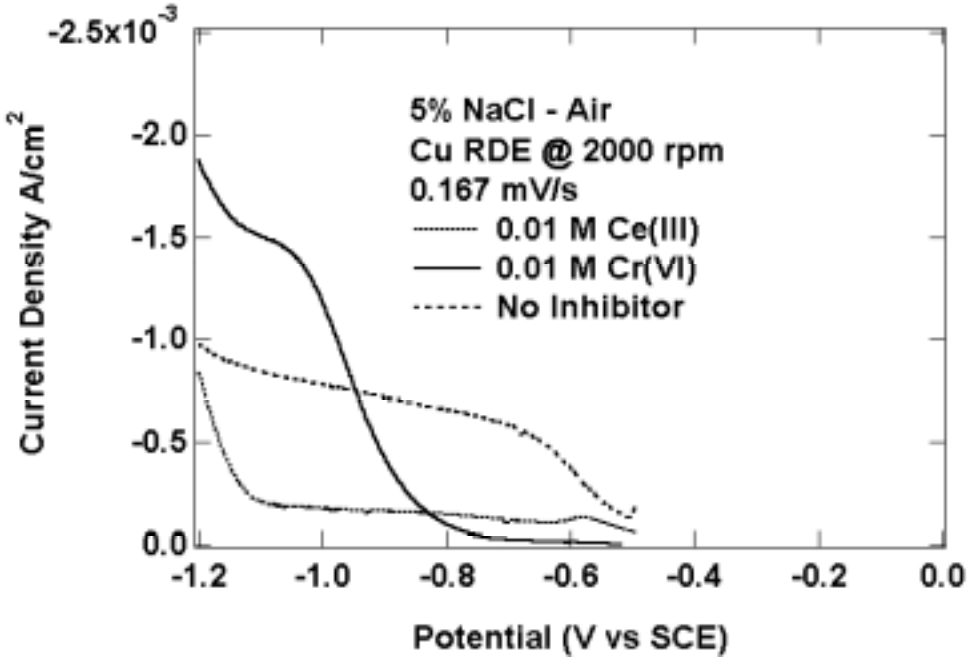

FIGURE 4. Current density vs potential for the cathodic polarization of a Cu RDE in 5% aerated NaCl containing 10 mM of Ce(III) or Cr(VI) inhibitors. The pH is 6.1.

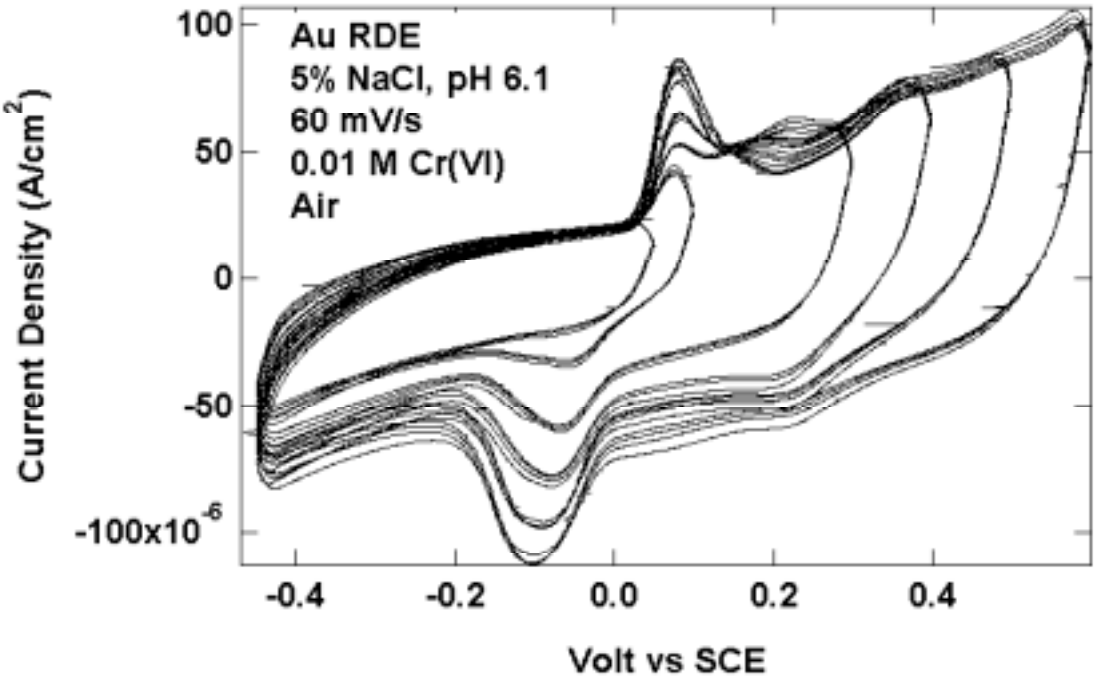

FIGURE 5. Cyclic voltammogram for a gold RDE (2000rpm) in the presence of Cr(VI) at pH 6. This is for the region where oxygen inhibition occurs. As can be seen peaks representing sub-monolayer electrosorption and desorption of an activated Cr(III) appear.

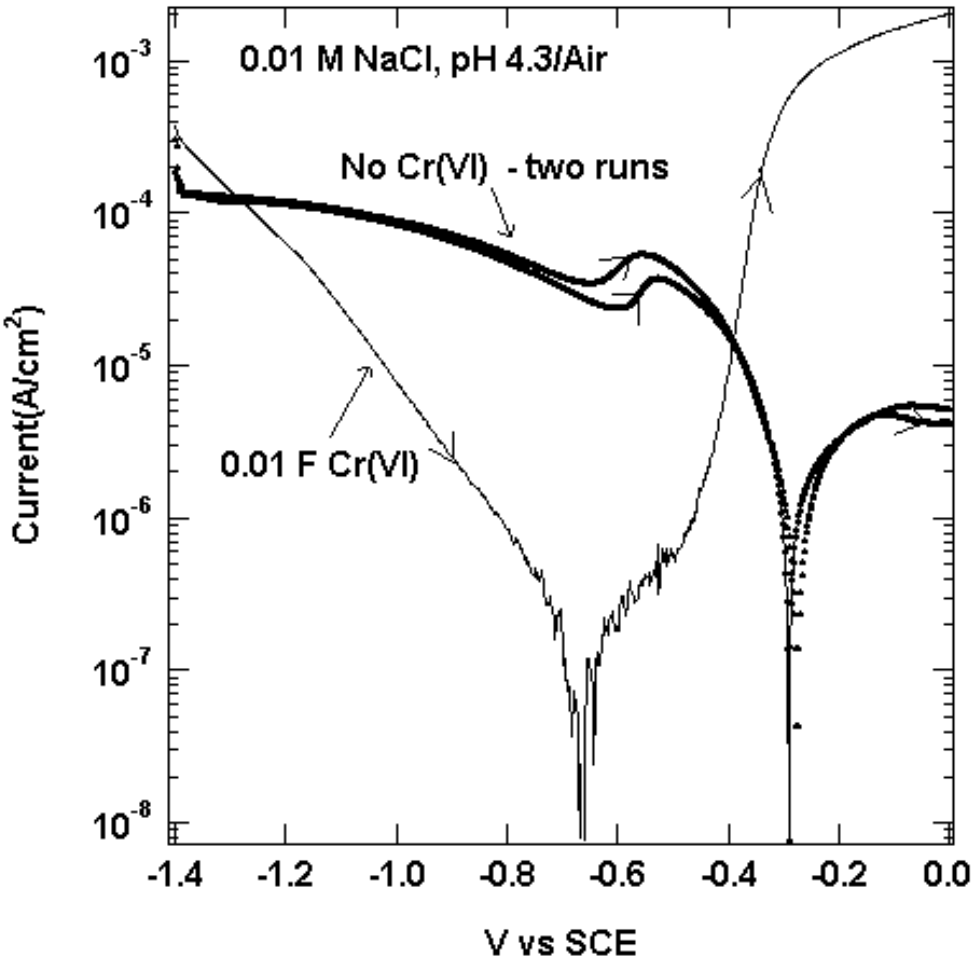

FIGURE 6. Polarization curves for Cu,Mg aluminide single crystal microelectrodes in pH 4.3 0.01 M NaCl. Scan rate is 10 mV/s cathodic to anodic potential.

INHIBITION OF AL ALLOY CORROSION BY CHROMATE

G. S. Frankel

Fontana Corrosion Center
The Ohio State University
Columbus, OH 43210

ABSTRACT

This paper summarizes some aspects of the activities in the author's lab during a 5-year MURI program funded by AFOSR. The focus of the work is the mechanism of Al alloy corrosion and the inhibition of corrosion by chromates, in particular chromates in solution. Four different projects are discussed: AFM-based studies, artificial crevice studies, EQCM studies and chromate release studies.

INTRODUCTION

Chromates are extremely effective and widely used as corrosion inhibitors for high strength Al alloys in aerospace applications. A combination of pressures, including environmental regulations on the use and handling of chromates, increased service life requirements of the fleet of airplanes, and the cost of preventive maintenance, has motivated the US Air Force to invest in efforts to find improved and environment-friendly methods of corrosion protection. A number of chromate-replacement systems have been developed in recent years, but none are as effective as chromate at inhibiting corrosion, especially for the high-strength Al alloys commonly used in aerospace applications. An Air Force Blue Ribbon Advisory Panel on Aircraft Coatings concluded that developing a better understanding of the mechanisms of aluminum corrosion and chromate inhibition is a top priority and a prerequisite for the development of a successful replacement. As a result of various research efforts over many years, considerable understanding of the mechanisms of Al corrosion and the inhibition

provided by chromate has already been developed. However, several key unresolved issues remain.

An international consortium of researchers from academia, industry and a national lab was formed as part of this AFOSR Multidisciplinary University Research Initiative program to address and resolve those issues regarding the mechanism of chromate inhibition. It should be noted that developing a chromate replacement was not the goal of this project. On the other hand, it is clear that the many efforts underway at a number of institutions to develop a conversion-coating/paint system to replace the standard chromate-containing protective systems are seeking guidance in making their systems more chromate-like. Most often that implies the desire to add functionality similar to the purported "self-healing" characteristic of chromates. It is considered that chromate can migrate from a reservoir somewhere in the conversion coating or primer to a distant active exposed site on the sample surface to inhibit the corrosion attack. A working hypothesis for why chromate is so effective an inhibitor is that it is a very soluble, higher-valent cation of an element with a lower-valent ion (Cr^{3+}) that is very poorly soluble and forms a protective film.

One goal of the MURI was to fully characterize and understand this migration and healing process. This involves understanding how chromate acts in organic primer coatings, in conversion coatings on Al alloys, and in solution as a dissolved species. Therefore, the work of this MURI team was loosely divided into those three realms, although there is considerable overlap. A fourth category on technique development, sample preparation and characterization contains critically important work that is not directly related to chromates. The perspective of this team was not limited, however, by this one view of the role of chromates. Other possible influences of chromates in organic coatings and conversion coatings were also investigated,

including the effect on cathodic kinetics, the effect of the chromate conversion coating (CCC) on the zeta potential of the surface, the effect on ion rectification, the effect on adhesion and protectiveness of organic coatings, pH buffering, rapid kinetics of coating deposition, and passivation of intermetallics.

Therefore, the work in this program addressed the following key questions related to the inhibition of Al dissolution by chromate:

1. What is the structure, composition, and formation mechanism of CCCs?
2. How and at what rate is chromate released from CCCs and primers?
3. Does chromate in CCCs and primers have a role other than dissolving and migrating to corrosion sites?
4. Does chromate in a primer affect the properties of the primer?
5. What is the speciation of chromium ions in solution?
6. How do chromates inhibit localized corrosion?
7. How do they affect anodic and cathodic kinetics of the Al matrix and common intermetallic particles?
8. How do they affect passivation and passive film properties?
9. Does chromate improve the adhesion of organic coatings?

This document summarizes the activities of one part of the MURI program.

SUMMARY OF PROJECTS

AFM-BASED STUDIES

The AFM is a very useful tool for documenting and quantifying the extent of corrosion and for in situ observation of corroding surfaces. One of the major contributions of the Frankel group as part of the MURI program was to develop two new AFM-based approaches for the study of corroding Al alloys: Scanning Kelvin Probe Force Microscopy (SKPFM)[1,2] and AFM scratching.[3,4,5]

SKPFM was a technique that had been developed for the study of semiconductor devices and not yet applied to corrosion prior to this MURI. It turns out that the technique is very well suited for corrosion studies because it is extremely sensitive to the distribution of charge across a surface. SKPFM is an easy, robust, and rapid means to map the practical nobility of a surface on a scale from tenths to tens of μm, which is the range that is relevant to Al alloy corrosion. It was determined that the measured signal is similar to a Volta potential, hence the use of the term Kelvin Probe in the name.[1,2] In contrast to a standard Kelvin probe, which nulls the capacitative current between a sample and a vibrating probe, the force between the sample and a conducting cantilever is nulled in the SKPFM. The Volta potential measured for a range of pure metals after removal from solution varies with the open circuit potential measured in the solution.[1] This is also true for a single metal exposed to different solutions in which it exhibits different open circuit potentials. The measured Volta potential for samples withdrawn from solution under potential control exhibit a slow decay associated with the oxide or double layer capacitance and a more permanent component associated with adsorbed species.[2] These studies validated the use of SKPFM, which must be applied ex situ, for relating the potential distribution across metal alloy surfaces to their corrosion behavior.

SKPFM was shown to be particularly useful for the study of Al alloys such as AA2024-T3, which exhibits high potential contrast associated with heterogeneities in the alloy on the order of tenths to tens of μm in size.[1,3] The intermetallic particles are clearly visible in the SKPFM potential maps, allowing a clear correlation of the localized corrosion behavior to the microstructure. Both AlCuFeMn and Al_2CuMg or S phase particles exhibit a high potential relative to the matrix for surfaces of samples polished without exposure to water, Figure 1. The high potential of the S phase particles results from the presence of a surface oxide layer. Removal of the oxide layer by scratching, sputter etching, or exposure to chloride solution results in a lowering or even reversal of the potential contrast.[2,6] On a polished surface, S phase particles corrode after a period of time during which their potential reaches that of the matrix.[2] After sputter etching of a polished surface, many S phase particles exhibit a lower potential than the matrix, and these sites tend to corrode upon exposure to chloride solutions.[6]

More details of the interactions of various parts of the sample surface can be determined by opening up windows in a protective organic coating over select areas of the microstructure.[6] In order for corrosion to proceed, both active anodes and active cathodes must be exposed. AlCuFeMn particles are the most active cathodes on the as-polished surface; in 0.5 M NaCl they will drive corrosion either at S phase particles or in the matrix if these areas are simultaneously exposed. Localized corrosion will usually not proceed if the exposed region contains only matrix phase or matrix phase + S phase particles. Some large S phase particles will corrode by dealloying even without simultaneous exposure of AlCuFeMn particles, but they do not convert to active cathodes and drive corrosion in the matrix phase. Exposure of a large area of AA2024 to 0.5 M NaCl results in local attack within AlCuFeMn particles and possibly the conversion of S phase particles to active cathodes after dealloying.

In situ scratching of the alloy surface with an AFM tip is another method that was developed in this work.[3,4,5] Scratching and other depassivation techniques have been used for some time to study repassivation and the conditions for stabilization of localized corrosion. AFM scratching allows for controlled scratching at select areas of a microstructure using controlled tip/sample forces. AFM scratching of pure Al in 0.5 M NaCl results in accelerated dissolution in the scratched region, or trenching, if performed in stagnant solution in the small Nanoscope IIIa electrochemical cell. Sustained localized corrosion does not occur because of depletion of oxygen in the small cell. If fresh solution is continually pumped into the cell during AFM scratching, deep pitting attack results from the breakdown caused by the tip because dissolved oxygen is replenished by the pumping action. Scratching during potentiodynamic scanning and while the 0.5 M NaCl solution is pumped through the cell results in pitting at potentials slightly below the pitting potential for an unscratched electrode. AFM scratching of AA2024-T3, even in a stagnant 0.5 M NaCl solution, results in immediate attack at the S phase particles even with the lightest scratching force because of destabilization of the somewhat protective oxide surface film on those particles.

These techniques, i.e. SKPFM and AFM scratching, were useful for illuminating various aspects of the effects of chromate on the corrosion process. AFM scratching of a pure Al sample upon immediate exposure to stagnant 0.5 M NaCl + 10^{-4} M $Na_2Cr_2O_7$ results in pitting similar to that found for the case of the pumped 0.1 M NaCl solution.[3] This example shows how chromate can act as a deleterious oxidizing agent under certain conditions. If the sample is allowed to be exposed to the 0.5 M NaCl + 10^{-4} M $Na_2Cr_2O_7$ solution for a period prior to scratching, the behavior is completely different. After a protective film is allowed to form, AFM scratching

(with an SiO_2 tapping mode cantilever) cannot destabilize the surface so that neither a pit nor a trench forms. No attack is evident.

The addition of 10^{-4} M $Na_2Cr_2O_7$ to the 0.5 M NaCl solution suppresses corrosion of AA2024-T3. Rather than a merging of the Volta potentials measured by SKPFM to a similar value, as is observed during exposure to pure chloride solution, the contrast at the intermetallic particles persists,[6] Figure 2. During AFM scratching in 0.5 M NaCl + 10^{-4} M $Na_2Cr_2O_7$, the breakdown of the S phase particles seen in pure chloride solutions is eliminated and pits form in the matrix phase instead. In solutions containing higher concentrations of dichromate, higher tip forces are required to cause breakdown. No corrosion was observed if a window containing cathodic area (AlCuFeMn particles) was pretreated in chromate solution and then simultaneously exposed to a pure chloride solution along with another un-pretreated area containing anodes (S phase and matrix). The same result was found if the anodic area was pretreated and the cathodic area was not. This shows that chromate can act as both cathodic and anodic inhibitor.

Since the behavior of S phase Mg is critical to the performance of AA2024, and Mg is a critical component of S phase, pure Mg was studied.[7] The rapid and massive attack of Mg in chloride solution in changed by the presence of a small amount of dichromate. In 0.5 M NaCl + 10^{-4} M $Na_2Cr_2O_7$, strong localized attack in the form of filiform-like corrosion is observed at specific low index twin boundaries.

ARTIFICIAL CREVICE STUDIES

One of possible explanations for the effect of chromates on Al alloy corrosion is anodic inhibition, in the sense that chromates might greatly reduce the local dissolution kinetics of Al alloys in pits or crevices. The repassivation potential is the lowest potential at which the critical current density for pit growth can be maintained. Since pits or acidic crevices must maintain a

minimum or critical current density in order to avoid repassivation, a decrease in the pit or crevice dissolution rate as a function of potential could inhibit localized corrosion by increasing the repassivation potential, which is the potential required to achieve the critical current density.

Artificial pit or “lead in pencil” electrodes have been used by researchers previously to study pit growth kinetics. The artificial pit electrode geometry forms a single pit in which the whole electrode area is active, generates a natural pit environment, and provides an ideal one-dimensional transport condition. The artificial crevice electrode is similar to the artificial pit electrode, except that a metal foil instead of a wire is used to create a recessed band instead of a recessed disk. Hydrogen bubbles can escape easier from this geometry, so artificial electrodes are useful for studying the localized corrosion kinetics of Al or Mg, in which copious hydrogen is evolved.

Dissolution kinetics for pits and crevices in aluminum and the effect of dichromate ions on the dissolution kinetics were investigated by using artificial crevice electrodes.[8,9] The aluminum artificial crevice electrodes were potentiostatically polarized over a range of potential in 0.1 M NaCl solution with and without dichromate ions. The anodic dissolution charge and cathodic charges for the hydrogen and dichromate reduction reactions were measured. The addition of dichromate ions does not suppress the active dissolution. This indicates that the mechanism of localized corrosion inhibition by dichromates is something other than anodic inhibition of Al dissolution in the pit or crevice environment. The relative amount of local cathodic reactions on Al increases by the addition of dichromate because of the dichromate reduction. The initial dissolution of aluminum in a crevice is ohmic-controlled. From the change in the dissolution current with time, the conductivity of the crevice and potential at the bottom of crevice are estimated. The conductivity and the bottom potential decrease with the

ratio of cathodic charge of hydrogen evolution to anodic dissolution charge. The conductivity in the crevice and thus the dissolution current seem to be controlled by hydrogen evolution and only indirectly by dichromate concentration.

In a follow-on study, the effect of four anions on dissolution kinetics of Al and Mg in chloride-containing solution was investigated using the artificial crevice technique.[9] Polarization curves for Al and Mg artificial crevice electrodes were obtained by first dissolving the artificial crevice electrode to a fixed depth at a high potential and then scanning the potential downward to the repassivation potential. Potential components were obtained by fitting the polarization curve to an equation describing activation overpotential and ohmic potential drops. Of chromate, dichromate, molybdate and nitrate, only nitrate inhibits the dissolution kinetics of Al artificial crevice electrodes, Figure 3. In contrast, all anions inhibit the dissolution kinetics of Mg artificial crevice electrodes. The results support the notion that the mechanism of localized corrosion inhibition of Al alloys by chromate must be something other than inhibition of anodic dissolution in an active pit or crevice.

ELECTROCHEMICAL QUARTZ CRYSTAL MICROBALANCE (EQCM) STUDIES

Characterization of electrochemical activity of intermetallic compounds and the Al matrix in AA2024 is critical for understanding corrosion behavior of this alloy. However, cathodic corrosion of Al and Al alloys makes it very difficult to determine the true cathodic kinetics using only electrochemical techniques. The electrochemical quartz crystal microbalance was used to directly measure the mass loss rate, and thus the anodic reaction rate, of thin film analogs in this alloy.[10] The thin films studied include pure Al, Al-4 Cu, which is an analog for the matrix phase, and Al_2Cu, which is an analog for θ phase and other high Cu cathodic intermetallic particles. The true cathodic reaction rate was calculated from the summation of the

net and the anodic current density. For pure Al in unbuffered 0.1 M NaCl, the anodic current density is large relative to the net current density, so the true cathodic current density is considerably larger than the measured net current density. The anodic current density and the cathodic current density are weakly dependent on potential and the presence of dichromate in the solution, even though the net current density shows stronger dependencies. The cathodic current density was almost identical to the net current density for Al_2Cu or θ phase because the anodic dissolution rate was very small compared to the cathodic reaction rate.

The effect of chromate in solution was studied by adding 10^{-2} or 10^{-4} M $Na_2Cr_2O_7$ to 0.1 M NaCl, and adjusting the pH to 6.2 by adding NaOH. The addition of dichromate decreases the net current density and the true cathodic current density. The largest effect was found for θ phase, though the effect was not as large as is found for AA2024-T3.

CHROMATE RELEASE STUDIES

The release of chromate ions from chromate conversion coatings (CCCs) on Al alloys was studied, and the effect of aging of CCCs on the chromate release kinetics was investigated. Chromate release from CCCs into aqueous solutions was monitored by measuring the change in the chromate concentration in solution using UV-vis spectroscopy.[11] Heat treatment of the CCC greatly reduces the chromate release rate. The chromate release rate also decreases with increasing aging time at room temperature. Work from the McCreery group in the MURI program showed that the steady state concentrations of Cr(VI) species in solutions contacting a CCC can be described by a Languirian adsorption/desorption equilibrium. In this work, a diffusion-control model for the release kinetics was proposed based on the notion that the CCC in an aqueous solution is a porous two phase structure consisting of a solid phase with adsorbed Cr(VI) species that is in local Langmuir-type equilibrium with an interpenetrating solution

phase. This model results in a concentration gradient of soluble Cr(VI) in the solution phase of the CCC as chromate is released. The concentration and diffusion coefficient of soluble Cr(VI) in CCC can be estimated with this model. The estimated diffusion coefficient tends to decrease with aging time suggesting that the CCC is modified with aging time, Figure 4.

SUMMARY

In summary, the work of this MURI has shown that there are several reasons why chromate is an extremely effective corrosion inhibitor for Al alloys:

1. Chromate can be stored in conversion coatings and as a pigment in paints.

2. CCC formation involves several sequential steps, including etching of aluminum oxide by fluoride, reduction of Cr^{VI} to Cr^{III}mediated by $Fe(CN)_6^{-3/-4}$, polymerization of $Cr^{III}_x(OH)_y$ and CrO_4^{-2} adsorption onto the $Cr^{III}_x(OH)_y$ backbone. The resulting CCC is a Cr^{III}-Cr^{VI} mixed oxide with an approximately 3:1 Cr^{III}:Cr^{VI} molar ratio, containing low levels of $Fe(CN)_6^{-3}$ and its degradation products. The distribution of Cr on the AA2024-T3 surface is uneven, with lower Cr levels on Cu-rich intermetallic particles.

3. Chromate is released from these CCC's and paint, particularly when they are scratched. The released chromate is in equilibrium with the chromate in the coatings, and higher pH favors Cr^{VI} release. Cathodic sites, which raise the local pH, may favor Cr^{VI} release. The concentration of Cr^{VI} in equilibrium with a CCC or $SrCrO_4$ pigment is approximately 10^{-4} to 10^{-3} M.

4. Chromate is mobile in solution and migrates to exposed areas on the Al alloy surface.

5. Chromate adsorbs on active corrosion sites of the surface and is reduced to form a monolayer of a Cr^{III} species. This monolayer inhibits further reduction of Cr^{VI}, but may adsorb a second layer of Cr^{VI} to form mixed oxide, depending on the pH.

6. This layer is effective at reducing the activity of both cathodic sites (Cu-rich IMC particles) and anodic sites in the matrix or at S phase particles. Inhibition in either or both cases is effected by blocking active sites, such as sites for O_2 adsorption, and reducing the tunneling rate of electrons through the inhibiting chromate film. Anodic inhibition involves reduction of localized corrosion initiation; localized corrosion growth is not inhibited by chromate, perhaps because chromate ions are fully protonated into an uncharged and inactive species in the low pH solutions that form in pits.

7. Adsorbed Cr^{VI} (unreduced) lowers the zeta potential and the pH of zero charge of Al oxide surfaces, which should inhibit chloride adsorption, consistent with the dipolar model for protective passive films.

8. $SrCrO_4$ pigments enhance the protective properties of even moderately good barrier coatings in the absence of obvious physical defects. They also improve adhesion of polymer coatings on AA2024-T3 surfaces, as do CCC's of a typical coating weight.

9. The combined properties of storage, release, migration, and irreversible reduction provided by chromate coatings underlie their outstanding corrosion protection. Of special note is the action of Cr^{VI} as a "suicidal inhibitor" in which reduction to Cr^{III} locks in the inhibiting film by converting mobile Cr^{VI} to insoluble and substitution inert Cr^{III}.

ACKNOWLEDGMENTS

This work was supported by the United States Air Force Office of Scientific Research under contract No F49620-96-1-0479.

REFERENCES

1. P. Schmutz and G. S. Frankel, *J. Electrochem. Soc.*, **145**, 2285 (1998).
2. V. Guillaumin, and G. S. Frankel, *J. Electrochem. Soc.*, **148**, B163-173 (2001).
3. P. Schmutz and G. S. Frankel, *J. Electrochem. Soc.*, **145**, 2295 (1998).
4. P. Schmutz and G. S. Frankel, *J. Electrochem. Soc.*, **146,** 4461 (1999).
5. D. Devecchio, and G. S. Frankel, " *Electrochem. Solid-State Lett.*, **3** 90 (2000).
6. P. Leblanc and G. S. Frankel, accepted for publication in *J. Electrochem. Soc.*
7. P. Schmutz, V. Guillaumin, S. Lillard, J. Lillard and G. S. Frankel, "Influence of Dichromate Ions on Corrosion Processes on Pure Magnesium," in preparation.
8. E. Akiyama and G. S. Frankel, *J. Electrochem. Soc.*, **146,** 4095 (1999).
9. Q. Meng, T. Ramgopal and G. S. Frankel, accepted for publication in *Electrochem. Solid-State Lett.*, 11/01.
10. Y. Baek and G. S. Frankel, in *Corrosion and Corrosion Protection*, J. D. Sinclair, E. Kalman, M. W. Kendig, W. Plieth, and W. H. Smyrl, eds, PV 2001- 22, The ECS Proceedings Series, Pennington, NJ (2001).
11. E. Akiyama, A. J. Markworth, J. K. McCoy, G. S. Frankel, L. Xia, and R. L. McCreery, submitted to *J. Electrochem. Soc.*, 11/01.

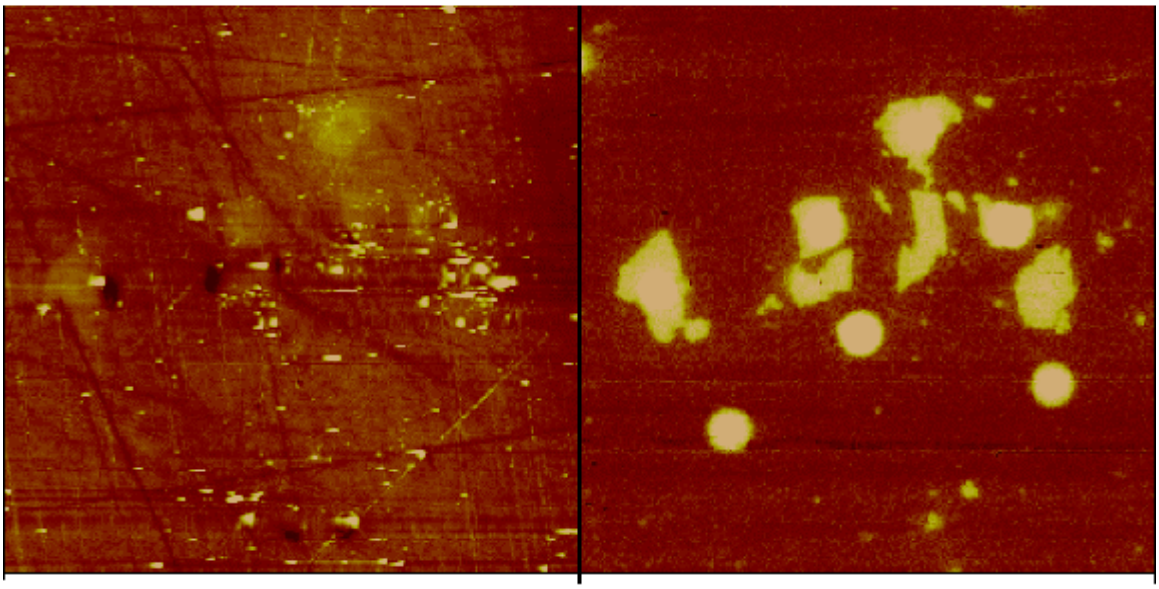

FIGURE 1. AFM image of intermetallic particles in AA2024-T3. Both images 80 x 80 μm, Left, topographical map with 100 nm z scale, right, Volta potential map with 1.5 V z scale.[1]

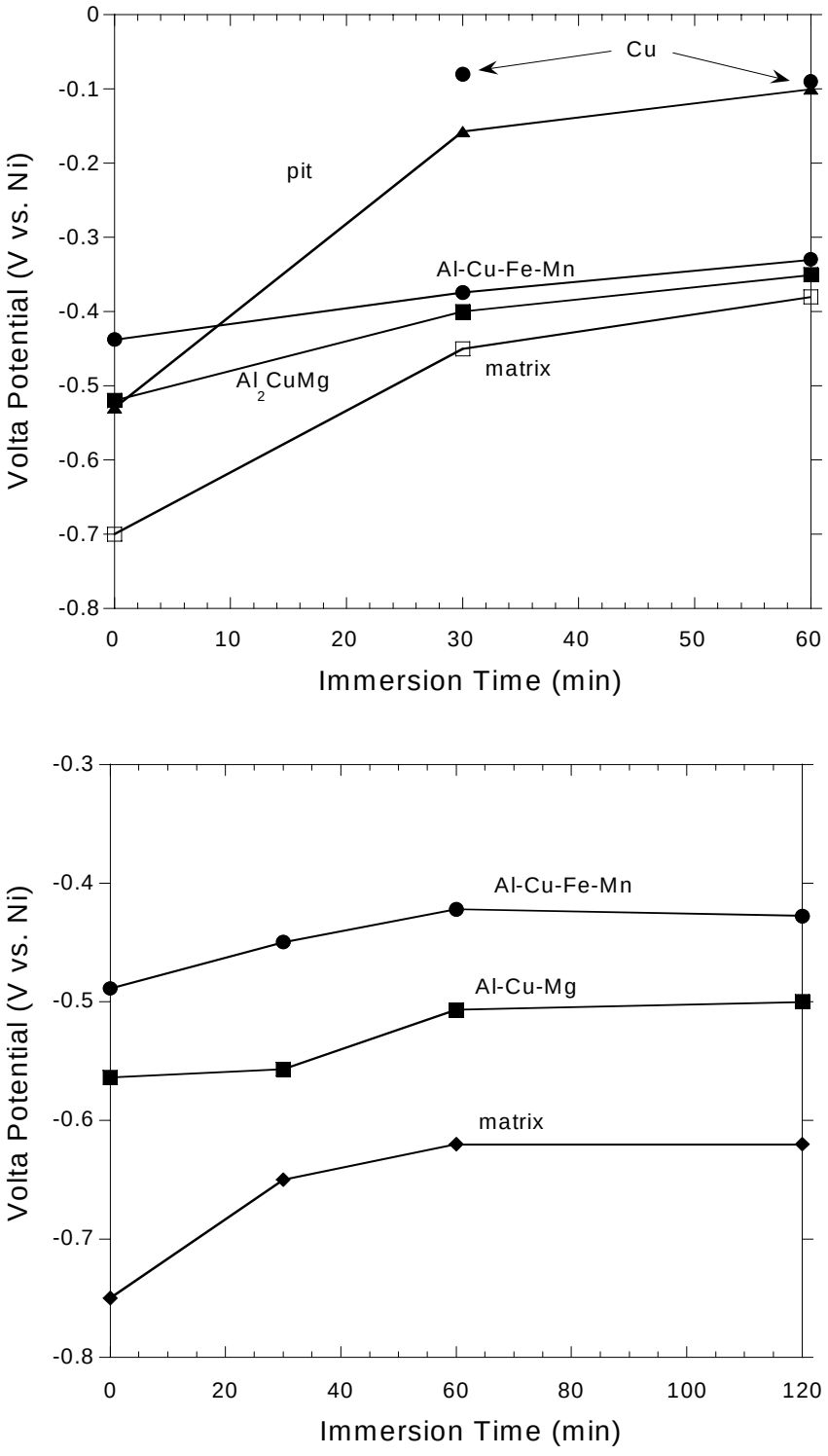

FIGURE 2. Volta potential change of matrix and intermetallic particles of AA2024-T3 in 0.5 M NaCl (left), 0.5 M NaCl + 10^{-4} M $Na_2Cr_2O_7$ (right).[6]

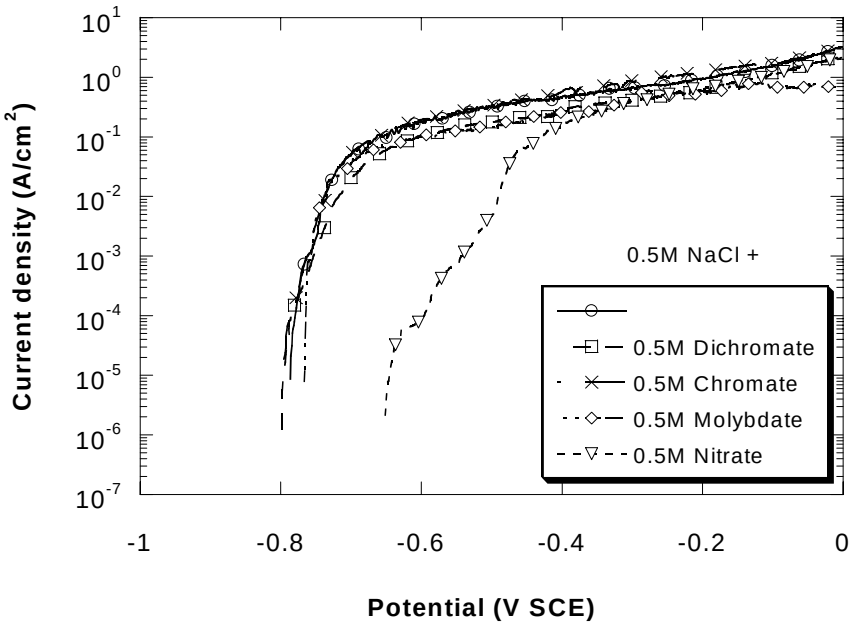

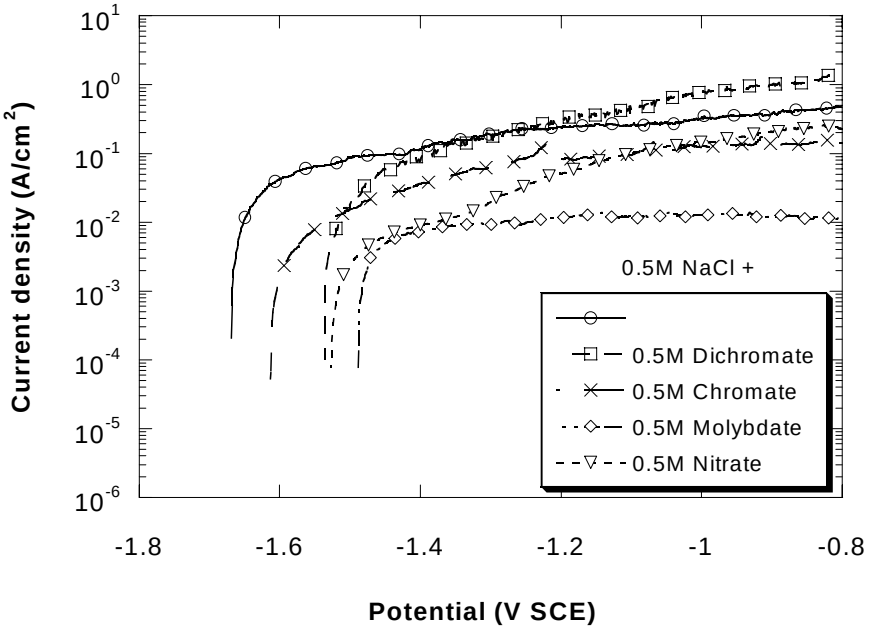

FIGURE 3. Effect of various inhibitor ions at a concentration of 0.5 M on dissolution kinetics in 0.5 M NaCl for artificial crevice electrodes of (a) Al, (b) Mg.[9]

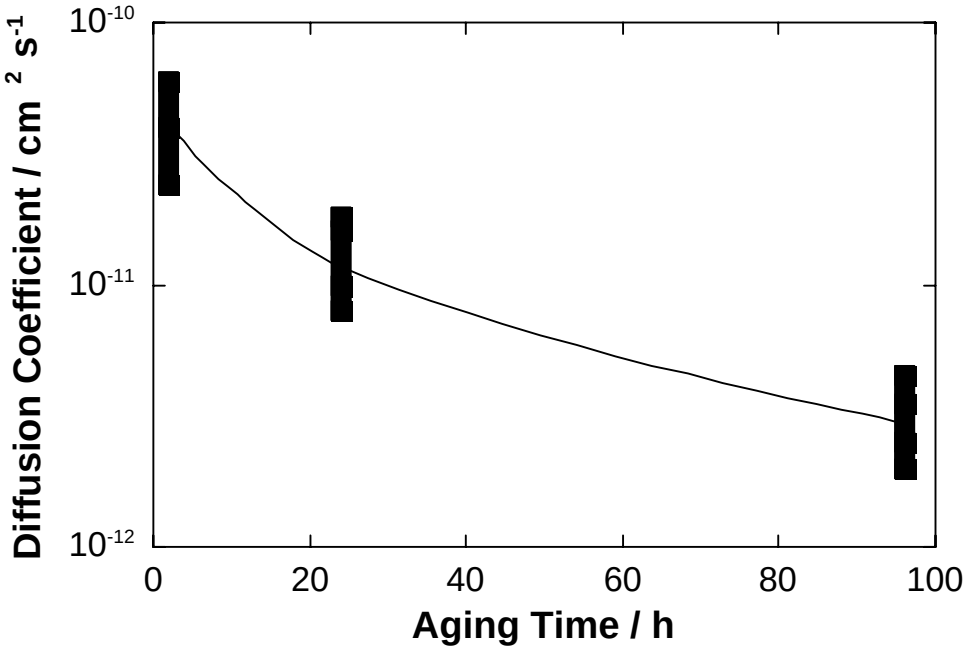

FIGURE 4. Estimated diffusion coefficient of Cr(VI) species in the CCCs on AA1100 as a function of aging time at RT.[11]

A SCANNING ELECTROCHEMICAL MICROSCOPY (SECM) STUDY OF HETEROGENEOUS REDOX ACTIVITY AT AA2024 SURFACES

Jesse Seegmiller and Daniel A. Buttry*

Department of Chemistry
University of Wyoming
Laramie, WY 82071-3838
Email: Buttry@uwyo.edu

ABSTRACT

Scanning electrochemical microscopy (SECM) is used to spatially resolve the cathodic redox activity at AA2024 alloy surfaces. Spatial mapping of the redox activity is achieved using a 10 micron diameter Pt probe microelectrode in a solution containing the protonated form of the electroactive molecule (dimethylamino) methylferrocene ($DMAFc^+$), which contains a Fe(II) redox center. The probe tip is brought near to the alloy surface while being held at a potential of 0.55 V versus Ag/AgCl , where $DMAFc^+$ is oxidized to $DMAFc^{2+}$ (i.e. the Fe(III) state). The AA2024 substrate is held at –0.85 V, where the $DMAFc^{2+}$ produced near the probe tip is reduced back to $DMAFc^+$. Images comprising spatial variation in the $DMAFc^+$ oxidation current at the probe tip are generated either by variation of the diffusive delivery of $DMAFc^+$ to the tip due to surface topology or by a positive feedback mechanism in which $DMAFc^+$ that had been oxidized at the probe tip is regenerated at the substrate. The images show the presence of locally high redox activity (i.e. higher probe currents over certain locations on the surface) which is attributed to the presence of intermetallic particles. Prolonged imaging at the same location leads to the appearance of larger regions of high redox activity. Optical microscopic inspection reveals these to be pits formed due to chemical etching caused by local generation of $DMAFc^{2+}$.

INTRODUCTION

A key feature of the corrosion behavior of the Cu-rich AA2000-series aluminum alloys, such as AA2024, is the presence of several types of second phase intermetallic particles embedded within the bulk of the alloy. The enhanced corrosion susceptibility of this alloy compared to pure Al is thought to be due to local galvanic cells that are established by virtue of

heterogeneous redox activity associated with the presence of these particles.[1-6] Specifically, some of these intermetallic particles (IP's) are thought to function as cathode sites at which the reducing power of Al appears and drives reduction of dioxygen. This causes oxidation of Al to Al(III) nearby, and can ultimately lead to pit initiation and growth. This tendency toward corrosion is dramatically reduced through the use of chromate-containing surface treatments,[7-12] and molecular level models have been proposed to account for this protection.[10]

The previous work in the area makes it clear that understanding the redox reactivity of IP's at the alloy surface is important. One approach to achieve this goal is to use probe techniques that allow one to spatially resolve compositional differences across the surface and to also resolve reactivity. For example, Frankel and coworkers have used scanning Kelvin probe force microscopy (SKPFM) to examine AA2024 surfaces.[13,14] This technique allows for the simultaneous measurement of topology and potential distribution for samples in air or vacuum. They found that the surface oxide and adsorption at the oxide can influence the measured Volta potential, and that both of these influences are affected by various solution treatments (prior to imaging). Other groups have used *in situ* atomic force microscopy (AFM) to examine the corrosion behavior of AA2024 (15). These workers studied the reactivity of this alloy in aqueous HCl, finding that dissolution occurs initially, followed by pit formation at later times.

Another approach that can be used to spatially image redox activity at a surface is scanning electrochemical microscopy (SECM). In this experiment, a microelectrode probe tip is rastered across a surface, producing an image.[16] The mechanism for imaging depends considerably on the electrochemical characteristics of the surface, the probe tip and any redox active molecules that are present in solution. Imaging typically relies on changes in the delivery of the redox active molecule to the probe tip, where these changes can be due to physical

blocking of diffusion of the molecule to the tip caused by topographic features on the (electrically insulating) surface or feedback, where the redox active molecule shuttles back and forth between the probe tip and the (electrochemically active) surface.[16] In the latter case, the currents measured at the probe tip are often substantially above those seen for a blocking surface, due to feedback enhancement.

An advantage of SECM is that it can be used in solution, under exactly the same conditions at which the alloy corrodes. This advantage has been previously exploited for studying corrosion processes. For example, White and Alkire used SECM to study the dissolution of sulfur species from inclusions in stainless steel.[17] Also, Serebrennikova and White used SECM to examine electroactive defect sites in the native film on aluminum.[18]

In this contribution SECM is used for the first time to image intermetallic inclusions at AA2024 surfaces. It is shown that these intermetallic particles are sites of enhanced redox activity. Further, it is shown that SECM can be used to produce oxidative stress locally at the surface, and that ultimately this can lead to pitting of the surface.

EXPERIMENTAL

MATERIALS

AA2024-T3 aluminum alloy samples were a gift from Prof. G. Frankel (Ohio State University). Chemicals were of reagent grade or better and were used as received. Water (18 MΩ) from a Millipore Nanopure system was used in all experiments. Disks were mechanically punched from the alloy sheet, and the disks were mounted at the end of a shaft and connected electrically for use as substrate electrodes in the SECM experiment. The exposed area of the AA2024 surface was 0.28 cm^2.

Pt probe tip microelectrodes were obtained from CH Instruments. They comprised 10 μm diameter Pt wire sealed into soft glass capillary tubing. A Ag/AgCl reference electrode was used in all experiments, and all potential are referenced to this electrode. Pt wire was used as a counter electrode. The SECM cell was Teflon, and the shaft with the alloy substrate electrode was introduced through an o-ring seal at the bottom of the cell.

Supporting electrolyte solutions were comprised of 5 mM (dimethylamino) methyl ferrocene (DMAFc) dissolved in either 10 mM sodium triflate (NaTf) or 10 mM sodium borate (NaB), and then adjusted to pH 7.75. Under these conditions the iron complex is predominantly in its soluble, protonated form, written as $DMAFc^{+}$ for convenience.

PROCEDURES

Samples were mechanically polished with 1 μm alumina powder suspended in odorless kerosene. They were then briefly (2 seconds) sonicated in hexane to remove polishing particles, rinsed thoroughly with hexane, air-dried and stored under hexane. After mounting in the SECM cell, the cell was filled with supporting electrolyte under conditions such that the alloy was never exposed to the aqueous solution without being held under potential control (typically –0.85 V). This was done in order to prevent corrosion of the surface and loss or evolution of the intrinsic redox reactivity of the IP's. In a typical experimental procedure, after filling the cell with supporting electrolyte, the cleanliness of the probe electrode would be checked by running a cyclic voltammogram.

INSTRUMENTATION

SECM experiments were done using a CHI-900 SECM (CH Instruments, Austin, TX). The instrument defines three axes for motion of the probe tip. The x,y plane is defined as the

plane of the AA2024 substrate electrode and the z axis is defined as the axis normal to this plane. For approach curves (see below), the tip is moved in 0.2 μm increments toward the surface (along the +z axis), with current measurements at each z position. For SECM imaging, the tip is rastered by moving it in 5 μm increments in the x direction (left to right in the figures, along the + x axis) with each x scan followed by a single increment of 5 μm in the y direction (top to bottom, along the + y axis). The residence time at each location is 0.05 s. Thus, an image comprises 1600 current values on a square grid and takes approximately 200 seconds to acquire (including the time required to move the tip back to the initial x position and increment along the y axis).

RESULTS AND DISCUSSION

Figure 1 shows a cyclic voltammogram (CV) using the 10 μm diameter Pt microelectrode as working electrode. One can clearly see the sigmoidal shape and plateau limiting current response that are characteristic of radial diffusion to microelectrodes.[16] The arrow shows the potential of 0.55 V that was used for the tip potential during SECM experiments.

Figure 2 shows the results for a typical tip approach curve at AA2024. In this experiment, the tip is first held far from the surface, and then is driven step-wise toward the surface, with the tip and substrate currents monitored after each increment along the z axis. In this experiment, the tip potential is held at 0.55 V, where $DMAFc^{+}$ (the Fe(II) form) is oxidized to $DMAFc^{2+}$ (the Fe(III) form), and the substrate potential is held at –0.85 V. At this potential any $DMAFc^{2+}$ that was produced at the tip and that had reached the substrate (due to proximity) would be reduced back to $DMAFc^{+}$, *if the substrate were in electrochemical contact with the solution*. Thus, positive feedback is possible under these conditions. This value of the substrate potential represents a compromise between more negative values, at which hydrogen evolution and bubble

formation would become problematic, and more positive values, where oxidation of the substrate might occur. It is especially important that anodic stripping of neither Fe nor Cu should occur at this value of the substrate potential. In contrast, given their redox potentials, both Mn and (especially) Mg may be anodically stripped at this potential.

Plate A shows a plot of tip current versus distance. Between z = 0 μm and z = 150 μm, the tip current decreases gradually due to slight passivation of the probe tip in the solution. Toward the end of the approach the current decreases abruptly as the tip approaches the surface, over the range of z values between 175 and 180 μm. The approximate position of the surface is indicated by the downward pointing arrow. The features of this curve are quite characteristic of previously reported tip approach curves.[16]

Plate B shows a plot of the substrate current during the same approach. The substrate current, which begins with a slightly anodic value, drifts slowly toward smaller values due to small residual redox activity of the substrate in the solution. As the tip approaches to within a few microns of the surface, the substrate current turns markedly in the cathodic direction, consistent with a feedback situation, as discussed above. These features have been reproduced many times for both the tip and substrate currents during approach.

Following the approach curve, the SECM experiment is used to image the surface by rastering the tip across the surface and simultaneously recording the tip current. The SECM image comprises a three dimensional map of the tip current projected onto the x,y plane. Figure 3 shows six SECM images for the AA2024 surface. These are grayscale images, with higher currents indicated by lighter regions of the image. In plate A, which was obtained in a NaTf solution containing the ferrocene redox reagent, the image clearly shows sites of very high redox activity. These are consistently seen at these surfaces, and can be imaged repeatedly, so long as

the substrate is maintained at –0.85 V. We believe these "redox hot spots" correspond to intermetallic inclusions present at the surface. White and coworkers have previously imaged low purity Al foils.[18] They saw similar features and also speculated that they were due to intermetallic particles. A more thorough analysis of the sizes and distributions of the features in these SECM images and their comparison to scanning electron microscopy images are now being done, which will aid in verifying this conclusion.

Plate B shows the results of changing the solution to 10 mM NaB. At first, the current decreases considerably, resulting in a steady graying of the image from top to bottom. Plate C, however, shows that the same features that had been observed in NaTf are also evident in NaB, albeit at lower absolute currents.

Repeated scanning in the same location leads to enlargement of the high current features. Optical microscopic inspection reveals these to be pits. We believe this pitting is induced by the oxidative stress produced under the probe tip. Note that the current density for producing $DNAFc^{2+}$ under the tip is ca. 5 mA cm^{-2}. Further studies are now being done to elucidate this effect.

CONCLUSIONS

For the first time, SECM imaging has revealed the presence of sites of high redox activity at AA2024 surfaces. In agreement with earlier speculation by White's group on the origin of similar sites at the surface of low purity Al foils, we attribute these to intermetallic inclusions. It is observed that they can be imaged stably for some time. However, prolonged imaging leads to pitting and surface damage. We expect that the use of SECM to characterize these surfaces will be quite useful in terms of understanding how localized redox reactivity changes with various chemical treatments, and are now undertaking several experimental studies toward that end.

ACKNOWLEDGEMENTS

We are grateful to the Air Force Office of Scientific Research for the generous support of this work.

REFERENCES

1. R. G. Buchheit, R. P. Grant, P. F. Hlava, B. Mckenzie and G. L. Zender, J. Electrochem. Soc. 144 (1997): p. 2621.
2. C. Blanc, B. Lavelle, and G. Mankowski, Corros. Sci. 39 (1997): p. 495.
3. T. J. Warner, M. P. Schmidt, F. Sommer and D. Bellot, Z. Mettallkd. 86 (1995): p. 494A.
4. A. Garnier and D. Tromans, Corrosion 35 (1979): p. 55.
5. G. S. Chen, M. Gao and R. P. Wei, Corrosion 52 (1996): p. 8.
6. L. F. Mondolfo, Aluminum Alloys: Structure and Properties ed. L. F. Mondolfo (London: Butterworths, 1976).
7. H. Bohni and H. H. Uhlig, J. Electrochem. Soc. 116 (1969): p. 906.
8. S. T. Pride, J. R. Scully, and J. L. Hudson, J. Electrochem. Soc. 141 (1994) : p. 3028.
9. F. Hunkeler and H. Bohni, Corrosion 37 (1981): p. 645.
10. J. Zhao, G. Frankel, and R. L. McCreery, J. Electrochem. Soc. 145 (1998): p. 2258.
11. A. C. Fraker and A. W. Ruff, Corrosion 27 (1971): p. 151.
12. R. G. Buchheit, M. A. Martinez and L. P. Montes, J. Electrochem. Soc. 147 (2000): p. 119.
13. V. Guillaumin, P. Schmutz, and G. S. Frankel, J. Electrochem. Soc. 148 (2001): p. B163.
14. T. Ramgopal, P. Schmutz, and G. S. Frankel, J. Electrochem. Soc. 148 (2001): p. B348.

15. K. Kowal, J. DeLuccia, J. Y. Josefowicz, C. Laird and G. C. Farrington, J. Electrochem. Soc. 143 (1996): p. 2471.
16. A. J. Bard, F.-R. Fan, and M. V. Mirkin, in Electroanalytical Chemistry, Vol. 18, A. J. Bard, Editor, p. 243, Marcel Dekker, NY (1994).
17. C. H. Paik, H. S. White, and R. C. Alkire, J. Electrochem. Soc. 147 (2000): p. 4120.
18. I. Serebrennikova, and H. S. White, Electrochem. Solid-State Lett. 4 (2001): p. B4.

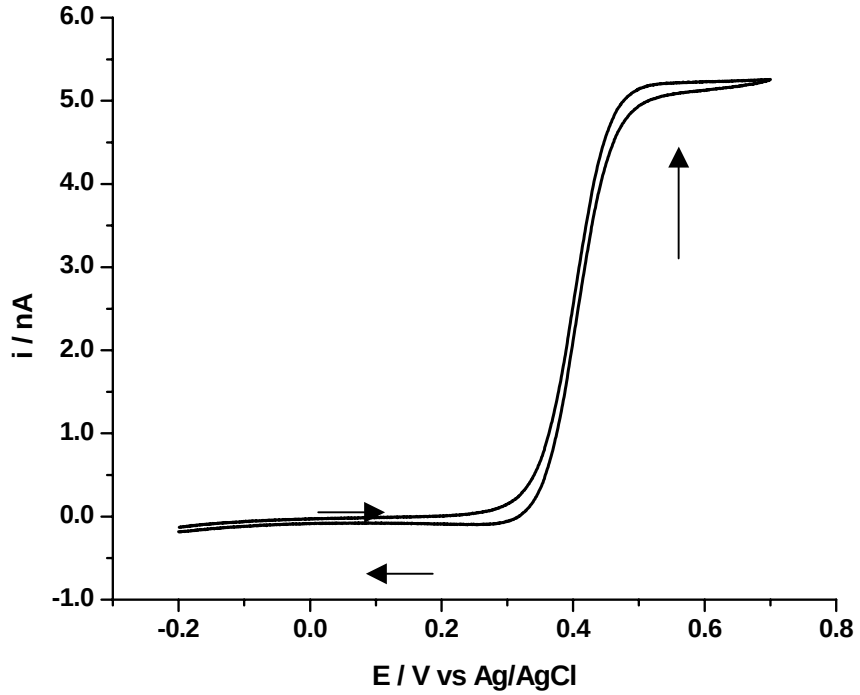

FIGURE 1. CV of 5 mM $DMAFc^{+}$ in 10 mM Na Tf. Scan rate: 0.1 V s^{-1}.

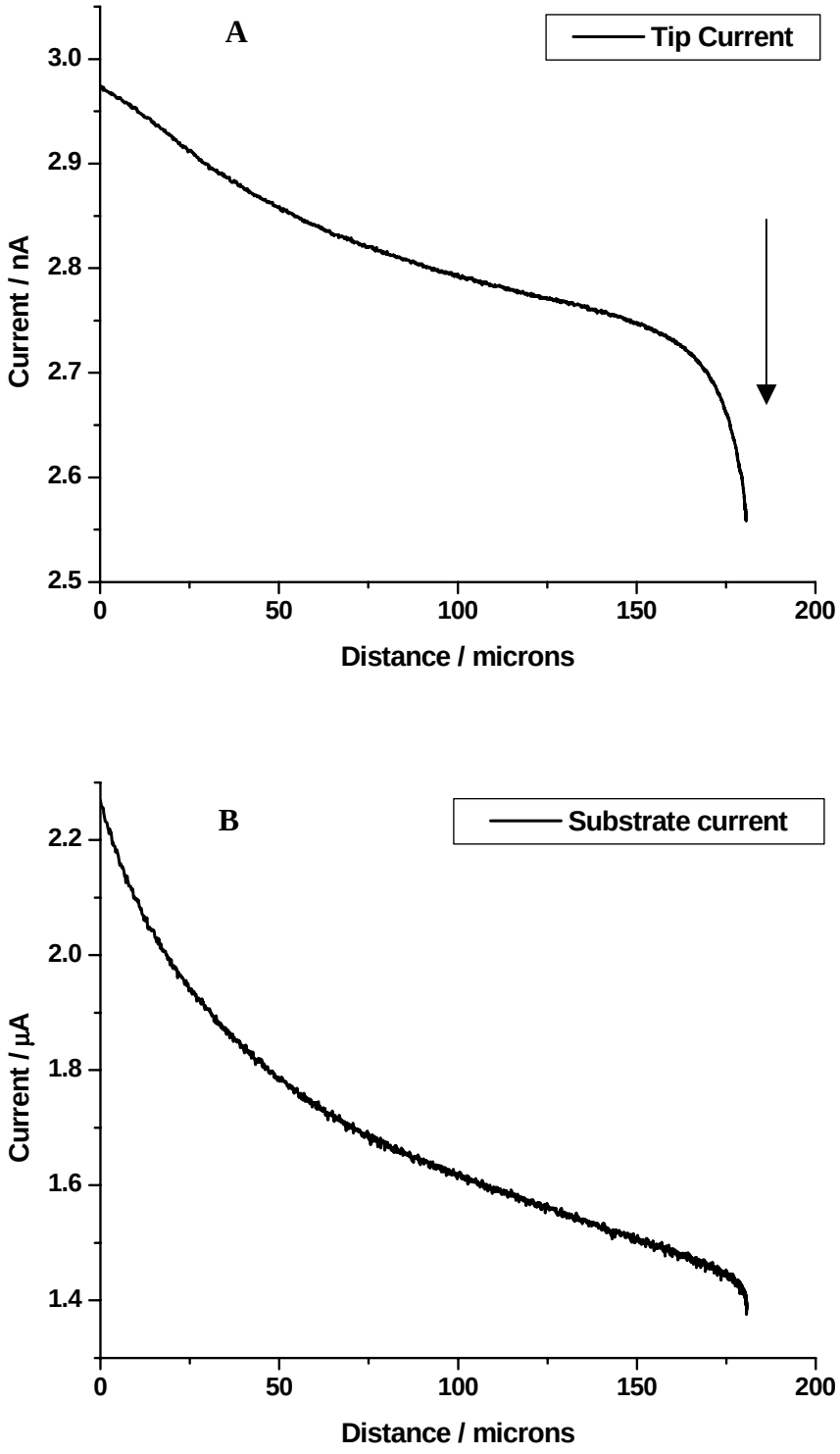

FIGURE 2. Approach curves at AA2024 in 5 mM $DMAFc^{+}$ + 10 mM NaTf. Plots are current versus (arbitrary) distance from initiation of the approach curve. Tip potential = 0.55 V, substrate potential = -0.85 V. Plate A: tip current. Plate B: substrate current. Termination of the approach curve occurs when the tip current has reached an arbitrarily chosen value.

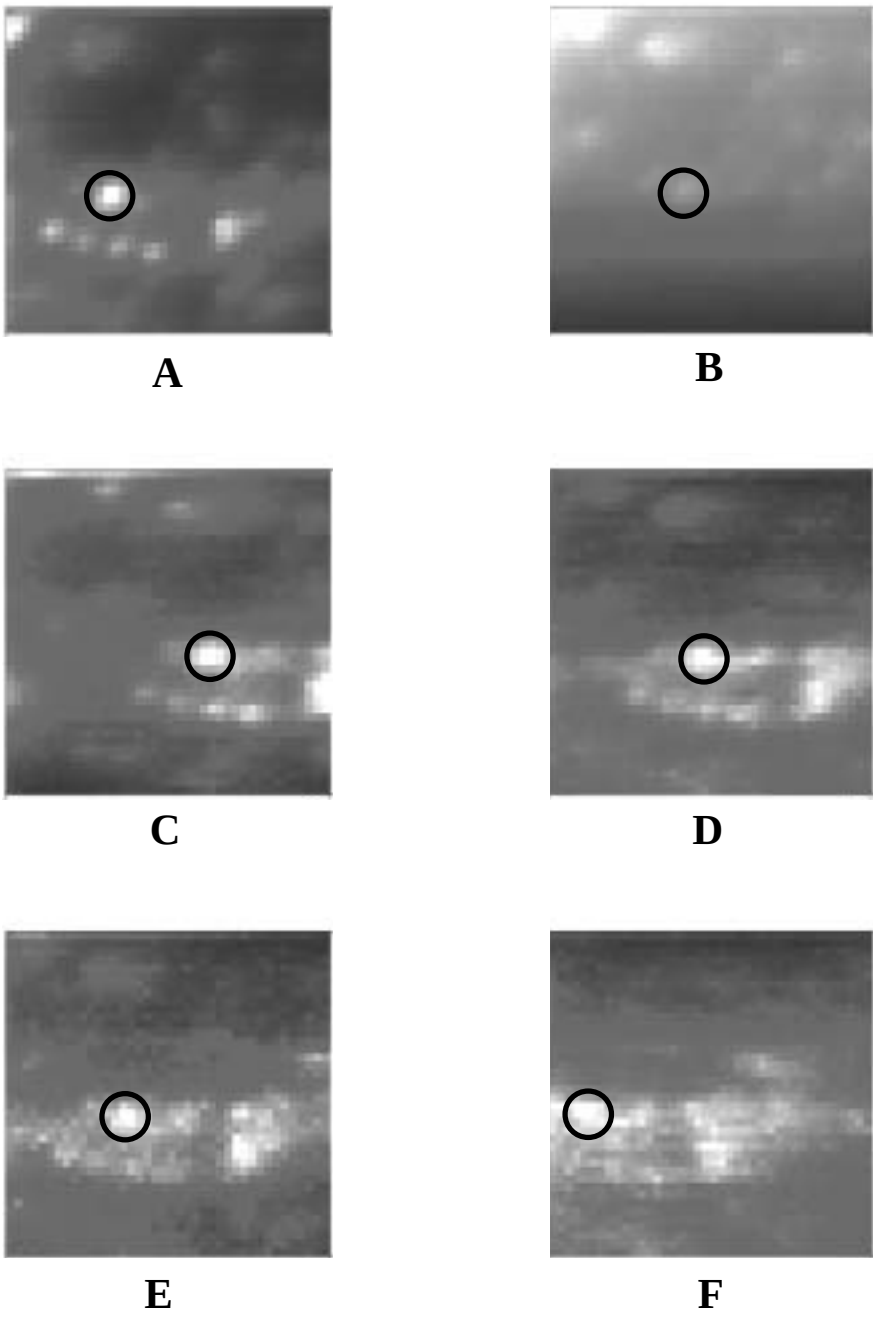

FIGURE 3. SECM images obtained after the approach curve shown in Figure 2. The circled feature is the same one in each image and is used to account for image drift. Image A is in 5 mM $DMAFc^+$ + 10 mM NaTf. Images B-F are in 5 mM $DMAFc^+$ + 10 mM NaB. Each image is 200 μm x 200 μm. Tip potential = 0.55 V, substrate potential = -0.85 V. The gray scale contrast corresponds to a minimum-maximum current range of: A) 5.47 – 6.65 nA, B) 1.77 – 4.91 nA, C) 0.77 – 0.92 nA, D) 0.73 – 0.90 nA , E) 0.72 – 0.87 nA, F) 0.67 – 0.86 nA. The scan history for each plate is: A) scan number 9, B), scan 10, C) scan 13, D) scan 16, E) scan 17, F) scan 19. The total elapsed time was 45 minutes.

AIRCRAFT COATINGS TESTING, CORROSION SENSORS IN COATINGS AND Mg-RICH COATINGS AS Cr-FREE PRIMERS FOR Al 2024 T-3

G. P. Bierwagen, S. Mabutt, X. Wang, M. Nanna, L. Ellingson and D. Tallman*

Depts. of Polymers & Coatings and Chemistry*
North Dakota State University
Fargo, ND 58105

ABSTRACT

Work has continued on testing in an accelerated exposure protocol present and future coatings systems for Al2024 substrates. This work has generated a proposed lifetime-of-corrosion-protection prediction method that was further examined during the last year for accuracy and applicability to all of the systems under test. The results of the testing will be presented as will a discussion of the lifetime prediction protocol.[1] Work has been performed on the use of embedded Pt wires in coatings together with electrochemical noise methods of data acquisition and analysis for use as a corrosion sensing system for Al 2024 substrates. This work has yielded *in situ* measurements of R_n, the electrochemical noise resistance, and other electrochemical parameters on substrates under exposure in a cyclic exposure chamber using the Prohesion exposure cycle.[2] Work has continued on the use of Mg-rich coatings as Cr-free primers for Al 2024 T-3. This system has shown that Mg-rich primers for Al using a stable particulate form of Mg can protect Al alloy substrate in a manner analogous to the way Zn-rich primers protect steel. Data will be presented on the primer by itself under Prohesion exposure and then as top-coated. The primer provides damage protection in scribed areas, and the reaction products of Mg oxidation do not immediately attack the Al substrate.[3]

INTRODUCTION

A. TESTING PROTOCOL FOR AIRCRAFT COATINGS OVER AL 2024 T-3

Work has been ongoing at North Dakota since 1996 under AFOSR sponsorship to develop improved test protocols for characterizing the protective lifetimes of complete aircraft coatings systems (Al 2024 T-3 Substrate + pretreatment + primer + topcoat). This protective

[1] A poster on further details of this work will be presented at this meeting by Stephen Mabutt.
[2] A poster on further details of this work will be presented at this meeting by Xianping Wang
[3] A poster on further details of this work will be presented at this meeting by Michael Nanna.

lifetime is against UV/humidity and cyclic salt fog exposure in accelerated test cabinets, thus judging the two components of exterior durability of coatings systems, UV radiation and corrosion resistance. This has been done to have a proper protocol available to judge and rank the new, chromate-free systems, which will be required of the Air Force in the near future, in comparison to the performance of existing, approved coating system. We have used the accelerated exposure cycle to UV/Prohesion environments according to the method ASTM D 5894-96, *Standard Practice for Cyclic Salt Fog/UV Exposure of Painted Metal (Alternating Exposures in a Fog/Dry Cabinet and a UV/Condensation Cabinet).* Coupling this exposure to electrochemical measurements and other characterization methods discussed by other NDSU researchers, we have developed a very powerful set of tools for objectively measuring, ranking and comparing aircraft coatings systems. We discuss the test protocol that we have judged most useful in giving rapid, accurate and objective numerical results for judging aircraft coatings systems, and present some of our more recent results from applying this protocol to existing AF coatings systems.

B. CORROSION SENSORS IN COATINGS

A long term goal of the aircraft coatings studies at NDSU has been the extension of laboratory electrochemical measurements on coated metals to *in situ* electrochemical measurements in coatings in actual exposure. We had projected that this might be possible when we began our examination of electrochemical noise methods (ENM) as applied to coated metals under ONR support in 1992.[1] Studies in our laboratory over the past two years have verified that these projections for *in situ* electrochemical measurements based on ENM were indeed true.[2,3,4] Using paired platinum wires embedded in a thick primer coating against the metal substrate as a working electrode/relative reference electrode, we have been able to extract ENM data that

enables us to follow the noise resistance and the localization index[5] as a function of time during the Prohesion Salt Fog Exposure Cycle. *We believe that this is the first reliable measurement of electrochemical properties of a coating/metal system during varying exposure conditions that has been recorded.* We have also applied spectral analysis methods to the ENM data, and have found for this sort of irreversible cycling of the sample, the maximum entropy transform provides the most easily usable form of the data in the frequency domain. The data and their implications are presentated and discussed below.

C. Mg-RICH COATINGS FOR THE CHROME-FREE CORROSION PROTECTION OF AIRCRAFT ALLOYS

In analogy to the Zn-rich coatings that are used to stop corrosion in steel by cathodic protection + other more complex effects, we have shown that Al 2024 T-3 can be protected by a primer that is an Mg-rich coating based on special particulate pigment grades of Mg from Eckard, AG. If the primer is formulated at or above the Critical Pigment Volume Concentration (CPVC)[6] of the Mg pigment, the primer provides cathodic protection to damaged areas of the coatings through sacrificial oxidation of the Mg preferentially to the Al, just as the Zn reacts to protect steel in Zn-rich coatings or galvanized steel at damaged areas of coated steel. This mode of protection holds until the amount of metal pigment consumed takes the system to the percolation threshold of the metal particles (in a random two-phase composite, this concentration is about 30 volume percent) and then the mode of protection is to seal the damage site stopping the oxidation of the metals. Because the forms of Mg oxidation products creat4ed at the damaged area do not create local pH's above the basic corrosion pH limits of Al, the protection stops the corrosion of the Al alloy that would take place at a damaged area of the coating system. With proper design of the polymer matrix of this type of primer (best results found with an

experimental epoxy-urethane-silane hybrid), a system that it is very stable underneath an aircraft polyurethane topcoat can be formulated. Recent studies in the exposure cycle described in section **I.A**., with alternating UV and cyclic salt fog exposure has shown almost no damage to a scribed Al 2024 T-3 test panel with no pretreatment coated with an optimally formulated Mg-rich primer and the ELT Air Force topcoat that has been exposed for 4500 hours. *This is the only completely chromate-free system that we know of that has shown this type of durability and corrosion protection for this length of exposure, and it exceeds the present chromate-based system in corrosion protection.*

RECENT STUDIES ON DEVELOPMENT OF A TEST PROTOCOL FOR AIRCRAFT COATINGS

A. RESULTS

The systems that have been examined on Al 2024 T-3 test panels are given in Table 1. The pretreatment and cleaning are describe in earlier publications from this laboratory.[7,8] In this round of experiments examining our test protocol, we emphasized the examination of systems with the Extended Life Topcoat, and give some sample details in Table 2. The complete test protocol is given in Figure 1.

This paper only reports the electrochemical results but the diagram has been included to emphasize the holistic approach to coating characterization. The ENM and EIS measurements were performed as discussed previously. We have been analyzing the lifetime of the coatings/substrate systems under examination by monitoring the electrochemical noise resistance, R_n, and the low frequency impedance modulus from EIS, $|Z|_{low\ f}$, versus exposure time. An analysis of such data for lifetime prediction has been developed in this laboratory[9] and was used to examine our recent $R_n(t)$and $|Z(t)|_{low\ f}$ data. The results are shown in Figures 2 and 3.

The electrochemical data implied that multi-layer flat topcoat has not provided much protection for the primer underneath it. Fast failure of (Primer + Flat Topcoat) might be a direct result of the topcoat formulation. To offer a flat appearance, the coating must have a rough surface scattering the incident light. It seems that the pigment volume concentration (PVC) of this flat topcoat has been formulated to exceed the critical pigment volume concentration (CPVC) so that the coarse coating surface can be achieved. This process has the effect of introducing voids into the coating, as there is insufficient resin present to fill the interstices between the pigment particles. The voids make the coating film less dense and leave open the pathways for ingress of corrosive species to the substrate. One of the alternatives to attain rough surface for low glass is to use new raw materials such as advanced fluoropolymers and encapsulated pigments.

After 116 weeks of long-term exposure, the systems (Self-Priming Topcoat) and (Primer + Glossy Topcoat) still maintained very high electrical resistances more than the order of $10^8 \Omega.cm^2$ in both tested batches. The results indicated excellent corrosion protection these systems have provided. Although (Self-Priming Topcoat) system slightly outperformed (Primer + Glossy Topcoat) system, the biggest gap in resistance between them was no more than a half of order of magnitude. The difference in their corrosion protective performance was smaller with longer exposure. At the end of exposure, their resistance values were almost the same, not showing distinct ranking between them. An extended exposure time is required to clearly differentiate their corrosion resistance under current exposure conditions.

The system of (Primer + Extended Life Topcoat), which was developed to replace the poor performance system (Primer + Flat Topcoat), has shown excellent corrosion resistance with relatively stable electrical resistance values after 95 weeks of exposure. The resistance was about

a half order lower than that of (Self-Priming Topcoat) and (Primer + Glossy Topcoat), but still above $10^8 \Omega.cm^2$ at the end of exposure. The new fluropolyurethane topcoat system has considerably outperformed the replaced system in terms of corrosion protection. Its excellent weathering and corrosion resistance are related to the favored chemical structures of the fluropolymer. The polymer has a combination of alkyl vinyl ether and fluoroethylene structures that provide high exterior durability. In addition, the topcoat with the fluropolymer usually has low water uptake in a high moisture containing environment because water has low solubility in the polymer. This type of fluropolymer can be easily modified by copolymerization with hydroxy- or carboxy-substituted vinyl ether comonomers to give improved properties. The functional groups on the alky vinyl ether units also make the polymer be easily incorporated into the coating formula. The fluropolymer with hydroxy groups can be cross-linked with aliphatic isocyanates under ambient conditions. Using the fluropolymer, the matt topcoat no longer needs to be formulated at PVC greater than the CPVC, the rough surface being achieved by the polymer/pigment aggregates in the coating.

The $\log[R_n(t)]$ vs t and $\log|Z(t)|_{low\ f}$ vs. t data continue to be very close to linear when considered after early exposure times, and this continues to provide lifetime estimation result consistent with some known exposure data.[9] An alternate electrode configuration was also introduced for R_n measurement with good results and agreement with earlier data.

B. CONCLUSIONS

Using a combination of electrochemical techniques, appearance assessments, surface characterization and visual inspection, a series of aircraft coating systems have been ranked successfully across a range of poor to excellent performance.

The single substrate technique has been shown to produce data that is comparable to noise data obtained from the more traditional bridge method.

THE USE ENM WITH EMBEDDED WIRES IN COATING FILMS AS AN *IN SITU* CORROSION SENSING METHOD

A. INTRODUCTION AND DISCUSSION

Organic coatings are very effective in protecting aircrafts from corrosion attacks. However, current aircraft coatings tend to degrade and loss effective protection due to aging or wearing as service time increases, and therefore, require removal and recoating lest the substrate corrosion became severe. The consequent maintenance cost is tremendous. In situ corrosion sensors could be attached directly to the coating surface and detect the coating degradation and substrate corrosion quantitatively at the very early stage without the need for extraneous electrolyte. Therefore, they may provide an early warning of the danger of significant structure degradation before it occurs. Consequently, it is applicable for condition-based maintenance of aircrafts, and other metal structures, which may significantly reduce the maintenance cost and promote safety. Due to the wide range of their potential applications, the developing of in situ corrosion sensors has been intensively studied in recent years. [10, 11, 12, 13, 14, 15, 16, 17]

However, these previous techniques are all based on Electrochemical Impedance Spectroscopy (EIS) methodologies, hence, require the applying of a perturbation signal (either a small potential or current signal) to the system being monitored, and measure the response. In our studies, we discovered that this perturbation signal may cause artificial damage to the coating system, (which leads to false alarm,) especially during long term monitoring. The main reason is that when the exposure condition is changing with time, as in the case of outdoor exposure, the

open circuit potential usually is not a constant value, and the use of 2-electrode configuration instead of 3-electrode conventional setup even worsens the drifting. Consequently, during the EIS measurement, the actually applied voltage is a small AC voltage signal plus a possibly large non-steady DC voltage, which will distort the EIS spectra especially in the low frequency region, and we also noticed that when environment change (temperature and/or humidity) was extremely fast about the electrode, (e.g. in fast wet-dry cycle), the DC drift could become 10 times larger than the applied AC signal during an EIS frequency sweeping, and cause severe artificial damage to the sample.

To alleviate these problems, Electrochemical Noise Methods (ENM) was applied in our corrosion sensor studies. Electrochemical noise is random fluctuations of potential or current, typically of low frequency (<10 Hz) and low amplitude. It originates (at least in part) from certain type of corrosion processes, (particularly in the case of localized corrosion, i.e. the initiation of pits and mechanical effects resulting from cracking and erosion processes.) Therefore, electrochemical noise is often regarded as a random (stochastic) phenomenon related to deterministic corrosion kinetics, and used to provide an indication of corrosion of the material.[18] Often being regarded as a complementary technique to EIS, ENM has also been used extensively to evaluate corrosion of metals and metal surfaces underneath organic coatings.[19,20] It is often considered as a non-intrusive technique since no external perturbation is applied to the test sample during the measurements. This feature makes ENM very promising for in situ monitoring of corrosion over long term period.

In our sensor studies, a novel *in situ* ENM technique derived from earlier work of S.J. Mabbutt and D.J. Mills[21] was proposed and tested. In this technique, two noble metal corrosion sensors were embedded into the coating (between the primer and topcoat,) and served as two

working electrodes, the metal substrate underneath the coating film was connected as reference. In our preliminary studies, good agreements were found between this new configuration and the conventional ENM configuration in immersion condition for these aircraft coatings systems being tested. This technique has several advantages over the surface-attached sensor technique: improved sensor steadiness by protecting sensors surface from environment attack; improved isolation between sensors, good for measure ENM on small samples; better adhesion to underneath film; higher sensitivity to small change in coating "resistance"; shows potential application for monitoring the impedance change of each coating layer during different exposure conditions, may be useful for studying the corrosion/degradation mechanism as well as designing new accelerated testing protocols for faster ranking and better simulation of outdoor exposure.

B. RESULTS

In this section, we present a summary of our results on our embedded electrode sensor studies. Figure 4 presents R_n, temperature, and LI (localization index) for aircraft coatings during two cycles of Prohesion exposure in a cyclic salt fog cabinet.

As far as we have been able to determine from searching the literature, this data represents the first tracking of electrochemical variables of this type during cyclic, varying, exposure conditions. R_n was calculated as the standard deviation of potential signal divided by the standard deviation of current signal during the same time period. The time period for calculating each R_n point is 60 seconds. LI is calculated as the standard deviation of the current noise divided by the root mean square of current. The value of R_n increased with time during the Dry Step, as water being driven out of the coating film with increasing dry time; and R_n decreased by around 5 orders of magnitude after the Fog step started, as a result of water penetration into the coating film. LI has been used to distinguish localized corrosion and general corrosion, however, in our

studies, the value of LI was often larger than it should be, which is probably due to the large variation in mean current.

ENM testing was also performed with controlled relative humidity under room temperature. Figure 5 and 6 showed the FFT and MEM results obtained from different relative humidity after 2100 and 2930 hours exposure in Prohesion, respectively. Both the FFT and MEM plots showed that the spectral noise resistance (R_{sn}) increased with decreasing relative humidity, implying less water content trapped inside the coating film. This also indicated that atmospheric corrosion are more likely to occur or may become worse when the environmental humidity goes higher. R_n from each relative humidity was also calculated after different exposure time, as given in Figure 7. The results showed that R_n decreased with increased humidity, and at similar humidity, sample with longer exposure time had smaller value of R_n, implying possible film degradation and loss of protection. The difference in R_n between different humidity became less significant as the humidity became lower; this was probably because the instrument was reaching its limit.

Direct ENM measurement during Prohesion cycling after different exposure time was performed and the R_{sn} results from MEM were given in Figure 8. A clear decreasing trend in R_{sn} was observed as the exposure time in Prohesion increased, which implied that this *in situ* sensing technique can successfully monitor the degree of coating degradation even in a fast changing environment.

C. CONCLUSIONS

The non-immersion exposure studies indicated that the proposed new ENM setup with embedded electrodes had the capability of recording noise data without leaving any negative effect to the sample in both ideal and non-ideal exposure conditions. The change in magnitudes of

the potential and current transient signals clearly indicated that the coating film was gradually losing its electrical resistivity as the exposure time increased. The calculated R_n and R_{sn} showed clear decreasing trend as the environmental humidity increased or as the aging time increased, implying change in film water content or possible film degradation and onset of corrosion. The large drop in both R_n and R_{sn} with increasing environmental humidity indicated that atmospheric corrosion are more likely to occur or may become more severe when the environmental humidity goes higher. The life time prediction calculated from data collected directly during Prohesion cycling showed good agreement with previous studies based on the same coating/substrate system. In summary, this new ENM technique with embedded electrode has very good feasibility to be applied on field to provide early warning of the onset of corrosion of aircraft materials in the same local environment; as well as to predict the life time of the actual coating system in the real exposure condition.

Mg-RICH COATINGS AS Cr-FREE PROTECTIVE PRIMERS FOR Al 2024 T-3

A. INTRODUCTION

This laboratory has worked for somewhat over two years on proof-of-concept and then the development of Mg-rich primers for aerospace alloys as a Cr-free protection system for Al 2024 T-3. We discuss below briefly the basics of the design of such a primer, the principles of its protective performance, electrochemical performance, and the accelerated testing of topcoat/Mg-rich primer/ 2024 systems.

Metal-rich primers act as stable protective coatings systems when the following are true:

a. The metal rich systems are properly formulated at or above the CPVC which puts all of the metal particles in electrical contact with each other as well as the metal substrate to which the primer is applied.
b. The particulate metal must be more reactive (below the metal to be protected in the oxidation potential series, eg. Zn below Fe, Mg below Al)[22]
c. The primer polymer matrix is not damaged by the reaction products of the sacrificial metal pigment.
d. The sacrificial metal pigment is not so small in size that it has such a high surface are that it reacts too fast in the presence of electrolyte.

All of these hold true in out situation, as the Eckart GmBH, ECKA™ metallic magnesium powder that we use in this system is relatively large (circa 75 μm number average particle size, total range 20 to 200 μm), the experimental epoxy-polyisocyanate-silane 'hybrid' polymer used in our primer is very stable to the MgO and $Mg(OH)_2$ oxidation products, and we formulated the system at a PVC≥ CPVC of 56% as determined both experimentally and by calculation.[6] A schematic diagram of a damaged portion of the prime we are describing is given in Figure 10.

B. EXPERIMENTAL RESULTS – ELECTROCHEMICAL PERFORMANCE

The electrochemical protection provided by this primer was examined by measuring the corrosion potential, E_{corr}, vs the saturated calomel electrode as a function of time when coated on Al 2024 T-3 and then immersed in neutral 3% NaCl solution. These data are shown for our Mg-rich primer at thre different PVC values in Figure 11,[23] below. The E_{corr} value begins at the E_{corr} of metallic magnesium, circa -1.50V to –1.60 V_{SCE} , and then moves to the mixed corrosion

potential for Al/Mg couple in 3% NaCl of circa -1.0 V.[22] One can see that the PVC effects the results, with the value at the CPV being the most stable.

Similarly, we were able to determine the CPVC experimentally by examining the low frequency EIS modulus, $|Z|_{low\ freq}$, vs PVC in similar immersion exposure as shown in Figure 12, below. One can see that |Z| goes through a maximum at the CPVC as seen previously in the work of Skerry and others (see ref. 6 for further details). Also, the $|Z|_{low\ freq}$ values drop with immersion exposure as common to most coatings.

C. EXPERIMENTAL RESULTS - PROHESION EXPOSURE PERFORMANCE

Q-Panel™ Al 2024 T-3 panels were primed with Mg-rich primer at CPVC film thickness of 4 mil and subsequently topcoated with Extended Lifetime™ topcoat at 3mil. A carbide tipped glass scribe was used to cut scribes marks through the coated panels. Panels were covered with electroplater's tape and the front borders sealed with a polysulfide epoxy curative. Panels were subsequently subjected up to 4,500 hours of Prohesion™ exposure in dilute Harrison's solution at pH~4.0. The visual results for the experimental epoxy-polyisocyanate-silane 'hybrid' polymer are shown in Figure 13, below. This system is entirely Cr-free, and uses no Cr-based pretreatments. As can be seen, no damage is seen to the system, and the only effects shown from the exposure are the white Mg oxidation products along the scribe line.

D. EXPERIMENTAL RESULTS – OTHER DATA

One of our concerns with this system is its safety in handling, especially flammability problems. We have encountered no problems in handling the Mg pigment, as it come dispersed in an organic solvent and is coated with a thin oxide coating. Normal safety precautions suffice, and spraying the Mg-rich primer causes no problems. A Modified Flammability test was

performed on Mg-rich coatings applied to Al 3015 substrate. Topcoated Mg-rich sample strips with dimensions 1″ by 6″ formulated at CPVC ~ 65 pigment volume concentration with magnesium powder and one of three binders were subjected directly to blue cone of the Bunsen burner flame for 30 seconds**.** Results from modified UL-94 flammability test, topcoated strips (A) Mannich base/BPA epoxy sample sustained combustion of Mg metal (FAILED TEST); (B) Zinc-rich dust epoxy sample, did not sustain combustion (PASSED TEST); (C) aromatic polyisocyanate sample sustained combustion of Mg metal (FAILED TEST); (D) hybrid epoxy-polyisocyanate sample did not sustain combustion of magnesium (PASSED TEST). (See Figure 14.)

E. SUMMARY AND CONCLUSIONS

Magnesium-rich coatings in three organic binders were applied to Q-panel™ Al 2024 T-3 at critical pigment volume concentrations and topcoated with Deft Extended Lifetime™ topcoat then exposed to Prohesion™ exposure in dilute Harrison' solution for up to 4,500 hours. Binder stability was found to be strongly influenced by the presence of magnesium metal and it's hydroxide, e.g., blistering observed at high and low pH's due to binder failure. It is believed Mg-rich coatings protect the AL 2024 T-3 surface in an analogous way that Zinc-rich coatings protect steel. However, the polydisperse nature of magnesium powder with its more varied particle size distribution permits a higher packing factor[6] than the zinc dust powders. Organic binders, such as epoxies with high dielectric constants appear to yield poorer cathodic coating systems in aggressive conditions that vary widely in pH

The aromatic polyisocyanate binder was better than the epoxy binder possibly due to its lower dielectric from isocyanate and urea linkages. Best performance was realized from the epoxy-polyisoscyanate-silane hybrid binder as it appeared to have some inorganic character. This

was shown by lower flammability, better stability in extreme acid and base conditions, as well as higher direct pull-off adhesion from the lightly wire-brushed Al 2420 T-3 panel. In summary, we have shown that cathodic protection of Al 2024 T-3 can be achieved simply by applying a Mg-rich primer formulated at CPVC, with an appropriate organic, or organic-silane modified binder with some given grade of magnesium powder to be used as the sacrificial anode. Of presently available aircraft topcoat systems, Deft's Extended Lifetime™ topcoat performed the best in combination with these Mg-rich primers.

SUMMARY

We have presented our recent results for our work on test protocols and lifetime prediction of protective performance for aircraft coatings. A usable protocol has been developed which should help verify the performance of new Cr-free coating systems as they are developed. We have also developed the first in situ electrochemical sensor system based on embedded electrodes and ENM methods for organic coatings protective performance and demonstrated its use in a cyclic salt fog accelerated exposure cabinet. And finally, we have shown that corrosion protection can be develop without the use of Cr for Al 2024 T-3 substrate by the use of an Mg-rich primer and a standard Air Force topcoat.

ACKNOWLEDGEMENTS

This work was supported at NDSU by the U.S. Air Force Office of Scientific Research under Grant F49620-99-1-0283, LtCol. Paul Trulove, Program Officer.

REFERENCES

1. Bierwagen, G.P., D.J.Mills, & D.E.Tallman, "Electrochemical Noise Methods as a Possible *In Situ* Corrosion Sensing Technique," *Proc. 12th International Corrosion Congress,* Vol.. 6, p. 4208-4218 (paper 576) Houston, TX (Sept. 3, 1993)
2. Xianping Wang*, Gordon Bierwagen & Dennis Tallman, "Electrode Configurations for *In situ* Electrochemical Impedance Measurements on Coated Metal Systems,' Paper 1297, Presented as a Poster at the 197th Meeting of the Electrochemical Society, Toronto, Canada, May 14-18, 2000
3. Xianping Wang, Gordon Bierwagen, & Dennis Tallman, "Use of Electrochemical Noise Methods (ENM) for *In Situ* Monitoring of Coatings Electrochemical Properties During Accelerated Exposure Testing," Paper 178 Presented at the 199th Meeting of The Electrochemical Society, Washington, DC, March 25-30, 2001
4. Xianping Wang, Gordon Bierwagen, & Dennis Tallman, "Embedded Electrodes for *In Situ* ENM Measurements on Coatings," submitted to **Prog. Organic Coatings**
5. D. A. Eden, "Electrochemical Noise," Ch. 69 in *Uhlig's Corrosion Handbook,* 2nd Ed., R. Ravie, ed. Electrochemical Society Series, John Wiley & Sons, New York (2000) pp.1227-37
6. G.P.Bierwagen, R.S.Fishman, T. Storsved, & J. Johnson, "Recent Studies of Particle Packing in Organic Coatings," **Prog. Organic Coatings, 35**(1999) 1-10
7. Gordon P. Bierwagen and Dennis E. Tallman, "Choice and Measurement of Crucial Aerospace Coating System Properties," **Prog. Organic Coatings, 41** (2001) 201-217

8. Gordon Bierwagen, D.E.Tallman, J. Li, S. Balbyshev, & M. Zuidone, "Electrochemical Noise Studies of Aircraft Coatings over Al 2024 T-3 in Accelerated Exposure Testing,' Refereed Paper 00427, CORROSION 2000, NACE Annual meeting, Orlando, FA, March 26-31, 2000
9. Gordon Bierwagen, Junping Li, Lingyun He, and Dennis Tallman "Fundamentals of the Measurement of Corrosion Protection and the Prediction of Its Lifetime in Coatings," Chapter 14 in *Proceedings of the 2nd International Symposium on Service Life Prediction Methodology and Metrologies*, Monterey, CA, Nov. 14-17, 1999, ACS Symposium Series # 805, J. Martin and D Bauer, ed., ACS Books, Washing ton, DC (2001) 316-350
10. T.C. Simpson, G.D. Davis, et al**., J. Electrochem. Soc., 136,** p.2761, 1989.
11. T.C. Simpson, H. Hampel, et al., **Corrosion, 46**, p.331, 1990.
12. T.C. Simpson, H. Hampel, et al., **Progress in Organic Coatings, 20**, p.199, 1992.
13. T.C. Simpson, in Proceedings of the 12th International corrosion Congress, Houston, TX, Sept. 1993, Vol. 1, p.157, NACE.
14. Amirudin, D. Thierry, **British Corrosion Journal, 30**, p.214, 1995
15. T.C. Simpson, P.J. Moran, et al., "Electrochemical Impedance Measurements for Evaluating and Predicting the Testing the Performance of Organic Coatings for Atmospheric Exposure", in ASTM STP 1000, *Corrosion Testing and Evaluation: Silver Anniversary Volume*, ASTM, Philadelphia, 397, (1990).
16. G.D. Davis, C.M. Dacres, (DACCO Sci, Inc., USA) Electrochemical Sensors for Evaluating Corrosion and Adhesion on Painted Metal Structures, US Patent 5859537 A 12, Jan. 1999.
17. G.D. Davis, C.M. Dacres, et al., **Material Performance,** p.46, Feb. 2000.

18. D.A. Eden, Chap. 69, *Uhlig's Corrosion Handbook*, 2nd Edition, R.Winston, Revie, 2000 John Wiley & Sons, Inc. (New York)

19. D.J. Mills, G.P. Bierwagen, et al., in Proceedings of the 12th International corrosion Congress, Houston, TX, Sept. 1993, Vol. 1, p.182-194, NACE.

20. J.R. Kearns, J.R. Scully, et al.Ed., *Electrochemical Noise Measurement for Corrosion Applications,* STP 1277, ASTM, West Conshohocken, PA (1996)

21. S.J. Mabbutt, D.J. Mills, **British Corrosion Journal, *33***, P158, 1998

22. Jones D. A., *Principles and Prevention of Corrosion*, 2nd Ed., (1996), Ch.3 and 13

23. Lisa Ellingson, Corrosion Studies for the Protection of Aluminum Alloys and Outdoor Bronze, Masters Thesis, North Dakota State University, June 2001

TABLE 1
Coating Systems Considered in Test Protocol Studies

System	**Primer**	**Topcoat**
Primer	Epoxy-Polyamide (DEFT 02-Y-040, MIL-P-23377G Type I Class C)	—
Self-Priming Topcoat	—	Polyurethane (DEFT 03-GY-374, Navy TT-P-2756)
Primer + Flat Topcoat	Epoxy-Polyamide (DEFT 02-Y-040, MIL-P-23377G Type I Class C)	Polyurethane (DEFT 03-GY-311, MIL-C-85285B, 36473, Type I)
Primer + Glossy Topcoat	Epoxy-Polyamide (DEFT 02-Y-040, MIL-P-23377G Type I Class C)	Polyurethane (DEFT 03-GY-277, Navy MIL-C-85285B Type I)
Primer + Extended Life Topcoat	Epoxy-Polyamide (DEFT 02-Y-040, MIL-P-23377G Type I Class C)	Fluro Polyurethane (DEFT 99-GY-1, Extended Life Topcoat)

TABLE 2
Coating Thickness Information on Recent Samples

Tested Panel	**Panel Number**	**Film Thickness (μm)**		
		Primer	**Topcoat**	**Total**
Primer	1	21.0	—	21.0
Self-Priming Topcoat	2	—	52.0 ± 1.4	52.0 ± 1.4
Primer + Flat Topcoat	2	19.3 ± 0.2	52.3 ± 0.5	71.5 ± 0.7
Primer + Glossy Topcoat	2	24.0 ± 0.0	55.9 ± 8.6	80.0 ± 8.5
Primer + Extended Life Topcoat	5	24.8 ± 1.8	42.8 ± 1.6	67.6 ± 0.6

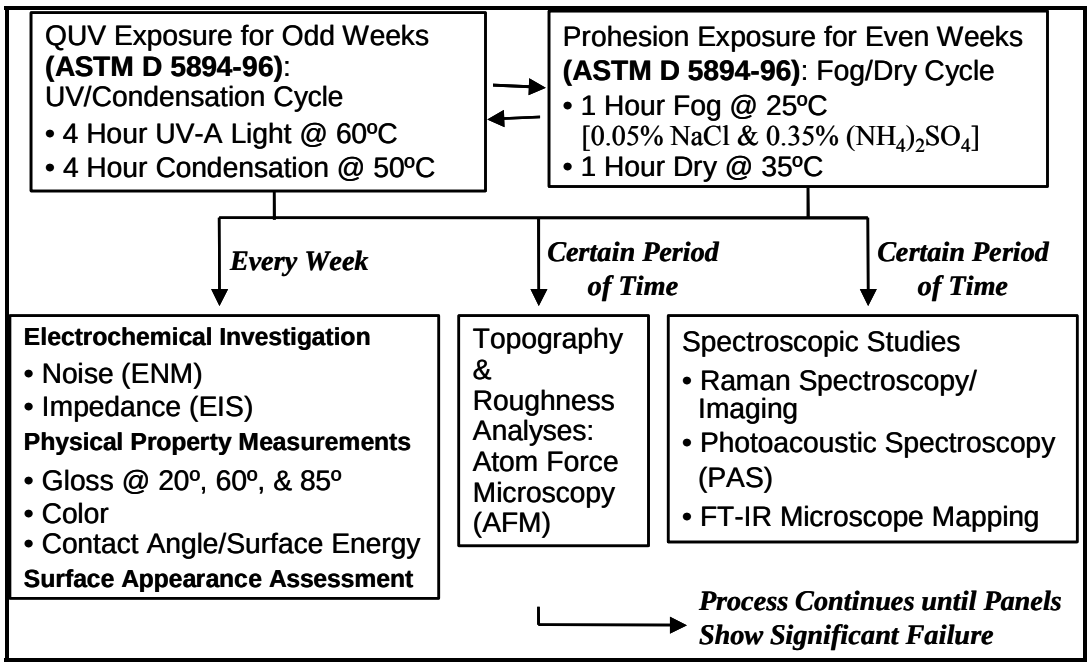

FIGURE1. Coating performance evaluation protocol

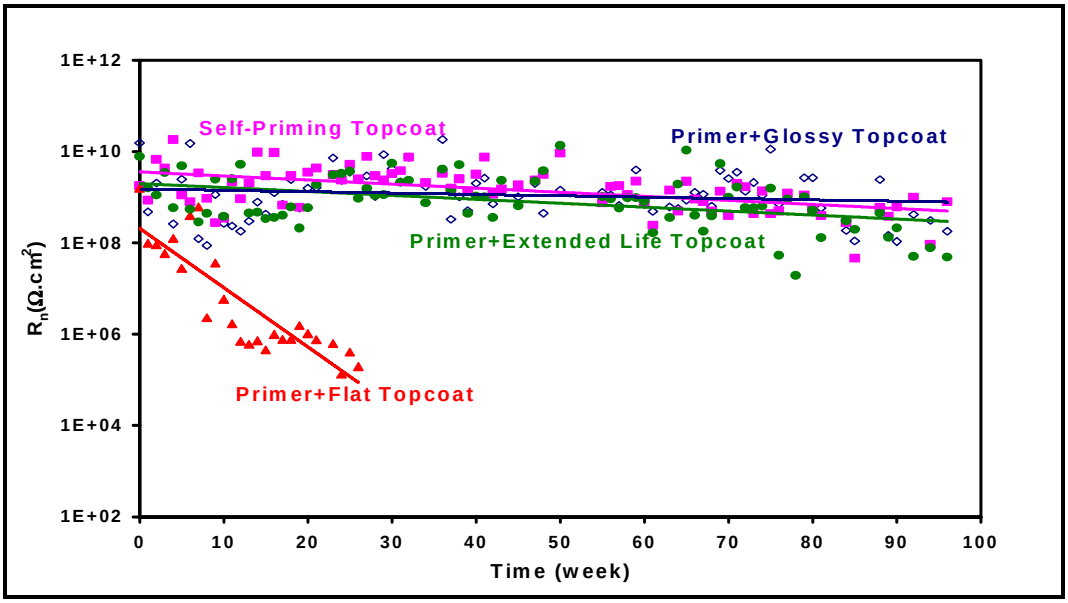

FIGURE 2. Recent R_n vs. time Data on Air Force Coatings Systems

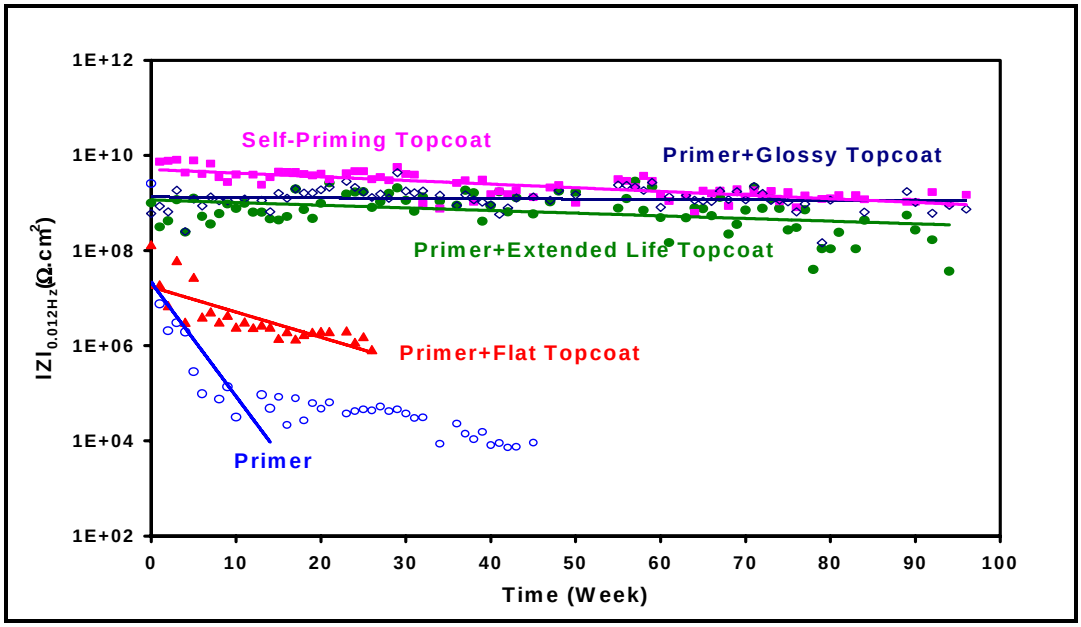

FIGURE 3. Recent $|Z|_{0.012\ Hz}$ vs. time Data on Air Force Coatings Systems

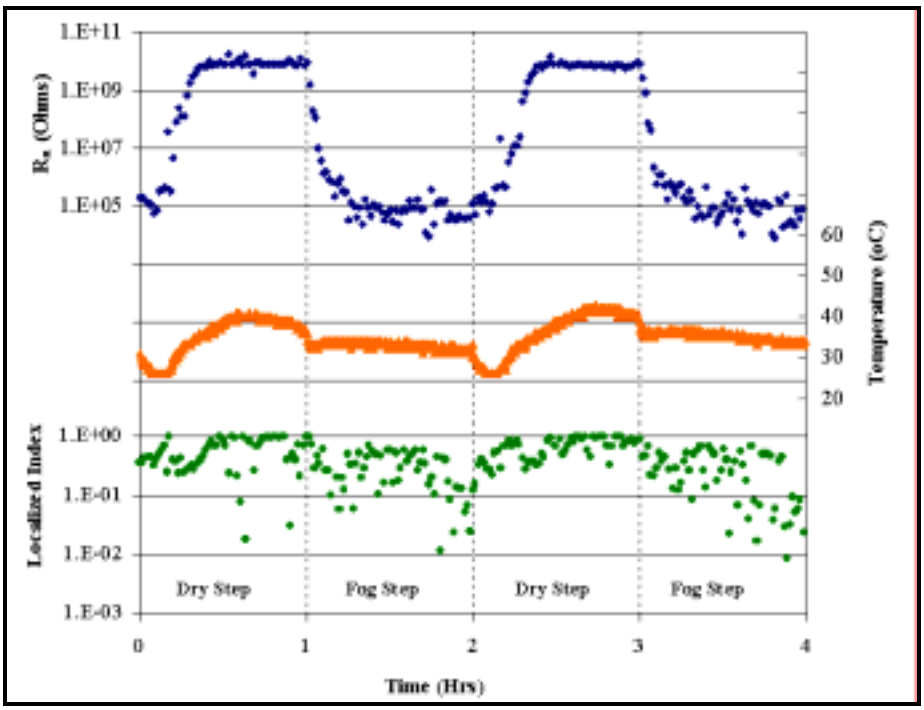

FIGURE 4. R_n, Temperature, and Localization Index vs. Time during 2 Prohesion cycles (after 2100 Hours Exposure in Prohesion)

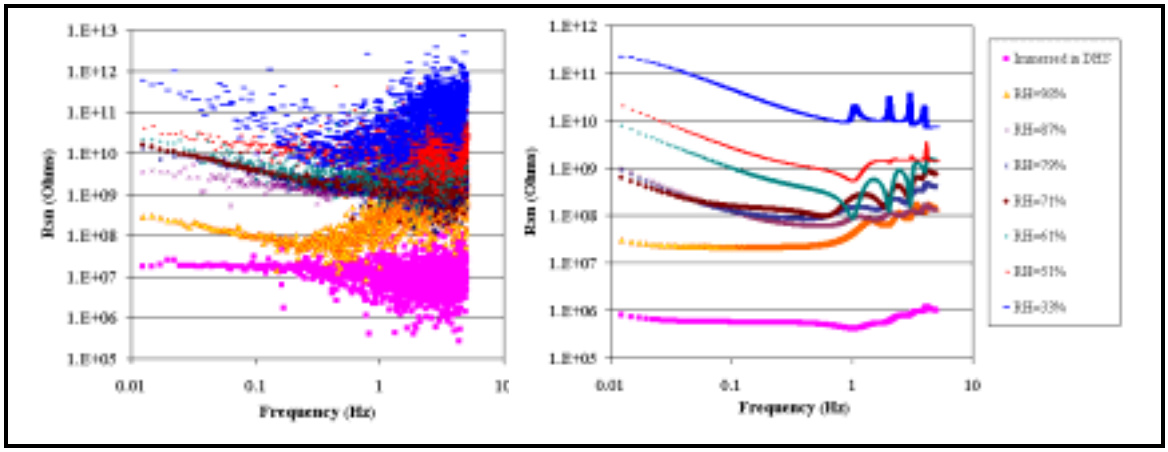

(a) FFT **(b) MEM**

Figure 5. R_{sn} Calculated from FFT and MEM as Function of Relative Humidity (after 2100 Hours Exposure in Prohesion)

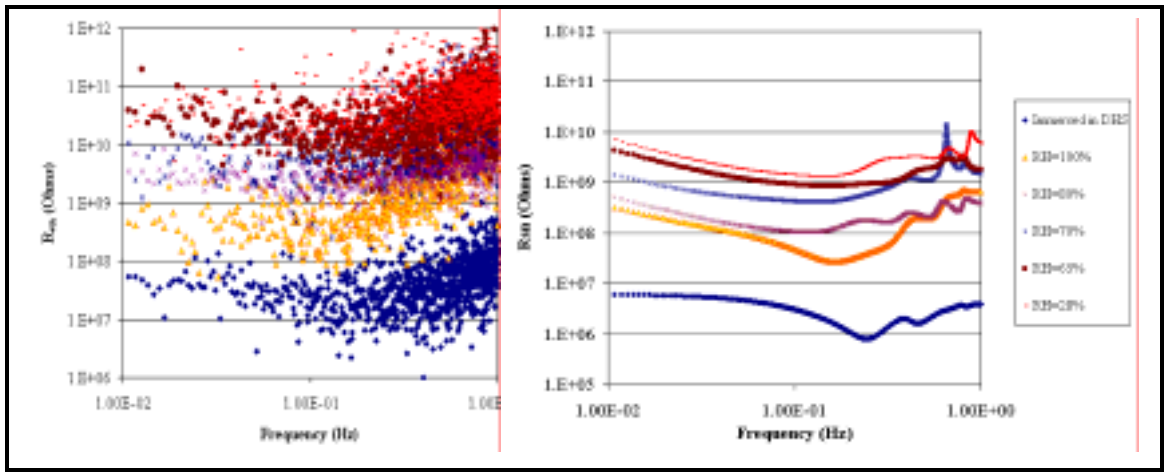

(a) FFT **(b) MEM**

FIGURE 6. R_{sn} Calculated from FFT and MEM as Function of Relative Humidity (after 2930 Hours Exposure in Prohesion)

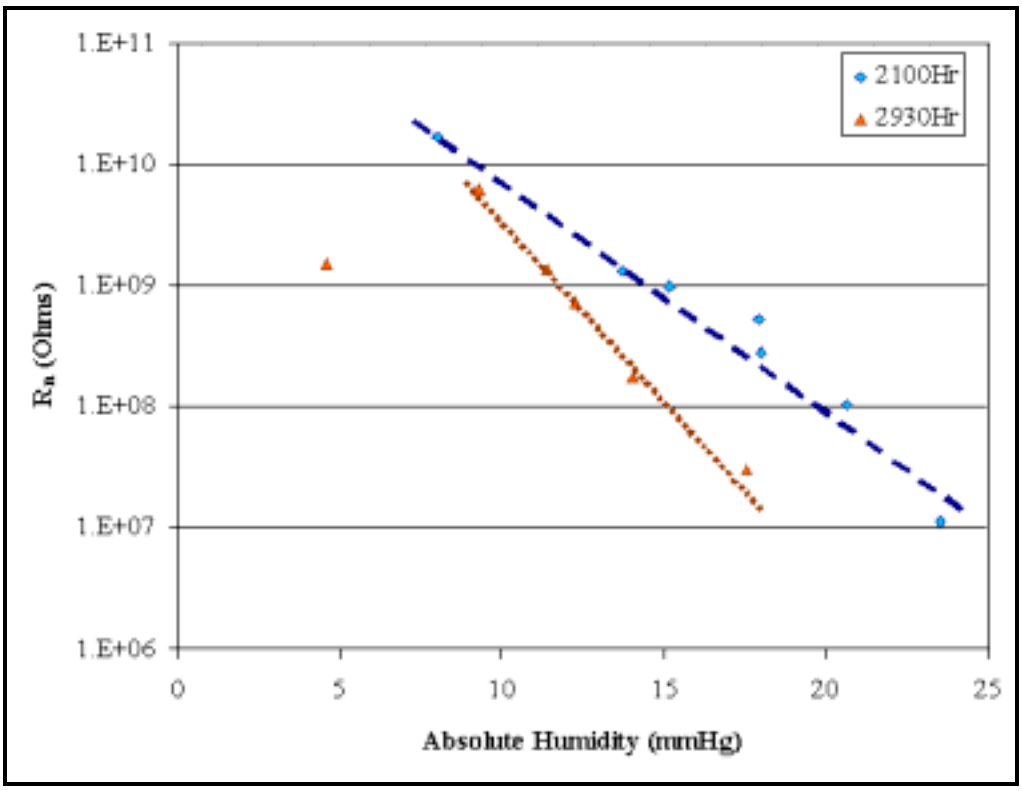

FIGURE 7. R_n vs. Absolute Humidity at Different Aging Time in Prohesion

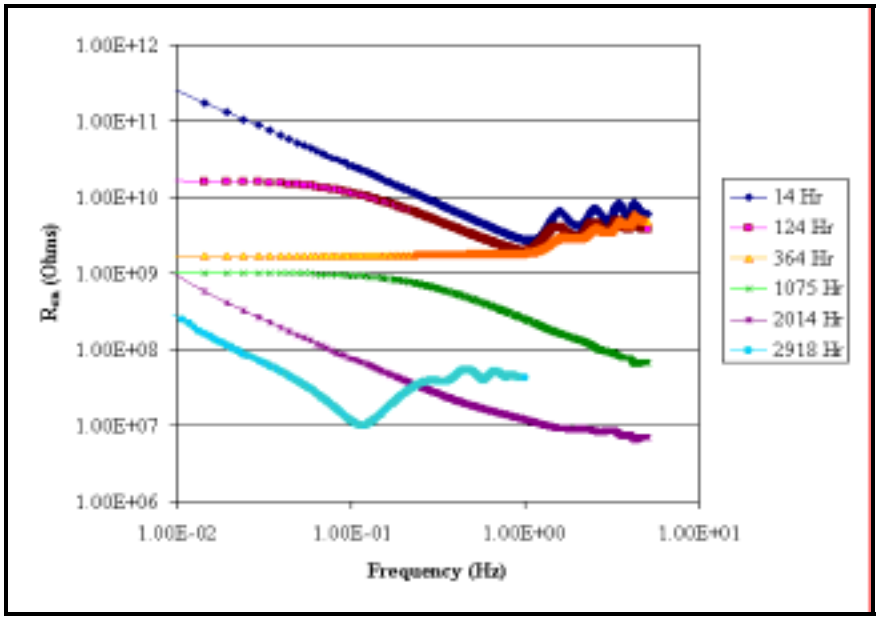

FIGURE 8. R_{sn} Measured directly during Prohesion Cycling at different Aging Times

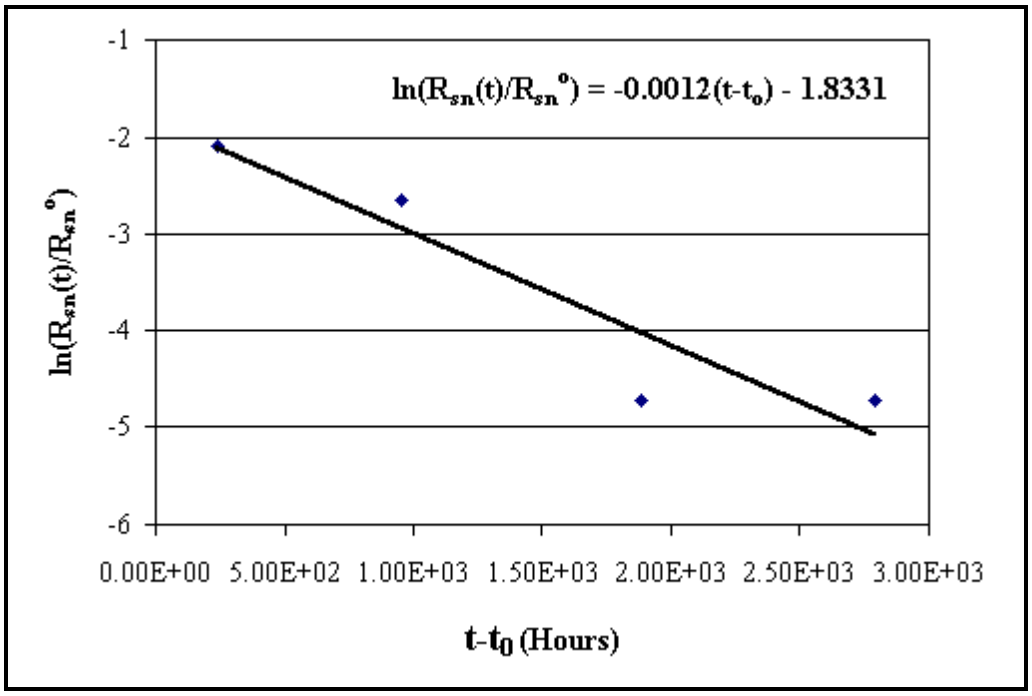

FIGURE 9. Calculation of Decay Constant for Life Time Prediction

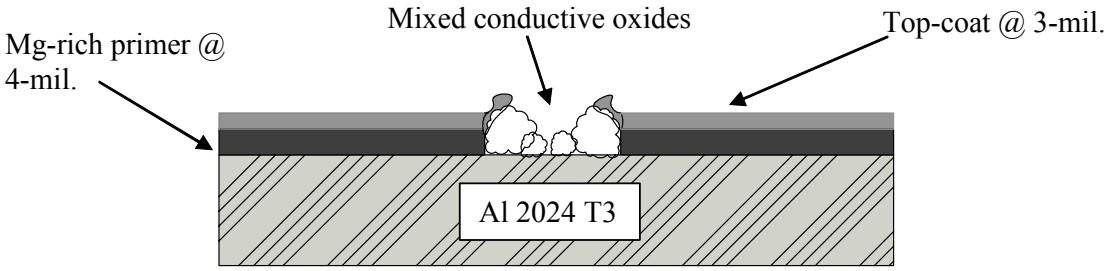

Figure 10 . Cathodic protection of top-coated Mg-rich coating over Al 2024 T-3 lengthy exposure to Harrison's solution. Porous mixed oxides of aluminum, copper, and magnesium remaining electrically connected to bulk of primer. So long as the binder is not degraded cathode area remains small relative to a larger electrically connected Mg-rich anode.

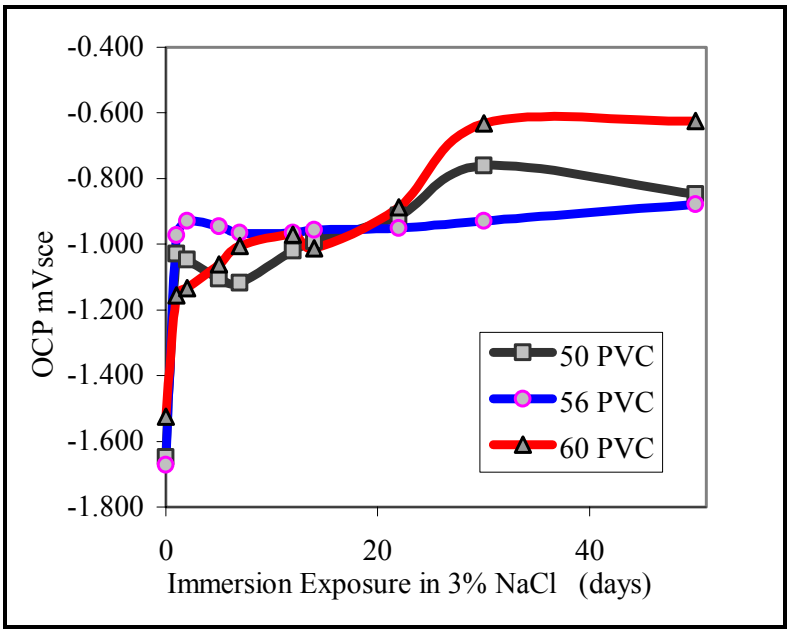

FIGURE 11. E_{corr} (vs SCE) vs PVC of Mg-rich primers at pH= 6.2 in 3% NaCl[23]

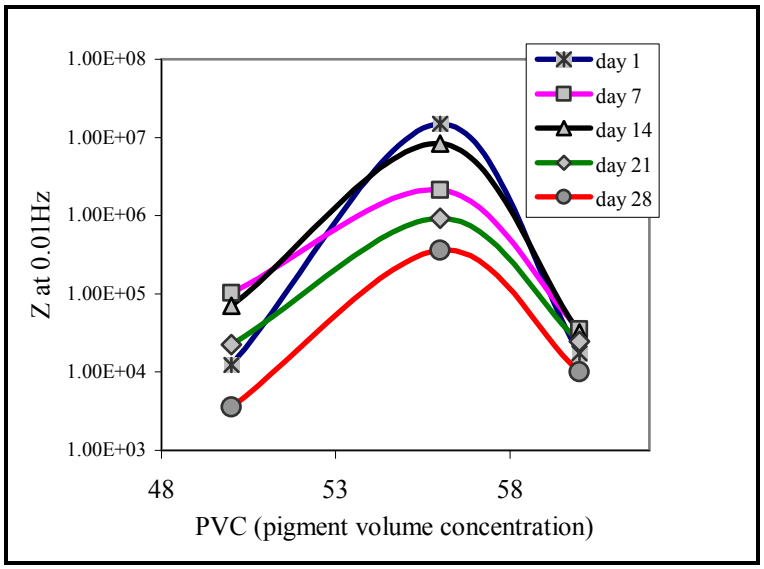

FIGURE 12. | Z| modulus at 0.01Hz vs PVC of Mg-rich primers at pH= 6.2 in 3% NaCl

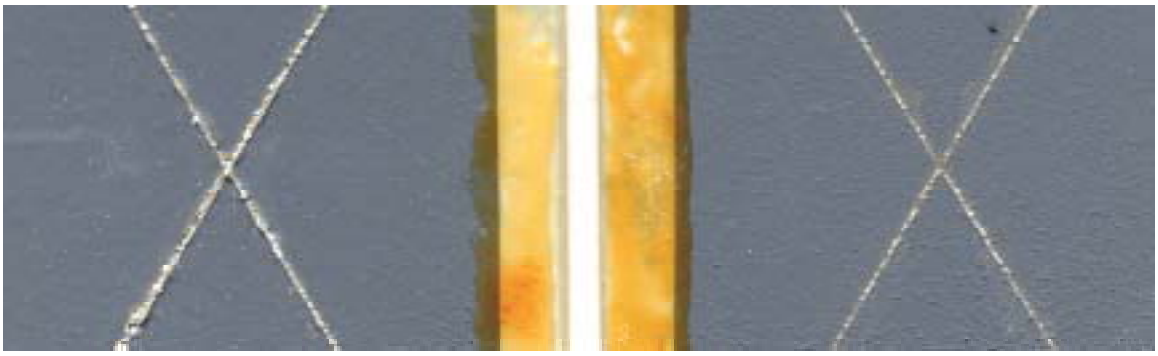

FIGURE 13. Hybrid epoxy-polyisocyanate topcoated with Extended Lifetime™ topcoat Prohesion™ exposure at 4,500 hours for Mg-rich primer at 4 mils and topcoat at 3 mils.

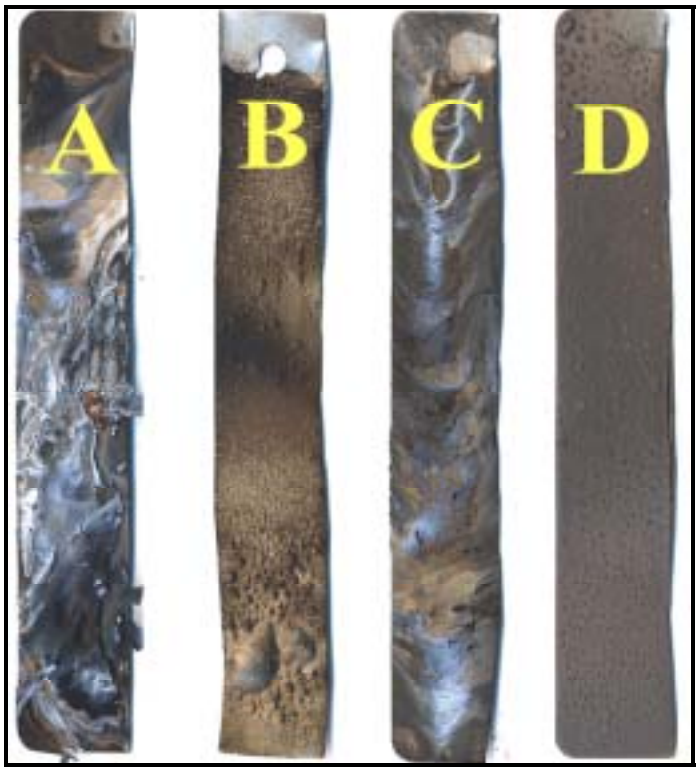

FIGURE 14. 1”x 6” metal filled coating strips at (CPVC) exposed to flame 30 seconds.

ELECTRODEPOSITION OF CONDUCTING POLYMER COATINGS ON ACTIVE METALS USING ELECTRON TRANSFER MEDIATION

D. E. Tallman,[1] C. Vang,[2] T. Underdahl,[1] G. G. Wallace,[3] and G. P. Bierwagen[2]

[1] Department of Chemistry and [2] Department of Polymers and Coatings
North Dakota State University
Fargo, ND 58105-5516

[3] Intelligent Polymer Research Institute
University of Wollongong
Wollongong NSW 2522, Australia

ABSTRACT

Our group is exploring a variety of electroactive conducting polymers (ECPs) as corrosion control coatings for aluminum alloys. A significant challenge in this area of research is the design and synthesis of processible polymers that form adhesive coatings on the metal substrate. The direct electrodeposition of ECPs on active metals such as iron and aluminum is an attractive approach but is complicated by the concomitant metal oxidation that occurs at the positive potentials required for polymer formation. In the case of aluminum and its alloys, the oxide layer that forms is an insulator that blocks electron transfer and impedes polymer formation and deposition. As a result, only patchy non-uniform polymer films are obtained. Electron transfer mediation is a well-known technique for overcoming kinetic limitations of electron transfer at metal electrodes. In this work, we report the use of electron transfer mediation for the direct electrodeposition of polypyrrole and polythiophene coatings onto alloys of aluminum (Al 2024-T3), focusing on the use of Tiron (4,5-dihydroxy-1,3-benzenedisulfonic acid disodium salt) for the electrodeposition of polypyrrole on Al 2024-T3. Typically, depositions were carried out under galvanostatic conditions at current densities of 1 mA/cm2, in which case the mediator reduced the deposition potential by nearly 500 mV compared to deposition performed in the absence of mediator. Polypyrrole deposition occurred with nearly 100% current efficiency and uniform adherent films were obtained. Results of the characterization of these films by optical microscopy, scanning vibrating electrode experiments, and electrochemical impedance spectroscopy will be presented.

INTRODUCTION

Electroactive conducting polymers (ECPs) are conjugated polymers that exhibit electronic conduction when partially oxidized or reduced. Examples of ECPs include polyaniline, polypyrrole, polythiophene and polyphenylenevinylene. These polymers continue to be of considerable research interest and are being explored for a variety of applications, including sensors, actuators, separation membranes, photochromic and photovoltaic devices, and corrosion control coatings.[1, 2] ECPs can be synthesized from the appropriate monomers by either chemical or electrochemical polymerization. Electrochemical polymerization is most often carried out at noble metal electrodes such as gold or platinum or sometimes at carbon electrodes.[1] The direct electrochemical polymerization of ECPs at active metal electrodes such as steel or aluminum is complicated by the concomitant corrosion of the metal at the positive potentials required for polymerization. In the case of aluminum, an electrically insulating oxide layer forms that blocks electron transfer and impedes polymer formation and deposition. As a result, only patchy non-uniform polymer films have been obtained.

If oxidation of the pyrrole monomer and/or subsequent formation and deposition of the polymer are kinetically limited at a metal electrode such as Al alloys, then electron transfer mediation may be useful in reducing the overpotential required for oxidation and deposition, perhaps alleviating the problems of Al corrosion. Electron transfer mediators, including various aromatic hydrocarbons and heterocycles, have the ability to lower the overpotential of such redox reactions and have been used as catalysts in organic and biological redox reactions.[3-6] Tiron® (4,5-dihydroxy-1,3-benzenedisulfonic acid disodium salt) has been shown to catalyze the electrodeposition of several conducting polymers (including polypyrrole) on platinum electrodes,

reducing the deposition potential by up to 200 mV.[7] To our knowledge this approach has not been applied to active metals such as aluminum and its alloys.

Our laboratory has been investigating various ECPs for use as corrosion control coatings.[8-12] In our previous studies, ECP coatings are typically formed by dissolving an appropriately derivatized ECP in an organic solvent and casting the film from the ECP solution. This solvent casting approach works reasonably well, but adhesion, cohesion and molecular weight of deposited polymer are somewhat limited by this approach. For these reasons, the direct deposition of ECPs on active metals is being explored in our laboratory. Since the introduction of ECPs for corrosion control by DeBerry[13] in 1985, a tremendous growth of research interest in this field has initiated. Conventionally and commercially, chromate based pigments are the primary corrosion inhibitors used in paint and coating systems. The protection mechanism by chromate ions has been well documented.[14, 15, 16] However, due to health and environmental concerns associated with chromate species, new technological coating approaches are being researched and developed as potential substitutes.

In this report we describe the use of electron transfer mediation for the direct electrodeposition of polypyrrole from aqueous solution onto Al 2024-T3 alloy, focusing on the use of Tiron (Figure 1) as the mediator.* In such experiments, Tiron serves as both the mediator and the dopant anion for the ECP. Furthermore, since Tiron is a complexing agent capable of binding metals ions such as aluminum and copper, it was anticipated that Tiron might also promote adhesion and/or otherwise stabilize the polypyrrole/Al alloy interface. Thus, the goal of this work was to develop a process for the direct electrodeposition of polypyrrole on Al and its alloys from aqueous solution using a minimum of surface preparation. In addition, preliminary

* Patent pending.

electrochemical corrosion performance of the electrodeposited polypyrrole coatings was also studied.

EXPERIMENTAL

MATERIALS

Aluminum alloy 2024-T3 was purchased from Q-Panel (Cleveland, OH). The metal substrate surface was prepared by polishing with 600-grit SiC paper followed by degreasing with hexane. Pyrrole and sodium *p*-toluene sulfonate (Na-*p*TS, 95%) were purchased from Aldrich and Tiron from Fluka. For the results reported here, the electrodeposition solution contained 0.05 M pyrrole monomer (freshly distilled) and either 0.05 M Tiron or 0.05 M Na-*p*TS. No additional electrolytes were used. The structures of pyrrole, Tiron and Na-*p*TS are depicted in Figure 1.

ELECTROCHEMICAL POLYMERIZATION.

Electrochemical polymerization/deposition was performed in a one-compartment 500 mL 3-electrode cell having an Al 2024-T3 working electrode, a platinum plate counter electrode, and a Ag/AgCl reference electrode. The working and counter electrodes had similar areas and were arranged parallel to one another to ensure uniform current distribution. The polypyrrole films were electrodeposited using the galvanostatic mode at a current density of 1 mA/cm^2 using an EG&G Princeton Applied Research Potentiostat/Galvanostat Model 273A. All potentials are reported versus the saturated Ag/AgCl reference electrode.

ELECTROCHEMICAL STUDIES.

The SVET (Applicable Electronics, MA) experiments were carried out by cutting into a 1-cm x 1-cm squares and masking by adhesive tapes such that only a 2-mm x 2-mm square

opening of the sample was exposed. The ECP coupons were artificially scribed to introduce a defect. The sample was mounted on Teflon stud and DHS was introduced into the exposed area. Scans were initiated within immersion of DHS with each scan consisted of 400 data points obtained on a 20 x 20 grid. All measurements were collected at the open circuit potential. Electrochemical impedance spectroscopy (EIS) measurements were performed in a three-electrode configuration. The configuration utilizes a Pt mesh and a saturated calomel electrode (SCE) as the counter and reference electrodes, respectively. All measurements were made on a Gamry PC4 Potentiostat (Gamry Instruments, Inc. Warminster, PA.). EIS measurements were carried out at the open circuit potential with a 5 mV AC voltage perturbation over the frequency range from 0.01 Hz to 5,000 Hz.

RESULTS AND DISCUSSION

Figure 2 shows potential-time curves for the galvanostatic deposition of polypyrrole (Ppy) at a current density of 1 mA/cm^2 on Al 2024-T3 in the presence of Tiron (curve 1) and, in a separate experiment, in the presence of Na-*p*TS (curve 2). No additional electrolyte was used in these experiments and, therefore, the anion of each salt also served as the counterion (dopant ion) in the deposited polymer. The deposition in the presence of Tiron was terminated at 750-seconds, at which point a continuous film was obtained (Figure 3). After an identical 750-second deposition in the presence of Na-*p*TS, the deposited polymer on the alloy surface was very patchy with numerous exposed bare alloy spots. The deposition was continued to the 1440-second mark (Figure 2, curve 2), at which point an apparently continuous film was obtained (Figure 3). However, closer inspection by optical microscopy revealed that bare patches of Al alloy remained in the Na-*p*TS polymer film, in spite of the 2-fold longer deposition time for the Na-*p*TS polymer (Figure 4).

Several additional observations are noteworthy from Figure 2. The open circuit potential (E_{oc}) was recorded for a few seconds prior to application of the current (at time zero). In the presence of 0.05 M Na-*p*TS (curve 2) the E_{oc} was –1.0 V (vs. saturated Ag/AgCl), whereas in the presence of 0.05 M Tiron (curve 1) the E_{oc} was ca. –0.6 V. Both solutions also contained pyrrole (0.05 M). The Tiron imparted a significantly more noble potential to the aluminum alloy (ca. 0.4 V), even before polymer deposition commenced. The most important observation from Figure 2 is that Tiron substantially reduced the potential for Ppy deposition at Al 2024-T3 by nearly 500 mV, from ca. 1.0 V (plateau region of curve 2, Figure 2) to ca. 0.5 V (plateau region of curve 1). Clearly this less positive polymerization potential should minimize complications from Al alloy corrosion and polymer overoxidation. The details of the mechanism of this process are still being investigated, but electron transfer mediation is clearly involved. It is also expected that film deposition occurs by a two-stage nucleation and growth process,[7] and the mediator could facilitate both of these stages. We conjecture that interaction of the Tiron with the aluminum oxide surface and subsequent electron transfer may be facilitated by hydrogen bonding interactions between the adjacent hydroxyl groups of Tiron and the oxide surface. It is possible that the mediator facilitates electron transfer at these defect sites, perhaps making available additional sites for nucleation and subsequent polymer growth. In-situ electrochemical AFM studies conducted in our laboratory (to be reported elsewhere) revealed a significant increase in the number of nucleation sites in the presence of Tiron, supporting this hypothesis.

We note that both the transient (nucleation) and steady-state (growth) regions of the potential-time curve of Figure 2 are shifted to lower potential in the presence of Tiron. This observation along with AFM and SEM studies of film morphology suggest that Tiron mediates

both the nucleation process at the alloy surface and the subsequent growth of the polymer particles.

Figure 5 illustrates preliminary SVET data for a typical scribed coupon of Ppy/Tiron. After 10 minutes of immersion in DHS, a small oxidation current was observed on the scribed area, with reduction current spread rather uniformly over the polymer surface. Although oxidation was clearly occurring within the defect area, no corrosion product was observed, as evident by the clean and shiny scribed area. The defect area remained shiny with continued immersion of up to 22 hours. These observations are in contrast to those for control experiments conducted with epoxy coatings, where oxidation and reduction were confined to the defect area and corrosion products were clearly evident.

The use of EIS for study of protective organic coatings has been well documented and was utilized for assessment of electrodeposited polypyrrole coatings. Bode plots of impedance modulus $|Z|$ versus frequency for electrodeposited Ppy/Tiron on Al 2024-T3 with a polyurethane topcoat at various stages of immersion in dilute Harrison solution and after various Prohesion® exposures are displayed in Figure 6. The data were collected between 0.01 Hz and 5000 Hz. The results obtained thus far indicate that the coating exhibits corrosion protection. On the first day of constant immersion and Prohesion® exposures, the low frequency impedance of the Al/Ppy/Polyurethane coating was 10^8 Ω to 10^9 Ω, values indicative of the good barrier properties of the polyurethane coating. As immersion and Prohesion® exposure times increased, a decrease in the low frequency impedance occurred, reflecting water and ion ingress into the coating system. However, upon further exposure, the low frequency impedance again increased, a behavior that has been observed for chromated coatings as well as other conducting polymer

coatings.[12] Such behavior is indicative of a dynamic interaction between the conducting polymer coating and the aluminum alloy surface, and is not observed with inactive primer coatings.[12]

Finally, the mediation approach illustrated here may have some generality. Figure 7 displays cyclic voltammograms of thiophene and catechol alone and together at a platinum electrode, illustrating mediation. The solvent in this case is dichloromethane since thiophene has limited solubility in water. Since Tiron is insoluble in dichloromethane, catechol was used as the mediator. Similar results were obtained when acetonitrile was used as the solvent. In these experiments, polythiophene electrodeposits on the platinum electrode at a lower potential in the presence of catechol. However, we have not yet been able to electrodeposit polythiophene films on the aluminum alloy, a consequence of the rather positive potential required to oxidize thiophene. These results are encouraging, however, since certain water-soluble (nitrogen containing) derivatives of thiophene oxidize at much less positive potentials, similar to pyrrole. We fully expect to be able to directly electrodeposit polymers of these derivatives on aluminum alloy. Results of these studies will be reported in due course.

CONCLUSIONS

Tiron (4,5-dihydroxy-1,3-benzenedisulfonic acid disodium salt) is an effective catalyst for the electrodeposition of polypyrrole on Al 2024-T3, lowering the deposition potential by nearly 500 mV. Continuous uniform polypyrrole films can be formed and alloy corrosion and polymer overoxidation during deposition are minimized. Corrosion studies including SVET, long-term constant immersion and Prohesion® exposure experiments on topcoated samples suggest an active control of the corrosion process. This mediated electrodeposition approach appears to be applicable to other conducting polymer systems.

ACKNOWLEDGEMENTS

This work was supported by the Air Force Office of Scientific Research, Grant Nos. F49620-99-1-0283, Program Manager LtCol Paul Trulove. The authors would like to express their appreciation to Jie He, Matthew Dewald, and Amy Richter for their assistance with the project.

REFERENCES

1. G. G. Wallace, G. M. Spinks, and P. R. Teasdale, "Conductive Electroactive Polymers, Intelligent Materials Systems,". Technomic Publishing Co., Inc., Lancaster, PA, 1997.
2. T. A. Skotheim, R. L. Elsenbaumer, and J. R. Reynolds, (eds.), "Handbook of Conducting Polymers." Marcel Dekker, Inc., New York, 1998.
3. C. P. Andrieux, J. M. Dumas-Bouchiat, and J. M. Saveant, *J. Electroanal. Chem. Interfacial Electrochem.*, 87, (1978): p. 39.
4. C. P. Andrieux, J. M. Dumas-Bouchiat, and J. M. Saveant, *J. Electroanal. Chem. Interfacial Electrochem.*, 87, (1978): p. 55.
5. C. P. Andrieux, J. M. Dumas-Bouchiat, and J. M. Saveant, *J. Electroanal. Chem. Interfacial Electrochem.*, 88, (1978): p. 43.
6. C. P. Andrieux and J. M. Saveant, *J. Electroanal. Chem. Interfacial Electrochem.*, 93, (1978): p. 163.
7. B. Zinger, *Journal of Electroanalytical Chemistry*, 244, (1988): p. 115.
8. D. E. Tallman, Y. Pae, G. Chen, and G. P. Bierwagen, *Annu. Tech. Conf. - Soc. Plast. Eng.*, 56th, 1234 (1998).
9. D. E. Tallman, Y. Pae, and G. P. Bierwagen, *Corrosion.*, 55, (1999): p. 779.
10. D. E. Tallman, Y. Pae, and G. P. Bierwagen, *Corrosion*, 56, (2000): p. 401.
11. J. He, V. Johnston-Gelling, D. E. Tallman, G. P. Bierwagen, and G. G. Wallace., *J. Electrochem. Soc.*, 147, (2000): p. 3667.
12. V. J. Gelling, M. M. Wiest, D. E. Tallman, G. P. Bierwagen, and G. G. Wallace, *Prog. Organic Coatings*, 43, (2001): p. 149.
13. D. W. DeBerry, *Journal of the Electrochemical Society*, 132, (1985): p. 1022.

14. Twite, R.L.; Bierwagen, G.P., *Progress in Organic Coatings*, 33, (1998): p. 91.
15. J. Sinko, *Progress in Organic Coatings*, 42, (2001): p. 267.
16. M.W. Kendig, A.J. Davenport, A.J., H.S. Isaacs, *Corrosion Science*, 34, (1993): p. 41.

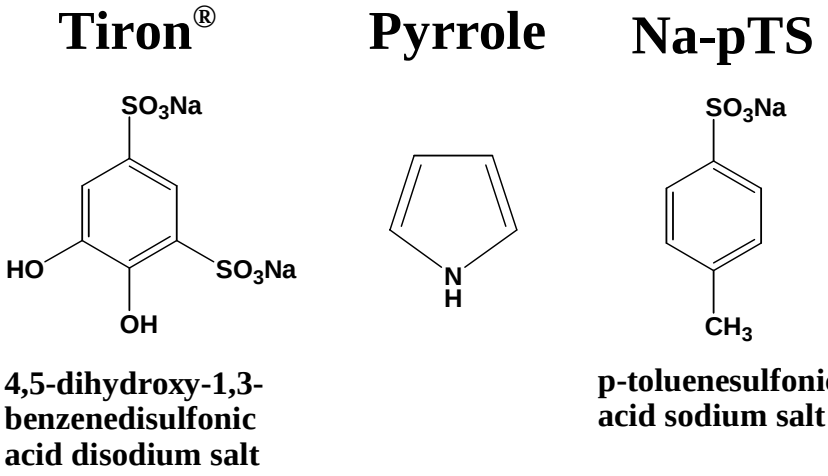

FIGURE 1. The structures of Tiron (4,5-dihydroxy-1,3-benzenedisulfonic acid disodium salt), pyrrole and *p*-toluene sulfonic acid sodium salt (Na-*p*TS).

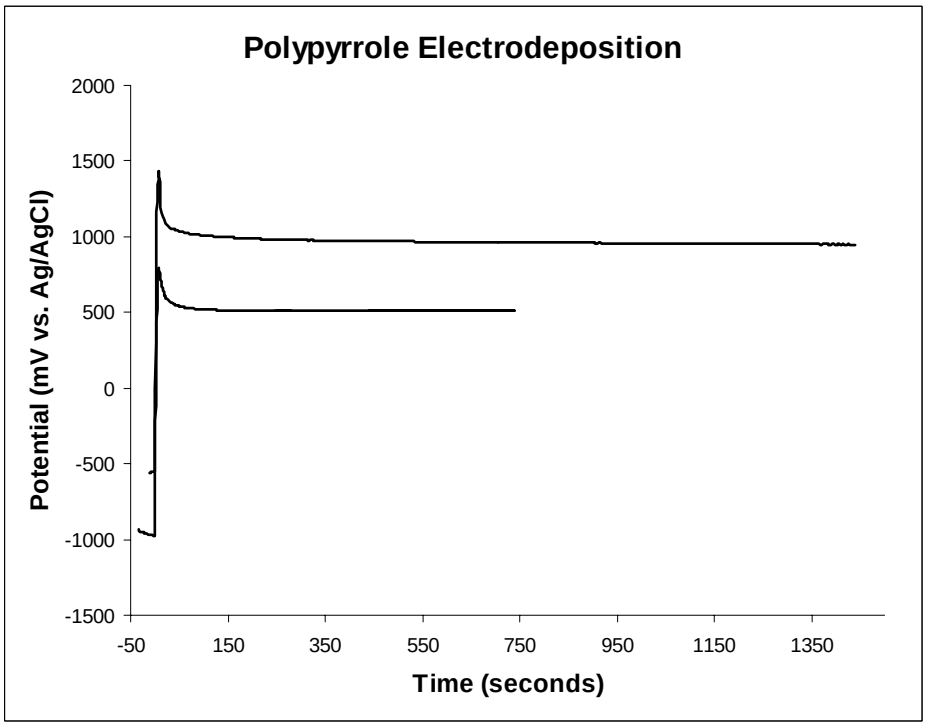

FIGURE 2. Potential-time curves for the galvanostatic deposition of polypyrrole on Al 2024-T3 at 1 mA/cm^2 current density in the presence of Tiron (curve 1) and in the presence of Na-*p*TS (curve 2).

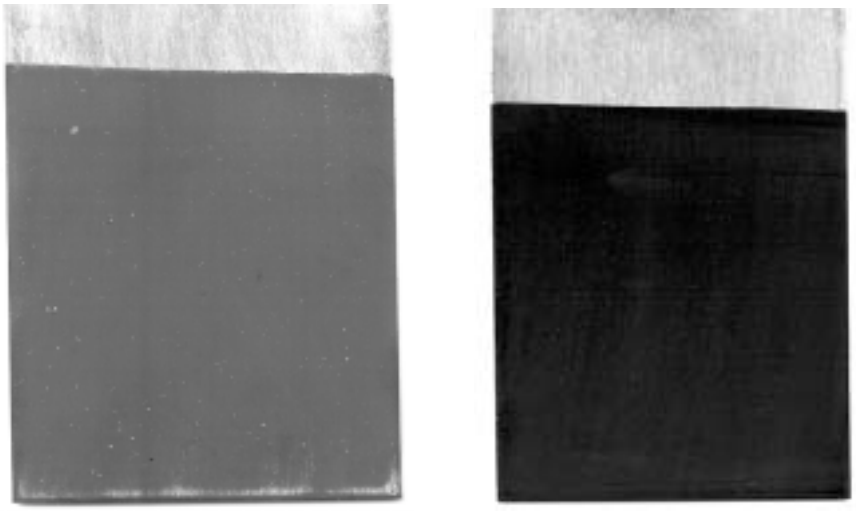

FIGURE 3. Photographs of polypyrrole films deposited galvanostatically in the presence of Na-*p*TS (1440-seconds deposition, left) and Tiron (750-seconds deposition, right).

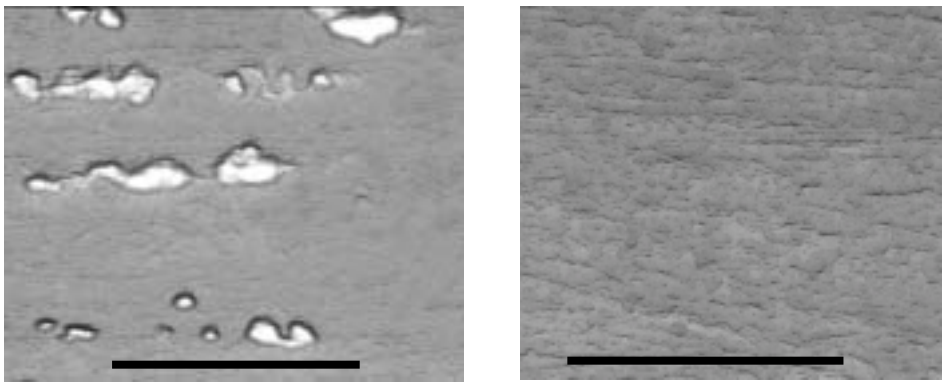

FIGURE 4. Optical micrographs of polypyrrole films deposited galvanostatically on Al 2024-T4 in the presence of Na-*p*TS (1440-seconds deposition, left) and Tiron (750-seconds deposition, right).

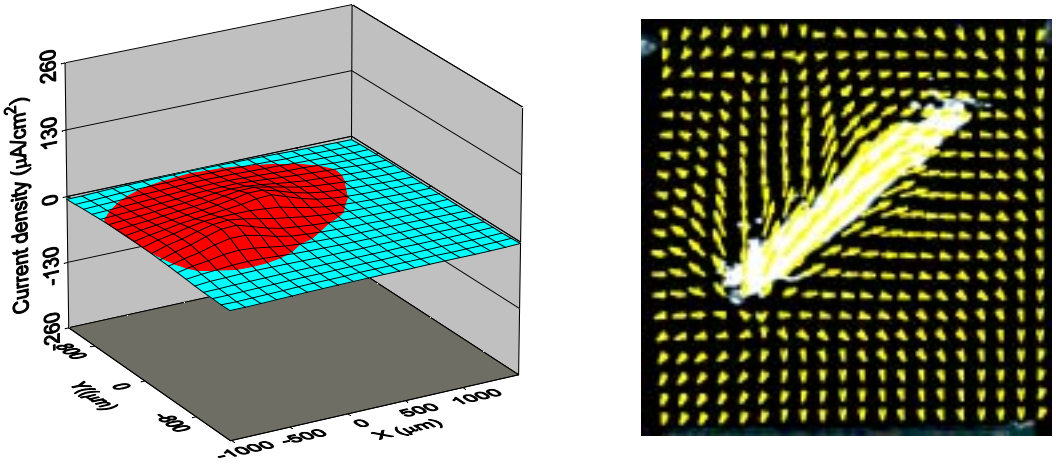

FIGURE 5. Current density map and optical micrograph for Ppy/Tiron on Al 2024-T3 immersed in dilute Harrison solution (DHS) for 10 minutes.

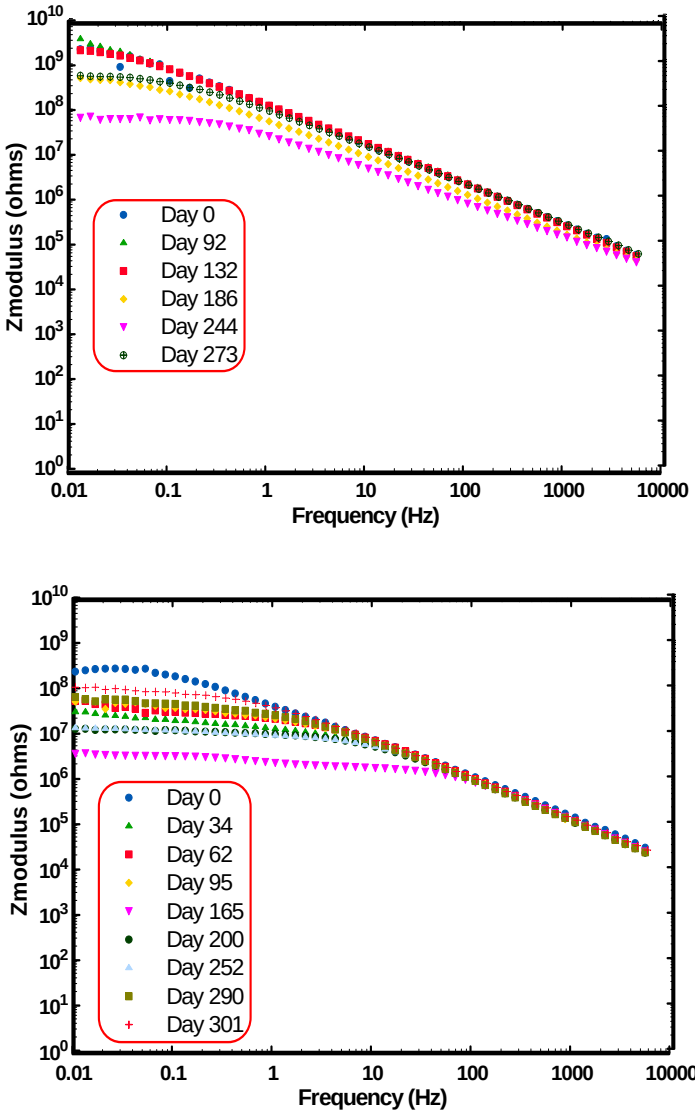

FIGURE 6. Bode plots of EIS data for electrodeposited polypyrrole on Al 2024-T3 alloy with polyurethane topcoat. Top – results from constant immersion experiments in dilute Harrison solution. Bottom – results from Prohesion exposure.

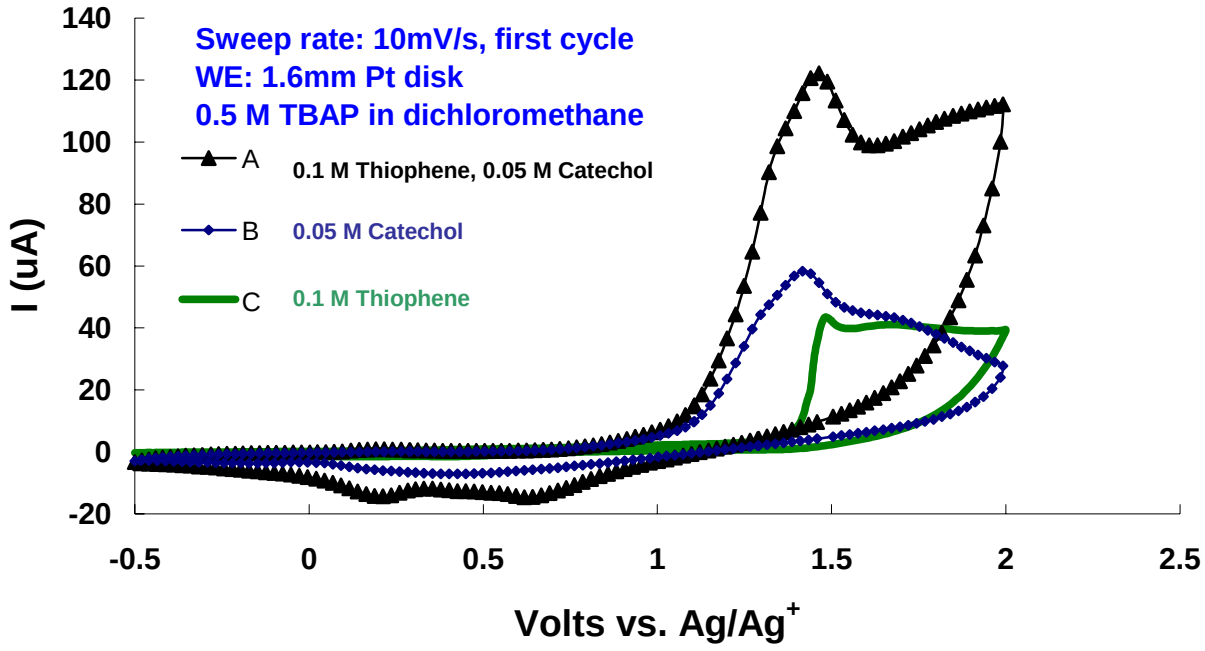

FIGURE 7. Cyclic voltammograms of thiophene and catechol in dichloromethane containing 0.5 M tetrabutylammonium perchlorate. (A) 0.1 M thiophene and 0.05 M catechol; (B) 0.05 M catechol; (C) 0.1 M thiophene.

QUANTITATIVE USE OF SPECTROSCOPY AND EFFECTIVE IRRADIATION DOSAGE DURING WEATHERING

S. G Croll and A. D. Skaja

Department of Polymers and Coatings
North Dakota State University
Fargo, ND 58105-5516

ABSTRACT

Integrity of the urethane topcoat is a crucial part of the overall coating system performance that protects the underlying metal substrate. Quantitative infrared spectroscopy was used to examine the chemical changes seen during weathering in the polymer and to measure the coating ablation. During weathering the ultraviolet absorbance of a typical urethane coating shows a tail into the visible region that increases with the weathering exposure period. Effective ultraviolet dosage can be calculated by integrating the spectrum of the incident radiation with the quantum yield for the degradation process and the ultraviolet absorption of the material under investigation. Depending on the form of the quantum yield, there is a clear acceleration of the absorption of damaging radiation because the absorbance increases with exposure. This non-linear relationship itself offers some possibilities on how to estimate a service lifetime; one could choose a value of the exposure period characteristic of the start of the acceleration in dosage, or one might choose the asymptote at which the dosage rate becomes very great. The ultraviolet tailing into the visible region is an example of an "Urbach" tail which is usually attributed to structural disorder that introduces electronic energy levels into the material's band-gap.

INTRODUCTION

Polyurethane coatings have a deserved reputation for durability in withstanding aggressive environments. One such application is providing durable topcoats for equipment that is protected from corrosion by a suitable corrosion inhibiting primer. In such multi-coat systems, the overall integrity of the substrate and its survival depends crucially on the continuing integrity of the topcoat [1]. The topcoat provides a barrier to penetration by atmospheric moisture and the corrosive components of the atmosphere that may originate as pollution, in addition to any appearance related properties that may be required for the equipment or installation. Thus

understanding the rate of degradation of urethane based coatings under attack by solar ultraviolet and the other elements that occur in weather is an important technological goal. Indeed, there has been a great deal of excellent work has been done in determining the chemical changes that occur during degradation of urethane coatings [2,3,4]. Much of the prior work determines the relative rate of appearance or disappearance of infrared bands in various polymers by comparison to another band, usually a carbon-hydrogen absorbance on the assumption that the CH band is a measure of the amount of polymer material that remains. Technologically useful polymers or additives may then be selected or designed by choosing the structure that suffers the least of these relative changes [5].

BACKGROUND

DETERMINATIONS OF COATING ABLATION AND STRUCTURAL CHANGES BY SPECTROSCOPY

Infrared spectroscopy is a very valuable technique for determining the chemical changes that occur during weathering of polymeric materials. It has been used to compare the durability performance of complicated proprietary polymers and to determine the actual chemical reactions during degradation in polymers whose structure is known. Since there are several possible reactions in urethanes and their progress may change with depth into the coating [6], for quantitative work it is necessary to make samples for examination that are as homogenous as possible and that can be examined in a spectroscopically straightforward manner. The polyester-urethane coatings were spin coated onto very polished, planar silicon or germanium disks. Neither silicon nor particularly, germanium have any absorbances in the infrared spectral region of interest for most polymer degradation studies. Thus quantitative study of the urethane absorbances may be achieved by the standard transmission technique. Although each sample

was marked so that the infrared beam would pass through the same location again after each exposure interval, the spin coating was used to ensure smooth, level coatings so that minor registration errors would not have significant impact on the results.

Another advantage of the smooth, level coatings was that interference fringes were apparent in the spectra and could be used to measure the changing thickness of the coatings as they were ablated during degradation. Both silicon and germanium have high refractive indices and so reflect an appreciable amount of light. The fringes come from the light reflected at the coating-air interface interfering with the light reflected at the coating-substrate interface. Similar fringes have been used in infrared spectroscopy for determining optical path length of cells for measuring liquids and gases and in establishing the parallelism of the end windows in such cells [7]. The fringe spacing is related to the optical path length between the reflecting surfaces by:

$$Dn = 1 / (2dn) \quad (1)$$

Where:

n = wavenumber,
Dn = difference in wavenumber between successive fringe maxima, or minima
d = thickness of film
n = refractive index of the coating film

Most polymers of widely different monomer composition have very similar values of refractive index, so it is plausible to assume that the overall refractive index of the polymer is insensitive to the chemical changes that occur during degradation. Thus the reciprocal of the fringe spacing is a measurement of the coating film thickness and changes in fringe spacing as a coating degrades will measure the changes in film thickness and thus the rate of ablation, i.e. degradation.

Other, physical means of measuring thin film thickness, e.g. by dial gauge or micrometer or induction gauge are not nearly so sensitive or accurate as this interferometric method. Further, when using changes in infrared absorbance height or area to follow the progress of the degradation chemistry, they values can be normalized by using the fringe spacing which is a measurement of the actual film thickness remaining. This has two, related advantages over using another infrared band, usually C-H band, as a reference: Firstly, changes in the reference moiety's concentration may now be investigated in addition to the other changes and secondly, the changes in band size with degradation exposure become an absolute measurement instead of being a relative measurement and so permits greater level of understanding. This can all be determined from the infrared spectra, otherwise a separate experiment and calibration would be necessary to follow the changes in CH concentration with film thickness or mass during degradation [5].

Absolute changes in spectroscopic absorbance can be used to deduce the relative importance of the peaks and other features of the ultraviolet adsorption spectrum of the polymer. If these features can be understood, then some insight may be possible into which of the chemical changes control the processes that govern degradation and perhaps how those processes change with degradation. Thus initial and predictable changes may be used to estimate the likely lifetime of a polymer coating in suitably defined circumstances.

The effect of ultraviolet radiation during the lifetime of a material depends on the spectral distribution of the radiation, its intensity, how much is absorbed by the material, and the quantum yield of the degradation process. This approach was taken to quantify this effective dosage and to determine its usefulness in estimating coating service lifetimes. Estimating product lifetime is a major technological and financial target for any user of construction or other materials since

product development and then maintenance costs are often very high. This article focuses on polymeric coatings, but the approaches may be useful for investigating other products.

The effective dosage can be calculated, as in the equation below [8]:

$$d_{eff}(?,t) = \int_{l_{min}}^{l_{max}} E_0(?,t)\left(1-10^{-A(?,t)}\right) f(?,t)\, d? \qquad (2)$$

Where:

d_{eff} = effective dosage at a given time [W/m^2] (will vary and accumulate with exposure)
l_{max}, l_{min} = maximum and minimum photolytically effective wavelengths
$E_0(l,t)$ = spectral irradiance, from sun or QUV etc. [W/m^2/nm]
$A(l,t)$ = coating absorption spectrum
$f(?l,t)$ = quantum yield of interest
t = exposure time
l = wavelength

Thus one can calculate the effective damaging dosage as it varies with exposure time. In fact, one can determine which parts of the coating adsorption spectrum are most important in the overall value. It is a quantity that incorporates the input (weather), the material properties (absorbance) together with an expression of the effect (quantum yield). If the effective dosage is an important parameter in determining service lifetime, then either it will be found to be a controlling variable in some crucial performance property or it will itself show some trends that can be used to deduce the progress of degradation. It is easy to see how an analogous expression could be generated to include the damage expressed in another property, the corresponding material property and the controlling variable in the weather, e.g. humidity.

In determining the effective dosage of the adsorbed radiation, the possibility exists that it changes as the coating degrades since it is known from many studies of degradation chemistry

that materials change as they degrade. Thus the equation above shows that it is necessary to know how the UV absorption and quantum efficiency of the crucial processes change. Only how the UV adsorption changes is reported here.

EXPERIMENTAL DETAILS

MATERIALS

Trimethylol propane (TMP) (Aldrich), Neopentyl Glycol (NPG) (Aldrich), Adipic Acid (AA) (Aldrich), Isophthalic Acid (IPA) (Aldrich), and Hexane diisocyanurate Trimer (HDI trimer) Desmodur N3300(Bayer) were used directly from the suppliers without further purification. The polyester was synthesized according to table 1 with no catalyst in a ramp cycle: 1hour at 160^{o}C, 2 hour at 180^{o}C, 2 hours at 190^{o}C, 2 hours at 200^{o}C, and hold temperature at 210^{o}C until acid value diminished below 10. The reaction was carried out in a reaction kettle with nitrogen purge, mechanical stirrer, thermocouple, and partial condenser.

An average of 5 hydroxyl functionality per chain, the ratio of isocyanurate was calculated 1:0.4, hydroxyl:isocyanurate. There was just enough isocyanurate to crosslink the film on a theoretical basis. This was done to speed up the degradation process.

APPLICATION

The samples were prepared by spin coat at 33% solids, at 4000 rpm for 10 seconds on 12 mm silicon discs and quartz slides. The solvent was 40% methyl ethyl ketone and 60% 1-methoxy-2-propanol acetate. The spin coater was a model WS-200-4NPP/RV from Laurell Technologies Corporation.

INFRARED SPECTROSCOPY

The infrared absorption spectra were obtained in transmission mode using a Nicholet Magna 850 Fourier transform spectrometer, FTIR. Substrates were polished silicon or germanium infra-red transmission windows, 13 mm diameter and 2 mm thick, available from Wilmad Glass. The technique is similar to that practiced by by van der Ven and Guerink [9]. These substrates are inert and dimensionally stable when exposed to the radiation, heat and moisture of the accelerated exposure environment used in this investigation as well as possessing suitable optical properties. Their size was chosen so that they fit into an atomic force microscope, AFM, as well as the FTIR; the AFM results will be reported separately. Each of the substrates was marked so that it could be put into the spectrometer at the same position with respect to the infrared beam after each exposure period. Since the coatings were spin coated onto these very flat substrates, they were quite insensitive to where they were located in the beam until appreciable degradation had taken place.

Analysis of the fringe spacing was done by curve fitting the IR absorbance spectra with a sin-squared wave in the portion between the carbonyl region and the CH stretch region. Nearby absorbance peaks were fit to Lorentzian peak shapes. The films used here were sufficiently thin that there were only two or three fringe maxima to use and so using the standard peak finding options in the spectroscopic software to get the maxima spacing did not give very reliable results.

DEGRADATION CONDITIONS

Although the ultimate application of the knowledge gained in this investigation is to estimate the service lifetime of such coatings in natural weathering, an accelerated exposure chamber was used. These chambers may not emulate natural exposure closely, but they do provide a controlled environment whereas natural exposure is variable and not completely

reproducible nor repeatable. The chamber used in this work was a QUV/SE made by the Q-Panel Company. The exposure of the panels was controlled in cycles according to ASTM D4587-91; the maximum coating temperature is 60°C for 4 hours when experiencing the ultraviolet radiation from the UVA fluorescent lamps and then there is a period of 4 hours with condensing humidity at 55°C. The substrates used had a diameter of only 13 mm, so they could all be accommodated in a single holder fabricated to occupy the space normally occupied by one standard 3 x 6 inch panel.

UV SPECTROSCOPY

The coatings were applied on quartz slides from Chemglass Inc. at the same thickness that were used to examine infrared spectroscopic changes (on silicon windows). A Cary 500 UV spectrometer was used to obtain the absorption spectra using a clean quartz slide to obtain the baseline.

RESULTS AND DISCUSSION

INFRARED SPECTROSCOPY

The change in thickness with exposure period, Figure 1, as determined by fringe spacing, is not distinguishable from a linear dependence. There is some noise in the data since the coatings were thin and produced three or fewer fringes for the curve fitting, but the linear relationship is also very characteristic of weight loss results [10, 11] wherever that approach is used to evaluate coating degradation. The linear reduction in the coating thickness implies that the degradation and ablation occur in a steady manner from a layer that remains essentially equivalent as it proceeds through the coating depth throughout the exposure period, or that loss of material is not controlled by the material remaining in the film on a time scale comparable

with the one week interval between testing. For example, there is no sign of diffusion limited kinetics. In either case, the material lost must be in low molecular weight fragments since it is fugitive and does not impede further erosion. Although these results do not have direct use in estimating a coating lifetime they are suggestive of some mechanistic approximations.

Multiplying peak area by fringe spacing shows how the concentration of CH and CO in the degrading films changes with exposure period, since this is equivalent to dividing by the remaining film thickness, see Equation (1).

Figure 2 shows how the carbonyl bands change in the infrared spectra. Figure 3 then shows how the concentration of carbonyl changes as calculated by the area of the peaks multiplied by the fringe spacing. The increase measured over 10 weeks approximately is approximately 25 %. As the exposure progresses, the data in this figure contains more variation, probably due to increased variation in degradation across each sample, and towards the end, there may have been microscopic locations that no longer had significant coating. Again, although there is some uncertainty in the data there appears to be a linear trend in carbonyl concentration.

Similarly Figure 4 shows that the CH concentration diminishes in a linear fashion at a rate that would be about 25% over ten weeks.

The CH concentration diminishes with exposure period which shows that it would be unwise to use it as a normalizing factor in analyzing spectra without a distinct calibration of film thickness. Changes in the CH concentration could easily mask another significant change if it were used unwittingly to normalize another band that changes with exposure. Deductions based on the relative increase or decrease with respect to a CH band must be viewed with caution unless the variation in CH is known independently.

For this polymer, there appears to be little that can be determined quantitatively in the OH, NH infrared spectrum around 3200 - 3600 cm^{-1}. Even if the (OH,NH) area is normalized using the fringe spacing there is no perceptible trend with exposure, even if the spectrum is fitted numerically and the contribution to the (OH,NH) area of the fringes is subtracted

There are some general conclusions that can be drawn from the quantitative changes in thickness and composition. If the thickness diminishes faster than the CH concentration is reduced, then the volatile fragments, on average, contain less CH than the previously intact polymer. Almost every polymer contains many more CH groups than other moieties. Thus it apparently requires only a modest fraction of the CH groups to be oxidized to CO containing groups for the CO groups to increase. If the concentration of CH in the degraded film is reduced to ¾ of its original concentration and the concentration of CO increases to 5/4 of its starting concentration, then the ratio in the degraded film should be 5/3 of its starting value. This is slightly larger than the spectroscopically determined increase, Figure 3, a ratio of 3/2. Inevitably, the chemistry of degradation involves more than the processes involved in the CH and CO absorbances, however in this case the link between the two seems to accounts for most of the ablation of the coating.

ULTRAVIOLET ABSORPTION

As in the quantification of the infrared results, the thickness change was used to adjust the UV absorbance since otherwise it is reduced as the optical path length through the coatings was reduced by weathering erosion. Thus changes in UV absorbance were determined that were a function only of how the material was changing, see Figure 5. It was interesting to see that this procedure clarified a nearly isobestic point at 295 nm better than the data displayed when uncorrected for thickness.

If UV absorbance is included in measuring the damaging dosage see Equation (2), then how and why it changes as the polymer degrades becomes important, particularly if it forms part of the means of predicting service life.

The UV absorbance shows several features. Even without thickness correction, there is an absorbance tail into the solar UV and visible region that is present in the pristine material and that increases with degradation (weeks of exposure). The peaks around 270 - 290 nm all diminish as the degradation period increases. There appear to be three distinguishable peaks in this region. In the data here, the tail increased as degradation proceeded but without developing any appreciable structure, no separate new peak appeared in the UV that would correspond to yellowing.

There are well documented cases of new chromophores generating obvious features [12, 13]. Although any peak caused by a new chromophore could be broadened due to multiple vibrational states splitting the peak and broadening from the material being a solid, but one would expect a maximum to become apparent. It is commonly reported that such tails are the result of absorbing moieties being generated by the chemistry of degradation, but sometimes this is asserted without any definite peaks being apparent. Other workers have discovered increased tailing without a defined maximum appearing in the UV [14, 15, 16]. These studies, together with the observation that even those results with a new maximum appearing seem also to get a larger, underlying tail, increases the motivation for seeking mechanisms and descriptions for this behavior that do not necessitate chemical changes producing specifically yellow chromophores.

Conventional analysis of spectroscopic changes focuses on suggestions of specific chemical changes to account for change in spectral features. For example, the usual explanation of a reduction in UV intensity when a polymer is irradiated is that the chromophore is being

destroyed by the radiation. Ultimately, that may well be true, but predicting the lifetime of a coating polymer requires knowledge of not only chemical changes but any processes that change the UV absorption.

As shown here, that part of the UV absorption spectrum that extends beyond ~295 nm gradually increases and broadens as the coating degraded. The carbonyl region in infra-red spectra taken during degradation also showed a broadening, Figure 2, which is consistent with the broadening in the ultraviolet, since the peaks around 260 - 290 nm are usually attributed to carbonyl n-π^* transitions. The three peaks in this region are probably due to fine structure typical of transitions that are smoothed out in solid materials. These peaks are often seen in polyester-urethanes or acrylic polymers [17]. Infrared carbonyl spectra show several bands that could easily account for splitting due to vibrational modes in the UV spectrum [18].

These samples were thin films, suitable for near UV transmission, and were visibly eroding but not changing color perceptibly. However, it is a common observation that many polymers in practical coatings "yellow" as they degrade. Clearly, the above encroachment of the blue end of the UV-visible spectrum in this model urethane corresponds to yellowing, and should be expected since urethanes are known to suffer yellowing. In conventional degradation studies, if a polymer "yellows", then the obvious change of color is used as a criterion of failure [19, 20]. Such specific chromophores may appear later as the chemical products of degradation become more concentrated but here these effects may be due to existing adsorption processes that are influenced somewhat as degradation proceeds.

Now, one of the differences between the infrared results and the UV spectra is that the carbonyl band area in the infrared increases in size, so the UV peaks might increase if they were detecting only the quantity of absorbing material present. However, they diminish considerably

as weathering proceeds. It is quite well known that n-π* transitions may be affected by solvent polarity [21] depending on how the various solute-solvent interactions affect the dipole moment on the chromophores and how energy levels in the ground and excited state are changed. One might expect that the intermolecular environment around the polymer chromophores becomes more polar as the polymer is oxidized during degradation. The polyester that was used to make the film was dissolved in four different solvents to investigate any solvent effect. UV absorbance was reduced significantly as the solvent environment changes (see Figure 6) just as the polymer absorbance changed during degradation.

The peak ultraviolet absorbance of the polyester solution chromophores moved to slightly shorter wavelengths as the solvent polarity and/or hydrogen bonding increased, which is very typical of n-π* transitions[21]. The Hansen solubility parameters for the solvents are given in Table 2.

The small peak center shift to higher energy is not apparent in the polymer films, which could be a result of experimental variation or that the polymer is not dilute in the films. However, the solvent effect correlates with the reduction in peak height during degradation, and thus rationalizes the absorption peak reduction with the apparently contradictory increase seen in the infrared carbonyl results. It does not correlate with the UV tailing because the n-π* peaks should move to shorter wavelengths, if anything. However, it is possible as the polymer degrades, although it becomes more polar, it may become more diverse at the molecular level and so electronic transitions are diversified and are smeared over a broader range.

ULTRAVIOLET ABSORPTION: TAILING

Regardless of associating the ultraviolet yellowing tail with a specific spectral peak the absorption in many materials varies exponentially with energy, an "Urbach" tail[22], for energies below that corresponding to the central peak:

$$a(l) = a_0 .\exp\left[\frac{hc}{l E_0}\right] \qquad (3)$$

Where;

l = wavelength
c = velocity of light
h = Planck's constant
E_0 = energy value interpreted as the width of the tail of localized states in a band gap

This equation was applied to the UV absorption obtained from the polyester-urethane polymer studied here (Figure7).

Linear regression of data in the diagram gave a characteristic energy of ~ 0.66 eV, which is consistent with literature values for polymers[23]**.** Usually, this exponential tail is attributed to thermal or structural disorder that provides electronic states that tail into the band gap for amorphous semiconductors[24]. Such analyses may give insight into the local molecular interactions that occur during weathering changes. The data here does not display identifiable trends with increasing degradation in the characteristic "Urbach" energy, E_0, , possibly because the UV spectra were obtained to calculate the effective dosage, not optimized for examining the tail of the absorbance.

Urbach found this exponential tail behavior in inorganic halides but it has since been found for many materials including glasses and amorphous semiconductors. Whatever the exact mechanism is for this tailing, the extended tail behavior must be a measure of a more

complicated density of states in which structural or compositional disorder perturb the electronic configurations. Polymers usually contain several different atoms, in a more or less random arrangement, so there is no easily identifiable bandgap as for a crystalline or amorphous semi-conductor material.

One literature reference has been found for organic systems[23]. In that work, the energy, E_0 was approximately 0.3 eV, for organic asphaltenes, which is similar in value to that found here, 0.66 eV. In the studies where this relationship has been used, E_0 is construed as an energy that represents the width of the tail of localized states in the band gap. The value of 0.66 eV found here, is small compared to the width of the band gap in insulators that are typically several electron volts. If ultraviolet induced degradation produces long-lived free radicals, one might expect these unpaired electrons to provide electronic states within the band gap[25] and thus to contribute to fairly low energy electronic absorptions and thus UV tails.

Since the UV absorbance tails examined here had the same value of E_0, within the uncertainty of the data, the increased UV-visible yellowing cannot be explained by changes in E_0. Thus the changes must instead come from an increase in the pre-exponential term in equation 3, a more complete form of which includes a term, E'_{bg}, that is taken to be comparable to the appropriate band gap[26]:

$$a(l) = a_0' . \exp\left[\frac{hc}{l E_0} - \frac{E'_{bg}}{E_0}\right] \qquad (4)$$

The same absorption spectra can be used to deduce a value for such a gap. One could chose a peak wavelength, 210 nm, and calculate the corresponding energy, 5.9 eV, and the peak deconvoluted with a center at 242 nm corresponds to an energy of 5.1 eV. However, inspection of this data did not reveal a trend in peak position with degradation period. This may be because

the spectra were obtained with polymer films thick enough to obtain accurate values for the near visible region for the effective dosage calculation (see later) and these films have very high absorbances centered around 210 nm so the detector's sensitivity and accuracy may be limited there.

An alternative approach is to employ "Tauc" gap analysis[27], an expression of the band gap used for amorphous semi-conductor materials. To use the Tauc approach, the square root of the absorbance divided by the wavelength is plotted against the reciprocal of the wavelength and the linear part is extrapolated to the abcissa to calculate the band gap energy of the amorphous material (Figure 8). Here the value was found to be 4.8 eV for the unexposed polymer, diminishing to 4.3 eV in exposed material. This magnitude is typical found for other polymers[25, 28] and somewhat lower, naturally, than the energies deduced from the peak centers. The major linear part in the Tauc plots occurred at wavelengths around 250 nm (see figure below) so it is the gap derived from the resultant of the peak ~242 nm and the stronger absorption that peaks around 210 nm. The arguments presented above suggest that the tailing cannot be associated with the small n-π* peaks, so the extrapolation was not done to deduce a "Tauc gap" for that transition. In addition, it is also more difficult to identify a linear portion in Figure 8 corresponding to those small peaks and thus get a good extrapolation to the abscissa.

One can question whether Tauc gap analysis is appropriate to polymers under such conditions since polymer absorption is usually a succession of peaks and not an adsorption edge, but at least it is another quantification that the Urbach energy, E_0 is a suitable, small fraction of an energy that probably represents a lower bound on a characteristic electronic transition as expected from Equation (4). An advantage here is that the "Tauc" gap is derived from the long wavelength side of the π-π* peak and so, again, may be connected to the processes governing the

yellowing. In fact, an alternative view for the utility of the Tauc analysis is that it might provide a consistent way of characterizing how these peaks either move or spread on the longer wavelength side as the degradation proceeds. Since the Tauc gap apparently moves slightly to lower energies as the degradation proceeds, it means that the peaks may be moving or spreading to lower energies and may thus contribute to the increased tailing. It is characteristic of a π-π^* transition to shift to longer wavelengths as its solvent environment becomes more polar[21] which is consistent with the need for a defining electronic transition, E'_{bg}, from Equation (4) to shift to lower energies and with a picture wherein the intermolecular environment becomes more polar as degradation proceeds. Unfortunately, selecting the "straight" part of the Tauc plots for the extrapolation is somewhat arbitrary and the extrapolation to the abcissa will be sensitive to the quality of the baseline in the original data, thus any conclusions drawn from the data must be tempered with practicality.

Since the model polyester-urethane gave "Tauc gap" energy values that appeared to diminish a little with exposure it would make the tailing absorbance increase in Equation (4) as required by the experimental results. Indeed, the transition modeled by the "Tauc gap" may be sensitive to the intermolecular disorder and diminish as the disorder increases[24] and thus be consistent with the overall picture here.

Although higher energy absorbance peaks are more distant from the solar UV-visible range, they are very important in defining the effective dosage response of the material because they may be the major contributors to the origin of the tailing. Explanations of yellowing that require development of new chromophores are frequently allied to infrared analysis of degradation chemistry[29]. Such analyses find infrared bands that attributable to species developed as the degradation develops. These new species then produce smooth featureless adsorption at

the blue end of the visible adsorption spectrum so that the material yellows[30]. The ideas presented here would account for such a smooth tailing, or yellowing, without the formation of specific chromophores and would account for it before the degradation chemistry develops to the point where new "yellow" moieties are present at sufficient concentrations to provide a maximum in the ultraviolet absorption.

ULTRAVIOLET ABSORPTION: EFFECTIVE DOSAGE

In order to properly measure the effect of UV exposure from Equation 2, one needs the quantum yield for the degradation process. There is very little data in the literature on quantum yields of degradation for suitable polymers that display any wavelength dependence. However, idealized data, most recently published by Bauer[31], can be used for discussion although there is no information on changes that may occur as degradation chemistry progresses. A calculation was performed with this quantum yield data, the UV absorption (above) and the solar spectrum; the results showed little trend with exposure time (weeks), see Figure 9. Another calculation was carried out using the same values of UV absorption and solar spectrum but by setting the quantum efficiency to unity at all wavelengths and exposure periods since it is, in truth, unknown. This second calculation showed a greatly increasing dosage rate with exposure. The points in Figure 9 were calculated for each week of exposure and the lines merely join those points.

Clearly, the nature of the quantum yield has a crucial rôle in determining the damaging UV dosage. The shape of the curves is very significant. Depending on the form of the quantum yield, there is a clear acceleration of the effect of damaging radiation. This non-linear relationship itself offers some possibilities on how to assess a service lifetime; one could choose a value of the exposure period characteristic of the start of the acceleration in damage, ~ 4 weeks

in this case, or one might choose a value that represents the asymptote as the damage rate increases greatly, ~ 10 weeks here. This is somewhat analogous to choosing a "yield" point or ultimate value of stress in mechanical properties of polymers.

A crucial part of the material absorbance lies within the solar spectral range and is increased by degradation processes leading to further increased UV energy absorption and an accelerating rate of degradation. In such cases, the response of the system to stimulus is to change its response so that it responds to a greater degree (positive feedback). A very simple algebraic model of this feedback might be:

$$d_{eff}(t) = \frac{d_{eff}(0)}{1 - k.t} \tag{5}$$

Where:

t = exposure period
$d_{eff}(t)$ = effective dosage as calculated from the experimental results using Equation (2)
$d_{eff}(0)$ = initial effective dosage, $t = 0$
k = parameter discussed below

In electronic circuits, very similar equations are used to calculate amplification controlled by feedback. This equation represents an increasing dosage rate that tends towards infinity at an exposure period of $1/k$. Further, it is easy to see that a graph of $d_{eff}(0)/d_{eff}(t)$ plotted as a function of exposure would be linear and have a slope of $-1/k$ and an intercept on the exposure period axis of $1/k$. The parameter, k, in this very simple equation represents the reciprocal of what might be construed as the ultimate (not necessarily useful) lifetime of the material. A simple test of this approach was done with the reciprocal of the effective dosage data calculated from the previous work and is presented in Figure 10.

There are perhaps too few data points in that graph for any strong conclusion, but if such a simple expression were found to describe the trend of effective dosage with exposure then careful experiments would allow an early estimate of the ultimate life. Although it is unlikely that such a simple relationship will prove to be applicable, understanding the shape of the non-linear response curve will be a valuable step in being able to estimate lifetimes. Further modeling techniques will be applied as more data becomes available.

CONCLUSIONS

Carbonyl concentration increases with degradation in polyester-urethane coatings as they oxidize as measured by infrared spectroscopy, but the corresponding n-π^* transition peaks in the UV absorption diminish as the degradation proceeds. By analogy to the effect of increasing solvent polarity and hydrogen bonding, the reduction in UV peak height seems to be attributable to the increasing polarity and/or hydrogen bonding within the polymer as it oxidizes due to degradation.

An absorbance tail into the longer wavelengths of the UV-visible region increases with degradation (weeks of exposure) and is clearly a major contributor to values calculated for the effective radiation dosage absorbed by the polymer. This encroachment of the blue end of the UV-visible spectrum in this model urethane corresponds to yellowing, and should be expected since urethanes are known to suffer yellowing. An explanation of "yellowing" during degradation that does not require the development of specifically yellow chromophores may be that it results from a broadening and diversification in the electronic transition associated with existing carbonyl groups. As the polymer is oxidized and degrades, the local intermolecular environment around the chromophores changes and spreads the transitions over a greater range.

This may describe yellowing that occurs before chemical degradation reaches the point of creating new structures that would provide chromophores in the visible region.

Since the π-π^* carbonyl peak is large, and if the increased tailing during degradation derives from existing features rather than from new chromophores, then the major contribution to the tailing would be from the π-π^* transition or other peaks at even shorter wavelengths, rather than from the much smaller n-π^* peaks closer to the visible region.

An exponential form fits the UV tailing very well and was used to calculate a value, 0.66 eV, for the "Urbach" energy characteristic of disordered materials that describes the tail in terms of electronic energy levels arising within the transition gap corresponding to the main UV absorption. This energy does not appear to change with exposure in this material, but the increase in tailing can be accounted for by the value of the transition gap being reduced slightly as degradation continues. Analyses, such as the approach of Tauc et al. may be useful as a quantification of the spreading, as degradation proceeds, of the larger UV peaks centered around 242 nm and 210 nm.

Depending on the form of quantum yield as a function of wavelength, effective UV dosage absorbed by the polyester-urethane coating accelerated as the coating degraded, similar to a "positive feedback" response. For this coating, and others with carbonyl functionality that oxidize further, the positive feedback in the effective adsorbed dosage may well be controlled by the presence and absorption of the carbonyls. The form of the acceleration lends itself to some choices that could be used to define the lifetime of the coating in terms of the rate of radiation absorption. One could choose a point at which the adsorbed dosage accelerates noticeably, or one could extrapolate to a point when adsorption of UV radiation has increased to an extremely large value. In this polymer, the feedback process, if it exists, may be determined by the

concentration and UV absorbing properties of carbonyl groups. If the causes for any non-linearity in the dosage response of a polymer as it changes due to degradation can be understood, then the functional form of the non-linearity may be deduced and thus bring prediction of service lifetime closer to reality.

Knowledge of the wavelength dependence of the quantum yield is very important in determining how much the individual UV adsorption peaks contribute to the radiation adsorption and is the subject of investigation. However, it is important that further attention is given to quantifying the exponential tailing (yellowing) that extends into the visible region because it is a major factor in energy adsorption regardless of the details of the quantum yield.

ACKNOWLEDGEMENTS

The authors would like to thank Dr. Rasmussen of the Chemistry Department at NDSU for access to the UV spectrometer and Dr. Mallik of the Chemistry Department, NDSU, for access to the computational chemistry facilities. This work was funded by the Air Force Office of Scientific Research under contract number F49620-99-1-0283.

REFERENCES

1. G. P. Bierwagen, D. E. Tallman, Prog. Org. Coatings, 41 (2001): p. 201
2. C. Wilhelm, J-L. Gardette, Polymer, 39 24 (1998): p. 5973
3. C. Wilhelm, A. Rivaton, J-L. Gardette, Polymer, 39, 5 (1998): p.1223
4. F. X. Perrin, M. Irigoyen, E. Aragon, J. L. Vernet, Polym. Deg. Stab., 70 (2000): p. 469

5. J. L. Gerlock, C. A. Smith, V. A. Cooper, T. G. Dusbiber, W. H. Weber, Polym. Deg. Stab., 62 (1998): p. 225

6. H. Kim, M. W. Urban, Langmuir, 16 (2000): p. 5382

7. M. Horák, A. Vítek, Interpretation and Processing of Vibrational Spectra (New York, NY: John Wiley and Sons, 1978)

8. J. W. Martin, Prog. Org. Coatings, 23 (1993): p. 49

9. L. G. J. van der Ven, P. J. A. Guerink, J. Oil and Colour Chemists Assoc., 74, 11 (1991): p. 401

10. S. G. Croll, "Assessment of TiO_2 pigment in coatings' durability using transmission infrared spectroscopy," 2nd. International Conference on Methodologies and Meterologies for Service Life Prediction, Monterey, California, November 1999.

11. G. Wypch, Handbook of Material Weathering, 2nd Ed. (Toronto, Ontario, Canada: ChemTec Publishing, 1995)

12. S. B. Maerov, J. Polym. Sci: A, 3 (1965): p. 487

13. S. M. Cohen, R. H. Young, A. H. Markhart, J. Polym. Sci: A-1, 9 (1971): p. 3263

14. A. Rivaton, F. Serre, J. L. Gardette, Polym. Deg. Stab., 62 (1998): p. 127

15. N. S. Allen, M. Edge, M. Rodriguez, C. M. Liauw, E. Fontan, Polym. Deg. Stab., 71 (2001): p. 1

16. P. K. Das, P. J. DesLauriers, D. R. Fahey, F. K. Wood and F. J. Cornforth, Polym. Deg. Stab., 48 (1995): p. 11

17. D. R. Bauer, M. C. Paputa Peck, R. O. Carter III, J. Coatings Tech., 59, 755 (1987): p. 103

18. B. Smith, Infrared Spectral Interpretation, A Systematic Approach (New York, NY: CRC Press, 1999)

19. N. S. Allen, M. Edge, M. Rodriguez, C. M. Liaw, E. Fontan, Polym. Deg. Stab., 71 (2001): p. 1

20. R. S. Davidson, J. Photochemistry and Photobiology B: 33 (1996): p. 3

21. E. D. Owen, "Basic photochemistry," Chapter 1 in "Photochemistry of Dyed and Pigmented Polymers," eds. N. S. Allen and J. F. Mckellar (Barking, England: Applied Science Publishers, 1980)

22. G. A. N. Connell, "Optical Properties of Amorphous Semiconductors," in "Topics in Applied Physics" Vol. 36 (1985) ed. M. H. Brodsky (New York, NY: Springer-Verlag)

23. O. C. Mullins, Y. Zhu, Appl. Spectroscopy, 46, 2 (1992): p. 354

24. S. K. O'Leary, S. R. Johnson, P. K. Lim, J. Appl. Phys, 82 (1997): p. 3334

25. R. Mishra, S. P. Tripathy, D. Sinha, K. K. Dwivedi, S. Ghosh, D. T. Khathing, M. Müller, D. Fink, W. H. Chung, Nucl. Inst. Meth. Phys. Res. B, 168 (2000): p. 59

26. S. John, M. Y. Chou, M. H. Cohen, C. M. Soukoulis, Phys. Rev. B, 37, 12 (1988): p. 6963

27. J. Tauc, R. Grigorovich, V. Vancu, Phys. Stat. Sol., 15 (1966): p. 627

28. S. Gupta, D. Choudhary, A.Sarma, J. Polym. Sci: B, 38 (2000): p. 1589

29. N. S. Allen, P. J. Robinson, N. J. White, D. W. Swales, Polym. Deg. Stab., 19 (1987): p. 147

30. A. Rivaton, F. Serre, J. L. Gardette, Polym. Deg. Stab., 62 (1988): p. 127

31. D. R. Bauer, Polym. Deg. Stab., 69 (2000): p. 307

TABLE 1
Composition of Polyester used to make the model urethane polymer network

Components	Molar ratio	Properties	
Neopentyl Glycol	3	Acid number	8.95
Trimethylol Propane	1	Hydroxyl number	166.5
Isophthalic Acid	1.714	Mol. Wt (No. avg.)	2899
Adipic Acid	1.286		

TABLE 2
Characteristics of solvents used to study the effect of solvent environment on UV absorbance for the polyester polymer.

	Hansen Solubility Parameter, (MPa)$^{1/2}$		
	Dispersion	Polar	Hydrogen Bonding
Dichloromethane	18.2	6.3	6.1
Tetrahydrafuran	16.8	5.7	8.0
Ethanol	15.8	8.8	19.4
Acetonitrile	16.4	17.4	6.8

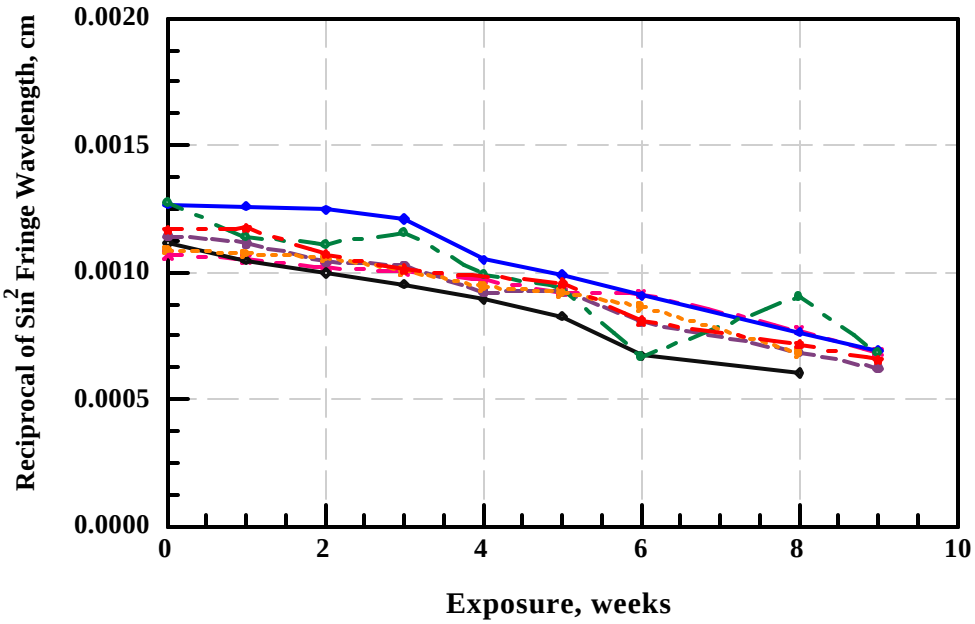

FIGURE 1. The change in coating film thickness with exposure period, determined by fringe spacing from infrared spectra.

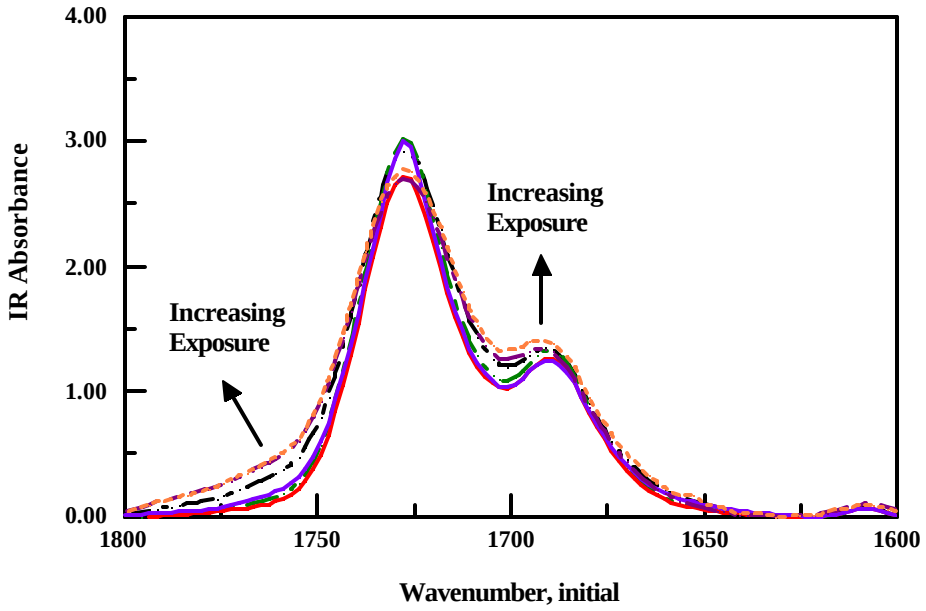

FIGURE 2. Infrared absorbance showing how the carbonyl peaks change with exposure.

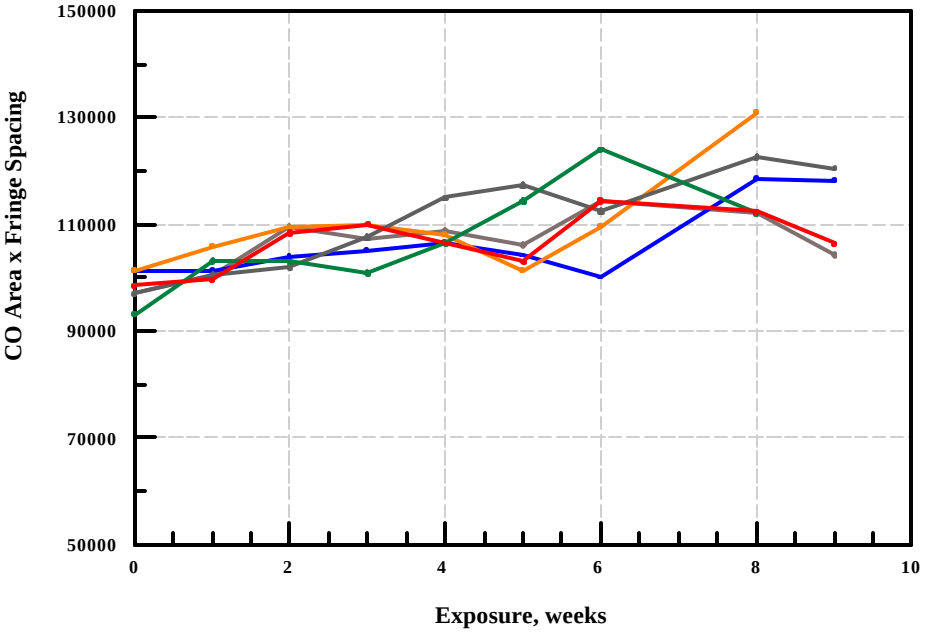

FIGURE 3. Change in carbonyl concentration during degradation from the infrared peak area and fringe spacing.

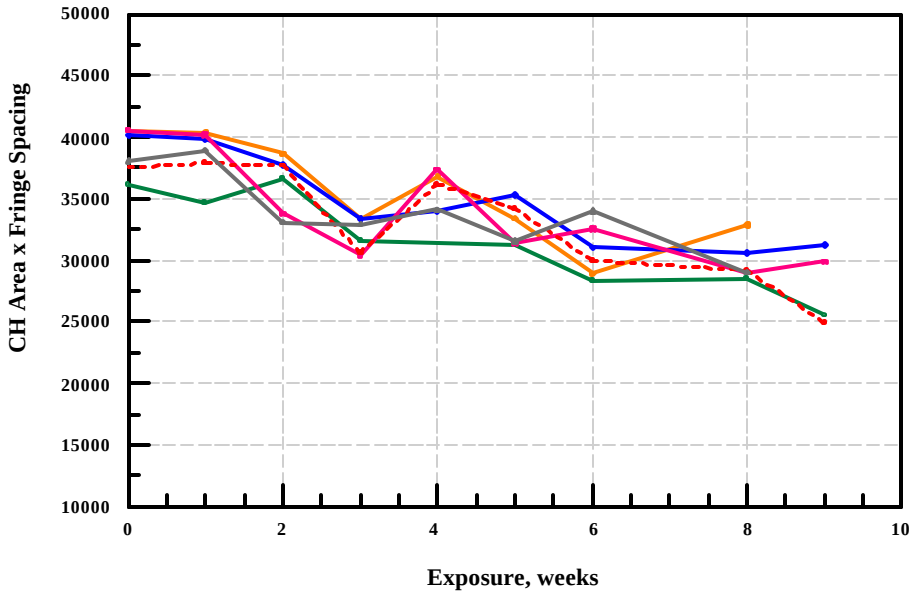

FIGURE 4. Reduction in CH concentration during degradation measured using the infrared peak area and fringe spacing.

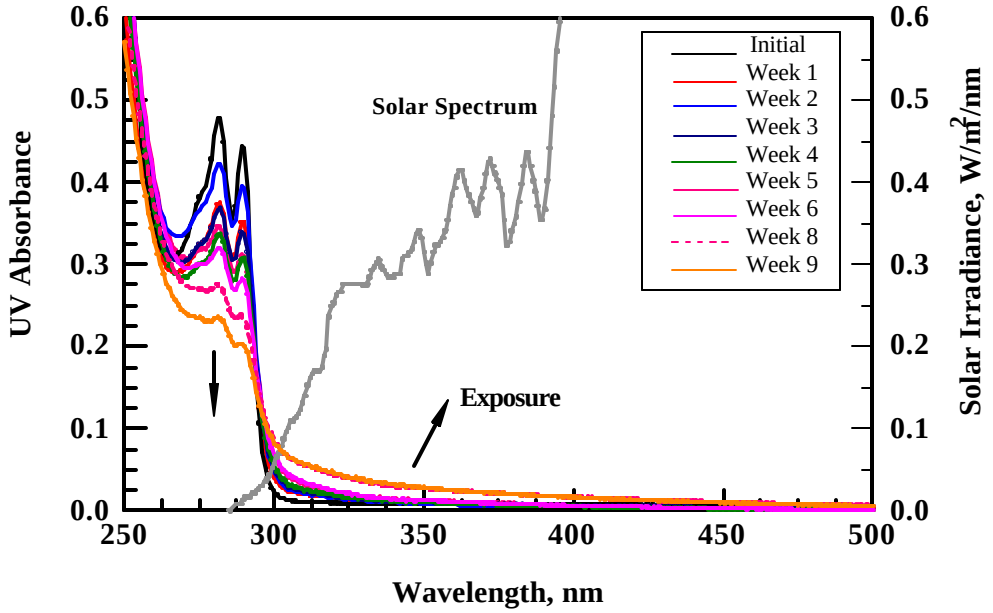

FIGURE 5. Ultraviolet absorption changes during exposure in accelerated weathering corrected for ablative thickness changes. Part of the solar spectrum is reproduced in the figure for comparison.

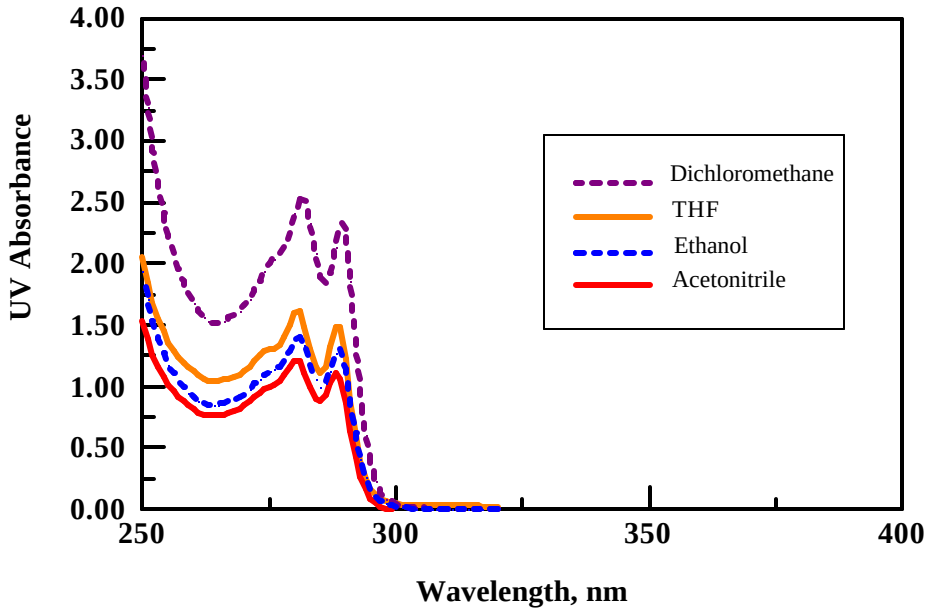

FIGURE 6. Effect of different solvents on the ultraviolet absorbance of the polyester component of the films; polymer concentration 0.1%.

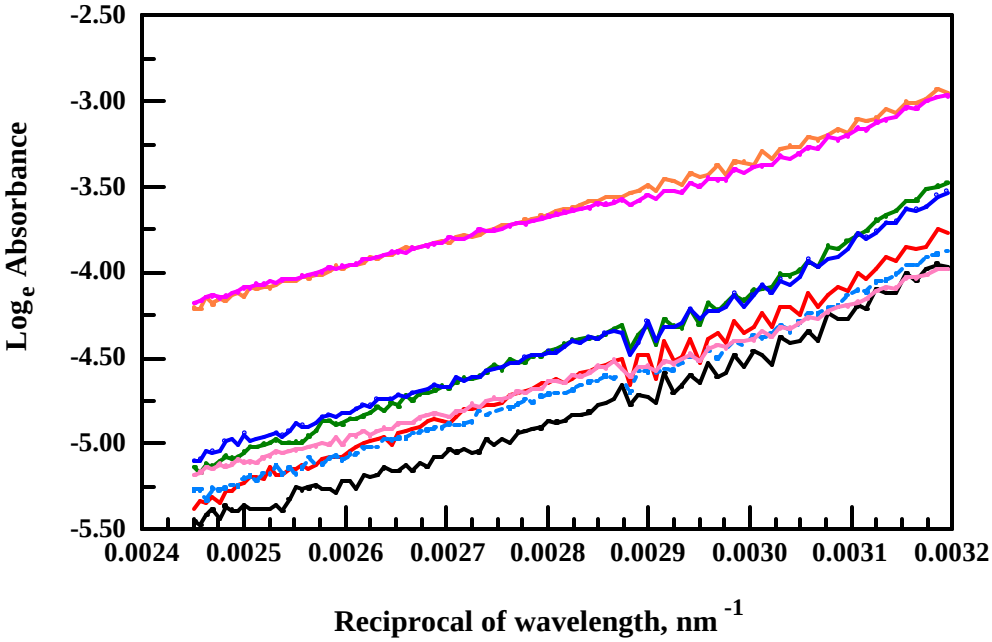

FIGURE 7. "Urbach" tail analysis of the ultraviolet spectra. The abscissa corresponds to wavelengths of 416 to 312.5 nm.

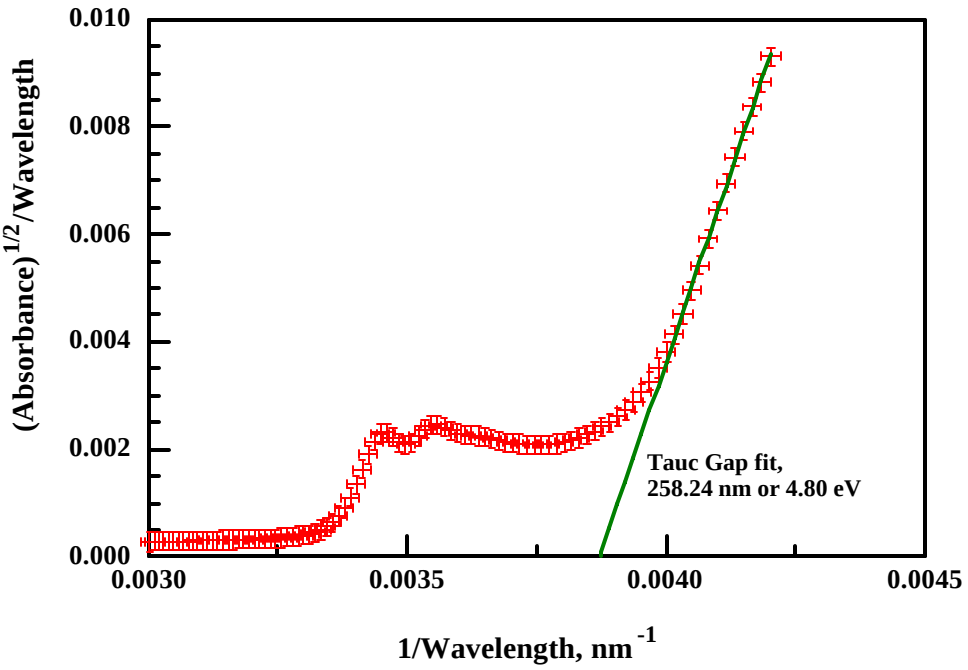

FIGURE 8(a). "Tauc" plot of the ultraviolet absoption for unexposed polyester urethane

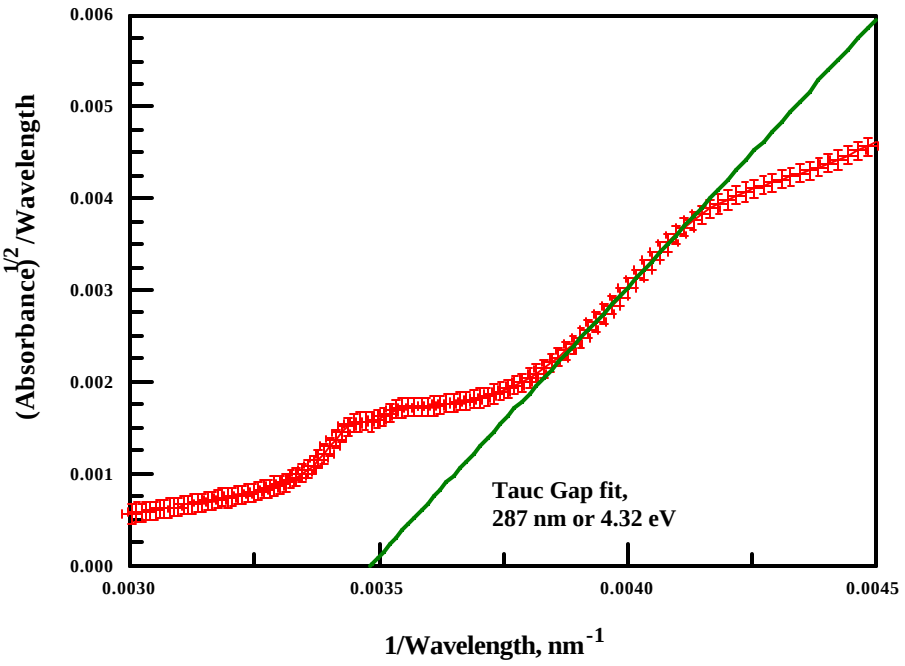

FIGURE 8(b) "Tauc" plot of the ultraviolet absorption for the polyester-urethane after nine weeks of accelerated weathering exposure.

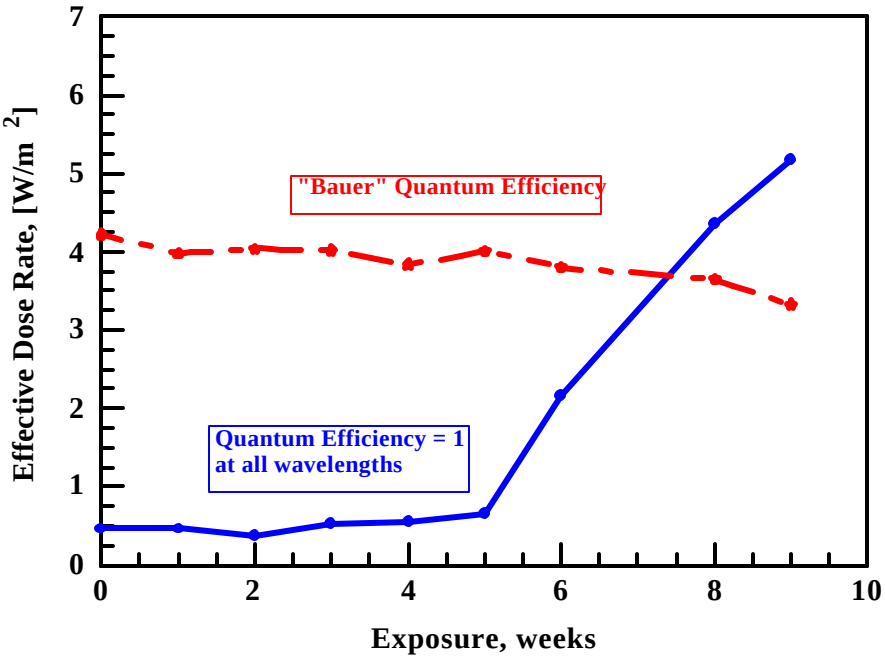

FIGURE 9. Calculation of Effective Dose rate when exposed to the solar spectrum: showing the effect of quantum efficiency function.

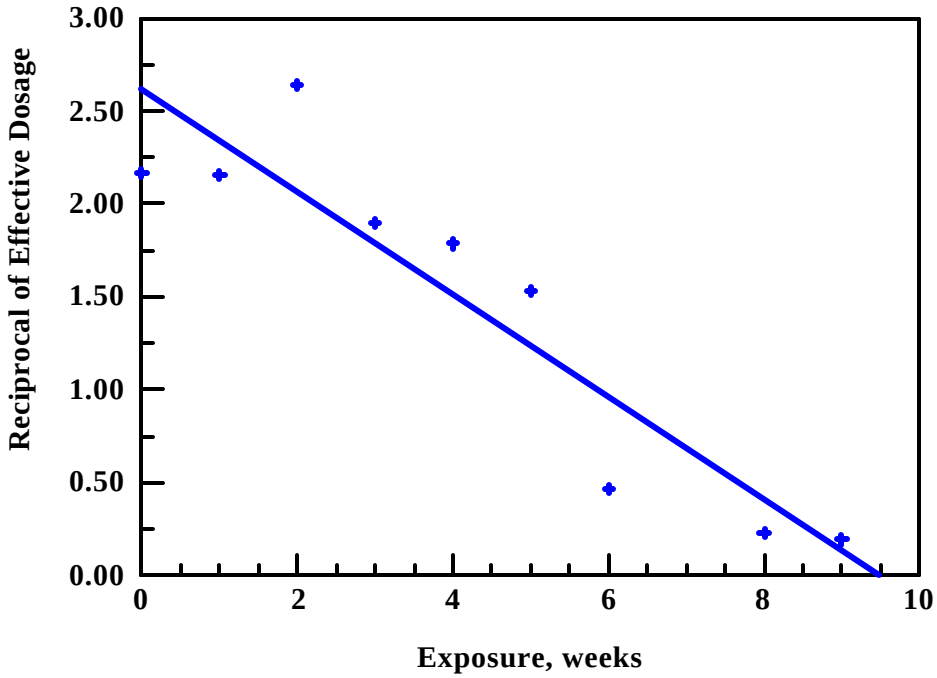

FIGURE 10. Reciprocal of Effective Dosage rate as a function of exposure period when the quantum yield is a constant (=1).

EVALUATION OF FUNCTIONALIZED POLYSILOXANES AS AIRCRAFT COATING PRIMERS

Philip Boudjouk*, Thomas E. Ready, and Seok-Bong Choi

Department of Chemistry
North Dakota State University
Fargo, North Dakota 58105

ABSTRACT

A variety of functionalized polysiloxanes have been successfully synthesized. These polysiloxanes have also been used to form inorganic/organic hybrid materials via conventional chemistry. Both the polysiloxanes themselves and the hybrid materials have been applied to Al 2024-T3 substrates for evaluation as coating primers. Ultra-thin polysiloxane /organic primers have been developed which promote topcoat adhesion > 1000 psi. Blending functionalized polysiloxanes with organic resins enhance the wettability and adhesion of the primers.

INTRODUCTION

Many aircraft currently in service, which utilize aluminum alloy s in their construction (i.e. the KC-135), have had their mandated service lifetime extended far beyond their original lifetime expectancy. Hence, corrosion protection has become an imperative for the continued deployment and performance of these aircraft. The most effective corrosion preventive primers in use today contain some form of chromate. However, chromates represent a significant environmental and occupational risk, which has called their continued use into question[1]. This has made the development of an effective, long term corrosion preventive coating, absent of chromates, a vital accomplishment toward maintaining available aircraft fleet numbers.

Several of the desirable characteristics inherent in a successful coating system are good barrier properties, the incorporation of active inhibitors, compatibility with pigments, and being environmentally innocuous.

As coatings on large aircraft are a significant endeavor, there are several criteria associated with the coating application which are important. These include a desire for spray - on application (either neat or aqueous solutions), an environmentally benign run off, and drying at ambient temperature within a reasonable timeframe (1 day).

The great preponderance of silicon-based coatings are based on either the polymerization of monomeric silicon precursors (sol-gel coatings) or high molecular weight silicones. Cross-linking functionalities in these coatings are generally introduced either by nucleophilic substitution or catalytic hydrosilation on the silicon atoms. The Boudjouk group has been examining the utility of well-defined, functionalized, oligomeric polysiloxanes synthesized either by dehydrogentative coupling[2] or hydrosilation as the principal matrix component in primer coatings.

There are several rationales to suggest *prima faci* that these oligomeric polysiloxane materials may serve as good candidates for this application. First, oligomeric, narrow polydispersity poly(methylhydrosiloxane) (PMHS) represents an affordable platform by which to access to highly functionalized silicone materials via an effective, facile, one pot process[2]. Second, the synthesic route to these materials allows for precise stoichiometric control of both the number and the type of functionalities on the polysiloxane backbone. Third, the resulting silicone materials are colorless, viscous liquids possessing low vapor pressures, which can be applied to substrates via solventless spraying with negligble volitile organic compounds (VOC's). Fourth, in most cases, the resulting polymers have long to infinite "pot life" compared to conventional sol-gels which have a rather tight and limited usage window.

In this work we provide some baseline data on oligomeric alkoxy-substituted polysiloxane homopolymers (a single type of functionality on the silicone backbone) as primer

coatings. In addition we report on the development of an ultra-thin, siloxane conversion coating and a three component primer coating based on an oligomeric alkyl-substituted polysiloxane.

EXPERIMENTAL PROCEDURES

SYNTHESIS OF ALKOXY-SUBSTITUTED POLYSILOXANE HOMOPOLYMER PRIMERS

Poly(methylhydrosiloxane) (**1**) was purchased from Aldrich and used without further purification. The synthesis of Poly(methylglycidoxysiloxane) (**2**, Figure 1) was described elsewhere. Poly(methyl, triethyleneglycol ethyl ether siloxane) (**3**, Figure 1) and poly(methylhexafluoro-2-propoxysiloxane) (**4**, Figure 1) were synthesized utilizing the same approach. The yields of **2**, **3**,& **4** were quantitative as measured by NMR.

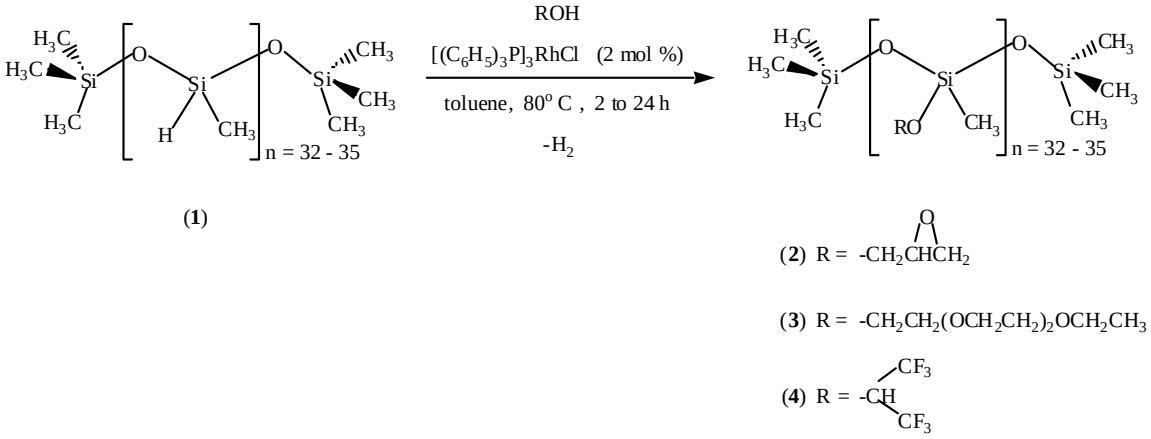

FIGURE 1. Synthesis of Functionalized Polysiloxane Homopolymers

ULTRA-THIN POLY(METHYLHYDROSILOXANE)-ALLYLGLYCIDOXYETHER (PMHS-AGE) PRIMERS

Ultra-thin PMHS-AGE primer coatings were formed on Al 2024-T3 substrates in two stages (Figure 2) using a synthetic methodology previously reported[3]: a.) platinum catalyzed

partial dehydrogenative coupling of PMHS to the aluminum surface, and b.) platinum catalyzed hydrosilation of the vinyl group in allylglycidyl ether (AGE). Each step of this process was monitored via the dissappearance of the Si-H bond (ν = 2155 cm $^{-1}$) using reflectance IR spectroscopy (Figure 3). Based on literature results[3], the film thickness of these coatings is estimated to be around 5 nm.

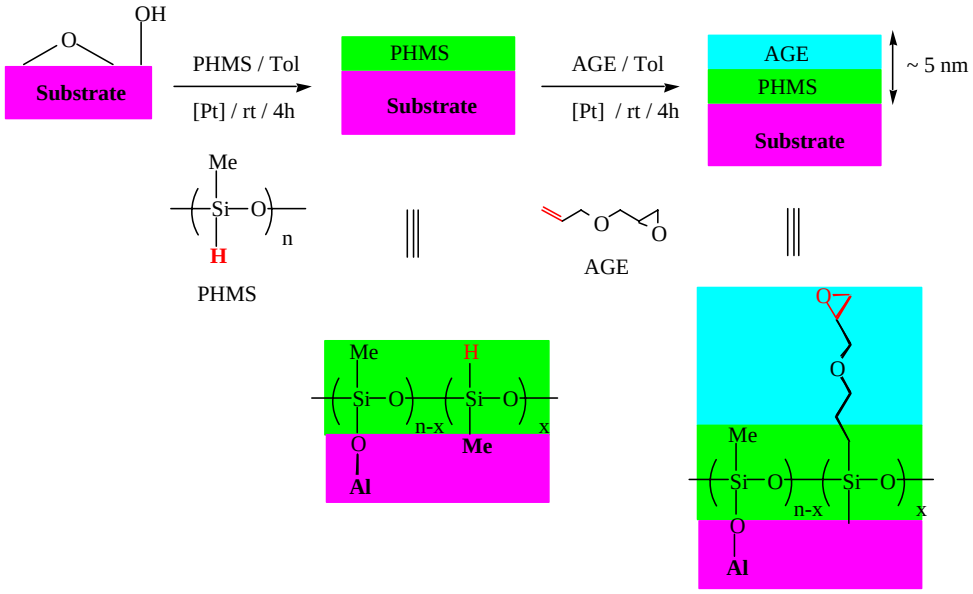

FIGURE 2. Formation of Ultra-thin Polysiloxane / AGE Primer Coatings

SYNTHESIS OF 3-COMPONENT ALKYL-SUBSTITUTED POLYSILOXANE (SGBA) PRIMER

Poly(methyl, glycidylpropylethersiloxane) was synthesized according to the literature. Diglycidyl bisphonol-A and poly(methyl, glycidylpropylethersiloxane) were then mixed together in a 1:1 (w/w) ratio. 1,3-bis(aminomethyl)cyclohexane was added to this mixture and stirred for 60 min. before application to form the 3-component SGBA primer.

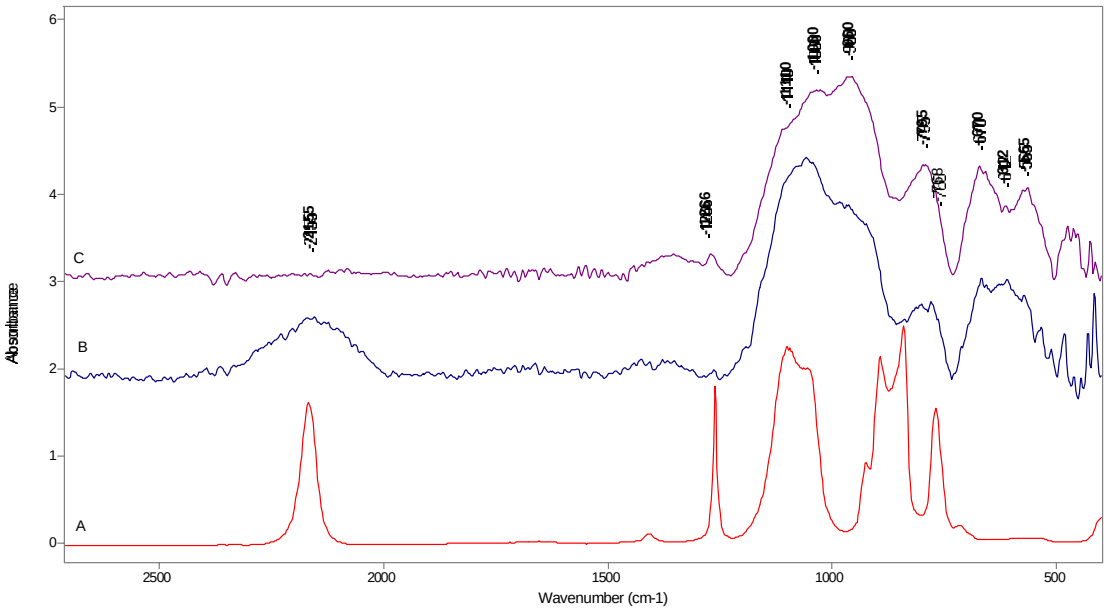

FIGURE 3. Reflectance Infrared Spectra of Ultrathin PMHS Hybrid Primer Coatings. *Bottom*: PMHS (solution IR); *Middle*: Ultrathin PMHS film on HF treated Al 2024-T3; *Top*: Ultrathin AGE film on Ultrathin PMHS film on HF treated Al 2024-T3. (Note: Si-H presence in Middle Spectrum and Si-H dissappearance in Top Spectrum)

COATING PREPARATION AND TESTING

Aluminum 2024-T3 test panels were purchased from Q-Panel. n-Butanol, i-butanol, and phosphoric acid was purchased from VWR and used without further purification or drying. Immediately prior to primer application, test panels were washed with acetone and submerged in an phosphoric acid bath consisting of n-butanol (40 v%), i-propanol (30 v%), water (20 v%), and phosphoric acid (10 v%) for 5 minutes. The panels were rinsed with de-ionized water and wiped dry. No conversion coatings were applied to the aluminum panels.

Primers, as described above, were applied neat with a wire wound, stainless-steel draw down bar, gauge 0.028. Films were formed at standing at ambient temperature for one day followed curing at 45^{o}C for five hours. Additional drying, as necessary, was done at ambient temperature. Primers **2** & **4** were dry to touch within 24 hrs. Primers **1** & **3** took 2 weeks to dry.

For comparisons, DEFT chromated epoxy primer was applied to test panels in the same fashion. Final film thicknesses were measured to be 2 μm using an Elcometer.

Each test panel was coated with either DEFT 03-GY-277 two component polyurethane topcoat or DEFT 99-GY-001 “Extended Life” topcoat using a wire wound, stainless-steel draw down bar. The topcoat was dried at ambient temperature for 1 day followed by curing at 45^{o}C for five hours. Total coating (primer and topcoat) thicknesses were measured using an Elcometer (model 106) to average of17 μm for the alkoxy-susubstituted siloxane primer coated samples. Similarly, the total coating thickness for the Ultra-thin primer coated samples was μm and 25 μm for the SGBA primer coated samples.

Contact angles of water droplets on the primer surface were measured as the average of 6 trials. Adhesion measurements (average of 12 trials) were made using ASTM pull-off test . First, primer adhesion was measured by pull-off of the primer (without topcoat) from the Al 2024-T3 substrate. Second, the topcoat adhesion was measured by pull-off of the topcoat from primer/topcoat coated Al 2024-T3 substrates.

Prohesion durations of scribed test panels (average of 3 trials) were made using a Q-Fog prohesion chamber with cyclic dry heat and dilute Harrison’s solution exposures. The duration times for each panel were judged by the first visual evidence of coating blistering, de-lamination, or other sign of damage to non-scribed portions of the panels.

Electrochemical Impedence Spectroscopy (EIS) was performed using an EIS900 (Gamry Instruments, Inc. Pennsylvania, U.S.A.). Electrochemical measurements were carried out in dilute Harrison’s solution at the open circuit potential. The counter electrode was a platinum mesh electrode with an area of 2.5 cm^2 and the area of the working electrode was 12.56 cm^2. The

reference electrode was a saturated calomel electrode (SEM). The frequency range of the applied potential was 0.001 to 60K Hz and the amplitude was 5 mV.

RESULTS

Water contact angles, polysiloxane primer adhesion to Al 2024-T3, and topcoat adhesions are listed in Table 1.

TABLE 1
Contact Angle and Adhesion of Alkoxy-Substituted Primers on Al 2024-T3 and Commercial Topcoats on Alkoxy-Substituted Primer Coated Al 2024-T3

Primer	**Contact Angle** (degrees)	**Primer Adhesion** (psi)	**PU Topcoat Adhesion** (psi)	**EL Topcoat Adhesion** (psi)
Cr Epoxy		600	600	700
(**1**)	95.1	600	90	250
(**2**)	55.2	650	650	620
(**3**)	74.6	300	275	250
(**4**)	103	100	50	100

PU = Deft Polyurethane Topcoat. EL = Deft “Extended Lifetime” Flourocarbon Topcoat

Prohesion durations for the scribed samples coated with alkoxy-substituted primer followed by topcoat are listed in Table 2.

TABLE 2
Prohesion Durations of Scribed Alkoxy-Substituted Primer/Commercial Topcoat Coated Al 2024-T3

Primer	**Scribed PU Topcoat Prohesion Duration** (hrs)	**Scribed EL Topcoat Prohesion Duration** (hrs)
Cr Epoxy	> 800	> 800
(**1**)	207	322
(**2**)	248	299
(**3**)	214	505
(**4**)	225	361

PU = Deft Polyurethane Topcoat, EL = Deft "Extended Lifetime" Flourocarbon Topcoat

Adhesion of the ultra-thin PMHS-AGE primer to Al 2024-T3 substrate was measured to be 800 psi. Adhesion of the polyurethane topcoat on bare uncoated Al 2024-T3 was 200 psi. The EIS of Al 2024-T3 sample coated with ultra-thin PMHS-AGE primer and DEFT polyurethane topcoat (Figure 3) shows that a moderate degree of initial corrosion protection (as indicated by the value of the low frequency impedance modulus) is afforded in relation to that imparted by samples coated with commercial chromated epoxy primer and polyurethane topcoat (i.e. note the low frequency values shown in Figure 3).

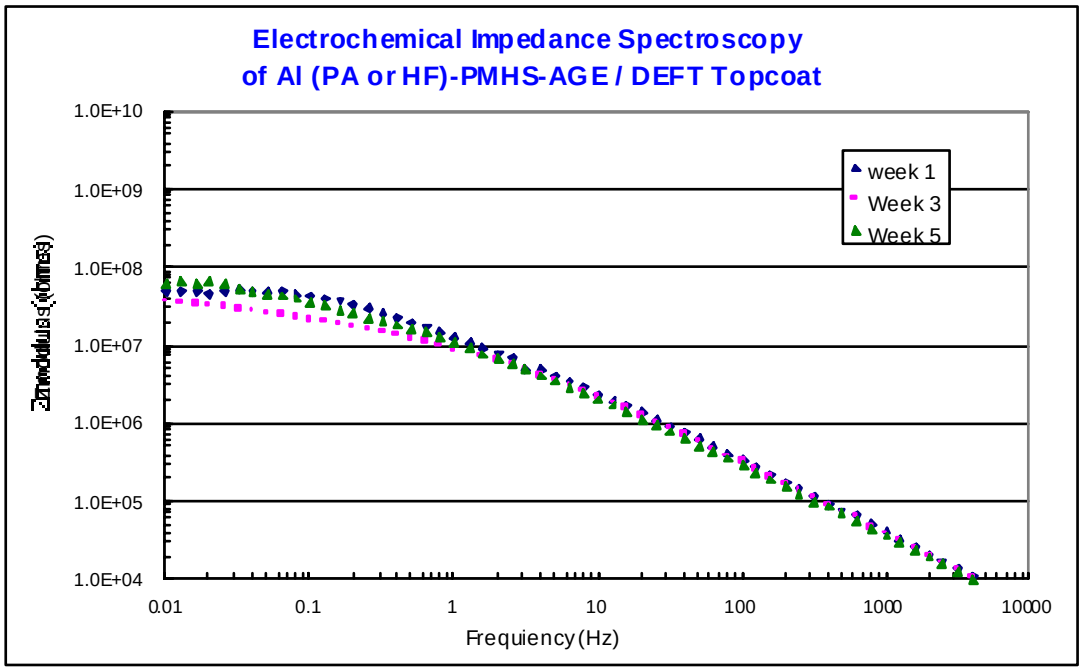

FIGURE 3. EIS for Al 2024-T3 Coated with Ultra-thin PMHS-AGE Primer and Polyurethane Topcoat

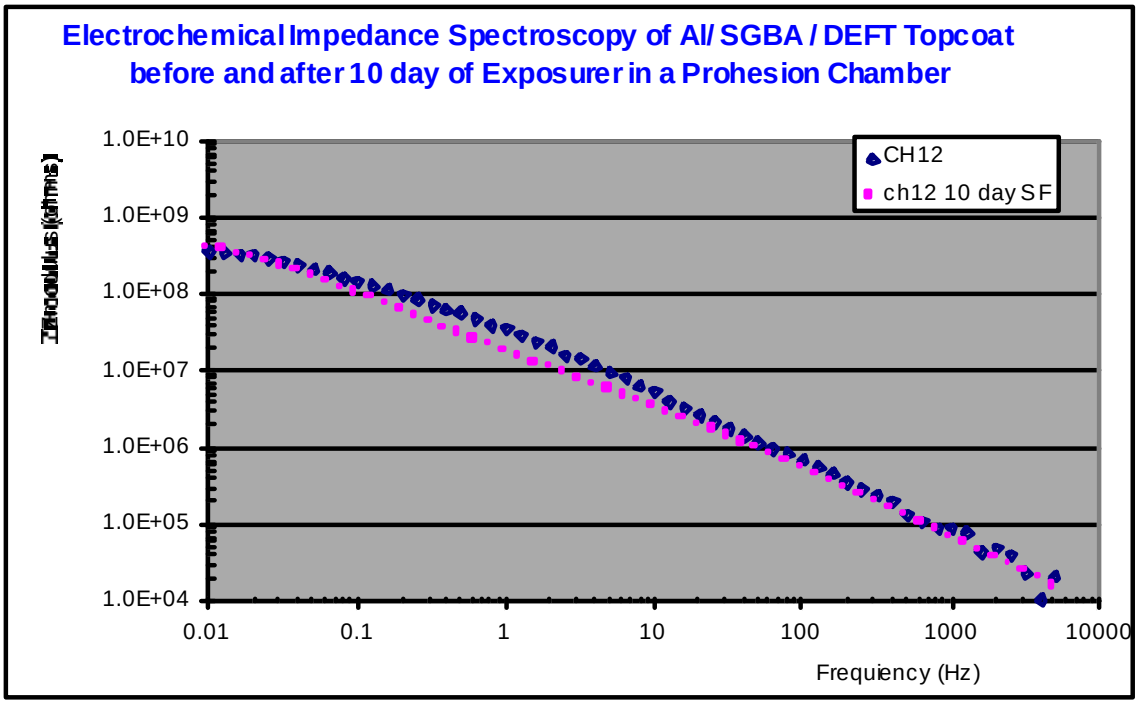

FIGURE 4. EIS for Al 2024-T3 Coated with SGBA Primer and Polyurethane Topcoat

Adhesion of the SGBA primer to Al 2024-T3 substrate and of the polyurethane topcoat to the SGBA primer was measured to be 800 psi. The EIS of Al 2024-T3 sample coated with SGBA primer and DEFT polyurethane topcoat (Figure 4) exhibits a much higher degree of initial corrosion protection is produced in relation to that imparted by samples coated with commercial chromated epoxy primer and polyurethane topcoat (i.e. note the low frequency values shown in Figure 3).

Separate sets of Al 2024-T3 coupons coated with SGBA primer only (no topcoat) or commercial chromated epoxy primer only (no topcoat) were placed in a prohesion testing. Periodically the coupons were removed for EIS measurements (Figures 5 & 6). These results show that the prohesion duration for the commercial chromated epoxy primer was slightly longer (30 days) compared to that for the SGBA primer (20 days).

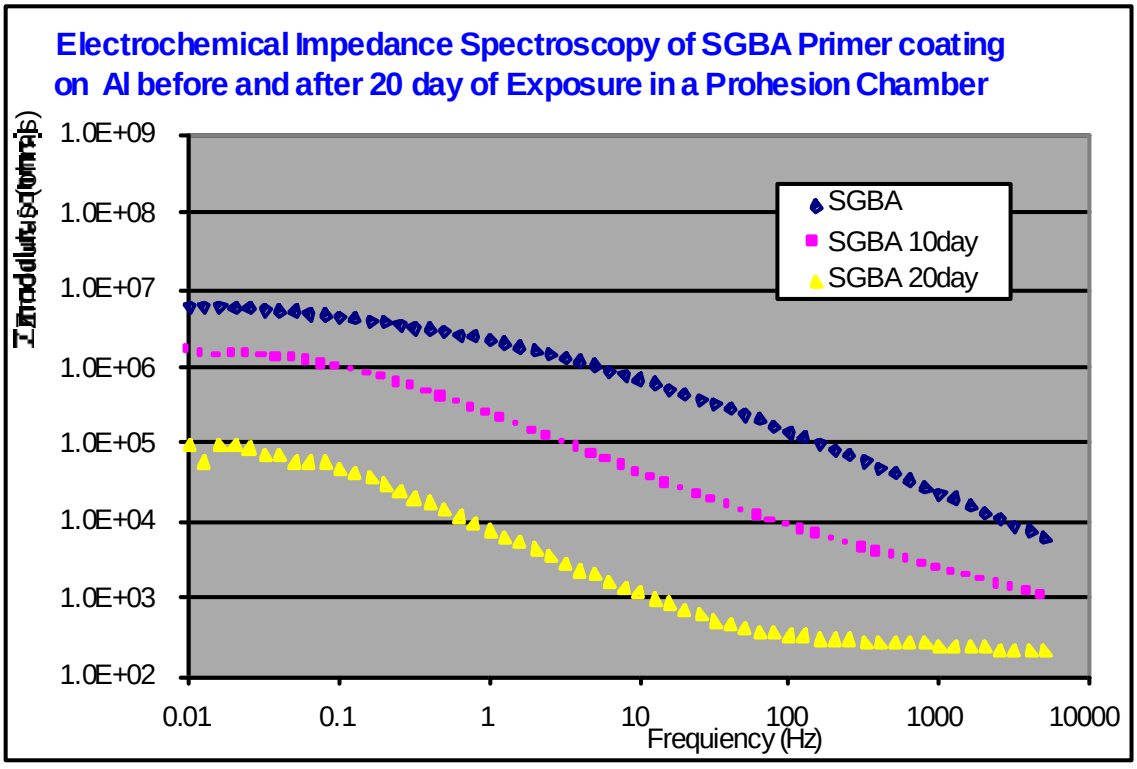

FIGURE 5. Periodic EIS for Al 2024-T3 Coated with SGBA Primer During Prohesion Testing

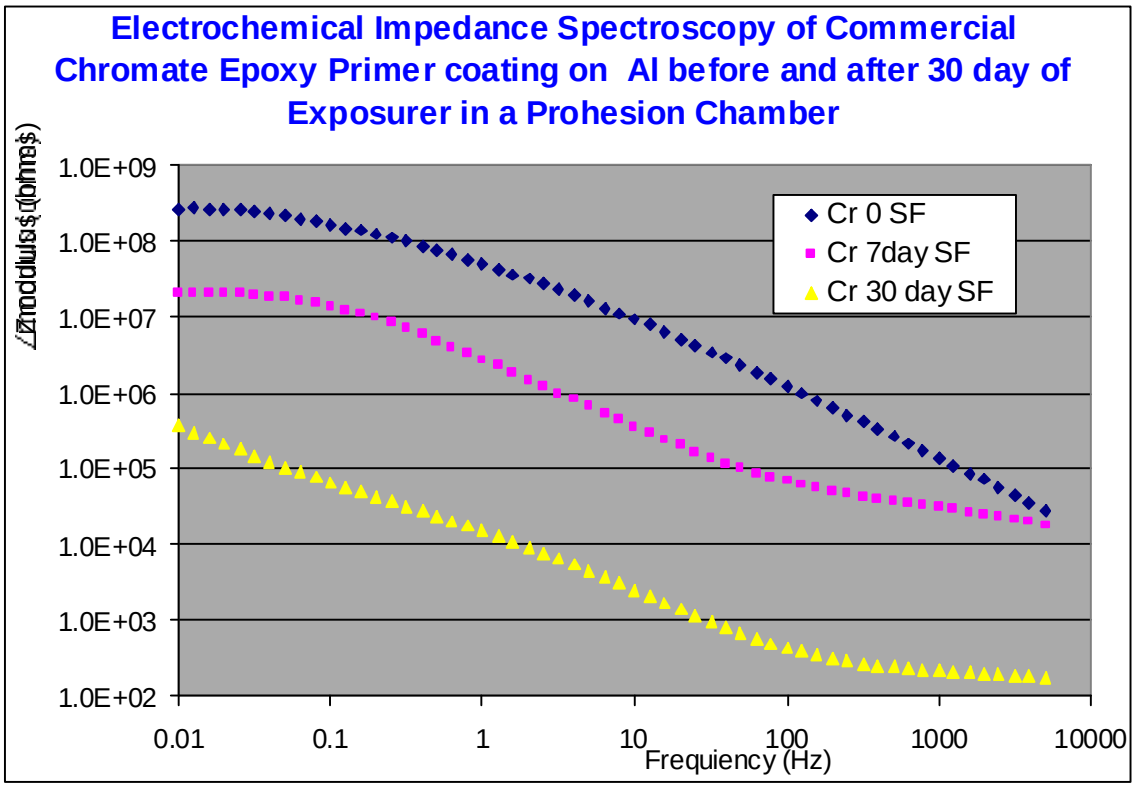

FIGURE 6. Periodic EIS for Al 2024-T3 Coated with Commercial Chromated Epoxy Primer During Prohesion Testing

DISCUSSION

The contact angle data for the alkoxy-substituted primers (Table 1) show that the surface energy of the polysiloxane films are generally high, but can be reduced by the incorporation of the appropriate alkoxy (i.e. glycidoxy) side chain on the silicone backbone. The generally hydrophobic nature of these films, suggest that that they may impart some barrier characteristics with regard to moisture exposure, but also adversely affects the wetability of these films by the polyurethane topcoat used.

Not surprisingly, the pull – off adhesion data (Table 1) for the alkoxy-substituted polysiloxanes vary greatly with type of alkoxy substituent present, with the PMHS primer (**1**) and the glycidoxy primer (**2**) exhibiting adhesion to the Al – 2024 surface comparable to that of

the commercial chromated epoxy primer. In the case of topcoat adhesion to the alkoxy-substituted primer coated Al – 2024, failure was at the primer topcoat interface, with glycidoxy polysiloxane (**2**) exhibiting topcoat adhesion comparable to that of the commercial chromated epoxy primer. In gross terms, the contact angles of the polysiloxane surfaces were inversely proportional to topcoat primer adhesion, but did not correlate to primer adhesion itself.

The prohesion durations for the alkoxy-substituted polysiloxane primer coated panels were greatly limited compared to the commercial chromated epoxy primer coated panels (Table 2). In the case of the alkoxy-substituted polysiloxane coated panels, panels coated with "Extended Life" topcoat showed slightly higher prohesion durations than those coated with the polyurethane topcoat. Interestingly, for the alkoxy-substituted silicone based primers, prohesion duration does not directly correlate to primer or topcoat adhesion.

Ultra-thin coating primers with a modicum of initial corrosion protection were produced. However, scale up for field implementation for existing aircraft is impractical.

CONCLUSIONS

The results concerning alkoxy-substituted polysiloxanes presented here are intended to serve as base-line data on their utility as coating primers. It should be noted that no performance enhancing fillers, extenders, pigments, or corrosion inhibitors were included in the formulations. These materials were used and applied as made.

In the case of the epoxy functionalized polysiloxanes, cohesive aluminum/primer/topcoat systems comparable to that achieved with the commercial chromated epoxy were achieved. Clearly, the unadulterated alkoxy-functionalized polysiloxanes are inferior to the chromated epoxy primer for corrosion protection. On the other hand, the three component primer based on

oligomeric poly(methyl, allylglycidoxysiloxane) exhibited performance levels close to that of the commercial chromated epoxy primer.

The SGBA primer results show that by using organic additives in conjunction with siloxane based compounds that unpigmented, non-inhibitor containing primers can be produced whose corrosion protection approaches that of commercial chromated epoxy primers.

REFERENCES

1. R. L. Twite, G. P. Bierwagen, *Prog. Org. Coatings*, **33**, (1998), 91.

2. a) M. Chauhan, B. P. S. Chauhan and P. Boudjouk, *Org. Lett.*, **2**, (2000), 1027-1029. b) B. P. S. Chauhan, P. Boudjouk, *Tetrahedron Lett.*, **41**, (2000), 1127-1130. c) T. E. Ready, B. P. S. Chauhan, and P. Boudjouk, *Macromolecular Rapid Commun.*, **22**, (2001), 654-657. d) B. P. S. Chauhan, T. E. Ready, Z. Al-Badri and P. Boudjouk, *Organometallics* **20**, (2001), 2725-2729.

3. a) Caser and Hirayama, *Appl. Surf. Sci.*, **143**, (1999), 256. b) Hirayama and Caseri, *J. Addhesion*, **72**, (2000), 51.

PHENOMENOLOGY OF LOCALIZED COATING FAILURE ON AA1100-H14

J. M. Williams*, O.M. Schneider[#], R.G. Kelly [#]

*Luna Innovations, Inc.
701 Charlton Ave
Charlottesville, VA 22903

[#]Department of Materials Science and Engineering
University of Virginia
116 Engineer's Way
Charlottesville, VA 22904

ABSTRACT

The global potential and the local potential associated with the intermetallic particles (IMCs) of the alloy combined to control blister initiation. Upon immersion in NaCl solutions, epoxy-coated panels experienced an increase in the OCP to near or above the mean pitting potential (due to solution uptake and oxygen transport through the coating) followed by a subsequent decrease in OCP (due to local passive layer breakdown by Cl^- at the bare metal surface), which coincided with observations of active blisters. Galvanic effects between the Al matrix and IMCs, known to contribute to the localized corrosion of bare Al alloys, were found to contribute to underfilm corrosion of AA1100-H14. The effect of varying chloride concentrations revealed a process that competed with potential control for blister initiation: water uptake by the coating. At low Cl^- concentrations, the degree of open circuit pitting was the controlling parameter for blister initiation whereas at high Cl^- concentrations water uptake dominated. Blister growth occurs on AA1100-H14 by way of anodic undermining, where a thin layer of Al matrix is dissolved underneath the organic coating causing detachment of the coating from the substrate. All blisters behaved as net anodes in the early stages of life. A fast shift to dominant cathodic activity occurred on AA1100-H14 if iron oxide deposited inside the blister.

INTRODUCTION

Blistering is usually one of the first signs of insufficient protection of organic coatings against corrosion. Blisters are local regions where adherence between the coating and the substrate has been lost, so that solution may accumulate and corrosion may begin. The

mechanism of blister growth depends on the type of electrochemical activity occurring inside the blister, *i.e.*, whether the blister shows anodic or cathodic activity. The modes of blister growth corresponding to cathodic or anodic activity are very different and operate under specific conditions.

Cathodic blistering occurs as a result of the production of an alkaline environment underneath the coating due to the cathodic reaction. The prerequisite for the development of cathodic blisters is that the substrate is capable of supporting a cathodic reaction, which in the case of neutral or alkaline environments is oxygen reduction. The loss of adhesion associated with corroding coated steel under cathodic conditions is known as cathodic delamination. It can occur either in the presence or in the absence of an applied potential. The major driving force for cathodic delamination in air is the reduction of oxygen, which produces hydroxyl ions and reaction intermediates[1-3]. The products of oxygen reduction are believed to be a destructive agent to the coating/substrate bond as the pH is high in the regions where the cathodic reaction is taking place. The value of the pH at the delamination front depends on the rate of reaction, shape of the delamination front, and the rate of hydroxyl ion diffusion away from the delamination front[4].

Growth occurs by a progression of delamination from the central anodic site; the detached regions of coating eventually swell with occluded blister solution as the blister takes shape. Separation of anodes and cathodes occurs because of differences in oxygen permeability at these sites so that a potential gradient exists between them, acting as a driving force for cathodic delamination. Therefore, the delamination front (cathode) is usually represented by positive potentials while the delaminated region (anode) is represented by negative potentials. pH values between 10 and 12 have been reported at the delamination front[4]. Koehler concluded

that delamination was due to saponification of the coating in his studies on polybutadiene-coated steel[5]. Saponification is the hydrolysis of esters in the presence of strong soluble bases. Anodic undermining represents a class of corrosion underneath an organic coating where the major separation process is anodic dissolution of the substrate under the coating. A thin layer of the substrate is selectively dissolved so that the organic coating becomes detached from the surface[6].

Aluminum is particularly susceptible to anodic undermining; it can also occur on coated steel under applied anodic potentials[4,7]. Anodic undermining bears a close relationship to pitting, although it tends to occur preferentially to pitting. The mechanism is activated by the presence of chloride, and it tends to prevent pit development in areas where pitting would normally be expected (*i.e.*, where the cathode is located). For this reason, significant corrosion damage is usually not observed at the cathodes in anodic undermining experiments[7]. The corrosion associated with anodic undermining occurs at a low rate initially. Growth occurs by way of a progressively advancing mode of crevice corrosion where the crevice, or anode, exists at the bare metal interface underneath freshly detached coating.

Anodic undermining is not as widely addressed in the literature as cathodic delamination. Galvanic effects and principles of crevice corrosion have been accepted as providing a suitable explanation for the undermining mechanism.

EXPERIMENTAL PROCEDURES

A five-step cleaning protocol was used to degrease alloy samples cut into 7.6 cm by 7.6 cm panels prior to the coating procedure. Panel thickness was approximately 1.13 mm (44.5 mils). Panel surfaces and edges were scrubbed with a sponge soaked in Alconox® and deionized water. A rinse with 18 MΩ-cm Milli-Q water (from a Millipore Milli-Q™ system) followed, and each panel was dried with forced air. Panels were then cleaned with sequentially

in isopropanol and hexane. The clear epoxy coating mixture used for all experiments was a 1:1:0.1 ratio of three components: resin, curing agent, and solvent. The resin was a bisphenol A-epichlorohydrin based epoxy solution manufactured by Shell with product name "Epon(R) Resin 1001-CX-75." The resin contained 16.3% methyl isobutyl ketone and 8.7% xylene with a remaining balance of the Epon resin. The second component of the coating mixture was 70% (by weight) fatty acid-polyethylene polyamine based polyamide curing agent with both high molecular weight and high viscosity and 30% xylene (by weight). The curing agent was also manufactured by Shell with product name "Epi-cure(R) 3115." In addition, the coating formulation contained butylcellosolve (ethylene glycol + monobutyl ether) acting as a solvent for increased viscosity.

Coating application consisted of a 25 second spin-coating procedure conducted at two different speeds. Each panel was centered on the spinning chuck of the KW4a spincoater (manufactured by Chemat Technology) and held in place by vacuum. Using the 10 mL syringe, approximately 1 mL of coating was released onto the center of the panel while sitting on the chuck. The spincoater spun at 8,000 rpm for 10 seconds followed by a 15 second spin at maximum speed of 10,000 rpm. In some cases, the vacuum was unable to hold panels to the chuck; such panels were damaged and immediately discarded. One spincoating sequence was usually enough to uniformly coat each panel. If necessary, the same spincoating sequence was run a second time to ensure uniform application. Following coating application, panels were allowed to cure inside a drying chamber containing Drierite® for a period of at least one week before immersion. Dry coating thickness averaged 10 μm over five readings with values ranging from 2 μm to 22 μm. The data were obtained with a PosiTector® Series 6000-NOS2 coating thickness gauge.

Water uptake of the epoxy coating was studied using freestanding thin films of the same coating formulation described above. Glass substrates were spincoated with the coating. After a two-week curing period inside a dessicator, the films were wetted with 18 MΩ-cm Milli-Q and cut along the edges with a scalpel blade. Using the blade, the intact coating was carefully detached from the glass substrate and allowed to dry in an evacuated dessicator. The freestanding film experiments used a three-electrode setup to run alternating OCP and EIS measurements in NaCl solutions of the following concentrations: 0.02M, 0.2M, 0.5M, and 2M.

RESULTS

BLISTER INITIATION

Blisters were grown on epoxy-coated substrates immersed in varying Cl^- concentrations under ambient conditions. Blister initiation times varied from five days to 2-3 months after initial exposure. Figure 1 shows AA1100-H14 blister initiation times versus immersion solution chloride concentration.

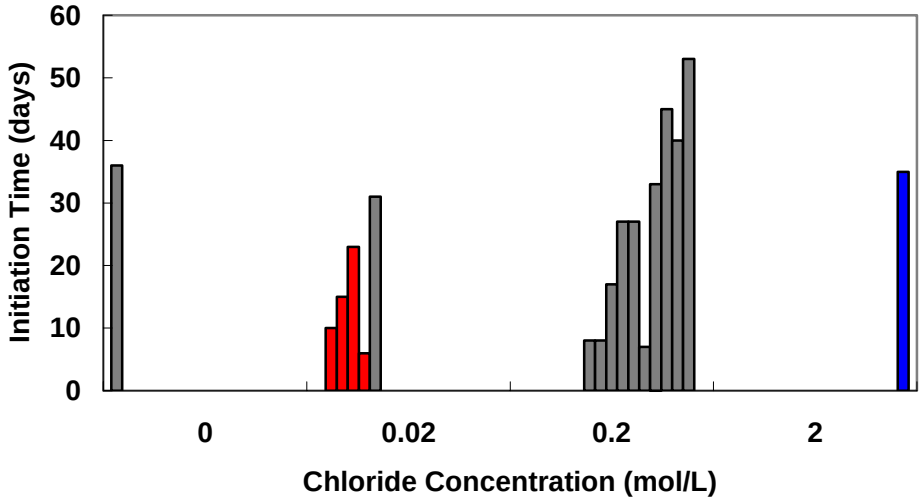

FIGURE 1. Blister initiation time vs. Cl^- concentration. The gray bars corresponding to 0M and 0.02M Cl^- represent blister initiation in 0.2M NaCl after an initial exposure to more dilute NaCl solutions.

More blisters formed in 0.2M NaCl than in any other immersion solution for coated AA1100-H14. As observed with the initiation time, the percentage of AA1100-H14 panels immersed in each NaCl solution that formed blisters showed a maximum at 0.2M.

Of the twelve-coated AA1100-H14 samples seeded with 1M NaCl salt islands, only two blisters initiated at a salt island site. The initiation time of these particular blisters did not differ significantly from the initiation times of non-island blisters.

BLISTER GROWTH RATES

Blister diameters were measured with the aid of a digital microscope camera at different points during blister life. Similar growth rates occurred for blisters grown in 0.02M and 0.2M NaCl immersion solutions. The AA1100-H14 blisters grown in 2M grew laterally very slowly, if at all. Figure 2 shows lateral growth rates for blisters in mm/day for times after which blisters were visually detected.

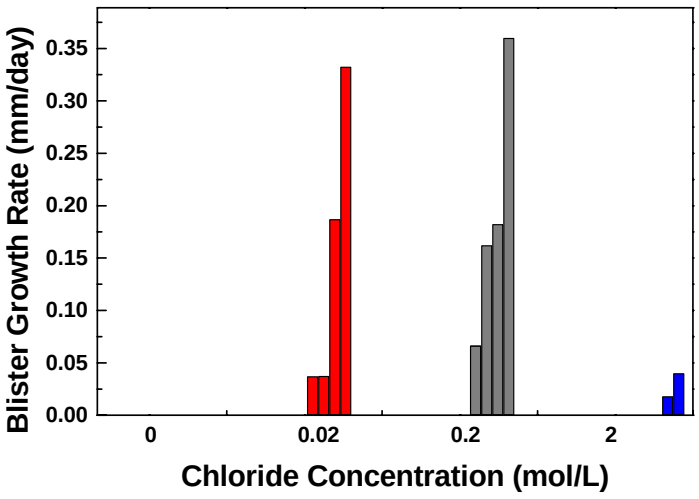

FIGURE 2. Lateral growth rates for different AA1100-H14 blisters in each immersion solution.

PHYSICAL OBSERVATIONS

AA1100-H14 blisters tended to be hemispherical in shape with circular growth. Blister formation was limited to one or two on each panel. The internal blister color ranged from milky white to no color. Gas bubbles were readily seen through the coating, as was corrosion product accumulation. Some blisters showed a defined circle of corrosion product at the center surrounded by concentric rings of more product. Infrequently, a dark reddish-brown center, later determined to contain Fe, appeared inside blisters, surrounded by corrosion product accumulation. Figure 3 shows photos of characteristic AA1100-H14 blister features.

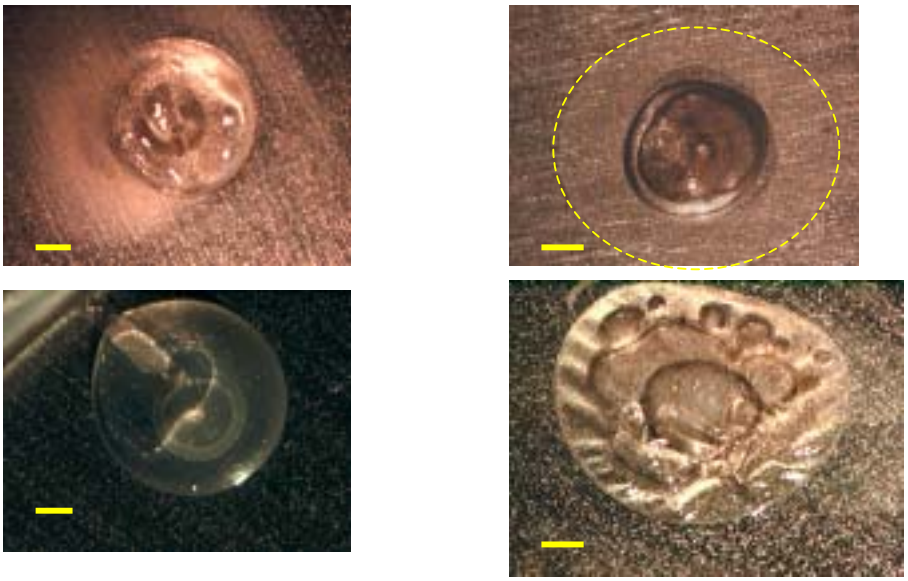

FIGURE 3. Digital photographs of characteristic AA1100-H14 blister features (neutral pH). (a) Colorless, hemispherical blister grown in 0.2M NaCl. (b) Active blister with delamination front highlighted by dashed line (0.2M NaCl). (c) 0.02M NaCl blister showing corrosion product rings near the center. (d) Large gas bubbles are easily seen through the coating of a blister grown in 0.2M NaCl.

OPEN CIRCUIT POTENTIAL BEHAVIOR

Daily OCP measurements show some variation during the course of blister life. In some cases, a sharp decrease in OCP on the order of 150–200 mV accompanied blister formation.

This distinct OCP decrease was not always seen, for instance, in the case of Cell 4 and Cell 6 blisters (see Figure 4 below) grown in 0.2M NaCl. However, OCP data for other 0.2M NaCl (and other Cl^- concentrations) blisters do show the distinct decrease. Metastable events were often seen during daily OCP measurements both before and after the appearance of a blister. Figure 4 shows daily global OCP fluctuations as active blisters initiate and grow.

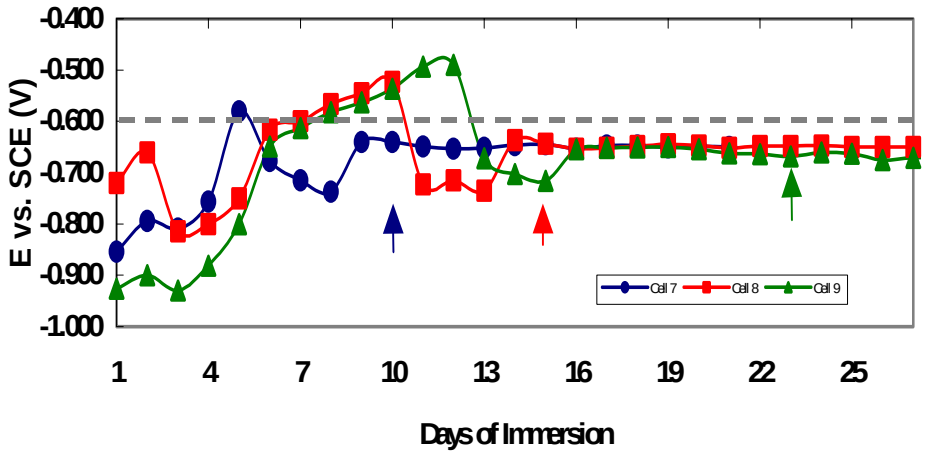

FIGURE 4. Daily open circuit potentials for 0.02M NaCl blisters showing distinct OCP decrease upon blister formation. Arrows indicate the day a blister was visible, and the dashed line indicates the pitting potential for AA1100-H14 in 0.02M NaCl.

ANODIC ACTIVITY INSIDE AA1100-H14 BLISTERS

AA1100-H14 blisters showed dominant anodic activity inside blister areas (represented by a blue color). AA1100-H14 blisters tended to show anodic activity. The area surrounding these blisters underneath the organic coating showed anodic activity, cathodic activity, or a combination of both.

CATHODIC ACTIVITY INSIDE AA1100-H14 BLISTERS

Cathodic activity was detected inside AA1100-H14 blisters that had a reddish-brown color located at their centers. Such blisters would show dominating cathodic activity with the surrounding areas outside of the blister containing some anodic activity underneath the epoxy coating. Figure 5 shows example photographs and SRET scans. Note that the surrounding area of the blister in Figure 5(b) denoted by anodic activity may be an exaggerated representation of the potential differences between the substrate and probe due to the height of the blister during signal conditioning.

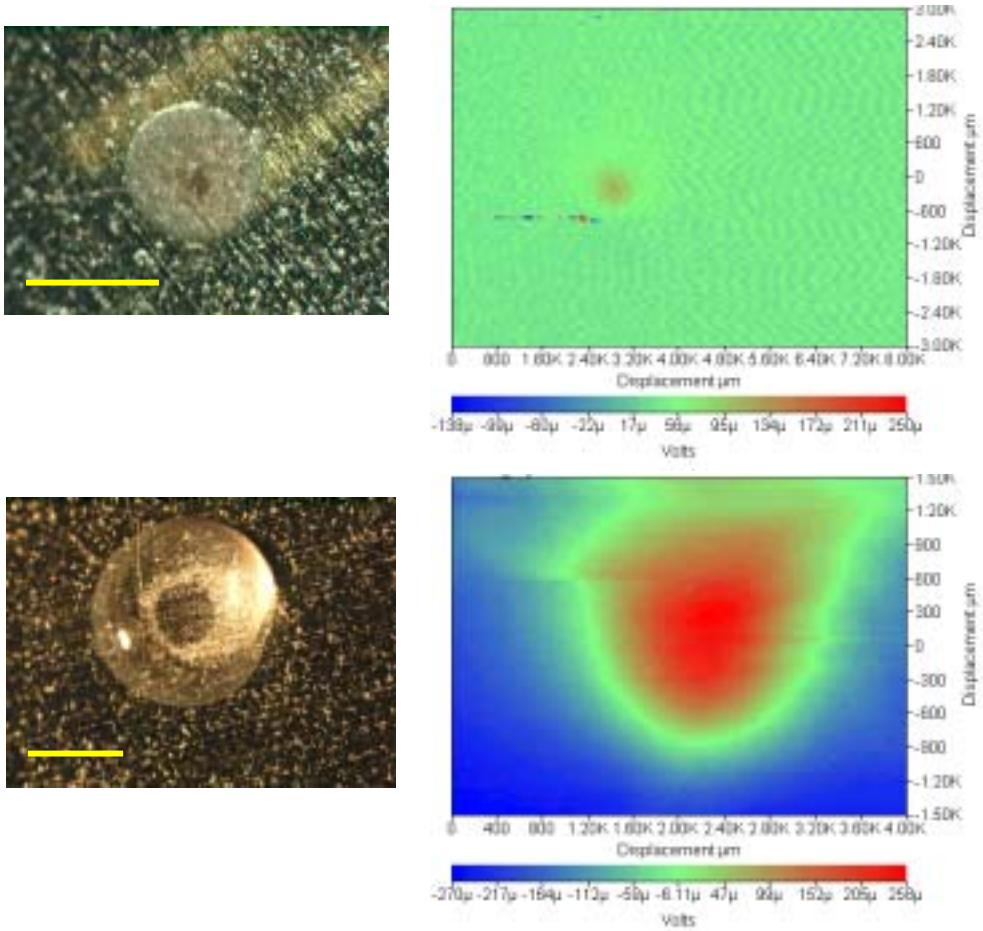

FIGURE 5. SRET scans and corresponding photographs of active AA1100-H14 blisters showing cathodic activity; photos taken same day as the scans (0.2M NaCl). (a) A dark brown deposit at the blister center causes the blister to exhibit positive electrochemical activity. (b) Scan showing a cathodic AA1100-H14 blister containing a dark center. The sharp line in scans (a) and (b) occurring at 600 µm (x-direction) is an artifact of the software.

BLISTER CORROSION MORPHOLOGY

Large salt deposits were found inside AA1100-H14 blisters in all NaCl concentrations. The most common form of corrosion attack found inside AA1100-H14 blisters grown in 0.02M and 0.2M NaCl was shallow pitting. The average pit depth was 10 μm while average pit width was 20 μm. These shallow pits were highly hemispherical in nature and often littered with constituent particles. EDX indicated that AA1100-H14 constituent particles mainly consisted of elemental Al (75+ wt.%), Si (5+ wt%), and Fe (less than 10 wt.%) in varying concentrations. Other elements included Cu (less than 5 wt.%), Zn (less than 2 wt.%), Na, and Cl. Shallow pitting was also found in 2M NaCl blisters.

A large density of shallow pitting was usually found at the blister center; however, pitting was found throughout the expanse of the blister area reaching all the way to blister edges. The symmetrical nature of the pitting found in AA1100-H14 blisters suggested a possible correlation to metallurgical features of the alloy, i.e., subgrain structure. Average feature sizes between an expanse of shallow pitting and the subgrain structure of polished AA1100-H14 are not related. The subgrain structure of AA1100-H14 is approximately three times the size of shallow pitting inside blisters.

For AA1100-H14 blisters containing corrosion product rings, the largest density of shallow pitting was again found at the blister center. Lower densities of pits were located in each section of the product rings. Figure 6 shows a series of CLSM images of a blister grown in 0.02M NaCl containing corrosion product rings near its center. Average pit depths are approximately 10 μm or less.

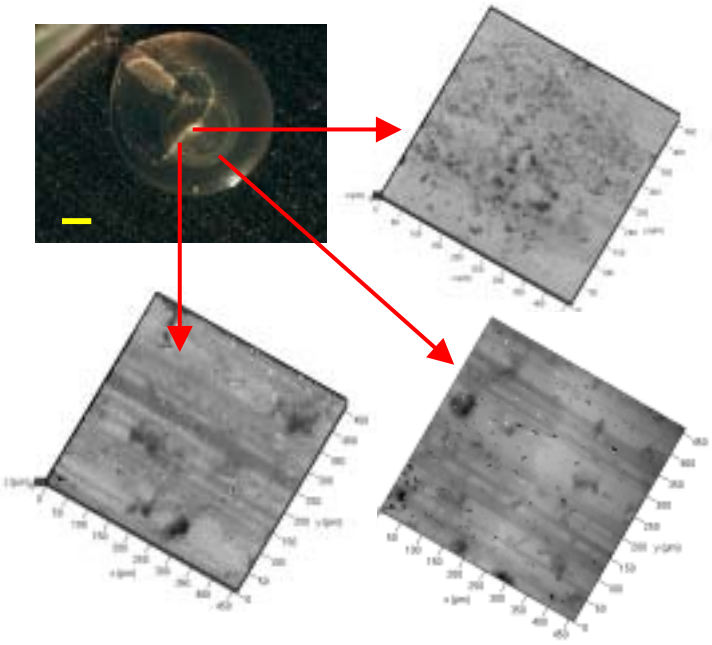

FIGURE 6. Digital photograph (a) and CLSM images (200x) of a three-week-old blister grown in 0.02M NaCl with corrosion product rings. (b) CLSM image of blister center showing the highest density of shallow pitting. (c) CLSM image of area between outer ring and center and (d) CLSM image of pitting at the corrosion product outer ring. The lesser density of pitting beyond the blister center is evident. Average pit depth is less than 10 μm.

FREESTANDING THIN FILMS AND COATING CAPACITANCE BEHAVIOR

Coating capacitance values, C_{coat}, were obtained through equivalent circuit model fits of impedance spectra of freestanding thin epoxy films. Assuming that capacitance changes are proportional to permittivity changes, the percentage of water uptake by the epoxy coating can be calculated directly from coating capacitance changes using the following equation[8]:

$$\Phi = (\mathrm{Log}C_t/C_0)/\log\varepsilon_{water}$$

where C_t is the coating capacitance at time t, C_0 is the capacitance at the start of the experiment (linearly extrapolated from $C_t(t)$ for $t \rightarrow 0$) and ε_{water} is the dielectric constant of pure water (~ 80

at 25°C). The distribution of water is assumed to be random and uniform throughout the coating. From the coating capacitance data, diffusion coefficients at each Cl^- concentration were calculated assuming a continuous model where each layer of thickness of the coating contributes to the overall film capacitance[9]. The calculated diffusion coefficients for water through freestanding epoxy coatings decreased from 6.43 x 10^{-11} cm^2/s to 3.92 x 10^{-12} cm^2/s for concentrations from 0.02 M to 2 M for an assumed coating thickness of 10 μm ± 3 μm error. The percentage of water uptake by the epoxy coating is shown in Figure 7. Note the highest percentage of water uptake occurred in films exposed to the more dilute 0.02M NaCl immersion solution.

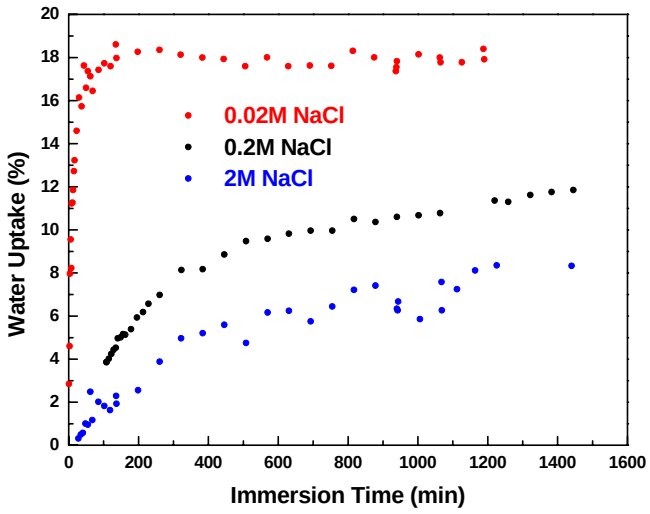

FIGURE 7. Percentage of water uptake by freestanding epoxy films determined using C_{coat} values. Films exposed to the lowest Cl^- concentrations exhibited the highest percentage of water uptake.

DISCUSSION

The blister framework presented here considers substrate heterogeneities and their contribution to the initiation and development of blisters. Constituent particles and intermetallic

compounds are known to produce widespread micro-galvanic activity in uncoated Al-Cu alloys. The critical role of copper, known to largely influence the corrosion properties of Al-Cu alloys in general, is likely to control and manipulate underfilm corrosion as well. It is suspected that the micro-galvanic activity at and below the substrate surface affects how the coating degrades and the resulting corrosion morphology associated with this degradation. This framework attempts to relate blister formation and growth to the microscopic electrochemical environment resulting from substrate heterogeneities. From there, the framework expands to show the relationship between the substrate and the macroscopic environment that develops as a consequence of microscopic galvanic activity.

BLISTER INITIATION

Blister initiation cannot occur without the formation of pathways through the coating that allow ion transport from the solution environment to the bare metal surface, whether through inherent pores within the coatings and/or other defects. The sources of these pathways or their formation as a result of water uptake, for example, are not addressed in this work. The assumption has been made, relative to this framework, that corrosion precludes blister formation so that the swelling of the coating due to osmotic pressure is a consequence of pitting phenomena underneath the coating.

Blister initiation on Al-Cu alloys appears to be potential-controlled. Blister initiation times decreased to only one or two days on AA1100-H14 as a result of potentiostatic holds at more noble potentials (higher than E_{pit}), like those of the approximate open circuit potential of AA2024-T3. These reduced initiation times compared to those seen on AA2024-T3 under OCP conditions. Most of the AA1100-H14 coated samples that initiated blisters under OCP conditions did so with a simultaneous decrease in the open circuit potential. An initial increase

in the global open circuit potential is mainly due to the uptake of water by the epoxy film and an increased cathodic reaction rate (ORR requires water as a reactant). The coated panel surrounding the tiny corrosion anode at the bottom of a pore or defect acts as a large cathode due to the ability of oxygen to permeate the film; as a consequence, the cathode-to-anode area increases. An increased cathodic reaction rate also causes an increase in the passive dissolution rate so that the potential has to increase to support the reaction, per mixed potential theory. In some cases, the global OCP measured for the first several days on coated AA1100-H14 rose above the measured pitting potential, as in Figure 4, so that stable pits were initiated prior to the appearance of a blister; however, blisters also initiated without the global OCP necessarily ever rising above E_{pit}. Metastable transients were observed in the measured global OCP frequently, both before and after the appearance of an active blister. These observations suggest that metastable pits may have been capable of causing blister formation below E_{pit}.

Another consideration is the alloy's tendency to pit at or near open circuit, most likely due to local clusters of Cu and Fe impurities. Any local increase in the potential of the Al matrix above E_{pit} (for the appropriate Cl^- concentration) near a Cu or Fe-containing particle can cause stable pitting due to the Cu and Fe-rich particles' tendency to enhance cathodic kinetics[10]. Therefore, local matrix potential increases in AA1100-H14 could be enough to induce pitting without a global OCP increase above E_{pit}.

The issue of whether the subsequent potential decrease is a consequence of blister formation or vice versa is entangled in the pitting kinetics on the alloy. Destabilization of the passive film occurs at local sites on the Al matrix upon chloride migration to the bare metal-solution interface. Following mixed potential theory, locally higher current densities at the bare metal sites where the passive layer has broken down cause a subsequent potential decrease,

reducing the rate of anodic dissolution and accelerating the ORR. The new dissolution rate is still higher than the passive dissolution rate of the alloy, so that pitting damage is more severe than it was before the passive layer was destroyed. An accelerated ORR can lead to enhanced delamination at cathodic sites and promote blister formation.

Pit stability on Al is dependent on changes in the local pit environment, mainly local pH and Cl^- concentration[11]. Occluded chemistries developed inside initiating blisters may be the key to continued pit stability on AA1100-H14 so that localized passive layer breakdown and the subsequent potential decrease depend solely on the support of the local blister environment. This explanation is not likely due to the induction time needed to develop an appropriate occluded solution to support stable pitting.

It is likely that blister formation is a consequence of the potential decrease occurring as a result of pitting; this is evidenced by the first observation of blisters at the "bottom" of a global OCP decrease, as seen in Figure 4. Blister initiation on AA1100-H14 is controlled by potential with the assistance of water uptake and oxygen transport through the coating, both of which are discussed in the next section.

Results of the freestanding thin film experiments were in agreement with results obtained in the literature[12-14]. The main finding was that water uptake decreased with increasing chloride concentration. With this result, it was expected that the most dilute of the tested immersion solutions, 0.02M NaCl, would show the greatest degree of blistering, and the most concentrated solution, 2M NaCl would show the least amount; however, the intermediate concentration of 0.2M NaCl was found to be the most aggressive chloride concentration by far for coated AA1100-H14. More blisters initiated at this Cl^- concentration than in any of the other tested immersion solutions. Coated AA1100-H14 panels immersed in high purity Milli-Q water did not

initiate blisters, likely due to the lack of chloride ions available to instigate pitting. The fact that the mid-range chloride concentration immersion solution displayed the highest degrees of blistering implies that there are two competing processes in blister initiation.

Just as the results presented in this work suggest that blister initiation is controlled by potential, solution environment factors such as water uptake and oxygen availability become competing factors for blister formation at specific ranges of Cl^- concentration. Potential differences, namely between the OCP and E_{pit}, control blister initiation at lower Cl^- concentrations while water uptake and oxygen transport direct blister formation at the higher chloride concentrations.

RESULTING SURFACE ANODE/CATHODE DEVELOPMENT

As mentioned previously, blister formation probably originates at a corroding IMC, which has been suggested to later become the center of the blister. Common phases found in AA1100-H14 include $FeAl_3$ and Fe_3SiAl_{12}. Fe, presumably in the form of iron oxides, was found to deposit at the center of some AA1100-H14 blisters. Blisters with Fe deposits exhibited cathodic activity as determined through SRET experiments. When describing blistering on steel due to paint defects, Funke reported observations of a brown spot located at the center of the blister, later determined to be simple rust by chemical analysis[15]. These blisters tended to be cathodic in nature, and Funke attributed a membrane of hydrated iron oxides covering the defect whose metallic base was corroding to furthering blister growth due to osmotic pressure effects. Anodic polarization at the bottom of the pore occurs once the area is depleted in oxygen due to blockage by semipermeable corrosion products. Circular cathodic regions develop around the anodic pore, setting up conditions for cathodic delamination discussed earlier for coated steel.

IMC corrosion of Fe-containing particles in AA1100-H14 and the formation of iron oxide precipitates on the substrate at the center of the blister alter the electrochemical activity inside AA1100-H14 blisters. The entire blister area becomes cathodic, and the development of the cathodic region throughout the blister occurs according to the cathodic delamination scenario posed for coated steel. Note that anodic activity that might be occurring underneath the iron oxide precipitate would not be detected during the SRET scan.

BLISTER GROWTH MECHANISM – ANODIC UNDERMINING VS. CATHODIC DELAMINATION

There are three possible mechanisms that can support blister growth on epoxy-coated AA1100-H14: (1) cathodic delamination, (2) anodic undermining, and (3) corrosion product wedging. Corrosion product wedging, which is heavy accumulation of product at the substrate/coating interface that forces coating detachment by mechanical force, has not been mentioned in this work previously. Evidence exists for and against both cathodic delamination and anodic undermining and will be discussed below.

Corrosion product wedging has been eliminated from consideration for three reasons. First, corrosion product accumulation usually occurred homogeneously throughout the blister area and tended to be of uniform thickness. Blisters that contained concentric rings and circles of product only at blister centers without heavy accumulation elsewhere continued to grow without product buildup near blister edges. Second, deeper pitting would be expected underneath corrosion product near blister edges due to crevice effects. SEM and CLSM examination did not reveal increased pit depth near blister edges. Evidence of episodic growth would be characterized by deep pitting patterns at the edges of each product ring; however, CLSM studies indicated reduced pitting within the ring areas compared to the blister center.

Third, a time factor would be required between growth spurts for adequate buildup of corrosion product to promote the wedge effect. Lateral blister growth rates tended to be linear for AA1100-H14 with no evidence of an incubation period prior to growth for corrosion product accumulation.

ANODE/CATHODE DEVELOPMENT

SRET data indicated that the majority of blisters grown on epoxy-coated AA1100-H14 showed purely anodic behavior with cathodic activity distributed outside of the blister underneath the coating. Only the few AA1100-H14 blisters with iron oxide deposits at their centers exhibited cathodic activity.

Potentials representing anodic activity were spread out through the entire expanse of the blister, all the way out to blister edges. Corrosion damage also extended to the edges of blisters. This implies that anodic undermining is the main mechanism of blister growth for AA1100-H14. AA1100-H14 susceptibility to anodic undermining was indicated by the potentiostatic hold experiments at the approximate open circuit potential of AA2024-T3 where blister growth was promoted by anodic polarization. The poor dry adhesion exhibited by AA1100-H14 eases anodic undermining by facilitating the progression of coating detachment from the substrate upon metal dissolution. A random distribution of adhesion throughout a coated substrate rationalizes random blister locations, in the absence of substrate heterogeneities.

Locally delaminated sites may act as local cathodes outside of the blister that support anodic undermining inside the blister. Recall that the locally delaminated sites were areas of small delamination where corrosion products collected, and no corrosion damage was detected inside these features; however, local delamination was only observed at chloride concentrations of 0.2M and above. For the 0.02M NaCl case, the cathodic reaction may be distributed over the

unblistered substrate immediately adjacent to the active blister without discrete local cathodes developing due to the decreased concentration of aggressive anion. SRET experiments over areas of local delamination were unable to detect any significant cathodic activity at these sites. It is assumed that these sites acted as cathodes due to the heavy accumulation of corrosion product with no appreciable corrosion damage (with the exception of crevice corrosion along the edges). The mechanism of delamination at these particular sites is unclear at this time. The effect of IR drop has also not been clarified with respect to the distance between potentially cathodic delaminated sites and the anodic blister. Locally delaminated sites were located across the expanse of each coated panel, and IR drop would become a problem the farther away these cathodic sites were from the anodic blister.

The possibility of cathodic delamination on AA1100-H14 may exist for cathodic AA1100-H14 blisters containing iron oxide deposits. As described above, the development of the cathodic region throughout the Fe-containing blister appears to occur according to the cathodic delamination scenario posed for coated steel. Deep pits greater than the typical shallow 10 μm depth for AA1100-H14 were observed underneath the iron deposits, providing the anodic center to support surrounding cathodic activity. Decreased pitting was detected radiating out from the central Fe deposit, supporting a central anode inside cathodic blisters.

LOCAL ELECTROCHEMICAL AND CHEMICAL BLISTER DEVELOPMENT

AA1100-H14 blisters tend to show either complete anodic or complete cathodic activity; SRET data did not indicate anode/cathode separation within each blister. Local OCP measurements taken with microelectrodes inside individual blisters, although weak in volume, provide some information regarding the galvanic nature of active blisters with the unblistered substrate and suggest whether a blister would be expected show either anodic or cathodic

activity. Table 16 compares global OCP values at the time of blister initiation with the local internal blister OCP and pH obtained prior to sampling. The 0.2M NaCl measurements reflect blisters with Fe-containing deposits at their centers.

Galvanic coupling between the blisters initiated in 0.02M NaCl and their respective substrates outside of the blister indicate that the unblistered substrate would be more active than the blister, with the blister serving as a net cathode. CE data reveals a few interesting points. Chloride was detected in concentrations greater than the bulk for both blisters, suggesting increased anion migration into the blister to compensate for amplified corrosion activity; detected Al^{3+} concentrations were 0.03M ($-0.510V_{SCE}$) and $8x10^{-4}$M ($-0.560V_{SCE}$). The latter aluminum cation concentration was the lowest Al^{3+} concentration detected and indicates little corrosion activity inside the blister. Reduced metal dissolution inside a growing blister suggests cathodic activity and would rationalize the high measured local OCP for the $-0.560V_{SCE}$ blister. The 0.02M NaCl local OCP measurements reflect early attempts at microelectrodes and blister sampling, and caution should be used when making conclusions about the local electrochemistry and chemistry of these blisters based on potentially large errors.

All of the 0.2M NaCl local OCP data reflects blisters containing iron (oxide) deposits and would be expected to behave as cathodes. pH values obtained for the blisters denoted by * support the local OCP measurements and the concept of cathodic blisters. Local OCP values were nobler than the potential of the unblistered substrate, and the high pH values (especially a value of 10) are consistent with cathodic activity. Low pH values inside blisters reflect high anodic dissolution rates. The differences in pH values may be reflective of the driving force for galvanic activity indicated by the potential differences between the blisters and the unblistered

substrates. For example, a larger driving force for coupling exists (~ 44 mV) for the high pH blister. The local OCP of $-0.807V_{SCE}$ is also consistent with cathodic activity.

The last value corresponding to 0.2M NaCl, $-0.963V_{SCE}$ indicates that the outside of the blister is nobler than the blister area, despite the tendency for Fe-containing blisters to exhibit cathodic activity; however, the unblistered substrate and blister OCPs are separated by only 5 mV. A slightly higher chloride and aluminum concentration detected in the 0.2M NaCl blister with a local OCP of $-0.963V_{SCE}$ provides little information with respect to the apparent anodic behavior of the blister.

It is likely that corrosion activity had been stifled for the blister represented by the first set of local OCP and pH values for 2M NaCl blisters. Local measurements were conducted over 200 days after blister initiation. pH values of 5 to 8 imply reduced amounts of Al^{3+} due to the low solubility of $Al(OH)_3$ in this pH range. CE data was available for the blister with a pH of 5.3, which was the youngest blister initiated at the time of local measurement. Chloride and aluminum were detected in relatively high concentrations compared to other blisters, 0.3M and 0.06M, respectively so that a correlation between local OCP, pH, and chemistry cannot be made with this set of data. The local OCP does indicate that the blister was anodic compared to the rest of the unblistered substrate, which would be expected, based on the deep pitting morphology seen inside the blister area upon examination.

It should be noted that acetate was detected in some AA1100-H14 blisters. Acetate is not a component of the electrolytic solutions used in CE testing; thus, the organic acid likely originates from the epoxy coating itself. Acetone as a cleaning agent has been proposed to account for the presence of acetate in a variety of circumstances[16], but acetate was detected in AA1100-H14 blisters even though acetone was not used in the alloy's cleaning procedure. The

presence of acetate in occluded blister solutions may be an indication of coating degradation, although possible sources in the coating formulation are unknown at this time.

RESULTING CORROSION MORPHOLOGY

The typical corrosion morphology for 0.02M and 0.2M NaCl blisters was shallow pitting that was, in general, uniformly distributed throughout the blister area. One contribution to such morphology is the poor dry adhesion as shown through POTS. With low adhesion between the epoxy coating and the AA1100-H14 substrate, it would be expected that blister growth laterally would be enhanced due to decreased forces that must be overcome in order for the coating to detach from the substrate. In this manner, lateral growth of corrosion pits that develop underneath the detached coating is facilitated since their formation relies on the geometry of the occluded site inside a blister, which is also not constrained by high adhesion. On AA1100-H14, pitting then would be expected to be wide and shallow because large pit depths are not required to compensate for the inability to grow outward.

AA1100-H14 corrosion morphology can also explained by growth due to anodic undermining, which bears a close relationship to pitting. A short incubation time would be necessary to allow sufficient metal dissolution to cause coating detachment. In this manner, blister growth would be largely irregular during the early stages of anodic undermining. In other words, a perfectly circular region of delaminated coating around an active blister at its periphery would be rare. Light microscope and CLSM studies have indicated that regions of the coating detach in individual round sections, such as those described in local delamination. Individual delaminated areas resemble small bubbles in the organic coating. Small pockets of occluded solution in each small delamination set up appropriate conditions for pitting and can cause pit shapes consistent with the detached region geometry. These observations suggest that episodic

growth in AA1100-H14 blisters may result from individual delaminated pockets in the coating that later coalesce into a larger, round delamination front, such as the one seen in Figure 3(b). Note that anodic activity was detected throughout both the swollen part of the blister in as well as in the delamination front, providing further evidence for anodic undermining.

General corrosion attack on the order of 2-3 μm was observed inside AA1100-H14 blisters that had been exposed to deaerated conditions. No appreciable blister growth was measured during the deaeration period; however, it has been suggested that reduced corrosion rates were supported during deaeration by the HER due to precipitation formation. The light general corrosion attack is consistent with metal dissolution that leads to anodic undermining, providing further evidence for the alloy's capacity for anodic undermining. Hemispherical pitting of the morphology usually seen under ambient conditions was also observed in the deaerated blister area, having likely occurred both before and after deaeration. Blister growth was not supported during deaeration by way of anodic undermining because the anodic dissolution rates were lowered significantly by the decrease in potential associated with elimination of the ORR.

CONCLUSIONS

Blister initiation is controlled by potential and the chloride concentration of the bulk solution for AA1100-H14. Upon immersion, the coated alloys experience global increases in the OCP (to near or above E_{pit}) associated with water uptake and oxygen transport through the coating and an increasing cathode-to-anode ratio. This potential increase is followed by a potential decrease associated with local sites of passive layer breakdown and pitting upon which simultaneous blister formation occurs. The tendency for single blister initiation on AA1100-H14

is related to the cathodic protection afforded by the subsequent potential decrease and the decreased local electrochemistry due to low particle density.

Blister growth appears to occur on AA1100-H14 by way of anodic undermining supported by results from SRET, dry adhesion tests, corrosion morphology in the blister area, local delamination morphology, blister initiation in sulfate + chloride electrolyte, and local blister environment characterization. The possibility of cathodic delamination as a mechanism for coated Al alloy blister growth has not been completely eliminated, although most of the results presented in this work better support anodic undermining. All blisters behave as net anodes in the early stages of life. A fast shift to dominant cathodic activity occurs on AA1100-H14 if iron oxide deposits inside the blister The epoxy coating detaches in a series of small areas of delamination that coalesce prior to new blister growth spurts. The formation and function of locally delaminated sites outside of active blisters is unclear at this time.

The effect of varying chloride concentrations revealed a competing process with potential control: water uptake by the coating. Slower water uptake occurs at high Cl^- concentrations (*i.e.*, 2M NaCl) reducing the amount of reactant water available for the cathodic reaction and decreasing the transport medium for cations to the coating/substrate interface to maintain electroneutrality.

ACKNOWLEDGEMENTS

The financial support of AFOSR (Paul Trulove) is gratefully acknowledged.

REFERENCES

1. Leidheiser, H. J. and Kendig, M. W., *Corrosion*, **32**, 69-76 (1976).

2. Dickie, R. A. and Smith, A. G., *Chemtech*, **10**, 31-35 (1980).

3. Leng, A., Streckel, H., Hofmann, K. and Stratmann, M., *Corrosion Science*, **41**, 599-620 (1999).

4. Leidheiser, H. J., *Corrosion*, **38**, 374-383 (1982).

5. Koehler, E. L., *Corrosion*, **40**, 5-8 (1984).

6. de Jong, H. F. and Moonen, W. A. J., *Aluminum*, **62**, 511-516 (1986).

7. Koehler, E. L., in *Localized Corrosion*, ed. R. W. Staehle, NACE, Houston, (1974).

8. Brasher, D. M. and Kingsbury, A. H., *Journal of Applied Chemistry*, **4**, 62 (1954).

9. Bellucci, F. and Nicodemo, L., *Corrosion*, **49**, 235-247 (1993).

10. Scully, J. C., Peebles, D. E., Romig, J. A. D., Frear, D. R. and Hills, C. R., *Met. Trans. A*, **23A**, 2641 (1992).

11. Frankel, G. S., *Journal of the Electrochemical Society*, **145**, 2186-2198 (1998).

12. Kittelberger, W. W. and Elm, A. C., *Industrial and Engineering Chemistry*, **38**, 695-699 (1946).

13. Leidheiser, H. J. and Wang, W., *Journal of Coatings Technology*, **53**, 77-84 (1981).

14. Brasher, D. M. and Nurse, T. J., *Journal of Applied Chemistry*, **9**, 96-106 (1959).

15. Funke, W., *Progress in Organic Coatings*, **9**, 29-46 (1981).

16. Kagwade, S. V., Clayton, C. R., Du, M. L. and Chiang, F. P., in *The Electrochemical Society Proceedings Series Proceedings of the Symposium on Surface Oxide Films*, J. A. Bardwell, p., The Electrochemical Society Proceedings Series, (1996).

CORROSION OF Al ALLOY 2024-T3

M.B. Vumirovic, N. Dimitrov and K. Sieradzki

Program in the Science and Engineering of Materials
Arizona State University
Tempe, Arizona 85387-6106

ABSTRACT

We briefly review the general phenomenology associated with the corrosion of Al Alloy 2024-T3. Copper redistribution is controlled by S-phase dealloying and matrix dealloying. Matrix dealloying of aluminum occurs owing to the increased pH that develops at the alloy/electrolyte interface owing to oxygen reduction. We summarize results of a detailed investigation aimed at determining the mechanism and magnitude of the oxygen diffusion – limited current density during corrosion of Al Alloy 2024-T3. Our results show that oxygen reduction occurs via the standard 4-electron mechanism and that the oxygen diffusion – limited current density has a value of ~ 25 $\mu A\ cm^{-2}$.

INTRODUCTION

The corrosion of commercial aluminum alloys is generally associated with the presence of microstructural heterogeneities, particularly intermetallic particles, that may be introduced deliberately for the enhancement of mechanical properties, or may arise from the presence of impurity elements. The intermetallics have different electrochemical properties from the matrix so local galvanic effects prevail leading to localized corrosion. High-strength Al-Cu-Mg alloys such as 2024 contain about 2-3 vol% of fine S'-phase (Al_2CuMg) particles in the alloy matrix. The S phase occurs as classical hemispherical cap particles on grain boundaries, with low energy interfaces on one bounding grain. The S' particles occur within the grains in a low energy morphology. The grain boundaries have much larger particles of S-phase. There are a variety of other particles in 2024, but the S-phase particles are probably most damaging from the

standpoint of localized corrosion, which penetrates along the Cu-depleted zones adjacent to the grain boundaries.

Alloying with copper is one of the chief ways of achieving high strength in aluminum alloys, but the presence of S and S' phases leads to a severe degradation of the corrosion performance. The detrimental effect of copper-containing intermetallics may be understood as a galvanic effect, though the details of this are often poorly described in textbooks. In the presence of chloride ions, corrosion of aluminum is promoted by anything that enhances the oxygen reduction reaction, thus raising the corrosion potential. Oxygen reduction is slow on top of the Al_2O_3oxide film, but rapid on corroded Cu-bearing intermetallics where copper protrudes through the oxide. The copper rich phases initially carry an oxide film that is more-or-less Al_2O_3. This film is gradually broken down to expose more copper, increasing the galvanic effect between the intermetallic and the matrix. The anodic reaction (pitting or intergranular corrosion) favors sites where copper has been depleted by precipitation of Cu-rich phases, especially around grain boundaries.

In equiaxed microstructures, stress-corrosion failure can occur as a consequence of this intergranular corrosion, but in aircraft, the 2000-series alloys are used in sheet form and have pancake-shaped grains that hinder intergranular crack propagation (these alloys are also normally clad with pure aluminum (this is not always necessary or desirable). On the other hand, corrosion fatigue is a transgranular process and is promoted by filiform and other forms of localized corrosion on coated Al alloy sheet.

COPPER REDISTRIBUTION

Copper redistribution occurs on the surface of copper containing aluminum alloys as a result of dealloying. There are two principal sources in the alloy: intermetallic copper containing

precipitate particles such as the orthorhombic S-phase in 2024, and copper in solid solution. Henceforth we refer to dealloying of matrix aluminum and the build-up of copper from solid solution as "*matrix dealloying*"[1]. S-phase dealloying occurs in virtually any electrolyte over the entire pH range[2]. The oxide on the surface of the S-phase is not very protective and a fluctuation (transient break-down event) or heterogeneity in the oxide exposes bare metal to the electrolyte. Once this event occurs, say in a neutral electrolyte, Mg dissolves into the electrolyte as the soluble Mg^{2+} cation. The remaining Cu forms a very high surface area porous sponge structure typical of dealloyed microstructures. Thus the S-phase is initially anodic, but after dealloying turns into a cathode for oxygen reduction. As long as the remnant Cu sponge remains mechanically and electrically connected to the Al matrix the corrosion potential is too low to allow for Cu dissolution by electrochemical means. However, if the particles of the Cu sponge become mechanically disconnected, the copper particle will dissolve at its corrosion potential in a Cl^- electrolyte and electrochemically plate back on to the aluminum alloy surface[2].

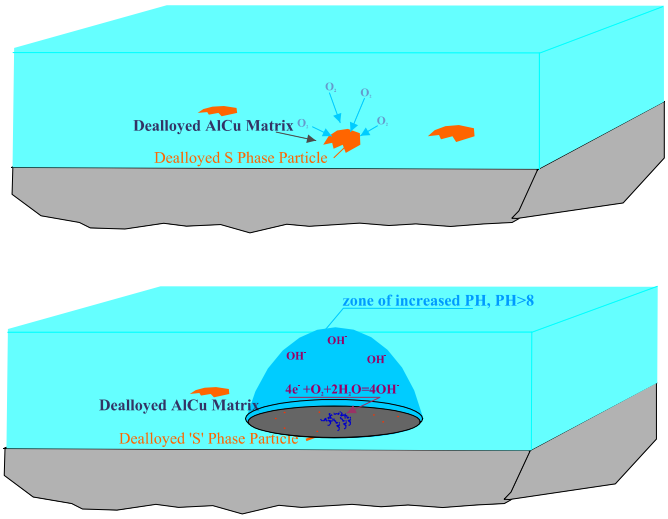

FIGURE 1. Schematic illustration of the growth of the zone of increased pH in the vicinity of a dealloyed S-phase particle. In the long-time limit the growth of the zone will be dictated by the geometry of overall mass transport in the electrolyte; either radial diffusion of O_2 toward the cathode or $(OH)^-$ diffusion radially away from the cathode.

On a bare metal surface, in a neutral chloride solution oxygen reduction occurs presumably according to the four-electron mechanism, $2H_2O + O_2 + 4e^- = 4(OH)^-$, which results in an increase in the pH of the electrolyte in the neighborhood of local cathodes. A Cu-rich remnant S-phase sponge can serve transiently as a high surface area cathode for this reaction. When this process becomes mass transport limited only the projected surface area of the porous cathode is available for oxygen reduction. As the pH increases to about 9 or 10, the passive oxide on the surface of the alloy matrix will chemically dissolve and aluminum will begin to selectively dissolve via the soluble AlO_2^- anion. A simple estimate of the time required to achieve a pH of about 10 at the metal solution interface yields a times of order 1 s. The time required for achieving a steady state concentration of hydroxyl ions through the thickness of the boundary layer is of order 10^3 s. As hydroxide is produced at a local cathode, it diffuses radially outward activating an ever increasing surface area surrounding the cathode to alkaline dissolution of aluminum. This scenario is illustrated in Figure 1.

In the long-time limit the growth of the zone will be dictated by the geometry of overall mass transport in the electrolyte; either radial diffusion of O_2 toward the cathode or $(OH)^-$ diffusion radially away from the cathode. The particles that serve as cathodes behave as microelectrodes with a diameter considerably smaller than the width of the diffusion boundary layer. Thus the zone of increased pH is initially planar (when the zone size is of the order of the cathode diameter) with Cottrellian current but eventually adopts the semispherical growth front that characterizes the diffusive field. The zone grows in this geometry until its radius is of the order of the diffusion boundary width (~ 50 μm) at which point the growth of the zone is cut off. Thus the diffusion boundary layer thickness sets an upper limit on the radius of the increased pH zone that can be developed by a single particle.

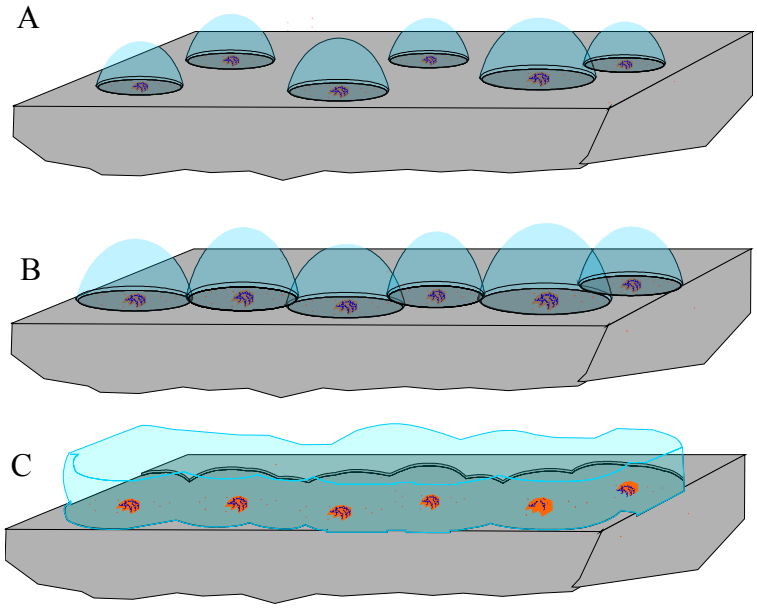

FIGURE 2. The de-alloyed S-phase behaves as an array of microelectrodes for the reduction of O_2 and the production of OH^-. Initially the S-phase particles behave as independent microelectrodes with hemispherical diffusion zones (A). As time evolves the 3D diffusion zones overlap (B) and eventually the diffusion zones become planar (C), as the entire surface is activated to AlO_2^- dissolution.

The dealloying process results in the agglomeration of solid solution Cu into Cu particles that also serve as cathodic sites that maintain the oxygen reduction process. Additionally, dissolution of aluminum will bring yet new precipitate particles to the surface, which can activate anodically and later turn in to oxygen reduction sites. This situation is further complicated since the cathodes have finite lifetimes. A copper particle can stop functioning as a cathode either because it eventually is undercut by alkaline dissolution of aluminum and becomes disconnected, or from build-up of a gel-like aluminum hydroxide which blocks the cathode from access to oxygen.

If we take the mean S-phase particle diameter to be 1μm, the average separation between particles will be 5.7 μm corresponding to 0.03 area fraction surface coverage of copper. Figure 2 illustrates the growth and overlap of a number of these zones of increased pH emanating from an array of these cathode microelectrodes. If the mean particle spacing is less than the diffusion boundary layer thickness, the hemispheres of increased pH overlap. As this occurs the diffusion field switches from radial to a one-dimensional field in the direction of the surface normal and

the current becomes Cottrellian. In this case, the entire surface is activated to matrix dealloying and a significant increase in the surface copper concentration develops.

Results of Rotation Disk Electrode (RDE) and Rotating Ring-Disk Electrode (RRDE) experiments on synthetically made model 2024 alloys (square array of 1 μm diameter copper disks 5 μm apart) have confirmed this scenario[1]. At 1500 rpm the diffusion boundary layer thickness is 13 μm. Thus the overlapping regions emanating from near-neighbor disks are cut-off and about 30% of the surface remains inactive to Al dissolution. Thus the surface coverage of copper as a function of time decreases with increasing rotation speed for speeds greater than about 1500 rpm. Figure 3 shows results obtained from RRDE demonstrating the important role of S-phase particles in the copper redistribution process.

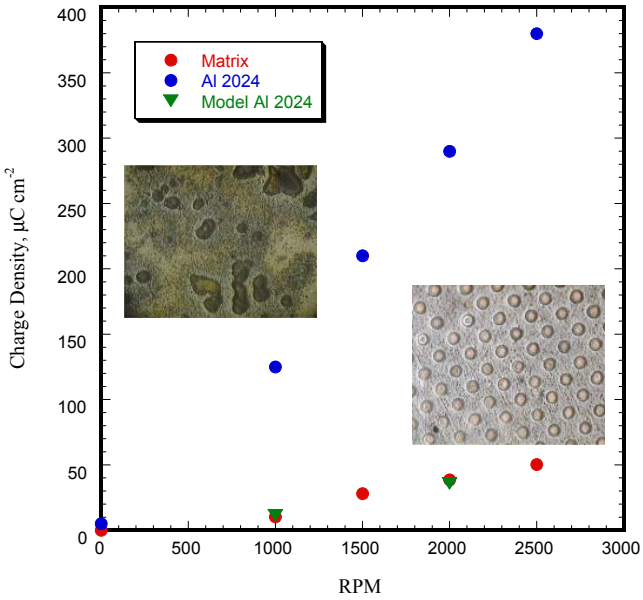

FIGURE 3. The amount of copper liberated (RRDE) during corrosion of Al alloy 2024-T3, Matrix 2024 (that models the matrix composition of 2024) and synthetic 2024 (Matrix 2024 containing 1 μm diameter Cu particles in the surface comprising ~ 0.03 area fraction of the surface). The differences (more copper liberated from 2024) indicate the important role of S-phase particles in the copper redistribution process.

OXYGEN REDUCTION RATES

Probably one of the most difficult parameters to characterize has been the magnitude of the diffusion - limited current density (DLCD) associated with oxygen reduction. This is

generally acknowledged to be a four electron (pH > 7) process operating at c.a. 100 μm cm^{-2}, on a film free metal surface. Figure 4 demonstrates the clear connection between the magnitude of this parameter and the surface coverage of copper on an Al 2024 alloy surface after just five minutes of corrosion. The surface Cu coverage was determined by a Pb underpotential deposition (UPD) assay that we developed[3].

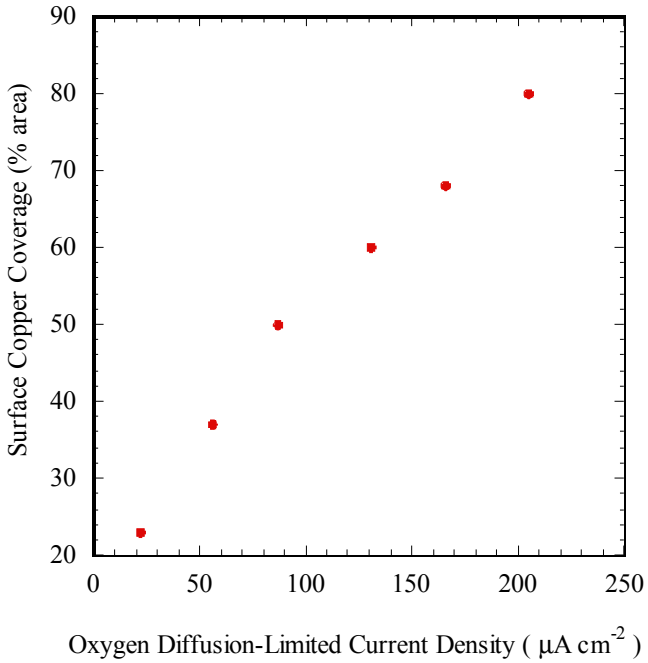

FIGURE 4. RDE results showing the surface copper coverage (Pb UPD assay) on an Al alloy 2024 after five minutes of immersion in 0.5 M NaCl as a function of the oxygen diffusion – limited current density (rotation speed). The source of the redistributed copper is matrix dealloying.

The general corrosion rate of the alloy and the subsequent extent of damage will depend on kinetics of the oxygen reduction at the copper enriched particles. In a recent study[1] we compared the kinetics of oxygen reduction on Al 2024 T3, a synthetic model Al 2024 T3 alloy, a planar Cu electrode and a lattice of copper particles embedded in an insulator (CEI samples) in 0.1 M Na_2SO_4. Both the synthetic alloy and the CEI sample contained 1.8 μm diameter Cu disks arranged in a square lattice with 9.5 μm near-neighbor spacing. This particle size and density was chosen to simulate the surface coverage of the S-phase on Al Alloy 2024-T3. We found that this configuration of Cu particles behaved as a microelectrode array for oxygen reduction. The

oxygen DLCD on the CEI microelectrode array and on a pure planar copper electrode in a stagnant, naturally aerated electrolyte was 20-30 µA cm^{-2} (Figure 5). These numbers differ significantly (by a factor of 4-5) from the numbers commonly accepted and used in the corrosion literature (i.e., 50 - 100 µA cm^{-2} [4]) and the immediate question is why? One possibility is that in a pH ~ 9 electrolyte in the near electrode vicinity, resulting from the ongoing oxygen reduction, a Cu surface may be oxidized so oxygen reduction may be under combined mass-transport and surface reaction – limited control.

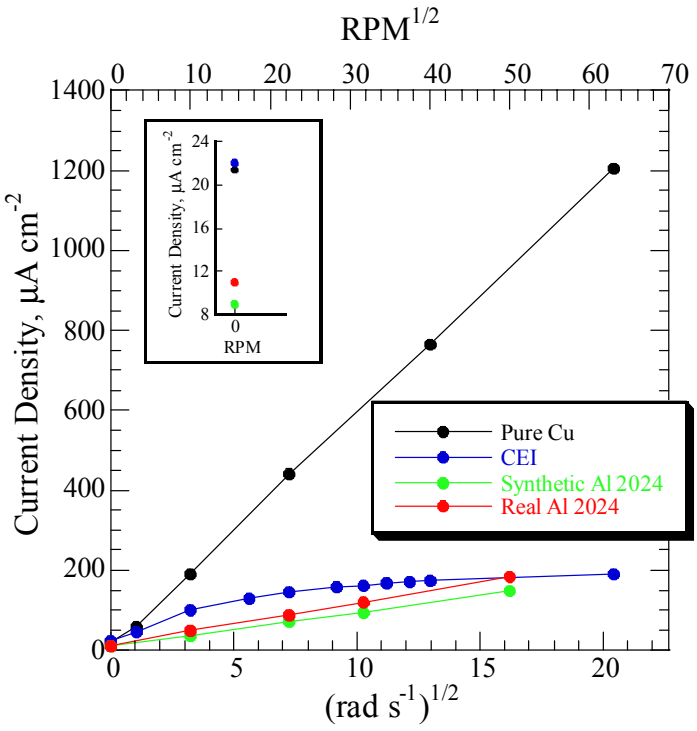

FIGURE 5. RDE results for the oxygen diffusion- limited current density on a planar Cu electrode (pure Cu), the CEI sample, synthetic Al 2024, and real Al 2024-T3. The planar Cu electrode shows linear behavior for the oxygen DLCD versus the square root of the rotation rate whereas the other samples show behavior indicative of microelectrode behavior. The inset shows the magnitude of the oxygen DLCD on these electrodes in an air-saturated stagnant electrolyte. The real and synthetic 2024 behavior is indicative of a net current resulting from anodic and cathodic processes. Note that the planar Cu and CEI samples yield almost identical results of 22 µA cm^{-2}.

In order to sort out these issues we performed a set of RDE experiments on planar copper and platinum electrodes to measure the oxygen DLCD in naturally aerated 0.1M Na_2SO_4 as a function of pH[5]. The pH employed was 1.5, 3, 5.5, 7.5, 10, 12, and 14. Solutions with pH values of 1.5 and 3 were made using 0.1 M Na_2SO_4 acidified with H_2SO_4 while solutions with pH values of 7.5; 10; 12 and 14 were made using 0.1 M Na_2SO_4 adjusted with NaOH. RDE

experiments were performed also on a Pt polycrystalline electrode in 0.1 M Na_2SO_4 (pH 5.5) and in 0.1 M Na_2SO_4 adjusted to pH 10. Each of the experiments designed to measure oxygen diffusion-limited current densities were at constant pH under a prescribed rotation rate by performing separately a cathodic as well as an anodic sweep at a sweep rate of 2 mV s^{-1}. The anodic sweeps had an initial potential just above the onset of hydrogen evolution. A saturated calomel electrode (SCE) was used as a reference electrode and a Pt sheet as a counter electrode. All the potentials in the text are reported vs SCE unless stated otherwise. A standard RDE device (Pine Instruments) together with a Pine Instruments bi-potentiostat (model AFRDE5) were used and a Nicolet 310 Digital Oscilloscope served to store data.

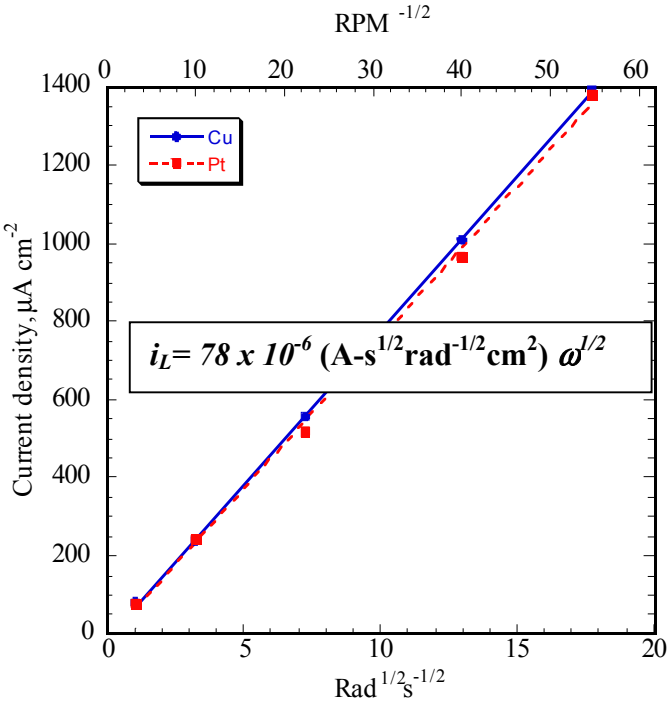

FIGURE 6. Results for the oxygen DLCD in a pH 10 electrolyte on planar polycrystalline Cu and Pt electrodes in the form of a Levich plot. Note that results over the entire range of pH investigated ((1.5 – 14) were virtually identical to the results shown in this figure, i.e., the kinetics of the oxygen DLCD was independent of pH.

Levich plots for the oxygen DLCD in the pH 10 electrolyte for Cu and Pt are shown in Figure 6. Note that the results for Cu and Pt virtually superimpose. The linear dependence of the current density on $\omega^{1/2}$ is indicative of diffusion limited process that is described by the

Levich equation, $i_L = 0.62nFD^{2/3}\nu^{-1/6}c_\infty\omega^{1/2}$. Here i_L is the diffusion limited current density, n is the number of transferred electrons, F is Faraday's constant, D the diffusion coefficient, ν the kinematic viscosity, ω the disc rotation rate and c_∞ the concentration of oxygen in the bulk solution. The experimentally obtained slopes on Cu and Pt are very close to the theoretically calculated slope (83.3 x 10^{-6} A $s^{1/2}rad^{-1/2}$ cm^{-2}) for a four electron (n = 4) reduction process for D = 1.93 x 10^{-5} cm^2 s^{-1} [6], ν =1.01 x 10^{-2} cm^2s^{-1} [7], and c_∞ = 2.25 x 10^{-7} mole cm^{-3} [8] in naturally aerated solutions. Markovic et al. used a rotating ring-disk electrode configuration to study of oxygen reduction on Pt (*hkl)* [9] in oxygen saturated 0.05 M H_2SO_4. They demonstrated that oxygen reduction on Pt occurred via the 4-electron mechanism and obtained a Levich slope of 463 x 10^{-6} A $s^{1/2}rad^{-1/2}cm^{-2}$ which agrees well with the theoretically calculated value (466 x 10^{-6} A $s^{1/2}rad^{-1/2}$ cm^{-2}) for n = 4. This slope is larger then the one obtained in the work presented herein by a factor of 5.9. This difference correlates with the difference in the concentration of oxygen in the electrolyte, 12.6 x 10^{-7} mole cm^{-3} [7] for the oxygen – saturated solution and 2.25 x 10^{-7} mole cm^{-3} [8] for the naturally aerated solution. Similar comparisons exist with results of Vasquez et al.[10] who investigated oxygen reduction on a pure copper electrode in oxygen - saturated borate solution. In that work the authors determined n = 3.8 for the electron pathway of the reaction. This result was obtained under the assumption that D = 1.9 x 10^{-5} cm^2 s^{-1}, ν =1 x 10^{-2} cm^2s^{-1}, and c_∞ is 12.6 x 10^{-7} mole cm^{-3}. We have estimated the slope of the Levich plots presented in [10] to be 440 x 10^{-6} A $s^{1/2}rad^{-1/2}cm^{-2}$. This slope is close to that obtained by Markovic et al. [9]on Pt in 0.05 M H_2SO_4 and differs from the one we obtained in the present study by a factor of 5.6. These results taken together lead us to conclude that a four-electron oxygen reduction mechanism takes place on copper in naturally aerated 0.1 M Na_2SO_4 solution.

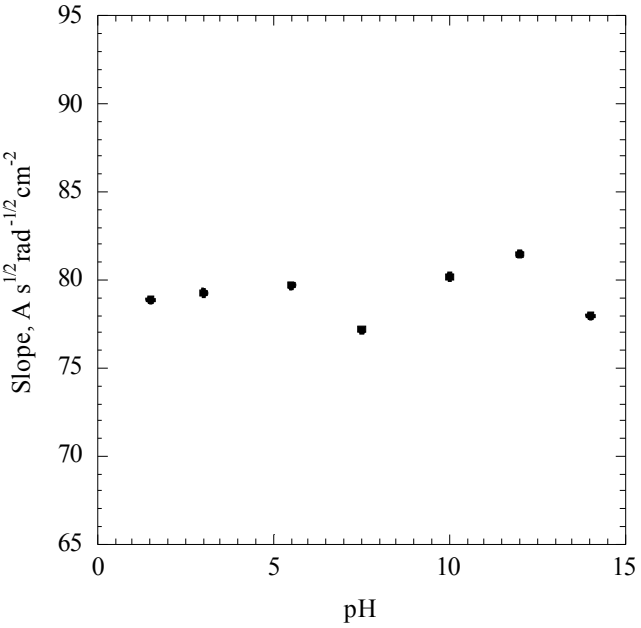

FIGURE 7. Summary of slopes obtained from the Levich plots for the oxygen DLCD on polycrystalline Cu electrodes as a function of solution pH.

Figure 7 summarizes the results for the slopes of the Levich plots as a function of pH. The average slopes of the lines obtained are 79 ± 3 x 10^{-6} A-s$^{1/2}$rad$^{-1/2}$cm^{-2}. This result is consistent with the theoretically predicted Levitch slope of 83.3 x 10^{-6} A-s$^{1/2}$rad$^{-1/2}$cm^{-2} for a four-electron reaction (n = 4) in naturally aerated solution. The results are consistent with those obtained by Markovic et al. on Pt [9] and therefore indicate the operation of a four-electron mechanism for oxygen reduction on Cu over the entire pH range examined.

CONCLUSIONS

Our studies of the oxygen diffusion – limited current density demonstrate that the CEI geometry behaves as a microelectrode array in the limit of a stagnant or very weakly stirred electrolyte. Under these conditions, the microelectrode array provides the same oxygen diffusion – limited current density as a planar Cu electrode. Thus, in a stagnant electrolyte, the synthetic 2024 alloy is as efficient as the real 2024 for oxygen reduction. Our RRDE results and those of Buchheit et al. [11], demonstrate the operation of a dissolution/back-plating copper redistribution

mechanism during corrosion of Al 2024-T3. This process is triggered by very small copper particles of order tens of nanometers in size that become mechanically disconnected from de-alloyed S-phase intermetallic particles. As long as the remnant de-alloyed copper sponge stays mechanically and electrically connected to the substrate no copper dissolution can take place. In this case, we can disregard particle size effects on dissolution since the corrosion potential is almost 1 V less than the reversible potential of copper.

The RDE studies of the oxygen diffusion – limited current density demonstrate that the synthetic 2024 (1.8 μm diameter Cu disks in a square array with 9.5 μm near-neighbor spacing) geometry behaves as a microelectrode array for oxygen reduction. Furthermore oxygen reduction on the surface of the real and synthetic alloys is quantitatively similar. During immersion of these alloys in 0.5 M NaCl, the only physical process that we can identify taking place on the surface of the real 2024 that does not occur on the synthetic 2024 is the operation of the dissolution/back-plating mechanism of copper redistribution. The difference in behavior for the surface coverage of Cu between 2024-T3 and the synthetic 2024 alloy is attributed to the operation of a dissolution/back-plating mechanism triggered by mechanical disconnection of Cu particles from de-alloyed porous S-phase. Comparison of the behavior of these two alloys allow us to conclude that the matrix de-alloying and dissolution/back-plating contribute about equally to the copper redistribution process during corrosion of Aluminum Alloy 2024-T3 in 0.5 M NaCl.

ACKNOWLEDGEMENT

We gratefully acknowledge discussions over the course of this investigation with R.C. Newman, and the AFOSR for support of this work under a MURI (F49620-96-1-0475).

REFERENCES

1. M.B. Vumirovic, N. Dimitrov and K. Sieradzki, *J. Electrochem. Soc.,* **149**, (2002).
2. N. Dimitrov, J.A. Mann, M. Vukmirovic, and K. Sieradzki, *J. Electrochem. Soc*, **147,** 3283 (2000).
3. N. Dimitrov, J.A. Mann, and K. Sieradzki, *J. Electrochem. Soc*., **146,** 98 (1999).
4. M.G.Fontana and N.D.Greene, Corrosion Engineering,McGraw-Hill, New York (1967), p. 315.
5. M. B. Vumirovic, N. Vasiljevic, N. Dimitrov and K. Sieradzki, "The Diffusion –Limited Current Density of Oxygen Reduction on Copper", *J. Electrochem. Soc*. in press. 2002.
6. N. A. Anastasijevic, Z. M. Dimitrijevic, and R. R. Adzic, *Electrochim. Acta*, **31**, 1125 (1986).
7. CRC Handbook of Chemistry and Physics, 66th ed.; R. C. Weast Ed; CRC Press: Boca Raton, Florida, 1986.
8. C.G. MacArthur, *J. Phys. Chem*., **20**, 495 (1916).
9. N. M. Markovic, H. A. Gasteiger, and P. N. Ross, Jr., *J. Phys. Chem*, **99**, 3411 (1995).
10. M. V. Vazquez, S. R. de Sanchez, E. J. Calvo, and D. J. Schiffrin, *J. Electroanal. Chem.*, **374**, 189 (1994)
11. R. G. Buchheit, M. A. Martinez, and L. P. Montes, *J. Electrochem. Soc.*, **147**, 119 (2000).

SELF-ASSEMBLED NANO-PHASE PARTICLE (SNAP) SURFACE TREATMENTS FOR AEROSPACE ALUMINUM ALLOYS

L.S. Kasten[1], M.S. Donley, V.N. Balbyshev[2], and D.J. Gaspar[3]

Air Force Research Laboratory, Materials and Manufacturing Directorate,
Nonmetallic Materials Division, Nonstructural Materials Branch, Coatings Research Group,
Wright-Patterson AFB, OH 45433-7750

ABSTRACT

The Air Force Research Laboratory is developing environmentally benign alternatives to the traditional chromated aircraft coating for aircraft corrosion protection, targeted to a 30+ year performance life cycle. Self-assembled NAno-phase Particle (SNAP), a new sol-gel system, has been created and analyzed and results will be presented. Aqueous solution processes are utilized to generate nanophase particles which produce a dense, protective thin film on metal substrates. The SNAP process enables inorganic functionality for bonding to the substrate and tailorable organic chemistry for interaction with subsequent polymer layers. Cross-linking agents are added to the solution to crosslink the particles to form an organic coating, chemically connecting the nanoparticles. The surface chemistry, bulk chemical structure, and crosslinker interactions in the SNAP coatings were determined through the application of a variety of surface analytical techniques. To investigate the surface chemistry of the films, complementary techniques of x-ray photoelectron spectroscopy (XPS), angle-resolved x-ray photoelectron spectroscopy (ARXPS), and Time-of-Flight Secondary Ion Mass Spectrometry (TOF-SIMS) have been utilized. The data indicates that the SNAP film has a uniform elemental chemistry from the near surface region through the bulk, and that the bulk of the film retains the expected organosilane character, which is formed in solution. The crosslinker works as expected due to the detection of C_xH_yON peaks associated with crosslinking. There are no large Si_xO_y cluster fragments detected in the standard or films. These results demonstrate how surface analytical techniques can greatly enhance research efforts in the development of organic coatings.

[1] University of Dayton Research Institute, 300 College Park, Dayton, OH 45469-0168
[2] Universal Technology Corp., 1270 N. Fairfield Rd., Dayton, OH 45432-2600
[3] Environmental and Molecular Sciences Laboratory, Pacific Northwest National Laboratory, Richland, WA 99352

INTRODUCTION

A novel application of sol-gel chemistry has been utilized to develop a new method of designing and building a coating from the molecular level upward. This method is called the Self-assembled NAno-phase Particle (SNAP) process, and it consists of forming functionalized siloxane nanoparticles *in-situ* in an aqueous sol-gel process, and then crosslinking the nanoparticles to form a thin, fully dense film. The SNAP process has been previously reported to make environmentally benign corrosion protection coatings.[1] These nanostructured coatings have been shown to provide an excellent barrier to corrosion in aluminum aerospace alloys, and other applications are envisioned. The ability to design coating components from the molecular level upward offers tremendous potential for creating multifunctional coatings demonstrating a nanoscience approach to coatings. However, to fully understand the film chemistry, accurate information on the chemical bonding of the film constituents is needed to characterize the organic film structure and chemistry.

Surface analysis, specifically X-ray photoelectron spectroscopy (XPS) and Time-of-Flight Secondary Ion Mass Spectrometry (TOF-SIMS), were used to obtain the chemical and structural information on the film. XPS was chosen for qualitative analysis of the surface chemistry of the SNAP films because it typically provides excellent quantitative elemental composition, chemical state information, and surface and bulk chemical bonding information. Although XPS works quite well on conductive samples, the analysis of nonconducting materials, such as organic coatings, is somewhat more complicated. Two things occur in the analysis of nonconductors – 1) lack of Fermi level alignment and 2) the buildup of positive charge on the surface induced by photoelectron emission. Existence of both phenomena results in an arbitrary

shift of the binding energy scale of the peaks, which makes detailed interpretation of spectra impractical without an accurate method to reference the peak shifts.

XPS analysis of non-conducting organic coatings entails two steps: data acquisition and "charge referencing". Charge referencing refers to the process by which a rational energy scale is determined in order to account for the binding energy shift due to charge accumulation. In acquiring the data, a low energy electron flood gun is used to provide consistent XPS peak energies. The gun emission is adjusted until the peak has the narrowest full width half max (FWHM) value with the highest signal intensity. Bart et al.[2] studied wide gap insulators with XPS and provided a set of recommendations for the analysis of insulators and for optimizing flood gun settings. Once a good spectrum is obtained, the peak position must be charge referenced. As cited in numerous literature references, charge referencing is most commonly accomplished by using "adventitious carbon" as a reference and setting the C 1s peak to a value of 285.0 eV.[3-5] This method may provide good accuracy when the carbon chemistry involves few chemical states, thereby producing a C 1s peak with a FWHM of less than 2 eV. However, if the carbon peak has a FWHM larger than 2.5-3.0 eV, this is indicative of multiple carbon chemical states and referencing the spectral data using the adventitious carbon method is not viable. Another peak must be used as a reference peak in this case, and care must be taken to ensure an appropriate reference peak is chosen.

The chemical structure of SNAP films was investigated using Time-of-Flight Secondary Ion Mass Spectrometry (TOF-SIMS). This technique was chosen because it typically provides excellent molecular level information in the analysis of organic-based coatings. In SIMS, the specimen surface is sputtered with a primary ion beam and atomic and molecular secondary ions sputtered off the sample are mass analyzed. Generally, the limited mass range of quadrupole and

magnetic sector instruments limit their utility in the analysis of organic materials. Additionally, many traditional SIMS instruments utilize a high intensity primary ion beam, which leads to fragmentation of molecular species to their atomic constituents and prevents useful analysis of organic films. In TOF-SIMS, a time-of-flight mass analyzer enables a very wide mass range of molecular ions to be detected, with very high mass resolution, which is ideal for the analysis of organic coatings.

In this work we have determined the surface chemistry, bulk chemical structure, and crosslinker interactions in the SNAP coatings through the application of a variety of surface analytical techniques. We also demonstrate that researchers involved in the development of organic coatings could benefit greatly from the demonstration and application of rigorous surface analytical techniques in the analysis of organic coatings.

EXPERIMENTAL

SAMPLE PREPARATION

Film specimens were prepared on Silicon {100} wafers sputter coated with high purity aluminum. The Al coated wafers were chosen as a substrate to replicate a metal surface similar to that of the AA2024 alloy and to provide a smooth surface for surface analysis, while removing any affects due to alloying elements. These wafers were cut into 1-inch by 1-inch specimens and solvent cleaned. SNAP solutions were made by drop-wise addition of GPTMS and TMOS in 3:1 ratio to a dilute solution of acetic acid in doubly distilled deionized water, as previously described.[1] The solution was continuously stirred during the addition. After all of the silanes had been added, the solution was aged in a covered container while still stirring for a given length of time. After the aging period, the SNAP solution was ready for addition of the coupling agent solution, crosslinking agent (diethylenetriamine, DETA), surfactant (3M FC-430 and FC-

171), and diluent (deionized water). Upon addition of these materials, the solution was immediately applied to the substrate by dip coating at a speed of 0.2 cm s^{-1}.

Specimens were prepared from several variations of the SNAP formulation, as listed in Table I. The thickness of the SNAP coating was determined to be nominally 1 μm. In order to reduce the sputter time required for analysis of the metal/organic coating interface, thinner coatings were required. Here the SNAP formulation was further diluted with deionized water to 50%, 30%, and 10%, as listed in Table I, and coated specimens were prepared from these dilute solutions. In addition, coatings were also prepared of uncrosslinked SNAP, and the individual TMOS and GPTMS precursors, again as listed in Table I. The coated wafers were air dried for at least 72 hours before any analysis was performed.

TABLE I: List of Samples for Analyses.

	TMOS:GPTMS ratio	Dilution ratio	Comments
SNAP	1:3	-	
50% SNAP	1:3	1:1	
30% SNAP	1:3	1:2	
10% SNAP	1:3	1:9	
SNAP unXL	1:3	-	Uncrosslinked, fresh
SNAP unXL aged	1:3	-	Uncrosslinked, aged 2 months
GPTMS	0:1	-	Precursor
TMOS	1:0	-	Precursor

XPS ANALYSES

XPS was used to determine the surface compositions of the coatings. The samples were mounted onto a stainless steel sample holder and fixed in place with copper clips and stainless steel screws. The coated specimens were analyzed using a Physical Electronics (PHI) 5700 multi-technique system. The XPS system was equipped with a hemispherical analyzer and a 16-channel detector, and a monochromatic Al x-ray source (having an energy of 1486.6 eV) was

used for the analysis, operated at 350 W. The analyzer was operated in the fixed analyzer transmission mode, with pass energy of 188 eV for survey scans and 23.5 eV for high resolution scans, corresponding to analyzer resolutions of 1.88 eV and 0.235 eV, respectively. The analysis area was 800 μm x 2000 μm, and the pressure in the system was below $1x10^{-9}$ Torr during analysis. Quantitative analysis was carried out using manufacturer supplied sensitivity factors. Likewise, curve fitting was performed using the manufacturer-supplied program.

To provide charge compensation of the specimen surface, an electron flood gun was used to supply low energy electrons to the specimen surface. The flood gun provided a consistent peak energy and width, and the lowest FWHM width with the highest intensity was obtained by flooding the sample with 1 eV electrons. Keeping the films thin (less than 1 μm) also decreased the effects of charging by allowing electrons to tunnel from the conducting metallic substrate. In addition, high resolution scans of elements present in the coating were taken on all specimens to check for damage due to x-rays and or the electron flood gun. There was no change in peak intensity or peak shape after 30 minutes of x-ray exposure.

XPS sputter depth profiling was performed on the SNAP films to investigate the bulk chemistry of the coated specimens. An argon ion beam was used to sputter away the surface and XPS measurements are taken after each sputter cycle. Argon ions were produced with beam energy of 3.0 keV and 10mPa argon pressure. Thickness measurements were made from sputter depth profiles of SNAP and diluted SNAP specimens relative to the depth profile of a standard with known thickness (1000 angstroms of silicon dioxide on silicon).

Angle-resolved x-ray photoelectron spectroscopy (ARXPS), also called grazing angle XPS, was used to compare near-surface content to bulk content. As the sample is tilted with respect to the detector, the measured distance in the sample (in the direction of the analyzer)

remains constant. When the collection angle between the detector and the surface decreases, the average sampling depth effectively decreases. Thus, changing the angle of acceptance between the sample and the detector to a smaller take-off angle (TOA) enhances surface sensitivity. Scans were taken at TOA of 15, 45 and 80 degrees. A TOA of 15 degrees detects photoelectrons from the near surface region and one of 80 degrees detects photoelectrons coming from deeper in the bulk. A 45 degree take-off angle is the typical position for general scans, and provides a data point in between. Using this technique, surface sensitivity enhancement allows the near surface region to be distinguished from the bulk of the film or coating. Angle revolved x-ray photoelectron spectroscopy data was collected with sample TOAs of 15°, 45°, and 80° degrees to the analyzer.

TIME OF FLIGHT SECONDARY ION SPECTROSCOPY (TOF-SIMS) ANALYSIS

The surface chemistry and chemical structure of SNAP films was investigated using Time-of-Flight Secondary Ion Mass Spectrometry (TOF-SIMS). Measurements were carried out on a Physical Electronics Model TRIFT II TOF-SIMS using a $^{69}Ga^{+}$ source in a high mass resolution mode. In this mode, a 15 kV, 600 pA (measured for a continuous ion beam; 0.1 pA during pulsed operation) electrodynamically bunched primary ion beam with a <1 ns pulse width is used. The mass resolution ($m/\Delta m$) in this mode is ≥ 9000, while the primary beam diameter is ~2-30 μm. Depth profiles were performed by alternating between a continuous ion beam rastered over a 40x40 μm area (the sputter crater) to slowly erode the film, and analysis of a 20x20 μm area within the sputter crater using a pulsed primary ion beam. For all analyses reported here, the positive secondary ions (+SIMS) were analyzed, as little or no information was present in the negative secondary ion mass spectra.

RESULTS AND DISCUSSION

XPS ANALYSES

Angle resolved XPS studies provided the relative atomic concentrations of the near surface (15 degree TOA) and subsurface or bulk (80 degree TOA) regions, as shown in Table II, for the various coating formulations. Comparison of data from the 10% and 100% SNAP films indicated no difference, within experimental error, between surface and subsurface composition. The elemental composition and percent relative concentration at 15 degree TOA is basically the same as the 80 degree TOA. Although slight chemical shifts from the near surface region to the surface region were detected, these are likely due to the presence of contamination-related species on the surface region. These data indicate that the SNAP film has a uniform elemental chemistry from the near surface region through the bulk.

TABLE II. Results of ARXPS measurements for SNAP and diluted SNAP show surface composition to be the same as the bulk.

10 % SNAP			
% Relative Atomic Concentration			
	15 TOA	45 TOA	80 TOA
Carbon	52	50	50
Silicon	16	16	14
Oxygen	32	34	35
Fluorine	0	<1	0
Nitrogen	1	1	1

100% SNAP			
% Relative Atomic Concentration			
	15 TOA	45 TOA	80 TOA
Carbon	53	51	49
Silicon	10	11	12
Oxygen	31	34	35
Fluorine	3	2	1
Nitrogen	2	3	3

Sputter depth profiling was performed on the SNAP films to investigate the thickness of the films made from the diluted SNAP formulations as discussed above. Film thickness determination was based on comparison of a standard specimen having a known thickness (1000 angstroms) of silicon dioxide on silicon. Thickness measurements were made of the SNAP

sample and the diluted SNAP specimens. A plot of the film thickness vs. SNAP concentration is presented in Figure 1, where the relationship is basically linear. These measurements confirm the assumption that the thinner films may be prepared from the dilutions of the SNAP formulation, up to at least a 10% solution. This confirmation combined with the results of the ARXPS measurements enable one to study thin film samples prepared especially for surface analytical studies and have confidence that the data will be representative of the analyses of the SNAP" films.

XPS survey spectra for SNAP, 10% diluted SNAP, and 50% diluted SNAP are shown in Figure 2. C, Si, O, F, and N were detected as the composition of the film. Si and O, of course, are the major components of the siloxane film. The nitrogen is from the crosslinking agent - diethylenetriamine (DETA), and fluorine is due to fluoride components of the surfactant (3M FC-430 and FC-171), which is used to aid in forming a uniform film.

Chemical state information was difficult to determine due to the nonconducting nature of the film. A critical underlying principle in obtaining accurate binding energy data from XPS analysis is that there exists intimate electronic connection between the sample and the spectrometer. During XPS analyses of the SNAP coatings, which are nonconducting organic coatings, there is no electronic contact between spectrometer and sample. This coupled with surface charge buildup from photoelectron emission results in a shift in the peak binding energies to higher values. This shift in binding energy makes spectra from these analyses very difficult to interpret, and at best only elemental, not chemical state, information could be determined. As mentioned in the introduction, a charge referencing method is used on the data, with adventitious carbon the most common peak used.

Where the "adventitious carbon" C 1s peak has been used in charge referencing XPS spectra of polymers,[3] the peak width has typically had a FWHM of 1.0 to 1.5 eV. In the analysis of the SNAP XPS data, it quickly became evident that this method was inadequate; it was apparent that complex carbon chemistry was present leading to a C 1s FWHM of 3.42 eV. Since several types of carbon chemical states are possible, curve fitting the C 1s peaks in the SNAP data proved to be unproductive. It was questionable as to where to place the peak, as demonstrated in Figures 3a and 3b - with the right edge or the center of the C 1s peak at 285.0 eV. Centering the peak at 285.0 eV is acceptable for a narrow peak, but in this case the broadness of the raw data peak complicates the peak referencing. Centering the peak does not allow room to fit a peak at higher binding energies for the C-O bonds, whereas placing the peak with its right edge at 285.0 eV does. However, one must realize that all spectral peaks will be shifted accordingly, depending on which position is chosen. When the spectra were charge referenced based on this "adventitious carbon" right edge assignment, the corresponding oxygen and silicon assignments were not close to the expected peak energies for Si-O bonds, and thus did not make chemical sense. Thus, the insulating nature of this organic coating made it difficult to assign binding energies with any confidence. Future work will need to be done to establish a charge referencing technique for this SNAP coating system.

For now, the XPS high resolution scans for Si 2p and O 1s are presented in Figures 4. The FWHM for both the silicon and oxygen peaks are 2.2 eV. Once a charge referencing technique is determined, the Si 2p peak should be fitted with the Si-O bonds of the orthosilicate found in the TMOS and of the silane in the GPTMS. Depending on the reference placement of the carbon peak, both silicon and oxygen bond energy values can differ by as much as 1.5 eV.

To summarize the ARXPS and XPS analyses, the data indicates that the SNAP film has a uniform elemental chemistry from the near surface region through the bulk. Sputter depth profile measurements showed a linear relationship between thickness and concentration which confirms the assumption that thinner films may be prepared from the dilutions of the SNAP formulation, up to at least a 10% solution. This confirmation combined with the results of the ARXPS measurements enable one to study thin film samples prepared especially for surface analytical studies and have confidence that the data will be representative of the analyses of the SNAP films. Binding energy assignments were difficult to make due to the insulating nature of this organic coating resulting in binding energy shifts. A charge referencing technique needs to be developed to obtain meaningful information concerning the surface chemistry, bulk chemical structure, and crosslinker interactions in the SNAP coating system.

TIME OF FLIGHT SECONDARY ION SPECTROSCOPY (TOF-SIMS) ANALYSIS

TOF-SIMS analysis was performed on the specimens listed in Table I for the various coating formulations. A portion of a typical + SIMS spectrum of the SNAP specimens is presented in Figures 5 (mass 0 – 250 amu) 6(mass 0 – 65 amu). Two key observations can be made from these data. First, the spectrum consists of discreet molecular fragments which are sputtered from the coating in clustered groups, as indicated in both figures 5 and 6. Since there is not a continuum of atomic species, these discreet fragments maintain their integrity in the sputter removal process and are thus identifiable. Second, the major spectral components are contained in the 0 – 200 amu mass region - high mass fragments above 200 amu are not observed in any significant intensity. These observations are consistent for films made from both the undiluted and the dilute SNAP formulations. The results of the TOF-SIMS analysis are

tabulated in Figure 7 for the Si_xO_y fragments observed in the analysis. Again, Si fragments with Si>3 are simply not observed in any significant intensity in the various SNAP specimens, and likewise not observed in the near surface, bulk, or near interface regions. The same observation is also made in the analysis of the TMOS films.

The results of the TOF-SIMS analysis of the relative content of SiC_xH_y fragments measured in the analysis of the SNAP specimens, the uncrosslinked SNAP films, and the TMOS and GPTMS films are presented in Figure 8. Specific mass peaks of interest are at 42 ($SiCH_2$) and 43 ($SiCH_3$) amu and 55 (SiC_2H_3) and 57 (SiC_3H_5) amu. These data indicate that the organosilane content of the SNAP films is basically unchanged from the TMOS and GPTMS precursors. Figure 9 shows C_xH_yON mass fragments associated with crosslinking. Masses for the bulk and near, mid and far interface regions are the same, which verifies that the crosslinker works as expected.

In summary, the TOF-SIMS data shows that the films retain the basic chemical arrangement of the siloxane macromolecules, which are formed in solution. These macromolecules are then interconnected through the crosslinking process. A model of this structure is presented below in Figure 10, which we call the “fuzzy tennis ball model”.

CONCLUSIONS

The surface chemistry, bulk chemical structure, and crosslinker interactions in the SNAP coatings were determined through the application of a variety of surface analytical techniques. Through ARXPS and XPS analyses, the data indicates that the SNAP film has a uniform elemental chemistry from the near surface region through the bulk. A linear relationship between thickness and solution concentration was determined by sputter depth profiling measurements, and therefore thinner films may be prepared from the dilutions of the undiluted

SNAP formulation to ease interface analyses. This confirmation combined with the results of the ARXPS measurements enable one to study thin film samples prepared especially for surface analytical studies and have confidence that the data will be representative of the analyses of the undiluted SNAP films.

The XPS and TOF-SIMS analyses are complementary concerning film uniformity, with no differences seen between surface and bulk. Additionally, from the TOF-SIMS analyses, the results show that the bulk of the film retains the expected organosilane character, which is formed in solution. There are no large Si_xO_y cluster fragments detected in the standard or films. The crosslinker works as expected due to the detection of C_xH_yON peaks associated with crosslinking.

Although the insulating nature of this organic coating resulted in XPS binding energy shifts (which made binding energy assignments difficult), the ARXPS and the TOF-SIMS results in combination support that the bulk of the SNAP film retains the expected organosilane character. There is little or no evidence of the large variation of other possible reactions occurring during film application and cure. However, more work needs to be done in two areas of this research: first, a charge referencing method for the XPS data must be developed and second, investigation of the adhesion properties of the coatings must be continued.

REFERENCES

1. Vreugdenhil, A. J., Balbyshev, V. N., and Donley, M. S., "Nanostructured Silicon Sol-Gel Surface Treatments for Al 2024-T3 Protection," *Journal of Coatings Technology*, Vol. 73, No. 915, 2001, pp.35-43.
2. Bart, F., Guittet, M. J., Henriot, M., Thromat, N., Gautier, M., and Duraud, J. P., "Surface Analysis of Wide Gap Insulators with XPS," *Journal of Electron Spectroscopy and Related Phenomena*, Vol. 69, 1994, pp. 245-258.
3. Beamson, G., and Briggs, D., *High Resolution of Organic Polymers*, Wiley, New York, 1992, p. 26.
4. Crist, B Vincent, *Handbooks of Monochromatic* Spectra, XPS International, Kawasaki, Japan, 1999.
5. Johanson, L., Campbell, J.M., Koljonen, K., and Stenius, P., "Evaluation of Surface Lignin on Cellulose Fibers with XPS," *Applied Surface Science*, Vol. 144-145, 1999, pp. 92-95.

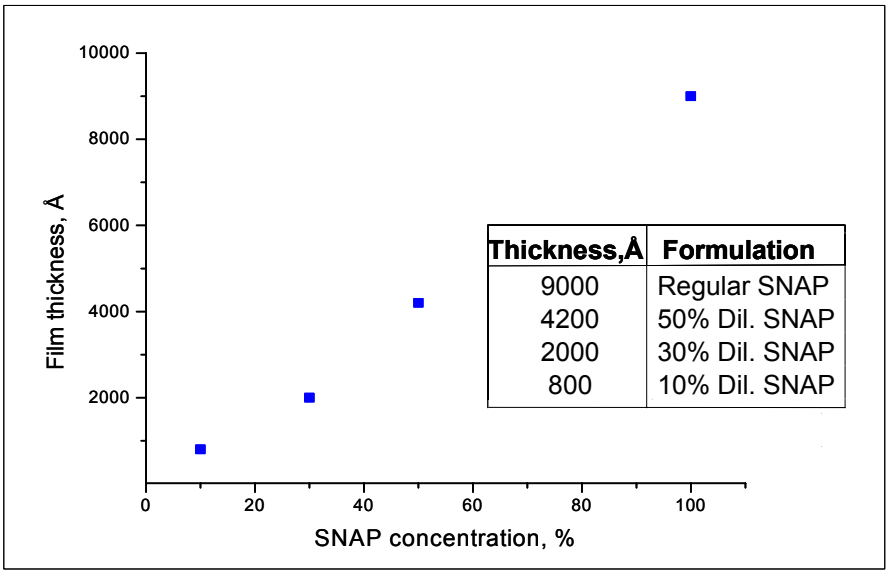

FIGURE 1. – Plot of Film Thickness vs. SNAP Solution Concentration.

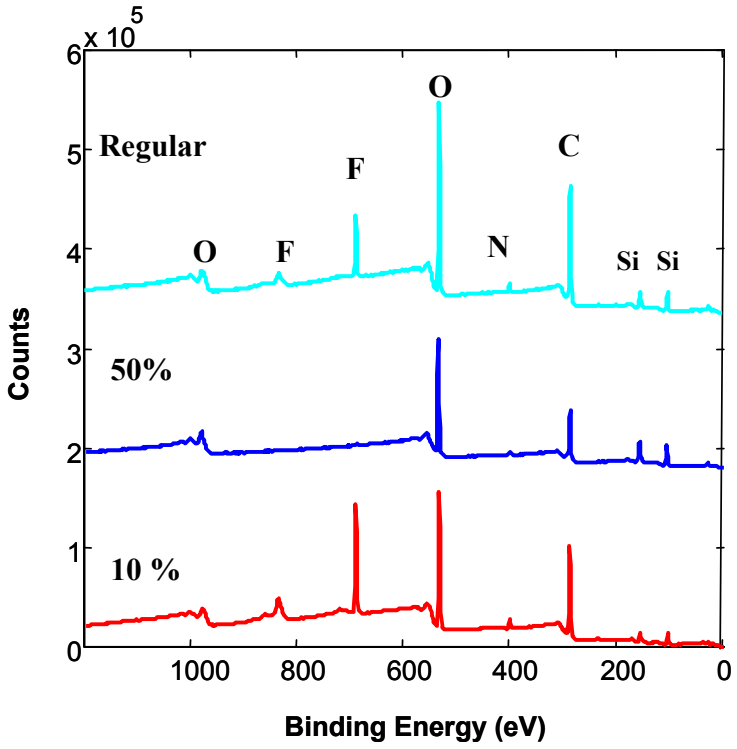

FIGURE 2. XPS Survey spectra of SNAP and dilutions of 10 and 50 percent show elemental compositions of the films.

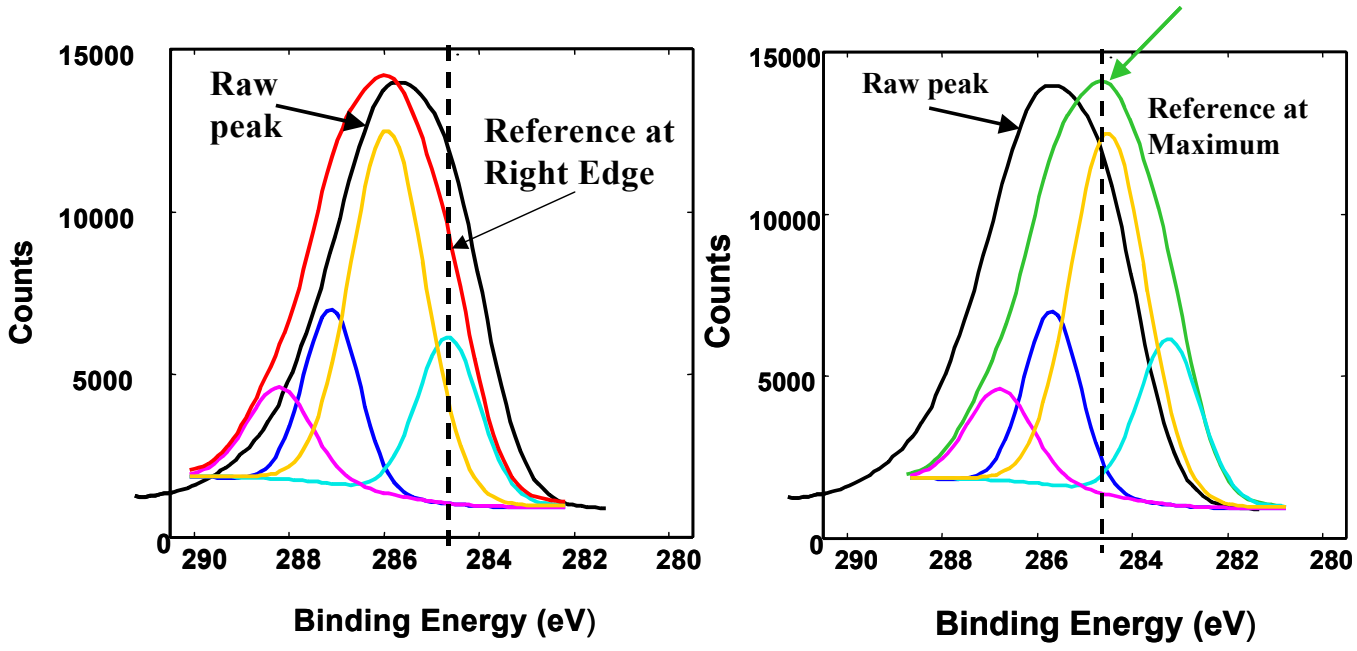

3a) 3b)

FIGURE 3. Curve fitting the C 1s peak when referenced at a) the right edge of peak and b) the maximum of peak. Fitted binding energy values are dependent on which part of the peak is positioned at the reference binding energy of 285.0 eV.

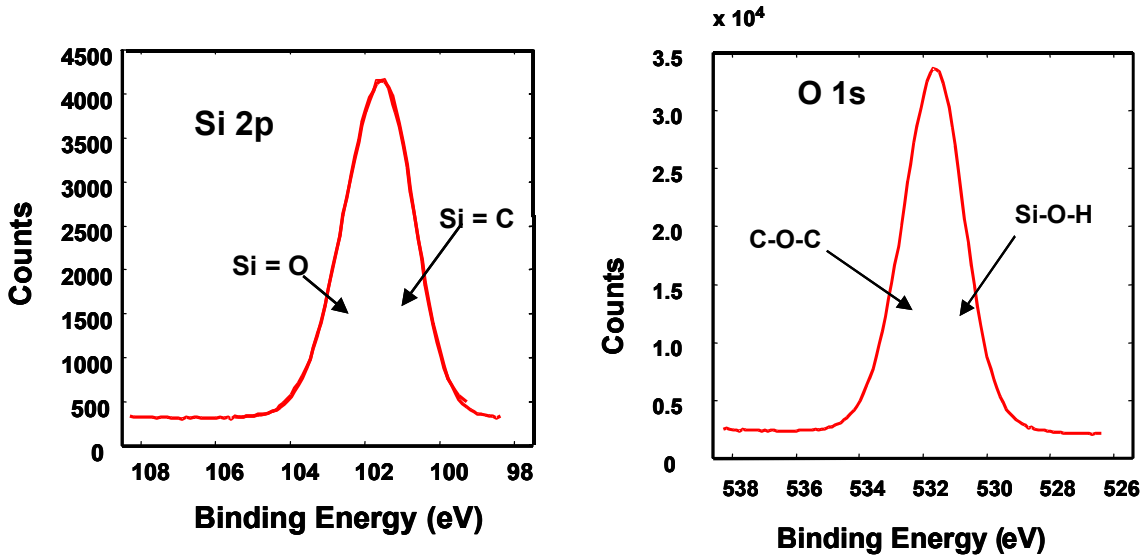

FIGURE 4. High resolution scans of the Si 2p and O 1s peaks.

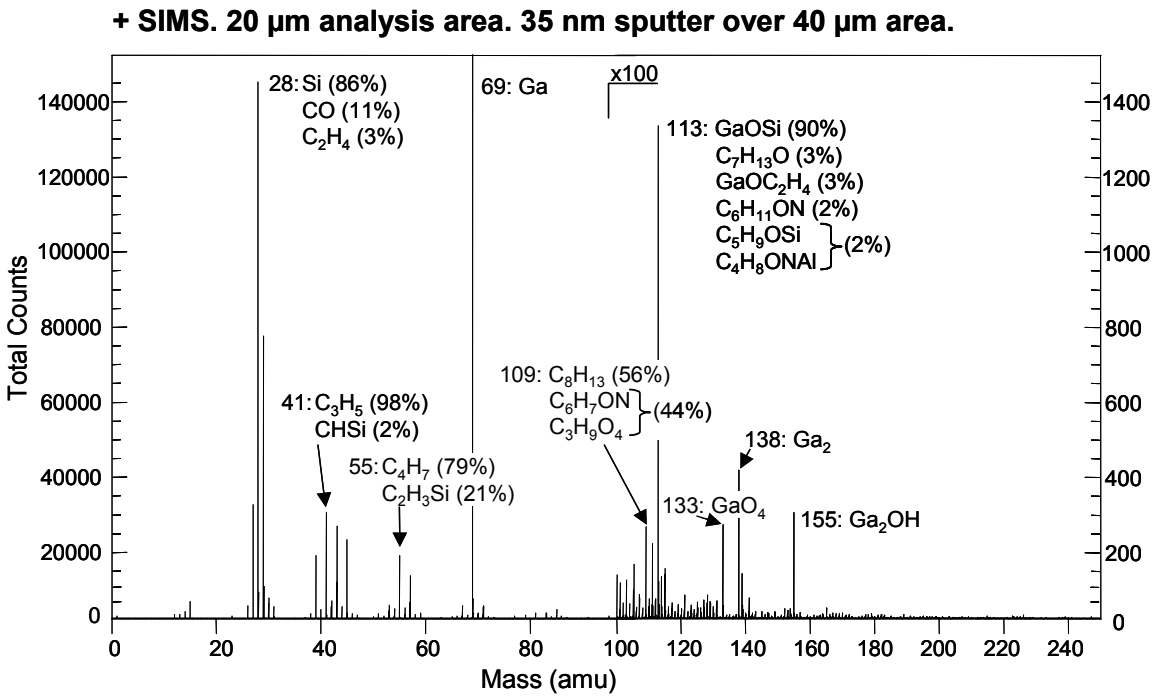

FIGURE 5. + SIMS spectrum of SNAP Coating, Mass 0 – 250 (amu)

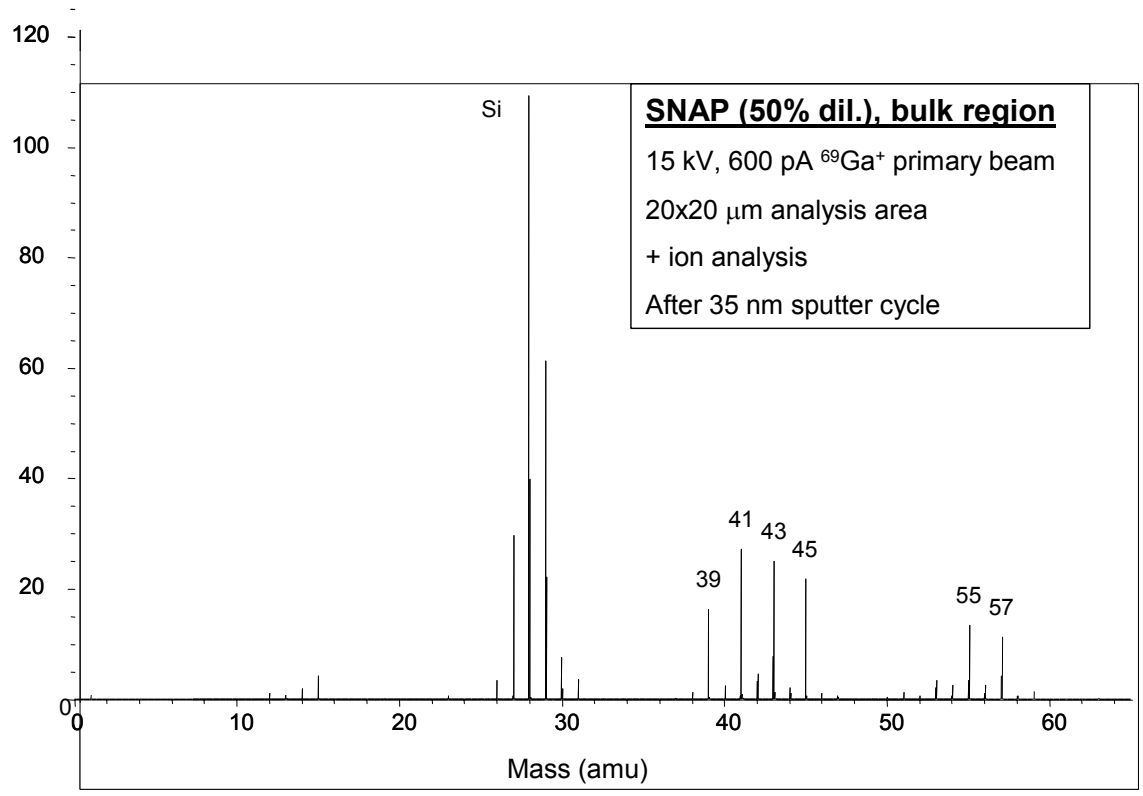

FIGURE 6. + SIMS spectrum of SNAP Coating, Mass 0 – 65 (amu)

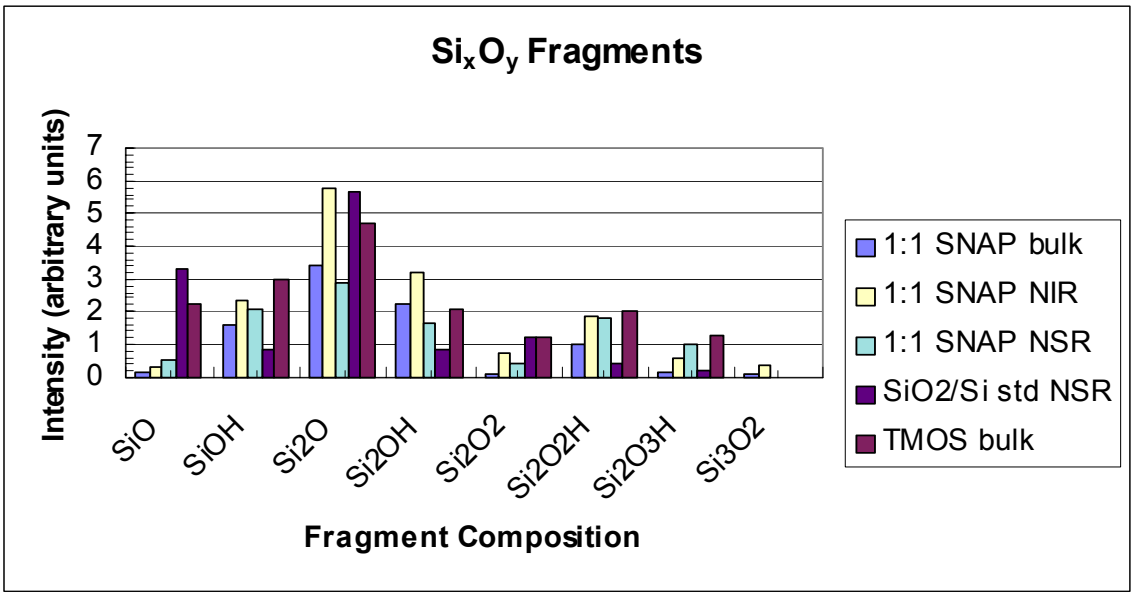

Si$_x$O$_y$ cluster fragments with Si > 3 not detected

FIGURE 7. Summary of TOF-SIMS Data for Si$_x$O$_y$ Fragments.

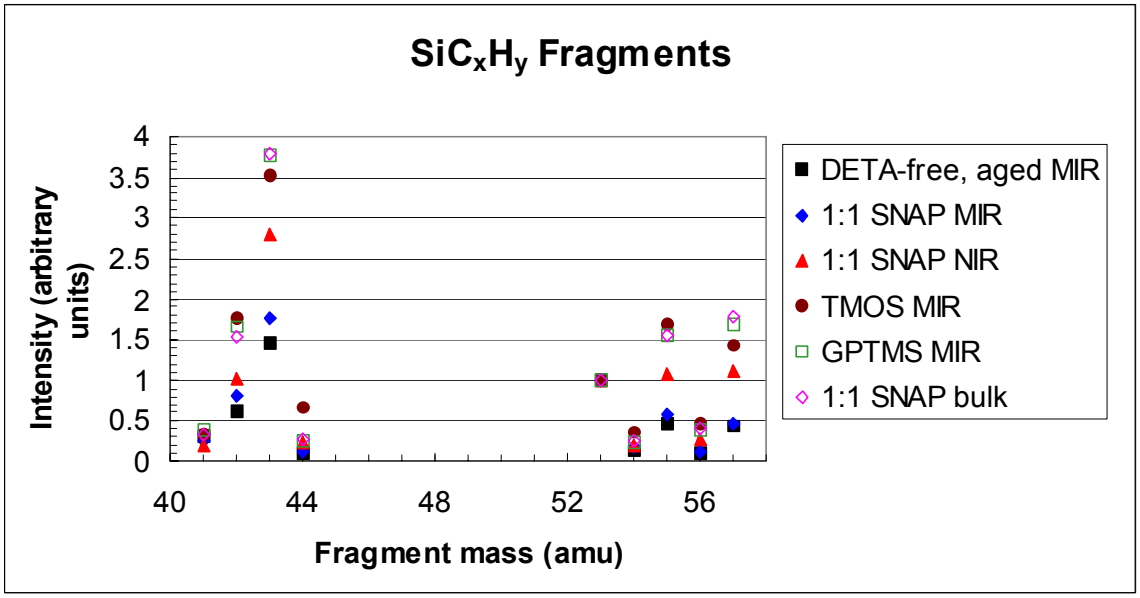

Organosilane content in bulk region is unchanged from precursor

FIGURE 8. Summary of TOF-SIMS Data for SiC$_x$H$_y$ Fragments.

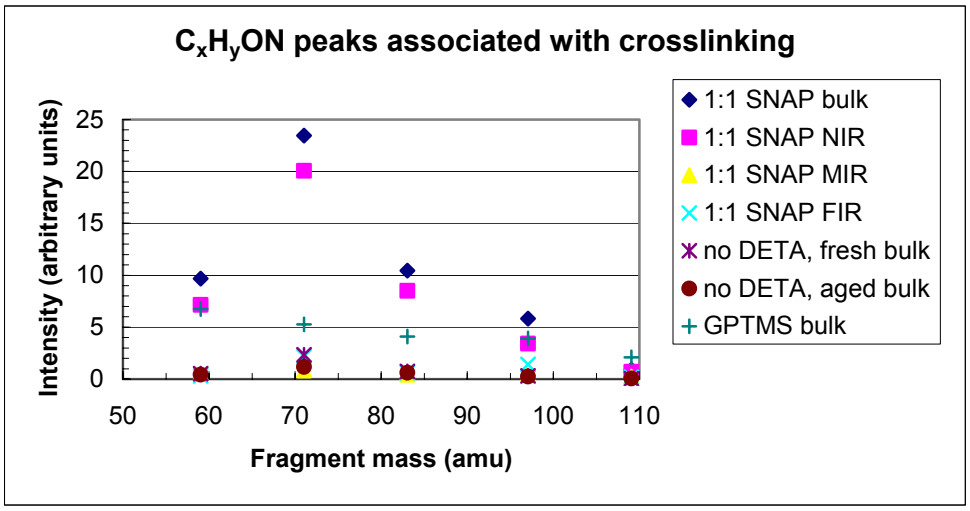

FIGURE 9. C_xH_yON mass fragments demonstrating the crosslinking in the film.

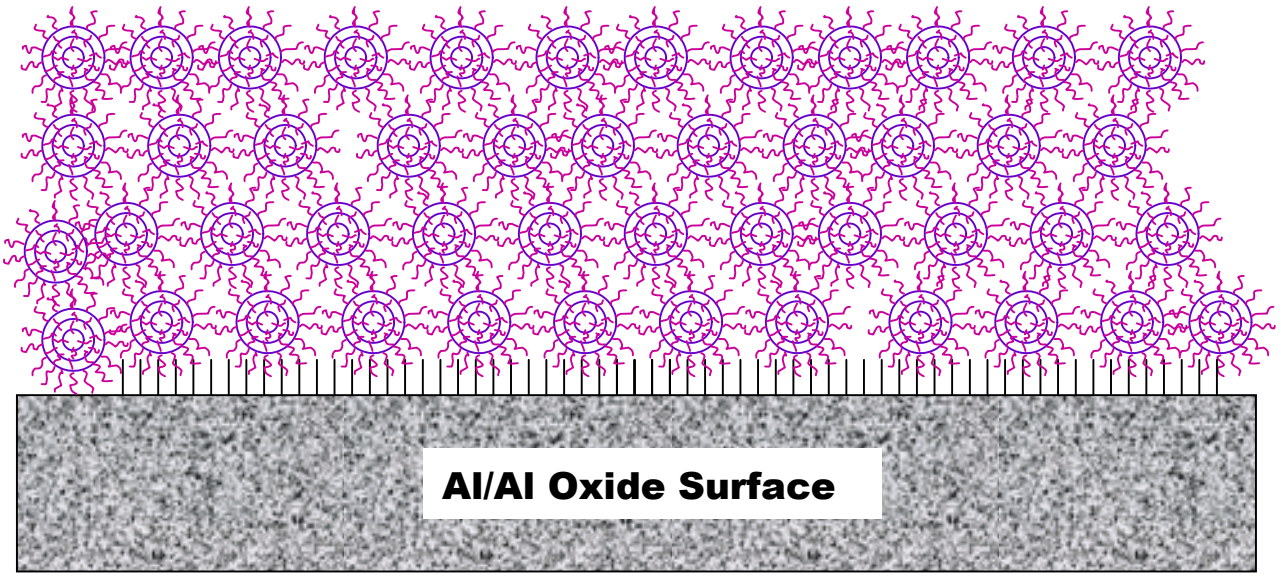

FIGURE 10. Model of SNAP coating on Aluminum/aluminum oxide surface shows the "fuzzy tennis ball" nature of the SNAP coating.

DEVELOPMENT OF PERMANENT FOUNDATION LAYER COATINGS FOR CORROSION PROTECTION OF AA2024-T3

J. A. Johnson,[*] T. D. Dang,[**] and N. N. Voevodin[***]

[*]Nonstructural Materials Branch
Air Force Research Laboratory
Wright-Patterson AFB, OH 45433

[**]Polymers Branch
Air Force Research Laboratory
Wright-Patterson AFB, OH 45433

[***]University of Dayton Research Institute
Dayton, OH 45469.

ABSTRACT

The Air Force has a requirement for the development of high performance aircraft coatings as an integral part of a long life chromate-free corrosion protection system. The basic theory and fundamentals regarding development of a 30+ year "permanent foundation layer" is outlined and the preliminary work regarding covalent bonding between the substrate and primer as well as long term acid hydrolysis resistance shows promise for further research. Organically functionalized sol-gel coatings were investigated as a method to obtain covalent adhesion between an AA2024-T3 substrate and a free radical cure organic primer. The mixed zirconate-silane coatings generated can covalently bond to an aluminum oxide surface through the zirconate component, while the allyl/vinyl silanes components provide the necessary functionality for incorporation into a free radical organic cure. The samples developed were shown via FTIR spectroscopy to contain the required unsaturated organic functionality and potentiodynamic scan (PDS) data show a shift of the corrosion potential to the more noble region for all formulations. The open circuit potential for the allyltrimethoxy silane-zirconate system was found to be -0.5 V, -0.35 V for vinyltriethoxy silane-Zr, and -0.25 V for allyltriethoxy silane-Zr systems. The requirement for long term acid hydrolysis resistance in an organic primer coating has prompted investigation into the use of benzoxazole based polymers as main components. The synthesis of a polyfunctional n-allyl pyrazole polybenzoxazole and difunctional oxy-allyl pyrazole benzoxazole monomer are outlined. Due to the inherent limitation of allyl functional groups toward self-polymerization, photoinitiated free radical cure coatings could not be obtained at ambient temperatures. However, a viable coating was obtained though the use of a difunctional thiol as a co-reactant in a free radical step-growth thiol-ene mechanism.

INTRODUCTION

The aging U.S. Air Force legacy aircraft fleet (e.g., KC-135, C-130, F-15, etc.) has a well-documented corrosion problem.[1] The currently used coating systems generally incorporate a chromated conversion coating (CCC) surface treatment (e.g., Alodine 1200S) and a solvent-borne epoxy-polyamide primer that is pigmented with a strontium chromate inhibitor. While this system is effective at reducing corrosion, the epoxy coating liberates relatively high levels of volatile organic content (VOC) and hazardous air pollutants (HAPs) upon application. Furthermore, toxic Cr^{6+} is present in both the surface treatment and coating. Both environmental and toxicity issues are compounded by the fact that this coating system is replaced every 6-8 years on average. The size of the aging legacy fleet of AA2024-T3 skinned aircraft is rather large and the current trend is to greatly extend these aircrafts' projected lifetimes, as much as four times the original estimate.[2] Given the environmental and economic impact of the de-paint/paint cycle as well as the reduction in aircraft mission readiness, the Air Force has a specific need for a surface treatment and primer coating system that will maintain adequate performance for a minimum of 30 years, a so-called "permanent foundation layer" (PFL). This layer should be non-chromated, provide adequate corrosion protection, and act as the interface between the substrate and a topcoat that will provide the necessary aesthetic and signature properties. In addition, the PFL should facilitate non-destructive evaluation (NDE) corrosion inspection techniques to eliminate the need to de-paint for scheduled inspection. Figure 1 is a proposed schematic that depicts the PFL layer (i.e., surface treatment and permanent primer) providing the required adhesion and corrosion protection in a complete coating system.

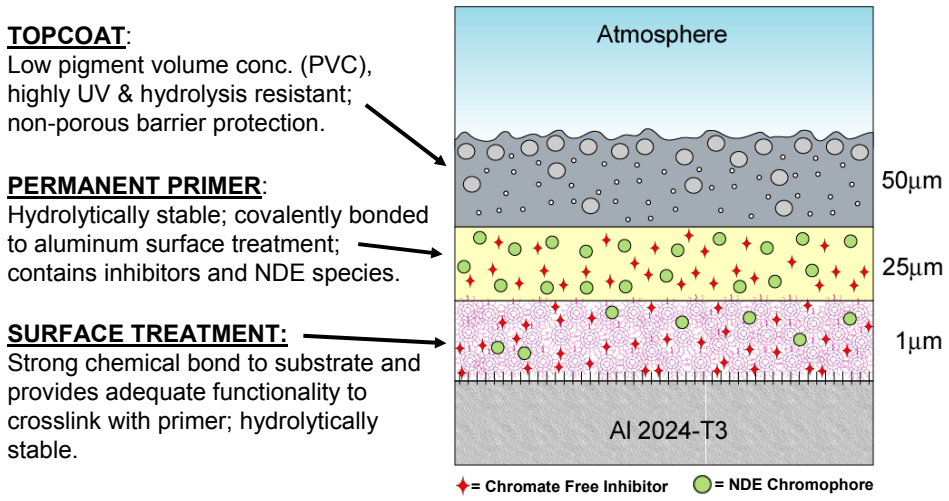

FIGURE 1. A proposed schematic of a permanent foundation layer (PFL) incorporated into an extended durability coating system for AA 2024-T3 skin aircraft. The PFL consists of the surface treatment and permanent primer and would be expected to last 30 years or more.

The Air Force Research Laboratory – Nonstructural Materials Branch (AFRL/MLBT) is actively pursuing the development of a PFL and has identified two key initial design requirements: a covalently bonded adhesion mechanism to the aluminum alloy substrate and hydrolytic stability of the polymer coating resin, particularly at low pH. The work presented in this communication does not address chromium-free inhibitor research or NDE techniques, but rather focuses on the development of novel surface treatments and polymeric resin materials for future PFL coating formulation development and testing.

SURFACE TREATMENT

The purpose of the surface treatment is to provide superior adhesion between the primer coating and substrate and, if possible, chemically alter the surface of the substrate, rending it less susceptible to corrosion. Since AA2024-T3 surfaces are primarily composed of mixed aluminum oxides, we have investigated the use of compatible sol-gel techniques to produce very thin films that are capable of covalently bonding to the oxide. While silanes and other silicon-

based sol-gel films are widely used as adhesion promoters for glass substrates,[3] the thermodynamic stability of the Al-O-Si bond that would provide the crucial covalent adhesion component for our systems is often disputed, despite reports of its existence.[4] The hydrogen bonding adhesion component of silicon-based sol-gels to aluminum oxide surfaces is expected to be quite high. Nevertheless, our initial work has been restricted to those chemistries that generate documented thermodynamically stable covalent bonds, namely zirconium based sol-gels.[5,6]

We are interested in utilizing the surface treatment as a covalent bonding bridge between the inorganic substrate and an organic primer coating. This inherently dictates that the surface treatment must also have the appropriate chemical functionality to react with the primer to ensure adhesion between the layers. Our prospective primer curing mechanism involves ultraviolet (UV) light initiated polymerization, thus, our surface treatment must have vinyl, allylic or another suitable functionality present. Due to the very limited number of organic functionalized zirconium sol-gel precursors available, our surface treatment will also include an appropriate amount of a functionalized silicon based precursor that can successfully co-react with the zirconium species. Previous work by AFRL/MLBT and a contractual effort with Boeing Inc. has produced viable zirconium/silicon hybrid sol-gel coatings that have shown increased adhesion and corrosion protection.[7] This technology involved the use of both tetrapropoxy orthozirconate (TPOZ) and glycidoxypropyl trimethoxysilane (GPTMS) sol-gel precursors. We have modified our formulations to include various UV curable functional species such as vinyl trimethoxy silane (VTMS), allyl trimethoxy silane (ATMS), and allyl triethoxysilane (ATES), shown in Figure 2, as substitutes for GPTMS.

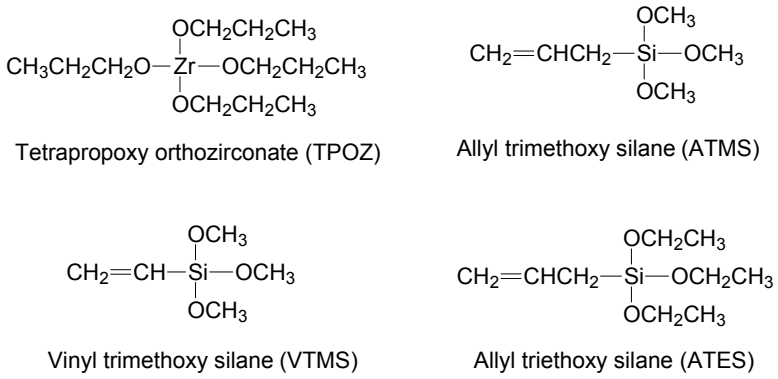

FIGURE 2. The sol-gel precursors utilized in the development of a UV curable organically functionalized surface treatment for AA2024-T3.

The purpose of using a mixed silicon/zirconium system is to generate a film that bridges the covalent substrate bonding of the zirconate with the organic functionality of the silane. The basic chemistry along with an idealized, albeit over-simplified, structure of a gradient hybrid sol-gel film is shown in Figure 3.

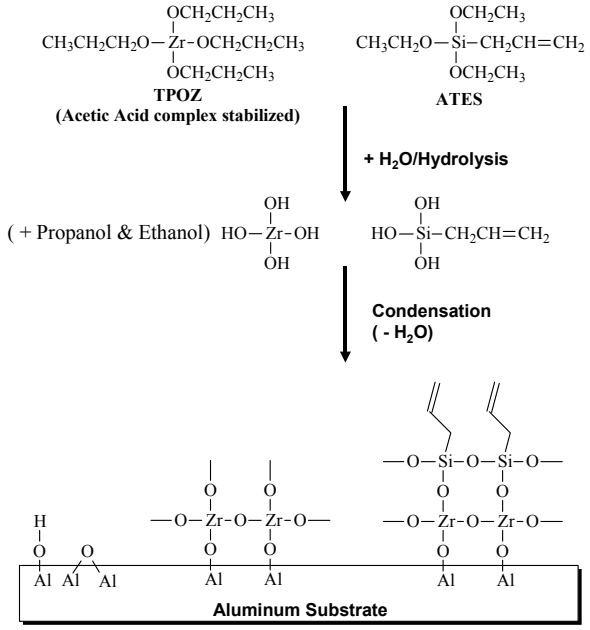

FIGURE 3. An idealized and simplified schematic of a Si-Zr hybrid sol-gel system used to generate a tailored organic functionality that is covalently bonded to an aluminum substrate.

PERMANENT PRIMER

Our permanent primer research is focused on development of hydrolyticly stable polymer binders that are capable of covalently bonding to an appropriate surface treatment under ambient conditions. The number of available coating technologies and chemistries for aircraft structures is quite limited due to the necessity of ambient cure conditions and physical size limitations. Hence, nearly every current coating system utilizes either the epoxy-amine or isocyanate-polyol (i.e. urethane) reactions. While these coatings perform marginally well over the current limited lifetime expectations, they are not inert to hydrolytic degradation nor can they provide adequate protection over the desired 30+ year lifetime. Epoxy-amine coatings, which are the mainstay of aircraft primers, are particularly susceptible to attack by acidic solvents. Upon exposure to acidic conditions, a reaction occurs with the tertiary amine linkages present at crosslink sites, resulting in the formation of a salt. The hydrophilic salt groups then increase the solubility of water in the film, thereby increasing water permeability and softening, making the film more susceptible to damage and exposing the metal surface to corrosive electrolyte.[8] The general order of hydrolytic stability for common aircraft coating chemical linkages is shown in Figure 4.

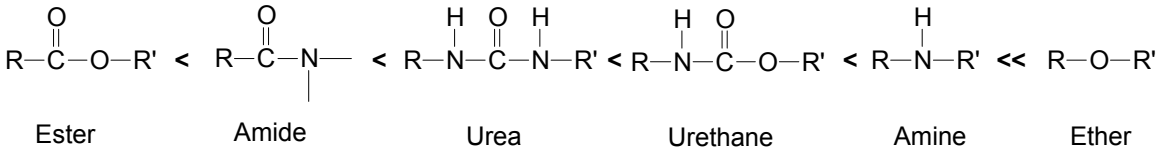

FIGURE 4. The general qualitative ranking of the hydrolytic stability of common polymer linkages found in ambient cure aircraft coatings.

The first design characteristic of a permanent primer resin is the utilization of oligomeric and/or polymeric components that have an inherently hydrolytically stable backbone structure.

This requirement eliminates nearly all of the conventional coating materials available to the formulator. Utilizing AFRL's prior experience with acid stable polymer architectures, we have begun investigation into the use of polybenzoxazole (PBO) based oligomers and polymers for the PFL application. PBO's (Figure 5) have superb resistance against acidic degradation, showing no molecular weight loss over time in concentrated phosphoric acid solution.

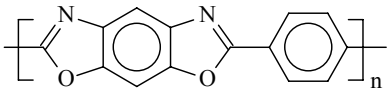

FIGURE 5. The basic chemical structure of a polybenzoxazole (PBO).

The second PFL design characteristic dictates that the crosslinking mechanism must also yield a hydrolyticly stable linkage. This inherently rules out the traditionally used epoxy-amine and urethane chemistries currently utilized. The ideal crosslinking mechanism is a free radical polymerization, which retains a very stable carbon-carbon main chain linkage. Several reviews summarizing the chemistry, advantages and disadvantages of UV cure coating systems are available.[9] The general scheme of this chain growth polymerization, induced by a UV activated inititator (I), is shown in Figure 6.

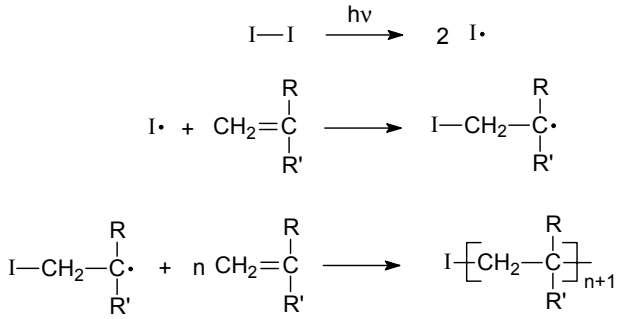

FIGURE 6. The general processes involved in a UV initiated free radical chain growth polymerization. The resultant polymer is extremely hydrolytically stable due to only carbon-carbon bonds present in the backbone.

There are several important formulation aspects to UV cure coating technology that must be considered. The reactivity of the unsaturated monomer or polyfunctional oligomers plays a critical role in the ability to obtain a fully cured (i.e., polymerized and crosslinked) coating without the need for excessive UV exposure and temperature. For this reason, nearly all commercial UV cure coatings are based on the highly reactive acrylate species. In general, acrylic coatings display very good hydrolysis resistance because the main polymer chain is not hydrolysable. However, in both acrylate and methacrylate systems the side group attached via the ester linkage can be hydrolyzed off, resulting in a significant change in the mechanical and barrier properties of the coating. While this phenomenon cannot occur with allyl and vinyl based polymers, there are no known coating formulations based entirely on these species due to their low reactivity towards self-polymerization. The general order of UV cure reactivity for unsaturated functional groups is given in Figure 7.

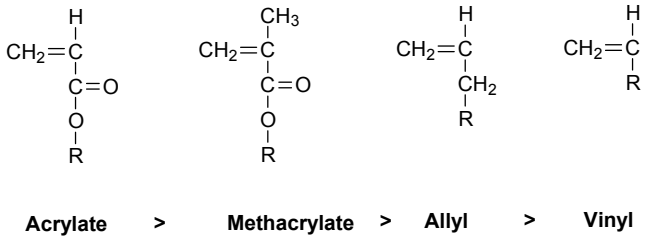

FIGURE 7. The general order of reactivity for UV curable functionalities. Allyl and vinyl (with the exception of vinyl ethers) are generally not reactive enough to self polymerize.

The original intention of the PFL coating development was to functionalize PBO oligomers with allyl groups and UV crosslink the oligomers together for curing. This approach is non-ideal for several reasons: the mechanism of chain growth polymerization precludes incorporation of the PBO moiety into the backbone structure of the polymer; the reactivity of the

allyl group is not high enough to obtain a significant molecular weight or crosslink density under ambient conditions; chain growth UV cure formulations inherently require that the starting components be relatively low viscosity liquids to allow enough molecular mobility for complete reaction to occur and not trap solvent in the film.

One alternative to conventional UV cure coatings that we are investigating is based on the "thiol-ene" reaction. This technique allows control of the backbone polymer structure because it is a two-component free radical step growth (versus chain growth) polymerization. As such, thiol-ene formulations require two separate reactive components, a poly-thiol species and a poly-unsaturated (i.e., allyl, vinyl, or alkene) compound. While it is not absolutely necessary, a photosensitive initiator such as benzophenone is usually added as well.[10] Upon UV irradiation, a hydrogen atom is abstracted from the thiol rendering a thiyl radical. The resultant radical then adds to the polyene double bond resulting in a thiol ether crosslink and radical transfer to the methine carbon. This radical then abstracts a hydrogen atom from another thiol reactant, completing the crosslinking reaction and re-initiating another reaction. The benzophenone ketyl radicals that were initially generated mostly dimerize into non-reactive pinacols. The general thiol-ene reaction scheme is represented in Figure 8 and Figure 9.

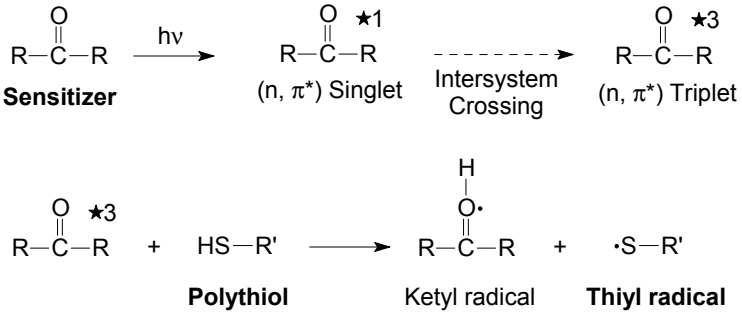

FIGURE 8. Initiation of the thiol-ene crosslinking reaction via a photosensitive species such as an aryl ketone.

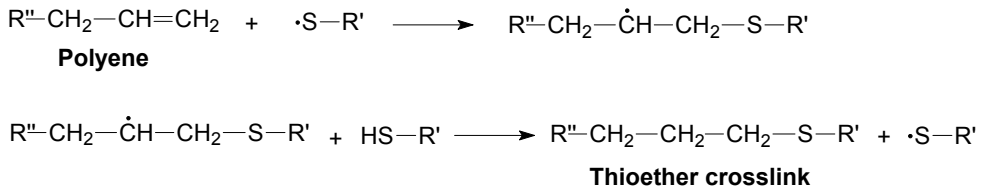

FIGURE 9. The free radical polymerization of a polyene and polythiol via hydrogen abstraction.

If the proper starting materials are chosen, the only hydrolytically susceptible linkage is that of the thioether, which is analogous to an oxyether linkage, one of the most stable in conventional coating chemical structures. Polyphenylene sulfide, which contains only thioether linked phenyl rings, has one of the best acid resistance properties of all industrial polymers. Excluding the use of chain growth polymerization to obtain a pure carbon backbone via acrylates or methacrylates, there must be some form of heteroatom linkages present. Of those available, the ethers/thioethers are probably the most suitable for this application and have the added effect of imparting additional flexibility to the film due to the ease of rotation around this type of bond. Thiol-ene based coating development began in the late 1970's and was very short lived due to the cost competitiveness of acrylates and the unpleasant odor of polythiols. It should also be noted that the limited work performed did not focus on enhancement of hydrolytic stability and included materials with ester linkages.

EXPERIMENTAL

FUNCTIONALIZED ZIRCONATE SOL-GEL FILMS

AA2024-T3 coupon substrates were first cleaned in a standard four bath cleaning process. Samples were first immersed in a ten-minute immersion in Oakite® Aluminum Cleaner 164 (alkaline detergent) with moderate air agitation at 55-60°C, followed by a two-minute immersion in distilled water at 50°C. Next, the coupons were immersed in a room temperature solution of Turco Smut-Go NC-B deoxidizer with moderate nitrogen gas agitation for ten

minutes. In the final bath the samples were rinsed in room temperature distilled water for two minutes. In an effort to reduce bath cross-contamination, the substrates are rinsed with flowing distilled water briefly before the second and forth steps. Finally, the coupons were blown dry with compressed air and stored covered until use.

Concurrently, two separate sols were formulated. The first sol was made by the addition of zirconium (IV) tetrapropoxide (Gelest, Inc.) to glacial acetic acid (J. T. Baker, Inc.) at a 1:4 molar ratio in a dry glove box and allowed to stir for 15 minutes. The stabilized zirconate sol was then removed from the glove box and water was added in a 10:1 $Zr:H_2O$ molar ratio. The second sol was made by combining glacial acetic acid with ATMS, ATES, or VTMS in a 3:1 molar ratio. All silanes were procured from Gelest, Inc. and used as received. After dilution with de-ionized water, the zirconate and silane sols were stirred separately for an additional fifteen minutes, after which, they were combined at a 1:3 molar ratio between Si and Zr. The mixed sols were allowed to stir for an additional thirty minutes, at which time additional excess water and 0.1g of surfactant solution (4.11 g FC-430 + 1.02 g FC-177 in 100mL water) was added. Immediately prior to film application, the sol-gel formulation was transferred to a Teflon® dip cell. The substrate coupons were dip coated one cycle using a Chemat Technology Inc. Model 201 dip-coater at a draw speed in the range of 10-12 cm/minute.

The resultant films were qualitatively characterized by glancing angle FTIR spectroscopy (Bruker Equinox 55) for the presence of allyl functional groups. The corrosion potentials of the sol-gel coated coupons, as well as an Alodine 1200 conversion coating and uncoated coupon, were determined from potentiodynamic polarization screening tests. Potentiodynamic polarization curves of specimens were taken in 3.5% NaCl solution at a rate of 0.5 mV/s, using a Gamry potentiostat PC3-300 (Gamry Instruments, Warminster, PA). An initial free corrosion

potential (open circuit potential, E_{oc}) measurement was taken and the scan range was (E_{oc}-20) mV to (E_{oc}+500) mV.

SYNTHESIS OF ALLYL FUNCTIONALIZED POLYBENZOXAZOLES

1H-pyrazole-3,5-dicarboxylic acid monohydrate (1.74 g, TCI America) was reacted with 2,2-bis(3-amino-4-hydroxyphenyl)hexafluoropropane (3.66 g, Daychem Inc.) in 83% polyphosphoric acid (33.5 g) at 180°C for 24 hours. Upon completion, the viscous product was precipitated in water and broken up using Waring blender in the presence of large amounts of water, yielding an off-white fibrous polymer. This precipitate was soxhlet extracted with hot water to remove any residual acid then vacuum-dried at 100°C for 24 hours. Allyl derivitization was performed by first dissolving sodium hydride (0.22 g) in anhydrous dimethylsulfoxide under nitrogen atmosphere. Next, the pyrazole-based PBO product (1.0 g) was added to the solution and stirred under mild heat until the polymer completely dissolved, forming a red colored homogenous solution. After the solution was cooled to room temperature, 0.3 g of allyl bromide was added and stirred under slight positive nitrogen pressure for 16 hours. During this time, the polymer solution turned yellow, indicating reaction completion. The product was precipitated into water and broken into a fine suspension using a Waring blender in the presence of large amounts of water to yield a yellow fibrous solid. This final product was then soxhlet extracted with hot hexane to remove any excess allyl bromide and the finally vacuum-dried at 100°C for 24 hours. The general reaction scheme is shown in Figure 10.

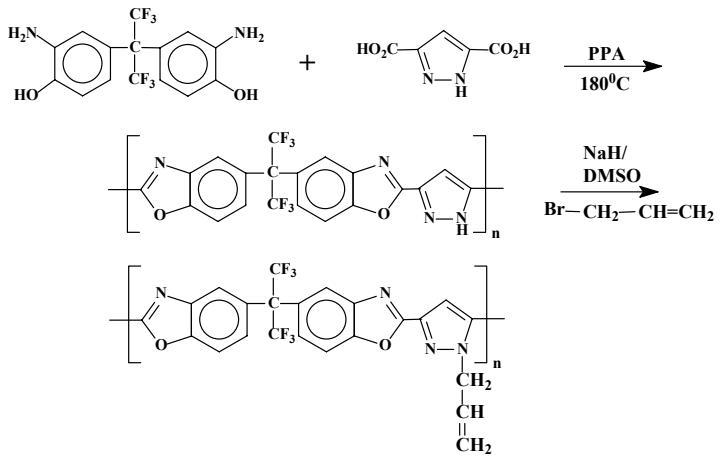

FIGURE 10. The reaction scheme used for synthesis of a 1H-pyrazole based PBO and subsequent n-allyl functionalization.

RESULTS AND DISCUSSION

FUNCTIONALIZED ZIRCONATE SOL-GEL FILMS

The resultant Zr/Si hybrid sol-gel films produced were defect free and very uniform in appearance. The FTIR spectra of each revealed the presence of the characteristic C-H and C=C stretches associated with the unsaturated allyl functionality. No depth profiling was performed at this time to determine the distribution of allyl functionality. An image of a typical Zr-VTMS sol-gel film as well as an abbreviated FTIR spectra compared against a pure zirconate sol-gel film are shown in Figure 11.

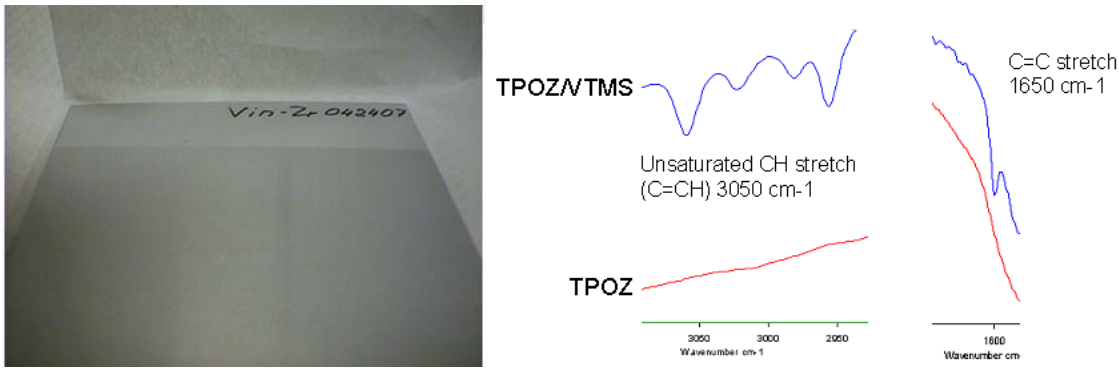

FIGURE 11. FTIR spectra of functionalized and unfunctionalized zirconate sol-gel films.

Potentiodynamic scan (PDS) data show a shift of the corrosion potential for the Zr based sol-gel systems to the more noble region, as compared with untreated substrate and Alodine surface treatment. The open circuit potential for Alodine surface treatment is around – 0.6 V, which is similar to bare aluminum. The open circuit potential for ATMS-Zr is -0.5 V, for Vin-Zr and Epoxy-Zr it is -0.35 V, and for ATES-Zr it is -0.25 V. All of the Zr-based coatings act to make the surface more noble. This phenomenon is most likely due to the covalent chemical interaction of the sol-gel film on the aluminum oxide surface layer. The results of the potentiodynamic scans are shown in Figure 12.

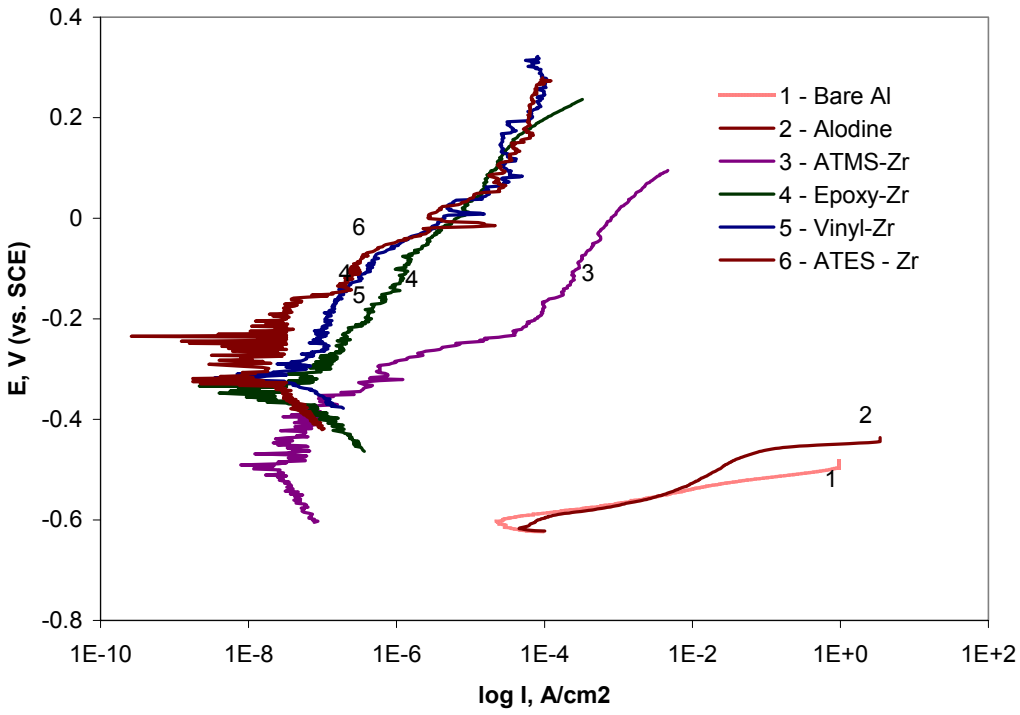

FIGURE 12. Potentiodynamic scans of various AA2024-T3 surface treatments.

ALLYL FUNCTIONALIZED POLYBENZOXAZOLES

Approximately 25 grams of the n-allyl pyrazole polybenzoxazole was recovered from the synthetic procedure and was soluble in both tetrahydrofuran (THF) and n-methyl pyrolidone

(NMP) solvents. The material displayed a high intrinsic viscosity, representative of a high molecular weight species. This was also verified by gel permeation chromatography results that indicated a repeat unit length of 3-6 units (~ 2,600 g/mol) and the ability to form thermoplastic films. Differential scanning calorimetry (DSC) results indicate a Tg in the range of 307-318° C for the crosslinked film since a crosslinking exotherm occurs around 240° C. The dimer oxy-allyl monomer synthesized was a crystalline solid soluble in NMP and is not an intrinsic film former. The structures of each product are shown in Figure 13.

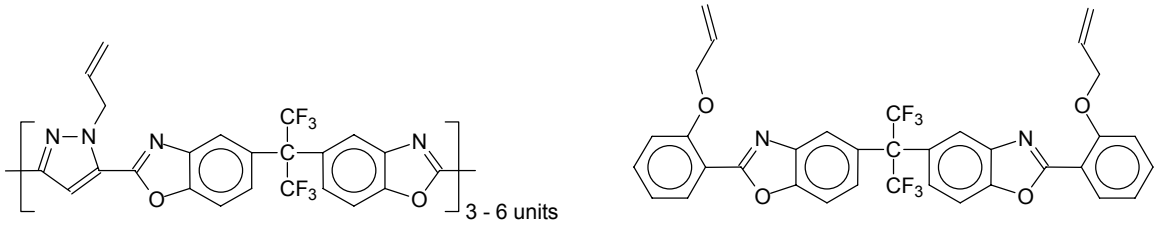

Polyfunctional n -allyl pyrazole PBO oligomer
25 grams synthesized

Difunctional oxy -allyl PBO monomer
5 grams synthesized

FIGURE 13. Chemical structures of the n-allyl oligomer and oxy-allyl monomer pyrazole based benzoxazoles that were synthesized.

Due to the small quantity of materials synthesized, only limited coating formulation efforts have been investigated thus far. The biggest limitation to the use of the current PBO materials is their solid phase at ambient temperature, which severely limits ambient cure rate when combined with the inherent low self reactivity of the allyl functionality. This property also dictates that a solvent be utilized to cast films. Since both materials are only soluble in THF or NMP, an additional problem results from the poor evaporation characteristics (THF is extremely volatile, while NMP is very slow) of the limited solvent choices, resulting in poor film quality.

Nevertheless, several attempts were made at solventborne formulations containing ~1wt% Irgacure 1700 photoinitiator with various blends of each material being irradiated with a

Fusion UV Model F300S (D bulb) source. Under ambient temperatures none of the formulations displayed full cure, however, under elevated temperature (~150° C) the n-allyl system displayed moderate crosslinking as observed by solvent resistance tests. The oxy-allyl material was observed to have a very low reactivity as indicated by reduced cure with increasing concentration in the formulations. Preliminary work on thiol-ene type crosslinking by incorporating a difunctional thiol (1,6-hexanedithiol) and benzophenone initiator does show promising results. A small amount of THF solvent was used to dilute the system to application viscosity, but was allowed to fully evaporate prior to cure. The presence of the dithiol species acted as a reactive diluent to prevent formation of a solid uncrosslinked film. Since this cure mechanism is step-growth, only the polyfunctional n-allyl material was suitable to obtain crosslinked films. Under ambient conditions and a stoichiometric ratio between both the n-allyl PBO and dithiol, a crosslinked film can be obtained with only 4 passes under the UV lamp. Initially, the resultant films are somewhat soft, but become increasingly hard after several minutes post cure as the system continues to crosslink. Excellent solvent resistance is observed as tested by double rubs with THF. Future work will include generation of samples for corrosion testing and thermal-mechanical testing. Additionally, samples will be made that incorporate crosslinking of the films on the allyl sol-gel surface treated aluminum to investigate the adhesion and corrosion resistance properties. A suitable accelerated test for hydrolysis resistance of coatings is currently being investigated and will be a major focus of all potential formulations.

CONCLUSIONS

- Organically functionalized sol-gel coatings were investigated as a method to obtain covalent adhesion between an AA2024-T3 substrate and a free radical cure organic primer. The

mixed zirconate-silane coatings generated can covalently bond to an aluminum oxide surface through the zirconate component, while the allyl/vinyl silanes components provide the necessary functionality for incorporation into a free radical organic cure. The samples developed were shown to contain the required unsaturated organic functionality and potentiodynamic scan (PDS) data show a shift of the corrosion potential to the more noble region for all formulations. The open circuit potential for the ATMS-Zr system was found to be -0.5 V, -0.35 V for Vin-Zr, and -0.25 V for ATES-Zr systems.

- The requirement for long term acid hydrolysis resistance in an organic primer coating has prompted investigation into the use of benzoxazole based polymers as main components. The synthesis of a polyfunctional n-allyl pyrazole polybenzoxazole and difunctional oxy-allyl pyrazole benzoxazole monomer were outlined. Due to the inherent limitation of allyl functional groups toward self-polymerization, photoinitiated free radical cure coatings could not be obtained at ambient temperatures. However, a viable coating was obtained though the use of a difunctional thiol as a co-reactant in a free radical step-growth thiol-ene mechanism.

- The basic theory and fundamentals regarding development of a 30+ year permanent foundation layer (PFL) was outlined and the preliminary work in this area presented shows promise for further research. Future work will focus on characterization and testing of hybrid sol-gel films for distribution of organic functional groups and the chemical interface between the substrate and film. Additional benzoxazole based materials, as well as other unsaturated non-hydrolizable species, will be obtained and evaluated with various poly-thiol co-reactants as protective films. The mechanism of adhesion between sol-gel and organic primer will be investigated by FTIR spectroscopy. The mechanical properties, acid

hydrolysis resistance, and corrosion protection properties of the PFL coating stack will be evaluated and compared against current systems.

ACKNOWLEDGEMENTS

The authors acknowledge Lt Col Paul C. Trulove for financial support under Air Force Office of Scientific Research Task # 2303 BL.

REFERNECES

1. Air Force Office of Scientific Research "Air Force Blue Ribbon Advisory Panel on Aircraft Coatings," Air Force Materiel Command, 1995.
2. National Research Council *Aging of U.S. Air Force Aircraft*; National Academy Press: Washington D.C., 1997.
3. Brinker, C. J.; Scherer, G. W. *Sol-Gel Science*; Academic Press: San Diego, 1990.
4. Leung, Y. L.; Zhou, M. Y.; Wong, P. C.; Mitchell, K. A. R.; Foster, T. *Applied Surface Science* **1992**, *59*, 23-29.
5. U.S. Patent 5,939,197; “Sol-Gel Coated Metal”, Blohowiak, K. Y.; Osborne, J. H.; Krienke, K. A.; The Boeing Company, 1999.
6. Hirai, S.; Shimakage, K.; Wada, K. *Journal of the American Ceramic Society* **1998**, *81*, 3087.
7. AFRL-ML-WP-TR-2001-4133 Technical Report, “Advanced Corrosion Resistant Aircraft Coatings”, Oct. 2000.
8. Zeno W. Wicks, J.; Jones, F. N.; Pappas, S. P. *Organic Coatings: Science and Technology*; John Wiley & Sons, Inc.: New York, 1992; Vol. Volume 1: Film Formation, Components, and Appearance.

9. Koleske, J. V. *"Free Radical Radiation Curing",* Federation Series on Coatings Technology; Blue Bell, PA, 1997.
10. Morgan, C. R.; Ketley, A. D. *Journal of Polymer Science: Polymer Letters Edition* **1978**, *16*, 75-79.

SPECTROSCOPIC INVESTIGATION OF SNAP SOLUTION CHEMISTRY

R. A. Mantz, V. N. Balbyshev[1], and M.S. Donley

Air Force Research Laboratory, Materials and Manufacturing Directorate,
Nonmetallic Materials Division, Nonstructural Materials Branch, Coatings Research Group,
Wright-Patterson AFB, OH 45433-7750

ABSTRACT

Current Air Force coating systems for corrosion protection rely on hexavalent chromium compounds to act as corrosion inhibitors. Due to the toxicity of hexavalent chromium compounds efforts are underway to develop environmentally benign alternatives. New coating systems with chemically tailored surfaces and interfaces have promise for attaining effective corrosion protection without toxic inhibitor compounds. The self-assembled nano-phase particle (SNAP) process is a hybrid sol-gel method that uses pre-formed nanosize organosilicate particles that are cross linked upon application. In order to better understand the coating properties, the solution chemistry of the SNAP solution has been investigated using NMR, GPC / light Scattering, and infrared spectroscopy.

INTRODUCTION

The aging U.S. Air Force legacy aircraft fleet (e.g., KC-135, C-130, F-15, etc.) has a well-documented corrosion problem.[1] Corrosion protection of aluminum-skinned aircraft and development of improved environmentally benign surface treatments for aluminum aerospace alloys are high priority topics for U.S. Air Force research. Current coating systems for aircraft corrosion protection are based on a traditional chromate surface treatment, primer, and topcoat. These coating systems generally incorporate a chromated conversion coating (CCC) surface treatment (e.g., Alodine 1200S) and a solvent-borne epoxy-polyamide primer that is pigmented with a strontium chromate inhibitor. A primary failure mechanism in traditional coating systems

[1] Universal Technology Corp., 1270 N. Fairfield Rd., Dayton, OH 45432-2600

results from a lack of hydrolytic stability at the substrate-coating interface. The loss of adhesion here allows accumulation of water and ions at this interface, which results in the formation of a corrosion cell. While this system is effective at reducing corrosion, toxic Cr^{6+} is present in both the surface treatment and coating.

However, the toxicity and carcinogenic properties of chromium has caused federal agencies, in particular the EPA, to impose severe restrictions on its use.[2] The U.S. Department of Health and Human Services has recently released the 9th Report on Carcinogens (January 2001) in which hexavalent chromium compounds, including the most widely used chromate corrosion inhibitor, strontium chromate, are listed as known human carcinogens. In addition, OSHA and the FDA all have restrictive exposure limits on hexavalent chromium compounds.[3]

Both environmental and toxicity issues are compounded by the fact that this coating system is replaced every 6-8 years on average. The size of the aging legacy fleet of AA2024-T3 skinned aircraft is rather large and the current trend is to greatly extend these aircraft projected lifetimes, as much as four times the original estimate.[4] Given the environmental impact of the de-paint/paint cycle, the Air Force has a specific need for a chromate free surface treatment and primer coating system that will provide adequate corrosion protection.

In order to address these needs the Air Force Research Laboratory has begun to develop new coating systems with chemically tailored surfaces and interfaces that may provide an effective approach for attaining effective corrosion prevention without incorporation of heavy metal inhibitors. Because AA2024-T3 surfaces are primarily composed of mixed aluminum oxides, we have investigated the use of compatible sol-gel techniques to produce very thin films that are capable of covalently bonding to the oxide. Silanes and other silicon-based sol-gel films are widely used as adhesion promoters for glass substrates,[5] and Al-O-Si bonds have been

observed for silane coatings providing a covalent adhesion component.[6] The hydrogen bonding adhesion component of silicon-based sol-gels to aluminum oxide surfaces is also expected to be quite large. The Self-assembled NAnophase Particle (SNAP) coating process is a hybrid sol gel coating process that is designed to provide superior adhesion between the primer coating and substrate and, if possible, chemically alter the surface of the substrate, rending it less susceptible to corrosion.[7]

In order to better understand the coating properties, the solution chemistry of the SNAP solution has been investigated using Size Exclusion Chromatography / light Scattering, infrared spectroscopy, and ^{29}Si NMR.

EXPERIMENTAL PROCEDURES

SNAP solutions were made by drop wise addition of 42.8 ml (0.194 moles) glycidoxypropyltrimethoxysilane (GPTMS) and 8.9 ml (0.06 moles) and tetramethoxysilane (TMOS) to 64.8 ml solution of 0.05 M acetic acid (Aldrich Chemical) in doubly distilled deionized (DDI) water (resistivity 18 MOhms cm). The solution was continuously stirred during the addition. All chemicals were reagent grade or better and used as received.

LIGHT SCATTERING

Static Light Scattering. Measurements were conducted with size exclusion chromatography (SEC) system with the Wyatt Technology DAWN® and Wyatt Technology Optilab® (refractive index) as detectors. The SEC pump system was a Waters Alliance 2690 using Shodex Ohpak SB-804, SB-802 HQ, and SB-G columns. The mobile phase was 50 mM acetic acid in water at a flow rate of 0.7 mL/min. Injection volumes were 10 or 15 μL

Dynamic Light Scattering. Dynamic light scattering (quasi-elastic) measurements were conducted using a Wyatt Technology DAWN® with a quasi-elastic light scattering detector at 110°. Samples were introduced into the detector using a syringe pump and 50 mM acetic acid in water.

INFRARED SPECTROSCOPY

Infrared spectra of the SNAP solutions were obtained using a Bruker Equinox 55 Fourier transform infrared spectrometer. Spectra of SNAP solutions were acquired with a resolution of 4 cm^{-1} using a cylindrical internal reflectance (CIR, SpectraTech) accessory with a zinc selenide crystal. Spectra are presented in ATR (attenuated total reflectance) units and are linear with respect to concentration. Single beam spectra of the samples were ratioed against a single beam background spectrum of the empty CIR cell.

NMR EXPERIMENTAL

^{29}Si NMR spectra were obtained on a Varian Inova 300 MHz NMR (59.557 MHz). Spectra were obtained using inverse gated decoupling direct observe pulse sequence with the following parameters: spectral width equal to 9800 Hz; 90° pulse width of 15 μsec, 30 seconds between acquisitions, and 512 transients acquired. ^{29}Si NMR chemical shifts were referenced to a tetramethylsilane in D_2O (δ = 0.00 ppm) external standard. SNAP solutions were prepared in 0.05 M d4-acetic acid D_2O solutions.

RESULTS AND DISCUSSION

A large amount of sol-gel research, including the work presented here, is based on silicon precursors because of their balance of reactivity and ease of handling, as well as their ready availability.[5] Silane sol-gel chemistry consists primarily of the sequential hydrolysis and

condensation reactions of alkoxysilane precursors to form three-dimensional siloxane networks. The hydrolysis reactions are typically catalyzed by acid or base conditions, initially producing a hydrolyzed silanol of the general form $(RO)_xSi(OH)_{4-x}$ and an alcoholic by-product. Subsequent condensation reactions occur to form siloxane bridges resulting in a substantial increase in molecular weight. The condensation reactions occur repeatedly. Given the multifunctionality of each silicon molecule, the condensation can occur repeatedly resulting in a high density of siloxane cross links. The products of these reactions are highly dependent on the catalysis conditions, solvent, and water content.[8]

One gauge that has been used to predict sol gel product properties is "r", the water silicate molar ratio.[5] At low r-values (≤4) the condensation products are generally polymeric linear or lightly branched siloxane chains. At high r values (>20) the condensation products are highly cyclic structures that form colloidal particles that coalesce into a three dimensional structure. Between low and high r-values lies a continuum of products. The SNAP process is performed at an r-value around 15. From this, one would expect products that consist largely of cyclic siloxane chains.

One limitation of the r-value is the tacit assumption that all silicate present is tetrafunctional with respect to hydrolysis and condensation. The SNAP solutions prepared in this work consist of both TMOS and GPTMS in a mole ratio of 1:3. In these solutions the most abundant silicate species is only capable forming three siloxane bonds. An alternative description that more applicable to SNAP solutions is "D" the molar ratio of water and alkoxide. For traditional sol gel materials, D is simply ¼ the value of r. SNAP solutions are prepared with a D value of 4.5. This simply indicates that when the SNAP solution is initially prepared there is 4.5 times more water than hydrolysable alkoxides. Traditional sol gel chemistry has often been

performed in alcohol with water added while the SNAP process is performed in an aqueous solvent. However, it is important to realize that during the hydrolysis of the alkoxide in the SNAP solution, alcohol is released into the solution.

Two SNAP solutions were examined, at 3 days and at 3 months after preparation using light scattering (Table 1). Replicate samples run using both static and dynamic light scattering after the solution had aged 3 days were consistent and had an average 1600 amu molecular weight. The average molecular radius determined by dynamic light scattering of the SNAP oligomers was 1.1 nm. After the solution had aged for 3 months the molecular weight had increased to 5200 amu. These molecular weights roughly correspond to 8 GPTMS and 3 TMOS molecules for the 3 day old solution and 26 GPTMS and 10 TMOS for the 3 month old solution. The change in molecular weight also corresponds to an expected 50% increase in the average molecular radius.

TABLE 1. SNAP Light Scattering Results for Two Samples
Tested After Aging 3 Days and 3 Months.

Sample	Sample Age	Light Scattering Technique	M_w (10^3 g/mol)	M_n (10^3 g/mol)	Average Molecular Radius
SNAP 1	3 Days	Static	1.67 ± 0.06	1.25 ± 0.05	
SNAP 2	3 Days	Static	1.62 ± 0.02	1.21 ± 0.02	
SNAP 1	3 Days	Dynamic	1.59 ± 0.01		1.1 nm
SNAP 1	3 Months	Static	5.6 ± 0.1	3.2 ± 0.1	
SNAP 2	3 Months	Static	4.9 ± 0.1	3.0 ± 0.1	

An infrared spectroscopy study of the SNAP solution was conducted as well. The SNAP solution was prepared and then recirculated through a cylindrical internal reflectance cell. The infrared band corresponding to the alkoxide, silanol, methanol, and the siloxane bridge were monitored (Figure 1). As expected the alkoxide absorption rapidly decreases along with the silanol, while the methanol and siloxane absorptions rise.

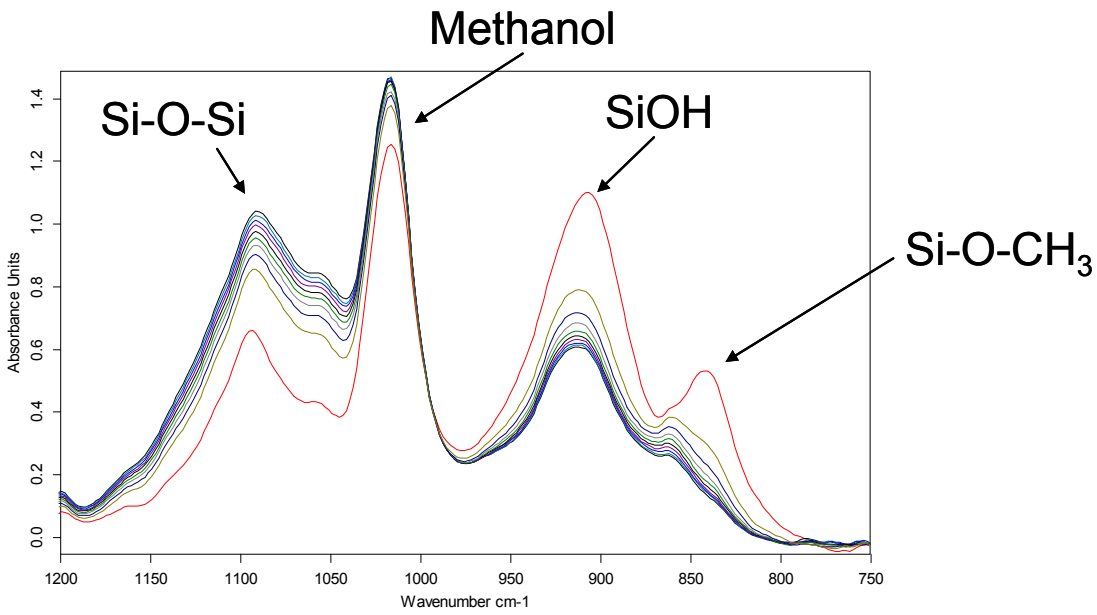

FIGURE 1. IR Spectra of SNAP Solution in a Cylindrical Internal Reflectance Cell. Spectra are shown at 10 hour increments.

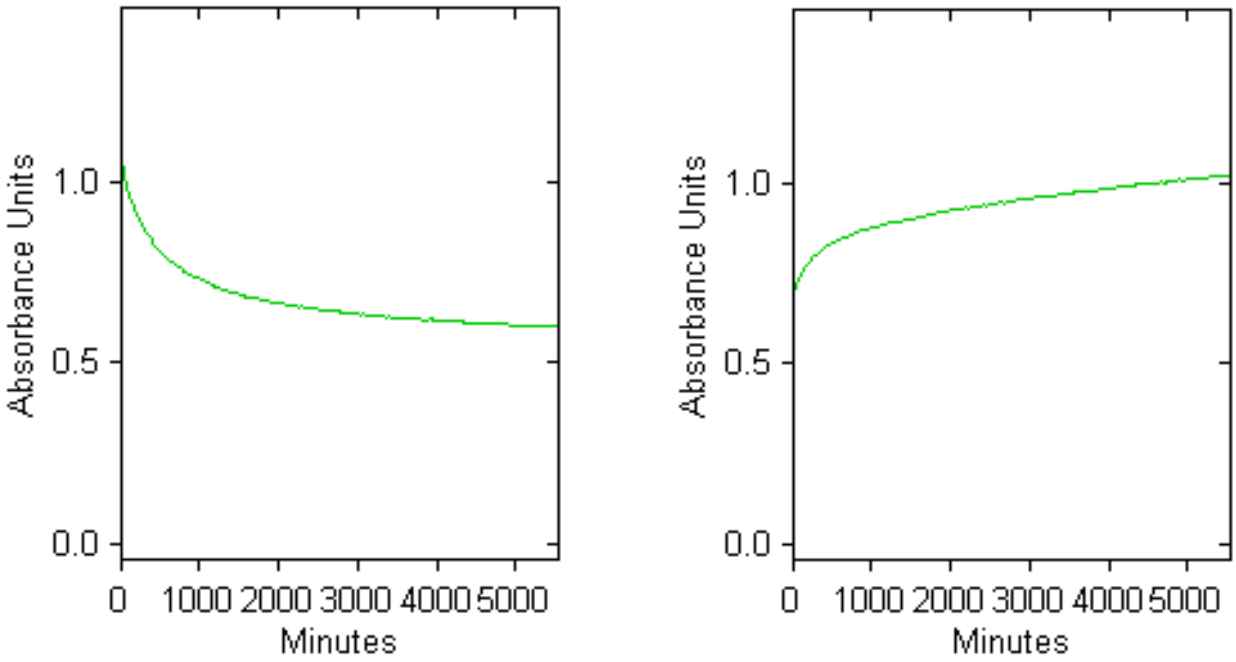

908 nm SiOH

1095 nm Si-O-Si

FIGURE 2. Slices of the Infrared Spectra Showing the Time Dependence of the IR Bands Corresponding to silanol and siloxane moieties.

Plotting specific infrared bands as a function of time reveals additional information about the hydrolysis and condensation reactions occurring in the SNAP solution (Figure 2). The infrared absorption at 908 nm is due to the presence of silanols. This absorption decreases rapidly but plateaus after about 60 hours. The absorption at 1095 nm corresponding to a siloxane bridge does not change as dramatically as the silanol absorption but it still changing after over 90 hours. Additional experiments need to be conducted in order to quantify the reaction rates.

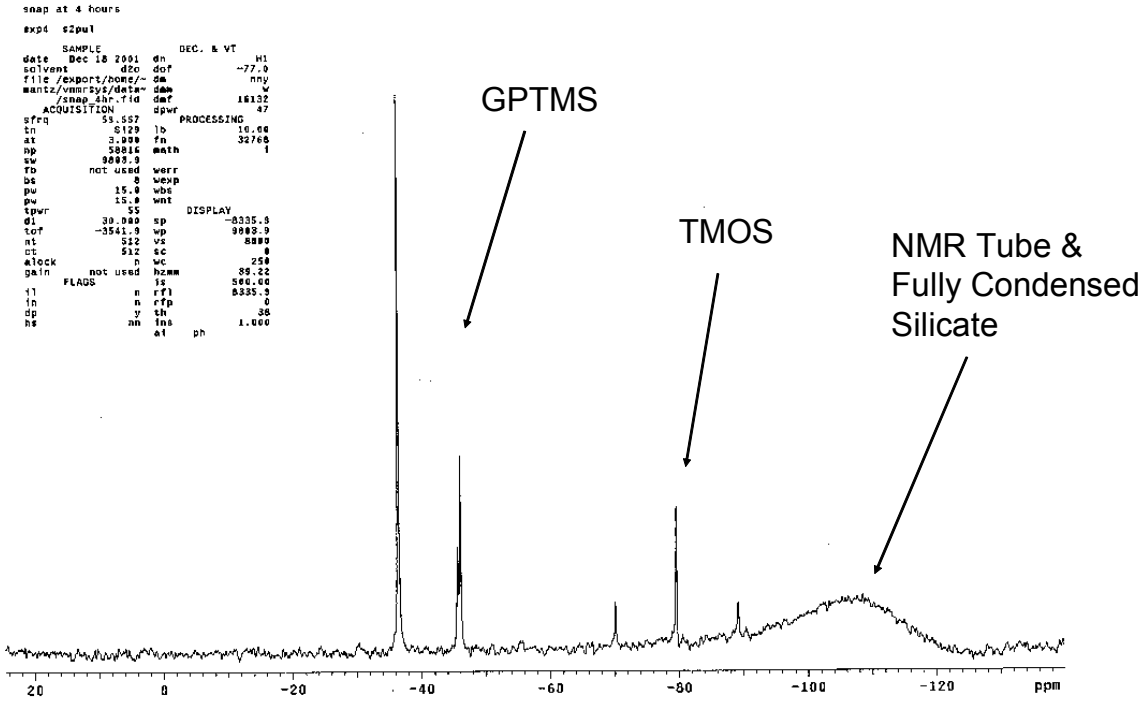

FIGURE 3. ^{29}Si NMR Spectrum of SNAP Solution Aged for 4 Hours.

NMR experiments were conducted in a manner similar to the infrared. Samples were prepared and spectra taken every 12 hours over a 17 day period. One difficulty is the acquisition time for ^{29}Si is over 4 hours. Any changes that occur during the acquisition are averaged. Reactions that occur rapidly, immediately after the solution is mixed are prone to error. Even with this difficulty NMR offers a powerful technique to study SNAP solution changes during

aging. Figure 3 is a typical ^{29}Si NMR spectrum that was acquired 4 hours after the SNAP solution was prepared. In this series of experiments the NMR tube interfered with the measurement of the intensities of the peaks due to TMOS. Future experiments will be conducted in polymer NMR tubes.

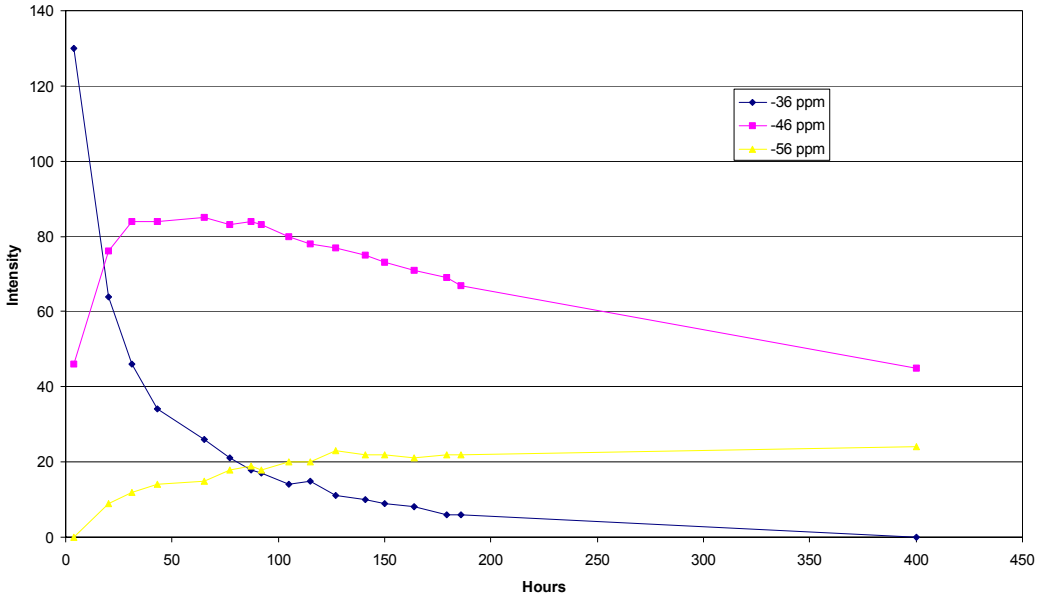

FIGURE 4. GPTMS Peak Intensities as a Function of SNAP Solution Age.

As the SNAP solution ages the peaks from each of the silicate species tended to move to higher field. As each silicate species undergoes successive hydrolysis and condensation reactions the resonance should shift to higher field. GPTMS has ^{29}Si NMR chemical shifts of -36, -46, and -56 ppm for the singly, doubly, and triply hydrolyzed silicate respectively. The reaction progression of a SNAP solution can be tracked from the intensities of the ^{29}Si NMR peaks due to either GPTMS or TMOS (Figure 4). In contrast to the infrared data previously discussed, the NMR data implies the SNAP solution changes more slowly. One difficulty that has been identified is the use of deuterated solvents. Both the hydrolysis and condensation reaction could

potentially be slowed by a deuterium isotope effect. Future NMR experiments should be conducted either in nondeuterated solvents or at least with a minimum of deuterated solvent present.

SUMMARY/CONCLUSIONS

Light scattering measurements indicate the SNAP oligomers have an average molecular weight of 1600 amu and an average molecular radius of 1.1 nm after aging 3 days. After 3 months the average molecular weight has grown to over 5200 amu. Both infrared and NMR measurements confirm that after preparation of the SNAP solution both the GPTMS and the TMOS rapidly hydrolyze to generate silicate species that slowly condense. ^{29}Si shows the stepwise hydrolysis and condensation of the silicon moieties.

ACKNOWLEDGMENTS

The authors acknowledge Lt Col Paul C. Trulove for financial support from the Air Force Office of Scientific Research and Wyatt Technology Corporation for providing the light scattering data.

REFERENCES

1. Air Force Office of Scientific Research "Air Force Blue Ribbon Advisory Panel on Aircraft Coatings," Air Force Materiel Command, 1995.
2. Fed. Regist., 12.4, 60, No. 170, 45947, 1995.
3. Environmental Health Information Service, U.S. Department of Health and Human Services Public Health Service National Toxicology Program, 9th Report on Carcinogens Revised January 2001. http://ehis.niehs.nih.gov/roc/.

4. National Research Council *Aging of U.S. Air Force Aircraft*; National Academy Press: Washington D.C., 1997.
5. Brinker, C. J. and Scherer, G. W., Sol Gel Science: The Physics and Chemistry of Sol-Gel Processing, Academic Press, New York, NY, 1990.
6. Leung, Y. L.; Zhou, M. Y.; Wong, P. C.; Mitchell, K. A. R.; Foster, T. *Applied Surface Science* **1992**, *59*, 23-29.
7. Vreugdenhil, A. J.; Balbyshev, V. N.; Donley, M. S.; *J. Coatings Tech*. **2001**, *73*, 35-43.
8. Schmidt, H., *J. Non-Cryst. Mat*., **1998**, *100*, 51.

ACOUSTIC AND THERMAL NDE TECHNIQUES FOR CHARACTERIZATION OF POLYMERIC COATINGS AND DETECTION OF LOCALIZED CORROSION

J. Hoffmann, M. Khobaib, S. Sathish, and N. Meyendorf

Center for Material Diagnostics
University of Dayton Research Institute
Dayton, OH 45469-0168

ABSTRACT

Corrosion is one of the limiting factors for extended use of aircraft. Nondestructive evaluation (NDE) has proven to foster early detection of defects and enhances the understanding of failure processes. This paper discusses the development of a multi-sensor nondestructive evaluation (NDE) approach to characterize aluminum alloy airframe structures under polymeric corrosion protective coatings. We employed acoustic and thermographic NDE techniques, including Scanning Acoustic Microscopy (SAM) and Fan Thermography.

BACKGROUND

Nondestructive characterization of corrosion protective coatings is of exceptional importance to enhance usability of coating systems and thus, to reduce the costs of aircraft maintenance and to avoid extensive environmental pollution. The possible failure of the coating leads to insufficient corrosion protection and finally to the failure of the Al alloy. Determination of mechanical and physical properties of the coating and the condition of the interface are required, both under different types of load and environmental exposure. Furthermore, it is necessary to detect corrosion damage in the aluminum alloy below the coating. To achieve this, the employment of high-resolution nondestructive evaluation (NDE) is necessary.

EXPERIMENTAL TECHNIQUES

SCANNING ACOUSTIC MICROSCOPY

Scanning acoustic microscopy (SAM) was performed by time-of-flight spectroscopy in the pulsed regime.[1,2] An electronic clock triggers at regular time intervals a signal generator (pulser) to sent high frequency voltage to an ultrasonic transducer causing vibrations of its piezoelectric unit. Pulse repetition rate can be as high as 2000 pulses per second. The clock also controls a time measuring circuit that operates simultaneously with the signal measurement. The transducer generates short, broadband ultrasonic pulses that are sent into the test material. If operated in reflection mode, the same probe detects the reflected waves, working alternately as sending and receiving unit. By recording C-Scans, SAM can be utilized to map either coating or interface properties. The SAM system includes a high frequency (50 MHz) focused ultrasound-transducer, which can be moved over the sample with high accuracy.

The SAM transducers used for coating inspection were highly focused. It is advisable to adjust the probe/sample-distance such that the sample part of interest (e.g. a sample interface) is at focal length distance. This will be indicated by maximal reflection since all incident waves are reflected if and only if the reflection occurs at focal length (Figure 1).

Besides longitudinal and shear wave inspection, acoustic microscopy has been used for generating and detecting surface waves. Figure 2 illustrates generation, propagation and detection of a surface wave. Rayleigh waves have narrow penetration depth and travel only short distances. Their velocity is slightly below shear wave velocity. Rayleigh waves enable high-resolution inspection of surface near material.[1]

THERMOGRAPHIC TECHNIQUES

Thermal imaging techniques are based on the fact, that every object emits electromagnetic waves. Spectral distribution and intensity of this radiation depends on the surface temperature. The wavelength dependent emissivity coefficient $\varepsilon(\lambda)$ describes the fraction of emitted radiation intensity from the real objects compared to the black body and is always smaller than 1. Unfortunately ε becomes very small for metals in the infrared range (0.1 or even less for aluminum surfaces at wavelength 10 μm). The sum of emissivity, transmissivity (τ) and reflectivity (ρ) has to be 1 for a selected material ($\varepsilon+\tau+\rho=1$). Therefore most metal surfaces are excellent mirrors for infrared radiation. For thermographic NDE of metallic parts, it is usually required to apply a black coating to their surfaces, which has to be removed after testing.

A well-established method is Flash Thermography, which provides a quantitative characterization of defects under coatings. Using this technique, a high-energy light pulse is deposited on the surface of examination. Some of the light is absorbed and converted into heat. An infrared (IR) camera observes the cooling process of the material. The material properties of coatings, as well as possible interface or substrate defects, influence heat diffusion and thus cause changes in the surface temperature with time.[3]

Disadvantage of this NDE principles is the low temperature contrast as well as high temperature dynamics (if thin layers are tested) that requires high sensitive and high-speed thermal cameras. To detect, for instance, the assumed delamination of a 400 μm coating on aluminum, a temperature dynamics of 50 K is necessary for a temperature contrast of approximately half a degree Kelvin. For thinner coatings the contrast increases, but the response time decreases. For a 100 μm coating, the maximum contrast appears only for the time of one

video frame (50ms) (Figure 3).[4] Therefore image averaging to enhance temperature resolution can not be used.

In the new approach, used for the present experiments (Figure 4), a hot air gun or fan replaces the flash lamps. In comparison to the flash lamps, this heating method deposits considerably less energy per time on the surface of examination. The sample heats up much slower, which allows observing the material response during the heating process over longer periods of time. Using image averaging, the sensitivity for detection of subsurface defects can be enhanced by an order of magnitude compared to conventional flash thermography. This is clearly demonstrated by computer simulation of thermal testing procedures. The lower heat deposition energy reduces the risk of coating damage. The main advantage is the very simple and inexpensive set-up that can easily applied for in-field testing.

Table 1 compares calculated temperature contrasts for a polymer coating with a 50 μm delamination (air gap). The data were obtained by either finite volume simulations for flash thermography[4] or by numerical modeling for fan thermography.[5] Equal geometrical and thermal parameters are assumed ($\lambda_{coating}$=0.17W /m·K; λ_{air}=0.025W /m·K; air velocity: 5m/s; α=15W/m^{2}K; air temperature 150^{o}C):

TABLE 1: Calculated temperature contrast from fan and flash thermography for polymer coatings on Al substrate with a delamination (50 μm air gap). Results for flash thermography from.[4]

Coating Thickness	100μm	200μm	300μm	400μm
Temperature Contrast for Fan Thermography	3.9 K	3.9 K	3.9 K	3.9 K
Maximum Temperature Contrast for Flash Thermography	4.7K	2.1K	1.1K	0.7K

SCANNING VIBRATING ELECTRODE TECHNIQUE

To understand and quantify the results obtained by SAM and Fan Thermography, well-established reference methods need to be employed. Scanning Vibrating Electrode Technique (SVET) proved to be very useful as an electrochemical technique to investigate corrosion activity at the coating/aluminum alloy interface. A complete description of SVET is available elsewhere [6]. SVET provides quantitative data and can distinguish between cathodic sites (negative current density) that basically indicate delamination and anodic sites (positive current density) revealing actual dissolution of the alloy.

RESULTS AND DISCUSSION

SAMPLES INVESTIGATED

At the present state of ongoing research efforts, all of the examined samples are basically AA2024-T3 substrates with a single layer epoxy/polyamine primer coating. The substrate was highly polished to simplify the interface response to incoming acoustic or thermal waves. The additives allowed within the epoxy matrix were some flowing agents, to obtain a smooth surface and nearly uniform coating thickness. Thickness evaluation with SAM was established earlier.[7] Samples with 1 mil (approximately 25 μm) and 1.5 mil (approximately 38 μm) coating thickness were investigated. These samples enable basic research to establish the NDE techniques and understand the correlation between NDE and electrochemical data.

SVET measurements were conduced with coatings exposed to Harrison's solution, an electrolyte containing 5 grams NaCl and 35 grams $(NH_4)_2SO_4$ in 1 liter of water. In each instance, Al 2024-T3 served as the substrate. Initially, the specimen coatings were intact (with no artificial damage), and the progress of corrosion activity was recorded by scanning a small area within the cell. The cell was formed by gluing a 1/8" high, 2" diameter slice of acrylic pipe

to the coated sample surface. Initially, corrosion damage was obtained by exposing the coated panel to Harrison's solution at open circuit potential. A small external potential was imposed if no corrosion was detected even after 100 hours of exposure.

COATING DELAMINATION DUE TO WATER EXPOSURE

Within the general sample parameters, the exact formulation of the epoxy/polyamine primer was varied for different sets of samples. For example, an experiment was planned to observe the development and growth of delamination. The coating formulation was chosen to minimize the number of hydrogen bonds to the substrate and to be highly hydrophilic. SAM C-scans were performed every 90 minutes. Ultrasonic reflections that characterize the coating/substrate interface were emphasized during evaluation. Since the SAM measurements involve water exposure of the samples, water was expected to diffuse easily in the polymer matrix and, eventually, to the substrate/coating interface. The C-scans enabled monitoring the development of micro-scale delamination that accumulates over time (Figure 5). Eventually, the coating lost contact to the substrate. This experiment helped to identify delamination defects and distinguish them from corrosion.

CORROSION DETECTION AT DELAMINATION SITES

Large, visible delamination was observed during exposure to Harrison's solution. This delamination can be easily detected with SAM. The solution fills the delaminated regions and acts as an electrolyte. Since the samples were polarized for an hour at +25 mV above the open circuit potential the creation of limited corrosion damage was expected.

A comparison of the coating and substrate reflection allows the identification of corrosion damage sites. In the substrate reflection C-scan, additional bright spots are observed within the

possible delaminated region. It was assumed that these spots reflect a corrosion damage feature. In addition, A–scans were recorded at an undamaged position, a site of delamination and a suspected corrosion spot. At the undamaged position, only the reflections from either the coating or substrate occur (Figure 6a). At a site of delamination, these two reflections are more separated in time as the distance between the two surfaces increases. An additional reflection from the coating backsurface/solution interface is observed (Figure 6b). Apparently, the water has penetrated into the open (delaminated) region separating the two materials. This reflection reveals negative amplitude, because the change of acoustic impedance from coating to water is negative as well. The additional bright spots in the C-scans correspond to large reflections caused by a large acoustic impedance change. This happens when the acoustic wave has to propagate from water into a hydrogen gas (H_2) bubble. This H_2 bubble, generated during active dissolution, indicates the presence of a corrosion pit underneath (Figure 6c).

NONDESTRUCTIVE EVALUATION OF CORROSION PROTECTION WITH SNAP COATINGS

Representative C-scans and corresponding electrochemical scans for a 38 μm thick coatings (90 hours exposure to Harrison's solution at open circuit potential) are presented in Figures 7 and 8. The coating formulation used provided reasonably good water resistance and adhesion capability. Thus, exposure to a corrosive environment was considered the main cause for the coating degradation observed.

The difference between the two samples is the application of a newly developed thin sol-gel initial layer prior to coating the epoxy primer. The sol-gel layer includes pre-formed, self-assembled nano-phase silane particles (SNAP). These SNAP coatings are considered to enhance corrosion resistance and adhesion to the substrate.[8]

The results indicate that the SNAP-coatings basically improve adhesion. Figure 7a presents a C-scan over a sample without additional SNAP layer. Several spots of delamination can be observed, which eventually lead to some severe accumulated corrosion activity. However, the measured current density does not show high peaks (maximum approximately 100 $\mu A/cm^2$) and is rather homogeneously distributed (Figure 7b).

In comparison, the SVET scan for the sample with additional SNAP layer shows no significant current density over almost the complete scan-area, except one negative (cathodic) peak (approximately –500 $\mu A/cm^2$) and one positive (anodic) peak (approximately 400 $\mu A/cm^2$) (Figure 8b). The SAM C-scan also detects these spots, but also several additional sites (Figure 8a). This is because of much higher lateral resolution of SAM.

The sample without SNAP pretreatment shown in Figure 7 is more severely damaged. A lot of image processing needed to be done, to visualize the minute detection in Figure 8a. These results indicate that SNAP pretreatment definitely improves adhesion capability and generally the corrosion resistance. However, if the primer coating fails, high-localized corrosion activity can lead to component failure.

EVALUATION OF FAN THERMOGRAPHY

AA 2024-T3 panels with artificially generated corrosion pits were used to quantify the Fan Thermography results. Different pit sizes were chosen. Exact pit topography was evaluated using White Light Interferometry before the panels were coated and Fan Thermography was employed. Since no coating defects were involved, the measured thermal contrast was solely due to the corrosion pits. The measurements on these samples yielded a correlation between thermal contrast and pit size especially, pit depth. Results obtained so far indicate a pit depth of approximately 110 μm to be the threshold for detection.

Ongoing work includes measurements on standardized samples. To prepare these samples, perfectly shaped triangle patterns have been cut into the 2024-T3 panels using laser ablation. The triangles have the size of typical corrosion pits; they are filled with an epoxy/alumina-composite to simulate corrosion byproducts. After careful polishing, the panels are coated with a typical aircraft coating system. For this experiment, actual military aircraft coatings were applied, i.e., a double-layer system consisting of an epoxy primer and a polyurethane topcoat. The overall coating thickness was approximately 120 μm. Two triangle arrays were prepared, each with 5 triangles with increasing size (triangle base length: 1mm, 2 mm, 3 mm, 4 mm, 5 mm). The upper triangle row is shallower (approximately 0.5 mm compared to 1 mm of the row below). The triangles are easily detected, as demonstrated in Figure 9. Furthermore, one can observe the increased thermal contrast for the deeper row.

These first results are valuable to improve the experimental set-up. For example, IR-camera optical arrays, arrangement of heat gun, camera and sample as well as air temperature are possible parameters to optimize improving the measurements. Additional noise reduction and enhancement of accuracy by a factor of 3 to 10 is possible if image averaging is used.

FAN THERMOGRAPHY COMPARED WITH SAM AND SVET

Figure 10 shows consecutive SVET, Fan Thermography and SAM images of exactly the same area of another coated sample. These scans were taken from an AA 2024-T3 panel coated with 50 μm thick epoxy coating. The sample was exposed for 125 hours at open circuit potential in Harrison's solution. SVET measurements were carried out first as discussed earlier. Figure 10a presents a vector overlay mapping of electrochemical current density superimposed over a video image. There are indications of delamination in the SVET video image. The longer vectors indicate increased corrosion activity underneath these delaminated regions.

Coating delamination or sites of corrosion are thermal barriers. If the test (object) surface is heated, the heat diffusion into the aluminum plate is inhibited in the delaminated or corroded region. This causes a change in the thermal response. Figure 10b shows a thermal contrast for corrosion below this coating. The spatial resolution was improved with a microscopic optic used in combination with the camera. The bright spots (higher surface temperature) indicate regions of reduced heat diffusion and correlate well with the SVET image.

The sample was then scanned with SAM (Figure 10c). The SAM scan clearly identifies the same three spots observed by SVET and Fan Thermography. Some additional spots are visible by SAM. This could be due to the rather poor performance of this coating and the fact that repeated heating and additional exposure in a water bath has a deteriorating effect on the sample.

These results demonstrate that the electrochemical and NDE techniques provide complimentary information about the state of the coating and there is a good possibility that integrating this information can provide the details of the health of the substrate beneath a coating exposed to corroding environment.

SUMMARY/CONCLUSIONS

The SAM system includes a high-frequency focused ultrasound-transducer, which can be moved over the sample with high accuracy. SAM C-scan enables detection of early stage delamination and monitoring of increasing delamination due to water exposure over time. Detected sites of delamination or corrosion can be verified by additional electrochemical studies. Different degradation processes in the polymers due to water exposure are evaluated.

Fan Thermography is a modified thermal NDE technique that has a high sensitivity for detection of corrosion below intact military coatings. This method revealed good potential for

detection of early stages of corrosion under intact coatings. The surface temperature is measured while the surface is heated with hot air. Delamination and corrosion size with corrosion byproducts is indicated by local hotspots. Model simulations show the advantages of these technique: high temperature contrast, high accuracy due to averaging of a large amount of video frames, low energy input to the surface, and simple application for in-field inspection. The strengths and limitations of this technique have been discussed by evaluating results obtained with corrosion standard samples.

ACKNOWLEDGEMENTS

Research was sponsored by DARPA AFOSR MURI under Grant No. F49620-96-1-0442. The authors would like to acknowledge the scientific and technical support of the AFRL/MLLP-Nondestructive Evaluation Branch, Materials and Manufacturing Directorate, Air Force Research Laboratory, Wright-Patterson Air Force Base, OH. We especially thank James Blackshire for providing the corrosion standard specimens examined in Figure 9 and Dr. Joel Johnson for preparing the coating specimens.

REFERENCES

1. A. Briggs (1992) Acoustic Microscopy. Oxford University Press, New York
2. V.K. Kinra, V.R. Iyer (1995) Ultrasonic measurement of the thickness, phase velocity, density or attenuation of a thin-viscoelastic plate. Ultrasonics 33: 95-109.
3. U. Netzelmann et al. (2001) Schichtprüfung mit Hochgeschwindigkeits-Thermographiekameras, Modellierung und Werkstoffcharakterisierung. FhG-IZFP Report 010111-TW
4. J Burgschweiger (1993) Simulation von Temperaturfeldern bei der zerstörungsfreien Werkstoffprüfung mittels der Impuls-Video- Thermographie. M.S. Thesis, University Magdeburg, Germany
5. N. Meyendorf et al. (2001) Early Detection of Corrosion in Aircraft Structures. Review of Progress in Quantitative Nondestructive Evaluation, Brunswick, ME
6. M. Khobaib, A. Rensi, T. Matikas, M.S. Donley (2001) Real Time Mapping of Corrosion Activity under Coatings. Progress in Organic Coatings 41:266-272
7. J. Hoffmann et al. (1999) Nondestructive characterization of corrosion protective coatings on Aluminum alloy substrates. Proceedings of Symposium S: Nondestructive Methods for Materials Characterization at MRS Fall Meeting ’99, Boston, MA
8. A. Vreugdenhil et al. (2001) SNAP: Characterization of the solution chemistry and film performance of a silicon sol-gel surface treatment for Al 2024-T3. to be published in Polymeric Materials: Science & Engineering 85

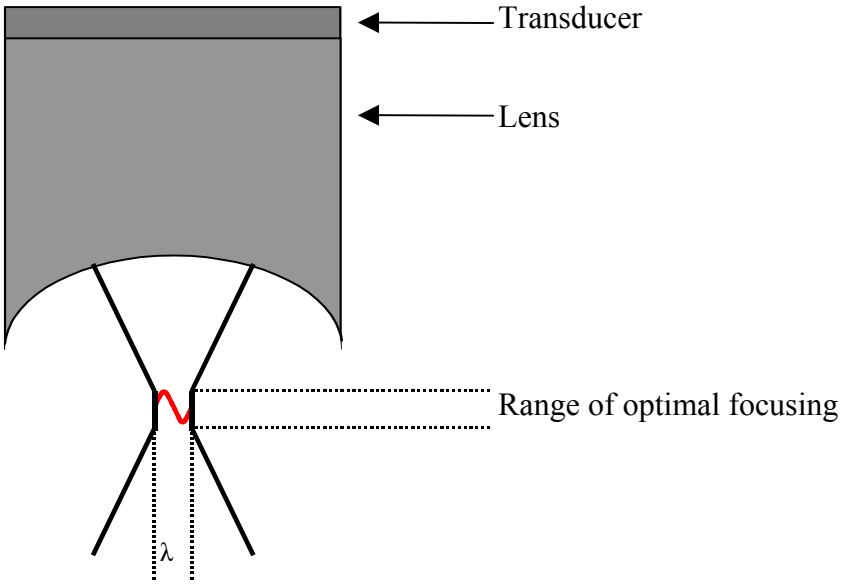

FIGURE 1. Focusing schematic; one wavelength is smallest possible focal point

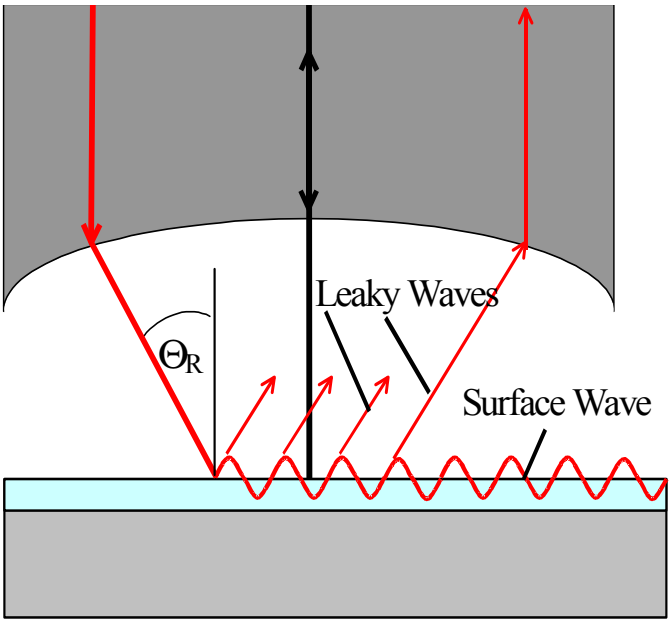

FIGURE 2. Scheme of surface wave generation and detection

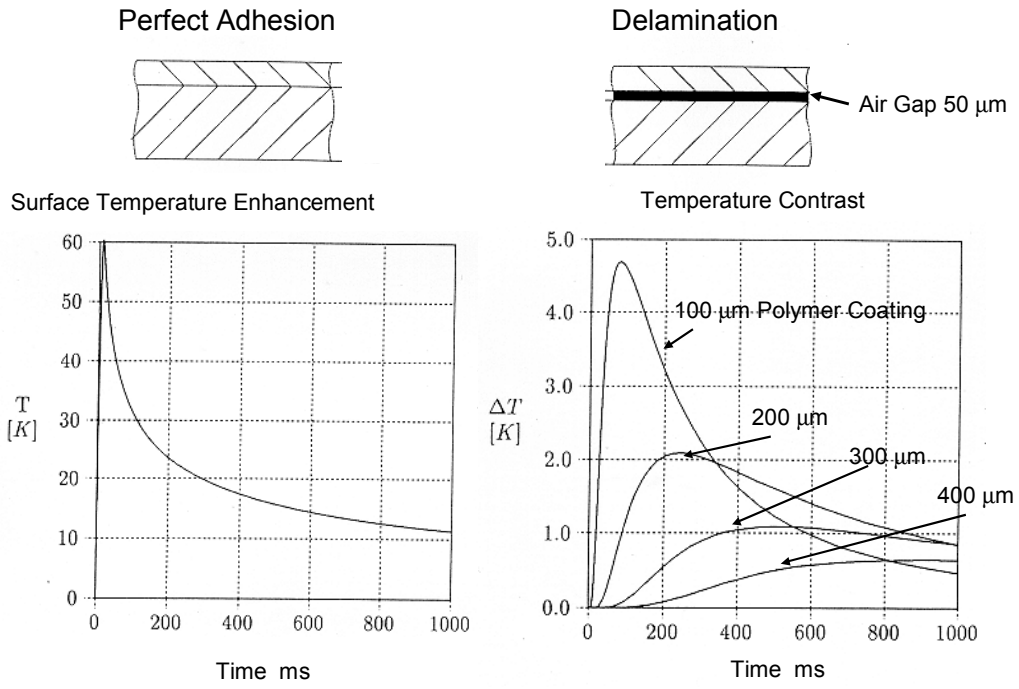

FIGURE 3. Simulation of surface temperature for flash thermography testing: Left: Surface temperature/ time diagram; Right: Temperature contrast due to a delamination.[4]

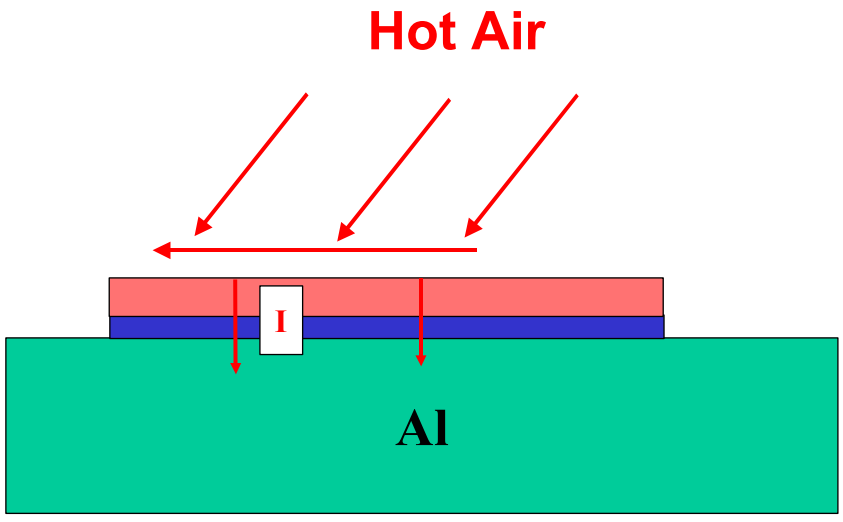

FIGURE 4. Principle of fan thermography

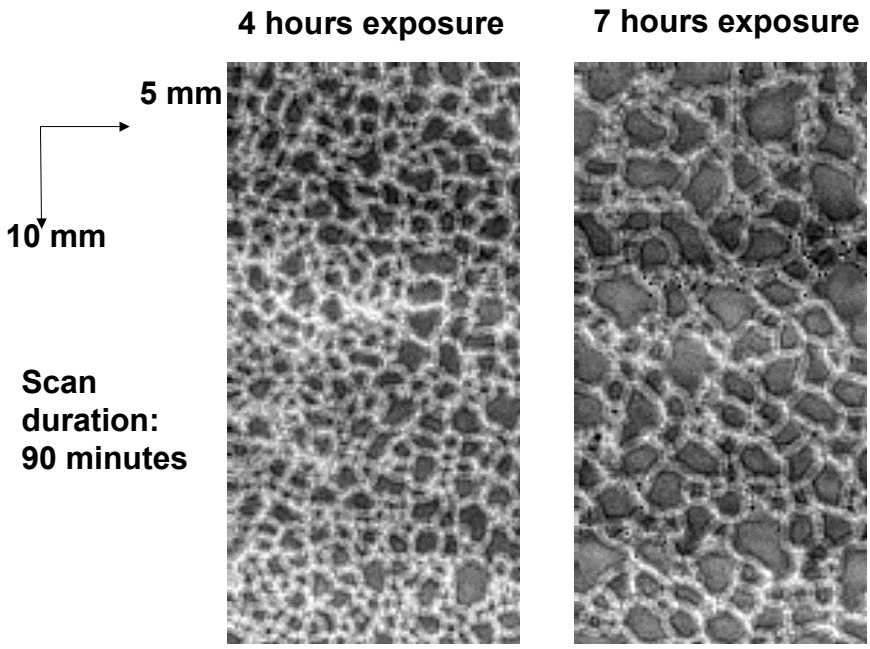

FIGURE 5. Formation of micro-delamination at epoxy coating/ 2024-T3 interface due to water exposure; right scan is measured 3 hours after left scan

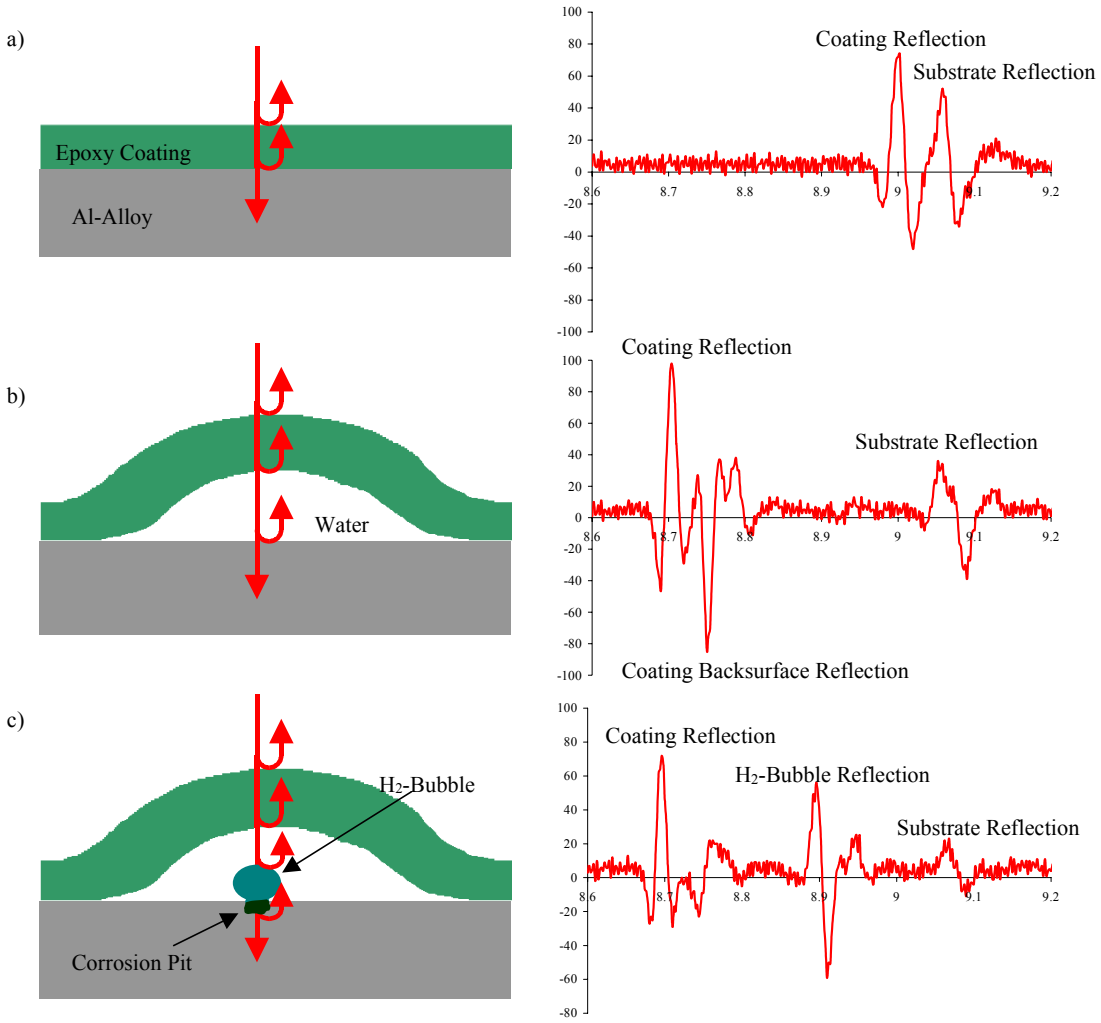

FIGURE 6. A-scans and schemes for different positions on epoxy coating sample, a) undamaged region, b) delaminated region, c) H_2-bubble above corrosion pit

a) b)

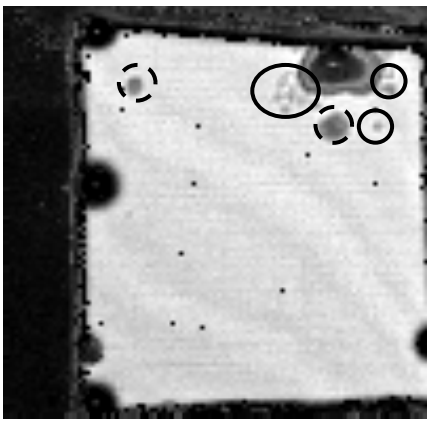

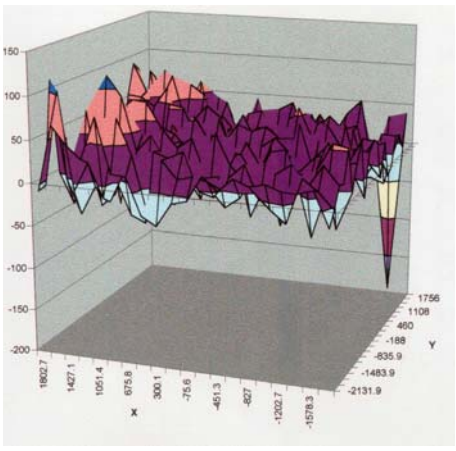

FIGURE 7. Epoxy coating, no SNAP layer; a) SAM C-scan: scan area: 6x6 mm^2, full line circles: hidden corrosion, dashed circles: hidden delamination, large visible delamination in upper right corner; b) SVET scan: 5x5 mm^2

a) b)

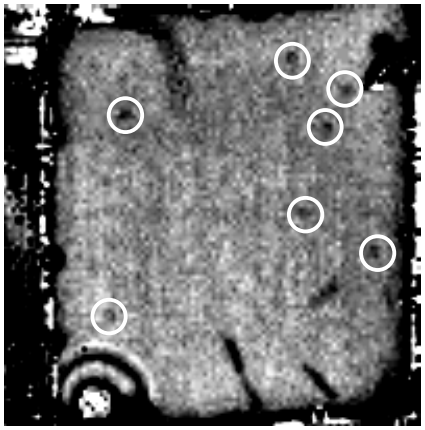

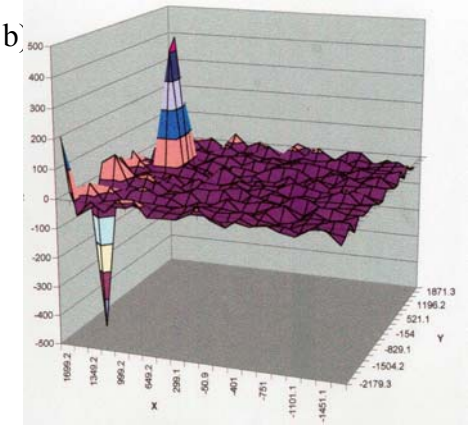

FIGURE 8. Epoxy coating, with SNAP layer; a) SAM C-scan: scan area: 6x6 mm^2, white circles: hidden corrosion b) SVET scan: 5x5 mm^2

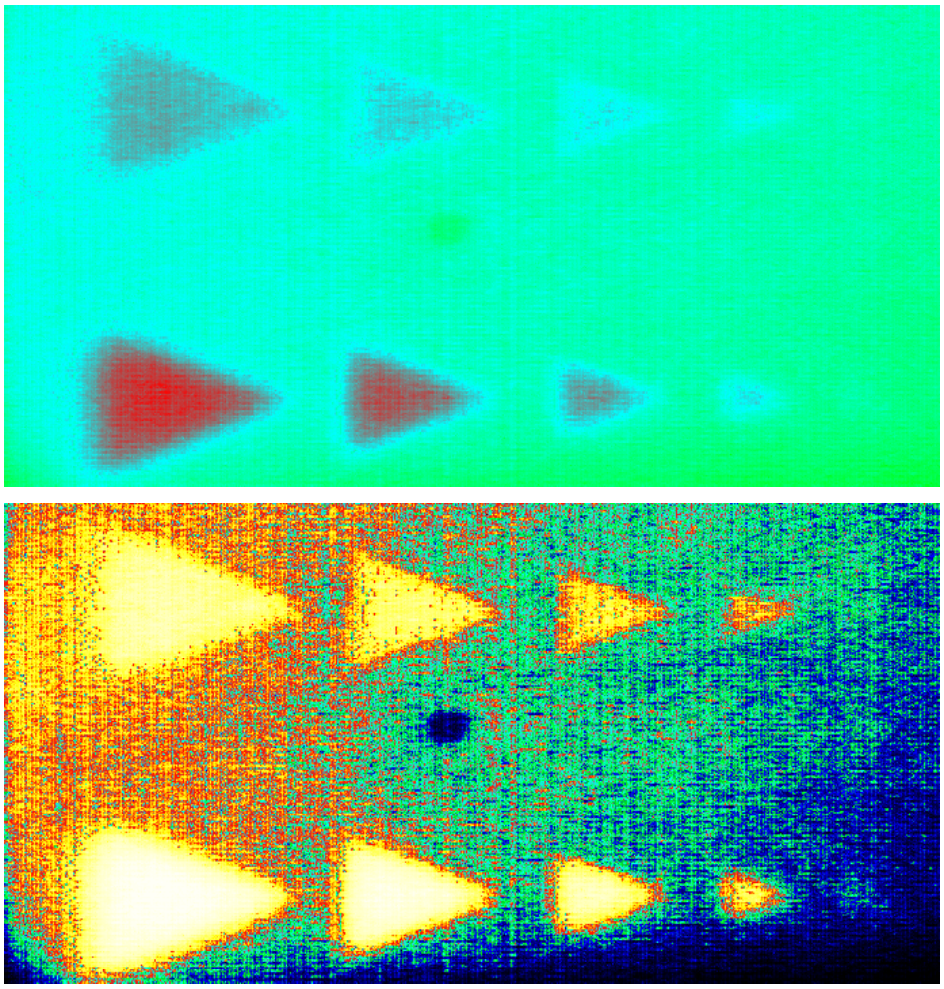

FIGURE 9. Detection of standardized defects under intact coating; top: linear contrast, bottom: enhanced contrast

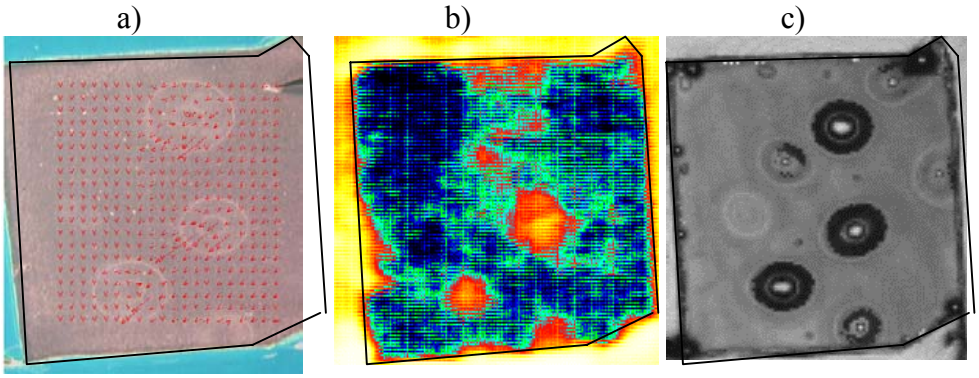

FIGURE 10. NDE imaging of same sample - 50 µm thick artificially damaged epoxy coating; a) SVET video image + current density vector overlay: vector area: 4x4 mm^2; b) Fan Thermography image: image area: 6x6 mm^2; c) SAM C-scan: scan area: 6x6 mm^2

THE DEVELOPMENT OF A MULTI-FUNCTIONAL COATING FOR AEROSPACE APPLICATIONS USING MOLECULAR- AND NANO-ENGINEERING METHODS: A MURI OVERVIEW

S.R. Taylor, J.R. Scully, R.G. Kelly, and G.J. Shiflet, University of Virginia Charlottesville, VA 22904; R.G. Buchheit, The Ohio State University, Columbus, Ohio 43210; W.J. VanOoij, University of Cincinnati, Cincinnati, OH; K. Sieradzki, Arizona State University, Tempe, Arizona 85387-6106; C.J. Brinker, University of New Mexico, Albuquerque, NM 87106, A.L. Moran, United States Naval Academy, Annapolis, MD 21402

ABSTRACT

The coating system presently used on military aircraft is constrained in function and limited to the use of chromate-based compounds for the mitigation of corrosion. Advances within the materials and chemical sciences have created an opportunity to identify a new multi-functional and environmentally compliant aerospace coating. By implementing advances in the molecular and nano-engineering, a coating is envisioned that will have the ability to: (1) sense corrosion and mechanical damage, (2) initiate mitigation responses to the sensed damage (chemical and mechanical), (3) provide corrosion protection and adhesion using environmentally compliant materials, and (4) improve fatigue resistance. This paper will provide an overview of a Multi-University Research Initiative (MURI) comprised of six U.S. academic institutions specifically targeted to identify the fundamental science that will enable the development of such a multi-functional coating. The enhanced functionality of this advanced coating system will be achieved through the incorporation of: (1) a field-replaceable, nano-engineered metallic cladding, (2) the use of molecular-engineering and self-assembled colloidal crystals, and (3) the development of new approaches for the identification, encapsulation, and delivery of environmentally compatible corrosion inhibitors, and that will optimize solubility and compatibility with the paint resins when used as inhibitive pigments, and (4) the optimization of organic coating adhesion through the use of environmentally compatible surface treatments. This significant undertaking is achievable through interactions between the MURI team, U.S. industry, and DoD laboratories. A summary of the organizational collaborations will be provided.

INTRODUCTION

The skin of military aircraft when received from the original equipment manufacturer (OEM) consists of AA2024-T3 sheet having a multi-layer coating system that provides corrosion

protection and mission function. This coating system is comprised of: (1) a commercially pure (e.g., AA1100) aluminum cladding, (2) a chromate-based conversion coating or chromate-sealed anodized oxide layer, (3) an epoxy-based (or polyurethane-based) primer coat containing chromate-based inhibitive pigments, and (5) a single color, low-gloss mission topcoat. Each of these material layers provides a specific function and collectively they interact to provide corrosion protection, both real-time and active, as well as some level of mission capability (e.g. low glint, ground camouflage). However, many of the materials most critical to the function of this current military aerospace coating system are either: (1) hazardous to worker health and safety, (2) hazardous to the environment, (3) removed and not replaced during the maintenance cycle, or (4) are extremely limited with regards to mission function. These limitations impose substantial costs to maintain worker safety and manage waste, and limit mission capability.

The majority of corrosion protection of current military aerospace coating systems as-received from the OEM is principally determined by the cladding. The cladding provides a homogenous, passive substrate that has excellent barrier properties and inherently low corrosion susceptibility[1]. This cladding is an excellent substrate for subsequent organic coatings[2-4]. However, it's surface is routinely augmented by a chromate conversion coating (CCC) to facilitate the corrosion protection provided by subsequent organic layers. The facility of CCC within the coating system appears not to be related to it's stand alone corrosion properties[5-9], but more to it's ability to enhance adhesion[10], especially as applied in the maintenance cycle[11].

The second-most important contributor to corrosion protection of OEM military aerospace coatings is from chromate-based inhibitive pigments contained within the primer layer. These inhibitive compounds (*e.g.*, strontium chromate, zinc tetraoxychromate, and zinc/potassium chromate[12]) have an optimum balance of solubility and inhibitor efficiency.

Thus, chromate is leached out of the primer coating at a rate sufficient to achieve the concentration at the metal/coating interface needed to mitigate corrosion, but do not solvate so fast such that the primer becomes porous or forms osmotic blisters[13]. The hexavalent chromium species (Cr^{6+}) within the primer and to a lesser extent within the CCC layer, through a combination of mobility and inhibitor efficiency have significant throwing power and can mitigate corrosion within physical breaches of the coating system and provide a self-healing character[10,14]. However, chromate-based materials are highly toxic and carcinogenic[15] and pose significant risks to workers and the environment, as well as costs in their management as a hazardous waste when either used in production or generated when removed during subsequent maintenance cycles.

This functional primer is then coated with a single color, low gloss topcoat. The topcoat provides very little, if any, benefit from the standpoint of corrosion protection[10]. It's primary function is to minimize glint during combat and provide some level of ground camouflage. In the context of emerging coating capabilities, current topcoats are very limited and static in nature, and are ultimately constraining with respect to mission capability.

The limitations of the OEM coating system described above are exacerbated in the course of depot maintenance. During the depot cycle, the aircraft coating will be stripped (through a combination of chemical strippers, blasting, and grinding) so that the skin can be inspected for corrosion and mechanical damage. Depainting eventually results in the removal of the cladding, thus exposing the underlying AA2024-T3 skin material. The localized corrosion susceptibility of AA2024-T3 and other current generation age-hardenable aerospace alloys is high due to the micro-galvanic couples created by inherent micro-structural and micro-chemical hetero-geneities[16-19]. This increased susceptibility can eventually effect structural integrity through the

loss of load-bearing cross-section, increased stress intensity at pits, or increased frame stress due to corrosion product buildup within lap splice joints. Exposure of AA2024-T3 substrate material for subsequent painting mandates the use of chromate conversion coatings and chromate-bearing primers to ensure adequate adhesion and corrosion protection. Thus, this crucial inspection cycle initiates an exacerbating effect to the worker safety, environmental, and cost issues discussed above.

The methods and materials used in present military aerospace coating systems present significant concerns with regards to worker and environmental safety, maintenance costs, and asset availability. Furthermore, there are imposed limits on mission safety due to the limited service-life of the cladding, the static nature of the topcoat color, and manner in which damage assessment is acquired and protection is delivered. Clearly, an expansion of these functional and material limitations is needed.

A timely intersection exists between the coating needs of the Air Force and tangible advances made in the materials, chemical, and engineering sciences on topics relevant to the components of aerospace coatings. These advances center on molecular and nano-engineered materials that can increase coating functionality beyond that of: (1) requisite stripping for inspection and removal of important OEM coating system components, (2) requisite chromate-based materials for corrosion protection, and (3) fixed color, low-gloss topcoats. Because of the interactive nature of coating system components, the successful development of a new multi-functional coating system will require deviation from the traditional mode for coating improvement, i.e. single component substitution, which has not been successful to date. This MURI team will develop an enhanced, multi-functional coating system through a new paradigm in which the entire coating system is redesigned. This coordinated approach will require the

concerted effort of a multi-disciplinary team of materials scientists, chemists, physicists, and coating scientists.

MURI OBJECTIVES

This collaborative team proposes to identify a new coating system that will significantly advance coating functionality and include the ability to:

(1) provide corrosion protection using environmentally compatible materials

(2) sense corrosion and mechanical damage of the aircraft skin

(3) initiate coating repair responses to sensed chemical and physical damage

(4) achieve optimal adhesion using environmentally compliant materials

(5) improve the fatigue resistance and mechanical integrity of the fuselage.

This significant advancement will be accomplished through the development of a new, total coating system and will include:

(1) the development of a field-replaceable, multi-functional, nano-engineered metallic cladding

(2) the use of molecular engineering, micro-electro-mechanical, and integrated circuit approaches to develop sensing capability of mechanical and environmental conditions of the surface of the aircraft.

(3) the development of new approaches for the identification, encapsulation, and delivery of environmentally compatible inhibitor compounds that will optimize solubility and compatibility with the paint resins when used as inhibitive pigments.

(4) the optimization of organic coating adhesion through the use of environmentally compatible surface treatments

This academic team will receive guidance and other assistance via interactions with U.S. industries (3M, Rowan Technologies, PRAXAIR, General Electric, Rockwell, and Boeing), DoD, (AFRL, ARL, NRL, NSWC) and DoE laboratories (Sandia National Labs). These partners will collaborate within one or more of the following types of interactions: (1) as an advisor, (2) as a technical partner that contributes materials and/or services, (3) as a fiscal contributor through student sponsorship

PAST AND SUGGESTED NEW DIRECTIONS

The fundamental strategy of this research initiative will be to: (1) Develop a field replaceable, nano-engineered cladding. This cladding will be made of such an alloy composition that it will be easily spray applied to achieve an amorphous structure with a high corrosion and enhanced mechanical properties. In addition, the thermally sprayed cladding may be made to possess active corrosion protection and sensing capabilities. (2) Augment adhesion without the use of chromate conversion coatings. This is facilitated by the presence of a field replaceable cladding to cover the AA2024-T3 substrate. (3) Identify non-chromate inhibitor(s) and identify molecular and nano-engineering strategies for delivery . Identified inhibitors will require micro/nano-containment to control solubility and could be used within the surface of the cladding or primer layer. (4) Develop sensing and healing strategies for corrosion and mechanical damage using nano- and molecular-engineering methods. Sensing strategies will be examined within the cladding, primer layer, and topcoat.

A. THERMALLY SPRAYED CLADDINGS WITH CORROSION INHIBITING CHARACTERISTICS

The current OEM cladding on military aircraft is a dilute, non-heat treatable alloy that is much lower in corrosion rate than the underlying substrate (AA2024-T3[1]). This quality

minimizes organic coating debonding and filiform corrosion[2-4] and provides superior field-corrosion resistance in lap/splice joints when compared to the bare substrate in the presence of chromates. However, current cladding compositions provide limited sacrificial cathodic protection of crevices, rivet holes, exfoliated regions, and cracks[1]. More importantly, this first line of defense against corrosion is often removed during the maintenance cycle, and presently cannot be replaced.

Thermal spray methods have been advanced to the point that rapidly quenched aluminum-based materials (*e.g.*, Al-Mg, Al-Zn, and Al-In-Sn) can now be applied to ferrous and precipitation age-hardenable aluminum alloys[20-21]. Thermal spraying allows the production of cladding compositions (*e.g.*, Al-In-Sn) that can attain the significant anodic potentials needed for suppression of localized corrosion and stress corrosion in high strength aluminum alloys[22]. The high cooling rates developed in this process (up to 10^7 degrees/s) also impart partitionless phase transformation, solute trapping, extend the solid solubility limits[23], and demonstrate capability of producing amorphous alloys[24]. Amorphicity in metals has the advantage of establishing micro-structural homogeneity (*i.e.*, elimination of second phase particles), thus reducing corrosion rates. Amorphicity also inhibits dislocation motion, which dramatically increases tensile strength and elastic modulus. Thus, the use of thermally sprayed aluminum claddings could provide significant electrochemical and mechanical advantage relative to current Alclad™.

Thermal spray coatings can be produced to have both graded chemical compositions and graded mechanical stresses. Graded compositions would allow the introduction of critical species only where they are needed (*e.g.*, at the surface), while a graded stress field would allow the production of compressive stresses[25] at the surface to mitigate mechanical fatigue similar to shot peening or cold working.

Advances in thermal spray technology are paralleled by achievements in the science of aluminum-based metallic glasses. Compositions identified at the University of Virginia can now be vitrified at reduced quench rates[26-29]. In addition, aluminum-based amorphous alloy chemistries have been produced (*e.g.*, inclusion of lanthanides) that not only improve resistance to localized corrosion[30] and possibly provide active corrosion protection, but also can be combined with a transition metal (TM – Fe, Ni, Co, Cr) to provide improved barrier protection. Several amorphous Al-TM-Ce alloys have been produced (*e.g.*, $Al_{85}Ni_{10}Ce_5$, $Al_{87}Co_{8.7}Ce_{4.3}$, and $Al_{90}Fe_xCe_{10-x}$), but have yet to be examined from the standpoint of self-healing. Since Ce is incorporated in the alloy in supersaturated solid solution, the opportunity exists to create oxidized layers of Al_2O_3 that contain CeO_2[31]. In the presence of moisture, soluble tetravalent Ce in the form of $Ce(OH)_2^{2+}$, could then migrate to cathodic sites, precipitate the less soluble trivalent form upon reduction, and block further cathodic activity, and hence corrosion[32].

Additional functionalities of the amorphous cladding is envisioned. These could be enhanced adhesion of subsequent topcoats by the inclusion of non-chromate adhesion promoters within the porosity of the cladding layer[33,34] or selective etching of the nano-crystalline structure, as well as the inclusion of sensing moieties within or on the surface of the cladding.

B. IDENTIFICATION OF NON-CHROMATE CORROSION INHIBITORS

Once the cladding is removed, corrosion protection by current military aerospace coatings is provided primarily from the chromate-based inhibitive pigments present within the primer layer[10]. Chromate pigments are unique within the current repertoire of inhibitors in that they have very high inhibitive power (*i.e.*, high efficiency at extremely low concentrations) even when used on the more susceptible Cu-bearing aluminum alloys[13]. This inhibitive power allows certain chromate compounds to be incorporated into primer resins such that they dissolve at a

sufficient rate to deliver an effective inhibitor dose to the metal substrate, yet not dissolve so fast so as to produce porosity or blistering. The effective water solubility for chromate pigments appears to be in the range of $5x10^{-3}$ mols CrO_4^{2-} L^{-1} (strontium chromate ($SrCrO_4$)) to $1.1x10^{-2}$ mols CrO_4^{2-} L^{-1} at 25° C (zinc yellow ($K_2CrO_4 \bullet 4ZnCrO_3 \bullet Zn(OH)_2 \bullet 2H_2O$))[12]. Other chromate compounds, e.g., zinc tetroxychromate ($ZnCrO_4 \bullet 4Zn(OH)_2$), require an acidic environment to achieve the proper solubility (used in acidified wash primers), while others, *e.g.*, zinc chromate, are too insoluble under any condition and can actually promote corrosion. Thus, the proper balance of inhibitive power and pigment solubility are requisite for total system performance. The selection of inhibitive pigments having the appropriate solubility is further complicated in that the precise solubility of the inhibitive pigment will be a function of the resin chemistry. The physical properties of the resin are, in turn, a function of the pigment volume concentration (PVC). Thus, once a reasonable compound has been identified based on solubility and inhibitive power characteristics, additional testing will require implementation into test resins using different loadings, and exposure to service-type environments.

Numerous compounds have been examined with the hope of providing a chromate replacement. These compounds include molybdates[35], vanadium-based compounds[36], boron-based compounds[37-39], and rare earth salts[40], among others, and have recently been examined for inhibitor efficacy on aerospace alloys[40-42]. To date, no single compound has demonstrated an effective inhibitive power (efficiency at specified concentration) comparable to chromate, much less with an appropriate pigment solubility.

A promising alternative to the use of a single inhibitive species is that of using synergistic combinations of two or more compounds. Synergy occurs when the inhibitive property of the combination exceeds the sum of the individual compounds. Synergistic combinations of

inhibitors have been examined extensively for steel in acidified[43-50] and neutral[51-54] aqueous environments, as well as for copper in neutral aqueous environments[55-56]. Numerous theories for synergy have emerged depending on whether active anions[44,48,55,58,59], cations[43,47,49,52,54], or organic species[53-54] are employed. However, a common theme throughout the literature is that one species adsorbs initially and bridges or facilitates the adsorption of the other species to produce a complex or layered barrier structure.

More germane to paints, synergistic combinations of paint additives have been explored since the late 1970's[60]. Examples include phosphates + borates, zinc phosphate + zinc nitrophthalate + zinc oxide, and more recently, zinc molybdate + zinc phosphate + a zinc salt of benzoic acid. This latter combination has been used in the DoD self-priming topcoat, which has unfortunately resulted in poor adhesion after limited service. This points out yet another hidden advantage of chromate pigments. In addition to having the appropriate balance of inhibitive power and solubility, an inhibitive pigment must not interfere with in-service adhesion, a property that is actually augmented by chromate pigments[61].

Recent studies have examined synergistic combinations of the previously described rare earth and transition metal salts[41,62,63]. Although these preliminary experiments have only examined 1:1 ratios of these materials at one concentration, synergistic effects have been observed using both electrochemical and pit morphology analyses. It is almost certain that the optimum ratio is something other than 1:1, and that an array of additional experiments is needed to identify the proper materials and ratio. Further, it is unlikely that the inhibitive compounds having the optimum corrosion protection properties will also have the optimum solubility characteristics needed for inclusion into a paint. Fortunately, numerous molecular and nano-

engineering packaging schemes are presently available to control compound solubility and delivery.

C. ENCAPSULATION AND DELIVERY STRATEGIES

As discussed above, a method is needed to provide control of solubility and delivery for a range of compounds so that they may be included within the paint formulation without compromising coating function. With specific regards to coatings, traditional microencapsulation strategies[64], in which the compound of interest is encased in a polymer sheath, were examined in the late '80's[65]. The results showed that the primer containing microencapsulated inhibitor were significantly better than the standard MIL-P-23377 primer containing strontium chromate. However, the inhibitor examined was a mixture containing a dichromate salt. This supports the feasibility of microencapsulation, but certainly points to the need for discovery of new inhibitor compounds.

The last 20 years have seen significant advancement in the polymer chemistry and methods used for microencapsulation, and many strategies for chemical release now exist. Release strategies can include sensitivity to mechanical stress, pH, chloride, and temperature, among others. While not explored in-depth, preliminary evidence has indicated that some of these new strategies show promise when used to encapsulate inhibitors for corrosion of steel[66].

Conventional microencapsulation has become a standard method in numerous industries, however there are emerging strategies that are showing considerable promise with regards to encapsulation and solubility control. Van Ooij has recently patented a process whereby chemical compounds of particulate materials, including nanoparticles, may be coated via plasma polymerization (PP) while suspended in a fluidized bed. PP can be used to apply an extraordinary range of polymer chemistries having a large range of properties e.g. monomer

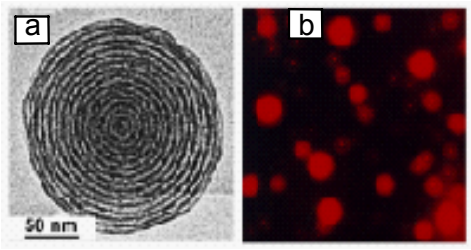

Figure 1. (a) TEM micrograph of hollow silica vesicle and b) Optical micrographs of rhodamine-encapsulated vesicles.[5]

type, cross-link density, thickness). This is essential for the generation of sheath chemistries that will be compatible with the coating matrix as well as control host dissolution. Recent experiments by Van Ooij have shown that highly soluble powders such as sodium carbonate, which normally dissolve in seconds in cold water, require 5 hours following PP treatment.

An additional approach for encapsulation of inhibitor compounds is that of using nano-structured (1-3 nm) hollow silica vesicles and hollow silica fibers formed by evaporation induced self-assembly of organic and inorganic precursors (Figure 1)[67]. The permeability of these silica vesicle walls can be controlled so that inhibitor delivery can be controlled. This approach of containment may provide an added optical advantage in that the silica vesicles are sufficiently small so as not to scatter light, which enables the formation of optically transparent reinforced nano-composites.

An alternate approach for holding on to and delivering water soluble, inhibitive pigments within paints is to immobilize the active species on an inert substrate, and then release the species as needed. This approach was devised for the retention and controlled release of molybdate species on activated alumina particles[68,69] in which the molybdate was delivered via an ion exchange reaction.

The preceeding method of immobilization/delivery is closely allied to another recently demonstrated approach in which Zn-Al hydrotalcite (HT) hosts were molecularly engineered to contain oxovanadate ions, then dispersed in an organic resin and shown to provide significant corrosion inhibition[70]. The host HT material is an important industrial material used as

absorbents, stabilizers, alkaline catalysts, and acid neutralizing agents[71,72], and consists of layers of mixed metal hydroxides separated by layers of anions and water (Fig. 2). The prototypical HT compound is the naturally occurring hydromagnesite whose formula is $Mg_6Al_2(OH)_{16}{\cdot}CO_3{\cdot}4H_2O$[73,74]. Structurally, the compound consists of $Mg(OH)_2$ layers. This layer is positively charged by substitution of Al^{3+} on Mg sites. This positive charge is offset by negatively charged carbonate situated in the interlayer. Layer-to-layer spacing in HT depends on the anion diameter[74].

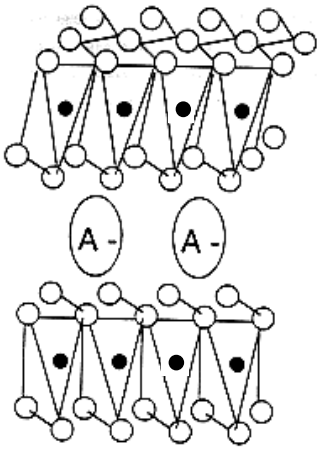

Figure 2. Layered structure characteristic of hydrotalcites. A-; anions, O: OH groups, • M(II) and M(III) cations.

There is great chemical variety in HTs because there are many different pairs of metals that can combine to form the positively charged layered hydroxide "host". In turn, each host structure can accommodate many different types of anions. Hydrotalcite compounds may be synthesized as powders by titration of one metal salt solution with another to induce precipitation[75-77]. Hydrotalcite coatings may be formed by sol-gel methods using metal alkoxides[78], and by reaction of a metal substrate with another metal salt solution in the presence of suitable anions[79].

Anions in hydrotalcites may exchange with anions in solution while the host structure remains stable. Exchange reactions are regularly employed to embed large electrochemically or catalytically active anions in HT[80-82]. The ability to participate in exchange also makes these compounds useful anion scavengers[83]. Exchange isotherms and equilibrium constants have been measured for simple mono- and divalent anions such as Cl^-, F^-, SO_4^{2-}, and CO_3^{2-}, etc. exchanged with NO_3^- [84]. These equilibrium constants range from about –0.6 to 2.0 and tend to increase as

the anion radius decreases and as anion valency increases. Exchange capacities are reported to range from 1 to 5 meq/gram making HTs very efficient inorganic anion scavengers[76,84]. Exchange characteristics also depend on the charge density in the mixed metal hydroxide layer, which in turn is dependent on the ratio of divalent to trivalent cations in the layer[85]. This ratio is adjustable at the time of synthesis allowing some measure of control over exchange characteristics.

Heat-treated or calcined HTs possess a "memory effect"[75,81,85,88] in that heat-treated materials will revert to HT upon contact with water and anions, and can therefore act as dessicants and anion scavengers. Differential scanning calorimetry and x-ray diffraction measurements show that thermal treatment of HTs up to about 200^{o}C induces dehydration. Treatment up to 500^{o}C induces dehydroxylation and loss of vaporizable anions such as carbonate, nitrate, oxalate, and acetate. Heating at up to 900^{o}C induces mixed metal oxide formation. Remarkably these partially or fully dehydrated mixed metal oxides produced from HT precursors, will rehydrate on contact with water, take up anions, and reform HT thereby conferring scavenging and desiccant characteristics.

Zeolitic host materials can be made by heat treatment of hydrotalcite precursors. These zeolite hosts can take-up a range of molecular species in the open galleries and have been used to absorb dyes[89], and molecular gases[90], and water. A zeolitic structure is produced by first synthesizing HTs with anion layers that contain a mixture of large vaporizable anions, and large non-vaporizable anions. Subsequent heat treatment at temperatures, usually ranging from 250^{o} to 400^{o}C, causes elimination of vaporizable anions leaving opens spaces in the structure. The extent of the open space in the structure depends on the diameter of the anions and the fraction of vaporizable anions in the layer. Gallery heights of 12 to 25 Å have been demonstrated[89]. Thus, a

wide range of nano- and molecular-engineering approaches are available for the containment and delivery of inhibitive components, but have yet to be fully exploited.

D. METHODS FOR SENSING AND SELF-REPAIR

The ability of an aircraft coating to sense damage, whether it be mechanical or chemical, and then initiate a protective measure is an extremely desirable characteristic. Recent work has used colorimetric agents within clear-coats to detect pH changes and hence anodic and cathodic regions on aerospace alloys[91]. While the limitations of such an approach in an actual commercial coating are apparent (*e.g.*, masking by pigments), it demonstrates one of the numerous modalities by which sensors can operate. In essence, changes in chemical (e.g. presence of corrodent) and mechanical (*e.g.*, stress state) conditions can be detected by molecular- and nano-scale sensors that are sensitive to shifts in energy outside of the visible spectrum, as well as other forms of energy (*e.g.*, magnetic). Multiple strategies for sensor implementation are envisioned in the proposed coating system, i.e. they could conceivably be used within any or all of the coating system layers: the cladding, the primer layer, or mission coat.

With regards to coating applications, there has been some effort to implement luminescent metal complexes as analytical chemical (oxygen) sensors in organic coatings. For example, the luminescence of a Ru(II) complex has been used to sense oxygen in polymer films[92]. Chemical affinity sensors have also been developed along the basis of long-period grating (LPG) concepts[93], in which an optical fiber is coated with a polymer whose refractive index is altered by the adsorption of a specific target chemical species. Such sensors could be located within the proposed coating system, either embedded in the cladding surface or elsewhere, but would need to be located in specific trouble regions of the aircraft because of the local nature of the sensing region. More importantly, the specificity of molecularly engineered

materials to target chemical moieties could be exploited into a miniaturized sensor that could be broadcast over the surface. To this end, the effort to develop intelligent photonic crystals are of importance[94,95]. Photonic crystals are structures in which the dielectric constant varies periodically in space. The periodicity is that of microscopic dielectric nanospherical particles instead of atoms. This produces many of the same phenomena for photons (light) as the atomic potential produces for electrons. In analogy to the diffraction of x-rays by atomic structures, mesoscale photonic crystals diffract light in the range of ultraviolet through the visible spectrum to near infrared.

Most current general methods for preparing these structures use self-organized surfactants, block copolymers, or colloidal particles as templates in conjunction with sol-gel techniques. Micro or nanospheres of mono-disperse polystyrene or silica can be self-organized through the phase transition of a colloidal suspension to form a face-centered (or body centered, depending on the initial volume fraction of colloidal particles) crystalline lattice that comprises a crystalline colloidal array (CCA)(see Figure 3). The CCA can be quenched into a polymer matrix permanently locking in ordering.

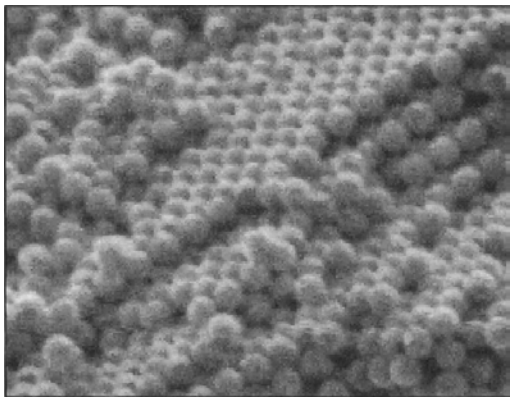

Figure 3. Scanning electron micrograph of a three-dimensional face-centered cubic CCA composed of 150 nm diameter silica spheres. The spheres had a polydispersity below one percent.

Most commercial polymer colloids or latex coatings employ polydisperse particle sizes and consequently do not form regular face-centered or body-centered cubic CCA. However, there is already considerable evidence within the literature that if highly monodisperse spherical particles are used in modified conventional latex coating formulations, CCA can be realized by appropriate control of

ionic strength, particle size uniformity, particle density, viscosity, etc.[96-98]. Many commercial latexes are made by copolymerization of acrylic acid or methacrylic acid which should be suitable matrices for the CCA.

Asher and co-workers have demonstrated that CCA's, quenched in a hydrogel, could be used for chemical sensing of analytes containing metal ions such as Pb^{2+} at the 0.1 μM concentration range. Such ion specificity is critical to accurate sensing of corrosion processes in Al alloys that have detectable signatures for dissolved cations such as Al^{3+} and Cu^{2+}. By incorporation of specific molecular recognition agents these materials can be tailored to respond to a large variety of stimuli including pH, ionic strength, chemical species, magnetic, thermal, electrical and ultrasound irradiation. Polyelectrolyte hydrogels can respond to an applied electric field (or voltage) by swelling. However, the typical hydrophilicity of hydrogels will be problematic for incorporation into an aerospace coating. Other polymer scaffolds for CCA's whose chemistry is more compatible with commercial coatings have not, but must, be examined.

SUMMARY

This paper has provided an overview of research program that seeks to develop the scientific framework for an environmentally compliant, multi-functional aerospace coating. This program is comprised of six academic institutions that will implement advances in nano-engineering to develop a coating that will have the ability to: (1) sense corrosion and mechanical damage, (2) initiate mitigation responses to the sensed damage (chemical and mechanical), (3) provide corrosion protection and adhesion using environmentally compliant materials, and (4) improve fatigue resistance. The enhanced functionality of this advanced coating system will be achieved through the incorporation of: (1) a field-replaceable, nano-engineered metallic cladding, (2) the use of molecular-engineering and self-assembled colloidal crystals, and (3) the

development of new approaches for the identification, encapsulation, and delivery of environmentally compatible corrosion inhibitors, and that will optimize solubility and compatibility with the paint resins when used as inhibitive pigments, and (4) the optimization of organic coating adhesion through the use of environmentally compatible surface treatments. This program is significantly bolstered by the technical steerage and contribution of U.S. industries and DoD laboratories.

ACKNOWLEDGEMENTS

The authors gratefully acknowledge the financial support of the Air Force Office of Scientific Research and the Department of Defense under contract number F49620-01-1-0352.

REFERENCES

1. *ASM Handbook* **13:**587-589 (1987).
2. G.M. Hoch, A Review of Filiform Corrosion, R.W. Staehle, J. Kruger, A. Agrawal, Ed., Localized Corrosion (NACE Houston, TX, 1974).
3. K. Nisancioglu, H. Let-Olsen, and O. Lunder, Electron Microscopic Investigation of Filiform Corrosion Morphologies on Aluminum, D. S. Scantlebury and M. W. Kendig, Ed., Advances in Corrosion Protection by Organic Coatings II (The Electrochemical Society, Pennington NJ, 1990).
4. L.F. Vega, F. Bovard, T. Nakayama, K. Ikeda, H. Sige, E.L. Colvin, Filiform Corrosion of Aluminum Alloys: Influence of Alloy Composition, R.G. Buchheit, M.R. Jaworski, and P.D. Chalmer, Ed., Surface Conversions of Al and Ferrous Alloys for Corrosion Resistance (CORROSION 2000 Research Topical Symposium, 2000).
5. P.L. Hagans and C.M. Haas, *Surf. Interface Anal.* **21:**65 (1994).

6. M.W. Kendig, A.J. Davenport and H.S. Isaacs, *Corr. Sci.* **34**:41 (1993).

7. F.W. Little, G.L. Bibbins, K.Y. Blohowiak, R.E. Smith, and G.D. Tuss,, *Corr. Sci.* **37:**349 (1995).

8. A.E. Hughes, R.J. Taylor and B.R. Hinton, *Surf. Interface Anal*., **25:**223 (1997).

9. G.O. Ilevbare, J.R. Scully, J. Yuan, and R.G. Kelly, *Corrosion* **56:**227-242 (2000).

10. C.N. Hunter, J.H. Osborne, and S.R. Taylor, *Corrosion* **56:**1059-1070 (2000).

11. R.B. Leggat, S.R. Taylor, R.G. Buchheit, and W. Zhang, 197th Meeting of The Electrochemical Society, Toronto, Ontario CAN (2000).

12. Z.W. Wicks, F.N. Jones, and S.P. Pappas, in *Organic Coatings, Science and Technology, Vol.2: Applications, Properties, and Performance* . (John Wiley and Sons, Inc., New York, 1994), vol. 2, pp. 183.

13. J. Sinko, Considerations on the Chem. and Action Mech. of Corr. Inh. Pigm. in Org. Ctgs, 6th Bien. Conf. on Sci. and Techn. of Org. Ctgs, Hilton Head, SC (Institute of Materials Science, 2000).

14. M.M. Madani, R.M. Simmons, K.M. Mann, Y.M. Sigonney, and R.D. Granata, Chromate Inhibition of Polymer-Coated AA2024-T3, 198th Meeting of the Electrochemistry Society, Phoenix, AZ (2000).

15. P. L. Hagans and C. N. Haas, in *ASM Handbook, Vol.5: Surface Finsihing* J. A. S. C.M. Cotell, and F.A. Smith, Ed. (ASM International, Metals Park, OH, 1994), vol. 5, pp. 405-411.

16. E.A. Starke, Jr. and J.T. Staley, *Prog. Aerospace Alloys* **32:**131-172 (1995).

17. J.R. Scully, T.O. Knight, R.G. Buchheit, and D.E. Peebles, *Corrosion Science* **35:**185 1993).

18. G.S. Chen, M. Goa, and R.P. Wei, *Corrosion* **52:**8 (1996).

19. R.G. Buchheit, *J. Electrochem. Soc.* **142:**3994 (1995).

20. M.J. Bayley and C. D. S. Tuck, *Industrial Corrosion* **10**, 5-12 (1992).

21. S.S. Birley, W. Hepples, N.J.H. Holroyd, The Corrosion Protection of Weldable 7XXX Aluminum Alloys by Al-based Arc Spray Coatings, E. A. Starke, Ed., 3rd Intl. Conference on Al Alloys, Charlottesville, VA .

22. H.H. Holroyd, NACE 10, R.P.G. and B. Ives, Ed. (NACE, Houston, TX).

23. K. D. Krishnanand, R.W. Cahn, in *Rapidly Quenched Metals,* N.J.Grant, B.C. Giessen, Ed. (MIT Press, Cambridge, MA, 1976) pp. 67-75.

24. T. Shymyreva and A. Ivanov, Characterization of the Thermal Spray Coatings Having Amorphous and Nanocrystalline Structures, United Thermal Spray Conference 99 (1999).

25. O. Kelser, J. Matejicek, S. Sampath, and S. Suresh, *Materials Science Forum* **308-31:**389-395 (1999).

26. Y. He, G.J. Shiflet and S.J. Poon, *J. of Alloys and Compounds,* **207/208:**349-354 (1993).

27. A. Inoue, K. Ohtera, and T. Masumoto, *Japanese Journal of Applied Physics* **27:**L736-L739 (1988).

28. T. Masumoto, *Materials Science and Engineering* **A179/A180:**8-16 (1994).

29. Y. He, S.J. Poon, and G.J. Shiflet, *Science* **241:**1640-1642 (1988).

30. J.E. Sweitzer, J.R. Scully, R.A, Bley, and J.W.P. Hsu, *J. Electroche. Soc. - Solid State Letters* **2:**267-270 (1999).

31. A.N. Mansour, S.J. Poon, Y. He, and G.J. Shiflet, *Surface Science Spectra* **2**, 31-44 (1993).

32. R.G. Buchheit, S.B. Mamidpally, P. Schmutz, and H. Guan, Ed., *Active Corrosion Protection in Chromate and Chromate-free Conversion Coatings* (NACE, Houston, TX, 2000).

33. G.D. Davis, *J. of Metals* **49:**25-27 (1997).

34. S. Kycek and P. Remer, *Mat. Sci. Forum* **308-32:**368-373 (1999).

35. M. Stern, *J. Electrochem. Soc.* **24:**787-806 (1958).

36. D. Bienstock and H. Field, *Corrosion*, **17**:87-90 (1961).

37. N. R. Whitehouse, *Polymer Paint and Colour J.* **178:**239 (1984).

38. J. Boxall, *Polymers, Paints and Colour J.* **174:**382-384 (1984).

39. B.R.W. Hinton, *Metal Finsihing* **Sept. '91, Oct. '91**, 55-61, 15-20 (1991).

41. H.E. Hager, C.J. Johnson, K.Y. Blohowiak, C.M. Wong, J.H. Jones, R.R. Taylor, R.L. Cook, Jr., *U.S.Patent 5,866,652* (The Boeing Company, U.S.A., 1999).

42. R.L. Cook and S.R. Taylor, *Corrosion* **56:**321-333 (2000).

43. Y. Feng, K.S. Siow, K.T. Teo, and A.K. Hsieh, *Corr. Sci.* **41:**829-852 (1999).

44. S. Sayed Azim, S. Muralidharan S. V. Iyer, B. Muralidharan, and T. Vasudevan, *Br. Corr. J.* **33:**297 (1998).

45. M.Mustafa. S.M. Shahinoor, amd I. Dulal, *Br. Corrosion J.* **32:**133-137 (1997).

46. S. Sayed Azim, S. Muralidharan, S. Venkatkrishna Iyer, *J. of Appl. Electrochem.* **25:**495-500 (1995).

47. D.D.N. Singh and A.K. Dey, *Corrosion* **49:**594-600 (1993).

48. M.A. Quraishi, J. Rawat, and M. Ajmal, *Corrosion* **55:**919-923 (1999).

49. G.N. Mu, T.P. Zhao, and T. Gu, *Corrosion* **52:**853-856 (1996).

50. M.A. Quraishi, S. Ahmed, and M. Ansari, *Br. Corrosion J.* **32**, 297-300 (1997).

51. J.M. Abd El Kader, A.A. Warraky, and A.M. Abd El Aziz, *Br. Corr. J.* **33:**152-157 (1998).

52. S. Rajendran, B.V. Apparao, and N. Palaniswamy, *Electrochem. Acta* **44:**533-537 (1998).

53. T. Suzuki, H. Nishihara, and K. Aramaki, *Corr. Sci.* **38:**1223-1234 (1996).

54. Y. Gonzalez, M.C. LaFont, N. Pebere, and F. Moran, *J. of Appl. Electrochem.* **26:**1259-1265 (1996).

55. Y. Feng, K.S. Siow, W.K. Teo, K.L. Tan, and A.K. Hsieh, *Corrosion* **53:**546-555 (1997).

56. S. Gonzalez, M.M. Laz, R.M. Souto, R.C. Salvarezza, and A.J. Arvia, *Corrosion* **49:**450-456 (1993).

57. K.T. Carron, M.L. Lewis, J. Dong, J. Ding, G. Xue, and Y. Chen, *J. Matl. Sci.* **28:**409-4103 (1993).

58. K. Aramaki and N. Hackerman, *J. Electrochem. Soc.* **116:**558 (1969).

59. N. Shikai and L. Yefen, Study of the Synergy Mech. of Acidic Inh., 8th Europ. Symp. on Corr. Inh. (1995).

60. S.A. Hodges,, W.A. Uphues, and M.T. Tran, *Surf. Coatings Australia* **34:**24-30 (1997).

61. A.T. Evans, J.D. Scantlebury, and L.M. Callow, The Adh. and Corr. of Chromate Cont. Ctgs on Al, J. D. Scantlebury and M. W. Kendig, Ed., Adv. in Corr. Prot. by Org. Ctgs II (ECS, Pennington, NJ, 1995).

62. R.L. Cook, Jr. M.S., University of Virginia (1995).

63. S. R. Taylor, An Examination of Possible Synergy Between Paired Combinations of Transition and Rare Earth Metal Salts, 197th Meeting of the ECS, Toronto, CAN (ECS, Pennington NJ, 2000).

64. C. Thies, in *Encyclopedia of Polymer Science and Engineering, 2nd Edition* e. a. H.G. Mark, Ed. (New York, 1987), vol. 9, pp. 724-745.

65. V.S. Agarwala, J.J. Delucia, L.J. Balin, Microencap. Crack Arrestment Comp. and Corr. Inh. for Org. Ctgs, D. J. Scantlebury and M.W. Kendig, Ed., Adv. In Corr. Prot. by Org. Ctgs (ECS, Pennington NJ, 1989).

66. D.G. Enos, C.R. Guilbert, C.F. Norman, J.A. Kehr, and C.E. Boyer, Improving the Damage Tolerancem and Extending the Service-Life of Fusion-Bonded Epoxy Coatings, ICCRCS (1998).

67. Y. Lu, H. Fan, A. Stump, T.L. Ward, T. Reiker, and C.J. Brinker, *Nature* **398:**223 (1999).

68. D.R. Robitaille, M.S. Vukasovich, H.F. Barry, *U.S. Patent 3,969,127*(Sherwin-Williams Co., U.S.A., 1976).

69. R. A. Cayless, . *U.S. Patent 4,459,155* (British Petroleum, U.S.A., 1984).

70. S.R. Taylor, E.A. Pehovaz, R.B. Leggat, et. al., "An Environmentally Compliant Corrosion Resistant and Electrically Conductive Inorganic Coating for Al Alloys" *Contract F49620-96-1-0305* (DARPA, 2000).

71. *Chemical and Engineering News* **77:**12 (1999).

72. *Chemical Week* **161:**27 (1999).

73. H.F.W. Taylor, *Min. Mag.* **39:**377 (1975).

74. S. Miyata, *Clay and Clay Miner.* **23:**369 (1975).

75. W. T. Reichle, *J. Catal.* **94:**547 (1985).

76. K. Itaya, H.C. Chang and I. Uchida, *Inorg. Chem.* **26:**624 (1987).

77. K.R. Popelmeir and S.J. Hwu, *Inorg. Chem.* **26:**3297 (1987).

78. T. Lopez, E. Ramos, P. Bosch, M. Asomoza, and R. Gomez, *Materials Letters* **30:**279 (1997).

79. R.G. Buchheit, M.D. Bode and G.E. Stoner, *Corrosion* **50:**205 (1994).

80. I. Sissoko, E.T. Iyagba, R. Sahai, and P. Biloen, *J. of Solid State Chem.* **60:**283 (1985).

81. M. A. Drezdzon, *Inorg. Chem.* **27:**4628 (1988).

82. E. T. Iyagba, Ph.D., University of Pittsburgh (1986).

83. J.K.G. Panitz and D.J. Sharp, "Th Use of HT as a Chloride Ion Getter for a Barrier Al Anodization Process" *Sandia Report CAND95-2300* (SNL, 1995).

84. S. Miyata, *Clay and Clay Minerals* **31:**305 (1983).

85. S. Miyata, *Clay and Clay Minerals* **28:**50 (1980).

86. A. Nemudryi, V.P. Isupov, and N.P. Kotsupalo, *Russ. J. of Inorg. Chem.* **28:**1575 (1983).

87. E.T. Devyatkina, N.P. Otsupalo, N.P. Tomilov, and A.S. Berger, *Russ. J. of Inorg. Chem.* **28:**801 (1983).

88. M.A. Ulibarri, J.M. Fernandez, F.M. Lbajos, and V. Rives, *Chen. Mater.* **3:**626 (1991).

89. H.W. Clark, in *European Patent Application* . (1986).

90. S. Miyata and T. Hirose, *Clay and Clay Minerals* **26:**441 (1978).

91. J. Zhang and G.S. Frankel, *Corrosion* **55:**957 (1999).

92. J.N. Demas and B.A. DeGraff, *Anal. Chem.* **63:**829A-837A (1991).

93. J. L. Elster, Corr. Monitoring in Aging Aircraft Using Opt. Fiber-based Chem. Sensors, 4th Joint DOD/FAA/NASA Conf. on Aging Aircraft, St. Louis, MO (2000).

94. J.H. Holtz and S.A. Asher, *Nature* **389:**829 (1997).

95. J.H. Holtz J.S.W. Holtz, C.H. Munro, and S.A. Asher, *Anal. Chem.* **70:**780 (1998).

96. J.W. Vanderhoff, E.B. Bradford, and W.K. Carrington, *J. Polymer Science Symposium No. 41* , 155 (1973).

97. S.T. Heckersley and A. Rudin, *J. Coatings Technol* **62:**89 (1990).

98. P.R. Sperry, B.S. Snyder, M.L. O'Dow, and P.M. Lesko, *Langmuir* **10:** (1994).

OPPORTUNITIES FOR NANO-STRUCTURED 'SOL-GEL-DERIVED' MATERIALS IN CORROSION INHIBITION

C. Jeffrey Brinker,[1,2] Evelyn M. Bond,[2] Hongji Chen,[2] Yi Yang,[2] George Xomeritakis,2
Hongyou Fan,[1] Kui Yu,[1] and Ricardo Pardey[3]

[1]Sandia National Laboratories, MS 1349
Albuquerque, New Mexico 87185
[2]Center for Micro-Engineered Materials
University of New Mexico
Albuquerque, New Mexico 87131
[3]PDVSA INTEVEP, P.O. Box 76343
Caracas, 1070 A, Venezuela

ABSTRACT

Evaporation induced self-assembly has been used to prepare new nanostructured materials with potential applications in corrosion inhibition. Using an aerosol approach, Ce has been incorporated into spherical particles with uniform and, in some cases, ordered pore morphologies. Leaching of these nanostructured particles shows that a steady amount of cerium is leached with time over a period of a week. Ordered lamellar polymer/silica nanocomposite films have been prepared that exhibit very low permeabilities, and these films could be applied as anti-corrosion coats. Finally, thermoresponsive poly-NIPAM/silica nanocomposite films have been prepared that could serve as environmentally sensitive gates to mediate the release of inhibitors.

INTRODUCTION

Self-assembly is the spontaneous organization of materials through noncovalent interactions (hydrogen bonding, Van der Waals forces, electrostatic forces, π-π interactions, etc.) with no external intervention. Self-assembly typically employs asymmetric molecules that are pre-programmed to organize into well-defined supra-molecular assemblies. Most common are amphiphilic surfactant molecules or polymers composed of hydrophobic and hydrophilic parts. In aqueous solution above the critical micelle concentration (cmc), surfactants assemble into micelles, spherical or cylindrical structures that maintain the hydrophilic parts of the surfactant in

contact with water while shielding the hydrophobic parts within the micellar interior. Further increases in surfactant concentration result in the self-organization of micelles into periodic hexagonal, cubic, or lamellar mesophases.

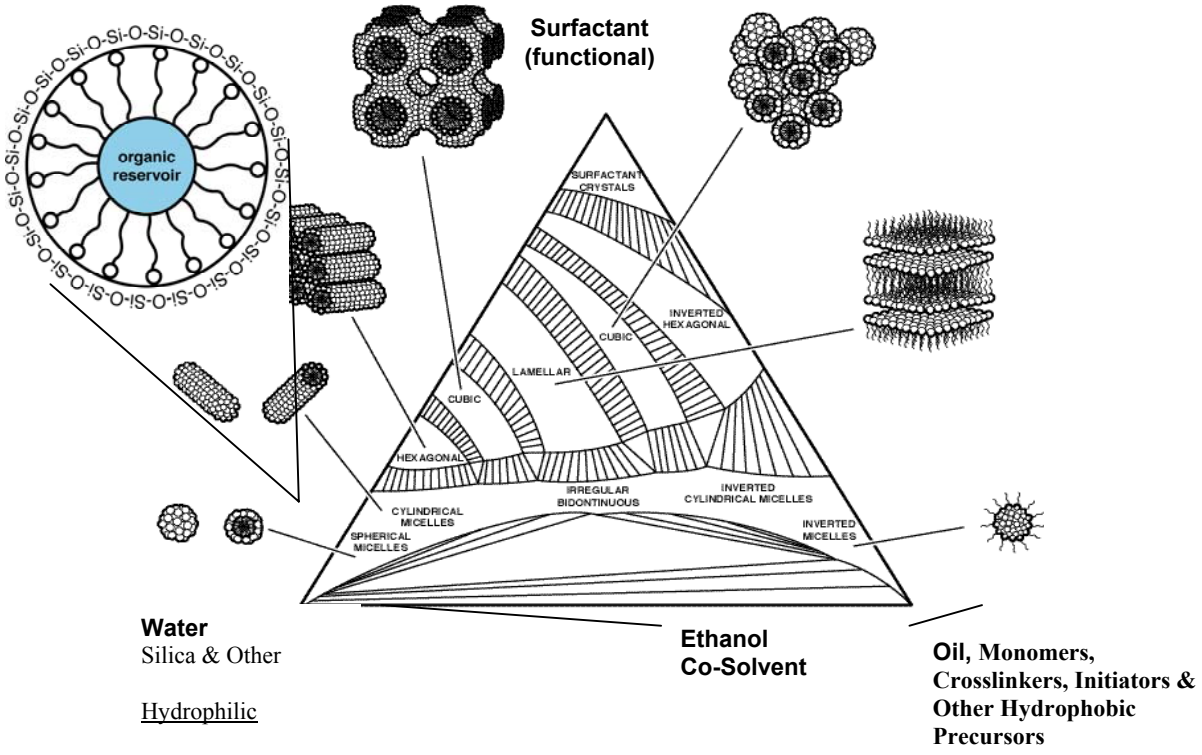

FIGURE 1. Schematic detergent (surfactant-oil-water)phase diagram.

Obviously such detergent mesophases do not themselves represent robust engineering materials suitable for nanotechnologies. It is noteworthy therefore that in 1992 Mobil researchers[1] discovered that surfactant self-assembly conducted in aqueous solutions of soluble silica species results in spontaneous co-assembly of silica-surfactant mesophases. Surfactant removal creates periodic mesoporous solids, essentially silica fossils of the liquid-crystalline assembly. Evaporation-Induced Self-Assembly (EISA) has been used in our group for the formation of thin film mesophases and aerosol particles. Using the generic detergent phase

diagram shown in Figure 1 as a conceptual guide, we can consider as oil a wide variety of hydrophobic, organic precursors and reagents (monomers, crosslinkers, oligomers, functionalized polymers, initiators, etc.). In a process not so unlike washing dishes, we use micelle formation to spatially separate and organize organic precursors (sequestered within the hydrophobic micellar interiors) and inorganic precursors (organized around the hydrophilic micellar exteriors). Further self-organization of micelles into periodic hexagonal, cubic, or lamellar mesophases simultaneously positions both the organic and inorganic precursors into precise 3-D arrangements. Beginning with a homogeneous solution of soluble silica and surfactant prepared in ethanol/water solvent with $c_o << cmc$, preferential evaporation of ethanol concentrates the depositing film in water and nonvolatile surfactant and silica species. The progressively increasing surfactant concentration drives self-assembly of silica-surfactant micelles and their further organization into liquid-crystalline mesophases.[2,3,4] The surfactant can be removed by pyrolysis or solvent washing. Subsequent aging, exposure to acid or base catalysts, or thermal treatment can solidify the silica skeleton, thereby locking in the desired mesostructure.

EISA has been used extensively in our group to prepare thin films of ordered mesophases.[2,5] Evaporation-induced self-assembly of liquid droplets can be used as a route to create ordered porous and composite powders.[6] Starting with an aerosol dispersion of the same precursor solutions used to create mesoporous or nanocomposite films, solvent evaporation creates a radial gradient of surfactant concentration within each droplet that steepens in time[7] and maintains a maximum concentration at the droplet surface. This surfactant enrichment induces silica-surfactant self-assembly into micelles and further organization into liquid-crystalline mesophases. The radial concentration gradient and presence of the liquid-vapor interface (which

serves as a nucleating surface)[8] causes ordered silica-surfactant liquid-crystalline (LC) domains to grow radially inward, rather than outward from a seed.[9]

Thin films and particles of controlled porosity prepared by EISA are of interest for their potential application in the controlled release of corrosion inhibitors. Using the aerosol assisted self-assembly described above, particles that contain monosized pores could be used to release a corrosion inhibitor in a controlled manner. Currently, chromate compounds are widely used as corrosion inhibitors for different metallic materials such as aluminium alloys.[10] Because of their high toxicity, it is desireable to replace chromates with environmentally friendly compounds. Studies have shown that among lanthanide compounds, $CeCl_3$ has the best performance as a corrosion inhibitor.[11,12] In this paper the aerosol assisted EISA of porous particles is extended to silica particles that encapsulate cerium chloride.

Another technique to delay corrosion would be to apply a coating that is impermeable to gases. Polymer-based barrier films find wide applications in packaging of products such as food, pharmaceuticals or electronics. In all cases the barrier material needs to have very low permeability to atmospheric penetrants such as oxygen or water vapor that may degrade the food/pharmaceuticals or attack the dielectric coatings of microelectronic devices. Yang et al.[13] point out that there are three main strategies to prepare effective barrier films, e.g. (1) Reducing the barrier permeability, which implies a polymer with increasingly glassy character, thus reducing the flexibility of the film; (2) Introducing reactive groups in the polymer, which will chemically react with the penetrant. In this case a saturation effect is expected; and (3) Increasing barrier tortuosity, e.g. adding impermeable slab-shaped flakes perpendicular to the diffusion direction, which will introduce significant transport resistance to the penetrant which will have to bypass around the flakes before transversing the barrier thickness. Eitzman et al.[14]

and Falla et al.[15] carried out modeling studies in order to estimate the permeability reduction of a polymer membrane loaded with a given amount of impermeable flakes and derived the following expression which is an upper limit for the ratio (D_o/D) of polymer permeability before and after flake incorporation:

$$D_o/D = 1 + \alpha^2 \phi^2 /(1-\phi) \quad (1)$$

where ϕ is the volume fraction occupied by the flakes (<1) and α is the flake aspect ratio (>1). For the range of values employed in their simulation, e.g. ϕ=0.05-0.2 and α=10-30, they predicted 10-100 times reduction in permeability of the membrane, which was consistent with experimental results of silicone/polycarbonate membranes as well.

A class of materials that shows potential for low permeability is the nanocomposite materials prepared in our lab by EISA that mimic nacre. Nacre is a natural material composed of alternating layers of aragonite (a crystalline form of calcium carbonate) and a rubbery biopolymer. It has evolved over millions of years to simultaneously provide strength, hardness, and toughness to a light weight material. For example abalone nacre composed of only 1 wt.-% polymer is twice as hard, and 1000 times tougher than its constituent phases.[16]

Two types of these hybrid inorganic/organic nanocomposites have been prepared. The first are based on poly(dodecylmethacrylate). [17] Polymerizable monomers, initiators, and crosslinkers are added to the system to produce a hybrid organic/inorganic hybrid material. Combined organic/inorganic polymerization locks in the nanocomposite architecture and covalently bonds the organic/inorganic interface. The beauty of this approach is its simplicity and efficiency: if we seek to prepare laminated organic/inorganic composites, many hundreds of alternating organic/inorganic layers can be assembled in seconds. Photo or thermally induced polymerization of the organic monomers and continued inorganic polymerization complete the

composite assembly process. The second type of hybrid inorganic/organic nanocomposites has been prepared using polymerizable amphiphilic diacetylene molecules as both structure-directing agents and monomers.[18] The self-assembly procedure is rapid and incorporates the organic monomers uniformly within a highly ordered, inorganic environment. Polymerization results in polydiacetylene (PDA)/silica nanocomposites that are optically transparent and mechanically robust. Conjugated polymer PDA/silica nanocomposite films with hexagonal, cubic, or lamellar order were fabricated through EISA and the resulting nanocomposite exhibits unique thermo-, mechano-, and solvato-chromic properties.

The hybid inorganic/organic nanocomposite materials described above display improved hardness over mesoporous silica films. Additionally, we have discovered that films of the nanocomposite materials display potential as gas impermeable membranes. The gas permeability of these nanocomposite materials will be explored in this paper.

Finally, new types of nanocomposite materials have recently been developed incorporating hydrogels. Hydrogels are polymers that are responsive to changes in external stimuli such as pH or temperature. These polymers have been used for controlled drug delivery[19] and micrometer-sized valves.[20] Polymers based on n-isopropylacrylamide (NIPAM) respond to changes in temperature and will swell at low temperatures and shrink at high temperatures (i.e. above 30ºC).[21] Clay nanocomposite materials have been prepared that incorporate poly-NIPAM.[22] These nanocomposite materials display a thermoresponsive behavior. Self assembled thin films and particles containing ordered nano-domains of hydrogel confined within silica have been prepared and the preliminary results are discussed in this paper.

EXPERIMENTAL PROCEDURES

Cerium chloride doped mesoporous silica particles were prepared using an aerosol reactor (Figure 2) operated at a volumetric flow rate of 2.6 l STP/min^{-1}. After collection on a filter, the particles were calcined at 425˚C (heating rate, 1˚ C/min^{-1}) in air for 3 hours. The particles were then characterized by TEM and nitrogen sorption. The precursor solutions were synthesized by the addition of the surfactant Brij-58 ($CH_3(CH_2)_{15}$-$(OCH_2CH_2)_{20}$-OH)) or Pluronic 123 ($(EO)_{20}(PO)_{70}(EO)_{20}$) to an acidic silica sol. The acidic sol is prepared by refluxing tetraethyl orthosilicate (TEOS), ethanol, water and dilute HCl (mole ratios: 1:3.8:5.3:10^{-5}) at 60˚ C for 90 min. The sol was diluted with ethanol (1:2) followed by addition of water and dilute HCl. Surfactants were added in the amounts needed to achieve initial surfactant concentrations c_0 ranging from 0.004 to 0.23 M. The final reactant mole ratios were 1 TEOS : 0-22 EtOH : 5-67 H_2O : 0.004 HCl : 0.006-0.23 surfactant. Cerium chloride was added to the final solution.

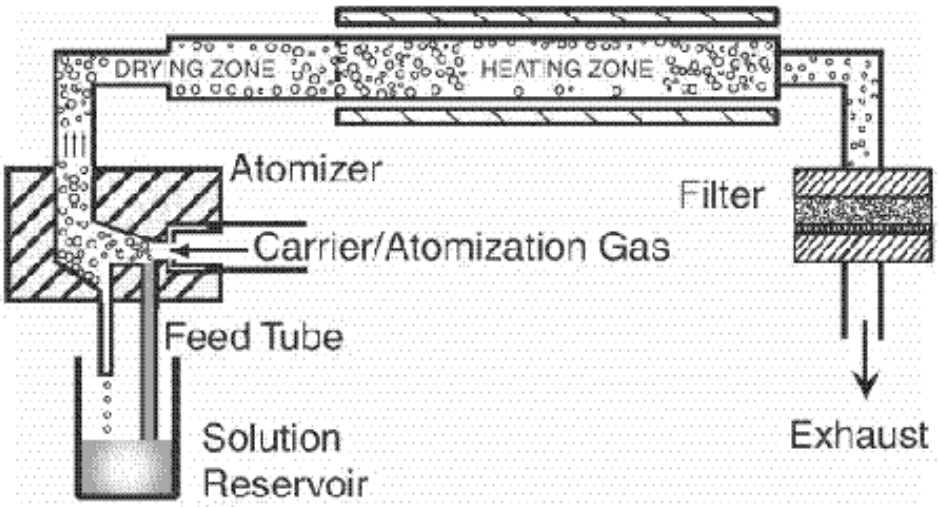

FIGURE 2. Diagram of aerosol reactor. Silica/surfactant/cerium salt aerosols were generated using a commercial atomizer (Model 3076, TSI, Inc., St Paul, MN) operated with nitrogen as a carrier/atomization gas.

Cerium containing particles were also prepared using a more hydrophobic cerium precursor, $Ce(TPS)_4(NH_3)_2$ (TPS = triphenylsiloxane ($OSi(C_6H_5)_3$)), the idea being to incorporate the organocerium precursor in the hydrophobic domains of the self assembled silica/surfactant mesophases. The molar ratios were 1 TEOS : 22 EtOH : 5 H_2O : 0.004 HCl : 0.05 Brij-58 : 0.1 Ce.

For the leaching experiment, the Ce particles were prepared from $CeCl_3$, Pluronic 123 (5% total weight) and ethanol. The final reactant mole ratios were1 TEOS : 22 EtOH : 5 H_2O : 0.004 HCl : 0.002 Pluronic 123: Ce 0.2. One gram of the particles were placed into a sealed bottle containing 100 ml DI water (pH~7) and were allowed to stir. At different times, the solution was removed and the UV absorption of the solution was analyzed using a Lambda 45 UV/VIS spectrometer. By measuring the UV absorption (in 253 cm^{-1}) of several different concentrations of $CeCl_3$ in DI water, a calibration curve was obtained, allowing us to quantify Ce release rates versus time.

The components used in the synthesis of the PDM/silica nanocomposite films are: TEOS, cetyltrimethylammonium bromide (CTAB), monomer (dodecylmethacrylate, DM), crosslinker (hexanedioldimethacrylate, HM), coupling agent (7-octenyltrimethoxysilane, OTS) and initiator (benzoin dimethylether, BME). The synthetic details have been previously described.[17] The mole ratios of the composite films described in this report were as follows: 1 TEOS : 22 ethanol : 5 H_2O : 0.004 HCl : 0.21 CTAB : 0.08 OTS: 0.16 DM: 0.02 HDM : 0.02 BME. The components used in the synthesis of the PDA/silica nanocomposite films are: TEOS, ethylene glycol functionalized diacetylenic surfactant (DA-EG_n), HCl and tetrahydrofuran (THF). The synthetic details have been previously described.[18] The molar ratios of the

PDA/silica nanocomposite films described in this report were as follows: 1 TEOS : 84.29 THF : 4.96 H_2O : 0.013 HCl : 0.11 DA-EG_5 : 0.02 10,12-pentacosadiynoic acid (PCA).

The gas transport properties of the silica/polymer nanocomposites were determined by depositing the membranes on the inside surface of commercial, tubular ceramic substrates provided by US Filter. The tubular supports had 7 mm ID 10 mm OD, and an asymmetric pore structure with a final inner layer of γ-Al_2O_3 with 50 Å nominal pore size. Before deposition, the supports were cut in 4-cm-long segments with a diamond wafering blade, ultrasonically cleaned in ethanol, and calcined for 3 hours at 450ºC in air. After calcination the tubular supports were immersed in the silica/polymer sol for 30 seconds, withdrawn at a speed of 7.6 cm/min, dried in ambient for 15 minutes and subsequently exposed to UV irradiation.

For gas transport measurements, the tubular supports were sealed against Viton gaskets inside a custom-made high-pressure stainless steel module. The gas of interest (CO_2, N_2, or CH_4) was introduced in the inner side of the tubular support (e.g. facing the silica/polymer layer) typically at a flow rate of 50-100 cc/min. The shell-side of the module was purged with a helium sweep stream and the composition of the permeating gas was determined by an on-line gas chromatograph equipped with a thermal conductivity detector. During the measurement, the volumetric flow rates of the retentate and permeate streams were measured with bubble flowmeters while the pressure at both sides of the membrane was kept at ambient. Permeation measurements at elevated temperatures were carried out by heating the membrane with the aid of a heating tape wrapped around the module and powered by a Varian controller. The permeability of each membrane was determined by taking into account the total volumetric flow at the permeate side, the % of the feed gas in the permeate, and the geometric area available for permeation.

The N-isopropylacrylamide (NIPAM) based films were prepared using a similar method as that for the PDM/silica nanocomposite films described above. Reactant molar ratios used were 1 TEOS : 22 ethanol : 5 H_2O : 0.004 HCl : 0.21 CTAB : 0.16 OTS: 0.32 DM: 0-0.04 HDM : 0.04 BME : 0.16 NIPAM. The sols were dipcoated on Si substrates in a dry box under N_2 at 0.85 cm/s. The NIPAM nanocomposite particles were prepared using the aerosol reactor described above. The reactant molar ratios used were 1 TEOS : 22 ethanol : 5 H_2O : 0.057 HCl : 0.21 CTAB : 0.16 OTS: 0.04 BME : 0.32 NIPAM. After the particles were collected, they were dried at 70º C for one hour and exposed to UV light.

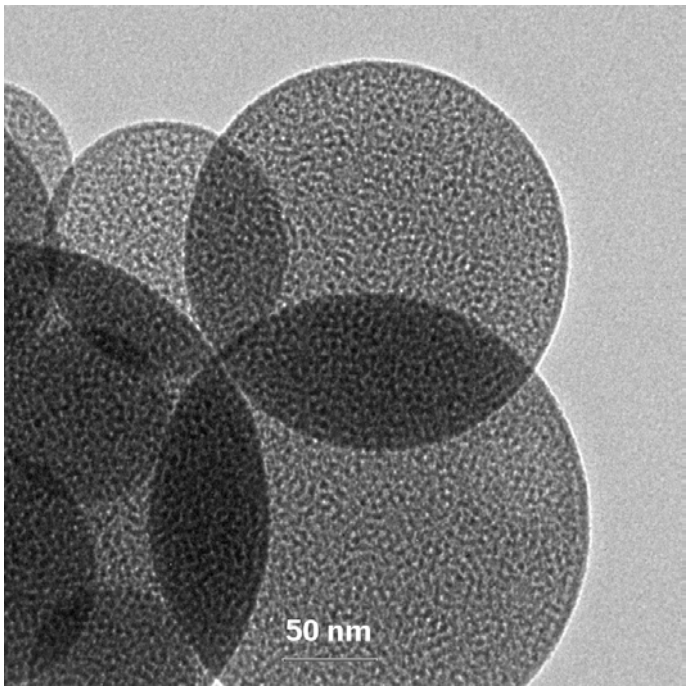

FIGURE 3. TEM image of mesoporous silica particles encapsulated with cerium chloride. The particles were prepared by using Brij-58 ($CH_3(CH_2)_{15}$-$(OCH_2CH_2)_{20}$-OH)). The molar ratios were 1 TEOS : 22 EtOH : 5 H_2O : 0.004 HCl : 0.05 Brij-58 : 0.1 Ce.

The swelling experiments were conducted by placing the samples in water at 1º C and 50º C for at least 4 hours. The samples were then removed from the water, blotted dry, and an x-ray diffraction spectrum of the sample was immediately taken. X-ray diffraction (XRD) spectra

were recorded on a Siemens D500 diffractometer using Ni-filtered CuKα radiation with λ = 1.5418 Å.

A JEOL JEM 2010 transmission electron microscope operated at 200 KeV was used to characterize the particles and films.

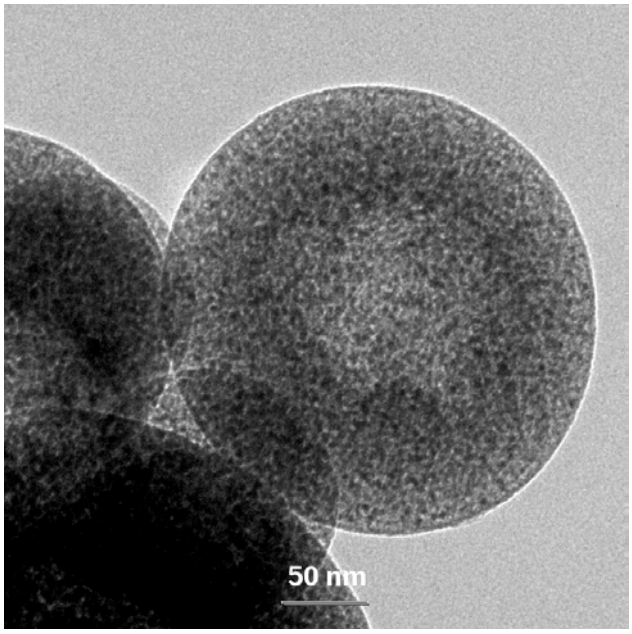

FIGURE 4. TEM image of mesoporous silica particles encapsulated with cerium chloride. The particles were prepared by using Brij-58 ($CH_3(CH_2)_{15}$-$(OCH_2CH_2)_{20}$-OH)). The molar ratios were 1 TEOS : 22 EtOH : 5 H_2O : 0.004 HCl : 0.05 Brij-58 : 0.2 Ce.

RESULTS

Figures 3 and 4 show two kinds of calcined particles containing cerium templated by 5% (by weight) Brij-58. The particles formed a worm-like structure with a uniform pore size of about 3 nm. For less doped particles (Figure 3), the cerium chloride salt dispersed uniformly within individual particles. After doubling the amount of cerium chloride, the salt re-crystallized as shown in Figure 4. Cerium chloride is shown in the figure as the darker spots.

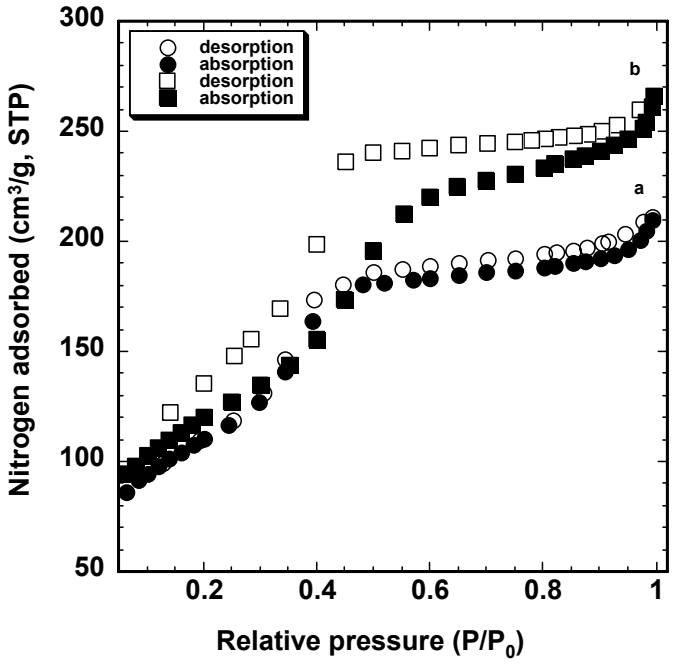

FIGURE 5. Nitrogen sorption isotherms of cerium chloride doped mesoporous silica particles. a: 0.1 mole cerium chloride, surface area: 430m^2/g, pore size 38Å; b: 0.2 mole cerium chloride, surface area: 400m^2/g, pore size 33Å.

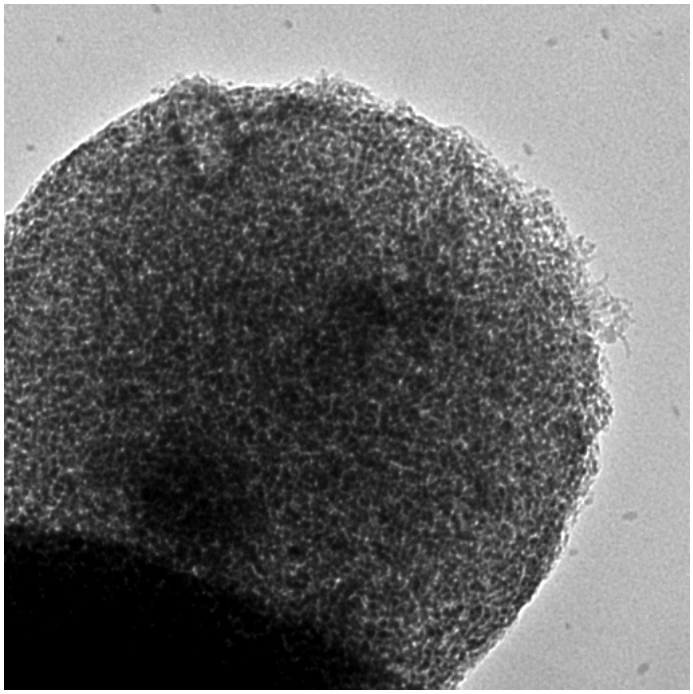

FIGURE 6. TEM image of mesoporous silica particles containing $Ce(TPS)_4(NH_3)_2$. The molar ratios were 1 TEOS : 22 EtOH : 5 H_2O : 0.004 HCl : 0.05 Brij-58 : 0.1 Ce.

Nitrogen isotherms show that both particles exhibit type IV isotherms which are characteristic of surfactant templated mesoporous materials (Figure 5). These particles exhibit great accessibility and uni-modal pore sizes. For the lower Ce concentration particles, the pore size was about 38 Å. As the amount of cerium chloride was doubled, the pore size became smaller (about 33 Å), which means that the cerium occupied a part of the pores.

Particles containing hydrophobic Ce have been prepared. Figure 6 shows the TEM image of mesoporous silica particles containing cerium using the compound $Ce(TPS)_4(NH_3)_2$ (TPS = triphenylsiloxane ($OSi(C_6H_5)_3$)). These particles also form a worm-like structure.

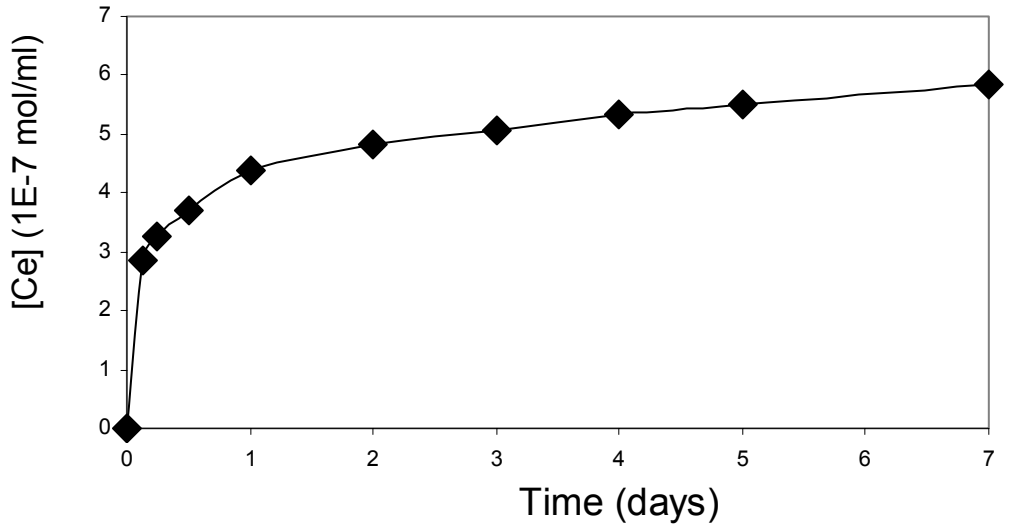

FIGURE 7. The leaching experiment of the particles containing cerium chloride. The concentration of cerium found in solution by UV is plotted versus time.

The particles used for leaching experiment were prepared using 5 % Pluronic 123 (by weight) in ethanol solution. The concentration of Ce as a function of time during leaching was calculated from a calibration curve. From Figure 7, we clearly see that after an initial transient, the cerium element is released slowly. By estimation, less than 5% of the cerium element was leached in 7 days.

The permeability data for the PDM/silica and PDA/silica nanocomposites have been measured and the results are shown in Table 1. The PDM/silica nanocomposite structure was lamellar, and the PDA/silica nanocomposite structure was hexagonal. The permeabilities were quite low. Also found in Table 1 are values for similar pure polyacrylate films for comparison.

TABLE 1. Permeabilities of polymers and polymer/silica composites.

Material	**Temp.**	**Permeability [Barrer] [1 B =10^{-10} cc-cm/cm^2-s-cmHg]**			
		He	CO_2	N_2	CH_4
PDM/Silica [a]	25ºC	0.08	0.12	0.05	0.067
PDA/Silica [b]	25ºC	0.058	0.018	0.018	0.025
Poly (decyl-acrylate)[23]	35ºC	54.5	265	18.4	55.9
Poly (octadecyl-acrylate)	35ºC	7.4	2.96	0.24	0.53

a. Assuming thickness L=150 nm
b. Assuming thickness L=56 nm

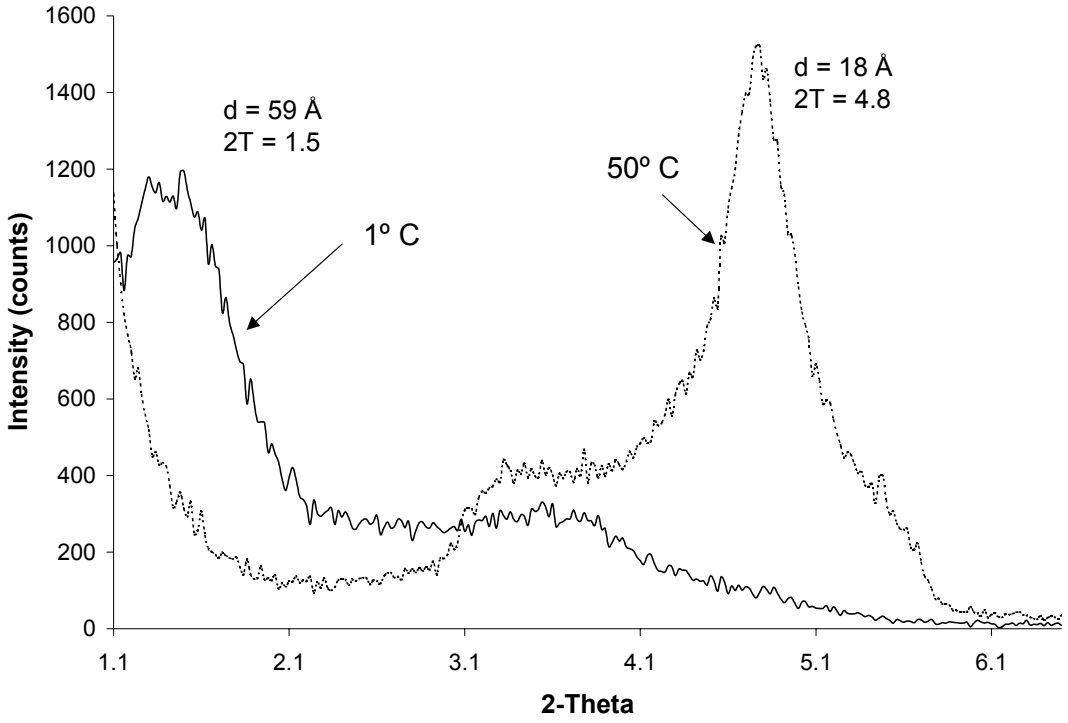

FIGURE 8. Thin film X-ray diffraction patterns of a NIPAM nanocomposite films exposed to 50º C and 1º C water.

A hydrogel/dodecylmethacrylate copolymer system was prepared by the addition of N-isopropylacrylamide (NIPAM) to the poly(dodecylmethacrylate) nanocomposite system described earlier.[17] The reactant molar ratios used were 1 TEOS : 22 ethanol : 5 H_2O : 0.004 HCl : 0.21 CTAB : 0.16 OTS: 0.32 DM: 0.04 HDM : 0.04 BME : 0.16 NIPAM**.** The XRD data of the films are consistent with a lamellar structure. Figure 8 shows XRD data for a thin film that had been exposed to 1º C water and 50º C water. The d-spacings for the sample at 50º C were 18 Å, compared to the d-spacing of 59 Å for the 1º C sample. This sample was cycled several times before order was lost.

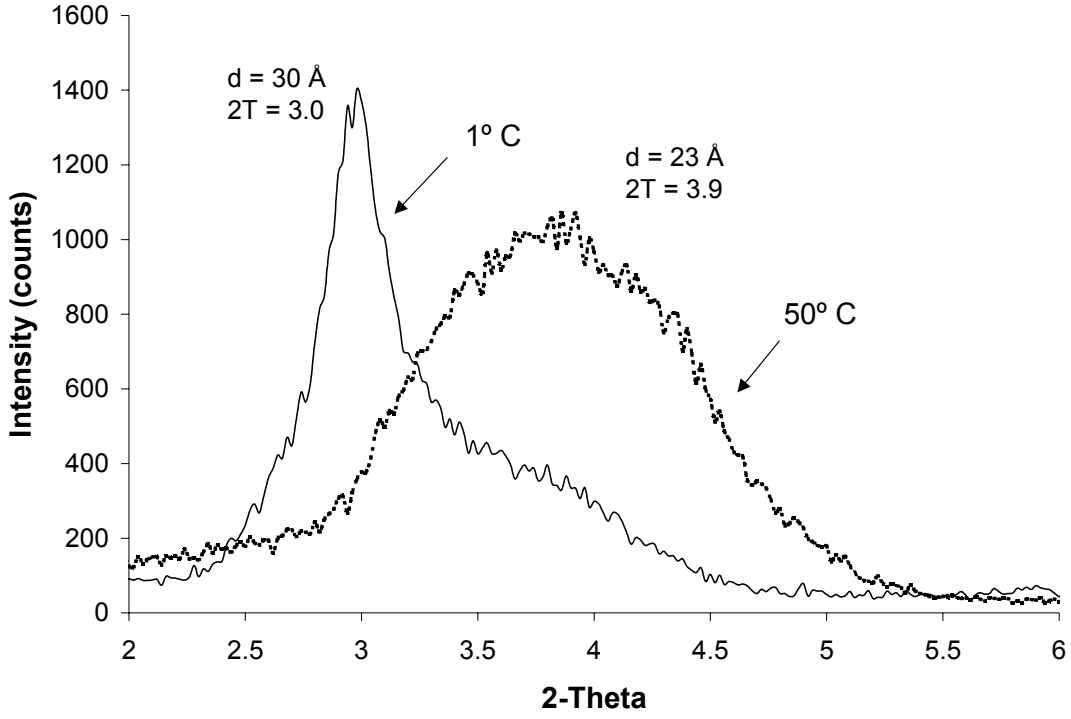

FIGURE 9. Thin film X-ray diffraction patterns of a NIPAM nanocomposite film exposed to 50º C and 1º C water.

Figure 9 shows the thermoresponsiveness of another film using a different formulation (1 TEOS : 22 ethanol : 5 H_2O : 0.004 HCl : 0.21 CTAB : 0.16 OTS: 0.32 DM : 0.04 BME : 0.16

NIPAM). This film did not show as large a change in the d-spacings. As shown, the 50º C sample had a broad peak centered at 23 Å and the 1º C sample had a much sharper peak centered at 30 Å. After several temperature cycles, the film was broken into two pieces, which were then exposed to 50º C or 1º C water. The TEM of the 1º C water sample is presented in Figure 10, which clearly show the lamellar structure of the films. The d-spacings as measured by TEM ranged from 22-27 Å for the 1º C water sample compared to 19-25 Å observed for the 50º C water sample (not shown). Overall, the d-spacings as measured by TEM were smaller for the 50º C sample than the 1º C sample, which is consistent with the XRD data.

FIGURE 10. TEM image of the NIPAM nanocomposite film exposed to 1º C water.

NIPAM nanocomposite particles have been prepared from a sol of composition 1 TEOS : 22 ethanol : 5 H_2O : 0.057 HCl : 0.21 CTAB : 0.16 OTS: 0.04 BME : 0.32 NIPAM. A TEM image of a polymerized, unwashed sample is shown in Figure 11. The image clearly shows a layered type structure within the particles.

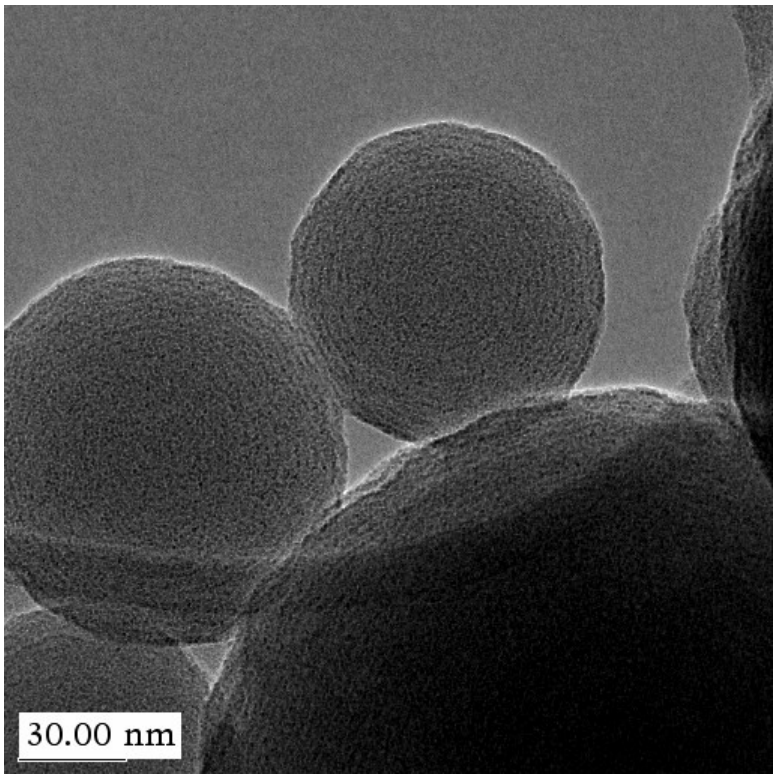

FIGURE 11. TEM image of NIPAM nanocomposite particles. The molar ratios used were TEOS : 22 ethanol : 5 H_2O : 0.057 HCl : 0.21 CTAB : 0.16 OTS: 0.04 BME : 0.32 NIPAM. The sample shown was polymerized by UV and unwashed.

DISCUSSION

Previously we have synthesized mesoporous silica nanoparticles based on the aerosol-assisted self-assembly process. Here we have extended this process to a new system in which hydrophilic and hydrophobic cerium compounds have been used as precursors. When the cerium compounds are placed into the precursor sol, the nanostructure was transformed from an ordered hexagonal mesophase to a worm-like or sponge phase. Depending on the cerium level, we observe by TEM either a uniform dispersion of the cerium or what appears to be recrystallization of cerium chloride within the nanostructured host. Both samples had very high surface areas (exceeding 400 m^2/g) and a controlled uni-modal pore size (~2.0-nm). Nitrogen sorption isotherms of cerium-doped particles showed that increasing the concentration of cerium chloride

in the precursor solution led to a decrease in pore size. This result can be explained by either the cerium ions remaining in the silica cell pore or by the cerium ions substituting for some of the silicon atoms in the structure.

By measuring the UV absorption of the leached cerium solution, we found an initial high leach rate. This is caused by the cerium on the surface or near the surface of the particles. After 24 hours, the release rate is nearly a constant. This is perhaps the result of the diffusion of the cerium within the particles. By estimation, less than 5% of the cerium element was leached in seven days. This is a small amount and we will continue these leaching experiments to determine how long we maintain linear rates.

Our group is currently exploring a new approach for preparation of polymer/silica composite barrier films based on self-assembly of organic precursor monomers in the presence of soluble silica. These barrier coatings exhibit several attractive features such as simple and rapid formation on large surface area and complex shape substrates by dip-coating and optical transparency, coupled with very low permeability guaranteed by the coexistence of a high aspect ratio inorganic silica-based phase and a polymer phase in intimate contact. Table 1 indicates that the intrinsic permeability of such silica/polymer coatings deposited on a commercial tubular ceramic support with a hexagonal or lamellar mesophases structure are significantly lower than the values reported in the literature for pure polymers,[23] despite the very low thickness (50-150 nm) of the former. By extrapolation of the pure polyacrylate data in Table 1, the permeablity of a poly(dodecyl) acrylate would be about 40. Therefore D_0/D for He for the PDM/silica nanocomposite film would be ~500. Assuming that the amount of silica and polymer are approximately equal within these nanocomposites, then $\Phi = 0.5$. Calculation from Equation 1 results in a flake aspect ratio (α) of ~30. The flake aspect ratio is defined as $2L/a$ where L =

length of flake and a = thickness of the flake.[14,15] From the XRD data, a typical d spacing for this formulation is 18 Å. Using this model, it can be calculated that the silica layers have a discontinuity approximately every 54 nm. These preliminary results indeed suggest that such silica/polymer coatings have great potential for barrier or related (e.g. corrosion) applications and can be considered an alternative to presently practiced polymer-based barriers and flake films.

The hydrogel nanocomposites described here have demonstrated thermoresponsiveness of self assembled nanostructures. The sample in Figure 8 showed a very large amount of swelling and shrinkage. The sample in Figure 9 showed a less extreme change in lamellar d-spacings than the sample in Figure 8. However, this particular sample was cycled several times without loss of response before the sample was "sacrificed" for the TEM experiment. Overall, the measured d-spacings for the 1º C sample from TEM were larger than the d-spacings measured for the 50º C sample (not shown). It is noted that the range of d-spacings seen for these samples is quite large, which correlates with the rather broad XRD peaks observed. These preliminary results show that responsive polymers can be incorporated in an ordered hybrid inorganic/organic matrix and still show a responsive behavior.

The NIPAM constituents were incorporated into particles by aerosol assisted EISA, which demonstrates that particles as well as films can be prepared from these thermoresponsive nanocomposite materials. It is envisioned that a hydrogel-containing nanocomposite particle could act as a controlled-release capsule that would be controlled by temperature or pH changes.

The previous examples of PDM/silica and NIPAM/silica nanocomposite materials have been lamellar in structure. However, other mesophases are of interest. Recently, poly(dodecylmethacrylate) based nanocomposite materials that retain order after calcination (which implies a non-lamellar structure) using the block copolymer Brij 56 have been prepared.

These nanocomposite films have a "worm-like structure" as determined by TEM. When confined to the nanopore of a 2-d mesophase, the contraction and dilation of the hydrogel could serve as a gate that could open and close to mediate release. Therefore, NIPAM nanocomposite films based on Brij 56 will be prepared with the expectation of preparing 2-d mesophases. Furthermore, other block copolymers such as Brij 58 and the Pluronics will be examined as potential surfactants to prepare NIPAM nanocomposites. Many other parameters remain to be explored as well. For example, the extent of polymerization, the amount of copolymer, the type of initiator, etc. could all affect the responsive behavior of the poly-NIPAM nanocomposites.

CONCLUSIONS

New materials that exhibit potential as corrosion inhibitors have been described. Porous silica particles were prepared that show linear Ce release rates. The hybrid inorganic/organic nanocomposite films have very low permeabilities compared to polymer coatings and could be useful for corrosion inhibition. Finally, new nanocomposite materials have been prepared that show a thermoresponsive behavior of interest for environmentally mediated controlled release.

ACKNOWLEDGMENTS

TEM investigations were performed in the Department of Earth and Planetary Sciences at the University of New Mexico. Sandia is a multiprogram laboratory operated by Sandia Corporation, a Lockheed Martin Company, for the United States Department of Energy under Contract DE-AC04-94 AL85000.

REFERENCES

1. C. Kresge, M. Leonowicz, W. Roth, C. Vartuli, J. Beck, Nature 359 (1992): p 710.

2. Y. Lu, R. Ganguli, C. Drewien, M. Anderson, C. Brinker, W. Gong, Y. Guo, H. Soyez, B. Dunn, M. Huang, J. Zink, Nature 389 (1997): p. 364.
3. P. J. Bruinsma, A. Y. Kim, J. Liu, S. Baskaran, Chem. Mater. 9 (1997): p. 2507.
4. M. Ogawa, J. Am. Chem. Soc. 116 (1994): p. 7941.
5. C. J. Brinker, Y. Lu, A. Sellinger, and H. Fan, Nature 389 (1997): p. 364.
6. Y. Lu, H. Fan, A. Stump, T. L. Ward, T. Rieker, and C. J. Brinker, Nature 398 (1999): p. 223.
7. G. V. Jayanthi, S. C. Zhang, and G. L. Messing, Aerosol Sci. Tech. 19 (1993): p. 478.
8. H. Yang, N. Coombs, I. Sokolov, G. A. Ozin, Nature 381 (1996): p. 589.
9. H. Yang, N. Coombs, G. A. Ozin, Nature 386 (1997): p. 692.
10. B.R.W. Hinton, D.R. Arnott, and N.E. Ryan, Metals Forum 7, 4 (1984): p. 11.
11. M. Bethencourt, F.J. Botana, J.J. Calvino, and M. Marcos, Corros. Sci. 40 (1998): p. 1803.
12. M. Bethencourt, F.J. Botana, M. Cauqui, M. Marcos, M. Rodringuez, J. Alloys Comp. 250 (1997): p 455.
13. Yang, C., E.E. Nuxoll and E.L. Cussler, *AIChE J*. 47 (2001): p. 295.
14. Eitzman, D.M., R.R. Melkote and E.L. Cussler, *AIChE J*. 42 (1996): p. 2.
15. Falla, W.R., M. Mulski and E.L. Cussler, *J.Membr.Sci*. 119 (1996): p. 129.
16. A. Jackson, J. Vincent, R. Turner, in Proceedings of the Royal Society of London Series B-Biological Sciences, Royal Society of Chemistry, London 1988, p. 415.
17. A. Sellinger, P. N. Weiss, A. Nguyen, Y. Lu, R. A. Assink, W. Gong, and C. J. Brinker, Nature 294 (1998): p. 256.
18. Y. Lu, Y. Yang, A. Sellinger, M. Lu, J. Huang, H. Fan, R. Haddad, G. Lopez, A. R. Burns, D. Y. Sasaki, J. Shelnutt, and C. J. Brinker, Nature 410 (2001); p. 913.

19. Y. Shin, J. H Chang, J. Liu, R. Williford, Y-K. Shin, and G. J. Exarhos, J. Control. Release 73, (2001): p 1.

20. D. J. Beebe, J. S. Moore, J. M. Bauer, Q. Yu, R. H. Liu, C. Devadoss, and B-H. Jo, Nature 404 (2000); p 588.

21. C. K. Chee, S. Rimmer, I. Soutar, and L. Swanson, Polymer 38 (1997): p. 483.

22. L. Liang, J. Liu, and X. Gong, Langmuir 16 (2000): p. 9895.

23. Mogri, Z. and D.R. Paul, *J.Membr.Sci*. 175 (2000): p. 253.

AMORPHOUS Al-Co-Ce ALLOY WITH POTENTIAL EXCELLENT CORROSION RESISTANCE

M. Gao, N. Unlu, M. Jakob, J. Scully and G.J. Shiflet

Department of Materials Science and Engineering
University of Virginia
Charlottesville, VA 22904-4745

ABSTRACT

The glass formation in the Al-Co-Ce system was investigated using differential scanning calorimetry (DSC) and x-ray diffraction (XRD). The glass formation range (GFR) was determined to cover compositions of less than 17 at.% cobalt and from 0 to 12 at. % cerium. Subsequent devitrification does not occur until relatively high temperatures (>300^{o}C), indicating good high thermal stability. The crystallization process in Al-Co-Ce is shown to be different from those in ternary Al-Ni(Fe)-Gd systems in that primary crystallization of fcc-Al was not observed in Al-Co-Ce alloys.

INTRODUCTION

The opportunity exists to create new metallic cladding alloys that exhibit a broad range of corrosion functions including active corrosion inhibition (i.e. self-healing), corrosion barrier properties, artificial cathodic protection, as well as resistance to crevice corrosion (e.g. alkaline or acidic dissolution) at faying surfaces in military components. One class of alloys that may be suitable for such cladding applications is an Al-based amorphous (glass) alloy system comprising selected rare earth and transition metal compositions.[1-4] Glass formation is promoted by certain transition metals such as Ni, Co, and Fe as well as rare earth elements such Gd, Ce, and Nd. Multifunctional behavior is possible because some of the same alloying elements that promote amorphous phase formation upon rapid cooling also have the potential to improve a range of corrosion properties. For instance, cerium has been widely examined as a corrosion

inhibitor in non- chromate conversion coatings on Al-base alloys. It was shown by Hinton and coworkers that cerium affects the oxygen reduction reaction on precipitation age hardened Al-base alloys by a cathodic inhibition mechanism, while a complex hydrated cerium oxide layer is formed on the surface.[5,6] Potentiodynamic tests also show a significant increase in E_{pit}.[7] Film formation occurs on or near local cathodic sites, due to the increase of the solution pH near the surface. Davenport and Isaacs found that the oxide layer on aluminum contains cerium in both trivalent and tetravalent state.[8] The different solubilities of the cerium species of different valence states give rise to an active corrosion protection, or self-healing.[9] Later, it was found that the presence of Ce(IV) species enhances the film formation on aluminum.[10] On the basis of these observations, accelerated cerium-based conversion coatings were developed for Al-base alloys using hydrogen peroxide as an oxidizing agent.[11] Cobalt compounds have also been investigated as a possible alternative to chromate conversion coatings. Potentiodynamic polarization measurements showed a slight increase in E_{pit} on aluminum in concentrated cobalt sulfate solution,[12] but cobalt conversion coatings formed in solutions containing Co(III) complexes (e.g. $[Co(NH_3)_6]_2[SO_4]_3$) are more promising candidates for protection of aluminum alloys.[13] The possibility of developing Al-Co-Ce alloys that contain cobalt and cerium in supersaturated solid solution would eliminate the need for the conversion coating process and, possibly, provide a nearly inexhaustible supply of inhibiting agent available within the cladding depending upon cladding thickness. If cobalt and cerium were present in an amorphous alloy cladding, then a renewable supply of oxidized Co (II and III) as well as Ce (III) and Ce(IV) would be available from within the clad alloy as these species became available through oxidation on the surface. Indeed, it has already been demonstrated that Ce(III) and Ce(IV) are present on passivated and oxidized Al-Fe-Ce alloys.[14-15] Some oxides and hydroxides of cobalt

and cerium are soluble at low pH.[9] Therefore, these potential inhibiting agents could be released from the oxide overlying such a cladding alloy when triggered by corrosion-induced acidification. Moreover, transition and rare earth metal additions to aluminum have been found to improve its corrosion barrier properties and resistance to pitting when these elements are retained in an amorphous solid solution.[16] These observations create the motivation to design an Al-Co-Fe alloy envisioned as a cladding material that may simultaneous support several corrosion functions.

EXPERIMENTAL PROCEDURE

All the alloys were synthesized from pieces of Al (99.999% purity), Co (99.9%) and Ce (99.9%) totaling ~5 grams in a Ti-gettered arc-melter in an argon atmosphere. The buttons were remelted four times to ensure chemical homogeneity, and the weight loss was less than 0.5%. The amorphous ribbons were made through melt-spinning on a copper wheel in a He atmosphere, creating typical ribbons of 1-3 mm in width and 15-30 μm in thickness. XRD was used to verify a wholly amorphous state of the as-spun ribbons. The continuous heating DSC scans were performed in a Perkin-Elmer DSC7 using a heating rate of $0.333 Ks^{-1}$ under flowing argon gas. The DSC was calibrated periodically with high purity standards of indium (99.999%) and aluminum (99.9995%). The sample weight was measured using 5-digit balance. The X-Ray diffraction (XRD) was performed on a Scintag diffractometer using CuKα radiation.

RESULTS AND DISCUSSION

The glass formation by liquid quenching in the binary Al-Ce system was found by Inoue et al.[1] in 1988 to lie in a compositional range of 7-10 at.% Ce. Ternary Al-Co-Ce systems were studied independently by He et al.[2] and Inoue[3] in 1988, and the atomic structure of amorphous

Al-Co-Ce alloys was investigated by Mansour et al.[4] later in 1994. A total of nine Al- Co-Ce alloy compositions were examined in the current study, seven of which are wholly amorphous. Based on our results and published data,[4] the glass formation range (GFR) in Al-Co- Ce in the Al-rich corner was completely determined, as indicated in Figure 1. It is seen that the GFR is extended to a broad range of 2-11 at.% Ce as the transition metal cobalt is added. The alloys with higher aluminum contents are ductile and can be bent up to 180° without fracture. However, an excess addition of cerium atoms tends to embrittle the glass, such as alloys $Al_{82}Co_7Ce_{11}$, $Al_{81}Co_8Ce_{11}$, and $Al_{80}Co_{10}Ce_{10}$.[3]

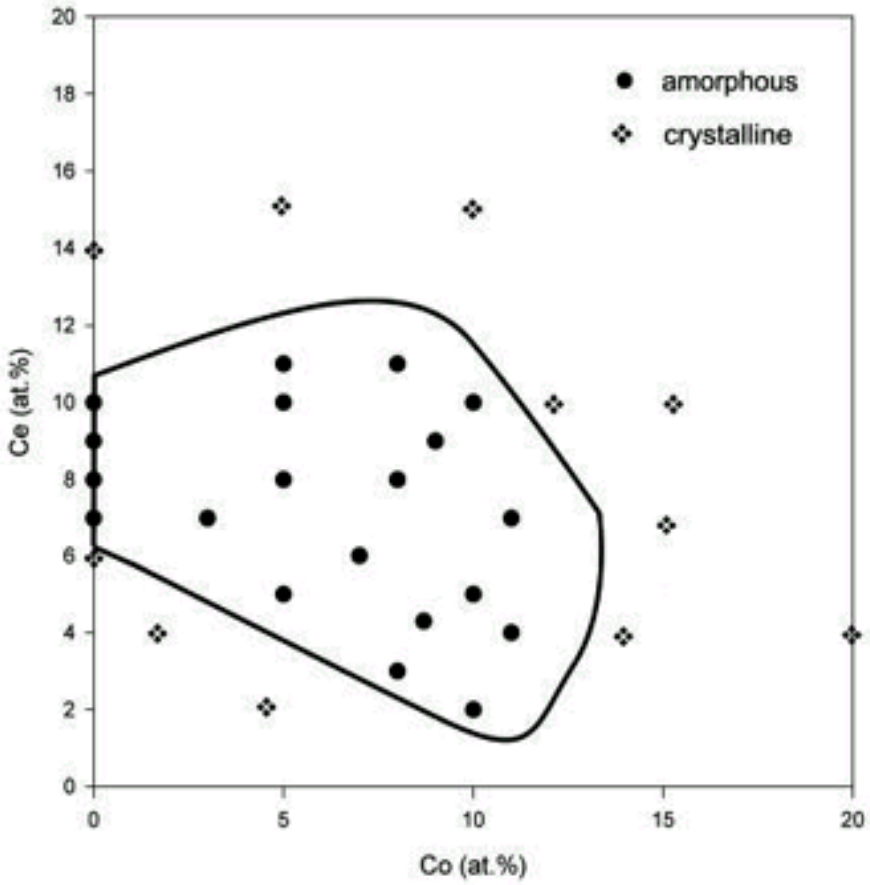

FIGURE 1. Composition range where Al-Co-Ce can be rapidly quenched into a wholly amorphous material. The points are taken from Inoue et al [1,3], He et al [2], Monsour et al [4] and the current work.

Figure 2 shows how the crystallization proceeds in five amorphous Al-Co-Ce alloys during continuous DSC heating. There is no glass transition T_g that can be resolved by conventional DSC scans for the alloys demonstrated. A maximum of three peaks are recorded when heating to 550^{o}C, which are related to different crystallization stages. Attention should be addressed to the shape of the first peaks. They are all symmetric, except that a little overlapping effect on the right shoulder in alloy $Al_{81}Co_8Ce_{11}$.

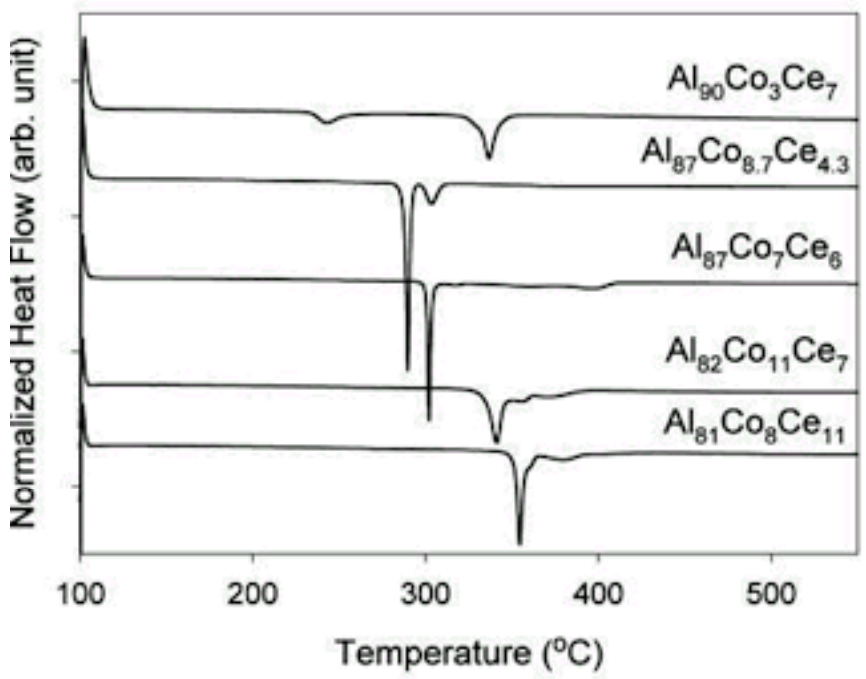

FIGURE 2. Differential scanning calorimetry data for five Al-Co-Ce alloys. As aluminum contend increases the first exothermic event moves to lower temperatures. Holding the aluminum content constant at 87 at.% and increasing cerium results in an increase in the first heat event, while holding cerium constant at 7 at.% and increasing cobalt content also results in a temperature increase.

In order to analyze how the microstructure evolves during continuous heating, the originally amorphous Al-Co-Ce alloys were heated within the DSC starting from 100^{o}C, and cooled

down to room temperature as soon as the crystallization stage (see Figure 2) of interest is finished. Then the sample was studied via XRD. The XRD patterns of alloy $Al_{90}Co_3Ce_7$ after heating to 270°C, 365°C and 550°C is shown Figure 3, together with the as-spun amorphous state for comparison. The only phase that can be identified unambiguously via XRD technique is fcc-Al. The binary compound phase $Al_{11}Ce_3$ has a tetragonal crystal structure at high temperature (>640°C) and transforms into an orthorhombic structure (T<640°C). Further work is necessary to identify all the devitrification products. Conventional electron diffraction experiments and analytical microscopy will provide useful additional structural and chemical data.

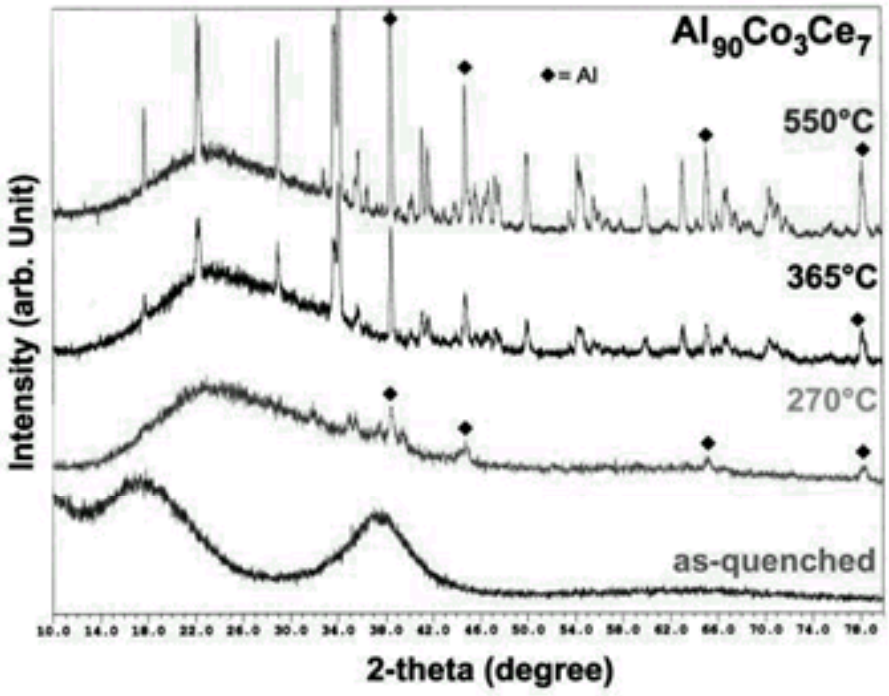

FIGURE 3. XRD results of continuously heating an $Al_{90}Co_3Ce_7$ wholly amorphous glass to the indicated temperatures in the DSC and then immediately cooling. The bottom curve is for the as quenched material illustrating it is amorphous. The 270 °C curve was heated to the temperature following the first heat event from DSC (see the same alloy in Fig. 2). The peaks are for fcc aluminum and an unknown compound. The 365 °C is for heating above the second exothermic event (Fig. 2). Additional compounds (unknown) are evident. The 550 °C pattern follows heating to a higher temperature to identify additional high temperature phases.

SUMMARY

The synthesis and mapping of Al-Co-Ce alloys into metallic glass was accomplished. The spectrum of formation chemistries extends from ca. 2 to 12 at. % Ce and 0 to 17 at%Co. This will allow a quantitative determination of corrosion properties with chemistry in this system. DSC experiments establishes that devitrification into various phases ranges from 240 ^{o}C in $Al_{90}Co_3Ce_7$ to 350 ^{o}C in $Al_{81}Co_8Ce_{11}$. Except for face centered cubic aluminum the crystalline products have not all been identified at this time.

ACKNOWLEDGEMENTS

A Multi-University Research Initiative (Grant No. F49602-01-1-0352) entitled "The Development of an Environmentally Compliant Multifunctional Coating for Aerospace Applications using Molecular and Nano-Engineering Methods" under the direction of Major Paul C. Trulove at AFOSR supported this study.

REFERENCES

1. Inoue, A., Ohtera, K., Kita, K., and Masumoto, T., *Jpn. J. Appl. Phys. Lett.*, 1988, **27**, L736- L739.
2. He, Y., Poon, S.J. and Shiflet G.J., *Science*, 1988, **241**, 1640.
3. Inoue, A., Ohtera, K., Kita, K., and Masumoto, T., *Jpn. J. Appl. Phys. Lett.*, 1988, **27**, L1796- L1799.
4. Mansour, A.N., Wong, C.P., and Brizzolara, R.A., *Physical Review B*, 1994, **50**, 401-412.
5. Hinton, BRW; Arnott, DR; Ryan, NE Met. Forum 17, 4 (1984): pp. 211-217.

6. Arnott, DR; Ryan NE; Hinton, BRW; Sexton, BA; Hughes AE Appl. Surf. Sci. 22/23, 1 (1985): pp. 236-351.
7. Hinton, B; Arnott, DR; Ryan, NE Mater. Forum 9, 3 (1986): pp. 162-173.
8. Davenport, AJ; Isaacs, HS J. Electrochem. Soc., 136, 6 (1989): pp.1837-1838.
9. Buchheit, RG; Mamidipally, SB; Schmutz, P; Guan, H Corrosion 2000, NACE, 67-92, 2000.
10. Aldykewicz, AJ; Davenport, AJ; Isaacs, HS J. Electrochem. Soc. 143, 1 (1996): pp. 147-154.
11. Hughes, AE; Hardin, SG; Wittel, KW; Miller PR Corrosion 2000, NACE, 47-66, 2000.
12. Kabasakaloglu, M; Aydin, H; Aksu, ML Materials and Corrosion 48, (1997), pp. 744-754.
13. Schriever, MP US005378293A Patent, 1993.
14. A. Mansour, C.A. Melendres, J. Electrochem. Soc., 142, 6 (1995): p. 1961-1968.
15. A. Mansour, C.A. Melendres, S.J. Poon, Y. He, G.J. Shiflet, J. Electrochem. Soc., 143, 2 (1996): p. 614-619.
16. J.E. Sweitzer, J.R. Scully, R.A. Bley, J.W.P. Hsu, Electrochem. And Solid State Letters, 2, 6 (1999): pp. 267-270.

THE RAPID DISCOVERY OF NEW CORROSION INHIBITORS USING COMBINATORIAL METHODS

B.D. Chambers [1], S.R. Taylor[1], and M.W. Kendig[2]

[1]University of Virginia
Charlottesville, VA

[2]Rockwell International, LLC
Thousand Oaks, CA

ABSTRACT

The search for alternate corrosion inhibitors must be accelerated. This is particularly true when considering the vast number of possible inhibitor combinations that should be examined for synergy. This paper examines the efficacy of using combinatorial methods to increase the rate of discovery of alternate corrosion inhibitors. The question arises as to what metric can be used for the rapid assessment of inhibitor performance. This study has examined simple DC potentiostatic polarization of 2024 wires in a series of inhibitors that had previously been characterized over a 10-day exposure period using electrochemical impedance spectroscopy. The ordinal correlation between short-term (2 hour) and long-term (10 day) electrochemical data was 100% using 100 mV DC polarization. There is likely a broad range of electrochemical and chemical methods that may be used for rapid screening of inhibitor compounds.

INTRODUCTION

Numerous compounds have been examined through the years with the hope of providing a chromate replacement. These compounds include molybdates[1], vanadium-based compounds[2], boron-based compounds[3-5], and rare earth salts[6], among others. Many of these compounds have been examined recently for inhibitor efficacy on aerospace alloys[6-8]. To date, however, no single compound has demonstrated an effective corrosion inhibition power (efficiency at specified concentration) comparable to chromate.

A promising alternative to the use of a single inhibitor species is that of using synergistic combinations of two or more compounds. Synergy occurs when the inhibitive property of the

combination exceeds the arithmetic sum of the individual components. Synergistic combinations of inhibitors have been examined extensively for steel in acidified[9-16] and neutral[17-20] aqueous environments, as well as for copper in neutral aqueous environments[21-22]. Numerous theories for synergy have emerged depending on whether active anions[10,14,21,24,25], cations[9,13,15,18,20], or organic species[19-20] are employed. However, a common theme throughout the literature is that one species adsorbs initially and bridges or facilitates the adsorption of the other species to produce a complex or layered barrier structure.

More germane to paints, synergistic combinations of paint additives have been explored since the late 1970's[26]. Examples include phosphates + borates, zinc phosphate + zinc nitrophthalate + zinc oxide, and more recently, zinc molybdate + zinc phosphate + a zinc salt of benzoic acid. This latter combination has been used in the DoD self-priming topcoat, which has unfortunately resulted in poor adhesion after limited service. This points out yet another hidden advantage of chromate pigments. In addition to having the appropriate balance of inhibitive power and solubility, an inhibitive pigment must not interfere with in-service adhesion, a property that is actually augmented by chromate pigments[27].

Recent studies have examined synergistic combinations of the previously described rare earth and transition metal salts[7,28,29]. Although these preliminary experiments have only examined 1:1 ratios of these materials at one concentration, synergistic effects have been observed using both electrochemical and pit morphology analyses. It is almost certain that the optimum ratio is something other than 1:1, and that an array of additional experiments is needed to identify the proper materials and ratio. Unfortunately, the predictive abilities and fundamental understanding of molecular systems with more than two or three different atomic species

remains extremely limited, so that one is faced with a tortuous matrix of experiments to identify the optimum inhibitor combination under a wide range of test conditions (e.g. pH, T).

One approach to increase the rate of material discovery is through combinatorial approaches[30-32]. Combinatorics, initially utilized in electronic materials development[33], has been more commonly associated with automated synthesis and high throughput screening for pharmaceutical research. In the combinatorial process, large arrays of material or chemical variables can be produced and screened to identify the optimum process or condition of interest. Creation of the combinatorial libraries is typically straightforward. However, the identification of a rapid detection method that can sensitively detect changes in the relevant parameter is not to be assumed and is often the rate limiting process in rapid discovery.

The corrosion protection properties of inhibitors can be electrochemically quantified in many different ways, however there are presently no specified electrochemical parameters that can be acquired rapidly (i.e. minutes) in the laboratory to predict long-term (i.e. years) corrosion protection. Yet, the desire is to screen thousands of chemical compounds with an infinite number of combinations in a vast number of environmental conditions (temperature, pH, concentration, etc.). This paper presents some initial experiments to identify rapid screening methods for the identification of effective inhibitor compounds.

EXPERIMENTAL METHODS

The purpose of the present experiments was to determine if short-term electrochemical measurements (ca. hour) could reproduce the findings of longer-term (10 day) data collected previously by electrochemical impedance spectroscopy (EIS).

MATERIALS

1/16" diamter 2024 wire (California Fine Wire) was obtained for use as electrodes in electrochemical testing using a multichannel microelectrode array (MMA). Metallography was carried out on the 2024 wire to examine the differences in grain structure between the 2024 wire and 2024 sheet. This metallography was carried out on the 2024 wire on both the wire end and a cross section along the length of the wire. Samples were etched with Keller's reagent (2.5 mL HNO_3, 1.5 mL HCl, 1 mL HF, 95 mL H_2O) to reveal the microstructure. Optical microscopy was used to examine the microstructure and revealed that the 2024 wire microstructure was qualitatively similar to that found in 2024 sheet used on aircraft. The 2024 sheet metallography was taken from a study on exfoliation in 2024 aluminum[34]. Comparison of the two microstructures qualitatively indicated that there is little difference between the as-received 2024 wire and 2024 sheet in place on aircraft skins.

ELECTROCHEMICAL CELL

Simultaneous testing of multiple electrochemical cells was accomplished by the use of the MMA analyzer (Scribner, Associates) with an array of electrochemical cells established within a conventional reaction frame. The MMA system is computer controlled and is attached to the electrodes in the reaction frame by means of an adapter. A schematic of the MMA reaction frame setup is shown below in Figure 1.

ELECTROCHEMICAL METHOD

Currents read by the MMA on the 2024 electrodes exposed to inhibitor and chloride solution were compared to findings of 2024 exposed to identical inhibitor and chloride solutions measured by EIS and verified by statistical pit analysis[8,28]. A good correlation between MMA

findings and EIS results would indicate that the MMA testing procedure could be used for rapid assessment of inhibitor performance.

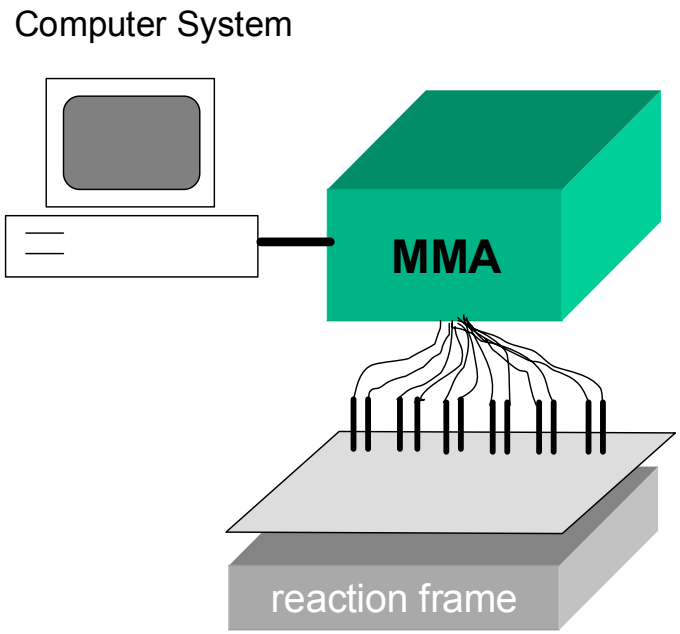

FIGURE 1. Schematic of MMA connection to reaction frame and computer controller.

Testing of several inhibitors was conducted previously by electrochemical impedance spectroscopy to obtain information on inhibitor performance on 2024 sheet exposed to chloride[8,28]. The testing was conducted by placing the 2024 sheet in 3.4 mM inhibitor, 0.6 M NaCl solution. EIS was conducted on the samples at initial exposure and exposures of 1,3,5 and 10 days. The results of the EIS testing for neutral pH solutions are presented below in Figure 2[8,28]. The inhibitors with the most consistent ranking of polarization resistance over the 10 day test were selected as target data for this study. Three compounds were selected for testing along with the control (no inhibitor): cerium chloride, yttrium chloride, and sodium metatungstate.

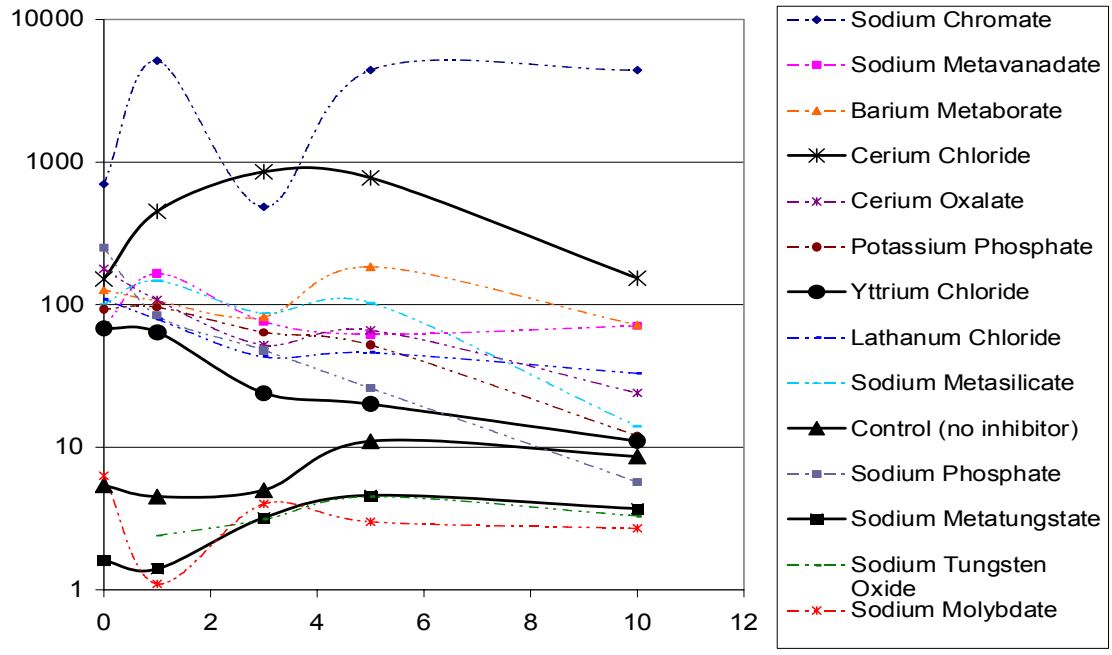

FIGURE 2. Polarization Resistance of 2024 sheet in 3.4 mM inhibitor, 0.6 M Cl^- solution[8,28]

MMA testing was performed for rapid assessment of the three inhibitors and control solutions that were mentioned above. Two-electrode potentiostatic polarization measurements were performed using two 1.75" 2024 wires attached as electrodes to the reaction frame. The wires were cut to 1.75" length to attach to the reaction frame with 3.3 cm of length exposed to the testing cell. One electrode in each cell was polarized 100 mV with respect to the other electrode. Ten reaction cells of the reaction frame were used in each testing interval. The current was measured between the two electrodes using an in-line ZRA. Current was measured over a time period of 9 hours.

Cells of the reaction frame were filled with a solution containing 3.4 mM inhibitor and 0.6 M NaCl to match the chemistries used in the previous EIS study[8,28]. 1.75 mL of solution was pipetted into each cell of the ten working cells of the reaction frame. Testing was conducted in this way on 11 cells containing no inhibitor, 11 cells containing cerium chloride, 9 cells

containing sodium metatungstate, 5 cells containing yttrium chloride, and 7 cells containing yttrium chloride adjusted to pH 7

RESULTS AND DISCUSSION

Results from the MMA testing were plotted to examine the current change over the course of the 9 hour test. An example plot of data from the MMA is shown below in Figure 3.

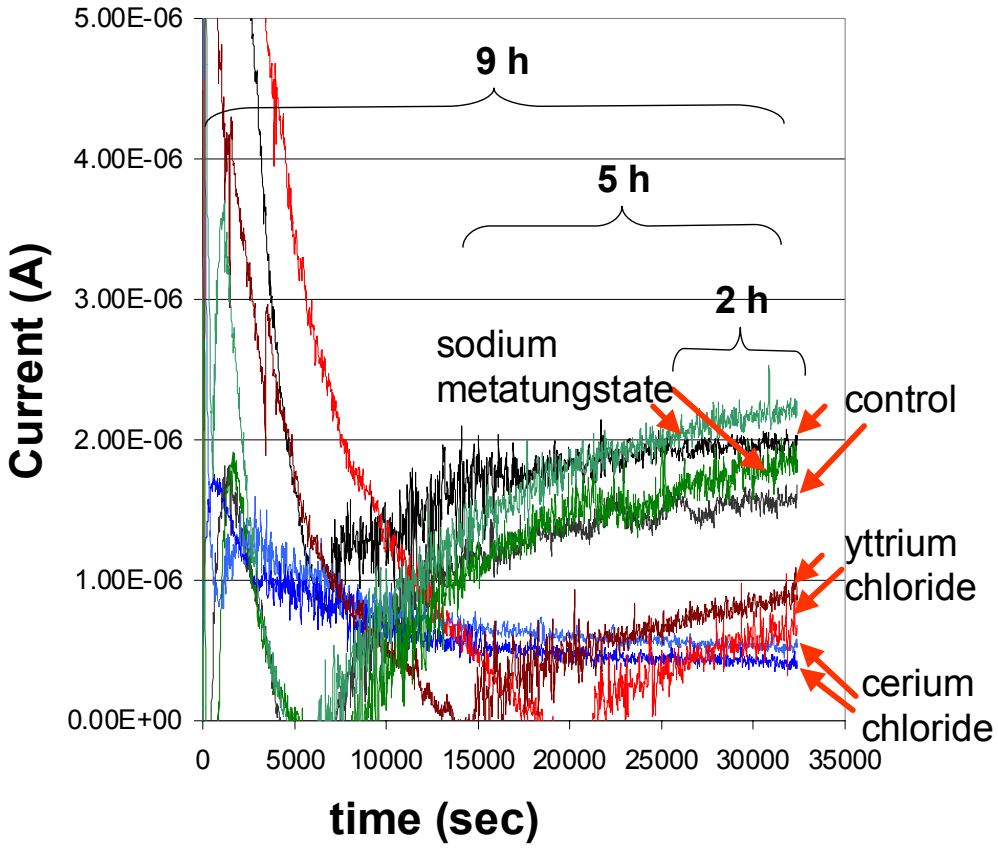

FIGURE 3. Example MMA galvanic current output a 2024/2024 wire couple with 100 mV DC bias.

The data collected from the MMA indicates the early instabilities in electrochemical measurements of this type. However, each system appears to be approaching a steady state near the ninth hour of testing. For this reason, the last two hours of the test data were selected as the most precise and were used to assess the inhibitor performance. Observations of the currents for

each inhibitor noted that electrochemical noise was present in all the cells tested but the amount of electrochemical noise varied depending on the contents of the cell. The cells containing cerium chloride possessed much less electrochemical noise in the currents measured and reached steady state the most quickly of all the cells. The cells containing the other inhibitors and the control took significantly longer to reach steady state and appeared to have much greater fluctuations in the current measured.

The inhibitor performance was based on the average current during the last two hours of the rapid screening test. The current was averaged over three different time periods: all 9 hours, the last 5 hours, and the last 2 hours of the test. The average current of the cells over the entire length of the test indicated a significant difference when compared to the average current of the last 5 hours and last 2 hours of the tests. Figure 4 shows the average current for the inhibitors and standard deviation using the currents from the entire duration of the test (9 hours). but has a significant statistical variance as noted by the large standard deviations. It can be seen in Figure 5 that the average current for the last two hours of the test, that the data is significantly more consistent as shown by the standard deviation. Unfortunately, the data indicated a significant accelerating effect of the corrosion rate of 2024 in the presence of yttrium chloride that was not observed in the previous EIS data.

At this point, the inhibitor testing using the MMA was altered to further imitate the conditions of the EIS testing by adjusting the pH of all solutions to 7. Figure 6 shows the average current for the inhibitors and standard deviations using the currents from the entire duration of the test conducted with neutral pH solutions. Figure 7 shows the average current for the last 2 hours of the test and once more demonstrated that the data taken at the end of the test is far more consistent than the entire 9 hour duration. After adjusting the pH of all solutions to 7

before testing, the yttrium chloride was found to be much more effective compared to its testing in unadjusted pH. With the assumption that low measured current indicates good inhibitor performance, the ordinal sequence of inhibitor performance is similar to the long-term EIS data.

The ranking of the inhibitor performance using the MMA testing results correlates 100% with the ranking of these four chemistries that were examined using both EIS and statistical pit analysis[28]. The correlation plot is shown in Figure 8.

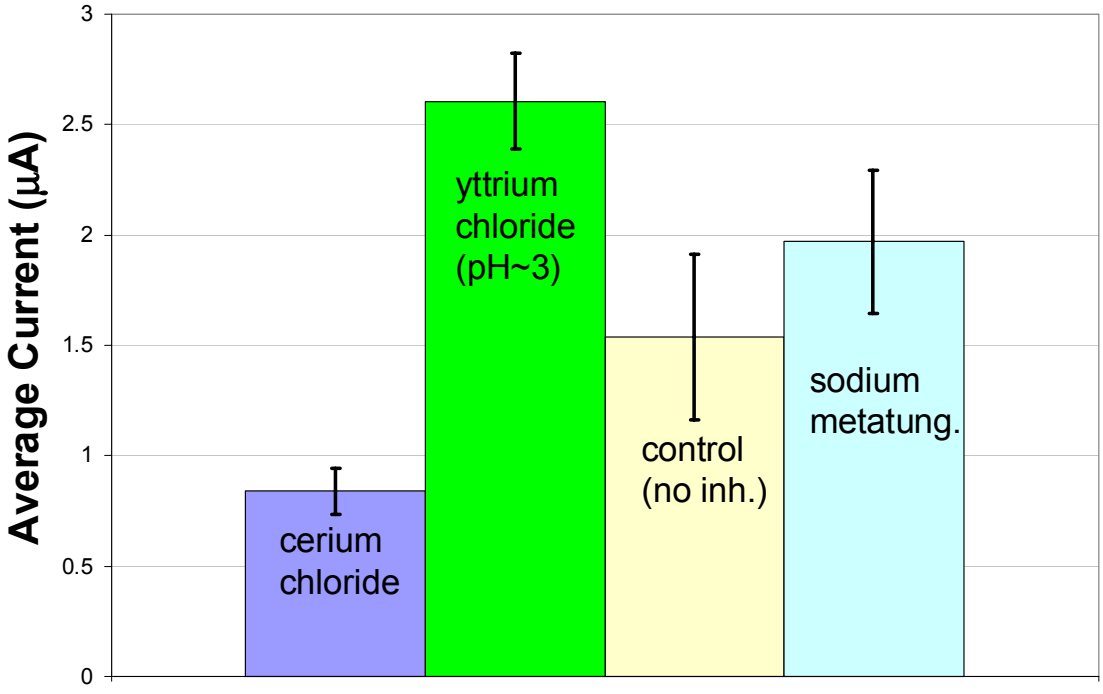

FIGURE 4. Average current of cells containing inhibitors over 9 hour test (pH unadjusted).

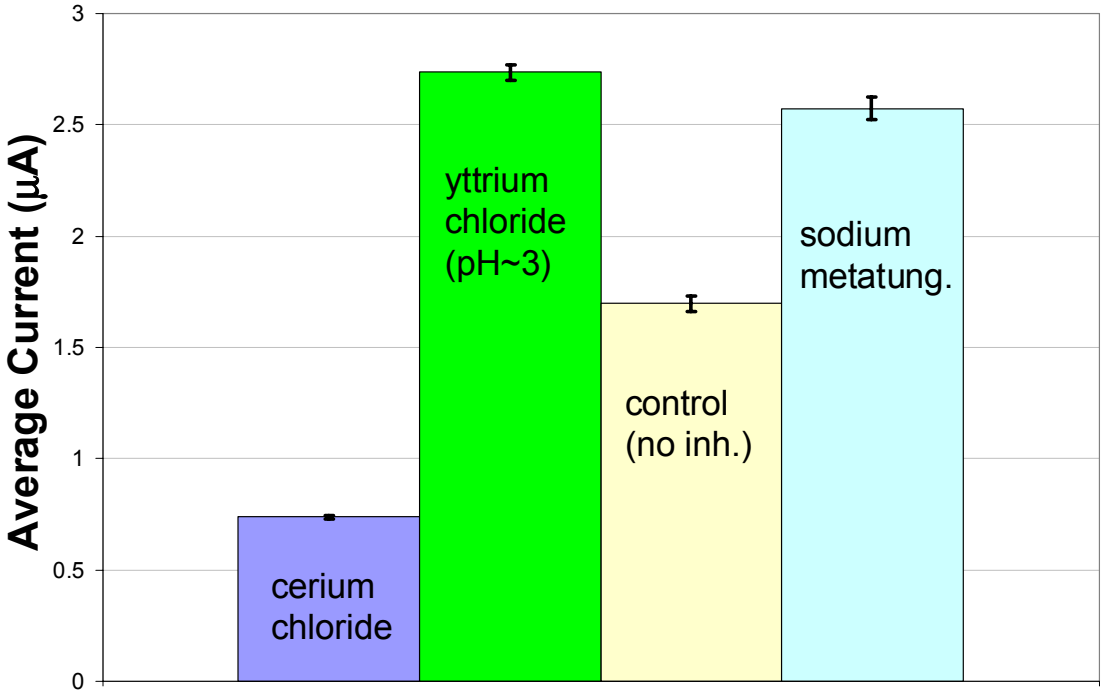

FIGURE 5. Average current of cells containing inhibitors during last 2 hours of 9 hour test (pH unadjusted).

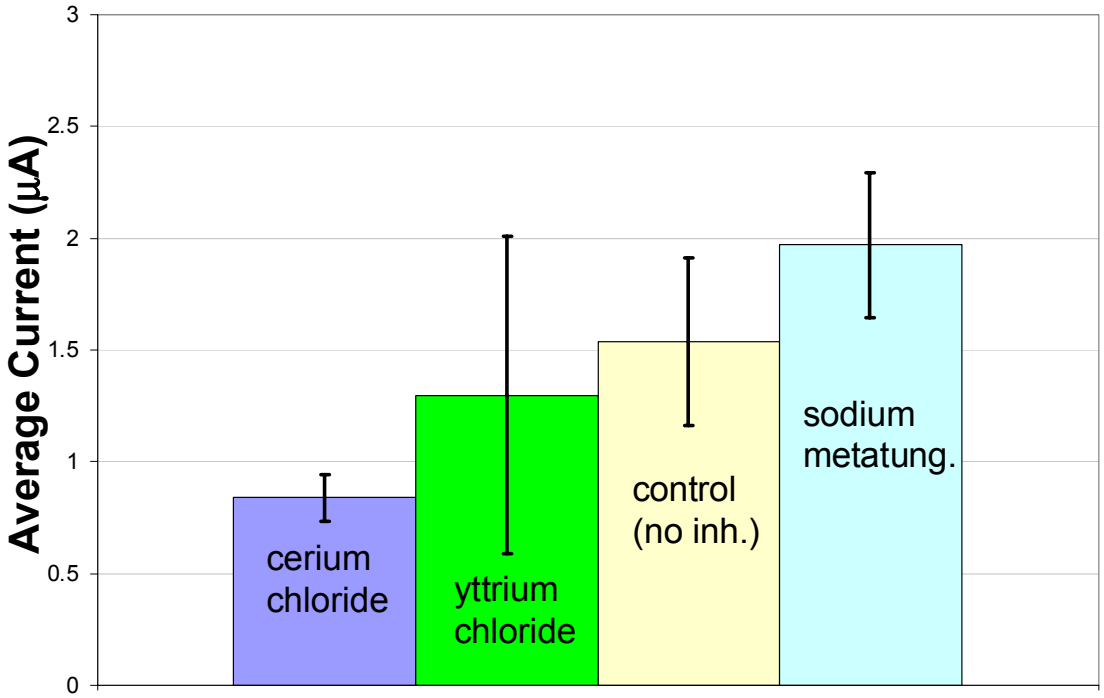

FIGURE 6. Average current of cells containing inhibitors over 9 hour test (pH adjusted to 7).

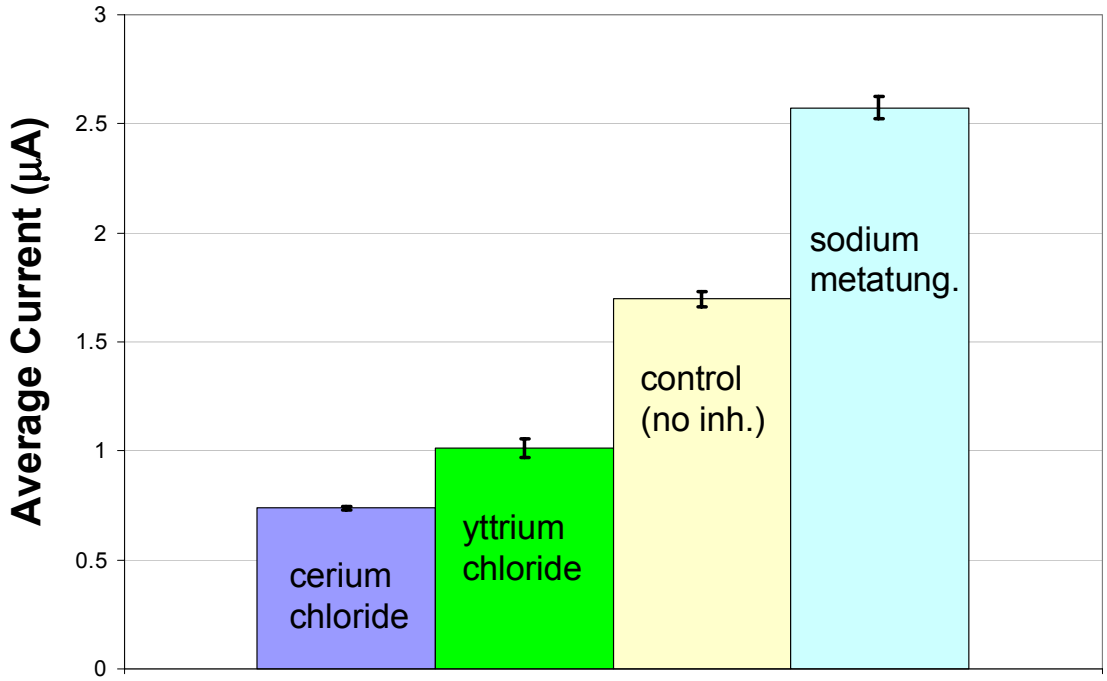

FIGURE 7. Average current of cells containing inhibitors during last 2 hours of 9 hour test

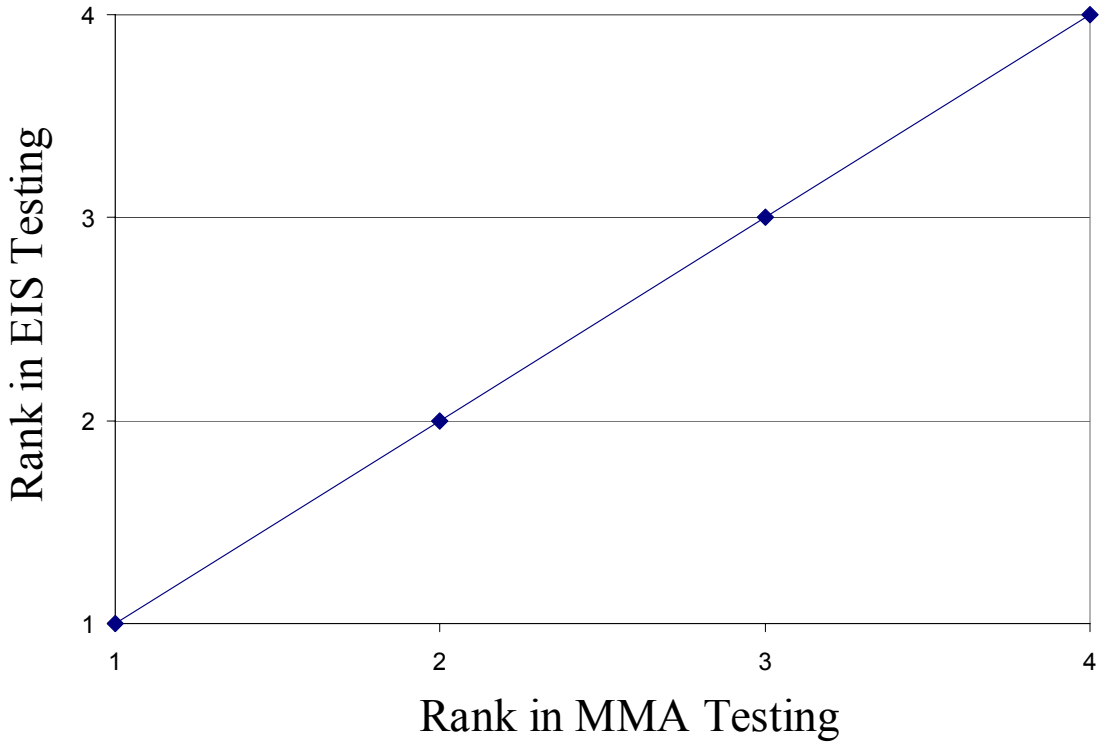

FIGURE 8. Comparison of inhibitor performance in EIS and MMA testing for cerium chloride, yttrium chloride, sodium metatungstate, and control (no inhibitor)

CONCLUSIONS

There are potentially a broad range of electrochemical methods for the rapid screening of inhibitor performance. This study has examined galvanic couples and simple DC potentiostatic polarization. Based on metallography and electrochemical results, the 2024 wire appears to be a suitable imitation of 2024 sheet for testing of inhibitor performance. The ordinal correlation between short-term (2 hour) and long-term (10 day) electrochemical data was 100% using 100 mV DC polarization of AA2024 wire for the inhibitors tested thus far. Future testing will examine electrochemical noise among other electrochemical and chemical approaches for the quantification of corrosion inhibitor performance.

REFERENCES

1. M. Stern, *J. Electrochem. Soc.* **24:**787-806 (1958).
2. D. Bienstock and H. Field, *Corrosion*, **17**:87-90 (1961).
3. N. R. Whitehouse, *Polymer Paint and Colour J.* **178:**239 (1984).
4. J. Boxall, *Polymers, Paints and Colour J.* **174:**382-384 (1984).
5. D. Bienstock and J. H. Field, *Corrosion* **17:**87-90 (1961).
6. B.R.W. Hinton, *Metal Finsihing* **Sept. '91, Oct. '91**, 55-61, 15-20 (1991).
7. H.E. Hager, C.J. Johnson, K.Y. Blohowiak, C.M. Wong, J.H. Jones, S.R. Taylor, R.L. Cook, Jr., *U.S.Patent 5,866,652* (The Boeing Company, U.S.A., 1999).
8. R.L. Cook and S.R. Taylor, *Corrosion* **56:**321-333 (2000).
9. Y. Feng, K.S. Siow, K.T. Teo, and A.K. Hsieh, *Corr. Sci.* **41:**829-852 (1999).
10. S. Sayed Azim, S. Muralidharan S. V. Iyer, B. Muralidharan, and T. Vasudevan, *Br. Corr. J.* **33:**297 (1998).

11. M.Mustafa. S.M. Shahinoor, amd I. Dulal, *Br. Corrosion J.* **32:**133-137 (1997).
12. S. Sayed Azim, S. Muralidharan, S. Venkatkrishna Iyer, *J. of Appl. Electrochem.* **25:**495-500 (1995).
13. D.D.N. Singh and A.K. Dey, *Corrosion* **49:**594-600 (1993).
14. M.A. Quraishi, J. Rawat, and M. Ajmal, *Corrosion* **55:**919-923 (1999).
15. G.N. Mu, T.P. Zhao, and T. Gu, *Corrosion* **52:**853-856 (1996).
16. M.A. Quraishi, S. Ahmed, and M. Ansari, *Br. Corrosion J.* **32**, 297-300 (1997).
17. J.M. Abd El Kader, A.A. Warraky, and A.M. Abd El Aziz, *Br. Corr. J.* **33:**152-157 (1998).
18. S. Rajendran, B.V. Apparao, and N. Palaniswamy, *Electrochem. Acta* **44:**533-537 (1998).
19. T. Suzuki, H. Nishihara, and K. Aramaki, *Corr. Sci.* **38:**1223-1234 (1996).
20. Y. Gonzalez, M.C. LaFont, N. Pebere, and F. Moran, *J. of Appl. Electrochem.* **26:**1259-1265 (1996).
21. Y. Feng, K.S. Siow, W.K. Teo, K.L. Tan, and A.K. Hsieh, *Corrosion* **53:**546-555 (1997).
22. S. Gonzalez, M.M. Laz, R.M. Souto, R.C. Salvarezza, and A.J. Arvia, *Corrosion* **49:**450-456 (1993).
23. K.T. Carron, M.L. Lewis, J. Dong, J. Ding, G. Xue, and Y. Chen, *J. Matl. Sci.* **28:**409-4103 (1993).
24. K. Aramaki and N. Hackerman, *J. Electrochem. Soc.* **116:**558 (1969).
25. N. Shikai and L. Yefen, Study of the Synergy Mech. of Acidic Inh., 8th Europ. Symp. on Corr. Inh. (1995).
26. S.A. Hodges,, W.A. Uphues, and M.T. Tran, *Surf. Coatings Australia* **34:**24-30 (1997).

27. A.T. Evans, J.D. Scantlebury, and L.M. Callow, The Adh. and Corr. of Chromate Conv. Ctgs on Al, J. D. Scantlebury and M. W. Kendig, Ed., Adv. in Corr. Prot. by Org. Ctgs II (ECS, Pennington, NJ, 1995).
28. R.L. Cook, Jr. M.S., University of Virginia (1995).
29. S. R. Taylor, An Examination of Possible Synergy Between Paired Combinations of Transition and Rare Earth Metal Salts, 197th Meeting of the ECS, Toronto, CAN (ECS, Pennington NJ, 2000).
30. E.W. MacFarland and W.H. Weinberg, *Trends in Biotechnology* **17:**107-115 (1999).
31. B. Jandeleit, D.J. Schaefer, T.S. Powers, et. al., *Angew. Chem. Intl. Ed.* **38:**2494 (1999).
32. J.C. Meredith, A. Karim, and E.J. Amis, *Macromolecules* **33** (2000).
33. J.J. Hank, *J. Mater. Sci.* **2:**964-971 (1970).
34. Maria Posada, L.E. Murr, C.S. Niou, D. Roberson, D. Little, Roy Arrowood, and Debra George, Exfoliation and Related Microstructures in 2024 Aluminum Body Skins on Aging Aircraft, *Materials Characterization* 38: 259-272 (1997).

CORROSION PROTECTION OF AA 2024-T3 BY ORGANOFUNCTIONAL SILANES

Wim J. van Ooij, J. Anna Lamar, Danqing Zhu and Matt Stacy

Department of Materials Science and Engineering
University of Cincinnati
Cincinnati, OH 45221-0012

ABSTRACT

A set of non-organofunctional silanes with closely related structures was applied to AA 2024-T3 substrates and characterized by polarization techniques and by several analytical tools including TOFSIMS and FTIR. The objective was to improve our understanding of the mechanism by which so-called bis-silanes protect aluminum alloys against various forms of corrosion. The silanes were BTSM, BTSE, BTSH and BTSO, bis-[trimethoxysilyl]methane, ethane, hexane and octane, respectively. They differ only in the number of ethylene groups between the two trialkoxysilyl groups. Variables in this study were, other than the molecular structure, the water/alcohol ratio of the silane solution, the pH and the age of the hydrolyzed solution. The results obtained by DC polarization and FTIR indicate that the most important factor in determining the corrosion protection performance is the hydrophobicity of the silane films. Thus, when hydrolyzed under optimum conditions, BTSO gave the best corrosion protection. In another part of this study various additions to silane films were studied. The additives were colloidal silica, an acrylate resin and TEOS. All additions resulted in an improvement of the corrosion protection capability of the films. An overall silane performance mechanism is presented.

INTRODUCTION

Organofunctional silanes, and especially, bis-silanes of the type $(XO)_3$-Si-$CH_2CH_2CH_2$-R-$CH_2CH_2CH_2$-Si-$(OX)_3$, where X is mainly CH_3 or C_2H_5, and R is an organic functional group, have been convincingly demonstrated to possess unique corrosion protection and paint adhesion properties, when used as metal pretreatments.[1-10] Not only aluminum alloys but metals such as steel, stainless steel, galvanized steel, and magnesium have all been protected from uniform and localized forms of corrosion.[1-6] As an example of the potential of such silanes, AA 2024-T3

alloy panels can be protected from corrosion in the B-117 salt spray test for 14 days without paint coating and more than 2000 hours when coated with a polyester powder or solvent-based paint. The optimum silane film thickness is of the order of only 0.2 μm. With paint coatings it was demonstrated that the paint thickness could be reduced by as much as 75% without losing performance in standard corrosion tests.[11]

Silanes have thus become an important candidate for chromate replacement in many metal-finishing industries, for instance in aerospace and the automotive industry. It is quite remarkable that it has taken so long before their capabilities were discovered. After all, silanes have been around for polymer-ceramic or polymer-metal bonding applications for many years.[12-14] However, the silanes used in those applications, while excellent coupling agents, do not provide significant corrosion protection. It was not until the discovery that bis-[triethoxysilyl]ethane (BTSE), previously only used as a silane crosslinker, i.e., mixed with monosilanes of the type $(XO)_3$-Si-$CH_2CH_2CH_2$-R,[12] could also be used by itself and then provided a much better corrosion protection than the monosilanes, that the literature on the use of silane for corrosion protection began to grow.

The underlying reasons why a film of BTSE, $(XO)_3$-Si-CH_2CH_2-Si-$(OX)_3$ is so much better and more stable than a film of, say, $(XO)_3$-Si-$CH_2CH_2CH_3$, are only poorly understood. No convincing mechanism has been put forward. It has been reported, though, that the bis-silanes such as BTSE, bis-[methoxypropylsilyl]amine ('bis-amino') and bis-[methoxypropylsilyl]-tetrasulfide ('bis-polysulfur'), can be considered conversion treatments: they convert part of the metal oxide into a silicate-like material with a very high density and ohmic resistance. This layer was assumed to be the cause of the striking difference between mono and bis-silanes.[5] It has been detected by TOFSIMS, IR, EIS and SEM/EDX.

In this paper we present new data on silane performance and characterization. A series of simple bis-silanes was selected with closely related structures, i.e., $(XO)_3$-Si-$(CH_2)_n$-Si-$(OX)_3$, with n = 1, 2, 6 and 8. These silanes did not contain an organofunctional group, as such groups might also interact with the metal, which would complicate the interpretation of the data. By varying the deposition conditions, such as pH, age of the solution, and the water/alcohol ratio, it was hoped to obtain useful information on the underlying mechanisms by which such silanes work and on the film structure or organization. In a second part of the paper we report on our first attempts to improve properties of silane films by making certain additions such as fine particles and organic resins. The rationale behind these experiments was to specifically improve the major corrosion-inhibiting properties identified in part one, such as thickness, density, hydrophobicity or others.

EXPERIMENTAL

MATERIALS

The silanes bis-[triethoxysilyl]methane (BTSM), bis-[triethoxysilyl]ethane (BTSE), bis-[triethoxysilyl]hexane (BTSH), bis-[triethoxysilyl]octane (BTSO) and tetraethoxysilane (TEOS) were all obtained from OSi Specialties (Tarrytown, NY). They were relatively pure laboratory products of >95% purity. They were used without further purification. The silanes bis-[trimethoxypropylsilyl]amine (bis-amino) and bis-[triethoxypropylsilyl]tetrasulfide (bis-polysulfur) were obtained from OSi Specialties as the commercial product A-1170 and A-1289, respectively. Vinyltriacetoxy silane (VTAS) was obtained from Gelest Inc. (Tullytown, PA). The bis-amino silane and VTAS were mixed in a 1.5/1 volume ratio without hydrolyzing them and stored until use.

AA2024-T3 and AA5005 panels of 100×150×0.5 mm³ were obtained from ACT, Hillsdale, MI. The water-borne acrylate resin Rhoplex K-3 was obtained from Rohm and Haas in Philadelphia, PA. Colloidal silica of type SNOWTEX PS-M (20 wt-%) was obtained from Nissan Chemical Industries Ltd. in Houston, TX.

SILANE SOLUTION PREPARATION AND APPLICATION

The silanes were mixed with DI water and ethanol to a 5 vol.-% silane content. Variables were the pH, the water/ethanol ratio and the time lapse between hydrolysis and metal treatment. Hydrolysis was done for a minimum of 24 hours at room temperature. The pH was adjusted with acetic acid. The metal sheets were cleaned several minutes at 70°C in AC 1055 alkaline cleaner from Brent America Inc. until water-break-free. After thorough rinsing with DI, the panels were dipped for 30 s in the hydrolyzed silane solution. They were then blow-dried with compressed air and cured at 100°C for 24 hours. The curing conditions were not varied in this work. Although not explicitly measured for the films discussed in this paper, it is known form previous work that the thickness of all films as prepared here (water/alcohol, acid to neutral pH, 5% concentration, blow drying) amounted to 150-200 nm.[6]

ADDITIONS TO THE SILANE FILMS

Silica was added to silane films by simply replacing the water used for the silane hydrolysis by the appropriate amount of colloidal silica sol and preparing the films as above. TEOS was added to an aged hydrolyzed 5% BTSE solution of pH = 4 (23 days old), by slowly adding a 5 vol.-% solution in ethanol until a BTSE/TEOS volume ratio of 80/20 was obtained. The solution remained clear. Film were prepared on AA2024-T3 panels immediately (see above) and again after aging the BTSE/TEOS mixture for 24 hours. The solution was still clear, i.e., the

TEOS had not condensed noticeably in that period. The acrylate resin was added by mixing 40 ml resin, 50 ml pure bis-amino/VTAS 5/1 mixture, (optionally) 10 ml colloidal silica sol and 100 ml DI water in a high-speed blender for 1-5 minutes. A film was deposited on the alkaline cleaned metal panels by using a drawdown bar. The films were cured in an oven at 130°C for 30 min.

CHARACTERIZATION AND TESTING OF SILANE FILMS

DC polarization was performed in 0.6 M aerated NaCl using a Gamry potentiostat and a saturated calomel electrode. A scan was recorded immediately after the OCP had stabilized (around 10 min.). TOFSIMS of freshly prepared silane films was performed on a Cameca Ion-Tof IV instrument equipped with a $^{69}Ga^{+}$ liquid metal ion gun. The samples were rinsed in hexane prior to analysis in order to remove siloxanes, a typical contaminant of silane films. Reflection-Absorption infrared (RAIR) spectra were recorded on a Win-Biorad instrument with a reflection-absorption attachment. The angle of incidence was 75°. A total of 100 scans were recorded per sample, using a 4 cm^{-1} resolution.

RESULTS

DC POLARIZATION TESTS OF SILANE FILMS

Some selected linear polarization results are presented in Figures 1-3. More DC polarization data for films deposited in different conditions are given in another paper. Figure 1 shows that films of BTSM, BTSE and BTSO prepared from solutions at their natural pH (no acetic acid added; pH 5.5-6) all provided corrosion protection in terms of reduction of both cathodic and anodic current, as compared with the blank panels, which was solvent and alkaline-cleaned but had no silane film. The corrosion potential did not change significantly, so both

anodic and cathodic currents were affected roughly equally. It should be noted that BTSO was hydrolyzed in dioxane/water here, as it was observed in preliminary experiments that hydrolysis in water/ethanol without any addition of acids (which catalyze hydrolysis) was much slower than for BTSM and BTSE. BTSM hydrolyzed the fastest and could also tolerate the highest water content (42%) of the four silanes that are compared in this paper.

It is further observed that of the three silanes shown here, BTSE provides the greatest reduction of the cathodic current and BTSO the least. The reduction in the case of BTSE is two orders of magnitude. All three films show a pitting potential of around –0.47 V. No pitting can be concluded in the curve of the blank panel. At the pitting potential, the reduction of the anodic current is two orders of magnitude for all three films.

Figure 2 shows a comparison for two BTSE films that were deposited from water/ethanol mixtures with different ratios. Both were hydrolyzed for at least one day. A significant difference is observed between the two. The film made with less water gives two orders of magnitude reduction in cathodic current, the one from higher water content only one order of magnitude. Further, the anodic curves for the two overlap, except that the film formed from lower water content indicate a pitting potential, the other one does not. The other silanes (not shown in this figure) confirmed both effects: lower cathodic current for less water and a clear pitting potential at –0.47 V for that film only. Both results were reproducible for all films.

In Figure 3 the cathodic curve are compared for the four silanes. In this experiment, the pH of the silane solutions was lowered by acetic acid, the hydrolysis time was three days and the water/ethanol ratio was the same for all silanes (5/90). It is now seen that BTSO has the greatest reduction of the cathodic current and BTSM (1½ orders of magnitude) has the lowest reduction. Again, these results were verified to be reproducible.

In conclusions of this section, it can be stated that the deposition conditions of a silane can greatly affect its performance. Further, if these conditions are optimized, the reduction in both cathodic and anodic currents can be about two orders of magnitude.

RAIR ANALYSIS OF SILANE FILMS

The major technique that could provide a clue as to why the deposition conditions affect the film performance is RAIR as it can probe the degree of hydrolysis of the silane. It has been published by us that thermal curing of a film does *not* hydrolyze a silane film further if it was deposited after incomplete hydrolysis. It requires a long time of immersion in a non-corrosive electrolyte to completely hydrolyze a partly hydrolyzed film on a metal *in situ*.[5] Figures 4-6 show RAIR results. In Figure 4, three spectra for BTSE are compared for films that were hydrolyzed in different conditions (pH, time, % water in the hydrolysis mixture). The main feature in the spectra is the intensity of the Si-O-C band relative to the Si-O-Si band. The former indicate hydrolysis, the latter shows the degree of siloxane formation (condensation) of the hydrolyzed silanol groups. This condensation occurs mainly during the curing step. Figure 4 thus shows that at pH = 6 the hydrolysis is far from complete, even at 18% H_2O in the solution. Even at pH = 4 (which is optimum for hydrolysis),[15] hydrolysis is incomplete after 3 days. Hydrolysis is almost complete for pH = 4, 18% H_2O after 3 days of hydrolysis (not shown here).

Figure 5 shows part of the spectra for films of BTSM, BTSE and BTSO films made from solutions with their maximum water content. BTSO was dissolved in dioxane/water mixtures, the others in water/ethanol. No acetic acid was added and the hydrolysis time was the same for all films. The pH was lower for the BTSM solution as the silanol groups are stronger acidic in that molecule. It is seen that the BTSO film is not very highly crosslinked and still contains a high degree of ester groups. The BTSE film is also incompletely hydrolyzed, but the BTSM film is

almost completely hydrolyzed and highly crosslinked. In this case, the lower pH is auto-catalyzing the hydrolysis to a certain extent.

In Figure 6 we present the spectra for the experiment shown earlier in Figure 3 in which the four silanes were deposited under identical conditions (90/5/5, 3 days, pH =4). It is seen that only BTSM is completely hydrolyzed. The others are incompletely hydrolyzed. The differences in crosslinking can be estimated by the shift of the Si-O-Si band, which shows that the BTSM film is highly condensed or crosslinked, and BTSO the least. Contact angle measurements, described in a different paper, also indicate that BTSO was the least hydrophilic and BTSM had the lowest contact angle, i.e., was the most hydrophilic.

TOFSIMS ANALYSIS OF SILANE FILMS

Positive and negative SIMS spectra of the four silane films of the experiment of Figure 3 are shown in Figures 7-10. They are, as expected, very similar. The silicone contamination, typical of silane films, is low in all films (typical peaks at +73 and +147 amu.) The major difference between the four films is the relative decrease in the intensity of Si peaks when going from BTSM to BTSO, and the corresponding increase of hydrocarbon peaks. This is most clearly seen in the ratio of the ions at +27, +29 (hydrocarbons) and +28 amu (Si^+). The 28/27 ratio is the highest in BTSM and the lowest in BTSO. These results, therefore, correspond well with the contact angle data published elsewhere [16].

The high-resolution capability of the TOFSIMS instrument allowed a unique identification of the identity of the peak at +27 amu. This peak analysis indicated that the peak at +27 amu consisted entirely of $C_2H_3^+$ and did not contain Al^+ in any of the SIMS spectra. This finding implies that none of the silane films compared here was porous.

EFFECT OF ADDITIONS TO SILANE FILMS

The silane bis-[triethoxypropylsilyl]tetrasulfide (bis-polysulfur) has been found to have a strong affinity for the AA2024-T3 alloy.[5] Therefore, this silane was used in experiments in which small amounts of silica were added in attempts to further improve the corrosion protection by this silane. Figure 11 shows DC polarization data in which it is seen that the bi-polysulfur silane by itself reduces the cathodic current by two orders of magnitude. The corrosion potential is lowered by about 50 mV, indicating an effect on the cathodic activity. Two curves for silica-loaded silane films are shown. At low silica content (28 mg per 100 ml 5% silane solution), the corrosion potential is decreased by another 300 mV and the anodic curve shows a tendency for the treated metal to passivate over a range of 200 mV. However, at higher silica levels (210 mg), the corrosion-inhibiting effects completely disappear and the cathodic curve is very close to the one for the untreated metal. It appears that the film becomes more porous at higher silica loading.

Figure 12 shows the effects of the addition of an acrylic resin the silane film, with and without colloidal silica. It is seen that the water-soluble silane used in this experiment (bis-amino/VTAS) lowers the cathodic current without affecting the corrosion potential, i.e., its effect is different from that of the bis-polysulfur silane used in Figure 11. It seems to have a barrier action only. Upon the addition of the resin, the curves shift further to lower currents, again without affecting the corrosion potential. When silica is also added to the silane, the corrosion potential increases by about 200 mV, which indicates a strong effect on the anodic reaction for this film. At –0.5 V, the current is 2½ orders of magnitude lower than for the untreated metal. The film thickness of this film ranged between 2 and 7 μm. The film was very scratch-resistant and could not be removed from the metal. A thick, cast film behaved like a rubbery material and

was highly flexible. More work on these promising materials, in which other resin materials are also included, is currently in progress.

In Figure 13 we show the effects of the addition of a small amount of pure TEOS to an old but clear solution of BTSE of pH = 4. The effect of the BTSE film itself on the polarization curves is not very strong, when compared with a fresh film, e.g., the one shown in Figure 3. This demonstrates that the silane molecules need to be predominantly monomeric in the solution. Oligomerization, which always occurs at a certain rate, with a minimum at pH = 4, impairs the formation of a highly protective film, in agreement with previous reports.[3,4] The addition of TEOS to the BTSE solution giving a 20/80 ratio, had only a minor effect on the polarization curves for a film prepared immediately after mixing. However, for a film made after one day of aging of the mixed solution (which was still clear), the cathodic current decreased by more than an order of magnitude. The shape of the curve has not changed very much, however, indicating primarily an increased barrier action. The results show promise for improving the performance of silane films further.

DISCUSSION AND CONCLUSIONS

The results presented in the previous section confirm that very thin films of simple bis-silane molecules can provide remarkably good corrosion protection of the AA2024-T3 alloy. However, several new conclusions can be drawn from the results presented here. The data shown in the polarization curves of Figures 1-3 and the IR spectra of Figures 4-6 indicate that the performance of the films depend on the molecular structure of the silane molecules and also on the deposition conditions. In Figures 1-2 it is seen that the shape of the polarization curve typically does not change. This implies that the reduction of the anodic and cathodic currents are predominantly the result of a barrier action of the silane film.

More specifically, it can be concluded that this barrier action is dependent on the permeability of the silane film to electrolyte. This permeability is closely related to the degree of hydrolysis of the film. If the film is completely hydrolyzed, the three-dimensional silane network becomes so hydrophilic that the film absorbs large amounts of electrolyte. This applies especially to BTSM, which has the lowest number of carbon atoms, so a crosslinked BTSM film is more hydrophilic than the other silane films. All silanes show the effect that a lower degree of silane hydrolysis in the solution is actually beneficial for its corrosion protection capabilities. This conclusion may be counter-intuitive, but is confirmed by polarization data presented here, and contact angle data and EIS data shown in another paper.[16] The EIS data, for instance, indicated that the BTSM film of Figures 1 and 3 were completely permeable to water, i.e., the film has an impedance at low frequency almost equal to that of the solution resistance. The contact angle data showed this film to be of higher surface energy than the other films.

Since a silane film with a very low degree of hydrolysis does not form a strong, crosslinked film, its performance will decrease if the degree of hydrolysis is very low. The film of BTSO in Figure 1 is poorly hydrolyzed, the film in Figure 3 was more hydrolyzed but still not completely, and it was still hydrophobic. The difference in performance is striking. Thus we arrive at the important conclusion that each silane will have its own optimum hydrolysis and deposition conditions. The rate of hydrolysis is not only dependent on the water/alcohol content, the pH of the solution, but also the molecular structure of the molecule. BTSO hydrolyzes more slowly than BTSM, as its molecular structure is much less soluble in water.

The results with BTSE shown in Figure 2 confirm this effect: if BTSE is more completely hydrolyzed (in the data of Figure 2 because of the higher water content in the

solution), its performance degrades, as the film becomes too hydrophilic and absorbs more electrolyte.

All the silane films, regardless of their structure, show the effect that films made from solutions with lower water content exhibit a knee in the curve, indicating a pitting potential (Figures 1 and 2). This knee disappears at higher water content, which parallels a lower corrosion performance. Although this effect is not completely understood, it can be concluded that films that are more insulating due to lower electrolyte content, show a tendency to pitting, similar to the pitting tendency of highly insulating oxide films.

The results shown for the addition of small amounts of silica to a silane film (Figure 11) and the phenomenon that the effect disappears at higher loading, point at the following mechanism. The bis-polysulfur silane was selected for this experiment as it has a passivating effect on the cathodic reaction, presumably by a reaction between the sulfur in the molecule and the copper-bearing intermetallic deposits in this alloy.[5] In figure 11, this effect manifests itself by a lowering of the corrosion potential. With a small amount of silica added, the film density increases and the film adsorbs less electrolyte. A pronounced knee (pitting potential) appears now in the anodic curve, in agreement with the lower conductivity of the film. EIS data (not shown in this paper) of similar filled films have indicated a higher overall resistance of the film. A higher content of silica probably induces porosity in the film. It becomes overpigmented, similar to a paint film with a pigment loading greater than the CPVC.

The effect of the resin addition (Figure 12) appears to be a pure barrier effect. The curve does not change in shape, nor does the corrosion potential shift. Here, the silica addition together with the resin, seems to have an effect on the anodic reaction. The silane in this experiment did not contain sulfur and the aluminum alloy did not contain copper. Thus, it is suspected that the

silica in combination with the resin has a passivating effect on the anodic reaction due to small amounts of silicate released by the silica. Alternatively, the silica could have a buffering effect on the pH of the anodic sites.

The negative effect of the aging of the BTSE solution and the positive effect of the addition of TEOS (Figure 13), suggest that oligomerized BTSE molecules no longer form a film that is well-organized and dense. The barrier action is largely lost. It should be noted that BTSE is the only bis-silane tested here that can form long, linear siloxane chains without a high strain in the molecule. This is shown in Figure 14. A ring structure could easily be formed. The other bis-silane cannot form that ring structure without steric hindrance or a high strain (BTSM), and, therefore they cannot form the extended, linear siloxanes of Figure 14. This explains the unusually high performance of BTSE in some cases.[3,4,16] It also provides an explanation for the difference between mono and bis-silanes. Mono-silanes cannot form the same high density of Si-O-Me bonds at the oxide interface as bis-silanes.

When TEOS is added to the aged BTSE solution that contained oligomers, it showed no effect immediately because the TEOS was, apparently, not hydrolyzed sufficiently. After one day, however, it was hydrolyzed and then clearly increased the barrier effect by crosslinking the BTSE oligomers. Such a crosslink is schematically shown in Figure 15. The dilution of the TEOS molecules by the more stable BTSE oligomers prevented the TEOS from condensing by itself. The mixture was more stable than a solution of TEOS alone.

In conclusion, we have presented evidence that an optimum bis-silane film is obtained from conditions with a certain degree of hydrolysis. Under those conditions, the film is sufficiently strong, adheres well to the substrate by providing a sufficient number of silanol groups that react with the metal oxide. On the other hand, the incomplete hydrolysis maintains a

certain hydrophobicity, so that the film has a good barrier action to the electrolyte. This optimum combination of properties cannot be obtained by mono-silanes. While silanes primarily work so well because of their barrier action, evidence has also been presented that the properties of silane films can be tailored by certain additions such as resins, pigments and TEOS. In certain cases, specific anodic or cathodic corrosion inhibiting effects have been suggested.

ACKNOWLEDGMENTS

This work was funded by the Air Force under contract No. F49620-01-1-0352 (MURI). The authors also acknowledge Tonya Shipp for performing the TOFSIMS analyses.

REFERENCES

1. 1. W. J. van Ooij and T. F. Child. CHEMTECH, 28, 26 (1998)
2. W. J. van Ooij, D. Zhu, Guru Prasad Sundararajan, Senthil K. Jayaseelan, Yuan Fu and Niranjan Teredesai. Surf. Engg. 16, 386 (2000)
3. V. Subramanian, Ph. D. Dissertation, University of Cincinnati, Department of Materials Science and Engineering, 1999.
4. V. Subramanian and W. J. van Ooij, CORROSION, 54, 204 (1998)
5. W. J. van Ooij and D. Zhu, CORROSION, 57, 413 (2001)
6. G. P. Sundararajan, M. S. Thesis, University of Cincinnati, Department of Materials Science and Engineering, 2000.
7. M. A. Petrunin, A. P. Nazarov, and Yu. N. Mikhailovski, J. Electrochem. Soc. 143, (1996) 251
8. M. Beccaria and L. Chiaruttini, Corros. Sci., 41, (1999) 885

9. P. R. Underhill and D. L. Duquesnay, Corrosion resistance imparted to alminum by silane coupling agents, in: K. L. Mittal (Ed), Silanes and Other Coupling Agents, Vol. 2., VSP, Utrecht, The Netherlands, 2000
10. P. Puomi, Ph. D. Dessertation, Åbo Akademi University, Department of Physical Chemistry, 2000
11. D. Zhu, S. K. Jayaseelan, , G. Prasad, Y. Fu, W.J. van Ooij, Proceedings of the US Navy & Industry Technology Information Exchange, Louisville, Ky, June 19-22, 2000 (on CD)
12. E.P. Plueddemann, "Silane Coupling Agents", 2nd Edition, Plenum Press, New York, 1991
13. K.L. Mittal, editor, "Silanes and other Coupling Agents", VSP, Utrecht, The Netherlands, 1992
14. K. L. Mittal (editor), Silanes and Other Coupling Agents, Vol. 2., VSP, Utrecht, The Netherlands, 2000
15. F. D. Osterholtz and E. R. Pohl, J. Adhesion Sci. Technol., Vol. 6, 127 (1992)
16. J.A. Lamar, D. Zhu and W.J. van Ooij, Corrosion Protection of 2024-T3 Aluminum Alloy by Bis-nonfunctional Silanes, Presented at Tri-Service Corrosion Conference in San Antonio, TX, January 14-18, 2002

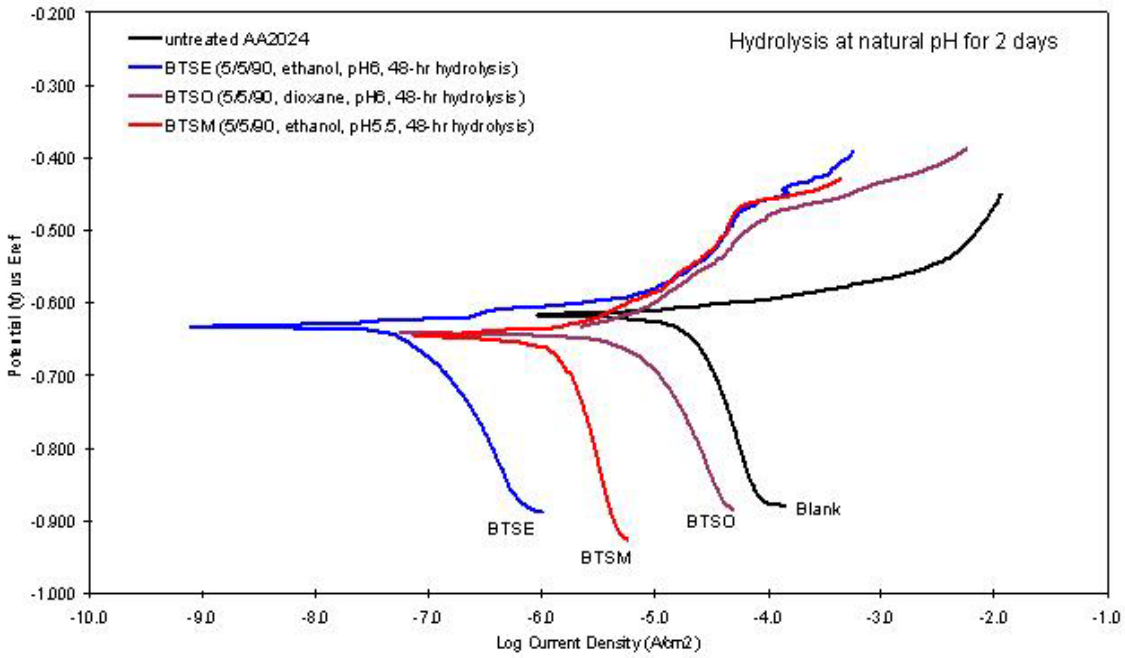

FIGURE 1. Polarization curves in aerated 0.6 M NaCl for films of BTSM, BTSE and BTSO on AA2024-T3 substrates. The 5% solutions were at their natural pH and had been hydrolyzed for 48 hours before film deposition. Solution compositions were 5/5/90 silane/water/ethanol for BTSM and BTSE, and silane/water/dioxane for BTSO. All films in this and subsequent figures were cured for 24 hours at 100°C, unless noted otherwise.

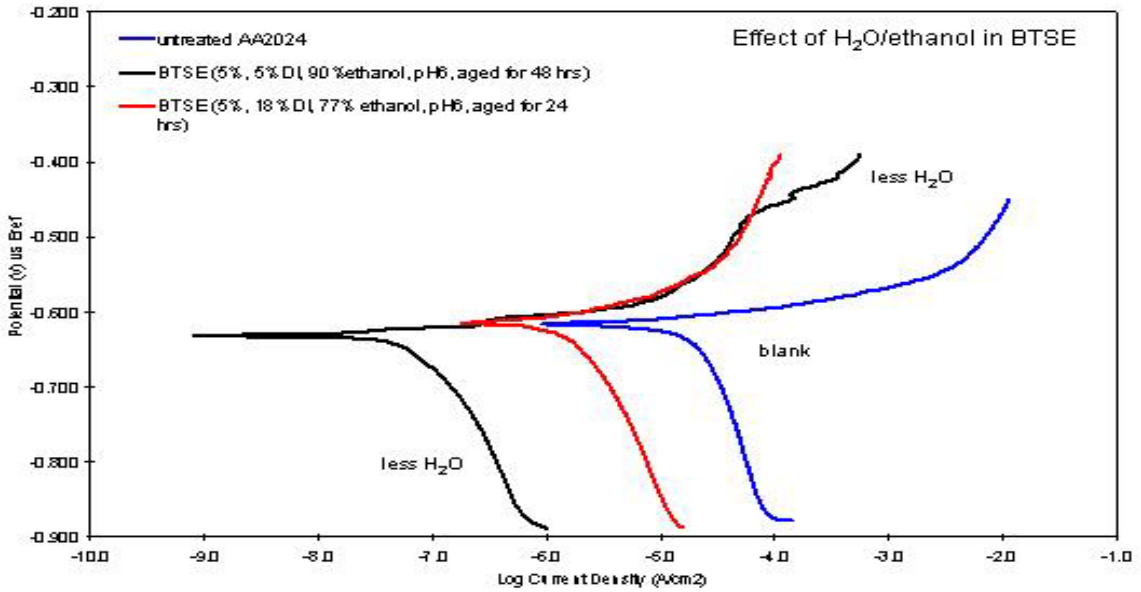

FIGURE 2. Polarization curves for films on AA2024-T3 substrates formed form BTSE/water/ethanol mixtures 5/5/90 and 5/18/77 at pH = 6. The 5/5/90 solution had been hydrolyzed for 48 hours, the 5/18/77 solution for 24 hours.

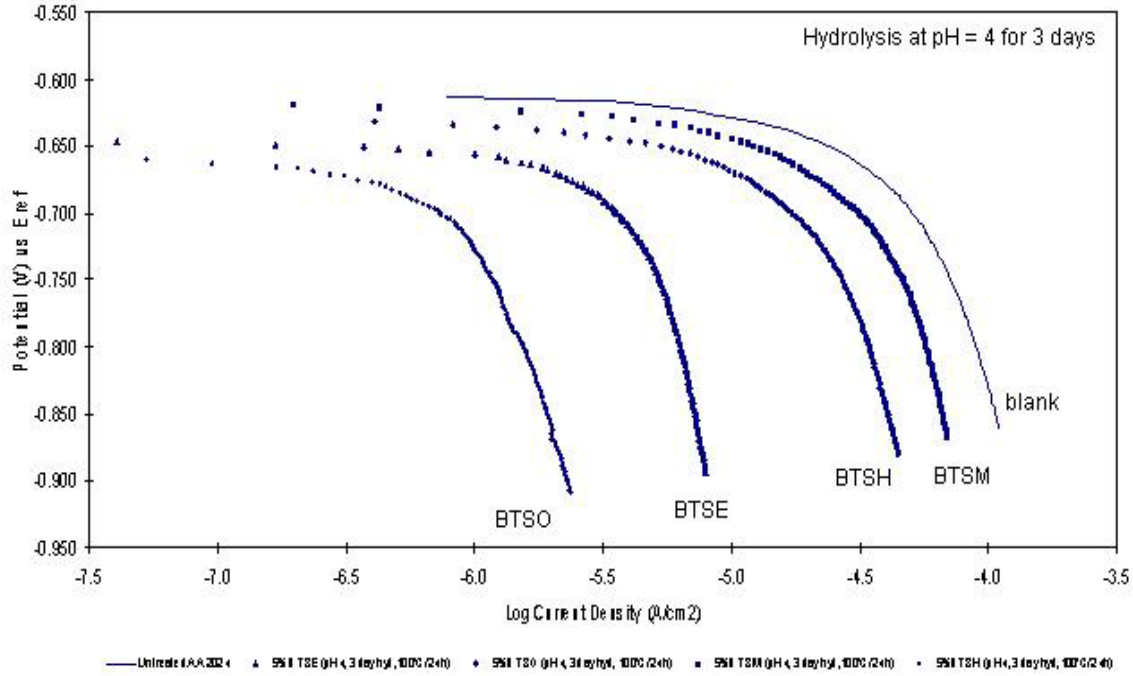

FIGURE 3. Cathodic polarization curves for films of BTSM, BTSE, BTSH and BTSO on AA2024-T3 substrates. Solution compositions were 5/5/90, silane/water/ethanol. The pH was adjusted to 4.0 by acetic acid. Hydrolysis was done for 72 hours.

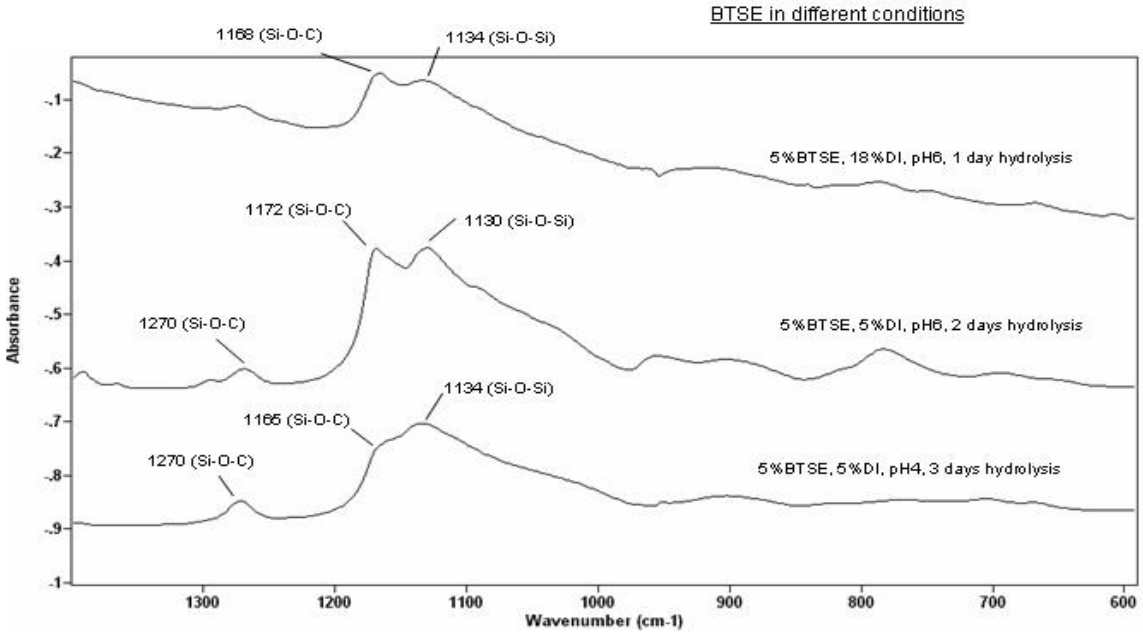

FIGURE 4. RAIR spectra of BTSE films on AA2024-T3 panels after deposition under different conditions.

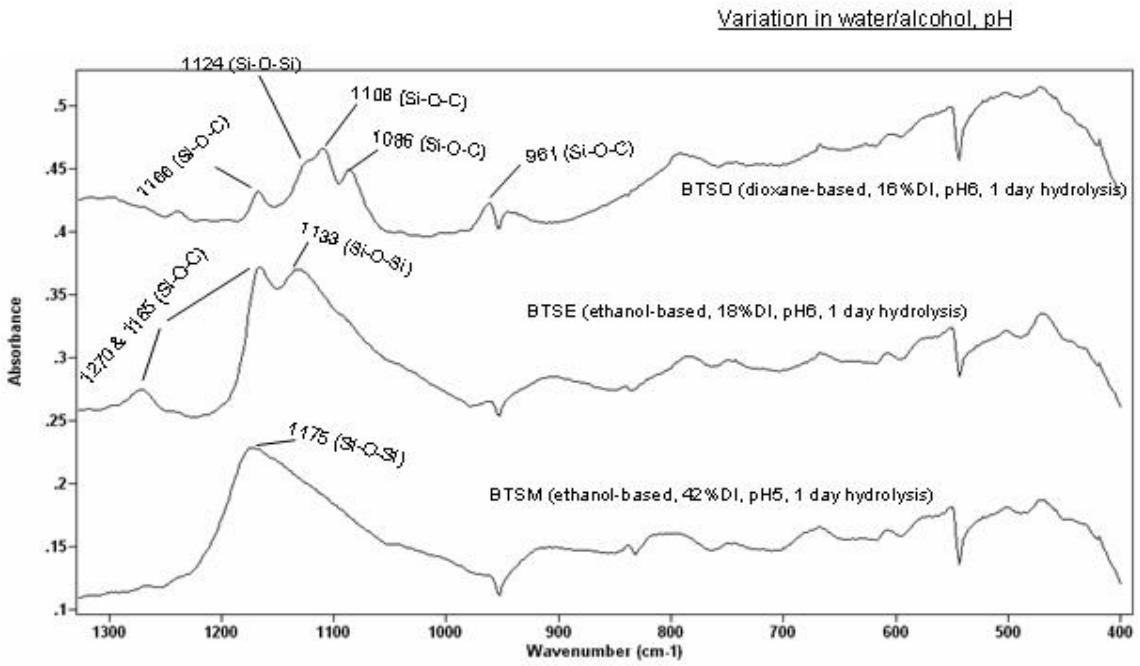

FIGURE 5. RAIR spectra of films of BTSM, BTSE and BTSO deposited on AA2024-T3 panels from silane/water/ethanol (BTSO dioxane) mixtures containing their maximum water content for dissolution. The time of hydrolysis was 24 hours.

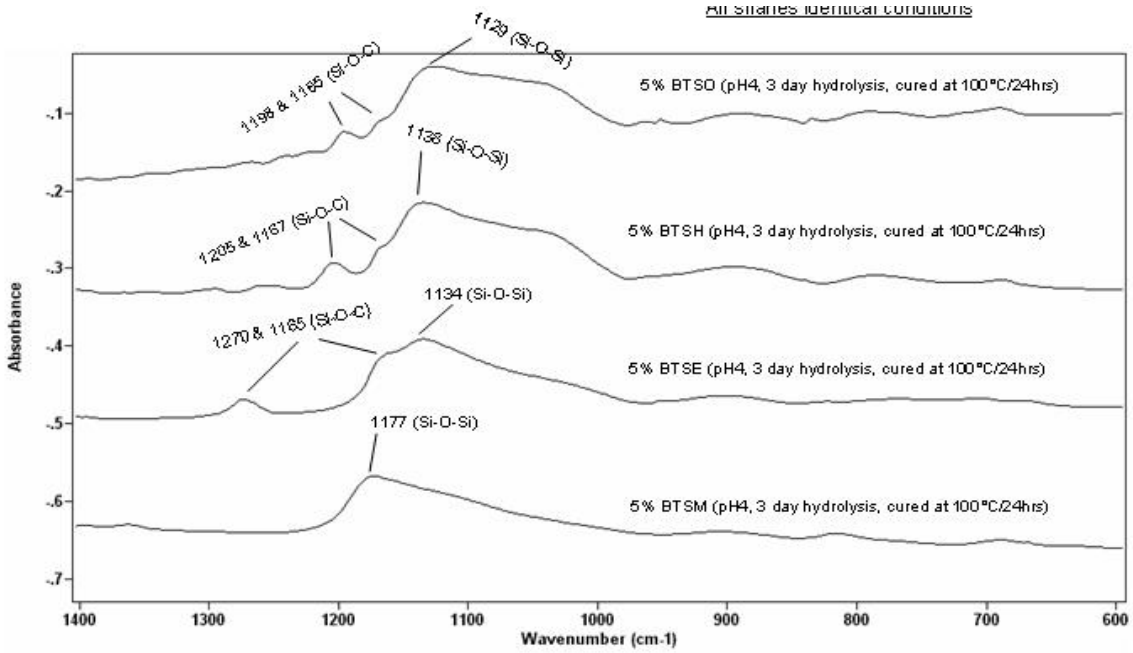

FIGURE 6. RAIR spectra of films of BTSM, BTSE, BTSH and BTSO deposited on panels of AA2024-T3 from silane/water/ethanol 5/5/90 solutions adjusted to pH = 4 and hydrolyzed for 72 hours.

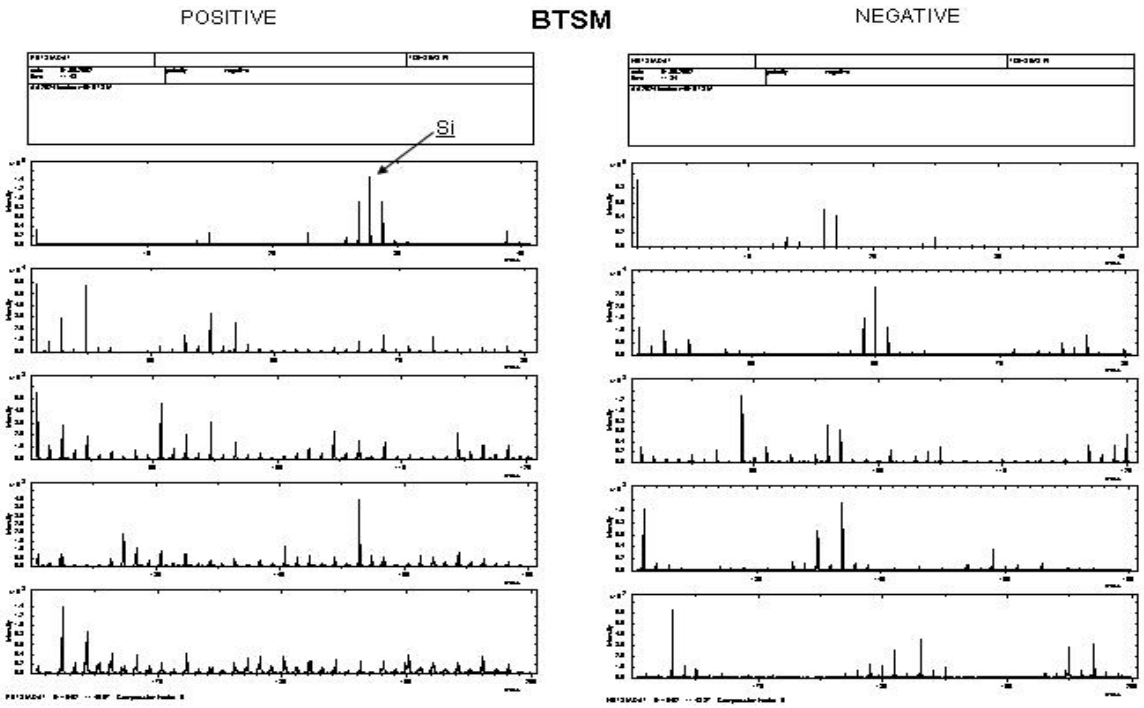

FIGURE 7. TOFSIMS spectra of a fresh film of BTSM on AA2024-T3 panel deposited from a silane/water/ethanol 5/5/90 solution of pH 4 and hydrolyzed for 72 hours.

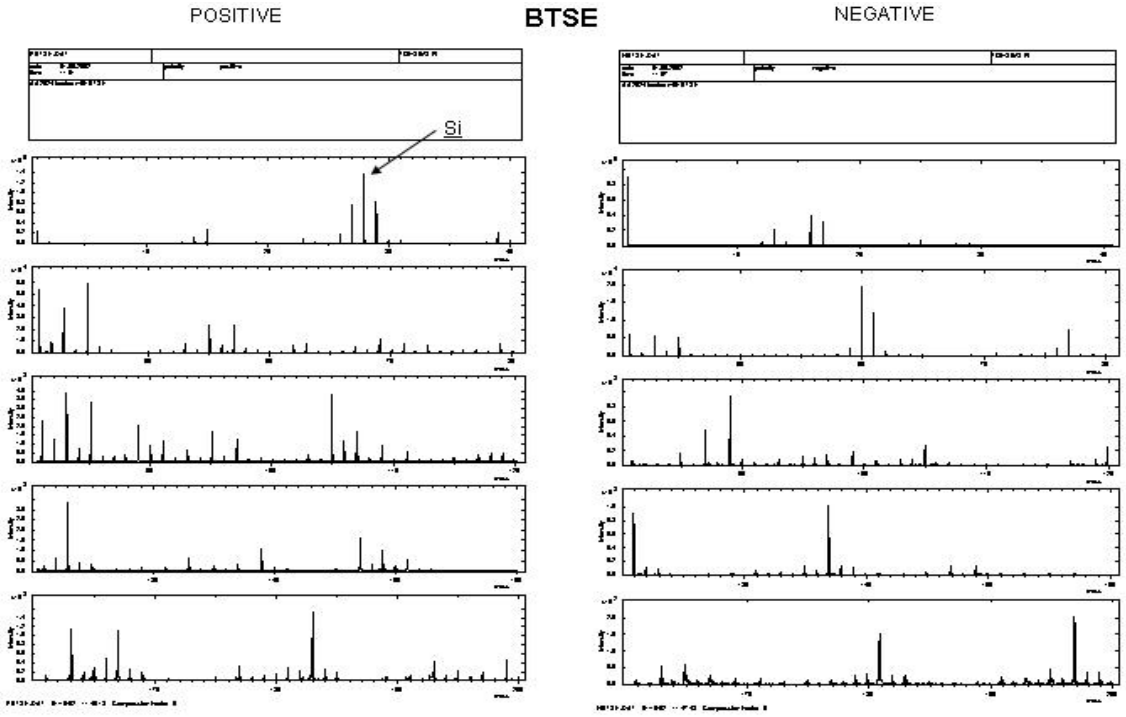

FIGURE 8. TOFSIMS spectra of a fresh film of BTSE on AA2024-T3 panel deposited from a silane/water/ethanol 5/5/90 solution of pH 4 and hydrolyzed for 72 hours.

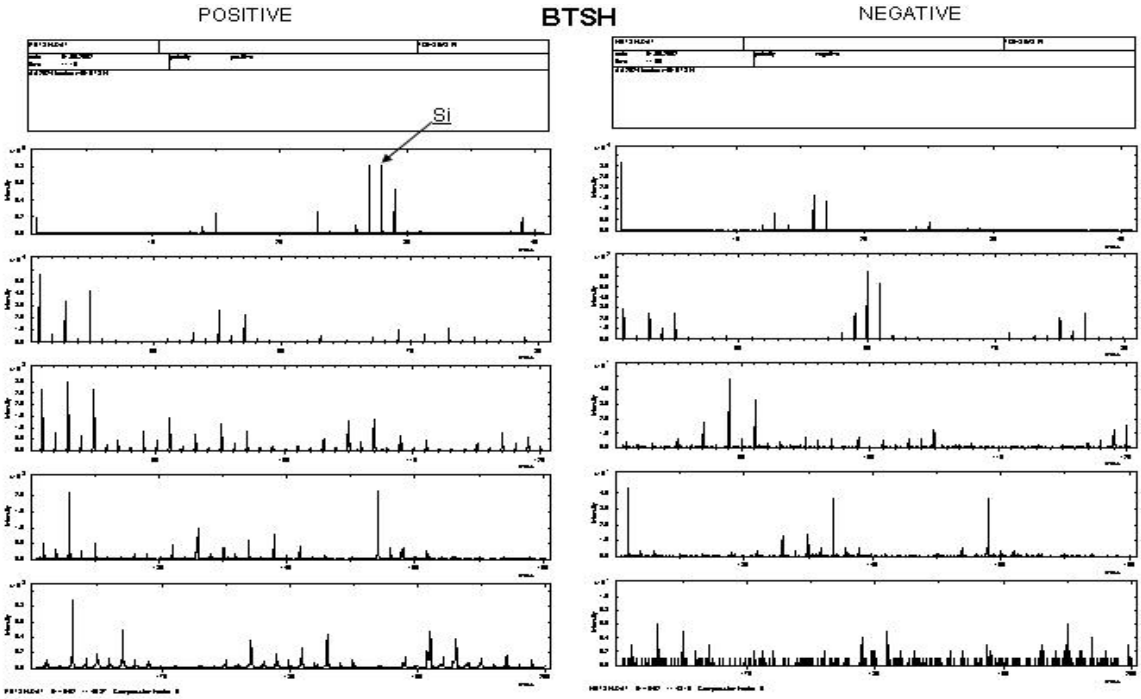

FIGURE 9. TOFSIMS spectra of a fresh film of BTSH on AA2024-T3 panel deposited from a silane/water/ethanol 5/5/90 solution of pH 4 and hydrolyzed for 72 hours.

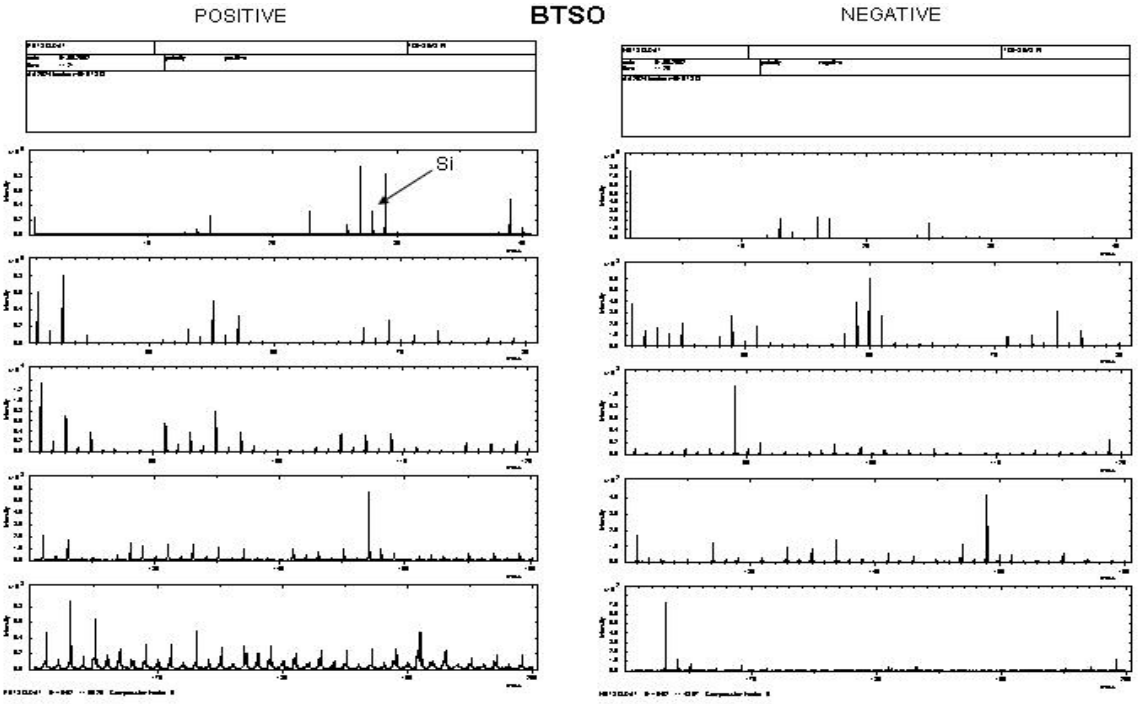

FIGURE 10. TOFSIMS spectra of a fresh film of BTSO on AA2024-T3 panel deposited from a silane/water/ethanol 5/5/90 solution of pH 4 and hydrolyzed for 72 hours.

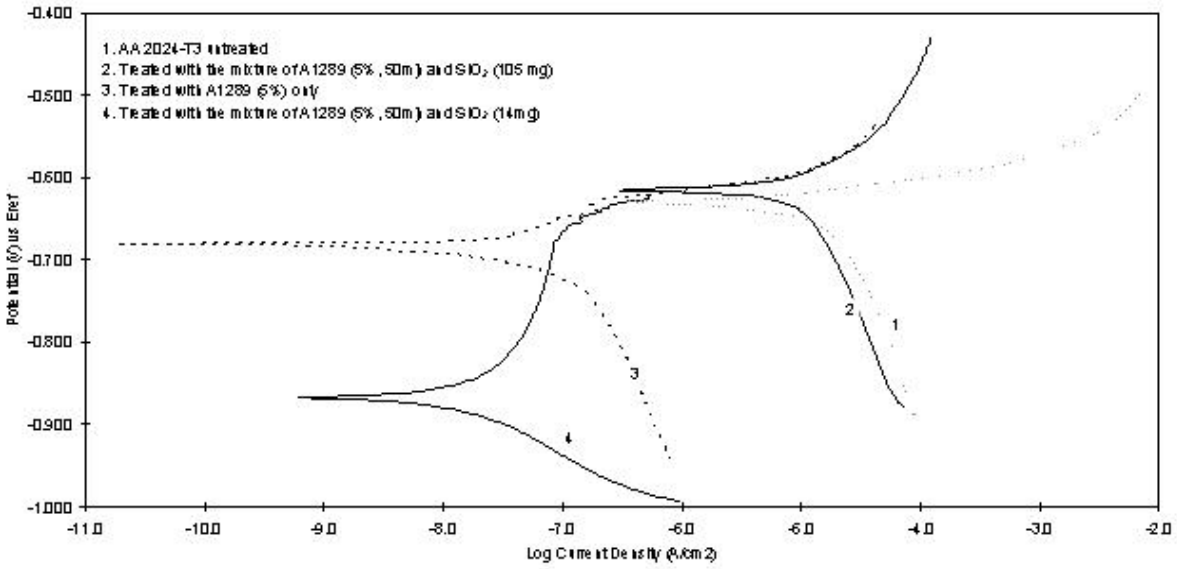

FIGURE 11. Polarization curves for films of bis-polysulfur silane on AA2024-T3 with and without colloidal silica addition. Solutions were silane/water/ethanol 5/5/90 and the silica contents were 28 and 210 mg per 100 ml solution.

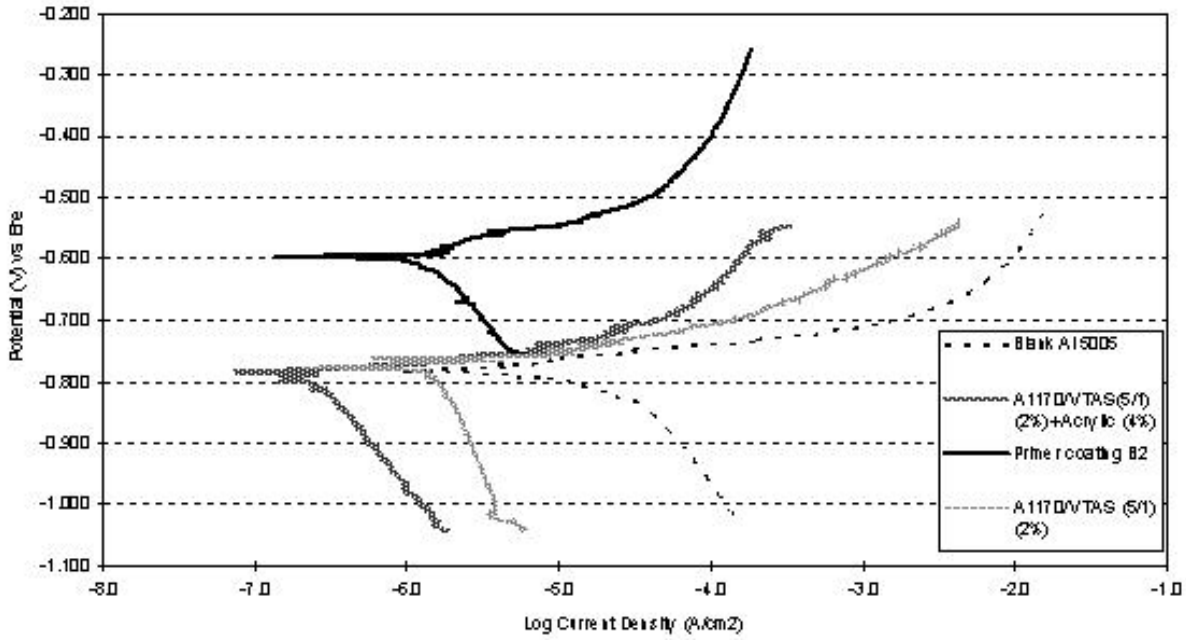

FIGURE 12. Polarization curves for films bis-amino/VTAS 5/1 mixtures on AA5005 panels, with and without addition of acrylic resin and colloidal silica. The primer coating of silane /resin/silica was prepared from 50 ml silane mixture (non-hydrolyzed), 40 ml resin, 10 ml colloidal silica (20% sol) and 100 ml DI water, and then baked at 130°C for 30 min.

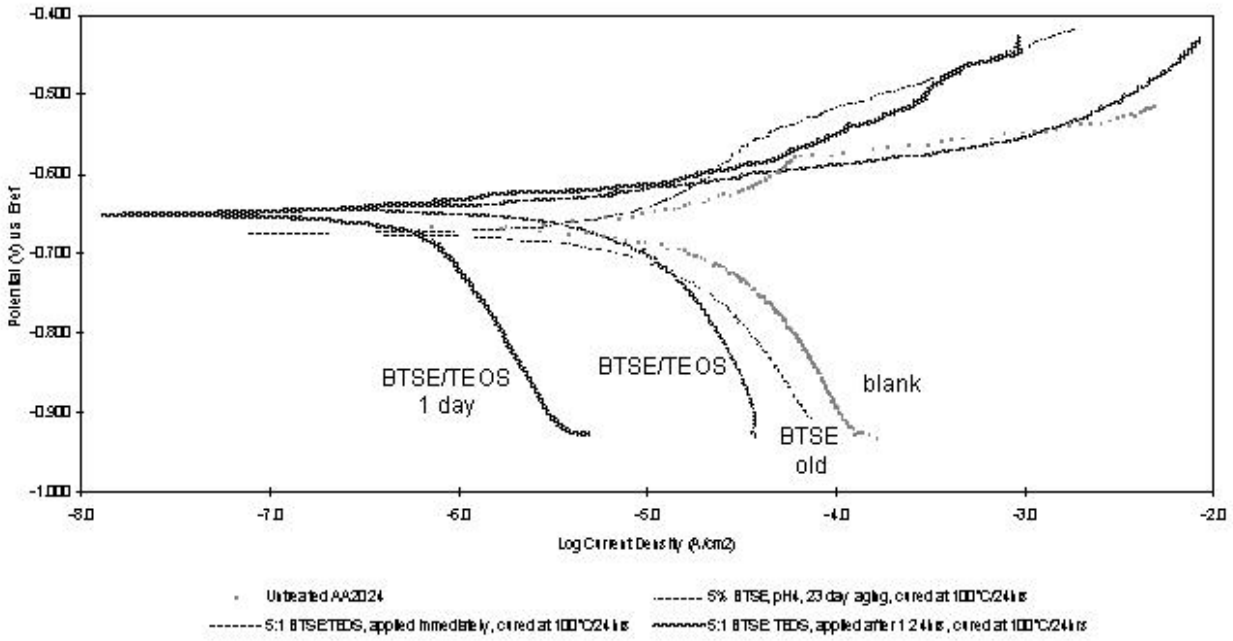

FIGURE 13. Polarization curves of silane film on AA2024-T3 panels deposited from a 23 day old 5% BTSE solution of pH = 4 and composition silane/water/ethanol 5/5/90, and from the same solution to which pure TEOS had been added. The BTSE/TEOS ratio was 80/20. After the TEOS addition a film was prepared immediately and another one after 24 hours aging.

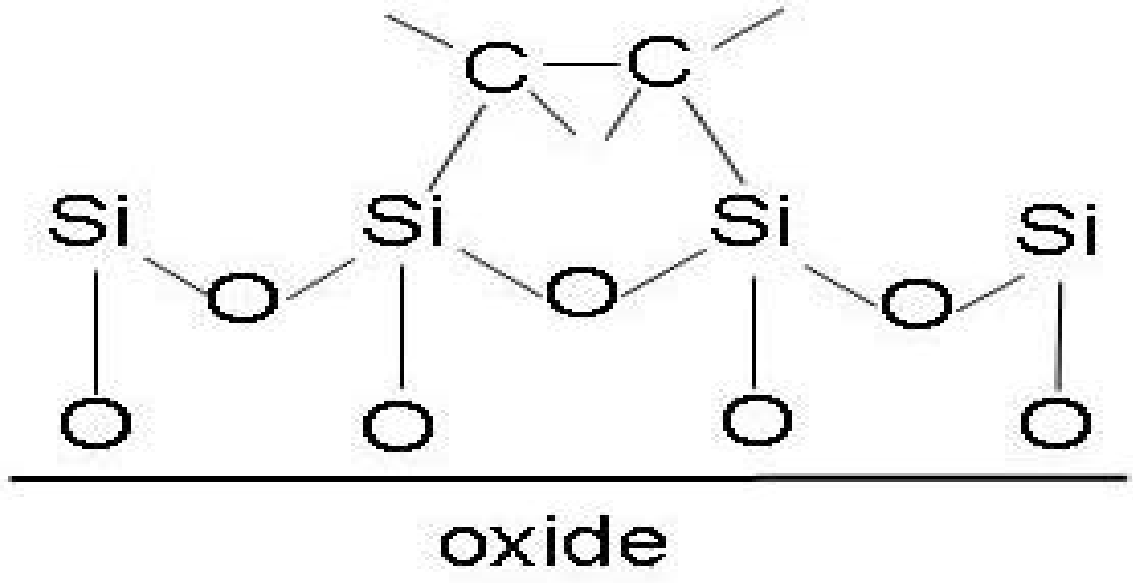

FIGURE 14. Proposed linear siloxane structure formed by BTSE on metals by ring formation.

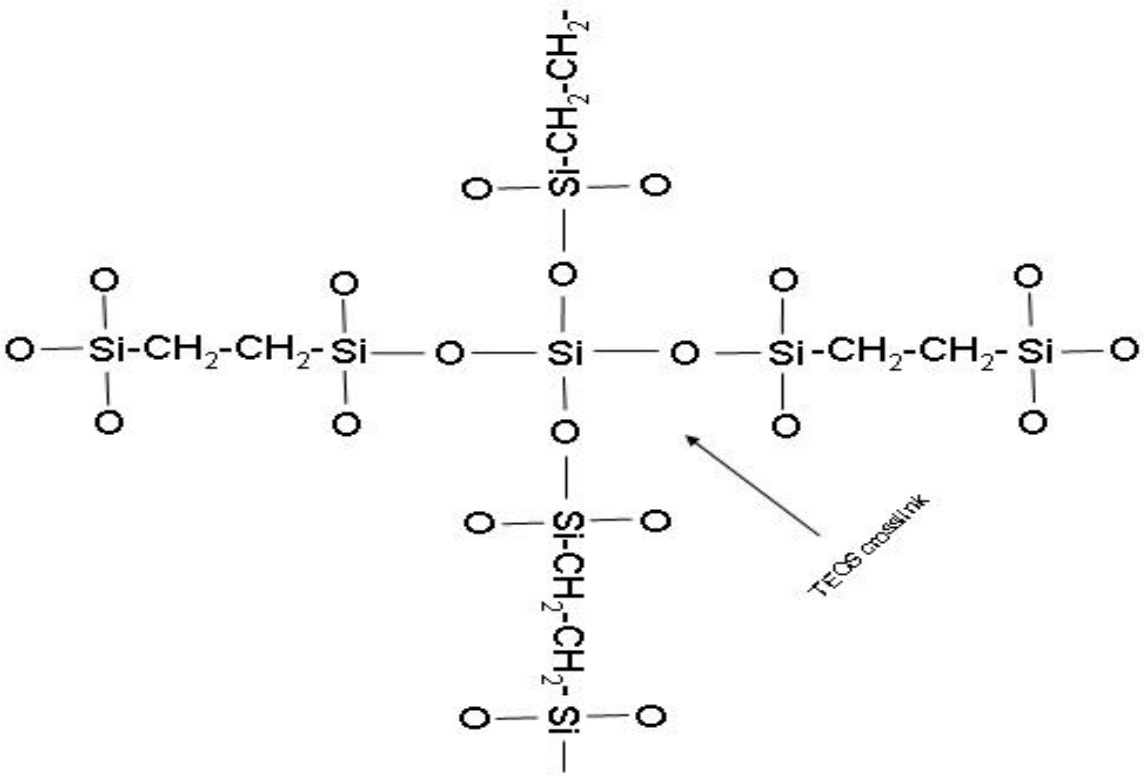

FIGURE 15. TEOS crosslink in aged BTSE solution containing oligomers.

PHOTONIC CRYSTAL STRUCTURES AS NANOENGINEERED COATINGS

K. Sieradzki, M. Vukmirovic, and V. Ratsko

Program in the Science and Engineering of Materials
Arizona State University
Tempe, Arizona 85387-6106

INTRODUCTION

A multifunctional aircraft coatings system must meet the following requirements:

- Integrated coating/sensor schemes must be flexible and conformal over large surface areas.
- Multifunctional sensors integrated into the coating must have components distributed over length scales consistent with the length scales over which corrosion and mechanical damage "nucleate" in airframe structures. These length scales range from 100 nm to 100 μm, and are set by the microstructure (e.g., mean size and separation of S-phase particles) of alloys such as Al alloy 2024.
- The coatings should yield spectroscopic signatures providing "markers" for detection of chemical and mechanical damage.
- The coatings should provide active corrosion protection schemes by incorporating inhibitors in analogy to the role of Cr^{6+} as a "self healing inhibitor" in currently employed chromate-based coating schemes. Sensors must be able to sense and identify corrosion processes and initiate measures to neutralize chemical damage.
- The coating/sensor scheme should have broad utility for integration of functionality such as on-demand color change.

- Ideally, the coating and integrated sensor system should be able to be maintained and replaced in the field.

Our approach to develop a sensor with on-board inhibitor delivery will is to use novel *photonic crystal structures* that can be incorporated into a polymer topcoat or total polymer coating system. Photonic crystals are structures in which the dielectric constant varies periodically in space. The periodicity is that of microscopic dielectric particles instead of atoms. This produces many of the same phenomena for photons (light modes) as the atomic potential produces for electrons. In analogy to the diffraction of x-rays by atomic structures, mesoscale photonic crystals diffract light in the range of ultraviolet through the visible spectrum to near infrared. There are numerous fabrication schemes ranging from micro-electronically fabricated structures to self-assembly of micro constituents. Most current general methods for preparing these structures use self-organized surfactants, block copolymers, or colloidal particles as templates in conjunction with sol-gel techniques. Micro or nanospheres of mono-disperse polystyrene, or silica can be self-organized into colloidal crystals by the following general scheme. In low ionic strength liquid media, the nano-spheres have a permanent net negative surface charge counterbalanced by positively charged counterions. Stray ions are also present in the suspension, decreasing the Debye screening length. The stray ions can be removed using ion-exchange resins and this allows the spheres to interact with short-range Coulombic repulsion and long-range van der Waals attraction. The colloidal suspension undergoes a phase transition from a disordered state to a face-centered (or body centered, depending on the initial volume fraction of colloidal particles) crystalline lattice forming crystalline colloidal arrays (CCA). The CCA can be quenched into a polymer matrix permanently locking in ordering.

By selecting for the quenching matrix a polymer that swells in response to a recognition event, the CCA becomes a large-scale sensor skin that continually monitors the airframe structure. A small change in the lattice constant of the mesoscopic ordered structure will be translated into a large detectable change in the Bragg diffraction properties of that structure. Since the scale of the periodicity can be chosen to be anywhere in the range from 20nm to 1000nm, health-inspection of the structure can be performed at a pre-selected range of frequencies anywhere between the infrared and the ultraviolet. In addition, recognition events causing the polymer matrix to swell from increased osmotic pressure (the result of a Donnan potential) can serve as a release mechanism for a corrosion inhibitor. The recognition events will take place through the reaction (and capture) of specific cations and anions by molecular recognition groups such as crown ethers and/or metallacrown ethers.

Therefore the sensor material is a three-dimensional (3D) periodic CCA of highly charged dielectric spheres embedded in an appropriate polymer network. One can typically produce layers of hundreds of microns in thickness incorporating about 1000 layers of (111) planes that orient parallel to the substrate, although we envision the use of thinner layers in

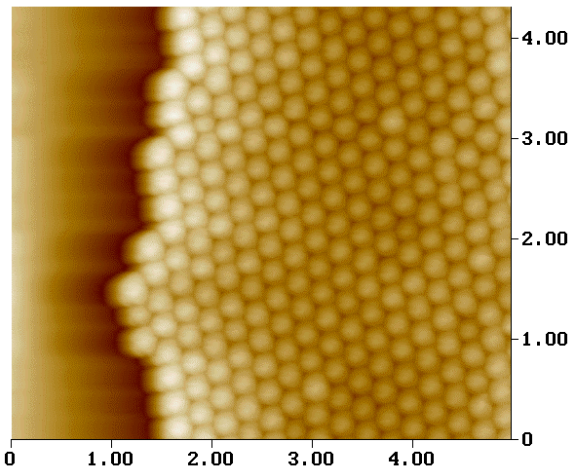

FIGURE 1. Non-contact atomic force microscopy image showing the development of the first monolayer of a self-assembled face centered cubic crystalline colloidal array. The unit of the x and y-axes is microns. A growth step runs almost vertically in the image at ≅1μm. The 270 diameter polystyrene spheres were assembled from a colloidal suspension obtained from Duke Scientific Corporation.

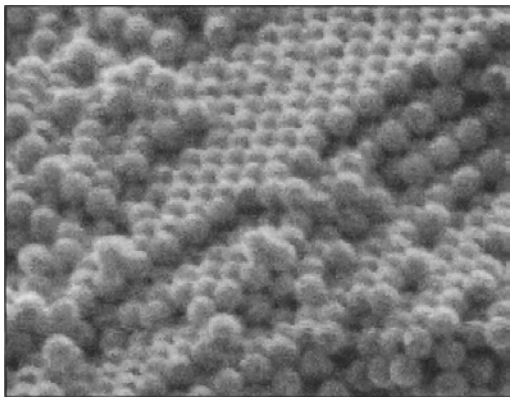

FIGURE 2. Scanning electron micrograph of a three-dimensional face-centered cubic CCA composed of 150 nm diameter silica spheres. The spheres had a polydispersity below one percent.

coating systems. Owing to the robust nature of the ordering process, it is easy to self-assemble these structures. Figure 1 is a non-contact AFM image obtained in our laboratory showing the growth of the first layer in a CCA composed of 270 nm polystyrene spheres.

Figure 2 shows a three-dimensional fcc CCA of silica nanospheres. The lattice constant of the crystals can be tailored by altering the particle size or tuning the attached electric charge. The sensor is interrogated by performing Bragg diffraction using a commercial UV-visible-near IR spectrophotometer. Sub-micron spatial resolution can be achieved with fiber-optic devices.

Since the diffraction obeys Bragg's law, $m\lambda = 2nd \sin\theta$. (where λ is the diffracted wavelength, m is the order of the diffraction, n is the index of refraction of the system (polymer matrix and colloids), d is the spacing of the diffracting planes, and θ is the incident angle between the incident light and the diffracting planes), the position of the Bragg peak will shift with a change in d resulting from an induced elastic strain. Such strains can result from a number of sources:

- When molecular recognition agents that are incorporated into the structure interact with specific chemical species, the monomer elements bearing the recognition elements undergo a change in solubility and/or charge state altering the gel volume and the CCA interplanar

spacing. Similar effects would result from the release of a corrosion inhibitor from the structure.

- Mechanical damage in the form of cracks (resulting from corrosion fatigue) has a recognizable elastic displacement field that can be sensed by the CCA.
- Thermal expansion.

INTELLIGENT PHOTONIC CRYSTALS

Most commercial polymer colloids or latex coatings employ polydisperse particle sizes and consequently do not form regular face-centered or body-centered cubic CCA. However, there is already considerable literature evidence that if highly monodisperse spherical particles are used in modified conventional latex coating formulations CCA can be realized by appropriate control of ionic strength, particle size uniformity, particle density, viscosity, etc[123]. Many commercial latexes are made by copolymerization of acrylic acid or methacrylic acid which should be suitable matrices for the CCA.

We are in the process of using two strategies for development of large scale crystals. One strategy for developing intelligent photonic crystals is based on the work of Asher's group[45]. They demonstrated that CCA as discussed above could be used for chemical sensing of analytes containing metal ions such as Pb^{2+} at the 0.1 μM concentration range. Such ion specificity is critical to accurate sensing of corrosion processes in Al alloys that have detectable signatures for dissolved cations such as Al^{3+} and Cu^{2+}. Additional functionality such as encapsulation of corrosion inhibitor into nano-porous or hollow colloidal particles or directly into a polymer matrix can at least in principle be accomplished in a seamless manner.

Asher's CCA were quenched into a hydrogel polymer matrix. Hydrogels are three-dimensional networks composed of hydrophilic flexible polymer chains with incorporated water.

Owing to bio-compatibility and the swelling/deswelling behavior of these materials, they have found important use in biological and medical applications as sensors and delivery systems owing to their ability for sustained drug release. These delivery systems have the ability to maintain drug concentrations in effective ranges for long periods of time and spatially target the drug to specific local sites. By incorporation of specific molecular recognition agents these materials can be tailored to respond a large variety of stimuli including pH, ionic strength, chemical species, magnetic, thermal, electrical and ultrasound irradiation. Polyelectrolyte hydrogels can respond to an applied electric field (or voltage) by swelling.

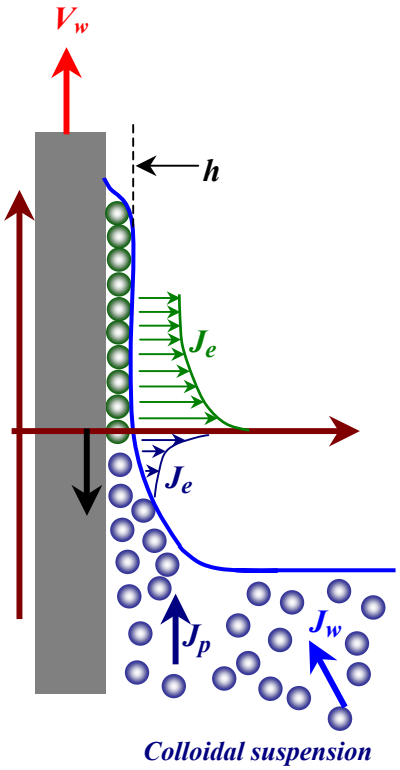

FIGURE 3. Schematic arrangement of colloidal crystal growth from "the melt" in the vicinity of the contact line. V_w is the pull rate, g is the crystal growth rate, h corresponds to the monolayer thickness, J_e, J_p, and J_w, are respectively the fluxes associted with evaporation, colloidal particles and water. Other parameters controlling growth include the concentration of colloidal particles in solution, interfacial tension which determine the meniscus shape, temperature and temperature gradients.

The other approach we are taking involves controlled evaporation and has many analogies to crystal growth from the melt. In this approach capillary and convective forces are used to structure colloidal particles in to regular close-packed arrays. Generally a clean substrate

is dipped in to a suspension of particles. Heterogeneous nucleation of the array initiates at the air contact line[678]. By carefully withdrawing the substrate and controlling a variety of parameters growth at the contact line ensues. This process is rapid in comparison to the formation of CCAs. Figure 3 is an illustration of the forces controlling growth.

FIGURE 4. Crystalline arrays of 800 nm polystyrene spheres grown the a 1:1 mixture of isopropyl alcohol and distilled water by evaporation using a fixed contact line (zero pull rate). (Image size 50 x 76 μm.) (A) polycrystalline growth showing 5-10 grain sizes. (B) and (C) polycrystalline growth showing twinned structures (D) single crystal

Various types of colloidal materials will be examined using solid spheres, "hollow" spheres and nanoporous particles. There are commercially available sources for highly monodisperse polystyrene and silica spheres ranging in size from 20 to 1000 nm which provides for considerable flexibility with respect to frequency response selection in the sensor element of the coating (e.g., Duke Scientific Corporation). We expect that size selection decisions will be

made in concert with MURI members including Airforce scientific personnel. Additionally, there are well known techniques for structuring metal and semiconductor nanoparticles in which

TABLE I. Characteristics of solvent and solvent mixtures used in evaporative crystal growth.

	Density (g/cm^3)	Dielectric constant	Viscosity (mPa s)
Water (H_2O)	0.99821 (@20°C) (p 6-3)	80.1	1.002 (@20°C) 0.890 (@25°C) 0.7977 (@30°C)
Methanol Methyl alcohol CH_3OH	0.7914	33.0	0.544 (@25°C)
Ethanol Ethyl alcohol CH_3CH_2OH	0.7893	25.3	1.074
Iso-propyl alcohol (2-propanol) $CH_3CH(OH)CH_3$	0.7855	20.18	2.038
Tert-butyl alcohol (2-propanol, 2-methyl) $C_4H_{10}O$	0.7887	12.47	4.312

for example metal or metal oxide colloidal particles are embedded in a silica shell of prescribed diameter in the 100 – 1000 nm range[9]. We will explore these approaches for the production of monodisperse colloidal particles of silica and/or polystyrene containing porous aluminum centers.

PRELIMINARY RESULTS

We have used evaporation techniques to grow colloidal crystals. Colloidal suspensions of 800 nm diameter polystyrene spheres were made using solvents described in Table I. High - resolution optical microscopy was used to study the self-assembly process. Some of our results are presented in Figure 4.

We are currently examining crystal growth using video microscopy and optical diffraction and future work will be aimed at optimizing the control parameters discussed above in order to obtain crystals that that diffract light at a single well-defined wavelength.

REFERENCES

1. J.W. Vanderhoff, E.B. Bradford, and W.K. Carrington, *J. Polymer Sci., Symposium No. 41*, p. 155, (1973).
2. S.T. Heckersley, and A. Rudin, *J. Coatings Tech*.,**62,** 89, (1990).
3. P.R. Sperry, B.S. Snyder, M.L. O'Dowd, and P.M. Lesko, *Langmuir,* **10,** 2619, (1994).
4. J.H. Holtz, and S.A. Asher, *Nature*, **389**, 829 (1997).
5. J.H. Holtz, J.S.W. Holtz, C.H. Munro, and S.A. Asher, *Anal. Chem*., **70,** 780 (1998).
6. V. Colvin, *Chem. Mat*. **11,** 2132 (1999).
7. Y. A. Vlasov, X-Zheng Bo, J. C. Sturm and D.J. Norris, *Nature*, **414,** 289, (2001).
8. A.S. Dimitrov and K. Nagayama*, Langmuir*, **12,**1303 (1996).
9. M. Alejandro-Arellano, T. Ung, A., Blanco, P. Mulvaney, L. M. Liz-Marzan, *Pure Appl. Chem*.,**72,** 257, (2000).

TRANSPORT OF CHEMICAL SPECIES THROUGH EPOXY COATINGS

W.Gan, H.Wang, and R.G.Kelly

Center for Electrochemical Science and Engineering
Department of Materials Science and Engineering
University of Virginia
Charlottesville, VA 22904

ABSTRACT

This paper focuses on the transport of chemical species through freestanding epoxy coatings by application of a permeation cell. Apparent diffusion coefficients for Cl^-, SO_4^{2-} and Na^+ were calculated and compared. Effects of solution species, concentration and pH were compared. For all species, lower feed solution concentrations lead to higher apparent diffusion coefficients. Lower pH values led to higher apparent diffusion coefficients for Cl^- and SO_4^{2-}, but lower diffusion coefficients for Na^+ at low Na^+ concentrations due to an increased contribution by hydronium ion to electroneutrality. Sodium transport was slightly higher in the film for sulfate feed solutions than for chloride feed solutions.

INTRODUCTION

Advances within the materials and chemical sciences have created a unique opportunity for the identification of a new multi-functional and environmentally compliant aerospace coating for military hardware. A new multi-functional coating system for military aircraft will be developed by implementing advances in molecular-and nano-engineering .

Many of the approaches for achieving a functional coating (*e.g.*, inhibitor release from encapsulants, polychromism, sensing) require the controlled release of chemical species. Quantitatively characterizing the pathways, mechanisms, and controlling parameters of the retention and release of the functional species is required to develop long-lived but rapidly responsive functional coatings.

Epoxies fulfill the role of an ideal binder for many high performances coating systems. The epoxy resin combines adhesion and corrosion resistance with chemical and heat resistance. It brings excellent mechanical and physical properties to the coating system. Curing agents are combined with epoxy resins to upgrade certain properties such as flexibility, light stability, and low temperature applications.[1]

This research aimed at deciding parameters playing roles on the permeate characteristics of the epoxy films through transport experiment. Quantitatively understand the effect parameters on transport of chemical species across coatings.

EXPERIMENTAL PROCEDURES

EPOXY FILMS PREPARATION

The recipe for the epoxy mixture used is shown in Table 1:

TABLE 1
The recipe of clean epoxy mixture

Components	Chemical name	Weight ratio
Resin	Epon(R) Resin 10001-CX-75	1
Curing agent	70%Epi-cure(R) 3115+30% xylene	1
Solvent	Butylcellosolve	0.5

Three components of epoxy mixture were hand-mixed by using the wooden end of a long tip. Then, the mixture was exposed to a vacuum to remove any trapped air bubbles. Film application consisted of a 25-second spin-coating procedure conducted at two speeds. Each 7.6 cm diameter round, glass substrates was centered on the spinning chuck of the KW4a spincoater (manufactured by Chemat Technology) and held in place by vacuum.[1] Using a 10-mL syringe, approximately 1mL of coating was released onto the center of the panel. The sample was then spun at 8,000 rpm for 10 seconds followed by a 15-second spin at the maximum speed of 10,000

rpm. Following that, films were allowed to cure inside a drying chamber containing Drierite® for a period of at least two weeks before starting the transport experiment. After a two-week curing period inside a dessicator, the films were wetted with 18 MΩ-cm Milli-Q water and cut along the edges with a scalpel blade. Using the blade, the intact coating was then carefully detached from the glass substrate and allowed to dry in an evacuated dessicator. The thickness of films were between 10 and 15μm.[1]

TRANSPORT EXPERIMENT

Transport experiments were conducted using the transport cell shown in Figure 1. A free-standing epoxy film divided the transport cell into feed chamber and permeate chamber. Eight types of feed solutions were studied as shown in Table 2. The initial permeate solution was 18 MΩ-cm Milli-Q water (from a Millipore Milli-Q ™ system) in all cases. After assembling the transport cells, 25 mL of feed solution and permeate solution were slowly filled in to both chambers at the same time. During the experiment, 40μL solution samples were withdrawn from the permeate solution chamber of every cell regularly, with 20μL being used for anion analysis and 20μL used for cation (sodium) analysis. In order to maintain the volume of permeate solution, 40μL 18 MΩ-cm Milli-Q water were then added to each permeate chamber. Concentrations of the different ions in samples were detected by Capillary Electrophoresis (CE) . Concentration-time data were recorded.

The apparent diffusion coefficients of anions and sodium were calculated according to equation (1).

$$\mathbf{D = b\ VT/(C_0A)}^{2} \qquad (1)$$

Where:

D——diffusion coefficient (cm^2/sec);

b —— the steady state studied ion flux, i.e., the linear slope of the concentration vs. time curve obtained by curve fitting to experimental data (mol/L·sec);
V —— the volume of the solution in each half cell (mL);
T —— the thickness of an epoxy film (μm);
C_0—— the concentration of the source ion solution (mol/L);
A —— the area of the film exposed to the solutions (cm^2) .

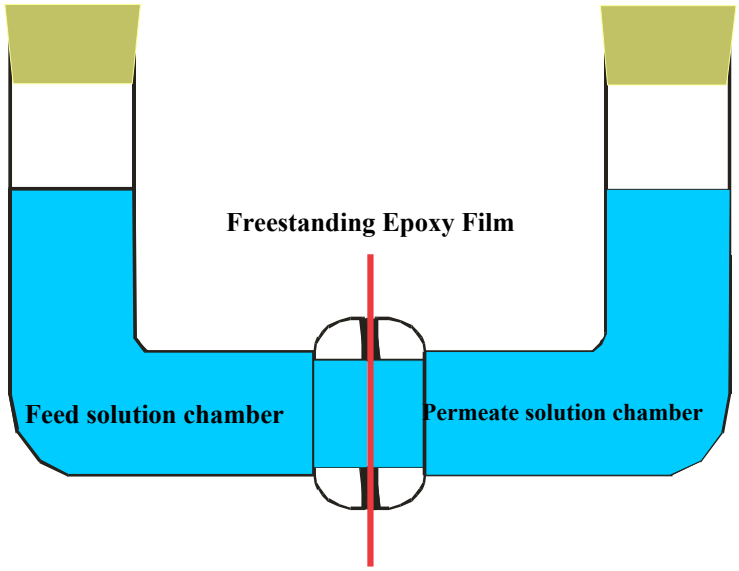

FIGURE 1. Schematic drawing for freestanding film cell setup for transport experiments [1]

TABLE 2
Feed solutions

Solution	Concentration(M)	pH
NaCl	0.02	2.0
NaCl	0.02	10.0
NaCl	2.0	2.0
NaCl	2.0	10.0
Na_2SO_4	0.02	2.0
Na_2SO_4	0.02	10.0
Na_2SO_4	2.0	2.0
Na_2SO_4	2.0	10.0

RESULTS

DIFFUSION COEFFICIENT

The concentration –time curves of Cl^-, SO_4^{2-} and Na^+ are shown in Figure 2–5.The diffusion coefficients and linearity of concentration–time curves (R^2) of Cl^- and SO_4^{2-} are shown in Tables 3 and 4. The apparent diffusion coefficients and linearity of Na^+ was shown in Table 5.

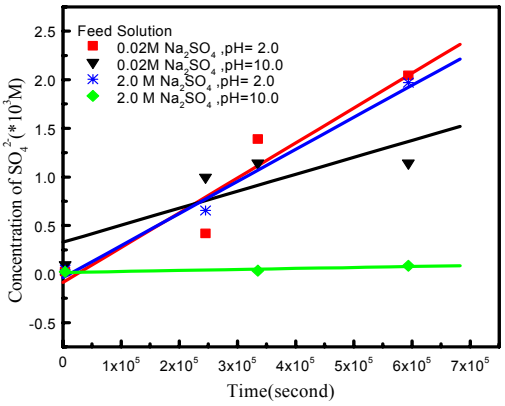

FIGURE 2. Transport of SO_4^{2-} from feed chamber to permeate chamber across freestanding epoxy films

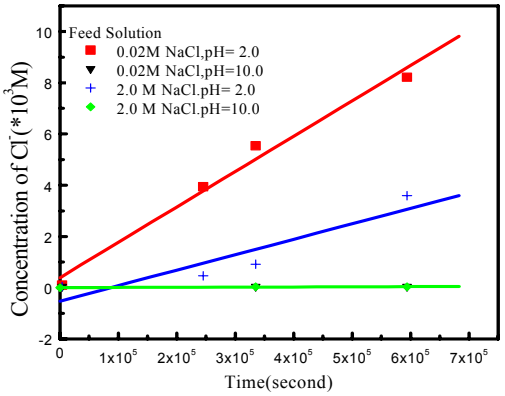

FIGURE 3. Transport of Cl^- from feed chamber to permeate chamber across freestanding epoxy films

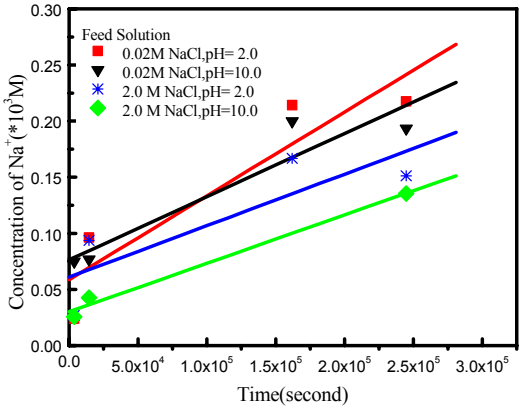

FIGURE 4. Transport of Na^+ from feed chamber to permeate chamber across freestanding epoxy films

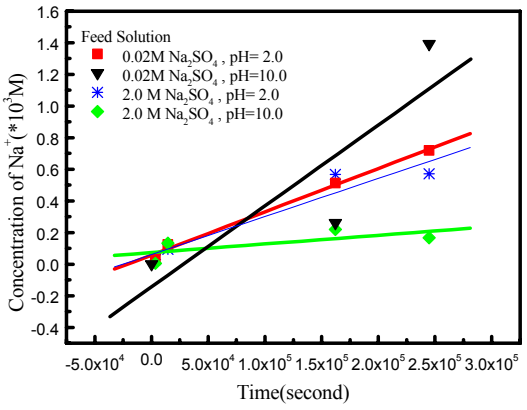

FIGURE 5. Transport of Na^+ from feed chamber to permeate chamber across freestanding epoxy films

TABLE 3
Diffusion coefficients and Linearity of concentration–time curves of Cl^- for epoxy films

Solution	$D_{Chloride}$ (cm^2/sec)	R^2 (Linearity of concentration –time fit line)
0.02M NaCl, pH= 2.0	$4.1*10^{-9}$	0.99
0.02M NaCl, pH=10.0	$2.0*10^{-12}$	0.99
2.0 M NaCl, pH= 2.0	$1.8*10^{-11}$	0.85
2.0 M NaCl, pH=10.0	$2.0*10^{-13}$	0.93

TABLE 4
Diffusion coefficients and linearity of concentration–time curves of SO_4^{2-} for epoxy films

Solution	$D_{sulfate}$ (cm^2/sec)	R^2 (Linearity of concentration –time fit line)
0.02M Na_2SO_4, pH= 2.0	$1.1*10^{-9}$	0.91
0.02M Na_2SO_4, pH=10.0	$5.1*10^{-10}$	0.71
2.0 M Na_2SO_4, pH= 2.0	$9.7*10^{-12}$	0.99
2.0 M Na_2SO_4, pH=10.0	$3.0*10^{-13}$	0.82

TABLE 5
Diffusion coefficients and linearity of concentration–time curves of Na^+ for epoxy films

Solution	D_{sodium} (cm^2/sec)	R^2 (Linearity of concentration –time fit line)
0.02M NaCl, pH= 2.0	$2.2*10^{-10}$	0.86
0.02M NaCl, pH=10.0	$1.7*10^{-10}$	0.89
2.0 M NaCl, pH= 2.0	$1.4*10^{-12}$	0.72
2.0 M NaCl, pH=10.0	$1.3*10^{-12}$	0.99
0.02M Na_2SO_4, pH= 2.0	$3.5*10^{-10}$	0.92
0.02M Na_2SO_4, pH=10.0	$7.5*10^{-10}$	0.74
2.0 M Na_2SO_4, pH= 2.0	$4.0*10^{-12}$	0.99
2.0 M Na_2SO_4, pH=10.0	$8.1*10^{-13}$	0.50

EFFECTS OF EXPERIMENTAL VARIABLES ON THE APPARENT DIFFUSION COEFFICIENTS

The effects of the experimental variables (feed solution, solution concentration, and pH) can be determined by calculating the difference of the average response for each of the first *k–1* levels from the average for the *kth* level by using equation (2):

ith factor effect = average response for level i –average response for level k [3] (2)

The diffusion coefficients of Na^+, Cl^- and SO_4^{2-} for transport through the epoxy coating were influenced by the each of the experimental variables to different degrees. All ions experienced higher transport rates for feed solutions of lower concentration, with ratios of conductivity at 0.02 M to conductivity at 2 M ranging up to 200:1 (for Na^+ in sulfate at pH 10). Most ratios were between 10 and 15. The solution pH also influenced the ionic transport through the coatings, with lower pH increasing transport rates for anions whereas it had no consistent effect on the transport rate of Na^+. Solution pH had the largest effect on Cl^- transport, with the apparent diffusion coefficient at pH 2 being 200x higher than when the permeate solution was pH 10. The effects on sulfate and sodium were substantially lower, with ratios on the order of 2 to 30. The nature of the anion in the feed solution also influenced the transport rate of Na^+, with higher rates being associated with sulfate solutions. Interestingly, the transport of chloride was more rapid than sulfate at pH 2, whereas it was slower than sulfate at pH 10.

DISCUSSION

It is important to realize the measurements presented here are couched in terms of apparent diffusion coefficients for ions through freestanding epoxy films. No external electric field was applied, but transport would be affected not only by concentration gradients but also by osmotic pressure gradients and the effect of the feed solution on the physicochemical characteristics of the polymer film. For example, it is known that low pH can damage these films irreversibly, increasing the transport of ions and water.[4] Thus, unlike in dilute aqueous solutions, the pH and nature of the anion can affect the important characteristics of the transport medium.

Kittelberger and Elm first investigated moisture ingress in organic coatings and concluded that the major driving forces for water transport through the coating were osmotic gradients .[5] Their work showed a relationship between the amount of dissolved salt in solution (expressed as osmotic pressure) and the amount of water uptake by the film (expressed as percentage weight gain). [1]As the amount of dissolved salt in the bulk solution increased, the absorption of water by the coating decreased non-linearly.[1] Kittelberger and Elm concluded that the degree of water uptake was a function of the activity of the water in solution due to differences in osmotic pressure between the bulk immersion solution and solution within the coating. [1] The decrease in the amount of water uptake with increasing salt concentration can be rationalized on the basis of simple thermodynamic reasoning. At equilibrium, the chemical potential of the water in the coating and in the bulk solution must be the same. [1]The maximum activity of water is obtained in pure water.[1] With the addition of a salt, the concentration of water in the bulk solution is decreased, decreasing its activity coefficient. Therefore, the activity of the water in the bulk solution is decreased causing the amount of water in the coating to decrease.[1] Water uptake likely occurs through hydrophilic groups in the coating and successively moves through polymer layers due to the kinetic motion of water molecules.[6] In the present work, there was more absorption of water expected in films exposed to the 0.02M feed solution than for those exposed to the 2.0M feed solution. It is possible that the absorption water carried with it hydrated Cl^-, SO_4^{2-} and Na^+ into the film. Once taken into the film, Cl^-, SO_4^{2-} and Na^+ diffused in the film by the driving force of concentration gradient, finally exiting the film and being detectable in the permeate chamber. The lower the concentration of feed solutions, the more hydrated Cl^-, SO_4^{2-} and Na^+ were carried into the film, leading to a larger concentration gradient in the film, and therefor higher fluxes into the permeate chamber. That might be the reason that

the lower the concentration of feed solution, the higher the diffusion coefficients of Cl^-, SO_4^{2-} and Na^+.

The effect of pH on the sodium transport is most likely due to competition by hydronium ion. Although electroneutrality would be maintained throughout the experiment, the higher mobility of hydronium would allow it to dominate the cation transport in the 0.02 M solution despite its slightly lower concentration. Note that in the 2.0 M concentration, there is no pH effect on sodium transport. The origin of the differing strength of the pH effect on chloride and sulfate are not clear.

SUMMARY

1. Transport measurements of ions through freestanding epoxy films have demonstrated that anion transport is increased at low pH, likely due to degradation of the polymer film.
2. Lower feed solution concentrations lead to higher apparent diffusion coefficients for all species. This effect is likely explained by increased water uptake at low feed solution concentrations that carries with it additional ions, leading to larger concentration gradients within the film and hence higher flux into the permeate chamber.
3. The apparent pH effect on sodium transport at low (0.02 M) concentration is likely an artifact of an increased transport contribution by hydronium under those conditions. At higher concentration (2 M), no pH effect on sodium transport is observed.

ACKNOWLEDGEMENTS

Technical discussions and assistance from Karen S. Ferrer, Jackie M. Williams and O.M.Schneider are gratefully acknowledged. A Multi-University Research Initiative (Grant No. F49602-01-1-0352) entitled “The Development of an Environmentally Compliant

Multifunctional Coating for Aerospace Applications using Molecular and Nano-Engineering Methods" supported this research under the direction of Lt.Col Paul C. Trulove at AFOSR.

REFERENCES

1. Jackie M. Williams, "Phenomenology of Localized Coating Failure on Copper-Containing Aluminum Alloys AA2024-T3 and AA1100-H14"(Master's thesis, University of Virginia, 2001)
2. N. R. Buenfeld,J.-Z, Zhang,Chloride Diffusion Through Surface-Treated Mortar Specimens, Cement Concrete Research, Vol. 28,No.5,pp.665-674,1998.
3. Richard F. Gunst, Robert L. Mason, How to construct fractional factorial experiments, Asqcquality press, Wisconsin, 1991,pp.17.
4. Schneider, O. M., R.G. Kelly, "In-Situ Confocal Studies of Coating Degradation",in preparation.
5. Kittelberger, W. W. and Elm, A. C., Industrial and Engineering Chemistry, 38, 695-699 (1946).
6. Hare, C. H., Protective Coatings: Fundamentals of Chemistry and Composition, Pittsburgh: Technology Publishing Co., (1994).

AUGMENTATION OF COATING FUNCTION USING HYDROTALCITES

F. Wong, H. Guan, S. Mahajanam, R.G. Buchheit

Department of Materials Science and Engineering
The Ohio State University
Columbus, Ohio 43210

ABSTRACT

This paper describes results from two related studies aimed at using hydrotalcite additives to organic coatings to impart self-healing and sensing functions without using chromium-based ingredients. The first part of the study describes the use of the structural memory effect associated with the hydration and dehydration of hydrotalcites, and how this can be used to detect water uptake in organic coatings by x-ray diffraction. The second part of the paper discusses the use of Al-Zn-vanadate hydrotalcite additives to epoxy resins. This hydrotalcite additive releases V and Zn inhibitors into contacting solutions and appear to impart a healing characteristics to organic coatings in laboratory experiments.

THE HYDROTALCITE MEMORY EFFECT AND SENSING COATNGS

INTRODUCTION

Hydrotalcites (HT) are complex crystalline compounds characterized by alternating layers of positively charged mixed metal hydroxide layers interleaved with layers of anions mixed with structural water molecules. HTs structures exhibit characteristic structural and chemical transformations when they are calcined at different temperatures. Structural changes are due to loss of interlayer water at low temperatures, loss of vaporizable interlayer anions at intermediate temperatures, and formation of metal oxides at high temperatures. Calcined HTs that are subsequently exposed to water will rehydrate and revert to their original HT structure. This phenomenon is referred to as the "structural memory effect", or more simply the "memory effect".

A specific example of this behavior is the Mg-Al-CO_3 HT compound $Mg_3Al(OH)_8 \cdot (CO_3)_{0.5} \cdot nH_2O$. At temperatures between 200° and 850°C Mg-Al-CO_3 HT decomposes to a MgO-like structure. Above 850°C, it transforms to a $MgAlO_2$ spinel. When exposed to aqueous solutions, calcined Mg-Al-CO_3 HT reverts to its original $Mg_3Al(OH)_8 \cdot (CO_3)_{0.5} \cdot nH_2O$ structure with kinetics that are influenced by the extent of structural transformation and the availability of free water.

We are using calcined HT powders dispersed in organic resins to sense water uptake as a prelude to substrate corrosion. In this section, we describe results illustrating the nature of the structural memory effect in Mg-Al-CO_3-HT. Results showing detection of water uptake in epoxy resins containing a HT additive are also presented.

EXPERIMENTAL PROCEDURES

Hydrotalcite, calcined derivatives, and coating preparation.

The Mg-Al-CO_3-HT powder was prepared using a co-precipitation methods carried out at room temperature by reacting aqueous solutions containing a mixture of $Mg(NO_3)_2 \cdot 6H_2O$, $Al(NO_3)_3 \cdot 6H_2O$, NaOH, and Na_2CO_3 in the ratio 3 : 1: 1.5 : 2. The mixture was maintained at pH 10 by dropwise addition of 1 M NaOH (1). After mixing and precipitation was completed, the resulting precipitate was aged in its mother solution at 70 °C for 24 hours. It was then filtered and washed with deionized water. The filtered precipitate was dried in an air oven at 70 °C overnight.

For calcination experiments, the synthesized Mg-Al-CO_3-HT powder was heated in air at 220 °C, 420 °C, 620 °C, 820 °C, and 1020 °C for one hour.

Sensing coatings were prepared by mixing 10 g of an epoxy resin with 2.42 g of calcined HT powder to create a loading level of 14.6% by weight. A 4.15 g aliquot of polyamide hardener

was added into the mixture, which was then stirred for 5-10 minutes. This mixture was then brush cast on to 2024-T3 sheet stock surfaces.

X-ray diffraction (XRD)

Powder XRD methods were used to detect the structural changes in the various HT samples. XRD was carried using powder techniques in a Scintag PAD-V diffractometer utilizing a Cu K_α source.

Exposure testing.

Calcined HT powders were exposed to water by immersion to aqueous solutions, exposure to humid air and exposure to aqueous solution when dispersed as an additive in the epoxy resin. For solution exposures, calcined HT powder was immersed in an 0.5 M NaCl solution overnight at ambient temperatures under gentle agitation. Humid air exposure was carried out by exposing dry calcined HT samples to flowing air humidified by bubbling through water prior to introducing it to an enclosed chamber. Exposure of coated alloys was carried out by contacting epoxy-coated surfaces to aerated 0.5 M NaCl solution. Transformation of calcined HT materials back to the hydrated form of the compound was tracked by XRD.

RESULTS

Figure 1 shows the changes in the diffraction pattern as Mg-Al-CO_3-HT is calcined at increasing temperatures. The "as-formed" pattern is derived from the fully hydrated HT structure. Calcination at temperatures between 220 ° and 820 °C, results in a pattern with three broad diffraction peaks, which are consistent with a MgO-like structure (1). Calcination at 1020 °C results in yet another distinct pattern consisting of a broad peak at about 12^o-15^o, and several sharp peaks between 20^o and 70^o. This pattern is consistent with a $MgAl_2O_4$ spinel structure.

Upon exposure to aqueous solution, the XRD patterns of calcined HTs exhibit distinct changes indicating structural alterations. Figure 2 shows the XRD patterns of calcined powders after immersion in 0.5 M NaCl solution for times indicated in the figure. The 100% peak for Mg-Al-CO_3 HT, which occurs at about 12^o, is clearly evident in the patterns of materials calcined at 220°C to 820°C. Diffraction peaks appear to be sharper, and the fully hydrated HT pattern is reproduced with greater fidelity for powders calcined at lower temperatures. The pattern from the material calcined at 1020^oC has changed from the $MgAl_2O_4$ spinel pattern, but does not show strong characteristics of HT even though it was exposed to solution for 9 days. The pattern from the powder calcined at 620^oC has two sharp peaks at about 32^o and 46^o not associated with HT. These peaks are also apparent in the pattern from the 1020^oC sample.

Exposure of calcined HTs to humid air also triggers the memory effect. Figure 3 shows XRD patterns for HT powders calcined at various temperatures, which are indicated in the figure. The duration of exposure is also indicated in the figure. Similar to the NaCl solution experiment, the diffraction pattern of fully hydrated HT is recognizable in HT powders calcined at 220 °C to 820 °C. The HT sample calcined at 1020 °C is much more resistant to reversion. This sample was exposed in the chamber for 7 days, but the sample still retains a pattern characteristic of the $MgAl_2O_4$ spinel. The broad peak at 10 to 25 degrees appears to be more intense than that of the other peaks, unlike the pattern for the material in its as-calcined form (Figure 1). This may indicate the onset of a sluggish structural transformation.

Figure 4 shows XRD patterns collected from epoxy coatings containing HT powders calcined at 220^oC, which were exposed to 0.5M NaCl solution. Structural changes in the calcined HT additive are apparent, but reversion to fully hydrated HT is not as clear as in solution or humid air exposures shown in Figs. 2 and 3. The 100% reflection of HT at about 12^o is

detectable superimposed on a broader reflection. A HT reflection at 35^{o} is also detectable. The strong reflection at 22^{o} appears to be masked by the diffuse background. Peaks at 39^{o}, 60^{o} and 62^{o} are absent.

CORROSION RESISTANCE AND SELF-HEALING OF Cr-FREE PRIMER COATINGS

INTRODUCTION

Hydrotalcite-like compounds (HT), so-called "anionic clays" are layered double hydroxides with the general formula $[M_{1-x}M'_x(OH)_2]^{x+}(X)_{x/m}.nH_2O$, where M=Zn(II), M′=Al(III) and X=$[V_{10}O_{28}]^{6-}$ (decavanadate) for this particular HT. The synthesis approach adopted here was co-precipitation in the presence of the pillaring anion ($V_{10}O_{28}^{6-}$).

In this section, we report on experiments aimed at demonstrating corrosion resistance and healing characteristics in epoxy primers containing Zn-Al hydroxide-vanadate hydrotalcites (HT-V). In this primer, healing characteristics are to be derived from anion exchange of chloride for oxyvanadate embedded in the hydrotalcite anion layer. We are using a simulated scratch cell combined with in situ electrochemical impedance spectroscopy, solution analysis and x-ray microchemical analysis to determine if characteristics of high corrosion resistance and self-healing are being exhibited.

EXPERIMENTAL PROCEDURES

HT-V Synthesis

HT-V samples were prepared using a co-precipitation method involving a vanadate precursor solution, and a precursor solution containing Al and Zn cations.

The vanadate solution was prepared by mixing 80g $NaVO_3$ with 2000ml DI water. The solution was stirred overnight for complete dissolution then filtered to remove any solid

contaminants. The solution was then acidified by addition of 2M HCl until the development of an orange coloration was noted. This occurred at a pH of about 4.5 and indicated the formation of the decavanadate ion $V_{10}O_{28}^{6-}$, which was the desired anion species for this particular synthesis. The decavanadate ion is the terminal species in vanadate polymerization at pH 4.5 (2).

The Al-Zn precursor solution was made by mixing 53.6g $ZnCl_2$ with 47.2g $AlCl_3 \cdot 6H_2O$ in 1000 ml DI water.

The vanadate precursor solution was neutralized to a pH of 6.5 with NaOH. Decavanadate is metastable in solutions up to pH 6.5 because of its slow reaction to metavanadate, which is the stable species in neutral solution. Neutralization does not lower the concentration of decavanadate over the time intervals of this synthesis.

The Zn-Al precursor solution was then added with mixing to the vanadate precursor solution slowly using a burette. NaOH additions were made to keep the pH within 0.1 pH units of 6.5 during the mixing of solutions. Addition of the Zn-Al precursor solution induced the formation of a solid precipitate. Once the Zn-Al precursor solution was consumed, the temperature of the mixture was elevated to 55^oC where it was held overnight.

The solid was filtered and washed until rinse solution, added to 5% $AgNO_3$ solution, no longer induced AgCl precipitation. Finally, the solid was washed with methanol to remove excess water. This process yielded a solid cake that was dried in the oven at 40^0C for 1-2 days. After drying, the cake was ground to a fine powder using a hand grinder. This was followed by ball milling with methanol for 1-2 days. The powder was dried in an oven at 40^0C for 1-2 days before any further use.

Primer coat preparation and application

Epoxy HT-V primers were prepared by mixing 10 g of epoxy resin with 6 g of HT-V powder until an even mixture was produced. Immediately prior to coating, 4.2 g of amine curing agent was added with stirring. Coatings were applied to 2mm thick 12" x 12" 2024 – T3 substrates using a rolling bar (#9). The substrates were prepared for priming by degreasing for 2 minutes in a solution consisting of 32.4g/L Na_2SiO_3 plus 48g/L Na_2CO_3 held at 65^0C. Sample surfaces were then deoxidized for 3 minutes by immersion in a solution consisting of 30g/L Sanchem 1000 plus 72mL/L HNO_3 held at 55^0C. After coating, primed surfaces were air dried overnight. Coating thicknesses ranging from 15 to 20μm were produced by this process. The resulting primer coatings that were deep yellow in appearance.

The simulated scratch cell and electrochemical testing

The simulated scratch cell consist of two surfaces separated by about 5mm with a rubber O-ring. One surface was primed with the HT-V primer; the other was bare simulating a defect. The cell permits examination for release of active agent from the coating into solution, deposition of the active agent on the defect, corrosion resistance of the simulated defect, and corrosion resistance of the original coating (3). The exposed area in the cell was 12.5cm^2 per cell side. The assembly was held together by compressing the O-ring between the two plates using nylon nuts and bolts. The cell was filled with 0.5M NaCl solution. The cell was also fitted with a Pt wire counter electrode and a port for a reference electrode so that three electrode electrochemical measurements could be made in situ. During operation, the cells were kept full and were agitated to prevent solution deaeration. The simulated scratch cell is shown in Figure 5.

Electrochemical Impedance Spectroscopy (EIS) was carried out on both the coated and uncoated sides of the simulated scratch cell. Spectra were collected from 100 kHz to 10 mHz on

the bare and coated sides of the cell using a 10 mV sine wave voltage signal. Spectra were interpreted using appropriate equivalent circuit models, or by inspection of data in Bode plots.

Solution analysis

Solutions were periodically extracted from the simulated scratch cells and were subject to chemical analysis by inductively coupled plasma-optical emission spectrometry (ICP-OES). Solution analysis was conducted to check for Zn and V leached from the primer into solution. The detection limit for these elements was 0.05 parts per billion (ppb).

Scanning Electron Microscopy (SEM) and Energy Dispersive Spectroscopy (EDS)

SEM was used to image the corroded AA2024-T3 surface and EDS helped in indicating the presence of zinc and vanadium on the bare surface.

RESULTS

Figure 6 shows the results of ICP-OES solution analysis on aliquots of electrolyte removed from the simulated scratch cell as a function of exposure time over 200 h. Soluble vanadium and zinc are detected in increasing concentrations up to 150 hours. Concentrations are in the part per million (ppm) levels with about twice as much V as Zn detected. For comparison, V and Zn release from vanadium conversion coatings are also reported. Vanadium was not detected above the instrumental limits of 0.05 ppb in control samples taken from solution in contact with bare 2024-T3. Zn was detected in control samples at concentrations up to 1.5 ppm. This probably resulted from alloy dissolution.

Figure 7 shows results from SEM and EDS illustrating the presence of Zn and V on the surface of bare 2024-T3, which served as the simulated defect in the simulated scratch cell experiments. Figure 7a shows a micrograph of the sample surface. This is characterized by many

small shallow pits and localized deposits of surface product. EDS of this surface product reveals trace concentrations of Zn and V as indicated in Figures 7b and c. EDS is not a particularly good method for surface analysis, but is it suitable for screening purposes. Detection limits for EDS operated in the manner used here are about 1 atomic percent. Neither Zn or V are present in the substrate at these concentrations, hence the positive indications for these metals implies that they were leached from the primer into the cell solution and deposited on the metal surface.

Figure 8 illustrates EIS responses collected from in situ simulated scratch cell testing. Figure 8a shows Bode magnitude and phase angle data collected from the primed side of the cell. Spectra are plotted representing the EIS response after 3, 216 and 432 hours of exposure. The spectra reveal an impedance response dominated by a coating capacitance at high frequencies, and a pore resistance at lower frequencies. A small portion of the capacitive response associated with defects is apparent at the lowest measured frequencies. The phase angle also shows that coating capacitance dominates at high frequencies and pore resistance dominates at lower frequencies. Over the exposure period, the pore resistances decreases as might be expected, as indicated a decrease in corrosion protection with increasing exposure time.

Figure 8b shows the EIS response of the bare side of the cell over the same exposure period. This side represents a bare metal defect. A solution resistance is detected at the highest measurement frequencies in this case. At intermediate frequencies, capacitance associated with the oxide film and incipient defects is observed. At the lowest frequencies an impedance response consistent with diffusion is observed. Over the course of the experiment, the total impedance of the bare surface increased as might be expected if vanadate and Zn species from the primer inhibited localized corrosion. In control experiments where the primer coated side of

the cell was replaced with a bare 2024-T3 surface, or a thick polyurethane coating was applied over the primer, no increase in corrosion resistance was detected.

Figure 8c shows the variation in pore resistance, R_p, of the coated side of the cell and the total impedance of the bare side of the cell, R_c, as a function of time. R_p decreases slightly from 2 to 1 Mohm·cm^2 over the 450-hour duration of the exposure. The impedance of the bare side increases by about an order of magnitude from its lowest to highest value during the exposure period. The greatest R_c values attained are about 0.4 Mohm·cm^2. This trend in behavior is consistent with the action of low concentrations of soluble inhibitors leached from the primer coating.

SUMMARY

Results from the first part of this study show that calcination of Mg-Al-CO_3 HT induces two distinguishable structural transformations. A transformation to material with a MgO-like structure occurs during calcination at 220°C to 820 °C. Transformation to a $MgAl_2O_4$ spinel occurs during calcination at 1020^{o}C. Exposure of calcined HTs exhibiting an MgO-like structure to an aqueous solution or humid air will cause reversion to fully hydrated HT. XRD reveals clear evidence of this transformation. Transformation of the spinel structure to hydrated HT has not been detected. Calcined HT powders have been dispersed in epoxy resins and applied to Al alloy surfaces. When coated surfaces are exposed to aqueous solutions structural transformation of the calcined to HT additive can be detected by XRD. This result opens the possibility of using HTs as additives for sensing the uptake of water as a prelude to undercoat corrosion.

Results from the second part of this study show that epoxy primers containing a 30 % Zn-Al-vanadate hydrotalcite additive provide corrosion protection to underlying substrates during exposure to chloride solutions. In simulated scratch cell experiments, evidence suggests that

these coatings can also heal defects. Specifically, Zn and V ions are detected in cell solutions indicating leaching. Zn and V are detected on the bare side of the cell suggesting that the interact with that surface. Finally the corrosion resistance of the bare side of the cell increases with exposure time in a manner suggesting that Zn and V slow localized corrosion.

ACKNOWLEDGEMENTS

Support for this work from the Air Force Office of Scientific Research is gratefully acknowledged.

REFERENCES

1. F. Millange, et al., J. Mater. Chem., 10, 1713 (2000).
2. J. Livage, Solid State Ionics, 86-88, 935 (1996).
3. J. Zhao, R. McCreery, G. Frankel, JES, 145, 2258 (1998)

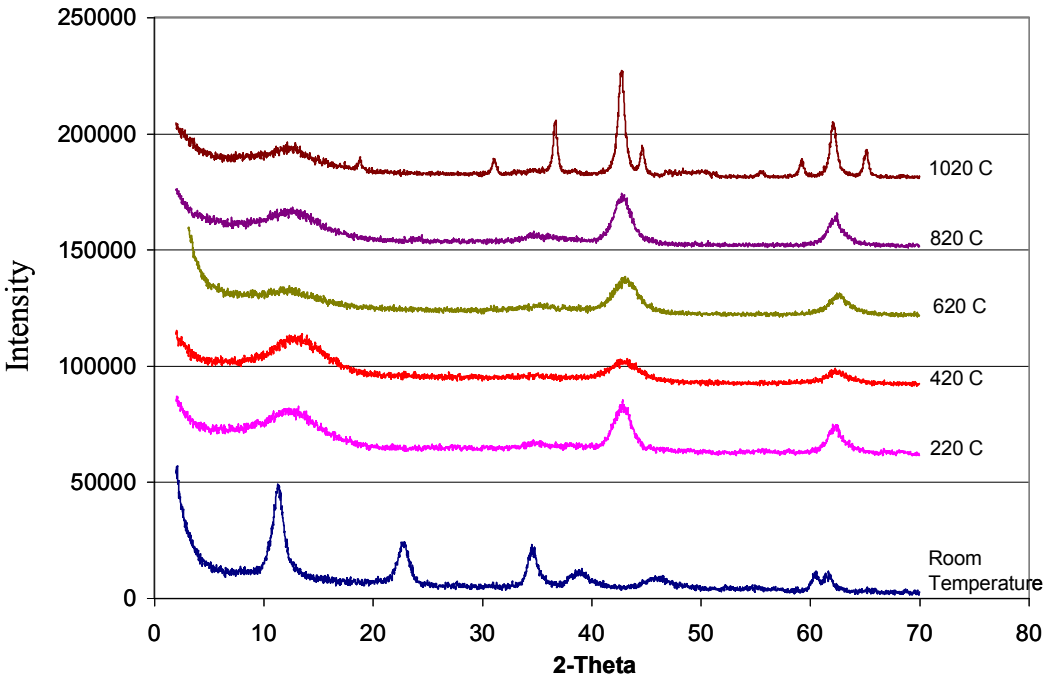

FIGURE 1. XRD patterns of HT calcined at different temperatures.

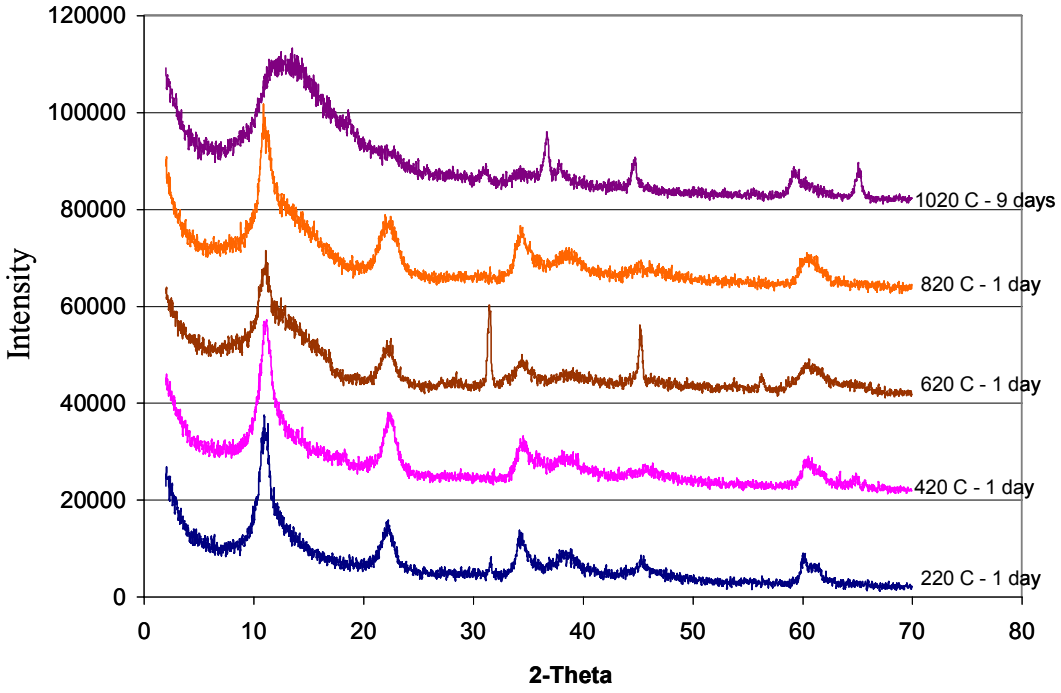

FIGURE 2. XRD patterns of HT immersed in 0.5 M NaCl

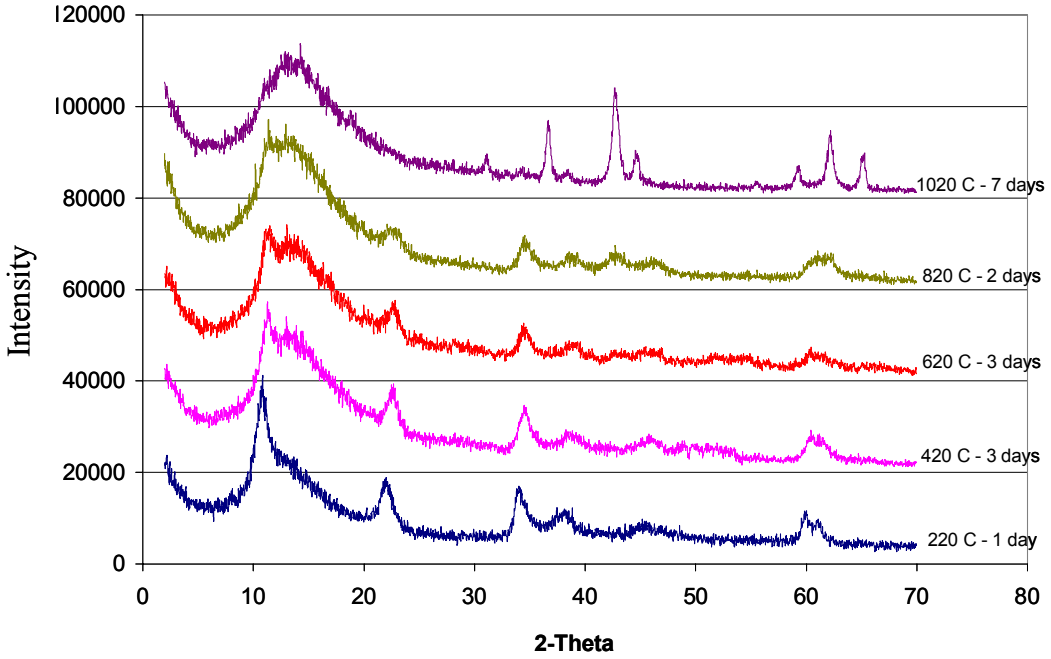

FIGURE 3. XRD patterns of HT put in a humid air chamber.

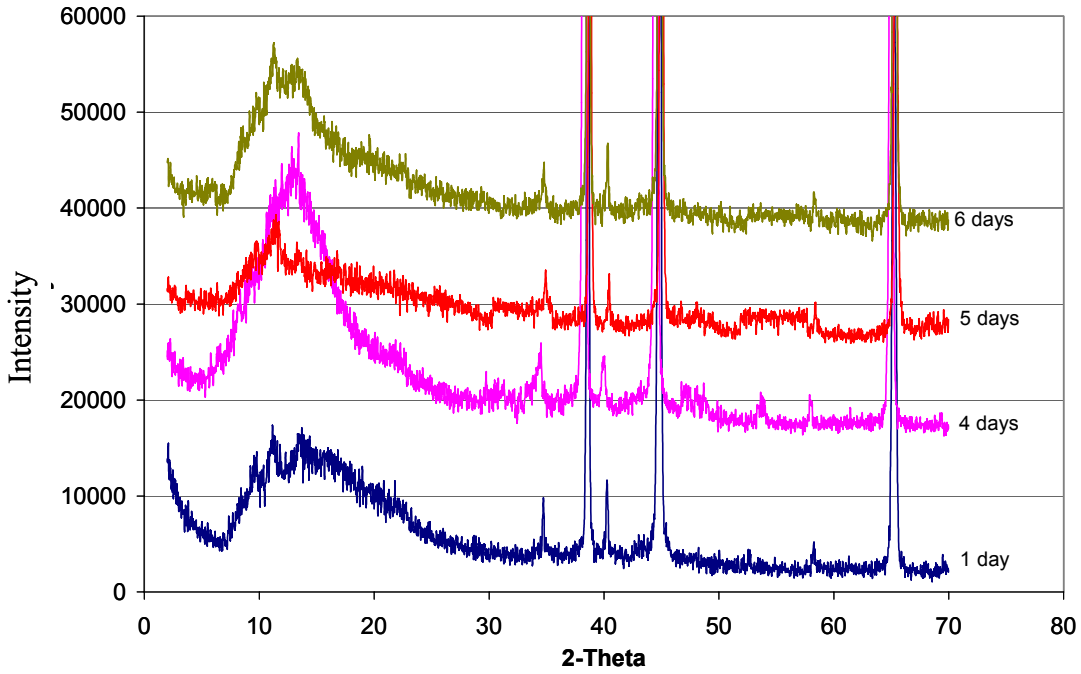

FIGURE 4. XRD patterns of HT applied as coating on 2024-T3 immersed in 0.5 M NaCl.

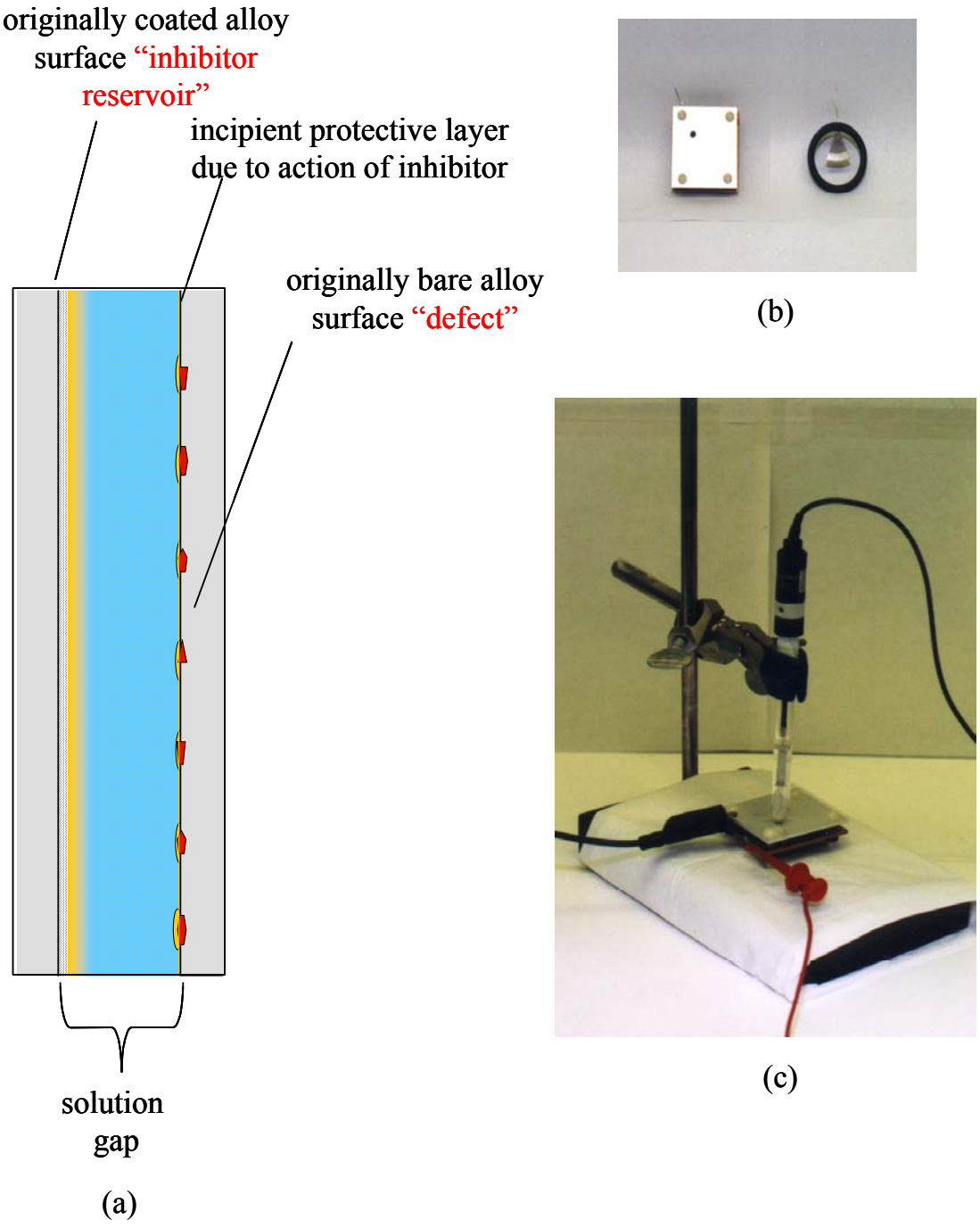

FIGURE 5. The simulated scratch cell. (a) Cross section illustration, (b) the assembled cell and Pt counter electrode inserted through the rubber O-ring, (c) the assembled cell with reference electrode.

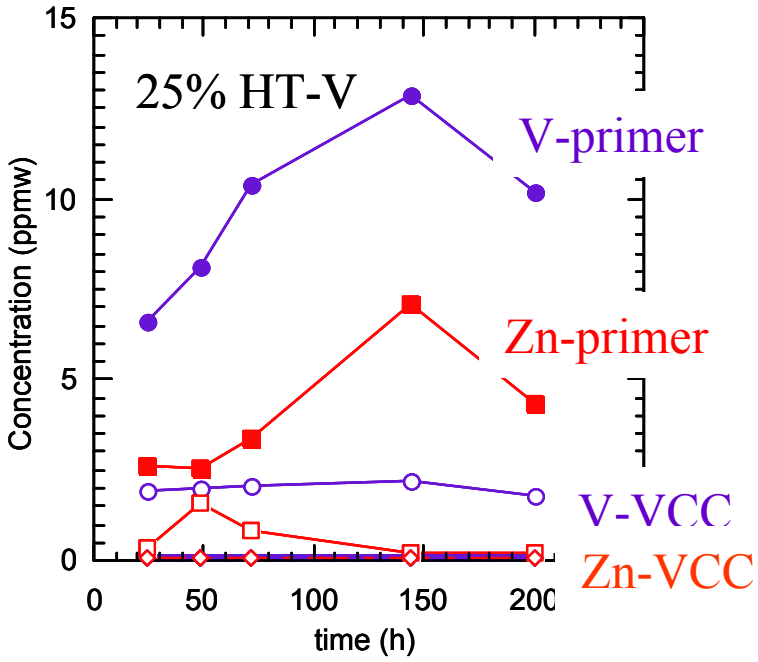

FIGURE 6. Concentrations of V and Zn determined by ICP-OES of solutions extracted from simulated scratch cell experiments.

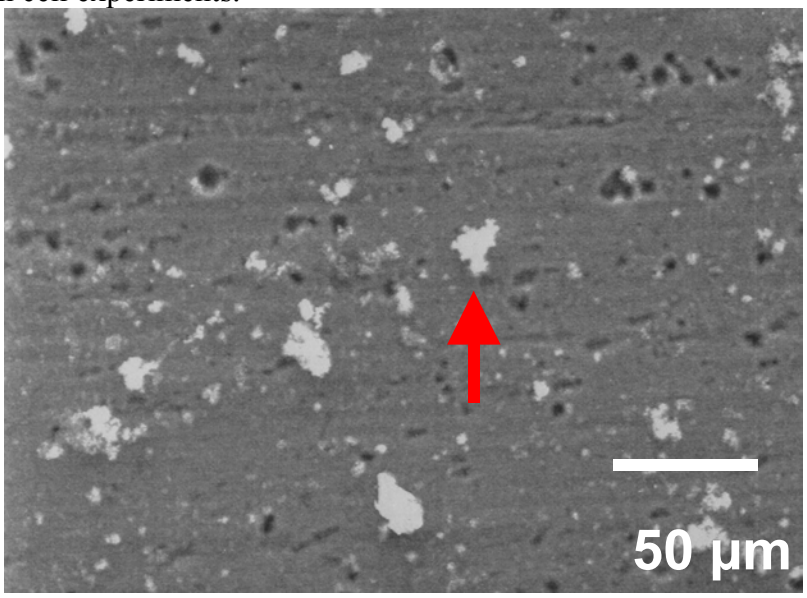

FIGURE 7a. SEM of a bare 2024-T3 surface exposed in a simulated scratch cell. The arrow indicates surface product analyzed by EDS.

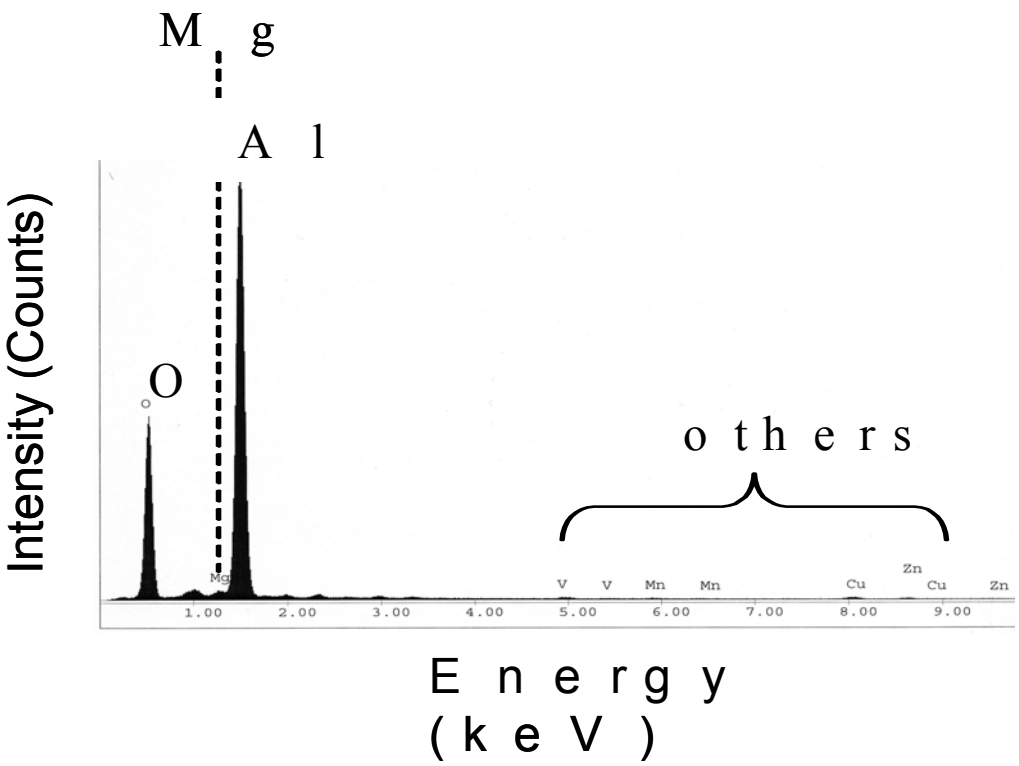

FIGURE 7b. Full EDS spectrum from the surface product particle in Fig.

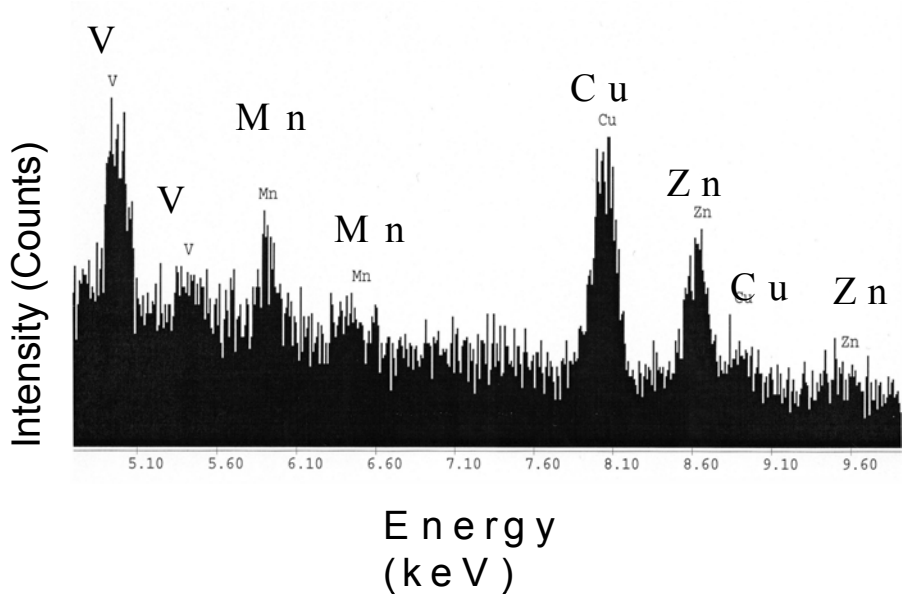

7a.

FIGURE 7c. EDS spectrum showing the V and Zn Ka characteristic peaks in the spectrum in Fig.7b.

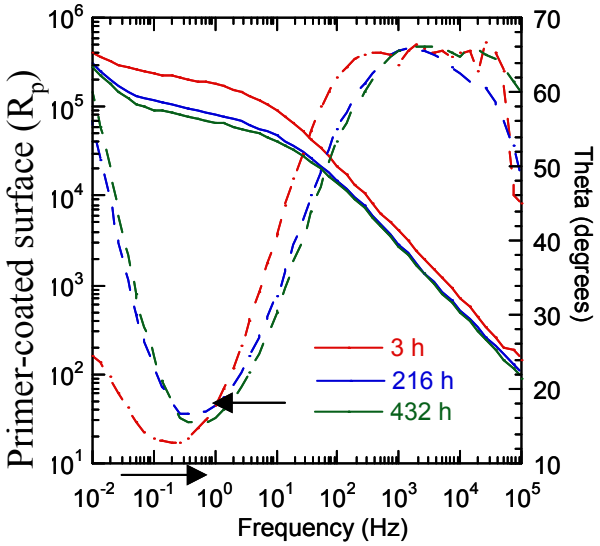

FIGURE 8a. Bode plots from the coated side in a simulated scratch cell experiment.

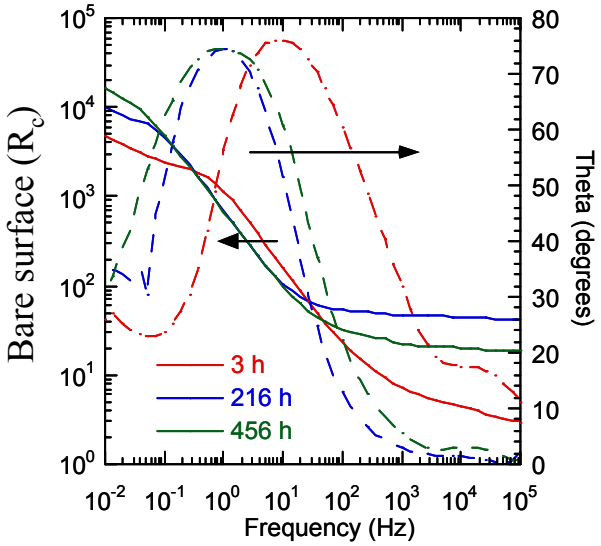

FIGURE 8b. Bode plots from the bare side in a simulated scratch cell experiment.

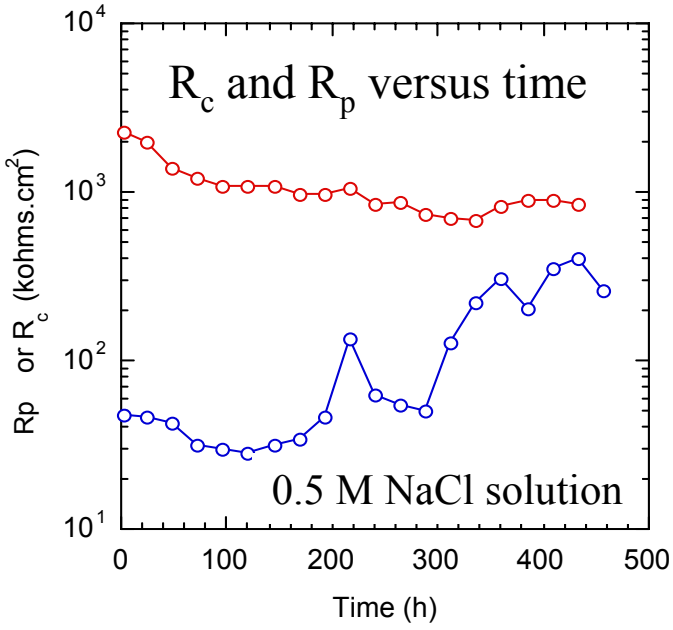

FIGURE 8c. Pore resistance, Rp, from the coated side, and total impedance, Rc, from the bare side of a simulated scratch cell plotted as a function of exposure time. The cell contains 0.5 M NaCl solution.

THERMAL SPRAYED ALUMINUM ALLOY CLADDING FOR AIRCRAFT SKIN REPLACEMENTS

B.J. Connolly, A.L. Moran
Department of Mechanical Engineering
United States Naval Academy
Annapolis, MD 21402

R.L. McCaw, J. Pugh
Naval Surface Warfare Center - Carderock Division C615
West Bethesda, MD 20817

K. Scandell
NAVSEA – Philadelphia C9733
Chesapeake, VA 23320

ABSTRACT

Although universally used, commercially available roll bonded aluminum claddings have limited corrosion fatigue performance in military applications. The goal of this effort, which is part of an Air Force MURI program to develop next generation multi-functional coating systems, is to replace these current claddings with a thermally sprayed aluminum or aluminum alloy coating. Specifically the new thermal sprayed cladding would be used to increase the corrosion fatigue lifetime of the aircraft skin. Thermally sprayed amorphous/nano-crystalline materials are desirable due to their ability to supersaturate desired alloying elements to produce superior corrosion performance as well as high strength, ductility, and wear resistance. The application of the thermal spray can be tailored to place the metal substrate in compression for improved fatigue resistance. Aluminum based metals will be thermally sprayed in air from powder stock on AA2024 thin sheet using several techniques including flame-arc, plasma, and HVOF spraying. In the first stage of this program the effect of compressive stresses introduced by thermal sprayed layers on fatigue life in ambient lab air will be investigated. Bending fatigue specimens of AA7075-T6, AA2024-T3 will be used as a control for comparison to AA2024-T3 specimens coated with thermally sprayed 99.0-99.8 wt% pure aluminum, and to conventional AA7075-Alclad, and AA2024-Alclad systems. Future stages of this project will investigate the effects of thermal sprayed coatings on corrosion fatigue lifetime as well as incorporating the use of exotic aluminum alloy systems (e.g., cerium additions) aimed at developing a multi-functional thermal sprayed coating system. This paper will discuss the advantages and disadvantages of the different thermal spray methods for producing advanced coatings as well as progress to date with the program.

INTRODUCTION

Atmospheric corrosion and subsequent localized corrosion in occluded geometries (i.e., intergranular corrosion, exfoliation, stress corrosion cracking, corrosion fatigue) play a dominant role in the structural integrity and lifetime of aircraft components. Decreased safety and increased operating costs are particularly detrimental and prohibitive in the case of an aging aircraft fleet. The total annual corrosion costs in the U.S. aircraft industry in maintenance, failures, and lost work hours have been estimated at billions of U.S. dollars.[1] More importantly, the safety risk due to corrosion was emphasized as a result of the Aloha Airline incident in 1988, where an aircraft operating over a saltwater environment lost a large section of its fuselage due to corrosion fatigue, resulting in the death of one crew member.

Corrosion is also a major concern and cost factor in the maintenance and operation of military aircraft. Exposure tests on board aircraft carriers have shown that the operating environment due to the combination of humidity, temperature, salt spray, and sulfur dioxide from carrier stack gases and the aircraft exhausts is extremely corrosive.[2] In many cases the maintenance hours due to corrosion for military aircraft is equal to or exceeds the actual flight hours logged.[3]

One of the most common and widely used corrosion mitigation methods used to protect aircraft components (i.e., skin, wing spars) in these environments is to metallurgically hot roll-bond a thin, electrochemically anodic layer of either pure aluminum or a binary aluminum alloy to either one or both sides of the structural component (usually an aluminum alloy in plate or sheet form). The clad material[(1)] not only provides an effective barrier to corrosive environments but also will preferentially corrode along bare edges, scratches, or corrosion sites that have

[(1)] The clad layer forms the base layer of a multi-component coatings system used for corrosion mitigation on military aircraft.

locally eliminated the clad material. Due to the electrochemical nature of the resultant galvanic couple the cladding will cathodically protect the substrate or inner core of material. The open circuit potential of the candidate clad material compared to that of the substrate or core material is the governing factor used to select material for the clad application. Pure aluminum is electrochemically anodic to Al-Cu alloys in the T3 or T4 temper and therefore is predominately used to clad 2XXX series aluminum alloys while an Al-1%Zn binary alloy is used to clad 7XXX series aluminum alloys due to their increased anodic nature compared to pure aluminum or 2XXX series alloys.[4]

Although the clad systems of 2XXX and 7XXX series aluminum alloys have proven to be an adequate corrosion protection system, the nature of the manufacturing steps required to produce them is not conducive to easy repair or refit. It is common practice to simply remove the clad material local to the damaged section of the aircraft. This, in effect, locally deprives a layer of corrosion mitigation to the structural element of the airframe. Furthermore, the nature of the manufacturing process limits the ability to use a cladding system on parts with complex geometries such as those found in many castings and extrusions. One option would be to replace the clad layer from the overall corrosion protection system with a more versatile metallic thermal sprayed coating[(2)] that could be easily applied and repaired in the fleet or at repair depots. Thermal spray technology has been offered as a global tool to achieve cost-effective preservation, condition-based maintenance, and restoration strategies for the Naval community.

Thermal spray aluminum technology has been proven to provide more than 20 years of maintenance-free service in the marine environment and can now be applied at a cheaper cost than traditional painting.[5,6,7] The U.S. Navy has been applying thermal sprayed aluminum

[(2)] In some cases highly corrosion resistant amorphous or amorphous/crystalline coatings may be produced.

coatings to high-corrosion areas aboard ships and to dry-dock facilities for over 15 years.[(3),8] Actual field applications, such as on weather decks, oil tanks, bilge tanks, freshwater tanks, fuel tanks, and steam valves, of aluminum coatings on steel substrates are testament to the success of the technology.[5]

Britain's military and aviation industries have also had experience with the use of thermal spray technology for corrosion mitigation, especially in the use of thermally sprayed sacrificial and barrier aluminum coatings on high-strength aluminum alloy components. Electrochemical and mechanical studies have been performed detailing the increased resilience to atmospheric corrosion and stress corrosion cracking of thermal spray coated Al-Cu-Mg alloy extrusions, Al-Zn-Mg extrusions, and Al-Mg castings[9] as well as the increased resilience to exfoliation and stress corrosion cracking of thermal spray coated, welded Al-Zn-Mg alloy plate.[10]

THERMAL SPRAY TECHNIQUES

Thermal spray is a generic term for a group of processes in which low to high melting point metals and alloys, ceramics, and some polymeric materials in the form of powder, wire, or rod are fed into a torch or gun with which they are heated to near their melting point. The resulting molten or semi-molten particles are accelerated in a gas stream and projected in a line-of-site manner against the surface of the substrate to be coated. On impact, the semi-molten

---

[(3)] Thermal Spray was introduced in the U.S. Navy in the mid-1940's as a means of conducting limited repairs on machinery components. Although this technology provided promise of a new repair medium, the expanded use was not fully explored until the late 1970's. It was not until 1981, when Military Standards/Quality Assurance Standards for thermal spray were developed and implemented under MIL-STD 1687. This standard was revised (MIL-STD 1687A) and has been further updated for a commercial American Welding Society standard (AWS C2.XX/99) that contains Navy unique definitions and requirements as an addendum. Intermediate Maintenance (IMA) within the Navy adopted this process of machinery repair in 1990 as the Machinery Equipment Repair and Restoration (MERR) process. MERR employs powder and wire flame spray technology. Currently thermal spray processes in the U.S. Navy comply with MIL-STD 1687A (MERR) and DOD-STD 2138 (Corrosion Control).

particles flow into thin, lamellar splats[4] adhering to the surface, overlapping and interlocking as they solidify.[5] A schematic representation of a thermal sprayed coating would be akin to a brick wall structure, where splat structures are entwined in complex arrays. Total coating thickness is usually achieved via multiple passes of the thermal spray device (please see Figure 1).[11,12,22,13]

The physical properties of the thermal spray coatings are principally dependent on the particle impact conditions, specifically the impact velocity and particle temperature. Substrate roughness and wetability also play important roles.

The chemistry of the deposited coating is largely determined by the composition of the feedstock (i.e., powder, rod, wire). The bond between the coating and the substrate is predominately mechanical with minimal to no chemical interaction at the interfacial layer.[6],[12] The integrity of the deposited coating is determined by three additional factors: 1) oxide content, 2) porosity, and 3) interfacial bond strength between the coating and the substrate as well as between individual splats.[11] These factors are dependent on the process parameters of the individual thermal spray techniques. The desired end-result coating characteristics define the criticality of the three factors and therefore the thermal spray technique selected for the application. Moreover, the deposition process/parameters of the thermal spray technique itself can substantially effect the structure of the coating. As a result, microstructures and properties of thermal sprayed coatings can be extremely varied. Therefore, detailed specification for a desired

---

[4] Splats result from impact, spreading, and rapid solidification of a high flux (millions of particles per cm^2/sec) of semi-molten particles ranging in size from 10-100 μm.

[5] The layered splat-based microstructure leads to intrinsic anisotropic properties in the direction perpendicular to the spray direction.

[6] The mechanism of bonding associated with a thermal spray coating to a substrate is not well understood but is thought to be due to mechanical interlocking of the solidifying and shrinking splats. Some interdiffusion of thermal spray coatings with the substrate has been observed in a few instances with unique combinations of material. There is also some evidence of chemical bonding in some coating/substrate systems due to the rupture of surface films on either the powder particles or the substrate resulting from the high-velocity impact associated with thermal spray techniques.

coating must include much more than just the composition of the starting powder or rod and the general type of thermal spray technique to be used.

Three of the most commonly used, commercially available thermal spray techniques include combustion flame spray, plasma spray, and high-velocity oxy-fuel (HVOF) spray. Each of the three techniques has distinct operating parameters and resulting characteristics. A summary of operating parameter is detailed in Table 1 and a brief description of each thermal spray technique is given below.

TABLE 1. Application Characteristics of Thermal Spray Techniques

Spray Process	Feed type	Flame/Arc Temperature (K)	Particle Velocity (m/sec)	Bond Strength (MPa)	Degree of Porosity (%)	Oxide Content (%)
Combustible Flame	powder	3000-3500	30-90	15 (ceramic) 30 (metal)	5-20	< 15
Plasma	powder	3500-14,000	500-650	15-25 (ceramic) 70 (metal)	1-7	< 7
HVOF	powder	3000-3500	850-1000	up to 90	< 1	< 5

FLAME SPRAY[(7)]

The flame spray technique uses combustible gases (i.e., acetylene, propane) mixed with oxygen as a heat source to melt and transport the coating material that may be in the form of powder, rod or wire. The gas inlet of a flame spray torch is usually axial with the powder feed introduced axially or perpendicular to the flame. The particles are melted in the flame and accelerated in the direction of the substrate to be coated. The flame spray technique is characterized by low capital investment, high deposition rates and efficiencies, relative ease of operation, and low cost of equipment maintenance.[12,22]

Typical process parameters for the flame spray technique are as follows. The flame temperature is in the range of 3000-3500 K while the flame velocity is usually between 80-100

(7) Invented by M.U. Schoop in 1911.

m/s. Powder particle sizes used in the flame spray process range from 5-100 μm. Spraying is usually performed in air at a distance of 120-250 mm with the powder feed rate on the order of 50-100 g/min and a transport gas flow rate of 3-5 Nl/min.[22]

Typical values for coating bond strength range from 15 MPa for ceramic coatings to 30 MPa for metallic coatings. Porosity is in the range of 5-20% and typical thicknesses are in the range of 100-2500 μm.[22]

The flame spray process produces low performance coatings when compared to other thermal spray techniques and are not usually employed when a high density, well-bonded coating is desired. Flame spray coatings exhibit lower bond strengths and higher porosity than most other thermal spray techniques.[12] The low performance is attributed to characteristic low flame velocity as well as low particle temperature achieved within the combustion flame.

ATMOSPHERIC PLASMA SPRAY[(8)]

Plasma spraying is achieved by utilizing a torch that sustains an electric arc within an inert gas between a tungsten cathode and a water-cooled copper anode. The arc ionizes the gas creating an high-pressure gas plasma. The resulting increase in gas temperature for a typical DC torch operating between 30 and 80 kW, in turn, increases the volume of the gas and, consequently, the gas pressure and velocity as it exits the torch nozzle. Coating powder is introduced at the hottest part of the flame at the torch exit where it is heated and accelerated by the plasma gas stream toward the substrate. The molten particles impact the substrate and are rapidly solidified at an approximate rate of 10^6 K/sec. Torch design is critical in determining the temperature and velocity achieved by the powder particles. Critical operating parameters include gas flows, power levels, powder feed rate, carrier gas flow, and standoff distance from the torch

[(8)] Invented and patented by R.M. Gage, O.H. Nestor, and D.M. Yenni in 1962.

to the substrate. An adequate standoff distance is required for the powder particles to achieve the necessary heat and velocity. Too great a standoff distance will allow the powder particles to cool and lose velocity. Powder size and variance also affect the heating and acceleration of the particle and therefore the quality of the coating. Powders with a tighter size distribution results in improved deposition efficiency and therefore higher quality in coatings.[12]

Typical process parameters for the plasma spray technique are as follows. The plasma temperature is on the order of 14000 K while the exit velocity at the plasma gun nozzle can reach 800 m/s or higher. Generally, higher particle velocities and temperatures above the melting temperature, but without excessive superheating, yield coatings with the highest densities and bond strengths. Powder particle sizes used in the flame spray process range from 5-100 μm. Spraying is usually performed in air at a distance of 60-130 mm with the powder feed rate on the order of 50-100 g/min and a transport gas flow rate of 3-10 Nl/min.[22]

Typical values for coating bond strength range from 15-25 MPa for ceramic coatings to 70 MPa for metallic coatings. Porosity is in the range of 1-7% and typical thicknesses are in the range of 50-500 μm.[22]

Plasma spray is predominantly used when applying thermal barrier coatings via a thermal spray technique. Plasma temperatures are sufficient to melt all materials and consequently plasma spray systems are routinely used to deposit oxide-based coatings. Plasma sprayed coatings have also seen widespread anti-corrosion applications in the transportation,[14] aerospace,[15] and aircraft industry.[16]

HVOF SPRAY[9]

The HVOF thermal spray technique is based on a novel variation of the combustion flame spraying technique. The improved coating properties are a result of a special torch/nozzle design. Fuel gas such as propylene, propane, or acetylene is mixed with oxygen and burned in a chamber. The products of this combustion are then allowed to expand through a specially designed nozzle where gas velocities can approach Mach 4. Powder is introduced axially in the nozzle where it is fully or partially melted and accelerated toward the substrate at supersonic speeds. Upon impact onto the substrate, the molten particles form very thin splats that bond strongly to the substrate and/or to any other splats in the vicinity.

Typical process parameters for the HVOF spray technique are as follows. The fuel gas flame temperature is in the range of 3000-3500 K while the exit velocity of the exhaust jet is about 2000 m/s. Powder particle sizes used in the flame spray process range from 5-40 μm. Spraying is usually performed in air at a distance of 150-300 mm with the powder feed rate on the order of 20-80 g/min.[22]

Typical values for coating bond strength can be as high as 90 MPa. Porosity is lower than 1% and typical thickness is in the range of 100-300 μm.[22]

The advent of the HVOF thermal spray technique has yielded fully dense high performance coatings. HVOF provides a very flexible coating system for most substrates. Industry has used HVOF extensively for over 15 years for manufacturing and repair, superior coating wear characteristics and corrosion mitigation and is predominately used as an alternative to hard chrome plating.

---

[9] Invented and patented by G.H. Smith, J.F. Pelton, and R.C. Eschenbach in 1958.

FATIGUE PERFORMANCE OF THERMAL SPRAY COATED METAL: INDUCED RESIDUAL STRESSES

Although corrosion protection is the primary task assigned to thermal spray coatings, the effect of the thermal sprayed coating on the physical properties, primarily the mechanical properties, of the substrate material must be documented and understood. Of particular importance in aerospace applications is the effect of thermal sprayed coatings on the fatigue lifetime of the substrate component.

Alternative corrosion mitigation systems such as anodization, sacrificial hot-rolled bond cladding,[17] and chrome plating[18] result in a loss of fatigue life in air of a coated material.[(10)] Drastic reduction of the fatigue life of components was observed due to cracking that initiated in the coating and penetrated into and propagated through the substrate material.

Fatigue crack initiation is a surface phenomena associated with the residual stress levels near the surface of a component.[19] Compressive residual stresses have been shown in high strength steels to increase the number of cycles to failure due to a mean stress effect.[20] A study comparing residual stress states of WC coated AA6061 showed that increased compressive residual stresses in the substrate surface at the coating/substrate interface will increase the fatigue lifetime of the component.[21] Results revealed that a HVOF coated component with a coating/surface interfacial compressive residual stress of 500 MPa has a fatigue lifetime 9 times that of HVOF coated component with a coating/surface interfacial compressive residual stress of 80 MPa and that a HVOF coated component with a coating/surface interfacial compressive residual stress of 760 MPa has a fatigue lifetime 34 times greater.[(11)]

[(10)] Although these corrosion mitigation systems reduce the fatigue life of a component in air, anodization and chrome plating increases the corrosion fatigue life of components exposed to aggressive aqueous environments.
[(11)] It should be noted that none of these three HVOF coated AA6061 specimens achieved the fatigue life of an uncoated specimen.

Some form of residual stresses will be present within a thermal spray component due to the inherent high temperatures associated with most thermal spray techniques and the possible differences in the coefficients of thermal expansion between the coating and the substrate. In order to understand the fatigue lifetime behavior of a thermal spray coated component, the nature of the residual stresses within the component must be known. Residual stresses due to the thermal coating application can be resultant of the following factors: 1) quenching stresses, generated during solidification of the lamella, 2) stresses generated during deposition during one pass of the thermal spray torch, 3) cooling stresses, generated in the coating and substrate while the sprayed specimen cools, and 4) phase transformation stresses, generated in the sprayed coating or substrate during spraying.[22]

EXPERIMENTAL PROCEDURE

The main objective of this paper is to investigate the effect of the application of corrosion mitigating coatings (i.e., hot roll-bonded Alclad, and various thermal sprayed coatings) on the aluminum alloy substrate's high cycle fatigue life as tested in lab air.

MATERIAL COMPOSITIONS AND CHARACTERISTICS

The substrate and control material of interest in this study is aluminum alloy AA2024-T3.[(12)] Chemical composition of the control substrate, the hot roll-bonded Alclad liner, and the aluminum powders used in each of the three thermal spray techniques is given is Table 2.

[(12)] Aluminum alloy AA7075-T6 was also used, for comparison purposes, to emphasize the loss of fatigue life in roll-bonded Alclad sheet product.

TABLE 2. Alloy chemical composition (wt%) for sheet and powder.

Material	Cu	Mn	Mg	Cr	Zn	Ti	Si	Fe	Al
AA2024-T3 (sheet and substrate of Alclad)	4.6	0.63	1.5	0.01	0.16	0.03	0.07	0.17	remain
AA1230 (2024 Alclad liner)	0.10	0.05	0.05	---	0.10	0.03	0.35	0.35	99.3
AA7075-T6 (sheet and substrate of Alclad)	1.6	0.03	2.6	0.19	5.7	0.02	0.09	0.29	remain
AA7072 (7075 Alclad liner)	0.10	0.10	0.10	---	1.1	0.05	0.35	0.35	remain
Flame spray grade powder	---	---	---	---	---	---	---	---	99.0
Plasma spray grade powder	---	---	---	---	---	---	---	0.11	99.8
HVOF spray grade powder	---	---	---	---	---	---	0.02	0.10	99.8

TABLE 3. Thermal spray powder characteristics, size.

Powder	Aluminum purity (wt %)	Average Particle Size (µm)	Sieve Analysis (% by weight – ASTM B214)		
			+270	+325	-325
Flame spray grade (+200/-375 mesh)	99.0	45-100			
Plasma grade (-325 mesh/-45µm)	99.8	45	---	0.5	99.5
HVOF grade (-270 mesh/+10µm)	99.8	10	1.2	2.0	96.4

THERMAL SPRAY APPLICATION

Three thermal spray techniques (i.e., combustion flame spray, plasma spray, and HVOF spray) were used to apply a 5-10 mils (125-250 µm) thick aluminum coating to AA2024-T3 test coupons. All coupon surfaces were grit blasted with SiC, washed in alcohol, and subsequently thermal sprayed in air according to the parameters listed for each spraying technique in Table 4. It should be noted that no post treatment was performed on any of the thermal sprayed test coupon surfaces prior to additional testing.

TABLE 4. System parameters for the three thermal spray techniques used.

System Parameter	Plasma Spray	HVOF Spray	Powder Flame Spray
System Model	Metco 7MC	Metco Diamond Jet DJ	Terodyn 3000
Gun type	Metco 7MB (GH nozzle - #1 port)	nozzle port #3	nozzle 210w
Primary Gas	Argon (100 psi)	Oxygen (150 psi)	Oxygen (34 psi)
Secondary Gas	Hydrogen (50 Psi)	Propylene (100 psi) Air (75 psi)	Propylene (54 psi) Air (50 psi)
Power	70-75 V (500 Amps)		
Spray Distance	4-6 inches	8 inches	6-8 inches
Spray Rate	6.5 lb/hr	3 lb/hr	15 lb/hr
Deposition Efficiency	80 %	80-85 %	90%
Deposition Rate	5.2 lb/hr	2.4-2.55 lb/hr	13.5 lb/hr
Travel Speed	hand held	hand held	hand held

FATIGUE TESTING

Fatigue testing was performed in lab air on a Satec/Instron universal fatigue testing machine with manual preload utilizing the small bend fixture (see Figure 1B). Double-notched fatigue bend specimens (see Figure 1A) machined from rolled sheet[13] were submitted to alternating loads (i.e., R= -1) of 60, 50, 40, and 30 ksi at 30 Hz. Three to four specimens were tested at each stress level. All tests were run until failure of the specimen and the cycles to failure recorded. Subsequently the data produced was used to generate a characteristic S-N curve. Fatigue test were performed on the following materials/specimens:

1) AA2024-T3 (as control)
2) AA2024-T3 Alclad
3) AA2024-T3 + 99.0% Al coating (via powder flame spray technique)
4) AA2024-T3 + 99.8% Al coating (via plasma spray technique)
5) AA2024-T3 + 99.8% Al coating (via HVOF spray technique)
6) AA7075-T6 (as control)
7) AA7075-T6 Alclad

RESULTS AND DISCUSSION

Figures 3, 4, and 5 display the results of the fatigue testing performed at 30 Hz in lab air. Figure 3 reveals the effect of applying a hot roll-bonded Alclad liner to the substrate of two high

[13] The sheet thickness of the substrate in all testing was 0.06 inches thick.

strength aluminum alloys (i.e., AA2024-T3: Figure 3A, and AA7075-T6: Figure 3B). Data from both alloys indicate that the application of an Aclad layer to the substrate results in a loss in fatigue lifetime. This is particularly evident at high fatigue cycles and low applied stress levels.

Figures 4A, B, and C display the results of the testing comparing the fatigue lifetimes of AA2024-T3 with the fatigue lifetimes of AA2024-T3 coupons coated with combustion flame spray, plasma spray, and HVOF spray techniques, respectively. Improvement in fatigue life is evident, once again predominately at high fatigue cycles and low applied stress levels, in the HVOF (Figure 4C) and combustion flame (Figure 4A) sprayed AA2024-T3 specimens with the HVOF coated samples having the greatest increase in lifetime. However the fatigue lifetimes of the plasma coated samples are not statistically different from the fatigue lifetimes of the AA2024-T3 control samples (Figure 4B). Figure 5 presents a summary and comparison of the fatigue lifetimes of AA2024-T3 coupons coated with the three thermal spray techniques shown in Figure 4. An investigation is now underway to determine what mechanisms are responsible for this behavior.

SUMMARY/CONCLUSIONS

- A loss of fatigue life was observed for roll-bonded aluminum clad AA2024 and AA7075 when compared to the fatigue life of AA2024 substrate and AA7075 substrate, respectively, when tested in ambient lab air.
- Longer fatigue lifetimes were observed for thermal spray coated AA2024 when compared to the AA2024 substrate.
- Therefore, fatigue lifetime of the tested material can be ranked as following in increasing order:

    1) AA2024 substrate + Alclad

2) AA2024 substrate

3) AA2024 substrate + 99.0-99.9 wt% Aluminum thermal spray coating (combustion flame spray and HVOF spray techniques only)

ACKNOWLEDGEMENTS

The authors would like to express their thanks to AFRL/AFOSR (monitor: LtCol Paul Trulove) for financial support of this project as part of the MURI consortium entitled “Multi-Functional Nano-Engineered Coatings for Aircraft Structural Materials”. The authors would also like to extend their appreciation to Mr. Steve Crutchley, Mr. Tony Antenucci, and Midn. Robert Kurrle from the United States Naval Academy for their technical assistance and work on this project.

A)

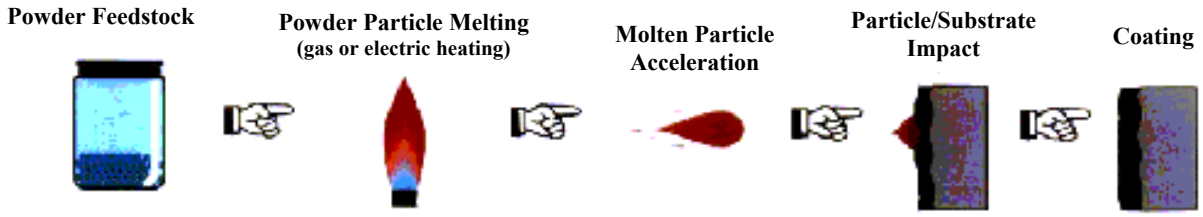

B)

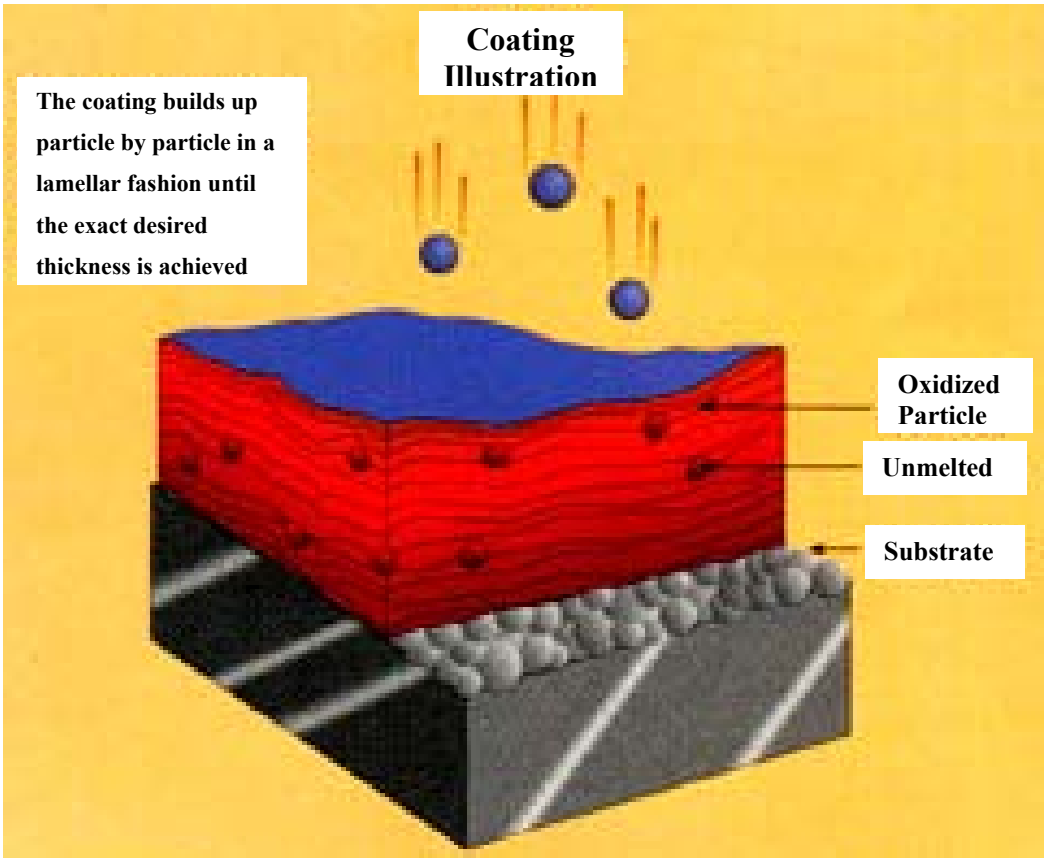

FIGURE 1. Schematics of thermal spray coating: A) Schematic illustrating the multiple stages of the thermal spray process. B) Schematic illustrating the intertwined "brick wall" splat structure characteristic of thermal spray coatings.
** figures provided by the International Thermal Spray Association

A)

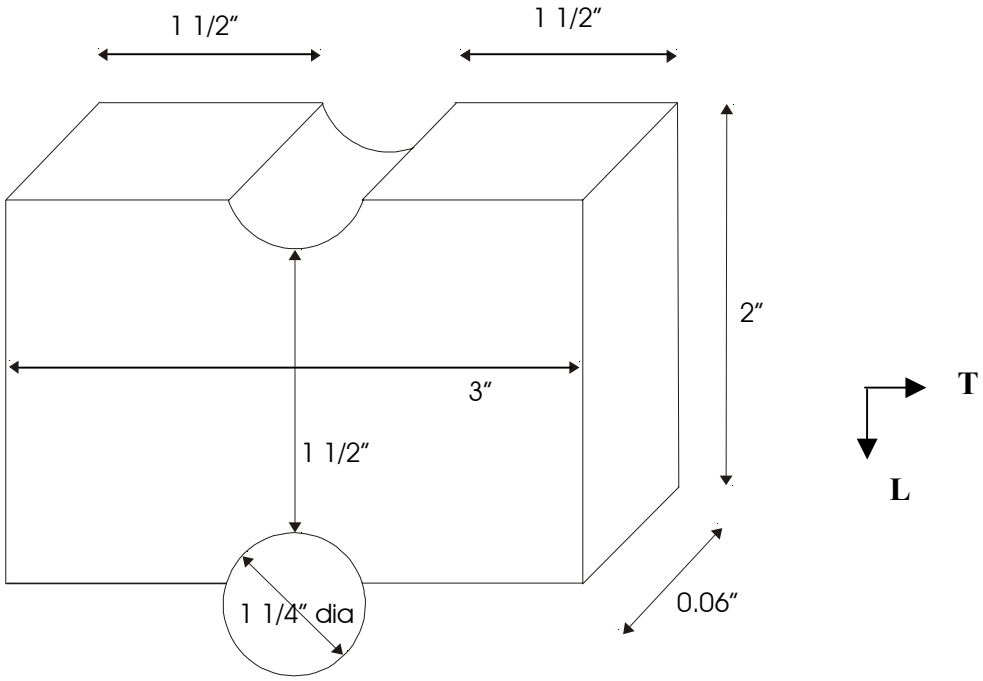

B)

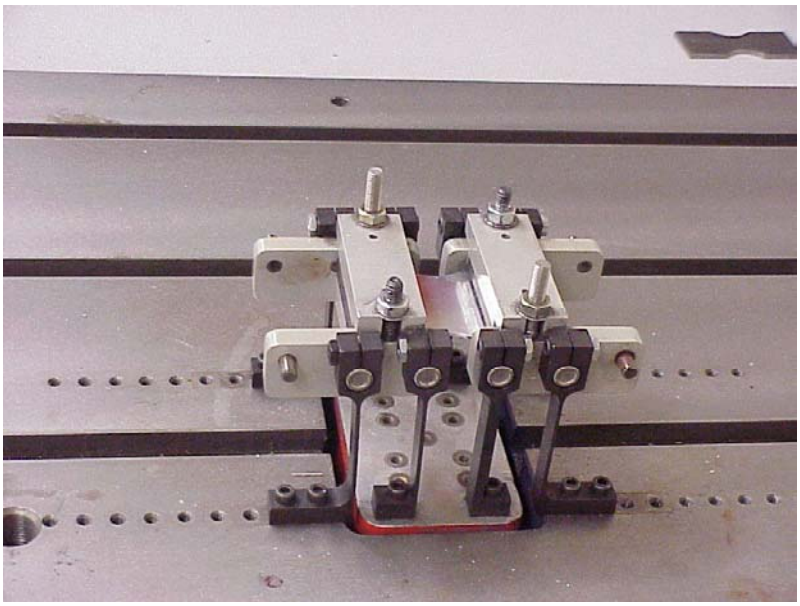

FIGURE 2. A) Bend specimen configuration used in all fatigue testing in this study indicating the configuration of the specimen to the rolling direction of the sheet material. B) Digital photo of the experimental setup utilizing a universal fatigue testing apparatus. A double-notched fatigue specimen can seen clamped in the bending fixture.

A)

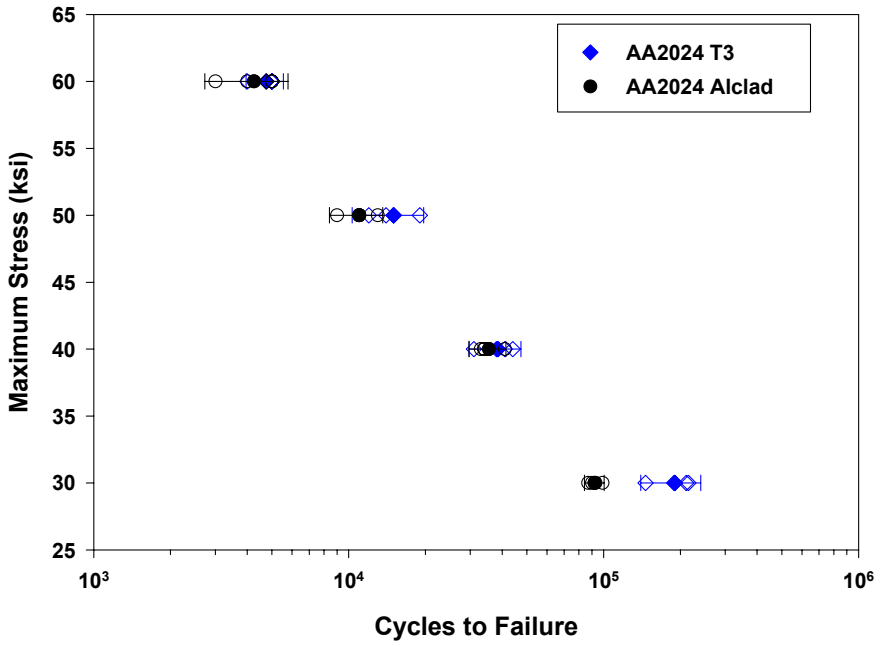

B)

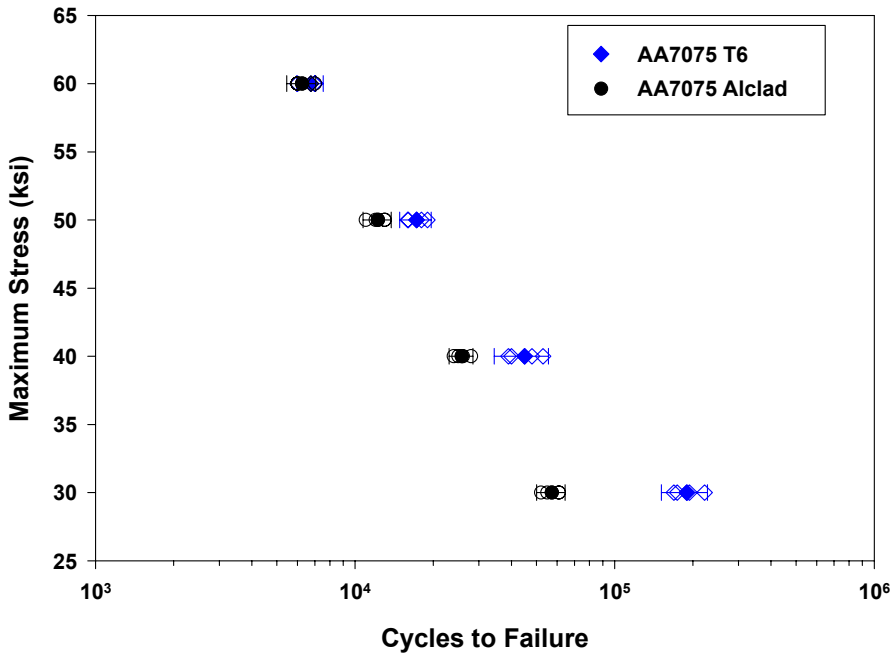

FIGURE 3. Results of cyclic fatigue tests in lab air at 30 Hz illustrating the effect of the application of a hot roll-bonded Alclad liner to the fatigue lifetime of the aluminum alloy substrate. A) AA2024-T3 (control) versus AA2024-T3 Alclad, and B) AA7075-T6 (control) versus AA7075-T6 Alclad.
Please note: the solid symbols indicate the mean of the data set at a given stress level, the open symbols indicate results from individual tests, and the error bars indicate the 95% confidence interval of the data for a given stress level.

A)

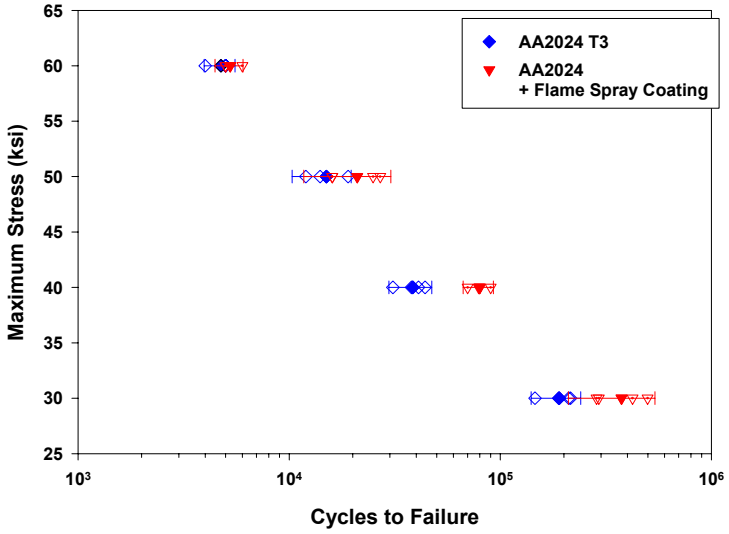

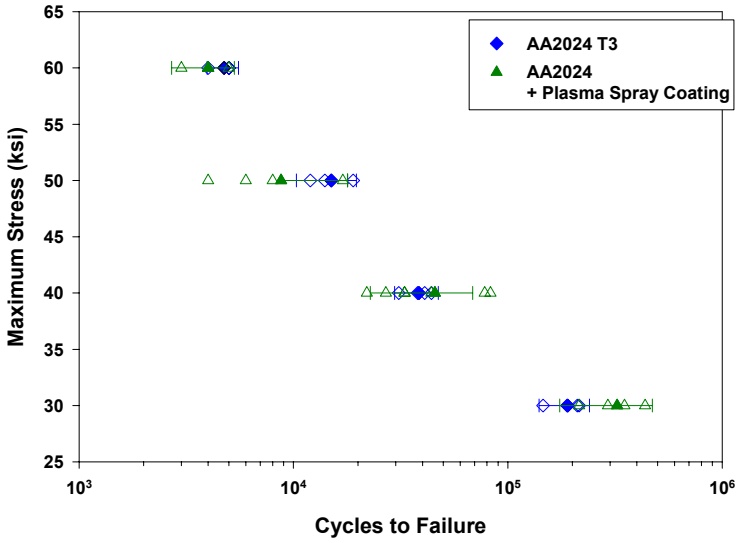

B)

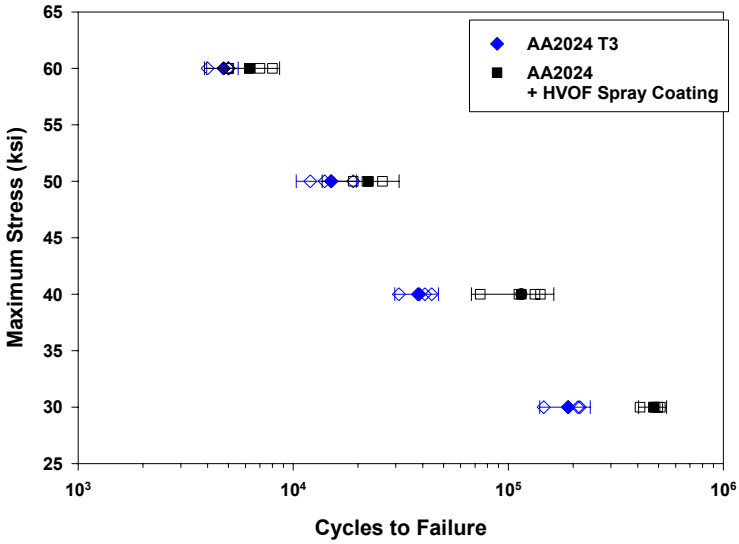

C)

FIGURE 4. Results of cyclic fatigue tests in lab air at 30 Hz illustrating the effect of the application of a thermal spray coating to the fatigue lifetime of the aluminum alloy substrate. A) AA2024-T3 (control) versus AA2024-T3 + 99.0 wt% Al flame spray coating, B) AA2024-T3 (control) versus AA2024-T3 + 99.8 wt% Al plasma spray coating , and C) AA2024-T3 (control) versus AA2024-T3 + 99.8 wt% Al HVOF spray coating.
Please note: the solid symbols indicate the mean of the data set at a given stress level, the open symbols indicate results from individual tests, and the error bars indicate the 95% confidence interval of the data for a given stress level.

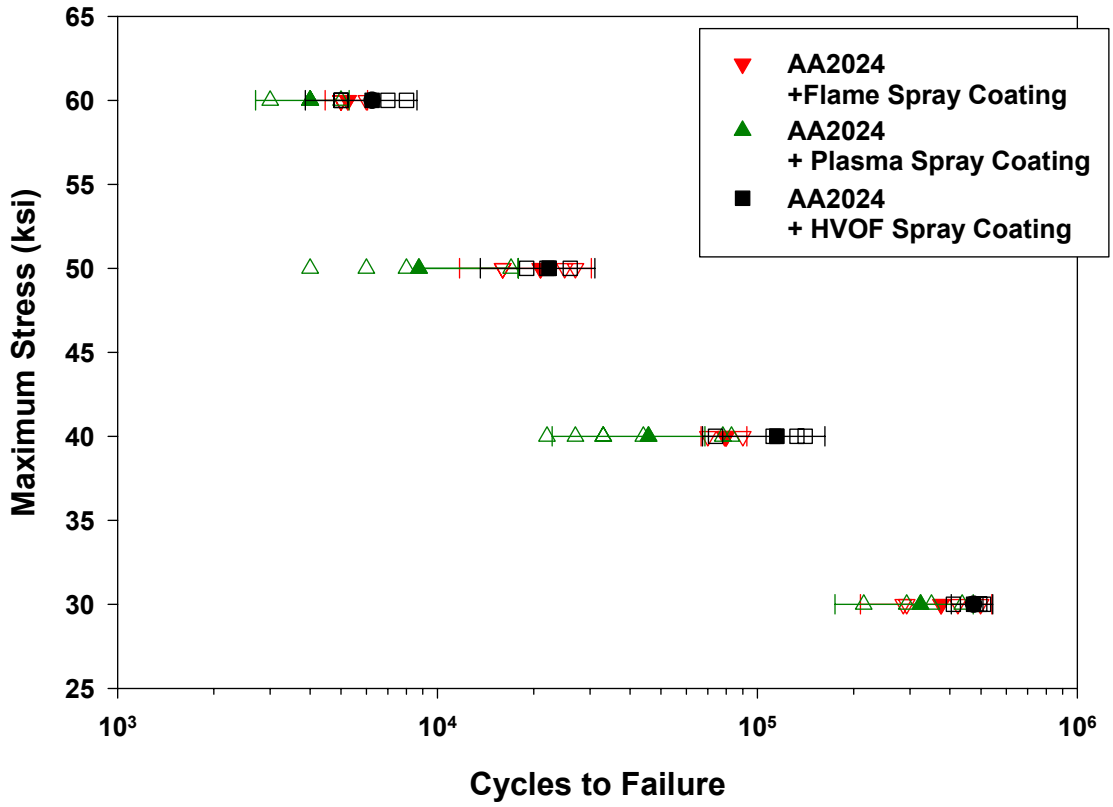

FIGURE 5. Results of cyclic fatigue tests in lab air at 30 Hz comparing the effect of the application of a thermal spray coating to the fatigue lifetime of the aluminum alloy substrate for the three thermal spray techniques presented in Figure 4.
Please note: the solid symbols indicate the mean of the data set at a given stress level, the open symbols indicate results from individual tests, and the error bars indicate the 95% confidence interval of the data for a given stress level.

REFERENCES

1. Agarwala, V.S., Bhagat, P.K., and Hardy, G.L., "Corrosion Detection and Monitoring of Aircraft Structures: An Overview," AGARD Conference Proceedings 565, Corrosion Detection and Management of Advanced Airframe Materials, (Seville, Spain: Oct. 1994).
2. Tankins, E., Kozol, J., and Lee, E.W., Journal of Materials Science, September (1995): pp. 40-44.
3. Ford, T., "Corrosion Control in the Royal Air Force," Aircraft Engineering and Aerospace Technology, Vol. 68 (1996): pp. 26-30.
4. Davis, J.R., Corrosion of Aluminum and Aluminum Alloys, ASM International, Metals Park, OH, (1999): pp.201-203.
5. Rogers, F.S., Journal of Thermal Spray Technology, Vol. 6, (3) September (1997): pp. 291-293.
6. Shaw, B.A., and Morton, A.G.S., "Final Report, Five Year Evaluation of Flame and Arc Sprayed Aluminum, Zinc, and 85/15 Zinc/Aluminum," DTNSRDC-SME-87-11, David Taylor Research Center, Bethesda, MD (1987).
7. Shaw, B.A., Leimkuhler, A.M., and Moran, P.J., "Corrosion Performance of Aluminum and Zinc-Aluminum Thermal Spray Coatings in Marine Environments," Testing of Metallic and Inorganic Coatings, ASTM STP 947, (Philadelphia, PA: American Society for Testing and Materials, 1987): pp. 246-264.
8. Scandell, K., McCaw, R., and Stowell, T., "High Velocity Oxy-Fuel (HVOF) Thermal Spray: an Alternative for Machinery Repair, Restoration, and Surface Conditioning," in Fleet Maintenance in the Joint Environment – Proceedings of the American Society of Naval Engineers Fifth Annual Fleet Maintenance Symposium, (1995).

9. Carter, V.E., and Cambell, H.S., British Corrosion Journal, Vol. 4, (1969): pp.15-20.

10. Hepples, W., Holroyd, N.J.H, and Birley, S.S., Aluminum Industry

11. Herman, H., and Sampath, S., "Thermal Spray Coatings," in Metallurgical and Protective Systems, (New York, NY: Chapman and Hall, 1996): pp. 261.

12. Tucker, R.C., "Thermal Spray Coatings," in Surface Engineering – Volume 5 ASM Handbook, (Materials Park, OH: ASM International): pp.497.

13. Sampath, S., and Herman, H., Journal of Thermal Spray Technology, Vol. 5, 4 (1996): pp. 445.

14. Nicoll, A.R., "Production Plasma Spraying in the Automotive Industry: A European Viewpoint," in 1994 Thermal Spray industrial Applications – proceedings of the 7th National Thermal Spray Conference, (Materials Park, OH: ASM International, 1994): pp.7-17.

15. Gougeon, P., Moreau, C., and Richard, F., "On-Line Control of Plasma Sprayed Particles in the Aerospace Industry," in Advances in Thermal Spray Technology - proceedings of the 8th National Thermal Spray Conference, (Materials Park, OH: ASM International, 1994): pp.149-155.

16. Varacalle, D.J., Lundberg, L.B., Crawmer, D.E., and Didier, P.A., "An Experimental Study of the Air Plasma Spraying of Aluminum Powder," in Advances in Thermal Spray Technology - proceedings of the 8th National Thermal Spray Conference, (Materials Park, OH: ASM International, 1994): pp.381-386.

17. Kaufman, J.G., Properties of Aluminum Alloys: Tensile, Creep, and Fatigue Data at High and Low Temperatures, ASM International, Materials Park, OH, (1999): pp. 295-297.

18. Quets, J.M., “High Cycle Fatigue Properties of Chrome Plated 7075-T73 Aluminum and 4340 Steel,” Union Carbide, Technical Note No. 91-03, 1991.

19. Landgraf, R.W., and Cherenenkoff, R.A., “Residual Stress Effects on Fatigue of Surface Processed Steels,” in Analytical and Experimental Methods for Residual Stress Effects in Fatigue, ASTM STP 1004, (Philadelphia, PA: American Society for Testing and Materials, 1988): pp. 1-12.

20. Koh, S.K., and Stephens, R.I., Fatigue Fracture in Engineering Materials Strucutres, Vol 14, 4 (1991): pp. 413-428.

21. McGrann, R.T.R., Greving, D.J., Shadley, J.R., Rybicki, E.F., Bodger, B.E., and Somerville, D.A., Journal of Thermal Spray Technology, Vol. 7, 4 (1998): pp. 546-552.

22. Pawlowski, L., The Science and Engineering of Thermal Spray Coatings, John Wiley and Sons, Chichester, England, (1995): pp. 139-146.

LOCALIZED CORROSION OF $Al_{90}Fe_5Gd_5$ AND $Al_{87}Ni_{8.7}Y_{4.3}$ ALLOYS IN THE AMORPHOUS, NANOCRYSTALLINE AND CRYSTALLINE STATES: Resistance to Micrometer-Scale Pit Formation

J.E. Sweitzer, G.J. Shiflet, J.R. Scully

Department of Materials Science and Engineering
University of Virginia
Charlottesville, VA 22904-4745

ABSTRACT

The role of isothermal aging on the localized corrosion behavior of $Al_{90}Fe_5Gd_5$ and $Al_{87}Ni_{8.7}Y_{4.3}$ alloys was characterized in 0.6 M NaCl solution. The pitting (E_{pit}) and repassivation (E_{rp}) potentials were both increased ~400 mV by the presence of transition and rare earth metal additions in supersaturated solid solution and amorphous structure. A statistical distribution in E_{pit} observed on small electrodes was due, in part, to the sensitivity of this critical potential to the presence of a population of critical surface flaws that serve as pit initiation sites. Mechanistic insight on the spacing of critical flaws was enabled by varying the tested electrode surface area. E_{rp} was not dependent on electrode surface area due to the similarity of pit depths in all electrode sizes. The critical potentials were also characterized after heat treating the amorphous ribbons isothermally at 150ºC for 25 hours and 550ºC for 1 hour. The former produced Al-rich nanocrystals embedded in the remaining amorphous matrix while the latter produced a fully crystalline condition containing intermetallic phases. Notably, the improved resistance to the formation of micrometer-scale pits was not lost compared to the fully amorphous condition when small Al-rich nanocrystals were present in an amorphous matrix. However, improvement in pitting corrosion resistance was completely lost in the fully crystallized condition as indicated by values for E_{pit} and E_{rp} that were similar to those of pure, polycrystalline aluminum.

INTRODUCTION

OPPORTUNITY FOR NEW METALLIC COATINGS

The opportunity exists to create new metallic coatings that exhibit a broad range of corrosion functions including active corrosion inhibition (i.e., self-healing), corrosion barrier properties, sacrificial cathodic prevention, as well as resistance to crevice corrosion (e.g.,

alkaline or acidic dissolution) at faying surfaces in military components. One class of alloys that may be suitable for such coatings is a recently discovered Al-rich glass alloy system based on rare earth and transition metal compositions. Multi-functionality is possible because some of the same alloying elements that promote amorphous phase formation upon rapid cooling also have attributes that could improve a range of corrosion properties.

This paper focuses on the ability of two selected amorphous Al-based metallic alloys to resist formation of micrometer scale pits. One critical issue is the concern that devitrification compromises the improved localized corrosion resistance associated with the amorphous state. The effects of heat treatment-induced devitrification on the pitting corrosion behavior of $Al_{90}Fe_5Gd_5$ and $Al_{87}Ni_{8.7}Y_{4.3}$ alloys were investigated in near-neutral NaCl solution.

PHYSICAL METALLURGY AND THERMAL STABILITY

It has been well established that a limitation of older as well as recently discovered Al-base metallic glasses is that they exist in a metastable form.[1-6] At room temperature the amorphous phase of Al-based glasses has been shown to be stable for up to two years.[3] However, such alloys tend to crystallize if heated with sufficient thermal energy to accelerate the kinetics of crystallization, nucleation and growth.[3-6] During a low temperature heat treatment, such homogeneous single phase amorphous alloys can transform into a nanocrystalline composite with the remaining amorphous phase as the matrix. Upon further heating, this amorphous/nanocrystalline composite microstructure then transforms into a fully crystalline state with the formation of transitional or equilibrium phases.[2-4] It is interesting to note that as-spun Al-base amorphous alloys and nanocrystalline composites exhibit improved mechanical properties. Hono[7] has reported tensile strengths of 800 MPa for aluminum-based alloys in the amorphous state and as high as 1500 MPa in a partially crystalline state after isothermal heat

treatment. In contrast, the tensile strength of 99.99% pure Al is 45 MPa and that of 2024-T3 is 485 MPa.[8]

Using differential scanning calorimetry (DSC), Goyal *et al.*[4] reported that all of the Al-Ni-Y alloy systems studied containing ≥80 at.% Al had a four stage crystallization process and the resulting phases were identified using x-ray diffraction (XRD) analysis. During the first stage indicated by an exothermic peak at 576 K, supersaturated α-Al precipitates formed in the amorphous matrix by a primary crystallization process. In the second stage (612 K), the remaining amorphous phase transformed eutectically into α-Al and Al_3Y. Stage three (655 K) can be thought of as the solid state precipitation of the ternary AlNiY phase from saturated α-Al. This ternary phase, being metastable, transforms into Al_3Y and Al_3Ni in the fourth stage (748 K), yielding equilibrium phases. Kwong *et al.*[5] and Cao *et al.*[1] reported a very similar crystallization sequence for Al-Ni-Y alloys with ≥85 at.% Al.

Csontos[3] also found that the $Al_{90}Fe_5Gd_5$ alloy had a three stage crystallization process. Microstructure changes were reported to occur at each transition temperature. The first exothermic peak (473 K) indicates the primary crystallization of a homogeneously dispersed, roughly spherical nanocrystalline phase embedded in the amorphous matrix. The second exotherm (663 K) indicates the transformation of the nanocrystals into lower energy metastable transition phases. These metastable transition phases transform into equilibrium phases of different compositions during the third exotherm temperature (753 K). Solute partitioning has been reported in the partially crystallized state containing α-Al nanocrystals embedded in an amorphous matrix.[3,7,9-11] Transition metal (TM) and rare earth elements (RE) are rejected from the α-Al phase due to the low solubility of these elements in f.c.c. aluminum.[8] The concentration of RE at the interface of the α-Al nanocrystal is higher than the bulk composition

while there is a general increase above the bulk concentration for TM in the amorphous matrix away from the interfacial region.[3,9,11] The increased concentration of RE at the interface and subsequent concentration gradient away from the nanocrystal suggests that the RE diffuses more slowly than the TM, most likely due to its larger atomic radii.[3,7,9-11]

A 25 hour heat treatment at 150°C was used in this study to obtain a partially crystallized state containing ~10 nm nanocrystals embedded in a remaining amorphous matrix, hereafter referred to as the nanocrystalline state. The volume fraction of precipitates can be as high as 40-50%. The measured concentrations of Al, Fe, and Gd in the nanocrystal was 95 at.%, 3 at.% and <2 at.%, respectively.[3] The Al concentration decreased to almost 87 at.% in the amorphous matrix, and approached the bulk concentration well into the matrix . A general build up of TM in the amorphous matrix to 7 at.% was observed, while a concentration gradient occurs for the rare earth element from the interface to the matrix. The RE maximum was 7 at.% at the nanocrystal/matrix interface and decreased to a concentration just below the bulk concentration in the matrix. This behavior has also been reported for other Al-TM-RE alloy systems.[7,9,10]

Performing a higher temperature heat treatment resulted in a fully crystalline microstructure with solute additions collected in equilibrium, intermetallic phases at the grain boundaries {$Al_3(Ni,Y)$[2,4], $Al_2(Ni,Y)$ and AlY_2;[2] $Al_2(Fe,Gd)$[12] and Al_4Gd[3]}. Csontos[3] found that nanocrystallization of $Al_{90}Fe_5Gd_5$ could be observed at temperatures as low as 100ºC but not at temperatures above 400ºC. Above this temperature, the nanocrystallization kinetics were so rapid that the transformation was bypassed in favor of the formation of transition/equilibrium phases. At a temperature of 550ºC, the microstructure of the amorphous $Al_{90}Fe_5Gd_5$ alloy was fully crystalline within 1 minute and continual grain growth occurred with increasing annealing time. Similar kinetics were observed for the $Al_{87}Ni_{8,7}Y_{4.3}$ alloy as well.

CORROSION PROPERTIES AND OBJECTIVE

Amorphous Al-TM-RE alloys have excellent corrosion resistance.[2,6,12,14,15] The mechanisms of the improved corrosion resistance of metallic glasses are related to amorphous structure[14,16] and/or alloying additions in supersaturated solid solution.[6,12,17-21] Pitting of polycrystalline high purity aluminum and precipitation age hardened aluminum alloys is commonly initiated at precipitate phases, constituent particles and grain boundaries.[22-32] Homo- and heterophase grain boundaries in crystalline alloys are areas of high local stresses, impurity segregation, precipitation and nanochemical heterogeneity that promote preferential nucleation of pits.[22-25,27-30] The amorphous structure eliminates microstructural heterogeneities as sites of localized corrosion initiation and accelerated attack.[12,14,16,33,34] Alloy additions may further improve resistance to localized corrosion by forming an improved passive film,[2,18,19,33-39] changing the kinetics of dissolution at localized sites,[20] or both. A more protective film may form on an amorphous material that is enriched in oxidized solute, with effects including hindering the migration of Cl^- ions through the film.[18,19] Alloy additions also reduce the ability of pits to dissolve at a sufficient rate and supply acidity via cation hydrolysis to maintain the critical local environment necessary for pit growth.[20,21]

However, little is known about the corrosion properties of Al-base amorphous alloys in various states of devitrification. All of the benefits cited above could potentially be lost after the formation of crystals with the structure and composition of the solvent element (e.g., f.c.c. aluminum). An important question is whether the formation of Al-rich nanocrystals in an amorphous matrix leads to a loss in the resistance to formation of micro-meter scale pits. The objective of this paper is to investigate the ability of partially devitrified Al-Ni-Y and Al-Fe-Gd alloys to resist formation of micrometer scale pits.

EXPERIMENTAL PROCEDURES

MATERIALS

Two Al-TM-RE metallic glass alloys, Al-Ni-Y and Al-Fe-Gd, were investigated. In particular, the compositions included $Al_{87}Ni_{8.7}Y_{4.3}$, $Al_{85}Ni_{10}Y_5$, and $Al_{85}Ni_5Y_{10}$ from the Al-Ni-Y family and $Al_{85}Fe_7Gd_8$, $Al_{90}Fe_{4.5}Gd_{5.5}$, and $Al_{90}Fe_5Gd_5$ from the Al-Fe-Gd family. Preliminary testing over these ranges of TM and RE compositions in several different aqueous environments revealed negligible differences in corrosion behavior in this range. Two alloys, $Al_{87}Ni_{8.7}Y_{4.3}$ and $Al_{90}Fe_5Gd_5$, were emphasized for more in-depth characterization and crystallization studies. Al-Ni-Y and Al-Fe-Gd alloys were fabricated using a single roller melt technique. Ingots of composition $Al_{87}Ni_{8.7}Y_{4.3}$ and $Al_{90}Fe_5Gd_5$ were produced by arc-melting elemental chips under an argon atmosphere. The purity of Al, Y, and Gd was 99.9%, Fe was 99.98%, and that of Ni was 99.99%. The metallic glass ribbons were prepared in a helium atmosphere using a 0.20 m diameter copper wheel with an approximate circumferential velocity of 45 m/s. The ribbons were formed with dimensions of 15-20 μm thick, 1-2 mm wide and up to several meters in length.[9] The as-spun ribbons were confirmed to possess a wholly amorphous structure using various techniques including x-ray and electron diffraction, dark field transmission electron microscopy (DFTEM), and high resolution electron microscopy.[3] High purity (99.999%) polycrystalline aluminum foils of the same dimensions as the metallic glass ribbons were tested for comparison. The Al foils were manufactured to dimensions of 2.5×2.5 cm and 20 μm thick and cut into ~1.4 mm×2.5 cm x 20 μm segments, similar to the dimensions of spun-melt ribbons.

HEAT TREATMENTS

Amorphous spun-melt ribbons were encapsulated in Pyrex or quartz tubes that were back-filled with argon gas. To partially crystallize the ribbons to form nanocrystals, the encapsulated samples were isothermally heat treated at 150ºC for 25 hours in a Precision® Gravity Convection Oven Model 16EG. A dark field transmission electron microscope (TEM) image of the $Al_{90}Fe_5Gd_5$ alloy in the nanocrystalline state is shown in Fig. 1 (a). A fully crystallized condition (Fig. 1 (b)) was achieved by heat treating for 1 hour at 550ºC in a Thermolyne® 480000 Furnace. Samples were allowed to air cool following their respective heat treatments. A TEM micrograph of crystalline $Al_{90}Fe_5Gd_5$ used in this study is shown in Fig. 1(b) after a 1 hour isothermal heat treatment at 550ºC. The microstructure consists of Al grains with equilibrium intermetallic phases at the grain boundaries. The grain size is approximately 400-600 nm. A TEM micrograph of the 99.999% pure polycrystalline Al foil is shown in Fig. 2. The grain size of pure Al was approximately 10-80 μm in the short transverse direction of the sheet. Grains were elongated in the rolling direction.[13,40]

ELECTROCHEMICAL TESTING

Alloy ribbon and Al foil samples were mounted on end in Buehler® Epoxide resin exposing a surface area of ~$2x10^{-4}$ cm^2 consisting of the foil cross-section (e.g., short transverse by long traverse surface of Al foil). These electrodes will be referred to as micro-band (mb) electrodes. This brand of epoxy was chosen, particularly for the metastable alloys, because it is a cold mounting compound. During curing the resin is reported to have a peak temperature of only 28ºC (82ºF) which was below the temperature associated with nanocrystal formation even at long times. Mounted samples were wet polished through 600 grit SiC paper. Final surface preparation included a successive polish to a 0.05 μm finish in alumina suspensions.

Complementary free standing (fs) electrodes with a larger exposed area, ~10^{-1} cm^2, were also tested to investigate the effects of surface area on critical potentials. The only surface preparation for these electrodes was a methanol rinse. The fs electrode exposes the as-spun metal ribbon, which has been shown to have less micro-scale roughness than a polished microelectrode by root mean square (RMS) average roughness over several surface profiles using atomic force microscopy. The polished surface (0.05 μm finish) had an average RMS roughness of 124 Å for amorphous $Al_{90}Fe_5Gd_5$ and $Al_{87}Ni_{8.7}Y_{4.3}$ while the as-spun materials had an average RMS roughness of 36.3 Å[1] on the side of the ribbon that contacted the wheel and an average RMS roughness of 21.5 Å on the opposite side. This issue will be discussed later when addressing pit stabilization potentials for the micro- and free standing electrodes since a rougher surface will typically form stable pits more easily.[41]

The working electrodes were tested using a 300 mL electrochemical flat cell equipped with a platinum mesh counter electrode, gas inlet and outlet ports, and a reference electrode port. All potentials were measured versus a saturated calomel electrode (SCE) scale with accuracy of ± 2 mV. A 0.6 M (3.5 wt.%) NaCl electrolyte was prepared using deionized water of 18 MΩ-cm resistivity and ACS certified reagents. This electrolyte was deaerated with N_2 gas and the open circuit potential was measured for approximately one hour followed by an anodic scan at 0.1 mV/s, and a reverse in scan direction at 0.05 mA. An EG&G Model 273A or Model 283 potentiostat under computer control was utilized with CorrWare™ Corrosion Measurement Software. E_{pit} was taken at the potential at which the current density, current normalized to total exposed area, reached a value two orders of magnitude higher than the passive current density, $i_{pass,}$ which ranged from 1-5 μA/cm^2. These parameters are clearly seen in the E-log i diagram

[1] It should be noted that AFM roughness measurements show only small-scale roughness. Both faces of the as-spun

for a high purity aluminum microelectrode (Fig. 3a). E_{rp} was taken as the potential where a distinct change in slope and characteristic shape of the reverse potentiodynamic scan was seen. E_{pit} and E_{rp} reflected micrometer scale pit formation and repassivation (Fig. 3b). Cumulative probability distribution plots were constructed from E_{rp} and E_{pit} data to compare the critical potential distributions for the amorphous, nanocrystalline, and crystalline alloys to pure polycrystalline aluminum foils. The survival probability P_s, defined as $^{n}/_{N+1}$ where n is the number of specimens surviving, i.e., not undergoing pit stabilization at applied potential E_{N-n} and N is the total number of specimens in the test population, was also used to compare the localized corrosion behavior of the alloys.[41] Pit depths on the mb electrodes were estimated at the end of E-I scans using Faraday's law assuming a single pit since the entire surface area of the electrode was observed to be recessed[2]. The actual pit depths were measured from sectioned electrodes. Scanning electron microscopy was used to measure the pit radii of the fs electrodes.

RESULTS

CRITICAL POTENTIALS ASSOCIATED WITH MICROMETER-SCALE PITTING

More positive mean values for E_{pit} and E_{rp} were achieved for amorphous and nanocrystalline $Al_{87}Ni_{8.7}Y_{4.3}$ and $Al_{90}Fe_5Gd_5$ compared to that of pure polycrystalline Al as well as crystalline $Al_{87}Ni_{8.7}Y_{4.3}$ and $Al_{90}Fe_5Gd_5$ (Table 1). The alloys lost their improved localized corrosion resistance in the fully crystalline state as indicated by similar values for E_{pit} and E_{rp} for the fully crystallized alloys and Al. No significant changes were seen in the passive current density and correlations between E_{pit} and i_{pass} were not obtained for any of the alloys.

---

ribbon possess other large-scale features such as broad ridges and ripples that may be observed through optical microscopy. These features were not present in the mb electrodes and the pure aluminum fs electrodes.

[2] The measured current is underestimated due to H_2 evolution in the artificial pits and, therefore, Q_{meas} is underestimated. Consequently, the pit depths calculated using Faraday's Law are underestimates of actual depth.

The values of E_{pit} and to a lesser extent E_{rp} were found to vary over successive measurements under each condition. The distributions are more evident on a cumulative probability plot. Fig. 4a shows the cumulative probability distributions of E_{corr}, E_{pit} and E_{rp} for pure Al in the micro-band electrode configuration. It shows the cumulative probability of obtaining a certain critical potential on polycrystalline Al. The median E_{pit} value for pure Al in the micro-band configuration was –0.348 V, which is elevated above reported E_{pit} values for pure Al in 0.6 M NaCl. However, the lowest recorded values of E_{pit} approached E_{rp}. Moreover, the mean E_{pit} and E_{rp} values for the larger surface area, free standing (fs) electrodes, -0.650 and -.806 V, respectively, are in good agreement with the published values for these conditions using large electrodes.[18-20,43,44] The mean value of E_{rp} for pure Al in the mb electrode configuration was –0.754 V and was quite reproducible as indicated by the steep slope on the cumulative probability distribution plot.

Fig. 4b shows the cumulative probability distributions of E_{corr}, E_{pit} and E_{rp} for $Al_{90}Fe_5Gd_5$ in the mb electrode configuration. It is interesting to note that E_{pit} and E_{rp} are elevated compared to Al while E_{corr} remains near –1 V. To compare all alloys to Al, E_{rp} was used due to its tight statistical distribution and lack of dependence on electrode surface area. The cumulative probability distributions in Fig. 5 and 6 clearly demonstrate the enhancement of E_{rp} for both the amorphous and nanocrystalline states in both alloys. Fig. 5 shows the cumulative probability of obtaining a given repassivation potential for pure Al compared to amorphous $Al_{87}Ni_{8.7}Y_{4.3}$ and $Al_{90}Fe_5Gd_5$. E_{rp} for both amorphous alloys is approximately 400 mV more positive than that of pure Al. Fig. 5 also shows that the behavior for $Al_{87}Ni_{8.7}Y_{4.3}$ and $Al_{90}Fe_5Gd_5$ are similar. For this reason the next series of plots will focus only on $Al_{90}Fe_5Gd_5$.

Fig. 6 shows the E_{rp} distributions for the amorphous, nanocrystalline and fully crystalline states of $Al_{90}Fe_5Gd_5$ in comparison to pure polycrystalline Al. Upon repassivation, the average pit size is large (>100 μm) so each of these data points represents a repassivation potential associated with pits that include considerable area fractions of the remaining amorphous matrix of the nanocrystalline state. That is to say that repassivated pits are much larger than the size of individual nanocrystals. Notably, the nanocrystalline alloy retained the improved resistance to micrometer size pit stabilization that was seen for the amorphous alloy as evident from similar values for E_{rp} for the amorphous and nanocrystalline conditions (Fig. 6). The median values for E_{rp} for the nanocrystalline materials were very similar to those of their amorphous counterparts and were enhanced as compared to the crystalline materials. The E_{rp} distribution for the crystalline state of $Al_{90}Fe_5Gd_5$, also plotted in Fig. 6, shows that the median E_{rp} value decreased over 400 mV to a value that is actually slightly less than that of pure polycrystalline Al. This was seen for both alloys (Table 1). Pit growth tests for the crystalline alloys suggest that repassivation is not by non-maintenance of the critical depassivating environment but by OH^- production since repassivation does not occur until the onset of net cathodic kinetics in the reverse polarization scan. Intermetallics were shown to increase the rate of the cathodic reaction that occurs within pits, yet E_{rp} was still more negative. In contrast, repassivation for the amorphous and nanocrystalline alloys and pure Al occurred by dilution of the critical depassivating environment and onset of repassivation as the dissolution process slowed in pits.

Fig. 7 shows the survival probability, P_s, versus potential for $Al_{90}Fe_5Gd_5$. The probability of pit stabilization ($1 - P_s$) is greater at more negative potentials for the fully crystalline condition compared to the nanocrystalline alloy. In general, the fully crystalline materials indicate a greater probability of stable pitting at a lower potential, while the amorphous and nanocrystalline

alloys would have to be exposed to a much higher potential to achieve the same probability of stable pit formation. Interestingly, nanocrystalline $Al_{90}Fe_5Gd_5$ had the lowest probability of breakdown and stabilization of micrometer scale pits[3] compared to amorphous $Al_{90}Fe_5Gd_5$. The crystalline alloy had a lower probability of surviving compared to pure Al specimens. The explanation for this behavior is likely linked to the microstructural differences between the two samples.

INSIGHT ON SPACING OF CRITICAL FLAWS

A tight statistical distribution for E_{rp} was always observed regardless of electrode size for pure polycrystalline Al as well as for both alloys. Moreover, small Al mb electrodes exhibited E_{rp} values that were similar to those on large fs electrodes (Table 1). In contrast, the statistical distribution in E_{pit} was always larger (Figures 4a and 4b, Table 1) in studies using small surface micro-band electrodes compared to large fs electrodes. Median E_{pit} was elevated above expected values for the crystalline Al mb electrodes when compared to large fs crystalline Al electrodes. Larger statistical distributions in E_{pit} were also seen in the cumulative probability plots for the alloys in the fully crystalline state using the micro band electrode. It is reasonable to speculate that this behavior is due to the microstructural heterogeneity of the crystalline condition that exists on the length scale of the mb electrode surface dimensions.

The elevation in E_{pit} and change in the distributions may give insight on the size of the critical flaw that leads to stabilization. Fig. 8(a) shows the cumulative probability for achieving a given E_{pit} value in the case of mb (10^{-4} cm^2) and fs (10^{-1} cm^2) electrodes of pure Al compared to amorphous $Al_{87}Ni_{8.7}Y_{4.3}$. A large statistical distribution of E_{pit} values was observed for pure polycrystalline Al mb electrodes, while the distribution for the larger surface area fs Al

[3] Numerous studies show that the pitting potential is associated with stabilization of pits already formed.[44,45]

electrodes was much tighter. In contrast, a tight distribution is seen for both the small mb and large free standing electrodes in the case of the amorphous $Al_{87}Ni_{8.7}Y_{4.3}$ alloy. In other words, there is no effect of electrode size on E_{pit}. The distribution in E_{pit} for amorphous $Al_{90}Fe_5Gd_5$ was larger and influenced more by surface area as seen in Fig. 8(b), but is still less distributed than data for polycrystalline Al. Fig. 9 summarizes the elevation in E_{pit} with decreasing electrode area as a function of alloy and heat treatment. For pure Al the elevation in E_{pit} for the mb electrode is almost 300 mV; from -0.647 V, a value in good agreement with the literature,[18-20,43,44] to -0.350 V. The elevation in the mean values for the amorphous and nanocrystalline $A_{87}Ni_{8.7}Y_{4.3}$ microelectrodes is relatively insignificant at 38 mV and 40 mV, respectively (Fig. 9(a)). A similar trend was also found for the $Al_{90}Fe_5Gd_5$ alloy in the amorphous and nanocrystalline states albeit with a greater elevation in E_{pit} as seen in Fig. 9(b). It is interesting to note that the trend is to have greater elevation of E_{pit} with decreasing surface area for crystalline compared to fully amorphous electrodes. That is to say, when the degree of μm scale microstructural heterogeneity is increased then small mb electrodes produce the greatest relative elevation in E_{pit} compared to larger fs electrodes.

It is interesting to note that E_{rp} is only slightly or slightly affected by electrode surface area. Fig. 10 verifies the similarity of E_{rp} for mb (10^{-4} cm^2) and fs electrodes (0.1 cm^2) of pure Al and amorphous $Al_{87}Ni_{8.7}Y_{4.3}$. The difference in median E_{rp} values for mb and free standing electrodes was only ~50 mV for pure Al and ~20 mV for amorphous $Al_{87}Ni_{8.7}Y_{4.3}$. Pits of several hundred micrometer diameter were repassivated at this critical potential (Fig. 11).

DISCUSSION

CORROSION BEHAVIOR AS A FUNCTION OF THE DEGREE OF CRYSTALLIZATION

The finding that the nanocrystalline state of the Al-TM-RE alloys retains the corrosion resistance of their amorphous counterparts is extremely promising for potential future applications of these high strength materials. In conventional precipitation age hardened materials, strength must often be sacrificed for improved corrosion resistance. E_{pit} and E_{rp} were enhanced for both the amorphous and nanocrystalline alloys as compared to their crystalline counterparts and pure polycrystalline Al (Fig. 4 and 5, Table 1). The amorphous structure of these alloys eliminates grain boundaries and second phase particles as sites of pit initiation,[22-32] while TM or RE in solid solution may improve the resistance to localized corrosion[2,17-19,33-39,43] by enriching solute in the passive film,[18,19,43] altering dissolution kinetics in pits,[20,46,47] changing the severity of the critical pit solution, or helping form insoluble compounds that destabilize pit growth.[21] It is difficult to determine whether E_{pit} data indicate that the oxide film is less prone to initiation when the metal is amorphous or that E_{pit} is raised due to pit growth and stabilization considerations. Data suggest that the critical flaw promoting stabilization for the amorphous alloys may not be as prone to initiation as the critical flaw responsible for pit stabilization in fully crystalline materials and requires a more positive potential to lead to stabilization. Moreover, once a pit has been initiated in the amorphous alloys a more severe depassivating pit chemistry may be required to sustain growth. This is suggested by elevated E_{rp} data.

Regarding pit initiation and growth in high strength nanocrystalline alloys, it is reasonable to assert that pits will be initiated more readily at the Al-rich f.c.c. nanocrystals, if they lack TM or RE solute. However, these pits may quickly face inhibited growth due to the solid solution solute gradient that exists at the nanocrystal/amorphous matrix interface.

Moreover, in the presence of the highly enriched solute concentration gradient at the interface, an even more severe depassivating pit chemistry may be required. Therefore, nanopits that reach the high TM and RE regions and grow into the amorphous matrix might be expected to require much higher applied potentials than pure Al in order to achieve and maintain stable pit growth conditions. This hypothesis will be examined in a subsequent paper using artificial pit studies simulating the conditions for active pit growth.

The fully crystalline alloys possessed slightly worse corrosion behavior than pure polycrystalline Al as characterized by slightly lower values for E_{pit} and E_{rp} (Table 1, Fig. 6-7). The almost pure Al, crystalline matrix of the heat treated alloy, devoid of TM and RE,[2-4] (Fig. 4) did not retain the localized corrosion resistance exhibited by the solid solution, amorphous matrix. Grain boundaries and intermetallic phases have been introduced as susceptible initiation sites[22-32] and pit growth is no longer hindered by TM and RE in solid solution because the beneficial alloy additions have been removed from solid solution and collected in intermetallics.

Two possible explanations for the finding that high purity polycrystalline Al performs slightly better than the crystalline alloys (Figures 6 and 7) are the higher population of grain boundaries and the presence of intermetallic phases in the crystalline alloy. Figures 1(b) and 2 show micrographs of the crystalline alloy and the pure Al foil. The size of the crystalline $Al_{90}Fe_5Gd_5$ grains is over 1000 times smaller than that found in pure polycrystalline aluminum. Considering that grain boundaries are a likely critical flaw for pitting,[28] a smaller grain size exposes more pitting initiation sites thereby degrading the corrosion resistance as compared to pure Al. Intermetallic phases may also degrade the pitting resistance of the crystalline alloys compared to pure Al as they introduce another easy pit initiation site.[48,49]

INSIGHT ON CRITICAL FLAWS RESPONSIBLE FOR PIT FORMATION

The mb electrodes showed larger statistical distributions in E_{pit}, and elevation in median E_{pit} values especially in the case of the crystalline materials. This elevation in E_{pit} is not likely due to differences in surface roughness between the microelectrodes and the free standing electrodes. The surface of the polished mb electrode is actually as rough or rougher than that of the fs electrodes. Conventional arguments suggest that stable pit formation would be an easier process on microelectrodes from the standpoint of easier occluded site formation based on surface roughness and mass transport.[41,51] E_{pit} values measured for amorphous $Al_{87}Ni_{8.7}Y_{4.3}$ mb electrodes were not elevated compared to the fs electrode (Fig. 8a and 9). This effect is demonstrated by plotting the difference between the median values of E_{pit} for the mb electrodes and the fs electrodes for pure Al, amorphous and nanocrystalline $Al_{87}Ni_{8.7}Y_{4.3}$ and $Al_{90}Fe_5Gd_5$ in Fig. 9 (a) and (b). One hypothesis links the elevation in the E_{pit} to differences in the structure between pure Al, the amorphous and the nanocrystalline alloys. The premise here is that by decreasing the electrode size to dimensions on the order of the spacing of the critical flaws that promote pit initiation and stabilization, then the total number of flaws on any randomly chosen at-risk exposed surface decreases. This may raise E_{pit} in a given upward scan because the possibility exists that some specimens will contain fewer flaws.[52] A greater probability of missing such a defect in the exposed "at-risk" surface of a small electrode, also, creates the possibility of large data scatter due to specimen-to-specimen variations. Conversely, if enough small electrodes are tested then there is a finite probability that some of the small electrodes will contain a fatal flaw and the foot of the cumulative probability plot for small electrodes will present data similar to that of large electrodes as seen in Fig. 8. This was also observed during pitting in stainless steel with Mn(FeCr)S inclusions and AA 2024-T3 containing S-Al_2CuMg,

both well-known pit sites.[52,53] Fig. 2 shows a TEM micrograph of the pure Al foil. The grain size is about 10-80 μm, which is on the order of the thickness of the Al mb electrode. Considering that grain boundaries are a likely critical site for pit initiation, E_{pit} would be elevated because the average number of exposed grains would be decreased from the order of 10^3 for a fs electrode (0.1 cm^2) to 10^1 for a mb (10^{-4} cm^2) as seen in Fig. 9. Similar arguments can be expressed regarding intermetallic particle spacing and large surface scratches or gouges in melt-spun cooled ribbons if they control pit initiation.

The elevation in E_{pit} for the amorphous $Al_{87}Ni_{8.7}Y_{4.3}$ mb electrodes (Fig. 8(a)) was insignificant compared to the fs electrode. This suggests that critical depassivating flaw, although more benign than grain boundaries or intermetallics, is far more closely spaced than any spacing on the order of the electrode dimensions. It is reasonable to speculate that as the electrode size is decreased to mb electrode dimensions, an ample population of the unknown critical flaws is still present on the amorphous surface and E_{pit} is not affected. Therefore, E_{pit} does not change over the electrode surface areas explored. For amorphous $Al_{90}Fe_5Gd_5$ (Fig. 8(b)), the elevation for mb electrodes was found to be significant for reasons not yet understood. The elevation in E_{pit} for amorphous $Al_{90}Fe_5Gd_5$ microelectrodes is most likely not due to inhomogeneities in the bulk material since TEM studies show a completely homogeneous matrix.[2,3,9,11] One hypothesis to explain this higher deviation and scatter in E_{pit} for amorphous $Al_{90}Fe_5Gd_5$ mb electrodes compared to amorphous $Al_{87}Ni_{8.7}Y_{4.3}$ mb electrodes is the differences in surface morphology. Very different surface morphologies have been discovered on the as-spun ribbons as seen in Fig. 12 (a) and (b). The images in Fig. 12 (a) and (b) are of the side of the ribbon not in contact with the rotating wheel during the melt-spinning process. This side is exposed during testing. The side in contact with the wheel has been shown to be similar for

amorphous $Al_{90}Fe_5Gd_5$ and $Al_{87}Ni_{8.7}Y_{4.3}$ and is very smooth except for large ridges. Fig. 12(a) shows the featureless, smooth surface for amorphous $Al_{90}Fe_5Gd_5$. If the critical flaw for an amorphous material is visible using AFM, this image would indicate that the spacing of a critical flaw is on the order of the dimensions of a microelectrode, thereby explaining the elevation in E_{pit} for this case. Fig. 12 (b) shows the dominant surface morphology for amorphous $Al_{87}Ni_{8.7}Y_{4.3}$. Surface inhomogeneities in the form of hemispherical roughness are present and are closely spaced compared to the microelectrode dimensions. If these inhomogeneities are critical flaws, Fig. 12 (b) explains the tight statistical distribution and lack of E_{pit} elevation for amorphous $Al_{87}Ni_{8.7}Y_{4.3}$ as the surface area of large fs or small mb electrode would contain many of these surface flaws.

INSIGHT ON REPRODUCIBILITY AND SIMILARITY OF E_{rp}

E_{rp} was independent of initial electrode surface area (Table 1 and Fig. 10) and the population of small initiation sites exposed on a polished surface. However, E_{rp} is likely dependent on the depth of the largest pit.[54] The reproducibility of E_{rp} suggests that pits of similar depths were repassivated on all electrodes. The pit depths of pure Al microelectrodes subjected to anodic polarization were determined from anodic charge to be 538 μm (650 μm actual) while the pit diameter observed on fs electrodes was observed to be approximately 479 μm (Fig. 3b). The pit depths of amorphous $Al_{87}Ni_{8.7}Y_{4.3}$ mb electrodes were 223 μm (315 μm actual), while the pit diameter observed on a fs electrode 308 μm (Fig. 11). Hence, similar pit depths are found and similar E_{rp} should be expected despite different electrode sizes.[54] Therefore, differences in E_{rp} as a function of alloy and heat treatment likely reflect intrinsic material differences and differences in critical pit chemistry,[55] not alteration of geometric conditions that produce differences in mass transport properties that likely govern repassivation tendencies.[54]

CONCLUSIONS

1. Solid solution TM and/or RE alloy additions as well as the amorphous structure of the as-solidified Al-Fe-Gd and Al-Ni-Y alloys significantly enhances E_{rp} compared to polycrystalline Al suggesting these materials are more resistant to corrosion damage caused by the growth of micrometer scale pits.
2. The nanocrystalline alloys retained the pit corrosion resistance of the amorphous alloys as indicated by retention of elevated E_{rp} even when 10-15 nm nanocrystals are embedded in the amorphous matrix.
3. Complete crystallization, involving depletion of TM and RE formerly in solid solution and the formation of intermetallic phases, degrades the corrosion resistance of the Al-TM-RE alloys as characterized by lower values of E_{pit} and E_{rp} compared to the fully amorphous phase and potentials similar to polycrystalline Al.
4. E_{rp} was very reproducible in both large (0.1 cm^2) and small (10^{-4} cm^2) electrodes owing to formation and repassivation of similar sized pits in both large and small electrodes. Therefore, differences in E_{rp} as a function of alloy heat treatment reflect intrinsic material differences and differences in critical pit chemistries, not alteration of geometric conditions that might affect the mass transport factors governing pit repassivation.
5. The spacing, population and identity of critical flaws compared to the electrode test area have a significant effect on the value and the variability of E_{pit}. This study suggests that the critical depassivating flaw for the amorphous material is not only more benign but smaller and more finely spaced than the proposed critical flaws, grain boundaries and second phase particles in the fully crystalline materials.

ACKNOWLEDGMENTS

A Multi-University Research Initiative (Grant No. F49602-01-1-0352) entitled *"The Development of an Environmentally Compliant Multifunctional Coating for Aerospace Applications using Molecular and Nano-Engineering Methods"* under the direction of Lt. Col. Paul C. Trulove at AFOSR supported this study. Electrochemical instrumentation and software in the Center for Electrochemical Science and Engineering are supported by EG&G Instruments and Scribner Associates, Inc. R. Bley and J. Hsu are acknowledged for AFM images.

REFERENCES

1. Cao, B., S. Li, and D. Yi, *J. Less Common Metals*, 171, (1991): p. 1.
2. Chmielewski, R., R. Sodhi, and S.J. Thorpe, in Corrosion, Electrochemistry, and Catalysis of Metastable Metals and Intermetallics," The Electrochemical Society, Inc., Pennington, NJ, (1993), p. 84.
3. Csontos, A.A., "*Phase Transformations in Al-Based Metallic Glasses*," M.S. Thesis, University of Virginia, Charlottesville, VA, (1996).
4. Goyal, A., B.S. Murty, and S. Ranganathan, *J. Mat. Sci*., 28, (1993): p. 6091.
5. Kwong, V., Y.C. Koo, S.J. Thorpe, and T. Aust, *Acta Metall. et Mater*., 39, 7 (1991): p. 1563.
6. Shiflet, G.J., *Glassy Metals*, (in Kirk-Othmer Encyclopedia of Chemical Technology), John Wiley & Sons, Inc., (1994): p. 656.
7. Hono, K., Y. Zhang, A. Inoue, and T. Sakurai, *Mat. Trans., JIM*, 36, 7 (1995): p. 909.
8. Davis, J.R., Aluminum and Aluminum Alloys, ASM International, Materials Park, (1993), p. 784.
9. Csontos, A. and G. Shiflet, *Nanostructured Materials*, 9, (1997): p. 281.

10. Hono, K., et al., *Scripta Metall. et Mater*., 32, 2 (1995): p. 191.

11. Csontos, A. and G. Shiflet, *The Effect of Gd on Nanocrystal Formation Kinetics in Al-Rich Metallic Glasses*, Sub. for Pub. in Chem. and Phys. of Nanostruc. and Related Non-Equil. Matls., UVa, Charlottesville, 1996.

12. Buchheit, R.G., G.E. Stoner, and G.J. Shiflet, *in The Application of Surface Analysis Methods to Environmental Material Interactions, PV 91-7,* The Electrochemical Society, Inc., (1990), p. 490.

13. Bley, R., Hsu, J., J.R. Scully, *Phil. Mag. Letters 2000*, 80, 2 (2000): p. 85.

14. Archer, M.D., C.C. Corke, and B.H. Harji, *Electrochim. Acta*, 32, 1(1987): p. 13.

15. Chen, H.S., *Metallic Glasses Update*. in *Micromechanics of Advanced Materials*. 1995, Murray Hill, NJ, TMS.

16. Szklarska-Smialowska, Z., Pitting Corrosion of Metals, NACE, Houston, TX, (1986), p. 431.

17. Frankel, G.S., et al., *J. Electrochem. Soc*., 136, 4 (1989): p. 1243.

18. Moshier, W.C., G.D. Davis, J.S. Ahearn, and H.F. Hough, *J. Electrochem. Soc*., 134, 11(1987): p. 2677.

19. Shaw, B.A., G.D. Davis, T.L. Fritz, and B.J. Rees, *J. Electrochem. Soc*., Vol. 138, 11(1991), p. 3288.

20. Frankel, G.S., R.C. Newman, C.V. Jahnes, and M.A. Russak, *J. Electrochem. Soc*., 140, (1993): p. 2193.

21. Szklarska-Smialowska, Z., *Corros. Sci*., 33, (1992), p. 1193.

22. Hunter, M.S., G.R. Frank, and D.L. Robinson, in *2nd Inter. Congress on Metal. Corr.,* Houston, NACE (1963).

23. Muller, I.L. and J.R. Galvele, *Corros. Sci*., 17, (1977): p. 179.

24. Garner, A. and D. Tromans, *Corrosion*, 35, 2 (1979): p. 55.

25. Urushino, K. and K. Sugimoto, *Corros. Sci*., 19, (1979): p. 225.

26. Buchheit, R.G., et al., *J. Electrochem. Soc*., 144, 8(1997): p. 2621.

27. Tomashov, N.D., G.P. Chernova, and N. Markova, *Corrosion*, 20, 5 (1964): p. 166t.

28. Szklarska-Smialowska, Z. and M. Janik-Czachor, *Corros. Sci*., 7, (1967): p. 65.

29. Tomashov, N.D., G.P. Chernova, and N. Markova, *Zaschita Metallov*, 6, (1970): p. 21.

30. Brauns, E. and W. Schwenk, *Eisenhuettenw*., 22, (1961): p. 387.

31. Scully, J.R., et al., *Met. Trans*., Vol. 23A, (1992): p. 2641.

32. Chen, G.S., M. Gao, and R.P. Wei, *Corrosion*, Vol. 52, 1 (1996): p. 8.

33. Mansour, A. and C. Melendres, *J. Electrochem. Soc*., 142, 6 (1995): p. 1961.

34. Mansour, A.N., et al., *J. Electrochem. Soc*., 143, 2 (1996): p. 614.

35. Mansour, A.N., et al., *Surface Sci. Spectra*, 2, 3 (1994), p. 184.

36. Mansour, A.N., S.J. Poon, Y. He, and G.J. Shiflet, *Surface Sci. Spectra*, 2, 1 (1993): p. 31.

37. Lee, H.J., et al., *Corros. Sci*., 38, 8 (1996): p. 1269.

38. Virtanen, S. and H. Böhni, *Corros. Sci*., 35, 1-4 (1993): p. 27.

39. Habazaki, H., A. Kawashima, K. Asami, and K. Hashimoto, *in The Application of Surface Analysis Methods to Environmental/Material Interactions*. *PV 91-7,* The Electrochemical Society, Inc., (1990), p. 467.

40. Shackelford, J.F., Intro. to Mater. Sci. for Eng., 4 ed, Prentice Hall, Upper Saddle River, NJ, (1996), p. 239.

41. Burstein, G.T. and P.C. Pistorius, *Corrosion*, 51, 5 (1995): p. 380.

42. Shibata, T. and T. Takeyama, "Stochastic Theory of Pitting Corrosion", *Corrosion*, 33, (1997): p. 243.

43. Davis, G.D., B.A. Shaw, B.J. Rees, and M. Ferry, *J. Electrochem. Soc*., 140, 4 (1993): p. 951.

44. Pride, S.T., J.R. Scully, and J.L. Hudson, *J. Electrochem. Soc*., 141, 11 (1994): p. 3028.

45. Pistorius, P.C. and G.T. Burstein, *Phil. Trans. Roy. Soc. Lond*., A341, (1992): p. 531.

46. Newman, R.C., *Corros. Sci.*, 25, 5 (1985): p. 341.

47. Frankel, G.S., *Corros. Sci.*, 30, (1990): p. 1203.

48. Bond, A.P., Bulling G.F., Domain, H.A., Billom, H., *J. Electrochem. Soc*, 13, (1996): p. 773.

49. Gehring, C.A., Peterson, M.H., Corrosion, 37, 4 (1981): p. 232.

50. Williams, D.E., C. Westcott, and H. Fleischmann, *J. Electrochem. Soc*., 132, 8 (1985): p. 1796.

51. Manning, P.E., D.J. Duquette, and W.F. Savage, *Corrosion*, 35, (1979): p. 151.

52. Ilevbare, G.O. and G.T. Burstein, *Corros. Sci*., 38, 12 (1996): p. 2257.

53. T. Suter, R.C. Alkire, *J. Electrochem. Soc*., 148, 1 (2001): p. B36-B42.

54. Frankel, G.S., Scully, J.R., Jahnes, C.V., *J. Electrochem. Soc*., 143, (1996): p. 1834.

55. J.E. Sweitzer, J.R. Scully, R.A. Bley, J.W.P. Hsu, Electrochem. And Solid State Letters, 2, 6 (1999), p. 267.

TABLE 1

Mean values of critical potential ranges (Volts vs SCE) reported for indicated materials at the 99% confidence level. Results reported for alloys are from microband electrodes.

MATERIAL	E_{pit} (V_{SCE})	E_{rp} (V_{SCE})
Pure Al		
Free standing[†]	-0.650 ± 0.034	-0.806 ± 0.033
Microelectrode[‡]	-0.376 ± 0.113	-0.754 ± 0.009
Amorphous[‡]		
$Al_{87}Ni_{8.7}Y_{4.3}$	-0.237 ± 0.030	-0.358 ± 0.011
$Al_{90}Fe_5Gd_5$	-0.099 ± 0.093	-0.304 ± 0.007
Nanocrystalline[‡]		
$Al_{87}Ni_{8.7}Y_{4.3}$	-0.133 ± 0.167	-0.371 ± 0.018
$Al_{90}Fe_5Gd_5$	+0.044 ± 0.130	-0.334 ± 0.009
Fully Crystalline[‡]		
$Al_{87}Ni_{8.7}Y_{4.3}$	-0.143 ± 0.194	-0.760 ± 0.008
$Al_{90}Fe_5Gd_5$	-0.499 ± 0.163	-0.798 ± 0.006

[†]Free standing electrode surface area is 10^{-1} cm^2

[‡]Microelectrode surface area is 10^{-4} cm^2

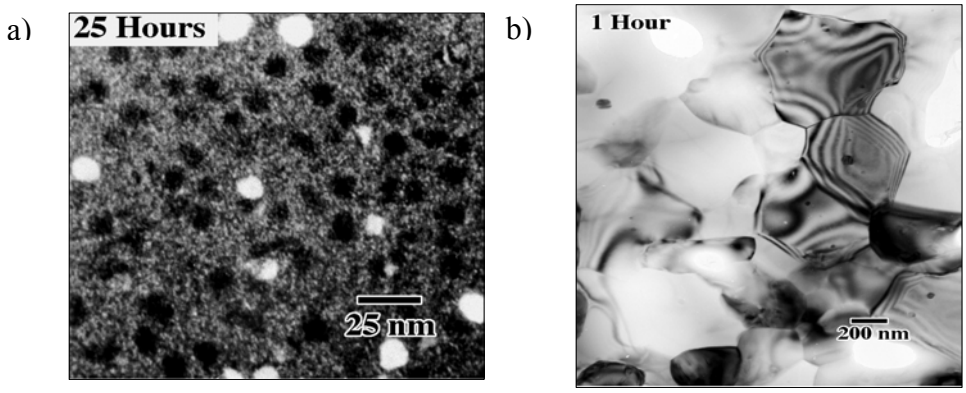

FIGURE 1. Dark field TEM image of nanocrystalline $Al_{90}Fe_5Gd_5$ obtained by heat treating an amorphous ribbon at 150°C for 25 hours (a), and bright field transmission electron microscope image of crystalline $Al_{90}Fe_5Gd_5$ obtained by heat treating an amorphous ribbon at 550°C for 1 h (b).[3]

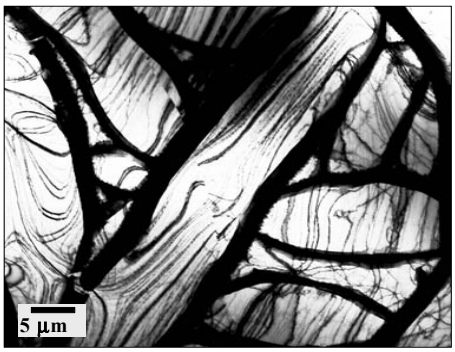

FIGURE 2. Transmission electron micrograph of pure polycrystalline Al foil.

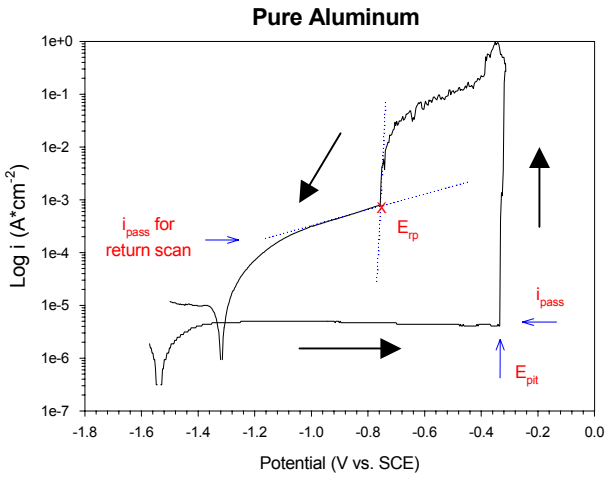

FFIGURE 3a. E-log i behavior showing the determination of E_{pit} and E_{rp} from an anodic potentiodynamic polarization experiement for pure Al. Electrode area is 10^{-4} cm^2. The arrows show the direction of the potential scan.

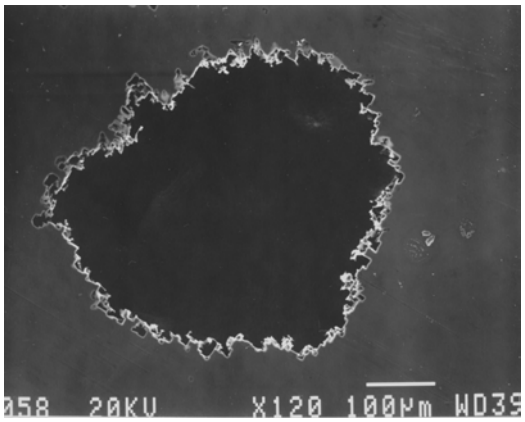

FIGURE 3b. Example of stable pit formed in polycrystalline Al after E-log(i) scan to determine E_{rp}.

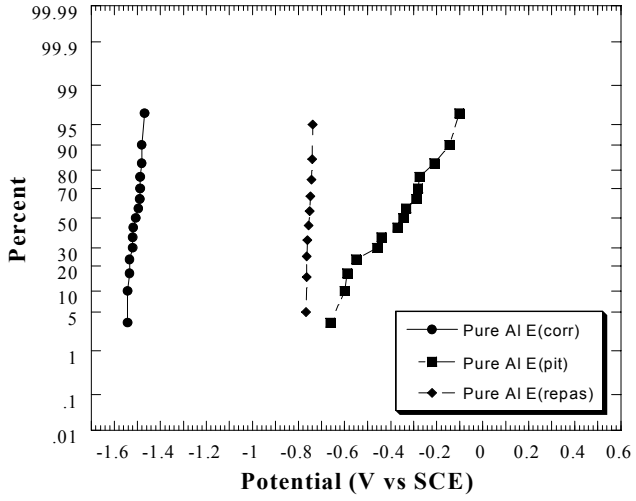

FIGURE 4a. Cumulative probability plot of E_{corr}, E_{pit}, and E_{rp} for high purity polycrystalline Al micro-band electrode (surface area of 10^{-4} cm^2) in deaerated 0.6 M NaCl.

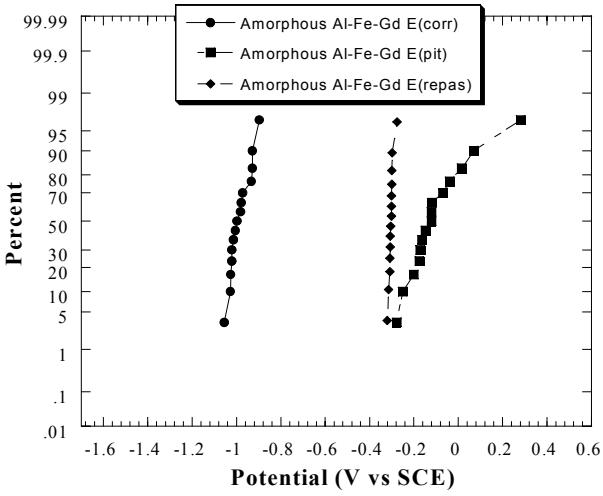

FIGURE 4b. Cumulative probability plot of E_{corr}, E_{pit}, and E_{rp} for $Al_{90}Fe_5Gd_5$ micro-band electrode (surface area of 10^{-4} cm^2) in deaerated 0.6 M NaCl.

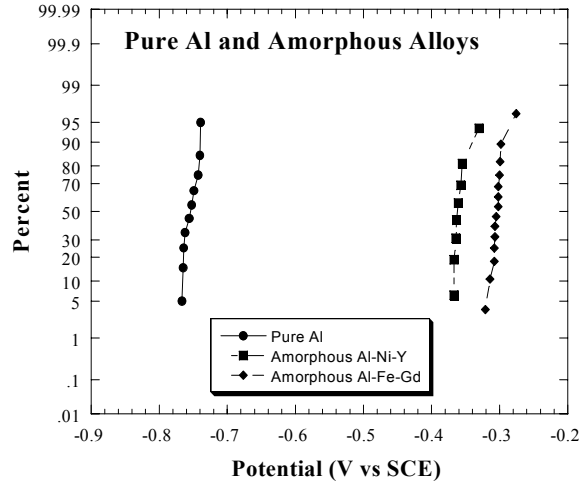

FIGURE 5. Cumulative probability plot of E_{rp} for pure Al and amorphous alloy micro-band electrodes (surface area of 10^{-4} cm^2) in deaerated 0.6 M NaCl showing the improved pit corrosion resistance of both amorphous alloys.

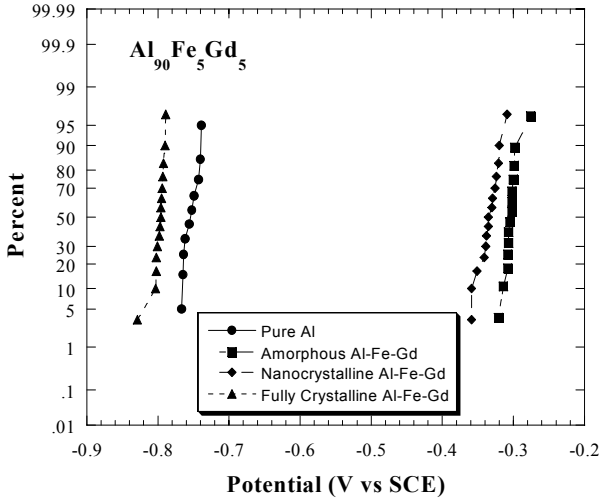

FIGURE 6. Cumulative probability plot of E_{rp} values for amorphous, nanocrystalline, and crystalline $Al_{90}Fe_5Gd_5$ micro-band electrodes (surface are of 10^{-4} cm^2) in comparison to pure Al in deaerated 0.6 M NaCl.

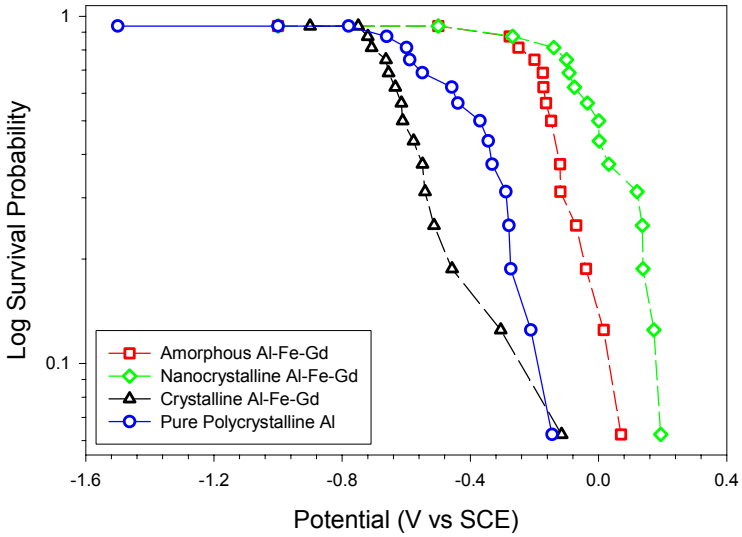

FIGURE 7. Survival probabilities with respect to stable pitting as a function of electrode potential for amorphous, nanocrystalline, and crystalline $Al_{90}Fe_5Gd_5$ in comparison to high purity, polycrystalline Al in deaerated 0.6 M NaCl. (micro-band electrode)

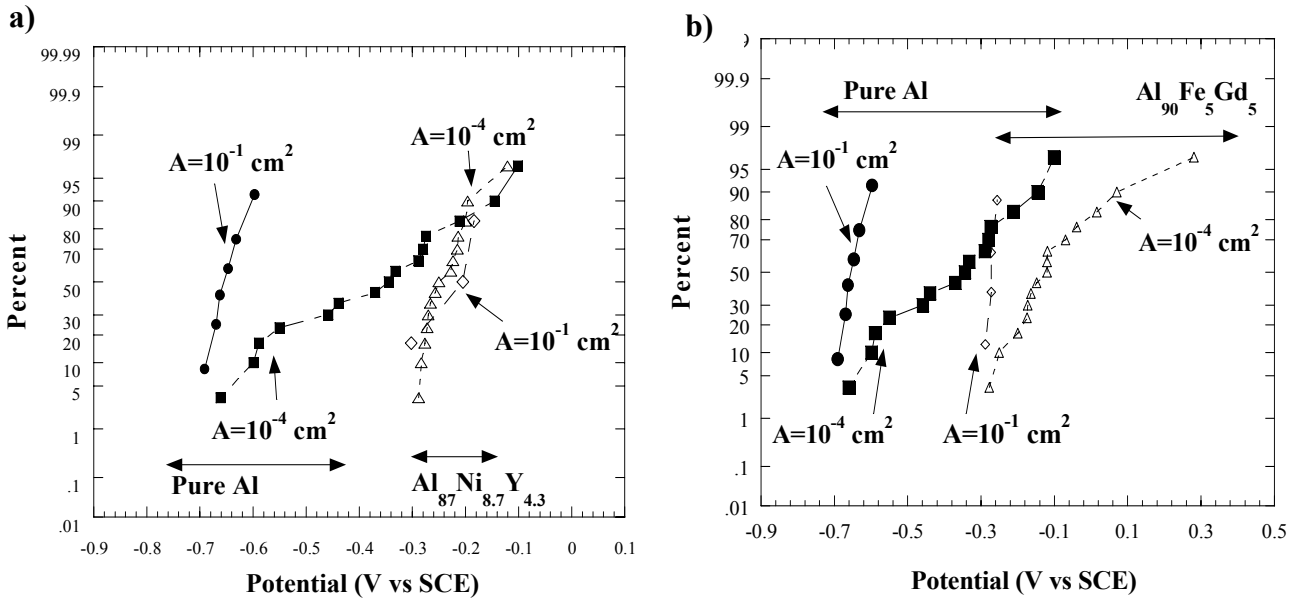

FIGURE 8. Cumulative probability plots of E_{pit} values for amorphous $Al_{87}Ni_{8.7}Y_{4.3}$ (a) and $Al_{90}Fe_5Gd_5$ (b) in comparison to polycrystalline Al for large and small surface area electrodes (deaerated 0.6 M NaCl). (•) Free standing polycrystalline Al, (+) micro-band polycrystalline Al, (◊) free standing amorphous alloy, (Δ) micro-band amorphous alloy. Free standing test surface area = 10^{-1} cm^2, microband area ~10^{-4} cm^2

a)

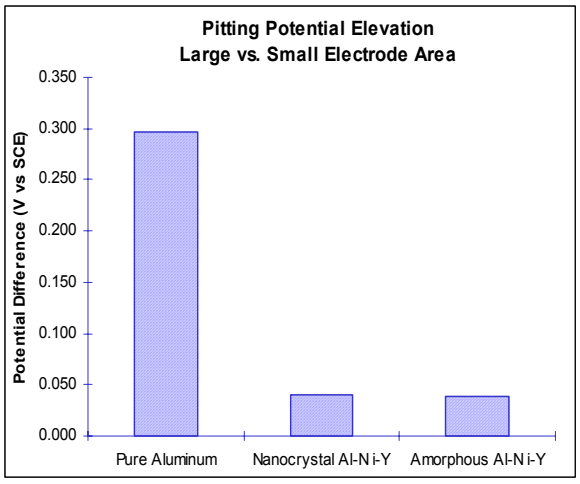

b)

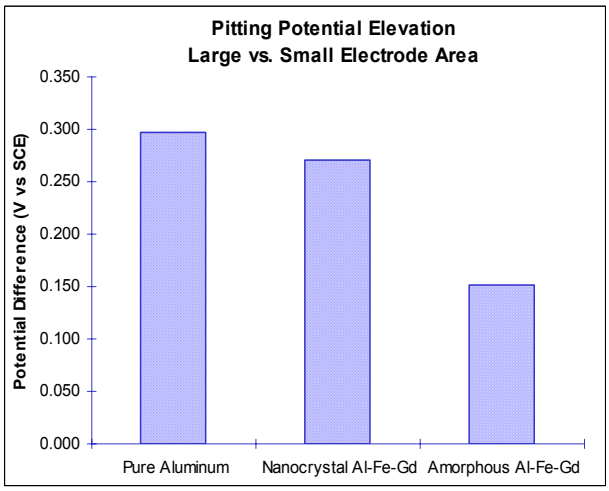

FIGURE 9. Elevation in E_{pit} given by the difference in the mean values of E_{pit} for microelectrodes compared to free standing electrodes. Cases shown are for amorphous and nanocrystalline $Al_{87}Ni_{8.7}Y_{4.3}$ (a) and $Al_{90}Fe_5Gd_5$ (b) in comparison to pure polycrystalline Al (deaerated 0.6 M NaCl).

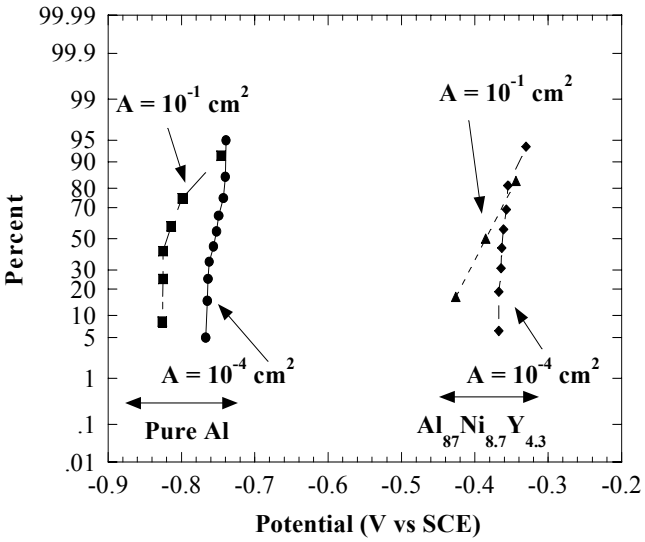

FIGURE 10. Cumulative probability distributions of E_{rp} for large and small pure Al and amorphous $Al_{87}Ni_{8.7}Y_{4.3}$ electrodes in deaerated 0.6 M NaCl demonstrating that E_{rp} is independent of initial electrode surface area.

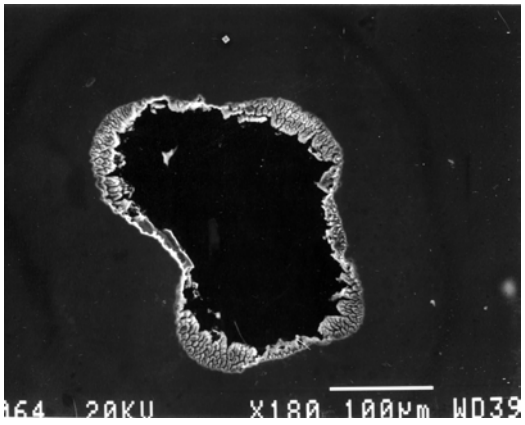

FIGURE 11. SEM-SEI micrograph of pit formed and repassivated in the amorphous $Al_{87}Ni_{8.7}Y_{4.3}$ material using a free standing electrode.

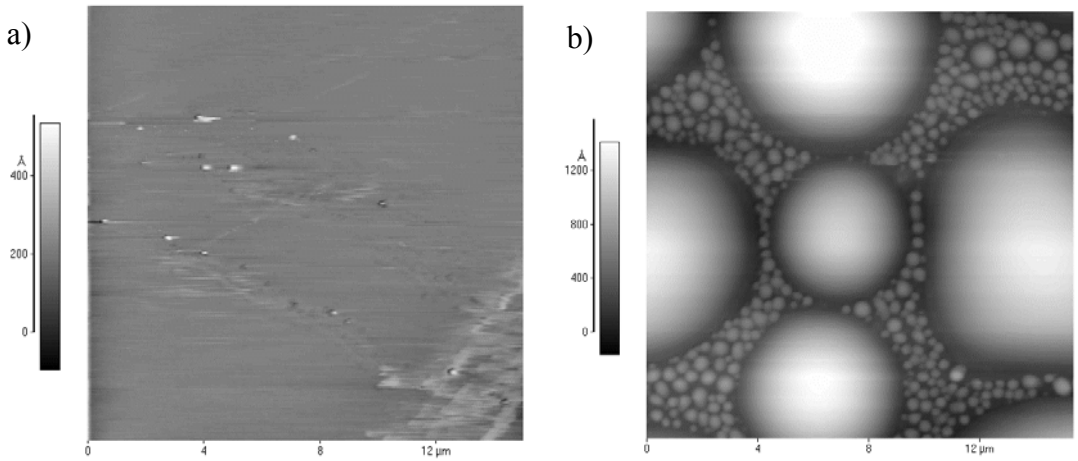

FIGURE 12. Atomic force microscope images of the surface morphologies of as-spun amorphous $Al_{90}Fe_5Gd_5$ (a) and amorphous $Al_{87}Ni_{8.7}Y_{4.3}$ (b).

THE DEVELOPMENT OF AN ADMICELLAR POLYMERIZATION PROCESS FOR DEPOSITING COATINGS ON ALUMINUM ALLOYS AND CREVICES

Olga Matarredona, Kha Mach, Steven Merchant, Ed O'Rear and Melissa Rieger

School of Chemical Engineering and Materials Science
University of Oklahoma

ABSTRACT

The main goal in this study was to assess the ability of ultra thin films of polystyrene and polypyrrole produced by admicellar polymerization to prevent corrosion within crevices on aluminum. The corrosion in model crevices coated with admicellar polystyrene was first investigated. Preliminary results showed that the admicellar polymerization of styrene provided a hydrophobic coating on aluminum flat plates and crevices. Water uptake into polystyrene coated crevices was significantly lower than in bare aluminum crevices. Corrosion inhibition was partially achieved within the polystyrene coated crevices. Preliminary voltammetry and impedance tests of polystyrene films suggest no significant protection by a barrier mechanism but protection by capillary repulsion. Thin polypyrrole films were also deposited onto aluminum alloy-7075 plates by admicellar polymerization. Two surfactants, dodecylbenzene sulfonic acid (DBSA) and pyrrole-2-carboxylic acid (P2C), were separately studied. The films formed with the P2C showed more adhesion and continuity than the films formed with DBSA. The oxidative polymerization of pyrrole, employed in admicellar polymerization, produced sulfuric acid; causing dissolution of the aluminum during the film formation, which resulted in the poor film quality and poor corrosion inhibition.

INTRODUCTION

Corrosion of aluminum alloys is a critical issue on many of the United States Air Force's older aircraft. Particularly problematic areas on these older aircraft occur around the faying surfaces and the crevices around fasteners. Such small locations usually lead to capillary uptake of water-drops from the environment, which mediate corrosion. Years of paint cleaning, parts replacement and repaint procedures during the maintenance and reconditioning lead to the removal of the original corrosion protection applied to the interfaces of the aluminum alloys and

ultimately severe corrosion problems. Thus, it would be beneficial to have a protection to eliminate the water uptake into the crevice locations and that could be applied directly to the undamaged fastener joint without removal of the fastener itself.

Researchers at the University of Oklahoma have experience in forming polymers within extremely small spaces using a process called admicellar polymerization[1-13]. This process is the surface analog of the emulsion polymerization process. The basis of the admicellar polymerization is the interaction of the surfactant with inorganic surfaces. It was found that certain characteristics of a surfactant-water solution could be adjusted in such a way as to produce surfactant aggregates on the inorganic surface in contact with the solution. Three main steps summarize the admicellar polymerization process: (i) *Admicelle Formation*: A bilayer of surfactant molecules is formed on the solid surface by adsorption from solution. (ii) *Monomer Adsolubilization*: A monomeric species that is nearly insoluble in water is introduced. The surfactant layer acts as a two-dimensional solvent at the interface. (iii) *Polymerization*: Thermally or photochemically activated initiators begin the polymerization. After the polymerization is completed, the outer layer of the surfactant admicelle can be removed by washing, to leave the polymer film exposed. Figure 1 depicts the admicellar polymerization process.

Using the admicellar process Wu et al were able to deposit thin films of polystyrene on porous alumina[3]. The process of admicellar polymerization has also been successfully implemented to form thin films on ceramic materials such as alumina and silica.[4,5] Tetrafluorethylene (Teflon), isoprene, butadiene, and styrene-diene copolymers have been polymerized on silica, titanium dioxide and alumina surfaces.[4,6] Funkhouser et al had moderate success depositing polypyrrole on flat aluminum surfaces using admicellar polymerization[14].

Recently, Yuan et al, using atomic force and scanning tunneling microscopy, were able to characterize the quality of the polypyrrole films formed on mica and alumina surfaces via admicellar polymerization. They determined that the films were smooth and continuous[12].

The focus of this research is to develop an admicellar polymerization process by which polymer thin films can be deposited into a into the small spaces between joints and fasteners of aluminum constructed aircraft for the purpose of corrosion inhibition. Two avenues of corrosion control will be examined: (1) Application of a hydrophobic polymer (e.g. polystyrene) film to prevent water uptake by capillary rise; (2) Deposition of a conductive polymer (e.g. polypyrrole) into the crevices as a electrochemical barrier to corrosion. This paper will to assess the chemical basis for the admicellar process on aluminum and the potential of the admicellar films to prevent corrosion.

EXPERIMENTAL PROCEDURES

The admicellar polymerization process was adapted from previous work to be applied on AA7075 aluminum alloy (i) 1x1 inch, 1 mm thick flat plates and (ii) 1 x1 inch depth crevice-like models. Sodium dodecylsulfate (SDS), Dodecylbenzene sulfonic acid (DBSA), and pyrrole-2-carboxylic acid (P2C) were the surfactants used to form the admicelle. Monomers used for this study were styrene and pyrrole 98%. Ammonium persulfate (APS) and AIBN were the compounds used to initiate the polymerization reactions of pyrrole and styrene respectively. All products were purchased from Sigma-Aldrich and used as received.

SURFACE PREPARATION

The samples were first brushed with commercial soap and water, followed by rinsing with Tetrahydrofurane (99.9% pure) to remove the paint. A Chromerge® solution was used as an acid wash to remove previous organic protective coating on the surface. Since Chromerge® contains chromium; elemental analysis was used to determine if any Cr remained on the surface after rinsing. No chromium was detected. Plates without pretreatment were simply cleaned with the 50/50 acetone-isopropanol mixture. Finally, the plates were rinsed with deionized water.

ADMICELLAR POLYMERIZATION PROCESS FOR STYRENE

The concentration of SDS was fixed to 6000 μM. SDS/Styrene concentration ratios and initiator/Styrene concentration ratios were varied. Monomer and initiator were dissolved in ethanol first. Adsorption time for the SDS was fixed to 4 hours. The temperature for the polymerization was fixed to 80 °C. One and two hour reactions were performed. Flat plates were placed in clean sealed plastic vials and 20 ml solution volumes were added. After the adsorption, the vials were heated up to 80°C. After the polymerization, the reaction was quenched by immersion of the vials in iced-water. The plates were then pulled out and rinsed with deionized water. Samples were then placed in the oven overnight.

ADMICELLAR POLYMERIZATION PROCESS FOR PYRROLE.

The AA-7075 plates were placed in a glass vial with 20 ml of deionized water, into which the surfactant was dissolved. Surfactant concentrations were varied below each respective critical micelle concentration (cmc) to prevent surfactant aggregation in the bulk solution. The solution set for 6 hours to allow the surfactant molecules to adsorb and equilibrate at the solid

liquid interface. The pyrrole monomer was then added and left for 12 hours to allow the solubilization into the admicelle. The ammonium persulfate was added in equimolar amounts to the pyrrole to initiate polymerization. When the solution was completely black, the plates were removed and rinsed with deionized water to remove excess surfactant and any polymer that had not adhered to the surface. The coated plates were set to dry in ambient air before electrochemical analysis was performed.

CONTACT ANGLE MEASUREMENTS.

Advancing contact angles on flat plates were measured by a Cahn DCA-322 dynamic contact angle analyzer, which used the Whilhelmy method for its calculations. Image analysis was employed to determine the static contact angles on the same samples.

CORROSION TESTING.

Three different corrosion baths were used to test the hydrophobic behavior of the coated and bare aluminum artificial crevices: 0.1 M NaCl, 3.5 w% NaCl and a solution developed by Dr. Rob Kelly at the University of Virginia[14]. Corrosion times were also varied from 24 h, 48 h to 168 h. Crevice-like models were built to simulate the corrosion process into a real crevice. 1x1 inch, 1 mm thick plates were held together to create ~ 0.15 mm width gaps in between. The corrosive solution was incorporated into the crevice by capillary forces. Then, the crevices were opened up for visual inspection.

ELECTROCHEMICAL TESTING.

Equipment used for polarization and impedance tests was the Solartron 1260 FRA with a Solartron 1287 Potentiostat. Electrochemical cell was made of an acrylic polymer (Cope Plastics, Oklahoma City, OK) and designed so small exposed area can be achieved for

reasonably equivalent crevice area. Each aluminum plate was tested at least three times at three different locations on the plate. The exposed area of the aluminum plate (working electrode, WE) for each test was 0.7 cm^2. The electrochemical cell held 45 mL of 3.5% NaCl solution with Platinum wire as the counter electrode (CE) and Saturated Calomel electrode as the reference electrode (RE). This electrochemical cell was set up for both polarization test and impedance test.

The polarization test was set up so that each sample was scanned 3 times after 10 minutes absorption in corrosion, and each of an hour after the first run. In the first scan, each sample was swept by a voltage range of +/- 0.015 V around its open circuit potential (OCP) at a very low scan rate of 0.01667 mV/s (ASTM G 61). The second scan was set at 1 mV/s scan rate and +/- 0.02 V range around OCP. The third scan was at a rapid scan rate of 10mV/s and +/- 0.3 V range around OCP. Corrosion rate was then calculated from these polarization experiments.

Impedance tests were performed on each sample at three locations. Frequency was swept from 10^5 to 10^{-2} Hz. Operating voltage is set at OCP with AC amplitude of 10 mV. Each run is separated by 1 hour to match each hour run in DC test.

RESULTS AND DISCUSSION

ADMICELLAR POLYSTYRENE

The polystyrene films were deposited onto flat AA70775 plates using admicellar polymerization of styrene with SDS surfactant. Scanning electron microscopy and specular reflectance FTIR confirmed the presence of a polystyrene uniform layer on the aluminum coated flat plates. Figure 3 shows a SEM photograph of the polystyrene thin coating on aluminum AA 7075, obtained at Styrene/SDS ratio of 5:1 and AIBN/Styrene ratio of 5:1. The reaction time was 2 hours and the pH was adjusted to 6. The polystyrene film appeared to cover the aluminum

exposed, however the presence of defects exposing minute amounts of aluminum cannot be ruled out.

Samples prepared under the conditions described above led to the modification of the substrates from hydrophilic to highly hydrophobic, to finally reach the optimum conditions to obtain a good coverage. Before the polymer was deposited onto the surface, the average advancing contact angle of the bare aluminum samples were 40°-60°. Admicellar polyystyrene samples polymerized at pH = 6 for 2 hours exhibited advancing contact angles that reached more than 100° in some cases. Additionally, when hydrophobic modified substrates were rinsed with water, water drops tended to bead up. This phenomenon is known as the "non-wettability effect". Figure 2 corresponds to water drops seating on both bare and polystyrene coated aluminum. In Figure 1a the coated aluminum surface exhibits high hydrophobicity observable from the 88º static contact angle obtained. On the other hand, Figure 1b presents a 44.5º static contact angle, characteristic of hydrophilic surfaces.

Corrosion testing was performed in a 3.5 w% NaCl solution. Corrosion times were also varied from 24 h, 48 h to 168 h. Tests were performed on two geometries: (1) fully immersed flat aluminum plates and (2) artificial crevices made of two flat plates. The artificial crevices were built from polymer coated flat aluminum plates held together with a gap of approximately 0.15 mm width and 1 inch length. The corrosive solution was drawn into the artificial crevices by capillary rise to expose the crevice in corrosive environments.

Preliminary results indicated that the admicellar polystyrene when fully immersed in chloride solutions afforded no corrosion inhibition, Figure 4. In contrast, the admicellar polystyrene when in the artificial crevices provided some corrosion protection, although water uptake was not completely avoided, Figures 5 and 6. In the case of long exposures, such as one

week, the protective characteristics of the polystyrene coated crevices can be seen in Figure 5 compared to the corrosion observed in crevices formed by uncoated aluminum. After one week of exposure to 3.5 wt% NaCl, the aluminum surface exhibited signs of mild corrosion however, the admicellar polystyrene seemed to delay the corrosion in the artificial crevices when compared to the bare aluminum sample. In the case of long exposures, the some of protective characteristics of the polystyrene were lost, probably by swelling of the polymer or by possible edge effects. In contrast, after 4 hours in 3.5% NaCl, non-treated aluminum crevices appeared fully wetted and the decreased to pH ~ 4, whereas polymer coated crevices only showed a small portion of wet area close to the edges. In addition, the pH of the crevice edge was neutral indicating no presence of corrosion by-products.

AFM was used to determine if the surfaces of polystyrene coated plates immersed in 3.5 wt % NaCl solution were indeed corroded. Figure 7 shows AFM images (100 x 100 micron) of coated and uncoated AA before and after corrosion inside the artificial crevice for 6 hours. As expected, the uncoated plates experienced corrosion after 6 hours in NaCl solution as evident by the increased roughness. However, increased roughness was also measured for the polystyrene coated aluminum. Based on work in this lab, because of the irregularity in roughness data caused by a random pitting process, AFM measurements here cannot determine the degree of corrosion only whether corrosion had occurred. Therefore it is unclear to what degree of corrosion was present under the polystyrene film, but it is believed that some corrosion occurred in the polystyrene coated crevice after 6 hours.

Uncoated and coated flat plates of aluminum samples were also tested on the plates using linear polarization. The potential shift in the corrosion potential, Figure 8, revealed that application of the admicellar polystyrene on the flat plates slightly increased the corrosion

inhibition of the aluminum. While the potential shift confirmed the present of the film, there was not a significant protection from the polystyrene by a barrier mechanism.

Electrochemical impedance spectroscopy (EIS) results showed a variation of overall impedance at different locations on the plate. The impedance of both uncoated and coated aluminum alloys varied from 10^3 Ohm.cm^2 to 10^6 Ohm.cm^2 in the first 5 hours immersed into 3.5 wt % NaCl (Figure 8). EIS results of the uncoated aluminum alloys implied that the aluminum used was heterogeneous. Both Frankel and Farrington [15, 16] also showed the heterogeneity of aluminum alloys from AFM study. The variations of the coated AAs also suggested that the film could not serve as a barrier protection on the flat plate.

The admicellar polystyrene appeared to have virtually no barrier properties to corrosion based on electrochemical impedance and polarization tests. AFM studies confirmed the presence of some corrosion on the polystyrene coated plates. The interesting phenomena was that in a crevice geometry, polystyrene appeared to reduce the amount of corrosion compared to bare AA 7075 samples and fully immersed AA 7075 coated with polystyrene. In the small spaces within the crevice geometry it appeared that the hydrophobic nature of the polystyrene film reduced the water uptake to some degree. As a result, the corrosion was delayed.

ADMICELLAR POLYPYRROLE

The admicellar polymerization of polypyrrole was performed using two surfactants, DBSA and P2C. Figure 9 shows polypyrrole formed on AA-7075 plates using DBSA and P2C as surfactants. From left to right, Sample A is an untreated, bare sample. Sample B is a pretreated, bare sample. The difference in color between A and B was due to the thicker oxide layer on the treated sample. Sample C and D are the films formed by DBSA and P2C, respectively, after rinsing. Corrosive spots on both the coated samples were also visible. The

films formed using the DBSA as the surfactant showed no continuity and very poor adhesion, as most of the black film would rinse off after polymerization. After examining DBSA concentrations below its cmc (6.3 e-4 M), it was determined visually that very little polypyrrole had been deposited on the AA-7075 plates.

Films formed using the P2C, Figure 9D as the surfactant showed much better continuity and adhesion, as most of the black film remained on the sample after rinsing. The cmc of the P2C was determined to be on the order of 10^{-3}M by means of the Wilhelmy-plate method using a Cahn-322 Dynamic Contact Angle Analyzer. There was no visual variation in the quality of the film as the concentration of surfactant was varied from 10^{-4} M to 10^{-3} M. It is proposed that the P2C performed better because of the similarity between the organic portion of the surfactant and the monomer. As a result, the concentration of pyrrole at the surface was greater since more monomer solubilizes into the admicelle; thus, better increased coverage on the AA-7075 plate. In addition to rinsing with water, a Scotch® tape test was employed to determine adherence. According to this method, the most adherent film was that formed with the P2C, followed by the film formed with the DBSA. In comparison, films of polypyrrole formed without a surfactant added showed no adherence to the aluminum.

Much of the problems with poor adhesion and film uniformity were attributed to corrosion taking place during the polymerization process. It was visually apparent that some corrosion had occurred during the polymerization process, as there were randomly located discolorations, characteristic of corrosion, on the aluminum. The oxidative polymerization of pyrrole using APS as the oxidant produces sulfuric acid, shown in Figure 10, as a by-product. This caused the surfactant/monomer solution's pH to drop from 6.5 to below 2. According to the Pourbaix diagram for aluminum, active corrosion of aluminum occurs at pHs lower than 4.5.

Therefore, as the polymerization of pyrrole proceeds with APS, the solution becomes increasingly acidic and destructive to the surface of the substrate. It is believe here that once the surface began to corrode, the admicelles were discontinuous or damaged thus interfering with the polymerization of pyrrole at the aluminum surface and ultimately the film quality.

A potential solution to this problem lies in the selection of an oxidant that will not form a strong acid as a by-product of the oxidative polymerization of pyrrole; particularly, oxidants whose by-products have relatively high pKa values. It is anticipated that the selection of such an oxidant would make the pH of the solution controllable, thus, minimizing corrosion.

Linear polarization performed on the uncoated plates was used for comparison with the polypyrrole-coated aluminum. Table 1 summarizes the results of the potential versus log of current density graphs for the aluminum samples with polypyrrole films formed by admicellar polymerization using the P2C. There was little difference in the corrosion behavior of the bare AA-7075 and the AA-7075 coated by admicellar polypyrrole. The poor corrosion inhibition was believed to be related to the problems with very low pHs formed during the polymerization of the pyrrole. Because acid forms during the polymerization of pyrrole with APS, it was believed that active dissolution of the native oxide prevented the formation of continuous and adherent films to the aluminum and caused poor corrosion protection from the polypyrrole.

CONCLUSIONS

Application of polystyrene films to aluminum alloys 7075-T6 using admicellar polymerization technique showed some improvements in corrosion protection inside crevice. Results from AFM surface characterization showed some modifications on the surface of the aluminum alloys after coating treatments. The results for coated AA plates from voltammetry and impedance experiments confirmed the present of the film, but did not indicate significant

protection by a barrier mechanism. However, admicellar coated crevice with polystyrene has showed promise of a delay for water up-take and improved corrosion protection.

The admicellar polymerization of pyrrole was attempted using two surfactants, DBSA and P2C. Use of the P2C yielded more uniform and adherent films of polypyrrole. However, film quality was poor. Electrochemical analysis using linear polarization confirmed the poor film formation and low corrosion inhibition. The polypyrrole problems were believed to be caused by dramatic decreases in pH resulting from the polymerization of pyrrole with APS. APS reacts to form sulfuric acid, causing the solution pH to decrease below 2. At pH< 4.5, the aluminum actively corrodes, preventing admicelles to remain at the aluminum surface.

ACKNOWLEDGEMENTS

This project is funded by U.S. Air Force DEPSCOR Grant # F49620-00-1-0241 and Oklahoma State Regents of High Education. Also, special thanks go to Don Neiser at Tinker Air Force Base, Harry Barraza and Wei-Li Yuan for AFM instructions.

REFERENCES

1. Wu J.; Harwell J.H.; O'Rear E.A. *Langmuir*, **3**(4), 531-537 (1987).
2. Wu J.; Harwell J.H.; O'Rear E.A. *J. Phys.Chem.,* **91**(3), 623-633 (1988).
3. Wu J.; Harwell J.H.; O'Rear E.A. *AICHE Journal,* **34**(9), 1511-1518 (1988).
4. O'Haver J.H, Harwell J.H.; O'Rear E.A.; Snodgrass L.J.; Waddell W.H. , *Langmuir,* **10**, 2588-2593 (1994).
5. Chen, H. Masters Thesis, University of Oklahoma (1992).
6. Lai C., Harwell J.H.; O'Rear E.A.; Komatsuzaki S.; Arai J.; Nakakawaji T.; Ito Y., *Langmuir*, **11**, 905-911 (1995)

7. Waddell W. H., O'Haver J.H.; Evans L.R.; Harwell J.H., *J. Appl. Polym. Sci.*, **55**(12), (1995).

8. Thammathadanukul V., O'Haver J.H.; Harwell J.H.; Osuwan N.N.;Waddell W.H., *J. Appl. Polym. Sci.*, **59**(9), 1427-1435 (1996).

9. O'Haver J.H., Harwell J.H.; Evans L.R.; Waddell W.H, *J. Appl. Polym. Sci.*, **59**(11), 1741-1750 (1996).

10. Grady B.P., O'Rear E.A.; Penn L.S.; Pedicini A. , *Polym. Comp.* **19**(5),579-587 (1998).

11. Cho G.; Glatzhofer D.T.; Fung B.M.; Yuan, W.-L.,O'Rear E. A., *Langmuir,* **16**, 4424-4429 (2000).

12. Yuan, W.-L.; O'Rear, E. A.; Cho, G.; Funkhouser, G. P.; Glatzhofer,D. T. *Thin Solid Films*, 385(1,2), 96-108 (2001).

13. H.J Barraza., M.J Hwa. K Blakley, E.A. O'Rear, B.P. Grady., *Langmuir,* **17**(17), 5288-5296 (2001).

14. G. Funkhouser , M. P. Arevalo, D.T. Glatzhofer, and

15. P. Schmutz, G.S. Frankel, *Journal of Electrochemical Society* **145**, (7).2295-2306 (1998).

16. G.C. Farrington, et al., *Journal of Electrochemical Society* **143**, (8) 2471-81(1996).

TABLE 1
A summary of results from linear polarization tests of films formed by admicellar polymerization of pyrrole using P2C surfactant.

	No Pretreatment	Pretreatment
E_{corr}	-728 mV	-709 mV
I_{corr}	1.22 E-6 (amp/cm^2)	3.23 E-6 (amp/cm^2)
$Rate_{corr}$	.014 mmPY	.036 mmPY

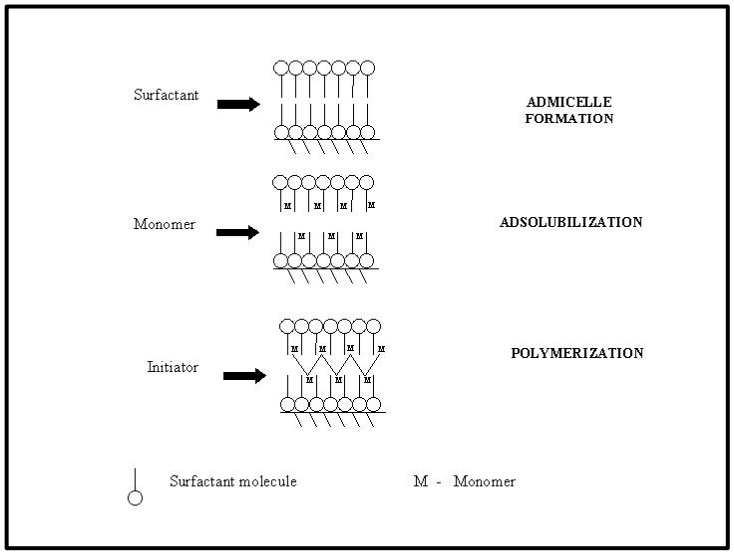

FIGURE 1. Schematic of the admicellar polymerization process.

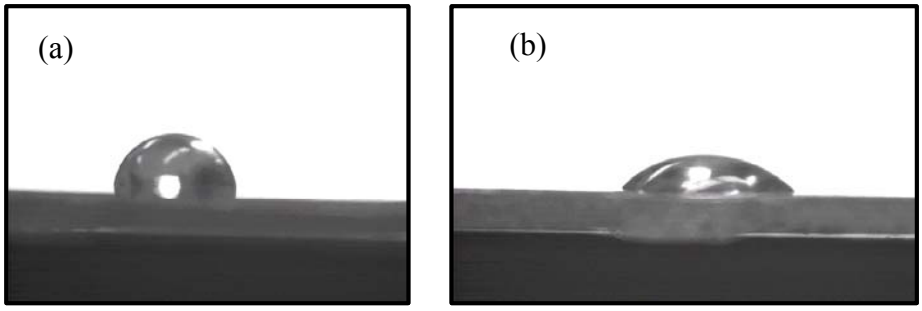

FIGURE 2. Static contact angles of water-drops in contact with aluminum 7075; (a) water drop on polystyrene modified aluminum, static contact angle is 88º; (b) water drop on bare aluminum, static contact angle is 44.5º.

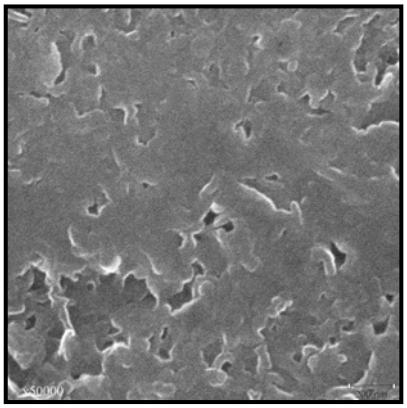

FIGURE 3. SEM image of polystyrene coated aluminum AA7075 flat plate (x50000).

FIGURE 4. A photograph illustrating the corrosion present after fully immersing the admicellar polystyrene/aluminum plate in 3.5 wt% NaCl for 48 h.

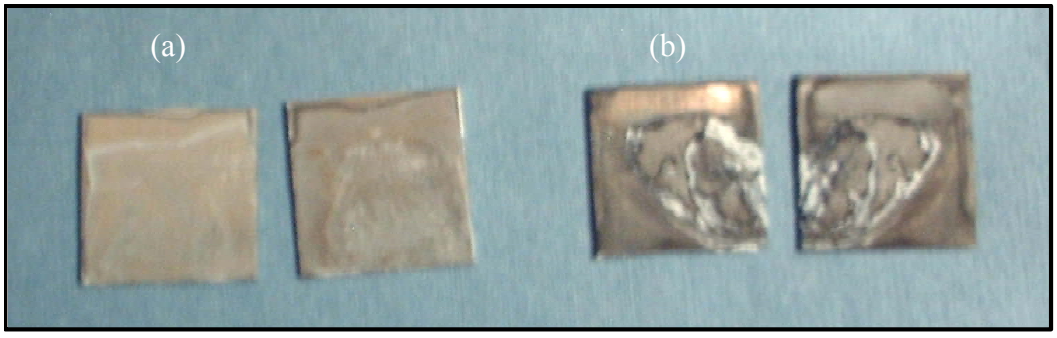

FIGURE 5. Aluminum AA7075 1x1 inch plates after 168h, 3.5 w% NaCl corrosion test by capillary effects in the interior of the artificial crevice, (a) Bare aluminum, (b) Polystyrene coated.

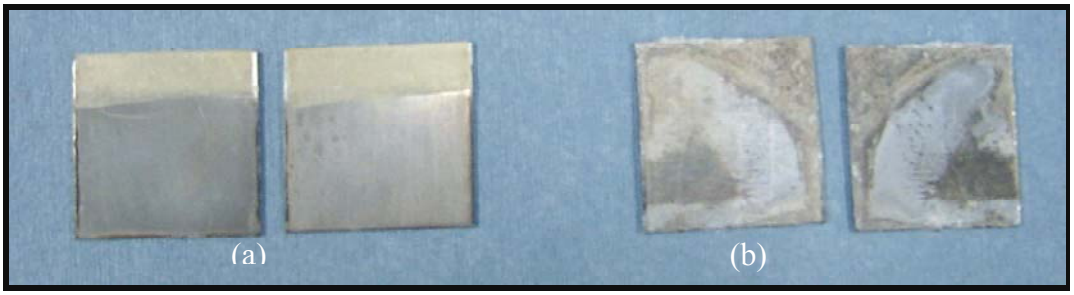

FIGURE 6. Aluminum AA7075 1x1 inch plates after 48h, 0.15 M NaCl corrosion test by capillary effects in the interior of the artificial crevice (a) Polystyrene coated, (b) Bare aluminum.

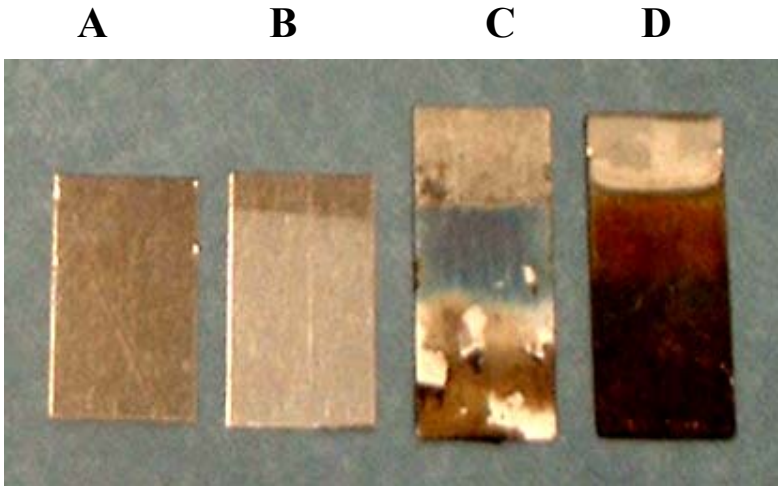

FIGURE 7. From left to right (A-D); A- bare sample; B- pretreated sample; C- film using DBSA; D- film using P2C.

TRANSIENT TRANSPORT IN FLAKE-FILLED FILMS USED FOR CORROSION PREVENTION

Nancy K. Lape, William H. Smyrl, and E.L. Cussler

Chemical Engineering and Materials Science
University of Minnesota
Minneapolis, MN 55455

ABSTRACT

Aligned mica flakes and colloidal zinc oxide can combine to reduce the acid permeability and increase the lag time in polyvinylalcohol membranes. The permeability is reduced up to ten times by the flakes, but is affected much less by the zinc oxide. The lag times are increased by up to 1000 times by a combination of flakes and reaction. The results can be estimated with theories for this transport, including variations with the square of the volume fraction of flakes and the first power of the zinc oxide concentration.

INTRODUCTION

This paper explores ways to reduce membrane transport so that the membrane may be used as a barrier. Such barriers have major commercial value, but not for the common objective of chemical separations.[1] Instead, such membranes can be used as packaging to retain food freshness or to prevent flavor loss. They can be used as coatings to retard corrosion.

Barrier membranes commonly use three strategies to reduce membrane transport. First, they can be made of organic or inorganic polymers, which are highly impermeable to the solutes of interest. This strategy has been the subject of over fifty years of intense, successful effort.[2] The second strategy for reduced membrane transport is to add impermeable flakes to a polymer continuum.[3-6] When the flakes are aligned parallel to the membrane surface, the amount of membrane transport can be reduced ten times or more because diffusion now follows a tortuous path. These reductions are the basis of several commercial products, including DuPont's SELAR plastic bottles.[9]

The third strategy for reducing membrane permeability is to incorporate reactive groups within the membranes.[11-23] In almost all cases, membrane transport is found to be reduced in unsteady state, often dramatically. However, membrane transport is only rarely reduced in the steady state.

In this paper we measure the reduction of membrane permeability by using all three strategies simultaneously. We are particularly interested in predicting the permeability reductions using only a single theory. In the following sections we will show how the effects of impermeable flakes and irreversible reaction can be combined to dramatically reduce membrane transport. We will also show that this combined effect can be predicted from theories for the three individual strategies mentioned above. To accomplish this, we begin by reviewing these theories.

THEORY

The theoretical background of these ideas is most easily described in terms of a specific experiment shown schematically in Figure 1. The experiment consists of two well-stirred compartments separated by a membrane. The right-hand compartment in the figure commonly contains 0.1 M HCl in water. The pH in the left-hand compartment, which initially contains only water, is measured as a function of time.

The concentration in the left-hand compartment, easily calculated from these pH measurements, often is well described by the equation[25,26]

$$\frac{C_1}{C_{10}} = \left[\frac{A}{V\ell}\right] DH\left(t - \frac{l^2}{6D}\right) \qquad (1)$$

where C_1 is the concentration in the receiving, left-hand compartment; C_{10} is the concentration in the donating, right-hand compartment; A and ℓ are the membrane area and length, respectively; V is the compartment volume; D and H are the membrane's diffusion and partition

coefficients; and t is the time. Note that the quantities in the square brackets are geometric properties of the experiment. In contrast, D and H are chemical properties of the membrane.

Equation (1) is often used to analyze membrane experiments in terms of a membrane permeability DH and a "lag time" $(\ell^2/6D)$. Because these two properties can be accurately measured experimentally, we can from one experiment determine both the diffusion coefficient D and the partition coefficient H. To be sure, Equation (1) is an approximation at times smaller than $(\ell^2/6D)$, when some solute leaks across the membrane. This solute concentration is a known function of time, but its small value makes it hard to measure. Additionally, the concentration C_1 must change at less than the first power of time at large times, because C_1 will approach a falling value of C_{10}. This concentration change is also known vs time, but yields no new information about the membrane. For intermediate times, Equation (1) has proved to be a simple, valuable method of analyzing data for over 80 years.

ALIGNED FLAKES

We can use Equation (1) to explore the effects of aligned flakes and of chemical reactions on membrane properties. For aligned flakes, the permeability P predicted to change from its value without flakes P_o to

$$\frac{P_o}{P} = 1 + \frac{\alpha^2 \phi^2}{1-\phi} \tag{2}$$

where ϕ is the volume fraction of flakes and α is the "aspect ratio" of the flakes.[3-6,27] This aspect ratio merits discussion. Any flake implicitly has three dimensions: a short dimension, often called the "thickness"; a long dimension, a "length"; and an intermediate dimension, called a "width". The aspect ratio is defined as half the width divided by the thickness. The length is predicted not to affect the apparent diffusion coefficient.

Equation (2) has been frequently verified experimentally, but the corresponding prediction for the lag time t_L has not been as solidly verified. The flakes increase the solute's path length across the membrane, resulting in a time lag t_L given by:[28]

$$t_L = \frac{l^2}{6D} = \frac{l^2}{6D_o}\ (1 + \alpha^2 \phi^2) \tag{3}$$

Note that both the diffusion coefficient and the lag time are independent of flake size, consistent with the results for periodic spheres[29] and for aligned cylinders.[30] Note also that both D and t_L vary with the square of the volume fraction ϕ^2. This is different from the prediction for spheres and cylinders that the variation will be linear with ϕ at small ϕ.

IRREVERSIBLE REACTIONS

The effects of fast, irreversible chemical reactions on the permeability and lag time have also been carefully investigated.[22,23] We should stress that our concern here is with irreversible reactions like:

$$2\ HCl + ZnO \xrightarrow{k_R} ZnCl_2 + H_2O \tag{4}$$

where k_R is the second order reaction rate constant. For such chemistry, the Thiele modulus $(k_R C_{20}\ \ell^2/D)^{1/2}$ is much greater than one, and the reverse reaction is near zero. Such reactions are different than the reversible reactions commonly emphasized in past studies.[18-21]

The effect of such fast irreversible reactions on the steady state permeability is predicted to be zero. The effect on the lag time, t_L, is predicted to be:[22]

$$t_L = \frac{l^2}{6D}\left(1 + \frac{3c_{20}}{H\nu C_{10}}\right) \tag{5}$$

where c_{20} is the concentration of reagent initially within the membrane and v is a stoichiometric coefficient. In deriving this prediction, species "2" is taken to be immobile, and v is the moles of reacting per mole of diffusing solute. For example, for the reaction given in Equation (4), the permeating reagent is HC*l*, the stationary reagent is zinc oxide, and the stoichiometric coefficient v is one half.

. The increase in lag time predicted by Equation (5) is large, often more than two orders of magnitude. This means that a barrier film which without reaction has a lag time of only a month will, with reaction, be effective for a decade. This effect has been verified experimentally, but only for a few, very rapid chemical reactions.

COMBINED EFFECTS

The simultaneous effects of both aligned flakes and chemical reactions have not been measured. Plausibly, we expect the result of these two effects will be a permeability like that in Equation (2) and a lag time equal to

$$t_L = \frac{l^2}{6D}\left(1+\alpha^2\phi^2\right)\left(1+\frac{3c_{20}}{H\nu\, C_{10}}\right) \qquad (6)$$

In other words, we should expect these effects to be synergistic. In past efforts,[3-6,24] flakes give an increase in lag time which is easily a factor of ten and reactions give more than a factor of 100. Thus we expect the combination will give us barriers whose lag times are increased by more than a thousand times.

EXPERIMENTAL

Polyvinylalcohol (PVA) barrier membranes including muscovite mica flakes and zinc oxide were prepared using the methods and materials described elsewhere.[40] To measure the permeability and lag time of these films, permeation experiments were performed using a diaphragm cell like that shown in Figure 1. To begin an experiment, distilled water was placed in

the "receiving" compartment, and a pH probe was inserted into the compartment. This pH probe was used to monitor the change in pH with time upon the addition of acid to the second, "donating" compartment. The details for these experiments appear elsewhere.[40]

RESULTS

The goal of this research is to explore how aligned flakes and irreversible chemical reactions can combine to improve the barrier properties of a thin film. For this exploration we want to compare diaphragm cell experiments with the theoretical predictions summarized above. For this comparison, we first show that the data behave as expected, both for aligned mica flakes and for reactive zinc oxide. We then show that these effects combine as expected, at least when the flakes are evenly distributed throughout the film.

We begin by reporting the general characteristics of our experiments. Hydrochloric acid diffusion through these films is consistent with Equation (1), as shown in Figure 3. In this figure, the concentration in the left-hand, receiving compartment in Figure 1 is plotted *vs*. time. The concentration is near zero until some lag time. It then rises linearly over the length of the experiment. For a pure polyvinylalcohol (PVA) film, the lag is shortest and the rise is steepest. This shows that transport in the pure PVA is fastest. For the other films, the lag is longer and the concentration rise is slower, an indication of the better barrier properties of these films.

The permeability of the barrier films, calculated from the slopes for data like those in Figure 3, is plotted for a variety of films in Figure 4. The data at the top of this figure give hydrochloric acid permeability as a function of the volume fraction of mica ϕ in films with a constant amount of zinc oxide. The solid line, which is the behavior expected from Equation 2, shows that the permeability varies with $[\phi^2/(1 - \phi)]$. These results are consistent with earlier studies of films loaded with flakes of mica, clay, and vermiculite.[4,24,31] They signal a reduced permeability due to increased tortuosity.

The data at the bottom of Figure 4 also show acid permeability, but now in the presence of initially different concentrations of zinc oxide in films with a constant volume fraction of

aligned mica flakes. The slightly increased permeability observed is inconsistent with the constant permeability expected on theoretical grounds and shown by the solid line. We are not sure of the reasons for this discrepancy; it may be due to the formation of aqueous droplets of reaction product solutions, like zinc chloride. We will return to this question in the discussion section which follows.

The lag times for a variety of barrier films are shown in Figure 5. Again, the data for films with a constant amount of zinc oxide and varying amounts of aligned mica flakes are shown at the top of this figure, and those for films with a constant amount of aligned flakes and varying concentrations of zinc oxide are shown at the bottom. The flake-filled films do agree with the theoretical prediction of Equations (3) and (6) which are shown as the solid line. This is a much better verification of this equation than has been possible with past data. The lag times caused by reactions of HC*l* with ZnO also agree with the predictions of Equations (5) and (6), shown as the solid line at the bottom of the figure. This agreement is an affirmation of our experimental procedure, because this theory had already been carefully verified.

When a barrier film contains both aligned flakes and reactive groups, the lag times can be increased more dramatically, as shown in Figure 6. More specifically, the lag times of some pure PVA films are less than 12 seconds, and the lag times of loaded films of the same thickness are over three hours. These increases can be predicted from Equation (6). Thus the effects of aligned flakes and reactive groups combine to make still more effective barriers.

DISCUSSION

The results above show that the barrier properties of most films can be dramatically improved by aligned flakes and chemical reactions. The aligned flakes both increase the lag before penetration and reduce the steady state permeability at longer times. Both effects are dependent upon to the shape and the volume fraction of the flakes. The changes are related to the square of the mica's aspect ratio. These changed lag and permeability are also proportional to the square of the volume fraction of flakes and to the amount of reagent present.

We have verified our predictions for the increased lag and the reduced permeability. In particular, for a volume fraction of 0.10 of flakes with an aspect ratio of 30, we find a lag time ten times larger and permeability which is ten times smaller. We can increase the loading to reduce the permeability further, by perhaps 100 times. However, doing so gives barrier films which are highly brittle and so potentially less useful.

We think that one good chance of improving barrier properties more than ten times is to focus on flakes with still larger aspect ratios. One possibility is flakes made of clay which are smaller than those of mica. Such flakes are smaller than the wavelength of light and so will have better optical properties than mica. Such optical properties may be important in consumer applications like food wrap, but they will be less important for pigment-filled films like paint. Another riskier possibility is to use as flakes the lamellar structures formed by block copolymers.[32-36] Such structures could offer flexible, rubbery films whose permeability is reduced by glassy lamellae. However, past efforts on this topic seem dismal failures, presumably because the blocks were poorly aligned.

Chemical reactions also increase the lag time before permeation in quantitative agreement with predictions without any adjustable parameters. This increased lag, which is over 100 times here, has been found to be over 1000 times in other cases.[22,23] Obtaining such dramatic increases in barrier properties requires that the reaction between the diffusing solutes and the immobile reactive groups be fast, i.e., that the Thiele modulus Φ be large:

$$\Phi^2 = \frac{k_R c_{20} l^2}{D} >> 1 \qquad (11)$$

Cases where the Thiele modulus is of order one have not been completely studied. Cases where the Thiele moduli are large for both directions of a reversible reaction appear to give smaller effects.

In contrast to these successful predictions, we do not predict correctly the observed change in steady-state permeability caused by chemical reaction. We are not sure why. We had

observed decreased steady state permeability for oxygen transport initially retarded by reaction with linoleic acid, but that reaction produced an interpenetrating polymer network in a composite made more brittle by the reaction. No such similar reaction exists here. We can speculate that the reaction with HC*l* changes solid particles of zinc oxide to similar particles of zinc chloride, and that these particles increase tortuosity over that in the original membrane. However, the increased tortuosity is not that large an effect, and osmotic effects should supply water to dissolve the zinc chloride. Still more tellingly, we have observed an unaltered permeability for HC*l* reacting with zinc oxide in water-swollen cellulose nitrate films, consistent with theory but not with the similar experiments here. We can only take solace in the fact that this unexplained decrease in permeability is at least improving the barrier's properties.

All of these results show that the effects of aligned flakes and chemical reactions are independent of the polymer chosen and of the size of flakes. For example, the dependent variables in Equations (2), (3), and (5) can always be written relative to the unmodified polymer. Thus if we start with a poor barrier and add 0.10 volume fraction of flakes of aspect ratio 30, we will decrease its high permeability and increase its short lag time by about ten times. If we start with an excellent barrier with the same volume fraction of the same flakes, we will decrease its low permeability and increase its large lag time by about ten times.

We also expect that these effects will be independent of flake size and reagent particle size as long as these sizes are small relative to the membrane thickness. This is explicit in results like Equations (2) and (3), which involve only the volume fraction of flakes and not this size. It is implied in Equation (5), which depends on the assumption of a large Thiele modulus given in Equation (11). This expectation implies a large apparent reaction rate constant $k_{R.}$ This apparent rate constant may get smaller as the size of the reagent particles gets larger. We plan to explore this point in future experiments.

The success of these experiments on model systems invites speculation about how similar effects can be realized under more practical conditions. We believe that three issues are key: additive wetting, flake alignment, and reaction kinetics. Additive wetting is the simplest to

understand. Both the flakes and any reactive particles must be completely wetted by the surrounding polymer to avoid any voids or cavities along their surfaces. These voids will serve as non-selective shunts for any mass transfer, and so severely compromise any efforts at barrier manufacture. Even small voids may be crippling because diffusion in the voids can be a million times faster than diffusion in the polymer continuum. We believe that such voids are one major reason why past efforts at composite barrier fabrication have sometimes been disappointing.

The second key question is how the flakes can be aligned parallel to the surface of the barrier film. This alignment is critical. For example, imagine 10% by volume of flakes of aspect ratio 30. If the flakes are aligned perpendicular to the membrane surface, they will increase the barrier resistance by 10%. If the same concentration of the same flakes is aligned parallel to the barrier surface, the flakes will increase the barrier resistance by 1000%. This topic is addressed elsewhere in the literature,[37-39] as well as in these proceedings.

The third key question concerns the enhancement of the lag times due to reactive groups within the barrier film. Here, the gains possible are potentially very large, but considerably less assured. We believe that the risk centers on having a reaction which is faster than the diffusion, i.e., a large Thiele modulus. This point seems sometimes to be ignored in patents on reactive barriers for oxygen because the patents report successful reaction equilibria, but no reaction kinetics. It may also be a problem in water barriers developed to protect microelectronics. Nonetheless, the improved barrier properties demonstrated by this work are so large that their continued study has enormous merit.

ACKNOWLEDGMENTS

E. D. Grassl helped with the microscopy. This work was primarily supported by the U.S. Air Force (AFOSR F49620-01-1-0333). Other support came from the Petroleum Research fund of the American Chemical Society (Grant 36528-AC9). Nancy K. Lape has a National Science Foundation Graduate School Fellowship.

REFERENCES

1. W.J. Koros, "Barrier Polymers and Structures: Overview," in Barrier Polymers and Structures, ed. W.J. Koros, ACS Symposium Series 423 (1990): p.1.
2. J. Branrup, E.H. Immergut, and E.A. Grulke, ed., Polymer Handbook, Vol. VI., 4th ed., (New York, NY: Wiley, 1999).
3. E.L. Cussler, S.E. Hughes, W.J. Ward, and R. Aris,. J. Memb. Sci. 38, (1988): p. 161.
4. D.M. Eitzman, "Diffusion in Flake-filled Barrier Membranes" (Ph.D. Thesis, University of Minnesota, 1992).
5. W.R Falla, M. Mulski, and E.L. Cussler, J. Memb. Sci. 119, (1996): p. 129.
6. W.A. Wakeham, and E.A. Mason, Ind. Eng. Chem. Fund. 18, (1974): p. 301.
7. T.C. Bissot, "Performance of High-Barrier Resins with Platelet-Type Fillers: Effects of Platelet Orientation", in Barrier Polymers and Structures, ed. W.J. Koros, ACS Symposium Series 423 (1990): p. 225.
8. D.M. Eitzman, R.R. Melkote, and E.L. Cussler, AIChE J. 42, (1996): p. 2.
9. DuPont data sheet, SELAR OH Barrier Resins. E.I. DuPont De Nemours & Company, Wilmington, DE.
10. A.S. Michaels, S.K. Chandrasekaran, and J.E. Shaw, AIChE J. 21, (1975): p. 985.
11. W.J. Gauthier and D. V. Speer, U.S. Patent No. 5,981,676. November 9, 1999.
12. K. Katsumoto and T.Y. Ching, U.S. Patent No. 5,776,361. July 7, 1998.
13. S.L. Schmidt, W.N. Collette, E.A. Coleman, and S.M. Krishnakumar, U.S. Patent No. 5,952,066. September 14, 1999.
14. D.V. Speer, C.R. Morgan, W.P. Roberts, and A. W. VanPutte, U.S. Patent No. 5,529,833. June 25, 1996.
15. T. Trinh, and D.V. Pham, U.S. Patent No. 5,429,628. July 4, 1995.

16. Wood, W.E. and N.J. Beaverson, U.S. Patent No. 5,492,947. February 20, 1996.
17. L.F. Vermeiren, Devlieghere, M. van Beest, N. de Kruijf, and J. Debevere, Trends in Food Sci. and Tech. 10, (1998): p. 77.
18. D.R. Paul, J. Polym. Sci. A2, 7 (1969): p. 1811.
19. D.R. Paul and W.J. Koros, J. Poly. Sci. Polym. Phys. 14, (1976): p. 675.
20. R.A. Siegel, Algebraic, J. Phys. Chem. 95, (1991): p. 2556.
21. K.F. Finger, A.P. Lemberger, T. Higuchi, L.W. Busse, and D.E. Wurster, J. Amer. Pharm. Assoc. 49, (1960): p. 569.
22. C. Yang, E.E. Nuxoll, and E.L. Cussler, AIChE J. 47, (2001): p. 295.
23. C. Yang and E.L. Cussler, AIChE J. 47, (2001): p. 2725.
24. W.J. Ward, G.L. Gaines, M.M. Alger, and T.J. Stanley, J. Memb. Sci. 55, (1991): p. 173.
25. J. Crank, The Mathematics of Diffusion, 2nd ed. (Oxford, U.K.: Oxford University Press, 1975).
26. H.A. Daynes, Proc. Roy. Soc. Lon. Ser. A 97, (1920): p. 286.
27. W.T. Brydges, S.T. Gulati, G. Baum, J. Mat. Sci. 10, (1975): p. 2044.
28. Perry, Diana, W.J. Ward, and E.L. Cussler, J. Memb. Sci. 44, (1989): p. 305.
29. J.C. Maxwell, Treatise on Electricity and Magnetism, vol. 1, 3rd ed. (London, U.K.: Claredon Press, 1892).
30. W. Strutt (Lord Rayleigh), Philos. Mag. 34,(1892): p. 481.
31. W.J. Ward, General Electric Corporation, correspondence to author, 1985.
32. J. Csernica, R.F. Baddour, and R.E. Cohen, Macromolecules 23, (1990): p. 1429.
33. P. L. Drzal, A.F. Halasa, and P. Kofinas, Polymer 41, (2000): p. 4671.
34. D.J. Kinning, E.L. Thomas, and J.M. Ottino, Macromolecules 20 (1987): p. 1129.
35. V. Premnath, J. Memb. Sci. 110, (1996): p. 133.

36. D.H. Rein, J. Csernica, R.F. Baddour, and R.E. Cohen, Macromolecules 23, (1990): p. 4456.

37. Tachi, K., C. Okuda, and S. Suzuki, J. Coat. Tech. 62, (1990): p. 43.

38. Tachi, K. and C. Okuda, J. Coat. Tech. 64, (1992): p. 71.

39. C. Yang, W. H. Smyrl, and E.L. Cussler, AIChE J., submitted (2002).

40. N.K. Lape, C. Yang, and E.L. Cussler, J. Memb. Sci., submitted (2002).

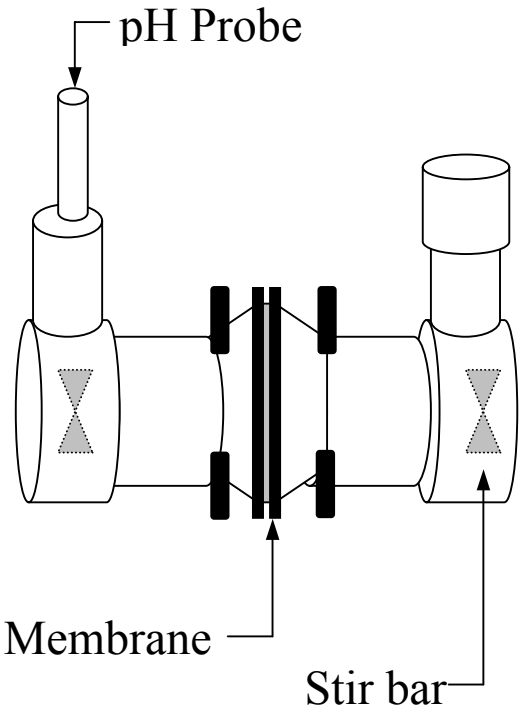

FIGURE 1. The Basic Experiment. Measurements of the concentration in the left-hand solution as a function of time give the permeability and the lag time central to the analysis presented here.

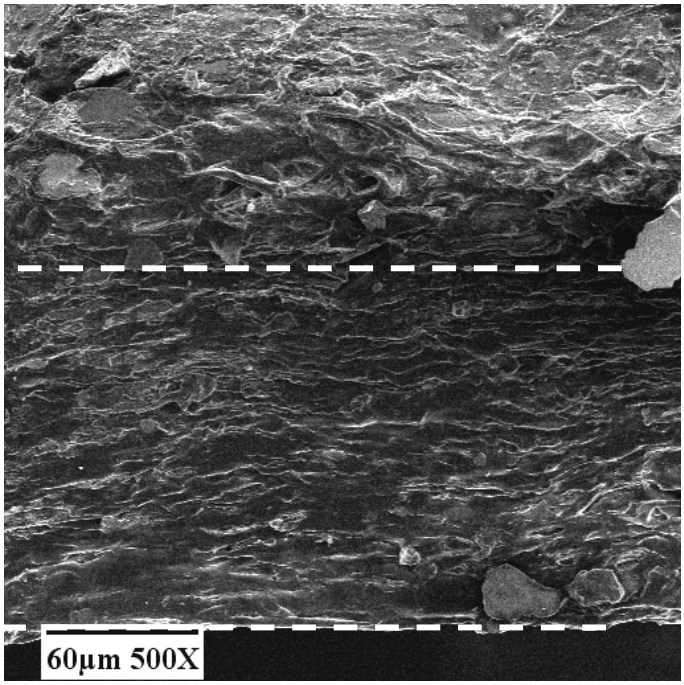

FIGURE 2. Cross-section of Flake-filled Reactive Membrane. This SEM micrograph shows aligned mica flakes with small zinc oxide inclusions in a polyvinylalcohol matrix. The cross-section is bounded by the dashed white lines.

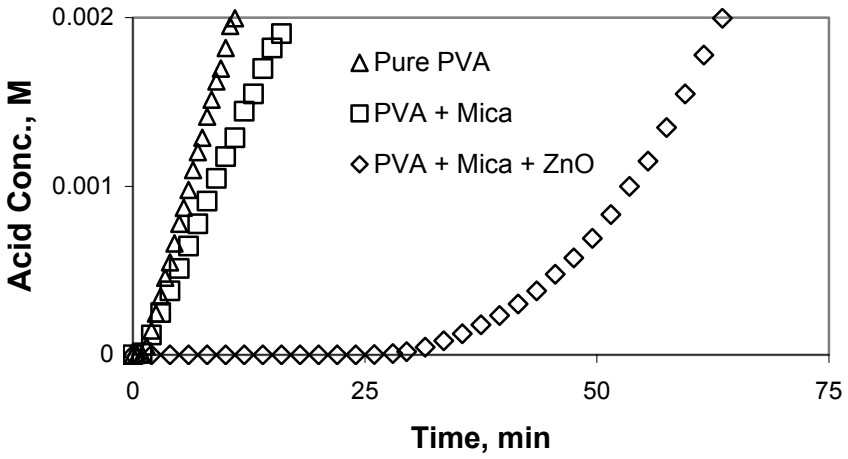

FIGURE 3. Typical Experimental Results. The permeability and lag time are found from data like these. As expected, the zinc oxide changes the unsteady state time lag more than the steady permeation.

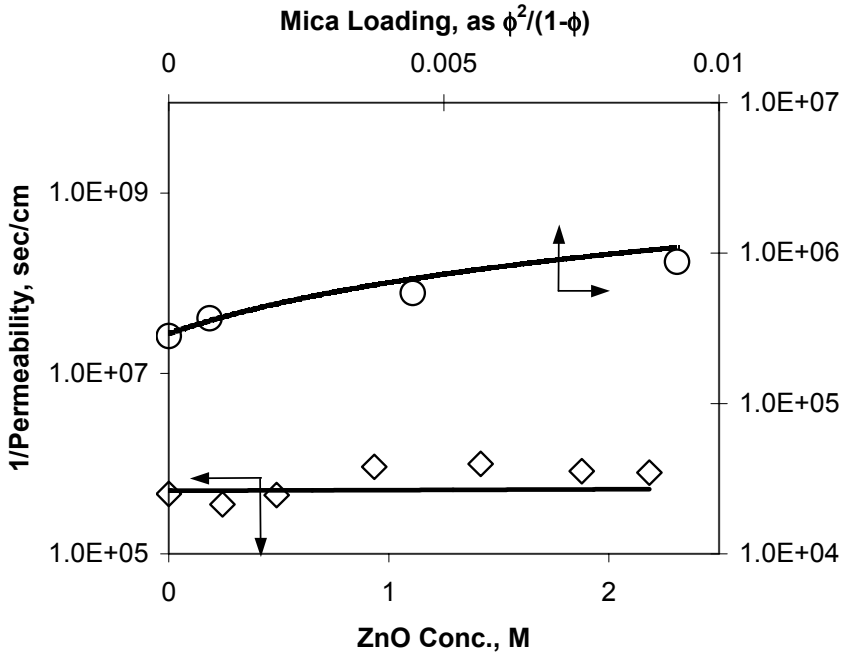

FIGURE 4. Permeability as a Function of Mica or Zinc Oxide Concentration. The solid lines are those predicted by Equation (2).

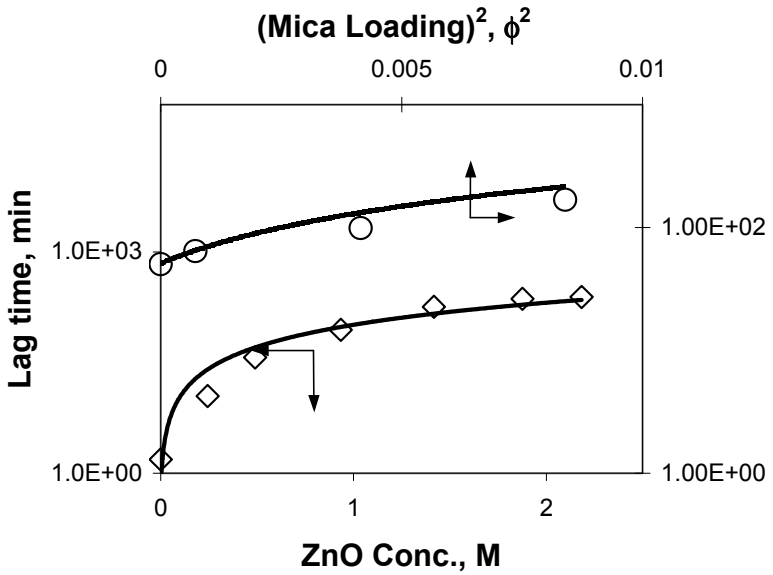

FIGURE 5. Lag Times as a Function of Mica or Zinc Oxide Concentration. The solid lines are those predicted by Equations (6).

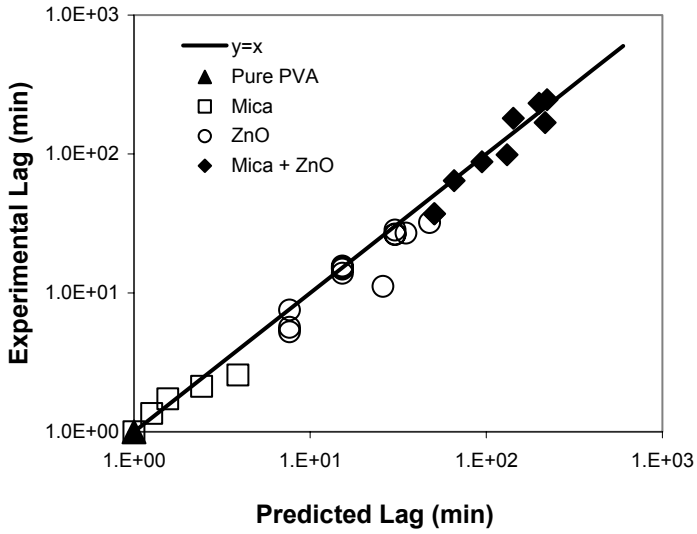

FIGURE 6. Predicted vs Experimental Lag Times. These experiments include aligned flakes and reactions, both individually and in combination. As a result, the data provide strong verification of Equation (6).

FLAKE ALIGNMENT IN COMPOSITE COATINGS

Chuanfang Yang, Allan Crasto*, W.H. Smyrl, and E.L. Cussler

Chemical Engineering and Materials Science
University of Minnesota
Minneapolis, MN 55455

ABSTRACT

Polymer coatings containing aligned mica flakes can reduce solute permeability by more than an order of magnitude. This permeability reduction can be used to reduce corrosion of aluminum coupons coated with mica-filled epoxy. The amount of permeability reduction, which depends on the flakes' volume fraction, shape, and alignment, is consistent with that predicted by published theories. The flake alignment is independent of the shear rate used to orient the flakes, consistent with fluid mechanics.

INTRODUCTION

Polymer coatings containing impermeable inorganic flakes can reduce solute permeability by ten or more times. As such, they can be used in coatings to reduce corrosion. As evidence of this, consider the coupons of aluminum 2024 shown in Figure 1(a). The coupons on the left are coated with epoxy; those on the right are coated with epoxy containing about 10 vol% mica, aligned roughly parallel to the surface of the metal coupons. As a quick test, these compounds were boiled in 0.5 M NaCl for weeks; salt fog experiments to supplement these measurements are in progress.

The epoxy-coated coupon corrodes much more quickly than the coupon coated with the epoxy-mica mixture. In particular, within one day and a half, corrosion is seen at the edge of the epoxy-coated coupon with the naked eye. The corrosion grows on the surface and penetrates deep inside the alloy. On the contrary, no corrosion is seen for the mica-filled epoxy-coated coupon within two weeks.

---

* University of Dayton

Details of this process are also shown in Figure 1. The optical micrographs of coupons coated with only epoxy and shown at the top of Figure 1(b) have evidence of some corrosion in the center of the coupon, and considerably more at the edge. In contrast, optical micrographs of the epoxy with aligned mica show no corrosion, even at the edge. Scanning electron micrographs of similar coupons, shown in Figure 1(c), have evidence of much more corrosion in the epoxy-coated coupons than in the epoxy plus mica coupons.

Thus coatings with aligned mica flakes provide substantially more corrosion protection than the same coatings without flakes. In this paper we want to explore the reasons for this result in two ways:

1) We will show that coatings with aligned flakes have dramatically reduced permeabilities. We believe this reduced permeability is the reason for the reduced corrosion.

2) We will show how shear influences flake alignment, and when Brownian motion can destroy it. This is important because unaligned flakes cause little changes in permeability.

To begin our exploration of these two implications, we review the theory of transport in these structures in the next section.

THEORY

Most simple theories for transport in composite media are based on a picture of impermeable bodies located periodically in a permeable continuum. If these bodies are spheres, the altered permeability is (Maxwell).

$$\frac{P_o}{P} = \frac{1 + \phi/2}{1 - \phi} \tag{1}$$

where P_o is the permeability of the continuum, P is that of the composite, and ϕ is the volume fraction of the impermeable bodies, in this case, the spheres. This volume fraction is often called the "loading". If the bodies are infinite cylinders aligned normal to the transport, the result is (Strutt)

$$\frac{P_o}{P} = \frac{1 + \phi}{1 - \phi} \tag{2}$$

where ϕ is now the loading of cylinders, not of spheres.

The results in Equations 1-2, which are supported by extensive experiments, are remarkable for three reasons. First, the change in permeability is independent of the size of the bodies. It doesn't matter if, the spheres are 10 nm or 10 mm in diameter; if they are present at the same volume fraction, their effect on the permeability is the same. Second, the relative permeability (P_o/P) is independent of the permeability of the pure continuum P_o. If P_o is 0.1 cm^2/sec or 10^{-8} cm^2/sec, the change caused by the impermeable bodies is still the same.

The third remarkable feature of Equations (1)-(2) is that the effects of spheres and cylinders are so similar and so small. After all, the entire result of the switch from spheres to cylinders is to replace a factor of ($\phi/2$) with a factor of ϕ. In either case, the effects are small; as Figure 2 shows, the effect of a loading ϕ of 0.1 is less than 20%.

FLAKES

The theories for transport in media with aligned impermeable flakes are very different:

$$\frac{P_o}{P} = 1 + \frac{\alpha^2 \phi^2}{1 - \phi} \tag{3}$$

where ϕ is now the loading of flakes and α is their aspect ratio, a measure of their shape. The definition of aspect ratio depends on the details of the flake alignment. For example, if the flakes are infinitely long, with a width of ($2d$) and a thickness of a, then their aspect ratio α is (d/a). This suggests a much larger effect than those expected for spheres or cylinders, as also seen from Figure 2. For example, for flakes at a loading ϕ equal to 0.1 and an aspect ratio of 30, Equation 3 predicts that P_o/P equals about 10. In other words, the flakes cause a permeability change of 1000%, a sharp contrast to the 15% expected for spheres or the 20% expected for cylinders.

EXPERIMENTAL

FILM PERMEABILITY

Film preparation and permeation measurements for polyvinyl alcohol (PVA) mica films are similar to those for PVA/ZnO films reported earlier (Yang et al., 2001), except that the ZnO particles are replaced by wet ground muscovite mica HiMod270 (Oglebay Orton Specialty Company, Kings Mountain, NC). This mica, of a specific gravity of 2.82, has the empirical formula as $KAl_2Si_3O_{10}(OH)_2 \cdot 5H_2O$. It was further exfoliated before use, following a process proposed by Barder (1951).

The preparation of mica-filled epoxy films is more complicated. We chose D.E.R. 331 as a standard epoxy resin and D.E.H.20 as the curing agent (Dow Chemicals, Midland, MI). The equivalent epoxy weight of D.E.R.331 is 189; the curing agent D.E.H.20 is an amine with five active hydrogens. A reactive diluent was used to reduce the high viscosity of the resin so that a better mixing can be achieved. The diluent, "Glydexx N-10" (ExxonMobil, Houston, TX), has an equivalent epoxy weight of 249. Surfactant modified mica ("SME") provided by the same company mentioned above was used as the filler as it has a better compatibility with the epoxy resin.

In our experiments, equal parts of resin and diluent are mixed in a beaker with magnetic stirring for an hour. Pre-weighed dry mica is then carefully added, and the mixture is stirred until a homogeneous suspension is obtained. The curing agent is then added and the mixture was stirred for 2.5 more hours at room temperature to effect partial curing. During this period, the viscosity of the mixture increases, which is helpful in reducing mica settling. The mixture is then cast on a Teflon Plate with a doctor blade. The shear rate is calculated as the ratio of blade velocity to gap. The wet film was immediately transferred to an oven for a cure at 50°C for 3 hours, followed by 100°C for two hours. In this way, the settling of mica is minimized. Finally, the film is cured for a week at room temperature.

The permeation experiments of the films are done on a diffusion cell consisting of two 40 cm^3 transparent compartments separated by the film. Initially, the left hand compartment is filled with 0.15M HC*l* and the right hand compartment contains distilled water. A pH probe attached to a Hach Sension 4 pH meter (Loveland, CO) monitors the downstream concentration of the acid. A Macintosh II si computer using Z-term 1.0.1 software records data continuously.

FLAKE ALIGNMENT

To determine the distribution of flake orientation in the film, wide angle X-ray diffraction techniques are used with a Siemens Microdiffractor. Powder diffraction of HiMod 270 mica shows that the 002 plane has the highest intensity at Bragg angle $2\theta = 8.9°$. Coincidentally, the 002 plane is also the cleavage plane of muscovite mica so the orientation of this plane reflects directly the orientation of mica flakes relative to the film surface.

In our experiments, we mount the film surface on the ZX plane, and define this angle as 0°. We then rotate the film around the X axis in the YZ plane at a step of 2° until it reaches 90°.

The highest absolute intensity is always found at rotation angle zero, indicating most flakes are aligned parallel to the surface of the film. We use this intensity as our reference, and plot the relative intensity as a function of rotation angle (orientation angle). Because relative intensity calculated with peak height or peak area makes little difference, we use peak height only.

CORROSION TESTING

The metal used for corrosion testing is A*l* 2024 aluminum alloy sheet (Corrosion Test Supplies, Maurepas, LA). It contains 4.4% Cu, 1.5% Mg and 0.6% Mn. We cut the sheet into 20 x 13 x 1.6 mm coupons and rounded the edges. The coupons are then polished, cleaned with isopropanol, and dried in air. To make the test specimen, each coupon is put into a cylindrical Teflon mold and sealed with a protective epoxy (EP21AR, Master Bond, Hackensack, NJ), with only one surface free of epoxy. After the epoxy is fully cured at room temperature, the test specimen is demolded. This protective epoxy, surrounding all but the face of the coupon, is over

0.5 cm thick and extremely resistant to acid and water permeation. The epoxy-free surface is then polished with 600-, 2400-, and 4000- grit sand paper in order, followed by a final polish with 1 μm alumina polishing powder. The bottom surface of the test specimen is polished also with 400-grit sand paper to make it flat so that the thickness of the future coating film on the coupon can be accurately measured with a micrometer within an error of 1 μm.

Epoxy coatings with and without mica flakes on the coupon are prepared following the same procedure described above. Because, as we will show, shear rate does not affect the alignment of the flakes, we can make the flake-contained coating on the aluminum coupon with either a blade of a paint knife. After oven curing, the test specimen is left in air for a week before use. These test coatings are more than 20 times thinner than the molded protective epoxy. Each test specimen with epoxy coating and mica-epoxy coating is put into 0.5N boiling NaCl solution for up to three weeks.

RESULTS

This research studies the permeability changes caused in films by aligned, impermeable flakes. Examples of such films, given in Figure 2, include films of epoxy and of polyvinyl alcohol (PVA). The epoxy system is chosen as a benchmark for corrosion resistant coatings. However, because this coating intended to be as impermeable as possible, permeability measurements are extremely tedious, lasting many weeks. As a result, we have also made measurements on PVA. While this coating is a poor barrier, permeability measurements are quick, typically only a few hours. Hence, we will make most of our measurements on PVA with checks on epoxy to show consistency.

In this research, we want to show how flakes can reduce permeability. We do so in three steps. First, we show the permeability reductions obtained. Second, we show that these reductions are predictable from simple theories. Third, we show how these permeability reductions are influenced by alignment of the flakes. Details are given in the following paragraphs.

The reduction in permeability caused by flakes is exemplified by the experimental results given in Figure 3. The delay, or lag time, is short for a pure epoxy film, and the concentration then increases very quickly. The lag time and the permeation rate are much slower for an epoxy film containing mica flake, even though the film containing flakes is somewhat thinner.

The permeability for experiments like that in Figure 3 is typically reduced about a factor of ten. In other words, if the permeability is 10^{-8} cm^2/sec in a pure polymer, it will be about 10^{-9} cm^2/sec in the same polymer but with added flakes. We can get larger permeability reductions by adding more flakes; indeed, reductions of more than 100 times are frequently observed. However, in our experiments, obtaining such high reductions requires films which are too brittle to make good coatings. We suspect that we may be able to get flexible coatings with still lower permeabilities if we replace the mica flakes with clay flakes, but we have not yet done so.

These flux reductions are consistent with the theory given in Equation (3). In particular, the steady state permeability varies with $(\phi^2/(1-\phi))$, as shown in Figure 4(a). This variation supports our contention that permeability is retarded by wiggles around the flakes, and not by gaps between flakes or necking into these gaps. If the gaps influenced mass transfer, then the reciprocal of permeability ($1/P$) would vary with ϕ. It does not. If the necking influenced mass transfer, then ($1/P$) would vary with $\phi \ln \phi$. It does not. Thus wiggles are the key.

The data in Figure 4(a) also allow us to estimate the flakes' shape. Because the slope on this plot is proportional to α^2, we can use these same data to estimate α. We get α equal to 18.

The data for the lag time give in Figure 4(b) imply similar conclusions. Again, the variation with ϕ^2 is consistent with predictions for wiggles, but not with expectations based on gaps between flakes or on necking into those gaps. The slope of these data also yields an aspect ratio of 18 Parenthetically, we have looked at these lag times more extensively in other work, including cases where the lag is altered both by flakes and by chemical reactions. Those results also fit existing theories.

Finally we turn to the issue of flake alignment. Our measurements of alignment distribution are given as a function of mica concentration, shear, and angle in Figure 5 The mica

concentrations of 5 and 10 wt% correspond to concentrations of 3.8 and 8.2 vol% of this system. The data in Figure 5 show no strong dependence of flake alignment on mica concentration.

The results in Figure 5 also show no significant dependence of flake alignment on the shear rate. This was for us at first counterintuitive; we had expected that more shear would give better alignment. The results imply that we merely need some small amount of shear to establish initial alignment, but we do not need continuing shear, which simply causes the flakes to periodically flip over.

CONCLUSIONS

Epoxy coatings with aligned mica flakes have dramatically less corrosion than the same coatings without added mica. This reduced corrosion results from a permeability which is typically a factor of ten lower when flakes are present. This lower permeability can be predicted from published theories. Curiously, flake alignment is easier than expected, engendered either by evaporation or modest shear.

ACKNOWLEDGEMENT

This work was primarily supported by the U.S. Air Force (AFOSR F49620-01-1-0333). Other support came from the Petroleum Research Fund of the American Chemical Society (Grant 36528-AC9).

REFERENCES

1. Chuanfang Yang, Allan Crasto , W.H. Smyrl, and E.L. Cussler, AIChE J., submitted (2002).
2. E.L. Cussler, S.E. Hughes, W.J. Ward and R. Aris, J. Memb. Sci. 38, (1988):P.161
3. W.R. Falla, M. Mulski and E.L. Cussler, J. Memb. Sci. 119, (1996): p.129.
4. D.M. Eitzman, R.R.Melkote and E.L. Cussler, AIChE J. 42, (1996):p.2.

5. S.W. Bailey, Reviews in Mineralogy, Volume 13: Micas, (Mineralogy Society of America, 1984).
6. W.S. Ho and K.K. Sirkar, Membrane Handbook, (Van Nostrand Reinhold, 1992).

a)

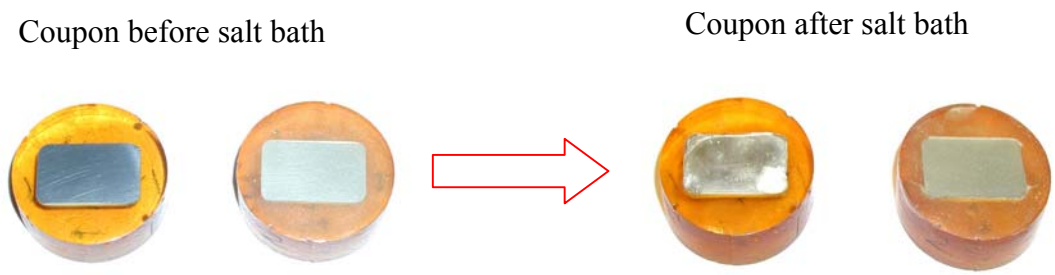

b)

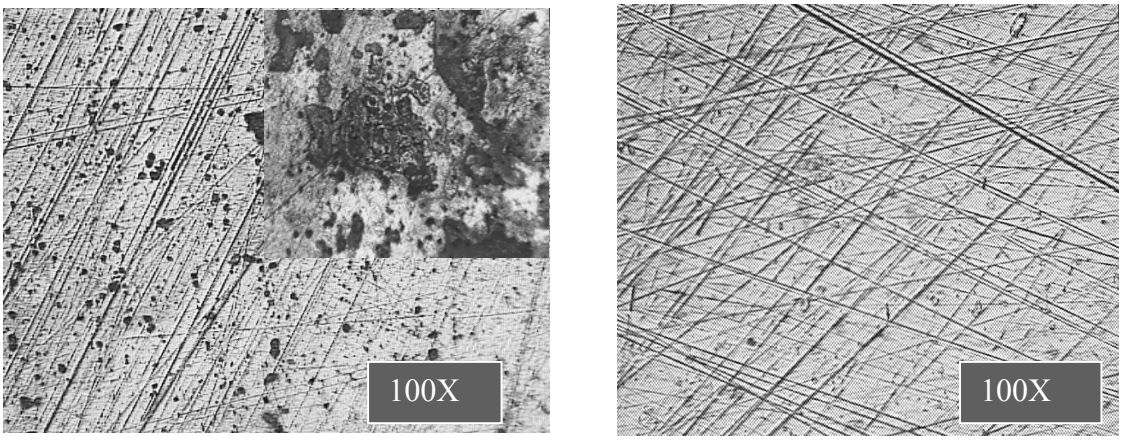

c)

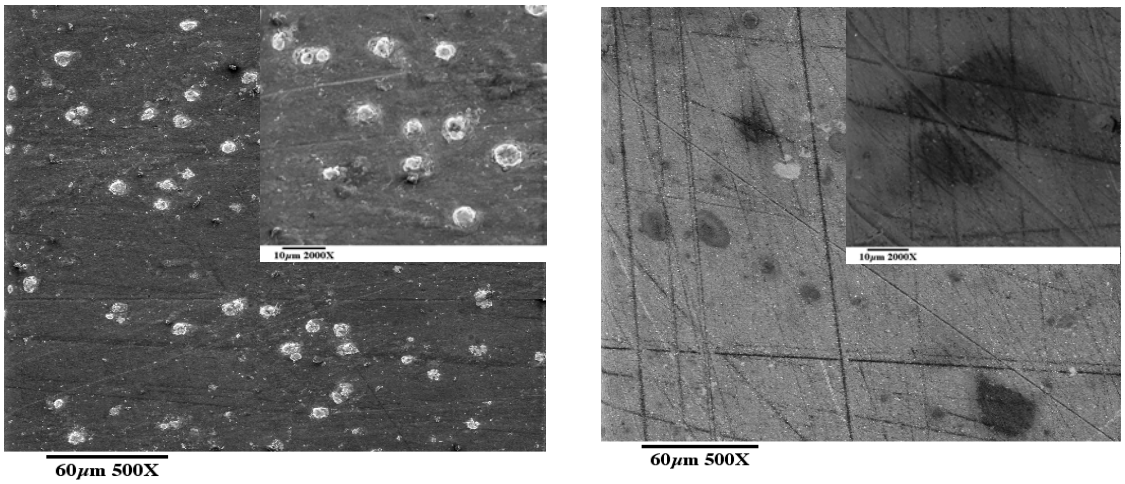

FIGURE 1. Corrosion of Al2024 Coupons Corrosion is much slower when the coating contains oriented mica flakes

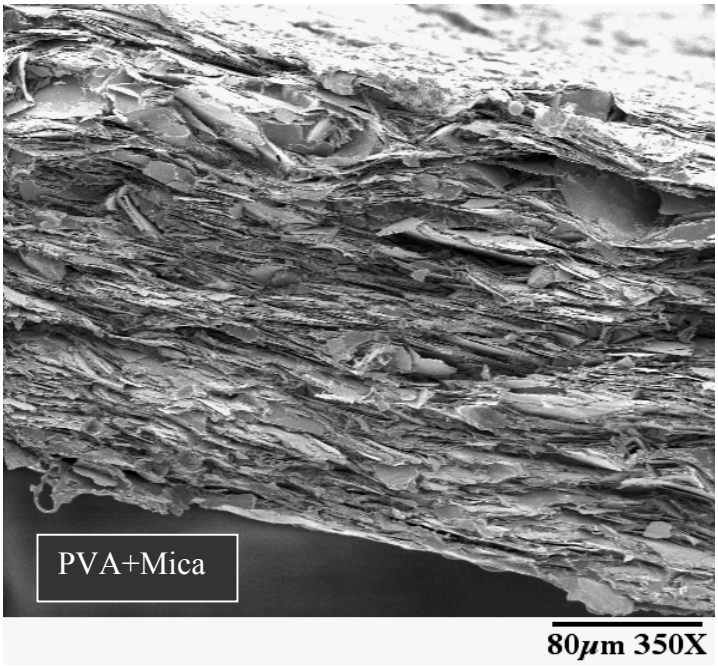

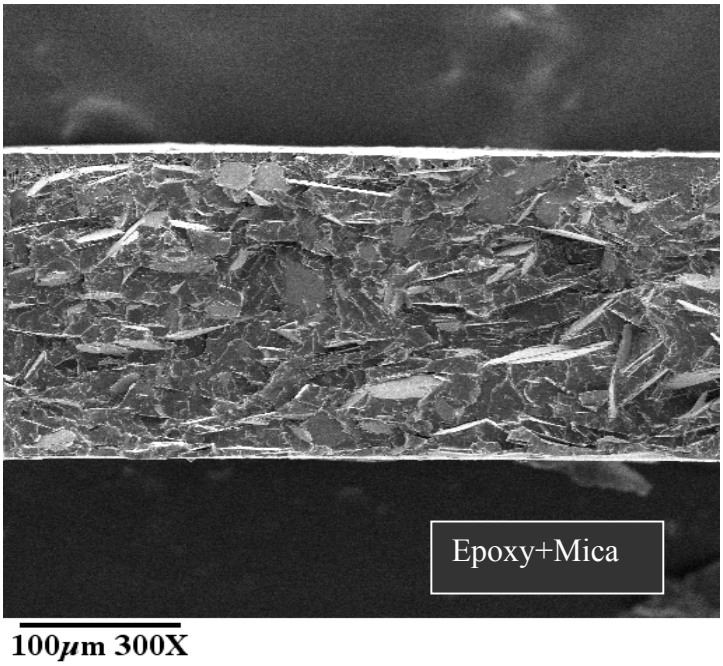

FIGURE 2. Coating Cross Section The flakes shown here are of muscovite mica. That in the top is orientated by evaporation; that in the bottom by shear

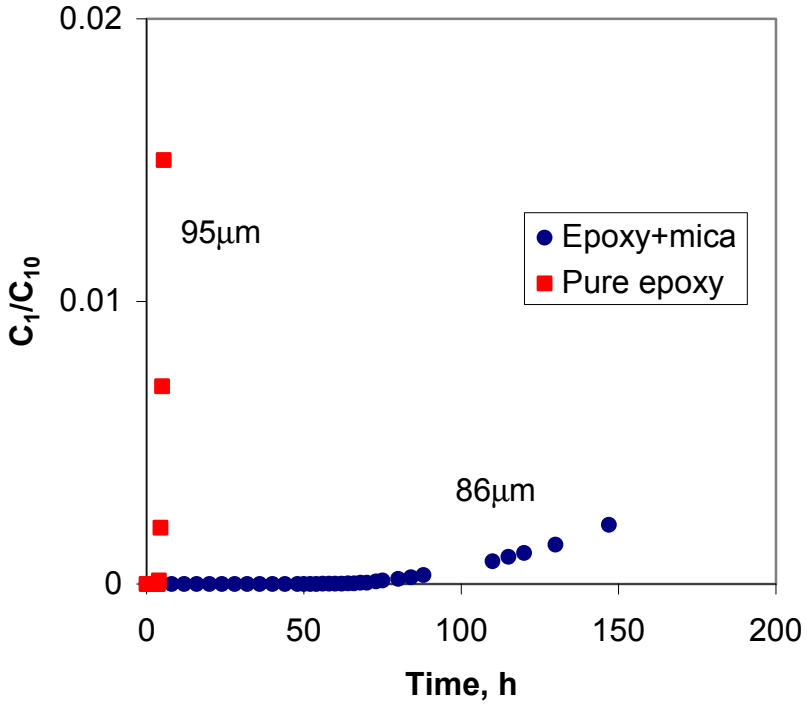

FIGURE 3. Acid leaking vs. Time The leak for a film without mica (the squares) is much faster than with mica (the circles)

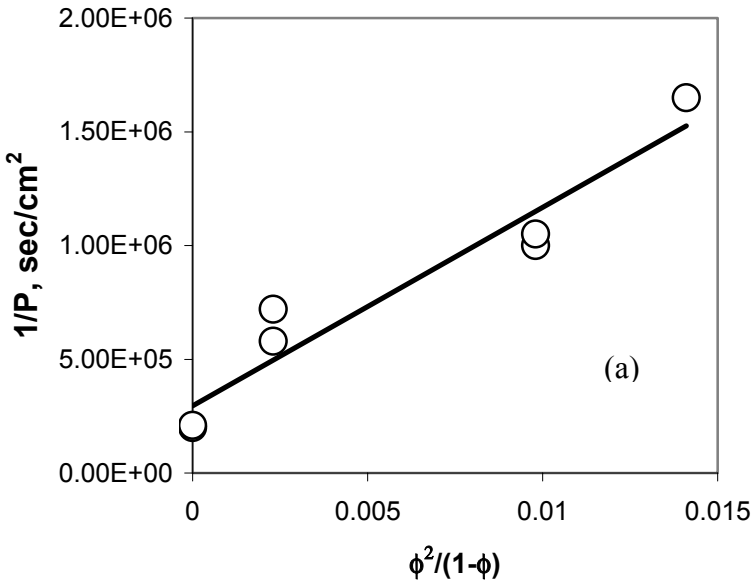

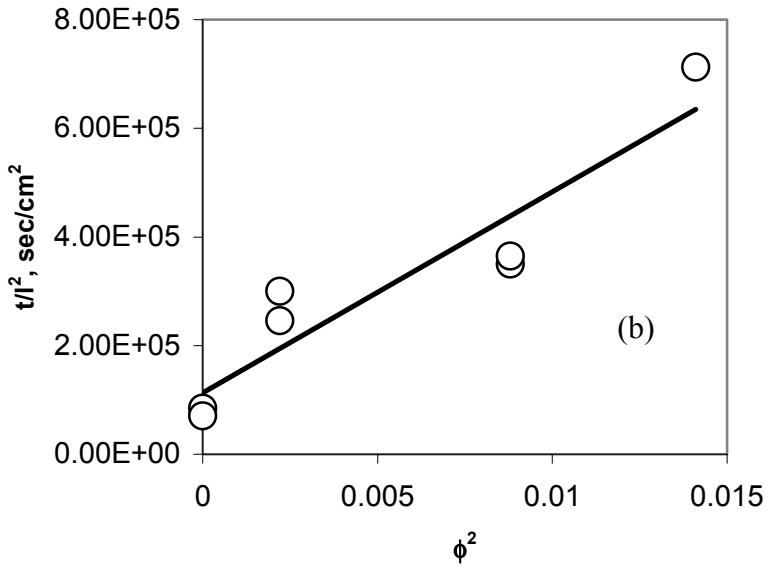

FIGURE 4. Permeability vs. Mica Loading ϕ Both permeability P and lag time t vary as suggested theoretically, including the prediction in Equation 3.

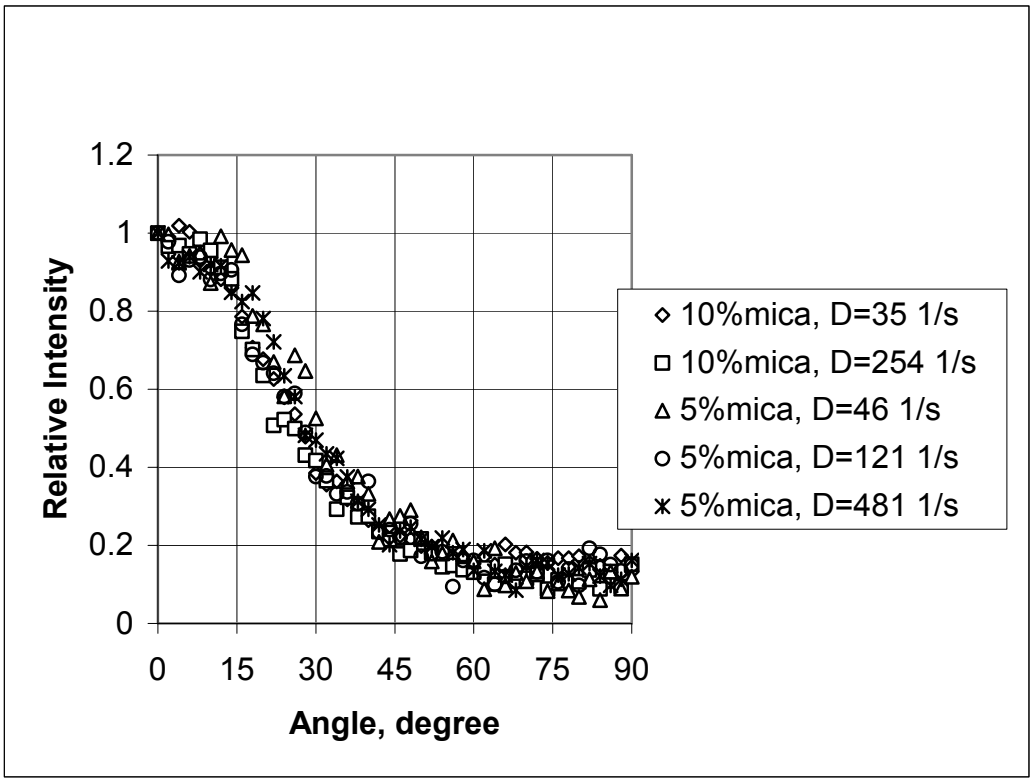

FIGURE 5. Flake Alignment vs. Angle The alignment, given as an X ray scattering intensity, is independent of loading ϕ and shear rate G.

SYNTHESIS OF SELF-ASSEMBLED NANOPHASE PARTICLES FROM ALKOXYSILANE SOLUTIONS

Raj Makote,* Mohammad Khobaib,* Chenggang Chen* and Edward Cussler[§]

*University of Dayton Research Institute, 300 College Park, Dayton OH 45469-0161
[§]University of Minnesota, Minneapolis MN 55455

INTRODUCTION

The corrosion protection of aluminum alloys in aircraft structures is increasing in importance, particularly in view of the extended use of aircraft well beyond their designed lifetimes. The conversion coatings currently used in these systems are based on toxic trivalent or hexavalent chromium salt solutions. The development of non-toxic, environmentally friendly coatings is an important task of the aircraft coating industry. Al-2024 T3 alloys have been used extensively in aircraft manufacturing and hybrid organic-inorganic polymeric coatings, prepared by simple sol-gel process [1-3], have proven to be a suitable alternative to chromate coatings on these materials. In this study we report on the development of coatings from self-assembled nanophase particles (SNAP) of organosilanes, examining in particular the effect of variations in the formulation and the incorporation of inorganic additives on the corrosion resistance of these coatings.

EXPERIMENTAL

SNAP was prepared from silane solutions. Various silanes were used (as received from Aldrich Chemicals), including tetramethoxysilane (TMOS), 3-glycidoxypropyltrimethoxysilane (GPTMS), methyltrimethoxysilane (MTMOS), and octyltrimethoxysilane OTMOS. Three different. crosslinkers were used: diethylenetriamine (DETA) $NH_2CH_2CH_2NHCH_2CH_2NH_2$; polyethyleneimine (PEI, MW ~600) $(NH_2CH_2CH_2\text{-})_x$ $[\text{-}N(CH_2CH_2NH_2)\ CH_2CH_2]_y$, and

Jeffamine D-230 (JA, MW ~230) $NH_2CH_2CH(CH_3)$-[-O-$CH_2CH(CH_3)$-]$_n$-NH_2. Montmorillonite clay (0.5% w/v) was also employed as an inorganic additive in some of the formulations.

AA2024-T3 panels (1"x3" or 3"x3") were cleaned in a standard four-bath cleaning process involving immersion in Oakite aluminum cleaner at 55-60^{o}C for 10 minutes, rinsing with distilled water, followed by 10 minute immersion in Turco Smut-Go deoxidizer for 10 minutes at 55-60^{o}C, and a final rinse with water. In a typical SNAP preparation TMOS and GPTMS were mixed in 1:4 mole ratios with water and stirred for two days at room temperature. In some cases MTMOS or OTMOS (0.5 and 0.25 mole ratio to TMOS, respectively) was added to these formulations. After two days of aging, the SNAP solution was ready for use. To this solution, a crosslinker such as DETA, PEI, or JA was added in a ratio such that one equivalent of GPTMS reacts with one equivalent of amine from the crosslinker. Precleaned aluminum panels were coated by a dip-coating method at a withdrawal rate of 5 cm/min. These panels were cured either at room temperature or at 100^{o}C for one day. A schematic of the SNAP formation is shown in Figure 1. After curing these panels, different tests were performed to study the corrosion resistance provided by the SNAP coating. Initial corrosion testing was performed via alternate immersion in a 3.5-percent NaCl solution and ambient air. The alternate immersion was continued for three weeks, and visual photographs of these panels are shown in Figures 2-4. Adhesion tests were conducted by immersing coated panels in boiling water for four hours. Microhardness tests were conducted using a Fischerscope HC100 microhardness tester, by an indentation method. SNAP particle size was measured using dynamic light scattering equipment manufactured by Precision Detectors, Inc. (PDDLS/batch mode). Montmorillonite clay (0.5

percent w/v) was added to the SNAP + crosslinker and the solution stirred for five minutes before coating panels, to investigate the effect of clay addition to SNAP.

RESULTS AND DISCUSSION

SNAP formation has been extensively studied by Donley and coworkers.[4-5] In these systems GPTMS and TMOS undergo hydrolysis and condensation reaction to form Si-O-Si linkages, which continue self-assembling to form nanosized particles. SNAP has reactive epoxy functionality. After the addition of a crosslinker, these formulations were coated on aluminum panels. Immersion in sodium chloride solution or dilute Harrison's solution was routinely used as a corrosion test for aluminum panels. SNAP coated and cured aluminum panels were placed in a 3.5-percent NaCl solution and dried in air alternately every 24 hours. Results after three weeks are shown in Figures 2 and 3. The upper row indicates panels cured at room temperature, while the bottom row panels were cured at 100^{o}C. It was observed that the addition of organosilanes such as MTMOS or OTMOS enhanced the corrosion-resistant properties of SNAP. After three weeks, the panels with OTMOS addition to the formulation showed no signs of corrosion. This organosilane has hydrophobic groups, which are included in SNAP. Because of increased hydrophobicity, these coatings are more corrosion resistant than coatings containing only TMOS in the formulation. Long alkyl chain compounds like OTMOS have a tendency to form organized micellar entities in solution. The addition of OTMOS has a structure-directing effect that helps to improve formation of SNAP. These panels did not show pitting or any other form of corrosion. This was presumably because of the evaporation of residual water and the formation of a denser film after curing.

As shown in Figure 3, SNAP coatings crosslinked with JA show enhanced resistance to corrosion compared to formulations cured with PEI and DETA. The DETA is a short-chain

crosslinker, while PEI, being a branched polymer, may not be good for uniform SNAP coatings. On the other hand, JA being a linear polymer with only terminal reactive amino groups, has a tendency to form a more organized structure and better corrosion-resistant coatings. Figure 3 indicates that JA panels demonstrated better corrosion resistance after three weeks of alternate immersion in 3.5-percent NaCl. The corrosion test performed by immersion in dilute Harrison's solution shows similar results.

Sol-gel or SNAP coatings are generally resistant to acid or base but are susceptible to hydrolysis. Cured panels were immersed in deionized boiling water for four hours to investigate the hydrolytic stability of the Si-O-Si linkage of these coatings. After removing TMOS and MTMOS, the panels showed cracks and poor adherence, but OTMOS panels performed much better due to their hydrophobic nature. Similar results were obtained for JA-crosslinked SNAP. It appears, therefore, that it is possible to improve the properties of coatings by the addition of hydrophobic organosilanes.

Curing of SNAP coatings alters its mechanical properties. The hardness of these coatings was determined by an indentation method. Vickers hardness numbers are reported in Table 1. Curing at higher temperature resulted in an increase in hardness. Evaporation of water and other solvents makes these coatings more crosslinked and dense. JA-crosslinked coatings were harder than the coatings crosslinked with DETA. Experiments are underway to study swelling properties of these coatings after exposure to salt solutions.

Formation of silica particles (20-50 nm) by the Stober process[6] is well documented. In most of the cases, silica particles are precipitated from TEOS solution using ammonium hydroxide as the catalyst. SNAP particles are grown in solution and not precipitated like silica particles. Hydrolysis and condensation of methoxy groups forms Si-O-Si bonds, and appropriate

ratios of TMOS and GPTMS formulations yield self-assembled particles. Again these are different from colloidal solutions stabilized by additives. The SNAP solution is homogeneous and transparent. It has been observed to be stable for a month without gelling. The size of these particles is of prime importance to form improved coating systems. A dynamic light scattering method was employed to evaluate particle size. Figure 5 indicates the average particle radius calculated using the Precision Detector, Inc. instrument. SNAP, after two days of aging, has an average particle size of about 1.74 nm, and after 10 days it grows to 4.84 nm. Further studies are underway to investigate the influence of particle size on properties of SNAP coatings.

An important aspect of these studies was to investigate the effect of inorganic additives such as clay, mica, alumina, etc. in enhancing the properties of SNAP coatings. Cussler and coworkers have extensively studied the barrier properties of membranes and films.[7-8] Montmorillonite clay (Na^+ form) was dispersed in the SNAP solution and, following the addition of JA crosslinker, was coated on AA2024-T3 aluminum panels. Photographs of the panels, after 10 days immersion in a 3.5-percent NaCl solution, are shown in Figure 6. It is clearly seen that panels cured at room temperature with no additive show similar behavior. However, panels cured at higher temperature (with the addition of clay to the coating formulation) performed demonstrated better corrosion resistance. This is probably due to reduction of interfacial voids between SNAP and clay at higher temperatures. Studies of the alignment of clay particles, dispersion ratios, etc. are under investigation.

CONCLUSIONS

The effect of organosilane addition to the SNAP system has been reported. MTMOS and OTMOS act as structure-directing agents for SNAP synthesis. It has also formed a hydrophobic effect on coatings on AA2024-T3 panels. Linear chain polymeric cross linker Jeffamine has

improved corrosion prevention ability of coatings. The particle size of a SNAP was found to be in the nano-range. In all cases, coatings cured at higher temperatures showed enhanced corrosion-resistance properties.

ACKNOWLEDGEMENTS

This work was supported by AFOSR Grant No. F49620-01-1-0333. We would also like to acknowledge Dr. M. S. Donley and his research group at AFRL/MLBT, WPAFB, OH for helpful discussions.

REFERENCES

1. Y. Joshua Du, M. Damron, and J. H. Osborne, *Progress in Organic Coatings 41* (2001) pp. 226-232.
2. V. Subramanian, and W. J. Van Ooij, *Surf. Eng. 15* (1999) p.168.
3. X. F. Yang, D. E. Tallman, and G. P. Bierwagen, *Surface and Coating Technology 140* (2001), p. 44.
4. A. Vreugdenhil, V. N. Balbyshev, and M. S. Donley, *J. Coatings Technology 73* (2001) p. 35.
5. M. Khobaib, L. B. Reynolds, and M. S. Donley, *Surface and Coating Technology 140* (2001), p. 16.
6. W. Stober, A. Fink, and E. Bohn, *J. Colloid Interface Sci. 26* (1968) p. 62.
7. E. L. Cussler, et al., *J. Membrane Sci. 38* (1988) p. 161.
8. E. L. Cussler, A. M. Gronda, and S. Buechel, *J. Membrane Sci. 165* (2000) p.177.

TABLE 1
Vickers Hardness Number for Coatings

Crosslinker	Cured at RT	Cured at 100°C
DETA	16.2	46.6
JA	18.2	29.4
PEI	25.7	41.3

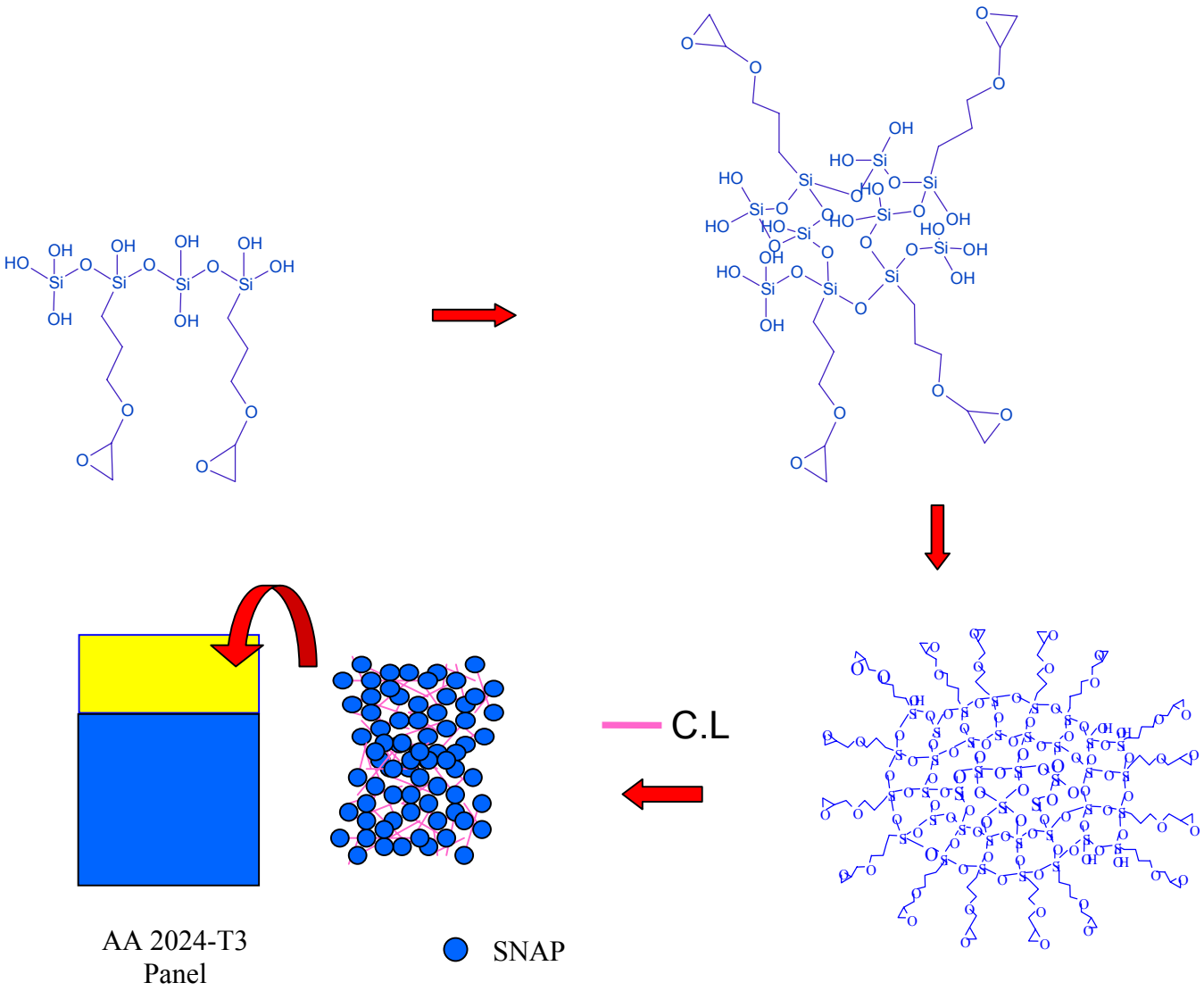

FIGURE 1: Schematic diagram of SNAP formation from silanes.

FIGURE 2: Effect of organosilanes on alternate immersion of coated aluminum panels in 3.5% NaCl solution. MTMOS and OTMOS were added into SNAP ormulations. Visual photographs taken after three weeks.

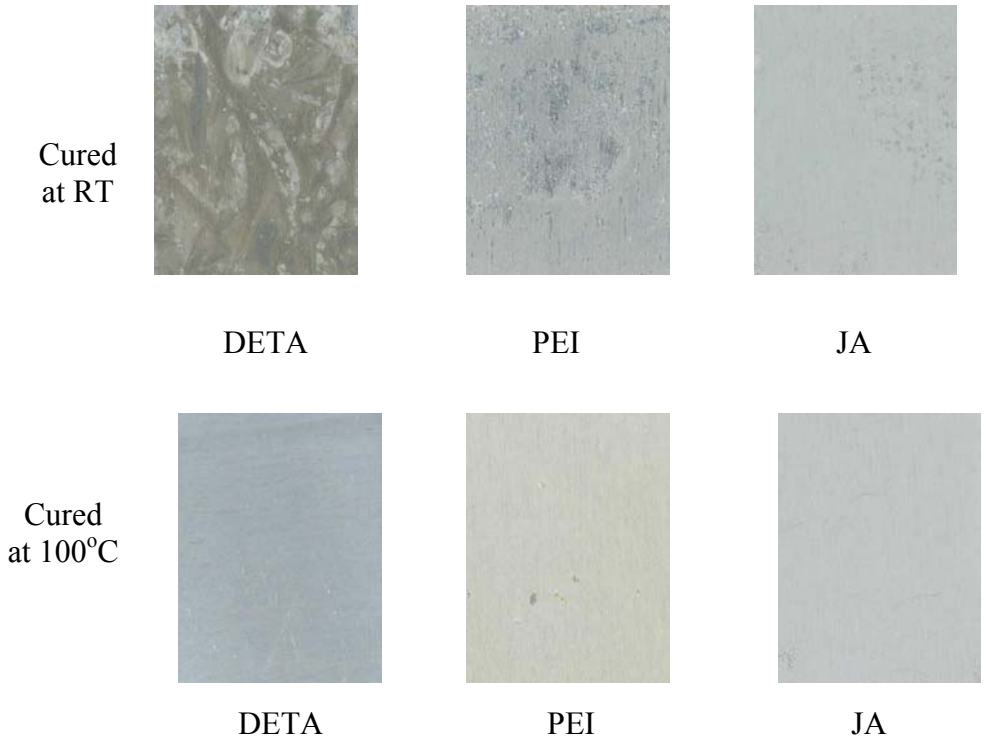

FIGURE 3: Effect of crosslinkers on alternate immersion of coated aluminum panels in 3.5% NaCl solution. DETA, PEI and JA were added into TMOS only SNAP formulations. Visual photographs taken after three weeks.

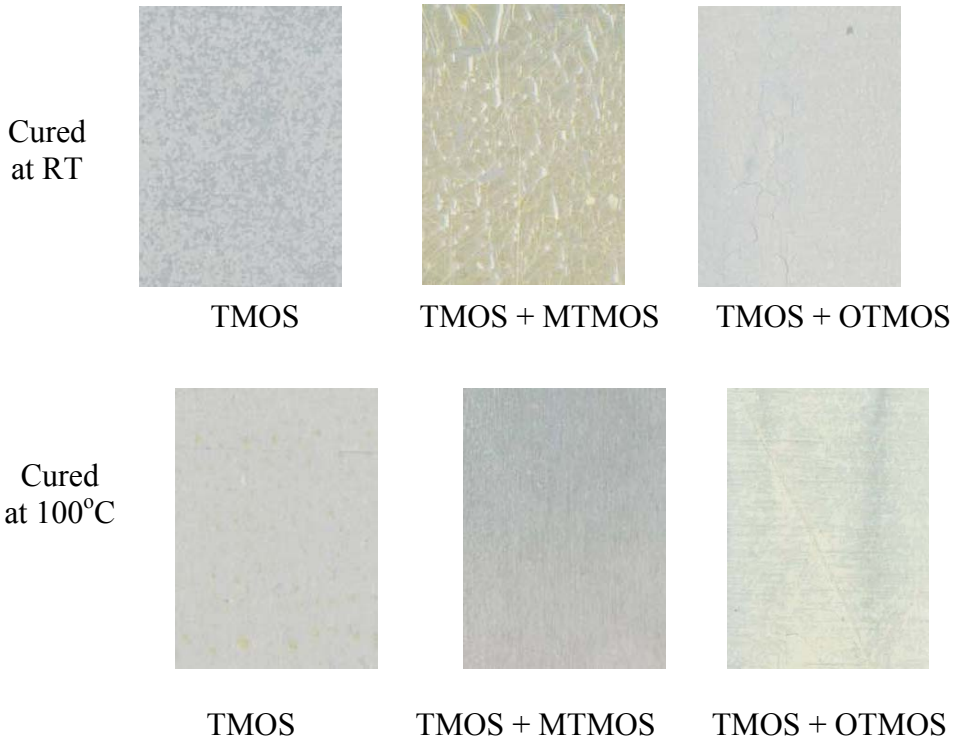

FIGURE 4: Effect of organosilanes on boiling water test of coated aluminum panels. Visual photographs taken after four hours in deionized boiling water.

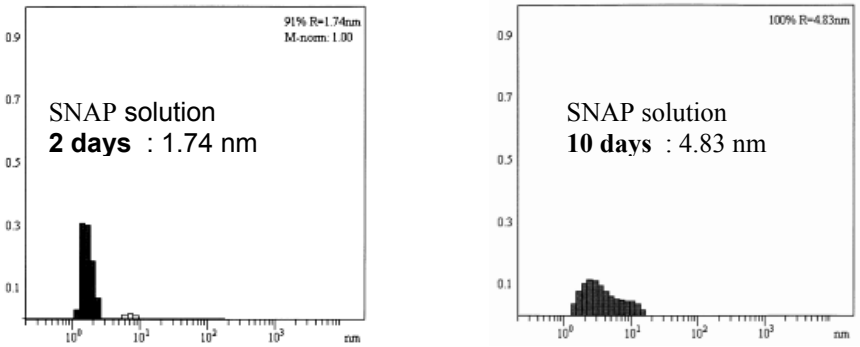

FIGURE 5: Particle size variation. TMOS+GPTMS only SNAP formulation. No crosslinker was added. Dynamic light scattering measurements in batch mode.

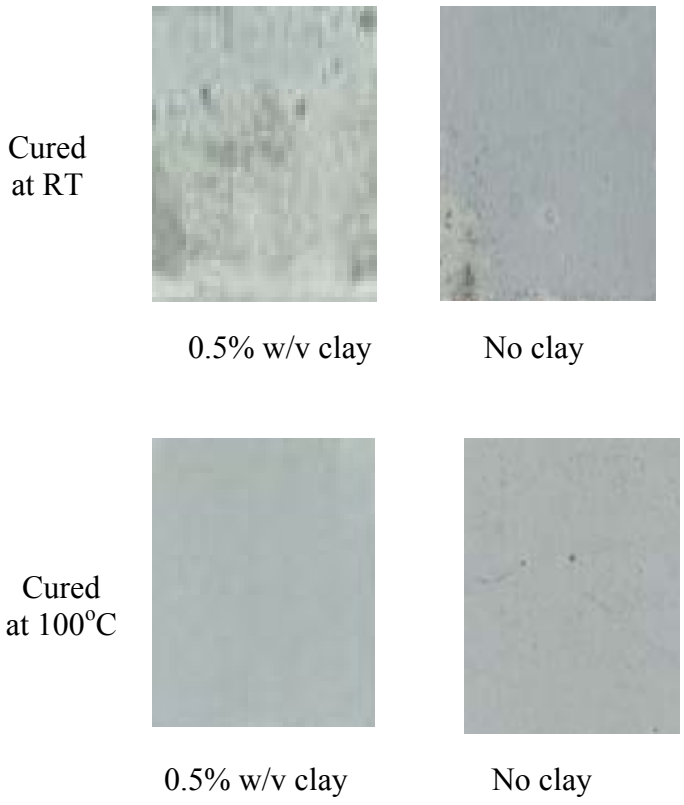

FIGURE 6: Effect of addition of montmorillonite clay to SNAP formulation. Photographs shown are JA crosslinked films immersed in 3.5% NaCl for 10 days.

LOCALIZED CORROSION GROWTH KINETICS IN Al ALLOYS

G. S. Frankel

Fontana Corrosion Center
The Ohio State University
Columbus, OH 43210

ABSTRACT

This paper describes recent work in the area of localized corrosion growth kinetics in Al alloys. Electrochemical and foil penetration experiments were used to study various tempers of AA2024 and found that intergranular corrosion growth kinetics are controlled by path length and not by grain boundary composition. The roles of grain boundary precipitates and the solute depleted zone on the intergranular corrosion of AA AA7150 were also investigated. An explanation for the effect of temper on intergranular corrosion (IGC) susceptibility was developed based on indirect influence of the grain boundary precipitates on the SDZ behavior. The foil penetration technique was used to study localized corrosion kinetics for AA7xxx alloys, which were found to be faster than for AA2024. A statistical model for IGC was developed. This model allows for determination of the nominal rate of penetration in any orientation. Finally, a novel technique was developed to understand the mechanism of IGC in Al alloys.

INTRODUCTION

The knowledge of localized corrosion growth kinetics is important from a practical point of view. Most high strength Al alloys widely used in aircraft structures are extremely susceptible to localized corrosion. While the total weight loss might be very small, local rates of attack can be very large and can lead to early catastrophic failure. A fundamental understanding of localized corrosion kinetics, including the effects of microstructure, potential, and solution environment on the development of localized corrosion, therefore, is critical for the development of predictive models.

Electrochemical techniques are commonly used for the study of localized corrosion growth[1]. Localized corrosion kinetics, such as pit growth kinetics, are often described by a relationship between current density and applied potential. However, there are several problems associated with the use of electrochemical techniques. First, the active area during localized corrosion is typically unknown and difficult to measure. Many assumptions regarding the number and morphology of localized corrosion sites are needed in order to translate measured current transients into localized corrosion growth rate. This is complicated by the fact that localized corrosion may take more than one form, such as pits, crevices, and intergranular attack. Also, in the case of Al alloys, hydrogen evolution within the pits or intergranular attack regions can consume a reasonable fraction of the anodic current, which makes the measured net current unrepresentative of the metal anodic dissolution kinetics due to the availability of local cathodic reactions. Finally, localized corrosion in a real structure occurs under open circuit conditions. Under open circuit conditions, it is impossible to use electrochemical techniques for the quantitative study of localized corrosion kinetics. The study of single pits, formed by various approaches such as implantation[2], laser irradiation[3], or the use of an artificial pit electrode[4], provides an alternative way to address the localized corrosion kinetics, but there is no assurance that the behavior of these configurations is the same as that of real pits that occur in practice. Non-electrochemical methods overcome many of these problems, and are useful for the study of localized corrosion growth kinetics.

The foil penetration technique is a non-electrochemical approach that was developed in the early 80s for the study of pit growth rate[5]. This technique offers advantages over electrochemical techniques because it measures the penetration time for the fastest-growing localized corrosion site for the determination of growth kinetics instead of using current density.

The foil penetration has been used recently to study localized corrosion behavior in AA2024-T3[6,7]. It was found that that localized corrosion can take circuitous paths while penetrating through a wrought Al alloy foil. Microfocal X-ray radiography indicated that the attack morphology was much more convoluted than a hemispherical pit[6]. The convoluted growth morphology of localized corrosion underscores the usefulness of the foil penetration technique for the measurement of growth kinetics. In fact, it was subsequently found that the growth kinetics of localized corrosion in AA2024-T3 exhibited a strong anisotropy at a controlled anodic potential; growth in the short transverse direction (through-thickness direction of a rolled plate) was found to be much slower than that in either the longitudinal or long transverse direction[7]. This is in contrast to the pitting potentials, which were almost identical for the different orientations[8]. The anisotropy occurred because pits that initiated on the surface often developed into intergranular corrosion (IGC) as they grew into the microstructure.

Pits and crevices have been shown to develop into other forms of localized corrosion, such as exfoliation or intergranular corrosion (IGC)[9,10,11]. Since the growth kinetics of IGC or exfoliation corrosion can be very different from pit growth kinetics, it is important to study them independently. However, only a few reports of quantitative measurements of the kinetics of IGC in Al alloys exist[12,13], and little is known about the influence of alloy microstructure on localized corrosion kinetics.

In this work, different approaches are taken to study localized corrosion kinetics in different Al alloys. The results can be used to enhance predictive models for localized corrosion in aging aircraft.

SUMMARY OF PROJECTS

FOIL PENETRATION AND ELECTROCHEMICAL STUDIES OF AA2024

Samples were given a solution heat treatment (SHT) in an air furnace at 492 ^{0}C for 1 h, followed by either a water quench or furnace cooling. AA2024 in the SHT + water quenched condition exhibited two breakdown potentials in a potentiodynamic polarization curve in 1 M NaCl, similar to the T3 temper. In contrast, SHT + furnace cooled AA2024 had only one breakdown potential, like the T8 temper. SHT + furnace cooled AA2024 is known to be susceptible to IGC, which supports the notion that breakdown in the T8 temper is caused by IGC. Foil penetration experiments found that the kinetics for penetration in the L direction were essentially the same for samples in the T3, T8, and SHT + water quench conditions, suggesting that growth kinetics are controlled by path length and not by grain boundary composition.

It was also reported previously that localized corrosion growth along L direction was almost independent of applied potential over a relatively wide range of potential (-610 to –490 mV SCE). In order to further examine the effect of potential on growth rate, penetration at +500 mV SCE was performed. The penetration rate at +500 mV SCE was only slightly faster than that at –490 mV SCE. One explanation for this behavior is that the anodic current at the bottom of the IGC crevices was largely consumed by cathodic reactions within the features rather than being provided by the potentiostat. This relative isolation of the IGC attack from the rest of the sample made the rate of attack almost independent of the applied potential at the exterior surface. A further discussion of this phenomenon is given below and in the section on Al/Cu artificial crevice experiments.

The repassivation behavior of localized corrosion in AA2024 was studied by first potentiodynamically polarizing T3 samples from OCP to –560 mV SCE, which is above the

second breakdown potential, and then scanning in the reverse direction to various potentials below the break in the reverse curve, E_{rc}. Metallographic cross section of a sample held at –720 mV SCE for 20 h indicates that that IGC growth was not sustained. It seems as if the sharp IGC crevices formed at high potentials were opened up by a more isotropic attack.

The effect of 0.2 M nitrate or 0.5 M sulfate addition on corrosion behavior in 1 M NaCl was studied because of the presence of relatively large amounts of nitrate and sulfate reported in real lap joints taken from airplanes. As in pure chloride, the breakdown potentials were almost independent of sample orientation relative to the rolling direction. As expected, addition of nitrate or sulfate increased both open circuit potential (OCP) and breakdown potential.

Potentiostatic experiments were performed to further examine the types of corrosion on the reverse scan. As described above, samples were potentiodynamically polarized to a current density $8x10^{-3}$ A/cm^2 (around –400 mV SCE), and then the scan was reversed. Samples held at –600 mV and at –630 mV SCE for 20 h after the reverse scan exhibited similar attack morphology: primarily IGC and exfoliation with similar depth into the microstructure. However, the measured current densities were very different and the net charge at -630 mV was about 5% of that at -600 mV. The lower anodic charges at –630 mV SCE was not reflected in a lesser extent of IGC attack, which suggests that the measured current density may not represent well the metal anodic dissolution kinetics. As discussed above, local cathodic reaction greatly affects the net current measurement under these potentiostatic conditions. This phenomenon is apparently enhanced by nitrate, a cathodic reactant.

Foil penetration experiments were performed by adding nitrate or sulfate into the chloride solution about 2-3 min after starting the experiments to exclude the possible inhibition effect on initiation of localized corrosion. The localized corrosion kinetics (still IGC) were not changed

by the addition of nitrate at –520 mV SCE. However, the IG attack density (number of grain boundaries attacked per unit cross section area) seems to decrease in nitrate containing solution.

The addition of sulfate does not change penetration kinetics at potentials of –520 and –580 mV SCE. The localized corrosion morphology is still IG attack in nature in sulfate-containing chloride solutions. But IG attack density seems to decrease in sulfate-containing solution as well.

ROLE OF GRAIN BOUNDARY PRECIPITATES AND SOLUTE DEPLETED ZONE ON IGC OF AA7150

Aluminum alloy AA7150 is known to be more susceptible to intergranular corrosion in the T6 temper than in the T7 temper. AA7150- T6 exhibits two breakdown potentials. The nature of attack associated with each breakdown is complex and varies with time. Short time polarization results in only pitting above the more active breakdown potential whereas 24 h potentiostatic polarization generates both pitting and IGC. The T7 temper exhibited only one breakdown potential exhibits only pitting during short time potentiostatic tests. However, 24 h potentiostatic tests show that the even the T7 temper is susceptible to IGC. Using analytical TEM, the copper concentration in the grain boundary precipitates of the T7 temper is seen to be much higher than for the T6 temper. However, the composition of the solute depleted zone is similar in both the T6 and T7 temper.

The breakdown potentials of the compositional analogs of the grain boundary precipitates in the T6 and T7 temper are below the breakdown potential of the alloy. The SDZ and the matrix behave similarly in neutral 0.5 M NaCl. However, in high Cu^{2+} solutions, the repassivation potentials of the matrix and the SDZ are above the breakdown potential of the alloy.

An explanation for the effect of temper was developed based on indirect influence of the grain boundary precipitates on the SDZ behavior. The notion is that dissolution of the grain boundary precipitates controls the microchemistry at the grain boundary. The dissolution of the T6 grain boundary precipitates results in a localized microchemistry containing a low Cu ion concentration. However, dissolution of T7 precipitates results in a relatively high localized concentration of Cu ions. The dissolution kinetics of the SDZ is ennobled in the presence of Cu ions, which makes the T7 temper more resistant to IGC than the T6 temper.

LOCALIZED CORROSION KINETICS FOR 7XXX ALLOYS

AA7075-T6 exhibits two breakdown potentials in Ar-deaerated 1 M NaCl, similar to AA2024-T3. Foil penetration experiments were performed on the three different sections, ST, L and LT, at -580 mV SCE and –725 mV SCE in oxygen-bubbled 1.0 M NaCl. The higher potential, -580 mV SCE, was used extensively in the work on AA2024, and is well above the second breakdown potential for AA7075-T6. The lower value, -725 mV SCE, is between the two breakdown potentials. At both potentials, the penetration rate for the ST section was the slowest and that for the L section was the fastest, with LT sections in between. The alloy exhibits a microstructure that is highly anisotropic and the attack was IG in nature.

The penetration rates for AA7075-T6 at -580 mV were higher than at -725 mV for every orientation, and somewhat slower than for AA2024-T3 at -580 mV, Figure 1. However, the penetration rates for AA7075-T6 at -725 mV SCE were considerably higher than for AA2024-T3 since the first breakdown potential for AA2024-T3 is about -675 mV, and no localized corrosion is observed at -725 mV SCE. The penetration rate for AA7075-T6 is faster at -725 mV than that for AA2024-T8 at -730 mV, which does have a lower breakdown potential.

Solutionized AA7178 with an equiaxed and large grained microstructure was tested. The penetration rate at –725 mV SCE was isotropic and similar to that for the L section of AA7075-T6. The attack for the solutionized AA7178 was pit-like rather than IGC.

STATISTICAL MODELING FOR IGC GROWTH

As indicated by our foil penetration studies, the growth kinetics of IGC of AA2024-T3 can be strongly anisotropic because the microstructural anisotropy results in a difference in intergranular path length for different orientations. The foil penetration technique measures the penetration time for the fastest growing localized corrosion site through the sample thickness direction. In the case of IGC growth, the measured fastest growing intergranular corrosion site can be regarded as the one taking the shortest intergranular corrosion path through the thickness direction providing local intergranular growth rate is independent of the sample orientation. Therefore, the statistical distribution of minimum intergranular corrosion path length provides a way to model IGC growth. The work was performed in collaboration with Prof. D. Wolfe of the Statistics Department of the Ohio State University.

Statistical models have been developed based on a simple "Brick Wall" model, in which grains in an ST section are considered to be rectangular with average width a and thickness b. A foil sample is assumed to have N layers of grains, so the total foil thickness, d, is equal to Nb. A sample of a given size is assumed to have a certain number of localized corrosion sites, m, that initiate on the surface and grow into the microstructure along different intergranular paths. $W_{i,D}$ is the total distance that the i^{th} intergranular site travels to get through k (k<N) layers to a depth of D=kb:

$$W_{i,D} = kb + \sum_{j=1}^{k-1} X_i(j) = kb + W_{i,D,H} \qquad (1)$$

where $X_i(j)$ is the horizontal distance that the i^{th} intergranular site will travel on the j^{th} layer, j=1, 2,….k-1. $W_{i,D,H}$ is the total horizontal distance that the i^{th} intergranular site travels. Since the foil penetration technique measures the rate of the fastest growing site, which is assumed to follow the shortest path length, it is of interest to know the minimum total horizontal distance for a given thickness sample. The probability distribution for the total horizontal distance was determined under different assumptions with varying complexity, as summarized below. Once the probability distribution function for total horizontal distance is determined, order statistics are used to determine the cumulative distribution function for minimum total distance.

The simplest model assumes that the horizontal distance at any layer follows a common uniform distribution over the interval [0,a], where a is average grain width. In other words, all grains are assumed to have width a, and the intersection of the IG path above a certain grain has equal probability of being any distance along that grain. However, this model does not fit the data well. From foil penetration experiments, the nominal depth of the fastest growing site in any orientation varies with $t^{1/2}$. It can be assumed that the local IGC dissolution rate is given by the nominal rate in the L direction since the attack is almost straight in the L direction. Therefore, the ratio of the total distance traveled divided by the nominal penetration rate in the ST direction for the 1.9 cm thick plate of AA202-T3 is:

$$\frac{d_{TOT}}{d_{ST}} = \frac{d_L}{d_{ST}} = \frac{0.3244t^{1/2}}{0.0756t^{1/2}} = 4.29 \qquad (2)$$

The simple uniform distribution model predicts a value for this ratio of about 2.3 rather than 4.3 because of over-simplification. In a real Al microstructure, grains have a distribution of sizes, so there is a chance for the horizontal length to be greater than the average grain size. Also, IGC might not take the shortest intergranular corrosion path because not all grain boundaries have

same susceptibility to IGC. The model fits the data quite well if the grains are assumed to have either a normal or gamma distribution of sizes, Figure 2.

A STUDY OF IGC IN AL ALLOYS USING AN ARTIFICIAL CREVICE ELECTRODE CELL

Foil penetration experiments have shown that the kinetics of IGC of AA2024-T3 are almost independent of potential for high potentials over a wide range. Since the attack is highly anisotropic and localized, it is unlikely that the potential independence is a result of mass-transport limitations. An alternative suggestion is that the anodic current in an IGC crevice (IGC develops crevice-like features) is primarily consumed within the crevice. The foil penetration technique measures the true anodic kinetics, but only the portion of the current that escapes from the IGC crevice (the net current) will respond to a change in applied potential. Also relevant is the view of 7xxx alloy IGC described above, in which Cu from GB particles affects the local dissolution kinetics. These thoughts and observations led to a new approach for addressing IGC in Al alloys.

The rate of dissolution of an artificial crevice sample consisting of a thin film of Al deposited on a Cu substrate was measured optically. A 5 μm film of Al (99.999%) was deposited on a 100 μm Cu foil by flash evaporation. Strips were sliced out of this Al/Cu foil and sandwiched between two thin acrylic sheets using epoxy resin. This assembly constituted the artificial crevice electrode. The artificial crevice electrodes were potentiostatically polarized at values between –600 and –200 mV SCE for 4 h. The potential control was then released and open circuit relaxation monitored for 2 more h. The progression of the dissolution of the Al film in 1 M NaCl on the Cu substrate was continuously recorded with a video camera, providing a measure of the anodic current density. As the Al dissolved, an increasingly larger area of Cu

was exposed. This Cu was, of course, electrically connected to the Al and available for cathodic reactions. The net current, I_{net}, was recorded from the potentiostat.

The crevice depth increased approximately with $t^{1/2}$ for about the first 20 min, and then with $t^{1/3}$ at longer times. The rate was independent of applied potential. Interestingly, dissolution continued at an approximately constant rate even under open circuit conditions, after the potential control was released. When the applied potential was released, all open circuit potentials converged toward a final common value close to –0.4V.

The Al anodic current density decreased with time from about 10 A/cm^2 to 0.1 or 0.2 A/cm^2 during the 6 h period. The net current was much less, and went negative at lower potentials. Figure 3 below shows that the net current density was much lower than the anodic current density, i.e. most of the current associated with the local anodic reaction was consumed by a local cathodic reaction that was almost as large.

SUMMARY

This paper describes recent work in the area of localized corrosion growth kinetics in Al alloys:

- Intergranular corrosion growth kinetics in AA2024 were found to be controlled by path length and not by grain boundary composition.
- An explanation for the effect of temper on intergranular corrosion (IGC) susceptibility was developed based on indirect influence of the grain boundary precipitates on the SDZ behavior.
- Localized corrosion kinetics for AA7xxx alloys were found to be faster than for AA2024.
- A statistical model for IGC was developed, which allows for determination of the nominal rate of penetration in any orientation.

- A novel technique was developed to understand the mechanism of IGC in Al alloys. The rate of local cathodic reactions was found to be extremely high for a Cu-lined crevice.

ACKNOWLEDGMENTS

This work was supported by the United States Air Force Office of Scientific Research under contract No F49620-99-1-0103

REFERENCES

1. G. S. Frankel, *Corros. Sci.*, **30**, 1203 (1990).
2. K. P. Wong and R. C. Alkire, *J. Electrochem. Soc.*, **137**, 3010 (1990).
3. D. W. Buzza and R. C. Alkire, *J. Electrochem. Soc.*, **142**, 1104 (1995).
4. H. S. Isaacs and R. C. Newman, *Corrosion Chemistry within Pits, Crevices and Cracks*, A. Turnbull, Eds., HMSO Books, London (1987).
5. F. Hunkeler and H. Bohni, *Corrosion*, **37**, 645 (1981).
6. A. Sehgal, G.S. Frankel, B. Zoofan and S. Rokhlin, *J. Electrochem. Soc.*, **147**, 140 (2000).
7. W. Zhang and G. S. Frankel, *Electrochem. and Solid-State Lett.*, **3**, 268 (2000).
8. W. Zhang and G. S. Frankel, *submitted to Electrochim. Acta* (2001).
9. M. Posada, L.E. Murr and R. M. Arrowood, *Microstructural Science*, **25**, 131 (1997).
10. A.L. Campuzano-Contreras, R. M. Arrowood, L. E. Murr and D. Little, *Microstructural Science*, **25**, 139 (1997).
11. G. H. Koch, *Corrosion '99, paper No.516*, NACE, Houston,TX (1999).
12. A. Rota and H. Bohni, *Werkst. und Korros.*, **40**, 219 (1989).

13. V. Guillaumin and G. Mankowski, *Critical Factors in Localized Corrosion*, P. M. Natishan, R. G. Kelly, G. S. Frankel, R. C. Newman, Eds., **PV 98-17**, p203, The Electrochemical Society, Pennington, NJ (1999).

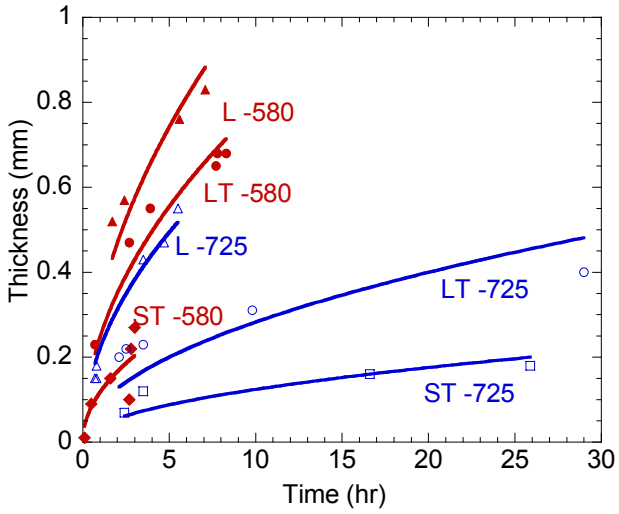

FIGURE 1. Foil penetration data for AA7075-T6 samples of various orientations (ST, LT, and L) in 1 M NaCl at two different potentials (-725 and -580 mV SCE).

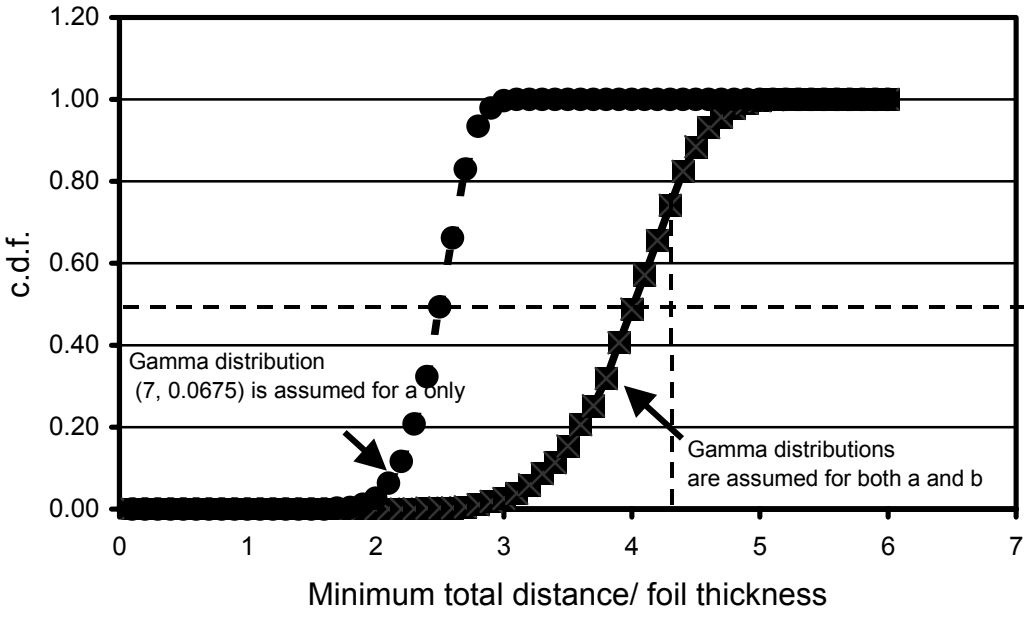

FIGURE 2. Cumulative distributions for the minimum total IG path length for penetration in the ST direction normalized by the foil thickness for the gamma distribution (4, 0.075) after the grain thickness is also assumed to have a gamma distribution.

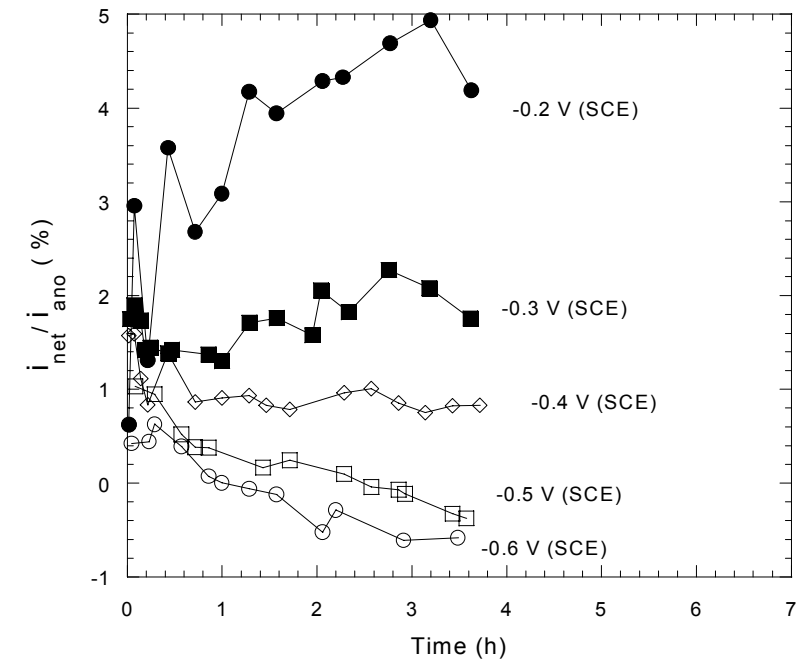

FIGURE 3. Ratio of net to anodic current for Al/Cu artificial crevice electrode at various potentials. Ratio becomes negative when net current is negative.

THE ROLE OF COATING HETEROGENEITIES IN THE LONG-TERM PERFORMANCE OF COATED ALUMINUM ALLOYS: DELINEATION OF IONIC PATHWAYS USING A MOLECULAR PROBE

P. Moongkhamklang and S. R. Taylor

Center for Electrochemical Science and Engineering
University of Virginia

ABSTRACT

The mode of ion entry through thin epoxy coatings was investigated using a chloride specific chromophore in conjunction with fluorescence microscopy. 10 μm thick epoxy coatings spin cast on glass slides were exposed to NaCl solutions at ambient and low (pH=3) pH for 1, 3, and 5 days. An additional material variable examined was the age of the material components as assessed from the date of manufacture. Following exposure to chloride solutions, the films were exposed to a chloride specific chromophore, 6-methoxy-N-ethylquinolinium iodide (MEQ). Fluorescence microscopy indicated that chloride ions were clustered in discrete sites on the surface of the coatings. The number of defect sites appeared qualitatively to increase with NaCl exposure time, but not to increase at low pH. This proof of concept experiment provides a new avenue for the characterization and quantification of coating degradation.

INTRODUCTION

One of the earliest proposed and most widely accepted mechanisms by which organic coatings provide corrosion protection is that of barrier protection.[1] It is now generally agreed that conventional organic coatings function by providing a barrier to ionic species[2] as opposed to water and oxygen.[3] However, the mode by which ions enter and move through the coating, i.e., via discrete sites vs. a homogeneous front, remains unclear.

Two divergent theories have been proposed for ionic transport through contiguous organic films as presented in reference.[4] One theory proposes that the flux of ions across the film is established by the presence of small imperfections or pores, which extend through the

thickness of the coating and have cross-sections that are larger than the free areas typically present between the molecular chains of the matrix.[5-7] An alternate theory proposes that the ions pass through the bulk matrix of the polymer film,[8] but that there are regional differences within a single coating with regards to ion selectivity.[9] These latter studies resulted in the proposed D (direct) and I (indirect) character of coating conductivity changes.

Recent research within these laboratories has examined the initial electrochemical phenomenon associated with coating breakdown on coated aluminum alloys using local electrochemical impedance spectroscopy (LEIM).[10-12] Admittance peaks observed during early times of chloride exposure and prior to visible corrosion have been attributed to local coating sites having reduced barrier properties, i.e., pores. These LEIM results were considered as direct confirmation of the coating pore concept. However, more recent experiments using various combinations of coating materials (vinyl, epoxy, polyurethane) and substrates (Au, Pt, Al, Cu) indicate that an alternate explanation for these admittance peaks is plausible. These experiments have indicated that an LEIM admittance peak observed on a coated alloy could result from a substrate site of low interfacial impedance covered by a coating whose general barrier properties are also intrinsically low but have been further reduced by uniform moisture and ion ingress. For example, the low interfacial impedance of the substrate could arise from an intermetallic (e.g., Al_2CuMg) or actively corroding site. Thus, the definitive linkage of an LEIM admittance peak to a coating pore that allows water and ion ingress, thus acting as the locus of underfilm corrosion, has not been conclusively made.

The origin of underfilm corrosion initiation and the precise interplay of the material and environmental factors that govern its evolution is unclear. If local chemical heterogeneities within the organic coating are responsible for ion entry, then their identification and elimination

could provide a means for dramatically improving paint performance. A more definitive approach for the identification of chemical heterogeneities and ion transport within the organic coating is needed.

Medical and biological researchers have significantly advanced the structural characterization of cells and cell membranes in recent years through the use of moiety specific chromophores.[13-14] This paper presents initial experiments that utilize an ion specific chromophore to identify the mode of ion entry through an epoxy coating. As mentioned, should ion channels be identified, an understanding of the material-related reasons for their existence will ultimately lead to improved resins for corrosion protection.

EXPERIMENTAL METHODS

SUBSTRATE

Microscope quality-glass slides (Fisher brand) were washed with Alconox® solution, rinsed with distilled water, and blown dry with air. These glass slides were subsequently wiped with acetone, ethanol, and hexane using lint-free wipes. The slides were left to air dry under ambient conditions, and stored in a closed desiccated cabinet to shield them from dust.

COATINGS

Cleaned glass slides were coated with a two-part epoxy solvated with butyl cellosolve. Part A consisted of bisphenol A-epichlorohydrin-based epoxy resin solution. Part B was composed of 70 wt% Epi-cure fatty acid polyethylenepolyamine-based polyamide curing agent and 30 wt% xylene. This specific epoxy resin is used as the binder resin in commercial primers for Air Force aircraft.

The coating was prepared by mixing equal amounts of part A and part B, and 8 wt% butyl cellosolve. Butyl cellosolve and xylene were used as solvents to reduce the viscosity for spin casting. Two batches of epoxy materials were used that differed in age of components. The samples in "batch 1" were made using a resin solution that was 2.5 years old and a curing agent that was 1.5 years old. The samples in "batch 2" were made from a resin solution that was, again, 2.5 years old, but the curing agent was 6.5 years old.

After mixing, the epoxy was allowed to set for 20 minutes prior to coating application. Air bubbles were removed from the resin of batch 1 using a vacuum chamber. This method was observed to leave small (< 5 μm diameter) air bubbles within the resin. In batch 2, a centrifuge was used to effectively remove the air from the mixed A and B materials. The coating was spin cast onto the cleaned glass slides using a spin caster to achieve a dry coating thickness of approximately 10 μm. Samples were then cured under ambient conditions in a desiccator for at least 48 hours before exposure to test environments.

EXPOSURE CONDITIONS

The coatings were exposed to 0.1 M NaCl solution at either ambient pH (ca. 5.5) or a pH adjusted to 2.5 (with HCl) using the ball-joint cell shown in Figure 1. A low pH was selected based on observations of increased ion flux through these resins starting at pH's below 3.[15] Samples were exposed for 1, 3 and 7 days. After exposure to NaCl solution, the samples were rinsed with distilled water and then exposed to 50 μM MEQ solution for 20 minutes. MEQ ($C_{12}H_{14}INO$) is a fluorescing molecule with a molecular weight of 315.15 grams per mole. It has absorption and emission wavelengths of 344 nm and 440 nm, respectively, and is also known to be sensitive to Br^-, I^- and SCN^-, but insensitive to NO_3^-, SO_4^{2-}, cations and pH.[16] The area of film exposed to MEQ was slightly larger than the region exposed to NaCl as shown in Figure 1(b).

This provided a control region for comparative purposes. MEQ (6-methoxy-N-ethylquinolinium iodide) is a chloride-sensitive fluorescence indicator.

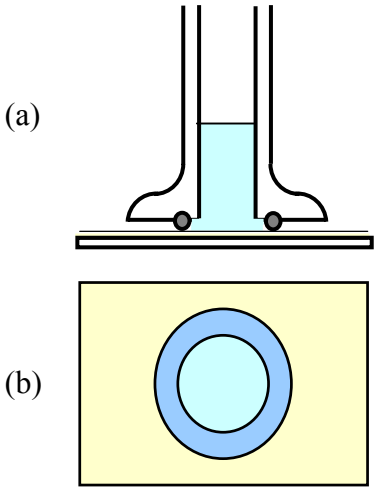

FIGURE 1: (a) Schematic showing exposure of a sample to NaCl solution using a ball-joint cell. (b) Schematic showing environments on surface of the sample.

MICROSCOPY

Steady state fluorescence microscopy was used to visualize MEQ-tagged chloride ions within and on the surface of the coating. Images of the sample surfaces were collected in both bright and fluorescent fields. In fluorescence mode, the wavelength of the incident light was selected to be in the range of the absorption spectrum of MEQ using a 340 nm filter, and the emitted light from the sample was collected through a 420 nm-long pass filter.

RESULTS AND DISCUSSION

Images of the coatings made from newer material components (batch 1) are shown in Figures 2, 3, 4, and 5. Images of the coating with no NaCl exposure or MEQ exposure (Figure 2) revealed no fluorescence signal in the fluorescent field, as expected. However, several dark spots were observed on the coating surface in bright field. These spots could be dust particles, but no further analysis has been performed at this time. A pattern within the epoxy was also observed, and is believed to be phase separation.

A second control experiment in which the surface of the coating was exposed to MEQ, but not to NaCl revealed results similar to those in Figure 2. Again, no features are observed in the fluorescent field indicating that there is no background chloride or other MEQ-sensitive moieties within the sample. Thus, it can be assumed that the observation of fluorescence in test experiments is solely attributable the NaCl exposure environment.

Figure 4 shows the bright and fluorescent field images of an epoxy coating that has been exposed to sodium chloride at pH 2.5 for 1 and 3 days followed by MEQ solution. Light colored (fluorescing) spots can be seen in the fluorescent field images on the right. The fluorescing sites observed in these images strongly suggest that chloride ions enter the polymer coating through discrete pathways. Experiments to examine the penetration characteristics of the chloride are in progress. Note that there is not a one-to-one relation between dark sites observed in the bright field and the light spots observed in the fluorescent field. Determination of the chemical nature and differences of these sites will be one of the long-term goals of this research.

Figure 5 illustrates coating surfaces after exposure to sodium chloride solution at ambient pH for 1, 3, and 7 days followed by MEQ staining. It can be qualitatively observed that the number of defect sites in the coating, as observed in both bright and fluorescence fields, appears to increase with NaCl exposure time. Quantitative assessment of differences has not been performed at this time because the method of experimentation requires the sacrifice of samples by the MEQ staining procedure. Once a coating has been extracted and stained, it is not re-immersed for continual study, so the images at different times do not represent a time lapse of a single specific site.

As seen previously, it was observed that not all sites in the bright field took up MEQ and fluoresced in the fluorescence field. This could be attributable to limited access of the MEQ to

chloride ions within the coating during the short MEQ soak times (20 minutes). It could also be due to the fact that there are different types of ionic pathways in the coating resin. Thus, further experiments to observe cross sections of NaCl exposed coatings in the fluorescence microscope will be performed to determine the transport depth of chloride ions and MEQ molecules in the coating. This may be a method to determine whether there are ionic pathways in the coating, and to clarify why some spots in bright field did not fluoresce.

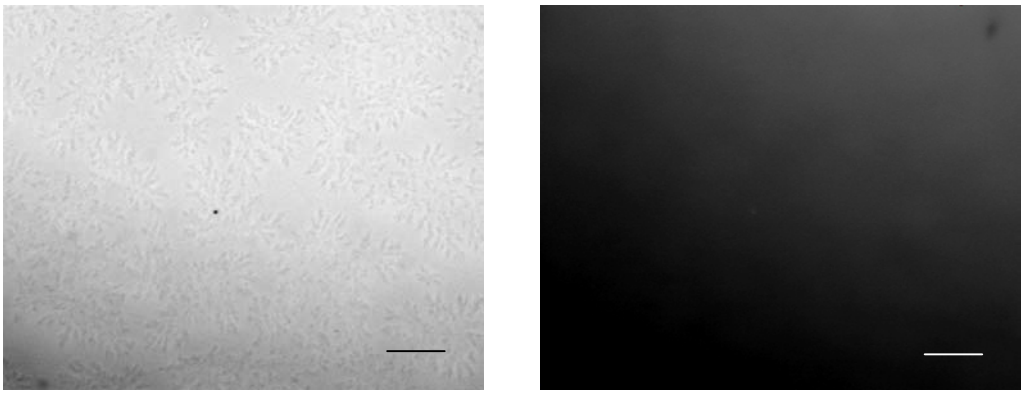

FIGURE 2. (a) A bright field image of initial surface of the coating (batch 1). (b) Fluorescence image of the same area as in a.

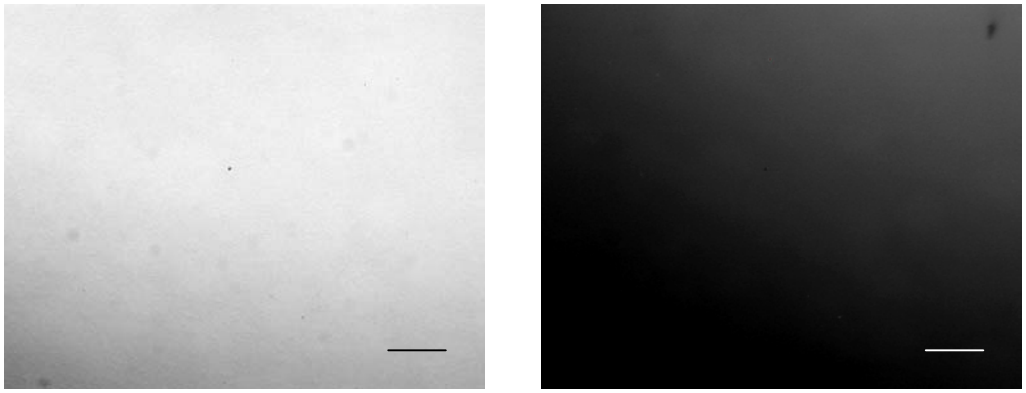

FIGURE 3(a) A bright field image of surface of the coating (batch 1) with MEQ exposure only. (b) Fluorescence image of the same area as in a.

At this time, no quantitative statement can be made about the differences in MEQ uptake between ambient pH and low pH exposures. This will be examined in subsequent experiments, and will require quantitative image analysis of numerous samples to establish distinct statistical trends.

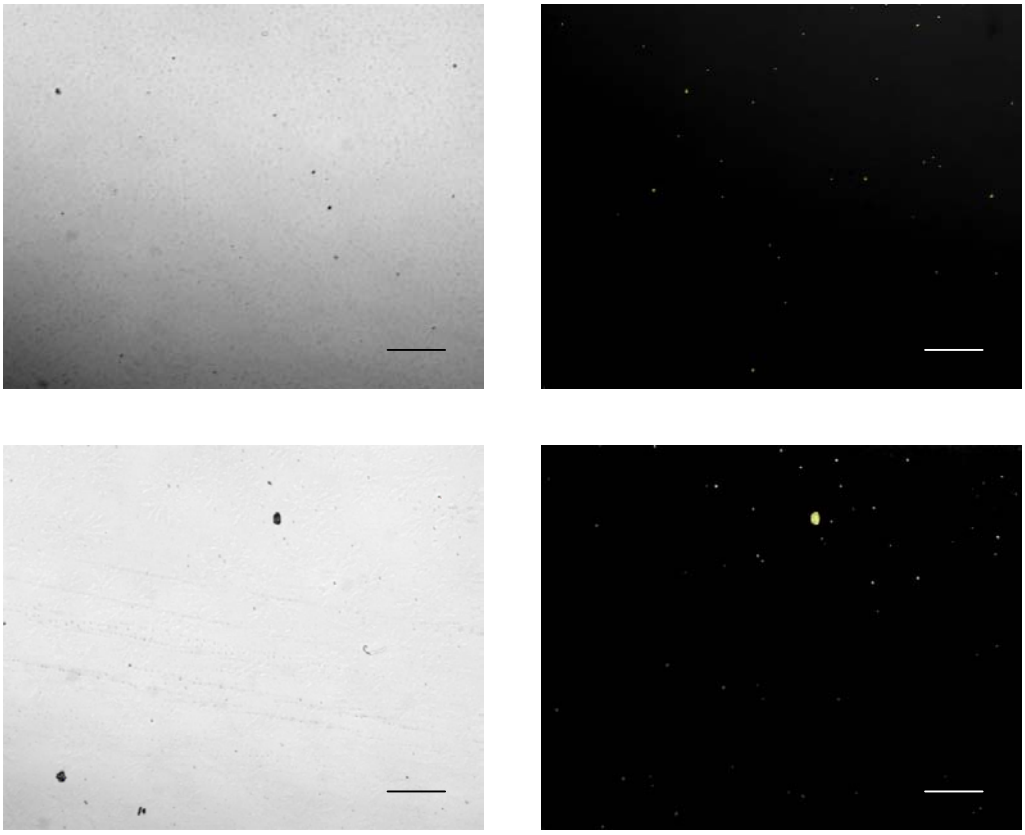

FIGURE 4. (a) A bright field image of the coating after 1 day of NaCl exposure at pH 2.5. (b) Fluorescence image of the same area as in a. (c) A bright field image of the coating after 3 days of NaCl exposure at pH 2.5. (d) Fluorescence image of the same area as in c.

Images of the coatings made with older material components (batch 2) are shown after exposure to NaCl solution at pH 2.5 and ambient pH in Figures 6 and 7, respectively. The pattern of phase separation is different and more pronounced from that of the coating made with

newer materials. Though qualitative at this time, the number of defect sites and film delamination in these coatings seems to be greater than in the previous batch with the same or even shorter periods of exposure. These defects appear to increase in number with longer NaCl exposure time, as seen previously.

These proof-of-concept experiments definitively reveal discrete sites of chloride ion uptake on the surfaces of thin epoxy coatings in the early stages of immersion. It will be important to understand the depth of ion penetration as a function of time. Experiments to examine film cross-sections are planned.

It is important to note that the present coating characterization have been performed while using a benign substrate, i.e., glass, so that the observed ion uptake is intrinsic to the coating and not a function of underfilm degradation as might occur in the blister chemistry of active blisters on AA2024. It will therefore be important to examine the role of the alloy substrate in the evolution of these ion gates. More importantly, an understanding of the material nature of the coating regions that take-up chloride is needed. Are these local regions similar in structure and chemistry? Do specific types lead to underfilm corrosion? If these coating heterogeneities can be characterized and eliminated, the corrosion protective properties of the resin can be dramatically improved. It is believed that these molecular-probe methods will provide an important step in the approach to the characterization of coating degradation processes.

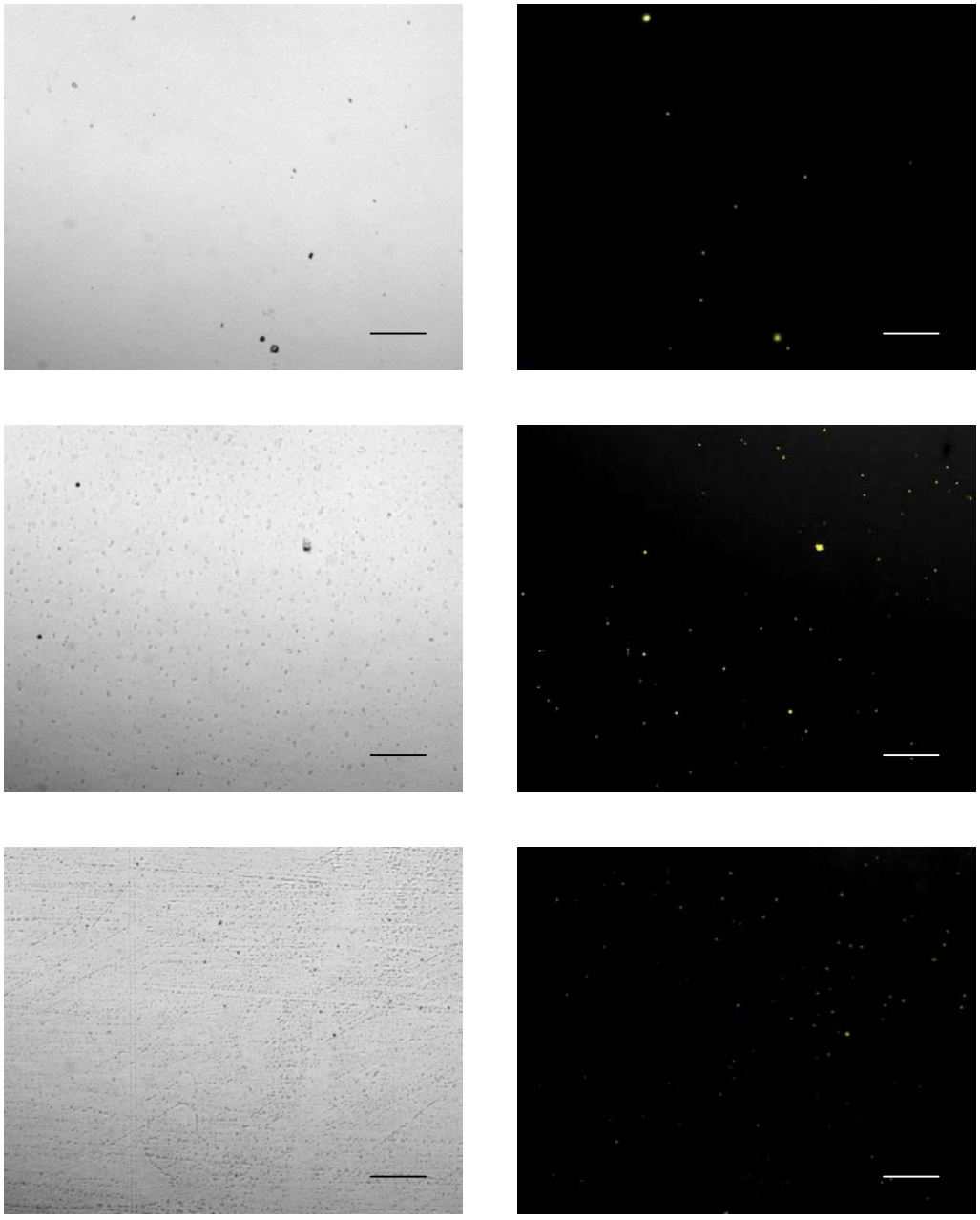

FIGURE 5 (a) A bright field image of the coating after 1 day of NaCl exposure at ambient pH. (b) Fluorescence image of the same area as in a. (c) A bright field image of the coating after 3 days of NaCl exposure at ambient pH. (d) Fluorescence image of the same area as in c. (e) A bright field image of the coating after 7 days of NaCl exposure at ambient pH. (f) Fluorescence image of the same area as in e.

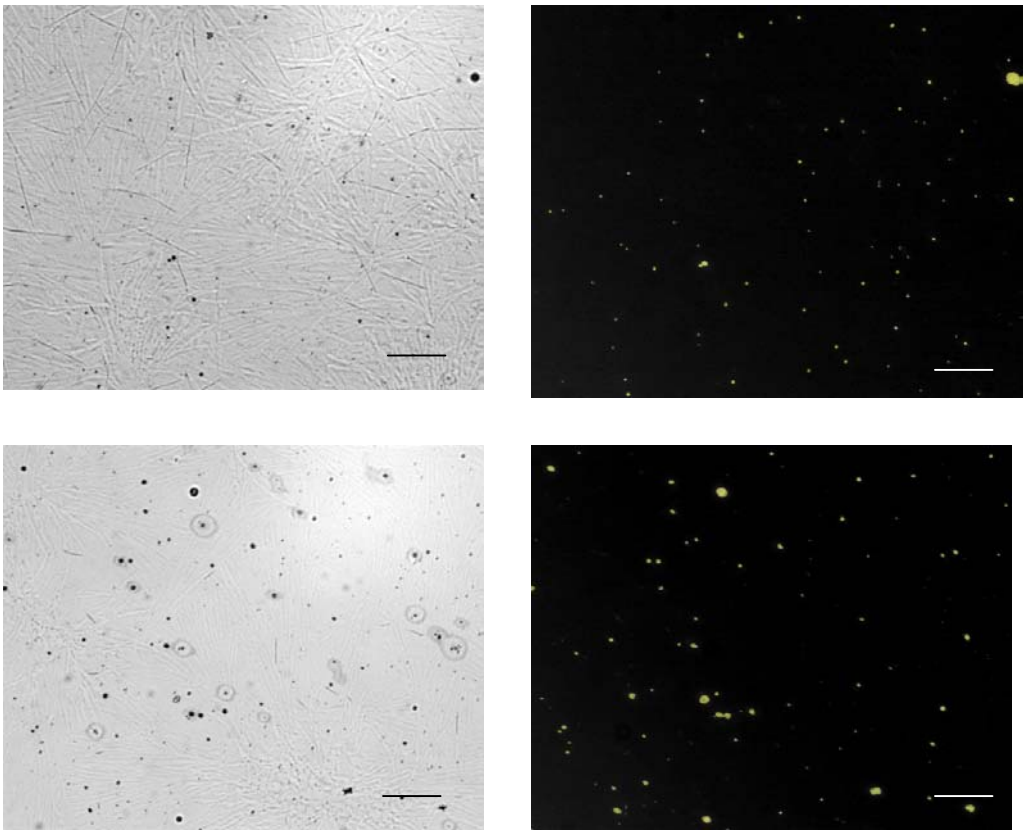

FIGURE 6. (a) A bright field image of the coating made with older materials after 1 day of NaCl exposure at pH 2.5. (b) Fluorescence image of the same area as in a. (c) A bright field image of the coating after 2 days of NaCl exposure at pH 2.5 . (d) Fluorescence image of the same area as in c.

CONCLUSIONS

These initial experiments utilize an ion specific chromophore to identify the mode of ion entry through an epoxy coating. Based on these initial experiments, the following conclusions can be made:

1. The use of MEQ has clearly indicated that following exposure to NaCl, chloride ions are clustered in discrete sites on the surface of epoxy resins. This is strongly suggestive of the discrete pore concept, however experiments to examine film penetration must be performed.

2. The number of defect sites in the coatings, as observed in both bright and fluorescent fields appears to increase with NaCl exposure time. Not all sites observed in bright field fluoresce in the fluorescent field. Whether different types of ionic pathways exist has yet to be shown.
3. The epoxy polymer phase separation morphology differs as a function of component material age. The number of spots, both in bright and fluorescence fields, appear to be greater in coatings made from older materials than those made from newer materials. Hence, the age of the resin will impact its performance, as intuitively expected.
4. At present, no quantitative distinction has been made between observation of films exposed to ambient and low pH environments. Image analysis techniques will be employed in subsequent experiments.

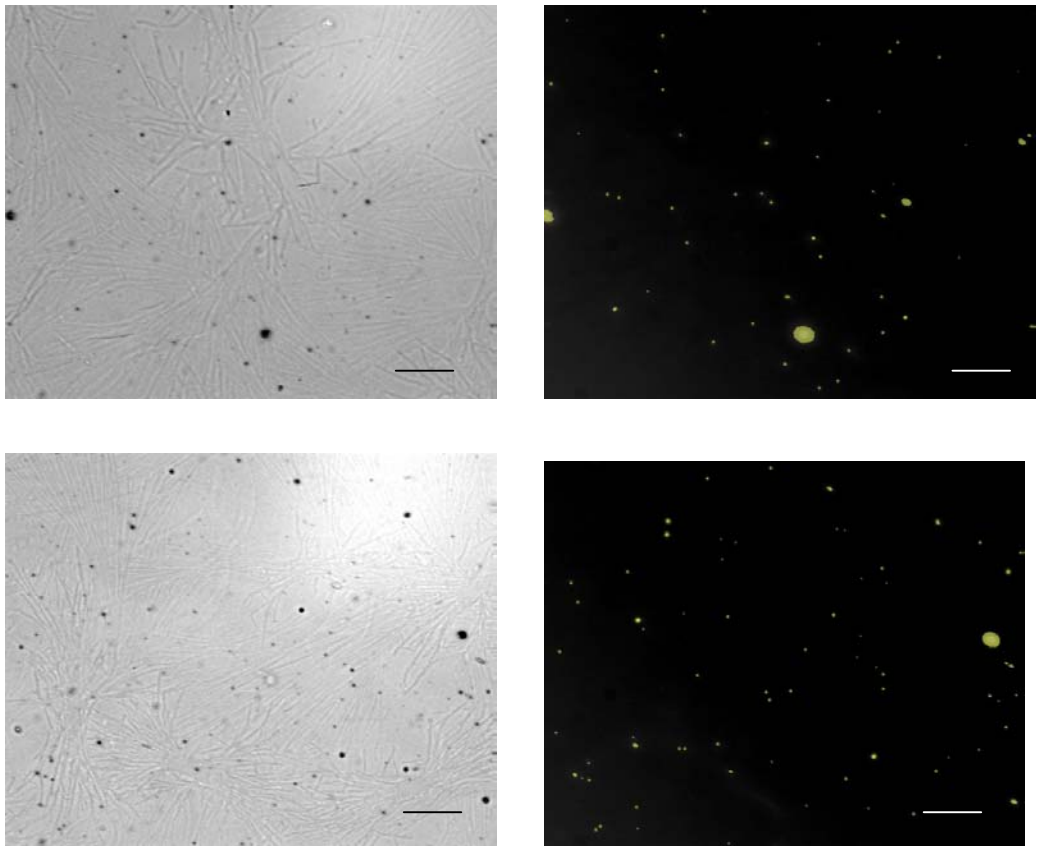

FIGURE 7. (a) A bright field image of the coating made with older materials after 1 day of NaCl exposure at ambient pH. (b) Fluorescence image of the same area as in a. (c) A bright field image of the coating after 2 days of NaCl exposure at ambient pH. (d) Fluorescence image of the same area as in c.

ACKNOWLEDGMENTS

The authors gratefully acknowledge the financial support of this research by the Air Force of Scientific Research through contract number F49620-96-1-0178. The authors would also like to thank Dr. Ammasi Periasamy and Colten Noakes at the W.M. Keck Center for Cellular Imaging, University of Virginia, for their assistance in fluorescence microscopy.

REFERENCES

1. C.H. Hare, *J. Protective Coatings and Linings*, Feb. 1989, pp. 59-69.
2. R.A. Dickie and A.G. Smith, *ChemTech*, Jan. 1980, pp. 31-35.
3. J.E.O. Mayne, *JOCCA*, **32**(352):481-487 (1949).
4. D. Greenfield and D. Scantlebury, *J. Corr. Sci. and Engr*., **Vol. 3**:paper 5 (2000), http://www.cp.umist.ac.uk/JCSE/,ISSN
5. M.W. Kendig and H. Leidheiser, Jr., *J. Electrochem. Soc*., **123**(7):982-989 (1976).
6. L. Beaunier, I. Epelboin, J.-C. Lestrade, an H. Takenouti, *Surface Technology*, **4**:237 (1976).
7. H. Corti, R. Fernandez-Prini, and D. Gomez, *Prog. Org. Coatings*, **10**:5-33 (1982).
8. J.E.O. Mayne, *Official Digest*, Feb. 1952, pp. 127-136.
9. E.M. Kinsella and J.E.O. Mayne, "Ionic Conduction in Polymer Films", in 3rd International Congress on Metallic Corrosion, Moscow 1966, pp. 117-120.
10. A.M. Mierisch and S.R. Taylor, *J. of Corr Sci. and Engr*., **Vol. 2**, Paper 30 (1999), http://www.cp.umist.ac.uk/JCSE.
11. A.M. Mierisch, J. Yuan, R.G. Kelly, and S.R. Taylor, *J. Electrochem. Soc.,* **146**(12):4449-4454 (1999).

12. S.R. Taylor, , *Prog. Org. Coatings*, **43**:141-148 (2001).

13. R.P. Hangland and I.D. Johnson, "Intracellular Ion Indicators", in Fluorescent Probes for Biological Activity, 2nd edition, Ed. by W.T. Mason, pp.40-15 (1999).

14. A. Takahashi, P. Camacho, J.D. Lechleiter, B. Herman, *Physiol. Rev*., 79:1088-1125 (1999).

15. R.G. Kelly, O. Schneider, and J. Yuan, ECS Proceedings Volume 99-1, Abstract #81, Phoenix, AZ, May 1998.

16. J. Birwersi and A.S. Verkman, *Biochemistry*, **30**:7879-7883 (1991).

IN-SITU CONFOCAL LASER SCANNING MICROSCOPY SURFACE METROLOGY STUDIES OF CORROSION ON AA 2024-T3: INFLUENCE OF ELECTROLYTE COMPOSITION ON THE CORROSION MORPHOLOGY OF BARE AA2024-T3

G. O. Ilevbare, O. Schneider, R.G. Kelly, J.R. Scully

Center for Electrochemical Science and Engineering
Department of Materials Science and Engineering
University of Virginia
Charlottesville, VA 22904-4745

ABSTRACT

The electrochemical behavior of bulk synthesized Al-Cu, Al-Cu-Mg, and Al-Cu-Fe-Mn intermetallic compounds as well as that of AA 2024-T3 have been studied and correlated with the morphology of attack at and around the intermetallic compounds present on the bare polished surface of AA 2024-T3. Exposures were conducted in four solutions: 0.1 M Na_2SO_4 + 0.005 M NaCl (pH 6), 0.1 M Na_2SO_4 + 0.005 M NaCl + 0.0001 M NaOH (pH 10), 0.1 M Na_2SO_4 + 0.005 M Cl^- (as $AlCl_3$) (pH 3) and 0.5 M NaCl (pH 6). Similar morphology of attack was observed at each type of intermetallic regardless of electrolyte composition. However, the rates of attack differed. These results suggest that the mechanism of the initial stages of local attack may be similar in all these electrolytes.

INTRODUCTION

Aluminum-based precipitation age hardened alloys containing Cu and Fe are prone to localized corrosion such as pitting induced by galvanic interactions between Cu-rich intermetallics compounds (IMC) and the Al-alloy matrix. These local galvanic cells, which induce pitting and alkaline attack, are often formed by Cu- and Fe-containing intermetallics or replated Cu.[1-13] In AA 2024-T3, pit initiation sites include Al-Cu-Mg particles,[1,2,7,11-13] the periphery of Cu-enriched Al-Cu-Mg particles that have been dealloyed of Al and Mg,[2] and the matrix adjacent to Al-Cu and Al-Cu-Fe-Mn particles.[1,8,10,11] Of these intermetallics, the Al-Cu-

Mg type is the most active. It is anodic to the Al-matrix and generally dissolves leaving a fine Cu-sponge (resulting from the de-alloying of both Al and Mg). Thus, with time it now becomes cathodic to the matrix.[1,2,12,13] Under certain conditions, some authors have observed rings of redeposited Cu around these Al-Cu-Mg precipitates.[14] As much as 60% of the intermetallics on the surface of an AA 2024-T3 sample could be of the Al-Cu-Mg type.[2,15] The Al-Cu, and Al-Cu-Mn-Fe types of intermetallic compounds are positive (serve as cathodic sites) relative to the Al-matrix.[16] As a result, Cu^{2+} ions dissolved in solution can be reduced readily on these particles.[1] The generation of OH^- ions at these particles due to the reduction of oxygen leads to alkaline attack of the Al adjacent to these particles, resulting in a trench-like attack morphology (trenching), which often forms a perimeter around the particle.[8,11,17,18] In addition, pitting can occur in the matrix in halide containing solutions.[16]

This work focuses on the comparison of the attack morphology of localized corrosion on AA 2024-T3 at these IMC studied in-situ in various electrolytes that simulate blister solutions under painted AA 2024-T3,[19] and the correlation of these observations to electrochemical data from AA 2024-T3 and the bulk synthesized analogues of the different types of IMC in the various solutions. Of interest is the effect of bulk solution pH and chloride concentration on the attack morphologies at IMC particles on bare polished AA 2024-T3 surfaces. In a subsequent paper, these results shall be compared to the corrosion processes observed in underpaint corrosion.[20,21]

The method applied for in-situ studies was Confocal Laser Scanning Microscopy (CLSM). CLSM significantly surpasses the capabilities of common optical microscopy to measure and quantify surface metrology.[8,22-24] A laser beam scans the surface of the sample in the x-y direction. A small pinhole is located in front of the detector at a position that is optically

conjugate to the focal point in the sample plane. The intensity of the light reflected from the sample on the focal plane is measured by the detector for each x-y-position. Most of the light scattered from out-of-focus planes is focused outside the pinhole and, therefore, does not reach the detector. This effect allows sharp imaging of a single sample plane known as a slice. By moving the sample surface stepwise through the focal plane (upwards and downwards) with a z-scanning stage, the three-dimensional surface topography can be calculated from assembly of the slices recorded at each z-step. This assembly is known as a stack. Data for surface roughness, surface profiles and pit depths can thus be obtained. In addition, a 2-dimensional (2D) microscopic image with extended depth-of-focus can be calculated. This process assigns a grey level to each image pixel, which corresponds to the brightest level at this x-y-position in all slices.

CLSM is a contact-free method.[8,22] CLSM has found extensive use in biology because it allows the three-dimensional (3D) *in-vivo* monitoring of transparent biological entities such as cells.[22] In materials science it has been used, for example, to study defects in thermal spray coatings.[23] The method has recently been applied to corrosion studies on bare aluminum alloy 2024-T3 (AA 2024-T3).[8,9,24] It was also shown to be a powerful tool for the in-situ study of underfilm corrosion.[20]

EXPERIMENTAL PROCEDURES

CLSM was carried out using a Zeiss model LSM 510 microscope. Imaging was performed with an argon laser (488 nm wavelength). The studies were conducted on 1.5 mm thick AA 2024-T3 sheets (from Kaiser) with the composition (major elements): Cu 4.5%, Mg 1.30%, Mn 0.62%, Fe 0.18%, Zn 0.10%, Si 0.093%, (in wt. %), balance Al. AA 2024-T3 coupons were cut from 90 by 120 cm sheets to squares of about 2.5 by 2.5 cm. One face of the

coupons was abraded with SiC paper (from 180 up to 1200 grit), and then polished with 1 μm diamond suspension. A thickness of about 0.1-0.3 mm of the sample was removed during the grinding and polishing processes.

SEM-EDS (Scanning Electron Microscopy-Energy Dispersive X-Ray Spectroscopy) studies were conducted on some samples to identify and analyze the intermetallic particles on the surface with a Jeol 840 SEM coupled to a Kevex EDS system at a voltage of 20 KV. Secondary Electron Images (SEI) were generated in all cases. In order to monitor the topography changes in-situ, a specially constructed flat electrochemical cell was mounted on the x-y-z-stage of the CLSM. A detailed description of the cell can be found elsewhere.[20] The electrolytes were not stirred, and there were several mm of electrolyte on the substrate in the flat cell. Prior to the introduction of any electrolyte, areas of interest for study were then selected with the 100x immersion objective lens of the CLSM. In some cases, some of the surface features that were studied were first chosen with the aid of the SEM. Imaging of the areas of interest commenced after the introduction of electrolyte into the flat cell, and any changes in surface morphology were monitored with time. 0.5 M NaCl (pH 6) was chosen as an example of a very corrosive environment. A solution containing 0.005 M NaCl + 0.1 M Na_2SO_4 (pH 6)[a] was chosen for its lower corrosivity. This composition has been used in previous studies.[16,25,26] It produces differences between OCP and the pitting potential (E_{pit}) in AA 2024-T3.[16] However, some galvanically induced pitting corrosion is still observed in this electrolyte because of the close proximity of OCP to pitting potential associated with the Al-matrix.[16] To examine the influence of the pH such as seen under blisters on painted Al 0.1 M Na_2SO_4 + 0.005 M NaCl + 0.0001 M

[a] This is referred to as the 'standard solution'.

NaOH (pH 10, "alkaline solution"), and 0.1 M Na_2SO_4 + 0.005 M Cl^- (as 0.00167 M $AlCl_3$) adjusted to pH 3 with H_2SO_4 ("acidic solution") were also used.[19]

Electrochemical studies were performed on high purity Al (99.998%), Cu (99.999%), AA 2024-T3 and bulk synthesized intermetallic castings: Al_2Cu (Al-Cu), Al_2CuMg (Al-Cu-Mg), and $Al_{20}Cu_2(MnFe)_3$ (Al-Cu-Mn-Fe). Open circuit potential (OCP) exposures followed by potentiodynamic polarization experiments were performed in the sulfates based electrolytes given above, at ambient temperature in a 3-electrode cell that was open to lab air. Details are discussed elsewhere.[16,27] The reference used was the saturated calomel electrode (SCE).

RESULTS

a) SEM-EDS

SEM-EDS results from bare polished surfaces of AA 2024-T3 samples indicated the presence of Al-Cu, Al-Cu-Mg and Al-Cu-Mn-Fe type intermetallic compounds. Al-Cu-Mg intermetallic particles were usually spherical while Al-Cu and Al-Cu-Mn-Fe intermetallics had blocky angular features (Figures 1a and 1b). Clustering of distinct Al-Cu and Al-Cu-Mn-Fe particles was especially observed.

Results from EDS analyses of the intermetallics particles on AA 2024-T3 prior to electrolyte exposure are presented in Table 1. Differences in apparent composition were observed amongst particles with the same elemental constituents. The compositions of some of the intermetallic particles were consistent with the stoichiometry of the most common intermetallics in AA 2024-T3, namely: θ-Al_2Cu, S-Al_2CuMg and $Al_{20}Cu_2(MnFe)_3$. Others were not. Other intermetallic particles contained distinct regions with differing composition. In some cases, regions containing an Al-Cu-Mg composition occurred next to regions, which predominantly contained an Al-Cu composition (Particles 5 in Table 1, and Figures 1a and 1b).

Si was detected in some of the spectra. Apart from the Si present in the alloy, another possible source of Si observed in the spectra might be from the SiC paper used in the grinding process.

b) ELECTROCHEMICAL STUDIES

Figure 2 compares the OCP values obtained after two hours of immersion for the different synthesized IMC and AA 2024-T3 in acidic (pH 3), near neutral (standard solution-pH 6), and alkaline (pH 10) solutions. All data points are the averages from at least four runs. These plots present comparisons in OCP in the pH 3 (Figure 2a) and pH 10 (Figure 2b) solutions with the standard pH 6 solution as departures from the diagonal line. Measurements close to the diagonal line indicate little or no difference in OCP. In acidic solution AA 2024-T3 showed a drop in potential compared with the alkaline and near neutral solutions within two hours of immersion. The OCP of AA 2024-T3 was much higher in the alkaline solution compared with the standard solution probably due to Cu replating (Figure 2b). The S-phase showed no significant dependence on pH. The OCP of $Al_{20}Cu_2(FeMn)_3$ was generally slightly more positive than that of Al_2Cu in the electrolytes. In the acidic solution, the values both intermetallics registered were much lower when compared with those recorded in the near neutral and alkaline solutions. The OCP of Al was lower at high pH. Notably, a galvanic potential driving force existed in each solution.

Figures 3a to 3f illustrate the overall E-log i behavior on AA 2024-T3, Al, Cu, and the Al-Cu, Al-Cu-Mg, and Al-Cu-Mn-Fe IMC in 0.1 M Na_2SO_4 + 0.005 M NaCl (pH6), 0.1 M Na_2SO_4 + 0.005 M NaCl + 0.0001 M NaOH (pH 10), and 0.1 M Na_2SO_4 + 0.005 M Cl^- (pH 3) after a 2 hour exposure at OCP. The horizontal lines shown in Figures 3a to 3d represent the mean OCP values of AA 2024-T3 in the respective environments (the lines are not shown in multiple pH plots, Figures 3e and 3f). In the pH 6 solution (Figures 3a and 3b), the OCP of Cu,

the Al-Cu, and the Al-Cu-Mn-Fe intermetallics are more positive than that of AA 2024-T3 (horizontal line) and far more positive than those of the Al-Cu-Mg intermetallic compound and Al. The Al-Cu-Mg intermetallic is not passive at OCP and exhibits a high dissolution rate upon anodic polarization. Figure 3b shows that the Al-Cu-Mn-Fe intermetallic is passive near the OCP of AA 2024-T3 but undergoes pitting at potentials above it. AA 2024-T3 pits at its OCP and large pits have been observed that extend into its matrix beyond any IMCs that might serve as initiation sites.[28] Cathodic kinetics were enhanced on all Cu-containing materials and AA 2024-T3 compared to high purity Al (Figure 3a) as noted by Prior and Kier for Al containing Fe and Cu.[5] The pH of the electrolyte (between 3 and 10) does not alter the enhancement of cathodic kinetics exhibited by the Cu-containing intermetallics, nor the relative position of the OCP values when compared with the behavior in the pH 6 electrolyte. The Al-Cu-Mg IMC shows a passive region in the pH 10 electrolytes (possibly due to Mg and Cu content) but none at pH 3 (Figures 3d and 3e). AA 2024-T3 showed the presence of a passive region in both the pH 3 and 10 electrolytes (Figure3e). No such passive region is seen in the pH 6 electrolyte. However, it should be noted that the OCP of AA 2024-T3 in the pH 3 electrolyte is much lower than in the pH 6 electrolyte (Figure 2). Anodic dissolution on the Al-Cu-Mg IMC and AA 2024-T3 proceeds at a faster rate in the pH 3 electrolyte compared with the pH 10 electrolyte (Figure 3e). Cathodic kinetics also proceeds at a faster rate on the Al-Cu and Al-Cu-Mn-Fe IMC in the pH 3 compared with the pH 10 electrolytes (Figure 3f). Compared with the pH 6 solution, the pitting potential on AA 2024-T3 is lower at pH 3, and higher at pH 10 possibly due to Cl^-/OH^- ratio (Figure 3g). It is now commonly accepted that the conventional pitting potential is a measure of stabilization of micropits that may have formed at potentials below the pitting potential.[29,30] Nevertheless, pitting potentials were determined using the criterion that pitting would have

occurred by the time the anodic current density of the specimen reached 3 x 10^{-5} Acm^{-2} and, hence, this apparent current density criterion was taken to be the pitting threshold for our various systems.[15,29,31-33] It was used purely as a basis for comparison for the susceptibility of pitting, and bears no other significance. Nonetheless, at this current density, enough anodic charge would have been passed so that pitting potentials reflected pit stabilization of pits large enough to include the matrix and not solely dissolution of a small region of S phase or metastable pitting. The cumulative probability plots (Figure 3g) were constructed using procedures reported elsewhere.[34] Of all the materials tested, AA 2024-T3 showed the most drastic changes in OCP and pitting potential as a function of pH. The mean OCP for AA2024-T3 was -0.665 ± 0.023 V(SCE), at pH 3, -0.466 ± 0.010 V(SCE) at pH 6, and –0.352 ± 0.079 V(SCE) pH 10, with all error values at a 95% confidence level (Figures 2a, 2b and 3g). Figure 3g also shows bands (depicted with vertical lines) for regions where the minimum and maximum OCP values for pure Cu, and the IMC fall in relation to AA 2024-T3 in the pH 3, 6 and 10.

c) IN-SITU CLSM STUDIES

Corrosion studies on bare, untreated AA 2024-T3 in the four different solutions described above were performed with CLSM. The observed galvanic corrosion morphological features associated with micron scale constituent particles could be divided into four different categories: (i) particles which corroded, (ii) particles which caused trenching in the adjacent matrix, (iii) particles which did not corrode at all during the time of immersion, (iv) pitting near intermetallic compounds. In addition matrix etching was observed in acidic solution.

Particles identified with EDX as Al-Cu-Mg particles started to corrode within ten minutes after exposure to standard solution. The corrosion behavior of the particle in Figure 1a composed of regions of Al-Cu-Mg and Al-Cu is shown in Figure 4a after 2 h immersion. The

Al-Cu-Mg phase corroded, whereas the Al-Cu-phase did not. Figures 4b to 4d show the corrosion of the particle from Figure 1b at selected times. After 13 minutes, the Al-Mg-Cu phase already showed corrosion at the surface. After 40 minutes, corrosion attack had occurred on the entire Al-Cu-Mg surface and had expanded into the matrix. The other sections of the constituent particle remained with slight indications of trenching in the matrix. After 110 minutes, other sites had developed corrosion pits within the matrix.

Different types of localized corrosion attack on large intermetallic particles were observed as well in the standard solution as in 0.5 M NaCl. In the standard solution, one hexagonally shaped particle started corroding at its center, leaving behind a great deal of corrosion product (Figure 5). The corroded area increased and covered the entire particle within a few hours. After the entire particle was involved, attack of the surrounding matrix occurred. Figure 6a shows a rectangular-shaped IMC on the AA 20204-T3 surface. The attack on this particle started with the formation of many tiny pits close to one edge (Figure 6b). In the early stages, the depth changes were too small to be resolved (Figure 6b), and the corrosion could only be made visible by the black spot in the extended depth-of-focus image. Later on, pit depths of >4 μm could be verified. The dissolution progressed through the rest of the particle (Figure 6c), and the attack of the matrix started before the particle was completely corroded. Precipitated corrosion products were observed around and on the particle (Figure 6d).

Figures 7a-7c show the formation of four larger pits on an IMC exposed to 0.5 M NaCl, of which three merged together. Two of these pits initiated at or close to the interface with the matrix, and the other two on the particle itself. The surrounding matrix exhibited pit formation, as well.

Figures 7d-7f show corrosion of a large IMC starting at several locations along the interface with the matrix. The total area (particle + corroded) remained fairly constant during the exposure time. This means that the IMC particle corroded, whereas the matrix itself was only slightly attacked, if at all in the vicinity of this large IMC particle. Otherwise, the total area would have increased with time. In the upper left area, pit formation was observed, which initiated at a small particle and grew to a size much larger than the original particle.

Individual IMC particles were attacked much earlier in 0.5 M NaCl solution compared with the standard (pH 6) solution. Figure 8 demonstrates this difference by comparing the attacked areas for the IMC from Figure 7 and Figure 5. Once corrosion has started also in standard (pH 6) solution significant corrosion rates (slope of Figure 8) can be achieved.

Trench formation occurred around particles in all electrolytes. An example from standard solution (pH 6) is given in Figures 9a and 9b. Both images show the same particle surrounded by a trench 2.5 μm wide. The particle itself had not been affected by corrosion at all after 1 day of exposure, still showing the polishing lines. The depth of the trench was about 3 μm. It was observed that in standard solution (pH 6), severe corrosion took place in large-sized indentations[b] made on a sample (~30 μm diameter). This prevented trenching at all nearby particles. These nearby particles were both of the Al-Cu and Al-Cu-Mn-Fe types. The particles that showed trenching had rather high Cu-concentrations (Table 2), with virtually no Mn or Fe suggesting they were Al-Cu. Indeed, several particles where no trenching occurred were identified by EDX as Al-Cu-Fe-Mn. In some cases, the matrix around some Al-Cu particles remained unattacked even though these were close to others, which trenched. In the alkaline solutions (pH 10), trenching appeared to be the most common form of corrosion, and sometimes

[b] Micro-hole put onto the metal surface that acted as an identification marker for surface features during microscopy.

involved more than a single IMC. Examples are given in Figures 9c to 9e. Deposition of corrosion products could be observed around all these trenched areas.

In acidic solution, trenching was observed as well. An example is given in Figure 9f. Even after 18 hours of exposure, the width of the trench was only about 0.5 to 1 μm, and the depth (in so far as not obscured by corrosion products) only 1.3 to 2.3 μm. Figure 9g shows an area originally containing 2 large IMC and a small one in-between, separated by a thin strip of matrix material. After 72 min of immersion in 0.5 M NaCl, one trench surrounding all three particles had formed, and the matrix between the IMC particles had corroded. In both alkaline and acidic solutions there were particles, which did not corrode and showed no trenching within the duration of the experiment (~1 day).

In several cases, a combination of cathodic trenching and anodic dissolution was observed in the same IMC particle cluster. This is shown in Figures 10a and 10b for the acidic solution. Within two hours, corrosion ended on some parts of the particle agglomerate (black areas), whereas other parts formed narrow trenches with time.

Figure 11 plots differences in corrosion rate in the different electrolytes when expressed by area attacked. For this plot, the localized corrosion occuring on larger sample areas (130 by 130 μm) was monitored with time (instead of monitoring individual intermetallic particles like in Figure 8), and related to the total IMC areas present at the beginning of the experiment. Again, it is obvious that the corrosion in concentrated chloride solution occured much more rapidly than in standard solution (pH 6). However, the influence of the pH could not be clarified. Even for different areas on the same sample (pH 10-data) very different corrosion rates were sometimes observed. Sometimes entire clusters of IMC showing similar behavior (trenching or no attack at all) were observed in these studies.

DISCUSSION

The shapes of the intermetallic phases found by SEM are consistent with the findings of other authors.[7-9,13,15,35-37] The variations in the chemical compositions of the different phases (Table 1) could be due to a number of reasons: (i) the interaction volume of the SEM-EDS beam may possibly be greater than the volume of the IMC, resulting in signals also being collected from the Al-matrix; (ii) selective dissolution during wet grinding; or (iii) an indication of more than one phase (transitional phases) of these IMC being present on the metal surface[c]. The increased Cu-content found after corrosion might be due to Cu replating or dealloying of other constituents.

The SEM-EDX observation of Al-Cu-Mg and Al-Cu phases adjacent to one another is confirmed by the findings of other authors who reported the occurrence of different intermetallic phases in very close proximity to one another.[38] This proximity may have promoted the selective dissolution of the Al-Cu-Mg phase, whereas the Al-Cu phase remained unattacked for a long time (Figure 1, 4). This is in agreement with the differences in OCP and E-log i behavior of the pure phases (Figures 2 and 3), which suggest that upon galvanic coupling the Al-Cu-Mg phase should undergo active dissolution, whereas Al-Cu phases should serve as a cathode. It is also possible that the proximity of the cathodic site even accelerates the corrosion of the Al-Cu-Mg. The corrosion of the matrix in the vicinity of this particle can be explained by the formation of sufficiently aggressive pit solution to promote attack of the Al-matrix. The reason for the initiation of corrosion (filiform-like) several μm below the original site of Al-Cu-Mg dissolution is unknown at this point (Figure 4d). One possibility is that it might have initiated at another

[c] It is possible that formation of one constituent particle can serve as a nucleation site for the next one.

defect(s) in the matrix, which was not previously identified by the imaging analyses carried out prior to exposure to electrolyte.

Compositional analyses of large-sized intermetallic particles (Figure 5 and 6) showing localized corrosion attacks were not performed. Based on the SEM/EDX analyses of other samples and a correlation between shape and composition, the IMC in Figure 5 was probably of the Al-Cu-Fe-Mn type, whereas the IMC in Figure 6 could be Al-Cu. Several factors might contribute to the localized attacks on these particles. The observed differences in local composition within the same particle (which have also been observed by other authors,[36] might be one reason. This compositional variation might lead to a galvanic couple within a particle (compare OCP differences in Figure 2), and initiate pitting within the particle (Figure 5, 7a and 7c), or dissolution beginning at the interface to the matrix (Figures 7d and 7f). The pitting of the particle as well as the matrix in Figure 7b might suggest the presence of small defects with a size close to the resolution of the microscope (< 500 nm), which serve as initiation sites. These may be Al-Cu-Mg particles. Based on the OCP of the Al-Cu and Al-Cu-Fe-Mn phases (Figure 2) alone, pitting would not be expected at the OCP of AA 2024-T3 for those particles. However corrosion attack on Al-Cu-Fe-Mn phases has been seen before in 0.1 M NaCl.[10]

The Al-Cu-Mg intermetallic would still dissolve in a galvanic couple with the other IMC, Cu or AA 2024-T3 at the pH values of 3 and 10 as shown based on the OCP data relative to the anodic behavior of Al-Cu-Mg (Figure 2). However, it should dissolve faster at pH 3 than at pH 10 (Figure 3e). The Al-Cu and Al-Cu-Fe-Mn particles will still serve as cathodic sites. The close proximity of the two different types of particles can explain the corrosion features shown in Figure 10, where corrosion of some particles and formation of narrow trenches at the interfaces to matrix material can be observed next to each other.

Cathodic trenching has been extensively discussed in the literature.[1,3,8,10,11,17,18] It is thought that the local increase in pH at the cathodic Al-Cu and Al-Cu-Fe-Mn particles attacks the oxide film at the interface to the alloy matrix. In the present work, it was found that the susceptibility to trenching is not the same for all particles (Table 2). The data in Table 2 suggested that Al-Cu particles trench faster than Al-Cu-Mn-Fe in standard solution. This could be due to differences in the cathodic current densities on Al-Cu, and Al-Cu-Mn-Fe IMC (Figure 3a). However, present experimental data did not show any significant differences that could explain the differences in trenching behavior. Differences in susceptibility to trenching at particles cathodic to the Al-matrix were also observed in the alkaline and acidic solutions. It was not confirmed by EDX whether the particles more susceptible to trenching in these solutions were Al-Cu. Cleary, further investigation is still required in this area as selective trenching of particles may have been limited to only the specific conditions under which the tests were carried out. Trenching might depend not only on the exact particle composition, and the intermetallic compound crystal plane exposed, but also on the microstructural and compositional details of the corrosion processes in the matrix close to each type of intermetallic. For instance, extensive re-crystallization of small grains next to the constituent particles could change the corrosion properties of the matrix. It is possible that acidic concentration fields oppose alkaline trenching. However, observations of trenching in the acidic electrolyte argue against this. The effect of the lower bulk pH is probably partially compensated by the larger cathodic currents occuring under acidic conditions, which in turn increases the local pH at the IMC site.

On the bulk synthesized IMC, a lower OCP was observed in acidic solutions, and the cathodic current densities were higher. Based on mixed potential theory an increase in cathodic current densities alone would result in a more positive OCP compared to neutral solutions. If the

anodic partial currents are larger in acidic solution too, a more negative OCP is possible. The passive layer on the compounds is probably thinner in a pH 3 environment, because Al-oxides are not stable under these conditions.[39] The same is true for the passive layer on the matrix of AA 2024-T3. That is why matrix etching was observed in the acidic STD-electrolyte, which contributes to the faster rate of anodic dissolution observed in the electrochemical experiments (Figure 3e).

As a result of the lower OCP registered by AA 2024-T3 in the pH 3 solution (-0.665 V(SCE)) compared with the OCP in the pH 6 solution (-0.466 V(SCE)), an increase in the possibilities of trenching of the AA 2024-T3 matrix around the Al-Cu and Al-Cu-Mn-Fe IMC particles embedded in the AA 2024-T3 matrix is predicated from Figure 3g. Following this line of reasoning, this relative risk should reduce in the pH 10 solution (-0.352 V(SCE)) due to the higher OCP registered by AA 2024-T3. However, the galvanic couples, which exist on AA 2024-T3, are far more complicated. For instance, the data in Figure 3g also predicts that with regard to these galvanic couples, at pH 3, a slower rate of dissolution of an Al-Cu-Mg IMC particle on the surface of AA 2024-T3 should result, while at pH 10, the rate of dissolution should be faster. However, data in Figure 3e show that the rate of dissolution is much faster at pH 3 compared with at pH 10 thus, the smaller difference in potential between the Al-Cu-Mg IMC and the AA 2024-T3 matrix in the galvanic couple is offset by its faster rate of dissolution. In addition, the Al-Cu-Mg IMC exhibits some degree of passivity at pH 10, which also counterbalances the effect of the larger potential difference that exists between the Al-Cu-Mg IMC and AA 2024-T3 at this pH. This might be a contributing factor to the higher pitting potential exhibited in the pH 10 solution by AA 20204-T3. The high rate of dissolution of the Al-Cu-Mg IMC might result in the faster formation of a dealloyed porous Cu-rich sponge and

islands, which in turn could promote trenching. The lower pitting potential (in spite of the passive region exhibited) of AA 2024-T3, and the higher anodic and cathodic current densities exhibited by the IMC suggests that the pH 3 solution is the most aggressive of the three environments with the same [Cl^-] concentration.

Figure 11 shows that at high chloride concentration the overall corrosion rate as observed by CLSM is much larger than for 0.1 M Na_2SO_4 + 0.005 M NaCl in the entire pH range investigated. The differences for the sulfate-based electrolyte are more subtle and show very low reproducibility. Agglomerates of certain IMC compounds can sometimes be found on AA 2024-T3. This is responsible for the low reproducibility of the data especially for the pH 10 electrolyte (Figure 11): One area had many particles supporting trenching and therefore showed a high corrosion rate. Other areas on the same substrate (probably clusters of Al-Cu-Fe-Mn phases) showed a low corrosion rate. A window of 130 x 130 μm is statistically insufficient to represent the behavior of the entire substrate and to analyze the influence of subtle changes in the environment. Larger areas must be analyzed, or, alternatively, more areas on one sample in combination with several samples would have to be analyzed to strengthen this statement. However, the increase in corrosion rate at high chloride concentrations is so significant that it is clearly visible in the Figure.

Based on electrochemical measurements, corrosion should be the fastest in the pH 3 electrolyte, where matrix etching could be observed in CLSM. This could explain why low pH blisters exhibit rapid attack in underpaint corrosion studies on coated AA 2024-T3.

CONCLUSIONS

1. Variations in composition were observed amongst particles with the same elemental constituents.

2. The composition of some of the intermetallic particles were consistent with the stoichiometry of the most common intermetallics in AA 2024-T3, namely: θ-Al_2Cu, S-Al_2CuMg and $Al_{20}Cu_2(MnFe)_3$.
3. EDS showed that some agglomerated intermetallic particles contained more than one phase. This led to different rates and morphologies of corrosion attack within one agglomerated particle.
4. The Al-Cu-Mg particles were the most active in all the electrolytes investigated on the bare polished samples and corroded rapidly.
5. Corrosion within some intermetallic particles was localized.
6. All Al-Cu and Al-Cu-Mn-Fe particles do not have the same propensity to promote trenching of the Al-matrix. Electrochemical studies of synthezised IMC suggest, that differences in the cathodic reaction rates on each IMC contribute to this behavior.
7. The morphology of initial stages of corrosion attack at the micro-scale at the intermetallic compounds on bare AA 2024-T3 is similar in all the electrolytes investigated. The influence of the bulk pH on effects caused by a local pH increase can be partially compensated by a change in cathodic reaction rate. Based on electrochemical measurements, corrosion should be the fastest in the pH 3 electrolyte, where matrix etching could be observed in CLSM.
8. Preliminary indications are that pitting in the matrix or at small matrix particles is more evident in 0.5 M NaCl than in other solutions used, particularly the pH 10 solution, which is supported by electrochemistry on Al-Cu-Mg and 2024-T3.

ACKNOWLEDGEMENTS

The authors gratefully acknowledge the AFOSR for the financial support of the project under contract number F49620-96-1-0178, with Lt Col. Paul Trulove, Ph.D., as program

director. PAR Instruments and Scribner Associates, Inc. are thanked for continuing support of electrochemical instrumentation and software in CESE.

REFERENCES

1. G.S. Chen, M. Gao, R.P. Wei, Corrosion, **52**, 8 (1996).
2. R.G. Buchheit, R.P. Grant, P.F. Hlava, B. McKenzie, G.L. Zender, J. Electrochem. Soc., **144**, 2621 (1997).
3. G.S. Chen, C.-M. Liao, K-C. Wan, M. Gao, R.P. Wei, ASTM STP 1298, W.A. Van Der Sluys, R.S. Piascik, R. Zawierucha, Eds., p.18, ASTM (1997).
4. J.R. Scully, T.O. Knight, R.G. Buchheit, D.E. Peebles, Corros. Sci., **35**, 185 (1993).
5. M.J. Pryor, D.S. Keir, J. Electrochem. Soc., **102**, 241C (1955).
6. R.G. Buchheit, J. Electrochem. Soc., **142**, 3994 (1995).
7. M. Büchler, J. Kerimo, F. Guillaume and W.H. Smyrl, J. Electrochem. Soc., **147**, 3691 (2000).
8. M.A. Alodan and W.H. Smyrl, J. Electrochem. Soc., **144**, L282 (1997).
9. M.A. Alodan and W.H. Smyrl, J. Electrochem. Soc., **145**, 1571 (1998).
10. P. Schmutz and G.S. Frankel, J. Electrochem. Soc., **145**, 2295 (1998).
11. T.Suter and R.C. Alkire, in Critical factors in Localized Corrosion III, Electrochemical Society Proceedings **98-17** p.118 (1999).
12. R.G. Buchheit, L.P Montez, M.A. Martinez, J. Micheal and P.F. Hlava, J. Electrochem. Soc., **146**, 4424 (1999).
13. V. Guillaumin and G. Mankowski, Corros Sci., **41**, 421 (1999).
14. N. Dimitrov, J.A. Mann and K Sieradski, J. Electrochem. Soc., **146**, 98 (1999).
15. C. Blanc, B. Lavelle and G. Mankowski, Corros Sci., **39**, 495 (1997).

16. G.O. Ilevbare, J.R. Scully, J. Yuan and R.G. Kelly, Corrosion, **56**, 227 (2000).

17. M. Büchler, T. Watari and W.H. Smyrl, Corros. Sci., **42**, 1661 (2000).

18. J.O. Park, C.H. Paik, Y.H. Huang and R.C. Alkire, J. Electrochem. Soc., **146**, 517 (1999).

19. A.M. Mierisch, J. Yuan, R.G. Kelly and S.R. Taylor, J. Electrochem. Soc., **146**, 4449 (1999).

20. O. Schneider, G.O.Ilevbare, J.R. Scully, R.G. Kelly, Electrochemical and Solid State Science Letters, **4**, B35 (2001)

21. O. Schneider, G.O.Ilevbare, J.R. Scully, R.G. Kelly, in preparation for J. Electrochem. Soc.

22. J. B. Pawley, Editor, *Handbook of Biological confocal Microscopy*, 2nd ed., Plenum Press, New York and London (1995).

23. N. Llorca-Isern, M. Puig, M. Español, *J. Therm. Spray Technol.*, **8**, 73 (1999).

24. F. Guillaume, L.F. Darfias-Mesias, M. Buchler and W.H. Smyrl, in Critical factors in Localized Corrosion III, Electrochemical Society Proceedings **98-17** p.155 (1999).

25. M. E. Inman, R. G. Kelly, S. A. Willard, and R. S. Piascik, "Coordinated Metallographic, Chemical and Electrochemical Analyses of Fuselage Lap Splice Corrosion", Proc. of the ASIP Conference, Atlanta, November 1996.

26. R.G. Kelly, O. Schneider and J. Yuan, ECS Meeting Abstract Vol. 99-1, Abstract #81, May, (1998).

27. G.O. Ilevbare and J.R. Scully, Corrosion, **57**, 134 (2001).

28. H. H. Strehblow, C. M. Melliar-Smith, and W. M. Augustyniak, J. Electrochem. Soc., **125**, 915 (1978).

29. S.T. Pride, J.R. Scully and J.L Hudson J. Electrochem. Soc., 141 (1994): p. 3028.

30. P. C. Pistorius P.C and G. T. Burstein, Phil. Trans. R. Soc. Lond., A 341 (1992): p. 531.

31. A. Broli and H. Holtan, Corros. Sci., 13, (1973): p. 237.

32. W. Zhang, S. Smialowska and G. S. Frankel, "Influence of Cr^{6+} Concentration and pH on Polarization Curves of AA 2024-T3", MURI report by G. S. Frankel, The Ohio State University, September 1998 p. 51.
33. M. Kendig, M. Cunningham, S. Jeanjacquet, and D. Hardwick, J. Electrochem. Soc., 144 (1997) p. 3721.
34. T. Shibata and T. Takeyama, Corrosion, 33 (1977) p. 243.
35. G.P. Halada, C.R. Clayton, M.J. Vasquez, J.R. Kearns, M.W. Kendig, S. L. Jeanjaquet, G.G. Peterson, G.S. McCarthy and G.L. Carr, in Critical factors in Localized Corrosion III, Electrochemical Society Proceedings **98-17** p.139 (1999).
36. T.J.R. Leclére, A.J. Davenport, J. Deakin, D. Raikes and R.C. Newman, in Critical factors in Localized Corrosion III, Electrochemical Society Proceedings **98-17** p.130 (1999).
37. P. Schmutz and G.S. Frankel, J. Electrochem. Soc., **145**, 2285 (1998).
38. P Campestrini, E.P.M. van Westing, H.W. van Rooijen and J.H.W. de Wit, Corrosion Science, **42**, 1853 (2000).
39. M. Pourbaix, "Atlas of electrochemical equilibria in aqueous solutions", 2nd edition, National Association of Corrosion Engineers, Houston, Texas 1974.

TABLE 1. EDS analyses (in At. %) of intermetallic particles before exposure to electrolyte.

Particle	Al	Cu	Mg	Mn	Fe
1	64.0	26.5	9.5	0.0	0.0
2	96.7	2.0	1.0	0.1	0.2
3	73.6	26.2	0.0	0.2	0.0
4	80.32	19.1	0.3	0.14	0.14
5-1	62.48	20.8	16.5	0.14	0.08
5-2	81.0	17.9	0.7	0.1	0.3
6	74.7	12.4	0.0	3.7	9.2
7	85.1	8.7	6.1	0.1	0.0
8	85.8	5.2	0.2	3.5	5.3
9	88.3	3.7	0.3	3.0	4.7
10	97.1	2.4	0.3	0.2	0.0

TABLE 2. EDS analyses (in At. %) of intermetallic particles after exposure to electrolyte.

Particle	Al	Cu	Mg	Mn	Fe	Corrosion
A	51.4	48.3	0.0	0.2	0.1	Trenched
B	64.8	34.8	0.0	0.2	0.2	Trenched
C	86.7	12.9	0.0	0.3	0.1	Trenched
D	77.6	8.7	0.0	5.1	8.6	No trench
E	80.2	7.3	0.0	5.2	7.3	No trench
F	76.1	8.6	0.0	5.5	9.8	No trench
G	71.5	28.0	0.0	0.0	0.5	No trench
H	77.4	21.8	0.0	0.3	0.5	Trenched
I	84.9	4.4	0.0	6.3	4.4	No trench
J	72.1	25.2	2.4	0.2	0.1	Trenched
K	75.9	7.6	0.0	6.4	10.1	No trench
L	95.6	3.1	0.5	0.4	0.4	Trenched
M	32.7	66.5	0.0	0.5	0.3	Trenched
N	65.4	34.6	0.0	0.0	0.0	Trenched
O	95.9	2.7	0.7	0.7	0.0	Dark part Close to N
P	85.3	14.7	0.0	0.0	0.0	Trenched

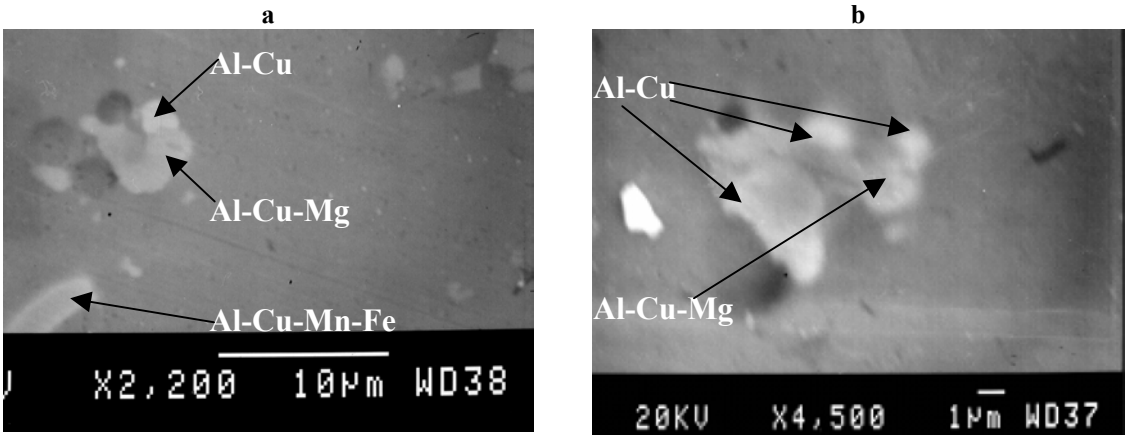

FIGURE 1. Secondary electron SEM images of intermetallic particles on AA 2024-T3. The three major types of IMC as identified by EDX are shown.

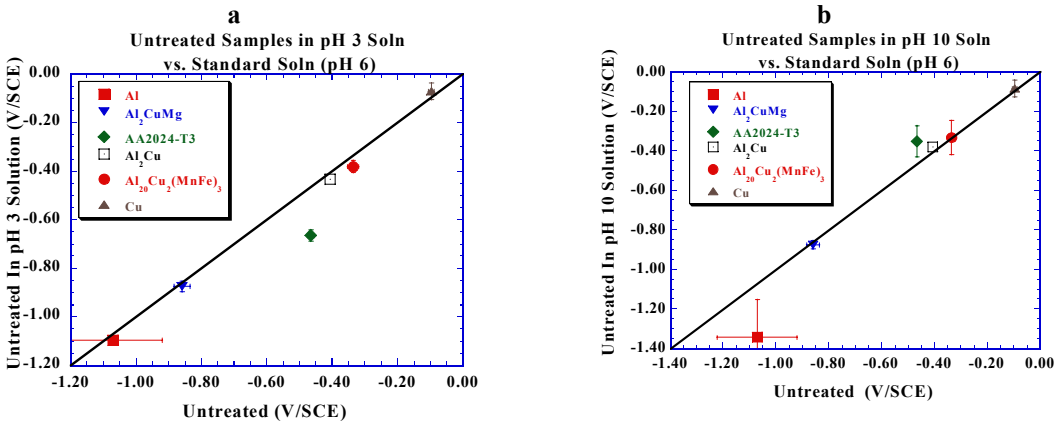

FIGURE 2. Open circuit potentials of untreated 99.998% Al, Al_2CuMg, AA 2024-T3, Al_2Cu, $Al_{20}Cu_2(MnFe)_3$, and 99.999% Cu in 0.1 M Na_2SO_4 + 0.005 M NaCl (pH 6) after 2 hours compared with those of their counterparts in (a) 0.1 M Na_2SO_4 + 0.005 M Cl^- (as 0.00167 M $AlCl_3$) adjusted to pH 3 with H_2SO_4, and in (b) 0.1 M Na_2SO_4 + 0.005 M NaCl + 0.0001 M NaOH, pH 10.

3a

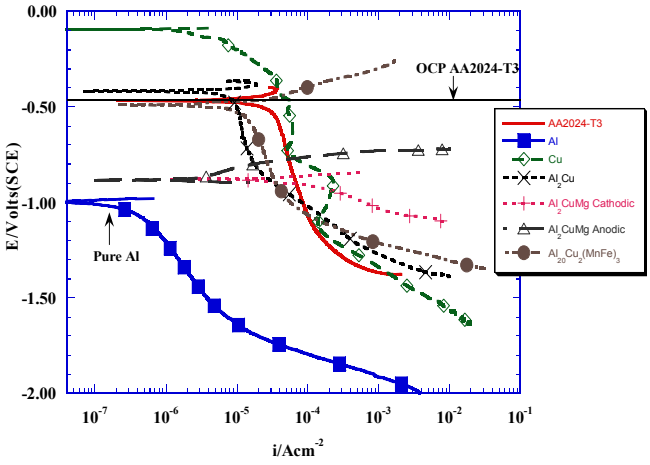

3b

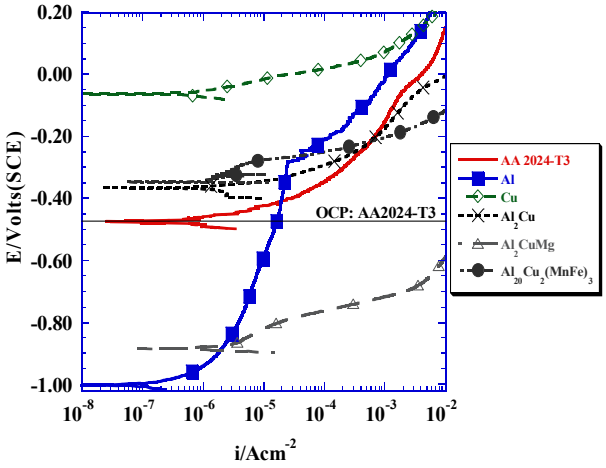

3c

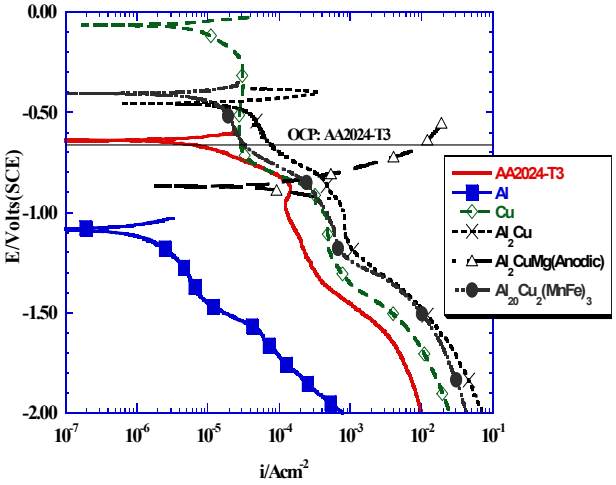

3d

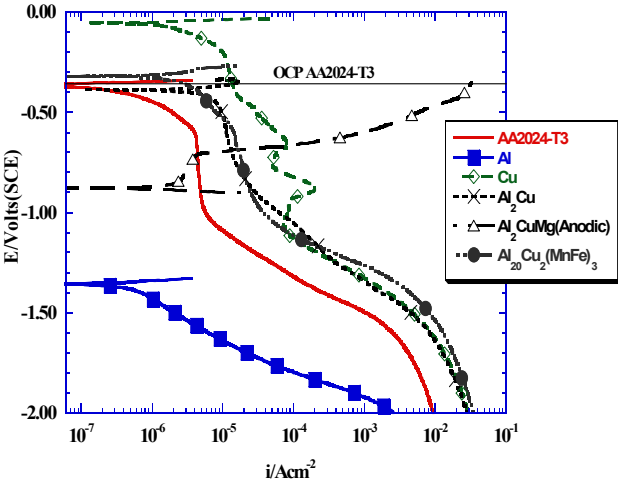

3e

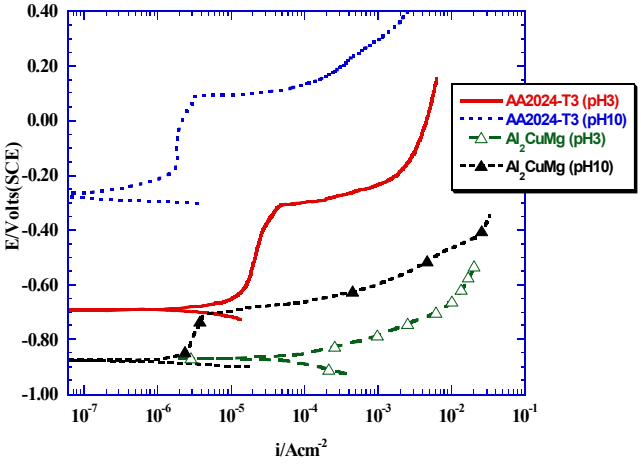

3f

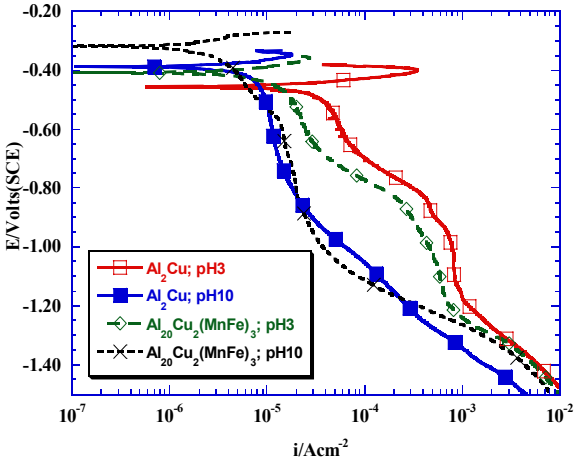

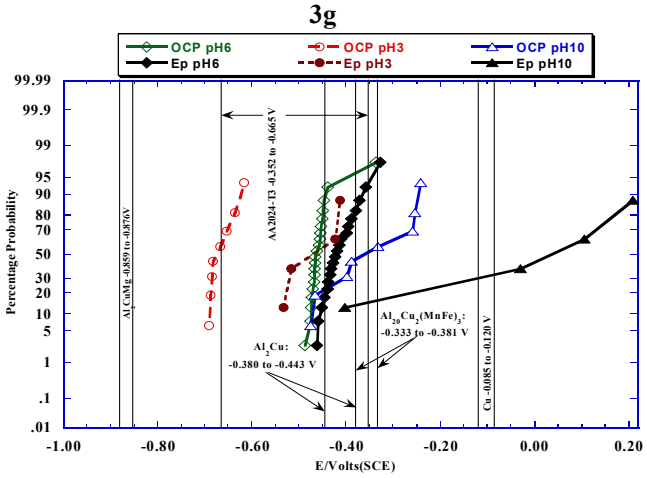

FIGURE 3. The E-logi behavior of stationary electrodes of AA 2024-T3, Al, Cu, θ-Al_2Cu S-Al_2CuMg, and $Al_{20}Cu_2(MnFe)_3$ at ambient aeration. (**3a**) Cathodic, (including anodic Al_2CuMg curve), and (**3b**) anodic, in 0.1 M Na_2SO_4 + 0.005 M NaCl; (**3c**) cathodic, (including anodic Al_2CuMg curve) in 0.1 M Na_2SO_4 + 0.005 M Cl^- (as 0.00167 M $AlCl_3$) adjusted to pH 3 with H_2SO_4; (**3d**) cathodic, (including anodic Al_2CuMg curve) in 0.1 M Na_2SO_4 + 0.005 M NaCl + 0.0001 M NaOH (pH 10); (**3e**) anodic, AA 2024-T3 and S-Al_2CuMg) in 0.1 M Na_2SO_4 + 0.005 M Cl^- (as 0.00167 M $AlCl_3$) adjusted to pH 3 with H_2SO_4 and 0.1 M Na_2SO_4 + 0.005 M NaCl + 0.0001 M NaOH (pH 10); (**3f**) Cathodic, θ-Al_2Cu and $Al_{20}Cu_2(MnFe)_3$ in 0.1 M Na_2SO_4 + 0.005 M Cl^- (as 0.00167 M $AlCl_3$) adjusted to pH 3 with H_2SO_4 and 0.1 M Na_2SO_4 + 0.005 M NaCl + 0.0001 M NaOH (pH 10); (**3g**) Cumulative probability of the OCP and the pitting potential of bare untreated AA 2024-T3 in 0.1 M Na_2SO_4 + 0.005 M NaCl (pH 6), 0.1 M Na_2SO_4 + 0.005 M Cl^- (pH 3), and 0.1 M Na_2SO_4 + 0.005 M NaCl + 0.0001 M NaOH (pH 10) under ambient aeration. There was a 2 h wait at OCP in all experiments. The vertical lines are the OCP indicated at the mean values attained amongst the 3 electrolytes listed above for each of the IMC, AA 2024-T3 and Cu.

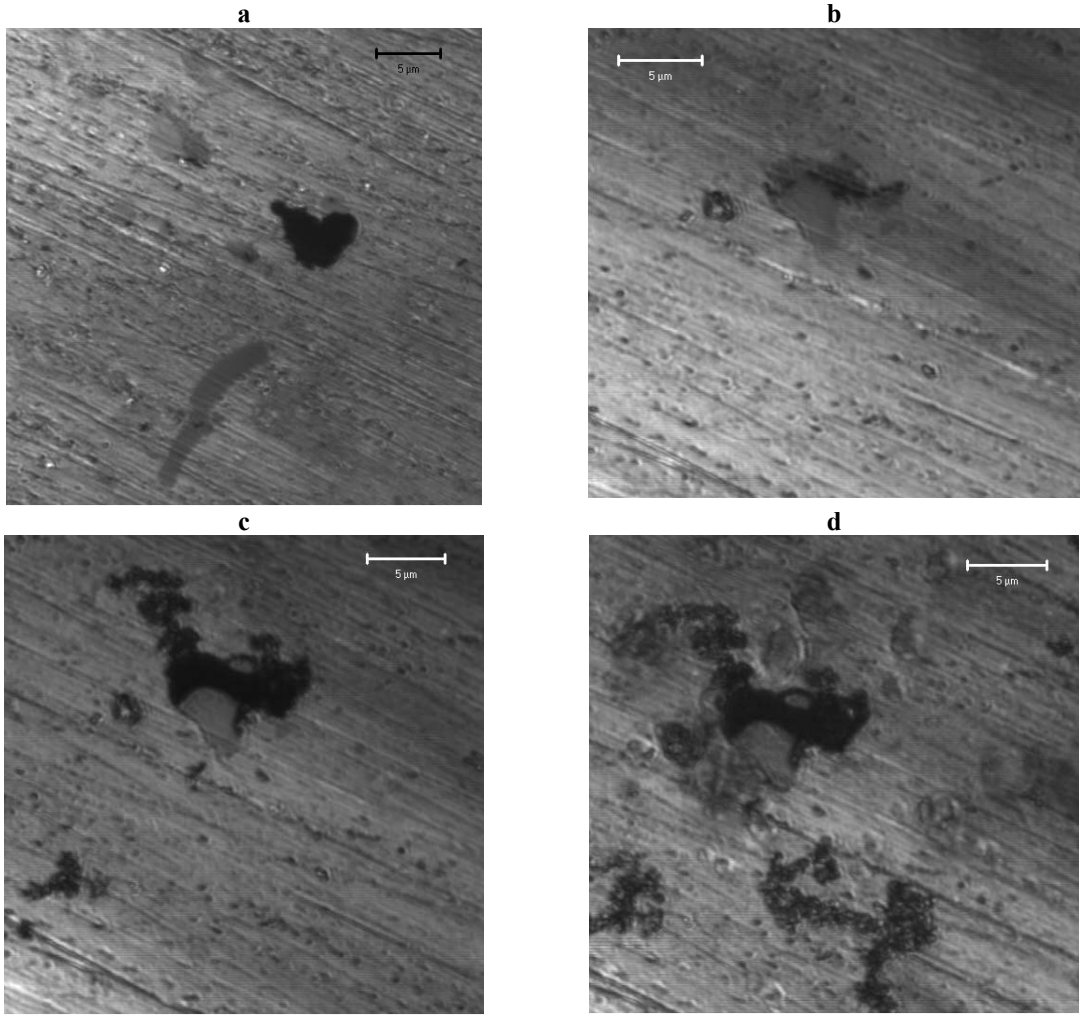

FIGURE 4. Selective Al-Cu-Mg corrosion on bare AA2024-T3: **(a)** CLSM image of the particle shown in Figure 1a after 2 h immersion in standard solution. **(b-d)** CLSM of the particle from Figure 1b during immersion in standard solution (immersion times: 13 minutes (b), 40 minutes (c), and 110 minutes (d)).

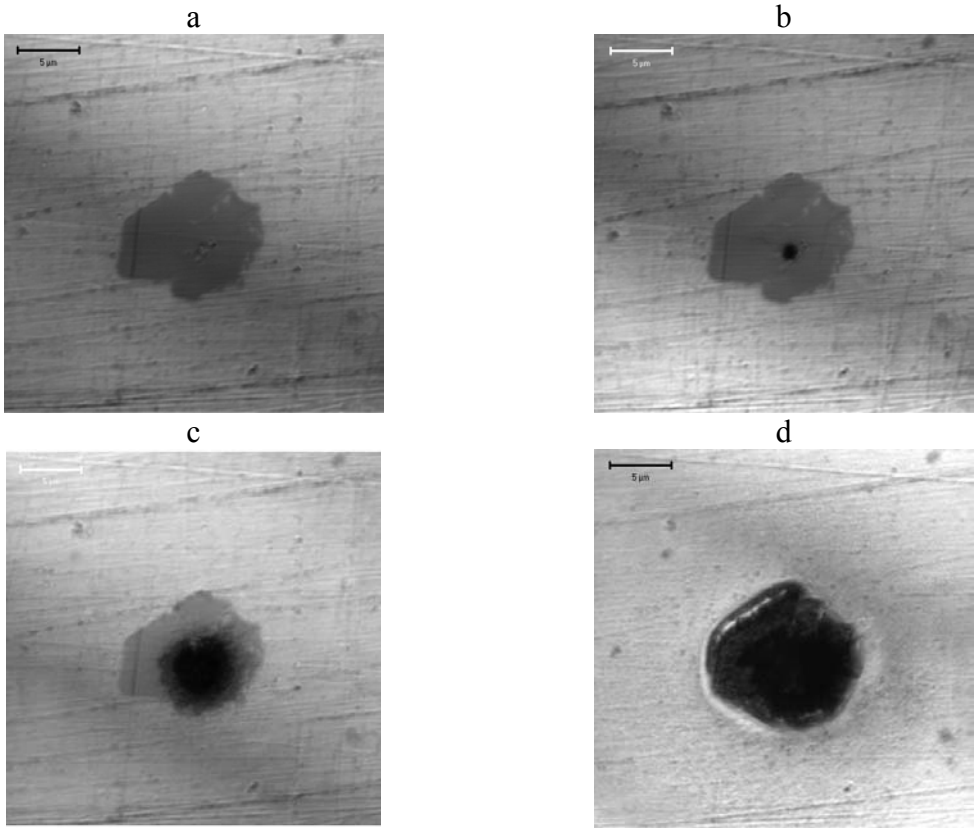

FIGURE 5. Intermetallic particle corroding on bare AA2024-T3 in 0.1 M Na_2SO_4 + 0.005 M NaCl. Immersion times: (a) 17 min (b) 83 min (c) 139 min and (d) 280 min.

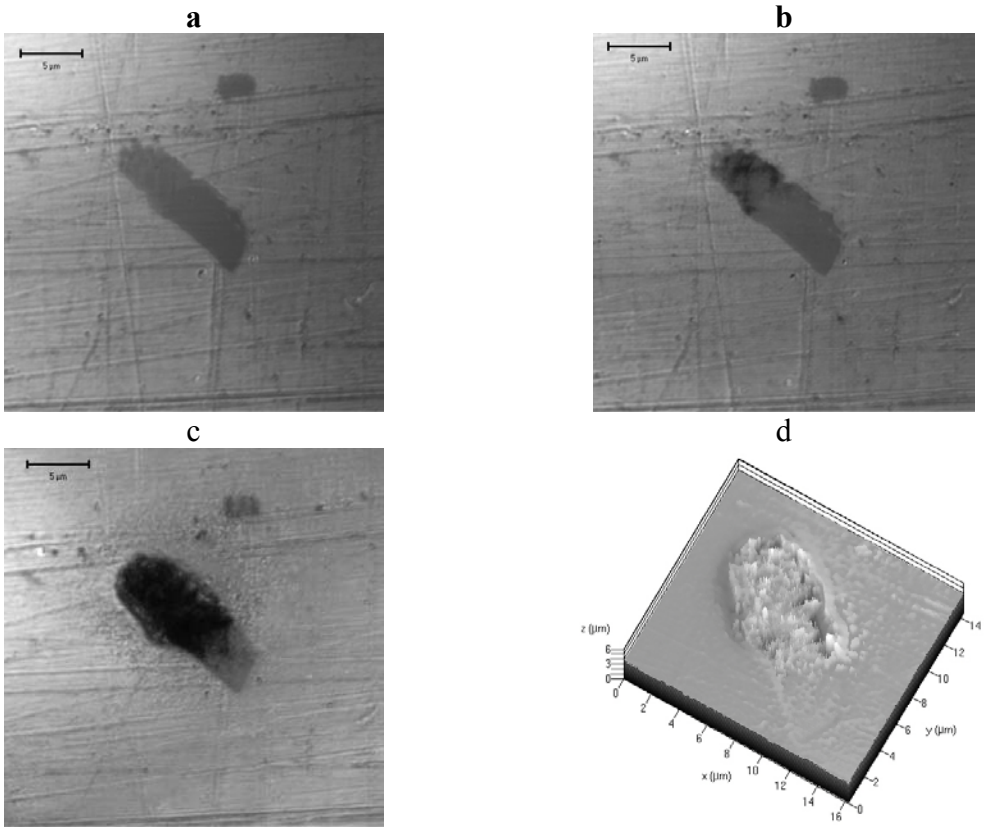

FIGURE 6. Corrosion attack on an intermetallic particle in 0.1 M Na_2SO_4 + 0.005 M NaCl (pH 6) after (a) 45 minutes (b) 147 minutes (c and d) 366 minutes.

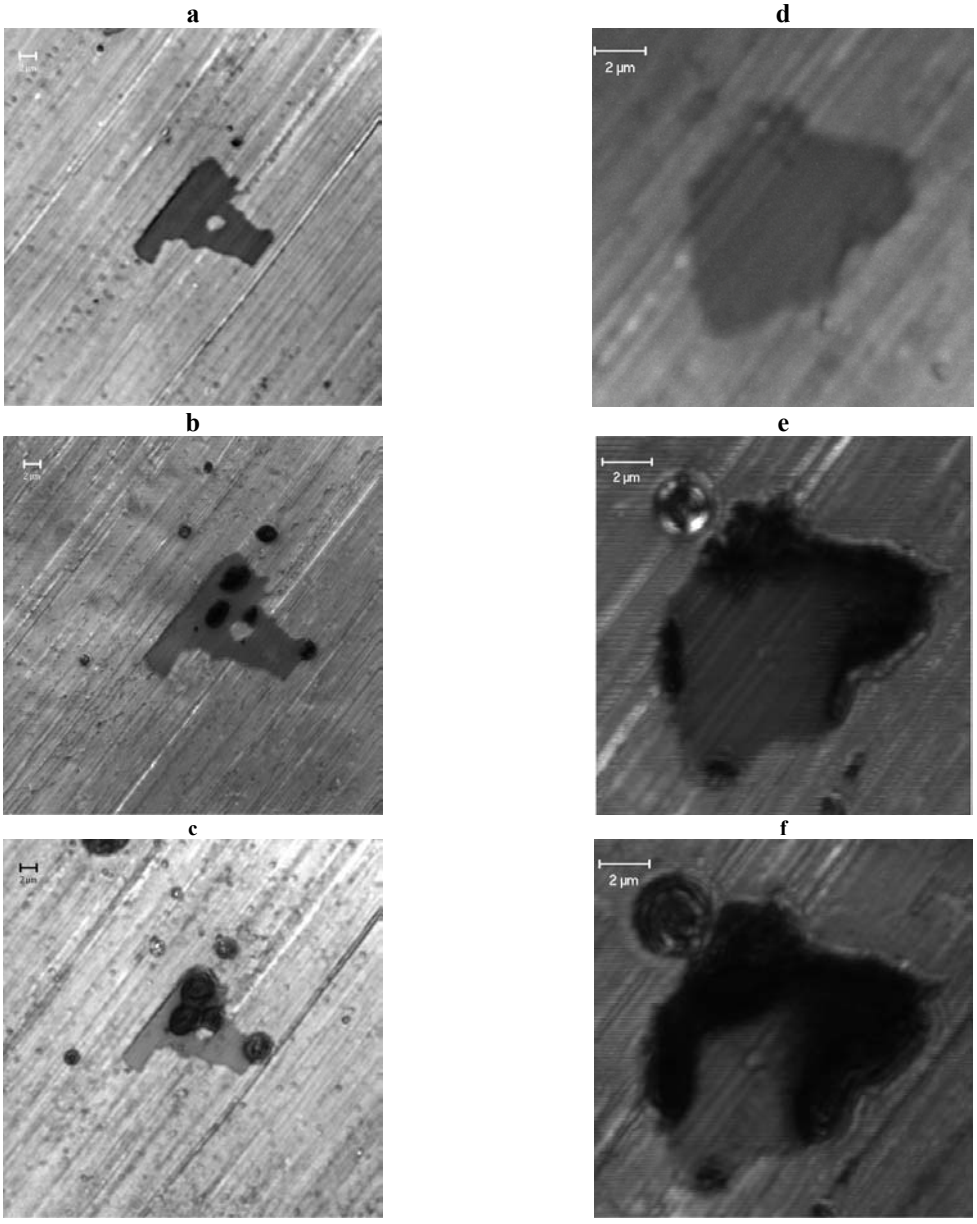

FIGURE 7. **(a to c)** Localized attack on IMC particle in 0.5 M NaCl (bar: 2 µm, immersion time (i.t.): (a) 0, (b) 50, and (c) 97 min); **(d to f)** dissolution of IMC particle in 0.5 M NaCl starting at he interface to the matrix (bar: 2 µm, i.t: (d) 0, (e) 22, and (f) 65 min). Pit growth at small particles in the matrix is also seen.

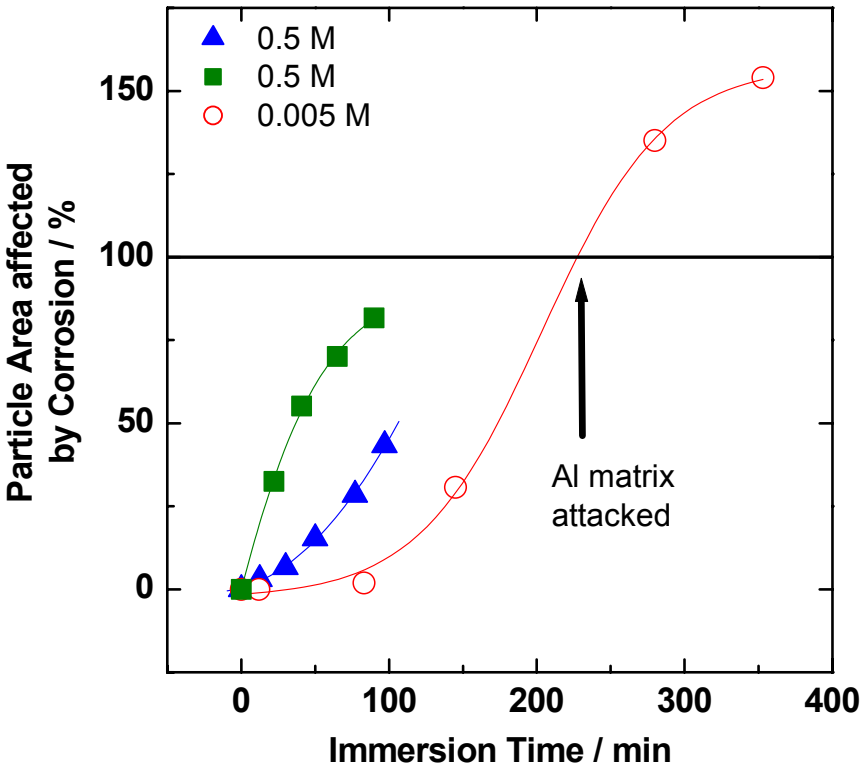

FIGURE 8. Comparison of the corrosion rate (based on the area affected by corrosion) of selected intermetallic particles on AA2024-T3 in 0.5 M NaCl (triangles, squares, particles from Figure 7) and 0.1 M Na_2SO_4 + 0.005 M NaCl (circles, particle from Figure 5). All areas are given relative to the particle size before corrosion. A value of more than 100% indicated that matrix material around the particle has corroded as well.

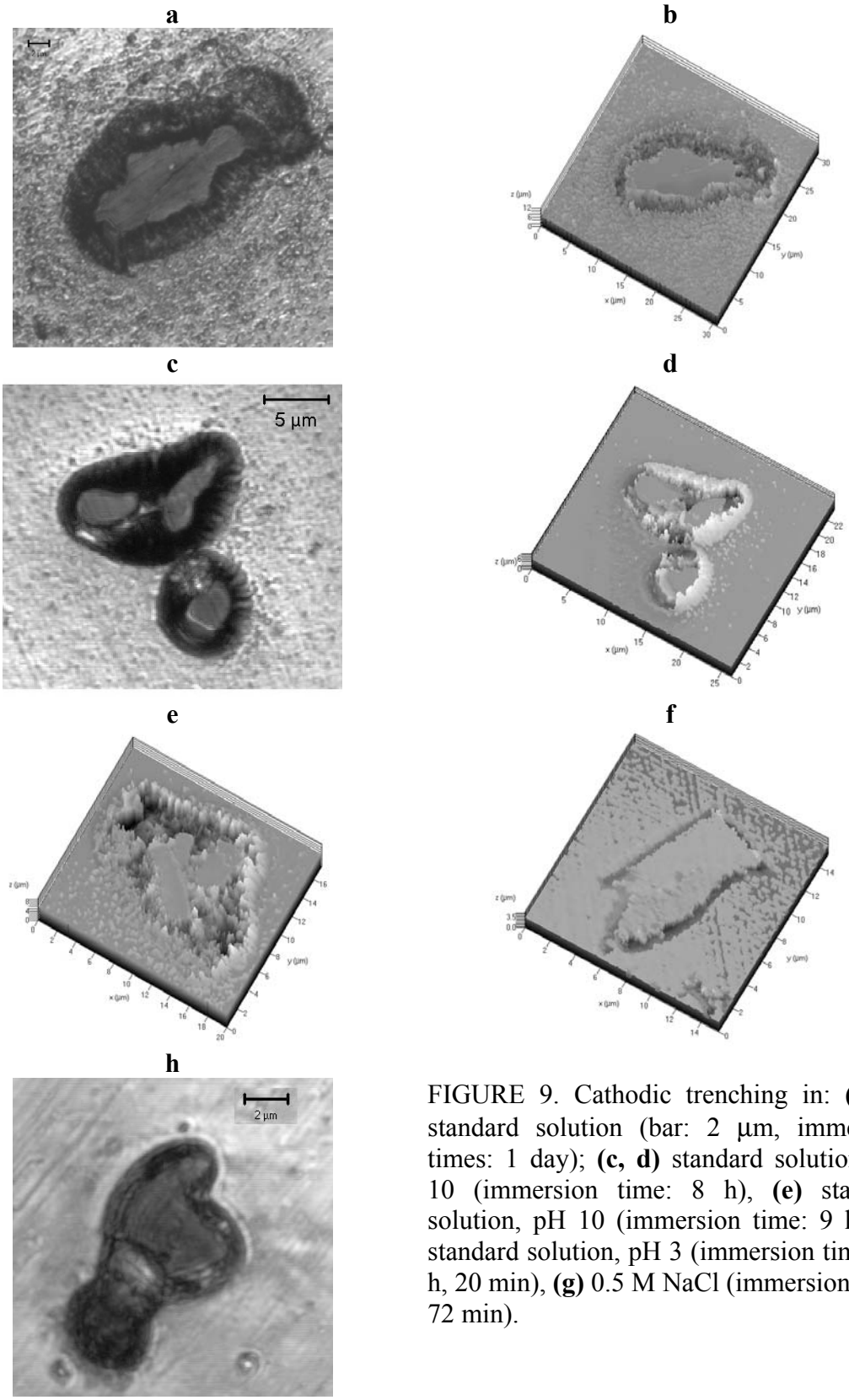

FIGURE 9. Cathodic trenching in: **(a, b)** standard solution (bar: 2 µm, immersion times: 1 day); **(c, d)** standard solution, pH 10 (immersion time: 8 h), **(e)** standard solution, pH 10 (immersion time: 9 h), **(f)** standard solution, pH 3 (immersion time: 18 h, 20 min), **(g)** 0.5 M NaCl (immersion time: 72 min).

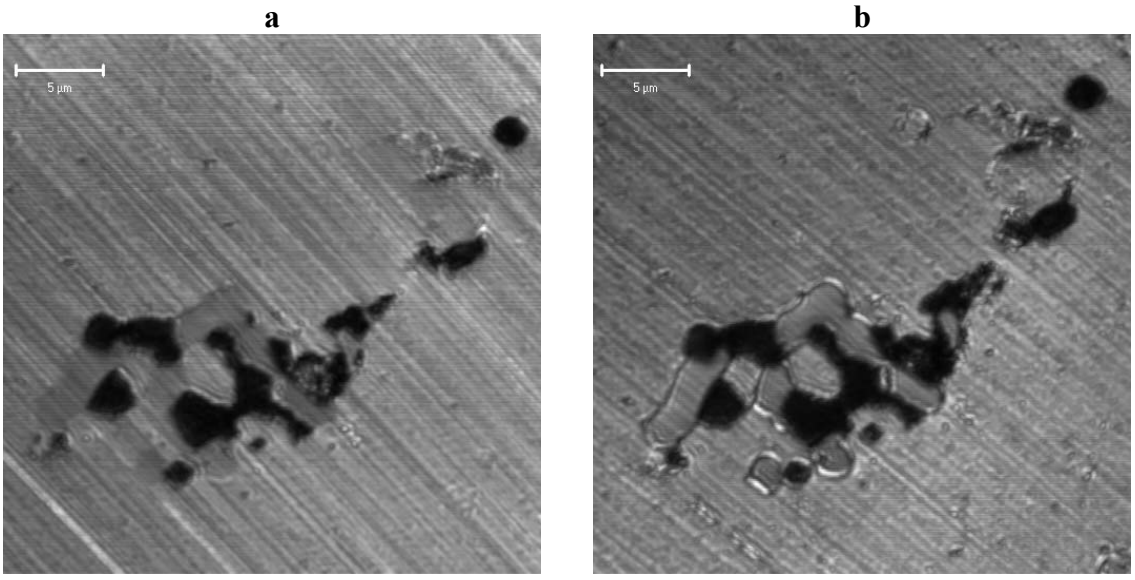

FIGURE 10. Cluster of intermetallic particles on bare AA 2024-T3, exposed to pH 3 0.1 M Na_2SO_4 + 0.005 l^-: (bar: 5 µm, immersion times: (a) 110, (b) 280 min).

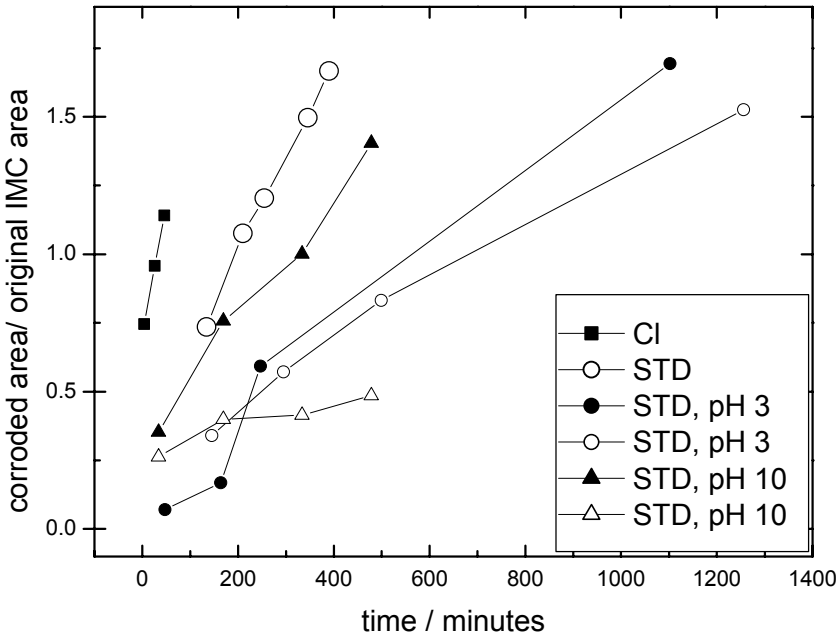

FIGURE 11. Increase of corroded area with time in different electrolytes: 0.5 M chloride (squares) and 0.1 M Na_2SO_4 + 0.005 M NaCl of pH 6 (large circles), 3 (small circles), and 10 (triangles). The areas analyzed were 130 by 130 µm, and the area affected by corrosion is given relative to the total area of IMC visible in the CLSM pictures before the onset of corrosion. Open and filled symbols are data from different regions on the same sample.

POSTER SESSIONS

DEVELOPMENT OF AN EXFOLIATION TEST PROCEDURE FOR USAF AGING AIRCRAFT PROGRAM

K.R. Cooper *, C. Franck [#], R.G. Kelly [#]

*Luna Innovations, Inc.
701 Charlton Ave, Charlottesville, VA 22903

[#]Department of Materials Science and Engineering, University of Virginia
116 Engineer's Way, Charlottesville, VA 22904

ABSTRACT

Wrought, high-strength aluminum alloys, such as AA 7075, widely used for aircraft structural components are susceptible to exfoliation corrosion in some temper conditions. In exfoliation, corrosion products formed by the selective attack of grain boundary regions force metal away from the body of the material, giving rise to a layered appearance, decreasing section thickness and affecting structural integrity. One of the objectives of the Air Force aging aircraft program is a quantitative assessment of the impact of exfoliation on structural integrity, including the ability to predict the extent of exfoliation with continued service. A lack of knowledge of the kinetics of exfoliation corrosion as a function of grain orientation hinders the quantitative assessment and prediction of its impact on structural integrity. The objective of this work is to develop a broadly-applicable test and analysis method that will provide a quantitative measure of the exfoliation growth kinetics as a function of grain structure and orientation relative to the rolling direction.

Peak-aged AA 7075 plate was used as the model system for the test protocol development. Parameters investigated included exposure environment and time, the effect of masking procedures to facilitate only S-T and S-L end-grain exposure, and orientation of the exposed material relative to the rolling direction (*i.e.*, longitudinal, transverse and short directions). Methods to quantify the magnitude and rate of exfoliation propagation are described.

INTRODUCTION

Wrought, high-strength aluminum alloys, such as aluminum association (AA) 7075 and AA 2024, widely used for aircraft structural components, are susceptible to intergranular attack and exfoliation corrosion in some temper conditions.[1] In exfoliation, corrosion products formed by the selective attack of grain boundary regions force metal away from the body of the material,

giving rise to a layered appearance and affecting structural integrity through the loss of load-bearing material and potentially acting as crack initiators.

The environment used in an accelerated test is critical. The corrosion behavior (*i.e.*, susceptibility and corrosion morphology) observed in field and service environments should be reproduced by the accelerated test. The current standard exfoliation test for 7xxx-series alloys (ASTM G-34, the EXCO test)[2] was developed in the late 1960's and has been criticized for employing an overly aggressive environment (initial pH ~ 0.4).[3,4] The EXCO test is reported to cause substantial surface attack during the first 24 hr of exposure and over-estimates the exfoliation susceptibility of aging conditions known to exhibit excellent resistance to this form of attack in the field (*i.e.*, T7x).[5] During the initial 24 hr, the pH increases from < 1 to ~ 3.[5] An alternative environment developed by Lee and Lifka in the early 1990's is based on the composition of the EXCO solution after the 48 hr exposure period, and uses 0.022 M $AlCl_3$ to achieve an initial pH ~ 3. Known as the ANCIT solution, this test environment reportedly more accurately reproduces the exfoliation behavior observed in field and service exposures.[5]

Little is known about the rate of intergranular corrosion and/or exfoliation in plate or sheet material as a function of orientation relative to the rolling direction. For example, it is unknown to what degree the global rate of intergranular attack, which has been demonstrated to be dependent on orientation for AA 2024-T3,[6] is determined by the microstructure (*i.e.*, grain structure) as opposed to the local rate of attack in a particular direction. On other words, is the local rate of grain boundary attack the same in the longitudinal direction as it is in the transverse direction? These unknowns have implications to the development of corrosion damage models for aircraft life prediction. If the local rates are the same in all directions than to predict the evolution of intergranular attack, and potentially exfoliation, one needs to know that rate (as a

function of environment, applied and residual stress, *etc*.) and the microstructure. If the local rates are not the same in all directions than each rate and the microstructure must be known to predict the damage evolution.

The objective of this work was to develop a test procedure that would facilitate quantification of the intergranular and/or exfoliation propagation rate in the orientations associated with rolled products (*i.e.*, L = longitudinal, T = transverse, and S = short; see Figure 1). To this end, the ideal test would prevent (or at least severely limit) the initiation of exfoliation on the L-T plane in order to facilitate the study of the intergranular corrosion propagation kinetics in the S-T and S-L directions. The tests described in this work examined the effect of: (1) exposure environment (EXCO *vs.* ANCIT), (2) exposure time, and (3) masking of the T/2 plane to the edge of a through-thickness hole that was designed to facilitate end-grain exposure and their corrosion only.

EXPERIMENTAL PROCEDURE

MATERIAL

A commonly employed high-strength aluminum alloy, AA 7075-T651, was used in this work. The nominal composition (in wt. %) is Al-5.6Zn-2.5Mg-1.6Cu and the microstructure is shown in

FIGURE 1. The grain size varied but was highly elongated in the rolling direction. This alloy is rated "highly susceptible" to exfoliation in the peak-aged (T6) condition.[1]

SPECIMEN DESIGN AND PREPARATION

The specimen configuration is illustrated in FIGURE 2. One inch thick AA 7075-T651 was cut at the T/2-plane and four 3/8" diameter holes were machined into each specimen. The

holes did not penetrate the full thickness of the specimen. The bottom of each hole was filled with epoxy to prevented corrosion of the bottom of the hole.

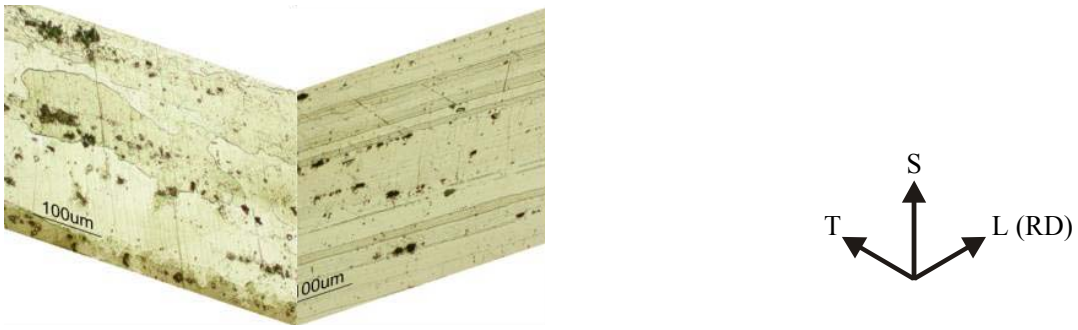

FIGURE 1. Microstructure of 1 in. thick plate of AA 7075-T651 used in this study. RD = rolling direction.

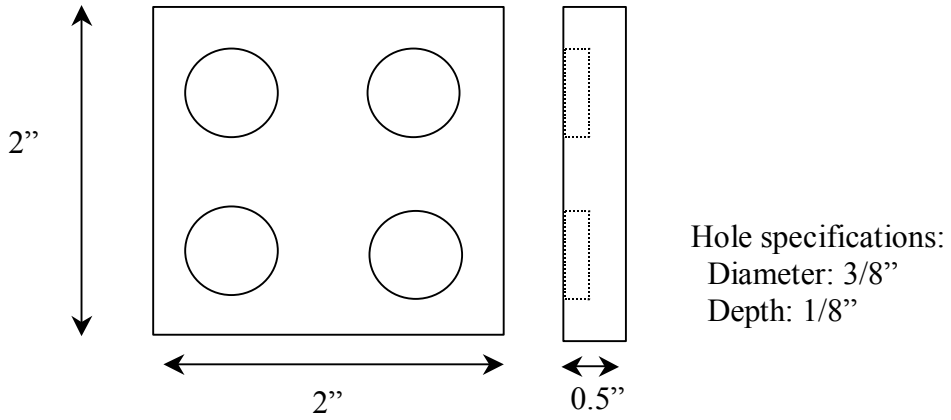

FIGURE 2. Specimen design for exfoliation test development. Each specimen had 4 non-through holes that served to expose end-grains.

In order to ensure that only the inside walls of the holes would be attacked most of the specimen was taped using electroplating tape and/or a peelable paint (XP-2000). For each sample, two holes were designated for the full exposure time (48 hr for EXCO or 96 hr for ANCIT) while the other two holes were exposed for half of the respective time period. This was

accomplished by covering two of the holes with electroplators tape for the first half of the exposure period, as indicated in FIGURE 3, at which time the tape was removed.

To examine the effect of masking right to the edge of the hole, for each pair of holes, one hole had a small exposed region around the hole and the second hole was completely masked off to the edge of the hole with peelable paint. FIGURE 3 illustrates the masking procedure and sequence, and the specimen exposed to the EXCO solution after the initial 24 hr period.

Therefore, each test specimen yielded 4 samples, one associated with each hole and of a different set of experimental conditions (*i.e.*, exposure time and masking condition).

TEST ENVIRONMENT

The tests environments were EXCO solution (4 M NaCl + 0.5 M KNO_3 + 0.1 M HNO_3, initial pH ~ 0.4) prepared as per ASTM G34[2] and ANCIT solution (4 M NaCl + 0.6 M KNO_3 + 0.022 M $AlCl_3$, natural pH ~ 3). All solutions were prepared with high purity water and reagent grade chemicals. The pH of the test solution was measured before and during the exposure with a calibrated pH electrode. The volume-to-area ratio was 40 mL/cm^2. It should be noted that ASTM G-34 recommends that this ratio not exceed 30 ml/cm^2.[2]

METALLOGRAPHIC SAMPLE PREPARATION

The intent was to examine and quantify the degree of exfoliation as a function of orientation (*i.e.*, relative to the RD). The layout for the metallographic specimens is illustrated in FIGURE 4. Each hole was cut in the rolling direction through the center of the hole. The resulting halves were then cut into three sections, to provide specimens in for cross sectional examination in the S-L and S-T directions, respectively. Before mounting the specimens for metallographic examination in epoxy, they were cleaned of corrosion products in concentrated

nitric acid for 5 min, thoroughly rinsed in water and dried. The epoxy-mounted samples were wet-polished to 1200 grit or additionally to 1 μm with alumina.

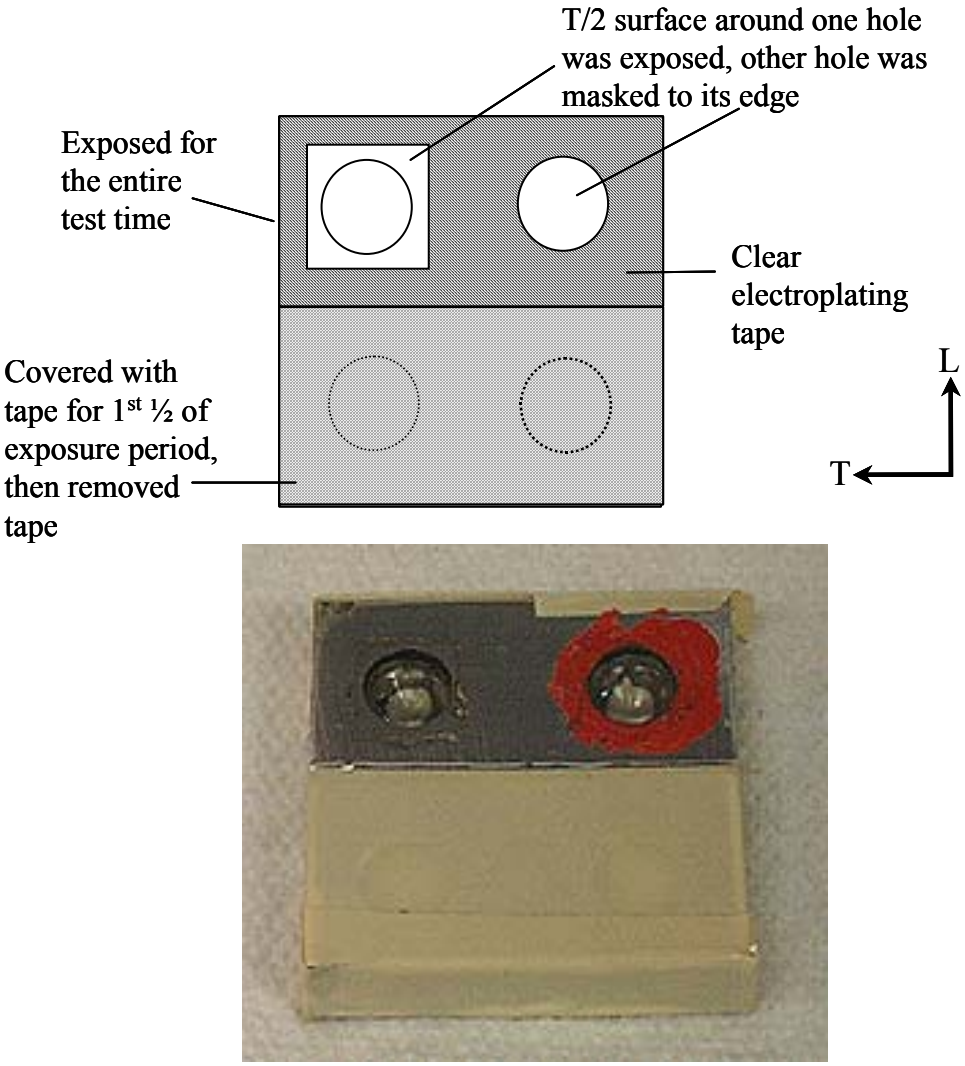

FIGURE 3. (a) Schematic of test specimen showing masking of T/2 surface as well as 2 of the 4 holes for the first ½ of the exposure period. (b) specimen exposed 24hr to EXCO solution, no tape had been removed yet.

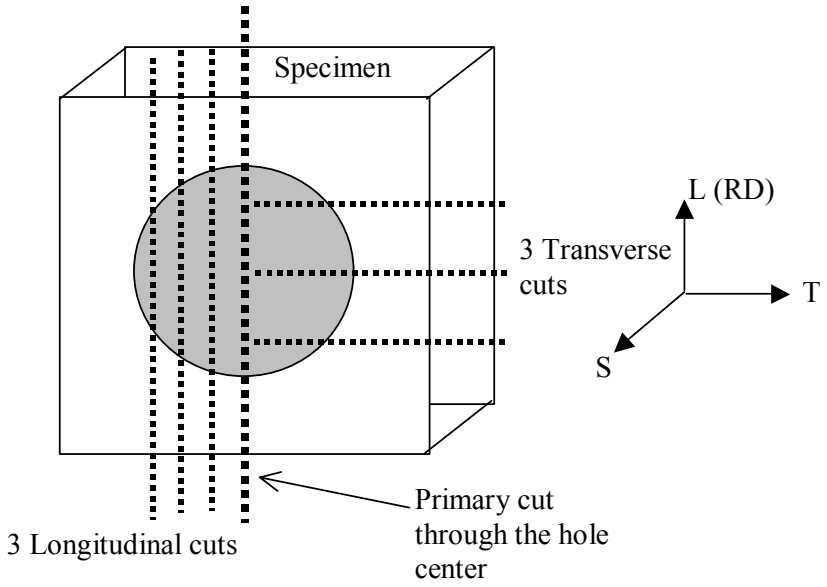

FIGURE 4. Schematic of specimen dissection for cross-sectional Metallography.

RESULTS AND DISCUSSION

SOLUTION PH DURING EXPOSURE

The measured pH of the EXCO and ANCIT test solutions is shown in Figure 5. The initial EXCO solution was very acidic (pH 0.4) and increased to pH 1.6 over the 48 hr exposure period. In contrast, the pH of the ANCIT solution was essentially constant at ~ 3 throughout the whole test period. The fact that the EXCO test solution pH did not increase to the expected value of about 3 within the test period was probably due to the use of a slightly larger volume-to-area ratio than typicall.[2]

QUALITATIVE ANALYSIS OF TEST SPECIMENS

Effect of Test Environment on Corrosion Morphology. The EXCO test excelled at producing extensive subsurface intergranular corrosion fissures but did not cause classic exfoliation (*i.e.*, uplifting of near-surface grains). In contrast, the ANCIT environment caused exfoliation although significant subsurface intergranular attack was not evident. These results are shown in FIGURE 6 and FIGURE 7, respectively.

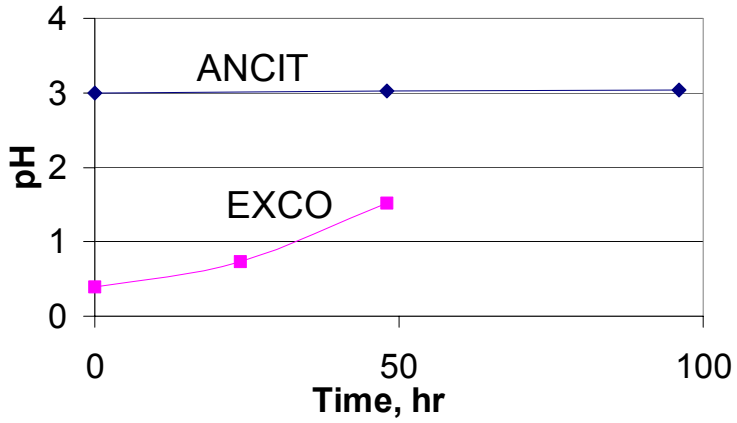

Figure 5. Bulk solution pH during 48 hr EXCO test.

The intergranular corrosion that caused the crack-like fissures was highly directional within the L-T plane. That is, the attack did not appear to wander out-of-plane. Some fissures were greater than 2 mm long in the L-direction. Extensive damage at the surface of the non-through hole was also observed (FIGURE 6). In addition, the fissures were predominately near the bottom of the machined hole, no fissuring was observed near the top of the hole. There are a number of reasons why this may have occurred. First, there may be differences in the susceptibility to exfoliation/intergranular attack through the thickness (S-direction) of the plate material.[4,7] For this work, however, this scenario is questionable because intergranular corrosion was observed at the top of the hole when the same material was exposed to the ANCIT solution (FIGURE 7). Alternatively, the difference in corrosion morphology in the EXCO could be due to differences in the local environment. The proximity of the solution within the top portion of the hole to the bulk made it relatively easy for the solution in that region to remain close to that of the bulk. In contrast, the solution close to the bottom of the hole would have reduced mass transfer with the bulk (because of longer diffusion and migration distance), and therefore would more easily achieve a slightly less aggressive environment, which may be more conducive to promoting intergranular attack. The less aggressive environment (*i.e.*, higher pH) is a result of

corrosion and subsequent hydrolysis of Al^{3+}.[8-10] Note that the pH measurements shown in Figure 5 are for the bulk environment and not the pH of the solution within the hole.

The requirement that a higher pH environment be established to promote intergranular attack (a prerequisite for exfoliation) is consistent with the observation of exfoliation of the sample exposed to ANCIT wherein the pH was near 3 to begin with. This reasoning does not, however, explain why we did not observe the extensive sub-surface crack-like fissures for the specimen exposed to ANCIT as was evident in the EXCO specimen.

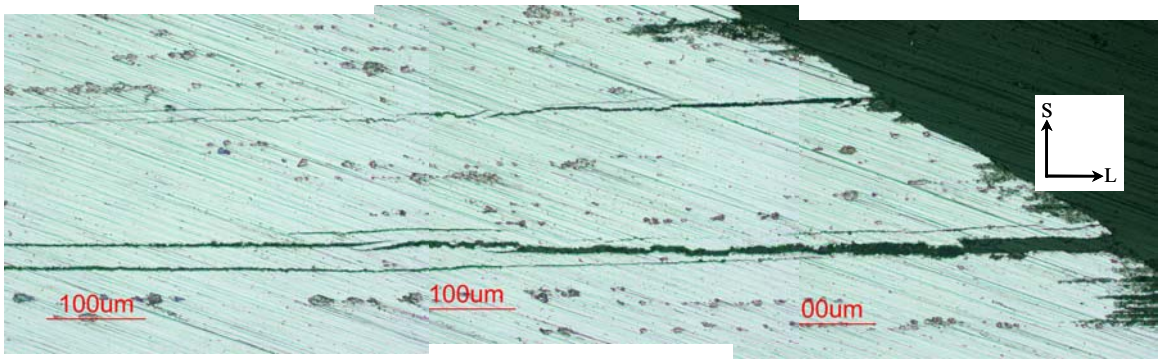

FIGURE 6. Extensive subsurface fissures in AA 7075-T6 after 48 hr exposure to EXCO.

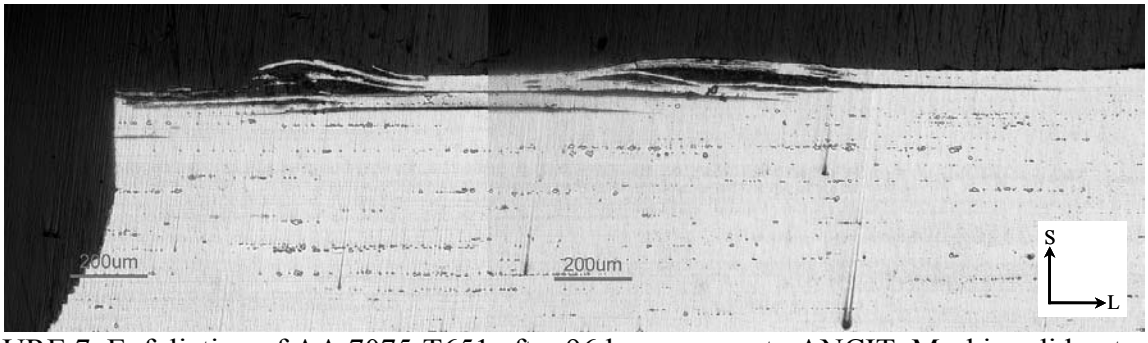

FIGURE 7. Exfoliation of AA 7075-T651 after 96 hr exposure to ANCIT. Masking did not reach to edge of the hole.

Effect of Masking To Edge of Hole. In general, masking with the peelable paint to the edge of the non-through hole (see FIGURE 3) tended to reduce the amount of exfoliation observed as compared to samples that were not masked to the edge of the hole during the test.

This general observation is demonstrated in the micrographs shown in FIGURE 8 (S-L orientation) and FIGURE 9 (S-T orientation) in which representative pictures show the amount of attack. Only specimens exposed to ANCIT solution are discussed here because exfoliation was not generally observed for specimens tested in EXCO (see previous discussion).

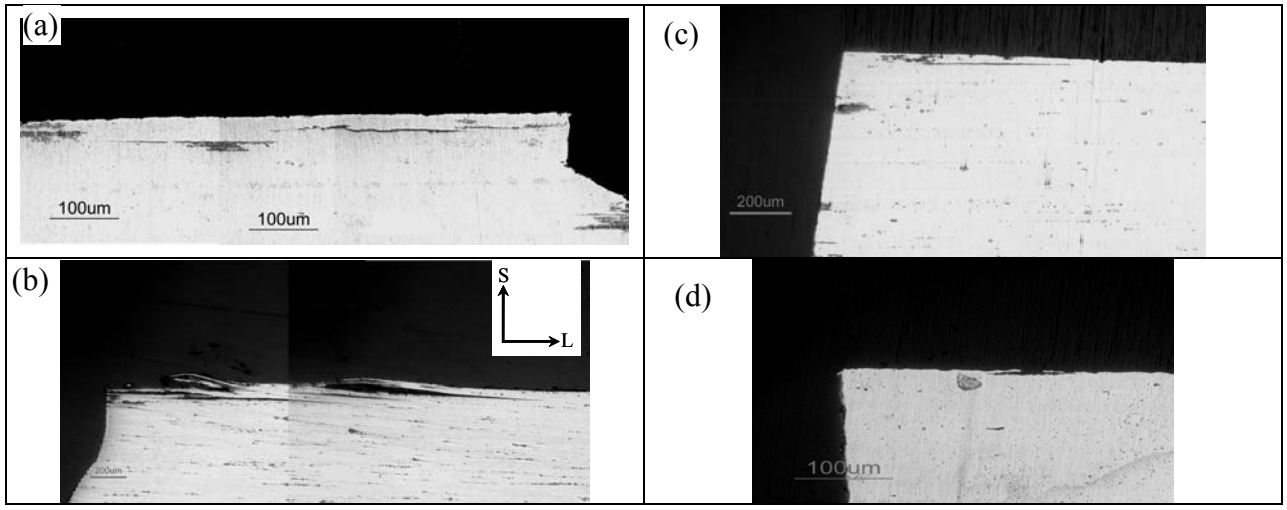

FIGURE 8. Exposure of AA 7075-T651 to ANCIT solution. (a) 48 hr, no masking to edge of hole, (b) 96 hr, no masking to edge of hole, (c) 48 hr, masking to edge of hole, (d) 96 hr, masking to edge of hole. In all cases L (or RD) is left to right and S is top to bottom.

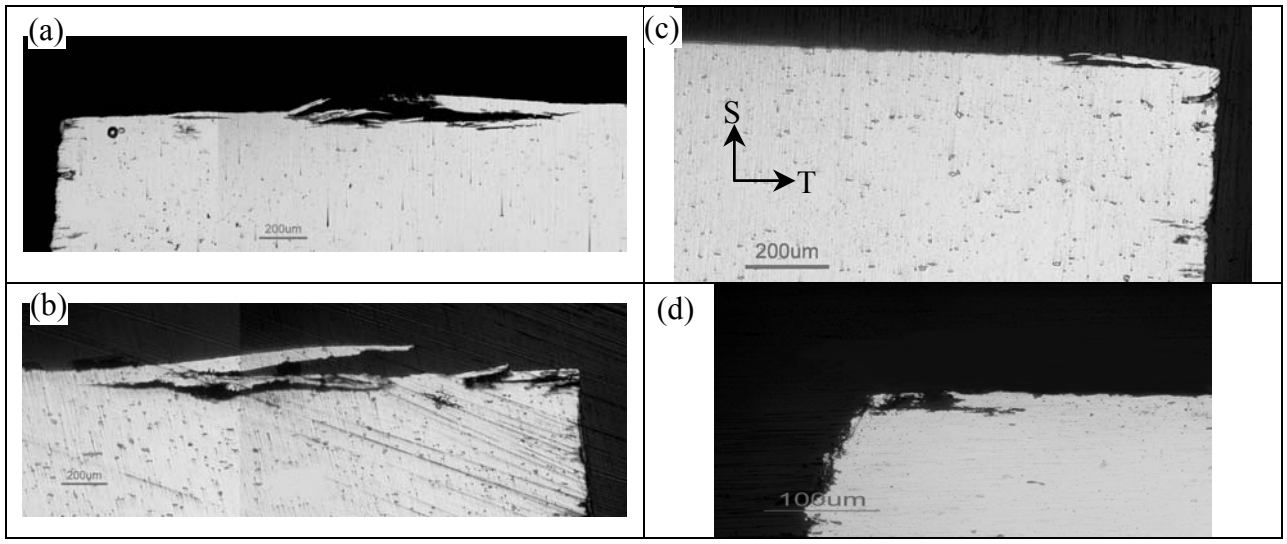

FIGURE 9. Exposure of AA 7075-T651 to ANCIT solution. (a) 48 hr, no masking to edge of hole, (b) 96 hr, no masking to edge of hole, (c) 48 hr, masking to edge of hole, (d) 96 hr, masking to edge of hole. In all cases T is left to right and S is top to bottom.

There are a number of scenarios that could explain the effect of masking. First, the L-T plane may have a higher density of sites that act as initiators of localized corrosion than the S-T or L-S planes. Such metallurgical features would include constituent particles or susceptible grain boundaries. If the development of intergranular corrosion that ultimately leads to exfoliation is related to the availability of these high susceptibility locations, than it is conceivable that the amount of exfoliation would be a function of the density of the culpable metallurgical feature. It is well known Al alloy pit initiation occurs at second-phase particles.[11-13] However, it is not clear if the area density of initiation sites is greater on the L-T plane than planes in the S-T or S-L orientations.

A second hypothesis is that masking the vast majority of the boldly exposed material significantly reduced the available area for the cathodic reaction. This would have the effect of decreasing the overall amount of corrosion and/or forcing the cathodic reaction to occur on the surface of the wall hole within the hole such that the acidic environment required to cause exfoliation may not have been maintained. The latter scenario implies that separation of anode and cathode are required support exfoliation. Localized corrosion, for example pitting,[11,14] and environmental cracking of aluminum alloys,[9,15] is associated with physical separation of the anodic and cathodic reaction sites.

The difficulty in introducing exfoliation from the wall of the hole as opposed to starting it from the T/x plane is problematic from the stand point of determining the kinetics of intergranular and exfoliation attack. In order to determine the rate of penetration via analysis of cross-sectional metallographs, it is necessary to know where the corrosion started (and where it ends). If the attack started, say as a pit, on the exposed L-T surface before changing direction to penetrate intergranularly in the L or T directions, than it is not possible to determine the rate of

attack in the L or T direction because the time at which the transition in direction of attack occurred is unknown. For this reason, future quantitative analysis of the exfoliation will be limited to samples that were masked to the edge of the hole. In this way, we can be assured that the attack began at the surface of the through-thickness hole.

QUANTITATIVE ANALYSIS OF EXFOLIATION

Quantitative analysis of each of exfoliated specimens consisted of determining two parameters: (1) the deepest intergranular penetration, and (2) the effective area loss. These data were obtained via a semi-automated procedure that consisted of either manually selecting the appropriate features, which was then analyzed by image analysis software. Alternatively, selection of appropriate features was also automatically detected by the image analysis software. For the latter scenario, the image was calibrated for brightness and contrast and thresholds for color were set to optimize selection of the relevant features.

For the purpose of illustrating the method, we analyzed specimens in which it appeared that the corrosion initiated on the S-T or S-L planes. However, because the specimens were not masked to the edge of the hole, we can not be certain that the attack initiated on the wall of the hole as opposed to on the L-T plane. FIGURE 10 demonstrates the quantitative analysis procedure.

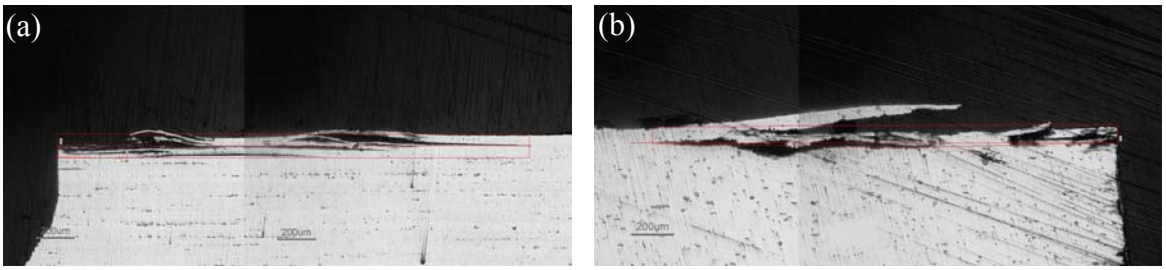

FIGURE 10. Examples of method to quantify exfoliation. AA 7077-T651, exposed 96 hr (a) S-L, (b) S-T direction. For each case, the greatest penetration and effective area loss is shown.

TABLE 1.
Preliminary results of quantification of exfoliation shown in Figure 10.
AA 7075-T651 exposed 96 hr ANCIT, samples not masked to edge of hole.

	L-direction,	T-direction
Greatest Penetration, mm	2.485	2.243
Effective area loss, mm^2	0.302 [a]	0.197 [b]

[a] in L-S plane, [b] in T-S plane

Based on the results shown in Table 1 and assuming that the attack initiated on the wall of the through-thickness hole, than it appears that the attack was no faster in the L direction than in the T-direction. This contrasts with what one might expect based on the aspect ratio of the grain structure, which was ~ 3 (*i.e.*, grains are ~ 3x larger in L-direction than T-direction), if the global or net penetration kinetics of intergranular attack are controlled by the grain structure, as proposed for AA 2024-T3.[6]

CONCLUSIONS

Exfoliation of AA 7075-T651 can be achieved through the described procedures. A modified (less aggressive) form of the EXCO solution, commonly referred to as ANCIT, was preferable to EXCO for inducing exfoliation within the specimens configuration used in this work. EXCO, on the other hand, was suitable for introducing extensive, subsurface crack-like fissures.

Complete masking the L-T surface suppressed exfoliation corrosion. The reason for this effect is not completely understood at this time but may be related to: (1) preferential initiation of localized corrosion occurs on L-T plane as opposed to on S-L and S-T planes, (2) very small cathode area reduced amount of attack, or (3) the cathodic reaction was forced to occur within the hole such that the local pH increased sufficiently that localized corrosion was suppressed. Additional unidentified mechanisms may also be in effect. Regardless of the precise cause of the

reduced exfoliation for completely masked specimens, the results complicates the fact that in order to facilitate quantification of the intergranular penetration kinetics as a function of orientation it is necessary to prevent or at least minimize initiation of localized corrosion on the L-T plane.

Two methods are proposed to quantify exfoliation that could be used by structural engineer for structural life analysis: greatest penetration distance and effective area loss. For the samples analyzed, maximum penetration in the L-direction only slightly exceeded that in the T-orientation. Although no significant anisotropy in attack is reported here, it should be noted than only a small number of specimens were analyzed. More analysis is required to confirm or refute the results presented.

ACKNOWLEDGEMENTS

This work was sponsored by AFRL/ WPAFB (Contract # F09650-00-DD-0018). The support is gratefully acknowledged.

REFERENCES

1. J. R. Davis, *ASM Specialty Handbook: Aluminum and Aluminum Alloys*. Materials Park, OH: ASM International, 1994.
2. ASTM, "Standard Test Method for Exfoliation Corrosion Susceptibility in 2XXX and 7XXX Series Aluminum Alloys (EXCO Test): G34-90," in *Annual Book of ASTM Standards - Metal Test Methods and Analytical Procedures*, vol. 03.02 Wear and Erosion; Metal Corrosion, R. A. Storer, Ed. Philadelphia, PA: ASTM, 1990, pp. 119-124.

3. B. W. Lifka and D. O. Sprowls, “Relationship of Accelerated Test Methods for Exfoliation Resistance in 7XXX Series Aluminum Alloys with Exposure to a Seacoast Atmosphere,” presented at Corrosion in Natural Environments, ASTM STP 558, 1974.
4. D. O. Sprowls, “Testing for Corrosion Types: Exfoliation,” in *Corrosion Tests and Standards: Applications and Interpretation*, R. F. Baboian, Ed. Philadelphia, PA: ASTM, 1995, pp. 218-224.
5. S. Lee and B. W. Lifka, “Modification of the EXCO Test Method for Exfoliation Corrosion Susceptibility in 7XXX, 2XXX and Aluminum-Lithium Alloys,” presented at New Methods for Corrosion Testing of Aluminum Alloys, ASTM STP 1134, 1992.
6. W. Zhang and G. S. Frankel, “Anisotropy of Localized Corrosion in AA 2024-T3,” *Electrochemical and Solid State Letters*, vol. 3, 2000.
7. T. J. Summerson and D. O. Sprowls, “Corrosion Behavior of Aluminum Alloys,” presented at Aluminum Alloys - Their Physical and Mechanical Properties, Charlottesville, VA, 1986.
8. C. J. Baes and R. E. Mesmer, *The Hydrolysis of Cations*, 2 ed. Malabar, FL: R.E. Krieger Publishing Company, 1976.
9. K. R. Cooper and R. G. Kelly, “Measurement and Modeling of Crack Conditions During the Environment-Assisted Cracking of an Al-Zn-Mg-Cu Alloy,” presented at Chemistry and Electrochemistry of Corrosion and Stress Corrosion Cracking, New Orleans, LA, 2001.
10. A. Turnbull, “The Solution Composition and Electrode Potential in Pits, Crevices and Cracks,” *Corrosion Science*, vol. 23, pp. 833-870, 1983.
11. Z. Szklarska-Smialowska, *Pitting Corrosion of Metals*. Houston, TX: NACE: Houston, TX, 1986.

12. T. Suter and R. C. Alkire, “Microelectrochemical Studies of Pit Initiation at Single Inclusions in Al 2024-T3,” *Journal of the Electrochemical Society*, vol. 148, pp. B36-B42, 2001.
13. P. Schumtz and G. S. Frankel, *Journal of the Electrochemical Society*, vol. 145, pp. 2295, 1998.
14. R. T. Foley, “Localized Corrosion of Aluminum Alloys - A Review,” *Corrosion*, vol. 42, pp. 277-288, 1986.
15. K. R. Cooper and R. G. Kelly, “Probing the Chemistry and Electrochemistry of Environment-Assisted Cracking of an Al-Zn-Mg-Cu Alloy,” presented at 198th Meeting of the Electrochemical Society, Corrosion and Corrosion Prevention of Low Density Metals and Alloys, Phoenix, AZ, 2000.

CORROSION CHEMISTRY DATA BASED ON CORRELATION BETWEEN ELECTROCHEMICAL SPECTROSCOPY AND SURFACE ANALYSIS

L.S. Kasten[1], N.N. Voevodin[1], M.Khobaib[1], M.S. Donley[2], Ryan Osterday[3]

[1]Research Institute, University of Dayton
300 College Park, Dayton, OH 45469-0168

[2]Air Force Research Laboratory
Materials & Manufacturing Directorate Nonstructural Materials Branch,
Bldg 654, Wright-Patterson Air Force Base, OH 45433-7750

[3]Southwestern Ohio Council for Higher Education
3155 Research Boulevard, Dayton, OH 45420-4015

ABSTRACT

A relatively new technique, the Scanning Vibrating Electrode Technique (SVET), allows *in-situ* examination of corrosion activity by probing the specimen potential and mapping anodic and cathodic areas during corrosion. In this research, we have used electrochemical microscopy[1] – the SVET - to investigate corrosion processes on aluminum alloys, inhibition actions of chromate, and candidates for chromate replacement on localized anodic/cathodic processes. SVET has been developed to allow in-situ examination of DC currents associated with localized corrosion activity – corrosion currents flow due to the presence of anodic and cathodic areas.[2] Since it is an *in-situ* technique, the SVET offers a method for directly observing the progress of corrosion. Using X-ray photoelectron spectroscopy (XPS) and Auger electron spectroscopy (AES), elemental and chemical information was obtained for the specific areas of anodic and cathodic activity based on the SVET analysis. Secondary electron microscopy (SEM) was used to image the surface.

INTRODUCTION

Aluminum alloys are used in aircraft because of their increased strength. However, the addition of other metals to increase strength increases the tendency for corrosion to occur. It has been shown that the presence of copper in the aluminum alloy is a site for galvanic coupling and therefore an initiation site for corrosion.

Samples were tested by SVET. SVET, which is a nondestructive technique, allows *in situ* examination of corrosion activity by mapping of anodic and cathodic areas during corrosion. This technique offers high resolution in current measurements on the order of 0.5 $\mu A/cm^2$. Since it is an *in situ* technique, the SVET offers a method for directly observing the progress of corrosion.

EXPERIMENTAL PROCEDURES

An accelerated corrosion site was prepared by placing two drops of $CuCl_2$ on specimens of Al1100. Specimen A was placed in a SVET cell and exposed to dilute Harrison's solution for 24 hrs. A second specimen B of Al1100 was exposed in a similar fashion to dilute Harrison solution for 24 hours in a SVET cell, and then 1 ml of 1% $Na_2Cr_2O_7$ solution in water was added to the SVET cell.

Following the SVET analyses, the two samples were transferred to the PHI 5700 Multitechnique system for surface analysis. The measurements were all made using a Physical Electronics PHI 5700 multi-technique system equipped with XPS, AES, and SEM. Base pressure was below 1 x 10^{-9} Torr. The samples were mounted onto stainless steal stubs and fixed in place with stainless steel screws. The XPS spectra were acquired using a monochromated Al Kα X-ray source (1486.7 eV energy) with a 400 μm analysis area. The AES data was acquired with a 5 keV electron beam. The XPS and AES data were taken at a 45^o take-off angle. SEM images were obtained with an electron beam energy of 5 keV and 10 nA current.

RESULTS

The results of the SVET, XPS, SEM, and Auger analyses for sample A are shown in Figures 1- 6. Figure 1 is an optical image of the two pits with the SVET vector overlay of current detected in these areas. Area 1 exhibits high anodic activity and area 2 shows cathodic activity. SVET did not detect any activity in area 3. However, there may have been activity occurring with the formation of the pit, and the area has since passivated. Figure 2 is the corresponding 2-D current density map showing high anodic activity in the upper left corner and cathodic activity to the right of it. The experiment continues by taking XPS and AES analyses in these three areas. XPS results are shown in Figures 3 and Table 1. Specimen A had a high concentration of aluminum oxide. Copper was not found in this oxide except at one cathodic sight (1 atomic %). There was a small amount of Si detected, probably originating from the silicon tape that masks the area for SVET analysis. Sulfur was detected, which is found in the Harrison's solution. Eleven areas were analyzed on this specimen with AES. Four representative areas are shown for the areas identified on the SEM image in Figure 4. The Auger results in Figure 5 show Al_2O_3 detected in all areas.

For specimen B, SVET test results are shown in Figure 6 and XPS relative atomic concentrations are given in Table 2. Specimen B had higher carbon content than specimen A and a lower concentration of aluminum oxide. Si and S were also detected on this sample. Cu was found at 0.2 atomic percent in the anodic and cathodic analysis areas and at 0.7 atomic percent in the passivated area. Surprisingly, Cr was not detected in spite of an exposure of the sample to a 1% $Na_2Cr_2O_7$ in water solution.

The direct comparison of areas 5 and 6 in the specimen exposed to chromate showed opposite surface compositions. Area 5 had higher carbon, lower Al and O concentrations, and

0.2% Cu. Area 6 had higher Al and O concentrations, lower carbon, and 0.7% Cu. Cr was detected on Area 6, which is far removed from the pitted area. No Cr was detected in the pit or near the pit.

SUMMARY / CONCLUSIONS

Review of the results left several questions for future experiments, such as why is the Cu concentration so low in areas where corrosion is occurring. The monolayer analyzed by XPS is highly oxidized, possibly due to the oxygen available in the Harrison's solution and or the oxygen in the air when the sample is removed. Depth profiling through this oxide may find higher copper levels in the oxide layer than what was detected at the very surface. The other question is why is Cr not detected in the active areas on the sample exposed to the $Na_2Cr_2O_7$. High levels of carbon were detected which may be carbon contamination present in the $Na_2Cr_2O_7$ itself before it was put into solution. Repeating the solution preparation with a new chemical could clear this up. Also, depth profiling would also show if the carbon is restricted to the surface or throughout the oxide layer.

REFERENCES

1. K. Ogle, V. Baudu, L. Garrigues, R. Nicolle, Proceedings of the 1999 Joint International Meeting of the Electrochemical Society, #582, (October 1999).

2. H.S. Isaaks, A.J. Aldykiewicz, D. Thierry, J.C. Simpson, Corrosion, 52, 63-168, (1996).

TABLES

TABLE 1.
Relative atomic concentrations (%) from XPS analyses of areas 1,2,3 identified in Figure 1.

RELATIVE ATOMIC CONCENTRATIONS (%)						
	C	O	Al	Si	S	Cu
#1 Anodic	23	53	16	5	3 (sulfate)	
#2 Cathodic	17	57	16	5	5 (sulfate)	
# 3 No Activity (Passivated)	19	55	20	3	3 (sulfate and sulfide)	1

TABLE 2.
Relative atomic concentrations (%) from XPS analyses of areas 4, 5, 6 identified in Figure 1.

RELATIVE ATOMIC CONCENTRATION (%)								
	C	O	Al	Si	S	N	Cu	Cr
#4 No Activity	54	30	9	5	2 (sulfate)	0.4	0.2	
#5 Anodic / Cathodic	55	30	7	5	2 (sulfate)	0.3	0.2	
#6 No Activity (Passivated)	30	46	17	3	2 (sulfate and sulfide)	0.2	0.7	1

FIGURES

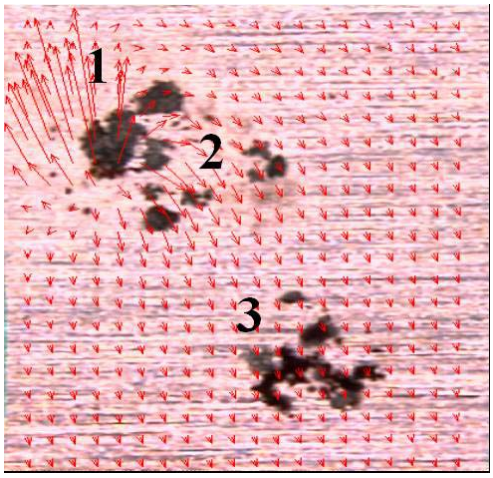

FIGURE 1. Optical image of two pits of specimen A with vector overlay showing current detected. In area 1, high anodic activity is detected and in area 2, cathodic activity is detected.

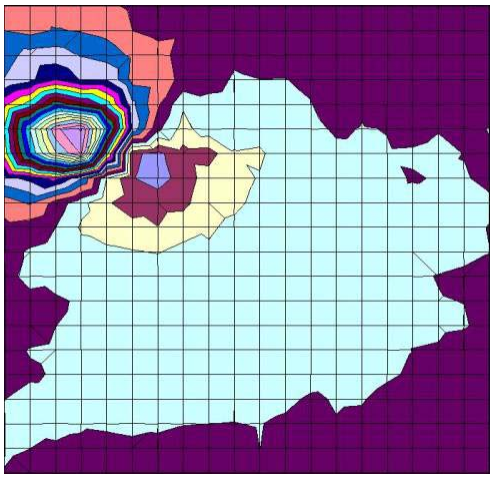

FIGURE 2. 2-D current density map from SVET test of specimen A.

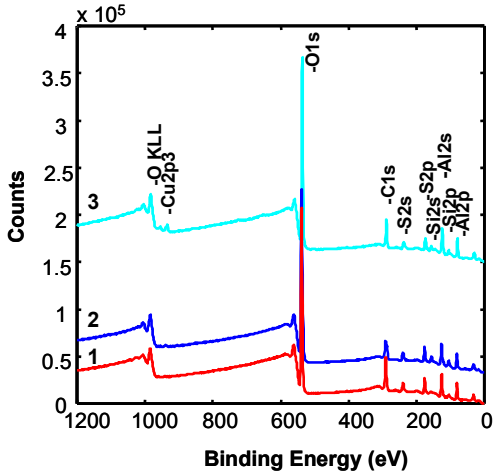

FIGURE 3. XPS survey scan of areas 1,2,3 identified in Figure 1.

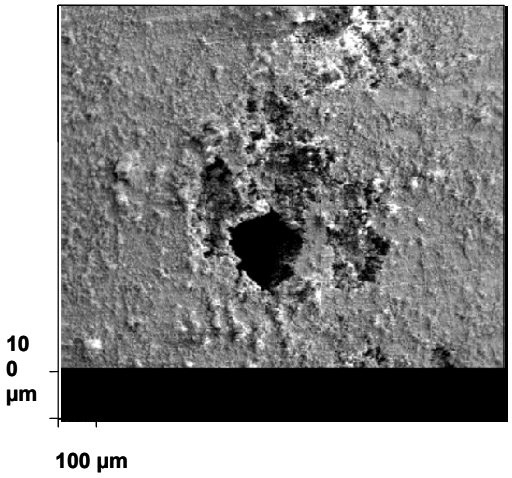

FIGURE 4. SEM of areas 1 and 2 identified in Figure 1 on the SVET image. Letters correspond to four analysis areas chosen for Auger electron spectroscopy.

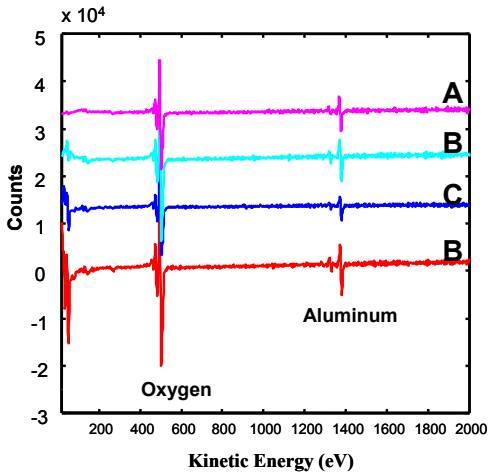

FIGURE 5. Auger spectra showing Al_2O_3 detected in all areas of pit in specimen A.

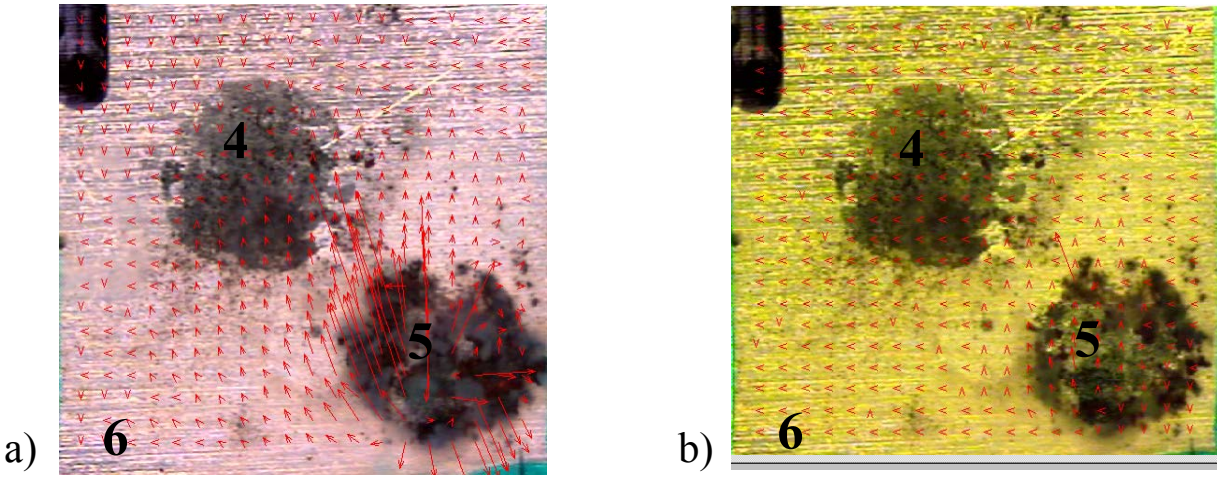

FIGURE 6. Optical image of two pits in specimen B with vector overlay showing current detected.

a) After Harrison's solution exposure. In area 5, high anodic activity is detected.

b) After chromate exposure. Anodic peak in area 5 significantly decreased.

INVESTIGATION AND EVALUATION OF THE PERFORMANCE OF AIRCRAFT COATINGS UNDER QUV/PROHESION ALTERNATING EXPOSURE

X.F.Yang[1,2], J.Li[2], A.M.Richter[1], D.E.Tallman[1], S.G.Croll[2] and G.P.Bierwagen[2]

[1]Department of Chemistry
[2]Department of Polymers and Coatings
North Dakota State University
Fargo, ND 58105

ABSTRACT

Last year, we reported our research on the weathering degradation of four types of aircraft coatings, namely a high gloss polyurethane coating, a low gloss polyurethane coating, a self-priming polyurethane coating and an extended life topcoat. In this paper, we shall report on the extension of this work on these coatings subsequent to last year's report. Because the low gloss polyurethane coating lasted only 25 weeks under QUV/Prohesion alternating exposure, we shall focus this report on the weathering stability of the other three coatings. The exposure tests lasted 120 weeks, or about 2 years. Impedance analysis showed that the low frequency (f = 0.012 Hz) impedance modulus $|Z|_{0.012}$ of the three coatings began to vary significantly after 100 weeks of exposure, with the lowest values falling in the range of 10^5 to 10^6 Ω. Such low values of $|Z|_{0.012}$ signify the end of the service life of the coatings. SEM/EDX were used to study the coatings after different exposure time intervals. From these results, an overview of the coating degradation process will be presented, the modes of chemical and the physical failure of the coatings will be discussed, and the overall performance of these coatings will be evaluated.

INTRODUCTION

Last year, we reported the performance of the four aircraft coating systems in QUV/Prohesion alternating exposure tests. These four coatings were: epoxy-polyamide primer coating (MIL-P-23377G Type I Class C) with polyurethane high gloss coating (Navy MIL-C-85285B Type I) system, Self-Priming topcoat (Navy TT-P-2756) by itself, Epoxy-Polyamide primer coating (MIL-P-23377G Type I Class C) with Fluoro Polyurethane (Extended Life

Topcoat) system and Epoxy-Polyamide primer coating (MIL-P-23377G Type I Class C) with low gloss polyurethane topcoat (MIL-C-85285B, 36473, Type I) system. The accelerated weathering exposure was conducted in a QUV chamber and a Prohesion® chamber alternately. After 25 weeks exposure, as we reported last year, the epoxy primer with low gloss polyurethane coating system totally lost function by adhesion failure. However, the other three coating systems were working well until the date of the report last year.

This paper shows the work done since last year. After about 120 weeks of exposure, these three coating systems had degraded, although they were still functional. In this paper, we shall discuss the coating degradation process and individual coating performance in two-year exposure.

In our previous work, we discussed the performance of epoxy primer with high gloss polyurethane coating under QUV exposure[1] and also discussed the coating degradation under different conditions. We found that QUV exposure is more damaging than QUV/Prohesion alternating exposure. This is because that UV radiation provides energy to the coating for polymer bond scission [2,3,4], and the continued higher temperature in the QUV chamber increases the coating degradation rate[5,6]. In this study, coating degradation in QUV/Prohesion alternating exposure will be discussed.

EXPERIMENTAL PROCEDURE

PANEL PREPARATION

The substrate was Al 2024-T3 alloy that was purchased from Q-panel Company. The aircraft coatings: epoxy-polyamide primer coating (MIL-P-23377G Type I Class C), self-priming polyurethane coating (Navy TT-P-2756), high gloss polyurethane coating and Fluoro polyurethane coating (extended life topcoat) were provided by DEFT Inc. The surface

pretreatment was: cleaning with methyl ethyl ketone (MEK), de-oxidation with phosphoric acid/alcohol solution and then, chromating with Alodine 1200s solution. Coating was applied by spraying the paint on the substrate with a Speedair (model 2Z366) professional spray gun and cured under ambient conditions.

ACCELERATED WEATHERING EXPOSURE:

According to the standard exposure method "ASTM D 5894-96, Standard Practice for Cyclic Salt Fog/UV exposure of Painted Metal (Alternating exposures in a Fog/Dry Cabinet and a UV/Condensation Cabinet)", the panels were transferred weekly between a QUV chamber and a prohesion chamber and the tests started with QUV exposure. In the QUV chamber, UV-A with a wave length of 340nm was used for UV radiation. The panels in the QUV chamber were exposed to UV radiation at 60^{o}C for 4 hours and condensation at 50^{o}C for another 4 hours. In the Prohesion® chamber, the panels were exposed to salt fog at 25 ^{o}C for 1 hour and dry-off at 35 ^{o}C for another 1 hour cyclically. The salt fog used was dilute Harrison's solution which contained 0.05% sodium chloride + 0.35% ammonium sulfate.

SEM STUDIES

The Scanning Electron Microscopy (SEM) used in this study was JSM-6300, produced by JEOL Company in MA, U.S.A., which was operated in 10^{-7} Torr vacuum. An Energy Dispersive X-ray Analysis (EDX) detector was attached in SEM, so X-ray analysis can be conducted on the surface in the SEM chamber.

EIS AND ENM STUDIES:

Electrochemical Impedance Spectroscopy (EIS) and Electrochemical Noise Measurement (ENM) were carried out on CMS 120 and CMS 300 systems that were produced by Gamry

Instruments, Inc, (Warminster, PA). The scanning frequency range for EIS was from 10 mHz to 100 KHz with 10 mV applied AC voltage. We focused on the low frequency results, because the EIS modulus in the low frequency was relative to the coating corrosion resistance.

RESULTS AND DISCUSSIONS

Figure 1a to 1d show the topography change of the extended life topcoat (ELT) in 123 weeks of exposure. During exposure, the pigment enriched surface of the ELT coating was eroded gradually. Therefore, after 64 weeks (Figure 1c), the surface became much flatter. After prolonging the exposure time, the coating surface became fractured.

Figure 1e shows the cross-section of the ELT coating after 123 weeks of QUV/Prohesion exposure. Although the enriched pigments at the surface layer had been lost, and the exposed surface was fractured, the coating bulk was still intact.

The high gloss (HG) polyurethane coating topography before and after 123 weeks of exposure are shown in Figure 2a and Figure 2b. Before exposure, HG coating surface was very smooth, so there were not many structures observed. After 123 weeks of exposure, however, degradation products fully covered the coating surface.

Figure 2c shows the cross-section of the HG coating after 123 weeks of exposure. There was not much change observed due to exposure. The pigments used in HG coating were not like those used in the ELT or the SP, they were small and their size was less than 1 μm.

Figure 3a and 3b show the Self-Priming (SP) polyurethane coating topography change upon exposure. After 123 weeks of exposure, the surface was cracked. When we inspected those cracks, we found that pigments exposed to the coating surface, and the cracks always developed following the edge of pigments. Therefore, breaking of bonds between the pigment and the polymer initiated the crack development in the coating surface.

From the coating cross-section in Figure 3c, we observed that pigments in the SP coating were much larger than those in the HG coating, that was, the pigment size in the SP was in 1 μm to over 5 μm range while it was less than 1 μm in the HG coating. We also observed that some pigments dropped off in the making cross-section and some pigments separated from the binder already. Since the adhesion between the pigment and the binder caused crack development, it is proposed that reducing pigment size may limit the size of cracks during the coating degradation.

The thickness of the coatings was measured before and after 123 weeks of exposure. In this test, three epoxy primer + ELT coated panels, two epoxy primer + HG coated panels and two SP coated panels were measured (Table 1). It was found that all of epoxy primer + ELT coating system lost more than 10 μm after 123 weeks. Recalling Figure 1, since we have observed ELT losing its pigment enriched surface, the thickness loss of the ELT coating is expected. In contrast, the thickness loss of the SP coated panels and the primer + HG coated panels were not significant in most of coating areas.

Table 2 shows EDX analysis on the coating surfaces before and after 123 weeks of exposure. To obtain general information of the coating surface, we analyzed at least 3 spots on the coating surface and listed the highest, the lowest and the average O/C and N/C ratios obtained. It was found that the significant change on these coating surfaces after exposure was the increase of O/C ratio. Therefore, the dominant coating degradation mode was coating oxidation. ELT coating is a Fluoro Polyurethane coating and the stability of F-C is expected to be high. However, no increase of F/C ratio on the coating surface was found.

EDX analysis also found that the ratio of pigments to carbon, Ti/C and Si/C, increased significantly after exposure. It was because the pigments were exposed on the coating surface after the coating polymer was damaged (Table 3).

The electrochemical property change of these three coatings during exposure was monitored with Electrochemical Impedance Spectroscopy (EIS). Our special interest is in the low frequency ($|Z|_{0.012Hz}$) modulus, because it indicates the coating resistance which is related to the coating corrosion resistance. In general, when the coating decreases its $|Z|_{0.012Hz}$ to 10^{-4} Ω, it signals the coating failure.

EIS results in Figure 4 show that in the first 20 weeks, the SP coating showed the highest $|Z|_{0.012Hz}$ value among these three coatings, near 10^{9} Ω, and the other two coating showed the $|Z|_{0.012Hz}$ slightly lower, around 10^{8} Ω. However, after 20 weeks, these three coatings showed similar $|Z|_{0.012Hz}$ in the subsequent one year. After 70 weeks, the $|Z|_{0.012Hz}$ value of the ELT coating diminished faster than the other two coatings. Recalling the SEM image in Figure 1c showing the pigment enriched surface was eroded from the coating bulk at that time, the accelerating reduction of the $|Z|_{0.012Hz}$ value after 70 weeks may be caused by the loss of pigment protection and the loss of significant thickness from the outer surface. After 100 weeks, the $|Z|_{0.012Hz}$ values of the three coatings varied in a wide range and the lowest $|Z|_{0.012Hz}$ value was down to 10^{6} Ω. It appeared that these three coatings were close to the end of their service life then in this exposure.

Adhesion tests were also conducted on these three coatings. Before exposure, all coatings possessed very good adhesion. We could not obtain an adhesion value before the coatings were exposed, because the glue used to join the testing dowels and the coating only stood 500 lb/in^2 loading and the glue adhesion always failed before the coating adhesion. Therefore, before exposure, the adhesion of all coatings was beyond 500 lb/in^2. After 123 weeks of exposure, however, the adhesion of the ELT coating system decreased to about 30 lb/in^2 and that of the HG coating system decreased to 50-75 1b/in^2. In contrast to these two coatings, the SP coating did

not show significant loss of adhesion after 2 years exposure. As before exposure, the adhesion of the SP coating and the Al substrate was still beyond 500 lb/in^2.

CONCLUSIONS

1. After 123 weeks of QUV/Prohesion alternative exposure, ELT, HG and SP coatings were degraded by oxidation. All of them lost thickness upon exposure. The major thickness loss occurred in ELT coating was due to the erosion of an outer pigment enriched surface layer.
2. The ELT pigment enriched surface protected the coating from degradation for more than one year. When this surface layer was eroded, the $|Z|_{0.012Hz}$ value for the coating decreased faster.
3. The cracks in the SP coating developed following the edges of pigments. The adhesion degradation between the pigment and the binder caused the development of cracks.
4. Among the three coatings, SP showed superior and durable adhesion to the panels in QUV/Prohesion alternating exposure. After 123 weeks of exposure, the adhesion was still over 500 lb/in^2 while the adhesion of the other coatings degraded remarkably in this period.

ACKNOWLEDGEMENT

We acknowledge S.A.Payne in NDSU for assistance on SEM studies, the cooperation of corrosion group in NDSU and the financial support by the Air Force Office of Scientific Research, Grant No F49620-99-1-0283.

REFERENCES

1. X.F.Yang, C.Vang, D.E.Tallman, G.P.Bierwagen, S.G.Croll and S.Rohlik, Polymer Degradation and Stability 74, (2001): p341.
2. R.L.Feller, Accelerated Aging, photochemical and Thermal Aspects, ed. D.berland, (J.Paul Getty Trust, 1994), p45.
3. Heung Kim and Marek W.Urban, Langmuir 16, (2000): 5382.
4. E.V.Schmid, Exterior Durability of Organic Coatings, (England, FMJ International Publications Ltd, 1988), p 108.
5. R.L.Feller, Accelerated Aging, photochemical and Thermal Aspects, ed. D.berland, (J.Paul Getty Trust, 1994), p144-165.
6. G.B.Bierwagen, Progress in Organic Coatings, 15 (1987): p179.

TABLE 1.
Thickness Loss of the Coatings after 123 Weeks of QUV/Prohesion Exposure (μm)

	Primer + HG	SP	Primer+ ELT
0wk	HG-1 74 ± 3.4 HG-2 86 ± 3.6	SP-1 53 ± 4.6 SP-2 51 ± 7.6	ELT-1 67 ± 5.2 ELT-2 68 ± 6.5 ELT-3 68 ± 4.1
123wks	HG-1 72 ± 4.5 HG-2 84 ± 4.3	SP-1 47± 2.7 SP-2 49 ± 5.6	ELT-1 55 ± 4.0 ELT-2 55 ±4.0 ELT-3 56 ± 3.2

TABLE 2
EDX analysis of the Coating Surfaces Before and After 123 weeks of QUV/Prohesion Exposure

		HG	SP	ELT
O/C	0 week low	0.18	0.35	0.13
	0 week high	0.31	0.55	0.31
	everage	0.26	0.47	0.22
	123 weeks low	1.07	0.97	0.98
	123 weeks high	2.81	1.85	1.36
	everage	1.79	1.28	1.17
N/C	0 week low	0.02	0.08	0.03
	0 week high	0.18	0.23	0.14
	everage	0.11	0.15	0.09
	123 weeks low	0	0	0.05
	123 weeks high	0.51	0.41	0.11
	everage	0.22	0.27	0.08

TABLE 3.
Pigment Contents on the Coating Surface

		HG	SP	ELT
Ti/C	0 week low	0.58	0	0.17
	0 week high	1.19	0.65	0.43
	everage	0.78	0.33	0.29
	123 weeks low	1.6	0.66	1.7
	123 weeks high	3.41	2.01	2.96
	everage	2.34	1.37	2.44
Si/C	0 week low	0.025	0.031	0.08
	0 week high	0.045	0.061	0.2
	everage	0.035	0.05	0.15
	123 weeks low	0.19	0.23	0.38
	123 weeks high	0.23	0.53	2.15
	everage	0.19	0.35	1.13

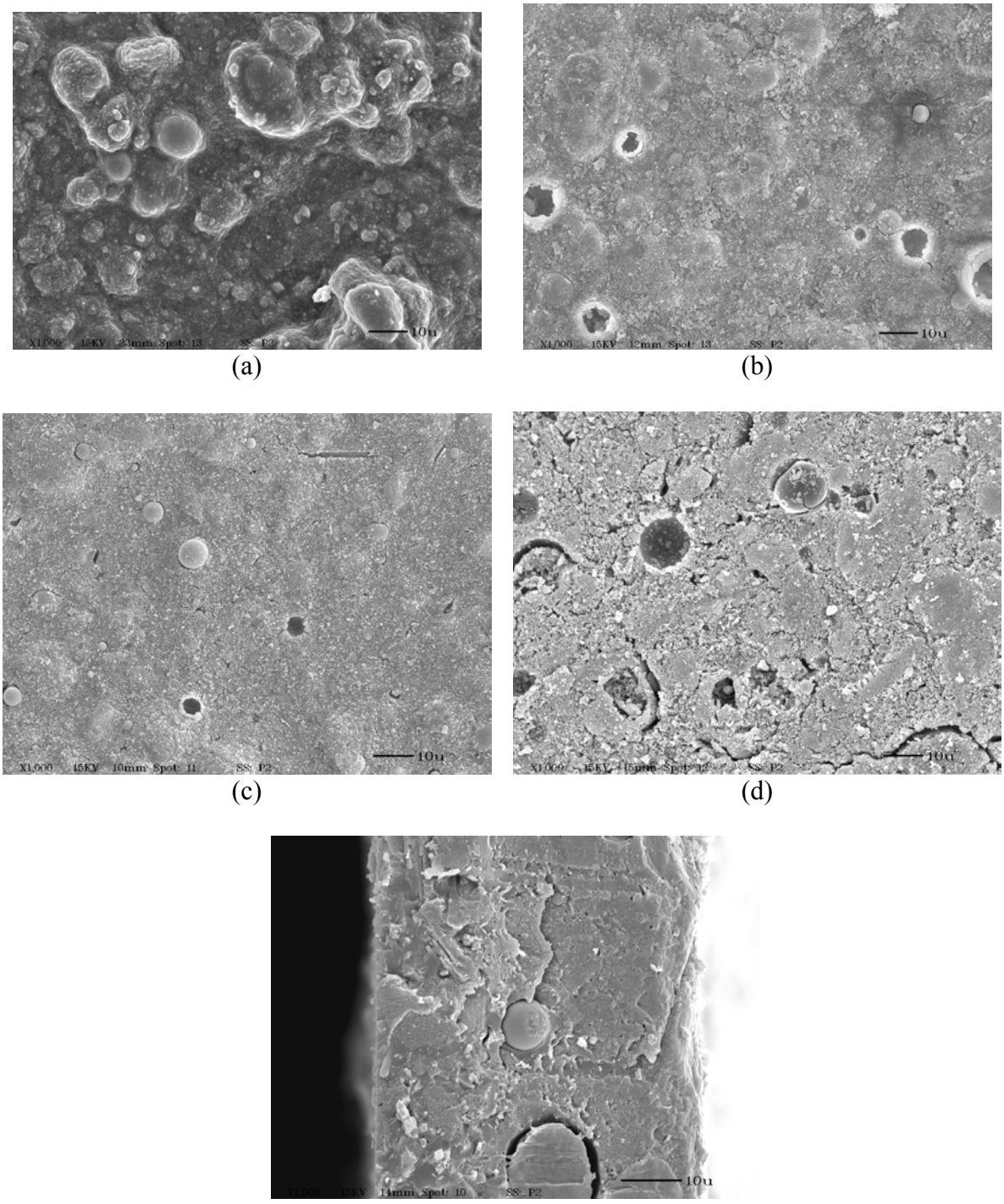

FIGURE 1. Epoxy primer + ELT coating system degradation under QUV/Prohesion alternating exposure: a) Before exposure, b) 47 weeks exposure, c) 64 weeks exposure, d) 123 weeks exposure, and e) the cross-section of the coating system after 123 weeks exposure.Epoxy primer + ELT coating system degradation under QUV/Prohesion alternating exposure: a) Before exposure, b) 47 weeks exposure, c) 64 weeks exposure, d) 123 weeks exposure, and e) the cross-section of the coating system after 123 weeks exposure.

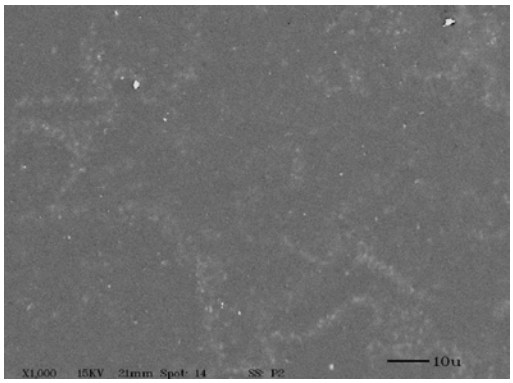

(a)

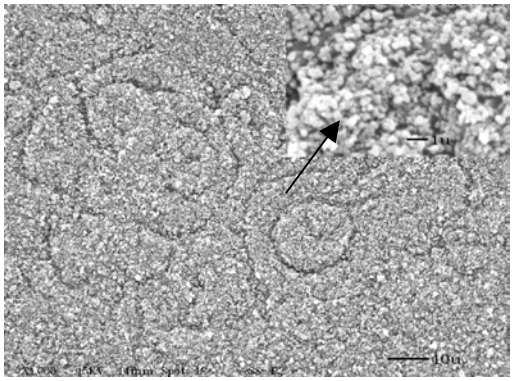

(b)

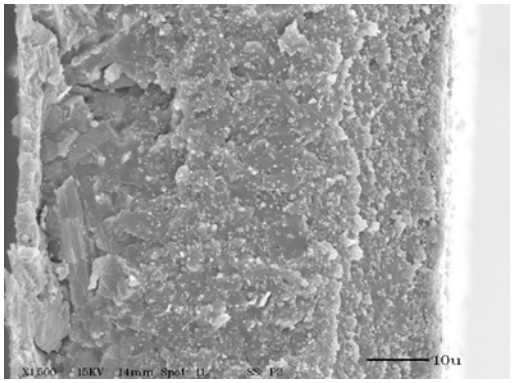

(c)

FIGURE 2. Epoxy + HG coating degradation under QUV/Prohesion alternating exposure: a) before exposure, b)after 123 weeks exposure, and c) the cross-section of the coating system after 123 weeks exposure.

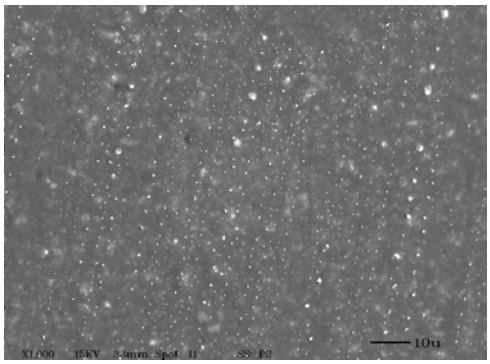

(a)

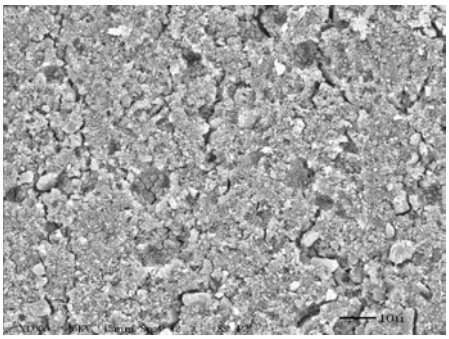

(b)

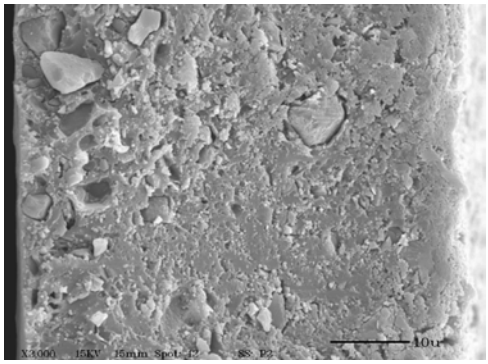

(c)

FIGURE 3. SP coating degradation under QUV/Prohesion alternating exposure: a) before exposure, b) after 123 weeks exposure, and c) the cross-section of the coating after 123 weeks exposure.

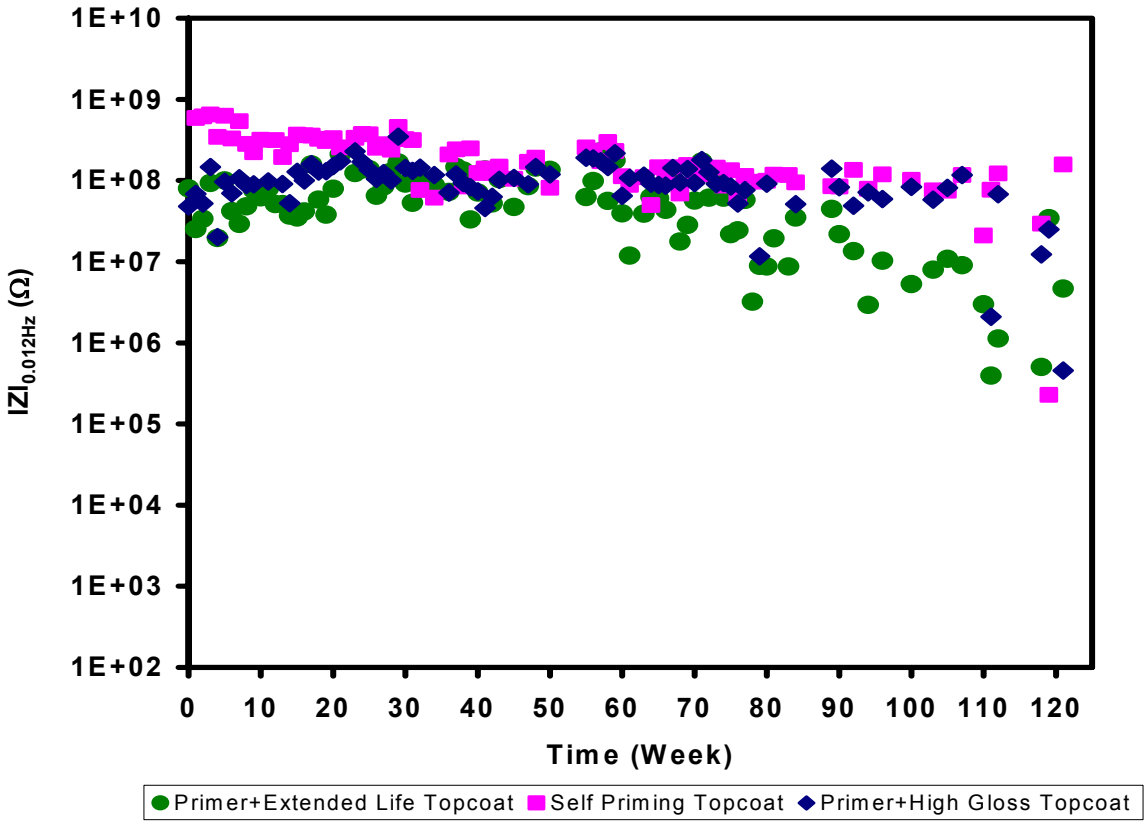

FIGURE 4. EIS measurements on the three coating systems in 121 weeks of QUV/Prohesion alternating exposure.

CERIUM CORROSION INHIBITOR IN POLYSILOXANE PRIMERS

Thomas E. Ready and Philip Boudjouk*

Department of Chemistry, North Dakota State University
Fargo, North Dakota 58105

ABSTRACT

Cerium has demonstrated promise as a corrosion inhibitor for Aluminum 2024 alloys, but with a modicum of the toxicity inherent in chromate inhibitors. We have examined in conjunction with polysiloxane primers. Cerium was incorporated into various stages of the primer coating process including direct application to the aluminum surface and blending with polysiloxane primers. The corrosion protection afforded by the inclusion of Cerium via the various methods was evaluated.

INTRODUCTION

Chromates have demonstrated exemplary capabilities as corrosion inhibitors and are widely utilized as an integral source of protection in coatings systems. This performance is attributed in part to the fact that Cr (VI) chromates are water-soluble and possess some degree of mobility within a coating as moisture enters the matrix[1]. More importantly, the Cr (VI) precursors are reduced to insoluble Cr (III) species, which form "self-healing" films with excellent barrier properties in corrosive environments[1]. The high toxicity of chromates has resulted in an initiative by the U.S. Environmental Protection Agency and the Occupational Safety and Hazard Administration to phase out their use in the near future.

Cerium compounds have been cited as possible environmentally acceptable alternatives to chromates in coating systems due to the formation of Ce (III) hydroxide films with good barrier properties and the drastically lowered toxicity of the cerium material[2]. Both Ce (III) and Ce (IV) precursors have been cited as corrosion inhibitors[2,3].

The Boudjouk group has been examining the utility of well-defined functionalized oligomeric polysiloxanes as the principal matrix component in primer coatings[4]. One objective is to study the feasibility of incorporating active corrosion inhibitors in polysiloxanes as direct replacements for chromated conversion / primer coatings. This work examines the corrosion inhibitory effects of ceric amonium nitrate (CAN)/ polysiloxane primer relative to polysiloxane primer, and compares both to that of standard chromated epoxy primers.

EXPERIMENTAL PROCEDURES

Iso-butanol was purchased from VWR and used without further purification or drying. The synthesis of Poly(methylglycidoxysiloxane) (**1**) (Figure 1) was described elsewhere[4d].

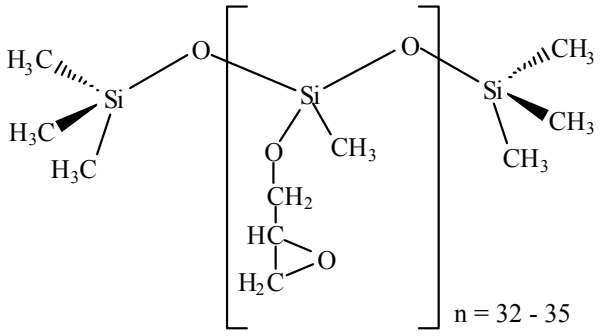

FIGURE 1: Poly(methylglycidoxysiloxane) (**1**)

Aluminum 2024-T3 test panels were purchased from Q-Panel. Immediately prior to primer application, test panels were washed with acetone and submerged in an phosphoric acid bath consisting of n-butanol (40 v%), i-propanol (30 v%), water (20 v%), and phosphoric acid (10 v%) for 5 minutes. The panels were rinsed with de-ionized water until a break-front film was present and wiped dry.

A ceric amonium nitrate solution was prepared by dissolving 1g of CAN in 20 ml of i-propanol. A ceric amonium nitrate/polysiloxane primer was prepared adding an aliquot (5ml) of the bright orange CAN solution to 5 ml of poly(methylglycidoxy-siloxane) (**1**) and stirred until a pale orange translucent solution was obtained.

Primers were applied with a wire wound, stainless-steel draw down bar. Films were formed at standing at ambient temperature for one day followed curing at 45^{o}C for five hours.

Each test panel was coated with either DEFT 03-GY-277 two component polyurethane topcoat or DEFT 99-GY-001 "Extended Life" topcoat using a wire wound, stainless-steel draw down bar. The topcoat was dried at ambient temperature for 1 day followed by curing at 45^{o}C for five hours.

Each type of sample was prepared and tested in triplicate. Prohesion[5] durations (average of 3 trials) were made using a Q-Fog chamber.

RESULTS

Ceric ammonium nitrate is an orange solid. Aqueous solutions of CAN we tested were converted to suspensions of pale yellow cerium (III) hydroxide via reductive hydrolysis within one half-hour. Iso-butanol solutions of CAN were stable for days as evidenced by retention of the orange color in the solution. The fact that the polysiloxane/CAN primer films were a translucent and orange in color as cast, dried, and cured is evidence that there was no qualitative reduction of cerium to Ce (III) during these processes.

Triplicate sets of scribed test panels were subjected to prohesion testing. The duration times were judged by the first visual evidence of coating blistering, de-lamination, or other signs of damage to non-scribed portions of the panels (i.e. Figure 2a-f).

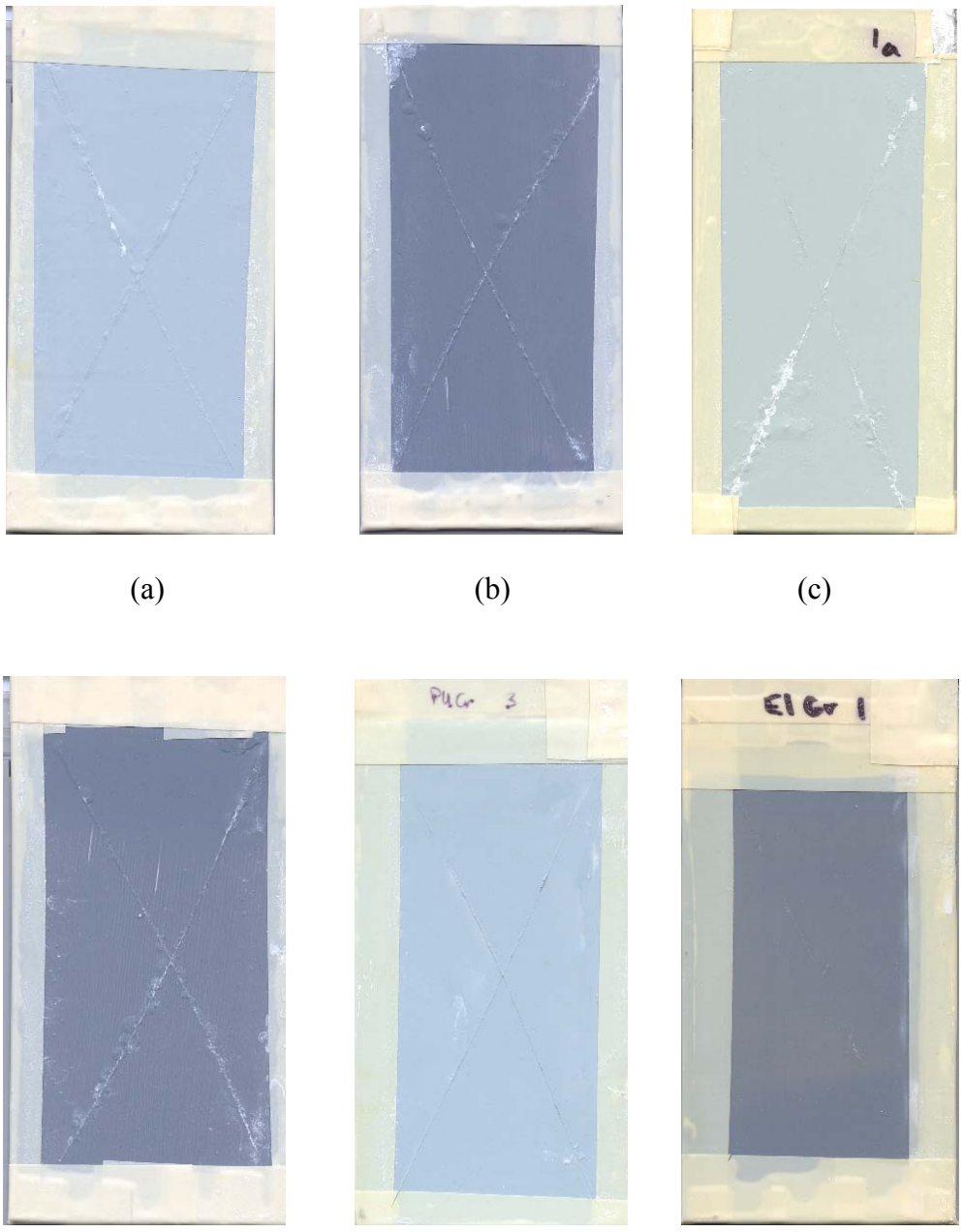

(a) (b) (c)

(d) (e) (f)

FIGURE 2: Al 2024 Panels after Prohesion Exposure
(a) Polysiloxane Primer / Polyurethane Topcoat (no Cerium) 248 hrs. exposure
(b) Polysiloxane Primer / Extended Life Topcoat (no Cerium) 299 hrs. exposure
(c) CAN Loaded Polysiloxane Primer / Polyurethane Topcoat 248 hrs.exposure
(d) CAN Loaded Polysiloxane Primer / Extended Life Topcoat 299 hrs exposure
(e) Cr-Epoxy Primer / Polyurethane Topcoat 800 hrs exposure
(f) Cr-Epoxy Primer / Extended Life Topcoat 800 hrs exposure

DISCUSSION

The mechanism of cerium corrosion inhibitory is ill defined compared to that of chromium. Our attempt here is to replicate the established chromate mechanism[1] by utilizing a "mobile", water soluble, cerium (IV) precursor, which will reduce to an insoluble barrier film (cerium (III) hydroxide) in a corrosive environment.

CONCLUSIONS

Two conclusions can be drawn from the prohesion duration results. First, the polysiloxane primer coatings, as constituted, are inferior (250 to 299 hrs prohesion duration) to the chromated epoxy primer (over 800 hrs prohesion duration). Second, there is no qualitative extension of coating life imparted by the presence of the cerium in the coatings as formulated.

REFERENCES

1. a) Waldrop, J. R.; Kendig, M. W. J. Electrochem. Soc. **145**, (1998), L11.

   b) Zhao, Frankel, G.; McCreery, R. L. J. Electrochem. Soc. **145**, (1998), 2258.

   c) Xia, L.; McCreery J. Electrochem. Soc. **145**, (1998), 3083.

   d) Xia, L; McCreery, J. Electrochem. Soc. **146**, (1999), 3696.

   e) Ramsey, McCreery J. Electrochem. Soc. **146**, (1999), 4076.

   f) Akiyama, E.; Frankel, G. S. c) Xia, L; McCreery, J. Electrochem. Soc. **146**, (1999) 4095.

   g) Kendig, M; Addison, R.; Jeanjaquet S. **146**, (1999), 4419.

   h) Schmutz, P.; Frankel, G. S. J. Electrochem. Soc. **145**, (1999), 4461.

   i) Jeffcoate, C. S.; Isaacs, H. S.; Aldykiewicz, A. J. Jr.; Ryan, M. P. J. Electrochem. Soc. **147**, (2000), 540.

   j) Xia, L; Akiyaa, E.; Frankel, G.; McCreery, R. J. Electrochem. Soc. **147**, (2000), 2556.

k) Frankel, G. S.; McCreery, R. L. *Interface*, **Winter**, (2001), 34.

2. Bethencourt, M; Botana, F. J.; Calvino, J. J.; Marcos, M; Rodriguez-Chacon, M. A. Corr. Sci. **40**, (1998),1803.

3. a) Bucheit, R. G.; Mamidipally, S. B.; Shmuts, P.; Guan, H. Corrosion **58**, (2002), 3.

   b) Li, F. B.; Thompson, G.E. J. Electrochem. Soc. **146**, (1999), 1809.

4. a) M. Chauhan, B. P. S. Chauhan and P. Boudjouk Org. Lett. **2**, (2000), p. 1027-1029.

   b) B. P. S. Chauhan, P. Boudjouk Tetrahedron Lett., **41**, (2000), 1127-30.

   c) T. E. Ready, B. P. S. Chauhan, and P. Boudjouk, Macromolecular Rapid Commun. **22**, (2001), p. 654-657.

   d) B. P. S. Chauhan, T. E. Ready, Z. Al-Badri and P. Boudjouk, Organometallic*s* **20**, (2001), p. 2725-2729.

5. ASTM G85,A5 is a cyclic salt-fog / dry heat exposure: 1 Hr fog (using dilute Harison's solution) followed by 1 hr dry (purging with fresh air) at 35 ^{o}C.

TUNABLE ISAM CORROSION PREVENTION COATINGS

Kevin R. Cooper[*], Michael B. Miller,[*] Keith W. Furrow,[*] and Robert G. Kelly[**]

[*]Luna Innovations, Inc.
2851 Commerce Street
Blacksburg, VA 24060

[**]Department of Materials Science and Engineering
University of Virginia
116 Engineer's Way
Charlottesville, VA 22904

ABSTRACT

Corrosion of metal structures is estimated to cost many billions of dollars annually. The most common methods of corrosion inhibition or prevention involve the application of heavy surface treatments (paints and primers) or conversion coatings using various processes that are strictly controlled and regulated due to toxicity and possible carcinogenic properties. A need exists to develop an alternate process that is capable of corrosion inhibition without the use or generation of hazardous materials, and that can be adapted to the coating of large surfaces. This report summarizes a recently initiated research program to develop tunable corrosion prevention coatings. To date the research has demonstrated a new coating process based on ionic self-assembled monolayers that 1) has **demonstrated corrosion inhibition** on 2024-T3 aluminum alloy, 2) **neither contains nor generates hazardous materials**, 3) offers the potential for tunabl or "**release on command**" capabilities, and 4) has **demonstrated practical application methods** including spraying and non-electrolytic brushing.

REVIEW OF IONIC SELF-ASSEMBLED MONOLAYER FILM FORMATION

Ionic self-assembled monolayers (ISAMs) are a recently developed[1,2,3] revolutionary technique that allows detailed structural control of materials at the molecular level combined with ease of manufacturing and low cost. The ISAM method involves the alternate dipping of a charged substrate into an aqueous solution of a cation followed by dipping in an aqueous solution of an anion at room temperature. Since the adsorption is based on the electrostatic attraction of interlayer charges, each layer is self-limiting in thickness and uniform at the

molecular level. This occurs because the film molecules are free to adjust their positions to improve the overall packing since they are not covalently bound to the substrate. Sequential layers are rapidly fixed by drying at room temperature and pressure. Multilayer films several microns in thickness are easily fabricated by repeating the dipping process with no limit to the number of layers that can be deposited. The resulting pliable films are mechanically very robust and are only removed by vigorous scraping.

FIGURE 1 shows the fundamental concept and simplified physical model behind the ISAM process, using polymer electrolytes. The substrate surface is thoroughly cleaned and charged through chemical processing. Schematically, a uniform one-dimensional distribution of anions at the outermost surface of the substrate is shown. The charged substrate is then dipped into a solution containing water soluble "cation" polymer molecules. Because the polymer chain is flexible, it is free to orient its geometry so a relatively low energy configuration is achieved. Some functional groups along the polymer chain have localized positive charges so experience attractive forces toward the negative substrate, and the chain bends in response to those forces. The net negative charge of the substrate surface is thus partially masked from other positive functional groups along the polymer chain. Those groups feel a net force due to the fixed positive functional groups bonded to the substrate, so move to form a net positive charge distribution on the outermost surface of the coated substrate. Since the polymer layer is neutral, negative charges with relatively loose binding to the polymer network pair up with the positive ions. In this way, the total energy of the layer configuration is relatively low. Subsequent monolayers may be added in bilayer pairs by alternately dipping the substrate into polyionic solutions, to produce a multi-layer thin-film structure as shown. Nanoparticles, appropriately

charged, can also be substituted for the appropriate polymer layers in the process, thereby incorporating their functionality into the film layers.

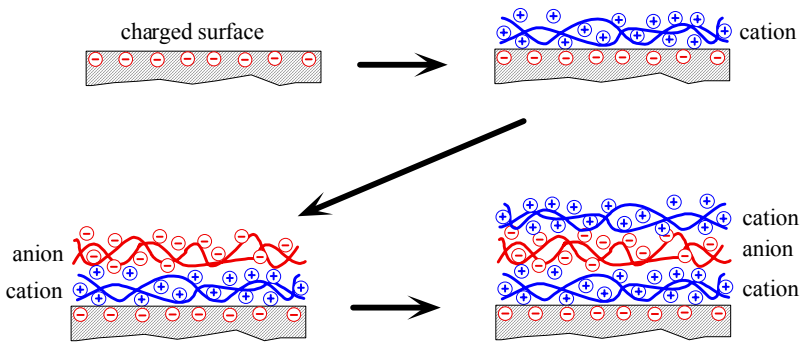

FIGURE 1. Basic ionic self-assembled multilayer (ISAM) process.

Polyelectrolyte self-assembly processing has specific advantages. Excellent nanoscale molecular level uniformity permits the fabrication of coatings with exceptional characteristics. Homogeneous mixtures of inorganic nanoparticles, including clay platelets, can be incorporated into the thin-films, and the ratio of polymer to nanoparticles controlled by adjusting bilayer thicknesses. Surfaces with extremely complex geometrical shapes may be coated uniformly due to the aqueous nature of the coating process. Ionic bonding of molecules in sequential layers inherently self-limits thickness and allows fabrication of very uniform coatings over the very large surfaces of aerospace structural systems or the very small surfaces of optical or electronic components. Synthesis is performed at room temperature and pressure. Avoidance of high-temperature binder burnout processing means that polyelectrolyte coatings may be created on nearly any solid material substrate, including ceramics, plastics, metals (with proper surface treatment to allow charging), semiconductors or organic films, without degrading or destroying the substrate. Capital equipment costs for basic fabrication are extremely low (the cost of large liquid containers), may be upscaled in size and volume, and may be easily automated. Capability

for thick multi-layer fabrication is allowed due to the uniformity of each layer and the avoidance of geometrical defects caused by conventional covalent bonding-based self-assembled monolayer approaches that allow deposition of only two or three superimposed layers. LUNA has demonstrated the synthesis of more than 2000 ISAM layers with good surface morphology[4,5,6]. Multi-layer structures allow the possibility of incorporating multiple functions into a single coating. Broad range of layer functionality is possible through incorporation of a wide range of inorganic nanoparticles to control of the electronic, conductive, optical, magnetic, thermal and mechanical properties,. High performance polymers may allow excellent thermal stability, mechanical properties and processability. Ionic self-assembly is an environmentally friendly process. Fabrication uses aqueous polyelectrolyte solutions and **no volatile organic compounds (VOCs).**

CORROSION INHIBITION

LUNA has demonstrated corrosion inhibition with two separate ISAM polymer anion-cation systems, polyamic acid (PAA) and polystyrene sulfonate (PSS). FIGURE 2 shows a standard aluminum alloy 2024-T3 coupon after exposure to salt fog testing, showing severe corrosion. FIGURE 3 shows four ISAM coated coupons after the same salt fog test, demonstrating a total absence of corrosion products. The films shown in the photo are, from left to right, PDDA/PAA (20 bilayers), PDDA/PSS (20 bilayers), PDDA/PAA (30 bilayers), and PDDA/PSS (30 bilayers).

FIGURE 2. LUNA uncoated aluminum 2024 coupon after salt fog test, showing severe corrosion.

FIGURE 3. ISAM coated aluminum 2024 samples after 168 hour salt fog test showing corrosion inhibition. "Speckle" in the photo is not corrosion, but reflectivity properties of the aluminum samples under the light of the photoflash.

FILM PERMEABILITY

Film permeability has been measured using cyclic voltammetry. Films are exposed to ionic solutions, and the capacitance of the film is measured. As the ions permeate the film, the capacitance changes. FIGURE 4 shows the type of graph obtained using this technique, where the current measured through the film is plotted as a function of applied voltage. The graphs are 'cyclic' because the voltage is varied from 0 to +150 mV, then from +150 mV down to –150 mV, and finally back to 0 again, producing the characteristic hysteresis plots shown in the figure. This is a powerful technique for determining relative permeability of thin films in comparison to a standard. FIGURE 4 is a plot of three different conditions. The wide plot (blue) is an uncoated

substrate and represents the background, or 100 percent permeability. The narrow plot (red) is for tetradecanemercaptan (C14), a thin organic film known from other measurements to be totally impermeable to aqueous electrolyte solutions. This represents the condition of zero permeability. The yellow trace was taken from a 50 Å thick film of ISAM fabricated Ultem PAA-PDDA. This plot indicates that the ISAM fabricated film is approximately 80% as impermeable as the C14. Again, this is for a five-bilayer ISAM film measuring only 50 Å, or 2 x 10^{-7} inch thick.

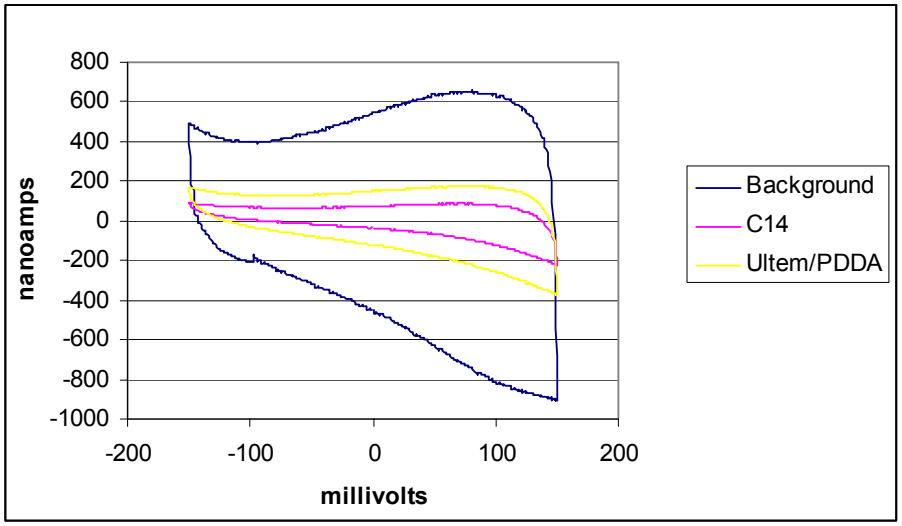

FIGURE 4. Cyclic Voltammetry measurments on ISAM PAA film.

BILAYER FUNCTIONALITY

LUNA has previously demonstrated the ease with which nanoparticles may be incorporated into the ISAM fabricated films. Nanoparticles will give the coatings their characteristic properties, and may be designed to give color, absorb or selectively reflect electromagnetic radiation or change optical properties or change ion permiability. FiIGURE 5 shows how nanoparticles are incorporated into the films through substitution of one of the

constituent cations in alternating layers. In this example, titanium dioxide is shown. This is a particularly useful nanoparticle, since it is transparent when the particles are sufficiently small (less than a few tens of nanometers), and it strongly absorbs ultraviolet radiation from sunlight that damages protective coatings and paints. Other nanoparticles of different constituents and sizes can be incorporated to produce various colors in the coating.

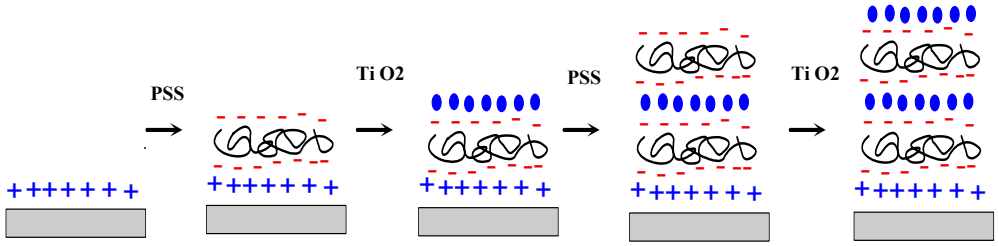

FiIGURE 5. ISAM-nanoparticle film fabrication.

Adjustment of the polymer constituents and layer thicknesses will enable the design of flexible coating layers. Previous LUNA coating research has shown that the polymer thickness is greatly affected by the processing conditions, in particular the pH of the aqueous solutions used and the degree of counterions and salts in the solution. Since the properties of the resulting coating are controlled by the individual layer constituents, it is a simple matter to create a coating process that incorporates a number of different polymeric and nanoparticle constituents that result in a flexible, corrosion inhibiting and appropriately colored coating.

TUNABLE ADHESION

Tunable or “release on command” ISAM coatings will allow the simple and quick application of mission coats for military applications. Release on command would also simplify maintenance and repairs when paint removal is required. A maintenance facility would not need

the capability to store, use and dispose of the harsh chemicals used to remove paint and primer layers.

The release on command potential of ISAM coating will be addressed by designing a cleaving layer whose adhesive or chemical bonds can be selectively broken under specific conditions as shown in FIGURE 6. The three potential mechanisms that will be investigated are radiation, enzymes and electrical charge. In the case of radiation or enzymes, the polymer chain or the functional group would contain a chemical linkage that could be cleaved under very specific conditions. Once enough bonds were cleaved the polymer would disentangle and release the ISAM layer. In all cases, the ISAM would be located beneath a topcoat and either on top or below a primer. In this location, the ISAM can operate effectively as a linkage that can be selectively broken on demand.

One of the Luna approaches to "release on command" coatings will combine multiphoton absorption processes with an appropriately designed ISAM molecule. Multiphoton processes are used for many investigations of chemical structure and analysis. These processes involved the absorption of two or more photons by a molecule. This absorption can be used to raise the energy of electrons to levels sufficient to disrupt bonds.

The ISAM coatings will be tailored to contain linkages that are engineered to make the layer susceptible to such multiphoton phenomena. For example, Resonance Enhanced Multiphoton Dissociation can be used to selectively break chemical bonds. Dissociation is achieved by delivering one (or more) non-resonant photons to an electronically and/or vibrationally excited molecule. For selectivity, the power and energy of these photons should be insufficient to cause ionization or dissociation of ground state molecules. The excited state of interest is achieved directly by resonant photon absorption or indirectly by intramolecular

vibrational energy redistribution from a resonantly achieved excited state. A chromophore for the resonant step can be designed into the molecule to be dissociated.

The method involving energy redistribution is of particular interest as it will allow a small number of absorption sites to serve as inputs for energy that can be used to break many bonds. One application of this method would be to tailor the ISAM so that part of it complexes with either a corrosive species or a dissolved metal ion. In this way areas of coating that have degraded and lost their protective capability will be selectively removed. The multiphoton techniques require high energy and are therefore most suitable for removing paint and or primer from localized areas.

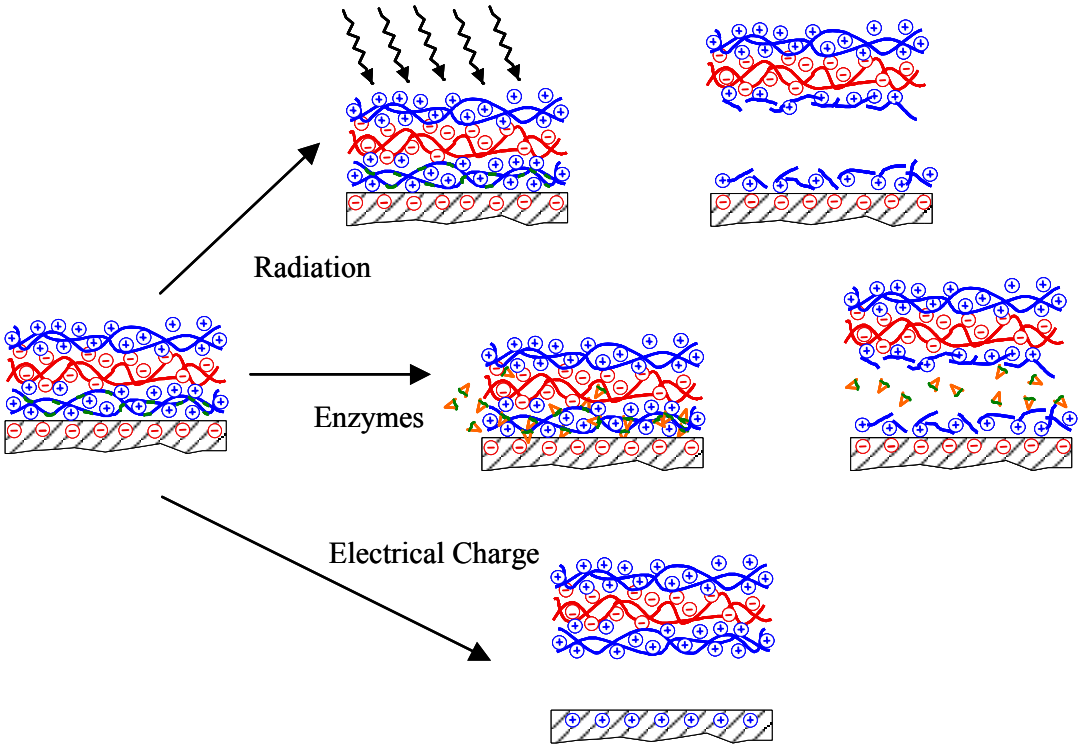

FIGURE 6. Three mechanisms for release on command functionality of an ISAM film

Enzymes are another means of specifically cleaving a chemical bond. The high specificity and efficiency of enzymes can be exploited to cleave the ISAM layer. Each enzyme

molecule has at least one active site that binds to a substrate specifically inserted into the ISAM polymer to form an enzyme-substrate complex. Then the enzyme catalyzes the bond cleavage. Once the bond is cleaved the electrical attractions that made the substrate molecule adhere to the active site no longer are present, and the cleaved ISAM layer can disengage itself from the active site thus freeing the enzyme to cleave another ISAM polymer.

The last method would be to reverse the charge on the substrate layer. This would be accomplished through electrical means or chemical means. Reversing the charge of one layer would result in a repulsive force separating the layers.

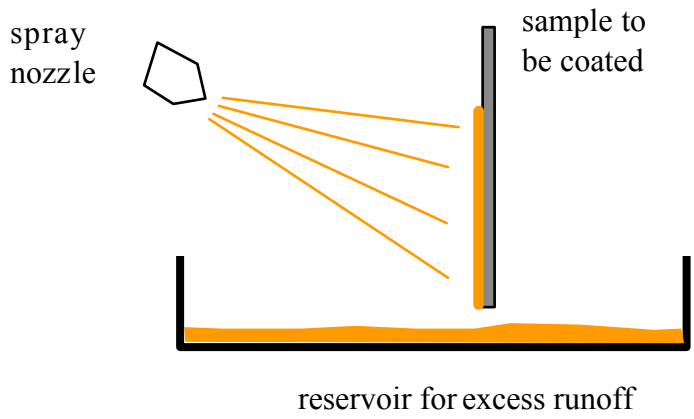

FIGURE 7. Schematic of spray ISAM film fabrication demonstration setup.

APPLICATION METHODS

Prior work by LUNA has demonstrated that a simple spray process is adequate to apply the coatings. A schematic drawing of this process is shown in FIGURE 7. ISAM cationic or anionic solution is sprayed on the sample, which is suspended over a reservoir that collects the excess solution as it runs off the sample. This setup is relatively easy to create in the laboratory using household spray bottles and petri dishes or beakers. Extension to standard spray application for larger panels in manufacturing processes would present no major obstacles.

FIGURE 8 is a photograph of the apparatus (two household spray bottles containing the anion and cation solutions) along with a microscope slide coated with the visible orange ISAM coating.

FIGURE 8. Spray Coating ISAM Film Fabrication Apparatus and Sample Film.

The design of a manufacturing process such as the one being considered here requires careful consideration of all aspects of material handling and storage and quality control in addition to the performance of the final product resulting from the process. In the proposed ISAM polymer film process, the following controls and parameters must be defined:

- Solution concentrations, upper and lower limits, and monitoring method,
- Solution pH, upper and lower limits, and monitoring method, and
- Rinse water quality, limits and monitoring method.

In addition, we must identify related process parameters such as:

- Solution storage capacity and storage container requirements (size, construction, material compatibility),
- Solution storage life requirements, both in-process and off-line,
- Process fluid flow volume and rate requirements, and

- Recycling and replenishment requirements.

In these areas and others, the relevant process requirements will be identified and quantified for a baseline manufacturing process capacity. Although the specific needs relate to the coating of large panels such as for aircraft, we will also perform these studies for smaller component applications. Process parameters will be evaluated for dip coating, spray coating and brush coating.

ACKNOWLEDGMENTS

The Air Force Research Laboratory is funding this project under Small Business Innovative Research Grant F49620-01-C-0053 technical monitor LtCol Paul C. Trulove.

REFERENCES

1. G. Decher and J.D. Hong, Makromol. Chem., Makromol. Symp. **46**, 321 (1991).
2. G. Decher, J.D. Hong, and J. Schimitt, Thin Solid Films **210/211**, 831 (1992).
3. M. B. Miller, *et al,* "Functionally tailored nanoparticle-based ionically self-assembled multilayer thin-films", Proceedings of SPIE Vol. 3324, March, 1998.
4. J.R. Heflin, et al., SPIE **3147**, 10 (1997)
5. A.C. Fou, O. Onitsuka, M. Ferreira, M.F. Rubner,and B.R. Hsieh, J. Appl. Phys. **79**, 7501 (1996).
6. O. Onitsuka, A.C. Fou, M. Ferreira, M.F. Rubner,and B.R. Hsieh, J. Appl. Phys. **80**, 4067

DESIGN AND SYNTHESIS OF NANOSTRUCTURED CORROSION RESISTANT COATING FOR AGING AIRCRAFT

J. B. Mecham*, R. J. Swavey and R.O. Claus

NanoSonic, Inc.
1485 S. Main St., Blacksburg, VA. 24060
* jbmecham@nanosonic.com

ABSTRACT

Our research involves the development of a coating system for the restoration of aging aircraft using an electrostatic self-assembly (ESA) method. This approach avoids the use of toxic solvents that are frequently utilized with current methods. Presently, the protective treatment utilizes a multi-step coating consisting of the following processes: electrochemical pretreatment of detail parts, primer, topcoat paint, sealant, water displacing topcoat and an add-on protective treatment involving a secondary treatment of detail parts. The novel ESA process permits the incorporation of multiple functionalities in a single material, with precise control over its nanostructure. NanoSonic has demonstrated the ability to form dense, micro-hard coatings of alternating polymers/metal oxides and metal oxide/metal oxide multilayers. This ability will be key in producing a barrier layer to protect the underlying metal layer from migrating species that result in corrosion of the substrate. Current work has involved the use of water dispersible epoxy adhesives that contain molybdenum oxides as anticorrosive barrier materials. Upcoming work will couple these materials with ultrahard metal oxide layers to form a multilayer anticorrosion system for use in aging aircraft and other applications where Al 2024-T3 alloy materials find utility.

INTRODUCTION

The objective of this work is to demonstrate the feasibility of using multifunctional materials to promote the corrosion resistance of aluminum using conventional coating and electrostatic self-assembly (ESA) methods.

Current work has focused on outlining a work plan and selection of material components in cooperation with our co-collaborator at Virginia Polytechnic Institute and State University, Dr.

Sean Corocoran of the Materials Science Engineering Department. Our progress to date is summarized below:

- Outlined a work plan for each stage of coating development.
- Acquired raw materials such as 2024-T3 aluminum and chemicals for surface treatments.
- Identified electrochemical screening tests to evaluate coating systems with the aid of Dr. Sean Corcoran of the Materials Science Engineering Department at Virginia Tech. Dr. Corcoran has purchased and installed two impedance systems during this period for this program.
- Produced first laboratory samples of epoxy-coated and Mo-oxide treated substrates for screening using electrochemical impedance.

Due to the complexity of the multi-component, multi-layer coating system, a plan of work was established to identify specifically the technical issues involved each coating layer. As we are in the initial stages of this investigation, an outline of the various development stages and a brief description of where our efforts will be focused is summarized below. Figure 1 illustrates our multilayer anti-corrosion coating system .

During stage 1, our multilayer coating systems have been applied to 1'' x 3'' coupons cut from larger sheets of 2024-T3 Aluminum alloy. Our commercially available epoxy primer falls under military specification MIL-PRF-23377G into which molybdenum oxide has been blended. Stage 2 will involve the inclusion of porous silicon oxide sub-micron particles to be used as moisture uptake materials. Determination of degree of drying needed to activate the silica, after being cast as thin films onto 2024-T3 coupons, will be investigated.

During stage 3, we will choose the most promising coating systems identified in Stages 1 and 2 and apply a mil-spec urethane topcoat to understand its impact on the full coating system

and its contribution to corrosion mitigation. Tests such as adhesion, impact resistance, and weatherability will be assessed at this time. A urethane coating supplied by Deft, with a military specification of MIL-PRF-85285C, will be used. Stage 4 will focus on the inclusion of ultrahard sub-micron alumina and silica nanoparticles The surface preparation of the epoxy coating will be investigated to effectively "charge" the inner-layer of the composite film so that it is compatible with ESA thin film fabrication techniques. The ESA approach toward thin film synthesis is illustrated in Figure 2.

Stage 5 will involve the incorporation of a thermoplastic polymeric material into the coating system as a release layer for to ease repair efforts. Applying heat to the repair area will raise the surface temperature above the flow point of the thermoplastic material allowing for easy removal and avoiding the need for abrasive surface treatments.

DISCUSSION

FORMULATION OF WATER-BASED EPOXY COATINGS

Our initial developmental focus has been to establish laboratory capabilities for the formulation and casting of water-based epoxy polymer primers onto 2024-T3 aluminum coupons which were purchased and cut to a convenient size of 1'' x 3''. The epoxy primer EPON 828, supplied by Resolution Performance Products, is the main polymer component in military specification MIL-PRF-23377G used in military aircraft structures. Through technical discussions with the vendor, it was determined that a water-based cross-linker is compatible with the EPON 828 resin, which will minimize environmental impact. Samples of the resin and cross-linker were obtained and coating formulations were prepared. Initial coatings were on average 70 mils thicker than the target thickness using a knife application bar due to the small

substrate size. Future coating attempts will be performed using a wire-wound rod for better accuracy.

Investigation into a secondary component to aid in scratch healing was also performed during this reporting period. Literature reports showed favorable scratch healing on iron substrates by the application of a molybdenum oxide to the metal surface and by incorporating the oxide into an epoxy resin primer.[1] The molybdenum is described as more environmentally acceptable than the chromate salts that are currently used for self-healing. Two commercial molybdenum oxides were purchased for use in 2024-T3 treatments. Further investigation of solution parameters such as concentration, pH, and exposure time, is needed. Future application of these materials by spray-coating will be evaluated as a means to simplify the procedure for use on larger surfaces.

ELECTROCHEMICAL ANALYSIS OF CORROSION

To determine feasibility of proposed coatings for the protection of Al alloys against corrosion, electrochemical impedance spectroscopy will be used to probe the electrical and electrochemical characteristics of coated Al alloy. Dr. Sean Corcoran's at Virginia Tech has obtained two impedance systems (Gamry PC4/750 Potentiostat and Impedance Spectroscopy System and a EG&G/PAR 263 A Potentiostat with a Solartron1260 Frequency Response Analyzer). Specifically, we are interested in the low-frequency impedance magnitude, coating resistance, and breakdown frequencies. We plan to measure the low-frequency impedance of our coating systems as well as coating resistance over the duration of several months exposure to aerated NaCl electrolyte at room temperature. It has been shown for several systems that a minimum value of 10^7 Ohm-cm for the low frequency impedance after a typical exposure of 60 days is required for "good" coating performance (providing service lifetimes on the order of

years).[2] This value however is not universal for all systems and represents only a minimum threshold for performance. This measurement will provide us one means of comparing our coating systems and to guide us in their development. The coating resistance, determined through circuit model fitting, will be used to estimate the initial defect area. We will also explore the use of the high-frequency and low-frequency breakpoints (determined from Bode magnitude plots) to estimate the defect area of our coatings over the duration of the NaCl exposure. This measurement, although involving many simplifying assumptions, will provide us some basis for comparing the rate of coating breakdown during each development phase. Promising coating systems identified through the above described impedance measurements will also be evaluated for scratch resistance. Artificial scratches will be made with a diamond stylus probe while the samples are being held potentiostatically at open circuit. The charge passed during scratch repassivation/healing will be assessed.

CONCLUSIONS

Our multilayer multi-component system provides us a unique opportunity to render aluminum substrates corrosion resistant while using an environmentally acceptable methodology. The multilayer system allows tailoring of specific performance goals by varying components in individual layers. We are optimistic that this approach will offer an alternative to today's state-of-the-art chromate-based anticorrosion systems.

ACKNOWLEDGMENTS

NanoSonic Inc. would like to thank the United States Air Force for its support of this research program under STTR grant No. F49620-01-C-0052 under the direction of technical monitor Lt Col Paul Trulove.

REFERENCES

1. K. Aramaki, Corrosion 55, 11 (1999): pp. 1020-1030.

2. J.R. Scully, S.T. Hensley, Corrosion Science 50, 9 (1994): pp. 705-716.

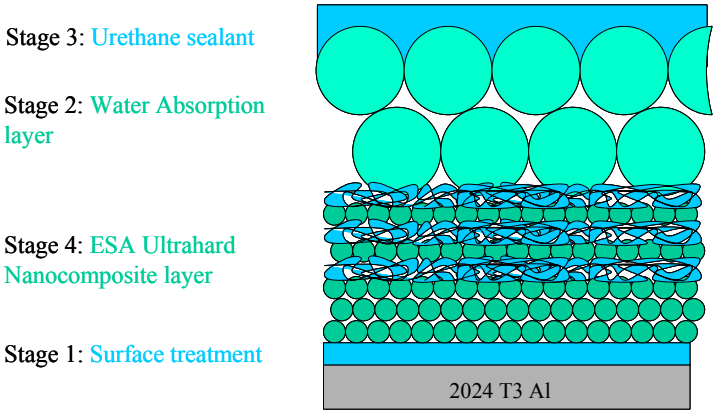

FIGURE 1. Graphical representation of the stages of our work plans.

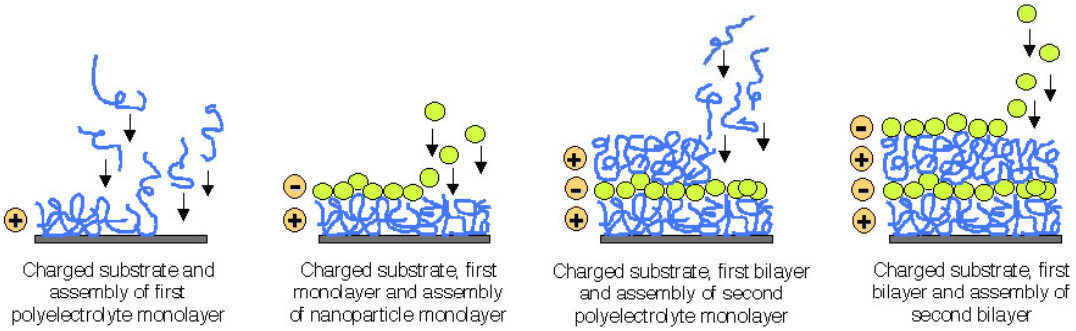

FIGURE 2. ESA processing of polymers in combination with water-soluble nanocluster quantum dots allows wide variation of coating properties, as required for corrosion-inhibiting films.

MONTE CARLO SIMULATIONS OF ENVIRONMENTAL DEGRADATION ON POLYMER COATINGS

Brian Hinderliter and Stuart Croll

Department of Chemistry
North Dakota State University
Fargo, North Dakota 58105

ABSTRACT

The degradation of a polymer coating and predicting the coating lifetime based on physical properties is economically important. The erosion of the surface of a coating was simulated using Monte Carlo techniques with terrestrial solar flux as the initiator for polymer segment cleavage and removal. The impact on the sensitivity of the polymer adjacent to the detached polymer segment can be increased or decreased in the model based on the chemistry of the remaining polymer matrix. Monte Carlo results are related to measurable properties; such as gloss, fracture toughness, and wetting contact angle, using various published correlations of the property to the surface topology. The simulated properties change through the lifetime of the coating in ways that are consistent with observed behavior. Apparently, complicated changes in many properties can be described by the repeated application of simple, random processes.

INTRODUCTION

The degradation of a polymer coating, and the related topic of predicting the lifetime based on important physical properties of the coating, have significant economic importance. Much effort is expended ranking coatings for various properties, predicting service lifetimes of coatings, and assessing likely remaining service life of a coating. Costs are associated with replacing a coating before it is necessary. We emulate the erosion of the surface of the coating using a Monte Carlo model using the solar spectrum photon flux as the initiator for polymer segment removal. The model is designed to predict behavior of coatings, though at this point, its generality has significance to the erosion of surfaces of any material due to a random process as the initiator to removal of a piece of the surface material.

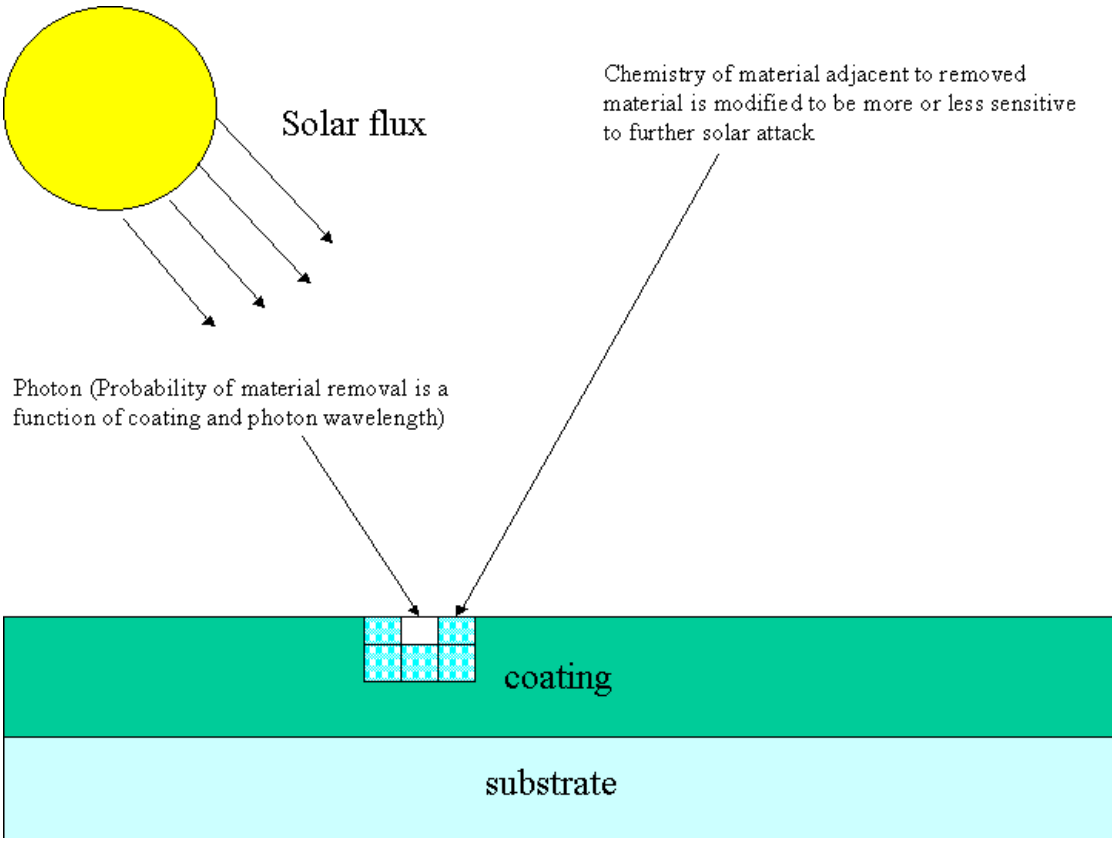

FIGURE 1. A photon initiates the degradation of a segment of the coating, which is volatilized or washed away. The adjacent polymer coating can either be sensitized or hardened against further photon initiated degradation.

The goal of the model is to be able, with appropriate chemical data related to degradation products for the coating, to predict coating lifetimes based on incident solar fluence. Additionally, the ability to correlate measurable and non-destructive properties, such as reflectance with lifetime may allow prediction of remaining service life based on other requirements, for example fracture toughness.

The most interesting aspect of the research so far is prediction of properties is functionally consistent with experimental results. These functional predictions are based on very general and simple assumptions of coating properties. The sigmoidal behavior of reflectance, for

example, can be predicted by repeated application of random processes in conjunction with a simple model of how reflectance is affected by surface roughness.

PREDICTING POLYMER COATING DEGRADATION

Several methods are available for the prediction of coating lifetime or rank candidate coatings. The methods can be broken into two divisions; first is experimental testing, including accelerated aging and extrapolation, and the second division is predictions based on modelling the system. One modelling method for predicting lifetime of a coating is to apply a damage function to the independent variables that correlate with the degradation. Independent variables that correlate to damage of coatings include such factors as solar spectrum and fluence, temperature, and humidity and water exposure. In this discussion, we focus on solar fluence. The damage function is a way to weight the affect of the particular free variable, in our case solar fluence, with a particular damage, for example change in gloss. The damage measures frequently used to define end of service life of a coating include loss of gloss, color change, fracture toughness, and erosion to substrate as examples. Focusing on solar irradiation as the initiator for coating degradation, an estimate for the damage as a function of solar irradiation is give by equation 1,[6] slightly modified to incorporate the variation with position and possibly material phase at that position.

$$D(x,t) = \int_{\lambda_{min}}^{\lambda_{max}} I_0(\lambda,t,x)(1-e^{-A(\lambda,x)})\phi(\lambda)d\lambda \qquad (1)$$

D is the instantaneous damage, or change in property in the coating at a particular material location, x and time, t. λ is the wavelength of the incident light with the subscripts min and max referring to the highest and lowest energy of the light in the incident spectrum. $A(\lambda,x)$ is the absorbance of the light of wavelength λ in the coating, since to produce the damage the light

must be absorbed in that material. $\phi(\lambda)$ is the damage function and gives the change in the particular damage being tracked due to a unit fluence of photons at a given wavelength and material phase. The damage function is likely different for different properties, for example $\phi^{gloss}(\lambda)$ for gloss is likely not the same as $\phi^{toughness}(\lambda)$ for fracture toughness. Damage function is the term used to weight the flux to account for responses in ionizing radiation damage studies, though quantum yield or spectral efficiency are frequently used to describe the same process at lower photon energies. The total damage over a length of time is the integral of the instantaneous over time $D_{total} = \int_0 D(t)dt$. To estimate the damage produced by a given flux, requires a function that relates the effectiveness of the photon of each energy to produce that damage. Generating a damage function experimentally entails measuring the change in one or several properties with time during a test series. Actual service conditions are likely to vary substantially from the exposure conditions used in testing. The testing may or may not accurately predict the ranking of coatings due to their damage susceptibility, when applied to actual service conditions. Additionally, the prediction of remaining service life of a coating based solely on the damage function requires the monitoring of the environmental conditions. A Monte Carlo model could help in correlating nondestructively measurable properties that could be used to measure one property, and predict remaining lifespan based on other properties. At a minimum, the Monte Carlo model results will allow more intelligent interpolation and extrapolation of damage functions. Monte Carlo modeling is a useful tool for taking damage functions generated experimentally and extending the data to predict other damage functions of interest.

1. CHEMISTRY

A chemical model and chemical analysis are being developed to predict the distribution of polymer segments that detach and are volatilized or can be washed away. The impact on the sensitivity of the polymer adjacent to the detached polymer segment can be increased or decreased in the Monte Carlo model based on the chemistry of the remaining polymer matrix, Figure 1. The affects of the modification of the material adjacent to a segment removed changes the predicted properties. In addition, the sensitivity and breakdown products of multi-phase materials are being investigated.

2. PHOTON FLUX

The flux of photons is a function of many variables including, but not limited to photon energy (wavelength), angle of surface relative to position of the sun, atmospheric conditions, season, and time of day. The penetration of UV and visible light into polymers is fairly low, for example in polyurethane attenuation to 0.10 of initial flux is x=14.7 μm at 340nm, and x=476 μm at 280nm.[7] Thus most of the visible and UV radiation will be absorbed near the surface of the coating, and the attenuation is even stronger in the presence of pigments. In addition, many of the degradation pathways require oxygen. The diffusion of oxygen into a coating results in a significantly higher concentration near the surface. Additionally, reactions relatively far from the surface may result in degradation fragments that need to diffuse from their origin and to a surface in order to escape. The loss of polymer fragments near the surface of the coating is less likely to result in recombination, compared to fragments diffusing out from deeper in the coating. Diffusion of oxygen in, diffusion of polymer segments out, and exponential attenuation of photon through a coating lead to the general observation that degradation is predominately a surface effect. We will, as chemistry details become available, incorporate

modification of subsurface chemistry into the model. The photon flux can be as high as 0.45 W/m^2 at midday in Florida. Using the solar spectrum, we calculate the integral photon flux as roughly $10^{18} \frac{photons}{m^2 sec}$. The photon fluence over a year is immense, and the probability of any particular photon initiating a segment rupture is low. A low probability of quantum efficiency for coating polymer degradation and the very high number flux of photons makes Monte Carlo techniques well suited for modelling the coating degradation.

3. MATERIALS

The Monte Carlo model allows the photon impinging on a region to modify the material in such a way to make it either more or less likely to be removed on subsequent photon impingements. Control can be set to remove a pixel impacted by a photon and the adjacent material modified to be more or less sensitive to future photon initiated erosion. The Monte Carlo model also allows the coating to be composed of multiple phases. These phases can either be randomly distributed, or clumped as in phase separation. The clumping presently consists of generation of random spheres where the radius and standard deviation of the radius can be input. The spheres are allowed to overlap. At low densities of the secondary phase, the spheres are predominately single. At higher densities of the second phase the secondary phase looks like the holes in a sponge. The two or many phases modeling option could be used to describe system containing pigment or extender particles which don't erode, just fall off when sufficiently free of surrounding matrix. Another multi-phase system might describe base material containing a dispersed UV absorber that requires a certain number of hits by photons before the chemistry is assumed to break down and erode. Obviously, it may be used to explore the behavior of a polymer system that separates into two or more distinct phases that have different durability.[4].

MODEL RESULTS

The initial surface is assumed to be flat, without defects. In all models, softening refers to the region around an eroded pixel becoming more likely to be eroded when impacted by subsequent solar radiation than the base material. Conversely, hardening results in the material being more resistant to erosion, either by being less likely to absorb the solar quanta, or if the light quanta is absorbed more likely to dissipate the energy without degradation.

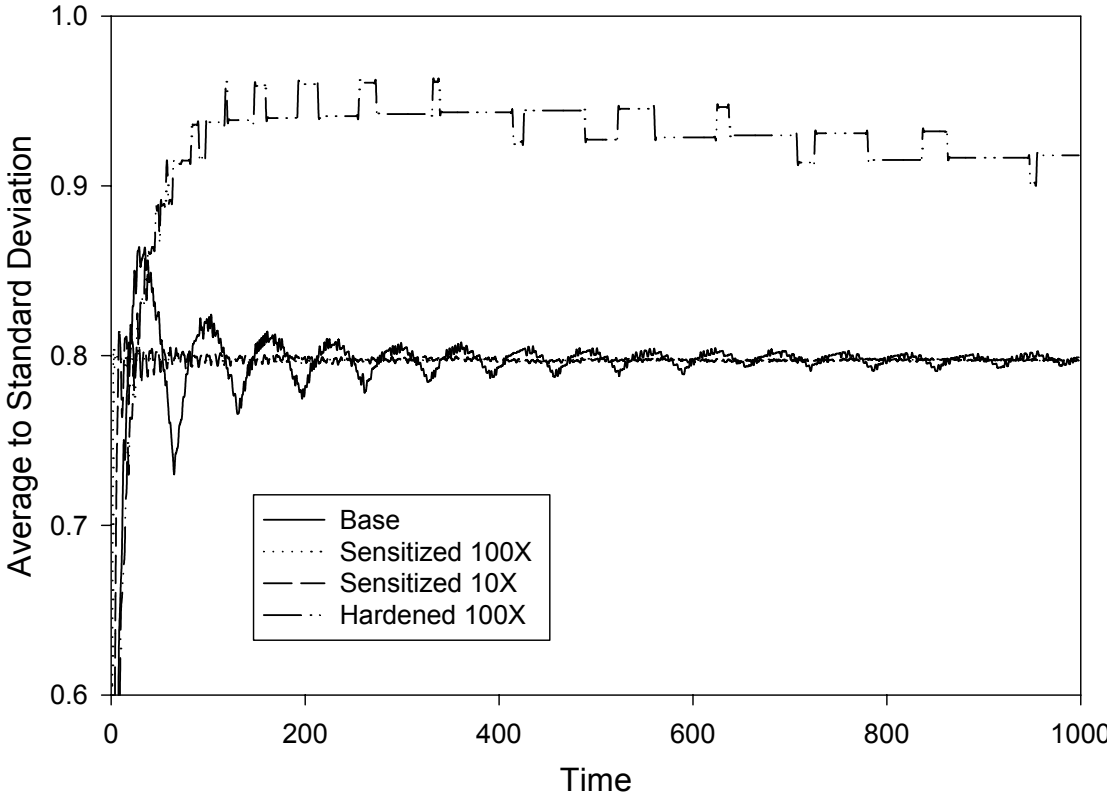

FIGURE 2. A measure of how close the distribution of surface topology is to Gaussian can be estimated by the ratio of the average deviation to the standard deviation of hole size. As the surface evolves, either sensitizing or hardening, the distribution of holes become Gaussian.

When the region adjacent to polymer segment eroded is unaffected, the distribution of holes quickly becomes a Gaussian distribution, Figure 2. The distribution of pit depths, if the surrounding material is modified, is not Gaussian initially. After long times, the distribution of

surface depths become Gaussian due to the entire surface being modified. The average to standard (root mean squared) deviation in depth predicts how close the distribution of pits is to a Gaussian distribution. The Gaussian distribution has an average to standard deviation of $\sqrt{\frac{2}{\pi}} \cong 0.80$. Initial roughness of many smooth surfaces has an average to standard deviation of 0.1 to 0.2, Bennett and Mattson.[2] In order to compare the model's prediction of behavior of a degrading system, a means to quantify the behavior is needed. Various theoretical and empirical equations are applied which take measures of the final physical state, in this case surface topology, and correlate to another measurable property. An example is the use of the standard deviation of the surface profile, which can be measured by an atomic force microscope (AFM) or other profilameters and used to predict the reflectance based on the equation of Bennett and Porteus.[1] The Monte Carlo generated surface may be parametrically compared to measurements of the true surface being modelled, for example depth profile distribution. This in turn can be used to predict integral properties, such as reflectance, wetting angle, and fracture toughness.

1. FRACTURE TOUGHNESS

A failure criterion of a coating may be crack propagation through to the base material. As the coating dries, it shrinks relative to the substrate resulting in planar, tensile stresses in the coating. Applying the Griffith crack criterion and using the maximum flaw size generated from the Monte Carlo model, an estimate of the relative strength of a coating can be predicted with time. We assume the coating is a nearly infinite plane. As an estimate of the reduction in coating strength we use $\sigma_G = \sqrt{\frac{2E\gamma_s}{\pi a}}$, where K_c is the fracture toughness, E is Young's modulus, γ_s is the surface energy per unit area, and a is the maximum flaw size. σ_G is the Griffith stress,

which is the critical stress above which the crack continues to progress to fracture. The coating has then failed.

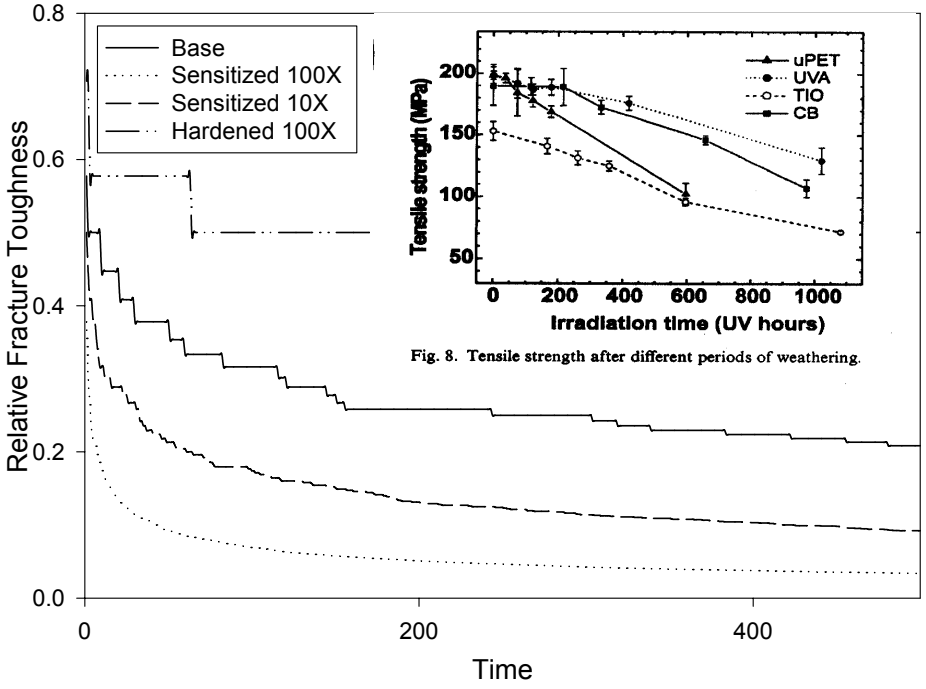

FIGURE 3. The strength of the coating decreases as defects in the coating become deeper and the coating thins.

The decrease in fracture toughness for the poly(ethylene terephthalate) coating used in ref. [3] is compared to the decrease in fracture toughness predicted by the Monte Carlo model for conditions in which the initial removal of a polymer segment results in a sensitization or hardening to erosion of adjacent material. The fracture toughness of thin films is difficult to test quantitatively due to such confounding parameters as variations in the thin film thickness and initial defect distribution. The spread in the predicted decrease in fracture toughness with time is too large to precisely define the functional form the decrease in fracture toughness takes as a function of time. The trends in the decrease in fracture toughness shown in Figure 3 show the Monte Carlo model and experimental data(inset plot) predict or show an early accelerated

decrease in the fracture toughness followed by a more gradual decrease. In an engineering system we would insert an initial distribution of holes consistent with the initial measurements of the coating prior to exposure and degradation. This initial defect distribution would decrease the initial steep slope seen in Figure 3. As expected, sensitizing the material adjacent to a removed segment reduces the fracture toughness more quickly, and vice versa. The coarse, step decrease in the case in which the material adjacent to a removed segment is hardened is due to only a few defects being generated over the timescale used. The change in fracture toughness for a two-phase system is given in Figure 4. The second phase in this example is 10% of the volume and consists of a secondary phase that is 100 times more sensitive than the base material. The dispersion of the second phase is either random, or taken as randomly dispersed spheres with a Gaussian distribution of given radius and standard deviation. The change in relative fracture toughness is least for a randomly dispersed secondary phase. The clumping of the sensitized phase results in quicker loss of toughness.

As with all the correlations used in this paper that relate surface topography to a physical property, other correlations exist. In this case the simple Griffith crack criterion is applied, though other models are available and can easily be incorporated. Additionally, many finite element codes are available and could be used to predict fracture toughness based on the materials and surface profile supplied by the Monte Carlo program.

2. REFLECTANCE

The reflectance is a non-destructive way to measure the progression of coating damage. Correlation between the parameter used to define coating failure and change in reflectance could be used to estimate remaining lifetime based on measuring the gloss. The specular reflectance calculated from the model is based on the model of Bennett and Porteus.[1].

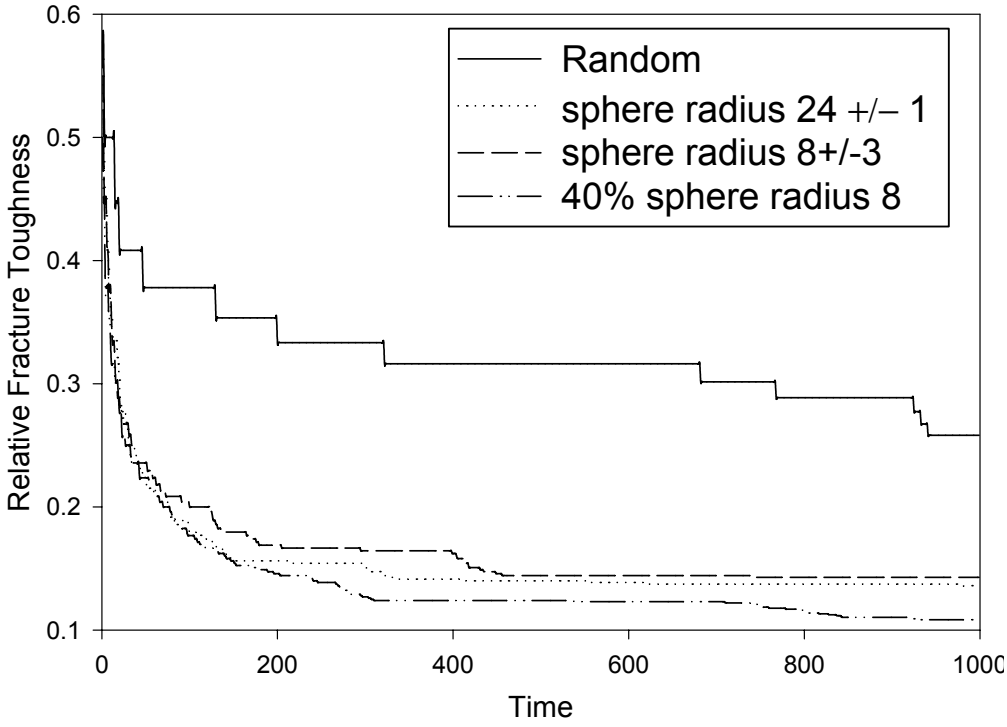

FIGURE 4. The strength of the multi-phase coating decreases as defects in the coating become deeper and the coating thins.

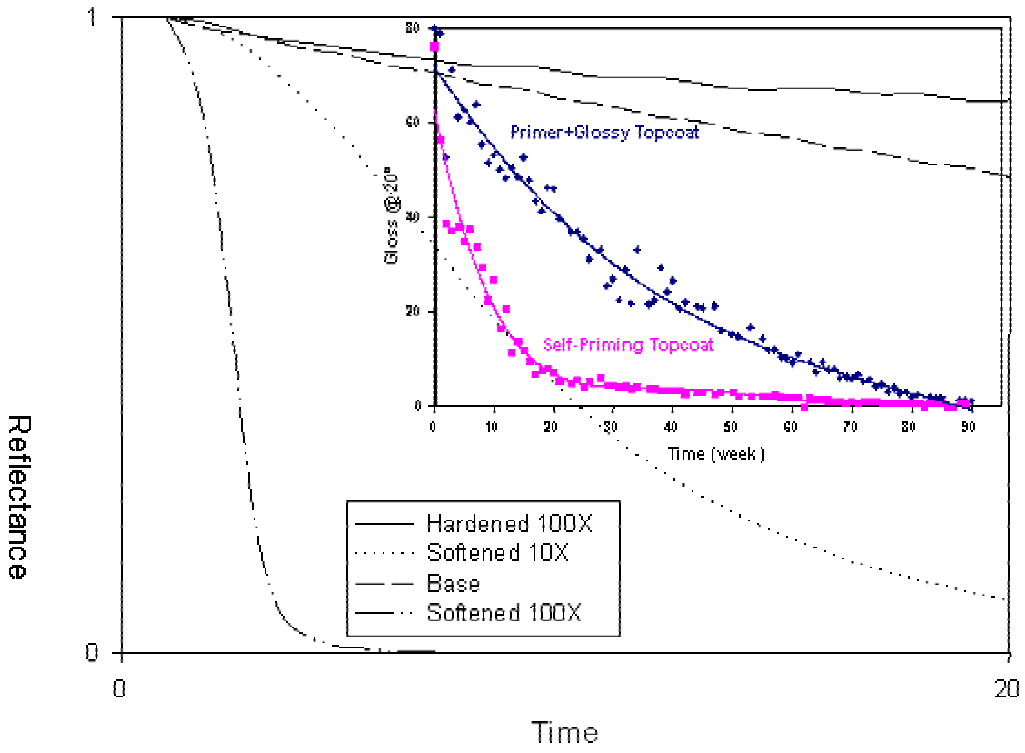

FIGURE 5. The reflectance decreases with coating degradation, due to increasing surface roughness. The model predicts the qualitative change in reflectance measured.

Specular reflectance for normal incidence:[1]

$$R_s = R_0 \exp[-(4\pi\sigma)^2/\lambda^2] \quad (2)$$

R_s is the specular reflectance and R_0 is the reflectance for a perfectly smooth surface of the same material. λ is the wavelength of the incident light and σ is the standard deviation of the surface from its mean level.

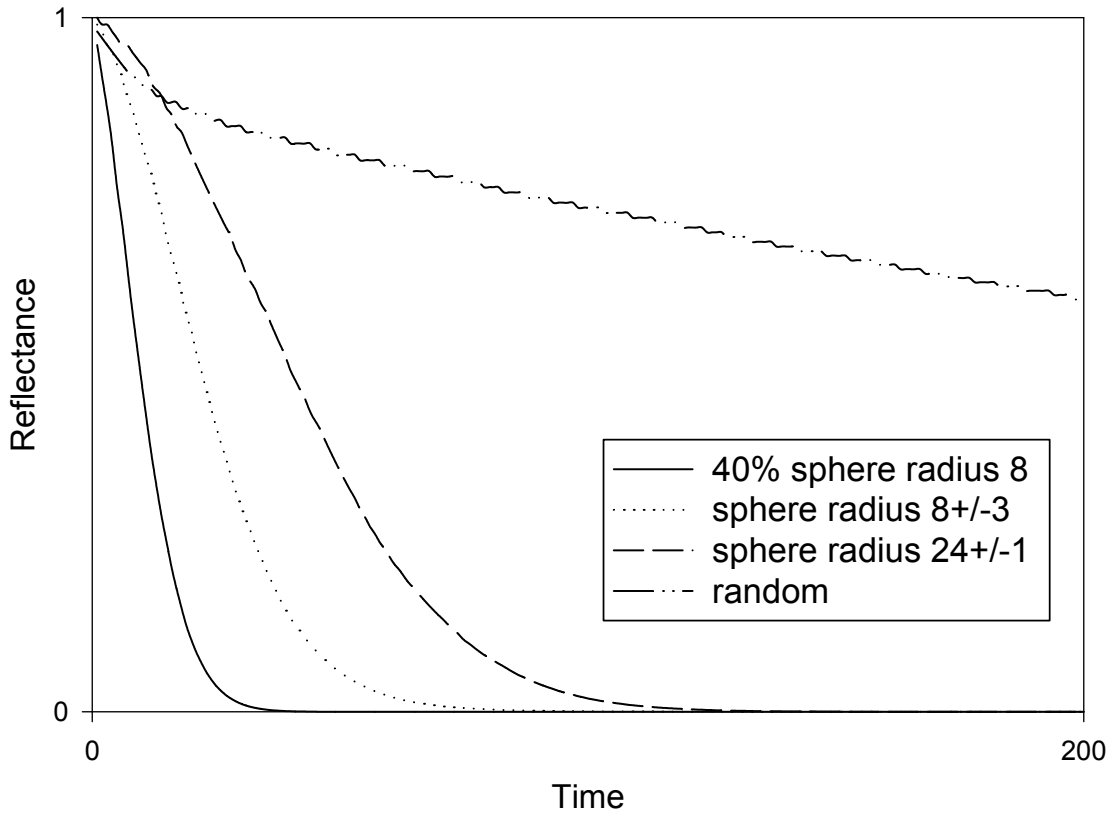

FIGURE 6. The reflectance of the coating is sensitive to the distribution of the secondary phase that is 100 times more sensitive to solar degradation. Also the fraction of the secondary phase effects the degradation of reflectance .

The Monte Carlo model of surface erosion as a function of solar spectral flux, Figure 5 predicts the sigmoidal decrease in reflectivity with exposure, which is consistent with experimental results. The softening of material adjacent to a removed segment results in a faster

degradation of the reflectance. The effect of the secondary phase, which is sensitized relative to the base material, is given in Figure 6. The higher the concentration of the secondary phase results in a faster degradation of gloss. The random distribution of secondary phase results in an accelerated degradation at early times, followed by a much slower degradation.

3. WETTING CONTACT ANGLE

The wetting angle changes with the roughness of the surface. At this point, we assume the chemistry of the surface does not change enough to alter the surface energy of the coating. The change in contact angle is a modified version of Young's equation, which incorporates the actual surface area to the projected surface.[5] We arbitrarily assume an initial wetting angle near 90 degrees, and at long times the change in wetting angle approaches 0 degrees, near complete wetting.

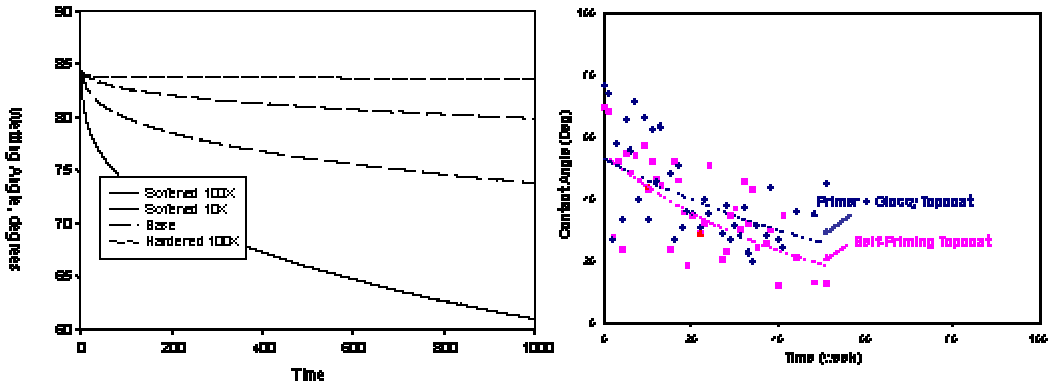

FIGURE 7. The wetting angle decreases as the coating degrades. The model predicts the change in wetting angle based only on the change in surface roughness.

The wetting of a surface is a function of the physical profile of the surface and the surface chemistry. We start by looking at the impact of the change in the surface roughness only, assuming the surface chemistry is unaffected. The assumption that the surface chemistry

unchanged during erosion, or equivalently the modified material has very similar surface energies between the solid surface and the vapor and liquid, can be relaxed later when chemical changes specific to a particular polymer are input. The defects must be much smaller than the dimension of the drop. An approximation for the effect of the surface roughness is:[5]

$$r(\gamma_{solid-vapor} - \gamma_{solid-liquid}) = \gamma_{liquid-vapor} cos\theta \tag{3}$$

where r is the ratio of the actual vs. projected area of solid contact with the solid phase. The γ's are the surface free energy between the subscripted phases. θ is the wetting angle. Assuming the wetting angle starts near 90 degrees for a flat surface,

$$r(\frac{\gamma_{solid-vapor} - \gamma_{solid-liquid}}{\gamma_{liquid-vapor}}) = \cos\theta \tag{4}$$

results in

$$\theta = arccos(r(\frac{\gamma_{solid-vapor} - \gamma_{solid-liquid}}{\gamma_{liquid-vapor}})) \tag{5}$$

We have assumed that the wetting angle of the initial surface before degradation is near 0 degrees, thus $(\frac{\gamma_{solid-vapor} - \gamma_{solid-liquid}}{\gamma_{liquid-vapor}})$ is chosen to be 0.1. Note that the equation 5 above cannot transition through a 90 degree angle since choosing $(\frac{\gamma_{solid-vapor} - \gamma_{solid-liquid}}{\gamma_{liquid-vapor}})$ to be 0 results in equation 5 being independent of r. The wetting angle is plotted in Figure 7. The softer the region adjacent to a removed segment the quicker the wetting angle changes. The inset plot of experimental data again shows great uncertainty, though the trends are consistent with the model's prediction. The wetting angle is not plotted for the two-phase system because the distribution of holes is not random when the second phase is clustered as spheres, and when the two phases may have potentially different wetting angles.

DISCUSSION

Being able to correlate a non-destructive measurement to a property of interest is useful since it allows, not only the prediction of service life based on an a priori estimate of the service environment, but also the ability to monitor and adapt the predicted service life based on the actual service environment without having to explicitly monitor that environment. The results of the Monte Carlo simulations are used to predict physical property changes in the coating, both those that define failure and those that are measurable in a non-destructive way. These changes can be related to measurable properties and may be correlated to lifetime predictions of in-service items.

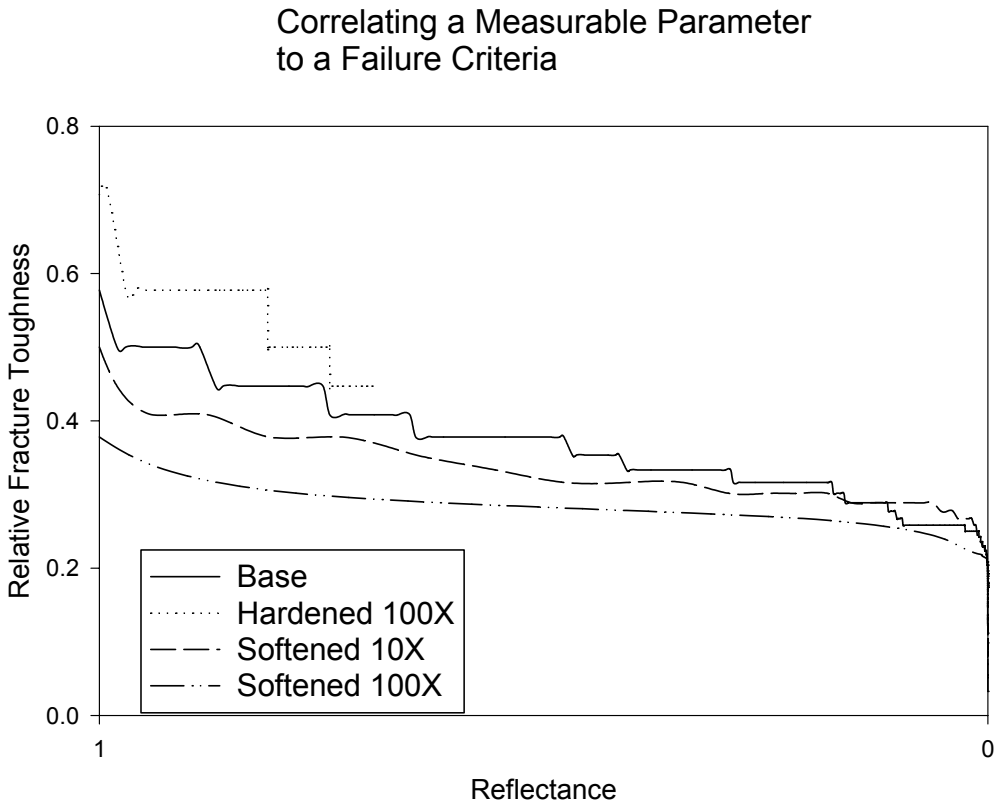

FIGURE 8. Failure criteria, such as fracture toughness can be correlated to a measurable property, such as reflectance.

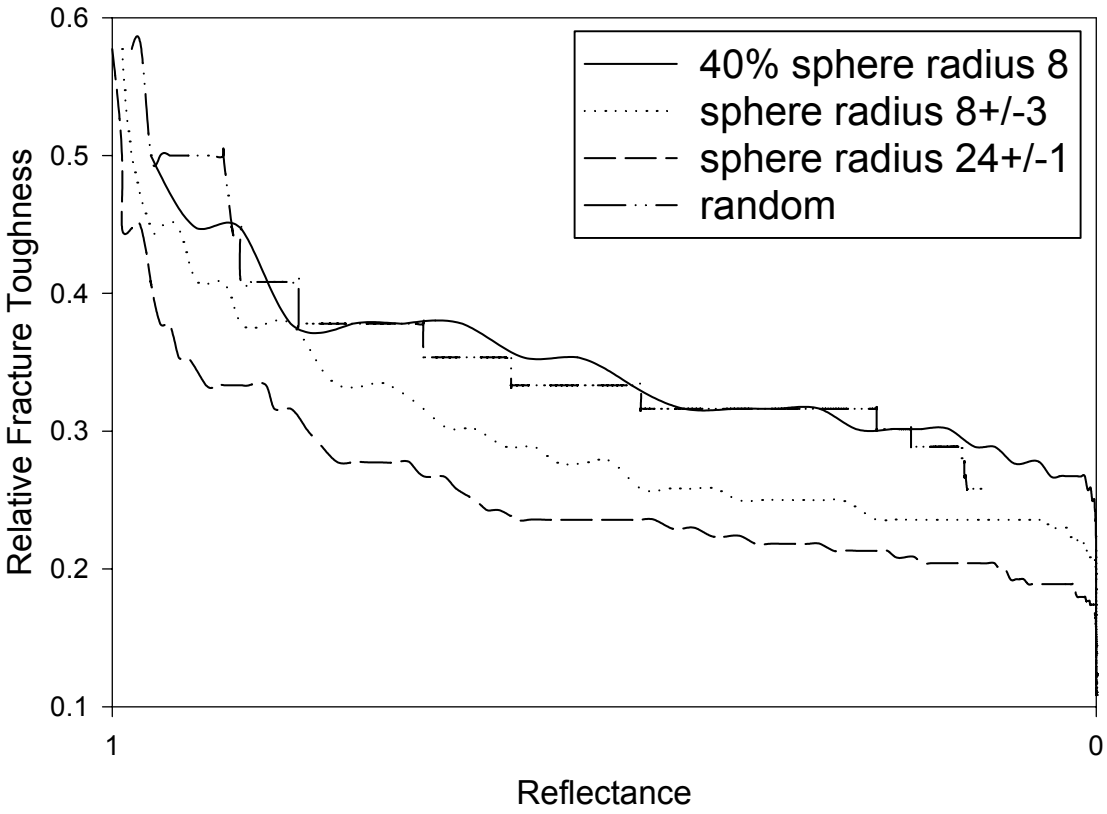

FIGURE 9. In a multiphase system failure criteria, such as fracture toughness can be correlated to a measurable property, such as reflectance.

As an example, the fracture toughness is plotted as a function of gloss, Figure 8 for a system where removal of a segment hardens or softens the adjacent material. Over a large portion of the reflectivity scale, the relative fracture toughness changes only slightly. This leaves only a very small time period early and late in coating life when the reflectivity is a good measure of toughness, for coatings that sensitize or harden adjacent material. A use of Monte Carlo may be to choose useful "pairs" of properties where the correlation is more sensitive to the extent of degradation. A major codicil in the accurate prediction of coating properties is the ability to generate a functional or correlation between a surface profile, and in the case of multiple phases the phase distribution, and the property or other damage being modelled. The

description of the property need not be an equation; a finite element or ray tracing routine could also be used to tie the Monte Carlo modelled surface to the predicted property.

CONCLUSIONS

We have created a Monte Carlo model to predict surface coating degradation and use the results to predict change in the coating properties with lifetime. The model presently predicts qualitative changes of system properties based on various theoretical and empirical models which take surface profile properties and relate them to measurable system properties related to coating lifetime, such as gloss, relative fracture toughness, and wetting contact angle. As noted in the introduction, the Monte Carlo model is quite general in its application of a random process to a surface that removes a portion of the surface, and then the surface topology is used to predict physical properties or future behavior. This type of application could apply to surfaces randomly eroded by solvent or corrosive species, for example. Presently we can model a random dispersion of phases, or control the size distribution of spherical secondary phase. This will be used to model the different phase domains in urethanes. The option is also used to model pigment particles that don't erode significantly, simply falling off when sufficient supporting matrix material is removed. Ultra-violet absorbers might also be modelled as a phase, requiring a certain number of hits by solar radiation before the chemistry breaks down and the pixel is removed. The Monte Carlo model uses an integral solar flux, though the ability to use the solar spectrum as chemical data for specific coatings as a function of wavelength becomes available. Erosion is limited to only surface regions in this work. The option to modify subsurface material by photon initiated photo-chemical reaction allowing easier erosion when that space becomes part of the surface is available contingent on data for the attenuation coefficient in the given coating for the specific wavelength. The model qualitatively reproduces the lifetime behavior of wetting angle,

reflectance, and fracture toughness for a single phase polymer coating. Further testing is presently underway to predict the degradation of a polyurethane coating, including the chemistry required for qualitative modelling. We plan future testing of pigmented systems to compare to the Monte Carlo models.

ACKNOWLEDGMENTS

This work was supported at NDSU by the U.S. Air Force Office of Scientific Research under Grant F49620-99-1-0283, LtCol. Paul Trulove, Program Officer.

REFERENCES

1. H. E. Bennett and J. O. Porteus, *Relation between surface roughness and specular reflectance at normal incidence*, Journal of the Optical Society of America **51** (1961), 123--129.
2. Jean M. Bennett and Lars Mattson, *Surface roughness and scattering*, Optical Society of America, Washington, DC, 1989.
3. G.J.M. Fecchine, M.S. Rabello, and R.M. Souto-Maior, *The effect of ultravolet stabilizers on the photodegradation of pol(ethylene terephthalate)*, Journal of Polymer Degradation and Stability **75** (2002), 153--159.
4. X. Gu, D. Raghavan, T. Nguyen, M. R. VanLandingham, and D. Yebassa, *Characterization of polyester degradation using tapping mode atomic force microscopy: Exposure to alkaline solution at room temperature*, Polymer Degradation and Stability **74** (2001), 139--149.
5. R. D. Hazlett, *On surface roughness effects on wetting phenomena*, Contact Angle, Wettability and Adhesion (1993), 173--181.

6. Jonathan W. Martin, *Quantitative characterization of spectral ultraviolet radiation-induced photodegradation in coating systems exposed in the laboratory and the field*, Progress in Organic Coatings **23** (1993), 49--70.

7. R. Zhang, H. Chen, H. Cao, C.M. Huang, P.E. Mallon, Y. Li, Y. He, T.C. Sandreczki, Y.C. Jean, R. Suzuki, and T. Ohdaira, *Degradation of polymer coating systems studied by positron annihilation spectroscopy. {IV}. oxygen effect of {UV} irradiation*, Journal of Polymer Science: Part B: Polymer Physics **39** (2001), 2035--2047.

STUDIES OF CORROSION AND PITTING INITIATION OF AA2024-T3 USING ATOMIC FORCE MICROSCOPY

G. S. Frankel and P. Leblanc

Fontana Corrosion Center, The Ohio State University
Columbus, OH, 43210, USA

ABSTRACT

The development of techniques linked to the atomic force microscope (AFM) has enabled the evaluation of physical and chemical properties of sub-micron structures. Scanning Kelvin Probe Microscopy (SKPFM) and in-situ AFM scratching have been particularly useful for studying corrosion phenomena. SKPFM generates a map of the potential distribution across a sample with a resolution of 100 nm. Furthermore, the open circuit potential of various pure metals in solution is linearly related to the Volta potential value measured in air immediately after exposure. SKPFM is a useful tool to assess the practical nobility of a surface. This technique has been successfully applied to the heterogeneous microstructure of AA2024-T3 and provided clear evidence regarding the shape, position, compositional inhomogeneities and local practical nobility of copper-rich intermetallic particles. The reactivity of these particles has been studied in detail. AFM scratching is an extremely controlled method to locally disturb the protective oxide film on a metal surface in solution. As with other approaches that utilize in situ scratching, the stability of the passive film and the tendency for stabilization of localized corrosion can be monitored. However, the lateral imaging capabilities of the AFM provides an approach to study the role of different microstructural features in the process of localized corrosion stabilization. Finally, AFM scratching can be used to open up small windows in a protective organic coating to reveal selected microstructural features. This allows the study of the corrosion behavior of these features in isolation from the rest of the microstructure or to study the interaction of different selected microstructural features. This approach is useful for understanding the interaction between different types of intermetallic particles in AA2024-T3.

INTRODUCTION

Localized corrosion is usually driven by microstructural heterogeneities.[1] For instance, in Al alloys, alloying elements added for increased strength are often segregated to and enriched in intermetallic particles. Such particles can be large constituent phases on the order of tens of

microns in size, or precipitated hardening particles nm in size. Localized corrosion typically initiates at the larger particles (micron size or larger), but the role of the particle in the localized corrosion process depends on the particle type. In AA2024-T3, there exist two primary types of large intermetallic particles: AlCuFeMn particles and S phase Al_2CuMg particles.[2] The FeMn-containing particles have a range of composition and are often themselves heterogeneous. These particles are typically considered to be cathodic to the matrix.[3] The S phase particles are more homogeneous, and are thought to be active owing to the high Mg concentration. It has been suggested that Mg and Al can dealloy from S phase particles, leaving a porous Cu-rich residue that might break apart and redistribute Cu across the sample surface, providing a large active cathode.[1]

Clearly, it is of interest to be able to understand the exact role of these intermetallic particles in the localized corrosion process. Owing to their small size, techniques with high spatial resolution are required to do so. A number of techniques with sub-micron resolution exist, such as SEM, EDS, AES, and TEM. This paper will summarize recent work utilizing a relatively new technique, the Scanning Kelvin Probe Force Microscope (SKPFM) to study the corrosion behavior of Al alloys.[4-8] The SKPFM is an AFM-based technique with sub-micron resolution. It is a robust technique that is relatively quick and simple to perform. It simultaneously provides topographic and potential maps of the same region of a sample surface.

It has been shown that, for distances greater than 100 nm from the surface, the potential measured by SKPFM is constant,[4] which corresponds to the conceptual definition of the Volta potential difference for a metal-solution interface. However, the separation between the influence of the surface dipoles and free charges contribution on the measured potential is theoretical and does not exist as such for a real solid-liquid interface. The influence of adsorbed dipoles

dominates closer to the surface, but also influences the potential measured at distances equal to or greater than 100 nm. Nonetheless, the overall nature of the potential measured by SKPFM justifies the description of it as the Volta potential difference.

EXPERIMENTAL

Scanning Kelvin probe force microscopy was performed with commercial AFMs (Nanoscope IIIa or Dimension 3100, Digital Instruments). These instrumente can measure the surface topography and potential distribution simultaneously on a line-by-line basis using metal-coated silicon cantilevers that are electrically conducting. The cantilevers were also obtained from Digital Instruments. The principle and details of the SKPFM measurement have been previously described. In short, it involves scanning the surface in tapping mode to determine the topography on a line-by-line basis. The cantilever is then lifted a fixed distance from the surface, typically 100 nm, and the tip is rescanned at this height in "lift mode". On the rescan, an AC voltage is applied to the tip, which stimulates oscillations of the cantilever in the presence of an electric field. The magnitude of the oscillations at the stimulating frequency, monitored by the AFM detection scheme, is nulled on a point-by-point basis on the rescan by adding a DC voltage that balances the field. This approach to potential distribution measurement is not possible in an aqueous solution because the large voltages applied to the tip would result in faradaic reactions. In this study, all potential mapping was performed in air. Since this technique is a nulling method, the output signal from the instrument was inverted; it has been shown previously that inversion of the signal is needed to obtain the expected polarity of the potential measurements. The values obtained are relative to the potential of the tip. The tips are only pseudo-references since their potential may vary with changes in the surface oxide. In order to avoid errors associated with variations in the tips or instabilities in the instrument electronics, the

potential measurements were calibrated by comparison to the potential measured on a pure Ni surface after immersion in DI H_2O. Ni was chosen as a reference because it was found to have a stable potential. All potential measurements are reported herein relative to that of a Ni sample. Consecutive measurements in air on a stable reference sample using different tips coated with the same metal showed potential difference of less than 50 mV, giving an indication of the reproducibility of this method.

Samples were cut from an AA2024-T3 sheet (nominal composition 3.8-4.9% Cu, 1.2-1.8% Mg, 0.3-0.9% Mn, 0.5% Fe, 0.5% Si, 0.25% Zn, 0.1% Cr, 0.05% Ti, balance Al). A non aqueous lubricating slurry (Blue Lube by Struers) was used during the surface preparation (grinding and polishing). The AA2024-T3 disks were mechanically ground with successively finer SiC paper through 1200 grit and polished with 6, 3, and 1 μm diamond paste. Prior to study, samples were cleaned ultrasonically with ethyl alcohol.

RESULTS AND DISCUSSION

EXPERIMENTS ON PURE METALS

In order to determine the usefulness of the scanning Kelvin probe force microscopy technique, potential measurements were made in air on a number of pure metal samples and compared to open circuit potential values determined on those samples immersed in aqueous solutions. The samples were immersed for 30 minutes in the solution before measurement to allow the open circuit potential to stabilize. Volta potentials are reported vs. the potential measured on a pure Ni sample, which served as a calibration standard. Ni was chosen as a reference because it was found to have a stable Volta potential. Figure 1 shows the relationship of open circuit potential for different metals in deionized water, 0.5 M NaCl, and 0.1 M Na_2SO_4 to the potential obtained in air with the Kelvin probe force microscope.[4] For samples exposed

to the chloride and sulfate solutions, both the open circuit potential in solution and the Volta potential difference in air after solution exposure were shifted in the active direction by around 150 mV relative to the values measured in and following DI water exposure. This suggests that adsorption of charged species at the electrode surface in chloride or in sulfate changed the dipole structure in the double layer and influenced the measured potential by the same value.

According to theoretical considerations, the measured potential should not be constant below 100 nm owing to the influence of image or dipole charges at the electrode surface.[9] To investigate this, the influence on the measured potential of the dipoles in the interphase region was studied as a function of the vertical tip-sample distance. Figure 2a shows the effect of tip-sample separation on the measured potential for pure Al directly after 30 min of immersion in DI water at OCP and one week later after storage in lab air.[4] At separation distances greater than about 100 nm, the potential is similar for the two cases, and independent of distance. This distance dependence of the potential with a constant domain above 100 nm is in good agreement with the literature.[9] It should be mentioned that this distance between the tip and the sample is not an absolute value because, during the tapping mode scan, the tip is already at a few tens of nm from the surface. In any case, it seems that above 100 nm the measured potential is constant and can be assumed to be the Volta potential difference. However, close to the surface, the measured potential changes with tip-sample separation, and the trend is different at the two times. Adsorption phenomena might be responsible for this difference. Indeed, after one week of storage in air, the surface might dehydrate, which could change the dipole structure. The influence of the adsorbed layer on the potential/distance relationship varies considerably for different metals. Ni shows almost no distance dependence over the full range of separation distances, Figure 2b.[4] The potential on Ni is also independent of the time in air. This suggests

the nickel oxide surface is very stable, and is the reason why Ni was chosen as a reference for the Volta potential difference measurements.

SPATIAL RESOLUTION

The advantage of the SKPFM over standard Scanning Kelvin Probes[10,11] is the improved spatial resolution owing to the small size of the probe and the separation of the probe from the sample surface. Figure 3 shows topographic and potential maps for a region of an as-polished sample of AA2024-T3.[6] Considerable debris resulting from the non-aqueous polishing and rinsing of the sample, is visible in the topographic image on the left. Also visible are scratches and some holes that might have resulted from corrosion or particle pull-out. Finally, there are some raised regions associated with intermetallic particles that are harder than the alloy matrix and polish slower. On the right is the Volta potential map of the same region. The intermetallic particles are clearly evident with high contrast. Figure 4 shows an SEM image of the same area.[6] The bright spots in the SEM image were found by EDS analysis to be intermetallic particles. They match up perfectly with the high potential features in the potential map of Figure 3. The large, blocky particles are the AlCuFeMn type and the three round particles, which are barely visible in the SEM image, are S phase particles. The secondary electron intensity in the SEM image is a convolution of topographic and chemical (z-number) effects. In contrast, the topographic and potential maps produced by the SKPFM separate these effects.

The limits of the spatial resolution capability of the SKPFM have not been fully investigated. Figure 5 shows an example of a small scan taken at the edge of an AlCuFeMn particle after exposure of the sample to 0.5 M NaCl for 10 min.[7] Trenching of the matrix around the cathodic particle was observed as well as some attack within the particle. The region

shown in Figure 5 is the trench along the side of the particle, which is in the bottom left part of the figure. The trench is seen to be associated with a high potential, likely as a result of Cu enrichment. Potential and topographic features smaller than 100 nm can be seen in the images.

BEHAVIOR OF PARTICLES IN AA2024-T3

The high Volta potential exhibited by the S phase particles in the as-polished condition relative to the matrix (Figure 3) is opposite of what would be expected given the relatively low potential reported for grains of S phase in a bulk fabricated analog sample[3] and the correlation presented above relating Volta potential measured by the SKPFM to corrosion potential. Figure 6 shows Auger depth profiles of the matrix, Al_2CuMg and AlCuFeMn particles collected simultaneously on a sample of AA2024-T3 directly after polishing in a non-aqueous polishing slurry. The surface of the intermetallic particles was covered with Al-Mg oxide (or hydroxide); Cu was depleted on the surface of both kinds of particles relative to the concentration beneath the surface. This measurement indicates that the noble potentials observed on these types of particles after polishing using SKPFM are not caused by surface enrichment of copper as might be expected. A more complex behavior has to be considered.

The oxide film formed on the reactive S phase particles during non-aqueous polishing provides some protectiveness to the surface. It has been shown that S-phase particles do not dissolve immediately upon exposure to 0.1 or 0.5 M NaCl [5,7]. The Volta potential of the different regions on the surface start out quite different, as evidenced by the contrast shown in potential map of the as polished sample. With time, these potentials merge to a single value and the contrast in the potential map decreases. This is shown in Figure 7 for various regions of samples exposed to 0.5 M NaCl.[5] Regions that are active pits go to a high potential similar in value to pure Cu exposed to the same solution. It was shown that S phase particles not

associated with a pit in the as-polished condition are eventually attacked when their potential reaches a value similar to that of the matrix. At this point, the protectiveness of the oxide film on the particle is reduced and localized attack at the particle can commence.

Sputter etching of the as-polished surface can change the behavior of the S-phase particles.[4,5] Partial removal of the oxide, as indicated by the O signal in the SAM tool in which the sputter etching was performed, resulted in the reversal in contrast for some, but not all, of the S-phase particles; after sputtering and exposure to air, they had a Volta potential lower than that of the matrix. Subsequent exposure to 0.5 M NaCl for 30 min resulted in dissolution of some, but not all, of the particles that had exhibited a low potential after sputter etching.[5]

SMALL EXPOSED AREAS

It is possible to expose small areas of a sample by coating the sample with a thin layer of a protective polymeric film and then scratching through the film at selected regions.[5] In this fashion, it is possible to expose regions containing only certain microstructural features or ratios of such features that are different than that given by the alloy microstructure.

A window exposing an area containing only a portion of an AlCuFeMn particle exhibited no corrosion upon 2 h exposure to 0.5 M NaCl. When such a particle was exposed with some surrounding matrix (but no large S-phase particles), considerable attack was found, and the extent of the attack increased as the fraction of the exposed area taken up by the AlCuFeMn particle increased, Figure 8.[5] This is what might be expected by simple galvanic corrosion considerations. AlCuFeMn inclusions are efficient cathodic regions and can drive corrosion reactions, not only at active S-phase particles but also in the matrix.

Interestingly, when an area containing typical S phase particles and matrix (no AlCuFeMn particles) was exposed to 0.5 M NaCl, no attack was seen after 120 min. This is the

same as was observed when only AlCuFeMn region was exposed. Clearly, localized corrosion only initiates in this system if there is simultaneous exposure of both active cathodes (AlCuFeMn particles) and an anodic site (S-phase particle or matrix). The absence of either anode or cathode prevents local attack. It should be noted that some S-phase particles were attacked when exposed to solution in a window that did not contain an AlCuFeMn particle. These reactive S phase particles were typically larger than average, and exhibited a lower Volta potential in the as-polished condition.

AFM SCRATCHING

In situ scratching of a passive metal with a sharp stylus has been used to assess repassivation behavior by localized removal of the passive film.[12-14] These and other studies have provided considerable insight into the nature of passivity and the kinetics of repassivation. Most of the prior work measured current transients generated under potential control. The effect of any local heterogeneities cannot be studied by simple scratching as there is no control over the placement of the scratch relative to the microstructure. Pressure applied by an AFM tip on the surface of a sample during in situ contact mode rastering is a form of scratching on the micro scale. An AFM tip can be placed directly on a feature of interest as determined by the topography or by ex situ SKPFM and the use of fiducial marks. Furthermore, the force applied by a tip can be controlled exactly.

In situ AFM scratching has been used to probe a number of different aspects of the protectiveness of the oxide film formed on Al and on different particles in the microstructure of Al alloys.[5,7,8,15]. A wide range of behavior was observed depending on the sample and the environment. Scratching of 99.99% Al or Al 1100 with a Si tip in the Nanoscope III environmental cell resulted in the formation of a smooth bottomed trench, Figure 9.[7,8]. The

depth of the trench depended on the AFM photodiode setpoint voltage, which is a measure of the scratching force. It is interesting that scratching of pure Al in 0.5 M concentrated NaCl resulted in uniform dissolution at a high rate and not in the formation of pits, even though Al might not be expected to repassivate spontaneously in this solution.

An explanation for this behavior can be given based on the concept that a critical current density is necessary to sustain pitting and prevent repassivation.[16] The rate of dissolution in a pit is on the order of A/cm2 over the first fractions of a second following breakdown. At open circuit, the high dissolution rate must be accompanied by an equally high rate of cathodic reaction, which in aerated 0.5 M NaCl is primarily oxygen reduction. Since the volume of electrolyte in the AFM cell was rather small (about 0.1 ml) and the cell was sealed, the supply of oxygen was finite and it quickly dropped to a level insufficient to maintain the required rate of anodic reaction. The result of continual film breakdown, accelerated dissolution and repassivation was the formation of a uniform trough. This is essentially erosion corrosion. This interpretation is supported by an experiment in which the 0.5 M NaCl solution was continually pumped through the AFM cell during scratching. Instead of accelerated uniform corrosion resulting in the formation of a flat-bottomed trough, scratching with solution flow at open circuit tended to result in sustained pitting.[8]

AFM scratching of AA2024-T3 in a more dilute chloride solution, 0.01 M NaCl, resulted in immediate dissolution of the S-phase particles,[7] even in a stagnant cell without pumping of the solution. The AlCuMnFe particles are apparently sufficiently catalytic to support enough cathodic reaction to sustain the localized attack even with a limited supply of oxygen.

CONCLUSIONS

Scanning Kelvin Probe Force Microscopy and in situ AFM scratching were shown to be useful techniques for the study of localized corrosion.

- SKPFM provides a potential map, which can be considered to be a map of the Volta potential difference, and represents the practical nobility of the surface. The Volta potential measured by SKPFM on pure samples in air following immersion in solution varies approximately linearly with the corrosion potential measured in that solution. It is sensitive to the excess charge and adsorbed dipoles.
- SKPFM provides clear visualization of the intermetallic particles in high strength Al alloys. The potential on the various particles and matrix changes with exposure and is related to the corrosion processes.
- The use of small exposure areas created by scratching through a thin protective polymeric film allowed the investigation of individual components of the microstructure in AA2024-T3. Both an active anode and cathode are required for localized corrosion, and the extent of attack depended on the area ratios of the anodes and cathodes.
- In situ AFM scratching provides information on the stability of the passive film and the ability of the system to stabilize localized attack.

ACKNOWLEDGEMENTS

This work was supported by the United States Air Force Office of Scientific Research under contract No F49620-96-1-0479.

REFERENCES

1. R. G. Buchheit, R. P. Grant, P. F. Hlava, B. McKenzie, and G. L. Zender, *J. Electrochem. Soc.*, **144,** 2621 (1997).
2. V. Guillaumin and G. Mankowski, *Corr. Sci.*, **41,** 421 (1999).
3. R. G. Buchheit, *J. Electrochem. Soc.*, **142,** 3994 (1995).
4. V. Guillaumin, P. Schmutz, and G. S. Frankel, *J. Electrochem Soc.*, **148,** B163 (2001).
5. P. Leblanc and G. S. Frankel, *J. Electrochem Soc.*, submitted (2001).
6. P. Schmutz and G. S. Frankel, *J. Electrochem. Soc.*, **145,** 2285 (1998).
7. P. Schmutz and G. S. Frankel, *J. Electrochem. Soc.*, **145,** 2298 (1998).
8. P. Schmutz and G. S. Frankel, *J. Electrochem. Soc.*, **146,** 4461 (1999).
9. J. O. M. Bockris and A. K. N. Reddy, Vol., (Plenum Press, New York,, 1970).
10. S. Yee, M. Stratmann, and R. A. Oriani, *J. Electrochem. Soc*, **138,** 55 (1991).
11. M. Stratmann and H. Streckel, *Corros. Sci.*, **30,** 681 (1990).
12. G. T. Burstein and D. H. Davies, *Corr. Sci.*, **20** (1980).
13. G. T. Burstein and R. C. Newman, *Electrochim. Acta*, **25,** 1009 (1980).
14. G. T. Burstein and P. I. Marshall, *Corr. Sci.*, **23,** 125 (1983).
15. D. Devecchio, P. Schmutz, and G. S. Frankel, *Electrochem. Solid-State Lett.*, **3,** 90 (2000).
16. G. S. Frankel, J. R. Scully, and C. V. Jahnes, *J. Electrochem. Soc*, **143,** 1834 (1996).

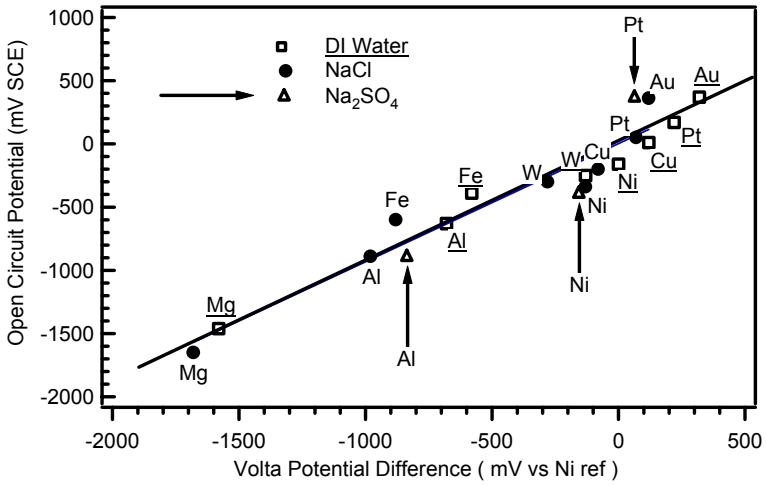

FIGURE 1: Comparison of the potential measured in air by Scanning Kelvin Probe Force Microscopy with open circuit measured in solution: in DI water (squares and underlined elemental symbols), in 0.5 M NaCl solution (filled dots) and in 0.1M Na_2SO_4 (triangles and indicated with an arrow) [4].

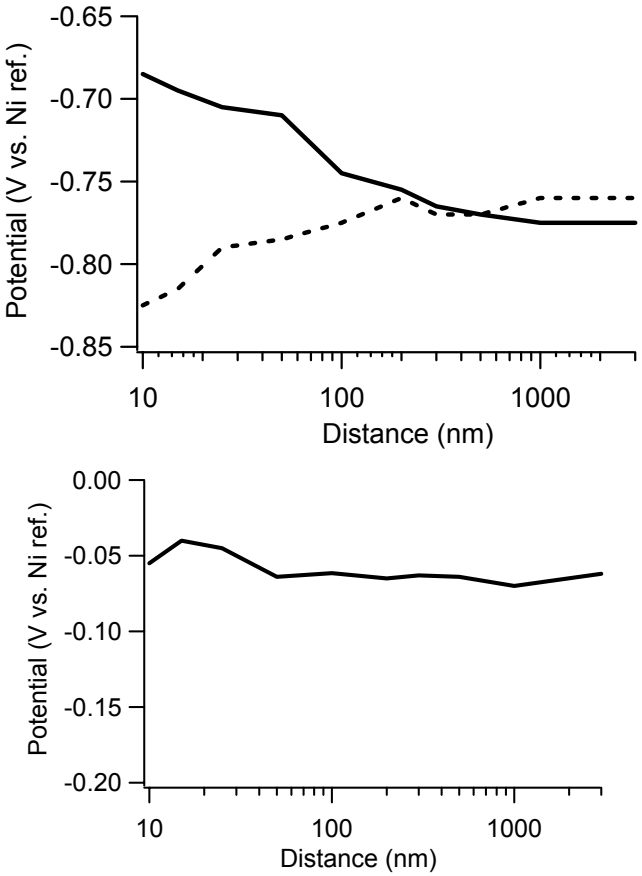

FIGURE 2: Potential measured as a function of tip-sample distance for a) pure Al after 30 min at OCP. Solid line, directly after removal from DI water, dashed line, 1 week later. b) pure Ni after 30 min of immersion in DI water at OCP.[4]

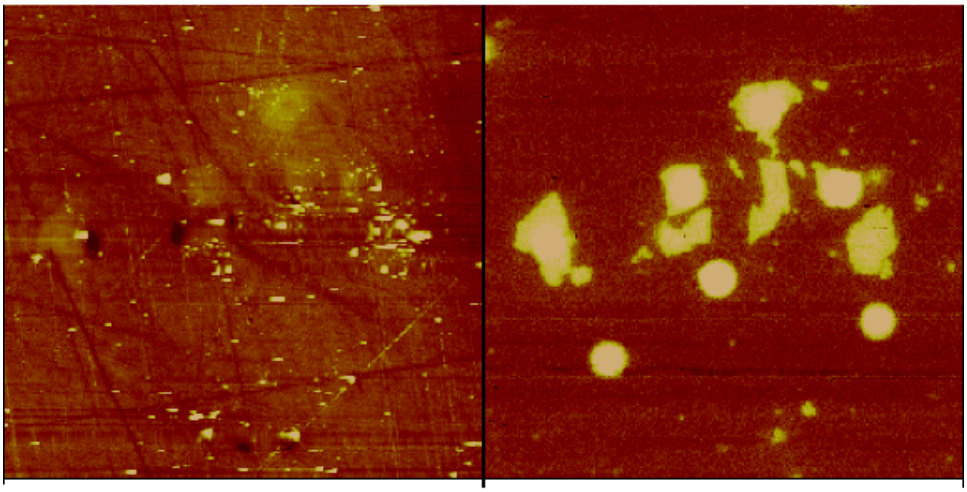

FIGURE 3. AFM image of intermetallic particles in AA2024-T3. Both images 80 x 80 µm, Left, topographical map with 100 nm z scale, right, Volta potential map with 1.5 V z scale.[6]

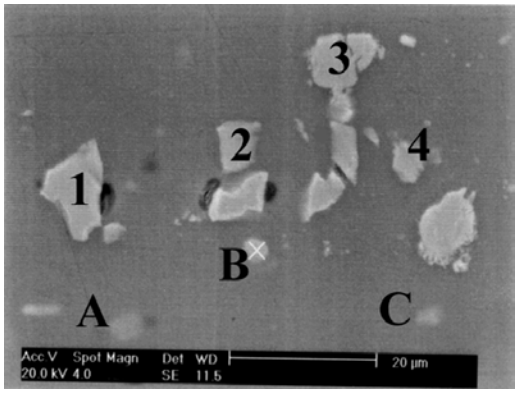

FIGURE 4. SEM image of the same region of the same sample as shown in Figure 3.[6]

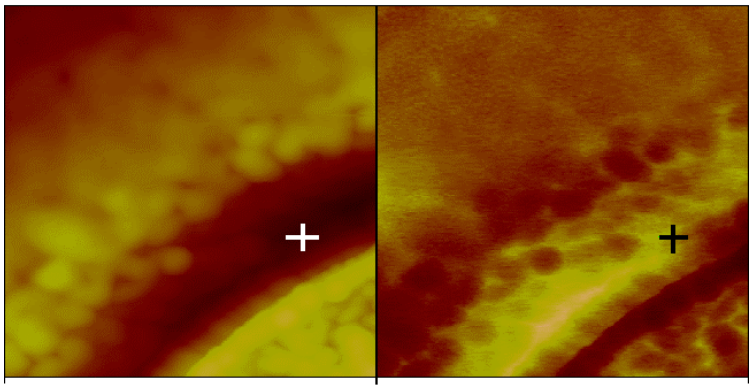

FIGURE 5. Topographic (left, z scale 600 nm) and Volta potential (right, z scale 0.5 V) maps of a region of AA2024-T3 sample exposed to 0.5 M NaCl for 10 min. The area of both maps is 1x1 µm. An AlCuFeMn particle is located at the bottom right of the images.[7]

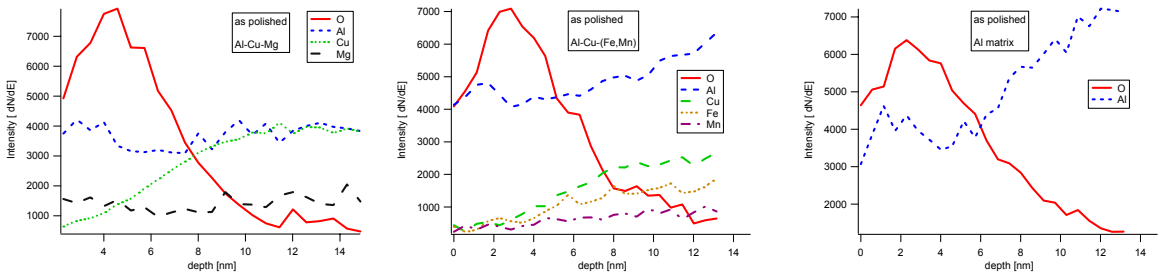

FIGURE 6. AES depth profile of an AA2024-T3 sample after polishing in non aqueous solution: (a) S phase Al_2CuMg particle, (b) AlCuFeMn particle and (c) Al matrix.

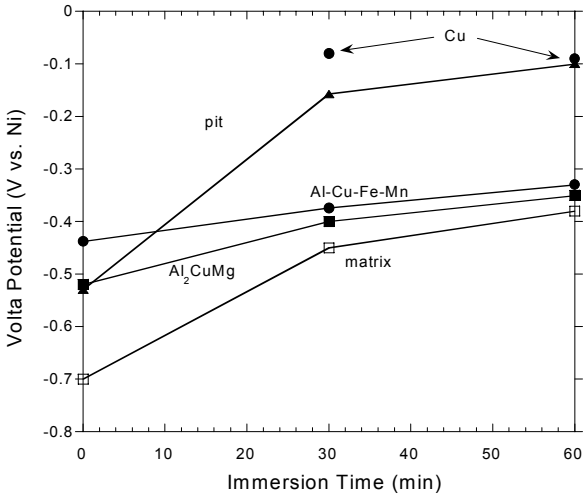

FIGURE 7. Volta potential change of pits, uncorroded matrix and uncorroded intermetallic particles in AA2024-T3 following immersion in 0.5 M NaCl for different periods of time. Volta potential of Cu given for comparison.[5]

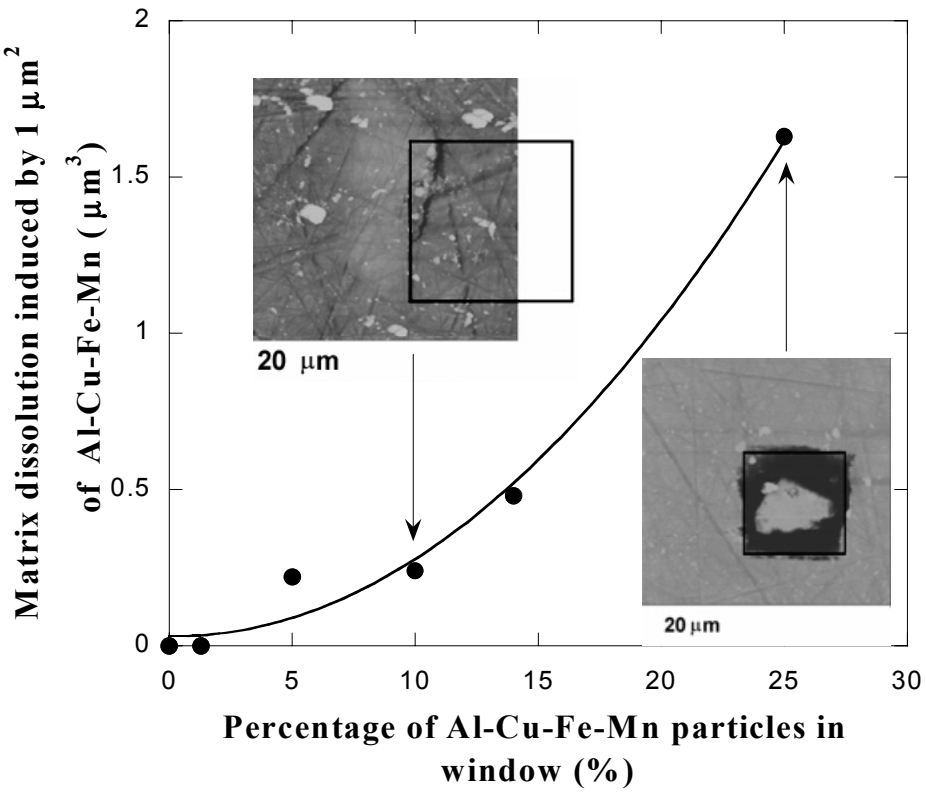

FIGURE 8: Effect of area fraction of Al-Cu-Fe-Mn in exposed window on matrix dissolution after 60 min exposure to 0.5 M NaCl.[5]

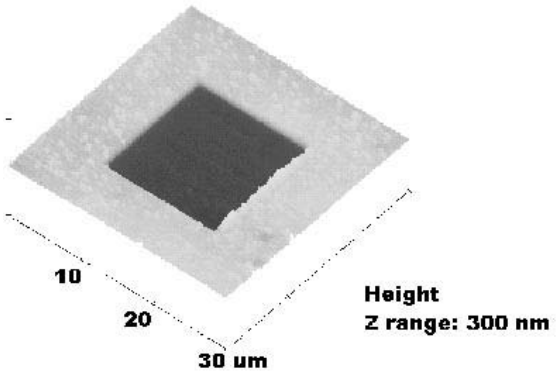

FIGURE 9. *In situ* topographic map of a 15 μm square hole in Al 99.99% obtained by contact mode scratching of the AFM tip in 0.5 M NaCl. Trench depth 75 nm.

AN ELECTROCHEMICAL AND SURFACE STUDY OF ADMICELLAR COATINGS ON ALUMINUM ALLOYS AND CREVICES

Kha Mach, Olga Matarredona, Steve Merchant, Melissa Rieger, and Edgar O'rear

School of Chemical Engineering and Materials Science
University of Oklahoma
Norman OK 73019

ABSTRACT

Corrosion of aluminum alloys is a growing issue for air force aging aircraft. The aluminum alloys (AAs) used in the construction of the tankers (e.g. KC 135) are prone to corrosive attack. Particularly critical locations for these aircraft are the interfaces between joints and crevices of the aluminum material. The main goal in this study is to assess the ability of ultra thin films produced by admicellar polymerization to prevent corrosion within crevices on aluminum.

The corrosion in model crevices coated with admicellar polystyrene was investigated using voltammetry and electrochemical impedance spectroscopy (EIS). Atomic Force Microscopy (AFM) was also used for examining the polymer film coverage and uniformity and for observing changes to the physical nature of the films prior to and after corrosion.

Preliminary results of voltammetry and impedance tests confirmed the present of the film but did not suggest significant protection by a barrier mechanism. The AFM images also showed some modifications on the surface of the aluminum alloys after coating treatments with admicellar polymerization technique. However, the capillary corrosion test indicated that within a crevice, admicellar polymerized thin layers have showed promise of a water-uptake delay and an improved corrosion protection.

INTRODUCTION

Corrosion of aluminum alloys is a growing issue for U.S. Military aircraft. For example, due to its age of greater than 40 years and the composition of the alloy the C/KC 135 tanker is prone to corrosive attack of the aluminum alloys used in its construction. Particularly critical locations for these aircraft are the interfaces between joints and faying surfaces of the aluminum material. After many years of use and maintenance, the original corrosion protection for crevices

has been removed. In these locations, capillary water uptake creates environments extremely prone to corrosion. Presently when corrosion is found in the crevices, the joints are opened and either cleaned or in extreme corrosive cases materials are replaced. It would be beneficial to have a protection process for mildly corroded areas and undamaged crevices that would not require removal or disabling of the aircraft body. Admicellar polymerization may provide a relatively easy and in situ method for providing protecting films in these crevices.

Admicellar polymerization, because of its ability to coat surfaces within tiny spaces, has great potential for applying thin films within the crevices of aircraft. Admicellar polymerization on alumina was first developed at University of Oklahoma [10-12]. It was shown that polymers such as polystyrene, polypyrrole, and polytetrafluoroethylene could be deposited as thin films in porous alumina powder.

The admicellar polymer process occurs in four steps: (1) Surfactant adsorption; (2) Monomer adsolubilization; (3) Polymerization inside the admicelle; (4) Rinsing of admicellar top bilayer. Using such a process, it is possible to say deposition of the polystyrene film on aluminum alloys in crevices by admicellar polymerization is feasible. The main goal in this study is to assess the ability of the polystyrene thin film produced by admicellar polymerization to prevent crevice corrosion on aluminum and to study corrosion behavior of aluminum alloys coated with polystyrene film in corrosive crevices.

Admicellar polymerization is a process that offers the ability to apply organic films to surfaces that are difficult to access such as pores and crevices. Previous studies have demonstrated the use of admicellar polymerization to form films of polystyrene and polypyrrole on alumina and silica surfaces [1-4]. Polystyrene films were used to change hydrophilic aluminum oxide powder into a hydrophobic material [1-3]. In order to prevent corrosion within the crevices,

two possible methods are proposed using the admicellar process: (1) prevent water uptake within the crevices by transforming aluminum within the crevice into a hydrophobic surface using polystyrene; (2) based on recent reports that conductive polymers reduce corrosion on aluminum alloys [4], apply a polypyrrole film inside the crevice.

EXPERIMENTAL PROCEDURES

MATERIALS PREPARATION

Aluminum Alloy 7075-T6 was obtained from Kaiser Aluminum Corporation, Houston, Texas. Plates (1 x 1 in.) were pretreated prior to polymerization using two methods. One method was to anodize the AA 7075 specimen in a 0.1 M solution of KCl at 15 V for one minute. A thick aluminum oxide layer was formed and was assumed to enhance surfactant adsorption. The second approach was cleaning in Tetrahydrofuran (THF) solution, followed by an immersion in a Chromerge solution, a mixture of H_2SO_4 and Chromic acid. The THF and Chromerge were used to dissolve any organic substances, which were left on the surface from the manufacturer. These two treatments were done after an initial washing process with ethanol and de-ionized water.

The surfactant used for the admicellar polymerization was Sodium dodecylsulfate (SDS). The initiator and polymer was 2,2 azo-bisisobutyronitrile (AIBN), and Styrene, respectively. They were as purchased and no other purification was made.

ADMICELLAR POLYMERIZATION

The admicellar polymerization was performed in a solution containing 6 mM of SDS, 30 mM of styrene 3 mM of AIBN. To dissolve the styrene and AIBN, 4 mL of ethanol was used for each compound separately before they were mixed. The solution was mixed well after adjusting

pH of the solution to 6. The 1 inch x 1 inch aluminum plates after pretreatment were put into a vial with 30mL of solution for 1 hour to allow surfactant to adsorb to the Al surface. Admicellar polymerization was initiated by heating the solution to 80^0C for 2 hours. After the reaction, the plates were taken out, rinsed with deionized water and air-dried. The admicellar process produced polystyrene films with contact angles greater than 90^0 as measured by a Cahn dynamic contact angle system.

CORROSIVE SOLUTIONS

Four different corrosion solutions were used for bare aluminum alloys corrosion testing with AFM: (1) 0.5 M NaCl; (2) 0.15 M NaCl; (3) 0.1 M KCl; and (4) Kelly's solution [5], which include 4mM nitrite, 4mM hydrogen carbonate, 2mM fluoride, 20mM chloride at pH = 9. For polarization and impedance tests, solution of 3.5 wt % NaCl (ASTM B 457) was used. All corrosion solutions were at room temperature, and 20 mL of the solution was used for each plate.

SURFACE CHARACTERIZATION USING AFM

Each aluminum plate was scanned at 3 different locations using Digital Instrument Multiple Mode AFM (Nanoscope III). AFM probe was scanned in a tapping mode. The scan size was 5 x 5 micron square. Samples of seven different corrosion times (1, 5, 25, 40, 60, 720, and 1440 minutes) were scanned to initiate the evaluation of AFM in corrosion characterization. Each image was processed using a plane fitting for any tilt corrections. The surface roughness analysis was done after the plane fitting. Roughness values from different locations on the plate were statistically average.

POLARIZATION (DC) AND IMPEDANCE (AC) TESTS

The equipment used for polarization and impedance tests was the Solartron 1260 FRA with a Solartron 1287 Potentiostat. Electrochemical cell was made of acrylic polymer (Cope Plastics, Oklahoma City, OK) and designed so small exposed area can be achieved for reasonably equivalent crevice area.

Each aluminum plate was tested at least three times at three different locations on the plate. The exposed area of the aluminum plate (working electrode, WE) for each test was 0.7 cm^2. The electrochemical cell held 45 mL of 3.5% NaCl solution with Platinum wire as the counter electrode (CE) and Saturated Calomel electrode as the reference electrode (RE). This electrochemical cell was set up for both polarization test and impedance test.

The polarization test was set up so that each sample was scanned 3 times after 10 minutes absorption in corrosion, and each of an hour after the first run. In the first scan, each sample was swept by a voltage range of +/- 0.015 V around its open circuit potential (OCP) at a very low scan rate of 0.01667 mV/s (ASTM G 61). The second scan was set at 1 mV/s scan rate and +/- 0.02 V range around OCP. The third scan was at a rapid scan rate of 10mV/s and +/- 0.3 V range around OCP. Corrosion rate was then calculated from these polarization experiments.

Impedance test was set up so than data from polarization test results can be compared to the impedance test results. Each sample was run with three impedance tests. Frequency was swept from 10^5 to 10^{-2} Hz. Operating voltage is set at OCP with AC amplitude of 10 mV. Each run is separated by 1 hour to match each hour run in DC test.

RESULTS

CORROSION CAPILLARY TEST OF POLYSTYRENE COATED CREVICE

Artificial crevices were built by two aluminum plates in parallel between a glass spacer. The crevices were oriented vertically and their openings were put to contact with the surface of underneath electrolyte solution (e.g. 3.5 wt % NaCl). This geometry was chosen so that the electrolyte flows into the crevice by capillary force and resultant corrosion could be studied. Figure 1 shows the results for a week exposure of (b) uncoated AA and (c) polystyrene coated AA with the solution of 3.5 wt. % NaCl using capillary corrosion geometry. Figure 1a shows the polystyrene coated AA fully immersed in the 3.5 wt % NaCl after 1 week. The picture of the inside of the polystyrene coated crevice (b) shows a less amount of corrosion visually than the uncoated crevice (c). However, comparing the fully immersed polystyrene coated sample to the coated crevice, it appeared that some protection was afforded to the crevice while the fully immersed and coated AA corroded at a similar. The results implied the admicellar polymerizing thin film has reduced and delayed the corrosion inside of the crevice and improved corrosion protection.

AFM CHARACTERIZATION

In an attempt to monitor corrosion on the coated aluminum samples, AFM was used to evaluate surface roughness of the aluminum samples. The surface roughness of the aluminum alloy 7075-T6 in various electrolyte solutions was first analyzed. For the first hour immersion as shown in Figure 2, the mean surface roughness varied dramatically. The irregularity observed in the roughness was because pitting corrosion of aluminum alloy occurs in solutions containing Cl^-. It is believed here that initially the aluminum oxide surface is attacked by Cl^-, creating pits. As the pits grow, the surface becomes very rough with many jagged peaks. As corrosion progresses

further, the jagged peaks, which are Al_2O_3 deposits, are dissolved by the electrolyte while the bottom of the pits is corroded at a slower rate because of diffusion limitations. Therefore, the surface roughness decreases as well. As corrosion continues, the surface will form new pits and holes at lower surface levels. These pits and holes will expand and smaller new peaks will appear. Farrington reported the same behavior on AA 2024-T3 explaining the fluctuation of surface roughness was due to two effects: (1) pitting dissolution of the aluminum surface and (2) redeposition of dissolved aluminum products on the aluminum surface (formation of peaks) [6]. Because of the irregularity in roughness data caused by a random pitting process, AFM measurements here cannot determine the degree of corrosion only whether corrosion has occurred.

After understanding the roughness from corroded 7075 AA plates, AFM was used to determine if the surfaces of polystyrene coated plates immersed in 3.5 wt % NaCl solution were corroded. Figure 3 shows AFM images (100 x 100 micron) of coated and uncoated AA before and after corrosion with the roughness values. The plates were corroded while in an artificial crevice geometry. As expected, the uncoated plates experienced corrosion after 6 hours in NaCl solution as evident by the increased roughness. However, increased roughness was also measured for the polystyrene coated aluminum. It is unclear to what degree of corrosion was present under the polystyrene film, but it is believed that some corrosion occurred in the polystyrene coated crevice after 6 hours.

DC POLARIZATION

Uncoated and coated samples were tested at many different locations on the plates using polarization. Polarization curves showed in Figure 4 were the common curves for admicellar polymerization coating on the flat plate. The corrosion rates (CRs) were slightly decreased on

the coated plate with a small shift in potential. However, the potential shift could only confirm the present of the film, but did not suggest significant protection by a barrier mechanism.

ELECTROCHEMICAL IMPEDANCE

Electrochemical impedance spectroscopy (EIS) results showed a variation of overall impedance at different locations on the plate. The impedance of both uncoated and coated aluminum alloys varied from 10^3 Ohm.cm^2 to 10^6 Ohm.cm^2 in the first 5 hours immersed into 3.5 wt % NaCl (Figure 5). EIS results of the uncoated aluminum alloys implied that the AAs used were heterogeneous. Both Frankel and Farrington [6, 7] also showed the heterogeneity of aluminum alloys from AFM study. The variations of the coated AAs suggested the film could not serve as a barrier protection on the flat plate.

DISCUSSION

The admicellar polystyrene appears to have virtually no barrier properties to corrosion based on electrochemical impedance and polarization tests. AFM studies confirmed the presence of some corrosion on the polystyrene coated plates. The interesting phenomena is that in a crevice geometry, polystyrene appears to reduce the amount of corrosion compared to bare AA 7075 samples and fully immersed AA 7075 coated with polystyrene. In the small spaces within the crevice geometry it appears that the hydrophobic nature of the polystyrene film reduces the water uptake to some degree. As a result, the corrosion is delayed.

CONCLUSIONS

Application of polystyrene films to aluminum alloys 7075-T6 using admicellar polymerization technique showed some improvements in corrosion protection inside crevice. Results from AFM surface characterization showed some modifications on the surface of the

aluminum alloys after coating treatments; yet, more images need to be scan to establish the statistical quantitative analysis. The results for coated AA plates from voltammetry and impedance experiments confirmed the present of the film, but did not indicate significant protection by a barrier mechanism. However, admicellar coated crevice with polystyrene has showed promise of a delay for water up-take and improved corrosion protection.

ACKNOWLEDGEMENTS

This project is funded by U.S. Air Force DEPSCOR Grant # F49620-00-1-0241 and Oklahoma State Regents of High Education. Also, special thanks go to Don Neiser at Tinker Air Force Base, Harry Barraza and Wei-Li Yuan for AFM instructions.

REFERENCES

1. J. Wu, J.H. Harwell, E.A. O'Rear, AiChE Journal (1988).
2. J. Wu, Ph.D. Dissertation, University of Oklahoma, 1987.
3. W. Yuan, Ph.D. Dissertation, University of Oklahoma, 2001.
4. K. Shah, Y. Zhu, G. Akundy, J. Iroh, O. Popoola, Key Eng. Mater. 197 (2001): p. 111-120.
5. K.S. Lewis, J. Yuan, R.G. Kelly, Journal of Chromatography A, 850 (1999): p. 375-80.
6. P. Schmutz, G.S. Frankel, Journal of Electrochemical Society 145, 7 (1998): p.2295-2306.
7. G.C. Farrington, et al., Journal of Electrochemical Society 143, 8 (1996): p. 2471-81.

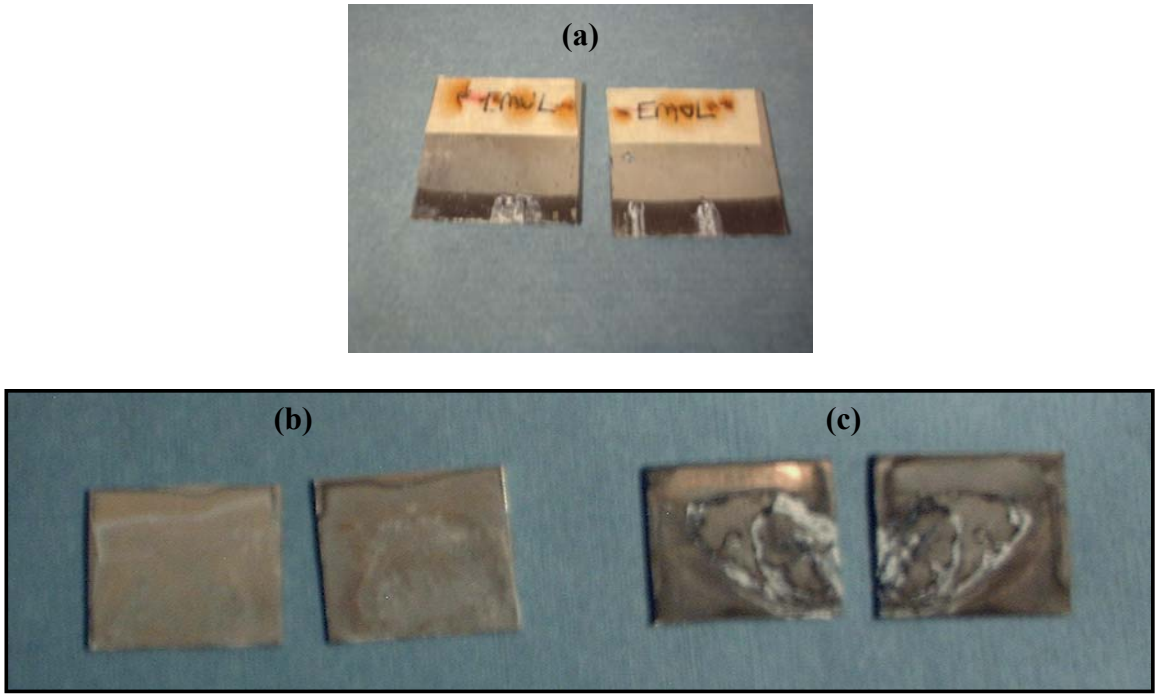

FIGURE 1: (a) Outside coated crevice; (b) Inside polystyrene coated crevice; (c) Inside uncoated crevice.

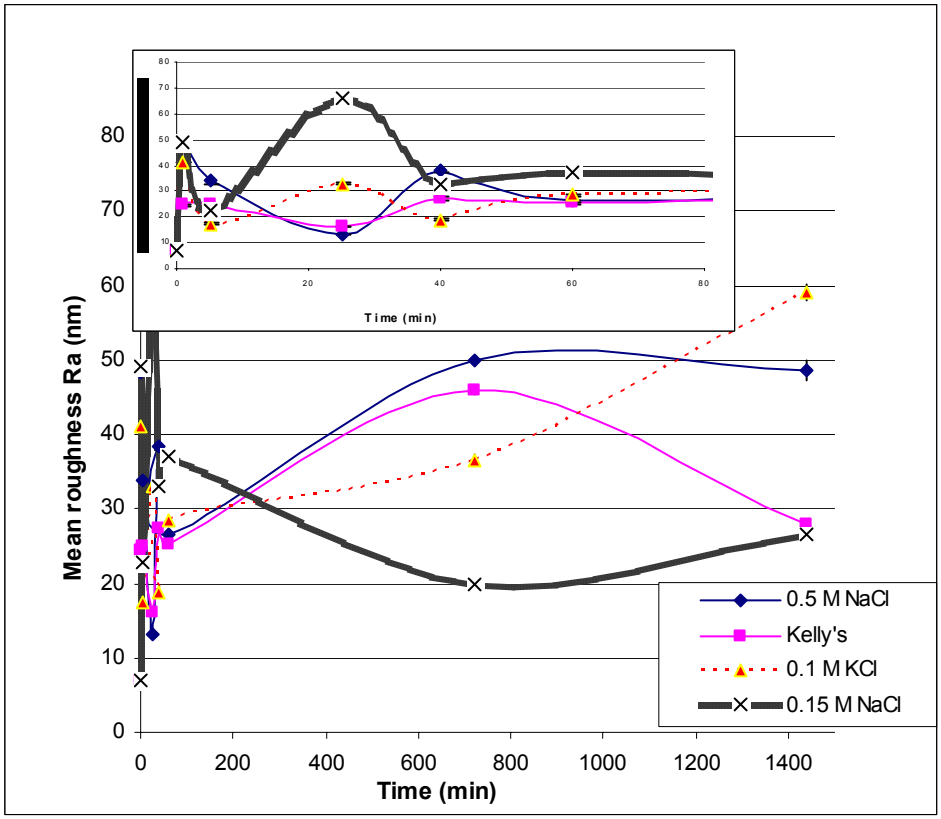

FIGURE 2: Average surface roughness, Ra versus time.

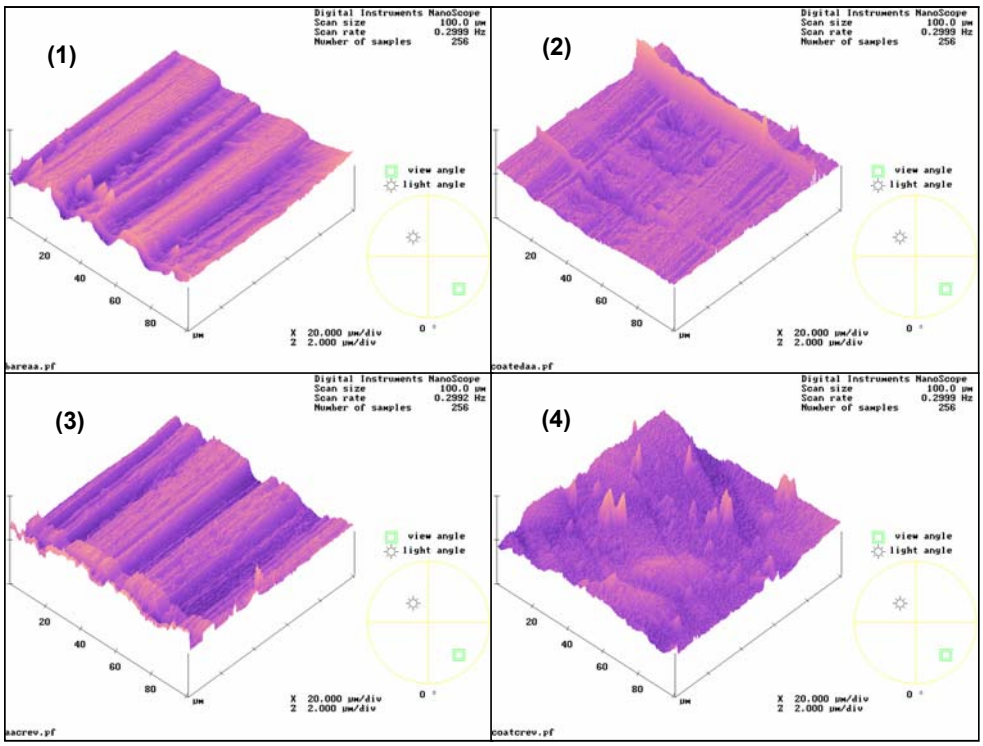

FIGURE 3: AFM images at different conditions (1): Bare AA (*Ra = 172 nm)* (2): Coated AA (*Ra = 140 nm)* (3): Corroded bare AA in crevice (*Ra = 184 nm)* (4): Corroded coated AA in crevice (*Ra = 156 nm)*

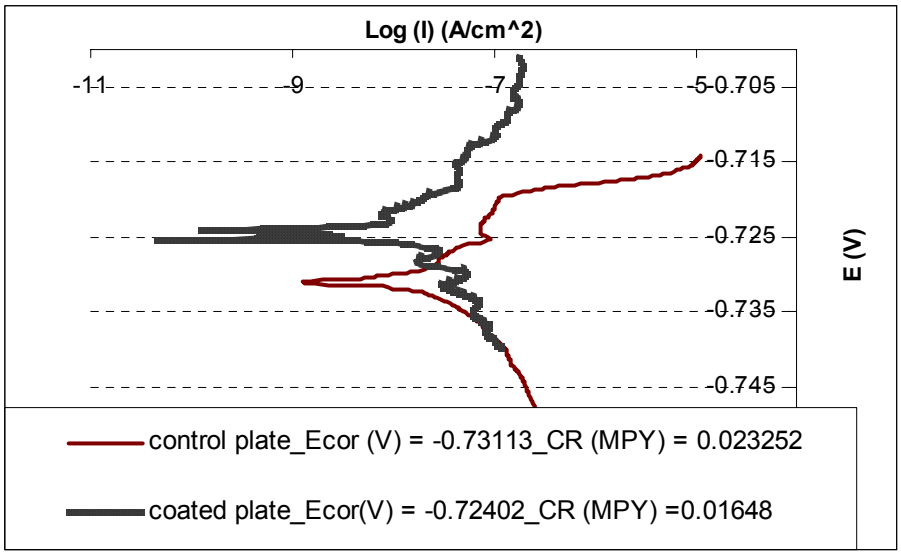

FIGURE 4: Typical polarization curves of uncoated and coated AA 7075-T6 using admicellar polymerization.

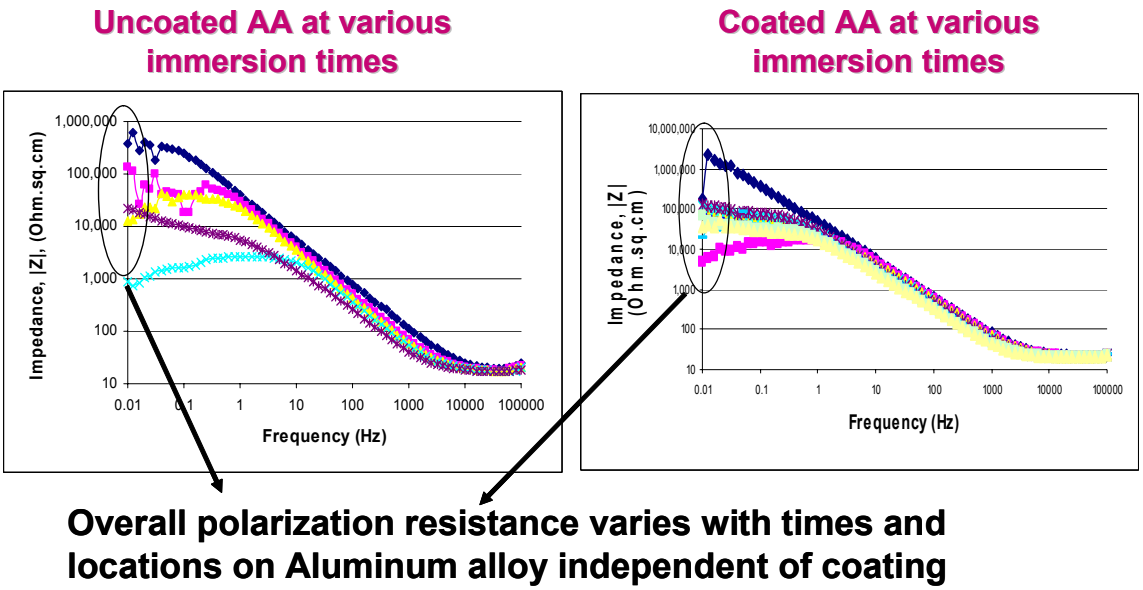

FIGURE 5: Variations of overall impedance with times an locations.

DEVELOPMENT OF AN ADMICELLAR POLYMERIZATION PROCESS FOR CREATING HYDROPHOBIC COATINGS ON ALUMINUM ALLOYS AND CREVICES

Olga M. Matarredona, Edgar A. O'Rear and Melissa M. Rieger

School of Chemical Engineering and Materials Science
University of Oklahoma
Norman OK 73019

ABSTRACT

Corrosion of aluminum alloys is a critical issue on many of the United States Air Force's older aircraft. Particularly, problematic areas on these older aircraft occur around the faying surfaces and the crevices between aluminum and steel layers. Years of paint cleaning, pieces replacement and repaint procedures during the maintenance and reconditioning lead to the removal of the original corrosion protection applied to the interfaces of the aluminum alloys and ultimately sever corrosion problems. Thus, it would be beneficial to have a coating that eliminates water uptake in the crevice locations and could be applied directly to the undamaged fastener joint without removal of the fastener itself. Admicellar polymerization can be used to deposit thin films to small spaces such as the crevices on aircraft. In the present study, the admicellar polymerization process has been adapted to deposit polystyrene onto aluminum alloy surfaces as the hydrophobic polymer. Flat and crevice-like models made of aluminum AA7075 have been used to simulate the crevices formed on aircraft. Characterization of the thin polystyrene film was performed using Scanning Electron Microscopy (SEM); Fourier Transfer Infrared Spectroscopy (FTIR) and Dynamic and Static contact angle measurements and corrosion tests. Preliminary results showed that the admicellar polymerization process provided a hydrophobic coating on aluminum flat plates and crevices. Water uptake into polystyrene coated crevices was significantly lower than in bare aluminum crevices. Corrosion inhibition was partially achieved.

INTRODUCTION

Until recently, most of the work has focused on corrosion on the outer skin of the aircraft. There are a wide variety of protective surface treatments available. These treatments are mainly based on the application of primers, topcoats and conversion coatings. Unfortunately, very little work has been done on the inhibition of corrosion in aluminum crevices and lap joints. The

original protection to the interfaces between steel fasteners, the aluminum wing skin and lap joints was afforded by the application of cadmium plating and/or chromate-based primers. However, paint removal and repainting procedures, applied year after year, cause the removal of these corrosion prevention agents that once covered fastener joints and other critical interfaces susceptible to corrosion attack. The easiest way to avoid corrosion is to create a barrier that blocks the contact between the metal surface and the water. This barrier can be applied in the form of a coating even before the damage has been caused, in order to prevent water uptake into the crevice-like locations. The hypothesis here is that a modification of the hydrophilic nature of the aluminum surface, by forming a thin hydrophobic polymer film inside the crevice, should stop the capillary forces that pull the water up into the gaps. This change in behavior was shown in modified alumina powder by Wu et al. in 1988[1]. This modification of the substrate surface can be achieved using a process called admicellar polymerization[1-13]. This process presents many advantages with respect to other conventional corrosion prevention techniques, such as the small amounts of chemicals that are needed, the water-base reaction solution, the variety of substrates and geometries it can be applied on, and the number monomers that can be polymerized by admicellar polymerization.

ADMICELLAR POLYMERIZATION

Admicellar polymerization is based on the formation of an ultrathin polymeric film inside a surfactant bilayer called an admicelle, which is adsorbed onto an inorganic surface by electrochemical forces. This phenomenon has been widely investigated on many types of substrates[1-13]. The process can be chemically and thermally activated with either water-soluble or virtually water-insoluble initiators. There are three basic steps to admicellar polymerization: (i) In the admicelle formation a bilayer of surfactant molecules is formed on the solid surface, (ii) at

equilibrium, the monomer in aqueous solution diffuses into the hydrophobic interior of the admicelle and (iii) in the last step free-radical initiators start the polymerization. After the polymerization is completed, the outer layer of the surfactant admicelle can be removed by washing, to leave the polymer film exposed. The schematic diagram for the admicellar process is shown in Figure 1.

The overall goal of this work is to establish an admicellar polymerization process for aluminum alloy substrates that will inhibit corrosion of the aluminum by preventing water uptake into crevices of aluminum-based aircraft. The admicellar polymerization process was adapted to deposit polystyrene onto aluminum alloy surfaces to act as a hydrophobic polymer film. The process uses sodium dodecylsulfate (SDS) to form the admicelles. The polymerization was thermally initiated with the virtually water-insoluble initiator 2,2'-azobisisobutyronitrile (AIBN). Flat and crevice-like models made of AA7075 were used to simulate the crevices formed on an aircraft. The work presented is geared towards understanding how process conditions such as pH, temperature and concentration affect the thin film properties, the hydrophobic behavior of the crevices and ultimately the corrosion inhibition inside the aluminum crevices. A fundamental investigation of the polymer, metal and aqueous interfaces has also been performed. Scanning electron microscopy has been used to qualify the film coverage and film uniformity of the thin polystyrene film. Dynamic and static contact angle measurements have been performed to investigate the affinity of polystyrene coated aluminum for water. Corrosion behavior of both untreated and coated aluminum samples was studied by visual inspection before and after exposure to different corrosion baths.

EXPERIMENTAL SECTION

MATERIALS

Aluminum alloy AA7075 plates were cut from commercial sheets provided by KAISER. Sodium dodecylsulfate (98% pure), styrene monomer (99% pure) and the initiator, 2,2'-azobisisobutyronitrile (AIBN), were provided by Aldrich Chemical Company, Inc.

PROCEDURE

The admicellar polymerization process was adapted from previous work[1-13] to be applied on AA7075 aluminum alloy (i) 1x1 inch, 1 mm thick flat plates and (ii) 1 x1 inch depth crevice-like models.

Surface Preparation. The samples were first brushed with commercial soap and water, followed by rinsing with Tetrahydrofurane (99.9% pure) to remove the paint. A Chromerge® solution was used as an acid wash to remove previous organic protective coating on the surface. Finally, the plates were rinsed with deionized water.

Admicellar polymerization process. The concentration of SDS was fixed to 6000 μM. Styrene was filtered with alumina powder for chromatography to remove the inhibitor. SDS/Styrene concentration ratios and initiator/Styrene concentration ratios were varied. Monomer and initiator were dissolved in ethanol first. The effect of the pH on the process was also studied. The pH was adjusted with concentrated H_2SO_4. Adsorption time for the SDS was fixed to 4 hours. The temperature for the polymerization was fixed to 80 °C. One and two hour reactions were performed. Flat plates were placed in clean sealed plastic vials and 20 ml solution volumes were added. After the adsorption, the vials were immersed in a preheated water bath at 80°C. After the polymerization, the reaction was quenched by immersion of the vials in iced-

water. The plates were then pulled out and rinsed with deionized water. After this, samples were placed in the oven overnight.

Contact Angle Measurements. Advancing contact angles were measured with a Cahn DCA-322 dynamic contact angle analyzer, which used the Whilhemy Method for its calculations. Static contact angles were measured by placing a drop of water on modified aluminum and on bare aluminum for comparison. A digital camera was employed for acquisition of images of the drops shape. The contact angle was determined with image analysis, by determining the angle formed between the line tangent to the surface of the drop at the water-air-metal interface point and the aluminum surface.

Scanning Electron Microscopy (SEM). Scanning electron microscopy was used to verify the presence of the polymeric film and to acquire images of the polymer distribution.

FTIR Analysis. Spectra of coated flat plates and coated crevice-like models were obtained by Specular Reflectance FTIR on a Nicolet Nexus 670 FTIR spectrometer.

Corrosion testing. Three different corrosion baths were used to test the hydrophobic behavior of the coated and bare aluminum artificial crevices: 0.1 M NaCl, 3.5 w% NaCl and a solution developed by Dr. Rob Kelly at the University of Virginia[14]. Corrosion times were also varied from 24 h, 48 h to 168 h.

RESULTS AND DISCUSSION

CONTACT ANGLES

The adjustment of the experimental conditions led to the modification of the nature of the substrates from hydrophilic to highly hydrophobic. Before the polymer was deposited onto the surface, the average advancing contact angle of the samples was 40°-60°. Admicellar polymerized samples performed advancing contact angles that reached more than 100° in some

cases. Additionally, when very hydrophobic modified substrates were rinsed with water, water drops tend to bead up. This phenomenon is known as the “non-wettability effect”. However, it was observed that the history of the sample played a determining role in the final dynamic contact angles obtained. Roughness increased the advancing contact angles on hydrophobic surfaces whereas in rough hydrophilic samples the advancing contact angles were decreased. Table 1 shows the average advancing contact angles obtained on flat plates polymerized at pH = 6 after 2 hours reaction process. Figure 2 depicts the variation of the advancing contact angle measurements with the concentration of initiator at fixed process conditions. It seems that the lowest concentration of AIBN provides a more hydrophobic substrate, probably due to a better coverage produced by longer polymer entangled chains along the surface. Figure 3 corresponds to water drops seating on both bare and polystyrene coated aluminum. In Figure 1a the coated aluminum surface exhibits certain hydrophobicity observable from the 88º static contact angle obtained. On the other hand, Figure 1b show the hydrophilic nature of bare aluminum with a 44.5º static contact angle.

SEM IMAGES

Scanning electron microscopy confirmed the presence of a polystyrene layer on the aluminum coated flat plates, as shown in Figure 4. However, it was unclear whether complete coverage was achieved because of the presence of holes on the surface. The nature of these holes could not be determined although they are believed to be inherent to the substrate.

FTIR ANALYSIS

FTIR spectra were obtained from both flat plates and the interior of crevice-like models. Characteristic peaks for polystyrene started to show at 3025 cm^{-1} at high concentrations of styrene. This confirmed the presence of the polymeric film on the surface.

CORROSION TESTING

Three different corrosion baths were used to test the affinity for water of the crevices and ultimately the corrosion inhibition inside the aluminum artificial crevices: 0.1 M NaCl, 3.5 w% NaCl and a solution developed by Dr. R. Kelly at the University of Virginia[14]. Corrosion times were also varied from 24 h, 48 h to 168 h. Artificial crevices were built from modified aluminum flat plates held together with a gap of approximately 0.15 mm width and 1 inch length. The corrosive solution was drawn into the artificial crevices by capillary rise to simulate the crevices actual conditions in a humid environment. This experiment was also run on bare aluminum crevices as the control samples. The samples were placed in sealed glass vials. After the corrosion testing period had elapsed the models were opened up for observation. Preliminary results indicated that corrosion inhibition in artificial crevices was partially achieved, although water uptake was not completely avoided. In the case of long exposures, such as one week, the protective characteristics of the polystyrene were lost, probably by swelling of the polymer or by possible edge effects. However, such was not the case for shorter exposure times. After 4 hours in 3.5% NaCl, non-treated aluminum crevices appeared fully wetted and the pH decreased to 4, whereas polymer coated crevices only showed a small portion of wet area close to the edges, and the pH on the wetted edge was neutral indicating no presence of corrosion by-products. A summary of the results obtained is shown in Figures 5 and 6.

CONCLUSIONS

Polystyrene thin films were deposited onto aluminum AA 7075 flat substrates using the admicellar polymerization process. Modified aluminum alloy specimens exhibited hydrophobic behavior after admicellar polymerization, confirmed from the high advancing contact angles obtained. At short exposure times, water uptake into polystyrene coated crevices was significantly lower than in bare aluminum crevices. Once the water penetration had occurred, corrosion inhibition on polystyrene coated samples was partially achieved. Modified samples showed a better response to the corrosion attack. However, at very long exposures to the corrosive environment, the polystyrene coating did not provide adequate corrosion protection.

AKNOLEDGEMENTS

This project is funded by the United States Air Force DEPSCOR Grant # F49620-00-1-0241 and the Oklahoma State Regents of Higher Education. Special thanks are given to Harry J. Barraza, Kha Mach, Steven Merchant and Orphius Islam Mohammad at the University of Oklahoma for help with experimental procedures dealing with corrosion and contact angle measurements. Also, appreciation is given to Don Neiser, Tinker Air Force Base for his contributions in defining the critical corrosion problems facing the U.S. Air Force.

REFERENCES

1. J. Wu; J.H. Harwell; E.A. O'Rear. *Langmuir*, **3**(4), 531-537 (1987).
2. J. Wu; J.H. Harwell; E.A. O'Rear. *J. Phys.Chem.,* **91**(3), 623-633 (1988).
3. J. Wu.; J.H. Harwell; E.A. O'Rear. *AICHE Journal,* **34**(9), 1511-1518 (1988).
4. J.H. O'Haver, J.H. Harwell; E.A. O'Rear; L.J. Snodgrass; W.H. Waddell. *Langmuir,* **10**, 2588-2593 (1994).
5. H. Chen. Masters Thesis, University of Oklahoma (1992).
6. C. Lai, J.H. Harwell; E.A. O'Rear; S. Komatsuzaki; J. Arai; T. Nakakawaji; Y. Ito. *Langmuir*, **11**, 905-911 (1995).
7. W. H. Waddell; J.H. O'Haver; L.R. Evans; J.H. Harwell. *J. Appl. Polym. Sci.*, **55**(12), (1995).
8. V. Thammathadanukul, J.H. O'Haver; J.H. Harwell; N.N. Osuwan; W.H. Waddell. *J. Appl. Polym. Sci.*, **59**(9), 1427-1435 (1996).
9. J.H. O'Haver, J.H. Harwell; L.R. Evans; W.H. Waddell. *J. Appl. Polym. Sci.*, **59**(11), 1741-1750 (1996).
10. B.P. Grady; E.A. O'Rear; L.S. Penn; A. Pedicini. *Polym. Comp.* **19**(5), 579-587 (1998).
11. G. Cho; D.T. Glatzhofer; B.M. Fung;, W.-L. Yuan; E.A. O'Rear. *Langmuir,* **16**, 4424-4429 (2000).
12. W.-L. Yuan;, E.A. O'Rear; G. Cho; G. P. Funkhouser; D. T. Glatzhofer. *Thin Solid Films*, 385(1,2), 96-108 (2001).
13. H.J. Barraza; M.J. Hwa; K. Blakley; E.A. O'Rear; B.P. Grady. *Langmuir,* **17**(17), 5288-5296 (2001).
14. K.S. Lewis; R.G. Kelly. *J.Chromat.* **850**, 375-380 (1999).

TABLE 1. Advancing contact angles of aluminum 7075 flat plates polymerized at pH = 6 after 2 hour reaction process. SDS concentration is 6000μM. Styrene/SDS concentration ratio is 5:1, AIBN/Styrene concentration ratio is 1:5 (95% confidence interval).

Sample #	Advancing Contact Angle °
1	92.9 ± 6.35
2	110.4 ± 12.56
3	109.1 ± 1.42
4	110.8 ± 9.90
5	94.9 ± 8.68
6	100.3 ± 2.18
7	105.0 ± 2.86
8	99.2 ± 0.98

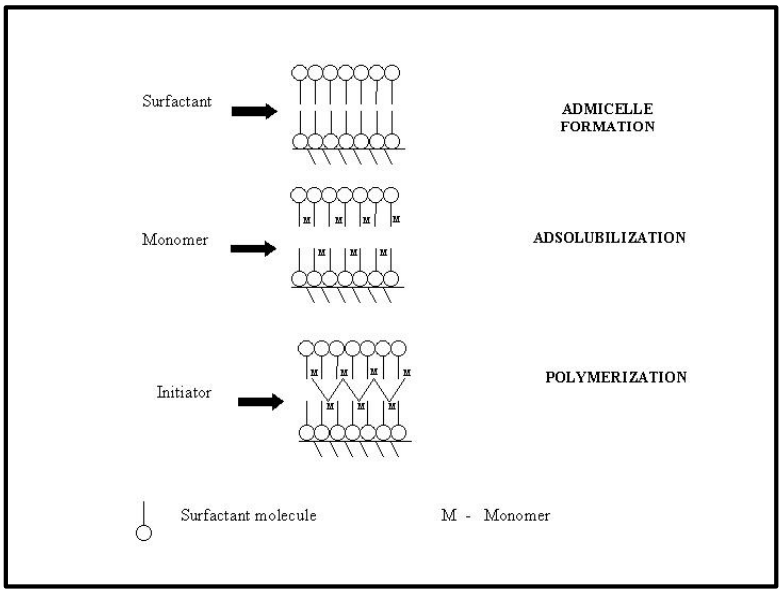

FIGURE 1. Schematic of the admicellar polymerization process.

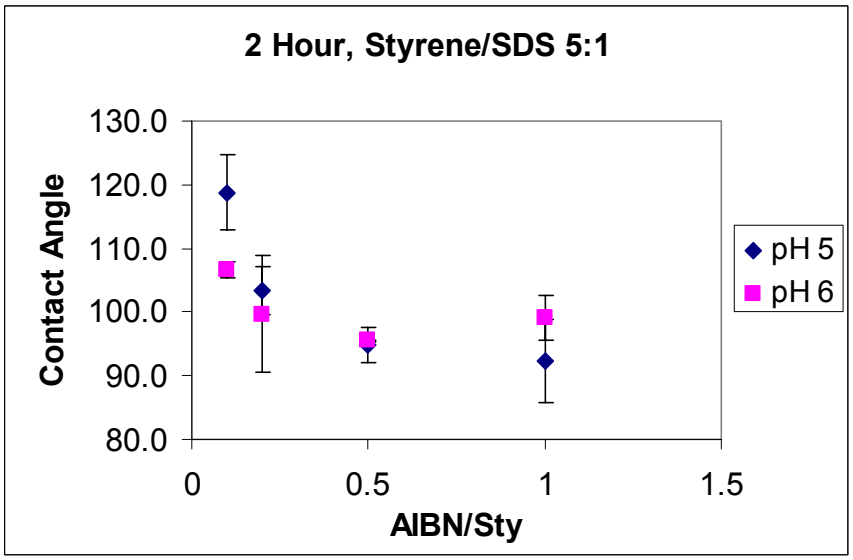

FIGURE 2. Effect of the concentration of AIBN on the average advancing contact angles obtained after polymerization on aluminum AA7075 flat plates for 2 hour at pH 5 and pH6. SDS concentration is 6000µM. Styrene/SDS ratio is 5:1 (95% confidence interval).

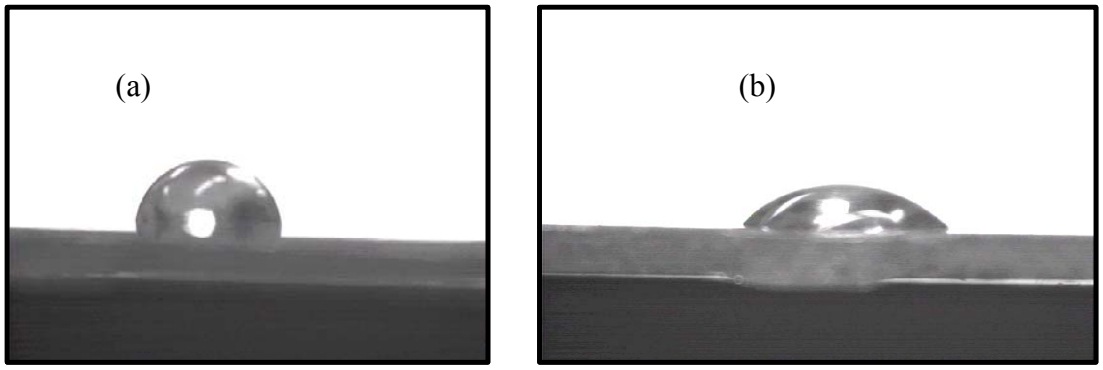

FIGURE 3. Static contact angles of water-drops in contact with aluminum 7075; (a) water drop on polystyrene modified aluminum, static contact angle is 88º; (b) water drop on bare aluminum, static contact angle is 44.5º.

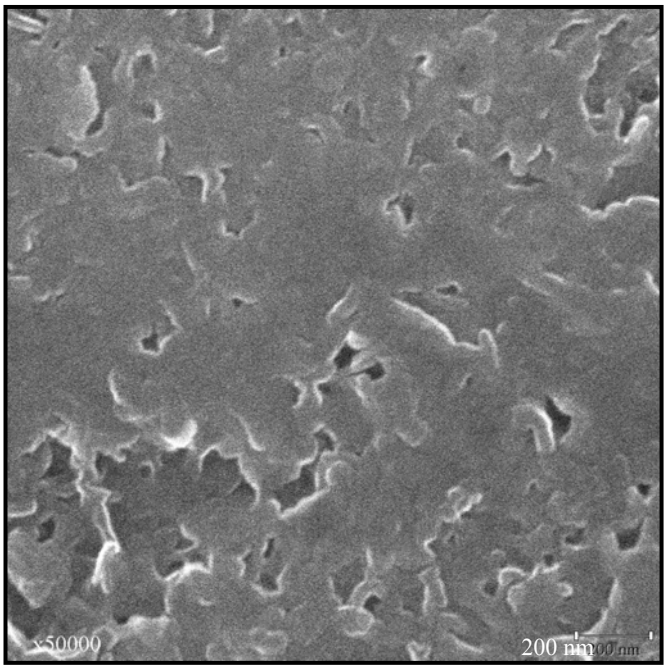

FIGURE 4. SEM image of polystyrene coated aluminum AA7075 flat plate (x50000).

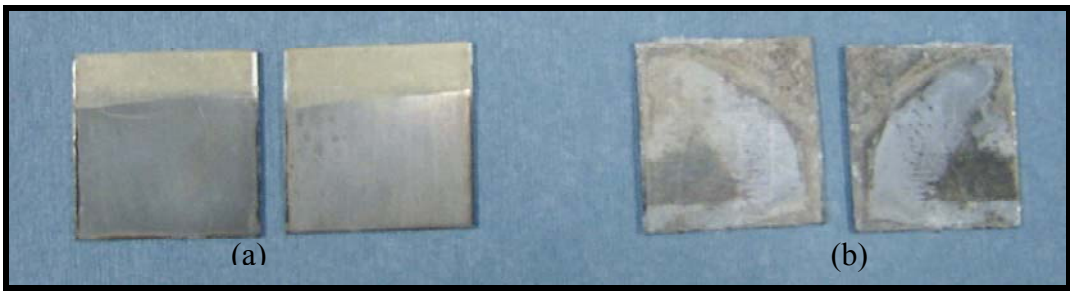

FIGURE 5. Aluminum AA7075 1x1 inch plates after 48h, 0.15 M NaCl corrosion test by capillary effects in the interior of the artificial crevice (a) Polystyrene coated, (b) Bare aluminum.

FIGURE 6. Aluminum AA7075 1x1 inch plates after 168h, 3.5 w% NaCl corrosion test by capillary effects in the interior of the artificial crevice, (a) Polystyrene coated, (b) Bare aluminum.

USE OF ELECTROCHEMICAL NOISE METHODS FOR IN SITU CORROSION MONITORING

Xianping Wang, Ryan Bennett, Kristopher Spenningsby & Gordon Bierwagen

Department of Polymers and Coatings,
North Dakota State University
Fargo, North Dakota 58105

ABSTRACT

Continued efforts were made to develop a practical corrosion sensor that could be used for in situ monitoring of corrosion. A novel method consisting of using embedded Pt wires or Pt/Au foils in coatings as electrodes and electrochemical noise methods of dada acquisition and analysis was investigated. This method utilizes an inversed ENM configuration, which uses the embedded noble metal as working electrodes, and the substrate (in this case Al 2024 T3) as reference electrode. In situ measurements were performed while the samples were under fast thermal and wet/dry cycling (Prohesion testing), both the electrochemical noise resistance calculated from time domain analysis and the spectral noise resistance from FFT and MEM showed a clear decreasing trend as the aging time increased, implying possible film degradation and onset of corrosion. Contrary to other electrochemical testing methods, such as EIS, this methods is capable of monitoring the change in the coating /metal system even in a fast changing environment without bringing any artificial damage to the system, therefore, is probably the best method for monitoring corrosion on field over long time period.

INTRODUCTION

Organic coatings are very effective in protecting aircrafts from corrosion attacks. However, current aircraft coatings tend to degrade and loss effective protection due to aging or wearing as service time increases, and therefore, require being stripped off and recoated before the substrate corrosion became severe. The consequent maintenance cost is tremendous. In situ corrosion sensor could be attached directly to the coating surface and detect the coating degradation and substrate corrosion quantitatively at the very early stage without the need for extraneous electrolyte. Therefore, they may provide an early warning of the danger of significant

structure degradation before it occurs. Consequently, it is applicable for condition-based maintenance of aircrafts, and other metal structures, which may significantly reduce the maintenance cost and promote safety. Due to the wide range of their potential applications, the developing of in situ corrosion sensors has been intensively studied in recent years. [1, 2, 3, 4, 5, 6, 7, 8]

However, these previous techniques are all based on Electrochemical Impedance Spectroscopy (EIS) methodologies, hence, require the applying of a perturbation signal (either a small potential or current signal) to the system being monitored, and measure the response. In our studies, we discovered that this perturbation signal may cause artificial damage to the coating system, (which leads to false alarm,) especially during long term monitoring. The main reason for that is, when the exposure condition is changing with time, as in the case of outdoor exposure, the open circuit potential usually is not a constant value, and the use of 2-electrode configuration instead of 3-electrode conventional setup even worsens the drifting. Consequently, during the EIS measurement, the actually applied voltage is a small AC voltage signal plus a non-steady DC voltage, which will distort the EIS spectra especially in the lower frequency region, and we also noticed that when the change was extremely fast, (e.g. in fast wet-dry cycle), the DC drift could even become 10 times larger than the applied AC signal during an EIS frequency sweeping, and cause severe artificial damage to the sample.

To alleviate these problems, Electrochemical Noise Measurements (ENM) was applied in our corrosion sensor studies. Electrochemical noise is random fluctuations of potential or current, typically of low frequency (<10 Hz) and low amplitude. It originates (at least in part) from certain type of corrosion processes, (particularly in the case of localized corrosion, i.e. the initiation of pits and mechanical effects resulting from cracking and erosion processes.) Therefore, electrochemical noise is often regarded as a random (stochastic) phenomenon related

to deterministic corrosion kinetics, and used to provide an indication of corrosion of the material.[9] Often being regarded as a complementary technique to EIS, ENM has also been used extensively to evaluate corrosion of metals and metal surfaces underneath organic coatings. [10,11] It is often considered as a non-intrusive technique since no external perturbation is applied to the test sample during the measurements. This feature makes ENM very promising for in situ monitoring of corrosion over long term period.

In our sensor studies, a novel *in situ* ENM technique derived from earlier work of S.J. Mabbutt and D.J. Mills[12] was proposed and tested. In this technique, two noble metal corrosion sensors were embedded into the coating (between the primer and topcoat,) and served as two working electrodes, the metal substrate underneath the coating film was connected as reference. In our preliminary studies, good agreements were found between this new configuration and the conventional ENM configuration in immersion condition for these aircraft coatings systems being tested. This technique has several advantages over the surface-attached sensor technique: improved sensor steadiness by protecting sensors surface from environment attack; improved isolation between sensors, good for measure ENM on small samples; better adhesion to underneath film; higher sensitivity to small change in coating impedance; shows potential application for monitoring the impedance change of each coating layer during different exposure conditions, may be useful for studying the corrosion/degradation mechanism as well as designing new accelerated testing protocols for faster ranking and better simulation of outdoor exposure.

EXPERIMENTAL

Bare aluminum Alloy 2024-T3 coupons with the size of 76.2×152.4×0.81 mm from Q-PANEL LAB PRODUCTS were used as the substrate. The bare panels were cleaned, degreased with methyl ethyl ketone, immediately followed by a surface pretreatment using phosphoric acid

then Alodine 1200s solution to form a dense oxide layer. After that, epoxy-polyamide primer (DEFT 02-Y-040, MIL-P-23377G Type I Class C) was spray applied. The film thickness of the primer was controlled within 15.2 ~ 22.9 μm. The primer was left for air dry for 20 hours, then a 200 mm Platinum wire (ϕ = 0.05 mm) was carefully attached to the primer surface with trace amount of super glue. One lead of the platinum wire was soldered to a copper electric wire, and the substrate was connected to a different electric wire through a rivet. Both junctions were carefully sealed with epoxy resin to ensure good insulation. After that, two layers of polyurethane topcoats (DEFT 03-GY-277, Navy MIL-C-85285B Type I) were air sprayed with equal thickness. The total thickness of the topcoat was controlled within 43.2 ~ 58.4 μm. The samples were left to cure in ambient condition for 1 month before testing.

ENM was performed through Gamry PC4/300TM electrochemical measurement system (Gamry Instruments, Inc. Willow Grove, PA). An application package called ESA400TM system (version 1.20) was used for both noise data acquisition and interpretation. Two identical samples with interconnected substrate were used as a pair for the ENM testing. (as shown in Figure 1.) The sampling frequency was 10 Hz. Both statistic analysis (noise resistance, R_n, calculated in time domain) and spectral analysis (Fast Fourier Transform (FFT) and Maximum Entropy Method (MEM)) were applied to interpret the data.

The feasibility of corrosion monitoring using this ENM technique was studied under two different non-immersion conditions, one is fast thermal/humidity cycling (or called Prohesion cycling test), the other is constant humidity and temperature control. Prohesion cycling test was performed using the Q-FOG Cyclic Corrosion Tester. The electrolyte solution for the fog was the dilute Harrison's solution (containing 0.35% $(NH_4)_2SO_4$, and 0.05% NaCl). Two steps were involved in the Prohesion exposure cycle: in step 1 (also called Fog Step), the samples were

sprayed with salt fog at 25 ^{o}C for 1 hour; and in step 2 (also called dry step), the samples were dried off at 35 ^{o}C for another 1 hour, then went back to step 1. In the constant humidity control, a series of saturated salt solutions (as shown in Table 1,) were used to achieve different relative humidity under room temperature.

RESULTS AND DISCUSSION

The potential and current fluctuations recorded directly during the Prohesion cycling at different exposure time were shown in Figure 2. The time for starting each data recording was 20 minutes after the Dry step started, so the external exposure condition should be theoretically the same when the data was collected at different exposure time. It is very interesting to notice that the magnitude of both the potential and current noise transient signals changed with exposure time; the magnitude of potential transient signals was below 0.015 V initially, but increased to around 0.025 V after 364 hours exposure, then it tended to stay relatively constant. The magnitude of the current transient signals followed a slightly different pattern, its original value was also very small, around 5.0×10^{-12} A, and it increased to about 2.5×10^{-11} A after 364 hours exposure, and it still kept increasing as exposure time increased; after 1075 hours exposure, the magnitude of current transients increased to around 4.0×10^{-10} A, and when the exposure time reached 2014 hours, the magnitude became about 1.0×10^{-9} A. The origin of these transient events is still unclear, but it is believed more likely caused by the fast evaporation of absorbed water in coating film from the previous Fog step, instead of localized pitting events. However, the change in magnitudes of the potential and current transient signals still clearly indicated that the coating film was gradually losing its electrical resistivity as the exposure time increased.

The time records of voltage and current fluctuations during two Prohesion cycles were given in Figure 3. This data was collected after 2100 hours exposure in Prohesion. Noise

resistance (R_n), Localized Index (LI), and exposure temperature (T) based on this data set were given in Figure 4. R_n was calculated as the standard deviation of potential signal divided by the standard deviation of current signal during the same time period. The time period for calculating each R_n point is 60 seconds. LI is calculated as the standard deviation of the current noise divided by the root mean square of current. The value of R_n increased with time during the Dry Step, as water being driven out of the coating film with increasing dry time; and R_n decreased by around 5 orders of magnitude after the Fog step started, as a result of water penetration into the coating film. LI has been used to distinguish localized corrosion and general corrosion, however, in our studies, the value of LI was often larger than it should be, which is probably due to the large variation in mean current.

ENM testing was also performed with controlled relative humidity under room temperature. Figure 5 and 6 showed the FFT and MEM results obtained from different relative humidity after 2100 and 2930 hours exposure in Prohesion, respectively. Both the FFT and MEM plots showed that the spectral noise resistance (R_{sn}) increased with decreasing relative humidity, implying less water trapped inside the coating film. This also indicated that atmospheric corrosion are more likely to occur or may become worse when the environmental humidity goes higher.

R_n from each relative humidity was also calculated after different exposure time, as given in Figure 7. The results showed that R_n decreased with increasing humidity, and at similar humidity, samples with longer exposure time had smaller value of R_n, implying possible film degradation and loss of protection. The difference in R_n between different humidity became less significant as the humidity became lower; this was probably because the instrument was reaching its limit.

Direct ENM measurement during Prohesion cycling after different exposure time was performed and the R_{sn} results from MEM were given in Figure 8. A clear decreasing trend in R_{sn} was observed as the exposure time in Prohesion increased, which implied that this *in situ* sensing technique can successfully monitor the degree of coating degradation even in a fast changing environment.

Further life time prediction based on earlier studies[13,14] was also performed. The decay constant, θ, as in Eqn. 1, has the dimension of time and could be used to estimate the corrosion rate and performance lifetime. The decay constant value of this sample was calculated from Figure 9, by plotting $\ln(R_{sn}(t)/R_{sn}^0)$ verses $(t-t_0)$, and the value of θ was the inverse of the slope of the exponential fit line. The calculated decay constant value for this coating system was 833 hours, and by defining the failure value $R_{sn}^{fail}=10^5$ Ohms, the predicted life time was around 59 weeks in Prohesion, which is very close to the previous study ($t_n^{fail}=61$ weeks) based on the same coating/substrate system.[15]

$$t_{sn}^{fail}=\theta\left[\ln\left(\frac{R_{sn}^0-R_{sn}^m}{R_{sn}^{fail}-R_{sn}^m}\right)\right]+t_0\approx\theta\left[\ln\left(\frac{R_{sn}^0}{R_{sn}^{fail}}\right)\right]+t \qquad (1)$$

CONCLUSIONS

The non-immersion exposure studies indicated that the proposed new ENM setup with embedded electrodes had the capability of recording noise data without leaving any negative effect to the sample in both ideal and non-ideal exposure conditions. The change in magnitudes of the potential and current transient signals clearly indicated that the coating film was gradually losing its electrical resistivity as the exposure time increased. The calculated R_n and R_{sn} showed clear decreasing trend as the environmental humidity increased or as the aging time increased,

implying change in film water content or possible film degradation and onset of substrate corrosion. The large drop in both R_n and R_{sn} with increasing environmental humidity indicated that atmospheric corrosion are more likely to occur or may become severer when the environmental humidity goes higher. The life time prediction calculated from data collected directly during Prohesion cycling showed good agreement with previous studies based on the same coating/substrate system. In summary, this new ENM technique with embedded electrode has very good feasibility to be applied on field to provide early warning of the onset of corrosion of aircraft materials in the same local environment; as well as to predict the life time of the actual coating system in the real exposure condition.

ACKNOWLEDGEMENTS

This work was supported by the Air Force Office of Scientific Research under Grant F 49620-99-1-0283, Lt. Col. Paul Trulove, Program Officer.

REFERENCES

1. T.C. Simpson, G.D. Davis, et al., J. Electrochem. Soc., 136, p.2761, 1989.
2. T.C. Simpson, H. Hampel, et al., Corrosion, 46, p.331, 1990.
3. T.C. Simpson, H. Hampel, et al., Progress in Organic Coatings, 20, p.199, 1992.
4. T.C. Simpson, in Proceedings of the 12th International corrosion Congress, Houston, TX, Sept. 1993, Vol. 1, p.157, NACE.
5. Amirudin, D. Thierry, British Corrosion Journal, 30, p.214, 1995
6. T.C. Simpson, P.J. Moran, et al., "Electrochemical Impedance Measurements for Evaluating and Predicting the Testing the Performance of Organic Coatings for Atmospheric Exposure",

in ASTM STP 1000, Corrosion Testing and Evaluation: Silver Anniversary Volume, ASTM, Philadelphia, 397, (1990).

7. G.D. Davis, C.M. Dacres, (DACCO Sci, Inc., USA) Electrochemical Sensors for Evaluating Corrosion and Adhesion on Painted Metal Structures, US Patent 5859537 A 12, Jan. 1999.
8. G.D. Davis, C.M. Dacres, et al., Material Performance, p.46, Feb. 2000.
9. D.A. Eden, Chap. 69, Uhlig's Corrosion handbook, 2nd Edition, R.Winston, Revie, 2000 John Wiley & Sons, Inc.
10. D.J. Mills, G.P. Bierwagen, et al., in Proceedings of the 12th International corrosion Congress, Houston, TX, Sept. 1993, Vol. 1, p.182-194, NACE.
11. Electrochemical Noise Measurement for Corrosion Applications, J.R. Kearns, J.R. Scully, et al., STP 1277, ASTM, West Conshohocken, PA (1996)
12. S.J. Mabbutt, D.J. Mills, British Corrosion Journal*, 33*, P158, 1998
13. Gordon Bierwagen, Junping Li, Lingyun He, and Dennis Tallman "Fundamentals of the Measurement of Corrosion Protection and the Prediction of Its Lifetime in Coatings," Chapter 14 in *Proceedings of the 2nd International Symposium on Service Life Prediction Methodology and Metrologies*, Monterey, CA, Nov. 14-17, 1999, ACS Symposium Series # 805, J. Martin and D Bauer, ed., ACS Books, Washing ton, DC (2001) 316-350
14. G. Bierwagen, J. Li, N. Davis, and D. Tallman, "Thickness Dependence of Electrochemical Properties of Organic Coatings" *Proceedings of 5th Nürnberg Congress – Creative Advances in Coatings Technology*, The Paint Research Association, Middlesex, UK, 1999.
15. J. Li. Ph.D. Disquisition, North Dakota State University, Fargo, ND (2001)

TABLE 1.
Relative humidity on saturated salt solutions

Type of Saturated Salt Solution	Relative Humidity at 25 ^{o}C
Pure water	100 %
KNO_3	92 %
KCl	84 %
NaCl	75 %
NH_4NO_3	62 %
$Ca(NO_3)_2$	51 %
$CaCl_2$	29 %

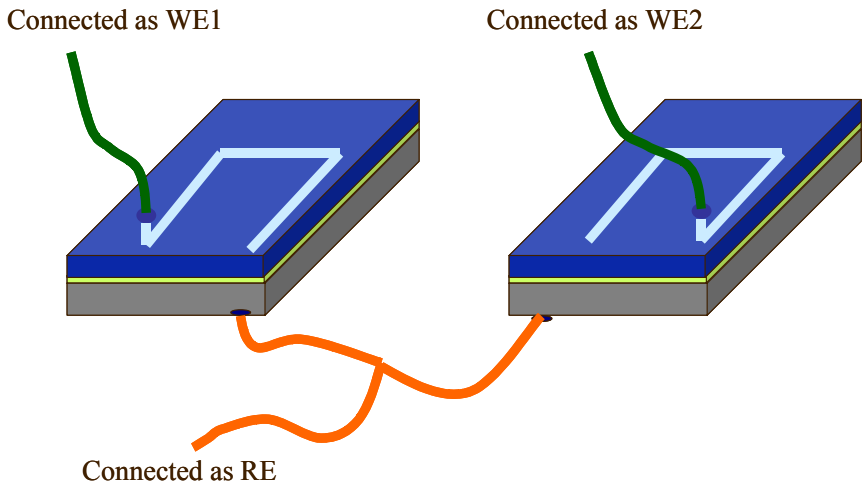

FIGURE 1. The Experimental Configuration Used in Our Design.

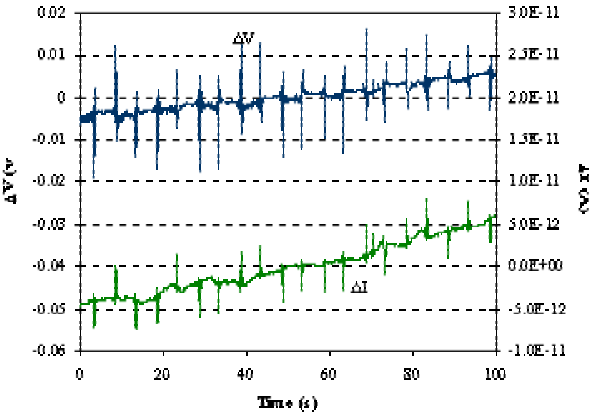

(a) after 14 Hours Exposure

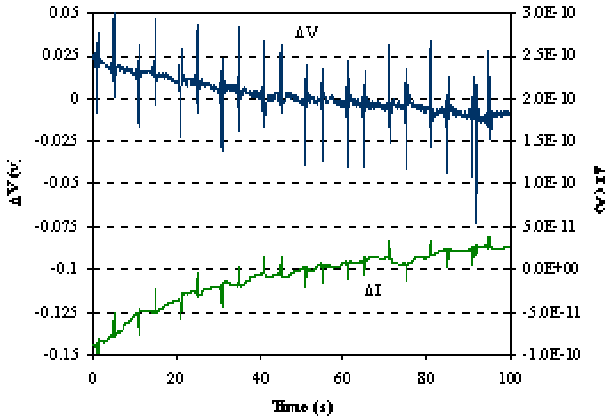

(b) after 364 Hours Exposure

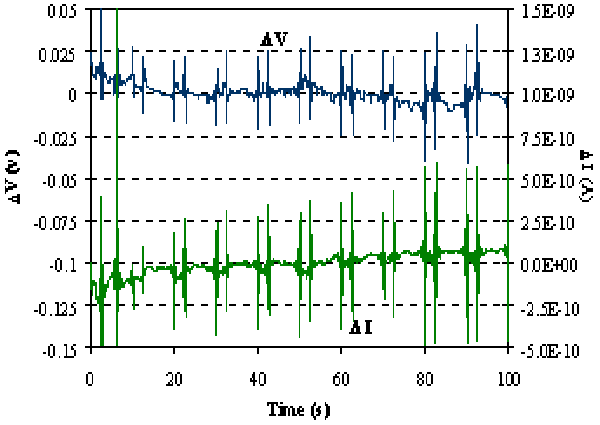

(c) after 1075 Hours Exposure

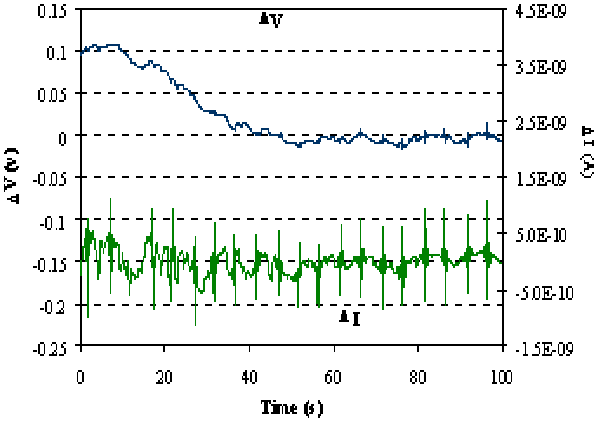

(d) after 2014 Hours Exposure

FIGURE 2. Time records of Voltage & Current Fluctuations at Dry Step 20 Minutes during Prohesion Cycling after different Exposure Time.

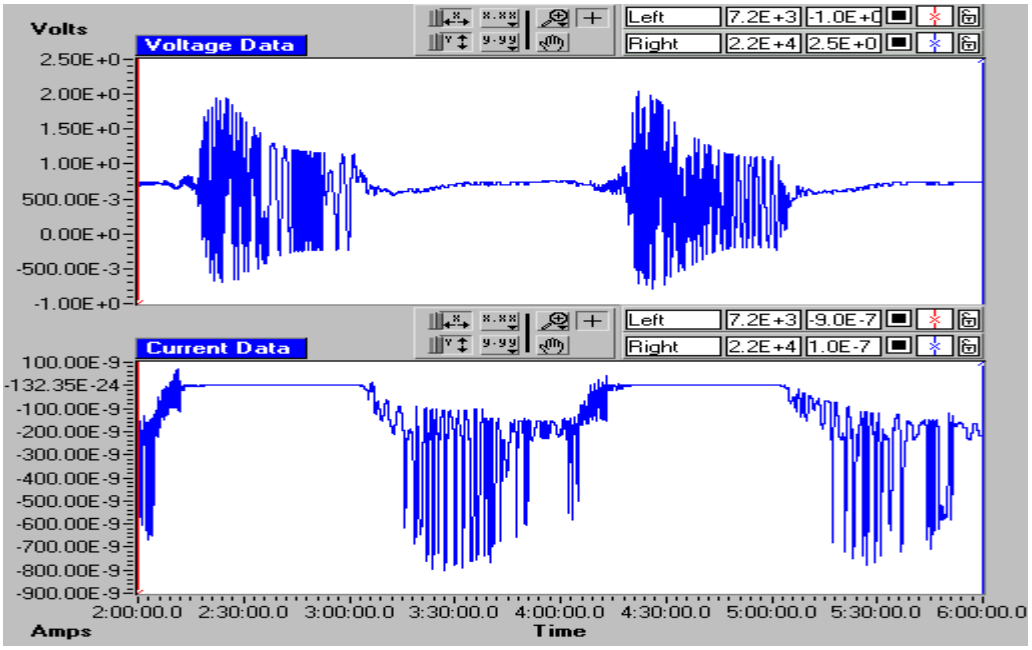

FIGURE 3. Time records of Voltage & Current Fluctuations during 2 Prohesion Cycles (after 2100 Hours Exposure in Prohesion).

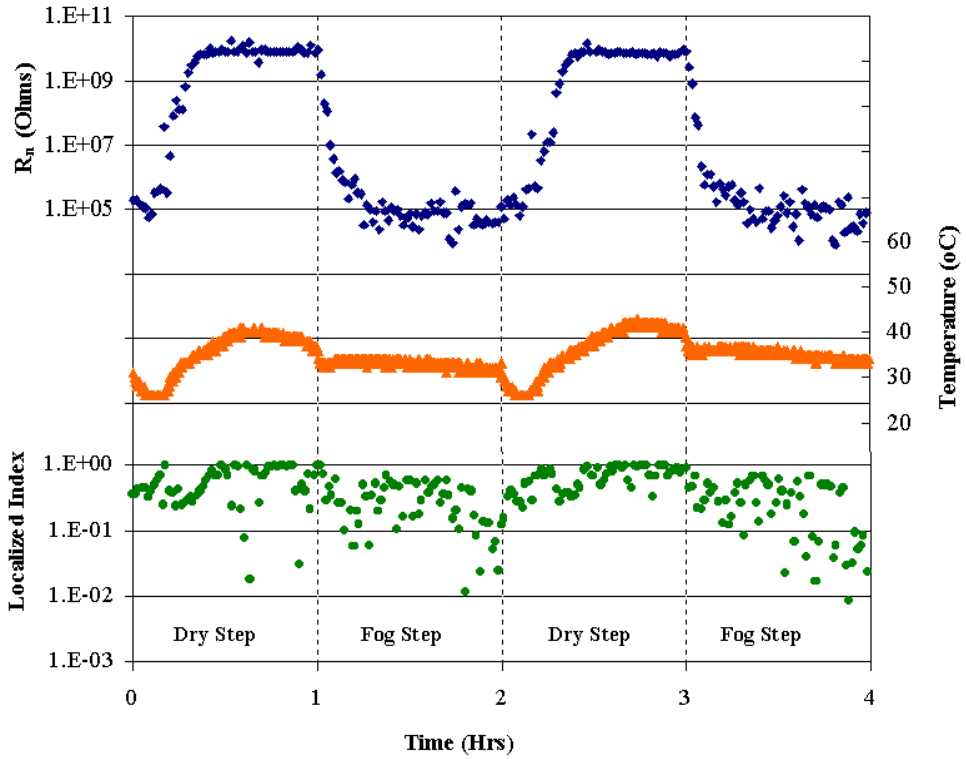

FIGURE 4. R_n, Temperature, and Localized Index vs. Time during 2 Prohesion cycles (after 2100 Hours Exposure in Prohesion).

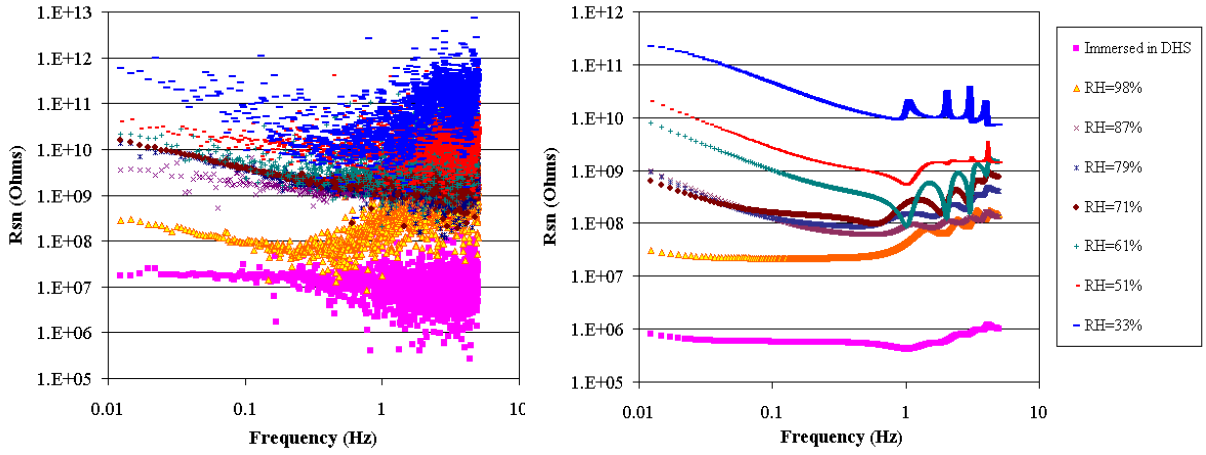

(a) FFT (b) MEM

FIGURE 5. R_{sn} Calculated from FFT and MEM as Function of Relative Humidity (after 2100 Hours Exposure in Prohesion).

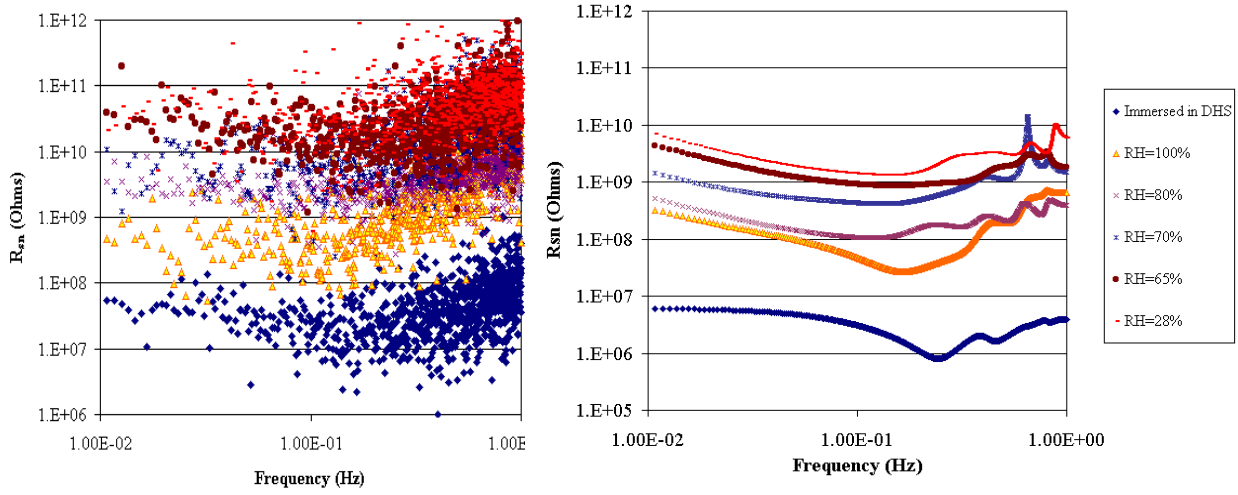

(a) FFT (b) MEM

FIGURE 6. R_{sn} Calculated from FFT and MEM as Function of Relative Humidity (after 2930 Hours Exposure in Prohesion).

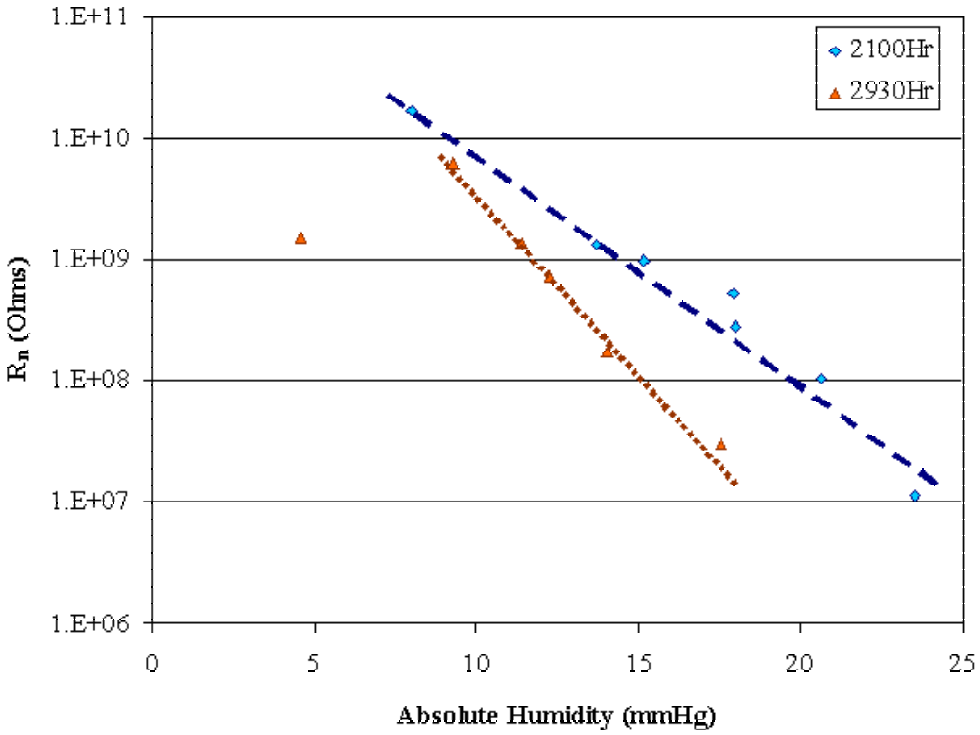

FIGURE 7. R_n vs. Absolute Humidity at Different Aging Time in Prohesion

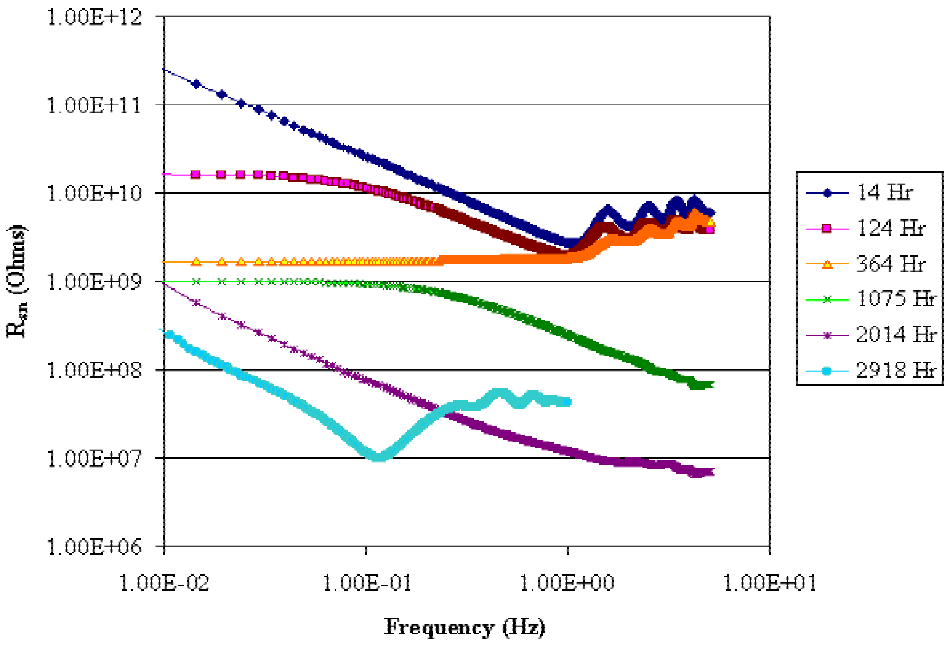

FIGURE 8. R_{sn} Measured directly during Prohesion Cycling at different Aging Time

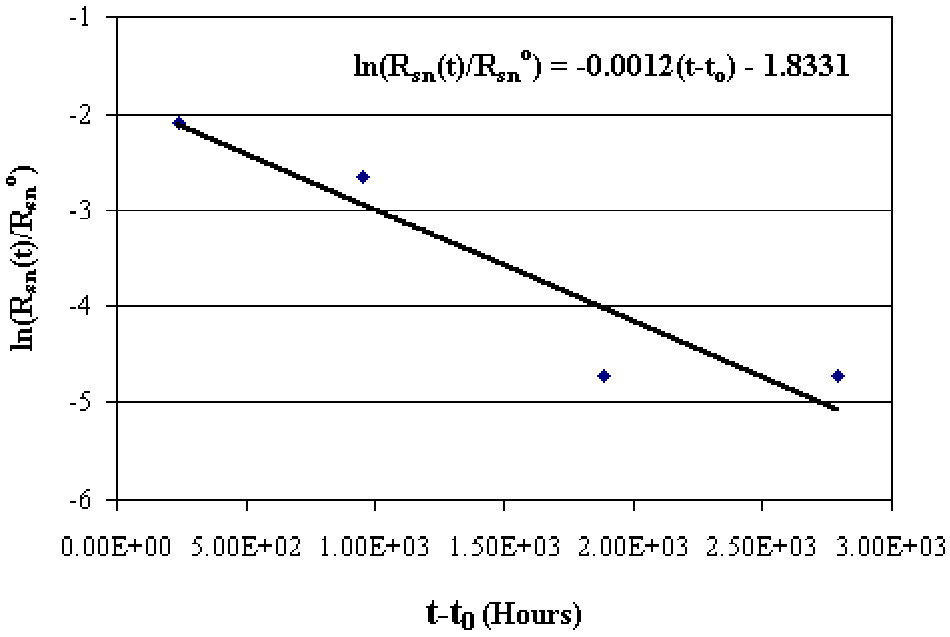

FIGURE 9. Calculation of Decay Constant for Life Time Prediction

THE STUDY OF POLYPYRROLE AS A CORROSION INHIBITOR OF ALUMINUM ALLOY 2024-T3

Victoria Johnston Gelling,[1,2] Jie He,[1] Dennis E. Tallman,[1] Gordon P. Bierwagen[2] and Gordon G. Wallace[3]

[1]Department of Chemistry, [2]Department of Polymers and Coatings
North Dakota State University
Fargo, ND 58105-5516
[3]Director, Intelligent Polymer Research Institute
University of Wollongong
Wollongong NSW 2522, Australia

ABSTRACT

Chromate surface treatments and chromate-containing epoxy primers are often used for the corrosion control of aluminum alloys. However, due to environmental concerns and adverse health effects surrounding such use of chromates, there is an intensive effort to find suitable replacements for chromate-based coatings. Electroactive conducting polymers (ECPs) continue to be of considerable interest as components of corrosion-resistant coating systems due to their conductivity and redox properties.

In this paper, the use of electrochemical techniques for the measurement of the corrosion inhibition provided to aluminum alloy 2024-T3 by ECP coatings will be discussed. The ECPs studied were poly(3-octyl pyrrole) (POP) doped with pTS^-/ClO_4^-, POP doped with pTS^-, POP doped with ClO_4^-, and poly(3-octadecyl pyrrole) (PODP) doped with pTS^-/ClO_4^-. The ECPs were applied as a thin (few micron) primer coating and, thus, were used in conjunction with a polyurethane topcoat. Electrochemical impedance spectroscopy (EIS) and the scanning vibrating electrode technique (SVET) were used to assess the corrosion behavior of these coating systems. While all of these ECP coatings appeared to provide some corrosion protection to AA 2024-T3, the best protection was provided by the ECPs containing pTS^- as a dopant.

INTRODUCTION

Pure aluminum forms a tightly adhering oxide layer that protects the underlying aluminum from rampant corrosion extremely well. Unfortunately, pure aluminum is also a very soft, malleable metal. In order for aluminum to be of any use as a structural metal, it must be alloyed with other metals. In aluminum alloy 2024-T3 (AA 2024-T3) aluminum has been

alloyed with copper (Cu, 4%), magnesium (Mg, 1.6%), manganese (Mn, 0.6%), silicon (Si, 0.5%), iron (Fe, 0.5%), zinc (Zn, 0.25%), titanium (Ti, 0.15%), chromium (Cr, 0.1%), and unspecified others (0.15%) as displayed in Table 1.[1]

TABLE 1
The chemical composition of AA 2024-T3

Cu	Mg	Si	Fe	Mn	Zn	Ti	Cr	Other	Al
3.8-4.9	1.2-1.8	0.5	0.5	0.3-0.9	0.25	0.15	0.1	0.15	Remainder

AA 2024-T3 has many desirable properties such as low density and high strength. However, AA 2024-T3 is susceptible localized corrosion problems such as pitting and intergranular corrosion.[2] The alloy also has a greater tendency to corrode than does pure aluminum. This susceptibility to localized corrosion is caused by the inherent nature of the copper-rich 2024-T3 aluminum alloy. This has created the need to understand the corrosion mechanisms that take place in aluminum alloys. An extensive amount of literature is available in the area of aluminum corrosion.[3-29]

Research is being conducted on the corrosion protection of copper-rich aluminum alloys. This is due to the necessity of replacing chromates, currently the most effective way of corrosion inhibition for aircraft aluminum.[30] However, with the knowledge that chromates pose an environmental and health threat, a replacement must be found. Electroactive conducting polymers (ECPs) have been suggested as a possible replacement for chromates.[31] Research has been conducted, starting with Deberry's work, to examine the corrosion protection afforded to steel and aluminum by polyaniline.[32] However, polypyrrole, the focus of this paper, has received

little attention when compared with polyaniline. Previous work from this laboratory on polypyrrole as a corrosion inhibitor has previously been published.[33,34]

EXPERIMENTAL

Aluminum alloy 2024-T3 panels were ordered from Q-Panel® in large quantities by batch number to reduce the possibility of minute differences in alloy material. Directly before coating, the 3" x 6" panels were polished using 600 grit Si-C sand paper for approximately 2 minutes until a uniform, blemish free surface was obtained. The polishing was followed by a hexane wash to degrease and clean the panel. The panels were wiped clean with Kimwipes® until the tissue used showed no black residue (caused by the Si-C sand paper). The ECPs were used as received from the Intelligent Polymer Research Institute (Wollongong, Australia) and are shown in Figure 1 below. The synthetic details and polymer characterization have been described elsewhere.[35]

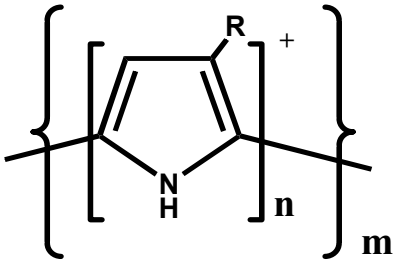

	R=	**Dopant(s)**	**Label**
Poly(3-octyl pyrrole)	$(CH_2)_7CH_3$	pTS^-/ClO_4^-	$POP/pTS^-/ClO_4^-$
Poly(3-octyl pyrrole)	$(CH_2)_7CH_3$	pTS^-	POP/pTS^-
Poly(3-octyl pyrrole)	$(CH_2)_7CH_3$	ClO_4^-	POP/ClO_4^-
Poly(3-octadecyl pyrrole)	$(CH_2)_{17}CH_3$	pTS^-/ClO_4^-	$PODP/pTS^-/ClO_4^-$

FIGURE 1. Poly(3-alkyl pyrrole).

1 % ECP solutions were made by dissolving the ECP in CCl_4 and CH_2Cl_2 (solvent ratio 50:50). Occasionally, CH_3CN was also used with the before mentioned solvents in which case the solvent makeup was CCl_4:CH_2Cl_2:CH_3CN in a ratio of 48:48:4. The polished and degreased panel was leveled, the ECP solution was pipetted on, and sufficient time was allowed to elapse for the solvents to evaporate. The resulting film was thin (usually ~2 to 5μm thick) and relatively uniform (standard deviations of thickness less than 1 μm). For some experiments the ECP coated panels were coated with a DEFT® polyurethane topcoat. This allowed for the comparison of the ECP/Polyurethane system with a system that was considered to be "standard". The standard system consisted of a polished, degreased AA 2024-T3 panel coated with a DEFT® chromated epoxy primer followed by a DEFT® polyurethane topcoat. The thickness of the chromated epoxy (Cr-Epoxy) was approximately 25 μm while the thickness of the polyurethane (topcoat) was 25 to 30 μm. The Cr-Epoxy coating was allowed to cure for one hour in an oven at 60 ° C after which it was removed, allowed to cool, and cured over night. The topcoat was applied the following day with a similar curing schedule.

ELECTROCHEMICAL IMPEDANCE SPECTROSCOPY

Gamry® Instrument's PC-3 or PC-4 was used to conduct the EIS experiments. An AC perturbation of 5 mV rms was applied to the sample. The frequency range studied was usually from 5000 Hz to 0.01 Hz, with the lower frequency sometimes extended to 0.001 Hz.

SCANNING VIBRATING ELECTROCHEMICAL TECHNIQUE

Current density above a substrate immersed in an electrolyte solution was mapped using the scanning vibrating electrochemical technique (SVET). The SVET used in this study was from Applicable Electronics (Forestdale, MA). The microelectrode used was an etched Pt/Ir

(80% / 20%) wire that had been coated with parylene and arced to expose the metal at the tip. The exposed metal was platinized to form a platinum black ball with a diameter of 20 μm. The microelectrode was placed ca. 100 μm above the surface of the sample.

The samples were prepared for scanning by taping off the sample, leaving only a 2 mm by 2 mm exposed area. The tape used in this study was a Polyester 5 adhesive tape (3M Company). Approximately 5 ml of dilute Harrison's solution was used for the immersion electrolyte. After immersion for 5 minutes, scans were initiated and 400 data points were collected by scanning in a 20 x 20 grid. For some experiments, an artificial defect was induced by scribing. All measurements were taken at open circuit.

GALVANIC COUPLING SCANNING VIBRATING ELECTRODE TECHNIQUE EXPERIMENT

Experiments were performed utilizing the SVET to better characterize the inhibition processes that occur while using ECPs on an aluminum substrate. For this experiment, aluminum 2024-T3 was coated with a 2 to 3 μm thick ECP coating. The ECP coated substrate was attached to uncoated aluminum 2024-T3 via a silver epoxy (Magnobond #8006) as shown in Figure 2 or a conductive lead tape. Scans were performed on the bare aluminum and the ECP sample by alternating between the two exposed areas.

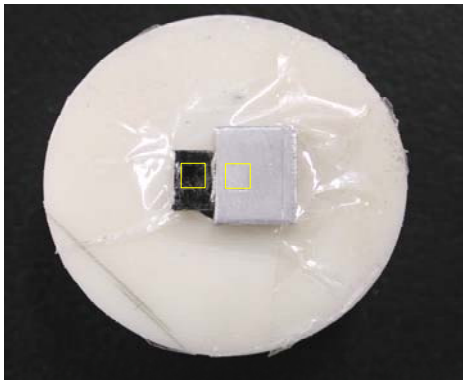

FIGURE 2. Galvanic SVET experimental cell.

RESULTS AND DISCUSSION

It was determined that the standard system was able to maintain its initial impedance value for over a year as shown in Figure 3a and 3b. Interestingly, after the initial decrease in impedance on day 329, the sample displayed an increase in impedance. This is attributed to the healing affect that chromates possess. In short, it has been found that the partial solubility of chromate is an important factor in its ability to "heal" a corroding area on an aluminum sample. It is said that chromates heal due to their solubility, which affords chromate the ability to migrate to the injured area and passivate the metal. However, the exact mechanism is still under debate.

The polyurethane topcoat was applied to POP/pTS^-/ClO_4^- on AA 2024-T3. By using a barrier coating in conjunction with the ECP, it was thought that an estimate of the corrosion protection afforded by the ECP in a real world scenario would be determined. This would also allow for the direct comparison of the impedance with that of a standard system that contained both the chromated epoxy primer and the polyurethane topcoat. As seen in Figure 3c and 3d, a high impedance, approximately 10^9 ohms at 0.01 Hz, was observed for the polyurethane coated POP/pTS^-/ClO_4^- throughout the study period, 1035 days of immersion in dilute Harrison's solution.

The polyurethane/POP/pTS^-/ClO_4^- displays no breakpoint frequency in the frequency range studied. It is suggested that the polyurethane/POP/pTS^-/ClO_4^- coating displays capacitive behavior even after 1035 days of immersion as shown in Figure 3d. The impedance of the polyurethane/POP/pTS^-/ClO_4^- coating may be at the limitations of the Gamry® Instruments, Inc. PC-3.

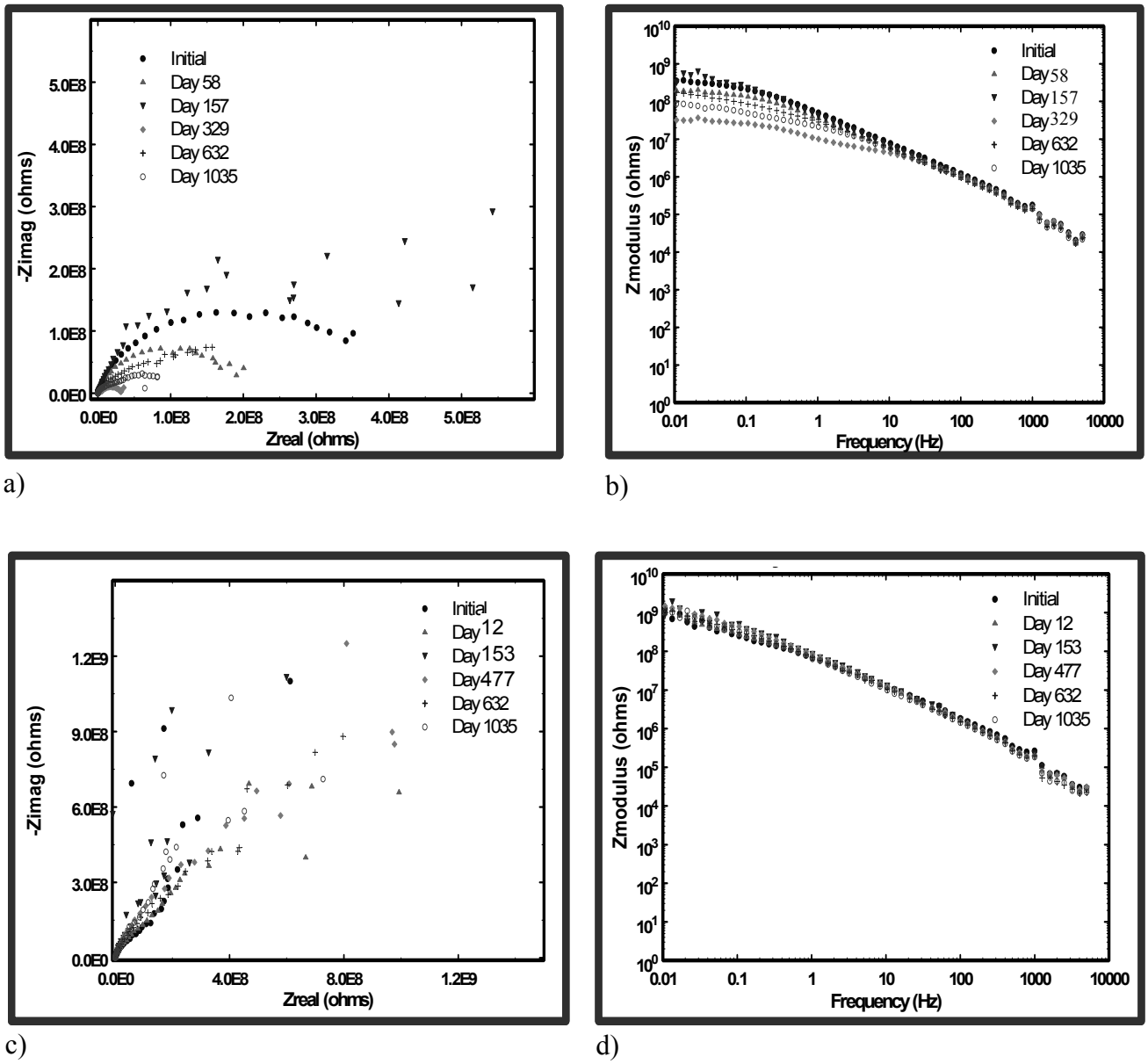

a) b)

c) d)

FIGURE 3. Electrochemical impedance spectroscopy of aluminum 2024-T3 coated with chromated epoxy and polyurethane topcoat (4a and 4b) POP/pTS^-/ClO_4^- and a polyurethane topcoat (4c and 4d) (exposed area = 7 cm^2).

SVET results have previously been reported by this laboratory for scribed plain epoxy and chromated-epoxy coatings on AA 2024-T3 immersed in dilute Harrison's solution.[36] In short, the onset of corrosion for AA 2024-T3 coated with an epoxy coating was observed within 20 minutes of immersion. The oxidation and reduction currents were confined within the defect area. The first detectable current for the chromated-epoxy coated AA 2024-T3 occurred after

approximately 5 hours of immersion. After 17 hours of immersion, large currents were observed (approximately 40 to 60 $\mu A/cm^2$ in magnitude). All currents appeared to be confined to the defect area.

POP/pTS^-/ClO_4^- displayed a delay in corrosion, with the first significant current flow observed at approximately 22-hours after immersion. By 26.6 hours, an oxidation peak is observed; interestingly, this occurred away from the induced defect. At the defect site, only cathodic currents were observed. The metal within the defect remained shiny throughout the immersion experiment with no visual evidence of corrosion products.

Results for the galvanic SVET experiments are presented below. Initially, low magnitude oxidation currents were observed when the AA 2024-T3 connected to POP/pTS^-/ClO_4^- coated AA 2024-T3 was scanned as shown in Figure 4. However, after 4 hours of immersion, corrosion at the AA 2024-T3 had virtually shut down, with mainly reduction currents observed at the AA 2024-T3. Even, after 21 hours of immersion, the uncoated AA 2024-T3 still maintained mostly cathodic currents as shown in Figure 5.

At this time, 21 hours of immersion, the sample was removed from the dilute Harrison's solution, the conductive Pb tape was cut, the experimental cell was refilled with dilute Harrison's solution, within 5 minutes of immersion in dilute Harrison's solution, the initial scan commenced. Interestingly, mostly anodic currents were observed at this time, 21 hours 5 minutes, as shown in Figure 6. After 20 and 60 minutes, as shown in Figures 7 and 8, much of the sample surface maintained anodic currents.

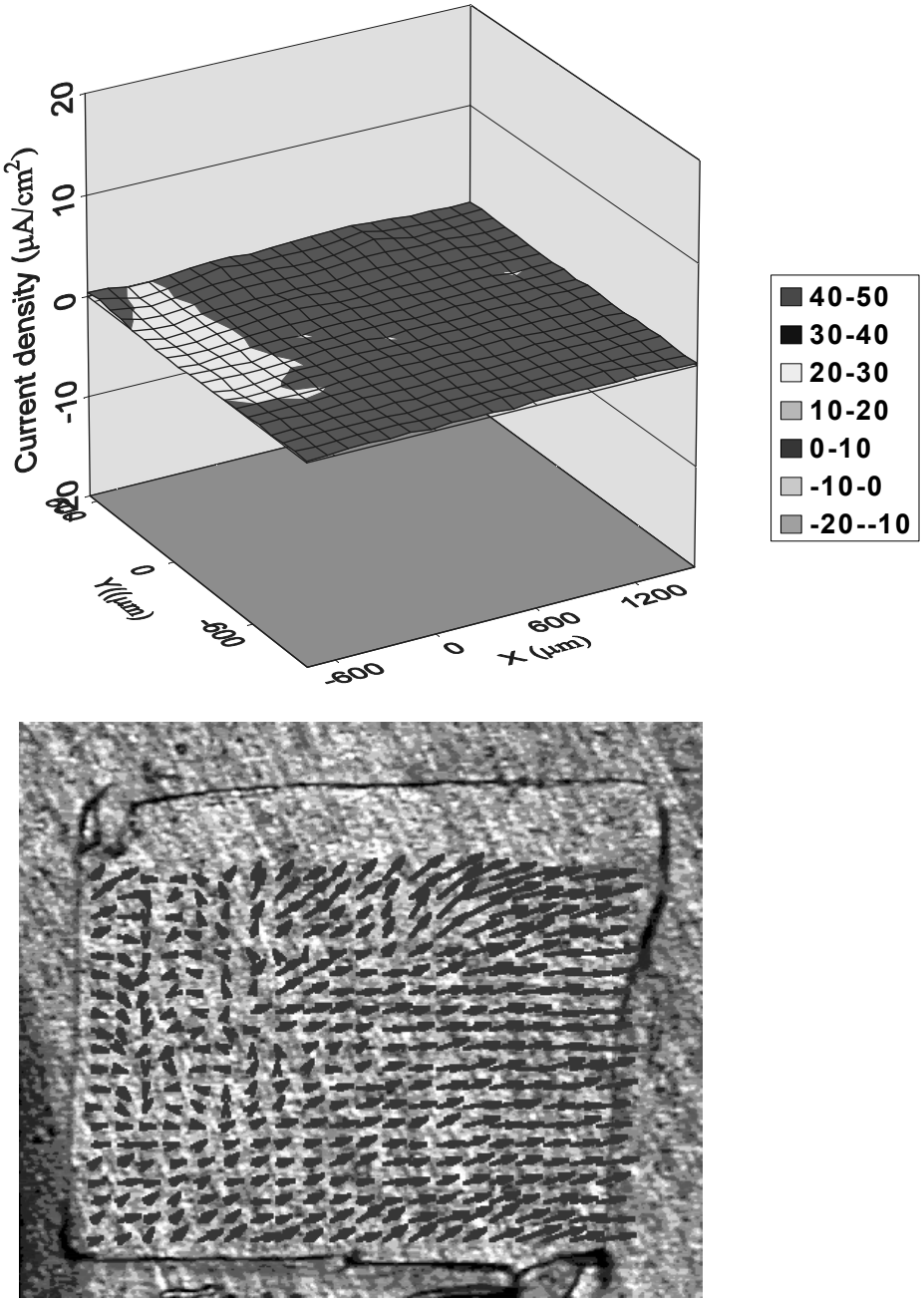

FIGURE 4. Scanning vibrating electrode technique results for AA 2024-T3 connected to a POP/pTS^-/ClO_4^- coated AA 2024-T3 after 5 minutes of immersion in dilute Harrison's solution.

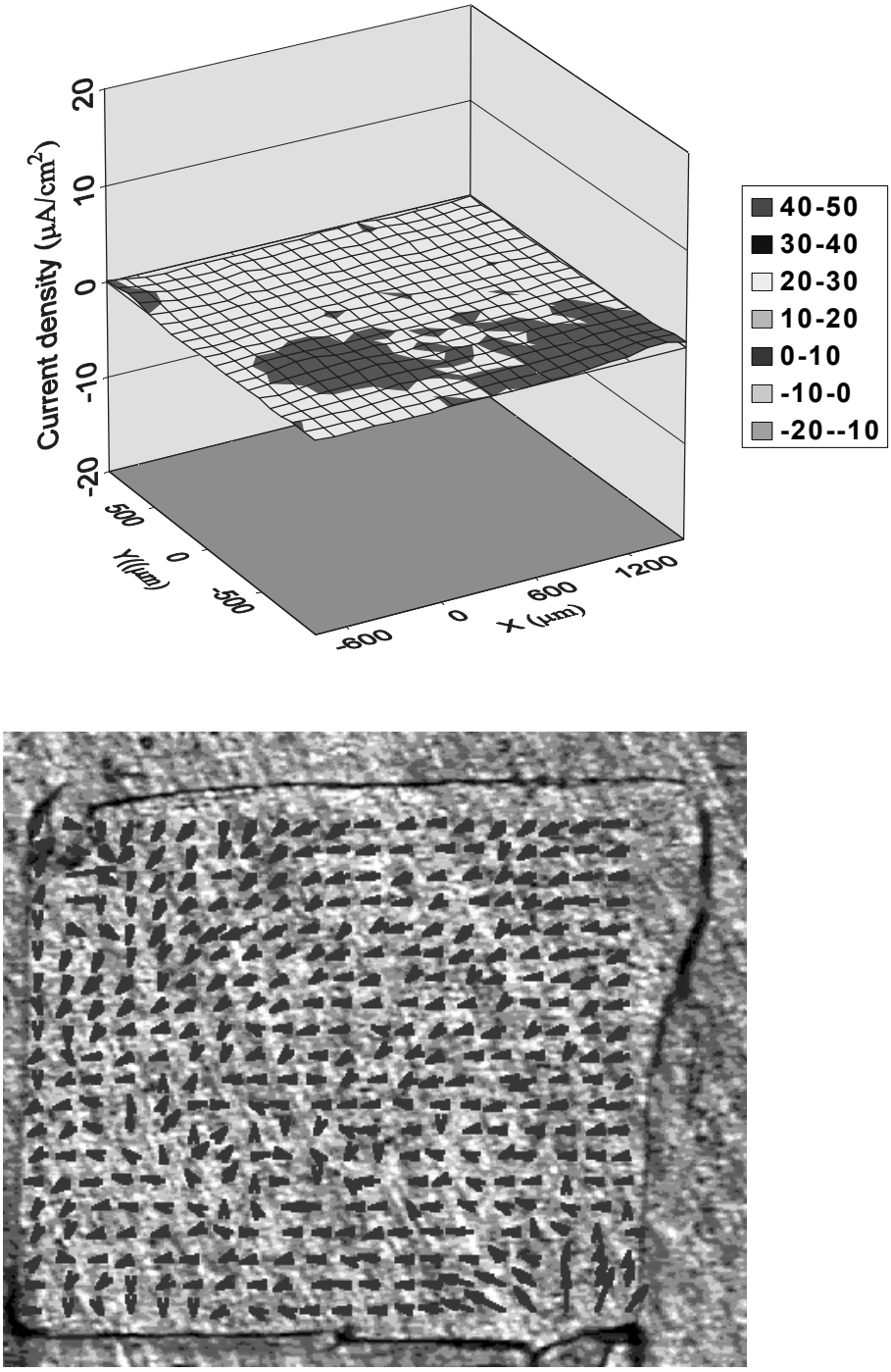

FIGURE 5. Scanning vibrating electrode technique results for AA 2024-T3 connected to a POP/pTS^-/ClO_4^- coated AA 2024-T3 after 21 hours of immersion in dilute Harrison's solution.

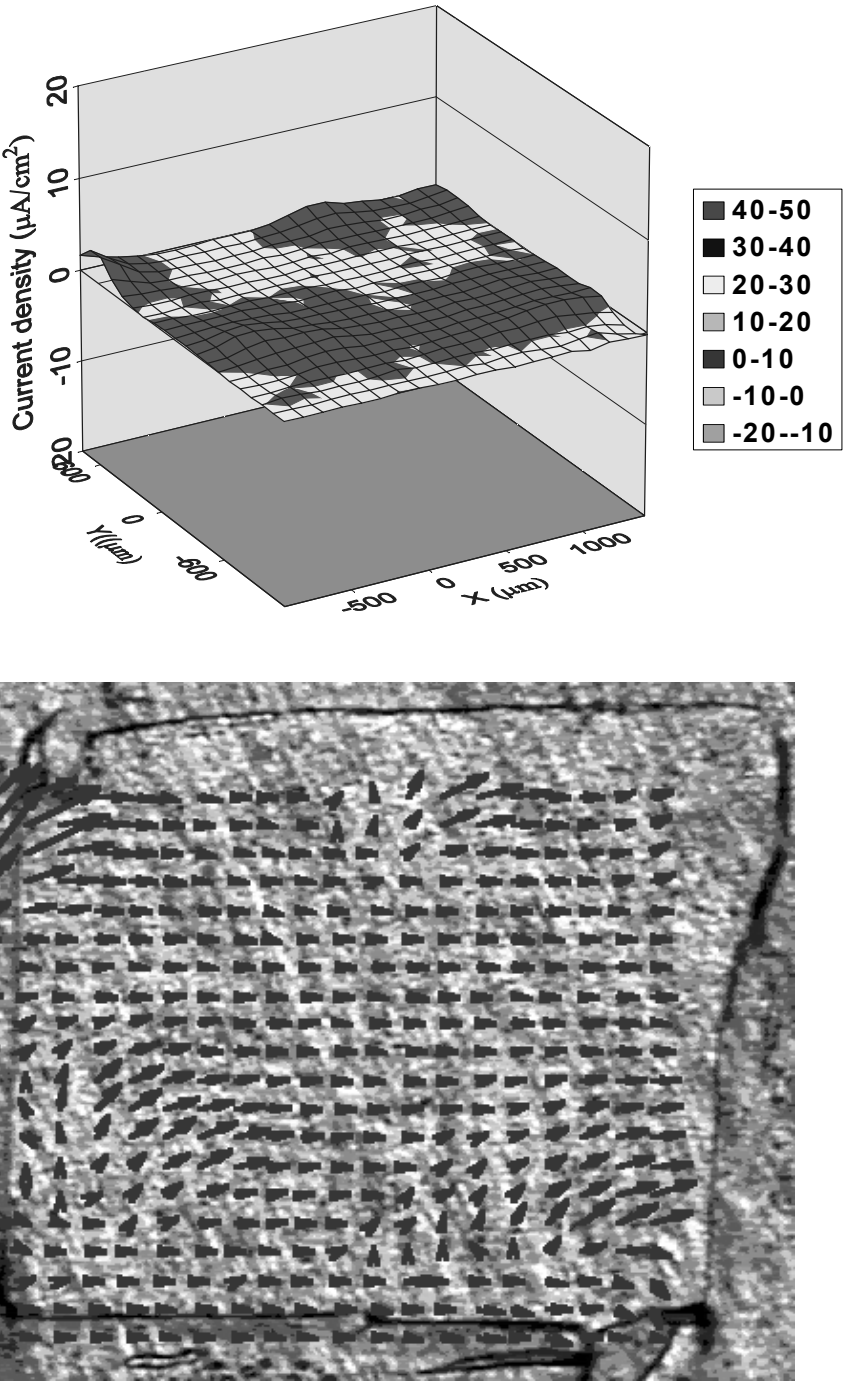

FIGURE 6. Scanning vibrating electrode technique results for AA 2024-T3 5 minutes after removing the connection to the POP/pTS^-/ClO_4^- coated AA 2024-T3 after 21 hours of immersion in dilute Harrison's solution.

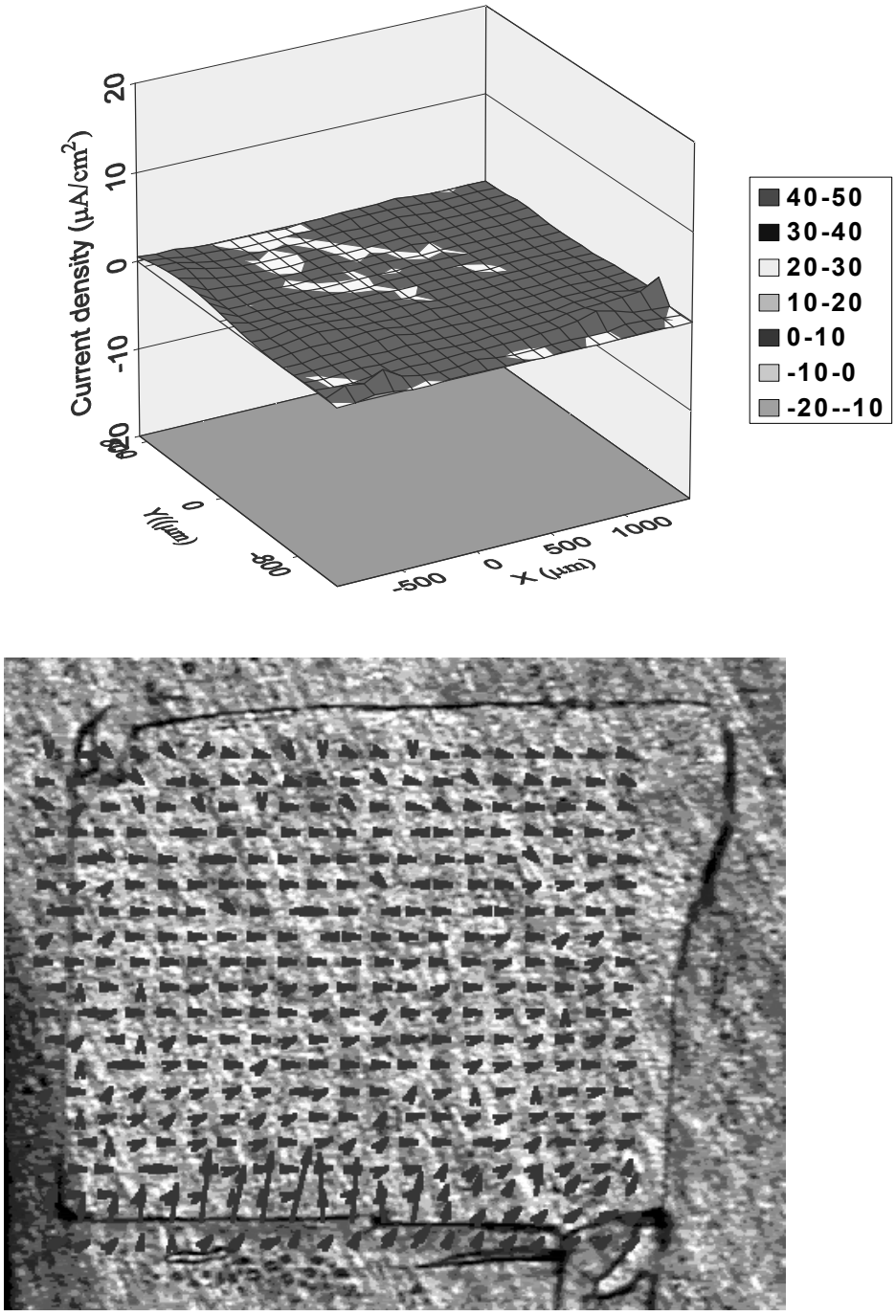

FIGURE 7. Scanning vibrating electrode technique results for AA 2024-T3 20 minutes after removing the connection to the POP/pTS^-/ClO_4^- coated AA 2024-T3 after 21 hours of immersion in dilute Harrison's solution.

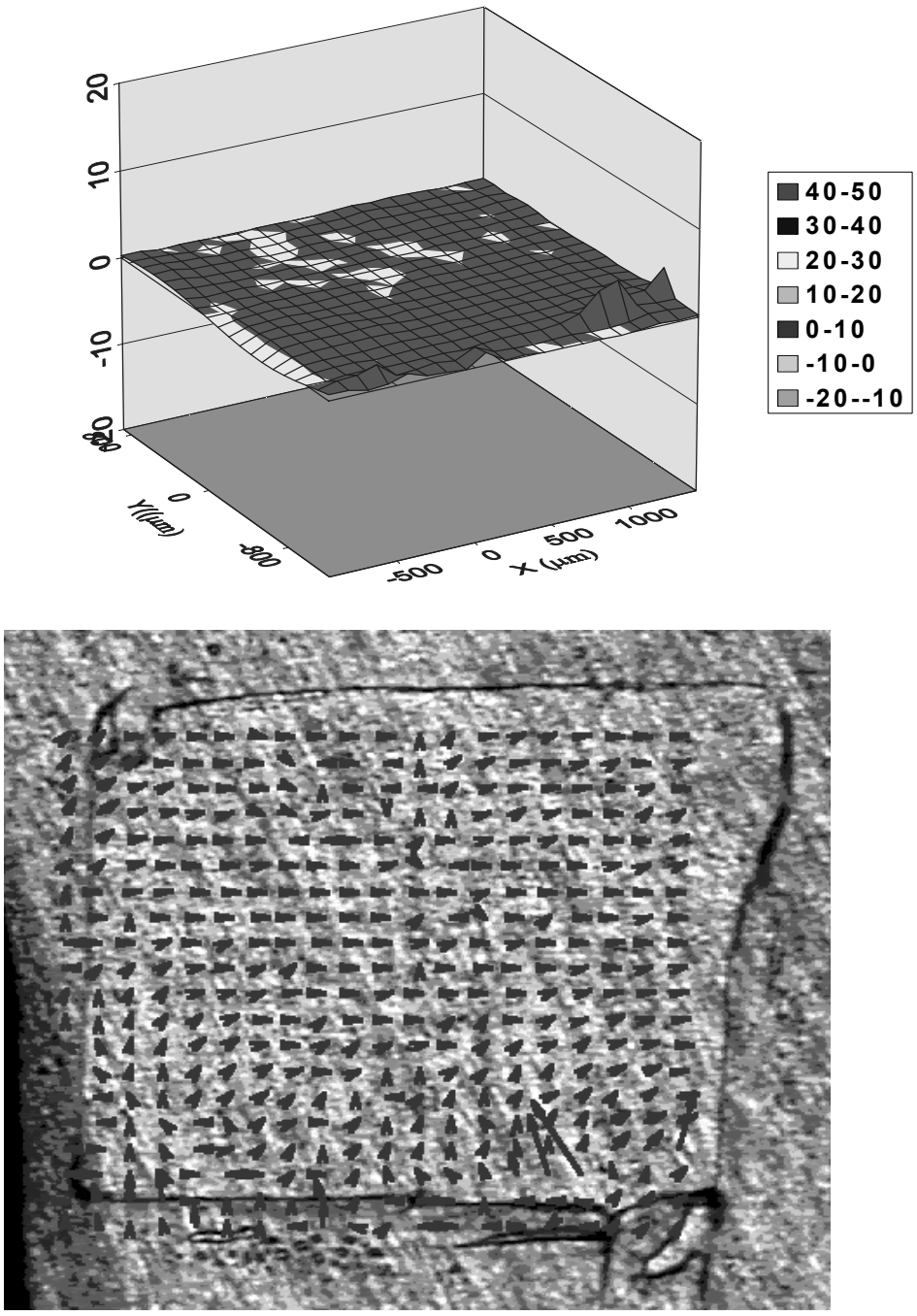

FIGURE 8. Scanning vibrating electrode technique results for AA 2024-T3 1 hour after removing the connection to the POP/pTS^-/ClO_4^- coated AA 2024-T3 after 22 hours of immersion in dilute Harrison's solution.

From the results presented above, it can be concluded that a galvanic interaction may be at least partially responsible for the corrosion inhibition properties of POP/pTS^-/ClO_4^-. The POP/pTS^-/ClO_4^- was able to delay the onset corrosion from occurring at a remote AA 2024-T3 panel that was electronically connected to a POP/pTS^-/ClO_4^- coated AA 2024-T3 via conductive Pb tape. Apparently, the POP/pTS^-/ClO_4^- was able to maintain the uncoated AA 2024-T3 at a more noble potential, therefore minimizing oxidation of the AA 2024-T3. It was initially thought that the rather noble potentials of conducting polymers might cause the oxidization and passivation of the AA 2024-T3 surface. If this oxidized layer was dense and tightly adhering, beneficial barrier properties would protect the underlying AA 2024-T3 for a period of time after the severance of the electronic connection.

Charge balance must be maintained and since predominately cathodic currents were observed at the uncoated AA 2024-T3 sample it was assumed that the corresponding anodic current was occurring at the POP/pTS^-/ClO_4^- coated AA 2024-T3. To verify this, a separate experiment was performed where scans were alternated between the uncoated AA 2024-T3 sample and the POP/pTS^-/ClO_4^- coated AA 2024-T3 sample. Results are presented in Figure 9. It is interesting to note that, once again, mainly cathodic currents were observed on the uncoated AA 2024-T3 sample and the POP/pTS^-/ClO_4^- coated AA 2024-T3 displayed only anodic currents. The anodic currents observed at the POP/pTS^-/ClO_4^- coated AA 2024-T3 could be due to either the oxidation of the underlying aluminum or the oxidation of the ECP.

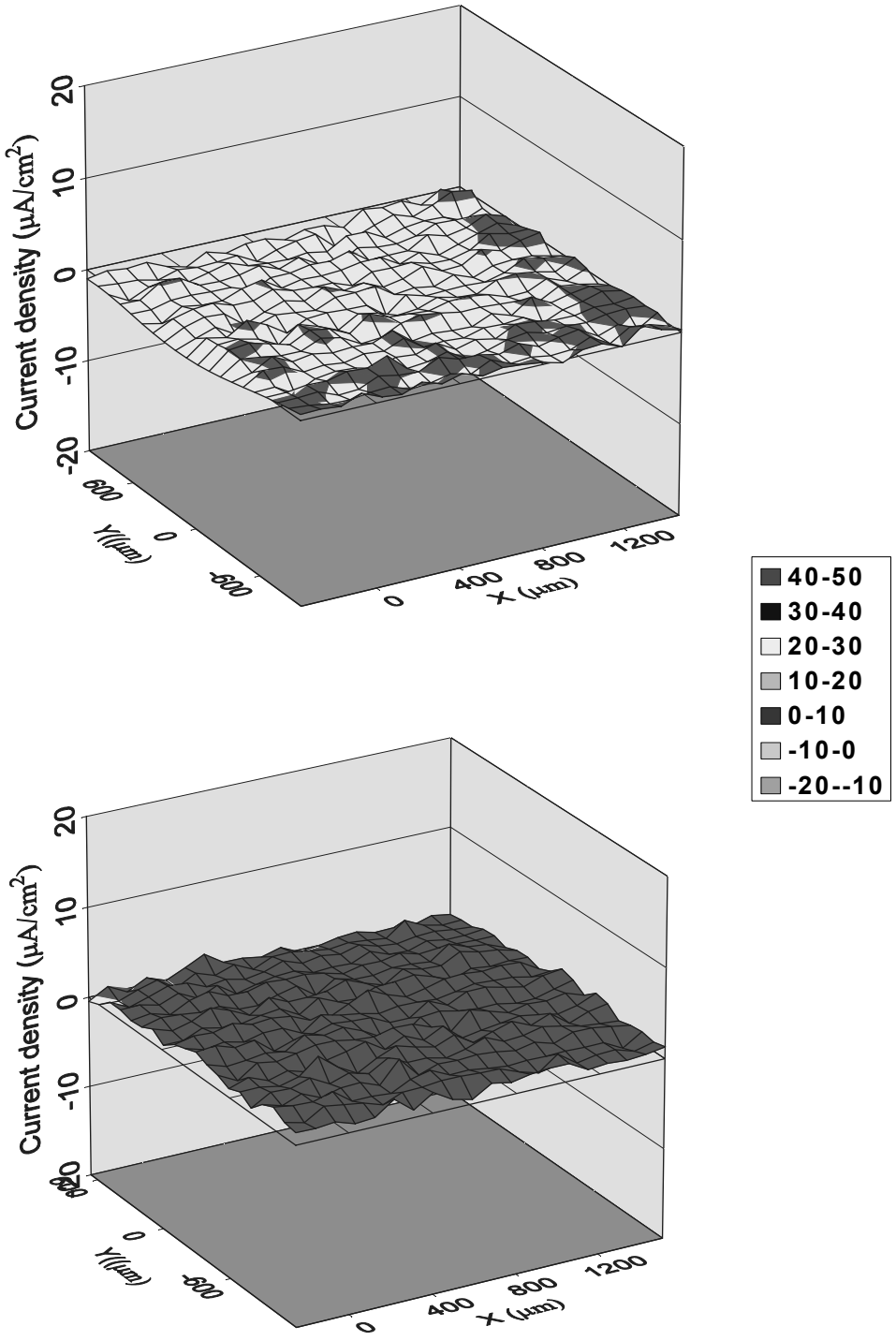

FIGURE 9. Scanning vibrating electrode technique results for AA 2024-T3 (top) connected to POP/pTS^-/ClO_4^- coated AA 2024-T3 (bottom) at 2 hours and 2 ½ hours, respectively.

CONCLUSION

One suggested mechanism of corrosion inhibition, therefore, is an ennobling of the uncoated AA 2024-T3 through a galvanic coupling with the POP/pTS^-/ClO_4^- coated AA 2024-T3. The ennobling effectively inhibits corrosion as long as the connection between the POP/pTS^-/ClO_4^- coated AA 2024-T3 and the uncoated AA 2024-T3 was maintained. As soon as the connection was severed, corrosion commenced at the uncoated AA 2024-T3, suggesting that no significant irreversible changes were made to the oxide layer. Therefore, long-term corrosion inhibition would require a constant electronic interaction with the ECP.

ACKNOWLEDGMENTS

I would like to acknowledge the Air Force Office of Scientific Research for funding this research, Grant No. F9620-96-0284 (North Dakota State University).

I am grateful to Dr. Chee O. Too and Dr. Syed A. Ashraf of the Intelligent Polymer Research Institute (University of Wollongong, Australia) for synthesis of the poly(3-octyl pyrrole) and poly(3-octadecyl pyrrole) used in this work.

REFERENCES

1. D. A. Jones. Principles and Prevention of Corrosion; (Prentice Hall: Upper Saddle River, NJ, 1996), p Pages.
2. D. Li,Y. Hu, B. Guo. Mater. Sci. and Eng., A280, (2000), 173-176.
3. F. Mansfield. Corrosion, 54, (1998), 595-597.
4. C. Andrieu,F. Dalard,J. J. Rameau,F. Alcouffe, M. Reboul. J. Mater. Sci., 33, (1998), 3177-3181.
5. M. A. Alodan, W. H. Smyrl. J. Electrochem. Soc., 145, (1998), 1571-1577.

6. D. J. Blackwood, A. S. L. Chong. British Corrosion Journal, 33, (1998), 219-224.

7. G. S. Frankel. J. Electrochem. Soc., 145, (1998), 2186-2198.

8. V. R. Crispim, J. J. G. D. Silva. Appl. Radiat. Isot., 49, (1998), 779-782.

9. H. Okada. Materials Performance, (1998), 54-61.

10. W. Li,A. Raman,R. Diwan, P. K. Bhattacharya. Corrosion-98, Paper #341, (1998).

11. R. C. Newman, K. Sieradzki. MRS Bulletin, (1999), 12-13.

12. R. C. Newman,S. G. Corcoran,J. Erlebacher,M. J. Aziz, K. Sieradzki. MRS Bulletin, (1999), 24-28.

13. P. J. E. Forsyth. Mater. Sci. and Tech., 15, (1999), 301-308.

14. B. Malki,A. Legris,J.-L. Pastol, D. Gorse. J. Electrochem. Soc., 146, (1999), 3702-3710.

15. N. Dimitrov,J. A. Mann, K. Sieradzki. J. Electrochem. Soc., 146, (1999), 98-102.

16. M. Mehmood,E. Akiyama,H. Habazaki,A. Kawashima,K. Asami, K. Hashimoto. Corr. Sci., 41, (1999), 477-499.

17. I. V. Murav'eva, Y. Y. Andreev. Protection of Metals, 35, (1999), 468-472.

18. G. E. Kiourtsidis,S. M. Skolianos, E. G. Pavlidou. Corrosion Science, 41, (1999), 1185-1203.

19. A. M. Mierisch,J. Yuan,R. G. Kelly, S. R. Taylor. J. Electrochem. Soc., 146, (1999), 4449-4454.

20. J. O. Park,C. H. Paik,Y. H. Huang, R. C. Alkire. J. Electrochem. Soc., 146, (1999), 517-523.

21. P. M. Natishan,W. E. O'Grady,E. McCafferty,D. E. Ramaker,K. Pandya, A. Russell. J. Electrochem. Soc., 146, (1999), 1737-1740.

22. E. McCafferty. J. Electrochem. Soc., 146, (1999), 2863-2869.

23. R. G. Buchheit,M. A. Martinez, L. P. Montes. J. Electrochem. Soc., 147, (2000), 119-124.
24. M. Verhoff, R. Alkire. J. Electrochem. Soc., 147, (2000), 1359-1365.
25. A. Sehgal,G. S. Frankel,B. Zoofan, S. Rokhlin. J. Electrochem. Soc., 147, (2000), 140-148.
26. S. Y. Yu,W. E. O'Grady,D. E. Ramaker, P. M. Natishan. J. Electrochem. Soc., 147, (2000), 2952-2958.
27. K. C. Emregul, A. A. Aksut. Corrosion Science, 42, (2000), 2051-2067.
28. K.-K. Lee, K.-B. Kim. Corrosion Science, 43, (2001), 561-575.
29. I. Serebrennikova, H. S. White. Electrochemical and Solid-State Letters, 4, (2001), B4-B6.
30. S. M. Cohen. Corrosion, 51, (1995), 71-78.
31. R. L. Twite, G. P. Bierwagen. Progress in Organic Coatings, 33, (1998), 91-100.
32. D. W. DeBerry. J. Electrochem. Soc., 132, (1985), 1022-1026.
33. V. J. Gelling,M. M. Wiest,D. E. Tallman,G. P. Bierwagen, G. G. Wallace. Progress in Organic Coatings, 43, (2001), 149-157.
34. J. He,V. J. Gelling,D. E. Tallman,G. P. Bierwagen, G. G. Wallace. J. Electrochem. Soc., 147, (2000), 3667-3672.
35. S. A. Ashraf,F. Chen,C. O. Too, G. G. Wallace. Polymer, 37, (1996), 2811-2819.
36. J. He,V. J. Gelling,D. E. Tallman, G. P. Bierwagen. J. Electrochem. Soc., 147, (2000), 3661-3666.

COATING PERFORMANCE EVALUATION PROTOCOL USING ELECTROCHEMICAL METHODS

S. J. Mabbutt,[1] J. Li,[1] Gordon P. Bierwagen,[1] and Dennis E. Tallman[2]

[1]Department of Polymers and Coatings, [2]Department of Chemistry
North Dakota State University
Fargo, ND 58105-5516

INTRODUCTION

The major components of modern aircraft are made from high strength aluminum alloys. The aluminum alloy 2024 – T3 constitutes most of the damage sensitive parts while 7075 – T6 forms those areas that need high strength. The composition and metallurgical structure of these alloys makes them particularly susceptible to localized corrosion when exposed to chloride containing environments. Normal life expectancy of a civil aircraft is about 10 years in major airlines and a further 10 years as a second hand airplane in smaller airlines. Military aircraft are currently expected to be in service for several decades longer than this. To ensure the functional integrity of an aircraft under harsh service conditions, organic coatings are primarily employed to provide protection. The aircraft may fly in different geographic areas where various levels of humidity from 0 to 100% and temperatures from -54 to 177°C are encountered. With the synergetic effects of shorter-wavelength UV light and coating degradation due to chemical attack monitoring of the protection afforded by the coating system is important.

Coating systems have traditionally contained chromium-based pigments and pretreatments as the basis for their corrosion protective properties, which has provided protection of seven years or greater before recoating is needed. The corrosion inhibiting process involves either adsorption of chromate species to previously formed corrosion products or deposition of an insoluble Al/chromate precipitate on the metal surface, which lead to the increases in

electrical resistance of the protective films and pitting corrosion potential of the protected aluminum alloy.[1, 2] The formation of chromate protective film is generally believed to be associated with destabilization of the passive aluminum oxide layer by corrosive species and reduction of chromate by the exposed aluminum.[3] The precise composition of the protective film varies with different conditions. Compared to other corrosion inhibitors, chromates exhibit a dynamic anticorrosive phenomenon in which chromate species slowly released from nearby chromate-containing pretreatment agents or organic coatings migrate to actively corroding sites and subsequently impede corrosion.[4] Unfortunately, chromium is a known carcinogen[5] and regarded as a hazardous substance which presents many problems in particular during the removal stage of the coating life cycle. Removal of chromium from coating material is therefore an important goal for the coatings industry and in this project alternative coating systems are examined using electrochemical and physical methods of monitoring performance.[6]

The tested panels were exposed to UV accelerated weathering and Prohesion accelerated corrosion environments according to ASTM D5894. UV/Prohesion exposure combines the synergistic effects of various environmental stresses in its cycles, which simulate damaging effects caused by the aggressive exposure conditions of aircraft coatings. Electrochemical Noise Measurement (ENM) and Electrochemical Impedance Spectroscopy (EIS) were used to assess the degradation of the coating systems in addition to physical techniques (not reported here). The final part of this paper gives some results from a new experimental configuration for Electrochemical Noise Monitoring. The development of the technique has been previously reported[7, 8, 9] and found to be potentially useful for monitoring in the field. The panels used for this work were steel substrate with epoxy primer and polyurethane top-coat, but successful application of the technique using Al substrate has been reported.[10]

EXPERIMENTAL

I. AIRCRAFT COATING SYSTEMS AND SUBSTRATE DETAILS

The substrate for the aircraft coatings were aluminum alloy 2024 –T3 panels 127.0 mm × 203.0 mm × 1.6 mm (5”× 8” × 0.063”). The aircraft coatings, epoxy primers and polyurethane topcoats, are provided by DEFT Inc. These coatings are either those are actually used or experimentally screened for the military planes of the US Air Force. As proprietary products, little information on the formulations of these aircraft coatings was available. Coating systems are listed with their manufacturer and military codes in table 1.

TABLE 1. Coating Systems

System	Primer	Topcoat
Primer	Epoxy-Polyamide (DEFT 02-Y-040, MIL-P-23377G Type I Class C)	—
Self-Priming Topcoat	—	Polyurethane (DEFT 03-GY-374, Navy TT-P-2756)
Primer + Flat Topcoat	Epoxy-Polyamide (DEFT 02-Y-040, MIL-P-23377G Type I Class C)	Polyurethane (DEFT 03-GY-311, MIL-C-85285B, 36473, Type I)
Primer + Glossy Topcoat	Epoxy-Polyamide (DEFT 02-Y-040, MIL-P-23377G Type I Class C)	Polyurethane (DEFT 03-GY-277, Navy MIL-C-85285B Type I)
Primer + Extended Life Topcoat	Epoxy-Polyamide (DEFT 02-Y-040, MIL-P-23377G Type I Class C)	Fluro Polyurethane (DEFT 99-GY-1, Extended Life Topcoat)

Prior to coating application, the substrate was cleaned with Methylethylketone (MEK), immediately followed by a surface pre-treatment. The pre-treatment consists of de-oxidation with a phosphoric acid/alcohol solution and chromating with an Alodine solution (chromic acid

solution). The formulas and procedures for surface pretreatment, which are recommended by the coating manufacturer, are described below.

Formula for Phosphoric Acid Solution

N-butyl alcohol	35.0 wt.%
Isopropyl alcohol	25.0 wt.%
DI water	22.0 wt.%
Phosphoric acid	18.0 wt.%

Formula for Alodine Solution

Alodine 1200s powder	7.6 g
DI water	1.0 l

Surface Pretreatment Procedure:

i) Clean the panel with MEK.
ii) Place the panel in the phosphoric acid solution for 3.5 minutes and then rinse it with tap water until a water break free surface of the panel is obtained.
iii) Place the panel in the Alodine solution for 2.5 minutes and then rinse it with de-ionized water.
iv) Dry the panel at room temperature and use it within 24 hours after surface pretreatment.

The coatings were spray applied to the standard application procedures provided by the coating manufacturer. The primer was allowed to air dry for 3 to 4 hours before the application of topcoat. All The topcoats, except for self-priming topcoat, were sprayed as two layers with the equal film thickness for each layer. The coated panels were left to dry under ambient conditions for several weeks prior to UV and Prohesion accelerated weathering. Coating thickness was measured at several points on the panel by Elcometer film thickness gauge and reported as the average thickness. Two batches of coated panels were used. Batch I includes four systems, and batch II has five. The systems and film thickness are listed in tables 2 and 3.

From batch I, 3 panels from each system were tested, two of which were characterized by electrochemical techniques. The third one was used for contact angle/surface energy

investigation, atom force microscopic (AFM) examination, and FTIR/photoacoustic spectroscopy analyses (non-electrochemical results not reported in this work).

TABLE 2. Coating thickness for Batch I

Tested Panel	Panel Number	Film Thickness (μm)		
		Primer	Topcoat	Total
Primer	3	19.4 ± 0.7	—	19.4 ± 0.7
Self-Priming Topcoat	3	—	53.0 ± 2.0	53.0 ± 2.0
Primer + Flat Topcoat	3	18.3 ± 1.4	57.3 ± 2.9	75.7 ± 2.1
Primer + Glossy Topcoat	3	17.6 ± 0.5	60.7 ± 1.3	78.3 ± 1.5

TABLE 3. Coating thickness for Batch II

Tested Panel	Panel Number	Film Thickness (μm)		
		Primer	Topcoat	Total
Primer	1	21.0	—	21.0
Self-Priming Topcoat	2	—	52.0 ± 1.4	52.0 ± 1.4
Primer + Flat Topcoat	2	19.3 ± 0.2	52.3 ± 0.5	71.5 ± 0.7
Primer + Glossy Topcoat	2	24.0 ± 0.0	55.9 ± 8.6	80.0 ± 8.5
Primer + Extended Life Topcoat	5	24.8 ± 1.8	42.8 ± 1.6	67.6 ± 0.6

Batch II incorporated all the previously tested systems plus the newly developed Fluro Polyurethane Extended Life Topcoat, which was examined under the exactly same exposure environments. In batch II, the characterization of the Fluro Polyurethane system was emphasized, and 5 panels from this system were chosen to test.

II. COATING AND SUBSTRATE DETAILS OF SPECIMENS FOR COMPARISON OF ENM TECHNIQUES

Two systems (coded F and I), each consisting of three coats on degreased, cold rolled and grit blasted mild steel panels. The coating thickness was approximately 240 μm**.** System (F**)** had a 150 μm epoxy primer containing aluminum pigmentation, a 40 μm tie coat and a 50 μm polyurethane topcoat. System (I) had a 150 μm anticorrosive coal tar epoxy primer, a 40 μm tie coat and a 50 μm silicone alkyd topcoat. Both systems F and I were highly protective systems evidence of this was the high (>1E8 ohms-cm^2) resistance values after > 10000 hrs in a prohesion test – salt fog at 25 C for 1hour followed by 35 C dry for 1 hour. The electrolyte solutions used for electrochemical testing were 3% NaCl for both coatings.

III. ASTM UV/PROHESION EXPOSURE PROCEDURE

The tested panels were exposed to UV/Prohesion environments according to the method ASTM D 5894-96, *Standard Practice for Cyclic Salt Fog/UV Exposure of Painted Metal (Alternating Exposures in a Fog/Dry Cabinet and a UV/Condensation Cabinet).* Starting the exposure in the QUV chamber, the panels were exposed to alternating periods of one week in a QUV chamber for fluorescent UV/condensation testing and one week in a Prohesion chamber for cyclic salt fog/dry testing. In our experiment, 340nm UV-A light was employed during the UV exposure in which a repetitive cycle included 4 hours of UV light at 60°C and 4 hours of condensation at 50°C. Diluted Harrison solution, 0.05% sodium chloride plus 0.35% ammonium sulfate, was the test electrolyte solution in Prohesion exposure whose own repetitive cycle consisted of two steps: salt fog at 25°C for 1 hour and dry-off at 35°C for 1 hour.

IV. COATING PERFORMANCE EVALUATION PROTOCOL

To perform more comprehensive characterizations on the coated systems an accelerated weathering and corrosion testing protocol for coating performance is graphically described in figure 1. This protocol combines electrochemical, chemical, and physical examination to investigate corrosion protection, surface change, and degradation of the samples during the accelerated weathering and corrosion exposures. This paper only reports the electrochemical results but the diagram has been included to emphasise the holistic approach to coating characterization.

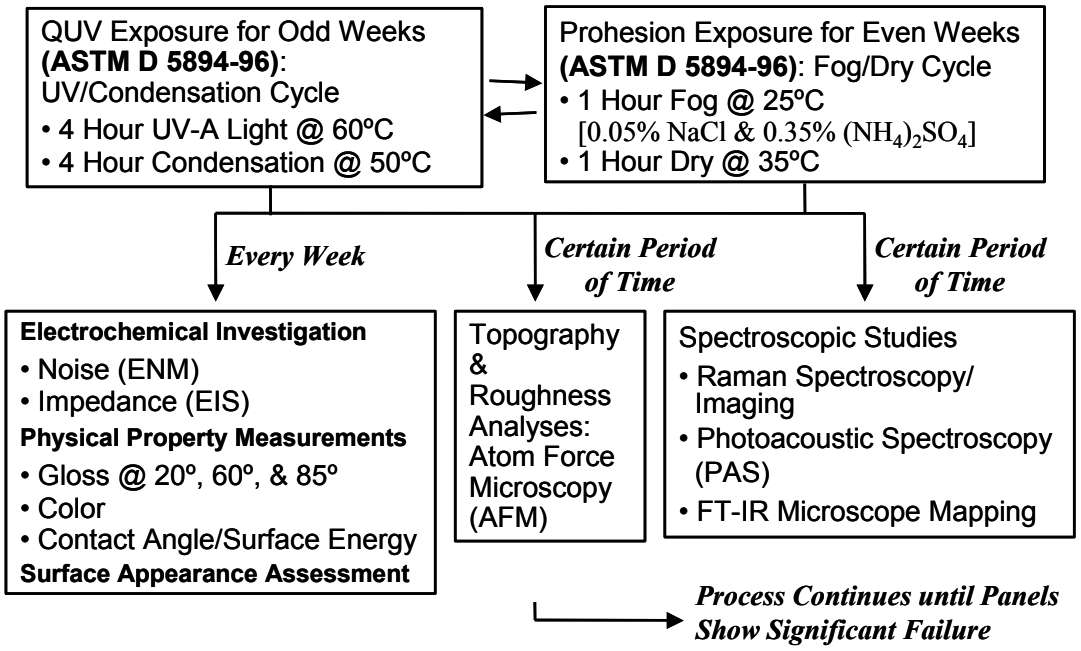

FIGURE 1. Coating performance evaluation protocol

V. ELECTROCHEMICAL MEASUREMENTS

Electrochemical measurements were conducted weekly on panels under UV/Prohesion exposure. ENM and EIS electrochemical measurements were taken with Gamry electrochemical measurement equipment. ENM was measured using the zero resistance ammeter (ZRA) mode

and EIS was done by EIS300 system in potentiostatic mode. The set-up for EIS and ENM measurements is shown in Figures 2 and 3. For ENM two nominally identical working electrodes (test panels) are used and these are connected with a salt bridge. This set-up is referred to as the bridge method. A Saturated Calomel reference electrode (SCE) is used to obtain potential relative to the working electrodes. The EIS measurements use just one working electrode a platinum counter electrode and a SCE. To construct the test cell, a glass cylinder with 40mm inside diameter and 60mm stem length and an O-Ring seal joint (Ace Glass Incorporated, Vineland, NJ) was held together with the panel by a clamp. Measurements were performed on the same area of the tested panel, the ENM experiment was done first, followed by the EIS experiment. All the measurements were carried out in a Faraday cage.

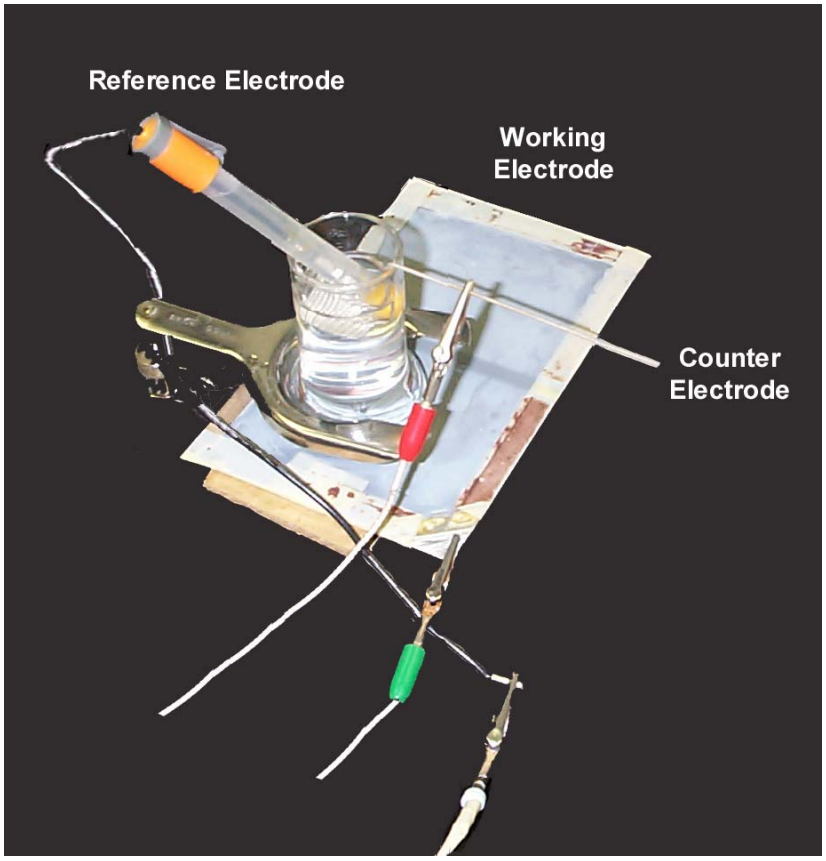

FIGURE 2. EIS set-up

For the ENM measurements, readings were taken every 0.2 second over a 51.2 second interval (block time). For each measurement 10 intervals (or blocks) were conducted. The scanning frequency range in the EIS experiment was from 10mHz to 100kHz at 10 points per decade with 10mV (rms) applied AC voltage. In the EIS experiment, before the AC voltage was imposed, a delay time was used to let the system open circuit voltage reach a stable value.

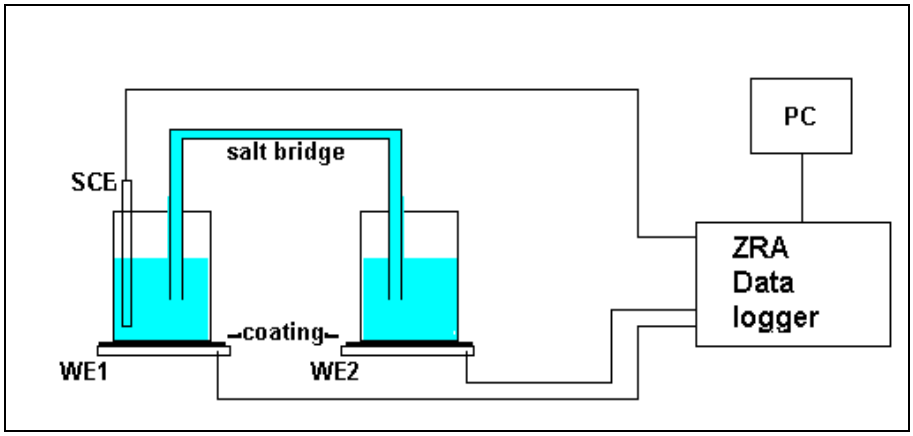

FIGURE 3. The two working electrode (traditional bridge method).

VI. ALTERNATIVE ELECTROCHEMICAL NOISE TECHNIQUE

The arrangement of the cells on the substrate, the software test parameters and the mathematical treatment of the data for the single substrate technique, were identical to those used in the bridge method. The data from the single substrate technique was obtained directly after the data from the bridge or traditional method, using the same cells but in different configuration, see Figure 4.

Note: The nature of the two techniques necessitates the use of different pairs of cells for any combination. This is because the SS technique uses only those cells attached to one panel. The

combination of cells shown in the Figure 4. are the minimum required to investigate all six areas 1A to 2C.

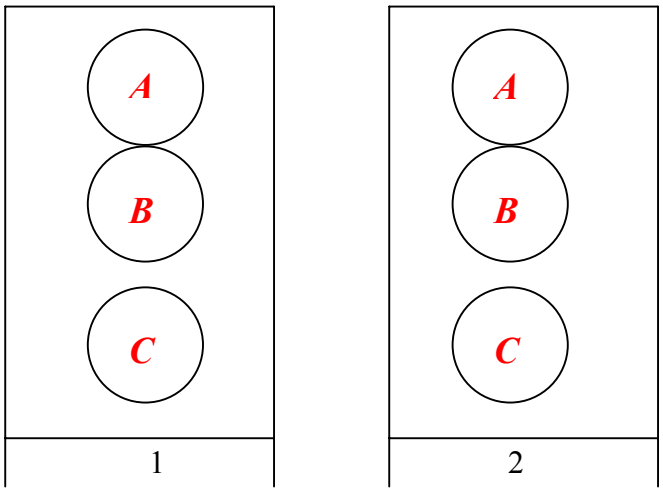

SS Technique
1 AB
1 BC
2AB
2BC

Two working elec.(Bridge Method)
12 AA
12 BB
12 CC

FIGURE 4. Schematic representation for the combination of cells to give pairs for the SS Technique and Bridge Method

The Single Substrate (SS) technique, shown in Figure 5, addresses the problem of needing two electrically isolated substrate elements required to make simultaneous potential and current noise measurements. The new arrangement was accomplished by replacing the two working electrodes (the substrate elements), with Saturated Calomel Electrodes (SCE's) connected to the working electrode inputs of the ZRA. The reference electrode connection from the ZRA was then made to the substrate, onto which cells were attached. The substrate then essentially replaces the solution (or the salt bridge) to complete the cell circuit. The potential of

the two SCE electrodes (WE1 & WE2 connections) are measured relative to the substrate (Ref. electrode connection), through the coatings of both cells, which are electrically in parallel, as with the bridge method. This does give a positive instead of negative value of potential because the electrical connections of the experiment are reversed. However, the formula for calculating the standard deviation (noise values) makes this irrelevant because the values are sign invariant. The voltage fluctuations that give rise to the noise value are the same as in the normal arrangement. Note that in the usual set-up WE1 and WE2 are assumed to be nominally identical. Using SCE's this assumption is closer to reality because of the greater stability of the electrode potentials compared to metal substrate.

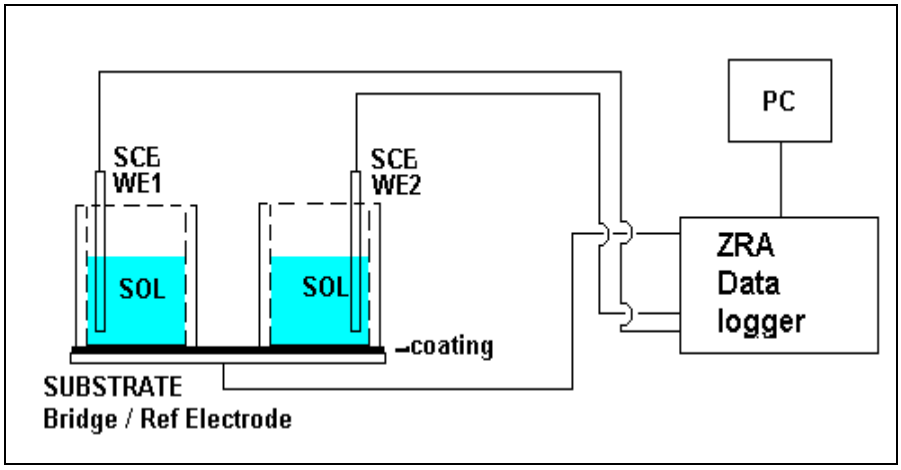

FIGURE 5. The single substrate technique

The current noise is measured between WE1 and WE2 as with the original set-up, using the ZRA. These signals are unlikely to arise in the calomel electrodes, which are generally considered to be low in noise. More likely is that they originate from ionic activity in the coating or at the coating substrate interface (thermal or shot noise) and this potential change is then imposed onto the saturated calomel electrodes. This is not considered a problem in this application because the

impedance of the electrodes are low at around 1 x 10^3 ohms compared to that of the coating at around 1 x 10^8 ohms.

RESULTS AND DISCUSSION

I. CONVENTIONAL EIS AND ENM RESULTS

The electrical resistance (R) of coated metal panels is a good indicator of corrosion protection performance of the coating system. Generally, the larger the value of the noise resistance or the modulus at low frequency ($|Z|_{low\ frequency}$) of coated metal panels when they exposed to corrosive environments, the higher the corrosion protection ability of the coating. Bacon, Smith and Rugg's work[11] reported in 1948, produced a numerical criterion for D.C. electrical resistance that can be used to evaluate coating corrosion resistance. This criterion of electrical resistance thresholds is graphically described in Figure 6. It was found that, if the electrical resistance of a coating falls between 10^6 Ω.cm^2 and 10^8 Ω.cm^2, then the corrosion protective performance of that coating is from fair to good. Above this value the coating is very good, though it is rare that coating resistance will excess the value of 10^{13} Ω.cm^2. Below 10^6 Ω.cm^2 the coating is poor. With the threshold being 10^4 Ω.cm^2 as the electrical resistance of the aluminum alloy substrate.

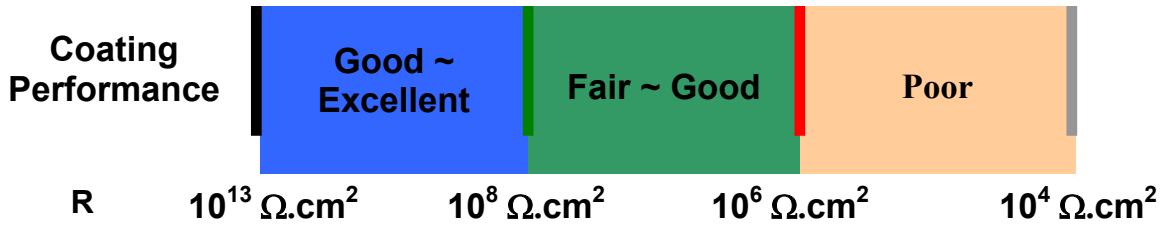

FIGURE 6. Resistance criterion to evaluate coating corrosion protection

The 2024-T3 aluminum alloy panels with chromate-pretreated surfaces were electrochemically measured over 12 weeks of UV/Prohesion exposure. After 3 weeks of exposure, electrical resistances of the panels had decreased to stable values: the R_n was 2.5×10^4 $\Omega.cm^2$ whilst the $|Z|_{0.012Hz}$ was 9.4×10^3 $\Omega.cm^2$. These were the averaged values of 4 pairs of the panels.

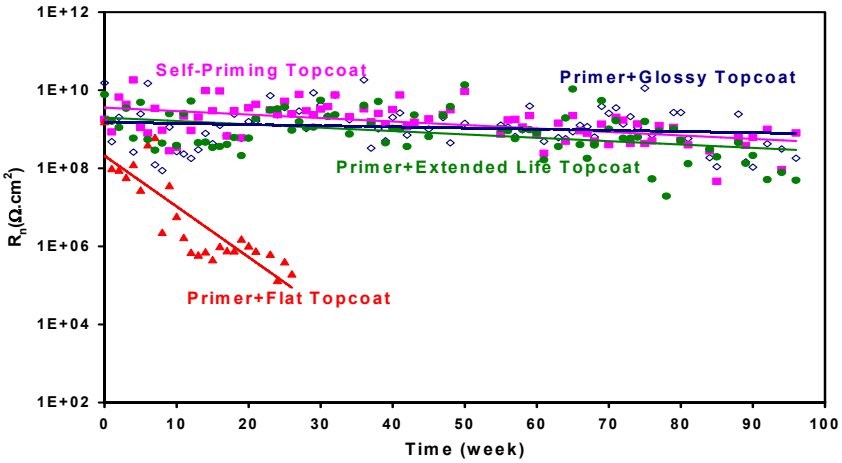

FIGURE 7. Noise resistance vs. UV/Prohesion exposure time for batch I panels

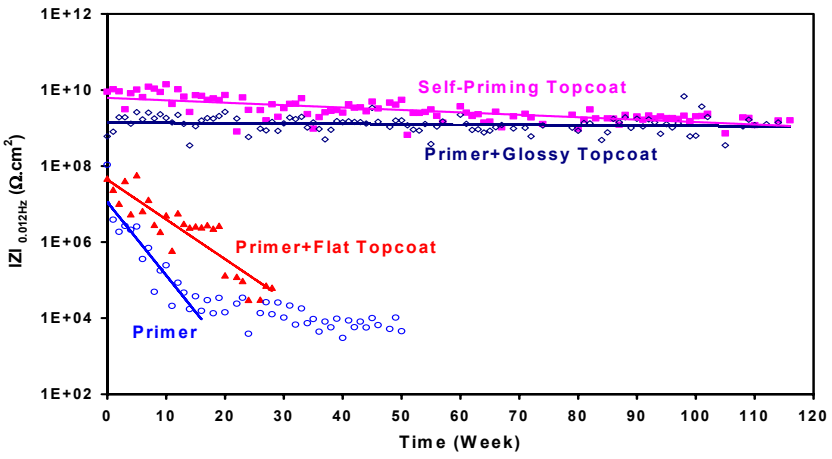

FIGURE 8. Noise resistance vs. UV/Prohesion exposure time for batch II panels.

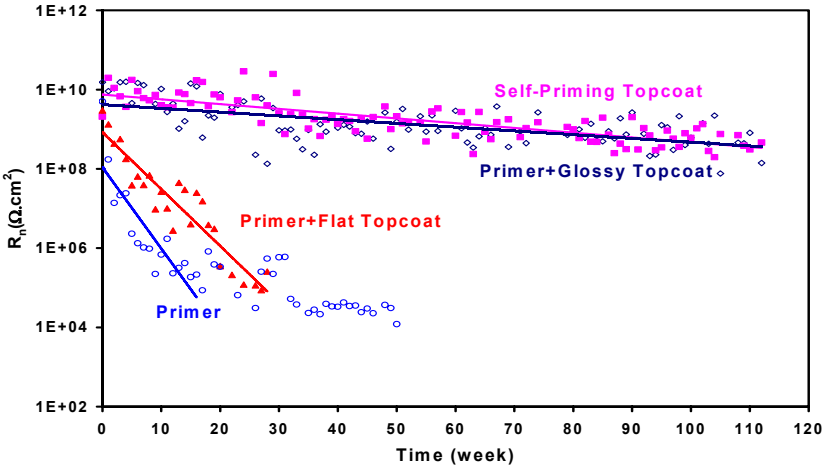

FIGURE 9. Impedance modulus vs. UV/Prohesion exposure time for batch I panels.

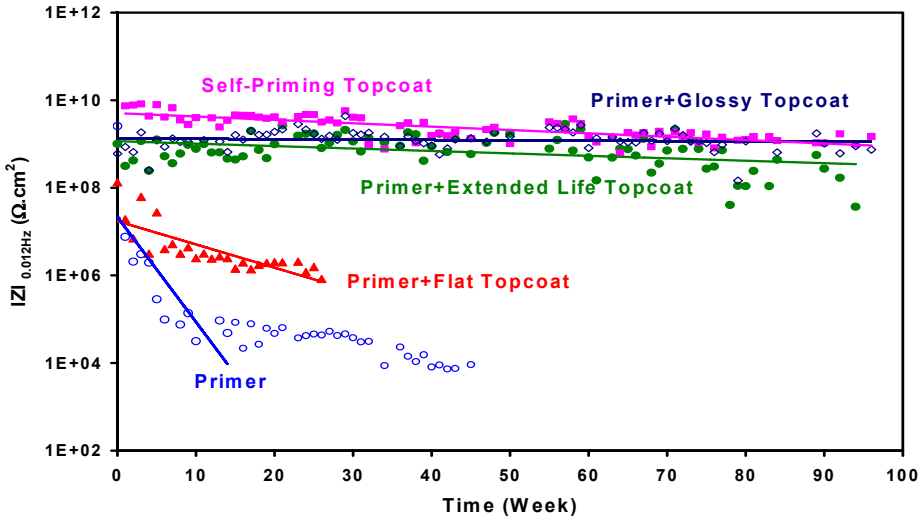

FIGURE 10. Impedance modulus vs. UV/Prohesion exposure time for batch II panels.

Figures 7, 8, 9, and 10 show resistance values against time for batch I and batch II panels. Batch II had one more coating system (Primer + Extended Life Topcoat), which is the experimental system, desired to replace (Primer + Flat Topcoat). Figures 7 and 8 are noise resistance (R_n) vs. exposure time and the Figures 9 and 10 are those of low frequency impedance modulus ($|Z|_{0.012Hz}$) vs. exposure time. These graphs of electrochemical resistance against

UV/Prohesion exposure time show that the noise data are more scattered than impedance data, especially for batch I panels. The values of R_n also seem to be larger than these of $|Z|_{0.012Hz}$ although less than a half of order in magnitude. However, in the long term, the orders of corrosion resistance ranked by R_n and $|Z|_{0.012Hz}$ for all the tested systems are consistent with each other for both batches. The electrochemical data had very good reproducibility and R_n or $|Z|_{0.012Hz}$ slopes of the trend lines were almost the same for the equivalent coating system in different batches.

At the beginning of exposure, all the coated systems, including the (Primer) system, showed high values of electrical resistance (R_n and $|Z|_{0.012Hz}$) values. However, the resistances of (Primer) and (Primer + Flat Topcoat) dropped quickly to reach a constant value about $10^4\ \Omega.cm^2$, which is essentially the value of the oxidized bare substrate. The exposure times during this process were 16 weeks for (Primer) and 25 weeks for (Primer + Flat Topcoat). The results clearly indicated that these two systems lost their corrosion protection rapidly and exhibited poor corrosion protective performance. The corrosion behavior of these two systems was reflected by the fast gloss loss and color change of the surface. The electrochemical data implied that multi-layer flat topcoat has not provided much protection for the primer underneath it. Fast failure of (Primer + Flat Topcoat) might be a direct result of the topcoat formulation. To offer a flat appearance, the coating must have a rough surface scattering the incident light. It seems that the pigment volume concentration (PVC) of this flat topcoat has been formulated to exceed the critical pigment volume concentration (CPVC) so that the coarse coating surface can be achieved. This process has the effect of introducing voids into the coating, as there is insufficient resin present to fill the interstices between the pigment particles. The voids make the coating film less dense and leave open the pathways for ingress of corrosive species to the substrate. One of

the alternatives to attain rough surface for low glass is to use new raw materials such as advanced fluoropolymers and encapsulated pigments.

After 116 weeks of long-term exposure, the systems (Self-Priming Topcoat) and (Primer + Glossy Topcoat) still maintained very high electrical resistances more than the order of $10^8 \Omega.cm^2$ in both tested batches. The results indicated excellent corrosion protection these systems have provided. Although (Self-Priming Topcoat) system slightly outperformed (Primer + Glossy Topcoat) system, the biggest gap in resistance between them was no more than a half of order of magnitude. The difference in their corrosion protective performance was smaller with longer exposure. At the end of exposure, their resistance values were almost the same, not showing distinct ranking between them. An extended exposure time is required to clearly differentiate their corrosion resistance under current exposure conditions.

The system of (Primer + Extended Life Topcoat), which was developed to replace the poor performance system (Primer + Flat Topcoat), has shown excellent corrosion resistance with relatively stable electrical resistance values after 95 weeks of exposure. The resistance was about a half order lower than that of (Self-Priming Topcoat) and (Primer + Glossy Topcoat), but still above $10^8 \Omega.cm^2$ at the end of exposure. The new fluropolyurethane topcoat system has considerably outperformed the replaced system in terms of corrosion protection. Its excellent weathering and corrosion resistance are related to the favored chemical structures of the fluropolymer. The polymer has a combination of alkyl vinyl ether and fluoroethylene structures that provide high exterior durability. In addition, the topcoat with the fluropolymer usually has low water uptake in a high moisture containing environment because water has low solubility in the polymer. This type of fluropolymer can be easily modified by copolymerization with hydroxy- or carboxy-substituted vinyl ether comonomers to give improved properties. The

functional groups on the alky vinyl ether units also make the polymer be easily incorporated into the coating formula. The fluropolymer with hydroxy groups can be cross-linked with aliphatic isocyanates under ambient conditions. Using the fluropolymer, the matt topcoat no longer needs to be formulated at PVC greater than the CPVC, the rough surface being achieved by the polymer/pigment aggregates in the coating.

II. ALTERNATIVE ENM RESULTS

Sample F was the epoxy primer coating with the polyurethane topcoat. The coating had been on test in the prohesion chamber for over two thousand hours and despite some degradation around the edges of the panel the main coating area was visually intact. This applied equally to the coating sample I; the epoxy primer with the silicone alkyd topcoat.

Figures 11 and 12 show R_n values calculated from noise data taken at the same time interval. Figures 13 and 14 use data obtained from tests week one (from above), then two further tests, test 2 at week four and test 3 at week six.

It can be seen in Figure 11 that the good visual appearance of the coating is reflected in the high R_n values from the data. The single substrate results and the bridge method results correlate well, mainly centered around $1x10^8$ ohms-cm^2. The closeness of the values from the two techniques indicates that the resistance of the coating is homogeneous. One of the bridge method R_n values is considerably higher on run 3 than those obtained by the other tests, this is considered an exception to the rule and reflects the nature of electrochemical data from organic coating tests.

Figure 12 shows a generally higher value of R_n for the silicone alkyd topcoat system compared to the polyurethane topcoat. The values from both techniques begin within half an

order of magnitude of each other but scatter increases with time. Run five has particularly bad scatter which is not typical of the data.

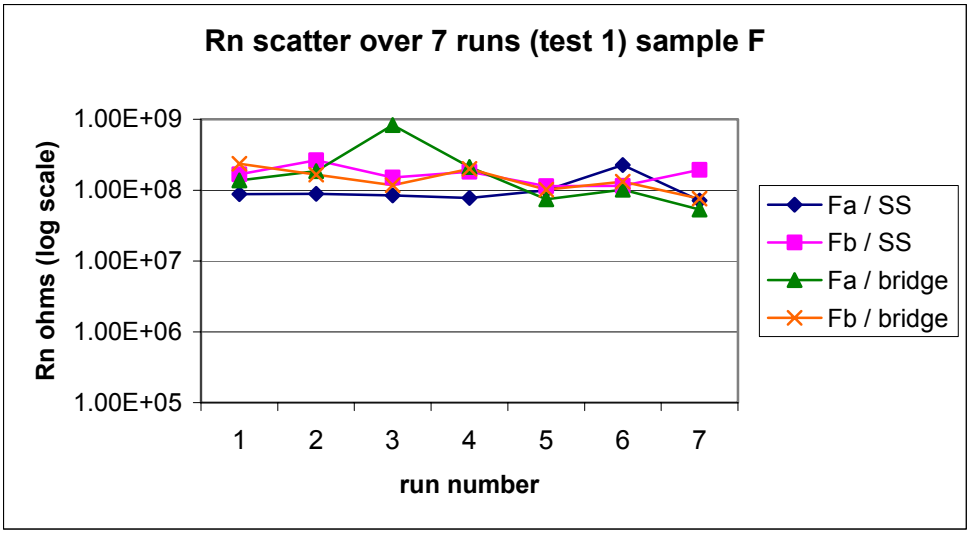

FIGURE 11. Polyurethane top-coat.

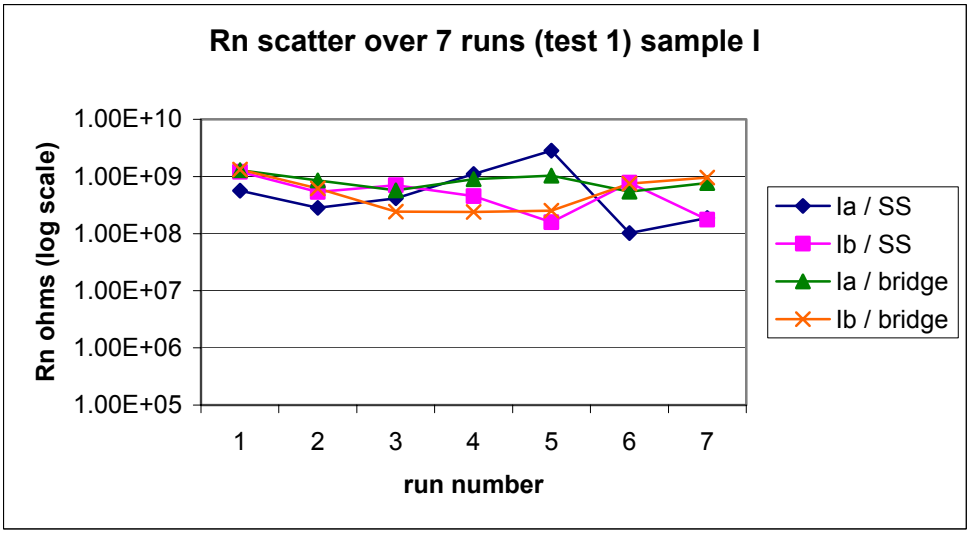

FIGURE 12. Silicone alkyd topcoat.

For the second test a longer period of time was allowed for the cells to settle before the readings were taken. Initially this was 10 minutes but this was increased to 45 for tests two and three. There was less scatter on the results from the single substrate technique which appears to indicate that the allowing the proper amount of time to let the system reach a steady state

condition with respet to electrolyte diffusion does play an important role in the acquisition of consistent data. The scatter of results from the bridge method is greater than that seen for the single substrate technique and this has been seen in previous work[vi]. Graphs of data scatter for tests two and three are not repeated here as there is little visual difference in the values. It is worth noting that the mean R_n values of the single substrate technique did not appear consistently in any order, in relation to the mean values of the R_n values from the bridge method.

Figures 13 and 14 show the averaged R_n values obtained from each technique over the three periods of time. They indicate the random nature of the order between the values from each technique and a typical spread of data from electrochemical tests on coating systems. However, by comparison of the R_n values and the order of magnitude range in which they fall, to the Bacon, Smith and Rugg criteria, useful information can be obtained as described previously. Both the ability of a coating to protect against corrosion in the first instance, or the state of an existing coating system that is already in service by monitoring against time could be assessed. By comparison of the results from the two techniques, it has been shown that coating information can be obtained by using the single substrate technique as a non-destructive monitoring method as an alternative to the more established bridge method.

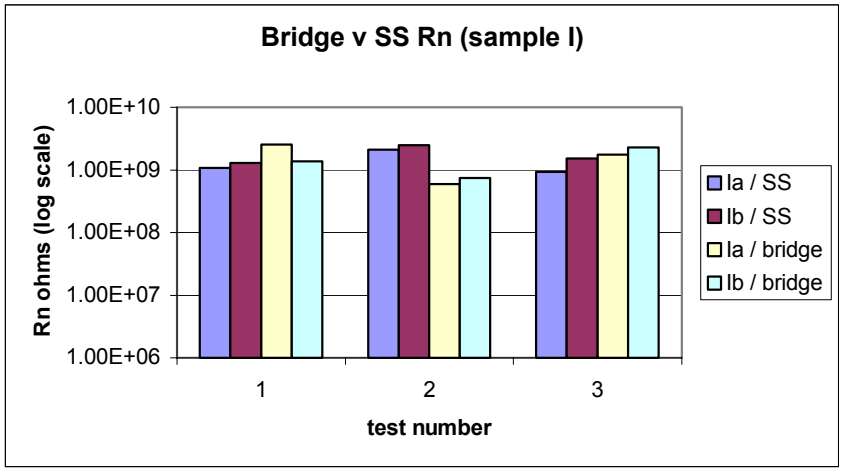

FIGURE 13. Silicone alkyd topcoat.

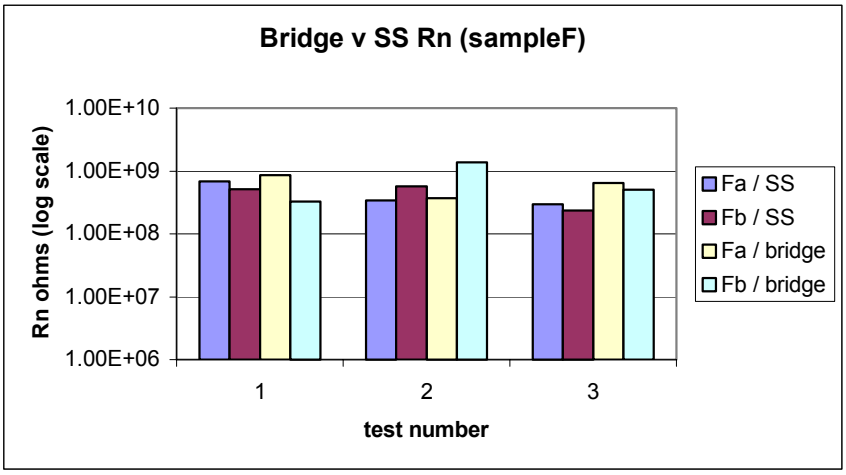

FIGURE 14. Polyurethane topcoat.

CONCLUSIONS

Using a combination of electrochemical techniques, appearance assessments, surface characterization and visual inspection, a series of aircraft coating systems have been ranked successfully across a range of poor to excellent performance.

The single substrate technique has been shown to produce data that is comparable to noise data obtained from the more traditional bridge method. The scatter of R_n values over six consecutive runs was visibly less than R_n values obtained from bridge method data. This was the seen to be the case with both coating systems tested and as with the bridge method the R_n values tracked the reduction of resistance with time for the single coat alkyd. The single substrate technique produced equally good data on the high resistance coating systems. From the graphs it can be seen that the relationship of R_n between both techniques is a random fluctuation with neither demonstrating a consistent higher or lower R_n value for a given specimen.

ACKNOWLEDGEMENTS

This work was supported at NDSU by the U.S. Air Force Office of Scientific Research under Grant F49620-99-1-0283, Lt. Col. Paul Trulove, Program Officer.

REFERENCES

1. J. Zhao, G. Frankel, and R. L. McCreery, (1998) "Corrosion Protection of Untreated AA-2024-T3 in Chloride Solution by a Chromate Conversion Coating Monitored with Raman Spectroscopy," *Journal of The Electrochemical Society, 145*, 7
2. S. T. Pride, J. R. Scully, and J.L. Hudson, (1994) "Metastable Pitting of Aluminum and Criteria for the Transition to Stable Pit Growth," *Journal of The Electrochemical Society, 141*, 11
3. M.W. Kendig, A.J. Davenport, and H.S. Isaacs, (1993) "The Mechanism of Corrosion Inhibition by Chromate Conversion Coatings from X-Ray Absorption Near Edge Spectroscopy (XANES)," *Corrosion Science, 34,* 1
4. J. He, V. J. Gelling, D. E. Tallman, and G. P. Bierwagen, (2000) "A Scanning Vibrating Electrode Study of Chromated-Epoxy Primer on Steel and Aluminum," *Journal of The Electrochemical Society, 147*, 10
5. R. L. Twite and G. P. Bierwagen, (1998) "Review of Alternatives to Chromate for Corrosion Protection of Aluminum Aerospace Alloys," *Progress in Organic Coatings, 33*, 2
6. Gordon Bierwagen, Junping Li, Lingyun He, and Dennis Tallman "Fundamentals of the Measurement of Corrosion Protection and the Prediction of Its Lifetime in Coatings," Chapter 14 in *Proceedings of the 2nd International Symposium on Service Life Prediction*

Methodology and Metrologies, Monterey, CA, Nov. 14-17, 1999, J. Martin and D Bauer, ed., ACS Books, Washington, DC (2001) 316-350

7. Mabbutt, S. J. and Mills, D. J. (1998) *British Corrosion Journal*, **33**, 2, pp158-160
8. Mabbutt, S. J. and Mills, D. J. (2000) Proc. EuroCorr, Queen Mary and Westfield College, London, UK.
9. Mabbutt, S. J. and Mills, D. J. (2001) *Surface Coatings International Pt. B: Coatings Transactions, 84,* pp 277-283
10. Wang, X., Bierwagen, G. P. and Mabbutt, S. J., (2001) Proc. EuroCorr, Lake Garda, Italy.
11. Bacon, B. C., Smith, J. J. and Rugg, F. M. (1948) *Ind. Eng. Chem*, **40**, pp 161-167.

DEVELOPMENT OF AN ADMICELLAR POLYMERIZATION PROCESS FOR DEPOSITING POLYPYRROLE ON ALUMINUM ALLOYS TO INHIBIT CORROSION

Steve Merchant, Melissa Rieger, and Ed O'Rear

School of Chemical Engineering and Materials Science
University of Oklahoma
Norman OK 73019

ABSTRACT

Thin polypyrrole films were formed and deposited onto aluminum alloy-7075 plates for the purpose of corrosion inhibition. Two surfactants, dodecylbenzene sulfonic acid (DBSA) and pyrrole-2-carboxylic acid (P2C), were separately studied to determine the effectiveness of each in this process. The films formed with the P2C showed more adhesion and continuity than the films formed with DBSA. The oxidative polymerization of polypyrrole, employed in admicellar polymerization, produced sulfuric acid. This caused the pH to drop to levels corrosive to aluminum. This reaction resulted in the poor film quality and, hence, poor corrosion inhibition.

INTRODUCTION

Electrically conducting polymers (ECPs), such as polypyrrole, have been of interest over the last twenty years because of their unique electrical and physical properties. Applications in biosensors, battery electrodes and semi-conductors have benefited from the use of ECPs. Recently, polypyrrole has been shown to protect against corrosion on a variety of substrates[1, 2]. Several mechanisms for the corrosion protection proposed suggest that the corrosion protection provided by polypyrrole and other ECPs results from charge transfer stabilization, substrate passivation, or the polymer acting as an electrolyte barrier[1, 3].

Electrochemical and oxidative chemical polymerization methods have been employed by researchers as the means by which the polypyrrole film is formed and deposited onto the

substrate. Electrochemical polymerization requires a conductive substrate, which is not always convenient or optimal. The oxidative chemical polymerization methods that have been studied involve the use of solvents including m-cresol[2] and chloroform[3], which are toxic and incompatible with aluminum and its alloys. A potential alternative to this is admicellar polymerization, which requires little solvent, and can be adapted to metallic and ceramic surfaces.

Admicellar polymerization, a process developed at the University of Oklahoma, enables the deposition of ultra-thin polymeric films on the surface of a wide range of substrates in an aqueous solution. Surfactants adsorb at the solid liquid interface to form ordered aggregates, admicelles, similar to micelles in bulk solution. Monomer molecules then solubilize in the organic medium formed at the interface by the admicelle. An initiator is then added to the solution to polymerize the monomer at the interface. Using this novel process, Wu et al were able to deposit thin films of polystyrene on porous alumina[4]. The researchers were able to show that capillarity of the surfactant solution resulted in the formation of polystyrene within the porous substrate. Later, Funkhouser et al had moderate success depositing polypyrrole on flat aluminum surfaces using admicellar polymerization[5]; employing sodium dodecyl sulfate as the surfactant. Recently, Yuan et al, using atomic force and scanning tunneling microscopy, were able to characterize the quality of the polypyrrole films formed on mica and alumina surfaces via admicellar polymerization. They determined that the films were smooth and continuous[6].

The focus of this research is to develop an admicellar polymerization process by which polypyrrole can be deposited onto a flat aluminum alloy surface and within a crevice geometry formed by fasteners and lap joints, particularly on aircraft, for the purpose of corrosion inhibition. Such a process would optimize the application of polypyrrole films by eliminating

dangerous solvents and the inconvenient constraint of making the substrate an electrode. It would also have the potential of forming a high quality film, which is very important in the process of corrosion inhibition. Admicellar polymerization makes the application of this process to crevices, lap joints, or other small openings viable due to the capillary behavior previously noted. Figure 1 shows the proposed admicellar polymerization process using pyrrole-2-carboxylic acid as the surfactant.

EXPERIMENTAL

MATERIALS

Dodecylbenzene sulfonic acid (DBSA), and pyrrole-2-carboxylic acid (P2C) were the surfactants used to form the admicelle. Pyrrole 98% and ammonium persulfate (APS) were the monomer and oxidant respectively. All products were purchased from Sigma-Aldrich and used as received.

METHODS

The experiments were performed on aluminum alloy 7075 plates from 1.5 to 2 in^2. Plates with and without pretreatment were studied. The pretreatment consisted of immersing the plates in a Chromerge® bath for 30 seconds and rinsing thoroughly with deionized water. The plates were then ultrasonically cleaned in a 50/50 mixture of acetone and isopropanol for 30 seconds, then rinsed and dried in an oven at 100^{oc} for 2 hours. This pretreatment was employed to; (1) remove organic films on the surface of the alloy left by the manufacturer that inhibits adsorption of the surfactant molecules, and (2) to create a thicker oxide layer on the surface of the alloy. Since Chromerge® contains chromium; elemental analysis was used to determine if any Cr

remained on the surface after rinsing. No chromium was detected. Plates without pretreatment were simply cleaned with the 50/50 acetone-isopropanol mixture.

The AA-7075 plates were placed in a glass vial with 20 ml of deionized water, into which the surfactant was dissolved. Surfactant concentrations were varied below each respective critical micelle concentration (cmc) to prevent surfactant aggregation in the bulk solution. The solution set for 6 hours to allow the surfactant molecules to adsorb and equilibrate at the solid liquid interface. The pyrrole monomer was then added and left for 12 hours to allow the adsolubilization into the admicelle. The ammonium persulfate was added in equimolar amounts to the pyrrole to initiate polymerization. When the solution was completely black, the plates were removed and rinsed with deionized water to remove excess surfactant and any polymer that had not adhered to the surface. The coated plates were set to dry in ambient air before electrochemical analysis was performed.

CHARACTERIZATION

Linear polarization resistance experiments (voltammetry) were used to characterize the effectiveness of the polypyrrole film as a corrosion inhibitor. This method involves measuring the current produced by sweeping the potential of the metal around its open circuit potential (E_{oc}). This process allows for the determination of the corrosion potential (E_{corr}), corrosion current (I_{corr}), and corrosion rate ($Rate_{corr}$) of the substrate.

The dried plates were placed in an electrochemical cell along with 40 ml of a 3.5% wt. solution of NaCl and a saturated calomel electrode as the reference. The potential of the sample was scanned from $^{+}/_{-}$ 15mV around the E_{oc} at a rate of .25 mV/sec using a Solartron 1287® potentiostat. Tafel plots were generated and analyzed to determine the E_{corr}, I_{corr}, and the $Rate_{corr}$ of the sample.

RESULTS AND DISCUSSION

FILM FORMATION

The admicellar polymerization of polypyrrole was performed using two surfactants, DBSA and P2C. The films formed using the DBSA as the surfactant showed no continuity and very poor adhesion, as most of the black film would rinse off after polymerization. After examining DBSA concentrations below its cmc (6.3 e-4 M), it was determined visually that very little polypyrrole had been deposited on the AA-7075 plates.

Films formed using the P2C as the surfactant showed much better continuity and adhesion, as most of the black film remained on the sample after rinsing. The cmc of the P2C was determined to be on the order of 10^{-3}M by means of the Wilhelmy-plate method using a Cahn-322 Dynamic Contact Angle Analyzer. There was no visual variation in the quality of the film as the concentration of surfactant was varied from 10^{-4} M to 10^{-3} M. It is proposed that the P2C performed better because of the similarity between the organic portion of the surfactant and the monomer. As a result, the concentration of pyrrole at the surface is greater since more monomer solubilizes into the admicelle; thus, better increased coverage on the AA-7075 plate.

To test the effect of the surfactant, the experiment was performed without the use of a surfactant. The result was a black film of moderate continuity and poor adhesion. After rinsing, a small portion of the film remained on the sample. In addition to rinsing with water, a Scotch® tape test was employed to determine adherence. According to this method, the most adherent film was that formed with the P2C, followed by the film formed with the DBSA. The film formed without surfactant showed no adherence.

Much of the problem with poor adhesion and film uniformity was attributed to the presence of corrosion taking place during the polymerization process. It was visually apparent

that some corrosion had occurred during the polymerization process, as there were randomly located discolorations, characteristic of corrosion, on the aluminum. Figure 2 shows polypyrrole formed on AA-7075 plates using DBSA and P2C as surfactants. From left to right, sample 1 is an untreated, bare sample. Sample 2 is a treated, bare sample. The difference in color between 1 and 2 was due to the thicker oxide layer on the treated sample. Sample 3 and 4 are the films formed by DBSA and P2C, respectively, after rinsing. The film on sample 3 appeared patch wise, while the film on sample 4 was continuous. The corrosive spots on the coated samples are also visible.

The oxidative polymerization of pyrrole using APS as the oxidant produces sulfuric acid, shown in figure 3, as a by-product. This caused the solution pH to drop from 6.5 to <2. The Pourbaix diagram of aluminum shows that active corrosion will occur at a pH lower than 4.5, indicating that the admicellar polymerization solution was destructive to the surface of the substrate.

A potential solution to this problem lies in the selection of an oxidant that will not form a strong acid as a by-product of the oxidative polymerization of pyrrole; particularly, oxidants whose by-products have relatively high pKa values. It is anticipated that the selection of such an oxidant would make the pH of the solution controllable, thus, minimizing corrosion.

CORROSION TESTING

Linear polarization performed on the uncoated plates was used for comparison with the polypyrrole coated aluminum. Figures 4 show the potential versus log of current density graphs for bare aluminum with and without the pretreatment described earlier. Table 1 summarizes the results from the graphs. Pretreatment of the AA-7075 plate caused a reduction in the I_{corr} resulting in a lower corrosion rate. It is believed that the reduction in I_{corr} was due to the increase

in oxide thickness from the pretreatment. This effect would show to have little influence on the corrosion behavior of the sample with polypyrrole films. Figure 5 shows the potential versus log current density graph for AA-7075 plates coated with the polypyrrole films formed without surfactant. Table 2 displays the corrosion results, which showed that there was little difference in the corrosion behavior from polypyrrole films formed without surfactant and the bare AA-7075.

Figure 6 shows results of the linear polarization tests for the samples with polypyrrole films formed by admicellar polymerization using the P2C. Table 3 summarizes the results of these tests. Again, there was little difference in the corrosion behavior of the AA-7075 coated by admicellar polymerization. This is also thought to be due to the chemistry occurring during the polymerization. The poor corrosion inhibition is believed to be related to the by-product formed during the polymerization of the pyrrole. During this process, APS molecules remove hydrogen atoms from pyrrole molecules forming sulfuric acid. This process drastically decreases the pH from the initial value of 6.5 to a value lower than 2. At pH values of 4 or lower, the corrosion of aluminum surfaces is accelerated due to the dissolution of their characteristic protective oxide layers. This is believed to be the dominant process occurring; inhibiting the formation of uniform films and reducing the potential protection afforded by the polypyrrole film. In this case, the dynamics occurring at the surface also influence the adsorption characteristics of the surfactant.

There is also very little protection provided to the substrate by the film as the corrosion rates for each case compared to that of the bare sample indicate.

CONCLUSIONS

The admicellar polymerization of pyrrole was attempted using two surfactants, DBSA and P2C. Use of the P2C yielded more uniform and adherent films of polypyrrole. However, film quality was poor. Electrochemical analysis using linear polarization confirmed the poor film formation and low corrosion inhibition. The polypyrrole problems were believed to be caused by dramatic decreases in pH resulting from the polymerization of pyrrole with APS. APS reacts to form sulfuric acid, causing the solution pH to decrease below 2. At pH< 4.5, the aluminum actively corrodes, preventing admicelles to remain at the aluminum surface.

Elimination of the low pH reached during the reaction could possibly be accomplished by employing either hydrogen peroxide or peracetic acid as the oxidant. This would disrupt the formation of a strong acid thus preventing the pH from reaching levels corrosive to aluminum and its alloys.

Along with experimentation with different oxidants, the future of this research includes the implementation of electrochemical impedance spectroscopy, FTIR and atomic force microscopy (AFM) to enhance the characterization process of the films produced by admicellar polymerization. The application of this process to simulated crevices will also be examined to determine its usefulness to similar geometries.

ACKNOWLEDGEMENTS

This project is funded by the United States Air Force DEPSCOR grant. Special thanks are given to the Oklahoma State Regents of Higher Education, Kha Mach, and Olga Matarredona.

REFERENCES

1. Iroh J.O., Su W., *Electrochimica Acta*, 46 (2000) 15-24
2. Shah, K., et.al., *Key Engineering Materials*, 197(2000) 111-120
3. Ferloni, P., et.al., *Electrochimica Acta*, (1996) 41(1) 27-33
4. Lee J.Y., Kim D.Y., Kim C.Y., *Synthetic Metals*, 74 (1995) 103-106
5. Lee Y.H., Lee J.Y., Lee D.S., *Synthetic Metals*, 114 (2000) 347-353
6. Wu J., Harwell J.H., O'Rear E.A., *Langmuir*, (1987) 3(4), 531-537
7. Yuan W.L., O'Rear E.A., Cho G., Funkhouser G.P., Glatzhofer D.T., *Thin Solid Films*, 385(2000) 96-108

TABLE 1
Summary of results from linear polarization tests of bare and pretreated samples

	No Pretreatment	Pretreatment
E_{corr}	-222 mV	-729 mV
I_{corr}	5.55 E-6 (amp/cm^2)	5.86 E-8 (amp/cm^2)
$Rate_{corr}$	.062 mmPY	.00066 mmPY

TABLE 2
Summary of results from linear polarization tests of films formed with no surfactant

	No Pretreatment	Pretreatment
E_{corr}	-724 mV	-717 mV
I_{corr}	1.03 E-6 (amp/cm^2)	4.76 E-6 (amp/cm^2)
$Rate_{corr}$	.011 mmPY	.053 mmPY

TABLE 3.
Summary of results from linear polarization tests of films formed by admicellar polymerization

	No Pretreatment	Pretreatment
E_{corr}	-728 mV	-709 mV
I_{corr}	1.22 E-6 (amp/cm^2)	3.23 E-6 (amp/cm^2)
$Rate_{corr}$	.014 mmPY	.036 mmPY

Step 1: Formation of admicelle

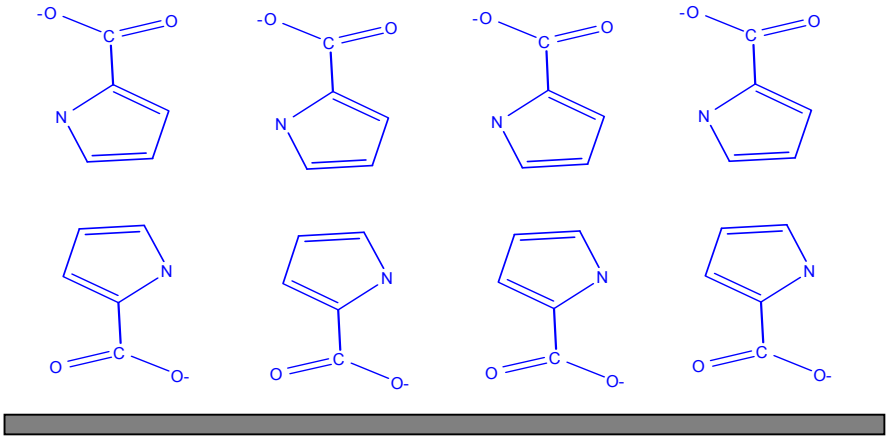

Step 2: Solubilization of Pyrrole

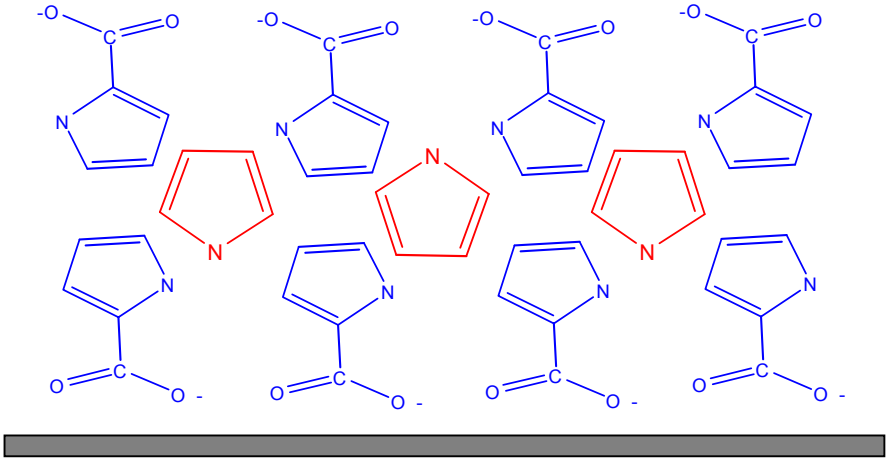

Step 3: Polymerization of Pyrrole

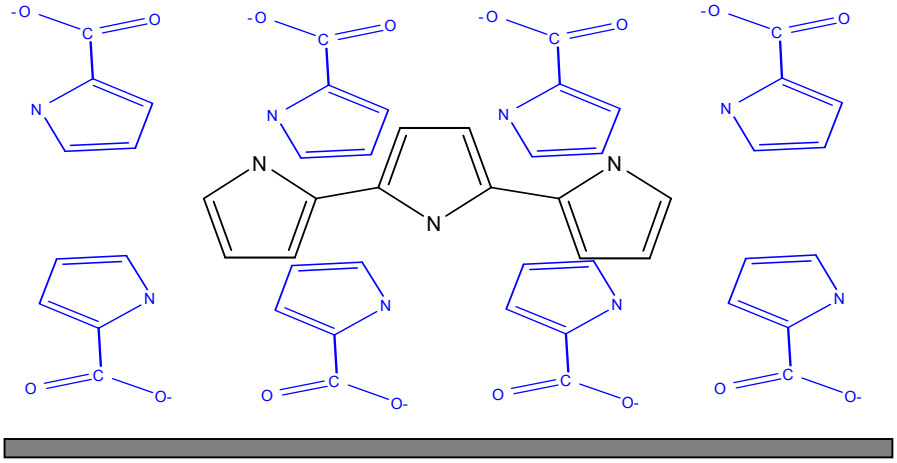

FIGURE 1. Proposed Admicellar Polymerization Process for Polypyrrole using P2C

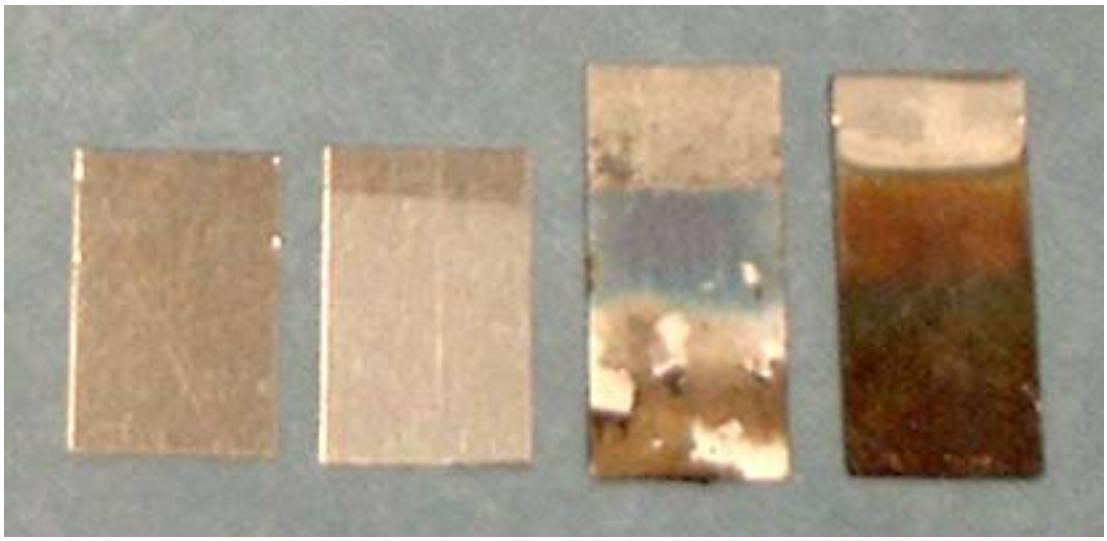

FIGURE 2. From left to right (1-4); 1- bare sample; 2- pretreated sample; 3- film using DBSA; 4- film using P2C

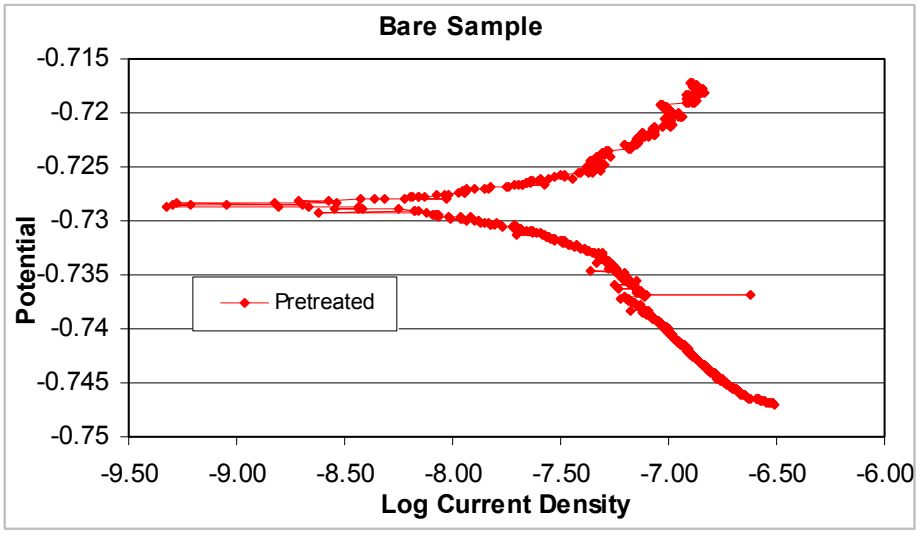

FIGURE 3. Linear polarization tests on *pretreated* AA-7075 to determine corrosion behavior

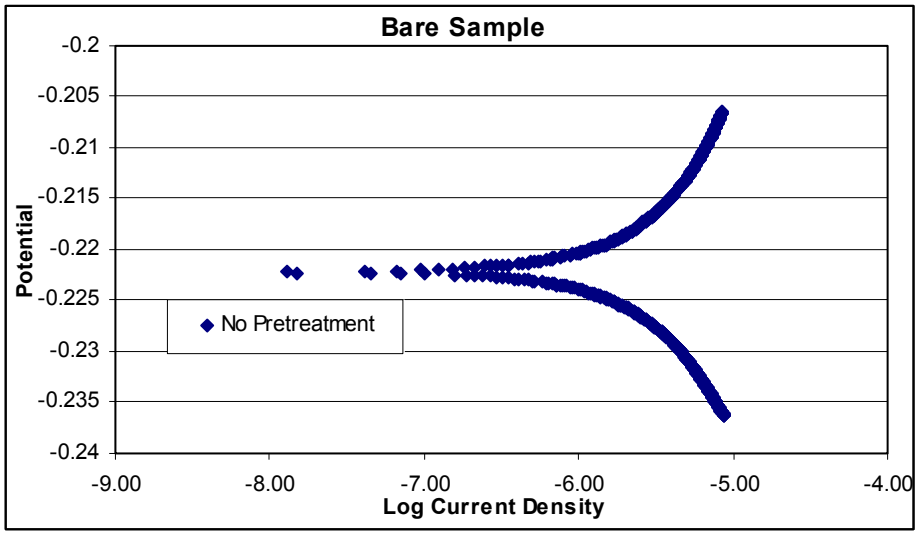

FIGURE 4. Linear polarization tests on AA-7075 to determine corrosion behavior

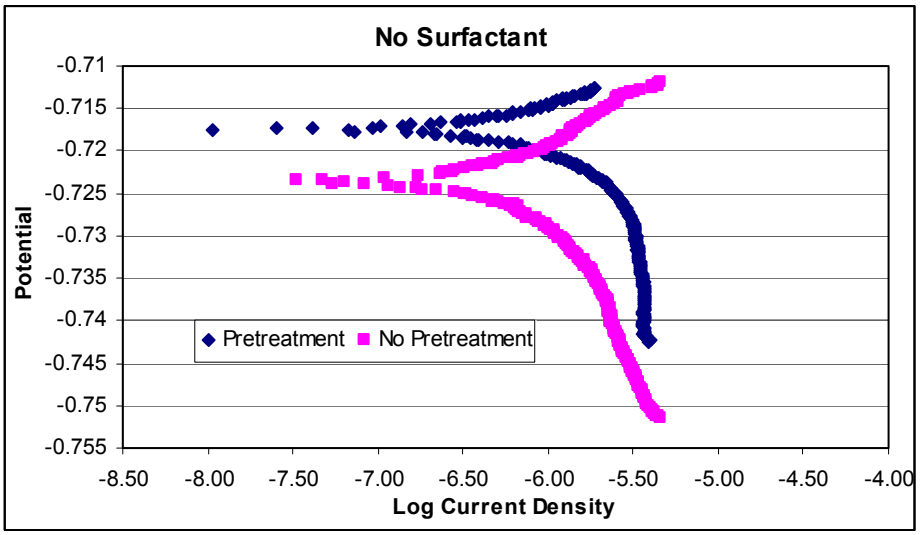

FIGURE 5. Linear polarization test on AA-7075 with polypyrrole film formed without surfactant.

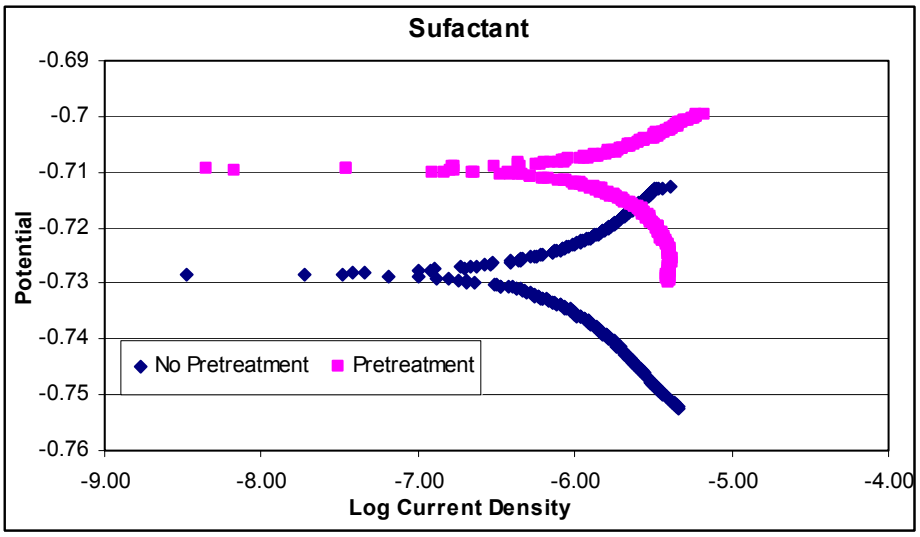

FIGURE 6. Linear polarization test on AA-7075 with polypyrrole film formed with surfactant.

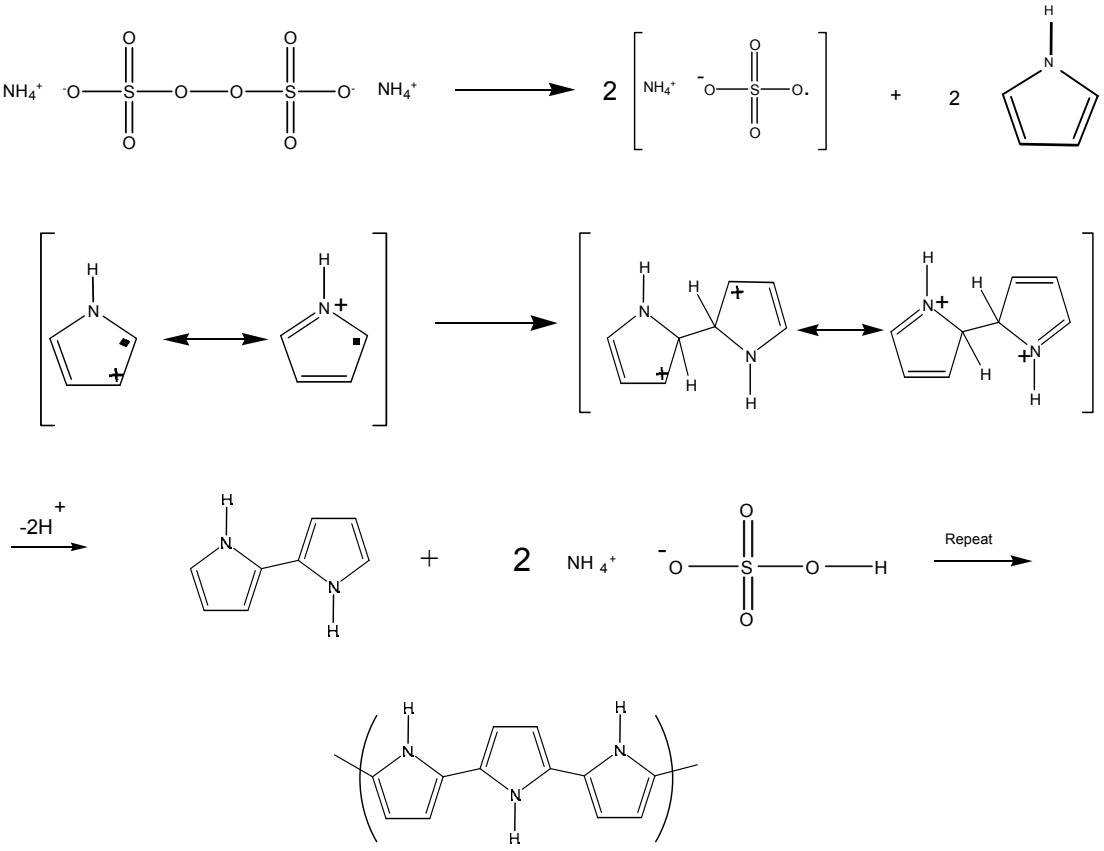

FIGURE 7. Oxidative polymerization of pyrrole using APS as oxidant

INVESTIGATION OF INTEGRATED COATING SYSTEM FOR CORROSION PROTECTION

Robert L. Parkhill
Sciperio, Inc.
5202-2 N. Richmond Hill Rd.
Stillwater, OK 74075

Olga Kachurina, Tammy L. Metroke, and Edward T. Knobbe
Environmental Institute (Oklahoma State University)
003 Life Science East
Stillwater, OK 74078

John Ostrander and Nicholas Kotov
Department of Chemistry (Oklahoma State University)
107 Physical Sciences
Stillwater, OK 74078

ABSTRACT

The corrosion resistance characteristics of an integrated multilayer coating system comprised of a layer-by-layer (LBL) stack and an organically-modified silicate (ormosil) have been analyzed using potentiodynamic polarization curve analysis. Results presented indicate that the LBL coating with Co^{+3} or Cr^{+6} followed by a hybrid ormosil coating, produced from a TEOS/VTMOS/MEMO mixture, yields a composite with enhanced corrosion-resistant coatings. Based on a comparison of the electrochemical data, there is a clear indication that the environmentally-compliant, nanostructured coating showed significant improvement over the hexavalent chromate treatment on AA 2024-T3. In addition, the baseline coating system without any corrosion-inhibiting additives, yields improvements evidenced through reduced corrosion current, and elevated corrosion- and pitting-potentials. Addition of corrosion inhibiting cations to the nanoengineered layers (e.g., Co^{+3}) provides additional performance improvements in all aspects of the pontentiodyanmic polarization curves (PPC) characterizations.

INTRODUCTION

The Air Force has identified corrosion of aluminum-skinned aircraft and the development of improved environmentally-compliant surface treatments for aluminum alloys (AA) to be topics of high priority. Changing federal regulations dictate the use of fundamentally new

surface treatment methods, which are capable of meeting more stringent environmental standards. Treatments that rely on the use of hexavalent chromium-based corrosion prevention compounds (e.g., Alodine 1200-type treatments) are expected to be removed based on environmental concerns. In the future, protective coatings must be compatible with near- and long-term environmental regulations, capable of large-scale application, and be easily integrated into current and future primer/topcoat paint systems.

A wide variety of novel coating processes have been developed as potential replacements for hexavalent chromium-based conversion coatings[1] as described in various reviews.[2] Some of the promising protection systems are derived from sol gel processing.[3-8] In reviews by Guglielmi et al. and Metroke et al., authors sited several different studies using sol-gel derived coatings as potential corrosion inhibiting systems for metal substrates.[4,5] Specific attributes, such as film adhesion, barrier properties, scratch resistance, and chemical inertness have been identified as primary features contributing to the corrosion protection of such systems. Sol-gel derived organically-modified ceramic (ormocer) coatings have been shown to provide exceptional corrosion protection on metal substrates.[5-8] When one considers the characteristic attributes of ormocer films (e.g., low temperature processing, chemical inertness, adhesion, diffusion barrier, absence of Cr(VI), etc.), it can be seen that sol-gel derived hybrid coatings represent one of the most promising approaches to the development of corrosion-inhibiting surface pretreatments.

The layer-by-layer assembly (LBL) developed by G. Decher is one of the newest methods of thin film deposition with potential use in the development of corrosion resistant coatings.[9] The LBL coating can be described as a sandwich-like structure with alternating layers of either charged polymers (polyelectrolytes) or a combination of oppositely charged polyelectrolytes and nanoparticles. The deposition of the films can be performed in a cyclic

manner, which is made possible by the overcompensation of surface charge, which often takes place when polyelectrolytes and other high molecular weight species are adsorbed to a solid-liquid interface.[10] The electrostatic and van-der-Waals attraction between a colloid and a layer of polyelectrolyte ensures facile adsorption. At the same time, the electrostatic repulsion between similarly charged species in solution limits the thickness of the newly formed adlayer of nanoparticles. Thereby, through repeated deposition of the oppositely charged layers, a uniform high quality film can be deposited.

LBL assembly also offers a unique method of incorporating ionic and oxide based corrosion inhibitors into individual sublayers.[11] Oxide corrosion protectors such as Co_2O_3, Cr_2O_3, CeO_2, ZrO_2, Mo_xO_y, and other species, can be incorporated in to the sublayer in the form of nanoparticles. Cationic and anionic species, such as Cr^{+6}, Co^{+3}, and NO_3^- can be incorporated into the sublayers through ion exchange. In comparison with mere incorporation of metal oxide nanoparticles and/or charged ions into the sol–gel, the LBL layering approach gives substantially greater density of the active species in the immediate vicinity of the AA surface.

In the present work, coating systems comprising LBL and ormosil layers have been investigated to determine the degree of corrosion resistance enhancement afforded by integration of the two components. By combining LBL coating attributes, such as versatile incorporation of corrosion inhibitors and high local activity of ionic species at the aluminum interface, with the barrier protection of an ormosil coating, a new coating system can be envisioned with improved corrosion protection and flexibility. To demonstrate that this concept is viable, multilayer LBL/Sol-Gel coating systems were prepared on 2024-T3 aluminum alloy substrates. Film attributes, such as morphology, were characterized using scanning electron microscopy (SEM) to determine coating compatibility, while corrosion-resistance and barrier performance of the

prepared LBL/Sol-Gel coatings were reported using PPC. Corrosion-resistance properties were assessed by comparing LBL/sol-gel treated aluminum 2024-T3 panels with comparable panels having a standard Alodine-1200 surface pretreatment.

EXPERIMENTAL

MATERIALS

Tetraethylorthosilicate, TEOS, 3-(trimethoxysilyl)propylmethacrylate, MEMO, and vinyltrimethoxysilane, VTMOS, were purchased from Aldrich or Gelest and were used as received. Swy-2 sodium montmorillonite (University of Missouri-Columbia, Source Clay Minerals Repository) was used as received without further modification.

COATING PROCEDURES

Layer-by-Layer (LBL) Assembly Preparation. Substrate materials were composed of 2024-T3 aluminum alloy. Test pieces were first washed vigorously with Citronox® soap and a soft bottle brush to reduce the concentration of residue from the manufacturing process, as well as any debris. The samples were then rinsed with copious amounts of deionized water (DI, 18.2MΩ /cm, Barnstead E-pure systems) and then dried at 100 °C for one hour. Subsequently, the samples were placed in closed glass containers containing acetone (Pharmco), and ultrasonicated (Fisher Scientific FS20) for about one hour, removed and allowed to dry.

Approximately 0.5 grams of montmorillonite clay (aluminosilicate platelets with dimension ranging from 1 to 5um in width and length and 5 to 50nm in thickness) was dispersed in about 100ml of DI water and ultrasonicated for two hours. The solution was allowed to stand for at least one day, the supernatant removed, and diluted to about 1:5 using deionized water.

In order to prepare PDDA-clay LBL layer assemblies, the aluminum alloy substrates were immersed in a 1% aqueous solution of poly(diallyldimethylammonium chloride), PDDA (Aldrich), for five minutes to allow for good adsorption of the polyelectrolyte (PE). The samples were removed from the PDDA solution and briefly rinsed with clean water from a plastic squeeze bottle to remove excess PE from the surface and edges. Subsequently, the samples were rinsed for 2 minutes using fresh deionized water and then transferred to another beaker containing clean water where they are rinsed for an additional 3 minutes.

The samples were then transferred to a beaker containing a 1% solution of poly(acrylic acid), or PAA, where the PE was allowed to adsorb for five minutes. The rinsing process was repeated, and the samples were immersed one more time for five minutes in PDDA and then rinsed again. The samples, while still wet, were immersed in the clay suspension and the particles were assembled for 10 minutes.

This process was repeated for up to 20 layers, with visually apparent buildup of PE and clay after only 4 layers. Producing the 20 layer samples may not be accomplished in one single experiment. Between layers, after the clay step and rinse, as required, the samples were dried with compressed air to remove as much water as possible and placed on end in a clean, dry, closed container. The experiment was then resumed in the following session. This was not found to affect the sample quality.

Sol-gel coating. Ormosils were prepared by mixing 5.6 ml TEOS, 7.6 ml VTMOS, 2.0 ml MEMO, and 9.8 ml 0.05 M HNO_3. The solutions were allowed to stir for one hour prior to film deposition. The Ormosil solutions were deposited onto cleaned or LBL-coated AA by a spray coating technique using an airbrush setup. Ormosil film thicknesses on bare aluminum alloy were approximately 10 microns as measured using a digital DeFelsko Series 6000 coating thickness gage. The coatings were allowed to dry at ambient conditions for at least 24 hours prior to their characterization.

CORROSION INHIBITORS

Nanoparticle-coated test coupons were immersed in 0.25 M $K_2Cr_2O_7$ for 30 minutes at ambient temperature or into a conversion coating solution developed by Schriever[12] at 140-150 °F for 30 minutes in order to introduce Cr^{+6} or Co^{+3} inhibitor ions, respectively. The Schriever conversion coating solution was prepared by mixing 55g/l NH_4NO_3, 26 g/l $Co(NO_3)_2{\cdot}6H_2O$, 26.4 g/l formic acid in 750 ml H_2O. The pH of this solution was adjusted to 7.0-7.1 with concentrated NH_4OH. Subsequently, 3.5 ml/l H_2O_2 (30 wt. %) and distilled H_2O were added to increase the volume to 1 L. The stock solution was heated to 140 °F for 30-90 minutes. The final pH was adjusted to 6.8-7.0 using concentrated NH_4OH. After immersion in the inhibitor solutions, the test coupons were rinsed with deionized water.

POTENTIODYNAMIC POLARIZATION MEASUREMENTS

Electrochemical measurements were performed using a BAS CV-50-W unit and a three-electrode cell equipped with a platinum counter electrode, a Ag/AgCl/Cl^- (3M KCl) reference electrode and a coated or non-coated AA 2024-T3 panel as the working electrode. AA working electrode panels, including uncoated control and coated test specimens, had an exposed area of 0.36 cm^2. All measurements were conducted in an aqueous 1M NaCl working solution at 25 ± 1

^{o}C. The reported values of potentials are given relative to the Ag/AgCl/Cl^- reference electrode. Oxygen was removed by purging the solution with purified nitrogen for approximately 30 minutes prior to the polarization measurements.

In order to reach steady corrosion potentials (E_{corr}), the electrodes were kept in the working solution for 30 minutes prior to electrochemical measurements with the electrical circuit open. Then, the acquisition of polarization curves was started from this open circuit potential, with a constant sweep of 1 mV/sec. Corrosion current values, I_{corr}, reported herein correspond to a 50 mV stretch between the cathodic and anodic parts of the polarization curve. Corrosion resistance was calculated using the equation $R_{corr} = 50mV/ 2I_{corr}$. This differs from the previously described definition of corrosion resistance(ref); however, this approach corresponds to the theory of electrochemical processes and complies with the ASTM G-59-97 standard for conducting potentiodynamic polarization resistance measurements. This method allows finding of the parameter R_{corr} for the entire pool of polarization curves collected in this study regardless of their shift along the abscissa. Pitting potentials, E_{pit}, were determined using the criterion described by Kelly et al wherein pitting would have occurred by the time the anodic current density of the specimen reached 3 x 10-5 A/cm^2(ref).

RESULTS AND DISCUSSION

BASIC DESCRIPTION OF A LBL/SOL-GEL COATING SYSTEM

The multilayer LBL/Sol-Gel coating system is composed of two layers on the aluminum alloy surface. The layer immediately adjacent to the aluminum alloy surface is derived from an aluminosilicate-polyelectrolyte composite, which may incorporate one or more active corrosion inhibitors (placed on or within a platelet by ion exchange) that are trapped within the exfoliated

aluminosilicate sheets. The top layer is made from an Ormosil coating exhibiting good barrier and corrosion resistance properties. Figure 1 shows a representative structure of a basic LBL/Sol-Gel coating system.

Although active corrosion inhibitor ions, such as Co^{+3} and Cr^{+6}, are expected to retain some of their mobility in the LBL/Sol-Gel coating system, we anticipate the inhibitor ions to be concentrated in the LBL layer; the uppermost portion of the LBL film may become sealed by the sol-gel film as curing may promote condensation reactions between the sol-gel film and the clay platelets, resulting in a thin, impermeable layer. The LBL layers in the vicinity of the aluminum alloy surface remain unchanged and serve as media for active inhibitor diffusion. In comparison with mere incorporation of metal oxide nanoparticles in the sol-gel layer, the layering approach gives substantially greater density of the active species in the immediate vicinity of the aluminum alloy surface.

Figure 2 shows a scanning electron microscopy image of the cross-section of a Co^{3+} inhibitor-doped LBL/Sol-Gel multilayer coating system. In this image, bare aluminum, LBL layer and the LBL layer can be clearly seen.

ELECTROCHEMICAL CORROSION RESISTANCE ANALYSIS OF FILM ASSEMBLIES

Potentiodynamic polarization curve analysis of bare aluminum and various LBL/hybrid coating film assemblies are shown in Table 1. Figure 3 shows potentiodynamic polarization curves for the coating systems under investigation.

Analysis of Standard Chromate Conversion Coating: Hexavalent chromium conversion coating was used as a control in this study due to its proven ability to act as a corrosion inhibitor for aluminum alloys (AA). Hexavalent chromium conversion coatings on the surface of AA were found to significantly improve the corrosion resistance, R_{corr}, from 8 $k\Omega cm^2$ for bare

aluminum to 143 $k\Omega cm^2$ for 2 minute immersion time. Similarly, E_{corr} values were found to shift to the more positive values from -720 mV for bare aluminum to -480 mV for hexavalent chromium conversion coated surfaces.

Analysis of LBL Film Containing No Inhibitor Ions: A significant increase in corrosion resistance was not observed upon coating the AA with 20 layers LBL film. R_{corr} values were found to be 10 $k\Omega cm^2$. However, E_{corr} and E_{pit} values increased from (-720 to –561) $k\Omega cm^2$ and (-654 to –533) $k\Omega cm^2$, respectively. This shift into the more positive potential region indicates the formation of a thin, barrier film on the substrate.

Analysis of LBL Film, Containing Corrosion Inhibiting Ions: Absorption of either Co^{+3} or Cr^{+6} inhibitor ions onto the LBL layers lead to an enhancement in corrosion resistance characteristics. R_{corr} was found to increase from 10 to (150-199) $k\Omega cm^2$; similarly, E_{corr} and E_{pit} values were found to increase from –561 mV and –533 mV to (-484 to –491) mV and (-464 to –465) mV, respectively.

Analysis of an Sol-Gel Derived Ormosil Film: There is a significant increase in corrosion protection afforded by coating the aluminum alloy with an Ormosil film as indicated by the increase in corrosion resistance, R_{corr}, from 8 $k\Omega cm^2$ for bare aluminum to 100 $k\Omega cm^2$ for AA coated with an Ormosil film. Similarly, an increase in E_{pit} values from –654 to –468 was observed, respectively.

Analysis of LBL/Sol-Gel Assemblies, Containing no Inhibitor Ions: There is an increase in the corrosion resistance, R_{corr}, from 8 $k\Omega cm^2$ for bare aluminum to 100 $k\Omega cm^2$ for AA /Sol-Gel and to 150 $k\Omega cm^2$ for LBL film /Sol-Gel. These results indicate that the LBL films are highly compatible with the sol- gel coating and provide additional protection when used in combination with the sol-gel coating, compared to the LBL film alone. The same conclusion is

inferred from corresponding changes in E_{corr} from –720 mV for bare aluminum to –473 mV for LBL film/Sol-Gel and from –654 mV to -316 mV for E_{pit} respectively.

Analysis of LBL/Sol-Gel Assemblies Containing Corrosion Inhibiting Ions: Introduction of known active corrosion inhibiting ions using the exchange capacity of clay and PAA in the protective film gives an increase of corrosion resistance, R_{corr}, from 8 $k\Omega cm^2$ for bare aluminum to 199 and 208 $k\Omega cm^2$ for Co^{+3} and Cr^{+6}, respectively. Introduction of the Ormosil in these systems exhibits a dramatic change of Epit into the positive potential region. For example, E_{pit} increased by more than 800 mV for the AA/Co^{+3}-exchanged LBL film when compared to the AA/Co^{+3}-exchanged LBL film /Sol-Gel, which is also an indication of improved corrosion protection imparted by the complex LBL/Sol-Gel protection system on the AA surface.

In review of the PPC results three specific conclusions were identified with regards corrosion protection based on LBL and integrated coating systems. (1)LBL as a single component system was not found to significantly enhance corrosion resistance. (2) LBL with a hybrid coating provided an enhancement of corrosion resistance properties over LBL and hybrid single component systems. (3) Ion-exchange with corrosion inhibiting ions led to a significant enhancement in corrosion resistance properties. Based on these three conclusions one can conclude that an integrated inhibitor-exchange LBL/sol-gel coatings system has great promise as an environmentally-benign replacement coating system for chromate conversion coatings.

CONCLUSIONS

The corrosion resistance behavior of aluminum 2024-T3 substrate coated with an integrated LBL/sol-gel coating system has been investigated. The corrosion resistance characteristics of an integrated multilayer coating system has been analyzed using

potentiodynamic polarization curve (PPC). Results presented have indicated that a LBL coating with Co^{+3} or Cr^{+6} followed by a hybrid ormosil coating produced from a TEOS/VTMOS/TMSPM mixture yields a composite with enhanced corrosion-resistant performance. PPC analyses of bare AA, Co^{+3} - and Cr^{+6} -exchanged layer-by-layer (LBL) film assemblies and a combination of ion-exchanged (IE) LBL films with sol–gel coatings revealed clear evidence that the integrated coating system provided enhance corrosion resistance. The baseline coating system, without any corrosion-inhibiting additive, yields improvements evidenced through reduced corrosion current, and elevated corrosion- and pitting-potentials. Addition of corrosion inhibiting cations to the nanoengineered layers (e.g., Co^{+3}) provides additional performance improvements in all aspects of the PCC characterizations. Based on these initial results, there is a clear indication environmentally-compliant, nanostructured coating shows significant improvement over the hexavalent chromate treatment on AA 2024-T3.

REFERENCES

1. (a) G. O. Ilevbare, J. R. Scully, Y. Yuan, R. G. Kelly, Corrosion, 56 (2000), 227; (b) . E. Hughes, R. J. Taylor, B. R. W. Hinton, Surface and Interface Analysis, 25 (1997), 223; (c) F. W. Lytle, R. B. Greegor, G. L. Bibbins, K. Y. Blohowiak, R. E. Smith, G. D. Tuss, Corrosion Science, 37 (1995), 349; (d) S. Jeffcoate, H. S. Isaacs, A. J. Aldykiewicz, M. P. Ryan, J. Electrochem. Soc. 147 (2000), 540; (e) L. Xia, R. L. McCreery, J. Electrochem. Soc. 15 (1998), 3083.

2. (a) A. Nylund, Aluminum Transactions, 2 (2000), 121; (b) C. J. E. Smith, K. R. Baldwin, S. A. Garrett, M. C. Gibson, M. A. H. Hewins, P. L. Lane, ATB Metallurgie, 37 (1997), 266; (c) J. Puippe, Galvanotechnik., 90 (1990), 3003; (d) R. L. Twite, G. P. Bierwagen, Progress in Organic Coatings, 33 (1998), 91.

3. R.L. Parkhill, T.L. Metroke, M.S. Donely, E.T. Knobbe, Prog. Org. Coat, 41 (2001), 261.

4. M. Guglielmi, J. Sol-Gel Sci. & Tech., 8 (1997), 443-449.

5. T.L. Metroke, R.L. Parkhill, E.T. Knobbe, Prog. Org. Coat, 41 (2001), 233.

6. M. Pilzand, H. Romich, J. Sol-Gel Sci. & Tech., 8 (1997), 1071-1075.

7. M. Shane, M.L. Mecartney, J. Mater. Sci., 25 (1990), 1537-1544.

8. M. Atik, P.L. Neto, L.A. Avaca, M.A. Aegerter, Ceram. Inter., 21 (1995), 403-406.

9. G. Decher, Science 277 (1997), 1232-1237. G. Decher, J. D. Hong, Thin Solid Films, 210/211 (1992), 831. G. Decher, J. D. Hong, Ber. Bunsen-Ges. Phys. Chem. Chem., 95 (1991), 1430. G. Decher, H. Haas, H. Mohwald, A. Kalachev, Physica B, 198 (1994), 89-91.

10. J. B. Schlenofff, H. Ly, M. Li, J. Am. Chem. Soc., 120 (1998), 7626-7634.

11. K. Ariga, Y. Lvov, I. Ichinose, Kunitake, . Appl. Clay Sci., 15 (1999), 137.

12. M. P. Schriever, U.S. Patent 5,551,994 (Sept. 3, 1996).

13. G. O. Ilevbare, J. R. Scully, J. Yuan, R. G. Kelly, Corrosion, 56 (2000), 227.

TABLE

TABLE 1
Electrochemical Characteristics of LBL/Sol-Gel Coating Systems Under Investigation

Composition	$I_{corr} \times 10^7$ (A/cm^2)	R_{corr} (kΩ·cm^2)	E_{corr} (mV)	E_{pit} (mV)
AA[2]	31	8	–720	–654
Hexavalent Chromium	1.74	143	-480	-439
AA/PDDA–Clay LBL (20 Layers)	25	10	–561	–533
AA/Sol–Gel	2.5	100	–510	–468
AA/PDDA–PAA–Clay LBL (20 Layers)/Sol–Gel	1.66	150	–473	–316
AA/Co^{3+}-IE PDDA–PAA–Clay LBL (20 Layers)	1.26	199	–491	–464
AA/Cr^{6+}-IE PDDA–PAA–Clay LBL (20 Layers)	1.2	208	–484	–465
AA/Co^{3+}-IE PDDA–PAA–Clay LBL (20 Layers)/Sol–Gel	1.25	199	–540	+342
AA/Cr^{6+}-IE PDDA–PAA–Clay LBL (20 Layers)/Sol–Gel	1.48	217	–200	+673

FIGURES

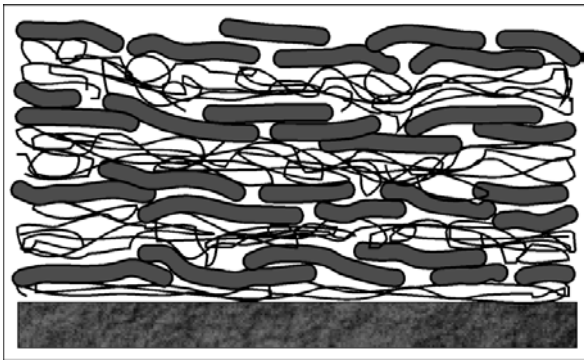

FIGURE 1 - Schematic representation of the LBL coating.

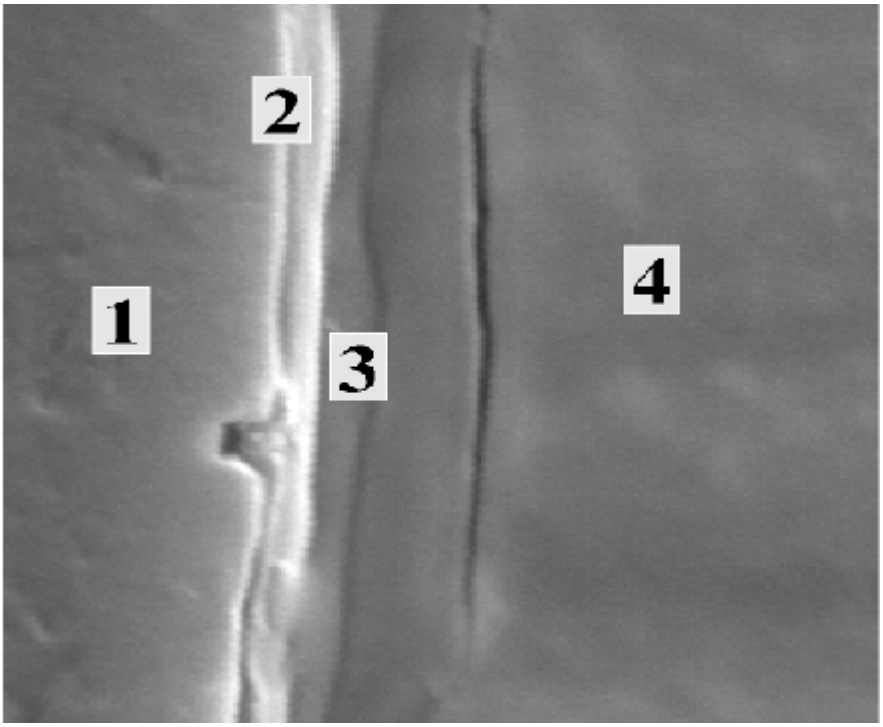

FIGURE 2. Scanning electron microscopy image of the cross-section of LBL/sol-gel coating: (1) aluminum, (2) LBL layer, (3) sol-gel layer (4) imbedding matrix.

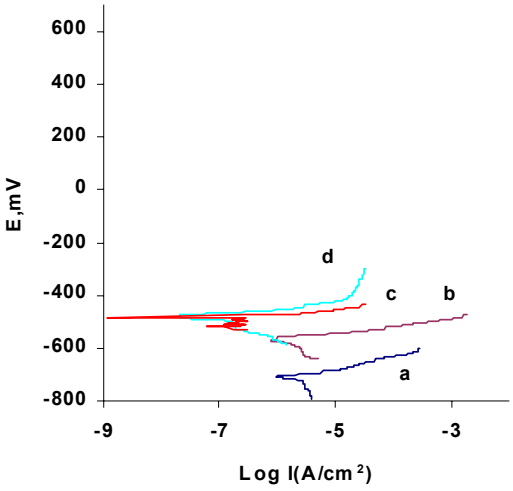

FIGURE 3a - Potentiodynamic polarization curves for (a) bare 2024-T3 aluminum alloy, (b) LBL film (20 layers), (c) hexavalent chromium conversion coating, (d) LBL film / Sol-Gel coating .

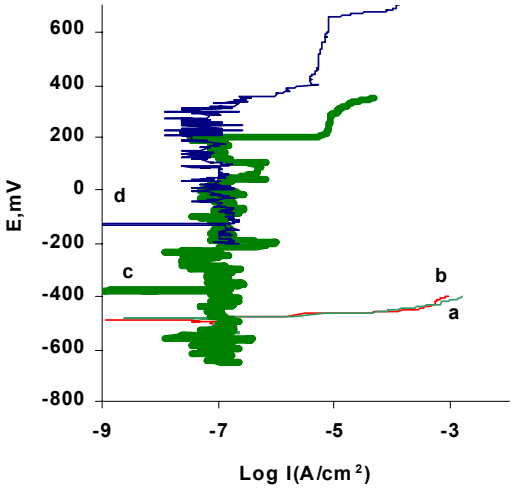

FIGURE 3b - Potentiodynamic polarization curves for (a) Co^{3+}-exchanged LBL film, (b) Cr^{6+}-exchanged LBL film, (c) Co^{3+}-exchanged LBL film /Sol-Gel, (d) Cr^{6+}-exchanged LBL film/ Sol-Gel .

FATIGUE LIFE PREDICTION OF CORRODED PARTS USING ARTIFICIAL NEURAL NETWORK ANALYSIS OF NDE DATA

E.B. Shell[1], R.G. Buchheit[2]

[1] Center for Material Diagnostics
University of Dayton Research Institute
Dayton OH
[2] Ohio State University
Department of Material Science and Engineering
Columbus OH

INTRODUCTION

Corrosion initiated fatigue failure in high strength aluminum alloys continues to be a serious concern in aging aircraft systems. There is little understanding of how to quantify corrosion damage during maintenance and depot inspections or how to relate NDE data of corrosion damage to residual fatigue life. This paper details a new approach to combining results of various NDE techniques to predict residual fatigue life of corroded components. Al 2024 fatigue specimens were corroded to produce a range of corrosion morphologies including intergranular, pitting, and general corrosion. These specimens were examined using ultrasonic inspection, optical profilometry, and microradiography. Image analysis was performed on the data to obtain statistics such as pit density, pit depth, surface asperity spacing, intergranular corrosion extent, and other parameters that may be relevant. These data will be input into an Artificial Neural Network (ANN) and used for residual fatigue life prediction. To benchmark ANN predictions, the residual fatigue life will be measured on the corroded samples. This multi-sensor approach enables the detection, characterization, and quantification of various forms of damage by utilizing the strengths of different techniques to combine for an enhanced analysis of

the material. This could result in an improved relationship between corrosion damage and residual fatigue life.

BACKGROUND

NDE NEEDS OF THE USAF

The requirements for NDE in the Air Force are changing. Due to overwhelming costs, both direct costs as well as those associated with planes being grounded, there is a movement to shift the strategy for dealing with aging aircraft.[1] Currently, the Air Force operates under a "find-it-fix-it" premise – any component suffering corrosion damage that is found must be repaired or removed from service if the projected cost of repair is too large. However, recent studies of condemned aircraft have shown that much of the corrosion damage that has been found has been largely cosmetic damage with little effect on the structural integrity of the component. So, a more cost-effective and reliable strategy – namely an "anticipate and manage" approach – must be implemented.

The implementation of this strategy will create new requirements and expectations that current NDE procedures do not address. Current NDE techniques are very capable of *finding* corrosion damage. However, most of these inspection techniques stop at that point, failing to actually *evaluate* or *quantify* the damage that is found. This leads to a dilemma that the Air Force does not want to deal with: spending large amounts of money and time repairing damage that may not be structurally meaningful. So, instead of simply finding corrosion, the expectation is that future NDE methods will be able to *find* corrosion, *quantify* the level of damage, and *help the inspector make an informed decision* as to the expected life of the component.

EFFECT OF CORROSION DAMAGE ON FATIGUE LIFE

The primary mechanism for crack initiation in a corroded specimen is through the result of a stress concentration at the root of corrosion pits.[2] This is fortunate, from an NDE point of view, as topological changes on the component surface due to pitting are relatively easy to locate and quantify. However, due to the stochastical nature of both corrosion pitting and fatigue crack initiation, it is difficult to develop and verify a model that relates the two. There have been numerous attempts at relating a measured corrosion pit depth to residual fatigue life.[3,4] However the success of these studies has been based on some rather simplistic assumptions concerning the morphology of the corrosive attack, e.g. treating fatigue-crack initiating pits as hemispherical defects. In practice, pits investigated by sectioning are usually highly tortuous, often following grain boundaries. In this type of damage, optical surface techniques cannot accurately measure the true damage depth while the assumptions made using radiography to determine pit depths are invalid since not all corrosion is surface bound.

There are no universal analytical formulas relating corrosion damage to residual fatigue life. However, certain trends may be seen upon close evaluation of testing data. Topological measurements made by white light interference microscopy (WLIM) have been shown to be somewhat relevant to fatigue life.[5] In general, it was found that residual fatigue life decreases with increasing number of pits, pit volume, surface roughness and maximum pitting depth. However, attempts to explain or quantitatively model the fatigue behavior entirely through a fracture mechanics-type analysis of topological data have been only mildly successful.

Empirical models relating corrosion damage to fatigue life are an alternate approach to this problem. The key to achieving an empirical relationship lies in obtaining data from numerous complementary techniques. For instance, profilometric data obtained by WLIM

contains much valuable and useful information about the surface and stress risers that are a result of pitting damage. However, by itself, it tells nothing about any damage that occurs just beneath the surface, such as intergranular (IG) corrosion, exfoliation, or tortuous pitting that is seen in anisotropic materials. Likewise, a technique like micro-focal radiography will give good data on general material/thickness loss and severe pitting damage, but would not be able to resolve the material loss due to IG corrosion and highly localized corrosion. Ultrasonic inspection, eddy current, and surface acoustic wave techniques would give information about internal and near-surface voids, crevices, cracks, and IG corrosion.

There is no easy way to combine the data from multiple input sources. Data fusion techniques are made difficult when the form of the data from the included NDE methods are not of the same form. While most NDE techniques included in this study result in picture-form data, the information in that picture has been pre-processed in order to get some relevant metrics. For instance, it would be nearly impossible for a neural network to extract the information that is contained in a Fourier transform of profilometry data without some form of pre-processing. So, one method of fully utilizing the information contained in NDE is to use numerical or image analysis to obtain metrics describing the corrosion damage, and then feed those metrics into a model, in this case powered by an artificial neural network.

ARTIFICIAL NEURAL NETWORKS

Artificial neural networks are mathematical models of a complex, nonlinear, parallel computer. In a functional sense, they operate like the human brain. In the brain, neurons accept electrical signals, process the sum of the inputs into the neuron nucleus, then send output signals across synapses to other neurons where similar operations occur. While a computer model of the brain, in the form of an ANN, cannot approach the complexity of nature's neural system, a

computer neural network can be trained to do simple pattern recognition, perform classification into one of several groups, or make numerical predictions. The same basic mathematical components of a natural neuron are present in the artificial neural network (Fig. 1). Input parameters (NDE metrics) are fed to the ANN on the left. These values are processed by a center hidden layer, and an output (residual fatigue life) is predicted on the right.

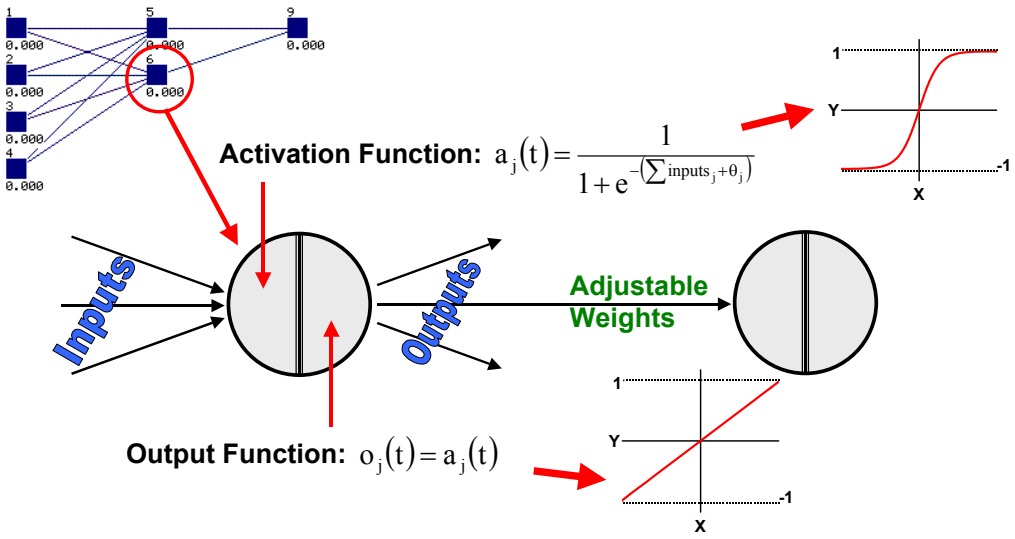

FIGURE 1. Structure of an ANN unit

There are numerous reasons for using an ANN to correlate the data from the various NDE sources. Foremost is the flexibility that is inherently a part of ANNs. ANNs are capable of modeling nonlinear effects because of the use of nonlinear transfer functions in the hidden layer. A large, unstructured network architecture may be used if little or no knowledge is available about the system. Alternatively, a tailored architecture may be used by restricting the structure of the network, or setting up weight sharing if there is prior knowledge about the system.

A second advantage of ANNs is that they are fault tolerant. They are said to have graceful performance degradation.[6] That is, with increasing noise in the input data, the quality of

the output usually degrades only slowly. Because corrosion and fatigue initiation processes are normally stochastic in nature, the analysis method that is used must be able to handle noisy data.

Finally, ANNs have the ability to make generalizations about the data. Classical statistical methods are designed to fit closely to the data, which can become troublesome with sparse or noisy data sets. ANNs are often able to determine trends in the data, even in the presence of large amounts of noise. An important limitation in ANN for predictive purposes arises because they are fundamentally interpolation based. There can be little confidence in predictions made outside of the training data range. For this reason it is important to include a full range of possible training conditions to have a robust ANN.

METHODS

Each individual NDE technique has its own strengths and weaknesses. Certain tools are adept at detecting specific corrosion attack morphologies while completely missing damage of a different form. An understanding of this information is critical to be able to design a residual life prediction methodology that will work over a range of damage types.

ULTRASONIC MEASUREMENT

Ultrasonic measurements conducted with high-frequency (20-200 MHz) transducers provide a mix of information concerning loss of thickness, internal corrosion morphology, and intergranular corrosion damage. The most convenient method is to inspect from the back (uncorroded) surface if it is accessible. This generally provides a smooth, flat surface for easy triggering and maximum transference of the signal into the test object. Then, echoes can be examined using both amplitude and time of flight (TOF) as criteria.

The amplitude of the back surface reflection gives information about the roughness of the surface. Areas with higher roughness will presumably have a higher percentage of high angle surface features, which scatter the acoustic signal and result in a lower reflection amplitude. The TOF of the acoustic signal before a peak is reached provides information about the depth of damage and/or the degree of pitting. This is especially helpful in specimens containing IG corrosion, since there are no easy nondestructive ways to reveal this type of damage.

Both of these types of information can be visualized in the form of C-scans. From these data sets, image analysis can be used to obtain metrics such as a 'quasi-roughness' from the amplitude image or the depth of the corrosion damage from a TOF image.

MICRORADIOGRAPHY

Microradiography has been used successfully in the determination of key corrosion damage parameters, such as pit depth.[4] Radiography essentially works as a shadow method where x-rays are focused through a specimen onto a recording medium. Areas of lesser thickness or density are identified through contrast differences in the obtained image. The lateral resolution of the micro radiography system is approximately 5 um while the depth resolution is dependent on the thickness of the specimen being investigated. Generally, the pit depth necessary for detection is around 1-2% of the thickness of the component. This thickness resolution limits the effectiveness of the method to components that have been subjected to severe pitting or a large loss of material due to corrosion at the surface. IG or exfoliation corrosion damage is usually not seen by radiographic methods, although occasionally a removed grain boundary is seen that happens to be at an angle parallel to the x-ray source.

WHITE LIGHT INTERFERENCE MICROSCOPY

White Light Interference Microscopy (WLIM) is a technique that obtains topographical data with a high vertical (3 nm) and lateral (0.2 μm) resolution. Although WLIM has a much higher resolution than either radiography or ultrasonic methods, the data obtained could be potentially misleading depending on the nature of the attack. If the material is highly anisotropic or the attack is intergranular, then profilometry would not provide an accurate picture of the level of damage. This is due to the line-of-sight limitation on profilometry data. If the corrosion path bends beneath the surface then profilometric data will not be as meaningful. Of course, there will be some meaningful information contained in the profilometry data. Still, it is dangerous to base a model completely on profilometric data without a clear understanding of the form or morphology of the damage.

Due to the high vertical and spatial resolution of the WLIM data, we are able to obtain several potentially meaningful metrics. A very accurate measurement of the deepest pit may be obtained, again under the assumption that there is no tortuous pitting. There are several forms of the roughness available (average, RMS, peak-to-peak, etc.). The total material volume removed by corrosion is available for clean pitting or uniform corrosion types of damage. The loss of cross-sectional area can also be calculated. This would directly affect the true stress that the specimen carries during fatigue loading. The surface fraction pitted is easily obtained by imposing a binary sort on the profilometry data using a pre-selected height (depth) threshold.

Finally, the Power Spectral Density (PSD) of the surface may be calculated. The PSD of a surface is obtained by calculating the Fourier transform of the data. This transforms the data from the spatial domain into the frequency domain so that the "power" of high frequency asperities may be investigated. In this context, the "power" of asperities refers to a combination

of the heights and density of a asperities at a given height amplitude. The Fourier transformation of a surface approximates the surface by the superposition of an infinite number of sine waves of varying power. So, as a surface is roughened by corrosion for example, the power of the higher frequency asperities increases, telling us that there are a greater number of large closely spaced peaks and valleys.

ARTIFICIAL NEURAL NETWORK ANALYSIS

It is not known presently which of these metrics are most relevant to fatigue crack initiation. However, through a self-guided training process for the ANN, the network will begin to learn which parameters have the greatest effect on crack initiation and what form that relationship should take. As ANN training proceeds, some of these metrics may be found to be unrelated or have a negligible impact on crack initiation and residual fatigue life. Others may be shown to contain redundant information (i.e. peak-to-peak roughness may contain the same information as the deepest pit as determined by WLIM). In these cases, the network architecture will be amended to consider only the relevant parameters in order to obtain a better fit and understanding of the relevance of each metric.

The final result of an ANN analysis is a model that takes some number of inputs (e.g., deepest corrosion damage depth, PSD, roughness, material lost) and predicts the residual fatigue life or effective stress intensity. This prediction can then be used to assess components and aid in retirement for cause decisions.

APPLICATION OF METHODS

Although the complete ANN analysis of the test specimens has yet to be completed, some preliminary NDE results show where these techniques have potential, either in the prediction of

residual fatigue life or in the general detection of certain forms of corrosion. Table 1 lists some of the measurable metrics that are thought to be relevant to crack initiation and residual fatigue life.

A small study has been performed to compare different types of NDE data obtained from visible, discrete pits. This study was conducted on an electrochemically-pitted specimen (Fig. 3a) that was produced through the work of Simon and Khobaib.[5] Three different techniques (WLIM profilometry, micro radiography, and ultrasonic imaging) were used to characterize the dimensions of the pits (Fig. 3b, c, and d, respectively). The comparison of these data sets provides an interesting look at the strengths and weaknesses of each technique.

TABLE 1
Corrosion metrics measured or calculated by NDE

Ultrasonic Testing	
D_{ultra}	Depth of damage, location of first signal detected from ultrasonic beam sent from the back wall (uncorroded surface)
SD_{ultra}	Standard Deviation of c-scan amplitude gated near corroded surface – related to the surface roughness
AI_{ultra}	Average intensity of the back wall reflection
MR_{ultra}	Depth of maximum reflection intensity – should give depth of IG damage
White Light Interference Microscopy	
R_a	Average roughness
R_q	RMS roughness
R_z	Peak-to-peak roughness
R_t	Peak-to-peak roughness
H_a	Histogram value – average surface depth
H_{sd}	Histogram value – standard deviation of surface depth
H_s	Histogram value – skew of surface depth
H_k	Histogram value – kurtosis (‘peakedness’) of surface depth
A_{corr}	Cross sectional area lost to corrosion
V_{corr}	Volume lost to corrosion
PSD	Power Spectral Density value at 30 mm^{-1}
Microradiography	
D_{rad}	Depth of damage, calculated from the grayscale level of the image
A_{rad}	Cross sectional area lost to corrosion

First, it should be emphasized that the information from each technique generally agrees with the other two. However, the low resolution (both lateral and depth) of the ultrasonic method provides a meaningful detailed comparison. For the profilometric and radiographic data, the data was despeckled to correct for discrete measurement noise in the WLIM image, was smoothed to reduce the noise due to film graininess in the radiographic image, and was corrected for an uneven x-ray source in the radiographic image. Subsequently, the height images were subtracted to obtain a difference image, which highlights differences in the two data sets (Fig. 4).

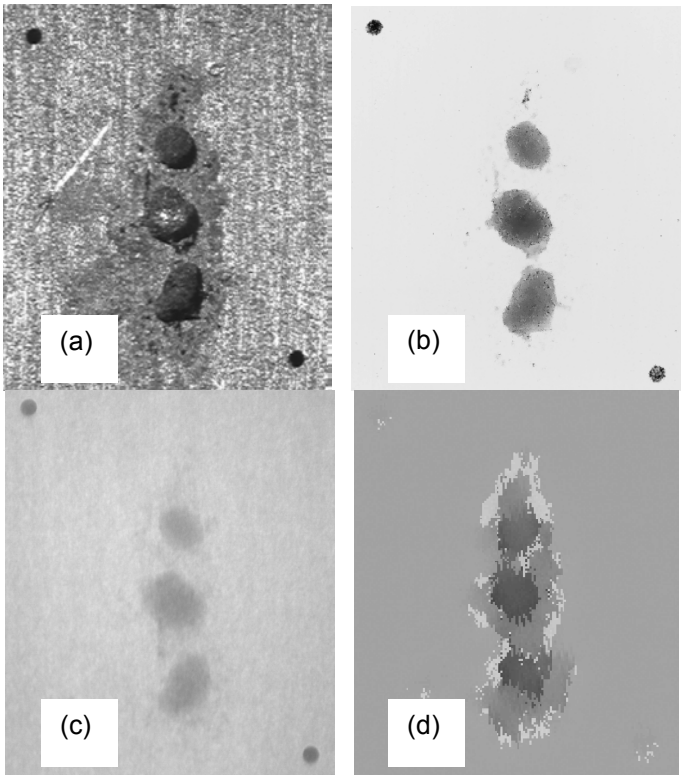

FIGURE 3. Corrosion pit images obtained by (a) optical microscopy, (b) WLIM profilometry, (c) microradiography, and (d) ultrasonic inspection

In this image, a couple of features are evident that highlight the capabilities of the two techniques. First, there is a region above the middle pit in which there is a discrepancy between

the two measurements. In this case, there is internal corrosion that profilometry could not detect, being a line of sight optical method. Using radiography, it is still uncertain the effect of this damage, since there is no way to tell the depth of the feature. On the other hand, there is a sharp, relatively deep (~80μm) pit below the three major pits. This pit was undetectable by microradiography, possibly due to the low thickness resolution of the method.

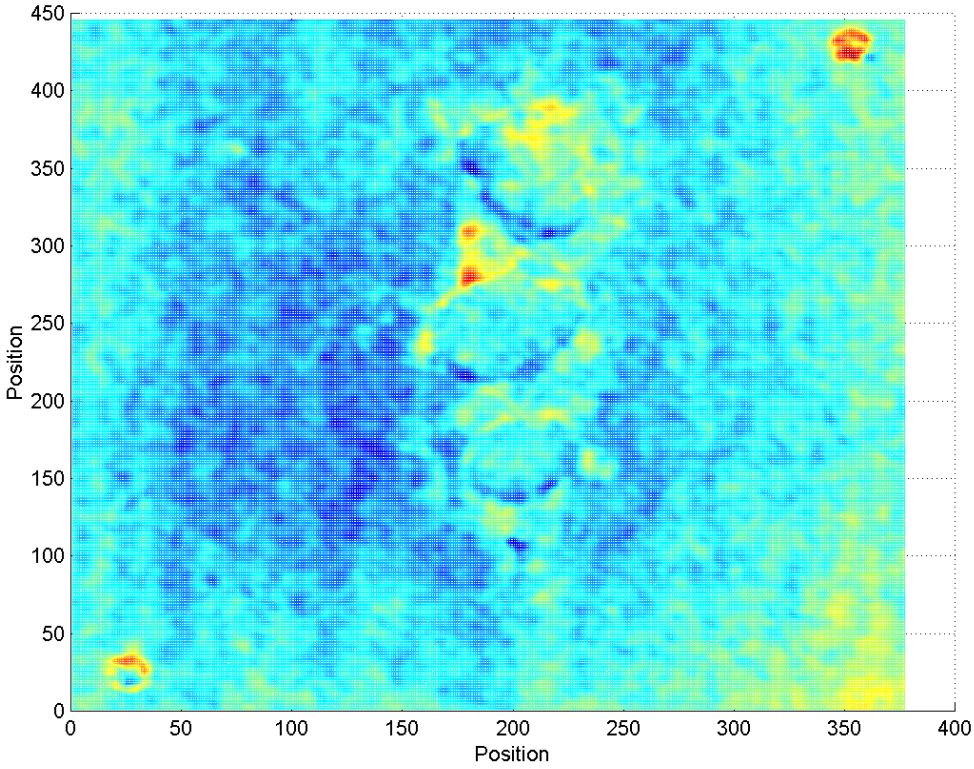

FIGURE 4. Image showing differences in the type of features that microradiography and profilometry can detect

In addition to this study, there are some expectations regarding the applicability of individual methods to specific forms of corrosion:

- Profilometry is expected to give some meaningful information concerning nearly all forms of corrosion. However, in the cases of IG or tortuous pitting corrosion, the profilometry data will probably not be as pertinent when predicting residual fatigue life.
- Microradiography will likely prove not useful in the case of IG corrosion or for shallow pitting.
- Ultrasonic inspection will be useful for the determination of the depth of damage in general corrosion or IG corrosion. However, under localized pitting conditions, low lateral resolution becomes a liability to the method.

FUTURE WORK

Fatigue results are not yet available for this study. After all NDE is performed on all specimens, the fatigue testing will be performed to determine the residual life. Residual life will be correlated to the NDE metrics using an ANN. This correlation will be compared to a more traditional statistical method as well as a model utilizing AFGROW,[7] a crack growth life prediction program developed by engineers at the Air Force Research Laboratory at Wright-Patterson Air Force Base.

REFERENCES

1. Peeler D (2001) Corrosion Damage Management: Supporting the Aging Fleet," Characterization of Materials and Devices, UDRI workshop, Dayton, OH
2. Suresh S (1998) Fatigue of materials. Cambridge University Press, Cambridge, New York
3. Sankaran KK, Perez R, Jata KV (2001) Effects of pitting corrosion on the fatigue beavior of aluminum alloy 7075-T6: modeling and experimental studies. Materials Science and Engineering A297:223-229

4. Rokhlin SI, Kim J-Y, Nagy H, Zoofan B (1999) Effect of pitting corrosion on fatigue crack initiation and fatigue life. Engineering Fracture Mechanics 62:425-444
5. Simon LB (1999) Influence of pitting corrosion on the loss of structural integrity in aluminum alloy 2024-T3. M.S. thesis, University of Dayton
6. Zell A, et.al. (1998) Stuttgart Neural Network Simulator User Manual, Version 4.2, University of Stuttgart: 18
7. http://fibec.flight.wpafb.af.mil/fibec/afgrow.html

EPOXY ADHESION TO HYDROTALCITE: CORRELTION BETWEEN CONTACT ANGLE AND ELECTROKINETIC MEASUREMENTS

R.B. Leggat and S.R. Taylor

Center for Electrochemical Science and Engineering
University of Virginia
Charlottesville, VA 22904

ABSTRACT

Hydrotalcite-based (HT) conversion coatings are being developed as an alternative to chromate conversion coatings (CCC). Efforts to date have focused on optimization of stand-alone corrosion resistance. Implementation of HT conversion coatings as part of a coating scheme (conversion coating, primer, and topcoat) will require adequate adhesion between HT and subsequent organic layers.

The practical adhesion (POTS) of epoxy to HT conversion coatings is compared with the surface chemistry of HT coatings assessed by contact angle and electrokinetic measurements. HT conversion coatings are Lewis bases with a dominant electrodynamic (γ^{LVW}) contribution to the surface tension. The dry epoxy POTS showed a reciprocal relation with the conversion coating IEP. Unfavorable acid-base interactions between the basic epoxy and the conversion coatings are decreased with decreasing basicity as indicated by the isoelectric point. The wet epoxy POTS was correlated with the total surface tension (γ^{total}) and the electrodynamic component of the surface tension (γ^{LVW}). Increased epoxy wettability would be expected for increasing HT γ^{total} and thus decreased void formation. Increased γ^{LVW} allows for bonding interactions in the presence of water where polar bonding would be disrupted.

INTRODUCTION

Hydrotalcite (HT) conversion coatings are nonchromate coatings formed on aluminum alloys by immersion in alkaline lithium salt solutions. The macroscopic structure of HT coatings consists of blade-like crystals. The atomic structure of HT consists of oxoanions (such as nitrate or carbonate) intercalated between lithium-aluminum hydroxide layers.

The corrosion resistance of hydrotalcite (HT) conversion coatings has been optimized for standalone corrosion resistance[1]. In practice, HT coatings will be used as part of a coating

system consisting of a primer and one or more topcoats. Sufficient adhesion between HT conversion coatings and subsequent organic layers will factor into the corrosion performance of a coating system with a HT conversion coating.

A number of mechanisms can contribute to adhesion including mechanical interlocking, adsorption, and electrostatic interactions[2]. Mechanical adhesion occurs by interlocking of the adhesive coating with surface asperities when sufficient wetting of the substrate has occurred. In the absence of complete wetting, voids at the interface compromise adhesion. It is believed that the blade-like HT morphology should provide good mechanical adhesion with subsequent layers, if the surface chemistry interactions are properly matched.

Adsorption can include primary (covalent) and/or secondary (dispersion, dipole, and hydrogen) bonding. Secondary forces can be probed by surface tension measurements. The surface tension (γ) can be separated into electrodynamic (dispersion and dipole) and acid-base contributions by the equation:

$$\gamma^{total} = \gamma^{LVW} + 2(\gamma+\gamma-)^{1/2} \quad [1]$$

where LVW is the electrodynamic (Liftshitz-van der Waal) contribution, and $\gamma+$ and $\gamma-$ are the electron accepting and electron donating components of the acid-base contribution[3].

Electrostatic interactions can be assessed by electrokinetic measurements. The zeta potential (ζ) is the potential at the hydrodynamically fixed plane. Other researchers have reported correlations between ζ and adhesion in polymers[4], composites[5,6], and organic coatings[7].

In the present study, contact angle and electrokinetic measurements were employed to characterize the surface tension and electrostatic character of HT coatings with different interlayer oxoanions. These results were correlated with practical adhesion tests for epoxy on HT coatings in the dry and wet state. Chromate conversion coatings (CCC) were used as a control.

EXPERIMENTAL METHODS

The pull off tensile strength (POTS) was used as a parameter to gauge the practical adhesion of epoxy on HT conversion coatings. HT coatings were applied to AA2024-T3 substrates by bath immersion as previously described[8,9]. Three HT chemistries using different lithium salts were prepared to examine the effect of the interlayer anion including carbonate (CO_3); nitrate (NO_3); and persulfate + nitrate (S_2O_8). CCC and degreased AA2024 were included as controls. Epoxy coatings (BPA based resin + polyamide hardener) were spin cast onto the HT treated panels (25-75 μm thick). The POTS was measured according to ASTM D4541 for dry coatings and after 24 hours exposure to deionized water.

HT particles that precipitated in the bath during sample preparation were collected for contact angle and electrokinetic measurements. CCCs were applied to Al powder (ca. 20 μm) for the powder studies. Contact angles were calculated using the rising height method. A liquid is allowed to wick through a cylinder of packed powder that is suspended from a microbalance. Washburn's equation was used to calculate the contact angle (θ) as shown in its most useful form:

$$\cos\theta = \frac{m^2}{t}\frac{\eta}{\rho^2 \gamma c} \qquad [2]$$

where t = time, m = mass of the wicked liquid, η = viscosity of the liquid, ρ = density of the liquid, γ = surface tension of the liquid; c = powder packing constant[10].

Contact angle measurements are useful in the determination of the acid-base properties of metal oxides[11]. The contact angles for a series of well-characterized liquids (water, diiodomethane, formamide, and ethylene glycol) were measured. Equation [1] was combined with Young's equation to determine the solid surface tension components (γLVW, γ+, γ-) from

the contact angle data. The equations were simultaneously solved for combinations of the probe liquids. As suggested in the literature, the probe liquid combinations consisted of diiodomethane, water and ethylene glycol or formamide[12]. The γ^{total} values determined from the two combinations (with ethylene glycol or formamide) represent the extrema for a range determined by various liquid combinations[13].

Electrophoresis was employed to measure ζ of the HT powders in 1mM KCl using the Smoluchowski equation:

$$\zeta = \mu\eta/\varepsilon\varepsilon_o \qquad [3]$$

where μ is the electrophoretic mobility, η is the solution viscosity, ε = solution dielectric constant, and ε_o = permittivity of free space[14]. ζ was measured as a function of pH to determine the iso-electric point (IEP), the pH where ζ changes sign. The IEP of CCC powders was determined by contact angle titration with buffered solutions. The pH where the contact angle is a maximum corresponds to the IEP[15].

RESULTS AND DISCUSSION

As can be seen in Table 1, the dry and wet epoxy POTS values for the HT conversion coatings fell between those observed for the degreased aluminum and the CCC. There was much scatter in the data which is commonly observed in pull-off test[16]. In addition, failure initiation and propagation can occur in any layer (HT coating or epoxy coating) or at any interface. Analysis of variance was employed to determine which treatments had significantly different POTS. Tukey's method indicated that at 95% confidence, the dry-state adhesion ranking was:

$$CCC > CO_3 \approx NO_3 > \text{Degreased} \approx S_2O_8,$$

while the wet-state adhesion ranking was:

$$CCC > CO_3 > S_2O_8 \approx NO_3 > \text{Degreased.}$$

The wet POTS was lower than the dry POTS for all treatments. It appears that the mechanical adhesion available through the HT morphology is not being achieved. This is most likely due to unfavorable surface chemistry interactions.

TABLE 1
Dry and wet epoxy POTS for HT conversion coated, CCC, and degreased AA2024-T3.

	Dry POTS (MPa)		**Wet POTS (MPa)**	
Treatment	**Mean**	**Std. Dev.**	**Mean**	**Std. Dev.**
Degreased	4.04	1.66	1.28	0.59
CCC	6.8	1.08	3.66	1.18
CO_3	5.35	1.34	2.47	0.99
NO_3	4.98	1.39	2.2	0.65
S_2O_8	3.91	1.92	2.32	0.38

Electrophoresis was used to measure the ζ of conversion coating powders as a function of pH. As can be seen in Table 2, the powders were all basic as indicated by the high IEP. The IEP of the CCC powders was found to be 8.2 by contact angle titration. This value is in agreement with the IEP of anodized aluminum in 0.01 M Oxo-Cr (VI) reported by Kendig, et al.[17]. Decreasing IEP was found to correlate with increasing dry POTS as seen in Figure 1. Amine-cured epoxies are considered to be basic polymer[18,19]. Unfavorable acid-base reactions between the epoxy and conversion coating would be expected to decrease as the IEP of the conversion coatings decreases. Interpretation of the IEP is complicated by the fact that the potential determining ions (H+ and OH-) also participate in acid-base type reactions i.e., the separation of electrostatic and acid-base interactions is intractable by this technique. Despite the fact that epoxies are Lewis bases, other researchers have reported negative ζ values for epoxies at neutral

pH[20,21]. This suggests that the wet epoxy POTS with HT conversion coatings is controlled by acid-base interactions and not electrostatics.

The surface tension components calculated from the rising height measurements are also shown in Table 2. The electrodynamic component (γ^{LVW}) was calculated from the contact angle data for diiodomethane, a completely non-polar liquid. The other components were calculated using using two combinations of probe liquids (diiodomethane, water, and a third polar liquid: formamide or ethylene glycol). The HT powders are Lewis bases (γ-) with a dominant electrodynamic component (γ^{LVW}). Increased wet epoxy POTS was observed for increasing γ^{total}. In the event of decreased wetting (γ^{total} solid < γ^{total} liquid), there would be decreased interfacial contact area and subsequent void formation. The wet POTS also correlated with γ^{LVW} as shown in Figure 2. This is in agreement with previous findings that wet adhesion increases with an increasing greater proportion of dispersive bonding[22,23]. Polar bonding increases the likelihood of water uptake and bond disruption. No correlation was observed between the acid-base components and adhesion performance (wet or dry).

TABLE 2

Isoelectric-Point (IEP) and surface tension components (γ^{LVW}, γ+, γ-, γ^{total}) for conversion coating powders. The surface tension components were calculated using two combinations of probe liquids (diiodomethane, water, and a third polar liquid: formamide (FA) or ethylene glycol (EG)).

Sample	IEP (pH)	γ^{LVW} (mN/m)	Liq 3	γ+ (mN/m)	γ- (mN/m)	γ^{total} (mN/m)
CCC	8.2±0.3	50.8	FA	0.7	28.1	59.4
			EG	0.0	34.8	53.4
CO3	11.1±0.2	38.8	FA	1.3	10.7	46.2
			EG	0.2	23.4	43.1
S2O8	11.3±0.1	33.6	FA	0.3	13.5	37.5
			EG	0.4	23.3	39.8
NO3	11.6±0.2	24.1	FA	0.6	15.4	30.2
			EG	0.1	24.5	26.5

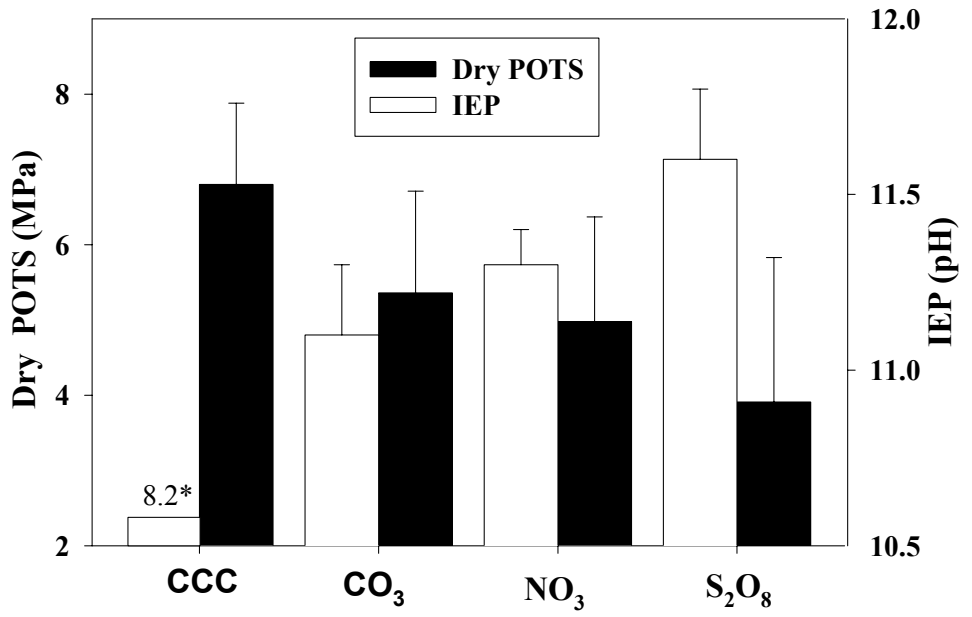

FIGURE 1. Dry POTS (left axis) and IEP (right axis) for CCC and HT conversion coatings. IEP of CCC listed to preserve scale of IEP of HT powders.

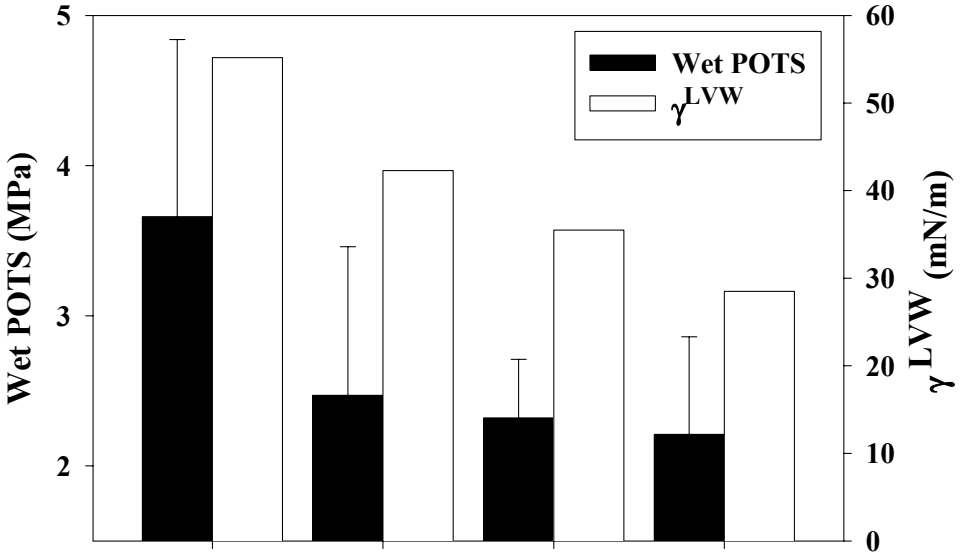

FIGURE 2. Wet POTS (left axis) and g LVW (right axis) for CCC and HT conversion coatings.

CONCLUSIONS

• HT conversion coatings are Lewis bases with a dominant electrodynamic (γ^{LVW}) contribution to the surface tension.

• The dry epoxy POTS showed a reciprocal relation with the conversion coating IEP. Unfavorable acid-base interactions between the basic epoxy and the conversion coatings are decreased with decreasing basicity as indicated by the IEP.

• The wet epoxy POTS was correlated with the total surface tension (γ^{total})and the electrodynamic component of the surface tension (γ^{LVW}). Increased epoxy wettability would be expected for increasing HT γ^{total} and thus decreased void formation. Increased γ^{LVW} allows for bonding interactions in the presence of water where polar bonding would be disrupted.

ACKNOWLEDGEMENTS

This work was supported by DARPA (Contract #49620-1-0305) under direction of Dr. Stephen Wax and Lt. Col. Paul Trulove (AFSOR). The use of the facilities of the Particle Science and Technology Center (UFL) is greatly appreciated. The authors gratefully acknowledge the assistance of Mr. S.A. Taylor.

REFERENCES

1. R.B. Leggat, E.A. Pehovaz-Diez, N.P. Cella, and S.R. Taylor, in *Corrosion and Corrosion Prevention of Low Density Metals and Alloys/ 2000*, B.A. Shaw, R.G. Buchheit, and J.P. Moran, Editors, PV 2000-23, p. 124, The Electrochemical Society Proceedings Series, Pennington, NJ (2001).
2. J.A. Baghdachi, *J. Coat. Technol.*, **69**, 8 (1997).
3. C.J. Van Oss, M.K. Chaudhury, and R.J. Good, *Chem. Rev.* **88**, 927 (1988).

4. H.-J. Jacobasch, K. Grundke, S. Schneider, and F. Simon, *J. Adhesion*, **48**, 57 (1995).

5. H.-T.Chiu and J.-H. Wang, *Polymer Composites*, **19**, 347 (1998).

6. A. Bismarck, D. Richter, C. Wuertz, and J. Springer, *Colloids and Surfaces A*, **159**, 341 (1999).

7. M. Kendig, *Corrosion*, **48**, 218 (1992).

8. R.G. Buchheit, M.D. Bode, and G.E. Stoner, *Corrosion*, **50**, 205 (1994).

9. R.G. Buchheit, C.A. Drewien, and G.E. Stoner in Corrosion Protection by Coatings and Surface Modification/ 1993, M.W. Kendig, K. Sugimoto, N.R. Sorensen Editors, PV 93-28, p. 212, The Electrochemical Society Proceedings Series, Pennington, NJ (1993).

10. C.J. Van Oss, R.F. Giese, Z. Li, K. Murphy, J. Norris, M.K. Chaudhury, and R.J. Good, *J. Adhesion Sci. Technol*., **6**, 413 (1992).

11. E. McCafferty and J.P. Wightman, *J. Adhesion Sci. Technol*., **13**, 1415 (1999).

12. A. Hollander, *J. Colloid Interface Sci.*, **169**, 493 (1995).

13. M. Gindl, G. Sinn, W. Gindl, A. Reiterer, and S. Tschegg, *Colloids and Surfaces A*, **181**, 279 (2001).

14. R.J. Hunter, *Zeta Potential in Colloid Science*, Academic Press, London (1989).

15. E. McCafferty and J.P. Wightman, *J. Colloid Interface Sci.*, **194**, 344 (1997).

16. J. Sickfeld, in *Adhesion Aspects of Polymeric Coatings*, K.L.Mittal, Editor, p. 543 Plenum Press, New York (1983).

17. M. Kendig, R. Addison, and S. Jeanjaquet, *J. Electrochem. Soc.*, **146**, 4419 (1999).

18. F.M. Fowkes, in *Encyclopedia of Polymer Science and Engineering*, supplemental vol., p. 1, John Wiley & Sons, New York (1989).

19. N. Dilsiz and J.P. Wightman, *Colloids and Surfaces A*, **164**, 325 (2000).

20. H.-T. Chiu and J.-H. Wang, *Polymer Composites*, **19**, 347 (1998).

21. A. Bismarck, G. Pfeifer and J. Springer, J. Adhesion Sci. Technol., 14, 661 (2000).

22. S.R. Taylor, G.L. Cahen and G.E. Stoner, *J. Electrochem. Soc*., **135**, 2943 (1988).

23. A. Carre and J. Shultz, *J. Adhes*., **15**, 151 (1983).

US ARMY TACOM ADOPTED CORROSION RATING SYSTEM

I. Carl Handsy
US Army Tank-Automotive Armaments Command
AMSA-TR-E/MEPS
Warren, MI 48397-5000
Handsyi@tacom.army.mil

John Repp
Corrpro Companies, Inc.
50 Tennessee Ave.
Ocean City, NJ 08226
Jrepp@corrpro.com

ABSTRACT

Corrosion is a major concern with military weapon systems that may be called to duty in any number of highly corrosive environments around the world. While designing a vehicle to resist corrosion in every possible environment is often impractical; knowing performance under these conditions can aid in the design and/or repair of current and future systems. For many years the Army has used a stage of corrosion rating system which looks at the severity of corrosive attack on components. Originally used for painted steel, this system identified stages of corrosion from 0 (no visible corrosion) to 4 (complete perforation of the base metal).

In 2000 the US Army Tank-Automotive Armaments Command (TACOM) adopted a new version of this rating system, updated for the systems they currently manage. This version was written to include the various stages of corrosion on base metals and coating/platings commonly used on components in current weapon systems. This document also included the addition of color photographs of actual components during the various stages of corrosive attack. TACOM, contractors and the accelerated corrosion test programs at Aberdeen Test Center (ATC) have used this rating system to evaluate the condition of vehicles and test samples. This is a comprehensive rating system that may be freely distributed (in its original form) to evaluate corrosive attack on systems and components in today's and tomorrow's military. The following pages contain the corrosion rating system adopted by the US Army TACOM. Copies of this rating system can be requested from TACOM or Corrpro Companies, Inc. (Corrpro).

INTRODUCTION

The pictures contained within this document represent corrosive attack that may be present on vehicle and weapon system components. Although every effort has been made to accurately depict the various stages of corrosion, not all stages for all types of materials are represented by the enclosed pictures. These pictures are intended to be used as a guideline during inspections, not to depict all forms and stages of corrosion. The overall rating given to a component should be based upon the narrative description of each stage below.

This document is meant to be used only to monitor corrosion occurring on metallic components and to accurately report the severity of corrosion on that component. No effort is made by this document to what constitutes a corrosion failure. This should be done on a system by system or component by component basis by the program management office responsible for that system.

STAGES OF CORROSION

The different stages of corrosion are described below. These are also highlighted in several of the pictures contained within this document. These figures are for informational purposes only and are not intended to be all-inclusive. The severity of corrosion should be determined by the narrative for the five (5) stages of corrosion listed below.

Stage 0 – No visible signs of corrosion or corrosive attack. No presence of white, red or black corrosion products. No presence of paint film blistering indicating corrosive attack. Discoloration of a coating system, other than caused by corrosion, is permissible.

Stage 1 – General surface corrosion is present. White, red and/or black corrosion products are present on the surface of the component being evaluated, but no significant attack is present. Minor blistering of the coating may have also occurred.

Stage 2 – Heavy corrosion products are present on the surface of the component. This is the beginning of base metal loss, however, no significant loss has yet occurred. Moderate white, red and/or black corrosion products are present on the component surface. Severe blistering of the paint may have also occurred.

Stage 3 – Corrosive attack has resulted in significant base metal loss. Reduction in the cross-section thickness of the component has occurred. Voluminous white, red and/or black corrosion products are present on the component. The structural integrity of the component may or may not be compromised. Pinholes, which may or may not penetrate through the base metal, may have developed.

Stage 4 – Perforation of the base metal has occurred. No metal remains at the point of severest corrosive attack. The component has lost structural integrity.

Painted Steel

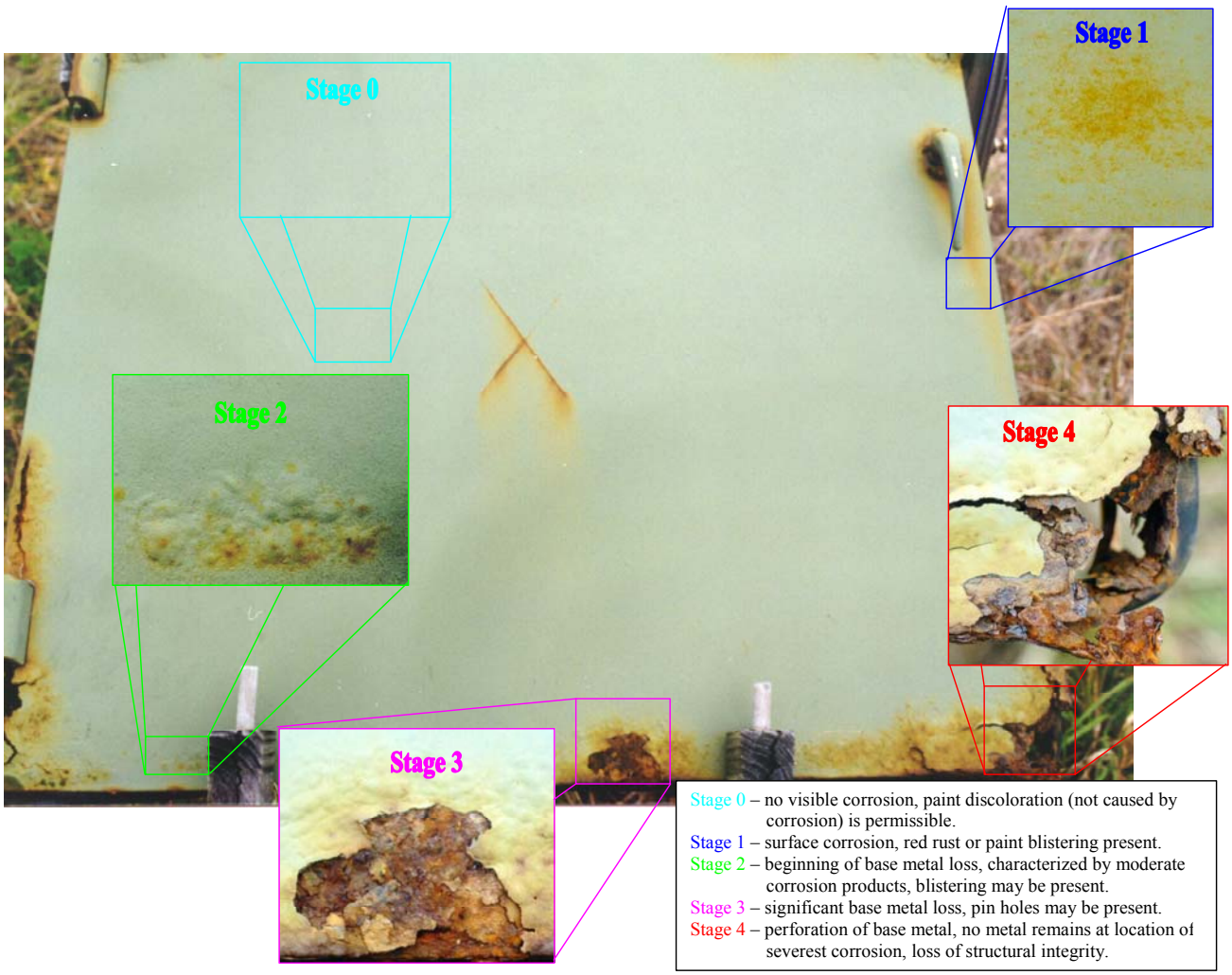

Stage 0 – no visible corrosion, paint discoloration (not caused by corrosion) is permissible.
Stage 1 – surface corrosion, red rust or paint blistering present.
Stage 2 – beginning of base metal loss, characterized by moderate corrosion products, blistering may be present.
Stage 3 – significant base metal loss, pin holes may be present.
Stage 4 – perforation of base metal, no metal remains at location of severest corrosion, loss of structural integrity.

Painted Galvanized Steel

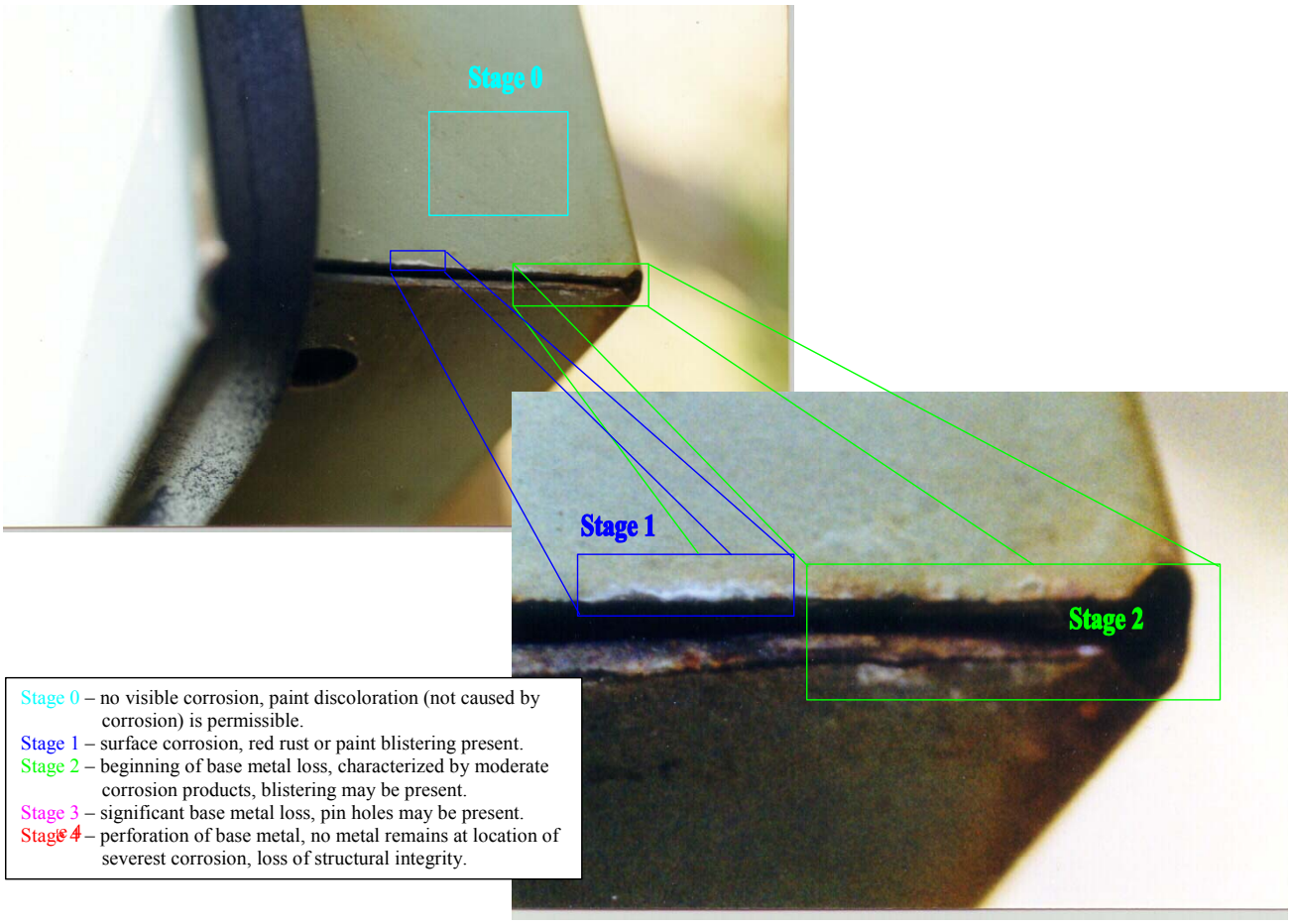

Stage 0 – no visible corrosion, paint discoloration (not caused by corrosion) is permissible.
Stage 1 – surface corrosion, red rust or paint blistering present.
Stage 2 – beginning of base metal loss, characterized by moderate corrosion products, blistering may be present.
Stage 3 – significant base metal loss, pin holes may be present.
Stage 4 – perforation of base metal, no metal remains at location of severest corrosion, loss of structural integrity.

Painted Aluminum

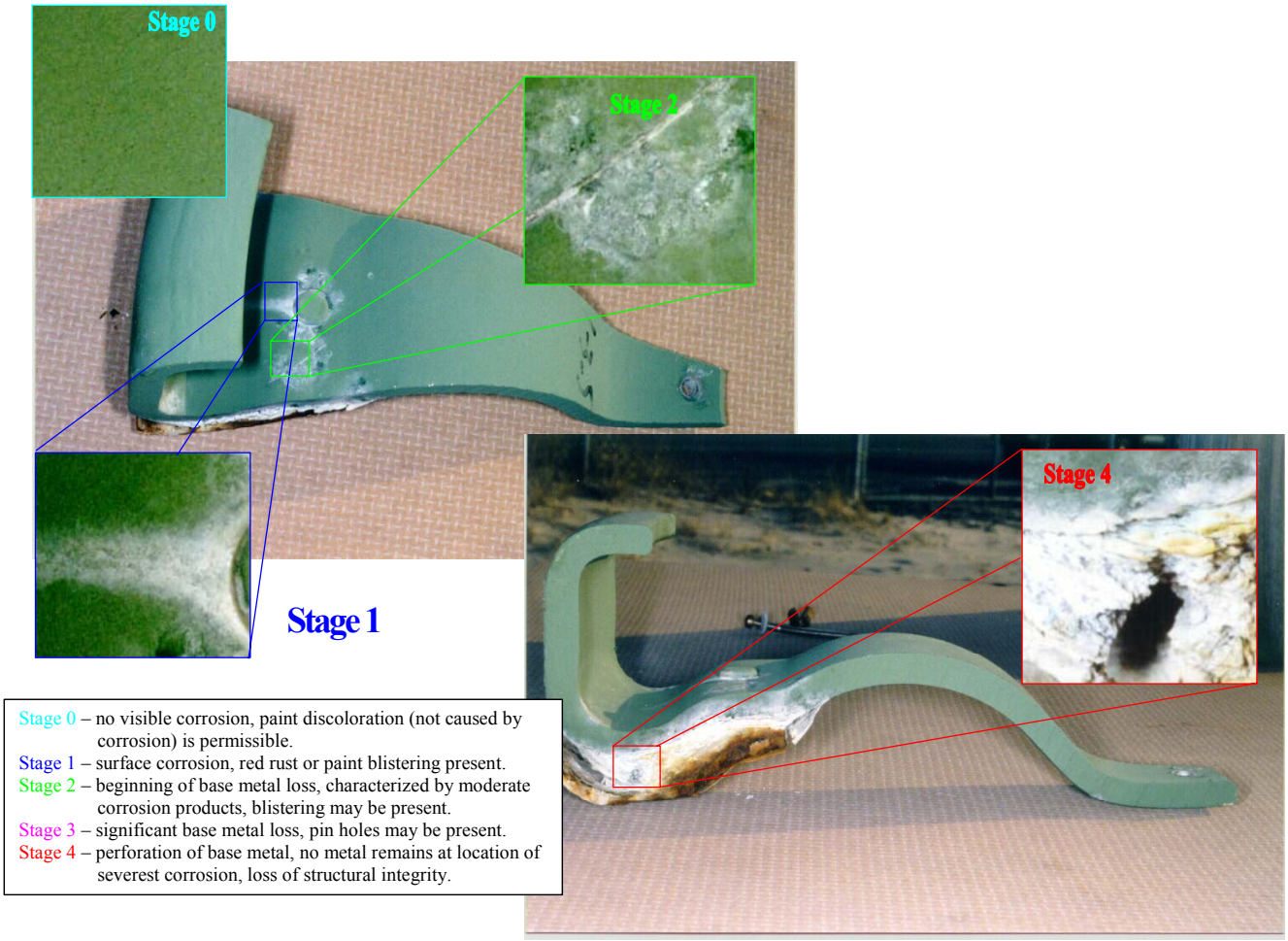

Stage 0 – no visible corrosion, paint discoloration (not caused by corrosion) is permissible.
Stage 1 – surface corrosion, red rust or paint blistering present.
Stage 2 – beginning of base metal loss, characterized by moderate corrosion products, blistering may be present.
Stage 3 – significant base metal loss, pin holes may be present.
Stage 4 – perforation of base metal, no metal remains at location of severest corrosion, loss of structural integrity.

Small Steel Components

Stage 0 – no visible corrosion, paint discoloration (not caused by corrosion) is permissible.
Stage 1 – surface corrosion, red rust or paint blistering present.
Stage 2 – beginning of base metal loss, characterized by moderate corrosion products, blistering may be present.
Stage 3 – significant base metal loss, pin holes may be present.
Stage 4 – perforation of base metal, no metal remains at location of severest corrosion, loss of structural integrity.

Small Aluminum Components

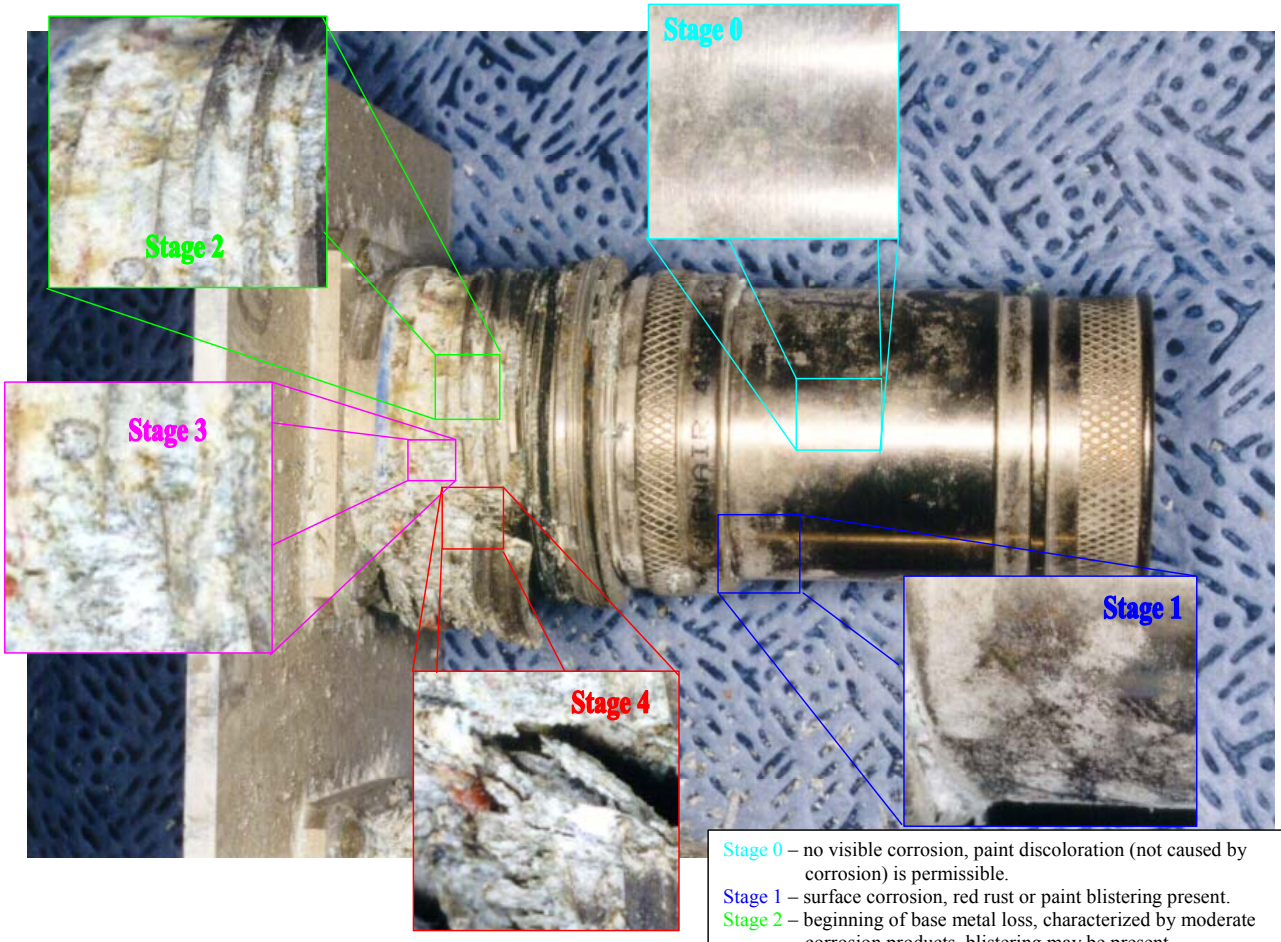

Stage 0 – no visible corrosion, paint discoloration (not caused by corrosion) is permissible.
Stage 1 – surface corrosion, red rust or paint blistering present.
Stage 2 – beginning of base metal loss, characterized by moderate corrosion products, blistering may be present.
Stage 3 – significant base metal loss, pin holes may be present.
Stage 4 – perforation of base metal, no metal remains at location of severest corrosion, loss of structural integrity.

PREDICTION OF CORROSION PROTECTION SYSTEM AGING BY THEORY-BASED DATA MINING

Maria Inman,[1] Patrick J. Moran,[2] Paul Koola,[3] Satheesh Ramachandran[3] and Perakath Benjamin[3]

[1] Faraday Technology, Inc.; [2] U.S. Naval Academy; [3] Knowledge Based Systems, Inc.

ABSTRACT

Corrosion damage to aging aircraft is the highest maintenance cost for the U.S. Air Force, and decreases the time that aircraft are available for missions. In order to continue using the aircraft beyond their design life, while staying within the budget constraints of the U.S. Air Force, maintenance costs must be decreased. This requires the capability to predict both degradation of the corrosion protection systems, as well as subsequent corrosion damage to aircraft structures, so that early action can be taken to avoid damage. The poster to be presented will describe the results from a U.S. Air Force Phase I SBIR program, which addresses the critical need for prediction of corrosion protection system aging and corrosion damage. The proposed approach is to enhance existing theoretical models for protection system breakdown and corrosion mechanisms, with sophisticated data mining processes to validate, refine or change those models. We will describe efforts to demonstrate the power of data mining to model one aircraft component and its associated corrosion protection system, specifically a coated lap splice joint. Experimental data used to develop and validate the data mining model will be presented. In future work, we intend to extend this approach to a wide range of protection systems and structures on aircraft, and develop broad models based on a combination of theory and data mining.

INTRODUCTION

Corrosion of aging aircraft is the single largest component of the total maintenance budget of the U.S. Air Force,[1] and will increase with time as structures are exposed to aggressive environments. The economic case for continued use of these aging aircraft can be made, as long as the cost of maintaining them does not exceed the cost of a new aircraft. Therefore, corrosion of aircraft structures must be detected and accurately predicted in order to implement cost-effective maintenance and repair strategies. The National Research Council Committee on Aging

of U.S. Air Force Aircraft concluded that *"…the major emphasis of the Air Force's technical and force management with regard to corrosion…should be focused on the early detection of corrosion and the implementation of effective corrosion control and mitigation practices so as to drastically reduce unscheduled repairs and replacement costs and aircraft downtime"* .[2]

Corrosion mitigation of aircraft structures is typically accomplished through the use of corrosion protection systems such as coatings, sealants, and appliques. However, these protection systems break down over time, allowing the ingress of aggressive, corrosive species into occluded sites on aircraft structures. To avoid the cost of corrosion, this breakdown must be anticipated, and the protection system either reinforced, repaired or replaced before damage occurs. A system that models the breakdown of specific corrosion protection systems and subsequent corrosion attack is required, one that is readily adaptable to all aircraft structures and components, and all types of protection systems. This model must utilize data that is easily collected by Air Logistics Center personnel for an aging aircraft, anticipate the onset of corrosion damage to that aircraft, and give action items that can be carried out to avoid that damage. This predictive model system is essential to reduction in maintenance costs and improvement in force readiness, and should improve understanding of the effect of continued service on corrosion protection systems, and therefore to the development of protection systems with longer lifetimes.

The approach taken in the proposed program is to enhance existing theoretical models or known concepts for coating breakdown and corrosion mechanisms, by combining sophisticated data mining processes with fundamental analysis, to validate, refine or change those models. Data mining processes are derived from the disciplines of machine learning, pattern recognition, and statistical analysis, and allow previously unknown relationships deeply buried in raw data to

be discovered. By combining this empirical process with theoretical knowledge of the problem under consideration, the modeling process can be enhanced and incorporate predictive capability.

The objective is to develop a software-based Faradaic Prediction Tool, for the lifetime and performance of a corrosion protection system for aircraft components, and the onset and propagation of corrosion resulting from coating degradation. The inputs to the Tool include the state of the coating and the environmental severity of the next base deployment. The output of the Tool would be an assessment of the state of the coating, and a prediction of the coating performance over time, using a database of impedance spectra, environmental severity and time. The Tool could also be used to down-select new coating formulations, for more rigorous testing. This paper describes initial efforts in developing the predictive algoritms for the software-based Tool, using data mining techniques, as well as equivalent circuit modeling. These techniques are described briefly below, followed by the experimental procedure, and the results to date.

PREDICTIVE ANALYSIS USING DATA MINING TOOLS

Data Mining is an emerging field that intelligently and automatically assists the operator to extract implicit and previously unknown information or relationships from data, enhancing the understanding of a problem or a decision making process. Useful facts deeply buried in raw data can be discovered; the facts become evident by taking the form of patterns and rules which can then be interpreted into useful knowledge. The knowledge gained can be used as a forecasting tool to predict future behaviors, based on historical data. Data mining tools include Decision Trees (which divide the data into hierarchical groups based on different variables of the selected data), Rule Induction (which is used to automatically explore target databases, discovering rules that characterize its contents), Neural Networks (which are a biologically inspired computational structure, that uses a set of processing elements analogous to neurons in the brain), and Data

Visualization (which is a way of representing information, so as to coherently disseminate the knowledge). Data mining processes use these techniques and tools in the following basic steps:

1) Understanding and/or formulating the problem: This step entails formulating a clear objective, in order to avoid bypassing valuable information, and to not be sidetracked with meaningless relationships.
2) Preparing the data: To make this process valuable, we need to "know" our data, what it encompasses, its limitations, and whether the patterns constitute knowledge that is useful. This will allow us to select the relevant variables to be considered.
3) Performing the mining operations: decide what algorithms or visualization tools to apply to the data set, including specifying a model, fitting the model to the data, and evaluating the model against the data with the purpose of refining the model based on the outcome it yields. This process is often repeated, until the true model emerges. This will allow the data mining process to understand the data, in terms of data characteristics and relevancy of information.
4) Analyzing the output: Does the result constitute knowledge? This step requires knowledge of the problem and the data to determine if the results are meaningful.
5) Interpreting and presenting the results: Making knowledge available and understandable for use by others is equally as important as the other four stages. Proper data visualization techniques are often used to accurately communicate the discovered knowledge.

PREDICTIVE ANALYSIS USING FUNDAMENTAL EQUIVALENT CIRCUIT PARAMETERS

Electrochemical impedance spectroscopy (EIS) has been used to analyze coating degradation, and provide relationships between short and long term behavior and EIS parameters. Hubrecht *et.al.*[3] showed that EIS measurements of coated metals contained 3

impedance arcs: the high frequency arc (f > 1 kHz) described the coating characteristics, the intermediate frequency arc (50 mHz < f < 1 kHz) described the double-layer capacitance and charge transfer resistance, and the low frequency arc (f < 50 mHz) described mass transfer of ionic species and water through the coating. The coating resistance was shown to correlate with changes in epoxy and alkyd paint structure by Compere *et.al*.[4] Scully[5] used EIS to monitor the performance of 4 epoxy polyamide coatings of varying thickness exposed to ASTM ocean water. The coating resistance and the 10 mHz impedance measured after 1, 5, 10, 50 and 200 days of exposure, demonstrated the ability to predict coating performance after 550 days of exposure. Scully showed that relative changes in the electrochemically active surface area could be determined from the 45^{o} breakpoint frequency. Similar analyses were performed in this program to determine the utility of parameter analysis for predictive purposes.

EXPERIMENTAL PROCEDURE

Al-2024 T3 panels (Q-Panel), 1″ x 4″ in size, were coated with a chromate conversion coating, formed by a 1 minute immersion in chromic acid. The panels were coated with a MIL-P-53030 chrome-free primer from Deft, Inc. (Irvine, CA). No topcoat was applied. This system was designed to give a “bad” coating which would fail within the program duration (6 months). The panels were exposed to two chemistries: dilute Harrison's solution (0.35 wt% $(NH_4)_2SO_4$ + 0.05 wt% NaCl) to simulate atmospheric conditions on boldly exposed surfaces, and an analog to simulate attack inside a crevice (Prof. Robert Kelly, University of Virginia - 20 mM NaCl + 4 mM $NaNO_2$ + 4 mM $NaHCO_3$ + 2 mM NaF). The pH’s (3.5, 7 and 9) were made alkaline by addition of NaOH or acidic by addition of H_2SO_4, and regularly adjusted. The solutions were continually aerated through gas bubblers laid on the bottom of each tank.

Three sample types were used: an unscribed coated panel, a scribed coated panel, and coated panels clamped together to form a simulated lap joint. The panels were suspended from fiberglass racks with polypropylene twine (Figure 1). Each day, the panels were removed from the tank by lifting up each rack and suspending it above the tank. In the evening, the panels were lowered back into the tank. This alternate immersion procedure, while not standard, accelerated coating system breakdown and corrosion of the substrate. To make EIS measurements, panels were removed from the racks, and placed in a simple flat cell. The cell was filled with solution from the tanks, and a platinum electrode was inserted into the cell to collect the EIS data using a 2-electrode technique. EIS spectra were taken for the unscribed and lap joint panels, scribe creep was estimated for the scribed panels, and blistering for all panels.

RESULTS/DISCUSSION

EIS SPECTRA AND EQUIVALENT CIRCUIT MODELING

Figure 2 shows an example of EIS data collected as a function of time, for an unscribed panel in dilute Harrison's solution at pH 3.5. The Bode plot shows a decrease in the impedance as a function of time. This behavior is expected for a coating that is degrading with time, and correlated visually with blistering on the surface of the panel. Equivalent circuit modeling was applied to each spectra. Two equivalent circuits were used to fit the data: 1) a Randles circuit to represent the coating when no corrosion was occurring or the corrosion beneath the coating, when the coating such that it was effectively transparent to the transfer of corrosive ions to the metal surface, and 2) a circuit representing the coating and corrosion underneath the coating (the high frequency semicircle described the coating, the low frequency semicircle described the

corrosion beneath the coating). Equivalent circuit parameters included constant phase elements for the coating and corrosion beneath the coating, the coating resistance, and charge transfer resistance. The breakpoint frequency was als recorded.

BLISTERING ON PANELS

Blistering was assessed in accordance with ASTM D714 "Standard Test Method for Evaluating Degree of Blistering of Paints". A decrease in the Blister Size No. implies an increase in the size of the blisters observed on the panel. Blistering was observed in all of the chemistries, although not on all of the panels. The blister size increased with decreasing pH.

ANALYSIS OF EQUIVALENT CIRCUIT PARAMETERS AND BLISTERING DATA FOR PREDICTIVE PURPOSES

Scully[5] and Hack and Murray[6] showed that equivalent circuit parameters such as coating resistance and the 10 mHz impedance, and the 45^{o} breakpoint frequency correlated with the visual blistering processes, for marine coatings. A similar, fundamental analysis of equivalent circuit parameters was done in this program to predict coating breakdown in simulated aircraft environments. Figure 3 shows the relationship between the coating resistance after 1 day, and the final blister size after 28 days of exposure. Figure 4 shows a relationship between the initial breakpoint frequency and the final blister size. These types of relationships are similar to those observed in the work by Hack, Murray and Scully, established for marine coatings, and could be used to predict long term performance based on short term data. However, these relationships must be better defined using longer tests and better coatings.

DATA MINING ANALYSIS OF EQUIVALENT CIRCUIT PARAMETERS AND BLISTERING DATA

Data mining was used in conjunction with laboratory testing and theoretical understanding, to examine current models of corrosion protection system degradation and crevice corrosion inside lap joints. Based upon the experimental data, predictive models were developed, which were calibrated as a function of solution pH, chemistry, initial coating thickness, and time. For each predictive model, two types of model were built:

(i) A model was calibrated using the 1-14 day data, to predict the 28^{th} day values

(ii) A model was calibrated using the 1-60 day data to predict the 75^{th} day values

The best predictive model developed using data mining tools was the prediction of the EIS spectral data. Some success was also obtained using the models to predict coating resistance data over the short term. However, models applied to the prediction of constant phase elements and the breakpoint frequency, did not perform as well.

Data Preparation Process: Edge frequencies were removed from the raw EIS data, as the data in this range of frequencies were unstable. The frequency range over which the models were calibrated were 0.01 to 6310 Hz. Missing data was filled through extrapolation. To account for the starting conditions, slopes were considered instead of using the original data. The day 1 slopes were calculated as the difference of the day 1 values and day 0 values, and the day 7 slopes were calculated as the difference of the day 7 values and day 0 values, etc. Two sets of files were prepared: 1-14 day calibration file, 28 day testing file; 1-60 day calibration file, 75 day testing file.

Modeling Framework: Due to the high levels of non-linearities, neural networks were employed to derive the predictive models. The architectures used were typically of a 3-layer

feed-forward type (with one hidden layer), with tan-hyperbolic transformations at all layers. The controllable parameters in the training process were the learning rate and the momentum rate. This architecture could be developed further, to build an algorithm for the prediction of EIS spectral data, as a function of time, environment and coating condition. Note: Mean Square Errors were tracked and used as the stopping criteria during the calibration process.

Raw EIS Spectral Data: Figure 5 shows the predicted versus actual EIS spectral data for the calibration data (1-14 day data) and the testing data (28^{th} day). Figure 6 shows the predicted versus the actual EIS spectral data on the calibration data (1-60 day data) and the testing data (75^{th} day). There is excellent agreement between the predicted and actual data, after 28 and 75 days. These results demonstrate the utility of data mining tools for predicting EIS spectral data as a function of time, based on the inputs of coating thickness and environment.

SUMMARY/CONCLUSIONS

In laboratory testing, panels of Al-2024-T3, coated with a chromate conversion coating and a MIL-P-53030 primer (Deft, Inc.), were exposed to chemistries simulating aircraft environments. Electrochemical impedance spectroscopy data and visual inspection of coated panels were collected over time. Rapid degradation of the coated panels was achieved, by the deliberate selection of poor coatings. Data mining analysis showed that prediction of EIS spectral data could be made as a function of time and chemistry. Also demonstrated were predictive relationships between equivalent circuit parameters and visual observations of coating breakdown. These efforts were built upon a fundamental understanding of coating breakdown and corrosion. Future work will develop a software module to predict EIS spectral data as a function of time, environment and corrosion protection system.

ACKNOWLEDGEMENTS

This research was supported by a SBIR Phase I grant from the U.S. Air Force (Contract Number: F33615- C-M-5602; Program Manager: Dr. Deborah Peeler). The technical assistance of Mr. Larry Gebhart during this program is very much appreciated.

REFERENCES

1 Scientific Advisory Board, *Report of the Ad Hoc Committee on Life Extension and Mission Enhancement for Air Force Aircraft, Vol. 1*, Exec. Summary. USAF Scientific Advisory Board Report No. SAB-TR-94-01. Washington, DC: Department of the Air Force, 1994.

2 *Aging of U.S. Air Force Aircraft,* Committee on Aging of U.S. Air Force Aircraft, National Academy of Science, Publication NMAB-488-2, National Academy Press, 1997.

3 Hubrecht J., Vereecken J. and Piens M. (1984), Corrosion Monitoring of Iron, Protected by an Organic Coating , with the Aid of Impedance Measurements, *J. Electrochem. Soc.*, **131**, 9, pp 2010-2015.

4 Compere C., Frechette E., and Ghali E. (1993), Corrosion Evaluation of Painted and Artificially Damaged Painted Steel Panels by AC Impedance Measurements, *Corrosion Science*, **34**, p 1259-1275.

5 Scully J.R. (1989), Electrochemical Impedance of Organic-Coated Steel: Correlation of Impedance Parameters with Long-Term Coating Deterioration, *J. Electrochem. Soc.*, **136**, 4, pp 979-990.

6 Murray, J.N. and H.P. Hack (1990), *Electrochemical Impedance of Organic Coated Steel; Final Report – Correlation of Impedance Parameters with Long-Term Coating Performance*, Report No. DTRC-SME-89/76, David Taylor Research Center, Bethesda, MD 20084-5000.

FIGURES

FIGURE 1: Test setup showing tanks and panels suspended from racks (left), one tank with panels suspended from racks above tank (middle) and in the tank (right).

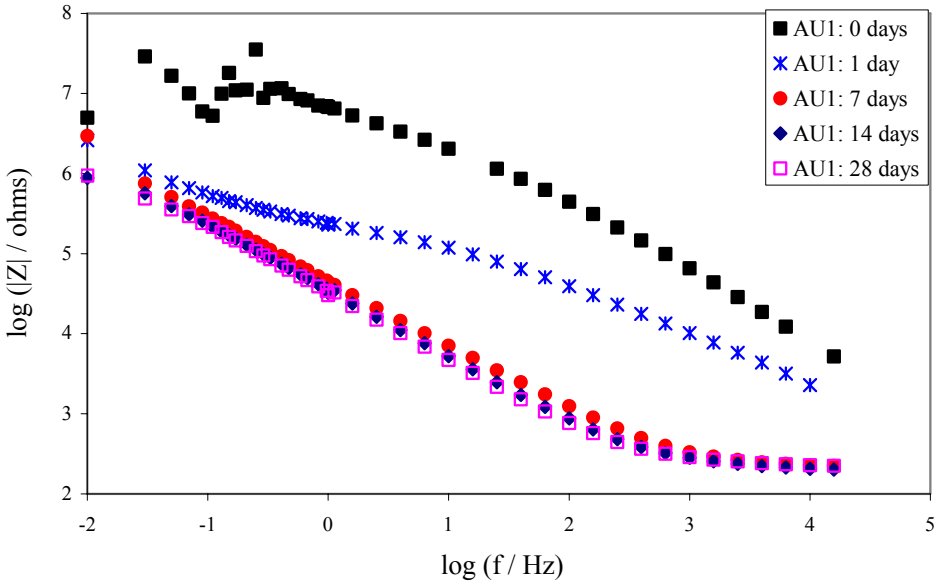

FIGURE 2: Bode plot showing changes in |Z| vs. frequency as a function of exposure time for unscribed panels in dilute Harrison's solution at pH 3.5

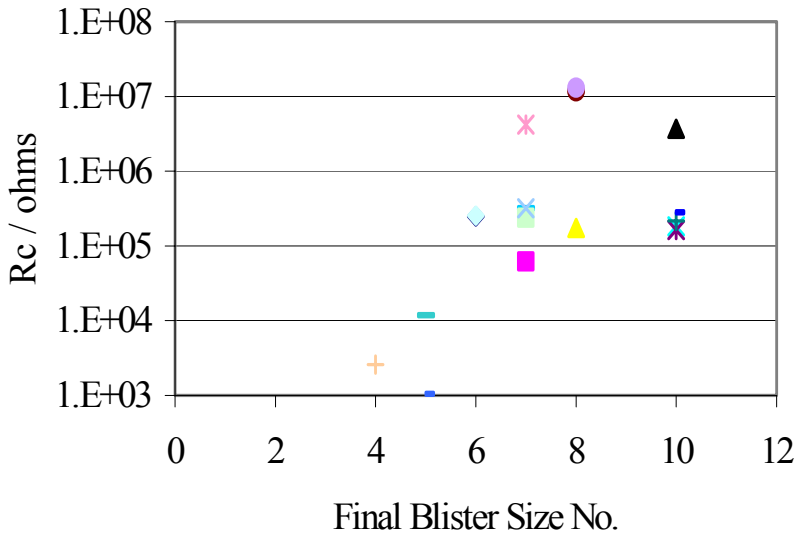

FIGURE 3: Relationship between coating resistance after 1 day and final blister size no., for the unscribed panels, exposed for 28 days.

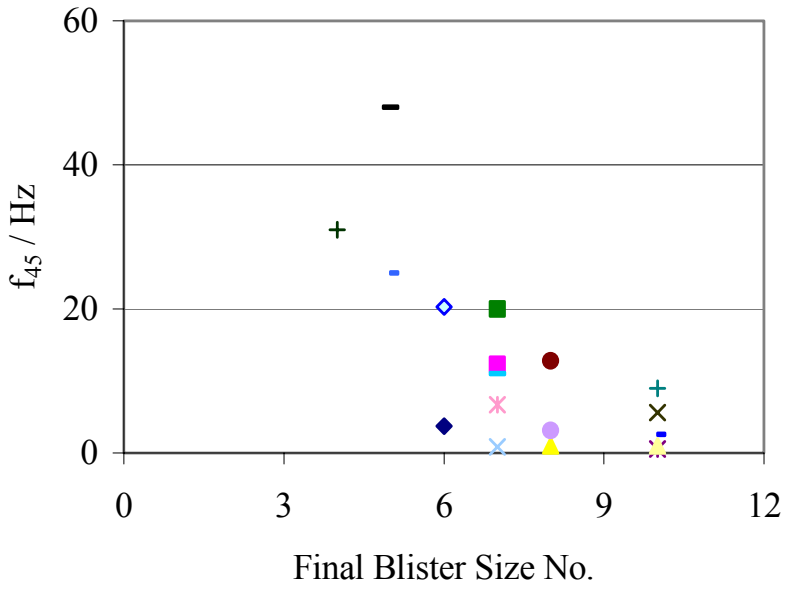

FIGURE 4: Relationship between the initial breakpoint frequency and final blister size, for unscribed panels, exposed for 28 days.

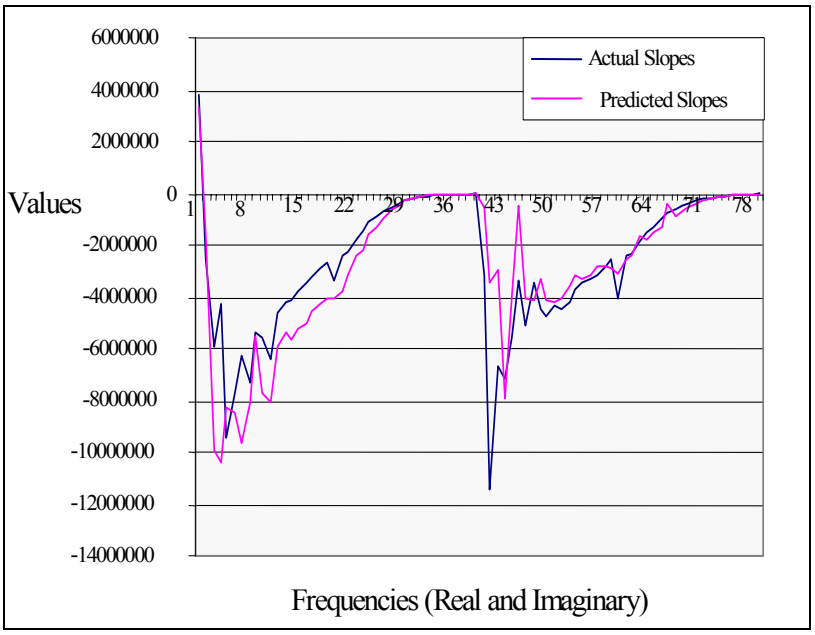

(a)

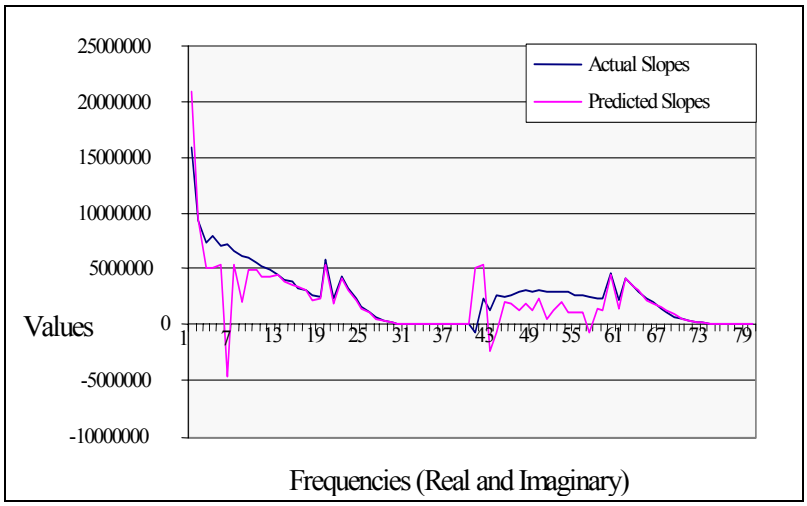

(b)

FIGURE 5: Comparison of prediction and actual spectral data, after 28 days; based on 1-14 day data. Chart (a) shows the calibration of the model using 1-14 day data. Chart (b) shows the predicted values for 28 days, versus the actual, based on the 1-14 day calibrated model.

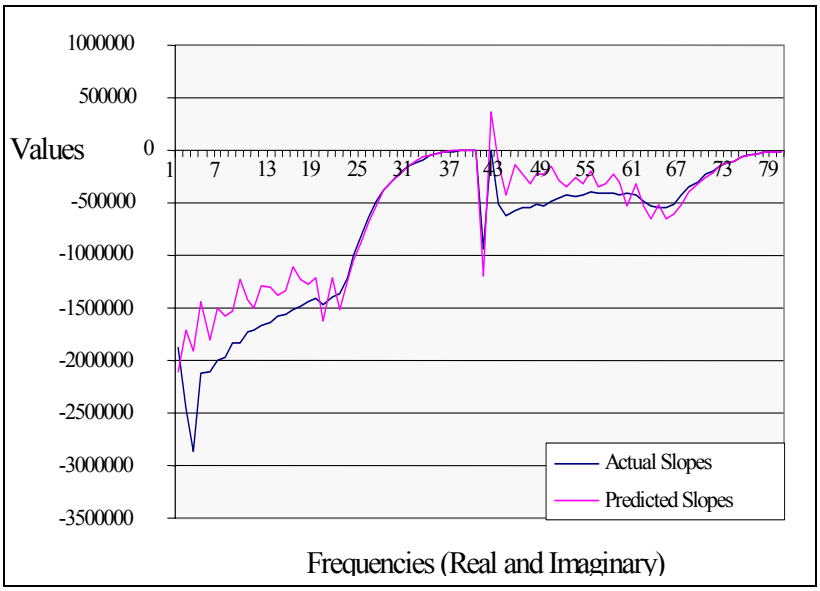

(a)

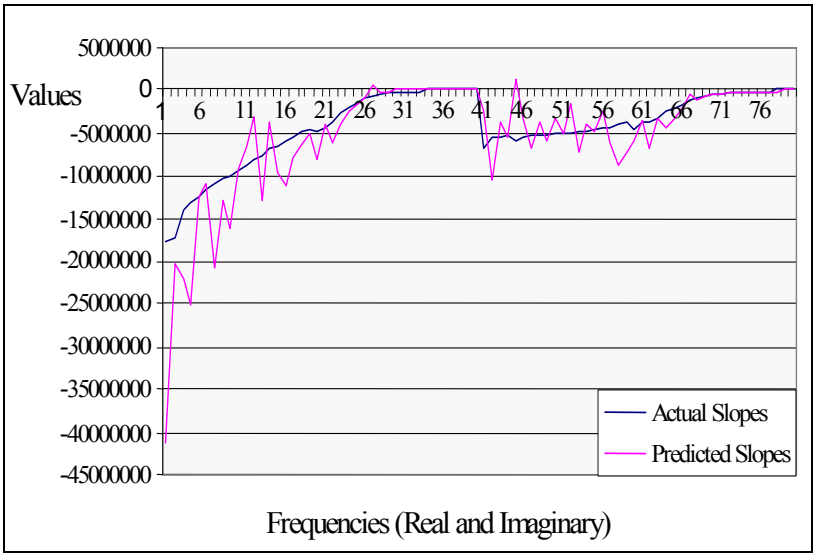

(b)

FIGURE 6: Comparison of prediction and actual EIS spectral data, after 75 days. These predictions are based on the 1-60 day data. Chart (a) shows the calibration of the model using the 1-60 day data. Chart (b) shows the predicted values for 75 days, versus the actual, based on the 1-60 day calibrated model.

NONDESTRUCTIVE QUANTIFICATION OF LOCALIZED CORROSION AND PREDICTION OF REMAINING FATIGUE LIFE

S. I. Rokhlin, J.-Y. Kim and B. Zoofan

The Ohio State University, Nondestructive Evaluation Program
Edison Joining Technology Center
Columbus OH 43221

ABSTRACT

The objective of this work is to develop a model-based experimental approach for prediction of a remaining fatigue life of a sample with pitting corrosion. It is done by measuring nondestructively parameters of the existing damage and by using the parameters in a model to predict the fatigue life. A quantitative microradiographic imaging method for measurements of pitting corrosion depth and morphology is described. The method is optimized as function of projection magnification. The accuracy of the developed technique is validated using different alternative methods: optical microscopy of the corroded samples, metallographic cross-sectioning, X-ray exposure at different angles and 3-D optical profilometry. The quantitative assessment of the microradiographic characterization of hidden corrosion is performed for reference samples with corroded areas covered by aluminum foils of varying thickness. The in situ surface acoustic wave monitoring of fatigue crack initiation and growth from corrosion pit has been performed for Al 2024-T3 alloy samples. The fatigue crack closure load at different stages of crack growth is determined from the surface wave reflection signals acquired at different levels of the fatigue load. The crack size is determined from the analysis of surface acoustic wave scattering amplitudes. The remaining fatigue life was predicted based on the fracture-mechanical model and using the measured parameters as the model input.

INTRODUCTION

It is known that pitting corrosion plays a role in triggering widespread fatigue crack initiation and reducing fatigue life of the aging aircraft. Therefore, it is important to size surface pits and associated fatigue cracks early in fatigue life in order to predict the remaining fatigue life and to prevent catastrophic failure. The effect of pitting on fatigue is not yet well understood, however, it is shown in ref. 1 and our own experiments[2] that the fatigue cracks are usually

initiated from the largest pits assuming homogeneous stress distribution in an unpitted sample. Thus, it is important to understand the effect of a single pit on fatigue life.

In this paper, a systematic experimental/model-based method to predict the remaining fatigue life of a sample with corrosion damage is developed. To this end, nondestructive techniques to measure parameters of the existing damage such as pit depth/diameter, crack depth and crack closure stresses is developed. Also a fatigue life prediction model is developed, it utilized the measured damage parameters as input for predicting the remaining fatigue life.

A quantitative microradiographic imaging technique for measurements of pitting corrosion depth and morphology is described. The method is optimized as function of projection magnification. The accuracy of the developed technique is validated using different alternative methods: optical microscopy of the corroded samples, metallographic cross-sectioning, X-ray exposure at different angles and 3-D optical profilometry. The quantitative assessment of the microradiographic characterization of hidden corrosion is performed for reference samples with corroded areas covered by aluminum foils of varying thickness.

An experimental ultrasonic technique is developed for in situ monitoring of fatigue crack initiation from a simulated pit and monitoring crack opening/closure stress with data acquired during fatigue cycling as a function of cycling load.[3] Surface acoustic wave reflections from the crack have been obtained as functions of fatigue load and number of cycles and from them the crack opening/closure loads have been determined. A model for surface acoustic wave scattering from cracks initiated from a surface pit is developed.[4] The depths of the fully and partially open cracks are determined.

Fatigue experiments and analyses for the fatigue crack initiation and propagation from a single artificial pit in Al 2024-T3 alloy have been performed to investigate the effect of pit depth

on fatigue life.[2] To predict the remaining fatigue life of the sample using measured damage parameters a fracture-mechanical model is developed.

MICRORADIOGRAPHY OF LOCALIZED CORROSION

EXPERIMENTAL SET-UP

A state-of-the-art imaging chain is integrated with a micro-focus X-ray source for characterization of fine localized corrosion in materials. A FeinFocus® 225 kV X-ray unit with 3-5 μm (0.0002 in.) focal size is used as an X-ray source. The tube head design allows placing the specimen at 5 mm away from the target allowing the highest projection magnification. A precise inspection positioning system specially designed for the system has three linear (with two micron resolution) and one rotating (with 0.01° resolution) computer controlled axis is used to control the position of the sample. One high-resolution linear axis is used for translation of the image intensifier. In addition an X-Y manipulator is used for positioning of the X-ray source. A 9-inch image intensifier integrated with a Sony CCD camera (XC-75) having standard frame rate of 30 frames/s is used for real-time radiography and also for alignment of the samples prior to film microradiography. Two additional TV cameras are used to monitor the exposure room and the position of the sample during the experiment inside the control room. The schematic of the microradiographic experimental setup developed for evaluation of micro-damage is shown in Figure 1.

MICRORADIOGRAPHIC DETECTABILITY

The microradiographic technique is distinguished by capability of producing images with high projection magnifications. The high-resolution images enable us a quantitative NDE of the corrosion micro-damage and fine fatigue cracks in Al 2024-T3 alloys. Since the size and the

normalized depth of a pit are critical to the fatigue life of a sample, the early detection of a micro-damage site is important. This necessitates for development of a quantitative assessment of the radiographic detectability. In characterizing the system detectability, the question of optimum magnification, and suitable X-ray system for field inspection can be addressed. The detectability of a radiographic system depends on contrast sensitivity and the system unsharpness. In the case of a microradiographic system a focal size of an X-ray source, projection magnification and unsharpness of an imaging chain play an important effect on detectability. The development of general concepts of microradiographic system characterization is very important. To find the detectability (the minimum visible depth Δh of a pit for a given pit diameter ϕ) we developed 1.6 mm Al 2024-T3 samples with artificial pits produced by EDM (electrical discharge machine) with precise depth control. To decrease the random noise in real-time images a DVS-3000 Hamamatsu image processor was used for fast averaging up to 252 frames.

The image of each artificial pit is captured for different projection magnifications in the range from 1X to 150X. After 252 frames averaging the pit image at each magnification was determined as visible, barely visible or invisible. The normalized brightness of the image for each pit reaches a maximum versus magnification and the image of the pit becomes invisible for small or very large magnifications. The data for visible, invisible and barely visible pit are collected in Figure 2 where normalized pit depths shown versus projection magnification. The dashed line indicates the boundary between visible and invisible regions. From this curve it is obvious that to detect a single pit at very low magnification the pit should be considerably deep.

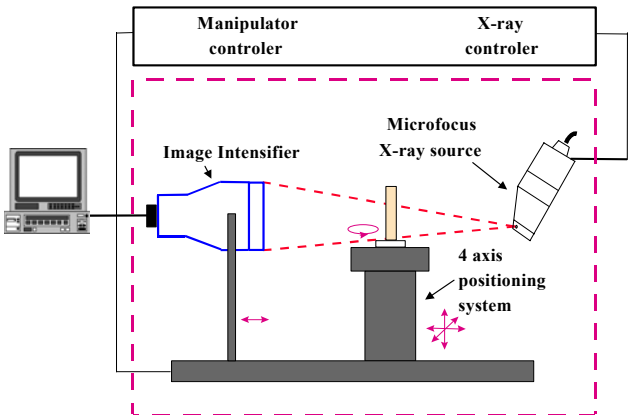

FIGURE 1. Schematic of the microradiographic system

The curve formed by two different curve branches; in the left branch the system detectability increases with magnification (pit threshold visibility contrast $\Delta h / h$ decreases) until it reaches the inherent contrast limitation of the radiographic system. The magnification at the curve dip represents the optimum projection magnification. This branch of the curve characterized by the decrease of the effect of receiving chain unsharpness due to geometrical magnification of the pit image size relative to the pixel size of the receiver. In this magnification range the effect of the detector unsharpness versus magnification is the dominant factor. On the right branch of the curve (after passing the dip) the system detectability gradually decreases. The detectability curve shows the strong effect of the system geometric unsharpness that increases versus magnification and becomes a dominant factor. The solid line with label Ug shows the variation of geometric unsharpness versus projection magnification *M*, *Ug =F (M-1)*, in which *F* is the focal spot size. The increase of the geometrical unsharpness with magnification gradually decreases the image contrast and the system detectability.

From Figure 2, it is observed that, for example, the minimum detectable pit depths are 30 μm and 150 μm for 20X and 5X magnifications, respectively. According to the single pit fatigue life model presented in Sec. 4, the pit can be detected approximately in 8% of the fatigue life

(marked as (A) in Figure 12) with 20X magnification whereas in 20% of the sample fatigue life marked as (B) in Figure 12) with 5X magnification. This demonstrates the importance of the system detectability for corrosion damage evaluation.

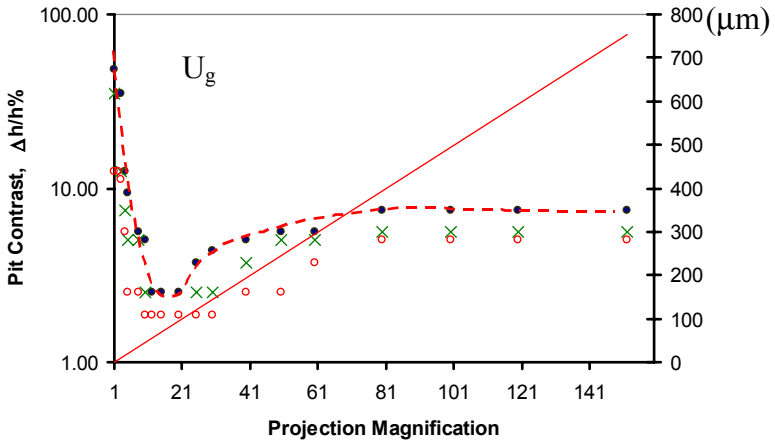

FUGURE 2. The detectability curve of different normalized pit depths at different projection magnifications

MICRORADIOGRAPHIC CHARACTERIZATION OF HIDDEN CORROSION

To simulate the effect of hidden corrosion different aluminum layers with thickness varying from 10 μm up to 9.6mm are added to a 1.6mm thick Al 2024-T3 sample with a corrosion site. The contrast sensitivity of the image of the deepest pit is measured and plotted vs. the total thickness. For the case of film microradiographs the measured optical densities of the corroded area and the base metal were used for contrast measurement and while for the real-time microradiography the brightness. The measured contrast sensitivities for each case are compared with the theoretical one in Figures 3 (a) & (b). Note that for all cases Δh is constant and I_S / I_D is negligible due to projection magnification. Film and real-time microradiographic evaluation of hidden corrosion show a reduction in the overall contrast sensitivity of images with thickness increase.

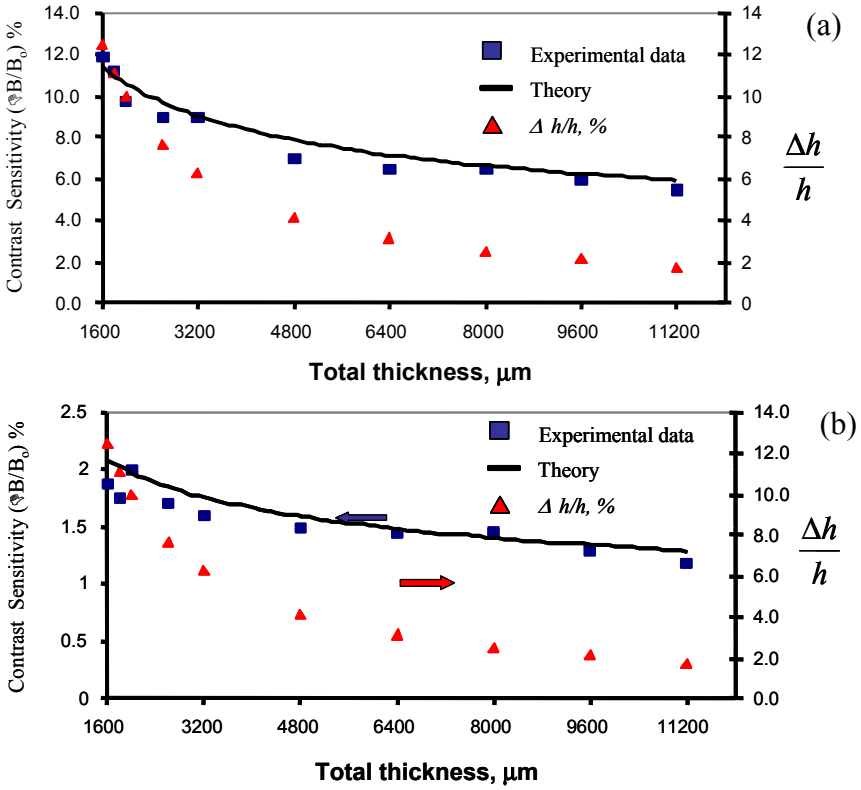

FIGURE 3 Contrast sensitivity measurements for the corroded sample covered by different aluminum layers. **(a)** Film microradiography **(b)** Real-time microradiography

IN SITU SURFACE ACOUSTIC WAVE TECHNIQUES

EXPERIMENT

The specimen used in the experiment was a standard fatigue sample [E-466-96-ASTM] with 1.6 mm thick Al 2024-T3 alloy. A controlled small pit with depth 250 μm and diameter 252 μm was generated by EDM. Fatigue tests were carried out on the servo-hydraulic mechanical testing system with 15 Hz cyclic loading. The stress range ($\Delta\sigma$) was 231 MPa and the stress ratio R was 0.1 so that the maximum stress level was 75 % of the yield stress. Post-fracture surfaces were examined with scanning electron microscope (SEM) fractographs and actual crack and pit sizes were measured. The dependence of sample fatigue life on the pit depth was also tested.

To monitor crack initiation and growth during the fatigue cycle, surface acoustic wave reflection from the pit and the crack was measured. A commercial wide band longitudinal wave transducer with center frequency 5 MHz was assembled with a specially designed polystyrene wedge for generating and receiving the surface wave signals, as shown in Figure 4. The design of this wedge is critical for acceptable signal-to-noise ratio.

For an in situ ultrasonic measurement during fatigue, the transducer is attached to the sample undergoing the fatigue test for collection of reflected signals at different fatigue load levels. The experimental system includes an ultrasonic pulser/receiver oscilloscope and a computer for fatigue control and data acquisition. At a predetermined number of cycles, the computer controlled fatigue load was changed to a step load (Figure 5) with recording of ultrasonic reflections at each step-load level. Recently, the data acquisition system has been improved to acquire ultrasonic data during the fatigue cycle without the step load.

INTERPRETATION OF ULTRASONIC RESULTS

As an example, Figure 6 shows surface wave reflection signals taken for two different load levels (100 lbs on the left (a) and 400 lbs on the right (b)) at different fatigue cycles. The surface wave reflection signal is composed of reflected waves from the pit and crack $A^{(1)}$ (first reflection), and the plate bottom $A^{(2)}$ (second) reflection of a mode-converted shear wave and the following multiple reflections in the plate (sample). As a result of the crack initiation and propagation amplitudes of both the first and second reflections change continuously. It is observed from Figure 6(b) that the signal starts to change due to crack initiation at 25,000 cycles. The signal is shifting in time and growing in amplitude.

The SEM fractograph at this number of cycles is shown in Figure 7(a). Whereas the reflection signal recorded at the load level 400 lb changes significantly as the number of cycles

increases, no change is observed until 52% of the fatigue life when signals are recorded at 100 lb load. Detailed interpretation of ultrasonic signals can be found in.[3] The SEM fractographs for cracks at different numbers of fatigue cycles are shown in Figure 7. In Figure 8(a) the normalized plate bottom (second) reflection versus the cyclic load is shown. Each curve begins to increase at a certain load level from near zero and then saturates at some load level, except for the case at 145,000 cycles when the fatigue crack is so large that it remains open during the whole cycle. The first load level corresponds to the crack mouth opening load and the second to the completely open crack. It is also noted that the crack opening loads change with the number of cycles.

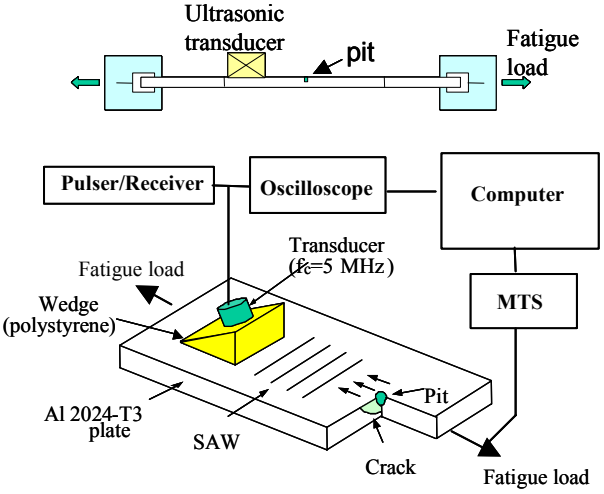

FIGURE 4. SAW monitoring of surface pit with a crack closure stresses

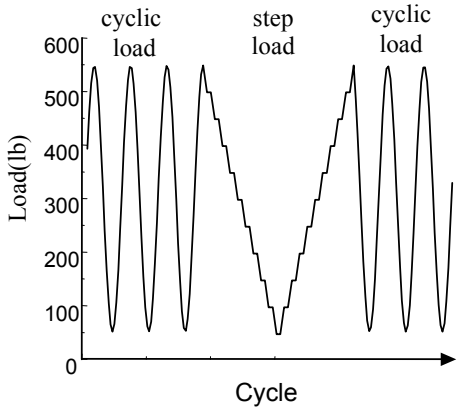

FIGURE 5. Load patterns to measure crack

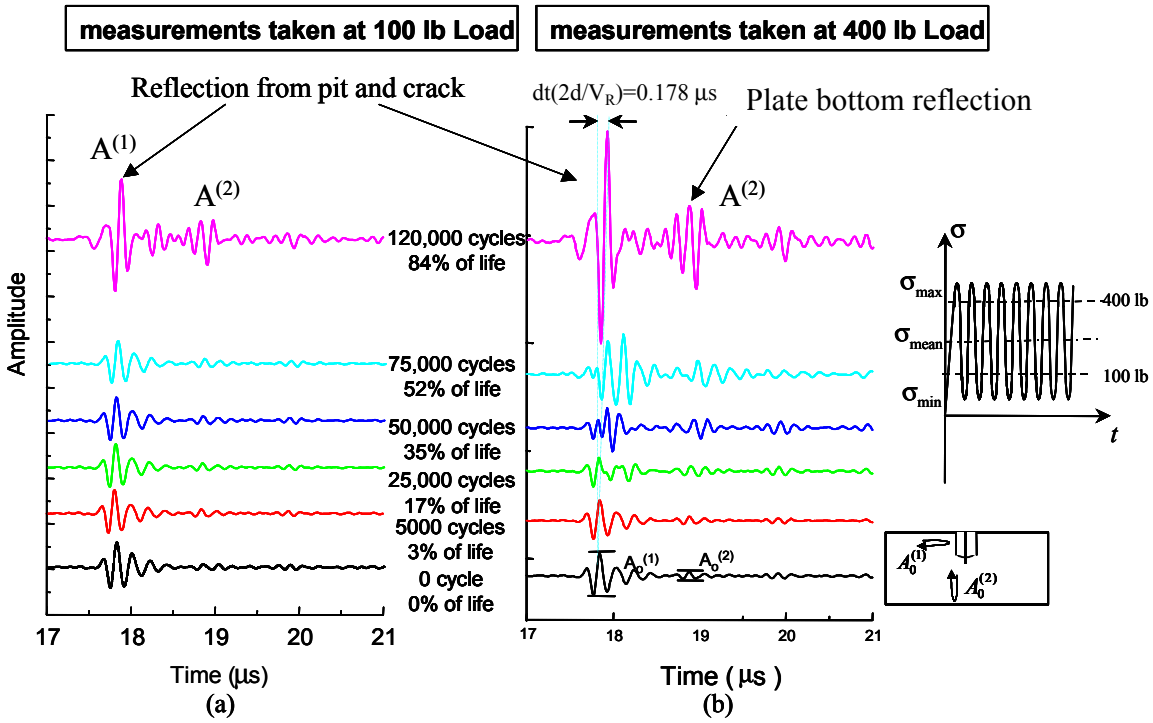

FIGURE 6. Change of reflection signal at different cycles for two different loads (a) 100 lb, (b) 400 lb.

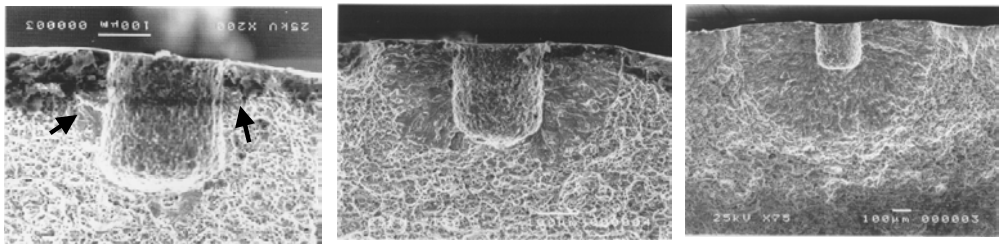

(a) (b) (c)

FIGURE **7.** SEM fractographs at (a) 25,000 cycles, (b) 65,000 cycles, (c) 130,000 cycles

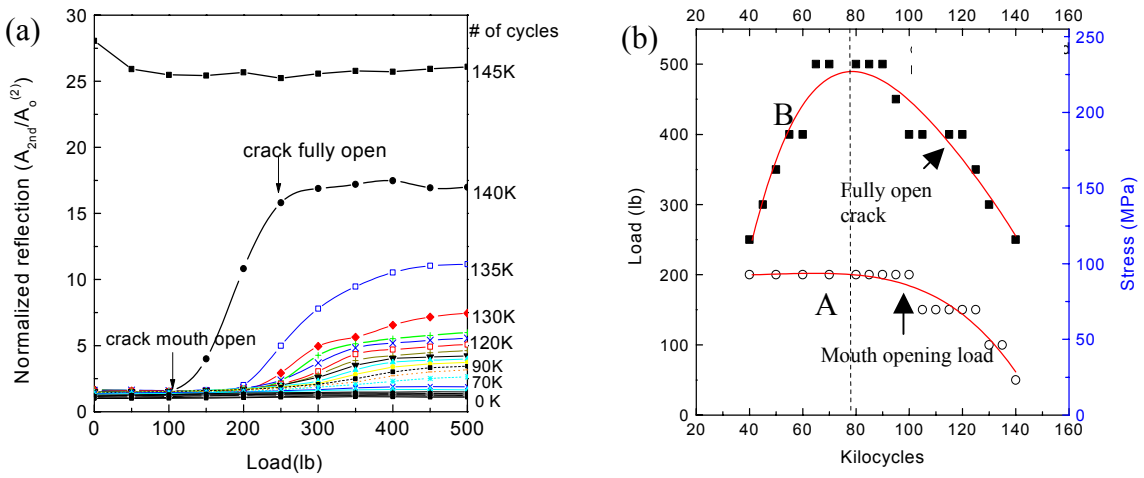

FIGURE 8. Determination of crack closure loads. (a) Change of plate bottom reflection vs. cyclic load at different numbers of fatigue cycles; (b) Crack closure (opening) loads vs. number of fatigue cycles.

MEASUREMENT OF CRACK CLOSURE LOADS

The loads at the beginning of crack mouth opening and at the completely open crack are determined from the plate bottom reflections and are shown in Figure 8(b). It is noted that the crack mouth opening load (A) is constant until around 100,000 cycles and then decreases, while the complete opening load (B) has its maximum at around 80,000 cycles. This result can be understood by considering the crack transition through the plastic zone caused by the pit under fatigue loading. The pit plastic zone produces the compressive closure force applied to the crack surface while the crack grows in the plastic zone. When the crack is short, the load to completely open the crack is just a little higher than the load of the crack mouth opening that is constant at this stage of crack growth. With its growth, the crack-fully-open load increases. When the crack grows out of the pit plastic zone, part of the crack surface is unloaded producing residual stress relief thus reducing the crack closure stresses. For the same reason, the crack-fully-opening load and crack-mouth-opening load decrease when the crack tip lies outside the plastic zone caused

by the pit. Assuming that the crack-fully-opening load reaches its maximum when the crack size is equal to the pit-induced plastic zone size, we estimate the plastic zone about 200 μm, which is in reasonable agreement with experiment. In Figure 9, the microradiographic images taken at 60,000 cycles under different loads are shown illustrating good agreements with ultrasonic data.

MODEL FOR CRACK DEPTH DETERMINATION

A low frequency scattering model has been proposed for determining the depth of a small crack emanating from the surface pit.[4] Consider the surface wave incident normally to corner cracks developed at the two sides of the pit (Figure 7(b)). The reflection coefficient can be represented as a sum of two contributions: integration over the pit surface (S_p) and the crack surface (S_c). Considering only the normal stress on the surface that is dominant in the low frequency range, the reflection coefficient can be expressed as:

$$R(\omega) \approx \frac{i\omega}{4P}\int_{S_p} u_I^{(1)}\sigma_{IJ}^{(2)} n_J dS + \frac{i\omega(1-\nu^2)}{3EP}\int_{\Gamma}\rho(\mathbf{r})K_I^2 dl \quad , \qquad (1)$$

where ω is the angular frequency, i the unit imaginary number, $u_I^{(1)}$ the scattered displacement field, $\sigma_{IJ}^{(2)}$ the incident stress field, n_J the inward normal vector to the flaw surface, K_I the stress intensity factor, ν Poisson's ratio, E Young's modulus and $\rho(\mathbf{r})$ the perpendicular distance from the origin to the line tangential to the crack front Γ.

To obtain the stress intensity factor, the stress of the incident surface wave is approximated by the bending stress in a plate:[4] $\sigma_{zz} = \sigma_o(1-2x/h^*)$ where the effective thickness of the plate $h^* = 0.6\lambda_R$. Next, we replace the crack on the pit with that on the through-thickness hole in the plate having the effective thickness (h^*) considering the ratio $d/h^* \approx 1$ where d is pit depth. Rokhlin et al.[2] used a similar approximate model for the analysis of fatigue

crack initiation and growth from a pit. We use the boundary correction factors of Raju and Newman[5] to calculate interpolated curves for the stress intensity factor at different crack configurations.

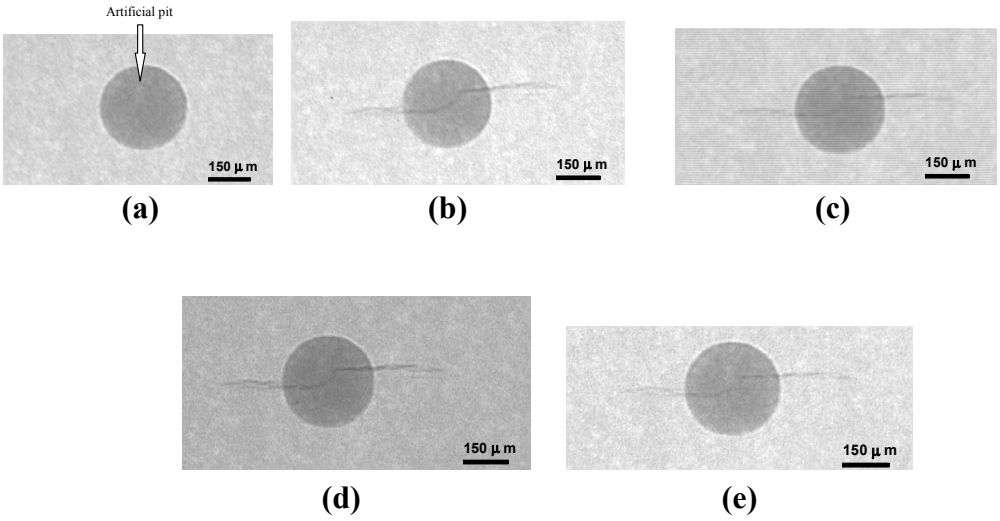

FIGURE 9. Microphotographs of fatigue sample after 60,000 cycles fatigue test with projection magnification 20X and optical magnification 5X. **(a)** No load. **(b)** Under 150lb load. **(c)** Under 350lb load. **(d)** Under 550lb load. **(e)** After removing the applied load indicating residual plastic deformation leading to crack opening

In Figure 10(a) the normalized first reflection versus crack depth is presented for samples with different pit diameters *D*. Due to signal interference between the two terms in Eq.(1), the amplitude of the reflection may increase or decrease depending on the pit diameter. In Figure 10(b), the size of the fully and partially open cracks at different number of cycles determined by comparing the measured and predicted reflection coefficients are shown.

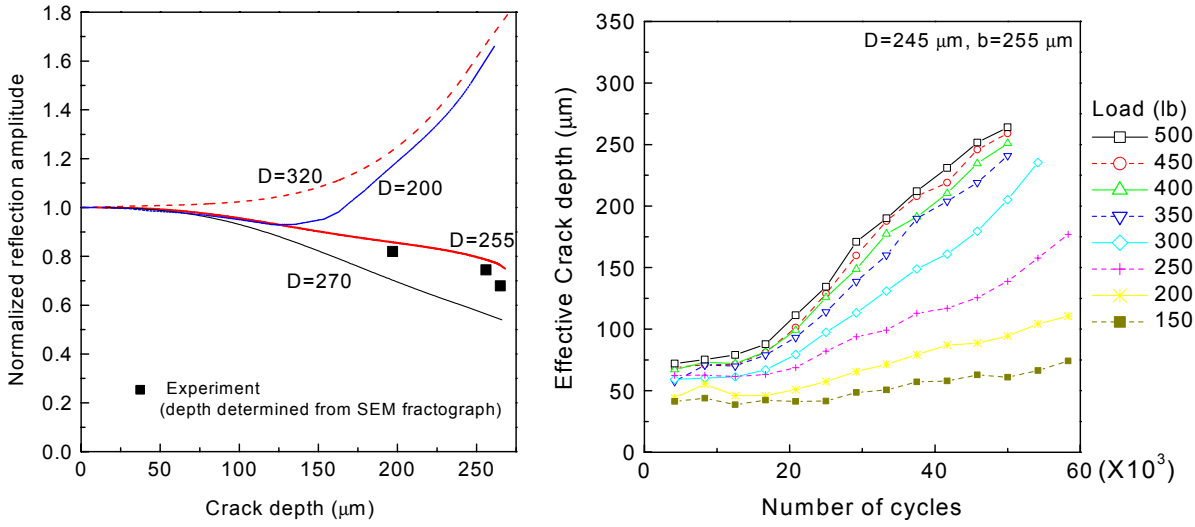

(a) (b)

FIGURE 10. (a) Model prediction of reflection coefficient of the corner cracks. (b) Typical example of crack depths determined at different numbers of fatigue cycle and under different load levels.

PREDICTION OF REMAINING FATIGUE LIFE

FATIGUE CRACK GROWTH ANALYSIS

The crack growth during the fatigue life can be predicted by the well-known Paris law, $da/dN=C[\Delta K(a)]^m$, where a is the crack length, N is the number of cycles, ΔK is the range of stress-intensity factor for the cyclic loading, and C and m are the material constants for the crack growth rate. For the Al 2024-T3 alloy and the fatigue parameters selected in the present study the Paris constants C and m of were taken to be $1.86\text{x}10^{-11}$ and 4.06 for the long crack[6] and $1.092\text{x}10^{-9}$ and 1.55 for the short crack based on the experimental results.[7]

Fractographic images in Figure 7 show that the fatigue cracks initiate at the edges of the pit with the highest stress concentration to form two corner cracks. These cracks grow separately on both sides of the pit, with shapes approximately a quarter circle, until the depth reaches that of the pit as shown in Figure 7(b). As these cracks grow further beyond the root of the pit, they

combine into a single semi-elliptical crack We define the period to this time as the first stage of the fatigue life and the remaining period to the failure of sample as the second stage. Therefore, the entire fatigue life can be divided into two different main stages with cracks of different geometry. The stress intensity factors for the first and second stages can be approximated using the crack propagation models proposed in ref. 2. The total fatigue life is thus calculated as sum of fatigue lives for the first and the second stages

$$N = \int_{a_i}^{d} \frac{da}{C[(\Delta K_1(a))]^m} + \int_{d}^{h-\varepsilon} \frac{da}{C[(\Delta K_2(a))]^m}. \qquad (2)$$

The lower limit a_i in the integration for the first stage can be the initial crack size from ultrasonic measurement for existing crack. The number of cycles for the second stage was calculated by using the second integral in Eq. (2) with upper limit of integration h-ε, where ε is determined from the fractograph for each sample.

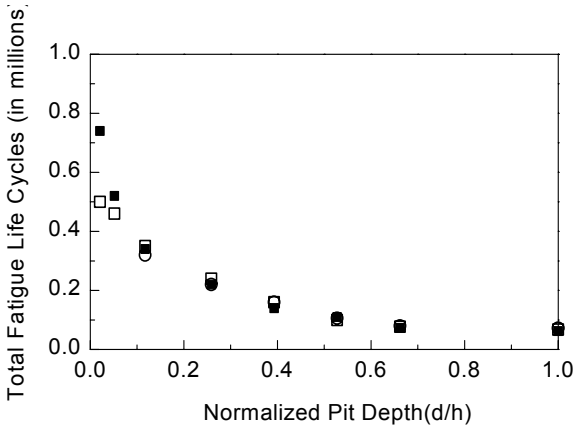

FIGURE 11. Measured and predicted fatigue lives vs. Normalized pit depth. ■ Experiment, □ Model Prediction (Corner crack model for 1st stage), ○ Model Prediction (Through-thickness crack model for 1st stage).

COMPARISON OF MODEL PREDICTION WITH EXPERIMENT

The experimental and calculated fatigue lives for samples with different pit depths are shown in Figure 11. It should be noted that the total number of fatigue cycles predicted by two

different models up to normalized pit depth d/h=0.1. The deviation of the model predictions from the experimental ones for shallow pits can be attributed to the initiation period taken to initiate a crack at a low stress concentrator.

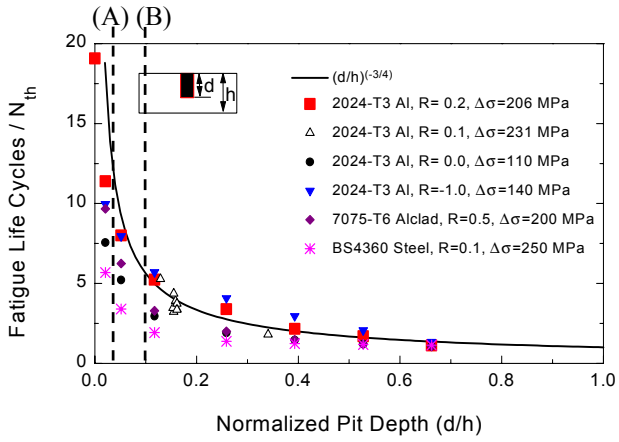

FIGURE 12. Comparison of experiment and empirical relation for normalized fatigue life vs. normalized pit depth. The normalization factor N_{th} is the fatigue life of the sample with through-thickness hole.

An empirical equation for the fatigue life of a sample with an arbitrary pit depth based on an experimental fatigue life for the reference sample geometry is proposed for field applications:

$$N = N_{th}(d/h)^{-(3/4)}, \qquad (3)$$

where N_{th} is the fatigue life of the sample with through-thickness hole, which is selected as an experimentally determined normalization parameter for the fatigue life of the sample with arbitrary pit depth. Such a representation factorizes for fatigue life problem by accounting for one normalization parameter depending on material fatigue properties, and the dependence on pit depth by one geometrical parameter (d/h). In Figure 12 the normalized fatigue life cycles versus the normalized pit depth is shown for different materials at different fatigue conditions together with approximation. As we can see the dependence of fatigue life on the pit depth is fitted well

by the proposed equation for data under different fatigue conditions. The simplicity of Eq. (3) should be noted in that the fatigue life of a sample with arbitrary pit depth can be predicted based on the experimentally determined fatigue life of the sample with through-thickness hole.

CONCLUSION

A quantitative microradiographic imaging method has been developed for measurements of pitting corrosion depth and morphology. The microradiographic characterization of hidden corrosion has also been performed for reference samples with corroded areas covered by aluminum foils of varying thickness. The in situ surface acoustic wave experiments for monitoring a fatigue crack initiated from a pit has been performed. The crack closure loads and the crack depths can be determined from the surface wave reflection signals acquired at different levels of the fatigue load and with the surface wave scattering model. The remaining fatigue life was predicted based on the fracture-mechanical model and using the measured parameters as the model input.

REFERENCES

1. Chen, G. S., Wan, K.-C., Gao, M., Wei, R. P., and Flournoy, T. H. (1996). *Mater Sci. Eng.* A219, 126
2. Rokhlin, S. I., Kim, J.-Y., Nagy, H. and Zoofan, B. (1999). *Eng. Frac. Mech.* 62, 425.
3. Rokhlin, S. I. And Kim, J.-Y. (2001). *Int. J. Fatigue*, submitted for publication.
4. Kim, J.-Y. and Rokhlin, S. I. (2001). *Int. J. Solids Struct.* Accepted for publication.
5. Raju, I. S. and Newman, J. C., Jr. (1979). In: *Fracture Mechanics-ASTM STP 677*, Smith, C. W. Ed., ASTM, New York, 411.Phillips, E. P. (1988). In: *Mechanics of Fatigue Crack Closure, ASTM STP 982*, J. C. Newman, Jr. and W. Elber, Eds., ASTM, New York, 505.
7. Philips, E. P. and Neuman, J. C. (1989). *Experimental Mechanics*, 221.

CORROSION PROTECTION OF 2024-T3 ALUMINUM ALLOY BY BIS-NONFUNCTIONAL SILANES

J. Anna Lamar, Danqing Zhu and Wim J. van Ooij*

Department of Materials Science and Engineering
University of Cincinnati
Cincinnati, OH 45221-0012

ABSTRACT

The effect of chain length of silane molecules on its resulting corrosion performance on AA 2024-T3 panels was studied using the following model silanes: bis-[trimethoxysilyl]methane (BTSM), bis-[triethoxysilyl]ethane (BTSE), bis-[trimethoxysilyl] hexane (BTSH), and bis-[triethoxysilyl]octane (BTSO). Corrosion performance of AA 2024-T3 treated with these silanes was evaluated in neutral sodium chloride solutions using electrochemical techniques, such as potentiodynamic polarization test and electrochemical impedance spectroscopy (EIS). It was found that BTSO with the longest chain length gave the best corrosion protection to AA 2024-T3; while BTSM with the shortest chain length performed the poorest. The corresponding contact angle measurements showed that the BTSO treated AA 2024-T3 surface is the most hydrophobic, while the BTSM treated surface is the most hydrophilic. This appears that a longer chain length would eventually generate a more hydrophobic silane treated metal system, and such hydrophobic nature would contribute to the corrosion protection of the system later on.

INTRODUCTION

Alondine® process as a standard chromating pretreatment is currently used for 2024-T3 aluminum alloy (AA 2024-T3 hereon) in aerospace industries. Although chromated AA 2024-T3 panels exhibit excellent corrosion performance, the use of this chromating pretreatment is still facing serious environmentally hazardous problems due to the high toxicity and carcinogenity of hexavalent chromium ions (Cr (VI)). A need for an alternative anticorrosion treatment has therefore arisen. Many chromium-free corrosion inhibitors have been explored. Among them, silane surface treatment is the one that has been drawing interests from various industries in

current years. The major benefits of this silane surface treatment include environmental compliance, economical application, and good corrosion inhibition and paint adhesion to a variety of metals.

Bis-trialoxysilanes (or bis-type silanes), with the general formula of $(RO)_3Si(CH_2)_3R'(CH_2)_3Si(OR)_3$ (where OR = hydrolyzable alkoxy group; R'=organic functionality), have been used as crosslinkers in adhesion industries for many years.[1] The function of these bis-type silanes as corrosion inhibitors for a variety of metals has only been found recently. An extensive study on this aspect has been carried out in our groups in the last few years.[1-8] Examples of bis-type silanes are bis-[triethoxysilylpropyl]ethane (BTSE), bis-[3-(triethoxysilyl)propyl]tetrasulfide (bis-sulfur silane), and bis-[trimethoxysilypropyl]amine (bis-amino silane) and their mixtures. Basically, silane surface treatment of metals is achieved by dipping the alkaline-cleaned metals into a dilute silane solution (e.g., 2 -5 vol.%) for a few seconds, followed by drying in air either at room temperature (RT) or at elevated temperatures (e.g., 100°C) for a certain period. During this treatment, the metal hydroxides (Me-OH) react chemically with silanols (Si-OH) generated from the hydrolysis of OR groups in the dilute silane solution. The covalent bonds in the form of metallo-siloxane (Me-O-Si) between the metal hydroxides and the silanes are thus formed, as illustrated in scheme 1.

$$\text{Me-OH (metal surface)} + \text{Si-OH (solution)} \Leftrightarrow \text{Me-O-Si (interface)} + H_2O$$

SCHEME 1. Condensation reaction between metal hydroxides and silanols at the interface

The excess Si-OH groups adsorbed on the metal surface condense with themselves, forming a siloxane (Si-O-Si) network on the outmost metal surface, as shown in scheme 2.

Si-OH (adsorbed) + Si-OH (adsorbed) ⇔ Si-O-Si (surface) + H_2O

SCHEME 2. Condensation reaction among silanols on the metal surface

Metals or alloys that can be protected by the above silanes include: Al and Al alloys, Steels (carbon steels and stainless steels), Zn and Zn-coated steels, Cu and Cu alloys, and Mg and Mg alloys.[2-8]

In our recent studies, the effects of some important processing parameters (like drying or curing temperatures of silane treated metals and hydrolysis time of silane solutions) and of the silane natures (such as functionalities) on the corrosion performance of the silane treated metals have been studied.[2-8] In the very recent study, it was found that the chain length or the number of CH_2 groups of bis-silane molecules also affected its resultant corrosion performance significantly. The study of the effect of the chain length is thus the major objective of this report.

In this report, four nonfunctional silanes (i.e., without R' group in the silane molecules), i.e., bis-[trimethoxysilyl]methane (BTSM), bis-[triethoxysilyl]ethane (BTSE), bis-[trimethoxysilyl] hexane (BTSH), and bis-[triethoxysilyl]octane (BTSO), were studied as model systems. AA 2024-T3 was used as the substrate for silane deposition. The silane treated AA 2024-T3 panels were then characterized by electrochemical techniques, such as potentiodynamic polarization tests and electrochemical impedance spectroscopy (EIS) in neutral 0.6 M sodium chloride solutions.

EXPERIMENTAL

MATERIALS

The silanes, BTSM, BTSE, BTSH, and BTSO were provided by OSi Specialties (Tullytown, CT). All silanes was used without further purification. The molecular structures of these silanes in their nonhydrolyzed states are shown in Figure 1. It is seen that the only difference among these silanes is the chain length or the number of CH_2 groups, with the BTSM molecule the shortest (i.e., 1 CH_2 group per molecule) and the BTSO molecule the longest (i.e., 8 CH_2 group per molecule).

2024-T3 Al alloy (AA 2024-T3) panels with the dimension of 10 cm × 15 cm × 0.06 cm (width × length × thickness) were purchased from ACT Inc (Hillsdale, MI).

PREPARATION OF SILANE SOLUTIONS

Before application, the OR groups of the silanes should be hydrolyzed to convert to active Si-OH groups for the subsequent condensation reactions mentioned above. 5 vol.% aqueous silane solutions were prepared by adding the silanes to the mixture of deionized (DI) water and ethanol. The ratio of silane/DI water/ethanol was 5/5/90 (v/v/v). The solution pH was adjusted to pH 4 by acetic acid, as this pH value was reported to favor the stability of silane solution.[9] All silane solutions were aged for at least 3 days before application, as was found in our preliminary work that the solutions could not hydrolyze sufficiently to produce enough Si-OH groups in the solutions within less than 3 days.

ALKALINE DEGREASING AND SILANE SURFACE TREATMENT

The AA 2024-T3 panels were degreased in a diluted alkaline cleaner (AC1055®) at 65 °C for 3-5 min, and then dried with compressed air. The cleaned AA 20204-T3 panels were dipped

into the 5% silane solutions for 30 s, and then dried using a hair dryer with cold air. The silane films deposited on a smooth metal surface (e.g., stainless steel) from a 5% solution is around 350 nm thick.[4] The silane-treated panels to be used for electrochemical testing were cured at 100°C for 24 hrs to obtain a crosslinked or denser structure in the silane treated AA 2024-T3 system.

ELECTROCHEMICAL TECHNIQUES

Potentiodynamic polarization tests were carried out on AA 2024-T3 panels with and without silane treatments in a 0.6M NaCl solution at pH 6.5. The silane-treated panels were cured at 100°C for 24 hrs and then pre-immersed in the electrolyte for 2 hrs before testing, in order to achieve a steady state. But the untreated AA 2024-T3 panels were tested immediately after exposed to the electrolyte. On average, 3 replicate samples were tested for each condition. The data were recorded, respectively, in anodic and cathodic directions, with a scan rate of 1mV. A commercial Saturated Calomel Electrode (SCE) and a platinum mesh were used as the reference and counter electrodes, respectively. The exposed area was fixed at 0.78 cm^2.

Electrochemical Impedance Spectroscopy measurements (EIS) were employed to evaluate the corrosion performance of the silane-treated AA 2024-T3 systems in a neutral 0.6 M NaCl solution. The silane treated panels were cured at 100°C for 24 hrs before measuring. The EIS measurements were carried out using an SR810 frequency response analyzer connected to a Gamry CMS100 potentiostat. The measured frequency range was from 10^{-2} to 10^5 Hz, with an AC excitation amplitude of 10 mV. SCE was used as the reference electrode and coupled with a graphite counter electrode. The surface area exposed to the electrolyte was 3.14 cm^2. The distance between the electrodes and the tested area was around 6 cm. Per decade, 6 experimental points were collected during the measurement around corrosion potential (E_{corr}) of the tested system.

RESULTS AND DISCUSSION

POTENTIODYNAMIC POLARIZATION TESTS

Figure 2 compares the cathodic polarization curves for AA 2024-T3 panels treated with BTSM, BTSE, BTSH, and BTSO, respectively. The curve for the untreated AA 2024-T3 panel is also shown here as a reference. It is seen that the cathodic curves of all silane treated AA 2024-T3 panels has been shifted to left more or less in comparison with that of the untreated panels. Among them, the curves for the panels treated with both BTSH and BTSE shifted even greater than those with BTSM and BTSO. The current densities at the cathodic potential of -0.85 V/SCE for the former two panels have been reduced by 1-2 decades as compared the untreated, while those for the latter two have only decreased < 1 decade. It should be, however, noted that the slope of the cathodic curves has not been changed much after the silane treatments. This indicates that the silanes studied here do not behave as cathodic inhibitors. The decrease in the cathodic current densities shown in Figure 2 is actually caused by the difficulty of the occurrence of cathodic reactions on the insulating surfaces of silane films in the initial period. As immersion goes on, more electrolyte penetrates into the films and eventually reaches the interface where more cathodic positions (i.e., cathodic second-phase particles at the alloy surface) are available for the cathodic reactions. Thus, an increase in the cathodic current density is expected after a long time of immersion.

Figure 3 presents the anodic curves for AA 2024-T3 panels treated with BTSM, BTSE, BTSH, and BTSO, respectively. The anodic current densities at -0.45 V/SCE for the BTSE, BTSO and BTSH treated panels (curves 3, 4, and 5) have decreased by at least two decades as compared with the untreated (curve 1). In the meanwhile, it is also noticed that the slope of these curves has increased remarkably, showing that these silanes act as effective anodic inhibitors.

The similar anodic behavior was also seen for bis-sulfur silane treated AA 2024-T3 system, and a plausible explanation was given elsewhere.[10] In general, it is thought that a highly crosslinked interfacial layer formed at the silane/metal interface is the major contribution to the corrosion inhibition of AA 2024-T3. The interfacial layer is primarily made up of metallo-siloxane (Si-O-Al) and siloxane (Si-O-Si). This interfacial layer, with a low porosity and a good adhesion to the substrate, heavily restricts pit growth underneath via retarding the transport of the corrosion products. The former causes severe "pore blocking" effect postponing the migration of the corrosion products in the vertical direction, while the latter limits that in the lateral direction. The BTSM treated panel (curve 2), on the contrary, does not show any significant changes in the anodic slope, implying that a similar interfacial layer may not be formed in the BTSM treated AA 2024-T3 system, and thus BTSM can not be used for corrosion protection of AA 2024-T3.

From Figures 2 and 3, a general conclusion drawn here is that BTSM with the shortest chain length cannot provide a good corrosion protection to AA 2024-T3; while the others with the longer chain lengths can be considered as anodic inhibitors for AA 2024-T3. In other words, a certain chain length of silane molecules is required for a good corrosion performance of metals.

EIS MEASUREMENTS

Figure 4 compares the EIS curves of the AA 2024-T3 panels treated with BTSM, BTSE, BTSH, and BTSO in the form of Bode plots. As is clearly seen in Figure 4a that the low-frequency impedance at 0.02 Hz ($Z_{0.02Hz}$) for the BTSO treated panel is the highest (curve 1), reaching 10^7 Ω. Both BTSH (curve 2) and BTSE (curve 3) treated panels give the $Z_{0.02Hz}$ values between 10^5 Ω to 10^6 Ω. The $Z_{0.02Hz}$ value of the BTSM treated panel, however, is only around 10^2 Ω (curve 4), which is the lowest among all the silane treated AA 2024-T3 panels. Correspondingly, the phase angle plots in Figure 4b show that the curve for the BTSO treated

panel is the broadest (curve 1); while that for the BTSM treated panel is the narrowest (curve 2). It is also noticed in Figure 4b that two time constants are shown on the curves for the silane treated AA 2024-T3 panels except that for the BTSM treated one. One time constant is centered at higher frequencies (~ 1000 Hz) and the other is at lower frequencies (~ < 1 Hz). The former is due to the outside silane film featured with siloxane bonds (Si-O-Si); while the latter is caused by the highly crosslinked interfacial layer dominated with both Si-O-Si and metallo-siloxane bonds (Al-O-Si in the case of AA 2024-T3). As mentioned above, this interfacial layer is also believed to be a major contribution to the corrosion protection provided by silanes. More detailed studies on the structural characterization of silane treated AA 2024-T3 system were reported elsewhere.[2-8,10]

It was reported previously[11] that low-frequency impedance can be used as a measure of the corrosion performance of polymeric coated systems, such as epoxy-coated steels. Thus, the difference in the $Z_{0.02Hz}$ values shown in Figure 4a can be explained by the different corrosion performance of these silane treated systems. Clearly, the BTSO treated system performs the best, followed by the BTSH and BTSE treated. The BTSM treated, on the contrary, behaves the worst. This suggests that the BTSM is not suitable for corrosion protection of AA 2024-T3, which is consistent with the polarization test results mentioned above. On the other hand, these EIS results once more conform that the chain length of silane molecules plays a key role in the corrosion protection of metals. The longer the chain length, the better the corrosion protection of metals.

CONTACT ANGLE MEASUREMENTS

To further clarify the action of chain length in the process of corrosion protection, contact angle measurements were conducted on the above panels using water. The result is shown in Figure 5. It is seen that the values of contact angle is linearly proportional to the chain length of the silane molecules. BTSO molecule has the longest chain length, and correspondingly, the BTSO treated AA 2024-T3 surface shows the most hydrophobic with the contact angle of >80°; whereas the surface treated with BTSM with the shortest chain length is the most hydrophilic, the contact angle of which is only around 65°. If combined the above electrochemical results, it can be seen that a good corrosion performance of BTSO is directly related to its highly hydrophobic nature. Such hydrophobic system is very likely caused by an extensive crosslinking during curing process. Since BTSO treated AA 2024-T3 shows the most hydrophobic surface, we therefore expect that the crosslinking in the BTSO system could be much more intensive as compared with the others. A longer chain length somehow enhances the crosslinking, forming a denser silane treated metal system. The corrosion performance of such denser silane/metal system has proven to be outstanding.[10] Since the BTSM with the shortest chain length could not give a denser film on AA 2024-T3, thus the corresponding corrosion performance is the poorest. A more detailed study on this aspect will be carried out in the future.

Corrosion performance of BTSE treated AA 2024-T3 panels was also evaluated using a 360-hr Salt Spray Test (SST). Figure 6 exhibits AA 2024-T3 panels with different treatments after the test. It is seen that both chromated (b) and BTSE-treated (c) AA 2024-T3 panels performed equally well; while the untreated (a) panel has been thoroughly corroded after only 20 hrs of exposure. This, again, conforms that a certain chain length (≥ 2 CH_2 groups per molecule) is needed for good corrosion protection of metals.

CONCLUSIONS

1. Polarization test results showed that AA 2024-T3 panels could be protected by BTSE, BTSH, and BTSO silanes, but not by BTSM. The former three silane molecules have longer chain lengths than BTSM, and act mainly as anodic inhibitors in the process of corrosion protection of AA 2024-T3. The corrosion performance of the BTSM treated AA 2024-T3 panel, on the contrary, is very poor. In other words, a certain chain length ($\geq$2 CH_2 groups per molecule) is required for the good resultant corrosion performance.
2. The results from EIS measurements were in good agreement with those obtained from polarization tests. BTSO treated AA 2024-T3 system showed the highest low-frequency impedance value, followed by BTSH and BTSE treated systems. The BTSM treated system, on the contrary, exhibited the lowest low-frequency impedance value, suggesting that BTSM is not suitable for the corrosion protection of metals.
3. Contact angle measurements indicated that the BTSO treated AA 2024-T3 surface is the most hydrophobic while the BTSM treated surface is the most hydrophilic. Correspondingly, the corrosion performance of the former is the best; whereas that of the latter is the worst.
4. The hydrophobic nature of silane treated metal systems, which is necessary for a good corrosion performance, is mainly determined by (1) the chain length of the silane molecules; and (2) the crosslinking degree in the system. In general, the longer the chain length, the more intensive the crosslinking in the system, and the better the corrosion performance.

ACKNOWLEDGMENT

The authors gratefully acknowledge the sponsorship of this research by the Air Force Office of Scientific Research under contract F49620-01-1-0352. Mr. Josh Hagen is also thanked here for the contact angle measurements.

REFERENCES

1. E. P. Plueddemann, Silane Coupling Agents, 2nd ed., Plenum Press, New York, 1991.
2. W. J. van Ooij and T. F. Child. CHEMTECH, 28, (1998) 26
3. V. Subramanian, Ph. D. Dissertation, University of Cincinnati, Department of Materials Science and Engineering, 1999.
4. G. P. Sundararajan, M. S. Thesis, University of Cincinnati, Department of Materials Science and Engineering, 2000.
5. W. J. van Ooij, D. Zhu, G. P. Sundararajan, S. K. Jayaseelan, Y. Fu and N. Teredesai. Surf. Engg. 16, (2000) 386
6. W. J. van Ooij and D. Zhu, CORROSION, 157(5), (2001) 413
7. V. Subramanian and W.J. van Ooij, CORROSION, 54, (1998) 204
8. D. Zhu and W. J. van Ooij, J. Adhesion Technol. Sci., accepted, 2002
9. F. D. Osterholtz and E. R. Pohl, J. Adhesion Sci. Technol., Vol. 6, 127 (1992)
10. D. Zhu and W. J. van Ooij, Corr. Sci. submitted, 2002
11. J. A. Grandle and S. R. Taylor, Corrosion, 50, (1994) 792

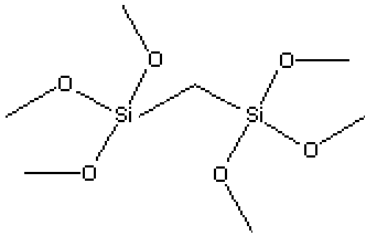

(a) BTSM

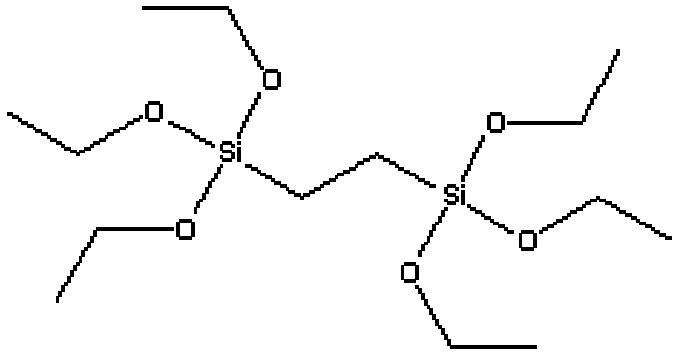

(b) BTSE

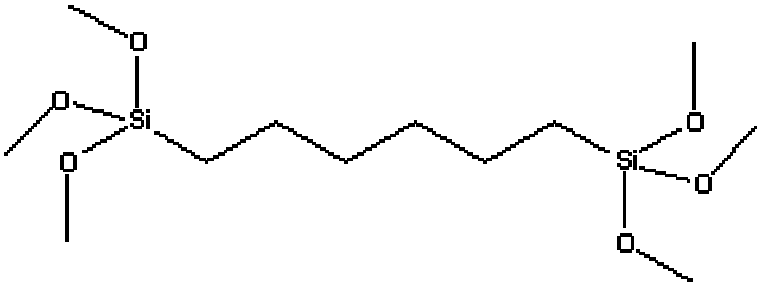

(c) BTSH

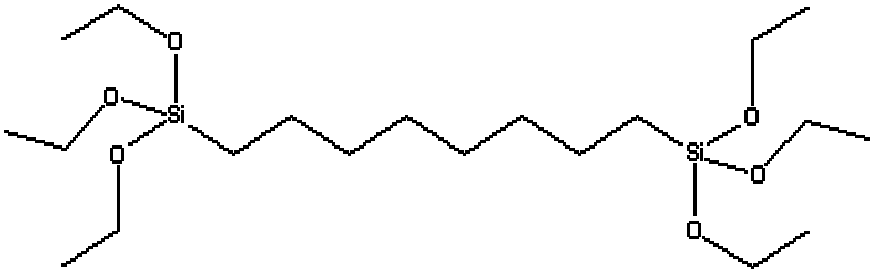

(d) BTSO

FIGURE 1. Molecular structures of the silanes studied here

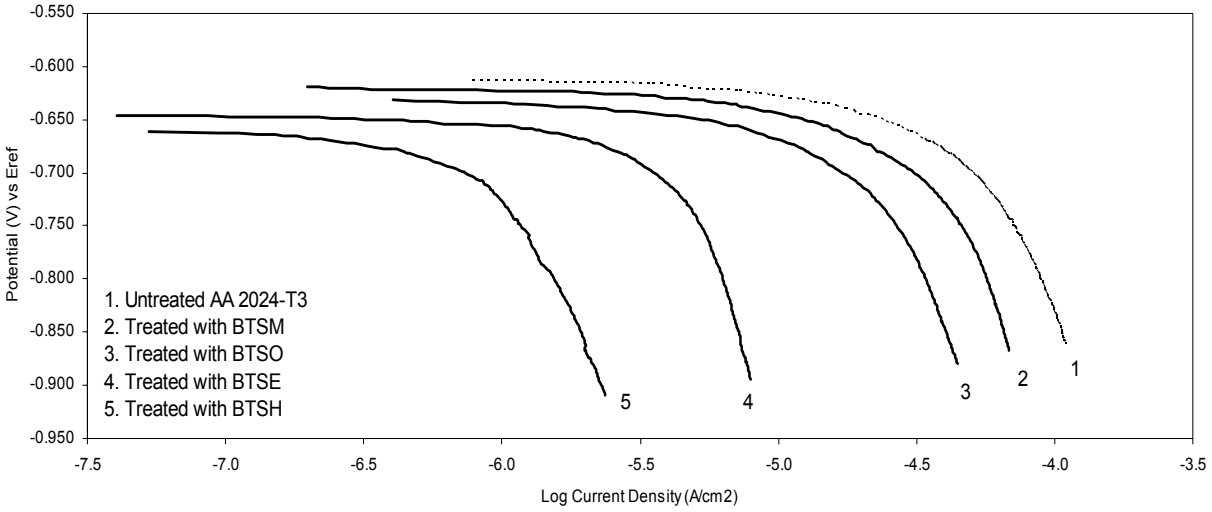

FIGURE 2: Cathodic polarization curves of AA2024 treated with silanes

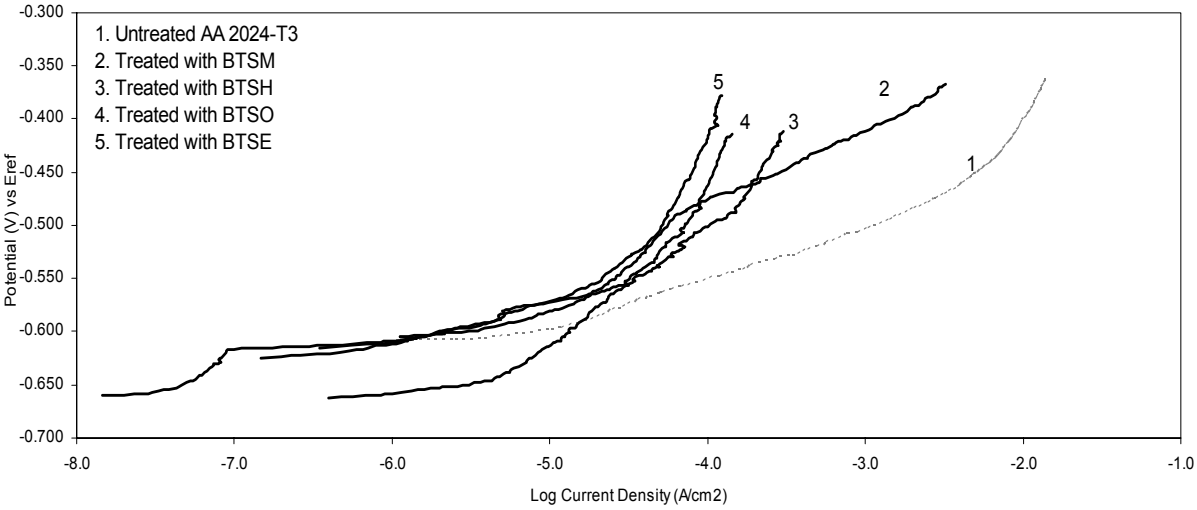

FIGURE 3. Anodic polarization curves of AA2024 treated with silanes

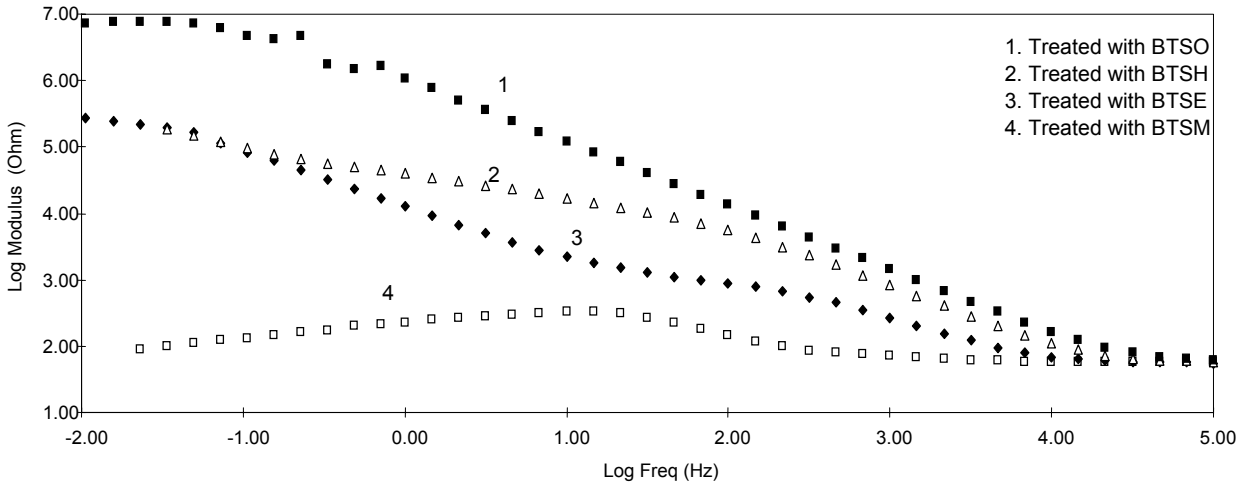

(a)

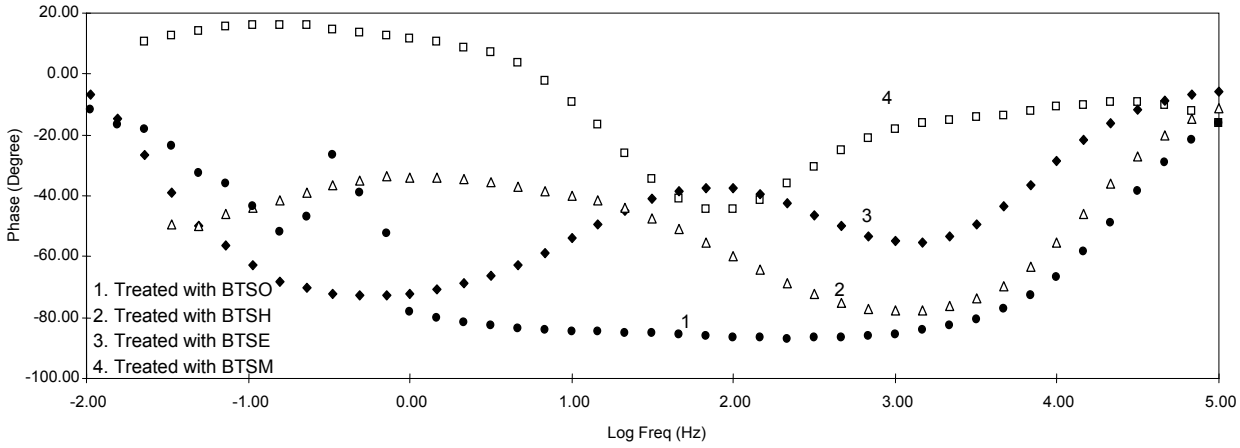

(b)

FIGURE 4. Bode plots of AA2024 treated with silanes, measured in 0.6M NaCl (exposed area: 3.14 cm^2); (a) impedance plot; and (b) phase angle plot

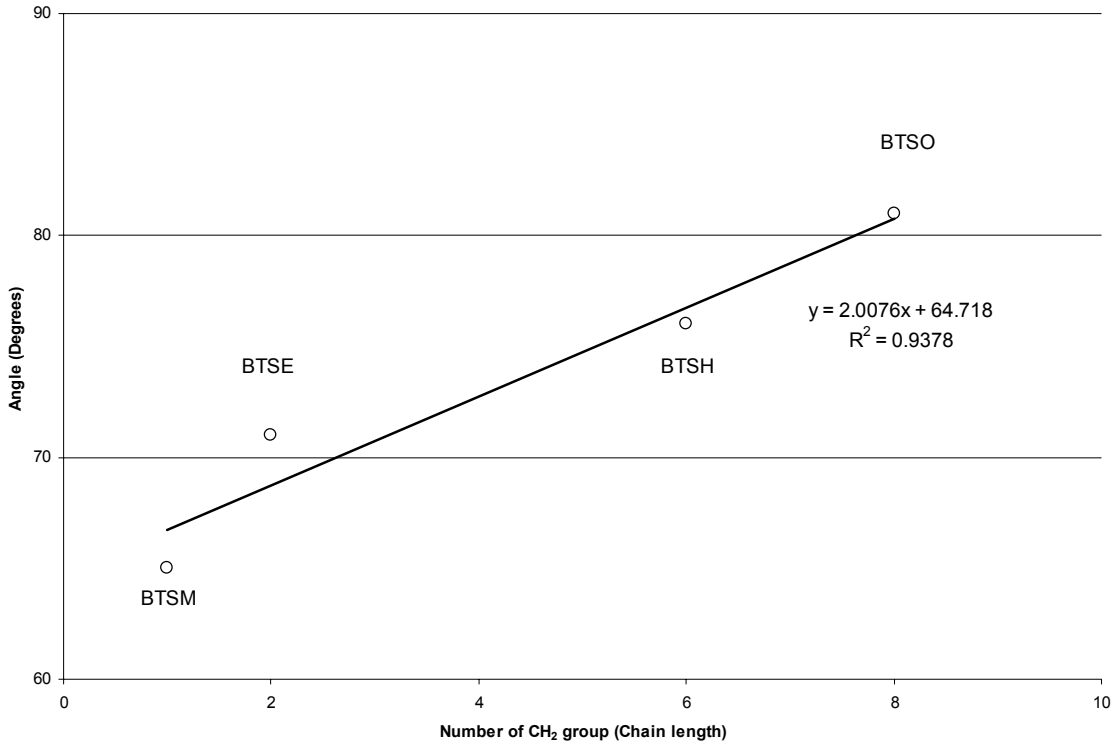

Figure 5. Contact angles of silane treated AA2024-T3 surfaces as a function of chain length (or the number of CH_2 group in the silane molecules)

(a) (b) (c)

FIGURE 6. AA 2024-T3 panels after 360-hr of salt spray test; (a) untreated; (b) chromated; and (c) BTSE-treated.

Chromate Conversion Coating Characterization Using Multichannel Microelectrode Analyzer (MMA)

W. Zhang,[a] B. Hurley,[b] and R. G. Buchheit[a]

[a] Department of Materials Science and Engineering and
[b] Department of Chemistry
The Ohio State University
Columbus, OH 43210

ABSTRACT

Chromate conversion coating (CCC) formation and breakdown was examined using 25 element Al wire electrode arrays. Arrays were interrogated using a multi-channel analyzer capable of separately recording currents from each electrode under open circuit or controlled potential conditions. During coating formation, electrodes exhibited a 30-second period of intense electrochemical activity characterized by large net currents. On any given element, net currents were predominantly anodic, cathodic, or mixed in polarity. Raman spectroscopy showed that the amount of Cr^{6+} in CCC continued to increase during electrochemically quiescent period suggesting continued CCC evolution. Breakdown potential distributions were found to increase with coating time up to 120 s, then stabilize. Breakdown was found to be more difficult on electrodes that were net cathodes during coating formation. Results also showed that the F^- activator and $Fe(CN)_6^{3-}$ accelerator in commercial CCC formulations strongly contribute to coating corrosion resistance.

INTRODUCTION

The structure and chemical composition of chromate conversion coatings (CCCs) have been the subject of numerous studies.[1-8] The findings of these studies show CCCs to be a mixture of chromium oxides, other components from coating bath, and components from substrate. Chromium is present in CCC in both Cr^{3+} and Cr^{6+} forms, with Cr^{6+} predominantly in the outer layer. Several mechanisms have been proposed to explain the excellent corrosion protection provided by CCCs. Among them are the barrier layer protection mechanism,[9,10] the bipolar membrane mechanism,[11,12] and the active corrosion protection mechanism.[3,8,13,14] Other

studies have been carried out on the formation of CCC. Commonly CCC formation is described as a redox reaction between chromate ions and substrate metals.[3,5,6] Chromates ions are reduced to non-soluble chromium oxide that forms on substrate as a protective layer. In accelerated chromium chromate coating formulations, $K_3Fe(CN)_6$ is present as an accelerator[2,5,6,15,16] for the Cr^{6+}/Cr^{3+}-Al^0/Al^{3+} redox couple. NaF is present as an activator[3,5] that dissolves any air-formed surface films and allows the conversion reaction to proceed.

CCC performance is usually assessed by salt spray or field exposure testing in harsh environments. Recently tests involving electrochemical impedance spectroscopy (EIS) have become more widely used.[17] Anodic polarization methods have not been widely used to evaluate CCC breakdown behavior probably because chromate conversion coated bulk electrodes do not usually show much improvement in pitting potential in concentrated chloride solution, although improvements in pitting potentials of CCC-coated 2024-T3 have been observed in 0.1M Na_2SO_4 + 0.005M NaCl solutions.[18,19] In this study, a multichannel microelectrode analyzer (MMA) was used to monitor the electrochemical activity on aluminum wire electrode arrays during coating formation and to measure the coating breakdown potentials of CCCs on Al. The effects of coating time, $K_3Fe(CN)_6$ and NaF on coating formation and breakdown were studied using this approach.

EXPERIMENTAL APPROACHES

MATERIALS AND ELECTRODE CONSTRUCTION

Aluminum wires, 0.5mm in diameter, with a purity of 99.999% were used to build 5 × 5 electrode arrays. A photograph of electrode array is shown in Figure 1(a). The distance between two adjacent wires in a row or a column is around 1 mm.

All the chemicals used in the study were ordered from commercial vendors and were of regent grade. Distilled water, with a resistivity of 18MΩ·cm, was used to make up all solutions.

CONVERSION COATING AND BREAKDOWN

Prior to use, the cross sections of electrode arrays were polished to 600 grit using SiC paper. Then the electrode arrays were immersed in dilute nitric acid for 1min to obtain a uniform surface across the array. The electrode array was then connected to the MMA and immersed in coating solution of designated chemistry for various times. The current evolution on each wire was recorded by the MMA at specified frequency (typically 50Hz). The array was then rinsed in distilled water and dried with gentle airflow. The electrode array was allowed to dry in air for 24hrs before potentiodynamic polarization measurement.

The coating bath used in this study contained 5.4 g/L CrO_3, 0.9g/L $K_3Fe(CN)_6$ and 0.9g/L NaF, which is close to the recommended Alodine 1200S bath.[20] The breakdown potential was measured by anodically polarizing the coated electrode array in 0.5M NaCl solutions at a scan rate of 0.2 mV/s starting from open circuit potential (OCP). All potentials reported are quoted versus the saturated calomel electrode (SCE).

MULTICHANNEL MICROELECTRODE ANALYZER (MMA)

A Model 900 MMA was used to monitor the current on each wire electrode during CCC formation and breakdown. The current on each electrode is measured on a ZRA capable of measuring up to 1μA with a resolution of 33pA. All channels are connected such that under open circuit conditions the net array current is zero, but individual electrode net currents can be monitored. Alternatively, the entire array can function as a working electrode in a three-electrode polarization experiment.

RAMAN SPECTROSCOPY

Raman spectra of CCCs of were collected using a Chromex 2000 spectrometer, with a standard interference band reject filter and EEV 15-11deep depletion CCD. A 785nm excitation and 180º backscattered sampling geometry were employed to obtain the Raman spectra. The area under 859cm^{-1} peak after baseline correction was used to indicate the amount of Cr^{6+} in CCCs.[7]

RESULTS

COATING FORMATION

Results of current transient measurements indicate that CCC formation can be characterized as a two-stage process: 1. During the initial 20-30s intense electrochemical activity occurs on the wire electrode array. 2. Further coating growth is under electrochemically quiescent conditions and appears to be predominantly chemical in nature. The wire can act as a net cathode or a net anode during coating formation. Most electrode wires changed polarity at least once during coating formation. Some electrodes showed extensive oscillation between anodic and cathodic behavior. Figure 1 shows the representative behaviors of these three types of electrodes.

CCC BREAKDOWN

During potentiodynamic anodic polarization, the CCC breaks down locally and stable pitting develops in the substrate. The potential at which this break occurs is termed the "breakdown" potential. Breakdown potential data were plotted as cumulative probability vs. breakdown potential.[21] Figure 2 shows the effect of coating time on breakdown potential distribution. These results clearly indicate CCCs inhibit anodic reactions even in 0.5M NaCl solution. Breakdown potentials increased with coating time up to 2 min. Increasing coating time

from 2 min to 5min did not increase the breakdown potential. Dramatic increases in breakdown resistance were achieved within the first 30s of immersion, where the median breakdown potential increased 250mV from –0.74V for bare Al to –0.49V. By comparison, the median breakdown potential increased by only an additional 90mV when coating time was increased from 30s to 300s. A similar increase in pitting potential with increasing coating time was observed Ilevbare et al.[18,19]

In Figure 3, breakdown potential data from conversion-coated electrodes was segregated according to the net current characteristics observed during the early stages of a 3min immersion in a CCC bath. "Net anodes" exhibited predominantly anodic current during the first 30 seconds of coating formation, "Net cathodes" exhibited predominantly cathodic current, and "Mixed character" electrodes exhibited significant currents of both polarity. Comparison of these breakdown potential distribution shows that net cathodes are possibly more resistant to breakdown than electrodes of mixed current character and net anodes.

Of the three main components of CCC bath, NaF has been classified as activator, and $K_3Fe(CN)_6$ as an accelerator.[15] Current results show that these two ingredients significantly affect coating breakdown potentials. Figure 4 shows the contributions of the ingredients in coating bath to the coating resistance to localized corrosion. The results show that CrO_3 alone does not improve the breakdown potentials of Al very much. When $K_3Fe(CN)_6$ was added to CrO_3, there was only a limited improvement in breakdown potential. When NaF was added to CrO_3, a significant increase in breakdown potential was observed. When both $K_3Fe(CN)_6$ and NaF were added to CrO_3, the breakdown potential was improved even further.

CR^{6+} CONCENTRATION IN CCC DETERMINED BY RAMAN SPECTROSCOPY

The Cr^{6+} component in CCC increases with coating time, as shown in Figure 5, indicating the build up of Cr^{6+} reservoir in CCCs or a thicker coating. This result is consistent with XANES results.[18,22]

DISCUSSION

CCC FORMATION PROCESS ON AL

Results from these experiments support the idea that CCC formation involves at least two steps (**7**): the electrochemical reduction of chromate and subsequent condensation polymerization of trivalent chromium oxide and the simultaneous chemical adsorption of chromate onto the trivalent chromium oxide. Electrochemical reduction occurs mainly during the early stages of coating growth where electrochemical activity is intense, and the resulting products provide basis for the adsorption and storage of chromate.[23,24] The continuous increase of Cr^{6+} component indicates that the adsorption process occurs during the whole coating process. These two steps provide a balanced corrosion protection scheme: chromate reduction results in formation of a Cr-rich mixed oxide for barrier layer protection and the chemical adsorption of Cr^{6+} forms the Cr^{6+} reservoir for later self-healing.

The results in Figure 3 show that net cathodes are more resistant to breakdown than net anodes. A simple interpretation can be made here. The polarity of a wire electrode during coating formation depends on the dominant reaction. If chromate reduction dominates, the wire electrode acts as net cathode; if Al oxidation dominates, the wire electrode acts as net anode. Since the Cr-rich mixed oxide layer is formed by chromate reduction, net cathodes are expected to provide

better barrier protection than net anodes. Further characterizations are necessary to understand this phenomenon.

EFFECTS OF COATING BATH CHEMISTRY ON COATING FORMATION AND BREAKDOWN BEHAVIOR

It has been observed that without F^- coating formation is very slow.[3] It is suggested that F^- dissolves the oxide film initially present on Al surface and activates the surface for chromate reduction.[3,5] During coating growth, F^- also dissolves a portion of the film and creates paths that will allow the solution keep in contact with the substrate and sustain the redox reactions. Otherwise, the surface will be completely passivated, film growth will stop and only a very thin film will form providing limited corrosion protection. The results from this experiment support the above arguments. As shown in Figure 6, when F^- is absent, the current drops very sharply in the first several seconds of coating formation. The smaller area under the curve measured in the absence of F^- indicates that the extent of the coating formation reaction is far less than when F^- is present. This can be explained by less available active Al surface area due to the absence of F^- and the formation of thin chromium oxide layer. This was confirmed by SEM observations. Figure 7 shows the surface morphology of pure Al after immersed in different coating bath chemistries. Without F^- in coating bath, there is little change on Al surface. With all three ingredients, the familiar mud-cracking pattern of CCCs was observed on Al.

It has been reported that when ferricyanide is added to coating bath, the coating weight, coating thickness, formation rate, and coating corrosion resistance are increased.[2,5,6,15,25] Comparison between the breakdown potential distributions with and without $Fe(CN)_6^{3-}$ indicates that the coating corrosion resistance is indeed increased when $Fe(CN)_6^{3-}$ is added to coating bath.

From the results shown in Figure 4 and the above discussions about the effects of NaF and $K_3Fe(CN)_6$ on CCC formation, it is concluded that to form a corrosion resistant conversion coating the addition of appropriate supplemental ingredients to the coating bath chemistry are as important as the primary film forming agent itself. In the case of CCCs, film-forming agent, CrO_3, is necessary to form CCC. But without the addition of F^- and $Fe(CN)_6^{3-}$ (or other chemicals in a different CCC process), a corrosion resistant coating will not form. This idea might be important in developing chromate-free coating systems. For example, Ce species have been known to be able to form conversion coatings on Al alloys.[26-28] However, some processes for forming cerium conversion coatings are either too long or involve acceleration by use of hot aqueous solutions or anodic polarization. In one accelerated Ce coating chemistry, H_2O_2 is used as accelerator, and Ce conversion coating can be formed in five minutes.[27]

SUMMARY

CCC formation and breakdown behavior are studied using the MMA. CCC formation includes at least two steps: the electrochemical reaction between chromate and Al and the buildup of chromate onto chromium oxides. Al can act as net anode and net cathode during coating formation. The change of polarity of wire electrode during coating formation indicates the non-uniformity of coating growth. The minor components in CCC bath chemistry are critically important for the formation of corrosion resistant coatings. Without F^-, Al surface passivates quickly and coating growth is extremely slow after first few seconds. Addition of $Fe(CN)_6^{3-}$ accelerates coating growth and increases the coating breakdown potential distribution. The importance of minor additions in coating bath suggests that in developing chromate-free

coating systems, efforts should also be made in identifying appropriate accelerants and activators.

ACKNOWLEDGEMENTS

This work was supported by the Strategic Environmental Research and Development Program and the Department of Army under contract no. DACA72-99-C-0002.

REFERENCES

1. J. A. Treverton and N. C. Davis, *Met. Technol.*, Oct., 480 (1977).
2. J. A. Treverton and N. C. Davis, *Surf. Interface Anal*, 3, 194 (1981).
3. H. A. Katzman, G. M. Malouf, R. Bauer and G. W. Stupian, *Applica. Surf. Sci.*, 2, 416 (1979).
4. F. W. Lytle, R. B. Greegor, G. L. Bibbins, K. Y. Blohowiak, R. E. Smith and G. D. Tuss, *Corros. Sci.*, 37, 349 (1995).
5. P. L. Hagans and C. M. Haas, *Surf. Interface Anal.*, 21,65 (1994).
6. A. E. Hughes, R. J. Taylor and B. R. W. Hinton, *ibid*, 25, 223 (1997).
7. L. Xia and Richard McCreery, *J. Electrochem. Soc.*, 145, 3083 (1998).
8. M. W. Kendig, A. J. Davenport and H. S. Isaacs, *Corros. Sci.,* 34, 41 (1993).
9. T. Biestek and J. Weber, translated from the Polish by A. Kozlowski, *Electrolytic and Chemical Conversion Coatings*, Portcullis Press Limited-Redhill, Poland (1976).
10. W. E. Pocock, *Met. Finish.*, 52, n12, 48 (1954).
11. N. Sato, *Corrosion*, 45, 354 (1989).
12. N. Sato, *Corros. Sci.*, 31, 1 (1990).
13. J. S. Wainright, O. J. Murphy and M. R. Antonio, *Corros. Sci.*, 33, 281 (1992).
14. J. Zhao, G. Frankel, and R. L. McCreery, *J. Electrochem. Soc.*, 145, 2258 (1998).

15. N. J. Newhard, Jr., *Met. Finish.*, n7, p. 49, n8, p.66 (1972).

16. L. Xia, and McCreery, *J. Electrochem. Soc.*, 146, 3696 (1999).

17. R. G. Buchheit, M. Cunningham and H. Jensen, *Corrosion*, 54, 61 (1998).

18. G. O. Ilevbare, J. R. Scully, J. Yuan, and R. G. Kelly, *Corrosion*, 56, 227 (2000).

19. G. O. Ilevbare, and J. R. Scully, *J. Electrochem. Soc.*, 148, B196 (2001).

20. Material Safety Data Sheet for Alodine 1200S, Henkel Corporation.

21. T. Shibata and T. Takeyama, *Corrosion*, 33, 243 (1977).

22. M. W. Kendig, A. J. Davenport and H. S. Isaacs, *Corros. Sci*. 34, 41 (1993).

23. A. L. Glass, *Mater. Prot.*, July, 26 (1968).

24. L. Xia, E. Akiyama, G. S. Frankel, and R. L. McCreery, *J. Electrochem. Soc.*, 147, 2556 (2000).

25. P. L. Hagans and C. M. Hass, " Chromate Conversion Coatings", p.405, *ASM Handbook, Vol. 5, Surface Engineering*, ASM International, Metals Park, OH (1994).

26. B. R. W. Hinton, D. R. Arnott and N. E. Ryan, *Met. Forum*, 7, 211 (1984).

27. B. R. W. Hinton, *J. Alloys Compd.*, 180, 15 (1992).

28. F. Mansfeld, Y. Wang, and H. Shih, *J. Electrochem. Soc.*, 138, L74 (1991).

FIGURES

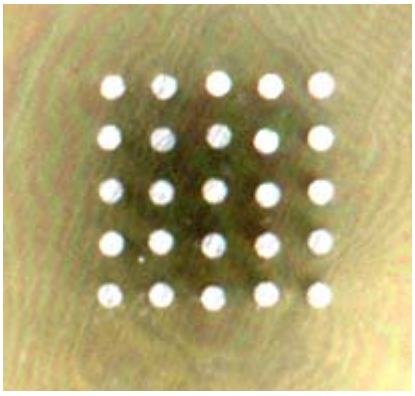

(a) electrode array

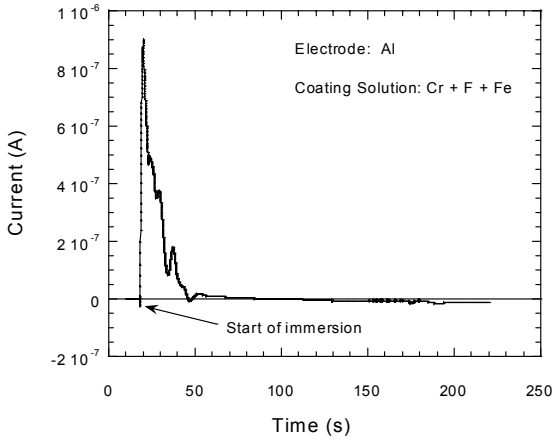

(b) net anode

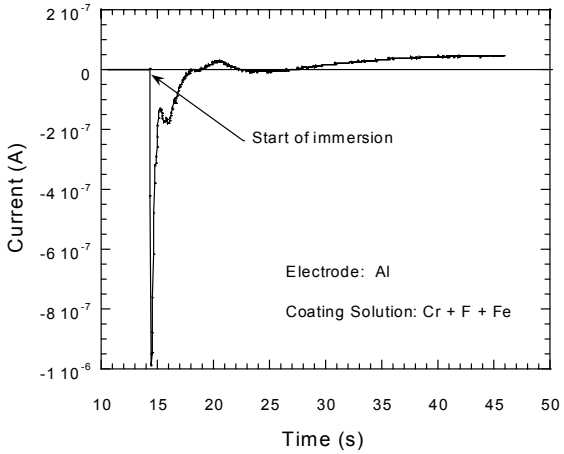

(c) net cathode

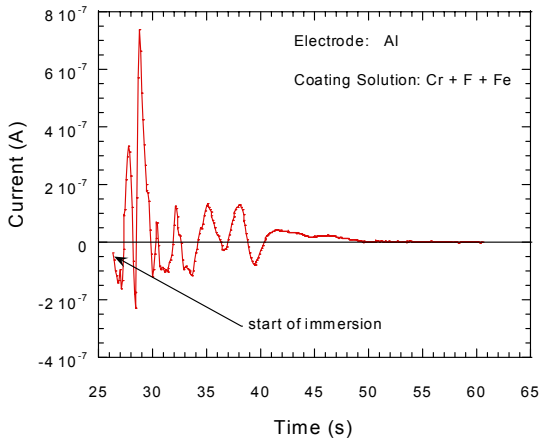

(d) mixed character

FIGURE 1. Electrode array and representative current vs. time behavior for electrodes during early CCC formation. In the coating solution notation, Cr, F and Fe stand for CrO_3, NaF and $K_3Fe(CN)_6$, respectively. The same notations are used for the rest figures.

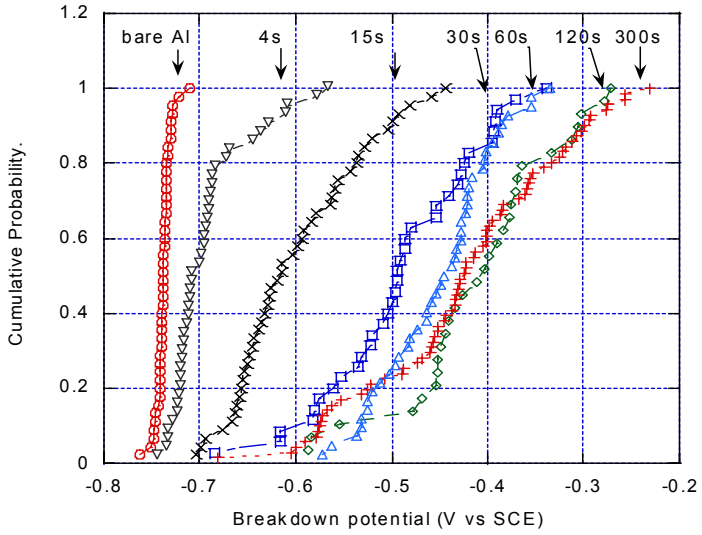

FIGURE 2. Effect of coating time on CCC breakdown potential distribution. Coating solution: CrO_3 + NaF + $K_3Fe(CN)_6$.

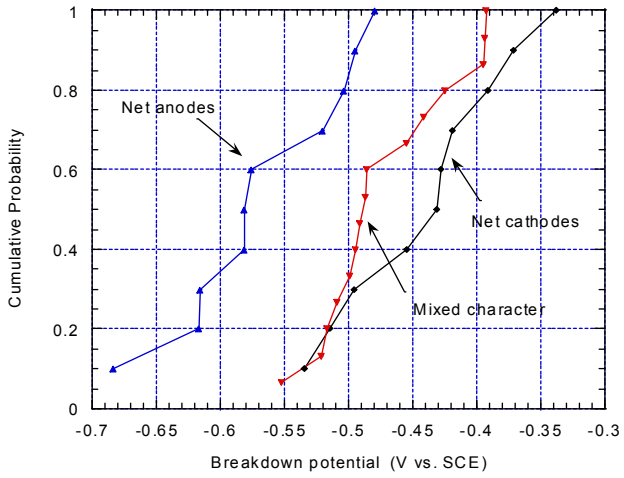

FGIURE 3. Effect of polarity during coating formation on coating breakdown potential distribution. Coating solution: CrO_3 + NaF + $K_3Fe(CN)_6$. Coating time: 3min.

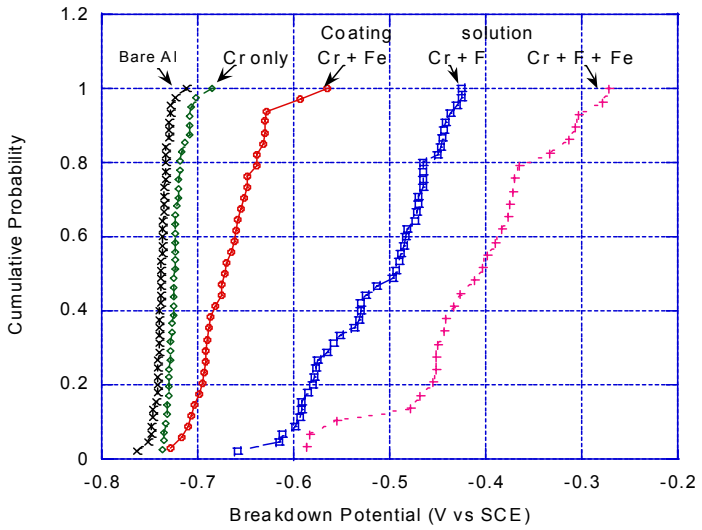

FIGURE 4. Relative contributions of coating bath components to coating breakdown potential. Coating time: 2min.

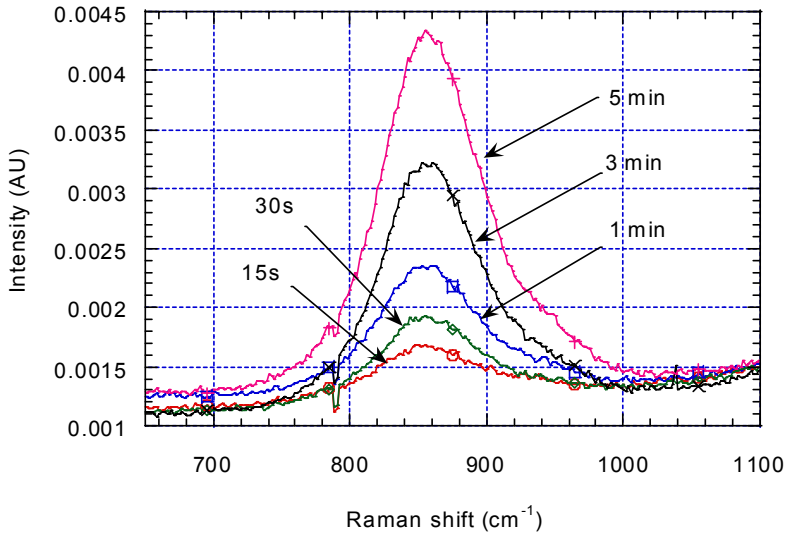

FIGURE 5. The intensity of the 860cm^{-1} band in Raman spectra increases with coating time, indicating the build-up of Cr^{6+} in CCCs. Coating solution CrO_3 + NaF + $K_3Fe(CN)_6$.

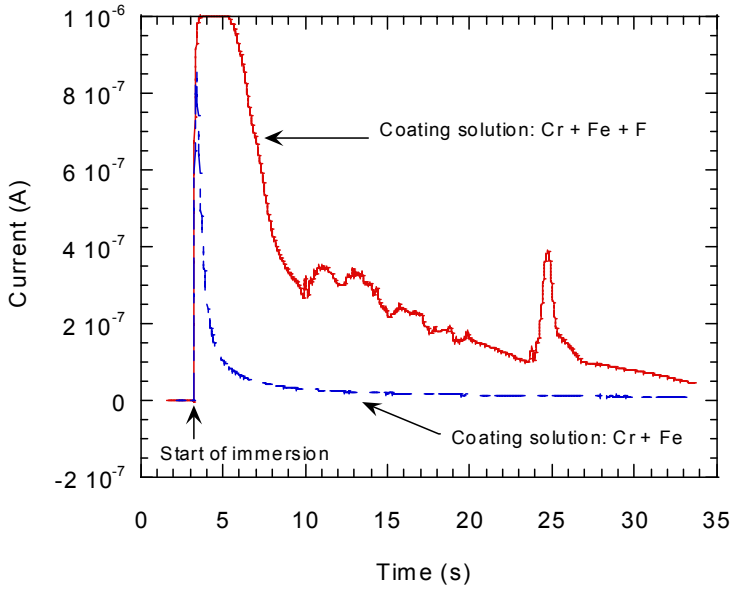

FIGURE 6. The effect of F^- on current evolution on Al during early CCC formation.

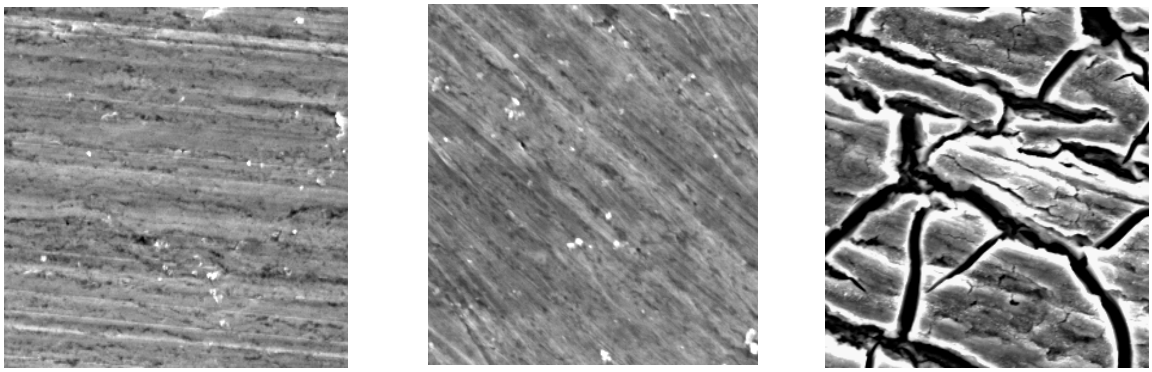

(a) bare Al (b) in $CrO_3 + Fe(CN)_6$ (c) $CrO_3 + Fe(CN)_6 + NaF$

FIGURE 7. Morphologies of coatings formed in different coating baths.